Malaysian Journal of Analytical Sciences (MJAS)
Published by Malaysian Analytical Sciences Society

Vol 26 No 1 (2022)

Vol 26 No 2 (2022)

Vol 26 No 3 (2022)

Vol 26 No 4 (2022)

Vol 26 No 5 (2022)

Vol 26 No 6 (2022)

2022

Malaysian Journal of Analytical Sciences Vol 26 No 1 2022

		Page
1.	SYNTHESIS AND MECHANISM STUDY OF NEW BIVALENT β-CARBOLINE DERIVATIVES (Kajian Sintesis dan Mekanisma Derivatif Bivalen β-karbolin Baharu) *Nurul Tasnim Noor Aaisa, Karimah Kassim, Nur Azzalia Kamaruzaman, Mazlin Mohideen*	1
2.	INSIGHT MECHANISTIC STUDY OF SAMARIUM OXIDE BASED CATALYST IN METHANATION REACTION (Kajian Mendalam Mekanistik Pemangkin Berasaskan Samarium Oksida dalam Tindak Balas Metanasi) *Salmiah Jamal Mat Rosid, Susilawati Toemen, Wan Azelee Wan Abu Bakar, Ahmad Zamani Ab Halim, Sarina Mat Rosid*	8
3.	ENHANCING TRYPSIN RECOVERY USING POLYMER-BASED AFFINITY ULTRAFILTRATION MEMBRANE: EFFECTS OF ELUTION pH AND DISPLACING SALTS (Meningkatkan Perolehan Tripsin menggunakan Membran Afiniti Ultrafiltrasi berasaskan Polimer: Kesan pH Pengeluatan dan Penggantian Garam) *Norhafiza Ilyana Yatim, Sofiah Hamzah, Maslinda Alias, Nora'aini Ali, Marinah Mohd Ariffin, Abdul Wahab Mohammad*	16
4.	BIOMIMETIC SYNTHESIS OF SILVER NANOPARTICLES USING *Eleusine indica* EXTRACT AND ITS ANTIBACTERIAL PROPERTIES (Sintesis Biomimetik Nanopartikel Perak Menggunakan Ekstrak *Eleusine indica* dan Ciri Antibakteria) *Ropisah Me, Muhammad Hafiz Istamam, Noor Hidayah Pungot, Nazlina Ibrahim, Alice Shanthi*	29
5.	MEASUREMENT OF SOLVENT PROPERTIES USING KAMLET-TAFT APPROACH FOR APPLICATION IN SYNTHESIS (Pengukuran Sifat Pelarut Menggunakan Pendekatan Kamlet-Taft untuk Penggunaan dalam Sintesis) *Tariqul Islam, A. B. M. Helal Uddin, Sahena Ferdosh, Md. Zaidul Islam Sarker*	39
6.	SYNTHESIS, CHARACTERIZATION, AND IN-SILICO STUDIES OF CINNAMIC ACID DERIVATIVES TOWARDS DENGUE VIRUS (Sintesis, Pencirian dan Kajian In-Siliko Sebatian Terbitan Asid Sinamik Terhadap Virus Denggi) *Anis Najwa Mohd Wahid, Nadia Mohamed Yusoff, Asnuzilawati Asari, Siti Nor Khadijah Addis, Hanis Mohd Yusoff, Habsah Mohamad, Fauziah Abdullah*	47
7.	EFFECT OF DEEP EUTECTIC SOLVENT ON TENSILE PROPERTIES AND BIODEGRADATION OF PECTIN WITH EGGSHELL BIOPLASTIC (Kesan Pelarut Eutektik kepada Sifat Tensil dan Biodegradasi Bioplastik Pektin dengan Cangkang Telur) *Non Daina Masdar, Rizana Yusof, Nur Amni Ramzani*	58
8.	SUPRAMOLECULAR ASSEMBLIES OF 1,2-DISUBSTITUTED CYCLOHEXANE AMIDE LIGANDS AND THEIR COORDINATION POLYMER: SYNTHESIS, CHARACTERISATION, AND CRYSTAL STRUCTURE (Himpunan Supramolekul Ligan Amida Sikloheksana 1,2-Tertukar Ganti dan Polimer	70

	Koordinatannya: Sintesis, Pencirian, dan Struktur Hablur) *Nur Shuhaila Haryani Haris, Nafisah Mansor, Maisara Abdul Kadir*	
9.	SPECTROSCOPIC FINGERPRINTING COMBINED WITH CHEMOMETRICS FOR PESTICIDE RESIDUE SCREENING ON ORGANIC PRODUCE: A CASE STUDY OF CHILI (Gabungan Cap Jari Spektroskopi dengan Kemometrik untuk Saringan Sisa Racun Perosak pada Hasil Organik: Kajian Kes ke atas Cili) *Intan Amirah Restu, Nur Fatin Zahra Mohamad Zhahir, Shum Mun-Hoe, Yong Chin Hong, Ng Jing Sheng, Syahidah Akmal Muhammad*	84
10.	ELICITATION OF INDUCED POLYKETIDE COMPOUNDS FROM A CO-CULTURE BETWEEN *Streptomyces* sp. STRAIN SUK10 AND *Fusarium* sp. AND THEIR ANTIBACTERIAL ACTIVITIES (Elisitasi Sebatian Poliketida Teraruh daripada Satu Kultur-bersama di antara *Streptomyces* sp. Strain SUK10 dan *Fusarium* sp. dan Aktiviti Antibakteria) *Muhammad Asyraf Zawawi, Nurul Izzati Rosdi, Noor Wini Mazlan, Mariam Taib, Kamariah Bakar, Noraziah Mohamad Zin, Siti Nordahliawate M. Sidique, Saif Aldeen Mohammad Fayiz Jaber, RuAngelie Edrada-Ebel*	96
11.	THE CONJUGATION AND CHARACTERISATION OF THERMORESONSIVE POLY (N-ISOPROPYLACRYLAMIDE) WITH TERNATIN BIOMOLECULE (Konjugasi dan Pencirian Poli (N-Isopropilakrilamida) dengan Biomolekul Ternatin) *Adrina Zulkifli, Farahiyah Najah Ab Samad, Nukman Ameen Rosli, Nurul Aina Jamaluddin, Nor Nadiah Mohamad Yusof, Noor Faizah Che Harun*	109
12.	CATALYTIC CONVERSION OF CELLULOSE TO LEVULINIC ACID USING SUPPORTED NOBLE METAL PALLADIUM CATALYST (Penukaran Bermangkin dari Selulosa ke Asid Levulinik Menggunakan Mangkin Disokong Logam Adi Paladium) *Puteri Nurain Syahirah Megat Muhammad Kamal, Norzahir Sapawe, Amin Safwan Alikasturi*	119
13.	PHYSICAL AND CHEMICAL DISCRIMINATION OF METHAMPHETAMINE TABLETS FOR FORENSIC INTELLIGENCE (Diskriminasi Fizikal dan Kimia bagi Pil Metamfetamin untuk Perisikan Forensik) *Noor Azlina Awang, Khai Lee, Way Koon Teoh, Vanitha Kunalan, Ahmad Fahmi Lim Abdullah, Kah Haw Chang*	130
14.	CATALYTIC NEUTRALIZATION OF ACIDIC PETROLEUM CRUDE OIL UTILIZING 2-METHYLIMIDAZOLE WITH ADDITION OF Cu/Ce(10:90)/Al_2O_3 CATALYST (Peneutralan Pemangkin Minyak Mentah Petroleum Berasid Menggunakan 2-Metilimidazol dengan Tambahan Mangkin Cu/Ce(10:90)/Al_2O_3) *Norshahidatul Akmar Mohd Shohaimi, Noraini Safar Che Harun, Hisyam Saufi Tajudin, Wan Azelee Wan Abu Bakar, Nurasmat Mohd Shukri, Nor Hakimin Abdullah, Ahmad Zamani Ab Halim*	152
15.	TEMPERATURE EFFECT ON THE ENCAPSULATION OF THE DRUG TETRACAINE HYDROCHLORIDE IN DIFFERENT CYCLODEXTRINS (Kesan Suhu Terhadap Pengkapsulan Dadah Tetrakain Hidroklorida dalam Siklodekstrin yang Berbeza) *Houria Boudjoras, Teffaha Fergoug, Mansour Azayez, Youcef Bouhadda, Noureddine Meddah-araibi, Cherifa Zelmat*	164

Malaysian Journal of Analytical Sciences (MJAS)
Published by Malaysian Analytical Sciences Society

SYNTHESIS AND MECHANISM STUDY OF NEW BIVALENT β-CARBOLINE DERIVATIVES

(Kajian Sintesis dan Mekanisma Derivatif Bivalen β-karbolin Baharu)

Nurul Tasnim Noor Aaisa[1,2], Karimah Kassim[2], Nur Azzalia Kamaruzaman[3], Mazlin Mohideen[1]*

[1]*Faculty of Pharmacy and Health Sciences,*
Universiti Kuala Lumpur Royal College of Medicine Perak, 30450 Ipoh, Perak, Malaysia
[2]*Institute of Science,*
Universiti Teknologi MARA, 40450 Puncak Alam, Selangor, Malaysia
[3]*National Poison Centre,*
Universiti Sains Malaysia, 11800 Minden, Pulau Pinang, Malaysia

**Corresponding author: mazlin.mohideen@unilkl.edu.my*

Received: 15 September 2021; Accepted: 30 December 2021; Published: 25 February 2022

Abstract

This study reports simple and straightforward methods for synthesizing new bivalent β-carboline compounds using L-tryptophan as a starting material with 1,4-dibromobutane as a dimerization linker. The synthetic route began with coupling L-tryptophan with formaldehyde via Pictet-Spengler condensation to afford tetrahydro-β-carboline, **T1** as the key intermediate. The reaction proceeded with decarboxylation of **T1** using potassium dichromate with acetic acid to afford β-carboline, **T2**. Subsequent alkylation of **T2** using 1,4-dibromobutane as the linker yielded intermediate **T3**, followed by dimerization to furnish the new bivalent β-carboline, **T4**. ^{1}H and ^{13}C NMR confirmed all the synthesized compounds. In addition, this study includes the proposed mechanism for the synthesis of a new bivalent β-carboline compound.

Keywords: synthesis, bivalent β-carboline, L-Tryptophan, Pictet-Spengler condensation, dimerization

Abstrak

Kajian ini melaporkan kaedah mudah dan secara terus untuk mensintesis sebatian baru bivalen β-karbolin menggunakan L-tryptofan sebagai bahan pemulaan dengan 1,4-dibromobutana sebagai penghubung dimerisasi. Laluan sintesis bermula dengan gandingan L-tryptofan dengan formaldehid melalui pemeluwapan Pictet-Spengler untuk mendapatkan tetrahidro-β-karbolin, **T1** sebagai kunci perantaraan. Tindak balas diteruskan dengan pendekarboksilan **T1** menggunakan kalium dikromat dengan asid asetik untuk menghasilkan β-karbolin, **T2**. Seterusnya alkilasi **T2** menggunakan 1,4-dibromobutana sebagai penghubung menghasilkan perantara **T3**, diikuti dengan dimerisasi untuk menghasilkan bivalen β-karbolin baharu, **T4**. Semua sebatian yang disintesis disahkan dengan ^{1}H NMR dan ^{13}C NMR. Sebagai tambahan, kajian ini merangkumi mekanisma yang dicadangkan untuk sintesis sebatian bivalen β-karbolin baharu.

Kata kunci: sintesis, bivalen β-Karbolin, L-Tryptofan, pemeluwapan Pictet-Spengler, dimerisasi

Introduction

β-carbolines are derived from a large group of heterocyclic compounds known as Norharmane (Figure 1), which have a 9H-pyrido[3,4-*b*]indole structural unit [1]. Furthermore, β-carboline can be classified as a synthetic and naturally occurring indole alkaloid with varying degrees of aromaticity that possess a planar tricyclic pyrido[3,4-*b*]indole ring system [2,3,4]. The core skeleton of β-carboline consists of a pyridine ring fused to an indole backbone (Figure 1).

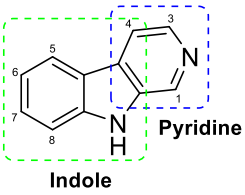


Figure 1. Core skeleton of β-carboline structure

β-carboline is a natural constituent found in plants, human tissues, body fluids, marine life, insects, and mammals [1]. Furthermore, β-carboline is also distributed in fungi and foods with broad pharmacological properties, including sedative, antithrombin, antimalarial, anti-HIV, and anti-inflammatory [5,6]. In addition, previous studies have reported that β-carboline, with its widespread biological properties, is commonly studied for its antitumor activity [7].

β-carboline alkaloid can be isolated from the seeds of a plant named *Peganum harmala,* which belongs to the family of Zygophyllaceae [4,7,8]. Other names for *Peganum harmala* include harmal, African rue, and Syrian rue. It is a perennial herbaceous, glabrous plant that can grow in semi-arid rangeland and sandy soils, especially in the Mediterranean region of North Africa and the Middle East [9]. β-carboline derivatives extracted from this plant are used mainly to treat various diseases, including asthma and jaundice. Despite its toxicity level, *Peganum harmala* has been used to treat a range of human ailments, as the health benefits outweigh the detrimental effects [10].

Interestingly, bivalent β-carboline alkaloids (Figure 2) elicited substantially greater bioactivity than the corresponding monomers. Thus, this suggests that bivalent compounds have better therapeutic potential and thus should be studied in future research [11].

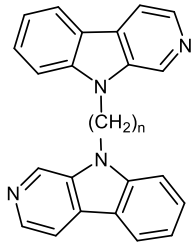


Figure 2. Example of a bivalent β-carboline structure

The bivalent β-carboline structure has two β-carboline monomers linked at positions-1, -2, -3, and -9 by carbon chains, heteroatoms, heterocyclic, amide esters, or amino-groups [11]. In addition, a previous study discovered that bivalent β-carboline elicited anticancer properties via a suitable linker, significantly improving activity by 100- to 500-fold over the corresponding monomers [5,12]. The improvement in anticancer activity might have occurred as the bivalent compound was more favourable to intercalating into DNA [5]. Therefore, bivalent β-carboline was expected to have significantly higher antitumor potency *in vitro* and *in vivo* than the corresponding monomers [12].

There are numerous reports of bivalent β-carboline derivatives. Daoud et al. investigated the anticancer activity of the bivalent β-carboline derivative B-9-3 (**1**) (Figure 3), which demonstrated potent anticancer activity against three cancer cell lines with IC_{50} values ranging from 3.58 μM–10.89 μM [13]. Chen et al. reported the synthesis and anticancer activity of a series of novel N^9-heterobivalent β-carboline (**2**) and (**3**) with strong cytotoxic activities against six cancer cell lines with IC_{50} values lower than 20 μM (Figure 3) [1].

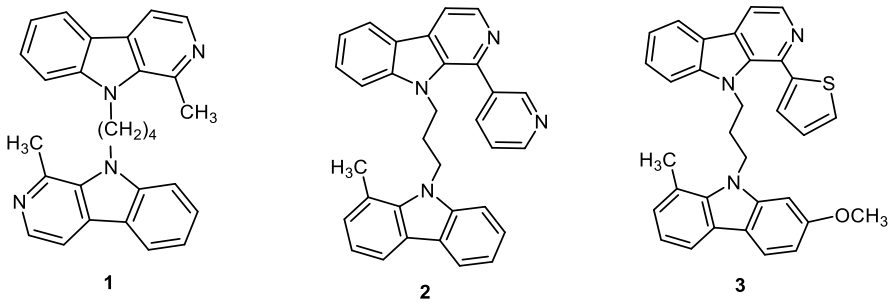


Figure 3. Reported bivalent β-carboline derivatives

Bivalent β-carboline, linked by suitable linkers, could significantly improve DNA-binding affinity as the dimerized compounds can bind to DNA through bis-intercalation mode, causing significant changes in DNA double helix structure [7,14,15]. The structural-activity relationships of the bivalent β-carboline compound indicated a few factors that determined antitumor activity; the common β-carboline moiety was very crucial for antitumor activity, the length of the linker affected antitumor potencies, four to six methylene units were more favourable, and the linker position in positions-1,-2,-3, and -9 were beneficial [14,16]. The problem statement that this study addresses is the importance of developing new anticancer drugs as cancer is currently one of the leading causes of major health problems worldwide. Thus, this study aims to synthesize a new bivalent β-carboline compound using the suitable length of 1,4-dibromobutane in position-9 in the four-step method using commercially available L-tryptophan as a starting material. The bivalent β-carboline was characterized using ^{1}H- and ^{13}C-NMR.

Materials and Methods

This section will describe a sequential decarboxylation and aromatization of tetrahydro-β-carboline-3-carboxylic acid **T1** to furnish β-carboline **T2**. This was followed by the dimerization reaction of the monomer β-carboline to form a new bivalent β-carboline **T4**.

Synthesis of tetrahydro-β-carboline (T1)

Tetrahydro-β-carboline-3-carboxylic acid (**T1**) was prepared through Pictet-Spengler condensation of L-tryptophan (**1**, 2.0 g, 9.8 mmol) with 37% formaldehyde (**2**, 0.98 mL, 32.63 mmol). The reaction started with 3 hours of stirring of L-tryptophan (**1**) and NaOH (0.4 g, 10 mmol) in a specific amount of water (200 mL). Then, 37% formaldehyde (**2**) was added to the solution, and it continued to reflux for 3 hours at room temperature. Upon completion, the reaction mixture was neutralized with glacial acetic acid, and the product was filtered off, washed well with water, and dried overnight.

Synthesis of β-carboline (T2)

Next, we attempted the decarboxylation-aromatization of tetrahydro-β-carboline-3-carboxylic acid (**3**, 1 g, 4.6 mmol) by stirring it in water (100 mL) at 100°C. The reaction continued to stir and heat with $K_2Cr_2O_7$ (9.5 g, 32 mmol) and acetic acid as a base (10 mL). Then, the reaction mixture was cooled by running it under tap water. Upon completion, sodium sulfite was added as a removing oxidizing agent. This was followed by the addition of 2.5 M NaOH drop by drop until it reached pH 7. The solution was extracted with ethyl acetate, and the combined organic layer was collected, washed with water and brine, and dried over anhydrous sodium sulfate. Lastly, the solution was evaporated. Yellowish solid, yield 47%, m.p. 199°C. ^{1}H-NMR (400 MHz, MeOD-d_4): δ 8.77 (s, 1 H), 8.26 (d, J = 5.5 Hz, 1 H), 8.17 (d, J = 7.8 Hz, 1 H), 8.08-8.07 (m, 1 H), 7.55-7.54 (m, 2 H), 7.27-7.23 (m, 1 H); ^{13}C NMR (101 MHz, MeOD-d_4): δ 137.0, 132.7, 129.1, 128.4, 121.4, 120.8, 119.5, 114.8, 111.5.

Synthesis of intermediate bivalent β-carboline (T3)

The intermediate **T3** was prepared by stirring β-carboline (**T2,** 0.5 g, 2.96 mmol) in anhydrous DMF (15 mL) at room temperature for 30 minutes, then 60% NaH dispersed in mineral oil (0.23 g, 5.92 mmol) and

appropriate 1,4-dibromobutane (0.7 mL, 5.92 mmol) was added. The reaction mixture continued to stir at room temperature, and upon completion, the mixture was poured into water, extracted with ethyl acetate, and washed with water and brine. Next, it was dried under anhydrous sodium sulfate, filtered, and evaporated. The final result of the reaction was an oily product. Dark brownish oil product, yield 98%, m.p. 188°C. ^{1}H NMR (400 MHz, $CDCl_3$): δ 8.39 (d, *J* = 5.9 Hz, 1 H), 8.31-8.27 (m, 2 H), 7.85 (d, *J* = 7.3 Hz, 1 H), 7.69 (d, *J* = 8.7 Hz, 2 H), 7.49 (d, *J* = 7.8 Hz, 1 H), 3.50 (d, *J* = 12 Hz, 2 H), 3.43 (d, *J* = 5.9 Hz, 2 H), 2.03-2.00 (m, 4 H); ^{13}C NMR (101 MHz, $CDCl_3$): δ 144.6, 136.2, 132.9, 132.3, 130.8, 123.5, 122.6, 119.6, 117.3, 111.2, 60.3, 44.4, 33.9, 29.7.

Synthesis of bivalent β-carboline (T4)

β-carboline (**T2**, 0.18 g, 1.09 mmol) in anhydrous DMF (6 mL) was added by stirring to a solution of intermediate (**T3**, 0.5 g, 1.64 mmol), 60% NaH dispersed in mineral oil (0.21 g, 5.49 mmol), potassium iodide (0.91 g, 5.49 mmol) in anhydrous DMF (10 mL). Next, intermediate **T3** was further reacted to form bivalent β-carboline **(T4)**. The reaction mixture was stirred at room temperature until the reaction was completed, and then it was poured into ice-cold water. After that, the reaction mixture was extracted with ethyl acetate and washed with water and brine. The combined organic layer was dried over anhydrous sodium sulfate, Na_2SO_4, and filtered. The purification process was conducted using column chromatography (DCM/MeOH 100:1 as the eluent) to furnish bivalent β-carboline **(T4)**. Dark brownish oil product, yield 13%, m.p. >270°C. ^{1}H NMR (400 MHz, $CDCl_3$): δ 8.93 (s, 2 H), 8.45 (d, *J* = 5.5 Hz, 2 H), 8.19 (d, *J* = 8.2 Hz, 2 H), 8.10 (d, *J* = 5.5 Hz, 2 H), 7.70-7.66 (m, 2 H), 7.52 (d, *J* = 8.4 Hz, 2 H), 7.36 (t, *J* = 7.5 Hz, 2 H), 5.06-5.00 (m, 4 H), 4.47 (t, *J* = 7.3 Hz, 4 H); ^{13}C NMR (101 MHz, $CDCl_3$): δ 143.3, 138.1, 137.5, 133.8, 132.0, 129.9, 122.6, 120.7, 118.5, 115.5, 110.1, 43.5.

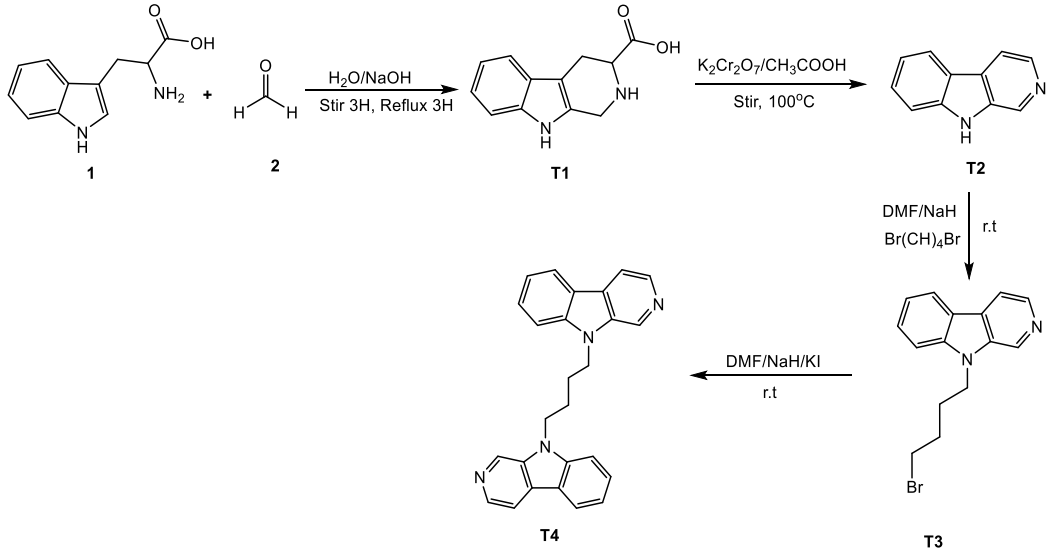
Results and Discussion

The desired bivalent β-carboline **(T4)** synthesis was performed in a four-step method starting from L-tryptophan **(1)** as outlined in Scheme 1. Firstly, the tetrahydro-β-carboline **(T1)** was prepared from the successful reaction of Pictet-Spengler condensation of L-tryptophan **(1)** with formaldehyde. The reaction was further reacted to form β-carboline **(T2)** with a 47% yield via decarboxylation by using potassium dichromate in the presence of acetic acid. Next, the β-carboline structure was alkylated at position-9 by the action of the strong base, NaH in anhydrous DMF, followed by the addition of 1,4-dibromobutane to successfully afford intermediate **T3** with a 98% yield. The intermediate **T3** was present in an oily product form. Finally, the intermediate **T3** was further reacted with β-carboline **(T2)** with a strong base, NaH in solvent anhydrous DMF, in the presence of potassium iodide. The reaction was carried out at room temperature to successfully afford the targeted compound, bivalent β-carboline **T4** (13%). The bivalent β-carboline **(T4)** underwent a purification process using column chromatography and furnished the oily product. ^{1}H NMR and ^{13}C NMR were utilized to characterize the chemical structures of all synthesized compounds in this study.

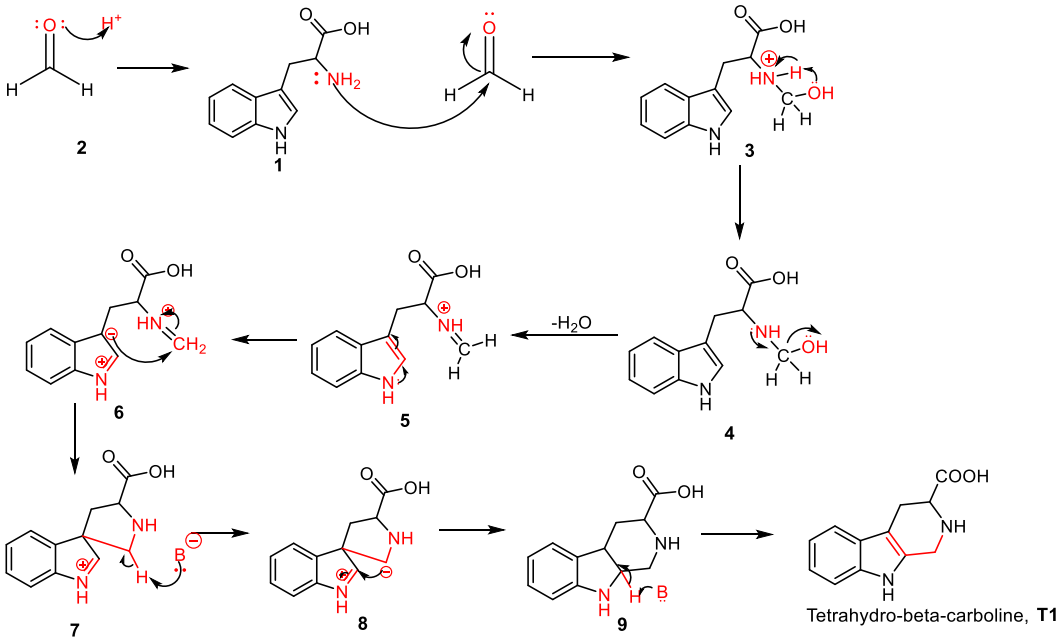
The proposed mechanism for the Pictet-Spengler condensation of L-tryptophan forming tetrahydro-β-carboline **T1** was outlined in Scheme 2. Initially, the mechanism started with the production of an iminium ion **3**, followed by the formation of an imine intermediate **5**, Schiff base, which removed H_2O. Next, the imine intermediate **5** underwent 6-endo-trig cyclizations involved in the base's action, forming a new ring, and the final product was tetrahydro β-carboline **(T1)**.

The proposed mechanism of the oxidation-decarboxylation of tetrahydro-β-carboline **(T1),** which produces β-carboline **(T2)**, is outlined in Scheme 3. Based on Scheme 3, the first step of the mechanism involved abstracting protons from tetrahydro-β-carboline **(T1)** by water. Then a new bond was formed: the double bond and functional group -COOH were removed, forming compound **10**. On the other hand, potassium dichromate that has been treated with acetic acid formed a chromic acid known as the common oxidizing agent for the oxidation reaction. Then, the strong nucleophile site of compound **10** attacked the electrophile site of chromic acid-water repeated proton abstraction in compound **11**. Next, the nucleophile site of -OH was abstracted proton from the α-carbon of compound **12**, forming a new bond. This double bond formed a new aromatic pyridine ring which successfully formed β-carboline **(T2)**.

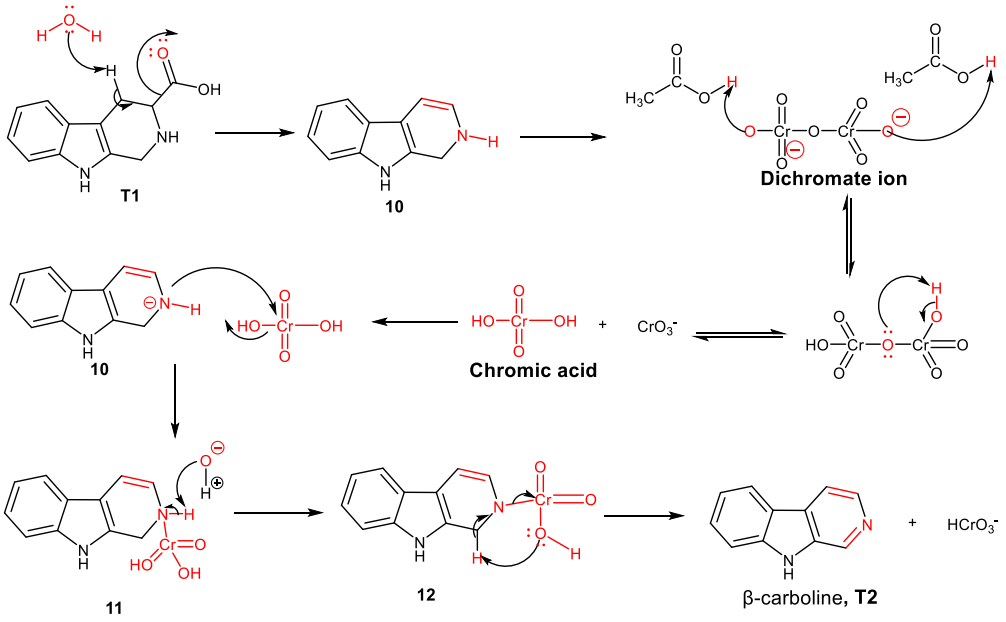
Lastly, the proposed mechanism for the new bivalent of β-carboline **(T4)** is outlined in Scheme 4. The mechanism started with the strong base, NaH, that abstracted protons from β-carboline (T2), producing a strong nucleophile site of compound **13**. Then, the strong nucleophile of N in compound **13** attacked the electrophile of C from the 1,4-dibromobutane, and it removed bromine since it is a good leaving group. Finally, the intermediate of bivalent β-carboline **(T3)** was successfully formed with NaBr. The intermediate bivalent β-carboline **(T3)** further reacted with the monomer β-carboline **(T2)** by the same reaction mechanism as the intermediate bivalent β-carboline **(T3)** to form a symmetrical structure of bivalent β-carboline **(T4)**.



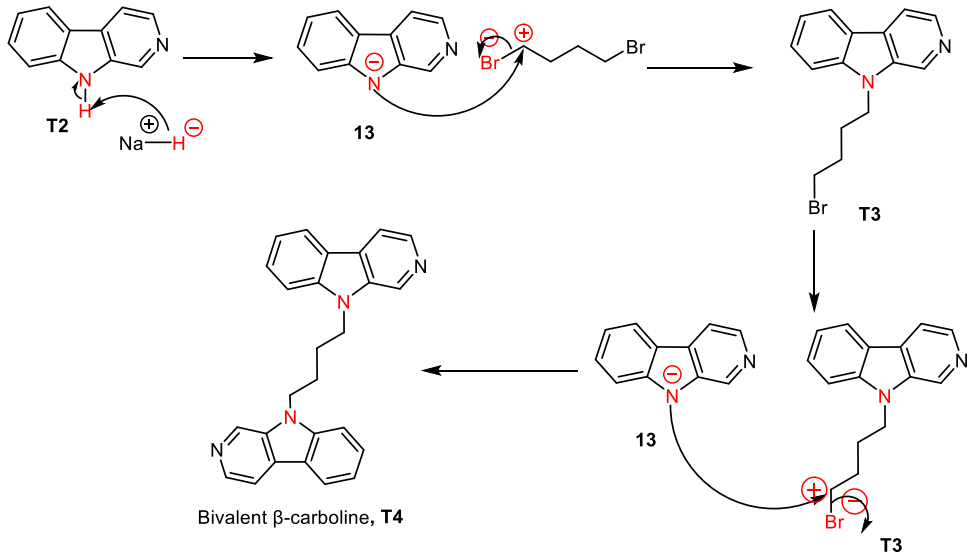
Scheme 1. Overall synthetic route for new bivalent β-carboline compound **T4**



Scheme 2. Proposed mechanism for the Pictet-Spengler condensation of L-tryptophan forming tetrahydro-β-carboline (**T1**)



Scheme 3. Proposed mechanism for the oxidation-decarboxylation of tetrahydro-β-carboline (**T1**) forming β-carboline (**T2**)



Scheme 4. Proposed mechanism for dimerization of β-carboline (**T4**)

Conclusion

In summary, this study has successfully synthesized a new bivalent β-carboline compound **(T4)** from the starting material L-tryptophan **(1)** with a 13% yield. The synthesis reaction is simple and straightforward, using commercially available, safe, and cheaper chemicals. Moreover, the mechanism for the synthesis route of the new bivalent β-carboline compound **(T4)** has been

proposed in this study for future reference. Future studies will evaluate the *in vitro* cytotoxicity potential of T4 in various cancer cell lines to determine its potential as an anticancer agent.

Acknowledgement

This study was supported by the Ministry of Higher Education Malaysia (MoHE) for the Fundamental Research Grant Scheme (FRGS) (FRGS/1/2019 /ST01/UNIKL/02) as well as the Faculty of Pharmacy and Health Sciences, Universiti Kuala Lumpur Royal College of Medicine Perak (UniKL RCMP) and the Institute of Science, Universiti Teknologi MARA (UiTM) for all of the facilities provided for the lab work. Huge thanks to the National Poison Centre, Universiti Sains Malaysia for their support of this project.

References

1. Chen, X., Guo, L., Ma, Q., Chen, W., Fan, W. and Zhang, J. (2019). Design, synthesis, and biological evaluation of novel n-acylhydrazone bond linked heterobivalent β-carboline as potential anticancer agents. *Molecules,* 24(16): 2950.
2. Ahmad, I., Fakhri, S., Khan, H., Jeandet, P. and Aschner, M. (2020). Targeting cell cycle by β-carboline alkaloids *in vitro*: Novel therapeutic prospects for the treatment of cancer. *Chemico-Biological Interactions*, 330: 109229.
3. Li, S., Yang, B., Zhang, Q., Zhang, J., Wang, J. and Wu, W. (2010). Synthesis and bioactivity of β-carboline derivatives. *Natural Product Communications*, 5(10): 1591-1596.
4. Sharma, S., Yadav, M., Gupta, S. P., Pandav, K. and Kumar, S. (2016). Spectroscopic and structural studies on the interactions of an anticancer β-carboline alkaloid, harmine with GC and AT specific DNA oligonucleotides. *Chemico-Biological Interactions*, 260: 256-262.
5. Du, H., Gu, H., Li, N. and Wang, J. (2016). Synthesis and biological evaluation of bivalent β-carbolines as potential anticancer agents. *Medicinal Chemistry Communications,* 7(4): 636-645.
6. Kumar, S., Singh, A., Kumar, K. and Kumar, V. (2017). Recent insights into synthetic beta-carbolines with anticancer activities. *European Journal of Medicinal Chemistry,* 142: 48-73.
7. Gu, H., Li, N., Dai, J., Xi, Y., Wang, S. and Wang, J. (2018). Synthesis and *in vitro* antitumor activity of novel bivalent beta-carboline-3-carboxylic acid derivatives with DNA as a potential target. *International Journal of Molecule Sciences,* 19(10): 3179.
8. Manasa, K. L., Yadav, S. S. and Nagesh, N. (2020). The β-carboline alkaloids in cancer therapy-recent advancements in this area. *Journal of Pharmacy and Biological Sciences*, 15(3): 1-27.
9. Nenaah, G. (2010). Antibacterial and antifungal activities of (beta)-carboline alkaloids of *Peganum Harmala* (L) seeds and their combinations effects. *Fitoterapia*, 81(7): 779-782.
10. Kuete, V. (2014). Physical, hematological, and histopathological signs of toxicity induced by African medicinal plants. *Toxicological Survey of African Medicinal Plants*, 2014: 635-657.
11. Dai, J., Dan, W., Scheinder, U. and Wang, J. (2018). β-carboline alkaloid monomers and dimers: Occurrence, structural diversity, and biological activities. *European Journal of Medicinal Chemistry,* 157: 622-656.
12. Chen, W., Zhang, G., Guo, L., Fan, W., Ma, Q., Zhang, X., Du, R. and Cao, R. (2016). Synthesis and biological evaluation of novel alkyl diamine linked bivalent β-carbolines as angiogenesis inhibitors. *European Journal of Medicinal Chemistry*, 124: 249-261.
13. Daoud, A., Song, J., Xiao, F. and Shang, J. (2014). B-9-3, a novel beta-carboline derivative exhibits anticancer activity via induction of apoptosis and inhibition of cell migration *in vitro*. *European Journal of Pharmacology,* 724: 219-230.
14. Shi, B., Cao, R., Fan, W., Guo, L., Ma, Q., Chen, X., Guoxian, Z., Qiu, L. and Song, H. (2013). Design, synthesis and *in vitro* and *in vivo* antitumor activities of novel bivalent β-carbolines. *European Journal of Medicinal Chemistry*, 60: 10-22.
15. Sun, R., Liu, R., Zhou, C., Ren, Z., Guo, L., Ma, Q. and Cao, R. (2015). Synthesis and biological evaluation of piperazine group-linked bivalent β-carbolines as potential antitumor agents. *Medicinal Chemistry Communications,* 6(12): 2170-2174.
16. Luo, B. and Song, X. (2021). A comprehensive overview of β-carboline and its derivatives as anticancer agents. *European Journal of Medicinal Chemistry*, 224: 113688.

Malaysian Journal of Analytical Sciences (MJAS)
Published by Malaysian Analytical Sciences Society

INSIGHT MECHANISTIC STUDY OF SAMARIUM OXIDE BASED CATALYST IN METHANATION REACTION

(Kajian Mendalam Mekanistik Pemangkin Berasaskan Samarium Oksida dalam Tindak Balas Metanasi)

Salmiah Jamal Mat Rosid[1]*, Susilawati Toemen[2], Wan Azelee Wan Abu Bakar[2], Ahmad Zamani Ab Halim[3], Sarina Mat Rosid[4]

[1]Unisza Science and Medicine Foundation Centre,
Universiti Sultan Zainal Abidin, Gong Badak Campus, 21300 Kuala Nerus, Terengganu, Malaysia
[2]Department of Chemistry, Faculty of Science,
Universiti Teknologi Malaysia, 81310 UTM Skudai, Johor, Malaysia
[3]Faculty of Industrial Sciences & Technology,
Universiti Malaysia Pahang, 26300 Gambang, Kuantan, Pahang, Malaysia
[4]Advanced Membrane Technology Research Centre (AMTEC),
Universiti Teknologi Malaysia, 81310 UTM Skudai, Johor, Malaysia

**Corresponding author: salmiahjamal@unisza.edu.my*

Received: 8 September 2021; Accepted: 1 January 2022; Published: 25 February 2022

Abstract

An understanding of the mechanism of chemical reactions is needed to optimize the reaction process and improve performance. The adsorption of reactant molecules, formation of reaction intermediates, and finally the distribution of products depend on the composition and surface structure of the catalyst. This research work deployed Fourier transform infrared (FTIR), high performance liquid chromatography (HPLC), and gas chromatography (GC) to identify the mechanism of Sm/Mn/Ru (60:35:5)/Al_2O_3 catalyst. The envisioned methanation reaction initially follows the Langmuir Hinselwood mechanism with the adsorption of CO_2 and H_2 gases on the catalyst surface. From the gaseous product, only methane peak was observed. Meanwhile, from the liquid product, methanol peak is observed at retention time 20 mins which accordance with standard methanol. Therefore, the final products acquired from the methanation reaction of Sm/Mn/Ru (60:35:5)/Al_2O_3 catalyst are CH_4, CH_3OH and H_2O.

Keywords: methanation, hydrogenation, samarium oxide, catalyst, mechanism

Abstrak

Pemahaman kepada mekanisme tindak balas kimia adalah perlu untuk mengoptimumkan proses tindak balas dan meningkatkan prestasi. Penjerapan molekul reaktan, pembentukan perantaraan tindak balas, dan taburan produk pada asasnya bergantung kepada komposisi dan struktur permukaan pemangkin. Kerja penyelidikan ini menggunakan inframerah transformasi Fourier (FTIR), kromatografi cecair prestasi tinggi (HPLC), dan kromatografi gas (GC) untuk mengenal pasti mekanisma mangkin Sm/Mn/Ru (60:35:5)/Al_2O_3. Tindak balas metana yang dipostulatkan adalah mengikut mekanisma Langmuir Hinselwood yang pada mulanya melibatkan penjerapan gas CO_2 dan H_2 pada permukaan mangkin. Daripada produk gas, hanya puncak metana

diperhatikan. Manakala, daripada produk cecair, puncak metanol diperhatikan pada minit ke 20 masa tahanan mengikut larutan piawai metanol. Oleh itu, produk akhir yang diperoleh daripada tindak balas metana mangkin Sm/Mn/Ru (60:35:5)/Al_2O_3 ialah CH_4, CH_3OH dan H_2O.

Kata kunci: metanasi, penghidrogenan, samarium oksida, pemangkin, mekanisma

Introduction

Nowadays, catalytic methanation reaction has been widely explored in order to convert CO_2 gas to CH_4 gas by reducing emission of greenhouse gases using metal oxide. The most conventional metal oxide catalyst used are nickel, cobalt, manganese, copper, iron and lanthanide element. The catalytic ability of metal oxide catalyst deteriorates after several hours of reaction time due to the carbon forming process. The formation of carbon can be avoided by adding a dopant to the metal oxide catalyst [1]. Rosid et al. revealed that dopants and metal-based oxides have varying functions in hydrogenation reactions [2]. The metal-based oxide incites the reaction via combining with CO_2 molecules to form carbonate species on the surface, while the dopant split the H_2 molecules and provides the H atoms required for further hydrogenation of the carbonate to form methane [3].

Carbon dioxide (CO_2) adsorption happens during carbonate species and carrier-related formate formation in H_2 presence [4, 5]. Many studies have proposed varying CO_2 methanation mechanisms. The first proposed mechanism refers to CO_2 reaction in a carrier, while H (ads) species generated in metals yield formate intermediate (COOH) at the interface of metal support. The CO (ads) species generated by formate are hydrogenated to methane [6]. Meanwhile, on second proposed mechanism, CO_2 (ads) and O (ads) dissociated directly on the metal surface. Subsequently, CO (ads) become hydrogenated to CH_4. The dissociation of CO (ads) denotes the rate determining step of the reaction [7].

Other than that, Marc. et al. also pointed out that the methanation process consists of three steps, of which the first step is to adsorb CO_2 on the catalyst chemically [8]. The second step is to separate CO_2 into surface-absorbed CO and O, and the final step is species reaction to separate it from H_2. The particular reaction process is known as Langmuir-Hinselwood mechanism [9]. However, most of the proposed mechanism involved alkaline earth metal dan transition metal which showed the formation of carbonate and formate species during reaction. Therefore, in this study the mechanistic study has been conducted over lanthanide element, which is samarium oxide catalyst in order to identify the mechanism pathway and product formed during the reaction occur. This study was conducted using FTIR, GC and HPLC for identification of product and by-product formed in methanation reaction.

Materials and Methods

Catalyst preparation

The catalyst was prepared by aqueous incipient wetness impregnation method. 5 g of samarium(III) nitrate was firstly weighed in a beaker and dissolved in a small amountof distilled water, then mixed together with a solution of $RuCl_3.xH_2O$ and $Mn(NO_3)_2.4H_2O$ salts according to the desired ratio. The catalyst solutions were stirred continuously for 30 minutes before 7 g of alumina was added to it. After that, the coated alumina was aging at 80 – 90 ^oC for 24 hours followed by calcination at 1000 ^oC for 5 hours using a ramp rate of 10 ^oC/min to remove all the metal counter ions and water present in the catalyst. Lastly, the sample was labelled as Sm/Mn/Ru (60:35:5)/Al_2O_3. All chemicals used in this study were purchased from Sigma Aldrich.

Catalytic screening

A gas mixture consisting of CO_2 and H_2 with a molar ratio of 1: 4 was continuously passed through the catalyst at a flow rate of 50.00 cm^3/min. Prior to starting the catalyst test, the reaction gas was introduced into the microreactor system without passing through the catalyst as a calibration. Then, the reaction gas was passed through a catalyst and the temperature is raised from room temperature (RT) to

400°C using FTIR Nicolet Avatar 370 DTGS spectrophotometer. The percentage of CO_2 conversion calculation is shown in Equation 1.

$$\% \text{ of } CO_2 \text{ conversion} = \frac{\text{Peak Area of } CO_2 \text{ calibration} - \text{Peak Area of } CO_2 \text{ conversion}}{\text{Peak area of } CO_2 \text{ calibration}} \times 100 \quad (1)$$

Mechanistic study

First, the catalyst was ground and placed in a glass tube, while air pre-treatment was executed for 30 minutes at 100 °C for catalyst sample activation. When the sample cooled to ambient temperature, H_2/CO_2 gas was installed into the microreactor system with the temperature increased to 400 °C. The product stream was gathered in a sample cell equipped with a KBr window and scanned through an in-situ Nicolet Avatar FTIR 370 DTGS spectrophotometer. Then, FTIR was used to analyze the catalyst powder to identify adsorbed materials on the catalyst surface. The liquid product of the reaction and methanol standard were analyzed by HPLC (Rezex ROA-Organic Acid), and methanol was detected using a 300 mm × 7.8 mm ID column with a refractive index (RI) detector. Meanwhile, gas products were analyzed by Hewlett Packard 6890 series gas chromatograph with Flame Ionization Detector (FID) and methane production was determined using an Equation 2.

$$\% \text{ Yield of } CH_4 = \frac{[CH_4] \text{ from GC}}{\% \text{ Conversion of } CO_2} \times 100\% \quad (2)$$

Results and Discussion

Marwood et al. and Sharma et al. confirmed the direct decomposition of CO_2 into CO and O [10, 11]. In this study, it seems that the direct decomposition of CO_2 is demonstrated. This proposal is very consistent with the fact that, as described by Solymosi et al. formate was not detected in excessive supports containing low concentrations of OH groups [12]. This was ascribed to hydrogen present in the reaction that hindered CO intermediates formation, thus yielding formate species.

Products analysis

Potential Sm/Mn/Ru (60:35:5)/Al_2O_3 catalyst reveal catalytic routes for methane as main product, methanol and water as a by-product. In this study, it seems that the direct decomposition of CO_2 is demonstrated. The FTIR spectrum of the gaseous product is presented in Figure 1. The spectrum shows that the peak is close to 2351 cm^{-1} due to the CO_2 stretching mode. At the same time, the stretching mode of CH_4 band at the wavenumber of 3014 cm^{-1} and C-H deformation mode at 1310 cm^{-1} [13] can be clearly detected starting at 250 ^oC reaction temperature. From the figure, it can be observed that no methane peak was appeared at room temperature (RT) and 100 ^oC indicating the absence of methane gas produced during the reaction. When the reaction temperature was raised to 400 ^oC, the highest CH_4 gas was formed with around 69% detected by GC-FID. This show that methane formation is advantageous at high reaction temperature [14]. No band of 3300-3600 cm^{-1} of water was observed in the FTIR spectrum because the silica trap system used in the reactor functions as adsorbed water. Interestingly, no CO intermediate was formed as there is no CO peak around 2080 cm^{-1} was detected. This shows that CO_2 gas is directly converted into CH_4 gas without producing CO gas as an intermediate.

As can be observed in Table 1, no methane gas was formed at room temperature (RT) and 100 ^oC of reaction temperature which agreed with the absence of methane peak (~3000 cm^{-1}) in FTIR spectra in Figure 1. However, when increasing reaction temperature to 200 ^oC, about 6% of CH_4 gas was formed from 65.52% of CO_2 conversion. This means that 59.09% of the reacted CO_2 was attained as a by-product. At a reaction temperature of 250 ^oC, the catalyst formed 20% CH_4 gas. Upon raising the reaction temperature to 400 °C (maximum value), the best 69% CH_4 gas was formed

as detected by GC-FID. Although CO_2 conversion is 100%, but the CH_4 gas formed only 69%. This might due to formation of methanol as side product for the catalysts (Refer Figure 2) as confirmed by HPLC analysis which showed the presence of peak at 20 minutes compatible with the retention time of standard methanol. As qualitatively, the presence of methanol was confirmed in the water product. This is because the peak area of 1.708 x 10^6 at 20.038 minutes coincided with the peak of standard methanol (not shown) at 19.122 minutes.

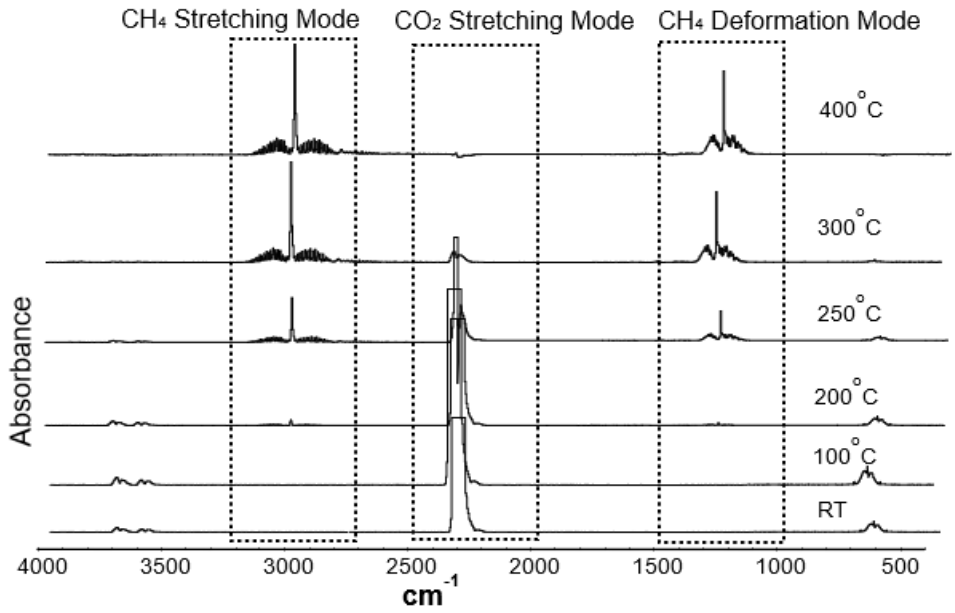


Figure 1. FTIR spectra of gaseous product at various reaction temperatures over calcined Sm/Mn/Ru (60:35:5)/Al_2O_3 catalyst

Table 1. Product analysis via *in-situ* reactions during methanation for Sm/Mn/Ru (60:35:5)/Al_2O_3 catalyst calcined on 1000 °C for 5 hours using GC-FID

Reaction Temperature (°C)	**Converted CO_2 (%)***		**Unreacted CO_2 (%)**
	% Formation of CH_4**	**% Formation of H_2O + with/without CH_3OH*****	
RT	-	0.00	100.00
100	-	0.31	99.69
200	6.43	59.09	34.48
250	20.85	71.67	7.48
300	31.11	65.67	3.22
350	48.91	49.95	1.14
400	68.87	31.13	-

*Converted CO_2 and Unreacted CO_2 was determined from FTIR as in Equation 1
**Formation of CH_4 was calculated from GC-FID as in Equation 2
***The presence of CH_3OH was confirmed with HPLC

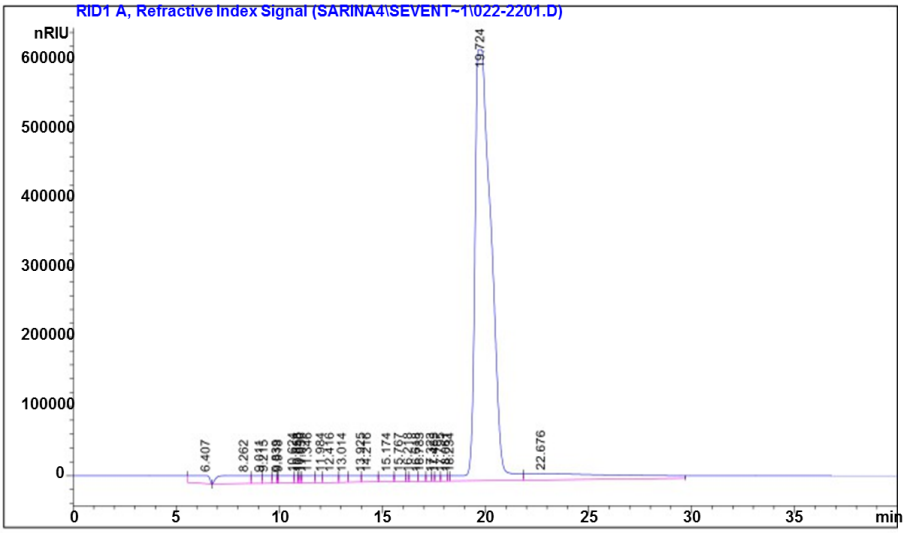


Figure 2. HPLC chromatogram of liquid product over calcined Sm /Mn/Ru (60:35:5)/Al_2O_3 catalyst

Methanation mechanism

The hydrogenation methanation adhered to the Langmuir-Hinshelwood mechanism, which reflected CO_2 and H_2 gases adsorption on the surface of catalyst. All CO_2 adsorption, dissociation, and reaction of the resolved species with H_2 had been established from in-situ FTIR experiments without any carbonate adsorption peak at 1760 and 1570 cm^{-1}. The FTIR spectra for catalyst during reaction is depicted in Figure 3. The spectra exhibited two broad O-H peak around 3443 and 1637 cm^{-1} corresponded to stretching and bending of adsorbed water on Al_2O_3 support [15, 16]. According to Narain et al., a peak band was noted at 1639 cm^{-1} for the similar temperature due to O-H bending derived from H_2O [17]. Initially, CO_2 and H_2 molecules were drawn to the catalyst surface (Step I) and directly coordinated the C atoms to generate inorganic carboxylate as proposed in Figure 4. The peak at 1116 cm^{-1} assigned to the CO species observed during the attachment of CO_2 to the catalyst surface at reaction temperature, 100°C [10]. This suggested the arrangement of C atoms attached to the catalyst surface (Step II). The adsorbed H_2 molecule was dissociated to active H atom species, and this was followed by CO_2 gas dissociation, as reported by Haldor [18] in Step III. The continuous flow of H_2 gas on the catalyst connects with oxygen atoms at the lone pair of electrons with higher electronegativity to form water (step IVa). This was supported with intense peak in the FTIR at reaction temperature, 200°C. A little peak at 1397 cm^{-1} was also observed at 200°C that correspond to the methoxy group (H_3C-O) as suggested in step IVb. Solymosi et al. described the peak around 1397 cm^{-1} on the catalyst surface foremost to the formation of methanol as a by-product [12]. When increased the reaction temperature to 250 – 300°C, the peak at 2892-2926 cm^{-1} was appeared which suggested free carbon from step III react directly with hydrogen to produce methane (step V). The intensity of C-H peak decreased at 350°C indicating that almost all CHx was released as CH_4 gas. At a reaction temperature of 400°C, all peak C-H groups disappeared which resulted higher CH_4 formation at this reaction temperature with 69% as stated in Table 1. This signifying the conversion of all species to CH_4, H_2O, and CH_3OH as the final yields.

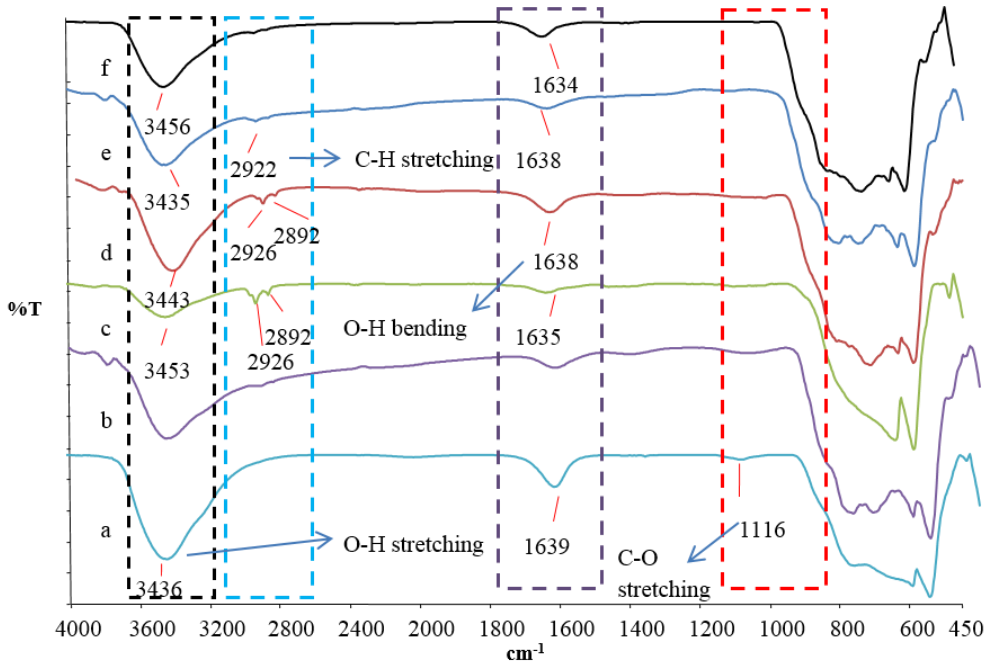


Figure 3. FTIR spectra of Sm/Mn/Ru (60:35:5)/Al_2O_3 catalyst surface at (a) 100ºC, (b) 200ºC, (c) 250ºC, (d) 300ºC, (e) 350ºC, and (f) 400ºC reaction temperature

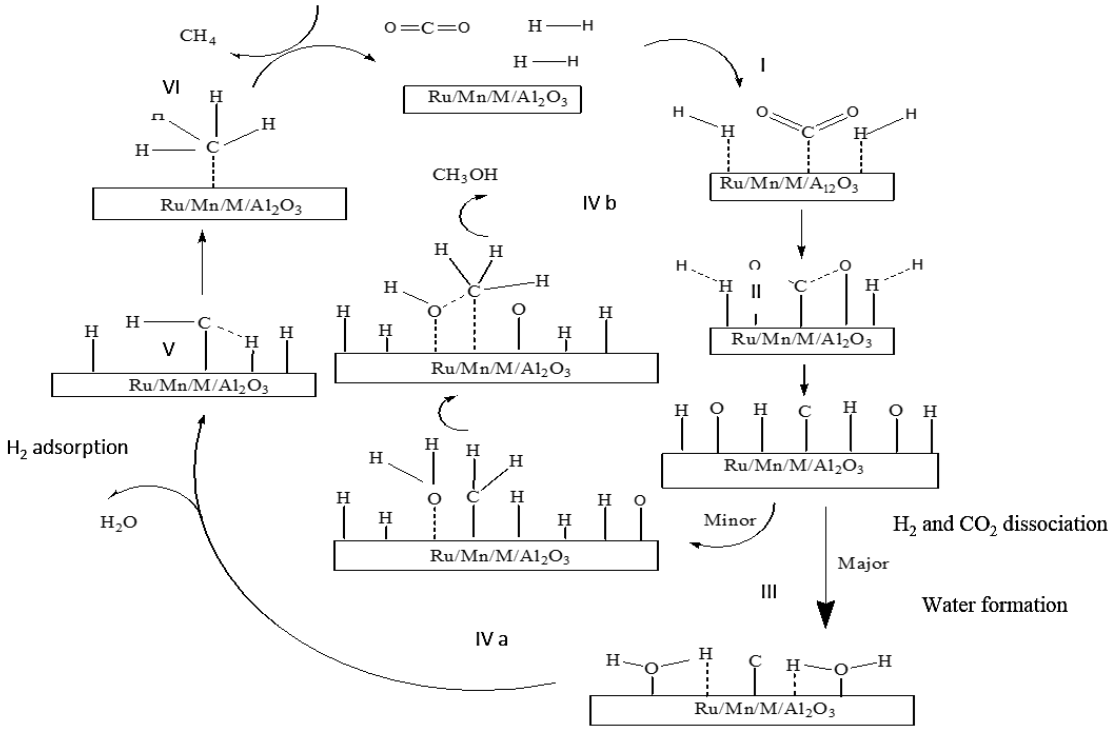


Figure 4. Proposed mechanism of M/Mn/Ru (60:35:5)/Al_2O_3, (M= Sm) calcined for 5 hours at 1000 ºC

Conclusion

This evaluation revealed compliance with the Langmuir Hinselwood mechanism, where CO_2 gas is first adsorbed, and then H_2-reactive gas is adsorbed on the catalyst surface. Based on the mechanistic approach, CH_4 was formed at temperature of 250 ºC and CO_2 peak was gradually decrease when the reaction temperature increased. The CO_2 conversion at 400ºC is 100%, with CH_4 formation of 69%. The others percent conversion was side products which are water and methanol, as detected by HPLC.

Acknowledgement

The authors gratefully acknowledge the Universiti Sultan Zainal Abidin and Universiti Teknologi Malaysia for financial support under GUP grant vote 13H34.

References

1. Asif Iqbal, M. M., Toemen, S., Abu bakar, W. A. W., Razak, F. I. A., Rosid, S. J. M. and Azelee, N. I. W. (2020). Catalytic methanation over nanoparticle heterostructure of Ru/Fe/Ce/γ-Al_2O_3 catalyst: Performance and characterization, *Renewable Energy*, 162: 513-524,
2. Rosid, S. J. M., Toemen, S., Iqbal, M. M. A., Bakar, W. A. W. A., Mokhtar, W. N. A. W. and Aziz, M. M. A. (2019). Overview performance of lanthanide oxide catalysts in methanation reaction for natural gas production. *Environmental Science and Pollution Research,* 26(36): 36124-36140.
3. Hu, D., Gao, J., Ping, Y., Jia, L., Gunawan, P., Zhong, Z., Xu, G., Gu, F. and Su, F. (2012). Enhanced Investigation of CO methanation over Ni/Al_2O_3 catalysts for synthetic natural gas production. *Industrial & Engineering Chemistry Research*, 51: 4875-4886.
4. Panagiotopoulou, P., Kondarides, D. I. and Verykios, X. E. (2008). Selective methanation of CO over supported noble metal catalysts: Effects of the nature of the metallic phase on catalytic performance. *Applied Catalysis A: General,* 344(1-2): 45-54.
5. Erdohelyi, A. (2021). Catalytic reaction of carbon dioxide with methane on supported noble metal catalysts. *Catalysts,* 11: 159.
6. Wang, X., Hong, Y., Shi, H., & Szanyi, J. (2016). Kinetic modeling and transient DRIFTS–MS studies of CO_2 methanation over Ru/Al_2O_3 catalysts. *Journal of Catalysis,* 343:185-195.
7. Fisher I.A. and Bell A.T. (1996). A comparative study of Co and CO_2 hydrogenation over Rh/SiO_2. *Journal of Catalysis,* 162: 54-65.
8. Marc J. Antoine Beuls, Patricio R. (2010). Catalytic production of methane from CO_2 and H_2 at low temperature: Insight on the reaction mechanism. *Catalyst Today*, 157: 462-466.
9. Gabor A. S. and Yimin L. (2010). Major success of theory and experiment-combined studies in surface chemistry and heterogeneous catalysis. *Top Catalyst,* 53: 311-325.
10. Marwood, M., Doepper, R. and Renken, A. (1997). *In-situ* surface and gas phase analysis for kinetic studies under transient conditions: The catalytic hydrogenation of CO_2. *Applied Catalysis A: General*. 151: 223-246.
11. Sharma, S., Hu, Z., Zhang, P., McFarland, E. W. and Metiu, H. (2011). CO_2 methanation on Ru-doped ceria. *Journal of Catalysis,* 278: 297-309.
12. Solymosi, F., Erdehelyi, A. and Bansagi, T. (1981). Methanation of CO_2 on supported rhodium catalyst. *Journal of Catalysis,* 68: 371-382.
13. Zamani, A. H., Shohaimi, N. A. M., Rosid, S. J. M., Abdullah, N. H. and Shukri, N. M. (2019). Enhanced low temperature reaction for the CO_2 methanation over Ru promoted Cu/Mn on alumina support catalyst using double reactor system. *Journal of the Taiwan Institute of Chemical Engineers*, 96: 400-408.
14. Rosid, S. J.M., Abu Bakar, W.A.W., Toemen, S., Yusoff, N. M., Azid, A. and Mokhtar, W. N. A.W. (2019). Investigation of active species in methanation reaction over cerium based loading. *Malaysian Journal of Fundamental and Applied Sciences,* 2018: 319-323.
15. Li, C., Sakata, Y., Arai, T., Domen, K. and Maruya, K. (1989). Carbon monoxide and carbon dioxide adsorption on cerium oxide studied by Fourier- transform infrared spectroscopy. *Journal of Chemical Society: Faraday Transaction*. 85(4): 929-943.
16. Stevens, R. W., Siriwardane, R. V and Logan, J. (2008). *In situ* Fourier transform infrared (FTIR) investigation of CO_2 adsorption onto zeolite materials. *Energy & Fuels*. 22(12): 3070-3079.

17. Narain, K., Yazdani, T., Bhat, M. M. and Yunus M. (2012). Effect on physico-chemical and structural properties of soil emended with distillery effluent and ameliorated by cropping two cereal plant spp. *Environmental Earth Sciences*, 66: 977-984.

18. Haldor Topsøe A/S, (2005). Methanation of CO over nickel mechanism and kinetics at high H_2/Co ratios. *Journal Physical Chemistry B*, 109(6): 2432-2438.

Malaysian Journal of Analytical Sciences (MJAS)
Published by Malaysian Analytical Sciences Society

ENHANCING TRYPSIN RECOVERY USING POLYMER-BASED AFFINITY ULTRAFILTRATION MEMBRANE: EFFECTS OF ELUTION pH AND DISPLACING SALTS

(Meningkatkan Perolehan Tripsin menggunakan Membran Afiniti Ultrafiltrasi berasaskan Polimer: Kesan pH Pengeluatan dan Penggantian Garam)

Norhafiza Ilyana Yatim[1], Sofiah Hamzah[2]*, Maslinda Alias[2], Nora'aini Ali[1,2], Marinah Mohd Ariffin[3], Abdul Wahab Mohammad[4]

[1]Higher Institution Centre of Excellence (HICoE), Institute of Tropical Aquaculture and Fisheries
[2]Faculty of Ocean Engineering Technology and Informatics
[3]Faculty of Science and Marine Environment
Universiti Malaysia Terengganu, 21030 Kuala Nerus, Terengganu, Malaysia
[4]Faculty of Engineering and Built Environment
Universiti Kebangsaan Malaysia, 43600 UKM Bangi, Selangor, Malaysia

**Corresponding author: sofiah@umt.edu.my*

Received: 27 August 2021; Accepted: 11 January 2022; Published: 25 February 2022

Abstract

Downstream processing of trypsin synthesis, which includes purification, is a major issue due to high complexity of the bio-suspension itself and the stress sensitivity of the desired target molecules. Therefore, an affinity membrane was fabricated in this study using polysulfone polymers and modified by chitosan to enhance biofouling resistance. To determine the optimum conditions for maximum trypsin adsorption and desorption during affinity ultrafiltration process, elution buffers and pH were investigated using various types of displacing salts (potassium chloride, KCl; sodium chloride, NaCl; magnesium chloride, $MgCl_2$; calcium chloride, $CaCl_2$) and elution pH (pH 4, 5, 6, 7, 8). The result showed that the buffer using KCl was identified as the best displacing salt as it recovered the highest trypsin of 78.84%, with a purification fold of 1.31. Trypsin recovery increased to 92% and 1.20 purification fold when the experiments were at pH 8. These buffers dissolved the interference chemical bonds comprising trypsin-trypsin inhibitor interactions and restore target trypsin to the permeate stream in an active state for maximum trypsin recovery. The information provided in this study represents a possible future avenue for developing an affinity membrane system.

Keywords: affinity, ultrafiltration, trypsin, elution pH, displacing salt creator

Abstrak

Pemprosesan hiliran sintesis tripsin, yang termasuk penulinan, adalah isu utama kerana kerumitan bio-pengampaian itu sendiri dan kepekaan tekanan molekul sasaran yang dikehendaki. Oleh itu, membran afiniti telah direka dalam kajian ini menggunakan polimer polisulfon dan diubahsuai oleh kitosan untuk meningkatkan rintangan bio-kotoran. Untuk menentukan keadaan optimum untuk penjerapan tripsin maksimum dan penyahjerapan semasa proses ultrafiltrasi perkaitan, penimbal pengeluat dan pH telah

disiasat menggunakan pelbagai jenis garam pengganti (kalium klorida, KCl; natrium klorida, NaCl; magnesium klorida, $MgCl_2$; kalsium klorida, $CaCl_2$) dan pH pengeluatan (pH 4, 5, 6, 7, 8). Hasilnya menunjukkan bahawa penimbal menggunakan KCl dikenal pasti sebagai garam pengganti terbaik kerana ia perolehan tripsin tertinggi sebanyak 78.84%, dengan lipatan penulenan 1.31. Perolehan tripsin meningkat kepada 92% dan 1.20 lipatan penulenan apabila eksperimen berada di pH 8. Penimbal ini telah melarutkan ikatan kimia yang menganggu yang terdiri daripada interaksi perencat tripsin-tripsin dan memulihkan tripsin sasaran ke aliran menelap dalam keadaan aktif untuk perolehan maksimum tripsin. Maklumat yang disediakan dalam kajian ini mewakili jalan masa depan yang mungkin untuk membangunkan sistem membran afiniti.

Kata kunci: afiniti, ultrafiltrasi, tripsin, pH pengeluat, pencipta pengganti garam

Introduction

Affinity ultrafiltration membranes have unfolded a new avenue in membrane technology due to the ability of membranes to bind specifically to target molecules/proteins via a specific interaction. This type of membrane results from a combination of two separation processes, namely affinity adsorption and ultrafiltration. It comprises the use of affinity ligands attached to the crosslinked or activated membrane matrix covalently. Ligands are bound to the target enzyme with different adsorption mechanisms and degrees of specificity, depending on the type of ligand used. This system conducts affinity adsorption and ultrafiltration in stages in ultrafiltration modules or separate systems [1].

The recent literature on the development of affinity chromatographic membranes describes highly diversity for proteins and enzyme purification in particular [2]. In fact, several recent studies have reported the rapid development of affinity membranes for protein recovery which increased gradually due to the need of this protocol to obtain high protein quality [3-6]. To meet the growing market demand for this enzyme, commercial production should focus either on innovating alternative procedures or modifying existing methods with slight improvement [7]. Based on the studies described above, affinity membrane chromatography has great potential to isolate a single protein fraction from protein mixture.

The target enzymes can be dissociated from the enzyme-ligand complex and passed through the affinity membranes by applying a suitable elution buffer on the system at the same operating pressure. Various buffers and conditions can be utilised for these studies; affinity-bound enzyme elution and elution using high-concentration salt solution are widely used [8]. This elution buffer breaks the connections between the target enzyme and ligand, lowers its binding affinity and forces the desired enzyme into the permeate stream.

Trypsin is one of the most well-known proteases and consists of serine endopeptidases [9]. Trypsin has a wide range of applications due to its strong proteolytic function and specificity of action, including its use as a critical intermediary in the manufacture of insulin, cell culture applications, research and production of recombinant proteins for clinical use, debriding agent in the wound care market, and oral treatment for inflammatory edema, hematoma and pain associated with diabetes [10, 11, 12].

In most cases, elution buffers were selected at random, most likely due to convenience or prior experience, although the final aim was to achieve a functional eluate [13]. However, several investigations have shown that elution conditions can substantially impact both the yield and specific activity of eluted products [14, 15]. The selected displacing salts are ensured to be soluble, non-denaturated, stable, transparent, ionic at relevant pH, pH stable, non-hazourdous and available [16].

The main benefit of ultrafiltration techniques over conventional separation methods such as chromatography, electrophoresis and conventional affinity separation is the high product throughput. Furthermore, ultrafiltration technologies are considerably easier to scale up, simple to clean and run, and relatively compact in design [17]. Although the use

of ultrafiltration is widespread, its potential in protein fractionation application has not been fully realised in the biotechnology industry due to lack of knowledge on the separation mechanism concepts and membrane fouling [18]. As a result, this study was conducted to determine the most efficient approach to increase the use of unltrafiltration in the biotechnology industry.

This study provides fundamental knowledge in designing a highly specific affinity ultrafiltration membrane for trypsin purification under proper pressure to selectively eliminate target enzyme-ligand complex as a retentate and simultaneously, other unbound impurities flow through membrane pores. Selectivity of polysulfone as a membrane material was due to its strong and thermally stable characteristics. The integration of chitosan with polysulfone was hypothesized to produce a hydrophilic segment on the membrane surface which can be an ideal method to combine both the advantages of hydrophilic and hydrophobic membranes. The use of ligands to support materials using activator (glutaraldehyde) can enhance the performance of affinity membranes. It is crucial to determine the best conditions for the trypsin recovery protocol; therefore, this study was conducted to identify the effects of displacing salt and pH of the buffer solution in separation process. In conclusion, with the integration of affinity chromatographic and high-performance ultrafiltration concept, it is believed that affinity ultrafiltration membrane will become common in the near future especially for protein and enzyme recovery.

Materials and Methods

Chemicals and raw materials

Membranes were produced using a ternary casting solution including polysulfone (PSf) as the polymer, N-methyl-2-pyrrolidone (NMP) as the solvent (provided by Merck), and water (H_2O) as the non-solvent. In this study, N-Methyl-2-Pyrrolidone (NMP) from MERCK Schuchard OHG, Germany, was used as a solvent for PES. As a coagulation medium, distilled water was employed. Fluka trypsin (Mw = 25 000 g/mol) was used as the target enzyme in this study. Trypsin inhibitor type III (ovomucoid) and trypsin (Mw = 25 000 Dalton) purchased from Sigma Aldrich were used for affinity ligand and adsorption study, respectively. Chitosan particle (Sigma Aldrich) was used for hydrophilic modification of asymmetric PSF membrane. Glutraraldehyde (Sigma Aldrich) was used for membrane activation to develop the affinity membranes. N-α-benzoly-L-arginine p-nitroanilide (BAPNA) was used for enzyme activity. Sodium acetate acetic acid buffer (solution), acetic acid solution, potassium chloride (KCl), sodium chloride (NaCl), calcium chloride ($CaCl_2$), and magnesium chloride ($MgCl_2$) were purchased from Sigma Chemical Co. (St Louis, Missouri) for affinity ultrafiltration experiments. All materials utilised in this study were of analytical grade.

Preparation of affinity membrane

For PSf membrane preparation, the weight of the binary dope was determined at 70 g. Then, 85 (wt.%) NMP was heated at 60 ˚C in a reactor flask for 10 minutes. The solvent was then gently infused with 15 (wt.%) polymer (PSf) until all polymers were dissolved and stirred at 300 to 400 rpm for about 8 hours at a constant temperature of 600 ˚C using a WiseStirTM Digital Overhead Stirrer from DAIHAN Scientific, Co., Ltd. To eliminate trapped air bubbles, the resulting polymer solution was immersed in an ultrasonic bath for about 3 hours. The prepared binary dope was then titrated with water as a non-solvent to produce the ternary dope and the stirrer was set to stir at a moderate speed. The presence of a drop of water that changed the colour of the binary dope solution indicated that the cloud point was achieved, and the volume of water titrated was recorded. The polymer solvent mixture was mixed again until all the components utilised were completely dissolved. Finally, the finished dope solution was put into a Schott bottle.

The affinity membrane (CH/PSf-60) was prepared with simple dry/wet phase inversion technique using an electrically casting machine at shear rate of 200 s^{-1} and then immersed directly into a coagulation bath for 24 hours. For surface modification, a native PSf membrane was immersed into the chitosan solution (0.1 wt.% in acetic acid with pH 5) for 60 minutes to deposit chitosan particles onto the membrane surface and dried in ambient air. The dried membrane was

then neutralized with NaOH solution (0.1 M in 50% of water-ethanol mixture) for 30 minutes to ensure that all chitosan acetate was converted to chitosan. To prevent osmotic cracking and to remove the remaining NaOH, the membrane was rinsed with 50% v ethanol solution for 3 times, and followed by washing with distilled water and stored in distilled water before use.

The membrane support (CH/PSf-60) was cut to an area of 14.6 cm^2 and incubated in an incubation shaker for 150 min in a reacting solution containing different amounts of 25 vol% glutaraldehyde (GTA) aqueous solution in 0.1 M sodium chloride and 0.1 M sodium acetate-acetic acid buffer (pH 7.4). From the reaction, excess glutaraldehyde was removed from the membrane by washing three times with 2 M acetic acid. The trypsin inhibitor was immobilized onto the active membrane for 180 minutes, and the adsorption capacity was measured every 30 minutes. The CH/PSf-60 membrane was referred to as an affinity membrane.

Affinity ultrafiltration experiment

A dead-end cell with a processing volume of 300 mL, and an effective permeation membrane area of 14.6 cm^2 was used for affinity ultrafiltration. This solution was drawn across the membrane using compressed nitrogen at a pressure of 5 bar. A washing step with 0.1 M phosphate buffer was used to eliminate unbound trypsin and contaminants. For the elution step, the bound trypsin was subsequently desorbed from the affinity membrane using 0.01 M Tris-HCl buffer with various displacing salts, namely KCl, NaCl, $CaCl_2$ and $MgCl_2$, and pH (pH 4, 5, 6, 7, 8). When the enzymes were firmly attached to the affinity membrane, it may be beneficial to pause the flow for 15 min after adding the eluent before proceeding with the elution. This phase allows additional time for dissociation to occur, which assists in the recovery of bound trypsin. The total protein content of the eluate was determined using the Bradford assay and trypsin activity.

Determination of total protein and enzyme activity

Protein concentration was calculated using Bradford method with Bovine Serum Albumin (BSA) as the standard. Using a UV-Vis spectrophotometer, absorbance and concentrations were determined by dissolving each 100 µL sample in 5 mL of Bradford reagent. The experiment was repeated with trypsin as the sample. Trypsin activity was assessed with minor changes [19] [12]. As a chromogenic substrate, BAPNA was utilised. Analiquot of the enzyme solution of 200 µL was added to the pre-incubated reaction mixture containing 1000 µL of BAPNA solution (dimethyl sulfoxide) and 200 µL of 0.05 M Tris-HCl. The mixture was incubated at 40°C for 10 min. The enzymatic process was halted by adding 200 µL of 30% (v/v) acetic acid and then centrifuged at 8000x g for 3 min at room temperature. Due to the production of p-nitroaniline, absorbance was used to assess trypsin activity at 410 nm using Equation 1.

$$q = \frac{(C_0 - C)\,V}{A} \quad (1)$$

where q is the amount of trypsin adsorbed onto the membrane ($mg.ml^{-1}$), C_0 and C are the total protein in the initial solution and the aqueous phase after adsorption, respectively ($mg.ml^{-1}$), V is the volume of the aqueous solution (ml), and A is the area of the membranes in the adsorption medium (cm^2).

Results and Discussion

Characteristics of affinity membrane

As seen in Figure 1(a), affinity membrane generally employs two separation concepts, namely affinity adsorption and ultrafiltration. It comprises the use of affinity ligands attached to the crosslinked or activated membrane matrix covalently. Depending on the ligand utilised, the ligands are attached to the target enzyme through different adsorption methods and specificity. Then, for ultrafiltration separation, a buffer media with sufficient pressure selectively excludes the target enzyme-ligand complex as a retentate while allowing other unbound contaminants to flow through the membrane pores. The target enzymes can be separated from the enzyme-ligand combination and processed through an amplification process. By introducing an appropriate elution buffer to the system at the same operating pressure, the target enzymes can be dissociated from the enzyme-ligand complex and passed through the affinity membranes. Figure 1(b) shows the schematic diagram of the developed affinity

membrane consisting of 15% PSf membrane. The PSf membrane underwent surface modification with chitosan to produce membrane hydrophilicity followed by an activation process using glutaraldehyde and immobilised using trypsin inhibitor as ligand.

The separation method of the affinity membrane is based on the affinity characteristics of the desired solute molecules. The selection of suitable membrane is one of the important elements influencing the separation performance of affinity ultrafiltration membrane. Large pore sizes and high porosity membrane matrix are necessary to avoid fouling while also allowing larger pollutants to flow through the membrane during the washing phase. The hydrophilic properties of the CH/PSf membrane enhances its ability to immobilise ligands and transmit trypsin during affinity ultrafiltration. Figure 2 depicts the surface morphology of native PSf 15 and affinity membrane after trypsin inhibitor was effectively adsorbed onto the CH/PSf membrane by glutaraldehyde activation.

Membrane activation with glutaraldehyde results in crosslinking, stabilising the membrane structure during ligand immobilisation [20]. As a result, this affinity membrane has rough and porous surface structure which improves the surface area, minimises mass transfer resistance and facilitates enzyme molecule diffusion. This results in a low diffusional resistance situation in the membrane, which contradicts to the packed bed affinity column, in which significant pressure drops constantly occur [21].

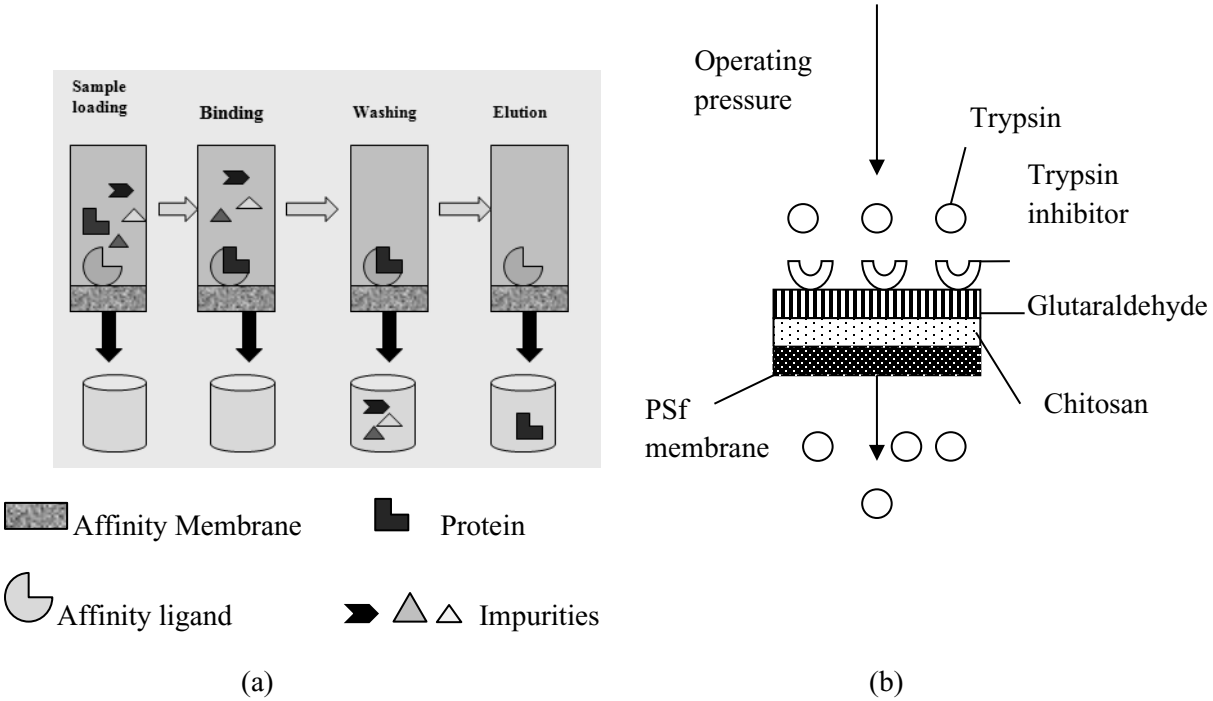


Figure 1. Graphical image of (a) protein purification protocols using affinity chromatographic membrane developed, and (b) synthesis of affinity membrane

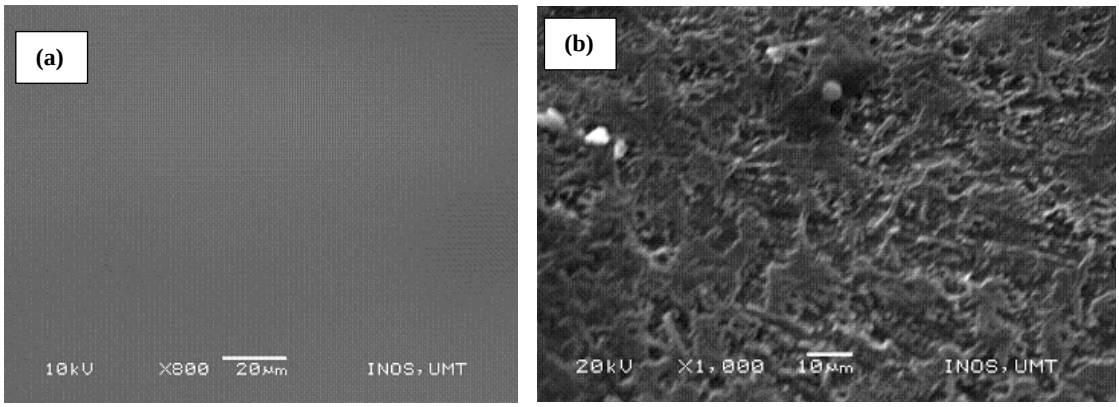


Figure 2. Surface morphology of (a) native membrane (PSf 15), and (b) affinity membrane (CH/PSf-60)

Figure 3 depicts the native membrane (PSf 15) and the affinity membrane by ATR-FTIR. The spectra represented the group of main compounds associated with the native membrane (PSf 15). After incorporating with chitosan, the band stretching was less intense due to the thin layer formation on the PSf 15 membrane. This band revealed the presence of O-H and N-H_2 groups in chitosan in affinity membrane (CH/PSf-60) ranging between 3200 and 3600 cm^{-1} [22,23]. The O–H stretching vibration peak (v=3200 to 3600 cm^{-1}) was reduced by crosslinking CH/PSf with glutaraldehyde (Figure 2 (b)). The wavelength at 2873 cm^{-1} exhibited C-H stretching due to aldehyde as well as duplet adsorption with peaks ascribed to the alkyl chain [24]. The band at 1657 cm^{-1} could be attributed to >C=O stretching (amide I) of the N-acetyl group in chitosan particles and a wavelength of 1722 cm^{-1} may be attributed to the presence of ethylenic chain [7].

The appearance of aldehyde peaks in the affinity membrane spectrum was due to the incomplete reactivity of glutaraldehyde with the chitosan OH groups during crosslinking network formation. As a bifunctional crosslinking, one aldehyde group may form a hemiacetal structure with hydroxyl groups of CH/PSf polymer chain while the other is unreacted associated with a certain conformation. The addition of a small amount of GTA may increase crosslinking chain with the formation of intermolecular covalent bonds between ligands and membrane (CH/PSf-60) via the availability of free amine group in affinity membrane (CH/PSf-60) [25]. Moreover, as a bi-functional reactive agent capable of reacting with the surface –OH groups of membrane and the amines groups of enzyme inhibitor, GTA could efficiently alleviate strong interaction between ligand and matrix apart from its ability to sustain ligand immobilization to be more resistant to pH changes and ionic strength.

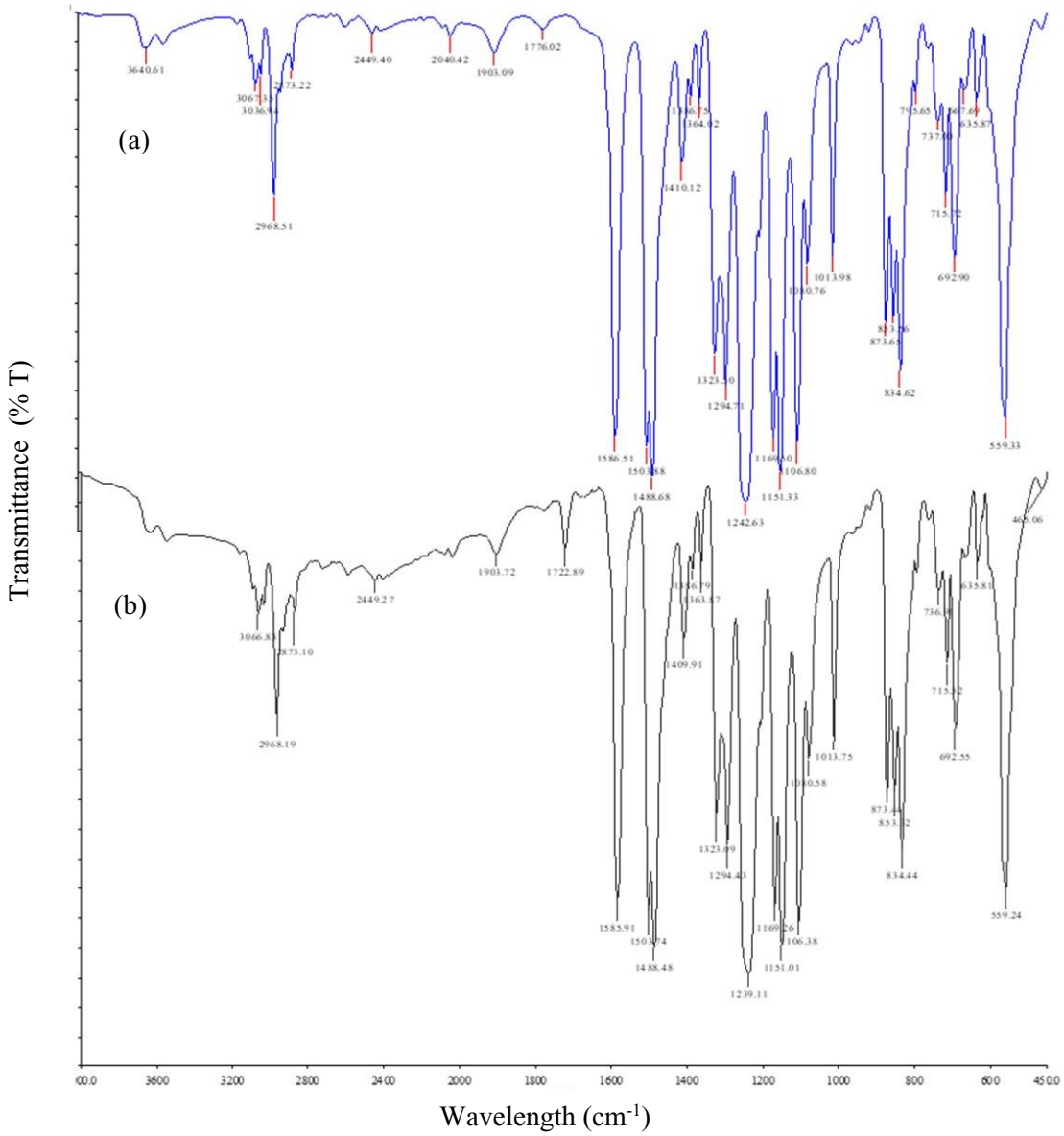


Figure 3. ATR-FTIR spectra of (a) native PSf15 and (b) affinity membrane

Effect of displacing salt in elution buffer

Other impurities and unbound molecules of the desired enzyme were removed using appropriate buffer solution during the washing stage. Although affinity chromatography membrane aims to target enzymes from their affinity ligands, an equally important aspect of this purification technique is the ability to release and recover isolated targets in active form.

A list of buffers and conditions can be applied for this recovery process, or the elution of affinity-bound enzymes using high-concentration salt solution [8] is commonly used. This elution buffer disrupts the interactions between the target enzyme and the ligand to reduce the binding affinity between them and force the desired enzyme in the permeate stream. In most cases, elution buffer options are targeted to obtain a functional eluate [26]. However, a number of studies

have demonstrated that elution conditions can significantly influence both the yield and specific activity of the eluted products [27].

In this study, four displacing salts (KCl, NaCl, $MgCl_2$ and $CaCl_2$) with 0.05 M ionic strength were added to the elution buffer to determine the ionic species that could enhance the dissociation of enzyme-ligand complex and trypsin transmission through affinity membrane. The results presented in Figures 4 and 5 exhibited a series of trypsin recovery in increasing order: $CaCl_2$ < NaCl < $MgCl_2$ < KCl. The main component in the adsorption mechanism is the affinity of positively charged trypsin and negatively charged sites on the membrane surface. The ionic bonding of this enzyme-ligand interaction can be affected by changing the physicochemical environment controlled by the displacing salts.

The pH 7 condition provided a favorable environment for trypsin adsorption with the help of electrostatic interaction that has dominated the adsorption. Trypsin was best adsorbed onto the affinity membrane with low positive charge as the electrostatic interactions between enzyme molecules decreased as the membrane increased. Moreover, in this favourable physicochemical environment, the amine groups of the trypsin molecules can undergo protonation to NH_3^+ [3], and these protonated amino groups on the surface of trypsin enhanced the electrostatic interaction between trypsin and affinity membrane. This observation is in agreement with the previous findings who found that the maximum adsorptive capacity of trypsin occureds around pH 7 [28].

The presence of displacing salts influenced the ionic strength of the elution buffer solution when KCl-HCl was added and then disrupted the electrostatic interaction of enzyme-affinity ligands, thus ionic exchange process occurred. K^+ cation is more electropositive, then the enzyme-ligand complex was dissociated and permeated through the membrane. Therefore, the trypsin recovery by KCl-HCl was highest at 78.8% with 1.31 purification fold. The properties of high chaotropic effect and salting of K^+ may destabilize the bonding between trypsin and trypsin inhibitor, leading to enhanced trypsin transmission [16].

The findings were attributed to different elution strengths of displacing ions during competition with trypsin in the affinity system. The trypsin recovery using the displacing salts such as NaCl-HCl, $MgCl_2$ and $CaCl_2$ were 65.0%, 69.3% and 40.6%, respectively. Compared to Ca^{2+}, Mg^{2+} with higher charge density is a better charge acceptor, thus it is expected to bind more tightly to the protein binding sites [29]. From the experimental observations, the addition of $CaCl_2$ converted the buffer solution to a cloudy solution, resulting in lower total protein readings and trypsin activity. This finding may be explained due to the formation of metal-enzyme complexes interaction. Calcium is a cosmotropic ion that can promote hydrophobic interaction with trypsin and may retain this enzyme on the membrane surface after elution [30]. Moreover, trypsin was assumed to have two binding sites, and the primary site has high affinity for calcium ions. This interaction has considerably stabilized the enzyme against denaturation [31] and was achieved by a conformational shift in the trypsin molecule, resulting in a more compact structure [32]. This change broke the bonding between trypsin and its ligand, and reduced trypsin transmission during the elution process.

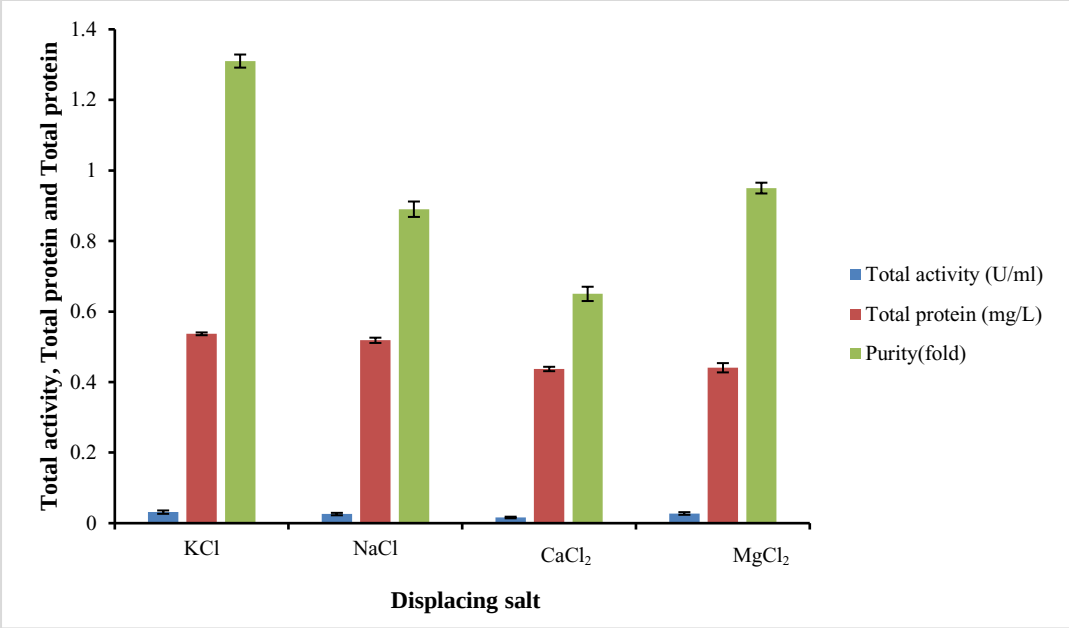


Figure 4. Effect of displacing salts of membrane parameters and data are presented as mean ± standard error (SE), $n = 3$

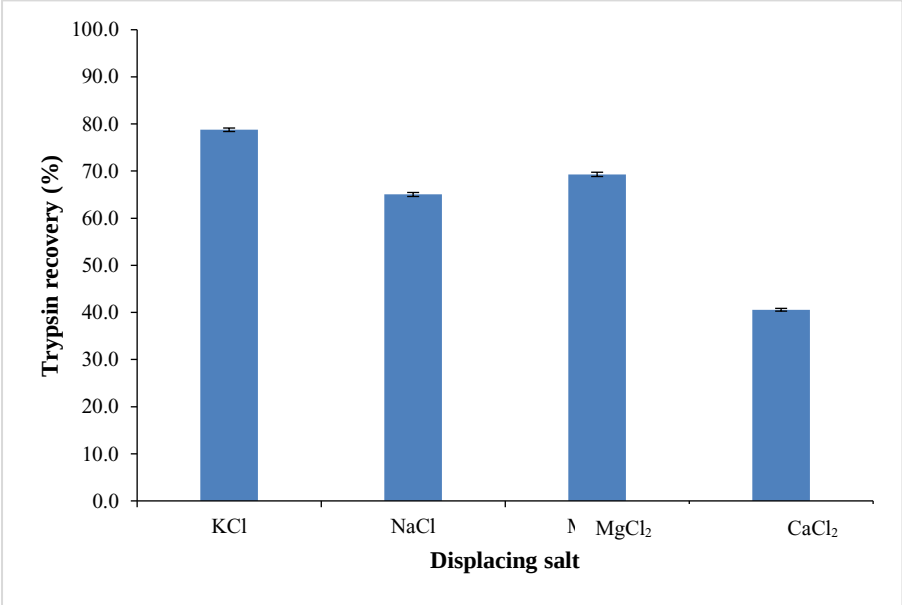


Figure 5. Effect of displacing salts on trypsin recovery activity and data are presented as mean ± standard error (SE), $n = 3$

Effect of elution pH

The adsorption behaviour in this study occurred mostly due to electrostatic interaction, and it is important to consider electrostatic interaction between trypsin molecules as well as between trypsin and membranes. pH can induce alteration in spatial structure of the

trypsin to affect the affinity of trypsin [33]. A small change in the pH of the solution can alter the electrical charge on proteins as well as membrane due to ionization or deionization of various acidic/basic groups on protein and membrane surface, which can cause either repulsive or attractive interactions [34]. The protein activity can be observed in Figures 6 and 7. The ionization of the charged groups on the ligand and/or the bound trypsin alters as the pH changes. This transition may directly influence the binding sites, reduce their affinity, or cause indirect changes in affinity through conformational changes.

Since the optimum adsorption of trypsin occurred at pH7, the trypsin recovery at this condition was 73.6%. This could be due to the fact that the electrostatic attraction of enzyme-ligand was strong and retained on the affinity membrane. Based on the optimum adsorption at pH 7, the pH of the elution buffer should be higher to break down the bonding of the enzyme and its ligand. Using an elution buffer at pH8, trypsin permeated into the membrane and resulted in about 92.0% recovery and 1.2 purification fold. An increase in the pH of elution buffer (pH 8) increased the dissociation of the sulfonic functional group of membranes and created a negative charge of the membrane. Therefore, electrostatic repulsion between enzyme-ligand was disrupted and thus trypsin dissociation occurred. An increase in the surrounding negative charge will cause the trypsin-ligand instability on the affinity membrane, increase the electrostatic repulsion and lead to high protein (trypsin) in eluent [35]. High OH^- anion will trigger enzyme aggregation as the net charge of the enzyme surface becomes zero. Therefore, there is no electrostatic repulsive force between trypsin-ligand [36]. The reduction of enzyme adsorption under alkaline pH could be attributed to the electrostatic repulsion between enzyme-membranes [37] and is responsible for lower adsorption, where thermodynamic entropy difference is the only force inducing the adsorption [38].

At lower pHs (6, 5 and 4), the decrease in protein activity due to trypsin recovery was 66.7%, 55.6%, and 50%, respectively. However, at extreme pH (acidic), the protein will be denatured [39]. Therefore, during the measurement of trypsin activity, the conformational changes of the trypsin molecules (denatured trypsin) at acidic pH affect the proper binding of the enzyme to the substrate, resulting in loss of the activity of the recovered trypsin in the permeate [40].

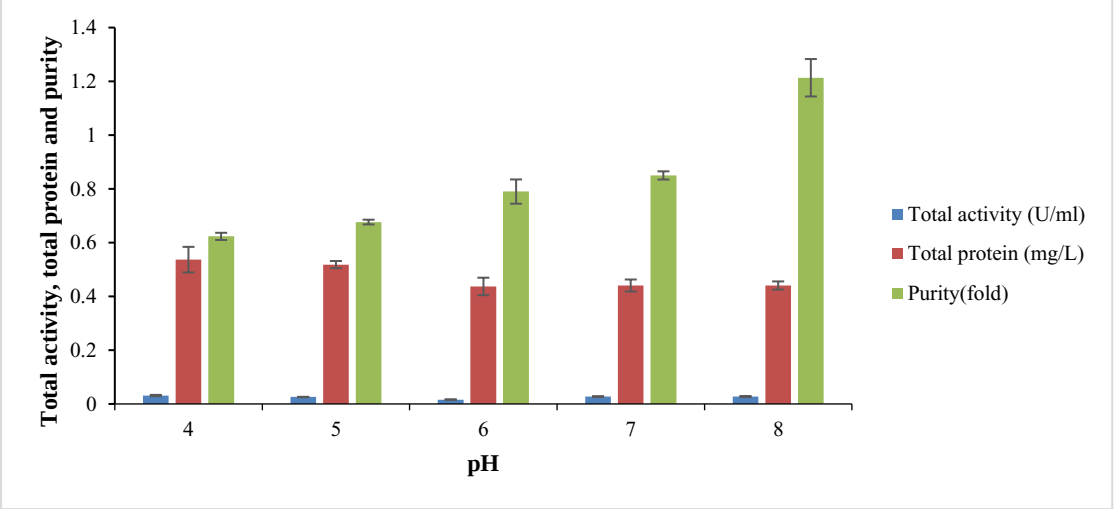


Figure 6. Effect of different pH on total protein, total activity and purity of affinity membranes using KCl buffer and data are presented as mean ± standard error (SE), $n = 3$

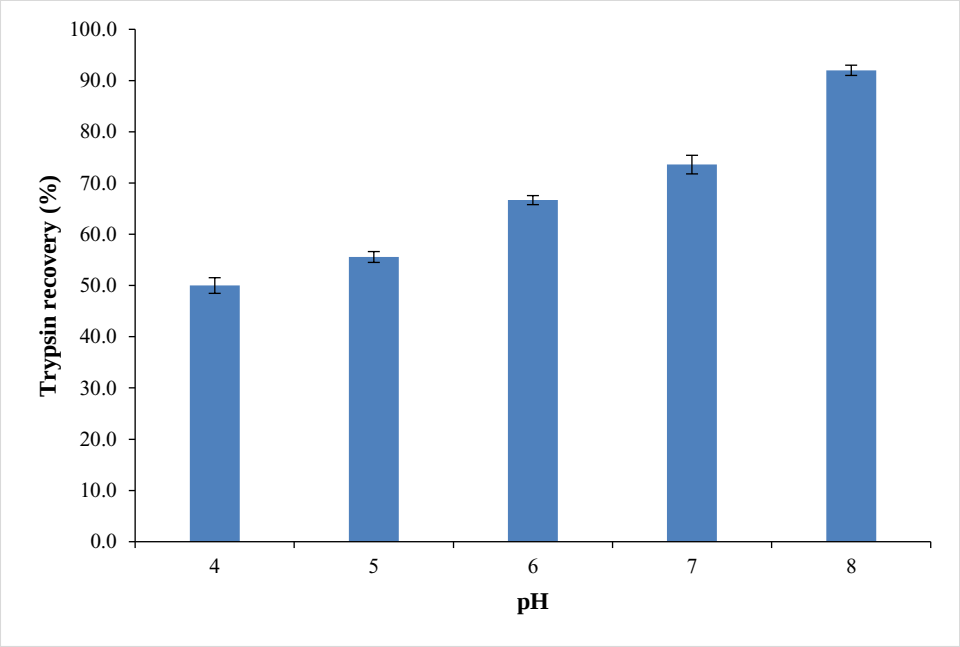


Figure 7. Effect of pH on trypsin recovery of affinity membranes using KCl buffer and data are presented as mean ± standard error (SE), $n = 3$

Conclusion

To conclude, this study suggests that the CH/PSf-60 membrane is the most appropriate membrane for trypsin separation. Furthermore, the modification of membrane with chitosan solution is a potential technique to mitigate fouling and improvemembrane lifespan as an excellent matrix material for developing an affinity membrane for trypsin separation and purification. Although the affinity membrane was well prepared, the physicochemical environment of the enzyme solution was also considered to obtain the greatest adsorption capacity. KCl as the displacing salt in the elution buffer solution was the optimum condition for trypsin recovery (78.8%). The recovery increased to 92% by setting the elution buffer pH at pH8. This study proved that the condition of elution buffer significantly influenced the degree of dissociation between the target enzyme and the affinity ligand, and enhanced the separation and purification performance. Thus, the fundamental chemical properties involved in the adsorption and desorption of proteins should be prioritized to develop affinity membrane protocols. The knowledge proposed in this study could be a good pathway for developing affinity membrane systems in the future.

Acknowledgement

The authors like to acknowledge Universiti Malaysia Terengganu for providing facilities and supporting this research.

References

1. Fane, A. G. and Radovich, J. M. (2020). Membrane systems. *Separation processes in biotechnology*. CRC Press: pp 209-262.
2. Kielkopf, C. L., Bauer, W. and Urbatsch, I. L. (2021). Considerations for membrane protein purification. *Cold Spring Harbor Protocols*, 2021(1): 102285.
3. Bayramoglu, G., Ozalp, V. C., Altintas, B. and Arica, M. Y. (2014). Preparation and characterization of mixed-mode magnetic adsorbent with p-amino-benzamidine ligand: Operated in a magnetically stabilized fluidized bed reactor for purification of trypsin from bovine pancreas. *Process Biochemistry*, 49(3): 520-528.

4. Ghosh, R. (2016). Bioseparations using integrated membrane processes. *Integrated Membrane Systems and Processes*: pp 23-34.
5. Khangembam, B. K. and Chakrabarti, R. (2015). Trypsin from the digestive system of carp *Cirrhinus mrigala*: Purification, characterization and its potential application. *Food Chemistry*, 175: 386-394.
6. Zamani, A. and Benjakul, S. (2016). Trypsin from unicorn leatherjacket (*Aluterus monoceros*) pyloric caeca: Purification and its use for preparation of fish protein hydrolysate with antioxidative activity. *Journal of the Science of Food and Agriculture*, 96(3): 962-969.
7. Sun, J., Yang, L., Jiang, M. and Xu, B. (2017). Stability and activity of immobilized trypsin on carboxymethyl chitosan-functionalized magnetic nanoparticles cross-linked with carbodiimide and glutaraldehyde. *Journal of Chromatography B*, 1054: 57-63.
8. Mondal, K. and Gupta, M. N. 2006. The affinity concept in bioseparation: Evolving paradigms and expanding range of applications. *Biomolecular Engineering*, 23: 59-76.
9. Poonsin, T., Simpson, B. K., Benjakul, S., Visessanguan, W. and Klomklao, S. (2017). Albacore tuna (*Thunnus alalunga*) spleen trypsin partitioning in an aqueous two-phase system and its hydrolytic pattern on Pacific white shrimp (*Litopenaeus vannamei*) shells. *International Journal of Food Properties*, 20(10): 2409-2422.
10. Mukherjee, S., Roy, D. and Bhattacharya, P. (2008). Comparative performance study of polyethersulfone and polysulfone membranes for trypsin isolation from goat pancreas using affinity ultrafiltration. *Separation and Purification Technology*, 60(3): 345-351.
11. Braia, M., Loureiro, D., Tubio, G., Lienqueo, M. E. and Romanini, D. (2017). Interaction between trypsin and alginate: An ITC and DLS approach to the formation of insoluble complexes. *Colloids and Surfaces B: Biointerfaces*, 155: 507-511.
12. Vatić, S., Mirković, N., Milošević, J. R., Jovčić, B. and Polović, N. Đ. (2021). Trypsin activity and freeze-thaw stability in the presence of ions and non-ionic surfactants. *Journal of bioscience and bioengineering*, 131(3): 234-240.
13. Lemma, S. M., Boi, C. and Carbonell, R. G. (2021). Nonwoven Ion-Exchange Membranes with High Protein Binding Capacity for Bioseparations. *Membranes*, 11(3): 181.
14. Soper, A. S. and Aird, S. D. (2007). Elution of tightly bound solutes from concanavalin A Sepharose: Factors affecting the desorption of cottonmouth venom glycoproteins. *Journal of Chromatography A*, 1154(1-2): 308-318.
15. Wang, L., Shen, S., He, X., Yun, J., Yao, K. and Yao, S.-J. (2008). Adsorption and elution behaviors of bovine serum albumin in metal-chelated affinity cryogel beds. *Biochemical Engineering Journal*. 42: 237-242.
16. Malmquist, G. and Lundell, N. 1992. Characterization of the influence of displacing salts on retention in gradient elution ion-exchange chromatography of proteins and peptides. *Journal of Chromatography A*, 627: 107-124.
17. Ghosh, R., Wan, Y. H. and Cui, Z. F. (2003). Parameter scanning ultrafiltration: rapid optimization of protein separation. *Biotechnology Bioengineering*. 81: 673-682.
18. Ghosh, R. and Cui, Z. F. (2000). Protein purification by ultrafiltration with pre-treated membrane. *Journal of Membrane Science*, 167: 47-53.
19. Jellouli, K., Bougatef, A., Daassi, D., Balti, R., Barkia, A. and Nasri, M. (2009). New alkaline trypsin from the intestine of Grey triggerfish (Balistes capriscus) with high activity at low temperature: Purification and characterisation. *Food Chemistry*, 116: 644-650.
20. Guo, W. and Ruckenstein, E. (2002). Crosslinked mercerized cellulose membranes for the affinity chromatography of papain inhibitors. *Journal of Membrane Science*, 197: 53-62.
21. Chen, T. -X., Nie, H. -L., Li, S. -B., Branford-White, C., Su, S. -N. and Zhu, L. -M. (2009). Comparison: Adsorption of papain using immobilized dye ligands on affinity membranes. *Colloids and Surfaces B: Biointerfaces*, 72: 25-31.

22. Boributh, S., Chanachai , A. and Jiraratananon, R. (2009). Modification of PVDF membrane by chitosan solution. *Journal of Membrane Science*, 342: 97–104.
23. Varghese, J. G., Kittur, A. A., Rachipudi, P. S. and Kariduraganavar, M. Y. (2010). Synthesis, characterization and pervaporation performance of chitosan-g-polyaniline membranes for the dehydration of isopropanol. *Journal of Membrane Science*, 364: 111-121.
24. Mansur, H. S., Sadahira, C. M., Souza, A. N. and Mansur, A. A. P. (2008). FTIR spectroscopy characterization of poly (vinyl alcohol) hydrogel with different hydrolysis degree and chemically crosslinked with glutaraldehyde. *Materials Science and Engineering C*, 28: 539-548.
25. Geng, L., Li, N., Xiang, M., Wen, X., Xu, D., Zhao, F. and Li, K. (2003). The covalent immobilization of trypsin at the galleries of layered γ-zirconium phosphate. *Colloids and Surfaces B: Biointerfaces*, 30: 99-109.
26. Firer, M. A. (2001). Efficient elution of functional proteins in affinity chromatography. *Journal of Biochemical and Biophysical Methods*, 49: 433-442.
27. Lee, W. -C., Chen, C. -H. (2001). Predicting the elution behavior of proteins in affinity chromatography on non-porous particles. *Journal of Biochemical and Biophysical Methods*, 49: 63-82.
28. Wu, J., Luan, M. and Zhao, J. (2006). Trypsin immobilization by direct adsorption on metal ion chelated macroporous chitosan-silica gel beads. *International Journal of Biological Macromolecules*, 39: 185-191.
29. Dudev, T. and Lim, C. (2014). Competition among metal ions for protein binding sites: determinants of metal ion selectivity in proteins. *Chemical reviews*, 114(1): 538-556.
30. de Gonzalo, G., and Lavandera, I. (Eds.). (2021). Biocatalysis for Practitioners: Techniques, reactions and applications. John Wiley & Sons.
31. Kishimura, H. and Hayashi, K. (2002). Isolation and characteristics of trypsin from pyloric ceca of the starfish Asterina pectinifera. *Comparative Biochemistry and Physiology Part B. Biochemistry and Molecular Biology*, 132: 485-490.
32. Klomklao, S., Benjakul, S., and Visessanguan, W. (2004) Comparative studies on proteolytic activity of spleen extracts from three tuna species commonly used in Thailand. *Journal of Food Biochemistry*, 28: 355–372.
33. Li, C., Han, Y., Gao, L., Zhang, Y. and Simpson, B. K. (2021). Development of a novel trypsin affinity material using a recombinant buckwheat trypsin inhibitor mutant with enhanced activity. *LWT*, 146, 111382.
34. Aravind, U. K., Mathew, J. and Aravindakumar, C. T. (2007). Transport studies of BSA, lysozyme and ovalbumin through chitosan/polystyrene sulfonate multilayer membrane. *Journal of Membrane Science*, 299: 146-155.
35. Purkait, M. K., Sinha, M. K., Mondal, P. and Singh, R. (2018). Introduction to membranes. *Interface science and technology*, Elsevier, 25: 1-37.
36. Gustafsson, H., Thörn, C. and Holmberg, K. (2011). A comparison of lipase and trypsin encapsulated in mesoporous materials with varying pore sizes and pH conditions. *Colloids and Surfaces B: Biointerfaces*, 87: 464-471.
37. Chen, N., Zou, J., Wang, S., Ye, Y., Huang, Y., Gadda, G. and Yang, J. (2009). Designing protease sensors for real-time imaging of trypsin activation in pancreatic cancer cells. *Biochemistry*, 48: 3519
38. Li, X., Zhang, Y. and Fu, X. 2004. Adsorption of glutamicum onto polysulphone membrane. *Separation and Purification Technology*, 37: 187-198.
39. Zhou, L., Liao, T., Liu, J., Zou, L., Liu, C. and Liu, W. (2019). Unfolding and inhibition of polyphenoloxidase induced by acidic pH and mild thermal treatment. *Food and Bioprocess Technology*, 12(11): 1907-1916.
40. Kim, J. S. and Lee, S. (2019). Immobilization of trypsin from porcine pancreas onto chitosan nonwoven by covalent bonding. *Polymers*, 11: 1462.

Malaysian Journal of Analytical Sciences (MJAS)
Published by Malaysian Analytical Sciences Society

BIOMIMETIC SYNTHESIS OF SILVER NANOPARTICLES USING *Eleusine indica* EXTRACT AND ITS ANTIBACTERIAL PROPERTIES

(Sintesis Biomimetik Nanopartikel Perak Menggunakan Ekstrak *Eleusine indica* dan Ciri Antibakteria)

Ropisah Me[1*], Muhammad Hafiz Istamam[1], Noor Hidayah Pungot[2], Nazlina Ibrahim[3], Alice Shanthi[4]

[1]Universiti Teknologi MARA, Cawangan Negeri Sembilan, Kampus Kuala Pilah, 72000 Kuala Pilah, Negeri Sembilan, Malaysia.
[2]Universiti Teknologi MARA, 40450 Shah Alam, Selangor, Malaysia
[3]Universiti Kebangsaan Malaysia, 43600 UKM Bangi, Selangor, Malaysia
[4]Universiti Teknologi MARA, Cawangan Negeri Sembilan, Kampus Seremban, 70300 Seremban, Negeri Sembilan, Malaysia.

**Corresponding author: ropisah@uitm.edu.my*

Received: 14 September 2021; Accepted: 18 December 2021; Published: 25 February 2022

Abstract

The biomimetic method, which relies on natural resources such as plant extracts, bacteria, and fungi, offers an alternative for synthesizing silver nanoparticles (AgNPs). The use of biomimetic method for synthesizing AgNPs have various benefits including cost effectiveness, low toxicity, and suitabiity for biomedical application. This study synthesizes plant mediated nanoparticle using *Eleusine indica* to determine its antibacterial activity. *Eleusine indica* methanol extract is treated with 1 mM of silver nitrate at room temperature (25-27 °C) for 24 hours. The resulting product is characterized using UV-Vis spectroscopy and transmission electron microscope (TEM). UV-Vis absorption spectroscopy displays a strong resonance centered on the surface of AgNPs at approximately 413 nm. Physical appearance of AgNPs as characterized by transmission electron microscopy (TEM) showed formation of AgNPs with average particle size of 20 nm. In the antibacterial activity of the synthesized AgNPs, minimum inhibitory concentration (MIC) and minimum bactericidal concentration (MBC) assays are performed. The plant mediated AgNPs has predicted bacteriocidal activity according to the ratio of MBC to MIC values against selected Gram-positive and Gram-negative bacteria. In this study, plant mediated AgNPs has been successfully synthesized by reduction of silver nitrate with *Eleusine indica* leaves methanol extract.

Keywords: Plant-mediated silver nanoparticles, *Eleusine indica*, UV-Vis analysis, transmission electron microscope, antibacterial activity

Abstrak

Kaedah biomimetik yang bergantung kepada sumber alam seperti ekstrak tumbuhan, bakteria dan kulat, menawarkan alternatif dalam sintesis nanopartikel perak (AgNPs). Penggunaan kaedah biomimetik dalam sintesis AgNPs mempunyai pelbagai kelebihan termasuk keberkesanan kos, ketoksikan yang rendah, dan kesesuaian dalam kegunaan biomedik. Objektif kajian ini adalah untuk mensintesis nanopartikel perak diperantara tumbuhan menggunakan *Eleusine indica* dan menentukan aktiviti antibakteria. Ekstrak metanol *Eleusine indica* telah dirawat dengan 1 mM larutan perak nitrat pada suhu bilik (25 – 27 °C) selama 24 jam. Sampel telah

dicirikan menggunakan spektroskopi UV-Vis dan mikroskopi transmisi elektron (TEM). Spektroskopi penyerapan UV-Vis menunjukkan resonans berpusat yang kuat atas permukaan AgNPs pada kira-kira 413 nm. Rupabentuk fizikal AgNPs yang dicirikan melalui mikroskopi transmisi elektron (TEM) menunjukkan pembentukan AgNP dengan purata saiz partikel 20 nm. Aktiviti antibakteria nanopartikel perak perantaraan-tumbuhan yang disintesis telah diasai melalui penentuan kepekatan perencatan minimum (MIC) dan kepekatan bakterisidal minimum (MBC). Gabungan nanopartikel perak perantaraan-tumbuhan diramal mempunyai aktiviti bacteriosidal berdasarkan nisbah nilai MBC kepada MIC terhadap bakteria Gram positif dan Gram negatif bakteria. Dalam kajian ini, AgNPs perantaraan-tumbuhan telah berjaya disintesis melalui penurunan perak nitrat dengan ekstrak metanol daun *Eleusine indica*.

Kata kunci: nanopartikel perak perantaraan-tumbuhan, *Eleusine indica*, analisa UV-Vis, mikroskopi transmisi elektron, aktiviti antibakteria

Introduction

Nanotechnology is developing - rapidly in the growing field with the applications of science and technology for the purpose of making new nanoscale materials [1]. Communication, electronics, chemistry, physics, robotics, biology, and medicine can benefit from nanotechnology research [2]. Different forms of nanoparticles (NPs) such as copper, zinc, titanium, magnesium, gold, alginate and silver have emerged, but silver NPs have proven to be the most effective since they have strong antimicrobial efficiency against bacteria, viruses and other eukaryotic microorganisms [1]

Conventional methods for synthesizing AgNPs, such as physical and chemical procedures, involved the usage of heavy equipment, substantial amounts of energy consumption, highly toxic and hazardous chemical compounds that can cause biological hazards and therefore, they are not environmentally sustainable and they are unsafe [3]. As a result, biomimetic nanoparticle syntheses or plant-mediated silver nanoparticles are often used because they are simple, cost-effective, environmentally friendly, and they are easily reproduced [4]. AgNPs synthesized in a biomimetic method - useful in a variety of fields, including optoelectronic devices [5], catalytic activities [6], and the food packaging industry [7]. AgNPs is has also be regarded as the agent of wound-healing, antioxidant, antimicrobial, antiviral, and anticancer [8].

Synthesis methods using either plant extract or fruit extract have several advantages over other biological approaches. This includes no requirement in cell culture that can take more time to produce which can scale up the synthesis process [9]. Plant extracts contain a wide range of metabolites that can act as capping and stabilizing agents and thus avoids the need to add these agents from other sources [3]. There are other studies whereby plant-mediated AgNPs have been investigated for the antibacterial properties such as using *Rhazya stricta* [10] and *Azhadirachta indica* [11] to synthesis AgNPs. This study aims to add the possibility of *Eleusine indica* as a plant candidate to synthesize AgNPs. *Eleusine indica* or locally known as sambau has been known to possess antioxidant, antibacterial and antiviral activities among others [12,13]. Thus, it is a good potential for producing AgNPs against bacterial candidates known to be pathogenic. The strategy involves the reduction of silver nitrate and the methanol extract of *Eleusine indica* which can be used as a reductant as well as a stabilizer. The synthesized AgNPs is evaluated for its physical characteristics and antibacterial activity against four pathogenic microorganisms.

In this study, an extract of *Eleusine Indica* is used in the synthesis of plant-mediated AgNPs, and the relation between AgNPs and the extract's metabolites, and evaluate its antibacterial properties The characterization of synthesized AgNPs is analyzed with the use of UV-Vis spectroscopy and transmission electron microscopy (TEM).

Materials and Methods

All the reagents purchased were of laboratory grade and used as received. Silver nitrate ($AgNO_3$) were purchased from R&M Chemicals, US. Methanol was purchased

from Sigma Aldrich, Germany. (3-[4,5-dimethylthiazol-2-yl]-2,5 diphenyl tetrazolium bromide) (MTT), Mueller Hinton agar and nutrient broth was obtained from Universiti Kebangsaan Malaysia. The fresh leaves of *Eleusine indica* were collected in Kuala Pilah, Negeri Sembilan. Authentication of this species was done by Forest Research Institute Malaysia (FRIM) where voucher specimen (FRI-51486) was deposited. Deionized water was used throughout the experiment.

Extractions of *Eleusine indica*

About 250 g of ground dried *Eleusine indica* leaves was soaked in 2500 mL of methanol for 72 hours at room temperature by using maceration technique [14]. The sample was filtered and concentrated by using rotary evaporator. The extract was placed in a fume hood until almost dried to obtain *Eleusine indica* methanol extract and kept in a vial for further analysis.

Biomimetic synthesis and characterization of silver nanoparticles

The biomimetic method was followed by Lee and Jun [15] with some modification. About 10 mL of *Eleusine indica* methanol extract was added drop by drop into 30 mL of 1 mM silver nitrate solution and was allowed to be reacted at room temperature for 24 hours at 25-27 ºC. The appearance of yellowish-brown color of the solution indicates the formation of silver nanoparticles [16]. The formation of plant-mediated AgNPs was analyzed using UV-Vis spectroscopy and TEM.

Characterization of plant-mediated silver nanoparticles

Physicochemical properties of the synthesized plant-mediated silver nanoparticles were characterized using UV-Vis spectra and TEM analysis. The UV-Vis spectra analysis was conducted using a UV 2450 Shimadzu double-beam spectrophotometer, operated at a resolution of 2 nm in the range from 300 to 500 nm. The formation of AgNPs was confirmed by transmission electron microscopy (TEM). TEM analysis of AgNPs was performed using a Philips CM12 instrument operated at an accelerating voltage at 80 kV. The size distribution of the AgNPs was calculated from the TEM images by measuring the diameter in nm of approximately 50 nanoparticles.

Evaluation of antibacterial activity

The antibacterial potential of the synthesized plant-mediated silver nanoparticles was determined using minimum inhibitory concentration (MIC) and Minimum Bactericidal Concentration (MBC) assays [17]. In the assay, four bacteria were tested with two Gram-positive bacteria (*Staphylococcus aureus*, *Bacillus subtilis*) and another two Gram-negative bacteria (*Escherichia coli*, *Enterobacter aerogenes*). MIC assay was performed in triplicate in a 96-well microtiter plate. Serial double dilutions of plant-mediated silver nanoparticles (AgNPs) varying from 100% to 1.562 % in nutrient broth were prepared in the MIC assay. Each dilution (100 µL) was dispensed into the wells and then 100 µL of the bacterial suspension in nutrient broth was incubated at 37ºC for 24 hours. After 24 hours, 10 µL of 0.2 mg/mL (MTT) solution was added into each well and incubated for another 2 hours. The solution color change from pale yellow to red/purple, which indicated biologically active bacteria [18]. MBC is the determination of the lowest concentration without colony growth on the agar plates. This was determined by plating 10 µL from each well that showed no growth on a Mueller Hinton agar plate. Plates was then incubated for further 24 hours at 37°C. Lowest concentration that shows no colony growth was determined as MBC.

Results and Discussion

Extractions of Eleusine indica

Dried ground Eleusine indica leaves was used in this study in order to enhance the surface area and optimize the extraction process (Figure 1). The percentage yield of the crude extract was calculated and presented in Table 1.

Methanol extraction resulted in moderate weight and percentage yield of Eleusine indica. Methanol is a polar solvent that can extract most of the key phytochemical compounds [19]. Compared with aqueous solvent, methanol solvent has less polarity which gives more efficiency in term of extraction because of its capability in degradation of cell wall. Thus, methanol provides excellent capability in extraction of secondary metabolites such as phenolics, glycosides, tannins, flavonoids, saponins, steroids and alkaloids [20, 21].

These secondary metabolites have polyhydroxy group that are suitable in reducing metal ions to nanoparticles [22]. According to Iberahim et al. [23], Eleusine indica methanol extract have several groups of metabolites including phenolics, glycosides, flavonoids and terpenoids. These metabolites substantiate the selection of Eleusine indica in this study to potentially act as reducing and stabilizing agent in the synthesis of AgNPs.

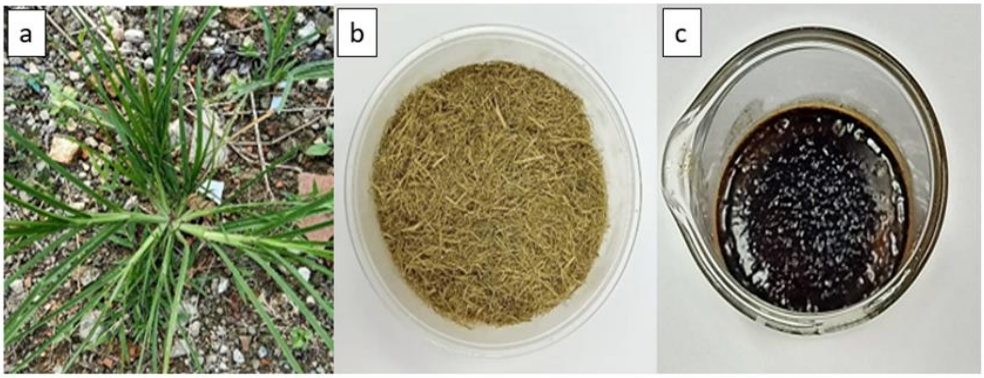


Figure 1. (a) *Eleusine indica* plant, (b) the dried ground leaves, (c) *Eleusine indica* methanol extract

Table 1. Percentage yield of *Eleusine indica* crude extract

Type of Crude Extract	Weight of Sample (g)	Weight of Crude (g)	Percentage of Crude Extract (%)
Methanol	250	13.3	5.32

Biomimetic synthesis and characterization of silver nanoparticles

Formation of silver nanoparticles in this study is monitored by color change. Figure 2 shows the color changes when the Eleusine indica methanol extract was mixed with a 1 mM $AgNO_3$ solution and treated at room temperature for 24 hours. The appearance of a yellowish solution in the reaction vessel indicated the formation of AgNPs due to excitation of surface plasmon resonance in the AgNPs [24,25].

Characterization of silver nanoparticles

Ultraviolet-visible spectroscopy (UV-Vis) and transmission electron microscopy (TEM) were used to characterize the synthesized AgNPs. As illustrated in Figure 3, the surface plasmon resonance of the AgNPs is centered at approximately 413 nm, indicating the presence of AgNPs in the solution. AgNPs are known to exhibit a UV-Visible absorption maximum in the range of 400-500 nm because of surface plasmon resonance [26]. The conduction band and valence band in AgNPs are relatively close to one other, allowing the electrons to travel freely. The collective oscillation of electrons of silver nano particles in resonance with the light wave produces a surface plasmon resonance (SPR) absorption band, which is caused by these free electrons [27]. According to Kerker [28], the absorbance of AgNPs depends mainly upon size and shape. thus, this will affect the absorbance of AgNPs that obtained.

The morphology and size distribution of plant-mediated AgNPs was analyzed using TEM micrograph. The TEM image in Figure 4 (left) shows that the particles are almost spherical. The particles size histograms of the plant-mediated AgNPs (Figure 4-right) suggest that the particles diameter is within the range of 10 nm to 55 nm

with an average size of 20 nm. Silver nanoparticles, in particular, have varying scale sizes depending on the type of plant extracts used [16]. For example, the silver nanoparticles synthesized using Plumbago auriculata leaves has average size between 15 to 30 nm [29]. [30] found that AgNPs synthesized using Datura stramonium leaf extract has average size of 15 to 20 nm. Based on the theory of quantum restraint, a smaller wavelength leads to a higher energy of the wave and a smaller particle size [31].

It has been reported that Eleusine indica extract contains 12 metabolites such as hydroxycinnamic acid, naringenin (flavanones), *2(3,4-dihydroxyphenyl)-7-hydroxy-5-benzenepropanoic acid,* antraquinone, caffeic acid derivative, caffeoyl glucose, hydroxybenzoic acid derivatives methyl 2-[cyclohex-2-en-1-yl(hydroxy)methyl]-3-hydroxy-4-(2-hydroxy ethyl)-3-methyl-5-oxoprolinate (aglycone) from the flavonoid and phenolic groups [12]. Active oxygen found in phenols, flavonoids, and triterpenoic acid can donate electrons into AgNPs to reduce silver precursors [32]. This reduction of silver ions to silver nanoparticles could be possibly due to -OH groups in flavonoids such as quercetin, which can be released during the tautomeric change of flavonoids from the enol to keto type that releases reactive hydrogen atoms that are responsible for the reduction of silver nanoparticles [33]. Figures 5 show the possible mechanism of reduction of silver ions to AgNPs by naringenin (flavonone) molecule.

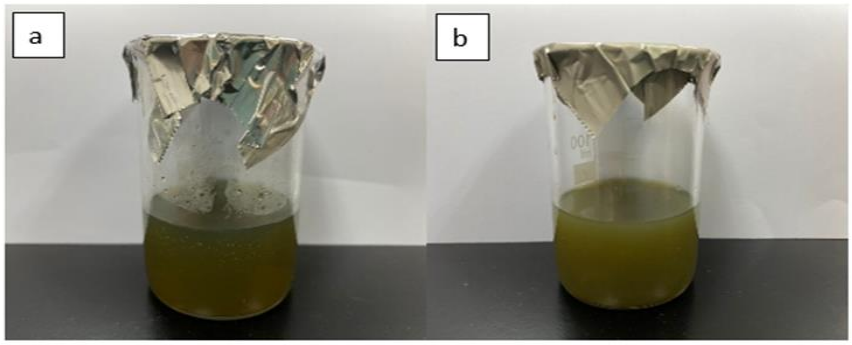


Figure 2. (a) *Eleusine indica* extract, (b) *Eleusine indica* extract mixed with silver nitrate after 24 hours

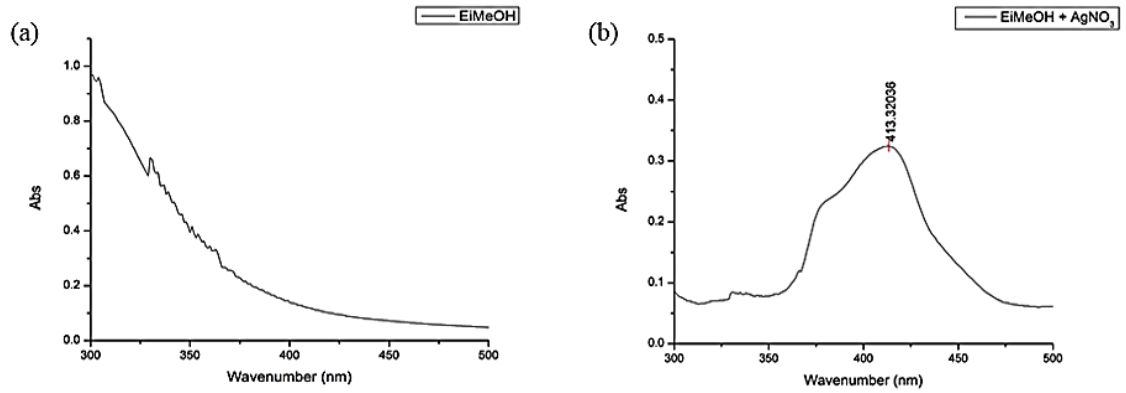


Figure 3. (a) UV-Vis absorption spectrum of Eleusine indica extract (EI-MeOH) and (b) synthesized silver nanoparticles (EI-MeOH-AgNPs)

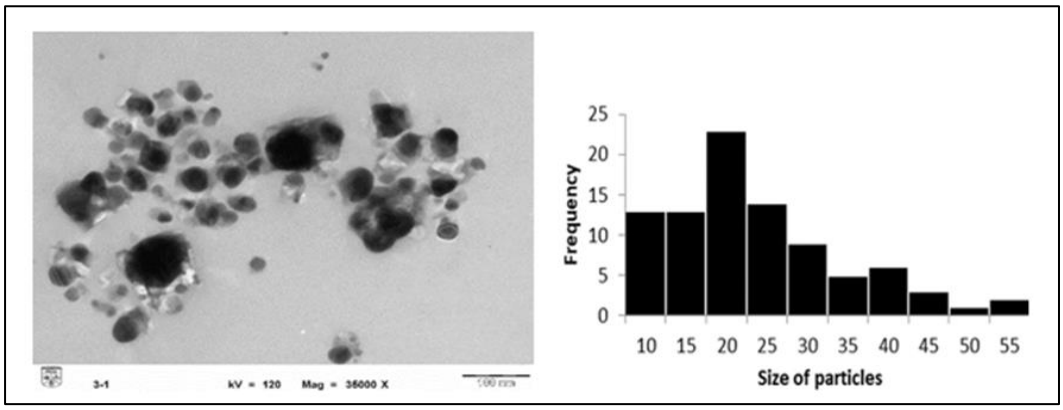


Figure 4. TEM micrograph and particle histogram

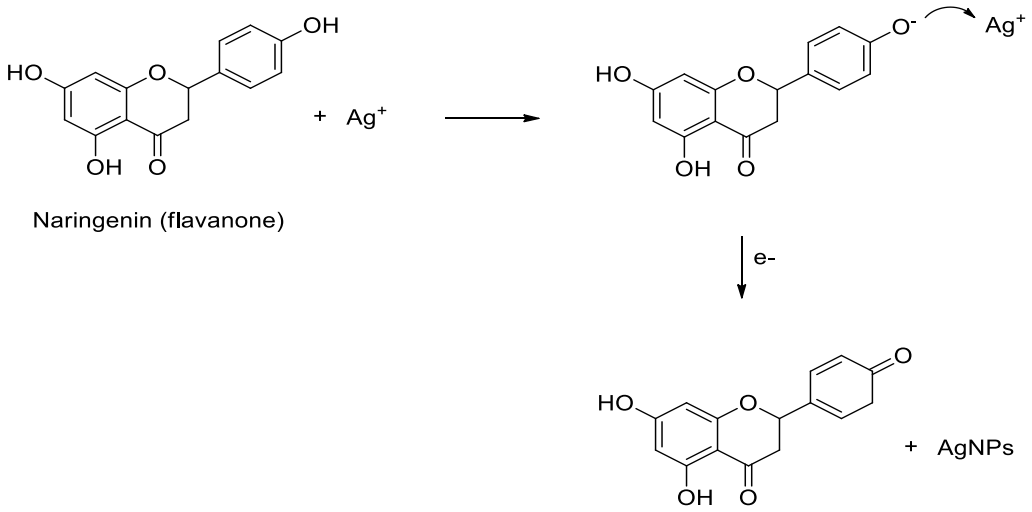


Figure 5. The proposed mechanism for the formation of plant-mediated AgNPs

Antibacterial activity of silver nanoparticles

The efficacy of AgNPs as promising antimicrobial has been experimentally tested against a wide range of medically important planktonic and sessile pathogenic microorganisms including bacteria, viruses, champignons, lichens and yeasts [34, 35]. In this study, the plant-mediated silver nanoparticles were tested against Gram-positive bacteria and Gram-negative bacteria. Table 2 shows the MIC and MBC test of synthesized silver nanoparticles against *Staphylococcus aureus*, *Bacillus subtilis*, *Escherichia coli* and *Enterobacter aerogenes*.

Based on the MIC and MBC values, the synthesized nanoparticle suggest the display of bacteriocidal potentials. The formal definition of a bactericidal agent is the ratio of MBC to MIC is ≤ 4, while a bacteriostatic agent has an MBC to MIC ratio of > 4 (CLSI). AgNPs antibacterial effects may be determined by the characteristics of certain bacterial species and the type of metabolite present in the plant [36] as well as the size

ranges and shapes of the AgNPs [27]. Theoretically, upon interaction with bacteria, nanoparticles bind with bacterial membrane which causes changes to both its physical and chemical nature. Nevertheless, the normal physiological process such as respiration and permeability of cells will be compromised [37]. Besides, the formation of various reactive nitrogen and oxygen species can be induced by nanoparticles that generates oxidative stress on DNA, and other important cell constituents which disrupt the overall functioning of bacterial cells.

Table 2. MIC and MBC test of silver nanoparticles synthesized by *Eleusine indica* against four bacteria

Bacteria	**MIC (µg/mL)**	**MBC (µg/mL)**	**MBC to MIC Ratio**
Staphylococcus aureus	12.5	12.5	1
Bacillus subtilis	1.56	1.56	1
Escherichia coli	6.25	12.5	2
Enterobacter aerogenes	3.13	6.25	2

Conclusion

In conclusion, the biomimetic method was demonstrated as a simple, safe, cost-effective, and ecofriendly preparation of AgNPs using *Eleusine indica* methanol extract. The synthesized plant-mediated AgNPs gave UV-Vis reading at 413 nm and have an average particle size of 20 nm. They showed potential antibacterial activity against Gram-positive and Gram-negative bacteria including *Staphylococcus aureus*, *Bacillus subtilis*, *Escherichia coli* and *Enterobacter aerogenes*. Thus, application of these synthesized AgNPs based on the findings may lead to valuable discoveries in various fields, including medical devices and in the pharmaceutical and biomedical industries. Toxicity studies of these AgNPs using human pathogens may open the door to a new range of antibacterial agents and the possibility to the use of AgNPs as antiviral agents.

Acknowledgement

The authors would like to acknowledge Ministry of Education for the financial support under Fundamental Research Grant Scheme (FRGS/1/ 2019/STG01/UITM/ 02/10) and Universiti Teknologi MARA, Negeri Sembilan Branch, Kuala Pilah Campus, Negeri Sembilan; Faculty of Applied Sciences, Universiti Teknologi MARA, Shah Alam Selangor; Faculty of Science & Technology and CRIM, Universiti Kebangsaan Malaysia, Bangi Selangor for providing the research facilities. Thanks also to Mr Yip Chee Wai for the invaluable guidance in the antibacterial assays. Not to be missed is our profound acknowledgement to Forest Research Institute Malaysia (FRIM), Mrs Syahida Emiza binti Suhaimi and Mr Mohd Aidil bin Nordin for helping in plant identification.

References

1. Logeswari, P., Silambarasan, S. and Abraham, J. (2015). Synthesis of silver nanoparticles using plants extract and analysis of their antimicrobial property. *Journal of Saudi Chemical Society*, 19(3): 311-317.
2. Safari, J. and Zarnegar, Z. (2014). Advanced drug delivery systems: Nanotechnology of health design a review. *Journal of Saudi Chemical Society*, 18(2): 85-99.
3. Rajeshkumar, S. and Bharath, L. V. (2017). Mechanism of plant-mediated synthesis of silver nanoparticles – A review on biomolecules involved, characterisation and antibacterial activity. *Chemico-Biological Interactions*, 273: 219-227.

4. Ahmed, S., Saifullah, Ahmad, M., Swami, B. L. and Ikram, S. (2016). Green synthesis of silver nanoparticles using *Azadirachta indica* aqueous leaf extract. *Journal of Radiation Research and Applied Sciences*, 9(1): 1-7.
5. Poulose, S., Panda, T., Nair, P. P. and Théodore, T. (2014). Biosynthesis of silver nanoparticles. *Journal of Nanoscience and Nanotechnology,* 14(2): 2038-2049.
6. Mosaviniya, M., Kikhavani, T., Tanzifi, M., Tavakkoli Yaraki, M., Tajbakhsh, P. and Lajevardi, A. (2019). Facile green synthesis of silver nanoparticles using *Crocus Haussknechtii Bois* bulb extract: Catalytic activity and antibacterial properties. *Colloids and Interface Science Communications*, 33(8): 100211.
7. Zhao, X., Zhou, L., Riaz Rajoka, M. S., Yan, L., Jiang, C., Shao, D. and Jin, M. (2018). Fungal silver nanoparticles: Synthesis, application and challenges. *Critical Reviews in Biotechnology*, 38(6): 817-835.
8. Larayetan, R., Ojemaye, M. O., Okoh, O. O. and Okoh, A. I. (2019). Silver nanoparticles mediated by *Callistemon citrinus* extracts and their antimalaria, antitrypanosoma and antibacterial efficacy. *Journal of Molecular Liquids*, 273: 615-625.
9. Roy, K., Sarkar, C. K. and Ghosh, C. K. (2015). Plant-mediated synthesis of silver nanoparticles using parsley (*Petroselinum crispum*) leaf extract: spectral analysis of the particles and antibacterial study. *Applied Nanoscience (Switzerland)*, 5(8): 945-951.
10. Shehzad, A., Qureshi, M., Jabeen, S., Ahmad, R., Alabdalall, A. H., Aljafary, M. A. and Al-Suhaimi, E. (2018). Synthesis, characterization and antibacterial activity of silver nanoparticles using *Rhazya stricta*. *PeerJ,* 2018(12): 1-15.
11. Lalitha, A., Subbaiya, R. and Ponmurugan, P. (2013). Green synthesis of silver nanoparticles from leaf extract *Azhadirachta indica* and to study its anti-bacterial and antioxidant property. *International Journal of Current Microbiology and Applied Sciences*, 2(6): 228-235.
12. Abdul, A. B., Al-Zubairi, A. S., Abdelwahab, S. I., Peng, C. Y., Mohan, S. and Elhassan, M. M. (2011). *Eleucine indica* possesses antioxidant, antibacterial and cytotoxic properties. *Evidence-Based Complementary and Alternative Medicine*, 2011: 965370.
13. Iberahim, R., Nor, N. S. M., Yaacob, W. A. and Ibrahim, N. (2018). *Eleusine indica* inhibits early and late phases of herpes simplex virus type 1 replication cycle and reduces progeny infectivity. *Sains Malaysiana*, 47(7): 1431-1438.
14. Devi, M., Devi, S., Sharma, V., Rana, N., Bhatia, R. K. and Bhatt, A. K. (2020). Green synthesis of silver nanoparticles using methanolic fruit extract of *Aegle marmelos* and their antimicrobial potential against human bacterial pathogens. *Journal of Traditional and Complementary Medicine*, 10(2): 158-165.
15. Lee, S. H. and Jun, B. H. (2019). Silver nanoparticles: Synthesis and application for nanomedicine. *International Journal of Molecular Sciences*, 20(4): 1-23.
16. Din, L. B., Mie, R., Samsudin, M. W., Ahmad, A. and Ibrahim, N. (2015). Biomimetic synthesis of silver nanoparticles using the *Lichen ramalina dumeticola* and the antibacterial activity. *Malaysian Journal of Analytical Sciences*, 19(2): 369-376.
17. Wang, W., Li, N., Luo, M., Zu, Y. and Efferth, T. (2012). Antibacterial activity and anticancer activity of *Rosmarinus officinalis L*. essential oil compared to that of its main components. *Molecules*, 17(3): 2704-2713.
18. Zarai, Z., Kadri, A., Ben Chobba, I., Ben Mansour, R., Bekir, A., Mejdoub, H. and Gharsallah, N. (2011). The in-vitro evaluation of antibacterial, antifungal and cytotoxic properties of *Marrubium vulgare L*. essential oil grown in Tunisia. *Lipids in Health and Disease*, 10(1): 161.
19. Ahmad, Aftab, Husain, A., Mujeeb, M., Khan, S. A., Alhadrami, H. A. A., & Bhandari, A. (2015). Quantification of total phenol, flavonoid content and pharmacognostical evaluation including HPTLC fingerprinting for the standardization of *Piper nigrum Linn* fruits. *Asian Pacific Journal of Tropical Biomedicine*, 5(2): 101-107.

20. Truong, D. H., Nguyen, D. H., Ta, N. T. A., Bui, A. V., Do, T. H. and Nguyen, H. C. (2019). Evaluation of the use of different solvents for phytochemical constituents, antioxidants, and in vitro anti-inflammatory activities of *Severinia buxifolia*. *Journal of Food Quality*, 2019: 8178294.
21. Gupta, M., Thakur, S., Sharma, A. and Gupta, S. (2013). Qualitative and quantitative analysis of phytochemicals and pharmacological value of some dye yielding medicinal plants. *Oriental Journal of Chemistry*, 29(2): 475-481.
22. Sahu, N., Soni, D., Chandrashekhar, B., Satpute, D. B., Saravanadevi, S., Sarangi, B. K. and Pandey, R. A. (2016). Synthesis of silver nanoparticles using flavonoids: hesperidin, naringin and diosmin, and their antibacterial effects and cytotoxicity. *International Nano Letters*, 6(3): 173-181.
23. Iberahim, R., Yaacob, W. A. and Ibrahim, N. (2015). Phytochemistry, cytotoxicity and antiviral activity of *Eleusine indica* (sambau). *AIP Conference Proceedings*, 1678: 1–5.
24. Shankar, S. S., Rai, A., Ankamwar, B., Singh, A., Ahmad, A. and Sastry, M. (2004). Biological synthesis of triangular gold nanoprisms. *Nature Materials*, 3(7): 482-488.
25. Kumar R, Ghoshal G, J. A. and G. M. (2017). Rapid green synthesis of silver nanoparticles (AgNPs) using (*Prunus persica*) plants extract: Exploring its antimicrobial and catalytic activities. *Journal of Nanomedicine & Nanotechnology*, 08(04): 2157-7439
26. Ashraf, J. M., Ansari, M. A., Khan, H. M., Alzohairy, M. A. and Choi, I. (2016). Green synthesis of silver nanoparticles and characterization of their inhibitory effects on AGEs formation using biophysical techniques. *Scientific Reports*, 2015(6): 1-10.
27. Zhang, X. F., Liu, Z. G., Shen, W. and Gurunathan, S. (2016). Silver nanoparticles: Synthesis, characterization, properties, applications, and therapeutic approaches. *International Journal of Molecular Sciences*, 17(9): 1534.
28. Kerker, M. (1985). The optics of colloidal silver: something old and something new. *Journal of Colloid and Interface Science*, 105(2): 297-314.
29. Singh, K., Naidoo, Y., Mocktar, C. and Baijnath, H. (2018). Biosynthesis of silver nanoparticles using *Plumbago auriculata* leaf and calyx extracts and evaluation of their antimicrobial activities. *Advances in Natural Sciences: Nanoscience and Nanotechnology*, 9(3): 035004.
30. Gomathi, M., Rajkumar, P. V., Prakasam, A. and Ravichandran, K. (2017). Green synthesis of silver nanoparticles using *Datura stramonium* leaf extract and assessment of their antibacterial activity. *Resource-Efficient Technologies*, 3(3): 280-284.
31. Narchin, F., Larijani, K., Rustaiyan, A., Ebrahimi, S. N. and Tafvizi, F. (2018). Phytochemical synthesis of silver nanoparticles by two techniques using *Saturaja rechengri Jamzad* extract: Identifying and comparing in vitro anti-proliferative activities. *Advanced Pharmaceutical Bulletin*, 8(2): 235-244.
32. Ramesh, A. V., Devi, D. R., Battu, G. R. and Basavaiah, K. (2018). A Facile plant mediated synthesis of silver nanoparticles using an aqueous leaf extract of *Ficus hispida Linn. f.* for catalytic, antioxidant and antibacterial applications. *South African Journal of Chemical Engineering*, 26(7): 25-34.
33. Jain, S. and Mehata, M. S. (2017). Medicinal plant leaf extract and pure flavonoid mediated green synthesis of silver nanoparticles and their enhanced antibacterial property. *Scientific Reports*, 7(1): 1-13.
34. Burdușel, A. C., Gherasim, O., Grumezescu, A. M., Mogoantă, L., Ficai, A. and Andronescu, E. (2018). Biomedical applications of silver nanoparticles: An up-to-date overview. *Nanomaterials*, 8(9): 1-25.
35. Mie, R., Samsudin, M. W., Din, L. B., Ahmad, A., Ibrahim, N. and Adnan, S. N. A. (2013). Synthesis of silver nanoparticles with antibacterial activity using the lichen *Parmotrema praesorediosum*. *International Journal of Nanomedicine*, 9(1): 121-127.
36. Kim, J. S., Kuk, E., Yu, K. N., Kim, J. H., Park, S. J., Lee, H. J. and Cho, M. H. (2007). Antimicrobial effects of silver nanoparticles. *Nanomedicine: Nanotechnology, Biology, and Medicine*, 3(1): 95-101

37. Salomoni, R., Léo, P. and Rodrigues, M. F. A. (2015). Antibacterial activity of silver nanoparticles (agnps) in *staphylococcus aureus* and cytotoxicity effect in mammalian cells. *The Battle Against Microbial Pathogens: Basic Science, Technological Advances and Educational Programs*, 2015: 851-857.

Malaysian Journal of Analytical Sciences (MJAS)
Published by Malaysian Analytical Sciences Society

MEASUREMENT OF SOLVENT PROPERTIES USING KAMLET-TAFT APPROACH FOR APPLICATION IN SYNTHESIS

(Pengukuran Sifat Pelarut Menggunakan Pendekatan Kamlet-Taft untuk Penggunaan dalam Sintesis)

Tariqul Islam[1], A. B. M. Helal Uddin[1], Sahena Ferdosh[2], Md. Zaidul Islam Sarker[1,3]*

[1]Faculty of Pharmacy
[2]Faculty of Science
International Islamic University Malaysia, 25200 Kuantan, Pahang, Malaysia
[3]Program Leader of Food Science Program, Cooperative Research, Education and Extension Services, Northern Marianas College, 501250, Saipan MP 96950, USA

**Corresponding author: mdzaidul.sarker@marianas.edu*

Received: 31 August 2021; Accepted: 11 January 2022; Published: 25 February 2022

Abstract

Solvents are an unavoidable part of pharmaceutical and chemical manufacturing/synthesis, most of them are toxic or hazardous. The study on toxic solvent replacement is ongoing over the world. Researchers are trying to overcome the hazardous issues that can be possible using the mixture of hydrogen bond donor (HBD) and hydrogen bond acceptor (HBA) solvent as a safe/recommended solvent mixture. This study presents the possibility for the replacement/limitation of dipolar aprotic solvent in drug synthesis using solvent-pair mixture where the Kamlet-Taft (KT) parameter works as a tool to alternate the uses of such types of toxic solvents. It has been simplified here among the many methods and equations of the KT approach. The polarity (π*), basicity (β), and acidity (α) of 10 pure solvents and 16 solvent-pair mixtures were measured spectroscopically, utilizing well-suited dyes or indicators. The highest absorption wavenumber value of indicators in the solution was selected and the simplified KT equations were used to determine the solvent properties (π*, β, α). Solvent mixtures were classified as per the solvent selection guideline of GSK2016 and CHEM21. Four pure solvents (tetrahydrofuran, dimethylformamide, dimethylsulfoxide, and acetone) exhibited low KT acidity, high KT basicity, and high KT polarity. Eight aqueous solvent mixtures (water-acetone, water-ethanol, water-isopropyl alcohol, water-dimethylsulfoxide, water-dimethylformamide, water-tetrahydrofuran), and two non-aqueous solvent mixtures (ethanol-dimethylformamide, ethanol-dimethylsulfoxide) showed low KT acidity and high KT basicity. Solvent classification by composite score showed that four solvent mixtures were as recommended and 5 mixtures were near to recommended solvent among 16 solvent mixtures. KT parameter was a simplified approach to determine which mixture can bind with active pharmaceutical ingredients (API) that is indicated by KT solvatochromic properties and solvent classification.

Keywords: Kamlet-Taft parameters, hazardous solvent, solvent-pair mixture, dipolar aprotic solvent, drug synthesis

Abstrak

Pelarut adalah bahagian yang tidak dapat dielakkan dalam pembuatan/sintesis farmaseutikal dan kimia, kebanyakannya beracun atau berbahaya. Kajian mengenai penggantian pelarut toksik sedang dijalankan di seluruh dunia. Penyelidik berusaha mengatasi masalah berbahaya yang mungkin dilakukan dengan menggunakan campuran pelarut penderma ikatan hidrogen (HBD) dan pelarut

ikatan hidrogen (HBA) sebagai campuran pelarut yang selamat/disyorkan. Kajian ini menunjukkan kemungkinan penggantian/pembatasan pelarut aprotik dipolar dalam sintesis ubat dengan campuran pasangan pelarut di mana parameter Kamlet-Taft (KT) berfungsi sebagai alat untuk mengganti penggunaan jenis pelarut toksik tersebut. Ini telah dipermudahkan di sini antara banyak kaedah dan persamaan pendekatan KT. Kekutuban (π*), asas (β), dan keasidan (α) daripada 10 pelarut tulen dan 16 campuran pasangan pelarut telah diukur dengan menggunakan spektroskopi, berdasarkan pewarna atau indikator yang sesuai. Nilai penyerapan gelombang tertinggi dari indikator dalam larutan dipilih dan persamaan KT digunakan untuk menentukan sifat pelarut (π*, β, α). Campuran pelarut dikelaskan mengikut garis panduan pemilihan pelarut GSK 2016 dan CHEM21. Empat pelarut tulen (tetrahidrofuran, dimetilformamida, dimetilsulfoksida, dan aseton) menunjukkan keasidan KT rendah, asas KT tinggi, dan kekutuban KT tinggi. Lapan campuran pelarut berasaskan air (air-aseton, air-etanol, air-isopropil alkohol, air-dimetilsulfoksida, air-dimetilformamida, air-tetrahidrofuran), dan dua campuran pelarut tidak berasaskan air (etanol-dimetilformamida, etanol-dimetilsulfoksida) menunjukkan keasidan KT rendah dan asas KT yang tinggi. Penggolongan terhadap 16 campuran pelarut berdasarkan skor komposit menunjukkan empat campuran pelarut adalah seperti yang disyorkan dan 5 campuran pelarut hampir dengan yang disyorkan. Parameter KT adalah pendekatan yang dipermudah untuk menentukan campuran mana yang dapat mengikat dengan bahan aktif farmaseutikal (API) yang ditunjukkan oleh sifat solvatochromic KT dan klasifikasi pelarut.

Kata kunci: parameter Kamlet-Taft, pelarut berbahaya, campuran pasangan pelarut, pelarut aprotik dipolar, sintesis ubat

Introduction

In 1976, Kamlet and Taft introduced a model to measure the solvatochromic properties, known as Kamlet-Taft parameters [1]. In 1997, Marcus brought some modifications in the measurement of KT parameters [2]. Various equations and indicators were used to calculate the KT parameters (KT acidity, KT basicity, and KT polarity) so that the appropriate result is obtained by averaging [3]. The most used indicators were N, N-dimethyl-4-nitroaniline, 4-nitro anisole, and N,N-dimethyl-3-nitro aniline for π* value; 4-nitroaniline, 4-nitrophenol, 4-aminoacetophenone and (tetramethyl ethylenediamine)(acetylacetonato)copper(II) perchlorate for β value; Cis-bis-(1,10-phenan throline)dicyanoiron(II), 2,6-dichloro-4-(2,4,6-triphenyl-1-pyridinio) phenolate, and 2,6-diphenyl-4-(2, 4, 6-tripheny-1-pyridinio) phenoxide/ phenolate for α value. The indicators were utilized in KT measurement because their UV variations are higher than the UV-Vis cutoff (310 nm) of the cyclic ketone [4]. In analysis, many specific equations are used to calculate the KT parameters that were prepared based on the indicators [2,5], and the concentration of the indicator greatly affects the result [6].

Solvents are categorized into four major types; recommended, problematic, hazardous, and highly hazardous based on health, safety, environment, and global harmonized system (GHS) hazards statements [7]. Most used solvents are hazardous as per the recommendation of the international conference on harmonization (ICH), Pfizer, GSK, and Sanofi [8,9], as shown in Table 1. Recently, KT parameters have been used to investigate the replacement/limitation of hazardous solvents using solvent-pair mixtures in synthetic chemistry. Most of the HBD-HBA solvent mixtures exhibit as solvent of recommended and problematic category [7,10,11], they can be applied in API [4,11] and non-API chemical [5,12,13] synthesis. The maximum use of safe solvents can minimize the health risks and negative impacts on the environment, which can be the most effective way to limit the use of hazardous solvents [14-17]. However, many methods; KT solvatochromic parameters using COSMO-RS [18], KT parameters using solvate ionic liquids [19] were more complex. Taking into consideration the advancement of the KT parameters in synthetic chemistry, the measurement technique has been simplified for determining the solvatochromic parameters. The 16 solvent-pair mixtures and 10 pure solvents were analyzed to determine the probability of application in replacing dipolar aprotic solvents (dimethylformamide, dimethylacetamide, N-methyl-2-pyrrolidone, pyridine etc.).

Table 1. Recommendation from Pfizer, GSK, Sanofi, and ICH regarding the use of the following solvents

Most Used Organic Solvents	**Concern in Use (Comment) [8, 9]**			
	Pfizer	**GSK**	**Sanofi**	**ICH**
Dimethylformamide (DMF)	Undesirable	Major issues	Substitution requested	To be limited
Dimethylacetamide (DMAC)	Undesirable	Major issues	Substitution requested	To be limited
N-methyl-2-pyrrolidone(NMP)	Undesirable	Major issues	Substitution requested	To be limited
Dichloromethane (DCM)	Undesirable	Major issues	Substitution advisable	To be limited
Chloroform	Undesirable	Major issues	No comment	To be limited
1,4-Dioxane	Undesirable	Major issues	Substitution requested	To be limited
Pyridine	Undesirable	No comment	Substitution advisable	To be limited
Diisopropyl ether (IPE)	Undesirable	Major issues	Substitution advisable	Unknown

Materials and Methods

Materials

Analytical reagent (AR) grade methanol (MeOH 99.9%), acetone (Ace 99.8%), tetrahydrofuran (THF 99.8%), dimethyl sulfoxide (DMSO 99.9%), and calcium chloride anhydrous (99.9%) were received from Merck KGaA, Germany. Ethanol (EtOH 99.8%) was purchased from HmbG chemicals, Malaysia. HPLC grade acetonitrile (ACN 99.99%), AR grade dichloromethane (DCM 99.9%) were purchased from QREC (Asia), Malaysia. AR grade dimethylformamide (DMF 99.99%), and isopropyl alcohol (iPrOH 99.99%) were received from Fisher Scientific, UK. Three solvatochromic indicators were purchased: N, N-dimethyl-4-nitroaniline 98% as indicator 1 from Alfa Aesar through Permula chemicals, Malaysia; 4-nitro aniline 99% (Indicator 2) and Reichardt's dye 90% or 2,6-diphenyl-4-(2,4,6-triphenyl-1-pyridinio) phenolate 90% as indicator 3 from Sigma-Aldrich. To avoid humidity contamination or light degradation, the samples and indicators were weighted cautiously. A microbalance (Brand: Mettler Toledo; model: AX-205) was used to prepare the samples by mass with an uncertainty of ±1×10-4 g.

Analytical condition of KT parameters

Organic solvents were dried to free residual water before analysis using calcium chloride anhydrous. Indicator concentration in the solvent was from 0.03 mM to 0.05 mM (for indicator 1 & 2) and 0.1 mM (for indicator 3). The indicator and solvent were mixed properly before analysis to limit a variety of UV absorption to 0.5-1.2. The desired UV spectra of the solution were determined at a resolution of 0.2 nm using a double beam UV-Vis spectrophotometer (Shimadzu, UV-1800). Every UV-Vis spectrum was performed in triplicate. During the UV analysis, the temperature has been controlled at 25±0.1 °C using a temperature controller (Shimadzu, TCC-240A).

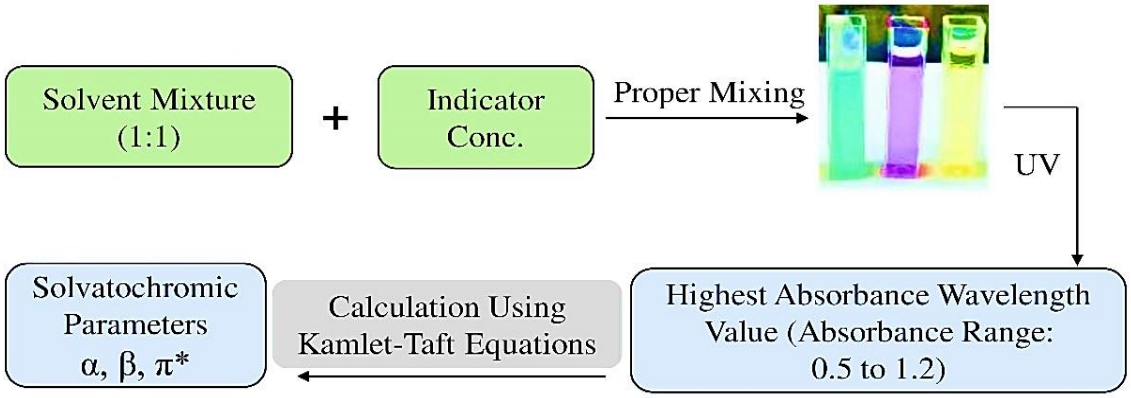


Figure 1. Measurement overview of solvatochromic parameters (π*, β, α) using the KT theory

Measurement equation of KT parameters

Three solvatochromic parameters i.e., KT polarity, KT basicity, and KT acidity were measured according to the original approach of KT theory using three equations (equation S1 to equation S3) [3,4]. The absorption wavenumber (V_{max}) from the highest wavelength value of the analytical sample was converted into KiloKaiser unit (1KK = 1000 cm^{-1}) to calculate the equations (1-3).

Statistical analysis

Experimental results were expressed as mean (n = 3) with uncertainty values and the data was analyzed using ANOVA and Dunnett's t-test in SPSS (version 20). *P values of 0.05 or less were regarded as significant.

Results and Discussion

The values of the measured wavenumbers (Vmax) and the obtained KT parameters have been expressed in Table 2 and Table 3. The absorbance range was established among the samples confined within 0.5 to 1.2. A total of ten pure solvents were analyzed to determine π*, β, and α. At the same time, sixteen mixed (HBD-HBA) solvents were also analyzed, involving eight aqueous and eight non-aqueous solvent pairs. In pure solvents, EtOH, MeOH, H_2O, iPrOH showed a high KT acidity and low KT polarity, whereas, DCM, ACN showed a low KT basicity. On the other hand, Ace, ACN, DMSO, DMF, and THF showed low acidity. In other words, the recommended solvents showed a high KT acidity, low KT basicity, and low KT polarity. In contrast, maximum problematic and hazardous solvents showed low KT acidity, high KT basicity, and high KT polarity except for DCM, iPrOH, and MeOH. Almost similar findings have been reported in the literature [20, 21].

Among the 16 mixed solvents, only four solvent mixtures i.e., H_2O-EtOH, H_2O-iPrOH, H_2O-DMSO, EtOH-DMSO were exhibited as recommended solvents, and the other 12 solvent mixtures were demonstrated as problematic in which 5 solvent mixtures (H_2O-Ace, EtOH-Ace, MeOH-Ace, H_2O-CAN, EtOH-CAN) showed as near to recommended solvent, as shown in Table 4. Eight aqueous (H_2O-MeOH, H_2O-Ace, H_2O-EtOH, H_2O-CAN, H_2O-iPrOH, H_2O-DMSO, H_2O-DMF, H_2O-THF) and two non-aqueous solvent mixtures (EtOH-DMF, EtOH-DMSO) showed a low KT acidity, low KT basicity, and high KT polarity. On the contrary, other non-aqueous solvent mixtures (EtOH-CAN, EtOH-Ace, EtOH-THF, MeOH-Ace, MeOH-DMF, MeOH-THF) showed a high KT acidity, low KT polarity, and low KT basicity, tabulated (Table 3). Similar results were found in the literature and previous work [6,11,12]. The solvent ranking was required for the application of mixed solvents that was prepared based on the GSK2016 and Innovative Medicines Initiative CHEM21 (IMI-CHEM21) solvent selection guideline [22]. The ranking of mixed solvents was ascertained from the minimum value of the GSK health and safety scores of HBA solvent using the equation (S4) [22].

Prat et al. and Byrne et al. stated that the commonly used solvents in drug synthesis and processing are hazardous, such as DMF, DMSO, NMP, DMAC, and pyridine, which are from dipolar aprotic solvents (HBA). IMI-CHEM21, GSK, Pfizer, ICH guidelines suggested that those solvents should be substituted/limited with safe solvents due to their toxic activities [7-9]. American Chemical Society (ACS) and Green Chemistry Institute (GCI) were investigating to replace such solvents in synthetic chemistry [23]. Duereh et al. stated that API has both HBD and HBA sites and dipolar aprotic (HBA) solvents have low KT acidity, high KT basicity, and high KT polarity. HBA solvents could easily create a strong chemical binding with the HBD site of API for these chemical properties [5].

Duereh et al. studied with 52 solvent mixtures and they reported that combinations of HBD-HBA allow the binding with API because solvent mixtures show low KT acidity, high KT basicity, and high KT polarity properties. For that, the solvent mixture can be used for the replacement of dipolar aprotic solvent. Although strong binding with API depends on physicochemical properties of solvent mixture. All mixtures who exhibited low KT acidity and high KT basicity, they are also capable to bind with the HBD site of API, can be selected for drug synthesis [4, 11, 13]. The solvent ranking was prepared to know which mixture is hazardous or problematic and which is recommended before being applied in synthesis. However, pure recommended solvents typically showed high acidity that is not capable to bind with the API. Therefore, when the solvent-pair mixtures show low KT acidity ($\alpha \approx 0$), high KT basicity ($\beta > 0.6$), and high KT polarity ($\pi^* > 0.6$), they offer a strong binding with the API [3, 11].

Indicator 1: Polarity (π^*) = $(28.10 - V_{max1}) / 3.52$ (1)

Indicator 2: Basicity (β) = $(0.984V_{max1} + 3.49 - V_{max2}) / 2.759$ (2)

Indicator 3: Acidity (α) = $(1.318V_{max1} - 47.7 + V_{max3}) / 5.47$ (3)

Composite score = $\sqrt{}$ (Safety score x Health score) (4)

Table 2 The properties of pure solvents from the wavenumber average (V_{max}) using the original approach of KT equations

Solvent	*V_{max}	*Polarity (π^*)	*V_{max}	*Basicity (β)	*V_{max}	*Acidity (α)
	(Mean ± SD)	(Mean)	(Mean ± SD)	(Mean)	(Mean ± SD)	(Mean)
EtOH	25.92 ± 0.06	0.62	25.80 ± 0.03	0.70	25.80 ± 0.02	0.82
MeOH	25.64 ± 0.02	0.70	25.66 ± 0.05	0.64	25.66 ± 0.02	1.00
Ace	25.66 ± 0.04	0.69	25.59 ± 0.03	0.49	25.59 ± 0.02	0.24
CAN	25.41 ± 0.02	0.76	25.39 ± 0.03	0.33	25.39 ± 0.01	0.38
i-PrOH	25.94 ± 0.02	0.61	25.91 ± 0.07	0.56	25.91 ± 0.01	0.60
DMSO	24.55 ± 0.02	1.01	24.57 ± 0.05	0.69	24.57 ± 0.01	0.10
DMF	25.07 ± 0.02	0.86	25.07 ± 0.02	0.71	25.07 ± 0.01	0.09
THF	26.05 ± 0.05	0.58	25.95 ± 0.05	0.48	25.95 ± 0.11	0.00
DCM	25.48 ± 0.03	0.74	25.43 ± 0.04	0.00	25.43 ± 0.06	0.04
H_2O	23.68 ± 0.02	1.26	23.64 ± 0.03	0.16	23.64 ± 0.14	1.27

Key: *P values ($P<0.05$) were regarded as significant. Uncertainty value of $\pi^* = \pm 8\times10^{-3}$, $\beta = \pm 6\times10^{-3}$, and $\alpha = \pm 8\times10^{-3}$

Table 3. The properties of mixed solvents from the wavenumber average (V_{max}) using the original approach of KT equations

HBD-HBA Mixture	*V_{max} (Mean ± SD)	*Polarity (π) (Mean)	*V_{max} (Mean ± SD)	*Basicity (β) (Mean)	*V_{max} (Mean ± SD)	*Acidity (α) (Mean)
Aqueous solvent mixture						
H_2O-MeOH	24.14 ± .02	1.12	24.14 ± 0.05	0.40	24.14 ± 0.03	0.82
H_2O-Ace	24.39 ± 0.03	1.05	24.39 ± 0.03	0.48	24.39 ± 0.01	0.68
H_2O-EtOH	24.31 ± 0.02	1.08	24.31 ± 0.03	0.48	24.31 ± 0.01	0.67
H_2O-CAN	24.51 ± 0.02	1.02	24.51 ± 0.04	0.41	24.51 ± 0.01	0.82
H_2O-iPrOH	24.62 ± 0.02	0.99	24.62 ± 0.03	0.57	24.62 ± 0.01	0.65
H_2O-DMSO	23.88 ± 0.02	1.20	23.88 ± 0.02	0.43		0.58
H_2O-DMF	24.08 ± 0.01	1.14	24.08 ± 0.02	0.48	24.08 ± 0.03	0.62
H_2O-THF	24.98 ± 0.02	0.89	24.98 ± 0.02	0.60	24.98 ± 0.01	0.64
Non-aqueous solvent mixture						
EtOH-CAN	25.46 ± 0.02	0.75	25.46 ± 0.05	0.51	25.46 ± 0.001	0.82
	25.64 ± 0.02	0.70	25.64 ± 0.03	0.59	25.64 ± 0.01	0.76
EtOH-DMF	25.36 ± 0.02	0.78	25.36 ± 0.04	0.65	25.36 ± 0.02	0.67
EtOH-DMSO	25.17 ± 0.02	0.83	25.17 ± 0.04	0.74	25.17 ± 0.01	0.60
EtOH-THF	25.81 ± 0.02	0.65	25.81 ± 0.02	0.64	25.81 ± 0.02	0.70
MeOH-Ace	25.54 ± 0.02	0.73	25.54 ± 0.03	0.56	25.54 ± 0.02	0.88
MeOH-DMF	25.32 ± 0.02	0.79	25.32 ± 0.02	0.63	25.32 ± 0.02	0.81
MeOH-THF	25.71 ± 0.05	0.68	25.71 ± 0.03	0.61	25.71 ± 0.02	0.84

Key: *P values ($P<0.05$) were regarded as significant. Uncertainty value of $\pi^* = \pm 7\times10^{-3}$, $\beta = 8\times10^{-3}$, and $\alpha = \pm 3\times10^{-3}$

Table 4. Ranking of the solvent-pair mixture from the minimum values of GSK health and safety score [22]

Solvent-pair (HBD-HBA)	GSK Scores of HBA Solvent				Composite Score (Rank)
	Safety	Health	Environmental	Waste	
H_2O-EtOH	7.7	8.9	6.7	4.2	8.3
H_2O-iPrOH	6.9	7.7	7.5	4.4	7.3
H_2O-DMSO	6.7	7.9	6.9	4.6	7.3
EtOH-DMSO	6.7	7.9	6.9	4.6	7.3
H_2O-Ace	6	7.7	7.7	3.3	6.8
EtOH-Ace	6	7.7	7.7	3.3	6.8
MeOH-Ace	6	7.7	7.7	3.3	6.8
H_2O-ACN	7.7	5.9	8.9	2.8	6.7
EtOH-ACN	7.7	5.9	8.9	2.8	6.7
H_2O-MeOH	7.1	4.9	8.4	4.0	5.9

Table 4 (cont'd). Ranking of the solvent-pair mixture from the minimum values of GSK health and safety score [22]

Solvent-pair (HBD-HBA)	GSK Scores of HBA Solvent				Composite Score (Rank)
	Safety	Health	Environmental	Waste	
H_2O-THF	4.9	5.9	5.2	3.5	5.4
EtOH-THF	4.9	5.9	5.2	3.5	5.4
MeOH-THF	4.9	5.9	5.2	3.5	5.4
H_2O-DMF	9	2.4	6.3	4.6	4.6
EtOH-DMF	9	2.4	6.3	4.6	4.6
MeOH-DMF	9	2.4	6.3	4.6	4.6

Keys: Recommended solvent-pairs (green highlight) = score 7-10, problematic solvent-pairs (yellow highlight) = score 4-7, hazardous solvent-pairs (red highlight) = score 0-4 are score ranges adopted from IMI-CHEM21 [7]

Conclusion

The Kamlet-Taft analytical approach was simple and efficient to measure the KT acidity, basicity, and polarity of solvents or solvent mixtures. However, the proper mixing and temperature control of the solvent and indicator was the prerequisite to get the correct result in KT analysis. The ranking of HBD-HBA combinations facilitated to find out a suitable solvent mixture to substitute hazardous solvents in drug synthesis. The highest yield was found when the solvent creates a strong interaction with the HBD site of API. It is possible if the solvent mixture carries low KT acidity and high KT basicity. The maximum use of this methodology could bring a revolutionary change in synthetic chemistry.

Acknowledgement

The authors are thankful to the Fundamental Research Grant Scheme of the Ministry of Education, Malaysia (GRANT NO: FRGS19-002-0610) and International Islamic University Malaysia for their support.

References

1. Kamlet, M. J., and Taft, R. W. (1976). The solvatochromic comparison method. I. The beta-scale of solvent hydrogen-bond acceptor (HBA) basicity. *Journal of the American chemical Society*, 98(2): 377-383.
2. Labban, A. S. and Marcus, Y. (1997). Solvatochromic parameters of ethanolamines. *Journal of the Chemical Society, Faraday Transactions*, 93(1): 77-79.
3. Islam, T., Sarker, M. Z. I., Uddin, A. H., Yunus, K. B., Prasad, R., Mia, M. A. R. and Ferdosh, S. (2020). Kamlet Taft parameters: A tool to alternate the usage of hazardous solvent in pharmaceutical and chemical manufacturing/synthesis-A gateway towards green technology. *Analytical Chemistry Letters*, 10 (5): 550-561.
4. Duereh, A., Guo, H., Honma, T., Hiraga, Y., Sato, Y., Lee Smith Jr, R. and Inomata, H. (2018). Solvent polarity of cyclic ketone (cyclopentanone, cyclohexanone): Alcohol (methanol, ethanol) renewable mixed-solvent systems for applications in pharmaceutical and chemical processing. *Industrial & Engineering Chemistry Research*, 57(22): 7331-7344.
5. Duereh, A., Sato, Y., Smith Jr, R. L., and Inomata, H. (2016). Analysis of the cybotactic region of two renewable lactone–water mixed-solvent systems that exhibit synergistic Kamlet–Taft basicity. *The Journal of Physical Chemistry B*, 120(19): 4467-4481.
6. Marcus, Y. (1994). The use of chemical probes for the characterization of solvent mixtures. Part 2. Aqueous mixtures. *Journal of the Chemical Society, Perkin Transactions 2*(8): 1751-1758.

7. Prat, D., Wells, A., Hayler, J., Sneddon, H., McElroy, C. R., Abou-Shehada, S. and Dunn, P. J. (2015). CHEM21 selection guide of classical-and less classical-solvents. *Green Chemistry*, 18(1): 288-296.
8. European Medicines Agency (2019), ICH guideline Q3C (R6) on impurities: guideline for residual solvents, step 5. https://www.ema.europa.eu/en/ich-q3c-r6-residual-solvents [Access online 08 October 2021].
9. Byrne, F. P., Jin, S., Paggiola, G., Petchey, T. H., Clark, J. H., Farmer, T. J., Hunt, A. J., McElroy, C. R. and Sherwood, J. (2016). Tools and techniques for solvent selection: green solvent selection guides. *Sustainable Chemical Processes*, 4(1): 1-24.
10. Prat, D., Hayler, J. and Wells, A. (2014). A survey of solvent selection guides. *Green Chemistry*, 16(10): 4546-4551.
11. Duereh, A., Sato, Y., Smith Jr, R. L. and Inomata, H. (2017). Methodology for replacing dipolar aprotic solvents used in API processing with safe hydrogen-bond donor and acceptor solvent-pair mixtures. *Organic Process Research & Development*, 21(1): 114-124.
12. Duereh, A., Sato, Y., Smith Jr, R. L. and Inomata, H. (2015). Spectroscopic analysis of binary mixed-solvent-polyimide precursor systems with the preferential solvation model for determining solute-centric Kamlet–Taft solvatochromic parameters. *The Journal of Physical Chemistry B*, 119(46): 14738-14749.
13. Duereh, A., Sato, Y., Smith Jr, R. L. and Inomata, H. (2015). Replacement of hazardous chemicals used in engineering plastics with safe and renewable hydrogen-bond donor and acceptor solvent-pair mixtures. *ACS Sustainable Chemistry & Engineering*, 3(8): 1881-1889.
14. Capello, C., Fischer, U. and Hungerbühler, K. (2007). What is a green solvent? A comprehensive framework for the environmental assessment of solvents. *Green Chemistry*, 9(9): 927-934.
15. Clark, J. H., and Tavener, S. J. (2007). Alternative solvents: shades of green. *Organic Process Research & Development*, 11(1): 149-155.
16. Jessop, P. G. (2011). Searching for green solvents. *Green Chemistry*, 13(6): 1391-1398.
17. Ashcroft, C. P., Dunn, P. J., Hayler, J. D. and Wells, A. S. (2015). Survey of solvent usage in papers published in organic process research & development 1997–2012. *Organic Process Research & Development*, 19(7): 740-747.
18. Sherwood, J., Granelli, J., McElroy, C. R. and Clark, J. H. (2019). A method of calculating the Kamlet–Abboud–Taft solvatochromic parameters using COSMO-RS. *Molecules*, 24(12): 2209.
19. Dolan, D. A., Sherman, D. A., Atkin, R., and Warr, G. G. (2016). Kamlet–taft solvation parameters of solvate ionic liquids. *ChemPhysChem*, 17(19): 3096-3101.
20. Marcus, Y. (1998). The properties of solvents. John Wiley & Sons, England: pp. 256
21. Marcus, Y. (1993). The properties of organic liquids that are relevant to their use as solvating solvents. *Chemical Society Reviews*, 22(6): 409-416.
22. Alder, C. M., Hayler, J. D., Henderson, R. K., Redman, A. M., Shukla, L., Shuster, L. E. and Sneddon, H. F. (2016). Updating and further expanding GSK's solvent sustainability guide. *Green Chemistry*, 18 (13): 3879-3890.
23. Hellsten, S., Qu, H. and Louhi-Kultanen, M. (2011). Screening of binary solvent mixtures and solvate formation of indomethacin. *Chemical Engineering & Technology*, 34(10): 1667-1674.

Malaysian Journal of Analytical Sciences (MJAS)
Published by Malaysian Analytical Sciences Society

SYNTHESIS, CHARACTERIZATION, AND IN-SILICO STUDIES OF CINNAMIC ACID DERIVATIVES TOWARDS DENGUE VIRUS

(Sintesis, Pencirian dan Kajian In-Siliko Sebatian Terbitan Asid Sinamik Terhadap Virus Denggi)

Anis Najwa Mohd Wahid[1], Nadia Mohamed Yusoff[1], Asnuzilawati Asari[1,2]*, Siti Nor Khadijah Addis[1], Hanis Mohd Yusoff[1,2], Habsah Mohamad[3], Fauziah Abdullah[4]

[1]*Faculty of Science and Marine Environment*
[2]*Advanced Nano Materials (ANoMa) Research Group, Faculty of Science and Marine Environment*
[3]*Institute of Marine Biotechnology*
Universiti Malaysia Terengganu, 21030 Kuala Nerus, Terengganu, Malaysia
[4]*Phytochemistry Programme, Natural Products Division,*
Forest Research Institute of Malaysia, 52109 Kepong, Selangor, Malaysia

**Corresponding author: asnu@umt.edu.my*

Received: 7 August 2021; Accepted: 18 December 2021; Published: 25 February 2022

Abstract

The dengue virus (DENV) has posed a serious global threat to human health for the past few decades. However, there are still no clinically approved antiviral drug available for the treatment of DENV. Cinnamic acid and its derivatives have attracted great attention due to their broad range of pharmacological properties. The present study aimed to synthesize and investigate the affinity of cinnamic acid derivatives against DENV. Six cinnamic acid derivatives (AC1-AC6) were synthesized by the reaction of substituted cinnamoyl chloride with the corresponding alcohol and amine. The structures of the compounds were confirmed by using ^{1}H and ^{13}C Nuclear Magnetic Resonance (NMR) and mass spectrometry. The synthesized compounds were then simulated for molecular docking to investigate their binding affinity to the protein target of DENV-2 NS2B/NS3 protease. The in-silico study reveals that the compound AC5 has the highest binding affinity and fit into the allosteric pocket of DENV-2 NS2B/NS3 serine protease with van der Waals interaction, C-H bonding and a few pi interactions such as π-cation, π-lone pair, π-π T-shaped as well as π-alkyl interaction.

Keywords: cinnamic acid, synthesis, anti-dengue virus, docking

Abstrak

Virus denggi (DENV) memberikan ancaman sejagat yang serius dalam kesihatan manusia sejak beberapa dekad yang lalu. Walau bagaimanapun, masih belum ada ubat anti-virus yang diluluskan secara klinikal bagi rawatan DENV. Asid sinamik dan terbitannya telah menarik banyak perhatian oleh kerana sifat farmakologi yang mempunyai julat yang luas. Kajian ini bertujuan untuk mensintesis dan menyiasat afiniti terbitan asid sinamik terhadap DENV. Enam terbitan asid sinamik (**AC1-AC6**) telah disintesis dengan tindakbalas penukargantian sinnamoil klorida dengan alkohol dan amina. Struktur sebatian telah disahkan dengan menggunakan ^{1}H dan ^{13}C Resonans Magnet Nukleus (NMR) dan spektrometer jisim. Sebatian yang telah disintesis kemudian disimulasikan dengan mengedok molekul untuk mengkaji sifat afiniti dengan protein sasaran iaitu protease DENV-2

NS2B / NS3. Kajian in-siliko mendedahkan bahawa sebatian **AC5** mempunyai afiniti pengikatan tertinggi dan dapat memasuki poket alosterik DENV-2 NS2B / NS3 protease serin dengan interaksi van der Waals, ikatan C-H dan beberapa interaksi pi seperti π-cation, π -lone pair, π-π berbentuk T dan juga interaksi π-alkil.

Kata kunci: asid sinamik, sintesis, anti-virus denggi, mengedok

Introduction

Dengue virus (DENV), the most significant virus in the *Flaviviridae* family with the highest morbidity and mortality rates, has been a serious global threat in the past few decades. The latest statistics from the World Health Organization (WHO) has shown an increasing trend of DENV infection throughout Malaysia with 127,407 reported cases in 2019. Despite this alarming issue, there is currently no effective vaccine nor antiviral treatment available for dengue patients. Prevention against DENV infection largely depends on controlling the mosquito vectors as well as on the use of the natural remedies. This underscores an urgent need to discover and develop a novel antiviral agent that is safe and effective in controlling dengue infection.

Cinnamic acid has gained a lot of interest due to its simple structure with great potential of pharmacological properties. It is a group of aromatic carboxylic acids, appearing naturally in the plant kingdom. Cinnamic acids occur in all green plants as well as the reproductive organs of flowering plants [1]. Cinnamic acids with varied substitution on the aryl ring, and their esters have been identified in natural bee products including honey and propolis [2]. It is also readily available from coffee beans, tea, cocoa, apples, tomatoes, and cereals [3]. It is a safe and extensive source of material due to its natural and low toxicity properties.

Cinnamic acid and its related molecules have a variety of biological activities, such as anticancer, antimalarial, antimicrobial and antioxidant [4,5]. Recently, cinnamic acid was reported to be an effective antiviral drug against Zika virus (ZIKV) [6]. It was found that cinnamic acid possessed anti-ZIKV properties against the post-entry stage of the ZIKV replication cycle, and inhibited RNA-dependent RNA polymerase (RdRp) activity. Additionally, cinnamic acid was also reported to have an excellent activity against *Tobacco mosaic virus* (TMV) in which most target compounds in this research exhibited good anti-plant virus activities [7]. One of the cinnamic acid derivatives also significantly inhibits hepatitis C virus (HCV) replication via the induction of oxidative stress [8].

Despite their rich medicinal tradition and remarkable biological activities, cinnamic acid derivatives and their potentials remained underutilized for several decades. Currently, the antiviral activity of cinnamic acid related molecules against dengue virus infection has never been experimentally addressed despite of its well-known therapeutic potential. In this study, six cinnamic acid derivatives have been synthesized and simulated for molecular docking to investigate their binding interactions to the protein target of DENV-2 NS2B/NS3 protease. Overall, this study demonstrated that cinnamic acid would be an excellent potential candidate for the development of antiviral drugs against DENV.

Materials and Methods

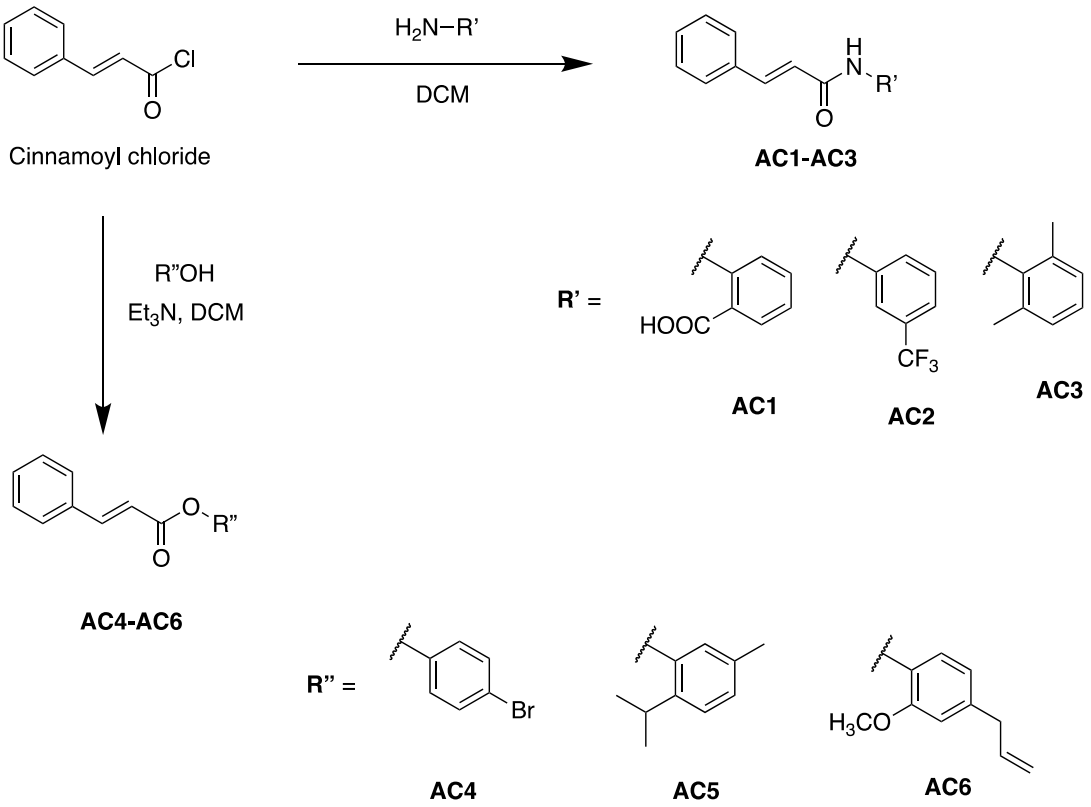
Chemicals and instrumentations

Ferulic acid, cinnamoyl chloride, anthranilic acid, 3-aminobenzotrifluoride, 2,6-dimethylaniline, 4-bromo benzyl alcohol, thymol, eugenol, anhydrous dichloromethane (DCM), triethylamine, hydrochloric acid (HCl), sodium bicarbonate ($NaHCO_3$), magnesium sulphate (Mg_2SO_4), hexane, ethyl acetate and acetone were purchased from standard commercial suppliers such as Sigma-Aldrich, Merck, Acrós Organics, Fisher Scientific, HmbG® Chemicals and R & M Chemical. All chemicals and solvents used in this study were of reagent grade (AR) and were used without further purification. Column chromatography was performed using silica gel 60 (230-400 mesh, Merck). Analytical thin-layer chromatography (TLC) was done on precoated silica gel 60 (F254, Merck) plates and visualized under UV 254 nm without treatment.

^{1}H and ^{13}C nuclear magnetic resonance (NMR) spectra were determined by Bruker Avance II 400 spectrometer in deuterated dimethyl sulfoxide (DMSO-d_6). The chemical shifts were reported in a ppm scale. The synthesized compounds were dissolved in dichloromethane (DCM) and analysed using Perkin Elmer GC-MS (Clarus 500 Chromatography/Mass Spectrometry).

Chemistry

The synthetic route of the synthesized compounds is described in Scheme 1.



Scheme 1. The synthetic work of cinnamic acid amide and ester derivatives

Synthesis of cinnamoyl amide derivatives (AC1-AC3)

Cinnamoyl chloride (0.40 g, 2.4 mmol) in anhydrous DCM (5 mL) was added dropwise at 0 ℃ to a stirred solution of 3.6 mmol of amine (anthranilic acid, 3-aminobenzotrifluoride and 2,6-dimethylaniline) in anhydrous DCM (10 mL). The mixture was stirred at 0℃ for 30 min and then at RT for 3 hours. After completion of the reaction, 10 mL of DCM was added. The solution was washed 3 times with 1 N HCl and 2 times with 1 N $NaHCO_3$. The separated organic layer was dried over Mg_2SO_4 and the solvent was evaporated completely to obtain a residue. The residue was purified by silica gel column chromatography to afford the desired products of **AC1-AC3** by using a solvent system of hexane and ethyl acetate.

2-cinnamamidobenzoic acid (AC1)

Colorless powder (0.34 g, 53 %), **AC1** was prepared from the reaction of cinnamoyl chloride (0.40 g, 2.4 mmol) with anthranilic acid (0.49 g, 3.6 mmol) in the same manner as described in Scheme 1, ^{1}H NMR (400MHz, DMSO-d_6): δ_H ppm, 11.38 (1H, s, NH) , 8.61 (1H, d, J = 7Hz, H-ar), 8.02 (1H, d, J = 6Hz, H-

ar), 7.74 (1H, t, *J* = 7Hz, H-ar), 7.66 (1H, d, *J* = 7Hz, CH), 7.62 (1H, t, *J* = 9Hz, H-ar), 7.44 (4H, m, H-ar), 7.19 (1H, t, *J* = 14Hz, H-ar), 6.89 (1H,d, *J* = 15Hz, CH); ^{13}C NMR (100MHz, DMSO-d_6): δ_C ppm, 117.5, 120.9, 123.4, 128.6, 129.4, 130.5, 131.6, 134.4, 134.8, 141.26 (CH-aromatic), 141.7 & 122.9 (C=C), 169.9 (C=O). HRESIMS (positive mode) m/z calculated for $[C_{16}H_{13}NO_3]^+$: 267, $[M+H]^+$; found: 268.2639.

N-(3-(trifluoromethyl)phenyl)cinnamamide (AC2)

Colorless powder (0.42 g, 61 %), **AC2** was prepared from the reaction of cinnamoyl chloride (0.40 g, 2.4 mmol) with 3-aminobenzotrifluoride (0.58 g, 3.6 mmol) in the same manner as described in Scheme 1, ^{1}H NMR (400MHz, DMSO-d_6): δ_H ppm, 10.57 (1H, s, NH) , 8.22 (1H, s, H-ar), 7.87 (1H, d, *J* = 8Hz, H-ar), 7.66 (2H, m, H-ar), 7.62 (1H, d, *J* = 4Hz, CH), 7.58 (1H, t, *J* = 8Hz, H-ar), 7.45 (4H, m, H-ar), 6.82 (1H, d, *J* = 16Hz, CH); ^{13}C NMR (100MHz, DMSO-d6): δ_C ppm, 115.7, 120.1, 123.2, 125.9, 128.3, 129.8, 1130.1, 130.5, 134.9, 140.4 (CH-aromatic), 141.4 & 122.1 (C=C), 164.5 (C=O). HRESIMS (positive mode) m/z calculated for $[C_{16}H_{12}NOF_3]^+$: 291, $[M+H]^+$; found: 292.0951.

N-(2,6-dimethylphenyl)cinnamamide (AC3)

Colorless powder (0.28 g, 46 %), **AC3** was prepared from the reaction of cinnamoyl chloride (0.40 g, 2.4 mmol) with 2,6-dimethylaniline (0.44 g, 3.6 mmol) in the same manner as described in Scheme 1, ^{1}H NMR (400MHz, DMSO-d_6): δ_H ppm, 9.52 (1H, s, NH) , 7.64 (2H, d, *J* = 7.0 Hz, H-aromatic), 7.57 (1H, d, *J* = 16.0 Hz, CH), 7.45 (3H, m, H-aromatic), 7.09 (3H, s, H-aromatic), 6.89 (1H, d, *J* = 16.0 Hz, CH), 2.00 (6H, s, CH_3); ^{13}C NMR (100MHz, DMSO-d_6): δ_C ppm, 18.6 (CH_3), 126.9, 128.1, 129.4, 130.1, 135.2, 135.5 (CH-aromatic), 163.9 (C=O), 140.1 & 122.2 (C=C). HRESIMS (positive mode) m/z calculated for $[C_{17}H_{17}NO]^+$: 251, $[M+H]^+$; found: 252.1391.

Synthesis of cinnamoyl ester derivatives (AC4-AC6)

Triethylamine (3 eq) was added into a stirred solution of 1 eq of alcohol (4-bromobenzyl alcohol, thymol, and eugenol) in anhydrous DCM (20 ml). The mixture was magnetically stirred for 0.5h at 0-5°C. Then, cinnamoyl chloride (1 eq) was slowly added to the mixture within a 15 min period. The reaction mixture was continued stirring for 0.5h at 0-5°C before being slowly removed to room temperature. Then, the stirring continued for another 24 h. The completion of the reaction was monitored by TLC. The solvent was evaporated by using a rotary evaporator and the compound was purified via column chromatography. Hexane/ethyl acetate was used as the eluent to afford the title ester products of **AC4**-**AC6**.

4-bromophenyl cinnamate (AC4)

Colorless powder (0.32 g, 43 %), **AC4** was prepared from the reaction of cinnamoyl chloride (0.40 g, 2.4 mmol) with 4-bromobenzyl alcohol (0.44 g, 2.4 mmol) in the same manner as described in Scheme 1, ^{1}H NMR (400MHz, DMSO-d_6): δ_H ppm, 7.69 (2H, m, H-aromatic) , 7.61 (1H, d, *J* = 16.0 Hz, H-aromatic), 7.52 (1H, d, *J* = 8.4 Hz, H-aromatic), 7.42 (3H, m, H-aromatic), 7.28 (1H, d, *J* = 8.4 Hz, CH), 6.55 (1H, d, *J* = 16.0 Hz, CH), 4.46 (1H, s, H-aromatic), 2.51 (1H, s, H-aromatic); ^{13}C NMR (100MHz, DMSO-d_6): δ_C ppm, 128.6, 129.0, 129.3, 130.7, 131.3, 134.7 (CH-aromatic). 142.4 &119.6 (C=C), 144.4 (C-O), 168.0 (C=O). HRESIMS (positive mode) m/z calculated for $[C_{15}H_{11}O_2Br]^+$: 303, $[M+H]^+$; found: 304.3010.

2-isopropyl-5-methylphenyl cinnamate (AC5)

Colorless powder (0.24 g, 35 %), **AC5** was prepared from the reaction of cinnamoyl chloride (0.40 g, 2.4 mmol) with thymol (0.36 g, 2.4 mmol) in the same manner as described in Scheme 1, ^{1}H NMR (400MHz, DMSO-d_6): δ_H ppm, 9.11 (1H, s, H-aromatic) , 7.92 (1H, d, *J* = 16.0 Hz, CH), 7.83 (3H, m, H-aromatic), 7.27-7.05 (2H, d, *J* = 8 Hz, H-aromatic), 6.97-6.61 (2H, m, H-aromatic), 6.56 (1H, d, *J* = 7.6 Hz, CH), 3.42 (3H, s, CH_3), 1.17 (6H, m, CH_3); ^{13}C NMR (100MHz, DMSO-d_6): δ_C ppm, 27.1-21.1 (CH_3), 123.2, 126.0, 126.8, 127.4, 129.1, 129.4, 135.7, 136.6, 137.2 (CH-aromatic), 146.8 & 116.0 (C=C), 148.1 (C-O), 165.6 (C=O). HRESIMS (positive mode) m/z calculated for $[C_{19}H_{20}O_2]^+$: 280, $[M+H]^+$; found: 281.1537.

4-allyl-2-methoxyphenyl cinnamate (AC6)

Colorless powder (0.33 g, 43 %), **AC6** was prepared from the reaction of cinnamoyl chloride (0.40 g, 2.4

mmol) with eugenol (0.39 g, 2.4 mmol) in the same manner as described in Scheme 1, ^{1}H NMR (400MHz, DMSO-d_6): δ_H ppm, 8.72 (1H, s, H-aromatic) , 7.54 (2H, m, H-aromatic), 7.48 (1H, d, J = 4.0 Hz, CH), 7.35 (3H, m, H-aromatic), 6.71 (2H, m, H-aromatic), 6.56 (1H, d, J = 4.0 Hz, CH), 3.74 (3H, s, CH_3) 3.25 (2H, d, J = 8.0 Hz, CH_2); ^{13}C NMR (100MHz, DMSO-d_6): δ_C ppm, 23.4 (CH_3), 115.9, 116.0, 123.3, 126.2, 148.3, 149.5 (CH-aromatic), 144.9 & 116.0 (C=C), 148.3 (C-O), 168.4 (C=O). HRESIMS (positive mode) m/z calculated for $[C_{18}H_{18}O_3]^+$: 282, $[M+H]^+$; found: 282.0887. Structures of synthesized cinnamic acid derivatives are shown in Figure 1.

Computational study

The synthesized derivatives (**AC1**-**AC6**) were simulated for molecular docking to investigate their binding affinity to the protein target of DENV type 2 (DENV-2) NS2B/NS3 protease, with Ser135, His51 and Asp75 as their catalytic triad amino acid residues. The virtual screening was carried out on the homology model of the DENV non-structural protein, NS2B/NS3pro developed by Wichapong et al. [16]. The DENV-2 NS2B/NS3pro model was built based on the DENV-2 complex cofactor-protease using the crystal structure of NS2B/NS3pro West Nile Virus (WNV) as the template. The protein structure was prepared as a macromolecule prior to docking using AutoDock version 1.5.6 package (www.autodock.scrips.edu). Briefly, the protein preparation was done by removing the native ligand, tetrapeptide inhibitor (Bz-Nle-Lys-Ar-H) and water molecules, the addition of polar hydrogen and Kollmann charges.

The 3D structures of all cinnamic acid derivatives were constructed and energetically optimized using ChemDraw Professional 16.0. The minimized structures were saved in sdf format before converted into pdb format using OpenBabel-3.1.1 software. The validation of the docking protocol was done by re-docking the inhibitor tetrapeptide (Bz-Nle-Lys-Ar-H) with the RMSD value not greater than 2.0 Å. The ligands were prepared by merging non-polar hydrogen and assigned a Gasteiger charge. The center of the grid box was employed around the protease active site at 23.038, 43.372, -0.316 in x, y, and z coordinates, respectively, with a box size of 60 × 60 × 60 dimensions and grid spacing 0.375 Å. The docking of ligands was run with the Lamarckian Genetics Algorithm (GA) search program applied to generate 100 runs. The binding modes of compounds were analyzed using Discovery Studio Client 2020 (www.accelrys.com). The identification of hit compound was identified based on the conformations with the ones of lowest free binding energy and of the most populated cluster.

Preparation of enzyme and ligand for docking

The structure of available DENV2, which is a complex of NS2B-NS3 protease (PDB code: 2FOM), is devoid of any ligand. Thus, to get an insight into the binding cavity we used coordinates of co-crystallized ligand from West Nile virus (PDB code: 2FP7) belonging to the same family as that of DENV and that shares the structural similarity of the catalytic triad. It is available in complex with the inhibitor tetrapeptide Bz-Nle-Lys-Arg-Arg-H. The structure of DENV2 complexed with the inhibitor tetrapeptide Bz-Nle- Lys-Arg-Arg-H was constructed by homology modelling method.

Results and Discussion

Chemistry

Six cinnamic acid derivatives (Figure 1) were successfully synthesized in moderate yield (35-61%) by modification of established methods [9]. The synthesis of the target compounds was straightforward, and the general synthetic pathway is illustrated in Scheme 1. Cinnamoyl chloride was reacted with various amines; anthranilic acid, 3-aminobenzotrifluoride and 2,6-dimethylaniline to produce the titled compounds of cinnamic acid amides (**AC1**, **AC2** and **AC3)**. For the synthesis of cinnamic acid ester derivatives, different alcohols; 4-bromobenzyl alcohol, thymol and eugenol were reacted with cinnamoyl chloride in DCM to afford the title compounds **AC4**, **AC5** and **AC6**. To optimize the reaction conditions, the polarity of the solvent medium from polar to non-polar was adjusted using DMSO, ethanol and tetrahydrofuran (THF) in the reaction of substituted cinnamoyl chloride with the corresponding alcohol and amine.

^{1}H and ^{13}C nuclear magnetic resonance (NMR) analysis confirmed the identity of all synthesized cinnamic acid derivatives. The presence of NH resonance peaks as observed in all three ^{1}H NMR spectra of **AC1**-**AC3** prove that the cinnamoyl amide derivatives were successfully synthesized. NH resonance which appears as singlet is found to be at the most downfield region (δ_H 11.38-9.52 ppm) for **AC1** to **AC3**. There is also a high-intensity singlet resonance in the upfield region at δ_H 2.17 ppm representing two methyl moieties presented in the **AC3** compound. For cinnamoyl ester derivatives, in the range of δ_H 7.41-7.70 ppm, multiple peaks can be observed in **AC4** indicating the presence of aromatic groups. Meanwhile, for **AC6** the peaks are in the range of δ_H 6.55-6.70 ppm. There are other high-intensity singlet resonances at δ_H 1.13-2.29 ppm and at δ_H 3.73 ppm respectively, representing methyl moieties presented in both compounds **AC5** and **AC6**. The alkene groups for all three compounds of **AC4**-**AC6** can be observed in the peak range of δ_H 6.51-6.57 ppm.

The resonance of the C=O group was clearly observed for all synthesized compounds at δ 169.9-163.8 ppm. The alkene group is also presented in all compounds which are in the range of δ 146.8-116.0 ppm. For the aromatic ring, the resonance carbon was found at the range between δ 129.8-123.3 ppm. Furthermore, the resonance for CH_3 moieties can also be observed for the compounds of **AC3**, **AC5** and **AC6** which are in the region δ 27.1-18.7 ppm.

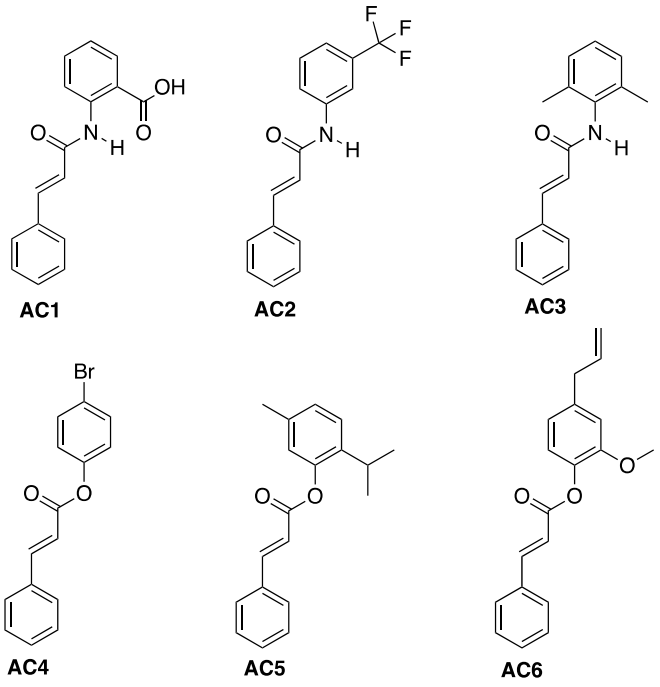


Figure 1. Structure of synthesized cinnamic acid derivatives

Molecular docking

The in-silico studies were conducted to investigate the binding interactions of the synthesized compounds **AC1**-**AC6** towards DENV-2 NS2B/NS3 protease and search for the best orientation of ligand-protease complex with the lowest free energy of binding (FEB). This step serves as a good tool to predict and match the desired binding site, understanding possible conformation of the compounds and further clarifies the binding interactions in the binding pocket [10].

DENV is a single-stranded RNA genome that encodes a single open reading frame (5-C-prM-E-NS1-NS2A-NS2B-NS3-NS4A-NS4B-NS5-3) with three structural and seven non-structural proteins [11]. The N-terminal of NS3 is a trypsin-like serine protease, which when combined with its co-factor can cleave the viral polyprotein [12]. Disruption of NS2B-NS3 protease inhibits viral replication [13]. This poses NS2B-NS3 protease of DENV-2 as a promising target for antiviral drug design [14].

The three catalytic triad amino acid residues were located in NS3 serine proteases namely His51, Asp75 and Ser135. The NS2B protease acted as an NS3 serine protease co-factor for an optimal catalytic activity [15]. The homology protein crystal structure generated by Wichapong et al., (2010) was used due to the lack of DENV-2 NS2B/NS3 serine protease inhibitor-bound 3D structures. Moreover, some of the protease database structures were found to have missing amino acid residues [16].

The Lamarckian genetic algorithm was employed in AutoDock version 1.5.6 to determine the binding modes and compounds conformation towards DENV-2 NS2B/NS3 protease homology protein crystal structure. In the preparation for docking simulation, only protease was retained as a part of the macromolecule file, while the Bz-Nle-Lys-Arg-Arg-H was extracted and saved as a positive control ligand. The ligand was extracted and re-docked into the binding site to evaluate the success of the docking method in reproducing the experimentally known complex.

The covalent map parameter was used during positive control docking simulation to constrain the molecular geometry of the peptide inhibitor. After that, all the synthesized compounds were docked with Wichapong et al., [16] homology crystal structure using the same parameter. The re-docked was carried out successfully with the root mean square deviation (RMSD) value of 1.23 Å. Henever et al. stated that the programs that able to poses the RMSD value in the range of 1.5-2 Å, depending on the ligand size, are considered to have performed successfully [17].

The synthesized compounds, **AC1**-**AC6** fit into the allosteric pocket of NS2B/NS3 serine protease. The free energy of binding (FEB) obtained was tabulated in Table 1. Figure 2 shows the overlay docked conformation of the cinnamic acid derivatives between the Wichapong et al. [16] homology model and Bz-Nle-Lys-Arg-Arg-H referenced ligand. The image was generated using Discovery Studio Visualizer 4.5.

The detailed ligand-binding site interaction in 2D structural views of all the compounds are shown in Figure 3 below. Compound **AC5** shows the lowest free energy of binding (-6.53 kcal mol^{-1}) indicating the highest binding affinity towards NS2B/NS3 protease of DENV-2 compared to the other five compounds [18]. Figure 3 also shows the poses and non-covalent interactions involved between the ligands and the protease-binding site. This compound showed a few van der Waals interaction, one C-H bonding interaction, one π-cation interaction, one π-lone pair interaction, one π-π T-shaped interaction, and two π-alkyl interactions with the amino acid residue in the DENV-2 NS2B/NS3 protease.

The presence of the aromatic group in the synthesized cinnamic acid derivatives enhances the possibilities of van der Waals interaction. Hence, we can see this interaction in all the synthesized compounds of **AC1**-**AC6**. Individually, van der Waals interaction was also observed in compound **AC5**, involving Ser135 (one of the catalytic triads) and other residues namely Asp129, Ser131, Gly151 and Thr134. Pi interactions such as π-π T-shaped interaction and π-lone pair interaction were also observed between the ester moiety of the synthesized compound with Tyr161 and Phe130, respectively. Meanwhile, another aromatic ring at cinnamic moiety of compound **AC5** appeared to have a π-cation interaction with the His51 (from the catalytic triad) and π-alkyl interactions with Val52. The π-cation interaction with the His51 suggested that the DENV-2 NS2B/NS3 replication was affected as His51 is one of the catalytic triads of NS2B required for replication activities [19].

Table 1. The free energy of binding (FEB) of compounds **AC1-AC6**

Compound	**FEB (kcal mol^{-1})**
Positive Control (peptide inhibitor)	-6.58
AC1	-6.11
AC2	-6.36
AC3	-6.45
AC4	-6.33
AC5	-6.53
AC6	-6.50

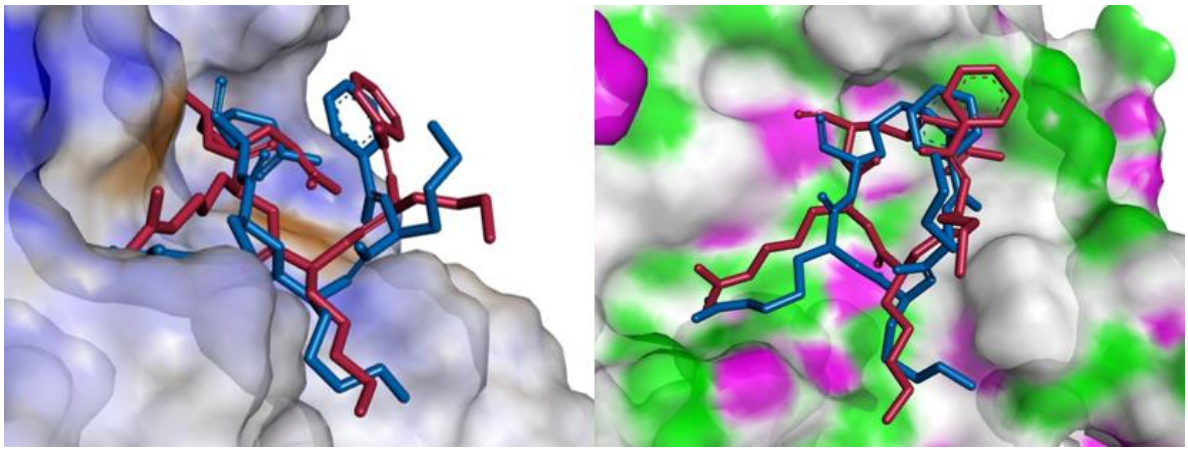


Figure 2. The overlay docked conformation of the cinnamic acid between the Wichapong et al. [16] homology model and Bz-Nle-Lys-Arg-Arg-H referenced ligand (red: original ligand conformation, blue: docked ligand conformation).

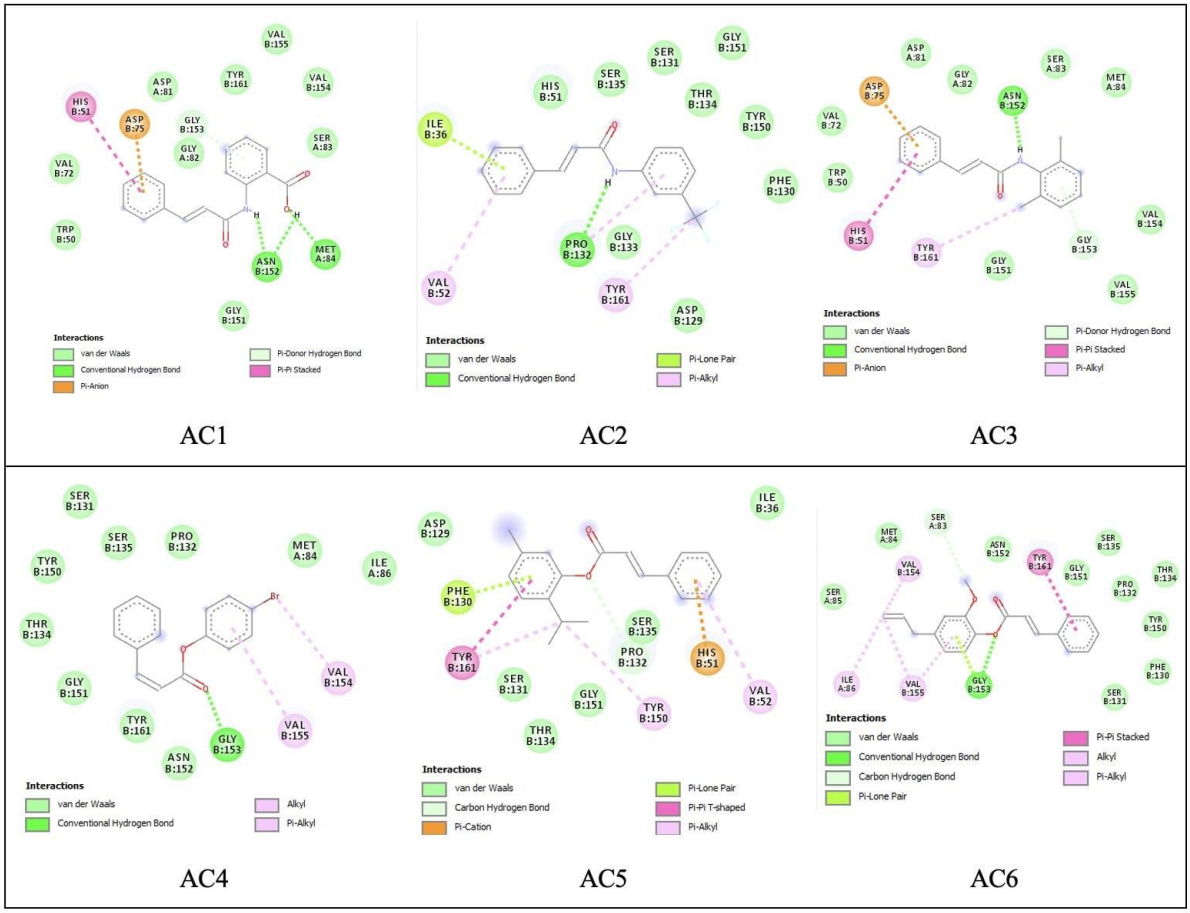


Figure 3. The 2D structural views of ligand-binding site interactions for synthesized compounds AC1-AC5

Conclusion

The present work has demonstrated that six cinnamic acid derivatives were successfully synthesized by the reaction of cinnamoyl chloride with various amines and alcohols. All synthesized compounds were characterized by ^{1}H and ^{13}C-NMR, and mass spectrometry. The significant molecular interaction between the synthesized compounds and DENV2 NS2B/NS3 protease were revealed by molecular studies indicating their potential activity as a protease inhibitor. The compound **AC5** is predicted to have a higher DENV-2 NS2B/NS3 protease inhibitor as it has the highest binding affinity, with a significant van der Waals force and pi interactions between the synthesized compound and the amino acid residues. Further verification studies such as *in-vitro*, toxicity analysis, and *in-vivo* analysis are required for identifying the possibilities of the cinnamic acid derivatives to be a lead molecule for anti-dengue drug development.

Acknowledgement

The authors would like to acknowledge the financial support from Ministry of Higher Education, Malaysia for Fundamental Research Grant Scheme FRGS 59580 (FRGS/1/2019/STG01/UMT/02/4). A sincere thanks to the Faculty of Science and Marine Environment, Universiti Malaysia Terengganu (UMT) for providing the space and facilities. We also would like to thank the Institute of Marine Biotechnology, Universiti Malaysia Terengganu for NMR services and analysis.

References

1. Martin-Tanguy, J., Cabanne, F., Perdrizet, E. and Martin, C. (1978). The distribution of hydroxycinnamic acid amides in flowering plants. *Phytochemistry*, 17(11): 1927-1928.
2. Mohammadzadeh, S., Shariatpanahi, M., Hamedi, M., Ahmadkhaniha, R., Samadi, N. and Ostad, S. N. (2007). Chemical composition, oral toxicity and antimicrobial activity of Iranian propolis. *Food Chemistry*, 103(4): 1097-1103.
3. Clifford, M. N. (1999). Chlorogenic acids and other cinnamates – nature, occurrence and dietary burden. *Journal of the Science of Food and Agriculture*, 79(3): 362-372.
4. De, P., Baltas, M. and Bedos-Belval, F. (2011). Cinnamic acid derivatives as anticancer agents-a review. *Current Medicinal Chemistry*, 18(11): 1672-1703.
5. Sova, M. (2012). Antioxidant and antimicrobial activities of cinnamic acid derivatives. *Mini-Reviews in Medicinal Chemistry*, 12(8): 749-767.
6. Amano, R., Yamashita, A., Kasai, H., Hori, T., Miyasato, S., Saito, S., Yokoe, H., Takahashi, K., Tanaka, T., Otoguro, T., Maekawa, S., Enomoto, N., Tsubuki, M. and Moriishi, K. (2017). Cinnamic acid derivatives inhibit hepatitis C virus replication via the induction of oxidative stress. *Antiviral Research*, 145: 123-130.
7. Chen, Y., Li, Z., Pan, P., Lao, Z., Xu, J., Li, Z., Zhan, S., Liu, X., Wu, Y., Wang, W. and Li, G. (2021). Cinnamic acid inhibits Zika virus by inhibiting RdRp activity. *Antiviral Research*, 192(11): 105117.
8. Wang, Y., He, F., Wu, S., Luo, Y., Wu, R., Hu, D. and Song, B. (2020). Design, synthesis, anti-TMV activity, and preliminary mechanism of cinnamic acid derivatives containing dithioacetal moiety. *Pesticide Biochemistry and Physiology*, 164(1): 115-121.
9. Abdul Rahim, N. H. C., Asari, A., Ismail, N. and Osman, H. (2017). Synthesis and antibacterial study of eugenol derivatives. *Asian Journal of Chemistry*, 29(1): 22-26.
10. Grinter, S. Z. and Zou, X. (2014). Challenges, applications, and recent advances of protein-ligand docking in structure-based drug design. *Molecules*, 19(7): 10150-10176.
11. Leung, D., Schroder, K., White, H., Fang, N. X., Stoermer, M. J., Abbenante, G., Martin, J. L., Young, P. R. and Fairlie, D. P. (2001). Activity of recombinant Dengue 2 Virus NS3 protease in the presence of a truncated NS2B co-factor, small peptide substrates, and inhibitors. *Journal of Biological Chemistry*, 276(49): 45762-45771.
12. Chiu, M. W., Shih, H. M., Yang, T. H. and Yang, Y. L. (2007). The type 2 dengue virus envelope protein interacts with small ubiquitin-like modifier-1 (SUMO-1) conjugating enzyme 9 (Ubc9). *Journal of Biomedical Science*, 14(3): 429-444.
13. Chen, W. N., Loscha, K. V., Nitsche, C., Graham, B. and Otting, G. (2014). The dengue virus NS2B-NS3 protease retains the closed conformation in the complex with BPTI. *FEBS Letters*, 588(14): 2206-2211.
14. Tomlinson, S., Malmstrom, R. and Watowich, S. (2012). New approaches to structure-based discovery of dengue protease inhibitors. *Infectious Disorders - Drug Targets*, 9(3): 327-343.
15. Preugschat, F., Yao, C. W. and Strauss, J. H. (1990). In vitro processing of dengue virus type 2 nonstructural proteins NS2A, NS2B, and NS3. *Journal of Virology*, 64(9): 4364-4374.
16. Wichapong, K., Pianwanit, S., Sippl, W. and Kokpol, S. (2010). Homology modeling and molecular dynamics simulations of Dengue virus NS2B/NS3 protease: Insight into molecular interaction. *Journal of Molecular Recognition*, *23*(3): 283-300.
17. Hevener, K., Zhao, W., Ball, D., Babaoglu, K., Qi, J., White, S. and Lee, R. (2009). Validation of molecular docking programs for virtual screening against dihydropteroate synthase. *Journal of Chemical Information and Modeling,* 49(2): 444-460.
18. Datar, P. A and Jadhav, S. R. (2015). Design and synthesis of pyrazole-3-one derivatives as hypoglycaemic agents. *International Journal of Medicinal Chemistry*, 2015: 1-10.

19. Noble, C. G., Seh, C. C., Chao, A. T. and Shi, P. Y. (2012). Ligand-bound structures of the dengue virus protease reveal the active conformation. *Journal of Virology*, 86(1): 438-446.

Malaysian Journal of Analytical Sciences (MJAS)
Published by Malaysian Analytical Sciences Society

EFFECT OF DEEP EUTECTIC SOLVENT ON TENSILE PROPERTIES AND BIODEGRADATION OF PECTIN WITH EGGSHELL BIOPLASTIC

(Kesan Pelarut Eutektik kepada Sifat Tensil dan Biodegradasi Bioplastik Pektin dengan Cangkang Telur)

Non Daina Masdar, Rizana Yusof *, Nur Amni Ramzani

Faculty of Applied Sciences,
Universiti Teknologi MARA, Perlis Branch, Arau Campus, 02600 Arau, Perlis, Malaysia

**Corresponding author: rizana@uitm.edu.my*

Received: 12 September 2021; Accepted: 21 December 2021; Published: 25 February 2022

Abstract

Pectin has excellent potential as a main source of bioplastic due to its biodegradability. However, the neat pectin-based film has poor chemo-physical properties and low mechanical performance. In this study, the pectin-based film is successfully modified by adding eggshell and deep eutectic solvent (DES), comprising choline chloride and malonic acid, as a filler and plasticiser to enhance the performance of bioplastic. Five pectin-based bioplastics were prepared: pectin/eggshell (without DES) and pectin/eggshell with each 1%, 2%, 3%, and 4% of DES. The bioplastics were characterised by the Fourier-transform infrared (FTIR) spectroscopy and inverted camera analysis. The presence of filler and the effect of different DES concentrations were studied based on mechanical properties, biodegradability, and water uptake. The results showed that the addition of different percentages of DES had decreased the tensile strength and increased the flexibility of the bioplastic. Biodegradability testing using compost soil demonstrated an increased degradation rate when a high concentration of DES (4%) was added. The DES of choline chloride and malonic acid shows high potential as a plasticiser in pectin/eggshell bioplastic.

Keywords: pectin, plasticiser, deep eutectic solvent, eggshell filler, bioplastic

Abstrak

Pektin berpotensi sebagai sumber utama bioplastik kerana sifat biodegradasinya. Walau bagaimanapun, bioplastik yang hanya berasaskan pektin sahaja mempunyai sifat kimia-fizikal yang lemah dan prestasi mekanikal yang rendah. Dalam kajian ini, filem bioplastik berdasarkan pektin telah berjaya diubah suai dengan menambahkan cangkang telur dan pelarut eutektik (DES), yang mengandungi kolin klorida dan asid malonik, sebagai pengisi dan pemplastik yang bertujuan untuk meningkatkan prestasi bioplastik. Lima bioplastik berasaskan pektin disediakan: pektin/cangkang telur (tanpa DES) dan pektin/cangkang telur dengan masing-masing 1%, 2%, 3%, dan 4% DES. Bioplastik yand dihasilkan dicirikan secara fizik menggunakan spektroskopi Fourier-penukaran inframerah (FTIR) dan analisis kamera terbalik. Kehadiran pengisi dan kesan kepekatan DES yang berbeza dikaji berdasarkan sifat mekanik, kebolehbiodegradasian, dan pengambilan air. Hasilnya menunjukkan bahawa penambahan peratus DES yang berbeza telah menurunkan kekuatan dan meningkatkan fleksibiliti bioplastik. Ujian biodegradasi menggunakan tanah kompos menunjukkan peningkatan kadar degradasi apabila peratus DES yang tinggi (4%) digunakan. DES bagi kolin klorida dan asid malonik menunjukkan potensi yang tinggi sebagai pemplastik di dalam bioplastik pektin/cangkang telur.

Kata kunci: pektin, pemplastik, pelarut eutektik, pengisi cangkang telur, bioplastik

Introduction

Petrochemical plastic materials are important in our daily lives. However, the vast amounts of plastic waste materials generated contribute to worldwide environmental concerns [1]. About 34 million tons of plastic trash is produced each year, with 93% ending in landfills and the seas. Furthermore, the disposal of non-biodegradable plastic leads to significant global warming, ozone depletion, eco-toxicity, eutrophication, and long-lasting decomposition [2]. Improper management of plastic causes a severe effect on the ecosystem. Thus, biodegradable plastic is the best alternative to reduce plastic waste, save the environment and sustain green global issues. The use of natural sources, such as cellulose, pectin, starch, chitosan, and alginate as food packaging materials has slowly replaced petrochemical plastics [3, 4, 5]. Pectin is a polysaccharide found abundantly in fruits like apple, orange, lemon, mango, grapes, and peach [1, 6]. It is very compatible as a biodegradable and edible biopolymer for food packaging. However, due to its poor chemo-physical properties and low mechanical performance, the pectin biofilm must be improvised by adding a plasticiser and organic filler accordingly to meet the food packaging requirements [1]. Like most polysaccharides, pectin is glassy at room temperature, causing defects such as cracking or curling in a film due to its shrinking, followed by water evaporation or rapid drying [7]. Gennadios et al. [8] asserted that these films are often fragile and rigid due to extensive interactions between the polymer molecules. Therefore, a filler is commonly used to improve the rigidity and strength of the biofilm [9, 10]. A natural bio filler such as eggshell has grown popular since they are environmentally friendly, renewable, cheap, and abundantly available [11, 12].

However, a biofilm made of pectin with eggshells is mostly brittle. A plasticiser is a useful compound in minimising film brittleness by reducing intermolecular forces among polymer chains, increasing their mobility, and improving mechanical properties [13] by holding the polymer bonds together [14]. Deep eutectic solvent (DES) is a new category of plasticiser that has been competently tested for polysaccharide biofilms in various methods [15, 16, 17, 18]. The two most common plasticisers in the polymer industry are *o*-hydroxyphenyl (HBP) and di-2-ethylhexyl phthalate (DEHP), known for their ability to disrupt the endocrine system, with carcinogenic and mutagenic properties [19]. Phthalate is not bonded to plastic; therefore, it will easily leak out into the human body, causing major health effects [20]. According to Mekonnen et al. [21], an ideal plasticiser significantly reduces the glass transition temperature (T_g), biodegradable, non-volatile, non-toxic, and have minimal leaching or migration properties. DES, comprising two self-associating components, met the requirements as a plasticiser in bioplastic [22, 23]. The ability of DES to swell inside biopolymers has enabled bioplastic plasticisation [19], as well as improved thermal stability and decreased the glass transition temperature (T_g) of bioplastics [24]. Previously, Shafie et al. [17] have successfully used DES as a plasticiser in pectin extracted from *Momordica charantia* or known as *peria*. According to their findings, DES caused different degrees of plasticisation via hydrogen bonds and ionic bonds with the polymer chains, which improved thermal stability, tensile properties, percentage of moisture absorption, and water vapour transmission rate of bioplastic. However, the strength of biofilm is reduced without fillers. Hence, this study investigates the compatibility of pectin/DES with eggshells as a natural filler. The pectin/eggshell bioplastic was developed with different concentrations of DES (choline chloride: malonic acid) to analyse bioplastic performance based on tensile strength, biodegradability, and water uptake.

Materials and Methods

Material and reagents

The commercial pectin from citrus was purchased from Sigma Aldrich, Malaysia. The choline chloride (ChCl), malonic acid, and sodium hypochlorite were purchased from Acros, Belgium, with 99% purity. All chemicals used are of analytical grade. The DES was prepared as

suggested by Abbot et al. [15], with a 1:1 ratio of ChCl and malonic acid. The mixture was magnetically stirred at 80 °C until the colourless liquid was formed and maintained as a liquid after 24 hours at room temperature. The eggshell powdered filler was prepared according to Kasmuri et al. [14]. The eggshells were crushed using a mortar and pestle and placed in a beaker. Sodium hypochlorite was added until all the eggshells were soaked and stirred using a glass rod until heat and bubble were released. The beaker was covered using aluminium foil and left for 24 hours before filtering and washing using distilled water. The dried eggshell sample was then dried in the oven and left to cool at room temperature. The eggshell sample was then ground into powder to obtain the size of 58 μm.

Preparation of pectin-based bioplastic

The pectin-based bioplastic was prepared according to Cataldo et al. [25] and Almeida et al. [26]. A volume of 3% (w/v) aqueous pectin was stirred at 70 °C until completely dissolved. About 1% to 4% wt of DES was added to the pectin solution and stirred to homogenise and form film-forming solutions. Approximately 3% wt of eggshell filler was added until completely dissolved. The well-dispersed aqueous dispersions were poured into Petri dishes and dried in the oven at 50 °C for 24 hours. The control was prepared without DES, i.e., 3% of aqueous pectin with 3% wt of eggshell as the filler.

Characterisation of DES

The thickness of the bioplastic was measured using a Digimatic thickness gauge (Model 547-301, Mitutoyo). At least five measurements were performed at different positions for each bioplastic, and the average thickness was calculated. The mechanical properties, including tensile strength, Young's modulus, and elongation at break, were determined using the Instron Universal Testing Instrument (Instron 3365, Instron, USA) equipped with a 1 kN load cell. The sample was cut into a rectangular shape with the size of 7 cm × 1 cm. The initial grip separation was 50 mm, with a crosshead speed of 5 mm min^{-1}. At least five replicates were performed for each film formulation. The soil burial test was conducted according to the ASTM D6003-96 standard method to determine the ability of bioplastics to degrade in compost soil. The initial mass of each bioplastic was weighed and recorded. The bioplastic was buried in compost soil, and the mass was recorded daily until fully degraded. The W_o (g) is the average of the initial bioplastic weight before being buried in soil samples, and the W_t (g) is the average weight of bioplastic at the time of measurement.

The following equation was used to calculate the weight loss of the sample:

$$\text{Weight Loss}(\%) = \frac{W_o - W_t}{W_o} \times 100 \quad (1)$$

The synthetic seawater was prepared by dissolving 35 g of sodium chloride in a total mass of 1000 g distilled water in a beaker. The bioplastic with the size of 1.5 cm × 2 cm was weighed before being immersed in the synthetic seawater. The samples were dried and reweighed at three days intervals. The percentage weight loss of the bioplastic was calculated using the following formula, where M_0 is the average initial mass of the sample, and M_1 is the average residual mass of the bioplastic after the test.

$$\text{Weight Loss } (\%) = \frac{M_0 - M_1}{M_0} \times 100 \quad (2)$$

The water uptake method was conducted according to Zárate-Ramírez et al. [27]. A 1.5 cm × 2 cm sample was cut, dried in the oven at 50 °C for 24 hours, and weighed as W_o. The sample was then immersed in distilled water for 10 seconds at room temperature and reweighed as W_t. The experiment was conducted in triplicate. Water uptake was calculated using the following equation:

$$\text{Water Uptake } (\%) = \frac{W_t - W_o}{W_o} \times 100 \quad (3)$$

Results and Discussion

FTIR analysis was carried out to analyse the functional group present in pure pectin, eggshell, and pectin/eggshell (P-E) composites (Figure 1). The O-H stretching, C=O stretching, and C-O stretching at 3440 cm^{-1}, 1746 cm^{-1}, and 1018 cm^{-1} characterise the structure of pectin.

According to Bichara et al. [28], the main peaks observed at 3436 cm^{-1}, 1743-1640 cm^{-1}, and 1103-1146 cm^{-1} represented the O-H, C=O, and C-O glycosidic bonds in pectin. Meanwhile, the pure eggshell showed peaks at 712, 876, and 1425 cm^{-1}, as similarly reported by Li et al. [29], who characterised calcite by an in-plane bending, out-of-plane bending, and asymmetric CO_3^{2-} stretching at the peaks of 713, 875, and 1424 cm^{-1}. Similar findings were also reported by Siriprom et al. [30] and Pradhan et al. [31]. The combination of pectin with eggshell in the composite film shows all peaks in individual pectin and eggshell. However, a C-O peak from CO_3^{2-} at 1424 cm^{-1} disappeared in the composite as the formation of new bonding is expected between the calcite of eggshell with the glycosidic bond of pectin. The pectin/eggshell composite is enhanced with the addition of DES as a plasticiser. Figure 1(b) shows the FTIR analysis on the increasing concentration of DES from 1% to 4% on the pectin/eggshell composite. As observed, the intensity peaks at 3350 cm^{-1} and 1000 cm^{-1} are slightly decreased when the concentration of DES increases. The IR spectra of all films are dominated by vibration, related to the presence of the pectin compound. A similar result was also reported by Gouveia et al. [32], indicating the interaction between pectin and the additives.

The images of bioplastic sample surfaces were analysed using an Olympus CKX53 inverted microscope (Figure 2). The bubbles trapped in the pectin/eggshell biofilm surfaces are due to the agitation process and the addition of the eggshell powder with pectin solution during sample preparation. The number of bubbles is reduced with the addition of a high percentage of DES, as shown in Figures 2(b) to 2(e). In general, it is also observed that the solubility of eggshell powder increases with the concentration of DES, especially at 3% to 4% of DES (Figure 2(d) and 2(e)). Kong et al. [33] stated that the addition of plasticiser might modify polymer chain intermolecular forces and reduce viscosity in the system. Thus, the DES enhances the dispersion of the added eggshells within the polymer matrices, which is expected to affect the mechanical performance of the bioplastics.

The thickness of the biofilms is an important characteristic that determines its purpose and function. A thin biofilm can lead to fragility and easily be torn, while a very thick biofilm has less flexibility. Table 1 shows the thickness of the pectin/eggshell biofilms. According to ASTM D885, the standard maximum thickness for plastic is 1 mm. Meanwhile, the pectin/eggshell bioplastic is the thinnest bioplastic with 0.0985 ± 0.01 mm. The thickness of bioplastic increases as the plasticiser is added from 1% to 4%, i.e., 0.0991 ± 0.01mm to 0.2687 ± 0.06 mm. The film tends to be thicker as the amount of DES increases. The result is congruent with Esposito et al. [34], which showed that the pectin film thickness increased as polyamines were added as a new cationic plasticiser for pectin-based edible (PEC) films. In this work, the thickness of the PEC films is doubled in the absence of glycerol.

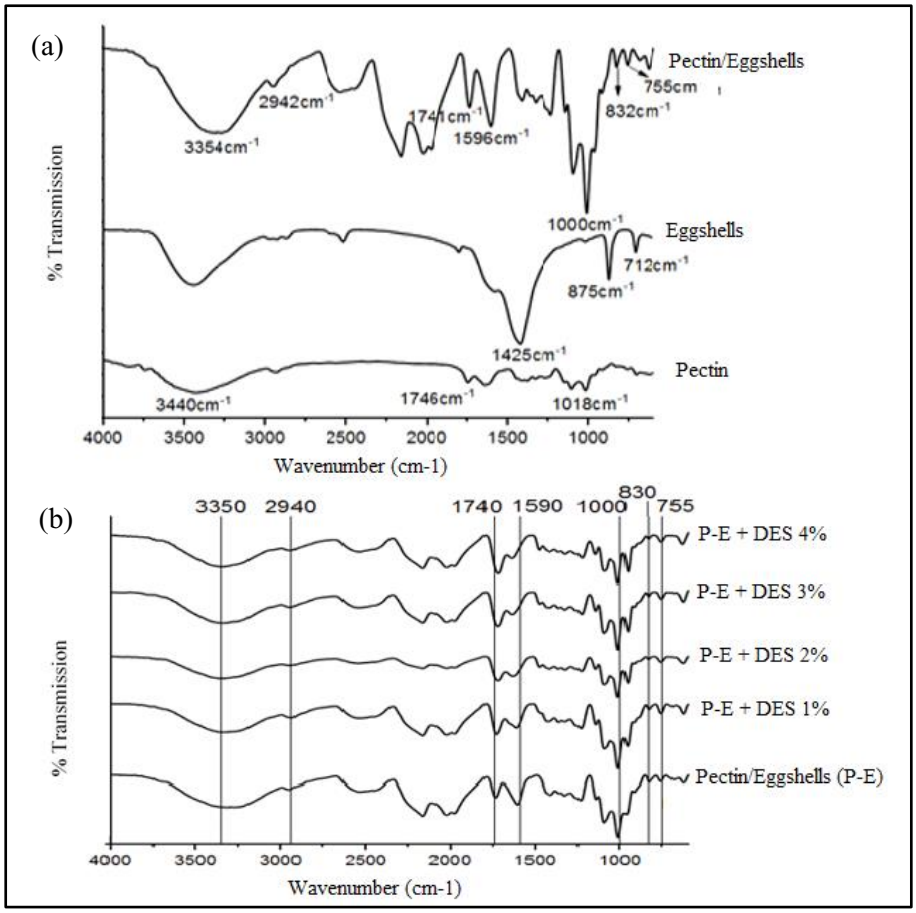
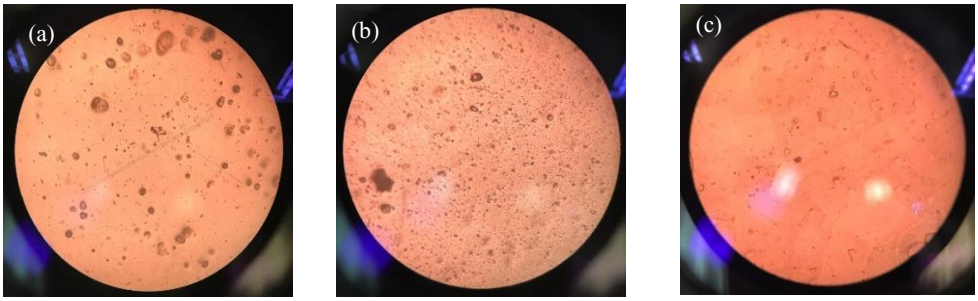


Figure 1. FTIR spectrum for (a) Pectin/Eggshell composite, pure eggshell, and pure pectin (b) Pectin/Eggshell composite with different DES concentrations



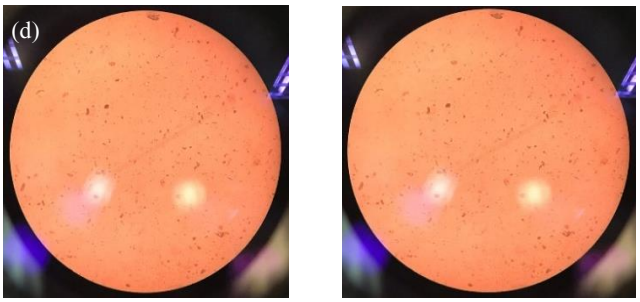


Figure 2. Bioplastic surface images in 4× magnification of (a) Pectin/Eggshell; (b) Pectin/Eggshell in DES 1%; (c) Pectin/Eggshell DES 2%; (d) Pectin/Eggshell DES 3%; and (e) Pectin/Eggshell DES 4%

Table 1. Thickness of pectin-based bioplastic

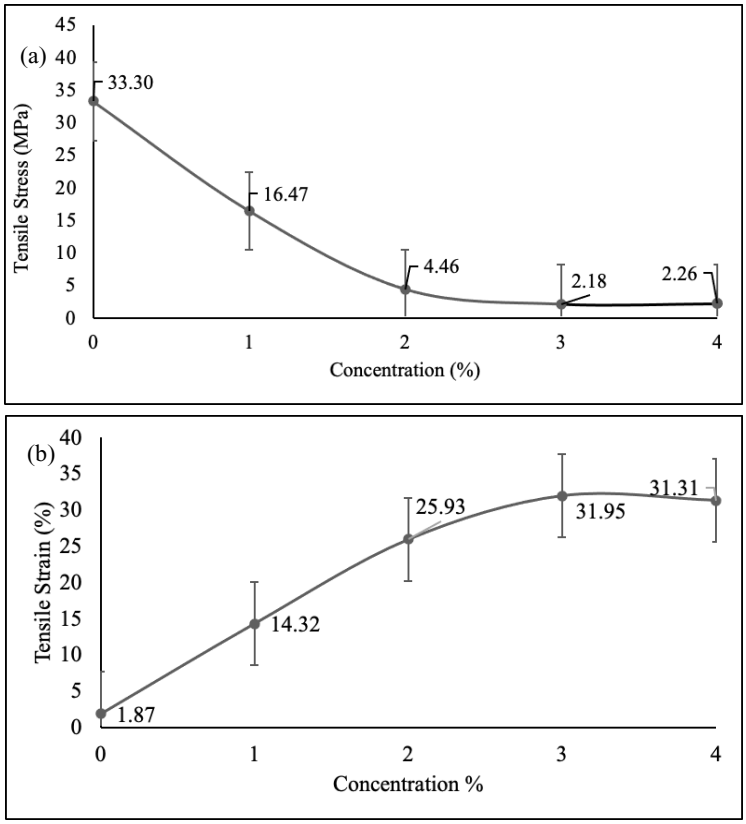
Sample Bioplastic	Thickness (mm)
Pectin/Eggshell (P-E)	0.0985 ± 0.01
P-E + DES 1%	0.0991 ± 0.01
P-E + DES 2%	0.1448 ± 0.02
P-E + DES 3%	0.2146 ± 0.02
P-E + DES 4%	0.2687 ± 0.06

The mechanical properties of the prepared bioplastic in 1% to 4% DES concentration were determined via tensile testing analysis. Figures 3(a-c) show the trend of tensile stress, strain, and modulus of the bioplastic at different DES concentrations. The results indicated that the pectin/eggshell bioplastic is the most rigid with high tensile stress at 33.30 MPa. As a filler, eggshells fill the space in the pectin polymer and increase the stiffness of bioplastic. The tensile strain of pectin/eggshell bioplastic is observed at 1.87%, with the modulus reaching 2754.00 MPa. A study by Kong et al. [33] stated that the addition of eggshell powder to polylactic acid (PLA) yielded a more rigid plastic than PLA only. The PLA/eggshell had superior tensile stress with 200% strain at break and a high modulus. Hence, a similar effect is observed in this study, where the addition of eggshells resulted in substantial improvement in the tensile strength and modulus of the pectin/eggshell bioplastic.

The DES was later added to pectin/eggshell as a plasticiser. The tensile stress and modulus are reduced from 33.30 to 16.47 MPa and 2754.00 to 774.00 MPa, with the addition of 1% DES to the pectin/eggshell. However, the addition of 1% DES caused the tensile strain to increase from 1.87% to 14.32%. The continual addition of DES from 1% to 3% has decreased the tensile stress from 16.47 to 2.18 MPa. A similar effect was observed on the modulus, which is reduced from 774.00 to 14.00 MPa with 1% to 3% DES. The opposite happened to tensile strain, which increased from 14.32% to 31.95% DES. The addition of plasticiser creates substantial intermolecular interaction between the polymer chains, preventing them from gathering close to each other, restricting the molecular chains to compact and cohesive strength in the sample. Thus, it can be concluded that DES has reduced the tensile stress of pectin/eggshell by subsequently weakening the hydrogen bonds between the pectin chains. Eggshells that caused the films to break after a certain force is applied. Muscat et al. [35], who previously used starch to make a film, stated that plasticisers diminish the strong intramolecular attraction between the starch chains. A similar

observation by Sanyang et al. [36] found that the tensile strength decreases with an increasing percentage of mixture glycerol/sorbitol/glycerol-sorbitol as the plasticiser increased from 15% to 45% on sugar palm starch films. However, the tensile strain value remains at the same range with 4% DES, which is 2.26 MPa. Similar results are observed for tensile strain and tensile modulus, i.e., constant at the addition of 4% DES. The addition of plasticiser did not significantly change the properties of bioplastic after 3%, indicating that at 3%, the liquid has swelled and filled up the free volume within polymer chains to prevent intermolecular interaction. Hence, the study only conducted only up to 4% of DES.

The biodegradability test was carried out to determine the weight loss of the pectin/eggshell after ten days in soil. The biodegradation process mainly depends on the moisture content and the presence of microorganisms in the ground. Figure 4 indicates the biodegradability behaviour in the weight loss of the bioplastic at a different DES percentage. All bioplastics show a continuous weight loss increase, with the bioplastic with 4% DES fully degraded (100%) on the third day and bioplastic with 1%, 2%, and 3% DES fully degraded on the fifth day. The pectin/eggshell composite without DES showed the highest percentage loss on the first day, but only 93% degraded on the fifth day and remained around 97% on the tenth day of the test. The higher percentage of DES concentration in bioplastic, led to a higher weight loss of the bioplastic. The bioplastic at 4% DES degrades faster than lower DES concentration. Kasmuri et al. [14] stated that the presence of the eggshell filler reduced the biodegradability rate since 95% of the eggshell is made up of calcium carbonate compounds, which mostly remained in the soil after the bioplastic had degraded. However, as proven by the tests, DES enhanced the biodegradability properties of bioplastic.



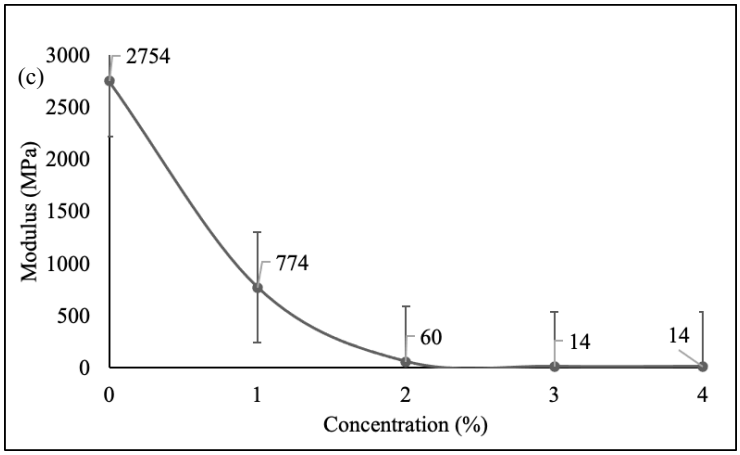


Figure 3. The properties of bioplastic in (a) tensile stress; (b) tensile strain and (c) modulus

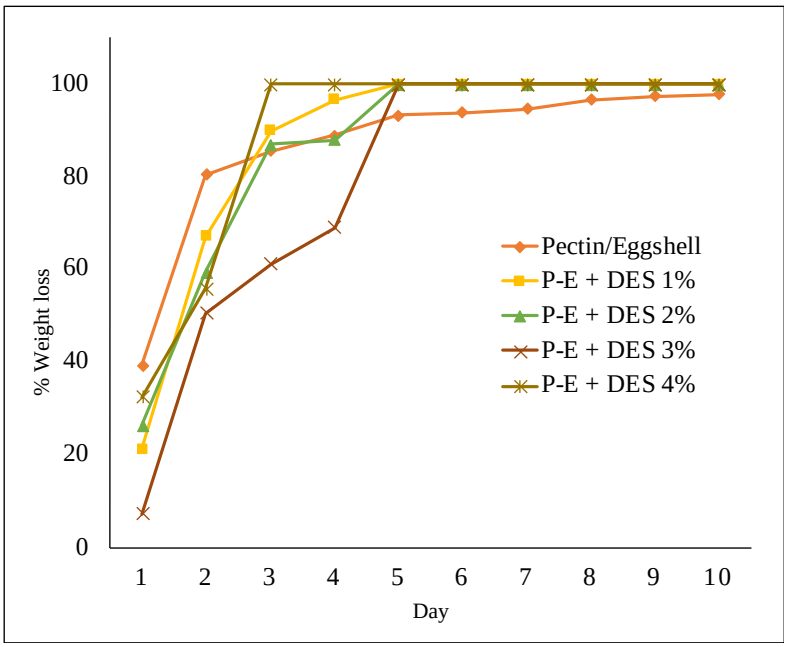


Figure 4. The percentage of weight loss of bioplastic in 10 days of biodegradability test in soil

Another biodegradability test was conducted in synthetic seawater. All bioplastics immediately swelled and curved when immersed in seawater. After one day in seawater, the pectin/eggshell bioplastic was fully degraded, but not the pectin/eggshell/DES bioplastics. Figure 5 shows the degradation of bioplastics in seawater. The result is contrary to the biodegradability test conducted in soil. In seawater, the bioplastic with a high DES concentration takes longer to degrade than those without DES. The inclusion of electrolytes from NaCl in synthetic seawater influenced bioplastic breakdown. According to Trindade et al. [37], ionic liquid shows the effect of salting out in salt solution. The same effect might be seen in the biofilm

containing DES. The added salt (NaCl) might compete with the ions in DES, causing the migration of NaCl molecules from the DES ions, decreasing the hydration and solubility of bioplastic-containing DES.

The analysis of water uptake was performed to measure the ability of bioplastic to absorb water with the addition of different concentrations (%) of DES. Figure 6 shows that the highest percentage of water uptake is at 1% concentration of DES, with 85% of water uptake. According to Suppakul et al. [38], the presence of hydroxyl group in plasticiser is strongly interacted with water molecules by forming hydrogen bonds. DES (choline chloride: malonic acid) consists of O-H bonds that interact directly with water, increasing the volume of the water uptake. However, when the percentage concentration of DES is more than 1%, the water absorption is reduced since the holding ability is weakened.

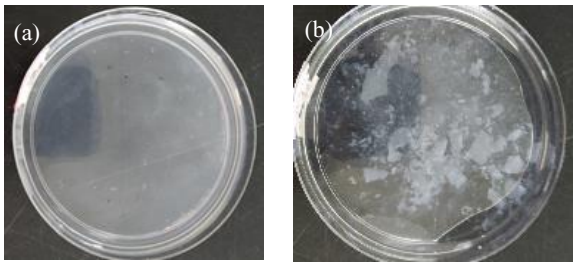


Figure 5. The images of (a) complete degradation of pectin/eggshell bioplastic and (b) incompleted degradation of pectin/eggshell/DES bioplastic in seawater

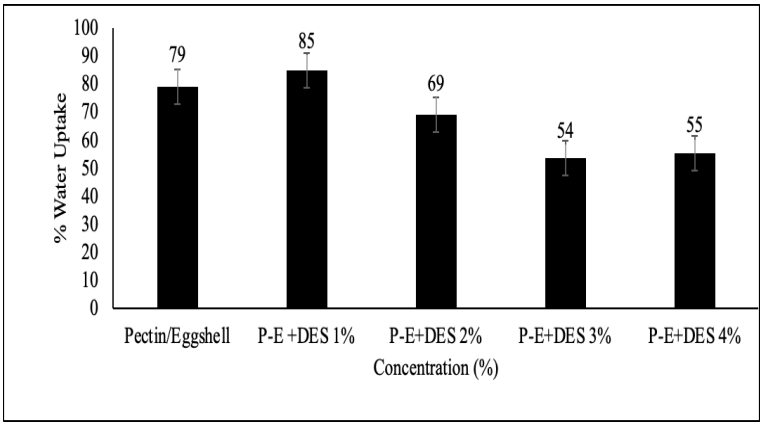


Figure 6. Percentage water uptake of bioplastics test in different concentration (%) of DES

Conclusion

The pectin/eggshell bioplastics with different concentrations of DES were successfully prepared. The eggshell and choline chloride: malonic acid are compatible with pectin, and no crystallisation occurred during the formation of biofilm. DES allowed the bioplastic to become more flexible by disrupting the polymer chains, causing an increase in elongation and a decrease in tensile strength of pectin/eggshell/DES. The higher concentration of DES leads to more flexibility and higher biodegradation in soil but with lower water uptake. These results indicated that

Choline chloride:malonic acid could be used as a potential plasticiser for pectin/eggshell bioplastic.

Acknowledgement

The authors are grateful for the financial support of the Fundamental Research Grant Scheme (FRGS) provided by the Ministry of Education, Malaysia, FRGS 5/3 (113/2019) and facilities in Universiti Teknologi MARA, Perlis Branch.

References

1. Šešlija, S., Nesic, A., Ruzic, J., Krusic, M. K., Velickovic, S., Avolio, R., Santagata, G. and Malinconico, M. (2018). Edible blend films of pectin and poly (ethylene glycol): Preparation and physico-chemical evaluation. *Food Hydrocolloids,* 77: 494-501.
2. Anastas, P. T. and Kirchhoff, M.M (2002). Origins, current status, and future challenges of green chemistry. *Accounts of Chemical Research*, 35(9): 686-694.
3. Fabra, M. J., Lopez-Rubio, A. and Lagaron, J. M. (2014). Biopolymers for food packaging application. *Smart Polymers and Their Application*, 15: 476-509.
4. Cavallaro, G., Lazzara, G. and Milioto, S. (2011). Dispersions of nanoclays of different shapes into aqueous and solid biopolymeric matrices. *Langmuir,* 27(3): 1158-1167.
5. Biddeci, G., Cavallaro, G., Blasi, F. D, Lazzara, G. Massaro, M. Milioto, S., Parisi, F., Riela, S. and Spinelli, G. (2016). Halloysite nanotubes loaded with peppermint essential oil as filler for functional biopolymer film. *Carbohydrate Polymers*, 152: 548-557.
6. Munarin, F., Tanzi, M.C. and Petrini, P. (2012). Advances in biomedical applications of pectin gels. *International Journal of Biological Macromolecules*, 51(4): 681-689.
7. Obara, S. and McGinity, W. (1995). Influence of processing variables on the properties of free films prepared from aqueous polymeric dispersions by a spray technique. *International Journal of Pharmaceutics,* 126 (1-2): 1-10.
8. Gennadios, A., Hanna, M. A. and Kurth, L. B. (1997). Application of edible coatings on meats, poultry and seafoods: a review. *LWT-Food Science and Technology,* 30(4): 337-350.
9. Pilla, S. (2011). Handbook of Bioplastic and *Biocomposites Engineering Applications.* ISBN 978 0-470-62607-8, Publisher John Wiley & Sons.
10. Abolibda, T. Z. (2015). Physical and chemical investigations of starch based bio-plastics. PhD Diss., University of Leicester.
11. Kang, D. J., Pal, K., Park, S. J., Bang, D. S., & Kim, J. K. (2010). Effect of eggshell and silk fibroin on styrene–ethylene/butylene–styrene as bio-filler. *Materials & Design,* 31(4): 2216-2219.
12. Toro, P. Quijada, R., Arias, J. L. and Yazdani-Pedram, M. (2007). Mechanical and morphological studies of poly (propylene)-filled eggshell composites. *Macromolecular Materials and Engineering,* 292(9): 1027-1034.
13. Vieira, M. G. (2011). Natural-based plasticizers and biopolymer films: A review. *European Polymer Journal,* 47(3): 254-263.
14. Kasmuri, N. and Abu Zait, M. S. (2018). Enhancement of bio-plastic using eggshells and chitosan on potato starch based. *International Journal of Engineering & Technology,* 7:110-115.
15. Abbott, A. P., Ballantyne, A. D., Conde, J. P., Ryder, K. S. and Wise, W. R. (2012). Salt modified starch: sustainable, recyclable plastics. *Green Chemistry,* 14(5): 1302-1307.
16. Galvis-Sánchez, A. C., Sousa, A. M. M, Goncalves, M. P. and Souza, H. K. S. (2016). Thermo-compression molding of chitosan with a deep eutectic mixture for biofilms development. *Green Chemistry* 18(6): 1571-1580.
17. Leroy, E., Decaen, P., Coativy, G., Pontoire, B., Reguerre, A. and Lourdin, D. (2012). Deep eutectic solvents as functional additives for starch based plastics. *Green Chemistry,* 14(11): 3063-3066.
18. Zdanowicz, M. and Johansson, C. (2016). Mechanical and barrier properties of starch-based films plasticized with two-or three component deep eutectic solvents. *Carbohydrate Polymers* 151: 103-112.

19. Shafie, M. H., Samsudin, D., Yusof, R. and Gan, C.Y. (2018). Characterization of bio-based plastic made from a mixture of Momordica charantia bioactive polysaccharide and choline chloride/glycerol based deep eutectic solvent. *International Journal of Biological Macromolecules*, 118: 1183-1192.
20. Malarvannan G, Onghena, M., Verstraete, S., Puffelen, E.V., Jacobs, A., Vanhorebeek, I., Verbruggen, C. A. T., Joosten, K. F. M., Berghe, G. V. D., Jorens, P. G. and Covaci, A. (2018). Phthalate and alternative plasticisers in indwelling medical devices in pediatric intensive care units. *Journal of Hazardous Materials,* 363: 64-72.
21. Mekonnen, T., Mussone, P., Khalil, H. and Bressler, D. (2013). Progress in bio-based plastics and plasticizing modifications. *Journal of Materials Chemistry A*, 1(43): 13379-13398.
22. Tome, L. I., Baiao, V., Silva, W. D. and Brett, M. A. (2018). Deep eutectic solvents for the production and application of new materials. *Applied Materials Today,* 10: 30-50.
23. Zhang, Q., Vigier, K. D. O., Royer, S. and Jerome, F. (2012). Deep eutectic solvents: Syntheses, properties and applications. *Chemical Society Reviews,* 41(21): 7108-7146.
24. Shamsuri, A. A. and Daik, R. (2012). Plasticizing eutectic-based ionic liquid on physicochemical. *BioResources*, 7(4): 4760-4775.
25. Cataldo, V. A., Cavallaro, G., Lazzara, G., Milioto, S. and Parisi, F. (2017). Coffee grounds as filler for pectin: Green composites with competitive performances dependent on the UV irradiation. *Carbohydrate Polymers*, 170: 198-205.
26. Almeida, C. M.R., Magalhaes, J.M.C.S., Souza, H.K.S. and Concalves, M.P. (2018). The role of choline chloride-based deep eutectic solvent and curcumin on chitosan films properties. *Food Hydrocolloids,* 81: 456-466.
27. Zárate-Ramírez, L. S., Bengoechea, C., Partal, P. and Guerrero, A. (2014). Thermo-mechanical and hydrophilic properties of polysaccharide/gluten-based bioplastics. *Carbohydrate polymers,* 112: 24-31.
28. Bichara, L. C, Alvarez, P. E., Bimbi, M. V. F, Vaca, H., Gervasi, C. and Brandan, S. A. (2016). Structural and spectroscopic study of a pectin isolated from citrus peel by using FTIR and FT-Raman spectra and DFT calculations. *Infrared Physics & Technology,* 76: 315-327.
29. Li, Y., Xin, S., Bian, Y., Xu, K., Han, C. and Dong, L. (2016). The physical properties of poly (l-lactide) and functionalized eggshell powder composites. *International Journal of Biological Macromolecules,* 85: 63-73.
30. Siriprom, W., Sangwaranatee, N., Hidayat, R., Kongsriprapan, S., Teanchai K. and Chamchoi, N. (2018). The physicochemical characteristic of biodegradable methylcellulose film reinforced with chicken eggshells. *Materials Today: Proceedings,* 5(7): 14836-14839.
31. Pradhan, A. K. and Sahoo, P. K. (2017). Synthesis and study of thermal, mechanical and biodegradation properties of chitosan-g-PMMA with chicken egg shell (nano-CaO) as a novel bio-filler. *Materials Science and Engineering: C,* 80: 149-155.
32. Gouveia, T. I. A. Biernacki, K., Castro, M. C. R., Goncalves, M. P. and Souza, H. K. S. (2019). A new approach to develop biodegradable films based on thermoplastic pectin. *Food Hydrocolloids,* 97:105175.
33. Kong, J., Li, Y., Bai, Y., Li, Z., Cao, Z., Yu, Y., Han, C. and Dong, L. (2018). High-performance biodegradable polylactide composites fabricated using a novel plasticiser and functionalized eggshell powder. *International Journal of Biological Macromolecules,* 112: 46-53.
34. Esposito, M., Pierro, P. D, Gonzales, C.R., Mariniello, L., Giosafatto, C. V. L and Porta, R. (2016). Polyamines as new cationic plasticisers for pectin-based edible films. *Carbohydrate polymers*, 153: 222-228.
35. Muscat, D. Adhikari, B., Adhikari, R. and Chaudhary, D. S. (2012). Comparative study of film forming behaviour of low and high amylose starches using glycerol and xylitol as plasticisers. *Journal of Food Engineering*, 109(2): 189-201.

36. Sanyang, M. L., Sapuan, S.M., Jawaid, M., Ishak, M.R. and Sahari, J. (2016). Effect of plasticiser type and concentration on physical properties of biodegradable films based on sugar palm (arenga pinnata) starch for food packaging. *Journal of Food Science and Technology*, 53: 326-336.
37. Trindade, J. R., Visak, Z. P., Blesic, M., Marrucho, I. M., Coutinho. J. A. P., Lopes, J. N. C. and Rebelo, L. P. N. (2007). Salting-out effects in aqueous ionic liquid solutions: Cloud-point temperature shifts. *The Journal of Physical Chemistry B*, 111(18): 4737-4741.
38. Suppakul, P., Chalernsook, B., Ratisuthawat, B., Prapasitthi, S. and Munchukangwan, N. (2013). Empirical modeling of moisture sorption characteristics and mechanical and barrier properties of cassava flour film and their relation to plasticizing–antiplasticizing effects. *LWT-Food Science and Technology,* 50(1): 290-297.

Malaysian Journal of Analytical Sciences (MJAS)
Published by Malaysian Analytical Sciences Society

SUPRAMOLECULAR ASSEMBLIES OF 1,2-DISUBSTITUTED CYCLOHEXANE AMIDE LIGANDS AND THEIR COORDINATION POLYMER: SYNTHESIS, CHARACTERISATION, AND CRYSTAL STRUCTURE

(Himpunan Supramolekul Ligan Amida Sikloheksana 1,2-Tertukar Ganti dan Polimer Koordinatannya: Sintesis, Pencirian, dan Struktur Hablur)

Nur Shuhaila Haryani Haris[1], Nafisah Mansor[1], Maisara Abdul Kadir[1,2]*

[1]Faculty of Science and Marine Environment,
[2]Advanced Nano Materials Research Group, Faculty of Science and Marine Environment,
Universiti Malaysia Terengganu, 21030 Kuala Nerus, Terengganu, Malaysia

**Corresponding author: maisara@umt.edu.my*

Received: 13 September 2021; Accepted: 18 December 2021; Published: 25 February 2022

Abstract

Supramolecular interactions such as hydrogen bonding, π-π stacking, Van der Waals interactions, and metal-ligand are important in stabilising the structure of molecules. In order to determine the presence of supramolecular interactions in two novel compounds, 1,2-disubstituted cyclohexane amide ligands, namely 1,2-bis[*N,N'*-6-(3-pyridylmethylamido)pyridyl-2-carboxyamido]cyclohexane (L1) and 1,2-bis[*N,N'*-6-(4-pyridylmethylamido)pyridyl-2-carboxyamido]cyclohexane (L2) were successfully synthesised and fully characterised by FTIR, ^{1}H and ^{13}C NMR and mass spectrometry, while the molecular formula was determined by elemental analysis. X-ray crystallography revealed that the folded conformations of both ligands were stabilised by intramolecular N-H···O=C and N-H···N hydrogen bonds at the pre-organised amide moieties. The crystal's structure was stabilised by weak face-to-face π-stacking interaction or centroid-centroid π-stacking interaction involving the two pendant pyridine rings. In the crystal structure of one-dimensional coordination polymer, there are two intermolecular hydrogen bonding interactions (N-H···O=C, d = 2.094 Å, D = 2.946 Å and d = 2.090 Å, D = 2.938 Å, N-H···O angle = 161.52°) formed between the pre-organised NH amide donors of a molecule of L1 in one coordination polymer and the amide carbonyl group of a molecule of L1 in an adjacent polymer that leads to the formation of 2-D hydrogen-bonded sheets extend in the *ac* diagonal.

Keywords: supramolecular, coordination polymer, cyclohexane, hydrogen bonding, racemic

Abstrak

Interaksi supramolekul seperti ikatan hidrogen, susunan π-π, interaksi Van der Waals dan logam-ligan adalah penting dalam menstabilkan struktur molekul. Dalam usaha mengenalpasti kehadiran interaksi supramolekul dalam dua sebatian baharu, ligan amida sikloheksana 1,2-tertukar ganti, iaitu 1,2-bis[*N,N'*-6-(3-piridilmetilamido)piridil-2-karboksiamido]sikloheksana (L1) dan 1,2-bis[*N,N'*-6-(4-piridilmetilamido)piridil-2-karboksiamido]sikloheksana (L2) telah disintesis dan dicirikan sepenuhnya dengan FTIR, ^{1}H dan ^{13}C NMR serta spektrometri jisim, manakala formula molekul ditentukan melalui analisis unsur. Kristalografi

sinar-X menunjukkan bahawa konformasi bagi kedua-dua ligan distabilkan oleh ikatan hidrogen intramolekul N-H···O=C dan N-H···N pada kawasan amida separa tersusun. Struktur hablur juga distabilkan oleh interaksi lemah susunan muka ke muka atau titik pusat ke titik pusat di antara gelang aromatik piridina. Dalam struktur hablur polimer koordinatan satu dimensi, terdapat dua ikatan hidrogen intermolekul (N-H···O=C, d = 2.094 Å, D = 2.946 Å dan d = 2.090 Å, D = 2.938 Å, N-H···O sudut = 161.52°) yang terbentuk di antara NH amida dari molekul L1 dalam polimer koordinatan dan karbonil amida dari molekul L1 dalam polimer bersebelahannya dan menghasilkan lapisan 2-D ikatan hidrogen yang bersambung ke diagonal *ac*.

Kata kunci: supramolekul, polimer koordinatan, sikloheksana, ikatan hidrogen, rasemik

Introduction

Supramolecular chemistry is often defined as 'the chemistry beyond the molecule' [1]. This term was introduced by Jean-Marie Lehn who won the Nobel Prize in Chemistry in 1987 together with Donald J. Cram and Charles J. Pedersen. They received the prize for their contributions to the synthesis of shape-selective and ion-selective receptors, in particular, the development of selective 'host-guest' complexes. In broader terms, supramolecular chemistry is defined as the self-assembly of small molecular subunits into large aggregates *via* weak intermolecular forces or reversible covalent bonding. The interactions commonly involved in the self-assembly process are hydrogen bonds, π-π interactions (stacking of aromatic rings), Van der Waals forces, cation-interactions, and metal-ligand (M-L) interactions [2]. The order of strength for the intermolecular interactions from very weak to very strong is broadly as follows: hydrophobic/hydrophilic interactions, Van der Waals forces, H-bonding interactions, electrostatic forces and metal coordination [3].

In general, the intermolecular interactions are individually weak, but by using multiple weak intermolecular forces within the assemblies, robust structures can be generated. Besides, the dynamic nature of noncovalent interactions endows supramolecular polymeric systems with many fascinating properties and functions, such as reversibility, adaptability, self-healing, and stimuli-responsiveness [4]. Hydrogen bonding interactions are commonly employed in supramolecular chemistry [5]. Hydrogen bonding occurs between a proton donor attached to an electronegative atom such as O, N, S, F or C (D-H) and an acceptor (A). The donor is partially positive hydrogen while the acceptor is a partially negative atom with unshared valence electrons or polarisable π electrons. The strength of hydrogen bonds is typically around 20 kJmol^{-1}, but can even be as strong as 163 kJmol^{-1} as has been reported for the F···HF interaction [6,7]. Weak interactions involving π-systems such as π-stacking interactions (π···π) are observed in many supramolecular systems [8]. Other weak interactions involving π-systems are C-H···π, cation···π and anion···π interactions. The C-H···π interaction is classified as weak H-bonding and have similar properties to the weak hydrogen bonds. Cation···π interactions occur between metallic or organic cations and π-bonded systems of the molecule.

Open chain molecules such as amide, thiourea, and urea are of interest because intermolecular amide-amide hydrogen bonding can promote the fabrication of well-defined assemblies of supramolecular chemistry [9]. Furthermore, amide ligands with the presence of pyridyl as one of the outstanding N or O-donor organic linkers have been effectively selected because they can connect metal centres through their pyridyl groups or the amide groups [10]. Thus, in this research, two novel amide compounds containing 1,2-disubstituted cyclohexane spacer were prepared (Figure 1). Compounds 1,2-bis[*N,N'*-6-(3-pyridylmethyl amido)pyridyl-2-carboxyamido]cyclohexane (L1) and 1,2-bis[*N,N'*-6-(4-pyridylmethylamido)pyridyl-2-carboxyamido]cyclohexane (L2) were synthesised from a racemic mixture of *trans*-1,2-diamino cyclohexane in two steps. The incorporation of a cyclohexyl spacer was anticipated to limit the relative arrangements of the two 2,6-pyridine dicarboxamide moieties as compared to common approaches of using aliphatic alkyl chains spacer [11].

The advantages of the pyridyl-amide ligands are the amide groups with both N-H hydrogen donor and C=O hydrogen acceptor can enhance the formation of hydrogen bonds and supramolecular structures. The isomerism and flexibility of ligands play important roles in permitting guest molecules such as anions to interact with the host molecules by using weak hydrogen bonding. The presence of aromatic rings from 1,2-disubstituted cyclohexane amide moieties and pyridine pendant groups is important to achieve well-defined frameworks with higher stability contributed by the supramolecular interactions of π-π stackings. In a work by Yusof et al. [12] the conformation of cyclohexane derived compound was stabilised by intramolecular hydrogen bonds and intermolecular N-H···O and C-H···O hydrogen bonds, which led to centrosymmetric dimers arrangement [12].

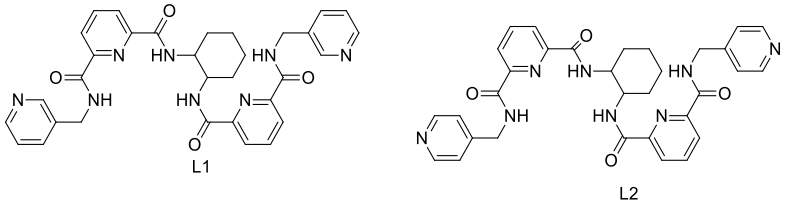


Figure 1. The structure of 1,2-bis[*N,N'*-6-(3-pyridylmethylamido)pyridyl-2-carboxyamido]cyclohexane (L1) and 1,2-bis[*N,N'*-6-(4-pyridylmethylamido)pyridyl-2-carboxyamido]cyclohexane (L2)

Materials and Methods

Synthesis of 1,2-bis[*N,N'*-6-(3-pyridylmethyl amido)pyridyl-2-carboxyamido]cyclohexane (L1)

1,2-bis[6-methoxycarbonyl)pyridyl-2-carboxyamido] cyclohexane (0.50 g, 1.1 mmol) and 3-aminomethylpyridine (0.22 mL, 2.3 mmol) were suspended in toluene (20 mL). The reaction mixture was heated at reflux for 72 hours, during which time a white solid precipitated. After cooling to room temperature, the solvent was removed in vacuo, the residue re-dissolved in dichloromethane (40 mL), washed with saturated aqueous sodium bicarbonate solution (2 × 100 mL), and the chlorinated extract was dried over magnesium sulphate. The solvent was removed in vacuum to give a sticky off-white solid. The solid was washed with diethyl ether, dried, and recrystallised from ethanol to give L1 as a white solid (0.55 g, 82%). Mp 250-252 °C. Anal. found: C, 64.19; H, 5.52; N 18.70. ($C_{32}H_{32}N_8O_4$) requires C, 64.84; H, 5.45; N 18.90%. ^{1}H (300 MHz; $CDCl_3$; Me_4Si) δ = 1.32 (2H, m, CH_2), 1.65 (1H, m, CH_2), 2.17 (1H, m, CH_2), 3.87 (1H, s, CH), 4.15 (2H, d, J = 11.43 Hz, CH_2), 7.23 (1H, m, pyH5), 7.82 (2H, m, pyH3, pyH4', pyH4), 8.28 (2H, m, pyH5'), 8.54 (2H, d, J = 4.81 Hz, pyH6'), 8.65 (2H, m, NH, pyH2') and 9.07 (1H, d, J = 8.38 Hz, NH). ^{13}C (75.1 MHz; $CDCl_3$; Me_4Si) δ = 23.1, 28.3, 45.1, 54.6, 123.9, 125.7, 125.9, 134.8, 136.7, 139.2, 148.1, 149.5, 149.9, 150.8, 161.1, 162.4. m/z (ES-MS) 592.2 (MH^+, 100), 593.6 (MH^+, 50%), 614.5 (MNa^+, 65%), 1204.2 ($M.H_2O+H)^+$, 30%). Selected IR bands (KBr disk, cm^{-1}): 3368 (m), 3267 (m), 2916 (s) 1627 (m), 1650 (s), 1527 (s), 1424 (m), 1306 (s). Crystals were obtained by slow evaporation of a methanol solution of L1 and copper nitrate.

Synthesis of 1,2-bis[*N,N'*-6-(4-pyridylmethyl amido)pyridyl-2-carboxyamido]cyclohexane hydrate L2·H_2O (L2)

1,2-bis[6-methoxycarbonyl)pyridyl-2-carboxyamido]cyclohexane (0.52 g, 1.2 mmol) and 4-aminomethylpyridine (0.24 mL, 2.4 mmol) were dissolved in hot toluene (20 mL) and heated at reflux for 72 hours. During the course of the reaction, a yellow solid precipitated. The solvent was removed in vacuum to give a yellow solid. The solid was re-dissolved in dichloromethane (40 mL), washed with saturated sodium bicarbonate solution (2 × 100 mL), and the chlorinated layer was dried over magnesium sulphate. The solvent was removed in vacuum to give a yellow oil which was triturated with hot ethyl acetate (5 mL) to give a brown solid. This solid was purified by column chromatography, eluting with 1:9 methanol–CH_2Cl_2 to give L2·H_2O as a brown solid (0.24 g, 33%). Mp 220 – 225 °C. Anal. found: C,

64.67; H, 5.89; N, 18.90. ($C_{32}H_{34}N_8O_5$) requires C, 64.84; H 5.45; N, 18.91%. ^{1}H (300 MHz; $CDCl_3$; Me_4Si) δ = 1.43 (2H, m, CH_2), 1.93 (2H, d, *J* = 6.73 Hz, CH_2), 2.14 (2H, d, *J* = 13.29 Hz, CH_2), 3.77 (1H, s, CH), 4.72 (2H, m, CH_2), 7.25 (2H, m, pyH3', pyH5'), 7.74 (2H, m, pyH3, pyH5), 8.32 (1H, m, pyH4), 8.54 (2H, d, *J* =5.70 Hz, pyH2', pyH6'), 9.15 (1H, d, *J* = 6.25 Hz, NH) and 9.75 (1H, t, *J* = 6.40 Hz, NH). ^{13}C (75.1 MHz; $CDCl_3$; Me_4Si) δ = 22.5, 28.9, 45.6, 54.0, 124.3, 125.6, 125.9, 139.8, 147.3, 148.9, 149.2, 149.9, 160.5, 161.8. *m/z* ES-MS) 592.3 (MH^+, 100%), 593.1 (MH^+, 75%). Selected IR bands (KBR disk, cm^{-1}): 3282 (m), 2923 (s), 1652 (s), 1671 (s), 1529 (s), 1444 (m), 672 (s). Crystals were obtained by slow evaporation of a methanol solution of L2 and copper perchlorate.

Synthesis of $\{[CdBr_2(L1)_4]\cdot 4H_2O\}_n$

$CdBr_2$ (0.0026 g, 0.010 mmol) was dissolved in water (5 mL), heated for 5 minutes, before being added dropwise to a solution of L1 (0.0120 g, 0.020 mmol) dissolved in methanol (15 mL). The resulting slightly cloudy solution was heated for 45 minutes to re-dissolve the precipitate and was left to evaporate at room temperature. The solution afforded $\{[CdBr_2(L1)_4]\cdot 4H_2O\}_n$ as colourless crystals in low yields (0.009 g, 24%). Mp 230-235ºC.

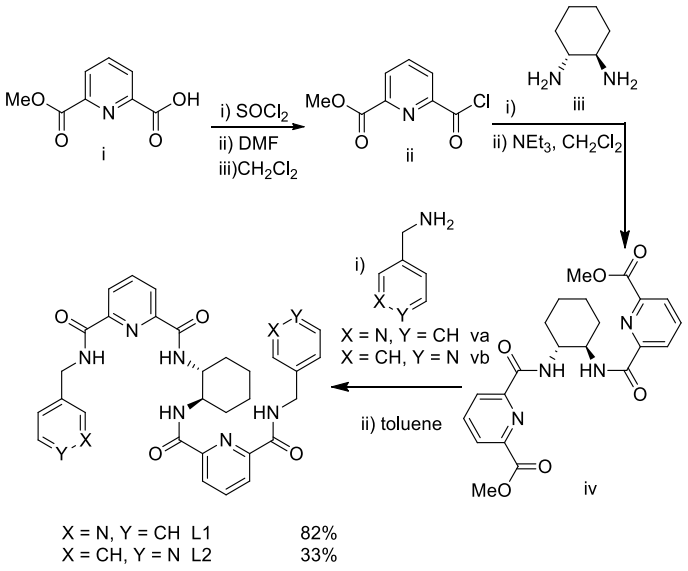
Results and Discussion

Compounds 1,2-bis[*N,N'*-6-(3-pyridylmethyl amido)pyridyl-2-carboxyamido]cyclohexane (L1) and 1,2-bis[*N,N'*-6-(4-pyridylmethylamido)pyridyl-2-carboxyamido]cyclohexane (L2) were synthesised from a racemic mixture of *trans*-1,2-diaminocyclohexane in two steps (Scheme 1). To synthesise the ligand, firstly, pyridine-2,6-dicarboxylic acid monomethyl ester (i) was reacted with thionyl chloride to produce 6-(methoxycarbonyl)pyridine-2-carboxylic acyl chloride (ii). Then, compound (ii) was reacted with 1,2-diaminocyclohexane (iii) with a 2:1 mol ratio to provide 1,2-bis[6-methoxy carbonyl)pyridyl-2-carboxyamido]cyclohexane (iv). At the second step, precursor (iv) and 3-aminomethylpyridine were suspended in toluene and heated at reflux for approximately 72 hours to give 1,2-bis[*N,N'*-6-(3-pyridylmethylamido)pyridyl-2-carboxy amido]cyclohexane (L1) (Scheme 1). The crude product of L1 was obtained as an off-white solid after being isolated after re-dissolved in hot ethanol. The insoluble solids were removed by filtration, and the filtrate was left to evaporate to afford L1 as a colourless powder in an 82% yield.

Ligand L2 was prepared with a similar procedure, but the 3-aminomethylpyridine was replaced with 4-aminomethylpyridine. The coordination chemistry of these ligands was investigated with a range of late transition metals, including cadmium(II), copper(II), cobalt(II), silver(I), and zinc(II). The focus of this synthesis was to produce coordination polymers that display anion coordinating pockets (Figure 2). Compounds L1 and $L2\cdot H_2O$ were found to preferentially crystallise from solutions containing metal salts. It showed that the ligands were insoluble in the metal salts solution and caused limitations to obtain metal complexes. Rectangular block-shaped colourless crystals of both compounds were obtained from several different reactions and were suitable for X-ray crystallography.

The FTIR spectra for the three compounds showed distinctive peaks for *ν*(N-H), *ν*(O-H), *ν*(C=N), *ν*(C=O), *ν*(Cd-N), and *ν*(N-O). As for compound L1, the *ν*(N-H) stretching displayed a broad peak due to the water molecule and the weak hydrogen bond interactions interrupted the chemical changes. The low frequency (N-H) stretching appeared at 3267 cm^{-1} showing that the steric effect occurred with the presence of methyl located near the amino group [13]. Meanwhile, the *ν*(N-H) bending was interpreted at 1527 cm^{-1} because of the hydrogen bond donor. The strong frequency band at 2916 cm^{-1} referred to *ν*(C-H) aromatics vibration respective to the formation of sp^3 hybridisation. The carbonyl *ν*(C=O) band shifted to the low frequency at 1650 cm^{-1} suggested the involvement of hydrogen bonds formed between the amide moieties and pendant pyridyl group [14]. In the IR spectrum, the high frequency above 3000 cm^{-1} regions is a signature area for recognition phenyl C-H stretching vibrations. The region below 2000 cm^{-1} showed very sharp and strong peaks [15]. The spectrum of L2 showed a close resemblance of the absorbance pattern

compared with L1. Compound L2 observed the appearance of amide stretching, ν_{str}(N-H) at 3282 cm^{-1}. A significant stretching vibration of ν_{str}(C-H) aromatics band attributed at 2923 cm^{-1}. Nevertheless, the wavenumbers captured in both compounds for *ν*(C=O) amide revealed a significant difference. Compound L2 recorded the appearance of the carbonyl stretching at wavenumbers 1647 cm^{-1}. The compounds showed bands at 1529 cm^{-1} which was ascribed to the N-H bending.



Scheme 1. The synthesis of L1 and L2

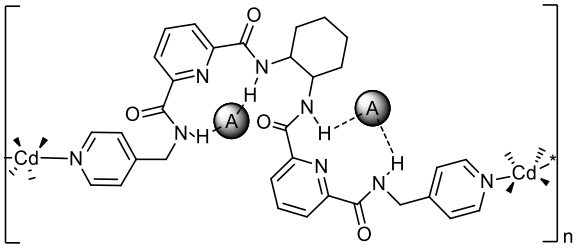


Figure 2. Coordination polymers that display anion coordinating pockets, where A in the circle represents anion

The ^{1}H NMR spectra of L1 were recorded in deuterated chloroform (Table 1). A signal that appears as a triplet at 9.09 ppm corresponding to the N-H protons of the pyridine core amide [16,17]. The signals for the cyclohexyl amide and the pendant pyridyl H2' are overlapped to give a broad singlet at 8.65 ppm. Another two signals (H6' at 8.54 and H5'at 8.28 ppm) were assigned to the pendant pyridine protons H6' and H5', while the multiplet near 7.82 ppm corresponded to the overlap between one triplet and doublets from the pyridine carboxamide H4 proton and the H4' of the pendant pyridine ring. The nearby doublet was assigned as the H3 and H5 hydrogen atoms from the pyridine core. The multiplets at 4.15 ppm arise from the CH_2 protons from the methylene linker adjacent to the pyridine rings. The cyclohexane protons are doublets that appear upfield at 3.87, 2.17, 1.65 and 1.32 ppm. The ESI-MS obtained on a methanol solution of

L1 revealed peaks for the parent ion $[L1+H]^+$ at m/z 591.2. Meanwhile, a peak at m/z 1204.2 corresponded to the hydrated dimeric species, $[(L1)_2 \cdot H_2O+H]^+$, while a hydrated trimeric species $[(L1)_3 \cdot H_2O+H]^+$ was observed at m/z 1793.2 in low relative abundance. There is also a peak observed for a sodium-containing ion, $[L1+Na]^+$, at m/z 614.5 (25%).

Based on the conditions employed for the synthesis of L1, the reaction of 6-(methoxycarbonyl)pyridine-2-carboxylic acyl chloride with a greater than two-fold excess of 4-aminomethylpyridine gave L2. Similar to the synthesis of L1, the reaction was heated at reflux for approximately 72 hours, and the formation of the product was monitored by TLC and NMR spectroscopy. Compound L2 was isolated by flash column chromatography techniques using the mixture of dichloromethane-methanol (9:1) as the eluting solvent system. Unfortunately, L2 was isolated in a much lower yield (33%) compared to L1. This is a consequence of the reduced nucleophilicity of the amine nitrogen compared to the 3-substituted precursor, as reported by Ikawa et al., 2011 [18]. Elemental analysis of the product obtained supports the isolation of the hydrate, $L2 \cdot H_2O$. In the ^1H NMR spectrum of $L2 \cdot H_2O$, the amide protons were observed downfield compared to L1, with a doublet at 9.75 ppm and a doublet at 9.15 ppm. The remaining signals between 7.25-8.54 ppm corresponded to the protons from the pyridine ring and the pyridine core. The methylene linker had a resonance at 4.72 ppm, while the cyclohexane protons showed signals at 3.77, 2.14, 1.93, and 1.43 ppm. The mass spectrometry indicated the presence of a dominant molecular ion corresponding to $[L2+H]^+$ at m/z 592.3 (100%).

Table 1. ^1H NMR data for L1 and L2

Proton signals	**L1**	**Proton signals**	**L2**
2H, m, CH_2	1.32		1.43
1H, m, CH_2	1.65	2H, d, CH_2	1.93
1H, m, CH_2	2.17	2H, d, CH_2	2.14
1H, s, CH	3.87		3.77
2H, d, CH_2	4.15	2H, m, CH_2	4.72
1H, m, pyH5	7.23	2H, m, pyH3', pyH5'	7.25
2H, m, pyH3, pyH4', pyH4	7.82	2H, m, pyH3, pyH5	7.74
2H, m, pyH5'	8.28	1H, m, pyH4	8.32
2H, d, pyH6'	8.54	2H, d, pyH2', pyH6'	8.54
2H, m, NH, pyH2'	8.65	1H, d, NH	9.15
1H, d, NH	9.07	1H, t, NH	9.75

X-ray crystallography

Crystal structure of L1

The particular crystals of L1 studied here were readily obtained from a methanol solution of copper nitrate and L1, consistent with the poor solubility of these compounds. Compound L1 crystallises in the triclinic space group *P*-1 with one molecule of L1 in the asymmetric unit. The structure reveals that this compound retained the two pre-organised amide hydrogen bond donor regions in the anticipated conformation (Figure 3), but as observed in molecule L1, these were arranged to form two separate pockets rather than one larger pocket. This arrangement is attributed to the planar arrangement of the substituents on the cyclohexane ring at the 1 and 2 positions.

In the conformation of L1 observed in the crystal structure, it appears there were intramolecular N-

H···O=C and N-H···N hydrogen bonds that stabilised the folded conformation. Figure 3 shows these hydrogen bonds have the following distances, N15-H15···O14 (*d* = 2.201 Å, *D* = 2.953 Å), N49-H49···O14 (*d* = 2.333 Å, *D* = 3.157 Å), N49-H49···N41 (*d* =2.308 Å, *D* = 2.697 Å), and N15-H15···N41 (*d* = 2.251 Å, *D* = 2.663 Å). The N-H···N angles are 106.78° and 108.41°, respectively.

Figure 4 shows that several intermolecular interactions were responsible for the formation of a dimeric arrangement of L1 in the solid state. The dimer was stabilised by four N-H···O=C hydrogen bonds between each molecule of L1 (N12-H12···O17, *d* = 2.158 Å, *D* = 3.000 Å; and N29-H29···O17 *d*= 2.111 Å; *D* = 2.951 Å).

The structure was further stabilised by π-π stacking interactions between the pyridine rings [19]. In the dimer, the pendant pyridyl group and the central pyridine core interact in an edge-to-face interaction, in which the C-H···π(centroid) distance is 2.912 Å. Adjacent dimers were then further involved in the π-stacking interactions involving one 2,6-pyridine dicarboxamide core of each molecule of L1 (Figure 5). The two pyridine cores formed a weak face-to-face π-stacking interaction (centroid-centroid distance 4.20 Å; angle 47.46°; centroid offset 1.32 Å). This ultimately resulted in a 1-D chain-like arrangement of the dimers.

Crystals of L2 were obtained from a methanol solution of copper perchlorate and compound L2. Like compound L1, compound L2 also crystallised in the triclinic space group *P*-1 but with two molecules of compound L2 in the asymmetric unit. The two molecules of L2 have similar conformations, with the major distinction between the two molecules being differences in bond lengths and angles. As observed in compound L1, intramolecular hydrogen bonding (*d* = 2.249-2.445 Å; N-H···N angles = 107.7 and 105.60°) pre-organised the NH functionalities of the compound to provide two anion pockets (Figure 6).

Like L1, one of these pockets was occupied by carbonyl oxygen of the other 2,6-pyridine dicarboxamide moiety (N-H···O, *d* = 2.380 Å ; *D* = 3.234 Å). Once again, intermolecular hydrogen bonding between the carbonyl oxygen (N-H···O) (*d* = 2.107 Å and *D* = 2.135 Å) and the pre-organised amide led to the formation of a dimer in the solid-state (Figure 7). Both molecules in the asymmetric unit demonstrated the same hydrogen bonding motifs with slightly different hydrogen bond distances (Table 2). One of the dimers had N-H···O hydrogen bond lengths of *d* = 2.109 - 2.137 Å, while the second dimer had hydrogen bond lengths of 2.106-2.153 Å. As observed in compound L1, the structures were also stabilised by intermolecular π-π stacking interactions. In the crystal packing, compound L2 was stabilised a centroid-centroid π-stacking interaction involving the two pendant pyridine rings (centroid-centroid distance 3.731 Å). The presence of excessive hydrogen-bonds networks in the compounds explains the huge range in the melting points for both compounds L1 and L2.

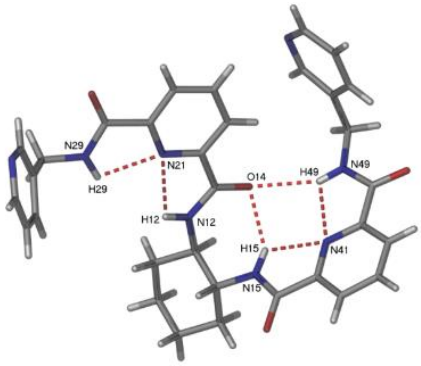


Figure 3. The asymmetric unit of compound L1, showing the presence of intramolecular N-H···O=C and N-H···N hydrogen bonds

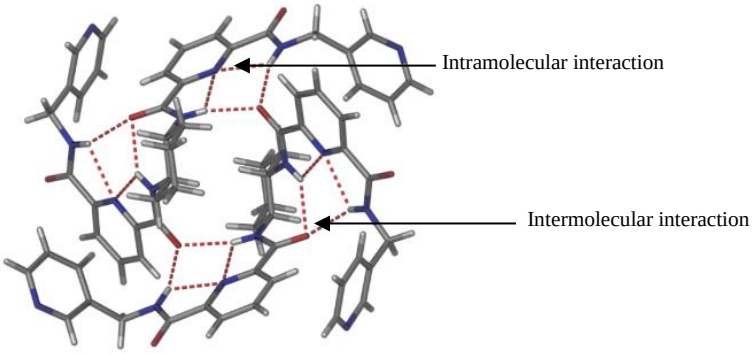


Figure 4. A perspective view of a dimer of L1 showing the weak intramolecular and intermolecular hydrogen bonds responsible for the conformation of L1 and the formation of the dimeric aggregate

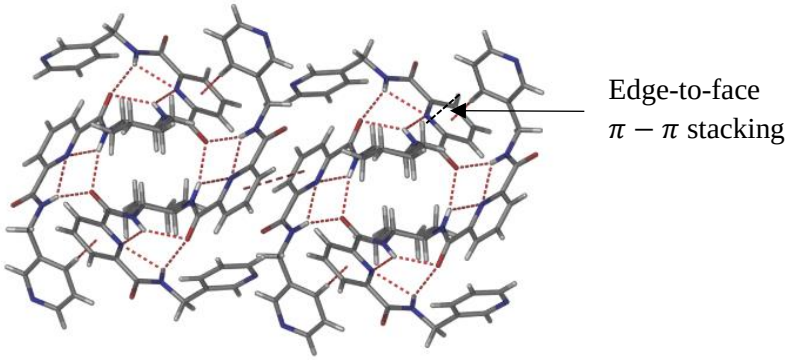


Figure 5. A perspective view of the π-π stacking interactions observed between the two pyridine cores of molecules of L1 that are involved in forming dimers

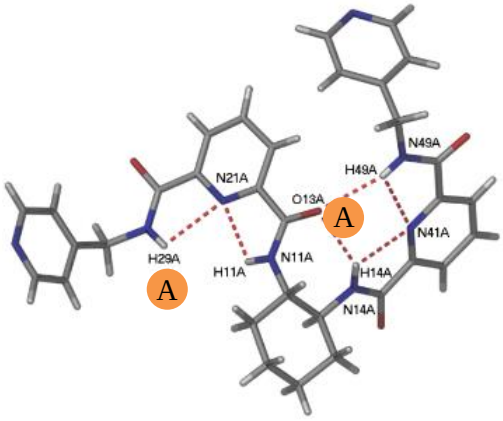


Figure 6. A perspective view of one of the molecules of L2 in the asymmetric unit, showing the pre-organizing intramolecular hydrogen bonding interactions that provided two potential anion pockets marked by A.

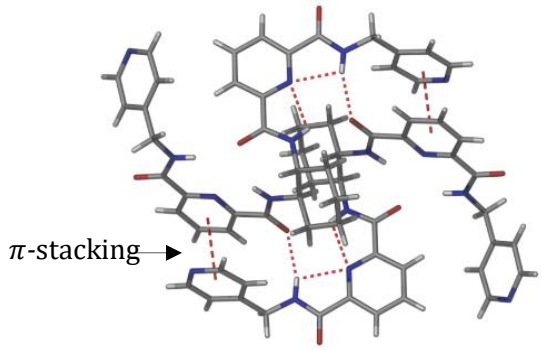


Figure 7. A perspective view of one of the dimers of compound L2, showing the intramolecular and intermolecular interactions, including the π-stacking interactions

Table 2. The asymmetric unit of hydrogen bond distances for L1 and L2

L1	
N15-H15···O14	*d* = 2.201 Å, *D* = 2.953 Å
N49-H49···O14	*d* = 2.333 Å, *D* = 3.157 Å
N49-H49···N41	*d* =2.308 Å, *D* = 2.697 Å
N15-H15···N41	*d* = 2.251 Å, *D* = 2.663 Å
L2	
N-H···O	*d* = 2.380 Å ; *D* = 3.234
N-H···O	*d* = 2.107 Å ; *D* = 2.135 Å
N-H···O	*d* = 2.109 - 2.137 Å
N15-H15···O14	*d* = 2.249 -2.445 Å

Crystal structure of CP-L1

Crystals of $\{[CdBr_2(L1)_2]\cdot 4H_2O\}_n$ were obtained from a methanol-water solution of L1 and cadmium bromide upon slow evaporation in 24% yield. Complex $\{[CdBr_2(L1)_2]\cdot 4H_2O\}_n$ was crystallised in the triclinic space group *P*-1 with one ligand L1, one cadmium atom (on a centre of inversion), two water molecules, and one bromide in the asymmetric unit (Figure 8). The cadmium atom adopts an octahedral coordination environment, with two bromide atoms in the axial positions and the equatorial positions occupied by four pyridyl donors from four separate molecules of L1. The Cd-N bond length is 2.453(4) Å and the Cd-Br bond length is 2.6805(5) Å, which is typically observed [20]. The Cd-Br bond distance was approximately 0.08-0.1 Å longer than the Cd-Br distance in compound 4.27, while the Cd-Cd distance in this compound is 16.765 Å.

The extended structure of compound CP-L1 is shown in Figure 9. Within the ligand, the pendant 4-pyridyl rings twisted backwards and forward relative to the 1,2-cyclohexane core with an -N-CH_2-CH_2-N- torsion angle of 56.3(2)° (Figure 9). This enabled the ligand to coordinate with two different cadmium centres which are also linked by a second molecule of L1.

Each cadmium is coordinated by four molecules of the ligand to generate a necklace-type 1-D coordination polymer. This coordination polymer was also

constructed from a dinuclear metallo-macrocylic repeating unit (Figure 9). Two types of ligand derived hydrogen bonding interactions are responsible for the internal conformation of the coordination polymers and the packing of adjacent 1-D coordination polymers in the solid-state. In the inter-polymer packing there are two intermolecular hydrogen bonding interactions in (N-H···O=C, d = 2.094 Å, D = 2.946 Å and d = 2.090 Å, D = 2.938 Å, N-H···O angle = 161.52°) formed between the pre-organized NH amide donors of a molecule of L1 in one coordination polymer and the amide carbonyl group of a molecule of L1 in an adjacent polymer (Figure 10(a)). The intermolecular hydrogen bonding led to the formation of 2-D hydrogen bonded sheets of the 1-D coordination polymers that extended in the *ac* diagonal (Figure 10(b)). Internally, each ligand within the coordination polymer adopts a conformation whereby the amide C=O forms a moderately strong N-H···O=C intramolecular hydrogen bonding interaction (d = 1.862 Å, D= 2.911 Å). This blocked one of the anion binding pockets of the ligand (Figure 10 (a)). In the 2-D crystal packing, the 1-D coordination polymers in each 2-D layer form C-H···π stacking interactions with 1-D coordination polymers in adjacent layers. These interactions occur between the pendant pyridyl rings of molecules of L1 in the adjacent layers (C-H-centroid distance 2.73 Å; angle 95.30°, centroid offset 1.39 Å Figure 10 (c). Weak intramolecular hydrogen bonding interactions of CP-L1 is shown in Table 3 while crystal data for CP-L1 is shown in Table 4.

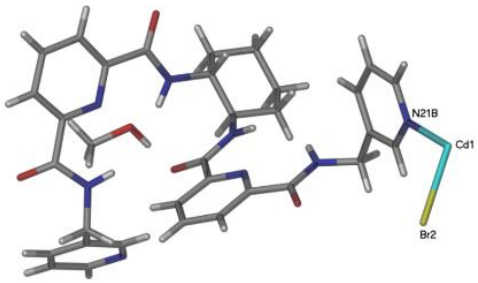


Figure 8. A perspective view of the asymmetric unit of compound CP-L1

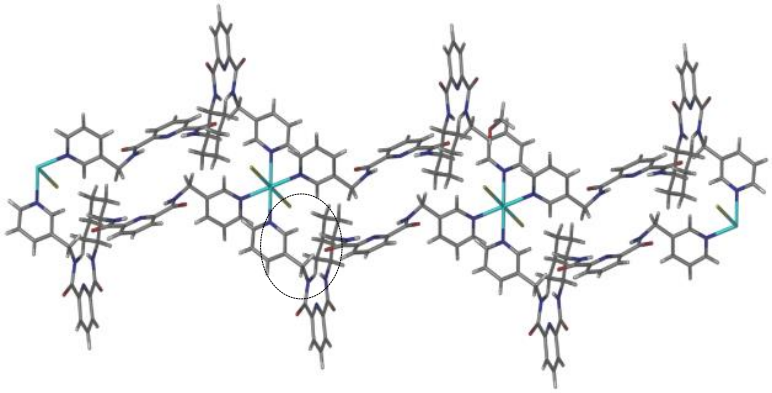


Figure 9. A perspective view of the extended structure of complex CP-L1

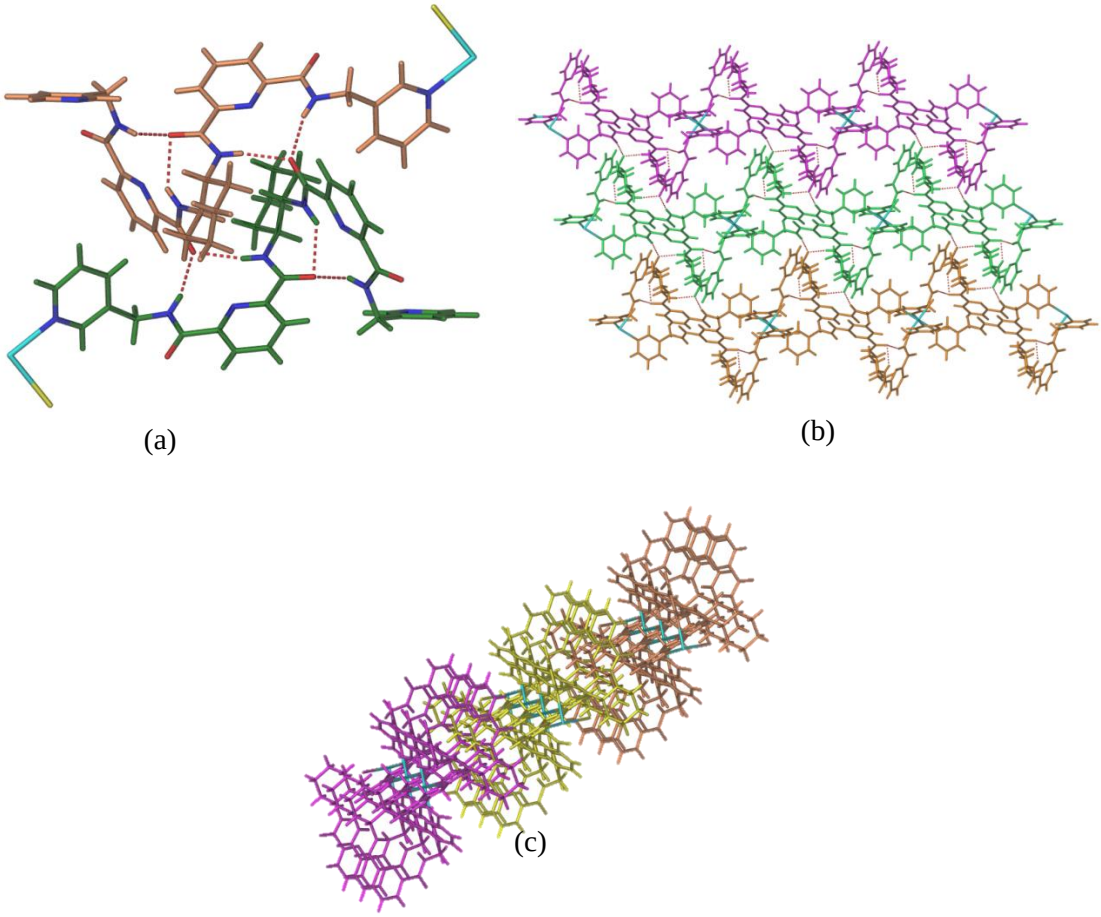


Figure 10. (a) A perspective view of intra- and the intermolecular hydrogen bonding in CP-L1 (b) The packing of 1-D coordination polymers into 2-D hydrogen bonded sheets (c) A perspective view of the crystal packing

Table 3. Weak hydrogen bonding of CP-L1

CP-L1	
N15-H15···O14	*d* = 2.201 Å, *D* = 2.953 Å
N49-H49···O14	*d* = 2.333 Å, *D* = 3.157 Å
N49-H49···N41	*d* =2.308 Å, *D* = 2.697 Å
N15-H15···N41	*d* = 2.251 Å, *D* = 2.663 Å
N-H···O	*d* = 2.380 Å ; *D* = 3.234
N-H···O	*d* = 2.107 Å ; *D* = 2.135 Å
N-H···O	*d* = 2.109 - 2.137 Å
N15-H15···O14	*d* = 2.249 - 2.445 Å

Table 4. Crystal data for L1, L2 and the CP-L1

Compound	**L1**	**L2**	**CP-L1**
Empirical formula	$C_{32}H_{32}N_8O_4$	$C_{32}H_{32}N_8O_4$	$C_{33}H_{36}BrCd_{0.50}N_8O_5$
Formula weight	592.66	592.66	760.81
Crystal system	Triclinic	Triclinic	Triclinic
Space group	*P*-1	*P*-1	*P*-1
a (Å)	9.0155(10)	13.0319(15)	9.4207(5)
b (Å)	12.1413(9)	15.1859(13)	11.4609(7)
c (Å)	13.7390(16)	16.7954(16)	16.1643(9)
α (º)	81.057(8)	111.971(8)	103.151(5)
β (º)	81.067(9)	103.352(9)	103.088(5)
γ (º)	78.114(8)	101.168(8)	97.360(5)
Volume ($Å^3$)	1441.9(3)	2965.8(5)	1625.38(16)
Z	2	4	2
Density (calculated) (Mg/m^3)	1.365	1.327	1.555
Absorption coefficient (mm^{-1})	0.094	0.091	1.638
F(000)	624	1248	778
Crystal size (mm^3)	0.30x0.13x0.09	0.35x0.08x0.04	0.20x0.08x0.04
Theta range for data (º)	2.91 – 29.86	2.47 – 28.24	2.57 – 29.94
Reflections collected	27261	34643	8454
Observed reflections [I>2s(I)]	7549	12267	5156
Data/restraints/parameters	7549/0/397	12267/0/793	8454/0/432
Goodness-of-fit on F^2	0.819	1.044	1.33
R_1 [I>2s(I)]	0.0604	0.0336	0.0485
wR_2 (all data)	0.2629	0.2629	0.1369
Largest diff. peak and hole ($e.Å^{-3}$)	0.194 and -0.213	1.369 and -0.775	1.049 and -0.727

Conclusion

In conclusion, two new 1,2-disubstituted cyclohexane amide ligands and one-dimensional coordination polymer were successfully prepared. L1 and L2 still maintained the pre-organisation of the 2,6-pyridine dicarboxamide in the solid states. X-ray crystallography also revealed that these three compounds crystallised in a triclinic crystal system with space group *P*-1. Several supramolecular interactions such as intramolecular and intermolecular hydrogen bonding interactions, π-π stacking interactions, C-H···π stacking interactions, and metal to ligand interactions were observed in the crystal structure in order to form a stable molecular architecture.

Acknowledgement

The authors thank the Ministry of Education of Malaysia and the Universiti Malaysia Terengganu for financial support through FRGS (vot. number 59579, FRGS/1/2019/STG01/UMT/02/3). The University of Adelaide is also acknowledged for the access to a single-crystal X-ray diffractometer for crystal-structure determination.

References

1. Lehn, J. M. (1988). Supramolecular chemistry-scope and perspectives molecules, supermolecules, and molecular devices (nobel lecture). *Angewandte Chemie International Edition in English*, 27(1): 89-112.

2. Lu, R., Zhang, X., Cheng, X., Zhang, Y., Zan, X. and Zhang, L. (2020). Medical applications based on supramolecular self-assembled materials from tannic acid. *Frontiers in Chemistry*, 8: 1-25.
3. Shuturminska, K., O'Malley, C., Collis, D. W. P., Conde, J. and Azevedo H.S. (2018). Displaying biofunctionality on materials through template self-assembly. *Self-Assembling Biomaterials*, 341-370.
4. Qin, B., Yin, Z., Tang, X., Zhang, S., Wu, Y., Xu, J. F. and Zhang, X. (2020). Supramolecular polymer chemistry: From structural control to functional assembly. *Progress in Polymer Science*, 100: 101167.
5. Deng, J. H., Luo, J., Mao, Y. L., Lai, S., Gong, Y. N., Zhong, D. C. and Lu, T. B. (2020). π-π Stacking interactions: Non-negligible forces for stabilizing porous supramolecular frameworks. *Science Advances*, 6(2): eaax9976.
6. Frey, P. A. (2004). Low barrier hydrogen bonds. *Encyclopedia of Biological Chemistry*, 2004: 594-598.
7. Wendler, K., Thar, J., Zahn, S. and Kirchner, B. (2010). Estimating the hydrogen bond energy. *The Journal of Physical Chemistry A*, 114: 9529-9536.
8. Castiñeiras, A., Fernández-Hermida, N., García-Santos, I., Gómez-Rodríguez, L., Gil, D. M. and Frontera, A. (2021). Supramolecular, spectroscopic and computational analysis of weak interactions in some thiosemicarbazones derived from 5-acetylbarbituric acid. *Journal of Molecular Structure*, 5: 131031.
9. Ghule, N. V., La, D. D., Bhosale, R. S., Kobaisi, M. A., Raynor, A. M., Bhosale, S. V. and Bhosale, S. V. (2016). Effect of amide hydrogen bonding interaction on supramolecular self-assembly of naphthalene diimideamphiphiles with aggregation induced emission. *ChemistryOpen*, 5(2): 157-163.
10. Rong, X., Lin, H., Liu, D., Wang, X., Liu, G. and Wang X. (2016). Solvothermal synthesis, structures and properties of two new octamolybdate-based compounds with tetrazole- and pyridyl-containing asymmetric amide ligands. *Inorganic Chemistry Communications*, 71: 9-14.
11. Haris, N. S. H., Mansor, N., Yusof, M. S. M., Sumby, C. J. and Kadir, M.A. (2021). Investigating the potential of flexible and pre-organized tetraamide ligands to encapsulate anions in one-dimensional coordination polymers: synthesis, spectroscopic studies and crystal structures. *Crystals*, 11: 77.
12. Yusof, M. S. M., Ayob, N. A. C., Kadir, M. A. and Yamin, B. M. (2008). 1, 2-bis [*N'*-(2, 2-dimethylpropionyl) thioureido] cyclohexane. *Acta Crystallographica Section E: Structure Reports Online*, 64(5): o937.
13. Shanmugharaj, A. M., Rhee, K. Y. and Ryu, S.H. (2006). Influence of dispersing medium on grafting of aminopropyltriethoxysilane in swelling clay materials. *Journal of Colloid and Interface Science*, 298(2): 854 -859.
14. Oprea, S., Potolinca, V. O. and Varganici, C. D. (2016). Synthesis and properties of polyurethane urea with pyridine-2,6-dicarboxamide moieties in their structure. *The Royal Society of Chemistry*, 6(108): 106904–106913.
15. Yalcin, S. P., Ceylan, U., Sarioglu, A. O. and Sonmez, M. (2015). Sythesis, structural, spectral (FT-IR, ^{1}H and ^{13}C NMR and UV-Vis), NBO and first order hyperpolarizability analysis of *N*-(4-nitrophenyl)-2, 2-dibenzoylacetamide by density functional theory. *Journal of Molecular Structure*, 1098: 400-407.
16. Basak, A., Ghosh, S. C., Das, A. K. and Bertolasi, V. (2005). A novel azetidinyl γ-lactam based peptide with a preference for β-turn conformation. *Organic and Biomolecular Chemistry*, 3: 4050-4052
17. Kushwaha, N., Saini, R. K. and Kushwaha, S. K. S. (2011). Synthesis of some amide derivatives and their biological activity. *International Journal of ChemTech Research*, 3(1): 203-209.
18. Ikawa, T., Nishiyama, T., Shigeta, T., Mohri, S., Morita, S., Takayanagi, S-I., Terauchi, Y., Morikawa, Y., Takagi, A., Ishikawa, Y., Fujii, S., Kita, Y. and Akai, S. (2011). *Ortho*-selective nucleophilic addition of primary aminesto silylbenzynes: synthesis of 2-silylanilines. *Angewandte Chemie*, 123: 5792-5795.

19. Hadadzadeh, H., Rezvani, A. R., Abdolmaleki, M. K., Ghasemi, K., Esfandiari, H. and Daryanavard, M. (2009). Pyridine-2,6-dicarboxylic acid (dipic): crystal structure from co-crystal to a mixed ligand nickel(II) complex. *Journal of Chemical Crystallography*, 40(1): 48-57.

20. Kadir, M. A., Yusof, M. S. M., Sumby, C. J (2018). Conjoint experimental and theoretical evaluation of zinc (II) coordination polymer as potential anion receptors for nitrate and chromate. *ASM Journal of Science*, 1: 136-146.

Malaysian Journal of Analytical Sciences (MJAS)
Published by Malaysian Analytical Sciences Society

SPECTROSCOPIC FINGERPRINTING COMBINED WITH CHEMOMETRICS FOR PESTICIDE RESIDUE SCREENING ON ORGANIC PRODUCE: A CASE STUDY OF CHILI

(Gabungan Cap Jari Spektroskopi dengan Kemometrik untuk Saringan Sisa Racun Perosak pada Hasil Organik: Kajian Kes ke atas Cili)

Intan Amirah Restu[1], Nur Fatin Zahra Mohamad Zhahir[1], Shum Mun-Hoe[1], Yong Chin Hong[1], Ng Jing Sheng[1], Syahidah Akmal Muhammad[1,2]*

[1]Environmental Technology Division, School of Industrial Technology, Universiti Sains Malaysia, 11800 USM, Penang, Malaysia
[2]Analytical Biochemistry Research Centre (ABrC), Inkubator Inovasi Universiti (I²U), Kampus SAINS@USM, Universiti Sains Malaysia, Lebuh Bukit Jambul, 11900 Bayan Lepas, Pulau Pinang

**Corresponding author: syahidah.muhammad@usm.my*

Received: 15 September 2021; Accepted: 30 December 2021; Published: 25 February 2022

Abstract

Pesticide detection for organic produce authentication requires laboratory work involving sample testing, which is generally arduous and time-consuming. In this study, a simple and reliable technique to produce an instant result for the pesticide screening of organic chili was developed, using attenuated total reflection-Fourier transform infrared (ATR-FTIR) spectroscopy. The resultant spectra observed in the region between 600-1800 cm^{-1} were further analyzed using principal component analysis (PCA) and orthogonal partial least square-discriminant analysis (OPLS-DA). Accordingly, the outcomes underline the potential for distinguishing chili samples sprayed with pesticides, such as cypermethrin, fenobucarb, and malathion, versus their organic counterparts. Furthermore, the models constructed by OPLS-DA were capable of classifying chili samples, yielding high-classification rates ranging between 91.67-100%. Thus, ATR-FTIR combined with chemometrics may be utilized as a potentially reliable screening tool for 'front-line' organic produce screening, where only flagged samples need to undergo further confirmation testing.

Keywords: chili, organic produce, pesticide screening, ATR-FTIR spectroscopy, principal component analysis

Abstrak

Pengesanan racun perosak untuk tujuan pengesahan hasil organik memerlukan kerja makmal yang melibatkan ujian sampel, yang biasanya sukar dan memakan banyak masa. Dalam kajian ini, satu teknik yang mudah dan berkesan dijalankan dengan menggunakan kaedah spektroskopi inframerah transformasi Fourier-pantulan keseluruhan dikecilkan (ATR-FTIR) bagi tujuan saringan racun perosak untuk sayuran cili organik. Spektrum yang dihasilkan dalam lingkungan antara 600-1800 cm^{-1} dianalisis dengan lebih lanjut dengan analisis komponen prinsipal (PCA) dan analisis ortagonal kuasa dua terkecil separa-diskriminan (OPLS-DA). Hasil kajian menunjukkan potensi yang baik dalam membezakan sampel cili yang disembur dengan racun perosak seperti cypermethrin, fenobucarb, dan malathion daripada sampel organik. Model yang dibina oleh OPLS-DA dapat

mengklasifikasikan sampel cili dengan kadar klasifikasi yang tinggi dalam lingkungan antara 91.67-100%. Oleh itu, penggabungan spektroskopi ATR-FTIR bersama aplikasi kimometrik dapat digunakan sebagai alat saringan yang berpotensi tinggi untuk pengesahan hasil organik, di mana hanya sampel yang dikenal pasti sahaja perlu menjalani ujian pengesahan dengan lebih lanjut.

Kata kunci: cili, hasil organik, saringan racun perosak, spektroskopi ATR-FTIR, analisis komponen prinsipal

Introduction

The demand for organic fruits and vegetables is growing in domestic and global markets alike, following consumers perceiving them as a healthier, safer, and more environmentally friendly option than non-organic types. Subsequently, there people have become increasingly apprehensive about the safety of the food that they consume on a daily basis. Accordingly, pesticide-free production is one of the most important factors influencing consumer preference for organic food options. Contrary to popular belief, however, some pesticides are permitted in organic farming as long as they have natural substances, such as hydrogen peroxide, lime sulfur, and copper sulfate, as ingredients [1]. Besides this, certain fairly low-risk synthetic pesticides are allowed in limited circumstances to manage pests and weeds, whereby their use markedly differs from the approach employed in non-organic farming.

It should be noted that organic fruits and vegetables may contain residues of synthetic pesticides, due to drift from neighboring non-organic farms or to irrigation contamination, originating at streams and groundwater polluted by synthetic fertilizers and pesticide runoff. According to the U.S. National Organic Program, the U.S. Environmental Protection Agency defines a level of tolerance in which organic claims are allowed for products containing synthetic pesticide residues as no more than 5% of said specified tolerance level [1]. In general, major manufactured pesticides are classified based on their chemical composition; examples include carbamates and dithiocarbamates, organophosphorus, and pyrethroids [2]. Malathion, an organophosphate insecticide, is especially prevalent as one of the oldest and widely-used active ingredients for pest control in fruits and vegetables [3]. Cypermethrin belongs to the class of pyrethroid insecticides, which are more effective and less toxic compared to organophosphates. Fenobucarb is a carbamate insecticide extensively implemented in controlling plant hopper, thrips, aphids, and whiteflies.

The increased utilization of pesticides has been associated with various health and environmental effects. Hence, maximum residue limits (MRLs) are defined by respective countries to monitor the level of pesticide chemical residues allowable in their food crops. The MRL represents the highest level of pesticide residue legally permitted in food crops [4]. In particular, the Malaysia Food Regulation 1985 in the 16th Schedule (Regulation 41) provides the MRLs for selected pesticides, as shown in Table 1. Standard techniques used for pesticide detection in fruits and vegetables, such as gas chromatography and high-performance liquid chromatography (HPLC), are often time-consuming and laborious. These methods necessitate sample destruction, lengthy test duration, controlled test conditions and expert lab skills, rendering them unsuitable for on-site analysis [5].

Therefore, a robust and quick technique capable of providing immediate results during organic produce screening for pesticides is currently necessary in the commercial world, particularly for the fast-moving consumer goods (FMCG) industry. As an alternative technique, attenuated total reflection-Fourier transform infrared (ATR-FTIR) spectroscopy represents an attractive option for pesticide detection in organic produce authentication, due to its non-destructive capability and portability, as well as its reliability in producing accurate results in a matter of minutes when combined with chemometrics [6]. Previous studies have shown that ATR-FTIR could be used to confirm the presence of organophosphate insecticides in vegetables [7]. Furthermore, data from several works also demonstrate the potential of ATR-FTIR, combined

with chemometrics, to solve adulteration and authentication issues for various food products, such as green tea, rice, and fruits [8, 9, 10].

Principal component analysis (PCA) is the most widely-used statistical procedure for interpreting large spectral data. As an unsupervised technique, it provides an overview of any patterns and groupings observable in studied samples, via a graphical representation in the form of 2D or 3D scatter plots [10]. However, it is not always possible to obtain differentiating features and adequate information directly from PCA models. On the other hand, supervised techniques such as orthogonal partial least squares-discriminant analysis (OPLS-DA) are often utilized to build classification models for further exploration of the data generated [11]. The combination of PCA and OPLS-DA may offer remarkable information for the classification and discrimination of the considered samples.

Chili (*Capsicum annuum L. var Kulai*) is one of the most widely cultivated and consumed vegetables in Malaysia [12]. The chili plant is highly susceptible to many diseases caused by insects, such as mites and thrips, resulting in the routine use of chemical insecticides to combat the problem. Therefore, this study aims to develop a screening method for the detection of pesticide presence in chili samples by using ATR-FTIR combined with chemometrics (PCA and OPLS-DA). The developed procedure can, thus, be utilized as a 'front-line' detection tool by food regulators prior to advanced laboratory testing, reserved only for flagged samples, resulting in cost and time-saving opportunities.

Table 1. The maximum residue limit for selected pesticides used in chili plant

Pesticide	**Molecular Formula**	**Classification**	**Maximum Residue Limit (mg/kg)**
Malathion	$C_{10}H_{19}O_6PS_2$	Organophosphate (OP)	2
Cypermethrin	$C_{22}H_{19}Cl_2NO_3$	Synthetic Pyrethroid (SP)	2
Fenobucarb	$C_{12}H_{17}NO_2$	Carbamate	0.5

Materials and Methods

Sample preparation

Three types of pesticides that were selected contained different concentrations and were in liquid form. The commercial pesticides, namely Wesco Malathion 57 (malathion, 57% w/w), Wesco Cyperin 550 (cypermethrin, 5.5% w/w), and Hoppergone (Fenobucarb, 50% w/w), were purchased from Volcano Agribusiness Sdn. Bhd. These pesticides were selected as they are frequently quantified in fruit and vegetable samples, and can be easily obtained from pesticide distributors [13]. The pesticides were diluted using distilled water, according to commercial formulations under Pesticides Act 1974, to replicate actual field conditions (Table 2). The prepared solutions were kept at room temperature and used within one week.

A total of 120 samples of organic chili (*Capsicum annuum L. var Kulai*) were purchased directly from a local certified farmer in Pulau Pinang. The farmer was aware of the aim of this study; hence the chance of including any fraudulent or inauthentic organic products in the dataset is minimized. The chili samples were left unwashed and randomly divided into four groups. In the first group, the chili samples were not treated and marked as group O (Organic). In the second, third and fourth groups, the chili samples were evenly sprayed with different pesticide solutions and marked as group M (Malathion), C (Cypermethrin), and F (Fenobucarb), respectively. All samples were left to dry for 2 hours so that the pesticide solution was evenly distributed over the surface of the chili prior to analysis.

Infrared spectroscopy measurements

The chili samples were scanned using a Perkin-Elmer Spectrum ATR-FTIR spectrophotometer. The equipment was connected to computer software

(Spectrum for Windows, Perkin-Elmer), and mid-infrared spectra were recorded in the wavenumber range of 4000-600 cm^{-1}, with a spectral resolution of 4 cm^{-1} at 16 scans. To simulate the on-site pesticide screening analysis, the whole chili was placed on the sample stage for direct measurement with no sample preparation. As a reference, the background spectrum of air was collected. Prior to each analysis, the ATR crystal surface was thoroughly cleaned with ethanol and wiped with clean tissue paper. The spectra for each of the three pesticide samples (cypermethrin, fenobucarb, and malathion) were also measured in ATR mode. Spectrum acquisition of each sample was repeated in triplicate under the same conditions, and an average spectrum was obtained.

Data pre-processing and chemometrics

Experimental data were subjected to chemometrics using SIMCA software (version 14.1, Umetrics, Sweden), wherein both unsupervised PCA and supervised OPLS-DA were performed for sample classification. The usual spectral region for mid-IR (4000-600 cm^{-1}) was observed and taken into account for the analysis; however, the fingerprint region between 1800-600 cm^{-1} was scrutinized further, due to this being the primary region where biomolecules absorb IR radiation [14]. Spectral pre-processing, such as first derivative transformation with third-degree polynomial, and standard normal variate (SNV) was applied to the IR data matrices to increase the predictive ability and accentuate any subtle features [15]. All variables were scaled and normalized using UV-scaling (unit variance) and log-10, respectively. The assessment of PCA's ability to detect and discriminate organic from pesticide-contaminated chili samples was made based on score plots observations, in which the principal component (PC) score plots were constructed using the first two resultant principal components. The OPLS-DA models were presented with several components based on the predictive performance from the internal sevenfold cross-validation by default, as suggested by the SIMCA software.

Table 2. Pesticide preparation according to commercial formulations

Pesticide	Amount Taken (mL)	Total Volume (solvent, mL)
Wesco Cyperin 550 (cypermethrin 5.5% w/w)	5	1000
Hoppergone (fenobucarb 50% w/w)	1.5	1000
Wesco Malathion 57 (malathion 57% w/w)	1.5	1000

Results and Discussion

ATR-FTIR spectral analysis of organic chili

The mid-FTIR spectrum of organic chili in the range of 4000-600 cm^{-1} is shown in Figure 1. As expected, the spectrum showed absorption bands corresponding to the vibrations of functional groups belonging to carotenoids, phenolic compounds and ascorbic acid, which corresponded to previously reported studies [16, 17]. A strong absorption band was observed at 3342.05 cm^{-1}, corresponding to characteristic stretching vibrations of O-H from amino acids. The small sharp cluster of peaks at 2900-2800 cm^{-1} was assigned to the C-H stretching band of methyl and methylene groups from the carboxylic acid structure. The medium-intensity peak at 1635 cm^{-1} corresponded to the C=O stretching, indicating the characteristic amide I band, while a low-intensity band at 1454 cm^{-1} was observed for the characteristic bending vibrations of C-H. The presence of polyphenols could be identified by the intense bands in the region of 1260-1180 cm^{-1}, caused by the stretching vibration of C-C-O and low-intensity C-H bending [16]. The functional groups associated with the absorption peaks identified from the spectra of the organic chili samples are summarized in Table 3.

ATR-FTIR spectral analysis of pesticides

The IR spectra of the three pesticides were also recorded to identify functional groups with unique absorption bands. As depicted in Figure 2, the green spectrum represents cypermethrin, the blue spectrum represents fenobucarb, and the red spectrum represents malathion. Each peak was contributed by a particular functional group present in the compound. In general, the pesticides revealed similar spectral patterns with a minimal shift of absorption band positions and intensity across the samples.

The C-H stretching in the two benzene rings of cypermethrin contributed to the stronger peaks within the wavenumber range of 3080–2820 cm^{-1}; thus, distinguishing this from the other two pesticides. The other, stronger peak which was more obvious for cypermethrin is the peak at 806 cm^{-1}, which is contributed by the C-Cl functional group, present in cypermethrin but not in fenobucarb or malathion. The peaks contributing to the fenobucarb cluster were mainly the N-H stretching at 3346 cm^{-1}, C=O stretching at 1718 cm^{-1}, C-O-C stretching at 1216 cm^{-1}, and C-N stretching at 1183 cm^{-1}. Malathion has a strong peak at 1013 cm^{-1}, mainly due to the presence of two P-O-C stretches. The P-O-C stretching was only observed in malathion as compared to cypermethrin and fenobucarb. Another prominent strong peak present only in malathion was observed at 654 cm^{-1}, mainly due to S=P-S-C stretching.

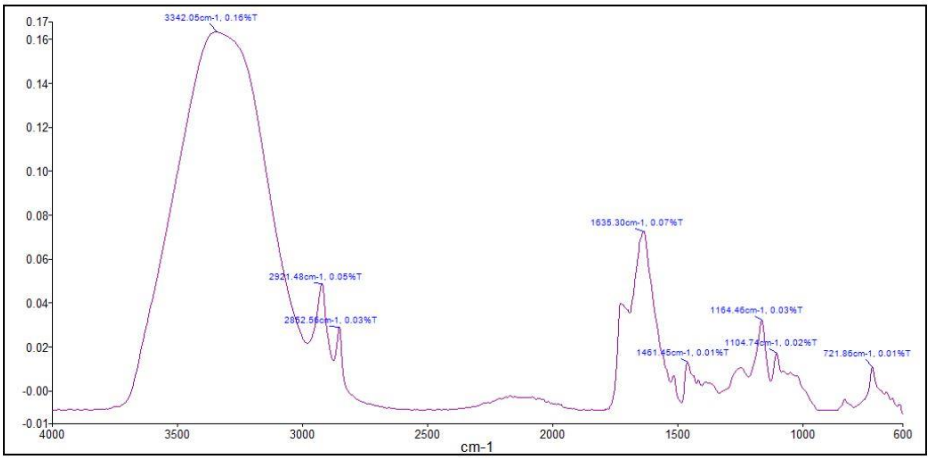


Figure 1. The FTIR spectrum of chili at wavenumber 4000-600 cm^{-1}

Table 3. The functional groups associated with absorption peaks identified in organic chili

Absorption Peak (cm^{-1})	**Possible Functional Group**
3342.05	O-H stretching from amino acids
2921.48 and 2852.56	C-H stretching (from CH_3 and CH_2 groups)
1635.3	C=O stretching of amide I band
1461.45	C-H bending
1164.46	C-C-O stretching
1104.74	C-H bending

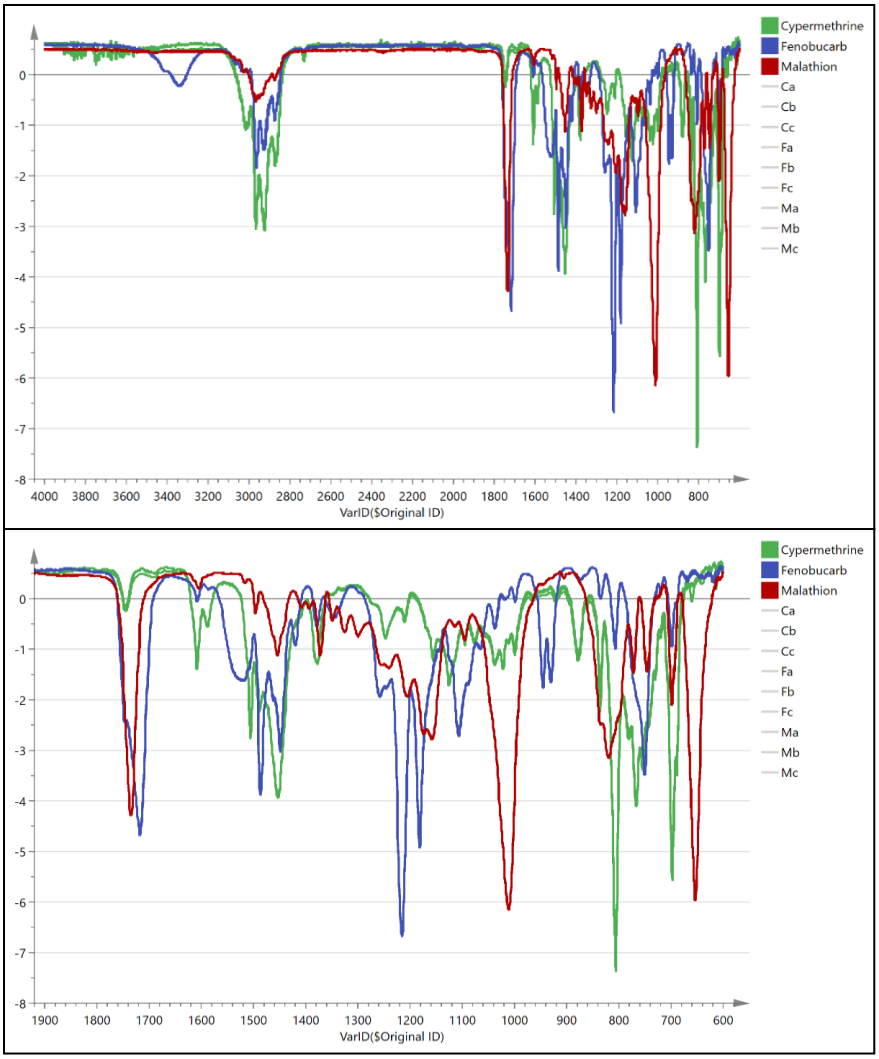


Figure 2. Full range FTIR spectra at wavenumber 4000–600 cm^{-1} (top) and the FTIR spectra enlarged at wavenumber 1900-600 cm^{-1} (bottom) for the three pesticides

Principal component analysis

Prior to analysis, the IR spectra of the chili samples were pre-processed to minimize data variation and overcome the dominating effect of strong peak absorbance over weaker absorbance intensity [18]. Selecting a proper spectral range may be beneficial in reducing the computational burden of the software in terms of variables. Hence, the spectral region 1800–600 cm^{-1} was selected for further analysis, due to the high positive correlations between changes in the composition and spectral response observed, which may be due to biomolecules' absorption of IR radiation occurring primarily in this region [14, 17].

As an unsupervised method, PCA was adopted for the initial exploratory data analysis, whereby the score plot reflected separation among the samples. PCA was applied to the dataset of 120 chili samples to detect outliers, as well as to predict possible patterns and trends of clustering. For a visual illustration and understanding, different classes of organic and pesticide samples were mapped and labeled with representative symbols. Figure 3(a) shows the score scatter plot for PCA overview using the first two principal components, PC1 (as in t1) and PC2 (as in t2). Most samples fell within Hotelling's T2 ellipse at

95% confidence intervals, with a few outliers. The combination of PC1 and PC2 explained 43.6% of the variation in the dataset. However, the organic and pesticide-contaminated samples could not be distinctly classified into two clusters, as some samples overlapped with each other. The presence of outliers may indicate experimental error due to sample preparation. Direct measurement of the samples without additional preparation may cause possible background noise, leading to inconsistencies.

PCA was performed further by plotting the individual score plots of each pesticide and organic sample, to allow better qualitative discrimination between sample groups. Results showed that a distinct separation into two clusters was observed in each of the scatter plots, meaning that PCA adequately captured relevant information within the dataset. As illustrated in Figure 3(b), the organic samples were well-segregated from cypermethrin-containing samples, with clearly defined clusters along PC2. When both PC1 and PC2 were combined, they contributed about 56.7% of the total variance, with some samples overlapping with each other. As for the outcome of PCA on organic samples and fenobucarb-containing samples (Figure 3(c), the result shows that the samples were well-distinguished, also mostly based on PC2. When both PC1 and PC2 were combined, these accounted for 57.5% of the total variance. Likewise, as shown in Figure 3(d), partially overlapping samples were observed in the score plot of organic and pesticide malathion-sprayed samples, with a total variance of 56.7%. This may be due to a low concentration of spiked malathion, making it difficult to differentiate between the IR spectra of both organic and pesticide-containing samples.

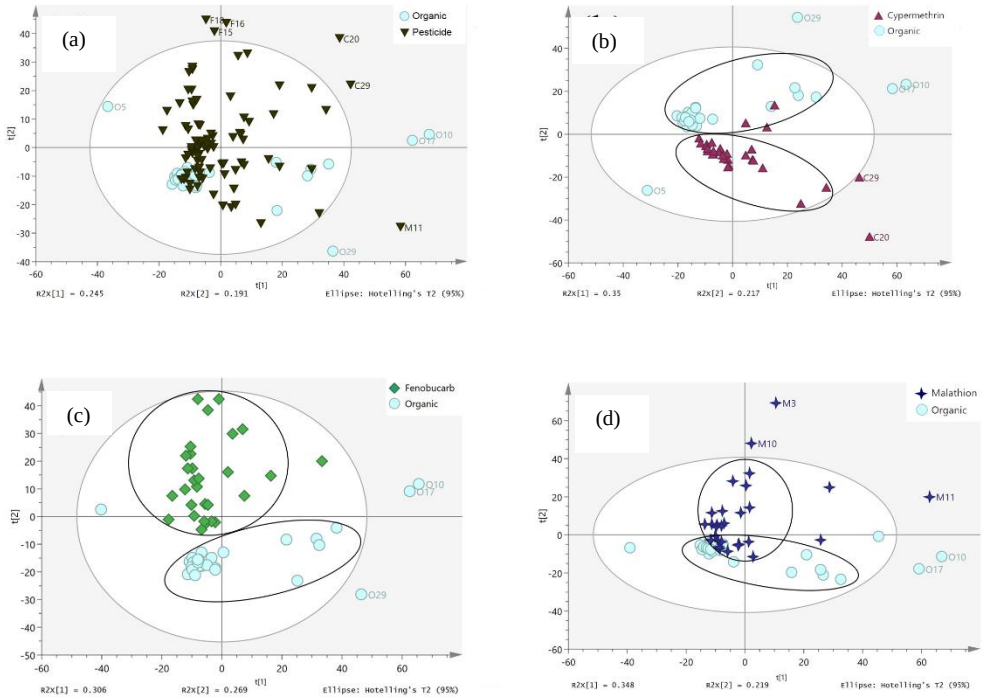


Figure 3. PCA score scatter plot based on PC1 and PC2 (a) organic and pesticide-contaminated samples, (b) organic and cypermethrin-contaminated samples, (c) organic and fenobucarb-contaminated samples, and (d) organic and malathion-contaminated samples

PCA was also performed on the IR spectra of neat cypermethrin, fenobucarb and malathion samples, to investigate the main variance among the three pesticides used in this study (Figure 4). The first two principal components explained 90.6% of data variation and showed observable clustering of the samples, according to the main active compound for the three pesticides.

Predictive models

As PCA had successfully distinguished the dataset into the observable cluster, a supervised OPLS-DA method was later performed using each dataset separately: organic with cypermethrin, organic with fenobucarb, and organic with malathion. The original dataset was divided into a training set and testing set, using an 80:20 ratio. Initially, 80% of the samples from the original dataset (24 samples from each class) were randomly selected as a training dataset, to build the predictive models aimed at differentiating organic and pesticide-contaminated chili samples. Classification rates were obtained from the internal sevenfold cross-validation by default in the SIMCA software. The remaining 20% of the samples (6 samples from each class) were set aside as an external validation test set, to evaluate the robustness of the predictive models. The overall efficiency of the models was assessed by observing the numbers of correctly and incorrectly assigned members of different classes for training and test datasets.

The score scatter plots displayed the samples by specific color-coded classes are shown in Figure 5. The four classes in the training set were organic chili (denoted as Organic Training Set), and organic chili that had been sprayed with pesticides: cypermethrin (denoted as Cypermethrine Training Set), fenobucarb (denoted as Fenobucarb Training Set), and malathion (denoted as Malathion Training Set). The scatter plots in OPLS-DA showed better separation between classes compared to PCA. As depicted in Figure 5, the samples in each cluster were more tightly grouped in OPLS-DA than in PCA.

The predictive model for organic and cypermethrin has a fitness of data (R^2) of 64.6%. The predictive ability (Q^2) was above moderate at 79.6%, with a total sum of variation ($R^2(Y)$) of 84.2%. The model for organic and fenobucarb has an R^2 of 62%, high predictive ability (Q^2) of 80.3%, and $R^2(Y)$ of 85.8%. For organic and malathion-contaminated samples, the predictive model has an R^2 of 78.1%, moderate Q^2 of 70.6%, and $R^2(Y)$ of 88.9%. The cross-validated analysis of variation (CV-ANOVA) for cypermethrin, fenobucarb, and malathion models reported *P*-values of 1.10×10^{-12}, 5.70×10^{-13}, and 3.15×10^{-7}, respectively. The results showed that the discrimination between organic and pesticide-contaminated chili samples was significant ($p < 0.05$).

The classification of the samples has been accurately performed (100% accuracy) for organic and cypermethrin models (Table 4), as well as organic and fenobucarb models (Table 5). In the case of organic and malathion models (Table 6), a single sample was misclassified into the organic class (91.67% accuracy), while all six organic chili samples fell accurately into their right cluster (100% accuracy). These results demonstrate the reliability of the models as a primary screening tool to detect the presence of pesticides in organic produce. It may help food regulators to ascertain whether the fruits or vegetables require further testing using more sophisticated instrumentation.

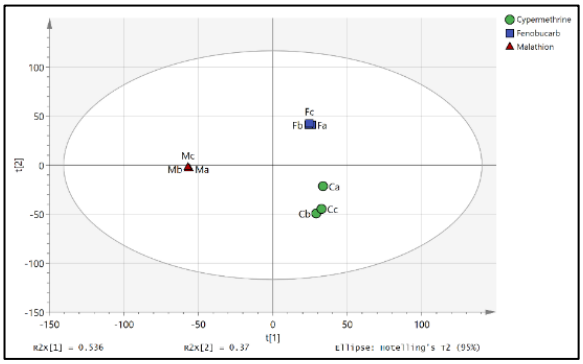


Figure 4. PCA score scatter plot according to the main active compound for the three pesticides

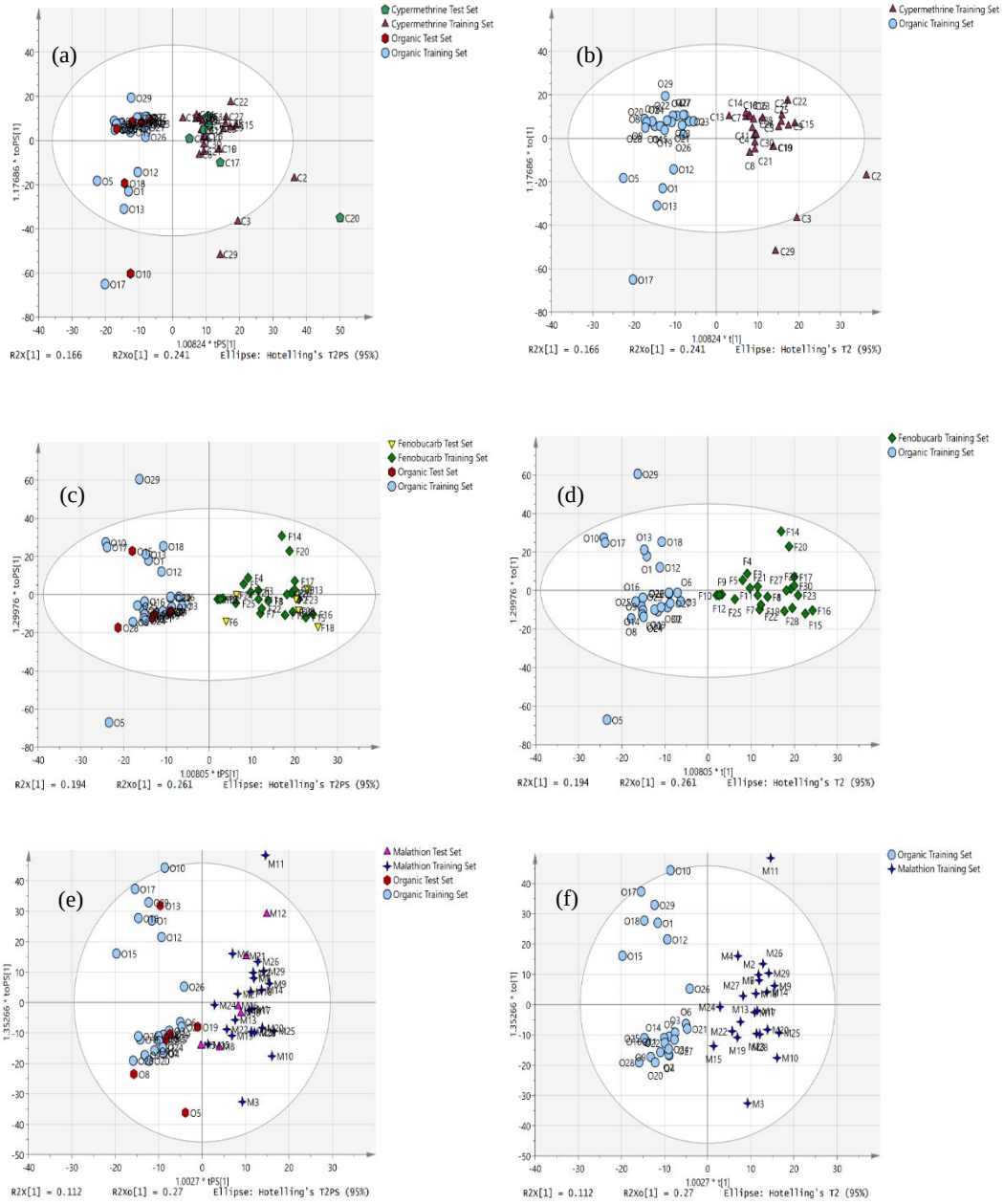


Figure 5. OPLS-DA scatter plots by the class of organic and pesticide-contaminated samples (a) training set for organic and cypermethrin, (b) predicted plot for organic and cypermethrin, (c) training set for organic and fenobucarb, (d) predicted plot for organic and fenobucarb, (e) training set for organic and malathion and (f) predicted plot for organic and malathion

Table 4. Misclassification table for organic and cypermethrin samples

	Members	Correct (%)	Organic Training Set	Cypermethrine Training Set
Organic Training Set	24	100	24	0
Cypermethrine Training Set	24	100	0	24
Test Set	12	100	6	6
Total	60	100	30	30

Table 5. Misclassification table for organic and fenobucarb samples

	Members	Correct (%)	Organic Training Set	Fenobucarb Training Set
Organic Training Set	24	100	24	0
Fenobucarb Training Set	24	100	0	24
Test Set	12	100	6	6
Total	60	100	30	30

Table 6. Misclassification table for organic and malathion samples

	Members	Correct (%)	Organic Training Set	Malathion Training Set
Organic Training Set	24	100	24	0
Malathion Training Set	24	100	0	24
Test Set	12	91.67	7	5
Total	60	100	31	29

Conclusion

The combination of ATR-FTIR and chemometrics can be utilized for preliminary screening of pesticides in organic produce, yielding benefits such as high speed, non-invasiveness, and simplicity of sample preparation. In general, distinguishing each pesticide was possible according to its functional groups, as analyzed by ATR-FTIR. Cypermethrin, for example, revealed stronger peaks contributed by C-H (from benzene rings) and C-Cl functional groups, whereas fenobucarb was identifiable by N-H stretching, C-O-C stretching, and C-N stretching. Malathion had strong peaks contributed by two P-O-C stretches and S=P-S-C stretching. The results also showed clear discrimination and classification between organic and pesticide-contaminated chili samples through PCA, and can be considered as a successful attempt, despite a few outliers observed in the process. With the use of OPLS-DA, it is possible to classify samples according to organic and pesticide-contaminated classes and predict

the residues of unknown pesticides. This study serves as an approach for pesticide screening of organic produce, thereby suggesting further investigation, based on the detection limit of pesticide residues for various fruit and vegetables, in ensuring more robust classification models.

Acknowledgment

The authors greatly acknowledge the funding provided by Universiti Sains Malaysia Bridging Grant (Khas) with Project Code: USM 304/PTEKIND/6316224, which has enabled this work to be conducted.

References

1. Winter, C. K. (2012). Pesticide residues in imported, organic, and "suspect" fruits and vegetables. *Journal of Agricultural and Food Chemistry*, 60(18): 4425-4429.
2. Akashe, M. M., Pawade, U. V. and Nikam, A. V. (2018). Classification of pesticides: A review. *International Journal of Research in Ayurveda and Pharmacy*, 9(4): 144-150.
3. Chatterjee, S., Das, S. K., Chakravarty, R., Chakrabarti, A., Ghosh, S. and Guha, A. K. (2010). Interaction of malathion, an organophosphorus pesticide with *Rhizopus oryzae* biomass. *Journal of Hazardous Materials*, 174(1–3): 47-53.
4. Munawar, A. and Hameed, S. W. (2013). Quantification of pesticide residues in vegetables by different chromatographic techniques. *Journal of Chromatography and Separation Techniques*, 4(8): 8-11.
5. Sadi, B. B., Vonderheide, A. P. and Caruso, J. A. (2004). Analysis of phosphorus herbicides by ion-pairing reversed-phase liquid chromatography coupled to inductively coupled plasma mass spectrometry with octapole reaction cell. *Journal of Chromatography A*, 1050(1): 95-101.
6. Ellis, D. I., Brewster, V. L., Dunn, W. B., Allwood, J. W., Golovanov, A. P. and Goodacre, R. (2012). Fingerprinting food: Current technologies for the detection of food adulteration and contamination. *Chemical Society Reviews*, 41(17): 5706-5727.
7. Xiao, G., Dong, D., Liao, T., Li, Y., Zheng, L., Zhang, D. and Zhao, C. (2015). Detection of pesticide (chlorpyrifos) residues on fruit peels through spectra of volatiles by FTIR. *Food Analytical Methods*, 8(5): 1341-1346.
8. Cheajesadagul, P., Arnaudguilhem, C., Shiowatana, J., Siripinyanond, A. and Szpunar, J. (2013). Discrimination of geographical origin of rice based on multi-element fingerprinting by high resolution inductively coupled plasma mass spectrometry. *Food Chemistry*, 141(4): 3504-3509.
9. Liu, Z., Yuan, Y., Zhang, Y., Shi, Y., Hu, G., Zhu, J. and Rogers, K. M. (2019). Geographical traceability of Chinese green tea using stable isotope and multi-element chemometrics. *Rapid Communications in Mass Spectrometry*, 33(8): 778-788.
10. Sârbu, C., Nacu-Briciu, R. D., Kot-Wasik, A., Gorinstein, S., Wasik, A. and Namieśnik, J. (2012). Classification and fingerprinting of kiwi and pomelo fruits by multivariate analysis of chromatographic and spectroscopic data. *Food Chemistry*, 130(4): 994-1002.
11. Cubero-Leon, E., De Rudder, O. and Maquet, A. (2018). Metabolomics for organic food authentication: Results from a long-term field study in carrots. *Food Chemistry*, 239(555): 760-770.
12. Lob, S., Aris, M. N. M., Sidique, S. N. M., Ibrahim, N. F. and Jin, X. (2017). Growth development and natural infection incidence of tobacco mosaic virus (TMV) on silicon-treated chilli (*Capsicum annuum* L.) cultivated in commercial soil. *Malaysian Applied Biology*, 46(3): 221-226.
13. Zaidon, S. Z., Hamsan, H. and Bin, H. Y. (2016). A review on pesticides occurrence in fruits and vegetables in Malaysia and their potential health risk among adults. *Indian Journal of Environmental Protection*, 36(10): 826-832.
14. Skolik, P., McAinsh, M. R. and Martin, F. L. (2019). ATR-FTIR spectroscopy non-destructively detects damage-induced sour rot infection in whole tomato fruit. *Planta*, 249(3): 925-939.

15. Devos, O., Downey, G. and Duponchel, L. (2014). Simultaneous data pre-processing and SVM classification model selection based on a parallel genetic algorithm applied to spectroscopic data of olive oils. *Food Chemistry*, 148: 124–130.
16. Ciulu-Costinescu, F., Neamţu, J., Popescu, M., Chirigiu, L., Simionescu, A., Bubulică, M. V. and Belu, I. (2015). Preliminary analysis of *Capsicum annuum* L. extracts. *Current Health Sciences Journal*, 41(4): 311-316.
17. Domínguez-Martínez, I., Meza-Márquez, O. G., Osorio-Revilla, G., Proal-Nájera, J. and Gallardo-Velázquez, T. (2014). Determination of capsaicin, ascorbic acid, total phenolic compounds and antioxidant activity of *Capsicum annuum* L. var. serrano by mid infrared spectroscopy (Mid-FTIR) and chemometric analysis. *Journal of the Korean Society for Applied Biological Chemistry*, 57(1): 133-142.
18. Ismail, D., Rahimi, A., Wan Ishak, W. R., Mahat, N. A. and Mat Desa, W. N. S. (2021). Classification model for detection and discrimination of inedible plastic adulterated palm cooking oil using ATR-FTIR spectroscopy combined with principal component analysis. *Malaysian Journal of Analytical Sciences*, 25(3): 388-398.

Malaysian Journal of Analytical Sciences (MJAS)
Published by Malaysian Analytical Sciences Society

ELICITATION OF INDUCED POLYKETIDE COMPOUNDS FROM A CO-CULTURE BETWEEN *Streptomyces* sp. STRAIN SUK10 AND *Fusarium* sp. AND THEIR ANTIBACTERIAL ACTIVITIES

(Elisitasi Sebatian Poliketida Teraruh daripada Satu Kultur-bersama di antara *Streptomyces* sp. Strain SUK10 dan *Fusarium* sp. dan Aktiviti Antibakteria)

Muhammad Asyraf Zawawi[1], Nurul Izzati Rosdi[1], Noor Wini Mazlan[1,2]*, Mariam Taib[1], Kamariah Bakar[2], Noraziah Mohamad Zin[3], Siti Nordahliawate M. Sidique[4], Saif Aldeen Mohammad Fayiz Jaber[5], RuAngelie Edrada-Ebel[5]

[1]Faculty of Science and Marine Environment
[2]Institute of Marine Biotechnology
Universiti Malaysia Terengganu, 21030 Kuala Nerus, Terengganu, Malaysia
[3]Center for Diagnostic, Therapeutic and Investigative Studies, Faculty of Health Sciences,
Universiti Kebangsaan Malaysia, Jalan Raja Muda Abd Aziz, 50300 Kuala Lumpur, Malaysia
[4]Faculty of Fisheries and Food Science,
Universiti Malaysia Terengganu, 21030 Kuala Nerus, Terengganu, Malaysia
[5]Strathclyde Institute of Pharmacy and Biomedical Sciences,
University of Strathclyde, The John Arbuthnott Building, 161 Cathedral Street, Glasgow G4 0RE, Scotland

**Corresponding author: noorwini@umt.edu.my*

Received: 3 November 2021; Accepted: 30 December 2021; Published: 25 February 2022

Abstract

Endophytes including bacteria and fungi produce an array of biologically active secondary metabolites. Different approaches have been applied in order to increase the probability production of new metabolites including mimicking the environment, media and the microbes. However, the use of single culture usually re-produces known compounds with known bioactivities. Therefore, co-culturing between *Streptomyces* sp. strain SUK10 and *Fusarium* sp. in the same media at different growth stages leads to direct interaction which may trigger the expression of "silent" biosynthetic pathway to produce novel secondary metabolites. In this study, we elicited the production of the unknown secondary metabolites from co-culture extracts by using high resolution liquid chromatography-mass spectrometry, while data was processed by utilizing the quantitative expression analysis software MZmine 2.40.1 and SIMCA P+ 15.0 coupled with macro analysis and supported with DNP database for dereplication studies. The results showed that only the extract from co-culture of F7S15 showed enhances antibacterial activity on the Gram-positive bacteria with minimum inhibition concentration (MIC) values of 5 mg/mL and 10 mg/mL against *Micrococcus* sp. and *Staphylococcus aureus*, respectively, compared with their independent and other co-culture extracts were non-active. However, all extracts were non-active on the Gram-negative bacteria. Our preliminary results showed that the potential of co-culture method leading the production of novel metabolites which could be explored for future antibacterial agents.

Keywords: co-culture, metabolomics, liquid chromatography-mass spectrometry, multivariate analysis, dereplication

Abstrak

Endofit termasuk bakteria dan fungus menghasilkan satu tatasusunan metabolit sekunder yang mempunyai keaktifan biologi. Pelbagai pendekatan telah digunakan bagi tujuan meningkatkan kebarangkalian penghasilan metabolit baru termasuk mengajuk persekitaran, media dan mikrob. Walaubagaimanapun, penggunaan kultur tunggal selalumya menghasilkan semula sebatian dengan bioaktiviti yang telah diketahui. Oleh itu, satu pengkulturan bersama di antara *Streptomyces* sp. strain SUK10 dan *Fusarium* sp. di dalam media yang sama di peringkat pertumbuhan yang berbeza, memacu kepada interaksi yang mungkin pencetus kepada ungkapan laluan biosintetik senyap untuk menghasilkan metabolit sekunder baru. Dalam kajian ini, kami telah memperolehi penghasilan metabolit sekunder yang belum diketahui daripada ekstrak kultur bersama dengan menggunakan kromatografi cecair-spektrometri jisim resolusi tinggi, sementara itu data telah dianalisis menggunakan perisian analisis ungkapan kuantitatif MZmine 2.40.1 dan SIMCA P+ 15.0 beserta analisis makro dan disokong oleh pengkalan data DNP bagi kajian dereplikasi. Keputusan telah menunjukkan bahawa hanya ekstrak daripada kultur bersama F7S15 telah menunjukkan peningkatan aktiviti antibakteria ke atas bakteria Gram-positif dengan nilai minimum kepekatan perencatan (MIC) 5 mg/mL dan 10 mg/mL melawan *Micrococcus* sp. dan *Staphylococcus aureus*, masing-masing, berbanding ekstrak kutur bebas dan kultur bersama yang lain adalah tidak aktif. Walaubagaimanapun, semua ekstrak tidak aktif ke atas bakteria Gram-negatif. Keputusan awal kajian kami telah menunjukkan potensi kaedah kultur bersama memacu penghasilan metabolit baru yang boleh diterokai bagi agen antibakteria masa hadapan.

Kata kunci: kultur bersama, metabolomik, kromatografi cecair-spektrometri jisim, analisis multivariat, dereplikasi

Introduction

Natural products have been rich sources of therapeutic agents as they inspire the advancement of synthetic methodologies to allow the possibility of making analogues of original lead compounds with improved pharmaceutical properties. For example, the secondary metabolites obtained from endophytic microbes are found to have antimicrobial, antiviral, anticancer, antioxidants, antidiabetic and immunosuppressant properties. The endophytic fungi and bacteria are known to produce these types of natural products that are potent for antibiotics [1]. They live inside the living plant tissues for at least a part of their life without causing any apparent disease symptoms in the host. Various bioactive metabolites are produced by endophytes that are proven to have potential to be anticancer, antioxidant, antifungal, antibacterial, antiviral and anti-insecticidal [2]. The induction of secondary metabolites is triggered by the interaction between the microorganisms, simulating the microbial competition for nutrition and space. Besides, the cultivation of the microbes is sustainable and reproducible in laboratory conditions. A well-known drugs-producer *Streptomyces* sp. belonging to actinobacteria varies in structures and has a great potential to be developed as therapeutic drugs for human use [3]. *Streptomyces* sp. is an aerobic, Gram-positive mycelial bacteria that disperse sporse as a method of reproduction and can develop branching vegetative hyphae in which the mycelium helps in scavenging nutrients from the surroundings [4]. *Streptomyces* sp. is able to synthesise potent secondary metabolites for medical applications such as antibiotics, herbicidal, antiparasitic, antitumor, antifungal and enzyme inhibiting agents as well as having the ability to inhibit various human pathogens including gancidin W [5], divergolides A-D [6], polycyclic anthraquinones [7], cyclic dipeptide [8-10] and xiamycin [11]. Meanwhile, a pathogenic fungus *Fusarium* sp. produces metabolites including naphthoquinones [12, 13], pyrones [14-16] and indole-acetic acids [17], naphthalenone derivatives [18] and aminobenzamide [19].

However, the discovery of new potential bioactive metabolites from independent cultures is challenging due to re-isolation of the known compounds with the same reported bioactivity. The re-occurrence of the known metabolites from an independent culture either of *Streptomyces* sp. SUK10 or *Fusarium* sp. may lead to similar bioactivities. Therefore, a co-culture method is introduced to challenge different strains instead of

individual strains. A co-culture is a process of culturing of two or more different microorganisms that mimic the complex microbial habitat in nature where they co-exist, leading to competition among them due to limited source and antagonism. Microbial community is a complex and dynamically changing consortium in which metabolic interactions between microbial species take place. The interaction between microbial communities often involves exchange of molecules for nutritional purposes that may benefit one or both species, which is known as symbiosis [20]. The co-cultures of different microbes in comparison to mono-cultures are increasingly being used in microbial natural product research as the interaction of two different microbes can increase the availability of existing natural products or may induce the expression of silent biosynthetic pathways resulting in new metabolites that are useful in the medical field [21].

A co-cultivation between *Streptomyces* sp. SUK10 and *Fusarium* sp. at different growth stages was carried out. Present study, the metabolomics approach was used to predict and identify potential novel bioactive components from the crude extracts, leading to the rapid and high-throughput assessment of metabolites. Metabolite profiling of the active metabolites in crude extracts of natural sources was supported by dereplication in which the novel compounds from the active groups were differentiated from known compounds that have been studied previously [22]. The dereplication method is a process for screening the known metabolites from the crude extracts before further scale-up or isolation work is undertaken, in order to avoid repetitive work.

High-resolution electrospray ionisation-liquid chromatography-mass spectrometry (HRESI-LCMS) data from both positive and negative ionisation modes were subjected to multivariate statistical analysis including unsupervised principal component analysis (PCA) and orthogonal partial least squares-discriminant analysis (OPLS-DA) to establish the optimal position of the discriminating plane, which would best separate classes. The high-resolution mass spectral data generated predicted molecular formulas used for dereplication of the secondary metabolites found in the crude extracts. Later in the final step of the metabolomics approach, the selected unique biomarkers were interpreted to putatively identify the novel metabolite using databases like Dictionary of Natural Products (DNP). The ultimate aim of this study was to fast track the identification of the metabolites from the co-culture extracts, which can lead to the decision-making of the optimum parameter for up-scaling of targeted metabolites responsible for biological activities. In future, the targeted metabolites will be isolated and absolute elucidation and identification of the molecule structures will be achieved using one and two dimensional-nuclear magnetic resonance (NMR) and high-resolution mass spectrometry (MS).

Materials and Methods

Preparation of microbial samples

A stock culture of *Streptomyces* sp. strain SUK10 was obtained from the Novel Antibiotics Laboratory, Programme of Biomedical Sciences, Faculty of Health Sciences, Universiti Kebangsaan Malaysia (UKM), Kuala Lumpur, while *Fusarium* sp. was obtained from the culture collection of Fungus Laboratory, Central Laboratory, Universiti Malaysia Terengganu (UMT). *Streptomyces* sp. SUK10 was originally isolated from the barks of *Shorea ovalis* [5] and *Fusarium* sp. was isolated from the roots of *Avicennia lanata* collected from Setiu Wetlands, Terengganu [13]. A 5 mm x 5 mm diameter plug containing *Fusarium* sp. mycelium was cut from the edge of the colony and placed in the middle of a new malt agar plate to establish a fresh and pure colony. The plates were incubated at 27 ± 2 °C (Vindon Scientific Ltd., UK) for 7-15 days. Meanwhile, *Streptomyces* sp. SUK10 was streaked onto fresh ISP2 agar plates and incubated at room temperature for 7-15 days.

Independent cultures

The International Streptomyces Project (ISP) medium was prepared by adding 10.0 g of malt extract, 4.0 g of D-(+)-glucose monohydrate, 4.0 g of yeast extract and 1 L of distilled water, vigorously shaken until completely mixed and dissolved. The pH was adjusted ranging at 7.2-7.4 using 10% NaOH or 36.5% HCl, and autoclaved at 121 ℃ for 15 minutes. The independent

cultures of *Streptomyces* sp. strain SUK10 and *Fusarium* sp. were achieved in which each active growing strain on the agar plate was cut into small cubes and transferred separately into seven 500 mL Erlenmeyer flasks containing 100 mL of ISP medium. The cultures were incubated in an orbital shaker and shaken at 150 rpm and 28 °C for 7 and 15 days (seven replicates). The metabolites were extracted twice with equal volumes of ethyl acetate, homogenised and filtered. The organic layer was discarded into a 500 mL round bottom flask using liquid-liquid extraction technique to obtain an organic solvent that was then concentrated under vacuum using a rotary evaporator (Büchi, Switzerland) to afford crude extracts ± 10.0 mg. The crude extracts were kept at 4 °C prior to analysis.

Co-cultivation between *Streptomyces* sp. strain SUK10 and *Fusarium* sp.

The co-cultivation between *Streptomyces* sp. strain SUK10 and *Fusarium* sp. was achieved including sets FS7, FS15, F7S15, and S7F15. The co-cultivation of sets FS7 and FS15 were obtained by mixing the agar cubes containing active growing *Streptomyces* sp. strain SUK10 and *Fusarium* sp. at initial incubation in the ISP broth. The incubation of co-cultivation of set FS7 was continued until day 7, while the co-cultivation of set FS15 was incubated until day 15. The co-cultivation of set F7S15 was obtained in which the agar plugs containing *Streptomyces* sp. strain SUK10 were introduced into the *Fusarium* sp. culture after 7 days of incubation, and the incubation was continued until day 15. The co-cultivation of set S7F15 was obtained in which the agar plugs containing *Fusarium* sp. mycelia were introduced into the *Streptomyces* sp. strain SUK10 culture after 7 days of incubation, and the incubation was also continued until day 15. A 100 mL of ISP broth was used for each culture and the incubation was done in an orbital shaker at 150 rpm and 28 °C (seven replicates). The metabolites were extracted twice with equal volumes of ethyl acetate, homogenised, and filtered. The organic layer was discarded into a 500 mL round bottom flask using liquid-liquid extraction technique to obtain an organic solvent that was then concentrated under vacuum using a rotary evaporator (Büchi, Switzerland) to afford crude extracts ± 15.0 mg. The crude extracts were kept at 4 °C prior to analysis.

Dereplication using HRESI-LCMS

The dereplication strategy on the crude extracts was performed using HRESI-LCMS and processed with the MZmine software 2.40.1, an in-house macro coupled with the Dictionary of Natural Products (DNP) 2015 and SIMCA P+ 15.0 (Umetrics AB, Umeå, Sweden). The procedure and programme for HRESI-LCMS was set up as described here [23]. 1 mg/mL of each extract was dissolved in methanol and analysed on an Accela HPLC (Thermo Scientific, UK) coupled with a UV detector at 280 and 360 nm and an Exactive-Orbitrap high-resolution mass spectrometer (Thermo Scientific, UK). A methanol blank was also analysed. The mass spectral data was processed using the procedure by MacIntyre et al. [23] which was established in the Natural Products Metabolomics Group Laboratory at Strathclyde Institute of Pharmacy and Biomedical Sciences (SIPBS) as described here [13, 23]. The LC-MS chromatograms and spectra were viewed using Thermo Xcalibur 2.1 or MZmine 2.40.1.

Antibacterial activity using agar disk-diffusion

An antibacterial activity of the extracts from independent and co-cultures was conducted using the agar disk-diffusion method as described here [24]. Each extract was diluted with 2-fold dilutions in dimethyl sulfoxide (DMSO) with concentration values of 0.156 mg/mL, 0.313 mg/mL, 0.625 mg/mL, 1.25 mg/mL, 2.50 mg/mL, 5.00 mg/mL and 10 mg/mL. The inhibition zone diameter (IZD) was measured to the nearest millimetres. Minimum inhibitory concentration (MIC) was taken as the lowest concentration of the extracts that shows the inhibition zone. MIC values of the extracts against the Gram-positive and Gram-negative bacteria were determined by averaging the results of three independent assays. Six strains of Gram-positive bacteria namely *Staphylococcus aureus*, *Bacillus cereus* and *Micrococcus* sp. and Gram-negative bacteria - *Vibrio cholera*, *Salmonella* sp. and *Escherichia coli* from glycerol stock were obtained from the Microbiology Laboratory, Institute of Marine Biotechnology, UMT.

Statistical analysis

All data were presented as mean ± SD and statistically analysed with One-Way ANOVA in the comparison between selected fractions using statistical analyses software PRISM ver. 5. Data were significantly different at $p < 0.05$.

Results and Discussion

Dereplication study on crude extracts

Each extract was screened on antibacterial activity at different concentrations: 10 mg/mL to 0 mg/mL. The inhibition zone diameter (IZD) was measured to the nearest millimetres. The results showed that the minimum inhibition concentration (MIC) values of the extracts against the Gram-positive and Gram-negative bacteria were determined by averaging the results of three independent assays (Table 1). The co-culture extract F7S15 revealed marginal antibacterial activity on *Micrococcus* sp. and *S. aureus* with MIC values of 5 mg/mL and 10 mg/mL, respectively, as compared to the non-active independent and other co-culture extracts. Meanwhile, the antibacterial activity on the Gram-negative bacteria showed that all extracts were non-active in this screening test, thereby supporting further investigation of the biologically-active compounds from the co-cultivation extracts.

Total ion chromatogram for the extract of co-cultivation between *Streptomyces* sp. strain SUK10 and *Fusarium* sp. F7S15 (Figure 1) showed the distribution of known and unknown compounds present in the extract (Table 2). The dereplication studies revealed that the co-culture extract F7S15 possessed certain types of compounds including macrocylic aromatic compounds such as macrolide- oligomycin A and cyclic peptolides-icosalide A1 and A3, which have also been previously isolated from different *Streptomyces* and fungi species, respectively (Table 2). The values and predicted formulas of unknown compounds are also shown (highlighted rows). The extracts of co-cultivation between *Streptomyces* sp. strain SUK10 and *Fusarium* sp. as well as the independent cultures were preliminarily screened on antibacterial activity and subjected to HRESI-LCMS prior to multivariate analysis. A dereplication study was performed to obtain the metabolomic profile of each extract.

The relationship between the occurrence of the metabolites in the independent and co-cultivation extracts and their bioactivity on antibacterial activity were evaluated through multivariate analysis. The PCA scores plot showed strong separation of the extracts (Figure 2a). There was clear separation between the co-culture extract of F7S15 from other extracts. The PCA loadings plot (Figure 2b) predicted the metabolites in the extracts. Meanwhile, a supervised multivariate OPLS-DA score plot analysis (Figure 2c) exhibited a distinctive separation between the active extract F7S15, while other extracts were the non-active group. These predicted antibacterial active compounds by MVA were indicated with their MZmine IDs as listed in Table 2. Peak IDs used in this table corresponded to those designated for the chromatogram as shown in Figure 1.

Table 1. Antibacterial activity for independent and co-culture extracts (calculated as mean value percentage viability) at different concentrations ranging at 10 mg/mL to 0 mg/mL. Highlighted rows showed enhanced antibacterial activity

Extracts	**Concentration of Crude Extract (mg/mL)**						
	***Micrococcus* sp.**						
	0.156	0.313	0.625	1.25	2.50	5.00	10.00
	Diameter of inhibition (mm)						
F7	n.d	n.d	n.d	n.d	n.d	n.d	n.d
F15	n.d	n.d	n.d	n.d	n.d	n.d	n.d
S7	n.d	n.d	n.d	n.d	n.d	n.d	n.d
S15	n.d	n.d	n.d	n.d	n.d	n.d	
FS7	n.d	n.d	n.d	n.d	n.d	n.d	n.d
FS15	n.d	n.d	n.d	n.d	n.d	n.d	n.d
F7S15	n.d	n.d	n.d	n.d	n.d	7.5 ± 0.6	8.7 ± 0.5
S7F15	n.d	n.d	n.d	n.d	n.d	n.d	8.0 ± 0
Oxytetracycline (30 µg)	35.7 ± 0.2						
	Staphylococcus aureus						
F7	n.d	n.d	n.d	n.d	n.d	n.d	n.d
F15	n.d	n.d	n.d	n.d	n.d	n.d	n.d
S7	n.d	n.d	n.d	n.d	n.d	n.d	n.d
S15	n.d	n.d	n.d	n.d	n.d	n.d	n.d
FS7	n.d	n.d	n.d	n.d	n.d	n.d	n.d
FS15	n.d	n.d	n.d	n.d	n.d	n.d	n.d
F7S15	n.d	n.d	n.d	n.d	n.d	n.d	n.d
S7F15	n.d	n.d	n.d	n.d	n.d	n.d	8.0 ± 0
Oxytetracycline (30 µg)	26.0 ± 1.4						

*Legend: extracts F7 = mono-culture *Fusarium* sp. incubation day 7; F15 = mono-culture *Fusarium* sp. incubation day 15; S7 = mono-culture *Streptomyces* sp. SUK10 incubation day 7; S15 = mono-culture *Streptomyces* sp. SUK10 incubation day 15; F7S15 = co-cultivation between *Fusarium* sp. and *Streptomyces* sp. SUK10 in which *Streptomyces* sp. SUK10 was added into *Fusarium* sp. culture after 7 days incubation and the incubation was continued until day 15; S7F15 = co-cultivation between *Fusarium* sp. and *Streptomyces* sp. SUK10 in which *Fusarium* sp. was added into *Streptomyces* sp. SUK10 culture after 7 days incubation and the incubation was continued until day 15; n.d: not detected; n=3.

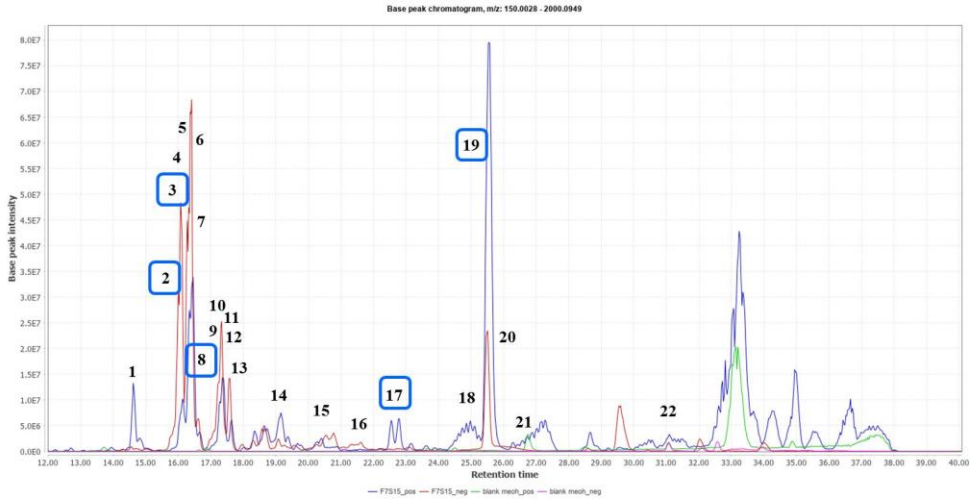


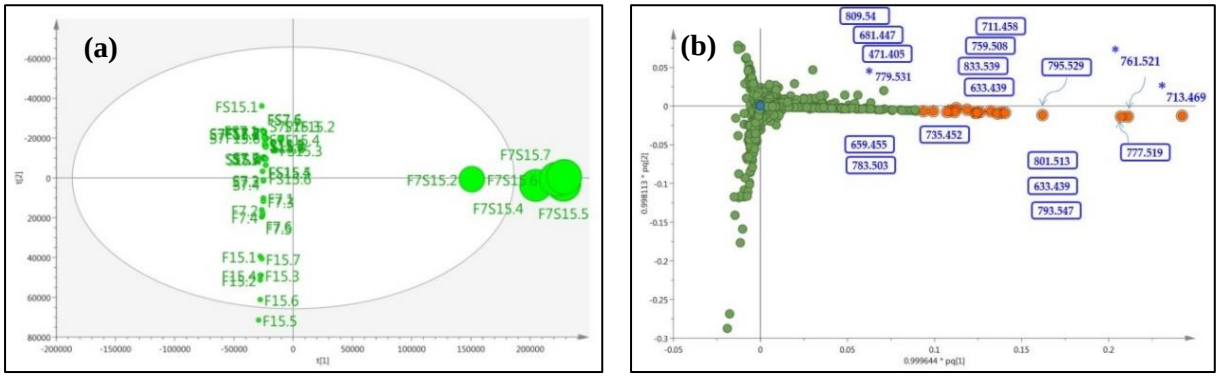
Figure 1. Total ion chromatogram for the extract of co-cultivation between *Streptomyces* sp. strain SUK10 and *Fusarium* sp. F7S15 (blue and red represent positive and negative ionization modes of F7S1 extract, respectively; green and pink represent positive and negative ionization modes of blank methanol, respectively). Dereplication of numbered peaks is shown on Table 1. Boxed in blue are the metabolites putatively identified using DNP database.

Table 2. List of compounds indicated on the total ion chromatogram for the extract of co-cultivation between *Streptomyces* sp. strain SUK10 and *Fusarium* sp. F7S15 that were putatively identified using DNP database. Peak IDs used in this table correspond to those designated for the chromatogram shown on Figure 1. Highlighted rows represent the unknown compounds as indicated with their MZmine IDs.

Peak ID	ESI Modes/ MZmine ID	Rt (min)	MS (*m/z*)	Molecular Weight	Chemical Formula	Chemical Name	Tolerance (ppm)	Sources	Peak Area
1	P_22521	14.58	274.2015	273.1943	$C_{14}H_{27}NO_4$	No hits			1.27E+08
2	N_2411	16.03	795.5293	796.5361	$C_{41}H_{80}O_{12}S$	bovine seminolipid	-1.1324	bovine spermatozoa	6.10E+08
3	P_21220	16.04	779.5308	778.5235	$C_{44}H_{74}O_{11}$	narasin D	0.5015	*Strep. aureofaciens*	2.75E+08
4	N_2409	16.19	633.4391	634.4464	$C_{30}H_{64}N_6O_4P_2$	No hits			3.81E+08
	N_2441	16.33	777.5188	778.5258	$CH_5NO_{15}P_4S_{12}$	No hits			8.40E+08
6	P_21679	16.35	801.5129	800.5056	$C_{10}N_3O_6PS_{16}$	No hits			3.80E+08
7	N_2435	16.36	759.5081	760.5154	$C_6HN_5O_3P_6S_{12}$	No hits			3.00E+08
8	P_21649	16.45	761.5204	760.5135	$C_{44}H_{72}O_{10}$	oligomycin A; 26-Demethyl, 12-deoxy	1.2529	*S. aureofaciens*	8.62E+08
9	N_2422	17.26	659.4550	660.4622	$C_{40}H_{70}OP_2S$	No hits			1.89E+08
10	P_21450	17.28	793.5469	792.5396	$C_2H_{18}NO_3P_{15}S_7$	No hits			4.10E+08
11	P_22522	17.32	833.5393	832.5320	$C_5H_9N_3O_8P_{14}S_5$	No hits			3.36E+08
12	N_2495	17.33	809.5449	810.5525	$C_2H_2N_3O_{19}P_9S_5$	No hits			2.12E+08
13	N_2496	17.58	777.5192	778.5264	$C_{38}H_{72}N_{10}O_3P_2$	No hits			1.69E+08

Table 2 (cont'd). List of compounds indicated on the total ion chromatogram for the extract of co-cultivation between *Streptomyces* sp. strain SUK10 and *Fusarium* sp. F7S15 that were putatively identified using DNP database. Peak IDs used in this table correspond to those designated for the chromatogram shown on Figure 1. Highlighted rows represent the unknown compounds as indicated with their MZmine IDs.

Peak ID	ESI Modes/ MZmine ID	Rt (min)	MS (*m/z*)	Molecular Weight	Chemical Formula	Chemical Name	Tolerance (ppm)	Sources	Peak Area
14	P_22523	19.10	783.5023	782.4957	$C_2H_4N_5O_5P_3S_{16}$	No hits			1.90E+08
15	N_2511	20.79	1556.0436	1557.0510	$C_{46}H_{88}N_9O_2P_9S_{15}$	No hits			1.11E+08
16	N_2549	21.62	1589.0730	1590.0803	$C_{41}H_{74}N_{14}O_{20}P_4S_{12}$	No hits			4.41E+07
17	P_22525	22.74	685.4392	684.4319	$C_{34}H_{60}N_4O_{10}$	icosalide A3	1.3669	fungus OSI 74159	9.07E+07
18	N_2408	25.38	711.4578	712.4649	$C_{38}H_{56}N_{12}O_2$	No hits			4.31E+08
19	P_21186	25.48	713.4698	712.4622	$C_{36}H_{64}N_4O_{10}$	icosalide A1	-0.1214	*Aureobasidium* sp. fungus OSI 59166	1.27E+09
20	N_2410	25.46	681.4474	682.4547	$C_{34}H_{63}N_6O_6P$	No hits			2.87E+08
21	P_21721	26.85	471.4048	470.3975	$C_{23}H_{51}N_8P$	No hits			8.99E+08
22	P_23269	31.03	523.3828	522.3755	$C_{27}H_{54}O_9$	1-Heptacosene-4,6,8,10,12,14,16, 18,24-nonol	-2.3912		4.07E+05



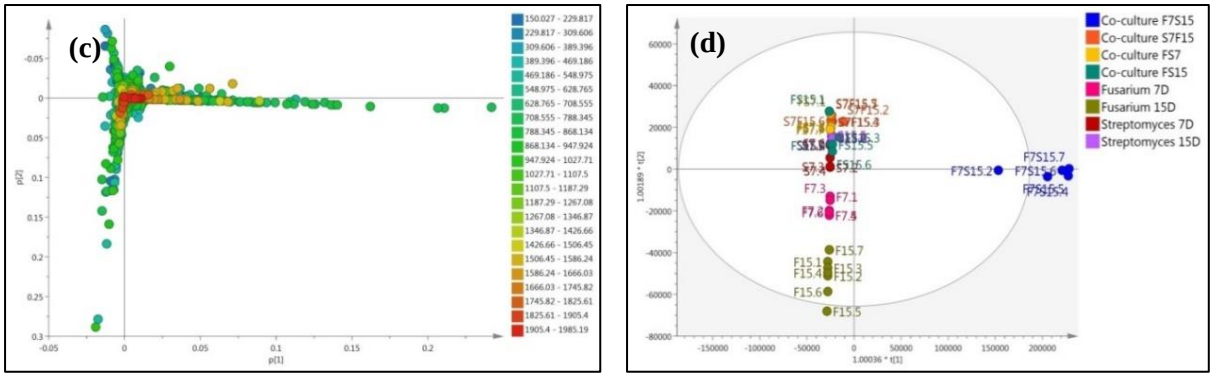
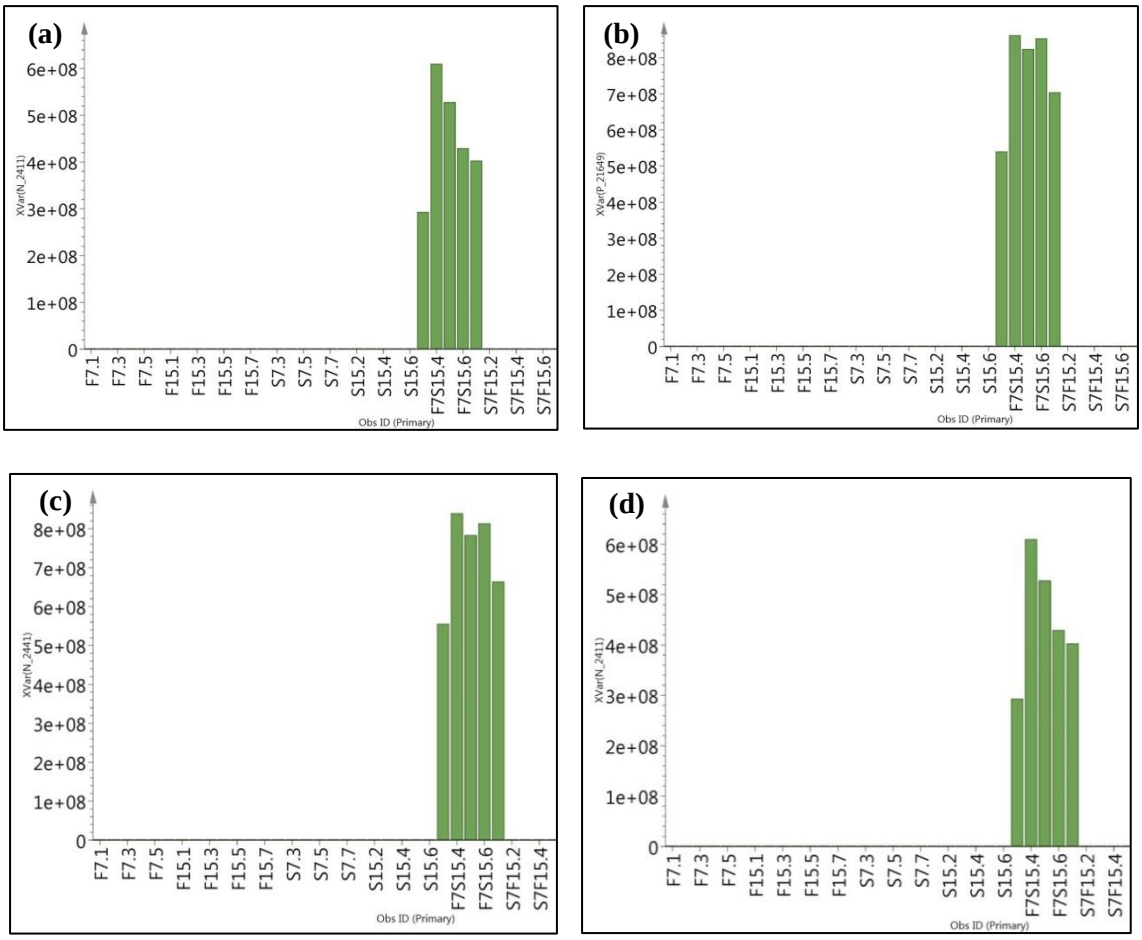


Figure 2. (a) Unsupervised PCA scores plot of mono- and co-cultivation extracts showed distinctive separation between the datasets. (b) PCA loadings plot showed the discriminating metabolites within the extracts. (c) OPLS-DA scores scatter plot of the extracts ($R^2(Y)$ = 1.00; Q^2 =0.998); Q^2(Y intercept). (d) Supervised OPLS-DA loadings plot showed the discriminating metabolites of the active co-culture extract F7S15 within the extracts. Asterisk specifies the identified metabolites from where the respective active extract F7S15. Legend: set F7.1-F7.7 = mono-culture *Fusarium* sp. incubation day 7; set F15.1-F15.7 = mono-culture *Fusarium* sp. incubation day 15; set S7.1-S7.7 = mono-culture *Streptomyce*s sp. SUK10 incubation day 7; S15.1-S15.7 = mono-culture *Streptomyces* sp. SUK10 incubation day 15; set F7S15.1-F7S15.7 = co-cultivation between *Fusarium* sp. and *Streptomyces* sp. SUK10 in which *Streptomyces* sp. SUK10 was added into *Fusarium* sp. culture after 7 days incubation and the incubation was continued until day 15; set S7F15.1-S7F15.7 = co-cultivation between *Fusarium* sp. and *Streptomyces* sp. SUK10 in which *Fusarium* sp. was added into *Streptomyces* sp. SUK10 culture after 7 days incubation and the incubation was continued until day 15, n=7.

The OPLS-DA loadings plot (Figure 2d) exhibited the discriminating metabolites in the active group F7S15 in which the ion peaks at *m/z* $[M+H]^+$ 713.469, 761.521, and 801.513 as well as *m/z* $[M-H]^-$ 777.519, 795.529, and 633.439 were outliers, indicating the presence of unique chemical profiles in the F7S15 extract. From the DNP database, it was putatively determined that the F7S15 extract contained polyketide and aromatic compounds [25-28] that perhaps contributed towards the antibacterial activity of F7S15. Some of the ion peaks in the F7S15 extract have been dereplicated as presented in Table 1. Characteristic metabolite for co-culture F7S15 extract observed at *m/z* $[M+H]^+$ 713.469 were putatively identified as icosalide A1, which has been identified from an *Aureobasidium* sp. fungus OSI 59166 [26, 29]. The ion peaks at *m/z* $[M+H]^+$ 761.521 and 779.531 were putatively identified as oligomycin A; 26-demethyl, 12-deoxy, and narasin D, respectively. Both compounds were isolated from *Streptomyces aureofaciens* [30, 31]. The *m/z* $[M-H]^-$ 795.529 was putatively identified as bovine seminolipid, which has been isolated from bovine spermatozoa [32]. Meanwhile, the ion peaks at *m/z* $[M+H]^+$ 801.513 and *m/z* $[M-H]^-$ 777.519 and 633.439 were the unidentified metabolites that were only produced in the active co-culture extract F7S15. The relative occurrence of the targeted putatively identified and unknown metabolites in the bioactive extract F7S15 is shown in Figure 3. Based on the predicted chemical formula of the unknown compounds, they may consist of at least one nitrogen atom that contributes to the presence of macrocyclic polyketide-membered rings. Isolation of polyketide compounds from *Streptomyces* sp. under normal condition is widely known [5, 33-35], and perhaps the discovery of most antibiotics in the market are from this species. However, the world is facing a multidrug resistant against bacteria. Thus, dual cultivation of different strains used in our preliminary study may enlighten the opportunity to discover more potential new drug candidates that could be further

explored. The optimization works in this study showed that the co-cultivation of F7S15 produced promising metabolites with enhanced antibacterial activity, which can be further scaled up to obtain larger volume extracts for isolation and identification of target metabolites that were absent in their parent culture. Our future study will focus on the identification of molecule structures of the unknown metabolites by using tandem mass spectrometry (MS/MS) analysis and one/two-dimensional nuclear magnetic resonance (1D/2D NMR) spectroscopy.



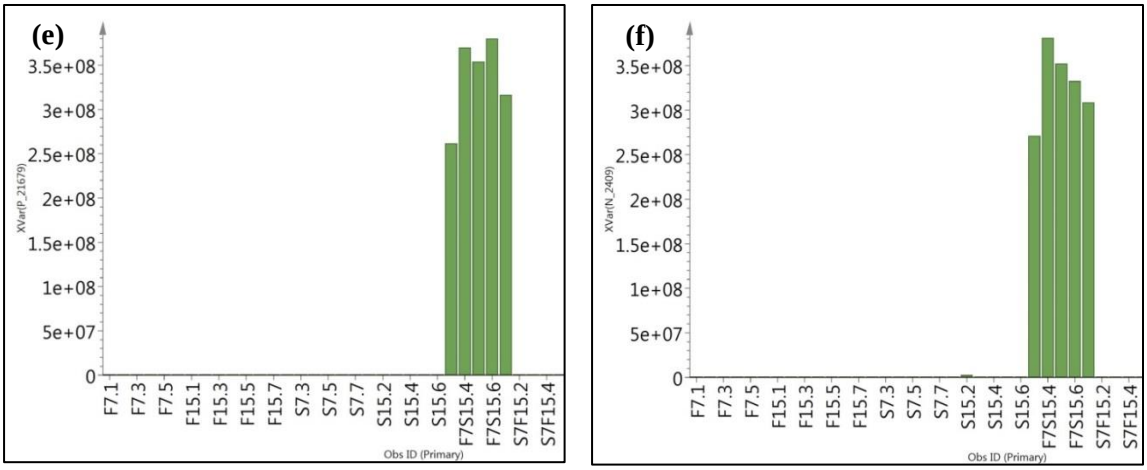


Figure 3. Relative abundance of target metabolites (a-f) which only present in the active co-culture extract of F7S15. Asterisk specifies the identified metabolites from where the respective active extract F7S15. (a) P_21186: *m/z* = 713.469, RT = 25.48 min; (b) P_21649: *m/z* = 761.521, RT = 16.45 min; (c) N_2496: *m/z* = 777.519, RT = 17.58 min; (d) N_2411: *m/z* = 795.529, RT = 16.03 min; (E) P_21679: *m/z* = 801.513, RT = 16.35 min; (F) N_2409: *m/z* = 633.439, RT = 16.19 min

Conclusion

The main aims in this study were to establish an optimum parameter to target and pinpoint the bioactive secondary metabolites directly from the extracts that were absent in the independent culture and subsequently imply the same parameter in the scale-up of the co-cultivation. By means of high-resolution liquid chromatography-mass spectrometry, the extracts obtained from mono- and co-cultivation were preliminarily screened for bioactive molecules and analyzed by multivariate analysis such as PCA and OPLS-DA. Dereplication study was used to screen the known metabolites and predict the novelty metabolites from the extracts which were not detected in single cultures, to avoid repetitive work on the same compounds with known bioactivity. Our future study will focus on the scale-up and isolation works of the targeted active metabolites from co-culture extract F7S15. In addition, identification of the molecule structures will be achieved using 1D and 2D-nuclear magnetic resonance (NMR) and high-resolution mass spectrometry (MS).

Acknowledgement

We wish to thank the Ministry of Higher Education Malaysia for the grant awarded to Noor Wini Mazlan FRGS/1/2018/STG05/UMT/03/2. The research described in this study has been done in IMB and Central Laboratory, UMT. The authors would like to thank Siti Aisha Mohd Radzi for assisting in the sample preparation.

References

1. Christina, A., Christapher, V. and Bhore, S. J. (2013). Endophytic bacteria as a source of novel antibiotics: an overview. *Pharmacognosy Reviews,* 7(13): 11.
2. Sarasan, M., Puthumana, J., Job, N., Han, J., Lee, J. S. and Philip, R. (2017). Marine algicolous endophytic fungi-a promising drug resource of the era. *Journal of Microbiology and Biotechnology*, 27(6): 1039-1052.
3. Berdy, J. (2005). Bioactive microbial metabolites. *The Journal of Antibiotics*, 58(1): 1-26.
4. Chater K. F., Losick, R. and Shapiro, L. (1984). Microbial development. *Cold Spring Habor Laboratory, Cold Spring Habor, New York*: pp. 89-116.
5. Zin, N. M., Baba, M. S., Zainal-Abidin, A. H., Latip, J., Mazlan, N. W. and Edrada-Ebel, R. (2017). Gancidin W, a potential low-toxicity antimalarial agent isolated from an endophytic Streptomyces SUK10. *Drug Design, Development and Therapy*, 11: 351.

6. Gao, H., Li, G. and Lou, H. X. (2018). Structural diversity and biological activities of novel secondary metabolites from endophytes. *Molecules*, 23(3): 646.
7. Liang, Y., Xie, X., Chen, L., Yan, S., Ye, X., Anjum, K., Huang, H. Lian, X. and Zhang, Z. (2016). Bioactive polycyclic quinones from marine Streptomyces sp. 182SMLY. *Marine Drugs,* 14(1): 10.
8. Cheng, C., Othman, E. M., Stopper, H., Edrada-Ebel, R., Hentschel, U. and Abdelmohsen, U. R. (2017). Isolation of petrocidin A, a new cytotoxic cyclic dipeptide from the marine sponge-derived bacterium Streptomyces sp. SBT348. *Marine Drugs,* 15(12): 383.
9. Gondry, M., Lautru, S., Fusai, G., Meunier, G., Ménez, A. and Genet, R. (2001). Cyclic dipeptide oxidase from *Streptomyces noursei*: Isolation, purification and partial characterization of a novel, amino acyl α, β-dehydrogenase. *European Journal of Biochemistry*, 268(6): 1712-1721.
10. Saadouli, I., Zendah El Euch, I., Trabelsi, E., Mosbah, A., Redissi, A., Ferjani, R. and Ouzari, H. I. (2020). Isolation, characterization and chemical synthesis of large spectrum antimicrobial cyclic dipeptide (l-leu-l-pro) from *Streptomyces misionensis* V16R3Y1 bacteria extracts. A novel ^{1}H NMR metabolomic approach. *Antibiotics*, 9(5): 270.
11. Ding, L., Münch, J., Goerls, H., Maier, A., Fiebig, H. H., Lin, W. H. and Hertweck, C. (2010). Xiamycin, a pentacyclic indolosesquiterpene with selective anti-HIV activity from a bacterial mangrove endophyte. *Bioorganic & Medicinal Chemistry Letters*, 20(22): 6685-6687.
12. Khan, N., Afroz, F., Begum, M. N., Rony, S. R., Sharmin, S., Moni, F. and Sohrab, M. H. (2018). Endophytic *Fusarium solani*: A rich source of cytotoxic and antimicrobial napthaquinone and aza-anthraquinone derivatives. *Toxicology Reports*, 5: 970-976.
13. Mazlan, N. W., Tate, R., Yusoff, Y. M., Clements, C. and Edrada-Ebel, R. (2020). Metabolomics-guided isolation of anti-trypanosomal compounds from endophytic fungi of the mangrove plant A*vicennia lanata*. *Current Medicinal Chemistry*, 27(11): 1815-1835.
14. Zhen, X., Mao, M. J., Wang, R. Z., Chang, S. S., Xiao, T. M., Wu, Y. X., Yu, Y., Song, Y. L., Chen, M. H. and Si, S. Y. (2021). Fusapyrone A, a γ-pyrone derived from a desert *Fusarium* sp. *Journal of Asian Natural Products Research*, 23(5): 504-511.
15. Choi, H. G., Song, J. H., Park, M., Kim, S., Kim, C. E., Kang, K. S. and Shim, S. H. (2020). Neuroprotective γ-pyrones from Fusarium Solani JS-0169: Cell-based identification of active compounds and an informatics approach to predict the mechanism of action. *Biomolecules*, 10(1): 91.
16. Gao, H., Li, G., Peng, X. P. and Lou, H. X. (2020). Fupyrones A and B, two new α-pyrones from an endophytic fungus, *Fusarium* sp. F20. *Natural Product Research*, 34(3): 335-340.
17. Luo, K., Rocheleau, H., Qi, P. F., Zheng, Y. L., Zhao, H. Y. and Ouellet, T. (2016). Indole-3-acetic acid in Fusarium graminearum: Identification of biosynthetic pathways and characterization of physiological effects. *Fungal Biology*, 120(9): 1135-1145.
18. Xiao, W. J., Chen, H. Q., Wang, H., Cai, C. H., Mei, W. L. and Dai, H. F. (2018). New secondary metabolites from the endophytic fungus Fusarium sp. HP-2 isolated from "Qi-Nan" agarwood. *Fitoterapia*, 130: 180-183.
19. Ibrahim, S. R., Mohamed, G. A., Al Haidari, R. A., Zayed, M. F., El-Kholy, A. A., Elkhayat, E. S. and Ross, S. A. (2018). Fusarithioamide B, a new benzamide derivative from the endophytic fungus *Fusarium chlamydosporium* with potent cytotoxic and antimicrobial activities. *Bioorganic & Medicinal Chemistry*, 26(3): 786-790.
20. Rodrigues Reis, C. E., Ogero D'Otaviano, L., Rajendran, A. and Hu, B. (2018). Co-culture of filamentous feed-grade fungi and microalgae as an alternative to increase feeding value of ethanol coproducts. *Fermentation*, 4(4): 86.
21. Kamdem, R. S., Wang, H., Wafo, P., Ebrahim, W., Özkaya, F. C., Makhloufi, G. and Proksch, P. (2018). Induction of new metabolites from the endophytic fungus *Bionectria* sp. through bacterial co-culture. *Fitoterapia*, 124: 132-136.

22. Harvey A. L., Edrada-Ebel, R. and Quinn, R. J. (2015). The re-emergence of natural products for drug discovery in the genomics era. *Nature Reviews Drug Discovery*, 14(2): 111-129.
23. Macintyre, L., Zhang, T., Viegelmann, C., Martinez, I. J., Cheng, C., Dowdells, C. and Edrada-Ebel, R. (2014). Metabolomic tools for secondary metabolite discovery from marine microbial symbionts. *Marine Drugs*, 12(6): 3416-3448.
24. Assaw, S., Mohd Amir, M. I. H., Khaw, T. T., Bakar, K., Mohd Radzi, S. A. and Mazlan, N. W. (2020). Antibacterial and antioxidant activity of naphthofuranquinones from the twigs of tropical mangrove Avicennia officinalis. *Natural Product Research*, 34(16): 2403-2406.
25. Chan, W. Y., Hickey, E. E., Khazandi, M., Page, S. W., Trott, D. J. and Hill, P. B. (2020). *In vitro* antimicrobial activity of narasin and monensin in combination with adjuvants against pathogens associated with canine otitis externa. *Veterinary Dermatology*, 31(2): 138-e26.
26. Boros, C., Smith, C. J., Vasina, Y., Che, Y., Dix, A. B., Darveaux, B. and Pearce, C. (2006). Isolation and identification of the icosalides--cyclic peptolides with selective antibiotic and cytotoxic activities. *Journal of Antibiotics*, 59(8): 486-494.
27. Dose, B., Niehs, S. P., Scherlach, K., Flórez, L. V., Kaltenpoth, M. and Hertweck, C. (2018). Unexpected bacterial origin of the antibiotic icosalide: two-tailed depsipeptide assembly in multifarious *Burkholderia* symbionts. *ACS Chemical Biology*, 13(9): 2414-2420.
28. Lysenkova, L. N., Saveljev, O. Y., Omelchuk, O. A., Zatonsky, G. V., Korolev, A. M., Grammatikova, N. E. and Shchekotikhin, A. E. (2020). Synthesis, antimicrobial and antiproliferative properties of epi-oligomycin A, the (33 S)-diastereomer of oligomycin A. *Natural Product Research*, 34(21): 3073-3081.
29. Jenner, M., Jian, X., Dashti, Y., Masschelein, J., Hobson, C., Roberts, D. M. and Challis, G. L. (2019). An unusual *Burkholderia gladioli* double chain-initiating nonribosomal peptide synthetase assembles 'fungal'icosalide antibiotics. *Chemical science*, 10(21): 5489-5494.
30. Khebizi, N., Boudjella, H., Bijani, C., Bouras, N., Klenk, H. P., Pont, F. and Sabaou, N. (2018). Oligomycins A and E, major bioactive secondary metabolites produced by *Streptomyces* sp. strain HG29 isolated from a Saharan soil. *Journal de Mycologie Medicale*, 28(1): 150-160.
31. Anadón, A. and Martínez-Larrañaga, M. R. (2014). Veterinary drugs residues: coccidiostats: 63-75.
32. Alvarez, J. G., Storey, B. T., Hemling, M. L., & Grob, R. L. (1990). High-resolution proton nuclear magnetic resonance characterization of seminolipid from bovine spermatozoa. *Journal of Lipid Research*, 31(6): 1073-1081.
33. Bekiesch, P., Oberhofer, M., Sykora, C., Urban, E. and Zotchev, S. B. (2019). Piperazic acid containing peptides produced by an endophytic *Streptomyces* sp. isolated from the medicinal plant *Atropa belladonna*. *Natural Product Research*, 35(7): 1090-1096.
34. Cho, E., Kwon, O. S., Chung, B., Lee, J., Sun, J., Shin, J. and Oh, K. B. (2020). Antibacterial activity of chromomycins from a marine-derived *Streptomyces microflavus*. *Marine Drugs*, 18(10): 522.
35. Qureshi, K. A., Bholay, A. D., Rai, P. K., Mohammed, H. A., Khan, R. A., Azam, F. and Prajapati, D. K. (2021). Isolation, characterization, anti-MRSA evaluation, and in-silico multi-target anti-microbial validations of actinomycin X2 and actinomycin D produced by novel S*treptomyces smyrnaeus* UKAQ_23. *Scientific Reports*, 11(1): 1-21.

Malaysian Journal of Analytical Sciences (MJAS)
Published by Malaysian Analytical Sciences Society

THE CONJUGATION AND CHARACTERISATION OF THERMORESONSIVE POLY (*N*-ISOPROPYLACRYLAMIDE) WITH TERNATIN BIOMOLECULE

(Konjugasi dan Pencirian Poli (*N*-Isopropilakrilamida) dengan Biomolekul Ternatin)

Adrina Zulkifli, Farahiyah Najah Ab Samad, Nukman Ameen Rosli, Nurul Aina Jamaluddin, Nor Nadiah Mohamad Yusof, Noor Faizah Che Harun*

Green Chemistry and Sustainable Engineering Technology, Polymer Technology Section, Universiti Kuala Lumpur (UniKL) MICET, Lot 1988, Kawasan Perindustrian Bandar Vendor, Taboh Naning, 78000 Alor Gajah, Melaka, Malaysia

**Corresponding author: noorfaizah@unikl.edu.my*

Received: 15 September 2021; Accepted: 4 January 2022; Published: 25 February 2022

Abstract

Poly (*N*-isopropylacrylamide) (PNIPAAm) is a well-known thermoresponsive polymer that shows a reversible coil-to-globule transition at the lower critical solution temperature (LCST) (32°C) in aqueous solution. Chemically modified PNIPAAm with hydrophilic/hydrophobic compound will tune its LCST. Below the LCST, PNIPAAm and its conjugate behave as an extended coil form in an aqueous solution, whereas it shrinks into a globule form above the LCST. In this study, a direct conjugate of PNIPAAm with a ternatin biomolecule and their physicochemical characterizations were investigated. Ternatin biomolecule is an anti-adipogenic cyclic peptide that has a potential as a new treatment approach for obesity and metabolic disorders. Poly (*N*-isopropylacrylamide)-chain transfer agent (PNIPAAm-CTA) was synthesized through reversible addition fragmentation chain transfer (RAFT) polymerization using 2-(Dodecylthiocarbonothioyltho)-2-methylpropanoic acid (DDMAT) as chain transfer reagent. One end-group of PNIPAAm-CTA was subsequently modified with maleimide to form PNIPAAm-Maleimide through aminolysis reaction. Thereafter, a carboxylic end-group of PNIPAAm-Maleimide was directly conjugated with a hydroxyl group of ternatin biomolecule (PNIPAAm-Ternatin) through esterification method. The chemical structure, molecular weight (Mw) and molecular weight distribution (Mw/Mn) of PNIPAAm were determined through the proton nuclear magnetic resonance (^{1}H-NMR), Fourier transform infrared (FTIR) and size exclusion chromatography (SEC) measurements. Moreover, the LCST of PNIPAAm and its conjugate were determined through light scattering intensity analysis. The results indicated that upon heating the solutions of PNIPAAm and its conjugates in 10 mM HEPES solution pH 7.4 at 25°C-40 °C, PNIPAAm-CTA, PNIPAAm-Maleimide and PNIPAAm-Ternatin solutions started to increase their light intensities at 32 °C, 34 °C and 35 °C, respectively. In conclusion, chemical structure modification of PNIPAAm could tune their LCST.

Keywords: poly (*n*-isopropylacrylamide), raft polymerization, ternatin biomolecule, conjugation, lower critical solution temperature

Abstrak

Poli (*N*-isopropilakrilamida) (PNIPAAm) adalah polimer termoresponsif terkenal yang menunjukkan peralihan gegelung-ke-globule yang boleh berbalik pada suhu larutan kritikal rendah (LCST) (32°C) dalam larutan akueus. PNIPAAm yang diubahsuai

secara kimia dengan sebatian hidrofilik/hidrofobik akan mengubahkan LCSTnya. Pada suhu di bawah LCST, PNIPAAm dan konjugatnya berbentuk gegelung di dalam larutan akueus, manakala ia akan mengecut menjadi bentuk globul pada suhu di atas LCST Dalam kajian ini, konjugasi secara langsung PNIPAAm dengan biomolekul ternatin dan sifat fizikokimianya dikaji. Biomolekul ternatin adalah peptida siklik anti-adipogenik. Ia berpotensi sebagai rawatan baharu untuk obesiti dan gangguan metabolik. Poli (*N*-isopropilakrilamida)-agen pemindahan rantai (PNIPAAm-CTA) disintesis melalui polimerisasi radikal hidup menggunakan asid 2-(dodekilthiokarbonothioiltho)-2-metilpropanoik(DDMAT) sebagai reagen pemindahan rantai. Selepas itu, satu kumpulan akhir pada PNIPAAm-CTA diubahsuai dengan maleimida untuk membentuk PNIPAAm-Maleimida melalui tindak balas aminolisis. Kemudian, kumpulan akhir karboksilik PNIPAAm-Maleimida dihubungkan secara langsung dengan kumpulan hidroksil pada biomolekul ternatin (PNIPAAm-Ternatin) melalui kaedah esterifikasi. Struktur kimia, berat molekul (Mw) dan taburan berat molekul (Mw/ Mn) bagi PNIPAAm dikaji melalui analisis proton resonans magnetik nuklear (^{1}H-NMR), spektroskopi inframerah Fourier transformasi (FTIR) dan kromatografi ekslusi saiz (SEC). Seterusnya, sifat LCST bagi PNIPAAm dan konjugatnya dikaji melalui analisis intensiti penyerakan cahaya. Hasilnya, setelah larutan PNIPAAm dan konjugat dalam larutan HEPES 10 mM pH 7.4 dipanaskan pada suhu 25-40 °C, intensiti cahaya bagi PNIPAAm-CTA, PNIPAAm-Maleimida dan PNIPAAm-Ternatin mula meningkat pada 32 °C, 34 °C dan 35 °C. Kesimpulannya, pengubahsuaian struktur kimia PNIPAAm dapat mengubah sifat LCST polimer.

Kata kunci: poli (*n*-isopropilakrilamida), pempolimeran raft, biomolekul ternatin, konjugasi, suhu larutan kritikal rendah

Introduction

Over the years, a great deal of effort has been devoted to the development of stimuli-responsive smart polymers that can provide a variety of applications for cosmetic, agriculture, biomedical and biotechnology [1-4]. Smart polymers are polymeric materials, in which the structure, function, and stability drastically change by slight changes in external stimuli. These stimuli could be temperature, pH, light, redox and/or photo [5-9]. In the case, whereby the external stimulus is the temperature change, the polymers are often referred as thermoresponsive polymers. Poly(*N*-isopropylacrylamide (PNIPAAm) is one of the well-known thermoresponsive polymer. PNIPAAm displays a lower critical solution temperature (LCST) of 33 °C [10-12]. PNIPAAm remains in coil conformation in water below LCST, meanwhile, it collapses into globule conformation above LCST [13, 14]. The LCST of PNIPAAm chain could be tuned by several approaches, such as modification of end-group with hydrophilic or hydrophobic compound, adding comonomers and/or changing its tacticity [15-17]. The introduction of hydrophilic compound into PNIPAAm chain leads to an increase of LCST, meanwhile, PNIPAAm incorporated with hydrophobic compound tends to decrease LCST. Moreover, a reported study demonstrated that PNIPAAm conjugated with a small interfering of ribonucleic acid (RNA) (siRNA) biomolecule using click chemistry tools tuned the LCST of PNIPAAm conjugates [18].

In the present study, a facile synthetic route for the conjugation of PNIPAAm with ternatin biomolecule was prepared to investigate the thermoresponsive behaviour. Ternatin biomolecule is a natural compound that is extracted from a plant, known as butterfly pea, or its scientific name *Clitoria ternatea* [19]. Ternatin is an anti-adipogenic cyclic peptide containing one or more *N*-methyl (or *N*-alkyl) amino acids [20, 21]. Furthermore, this study hypothesised that the modification of PNIPAAm chain with hydrophilic compound end-group and ternatin biomolecule would tune the thermoresponsive behaviour of PNIPAAm. Concisely, this study prepared PNIPAAm and its conjugate through controlled living radical polymerisation and esterification techniques (Figure 1). It is expected that the prepared facile synthetic route for the conjugation of thermoresponsive polymer with biomolecule and the resulted thermoresponsive behaviour in this study would be useful for further related field studies.

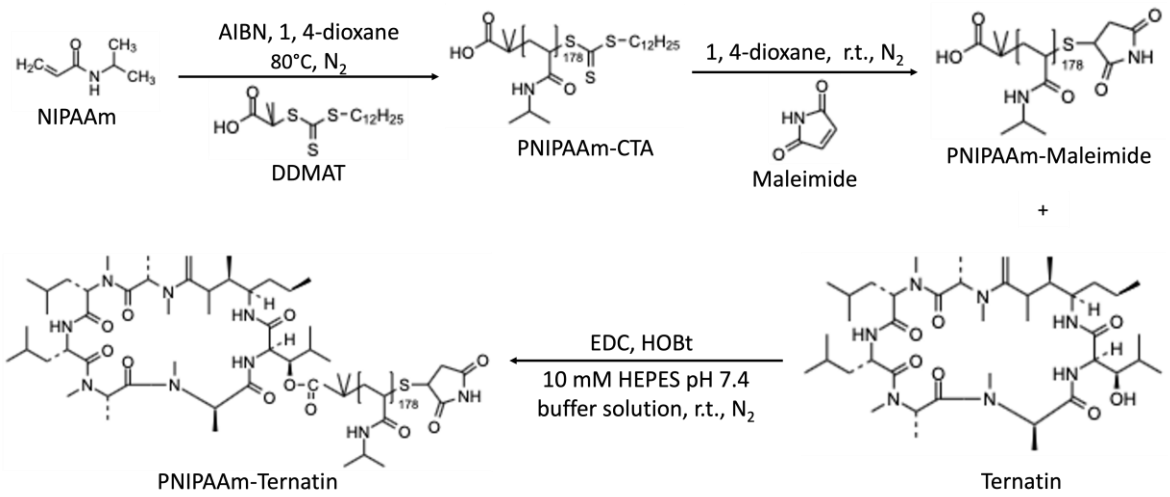


Figure 1. Synthetic route of PNIPAAm-Ternatin conjugation

Materials and Methods

Materials

N-Isopropylacrylamide (NIPAAm), 2-(Dodecylthiocarbonothioyltho)-2-methylpropanoic acid (DDMAT), 2,2'-Azobis(2-methylpropionitrile) (AIBN), 1,4-dioxane, diethyl ether, ethanolamine, maleimide, tributylphosphine (TBP), HEPES solution, N-ethyl-N'-(3-dimethylaminopropyl) carbodiimide (EDC), 1-Hydroxybenzotriazole (HOBt), tetrahydrofuran (THF) and acetonitrile were purchased from Sigma-Aldrich, Malaysia. NIPAAm was purified by recrystallisation from n-hexane and dried in a vacuum. AIBN purification was performed by recrystallisation from cold methanol. Prior to the usage, 1,4-dioxane was purified using reflux condenser. Ternatin was purchased from Cayman Chemical (Ann Arbor, Michigan, USA). Deuterated methanol (MeOD) was purchased from Merck and it was used without further purification.

Synthesis of PNIPAAm–CTA

PNIPAAm-CTA was synthesised by dissolving NIPAAm (3.0 g, 30.0 mmol), DDMAT (110 mg, 0.3 mmol), AIBN (2.5 mg, 0.015 mmol) in 1,4-dioxane (10 mL) ([NIPAAm]: [DDMAT]: [AIBN] = 100: 1: 0.05, respectively). The solution was stirred at room temperature until a homogeneous mixture was formed. Next, the nitrogen gas was purged into the reaction for 15 minutes. The mixture was stirred and heated in an 80 °C oil bath for 12 hours. After 12 hours, the reaction solution was precipitated into cold diethyl ether to remove the unreacted monomer. The produced polymer was filtered using vacuum pump and dried in a desiccator for a day. Finally, the polymer was collected, weighted and stored in the refrigerator.

Synthesis of PNIPAAm–maleimide

PNIPAAm–Maleimide was synthesised by dissolving PNIPAAm-CTA (1.5 g, 0.27 mmol), ethanolamine (1.6 g, 27.20 mmol) and maleimide (0.26 g, 2.72 mmol) into the 1,4-dioxane (5 mL). The solution was stirred at room temperature until a homogeneous mixture was formed. Next, the nitrogen gas was purged into the reaction for five minutes. After five minutes, TBP (0.10 mL, 0.54 mmol) was added to the mixture ([PNIPAAm–CTA]: [maleimide]: [TBP]: [ethanolamine] = 1: 10: 2: 100, respectively). The mixture was stirred at room temperature for six hours. After six hours, the reaction solution was precipitated into cold diethyl ether to remove the unreacted monomer. The produced polymer was filtered using a vacuum pump and dried in a desiccator for a day. The polymer was collected, weighted and stored in the refrigerator.

Synthesis of PNIPAAm–ternatin

PNIPAAm–Maleimide solution was prepared by dissolving PNIPAAm-Maleimide (33.33 mg, 0.02 mmol) into 4 mL of 10 mM HEPES pH 7.4 buffer solution. The mixture was stirred for 20 hours at room temperature. After 20 hours, EDC (3 mg, 0.02 mmol) and HOBt (1 mg, 0.01 mmol) were added to the mixture and stirred continuously for three hours at room temperature to activate the carboxylate group. Next, the nitrogen gas was purged into the reaction for 15 minutes and 0.5 mL of 10 ppm ternatin was slowly added to the mixture. After 15 minutes, the mixture was stirred for 20 hours at room temperature. Thereafter, 4 mL of 10 mM HEPES pH 7.4 buffer solution was added to the mixture and cooled at room temperature. After two days, it was purified by centrifugation using ultra centrifugal filter (MWCO 3kDa, Millipore) to remove the unreacted molecules. Finally, the produced PNIPAAm-Ternatin was collected and stored in the refrigerator.

Molecular weight and molecular weight distribution

The polymer molecular weight and molecular weight distribution (Mw/Mn) was measured by using Waters® ACQUITY® Advanced Polymer Chromatography™ (APC) with THF, which was used as an eluent at a flow rate of 1.0 mL/min at 40°C using the standard polystyrene. The ACQUITY UPLC Refractive Index Detector ACQUITY APC Column were used.

Chemical structure characterisations

Fourier transform infrared (FTIR) spectra of the PNIPAAm-CTA and PNIPAAm-Maleimide were recorded with FTIR Nicolet 510 spectrometer in the 4,000 cm^{-1} – 400 cm^{-1} range. The samples were prepared by grinding the polymer with KBr pellets and compressing the mixture to form disks. For PNIPAAm-Ternatin, FTIR spectra was recorded with Shimadzu FTIR-8300 instrument in the 4,000 cm^{-1} - 600 cm^{-1} range. The polymer chemical structure and the conjugated polymers were also characterised using ^1H NMR spectra. It was conducted on a Bruker Spectrospin 400 MHz UltraShield Spectrometer. Chloroform-d ($CDCl_3$) and methanol-d (MeOD) were used as solvents.

Reversed-phase high-performance liquid chromatography analysis

Reversed-phase high-performance liquid chromatography (RP-HPLC) analysis was used to separate, identify and quantify each component in the produced polymer conjugated with ternatin. For polymer-peptide conjugate, the HPLC gradients consisted of eluent A with 0.1% formic acid in water and eluent B with 0.1% formic acid in acetonitrile. The flow rate was maintained at 0.5 mL/min, detected at 200 nm and the column temperature was at room temperature.

Light scattering intensity analysis

Light scattering intensity analysis was performed to determine the LCST of polymer by using Zetasizer Nano (Malvern Instrument Ltd.) at a detection angle of 173°. The sample solutions were prepared by dissolving the polymer, ternatin and its polymer conjugates in 10 mM HEPES solution (pH 7.4) (sample solution concentration at 0.5 mg mL^{-1}). It was measured at various temperatures from 25°C to 40°C. The results were presented as mean value of count rate in kilo counts per second (kcps) and the standard deviation was obtained from three times repetitions.

Results and Discussion

Chemical structure characterisation of PNIPAAm-CTA and PNIPAAm-Maleimide

The synthesised PNIPAAm-CTA possessed molecular weight, Mw at 20140 g/mol and had a narrow molecular weight distribution (Mw/Mn) of 1.26. The obtained molecular weight of PNIPAAm-CTA was purely theoretical. Furthermore, a quite narrow molecular weight distribution suggested that a successful controlled polymerization of PNIPAAm.

The chemical structure of PNIPAAm-CTA and PNIPAAm-Maleimide were characterised by ^1H NMR and FTIR analysis. The ^1H NMR spectrum of PNIPAAm-CTA in Figure 2 showed the presence of signal characteristic of PNIPAAm at δ = 3.9 ppm for CH connected to the NH, 1.15 ppm for CH_3, 1.61 ppm ($-CH_2-$) and 2.13 ppm (-CH-) [22, 23]. The formation of PNIPAAm-CTA was proven by the existence of trithiocarbonate functionality at the PNIPAAm-CTA

end-group, which was demonstrated in the ^{1}H NMR spectrum through the peak at 0.88 ppm (CH_3–$(CH_2)_{10}$–CH_2–S–) [24]. Furthermore, the ^{1}H NMR spectrum of PNIPAAm-Maleimide (Figure 3) confirmed the existence of maleimide at the peak of 8.55 ppm which belong to the -NH group in maleimide [25]. The disappearance of the peak at 0.88 ppm for trithiocarbonate group in the spectrum suggested the successful conversion into PNIPAAm-Maleimide through aminolysis reaction [26].

PNIPAAm-CTA and PNIPAAm-Maleimide chemical structures were further confirmed through FTIR analysis. In Figure 4, the FTIR spectrum for PNIPAAm-CTA showed that the formation was proven by the C=S stretching band of the chain at 1,065 cm^{-1} [27]. The C=S group was belong to the trithiocarbonate end in PNIPAAm-CTA. The FTIR spectra for PNIPAAm-CTA also represented the N-H stretch at 3,414 cm^{-1}, carbonyl group (C=O) at 1,554 cm^{-1} and 1,643 cm^{-1}, and C–N stretching at 1,462 cm^{-1} [28]. The FTIR spectrum for PNIPAAm–Maleimide showed that the aminolysis reaction was succeeded because the C=S stretching band (1,050 cm^{-1} – 1,080 cm^{-1}) of the trithiocarbonate end was no longer being observed after the aminolysis reaction [29]. Furthermore, there was a peak at 1,743 cm^{-1} for maleimide C=O stretching. For symmetric C-N-C stretch, the peak was situated at 1,457 cm^{-1}, which affirmed the existence of maleimide [30]. The FTIR absorption band, which was around 3,300 cm^{-1} – 3,500 cm^{-1} covered N-H stretching group bands in PNIPAAm and maleimide [31]. These results confirmed the polymerisation of PNIPAAm-CTA and the modification of its end-group to produce PNIPAAm-Maleimide.

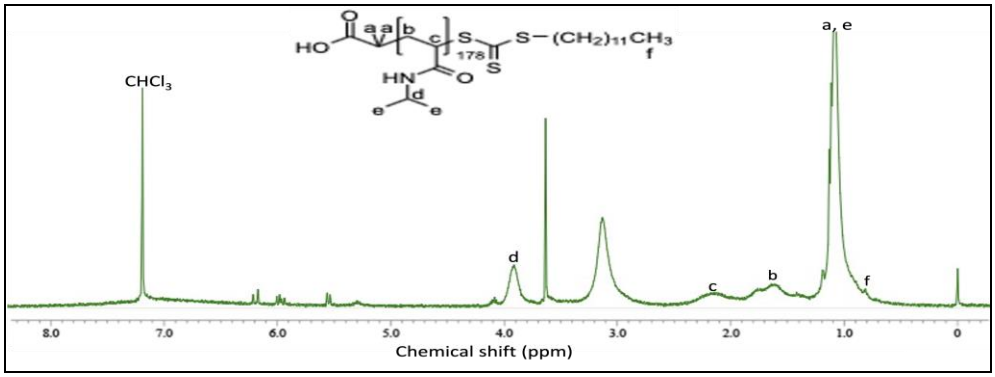


Figure 2. ^{1}H NMR spectrum of PNIPAAm-CTA

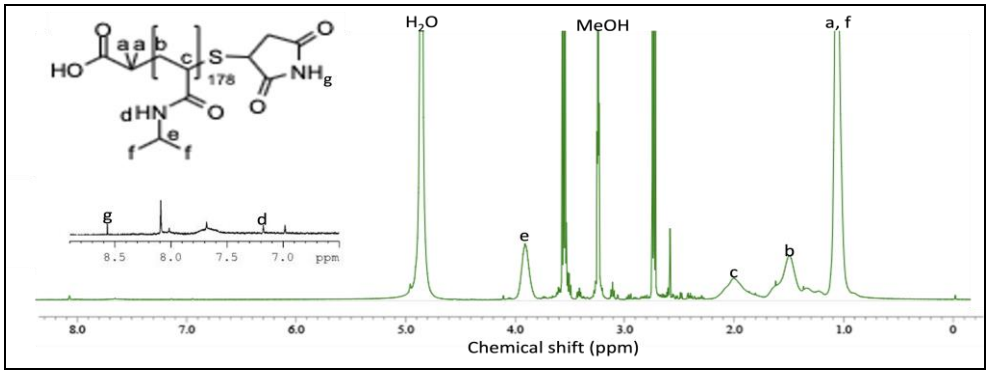


Figure 3. ^{1}H NMR spectrum of PNIPAAm-Maleimide

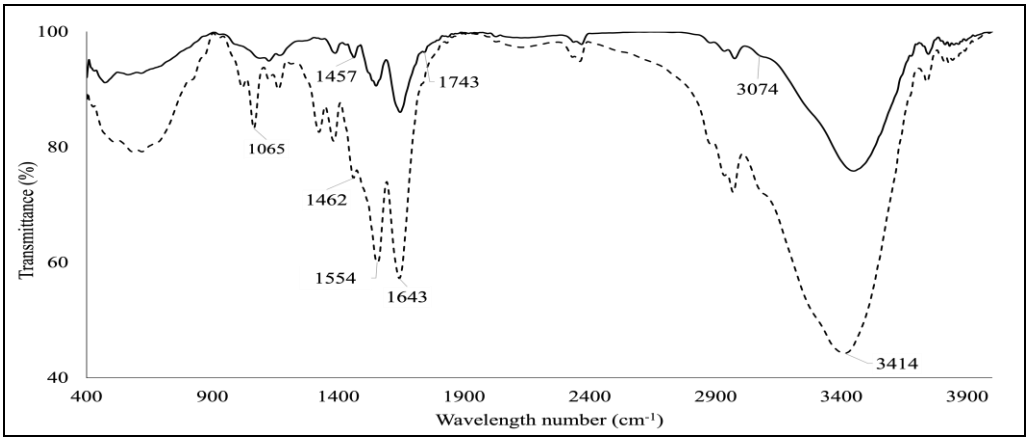


Figure 4. FTIR analysis for PNIPAAm-CTA (dash-line) and PNIPAAm-Maleimide (straight-line)

Characterisations of PNIPAAm-Ternatin conjugate

The esterification method was used to synthesise the PNIPAAm-Ternatin. The chemical structure of PNIPAAm-Ternatin was confirmed by the FTIR. In Figure 5 (a) showed the FTIR analysis for PNIPAAm-Ternatin, whereby the band at 1,635 cm^{-1} and 1,185 cm^{-1} were attributed to the C=O and C-O stretching frequencies of ester linkage, respectively [32]. Therefore, it was suggested that the PNIPAAm-Ternatin was successfully synthesised through esterification method. A broad stretch at 3,286 cm^{-1} was indexed to the NH group in ternatin [33]. The NH stretching group in PNIPAAm and maleimide at 3,300 cm^{-1} – 3,500 cm^{-1} were overlapped by the broad stretch of OH group in the ternatin [34].

The HPLC chart for PNIPAAm-Ternatin is shown in Figure 5 (b). The purpose of this analysis was to identify the retention time of ternatin, PNIPAAm-Maleimide and PNIPAAm-Ternatin and also to calculate the concentration and conjugation percentages of ternatin biomolecule to PNIPAAm chain. As a result, it was confirmed that the peak at the retention time of 2.57 minutes and 3.06 minutes for ternatin and PNIPAAm-Ternatin, respectively, clearly appeared in the HPLC chart. The concentration and conjugation percentages of PNIPAAm-Ternatin were obtained at 8.75 ppm and 87.5%, respectively, which was calculated based on ternatin calibration. Consequently, the collected PNIPAAm-Ternatin through RP-HPLC was purified using centrifugation against 10 mM HEPES pH 7.4 buffer solution and conducted for further analysis.

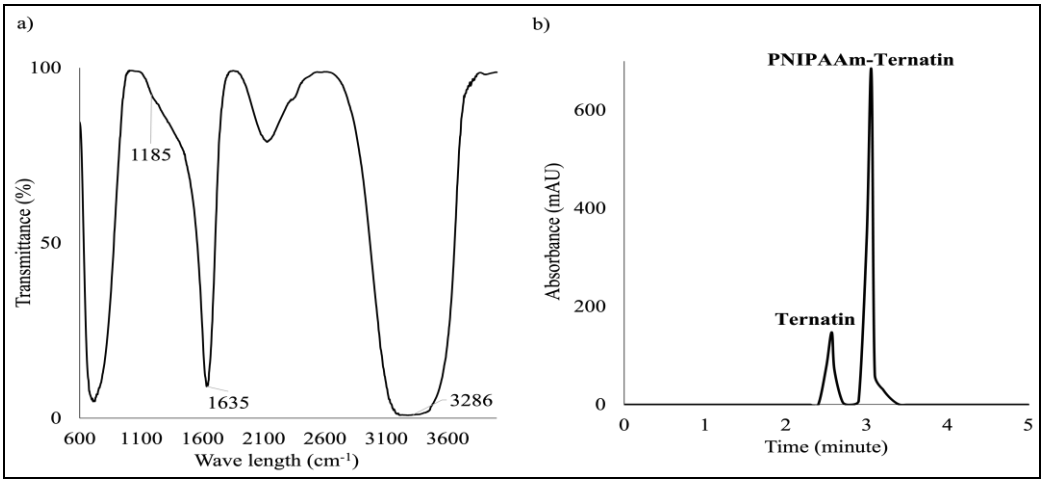


Figure 5. (a) FTIR analysis and (b) HPLC analysis for PNIPAAm-Ternatin

Thermoresponsive behaviour of PNIPAAm and its conjugate

The LCST of PNIPAAm and its conjugate were determined by light scattering intensity analysis. The resulting light scattering intensity of PNIPAAm and its conjugate are shown in Figure 6(a) for PNIPAAm-CTA, Figure 6(b) for PNIPAAm-Maleimide and Figure 6(c) for PNIPAAm-Ternatin. Upon heating solutions of PNIPAAm-CTA, PNIPAAm-Maleimide and PNIPAAm-Ternatin in 10 mM HEPES pH 7.4 from 25 °C to 40 °C, it could be seen that light scattering intensity of PNIPAAm-CTA started to increase at a temperature of 32 °C, whereas the change was shifted to the temperature at 34 °C in the case of PNIPAAm-Maleimide and at 35 °C for PNIPAAm-Ternatin. The increased light scattering intensity of PNIPAAm and its conjugate were due to the aggregation of globule form of PNIPAAm chain above the LCST [35]. The modification of chemical structure of PNIPAAm with hydrophilic or hydrophobic compound tuned the LCST of PNIPAAm [36]. Based on this study, the LCST for PNIPAAm-Maleimide and PNIPAAm-Ternatin were higher when compared to the LCST of PNIPAAm-CTA. This was due to the addition of hydrophilic maleimide compound and ternatin biomolecule at end-group of PNIPAAm chain that improved the LCST of the polymer. Therefore, the results indicated that the addition of hydrophilic compound increased the LCST of PNIPAAm. The small changes of LCST for PNIPAAm-Ternatin solution upon heating suggested that the conjugation of PNIPAAm with ternatin biomolecule did not contribute any effect on the thermoresponsive behaviour of PNIPAAm chain.

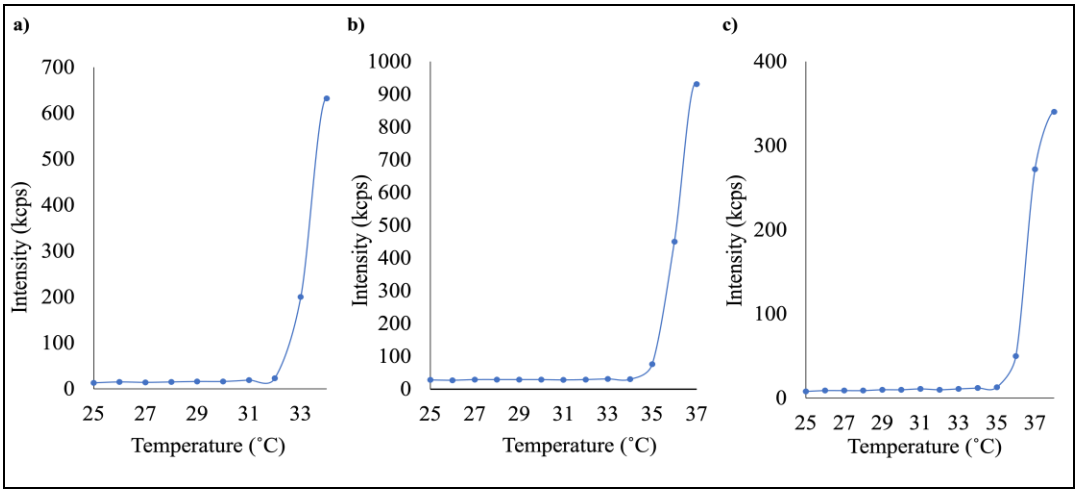


Figure 6. Light scattering intensities of (a) PNIPAAm-CTA, b) PNIPAAm-Maleimide and c) PNIPAAm-Ternatin solution at an indicated temperature in 10 mM HEPES pH 7.4 buffer solution

Conclusion

A thermoresponsive PNIPAAm conjugate was designed with ternatin biomolecule through controlled living radical polymerisation and esterification techniques. The synthesised PNIPAAm-CTA possessed molecular weight, Mw of 20140 g/mol and had quite a narrow molecular weight distribution (Mw/Mn) of 1.26, which revealed that the synthesised PNIPAAm through RAFT polymerisation was in a controlled structure. Moreover, PNIPAAm-Ternatin with conjugation percentage of 87.5% was successfully prepared through esterification technique. The synthesised PNIPAAm-CTA had a LCST at 32 °C. Meanwhile, the modification of PNIPAAm chain end-group by the addition of hydrophilic compound of maleimide (PNIPAAm-Maleimide) and the introduction of ternatin biomolecule (PNIPAAm-Ternatin) increased the LCST of PNIPAAm to 34 °C and 35 °C, respectively. Therefore, reported synthesised PNIPAAm and its chemical modifications are expected to provide a fundamental knowledge for further design and an excellent flexibility in tailoring for specific usage, particularly in the bioengineering and biomedical studies. Further studies on this topic are now in progress.

Acknowledgements

The authors thank the Ministry of Higher Education (MOHE) Malaysia for the financial support provided via the Fundamental Research Grant Scheme [ref no. FRGS/1/2018/STG05/UNIKL/02/5]. The authors also thank Universiti Kuala Lumpur Malaysian Institute of Chemical and Bioengineering Technology, Melaka, Malaysia for providing resources and necessary facilities for FTIR, HPLC and Light Scattering Intensity analyses. The authors also thank the Nuclear Magnetic Resonance Laboratory, University Industry Research Laboratory, Universiti Teknologi Malaysia, Johor, Malaysia for ^{1}H NMR analysis.

References

1. Hoffman, A. S. and Stayton, P. S. (2007). Conjugates of stimuli-responsive polymers and proteins. *Progress in Polymer Science,* 32(8-9): 922-932.
2. Martens, P. J., Bryant, S. J. and Anseth, K. S. (2003). Tailoring the degradation of hydrogels formed from multivinyl poly (ethylene glycol) and poly (vinyl alcohol) macromers for cartilage tissue engineering. *Biomacromolecules,* 4(2): 283-292.
3. Tan, L., Liu, J., Zhou, W., Wei, J. and Peng, Z. (2014). A novel thermal and pH responsive drug delivery system based on ZnO@PNIPAM hybrid nanoparticles. *Materials Science and Engineering: C,* 45(1): 524-529.
4. Tian, Y., Wei, X., Wang, Z. J., Pan, P., Li, F., Ling, D., Wu, Z. L. and Zheng, Q. (2017). A facile approach to prepare tough and responsive ultrathin

physical hydrogel films as artificial muscles. *ACS Applied Materials & Interfaces,* 9(39): 34349-34355.

5. Bajpai, A., Shukla, S. K., Bhanu, S. and Kankane, S. (2008). Responsive polymers in controlled drug delivery. *Progress in Polymer Science,* 33(11), 1088-1118.
6. Xiong, X., Del Campo, A. and Cui, J. (2019). Photoresponsive polymers. *Smart Polymers and Their Applications,* 1: 87-153.
7. Swift, T., Swanson, L., Geoghegan, M. and Rimmer, S. (2016). The pH-responsive behaviour of poly (acrylic acid) in aqueous solution is dependent on molar mass. *Soft Matter,* 12: 2542-2549.
8. Elbert, J., Mersini, J., Vilbrandt, N., Lederle, C., Kraska, M., Gallei, M., Stuhn, B., Plenio, H. and Rehahn, M. (2013). Reversible activity modulation of surface-attached grubbs second generation type catalysts using redox-responsive polymers. *Macromolecules,* 46(11): 4255-4267.
9. Lustig, S. R., Everlof, G. J. and Jaycox, G. D. (2001). Stimuli-responsive polymers. 5. Azobenzene modified polyaramides containing atropisomeric binaphthyl linkages: Tuning chiroptical behavior with light and heat. *Macromolecules,* 34(7): 2364-2372.
10. Schild, H. (1992). Poly(n-isopropylacrylamide): Experiment, theory and application. *Progress in Polymer Science,* 17(2): 163-249.
11. Abbott, L. J., Tucker, A. K. and Stevens, M. J. (2015). Single chain structure of a poly(n-isopropylacrylamide) surfactant in water. *The Journal of Physical Chemistry B,* 119 (9): 3837-3845.
12. Hirokawa, Y. and Tanaka, T. (1984). Volume phase transition in a nonionic gel. *The Journal of Chemical Physics,* 81 (12): 6379-6380.
13. Cook, M. T., Haddow, P., Kirton, S. B. and McAuley, W. J. (2020). Polymers exhibiting lower critical solution temperatures as a route to thermoreversible gelators for healthcare. *Advanced Functional Materials,* 31(8): 2008123.
14. Irani, C. A. and Cozewith, C. (1986). Lower critical solution temperature behavior of ethylene propylene copolymers in multicomponent solvents. *Journal of Applied Polymer Science,* 31(6): 1879-1899.
15. Maeda, Y., Higuchi, T. and Ikeda, I. (2000). Change in hydration state during the coil−globule transition of aqueous solutions of poly(n-isopropylacrylamide) as evidenced by FTIR spectroscopy. *Langmuir,* 16(19): 7503-7509.
16. García-Peñas, A., Biswas, C. S., Liang, W., Wang, Y., Yang, P. and Stadler, F. J. (2019). Effect of hydrophobic interactions on lower critical solution temperature for poly (n-isopropylacrylamide-co-dopamine methacrylamide) copolymers. *Polymers,* 11 (6): 991.
17. Ashbaugh, H. S. and Paulaitis, M. E. (2006). Monomer hydrophobicity as a mechanism for the LCST behavior of poly (ethylene oxide) in water. *Industrial & Engineering Chemistry Research,* 45(16): 5531-5537.
18. Che Harun, N., Takemoto, H., Nomoto, T., Tomoda, K., Matsui, M. and Nishiyama, N. (2016). Artificial control of gene silencing activity based on siRNA conjugation with polymeric molecule having coil-globule transition behavior. *Bioconjugate Chemistry,* 27(9): 1961-1964.
19. Nair, V., Bang, W. Y., Schreckinger, E., Andarwulan, N. and Cisneros-Zevallos, L. (2015). Protective role of ternatin anthocyanins and quercetin glycosides from butterfly pea (*Clitoria ternatea* Leguminosae) blue flower petals against lipopolysaccharide (LPS)-induced inflammation in macrophage cells. *Journal of Agricultural and Food Chemistry*, 63(28), 6355-6365.
20. Carelli, J. D., Sethofer, S. G., Smith, G. A., Miller, H. R., Simard, J. L., Merrick, W. C., Jain, R. K., Ross, N. T. and Taunton, J. (2015). Ternatin and improved synthetic variants kill cancer cells by targeting the elongation factor-1a ternary complex. *eLife*, 4: e10222.
21. Kobayashi, M., Kawashima, H., Takemori, K., Ito, H., Murai, A., Masuda, S., Yamada, K., Uemura, D. and Horio, F. (2012). Ternatin, a cyclic peptide isolated from mushroom, and its derivative suppress hyperglycemia and hepatic fatty acid synthesis in spontaneously diabetic KK-AY mice. *Biochemical and Biophysical Research Communications,* 427(2): 299-304.

22. Kuo, S.-W., Hong, J.-L., Huang, Y.-C., Chen, J.-K., Fan, S.-K., Ko, F.-H. and Chang, F.-C. (2012). Star poly(n-isopropylacrylamide) tethered to polyhedral oligomeric silsesquioxane (POSS) nanoparticles by a combination of ATRP and click chemistry. *Journal of Nanomaterials,* 2012: 1-10.
23. Coronado, R., Pekerar, S., Lorenzo, A. T. and Sabino, M. A. (2010). Characterization of thermo-sensitive hydrogels based on poly(n-isopropylacrylamide)/hyaluronic acid. *Polymer Bulletin*, 67(1): 101-124.
24. Ma, Y.-M., Wei, D.-X., Yao, H., Wu, L.-P. and Chen, G.-Q. (2016). Synthesis, characterization and application of thermoresponsive polyhydroxyalkanoate-graft-poly(n-isopropylacryl amide) *Biomacromolecules*, 17(8): 2680-2690.
25. Avila, A., Chinchilla, R. and Nájera, C. (2012). Enantioselective Michael addition of α,α-disubstituted aldehydes to maleimides organocatalyzed by chiral primary amine-guanidines. *Tetrahedron: Asymmetry*, 23(24): 1625-1627.
26. Ho, T. H., Levere, M., Soutif, J.-C., Montembault, V., Pascual, S. and Fontaine, L. (2011). Synthesis of thermoresponsive oxazolone end-functional polymers for reactions with amines using Thiol-Michael addition "click" chemistry. *Polymer Chemistry*, 2(6): 1258.
27. Lai, J. T., Filla, D. and Shea, R. (2002). Functional polymers from novel carboxyl-terminated trithiocarbonates as highly efficient RAFT agents. *Macromolecules,* 35(18): 6754-6756.
28. Roach, P., McGarvey, D., Lees, M. and Hoskins, C. (2013). Remotely triggered scaffolds for controlled release of pharmaceuticals. *International Journal of Molecular Sciences,* 14(4): 8585-8602.
29. Willcock, H. and O'Reilly, R. K. (2010). End group removal and modification of RAFT polymers. *Polymer Chemistry,* 1(2): 149-157.
30. Shen, G. (2004). X-ray photoelectron spectroscopy and infrared spectroscopy study of maleimide-activated supports for immobilization of oligodeoxyribonucleotides. *Nucleic Acids Research,* 32(20): 5973-5980.
31. Icriverzi, M., Rusen, L., Sima, L. E., Moldovan, A., Brajnicov, S., Bonciu, A., Mihailescu, N., Dinescu, M., Cimpean, A., Roseanu, A. and Dinca, V. (2018). *In vitro* behavior of human mesenchymal stem cells on poly (n-isopropylacrylamide) based biointerfaces obtained by matrix assisted pulsed laser evaporation. *Applied Surface Science,* 440: 712-724.
32. Smith, B. (2020). The C=O bond, Part VI: Esters and the rule of three. Access from https://www.spectroscopyonline.com/view/co-bon-part-vi-esters-and-rule-three. [Access online on 12 August 2021].
33. Ludin, N. (2018). Utilization of natural dyes from zingiber officinale leaves and *Clitoria ternatea* flowers to prepare new photosensitisers for dye-sensitised solar cells. *International Journal of Electrochemical Science,* (1): 7451-7465.
34. Ramesh, S., Sivasamy, A. and Kim, J. (2012). Synthesis and characterization of maleimide-functionalized polystyrene-SiO_2/TiO_2 hybrid nanocomposites by sol–gel process. *Nanoscale Research Letters,* 7(1): 350.
35. Chung, J., Yokoyama, M., Yamato, M., Aoyagi, T., Sakurai, Y. and Okano, T. (1999). Thermo-responsive drug delivery from polymeric micelles constructed using B lock copolymers of poly(n-isopropylacrylamide) and poly(butylmethacrylate). *Journal of Controlled Release,* 62(1-2), 115-127.
36. Yang, L., Fan, X., Zhang, J. and Ju, J. (2020). Preparation and characterization of thermoresponsive poly (n-isopropylacrylamide) for cell culture applications. *Polymers,* 12(2): 389.

Malaysian Journal of Analytical Sciences (MJAS)
Published by Malaysian Analytical Sciences Society

CATALYTIC CONVERSION OF CELLULOSE TO LEVULINIC ACID USING SUPPORTED NOBLE METAL PALLADIUM CATALYST

(Penukaran Bermangkin dari Selulosa ke Asid Levulinik Menggunakan Mangkin Disokong Logam Adi Paladium)

Puteri Nurain Syahirah Megat Muhammad Kamal, Norzahir Sapawe, Amin Safwan Alikasturi*

Universiti Kuala Lumpur Branch Campus Malaysian Institute of Chemical and Bioengineering Technology, Lot 1988 Vendor City, Taboh Naning, 78000 Alor Gajah, Melaka, Malaysia

**Corresponding author: aminsafwan@unikl.edu.my*

Received: 15 September 2021; Accepted: 30 December 2021; Published: 25 February 2022

Abstract

In resolving the current energy crisis, it is vital to effectively use the abundant biomass to produce platform chemicals, for instance levulinic acid (LA). LA is very flexible for the formation of high value-added chemicals as it belongs to the family of carboxyl and ketone. This valuable platform chemical can be produced from cellulose (the most abundant biomass in nature). Palladium (Pd) as a noble metal was incorporated with catalyst supports (silica-alumina; SiO_2-Al_2O_3 and gamma-alumina; γ-Al_2O_3) by using wet impregnation method, aiming for 4 wt.% of noble metal on supports followed by catalyst calcination at 500 ˚C. The catalyst was characterized using Fourier-transform infrared spectroscopy (FTIR) and Brunauer–Emmett–Teller (BET). The effects of reaction parameters such as agitation speed, reaction temperature, and cellulose loading were investigated using this catalyst in a semi-batch reactor for 8 hours. The highest conversion of cellulose (73.9%) and yield of LA (43.3%) was achieved under these conditions: agitation speed of 1100 rpm, reaction temperature of 200 ˚C, and cellulose loading of 1.5 g with pre-reduction of Pd/SiO_2-Al_2O_3 catalyst (surface area and pore volume up to 485.6 m^2/g and 0.2459 cm^3/g, respectively) at 150 ˚C and agitation speed of 1300 rpm (in 5 bars of hydrogen, H_2 for 1 hour).

Keywords: Pd/SiO_2-Al_2O_3, cellulose, hydrolysis, levulinic acid

Abstrak

Dalam menyelesaikan krisis tenaga semasa, adalah sangat penting untuk menggunakan biojisim yang berkesan dalam menghasilkan bahan kimia platform seperti asid levulinik (LA). LA sangat fleksibel untuk pembentukan bahan kimia bernilai tinggi, kerana ia tergolong dalam keluarga karboksil dan keton. Bahan kimia platform yang berharga ini boleh dihasilkan dari selulosa (biojisim yang paling banyak terdapat di alam semula jadi). Paladium (Pd) sebagai logam adi boleh digabungkan dengan penampung mangkin (silica-alumina; SiO_2-Al_2O_3 and gamma-alumina; γ-Al_2O_3) yang dihasilkan menggunakan kaedah impregnasi basah yang bertujuan untuk 4% logam adi pada penampung mangkin diikuti oleh kalsinasi mangkin pada suhu 500 ˚C. Mangkin dicirikan menggunakan spektroskopi inframerah transformasi Fourier (FTIR) dan *Brunauer–Emmett–Teller* (BET). Kajian mengenai pengaruh parameter reaksi seperti kelajuan pengadukan, suhu tindak balas, dan pemuatan selulosa disiasat menggunakan mangkin ini dalam reaktor semi-kelompok selama 8 jam. Penukaran selulosa tertinggi (73.9%) dan hasil LA (43.3%) dicapai dalam keadaan ini; kelajuan pengadukan 1100 rpm, suhu tindak balas 200 ˚C, dan pemuatan selulosa 1.5 g

dengan pra-pengurangan mangkin Pd/SiO_2-Al_2O_3 (luas permukaan dan isi pori 485.6 m^2/g dan 0.2459 cm^3/g, masing masing) pada suhu 150 ˚C dan kelajuan pengadukan 1300 rpm (dalam 5 bar hidrogen, H_2 selama 1 jam).

Kata kunci: Pd/SiO_2-Al_2O_3, selulosa, hidrolisis, asid levulinik

Introduction

Cellulose, a part of biomass, is a major component of lignocelluloses as it comprises 40-50% of lignocellulose composition. It is formed by dehydration and condensation of glucose produced from photosynthesis [1]. Starch, which is likewise created by photosynthesis but having a different characteristic than cellulose, can be classified as biomass. Starch, a polymer with α-1→4 glycosidic linkages, is soluble in hot water and is the main constituent of corn, potato, and rice. Even though considerable attention has been given to the production of fuels and chemicals, starch should be prioritized as a dietary source [2].

Furthermore, the amount of cellulose is so enormous that it is wasteful to simply let it decompose without exploring its potential benefits. The commercial feasibility of producing sugar alcohols such as sorbitol and mannitol, which are particularly valuable in the food sector as sweeteners and preservatives, by using hydrogenation method is one way to utilize this enormous resource [3]. When it comes to catalytic cellulose hydrolysis, LA is the main product produced after cellulose undergoes a few processes; 1) hydrolysis 2) dehydration and 3) rehydration [4]. Figure 1 shows the reaction pathway for the production of LA from cellulose.

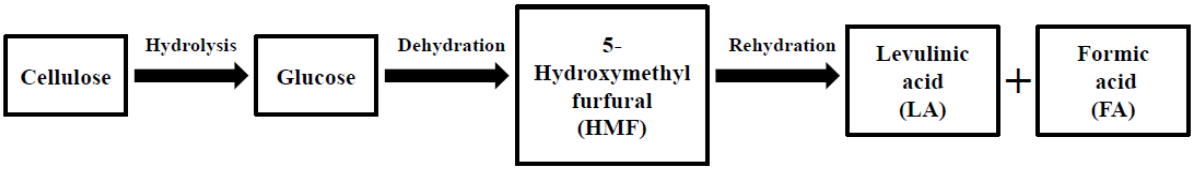


Figure 1. Reaction pathway for the production of LA from cellulose

LA is a water-soluble, organic compound that comes from the family of carboxylic acid and ketone, possessing a wide range of reactivity and functionality [5]. These two functional groups cause LA to be a very versatile building block for a vast chemical transformation of high-value organic chemicals, resin precursors, polymers precursors, and fuel additives with plenty of potential industrial applications [4]. Succinic acid and maleic anhydride are two high value-added chemicals that can be synthesized from LA and are useful in the food and textile industries, respectively. Aside from that, LA can be utilized as a starting material for the production of γ–valerolactone, as well as ethyl and methyl levulinate, making it a potential alternative to petroleum-based fuels or chemicals [6]. Aside from choosing LA as the final product, the reaction can be tuned up to produce various products with high yields, such as 5-hydroxymethylfurfural (HMF) and formic acid (FA).

Over the past decade, homogeneous catalysts have been used in many applications, including LA synthesis (using acids). Despite its efficiency, there are a few drawbacks to use this type of acid in the system, including the generation of additional wastes due to the difficulties of separation and recovery (environmental pollution). Besides that, this catalyst leads to equipment corrosion [7]. As a result, many researchers nowadays prefer to use heterogeneous catalysts in their systems, especially solid catalysts to overcome the issues that arise from the homogenous catalyst. Metal oxides, supported metals (nickel, Ni), H-form zeolites, carbonaceous acids, heteropoly acids, acid resins, magnetic acids, and functionalized silicas are the

examples of solid catalysts that have garnered attention as promising and appealing catalysts for the hydrolysis of cellulose [8].

Recently, there has been a noticeable growth towards employing cheap, non-noble metal-based catalysts such as Ni, yet the study on this catalyst's stability and recyclability needs to be emphasized as leaching and sintering can be mainly responsible for the decreasing catalytic activity [9]. Hence, in this research study, Palladium (Pd), a noble metal that can be regenerated and recycled up to 20 times without observing any significant loss of activity [10] was utilized as a catalyst. Even though Pd is relatively expensive when used individually, Pd can be incorporated into high dispersion and narrow sizes distribution of catalyst support such as silica (SiO_2) and alumina (Al_2O_3). Despite the high cost of Pd, it is widely acknowledged for its high chemical stability and catalytic abilities [11].

Therefore, this research was conducted to study the effects of various reaction conditions such as agitation speed, temperature, and substrate loading on the production of LA from cellulose using noble metal, Pd supported on different catalyst supports such as silica-alumina (SiO_2 -Al_2O_3) and gamma-alumina (γ-Al_2O_3). As a result, the most suitable catalyst that was effective in the conversion of cellulose to LA (under the conditions studied) could be determined throughout the experiments.

Materials and Methods

Materials

For the synthesis of catalyst, palladium (II) nitrate ($Pd(NO_3)_2$) with 40% w/w of Pd, SiO_2-Al_2O_3 grade 135 ($\leq$100%), and γ-Al_2O_3 (99.9%) were purchased from Sigma Aldrich and Alfa Aesar, respectively. As for the experimental work, microcrystalline cellulose (extra pure, 100%) from Acros Organics was used as substrates. In addition, glucose (>99.9%), HMF (>98%), LA (>98%), FA (>98%), and furfural (>99.9%) were used for standard reference calibration purposes. All the chemicals were analytical grade without further purification and distilled (DI) water was used for all the experiments.

Catalyst preparation

The solid noble catalyst was prepared using wet impregnation method. This method aimed to provide 5 g of 4 wt.% Pd on SiO_2-Al_2O_3 support. About 4.8 g of SiO_2-Al_2O_3 was weighed and spread on a petri dish. Then, 0.5 g of $Pd(NO_3)_4$ was dissolved in the minimum amount of DI water necessary to wet the SiO_2-Al_2O_3 support; this was found to be 3.3 ml of DI for 4.8 g of SiO_2-Al_2O_3. The diluted $Pd(NO_3)_4$ was dropped to the spread SiO_2-Al_2O_3 carefully using a syringe. The dropping was done in a circular motion where each $Pd(NO_3)_4$ droplet was at different point. After that, the $Pd(NO_3)_4$ was pressed using a spatula to achieve a homogenous mixture between $Pd(NO_3)_4$ and SiO_2-Al_2O_3. The prepared catalyst was dried using an oven at 110 ˚C for 12 hours to remove the excess moisture prior to calcination. The catalyst was then calcined at 500 ˚C for 5 hours. The catalyst was stored in a vial sealed with parafilm, and stored in desiccator prior to analysis and experimental work. The method was repeated to prepare 4 wt.% Pd on γ-Al_2O_3 support.

Catalyst characterization

The Fourier-transform infrared spectroscopy (FTIR) analysis was conducted with a Nicolet iS10 FTIR with a spectral resolution of 8 cm^{-1} at room temperature and accumulation of 5 scans in an open beam air background [12]. The spectrum ranged from 4000 cm^{-1} to 400 cm^{-1}. The Brunauer–Emmett–Teller (BET) method was used to determine the surface area and pore volume using Micromeritics 3Flex where the catalyst was degassed at 150 ˚C for 12 hours in N_2 prior to analysis.

Experimental procedure

The pre-reduction of catalyst and the experimental work for the catalytic conversion of cellulose to LA were carried out in a 100 ml stainless steel semi-batch reactor. The pre-reduction of catalyst was conducted with 5 bar of hydrogen gas (H_2). The desired temperature (130 ˚C and 150 ˚C) and agitation speed (600 rpm and 1300 rpm) were set according to the parameters studied for 1 hour. As for the reaction work, after the pre-reduction of catalyst, cellulose was loaded into the reactor containing catalyst and distilled water. The air inside the reactor was purged out using N_2

about three times. Once the desired temperature (170 ˚C and 200 ˚C) had been achieved, the stirring speed (1300 rpm) and timer were set accordingly. The reaction took place for 8 hrs. The samples were collected at the time interval of 0 min, 30 min, 60 min, 120 min, 180 min, and 480 min by opening the valve of the sample port. After releasing the gas inside the reactor, to stop the reaction, the reactor was quenched into a beaker with cold water.

The remaining solid product was collected and filtered using filter paper before drying in the oven at 100 ˚C overnight. The weight was recorded regularly until a constant weight of ±0.005 g was achieved. This data was essential for the calculation of cellulose conversion to products. The final weight of cellulose and cellulose conversion was calculated using Equations 1 and 2, respectively.

The weight of the cellulose could only be obtained at the end of the experiment because the reactor used was a semi-batch reactor. Thus, the remaining solid product could not be collected during the reaction process.

Product analysis

The liquid products were filtered to remove any impurities and analyzed using a High-Performance Liquid Chromatography (HPLC) system: Sugar SH1011 (SHODEX, Japan) with ion exclusion mode (column's physical size: 8.0 mm I.D X 300 mm) and UV as column and detector, respectively. An aqueous solution of sulphuric acid (0.05 M) at a flow rate of 1 ml/min was used as mobile phase and the column temperature was set at 40 ˚C [8].

$$\text{Weight}_{\text{final cellulose}}\,(a) = \text{Weight}_{\text{solid product after drying}} - \text{Weight}_{\text{filter paper}} - \text{Weight}_{\text{catalyst}} \quad (1)$$

$$\text{Cellulose conversion (\%)} = \frac{a - \text{Weight}_{\text{initial cellulose}}}{\text{Weight}_{\text{initial cellulose}}} \times 100\% \quad (2)$$

Results and Discussion

Catalyst characterization (FTIR)

The validation of the decomposition of precursor (nitrate) in the synthesized catalyst after calcination at 500˚C was verified by FTIR analysis. A FTIR spectrum comparison between catalysts before and after calcination was conducted, and the findings are presented in Figures 2 and 3. Table 1 shows the summary of the functional group present in this study.

Based on Figures 2 and 3, a similar trend of FTIR spectrum was obtained for each of the catalysts. The spectral range of 3600-3200 cm^{-1} and 1700-1600cm^{-1} were assigned to the stretching and bending modes of absorbed water molecules through hydrogen bonding, respectively [13,14]. The presence of C-O stretching band at the spectral range of 2400-2300 cm^{-1} represented atmospheric carbon dioxide (CO_2), an impurity and sign that contamination might have occurred [15,14].

The FTIR spectrum around 1450-1300 cm^{-1} proved the presence of nitrate precursor (NO_3^-) in the catalyst (before calcination) [16,17]. The diminishing intensity of the catalyst's peak after calcination implied that the decomposition of nitrate was successful at the calcination temperature of 500 ˚C [14]. As a result, it can be concluded that calcination temperature of 500 ˚C is effective in removing nitrate precursor. On the other hand, an extra peak was discovered from the FTIR spectra analysis for Pd/SiO_2-Al_2O_3 (Figure 2) at the range of 1200-1000 cm^{-1}, showing the presence of Si-O-Si [18,19].

Table 1. Summary of the functional group present in this study

Region	Wavelength (cm^{-1})	Peak Assignment
I	3600-3200	O-H stretching, strong, broad
II	2400-2300	C-O stretching
III	1700-1600	O-H bending
IV	1450-1300	NO_3^- (nitrate)
V	1200-1000 (for Pd/SiO_2-Al_2O_3)	Si-O-Si

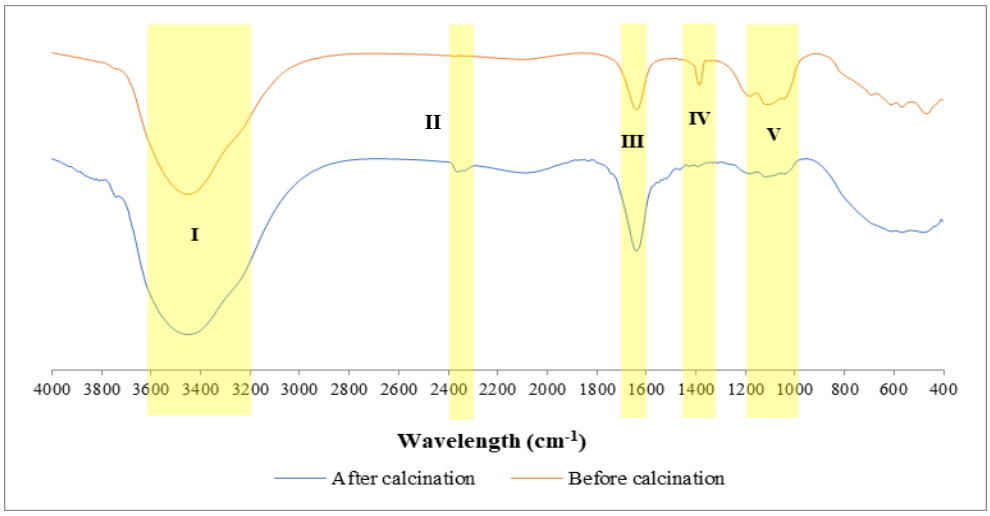


Figure 2. FTIR spectra before and after calcination for catalyst Pd/SiO_2-Al_2O_3

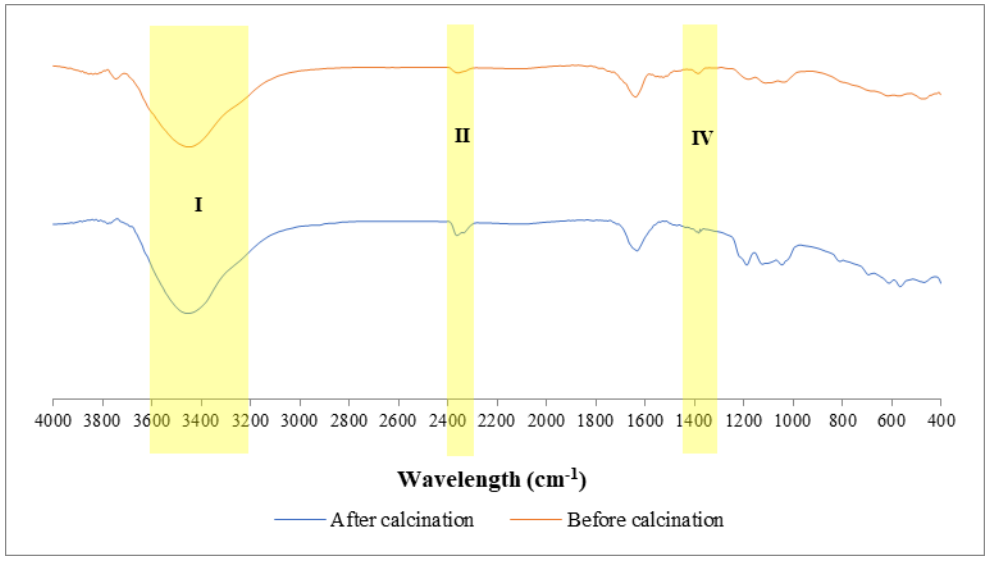


Figure 3. FTIR spectra before and after calcination for catalyst Pd/γ-Al_2O_3

Catalyst characterization (BET)

In heterogeneous catalysts, specific area and pore volume are significant factors to consider especially for the supported catalyst. The BET surface area and pore volume of raw supports and catalysts are listed in Table 2.

Based on Table 2, an increasing trend of surface area and pore volume was observed from raw SiO_2-Al_2O_3 to catalyst Pd/SiO_2-Al_2O_3 (after calcination). The surface area increased from 217.6 m^2/g to 485.6 m^2/g and the pore volume increased from 0.1068 cm^3/g to 0.2459 cm^3/g, which could be explained by the elimination of organic matters where many new pores were formed during the calcination [20]. However, for catalyst Pd/γ-Al_2O_3, the trend of the result was converse from that of the Pd/SiO_2-Al_2O_3 (after calcination) as the surface area and pore volume decreased from raw γ-Al_2O_3 to Pd/γ-Al_2O_3 possibly due to aggregation of catalyst, resulting in losing the surface area and decreasing the pore volume [21].

Catalyst Pd/SiO_2-Al_2O_3 possessed a high pore volume (0.2459 cm^3/g) and surface area (485.6 m^2/g) compared to catalyst Pd/γ-Al_2O_3 (pore volume and surface area of 0.0296 cm^3/g and 79.4 m^2/g, respectively) (Table 2). This could be due to the combination of materials such silica (SiO_2) and alumina (Al_2O_3) that significantly increased the porosity and surface area [22]. Moreover, this observation could be related to the findings according to Table 2 where the pore volume and surface area of the combined materials (SiO_2-Al_2O_3) were two times larger than raw γ-Al_2O_3.

Table 2. BET surface area, pore volume and particle size of raw supports and catalysts

Sample	Surface Area[a] (m^2/g)	Pore Volume[b] (cm^3/g)
SiO_2-Al_2O_3	217.6	0.1068
Pd/SiO_2-Al_2O_3 (After calcined)	485.6	0.2459
γ-Al_2O_3	101.3	0.0504
Pd/γ-Al_2O_3 (After calcined)	79.4	0.0296

[a]: Surface area is obtained from BET method,
[b]: Pore volume is obtained from BET method

Effects of agitation speed during pre-reduction of catalyst and reaction work

Based on Figure 4, at higher agitation speed, an increasing trend in the yield of LA was observed for both of the catalysts. This increasing trend of yield was also seen for HMF and FA, except for glucose possibly because glucose was converted to other products (HMF, LA, and FA). LA produced from cellulose was at the highest (33.5%) when the reaction agitation speed was at 1100 rpm with pre-reduction of Pd/SiO_2-Al_2O_3 catalyst at 1300 rpm. Up to 20.6% of cellulose was successfully converted to products. This high conversion of cellulose and production of LA might be due to the high agitation speed during the reaction; increasing the agitation speed increases the contact area and relative velocity between the two phases, and hence diminishes any external diffusion limitations [23]. Furthermore, the higher surface area and pore volume of Pd/SiO_2-Al_2O_3 catalyst (485.6 m^2/g and 0.2459 cm^3/g, respectively) caused the high conversion of cellulose and yield of LA as these properties led to the high availability of catalytic activity sites [24]. Thus, high catalytic activity could occur during the reaction compared to the usage of Pd/γ-Al_2O_3 catalyst, which possessed a smaller surface area and pore volume of 79.4 m^2/g and 0.0296 cm^3/g, respectively. Owing to these properties, an increment of only 6.4% of LA

yield was observed for catalyst Pd/γ-Al_2O_3 when an increase of reaction speed from 200 rpm to 1100 rpm was employed, with 12.2% of cellulose being converted to products.

Even though the usage of high agitation speed during the pre-reduction catalyst (activation) is not as crucial as high temperature [25], increasing agitation speed during the pre-reduction of catalyst might improve the performance of the catalyst by increasing the surface contact of the catalyst with H_2 which can activate the catalyst prior to the reaction [26]. The pre-reduction for both of the catalysts was aimed to reduce palladium oxide to metallic Pd. As a result, it can be concluded that the reaction agitation speed of 1100 rpm with the catalyst pre-reduction agitation speed at 1300 rpm was the most ideal condition in this study for further experimentation.

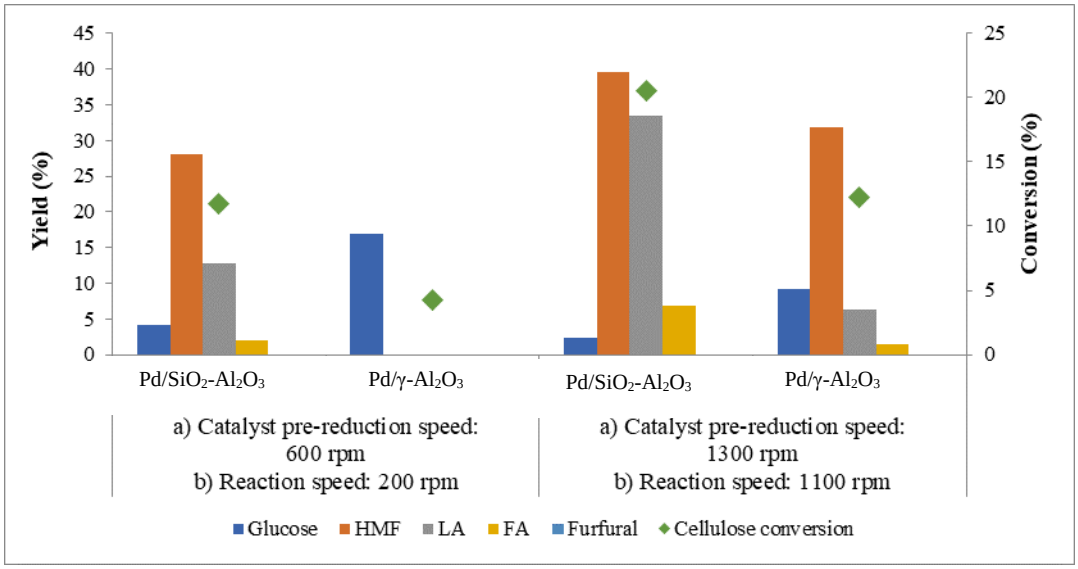


Figure 4. Effects of agitation speed on the conversion of cellulose to LA at 8 hours. Note: a) Catalyst pre-reduction condition: 0.5 g of catalyst, and 5 bar of H_2 at 130 ˚C for 1 hour; b) Reaction condition: 4 g of cellulose, 0.5 g of catalyst, reaction temperature of 170 ˚C, and reaction time of 8 hours.

Effects of temperature during pre-reduction of catalyst and reaction work

Temperature plays a significant role in the production of LA from cellulose, particularly at higher temperatures as demonstrated in a previous study [27]. The effects of temperature on the production of LA from cellulose at different cellulose loading is shown in Figure 5.

Based on Figure 5, a significant increment in the conversion of cellulose and production of LA was observed when the reaction temperature increased from 170 ˚C to 200 ˚C with catalyst pre-reduction at 150 ˚C. Except for glucose, the production of intermediate products and by-products such as HMF and FA, respectively also increased as the reaction temperature rose. According to this study, as the temperature increased (from 170 ˚C to 200 ˚C), the cellulose conversion increased gradually from 20.6% to 73.9% when Pd/SiO_2-Al_2O_3 catalyst (pre-reduction of catalyst at the temperature of 150 ˚C) was employed in the system where the highest LA was produced (up to 43.3%) possibly since the higher reaction temperature accelerated the rate of chemical reaction and provided a faster route for the cellulose to convert to products [8]. Furthermore, a higher reaction temperature promotes greater contact between cellulose and water molecules, resulting in a complete process of cellulose bond breaking to form LA [28]. A similar trend of results was observed with Pd/SiO_2-Al_2O_3 catalyst when

$Pd/\gamma\text{-}Al_2O_3$ catalyst was employed in the system; the conversion of cellulose and yield of LA increased as the reaction temperature increased. However, the conversion of cellulose and yield of LA were lower using $Pd/\gamma\text{-}Al_2O_3$ catalyst in the system compared to $Pd/SiO_2\text{-}Al_2O_3$ catalyst. The conversion of cellulose and yield of LA were only up to 37.1% and 9.5%, respectively.

Moreover, one of the parameters that improved the catalyst efficiency was increasing the temperature from 130 ˚C to 150 ˚C during the pre-reduction of the catalyst. It is advised to heat the catalyst at a high temperature during the catalyst pre-reduction for the metal to finely disperse on the support. Under these high temperatures during heating the catalyst, the mobility of the catalyst can be enhanced, increasing the active site of the catalyst, and thus greatly influencing the catalytic activity [25].

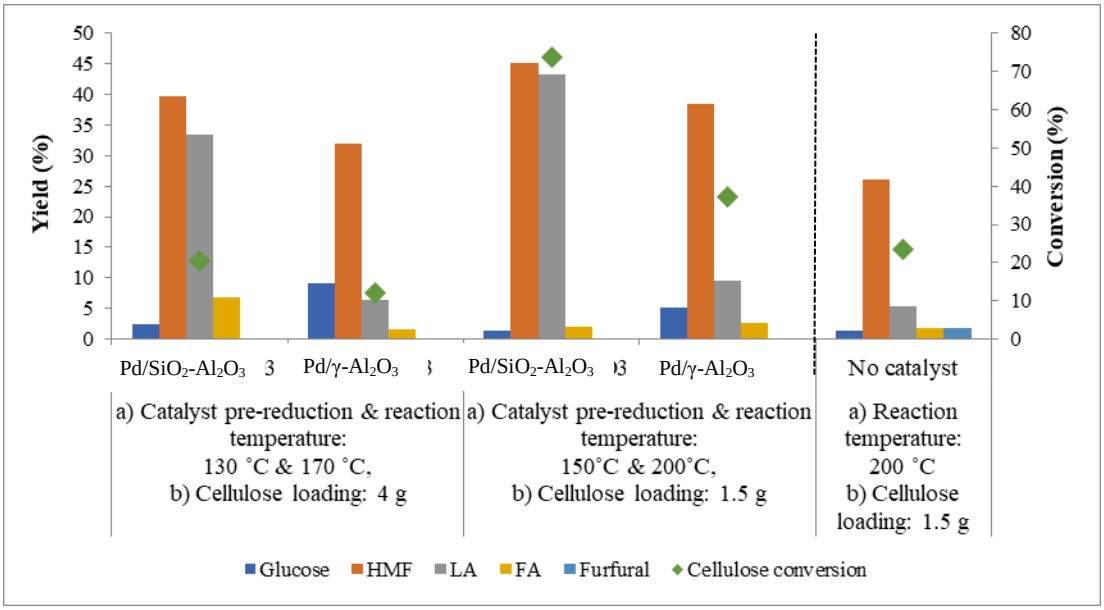


Figure 5. Effects of temperature on the conversion of cellulose towards LA at 8 hours. Note: a) Catalyst pre-reduction condition: 0.5 g of catalyst, agitation speed of 1300 rpm, and 5 bar of H_2 for 1 hour; b) Reaction condition: 0.5 g of catalyst, agitation speed of 1100 rpm, and reaction time of 8 hours

Effects of substrate loading

Based on Figure 5, the yield of LA increased gradually for all the catalysts ($Pd/SiO_2\text{-}Al_2O_3$ and $Pd/\gamma\text{-}Al_2O_3$) when 1.5 g of cellulose was used in the reaction (under high-temperature conditions). Increasing the substrates loading might lead to the increasing cellulose availability for the conversion, with a high concentration of LA being produced; however, the yield of LA was shown to eventually decrease as the cellulose loading increased. This might be due to the reactivity diminution or insufficient catalyst dosage for the additional cellulose [4].

Moreover, a blank experiment (without catalyst) was conducted for reference purposes. It was conducted under the ideal condition highlighted in this study. LA produced was at its lowest (5.3%) compared to the other reactions that used catalyst. This might be due to the side reaction that occurred during the reaction where it resulted in the production of furfural [29]. According to Figure 5, it can be highlighted that the production of HMF was more favorable if no catalyst was employed in the system.

Figure 6 shows the reaction profile of reaction using Pd/SiO_2-Al_2O_3 under the high condition in cellulose depolymerization, leading to the formation of LA. According to Figure 6, the yield of all products (HMF, LA, and FA) increased overtime except for glucose. An increasing yield of glucose was reported until 2 hours of reaction, then the yield subsequently decreased. This might be due to the glucose already being used up in converting to other products. Since the hydrolysis of cellulose to glucose was the rate-determining step, once glucose was formed, it was much easier to break down the glucose bond to other products. Hence, it resulted in the formation of HMF (5.73%), LA (17.4%), and FA (0.77%) at the 30 min of reaction time. As a result, 73.9% of cellulose was converted to products, and 43.4% of LA yield was produced at the end of the reaction.

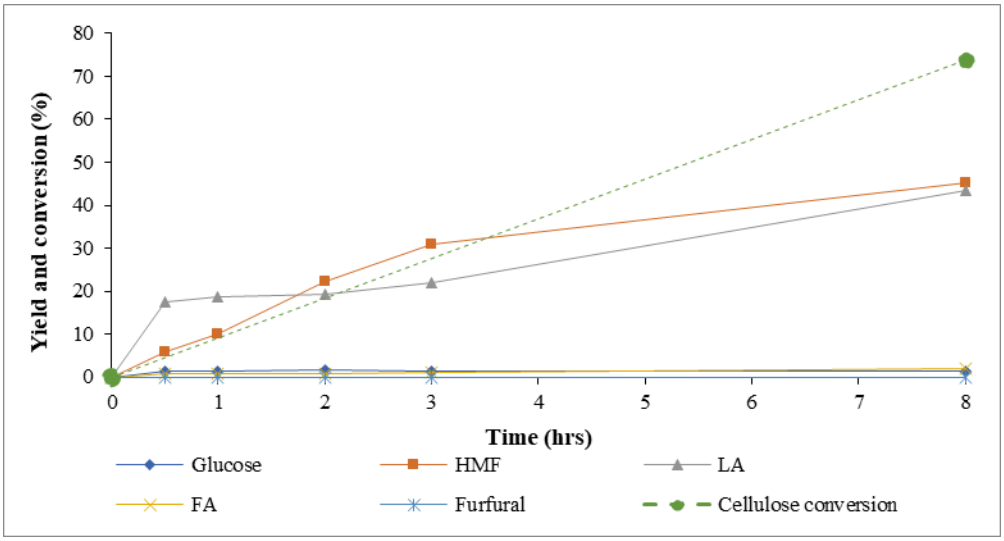


Figure 6. Reaction profile for catalyst Pd/SiO_2-Al_2O_3. Note: Reaction condition: 1.5 g of cellulose, 0.5 g of catalyst (pre-reduction at an agitation speed of 1300 rpm in H_2 at 150˚C for 1 hour), reaction temperature of 200 ˚C, agitation speed of 1100 rpm, and reaction time of 8 hours.

Conclusion

From this research, it can be concluded that the conversion of cellulose to LA is highly influenced by the reaction parameters: agitation speed (1100 rpm), temperature (200 ˚C), and substrate loading (1.5 g) with catalyst pre-reduction at the temperature of 150 ˚C and stirred at 1300 rpm for 1 hour. It was observed that under these conditions, the LA produced was at the highest which was 43.3% and the conversion of cellulose was up to 73.9%. Moreover, the higher surface area (485.6 m^2/g) and pore volume (0.2459 cm^3/g) of Pd/SiO_2-Al_2O_3 catalyst showed better performance to produce LA from cellulose compared to Pd/γ-Al_2O_3.

Acknowledgments

The authors would like to express their highest gratitude for the financial support from the Ministry of

Higher Education (MOHE) (under the Fundamental Research Grant Scheme, FRGS/1/2018/ TK02/UNIKL/02/3), Universiti Kuala Lumpur Malaysian Institute of Chemical and Bioengineering Technology (UniKL MICET), and Majlis Amanah Rakyat Malaysia (MARA).

References

1. Caretto, A. and Perosa, A. (2013). Upgrading of levulinic acid with dimethylcarbonate as solvent/ reagent. *Sustainable Chemistry & Engineering*, 1(8): 6-11.
2. Dhepe, P. L. and Fukuoka, A. (2007). Cracking of cellulose over supported metal catalysts. *Catalysis Surveys from Asia*, 11(4): 186-191.
3. Shrotri, A., Kobayashi, H. and Fukuoka, A. (2018). Cellulose depolymerization over heterogeneous catalysts. *Accounts of Chemical Research*, 51(3): 761-768.
4. Peng, L., Lin, L., Zhang, J., Zhuang, J., Zhang, B. and Gong, Y. (2010). Catalytic conversion of cellulose to levulinic acid by metal chlorides. *Molecules*, 15: 5258-5272.
5. Signoretto, M., Taghavi, S., Ghedini, E. and Menegazzo, F. (2019). Catalytic production of levulinic acid (LA) from actual biomass. *Molecules (Basel, Switzerland)*, 24(15): 1-20.
6. Jeong, H., Jang, S., Hong, C. and Kim, S. (2016). Levulinic acid production by two-step acid-catalyzed treatment of *Quercus mongolica* using dilute sulfuric acid. *Bioresource Technology*, 225: 1-28.
7. Thunyaratchatanon, C., Sinsakullert, W., Luengnaruemitchai, A. and Faungnawakij, K. (2019). 5-hydroxymethylfurfural production from hexose sugars using adjustable acid- and base-functionalized mesoporous SBA-15 catalysts in aqueous media. *Biomass Conversion and Biorefinery*, 2019: 1-15.
8. Li, G., Liu, W., Ye, C., Li, X. and Si, C. L. (2018). Chemocatalytic conversion of cellulose into key platform chemicals. *International Journal of Polymer Science*, 2018: 1-20.
9. Li, X., Zhang, L., Wang, S. and Wu, Y. (2020). Recent advances in aqueous-phase catalytic conversions of biomass platform chemicals over heterogeneous catalysts. *Frontiers in Chemistry*, 7(948): 1-21.
10. Xu, S., Yan, X., Bu, Q. and Xia, H. (2017). Catalytic conversion of cellulose into polyols using carbon-nanotube-supported monometallic Pd and bimetallic Pd–Fe catalysts. *Cellulose*, 24(6): 2403-2413.
11. Yoshimura, A., Tochigi, S. and Matsuno, Y. (2021). Fundamental study of palladium recycling using "dry aqua regia" considering the recovery from spent auto-catalyst. *Journal of Sustainable Metallurgy*, 7(1): 266-276.
12. Kamal, P. N. S. M. M., Mohamad, N. I., Serit, M. E. A., Rahim, N. S. A., Jimat, N. I. and Alikasturi, A. S. (2020). Study on the effect of reaction and calcination temperature towards glucose hydrolysis using solid acid catalyst. *Materials Today: Proceedings*, 31(8)*:* 282-286.
13. Benkhaled, M., Morin, S., Pichon, C., Thomazeau, C., Verdon, C. and Uzio, D. (2006). Synthesis of highly dispersed palladium alumina supported particles: Influence of the particle surface density on physico-chemical properties. *Applied Catalysis A: General*, 312(1–2): 1-11.
14. Yabushita, M., Kobayashi, H., Hara, K. and Fukuoka, A. (2014). Quantitative evaluation of ball-milling effects on the hydrolysis of cellulose catalysed by activated carbon. *Catalysis Science and Technology*, 4(8): 2312-2317.
15. Anderson, I. E., Shircliff, R. A., MacAuley, C., Smith, D. K., Lee, B. G., Agarwal, S., Stradins, P. and Collins, R. T. (2012). Silanization of low-temperature-plasma synthesized silicon quantum dots for production of a tunable, stable, colloidal solution. *Journal of Physical Chemistry C*, 116(6): 3979-3987.
16. Zhang, H., Huang, H., Ji, Y., Qiao, Z., Zhao, C. and He, J. (2010). Preparation, characterization, and application of magnetic Fe-SBA-15 mesoporous silica molecular sieves. *Journal of Automated Methods and Management in Chemistry*, 2010(1463–9246): 323509.

17. Amadine, O., Essamlali, Y., Fihri, A., Larzek, M. and Zahouily, M. (2017b). Effect of calcination temperature on the structure and catalytic performance of copper-ceria mixed oxide catalysts in phenol hydroxylation. *RSC Advances*, 7(21): 12586-12597.
18. Yadav, M. K., Kothari, A. V. and Naik, D. G. (2009). Morphological silica-supported acid catalyst for esterification of aliphatic fatty acid. *Green Chemistry Letters and Reviews*, 2(3):181-197.
19. Shah, K. A., Parikh, J. K., Dholakiya, B. Z. and Maheria, K. C. (2014). Fatty acid methyl ester production from acid oil using silica sulfuric acid: Process optimization and reaction kinetics. *Chemical Papers*, 68(4): 472-483.
20. Amadine, O., Essamlali, Y., Fihri, A., Larzek, M. and Zahouily, M. (2017a). Effect of calcination temperature on the structure and catalytic performance of copper-ceria mixed oxide catalyst in phenol hydroxylation. *RSC Advances*, 7:12586-12597.
21. Inmanee, T., Pinthong, P. and Jongsomjit, B. (2017). Effect of calcination temperatures and mo modification on nanocrystalline (γ-χ)-Al_2O_3 catalysts for catalytic ethanol dehydration. *Journal of Nanomaterials*, 2017(2011): 1-9.
22. Rahmati, M., Huang, B., Mortensen, M. K., Keyvanloo, K., Fletcher, T. H., Woodfield, B. F., Hecker, W. C. and Argyle, M. D. (2018). Effect of different alumina supports on performance of cobalt Fischer-Tropsch catalysts. *Journal of Catalysis*, 359: 92-100.
23. Ahlkvist, J. (2013). Formic and levulinic acid from cellulose via heterogeneous catalysis. Doctoral dissertation, Umeå Universitet.
24. Klinghoffer, N. B., Castaldi, M. J., Nzihou, A. (2012). Catalyst properties and catalytic performance of char from biomass gasification. *Industrial and Engineering Chemistry Research*, 51(40): 13113-13122.
25. Fadoni, M. and Lucarelli, L. (1999). Temperature programmed desorption, reduction, oxidation and flow chemisorption for the characterisation of heterogeneous catalysts. Theoretical aspects, instrumentation and applications. *Studies in Surface Science and Catalysis*, 120: 177-225.
26. Shim, W. G., Lee, J. W. and Kim, S. C. (2008). Analysis of catalytic oxidation of aromatic hydrocarbons over supported palladium catalyst with different pretreatments based on heterogeneous adsorption properties. *Applied Catalysis B: Environmental*, 84(1-2): 133-141.
27. Yuan, Z., Long, J., Xia, Y., Zhang, X. and Wang, T. (2016). Production of levulinic acid from *Pennisetum alopecuroides* in the presence of an acid catalyst. *Bioresources*, 11(2): 3511-3523.
28. Watanabe, M., Aizawa, Y., Iida, T., Aida, T. M., Levy, C., Sue, K. and Inomata, H. (2005). Glucose reactions with acid and base catalysts in hot compressed water at 473 K. *Carbohydrate Research*, 340: 1925-1930.
29. Liu, L., Li, Z., Hou, W. and Shen, H. (2018). Direct conversion of lignocellulose to levulinic acid catalyzed by ionic liquid. *Carbohydrate Polymers*, 181(7): 778-78.

Malaysian Journal of Analytical Sciences (MJAS)
Published by Malaysian Analytical Sciences Society

PHYSICAL AND CHEMICAL DISCRIMINATION OF METHAMPHETAMINE TABLETS FOR FORENSIC INTELLIGENCE

(Diskriminasi Fizikal dan Kimia bagi Pil Metamfetamin untuk Perisikan Forensik)

Noor Azlina Awang[1,2], Khai Lee[1], Way Koon Teoh[1], Vanitha Kunalan[3], Ahmad Fahmi Lim Abdullah[1], Kah Haw Chang[1]*

[1]Forensic Science Programme, School of Health Sciences,
Universiti Sains Malaysia, 16150 Kubang Kerian, Kelantan, Malaysia
[2]Department of Chemistry Malaysia (Kelantan Branch), 16100 Panji, Kota Bharu, Malaysia
[3]Narcotics Division, Forensic Science Analysis Centre,
Department of Chemistry, Jalan Sultan, 46661 Petaling Jaya, Selangor, Malaysia

**Corresponding author: changkh@usm.my*

Received: 16 September 2021; Accepted: 10 November 2021; Published: 25 February 2022

Abstract

Illicit methamphetamine seizures have risen significantly worldwide, and its widespread use threatens societal well-being. Thus, attention from various parties is required to stem methamphetamine trafficking; however, routine forensic analysis is generally limited to identifying and quantifying the controlled substances according to standard operating procedures. Although further analytical characterization and drug profiling via physical and chemical methods is not routinely conducted, it warrants further exploration for forensic comparison and intelligence. In this study, the physical and chemical profiles of seized illicit methamphetamine tablets were obtained employing various analytical techniques, including physical examination, attenuated total reflectance-Fourier transformed infrared (ATR-FTIR) spectroscopy, thin layer chromatography (TLC), and gas chromatography (GC). Physical characterization did not enable the identification of methamphetamine, but sample discrimination based on unique logos and dimensions was achieved. Based on ATR-FTIR and principal component analysis results, caffeine was found to be the most common adulterant, while the dyes used in the composition were identified via TLC analysis. GC analysis results confirmed the presence of methamphetamine and its quantity. Overall, a methamphetamine tablet profiling strategy was implemented to gather important information regarding the similarities and differences among illicit methamphetamine tablets, potentially beneficial for sample-to-sample, case-to-case, and seizure-to-seizure comparisons.

Keywords: forensic science, methamphetamine, drug profiling, physical examination, chemical analysis

Abstrak

Rampasan metamfetamin haram telah meningkat dengan ketara di seluruh dunia and penggunaannya secara meluas telah mengancam kesejahteraan masyarakat. Justeru, perhatian daripada pelbagai pihak adalah diperlukan untuk mengurangkan penjualan metamfetamin. Namun begitu, analisis forensik rutin secara umumnya dihadkan kepada pengenalpastian dan pengkuantitian bahan terkawal berdasarkan prosedur operasi standard. Sungguhpun pencirian analitikal dan pemprofilan dadah seterusnya melalui kaedah fizikal dan kaedah kimia tidak dilaksanakan secara rutin, hal ini membolehkan penerokaan selanjutnya untuk perbandingan dan perisikan forensik. Dalam kajian ini, profil fizikal and profil kimia pil metamfetamin haram

yang dirampas telah diperoleh dengan menggunakan pelbagai teknik analitikal, termasuk pemeriksaan fizikal, spektroskopi transformasi inframerah Fourier dengan pantulan keseluruhan dikecilkan (ATR-FTIR), kromatografi lapisan nipis (TLC) dan kromatografi gas (GC). Pencirian fizikal tidak membolehkan pengenalpastian metamfetamin tetapi diskriminasi sampel berdasarkan logo dan dimensi unik telah dicapai. Berdasarkan keputusan ATR-FTIR dan analisis komponen utama, kafien dinampakkan sebagai bahan adukan yang paling lazim, manakala pewarna yang digunakan dalam kandungan telah dikenal pasti melalui analisis TLC. Keputusan analisis GC telah memastikan kehadiran metamfetamin and kuantitinya. Secara keseluruhannya, satu strategi pemprofilan pil metamfetamin telah dilaksanakan untuk mengumpulkan maklumat penting berkenaan dengan kesamaan dan perbezaan antara pil metamfetamin haram. Hal ini berpotensi dalam memanfaatkan perbandingan sampel kepada sampel, kes kepada kes, dan rampasan kepada rampasan.

Kata kunci: sains forensik, metamfetamin, pemprofilan dadah, pemeriksaan fizikal, analisis kimia

Introduction

Methamphetamine acts on the central nervous system by stimulating excessive dopamine secretion [1]; thus, it has become one of the most abused stimulants worldwide, as evidenced by a sevenfold increase in global seizures thereof over the past two decades [2]. Although methamphetamine possession, trafficking, and manufacture is strictly enforced and punishable by law worldwide, cases of its abuse are increasing globally, especially in the United States, Europe, Australia, and New Zealand [2]. Users in East and South-East Asia account for more than 30% of the total estimated worldwide users of amphetamine-type stimulant (ATS) [2]. The severe societal well-being deterioration associated with illicit methamphetamine use necessitates collective strategic action, both domestically and internationally.

In recent years, methamphetamine manufacture in the United States, China, and the Islamic Republic of Iran has reportedly decreased, but a significant expansion of illicit methamphetamine drug trafficking has been encountered in Mexico, as well as in East and South-East Asia [3,4], suggesting a gradual shift in this illicit black market from North America to East and South-East Asia. Malaysia, the country where the present study was based, has reported a sharp increase in seized methamphetamine since 2015, wherein approximately 5.8 tons of crystalline methamphetamine and more than 1.6 million illicit methamphetamine tablets had been seized law enforcement authorities in 2019 alone [2]. Recent statistics and trend analyses have indicated that the expansion of the methamphetamine black market in East and South-East Asia has been driven by supply, as the organized crime groups have adapted their trafficking routes in response to law enforcement operations [5,6]. In fact, the growing methamphetamine manufacture in the region has also been supported by an increase in the diversion and trafficking of precursors and related chemicals [6].

Methamphetamine can appear in various forms: as an oily paste consisting of methamphetamine free-base, as a solid, which is the methamphetamine salt form, whereby high-purity methamphetamine salt can appear in crystalline form, commonly termed as “crystal” or “ice”. Methamphetamine is also commonly processed into tablet form known as “Yaba” tablets in Asia, especially in the golden triangle region bounded by Thailand, Laos, and Myanmar. Countries such as Malaysia, Australia, and China are inundated by transnational drug trafficking [7]. Transnational efforts to identify and disrupt the supply chain are therefore crucial. In routine forensic analysis, testing is frequently limited to identifying and quantifying the controlled substance in the illicit drug sample. However, limited information is retrieved regarding the source of origin, supply, trafficking, and distribution network thereof without further post-seizure profiling studies. Studies focused on the profiling of methamphetamine have been conducted, generally employing gas chromatographic techniques [8-10]. However, analytical characterization via physical and chemical methods is less likely to be conducted in forensic laboratories, and therefore gathering further information is required for subsequent forensic comparisons and intelligence. In non-ideal clandestine

laboratory production, the chemical composition of illicit drugs can vary significantly [11]. Illicit drug profiling involving the characterization of seized samples in a systematic manner should be conducted to elucidate the connection between suppliers, distributors, and users [11]. In this study, the physical and chemical profiles of illicit methamphetamine tablets were investigated employing various analytical techniques. Integrated approach for profiling illicit drugs could potentially support forensic intelligence [11-13] and be particularly useful for law enforcement authorities.

Materials and Methods

Standards and samples

Illicit methamphetamine tablets (164 samples) seized between January 2019 and December 2020 were used in this study. Methamphetamine, ephedrine, and caffeine standards were sourced from certified reference material suppliers, while various sugars, including glucose, lactose, dextrose, maltose, and mannitol were obtained from Merck (Whitehouse Station, NJ). For thin layer chromatography (TLC) analysis, various dye standards, including Amaranth, Rhodamine B, Erythrosine BS, Carmoisine, Red 2G, Ponceau 4R, Tartrazine, Sunset Yellow, Fast Green, Green S, and Brilliant Blue were sourced from Merck (Whitehouse Station, NJ). All solvents used, including glacial acetic acid, 25% w/w ammonia (S.G. 0.880), acetone, methanol, 2-propanol, n-butanol, and butanone, were of analytical grade. Nortriptyline HCl was used as the internal standard (IS) for gas chromatography (GC) analysis. Chloroform and methanol used to dissolve the standards and samples were of GC grade and were sourced from Merck (Whitehouse Station, NJ).

Physical examination

Physical examination was performed on the seized tablets by observation of the stamp or logo on each tablet, and that of their respective colors. The diameter and thickness of each sample (± 0.02 mm) were also measured using vernier calipers, while the weight (± 0.01 mg) was determined using an analytical balance. All physical characteristics were recorded and compared.

Attenuated total reflectance-fourier transform infrared spectroscopy

Various drug and adulterant standards, and the illicit methamphetamine samples in powdered form were analyzed directly using a Bruker Fourier transformed infrared (FTIR) Tensor 27 instrument (Bruker Corporation, Billerica, MA) equipped with a single-reflection zinc selenide attenuated total reflectance (ATR) sampling accessory, at a controlled ambient temperature (≈25˚C). Approximately 10 mg of the standard or sample was placed onto the ATR crystal to obtain their ATR-FTIR profiles. A background spectrum was recorded before each analysis run and absorbances were measured in the wavelength range between 4000 and 600 cm^{-1}. The resolution was set at 4 cm^{-1} and 16 scans were performed. The built-in software, OPUS 7.0.122 (Bruker Corporation, Billerica, MA) was utilized for spectrum acquisition. All spectra were recorded in duplicate, compared, and the differences evaluated. A repeatability test was performed by analyzing a representative sample thrice. A reproducibility test was also performed by analyzing a representative sample on three consecutive days. All spectral data were reported as absorbance values at each data point for subsequent interpretation and comparison.

It is often the case that the illicit drugs seized in forensic cases are normally in the form of mixture, which not only contain the drug alone but also adulterants and/or diluents. The influence of mixture composition on the respective ATR-FTIR profiles was investigated. Mixture samples consisting of methamphetamine and different adulterants in varying quantities were prepared. Based on the literature search, caffeine, ephedrine, and various sugars are more common [14,15]. Caffeine is a legal substance, inexpensive and readily available. The stimulant properties of caffeine could also create milder but very similar effect of methamphetamine. Ephedrine is the precursor during manufacturing, usually through Nagai pathway. On the other hand, sugars do not contribute to any additional effects on the methamphetamine but used to dilute or add the bulk of the illicit drugs. Being legal and readily available, sugars give greater margin to the illicit drug manufacturers [14,15]. In this study,

four commonly reported adulterants were used, namely caffeine, ephedrine, lactose, and mannitol. The mixtures (w/w) of methamphetamine and the respective adulterant were prepared at 100%, 90%, 75%, 50%, 25%, 10%, and 0%. All the prepared mixtures then underwent ATR-FTIR analysis.

For statistical analysis, data points of regions with noticeable variations, in the ranges of 3200-2550 cm^{-1} and 1800-600 cm^{-1}, were used. Data points of all ATR-FTIR spectra were transferred into Microsoft Excel® (Redmond, WA) and normalized to remove any possible variation resulting from inconsistent sample quantity. This was done by dividing the absorbance value at each data point to the total absorbance under the spectrum of the standards and samples. The normalized data were then analyzed using Minitab 18 software (Minitab Inc., State College, PA). Principal component analysis (PCA) was implemented for the characterization of illicit methamphetamine samples, and any potential differences among the samples were evaluated.

Thin layer chromatography

Prior to TLC analysis, the dye was extracted from the tablets to remove any sugars, fats, or other substances contained in a tablet [16,17]. The presence of any sugar might cause blurring of the spots upon TLC analysis [18]. Therefore, acidification coupled with alkaline treatment on the samples was suggested for the extraction of dye from tablet-coating formulations [17-19].

Dyes present in the samples were extracted for TLC analysis according to the following procedure. Approximately 10 mg of powdered sample was transferred into a vial. Acetic acid (5% v/v) was added to the vial, followed by the introduction of a knotted piece of white knitting wool, 5 cm in length. Knitting wool was knotted to avoid disassembling of the thread. Note that the wool was firstly washed with dilute ammonium hydroxide and water to minimize the effect of possible interference and to enhance the absorption of dye onto the treated wool. Warming of the mixture in a temperature range of 70-80ºC allowed the transfer of dye onto the knitting wool, and the entire procedure was complete within approximately 15 min. Then, the wool was carefully removed using tweezers and washed thoroughly with distilled water. The treated wool, now visibly colored, was dried and then placed into another vial. Dye extraction was performed by adding 1 mL of a solution consisting of equal volumes of acetone and 3N ammonia and warming for 15 min between 70-80ºC, after which time the wool was removed from the vial. Finally, the resultant dye solution was gently warmed in a water bath to evaporate the solvent and concentrate the solution. All the targeted dye standards were prepared following the above-described procedure for comparison.

TLC separation was performed using silica gel 60 F254 (Merck, Darmstadt, Germany). Four solvent systems were evaluated to select the optimal system for the separation of dyes possibly contained in illicit methamphetamine tablets. The four solvent systems were as follows:

(1) Solvent system A- isopropanol: ammonia (4:1)
(2) Solvent system B- n-butanol: glacial acetic acid: water (10:5:6)
(3) Solvent system C- acetone: butanone: ammonia: water (60:140:1:60)
(4) Solvent system D- isopropanol: ammonia: water (7:2:1)

The various dye solutions obtained from the samples were analyzed using the optimal solvent system. All the visible bands were compared to those of the reference dye standards. The TLC plates were also visualized under UV light to detect the presence of fluorescent spots. Any potential differences among the illicit drugs samples were evaluated based on their TLC profile and the respective dyes contained in the tablets were identified.

Gas chromatography

A methamphetamine standard containing a precisely known concentration thereof was used in both qualitative and quantitative analyses using gas chromatography-mass spectrometry (GC-MS) and a gas chromatography-flame ionization detector (GC-

FID), respectively. Prior to sample analysis, a calibration curve was constructed using the data obtained from the GC-FID analysis of methamphetamine calibration standards in a concentration range of 0.10 – 1.40 mg/mL. Such calibration range had allowed the determination of concentration of the target substance within an illicit tablet. Note that the GC method was adapted from United Nations Office on Drugs and Crime [20] and is utilized in the country of study for routine forensic analysis.

A Perkin Elmer Clarus 600 Gas Chromatographic system coupled with Mass Spectroscopy (MS) (Perkin Elmer, Waltham, MA) was used to confirm the presence of methamphetamine using a HP-5 capillary column (30 m × 0.25 mm i.d., 0.25 µm film thickness) (Agilent Technologies, Santa Clara, CA). Purified helium gas (99.99%) was used as the carrier gas at a constant flow rate of 1.5 mL/min. The front injection temperature was set to 270°C. The initial temperature was 80°C, and it was held for 1 min. The temperature was then increased to 200°C at 30°C/min, followed by a further increase to 270°C at 50°C/min. The final temperature was held for 1.0 mins. The temperature of the transfer line of the MS detector was set to 280°C. The data acquisition rate was 1.0 sec/scan and mass fragments were collected in the 50–500 m/z range. Turbomass Ver 5.4.2 Properties (Perkin Elmer, Waltham, MA) was used for data analysis. The spectra of the target compounds were interpreted, evaluated, and the resultant peaks were identified using the mass spectral library (NIST MS 2014 version 2.2) (National Institute of Standards and Technology, Gaithersbury, MD).

An Agilent 7890B Gas Chromatography system equipped with a split/splitless injector, and an FID (Agilent Technologies, Santa Clara, CA) was used for methamphetamine quantification upon positive identification based on GC-MS results. Liquid injection was performed at a constant inlet temperature of 270°C. Chromatographic separation was achieved using a HP-5 capillary column (30 m × 0.32 µm i.d., 0.25 µm film thickness). Purified helium gas (99.99%) was used as the carrier gas at a constant flow rate of 0.6 mL/min. The initial oven temperature was set at 150°C and held for 1 min. A temperature ramp of 30°C/min was selected to reach the maximum of 270°C and held for 2.5 min. Hydrogen flow, air flow, and the make-up flow were supplied to the detector at 30, 400, and 29.4 mL/min, respectively. Standard solution (1 µL) was introduced into the injector port. Chemstation software (Rev. B.04.02, Agilent, Santa Clara, CA) was used for GC automation and data analysis. All standards and IS were identified by comparison of the retention times.

The drug samples were prepared by weighing an accurately weighed amount of the powdered sample into a 10 mL volumetric flask. The sample was then dissolved using the IS solution to the levelling of mark and ultrasonicated for five minutes to allow for complete dissolution. An IS solution with a concentration of 0.60 mg/mL nortriptyline HCl was used. The solution formed upon the sonication was transferred into GC vial and properly labelled. All prepared samples were then introduced into the GC systems.

Upon analysis by GC-FID, the area under the chromatogram of each peak was integrated and the peak area ratio of the target substance was determined. The percentage of methamphetamine was calculated using Equation 1.

$$\% \text{ methamphetamine} = [(\text{Concentration} \times 10)/\text{weight of sample taken}] \times 100\% \quad (1)$$

where concentration is in mg/mL; 10 is the volume of dissolved sample in a 10 mL volumetric flask, and weight of sample taken is measured in mg. The purity among all the samples tested in this study was then compared.

Drug profiling strategy

A drug profiling scheme involving the physical characterization and chemical analyses of illicit methamphetamine tablets was conducted in that order. A comparative study was performed on the samples

and possible differences were determined on a case-by-case basis.

Results and Discussion

A total of 164 seized illicit methamphetamine tablets were analyzed in this study. Among them, six were green in color (3.7%), differing from the commonly encountered red tablets (96.3%). Therefore, the six green samples were labelled as G01-G06, while the remaining 158 samples were labelled as S001–S158.

Physical examination

Color

The samples analyzed in this study were predominantly red. However, the red color of each tablet differed slightly in terms of the hue, likely due to the use of different dyes. Some tablets appeared cherry-red, while some were maroon in color. Such variation in color could be due to the presence of different dyes or combinations of dyes that had been used in the manufacturing process, which can be determined by chemical analysis of the dye composition. In addition to the red tablets, six tablets were green in color. Generally, only one or two such green tablets are encountered in larger packages of seized samples containing 100 or 200 tablets.

Logo variant

All the methamphetamine tablets were round in shape with a deep convex center. A specific logo was observed on one of the sides, consisting of the letter's "w" and "y", as shown in Figure 1. However, different variations of the logo were noted, whereby "wY", "WY," or "wy" were present. In our case, the "wY" logo was dominant with 155 out of 164 samples (94.5%) being stamped with it [Figure 1(a)-(d)]. A slight variation in the size and positioning of the markings was also noted among the "wY"-labelled tablets, likely due to the use of different tableting machines. Some of the tablets exhibited deeply stamped logos, whereby the two letters could be seen clearly (Figure 1(a)-(b)), while most of the logos appeared very faint (Figure 1(c)-(d)).

Previous studies have indicated that such variations are a result of manufacture by different drug syndicates [21]. Tablets with the "wY" insignia were the most common in the sample set, and it is believed that they are produced by the United Wa State Army [21]. The other two variants, that is tablets bearing the "WY" and "wy" logos, were not common, being noted on only two (1.2%) [Figure 1(e)] and one sample (0.6%), respectively, [Figure 1(f)]. Reportedly, the former variant likely originated from the Myanmar National Defense Alliance Army, while the latter was produced by the Shah United Army 15. The "Wy" insignia was not observed among our seized samples; neither were other less common variants, such as "R", "OK", "888", and "Ã/99" [21,22]. None of the tablets bore an imprint on the reverse side.

The presence of a logo indicated the unique physical characteristics of the methamphetamine tablets, as it appeared on most of our tested samples. However, drug syndicates and trafficking groups other than those mentioned above reportedly stamp the same logos on their tablets, essentially counterfeiting illicit methamphetamine tablets [21,23]. As the samples tested in this study had all been seized, they could have been exposed to unknown physical and environmental conditions; thus, the faintness of the markings and/ or the rough texture of some tablets possibly resulted from exposure to moisture or due to transport and handling practices. Tablets whereby the logo on the surface could not be clearly determined through visual observation accounted for 3.7% of the total samples, or six out of 164 samples.

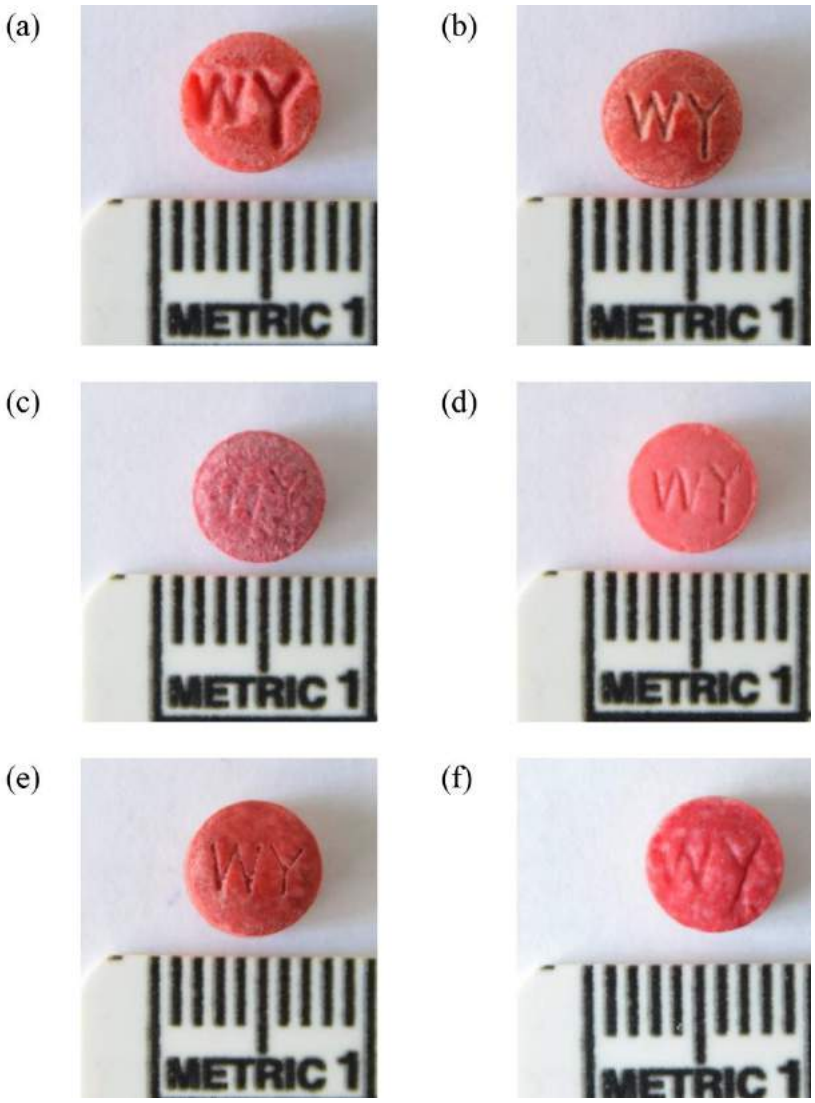


Figure 1. Physical observation of illicit drug tablets encountered in this study.

Dimensions

In terms of size, all of the tablets appeared very similar to each other, and the average diameter and thickness were 6.21 ± 0.21 mm and 3.06 ± 0.14 mm, respectively. Four of the samples were slightly larger in diameter, especially S077, measuring 8.16 mm in diameter. On the other hand, the diameter of S001 was relatively smaller at only 5.60 mm. The weight of each tablet was directly related to its dimensions. In this study, the average weight of the tablets was 97.63 ± 32.52 mg, but the range was from 26.50 mg to 474.95 mg, showing significant variation. The heaviest sample was S017, although its diameter and thickness were within the dimension range of the dominant group. Figure 2 illustrates the number and percentage of samples with a certain diameter, thickness, and weight.

In most instances, drug tablets produced using the same tableting machine present uniform dimensions and thickness [24]. A tableting machine compresses pharmaceutical powder with a specific formulation into tablet form, resulting in the production of tablets with uniform size, shape, and weight [24,25]. Thus, the variation in the physical characteristics could be as a

result of the use of different tableting machines in the production step [21,23]. Any differences in terms of the punches and dies of a tableting machine could potentially produce tablets that differ in diameter [21]. Tablet thickness could be affected by the compressive force, even when a consistent ingredient fills of the die is practiced [21,26]. Tablet weight is governed by the volume of the ingredient filling the die cavity in a tableting machine, and the size of the granule and void space would influence the weight [21].

For forensic intelligence, our findings suggested that the majority of illicit drug samples were likely to have similar physical characteristics, but several samples that showed significant variation from the dominant group were identified. Taking note of such variation could be beneficial for differentiating between batches and manufacturers, at least for sample-to-sample, case-to-case, and seizure-to-seizure direct comparisons [27]. The physical examination would additionally be supported by the information obtained from the chemical analyses for forensic characterization.

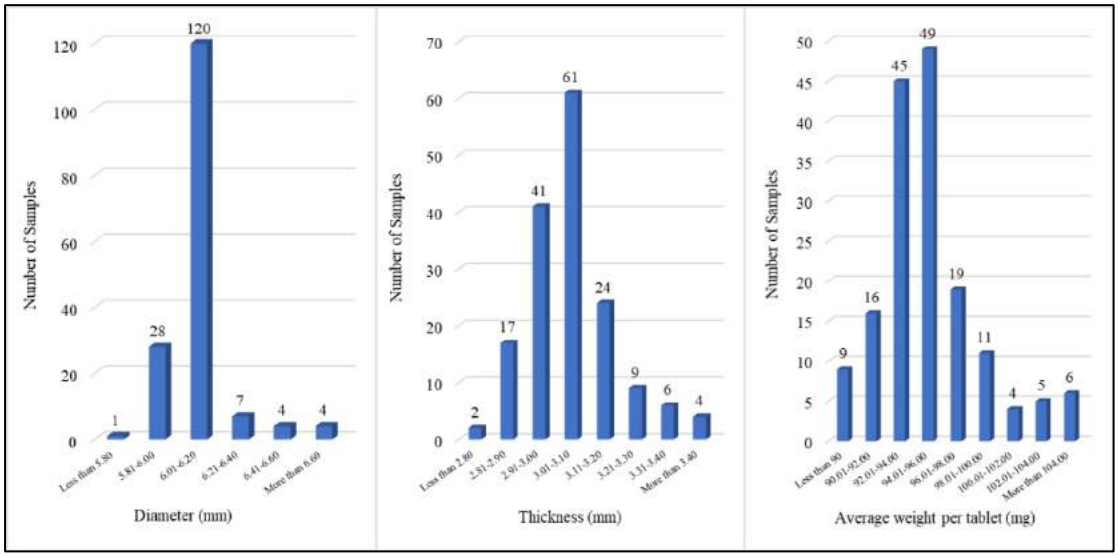


Figure 2. The number and percentages of samples in term of their (a) diameters, (b) thicknesses and (c) weights

ATR-FTIR analysis

ATR-FTIR spectral comparison of illicit drug samples and standards

ATR-FTIR spectroscopy is a useful technique for analyzing and identifying samples, as well as for comparing various samples in numerous forensic applications [28,29]. All 164 illicit drug samples (158 red-colored and 6 green-colored samples) were analyzed using ATR-FTIR spectroscopy to determine their structure, compare their spectra with that of the methamphetamine standard, and to differentiate the seized samples. Prior to determination and comparative studies, repeatability and reproducibility tests were performed. A representative sample (S001) from the same seizure was used in the repeatability study, showing close agreement between three successive measurements under the same conditions [Figure 3(a)]. In the reproducibility study, no differences were observed in ATR-FTIR spectra when S100 was analyzed thrice on three consecutive days [Figure 3(b)], indicating that ATR-FTIR spectroscopy is capable of generating comparable results from multiple analyses and preparations of the same sample. For both repeatability and reproducibility tests, the intensity of three major peaks appearing at 1691, 1653 and 743 cm^{-1} were respectively measured, and their relative standard deviations were determined to be less than 5%.

Complex interacting vibrations were evident in the ATR-FTIR spectra of both the standards and samples. Figure 4 depicts the ATR-FTIR spectra of the methamphetamine standard and common adulterants, including caffeine, ephedrine, and various sugars [14,15], added during the manufacture of illicit methamphetamine tablets.

With reference to (Figure 4(a)), the absorbance pattern of methamphetamine contained major peaks in regions ranging from 3200 to 2550 cm^{-1} and 1800 to 650 cm^{-1} [29-31]. Broad absorbance bands were observed at 2972, 2726, and 2457 cm^{-1}, and were attributed to C-H ($C-CH_3$), NH_2, and C-N-C stretching vibrations, respectively. Meanwhile, two sharp absorbance peaks were also observed at 699 cm^{-1} and 747 cm^{-1}, likely arising from the aromatic C-H out-of-lane bending vibration. The existence of an aromatic ring stretching vibration (C=C-C) at 1602 cm^{-1} could be unique to aromatic ring bonding, while the absorbances at 1454, 1386, and 1046 cm^{-1} likely arose due to C-H bond deformation in the chemical structure. Absorbance peaks in the region of 1192 cm^{-1} possibly represented C-N stretching in a secondary amine structure of methamphetamine.

The ATR-FTIR profile of ephedrine (Figure 4(c)) appeared very similar to that of methamphetamine due to their similar structure. However, the distinguishing feature of the ephedrine spectrum was the presence of additional absorbance bands at 3400 and 3200 cm^{-1} ascribed to hydroxyl stretching. Additionally, the absorbance peaks of ephedrine appeared weaker than those of methamphetamine in the region of 2400-3100 cm^{-1}.

In the spectrum of caffeine (Figure 4(b)), prominent absorbance peaks were evident in the region of 1655-1705 cm^{-1}, attributed to C=O bond vibration, C=C bonds of cyclic hydrocarbons, and/or C=N bond stretching. The ketone group present in caffeine gave rise to peaks at 1025 and 1237 cm^{-1}. Additionally, C-N stretching gave rise to an absorbance peak at 1359 cm^{-1}, while C=C vibration contributed to the peak at 1486 cm^{-1}.

From the ATR-FTIR spectra of the five types of sugars tested in this study, glucose [Figure 4(d)] and dextrose (Figure 4(h)) had very similar profiles. As disaccharides, the spectra of lactose [Figure 4(e)] and maltose [Figure 4(f)] also appeared very similar to each other. Lastly, the spectrum of mannitol [Figure 4(g)], a type of sugar alcohol used as sweetener, was distinct, containing two intense absorbances at 1074 and 1015 cm^{-1}. Absorbance peaks in the ATR-FTIR profiles of sugars arise predominantly from skeletal C-C vibrations (1300-700 cm^{-1}), methyne C-H bending (1350-1330 cm^{-1}), and H-bonded OH stretching (3570-3200 cm^{-1}).

Visually, two unique ATR-FTIR spectral patterns were observed for the illicit drug samples tested in this study, as depicted in Figures 4(i) and 4(j). Careful analysis suggested that pattern A (Figure 4(i)) contained peaks similar to those of caffeine, while pattern B (Figure 4(j)) resembled the spectrum of mannitol. In this study, only one sample, namely S077, showed ATR-FTIR profile of pattern B. Experimental results can be used to determine the major adulterant added to the composition of illicit drug tablets during the manufacturing process. It was noted that the choice of adulterants can differ among the drug distributors and manufacturers, due to factors such as user preference, drug syndicate "trade-marks," the availability of these substances, and differing strategies for increasing the profit margin [32,33]. The ATR-FTIR profiles of the six green tablets did not differ from those of the red tablets, suggesting that the tablets had a similar composition, with the exception of the dye.

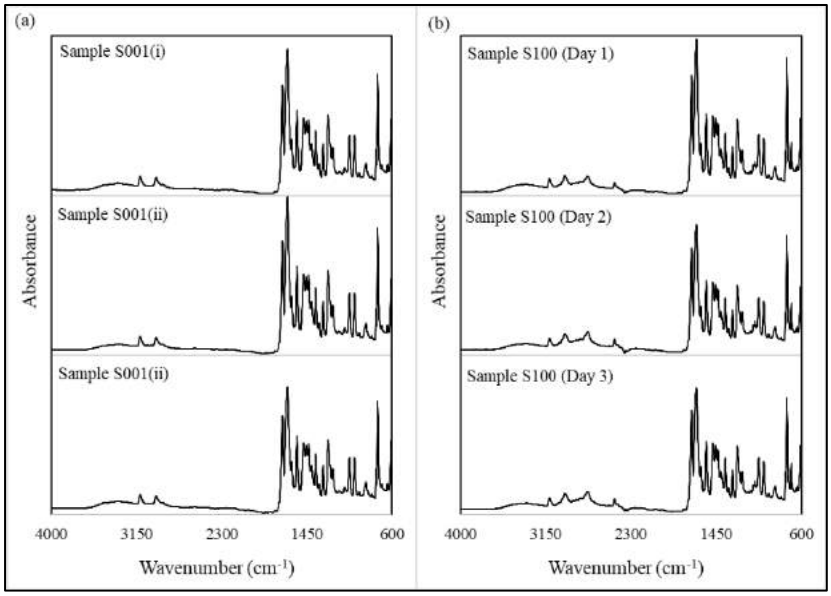


Figure 3. (a) Repeatability test using sample S001 as representative sample, and (b) reproducibility test using sample S100 as representative sample

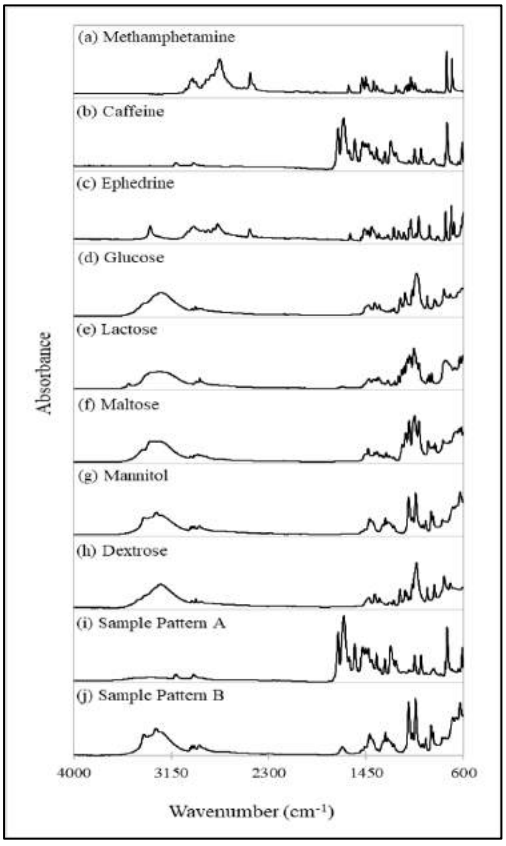


Figure 4. ATR-FTIR spectra of drug standards and seized illicit drug samples in the region of 4000 to 600 cm^{-1}

ATR-FTIR spectral comparison of adulterated methamphetamine at varying percentages

To further evaluate the inclusion of adulterants and their influence on the resultant ATR-FTIR profiles, varying ratios of methamphetamine and adulterants were prepared, and the spectra of the mixtures were examined. Figure 5 illustrates the comparison of the ATR-FTIR profiles of the methamphetamine standard containing varying adulterant amounts.

As evident in Figure 5, the ATR-FTIR profile of methamphetamine changed upon the addition of adulterants, regardless of the choice of adulterant. With increasing adulterant content, the prominent methamphetamine absorbance peaks gradually reduced in intensity or became concealed by the intense peaks originating from the adulterant. For instance, an increase in caffeine content in a mixture led to a gradual decrease in the intensity of the main absorbance peak at 699 cm^{-1}. When methamphetamine content reached 25% in the mixture, the peak was no longer detectable. Additionally, the broad absorbances within the wavenumber region of 3100-2400 cm^{-1} also underwent significant changes. On the other hand, absorbance peaks arising from caffeine were evident in the range of 1655-1705 cm^{-1} for a mixture containing 25% caffeine. Absorbance peaks in this region became more intense with increasing caffeine content. From Figure 5(a), the absorbance peaks attributed to methamphetamine were virtually absent for a mixture containing > 75% caffeine, and the spectrum resembled that of the pure caffeine standard. Based on the ATR-FTIR spectra of the methamphetamine and ephedrine standards, the spectrum of their mixture contained an additional peak at 3340 cm^{-1} due to the presence of a hydroxyl group in ephedrine (Figures 5(b)). When sugars were added to the composition, the dominant peaks from methamphetamine also decreased in intensity, gradually being replaced by the peaks arising from the sugars. In other words, the ATR-FTIR profile of the mixture started to resemble that of the sugars with increasing sugar concentration (Figures 5(c) and (d)).

Regardless of the adulterant added, the peaks ascribed to methamphetamine remained prominent in the ATR-FTIR spectrum when methamphetamine content was 75% and above. However, with the addition of 50% or more of any adulterant, the presence of methamphetamine was challenging to confirm using the ATR-FTIR profile of the mixture. A previous study has suggested the potential of using ATR-FTIR spectra to identify methamphetamine when the concentration thereof is >30% [34]; however, the presence of adulterants impeded the determination of methamphetamine in our study. In our case, at least 75% methamphetamine content was required for confident determination of its presence in a mixture. Thus, the ATR-FTIR technique has several limitations, particularly when the screening for the presence of methamphetamine as a controlled substance. However, the ATR-FTIR technique could be applied in clandestine laboratory settings where illicit drugs of very high purity have been synthesized prior to the packaging stage. In such cases, ATR-FTIR spectroscopic analysis would allow for rapid determination and portable on-site detection.

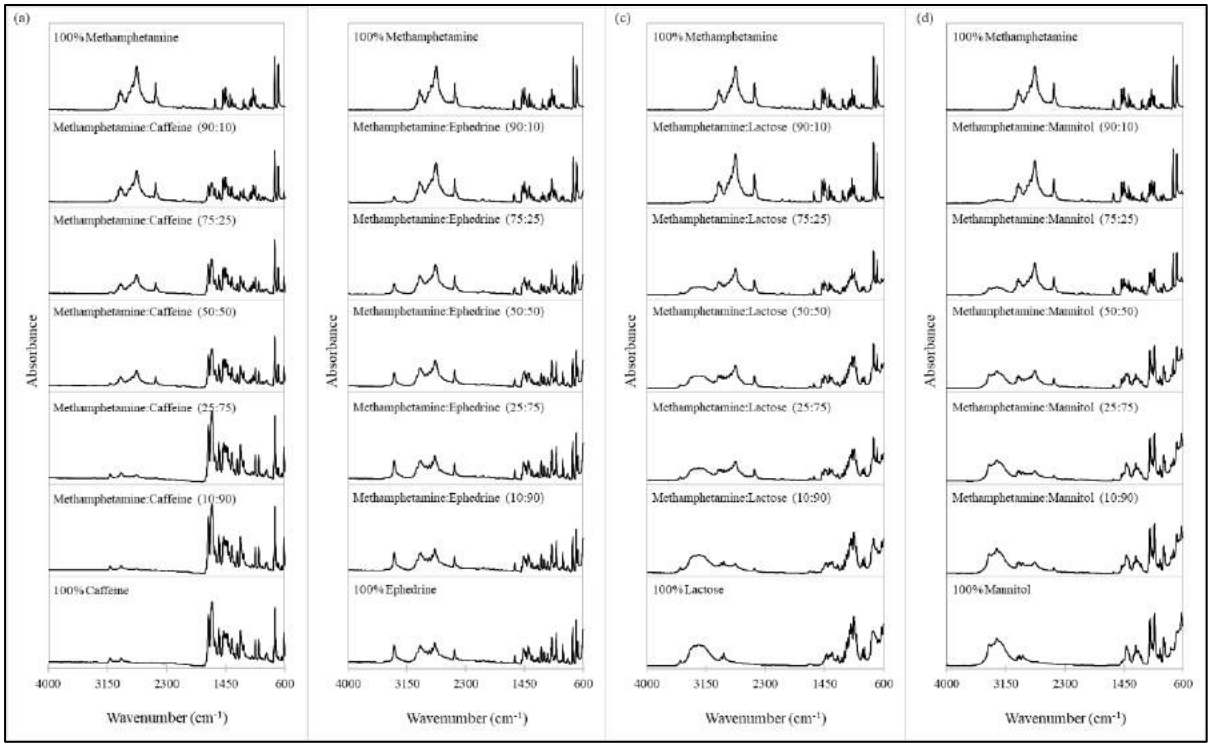


Figure 5. ATR-FTIR profiles of methamphetamine with varying percentage of adulterants

PCA decomposition of ATR-FTIR profiles

Our findings indicated that the determination of methamphetamine presence in illicit drug tablets using ATR-FTIR spectroscopy could be challenging. However, the identity of the adulterant in an illicit drug pill could be determined via this technique based on the obtained spectrum, and consequently, samples of differing composition can be differentiated. PCA was performed to decompose the large dataset into a smaller set that represented the variability of all the 164 samples tested in this study. Prior to the PCA, the ATR-FTIR spectra were pre-treated and normalized. From the ATR-FTIR spectra in Figure 4, the regions with noticeable variations among the standards and samples, namely those ranging from 3200 to 2550 cm^{-1} and 1800 to 650 cm^{-1}, were subjected to PCA. Figure 6 illustrates the two-dimensional score plot upon PCA decomposition of data for the 164 illicit drug samples and related standards.

The majority of the illicit drug samples tended to locate closely, as seen for cluster P in the score plot (Figure 6). These samples were clustered together with the caffeine standard, suggesting the similarity in their ATR-FTIR profiles. This observation was supported by the visual comparison of their ATR-FTIR spectra, wherein they appeared very similar, as demonstrated in Figures 4(b) and 4(i). On the other hand, the S077 sample was located away from the cluster P, while being close to the sugar standards, denoted as cluster Q. S077 could have been adulterated with any sugar, most likely mannitol, based on the similarities of its ATR-FTIR profile with that of mannitol (Figure 4(g)). The PCA grouped the green samples into cluster P, as the color did not contribute to significant changes in the ATR-FTIR profile.

The PCA score plot indicated that all the illicit drug samples were located very far away from the methamphetamine standard data point, found in the right bottom corner. This observation implied that the absorbance peaks comprising the ATR-FTIR profile of the methamphetamine standard were not useful for determining its presence in the illicit drug tablets, as

they were concealed by the peaks originating from the adulterants. It was noted that the ephedrine standard was located close to methamphetamine (cluster R), indicating significant similarities between their ATR-FTIR profiles. Generally, PC1 (52.8%) discriminated the majority of the samples from the standards and adulterants, including methamphetamine, ephedrine, and various sugars. PC2 (26.9%) further separated the methamphetamine and ephedrine standards from the data points consisting of various sugars. The presence of adulterant had modified the ATR-FTIR profiles of methamphetamine. As evident in Figure 7 demonstrating the score plot decomposing drug samples and the standard-adulterant mixtures, data points of the mixture carrying greater percentage of adulterant, in this case caffeine, had been dispersed away from cluster R to cluster P. Majority of the drug sample tested in this study could have contained less than 25% active compound and adulterated with caffeine. The sample S077 might have also contained a percentage of methamphetamine at a level of less than 10% and adulterated with sugar, probably mannitol based on the ATR-FTIR spectrum.

In this study, the discrimination of illicit drug samples was possible through the use of ATR-FTIR spectroscopy by recognizing the corresponding pattern and comparing it to that of the standards and adulterants. PCA allowed for more objective clustering and discrimination. The majority of the illicit drug samples tested in this study were adulterated with caffeine, except for one sample, namely S077, that likely contained mannitol. The literature has suggested the preference for utilizing caffeine as the adulterant during illicit drug production probably due to the similar stimulant effect of caffeine as in methamphetamine [15,23]. Perhaps more samples from different regions of the country should be included in future profiling activities to evaluate if the choice of caffeine was restricted to the east coast of the country, or generally, across the country and in nearby countries.

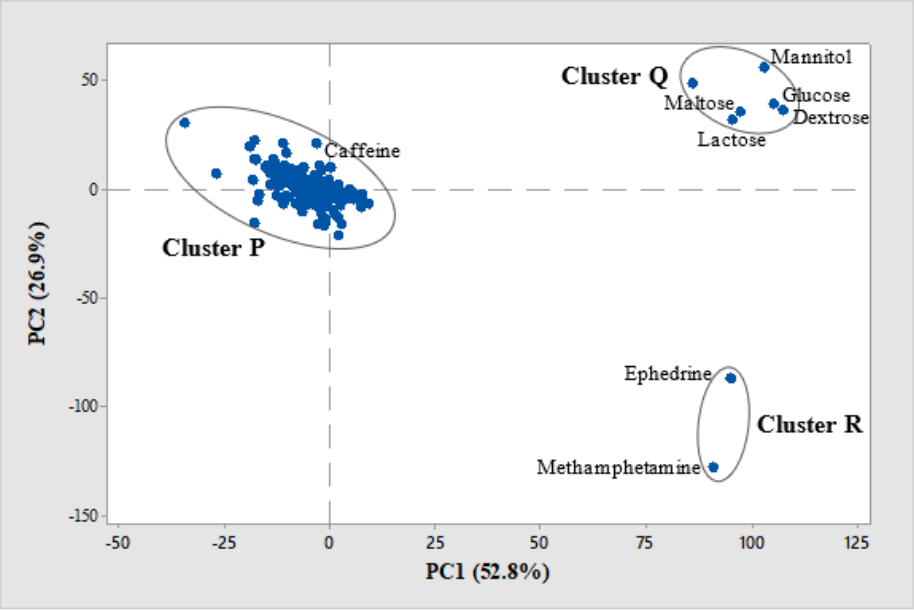


Figure 6. Decomposition of 164 samples and standards into two-dimensional score plot

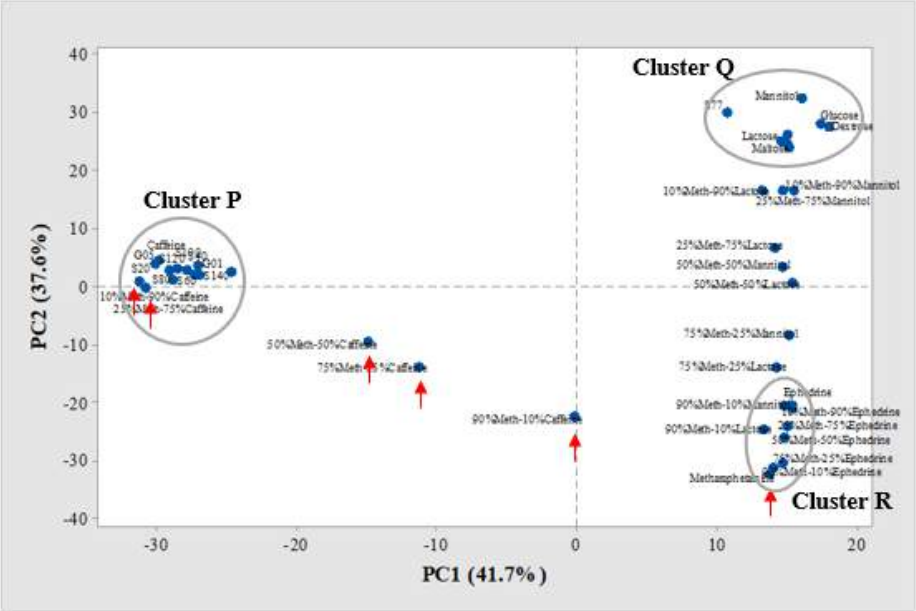


Figure 7. Decomposition of drug samples and standard-adulterant mixture into two-dimensional score plot

TLC analysis

Choice of Solvent System

Prior to TLC analysis, the dye was extracted from the tablets to remove any sugars, fats, or other substances contained therein [16,17] that could potentially cause blurring of the spots upon analysis [18]. Thus, the dye was transferred to a piece of wool via acidification and subsequently stripped from the wool by alkaline treatment [17-19,35]. All the dye standards used in this study underwent the same procedure as did the negative control. Upon TLC analysis, all the standards developed colored spot(s) on the plate when various solvent systems were applied, and their respective retention factor (R_f) values are given in Table 1.

Among the dye standards, the Rhodamine B dye standard exhibited strong fluorescence under long-wave UV light illumination; Erythrosine BS fluoresced weakly. Adequate separation of the dye standards could not be achieved using solvent systems B or C for TLC analysis. These solvent systems were excessively polar, and the dye components moved high up the plate due to insufficient interaction with the stationary phase. Solvent system A consisting of isopropanol and ammonia (4:1 v/v) reportedly achieves effective separation of synthetic food colorants with minimum tailing effects [17]. However, it was found that certain dye standards were not adequately separated using solvent system A, as evident from the very close R_f values of the color spots formed by Tartrazine and Brilliant Blue. The color spot generated from Brilliant blue dye was also very close to those formed by the two green-colored dye standards used in this study, namely Fast Green and Green S. These occurrences hamper interpretation, especially in the analysis of green tablets. In fact, the green color may be the result of a blue and yellow dye mixture.

Favorable separation among the dye standards was achieved with silica gel plates eluted with solvent system D consisting of isopropanol, ammonia, and water in a volume composition of 7:2:1, especially in the case of the red dyes. Furthermore, the greater separating distance between the spots formed by Tartrazine and Sunset Yellow dye standards resulting from the use of solvent system D would allow for more confident discrimination between these two dyes potentially found in the green tablets. Thus, solvent system D was used for the subsequent determination of dye components in the illicit drug samples.

Table 1. R_f values of the color dye standards upon TLC analysis

Standard	Solvent system A	Solvent system B	Solvent system C	Solvent system D
Amaranth	0.81	0.81	1.00	0.64
Carmoisine	0.88	0.91	1.00	0.70
Erythrosine BS	(0.93)	(0.94)	(1.00)	(0.82)
Ponceau 4R	0.81	0.87	1.00	0.65
Rhodamine B	(0.90)	(0.90)	(1.00)	(0.82)
	(0.74)	(0.87)	(0.88)	(0.76)
	(0.71)		(0.80)	(0.65)
Red 2G	0.84	0.90	1.00	0.73
Tartrazine	0.78	0.87	1.00	0.64
Sunset Yellow	0.83	0.88	1.00	0.73
Fast Green	0.83	0.88	1.00	0.68
	0.80	0.86		0.65
Green S	0.78	0.81	1.00	0.64
	0.72			
	0.64			
Brilliant Blue	0.77	0.87	0.95	0.73

( ) indicates fluoresced colored spot under UV illumination

Determination of dye components in illicit drug samples

In pharmaceutical products, the addition of color aids in enhancing drug acceptability, discrimination among different drugs, and prevents counterfeiting 18. In illicit drugs, dyes are used to improve their external appearance, and to render them readily identifiable on the drug scene [36]. Figure 8 illustrates the percentages of drug samples that contained specific dye components. Upon examination, a total of 151 samples (95.6%) contained Ponceau 4R as the only dye. In addition to Ponceau 4R, Erythrosine BS (0.6%), Sunset Yellow (1.9%), and Tartrazine (0.6%) were also concurrently detected in certain drug samples, suggesting that the dye used during the manufacturing of certain drug samples was not restricted to a single type. Only two samples were found to be unique and not to contain Ponceau 4R (1.3%), namely S001 and S002, which contained Rhodamine B and Erythrosine BS. The six green-colored illicit drug samples were classified into two separate groups, according to whether they contained Tartrazine and Brilliant Blue (66.7%), or Ponceau 4R as well (33.3%). However, the presence of Ponceau 4R in the two green-colored samples possibly originated from contamination by red-colored tablets as they were all placed in the same packaging.

TLC analysis contributed significantly to the identification of the various dyes contained in the illicit drug samples. Importantly, the dye must be carefully extracted from the samples to ensure satisfactory TLC separation. Ponceau 4R was the most commonly used dye in red-colored samples, but a mixture of dyes was also encountered. Based on TLC analysis results, at least seven different groups of illicit drug samples were determined.

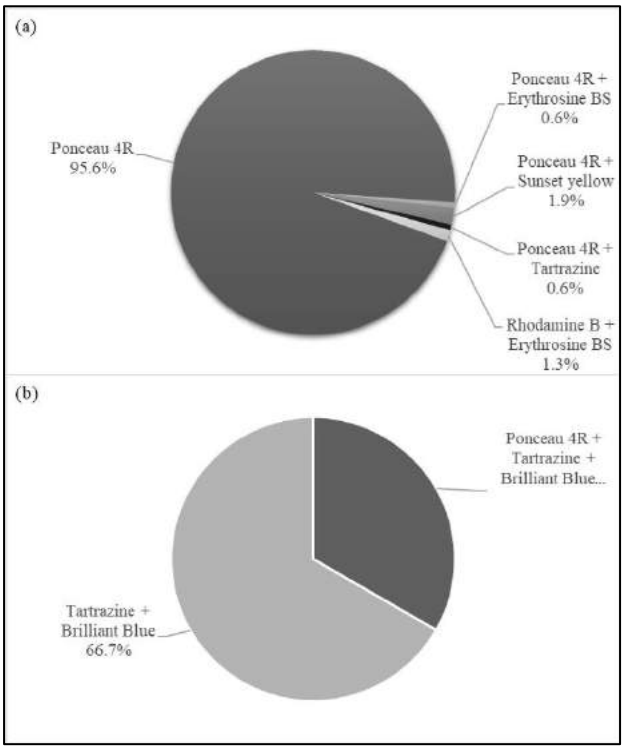


Figure 8. Percentages of samples of varying dye composition in (a) red-colored and (b) green colored illicit drug samples tested in this study

Gas chromatographic analysis

Confirmation of methamphetamine presence

Due to the excellent sensitivity of GC-MS, it was chosen to confirm the presence of methamphetamine [8,11]. Figure 9 shows a representative chromatogram showing methamphetamine and IS peaks upon sample analysis. The methamphetamine and IS peaks appeared at 3.72 and 7.27 min, respectively. The presence of caffeine was also evident in the majority of samples, supporting the findings of ATR-FTIR analysis. The caffeine peak dominated the chromatogram, appearing at a retention time of 6.33 min. The mass spectrum of methamphetamine displayed an M-1 peak with an m/z ratio of 148. The base peak was found at m/z 58, followed by m/z 91 and 134.

Of the 164 samples tested in this study, 162 of them were found to contain methamphetamine; samples S077 and G02 did not. A probability index of greater than 80% was considered for a positive determination of methamphetamine. It was noted that physical examination alone could not confidently indicate the presence of methamphetamine. As evident in these two samples, the target substance was not detected using our analytical method, either because it was absent, or its content was too low for detection.

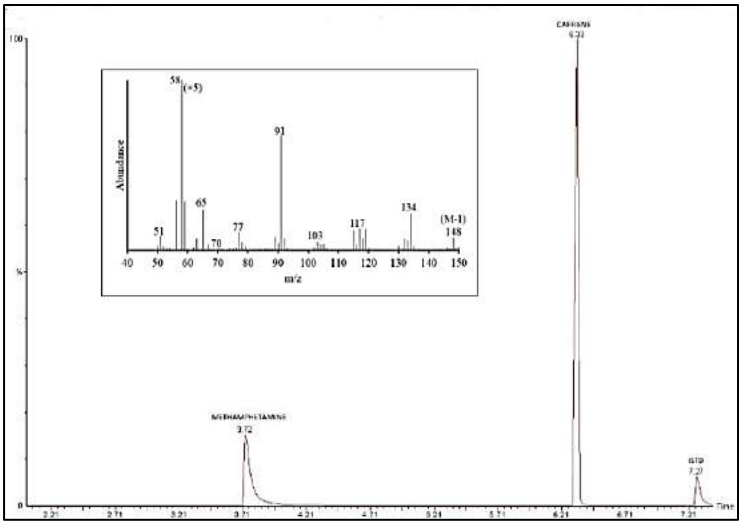


Figure 9. Representative chromatogram showing the peaks of methamphetamine, caffeine, and IS upon GC-MS analysis of sample S001 (Inset: mass spectrum of methamphetamine)

Quantification of methamphetamine in illicit drug tablets

A calibration curve was constructed using the GC-FID analysis results obtained for methamphetamine solutions of varying concentrations and linear least regression analysis, and the percentage of methamphetamine (w/w) in each illicit drug tablet was determined, as shown in Figure 10.

The mass of methamphetamine in individual samples was found to vary. Most of the samples contained 15.01% – 17.50% w/w of methamphetamine, accounting for 64.8% of the total samples. In fact, > 98% of the samples (159 samples) were found to contain < 20% methamphetamine. Our experimental data indicated that most of the tablets had been adulterated with caffeine to add bulk during the manufacturing and tableting processes; however, caffeine quantification was not pursued in this study. Considering the w/w ratios and the tablet weight, approximately 16 mg of methamphetamine was generally present in a single tablet.

Several samples were distinct in terms of their methamphetamine content, which was either significantly higher or lower than the average, allowing for their discrimination from the majority groups. The two samples with a relative higher percentage of methamphetamine were S082 (35.04% methamphetamine) and S094 (56.60% methamphetamine). In other words, they contained significantly lower amounts of adulterant. The empty space between the granules may have been larger, reducing their measured weights [21]. On the other hand, five samples (3.08%) were found to contain <10% methamphetamine. The lowest methamphetamine content was found in sample S002, wherein only 10 mg methamphetamine was detected for all 300 tablets encountered in a single packaging. The remaining w/w percentage of each tablet was principally made up of the adulterant. Samples with such low methamphetamine content are not commonly encountered as their effects upon consumption would be diminished. The other four samples within the same group contained approximately 7% methamphetamine.

Thus, the presence methamphetamine in seized drug samples was confirmed based on GC-MS analysis results and its quantity was determined through the GC-FID analysis. In this study, 98.7% of the samples contained methamphetamine, and only several tablets contained either very high or very low levels of methamphetamine.

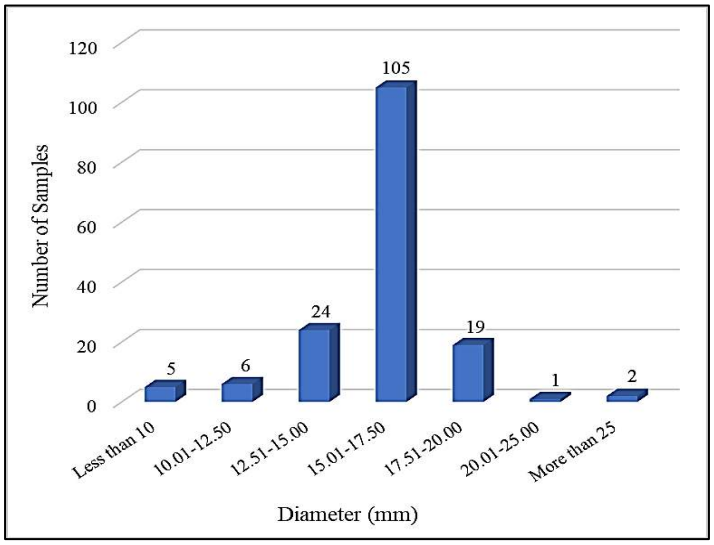


Figure 10. Percentages of methamphetamine (w/w) of 162 illicit drug tablets positively confirmed by GC-MS

General discussion

Based on physical characterization and chemical analyses results, valid information was retrieved regarding the composition of illicit drug samples [37]. In routine forensic analysis, the ultimate objective is to detect the presence of a controlled substance and quantify it. However, more in-depth analysis of illicit drug samples could contribute to a greater comparative study to gather information regarding sample-to-sample, case-to-case, seizure-to-seizure connections, especially when a large number of samples are encountered by the enforcement authorities [38-41]. To a certain extent, this approach could contribute to establishing the origins of illicit drug samples, the possible manufacturing pathway, as well as the potential trafficking and distribution network [42-43], enabling the tracking of drug syndicates or manufacturers.

In this study, illicit drug samples from various seizures were profiled for possible clustering or discrimination among them. Although physical characterization did not provide information on the identity of the substance in the illicit drugs, it allowed for the discrimination of a few samples from the major groups due to their unique physical appearance, especially in relation to their respective logos, diameter, thickness, and weight. ATR-FTIR analysis coupled with PCA indicated that the majority of the illicit drug samples were adulterated with caffeine. TLC analysis enabled the identification of the dyes that had been added to the tablets, whereby Ponceau 4R was found to be the most commonly used dye. Lastly, GC-MS analysis enabled the determination of the presence of methamphetamine as well as that of its content in each tablet through GC-FID. All the analytical results are summarized in Figure 11; the classification of samples into several groups was based on the drug profiling results. The proposed strategy can be used by law enforcement agencies and forensic laboratories to profile illicit drugs, in this case, methamphetamine tablets. Illicit methamphetamine samples tested in this study had demonstrated certain degree of physical and chemical differences. Differentiation among drug samples would be advantageous for sample-to-sample and seizure-to-seizure comparison. It was noted that this profiling study could have been restricted by the availability of methamphetamine samples, limited to the east coast region of Malaysia. A greater number of samples, perhaps from different regions of the country, would

provide information of the current situation of illicit methamphetamine in the country. Nonetheless, data from such analytical endeavors should be further collated as it is necessary for wider forensic intelligence to provide information on the possible connection among seized samples to law enforcement authorities.

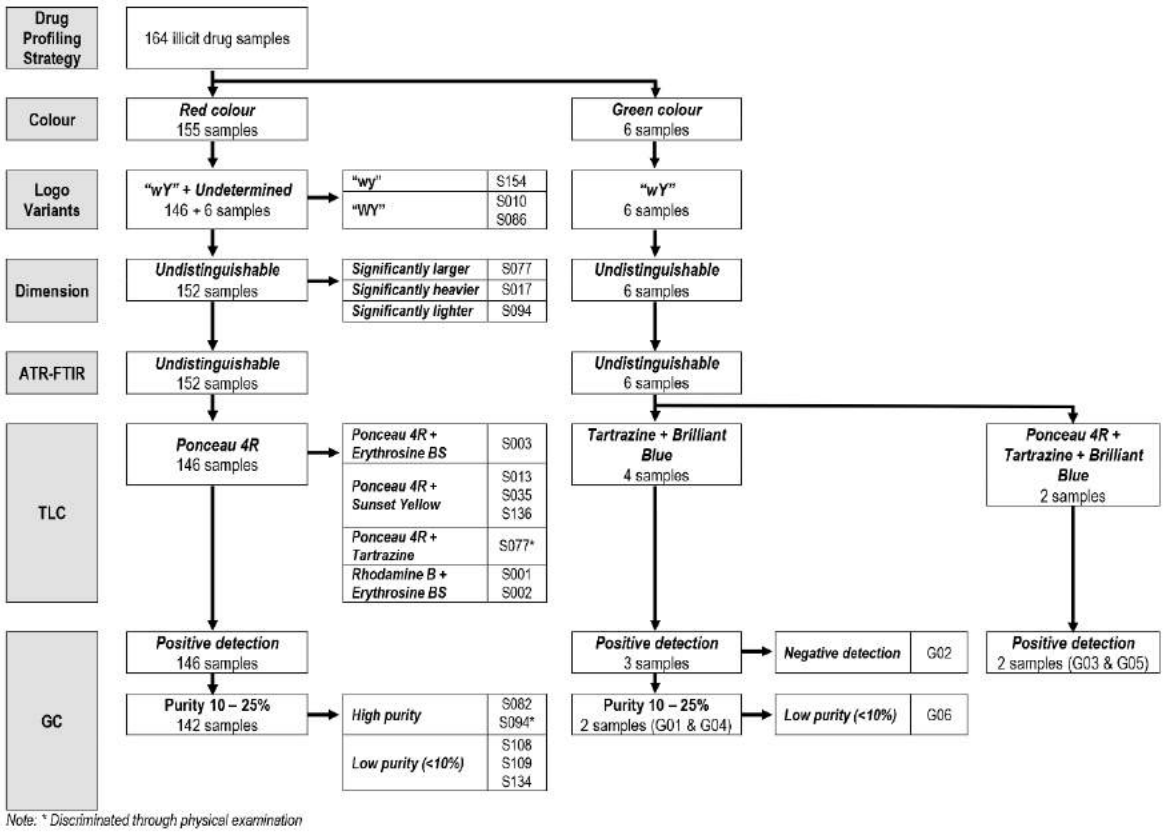


Figure 11. Drug profiling strategy and grouping of illicit drug samples

Conclusion

Forensic drug profiling was conducted with the aim of benefiting forensic investigation and intelligence. In this study, samples were differentiated based on several physical and chemical characteristics, allowing sample-to-sample comparison. With a greater number of illicit drug samples being processed, the linkages between seizures could be revealed, beneficial for tracking down the sources of these illicit drugs on the black market and their related distribution chain. Drug profiling strategies on a global level in accordance with comparative analyses of illicit drug samples would be advantageous for uncovering complex trafficking networks. This information could advance the body of knowledge useful to drug-related investigations and intelligence.

Acknowledgement

The authors thank the financial support via the USM RUI grant (1001/PPSK/8012236).

References

1. National Institute on Drug Abuse (2021). Methamphetamine. Access from https://www.drugabuse.gov/publications/drugfacts/methamphetamine. [Access online 29 May 2021].

2. United Nations Office on Drugs and Crime (2020). Drug use and health consequences. Vienna: United Nations Office on Drugs and Crime.
3. United Nations Office on Drugs and Crime (2020). Synthetic drugs in east and southeast Asia: Trends and patterns of amphetamine-type stimulants and new psychoactive substances. Vienna: United Nations Office on Drugs and Crime.
4. United Nations Office on Drugs and Crime (2020). Drug supply. Vienna: United Nations Office on Drugs and Crime.
5. Hamdan, R., Nik Hassan, N. F., Mat Desa, W. N. S., Kunalan, V., Sulaiman, M. and Abdullah, A. F. L. (2015). Characterisation of seized clandestine methamphetamine in Malaysia. *Malaysian Journal of Forensic Sciences*, 6(1): 20-29.
6. United Nations Office on Drugs and Crime (2020). Synthetic drugs in east and southeast Asia: Latest developments and challenges. Vienna: United Nations Office on Drugs and Crime.
7. Libby H. (2018). Myanmar's meth crisis reaches as far as Australia. ABC News. Access https://www.abc.net.au/news/2018-07-29/myanmars-meth-crisis-reaches-australia/10044502 [Access online 29 May 2021].
8. Puthaviriyakorn, V., Siriviriyasomboon, N., Phorachata, J., Pan-ox, W., Sasaki, T. and Tanaka, K. (2002). Identification of impurities and statistical classification of methamphetamine tablets (Ya-Ba) seized in Thailand. *Forensic Science International*, 126(2): 105-113.
9. Sennello, L. T. (1971). GLC determination of methamphetamine hydrochloride in methyl acrylate-methyl methacrylate sustained-release tablets. *Journal of Pharmaceutical Sciences*, 60 (4): 595-596.
10. Mitrevski, B. and Zdravkovski, Z. (2005). Rapid and simple method for direct determination of several amphetamines in seized tablets by GC–FID. *Forensic Science International*, 152 (2-3): 199-203.
11. United Nations Office on Drugs and Crime (2001). Drug characterization/impurity profiling – Background and concept. Vienna: United Nations Office on Drugs and Crime.
12. Dufey, V., Dujourdy, L., Besacier, F. and Chaudron, H. (2007). A quick and automated method for profiling heroin samples for tactical intelligence purposes. *Forensic Science International*, 169:108-117.
13. Esseiva, P., Dujourdy, L., Anglada, F., Taroni, F. and Margot, P. (2003). A methodology for illicit heroin seizures comparison in a drug intelligence perspective using large databases. *Forensic Science International*, 132(2): 139-152.
14. European Monitoring Centre for Drugs and Drug Addiction (2009). Methamphetamine: A european union perspective in the global context. Portugal: European monitoring centre for drugs and drug addiction.
15. Cole, C., Jones, L., Mcveigh, J., Kicman, A., Syed, Q. and Mark, A. B. (2010). A guide to adulterants, bulking agents and other contaminants found in illicit drugs. Faculty of Health and Applied Social Sciences, Liverpool John Moores University, Liverpool.
16. De Andrade, F. I., Florindo Guedes, M. I., Pinto Vieira, Í. G., Pereira Mendes, F. N., Salmito Rodrigues, P. A., Costa Maia, C. S., Marques Ávila, M. M. and de Matos Ribeiro, L. (2014). Determination of Synthetic Food Dyes in Commercial Soft Drinks by TLC and Ion-pair HPLC. *Food Chemistry*, 157: 193-198.
17. Dixon, E. A. and Renyk, G. (1982). Isolation, separation, and identification of synthetic food colors. *Journal of Chemical Education*, 59(1): 67-69.
18. Kucharska, M. and Grabka, J. (2010). A review of chromatographic methods for determination of synthetic food dyes. *Talanta*, 80(3): 1045-1051.
19. Fadil, F. A. and McSharry, W. O. (1979). Extraction and TLC separation of food, drug, and cosmetic dyes from tablet-coating formulations. *Journal of Pharmaceutical Sciences*, 68(1): 97-98.
20. United Nations on Office Drugs and Crime (2006). Recommended methods for the identification and analysis of amphetamine, methamphetamine and their ring-substituted analogues in seized materials. Vienna: United Nations Office on Drugs and Crime.

21. Adam, P., Natakankitkul, S., Sirithunyalug, J. and Aramrattana, A. (2005). Physio-chemical profiles of methamphetamine tablets. *CMU Journal*, 4(1): 65-70.
22. Adam, P., Natakankitkul, S., Sirithunyalug, J. and Aramrattana, A. (2004). Drug characterization of methamphetamine tablets – a scientific tool to help identify drug production and trafficking networks. In: The third Australasian drug strategy conference – preventing and reducing substance abuse, 4-6 May 2004, Alice Springs, Australia.
23. Li, T., Hua, Z., Meng, X. and Liu, C. (2018). A Simple and effective physical characteristic profiling method for methamphetamine tablet seized in China. *Journal of Forensic Sciences*, 63(2): 541-547.
24. Haywood, A. and Glass, B. D. (2011). Pharmaceutical excipients - where do we begin? *Australian Prescriber*, 34(4): 112-114.
25. Armstrong, N. (2006). Tablet manufacturer. In: Encyclopedia of pharmaceutical technology (3rd edition). Marcel Dekker, New York.
26. Gordon, R. E., Rosanske, T. W. and Fonner, D. E. (1990). Granulation technology and tablet characterization. In: Pharmaceutical dosage forms. Marcel Dekker, New York.
27. Cole, M. D. (2003). The analysis of controlled substances. John Wiley and Sons Ltd Wiley, New Jersey.
28. Bunaciu, A. A. and Aboul-Enein, H. Y. (2021). Adulterated drug analysis using FTIR spectroscopy. *Applied Spectroscopy Reviews*, 56 (5): 423-437.
29. Mail, R., Teoh, W. K., Kunalan, V., Chang, K. H. and Abdullah, A. F. L. (2021). Quick discrimination of seized erimin-5 tablets by attenuated total reflectance-Fourier transform infra-red spectroscopy. *Australian Journal of Forensic Sciences*, In Press.
30. Liu, C-M., Han, Y., Min, S-G., Jia, W., Meng, X. and Liu, P-P. (2018). Rapid qualitative analysis of methamphetamine, ketamine, heroin, and cocaine by Fourier transform infrared spectroscopy (FTIR). *Forensic Science International*, 290: 162-168.
31. He, X., Wang, J., You, X., Niu, F., Fan, L. and Lv, Y. (2020). Classification of heroin, methamphetamine, ketamine and their additives by attenuated total reflection-Fourier transform infrared spectroscopy and chemometrics. *Spectrochimica Acta Part A: Molecular and Biomolecular*, 241: 118665.
32. Chan, K. W., Tan, G. H. and Wong, R. C. S. (2012). Gas chromatographic method validation for the analysis of major components in illicit heroin seized in Malaysia. *Science and Justice*, 52(1): 9-16.
33. Broséus, J., Gentile, N. and Esseiva, P. (2016). The cutting of cocaine and heroin: A critical review. *Forensic Science International*, 262: 73-83.
34. Hughes, J., Ayoko, G., Collett, S. and Golding, G. (2013). Rapid quantification of methamphetamine: Using attenuated total reflectance Fourier transform infrared spectroscopy (ATR-FTIR) and chemometrics. *PLoS One* 8(7): e69609.
35. Abdullah, A. F. L., Abraham, A. A., Sulaiman, M. and Kunalan, V. (2012). Forensic drug profiling of erimin-5 using TLC and GC-MS. *Malaysian Journal of Forensic Sciences*, 3 (1): 11-15.
36. Joyce, J. R. (1980). The identification of dyes in illicit tablets. *Journal of Forensic Science Society*, 20(4): 247-252.
37. Chiarotti, M., Fucci, N. and Furnari, C. (1991). Comparative analysis of illicit heroin samples. *Forensic Science International*, 50(1): 47-56.
38. Barnfield, C., Burns, S., Byrom, D. L. and Kemmenoe, A. V. (1988). The routine profiling of forensic heroin samples. *Forensic Science International*, 39(2): 107-117.
39. Johnston, A. and King, L. A. (1988). Heroin profiling: Predicting the country of origin of seized heroin. *Forensic Science International*, 95(1): 47-55.
40. Yusoff, M. Z., Chang, K. H. and Abdullah, A. F. L. (2017). Attenuated total reflectance – Fourier transform infra-red spectral profiling of illicit heroin for forensic intelligence. *Australian Journal of Forensic Sciences*, 50(5): 543-551.

41. Collins, M., Huttunen, J., Evans, I. and Robertson, J. (2007). Illicit drug profiling: The Australian experience. *Australian Journal of Forensic Sciences*, 39(1): 25-32.
42. Dams, R., Benijts, T., Lambert, W. E., Massart, D. L. and De Leenheer, A. P. (2001). Heroin impurity profiling: Trends throughout a decade of experimenting. *Forensic Science International*, 123(2-3): 81-88.
43. United Nations on Office Drugs and Crime (2005). Methods for impurity profiling of heroin and cocaine - manual for use by national drug testing laboratories. Vienna: United Nations Office on Drugs and Crime.

Malaysian Journal of Analytical Sciences (MJAS)
Published by Malaysian Analytical Sciences Society

CATALYTIC NEUTRALIZATION OF ACIDIC PETROLEUM CRUDE OIL UTILIZING 2-METHYLIMIDAZOLE WITH ADDITION OF Cu/Ce(10:90)/Al_2O_3 CATALYST

(Peneutralan Pemangkin Minyak Mentah Petroleum Berasid Menggunakan 2-Metilimidazol dengan Tambahan Mangkin Cu/Ce(10:90)/Al_2O_3)

Norshahidatul Akmar Mohd Shohaimi[1]*, Noraini Safar Che Harun[1], Hisyam Saufi Tajudin[1], Wan Azelee Wan Abu Bakar[2], Nurasmat Mohd Shukri[3], Nor Hakimin Abdullah[4], Ahmad Zamani Ab Halim[5]

[1]Faculty of Applied Sciences,
Universiti Teknologi MARA Pahang, Bandar Tun Abdul Razak Jengka, Pahang, Malaysia
[2]Faculty of Sciences,
Universiti Teknologi Malaysia, Johor Bahru, Johor, Malaysia
[3]School of Health Sciences,
Universiti Sains Malaysia, Health Campus, 16150 Kubang Kerian, Kelantan
[4]Advanced Materials Research Centre (AMRC), Faculty of Bioengineering and Technology,
Universiti Malaysia Kelantan, Locked Bag 100, 17600 Jeli, Kelantan
[5]Faculty of Industrial Sciences & Technology,
Universiti Malaysia Pahang, 26300 Gambang, Kuantan, Pahang, Malaysia

**Corresponding author: akmarshohaimi@uitm.edu.my*

Received: 22 December 2021; Accepted: 3 February 2022; Published: 25 February 2022

Abstract

The presence of naphthenic acid (NA) in crude oil leads to corrosion problems within oil refineries which may increase the maintenance cost and produce lower quality of crude oil. The objective of this study is to reduce the total acid number (TAN) of Petronas Penapisan Melaka (PPM)'s crude oil (TAN = 2.43 mgKOH/g) using 2-methylimidazole with the aid of Cu/Ce (10:90)/Al_2O_3 catalyst through the catalytic neutralization technique. A 10% of 2-methylimidazole in ethanol solution was used as the acid removal agent. Cerium oxide based catalysts with copper as a dopant were supported onto alumina and calcined at different calcination temperatures of 800 ℃, 900 ℃ and 1000 ℃. The potential catalyst was characterized by using TGA-DTG, FTIR and XRD for its physicochemical properties. The results showed TAN was reduced to 0.53 mg KOH/g with 78.2% reduction at catalyst calcination temperature of 900 ℃, 0.5% catalyst loading, reaction temperature of 27 ℃ and 10 minutes reaction time. The small particle size of catalyst calcined at 900 ℃ which was 18.02 nm led to bigger surface areas that enhanced the neutralization process. These structural properties contributed to the excellent catalytic performance which removed the NAs in the PPM's crude oil and concurrently reduced the TAN value below than one.

Keywords: catalyst, catalytic neutralization, crude oil, naphthenic acid

Abstrak

Kehadiran asid naftenik (NA) dalam minyak mentah membawa kepada masalah kakisan dalam kilang penapisan minyak yang boleh meningkatkan kos penyelenggaraan dan menghasilkan minyak mentah yang berkualiti rendah. Objektif kajian ini adalah untuk mengurangkan jumlah asid (TAN) minyak mentah Petronas Penapisan Melaka (PPM) (TAN = 2.43 mgKOH/g) menggunakan 2-metilimidazol dengan bantuan mangkin Cu/Ce (10:90)/ Al_2O_3 melalui teknik peneutralan pemangkin. 10% daripada 2-metilimidazol dalam larutan etanol digunakan sebagai agen penyingkiran asid. Pemangkin berasaskan serium oksida dengan kuprum sebagai dopan disokong pada alumina dan dikalsinkan pada suhu pengkalsinan berbeza 800 ℃, 900 ℃ dan 1000 ℃. Mangkin berpotensi dicirikan dengan menggunakan TGA-DTG, FTIR dan XRD untuk sifat fizikokimianya. Keputusan menunjukkan TAN dikurangkan kepada 0.53 mg KOH/g dengan pengurangan 78.2% pada suhu pengkalsinan mangkin 900 ℃, 0.5% pemuatan mangkin, suhu tindak balas 27 ℃ dan 10 minit masa tindak balas. Saiz zarah kecil pemangkin yang dikalsinkan pada 900 ℃ iaitu 18.02 nm membawa kepada kawasan permukaan yang lebih besar yang meningkatkan proses peneutralan. Ciri-ciri struktur ini menyumbang kepada prestasi pemangkin yang sangat baik yang mengeluarkan NA dalam minyak mentah PPM dan secara serentak mengurangkan nilai TAN di bawah satu.

Kata kunci: mangkin, peneutralan pemangkin, minyak mentah, asid naftenik

Introduction

Nowadays, crude oil had become one of the most important source of energy in the world. Since raw petroleum is an important source of energy, it is imperative to overcome the issue of acidic crude oil to have better oil production [1]. In recent years, acidic crude oil production has raised by 0.3% per year worldwide. The naphthenic acid (NA) compound present in crude oil leads to the high acidity of oil. The term “naphthenic acids” is used to account for all carboxylic acids present in crude oil including acyclic and aromatic acids, which is also referred to as complicated mixtures [2].

The acidity of petroleum crude oil is measured by its total acid number (TAN), which refers the number of milligrams of KOH required to reduce the corrosiveness in one gram of oil [3]. Currently, the treatment for acidic oil either relies upon weakening or caustic washing techniques to decrease the TAN number of overwhelming rough oils. Moreover, neither of these method is altogether attractive. For example, even though mixing high TAN unrefined petroleum with a low TAN unrefined petroleum might decrease the NAs content to a worthy level, the acidic mixes still remain [1]. Burning treatment can also considerably evacuate NAs, but the procedure creates critical measures of wastewater and emulsion that are problematic to treat. Specifically, once an emulsion is formed, it is exceptionally hard to evacuate [4, 5]. A series of homogeneous basic catalysts are widely used in the petroleum industry such as KOH and NaOH but these types of catalysts would induce an emulsion problem and no catalyst recovery. Solid acid catalysts have attracted a lot of attention in recent years in various industrial organic transformations, owing to their non-toxicity, non-corrosiveness, low cost, easy handling, recovery, and reusability. Among the several mesoporous materials, such as MCM-41 and SBA-16, the most important amphoteric substance is ɣ-alumina (ɣ-Al_2O_3), which is commercially accessible. It has been employed directly as a catalyst and as a catalyst support material in the automotive and petroleum industries due to its combination of textural features such as surface area, pore volume, and pore size dispersion.

Due to the fact that crude oil upgrading is important to ensure the crude oil produced is in a high quality with a good price, an extensive treatment will be carried out for the high acidic crude oil. In this study, the catalytic neutralization technique was introduced utilizing a 2-methylimidazole in ethanol solution with the aids of copper doped cerium based catalyst with alumina as a support.

Materials and Methods

Catalyst preparation and characterization

In this study, cerium oxides were used as catalysts of interest and supported onto alumina with copper as a dopant. Cerium nitrate and copper nitrate were chosen as the metal precursor as it is easily soluble in water.

The ratio of based-dopant used was 10 (dopant) to 90 (base) according to the metal precursor molar ratio and then calcined at a temperatures of 800 ℃, 900 ℃, and 1000 ℃ [6]. An aqueous Incipient Wetness Impregnation (IWI) method was used to prepare the catalyst. According to the desired ratio, each of the metal salts was weighted in a beaker and it was dissolved in small amount of distilled water. To homogenize the mixture, the solutions were mixed together and the mixture solution was stirred continuously by magnetic bar for 30 minutes at 27 ℃. The alumina (Al_2O_3) beads as a support material were immersed into the catalysts solution for 1 hour and the supported catalysts were transferred onto an evaporating dish covered with glass wool [7, 8].

To remove water and allow good coating of catalyst solution on the surface of alumina, it was then aged inside an oven at 80-90 ℃ for 24 hour. To eliminate all the metals precursor, excess water and impurities, this steps were followed by calcination in the furnace at 800 ℃ for 5 hours using a ramp rate of 5℃/min [9]. The preparation of the best catalyst was further optimized at temperatures of 900 ℃ and 1000 ℃ [4]. To study its physicochemical properties, the potential catalyst was characterized by a several methods. The data obtained were exceedingly valuable to comprehend the relationship between catalyst properties and its catalytic performance towards the neutralization activity. The characterization techniques that were used are X-ray Diffraction Spectroscopy (XRD), Fourier Transform Infrared Spectroscopy (FTIR), and Thermal Gravimetry Analysis (TGA-DTG) [10].

Feedstock and basic chemical

The materials were purchased from QReCTM and used as supplied. Feedstock used in this study was obtained from Petronas Penapisan Melaka (PPM), Malaysia with TAN of 2.43 mg KOH/g. In this study, the 2-propanol and toluene was used as titration solvents. The indicator used in the neutralization reaction is a phenolphthalein solution, 1% (w/v) in ethanol. Potassium hydroxide pellets and barium hydroxide were utilized as titrants [11, 12].

Catalytic neutralization reaction

Crude oil and 2-methylimidazole solution in ethanol by a certain mass ratio was stirred. A total of 10% (w/w) of imidazole derivative solutions in ethanol and cerium oxide as catalyst were added to Petronas Penapisan Melaka (PPM)'s crude oil. Then the mixture solution was put into 2 neck round bottom flask equip with a magnetic stirrer and thermometer to control the constant temperature. Parafin oil was used to ease the maintaining of the constant temperature that was 27 ℃, 40 ℃, 50 ℃ and 60 ℃ [13]. The mixture then was stirred at the various temperatures for 5, 10 and 15 minutes to study the effect of reaction time [2]. After the extraction process, the mixture was put into a centrifuge container and was centrifuge with a speed of 50×106 rpm for 30 minutes. The mixture was centrifuged to achieve the gravity separation of the reagent with the acidic compounds extracted from the crude oil sample. The reagent with ionic liquid was on top of the centrifuge tube, while the neutralized crude oil was collected at the bottom of the tube [9].

Total acid number (TAN) determination

A 0.2 g Melaka crude oil sample after neutralization treatment was measured and placed in a titration beaker. The titration solvent, 40 mL with a mixture of 2-propanol: toluene: distilled water (50:49.5:0.5) was poured into the crude oil sample in the titration beaker. Then, the petroleum crude oil sample was titrated with potassium hydroxide and barium hydroxide solution (0.01 mol/L).

TAN value for Melaka's crude oil (TAN = 2.43 mg KOH/g) was determined by semi-micro colour indicator titration method. The indicator used was phenolphthalein solution, 0.1 mL where the stable red colour was observed and indicated the end-point for the titration method. The titration method was performed on Melaka's crude oil before and after the catalytic neutralization reaction. In order to express the results, the TAN of the sample was calculated in milligrams of potassium hydroxide per gram of sample (mg KOH/g) by using Equation 1.

$$\text{TAN} = 56.1 \times c \times \frac{(V_{KOH} - V_B)}{m} \quad (1)$$

where 56.1 is the molecular mass of KOH (g/mol), c is the concentration of the standard volumetric potassium hydroxide solution (mol/L), V_{KOH} is the volume of titrant used to reach the equilibrium point (mL), V_B is the volume of titrant required for the blank titration (mL), and m is the sample mass (g).

Results and Discussion

Thermogravimetry analysis-differential thermal gravimetry (TGA-DTG)

TGA-DTG analysis was studied to obtain thermal stability of potential catalyst after being aged overnight in an oven at 80-90 ℃ [1]. TGA profile exhibited some well-defined sections of weight loss accompanied by different slopes of thermogravimetric trace (weight loss rate). The thermogram of the Cu/Ce(10:90)/Al_2O_3 catalyst showed three phases of weight loss as depicted in Figure 1 while the Table 1 tabulated the type of species deduction corresponding to the heating temperature.

The weight loss in the range of 100-200 ℃ was due to the loss of physisorbed water molecules and was assigned to the evaporation of chemically adsorbed water molecules[14]. Between the temperature of 200–380℃, the weight loss was attributed to the loss of hydroxyl molecules and lastly the weight loss at the range of 380–650℃ was due to the decomposition of nitrate precursors as shown in equation

$$2Ce(NO_3)_3 \rightarrow 2CeO_2 + 6NO_2 + O_2 \quad (2)$$

The theoretical mass loss when the nitrates were decomposed can be calculated in terms of the final mixture form (CeO_2/Al_2O_3) from 650 ℃ to 1000 ℃ for being a stable form [15]. From the overall of TGA–DTG analysis, it can be concluded that thermal treatment had eliminated the impurities and water from the materials with 14.50% of total weight loss in 8.15 mg of catalyst and the pure metal oxide was obtained after heating at 650 ℃ [16].

This observation is in agreement with the result shown in Figure 5 where by using Cu/Ce (10:90)/Al_2O_3 catalyst calcined at 900 ℃, the TAN value of PPM's crude oil can be reduced from the original TAN value as the catalyst calcined at this temperature show complete formation of metal oxide. The detailed weight loss and the deduction for each stages of weight loss is presented in Table 1.

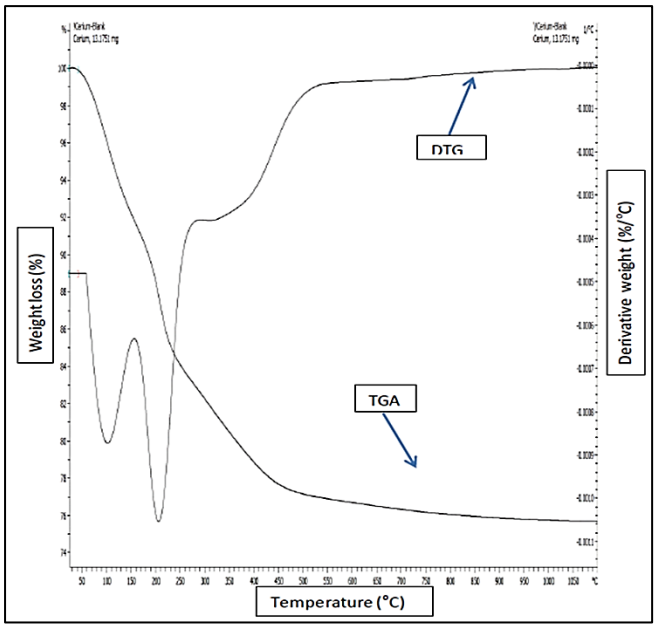


Figure 1. TGA-DTG thermogram of Cu/Ce (10:90)/Al_2O_3 catalyst after aging in an oven for 24 hours at 80-90 ℃

Table 1. TGA analysis results for Cu/Ce (10:90)/Al_2O_3 catalyst

Heating Temperature, ºC	Weight Loss, %	Deduction
100-200	14.50	Loss of crystal water and surface water molecule
200-380	8.20	Complete removal of water and formation of pure metal oxide
380-650	1.30	Loss of nitrate compound and surface hydroxyl molecule

X-ray diffraction

The XRD diffractogram for the bimetallic catalyst of Cu/Ce (10:90)/Al_2O_3 calcined at different temperatures of 800 ℃, 900 ℃, and 1000 ℃ were compiled in Figure 2. From the XRD diffractogram pattern, it can be seen that Cu/Ce(10:90)/Al_2O_3 catalyst calcined at 800 ℃ and 900 ℃ were less crystalline compared to the catalyst calcined at 1000 ℃. Typically, the calcination process of a catalyst involves the loss of chemically bound water or precursors, modification of the texture through sintering, modification of the structure, generation of an active phase and stabilization of mechanical properties which result in the development of an increased surface area of these catalysts [17].

The polycrystallinity phase of the catalyst calcined at 800 ºC and 900 ºC was dominated by the CeO_2 face-centered cubic (fcc) species and some of the alumina orthorhombic (o) phase. The broadening of CeO_2 peak calcined at 800 ℃ and polycrystalline of CeO_2 calcined 900 ℃ were attributed to the presence of a mixture of metal oxides and also due to loose arrangement of atom in the compound [18]. The high crystallinity of CeO_2 peak observed at 1000 ºC calcination temperature is in agreement with the finding from [19] who stated that the size of catalyst will increase as it was calcined at high temperature. Increasing in particle size of catalyst will lead to the smaller surface area. Therefore, 900 ℃ was an ideal calcination temperature for Cu/Ce (10:90)/Al_2O_3 catalyst in order to reduce the NAs content of PPM's crude oils.

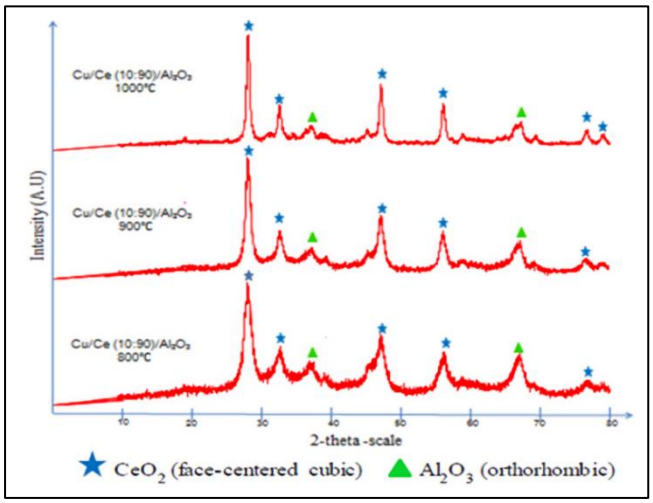


Figure 2. The XRD diffractograms of Cu/Ce(10:90)/Al_2O_3 catalyst calcined at temperatures of 800, 900 and 1000 ℃ for 5 hours

Fourier transform infrared spectroscopy

The FTIR spectra of Cu/Ce (10:90)/Al_2O_3 is shown in Figure 3. The peaks assignments for the catalyst is tabulated in Table 2. The results showed a group assignment for peak at 567.46 – 541.32 cm^{-1} at calcination temperature of 900 ℃ before and after neutralization process was due to the stretching mode of metal oxide group which resulted from the complete formation of pure metal oxide catalyst as also reported by Roy and Bhattacharya [20]. Based on the figure, it can be observed that after deacidification process (b), the new peak appeared at stretching frequency of 1310.65, 1478.24, 2810.87, and 2987.87 due to the attachment of impurities on the surface of the catalyst. It could be suggested that the catalyst should be pre-treated before use in the next cycle of reaction.

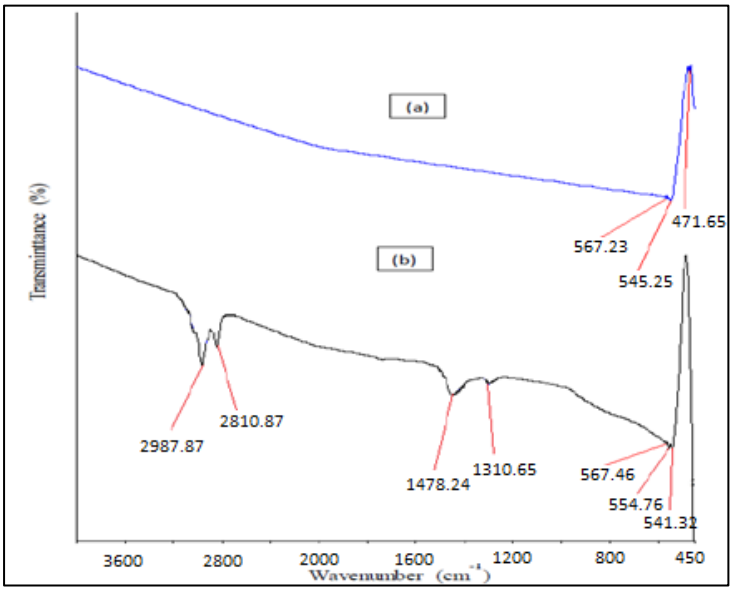


Figure 3. FTIR spectra of Cu/Ce (10:90)/Al_2O_3 catalyst at calcination temperatures of 900 ℃, (a) before neutralization reaction (b) after neutralization reaction

Wavenumber, cm^{-1}	**Peak Assignment**
2987.87 and 2810.87	sp^3 C-H stretching
1478.24	sp^2 C-H stretching
1310.65	Stretching mode of free nitrate (NO_3^-) group from metal precursors
567.46 – 541.32	Stretching mode of Metal=Oxygen (M=O)

Table 2. FTIR peak assignment of Cu/Ce (10:90)/Al_2O_3 catalyst

Effect of reagent concentration towards crude oil TAN without catalyst

Shi et al. [13] had reported the effect of different imidazole derivatives on the reduction of TAN value of PPM's crude oil. It could be seen that when ethanol was used to extract NA from crude oil, the acid removal rate reached up to 17.6%. The polar NAs could be partially dissolved in alcohol especially the smaller molecular weight ones with larger polarity were more easily dissolved in ethanol according to the

similar dissolve mutually theory. Due to this theory, when imidazole derivatives were added into ethanol solution, the acid removal rate was significantly improved. The stronger the alkalinity of imidazole derivatives, the easier the reaction to occur because NA is a weak acid.

Figure 4 shows various amount of 2-methylimidazole concentration from 5% to 15% that were tested in order to reduce the TAN of untreated PPM's crude oil sample. When higher percentages of 2-methylimidazole were used, the TAN value of PPM's crude oils was further decreased. The best result showing the highest concentration of 2-methylimidazole (15%) reduced TAN value from 2.43 mg KOH/g to 1.10 mg KOH/g is when the percentage removal of NA was 55%.

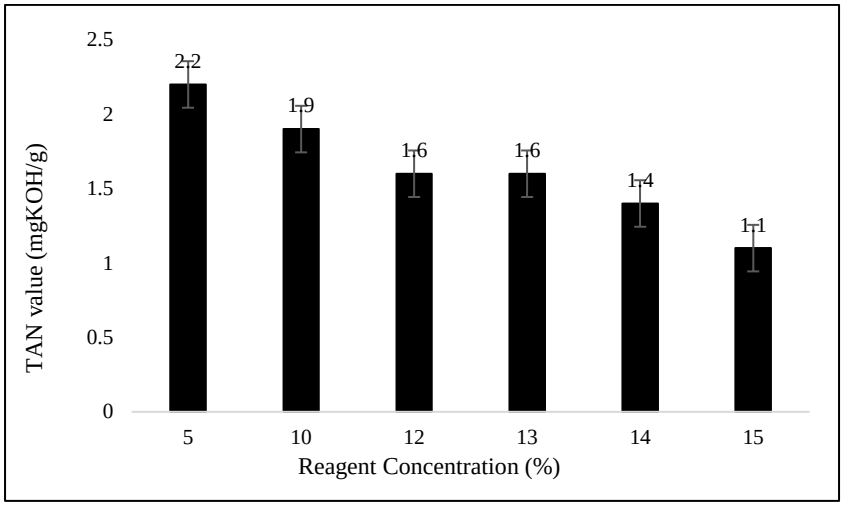


Figure 4. Effect of different reagent concentration towards TAN value without presence of catalyst

Effect of catalyst calcination temperature

An investigation on this parameter was conducted to determine the effect of calcination temperature on the alumina supported catalyst by using 10% of 2-methylimidazole. Figure 5 showed the trends of TAN value based on different catalyst calcination temperature. The trend of TAN value of PPM's crude oils decreased from calcination temperature of 800 ℃ to 900 ℃ and increased when the catalyst calcined at 1000 ℃. The catalysts which calcined at lower calcination temperatures (800 ℃) showed poor performance in this study while the catalyst functioned well in the removal of NAs process when calcined at a medium calcination temperature of 900 ℃. At 900 ℃ calcination temperature, it showed an improvement in reducing acidic content of crude oil due to the larger surface area of the catalyst from smaller particle size as supported from the BET results obtained by [4]. Thus, it provided sufficient surface sites for an excellent NAs removal process [21].

Lower performance was shown by this catalyst calcined at 1000 ℃, which gave TAN value of 1.87 mg KOH/g which is above than one. This is probably due to the fact that increasing calcination temperature will increase particle size of the catalyst which leads to a smaller surface area because of high crystallinity of the catalyst observed by the narrow peak as shown by diffractogram in XRD analysis. Therefore, 900℃ was selected as the ideal calcination temperature for removal of NA for PPM's crude oil samples [6].

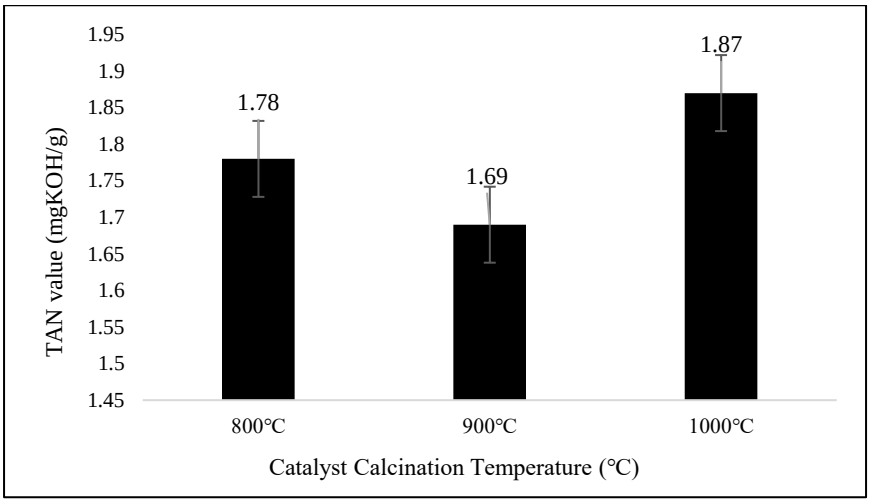


Figure 5. Effect of different calcination temperature towards TAN value

Effect of catalyst loading

Catalyst loading is the percentage of the catalyst used by calculating the weight of catalyst used over mass of crude oil. In this study, this parameter was observed to study the effectiveness and efficiency of various catalyst loading towards TAN value. Figure 6 showed the trend of TAN value for PPM's crude oil based on different catalyst loading. The trend of TAN value for PPM's crude oils was decreasing with an increase in the percentage of the catalyst loading. It could be seen that the highest catalyst loading of 0.5% successfully reduced TAN value to 0.53 mg KOH/g while the lowest loading percentages that was 0.1% only reduced the TAN value to 1.69 mg KOH/g. An increased in the catalyst loading made the catalytic reaction became faster and more efficient.

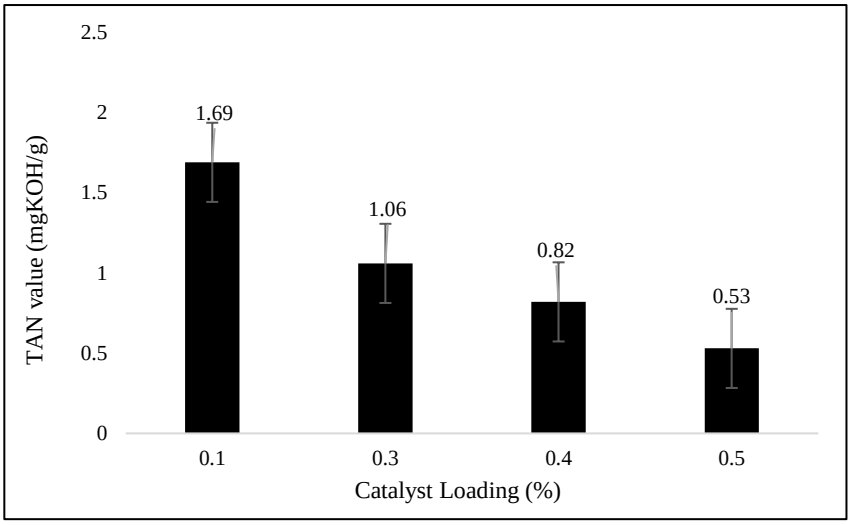


Figure 6. Effect of different percentage of catalyst loading towards TAN value (Catalyst calcination temperature: 900 ºC)

Effect of reaction temperature

In this study, different reaction temperatures were studied for catalytic neutralization process on PPM's crude oils. The temperature can be used to determine the speed of the neutralization reaction and can also decrease the viscosity of the crude oil, making the crude oil more accessible to the 2-methylimidazole. The trend of TAN for PPM's crude oils was increased when the reaction temperature increased as shown in Figure 7.

The percentage of catalytic neutralization activity decreased from 27 ℃ until 40 ℃ for PPM's crude oil samples as the TAN value for 27 ℃ reduced from 2.43 to 0.53 mg KOH/g while at 40 ℃, TAN reduced from 2.43 to 0.74 mg KOH/g and at 50 ℃ it decreased to 1.24 mg KOH/g and lastly, for 60 ℃ the TAN decreased from 2.43 to 1.44 mg KOH/g. This was because the reaction occured at higher temperature was not profitable for the reaction between 2-methylimizadole and NAs in crude oil as the higher temperature can increase the viscosity of the crude oil. This occurrence probably stabilized the NA in crude oil and inhibited the reagent to react with NA effectively. In addition, this study offered an environmental friendly process because lower reaction temperature can lead to lower energy consumption and at the same time can reduce air pollution [3].

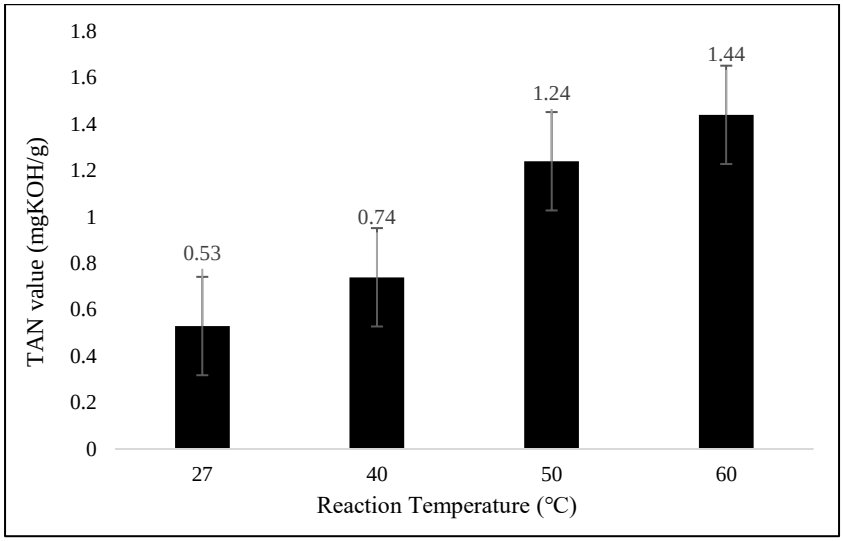


Figure 7. Effect of different reaction temperature towards TAN value (Catalyst calcination temperature: 900 ℃, catalyst loading: 0.5%)

Effect of reaction time

The effect of different reaction times on the neutralization process with Cu/Ce (10:90)/Al_2O_3 catalyst calcined at 900 ℃ with addition of 0.5% catalyst loading, 10% of 2-methyl imidazole concentration, and reaction temperature of 27 ℃ was performed on PPM's crude oils shown in Figure 8. The results illustrated that the TAN values decreased when the reaction time was increased from 5 to 15 minutes. This substantial reduction of the TAN value was attributed to the elevated opportunity for a reaction between 2-methylimidazole aided by a catalyst and NA in the crude oil. The longer the reaction time, the longer the duration for which the solution was stirred, which consequently meant the more markedly the 2-methylimidazole aided by Cu/Ce (10:90)/Al_2O_3 catalyst in the solution reacted to remove NA in PPM's crude oils.

According to Shi et al. [13] when the reaction time was increased above 15 minutes, the TAN values became constant for PPM's crude oil samples. This is because after 15 minutes, reagent successfully reduced and removed all NAs in crude oils. As a longer reaction time will only consume more energy, the optimum reaction time recommended is 10 minutes for the basic chemical to remove NA effectively and the best TAN value reduced is to 0.53 mg KOH/g for PPM's crude oils. It was observed that the acid-removal rate was increased by increasing the reaction time from 5 minutes to 10 minutes at 27 ℃, but showed very small improvement of TAN value when the reaction time is between 10 minutes and 15 minutes. TGA–DTG analysis concluded that thermal treatment had eliminated the impurities and water from the materials with 14.50% of total weight loss in 8.15 mg of catalyst and the pure metal oxide was obtained after heating at 650 ℃.

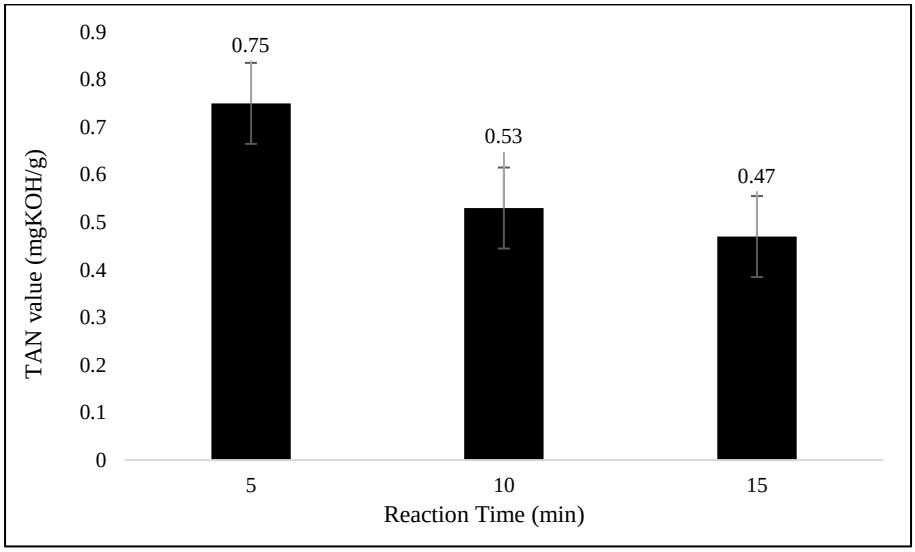


Figure 8. Effect of the different reaction times on the TAN values of PPM crude oils

Conclusion

The catalytic neutralization technique had successfully been applied in this study for the removal of NA and simultaneously solved the corrosion and emulsion problem by meeting the PETRONAS benchmark for TAN value less than 1 mg KOH/g. PPM's crude oil which possessed an initial TAN value of 2.43 mg KOH/g was reduced to 0.53 mg KOH/g with addition of 10% of 2-methylimidazole, catalyst calcination temperature of 900 ℃, 0.5% of Cu/Ce (10:90)/Al_2O_3 catalyst loading (4 beads), reaction temperature of 27 ℃ and reaction time of 10 minutes. XRD results revealed the polycrystallinity phase of the catalyst which was dominated by the CeO_2 face-centered cubic (fcc) species and some of the alumina orthorhombic (o) phase. As a recommendation for further study, other instruments to characterize the physicochemical properties of catalyst such as Brunauer–Emmett–Teller (BET), and Transmission Electron Microscopy (TEM) could be implemented.

Acknowledgement

The authors acknowledged the funding from Research Grant, FRGS with Grant No.: 011000190001 (File no.: 600 IRMI/FRGS 5/3 (108/2019)).

References

1. Shohaimi, N. A., Mohd Halim, N. S., Ab Halim, A. Z., Mohd Shukri, N. and Abdullah, N. H. (2020). Catalytic study of Ni/Ce/Al_2O_3 and Ni/Ca/Al_2O_3 on the removal of naphthenic acid from petroleum crude oil utilizing sodium thiocyanate in ethanol. *Petroleum Science and Technology,* 38(6): 602-608.
2. Sun, Y. and Shi, L. (2012). Basic ionic liquids with imidazole anion: New reagents to remove naphthenic acids from crude oil with high total acid number. *Fuel*, 99: 83-87.
3. Cho, K., Rana, B. S., Cho, D. W., Beum, H. T., Kim, C. H. and Kim, J. N. (2020). Catalytic removal of naphthenic acids over Co-Mo/γ-Al_2O_3 catalyst to reduce total acid number (TAN) of highly acidic crude oil. *Applied Catalysis A: General,* 606: 117835.
4. Shukri, N. M., Bakar, W. A., Jaafar, J. and Majid, Z. A. (2015). Removal of naphthenic acids from high acidity Korean crude oil utilizing catalytic deacidification method. *Journal of Industrial and Engineering Chemistry*. 28: 110-116.
5. Wu, C., De Visscher, A. and Gates, I. D. (2019). On naphthenic acids removal from crude oil and oil sands process-affected water. *Fuel*, 253: 1229-1246.
6. Shukri, N. M., Bakar, W. A., Jaafar, J. and Majid, Z. A. (2015b) Optimization of basic catalyst with ammoniated polyethylene glycol for the removal of naphthenic acid from petroleum crude oil by Box–Behnken design. *Clean Techn Environ Policy Clean Technologies and Environmental Policy*, 17(8), 2387-2400.
7. Zamani, A. H., Shohaimi, N. A. M., Rosid, S. J. M., Abdullah, N. H. and Shukri, N. M. (2019). Enhanced low temperature reaction for the CO_2 methanation over Ru promoted Cu/Mn on alumina support catalyst using double reactor system. *Journal of the Taiwan Institute of Chemical Engineers*, 96: 400-408.
8. Shohaimi, N. A. M., and Marodzi, N. F. S. (2018). Transesterification of waste cooking oil in biodiesel production utilizing CaO/Al_2O_3 Heterogeneous Catalyst. *Malaysian Journal of Analytical Sciences*, 22(1): 157-165.
9. Aziz, N. H., Shohaimi, N. A. M. and Che Harun, N. S. (2021). The effectiveness of Ni/Ce/Al_2O_3 catalyst in the extraction of naphthenic acids from acidic crude oil. *Materials Science Forum*, 1025: pp. 284-289.
10. Shohaimi, N. A. M, Jelani, N., Ab Halim, A. Z., Abdullah, N. H. and Shukri, N. M. (2021). Catalytic neutralization of naphthenic acid from petroleum crude oil by using cerium oxide catalyst and 2-methylimidazole in polyethylene glycol. *Recent Innovations in Chemical Engineering*, 14(3): 219-227.
11. Shohaimi, N. A. M., Jaafar, J. and Bakar, W. A. W. A. (2015). Catalytic deacidification optimization of Korean crude oil based on response surface methodology. *Clean Technologies and Environmental Policy*, 17(6), 1513-1522.
12. Shohaimi N.A.M, Bakar, W. A. W. A. and Jaafar, J. (2014). Catalytic neutralization of acidic crude oil utilizing ammonia in ethylene glycol basic solution. *Journal of Industrial and Engineering Chemistry*, 20(4): 2086-2094 .
13. Shi, L. J., Shen, B. X., Wang, G. Q. (2008). Removal of naphthenic acids from beijiang crude oil by forming ionic liquids. *Energy & Fuels Energy Fuels.* 22(6): 4177-4181.
14. Shohaimi, N. A. M., Bakar, W. A. W. A. and Jaafar, J. (2014). Catalytic neutralization method for naphthenic acid removal in crude oil by alumina supported Ca and Ba catalysts. *Petroleum Science and Technology*, 32(19): 2365-2375.
15. Dias, A. P. S., Bernardo, J., Felizardo, P. and Neiva Correi, M. J. (2012). Biodiesel production over thermal activated cerium modified Mg-Al hydrotalcites. *Energy.* 41: 344-353.
16. Alouche, A. (2008). Preparation and characterization of copper and/or cerium catalysts supported on alumina or ceria. *Jordan Journal of Mechanical and Industrial Engineering*, 2: 111-116.
17. Bakar, W. A. W. A., Ali, R., Sulaiman, N. and Rahim, H. A. (2010). Manganese oxide doped noble metals supported catalyst for carbon dioxide methanation reaction. *Iranian Journal of Science and Technology Transactions*. 17: 115-123.

18. Lamonier, C., Bennani, A., D'Huysser, A., Aboukais, A. and Wrobel, G. (1996). Evidence for different copper species in precursors of copper-cerium oxide catalysts for hydrogenation reactions: An X-ray diffraction, EPR and X-ray photoelectron spectroscopy study. *Journal of Chemical Society Faraday Transaction*, 92(l): 131-136.
19. Bueno-Ferrer, C., Parres-Esclapez, S., Lozano-Castello, D. and Bueno-Lopez, A., (2010). Relationship between surface area and crystal size of pure and doped cerium oxides. *Journal of Rare Earths*, 28: 647-656.
20. Roy, A. and Bhattacharya, J., (2011). Microwave-assisted synthesis and characterization of CaO nanoparticles. *International Journal Nanoscience,* 10(41): 3-8.
21. Li, X., Zhu, J., Liu, Q. and Wu, B., (2013). The removal of naphthenic acids from dewaxed VGO via esterification catalyzed by Mg–Al hydrotalcite. *Fuel Processing Technology*, 111: 68-77.

Malaysian Journal of Analytical Sciences (MJAS)
Published by Malaysian Analytical Sciences Society

TEMPERATURE EFFECT ON THE ENCAPSULATION OF THE DRUG TETRACAINE HYDROCHLORIDE IN DIFFERENT CYCLODEXTRINS

(Kesan Suhu Terhadap Pengkapsulan Dadah Tetrakain Hidroklorida dalam Siklodekstrin yang Berbeza)

Houria Boudjoras, Teffaha Fergoug, Mansour Azayez*, Youcef Bouhadda, Noureddine Meddah-araibi, Cherifa Zelmat

Laboratory of Physical Chemistry of Macromolecular and Biological Interfaces,
Faculty of Exact Sciences,
University of Mustapha Stambouli, Mascara, Algeria

**Corresponding author: m.azayez@univ-mascara.dz*

Received: 25 September 2021; Accepted: 30 December 2021; Published: 25 February 2022

Abstract

The encapsulation of tetrakain hydrochloride (TC-HCl) in α-cyclodextrin (α-CD), β -cyclodextrin (β-CD) and hydroxypropyl-β-cyclodextrin (HPβ-CD) has been studied by UV-Visible at different temsperatures. The appearance of isosbestic points as well as hyperchromic and bathochromic shifts on the different UV-Visible spectra confirm the complexes formation. From the complexation constants values the stability of the 1:1 type complexes is in the order of α-CD < HPβ-CD < β-CD and decreases with increasing temperature for each complex. All complexation processes are spontaneous, with a favorable enthalpic contribution and an unfavorable entropic term as deduced from Van't Hoff plot analysis. The negative values obtained for ΔCp ° indicate that the apolar part of TC-HCl is encapsulated in the cavities of the CDs.

Keywords: UV-Vis spectrophotometry, cyclodextrins, tetracaine drug, temperature effect, Van't Hoff analysis

Abstrak

Pengkapsulan tetrakain hidroklorida (TC, HCl) dalam α-siklodekstrin (α-CD), β-sikloododekstrin (β-CD) dan hidroksipropil-β-siklodekstrin (HPβ-CD) telah dikaji mengunakan spektrofotometri UV-cahaya nampak pada suhu yang berbeza. Kemunculan titik isosbestik serta pergeseran hipokromik dan bathokromik pada spektrum UV-cahaya nampak yang berbeza mengesahkan pembentukan kompleks. Daripada nilai pemalar kompleks, kestabilan kompleks jenis 1: 1 berada dalam urutan α-CD <HPβ-CD <β-CD dan menurun dengan kenaikan suhu bagi setiap kompleks. Semua proses pengkompleksan adalah spontan, dengan sumbangan entalpik yang menggalakkan dan istilah entropik yang tidak menguntungkan seperti hasil analisis plot Van't Hoff. Nilai negatif yang diperoleh untuk ΔCp ° menunjukkan bahawa bahagian tidak berkutub TC-HCl dikemas dalam rongga CD.

Kata kunci: spektrofotometri UV-cahaya nampak, siklodekstrin, dadah tetrakain, kesan suhu, analisis Van't Hoff

Introduction

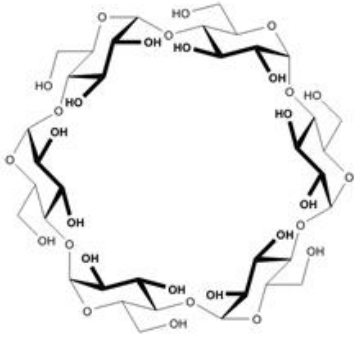
The administration of local anesthetics such as tetracaine or procaine during ophthalmologic or dentistry surgeries often shows adverse side effects such as irritations and sometimes cardiac arrhythmias and neurological after effects [1-3]. To reduce these discomforting effects an alternative approach consisting in reformulating these anesthetics as

molecular complexes with adapted complexing agents, has emerged. In this option, the complexing agent is generally a molecule with a peculiar structural conformation shaping a hydrophobic pocket-like site suited to fully encompass the anesthetic molecule or a part of it. Molecules such as cyclodextrin, crown-ether and calixarene are examples of these complexing agents and they operate based on the molecular recognition principle better known as host-guest interaction [4-6].

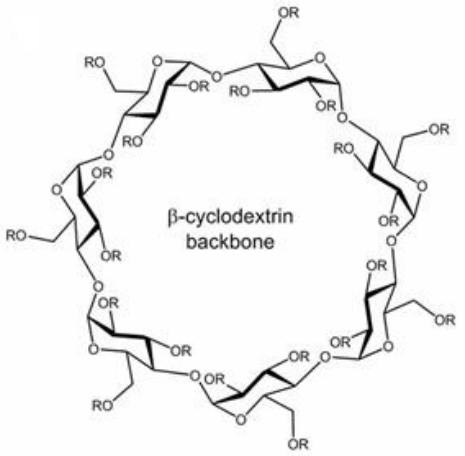
Cyclodextrins (CDs) represent the most used molecules in host-guest processes because of their biodegradability, non-toxicity and aqueous solubility. They are cyclic oligomers comprising many α(1,4) bound glucopyranose units. They are often schematized in the form of a torus-shaped molecule having a dual nature with hydrophilic external faces and a hydrophobic cavity making them able to form non-covalently bonded inclusion complexes with a variety of hydrophobic molecules in an aqueous solution. The size of each cyclodextrin (CD) varies according to the number of glucose units forming the structure (α-, β- and γ-CD contain respectively 6, 7 and 8 units of D-glucopyranosyl) [7-9] (Figure 1a). The stability of the formed complex is therefore depending partly on the size compatibility between the host and the guest molecule and in the other part on the nature of interacting forces. According to the chemical nature of the guest molecule different interactions may take place as Van der Waals interactions, hydrophobic effect, solvent reorganization, hydrogen bonding, charge transfer, etc. [10, 11]. So, structural information such as complex stoichiometry and geometry are important to know as well as thermodynamic parameters as the association constant, the variation of the free enthalpy (ΔG^0) and the entropy (ΔS^0) of binding. All these are necessary to achieve the best formulation of these complexes [12, 13].

In this present study, the formation of complexes made of tetracaine-hydrochloride (TC-HCl) and different CDs in an aqueous solution are investigated by UV-Visible spectrophotometry from a thermodynamic point of view. The guest molecule (Figure 1b) is a potent local anesthetic, primarily used for topical anesthesia and spinal block, but has a fairly toxic effect resulting in cauda equina syndrome among other compelling side effects [14]. Chemically, TC-HCl is an amino ester where the ester group links a hydrophilic ammonium group to an aromatic lipophilic ring. These peculiarities allow TC-HCl to behave both as a surfactant molecule and as a weak acid with a PKa of 8.5 [15].

(a)



α-CD



R=$CH_2CHOHCH_3$ for HPβ-CD

(b)

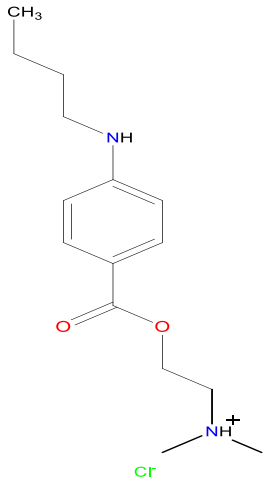


Figure 1. Chemical structures of: (a) CDs, (b) tetracaine hydrochloride

Materials and Methods

Materials

4-(Butylamino)benzoic acid 2-(dimethylamino)ethyl ester monohydrochloride, called tetracaine hydrochloride (TC-HCl) was obtained from Sigma in the crystalline form and was used without further purification. The β-cyclodextrin (β-CD), *α*-cyclodextrin (α-CD), and hydroxypropyl-*β*-cyclodextrin (HPβ-CD) were purchased from Sigma. 6-Hydroxypropyl-β-cyclodextrin (HPβ-CD), containing an average of 0.64 hydroxypropyl groups per glucopyranose unit. All of them, with 99% purity or greater, were used without further purification. All the solutions were freshly prepared with a distilled/deionized water of a conductivity value lower than 2 µS/cm. The homogeneity of the initial solutions was assured by sonicating them in an ultrasonic bath.

UV-Vis measurements

The UV-Vis spectra were recorded with a Specord 200plus double-beam UV-Vis spectrophotometer (Germany), from 190 to 400 nm with 1 nm intervals at 15, 20, 25 and 37 °C, which temperature was kept constant with thermostated cell. Data acquisition of UV-Vis spectra was performed with software (Winspec) supported by the manufacturer and converted to ASCII format for their analysis. On the experiments with the Drug/water binary systems, the (TC-HCl) concentration was varied from 0 to 0.1mM, while for the CD/Drug/water ternary systems, the drug concentration was kept constant at 10^{-5} mol.l^{-1} and CD concentration was varied from 0 to 10 mmol.l^{-1}.

Modeling stoichiometry and association constants

Assuming that a 1:1 complex between any CD and the drug is formed, the following chemical equilibrium takes place.

$$CD + G \leftrightarrows CD\text{-}G \quad (1)$$

If one takes that the activity coefficients of all species are equal to unity, the equilibrium constant K can be written as:

$$K = \frac{[CD-G]}{[CD][G]} \quad (2)$$

The laws of mass conservation for all species require that

$$[CD]_0 = [CD] + [CD-G] \quad (3)$$

$$[G]_0 = [G] + [CD-G] \quad (4)$$

with $[CD]_0$: initial (total) concentration of host molecule, $[G]_0$: initial (total) concentration of the guest molecule. [CD], [G], [CD-G]: equilibrium concentrations of host, guest and complex respectively. The combination of these equations gives the expression of K the equilibrium constant as a function of initial concentrations of the host and the guest molecules as well as one of the formed complexes:

$$K = \frac{[CD-G]}{([CD]_0 - [CD-G])([G]_0 - [CD-G])} \quad (5)$$

So, to compute the equilibrium constant one has to determine the concentration of the formed complex since all other quantities are available. This quantity can be extracted from any technique for which intensity variation is proportional to the concentration of the complex. Amongst all available techniques, UV-Vis spectrophotometry represents the most used technique because of its simplicity and repeatability. For this technique, it is well known that the absorbance or optical density is proportional to the concentration of the absorbing chromophore so the observed absorbance for a system constituted of CD, guest and complex species is expressed as:

$$A_{abs} = A_{CD} + A_G + A_{CD-G} \quad (6)$$

A_{CD}, A_G and $A_{CD\text{-}G}$ represent respectively the absorbance of the host, the guest and the complex. Taking that the length of the optical path is fixed to 1 cm, the different absorbances can be expressed as a function of the molar extinction coefficients ε of each absorbing species in solution.

$$A_0 = \varepsilon_G [G]_0 \quad (7)$$

$$A_{CD} = \varepsilon_{CD}([CD]_0 - [CD-G]) \quad (8)$$

$$A_G = \varepsilon_G([G]_0 - [CD-G]) \quad (9)$$

$$A_{CD-G} = \varepsilon_{CD-G}[CD-G] \quad (10)$$

where A_0 represents the absorbance of the drug in absence of cyclodextrin and A_{CD}, A_G and $A_{CD\text{-}G}$ are absorbances of CD, Guest and the complex in the solution. Assuming that CD doesn't absorb light in the near-UV-Visible domain and combining equations 5 to 10 gives after a rearrangement the following equation (11) [16].

$$\Delta A = [\varepsilon_G - \varepsilon_{CD-G}]\left[\left([G]_0 + [CD]_0 + \frac{1}{K}\right) - \sqrt{\left(\left([G]_0 + [CD]_0 + \frac{1}{K}\right)^2 - 4[G]_0[G]_0\right)}_0\right] \quad (11)$$

which relates the difference in absorbance $\Delta A = A_{abs} - A_0$ to the equilibrium constant K. The use of a nonlinear regression permits to extract simultaneously the values of Δε and K from the experimental curve of the variation of ΔA versus [CD].

Results and Discussion

The UV-Visible spectra of the drug TC-HCl in an aqueous solution at different concentrations at 25 °C are reported on Figure 2(a).

It can be observed that the spectra show three peaks centered at wavelength 190, 227 and 312 nm, corresponding to π-π* and n-π* electronic transitions of the unsaturated C = C bonds of the aromatic ring and the non-binding doublets of the nitrogen and the oxygen atoms [17]. With increasing drug concentration no significant wavelength shift occurs but the absorbance (A) increases obeying to a typical Lambert-Beer law (2*b*). This means that in this concentration range the solutions are dilute and no important intermolecular interactions exist as well as any solvent effect. From the linear fitting of the absorbance data as a function of drug concentration, the molar absorption coefficient, ε=20604 is determined for λ_{max}=312nm. The extracted value is comparable to one published by Merino *et al* for procaine hydrochloride anesthetic which possesses an identical chromophore as tetracaine, they reported a value of ε=19825 for λ_{max}=311nm [18].

Figure 3 shows the UV spectra of aqueous solutions of TC-HCl at a constant concentration of 10^{-5}M in the absence and the presence of β-CD, at three different temperatures. The analysis of the obtained three spectra shows the presence of isosbestic points which indicates the occurrence of chemical equilibrium between the free and the complexed TC-HCl. For the spectrum at 15°C both absorbance and wavelength variations (ΔA and Δλ) are obvious but for the spectra at 25 and 37°C the wavelength shift Δλ diminishes considerably with temperature increase. When the same sets of experiments are

conducted with α-CD and HPβ-CD instead of β-CD different behaviors are noted as shown in Figure 4.

Figure 4 shows, as an example, the experiments performed at 25 °C. For α-CD only one isosbestic point is visible at λ=329 nm and only absorbance variation ΔA is observed. For HPβ-CD both ΔA and Δλ variation are noticeable and many isosbestic points close to ones observed for β-CD appear. All these observations underline that an inclusion complexation has occurred between these CDs and the drug [19]. These results agree with ones reported by García et al. using the fluorimetry method [20].

The analysis of the obtained three spectra shows the presence of isosbestic points which indicates the occurrence of chemical equilibrium between the free and the complexed TC-HCl. For the spectrum at 15°C both absorbance and wavelength variations (ΔA and Δλ) are obvious but for the spectra at 25 and 37°C the wavelength shift Δλ diminishes considerably with temperature increase. When the same sets of experiments are conducted with α-CD and HPβ-CD instead of β-CD different behaviors are noted as shown in Figure 4.

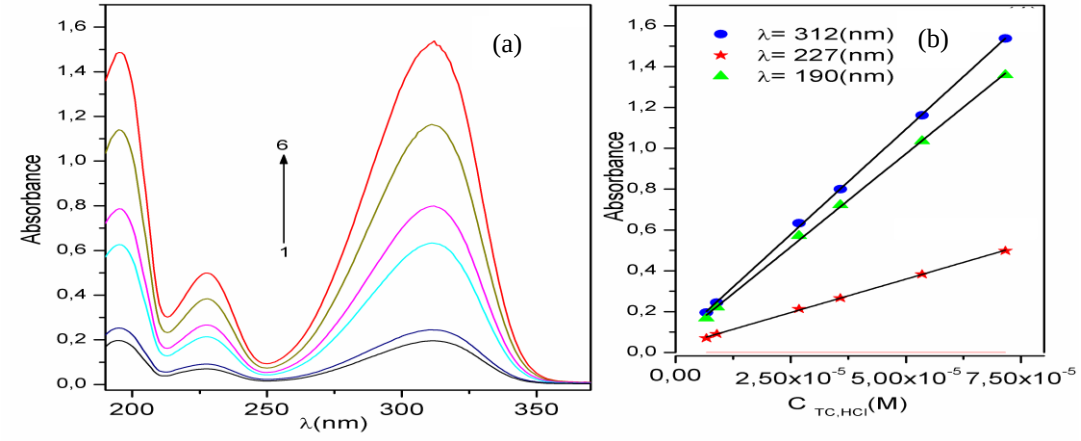


Figure 2. (a) UV-Visible spectra of aqueous solution of TC-HCl for different concentrations at 25°C. 1) 3.43x10^{-6}M, 2) 5.52 x 10^{-6} M, 3) 9.2 x 10^{-6} M, 4) 1.48 x 10^{-5}M, 5) 3.1 x 10^{-5} M, 6) 5 x 10^{-5}M. (b) Absorbance as function of concentration for different wavelengths.

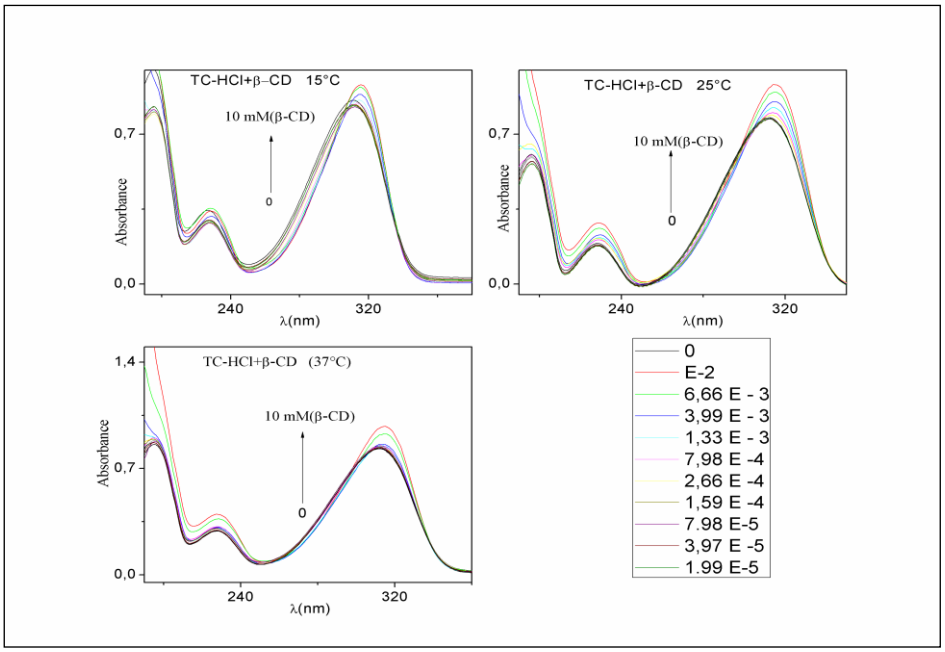


Figure 3. UV-Visible spectra of aqueous solutions of tetracaine hydrochloride (TC-HCl) 10^{-5}M with different amounts of β-CD (0-10mM) at different temperatures

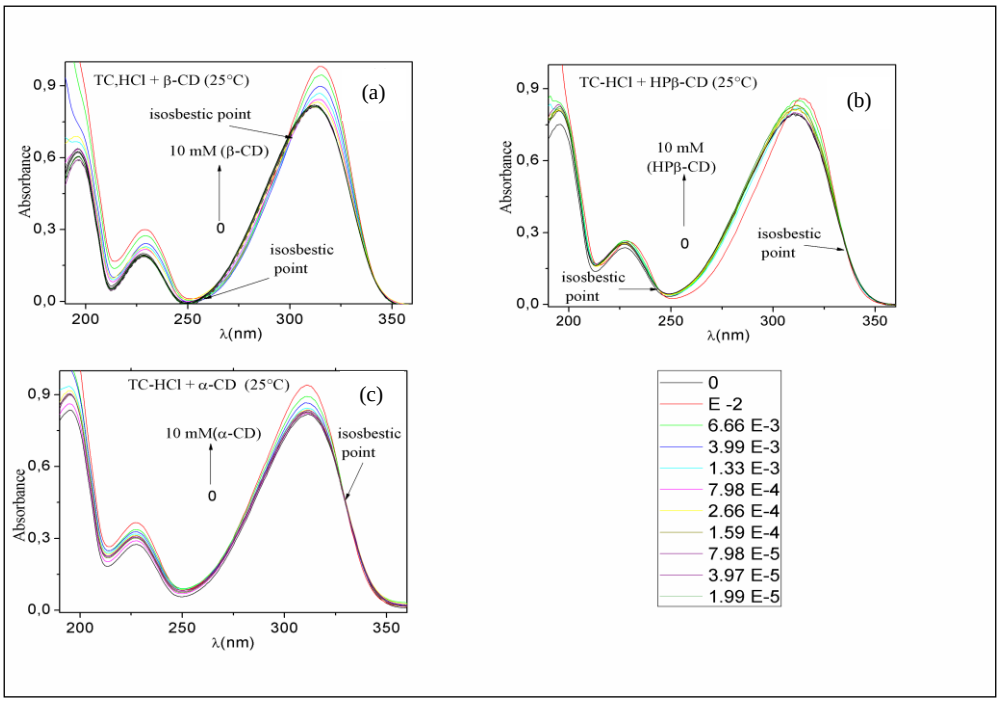


Figure 4. UV-Visible spectra of aqueous solutions (TC-HCl) 10^{-5}M in the presence of different host molecules. (a) β-CD, (b) HPβ-CD and (c) α-CD at 25 °C

In order to confirm the formation of complexes the same set of experiments were carried out in the presence of d-(+)-glucose at amounts analogous to ones used for CD's experiments at 25 °C. Because CDs are oligomers of glucose molecule units, they have mainly the same elemental composition but different spatial conformational characteristics. With this choice one tries to preserve the solvent-molecule interaction (water-CD interaction are supposed close to water-glucose one) and letting the geometry differences be the only influencing parameter. From Figure 5 it is easy to note that for d-(+)-glucose no isosbestic points exist, only a slight red shift of the order of 1 nm is obtained with a very weak effect on absorbance values.

From the variation of the curve of ΔA against CD concentration it is possible to extract the K values by a nonlinear regression method [19]. As an example, Figure 6 shows the variation of ΔA against CD's concentration at T=25°C. The same method was applied for all the studied systems at different temperatures and the corresponding association constants are reported in Table 1.

The dependence of equilibrium constants with the temperature can be noticed in Table 1, where the affinity of all cyclodextrins for the drug decreases as long as the temperature increases. Our results at T=25 °C agree with the findings of Takisawa and al. [21] who studied the inclusion of TC-HCl into α-CD and β-CD using the potentiometric method using drug-sensitive electrodes. They reported that the (β-CD/TC-HCl) formed complex is more stable than (α-CD/TC-HCl) one. From the preceding results, it is possible to determine some thermodynamic parameters of complexation from the variation of R$\ln K$ against $1/T$. Figure 7 shows the Van't Hoff plots of all association processes using both linear ($\Delta C_p°=0$) and non-linear ($\Delta C_p°\neq0$) fitting functions.

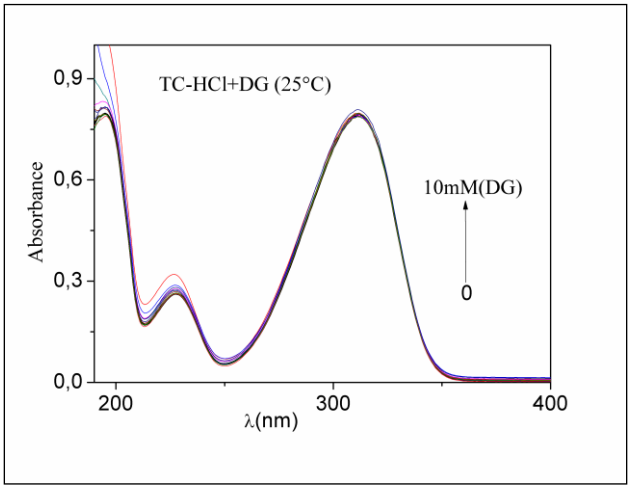


Figure 5. UV-Vis spectra of aqueous solutions of TC-HCl (10^{-5}M) for different amounts of d-(+)-glucose

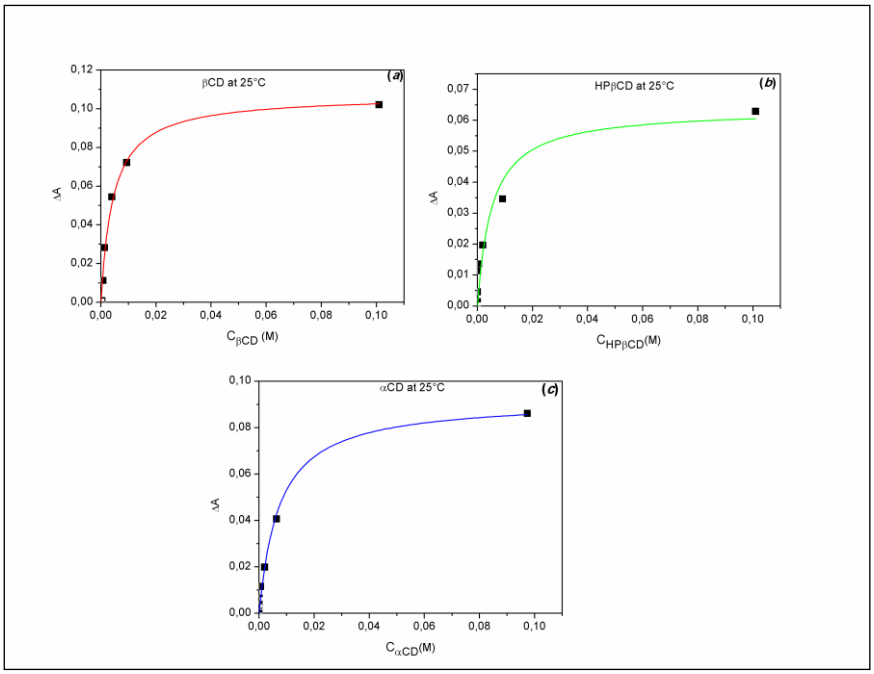


Figure 6. Non-Linear fitting of the variation of ΔA as a function of CD's concentration at 25°C for λ=310 nm

Table 1. Values of the association constant (K_{CD}) at different temperatures, obtained from UV-Vis measurements for the complex β-CD/TC-HCl, HPβ-CD/TC-HCl and α-CD/TC-HCl

T (°C)	***K*** **α-CD (l.mol^{-1})**	***K*** **β-CD (l.mol^{-1})**	***K*** **HPβ-CD (l.mol^{-1})**
15	155 ± 2	293 ± 26	285 ± 22
20	152 ± 14	263 ± 20	234 ± 12
25	137 ± 24 252 ± 14$^{(**)}$	229 ± 36 1090 ± 40$^{(**)}$	193 ± 81
37	76 ± 5.58	121 ± 9.6	91 ± 20

(**): reference [21]

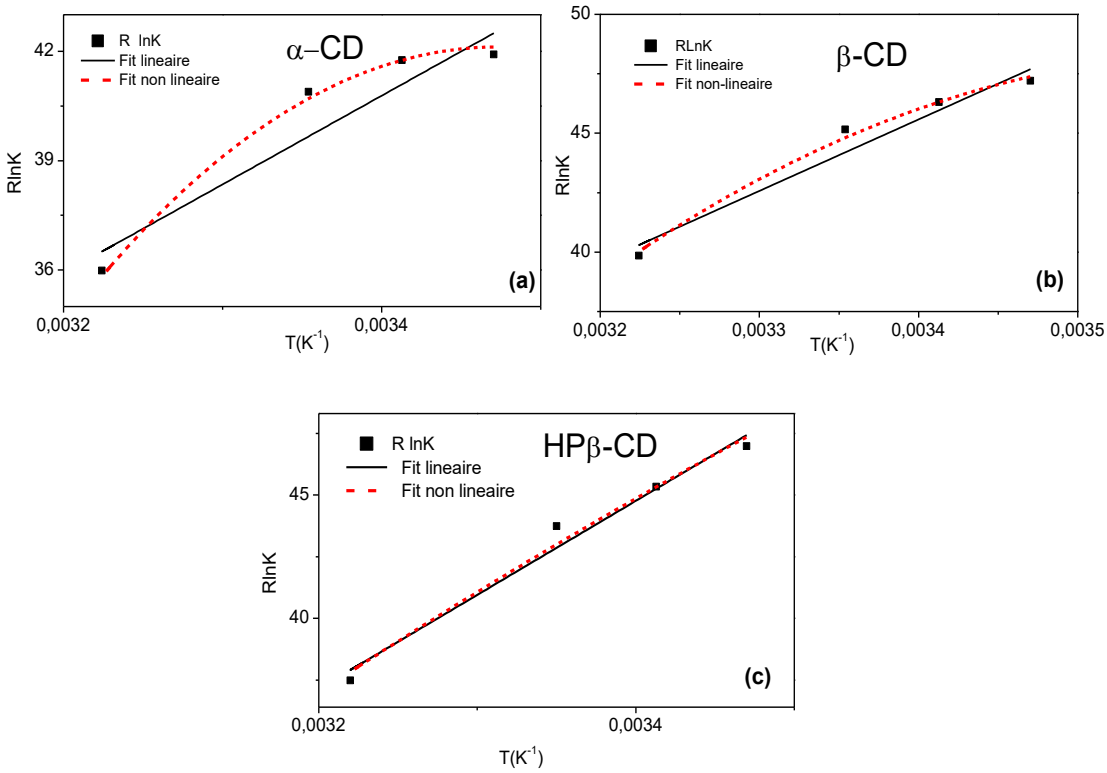


Figure 7. Van't Hoff plot for the association of TC-HCl with a) *α*-CD, *b)* β-CD and c) HPβ-CD

From the slopes of the linear fits of the data to the classical Van't Hoff equation *(R*ln*K= −ΔH°/T + ΔS°),* values of *ΔH°* equal to -24.3, -30.06 and -38.08 Kj.mol^{-1} are obtained respectively for α-CD, β-CD and HPβ-CD complexes (Table 2). Negative values of the binding enthalpy are the sign that the drug establishes favorable interactions with cyclodextrins. In such association, the enthalpy change is the result of two main conflicting contributions: the favorable enthalpy associated with van der Waals forces coupled to the host/guest hydrogen bonds formation and the unfavorable enthalpy associated with the desolvation of the guest polar groups [11-13]. Van der Waals interactions become maximal when a perfect size fitting between cyclodextrin and the drug takes place while the hydrogen bonds formation optimization is reached when drug polar groups prefer forming hydrogen bond with the cyclodextrin prior to the surrounding water molecules. Thus, an unfavorable binding enthalpy usually indicates that the desolvation is not enough to permit the inclusion of the guest molecule. However, the enthalpic contribution is not the sole provider of the stabilization of the complex and one has to consider the entropic contribution *ΔS°*. Two major terms contribute to the entropy of binding; the first one is the favorable desolvation entropy change which originates from the release of water molecules as the drug molecule and the binding cavity undergo desolvation upon binding [11-13].

The second term is related to the conformational entropy change which is almost always unfavorable since during the binding process both the drug and the cyclodextrin molecules induce the loss of conformational degrees of freedom. Thus, for our studied system, from the intercepts of Van't Hoff plot, *ΔS°* values equal to −41.8, -56.63 and -84.73 J.K^{-1}.mol^{-1} are extracted for α-CD, β-CD and HPβ-CD complexes respectively (Table 2). For all cases it can be observed that the drug bind to CDs with a favorable enthalpic term *(ΔH° < 0)* and an unfavorable entropic term *(ΔS° < 0)*. All processes are exothermic and enthalpy driven (*|ΔH°| > T|ΔS°|*), as usually found for such associations [10, 22]. With its negative entropy *ΔS° < 0* the complexation seems

to be mainly driven by Van der Waals attractive forces ($\Delta H° < 0$; $\Delta S° < 0$) and solvent reorganization effects. The contribution coming from the hydrophobic effect seems to be negligible especially for HPβ-CD ($\Delta S°$ =-84 J.mol^{-1}.K^{-1}).

For HPβ-CD a linear relationship has been found in the Van Hoff plot, revealing independence of both the $\Delta H°$ and the $\Delta S°$ of the association processes with *T*. For β-CD and α-CD, Van Hoff plots are better described by nonlinear curves as usually reported for this kind of processes by different authors [10, 22]. With its hydroxypropyl hydrocarbon chains the HPβ-CD second rim is a relatively flexible structure compared to one belonging to native βCD which is more rigid since hydrogen bonds belt is thought to exist all around the rim. These hydrocarbon chains can hinder the complete inclusion of the guest molecule and decrease the desolvation process and thus diminish the strength of the desolvation positive entropy contribution. So, the contribution of solvent reorganization and hydrophobic effects couldn't be similar in both inclusion processes which make the binding of β-CD and TC-HCl energetically more favorable than that of HPβ-CD with TC-HCl. The proposed architecture of the complexes formed can then be illustrated in Figure 8.

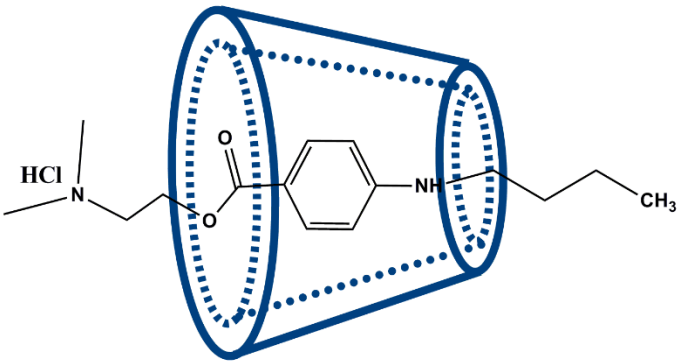


Figure 8. Architecture of inclusion complexes TC-HCl/CD

The negative value of all the ΔC_p° in table 2 obtained from the fitting of the experimental data with the non-linear Van Hoff equation ($R.\ln K = [-(\Delta H° + (T-T_o)\ \Delta C_p^\circ)/T + \Delta S° + (\Delta C_p^\circ \ln(T/T_o))]$) are close to values generally found when apolar solutes are encapsulated in CD's [23]. The difference found in the values of ΔC_p° for β-CD and HPβ-CD confirm the fact that the β-CD complex is more stable than the HPβ-CD one probably due to the diminution of the OH groups on the HPβ-CD molecule, which limit the formation of hydrogen bonds with the surrounding water.

The β-CD secondary face diameter is larger than the α-CD one and could better accommodate the inclusion of a guest molecule bearing a benzene structure. This hypothesis is confirmed by the appearance of shifts of the absorbance and wavelength λ and consequently the attractive Van der Walls interactions must be optimal for the TC-HCl/β-CD complex compared to the TC-HCl/α-CD one. The hyperchromic effect is usually attributed to the dissociation of the hydrogen bonds and the bathocromic is related to change of drug surrounding environment which become more apolar. According to Bernardi's theoretical DFT calculation in water the terminal nitrogen end of tetracaine possesses appreciable hydrophilicity which can reach the ester function close to the benzene cycle whereas the hydrocarbon butyl chain is completely hydrophobic [23, 24]. So, it can be proposed that the drug penetrates deeply in the β-CD cavity to an extent where both hydrophobic butyl chain and the benzene aromatic structure are influenced by the cavity walls which explain the simultaneous variation of ΔA and Δλ. For α-CD because of its narrower rim diameter only hydrophobic chain is penetrated and hyperchromic signature is revealed by UV-Visible spectrophotometry.

Table 2. Values of ΔH°; ΔS°, and ΔC_P^0 for the association of TC-HCl with different CDs obtained from the linear and nonlinear fitting of Van't Hoff equation

CD	Fitting	ΔH° (KJ.mol^{-1}) linear	ΔS° (J.mol^{-1}.K^{-1})	ΔC_P^0 (J.mol^{-1}.K^{-1})
α-CD	Linear	-24.3 ± 7.74	-41.8 ± 25.9	-
	Nonlinear	-23.0 ± 0.077	-39.29	-2311 ± 464.4
β-CD	Linear	-30.06 ± 6.68	-56.63 ± 22.4	-
	Nonlinear	-29.23 ± 0.00	-53.40 ± 4.81	-1000 ± 4.85
HPβ-CD	Linear	-38.08 ± 6.06	-84.73 ± 20	-
	Nonlinear	-37.78 ± 5.10	-83.57 ± 17.08	-300

Conclusion

Employing the spectrophotometry technique for the inclusion complexation of tetracaine hydrochloride in different type of CDs (α-CD, β-CD and HPβ-CD) was demonstrated. The occurrence of the complexation is confirmed by the appearance of isosbestic points, hyperchromic and bathochromic shift effects on the UV-Visible spectra. From the values of complexation constants, the strength of the complexation increases from α-CD to β-CD in accord with the majority of the studies earlier reported by different authors with other techniques. From the Van't Hoff analysis, the studied complexation processes are spontaneous, with a favorable enthalpic contribution and an unfavorable entropic term. This means that the complexation seems to be driven by Van der Waals attractive forces (ΔH° < 0; ΔS° < 0) and to the solvent reorganization effects. Van't Hoff plots well show that for the drug/HPβ-CD association process linear fitting function is sufficient to describe the phenomena. However, for the α-CD and β-CD a non-linear fitting is necessary (ΔCp°≠0) to characterize their association with the drug.

Acknowledgement

The authors would like to thank the general directorate of scientific research and technological development, Algeria for the financial support.

References

1. Mary Ann Vann, M. D., Babatunde O. Ogunnaike, M. D. and Girish P. Joshi, M.B. (2007). Sedation and anesthesia care for ophthalmologic surgery during local/regional anesthesia. *Anesthesiology,* 107(3): 502-508.
2. Glantz, L., Drenger, B. and Gozal, Y. (2007). Perioperative myocardial ischemia in cataract surgery patients: general versus local anesthesia. *Anesthesia & Analgesia,* 91(6): 1415-1419.
3. Cherobin, A. C. F. P. and Tavares, G. T. (2020). Safety of local anesthetics. *Anais Brasileiros de Dermatologia,* 95 (1):82-90.
4. Ariga**,** K. and Kunitake, T. (2006). Supramolecular chemistry-fundamentals and applications. Springer-Verlag Berlin, Heidelberg: pp. 207-238.
5. Torchilin, V. P. (2006). Multifunctional nanocarriers. *Advanced Drug Delivery Reviews*, 58(14): 1532-1555.
6. Loftsson, T. and Masson, M. (2001). Cyclodextrin in topical drug formulation: Theory and practice. *International Journal of Pharmaceutics*, 225(1-2): 15-30.
7. Frömming, K. H. and Szejtli, J. (1994). Cyclodextrin in pharmacy. Klumer Academies Publishers, Dordrecht: pp. 1-18.
8. Martin Del Valle, E. M. (2004). Cyclodextrins and their uses: A review. *Process Biochemistry*, 39: 1033-1046.
9. Maheriya, P. M. (2017). Cyclodextrin: A promising candidate in enhancing oral bioavailability of poorly water soluble drugs. *Bioequivalence &Bioavailability*, 3(3): 60-63.

10. Junquera, E. and Aicart, E. (1997). Potentiometric study of the encapsulation of ketoprophen by hydroxypropyl-β-cyclodextrin. Temperature, solvent, and salt effects. *Journal Physical Chemistry. B*, 101(36), 7163–7171.
11. Astray, G., Mejuto, J. C., Morales, J., Rial-Otero, R. and Simal-Gándara, J. (2010). Factors controlling flavors binding constants to cyclodextrins and their applications in foods. *Food Research International*, 43 (4): 1212-1218.
12. Rekharsky, M. V. and Inoue, Y. (1998). Complexation thermodynamics of cyclodextrins. *Chemical Reviews*, 98(5): 1875-1918.
13. Santos, C. I. A. V., Ribeiro, A. C. F. and Esteso, M. A. (2019). Drug delivery systems: Study of inclusion complex formation between methylxanthines and cyclodextrins and their thermodynamic and transport properties. *Biomolecules*, 9(5): 196-216.
14. Hugh, C., Hemmings, Jr. and Talmage D. E. (2019). Pharmacology and physiology for anesthesia: Foundations and clinical application, Elsevier, Philadelphia. pp: 20-43.
15. Shibata, A., Ikawa, K. and Terada, H. (1995). Site of action of the local anesthetic tetracaine in a phosphatidylcholine bilayer with incorporated cardiolipin. *Biophysical Journal*, 69(2): 470-477.
16. Schalley, C. (2007). Analytical methods in supramolecular chemistry. Wiley-VCH Verlag GmbH & Co. KGaA, Weinheim. pp: 419-471.
17. Nouiri, M. A., Fergoug, T., Azayez, M., Boujores, H., Zelmat, C. and Bouhadda, Y. (2017). Experimental and theoretical study of tetracaine-hydrochloride β-cyclodextrin complexation. *Journal of Materials Environmental Sciences*, 8(5): 1589-1598.
18. Merino, C., Junquera, E., Jiménez-Barbero, J. and Aicart, E. (2000). Effect of the presence of β-cyclodextrin on the solution behavior of procaine hydrochloride. spectroscopic and thermodynamic studies. *Langmuir*, 16(4): 1557-1565.
19. Mura, P. (2014). Analytical techniques for characterization of cyclodextrin complexes in aqueous solution: A review. *Journal of Pharmaceutical and Biomedical Analysis*, 101: 238-250.
20. García, I., Brandariz, I. and Iglesias, E. (2010). Fluorescence study of tetracaine-cyclodextrin inclusion complexes. *Journal of Supramolecular Chemistry*, 22(4): 228-236.
21. Takisawa, N., Shirahama, K. and Tanaka, I. (1993). Interactions of amphiphilic drugs with α-, β-, and γ- cyclodextrins. C*olloid and Polymer Science*, 271: 499-506.
22. Cano, J. Rodriguez, A. Aicart, E. and Junquera, E. (2007). Temperature effect on the complex formation between tricyclic antidepressant drugs (amitriptyline or imipramine) and hydroxypropyl-β-cyclodextrin in water. *Journal of Inclusion Phenomena and Macrocyclic Chemistry*, 59: 279-285.
23. Bernardi, R. C., Gomes, D. E. B., Pascutti, P., Ito, A. S. and Ota, A. T. (2006). Theoretical studies on water–tetracaine interaction. *International Journal Quantum Chemistry*, 106: 1277-1282.
24. Bernardi, R. C. Gomes, D. E. B. Ito, A. S. Ota, A. T. Pascutti, P. G. and Taft, C. (2007). Density functional and molecular dynamics simulations of local anesthetics in 0.9% NaCl solution. *Molecular Simulation*, 33(14): 1135-1141.

Malaysian Journal of Analytical Sciences Vol 26 No 2 2022

1.	COMPARATIVE STUDY ON VISCOSITIES, STRESS RELAXATION, CURING AND MECHANICAL PROPERTIES OF SEPIOLITE AND SILICA FILLED NATURAL RUBBER COMPOSITES (Kajian Perbandingan Mengenai Kelikatan, Kelonggaran Tekanan, Penyembuhan dan Sifat Mekanikal Komposit Getah Asli dengan Sepiolit dan Silika) *Nabil Hayeemasae, Ajaman Adair, Abdulhakim Masa*	176
2.	A SHORT REVIEW ON THE INFLUENCE OF THE PREPARATION METHOD ON THE PHYSICOCHEMICAL PROPERTIES OF Mg/Al HYDROTALCITE FOR GLUCOSE ISOMERIZATION (Ulasan Ringkas Mengenai Pengaruh Kaedah Penyediaan Terhadap Sifat-Sifat Fizikokimia Mg/Al Hidrotalsit untuk Pengisomerisasi Glukosa) *Munirah Zulkifli, Noor Hidayah Pungot, Nazrizawati Ahmad Tajuddin, Mohd Fadhlizil Fasihi Mohd Aluwi, Nor Saliyana Jumali, Zurina Shaameri*	191
3.	OPTIMIZATION PARAMETERS FOR ELECTROPOLYMERIZATION OF MELAMINE IN DEEP EUTECTIC SOLVENT (Pengoptimuman Parameter Elektropempolimeran Melamin Dalam Pelarut Eutektik Dalam) *Yeet Hoong Chang, Pei Meng Woi, Yatimah Alias*	202
4.	PREPARATION AND ADSORPTION STUDIES OF MOLECULARLY IMPRINTED POLYMER FOR SELECTIVE RECOGNITION OF TRYPTOPHAN (Penyediaan dan Kajian Penjerapan Polimer Molekul Tercetak untuk Pengecaman Selektif Triptofan) *Nur Habibah Safiyah Jusoh, Faizatul Shimal Mehamod, Noor Fadilah Yusof, Abd Mutalib Md Jani, Faiz Bukhari Mohd Suah, Marinah Mohd Ariffin, Nur Asyiqin Zulkefli*	215
5.	THE CHEMICAL PROPERTIES and ANTI-ACNE ACTIVITY DETERMINATION of Swietenia macrophylla SEED EXTRACTS (Penentuan Ciri Kimia dan Aktiviti Anti-Jerawat Ekstrak Biji Swietenia Macrophylla) *Non Daina Masdar, Noor Hafizah Uyup, Zamzila Erdawati Zainol, Muhammad Akmal Roslani, Siti Nur Syarifa Anuar, Muhamad Azhar Zulkafle*	229
6.	ESTIMATION OF METHANE PRODUCTION VIA ANAEROBIC CO-DIGESTION OF FOOD WASTE AND SLUDGE BY BIOCHEMICAL METHANE TEST (Anggaran Pengeluaran Metana Melalui Pencernaan Bersama Anaerobik Sisa Makanan dan Enap Cemar oleh Ujian Potensi Metana Biokimia) *Nur Anisah Abdul Latif, Zuhaida Mohd Zaki, Faeiza Buyong*	241

7. POTENTIAL APPLICATIONS OF CONDUCTING POLYMER/TUNGSTEN DISULFIDE COMPOSITES: A MINI REVIEW 251
(Aplikasi Potensi Konduktif Polimer/ Tungsten Disulfida komposit: Ulasan Mini)
Siti Nor Atika Baharin, Nur Solehah Samsudin, Nur Farahin Suhaimi, Kavirajaa Pandian Sambasevam

8. DIASTEREOSELECTIVE REDUCTION OF ENDOCYCLIC β-ENAMINO ESTER: AN APPROACH TO PREPARE DIASTEREOPURE MULTISUBSTITUTED PYRROLIDINE β-AMINO ESTERS 269
(Penurunan Diastereoselektif Terhadap Ester β-Enamino: Sebuah Pendekatan untuk Menyediakan Ester β-Amino Pirolidin Multi-Terganti Diastereotulen)
Ayisy Amirul Afti, Zurina Shaameri, Ahmad Sazali Hamzah, Nor Saliyana Jumali

9. CHROMIUM (VI) ANALYSIS IN EFFLUENTS USING LIQUID-LIQUID EXTRACTION COUPLED WITH FLAME ATOMIC ABSORPTION SPECTROMETRY 283
(Analisis Kromium (VI) dalam Efluen Menggunakan Pengekstrakan Cecair-Cecair Bersama Spektrometri Serapan Nyalaan Atom)
Nguyen Cong-Hau, Le-Thi Anh-Dao, Nguyen Thanh-Nho, Le-Thi Huynh-Mai, Le Nhon-Duc, Do Minh-Huy

10. KAFFIR LIME OIL QUALITY GRADING USING NON-LINEAR SUPPORT VECTOR MACHINE WITH DIFFERENT KERNELS 295
(Penentuan Kualiti Minyak Limau Purut Dengan Menggunakan Mesin Vektor Sokongan Bukan Linear Dengan Kernel Berbeza)
Nor Syahira Jak Jailani, Zuraida Muhammad, Nor Salwa Damanhuri, Muhd Hezri Fazalul Rahiman, Mohd Nasir Taib

11. DIRECT CATALYTIC CONVERSION OF CELLULOSE INTO FORMIC ACID BY SUPPORTED PHOSPHOTUNGSTIC ACID CATALYST 303
(Penukaran Terus Selulosa Kepada Asid Formik Menggunakan Pemangkin Asid Fosfotungstik yang Disokong)
Nor Liyana Zakira Zabidi Adil @ Zaibidai Adil, Farah Wahida Harun, Syaza Azhari, Lailatun Nazirah Ozair, Shikh Mohd Shahrul Nizan Shikh Zahari, Tengku Shafazila Tengku Saharuddin

12. THE PREPARATION AND APPLICATION OF ZINC SULFIDE AS PHOTOCATALYST FOR WATER REMEDIATION: A MINI REVIEW 318
(Penyediaan dan Aplikasi Zink Sulfida sebagai Pemangkin Cahaya untuk Rawatan Air: Ulasan Ringkas)
Kavirajaa Pandian Sambasevam, Jamilin Rashida Adnan, Izyan Najwa Mohd Norsham, Siti Nor Atika Baharin

13. PREPARATION OF EXTRACTED MAGNETITE FROM AN INDUSTRIAL WASTE MILL MODIFIED BY CETYL TRIMETHYL AMMONIUM BROMIDE FOR CADMIUM ION REMOVAL FROM AQUEOUS SOLUTION 334
(Penyediaan Magnetit daripada Sisa Buangan Sisik Besi yang Dimodifikasikan oleh Setil Trimetil Ammonium Bromida untuk Menyerap Kadmium Ion daripada Larutan Akues)
Nur Asyikin Ahmad Nazri, Raba' ah Syahidah Azis, Hasfalina Che Man, Ismayadi Ismail

14. THERMAL DECOMPOSITION OF CALCIUM CARBONATE IN CHICKEN EGGSHELLS: STUDY ON TEMPERATURE AND CONTACT TIME 347
(Penguraian Kalsium Karbonat dalam Kulit Telur Ayam: Kajian Mengenai Suhu dan Masa)

Nadia Razali, Nurriswin Jumadi, Adlin Yasmin Jalani, Nurhanim Zulaikha Kamarulzaman, Khairul Faizal Pa'ee

15. DEVELOPMENT AND OPTIMIZATION OF A RAPID RESOLUTION LIQUID CHROMATOGRAPHY METHOD FOR CYANIDIN-3-O-GLUCOSIDE IN RAT PLASMA 360
(Pembangunan dan Pengoptimuman Kaedah Kromatografi Cecair Resolusi Pantas untuk Sianidin-3-O-Glukosida Klorida di dalam Plasma Tikus)
Nadiratul Asyikin Sauji, Wan Amir Nizam Wan Ahmad, Liza Nordin, Ruzilawati Abu Bakar

16. CHEMICAL CHARACTERISATION OF BIOCHAR FROM OIL PALM FROND FOR PALM OIL MILL SECONDARY EFFLUENT TREATMENT 370
(Analisis Sifat Kimia Biochar Daripada Pelepah Kelapa Sawit Untuk Rawatan Air Sisa Sekunder Kilang Pemprosesan Kelapa Sawit)
Nadia Razali and Nurhanim Zulaikha Kamarulzaman

17. ADSORPTION OF METHYLENE BLUE FROM AQUEOUS SOLUTIONS BY ACTIVATED CARBON PREPARED FROM BANANA TRUNK USING ZINC CHLORIDE ACTIVATION 384
(Penjerapan Metilena Biru daripada Larutan Akueus oleh Karbon Teraktif yang Disediakan dari Batang Pisang secara Pengaktifan Zink Klorida)
Zaidi Ab Ghani, Muhammad Taufiq Hafizuddin R. Azemi, Mohd Hafiz Yaacob, Noor Hafizah Uyup, Lee Sin Ang, Nor Azliza Akbar

18. INITIATIVES IN UTILIZING NATURAL REAGENTS AND NATURAL MATERIALS FOR CHEMICAL ANALYSIS: TALENT AND CHALLENGE FOR ASEAN IN NEW NORMAL CHEMICAL ANALYSIS 399
(Inisiatif dalam Penggunaan Reagen Semulajadi dan Bahan Semulajadi bagi Analisis Kimia: Bakat dan Cabaran untuk ASEAN dalam Analisis Kimia Norma Baru)
Kanokwan Kiwfo, Pei Meng Woi, Chalermpong Saenjum, Treethip Sukkho, Kate Grudpan

19. OPTIMISATION OF THE EXTRACTION METHOD OF RED Christia vespertilionis LEAVES TO YIELD BIOACTIVE PHTYOCHEMICALS AS MONITORED BY GAS CHROMATOGRAPHY-MASSSPECTROMETRY 415
(Pengoptimuman Kaedah Pengekstrakan Pada Daun Merah Christia vespertilionis untuk Menentukan Fotokimia Bioaktif Melalui Kromatografi Gas-Spektrometri Jisim)
Izzah Farhah Zambari, Sitti Rahma Abdul Hafid, Nur Airina Muhamad

20. ESSENTIAL MINERALS AND HEAVY METALS ANALYSIS OF PENANG ASSAM LAKSA USING ATOMIC ABSORPTION SPECTROMETRY, FLOW INJECTION MERCURY SYSTEM, AND INDUCTIVELY COUPLED PLASMA OPTICAL EMISSION SPECTROMETRY 429
(Analisis Mineral Penting dan Logam Berat Asam Laksa Pulau Pinang Menggunakan Spektrometri Penyerapan Atom dn Spektrometri Pancaran Optik Induktif Gabungan Plasma)
Phang Hui Lee, Koo Pooi Ling, Lim Gin Keat, Oo Chuan Wei, Tan Kean Chye

Malaysian Journal of Analytical Sciences (MJAS)
Published by Malaysian Analytical Sciences Society

COMPARATIVE STUDY ON VISCOSITIES, STRESS RELAXATION, CURING AND MECHANICAL PROPERTIES OF SEPIOLITE AND SILICA FILLED NATURAL RUBBER COMPOSITES

(Kajian Perbandingan Mengenai Kelikatan, Kelonggaran Tekanan, Penyembuhan dan Sifat Mekanikal Komposit Getah Asli dengan Sepiolit dan Silika)

Nabil Hayeemasae[1,2], Ajaman Adair[3], Abdulhakim Masa[2,4]*

[1]*Department of Rubber Technology and Polymer Science, Faculty of Science and Technology*
[2]*Research Unit of Advanced Elastomeric Materials for BCG Economy, Faculty of Science and Technology*
Prince of Songkla University, Pattani Campus, 94000 Pattani, Thailand
[3]*Department of Cosmetic Science and Beauty, Faculty of Science Technology and Agriculture,*
Yala Rajabhat University, 95000 Yala, Thailand
[4]*Rubber Engineering & Technology Program,*
International College, Prince of Songkla University,
90110 Hat Yai, Songkhla, Thailand

**Corresponding author: abdulhakim.m@psu.ac.th*

Received: 1 November 2021; Accepted: 3 February 2022; Published: 28 April 2022

Abstract

In the present study, natural rubber composites filled with sepiolite and silica were prepared. The effects of the two fillers by loading (1–10 phr) on viscosities, stress relaxation, curing, and mechanical properties of the composites were investigated. Viscosity of rubber usually increased with filler loading about 7–22% with sepiolite and about 3–37% with silica, depending on filler content. Smaller rate of stress relaxation was found with sepiolite filler in comparison with silica filler. Furthermore, shorter curing cycle with greater crosslink density and hot temperature reversion resistance were achieved through the use of sepiolite filler in NR. Lorenz-Parks and Kraus models utilized for assessing rubber-filler interactions revealed stronger interactions of sepiolite filler with the rubber matrix. As a result of the good interactions between sepiolite filler and rubber matrix, larger reinforcement indexes and tensile strengths were achieved with sepiolite filler in comparison with silica filler. This was due to the higher aspect ratio of sepiolite (~5.32) compared to that of silica (~1.09) as demonstrated by SEM analysis. The highest tensile strength was achieved at 1 phr sepiolite loading which was about 17% improvement over unfilled sample.

Keywords: composites, fillers, rubber, sepiolite, silica

Abstrak

Komposit getah asli yang diisi dengan sepiolit dan silika telah disediakan dalam kajian ini. Kesan kedua-dua pengisi dengan memuatkan (1-10 phr) pada kelikatan, kelonggaran tekanan, tempoh pematangan dan sifat mekanikal komposit telah disiasat. Kelikatan getah biasanya meningkat dengan pengisi yang memuatkan dari 7-22% dengan sepiolite dan kira-kira 3-37% dengan silika, bergantung kepada kandungan pengisi. Kadar kelonggaran tekanan yang lebih kecil didapati dengan sepiolit berbanding

dengan pengisi silika. Juga, tempoh pematangan yang lebih pendek dengan ketumpatan sambung silang yang lebih tinggi dan rintangan perkembalian suhu panas dicapai dengan menggunakan pengisi sepiolit dalam getah asli. Model Lorenz-Parks dan Kraus yang digunakan untuk menilai interaksi pengisi getah mendedahkan interaksi yang lebih kuat dari pengisi sepiolit dengan matriks getah. Indeks pengukuhan yang lebih tinggi dan kekuatan tegangan dicapai dengan pengisi sepiolit daripada pengisi silika. Ini disebabkan oleh interaksi pengisi getah yang lebih baik yang timbul daripada nisbah aspek sepiolit yang lebih tinggi (~ 5.32) daripada silika (~ 1.09) seperti yang kemudiannya didedahkan oleh analisis SEM. Kekuatan tegangan tertinggi dicapai pada 1 phr pemuatan sepiolite iaitu kira-kira 17% peningkatan berbanding sampel yang tidak diisi.

Kata kunci: komposit, pengisi, getah, sepiolit, silika

Introduction

Generally, introducing one or more fillers is a strategy for improving the properties of natural rubber (NR). The use of a filler is convenient, effective, and relatively cheap for enhancing the properties of rubber [1, 2]. Among the different properties, modulus, tensile strength, tear strength, abrasion resistance, and service life of rubber can be improved, depending on size and shape of filler particles as well as the filler-matrix interactions [3, 4]. Various types of filler have been applied in rubber composites, and carbon black and silica are the most commonly used fillers in the rubber industries [5, 6]. Several studies have tested sepiolite filled rubber composites since sepiolite has unique needle-like particle shape with tunnel-like micropore channels, possibly improving the thermal, mechanical, and barrier properties of the composites [7-11].

Sepiolite belongs to nontoxic phyllosilicates, is abundant in the nature, and has a low cost. Regarding its chemical structure, sepiolite comprises microcrystalline-hydrated magnesium silicate with the unit cell formula $Si_{12}Mg_8O_{30}(OH,F)_4].(H_2O)_4 \cdot 8H_2O$ [11]. It is microfibrous with 2–10 μm particle length and tunnel-like micropore channels, providing efficient adsorption and high specific surface area for strong interaction with the rubber matrix. Comparative studies of sepiolite with other fillers, assessing reinforcing abilities, have been conducted recently [7, 9, 12-14]. Bokobza et al. [7, 9] investigated the relation of filler shape (silica particles and sepiolite fibers) with the mechanical properties of NR and styrene butadiene rubber (SBR), prepared by sol-gel process. They demonstrated that the sepiolite filler imparted more reinforcement in comparison with the spherical silica particles in NR. However, it had less interaction with SBR because the sepiolite interacts less with SBR than NR, leading to poor interaction between the rubber and filler and poor dispersion in the SBR matrix. Bhattacharya et al. [12] investigated the impact of various nanofillers, namely, montmorillonite clay, sepiolite, hectorite, carbon nanofiber, and expanded graphite, and their dispersion methods on the properties of NR nanocomposites. They found that the mechanical and physical properties, including modulus, tear, and tensile strength, depended strongly on specific surface area, aspect ratio, filler volume fraction, and dispersion of filler. Lowe et al. [13] prepared NR nanocomposites reinforced with unmodified and modified clay and sepiolite. They observed that overall better properties were obtained for nanocomposites filled with clay. In case of sepiolite filler, the modified sepiolite exhibited relatively small improvements (only 3%) compared to the neat sepiolite. Winya and Hansupalak [14] compared the effects of sepiolite and silica on mechanical properties and thermal stability of NR/EPDM blend. They reported that both properties were similar for the two fillers, in the loading range investigated (0–12.5 phr), but the sepiolite was preferred over silica, as a lower loading achieved comparable mechanical and thermal properties.

Up to now, there is little work studying property changes of sepiolite and silica filled NR composites in the literature. The objective of the current study was to understand the effects of the two types of filler (i.e., sepiolite and silica) by small loading level on mechanical properties of NR composites. The study results are discussed considering certain properties, including viscosity, stress relaxation, curing, and tensile properties. The rubber-filler interactions are discussed based on Lorenz-Parks and Kraus models.

Materials and Methods

Materials

Table 1 summarizes the details of the various chemical ingredients utilized in compound preparation and their quantities expressed in part(s) per hundred parts of rubber (phr). All the ingredients were used as received.

Preparation of composites

The composites of NR with sepiolite or silica filler were prepared on a laboratory-sized two-roll mill with a 1.5 mm nip and a 12 cm guide. The chemical ingredients were added in the sequence displayed in Table 2. NR was firstly masticated for 2 min, followed by incorporation of ZnO and stearic acid, and milled for 1 min. The filler (sepiolite or silica) was then added to the mix and milled for 9 min. Next, MBTS was fed to the mix and milled for 2 min. Finally, sulfur was added to the mix and milled for 1 min. After completion of the mixing with total mixing time of 15 min, the rubber compounds were then vulcanized through compression molding with a hydraulic press at 160 °C following their respective curing times (t_{90}) in order to obtain 1 mm thick vulcanized sheets.

Table 1. Formulation of the NR compounds

Chemical	Supplier
NR (Standard Thai Rubber graded 5L, STR 5L)	Chalong Concentrated Natural Rubber Latex Industry Company Limited, Songkhla, Thailand
Zinc oxide (ZnO)	Imperial Chemical Company Limited, Pathumthani, Thailand
Stearic acid	Global Chemical Company Limited, Samut Prakarn, Thailand
2,2'-Dithiobisbenzothiazole (MBTS)	Shanghai Rokem Industrial Company Limited, Shanghai, China
Sulfur	Siam Chemical Company Limited, Samut Prakan, Thailand
Sepiolite clay	Guangzhou Billion Peak Chemical Technology Company Limited, Guangzhou, China
Precipitated silica (Ultrasil VN3)	Evonik Industries AG, Essen, Germany

Table 2. Formulation of the NR compounds

Chemicals	Quantity (phr)		Mixing time (min)
	NR/sepiolite	NR/silica	
NR	100	100	2
Stearic acid	1	1	1
ZnO	3	3	
Sepiolite clay	0, 1, 3, 5, and 10	-	9
Silica	-	0, 1, 3, 5, and 10	
MBTS	1.5	1.5	2
Sulfur	1.5	1.5	1
Total mixing time (min)			**15**

Mooney viscosity and Mooney stress relaxation measurement

Mooney viscosity and Mooney stress relaxation of the different rubber composite samples were investigated through the use of a Mooney viscometer, MV 3000 Basic (MonTech, Germany), according to ASTM D1646. The tests were carried out at 100 °C using the large rotor. The stress relaxation was fit with the power law model in equations 1 and 2:

$$M = kt^{a}, \quad (1)$$

$$\log M = \log k + a \log t, \quad (2)$$

where M refers to the torque during relaxation, k is a constant, t is the relaxation time, and the relaxation rate a denotes the slope visible in a log-log plot of M versus t.

Curing characteristics

The curing characteristics of the NR compounds, in terms of maximum torque (M_H), torque difference (M_H-M_L), cure time (t_{90}), and cure rate index (CRI), were determined at 160 °C through the use of a moving die rheometer (Montech MDR 3000 BASIC, Buchen, Germany). The CRI was defined by equation 3.

$$CRI = \frac{100}{t_{90} - t_{s1}} \quad (3)$$

Reversion resistance

The measurement of the reversion resistance of the composites at elevated temperature was performed using the percentage of reversion in the rubber compound after 300s, from the time at maximum torque (R_{300}), as shown in equation 4 [15, 16]:

$$R_{300} = \frac{M_H - M_{300}}{M_H} \times 100, \quad (4)$$

where M_H is the maximum torque in the curing curve and M_{300} is the torque at 300s after M_H.

Rubber-filler interactions

The extent of these filler-matrix interactions was estimated through the use of the Lorenz-Parks [17] and Kraus models [18]. The Lorenz-Parks model is as follows:

$$\frac{Q_f}{Q_g} = ae^{-z} + b, \quad (5)$$

where Q is the amount of solvent absorbed, f and g indexes refer to filled and gum rubber vulcanizates, a and b are constants (the model parameters tuned to fit data), and z denotes the weight fraction of filler. The Q can be obtained via equation 6 [19]:

$$Q = \frac{\text{Swollen wt. - Dried wt.}}{\text{Original wt.}}. \quad (6)$$

The Kraus equation is as follows:

$$\frac{V_{ro}}{V_{rf}} = 1\text{-}m\left(\frac{f}{1\text{-}f}\right), \quad (7)$$

where V_{ro} and V_{rf} refer to the volume fractions of elastomer in the solvent swollen gum vulcanizate and filled sample, f is the volume fraction of filler, and m is the rubber-filler interaction parameter. V_{rf} is expressed by the equation of Ellis and Welding [20], as follows:

$$V_{rf} = \frac{(W_d - fW_0)/\rho_r}{(W_d - fW_0)/\rho_r + A_s/\rho_s}, \quad (8)$$

where W_d and W_0 are the deswollen and the initial weights of the composite samples, f is the volume fraction of filler in the composite, ρ_r is the density of rubber, A_s is the content of solvent absorbed, and ρ_s is the density of solvent. V_{ro} is given by equation 9:

$$V_{ro} = \frac{(W_d - W_f/\rho_r)}{(W_d - W_f/\rho_r + W_s/\rho_s)}, \quad (9)$$

where W_f denotes the weight of filler in the composite sample.

Tensile properties

The tensile properties including tensile strength, elongation at break, and reinforcement index (the ratio of the moduli at 300 and 100% elongations, or M300/M100, RI) of crosslinked NR composites were studied through the use of a universal tensile testing machine, LR5K Plus (LLOYD Instruments, UK) in accordance with ISO 37. The averages of five dumbbell-shaped specimens are reported, and the test was conducted at ambient temperature with a crosshead speed of 500 mm/min. The RI was defined by equation 10 [21-23]:

$$\text{Reiforcement Index, RI} = \frac{\text{M300}}{\text{M100}} \quad (10)$$

where M300 and M100 refer to the stresses at 100% and 300% strains, respectively.

Morphological test

The dispersion of sepiolite and silica fillers throughout the rubber matrix was investigated through the use of a scanning electron microscope (SEM; FEI Quanta 400 FEG, the Netherland). All composite specimens were immersed in liquid nitrogen and subsequently fractured before sputter-coating with gold in order to eliminate electrostatic charge buildup during examination. The SEM photomicrographs of cut surfaces were taken at magnification of 500x.

Results and Discussion

Mooney viscosity and Mooney stress relaxation measurement

The Mooney viscosities of the NR composite compounds filled with sepiolite or silica are shown in Figure 1. It is observed that in general the Mooney viscosity increased with filler loading. This is usually attributed to hydrodynamic effects, following the Guth and Gold equation [24].

$$\eta_{rel} = \frac{\eta_f}{\eta_u} = 1+2.5\phi + 14.1\phi^2 \quad (11)$$

where η_{rel} is the relative Mooney viscosity, η_f refers to the Mooney viscosity of filled rubber composite, η_u denotes the Mooney viscosity of neat rubber compound, and ϕ is the volume concentration of filler. As the filler loading increases, the viscosity should increase. However, a reduction of viscosity after adding 5 phr silica was observed, which was probably attributed to the formation of large silica aggregation as will be discussed later.

Figure 2 illustrates the Mooney stress relaxation rates of the composite compounds. The filler content had a great effect on the rate of relaxation, and the relaxation rates of sepiolite filled NR composites were slower than those of the silica filled ones. It has been reported that the choice of filler and its interactions with the polymer matrix considerably impacted the rate of stress relaxation. Interactions between filler particles and rubber chains hindered the molecular mobility, thus decreasing the relaxation rate [25, 26]. Considering the type of filler, composites filled with sepiolite relaxed slower than the silica filled ones. Since stronger interactions between filler and rubber matrix could better retard the relaxation rate as mentioned earlier, it is assumed that sepiolite gave stronger filler-matrix interactions than silica. The stronger filler-rubber interaction of sepiolite was attributed to the smaller size with higher aspect ratio of sepiolite dispersion in the rubber matrix as will be discussed later in the morphological observation part. The higher aspect ratio provided the higher surface area to interact with the rubber through chain entanglement and physical adsorption of rubber molecules onto the filler surfaces. It is well accepted that surface area is a major factor in the rubber composite structure. The larger the surface area of the filler is, the higher the possibility of filler-rubber contact takes place, resulting in efficient retardation of rubber molecules during relaxation.

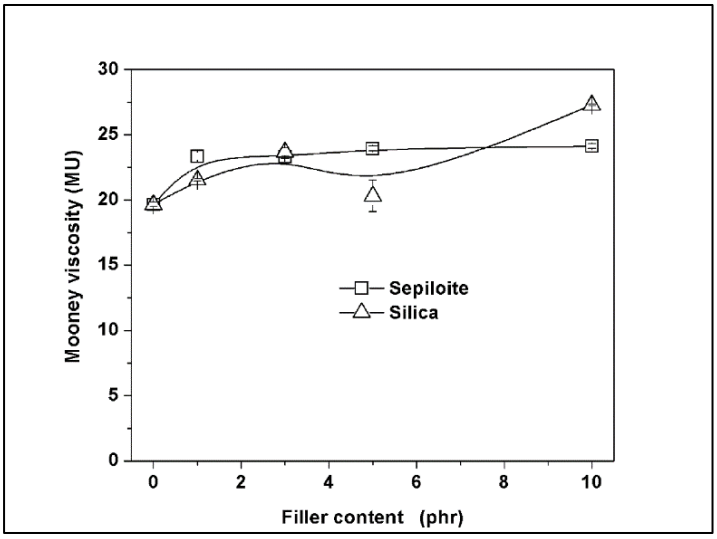


Figure 1. Mooney viscosities of NR compounds filled with sepiolite or silica

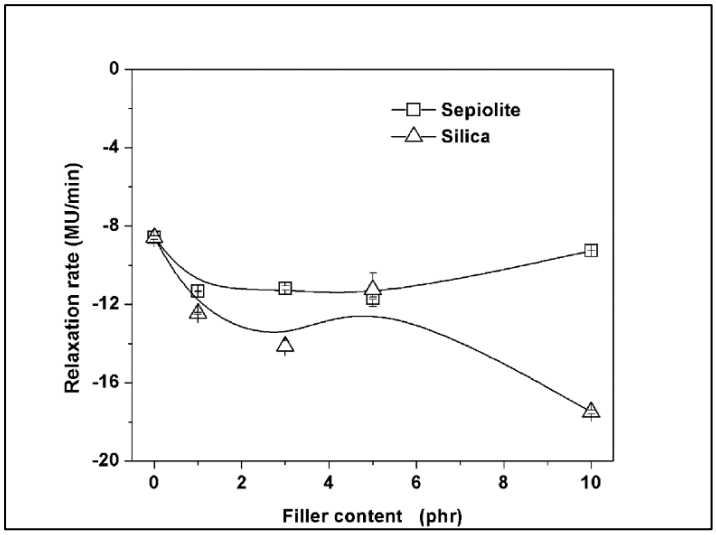


Figure 2. Mooney stress relaxation rates of NR compounds filled with sepiolite or silica

Curing characteristics

Curing properties in terms of M_H, M_H-M_L, t_{90}, and CRI, obtained from rheometric tests of the different rubber compounds, are presented in Figure 3(a)–Figure 3(d). It is noticed that the changes in curing properties were more pronounced for the sepiolite filled compounds in comparison with those for the silica filled ones. The M_H and M_H-M_L (Figures 3(a) and 3(b)) tended to increase with sepiolite loading, while they were approximately constant when silica was incorporated to the NR compounds. It is well known that M_H and M_H-M_L are related to molecular rigidity and crosslink density, respectively, for rubber compounds. The higher molecular rigidity and crosslink density were achieved with sepiolite filler because of the larger aspect ratio and surface area for contacting with the rubber molecules. The adsorbed rubber chain fragments on filler surfaces forming physical interaction restrict the chain mobility in the rubbery matrix and serving as additional crosslinks in the

composites. Consequently, the rigidity and crosslink density of the composites were improved. It has been reported that large improvements in M_H and M_H-M_L for composites with small filler loadings are attributed to stronger rubber-filler interactions [27-29]. Therefore, stronger interactions of rubber and filler can be assumed for sepiolite compared to those for silica in filled NR compounds.

Considering t_{90} of both sepiolite and silica filled compounds (Figure 3(c)), different phenomena are observed based on the filler type. Incorporation of sepiolite in NR tended to reduce t_{90}, while silica slightly prolonged it. A reduction of the t_{90} in sepiolite filled composites can be explained by the magnesium oxide (MgO) contained in the sepiolite structure. It is generally accepted that MgO is an activator of vulcanization reaction in rubber compounds, as it acts as a cation activating the crosslinking process at the diene backbone of the rubber [30]. On the contrary, the slight increase in t_{90} noticed for the silica filled compounds was probably a result of the highly polar nature of silica, leading to the absorption of the curing ingredients, including ZnO, stearic acid, and accelerators, and thereby resulting in a delayed curing process [31, 32].

The influence of metal oxide in sepiolite filled compounds on vulcanization process was later confirmed by increased CRI (Figure 3(d)), which indicated that curing reactions occurred faster with sepiolite filler than with silica filler. The CRI is a measure of rate of vulcanization based on the difference between cure time and scorch time. The higher the value of cure index, the faster the curing process [30].

Reversion resistance

Reversion resistances, R_{300}, for the composites with sepiolite or silica filler in NR vulcanizates were estimated by exposing the rubber composites to shear at an elevated temperature for a certain period of time. A larger R_{300} indicates more reversion [15, 33]. Figure 4 illustrates the reversion resistances of NR composites filled with sepiolite and silica. It is observed that the filler type and loading had a considerable effect on R_{300} within the experimental range probably because of relatively small filler loading. However, a larger R_{300} was seen for the silica filled NR composites, indicating that they had poorer reversion resistance in comparison with sepiolite filler. This can be because the greater sepiolite dispersion and better rubber-filler interactions improved the crosslink density of sepiolite filled NR composites. The better filler dispersion to gather with the higher overall crosslinking degree retarded the mobility of the rubber chains, and this enhanced the thermal stability of the rubber composites [8]. Furthermore, sepiolite itself could contribute to thermal stabilization and flame retardant properties of the filled polymer, as it served as a heat quencher and an initiator for formation of char on the polymer surface, inhibiting diffusion of oxygen [10].

Rubber-filler interactions

In order to evaluate the extent of interactions between rubber and filler, Lorenz-Parks and Kraus models were employed. Figure 5 presents Lorentz-Parks plot for the NR composites filled with sepiolite and silica. The value of rubber-filler interaction (Q_f/Q_g) generally reduced with sepiolite content but remained almost constant for the silica filled composites. Since the Q ascribed to the amount of solvent absorbed by rubber sample, the reduction of Q_f/Q_g was due to the better restricted diffusion of solvent molecules through the rubber matrix, resulting from greater extent of interaction between rubber and filler. The smaller value of Q_f/Q_g denotes stronger filler-matrix interactions [19, 28, 34, 35]. Since the Q_f/Q_g of sepiolite filled NR composites was below that of the silica filled composite at each loading level, the stronger rubber-filler interactions were achieved in the sepiolite filled composites. In contrast, the constant value of Q_f/Q_g in the composites filled with silica implies less interaction between silica and rubber matrix.

The rubber-filler interactions were further confirmed through the use of the Kraus model (plot of volume fraction ratio (V_{ro}/V_{rf}) versus volume ratio of filler (f/1-f)), and the results are displayed in Figure 6. It was observed that V_{ro}/V_{rf} decreased with filler loading. The negative slope in the plot of V_{ro}/V_{rf} versus f/1-f is an

indication of a good reinforcing effect [19, 28]. The negative slope was due to strong rubber-filler interaction, resulting from a reduction of the solvent uptake (solvent sorption) in the rubber composites. Consequently, the V_{rf} value decreases, resulting in a reduction in V_{ro}/V_{rf} value (V_{ro} is constant). More negative slope is noticed for the composites with sepiolite filler, implying that sepiolite was more effective in reinforcing the composite than the silica.

Based on the Lorenz-Parks and Kraus models, it is confirmed that sepiolite provided stronger rubber-filler interactions of the two fillers, leading to greater reinforcement within the range tested in the present study. The good interactions between sepiolite and rubber were attributed to the fact that the rubber chains can easily interact with the narrow channels in the sepiolite structure [9, 36]. Moreover, the larger specific surface area of sepiolite (364 m^2/g) [36] over silica (175 m^2/g) [37] may facilitate the rubber-filler interactions.

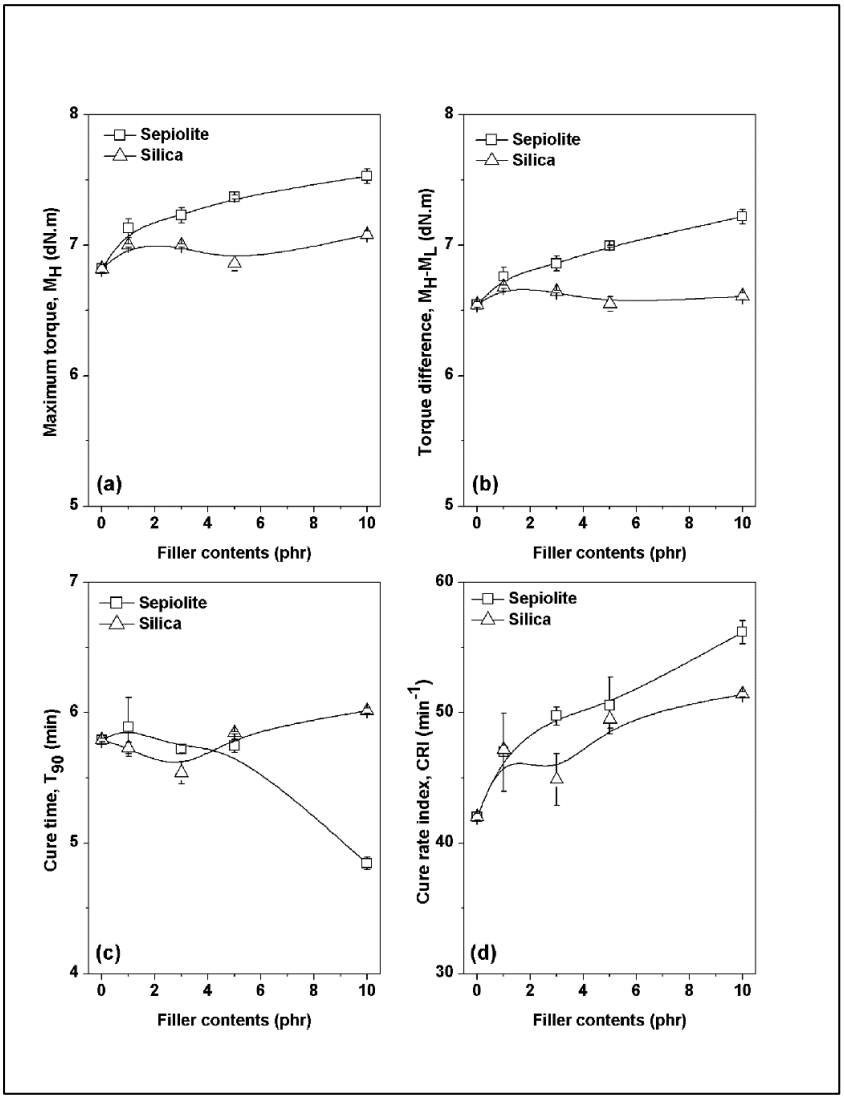


Figure 3. Curing properties in terms of (a) maximum torque, (b) torque difference, (c) cure time, and (d) cure rate index for the NR composites filled with sepiolite or with silica

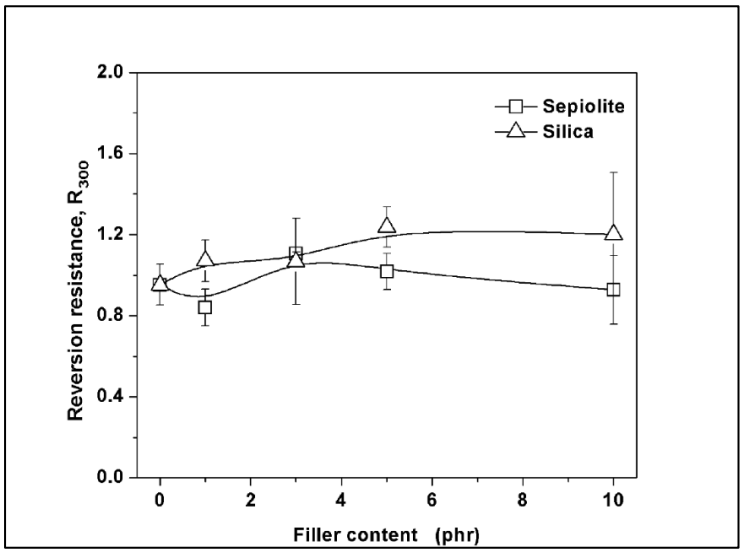


Figure 4. Reversion resistances of NR composites filled with sepiolite or with silica

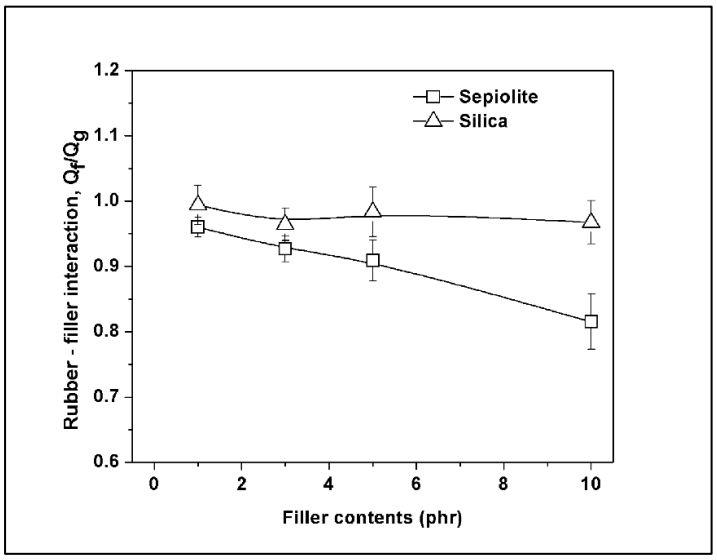


Figure 5. Lorentz-Parks plot of NR composites filled with sepiolite or silica

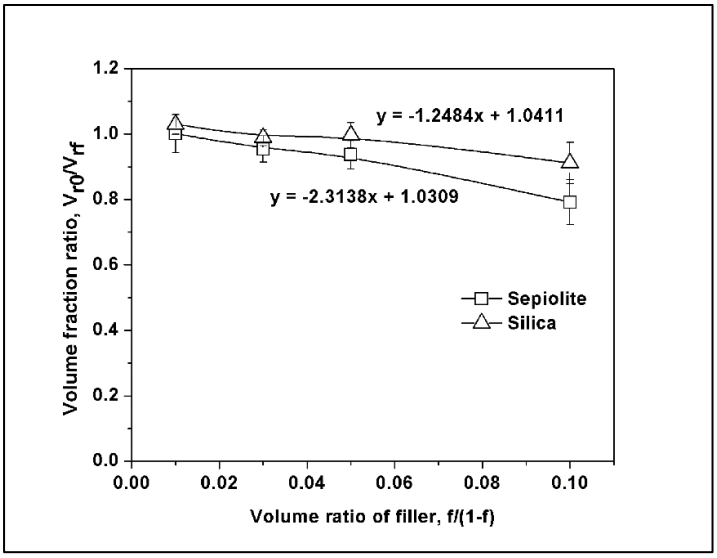


Figure 6. Kraus plot of NR composites filled with sepiolite or silica

Tensile properties

Figure 7 displays reinforcement index (M300/M100) for the NR composites filled with the two tested fillers. It is generally observed that the reinforcement index of sepiolite filled NR composite was greater than that of the silica filled composite. This was simply due to the stronger interactions between rubber and sepiolite filler, as previously discussed. The tubular-shaped with high specific surface area of sepiolite may act as stress transferring agent, which would increase the reinforcing index. This finding is in agreement with previous literature [5, 7, 9, 38], reporting that sepiolite fibers provided more reinforcement than spherical silica particles due to their high aspect ratio. The aspect ratios of sepiolite and silica found in the current study were approximately 5.32 and 1.09, respectively, which are in line with the previous report [38].

Figure 8 displays the variation in tensile strength of NR composites filled with sepiolite and silica. It can be clearly noticed that incorporation of sepiolite provided slightly higher tensile strength than silica, because of the better rubber-filler interactions. The highest tensile strength was about 17% improvement over unfilled sample found at 1 phr sepiolite loading, probably due to the greatest rubber-filler interactions as previously suggested by the stress relaxation and filler-rubber interaction results (Figures 2, 5, and 6). As a result of filler incorporation, the extensibility of rubber usually decreases due to either good rubber-filler interactions, restricting the movements of rubber chains, or poor filler dispersion, with agglomerates serving as stress concentration points. Thus, the elongation at break of composites reduced with filler loading, as presented in Figure 9. Similar observation was found in previous report [30]. The better rubber-filler interactions of sepiolite provided a slightly superior extension capability, particularly at low filler loadings.

In case of NR composites filled with silica, the highest tensile strength was found at 5 phr (about 12% over neat NR) which was considered to be optimum. Further increase in the silica incorporation slightly reduced the tensile strength because of the increment of silica aggregation, as will be discussed later in the morphological part. The aggregation of silica served as stress concentration point, resulting in a reduction of elongation at break. It is also found that the tensile strength of NR composites filled with sepiolite and silica was not much different due to relatively small filler loading. However, smaller loading of sepiolite required to obtain maximum tensile strength than silica would be benefited for preparation of rubber composite containing small filler loading.

Morphological property

Figure 10 presents the SEM micrographs of cryo-fractured surfaces of sepiolite (Figures 10(a) and 10(b)) and silica (Figures 10(c) and 10(d)) filled NR composites. It is noticed that the morphology of rubber composites comprises different sizes and shapes of filler dispersion, based on loading and type of filler. In the composites filled with sepiolite (Figures 10(a) and 10(b)), small size of filler with tubular-shaped was dispersed throughout the rubber matrix. The length (L) and diameter (D) of sepiolite in NR/Sepiolite 1 were about 1.34 - 3.15 μm and 0.34 - 0.91 μm, respectively. Meanwhile, they were about 2.45 - 5.50 μm and 0.45 - 1.12 μm, respectively, in NR/Sepiolite 5. Thus, the average aspect ratios of rubber composites filled with 1 and 5 phr sepiolite were about 5.32 ± 3.44 and 4.88 ± 3.36, respectively. Less amount of tubular-shaped particulates was observed in sample containing 1 phr sepiolite due to small amount of sepiolite added. However, such dispersion is sufficient to assist the stress transfer to each other. Large size of sepiolite aggregation was seen when the sepiolite loading was up to 5 phr. Such dispersion would be responsible for a reduction in tensile strength and elongation at break.

Considering the composites filled with silica, the L and D of silica in NR/Silica 1 (Figure 10(C)) ranged within 0.46 - 3.02 μm and 0.44 - 2.80 μm, respectively, whereas they were within 1.34 - 6.72 μm and 1.12 - 7.05 μm, respectively, for NR/Silica 5 sample (Figure 10(D)), resulting in the aspect ratio of about 1.06±0.04 for NR/Silica 1 and 1.03 ± 0.2 for NR/Silica 5. It was also found that the size of silica dispersion increased with filler loading, suggesting that filler-filler interaction was preferred at high silica loading. Smaller aspect ratio of silica dispersion than those of sepiolite can be confirmed which was in well agreement with previous report [39].

Based on the SEM observation, it is clearly evident that the aspect ratio of sepiolite dispersion was greater than that of silica. The higher aspect ratio created larger surface area contact between rubber and filler, providing better stress transfer between the components. Therefore, the better restricted chain relaxation and the higher tensile properties were obtained with incorporation of sepiolite.

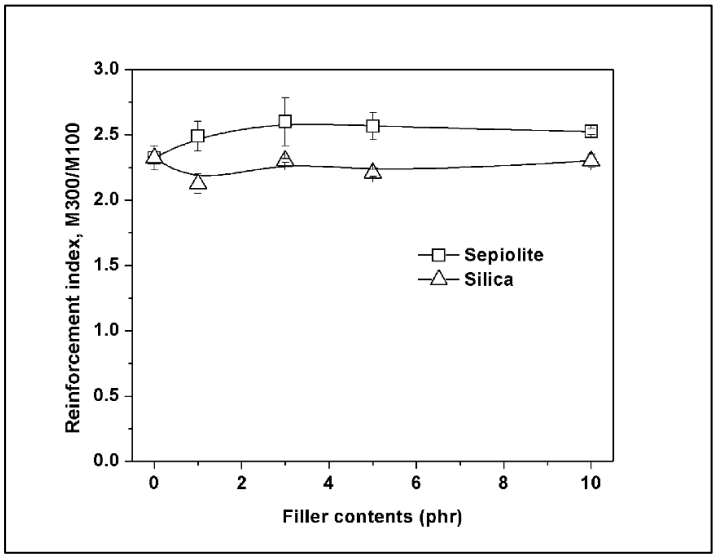


Figure 7. Reinforcement index (M300/M100) of NR composites filled with sepiolite or silica

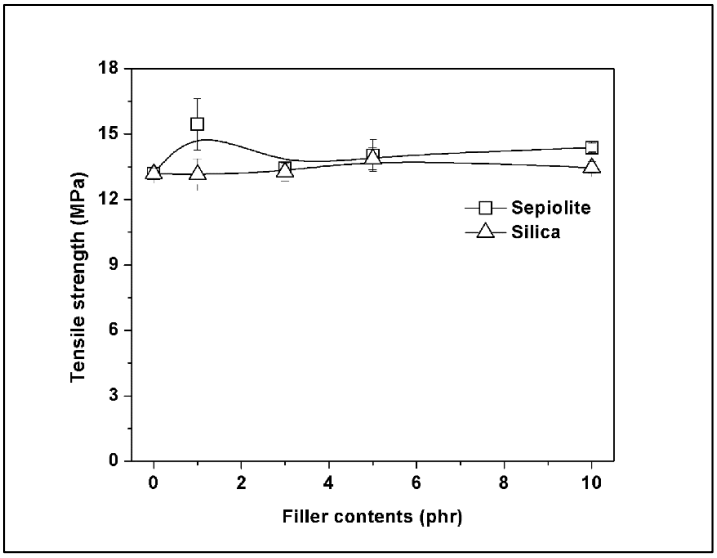


Figure 8. Tensile strength of NR composites filled with sepiolite or silica

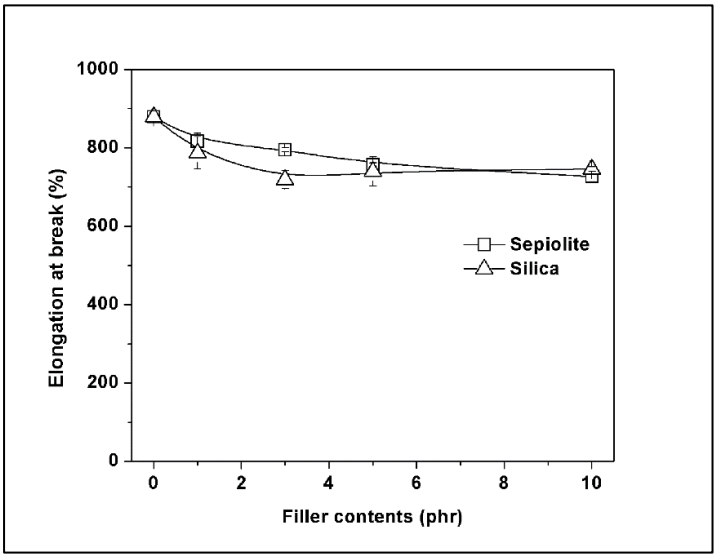


Figure 9. Elongation at break of NR composites filled with sepiolite or silica

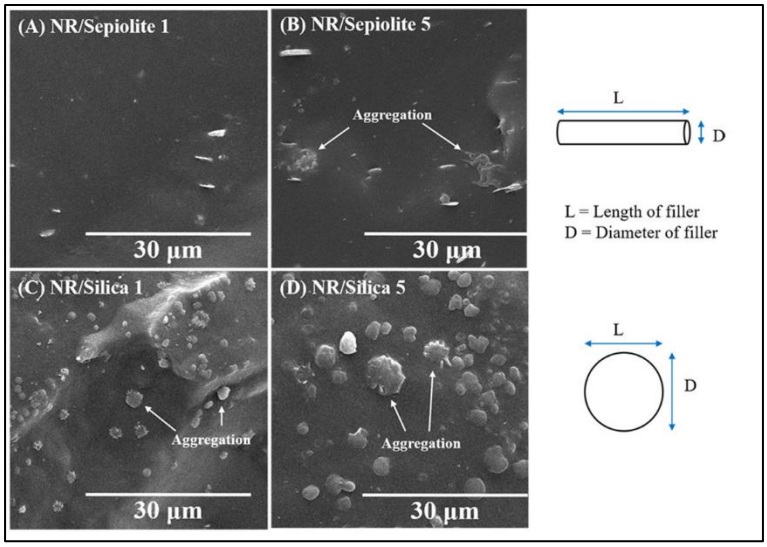


Figure 10. SEM micrographs of NR composites: (a) NR/Sepiolite 1 phr, (b) NR/Sepiolite 5 phr, (c) NR/Silica 1 phr, and (d) NR/Silica 5 phr at 500x

Conclusion

Composites of NR filled with sepiolite or with silica were prepared in the present study, and the influence of filler type and loading level on properties of the composites was investigated. From Mooney viscosity, stress relaxation, and rheometric tests, the results revealed that sepiolite filled NR exhibited a slower relaxation rate with larger torque difference and better reversion resistance than that with the silica filled compounds, suggesting better rubber-filler interactions than in silica filled composites. Increased addition of filler improved the viscosity of rubber by approximately 7 - 22% with sepiolite and approximately 3 - 37% with silica, depending on filler loading. The stronger rubber-filler interactions in the sepiolite filled composites were later confirmed through the use of the Lorenz-Parks and Kraus models. The greater extent of interaction between rubber and filler resulted in the greater restricted diffusion of solvent molecules through the rubber matrix. As a result of the good interactions between sepiolite filler and rubber matrix, larger reinforcement indexes and tensile strengths were achieved with sepiolite filler than with silica filler in the composites. This was due to the higher aspect ratio of sepiolite (~5.32) compared to that of silica (~1.09) as revealed by SEM analysis. The highest tensile strength was achieved at 1 phr sepiolite loading which was about 17% improvement over unfilled sample.

Acknowledgement

This research was supported by Prince of Songkla University (Grant No. UIC6402030S).

References

1. Chang, B. P. P., Gupta, A., Muthuraj, R. and Mekonnen, T. (2021). Bioresourced fillers for rubber composites sustainability: current development and future opportunities. *Green Chemistry*, 23: 5337-5378.
2. Maslowski, M., Miedzianowska, J. and Strzelec, K. (2019). Natural rubber composites filled with crop residues as an alternative to vulcanizates with common fillers. *Polymers*, 11(6): 972.
3. Bokobza, L. (2017). Mechanical and electrical properties of elastomer nanocomposites based on different carbon nanomaterials. *Journal of Carbon Research*, 3(2): 10.

4. Anand, A., Nussana, L., Sham Aan, M. P., Ekwipoo, K., Sangashetty, S. G. and Jobish, J. (2020). Synthesis and characterization of zno nanoparticles and their natural rubber composites. *Journal of Macromolecular Science, Part B,* 59(11): 697-712.
5. Bokobza, L. (2019). Natural rubber nanocomposites: a review. *Nanomaterials*, 9(1): 12.
6. Roy, K., Debnath, S. C. and Potiyaraj, P. (2020). A critical review on the utilization of various reinforcement modifiers in filled rubber composites. *Journal of Elastomers and Plastics,* 52(2): 167-193.
7. Bokobza, L. and Chauvin, J. P. (2005). Reinforcement of natural rubber: use of in situ generated silicas and nanofibres of sepiolite. *Polymer,* 46(12): 4144-4151.
8. Chen, H., Zheng, M., Sun, H. and Jia, Q. (2007). Characterization and properties of sepiolite/polyurethane nanocomposites. *Materials Science and Engineering: A,* 445-446: 725-730.
9. Bokobza, L., Leroy, E. and Lalanne, V. (2009). Effect of filling mixtures of sepiolite and a surface modified fumed silica on the mechanical and swelling behavior of a styrene-butadiene rubber. *European Polymer Journal,* 45(4): 996-1001.
10. Zhan, Z., Xu, M. and Li, B. (2015). Synergistic effects of sepiolite on the flame retardant properties and thermal degradation behaviors of polyamide 66/aluminum diethylphosphinate composites. *Polymer Degradation and Stability*, 117: 66-74.
11. Zaini, N. A. M., Ismail, H. and Rusli, A. (2018). Thermal, flammability, and morphological properties of sepiolite filled ethylene propylene diene monomer composites. *Malaysian Journal of Analytical Sciences,* 22(5): 899-905.
12. Bhattacharya, M., Maiti, M. and Bhowmick, A. K. (2008). Influence of different nanofillers and their dispersion methods on the properties of natural rubber nanocomposites. *Rubber Chemistry and Technology*, 81(5): 782-808.
13. Lowe, D. J., Chapman, A. V., Cook, S. and Busfield, J. J. C. (2011). Natural rubber nanocomposites by in situ modification of clay. *Macromolecular Materials and Engineering,* 296(8): 693-702.
14. Winya, N. and Hansupalak, N. (2016). A comparison between the effects of sepiolite and silica on mechanical properties and thermal stability of NR/EPDM blend. *MATEC Web of Conferences,* 6: 04003.
15. Khang, T. H. and Ariff, Z. M. (2012). Vulcanization kinetics study of natural rubber compounds having different formulation variables. *Journal of Thermal Analysis and Calorimetry,* 109(3): 1545-1553.
16. Hayeemasae, N. and Masa, A. (2020). Relationship between stress relaxation behavior and thermal stability of natural rubber vulcanizates. *Polímeros,* 30(2): e2020016.
17. Lorenz, O. and Parks, C. R. (1961). The crosslinking efficiency of some vulcanizing agents in natural rubber. *Journal of Polymer Science,* 50(154): 299-312.
18. Kraus, G. (1965). Interactions of elastomers and reinforcing fillers. *Rubber Chemistry and Technology,* 38 (5): 1070-1114.
19. Swapna, V. P., Stephen, R., Greeshma, T., Sharan, D. C. and Sreekala, M. S. (2016). Mechanical and swelling behavior of green nanocomposites of natural rubber latex and tubular shaped halloysite nano clay. *Polymer Composites,* 37(2): 602-611.
20. Ellis, B. and Welding, G. N. (1964). Techniques of polymer science. society of the chemical industry, London: pp. 46-46.
21. Lee, J. Y., Kim, S. M. and Kim, K. J. (2015). Observation of interfacial adhesion in silica-nr compound by using bifunctional silane coupling agent. *Polymer Korea,* 39(2): 240-246.
22. Saramolee, P., Sahakaro, K., Lopattananon, N., Dierkes, W. K. and Noordermeer, J. W. (2015). Compatibilization of silica-filled natural rubber compounds by combined effects of functionalized low molecular weight rubber and silane. *Journal of Elastomers and Plastics*, 48(2): 145-163.
23. Mohamad Aini, N. A., Othman, N., Hussin, M. H., Sahakaro, K. and Hayeemasae, N. (2019). Hydroxymethylation-modified lignin and its effectiveness as a filler in rubber composites. *Processes,* 7(5): 315.

24. Sajjayanukul, T., Saeoui, P. and Sirisinha, C. (2005). Experimental analysis of viscoelastic properties in carbon black-filled natural rubber compounds. *Journal of Applied Polymer Science*, 97(6): 2197-2203.
25. Maria, H. J., Lyczko, N., Nzihou, A., Joseph, K., Mathew, C. and Thomas, S. (2014). Stress relaxation behavior of organically modified montmorillonite filled natural rubber/nitrile rubber nanocomposites. *Applied Clay Science*, 87: 120-128.
26. Gabriel, D., Karbach, A., Drechsler, D., Gutmann, J., Graf, K. and Kheirandish, S. (2016). Bound rubber morphology and loss tangent properties of carbon-black-filled rubber compounds. *Colloid and Polymer Science*, 294: 501-511.
27. Honorato, L., Dias, M. L., Azuma, C. and Nunes, R. C. R. (2016). Rheological properties and curing features of natural rubber compositions filled with Fluoromica ME 100. *Polimeros*, 26(3): 249-253.
28. Mondal, D., Ghorai, S., Rana, D., De, D. and Chattopadhyay, D. (2019). The rubber-filler interaction and reinforcement in styrene butadiene rubber/devulcanize natural rubber composites with silica-graphene oxide. *Polymer Composites*, 40(S2): E1559-E1572.
29. Lopez-Manchado, M. A., Arroyo, M., Herrero, B. and Biagiotti, J. (2003). Vulcanization kinetics of natural rubber-organoclay nanocomposites. *Journal of Applied Polymer Science*, 89(1): 1-15.
30. Masa, A., Krem-ae, A., Ismail, H. and Hayeemasae, N. (2020). Possible use of sepiolite as alternative filler for natural rubber. *Materials Research*, 23(4): e20200100.
31. Sridharan, H., Guha, A., Bhattacharyya, S., Bhowmick, A. K. and Mukhopadhyay, R. (2019). Effect of silica loading and coupling agent on wear and fatigue properties of a tread compound. *Rubber Chemistry and Technology*, 92(2): 326-349.
32. Ansarifar, M. A., Chugh, J. P. and Haghighat, S. (2000). Effects of silica on the sure properties of some compounds of styrene-butadiene rubber. *Iranian Polymer Journal*, 9(2): 81-87.
33. Kok, C. M. (1987). The effects of compounding variables on the reversion process in the sulphur vulcanization of natural rubber. *European Polymer Journal*, 23(8): 611-615.
34. Wu, X., Lin, T. F., Tang, Z. H., Guo, B. C. and Huang, G. S. (2015). Natural rubber/graphene oxide composites: effect of sheet size on mechanical properties and strain-induced crystallization behavior. *eXPRESS Polymer Letters*, 9(8): 672-685.
35. Ismail, H., Omar, N. F. and Othman, N. (2011). Effect of carbon black loading on curing characteristics and mechanical properties of waste tyre dust/carbon black hybrid filler filled natural rubber compounds. *Journal of Applied Polymer Science*, 121(2): 1143-1150.
36. Bhattacharya, M. and Bhowmick, A. K. (2008). Polymer-filler interaction in nanocomposites: New interface area function to investigate swelling behavior and Young's modulus. *Polymer*, 49(22): 4808-4818.
37. Kaewsakul, W., Sahakaro, K., Dierkes, W. K. and Noordermeer, J. W. (2013). Optimization of rubber formulation for silica-reinforced natural rubber compounds. *Rubber Chemistry and Technology*, 86(2): 313 - 329.
38. Locatelli, D., Pavlovic, N., Barbera, V., Giannini, L. and Galimberti, M. (2020). Sepiolite as reinforcing filler for rubber composites: from the chemical compatibilization to the commercial exploitation. *KGK Kautschuk Gummi Kunststoffe*, 73: 26-35.
39. Abdul Salim, Z. A. S., Hassan, A. and Ismail, H. (2018). A review on hybrid fillers in rubber composites. *Polymer-Plastics Technology and Engineering*, 57(6): 523-539.

Malaysian Journal of Analytical Sciences (MJAS)
Published by Malaysian Analytical Sciences Society

A SHORT REVIEW ON THE INFLUENCE OF THE PREPARATION METHOD ON THE PHYSICOCHEMICAL PROPERTIES OF Mg/Al HYDROTALCITE FOR GLUCOSE ISOMERIZATION

(Ulasan Ringkas Mengenai Pengaruh Kaedah Penyediaan Terhadap Sifat-Sifat Fizikokimia Mg/Al Hidrotalsit untuk Pengisomerisasi Glukosa)

Munirah Zulkifli[1,2], Noor Hidayah Pungot[1,2]*, Nazrizawati Ahmad Tajuddin[1], Mohd Fadhlizil Fasihi Mohd Aluwi[3], Nor Saliyana Jumali[4], Zurina Shaameri[1,2]

[1]School of Chemistry and Environment, Faculty of Applied Sciences,
Universiti Teknologi MARA, 40450 Shah Alam, Selangor, Malaysia
[2]Organic Synthesis Laboratory, Institute of Science,
Universiti Teknologi MARA Puncak Alam Campus, 42300 Bandar Puncak Alam, Selangor, Malaysia
[3]Faculty of Industrial Sciences and Technology,
Universiti Malaysia Pahang, Lebuhraya Tun Razak, 26300 Gambang, Kuantan, Pahang, Malaysia
[4] Department Chemistry, Kulliyyah of Science,
International Islam University Malaysia, 25200 Bandar Indera Mahkota, Kuantan, Pahang, Malaysia

**Corresponding author: noorhidayah977@uitm.edu.my*

Received: 15 September 2021; Accepted: 3 February 2022; Published: 28 April 2022

Abstract

Hydrotalcite ($Mg_6Al_2(OH)_{16}CO_34H_2O$) is a naturally occurring anionic clay with a layered crystal structure. Hydrotalcites is classified as heterogeneous catalysts that exhibit an excellent separation post-reaction. Furthermore, commercial hydrotalcites are environmentally friendly. Organically synthesised hydrotalcites have attracted numerous researchers. The compounds are crucial solid base materials for several organic reactions, such as the Aldol condensation, Knoevenagel, Claisen-Schmidt, and Michael addition reactions. The present review covers the synthesis of magnesium aluminide (MgAl) hydrotalcites with varying magnesium to aluminium (Mg/Al) molar ratios employed to prepare the catalyst. Additionally, the characterisation of MgAl hydrotalcites with X-ray diffraction (XRD), Brunauer-Emmett-Teller (BET), and scanning electron microscopy (SEM) are highlighted. The instruments were utilised to identify the physicochemical properties of the catalyst, including crystallinity, surface area, and morphology. The catalytic activity of MgAl hydrotalcite was explored in the isomerisation of glucose into fructose as a model reaction for the catalytic performance.

Keywords: MgAl hydrotalcite, Mg/Al molar ratio, physicochemical properties, catalytic activity

Abstrak

Hidrotalsit ($Mg_6Al_2(OH)_{16}CO_34H_2O$) ialah tanah liat anionik yang wujud secara semula jadi dengan struktur kristal berlapis. Hidrotalsit dikelaskan sebagai pemangkin heterogen yang mempamerkan pemisahan selepas tindak balas yang sangat baik. Tambahan pula, hidrotalsit komersial adalah mesra alam. Hidrotalsit yang disintesis secara organik telah menarik ramai

penyelidik. Sebatian tersebut merupakan bahan asas pepejal yang penting untuk beberapa tindak balas organik, seperti tindak balas kondensasi Aldol, Knoevenagel, Claisen-Schmidt, dan penambahan Michael. Ulasan semula ini meliputi sintesis magnesium aluminida (MgAl) hidrotalsit dengan pelbagai nisbah molar magnesium kepada aluminium (Mg/Al) digunakan untuk menyediakan mangkin. Selain itu, pencirian hidrotalsit MgAl dengan pembelauan sinar-X (XRD), Brunauer-Emmett-Teller (BET), dan mikroskop elektron pengimbasan (SEM) diserlahkan. Instrumen ini telah digunakan untuk mengenal pasti sifat fizikokimia mangkin, termasuk kehabluran, luas permukaan, dan morfologi. Aktiviti pemangkin hidrotalsit MgAl telah diterokai dalam pengisomeran glukosa kepada fruktosa sebagai tindak balas model untuk prestasi pemangkin.

Kata kunci: MgAl hidrotalsit, nisbah molar Mg/Al, sifat-sifat fizikokimia, aktiviti pemangkin

Introduction

Hydrotalcite is a magnesium-aluminium hydroxy-carbonate, a naturally occurring mineral with the chemical composition $Mg_6Al_2(OH)_{16}CO_34H_2O$ that exhibits a layered crystal structure [1]. The layers consist of positively charged hydroxide layers, while the interlayers contain carbonate anions and water molecules, as displayed in Figure 1. The general formula of hydrotalcites is $[M^{2+}_{(1-x)}M^{3+}_x(OH)_2]_{x+}(A_{x/n})^{n-}.yH_2O$, where M^{2+} and M^{3+} are the metal components with divalent and trivalent cations, respectively, and A^{n-} is an interlayer anion [2]. Aluminium (Al) is partially substituted in magnesium hydroxide ($Mg(OH)_2$) and is a brucite structure in magnesium aluminide (MgAl) hydrotalcite, the typical representation of hydrotalcites [3]. The charge imbalance when a trivalent cation replaces the divalent is counterbalanced by the placement of available anions, such as CO_3^{2-}, NO_3^-, Cl^-, SO_4^{2-}, and OH^-, in the interlayers along with water molecules [4].

The MgAl hydrotalcites are solid bases that exhibit potential catalytic activity and good stability under required reaction conditions [6]. Moreover, hydrotalcites possess two representative and prominent properties, the ability to capture and exchange organic and inorganic anions and the memory effect due to their unique structures [7]. The unique characteristics resulted in the wide range of applications of the compounds as anion exchangers, absorbing agents, stabilisers for polymers, catalysts, electroactive materials, and pharmaceuticals. Hydrotalcite is classified as a heterogeneous catalyst with numerous advantages over homogeneous catalysts, including catalyst reusability, high purity by-products, and good separation and purification [8]. The wide applications of hydrotalcite catalysts have brought more functionality to the industry. Researchers in the scientific field generally employ hydrotalcite catalysts in organic synthesis reactions [9]. The catalysts are regarded as crucial solid base materials for various organic reactions, including Aldol condensation [10], Knoevenagel [11], Claisen-Schmidt [12], and Michael addition [13] reactions.

Numerous methods, such as co-precipitation, urea, sol-gel, and hydrothermal synthesis, could be utilised to prepare MgAl hydrotalcite [14, 15]. In this review, the preparation of MgAl hydrotalcite via co-precipitation, urea, and simple methods are discussed in detail. Furthermore, the current review highlights the characterisation of MgAl hydrotalcites with X-ray diffraction (XRD), Brunauer-Emmett-Teller (BET), and scanning electron microscopy (SEM). The instruments identified the physicochemical properties of the catalyst, including crystallinity, surface area, and morphology. The catalytic properties of MgAl hydrotalcite as base catalysts were confirmed by the isomerisation of glucose to fructose. The influence of the preparation method on the physicochemical properties and activity of MgAl hydrotalcites as solid base catalysts based on the characterisation results and the catalytic activities observed are discussed and compared.

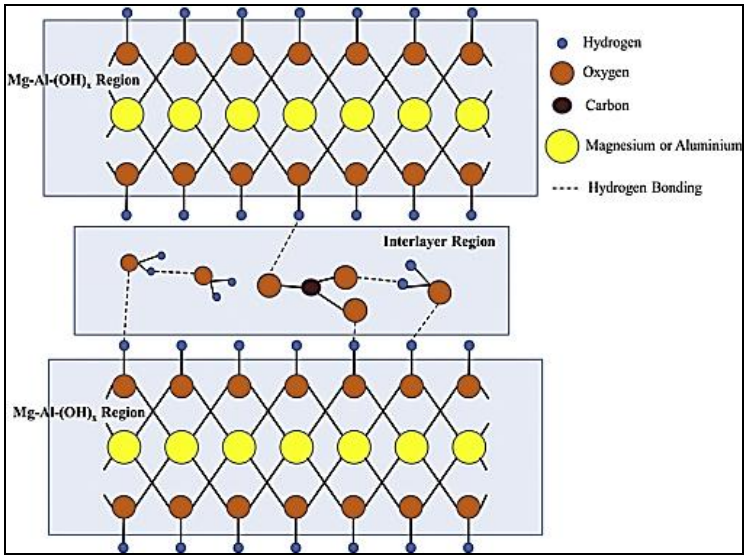


Figure 1. MgAl Hydrotalcite Structure [5]

Preparation of MgAl hydrotalcite catalyst

Researchers have employed numerous methods to synthesise MgAl hydrotalcite catalysts, such as co-precipitation, urea, and simple methods. The techniques are applicable in the isomerisation of glucose into fructose. The most common method to prepare hydrotalcite catalyst is the co-precipitation method. The pH of the solution plays a vital role in the technique. If the pH of the solution utilised is low, not all ions would precipitate, while a high pH would result in the dissolution of the metallic ions present [5]. Consequently, it is essential to control the pH of the solution to obtain the hydrotalcite catalyst successfully. Park et al. [14] performed the preparation of MgAl hydrotalcite catalyst via the co-precipitation method by adding aqueous solution B, sodium hydroxide and sodium carbonate in distilled water dropwise into solution A that consisted $Mg(NO_3)_2.6H_2O$ and $Al(NO_3)_3.9H_2O$ dissolved in distilled water. During the addition of solution B into solution A, the pH of the solution need to be maintained at approximately 9.5. The resulting solution was vigorously stirred at room temperature for 18 h before proceeding with the filtration process by washing it with distilled water several times. Subsequently, the solid product was dried overnight at 100 °C. The molar magnesium to aluminium (Mg/Al) ratio utilised in the study was three. The report found that the ratio resulted in a promising catalyst for various base-catalysed reactions due to its excellent base catalytic properties.

The utilisation of varying Mg/Al molar ratios affected the catalytic performance of the MgAl hydrotalcites catalyst obtained [16]. Kang et al. prepared MgAl hydrotalcite via the co-precipitation method with different Mg/Al atomic ratios of from 0.5 to 3.5, which was dissimilar to the investigation by Park et al., where the only Mg/Al molar ratio employed was three. In a similar investigation to [14], Yu et al. reported synthesising fresh, calcined, and rehydrated MgAl hydrotalcite catalysts with the Mg/Al ratio of three [17]. The calcined MgAl hydrotalcite was prepared by calcining the synthesised MgAl hydrotalcite at 450 °C for 10 h in an airstream. In contrast, the rehydrated MgAl hydrotalcite was obtained by hydrating the calcined MgAl hydrotalcite in decarbonated water with vigorous stirring in an inert atmosphere at 60°C for a day followed by filtration and drying overnight at 80 °C.

Urea hydrolysis is one of the techniques employed to acquire MgAl hydrotalcite. The alternative precipitating agent utilised in the method is urea, while the co-precipitating technique employs Na_2CO_3 as the

precipitating agent [5]. The MgAl hydrotalcite with Mg/Al = 3 was prepared by Park et al. [16] according to this procedure. A solution of $Mg(NO_3)_2.6H_2O$, $Al(NO_3)_3.9H_2O$, urea, and distilled water was added into a three-neck flask equipped with a condenser . The reaction was conducted at 95℃ for two days, while the pH of the solution was measured every 15 min during the hydrolysis. After the reaction was completed, the resulting mixture was cooled in an ice bath for 30 minutes, filtrated, washed, and dried at 80 ℃. Another method employed by the same researchers was the simple method. The technique was based on the hydration of metal oxides obtained by calcination of metal nitrates in the air at 450 ℃ for 10 h. Subsequently, suitable amounts of MgO and Al_2O_3 were dissolved in distilled water, and the resulting solution was aged at 60 ℃ for a week. A white precipitate was obtained after the solution was filtered and dried overnight at 80 ℃. The method was simpler than the other two techniques as no particular controlled variables were involved with metal oxides [7].

Characterization of MgAl hydrotalcite catalyst

The formation of MgAl hydrotalcite was confirmed with various characterisation tools such as XRD, SEM, and BET. The XRD is one of the most common characterisation tools employed to confirm the layered structure of hydrotalcite. Park et al. [16] reported that the typical XRD pattern of MgAl hydrotalcite exhibits definite crystalline phases observable in fresh catalyst obtained from every method, attributing to the reflections of 2θ = 11.6° (003), 23.3° (006), 34.8° (009), 60.7° (110), and 62.0° (113), as shown in Figure 2. The results indicated that the MgAl hydrotalcite with Mg/Al = 3 retained the layered double hydroxide structures even though they are prepared differently. The XRD patterns in Figure 2(b) demonstrated a slight shift of the peaks at the (003) plane, depending on the preparation method employed. The observation was due to the different anions located in the interlayer spaces of the hydrotalcite procured from the three preparation techniques.

Figure 3 displays the XRD pattern of the MgAl hydrotalcite synthesised by Yu et al. [17]. Only the synthesised and rehydrated MgAl hydrotalcites exhibited the characteristic hydrotalcite XRD peaks similar to the planes reported by Park et al. [16]. No XRD peaks corresponded to the layered structure of hydrotalcite in the calcined MgAl hydrotalcite due to the destruction of the structure by the calcination process. Conversely, the calcined MgAl hydrotalcite maintained the spinel structure of MgAl mixed oxide. Surprisingly, the rehydrated MgAl hydrotalcite preserved the layered structure of hydrotalcite, proving the memory effect of hydrotalcite.

Figure 3 exhibits the XRD peaks for (003) planes in the rehydrated MgAl hydrotalcite, which was much broader compared to the synthesised MgAl hydrotalcite. The observation was due to the exfoliation and vertical breaking of layers in the structure of hydrotalcite, resulting in a smaller crystallite size of the rehydrated MgAl hydrotalcite. A report demonstrated the XRD patterns of MgAl hydrotalcites synthesised with different Mg/Al atomic ratios between 0.5 and 3.5 (Figure 4). The catalysts with the Mg/Al atomic ratios of 0.5 and 1.5 were the least developed. The lower the Mg/Al atomic ratio, the more the peaks shifted towards higher values, attributing to a decreased *d*-spacing between the hydroxide layers, resulting in reduced distance between layers of MgAl hydrotalcite as the Al content was elevated [16].

The XRD peaks on the (003) plane were applied in the Scherrer equation to calculate the crystallite size of the MgAl hydrotalcites. Specific surface areas (S_{BET}) of the MgAl hydrotalcites were determined via the BET plot. Park et al. found that different preparation methods of MgAl hydrotalcite significantly impacted the crystallite size and S_{BET}. The MgAl hydrotalcite prepared via co-precipitation (HT_P) demonstrated the smallest crystallite size and the highest S_{BET} compared to the urea (HT_U) and simple (HT_S) techniques (Table 1). Yu et al. [17] reported that the crystallite size of the synthesised (HT_A) and rehydrated MgAl (HT_R) hydrotalcites could be calculated as the catalysts prepared through the co-precipitation method but under different conditions retained their LDH structure. Nonetheless, the calcined MgAl (HT_C) hydrotalcite

did not produce results for crystallite as the structure of the catalyst was destroyed during the calcination process.

Kang et al. [16] concluded that as the Mg/Al atomic ratio decreased, the S_{BET} increased even at the Mg/Al ratio of 1.0 (Figure 4). Nonetheless, based on the XRD characterisation, the 1.0 sample exhibited lower S_{BET} due to the unsuccessful formation of layered structures. Additionally, the catalyst produced with the Mg/Al ratio of 1.5 demonstrated the most significant S_{BET} and the smallest crystallite size. Consequently, the crystallite size was strongly affected by the preparation method as the growth of the hydrotalcite layers and the degree of layer stacking differed greatly depending on the preparation method. Resultantly, the surfaces of the active sites had different exposures to reactants, resulting in varying catalytic activities of the MgAl hydrotalcites [14].

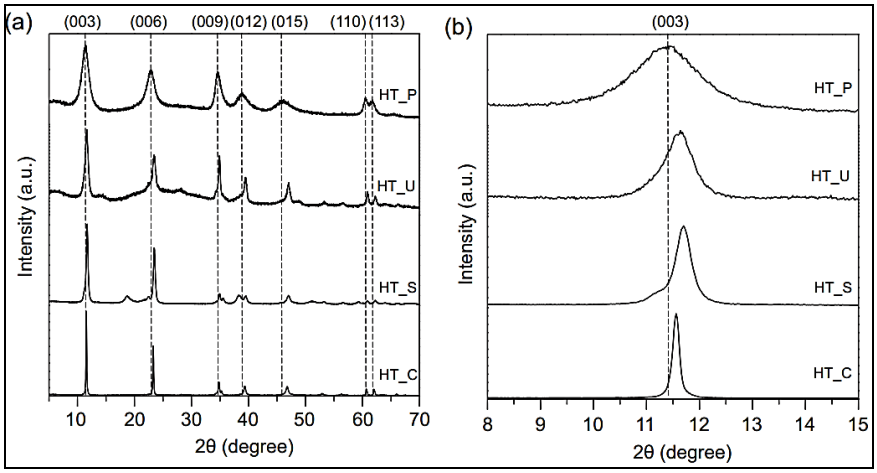


Figure 2. XRD patterns of MgAl hydrotalcite catalyst (HT_P = Co-precipitation, HT_U = Urea, HT_S = Simple & HT_C = Purchased from Sigma-Aldrich) [14]

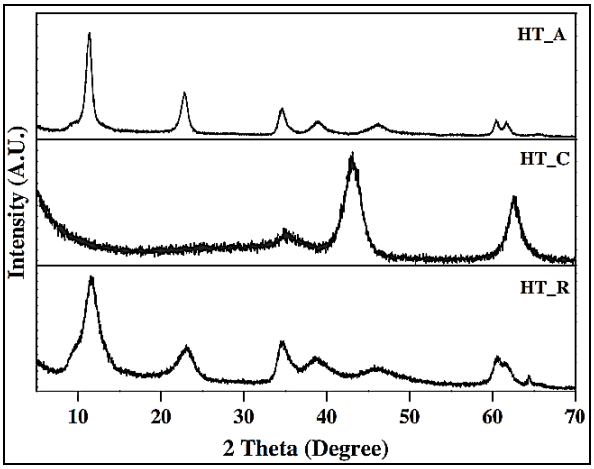


Figure 3. XRD patterns of MgAl hydrotalcite catalyst (HT_A = Synthesized MgAl hydrotalcite, HT_C = Calcined MgAl hydrotalcite & HT_R = Rehydrated MgAl hydrotalcite) [17]

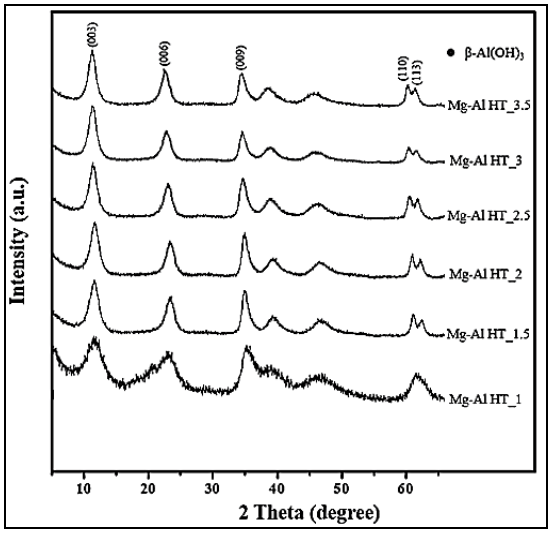


Figure 4. XRD patterns of MgAl hydrotalcite catalyst with different Mg/Al atomic ratio (1.0 – 3.5) [16]

Table 1. Crystallite size and specific surface areas of the Mg-Al hydrotalcite catalyst

Catalyst Used	Synthesis Method	Mg/Al Atomic Ratio	Crystallite Size (nm) (At (003) plane)	S_{BET} (m^2g^{-1})	Ref
Mg-Al	Co-precipitation (HT_P)	3.0	5.80	141.0	[14]
	Urea (HT_U)	3.0	12.6	36.6	
	Simple (HT_S)	3.0	21.3	1.3	
Mg-Al	Co-precipitation (HT_A)	3.0	9.9	68.9	[17]
	(HT_C)	3.0	-	158.5	
	(HT_R)	3.0	4.1	88.8	
Mg-Al	Co-precipitation (HT_1.0)	1.0	-	86.3	[16]
	(HT_1.5)	1.5	3.9	204.5	
	(HT_2.0)	2.0	4.7	110.7	
	(HT_2.5)	2.5	4.6	130.1	
	(HT_3.0)	3.0	4.7	109.0	
	(HT_3.5)	3.5	5.2	89.1	
Mg-Al	Co-precipitation (HT_1.0)	1.0	7.9	147	[18]
	(HT_1.5)	1.5	8.4	131	
	(HT_2.0)	2.0	10.3	110	
	(HT_3.0)	3.0	8.1	37	
	(HT_5.0)	5.0	6.8	23	

Upare et al. [18] reported XRD patterns for all the samples with rehydrated Mg/Al ratios from 1.0 to 5.0 (Figure 5). Based on the XRD characterisation, an increase of Mg/Al ratio was slightly shifted to a lower angle on the (003) plane at 2θ of 11.4° corresponding to the interlayer anion. This observation indicating that the interlayer spacing and unit cell parameter increased with Mg/Al ratio of the rehydrated hydrotalcite [18]. Additionally, the crystallite size increases from 7.9 to 10.3 nm as the rehydrated hydrotalcite with Mg/Al ratio increases from 1.0 to 3.0. Conversely, the crystallite size decreases from 10.3 to 6.8 nm as Mg/Al ratio decreases from 3.0 to 5.0.

Apart from XRD and BET analysis, SEM analysis also can be employed to confirm the structure of MgAl hydrotalcites and to prove the crystallite size calculated from the XRD analysis. The characteristic layered structures of the synthesised MgAl hydrotalcites were composed of platelet-like particles that agglomerated in different ways depending on the preparation method, as shown in Figure 6. In particular, the HT_P MgAl hydrotalcite with the smallest crystallite size exhibited a sand-rose morphology (Figure 6(a)) [14]. Kang et al. [16] observed a similar sand-rose morphology, indicating that the co-precipitation method successfully produced the layered MgAl hydrotalcite structure (Figure 7). The findings might be due to the surfaces being easily exposed to reactants, which strongly affected the catalytic activity of the catalysts [14]. Consequently, Park et al. reported that MgAl hydrotalcites prepared according to the co-precipitation procedure could be expected to exhibit superior activity over other hydrotalcite catalysts in base-catalysed reactions [14].

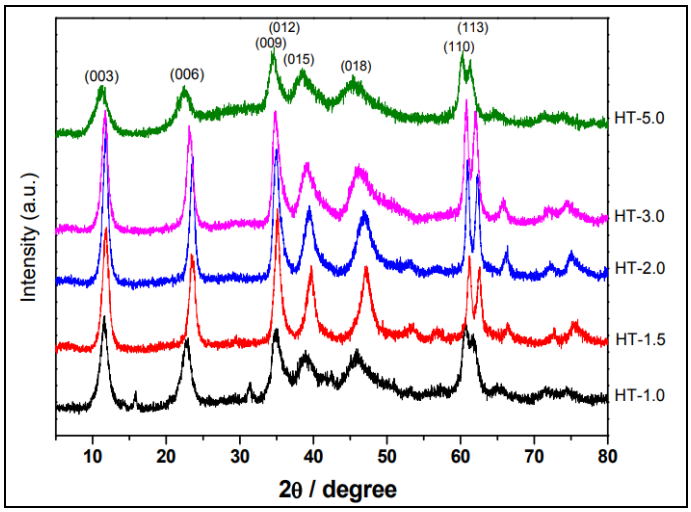


Figure 5. The XRD patterns of the rehydrated MgAl hydrotalcite catalyst synthesised with different Mg/Al atomic ratios (1.0–3.5) [18]

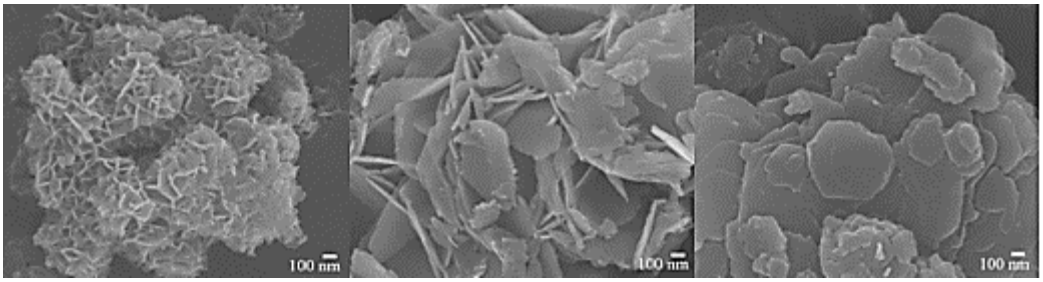


Figure 6. SEM images of (a) HT_P (b) HT_U (c) HT_S [14]

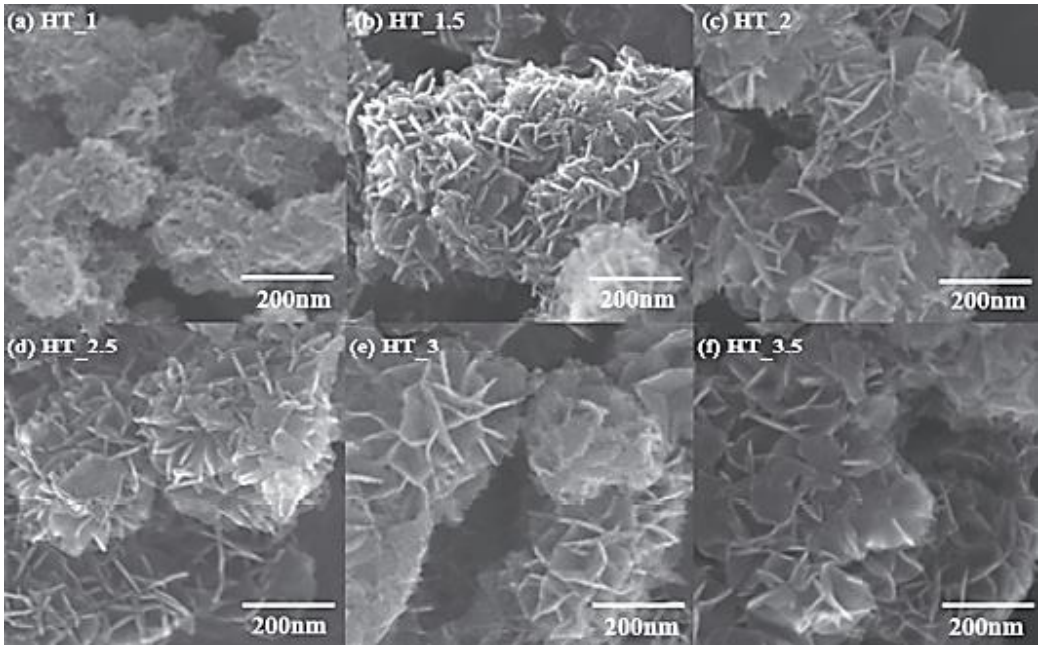


Figure 7. SEM images of MgAl hydrotalcite with different Mg/Al atomic ratio [16]

Catalytic reaction in the isomerization of glucose to fructose

Glucose isomerisation was employed as a model reaction to explore the catalytic activity of the synthesised MgAl hydrotalcites. The isomerisation of glucose into fructose is a critical step in biomass conversion technologies [19]. Generally, the isomerisation of glucose into fructose was conducted in a batch-type glass reactor with glucose as the reactant, MgAl hydrotalcite as the catalyst, and dimethylformamide. The reaction was conducted at 100°C for 3 h. After the reaction was completed, the reactor was cooled in an ice bath, followed by filtrating the resultant solution to separate the catalyst. Lastly, the filtrate was analysed with HPLC equipped with a UV-Vis detector. Table 2 tabulates the catalytic activity of the synthesised MgAl hydrotalcite as a solid base catalyst in the isomerisation of glucose into fructose, as reported by Park et al., Yu et al., and Kang et al. [14, 16, 17]. According to Park et al. [14], the MgAl hydrotalcite prepared by co-precipitation produced the highest fructose yield at 25% compared to the other methods. Moreover, since the method fabricated the smallest crystallite size with abundant surface base sites, numerous researchers utilised MgAl

hydrotalcite catalyst prepared with the co-precipitation technique to convert glucose into fructose [14].

Yu et al. [17] found that the highest fructose yield (30%) was obtained when the rehydrated MgAl hydrotalcite catalyst was employed. The results were due to the abundant and selective surface base sites for glucose isomerisation were produced during the rehydration process. Meanwhile, Kang et al. [16] studied the effects of Mg/Al with different ratios on the catalytic activity of MgAl hydrotalcite. They reported that the MgAl hydrotalcite with an Mg/Al ratio of 1.5 produced the highest fructose yield (42%). The increased catalytic activity of the MgAl hydrotalcite during the isomerisation of glucose into fructose was assumed to be due to the small crystallite size obtained by co-precipitation of Mg/Al with the molar ratio of 1.5. Theoretically, the larger the surfaces of the MgAl hydrotalcite exposed to the reactants, the catalyst would exhibit a better catalytic activity.

A report demonstrated by Upare et al. on glucose isomerization, 1-butanol was used as the solvent. It is noted to be very effective in preventing the formation of humin based on their previous study [18]. The uniqueness of 1-butanol as a solvent for glucose isomerization showed that there is no leaching of Mg ions from the hydrotalcite catalyst compared to other solvents such as water, ethanol and dimethylformamide [18]. Notably, the rehydrated MgAl hydrotalcite catalyst with Mg/Al ratio of 2.0 is the excellent catalyst for the isomerization of glucose into fructose with the highest percent yield (51%). The fructose yield increased from Mg/Al ratio of 1.0 to 2.0, however, it decreased from Mg/Al ration of 2.0 to 5.0. These results showed that the high rehydrated Mg/Al ratio were not favourable in the formation of fructose [18].

Apart from using the combination of 1-butanol and hydrotalcite catalyst in glucose isomerisation, ethanol is one of the solvent used in this reaction. Yabuhita et al. found that the use of ethanol enhance the fructose yield and thus, obtained 50% yield which is quite higher compared to other results (Table 2). Furthermore, the removal of ethanol after the reaction is much simpler as its boiling point is quite low than water [20]. By having Mg/Al molar ratio of 3, Yabushita et al. [20] successfully acquired the formation of fructose within a short time.

Table 2. Recent studies on MgAl hydrotalcite for Isomerization of Glucose into Fructose

Synthesis Method	Mg/Al atomic ratio	Conditions	Conversion of glucose (%)	Selectivity of fructose (%)	Yield for fructose (%)	Ref
Co-precipitation			38	65	25	
Urea	3.0	At 100°C for 3 h	22	69	14	[14]
Simple			21	71	13	
Co-precipitation						
Synthesized HT			48	53	25	
Calcined HT	3.0	At 100°C for 5 h	75	32	23	[17]
Rehydrated HT			63	47	30	
Co-precipitation						
HT	1.0		25	98	24	
	1.5		62	71	42	
	2.0	At 100°C for 5 h	58	73	41	[16]
	2.5		55	70	39	
	3.0		48	81	40	
	3.5		47	79	38	

Table 2 (cont'd). Recent studies on MgAl hydrotalcite for Isomerization of Glucose into Fructose

Synthesis Method	Mg/Al atomic ratio	Conditions	Conversion of glucose (%)	Selectivity of fructose (%)	Yield for fructose (%)	Ref
Co-precipitation						
Rehydrated (HT/1-Butanol)	1.0	At 120°C for 5 h	46	65	30	[18]
	1.5		59	83	49	
	2.0		62	82	51	
	3.0		66	70	46	
	5.0		72	58	42	
Co-precipitation (HT/Ethanol)	3.0	At 90°C for 2 h	61	83	50	[20]

Conclusion

Based on the comprehensive literature review, it could be concluded that the preparation method of MgAl hydrotalcite strongly influenced the growth and stacking of its layers and the type of anions intercalated during the formation of the layered structure. The unique characteristics of the MgAl hydrotalcites led to varied crystallite sizes and morphologies. The co-precipitation method was more favourable than the urea and simple methods to fabricate MgAl hydrotalcites with surfaces that consist of numerous basic sites. Furthermore, different Mg/Al molar ratios also affected the formation and catalytic activity of the synthesised MgAl hydrotalcite. The catalytic activity of the synthesised MgAl hydrotalcite was observed in the isomerisation of glucose into fructose. The MgAl hydrotalcite prepared via co-precipitation produced the highest fructose yield as its small crystallite size and sand-rose morphology result in significant exposure of its surface active sites to the reactants.

Acknowledgement

The authors acknowledge the generous support of Organic Synthesis Research Laboratory, Institute of Science (IOS), Universiti Teknologi MARA, Puncak Alam Campus and Faculty of Applied Sciences, Universiti Teknologi MARA (UiTM), Shah Alam as well as the financial support of the Ministry of Higher Education, Malaysia FRGS Grant [600-RMC/SRC/5/3 (024/2020)].

References

1. Dębek, R., Motak, M., Grzybek, T., Galvez, M. E. and Da Costa, P. (2017). A short review on the catalytic activity of hydrotalcite-derived materials for dry reforming of methane. *Catalysts*, 7(1): 32.
2. Gomes, J. F. P., Puna, J. F. B., Gonçalves, L. M. and Bordado, J. C. M. (2011). Study on the use of MgAl hydrotalcites as solid heterogeneous catalysts for biodiesel production. *Energy*, 36(12): 6770-6778.
3. Baskaran, T., Christopher, J. and Sakthivel, A. (2015). Progress on layered hydrotalcite (HT) materials as potential support and catalytic materials. *RSC Advances*, 5: 98853-98875.
4. Tsujimura, A., Uchida, M. and Okuwaki, A. (2007). Synthesis and sulfate ion-exchange properties of a hydrotalcite-like compound intercalated by chloride ions. *Journal of Hazardous Materials*, 143(1–2): 582-586.
5. Sikander, U., Sufian, S. and Salam, M. A. (2017). A review of hydrotalcite based catalysts for hydrogen production systems. *International Journal of Hydrogen Energy*, 42: 19851-19868.
6. Delidovich, I. and Palkovits, R. (2015). Structure-performance correlations of Mg-Al hydrotalcite catalysts for the isomerization of glucose into fructose. *Journal of Catalysis*, 327: 1-9.

7. Lee, G., Kang, J. Y., Yan, N., Suh, Y. W. and Jung, J. C. (2016). Simple preparation method for Mg–Al hydrotalcites as base catalysts. *Journal of Molecular Catalysis A: Chemical*, 423: 347-355.
8. Nur Fazira Edlina, I., Nazrizawati, A. T., Erma Hafiza, I. A. Z. and Noraini, H. (2020). MgAl mixed oxide derived alkali-free hydrotalcite for transesterification of waste cooking oil to biodiesel. *ASM Science Journal*, 13: 1-7.
9. Nope, E., Sathicq, G., Martinez, J., Rojas, H., Luque, R. and Romanelli, G. (2018). Hydrotalcites in Organic Synthesis: Multicomponent Reactions. *Current Organic Synthesis*, 15(8): 1073-1090.
10. Kikhtyanin, O., Kadlec, D., Velvarská, R. and Kubička, D. (2018). Using Mg-Al mixed oxide and reconstructed hydrotalcite as basic catalysts for aldol condensation of furfural and cyclohexanone. *ChemCatChem*, 10(6): 1464-1475.
11. Jadhav, A. L. and Yadav, G. D. (2019). Clean synthesis of benzylidenemalononitrile by Knoevenagel condensation of benzaldehyde and malononitrile: Effect of combustion fuel on activity and selectivity of Ti-hydrotalcite and Zn-hydrotalcite catalysts. *Journal of Chemical Sciences*, 131(8): 79.
12. Arias, K. S., Climent, M. J., Corma, A. and Iborra, S. (2016). Chemicals from biomass: Synthesis of biologically active furanochalcones by claisen–schmidt condensation of biomass-derived 5-hydroxymethylfurfural (HMF) with acetophenones. *Topics in Catalysis*, 59(13–14): 1257-1265.
13. Mokhtar, M., Saleh, T. S. and Basahel, S. N. (2012). Mg-Al hydrotalcites as efficient catalysts for aza-Michael addition reaction: A green protocol. *Journal of Molecular Catalysis A: Chemical*, 353-354: 122-131.
14. Park, S., Kwon, D., Kang, J. Y. and Jung, J. C. (2019). Influence of the preparation method on the catalytic activity of Mg-Al hydrotalcites as solid base catalysts. *Green Energy and Environment*, 4(3): 287-292.
15. Labuschagné, F. J. W. J., Wiid, A., Venter, H. P., Gevers, B. R. and Leuteritz, A. (2018). Green synthesis of hydrotalcite from untreated magnesium oxide and aluminum hydroxide. *Green Chemistry Letters and Reviews*, 11: 18-28.
16. Kang, J. Y., Lee, G., Suh, Y. W. and Jung, J. C. (2017). Effect of Mg/Al atomic ratio of Mg–Al hydrotalcites on their catalytic properties for the isomerization of glucose to fructose. *Journal of Nanoscience and Nanotechnology*, 17(11): 8242-8247.
17. Yu, S., Kim, E., Park, S., Song, I. K. and Jung, J. C. (2012). Isomerization of glucose into fructose over Mg-Al hydrotalcite catalysts. *Catalysis Communications*, 29: 63-67.
18. Upare, P. P., Chamas, A., Lee, J. H., Kim, J. C., Kwak, S. K., Hwang, Y. K., and Hwang, D. W. (2020). Highly efficient hydrotalcite/1-butanol catalytic system for the production of the high-yield fructose crystal from glucose. *ACS Catalysis*, 10(2): 1388-1396.
19. Huang, H., Meng, X. G., Yu, W. W., Chen, L. Y. and Wu, Y. Y. (2021). High selective isomerization of glucose to fructose catalyzed by amidoximed polyacrylonitrile. *ACS Omega*, 6(30): 19860-19866.
20. Yabushita, M., Shibayama, N., Nakajima, K. and Fukuoka, A. (2019). Selective glucose-to-fructose isomerization in ethanol catalyzed by hydrotalcites. *ACS Catalysis*, 9(3): 2101-2109.

Malaysian Journal of Analytical Sciences (MJAS)
Published by Malaysian Analytical Sciences Society

OPTIMIZATION PARAMETERS FOR ELECTROPOLYMERIZATION OF MELAMINE IN DEEP EUTECTIC SOLVENT

(Pengoptimuman Parameter Elektropempolimeran Melamin Dalam Pelarut Eutektik Dalam)

Yeet Hoong Chang[1], Pei Meng Woi[1,2]*, Yatimah Alias[1,2]

[1]*Department of Chemistry, Faculty of Science*
[2]*University Malaya Centre for Ionic Liquids (UMCiL)*
University of Malaya, 50603 Kuala Lumpur, Malaysia

**Corresponding author: pmwoi@um.edu.my*

Received: 15 September 2021; Accepted: 10 December 2021; Published: 28 April 2022

Abstract

Polymelamine is a new class of polymer that possess electrocatalytic behavior in dopamine (DA) detection. Our previous studies have successfully replaced the conventional acidic electrolyte to deep eutectic solvent (DES) has open the opportunity for a greener solvent in used. Herein we report the optimization process of melamine electropolymerize in DES- reline. Various electrochemical techniques have been employed to studies the ideal parameters. The optimum potential window, scan rate, and number of scan cycles were recorded as -0.20 V – 1.60 V, 50 mV s^{-1} and five scan cycles, respectively. Cyclic voltammetry (CV) was employed in the electropolymerization of melamine to optimize the redox behavior of polymelamine film on electrode surface. The growing of polymer film which indicated by the increased of reduction current can be well-controlled by the slow scan rate and optimum scan cycles which leads to strong adhesion and uniform morphology. Amperometry sensing on DA was performed to study and compare the sensitivity and limit of detection for the polymers synthesized in varied parameters. A brief discussion on the principal polymerization factors that would affecting the electrocatalytic behavior of melamine is included.

Keywords: deep eutectic solvent, electropolymerization, melamine, optimization

Abstrak

Polimelamin adalah kelas polimer baharu yang mempunyai tingkah laku elektromangkin dalam pengesanan dopamin (DA). Kajian yang dilaporkan terdahulu menujukkan kerjayaan penggantian elektrolit berasid konvensional kepada pelarut eutektik (DES). Kerjayaan ini membuka peluang untuk pelarut yang lebih mesra alam digunakan. Dengan ini, kami melaporkan proses pengoptimum elektropolimerisasi melamin dalam DES-relin. Pelbagai teknik elektrokimia telah digunakan untuk mengkaji parameter yang terbaik. Julat keupayaan, kadar imbasan dan bilangan kitaran imbasan yang terbaik dicatat pada -0.20 V – 1.60 V, 50 mVs^{-1} dan lima kitaran imbasan. Siklik voltametri (CV) telah digunakan dalam elektropolimerisasi melamin untuk mengoptimumkan tingkah laku elektropemangkinan lapisan polimelamin pada permukaan elektrod. Pertumbuhan lapisan polimer yang ditunjukkan dalam penainkkan arus penurunan boleh dikawal baik dengan kadar imbasan yang perlahan dan kitaran imbasan optimum untuk mencapai lekatan yang kuat dan morfologi yang seragam. Penderiaan amperometri pada DA telah dijalankan untuk mengkaji dan membandingkan kepekaan dan had pengesanan rendah untuk polimer yang disintesis dalam

parameter yang berbeza-beza. Perbincangan ringkas tentang faktor-faktor elektropolimerisasi yang mempengaruhi tingkah laku elektromangkin melamin telah disertakan.

Kata Kunci: pelarut eutektik dalam, elektropempolimeran, melamin, pengoptimuman

Introduction

Heretofore, the polymers such as polyisoprene, polystyrene, polythiophene, polyaniline, polypyrrole, formaldehyde resin and their by-products have been examined extensively as promising candidates in sensor development. A novel class of conducting polymer - polymelamine (PME) was proposed. PME is made from the nitrogen-rich melamine (1,3,5-Triazine-2,4,6-triamine) which is a heterocyclic organic compound. The synthesis methods of PME included chemical, electrochemical, photo-initiating, biocatalytic, and plasma polymerization. Among all, electropolymerization is commonly employed due to its advantages in facile engineer the morphology, thickness, density, and growing rate of the polymer. PME can be synthesized easily using electropolymerization technique by oxidize the amino groups found in melamine. In the discipline of electrochemistry, PME has been employed as a stable matrix to enhance the effective immobilization of nanomaterials on it. It is also employed as electrochemical sensor owing to the existence of numerous active groups such as nitrogen and amine. PME and its offshoots were soon utilized extensively in sensing of different neurotransmitters, pharmaceutic particles, and toxic heavy metals [1-3]. Moreover, PME composited with nanocarbon demonstrated high specificity and exhibited exceptional catalytic reaction over broad extent of molarity [4].

Deep eutectic solvent (DES) draws great attention lately owing to their solvation potential, conductivity, simple synthesis method, cost effective and many are biodegradable [5]. DES are commonly applied in two principal fields: metal processing (metal electropolishing, metal dissolution, metal deposition) and as synthesis solvent [6-8]. Reline (a Type III DES) was employed as stimulant and reducing mediator for polymerization of hydrophilic monomer at temperature close to ambient [9]. Reline and glyceline (a Type III DES) were proposed to substitute typical aqueous solution in free-radical polymerization of acrylamide [10]. The outcome shows the polymer synthesized has similar molecular mass compared to the polymer synthesized in aqueous solution. Moreover, polyaniline synthesized in DES demonstrated exceptional conductivity reported at 50 S cm^{-1} [11]. The polyaniline shows excellent reversibility to doping/dedoping mechanisms which indicated rapid charge transfer. Furthermore, Type I DES has effectively utilized as a cationic catalyst for epoxy resin curing [12].

Despite that, DES being the synthesis solvent particularly in the formation of polymers are rarely examined in terms of polymerization parameters. Conventionally, electropolymerization of melamine was conducted in acidic electrolyte [1]. Acidic electrolyte with pH less than two is the key for the growth and establishment of radical cations that required in rate-limiting step during the electropolymerization of melamine. In accordance with our published work, we have successfully superseded the conventional acidic electrolyte with DES. PME synthesized in DES manifests excellent sensitivity, specificity, and stability [13]. In this work, we focus on the optimization of polymerization parameters, and discuss the effect of these parameters in polymerization of melamine. Reline is selected as study target due to the enlightenment of the novel perception asserted that chloride ion (Cl^-) is the vital factor for PME formation [14]. Reline is a mixture of choline chloride and urea in 1:2 ratio, urea molecules offer plentiful positive hydrogen bonding spot to adopt the Cl^- negative ion into their polar matrix [15]. PME synthesized in reline is then applied in electrochemical qualification and quantification of dopamine (DA).

Materials and Methods

Materials

Melamine monomer, choline chloride, ethylene glycol, urea, glycerol, dopamine (DA), potassium dihydrogen

phosphate (KH_2PO_4) and potassium hydrogen phosphate (K_2HPO_4) were purchased from Sigma Aldrich. Ultra-pure deionized (DI) water with a resistance of 18.3 MΩcm (Merck Synergy) was used in all sample preparations. All the chemical reagents were of analytical grade and were used without further purification.

Instrumentation

The surface morphology of the bare and modified sensor was studied by using Horizontal Attenuated Total Reflectance-infrared spectroscopy (HATR-IR, PerkinElmer, Inc). All electrochemical experiments were carried out by Autolab potentiostat/galvanostat PGSTAT-302N with an ordinary three electrodes system, containing glassy carbon electrode (GCE) (ALS-Japan, diameter = 3.0 mm, surface area = 0.071 cm^2) as working electrode, a platinum braid wire (BASi, diameter = 1.0 mm, surface area = 0.008 cm^2) as counter electrode and sodium chloride (KCl) saturated Ag/AgCl (BASi) as the reference electrode. All the potential readings were referred to Ag/AgCl unless stated elsewhere. A pseudo reference electrode (Ag wire, BASi, diameter = 1.0 mm, surface area = 0.008 cm^2) was employed for electrochemical polymerization of polymer in DES or mixtures. The referred reading of the pseudo wire with respect to the Ag/AgCl electrode was at + 90 mV. Amperometry analysis of DA was conducted at constant potential (0.20 V) in PBS (0.10 M, pH 7.0).

Preparation of deep eutectic solvent

Type III DES - reline was prepared by mixing choline chloride into urea, in 1:2 molar ratio. The mixture was heat under oil bath with control temperature from 55ºC to 60ºC until a clear solution was obtained. Reline was then set aside to cool down to ambient temperature prior served as supporting electrolyte for the electropolymerization of melamine.

Preparation of 0.10 mM melamine(reline) solution

A 10.0 mM of melamine was prepared by mixing 5.0 mg of melamine into 4.0 mL reline followed by ultrasonication for 30 minutes until a homogeneous solution is achieved. The as-prepared melamine solution was named as melamine(reline).

Synthesis of PME(reline)/GCE

GCE was gently polished with 0.05 µM alumina slurry and then rinsed with DI water and ethanol a few times until a clean mirror-like surface was obtained. A clean GCE was then immersed into melamine(reline) solution and CV was scanned from the studied potential window at various scan rates for different number of cycles as part of the optimization studies. The fabricated PME(reline)/GCE was gently rinsed with DI to wash off the monomer residue and then set to dry in ambient condition before used.

Preparation of phosphate buffer solution

Phosphate buffer solution (PBS) was used as supporting electrolyte in amperometry sensing of DA. 27.2 g of KH_2PO_4 and 34.8 g of K_2HPO_4 were individually poured into 1.0 L volumetric flask and added with DI until meniscus line forming solution A (0.20 M) and B (0.20 M), respectively. PBS (0.10 M, pH 7.0) was prepared by mixing 39.0 mL solution A and 61.0 mL solution B follow diluted with DI to 200 mL. The pH value of the buffer solution was confirmed with pH meter (model pH 700, Eutech Instruments).

Preparation of DA stock solution

1000 µM of DA stock solution was prepared by adding 0.015 g DA into 100 mL volumetric flask and added DI until meniscus. DA solution was freshly prepared daily and kept in refrigerator at 4ºC before used for not more than 12 hours. A layer of aluminum foil was used to cover the stock solution to avoid contact with light.

Results and Discussion

Optimization of potential window for melamine electropolymerization

To understand the effect of applied potential window on the melamine electropolymerization process, repeated CV cycling tests were carried out on melamine dissolved in reline. To begin with the potential window investigation, parameters of melamine concentration, scan rate, scan cycles, and temperature were fixed at 10.0 mM, 50 mV s^{-1}, five scan cycles and 25°C, respectively. Figure 1 shows the

electropolymerization of melamine at fixed starting potential (-0.20 V) and ended with varied potentials: 1.20 V, 1.40 V, 1.60 V, and 1.80 V. The electropolymerization behavior of melamine in reline was different from the conventional electrolyte - H_2SO_4 as in previous literature [14]. In conventional electrolyte, a cathodic peak at around + 0.85 V was noticed owing to the coupling among the melamine molecules and carbonyl groups (C=O and/or C-O) from the DES instead of head-to-head linking of amine groups betwixt the melamine molecules [13]. Figure 1(c) illustrated an anodic peak at 1.20 V was observed for the electropolymerization of melamine from -0.20 to 1.60 V. The anodic peak was due to functionalization of melamine monomers with carbonyl groups (C=O) attributed from the reline and forming an electroactive PME functionalized DES. Likewise, an anodic peak at about 1.20 V was observed in Figure 1(b) for applied potential window -0.20 - 1.40 V, indicating the formation of PME. However, it noticed that the peak current was lower as compared to the electropolymerization of melamine at -0.20 to 1.60 V, indicating the limit of charge depository of polymer formed at -0.20 - 1.40 V. Noted that in Figure 1(a) and Figure 1(d), no anodic peak was observed with the applied potential. This is probably due to a narrow potential window restricts the charge depository ability of monomer during polymerization, while a wide potential window will lead to overoxidation of polymer, causing breakage of polymer chain [16]. From these, it was concluded that potential range from -0.20 V to 1.60 V is well suited to carry out the melamine electropolymerization for the PME formation.

To further verify how the tuning of potential window affecting the performance of PME in dopamine (DA) sensing, all the PME/GCE electrodes synthesized in varied potential window were further tested in two aspects: sensitivity and limit of detection (LOD). In amperometry setting, DA is oxidised at potential 0.20 V [13]. Therefore, amperometry was scanning at fixed potential (0.20 V) with additional of DA with concentration ranging from 100 - 1200 μM in PBS (0.10 M, pH 7.0) as shown in Figure 2. Sensitivity and LOD were then calculated based on the amperometric results and summarized in Figure 3 and Table 1. Naming of PME was based on the maximum applied potential e.g., PME synthesized in reline with potential window applied at -0.20 - 1.20 V is named as PME(reline +1.20 V). Based on Figure 2, it was noticed that the amperometry result of PME(reline +1.60 V) recorded the highest current response as compared to the other PME. Figure 3(A) and (B) illustrated the calculated sensing sensitivity and LOD of DA at PME(reline), respectively. Noted that the sensing of DA at PME(reline +1.60 V) recorded the highest sensitivity and lowest LOD recorded at 0.044 $\mu A\ \mu M^{-1}\ cm^{-2}$ and 0.198 μM, respectively which are in line with amperometry result shown in Figure 2. The sensitivity line graph of over-potential showed increment from +1.20 V and reached maximum at +1.60 V. At the same time, LOD obey the opposite relationship and reaching the minimum LOD at +1.60 V. In case, further widen the potential window of PME(reline) to +1.80 V, the electrode sensing capability has reduced drastically where the LOD did not showed any improvement and has been increased 10-fold recorded at 2.070 μM compared to +1.60 V. The result justified the optimized potential window for electropolymerization of melamine is -0.20 V to +1.60 V.

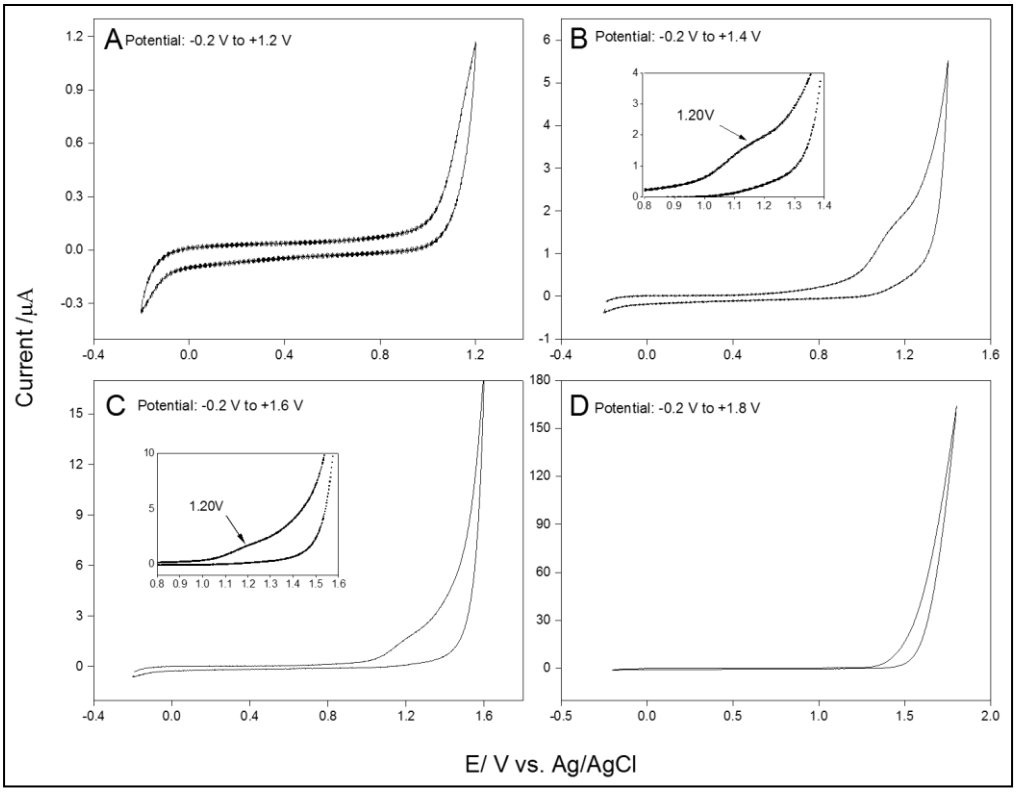


Figure 1. Electropolymerization of melamine (10.0 mM) in reline scanning with varied potential window a) -0.20 to 1.20 V, b) -0.20 to 1.40 V, c) -0.20 to 1.60 V, and d) -0.20 to 1.80 V at 50 mV s^{-1} with five scan cycles

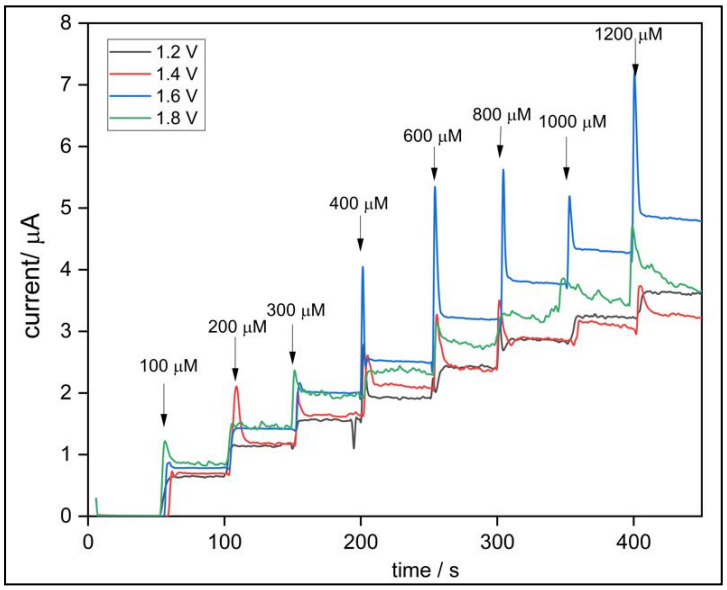


Figure 2. Amperometry results of PME synthesized in different potential window. All the amperometry test were scanned at a fixed potential (0.20 V) with additional of DA with concentration ranging from 100 - 1200 μM in PBS (0.10 M, pH 7.0)

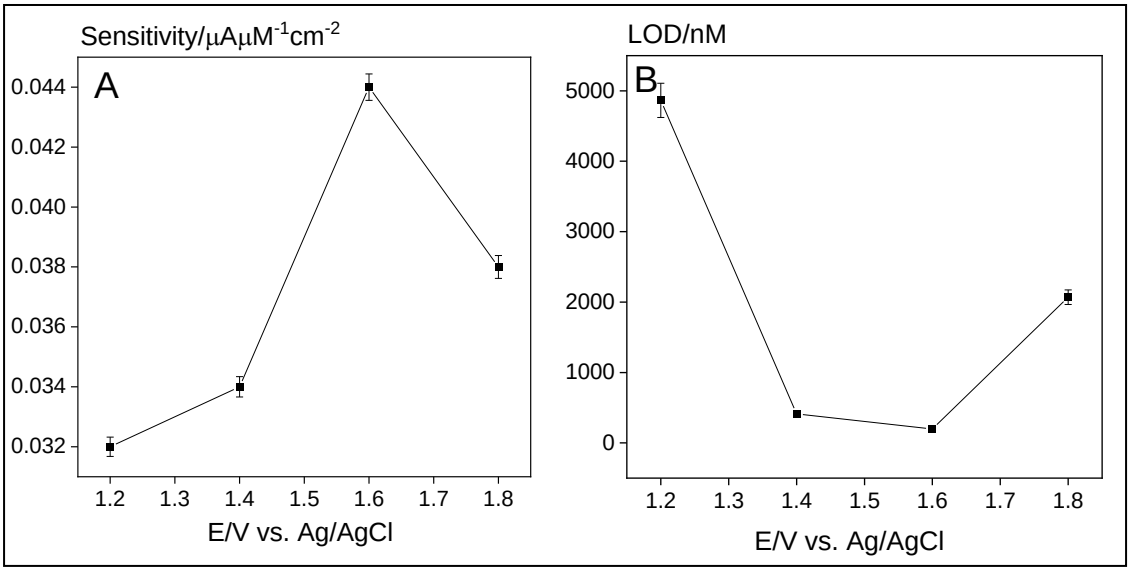


Figure 3. Graphs of (a) sensitivity and (b) LOD results versus varied potential window applied for electropolymerization of melamine in reline.

Table 1. Optimization studies for electropolymerization of melamine in reline, DA as model analyte; sensing with amperometry at 0.20 V vs Ag/AgCl: Effect of electropolymerization potential window, effect of scan rate and effect of scan cycles

Parameter Varied		**Eutectic Solvent**	**Sensitivity / μA μM^{-1} cm^{-2}**	**LOD / μM**
Potential (V)	1.2	reline	0.032	4.8640
	1.4	reline	0.034	0.4110
	1.6	reline	0.044	0.1980
	1.8	reline	0.038	2.0700
Scan rate (mV s^{-1})	10	reline	0.035	0.4450
	25	reline	0.044	0.3260
	50	reline	0.044	0.1980
	75	reline	0.046	1.0770
	100	reline	0.045	0.7860
Scan cycles	3	reline	0.038	0.6800
	5	reline	0.044	0.1980
	10	reline	0.039	1.1800
	15	reline	0.044	0.5680

Optimization of scan rate for melamine electropolymerization

Figure 4 illustrates the electropolymerization behavior of melamine in different scan rates. Scan rate determine the time taken to complete one polymerization cycle. In this study, the recorded voltammogram was not able to distinct any significant observation to relate the effect of scan rate on polymerization of melamine. Thus, these electrodes prepared at 10, 25, 50, 75, and 100 mV s^{-1} scan rates were analyzed using the amperometry technique to investigate the performance in DA sensing. Figure 5 displays the amperometry plot of PME whereas Figure 6 displays the calculated sensitivity and LOD based on the amperometry results obtained.

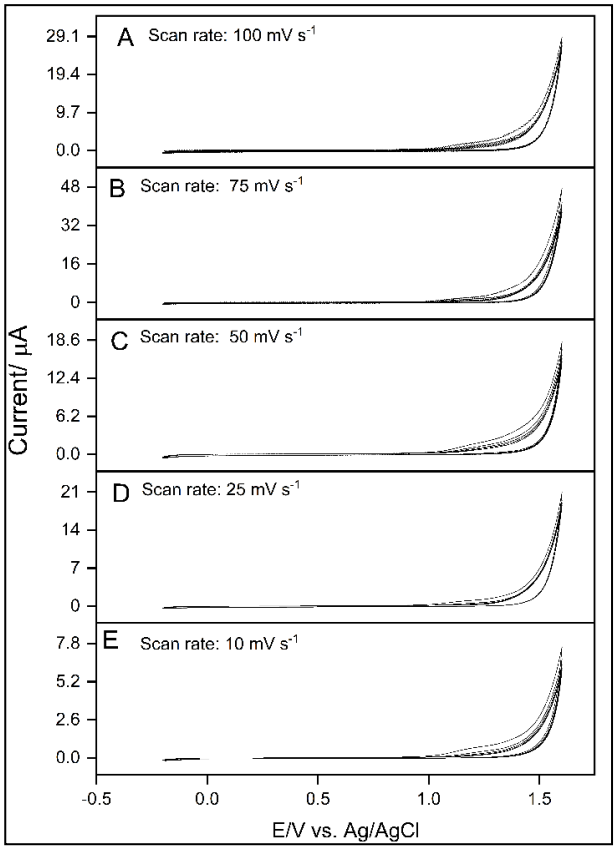


Figure 4. Electropolymerization of melamine (10.0 mM, -0.20- 1.60 V, five cycles) in reline scanning with varied scan rate (10, 25, 50, 75, and 100 mV s^{-1})

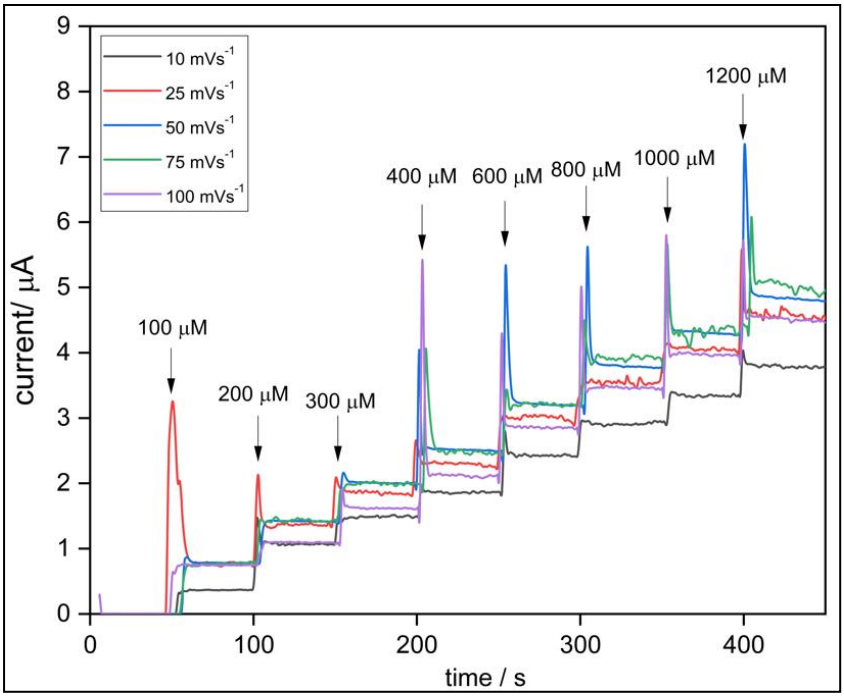


Figure 5. Amperometry results of PME synthesized in different scan rates. All the amperometry test were scanned at a fixed potential (0.20 V) with additional of DA with concentration ranging from 100 - 1200 μM in PBS (0.10 M, pH 7.0)

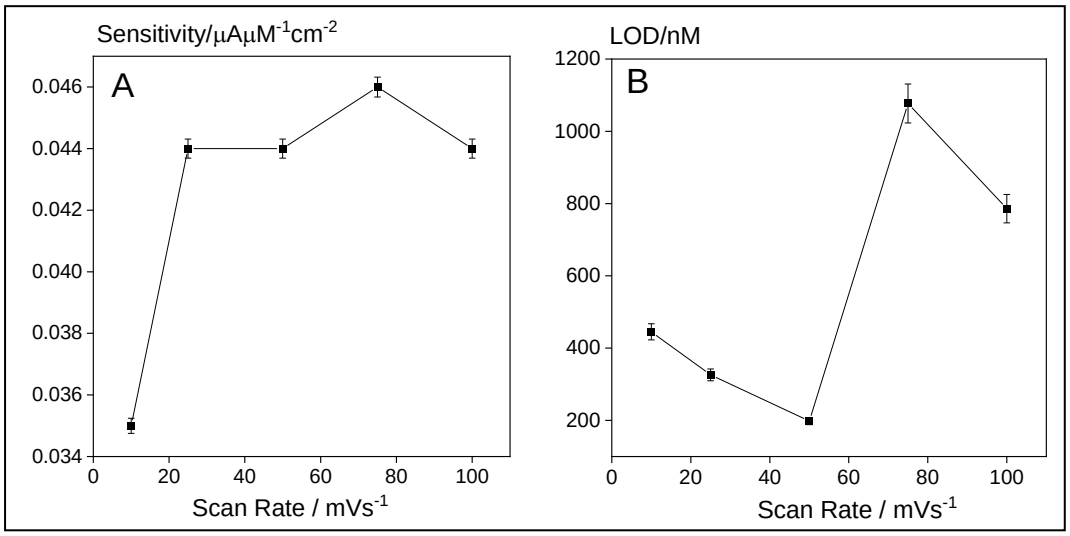


Figure 6. Graphs of (a) sensitivity and (b) LOD results versus varied scan rates applied for electropolymerization of melamine in reline

The result of amperometry sensing of DA at PME/GCE synthesized with varied scan rates are display in Figure 5. Based on Figure 5, the amperometry plots of PME(reline 75 mV s^{-1}) and PME(reline 50 mV s^{-1}) were very close to each other, unable to differentiate which scan rate gives the best outcome. Figure 6(a) and (b) show the fluttered of sensitivity and LOD of varied scan rates applied in electropolymerization of melamine (10.0 mM) in reline. The scan rate applied was varied from 10 to 100 mV s^{-1}. PME(reline) synthesized with 10 mV s^{-1} is named as PME(reline 10 mV s^{-1}) in accordance to the scan rate applied. As shown, the PME(reline 50 mV s^{-1}) was selected as the ideal scan rate where the sensitivity and LOD reported at 0.044 μA μM^{-1} cm^{-2} and 0.198 μM, respectively. In this case, PME(reline 75 mV s^{-1}) and PME(reline 25 mV s^{-1}) demonstrated the excellent sensitivity at 0.046 μA μM^{-1} cm^{-2} and 0.044 μA μM^{-1} cm^{-2}, respectively. However, both PME(reline 75 mV s^{-1}) and PME(reline 25 mV s^{-1}) showing much poorer sensing capability with LOD recorded at 1.077 μM and 0.326 μM, respectively as indicate in Table 1. It is noted that the change of polymerization scan rate affecting the LOD significantly. This is due to the low signal strength and high signal noise. Higher scan rate will result in branched polymer that have side chains growing out from the main chain. Branched polymer exhibits lower density and less packing where the analyte would be easily to move into the polymer cavity during the electrocatalytic activity, thus inducing flux of analyte molecules or ions at the electrode-electrolyte interface which result in a great fluctuation (noise) [17]. Whereas lower scan rate develops linear polymer which are very dense and compact, resulting there would be almost no channel for analyte to approach the electrode and hence reduced the signal strength and increased the LOD.

Optimization of scan cycles on melamine electropolymerization

Scan cycles influences the polymer film thickness and sensing characteristics. The optimum scan cycle was investigated using constant conditions *i.e.*, 10.0 mM melamine in reline electrolyte at room temperature with CV scanned from -0.20 V - 1.60 V. The growing of polymer film was indicated from the increase of the reduction current. Figure 7 illustrates the electropolymerization behavior of melamine in different scan cycle. Different scan cycles lead to different thickness of polymer on the surface of GCE. Unfortunately, the voltammogram could not show any significant result to relate the effect of scan cycle on polymerization behaviour of melamine as scan cycle are served to control the thickness the polymer film. Therefore, amperometry was employed to study the effect of polymer thickness on its sensing properties. Figure 8 shows the electrocatalytic performance of PME synthesized in different scan cycles. Scan cycles of five shows the steady increase of current with the increase of DA concentration, it also demonstrates the highest current response among all. Based on Figure 9(a) and (b), the optimum polymeric film can be obtained in five scan cycles, due to the sharp enhancement of sensitivity that has been recorded. When the scan cycles are increased to ten, it caused a minor decreased on LOD, further increasing of scan cycles to 15 attributed to a steeply decrease in sensitivity and raising of LOD. Such phenomenon was presumably due to excess polymer deposited on the GCE surface which blocking the electron transfer that needed for the DA oxidation process. As deduced from the higher charge transferred during polymerization, thin polymer films are usually superior in sensing studies due to better conductivity and easier in accessing analyte. Hence, five scan cycles were used for film formation.

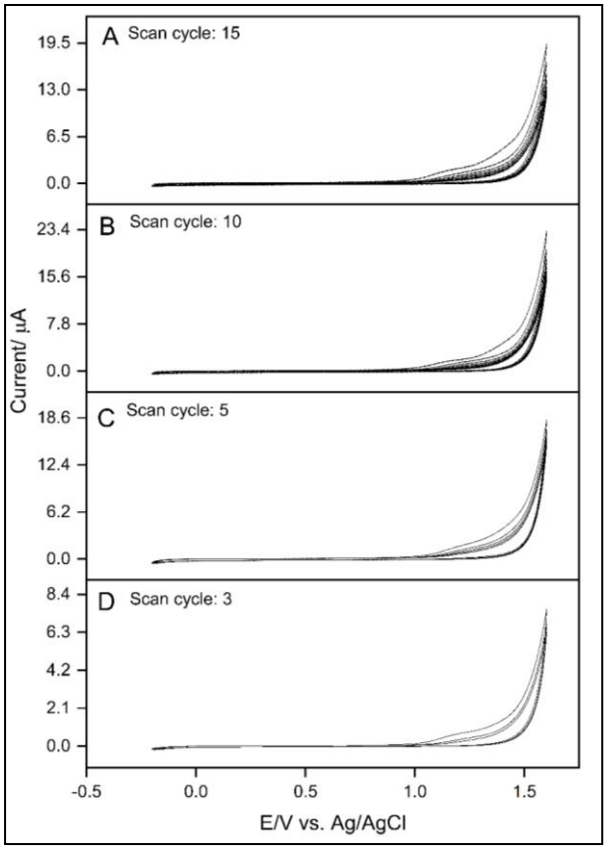


Figure 7. Electropolymerization of melamine (10.0 mM, -0.20- 1.60 V, 50 mV s^{-1}) in reline scanning with varied scan cycle (3, 5, 10 and 15)

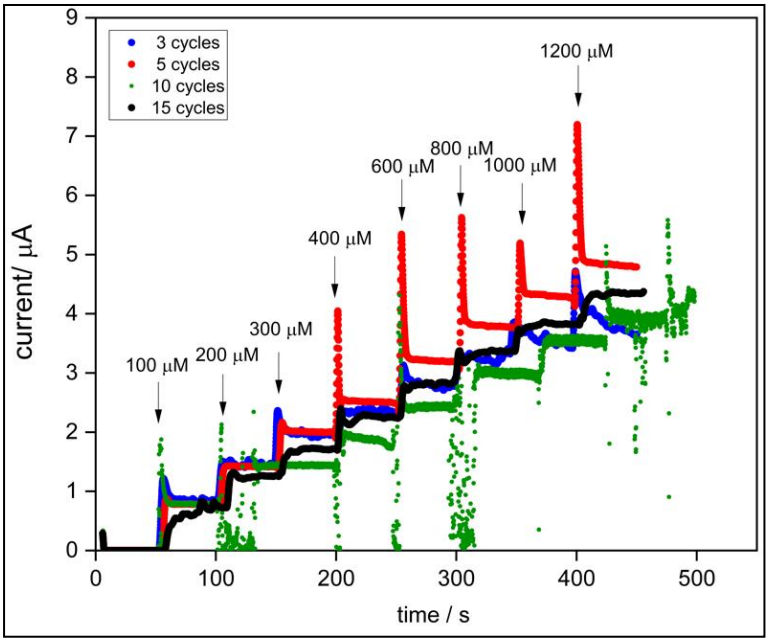


Figure 8. Amperometry results of PME synthesized in different scan cycles. All the amperometry test were scanned at a fixed potential (0.20 V) with additional of DA with concentration ranging from 100 - 1200 μM in PBS (0.10 M, pH 7.0)

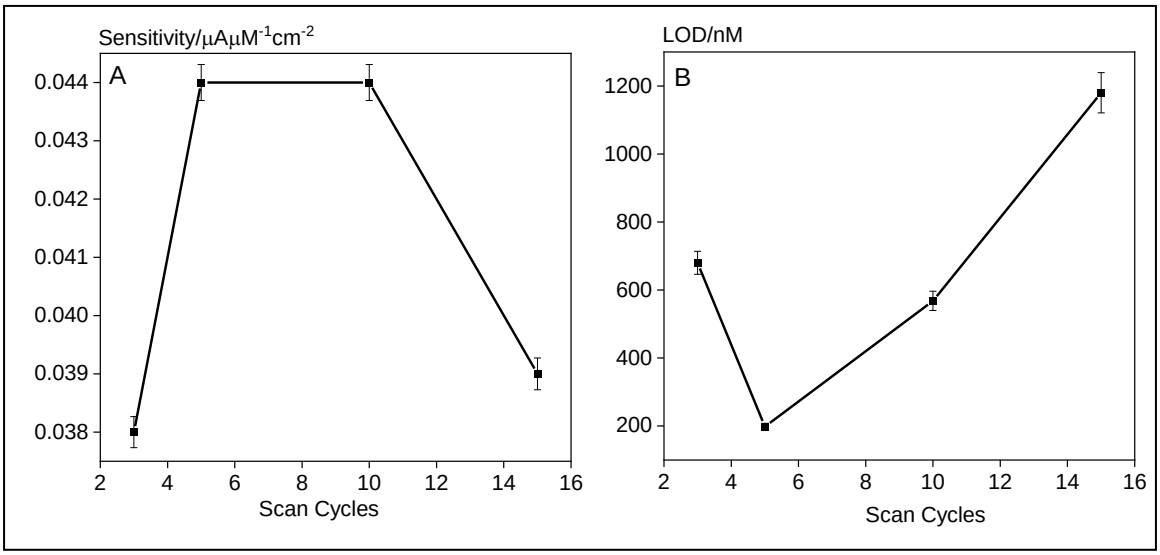


Figure 9. Graphs of (a) sensitivity and (b) LOD results versus varied scan cycles applied for electropolymerization of melamine in relin

Conclusion

Hereby reports the novel studies of optimization parameters for melamine electropolymerizes in DES, reline. Different parameters including potential window, scan rate, and number of scan cycles were manipulated in preparing PME in DES. Amperometry sensing on DA was conducted to compare the sensitivity and limit of detection for the PME prepared in different parameters. The optimum polymerization parameters for melamine were discovered as -0.20 V – 1.6 V, 50 mVs^{-1}, and five scan cycles, respectively. The effect of each parameter on the electrocatalytic behavior of PME has been clarified. With the successful optimization, PME(reline)/GCE with high sensitivity and low limit of detection recorded at 0.044 $\mu A\ \mu M^{-1}\ cm^{-2}$ and 0.198 μM has achieved. Proportionally, contemporary potential polymers can be construct by manipulating the parameters accordingly.

Acknowledgement

This work is financially supported by Impact Oriented Interdisciplinary Research Grant IIRG013B-2019 and Frontier Research Grant FG030-17AFR by the Universiti Malaya.

References

1. Gupta, P. and Goyal, R. N. (2014). Polymelamine modified edge plane pyrolytic graphite sensor for the electrochemical assay of serotonin. *Talanta,* 120: 17-22.
2. Kesavan, S., Kumar, D. R., Lee, Y. R. and Shim, J. J. (2017). Determination of tetracycline in the presence of major interference in human urine samples using polymelamine/electrochemically reduced graphene oxide modified electrode. *Sensors and Actuators B: Chem,* 241: 455-465.
3. Khosropour, H., Rezaei, B., Alinajafi, H. A. and Ensafi, A. A. (2021). Electrochemical sensor based on glassy carbon electrode modified by polymelamine formaldehyde/graphene oxide nanocomposite for ultrasensitive detection of oxycodone. *Microchimica Acta*, 188(1): 1.
4. Farida, A. N., Fitriany, E., Baktir, A., Kurniawan, F. and Harsini, M. (2019). Voltammetric study of ascorbic acid using polymelamine/gold nanoparticle modified carbon paste electrode. *IOP Conference Series: Earth Environmental Science*, 217: 012004.
5. Qin, H., Hu, X., Wang, J., Cheng, H., Chen, L. and Qi, Z. (2020). Overview of acidic deep eutectic solvents on synthesis, properties and applications. *Green Energy and Environment*, 5(1): 8-21.
6. Zante, G. and Boltoeva, M. (2020). Review on hydrometallurgical recovery of metals with deep eutectic solvents. *Sustainable Chemistry*, 1(3): 238-255.
7. Cen, P., Spahiu, K., Tyumentsev, M. S. and Foreman, M. R. S. J. (2020). Metal extraction from a deep eutectic solvent, an insight into activities. *Physical Chemistry Chemical Physics*, 22(19): 11012-11024.
8. Paiva, A., Craveiro, R., Aroso, I., Martins, M., Reis, R. L. and Duarte, A. R. C. (2014). Natural deep eutectic solvents – solvents for the 21st century. *ACS Sustainable Chemistry & Engineering*, 2(5): 1063- 1071.
9. Mendonça, P. V., Lima, M. S., Guliashvili, T., Serra, A. C. and Coelho, J. F. (2017). Deep eutectic solvents (DES): Excellent green solvents for rapid SARA ATRP of biorelevant hydrophilic monomers at ambient temperature. *Polymer*, 132: 114-121.
10. Sánchez-Leija, R. J., Torres-Lubián, J. R., Reséndiz-Rubio, A., Luna-Bárcenas, G. and Mota-Morales, J. D. (2016). Enzyme-mediated free radical polymerization of acrylamide in deep eutectic solvents. *RSC Advances,* 6(16): 13072-13079.
11. Fernandes, P. M. V., Campiña, J. M., Pereira, N. M., Pereira, C. M. and Silva, F. (2012). Biodegradable deep-eutectic mixtures as electrolytes for the electrochemical synthesis of conducting polymers. *Journal of Applied Electrochemistry*, 42(12): 997-1003.
12. Mąka, H., Spychaj, T. and Adamus, J. (2015). Lewis acid type deep eutectic solvents as catalysts for epoxy resin crosslinking. *RSC Advances*, 5(101): 82813-82821.

13. Chang, Y. H., Woi, P. M. and Alias, Y. B. (2021). Electrochemical characterization of melamine electropolymerized in deep eutectic solvents for selective detection of dopamine. *Electrocatalysis,* 12(3): 238-250.
14. Chen, S., Liu, S., Wen, A., Zhang, J., Nie, H., Chen, J., Zeng, R., Long, Y., Jin, Y. and Mai, R. (2018). New insight into electropolymerization of melamine. I: Chloride promoted growth of polymelamine in different pH medium. *Electrochimica Acta*, 271: 312-318.
15. Migliorati, V., Sessa, F. and D'Angelo, P. (2019). Deep eutectic solvents: A structural point of view on the role of the cation. *Chemical Physics Letters,* 2: 100001.
16. Li, R., Lin, C. W., Shao, Y., Chang, C., Yao, F. K., Kowal, M., Wang, H., Yeung, M., Huang, S. C. and Kaner, R. (2016). Characterization of aniline tetramer by MALDI TOF mass spectrometry upon oxidative and reductive cycling. *Polymers*, 8(11): 401.
17. Gabrielli, C., Huet, F. and Keddam, M. (1993). Fluctuations in electrochemical systems. I. General theory on diffusion limited electrochemical reactions. *The Journal of Chemical Physics*, 99: 7232.

Malaysian Journal of Analytical Sciences (MJAS)
Published by Malaysian Analytical Sciences Society

PREPARATION AND ADSORPTION STUDIES OF MOLECULARLY IMPRINTED POLYMER FOR SELECTIVE RECOGNITION OF TRYPTOPHAN

(Penyediaan dan Kajian Penjerapan Polimer Molekul Tercetak untuk Pengecaman Selektif Triptofan)

Nur Habibah Safiyah Jusoh[1], Faizatul Shimal Mehamod[2]*, Noor Fadilah Yusof[3], Abd Mutalib Md Jani[4], Faiz Bukhari Mohd Suah[5], Marinah Mohd Ariffin[1], Nur Asyiqin Zulkefli[1]

[1]*Faculty of Science and Marine Environment*
[2]*Advanced Nano Materials (ANoMA) Research Group, Faculty of Science and Marine Environment*
Universiti Malaysia Terengganu, 21030 Kuala Nerus, Terengganu, Malaysia
[3]*School of Chemical and Energy Engineering, Faculty of Engineering,*
Universiti Teknologi Malaysia, 81310 Skudai, Johor Bahru, Malaysia.
[4]*Faculty of Applied Sciences,*
Universiti Teknologi MARA, Perak Branch, Tapah Campus, 35400 Perak, Malaysia
[5]*School of Chemical Sciences,*
Universiti Sains Malaysia, 11800 Minden, Pulau Pinang, Malaysia

**Corresponding author: fshimal@umt.edu.my*

Received: 13 September 2021; Accepted: 18 December 2021; Published: 28 April 2022

Abstract

One of the effective technologies in molecular recognition is based on the molecular imprinting process. In this work, the polymers were prepared by bulk polymerization, using methacrylic acid and ethylene glycol dimethacrylate as the functional monomer and crosslinking agent, respectively. The polymers were characterized by Fourier transform infrared spectroscopy, scanning electron microscopy and surface area and porosity analyses. Several parameters influencing the adsorption efficiency of Tryptophan (Tryp) such as adsorbent dosage, contact time, pH of sample solution as well as selectivity and reproducibility study, have been evaluated. The Tryptophan-imprinted polymer (Tryp-IP) showed significantly higher removal efficiency and selective binding capacity towards Tryp compared to non-imprinted polymer (NIP). The adsorption isotherm demonstrated that the Tryp-IP followed Langmuir isotherm model, indicating the Tryp-IP owning the homogenous surface type of adsorbent. In contrast, the NIP fit with the Redlich-Peterson model, indicating that mechanism adsorption is a mixed type. The kinetic study revealed that pseudo-second order was the appropriate kinetic model for Tryp-IP and the adsorption kinetic of NIP appeared to fit with pseudo-first order.

Keywords: molecularly imprinted polymer, tryptophan, adsorption study

Abstrak

Salah satu teknologi yang efektif dalam pengecaman molekul adalah berdasarkan proses pencetakan molekul. Dalam kajian ini, polimer telah disediakan melalui pempolimeran pukal, masing-masing menggunakan asid metakrilik dan etilena glikol dimetakrilat sebagai monomer berfungsi dan agen tautsilang. Polimer dicirikan oleh spektroskopi inframerah transformasi Fourier, pengimbasan mikroskop elektron dan analisis luas permukaan dan keliangan. Beberapa parameter yang mempengaruhi kecekapan penjerapan Triptofan (Tryp) seperti dos penjerap, masa sentuhan, pH larutan sampel serta kajian selektiviti dan kebolehulangan telah dinilai. Polimer tercetak-

Triptofan (Tryp-IP) menunjukkan kecekapan penyingkiran dan kapasiti pengikatan yang lebih tinggi terhadap Tryp berbanding polimer tidak dicetak (NIP). Isoterma penjerapan menunjukkan bahawa Tryp-IP mematuhi model isoterma Langmuir, ini menunjukkan Tryp-IP memiliki jenis penjerap permukaan homogen. Sebaliknya, NIP mematuhi model Redlich-Peterson, menunjukkan mekanisme penjerapan adalah jenis campuran. Kajian kinetik mendedahkan bahawa tertib pseudo-kedua adalah model kinetik yang sesuai untuk Tryp-IP dan kinetik penjerapan NIP kelihatan lebih sesuai dengan tertib pseudo-pertama.

Kata kunci: polimer tercetak molekul, triptofan, kajian penjerapan

Introduction

Tryptophan (Tryp) is one of the essential amino acids that is necessary for normal growth and it also acts as a precursor for several bioactive compounds such as nicotinamide (vitamin B6), serotonin, melatonin, tryptamine, kynurenine, and xanthurenic acids [1]. Tryp cannot be synthesized in the human body. However, it can be supplied via our dietary intake such as high protein food and fiber rich food like banana, soy, egg and rice. Even though the Tryp in the human body is relatively low, its potency is very significant. It is one of the amino acids capable of passing through the blood- brain barrier, which makes it very important for protein synthesis in our body [2]. Previous studies have shown that Tryp deficiency in the body can affect mood or cause depressive symptoms, whereas low serotonin levels contribute to increased anxiety and depression [3]. Since Tryp acts as a precursor for serotonin synthesis, the level of serotonin depends on the concentration of Tryp in the body [4]. From this point of view, it is crucial to determine the level of Tryp in the body to monitor this condition. At present, many technologies have been applied for the determination of Tryp, such as electrochemical sensors [5], high-performance liquid chromatography (HPLC) [6], solid-phase extraction-liquid chromatographic-tandem mass spectrometric (XLC-MS/MS) [7] and tandem mass spectrometer [8]. These techniques are very selective and precise; however, they often require pre-treatment steps, expensive and complicated instruments, skilled operators and a lot more time [9]. For these reasons, attention has been focused on the adsorption method due to its low cost and ease of operation. The latest development of adsorbent material for the determination and removal of Tryp/ Tryp derivatives such as polymeric resin [10], gold nanoparticles [11] and activated carbon [12], has shown outstanding results for the adsorptive capacity of Tryp.

In recent years, the low-cost adsorbent materials fabricated from molecular imprinting technology have attracted much attention due to the high selectivity and simple preparation method, which gives the technology a broad range of applications. Molecularly imprinted polymer (MIP) is an adsorbent from the imprinting technique with specific binding sites, shape and size towards the imprinted analyte called template. The molecular imprinting technique is a process that involves the polymerization reaction of functional monomers with the template molecule, thus allowing the formation of polymer networks to possess binding sites complementary with the template molecule [13]. MIP has several advantages which include low cost, ease of preparation, high stability and high selectivity and affinity. In addition, MIP is an insoluble substance with high durability under extreme pH conditions, organic solvents and high temperatures [14]. In general, many researchers favored the non-covalent approach due to the straightforward procedure, easy template removal as well as the fact that imprinted polymer can be used in various applications because most of the biomolecular interaction were non-covalent bond [15]. During pre-polymerization, functional monomers and template interaction are formed by self-assembly *via* non-covalent interactions, such as hydrogen bond, ionic interaction, hydrophobic interaction, and Van der Waals interaction [16]. Therefore, the present work highlights the application of MIP as a versatile material for selective determination of Tryp molecule. Tryptophan-imprinted polymer designated as Tryp-IP was prepared by bulk polymerization. Figure 1 shows a schematic for the formation of MIP for Tryp *via* the imprinting technique. The process involves methacrylic acid (MAA), ethylene glycol dimethacrylate (EGDMA) and azobisisobutyronitrile (AIBN) as the functional monomer, cross-linker and initiator, respectively. Once

the polymerization is complete, the removal of the template from the polymer matrix, leaves the cavities that are ideally complementary in terms of size, shape, and function to the template analyte. The corresponding non-imprinted polymer (NIP) was synthesized as a control sample.

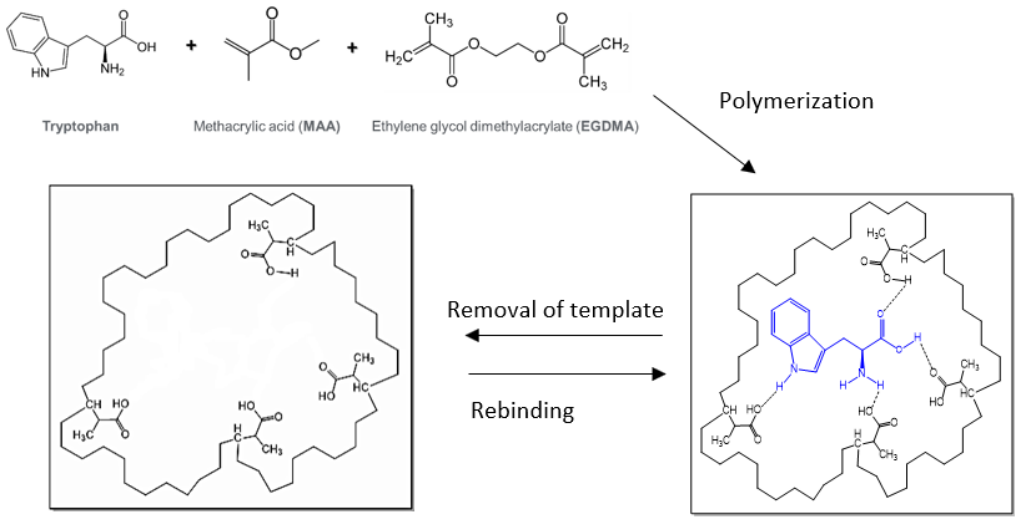


Figure 1. Schematic of the molecular imprinting process for Tryp

Materials and Methods

Materials

Tryptophan (Tryp), kynurenine (Kyn), tyrosine (Tyr), phenylalanine (Phe), methacrylic acid (MAA), ethylene glycol dimethacrylate (EGDMA), and azobisisobutyronitrile (AIBN) were purchased from Sigma Aldrich, Germany whereas methanol, acetic acid, sodium hydroxide (NaOH), hydrochloric acid (HCl) were supplied by R&M Chemicals, UK.

Preparation of Tryp-imprinted polymer

The preparation of Tryp-IP was carried out by the bulk polymerization method [17, 18]. Initially, Tryptophan (Tryp, 1 mmol) was dissolved in water/methanol (1:3 v/v). Then the functional monomer (MAA, 10 mmol), cross-linker (EGDMA, 30 mmol) and initiator; (AIBN) were added into the glass tube to allow the polymerization process to occur. Then, the mixture was stirred until homogeneous and purged with nitrogen gas before being placed in an oil bath at 60 °C for 48 hours. Upon completion of the polymerization reaction, the polymers obtained were crushed, ground, and sieved. The polymers were treated with methanol and acetic acid in a 9:1 v/v ratio by Soxhlet extraction to remove the template molecules. The obtained polymers were stored at room temperature for further characterization. Finally, the non-imprinted polymer (NIP) as a control sample was prepared using the same method but in the absence of the template.

Characterization of the polymers

The polymers were characterized by attenuated total reflection-Fourier transform infrared spectroscopy (ATR-FTIR). The spectra were recorded from 500 cm^{-1} to 4000 cm^{-1}. Then, the surface morphology of polymers was observed by Scanning Electron Microscopy (SEM). Each polymer was mounted on the stubs and coated with gold for protection from the electron beam. Next, the determination of the specific surface area, pore volume and pore diameter were performed by porosity analyzer using Bruner-Emmett-Teller (BET) and Barrett-Joyner-Halenda (BJH) technique.

Adsorption studies

The adsorption studies were conducted by batch rebinding experiment, which was performed in an aqueous medium [19]. First, 1 ppm of Tryp solution was prepared and mixed with a different mass of Tryp-IP (1, 3, 5, 7, 9 mg) while maintaining other parameters at optimal conditions. After the adsorption process, the Tryp solution was analyzed using a UV-Vis spectrometer to determine the remaining Tryp molecule by observing its final concentration. Then, the percentage removal and adsorption capacity of Tryp-IP towards Tryp was calculated using equations (1) and (2), respectively [20]:

$$\% \text{ removal} = \frac{C_i - C_f}{C_i} \times 100 \quad (1)$$

$$Q_e = \frac{(C_i - C_f)V}{W} \quad (2)$$

In the equations above, C_i and C_f are initial and final concentrations (mg/L) of Tryp solutions, respectively, Q_e (mg/g) is the quantity of total adsorption of Tryp molecules, V (L) is the volume of the solution and W (g) is the weight of polymers.

The interaction and adsorption mechanism of Tryp-IP and Tryp were further studied by fitting equilibrium data into the isotherm models. The adsorption equilibrium data obtained were fitted into Langmuir, Freundlich and Redlich-Peterson isotherm models. Langmuir isotherm is often associated with adsorption on the surface of homogeneous sites within the adsorbent and occurs in a monolayer pattern. Nevertheless, Freundlich isotherms apply to adsorption processes that occur on heterogeneous surfaces. Redlich-Peterson isotherm is a three-parameter isotherm which combines Langmuir and Freundlich isotherms. The Langmuir, Freundlich and Redlich-Peterson equation can be written in the following linear form as stated in equations (3), (4) and (5), respectively [21].

$$\frac{C_e}{Q_e} = \frac{1}{BQ_o} + \frac{C_e}{B} \quad (3)$$

$$\ln Q_e = \ln K_F + \frac{1}{n} \ln C_e \quad (4)$$

$$\ln \frac{C_e}{Q_e} = \beta \ln C_e - \ln A \quad (5)$$

In equations (3), (4) and (5), Q_e is the equilibrium adsorption capacity (mg/g), C_e is the equilibrium concentration of adsorbents at equilibrium (mg/L), and Q_o is the maximum adsorption capacity of the adsorbents (mg/g). B (L/mg) is the Langmuir adsorption constant, while K_F (mg/g) is the Freundlich adsorption equilibrium constants indicating the sorption capacity and 1/n represents the intensity of the adsorption. Meanwhile, A (Lg^{-1}) is Redlich-Peterson isotherm constant and β is the exponent that lies between 0 and 1. The favorability of the Langmuir isotherm was expressed by a dimensionless constant called the separation factor (RL), as shown in equation (6).

$$RL = \frac{1}{1 + B(C_e)} \quad (6)$$

where RL values indicate the adsorption to be unfavorable when RL > 1, linear when RL = 1, favorable when 0 < RL< 1, and irreversible when RL = 0 [21].

Adsorption kinetic study

Adsorption kinetics was studied to determine the kinetic behavior and rate-controlling step for the adsorption process of Tryp-IP. The experiments were conducted using 1 ppm of Tryp solution mixed with 9 mg of Tryp-IP. The kinetics of Tryp uptake by Tryp-IP were analyzed using a UV-Vis spectrometer. The time was set at 0 to 180 min. Two adsorption kinetic models, namely pseudo-first-order and pseudo-second-order, were tested and fitted into the adsorption kinetic data. The pseudo-first and pseudo-second order equations can be expressed in equations (7) and (8), respectively,

$$\ln(q_e - q_t) = \ln q_e - k_1 t \quad (7)$$

$$\frac{t}{q_t} = \frac{1}{k_2 q_e^2} + \frac{t}{q_e} \quad (8)$$

where q_t and q_e (mg/g) represent adsorption capacities at time and equilibrium, respectively, while k_1 and k_2 represent rate constants at equilibrium [22]. Furthermore, the favorability of kinetic models was calculated by standard deviation formula, Δq (%) and relative error, RE (%) as in the following equations:

$$\Delta q(\%) = \sqrt{\frac{[(Q_{e,exp} - q_{e,cal})/Q_{e,exp}]^2}{N-1}} \times 100 \quad (9)$$

$$RE\ (\%) = \frac{|q_{e,cal} - Q_{e,exp}|}{Q_{e,exp}} \times 100 \quad (10)$$

where N is the amount of data points fitted to the plot, $Q_{e,exp}$ and $q_{e,cal}$ (mg/g) are the experimental and calculated adsorption capacities, respectively. A lower Δq (%) gives the desired fitness of polymer to the kinetic model [20].

Effect of pH study

1 ppm of Tryptophan solution was prepared, and the pH was adjusted in the range of 4, 5, 7, 9, 11 and 13, by adding diluted HCl and NaOH. The experiment was carried out by mixing each solution with 9 mg of Tryp-IP. An independent analyte solution was analyzed and the optimum pH for optimum adsorption was determined.

3

Effect of selectivity study

In the selectivity study, the molecular structural analogues of Tryptophan; kynurenine, tyrosine and phenylalanine were tested for the binding performance with Tryp-IP. Firstly, 1 ppm of analyte concentrations were prepared separately and mixed with 9 mg of Tryp-IP. Then, the solutions were analyzed using UV-Vis spectrometer. The distribution coefficient (kd) was calculated based on the equation 11.

$$k_d = \frac{(C_i - C_f)}{C_f}\left(\frac{V}{W}\right) \quad (11)$$

where k_d is the concentration ratio between two solutions, C_i and C_f are initial and final concentrations of each compound, respectively. V (L) is the volume of the solution and W (g) is the weight of polymers [23]. The adsorption capacity of the polymer increases as the value of k_d increases. Selectivity coefficient (k), which indicates the selectivity of Tryp over the competitive compounds was calculated based on the equation 12 below:

$$k = \frac{k_d(\text{Tryp})}{k_d(\text{Kyn/Tyr/Phe})} \quad (12)$$

Relative selectivity coefficient (k') was determined by comparing the ratio of Tryp-IP and NIP as equation 13 below:

$$k' = \frac{k\,(\text{Tryp-IP})}{k\,(\text{NIP})} \quad (13)$$

Reproducibility study

A reproducibility study was explored to evaluate the practical application of the prepared adsorbent. Firstly, 1 ppm of Tryp solution was mixed with nine sets of Tryp-IP (9 mg) at the optimal time taken. Then, each solution was evaluated by UV- Vis spectrometer and its adsorption capacity were calculated.

Results and Discussion

FTIR characterization

Figure 2 shows the FTIR spectra of Tryp, Tryp-IP before and after template removal and the NIP. From the Tryp spectrum in Figure 2(a), a peak at 3400 cm^{-1} and 3012 cm^{-1} were observed, indicating a peak for NH stretching from the indole group and alkene C-H stretching, respectively. The IR peaks obtained at 1654 cm^{-1} and 1575cm^{-1} show the COO- and NH asymmetric stretching vibrations, respectively [9]. Due to the high cross-linking agent, all polymers show similar vibration peaks with almost the same IR spectrum. Based on Figure 2(b), the IR broad peaks obtained around 3471 cm^{-1} – 3275 cm^{-1} show a strong interaction between the NH group of Tryp and the O-H group of the MAA monomer through hydrogen bonding [24]. The aromatic stretching of C-H appeared at 2985 cm^{-1} at a lower intensity indicating the presence of Tryp in the polymer. After removal of Tryp Figure 2(c), the IR spectrum showed the complete disappearance of Tryp characteristic. The intensity of C=O from MAA at 1724 cm^{-1} increased. In comparison with Figure 2(b), the C=O absorption peak shifted from 1716 cm^{-1} to 1724 cm^{-1}, indicating the rupture of the hydrogen bond. In Figure 2(d), the IR spectrum for NIP is expected to be similar to Tryp-IP after the template is removed, where the C-H stretching vibration of MAA appeared at 2985 cm^{-1}. The schematic from Figure 1 is used to confirm all the functional groups present in the polymers for the FTIR spectra.

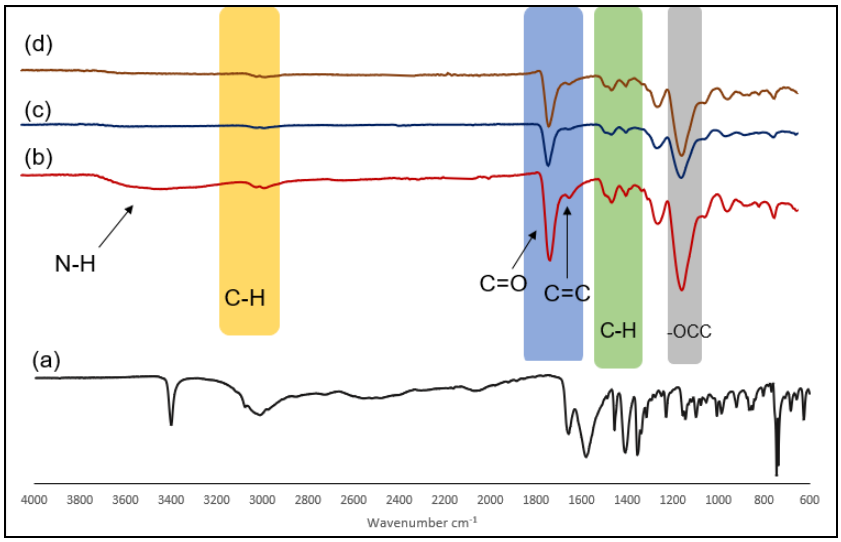


Figure 2. FTIR spectrum of (a) Tryp, (b) Tryp-IP before and (c) Tryp-IP after removal of the template and (d) NIP

SEM analysis

Figures 3(a) and 3(b) show the SEM micrographs for Tryp-IP and NIP, respectively. Bulky particles with the size in the range of a few microns is observed. This morphological feature is typical for polymers synthesized by the bulk polymerization approach. Furthermore, agglomeration is observed in Tryp-IP and NIP, and this is expected due to the high molar ratio of monomer to cross-linker (10:30) used in this study [24, 25]. Based on previous studies, bulk polymerization using the optimum molar ratio (4:20) can give a morphological image in heterogeneous irregular shapes and sizes due to crashing, grinding, and sieving processes [26]. Besides, the molar ratio of the cross-linker played a significant role in controlling the morphology of the polymer where it can form a rigid surface of the primary particles, which makes it difficult to agglomerate [27]. As in a previous study reported in the literature, the polymer morphology changes when the cross-linker ratio exceeds the optimum level within the polymer structure, resulting in the hard segment and a reduction in the polymer matrix binding sites [24].

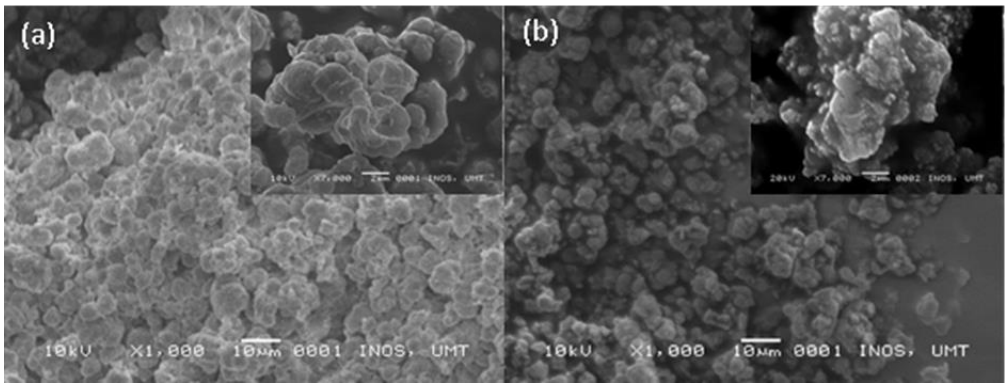


Figure 3. SEM micrograph of (a) Tryp-IP and (b) NIP

BET surface area analysis and porosity

BET analysis was carried out to determine the specific surface area and porosity properties of the Tryp-IP and NIP. Table 1 shows the results of surface area, pore volume and pore diameter of the polymers. The average pore diameters of Tryp-IP and NIP were in the range of 2–50 nm, indicating that both polymers have a mesoporous structure [20, 28]. However, Tryp-IP has larger a surface area and slightly larger total pore volume than the NIP. The increased surface area in Tryp-IP reflects the effect of the imprinting process, which occurred when the presence of the Tryp as a template during MIP synthesis resulted in the formation of pores or imprinted cavities [29, 30]. Based on previous studies, high molar ratios of monomers to the cross-linker resulted in non-specific interactions, while low ratios lead to inadequate functional sites [31]. Consequently, the agglomeration of the polymers particle resulted in the reduction of surface area and the number of active sites of polymers.

Table 1. BET surface area, pore volume and pore diameter

Polymer	Surface area ($m^2 g^{-1}$)	Pore volume ($cm^3 g^{-1}$)	Pore diameter (nm)
Tryp-IP	6.4519	0.022482	13.94
NIP	4.0351	0.016078	15.94

Adsorption isotherm study

The effect of the mass polymer was investigated to get the optimum mass for Tryp-IP. Based on Figure 4, it was observed that the percentage removal of Tryp increased with the increase of polymer mass. The maximum percentage removal achievable by Tryp-IP and NIP were 82% and 70%, respectively. An increase in polymer mass appears to increase the number of active sites and surface area for Tryp adsorption [32, 33]. Due to the absence of a template during the NIP synthesis, the non-specific cavities are formed, thus lower percentage removal of NIP than Tryp-IP. Based on Figure 4, the percentage removal increased until it reached the optimum level at 5 mg, indicating that all cavities were filled with Tryp molecules. However, a previous study agreed that a further increase in polymer mass could lead to adsorbent aggregation resulting in a decrease in the adsorption sites [34]. Hence, an increase in polymer mass does not increase the adsorption of Tryp.

Figure 5 is the isotherm models used in this study to fit the experimental data to predict the adsorption mechanism. Based on the isotherm parameter in Figures 5(a) and 5(b), the adsorption mechanism for Tryp-IP followed the Langmuir isotherm model and NIP followed the Redlich-Peterson isotherm which gave the highest R^2 value. The Langmuir isotherm was described as monolayer adsorption of Tryp onto Tryp-IP. The possible way for monolayer adsorption is for the adsorption to take place on the homogenous surface of the polymer matrix [35]. The similar observation was reported by the adsorption of D-Tryp onto polymer matrix [36]. To further strengthen the important features of the Langmuir isotherm model, the dimensionless constant separation factor (RL) was calculated [37]. RL values were found in the range of 0.017-0.009, which confirms adsorption of Tryp onto Tryp-IP was good. For the NIP, the data was fitted to the Redlich-Peterson model which, incorporates the features of both Langmuir and Freundlich isotherm. This can be applied as a homogeneous and heterogeneous system due to its versatility [38]. The parameters calculated for the three isotherms are tabulated in Table 2. From the data obtained, the maximum adsorption capacity for Tryp onto Tryp-IP was found to be 0.98 mg/g, which was seven times lower than the NIP (7.325 mg/g). The similar finding was reported by Hasanah et.al, which might be due to the non-specific recognition sites in NIP and therefore, made it swells better in polar solvent [39].

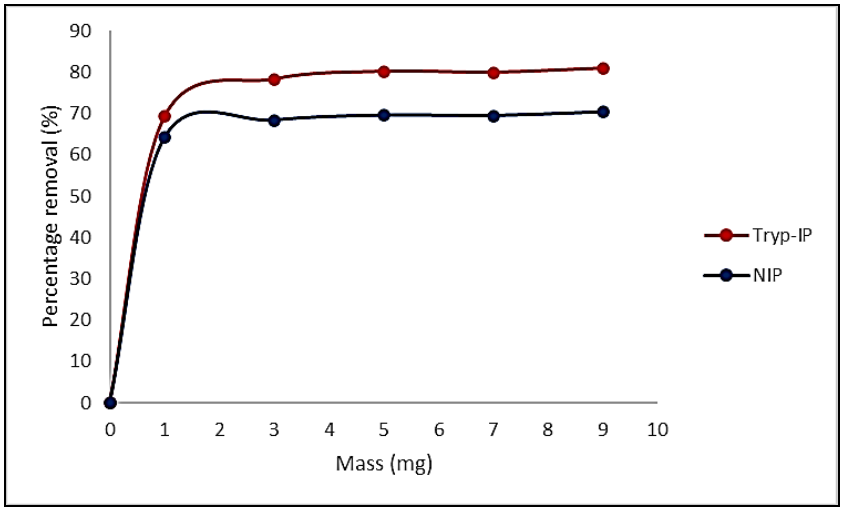


Figure 4. Effect of mass polymer on adsorption Tryp by Tryp-IP and NIP

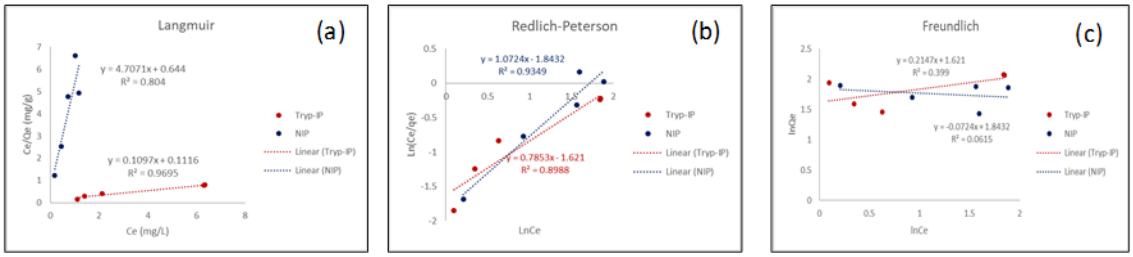


Figure 5. Adsorption isotherms of Tryp-IP and NIP using models (a) Langmuir (b) Redlich-Peterson (c) Freundlich

Table 2. Isotherm parameter for adsorption of Tryp by Tryp-IP and NIP

Polymer	Langmuir			Redlich-Peterson			Freundlich		
	Q_o	B	R^2	ß	A	R^2	1/n	K_F	R^2
Tryp-IP	0.98	9.116	0.9695	0.7853	5.058	0.8988	0.2147	5.058	0.399
NIP	7.325	0.212	0.804	1.0724	6.3167	0.9349	-0.0724	6.3167	0.0615

Adsorption kinetic study

The effect of contact time on the binding capacity of polymers is important to evaluate the binding efficiency in adsorption studies. It has been observed that the adsorption of Tryp onto the polymer surface increases with prolonging the contact time up to achieve equilibrium [40]. In Figure 6, initially, the adsorption rate of Tryp onto the polymeric surface was accelerating due to the abundant number of empty adsorption sites that can be accessed and less mass transfer resistance which allowed the active sites to capture the target analyte. However, with the progress of time, the number of active sites decreases, the imprinted cavities are gradually filled

with Tryp and the mass transfer resistance of Tryp to the active sites increases. Thus, the adsorption rate decreases and the removal percentage decreases slowly [41]. Finally, the adsorption equilibrium was reached within 120 min for Tryp-IP and 150 min for NIP. There is no change in the percentage removal if the time is prolonged because the polymer binding sites have been occupied with the Tryp. Therefore, it could be observed that Tryp-IP exhibited slightly higher percentage removal and faster mass transfer than the NIP, which could be attributed to the imprinting effect of Tryp [35, 42].

The adsorption mechanism was further evaluated by two of the most widely used kinetic models which is pseudo-first order kinetics, and pseudo-second order kinetic models. The results shown in Table 3 indicates that the R^2 value of Tryp-IP is most fitted with pseudo-second order (R^2 =0.9698) whereas the R^2 value for pseudo-first order is 0.2195. In the pseudo-second-order model, the theoretical and experimental adsorption capacity values were in good agreement. Therefore, the pseudo-second-order adsorption mechanism is predominant and the rate-limiting step at the surface involving a chemisorption process between Tryp and cavities of Tryp-IP [38].

Moreover, the values of Δq and RE were found to be low compared to pseudo-first order which means the accuracy and validity of the kinetic model were better equipped with pseudo second order. However, NIP appeared to be more suitable with pseudo-first order with the highest R^2 value (0.9107). It was expected that the rate of adsorption is proportional to the number of unused sites and the rate-limiting step was physisorption [39]. As in the case of Tryp-IP where Δq and RE values of NIP were exceedingly low for pseudo-first-order compared to pseudo-second order, these values indicate the accuracy of this kinetic model. Furthermore, the adsorption capacity Q_e (Table 3) for Tryp-IP (10.0336) was lower than NIP (11.3958). This result is due to the absence of specific recognition sites in the NIP, thus leading to the physical adsorption and random interaction of the Tryp molecule with the functional group of MAA in the polymer chain [43].

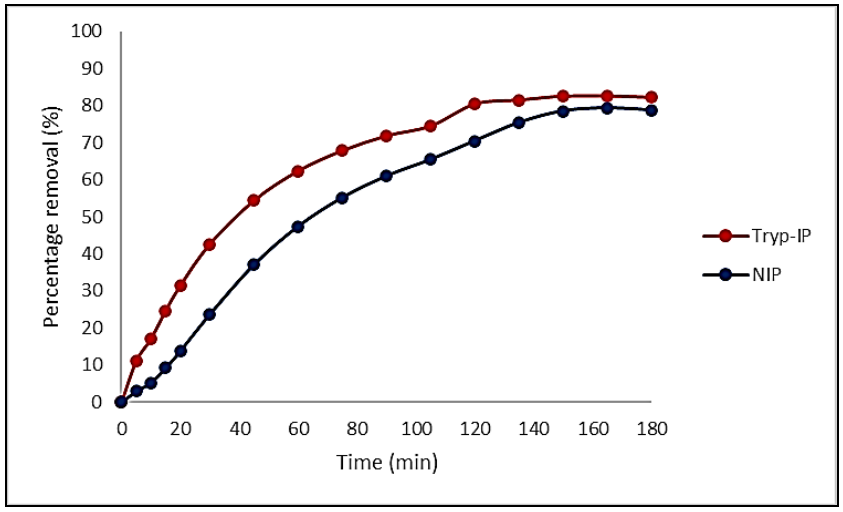


Figure 6. Effect of contact time on adsorption Tryp by Tryp-IP and NIP

Table 3. Kinetic parameter for adsorption of Tryp by Tryp-IP and NIP

Polymer	Model	Kinetic Parameters					
		y = mx + c	Q_e (mg/g)	Q_e (mg/g)	Δq (%)	RE (%)	R^2
Tryp-IP	Pseudo-first-order	y= -0.0223x +1.909	10.0336	6.746	8.464	32.78	0.2196
	Pseudo-second-order	y= 8.0813x +2.902		12.3001	5.826	22.56	0.9698
NIP	Pseudo-first-order	y= -0.017x +2.478	11.3958	11.9174	1.18	4.58	0.9107
	Pseudo-second-order	y= 0.0353x +7.9307		28.3286	38.37	149	0.3772

Effect pH study

The pH of the adsorption medium is the most critical parameter influencing the adsorption capacity [29]. In this analysis, a pH of 4-13 has been selected. Figure 7 shows that the highest percentage removal was obtained when the pH is in acidic condition and the percentage removal decreases as the pH increases (base condition). This condition might be due to the interaction of hydrogen bonding between the surface of the carboxylic group of MAA and the functional group of Tryp. As shown in Figure 7, the highest percentage removal of Tryp appeared when the pH became acidic. This observation occurred as a result of the zwitterionic Tryp and the large electronegativity of the oxygen atom of the carbonyl group in the polymers [43]. However, when the pH value becomes basic, Tryp exists as an anion and diffuses very slowly into the polymer surface [44]. Therefore, pH 5 was chosen as the optimal pH throughout this study.

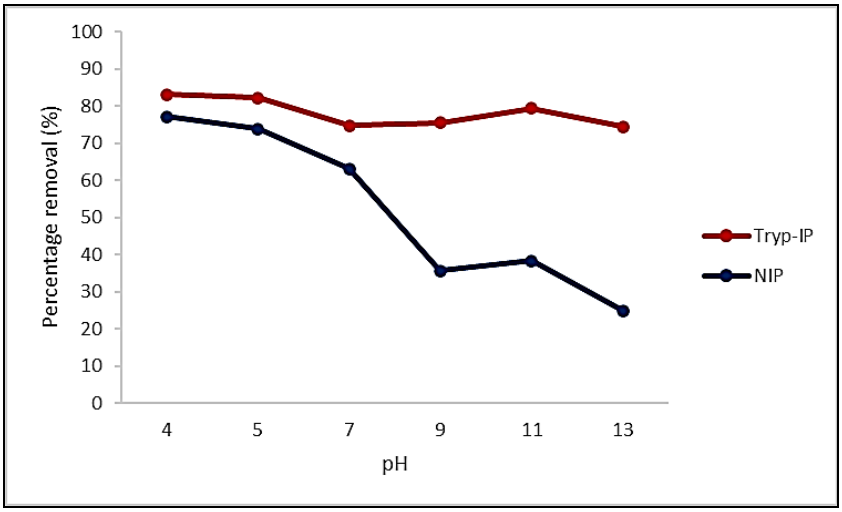


Figure 7. Effect of pH on adsorption Tryp by Tryp-IP and NIP

Effect of selectivity study

To study the selectivity of Tryp-IP and NIP, the recognition of Tryp was compared with tyrosine, phenylalanine and kynurenine as potential interferences. Table 4 shows the k_d values of each molecule in the Tryp-IP and the NIP. According to the Table 4, Tryp has higher k_d values compared to the other molecules in the Tryp-IP, which means that high specific recognition ability for Tryp is associated with a unique complementary form of the binding sites [42]. In contrast with the NIP, tyrosine gave a higher k_d value compared to Tryp. This is due to the non-specific

cavities existing in the NIP. Furthermore, the k values indicate that the polymer has selective behavior for the template in the presence of other molecules. The larger the k values, the higher the selectivity of the polymer towards the template compared to the other molecule [23]. For the Tryp-IP, the k values are higher than for the NIP, which means that Tryp-IP has selective behavior for Tryp as calculated in Equation 12. In order to show the efficiency of Tryp-IP for selective separation of Tryp against NIP, the k' values were calculated according to Equation 13. The larger the k' values the more selective is the Tryp-IP against NIP for the template toward the other molecules [41]. It can be concluded that the Try-IP has greater molecular recognition towards its template molecule.

Table 4. Selectivity study constant for Tryp-IP and NIP

	Tryp-IP		**NIP**		**k'**
	k_d	K	k_d	k	
Tryptophan	1.5751	-	1.2175	-	-
Kynurenine	0.7495	2.1015	0.8407	1.4482	1.451112
Tyrosine	0.5309	3.958	1.3346	0.9123	4.338485
Phenylalanine	0.8392	4.7168	0.7567	1.609	2.93151

Effect of the reproducibility study

The reproducibility performance of the Tryp-IP was evaluated by comparing the adsorption capacity for each adsorption process of Tryp-IP. The result in Figure 8 revealed that the percentage removal of Tryp did not show a significant change (80% to 83%) for each repeated usage. The Tryp-IP can be used at least nine times while maintaining its percentage removal of more than 80%, reflecting the excellent precision and reproducibility of the proposed polymer. Therefore, Tryp-IP showed good stability and could maintain its adsorption capacity at a constant value.

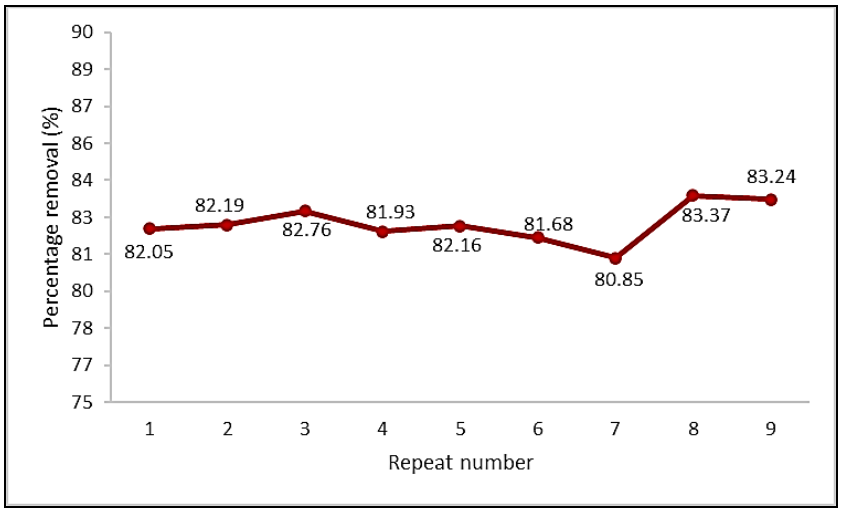


Figure 8. Effect of reproducibility of Tryp-IP

Conclusion

In this study, Tryp-IP and NIP were successfully synthesized through bulk polymerization and used as an adsorbent for tryptophan detection. FTIR, SEM, and BET were used to analyze the physical and chemical characterizations, which revealed evidence of chemical interaction, surface morphology, and cavities of the polymer matrix; all of which are responsible for the binding ability of the polymer. Hence, the adsorption studies have revealed that Tryp-IP has a greater removal percentage, selectivity, and stability than the NIP.

Acknowledgments

We would like to thank the Ministry of Higher Education Malaysia for the project funding support under Fundamental Research Grant Scheme (FRGS/1/2018/STG01/UMT/02/6 – Vot: 59493) and Universiti Malaysia Terengganu.

References

1. Friedman, M. (2018). Analysis, nutrition, and health benefits of tryptophan. *International Journal of Tryptophan Research*, 11: 1178646918802282.
2. Richard, D. M., Dawes, M. A., Mathias, C. W., Acheson, A., Hill-Kapturczak, N. and Dougherty, D. M. (2009). L-tryptophan: basic metabolic functions, behavioral research and therapeutic indications. *International Journal of Tryptophan Research*, 23(2): 45-60.
3. Lindseth, G., Helland, B. and Caspers, J. (2015). The effects of dietary tryptophan on affective disorders. *Archives of Psychiatric Nursing*, 29(2): 102-107.
4. Jenkins, T. A., Nguyen, J. C. D., Polglaze, K. E. and Bertrand, P. P. (2016). Influence of tryptophan and serotonin on mood and cognition with a possible role of the gut-brain axis. *Nutrients*, 8(1): 56.
5. Sundaresan, R., Mariyappan, V., Chen, S.-M., Keerthi, M. and Ramachandran, R. (2021). Electrochemical sensor for detection of tryptophan in the milk sample based on $MnWO_4$ nanoplates encapsulated RGO nanocomposite. *Colloids and Surfaces A: Physicochemical and Engineering Aspects*, 625: 126889.
6. Capuron, L., Ravaud, A., Neveu, P. J., Miller, A. H., Maes, M. and Dantzer, R. (2002). Association between decreased serum tryptophan concentrations and depressive symptoms in cancer patients undergoing cytokine therapy. *Molecular Psychiatry*, 7(5): 468-473.
7. de Jong, R. A., Nijman, H. W., Boezen, H. M., Volmer, M., Klaske, A., Krijnen, J., van der Zee, A. G. J., Hollema, H. and Kema, I. P. (2011). Serum tryptophan and kynurenine concentrations as parameters for indoleamine 2, 3-dioxygenase activity in patients with endometrial, ovarian, and vulvar cancer. *International Journal of Gynecologic Cancer*, 21(7): 1320-1327.
8. Onesti, C. E., Boemer, F., Josse, C., Leduc, S., Bours, V. and Jerusalem, G. (2019). Tryptophan catabolism increases in breast cancer patients compared to healthy controls without affecting the cancer outcome or response to chemotherapy. *Journal of Translational Medicine*, 17(1): 1-11.
9. Tian, Y., Deng, P., Wu, Y., Ding, Z., Li, G., Liu, J. and He, Q. (2019). A simple and efficient molecularly imprinted electrochemical sensor for the selective determination of tryptophan. *Biomolecules*, 9(7): 294.
10. Jiao, P., Wei, Y., Zhang, M., Zhang, X., Zhang, H. and Yuan, X. (2021). Adsorption separation of l-tryptophan based on the hyper-cross-linked resin XDA-200. *ACS Omega*, 6(3): 2255-2263.
11. Lee, D., Hussain, S., Yeo, J. and Pang, Y. (2021). Adsorption of dipeptide L-alanyl-L-tryptophan on gold colloidal nanoparticles studied by surface-enhanced Raman spectroscopy. *Spectrochimica Acta Part A: Molecular and Biomolecular Spectroscopy*, 247: 119064.
12. Belhamdi, B., Merzougui, Z., Laksaci, H. and Trari, M. (2019). The removal and adsorption mechanisms of free amino acid l-tryptophan from aqueous solution by biomass-based activated carbon by H_3PO_4 activation: regeneration study. *Physics and Chemistry of the Earth, Parts A/B/C*, 114: 102791.

13. Mehamod, F. S., KuBulat, K., Yusof, N. F. and Othman, N. A. (2015). The development of molecular imprinting technology for caffeine extraction. *International Journal of Technology*, 6(4): 546-554.
14. Samarth, N. B., Kamble, V., Mahanwar, P. A., Rane, A. V. and Abitha, V. K. (2015). A historical perspective and the development of molecular imprinting polymer-A review. *Chemistry International*, 4: 202-210.
15. Mujahid, A. and Dickert, F. L. (2016). Molecularly Imprinted polymers: principle, design, and enzyme-like catalysis. *Molecularly Imprinted Catalysts: Principles, Syntheses, and Applications*, pp. 79-101.
16. Zhang, H., Ye, L. and Mosbach, K. (2006). Non-covalent molecular imprinting with emphasis on its application in separation and drug development. *Journal of Molecular Recognition: An Interdisciplinary Journal*, 19(4), 248-259.
17. Yusof, N. F., Mehamod, F. S., Kadir, M. A. and Suah, F. B. M. (2018). Characteristics of adsorption isotherm and kinetic study for newly prepared Co2+-imprinted polymer linkage with dipicolinic acid. *IOP Conference Series: Materials Science and Engineering*, 440(1): 012005.
18. Yusof, N. F., Mehamod, F. S. and Suah, F. B. M. (2018). The effect of RAFT polymerization on the physical properties of thiamphenicol-imprinted polymer. *E3S Web of Conferences*, 67(12): 03050.
19. Abdul Hamid, N. S., Naseeruteen, F., Wan Ngah, W. S., Yusof, N. F., Mehamod, F. S. and Mohd Suah, F. B. (2020). Synthesis of chitin-ionic liquid beads as potential adsorbents for methylene blue. *Malaysian Journal of Chemistry*, 22(2): 98-110.
20. Yusof, N. F., Mehamod, F. S. and Suah, F. B. M. (2019). Fabrication and binding characterization of ion imprinted polymers for highly selective Co2+ ions in an aqueous medium. *Journal of Environmental Chemical Engineering*, 7(2): 103007.
21. Ayawei, N., Ebelegi, A. N. and Wankasi, D. (2017). Modelling and interpretation of adsorption isotherms. *Journal of Chemistry*, 2017: 3039817.
22. Alveroglu, E., Balouch, A., Khan, S., Mahar, A. M., Jagirani, M. S. and Pato, A. H. (2021). Evaluation of the performance of a selective magnetite molecularly imprinted polymer for extraction of quercetin from onion samples. *Microchemical Journal*, 162: 105849.
23. Fareghi, A. R., Moghadam, P. N., Khalafy, J., Bahram, M. and Moghtader, M. (2017). Preparation of a new molecularly imprinted polymer based on self-crosslinkable cellulose acrylate in aqueous solution: A drug delivery system for furosemide. *Journal of Applied Polymer Science*, 134(48): 45581.
24. Prabakaran, K., Jandas, P. J., Luo, J., Fu, C. and Wei, Q. (2021). Molecularly imprinted poly (methacrylic acid) based QCM biosensor for selective determination of L-tryptophan. *Colloids and Surfaces A: Physicochemical and Engineering Aspects*, 611: 125859.
25. Azodi-Deilami, S., Abdouss, M. and Seyedi, S. R. (2010). Synthesis and characterization of molecularly imprinted polymer for controlled release of tramadol. *Central European Journal of Chemistry*, 8(3): 687-695.
26. Wang, L., Zhi, K., Zhang, Y., Liu, Y., Zhang, L., Yasin, A. and Lin, Q. (2019). Molecularly imprinted polymers for gossypol via sol–gel, bulk, and surface layer imprinting—a comparative study. *Polymers*, 11(4): 602.
27. Xia, Q., Yun, Y., Li, Q., Huang, Z. and Liang, Z. (2017). Preparation and characterization of monodisperse molecularly imprinted polymer microspheres by precipitation polymerization for kaempferol. *Designed Monomers and Polymers*, 20(1): 201-209.
28. Madikizela, L. M., Zunngu, S. S., Mlunguza, N. Y., Tavengwa, N. T., Mdluli, P. S. and Chimuka, L. (2018). Application of molecularly imprinted polymer designed for the selective extraction of ketoprofen from wastewater. *Water SA*, 44(3): 406-418.
29. Hasanah, A. N., Susanti, I., Marcellino, M., Maranata, G. J., Saputri, F. A. and Pratiwi, R. (2021). Microsphere molecularly imprinted solid-phase extraction for diazepam analysis using itaconic acid as a monomer in propanol. *Open Chemistry*, 19(1): 604-613.

30. Yusof, N. F., Mehamod, F. S., & Suah, F. B. M. (2020). Adsorptive removal of bis (2-ethylhexyl) phthalate using an imprinted polymer: isotherm and kinetic modelling. *International Journal of Environmental Analytical Chemistry*, 2020: 1-12.
31. Song, S., Wu, A., Shi, X., Li, R., Lin, Z. and Zhang, D. (2008). Development and application of molecularly imprinted polymers as solid-phase sorbents for erythromycin extraction. *Analytical and Bioanalytical Chemistry*, 390(8): 2141-2150.
32. Albadarin, A. B., Mangwandi, C., Ala'a, H., Walker, G. M., Allen, S. J. and Ahmad, M. N. M. (2012). Kinetic and thermodynamics of chromium ions adsorption onto low-cost dolomite adsorbent. *Chemical Engineering Journal*, 179: 193-202.
33. Gomes, C., Sadoyan, G., Dias, R. and Costa, M. R. P. F. N. (2017). Development of molecularly imprinted polymers to target polyphenols present in plant extracts. *Processes*, 5(4): 72.
34. Mor, S., Chhoden, K. and Ravindra, K. (2016). Application of agro-waste rice husk ash for the removal of phosphate from the wastewater. *Journal of Cleaner Production*, 129: 673-680.
35. Bakhtiar, S., Bhawani, S. A. and Shafqat, S. R. (2019). Synthesis and characterization of molecular imprinting polymer for the removal of 2-phenylphenol from spiked blood serum and river water. *Chemical and Biological Technologies in Agriculture*, 6(1): 1-10.
36. Jin, Y., Liu, C. C., Sun, X. H., Lee, K. J., Jung, Y. A. and Row, K. H. (2012). Adsorption isotherms of tryptophan enantiomer on d-tryptophan molecular imprinted polymer. *Asian Journal of Chemistry*, 24(6): 2461-2466.
37. Hameed, B. H., Ahmad, A. L. and Latiff, K. N. A. (2007). Adsorption of basic dye (methylene blue) onto activated carbon prepared from rattan sawdust. *Dyes and Pigments*, 75(1): 143-149.
38. Kumar, V. (2019). Adsorption kinetics and isotherms for the removal of rhodamine B dye and Pb^{2+} ions from aqueous solutions by a hybrid ion-exchanger. *Arabian Journal of Chemistry*, 12(3): 316-329.
39. Hasanah, A. N., Dwi Utari, T. N. and Pratiwi, R. (2019). Synthesis of atenolol-imprinted polymers with methyl methacrylate as functional monomer in propanol using bulk and precipitation polymerization method. *Journal of Analytical Methods in Chemistry*, 2019: 9853620.
40. Yusof, N. F., Mehamod, F. S., Jusoh, N., Amin, K. A. M. and Suah, F. B. M. (2017). Ion-imprinted polymer-based on picolinic acid as a co-functional monomer for highly selective sorption of Cu(II) ions in an aqueous solution. *AIP Conference Proceedings*, 1885: 020017.
41. Abouzarzadeh, A., Forouzani, M., Jahanshahi, M. and Bahramifar, N. (2012). Synthesis and evaluation of uniformly sized nalidixic acid–imprinted nanospheres based on precipitation polymerization method for analytical and biomedical applications. *Journal of Molecular Recognition*, 25(7): 404-413.
42. Pan, J., Li, L., Hang, H., Ou, H., Zhang, L., Yan, Y. and Shi, W. (2013). Study on the nonylphenol removal from aqueous solution using magnetic molecularly imprinted polymers based on fly-ash-cenospheres. *Chemical Engineering Journal*, 223: 824-832.
43. Kong, Y., Zhao, W., Yao, S., Xu, J., Wang, W. and Chen, Z. (2010). Molecularly imprinted polypyrrole prepared by electrodeposition for the selective recognition of tryptophan enantiomers. *Journal of Applied Polymer Science*, 115(4), 1952-1957.
44. Monier, M., Abdel-Latif, D. A. and Nassef, H. M. (2015). Preparation of l-tryptophan imprinted microspheres based on carboxylic acid functionalized polystyrene. *Journal of Colloid and Interface Science*, 445: 371-379.

Malaysian Journal of Analytical Sciences (MJAS)
Published by Malaysian Analytical Sciences Society

THE CHEMICAL PROPERTIES AND ANTI-ACNE ACTIVITY DETERMINATION of *Swietenia macrophylla* SEED EXTRACTS

(Penentuan Ciri Kimia dan Aktiviti Anti-Jerawat Ekstrak Biji *Swietenia Macrophylla*)

Non Daina Masdar[1], Noor Hafizah Uyup[1], Zamzila Erdawati Zainol[2], Muhammad Akmal Roslani[2], Siti Nur Syarifa Anuar[1], Muhamad Azhar Zulkafle[3]*

[1]*Department of Chemistry*
[2]*Department of Marine*
[3]*Department of Biology*
Faculty of Applied Sciences,
Universiti Teknologi MARA, Perlis Branch, Arau Campus, 02600 Arau, Perlis, Malaysia

**Corresponding author: azharz@uitm.edu.my*

Received: 7 October 2021; Accepted: 18 December 2021; Published: 28 April 2022

Abstract

Acne is a common skin disorder usually treated using antibiotics and drugs. However, until today, dermatologists struggle to treat acne resistance towards topical treatment over a long period. One of the solutions is using natural bioactive compounds from plant extracts. In this work, *Swietenia macrophylla* seeds oil, rich in active compounds, was used to inhibit acne-causing bacteria, i.e., *Propionibacterium acnes*, *Staphylococcus aureus*, and *Staphylococcus epidermidis*. The seed powder sample was extracted using the Soxhlet extraction method in three different solvents for six hours and ten cycles. The seed extracts were analysed using a gas chromatography-mass spectrophotometer (GC-MS), and a disc diffusion assay was performed to analyse the antibacterial activities. The heavy metal analysis was determined by inductively coupled plasma atomic emission spectroscopy (ICP-OES). The results show that bioactive compound yields are 37-72%. Eugenol and isoeugenol compounds are the main constituents in the oil extracts with 98% and 97% quality. The compounds also demonstrated inhibitory activities towards all tested bacteria, with inhibition zones between 11 and 22 mm on 30 µg tetracycline discs. These compounds without isolation work also showed inhibitory activity against all bacteria tested with inhibition zones ranging from 11 to 21 mm.

Keywords: *Swietenia macrophylla*, acne, natural treatment, *Propionibacterium acne*, *Staphylococcus epidermidis*

Abstrak

Jerawat adalah penyakit kulit biasa dan selalunya dirawat menggunakan antibiotik dan ubat-ubatan. Namun, sehingga hari ini, pakar dermatologi masih belum dapat merawat ketahanan jerawat terhadap rawatan permukaan dalam jangka masa panjang. Salah satu penyelesaiannya adalah menggunakan sebatian bioaktif semula jadi dari ekstrak tumbuhan. Dalam kajian ini, minyak biji *Swietenia macrophylla* yang kaya dengan sebatian aktif, digunakan untuk merencat bakteria penyebab jerawat iaitu *Propionibacterium acnes*, *Staphylococcus aureus*, dan *Staphylococcus epidermidis*. Sampel serbuk biji diekstrak menggunakan kaedah pengekstrakan Soxhlet dalam tiga jenis pelarut berbeza selama enam jam dan sepuluh kitaran. Analisis hasil ekstrak dijalankan menggunakan kromatografi gas-spektrofotometer jisim (GC-MS) dan asai cakera resapan dilakukan untuk menganalisis aktiviti antibakteria. Analisis logam berat pula ditentukan melalui spektrometri pancaran optikal-plasma gandingan

aruhan (ICP-OES). Hasil kajian menunjukkan bahawa hasil sebatian bioaktif ialah 37-72%. Sebatian eugenol dan isoeugenol merupakan sebatian utama dalam sampel ekstrak minyak dengan kualiti 98% dan 97%. Sebatian tanpa kerja pengasingan ini juga menunjukkan aktiviti perencatan terhadap semua bakteria yang diuji dengan zon perencatan berjulat antara 11 hingga 21 mm.

Kata kunci: *Swietenia macrophylla*, jerawat, rawatan semula jadi, *Propionibacterium acne, Staphylococcus epidermidis*

Introduction

IntroductionAcne is a specific skin disease in dermatology. The skin problem occurs in pre-pubertal individuals, teenagers, and adults. It usually occurs in 14 to 17 years old girls and 16 to 19 years old boys. Those affected would experience distressing self-esteem and social relationships due to the inflammatory lesions and scarring effects [1]. Several factors that trigger acne include genetics, gender, youth, stress, and smoking habit [2]. The proliferation of bacteria such as *Propionibacterium acnes* in clogged pores causes the problem to worsen, especially when the body releases enzymes to break down the sebum, causing inflamed pores [3]. The main goal of acne treatment is to control the existing acne lesions, prevent permanent scarring, and reduce the disorder. According to Vora et al. [4], acne may be treated by topical and systemic therapies, such as antibiotics, comedolytic agents, and anti-inflammatory drugs such as clindamycin, salicylic acid, and isotretinoin.

The use of natural products or non-drug treatments is preferable and acceptable due to organic awareness of remedial solutions. Moreover, natural products, especially skincare, are safer than synthetic products [5]. Even though various herbal products such as orange peel, neem, jojoba oil, and turmeric are used for acne treatment, the research on natural medication continues due to the tolerance resistance of *P. acnes* towards the commercially available antibiotics [6-7]. *Swietenia macrophylla* is a common plant species that grows wildly in Malaysia. It is known as the “sky fruit” or tunjuk langit, as the fruits seem to point upwards to the sky (Figure 1). *Swietenia macrophylla* is abundant in more than 40 countries, including Brazil, Bolivia, Mexico, Guatemala, Peru, and other central American countries [8]. In Malaysia, the locals usually consume the *S. macrophylla* seeds to treat high blood pressure, diabetes, increase blood circulation, and relieve body pain [9]. The *S. macrophylla* seeds are also widely used in healthcare and skincare products [10]. Due to the numerous pharmacological activities of *S. macrophylla* extract, *including* antimicrobial, anti-inflammatory, antioxidant, antidiabetic, antifungal, and antimalaria [11], the *S. macrophylla* extract is suitable to be explored and utilised in an acne treatment regime.



Figure 1. Photo image of *Swietenia macrophylla tree* and seeds (insert)

Hence, this study explored the properties of seed extract as the novel ingredient for acne treatment. The Soxhlet extraction method was performed to investigate the extraction yield in three different extraction solvent systems (methanol, ethyl acetate, and methanol: ethyl acetate mixture). The bioactivities of the extracts were analysed using a gas chromatography-mass spectrophotometer (GC-MS), and the heavy metals elements were determined using the inductive coupled plasma optical emission spectrometry (ICP-OES). A biochemical test and the disc diffusion assay method were conducted to determine the antibacterial activity against *P. acnes, Staphylococcus aureus, and Staphylococcus epidermidis*.

Materials and Methods

Material and reagents

Tetracycline (30 µg) was purchased from Sigma Chemicals (St. Louis, MO, USA), Mueller Hinton agar (MHA), Mueller Hinton broth, nutrient agar (NA) and nutrient broth used for the determination of antibacterial activity were purchased from Merck (M) Sdn. Bhd. and Thermo Fisher Scientific (M) Sdn. Bhd. All chemicals and solvents used in the experiment were analytical grades with above 98% purity. The reagents were supplied by the Chemistry Laboratory 2 and 4, UiTM Perlis Branch. The methanol, ethyl acetate, and 1:1 ratio of methanol: ethyl acetate mixtures were prepared and used to extract the *S. macrophylla* seeds sample. *P. acnes*, *S. aureus*, and *S. epidermidis* were obtained from the Biology Laboratory, UiTM Perlis Branch.

Preparation of *Swietenia macrophylla* samples extract

The *S. macrophylla* seeds were collected from the trees in Jitra, Kedah. The seeds were washed with tap water to remove dust and other inert materials. The cleaned samples were air-dried for two days. Then, the samples were ground into powder using an electrical blender. About 5.0 g of powdered seed sample was mixed with 150 mL of extraction solvent (methanol, ethyl acetate, and methanol-ethyl acetate mixture) and extracted using the Soxhlet apparatus for 6 h. The filtrate was then concentrated using a rotary evaporator to remove the solvent, and the yield percentage was expressed in w/w% and stored in a vacuum desiccator for further analysis. The yield percentage was calculated using the following equation:

$$\% \text{ yield} = [M_1 - M_o] \times 100 \quad (1)$$

where M_1 = mass of sample (g) and M_o = mass of the extract (g)

The chemical properties of SME

The chemical properties of SME were analysed using a GC-MS (Model Agilent 6890 equipped with 5MS, 30 m × 0.25 mm i.d. capillary column coated with 0.25 µm film and coupled with Agilent Chemstation software of NIST/Wiley Library). A volume of 0.1 mL samples extracts was derivatised with 100 µL N, O-Bis(trimethylsilyl)trifluoroacetamide (BSTFA) for 30 min in a sealed 2 mL vial. Then 0.1 µL of derivatised samples were analysed by the GC-MS, and the data was recorded, according to Hashim et al. [11].

The elemental analysis was determined using the ICP-OES (Model Thermo Scientific ICAP6000 Series). The multi-element of the standard solution was prepared from a 10-ppm stock solution in different concentrations at 0.01 ppm, 0.1 ppm, 1.0 ppm, and 10 ppm. Approximately 0.5 g of sample was digested with 8 mL of 65% nitric acid and 2 mL of concentrated hydrogen peroxide in microwave digestion. The sample was treated in the microwave digester for 15 min at 180 °C of 500 W. The treated sample mixture was cooled and diluted to 10 times concentration with distilled water prior to ICP-OES analysis.

The antibacterial analysis

The MHA and NA media were prepared according to the manufacturer's instructions. Approximately 38.0 and 28.0 g of the MHA and NA powders were weighed to prepare 1000 mL agar and poured into conical flasks. The powder was dissolved in distilled water and continuously stirred until homogenised. The agar solution was sterilised using an automatic autoclave at 121 °C for 15 min. The agar was cooled to 45 to 50 °C before being poured into sterile Petri dishes. These agars were stored upside down in a chiller of 4 to 8 °C before being used.

The bacteria were subcultured by the streaking method. The inoculation loop was sterilised and cooled for a few seconds before dipping into the bacterial solution and streaked in a zigzag motion on the agar. This method was repeated three times for each bacterium. The inoculating loop was sterilised each time before subculturing the bacteria. The agar plates of *S. aureus* and *S. epidermidis* were incubated at 37 °C for 18 to 24 h in an inverted position [12].

The *P. acnes* was subcultured using a different method since it is a facultative anaerobic. It grows best under limited oxygen (0-20%), and the growth rate was reduced at high oxygen concentration [14]. The cultured plate was incubated under anaerobic

conditions [13], i.e., inside a candle jar to provide a suitable condition for the *P. acnes* to grow at 37 °C for 72 h [15]. The biochemical tests involved were the catalase, the methyl red/Voges-Proskauer (MR-VP), and Gram staining to identify the desired bacterial interaction activities.

The catalase test was performed according to Habib et al. [16], whereby *S. aureus* and *S. epidermidis* were streaked onto MHA, and *P. acnes* was streaked onto NA to obtain bacterial colonies. The plates were incubated for 24 h and 72 h, respectively. Each bacterial colony was mixed with 2 to 3 drops of 3% hydrogen peroxide, where the formation of bubbles indicated positive results.

The methyl red (MR) and Voges-Proskauer (VP) test utilised the MR-VP broth. The MR-VP broth was prepared according to the manufacturer's recommendation. About 17g of broth powder was weighed to prepare 1000 mL MR-VP broth and sterilised at 121 °C for 15 min. The MR-VP broth was then incubated at 37 °C for 24 h and 48 h, respectively, for the VP and MR tests. The VP and MR test method. Approximately 1 mL of MR-VP broth was poured into test tubes. The VP test involved the addition of each bacterial colony, 0.6 mL of 5% α naphthol, and 0.2 mL of 40% of potassium hydroxide to test tubes. Meanwhile, the MR test involved the addition of five drops of methyl red to test tubes containing bacterial colonies. Then, the test tubes were shaken gently and left undisturbed for 10 to 15 min. The colour changes from yellow to red of the sample showed a positive result.

The Gram staining test method was performed according to Shinkafi and Ndanusa [17]. A loopful of bacteria was heat-fixed onto a slide. A drop of crystal violet, followed by the decolouriser, iodine, and safranin, was added onto the bacteria on the slide for 1 min and was washed off with distilled water. The slide was blotted to dry before being observed under the light microscope at 100× magnifications and recorded.

The disc diffusion assay method to test antibacterial activities was performed according to Park et al. [14]. Approximately 100 µL of each bacterial suspension was used and spread on MHA using a sterile cotton swab (for *S. aureus and S. epidermidis*) and NA (for *P. acnes*). Each disc impregnated with antibiotics was gently pressed down to ensure that the disc was completely in contact with the agar surface and did not fall when inverted. The streptomycin antibiotic disc was used as a positive control, while the extraction solvent, i.e., methanol, ethyl acetate, and 1:1 ratio of methanol: ethyl acetate mixture, was used as the negative control. The experiment was done in triplicate for each bacterium. The plates were incubated at 37 °C for 24 h (*S. aureus* and *S. epidermidis*) and 37 °C for 72 h in a candle jar to retain the anaerobic condition for *P. acnes*. The antibacterial activity was measured based on the diameter of the inhibition growth zone.

Results and Discussion

The *S. macrophylla* seed was extracted using the Soxhlet extraction method in three different solvent systems; methanol aqueous, ethyl acetate, and 1:1 methanol-ethyl acetate mixture. Table 1 shows that the 1:1 ratio of methanol-ethyl acetate solvent mixture produces the highest percentage of crude oil extract (72.68%), followed by ethyl acetate (67.55%) and aqueous methanol (37.65%). All solvents used can extract the crude oil in 6 h extraction time. Do et al. mentioned that methanol solvent is generally more efficient in extracting lower molecular weight polyphenols [18]. In this experiment, the combination of methanol-ethyl acetate organic solvent facilitates a suitable extraction of all soluble compounds in both solvents. According to Nawaz et al., using a combination of polar and nonpolar solvents can increase the excellent quality of extraction yield from the bean and other legume seeds [19]. Furthermore, Che Sulaiman et al. reported that the extraction yield of organic samples is also dependent on the extraction times, extraction temperatures, and solvent ratios [20].

Table 1. Percentage Yield of Swietenia macrophylla Seed's Extract in a different solvent

Solvent Types	Mass of Dried Powder (g)	Mass of Oil Crude Extract (g)	% Yield
Methanol	5.07 ± 0.02	1.90 ± 0.45	37.65
Ethyl Acetate	5.04 ± 0.02	3.40 ± 0.18	67.55
Methanol: Ethyl Acetate	5.04 ± 0.03	3.67 ± 0.49	72.68

The phytochemical compounds in the *S. macrophylla* seed extract were analysed using GC-MS analysis. About 13 compounds were successfully identified in the methanol extract, 20 in the ethyl acetate extract, and 12 in the 1:1 methanol-ethyl acetate mixture as terpenoids, flavonoids, and limonoids. The compounds obtained strongly depended on the nature of extracting solvent due to different antioxidant compounds that vary their chemical characteristics and polarities. The most extracted compounds were reported in ethyl acetate, methanol, and 1:1 methanol-ethyl mixture due to the semipolar-polar compounds [21]. The number of extracted compounds in the 1:1 methanol-ethyl acetate extract is less than ethyl acetate alone because the elution strength of ethyl acetate decreased due to the polarisation effect of methanol. The extraction process yielded seven compounds in methanol extract, five compounds in ethyl acetate extract, and two compounds in the 1:1 methanol-ethyl acetate mixture, with more than 80% quality compared to the GC-MS reference library software (Table 2). In Table 2 show that silane methoxytrimethyl-, disiloxane hexamethyl, and 2,2,2-trifluoro-N-(trimethylsilyl)- are the major bioactive compound present in *S. macrophylla* seed extract, with the under peak percentage area of more than 23.57%. A previous study by Azhari et al. [22] stated that several compounds of limonoids such as phenol, 2-methoxy-4-(1-propenyl)-, and eugenol were also found in *S. macrophylla seed* extract using the maceration method. In this work, compounds such as phenol, 2-methoxy-4-(1-propenyl)-, (E)-(isoeugenol), silane, [2-methoxy-4-(1-propenyl) phenoxy] trimethyl- (isoeugenol), and eugenol are present in the sample. As reported in previous works, these compounds possess effective antifungal and antibacterial activities [23-25]. According to Sharma et al. [26], phytocompounds present in chloroform and methanol seed extracts are responsible for the varied antioxidant and antimicrobial activities.

The concentration of arsenic (As), lead (Pb), cadmium (Cd), nickel (Ni), mercury (Hg), and copper (Cu) in *S. macrophylla* seed powder was analysed using ICP-OES. Table 3 shows the result of heavy metal concentration in the crude oil extract sample. Only low concentrations of mercury are detected in the sample, i.e., 0.080 ppm. The result revealed that the *S. macrophylla* seed powder is low in heavy metal content. Hence, it is considered a safe ingredient in medication or cosmetic products. According to the U.S. Food and Drug Administration (USFDA) limits regulation, the accepted concentration of mercury must be less than 1 ppm (1 mg/kg), i.e., safe to be used as new constituents in products [31].

The images of catalase test (CT), Voges Proskauer (VP), and Gram staining test (GST) of Gram-positive bacteria (*S. aureus, S. epidermidis*, and *P. acnes* [facultative anaerobic bacteria]), are shown in Figures 2 - 4. Figure 2 shows a positive CT result, whereby bubbles are observed at 10 min observation. The finding is similar to the study by Mustafa [30], Kallstrom et al. [31], and Cauich-Sanchez et al. [32]. The catalase acts as a catalyst in breaking down the hydrogen peroxide into water and oxygen to form an oxygen bubble produced by the bacteria. The VP test was conducted to measure the production of acetyl methyl carbinol, as shown in Figure 3. *S. aureus* and *P. acnes* show positive results, where the color of the solution change to red. In contrast, the colour of the *S. epidermidis* solution remains unchanged. This result

is similar to Shinkafi and Ndanusa [17], whereby the colour change from light yellow to slightly red in the *S. aureus* and *P. acnes* tests indicated positive results. Whereas the colour of the solution in the *S. epidermidis* tube did not change, indicating a negative result. Further validation analysis for *S. aureus*, *S. epidermidis*, and *P. acnes* were carried out using the methyl red (MR) test (Figure 4). The unchanged colour of the MR solution of *S. aureus* and *P. acnes* indicates positive results. On the contrary, the colour of the *S. epidermidis* solution changed from light yellow to red. The researcher also stated that *S. aureus* and *P. acnes* showed negative results when the colour of the MR solution remained unchanged. This is contradictory to *S. epidermidis*, which showed positive results when the light-yellow solution slightly changed to red. The purpose of the MR test is to determine the ability of the bacteria to oxidise glucose and produce a high concentration of acidic products.

Table 2. Phytocompounds in SME in different extraction solvents by using GC-MS

Retention Time (min)	**Area (%)**	**Name of Compound**	**Bioactivity**	**Solvent**
1.300	45.76	Silane, methoxytrimethyl-	NR	Methanol
1.545	23.57	Disiloxane, hexamethyl-	NR	
4.409	0.34	Benzene-1-ethyl-3-methyl-	NR	
4.540	0.16	Benzene-1,3,5-trimethyl-	NR	
4.723	0.12	Benzene, 1-ethyl-2-methyl-	NR	
4.997	0.57	Benzene, 1,2,3-trimethyl-	NR	
5.535	0.18	Benzene, 1,2,3-trimethyl-	NR	
1.923	25.84	Disiloxane, hexamethyl-	NR	Ethyl acetate
2.414	34.13	Acetamide, 2,2,2-trifluoro-N-(trimethylsilyl)-	NR	
13.205	0.11	Phenol, 2-methoxy-4-(1-propenyl)-, (E)-	Antifungal [21],	
13.239	0.15	Eugenol	Antibacterial, Anti-inflammatory [22], Antioxidant [23]	
14.988	0.12	Silane, [2-methoxy-4-(1-propenyl) phenoxy] trimethyl-	Antifungal [20]	
1.631	2.77	Silane, methoxytrimethyl-	NR	Methanol: ethyl acetate (1:1)
5.660	0.15	Benzene, 1,2,4-trimethyl-	NR	

NR – Activity of compound is not reported

Table 3. Heavy metal concentration in *Swietenia macrophylla* seed's powdered sample using ICP-OES

Heavy Metal	Concentration (ppm)
As	0
Pb	0
Cd	0
Ni	0
Hg	0.080
Cu	0

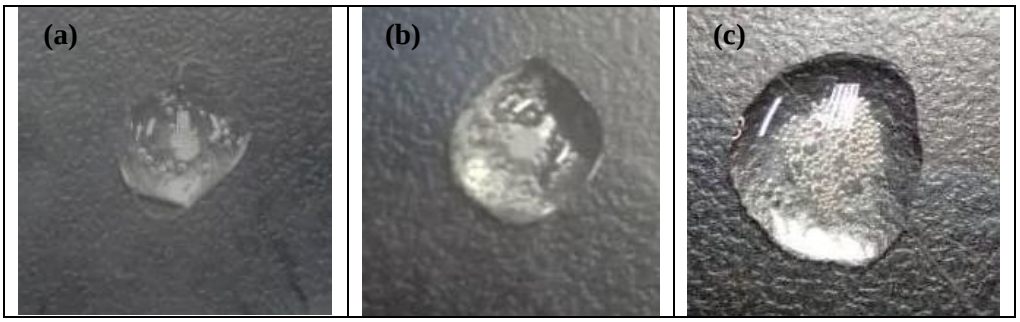


Figure 2. The photo images of catalase test of (a) *S. aureus*, (b) *S. epidermidis*, and (c) *P. acnes*

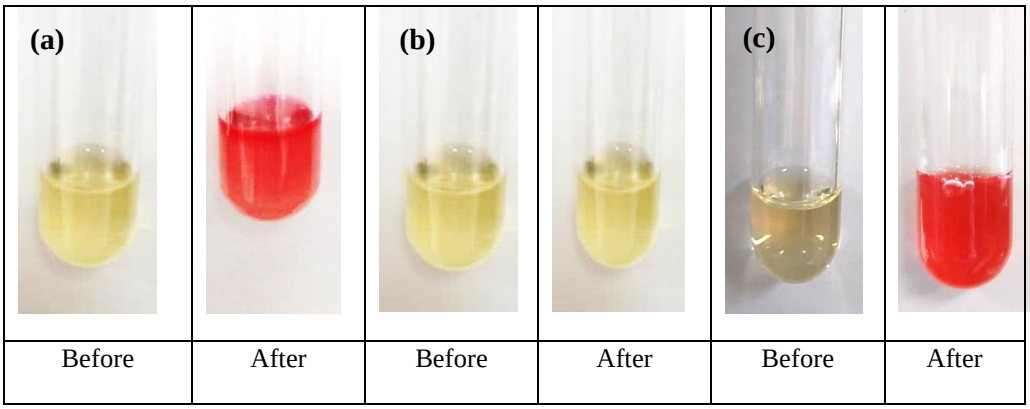


Figure 3. The photo images of Voges Proskauer (VP) test of (a) *S. aureus* (b) *S. epidermidis* (c) *P. acnes*

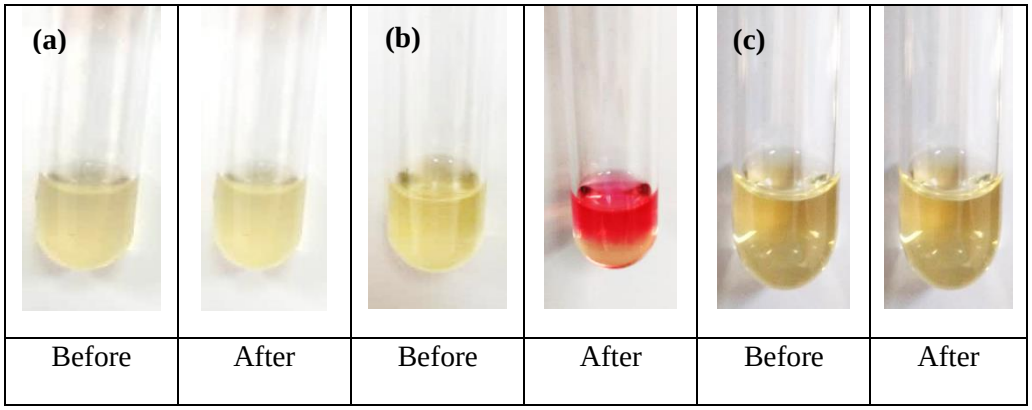


Figure 4. Photo images of methyl red (MR) test of (a) *S. aureus*, (b) *S. epidermidis*, and (c) *P. acnes*

The Gram-staining analysis was performed to determine the Gram-positive and Gram-negative bacteria based on the bacterial cell wall colour using an Olympus CKX53 inverted microscope (Figure 5). The Gram-positive bacteria, i.e., *S. aureus*, *S. epidermidis*, and *P. acnes*, were observed in this analysis. The results showed that the bacteria appear violet with aggregated grape-like clusters under 100× magnification [16]. In contrast, the *P. acnes* is visualised as violet with a rod-like bacillus structure [33], as shown in Figure 5(c). According to Panawala [34], the bacteria appear violet under the microscope due to the thick peptidoglycan cell wall and teichoic acid composition.

The inhibition zones of the three bacteria species were determined using the disc diffusion assay method, as shown in Figure 6 and Table 4. The disc assay method is a rapid determination of antibacterial activity by measuring the diameter of the inhibition zone that resulted from the diffusion of the phytochemical compound into the medium surrounding the disc [35]. Table 4 shows the inhibition zone category and bacterial inhibition zone in 30-disc tetracycline concentration (µg/disc).

The inhibition of bacteria towards the sample extract was expressed as susceptible, intermediate, and resistant according to international standards (ISO 20776-1). Susceptible is when the bacteria are inhibited *in vitro* by a drug concentration with high therapeutic properties. Meanwhile, intermediate is when the bacteria are inhibited in vitro by a drug with uncertain therapeutic effects. For resistance, the bacteria are inhibited in vitro by a drug with a high chance of therapeutic failure [36].

Figure 6 shows *P. acnes* is minimally inhibited in the methanol and 1:1methanol-ethyl acetate extracts. In comparison, the inhibition zone of the *S. aureus* is more prominent than in tetracycline (antibiotic control). Table 4 shows the results of the inhibition zone of the bacteria tested. *S. aureus* is susceptible in methanol and 1:1 methanol-ethyl acetate extracts, as the zone of inhibition more than 19.00 ± 0.00 mm, while *S. epidermidis* is resistant towards ethyl acetate and 1:1 methanol-ethyl acetate extracts at 13.00 ± 1.00 mm and 13.00 ± 2.31, respectively.

Meanwhile, *P. acnes* exhibits resistant, intermediate, and susceptible properties in 1:1 methanol-ethyl acetate, methanol, and ethyl acetate extract respectively. Aditi and Hossain [37] reported that *S. aureus* acquired resistance easily, a good bio-indicator model for surveillance studies of antimicrobial resistance [38]. *S. aureus* and *P. acnes* in ethyl acetate extraction solvent showed a more significant inhibition zone but slightly lower inhibition of *S. epidermidis*. In a nutshell, for antibacterial activity, all extracts showed a high therapeutic capability towards *S. aureus* and *P. acnes* but are less effective against *S. epidermidis*.

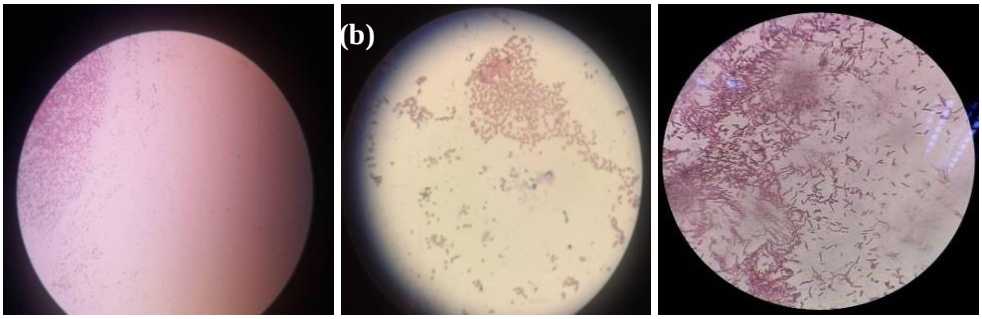


Figure 5. Photo images of Gram Staining Test in 100X Magnifications of (a) *S. aureus* (b) *S. epidermidis*, and (c) *P. acnes*

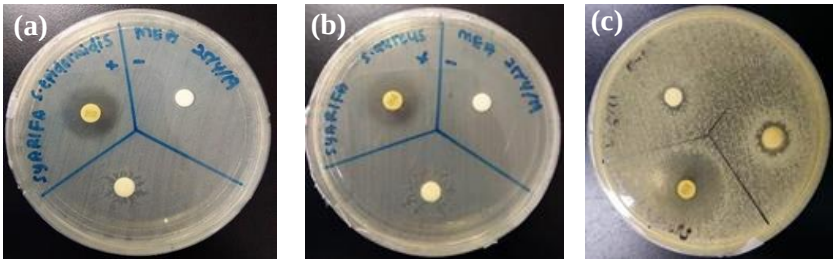


Figure 6. Inhibition zone photo images of the test discs (a) *S. epidermidis*, (b) *S. aureus*, and (c) *P. acnes* of SME in 1:1 methanol-ethyl acetate mixture

Table 4. Inhibition zone category in tetracycline and inhibition zone on bacterial growth activities in different extraction solvent

Antibiotic	**Inhibition zone (Category)**		
Tetracycline (control) in 30-disc (µg/disc)	*S. aureus* (± n) 18.33 ± 0.58	*S. epidermidis* (± n) 18.67 ± 0.58	*P. acnes* (± n) 21.33 ± 1.53
Sample in the different extraction solvent	**Inhibition zone (Bacterial Growth)**		
Methanol	20.67 ± 6.03	18.67 ± 14.15	16.33 ± 5.69
Ethyl acetate	16.67 ± 6.66	13.00 ± 1.00	19.00 ± 4.36
Methanol: Ethyl acetate (1:1)	21.67 ± 11.72	13.00 ± 2.31	11.00 ± 1.73

*R- resistant (≤14 mm), I- intermediate (15-18 mm), S-susceptible (≥19 mm) [9]
*The values were presented in mean ± SD, where n=3

Conclusion

The properties of *S. macrophylla* seeds in three different extraction solvents were successfully determined. Three new compounds, phenol, 2-methoxy-4-(1-propenyl)-, (E)-Eugenol; and silane, [2-methoxy-4-(1-propenyl) phenoxy] trimethyl, were successfully extracted from *S. macrophylla* seeds using ethyl acetate solvent. The highest extraction yield is obtained in the 1:1 methanol-ethyl acetate mixture (72.68%), followed by ethyl acetate (67.55%) and methanol (37.65%). From the disc diffusion assay, *S. epidermidis and P. aureus* are susceptible towards

methanol and 1:1 methanol-ethyl acetate extracts. In contrast, *P. acnes* is susceptible towards ethyl acetate extract. The result showed that *S. macrophylla* seeds extract is an effective ingredient for treating acne due to positive inhibition towards three acne-causing bacteria and is considerably low in heavy metal contents.

Acknowledgement

The authors are sincerely grateful to UiTM Perlis Branch, Arau Campus, to provide the research facilities. High appreciation also goes to the Frontier Applied Science and Technology research group (FAST) for completing this work.

References

1. Zaghloul, S. S., Cunliffe, W. J. and Goodfield, M. J. D. (2005). Objective assessment of compliance with treatments in acne. *British Journal of Dermatology*, 152(5): 1015-1021.
2. Fox, L., Csongradi, C., Aucamp, M., Du Plessis, J. and Gerber, M. (2016). Treatment modalities for acne. *Molecules*, 21(8): 1-20.
3. Savage, A. E. O. (1985). *United States Patent*, 19(54): pp. 19.
4. Vora, J., Srivastava, A. and Modi, H. (2018). Antibacterial and antioxidant strategies for acne treatment through plant extracts. *Informatics in Medicine Unlocked*, 13: 128-132.
5. Afsar, Z. and Khanama, S. (2016). Formulation and evaluation of polyherbal soap and sanitiser. *International Research Journal of Pharmacy*, 7(8): 54-46.
6. Platsidaki E. and Dessinioti C. (2018). Recent advances in understanding *Propionibacterium acnes* (*Cutibacterium acnes*) in acne. F1000Research, 7(F1000 Faculty Rev:1953).
7. Tan, A. U., Schlosser B. J. and Paller, A.S. (2017). A review of diagnosis and treatment of acne in adult female patients. *International Journal of Women's Dermatology*, 4(2): 56-71.
8. Eid, A. M. M., Elmarzugi, N. A. and El-Enshasy, H. A. (2013). A review on the phytopharmacological effect of *Swietenia macrophyll*a. *International Journal of Pharmacy and Pharmaceutical Sciences*, 5(3): 47-53.
9. Suliman, M. B. (2018). Preliminary phytochemical screening and thin layer chromatography analysis of *Swietenia Macrophylla King* methanol extracts. *Chemistry of Advanced Materials*, 3(1): 1-7.
10. Durai, M., Balamuniappan, G. and Geetha, S. (2016). Phytochemical screening and antimicrobial activity of leaf, seed and central-fruit-axis crude extract of *Swietenia macrophylla King*. *Journal of Pharmacognosy and Phytochemistry*, 181(53): 181-186.
11. Hashim, M. A., Yam, M. F., Hor, S. Y., Lim, C. P., Asmawi, M. Z. and Sadikun, A. (2013). Anti-hyperglycaemic activity of *Swietenia macrophylla king* (*meliaceae)* seed extracts in normoglycemic rats undergoing glucose tolerance tests. *Chinese Medicine* (United Kingdom), 8(1): 1-8.
12. Wu, Q., Li, Y., Hu, H., Wang, M., Wu, Z. and Xu, W. (2012). Rapid identification of *Staphylococcus aureus*: FISH versus PCR methods. *Laboratory Medicine*, 43(6): 276-280.
13. Naghdi, N. and Ghane, M. (2017). A comparison of culture and PCR methods for identifying *Propionibacterium* acnes in lesions isolated from patients with acne. *Turkish Journal of Medical Sciences*, 47(3): 967-972.
14. Park, J., Lee, J., Jung, E., Park, Y., Kim, K., Park, B., Jung, K., Park, E., Kim, J. and Park, D. (2004). *In vitro* antibacterial and anti-inflammatory effects of honokiol and magnolol against *Propionibacterium* sp. *European Journal of Pharmacology*, 496(1): 189-195.
15. Nirmal, N. P. and Panichayupakaranant, P. (2014). Anti-propionibacterium acnes assay-guided purification of brazilin and preparation of brazilin rich extract from *Caesalpinia sappan* heartwood. *Pharmaceutical Biology*, 52(9): 1204-1207.
16. Habib, F., Rind, R., Durani, N., Latif Bhutto, A., Buriro, R. S., Tunio, A., Aijaz, N., Lakho, S., Ghulam, B. and Shoaib, M. (2015). Morphological and cultural characterization of *Staphylococcus aureus* isolated from different animal species. *Journal of Applied, Environmental and Biological Sciences*, 5(2): 15-26.

17. Shinkafi, S., and Ndanusa, H. (2013). Antibacterial activity of citrus lemon on acne *vulgaris* (pimples). *International Journal of Science Inventions Today*, 2(5): 397-409.
18. Do, Q. D., Angkawijaya, A. E., Tran-Nguyen, P. L., Huynh, L. H., Soetaredjo, F. E., Ismadji, S. and Ju, Y. H. (2014). Effect of extraction solvent on total phenol content, total flavonoid content, and antioxidant activity of *Limnophila aromatica*. *Journal of Food and Drug Analysis*, 22(3): 296-302.
19. Nawaz, H., Shad M. A., Rehman, A. N., Andaleeb, H. and Ullah, N. (2020). Effect of solvent polarity on extraction yield and antioxidant properties of phytochemicals from bean (*Phaseolus vulgaris*) seeds. *Brazilian Journal of Pharmaceutical Sciences*, 56: 17129.
20. Che Sulaiman I. S. and Basri, M. (2017). Effects of temperature, time, and solvent ratio on the extraction of phenolic compounds and the anti-radical activity of *Clinacanthus nutans* Lindau leaves by response surface methodology. *Chemistry Central Journal*, 11(1): 54.
21. Akbar A., Soekamto N. H., Firdaus and Bahrun (2021) Antioxidant of n-hexane, ethyl acetate and methanol extracts of *Padina* sp. with DPPH method. *Earth and Environmental Science* 800: 012019.
22. Azhari, Nour, H., Mohammed, Sulieman, B., Mashitah, Yousf, M. and Adam, M. M. (2016). Bioassay-guided isolation and identification of antifungal compounds from seeds of *Swietenia macrophylla* King. *Australian Journal of Basic and Applied Sciences*, 10(17): 55-62.
23. Aquirre-Becerra H., Pineda-Noeto S. A., Garcia-trejo J.F., Guevara-Gonzalez R. G., Feregrino-Perez A. A., Alerez-Mayorga B. L. and Rivera-Pastrana D. M. (2020). Jacaranda flower (*Jacarand mimosifolia*) as alternaive for antioxidant and antimicrobial use. *Heliyon*, 6(12): e05802.
24. Eid A., Elmarzugi N. and El-Enshasy H. (2013). A review on the phytopharmacological effect of *Swietenia macrophylla. International Journal of Pharmacy and Pharmaceutical Sciences*, 5: 47-53.
25. Moghadamtousi S. Z., Goh B. H., Chan C. K., Shabab T. and Kadir, H. A. (2013). Biological activities and phytochemicals of *Swietenia macrophylla* King. *Molecules*, 18: 10465-10483.
26. Sharma S., Kumari A., Dhatwalia J., Guleria I., Lal S., Upadhyay N., Kumar V. and Kumar A., (2021), Effect of solvents extraction on phytochemical profile and biological activities of two *Ocimum* species: A comparative study. *Journal of Applied Research on Medicinal and Aromatic Plants*, 25(2021): 100348.
27. Koeduka, T. (2014). The phenylpropene synthase pathway and its applications in the engineering of volatile phenylpropanoids in plants. *Plant Biotechnology*, 2014: 14-0801.
28. Nejad, S. M., Özgüneş, H. and Başaran, N. (2017). Pharmacological and toxicological properties of eugenol. *Turkish Journal of Pharmaceutical Sciences*, 14(2): 201.
29. Bendre, R. S., Rajput, J. D., Bagul, S. D. and Karandikar, P. S. (2016). Outlooks on medicinal properties of eugenol and its synthetic derivatives. *Natural Product Chemistry Research*, 4(3): 1-6.
30. Mustafa, H. S. I. (2014). *Staphylococcus aureus* can produce catalase enzyme when adding to human WBCs as a source of productions in human plasma or serum in the laboratory. *Open Journal of Medical Microbiology*, 04: 249251.
31. Kallstrom, G., Chang, T., Albertson, M., Morilla, D., Fisher, M. A. and Eberly, B. (2011). Recovery of a catalase-negative *Staphylococcus epidermidis* strain in blood and urine cultures from a patient with pyelonephritis. *Journal of Clinical Microbiology*, 49(11): 4018-4019.
32. Cauich-Sanchez, P., Alatriste-Mondragon, F., Garcia-Cano, E. and Aquino-Santiago, C. (2001). Identification of anaerobic nonsporeforming gram-positive bacilli by biochemical tests and gas-liquid chromatography. *Revista Latinoamericana de Microbiologia*, 43(1): 27-35.
33. Rolf, L. (2011). Propionibacterium acnes and its phages department of clinical sciences. Department of Clinical Sciences, Lund University: pp. 1-85.

34. Kuntom, A. and Kifli, (1998). Properties of soaps derived from distilled palm stearin and palm kernel fatty acids. *Journal of Surfactants and Detergents*, 1(3): 329-334.
35. Panawala, L. (2017). Difference between gram positive and gram-negative bacteria. *Epedıaa*, 3: 1-13.
36. Tenover F. C. (2019). Antimicrobial susceptibility testing. *Encyclopedia of Microbiology (Fourth Edition)*: pp. 166-175.
37. Rodloff, A., Bauer, T., Ewig, S., Kujath, P. and Müller, E. (2008). Susceptible, intermediate, and resistant – the intensity of antibiotic action. *Deutsches Aerzteblatt Online*, 105(39): 657-662.
38. Aditi, F. Y., Rahman, S. S. and Hossain, M. M. (2017). A study on the microbiological status of mineral drinking water. *The Open Microbiology Journal*, 11: 31.
39. Hepp, N. M., Mindak, W. R., Gasper, J. W., Thompson, C. B. and Barrows, J. N. (2014). Survey of cosmetics for arsenic, cadmium, chromium, cobalt, lead, mercury, and nickel content. *Journal Cosmetic Sciences*, 65(3): 125.

Malaysian Journal of Analytical Sciences (MJAS)
Published by Malaysian Analytical Sciences Society

ESTIMATION OF METHANE PRODUCTION VIA ANAEROBIC CO-DIGESTION OF FOOD WASTE AND SLUDGE BY BIOCHEMICAL METHANE TEST

(Anggaran Pengeluaran Metana Melalui Pencernaan Bersama Anaerobik Sisa Makanan dan Enap Cemar oleh Ujian Potensi Metana Biokimia)

Nur Anisah Abdul Latif[1], Zuhaida Mohd Zaki[2], Khor Bee Chin[3], Faeiza Buyong[1]*

[1]*Faculty of Applied Sciences,*
Universiti Teknologi MARA, 40450 Shah Alam, Selangor, Malaysia
[2]*Faculty of Civil Engineering,*
Universiti Teknologi MARA, 13500 Permatang Pauh, Pulau Pinang, Malaysia
[3]*Indah Water Konsortium Sdn. Bhd., Damansara Height, 50490 Kuala Lumpur, Malaysia*

**Corresponding author: faeiza@uitm.edu.my*

Received: 28 December 2021; Accepted: 27 February 2022; Published: 28 April 2022

Abstract

Biochemical methane potential (BMP) tests are extensively used in many studies related to anaerobic co-digestion (AcoD) to evaluate biogas production and determine the potential methane yield between various substrates at specific retention times and parameters. AcoD is a process of mixing two or more substrates in a digester that could help to improve the methane yield as compared to mono-digestion with the same substrates. This study evaluates the methane production efficiency via AcoD of food waste and thickened sludge by using the BMP tests. The substrates used for this study were wastes from non-dairy creamer, coffee, and mixed food waste with sludge. Additionally, thickened sludge as an inoculum was used for the BMP test. The samples characterisation was analysed according to standard and HACH methods. The thickened sludge was set up at a ratio of 1:1 as a control, while the food wastes sample with sludge was set up at a ratio of 1:2. The initial pH was adjusted in a range of 6.5-7. The BMP test setup was done using a 125mL serum bottle in triplicates for 31 days in an incubator at 37°C. The results showed that the highest methane production of the BMP was from thickened sludge itself which is 18.275 ± 3.3 mL CH_4/gVS, followed by non-dairy creamer waste with thickened sludge, mixed food waste with sludge and coffee waste with thickened sludge which are 17.865 ± 6.2 mL CH_4/gVS, 17.825 ± 0.05 mL CH_4/gVS and 14.797 ± 0.01 mL CH_4/gVS respectively. In conclusion, the pre-treatments process is highly recommended in order to improve biogas production.

Keywords: anaerobic co-digestion, biochemical methane potential, experimental methods, food wastes, methane production

Abstrak

Ujian potensi metana biokimia (BMP) digunakan secara meluas dalam banyak kajian berkaitan penghadaman bersama anaerobik (AcoD) untuk menilai pengeluaran biogas dan menentukan potensi hasil metana antara pelbagai substrat pada masa dan parameter pengekalan tertentu. AcoD merupakan suatu proses mencampurkan dua atau lebih substrat dalam pencerna yang boleh meningkatkan hasil metana berbanding mono-pencernaan dengan substrat yang sama. Kajian ini bertujuan menilai kecekapan pengeluaran metana oleh AcoD bagi sisa makanan dan enap cemar pekat menggunakan ujian BMP. Substrat yang digunakan

untuk kajian ini ialah sisa daripada krimer bukan tenusu, kopi, dan sisa makanan yang bercampur dengan enap cemar. Enap cemar pekat digunakan untuk ujian BMP sebagai inokulum. Pencirian sampel dianalisis mengikut kaedah standard dan HACH. Enap cemar yang menebal telah disediakan dalam nisbah 1:1 sebagai kawalan, manakala sampel sisa makanan dengan enap cemar disediakan dalam nisbah 1:2. Nilai pH awal diselaraskan dalam julat 6.5–7. Persediaan ujian BMP dilakukan menggunakan botol serum 125mL sebanyak tiga kali ganda selama 31 hari dalam inkubator pada suhu 37^{o}C. Hasil kajian menunjukkan bahawa pengeluaran metana BMP tertinggi adalah daripada enap cemar pekat itu sendiri, iaitu 18.275 ± 3.3 mL CH_4/gVS, diikuti sisa krimer bukan tenusu dengan enap cemar pekat, sisa makanan bercampur dengan enap cemar, dan sisa kopi dengan enap cemar pekat, masing-masing 17.865 ± 6.2 mL CH_4/gVS, 17.825 ± 0.05 mL CH_4/gVS, dan 14.797 ± 0.01 mL CH_4/gVS. Kesimpulannya, proses pra-rawatan amat disyorkan untuk meningkatkan pengeluaran biogas.

Kata kunci: pencernaan bersama anaerob, potensi metana biokimia, kaedah eksperimen, sisa makanan, penghasilan metana

Introduction

The amount of sewage sludge is continuously increasing as a surplus of the wastewater treatment process due to increased population. The higher percentage of households connected to the main wastewater treatment plants (WWTPs) also contributes to the higher production of sewage sludge [1, 2]. Nevertheless, improper handling and untreated sewage sludge may lead to environmental impacts and public health problems. This is because sewage sludge is characterised by its high concentrations of solids and organic matter, with the presence of nutrients, organic and inorganic pollutants and pathogens that create odour problems. Nowadays, there are several alternative techniques which are applied for sewage sludge disposal, such as incineration, landfills, compost, recycling, and anaerobic digestion (AD). AD is a proven technology and one of the most feasible techniques applied for the treatment of sewage sludge in many countries due to its lower operational cost, reduced chemical oxygen demand (COD), decreased pollutants discharged into the environment, and production of energy-rich biogas [3, 4, 5].

Besides that, anaerobic digestion (AD) is also known as the most efficient process for the treatment of municipal solid waste and wastewater sludge [6, 7]. In general, anaerobic digestion (AD) is the process in which organic waste such as bio-waste, animal manure, sludge, crops, and other biomasses are biologically degraded in the absence of oxygen and converted into a form of biogas and other organic compounds as end products [6, 7]. The food waste also can be characterised by its high percentage of biodegradability, moisture content around (> 70%), volatile solids (> 95%), with numerous amounts of lipids [8] that will enhance the AD performance. Other than that, the methane gas obtained from the AD process can be used to generate electricity and for heating purposes. Sewage sludge is characterised by its high concentration of solids and organic matter, with the presence of nutrients, organic and inorganic pollutants, and pathogens. According to Appels et al., [6], fuels can be produced by using sewage sludge. It can also be used as an inoculum in the anaerobic digestion process by considering its characteristics. Thus, anaerobic co-digestion (AcoD) is the process of mixing two or more substrates in a digester that could improve methane production from 25% to 400% as compared to the mono-digestion [9-13] of the same substrates [14,15].

Non-dairy creamer (NDC) and coffee are from the food and beverages industry. However, the NDC contains no lactose. It is a substitute product for milk or cream in the form of a liquid or powder which produces high water dissolved fat emulsion that is made up from vegetable oil (30% hydrogenated coconut or palm oil) for the purpose of reducing the amount of milk or replacing the milk powder in oatmeal, baked goods, coffee and others [16]. Huang et al.,[17] stated that NDC is made up of 60-65% glucose or corn syrup, 2-5% sodium caseinate, stabilisers, and emulsifiers [18], and it contains about 1.2% of minerals, 8.5% of protein, 32.5% of fat, and the highest percentage is carbohydrate at 58%. The liquid waste and sewage sludge are the by-products of the NDC industry. The improper processing of the NDC wastewater will affect

the environment. The sewage sludge and wastewater from NDC contain high organic matter such as proteins, lipids, and carbohydrates [19-21] While the coffee processing effluent is highly acidic, has high chemical oxygen demand (COD), and also contains a high amount of organic matter and suspended solids [22-23], the foul odour and eutrophication occurs due to the dark brown colour of the effluent which was produced from the coffee processing plants due to the decomposition of lignin (humic acid, tannin) with different macromolecules such as caffeine and polyphenols (melanoidins). Cardenas et al., [24] cited that melanoidins consist of ligands (polysaccharides, tannins), which hardly degrade biologically [25]. Thus, AD is considered as an alternative method to treat both NDC and coffee waste.

In addition to that, AD can be applied experimentally via the biochemical methane potential (BMP) test by determining the biodegradability of waste biomass and wastewater and also the methane potentiality [26]. The BMP experimental test is usually suitable for small-scale (batch) analysis (lab-work) which is costly, and time-consuming, with analysis within 20 to >100 days [27] compared to the BMP theoretical test. Several parameters influence the determination of BMP experimental tests such as the inoculum-substrate ratio, pH, temperature, retention time, chemical oxygen demand (COD), total solids (TS), moisture content, volatile solids (VS), and others [28]. The objective of this study is to evaluate the methane production via anaerobic co-digestion of food waste and sludge by using the BMP experimental method.

Material and Methods

Sample collection

Substrate and inoculum

Food waste samples as substrates (coffee, non-dairy creamer waste and mixed food waste) were obtained from the food manufacturing industry and the IWK sludge (thickened) was used as inoculum. All food wastes and thickened sludge were supplied by Indah Water Konsortium Sdn. Bhd (IWK), whose WWTP plant is located at IWK Sewage Treatment Plant, Kuala Lumpur. Then, the collected samples were degassed or pre-incubated to deplete the residual biodegradable organic material present in them [29]. Table 1 presents the setup of substrates used for this study.

Table 1. Substrates for BMP, and S/I ratio

Inoculum & Substrates	Label	Substrate/inoculum Ratio, S/I
Thickened sludge (inoculum)	IWK Sludge	1:1
Non-dairy creamer waste + inoculum	Co-digestion 1	1:2
Coffee waste + inoculum	Co-digestion 2	1:2
Mixed food wastes + inoculum	Co-digestion 3	1:2

Analytical method

Sample characterization

The characterisations of the substrate (food waste) and inoculum (thickened sludge) conducted for this study are the moisture content, Volatile Matter, pH, temperature, Total Solid (TS) and Volatile Solid (VS), chemical oxygen demand (COD), alkalinity and volatile fatty acid (VFA). Thus, all these parameters were measured according to the Standard Methods [30] except for the alkalinity and VFA, which used the HACH method. About 200mL of the sample was placed in a 500 mL beaker. The pH meter was calibrated first at pH 4, 7 and 10, and then the pH of the samples was measured by using the pH meter (Orion Star A111 pH meter). In order to do that, moisture and TS were determined by drying the samples at 105 $^{\circ}$C overnight and for 4 hours at a constant weight [30]. While the previous sample from the moisture content and TS was heated by furnace at 550 $^{\circ}$C for 2 hours and 15 minutes to measure the volatile matter and VS. Chemical oxygen demand (COD) was performed by using and preparing the high

range COD standard reagents (200-15000 mg/L), blank, and samples. Each sample was diluted by 1:10 time's dilution, and about 2.0 mL of the sample was filled into the high range COD reagent vial. Thus, the samples were placed into the COD reactor within 2 hours at 150 °C. Then, the readings of the COD were analysed by using the spectrophotometer.

However, for alkalinity, the digital titration cartridge, sulfuric acid 1.600±0.008 N was used (based on the HACH method procedure). About 10mL of the sample volume was titrated with a digital titration cartridge, and the titration was stopped at a pH 4.5. Then, the counter (at the digital titrator) showed the digits for the first endpoint, and the digits were multiplied with the digit multiplier (x10) for samples in the range of 1000-4000 (mg/L as $CaCO_3$). Thus, the exact volume (mg $CaCO_3$/L) total alkalinity was recorded. Lastly, for the VFA test method, about 0.5 mL of deionized water and samples (the filtrate or supernatant) were placed separately on a sample cell. An amount 1.5 mL of ethylene glycol was added to each sample cell, and then it was swirled, followed by adding 0.2 mL of 19.2N sulfuric acid. Then, the sample cell was boiled for 3 minutes. The sample cell was immersed into cool water at 25 °C (until the cells feel cold). 0.5 mL of Hydroxylamine hydrochloride solution, 2.0 mL of 4.5N sodium hydroxide standard solution, 10 mL of ferric chloride sulfuric acid solution, and 10 mL of deionized water was added to each sample cell and the cell was inverted to mix. 10 mL of the blank solution and prepared sample were transferred to a clean sample cell. The sample cell was inserted into the cell holder and the results were shown in mg/L HOAC.

Sample preparation

BMP experimental test

The BMP experimental test was performed in 125 mL serum bottles for the AD process [31] with a working volume of 70% and 30% remaining for the gas production as shown in Figure 1 [32]. Food waste samples such as coffee and non-dairy creamer were used as a substrate, while the IWK sludge (thickened sludge) was an inoculum. The initial pH was adjusted at a range of 6.5-7. After mixing and adding the samples into the serum bottle, the nitrogen gas was purged immediately in the headspace of the bottles for 3 minutes to remove the presence of air, which creates an anaerobic condition in the system [33], prior to sealing the serum bottles. All serum bottles were placed into an incubator at 37 °C, which is the optimum temperature for microbial activities [34] within the retention period of 31 days [35]. Every batch of AD was set up according to a 1:1 ratio for control and a 1:2 ratio of food waste to sludge. The serum bottles were placed into a rotary shaker once a day for 15 minutes to ensure the mixtures were well shaken. All experiments were performed in triplicate. An inoculum filled with water, with no substrate added, was used as a blank assay for the background of the methane yield. The gas sample produced was abstracted from the serum bottle and was then analysed by Gas Chromatography (GC) Agilent 7890A (30m x 32 µm x 0.25 µm).

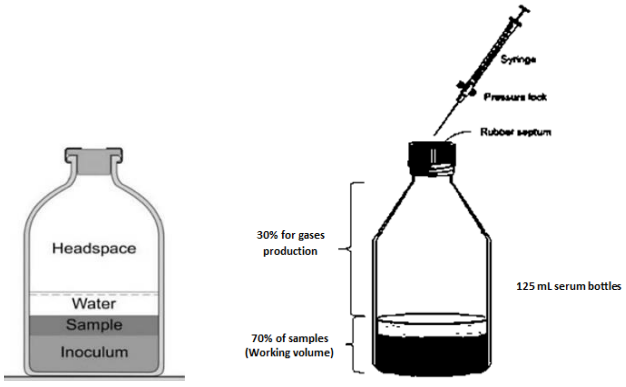


Figure 1. 125 mL of serum bottles set up [31]

Results and Discussion

Sample characterization

The results of the characterization of all samples are summarized in Table 2. The pH for non-dairy creamer waste (NDC), coffee waste, thickened sludge, and mixed food waste with sludge was in the range of slightly neutral to alkaline. The highest pH observed was in coffee waste. During the methanogenesis stages of AD, the methanogenic bacteria are highly sensitive to pH, so the optimum pH for methanogenic bacteria activities is within a range of 6.8-7.2 [36-37], as supported by Lusk [38]. The digester should be maintained at a pH near 7.0 to enhance biogas production, while a low pH would create the accumulation of volatile fatty acids (VFA) which results in the inhibition of the digestion process [39-40]. For a proximate analysis, the information on the moisture content (MC), volatile matter (VM) and others were obtained, which is important to determine the potentiality and suitability of the biomass [41]. From the results in Table 2, the MC for all raw samples is more than 90%, which shows that the water content of each sample was high, which means the raw materials have sufficient MC for anaerobic digestion, as the moisture content of the food waste in the substrate is between 95 - 97% from his study [42]. The volatile matter (VM) for all the samples was in the range of 66-80%. Thus, the fraction of VM for all the samples showed its potential to produce higher biogas production [43-44]. The thickened sludge and mixed food waste produced the higher chemical oxygen demands (COD) with 18790 ± 96.44, and 12,516 ± 92.38 mg/L respectively. According to Treagust [45], the COD of coffee wastewater reaches up to 50,000 mg/L. Toxic chemicals such as tannis, alkaloids (caffeine) and polyphenolics can be found in coffee wastewater in small amounts. The COD values measured the oxygen needed to oxidize all organic material present within substances [46]. The higher the COD values, the higher the potential of substances to produce methane.

The total solids (TS) of the substrates mainly started from < 7%. TS measures the suspended and dissolved solids in water. Coffee waste has the greater TS value, with 7.32%, compared to others. Volatile solids (VS), are described as the organic matter present in the wastewater which is important for AD performances that would enhance the higher production of methane. The VS value for food waste and sludge is at a range of 40-70%. Alkalinity is a very important parameter in the AD process. Alkalinity helps to avoid the failure of the digester and causes the inhibition of methanogenic bacteria activities by preventing the pH drop. The alkalinity of NDC, coffee waste, thickened sludge, and mixed food waste with sludge was 900 ± 1.48, 794.83 ± 1.56, 3012.5 ± 1.75 and 3337.5 ± 0.89 mg $CaCO_3$/L. Volatile fatty acid (VFA) is another option to justify the availability of the raw materials used in AD for the production of methane. Like other common factors of AD such as pH, alkalinity, and COD, the VFA gives information on the process status [47]. The hydraulic loading, temperature, and organic loading might affect the concentration of VFA. According to Yu et al. [48], the accumulation of VFA will interrupt the digester buffer capacity, leading to acidification and the failure of system performance by inhibiting the methanogenic bacteria activities. Thus, the VFA readings for all the samples were 6510 ± 25.39, 2410.33 ± 27.94, 211 ± 23.81, and 707.33 ± 57.66 mg/L which represents the NDC, coffee waste, thickened sludge, and mixed food waste with sludge. There are many studies on the effects of VFA content that might affect AD efficiency.

Table 2. The results of the characterization of samples

Parameters	Non-Dairy Creamer waste (NDC)	Coffee waste	Mixed Food waste with sludge	Thickened sludge
pH	7.46 ± 0.01	11.55 ± 0.08	7.07 ± 0.03	7.09 ± 0.03
Moisture Content (%)	99.34 ± 0.02	90.05 ± 0.03	95.53 ± 0.02	96.21 ± 0.01
Volatile Matter (%)	80.03 ± 1.82	73.59 ± 1.18	66.07 ± 2.08	68.97 ± 0.002
Chemical Oxygen Demands (mg/L)	8400 ± 52.92	7843.33 ± 32.15	12516.67 ± 92.38	18790 ± 96.44
Total Solid (%)	0.68 ± 0.18	7.32 ± 0.02	4.49 ± 0.03	4.11 ± 0.06
Volatile Solid (%)	70.84 ± 0.08	44.68 ± 0.002	67.11 ± 0.06	69.18 ± 0.001
Alkalinity (mg $CaCO_3$/L)	900 ± 1.48	794.83 ± 1.56	3337.5 ± 0.89	3012.5 ± 1.75
Volatile Fatty Acids, VFA (mg/L)	6510 ± 25.39	2410.33 ± 27.94	707.33 ± 57.66	211 ± 23.81

BMP experimental test

The BMP experimental test was performed in 125 mL serum bottles for the AD process [31] with a working volume of 70% and 30% remaining for the gas production as shown in Figure 1. Constant BMP experimental results were achieved for all samples after the retention time of 31 days for the anaerobic digestion process took place. The BMP assays are assumed to be finished when the daily production is less than 1% or when the cumulative graph shows a constant trend of methane production which indicates the organic substances are fully degraded. The microorganisms no longer have enough nutrients for digestion purposes. Figure 2 shows the methane production of co-digestion 1, co-digestion 2, co-digestion 3, and thickened sludge. The lag phase, which is the time of adaptation for inoculum to a new environment or medium, stopped around 7 days, in this study. According to the curves in Figure 2, it can be observed that the methane production was initially slow, but continuously increased at around 20 days. There was a constant production of methane from day 20 until day 31. Thus, it took almost 20 days for all the methane to be produced from the substrates. It can be seen that the highest methane production was from the thickened sludge which is 18.275 ± 3.3 mL CH_4/gVS, followed by the non-dairy creamer waste with sludge (co-digestion 1) that is 17.865 ± 6.2 mL CH_4/gVS and mixed food waste with sludge (co-digestion 3) at 17.825 ± 0.05 mL CH_4/gVS. While, the lowest methane production is from coffee waste with sludge (co-digestion 2) which is 14.797 ± 0.01 mL CH_4/gVS.

Co-digestion 2 shows the lowest production of methane compared to co-digestions 1 and 3. The coffee waste itself is characterized as lipids, cellulose, lignin-rich biomasses. Lignin (humic acid, tannin) has different macromolecules such as caffeine and polyphenols (melanoidins). Cardenas et al.,2009 [24] cited that, melanoidins consist of ligands (polysaccharides, tannins), which hardly degrade biologically [24]. The cellulose and lignin make the lignocellulosic biomass a great prospect for biogas production through AD. However, it is still considered difficult for it to be degraded and digested. Somehow, the study also highlighted that lower methane potentials of about 0.16 - 0.35 CH_4 m3/kg VS of food waste are rich-lignocellulosic fractions and have low lipids content, such as fruit and vegetable residues and brewery waste. Moreover, the coffee waste shows that the highest pH, which is 11.55 ± 0.08, is very alkaline. It will affect biogas productivity. As mentioned before, it has been proved that the optimum pH for methanogenic bacteria activities is within a range of 6.8-7.2, which will give a

significant effect on biogas yield [36-37]. Co-digestion 1 shows that the second-highest methane yield is 17.865 ± 6.2 mL CH_4/gVS. This is because NDC contains high organic matter with about 1.2% minerals, 8.5% protein, 32.5% fat, and the highest percentage is carbohydrates (58%) [18-21]. Protein and carbohydrate-rich substrates are considered to be easily degradable, and lipids have less of a hydrolysis rate [48]. Thus [42, 49], higher methane yields can be achieved from food wastes rich in lipids, such as easily degradable carbohydrates.

The reading of the methane yields for co-digestion 3 (mixed food waste with sludge) is slightly similar to co-digestion 1 which is 17.825 ± 0.05 mL CH_4/gVS. The COD of co-digestion 3, which is 12516.67 ± 92.38 mg/L, is higher compared to co-digestion 1 and co-digestion 2. However, the COD for the thickened sludge, which is 18790 ± 96.44 mg/L, shows the highest yield compared to the others. This shows that most of the organic matter is contained in both co-digestion 3 and the thickened sludge. It can be summarised from Figure 2, that the solely thickened sludge has the potential to produce a higher methane yield without adding any substrate. As we informed, the mixed food waste with sludge consists of coffee and non-dairy creamer waste. Thus, there is the mixing of protein, carbohydrates, and lipids with lignin groups of waste within it. These can act as a reason for the lower methane yield of co-digestion 3 compared to the inoculum which is solely thickened sludge. Therefore, the pre-treatment to the substrate is suggested either by biological, chemical, or thermal treatments to improve the substrate's potential in producing methane. This study has proven different substrates have different characteristics, as can be seen in the proximate analysis of the raw materials. Thus, pre-treatment approaches can be taken to enhance the efficiency of methane generation.

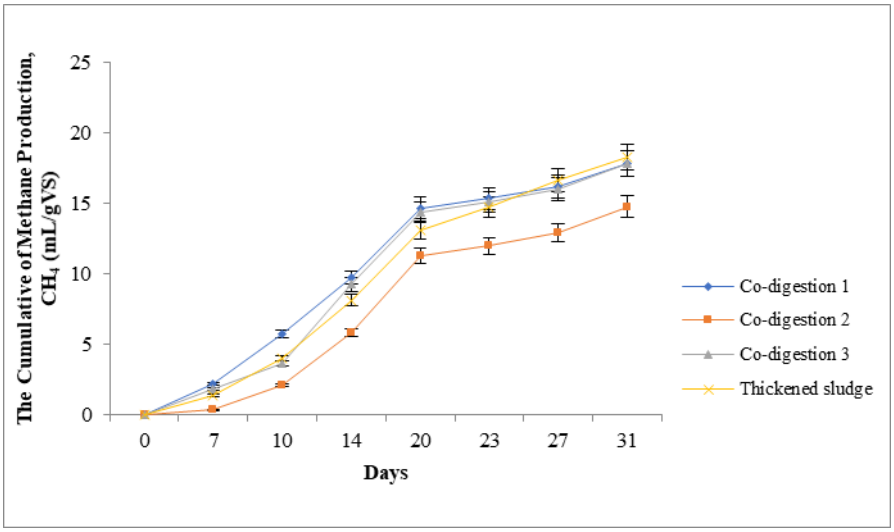


Figure 2. The cumulative BMP experimental test of methane production for co-digestions and inoculum

Conclusion

The NDC and coffee industry play an important role by providing good handling and processing wastewater management in order to achieve and maintain environmental stability. Nevertheless, the BMP experimental test results indicate that there is a potential for a single inoculum (thickened sludge), and the co-digestion of different wastes such as coffee waste, non-diary creamer waste, and the sample of mixed food waste with sludge would produce a methane yield within the 31 days of the AD process. However, it is also possible to inhibit the AD process if the nutrients are imbalanced. For further observation, an effective and environmentally friendly pre-

treatments process is highly recommended to improve biogas production.

Acknowledgements

The authors would like to thank Universiti Teknologi MARA and IWK for awarding the grant ((100-RMC 5/3/SRP PRI (026/2020)). Special appreciation to the Faculty of Applied Sciences, UiTM, and IWK for providing the facilities to conduct this study.

References

1. Werther, J. and Ogada, T. (1999). Sewage sludge combustion. *Progress Energy Combustion,* 25: 55-116.
2. Appels, l., Baeyens, J., Degrève, J. and Dewil, R. (2008). Principles and potential of the anaerobic digestion of waste-activated sludge. *Progress Energy Combustion,* 34: 755-781.
3. Appels, L., Degrève J., Van der Bruggen, B., Van Impe, J., and Dewil, R. (2010). Influence of low temperature thermal pre-treatment on sludge solubilisation, heavy metal release and anaerobic digestion. *Bioresource Technology,* 101: 5743-5748.
4. Angelidaki, D., Karakashev, D.J. Batstone, C.M, Plugge, A.J.M. (2011). Stams, biomethanation and its potential. *Methods in Enzymology*, 494: 327-351.
5. Ward, A. J., Hobbs, P. J., Holliman, P. J. and Jones, D. L. (2008). Optimization of the anaerobic digestion of agricultural resources. *Bioresource Technology,* 99: 7928-7940.
6. Appels, L., Joost, L., Degrève, J., Helsen, L., Lievens, B. and Willems, K. (2011). Anaerobic digestion in global bio-energy production: potential and research challenges. *Renewable Sustainable Energy Reviews,* 15: 4295-4301.
7. Nasir, I. M., Tinia, I. M. G. and Rozita, O. (2012). Production of biogas from solid organic wastes through anaerobic digestion: a review. *Applied Microbiology Biotechnology,* 95: 321-329.
8. Zhang, J., Wang, Q., Zheng, P. and Wang, Y. (2014). Anaerobic digestion of food waste stabilized by lime mud from paper-making process. *Bioresource Technology,* 170: 270-277.
9. Astals, S., Nolla-Ardevol, V. and Mata-Alvarez, J. (2013). Thermophilic co-digestion of pig manure and crude glycerol: process performance and digestate stability. *Journal of Biotechnology*, 166: 97-104.
10. Chen, J. H., Lin, C. C. and Wang, K. S. (2013). Potential of methane production by thermophilic anaerobic co digestion of pulp and paper sludge with pig manure. *Journal Biobased Material Bioenergy,* 7: 300-304.
11. Giuliano, A., Bolzonella, D., Pavan, P., Cavinato, C. and Cecchi, F. (2013). Co-digestion of livestock effluents, energy crops and agro-waste: Feeding and process optimization in mesophilic and thermophilic conditions. *Bioresource Technology,* 128: 612-618.
12. Astals, S., Ariso, M., Galí, A. and Mata-Alvarez, J. (2011). Co-digestion of pig manure and glycerine: experimental and modelling study. *Journal Environmental Management,* 92: 1091-1096.
13. Fraizer, R. S., Hamilton, D. and Ndegwa, P. M. (2011). Anaerobic digestion: biogas utilization and cleanup. Oklahoma Cooperative Extension Service.
14. Cavinato, C., Fatone, F., Bolzonella, D., Pavan, P. (2010). Thermophilic anaerobic co-digestion of cattle manure with agro-wastes and energy crops: comparison of pilot and full scale experiences. *Bioresource Technology,* 101:545-50.
15. Shah, F. A., Mahmood, Q., Rashid, N., Pervez, A., Raja, I. A and Shah, M. M. (2015). Co-digestion, pretreatment and digester design for enhanced methanogenesis. *Renewable Sustainable Energy Reviews,* 42: 627-642.
16. Dedin, F., Rosida, Mulyani, T. and Reshita Septalia, L. (2016). A comparative study of non-dairy cream based on the type of leguminosae protein source in terms of physico chemical properties and organoleptic. *Agriculture and Agricultural Science Procedia,* 9: 431-439.
17. Huang, X., Lee, E. J. and Ahn, D.U. (2019). Development of non-dairy creamer analogs/mimics for an alternative of infant formula using egg white, yolk, and soy proteins. *Asian-Australasian Journal of Animal Sciences,* 32(6): 881-890.

18. Ramesh, C.C, Kilara, A. and Shah, N. P. (2008). Dairy processing and quality assurance. 1st Edition., Wiley Blackwell Publishing, A. John Wiley and Sons Inc., New York.
19. Dewi, E. R. S., Legowo, A. M. and Izzati, M. (2016). Absorption of organic compounds by *Saccharomyces cerevisiae* on industrial waste media. *International Journal of Applied Environmental Science,* 11(1): 27-36.
20. Dewi, E. R. S., Legowo, A. M., Izzati, M. and Purwanto (2016). Kinetic growth of Saccharomyces cerevisiae in non dairy creamer wastewater medium. *Journal of Environmental Studies*, 2(1): 1-5.
21. Triyaswati, D. and Ilmi, M. (2020). Lipase-producing filamentous fungi from non-dairy creamer industrial waste. *Microbiology and Biotechnology Letters,* 48(2): 167–17.
22. Navitha, K. and Kousar, H. (2018). A comparative study on the potential of *Aspergillus niger* and *Aspergillus favus* for the treatment of coffee processing effluent. *International Journal Environmental Ecology Family and Urban Studies,* 8(4):17-22.
23. Sahana, M., Srikantha, H., Mahesh, S. and Swamy, M.M. (2018). Coffee processing industrial wastewater treatment using batch electrochemical coagulation with SS and Fe electrodes and its combinations recovery and reuse of sludge. *Water Science Technology,* 78: 279-289.
24. Cardenas, A., Zayas, T., Morales, U. and Salgado, L. (2009). Electrochemical oxidation of wastewaters from the instant coffee industry using a dimensionally stable RuIrCoOx anode. *ECS Transactions,* 20(1): 291-299.
25. Péerez, T.Z., Geissler, G. and Hernandez, F. (2007). Chemical oxygen demand reduction in coffee wastewater through chemical flocculation and advanced oxidation processes. *Journal Environmental Sciences*, 19: 300-305.
26. Remigi, E.U., Buckley, C.A. (2006). Co-digestion of high strength/toxic organic effluents in anaerobic digesters at wastewater treatment works; water research commission: Pretoria, South Africa.
27. Da Silva, C., Astals, S., Peces, M., Campos, J. L. and Guerrero, L. (2018). Biochemical methane potential (BMP) tests: Reducing test time by early parameter estimation. *Waste Management,* 71: 19-24.
28. Raposo, M. M. M., Castro, M. C., Belsley, M. and Fonseca, A. M. C. (2011). Push pull bithiophene azo-chromophores bearing thiazole and benzothiazole acceptor moieties: Synthesis and evaluation of their redox and nonlinear optical properties. *Dyes Pigments*, 91:454-465.
29. Yan (2014). Romania to develop national strategy to reduce food waste: Minister. Access from http://news.xinhuanet.com/english/world/2014-04/01/c_133230744.htm [Accessed date 03.09.14]
30. APHA (1998). Standard methods of examination of water and wastewater. 20th ed. American Water Works Association, Water Pollution Control Federation, American Public Health Association, Washington DC.
31. Angelidaki, I., Alves, M., Bolzonella, D., Borzacconi, L., Campos, J. L., Guwy, A. J. and van Lier, J. B. (2009). Defining the biomethane potential (BMP) of solid organic wastes and energy crops: a proposed protocol for batch assays. *Water Science and Technology,* 59(5): 927-934.
32. Ramatsa, I., Sibiya, N. and Huberts, R. (2014). Effect of nutrients addition during anaerobic digestion of potato peels and maize husk. *International Conference on Chemical, Environmental & Metallurgical Engineering,* 2014: pp. 15-16.
33. Ebner, J. H., Labatut, R. A., Lodge, J. S., Williamson, A. A. and Trabold, T. A. (2016). Anaerobic co-digestion of commercial food waste and dairy manure: Characterizing biochemical parameters and synergistic effects. *Waste Management,* 52: 286-294.
34. Sibiya, N. T., Edison, M. and Habtom, B. T. (2014). Effect of temperature and pH on the anaerobic digestion of grass silage. *International Conference on Chemical Engineering & Advanced Computational Technologies,* 2014: 198-201.
35. Nielfa, A., Cano, R. and Fdz-Polanco, M. (2015). Theoretical methane production generated by the co-digestion of organic fraction municipal solid waste and biological sludge. *Biotechnology Reports*, 5, 14-21.

36. Turovskiy, I. S. and Mathai, P.K. (2006). Wastewater sludge processing. New York: Wiley
37. Cioabla, A. E., Ionel, I., Dumitrel, G.-A. and Popescu, F. (2012). Comparative study on factors affecting anaerobic digestion of agricultural vegetal residues. *Biotechnology for Biofuels,* 5(1): 39.
38. Lusk, P. (1999). Methane recovery from animal manures the current opportunities casebook. National Renewable Energy Laboratory, NREL/SR-580-25145.
39. Parkin, G. F. and Owen, W. F. (1986). Fundamentals of anaerobic digestion of wastewater sludges. *Journal of Environmental Engineering,* 112: 867-920.
40. Pearse, L.F., Heittiaratchi, J.P. and Kumar, S. (2018). Towards developing a representative biochemical methane potential (BMP) assay for landfilled municipal solid waste-a review. *Bioresource Technology,* 254: 312-324.
41. Brito, J. O., Barrichello, L. E. G. and Trevisan, J. F. (1978). Condicoes climaticas e suas influencias sobre a producao de resinas de pinheiros tropicais, Piracicaba, 16: 37-44
42. Labatut, R., Angenent, L.T. and Scott, N., (2011). Biochemical methane potential and biodegradability of complex organic substrates. *Bioresource Technology,* 102(3): 2255-2264.
43. Vassilev, S., Baxter, D., Andersen, L. and Vassileva, C. (2010). An overview of the chemical composition of biomass. *Fuel,* 89: 913-933.
44. Demiral, I. and Ayan, E.A. (2011). Pyrolysis of grape bagasse: Effect of pyrolysis conditions on the product yields and characterization of the liquid product. *Bioresource Technology,* 102: 3946-3951.
45. Treagust, J. (1994). Coffee waste water treatment. B.Sc. (Hons.) dissertation. Cranfield, United Kingdom: Cranfield University.
46. Watershed Protection Plan Development Guidebook (2015). Description of commonly considered water quality constituents [Access date 10 October 2015].
47. Boe, K., Batstone, D. J. and Angelidaki, I. (2007). An innovative online VFA monitoring system for the anerobic process, based on headspace gas chromatography. *Biotechnology and Bioengineering,* 96(4): 712-721.
48. Mata-Alvarez, J., Dosta, J., Romero-Güiza, M., Fonoll, X., Pecesa, M. and Astals, S., (2014). A critical review on anaerobic co-digestion achievements between 2010 and 2013. *Renewable Sustainable Energy Review,* 36: 412-427.
49. Meng, Y., Li, S., Yuan, H., Zou, D., Liu, Y., Zhu, B., Chufo, A., Jaffar, M. and Li, X., (2015). Evaluating biomethane production from anaerobic mono- and co-digestion of food waste and floatable oil (FO) skimmed from food waste. *Bioresource Technology,* 185: 7-13.

Malaysian Journal of Analytical Sciences (MJAS)
Published by Malaysian Analytical Sciences Society

POTENTIAL APPLICATIONS OF CONDUCTING POLYMER/TUNGSTEN DISULFIDE COMPOSITES: A MINI REVIEW

(Aplikasi Potensi Konduktif Polimer/ Tungsten Disulfida komposit: Ulasan Mini)

Siti Nor Atika Baharin[1], Nur Solehah Samsudin[1], Nur Farahin Suhaimi[1], Kavirajaa Pandian Sambasevam[1,2]*

[1]*Advanced Material for Environmental Remediation (AMER) Research Group, Faculty of Applied Sciences, Universiti Teknologi MARA, Cawangan Negeri Sembilan, Kampus Kuala Pilah, 72000 Kuala Pilah, Malaysia*
[2]*Electrochemical Material and Sensor (EMaS) Group, Universiti Teknologi MARA,40450 Shah Alam, Selangor, Malaysia*

**Corresponding author: kavirajaa@live.com*

Received: 22 July 2021; Accepted: 4 January 2022; Published: 28 April 2022

Abstract

Recent works on many types of synergistic conducting polymers/tungsten disulfide (CP/WS_2) composites are thoroughly covered in this mini review. Data were gathered from over 60 scientific research papers from all over the world and published within the last decade (2012-2021). CPs are as versatile materials because of their remarkable advantages over other traditional materials. These advantages include wide and adjustable electrical conductivity, high mechanical flexibility, high capacitance, and low manufacturing cost. However, CPs do possess limitations in terms of stability, processability, and mechanical strength. As a result, CPs are frequently integrated with inorganic fillers such as metal sulfide. WS_2 has garnered significant attention among metal sulfides when combined with CPs, where it improves chemical/thermal stability and provide good processability to the CPs/WS_2 composites. Hydrothermal procedures and solvothermal techniques were all mentioned and discussed as relevant synthesis methods. As a result, hybridized CP/WS_2 composites have shown prospects in terms of functionality and applicability. Sensors, energy storage, and electrical applications are among the areas that experienced enhanced performance by using CP/WS_2. A brief discussion of the mechanisms underlying these successful applications is also included. This mini review is meant to provide readers with information on CP/WS_2 and, as a result, instill interest in new research topics.

Keywords: conducting polymer, tungsten disulfide, sensors, supercapacitors, photocatalyst

Abstrak

Terdapat banyak jenis komposit yang terdiri daripada konduktif polimer/tungsten disulfida (CP/WS_2) telah dibincangkan di dalam ulasan mini ini. Data yang telah dikumpulkan telah diperolehi dari lebih 60 penyelidikan saintifik dari seluruh dunia selama sepuluh tahun sebelumnya. CP merupakan bahan kimia yang serba boleh kerana mempunyai kelebihan yang luar biasa berbanding bahan tradisional yang lain, termasuk kekonduksian elektrik yang luas dan boleh laras, fleksibiliti mekanikal yang tiggi, kapasitans yang tinggi dan kos pembuatan yang rendah. Walau bagaimanapun, CPs mempunyai batasan dari segi kestabilan, kebolehkerjaan dan kekuatan mekanikal. Oleh itu, CP sering digunakan bersama dengan pengisi bukan organik seperti sulfida logam. Di antara sulfida logam, WS_2 telah mendapat perhatian yang signifikan jika digabungkan dengan CP kerana dapat meningkatkan kestabilan kimia/haba serta menambahbaik ciri-ciri pemprosesan dalam komposit CP/ WS_2. Antara kaedah sintesis yang relevan yang telah dibincangkan dalam kajian mini ini adalah proses hidrotermal dan teknik solvotermal.

Hasilnya, komposit CP/WS_2 yang dihibridisasi telah menunjukkan penningkatan dari segi fungsi dan kebolehgunaan. Penggunaan CP/WS_2 dalam bidang sensor, penyimpanan tenaga dan aplikasi elektrik dapat meningkatkan keupayaan mereka. Perbincangan ringkas mengenai mekanisme aplikasi yang berjaya turut disertakan. Akhir sekali, tujuan kajian mini ini adalah untuk memberi maklumat kepada pembaca mengenai CP/WS_2 dan menarik minat mereka untuk menghasilkan suatu kajian penyelidikan yang baharu.

Kata kunci: konduktif polimer, tungsten disulfida, pengesan, superkapasitor, fotomangkin

Introduction

Conducting polymers (CPs) are a unique class of materials with a π-conjugated system that corresponds to its electrical conductivity. The success of CPs as synthetic metals was discovered in the late seventies by Hideki Shirakawa and his team by accidental addition of excess halides in the reaction medium of polyacetylene. Since then, CPs were widely studied upon in terms of their significant properties such as large conducting mechanisms, electrical properties, adjustable electrochemical properties, and easy processing. Currently, the CPs family consists of polyacetylene (PA), polyaniline (PANI), polypyrrole (PPy), poly(phenylene vinylene) (PPV), poly(3,4-ethylene dioxythiophene) (PEDOT), polyfuran (PF), and other polythiophenes (PTh) and its' derivatives [1]. Due to their fascinating properties, CPs have received widespread attention from both the industrial community and researchers, especially in the study of supercapacitors, sensors, fuel cells, and photocatalysis for their wide range of applications. Figure 1 summarizes far-famed CPs that correspond to their applications.

Although CPs have become the interest of many communities, they still possess a few drawbacks such as high recycling instability [2], high defect sites from poor temperature tolerance [3], slow exchange of ions [4], and inconsistent solubility [5]. Therefore, enormous effort has been undertaken to incorporate various types of filler such as carbon materials, polymers and inorganic compounds into the CPs' matrix to enhance its properties. Particularly, in recent decades, many attempts were made to produce CPs-inorganic hybrid materials, where the integration of inorganic fillers into CPs may enhance the stiffness, toughness, and dimension stability of the resulting hybrid materials [6]. Among the inorganic fillers, transition metal dichalcogenides (TMDC) were the most favored due to considerable bandgaps in the range of 1-2eV, which is applicable for sensing, nanoelectronics, and photonics [7]. Considering metal sulfides are a class of TMDC, it is an excellent candidate to improve the CPs' properties in terms of conductivity, thermal stability [8], capacitance activity, and cyclic stability[9]. This is because by supplying electrons or withdrawing electrons to or from the transition state of reaction, the transition metal retains a good source of electrons from the partially filled d-subshell. CPs eventually have more free-moving electrons obtained from metal sulfide and therefore exhibits better electrical conductivity. In a study reported by Ramesan 2013, it was found that when PPy and cadmium sulfide (CdS) were combined, the nanocomposite's alternating current conductivity was greater than pristine PPy. Meanwhile, the highest generated direct current electrical conductivity was obtained when a higher amount of CdS were added [10].

In addition, metal sulfide is outstanding because it generates excellent characteristics due to its two-dimensional (2D) structure that exhibits tunable band gaps in the visible to near-infrared spectrum [11] and exceptional physicochemical properties [12]. Among the metal sulfides, tungsten disulfide (WS_2) possesses considerable advantages too, which is comparable to other existing metal sulfides. Tungsten is a d-block element from period 6 and sulfur is a p-block element from period 3. Interestingly, the band-gap of WS_2 changed from an indirect band-gap of 1.4 eV to a direct band-gap of 20 eV when a 2D material was isolated by a simple mechanical exfoliation technique from the bulk material. Due to the wide bandgap, WS_2 is seen as an interesting material for many areas of application, especially in the industry of solid lubricant, lithium-ion

battery, catalytic degradation, and electronic devices. By considering the pros and cons of both CPs and WS_2, numerous synthetic approaches have been developed with different morphologies, structures, and properties to satisfy the demands of different applications. WS_2 has been investigated with several types of CPs such as PANI, PPy and PEDOT. In the past decade, CP/ WS_2 composites have been found to have potential in several applications such as in supercapacitors, electronic components and sensors and actuators. However, a simple search in the SCOPUS database with a combined search string specifically on CPs and WS_2 only resulted in less than 50 papers, indicating that more extensive research is needed to cultivate and promote the CP/WS_2 binary composites. Therefore, this mini-review is an attempt to scrutinize the potential applications of CP/WS_2 composites and its benefits.

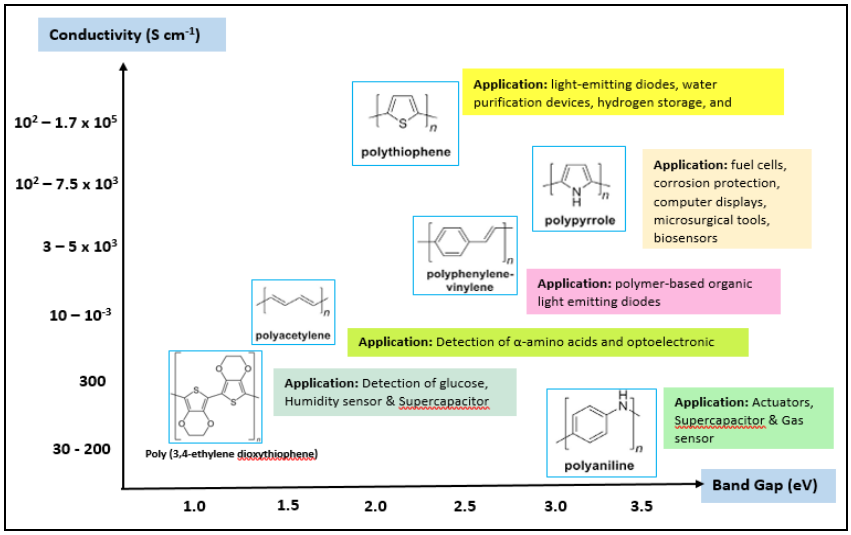


Figure 1. Various types of CPs assigned to a specific range of conductivity and band gap including their existing applications

Brief history of tungsten disulfide composites

Tungsten disulfide (WS_2) or also known as tungstenite is an inorganic compound which is composed of tungsten and sulfur with a molar mass of 247.98 g/mol. In the past, WS_2 has shown great potential for a high-temperature solid lubricant used in space as jotted in the National Aeronautics and Space Administration (NASA) record (History of Tungsten Disulfide (WS_2), 2018). The idea was initiated due to inefficient spacecraft mechanisms which cannot be inspected or maintained after launched. It was discovered that some parts of the spacecraft were not well-lubricated. On top of that, any satellite components that are subject to sliding wear must be properly lubricated to withstand the requirements of the mission. In that sense, WS_2 became the promising candidate due to its anti-friction properties that attributed by its crystal structure, which consists of hexagonal close-packed atomic tungsten layers sandwiched between two hexagonally closed atomic layers of sulfur. Weak Van der Waals forces that hold two adjacent sulfur layers allow them to slide for lubrication purposes [13]. Progressively, the success of WS_2 as a layered structure has expanded due to their interesting anisotropic behavior, great diversity in other physical properties and its advantages for various applications when added to base oil under specific laboratory test conditions. The composition of WS_2 with folded triple-layer of S-W-S sheets enables the atoms within each triple layer to be held by potential carbon-carbon bond. Each bond is clenched by weak Van der Waals interactions. This anisotropic nature of WS_2 therefore opens an opportunity to be

incorporated into different types of polymer matrices, resulting in high strength moduli and a good ability for shock absorption [14].

Synthesis method of WS_2

The synthesis of WS_2 composite usually involves multiple steps. Pristine WS_2 must be prepared prior to the integration with a specific CP. Then, WS_2 can be utilised to synthesise CP/WS_2 composite commonly via chemical oxidative method [15]. Every synthetic route for metal disulfide (MS_2) synthesis offers different outputs. The synthesised material can be tailored in order to develop various functions and applications for the metal sulfide [16]. For WS_2, every type of synthetic methods conducted possess several pros and cons depending on the processes involved. Hydrothermal and solvothermal syntheses are a few of the existing methods to synthesise WS_2 that have different synthetic route and its own significance.

Hydrothermal synthesis

Hydrothermal synthesis has been reported as an appealing method due to its simple procedure and productivity. Due to its advantages of low temperature, large-scale development and simple synthesis, it is an environmentally friendly technique for the preparation of various nanostructures [17]. In addition, hydrothermal method leads to the development of nanoscale products under supercritical pressure, which is cumbersome via classical routes. In this method, sodium thiosulfate and hydroxylamine sulfate are the important chemical ingredients. Hydroxylamine sulfate not only acts as the source of sulfur, but is also utilised as a strong acid to establish an acidic state for the nanoparticles that may form. Moreover, WS_2 can also be produced with a chrysanthemum-like nanostructure via hydrothermal synthesis. According to Tang et al. [18], the addition of pluronic and cetyltrimethyl ammonium bromide (CTAB) significantly affect the growth and final morphology of the WS_2. The resulted self assembled chrysanthemum-like nanostructures were grown prior to a fast nucleation of amorphous primary particles and slow aggregation of nanosheets [19]. Prominently, this method is interesting since large-scale metal sulfide composite can be achieved via this technique. However, this method is limited to aqueous precursors which might restrict the control over certain optimisations like temperature, reaction time, and type of solvent.

Solvothermal synthesis

Typically, solvothermal synthesis is a technique for preparing a variety of materials such as ceramics, polymers, metals and semiconductors. It might imitate the hydrothermal synthesis method but what differentiate both of them is the precursor type. Both hydrothermal and solvothermal synthesis use aqueous and non-aqueous precursor solution, respectively [20]. This method may adjust certain experimental parameters including temperature of reaction, time of reaction, type of solvent, type of surfactant, and type of precursor to ensure precise control of the size, distribution of shape and crystallinity of the nanostructure product. Focusing on WS_2, one step exfoliation-restacking technique is invalid to be employed even though WS_2 has similar chemical structure with MoS_2. The reason why this restacking technique makes the WS_2 layered nanocomposites difficult to obtain is because the precursor does not have optimum concentration. Hence, the solvothermal method is used to increase the amount of lithium introduced in WS_2 in order to improve processability [21].

Applications of conducting polymer/tungsten disulfide

The electrical properties of polymeric materials have piqued researchers' attention in the field of solid-state electronics. Generally, CPs by nature reveal poor electrical conductivity due to the absence of free moving electrons to enable the conduction process. However, when the CPs undergoes doping treatment with oxidizing or reducing agent, they can exhibit reasonable conductivity [22]. As a result of the presence of both the polymer and the filler material, a range of inorganic materials may be integrated into CPs with improved characteristics. Metal sulfide appears to be a superior alternative for making hybrid CP composites than metal oxide and other carbon derivatives. Metal sulfide is not only inexpensive and abundant in nature, but it also performs well in faradic redox reactions, making it useful in the fuel cell

business. When it comes to the WS_2 nanostructure, the weak Van der Waals interactions indicate that it is anisotropic, and it is well known for its high strength moduli and shock absorption capabilities [14]. However, WS_2 has a drawback in the form of short cycle stability, which causes the capacitance to rapidly degrade. As a result, including WS_2 into CP matrices might be a promising method to improve the stability and combine favourable physical properties of both organic and metallic components while retaining capacitance in a single composition [23].

Polyaniline/Tungsten Disulfide (PANI/WS_2)

Since PANI is one of the most promising CP with enhanced properties, researchers actively synthesize and analyze the PANI composites in numerous applications. A lot of papers were published on the preparation of conducting composites of PANI, such as PANI/TiO_2, PANI/ZrO_2, PANI/Fe_3O_4, PANI/MoO_3, PANI/zeolite, PANI/WO_3, PANI/MnO_2 and PANI/WS_2 from metal sulfide groups [24]–[31]. Despite many papers have been published regarding PANI composites, PANI/WS_2 are still lagging in terms of research and have limited source of information. Only a few reports were found using PANI/WS_2 in the fabrication of micro supercapacitor microrobots and its incorporation with chlorin e6 (Ce6) to give a triple-synergistic strategy in tumor treatment [32]. In a study by Stejskal et al. [33] PANI/WS_2 was fabricated through in situ polymerisation. The flake-like semiconducting particles of WS_2 were coated with a thin film of PANI during the oxidation of aniline. In addition, scanning electron microscopy (SEM) analysis of PANI/WS_2 revealed a porous nature and seems to be robust, where the WS_2 particles interlinked the PANI nanorods. This is probably due to the fact that, WS_2 naturally exists as a stack layered material, where the incorporation of PANI provides additional strength to the whole structure.

Humidity sensors

Humidity is another critical parameter that significantly affects the operation of electronic components in the determination of geographical distribution and the maximum intensity of precipitation, biosphere and surface hydrology. Measurements of humidity or moisture level in the human body could be beneficial in evaluating a variety of physiological and metabolic conditions. Since low humidity has adverse effects on human health, the existence of humidity sensor is important in interpreting the growth, repair and aging mechanisms to regulate internal body conditions [34]. Manjunatha et al. [31] reported on the preparation of PANI/WS_2 composite by in situ polymerisation technique and demonstrated an excellent humidity sensing compare to pure WS_2 as reported by Guo et al [35]. Typically, PANI/WS_2 exhibits enhanced humidity sensing properties due to its porous nature. The porous nature is of paramount interest for the adsorption of water molecules, which is also an important aspect in developing humidity sensors. Consequently, the agglomerated flower-like structure with highly microporous nature of PANI/WS_2 is assumed to have an important role in the humidity sensing behaviour of the composite. Typically, the water vapour could find its way through micropores of PANI/WS2 to react and give response in the sensing mechanism. Figure 2 shows a uniform distribution of WS_2 micro-sized sheets in the matrix of PANI from the observation of a field emission scanning electron microscope (FESEM) micrograph of the composite with magnification 12kx.

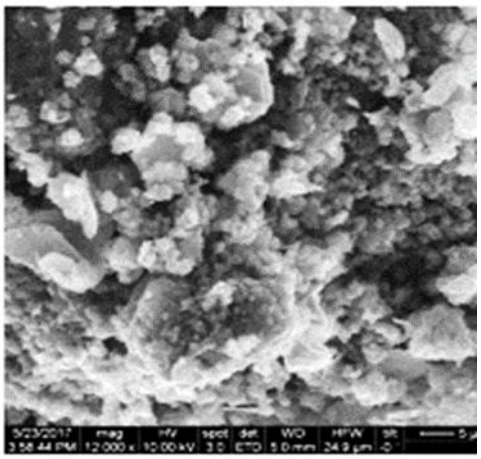


Figure 2. Field emission scanning electron micrograph of the PANI/WS_2 composite with 12000x magnification [31]

Ammonia gas sensor

The application of gas sensors in industries of environmental analysis, automotive, medical applications and indoor air quality controls have been developed for more than a decade ago due to the enforcement of the Occupational Safety and Health (OSHA) regulations against volatile hazardous gases [36]. Among the hazardous gases, ammonia (NH_3) has received major attention in the field of gas sensors due to its abundance in chemicals manufacturing industries and applied in diverse areas around the world [37]. Hybrid PANI/WS_2 composite promises a synergetic effect for NH_3 gas detection. The mechanism of NH_3 gas sensing by PANI/WS_2 can be proposed based on electron donation concept. Complementary to each other, PANI is a p-type conducting polymer with a linear conjugation of π−electronic system, while WS_2 is an n-type semiconductor whose band gap increases with the decrease in the number of stacked layers. The fact that NH_3 could donate electrons to the p-type PANI resulted in a decrease in the hole-transport concentration and next, deprotonation reaction caused the resistance of PANI to incline. Consequently, PANI/WS_2 showed high selectivity towards NH_3 gas with long term stability and repeatability [38]. The magnificent sensing capability of PANI/WS_2 sensor in humid environments and at room temperature makes it a suitable candidate for environmental monitoring devices [39].

Supercapacitor

Self-propelled supercapacitor device based on WS_2 nanoparticles-polyaniline/platinum (PANI/Pt) microrobot design opened a new insight that it can act as an on-demand reconfigurable device owing to its superior capacitance of 14000 μFcm^{-2} with energy density and power density of 0.07 $mWhm^{-2}$ and 120 mWm^{-2}, respectively [40]. Due to great capacitance result exerted by this microbot, it is expected to be proficient for on-demand construction and adjustment of the electronic devices. The fabrication of this autonomous WS_2NPs-PANI/Pt self-propelled microsupercapacitor for on-site electronics delivery in the circuit involved an electrodeposition process using cyclopore polycarbonate membrane as a template. WS_2NPs-PANI/Pt micromotors (μ-motor) fabrication process is shown in Figure 3.

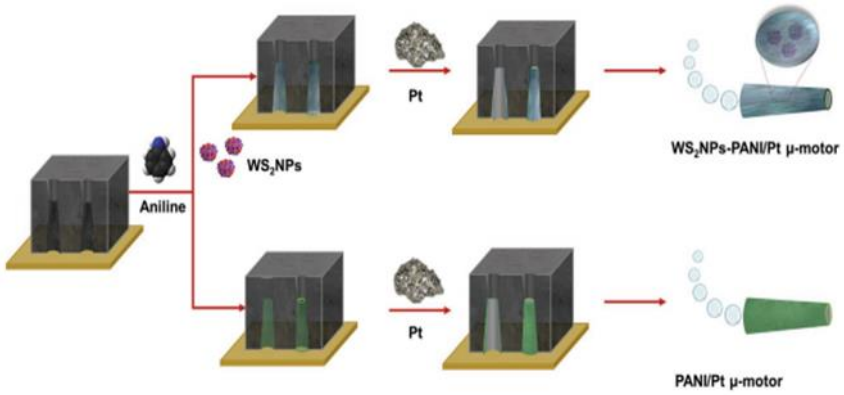


Figure 3. Schematic representation of WS_2NPs-PANI/Pt μ-motor fabrication process. Reproduced with permission from ACS [40].

Polypyrrole/Tungsten Disulfide (PPy/WS_2)

The integration between PPy and WS_2 nanocomposites exhibited a conductivity higher than the pristine WS_2 at ambient temperature [37]. In addition, WS_2 coated with PPy has benefit of wettability. In simple words, wettability is the ability of surface to reduce the surface tension of the liquid that is in contact with it and allow the liquid to spread over the surface and wet [41]. Wettability is important in adhesion as it provides quality for adhesive bonding and coating. Besides, synthesis of PPy/WS_2 can be steered by in-situ oxidative polymerization. The oxidation of pyrrole yields water-insoluble pyrrole oligomers that is further adsorbed on an immersed surfaces and continually grow the PPy chains. Typically, the process started with adsorption where the PPy patches are reinforced into chain colonies and are then grown slowly, resulting in uniform brush-like coating on the entire film [42] to the extent whenever the substance are still available, additional PPy globules will continuously be produced. The PPy globules are produced on hydrophilic PPy films or in surrounding aqueous phase and the globules stick to the film surface. In this context, the deposition of CPs are hydrophilic or hydrophobic surface dependent [43]. The product therefore generally consists of two phases which involve a thin polymer film deposited on the substrate and globular PPy. These two phases were demonstrated by the morphology analysis where, at a composition of 23.7 wt.% of PPy content, WS_2 flakes readily become coated with PPy. Furthermore, the appearance of additional PPy globules was due to the increment of the PPy content up to 38.3%. The idea of uniform PPy coating on WS_2 is due to the different hydrophobicity of pyrrole oligomers in conjunction to the fact that WS_2 is mildly hydrophilic [41].

Hydrogen evolution reaction

Hydrogen evolution reaction (HER) is basically a water splitting technology which found importance in energy storage based on hydrogen evolution. The combination of PPy and WS_2 seems to be a promising composite in the HER catalytic process due to the enhanced conductivity and wettable properties of this composite. Stejskal and co-workers [41] prepared PPy/WS_2 in various ratio of pyrrole monomer. The study revealed that excess of PPy globules would block the active edges of WS_2 in HER, despite of improved conductivity. However, a significant result was attained upon physical mixing of the PPy and WS_2 as a result of proton abundancy which was responsible for capacitive charging process in HER.

In Vivo drug release

Traditional drug delivery medications, such as oral administration and injections, tend to deliver greater drug concentrations than necessary, which may cause side effects in patients. Therefore, externally controlled drug delivery systems are of special relevance for study because they enable for drug delivery control from outside the body [44]–[46]. Particular interest on PPy functionalized WS_2 was paid by Hsiao and co-workers [47] since the composite possesses excellent synergistic properties to fine-tune the electrical properties to enable an electrically active nanocarrier system for an effective drug delivery to the target organ. The study revealed that a large quantity of anti-cancer drug, such as 5-fluorouracil (5-FC), be effectively delivered (90%) in the presence of electrical stimulation. They also successfully reported could that no toxic effect was evident in the electrical stimulation of PPy/WS_2.

Poly (3,4-ethylenedioxythiophene: Poly (Styrene Sulfonate)/Tungsten Disulfide (PEDOT: PSS/WS_2)

Poly(3,4-ethylenedioxythiophene): poly(styrene sulfonate)/tungsten disulfide, PEDOT:PSS/WS_2 is one of the ternary CPs composites as a potential material in thermoelectric applications due to its various benefits such as adjustable electrical conductivity and solution processability [49, 50]. PSS is a polymer surfactant, which enhances the dispersion and stability of PEDOT in water and other solvents [50]. PEDOT:PSS is well-known in the thermoelectric field for its excellent mechanical flexibility, low thermal conductivity, water solubility and processability [51]. As PEDOT:PSS went through a small treatment via direct vacuum filtration, the composite has been enhanced with high

electrical conductivity. Since then, research related with incorporation of inorganic nanostructures with PEDOT:PSS to enhance the thermoelectric performances has been expanding [49].

The introduction of PEDOT:PSS into WS_2 resulted in a composite that facilitated the charge carriers to move along the polymer chains, which effectively improved the charge transfer within the composite [52]. The fabrication technique was utilized due to the poor conductivity of WS_2, where the lateral transfer of electrons along the lamella structure of the WS_2 nanostructures were blocked, making the electron transfer inefficient. PEDOT:PSS also acts as spacers to avoid restacking of WS_2 and provide plenty of channels to enhance the charge transport. Moreover, synthesized the PEDOT:PSS/WS_2 thin film synthesized may easily be peeled off and transferred to another substrate, resulting in more potential applications. Therefore, stronger performing thermoelectric composite such as PEDOT:PSS/WS_2 carries better properties rather than the pristine PEDOT:PSS and pristine WS_2 [52].

Schottky diodes

In a study by Ortiz et al. [53], PEDOT:PSS/WS_2 Schottky nano-diode was constructed through hetero-junction of a hole transporting CP with an n-type semiconductor. In order to fabricate this composite, individual PEDOT:PSS was synthesized via electrospinning while the mono- and multi-layer WS_2 flakes were synthesized via chemical vapor deposition (CVD). These combination methods are developed from a previous research that implemented electrochemical polymerization techniques [54]. The previous experiment demonstrated poor device operation due to undesirable chemical reactions with the inorganic semiconductor. In terms of performance, the equations in standard thermionic emission model of a Schottky junction were used and from there it exerts an ideality parameter of 1.9 and a barrier height of 0.58 eV. Far from being ideal, the high ideality parameter measured value for this device may be contributed by the recombination of hole and electrons at the interface or the presence of interface states at the CP/WS_2 interface. Even so, upon large surface to volume ratio of the film, semiconductor carrier density is tunable via a back-gate bias and the reversible change of barrier height makes it potentially useful as a sensor [53].

Supercapacitor

In the organic semiconducting family, PEDOT has triggered worldwide interest owing to its development as pioneer for electronically conducting polymers (ECPs). However, the fact that PEDOT has outstanding electrochemical properties is still insufficient for it to meet the needs of practical applications. To overcome the problem, WS_2 has been incorporated into PEDOT to accelerate its applications in the fields of various devices, especially for the supercapacitors [55]. Nevertheless, to excel as high-performance supercapacitors, PEDOT/WS_2 may need to form a ternary composite with another compound. The combination of the three components in nanoscale creates a synergistic effect and higher potential in the faradaic processes Xia et al. [34]. For instance, a recent study in the electrical field by Liang et al. [56]reported that the use of poly(3,4-ethyleenedioxythiophene)-poly(ethylene glycol)-tungsten disulfide (PEDOT-PEG-WS_2) as ternary compounds exhibited good performance as a supercapacitor. PEDOT-PEG-WS_2 nanocomposite was prepared via electrochemical self-assembly of PEDOT and WS_2 nanosheets in the presence of PEG.

This ternary composite has resulted in a unique three-dimension interpenetrating porous network (3D-IPN) in nano-/micro scale. The addition of 5% PEG surfactant has effectively stabilized the WS_2 nanosheets that coexist with additional electrolytes. 3D-IPN materials has gained attention for its high-volume ions transport system and utilization of limited space that allows enhancement of energy storage capacity. Moreover, the 3D-IPN confined to metal-organic framework helps to build and verify automotive hydrogen storage systems that will allow hydrogen-fueled vehicle platforms to meet customer specifications. The optimization of PEDOT-PEG-WS_2 nanocomposite has been developed from the WS_2 contents and CV cycles adjustment. Based on their CV area and specific capacity of each sample, it was found that the as-prepared PEDOT-PEG-WS_2 nanocomposite has reached maximum specific capacity by adding 2.7% WS_2 in solution and 50 electrodeposition cycles.

Other than that, electrochemical properties of the engineered 3D IPN-PEDOT-PEG-WS_2 nanocomposite were recognized and compared with PEDOT-PEG [56].

Organic photovoltaic cells

OPV is an electrical device that converts light directly into electricity by photovoltaic cells, which combine physical and chemical phenomenon. The great characteristics such as low cost, light weight, flexible and scalability through roll-to-roll coating processes make OPV is great for green technology. The performance of OPV can be improved by a few ways including device structure optimization, conversion of light to suitable absorbance wavelengths and synthesis of new short band-gap polymers. PEDOT:PSS is familiar in hole-extraction layers (HEL) which works as buffer layers between the active layer and electrode. Recently, researchers have discovered that MoS_2 based OPVs utilizing PEDOT:PSS HEL, possesses better performance due to increased hole extraction and light absorption [57]. This finding has opened a venue for WS_2 to replace traditional MoS_2 as HEL in OPVs since it is structurally similar to MoS_2 with some expectation to enhance device performance equally or better. Surprisingly, a study by Lin and co-workers [58] exhibited excellent results of the OPV device performance through the implementation of an WS_2 HEL layer combined with the indium tin oxide (ITO) anode, PEDOT:PSS layer, poly (3-hexylthiophene) (P3HT) and phenyl-C61-butyric acid methyl ester (PCBM) [58]. In this study, WS_2 nanosheets were obtained by a simple ultra-sonication method and were uniformly spin coated on a ITO/glass as visualized in Figures 4 (a) and (b). Next, the hole-extraction efficiency of WS_2 was amplified by a UV-ozone treatment which at the same time empowered the OPV device.

In another study by Le and co-workers [59], the effect of WS_2 upon UVO treatment was investigated by introducing WS_2 into CP composites such as PEDOT:PSS, P3HT:PCBM and lithium fluoride/aluminum (LiF/Al) [59]. As expected, the change in work function of WS_2 due to UVO treatment enhanced its hole-extraction properties. The power conversion efficiency (PCE) of the OPV with WS_2/PEDOT:PSS was 3.07%, which is superior compared to the OPV with only PEDOT:PSS layer of 2.87%. Therefore, the study agreed on a deduction that high PCE resulted from the efficiency of charge separation and collection processes by WS_2/PEDOT:PSS.

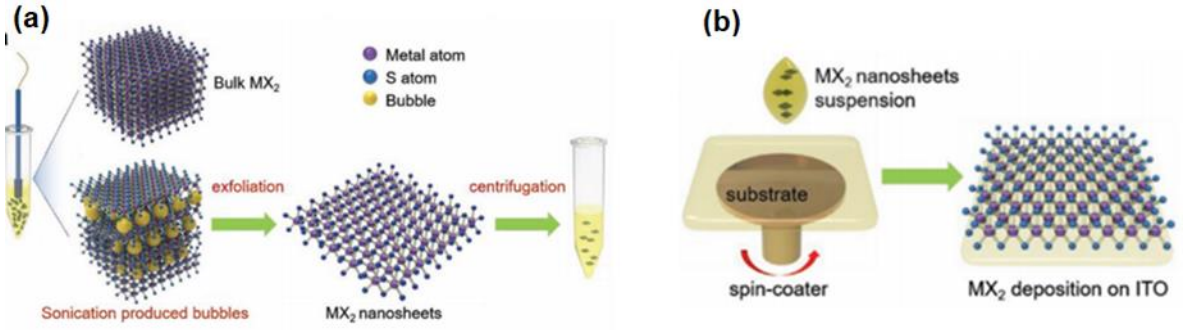


Figure 4. (a) Sonication assisted liquid exfoliation to prepare WS_2 and (b) deposition of WS_2 or MoS_2 onto ITO substrate via spin coating technique

Polyfluorene/ Tungsten Disulfide (PFO/ WS_2)

Polyfluorene (PFO) is an attractive material for display applications such as light source in organic light emitting diodes (LED) due to efficient blue light emission, good solubility and high mobility. Light absorption of PFO in the UV region falls

approximately at 380 nm. Beyond the desired blue emission at 425 nm, a green component close to 530 nm can either be attributed to intermolecular interactions or oxidation-induced keto defects that cause aggregates to form [60]. According to Luccio et al. [61], even though the energy emission is low, the removal of the inter-chain interaction enhanced the color purity and luminescence stability of PFO/WS_2. Considering WS_2, both fullerene-like nanoparticles (F-WS_2-NP) and nanotube (WS_2-NT) structures work differently. F-WS_2 is more into lubricating fluids, self-lubricating coatings and medical devices. Meanwhile, WS_2-NT is great at improving the mechanical properties of CP composites [61]. With respect to that, the addition of inorganic nanomaterial like WS_2 ensures color emission tunability. Not to mention, the exhibited optical and electrical properties of PFO/WS_2 depends on the number of WS_2 layer present [61]. The surface morphology of PFO has a smooth appearance at a glance as shown in Figure 5 (a). Meanwhile, SEM images of PFO/WS_2 nanocomposite films showed high dispersion of WS_2 nanotubes upon various WS_2 concentration from 10 wt.% to 50 wt.% as displayed in Figure 5 (b–d). It is observed that the dispersion of the WS_2-NT is quite homogeneous for all the concentrations investigated, even though some nanotube agglomerates remain. This finding suggests a further study is needed either on the purification of nanotubes or the preparation of the blend.

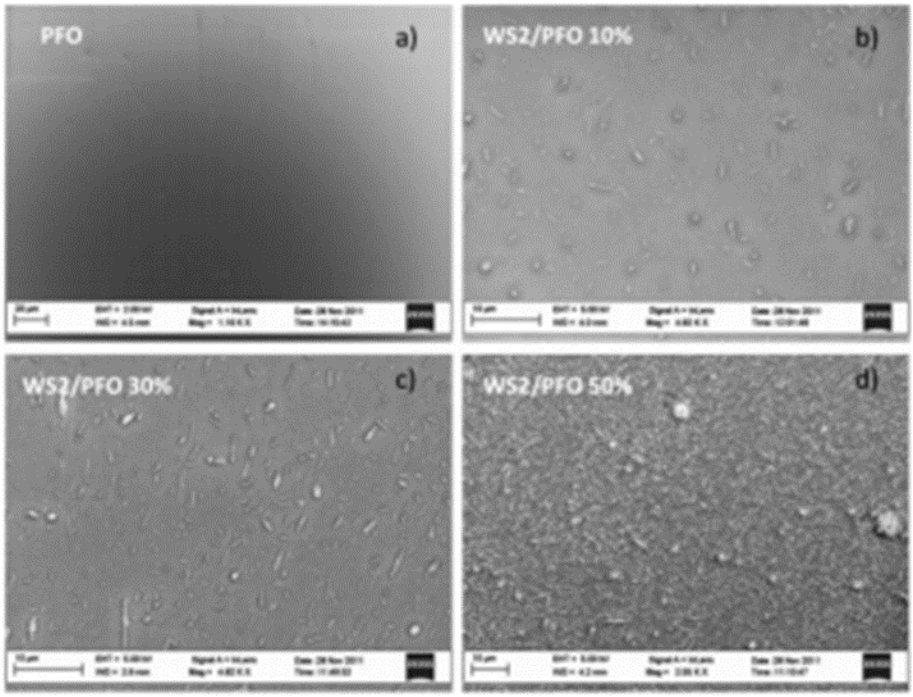


Figure 5. Scanning electron microscope images of a) bare PFO, and PFO/WS_2 nanocomposites at b) 10 wt.% c) 30 wt.% and d) 50 wt.% [61].

Organic light-emitting diode

An organic light-emitting diode (OLED) is a light emitting diode in which organic layers are responsible for light emission. The light emitted by OLED follows the basic principal of electroluminescence in which a material acts in response to the electrical field applied across it [62]. In context of CP/WS_2, PFO has recorded an investigation where PFO matrix and WS_2 nanotubes were combined to prepare PFO/WS_2 blends with various loadings of 10 wt.%, 30 wt.%, and 50 wt.%. The fabrication of these homogeneously dispersed PFO/WS_2 composites were influenced by two major steps including the WS_2 nanotube purification and the blend preparation. An optimization on the threshold

voltage has recorded the highest voltage of 4.7 V when 30% of WS_2 was integrated with PFO, and surprisingly the threshold voltage depreciated at 50% of WS_2 and recorded 4.1 V which was almost similar to pure PFO. Compared to pure PFO, the devices containing the nanocomposites has poor efficiency. This is because the electrical data exhibited that the PFO/WS_2 nanocomposite device of WS_2 showed fluctuated performances with increasing wt.%. Such unsynchronized data of threshold voltage and efficiency of the tailored material might be contributed by several factors such as unbalanced charges and electrode interfaces. It also could be due to the change of the device working point or total applied power [61]. Table 1 summarizes various CPs/WS_2 composites with its respective summary on desired applications and advantages.

Table 1. Summary of CP/WS_2 in various application and their significant advantages

Conducting Polymer/WS_2	**Application**	**Advantage**	**Remarks**	**Ref.**
PANI/WS_2	Dye sensitized solar cell (DSSC)	Higher conversion efficiency of WS_2 compare to platinum counter-electrode. Relatively cheaper cost compares to platinum.	Nano-sheets of WS_2 and nano-rods of PANI were used in the investigation.	[63]
	Supercapacitor	The higher composition of PANI in the WS_2 matrix has enhanced the supercapacitor performance.	Conductivity: 65.7 S/m; Specific capacitance: 441 at 0.5A/g.	[64]
	Supercapacitor	Exhibited excellent electrochemical properties and high frequency response.	High capacitance of 180 $\mu Fcm^{-}{}_2$ at 1_20 Hz. Potential use in energy storage device.	[65]
	Sensor	The sensor showed an excellent result under humid environment which can be utilized in the respiratory gases.	Ammonia sensor	[39]
PPy/WS_2	Drug release	Biocompatible Non-invasive electrically stimulating drug release system	5-fluorouracil (anticancer drug)	[47]
	Potential use in medium-frequency devices such as humidity and gas sensors.	Excellent operation in terms of AC conductivity and dielectric properties.	PPy with 40 wt% of WS_2 possessed highest conductivity of 5.081 x 10^{-3} S/cm.	[66]

Table 1 (cont'd). Summary of CP/WS_2 in various application and their significant advantages

Conducting Polymer/WS_2	**Application**	**Advantage**	**Remarks**	**Ref.**
PPy/WS_2	Humidity sensor	Excellent long term-stability.	Response/recovery = 5_2/58 s, respectively. Long term stability up to 60 days at 55 and 95% relative humidity.	[67]
PEDOT/WS_2	Electrochemical sensor	WS_2 has enhanced the denseness and smoothness of PEDOT morphology. The ternary composite of SWCNT/WS_2-PEDOT showed good linear response in the range of 0.00_2 – 0.9 μM with low LOD of 0.7 nM in the Vitamin B_2 detection.	The study involves molecularly imprinted polymer of WS_2-PEDOT in the presence of Vitamin B_2 as the template.	[68]
	Supercapacitor	The supercapacitor showed long-term stability up to 5000 cycles by retaining 83.3% of initial areal capacitance.	Hybrid material of ternary composites consist of PEDOT, MeOH, PEG and WS_2 were prepared using simple co-electrodeposition method.	[69]
	Schottky diode	Novel material of PEDOT/WS_2 used for the first time in nano-diodes. The perfect ambient tolerance of the diode makes it an ideal candidate for gas or light sensors.	The combination of PEDOT and WS_2 has resulted in rectification ratio of 1_2 and a turn-on voltage of 1.4 V.	[53]
	Miniature-supercapacitor	Simple and cost-effective fabrication of WS_2/PEDOT:PSS ternary composite. Improved flexibility in the miniaturized supercapacitor.	The WS_2/PEDOT:PSS supercapacitor recorded a high conductivity of 44 S/cm, high areal specific capacitance of 86 $mFcm^{-}{}_2$, and 107% capacitance retention after 5000 cycles.	[70]

Table 1 (cont'd). Summary of CP/WS_2 in various application and their significant advantages

Conducting Polymer/WS_2	**Application**	**Advantage**	**Remarks**	**Ref.**
Polythiophene/WS_2 (PTh/WS_2)	Functionally designed PTh/WS_2	Shown good magnetic effect which could find potential use in microwave absorbing materials.	Modified liquid phase oxidative polymerization that controls interface PTh-based layered material.	[71]
	Functionally designed coating method for Pth/WS_2	Electro-conductivity and mechanical properties of WS_2 has been enhanced via the tailor-made functionalization.	Potential use in drug release control.	[72]
PFO/WS_2	Organic Light Emitting Diodes	PFO with 30% of WS_2 showed a threshold voltage of 4.7 V when 30% of WS_2.	PFO/WS_2 has been tested for the first time as OLED and it opens the door for new avenues for this composite material.	[61]

Conclusion

A widespread overview of CP composites has been studied in the context of their properties and existing applications. WS_2-based CPs offer a very broad and promising field of research, not only due to its enhanced properties but also because of the chances to achieve multifunctional nano systems from the synergic effect between CP and WS_2. In this mini-review, CP/WS_2 composite showed the best performance as energy storage material followed by electronic components and sensors. CP/WS_2 is a great choice for energy storage since it shows high capacitive behaviour even in a micro-sized supercapacitor. As a matter of fact, this material composite deserves a place in electronic and biomedical industries. Based on the findings and limitation of this research, some improvement can be made on low energy emission by PFO/WS_2. As abovementioned, WS_2 nanotubes were not fully homogenous in the PFO matrix. Henceforth, future research might consider nanotube purification in the fabrication of PFO/WS_2. Besides, CP/WS_2 can also consider more formation of ternary compounds inspired from the PEDOT-PEG-WS_2 composite. This is because the initiative of using ternary compound can strengthen the connection between CP and inorganic filler, thus exhibiting remarkable performance in supercapacitors due to better electrons transport.

Acknowledgement

The authors would like to thank Fundamental Research Grant Scheme (FRGS) [FRGS/1/2019WAB05/ UITM/02/5] for the financial assistance.

References

1. Das, T. K. and Prusty, S. (2012). Review on conducting polymers and their applications. *Polymer - Plastics Technology and Engineering*, 51(14): 1487-1500.
2. Mohd Norsham, I. N., Baharin, S. N. A., Raoov, M., Shahabuddin, S., Jakmunee, J. and Sambasevam, K. P. (2020). Optimization of waste quail eggshells as biocomposites for polyaniline in ammonia gas detection. *Polymer Engineering and Science*, 60(12): 1-13.

3. Sambasevam, K. P., Mohamad, S. and Phang, S.-W. (2015). Enhancement of polyaniline properties by different polymerization temperatures in hydrazine detection. *Journal of Applied Polymer Science*, 132(13): 41746.
4. Kumar, R., Singh, S. and Yadav, B. C. (2016). Conducting polymers: Synthesis, properties and applications conducting polymers. *International Advanced Research Journal In Science,Engineering and Technology*, *2*(11): 110-124.
5. Kaur, G., Adhikari, R., Cass, P., Bown, M. and Gunatillake, P. (2015). Electrically conductive polymers and composites for biomedical applications. *RSC Advances*, 5(47): 37553-37567.
6. Yu, M., Huang, R., He, C., Wu, Q. and Zhao, X. (2016). Hybrid composites from wheat straw, inorganic filler, and recycled polypropylene: morphology and mechanical and thermal expansion performance. *International Journal of Polymer Science*, 2016: 1-12.
7. Huo, N., Yang, S., Wei, Z., Li, S. S., Xia, J. B. and Li, J. (2014). Photoresponsive and gas sensing field-effect transistors based on multilayer WS_2 nanoflakes. *Scientific Reports*, 4: 1-9.
8. Ajibade, P. A. and Mbese, J. Z. (2014). Synthesis and characterization of metal sulfides nanoparticles/poly(methyl methacrylate) nanocomposites. *International Journal of Polymer Science*, 2014: 1-8.
9. Abdel Maksoud, M. I. A., Fahim, R. A., Shalan, A. E., Abd Elkodous, M., Olojede, S. O., Osman, A. I., Farrell, C., Al-Muhtaseb, A. H., Awed, A. S., Ashour, A. H. and Rooney, D. W. (2021). Advanced materials and technologies for supercapacitors used in energy conversion and storage: a review. *Environmental Chemistry Letters*, 19(1): 375-439.
10. Ramesan, M. T. (2013). Synthesis, characterization, and conductivity studies of polypyrrole/copper sulfide nanocomposites. *Journal of Applied Polymer Science*, 128(3): 1540-1546.
11. Ahmad, H., Kamarudin, S. K., Minggu, L. J. and Kassim, M. (2015). Hydrogen from photo-catalytic water splitting process: A review. *Renewable and Sustainable Energy Reviews*, 43: 599-610.
12. Ke, X., Dai, K., Zhu, G., Zhang, J. and Liang, C. (2019). In situ photochemical synthesis noble-metal-free NiS on CdS-diethylenetriamine nanosheets for boosting photocatalytic H_2 production activity. *Applied Surface Science*, 481: 669-677.
13. Takahashi, A., Tetuko, J. and Hashimoto, K. (2018). Evaluation of friction characteristics and low friction mechanism of tungsten disulfide for space solid lubricant at elevated temperature in a vacuum. *Proceedings of the 44th Aerospace Mechanisms Symposium,* 2018: pp. 113-126.
14. Sade, H. and Lellouche, J. (2018). Preparation and characterization of WS_2@SiO_2 and WS_2@PANI core-shell nanocomposites. *Nanomaterials*, 8(3): 156.
15. Li, H., Yu, C., Chen, R., Li, J. and Li, J. (2012). Novel ionic liquid-type Gemini surfactants: Synthesis, surface property and antimicrobial activity. *Colloids and Surfaces A: Physicochemical and Engineering Aspects*, 395: 116-124.
16. Chandrasekaran, S., Yao, L., Deng, L., Bowen, C., Zhang, Y., Chen, S., Lin, Z., Peng, F. and Zhang, P. (2019). Recent advances in metal sulfides: from controlled fabrication to electrocatalytic, photocatalytic and photoelectrochemical water splitting and beyond. *Chemical Society Reviews*, 48(15): 4178-4280.
17. Ashraf, W., Fatima, T., Srivastava, K. and Khanuja, M. (2019). Superior photocatalytic activity of tungsten disulfide nanostructures: role of morphology and defects. *Applied Nanoscience*, 1(1): 1-15.
18. Tang, G., Tang, H., Li, C., Li, W. and Ji, X. (2011). Surfactant-assisted hydrothermal synthesis and characterization of WS_2 nanorods. *Materials Letters*, 65(23–24): 3457-3460.
19. Cao, S., Liu, T., Hussain, S., Zeng, W., Pan, F. and Peng, X. (2014). Synthesis and characterization of novel chrysanthemum-like tungsten disulfide (WS_2) nanostructure: structure, growth and optical absorption property. *Journal of Materials Science: Materials in Electronics*, 26(2): 809-814.

20. Zhang, D., Liu, T., Cheng, J., Liang, S., Chai, J., Yang, X., Wang, H., Zheng, G. and Cao, M. (2019). Controllable synthesis and characterization of tungsten disulfide nanosheets as promising nanomaterials for electronic devices. *Ceramics International*, 45(9): 12443-12448.
21. Sun, S., Li, Z. and Chang, X. (2011). Synthesis and structural characterization of tungsten disulfide nanomaterials. *Materials Letters*, 65(19-20): 3164-3166.
22. Ramesan, M. T. (2013). Synthesis, characterization, and properties of new conducting polyaniline/copper sulfide nanocomposites. *Polymer Engineering and Science,* 2013: 1-8.
23. Flores, A., Naffakh, M., Díez-Pascual, A. M., Ania, F. and Gómez-Fatou, M. A. (2013). Evaluating the reinforcement of inorganic fullerene-like nanoparticles in thermoplastic matrices by depth-sensing indentation. *Journal of Physical Chemistry C*, 117(40): 20936-20943.
24. Li, S., Liu, A., Yang, Z., Zhao, L., Wang, J., Liu, F., You, R., He, J., Wang, C., Yan, X., Sun, P., Liang, X., and Lu, G. (2019). Design and preparation of the WO_3 hollow spheres@ PANI conducting films for room temperature flexible NH_3 sensing device. *Sensors and Actuators B: Chemical*, 289: 252-259.
25. Ma, Y., Qiao, M., Hou, C., Chen, Y., Ma, M., Zhang, H. and Zhang, Q. (2015). Preparation of polyaniline (PANI)-coated Fe_3O_4 microsphere chains and PANI chain-like hollow spheres without using surfactants. *RSC Advances*, 5(125): 103064-103072.
26. Shyaa, A. A., Hasan, O. A. and Abbas, A. M. (2015). Synthesis and characterization of polyaniline/ zeolite nanocomposite for the removal of chromium(VI) from aqueous solution. *Journal of Saudi Chemical Society,* 19(1): 101-107.
27. Prasanna, B. P., Avadhani, D. N., Muralidhara, H. B., Chaitra, K., Thomas, V. R., Revanasiddappa, M. and Kathyayini, N. (2016). Synthesis of polyaniline/ZrO_2 nanocomposites and their performance in AC conductivity and electrochemical supercapacitance. *Bulletin of Materials Science*, 39(3): 667-675.
28. Khademian, M. and Eisazadeh, H. (2015). Preparation and characterization emulsion of PANI-TiO_2 nanocomposite and its application as anticorrosive coating. *Journal of Polymer Engineering*, 35(6): 597-603
29. Jiang, Feiran, Li, W., Zou, R., Liu, Q., Xu, K., An, L. and Hu, J. (2014). MoO_3/PANI coaxial heterostructure nanobelts by in situ polymerization for high performance supercapacitors. *Nano Energy*, 7: 72-79.
30. Ghani, S. A. and Young, H. C. (2010). Conductive polymer based on polyaniline-eggshell powder (PANI-ESP) composites. *Journal of Physical Science*, 21(2): 81-97.
31. Manjunatha, S., Chethan, B., Ravikiran, Y. T. and Machappa, T. (2018). Room temperature humidity sensor based on polyaniline-tungsten disulfide composite. *AIP Conference Proceedings*, 1953.
32. Wang, J., Pang, X., Tan, X., Song, Y., Liu, L., You, Q., Sun, Q., Tan, F. and Li, N. (2017). A triple-synergistic strategy for combinational photo/radiotherapy and multi-modality imaging based on hyaluronic acid-hybridized polyaniline-coated WS_2 nanodots. *Nanoscale*, 9(17): 5551-5564.
33. Stejskal, J., Mrlík, M., Plachý, T., Trchová, M., Kovářová, J. and Li, Y. (2017). Molybdenum and tungsten disulfides surface-modified with a conducting polymer, polyaniline, for application in electrorheology. *Reactive and Functional Polymers*, 120: 30-37.
34. Xia, X., Hao, Q., Lei, W., Wang, W., Sun, D. and Wang, X. (2012). Nanostructured ternary composites of graphene/Fe_2O_3/polyaniline for high-performance supercapacitors. *Journal of Materials Chemistry*, *22*(33): 16844-16850.
35. Guo, H., Lan, C., Zhou, Z., Sun, P., Wei, D. and Li, C. (2017). Transparent, flexible, and stretchable WS_2 based humidity sensors for electronic skin. *Nanoscale*, 9(19): 6246-6253.
36. Kim, S. J., Hwang, I. S., Kang, Y. C. and Lee, J. H. (2011). Design of selective gas sensors using additive-loaded In_2O_3 hollow spheres prepared by combinatorial hydrothermal reactions. *Sensors*, 11(11): 10603-10614.

37. Xu, B. H., Lin, B. Z., Chen, Z. J., Li, X. L. and Wang, Q. Q. (2009). Preparation and electrical conductivity of polypyrrole/WS_2 layered nanocomposites. *Journal of Colloid and Interface Science*, 330(1): 220-226.
38. Jha, R. K., Wan, M., Jacob, C., & Guha, P. K. (2018). Ammonia vapour sensing properties of in situ polymerized conducting PANI-nanofiber/WS_2 nanosheet composites. *New Journal of Chemistry*, 42(1): 735-745.
39. Liu, G., Zhou, Y., Zhu, X., Wang, Y., Ren, H., Wang, Y., Gao, C. and Guo, Y. (2020). Humidity enhanced ammonia sensing of porous polyaniline/tungsten disulfide nanocomposite film. *Sensors and Actuators B: Chemical*, 323: 128699.
40. Mayorga-Martinez, C. C., Moo, J. G. S., Khezri, B., Song, P., Fisher, A. C., Sofer, Z. and Pumera, M. (2016). Self-propelled supercapacitors for on-demand circuit configuration based on WS_2 nanoparticles micromachines. *Advanced Functional Materials*, 26(36): 6662-6667.
41. Stejskal, J., Acharya, U., Bober, P., Hajná, M., Trchová, M., Mičušík, M., Omastová, M., Pašti, I. and Gavrilov, N. (2019). Surface modification of tungsten disulfide with polypyrrole for enhancement of the conductivity and its impact on hydrogen evolution reaction. *Applied Surface Science*, 492(5): 497-503.
42. Kapralova, V. M., Sapurina, I. Y. and Sudar', N. T. (2018). Variation in the conductivity of polyaniline nanotubes during their formation. *Semiconductors*, 52(6): 816-819.
43. Stejskal, J., Sapurina, I. and Trchová, M. (2010). Polyaniline nanostructures and the role of aniline oligomers in their formation. *Progress in Polymer Science*, 35(12): 1420-1481.
44. Hailemeskel, B. Z., Addisu, K. D., Prasannan, A., Mekuria, S. L., Kao, C. Y. and Tsai, H. C. (2018). Synthesis and characterization of diselenide linked poly(ethylene glycol) nanogel as multi-responsive drug carrier. *Applied Surface Science*, 449: 15-22.
45. Timko, B. P. and Kohane, D. S. (2012). Materials to clinical devices: Technologies for remotely triggered drug delivery. *Clinical Therapeutics*, 34(11): S25-S35.
46. Wu, S. Y., Chou, H. Y., Yuh, C. H., Mekuria, S. L., Kao, Y. C. and Tsai, H. C. (2018). Radiation-sensitive dendrimer-based drug delivery system. *Advanced Science*, 5(2): 1700339.
47. Hsiao, P. F., Anbazhagan, R., Tsai, H.-C., Rajakumari krishnamoorthi, Lin, S.-J., Lin, S.-Y., Lee, K.-Y., Kao, C.-Y., Chen, R.-S. and Lai, J.-Y. (2020). Fabrication of electroactive polypyrrole-tungsten disulfide nanocomposite for enhanced in vivo drug release in mice skin. *Materials Science and Engineering: C*, 107: 110330.
48. Bubnova, O., Khan, Z. U., Malti, A., Braun, S., Fahlman, M., Berggren, M. and Crispin, X. (2011). Optimization of the thermoelectric figure of merit in the conducting polymer poly(3,4-ethylenedioxythiophene). *Nature Materials*, 10(6): 429-433.
49. Jiang, Fengxing, Xiong, J., Zhou, W., Liu, C., Wang, L., Zhao, F., Liu, H. and Xu, J. (2016). Use of organic solvent-assisted exfoliated MoS_2 for optimizing the thermoelectric performance of flexible PEDOT:PSS thin films. *Journal of Materials Chemistry A*, 4(14): 5265-5273.
50. Sun, K., Zhang, S., Li, P., Xia, Y., Zhang, X., Du, D., Isikgor, F. H. and Ouyang, J. (2015). Review on application of PEDOTs and PEDOT:PSS in energy conversion and storage devices. *Journal of Materials Science: Materials in Electronics*, 26(7): 4438-4462.
51. Wei, Q., Mukaida, M., Kirihara, K. and Ishida, T. (2014). Experimental studies on the anisotropic thermoelectric properties of conducting polymer films. *ACS Macro Letters*, 3(9): 948-952.
52. Wang, T., Liu, C., Wang, X., Li, X., Jiang, F., Li, C., Hou, J. and Xu, J. (2017). Highly enhanced thermoelectric performance of WS_2 nanosheets upon embedding PEDOT:PSS. *Journal of Polymer Science, Part B: Polymer Physics*, 55(13): 997-1004.
53. Ortiz, D. N., Vedrine, J., Pinto, N. J., Naylor, C. H. and Charlie Johnson, A. T. (2016). Monolayer WS_2 crossed with an electro-spun PEDOT-PSS nano-ribbon: Fabricating a Schottky diode. *Materials Science and Engineering B: Solid-State Materials for Advanced Technology*, 214: 68-73.

54. Kim, M. S., Yun, S. J., Lee, Y., Seo, C., Han, G. H., Kim, K. K., Lee, Y. H. and Kim, J. (2016). Biexciton emission from edges and grain boundaries of triangular WS_2 monolayers. *ACS Nano*, 10(2): 2399-2405.
55. Li, Y., Niu, J., Xue, T., Duan, X., Tian, Q., Wen, Y., Lu, X., Xu, J., Lai, L., Chang, Y., Li, Z., Zhao, X. and Chen, Y. (2020). Multifunctional porous nanohybrid based on graphene-like tungsten disulfide on poly(3,4-ethoxylenedioxythiophene) for supercapacitor and electrochemical nanosensing of quercetin. *Journal of The Electrochemical Society*, 167(4): 047512.
56. Liang, H., Zhang, B. Q. and Song, J. M. (2019). Synthesis of textured tungsten disulfide nanosheets and their catalysis for benzylamine coupling reaction. *ChemCatChem*, 11(24): 6288-6294.
57. Gu, X., Cui, W., Li, H., Wu, Z., Zeng, Z., Lee, S. T., Zhang, H. and Sun, B. (2013). A solution-processed hole extraction layer made from ultrathin MoS_2 nanosheets for efficient organic solar cells. *Advanced Energy Materials*, 3(10): 1262-1268.
58. Lin, Y., Adilbekova, B., Firdaus, Y., Yengel, E., Faber, H., Sajjad, M., Zheng, X., Yarali, E., Seitkhan, A., Bakr, O. M., El-Labban, A., Schwingenschlögl, U., Tung, V., McCulloch, I., Laquai, F. and Anthopoulos, T. D. (2019). 17% efficient organic solar cells based on liquid exfoliated WS_2 as a replacement for PEDOT:PSS. *Advanced Materials*, 31(46): 1902965.
59. Le, Q. Van, Nguyen, T. P. and Kim, S. Y. (2014). UV/ozone-treated WS_2 hole-extraction layer in organic photovoltaic cells. *Physica Status Solidi - Rapid Research Letters*, 8(5): 390-394.
60. Fukumaru, T., Toshimitsu, F., Fujigaya, T. and Nakashima, N. (2014). Effects of the chemical structure of polyfluorene on selective extraction of semiconducting single-walled carbon nanotubes. *Nanoscale*, 6(11): 5879-5886.
61. Di Luccio, T., Borriello, C., Bruno, A., Maglione, M. G., Minarini, C. and Nenna, G. (2013). Preparation and characterization of novel nanocomposites of WS_2 nanotubes and polyfluorene conductive polymer. *Physica Status Solidi (A) Applications and Materials Science*, 210(11): 2278-2283.
62. Zou, S. J., Shen, Y., Xie, F. M., Chen, J. De, Li, Y. Q. and Tang, J. X. (2020). Recent advances in organic light-emitting diodes: Toward smart lighting and displays. *Materials Chemistry Frontiers*, 4(3): 788-820.
63. Ahmad, M. S., Rahim, N. A., Syed shahabuddin, Mehmood, S. and Khan, A. D. (2021). Effect of WS_2 nano-sheets on the catalytic activity of polyaniline nano-rods based counter electrode for dye sensitized solar cell. *Physica E: Low-Dimensional Systems and Nanostructures*, 126: 114466.
64. Gopalakrishnan, K., Sultan, S., Govindaraj, A. and Rao, C. N. R. (2015). Supercapacitors based on composites of PANI with nanosheets of nitrogen-doped RGO, BC 1.5 N, MoS_2 and WS_2. *Nano Energy,* 12: 52-58.
65. De Adhikari, A., Shauloff, N., Turkulets, Y., Shalish, I. and Jelinek, R. (2021). Tungsten-disulfide/polyaniline high frequency supercapacitors. *Advanced Electronic Materials*, *7*(6): 2100025.
66. Sunilkumar, A., Manjunatha, S., Ravikiran, Y. T., Revanasiddappa, M., Prashantkumar, M. and Machappa, T. (2021). AC conductivity and dielectric studies in polypyrrole wrapped tungsten disulphide composites. *Polymer Bulletin*, 2021: 1-17.
67. Sunilkumar, A., Manjunatha, S., Machappa, T., Chethan, B. and Ravikiran, Y. T. (2019). A tungsten disulphide–polypyrrole composite-based humidity sensor at room temperature. *Bulletin of Materials Science*, 42(6): 271.
68. Zhang, Z., Xu, J., Wen, Y. and Wang, T. (2018). A highly-sensitive VB_2 electrochemical sensor based on one-step co-electrodeposited molecularly imprinted WS_2-PEDOT film supported on graphene oxide-SWCNTs nanocomposite. *Materials Science and Engineering: C*, 92: 77-87.

69. Liang, A., Cai, Y., Wang, J., Xu, L., Zhou, W., Xue, Z., He, Y., Xu, J. and Duan, X. (2021). Co-electrodeposited porous poplar flower-like poly(hydroxymethyl-3,4-ethylenedioxythiophene)/ PEG/WS_2 hybrid material for high-performance supercapacitor. *Journal of Electroanalytical Chemistry*, 891: 115261.
70. Liang, A., Li, D., Zhou, W., Wu, Y., Ye, G., Wu, J., Chang, Y., Wang, R., Xu, J., Nie, G., Hou, J. and Du, Y. (2018). Robust flexible WS_2/PEDOT:PSS film for use in high-performance miniature supercapacitors. *Journal of Electroanalytical Chemistry*, 824: 136-146.
71. Ben Ishay, R., Harel, Y., Lavi, R. and Lellouche, J.-P. (2016). Multiple functionalization of tungsten disulfide inorganic nanotubes by covalently grafted conductive polythiophenes. *RSC Advances*, 6(92): 89585-89598.
72. Raichman, D., Ben-Shabat Binyamini, R. and Lellouche, J. P. (2016). A new polythiophene-driven coating method on an inorganic INT/IF-WS_2 nanomaterial surface. *RSC Advances*, 6(6): 4490-4504.

Malaysian Journal of Analytical Sciences (MJAS)
Published by Malaysian Analytical Sciences Society

DIASTEREOSELECTIVE REDUCTION OF ENDOCYCLIC β-ENAMINO ESTER: AN APPROACH TO PREPARE DIASTEREOPURE MULTISUBSTITUTED PYRROLIDINE β-AMINO ESTERS

(Penurunan Diastereoselektif Terhadap Ester β-Enamino Endosiklik: Satu Pendekatan untuk Menyediakan Ester β-Amino Pirolidin Multi-Penukarganti Diastereotulen)

Ayisy Amirul Afti[1]*, Nor Saliyana Jumali[1], Mohd Fazli Mohammat[2], Zurina Shaameri[2], Ahmad Sazali Hamzah[2]

[1] *Department of Chemistry, Kulliyyah of Science, International Islamic University Malaysia, 25200 Kuantan, Pahang, Malaysia.*
[2] *Organic Synthesis Research Laboratory, Institute of Science (I.O.S), Universiti Teknologi MARA, 42300 Bandar Puncak Alam, Selangor, Malaysia.*

**Corresponding author: ayisy.aaba@live.iium.edu.my*

Received: 26 November 2021; Accepted: 27 February 2022; Published: 28 April 2022

Abstract

A set of chiral multi-substituted pyrrolidine diastereomers containing β-amino ester moiety (**5a-c**) were successfully synthesized from 4-carbethoxy-3-hydroxy-2-oxo-5-phenyl-3-pyrroline (**1**). The key intermediate endocyclic β-enamino ester (**4**) was prepared by methylamination of precursor **1**, followed by acid-catalyzed reduction of **4** using sodium cyanoborohydride to obtain target products (**5**) with moderate diastereoselectivity. Other exploration on the reduction of **4** includes the use of sodium triacetoxyborohydride in acetic acid and catalytic hydrogenation which are subsequently compared with the aforementioned approach in terms of selectivity. Several plausible reaction mechanisms have been proposed based on experimental data.

Keywords: pyrrolidine; β-enamino ester; diastereoselective reduction; catalytic hydrogenation; sodium cyanoborohydride.

Abstrak

Satu set diastereomer pirolidin multi-penukarganti kiral yang mengandungi bahagian ester β-amino (**5a-c**) telah berjaya disintesis daripada 4-karbetoksi-3-hidroksi-2-okso-5-fenil-3-pirolin (**1**). Perantara utama, ester β-enamino endosiklik (**4**), telah disediakan melalui metilaminasi pendahulu **1.** Kemudian, penurunan bagi **4** yang dimangkinkan oleh asid menggunakan natrium sianoborohidrid menghasilkan produk sasaran **5** dengan diastereoselektiviti yang sederhana. Tatacara lain untuk menurunkan **4** termasuk penggunaan natrium triasetoksiborohidrid dalam asid asetik dan penghidrogenan mangkin telah dibandingkan dengan kaedah terdahulu dari sudut selektiviti. Di sini, kami menghuraikan beberapa mekanisme tindakbalas yang munasabah daripada hasil eksperimen ini.

Kata kunci: pirolidin; ester β-enamino; penurunan diastereoselektif; penghidrogenan mangkin; natrium sianoborohidrid.

Introduction

β-enamino esters **A** are recognized as versatile building blocks in the synthesis of various interesting alkaloids [1] including bi- and tricyclic heterocycles such as pyrrolopyrimidines [2], pyrroloquinolines [3], indoles [4], pyrrolizidines and indolizidines [5, 6] (Figure 1). The multifunctionality of these compounds resides in the simultaneous presence of a nitrogen atom, a carbon-carbon double bond, C=C (which when reduced, gives rise to one or two chiral centre(s) and enhances the nucleophilicity of the nitrogen via the localization of its lone pair electrons) and an ester group for further chain extension or ring closure [7, 8].

Owing to their role as key intermediates for synthesizing naturally occurring compounds (Figure 2), this class of functional group has been of crucial interest to researchers especially for the chemistry of its enantio- and diastereoselective reductions.

Excellent enantioselectivity of catalytic hydrogenation over palladium hydroxide, $Pd(OH)_2$ enables the preparation of (+)-calvine, an alkaloid piperidine isolated from coccinellid beetles of the genus *Calvia* [9]. Hydrogenations in the presence of 10% platinum on carbon (Pt/C) and 10% palladium on carbon (Pd/C) offers high diastereoselectivity to reduce β-enamino esters with exocyclic C=C in the asymmetrical syntheses of (+)-laburnine and (+)-tashiromine, respectively. While the ones with endocyclic double bond can be reduced using platinum dioxide-catalyzed hydrogenation with a large diastereomeric excess (d.e. = 90%) as described in the synthetic approach of constructing (-)-isoretronecanol [10, 11].

Apart from that, chemical reduction by sodium triacetoxyborohydride, $NaBH(OAc)_3$ in acetic acid provides greater diastereoselectivity for enamino esters with endocyclic C=C rather than their exocyclic and acyclic counterparts [10], while in the presence of magnesium iodide (MgI_2), near quantitative yield can be achieved [12]. Sodium cyanoborohydride, $NaBH_3CN$ is a versatile reducing agent known for its ability to yield diastereopure β-amino esters as mentioned in the preparation of (±)-lythrancepine (II) and (III) [8].

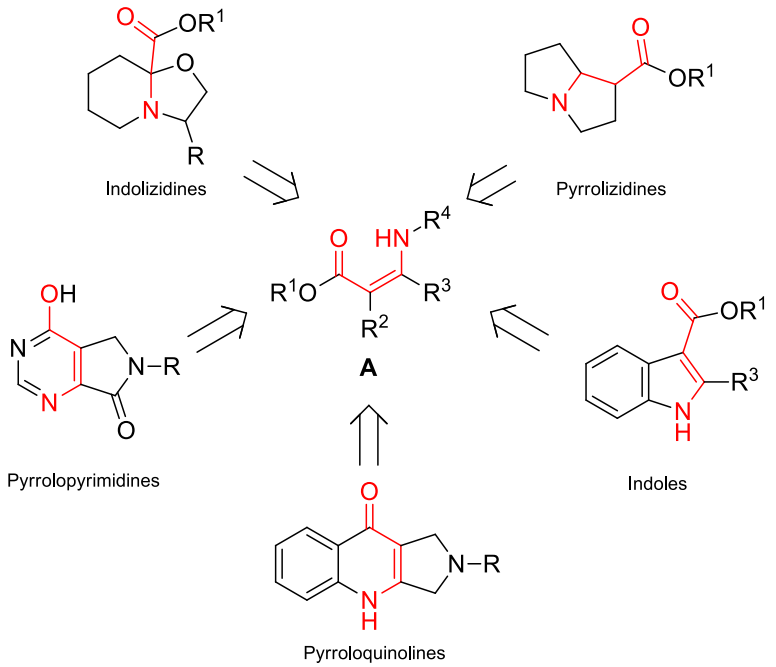


Figure 1. Bi- and tricyclic alkaloids derived from β-enamino esters

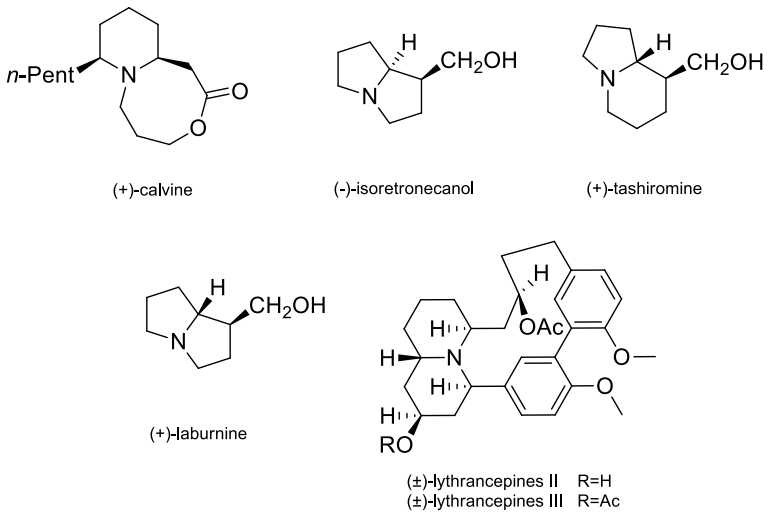


Figure 2. Naturally occurring compounds derived from selective reductions of β-enamino esters

Notably, some studies report that catalytic hydrogenations portray superior selectivity over chemical reductions when involving exocyclic and acyclic β-enamino esters [10, 13]. To our knowledge, there is yet any reported work that specifically discusses the chemistry behind the reduction of endocyclic β-enamino esters – i.e. comparison between the two approaches.

Ergo, in this short study, we describe an experiment to reduce β-enamino ester (**4**) containing endocyclic C=C. The procedures explored include hydrogenation with either 10% Pd/C or 20% $Pd(OH_2)$/C along with reduction using either $NaBH(OAc)_3$ in acetic acid or $NaBH_3CN$ in acidic medium. Different approaches are believed to have distinct stereochemical controls and effectiveness over the reduction protocols.

Materials and Methods

All reagents and solvents were supplied by R&M Chemicals, Merck KgaA and Acros Organics. The reactions were monitored by TLC on silica gel 60 F254 plates, Merck (layer thickness 0.25 mm) and visualized with UV light (254 and 365 nm) and $KMnO_4$ solution as the staining reagent. For product purification using column chromatography, Merck silica gel (230-400 mesh particle size) was used. Infrared spectra were recorded on Varian 3100 Excalibur Series FT-IR spectrometer in the range of 4000-400 cm^{-1}. ^{1}H-, ^{13}C- and 2D NMR spectra were captured on JEOL-400 (^{1}H 400 MHz, ^{13}C 101 MHz) NMR spectrometer.

Multicomponent reaction (MCR) to synthesize 4-carbethoxy-3-hydroxy-2-oxo-5-phenyl-3-pyrroline (1)

The method was adapted from literature [15]. Sodium diethyl oxalacetate (5.01 g, 24 mmol), benzaldehyde (2.4 mL, 24 mmol) and aqueous ammonia (8.0 mL, 119 mmol) were suspended in ethanol (70 mL) and refluxed. After an hour and 15 minutes, the reflux was stopped and once the mixture cooled down to room temperature, it was added to an ice bath. The mixture was acidified with concentrated HCl until it reached pH 2 while being constantly stirred. The resulting precipitate was filtered by suction and washed with distilled water. The solid was dried under vacuum overnight to give the product, 4-carbethoxy-3-hydroxy-2-oxo-5-phenyl-3-pyrroline, as a white solid (Yield: 2.67 g, 42%).

Analytical data: FT-IR (ATR) $\bar{\upsilon}$ (cm^{-1}) 3370 (O-H), 3311 (N-H), 2994 (C-H), 1689 (C=O); ^{1}H-NMR (400 MHz, CD_3OH) δ(ppm) 7.32-7.22 (m, 5H, ArH), 5.23 (s, 1H, ArC<u>H</u>NH), 4.10-4.01 (m, 2H, OCH_2), 1.06 (t, J = 7.1 Hz, 3H, CH_3); ^{13}C-NMR (101 MHz, CD_3OH) δ(ppm) 167.4 (C=<u>C</u>-OH), 163.5 (O-C=O), 155.0

(NHC=O), 137.4 (ArC-CH), 128.2 (ArCH), 127.9 (ArCH), 127.1 (ArCH), 114.0 (C=C-C=O), 60.1 (OCH_2), 57.3 (ArCHNH), 13.0 (CH_3).

Leuckart reaction to synthesize 3-amino-4-carboethoxy-2-oxo-5-phenyl-3-pyrroline (2)

The method was adapted from literature [2]. To a suspension of 4-carbethoxy-3-hydroxy-2-oxo-5-phenyl-3-pyrroline (**1**) (2.01 g, 8 mmol) in ethanol (40 mL), ammonium formate (1.03 g, 16 mmol) was added while stirring. After heating under reflux for 24 hours with TLC monitoring, the mixture was left to cool to room temperature. The solvent was evaporated under reduced pressure and the crude product was purified using column chromatography (petroleum ether/ethyl acetate: 2/1) to yield the product, 3-amino-4-carboethoxy-2-oxo-5-phenyl-3-pyrroline, as a white solid (Yield: 1.23 g, 62%).

Analytical data: TLC (Petreoleum ether/ethyl acetate : 2/1, R_f = 0.26); FT-IR (ATR) $\bar{\upsilon}$ (cm^{-1}) 3482 (N-H), 3385 (N-H), 3278 (N-H), 2965 (C-H), 1718 (conj. C=O), 1679 (C=O), 1625; ^{1}H-NMR (400 MHz, CD_3OH) δ(ppm) 7.28-7.19 (m, 5H, ArH), 5.16 (s, 1H, ArCHNH), 4.57 (s, 2H, NH_2), 4.06-3.99 (m, 2H, OCH_2), 1.07 (t, J = 7.1 Hz, 3H, CH_3); ^{13}C-NMR (101 MHz, DMSO-d_6) δ(ppm) 167.3 (O-C=O), 164.8 (NHC=O), 147.4 (C=C-NH_2), 140.3 (ArC-CH), 128.6 (ArCH), 128.0 (ArCH), 127.7 (ArCH), 103.3 (C=C-C=O), 59.3 (OCH_2), 57.8 (ArCHNH), 14.7 (CH_3).

Hydrogenation of 3-amino-4-carboethoxy-2-oxo-5-phenyl-3-pyrroline (2) over 10% Pd/C

This is our in-house method [19]. To a stirred solution of 3-amino-4-carboethoxy-2-oxo-5-phenyl-3-pyrroline (**2**) (0.50 g, 2.03 mmol) in acetic acid (50 mL), 10% Pd/C (0.30 g, 0.26 mmol) was added slowly. The reaction mixture was stirred vigorously under hydrogen atmosphere at 1 atm with TLC monitoring. After 22 hours, the reaction was stopped and the catalyst was filtered through Celite. The solvent was removed from the filtrate under reduced pressure to give a white solid. From TLC, FT-IR and NMR characterization experiments, it was concluded that the starting material **2** was recovered.

Analytical data: TLC (Petreoleum ether/ethyl acetate : 2/1, R_f = 0.26); FT-IR (ATR) $\bar{\upsilon}$ (cm^{-1}) 3482 (N-H), 3385 (N-H), 3278 (N-H), 2965 (C-H), 1718 (conj. C=O), 1679 (C=O), 1625; ^{1}H-NMR (400 MHz, DMSO-*d*6) δ(ppm) 9.10 (s, 2H, NH_2), 7.27-7.12 (m, 5H, ArH), 6.46 (s, 1H, NHC=O), 5.06 (s, 1H, ArCHNH), 3.91 (qt, J = 11.0, 3.5 Hz, 2H, OCH_2), 0.98 (t, J = 7.1 Hz, 3H, CH_3); ^{13}C-NMR (101 MHz, DMSO-d_6) δ(ppm) 167.3 (O-C=O), 164.8 (NHC=O), 147.4 (C=C-NH_2), 140.3 (ArC-CH), 128.6 (ArCH), 128.0 (ArCH), 127.7 (ArCH), 103.3 (C=C-C=O), 59.3 (OCH_2), 57.8 (ArCHNH), 14.7 (CH_3).

Synthesis of 4-carboethoxy-3-methylamino-2-oxo-5-phenyl-3-pyrroline (4)

The method was adapted from literature [2]. To a suspension of 4-carbethoxy-3-hydroxy-2-oxo-5-phenyl-3-pyrroline (**1**) (1.94 g, 8 mmol) in ethanol (40 mL), aqueous methylamine (40%) (1.4 mL, 16 mmol) was added while stirring. After heating under reflux for 24 hours with TLC monitoring, the mixture was left to cool to room temperature. After cooling in an ice bath, the resulting white crystals were filtered to give the product, 4-carboethoxy-3-methylamino-2-oxo-5-phenyl-3-pyrroline, as white crystals (Yield: 1.41 g, 69%).

Analytical data: TLC (Ethyl acetate, R_f = 0.83); FT-IR (ATR) $\bar{\upsilon}$ (cm^{-1}) 3351 (N-H), 2980 (C-H), 1698 (C=O), 1667 (C=O), 1633; ^{1}H-NMR (400 MHz, $CDCl_3$) δ(ppm) 7.30-7.20 (m, 5H, ArH), 6.48 (s, 1H, CH_3NH), 5.14 (s, 1H, ArCHNH), 4.04-3.93 (m, 2H, OCH_2), 3.34 (s, 3H, CH_3NH), 1.71 (s, 1H, CH_3NH), 1.03 (t, J = 7.1 Hz, 3H, CH_3); ^{13}C-NMR (101 MHz, $CDCl_3$) δ(ppm) 167.9 (O-C=O), 166.6 (NHC=O), 147.1 (C=C-$NHCH_3$), 138.9 (ArC-CH), 128.4 (ArCH), 128.1 (ArCH), 127.4 (ArCH), 104.8 (C=C-C=O), 59.5 (OCH_2), 57.9 (ArCHNH), 30.2 ($NHCH_3$), 14.1 (CH_3).

Hydrogenation of 4-carboethoxy-3-methylamino-2-oxo-5-phenyl-3-pyrroline (4) over 10% palladium on carbon (Pd/C)

This is our in-house method [19]. To a stirred solution of 4-carboethoxy-3-methylamino-2-oxo-5-phenyl-3-pyrroline (**4**) (0.50 g, 1.92 mmol) in acetic acid (10 mL), 10% Pd/C (0.20 g, 0.19 mmol) was added

slowly. The reaction mixture was stirred vigorously under hydrogen atmosphere at 1 atm with TLC monitoring. After 24 hours, the reaction was stopped and the catalyst was filtered through Celite. The solvent was removed from the filtrate under reduced pressure and the residue was purified by column chromatography (gradient elution) to yield the diastereomers of 4-carbethoxy-3-methylamino-2-oxo-5-phenylpyrrolidine as yellow oils; *cis-trans* **5a** (Yield: 51.9 mg, 10.3%), *all-trans* **5b** (Yield: 22.9 mg, 4.5%) and *all-cis* **5c** (Yield: 48.3 mg, 9.6%).

Analytical data: FT-IR (ATR) $\bar{\upsilon}$ (cm^{-1}) 3395 (N-H), 3200 (N-H), 2981 (C-H), 1698 (C=O), 1646 (C=O); *cis-trans* **5a**: TLC (Ethyl acetate, R_f = 0.53); ^{1}H-NMR (400 MHz, CD_3OH) δ(ppm) 7.38-7.28 (m, 5H, ArH), 4.98 (d, J = 4.8 Hz, 1H, H-5), 4.57 (s, 1H, $CH_3N\underline{H}$), 4.19-4.16 (dq, 2H, OCH_2), 3.60 (d, J = 8.4 Hz, 1H, H-3), 3.31 (m, 1H, H-4), 2.45 (s, 3H, $C\underline{H_3}NH$), 1.24 (t, J = 7.6 Hz, 3H, CH_3); ^{13}C-NMR (101 MHz, CD_3OH) δ(ppm) 176.0 (NHC=O), 171.1 (O-C=O), 140.4 (Ar$\underline{C}$-CH), 128.8 (ArCH), 128.1 (ArCH), 125.8 (ArCH), 61.4 (C-3), 60.8 (OCH_2), 58.0 (C-5), 53.9 (C-4), 34.0 ($NHCH_3$), 13.2 (CH_3). *all-trans* **5b**: TLC (Ethyl acetate, R_f = 0.13); ^{1}H-NMR (400 MHz, CD_3OH) δ(ppm) 7.40-7.31 (m, 5H, ArH), 4.73 (d, J = 8.2 Hz, 1H, H-5), 4.22-4.11 (m, 2H, OCH_2), 3.95 (d, J = 9.6 Hz, 1H, H-3), 3.01 (dd, J = 9.8, 8.5 Hz, H-4), 2.51 (s, 3H, $C\underline{H_3}NH$), 1.18 (t, J = 7.3 Hz, 3H, CH_3); ^{13}C-NMR (101 MHz, CD_3OH) δ(ppm) 175.6 (NHC=O), 173.4 (O-C=O), 140.0 (Ar$\underline{C}$-CH), 128.6 (ArCH), 128.3 (ArCH), 126.4 (ArCH), 62.7 (C-4), 61.4 (OCH_2), 58.2 (C-3), 55.4 (C-5), 32.2 ($NHCH_3$), 13.1 (CH_3). *all-cis* **5c**: TLC (Ethyl acetate, R_f = 0.31); ^{1}H-NMR (400 MHz, CD_3OH) δ(ppm) 7.38-7.29 (m, 5H, ArH), 5.11 (d, J = 6.4 Hz, 1H, H-5), 4.05 (d, J = 6.9 Hz, 1H, H-3), 3.86 (t, J = 6.9 Hz, 1H, H-4), 3.73-3.67 (m, 1H, OCH_2), 3.57-3.51 (m, 1H, OCH_2), 2.63 (s, 3H, $C\underline{H_3}NH$), 0.71 (t, J = 7.1 Hz, 3H, CH_3); ^{13}C-NMR (101 MHz, CD_3OH) δ(ppm) 174.6 (NHC=O), 169.4 (O-C=O), 136.6 (Ar$\underline{C}$-CH), 128.2 (ArCH), 126.3 (ArCH), 61.3 (C-3), 60.7 (OCH_2), 56.8 (C-5), 51.2 (C-4), 33.6 ($NHCH_3$), 12.5 (CH_3).

Hydrogenation of 4-carboethoxy-3-methylamino-2-oxo-5-phenyl-3-pyrroline (4) over 20% palladium hydroxide on carbon ($Pd(OH)_2$/C)

This method was adapted from our in-house method [19]. To a stirred solution of 4-carboethoxy-3-methylamino-2-oxo-5-phenyl-3-pyrroline (**4**) (0.50 g, 1.92 mmol) in acetic acid (10 mL), 20% $Pd(OH)_2$/C (0.13 g, 0.19 mmol) was added slowly. The reaction mixture was stirred vigorously under hydrogen atmosphere at 1 atm with TLC monitoring. After 24 hours, the reaction was stopped and the catalyst was filtered through Celite. The solvent was removed from the filtrate under reduced pressure and the residue was purified by column chromatography (gradient elution) to yield the diastereomers of 4-carbethoxy-3-methylamino-2-oxo-5-phenylpyrrolidine as yellow oils; *cis-trans* **5a** (Yield: 11.4 mg, 2.2%), *all-trans* **5b** (Yield: 0.7 mg, 0.1%) and *all-cis* **5c** (Yield: 10.3 mg, 2.0%).

Analytical data: FT-IR (ATR) $\bar{\upsilon}$ (cm^{-1}) 3358 (N-H), 3193 (N-H), 2982 (C-H), 1698 (C=O), 1646 (C=O); *cis-trans* **5a**: TLC (Ethyl acetate, R_f = 0.43); ^{1}H-NMR (400 MHz, $CDCl_3$) δ(ppm) 7.34-7.25 (m, 5H, ArH), 6.58 (s, 1H, $CH_3N\underline{H}$), 4.98 (d, J = 3.7 Hz, 1H, H-5), 4.21-4.12 (m, 2H, OCH_2), 3.58 (d, J = 8.2 Hz, 1H, H-3), 3.27 (dd, J = 4.1 Hz, H-4), 2.46 (s, 3H, $C\underline{H_3}NH$), 1.23 (t, J = 7.1 Hz, 3H, CH_3); ^{13}C-NMR (101 MHz, $CDCl_3$) δ(ppm) 175.1 (NHC=O), 170.8 (O-C=O), 140.5 (Ar$\underline{C}$-CH), 129.2 (ArCH), 126.0 (ArCH), 125.7 (ArCH), 61.3 (C-3), 60.7 (OCH_2), 57.6 (C-5), 54.1 (C-4), 35.4 ($NHCH_3$), 14.1 (CH_3). *all-trans* **5b**: TLC (Ethyl acetate, R_f = 0.11); ^{1}H-NMR (400 MHz, Acetone-d_6) δ(ppm) 7.38-7.30 (m, 5H, ArH), 4.71 (d, J = 8.4 Hz, 1H, H-5), 4.15-4.12 (m, 2H, OCH_2), 3.60 (d, J = 9.6 Hz, 1H, H-3), 2.80 (m, 1H, H-4), 2.40 (s, 3H, $C\underline{H_3}NH$), 1.16 (t, J = 7.2 Hz, 3H, CH_3); ^{13}C-NMR (101 MHz, Acetone-d_6) δ(ppm) 173.8 (NHC=O), 172.0 (O-C=O), 141.2 (Ar$\underline{C}$-CH), 128.7 (ArCH), 128.2 (ArCH), 126.4 (ArCH), 64.4 (C-3), 60.8 (OCH_2), 57.8 (C-5), 57.6 (C-4), 33.9 ($NHCH_3$), 13.6 (CH_3). *all-cis* **5c**: TLC (Ethyl acetate, R_f = 0.26); ^{1}H-NMR (400 MHz, $CDCl_3$) δ(ppm) 7.33-7.29 (m, 3H, ArH), 7.18-7.16 (m,

2H, ArH), 6.64 (s, 1H, $CH_3N\underline{H}$), 5.00 (d, J = 9.6 Hz, 1H, H-5), 4.10 (d, J = 9.1 Hz, 1H, H-3), 3.81-3.76 (m, 1H, H-4), 3.73-3.61 (m, 2H, OCH_2), 2.15 (s, 3H, $C\underline{H}_3NH$), 0.93 (t, J = 7.3 Hz, 3H, CH_3); ^{13}C-NMR (101 MHz, $CDCl_3$) δ(ppm) 175.3 (NHC=O), 169.7 (O-C=O), 137.7 (Ar$\underline{C}$-CH), 128.8 (ArCH), 127.2 (ArCH), 126.9 (ArCH), 61.2 (C-4), 59.4 (C-3), 57.6 (C-5), 52.1 (OCH_2), 31.1 ($NHCH_3$), 13.8 (CH_3).

Reduction of 4-carboethoxy-3-methylamino-2-oxo-5-phenyl-3-pyrrolines (4) by sodium triacetoxyborohydride ($NaBH(OAc)_3$)

The method was adapted from literature [9]. A solution of $NaBH(OAc)_3$ was prepared by the addition of sodium borohydride ($NaBH_4$) (0.73 g, 19 mmol) to glacial acetic acid (5.6 mL, 96 mmol) at 0 °C and the mixture was stirred for 30 minutes at room temperature with some evolution of hydrogen gas. Then, 4-carboethoxy-3-methylamino-2-oxo-5-phenyl-3-pyrroline (**4**) (1.01 g, 4 mmol) in acetonitrile (25 mL) was transferred into the previous mixture. The resulting mixture was stirred vigorously for 48 hours before being neutralized by saturated Na_2CO_3 solution. Upon extraction by dichloromethane, the organic phase was washed with brine and dried over anhydrous $MgSO_4$. The solvent was removed from the organic phase *in vacuo* to give a white solid**.** From TLC, FT-IR and NMR characterization experiments, it was concluded that the starting material **4** was recovered.

Analytical data: TLC (Ethyl acetate, R_f = 0.79); FT-IR (ATR) $\bar{\upsilon}$ (cm^{-1}) 3351 (N-H), 2980 (C-H), 1698 (C=O), 1667 (C=O), 1633; ^{1}H-NMR (400 MHz, $CDCl_3$) δ(ppm) 7.30-7.21 (m, 5H, ArH), 6.43 (s, 1H, $CH_3N\underline{H}$), 5.14 (s, 1H, Ar$C\underline{H}$NH), 4.04-3.93 (m, 2H, OCH_2), 3.35 (s, 3H, $C\underline{H}_3NH$), 1.70 (s, 1H, $CH_3N\underline{H}$), 1.03 (t, J = 7.1 Hz, 3H, CH_3); ^{13}C-NMR (101 MHz, $CDCl_3$) δ(ppm) 167.9 (O-C=O), 166.6 (NHC=O), 147.1 (C=$\underline{C}$-$NHCH_3$), 138.9 (Ar$\underline{C}$-CH), 128.4 (ArCH), 128.1 (ArCH), 127.4 (ArCH), 104.8 (C=$\underline{C}$-C=O), 59.5 (OCH_2), 57.9 (ArCHNH), 30.2 ($NHCH_3$), 14.1 (CH_3).

Reduction of 4-carboethoxy-3-methylamino-2-oxo-5-phenyl-3-pyrroline (4) by sodium cyanoborohydride ($NaBH_3CN$)

The method was adapted from literature [8]. Traces of bromocresol green was added to 4-carboethoxy-3-methylamino-2-oxo-5-phenyl-3-pyrroline (**4**) (1.00 g, 4 mmol) in methanol (20 mL) while stirring followed by $NaBH_3CN$ (0.97 g, 15 mmol). Dilute MeOH-HCl mixture was added dropwise until the colour of the reaction mixture turned yellow. More MeOH-HCl was added to the mixture periodically to maintain the yellow colour (pH ~4) with TLC monitoring. After 24 hours, the reaction was quenched by dropwise addition of 0.1 N NaOH solution (saturated with NaCl) until the mixture turned blue. The crude product was extracted by ethyl acetate and the organic phase was washed with brine and dried over anhydrous $MgSO_4$. The solvent was evaporated under vacuum and the residue was purified by column chromatography (gradient elution) to give the diastereomers of 4-carbethoxy-3-methylamino-2-oxo-5-phenylpyrrolidine; *all-trans* **5b** (Yield: 174.7 mg, 34.7%) and *all-cis* **5c** (Yield: 97.6 mg, 19.4%).

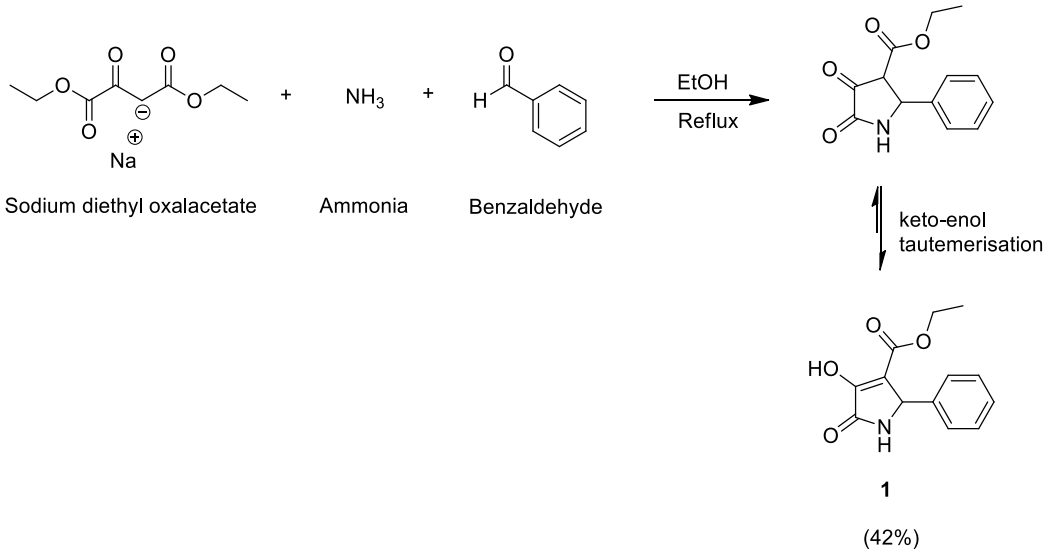
Analytical data: FT-IR (ATR) $\bar{\upsilon}$ (cm^{-1}) 3391 (N-H), 3306 (N-H), 2977 (C-H), 1718 (C=O), 1698 (C=O); *all-trans* **5b**: TLC (Ethyl acetate, R_f = 0.49); ^{1}H-NMR (400 MHz, $CDCl_3$) δ(ppm) 7.37-7.31 (m, 5H, ArH), 6.42 (s, 1H, $CH_3N\underline{H}$), 4.78 (d, J = 8.2 Hz, 1H, H-5), 4.18-4.16 (m, 2H, OCH_2), 3.84 (d, J = 9.6 Hz, 1H, H-3), 3.06 (t, J = 8.9 Hz, 1H, H-4), 2.16 (s, 3H, $C\underline{H}_3NH$), 1.20 (t, J = 7.1 Hz, 3H, CH_3); ^{13}C-NMR (101 MHz, $CDCl_3$) δ(ppm) 173.9 (NHC=O), 171.7 (O-C=O), 139.5 (Ar$\underline{C}$-CH), 129.0 (ArCH), 128.7 (ArCH), 126.5 (ArCH), 63.6 (C-3), 61.7 (OCH_2), 57.9 (C-5), 55.9 (C-4), 31.1 ($NHCH_3$), 14.1 (CH_3). *all-cis* **5c**: TLC (Ethyl acetate, R_f = 0.26); ^{1}H-NMR (400 MHz, $CDCl_3$) δ(ppm) 7.33-7.29 (m, 3H, ArH), 7.18-7.16 (m, 2H, ArH), 6.64 (s, 1H, $CH_3N\underline{H}$), 5.00 (d, J = 9.6 Hz, 1H, H-5), 4.10 (d, J = 9.1 Hz, 1H, H-3), 3.81-3.76 (m, 1H, H-4), 3.73-3.61 (m, 2H, OCH_2), 2.15 (s, 3H, $C\underline{H}_3NH$), 0.93 (t, J = 7.3 Hz, 3H, CH_3); ^{13}C-NMR (101 MHz, $CDCl_3$) δ(ppm) 175.3 (NHC=O), 169.7 (O-C=O), 137.7 (Ar$\underline{C}$-CH), 128.8 (ArCH), 127.2 (ArCH), 126.9 (ArCH), 61.2 (C-4), 59.4 (C-3), 57.6 (C-5), 52.1 (OCH_2), 31.1 ($NHCH_3$), 13.8 (CH_3).

Results and Discussion

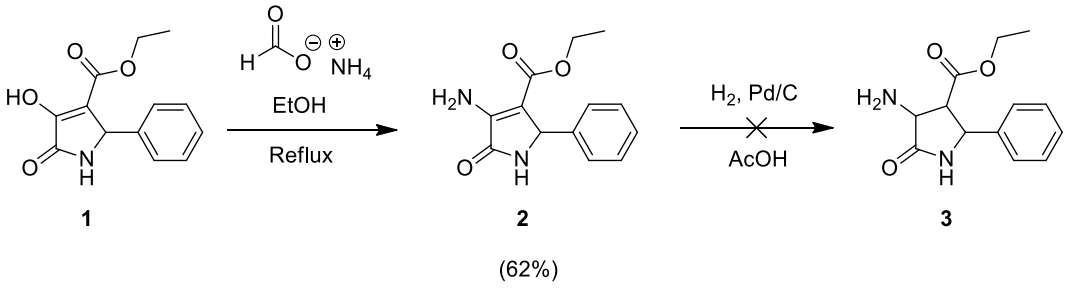
4-carbethoxy-3-hydroxy-2-oxo-5-phenyl-3-pyrroline (**1**) were prepared through one-pot multicomponent reaction (MCR) by refluxing equimolar sodium diethyl oxalacetate and benzaldehyde with excess aqueous ammonia in ethanol as developed by Metten et. al. (Scheme 1) [15]. The product was more stable in the enol rather than the keto form, consistent with previous findings [16-19]. The moderate yield was compromised for the ease of the purification process and overall facile procedure.

Afterwards, treatment of **1** with ammonium formate gave enamino ester **2** with a good yield via Leuckart reaction (Scheme 2) [2,3]. Hydrogenation of **2** in the presence of 10% Pd/C in acetic acid for 22 hours was ineffective, recovering the starting material. To our best knowledge, there is yet to be a report on a successful reduction of primary enamino esters such as **2**. Wang and co-workers described that the enamino group has to be protected prior to the hydrogenation to gain successful conversions [20]. Other works of literature suggested that there should be at least one substituent on the enamino functionality for the procedure to work [7-13]. Perhaps, the conjugated π system and alternating intramolecular hydrogen bonding form very stable 6-membered resonance structures (Figure 3) therefore preventing interaction with the metal catalyst.

However, methylamination of **1** in the presence of formic acid afforded secondary β-enamino ester (**4**), which was then reacted through four different reduction systems (Scheme 3).



Scheme 1. Synthesis of 4-carbethoxy-3-hydroxy-2-oxo-5-phenyl-3-pyrroline (**1**) via one-pot MCR



Scheme 2. Amination of **1** and the attempt to catalytically hydrogenate **2** over Pd/C

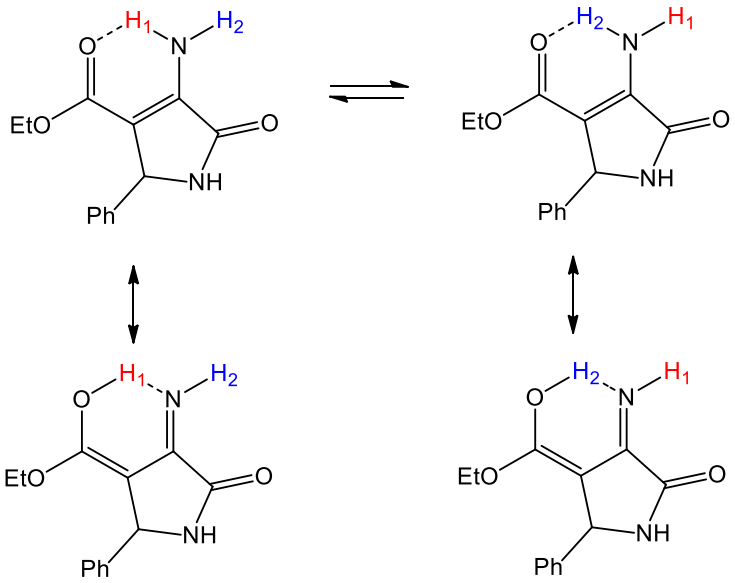
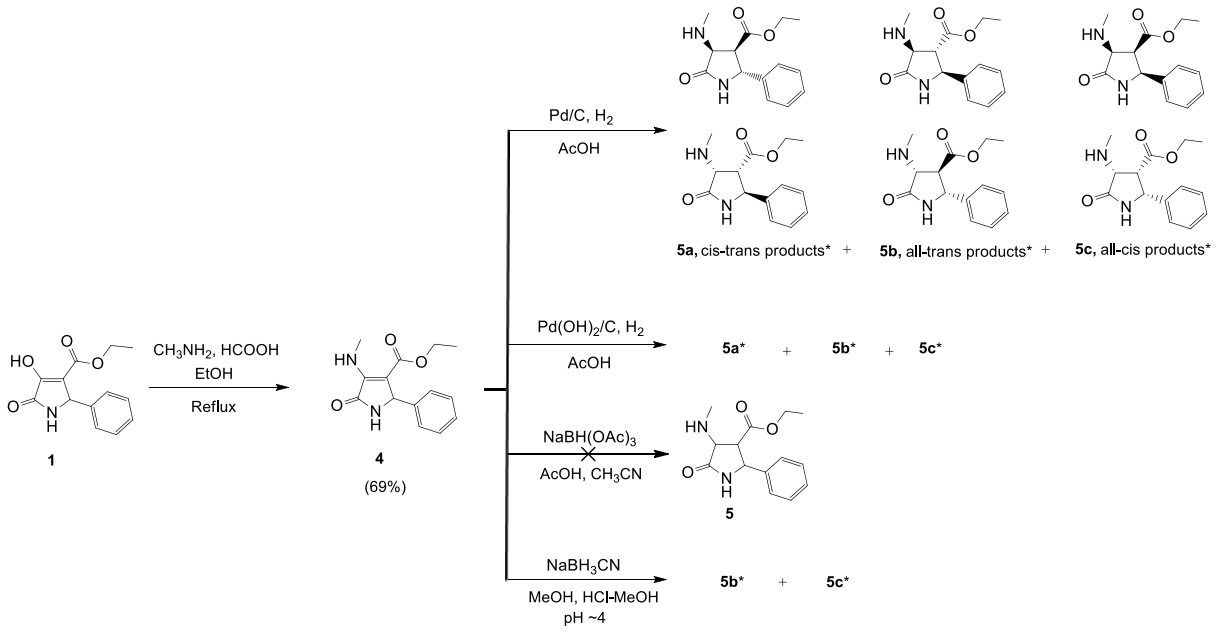


Figure 3. Intramolecular hydrogen bonding and the resonance structures of **2**.



* The absolute configuration was not determined. Thus, both possible enantiomers are displayed.

Scheme 3. Methylamination of **1** and various reduction protocols of **4**.

Pd/C hydrogenation of **4** displayed low diastereoselectivity (d.r. = 42 : 19 : 39) of three separable mixtures of β-amino ester diastereomers (**5a-c**) with low yields (4 to 10%) (Table 1). Hydrogenation of **5** in the presence of $Pd(OH)_2$ on charcoal was more diastereoselective (d.r. = 51 : 3 : 46) than Pd/C but afforded an even poorer yield (0.1 to 2.2%) of isomers (**5a-c**). Both catalytic processes involved the syn addition of hydrogens onto the double bond resulting in a nearly equivalent d.r. of **5a** (*cis-trans*) and **5c** (*all-cis*) products with a minor anti addition causing the formation of **5b** (*all-trans*) product, in agreement with one of our previous findings [17].

The treatment with sodium borohydride, $NaBH_4$ and acetic acid to form *in situ* sodium triacetoxyborohydride, $NaBH(OAc)_3$ failed to reduce compound **4**. On the other hand, reduction using sodium cyanoborohydride ($NaBH_3CN$) in acidic medium gained the mixture of **5b** and **5c** diastereomers, giving superior stereochemical control (d.r. = 64 : 36) than catalytic hydrogenations, with better yields. Deustch et. al. observed similar diastereomeric selectivities when reducing acyclic β-enamino ester derivatives by the same protocol [8].

Table 1. Stereoselective reduction of **4**

Reducing Agent	**Isolated Product Yield (%)***			**Diastereomeric ratio (d.r.)****
	5a	**5b**	**5c**	
Pd/C, H_2	10.3	4.5	9.6	42 : 19 : 39
$Pd(OH)_2$/C, H_2	2.2	0.1	2.0	51 : 3 : 46
$NaBH(OAc)_3$	-	-	-	-
$NaBH_3CN$	-	34.7	19.4	64 : 36

*Isolated yield of each diastereomeric product obtained after purification by column chromatography.
**Diasteremeric ratio (d.r.) was determined based on the isolated yield after column chromatography.

All resulting diastereomers were studied through nuclear magnetic resonance (NMR) experiments to assign their configurations. For instance, Nuclear Overhauser Effect Spectroscopy (NOESY) correlation between the hydrogen at C-4 (3.01 ppm) and aryl proton (7.35 ppm) in **5b** (*all-trans*) product confirmed that both the hydrogen and the phenyl ring are on the same side (Figure 4) whereby in **5c** (*all-cis*) product, the correlation between the hydrogens at C-4 (3.86 ppm) and C-5 (5.11 ppm) were observed, indicating their close proximities to each other. This claim is supported by the low proton NMR (^{1}H-NMR) chemical shift value of the hydrogen on C-4 of **5b** compared to that of **5c** due to the anisotropic effect of being near the phenyl ring. Moreover, **5b** diastereomer showed significantly higher values of $J_{4,5}$ coupling constant than **5c** (Table 2).

Alternatively, the assignment of *cis*-configuration between protons on C-4 and C-5 of **5c** isomer can be further proven by another anisotropy experienced by protons of its ester moiety indicated by their lower chemical shift values in comparison to those of **5a** (*cis-trans*) and **5b** diastereomers. On another note, the NOESY correlation between the hydrogen on C-4 (3.01 ppm) with methylamine proton (2.51 ppm) of **5b** led to the notion that the protons on C-3 and C-4 were *trans* to each other while for **5a**, its C-4 proton (3.35 ppm) correlated with the one on C-3 (3.60 ppm) thus they were assigned as *cis*.

The mechanistic pathway that we proposed for these catalytic hydrogenations is displayed in Scheme 4. Syn addition of hydrogens on either side of the C=C of the enamino ester caused both the methylamine and ester groups to be on the same side. These structural changes

gave rise to steric clashes between the ester and phenyl ring that determined which conformer was more favourable. The steric strain in **5c** (ester and phenyl groups located near to each other) contributed to a slightly lower yield compared to the thermodynamic product **5a** (the groups were on opposite sides).

Anti addition of hydrogens by metal-catalysed hydrogenation was initiated by the formation of an enolate intermediate through the protonation of one of the prochiral centres which are C-3 in **5b**, the less hindered site (Scheme 4). The following step involved the addition of another hydrogen on C-4 selectively to form a stable conformer whereby the ester group and phenyl ring were situated on different planes (lower steric strain) thus resulting in the *trans*-position between the hydrogens on C-3 and C-4 [10].

$NaBH_3CN$ reduction began with a rate-determining step of acid protonation on C-4 of **4** from either side of the C=C of the enamino ester, thus forming respective iminium intermediates (Scheme 5) [21]. Then, an attack by cyanoborohydride from the less crowded site (away from the phenyl ring) restored the nitrogen lone pair electrons. The reagent selectively favoured the formation of **5b** over **5c** due to the greater strain between ester and phenyl groups in **5c**, consequently causing the latter to be less energetically stable.

The poor yield of $Pd(OH)_2$ hydrogenation compared to Pd/C and the unsuccessful reduction by $NaBH(OAc)_3$ can be explained by the bulkiness of the reagent structures causing severe steric hindrance that antagonized the reactions.

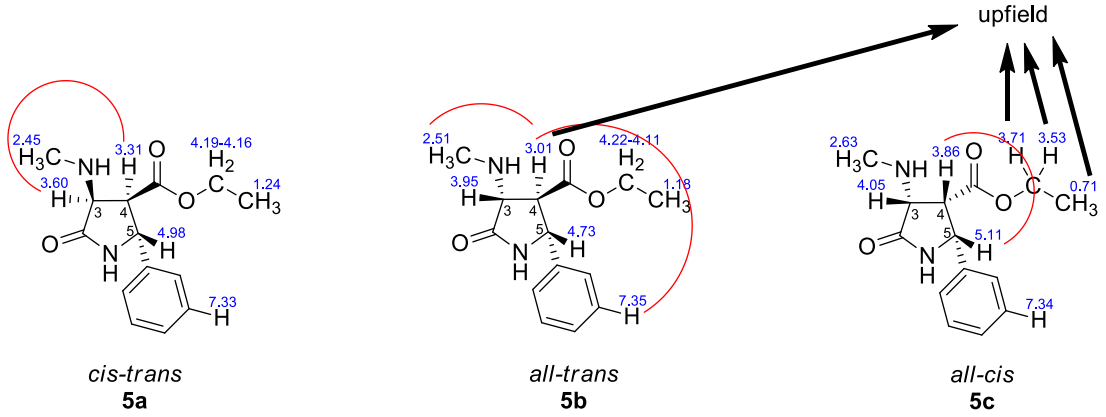
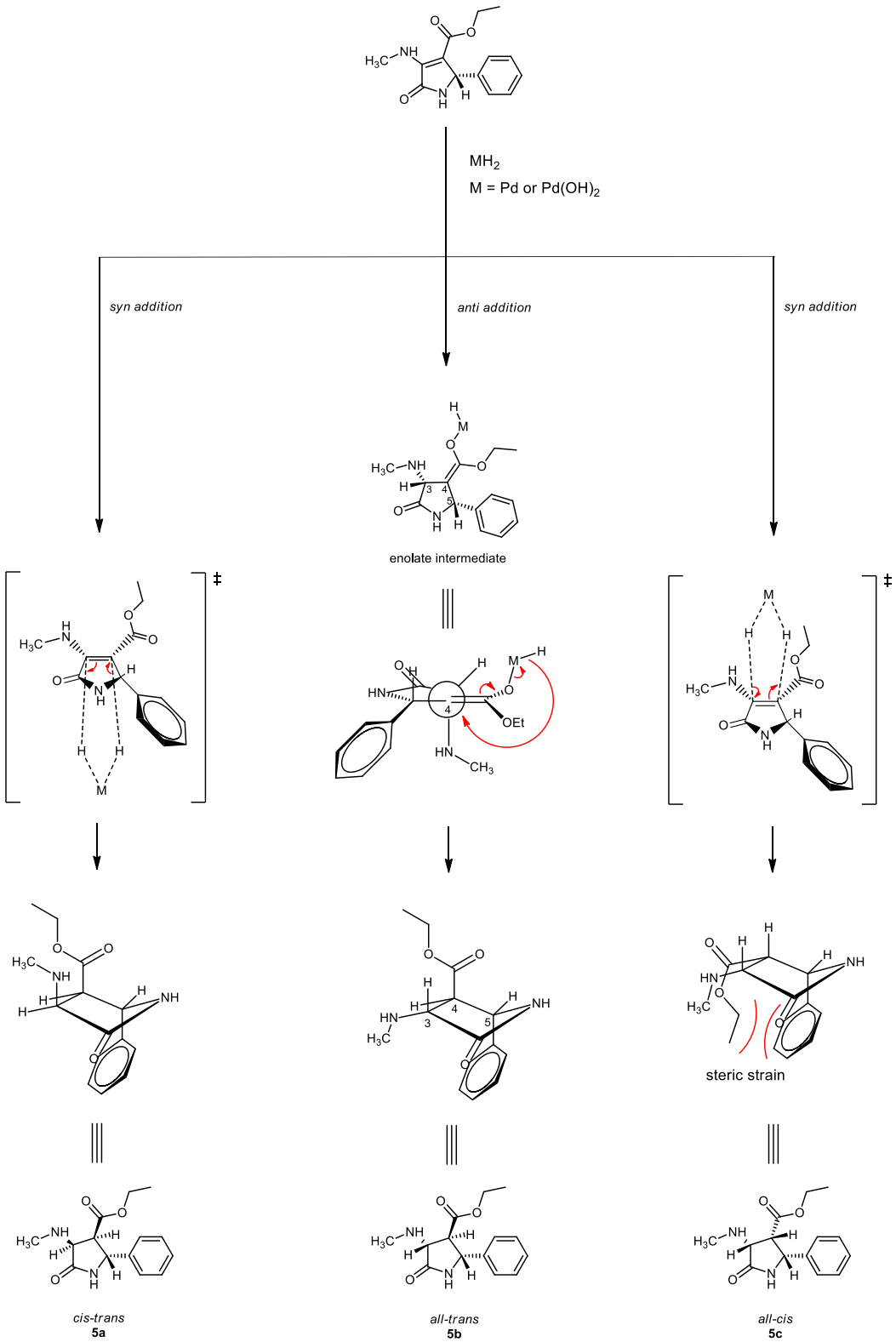


Figure 4. ^{1}H-NMR shift values and NOESY correlations of diastereomers **5a-c**

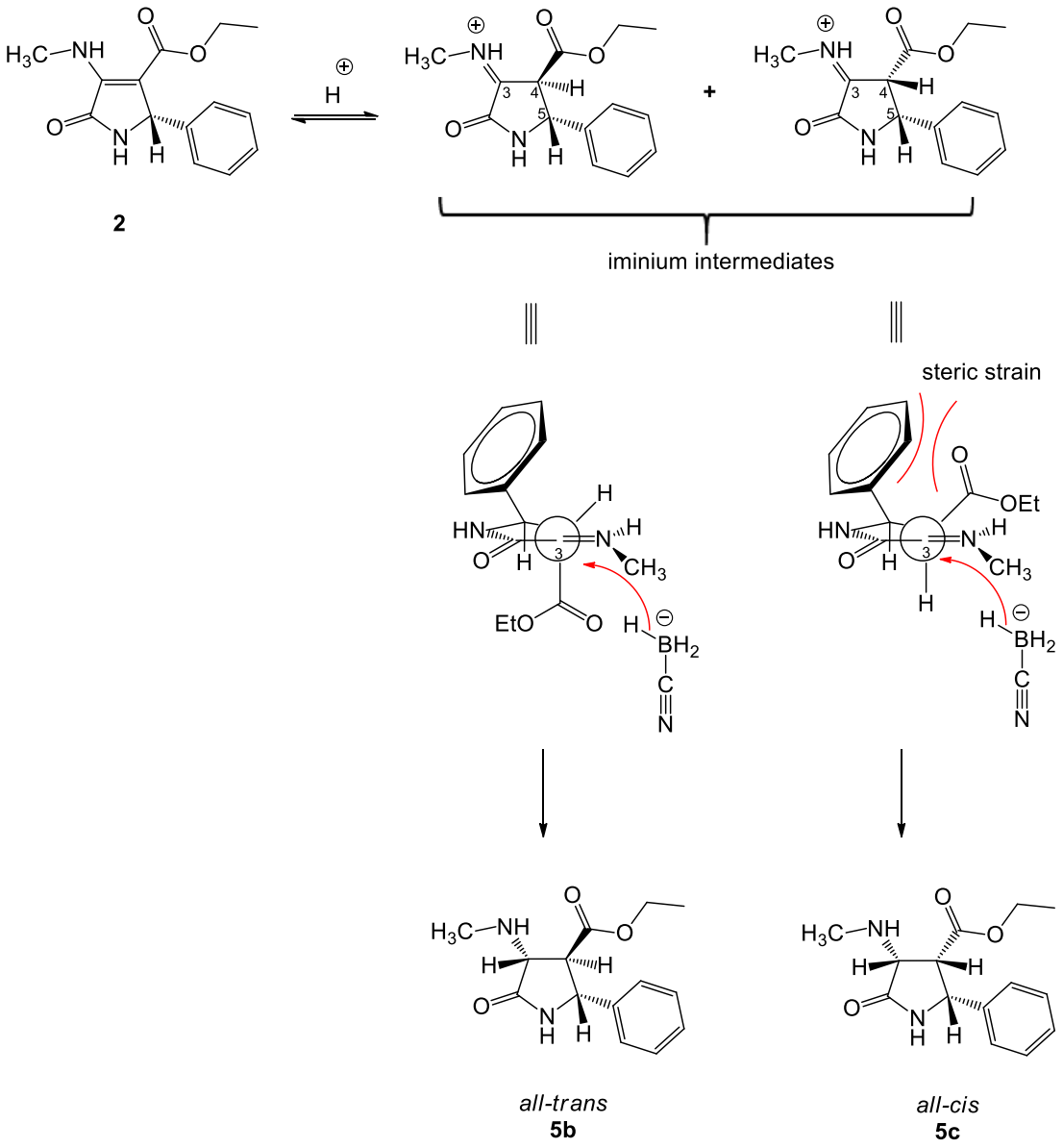
Table 2. Selected ^{1}H-NMR data for diastereomers **5a-c** in methanol-d_4

Compound	Shift value, δ (ppm)			Coupling constant, J (Hz)		
	H-3	H-4	H-5	H-3	H-4	H-5
5a	3.60	3.35	4.99	8.4	–*	4.8
5b	3.95	3.01	4.73	9.6	8.5	8.2
5c	4.05	3.86	5.11	6.9	6.9	6.4

*H-4 of **5a** showed a multiplet pattern



Scheme 4. Proposed mechanistic pathways for Pd and $Pd(OH)_2$ hydrogenation of **4**



Scheme 5. Plausible reaction mechanism for reduction of **4** by $NaBH_3CN$.

Conclusion

Overall, the stereochemical control for this class of functional group depends strongly on the position of the ester group in regards to the phenyl ring after the protonation/reduction steps i.e. if they are on the same plane, the lower the preference for the formation of said diastereomer. This brief experiment shows that endocyclic β-enamino ester (**4**) can be reduced with excellent diastereoselectivity by $NaBH_3CN$ (d.r. = 64 : 36), in addition to its moderate turnover percentage (54.1%). Hydrogenations on Pd and $Pd(OH)_2$ surfaces suffered from poor selectivities (d.r. = 42 : 19 : 39 and d.r. = 51 : 3 : 46, respectively) and yields (0.1 to 10.3%) with unexpected anti additions of hydrogens while $NaBH(OAc)_3$ reduction recovered the starting material. Nevertheless, we have successfully employed some of these reduction strategies to prepare chiral

cyclic β-amino ester with satisfying diastereomeric purity.

Acknowledgement

We would like to thank University Teknologi MARA (UiTM) for providing the facilities to conduct the research and International Islamic University Malaysia (IIUM) along with the Malaysian Ministry of Higher Education (MoHE) for the financial support (FRGS/1/2017/STG01/UIAM/03/2 [Project ID: 11794]).

References

1. Xin, D., & Burgess, K. (2014). A Chemoselective Route to β-Enamino Esters and Thioesters. *Organic Letters*, *16*(8), 2108-2110.
2. Southwick, P. L., & Hofmann, G. H. (1963). Compounds in the pyrrolo[3,4-*d*]pyrimidine series. Syntheses based on 2, 3-dioxopyrrolidines. *The Journal of Organic Chemistry*, *28*(5), 1332-1336.
3. Madhav, R., Dufresne, R. F., & Southwick, P. L. (1973). The preparation of derivatives 9-oxo-2,3,4,9-tetrahydro-1*H*-pyrrolo[3,4-*b*]quinoline and 7-oxo-7,9,10,11-tetrahydro-8*H*-benzo[*h*]pyrrolo [3,4-*b*]quinoline. *Journal of Heterocyclic Chemistry*, *10*(2), 225-228.
4. Jia, Z., Nagano, T., Li, X., & Chan, A. S. (2013). Iodide-Ion-Catalyzed Carbon–Carbon Bond-Forming Cross-Dehydrogenative Coupling for the Synthesis of Indole Derivatives. *European Journal of Organic Chemistry*, *2013*(5), 858-861.
5. David, O., Fargeau-Bellassoued, M. C., & Lhommet, G. (2002). A short and convenient synthesis of chiral heterocyclic β-enamino esters from halogeno acetylenic esters. *Tetrahedron Letters*, *43*(19), 3471-3474.
6. Calvet, S., David, O., Vanucci-Bacqué, C., Fargeau-Bellassoued, M. C., & Lhommet, G. (2003). Chiral heterocyclic β-enamino esters: convenient synthesis and diastereoselective reduction. *Tetrahedron*, *59*(33), 6333-6339.
7. Hart, D. J., Hong, W. P., & Hsu, L. Y. (1987). Total synthesis of (±)-Lythrancepine II and (±)-Lythrancepine III. *The Journal of Organic Chemistry*, *52*(21), 4665-4673.
8. Deutsch, H. M., Ye, X., Shi, Q., Liu, Z., & Schweri, M. M. (2001). Synthesis and pharmacology of site specific cocaine abuse treatment agents: a new synthetic methodology for methylphenidate analogs based on the Blaise reaction. *European Journal of Medicinal Chemistry*, *36*(4), 303-311.
9. Calvet-Vitale, S., Vanucci-Bacqué, C., Fargeau-Bellassoued, M. C., & Lhommet, G. (2005). Stereocontrolled reduction of chiral pyrrolidine and piperidine β-enamino esters: formal enantioselective synthesis of (+)-calvine. *Tetrahedron*, *61*(32), 7774-7782.
10. David, O., Blot, J., Bellec, C., Fargeau-Bellassoued, M. C., Haviari, G., Célérier, J. P., & Gardette, D. (1999). Enamino ester reduction: A short enantioselective route to pyrrolizidine and indolizidine alkaloids. Synthesis of (+)-laburnine,(+)-tashiromine, and (−)-isoretronecanol. *The Journal of Organic Chemistry*, *64*(9), 3122-3131.
11. Haviari, G., Célérier, J. P., Petit, H., & Lhommet, G. (1993). Asymmetric synthesis with chiral hydrogenolysable amines. A short synthesis of (-)-isoretronecanol. *Tetrahedron letters*, *34*(10), 1599-1600.
12. Zhang, X., Mi, N., Liu, H., & Liu, Y. (2019). An approach to highly efficient reduction of β-enamino esters: A convenient synthesis of β-amino esters. *Journal of Chemical Research*, *43*(5-6), 196-200.
13. Cimarelli, C., & Palmieri, G. (1996). Stereoselective reduction of enantiopure β-enamino esters by hydride: a convenient synthesis of both enantiopure β-amino esters. *The Journal of Organic Chemistry*, *61*(16), 5557-5563.
14. Furukawa, M., Okawara, T., Noguchi, Y., & Terawaki, Y. (1979). Asymmetric syntheses of β-amino acids by the reduction of enamines. *Chemical and Pharmaceutical Bulletin*, *27*(9), 2223-2226.
15. Metten, B., Kostermans, M., Van Baelen, G., Smet, M., & Dehaen, W. (2006). Synthesis of 5-aryl-2-oxopyrrole derivatives as synthons for highly substituted pyrroles. *Tetrahedron*, *62*(25), 6018-6028.

16. Mohammat, M. F., Najim, N., Mansor, N. S., Sarman, S., Shaameri, Z., Zain, M. M., & Hamzah, A. S. (2011). Synthesis and bioactivity of some 2-oxo-5-aryl-3-hydrazone and 2-oxo-5-aryl-4-hydrazone pyrrolidine derivatives. *ARKIVOC: Online Journal of Organic Chemistry*.
17. Mohammat, M. F., Mansor, N. S., Shaameri, Z., & Hamzah, A. S. (2015). Diastereoselective Reduction of 2,3-Dioxo-4-carboxy-5-substituted Pyrrolidines Using $NaBH_4$/AcOH and Heterogenous Hydrogenation Reactions. *Journal of the Korean Chemical Society*, *59*(1), 31-35.
18. Rashid, F. N. A. A., Mohammat, M. F., Shaameri, Z., & Hamzah, A. S. (2019). Synthesis of novel 3,4-fused pyrazolidinone γ-lactam bicyclic moieties from 2,3-dioxo-4-carboxy-5-(substituted) pyrrolidines. *Organic Communications*, *12*(3), 121-131.
19. Rashid, F. N. A. A., Mohammat, M. F., Bouchamma, F. E., Shaameri, Z., & Hamzah, A. S. (2020). Facile Reduction of β-Enamino Oxopyrrolidine Carboxylates Mediated by Heterogeneous Palladium Catalyst. *Russian Journal of Organic Chemistry*, *56*(6), 1082-1088.
20. Wang, G. T., Chen, Y., Wang, S., Gentles, R., Sowin, T., Kati, W., ... & Kempf, D. (2001). Design, synthesis, and structural analysis of influenza neuraminidase inhibitors containing pyrrolidine cores. *Journal of medicinal chemistry*, *44*(8), 1192-1201.
21. Borch, R. F., Bernstein, M. D., & Durst, H. D. (1971). Cyanohydridoborate anion as a selective reducing agent. *Journal of the American Chemical Society*, *93*(12), 2897-2904.

Malaysian Journal of Analytical Sciences (MJAS)
Published by Malaysian Analytical Sciences Society

CHROMIUM (VI) ANALYSIS IN EFFLUENTS USING LIQUID-LIQUID EXTRACTION COUPLED WITH FLAME ATOMIC ABSORPTION SPECTROMETRY

(Analisis Kromium (VI) dalam Efluen Menggunakan Pengekstrakan Cecair-Cecair Bersama Spektrometri Serapan Nyalaan Atom)

Nguyen Cong-Hau[1], Le-Thi Anh-Dao[1], Nguyen Thanh-Nho[1]*, Le-Thi Huynh-Mai[2], Le Nhon-Duc[3], Do Minh-Huy[1]

[1]Faculty of Environmental and Food Engineering,
Nguyen Tat Thanh University, Ho Chi Minh City, Vietnam
[2]Faculty of Chemistry,
University of Science, Vietnam National University Ho Chi Minh City, Vietnam
[3]Warrantek Joint Stock Company, Testing Center, Can Tho City, Vietnam

**Corresponding author: ntnho@ntt.edu.vn*

Received: 1 September 2021; Accepted: 10 January 2022; Published: 28 April 2022

Abstract

Simple sample preparation was investigated and developed to selectively determine Cr(VI) in wastewater samples or effluents based on the liquid-liquid extraction principle using tetrabutylammonium hydrogensulfate (TBAHS) as the ion-pair reagent in an acidic medium. TBAHS was prepared in an organic solvent to improve the extraction efficiency. The extracted Cr(VI) in the organic phase endured the acid digestion, and its atomic absorption was measured at 357.9 nm. The influences of several working parameters, namely, organic solvents (methyl isobutyl ketone-MIBK, dichloromethane-DCM, and chloroform), pH values (lower than 1.0, 1.0, 2.0, and 3.0) in the aqueous phase, TBAHS concentrations in the organic solvent (0.02, 0.04, 0.05, and 0.06 mol L^{-1}), extraction duration (from 3 to 30 minutes), number of extraction cycles (single or repeated extraction), sample preservation duration at ambient temperature, and co-existence of Cr(III) in the sample matrices, were investigated to discover the optimized working parameters. The results showed that dichloromethane (DCM) was the most effective extraction solvent. The most favorable conditions for complex formation were determined as follows: a pH of around 1.0 to 3.0; 0.05 mol L^{-1} TBAHS prepared in DCM, triple extraction, and a shaking duration of 15 minutes for each extraction cycle. The calibration curve was linear in the range of 0.05, 0.10, 0.20, 0.40, 0.60, 0.90, 1.2, 1.5 and 2.0 mg L^{-1}, and the regression equation was $y = 0.1068x + 0.0012$ with $R^2 = 0.9994$, exhibiting goodness of linearity. The method detection and quantification limit values were estimated to be 0.012 mg L^{-1} and 0.04 mg L^{-1}, respectively. The repeatability (RSD_r = 0.71%) and reproducibility (RSD_R = 1.1%) were favorable according to the requirements presented in Appendix F of AOAC (2016) for analytical method validation. The proposed method was applied to real wastewater samples and spiked samples, showing very low Cr(VI) concentrations for most samples and proper recoveries (91.1-109%).

Keywords: Cr(VI), Cr(III), liquid-liquid extraction, TBAHS, dichloromethane, DCM, ion-pair reagent

Abstrak

Penyediaan sampel yang mudah telah dikaji dan dibangunkan bagi penentuan terpilih Cr(VI) di dalam air sisa atau efluen berdasarkan prinsip pengekstrakan cecair-cecair menggunakan tetrabutylammonium hidrogensulfat (TBAHS) sebagai reagen pasangan ion di dalam medium berasid. TBAHS telah disediakan dalam pelarut organik bagi tujuan meningkatkan keberkesanan pengekstrakan. Cr(VI) yang telah diekstrak di dalam fasa organik melalui penghadaman asid, dan serapan atom telah diukur pada 357.9 nm. Pengaruh parameter seperti pelarut organik (metil isobutil keton-MIBK, diklorometana-DCM, dan klorofom), nilai pH (dibawah 1.0, 1.0, 2.0 dan 3.0) di dalam fasa akues, kepekatan TBAHS di dalam pelarut organik (0.02, 0.04, 0.05, dan 0.06 mol L^{-1}), tempoh pengekstrakan (dari 3 hingga 30 minutes), bilangan kitaran pengekstrakan (pengekstrakan tunggal atau ulangan), tempoh pengawetan sampel pada suhu sekitar, dan kehadiran bersama Cr(III) dalam matrik sampel turut dikaji untuk penentuan parameter kerja yang optimum. Hasil kajian menunjukkan diklorometana (DCM) paling efektif sebagai pelarut pengekstrakan. Keadaan paling baik untuk penghasilan kompleks ditentukan seperti berikut: pH antara 1.0 hingga 3.0; 0.05 mol L^{-1} TBAHS disediakan dalam DCM, tiga kali pengekstrakan, dan masa goncangan ialah 15 minit bagi setiap kitaran pengekstrakan. Lengkung kalibrasi adalah linear pada julat 0.05 hingga 2.0 mg L^{-1}, dan persamaan regresi ialah $y = 0.1068x + 0.0012$ dan $R^2 = 0.9994$. Had pengesanan dan kuantifikasi telah dihitung masing-masing pada 0.012 mg L^{-1} and 0.04 mg L^{-1}. Kebolehulangan ($RSD_r = 0.71\%$) dan kebolehhasilan semula ($RSD_R = 1.1\%$) adalah baik berdasarkan keperluan yang dinyatakan dalam Appendix F of AOAC (2016) bagi validasi kaedah analisis. Kaedah yang dicadang ini telah digunapakai bagi analisis sampel air sisa sebenar dan sampel yang dipaku, ia menunjukkan kepekatan Cr(VI) yang rendah dan perolehan semula yang baik (91.1-109%).

Kata kunci: Cr(VI), Cr(III), pengekstrakan cecair-cecair, diklorometana, reagen pasangan ion

Introduction

Chromium (Cr) has been known as the non-essential and toxic element for human beings and animals despite existing in trace quantities [1, 2]. The emission of Cr into the environment is mainly derived from metallurgical, electroplating, pigments, etc. The two most common species of chromium are Cr(III) and Cr(VI), whereby Cr(VI) exhibits remarkably high toxicity due to its higher solubility and flexibility than Cr(III) [3, 4], 100 times more toxic than Cr(III). Many studies have indicated death risks from lung cancers during working and direct exposure to Cr(VI). Moreover, Cr(III) is considered an essential micro-nutrient and is responsible for blood glucose control and lipid metabolism in mammals. Because of their toxicity differences, the determination of total Cr concentrations did not provide enough reliable and accurate information to evaluate the toxicity potentials toward the environment. Additionally, the selective determination of Cr species has helped the scientists to recognize their origins and behaviors to find adequate solutions to remove these exposed pollutants from the environment. Modern instrumental methods using ICP-OES or ICP-MS coupled with liquid chromatography have met the requirements for direct analysis of Cr species in various sample matrix due to their selectivity and sensitivity [5, 6]. However, such methods are costly and not easily equipped in many laboratories. Therefore, another cheap, convenient, simple, and effective analytical method by using selective solvent or liquid-liquid extraction techniques (LLE) and measured on the Flame-Atomic Absorption Spectrometry (F-AAS) analysis, a common instrument for metal(loid)s quantification in various environmental laboratories, should be developed for Cr(VI) detection in complicated sample matrices such as wastewater.

For trace analysis of metal ions, solvent extraction has become a popular technique to serve the analyte enrichment and/or matrix removal purposes. Moreover, such techniques allow to easy control of the volumes of the aqueous and organic phases, which makes them possible to be coupled with any potentially suitable analytical methods for determining various metal ions. Typically, the volume of organic solvent used in the extraction is smaller than that of the sample volumes, resulting in higher enrichment factors and lower method limits of detection and quantification. At the industrial scale, solvent extraction has been utilized in chemical industries for the purification of chemical elements and/or for the separation and concentration of metals of interest [7, 8]. However, for the analytical

method development, the single application of organic solvents is usually faced with a lack of selectivity. Therefore, in order to enhance the selectivity of the LLE, complexing agents in organic solvents could be used. The separation of Cr(III) and Cr(VI) using ion-exchange and/or complex reagents in organic solvent have gained considerable interests among the scientists since the last few decades, e.g., zephyramine [9], bis(2-ethyl hexyl phosphoric acid) in benzene [10], diphenyl carbazide with isoamyl alcohol [11], and 4-methyl-3-pentene-2-one [12]. In 2009, Kalidhasan and Rajesh published the determination of Cr(VI) based on the LLE using tetrabutylammonium iodide (TBAI) as an ion-pair reagent in methyl isobutyl ketone (MIBK) used as the extraction solvent [8]. The ion-pair complex was back-extracted using ascorbic acid to convert Cr(VI) into free Cr(III) before spectrophotometric measurement for quantification purposes. The extraction of Cr(VI) using TBAB as the ion-pair reagent in dichloromethane was performed with 95% recovery [13].

As an emerging country with rapid development in industrialization and urbanization, Vietnam has been facing the risk of serious water pollution, as the heavy metals discharged from industrial activities have identified as a threat to public health and the safety of the ecosystem. Notably, the wastewater from the mechanical, electronic, dyeing, and tanning industries, etc., potentially has high concentrations of heavy metals, e.g., Cr, and in many cases, may exceed the permitted levels. In the present study, we employed the liquid-liquid extraction (LLE) using tetrabutylammonium sulfate (TBAHS) as the ion-pair reagent prepared in the extraction solvent of dichloromethane to separate Cr(VI) from the effluents into the organic phase before measuring the quantity using Flame Atomic Absorption Spectrometry (F-AAS). The preparation of TBAHS in the organic solvent instead of in water aimed to assist the chemical reaction between the analyte and the complexing agent, then to increase the extraction yield for quantification purposes. The parameters related to the LLE namely the concentrations of ion-pair reagent, extraction pH and solvents, reaction duration, numbers of extraction cycles (repeated extraction), and sample preservation as the co-existence of Cr(III), were evaluated to discover the optimized analytical conditions for real wastewater application. Moreover, in this current study, the ion-pair reagent was prepared in the extraction organic solvent instead of in the aqueous phase to increase the extraction efficiency, minimize the interferences of co-existing ions and substances, and improve the recovery of the proposed analytical method for quantification purposes.

Materials and Methods

Chemicals and reagents

All chemicals and reagents, including a stock solution of 1000 mg L^{-1} chromium (III), methyl isobutyl ketone (MIBK), dichloromethane (DCM), and chloroform, were of the analytical grade and purchased from Merck (Germany). A stock solution of 1000 mg L^{-1} chromium (VI) solution was prepared from potassium dichromate (≥ 99.9%, Merck, Germany). Working standard solutions of Cr(VI) were prepared daily by appropriate dilution of the 1000 mg L^{-1} stock solution using deionized water (DIW, Millipore, USA) before each use. Ion-pair reagents of 0.05 mol L^{-1} tetrabutylammonium hydrogensulfate (TBAHS) in extraction solvents namely dichloromethane (DCM), methyl isobutyl ketone (MIBK), and chloroform were prepared by dissolving 7.608 g of TBAHS in 500 mL of each of these solvents to obtain three different solutions used as the extraction solvent. Sulfuric acid of 1.0 mol L^{-1} was prepared by properly diluting the concentrated sulfuric acid in DIW. The Cr(VI) standard solution of 1.0 mg L^{-1} was prepared and used for evaluating the effects of various analytical parameters in the LLE, including types of organic solvents, pH index in the aqueous phase, ion-pair reagent concentrations in the extraction organic solvent, shaking duration per each extraction cycle, and the numbers of extraction cycles (single or repeated extraction). For the assessment of sample preservation at the ambient temperature, primarily due to the effects of Cr(III) co-existence, Cr(III) and Cr(VI) standard solutions were spiked into real wastewater samples to obtain the concentrations of both species at 1.0 mg L^{-1}.

Liquid-liquid extraction

The single factor experiment of the standard solution was used for optimizing the liquid-liquid extraction (LLE). The LLE was set up as follows: 1.00 mL of 10 mg L^{-1} Cr(VI) was added to 40 mL glass vial with a cap. The solution pH was adjusted to different investigated values, namely below 1.0, 1.0, 2.0, and 3.0 using 1.0 mol L^{-1} sulfuric acid and sodium hydroxide solutions. Then, 5.00 mL of TBAHS with various concentrations of 0.02, 0.04, 0.05, and 0.05 mol L^{-1} in the extraction organic solvents was added to the sample liquids to carry out the LLE. Three different organic solvents of methyl isobutyl ketone or MIBK, dichloromethane or DCM, and chloroform were investigated to discover the most suitable extraction solvent. The extraction was carried out by shaking the sample glass vial for a certain duration (3, 5, 10, 15, 20, 25, and 30 minutes). Single, double, and triple extractions were evaluated to find out the number of repeated extractions required for the highest recovery. All the organic phases were collected and transferred to another glass vial before being evaporated to the volume of around 1 mL by gentle heating at 60-70 ºC. Next, approximately 1 mL of concentrated nitric acid was added. The mixture was continued to heat until the volume observed was nearly 0.3-0.5 mL (do not heat to dry). Finally, the residue in the reaction vial was dissolved carefully in DIW and transferred to a 10-mL volumetric flask. The solution was filtered through a 0.45-µm membrane before measurement at 357.9 nm on an atomic absorption spectrometer.

Flame atomic absorption spectrometry for determining Cr(VI)

Cr(VI) determination after LLE was performed on a flame atomic absorption spectrometer (AA-6650 Shimadzu, Japan), equipped with a chromium hollow cathode lamp, an air-acetylene flame atomizer. The wavelength, lamp current, and spectral bandwidth used were 357.9 nm, 10 mA, and 0.5 nm, respectively. The burner height was 12 mm and the gas flow rate were 3.0 L min^{-1}. The background correction using a Deuterium lamp was applied for all measurements. The calibration curve was developed based on the linear relationship between the Cr(VI) standard concentrations (i.e., 0.05, 0.10, 0.20, 0.40, 0.60, 0.90, 1.2, 1.5 and 2.0 mg L^{-1}) prepared in 0.5% (v/v) nitric acid and the respective absorbance. The method limits of detection and quantification (MLD and MLQ) were determined by simultaneously analyzing 11 blank samples using the optimized LLE and F-AAS measurement. The estimated average concentration value ($\bar{x}$) and standard deviation (SD) were calculated to apply in the following relationships [14, 15]: MLD = $\bar{x}$ + 3SD and MLQ = 10/3*MLD. The repeatability and reproducibility were evaluated by calculating $\%RSD_r$ and $\%RSD_R$ for intra-day (six replicates, n = 6) and inter-day (three separate days). The trueness of the method was evaluated based on the recovery of the spiked samples.

Application of the proposed method to determine Cr(VI) in real effluent samples

A total number of 10 wastewater samples or effluents were randomly collected from several industrial parks around Ho Chi Minh City, based on ISO 5667-3:2003 [16] and ISO 5667-10:2020 [17]. The effluents were collected from the wastewater drain pipes of textile and electronics factories. The samples were contained in acid-washed polyethylene bottles, filtered through a 0.45-µm membrane (GE Whatman Membrane Filters, GF/F), and stored at freezing conditions (−10 ºC) until further analysis. These samples were analyzed by the proposed analytical method using the LLE procedure for the selective determination of Cr(VI). Besides, the Cr(VI) standard solution was spiked to these collected effluents to carry out the recovery test based on the real sample matrices, which aimed to assess the matrix effects on the analytes of interest.

Results and Discussion

Effects of extraction solvents

There are two possible ways for the extraction of Cr(VI from the aqueous phase to the organic phase. A common approach is the formation of an ion-pair complex in the aqueous phase, using an ion-pair reagent in water. The formed complex was extracted using a suitable organic solvent. However, the produced TBA^+–$HCrO_4^-$ ion-pair complex is less polar, and therefore poorly interactive with water. The molecule has a large molecular size, and thus is less stable in water, lowering extraction efficiency. Another

approach is to prepare the ion-pair reagent in organic solvents and carry out the LLE between aqueous and organic phases. In the present study, to enhance the extraction efficiency and minimize the interferences of co-existing ions and substances, the later approach was applied, i.e., the TBAHS was prepared in organic solvents, then used for LLE. The formation of an ion-pair complex could happen at the interface between the aqueous and organic phases (mostly in the aqueous phase) due to shaking effects. Such affects allow for the analyte of interest to be transferred into the organic solvent due to the stronger interaction formed by the ion-pair complex with organic solvents [8]. In the present study, three organic solvents were investigated for their potential use as extraction solvents, i.e., MIBK, DCM, and chloroform. The extraction yield (%) of Cr(VI) in the solvents (i.e., performing a single extraction within 10 minutes) is presented in Figure 1.

In descending order, the highest yield was obtained in DCM (97.4%), followed by chloroform (70.9%), and MIBK (26.9%). The differences in extraction yields could be due to the differences in the polarity of these solvents, of which MIBK has a relatively high polarity, and thus was less effective for extraction of Cr(VI). Meanwhile, DCM (polarity index of 3.1) and chloroform (polarity index of 4.1) are less polar than MIBK [18, 19], thus exhibiting higher extraction efficiency. Between DCM and chloroform, the former exhibited a better extraction efficiency, which may be due to the lower polarity and larger size of DCM molecules that allow for more favorable solvation for the ion-pair complex. The ion-pair complex is large in size, held by relatively weak electrostatic forces (Figure 3) but possesses enough stability to be effectively extracted to the organic phase [20]. Due to the large size of the formed complex, the organic solvents with larger molecule sizes may provide favorable conditions for better extraction yields than that of smaller molecule sizes under the same working parameters. Comparing between CCl_4 and $CHCl_3$ as the extraction solvent, CCl_4 with lower polarity was reported to perform higher extraction efficiency [21, 22]. Therefore, in this current study, an ion-pair reagent of TBAHS was prepared in DCM as a lower polar extraction solvent for further experiments and investigations to assure the highest extraction yield.

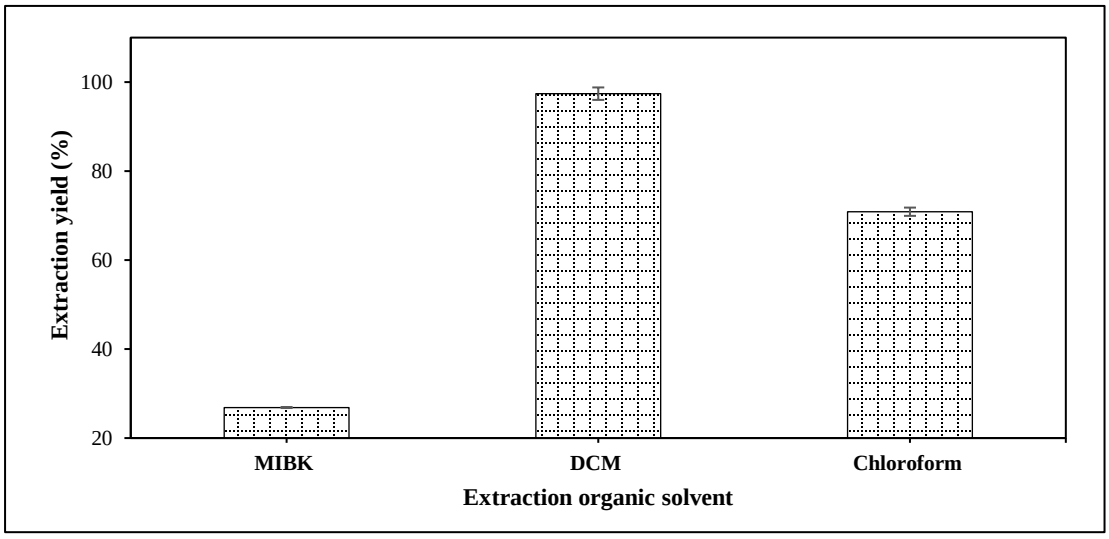


Figure 1. The Cr(VI) extraction efficiency using different extraction organic solvents

Effects of pH index in the aqueous phase

Depending on pH, predominant speciation of chromium could be changed to reach chemical equilibrium, which typically includes the formation of chromate (CrO_4^{2-}), dichromate ($Cr_2O_7^{2-}$), hydrogen chromate ($HCrO_4^-$), chromic acid (H_2CrO_4), hydrogen dichromate ($HCr_2O_7^-$), trichromate ($Cr_3O_{10}^{2-}$), and tetrachromate ($Cr_4O_{13}^{2-}$) [23, 24]. For instance, $HcrO_4^-$,

$Cr_2O_7^{2-}$, and H_2CrO_4 dominated the acid medium [25]. The different chromium species in water remarkably influence the extraction efficiency. The effects of pH on the extraction efficiency were investigated in the pH range from under 1.0 to 3.0. The extraction yield at different pH values is presented in Figure 2.

The results showed that the Cr(VI) ion quantitatively formed an ion-pair complex with TABHS at all the investigated pH, resulting in the extraction yields higher than 90%. Extraction yields generally remained unchanged within the ranges of pH tested in this current study (i.e., from less than 1.0 to 3.0). This phenomenon could be attributed to Cr(VI) mostly existing as $HCrO_4^-$ in the medium with a pH < 4.0, whereby the association was well-formed due to the big radius of $HCrO_4^-$[26]. The TBA^+–$HCrO_4^-$ ion association was formed in the interaction between the two phases (mostly in the aqueous phase) according to the following schematic representation (Figure 3). Therefore, the favorable pH for complex formation may vary in a relatively wide range, and pH adjustment in the sample preparation was not strictly (from very acidic, pH lower than 1.0, to pH of 3.0) [8, 20]. At pH > 4, lower extraction efficiency has been reported in previous publications, e.g., Ouejhani et al. [7], Baig et al. [21], and Kalihasan et al. [20]. The lower extraction yield of Cr(VI) in the alkaline medium could be explained due to the presence of dominant species, the CrO_4^{2-} and its potential hydrolysis [27]. In the present study, we did not investigate the extraction at high alkaline pH. The pH around 1.0 was chosen for further experiments and investigations due to the easy and convenient adjustment.

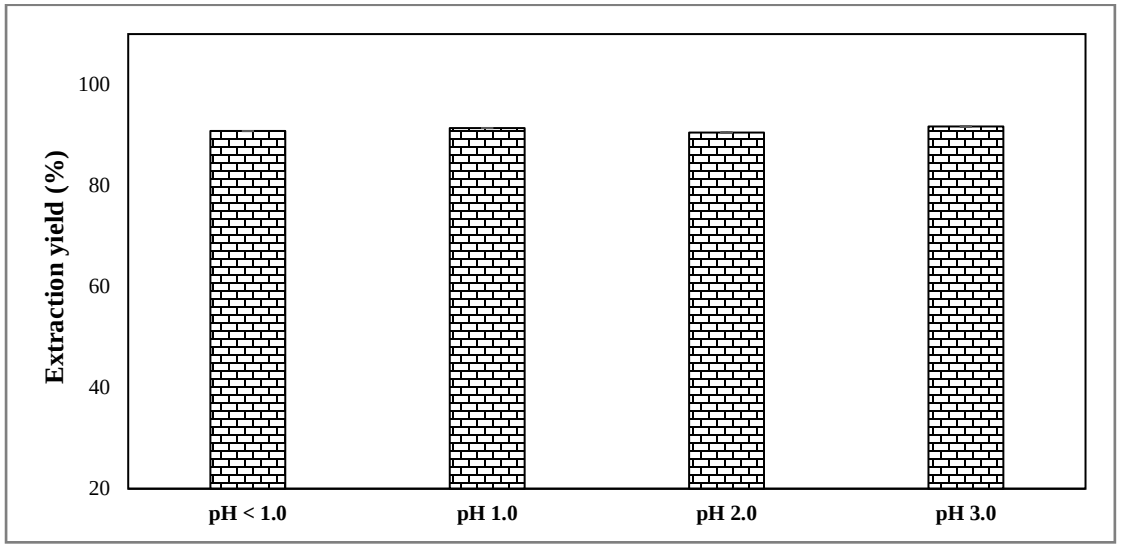


Figure 2. The Cr(VI) extraction efficiency at different pH

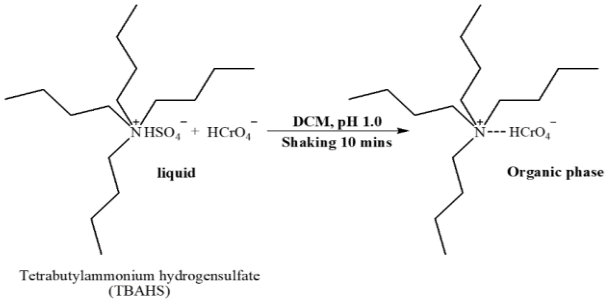


Figure 3. The chemical reaction for the formation of the ion-pair association

Effects of ion-pair reagent-TBAHS concentrations in DCM

As mentioned before, the ion-pair reagent of TBAHS was prepared in DCM to maximize the extraction efficiency [13]. The effects of TBAHS concentrations on the recovery were assessed, and the results are presented in Figure 4. It has been known that the formation of the ion-pair complex happens at the interface between two phases. However, the lower TBAHS concentration in the organic phase could lead to the lower concentrations of TBAHS as the ion-pair reagent at the interface, hence ineffective complexation between TBAHS and Cr(VI). Therefore, higher TBAHS concentrations were required to provide high TBAHS contents for favorable for ion-pair formation. Moreover, as shown in Figure 4, the chemical equilibrium was shifted forward to form the ion-pair complex when the concentrations of reactants (TBAHS) were higher. The increasing recovery as the concentration of TBAHS in DCM was increased was observed as the lowest (67.1%) and highest (103%) recovery was obtained at 0.02 mol L^{-1} and 0.05 mol L^{-1}, respectively. The TBAHS concentration of 0.04 mol L^{-1} resulted in relatively lower recovery (98.5%) and poorer precision (%RSD of 1.2%) than that of 0.05 mol L^{-1} (recovery of 103% and %RSDs of 0.68%). Based on the results, the 0.05 mol L^{-1} TBAHS in DCM was used for further experiments to ensure the most favorable recovery and precision.

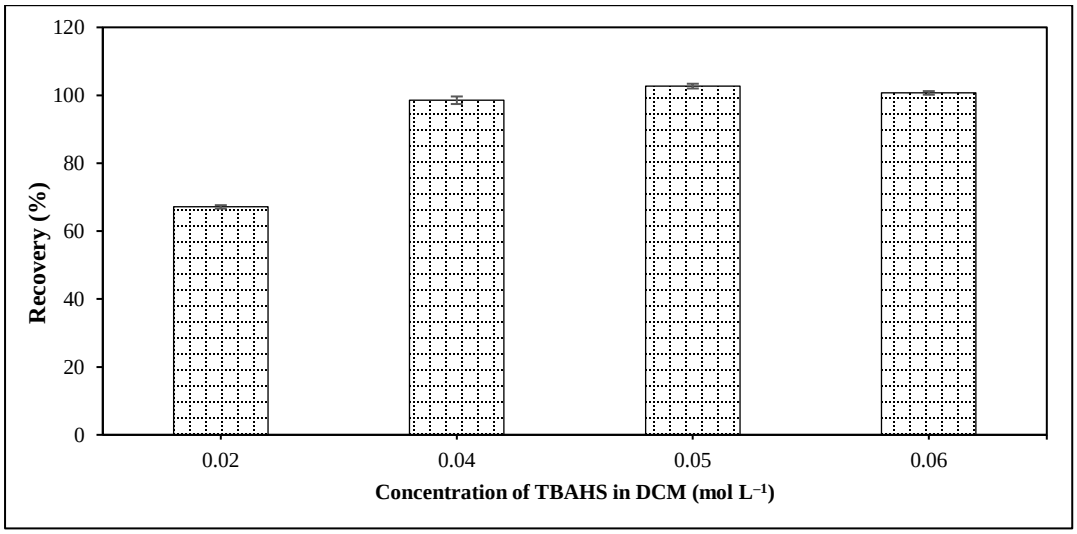


Figure 4. The extraction efficiency of Cr(VI) at different TBAHS concentrations in DCM

Effects of shaking duration and numbers of extraction cycles

During the extraction period, the shaking activity increases the interaction between Cr(VI) in the aqueous phase (wastewater samples) and the ion-pair reagents in the organic phase (DCM) at the interface of the two phases, and thus increases the chances for the formation of the ion-pair complex in the organic phase. The effects of shaking duration on the Cr(VI) recoveries are illustrated in Figure 5, which indicates that the longer shaking duration led to higher recoveries (i.e., 80.4% to 101%). We suggest that it is necessary to apply sufficient shaking for a certain duration to equilibriate the complex formation via a chemical reaction in the complicated wastewater matrices. In the present study, the recoveries mostly remained unchanged in the extraction performed for more than 15 minutes for each extraction cycle. Therefore, 15 minutes was determined as the shaking duration for each cycle of the extraction. In addition, to ensure the quantitative extraction of Cr(VI), the number of extraction cycles (i.e., repeated extraction)

was investigated. Double and triple extraction procedures were compared for their respective recoveries. The results showed higher recovery in triple than double extractions (i.e., 89.6% and 104%, respectively), which reflected the high partition coefficient of the complex in the organic phase.

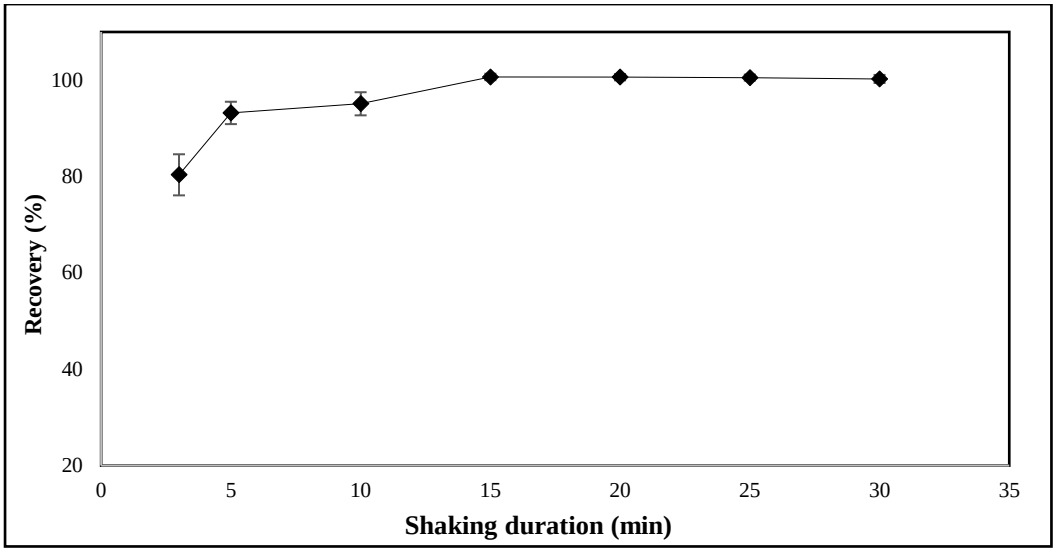


Figure 1. The variability of Cr(VI) recoveries at different shaking duration values (from 3 to 30 minutes), using 5.0 mL of DCM containing 0.05 mol L^{-1} TBAHS for 1.00 mg L^{-1} Cr(VI) standard solution

Effect of sample preservation on Cr(VI) analysis

The effects of sample matrices were investigated to obtain the most favorable sample preservation conditions at the ambient temperature. Cr(III) and Cr(VI) standard solutions were spiked into the real wastewater samples with free chromium to obtain the concentrations of 1.0 mg L^{-1} for both species to calculate the recoveries of Cr(VI) at different preservation duration values at the ambient temperature. The sample preparation for Cr(VI) analysis was carried out based on the optimized conditions, as shown in Figure 6.

The filtered sample solution endured FAAS measurement at 357.9 nm for quantification purposes. The results in Figure 7 showed that the immediate extraction within an hour resulted in no significant changes in the concentration of Cr(VI) as compared to its initial concentration, while the longer preservation duration resulted in lower recoveries (53.0% and 35.3% for 24-and 48-hour preservation, respectively). The result could be due to the presence of organic matters in the wastewater that may reduce Cr(VI) into Cr(III) [28, 29] and/or the presence of other substances that may interfere in the formation of Cr(VI) and the ion-pair reagent complexes. Therefore, to ensure reliable and accurate results, the wastewater samples should be analyzed right after being transported to the laboratory (within around one hour) or preserved at freezing temperature to minimize the conversion of Cr(VI) into Cr(III).

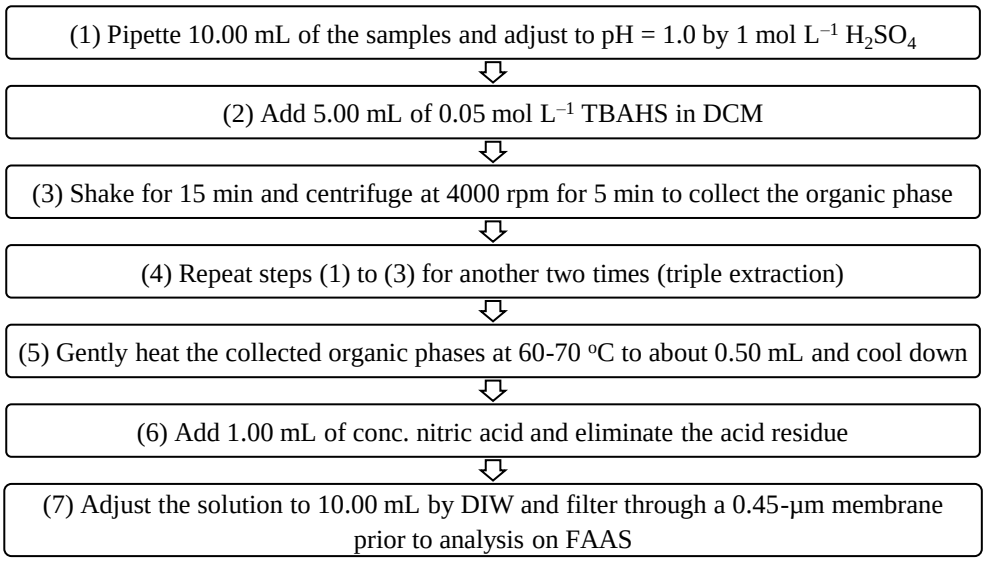


Figure 6. Optimized preparation procedure for Cr(VI) analysis

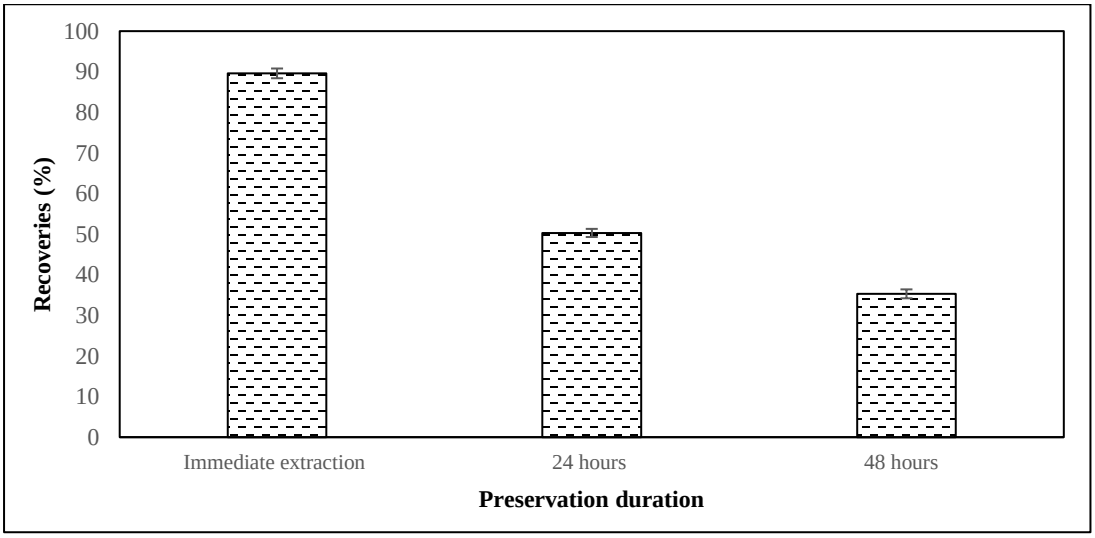


Figure 7. Recoveries of Cr(VI) in spiked samples with the co-existence of Cr(III) at different preservation duration values

Analytical method performance for analyzing Cr(VI)

The selective determination of Cr(VI) in wastewater following LLE with ion-pair reagent using FAAS was evaluated. The results are presented in Table 1. The estimated MDL and MQL were lower than regulated values in QCVN 24: 2009/BTNMT (National Technical Regulation on Industrial Wastewater) for industrial wastewater disposed to domestic and non-domestic water sources (0.05 and 0.1 mg L^{-1}) [30]. Therefore, the analytical method could be applied for industrial wastewater control and management of Cr(VI) content. The calibration curve was established based on the linear relationship between the chromium

concentrations and their atomic absorption values, which exhibited goodness of linearity (R^2 = 0.9994). The $\%RSD_r$ and $\%RSD_R$ were used to evaluate the repeatability (within one day) and reproducibility (for three separate days) of the proposed analytical method, which proved favorable according to the Appendix F of AOAC (2016) [31]. Besides, the recoveries varied from 91.1 to 109%, demonstrating the result accuracy obtained via the proposed method.

Table 1. Parameters for analytical method performance

Regression Equation	R^2	MDL (mg L^{-1})	MQL (mg L^{-1})	RSD_r (%)	RSD_R (%)	Recoveries (%)
y = 0.1068x + 0.0012	0.9994	0.012	0.040	0.71	1.1	91.1-109

The variability of Cr(VI) in the effluents

The sample preparation for Cr(VI) analysis in real wastewater samples or effluents was carried out based on the optimized procedure in Figure 6. The results of Cr(VI) analysis in real effluent samples are shown in Table 2. Most of the wastewater samples exhibited remarkably low Cr(VI) (i.e., below MQL values of 0.040 mg L^{-1}). The highest Cr(VI) in wastewater was determined as 0.37 mg L^{-1}. The Cr(VI) standard solution was spiked into all these samples for the recovery test, which demonstrated favorable recovery values (91.1-109%) according to the Appendix F of AOAC (2016) [31]. The recovery test was conducted to examine the matrix effects (mostly from the co-existing ions and organic matters present in wastewater). Therefore, the obtained high recoveries obtained in the test demonstrated the effectiveness of the LLE using the ion-pair reagent (TBAHS) for selective determination of Cr(VI) in complicated sample matrices.

Table 2. Analytical results of Cr(VI) in wastewater samples and recovery tests

Sample code	Cr(VI) (mg L^{-1})	Spiked Cr(VI) (mg L^{-1})	Recoveries (%)	RSD for Recoveries (%)
S1	n.d	1.00	96.8	1.6
S2	n.d	1.00	91.1	2.1
S3	0.37	1.00	109	1.1
S4	n.d	1.00	102	1.8
S5	0.22	1.00	94.3	1.8
S6	n.d	1.00	95.3	1.8
S7	n.d	1.00	99.7	1.7
S8	n.d	1.00	96.8	1.1
S9	0.18	1.00	96.2	1.1
S10	n.d	1.00	96.8	1.4

n.d: not detected

Conclusion

The proposed analytical method for determining Cr(VI) in wastewater or effluents demonstrated its good sensitivity and selectivity. The measurement was performed on an inexpensive and common technique of FAAS following the liquid-liquid extraction with

TBAHS as the ion-pair reagent. The TBAHS was prepared in the organic solvent to improve the extraction efficiency due to the low potential of interferences. Dichloromethane (DCM) was found to be the most favorable organic solvent for the extraction process. Various analytical parameters related to the extraction procedure were investigated to discover the optimized working parameters, including 0.05 mol L^{-1} TBAHS as the ion-pair reagent in DCM, aqueous sample with pH index in the range of around 1.0 to 3.0 (i.e., before the extraction), triple extraction cycle or triple extraction, and 15 minutes of shaking duration for each cycle. The calibration curve was established using a standard solution with a concentration ranging from 0.05 to 2.0 mg L^{-1} based on the linear relationship between Cr concentrations and the respective atomic absorption values at the wavelength of 357.9 nm. The method limit of detection and quantification values were estimated as 0.012 mg L^{-1} and 0.040 mg L^{-1}, respectively. This proposed analytical method could serve as a simple and low-cost procedure to determine the severely low concentrations of Cr(VI) in wastewater samples or effluents, which indicated proper recoveries (91.1-109%) for spiked samples based on the Appendix F of AOAC (2016). Moreover, the LLE approaches coupled with the addition of ion-pair reagents may be applied for quantitative and qualitative analysis of other ion metals for trace analysis purposes.

Acknowledgment

The authors would like to express our gratitude and appreciation to Nguyen Tat Thanh University and University of Science, Vietnam National University Ho Chi Minh City, Vietnam for their assistance and support throughout this study.

References

1. Ali, H., Khan, E. and Ilahi, I. (2019). Environmental chemistry and ecotoxicology of hazardous heavy metals: environmental persistence, toxicity, and bioaccumulation. *Journal of Chemistry*, 2019 (6730305): 1-14.
2. Tchounwou, P. B., Yedjou, C. G., Patlolla, A. K. and Sutton, D.J. (2012). Heavy metal toxicity and the environment. Springer.
3. Saha, R., Nandi, R. and Saha, B. (2011). Sources and toxicity of hexavalent chromium. *Journal of Coordination Chemistry*, 64(10): 1782-1806.
4. Oliveira, H. (2012). Chromium as an environmental pollutant: Insights on induced plant toxicity. *Journal of Botany*, 2012(375843): 1-8.
5. Jia, X., Gong, D., Xu, B., Chi, Q. and Zhang, X. (2016). Development of a novel, fast, sensitive method for chromium speciation in wastewater based on an organic polymer as solid phase extraction material combined with HPLC–ICP-MS. *Talanta*, 147: 155-161.
6. Séby, F. and Vacchina, V. (2018). Critical assessment of hexavalent chromium species from different solid environmental, industrial and food matrices. *Trends in Analytical Chemistry*, 104: 54-68.
7. Ouejhani, A., Dachraoui, M., Lalleve, G. and Fauvarque, J.-F. (2003). Hexavalent chromium recovery by liquid-liquid extraction with tributylphosphate from acidic chloride media. *Analytical Sciences,* 19(11): 1499-1504.
8. Kalidhasan, S. and Rajesh, N. (2009). Simple and selective extraction process for chromium (VI) in industrial wastewater. *Journal of Hazardous Materials*, 170(2-3): 1079-1085.
9. Noro, J., Maruyama, K. and Komatsu, Y. (2002). Separation of chromium (III) and chromium (VI) by the combination of solvent and ion exchange methods. *Analytical Sciences/Supplements Proceedings of IUPAC International Congress on Analytical Sciences,* 2001: 1333-1336.
10. Islam, F. and Biswas, R. (1979). The solvent extraction of chromium (III) with bis-(2-ethyl hexyl) phosphoric acid in benzene and other solvents. *Journal of Inorganic and Nuclear Chemistry*, 41(2): 229-233.
11. Gardner, M. and Comber, S. (2002). Determination of trace concentrations of hexavalent chromium. *Analyst*, 127(1): 153-156.
12. Shinde, V. and Khopkar, S. (1970). Extraction of chromium (VI) with 4-methyl-3-pentene-2-one and subsequent photometric determination as diphenylcarbazide complex. *Fresenius' Zeitschrift für analytische Chemie*, 249(4): 239-241.

13. Venkateswaran, P. and Palanivelu, K. (2004). Solvent extraction of hexavalent chromium with tetrabutyl ammonium bromide from aqueous solution. *Separation and Purification Technology*, 40(3): 279-284.
14. Konieczka, P. and Namiesnik, J. (2016). Quality assurance and quality control in the analytical chemical laboratory: A practical approach, CRC Press.
15. Ellison, S. L., Barwick, V. J. and Farrant, T. J. D. (2009). Practical statistics for the analytical scientist: A bench guide, Royal Society of Chemistry.
16. ISO 5667-3:2003 (2003). Water quality-Sampling-Part 3: Guidance on the preservation and handling of water samples.
17. ISO 5667-10:2020 (2020). Water quality-Sampling-Part 10: Guidance on sampling of waste waters.
18. Wypych, G. (2001). Handbook of solvents, ChemTec Publishing.
19. Polarity Index. https://macro.lsu.edu/howto/solvents/polarity%20index.htm. [Assess online 20 December 2020].
20. Kalidhasan, S., Ganesh, M., Sricharan, S. and Rajesh, N. (2009). Extractive separation and determination of chromium in tannery effluents and electroplating waste water using tribenzylamine as the extractant. *Journal of Hazardous Materials*, 165(1-3): 886-892.
21. Baig, J. A., Kazi, T. G., Elci, L., Afridi, H. I., Khan, M. I. and Naseer, H. M. (2013). Ultratrace determination of Cr (VI) and Pb (II) by microsample injection system flame atomic spectroscopy in drinking water and treated and untreated industrial effluents. *Journal of Analytical Methods in Chemistry*, 2013: 629495
22. Sereshti, Khojeh, V. and Samadi, S. (2011). Optimization of dispersive liquid–liquid microextraction coupled with inductively coupled plasma-optical emission spectrometry with the aid of experimental design for simultaneous determination of heavy metals in natural waters. *Talanta*, 83(3): 885-890.
23. Tandon, R., Crisp, P., Ellis, J. and Baker, R. (1984). Effect of pH on chromium (VI) species in solution. *Talanta*, 31(3): 227-228.
24. Kalidhasan, S. and Rajesh, N. (2009). Simple and selective extraction process for chromium (VI) in industrial wastewater. *Journal of Hazardous Materials*, 170(2-3): 1079-1085.
25. Sperling, M., Xu, S. and Welz, B. (1992). Determination of chromium (III) and chromium (VI) in water using flow injection on-line preconcentration with selective adsorption on activated alumina and flame atomic absorption spectrometric detection. *Analytical Chemistry*, 64(24): 3101-3108.
26. Palmer, C. D. (1994). Natural attenuation of hexavalent chromium in ground water and soils: Superfund Technology Support Center for Ground Water.
27. Leśniewska, B., Jeglikowska, A. and Godlewska-Żyłkiewicz, B. (2016). Chromium speciation in wastewater and sewage by solid-phase extraction using a new diphenylcarbazone-incorporated resin. *Water, Air, & Soil Pollution*, 227(8): 1-10.
28. Zhang, L. and Lay, P. A. (1996). EPR Spectroscopic studies of the reactions of Cr (VI) with l-ascorbic acid, l-dehydroascorbic acid, and 5, 6-O-isopropylidene-l-ascorbic acid in water. 1 Implications for chromium (VI) genotoxicity. *Journal of the American Chemical Society*, 118(50): 12624-12637.
29. Xu, X.-R., Li, H.-B., Li, X.-Y. and Gu, J.-D. (2004). Reduction of hexavalent chromium by ascorbic acid in aqueous solutions. Chemosphere, 57(7): 609-613.
30. QCVN 24:2009/BTNMT (2009). National Technical Regulation on Industrial Wastewater.
31. Appendix F of AOAC (2016). Guidelines for Standard Method Performance Requirements.

Malaysian Journal of Analytical Sciences (MJAS)
Published by Malaysian Analytical Sciences Society

KAFFIR LIME OIL QUALITY GRADING USING NON-LINEAR SUPPORT VECTOR MACHINE WITH DIFFERENT KERNELS

(Penentuan Kualiti Minyak Limau Purut Dengan Menggunakan Mesin Vektor Sokongan Bukan Linear Dengan Kernel Berbeza)

Nor Syahira Jak Jailani[1]*, Zuraida Muhammad[2], Nor Salwa Damanhuri[2], Muhd Hezri Fazalul Rahiman[1], Mohd Nasir Taib[1]

[1]College of Engineering,
Universiti Teknologi MARA, 40450 Shah Alam, Selangor, Malaysia
[2]College of Engineering,
Universiti Teknologi MARA,
13500 Permatang Pauh, Pulau Pinang, Malaysia

**Corresponding author: norsyahira_jakjailani@yahoo.com*

Received: 23 September 2021; Accepted: 5 February 2022; Published: 28 April 2022

Abstract

Nowadays, Kaffir lime oil is one of the highly demand in the industries and sold with various market prices. But sometime the most expensive price of kaffir lime oil does not guarantee the best quality of this oil. Currently, kaffir lime oil quality grading is based only on human sensory evaluation such as smell and visual which accompanying with confusion and inconsistent result. This is due to human sensory evaluations have limitations such as easily fatigue and unable to manage mass products of the oil in time. This paper presents the classification of significant chemical compound of kaffir lime oil in the oil quality grading by using Non-Linear Support Vector Machine (NSVM). The objective of this study is to classify the quality of kaffir lime oil whether it is high or low in quality only by tuning the two different kernels into NSVM. This project has used up to 90 samples of kaffir lime oil data from various high to low quality to prepare NSVM with two different kernels. The implementation of this project was performed by using MATLAB version R2020A. The result appeared NSVM model with RBF kernel is better than NSVM model with Polynomial kernel. It was discovered that RBF kernel was able to generate 100% accuracy, specificity, precision, and sensitivity compared to Polynomial kernel. Since the finding and outcome were effective and significant, thus this study contributes a lot of benefits for future study especially in kaffir lime field.

Keywords: non-linear support vector machine, radial basis function, polynomial, kaffir lime oil, high/low quality

Abstrak

Saat ini, minyak limau purut mendapat permintaan tinggi di industri, dan dijual dengan harga yang berbeda di pasar. Tetapi harga minyak limau purut yang mahal tidak menjamin kualiti tinggi minyak ini. Pada masa ini, penilaian kualiti minyak limau purut berdasarkan penilaian deria seperti hidung dan mata menimbulkan kekeliruan dan hasil yang tidak konsisten. Ini kerana penilaian deria mempunyai batasan dan mudah letih dan tidak dapat menangani banyak sampel sekaligus. Oleh itu, kajian inimembentangkan klasifikasi sebatian kimia yang penting dalam minyak limau purut untuk gred kualiti minyak dengan

menggunakan Mesin Vektor Sokongan Bukan Linear (NSVM). Objektif kajian ini adalah untuk mengklasifikasikan kualiti minyak limau purut sama ada berkualiti tinggi atau rendah dengan menyesuaikan dua kernel yang berbeza ke dalam NSVM. Projek ini menggunakan 90 sampel data minyak limau purut dari berkualiti tinggi hingga rendah untuk melatih NSVM dengan kernel yang berbeza. Pelaksanaan projek ini dilakukan dengan menggunakan MATLAB versi R2020A. Hasilnya menunjukkan model NSVM dengan kernel RBF lebih baik daripada model NSVM dengan kernel Polinomial. Didapati kernel RBF mampu menghasilkan ketepatan, kekhususan, ketepatan, dan kepekaan 100% berbanding dengan kernel Polinomial. Penemuan dan hasil ini berkesan dan signifikan sekali gus akan mendorong dan memberi banyak faedah untuk kajian masa depan terutama dalam bidag limau purut

Kata kunci: mesin vektor sokongan bukan linear, fungsi asas radial, polinomial, minyak limau purut, kualiti tinggi/rendah

Introduction

Kaffir lime oil or scientifically known as Citrus Hystrix which is originate from Rutacae family can be found in most Asian Countries. It was widely consumed in Asian dishes and other few industries such as aromatherapy, medicines, and fragrances. Despite all, Kaffir lime oil can also be obtained from its peels and leaves. Currently, the oil quality grading was performed manually based on human sensory evaluation. It was observed based on the physical properties of the samples. Human experienced and perception on the oil long-lasting aroma, color and odor is the only method to classify the quality of the oil. Natural sensory quality evaluation method like this produces less accuracy and subjective as it may vary from everyone. Usually, the result performed by natural sensory train grader were not consistent since it may vary to each other and the process itself take a high time consuming in the procedure [1-3]. Many researchers encountered that essential oil can be classified based on their chemical compound. This method of classification is more accurate compared to the human sensory evaluation [4]. The chemical compounds of essential oil need to be analyzed in order to classify the grading of their quality [5].

The quality of kaffir lime oil can be determined based on their abundances of major chemical compound. Many researchers found the major chemical compound of kaffir lime oil was monoterpene components. The monoterpene components discovered were Citronellal, Limonene, β-pinene, α-pinene and Sabinene [6-9] Besides that, caryophyllene was also identified by Ngan et al., researcher from Vietnam [10] and terpinene-4-ol was found by Hongatanaworkit & Buchbauer as another major compounds of kaffir lime oil [11].

Furthermore, to overcome the inconsistent result of classifying oil grading and the amount time consuming, this project proposed a latest technique of classifying major compounds in Kaffir lime essential oil using Non-Linear Support Vector Machine (NSVM) to perform the automated grading. A SVM is a method in supervised learning that usually used for classification. SVM is used to overcome the problem of classification and regression with linear or non-linear data [12, 13]. However, NSVM will be applied when the data consumed can't be easily separated with linear line. Therefore, the kernels ought to be used to make non-separable data into separable data. Kernels is used to map out the data from the vector input into the high dimension vector space [12]. In this project, the RBF kernel and polynomial were choosing to be tuning into NSVM. The abundance percentages (%) of major compounds act as an input and will be supplied to NSVM model develops by kernel. The output will determine the quality of kaffir lime oil whether it is low or high in quality. Hence, the oil quality and grading of kaffir lime will be classified by using an automated intelligent nonlinear support vector machine (NSVM) which regards to their chemical compounds and reduce the time-consuming during grading processes.

Materials and Methods

Sample preparations

The 90 samples data of kaffir lime oil that contains high and low in quality were used in this study that contains high and low quality. These data were

obtained from 15 samples kaffir lime oil before applying synthetic data. 12 samples of kaffir lime oil obtained in the market with different various brands. All 12 brands kaffir lime oil was sent to Forest Research Institute Malaysia (FRIM) to extract the chemical compound by applying gas chromatography-mass spectrometry (GC-MS). It was found kaffir lime oil has almost 96 chemical compounds. Another three samples kaffir lime oil data get from previous researcher[7, 9, 14].

Z-score technique

The Z-score technique was utilised to group the data and assign an explicit grouping to the data population sample in this study. Previous studies have used Z-score approaches to establish a specific set, with Z-score being a widely used application for standardising data and calculating a factor score. Thus, the Z-score technique was applied to identify the significant chemical compound of kaffir lime oil [4]. In this technique, the two significant chemical compounds of kaffir lime oil were found, which were β-pinene, limonene, linalool, citronellal, and terpinene-4-ol. The five chemical compounds were used as a marker compound for the NSVM classification method. Table 1 shows samples kaffir lime oil was used in this project and its significant chemical abundance (%). There are 11 HIGH samples and 4 LOW samples of kaffir lime oil. Samples AA, AB and AC got from previous researcher that were extract directly from kaffir lime, so they were labelled as a high quality. Another. 8 samples HIGH kaffir lime oils are traded as high quality by certified trader and some of them were published as high-quality kaffir lime oil

The quality of kaffir lime oil was determined based on its chemical abundance (%). The higher the abundance(%) of this chemical, the higher quality of kaffir lime oil [6, 8, 15–17].

Table 1. Significant Kaffir lime chemical constituents used for classification (Group' 1' for HIGH quality and '2' for LOW quality

	Abundance (%)					**Group**
	β-pinene	**Limonene**	**Linalool**	**Citronellal**	**Terpinen-4-ol**	
AA	16.8	19.8	1	7.8	2.8	1
AB	8.974	28.649	0.541	8.29	0.47	1
AC	9.321	26.446	0.687	6.63	1.0541	1
WS	1.42	0.52	7.19	60.06	0.99	1
FF	0.6	0.46	5.68	54.73	0.62	1
T	18.13	22.7	0.44	0	11.15	1
SS	0.56	0.37	7.4	79.39	0	1
SE	10.47	15.06	1.85	28.32	5.98	1
S	16.37	24.39	0.38	0	10.84	1
NL	1.16	0.42	7.35	60.65	0.85	1
DE	16.19	23.01	0.8	4.45	9.93	1
SP	0	16.8	2.48	0	0	2
C	0.19	18.49	2.14	0	0	2
B	0	0	12.38	51.05	0	2
LL	2.19	50.61	7.14	0	0	2

Synthetic data

All 15 data was added with synthetic data to become 90 samples data to increase the performances classification method[18]. Synthetic data was created by adding the SNR signal to the original input-output data. The synthetic data equations can be represented as follows, as recommended by Sevgi [19]:

$$Ysynthetic = Y_{\mathrm{NSVM}} + Y_{SNR} \quad (1)$$

The original NSVM input-output data is Y_{NSVM}, and the SNR signal or random noise is Y_{SNR}. The trend of the original data and original data with synthetic data should be the same. The calculation minimum, maximum and median of synthetic data are done to support the trend similarity.

Data pre-processing

Data pre-processing done for this experiment consists of a holdout cross-validation strategy for splitting data. The data is divided into ratios 80%:20% for training data and for testing data that was recommended by the authors [5, 20-22], which were for training data set it has 72 samples while the testing data has 18 samples. The ratio is applied in that manner due to the higher number of the training data collected, hence the higher accuracy results appeared on the model [22]. On the other hand, the difference between these two data sets is that the training data is used in model creation while the test data is performed as the model output prediction.

Build the NSVM classifier model

In the real world, data is rarely linearly separable. Most are non-linear. NSVM is modified by entering the kernel functions into SVM. There are a few types of kernel functions of NSVM: polynomial, quadratic, RBF, and sigmoid [23]. When using NSVMs in practice, it's especially vital to pick the correct kernel parameters. Thus, this experiment will test two different kernels to find the best kernel for modelling the quality kaffir lime oil grading. The two different kernels are the Polynomial kernel and RBF kernel. In general, the RBF kernel is a good starting point. This kernel nonlinearly maps samples into a higher-dimensional space to handle the case where the relationship between class labels and attributes is non-linear, unlike the linear kernel[24]. The polynomial kernel is selected because this kernel gives 100% accuracy for agarwood oil grading in a previous study [20] compared to the RBF kernel that is given only 89.5% [25].

The compounds gathered from the 90 samples of kaffir lime oil were used to train NSVM with Polynomial kernel and RBF kernel. The abundances (%) of the chemical compounds act as input, and this input were fed into NSVM model development, and hence the output is set to be either '1' or low '2' quality. All the analytical work was performed automatically by using MATLAB software version R2020A. Figure 1 shows the flowchart of NSVM modelling.

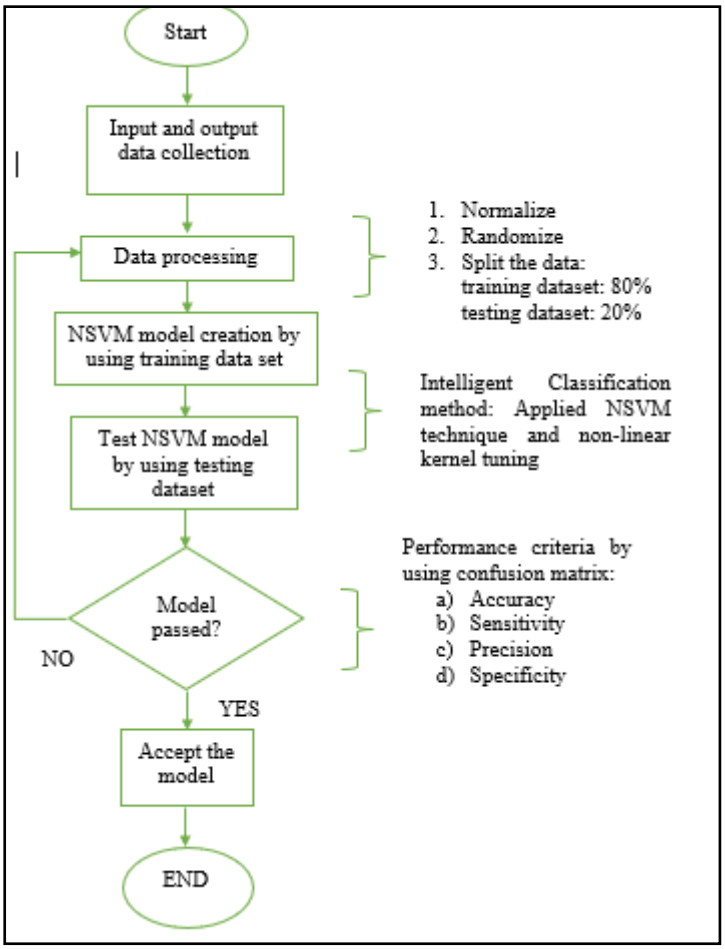


Figure 1. Flowchart NSVM modelling

Performance's measure

The performances for NSVM modelling were measured by using the confusion matrix. Other than that, measurements such as accuracy, sensitivity, specificity, precision, and Mean Absolute Error (MAE) would also be used to obtain more granular and precise model-building results. The accuracy (ACC) is defined as the effectiveness of the classifier. The calculation of the accuracy is as follows [29]:

$$ACC=(TP+TN)/(TP+FN+FP+TN) \quad (2)$$

Sensitivity (SENS) is defined as the rate of a true positive. The effectiveness of a classifier to identify the high quality of kaffir lime is as follow [29]:

$$SENS=TP/(TP+FN) \quad (3)$$

The specificity (SPEC) is interpreted as the rate of the negative. The effectiveness of a classifier to identify the low quality of kaffir lime is as follows [29]:

$$SPEC=TN/(TN+FP) \quad (4)$$

Precision (PREC) is interpreted how often it is correct when it predicts high quality of kaffir lime oil as follow:

$$PREC=TP/(TP+FP) \quad (5)$$

Results and Discussion

The confusion matrix result is shown in Table 2 for the polynomial kernel and Table 3 for the RBF kernel. Where TP (True positive): Classified as HIGH quality and the actual was HIGH quality, FP (False positive): Classifies as HIGH quality but the real is LOW quality, FN (False negative): classified as HIGH quality, but the actual was LOW quality and TN (True negative): classified as LOW negative and the actual is LOW quality. From the result in table 2 and table 3, the value of TP for Polynomial and RBF were 14 and the value of FN for both kernels is also the same, which is 0. FP value for table 1 was 4, while FP value in table 2 was 0. TN value in table 1 was 0 while TN value in table 2 was 4. This result shows that RBF kernel is better than the polynomial kernel because the best model does not have value of FP and FN.

Table 4 shows the comparison performances between the polynomial kernel with RBF kernel. It is clearly showing that RBF kernel is way better than polynomial. RBF kernel can reach up to 100% of its accuracy, sensitivity, specificity, precision, and 0% mean absolute error (MAE) compared to the polynomial kernel which only manage to achieve 100% in its sensitivity, 66.78% accuracy precision, and 0% specificity, and 0.22 for MAE. In general, the lower the MAE, the better a model's ability to match a dataset. We may compare the MAE of two distinct models to see which one delivers a better fit to a dataset when comparing them.

Table 2. Confusion matrix for polynomial

Data Class N=18	**Classified as HIGH**	**Classified as LOW**
actual HIGH	TP=14	FP=4
actual LOW	FN=0	TN=0

Table 3. Confusion matrix for RBF

Data Class N=18	**Classified as HIGH**	**Classified as LOW**
actual HIGH	TP=14	FP=0
actual LOW	FN=0	TN=4

Table 4. Confusion performances between polynomial kernel and RBF kernel

Performances	**Polynomial (%)**	**RBF (%)**
Accuracy	66.78	100
Sensitivity	100	100
Specificity	0	100
Precision	66.78	100
MAE	0.22	0

Conclusion

This paper has successfully evaluated the Kaffir lime oil quality either high or low by tuning in polynomial kernel and radial basis function (RBF) kernel into NSVM. The result shows RBF kernel was able to produce 100% in its accuracy, specificity, precision, and sensitivity compared to Polynomial kernel which was able only to produce 77.78% in its accuracy, 100% sensitivity, 0% specificity and 77.78% precision. Hence it is also can be concluded that RBF kernel parameter better than polynomial for kaffir lime oil grading classification. Since the finding and outcome were effective and significant, thus this study contributes a lot of benefits for future study especially in kaffir lime field.

Acknowledgements

A highly appreciate this research funder, the Malaysia Ministry of Higher Education's Fundamental Research Grant Scheme (FRGS-RACER). This research was supported by FRGS Grant no 600-IRMI/FRGS-RACER 513(115/2019) for my financial support. The authors wish to thank Universiti Teknologi MARA, Cawangan Pulau Pinang and Faculty of Electrical Engineering, Universiti Teknologi MARA, Cawangan Pulau Pinang for their endless technical assistance.

References

1. Abas, M. A., Zubir, N. S. A., Ismail, N., Yassin, I. M., Ali, N. A. M., Rahiman, M. H. F. and Taib, M. N. (2017). Agarwood oil quality classifier using machine learning. *Journal of Fundamental and Applied Sciences*, 9(4): 62-76.
2. Haron, M. H., Taib, M. N., Ismail, N., Mohd Ali, N. A. and Tajuddin, S. N. (2019). Statistical analysis of agarwood oil compounds based on GC-MS data. *9th IEEE Control System Grad. Research Colloquium:* pp. 27-30.
3. Azah, M. N., Husni, S. S., Mailina, J., Sahrim, L., Majid, J. A. and Faridz, Z. M. (2013). Classification of agarwood (gaharu) by resin content. *Journal of Tropical Forest Science*, 2013: 213-219.
4. Ismail, N., Azah, M. A. N., Jamil, M., Rahiman, M. H. F., Tajuddin, S. N. and Taib, M. N. (2013). Analysis of high quality agarwood oil chemical compounds by means of SPME/GC-MS and Z-score technique. *Malaysian Journal of Analytical Sciences*, 17(3): 403-413.
5. Jantan, H., Yassin, I. M., Zabidi, A., Ismail, N. and Ali, M. M. (2017). Differentiation of agarwood oil quality using support vector machine (SVM). *Journal Engineering Applied Sciences*, 12(15): 3810-3812.
6. Mohd Sauid, S. and Aswandi, F. A. (2018). Extraction methods of essential oil from kaffir lime (*Citrus hystrix*): A review. *Malaysian Journal of Chemical Engineering and Technology*, 1: 56-64.
7. Kasuan, N., Muhammad, Z., Yusoff, Z., Fazalul Rahiman, M. H., Taib, M. N. and Haiyee, Z. A. (2013). Extraction of *Citrus hystrix* DC (kaffir lime) essential oil using automated steam distillation process: analysis of volatile compounds. *Malaysian Journal of Analytical Sciences*, 17: 359-369.
8. Haiyee Z. A. and Winitkitcharoen, C. (2012). Extraction of volatile oil from kaffir lime leaves (*Citrus hystrix*) using pressurize liquid extraction. *International Journal Food, Nutrition Public Health*, 5: 201-210.
9. Muhammad, Z., Yusoff, Z. M. and Nordin, M. N. N. (2013). Steam Distillation with induction heating system: analysis of kaffir lime oil compound and production yield at various temperatures. *Malaysian Journal of Analytical Sciences*, 17(2): 340-347.
10. Ngan, T. T. K., Hien, T. T., Tien, L. X., Anh, T. T., Quan, P. M., Cang, M. H. and Toan, T. Q. (2019). Physico-chemical profile of essential oil of kaffir lime (*Citrus hystrix* DC) grown in An Giang Province, Vietnam. *Asian Journal Chemistry*, 31(12): 2855-2858.
11. Hongatanaworkit, T. and Buchbauer, G. (2007). Chemical composition and stimuating effect of *Citrus hystrix* oil on human. *Flavour Fragrance Journal*, 22(4): 443-449.
12. Dewi, C. and Basuki, A. (2018). Identifying citronella plants from UAV imagery using support vector machine. *Telkomnika*, 16(4): 1877–1885.

13. Windha Mega, P. D. and Haryoko (2019). Optimization of parameter support vector machine (SVM) using genetic algorithm to review go-jek's services. *4th International Conference Information Technology, Information System, and Electrical Engineering*, 6: 301-304.
14. Zakiah, M. Y., Zuraida, M., Nurhani, K., Mohd, H. F. R. and Mohd, N. T. (2013). Effect of temperature on kaffir lime oil by using hydro-diffusion steam distillation system. *Malaysian Journal of Analytical Sciences,* 17(2), 326-339.
15. Lubinska-Szczygieł, M., Różańska, A., Namieśnik, J., Dymerski, T., Shafreen, R. B., Weisz, M., ... & Gorinstein, S. (2018). Quality of limes juices based on the aroma and antioxidant properties. *Food Control*, 89: 270-279.
16. An, T. N. T., Ngan, T. T. K., Van, C. K., Anh, H. L. T., Minh, L. V. and Ay, N. V. (2021, March). The major and minor components of Kaffir Lime (*Citrus hystrix* DC) essential oil in the steam distillation process. In *IOP Conference Series: Materials Science and Engineering*, 1092(1): 012082.
17. Jailani, N. S. J., Muhammad, Z., Rahiman, M. H. F. and Taib, M. N. (2021). Analysis of kaffir lime oil chemical compounds by gas chromatography-mass spectrometry (GC-MS) and Z-Score technique. In *2021 IEEE International Conference on Automatic Control & Intelligent Systems:* pp. 110-113.
18. Ismail, N., Rahiman, M. H. F., Taib, M. N., Ali, N. A. M., Jamil, M. and Tajuddin, S. N. (2014). Application of ANN in agarwood oil grade classification. In *2014 IEEE 10th International Colloquium on Signal Processing and its Applications*: pp. 216-220.
19. Sevgi, L. (2007). Synthetic radar-Signal environment: Computer generation of signal, noise, and clutter. *IEEE Antennas and Propagation Magazine*, 49(5): 192-198.
20. Ismail, N. S., Ismail, N., Rahiman, M. H. F., Taib, M. N., Ali, N. A. M. and Tajuddin, S. N. (2018, October). Polynomial tuned kernel parameter in SVM of agarwood oil for quality classification. In *2018 IEEE International Conference on Automatic Control and Intelligent* Systems: pp. 77-82.
21. Ariffin, B. M., Ismail, N., Ali, N. A. M., Rahiman, M. H. F., Tajuddin, S. N. and Taib, M. N. (2018). Multilayer perceptron (MLP) tuned kernel parameter in support vector machine (SVM) for agarwood oil compounds quality classification. *J. Tomography System and Sensors Application*, 1(1): 1-15.
22. Raif, M. A. A., Ismail, N., Ali, N. A. M., Rahiman, M. H. F., Tajuddin, S. N. and Taib, M. N. (2019). Quadratic tuned kernel parameter in Non-linear support vector machine (SVM) for agarwood oil compounds quality classification. *Indonesia Journal Electronic Engineering Computer Science*, 17(3): 1371-1376.
23. Patle, A. and Chouhan, D. S. (2013). SVM kernel functions for classification. In *2013 International Conference on Advances in Technology and Engineering*, pp. 1-9.
24. Apostolidis-Afentoulis, V. and Lioufi, K. I. (2015). SVM classification with linear and RBF kernels: pp. 1-7.
25. Kamarulzaini, K. A. A., Ismail, N., Rahiman, M. H. F., Taib, M. N., Ali, N. A. M. and Tajuddin, S. N. (2018). Evaluation of RBF and MLP in SVM kernel tuned parameters for agarwood oil quality classification. In *2018 IEEE 14th International Colloquium on Signal Processing & Its Applications*, pp. 250-254.

Malaysian Journal of Analytical Sciences (MJAS)
Published by Malaysian Analytical Sciences Society

DIRECT CATALYTIC CONVERSION OF CELLULOSE INTO FORMIC ACID BY SUPPORTED PHOSPHOTUNGSTIC ACID CATALYST

(Penukaran Terus Selulosa Kepada Asid Formik Menggunakan Pemangkin Asid Fosfotungstik yang Disokong)

Nor Liyana Zakira Zabidi Adil @ Zaibidai Adil, Farah Wahida Harun, Syaza Azhari, Lailatun Nazirah Ozair, Shikh Mohd Shahrul Nizan Shikh Zahari, Tengku Shafazila Tengku Saharuddin*

Faculty of Science and Technology,
Universiti Sains Islam Malaysia, Bandar Baru Nilai, 71800 Nilai, Negeri Sembilan

**Corresponding author: shafazila@usim.edu.my*

Received: 15 August 2021; Accepted: 11 January 2022; Published: 28 April 2022

Abstract

This study aims to prepare phosphotungstic acid supported on hydrotalcite (PTA-HT) for one-pot hydrothermal cellulose conversion into formic acid (FA). In this study, different percentages of PTA on HT (1, 5, 10, 15, 20, 25, and 33%) were prepared and the catalytic activity was observed for two different parameters such as time (1 to 5 hours) and reaction temperature (160 to 240 °C). The prepared catalysts were characterized using Fourier transform infrared (FTIR), X-ray powder diffraction (XRD), Brunauer-Emmet-Teller (BET) and field emission scanning electron microscopy-energy dispersive X-ray spectrometry (FESEM-EDX), while the production of FA was determined using ultra high-performance liquid chromatography (UHPLC). To avoid bias, raw PTA and calcined HT were compared with varying percentages of supported PTA. PTA-HT was successfully prepared through the impregnation method as confirmed by XRD, FTIR, BET and FESEM-EDX. According to the results, the optimum condition for cellulose conversion into formic acid was when 25% PTA-HT was applied at 220 °C for 4 hours, with a 30% cellulose conversion and 18 % FA yield. Due to the acidity and redox properties of PTA, it has been demonstrated that PTA-HT increased the catalytic activity by two-fold when compared to calcined HT alone (8%). The significance of this finding opens new suggestion of bifunctional catalyst in cellulose conversion into FA.

Keywords: catalyst, cellulose, formic acid, hydrothermal, phosphotungstic acid

Abstrak

Tujuan kajian ini adalah untuk menyediakan asid fosfotungstik yang disokong dengan oleh hidrotalsit (PTA-HT) bagi proses hidroterma penukaran selulosa kepada asid formik. Di dalam kajian ini, perbezaan peratus PTA ke atas HT (1, 5, 10, 15, 20, 25 dan 33%) telah disediakan dan aktiviti pemangkinan telah dijalankan terhadap dua parameter iaitu masa (1 jam hingga 5 jam) dan suhu (160 hingga 240 ℃). Pemangkin yang telah disediakan diperincikan menggunakan inframerah transformasi Fourier (FTIR), pembelauan sinar-X (XRD), Brunauer-Emmet-Teller (BET) and mikroskopi imbasan pancaran medan-spektrometri tenaga serakan sinar-X (FESEM-EDX) manakala asid formik yang terhasil ditentukan menggunakan kromatografi cecair berprestasi ultra tinggi (UHPLC). Bagi mengelakkan keputusan yang berat sebelah dalam kajian, PTA tulen dan HT yang dikalsin telah dibandingkan dengan perbezaan peratus PTA yang disokong. PTA-HT yang telah disediakan melalui kaedah

impregnasi dicirikan oleh XRD, FTIR, BET dan FESEM-EDX. Berdasarkan keputusan, keadaan yang paling optimum bagi penukaran selulosa kepada asid formik adalah apabila 25% PTA-HT digunakan pada 220 °C selama 4 jam dengan menghasilkan 30% penukaran selulosa dan 18% penghasilan asid formik. Oleh kerana ciri-ciri asid dan redoks yang dimiliki oleh PTA, keputusan kajian telah menunjukkan bahawa PTA yang disokong oleh HT meningkatkan aktiviti pemangkin sebanyak dua kali ganda berbanding HT yang telah dikalsin yang hanya menghasilkan 8% asid formik. Kepentingan kajian ini akan membuka cadangan baru terhadap penggunaan pemangkin dwifungsi dalam penukaran selulosa kepada asid formik.

Kata kunci: pemangkin, selulosa, asid formik, hidroterma, asid fosfotungstik

Introduction

Biomass is a great alternative for carbon sources in the production of platform chemicals as biomass originated from plants and animals [1]. Numbers of researches focused on forestry and agricultural residues as it is non-edible to address food competition issues such as wood [2], corncob waste [3] and rice husk [4]. Plant biomass is made up of three main constituents: cellulose, hemicellulose and lignin. Among these constituents, cellulose has the highest percentage and play important structural function for plant cell walls [5, 6]. Cellulose is a polymer that is highly crystalline due to rigid intermolecular bonds of hydrogen to hydroxyl group and oxygen with nearby glycosidic rings [7, 8]. Glycosidic bonds of cellulose causes difficulty in depolymerizing cellulose, which required highly reactive catalyst and rigorous experimental conditions. In converting cellulose, many techniques have been studied such as pretreatment of cellulose using ball-milling [9], addition of oxidant [10], Fenton reaction [11-13], hydrolysis [14, 15], ozonation [2] and oxidation [16]. A successful cellulose conversion provides production of important chemicals such as formic acid [17-19], lactic acid [20, 21], levulinic acid [22] and acetic acid [23]. Industries have been eyeing formic acid (FA) due to its nontoxicity, noncorrosive, easy handling and readily biodegradable qualities [24]. Formic acid is the most basic form of carboxylic acid and is commonly used as a byproduct in a variety of applications such as agriculture [25], cosmetics [26], textile [27] and pharmaceuticals [28].

Mineral acids such as hydrochloric acid, sulfuric acid and phosphoric acid have previously been used as acid catalysts for cellulose conversion due to their strong acidity and low cost, but these catalysts are highly corrosive [29-33]. Therefore, improvement had been made to convert cellulose using solid acid catalyst such as heteropoly acid [16], zirconia, zeolite and montmorillite [34]. The advantageous of using solid catalyst is that it is less corrosive, easier to handle, and separates the catalyst from the reaction medium. Among all catalysts, heteropoly acid (HPA) catalyst appears to be the most promising due to its strong Bronsted acidity and redox property [35] that able to hydrolyze and oxidize cellulose into FA. Nevertheless, drawbacks of homogenous HPA are low thermal stability, low surface area and easily soluble in polar solvent [35]. Supporting HPA on a suitable support is one way to heterogenized HPA, which can improve product yield, selectivity, and reduce HPA's drawbacks by providing more active sites and making it more porous [14, 22, 35, 36]. In addition, hydrotalcite (HT), a potential support material with a high surface area and basic properties that may aid in the catalytic conversion of cellulose, is one such material that has been widely used–in flame retardance, neutralizing additives, a base catalyst for cellulose conversion and adsorbent [37-40]. Therefore, in this work, cellulose conversion into FA by different percentages of PTA ($H_3PW_{12}O_4$) supported with HT ($Mg_6Al_2CO_3(_{16})\cdot 4H_2O$) were investigated to see the effects of temperature, time and PTA amount towards the production of FA.

Materials and Methods

Materials

All reagents were analytical grade and used without further purification such as hydrotalcite (Sigma-Aldrich), microcrystalline cellulose and ethanol 99.5% (Systerma) while formic acid 98-100% HPLC grade, tungstophsphoric acid hydrate, orthophosphoric acid and potassium dihydrogen phosphate were purchased from Merck.

Preparation of catalyst

The catalyst preparation starts with the reconstruction pathway in which commercial HT was calcined at 450 °C for 4 hours under nitrogen gas to remove carbonate ions. This step is to allow anions from raw PTA solution to enter into the empty interlayer region later [41]. The raw PTA was dissolved into deionized water to the desired amount (1, 5, 10, 15, 20, 25 and 33% by w/w%). Meanwhile, calcined HT was dissolved in another beaker. Subsequently, dissolved PTA was added dropwise into calcined HT solution. At this step, calcined HT will reconstruct into its original shape with new interlayer anions from PTA. This is because calcined HT regains its original structure when exposed to the aqueous solution [42]. Then, the mixture was stirred for 4 hours to ensure that PTA and calcined HT until both solutions were well-mixed. Lastly, the mixture was dried overnight to remove the water from the mixture forming a solid containing PTA and calcined HT.

Catalytic experiment

Cellulose conversion was conducted in a 100 mL hydrothermal reactor in which the contents of catalyst and cellulose fed were 0.1 g and 0.05 g respectively. Then, about 50 mL of deionized water was added. The reactor was tightened and placed inside an oven. Once reaction temperature and time were up, the cellulose conversion started. As soon as the required temperature and time were reached, the liquid product was filtered using a syringe filter and the solid residue was filtered using a vacuum pump. Cellulose conversion was calculated according to Equation 1. The concentration of FA was analyzed using the UHPLC system (1290 Infinity, Agilent Technologies) using Zorbax SB C18 column with an internal diameter of 21.2mm and 5µm particle size. The UHPLC system was connected with a DAD detector measuring at 210 nm. 10 mM phosphate buffer with pH adjusted to pH 2 was prepared, filtered and degassed. The concentration of FA from the sample was identified by comparing the retention times with standards. Standards calibration was used for FA quantification. The yield of FA was calculated using Equation 2 [43].

$$\text{Cellulose conversion} = \frac{\text{Cellulose fed} - (\text{Solid residue} - \text{Catalyst})}{\text{Cellulose fed}} \text{x} 100\% \quad (1)$$

$$\text{Formic acid yield} = \frac{\text{Liquid product}}{(\text{Stoichiometric coefficient FA from glucan})(\frac{\text{Cellulose fed}}{\text{Mass of glucan}})} \text{ x } 100 \quad (2)$$

Catalyst characterization

Nitrogen adsorption was done to differentiate specific surface area, pore size distribution and pore volume of PTA-HT, raw PTA, calcined HT and raw HT using Brunner-Emmet-Teller (BET) model 3 Flex Micromeritics. BET analysis started with degassing the sample to remove unwanted adsorbed molecules inside the sample pore. The thermal condition of degassing is prior to thermal gravimetric analysis to ensure that the sample was not destroyed during degassing. After degassing, the sample was placed inside the sample tube and liquid nitrogen was filled inside the dewar and placed below the sample tube for BET analysis. Then, phase characterization was carried out by X-ray diffraction (XRD) model Mini Flex 600, Rigaku with Cu Kα 1.54 (40 kV, 40 mA) X-ray radiation source at angle range 3^{θ} to 90^{θ}. In order to identify the crystalline phase compositions, the diffraction patterns were matched with Crystallography Open Database (COD). Chemical functional groups identification was carried out using Fourier Transform Infrared (FTIR) model Nicolet™ iS50 FTIR Spectrometer, Thermo Scientific. FTIR sample was grind using pestle and mortar until it become fine and thin. The sample analysis started after placing the sample onto the detector and background scanning was done. Then, surface morphology of sample was confirmed by Field Emission Scanning Electron Microscope (FESEM) model JSM-IT 800 FESEM, Joel with accelerating voltage 20 kV. Sample was coated with platinum using JEOL Smart Coater. The FESEM images were paired with Energy Dispersive X-ray Analysis (EDX) model Ultimax 45

Oxford to confirm the presence of elemental composition of each sample.

Results and Discussion

Catalytic activity

Three parameters were investigated to find the best conditions for FA production from cellulose using the PTA-HT catalyst: reaction time, temperature, and amount of PTA. The influence of reaction time towards FA production is displayed in Figure 1. To determine the best reaction time, the temperature and amount of PTA were kept constant at 180 ℃ and 5%, respectively. From the results, FA yield increased gradually from 0.08% to 0.22% between 1 to 3 hours of the reaction time. The value then increased slightly to 0.24% at 4 hours and remained constant until 5 hours. In the case of cellulose degradation, a longer reaction time allowed higher degradation rates ranging from 15% to 42% and does not achieve a plateau. From the result, it is observed that reaction condition for both cellulose degradation and FA yield at 180 ℃ is very mild although the reaction time varies from 1 hour to 5 hours. This can be seen when the reaction time was prolonged to 5 hours the cellulose degradation is slightly increased from 30 to 44% while FA yield remain constant as shown in Figure 1. Degradation of cellulose can be done independently without the presence of catalyst as reported in previous journal [44]. However, high temperature of water was required range 320 to 400 ℃ but cellulose was able to degrade into cellobiose, glucose and fructose [44]. Another study of cellulose degradation without presence of catalyst also observed the same trend where at 180℃ degradation products such as acids, furans and sugar were not detectable with only 12% cellulose converted [45]. Meanwhile, as shown in Figure 1, our experiment shows that at 180 ℃, cellulose degradation increases as reaction time prolonged and FA was detectable and reached a plateau at 4 hours reaction time. The production of FA which may cause by the presence of 5% PTA-HT that enhance cellulose degradation. This is because PTA contains tungsten ions and oxygen ions that does have an effect on hydrolysis and oxidation. Although hydrolysis mainly took place in a high temperature water medium, the production of the targeted product requires oxidation of cellulose where PTA provide additional oxygen located at bridging and terminal oxygen atom. However, the reaction time, water temperature and acidic strength of PTA was only able to hydrolyse cellulose but this condition is not enough to produce more FA. Hence, to improve this, we further with the next condition at 4 hours reaction time with the same amount of PTA to determine the suitable temperature and amount of PTA on HT catalyst.

Subsequently, the effect of reaction temperature on FA production was examined by varying the reaction temperature from 160 to 280 ℃. As illustrated in Figure 2, a noticeable increment can be seen towards cellulose degradation from 9% to nearly 50% with prolonged temperature. FA yield also showed better improvement with a maximum yield of 13.36% at 240 ℃. However, a very slight change in FA yield was observed between 220 ℃ (13.05 %) and 240 ℃ (13.36%). From the graph, the trend of FA yield started to decrease at 250 to 280 ℃ although cellulose degradation increases. The suggested mechanism pathway started with cellulose undergoes hydrolysis which form glucose [46]. The glucose further dehydrated into hydroxymethylfurfural (HMF) where later rehydrated into levulinic acid and decomposed into FA [47]. It is reasonable to speculate that higher temperature promotes degradation of cellulose as stated in [48] where cellulose can be degraded without the presence of acid at high temperature. However, previous journal [45] only highlighted the production of monosaccharides but our study proved that with the presence of PTA it enhances cellulose degradation route until FA was produced at suitable temperature. This occurs due to Brönsted acidity of PTA that highly protonate ions during reaction took place. Although, production of FA was a success, FA is an unstable compound which can easily decomposed into CO_2 [43][9]. Hence, selecting 220℃ as our reaction temperature is reasonable to avoid decomposition of FA.

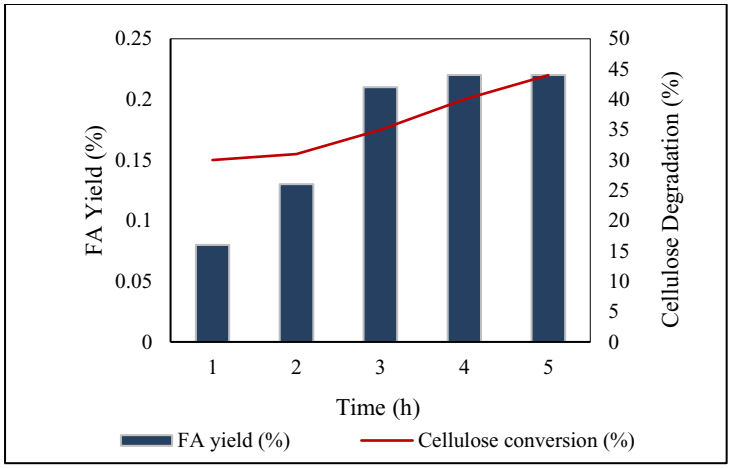


Figure 1. Effect of reaction time on cellulose conversion and FA yield by PTA-HT catalyst. Reaction condition: 0.05 g cellulose, 0.1 g PTA-HT, the temperature at 180 ℃ and PTA loading on HT is 5%

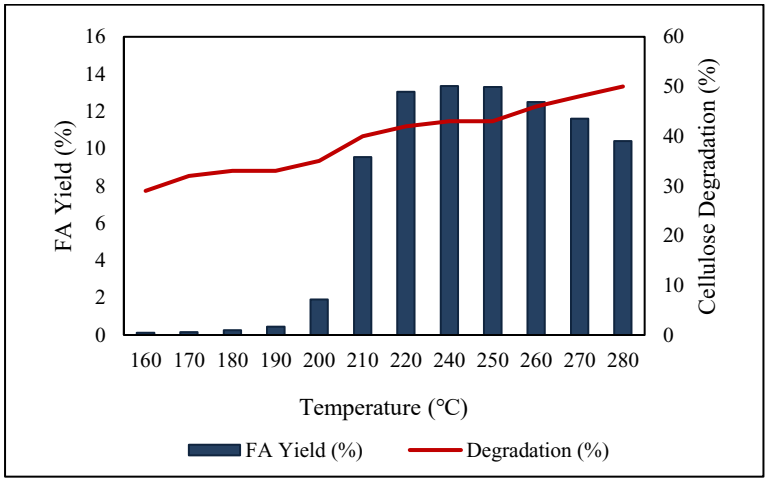


Figure 2. Effect of reaction temperature on cellulose conversion and FA yield by PTA-HT catalyst. Reaction condition: 0.05 g cellulose, 0.1 g PTA-HT, 5% PTA-HT and 4 hours reaction time

The influence of PTA amount supported on calcined HT was displayed in Figure 3. This investigation was compared with blank experiment where catalyst was not included during cellulose degradation. In Figure 3, although cellulose was degraded in blank experiment, FA yield was not obtained. However, other reactors that contained PTA-HT yielded FA. This phenomenon is possible to occur due to PTA criteria that is highly protonic acid which speed up the cellulose degradation [41]. Hence, FA can be obtained in 4 hours under 220 ℃ water temperature. A factor that allows hydrolysis to happen in blank experiment is when water medium is heated to high temperature but as observed our solid acid catalyst improves the hydrolysis rate and react further to form FA. Furthermore, the degradation rate in blank experiment was lesser as compared when PTA-HT was presence. The formation of FA occurred due to cascade reaction in which dehydration and rehydration took place before FA was formed. So as Brönsted acid was placed in the medium, hydrogen ions were highly dissociated which speed up dehydration of glucose into HMF which later

rehydrate into FA [44]. From our experiment, FA production depends on the acidic strength of our catalyst as FA yield increase with increasing amount of PTA but the FA yield was inconsistent. However, FA yield drops drastically to 0.08% when 33% of PTA-HT was placed in reaction medium while highest yield of FA (18%) was observed with 25% amount of PTA. To our surprise, calcined HT alone produce 8% FA which initially function as catalyst support.

Based on previous literature, calcined HT contains medium-strong Lewis basic O^{2+}-Mn^{n+} pairs and isolated O^{2-} as strong basic sites which promote production of FA compared with uncalcined HT that contain weak basic sites [49]. After cellulose was hydrolyze, glucose was not dehydrated into HMF instead isomerizes into fructose and retro-aldol forming glycolic acid. Then, dehydrated into lactic acid which later degraded into FA [50,51, 38]. From this, we understand that two possible routes occurred during FA production as illustrated in Scheme 1. PTA and HT when combined together consist of both acid and base sites. Having Brönsted acid feature increase degradation rate of cellulose while the basic site of calcined HT hindered decomposition of FA into carbon dioxide. 25 % PTA-HT was chosen to further investigate and characterize its properties in relation to the catalytic reaction. 25% PTA-HT was compared with calcined 25% PTA-HT to observe any difference in FA production. Cellulose degradation from calcined 25% PTA-HT was better than blank and calcined HT. The FA yield decreased drastically when PTA loading are more than 25%. This might happen due to leaching of PTA. Another similar study, compared uncalcined tungsten-based zirconia and calcined tungsten-based zirconia reported the same result [52]. From Figure 4, the UHPLC result shows the formation of FA together with other by-products that was obtained during FA production. Although other by-products were obtained, FA peak is one of the highest compared to the others.

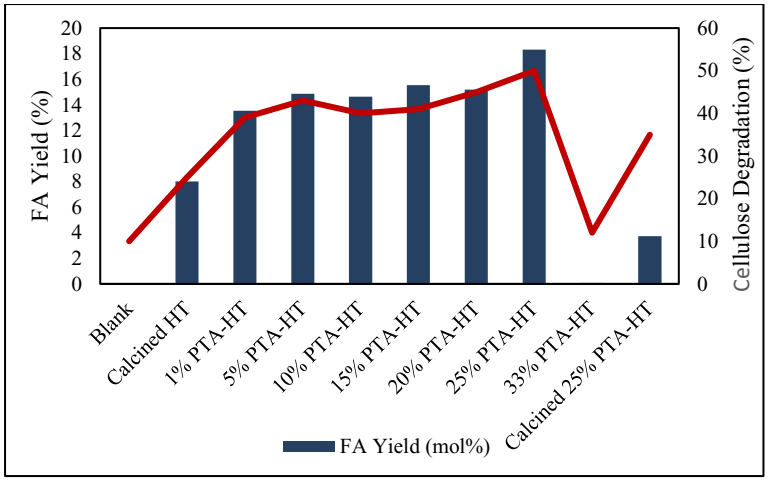


Figure 3. Effect of percentage PTA loading on HT on cellulose conversion and FA yield by PTA-HT catalyst. Reaction condition: 0.05 g cellulose, 0.1 g PTA-HT and temperature at 220 °C

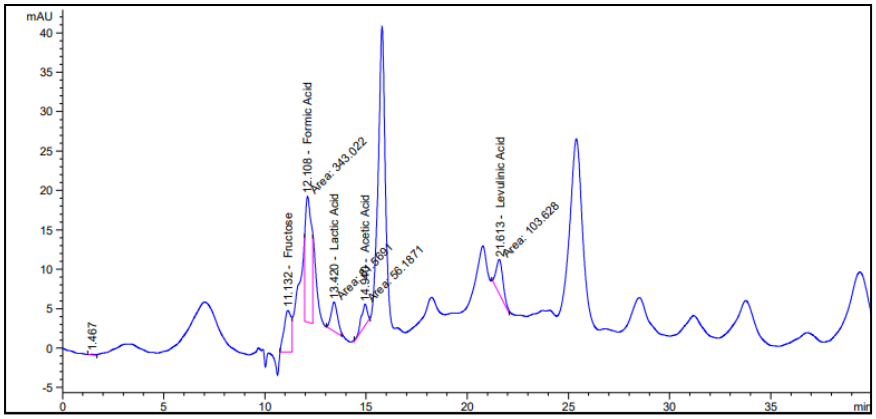


Figure 4. HPLC analysis of cellulose degradation with 0.1g 25% PTA-HT, 4 hours reaction time at 220 ℃

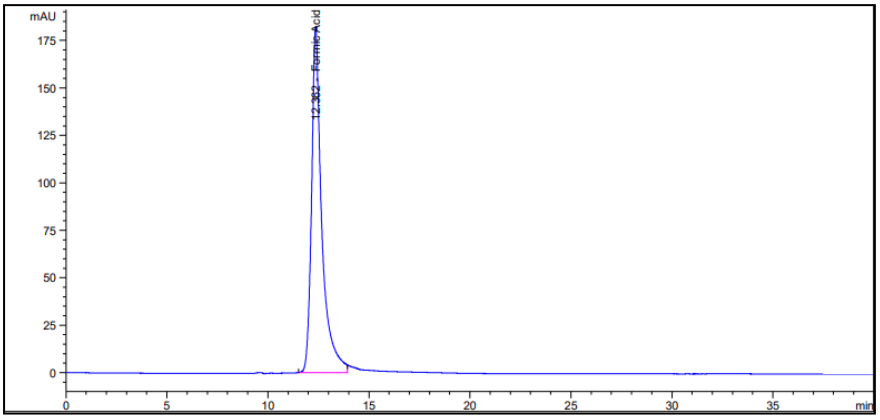
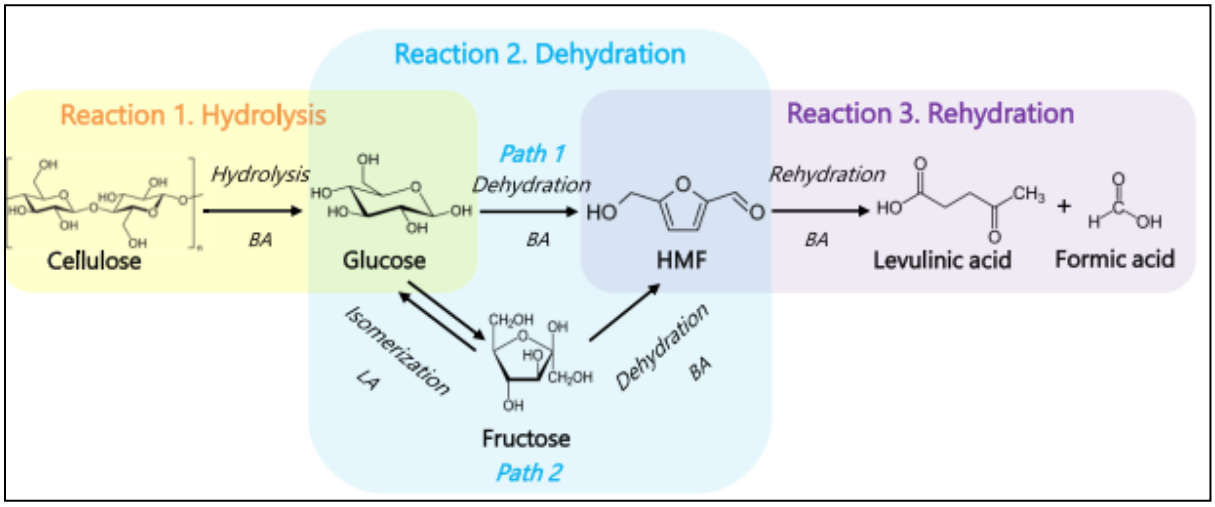


Figure 5. HPLC result for standard FA



Scheme 1. Mechanism pathway of cellulose degradation into FA [51]

Nitrogen adsorption-desorption analysis

BET measurement has been carried out on raw HT, raw PTA, calcined HT and 25% PTA-HT. The objective of this test is to evaluate the significance of impregnating PTA with calcined HT. One of the drawbacks implementing PTA as homogenous catalyst is because of its low surface area and difficulty to reuse. Hence, having large surface area and porous catalyst support can overcome this. Few journals have reported supported PTA with zirconia, activated carbon and carbon foam but as far as our knowledge there is no PTA supported with calcined HT for cellulose degradation study. As shown in Table 1, raw PTA have the lowest specific surface area as compared to 25% PTA-HT. The main reason to calcined HT is to provide larger surface area and porous surface to support PTA and open more active sites during cellulose degradation. If raw HT was not calcined and impregnated with PTA, we assumed that our catalyst will not be well supported as the surface area for raw HT is small compared to calcined HT. The specific surface area of 25% PTA-HT was significantly lesser than calcined HT is because PTA was deposited inside the pores of calcined HT. Hence, it is important to calcined HT so that the surface area is still larger despite being deposited with PTA.

Table 1. BET analysis of raw HT, calcined HT and 25% PTA-HT

Sample	Specific Surface Area (m^2/g)
Raw HT	10.63
Raw PTA	3.91
Calcined HT	206.62
25% PTA-HT	163.39

XRD analysis

XRD patterns of raw HT (2θ=11.58˚, 23.31˚, 34.42˚, 34.80˚, 35.30˚, 39.32˚, 46.71˚, 52.84˚, 56.32˚, 60.65˚and 61.98˚) and raw PTA (2θ=6.89˚, 8.62˚, 9.33˚, 9.5˚, 10.97˚, 11.66˚, 16.09˚, 17.41˚, 17.83˚, 18.60˚and 19.46˚) showed the typical crystalline structure of Mg-Al layered double hydroxides and phosphotungstic acid respectively. Meanwhile, the XRD peak of calcined HT showed significant difference as crystallinity of raw HT was destructed and formed amorphous mixed oxide phase. This can be seen at 2θ=26.55˚, 29.54˚, 39.52˚ and 62.32˚ that showed an appearance of $MgAl_2O_4$ (spinel) (COD Card No. 5000120). Calcination of HT also gave rise to weak and broad peaks that correlated to MgO known as periclase (COD Card No. 9013246) at 2θ=34.78˚, 43.29˚, 60.70˚ and 79.03˚. As shown in Figure 6, XRD peak of 25 % PTA-HT showed the presence of MgO at 2θ= 38.39˚, $MgAl_2O_4$ (2θ=43.01˚, 62.95˚ and 79.77˚) and (2θ=18.59˚, 28.66˚, 34.79˚ and 47.24˚). This phenomenon is related to calcination of HT that will generate mixed oxide and surface defects. Hence, after calcination of HT at 450 ℃ for 4 hours, original structure of HT lost water and carbonate ions [53]. Removing water and carbonate ions that located at interlayer region will allow incorporation of PTA in MgO framework. Therefore, it is observed that 25% PTA-HT peak follows calcined HT peak. From Figure 4, cellulose peak was observed in sample 25% PTA-HT after reaction because this sample was only separated from liquid product using vacuum filter. Although most peaks appear in 25% PTA-HT after reaction sample, there is missing peak of periclase which might cause from leaching due to reaction condition. However, most of the peaks are maintained in 25% PTA-HT after reaction sample.

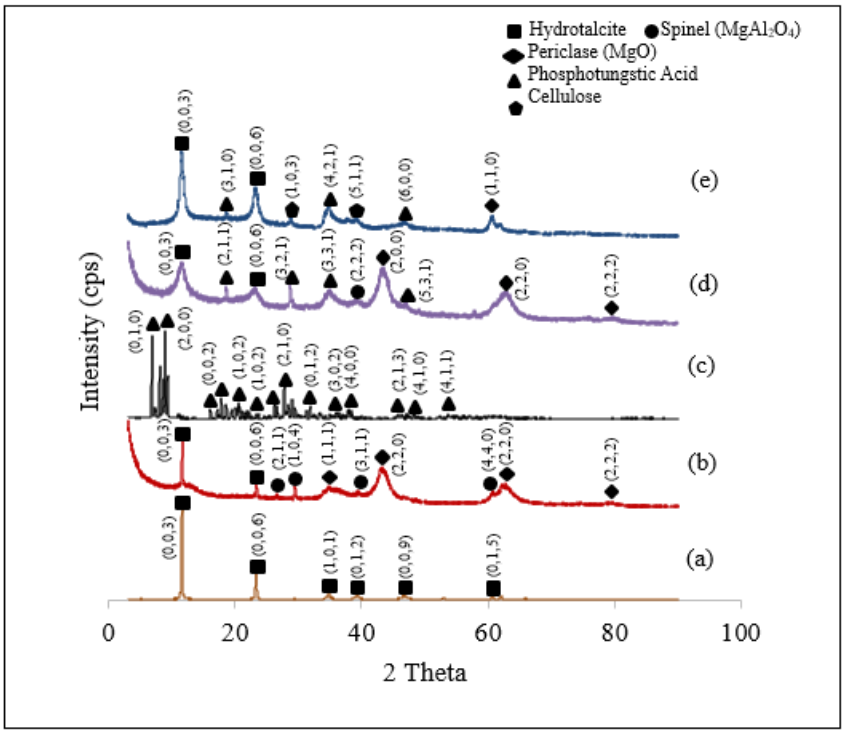


Figure 6. XRD patterns of (a) Raw HT, (b) Calcined HT, (c) Raw PTA, (d) 25% PTA-HT and (e) 25% PTA-HT after reaction

Infrared spectroscopy

IR spectroscopy was used to confirm the presence of PTA after impregnated with calcined HT. As shown in Figure 7, raw PTA was observed to have significant peaks of Keggin HPA at 1071 cm^{-1} (P-O), 970 cm^{-1} (W=O), 899 cm^{-1} (W-O-W) and 729 cm^{-1} (W-O-W) that attributed to stretching vibrational peaks of Keggin anions [54]. The peaks were not obvious because for 25% PTA-HT only 0.025g of PTA impregnated with 0.1g calcined HT. In the case of raw HT, peaks observed at low peaks range between 900-500 cm^{-1} corresponded to metal hydroxides such as $Mg(OH)_2$ and $Al(OH)_3$ [55]. Meanwhile, peaks near 937 cm^{-1} were caused by Mg-O and Al-O. The characteristic peak of raw HT is at 1359 cm^{-1} which is the carbonate and 3403 cm^{-1} for O-H group [56]. The disappearance peaks of metal hydroxides and weak peak of O-H at 3442 cm^{-1} in calcined HT is due to loss of water [57, 58]. IR spectra for 25% PTA-HT, showed the appearances of P-O (1003 cm^{-1}), W=O (801 cm^{-1}), W-O-W (700 cm^{-1}) and Mg-O and Al-O (501 cm^{-1} to 532 cm^{-1}) peaks, which indicated the successful impregnation between PTA and HT. This result can be confirmed with XRD analysis and EDX analysis that can show elements present in the sample.

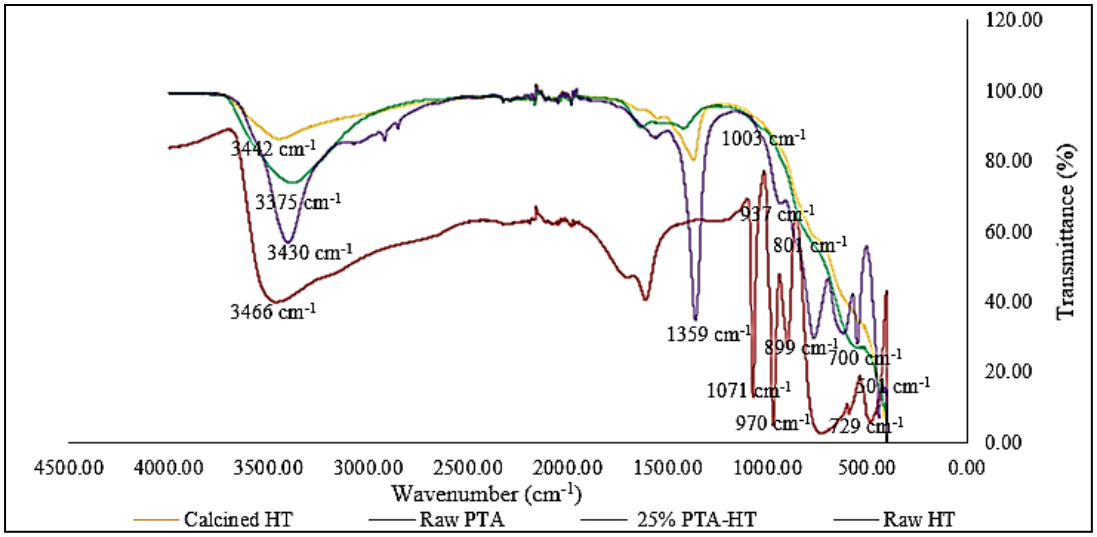


Figure 7. FTIR spectra of raw PTA, raw HT, calcined HT and 25% PTA-HT

FESEM-EDX analysis

FESEM was used to characterize the surface morphology of calcined HT and 25% PTA-HT as shown in Figure 8. Both calcined HT and 25% PTA-HT displayed a similar pattern of particles with irregular shapes. This is because small amount of PTA was impregnated with calcined HT which does not provide any distinguish pattern between calcined HT and 25% PTA-HT. Hence, EDX analysis is important for us to detect the presence of PTA incorporated with calcined HT that can be observed in Figures 9 and 10. As reported before, phosphorus-based HPAs are slightly more acidic than silicon-based HPAs [58]. The importance of tungsten (W) and oxygen (O) inside PTA is their proton affinity which contribute to its acidic site. As shown in Figure 7, the presence of tungsten (W), phosphorus (P) and oxygen (O) indicated the core elements of PTA. Calcination of HT remove carbonate and water at the interlayer and formed mixed oxide where only magnesium (Mg), aluminum (Al) and oxygen were present in Figure 8. The empty interlayer region will be filled with PTA elements and regains its original structure. The unlabeled peaks were carbon tape used for imaging. Both EDX results showed high intensity of Mg, O and Al peaks which shows that calcined HT is more dominant in 25% PTA-HT. Hence, there is no significant difference between FESEM images and FTIR results. Although, calcined HT was dominant the amount of PTA far important towards FA production.

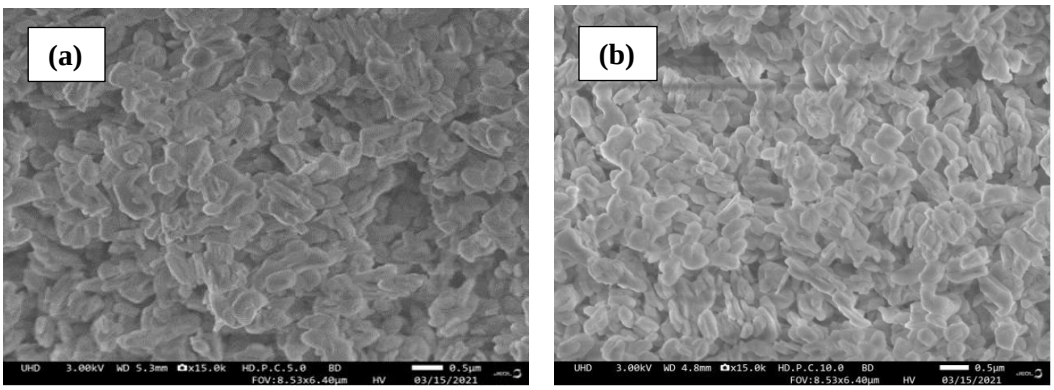


Figure 8. FESEM image of (a) calcined HT and (b) 25% HTA-PTA

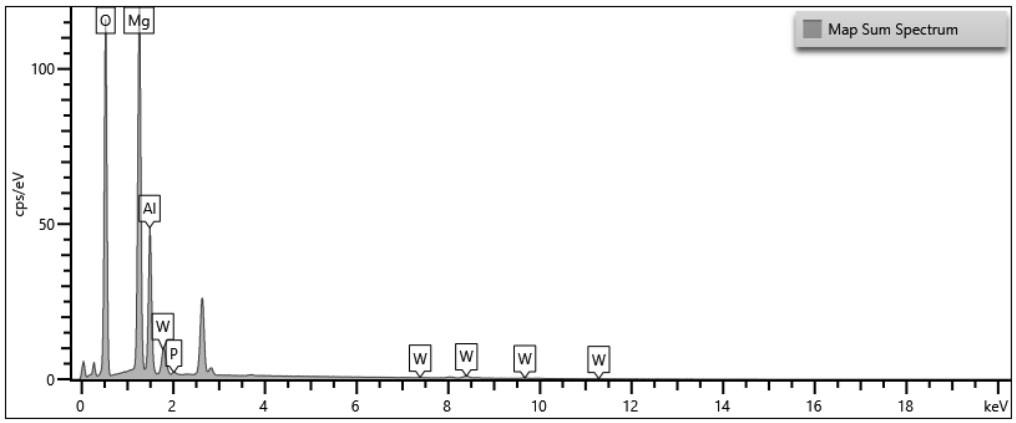


Figure 9. EDX analysis of 25% PTA-HT. Core elements belong to PTA were tungsten (W), phosphorus (P) and oxygen (O). Meanwhile, magnesium (Mg) and aluminum (Al) belong to HT

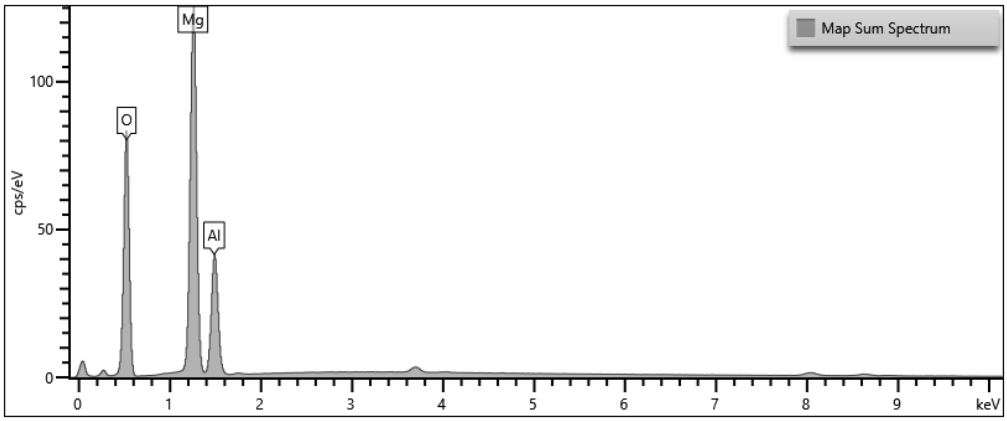


Figure 10. EDX analysis of calcined HT. Core elements belong to calcined HT were magnesium (Mg) and aluminum (Al) belong to HT

Conclusion

From our results, the FA production follows two possible routes contributed by Brönsted acid of PTA and basicity of calcined HT. The basicity of calcined HT may also promote formation of FA while performs well as catalyst support. Although calcined HT is dominant in the catalyst, acidity of PTA plays major role in degrading cellulose into FA. As reported, at optimum condition, 18% FA was yielded together with 30% cellulose degradation which was two times higher than calcined HT alone. To conclude this, the temperature and acidity of catalyst influence the cellulose degradation into FA. However, suitable temperature acidity is required to avoid decomposition of FA. Meanwhile, reaction time have minimal effect towards FA yield. The cellulose degradation can be done independently in water medium but regards to temperature and acid catalyst, the reaction was enhanced. Through catalyst characterization, PTA was successfully impregnated with calcined HT as proved from our results. According to the finding, FA was successfully produced in moderate amounts. Optimum condition for FA yield was as follows: 220℃, 4 hours with 25% catalyst loadings.

Acknowledgement

Authors thank Fundamental Research Scheme Grant (FRGS/1/2019/STG01/USIM/03/1) from Ministry of Education Malaysia for the financial support and Universiti Sains Islam Malaysia for laboratory facilities.

References

1. Foong, S. Y., Liew, R. K., Yang, Y., Cheng, Y. W., Yek, P. N. Y., Mahari, W. A. W., ... and Lam, S. S. (2020). Valorization of biomass waste to engineered activated biochar by microwave pyrolysis: progress, challenges, and future directions. *Chemical Engineering Journal*, 389: 124401.
2. Mamleeva, N. A., Autlov, S. A., Bazarnova, N. G. and Lunin, V. V. (2016). Degradation of polysaccharides and lignin in wood ozonation. *Russian Journal of Bioorganic Chemistry*, 42(7): 694-699.
3. Ribeiro, L. S., de Melo Órfão, J. J. and Pereira, M. F. R. (2017). Simultaneous catalytic conversion of cellulose and corncob xylan under temperature programming for enhanced sorbitol and xylitol production. *Bioresource Technology*, 244: 1173-1177.
4. Scapin, E., Rambo, M. K. D., Viana, G. C. C., Marasca, N., Lacerda, G. E., Rambo, M. C. D. and Fernandes, R. D. M. N. (2019). Sustainable production of furfural and 5-hidroximetilfurfural from rice husks and soybean peel by using ionic liquid. *Food Science and Technology*, 40: 83-87.
5. Dalena, F., Basile, A. and Rossi, C. (Eds.). (2017). *Bioenergy systems for the future: Prospects for biofuels and biohydrogen*. Woodhead Publishing.
6. Tursi, A. (2019). A review on biomass: importance, chemistry, classification, and conversion. *Biofuel Research Journal*, 6(2): 962-979.
7. Nur, N. D., Nur, W. M. Z., Ahmad, H. M., Nor, M. A. and Sheikh, A. I. S. M. G. (2020). Study on the oxidation and properties of dihydroxyl cellulose using different amounts of sodium periodate. *Malaysian Journal of Analytical Sciences*, 24(6): 830-837.
8. Prasad, S. and Ingle, A. P. (2019). Impacts of sustainable biofuels production from biomass. In *Sustainable Bioenergy*, Elsevier. pp. 327-346.
9. Wattanapaphawong, P., Sato, O., Sato, K., Mimura, N., Reubroycharoen, P. and Yamaguchi, A. (2017). Conversion of cellulose to lactic acid by using ZrO_2–Al_2O_3 catalysts. *Catalysts*, *7*(7): 221.
10. Hou, Y., Lin, Z., Niu, M., Ren, S. and Wu, W. (2018). Conversion of cellulose into formic acid by Iron(III)-catalyzed oxidation with O_2 in acidic aqueous solutions. *ACS Omega*, 3(11): 14910-14917.
11. Zhang, M. H., Dong, H., Zhao, L., Wang, D. X. and Meng, D. (2019). A review on Fenton process for organic wastewater treatment based on optimization perspective. *Science of the Total Environment*, 670: 110-121.

12. Morone, A., Mulay, P. and Kamble, S. P. (2019). Removal of pharmaceutical and personal care products from wastewater using advanced materials. *Pharmaceuticals and Personal Care Products: Waste Management and Treatment Technology*, 2019: 173-212.
13. Ma, J., Zhang, K., Huang, M., Hector, S. B., Liu, B., Tong, C., ... and Zhu, Y. (2016). Involvement of Fenton chemistry in rice straw degradation by the lignocellulolytic bacterium *Pantoea ananatis* Sd-1. *Biotechnology for Biofuels*, 9(1): 1-13.
14. Awudu, F. (2018). Hydrolysis of Cellulose and Biomass using Blue Molybdenum (Doctoral dissertation, East Tennessee State University).
15. Gromov, N. V., Medvedeva, T. B., Rodikova, Y. A., Babushkin, D. E., Panchenko, V. N., Timofeeva, M. N., ... and Parmon, V. N. (2020). One-pot synthesis of formic acid via hydrolysis–oxidation of potato starch in the presence of cesium salts of heteropoly acid catalysts. *RSC Advances*, 10(48): 28856-28864.
16. Cheng, C., Wang, J., Shen, D., Xue, J., Guan, S., Gu, S. and Luo, K. H. (2017). Catalytic oxidation of lignin in solvent systems for production of renewable chemicals: A review. *Polymers*, 9(6): 240.
17. Albert, J. (2017). Selective oxidation of lignocellulosic biomass to formic acid and high-grade cellulose using tailor-made polyoxometalate catalysts. *Faraday Discussions*, 202: 99-109.
18. Chen, X., Liu, Y. and Wu, J. (2020). Sustainable production of formic acid from biomass and carbon dioxide. *Molecular Catalysis*, 483: 110716.
19. Voß, D., Dietrich, R., Stuckart, M. and Albert, J. (2020). Switchable catalytic polyoxometalate-based systems for biomass conversion to carboxylic acids. *ACS Omega*, *5*(30), 19082-19091.
20. Doungsri, S., Rattanaphanee, P. and Wongkoblap, A. (2019). Production of lactic acid from cellulose using solid catalyst. In *MATEC Web of Conferences*, 268: 07006).
21. Sun, Y., Shi, L., Wang, H., Miao, G., Kong, L., Li, S. and Sun, Y. (2019). Efficient production of lactic acid from sugars over Sn-Beta zeolite in water: catalytic performance and mechanistic insights. Sustainable *Energy & Fuels*, 3(5): 1163-1171.
22. Ramli, N. A. S. and Amin, N. A. S. (2015). Fe/HY zeolite as an effective catalyst for levulinic acid production from glucose: characterization and catalytic performance. *Applied Catalysis B: Environmental*, 163: 487-498.
23. Bhorodwaj, S. K. and Dutta, D. K. (2011). Activated clay supported heteropoly acid catalysts for esterification of acetic acid with butanol. *Applied Clay Science*, 53(2): 347-352.
24. Hietala, J., Vuori, A., Johnsson, P., Pollari, I., Reutemann, W. and Kieczka, H. (2016). Formic acid. *Ullmann's Encyclopedia of Industrial Chemistry*, 1: 1-22.
25. Ricke, S. C., Dittoe, D. K. and Richardson, K. E. (2020). Formic acid as an antimicrobial for poultry production: A review. *Frontiers in Veterinary Science*, 2020: 563.
26. Johnson Jr, W., Heldreth, B., Bergfeld, W. F., Belsito, D. V., Hill, R. A., Klaassen, C. D., ... and Andersen, F. A. (2016). Safety assessment of formic acid and sodium formate as used in cosmetics. *International Journal of Toxicology*, 35(2): 41S-54S.
27. Kos, L., Michalska, K., Żyłła, R. and Perkowski, J. (2014). Effect of formic acid on pollutant decomposition in textile wastewater subjected to treatment by the Fenton method. *Fibres & Textiles in Eastern Europe*, 22, 135-139.
28. del Barrio, M. A., Hu, J., Zhou, P. and Cauchon, N. (2006). Simultaneous determination of formic acid and formaldehyde in pharmaceutical excipients using headspace GC/MS. *Journal of Pharmaceutical and Biomedical Analysis*, 41(3): 738-743.
29. Higgins, F. J. and Ho, G. E. (1982). Hydrolysis of cellulose using HCl: a comparison between liquid phase and gaseous phase processes. *Agricultural Wastes*, 4(2): 97-116.
30. Goldstein, I. S., Pereira, H., Pittman, J. L., Strouse, B. A. and Scaringelli, F. P. (1983, January). Hydrolysis of cellulose with superconcentrated hydrochloric acid. In *Biotechnol. Bioeng. Symp.;(United States)*, 13: No. CONF-830567. North Carolina State Univ., Raleigh.

31. Dussán, K. J., Silva, D. D., Moraes, E. J., Arruda, P. V. and Felipe, M. G. (2014). Dilute-acid hydrolysis of cellulose to glucose from sugarcane bagasse. *Chemical Engineering Transaction*, 38: 433-438.
32. Alcañiz-Monge, J., El Bakkali, B., Trautwein, G. and Reinoso, S. (2018). Zirconia-supported tungstophosphoric heteropolyacid as heterogeneous acid catalyst for biodiesel production. *Applied Catalysis B: Environmental*, 224: 194-203.
33. Anggorowati, H., Jamilatun, S., Cahyono, R. B. and Budiman, A. (2018). Effect of hydrochloric acid concentration on the conversion of sugarcane bagasse to levulinic acid. In *IOP Conference Series: Materials Science and Engineering*, 299(1): p. 012092.
34. Huang, P. and Yan, L. F. (2017). Efficient degradation of cellulose in its homogeneously aqueous solution over 3D metal-organic framework/graphene hydrogel catalyst. *Chinese Journal of Chemical Physics*, 29(6): 742.
35. Sivasubramaniam, D., Amin, N. A. S., Ahmad, K. and Ramli, N. A. S. (2019). Production of ethyl levulinate via esterification reaction of levulinic acid in the presence of ZrO_2 based catalyst. *Malaysian Journal of Analytical Sciences*, 23(1): 45-51.
36. Demesa, A. G., Laari, A., Sillanpää, M. and Koiranen, T. (2017). Valorization of lignin by partial wet oxidation using sustainable heteropoly acid catalysts. *Molecules*, 22(10): 1625.
37. Zhang, Z., Wang, B., Zhang, Y., Zhang, G. and Wang, Y. (2019). Study on the synthesize, characterization, and conductive performance of nickelzircomolybdnum heteropoly acid salt with Keggin structure. *Advances in Polymer Technology*, 2019: 501593.
38. Guarin, C., Gavila, L., Constanti, M. and Medina, F. (2018). Impact of cellulose treatment with hydrotalcites in hydrothermal catalytic conversion. *Chemical Engineering Science*, 179: 83-91.
39. Ziyat, H., Naciri Bennani, M., Hajjaj, H., Mekdad, S. and Qabaqous, O. (2018). Synthesis and characterization of crude hydrotalcite Mg–Al–CO_3: study of thymol adsorption. *Research on Chemical Intermediates*, 44(7): 4163-4177.
40. Li, T., Miras, H. N. and Song, Y. F. (2017). Polyoxometalate (POM)-layered double hydroxides (LDH) composite materials: design and catalytic applications. *Catalysts*, 7(9): 260.
41. Omwoma, S., Chen, W., Tsunashima, R. and Song, Y. F. (2014). Recent advances on polyoxometalates intercalated layered double hydroxides: From synthetic approaches to functional material applications. *Coordination Chemistry Reviews*, 258: 58-71.
42. Sasaki, M., Fang, Z., Fukushima, Y., Adschiri, T. and Arai, K. (2000). Dissolution and hydrolysis of cellulose in subcritical and supercritical water. *Industrial & Engineering Chemistry Research*, 39(8): 2883-2890.
43. Paksung, N., Pfersich, J., Arauzo, P. J., Jung, D. and Kruse, A. (2020). Structural effects of cellulose on hydrolysis and carbonization behavior during hydrothermal treatment. *ACS Omega*, 5(21): 12210-12223.
44. De Guzman, D. and De Leon, R. (2021). Preliminary optimization and kinetics of $SnCl_2$-HCl catalyzed hydrothermal conversion of microcrystalline cellulose to Levulinic acid. *Journal of Renewable Materials*, 9(1): 145.
45. Wang, K., Liu, Y., Wu, W., Chen, Y., Fang, L., Li, W. and Ji, H. (2020). Production of levulinic acid via cellulose conversion over metal oxide-loaded MOF catalysts in aqueous medium. *Catalysis Letters*, 150(2): 322-331.
46. Li, X., Lu, X., Nie, S., Liang, M., Yu, Z., Duan, B., ... and Si, C. (2020). Efficient catalytic production of biomass-derived levulinic acid over phosphotungstic acid in deep eutectic solvent. *Industrial Crops and Products*, 145: 112154.
47. Lauermannová, A. M., Paterová, I., Patera, J., Skrbek, K., Jankovský, O. and Bartůněk, V. (2020). Hydrotalcites in construction materials. *Applied Sciences*, 10(22): 7989.

48. Gromov, N. V., Taran, O. P., Delidovich, I. V., Pestunov, A. V., Rodikova, Y. A., Yatsenko, D. A., ... and Parmon, V. N. (2016). Hydrolytic oxidation of cellulose to formic acid in the presence of Mo-VP heteropoly acid catalysts. *Catalysis Today*, 278: 74-81.
49. Guarin, C., Gavila, L., Constanti, M. and Medina, F. (2018). Impact of cellulose treatment with hydrotalcites in hydrothermal catalytic conversion. *Chemical Engineering Science*, 179: 83-91.
50. Delidovich, I. and Palkovits, R. (2015). Structure–performance correlations of Mg–Al hydrotalcite catalysts for the isomerization of glucose into fructose. *Journal of Catalysis*, 327: 1-9.
51. Tulaphol, S., Hossain, M. A., Rahaman, M. S., Liu, L. Y., Phung, T. K., Renneckar, S., ... and Sathitsuksanoh, N. (2019). Direct production of levulinic acid in one pot from hemp hurd by dilute acid in ionic liquids. *Energy & Fuels*, 34(2): 1764-1772.
52. Dandach, A., Vu, T. T. H., Fongarland, P. and Essayem, N. (2019). ZrW catalyzed cellulose conversion in hydrothermal conditions: Influence of the calcination temperature and insights on the nature of the active phase. *Molecular Catalysis*, 476: 110518.
53. Tian, J., Wang, J., Zhao, S., Jiang, C., Zhang, X. and Wang, X. (2010). Hydrolysis of cellulose by the heteropoly acid $H_3PW_{12}O_{40}$. *Cellulose*, 17(3): 587-594.
54. Xiaohua, C., Jie, R., Changlong, X., Zhang, K., Changchao, Z. H. A. N., and Jian, L. A. N. (2013). Preparation, characterization of Dawson-type heteropoly acid cerium (III) salt and its catalytic performance on the synthesis of n-butyl acetate. *Chinese Journal of Chemical Engineering*, 21(5): 500-506.
55. Julianti, N. K., Wardani, T. K., Gunardi, I. and Roesyadi, A. (2017). Effect of calcination at synthesis of Mg-Al hydrotalcite using co-precipitation method. *The Journal of Pure and Applied Chemistry Research*, 6(1): 7.
56. Jia, Y., Fang, Y., Zhang, Y., Miras, H. N. and Song, Y. F. (2015). Classical Keggin intercalated into layered double hydroxides: facile preparation and catalytic efficiency in Knoevenagel condensation reactions. *Chemistry–A European Journal*, 21(42): 14862-14870.
57. Liu, G., Yang, J. and Xu, X. (2020). Synthesis of hydrotalcite-type mixed oxide catalysts from waste steel slag for transesterification of glycerol and dimethyl carbonate. *Scientific Reports*, 10(1): 1-14.
58. Roohollahi, G. and Ehsani, M. (2019). An investigation into the effect of hydrotalcite calcination temperature on the catalytic performance of mesoporous Ni-MgO-Al_2O_3 catalyst in the combined steam and dry reforming of methane. *Iranian Journal of Oil and Gas Science and Technology*, 8(4): 64-84.
59. Bardin, B. B., Bordavekar, S. V., Neurock, M. and Davis, R. I. (1998). Analysis of kegging-type heteropoly compounds evaluated by catalytic probe reaction sorption microcalorimetry and density functional quantum chemical calculations. *Journal Physical Chemistry*, 102: 10817-10825.

Malaysian Journal of Analytical Sciences (MJAS)
Published by Malaysian Analytical Sciences Society

THE PREPARATION AND APPLICATION OF ZINC SULFIDE AS PHOTOCATALYST FOR WATER REMEDIATION: A MINI REVIEW

(Penyediaan dan Aplikasi Zink Sulfida sebagai Pemangkin Cahaya untuk Rawatan Air: Ulasan Ringkas)

Kavirajaa Pandian Sambasevam, Jamilin Rashida Adnan, Izyan Najwa Mohd Norsham, Siti Nor Atika Baharin*

Advanced Material for Environmental Remediation (AMER) Research Group,
Faculty of Applied Sciences,
Universiti Teknologi MARA, Cawangan Negeri Sembilan, Kampus Kuala Pilah, 72000 Kuala Pilah, Negeri Sembilan, Malaysia

**Corresponding author: atikabaharin@uitm.edu.my*

Received: 2 September 2021; Accepted: 7 March 2022; Published: 28 April 2022

Abstract

ZnS has gained attention as an effective photocatalyst for the photocatalytic degradation method in wastewater treatment. Photocatalysis is believed to be a promising solution to solve the problem of water pollution and remove organic pollutants. Apart from other photocatalysts such as ZnO, TiO_2 and MoS_2, ZnS is a developing photocatalyst in this degradation method due to its large bandgap energy. This review paper comprehensively considered the preparation (hydrothermal, solvothermal, low temperature, green synthesis, solid-state reaction, and microwave-assisted synthesis) of ZnS, application, and some challenges that have been faced by photocatalytic degradation methods. The adsorption and photocatalytic properties of ZnS depend on the different morphology and size formed by different methods. ZnS modification presents higher decomposition efficiency in removing organic pollutants.

Keywords: metal disulfide, organic pollutants, photocatalytic degradation, sustainable water management

Abstrak

ZnS mendapat perhatian sebagai pemangkin cahaya yang terbaik untuk melakukan rawatan terhadap air yang tercemar. Fotokatalisis dipercayai sebagai penyelesaian dalam menyelesaikan masalah air yang tercemar dan menyingkirkan pencemaran semulajadi yang terdapat di dalam air. Selain daripada pemangkin cahaya seperti ZnO, TiO_2 dan MoS_2, ZnS dijadikan sebagai pemangkin cahaya dalam kaedah pemulihan air kerana ZnS mempunyai tenaga jurang pita yang tinggi. Kertas kajian ini merangkumi cara penyediaan (hidroterma, solvoterma, teknik suhu rendah, sintesis hijau, tindak balas keadaan pepejal, dan sintesis berteraskan gelombang mikro) ZnS, aplikasi dan beberapa cabaran yang perlu di hadapi dalam proses rawatan air. Ciri-ciri penyerapan dan fotokatalitik ZnS bergantung kepada perbezaan struktur permukaan dan saiz yang terbentuk dari perbezaan penyediaan. Pengubahsuaian ZnS menunjukkan kecekapan penguraian yang tinggi kepada pencemaran semulajadi.

Kata kunci: logam disulfida, pencemar organik, penyingkiran fotokatalitik, pengurusan lestari air

Introduction

Filtration, chemical precipitation, ion exchange adsorption, electro deposition and membrane system are several conventional methods of water treatment. However, they exhibit slow and non-destructive effects on some organic contaminants [1]. Application of advanced oxidation methods such as photodegradation is significant due to their complete degradation without leaving any by-product behind. Photocatalysis has been widely studied because it requires an exceptionally simple procedure to generate free radicals that can degrade organic pollutants [2]. Photocatalytic study can be defined as the ability of some materials to speed up a certain reaction as a catalyst in combination with light including sunlight, UV and visible light. The term 'photocatalytic' designated reactions accelerated by light but maintaining the same course as the thermal reactions [3]. Photocatalytic activity is influenced by the crystal structure, particle size, band gap, dispersibility and hydroxyl of the catalyst. Photocatalytic degradation is a study that is still currently developing. Semiconductor photocatalysts play an important role in photocatalytic activities. Various studies were widely carried out by many researchers around the globe. Among all semiconductors, titanium dioxide (TiO_2) is the most frequently used photocatalyst in study and research regarding oxidation of organic pollutants. However, its high potential for charge recombination has become a limiting factor of TiO_2 for sunlight photocatalytic applications [4].

Meanwhile, the single semiconductor which is the photocatalyst only consists of one medium of photocatalyst to degrade organic pollutant that shows ineffective degradation rates, such as bismuth vanadate ($BiVO_4$), zinc oxide (ZnO) and cadmium selenide (CdSe) [5]. ZnS is a II-VI semiconductor material that exhibits a high excitation energy which is approximately 40 meV. ZnS also has a band gap energy of 3.7 eV and ZnS can be used as semiconductor photocatalyst to degrade pollutants due to its non-toxic nature, highly negative reduction potential of excited electrons and high rate of formation of electron-hole pairs that leads to higher conduction band position in aqueous media [6,7]. A study reported that ZnS is an important inorganic material for various applications such as solar cell, field effect transistor, photoconductors, sensors, light-emitting materials and optical coating [8]. Moreover, ZnS is chosen to be a photocatalyst because of its direct wide band gap (e.g., = 3.7 eV), good mechanical stability, highly efficient conductivity, and high electron transfer ability, aside from the ZnS nanoparticle having a high rate of success when doped with the polyaniline matrix [6,5]. Thus, this mini review aimed to examine the recent preparation technique of ZnS and its application as a photocatalyst in water remediation.

Fundamental of photocatalytic degradation

Photocatalytic degradation technology is one of the advanced oxidation processes (AOP) that involves semiconductor photocatalyst and oxygen to produce radicals in which the activity is influenced by the crystal structure, particle size, band gap, dispersibility and hydroxyl of the catalyst. The basic principle of photocatalyst activation mechanism can be seen in Figure 1. During this reaction, these photons contribute to the excitation of electrons (e^-) on the surface of photocatalyst in the valence band when the energy of the photons is higher than the band gap which makes the e^- rise up into the conduction band and causes the production of a hole (h^+) in the valence band. These separated holes and electrons can recombine and release the absorbed energy to form heat. The excited electrons that are now in the conduction band (e^-_{CB}) will react with oxygen (O_2) to form superoxide radicals (O_2^-) or hydroperoxide radicals (HO_2). Next, these reactive oxygen species will be used for the degradation of pollutants into water (H_2O) and carbon dioxide (CO_2). O_2^- can be further used again in secondary degradation steps where these reactions could result in the oxidation of water molecules at the positive hole in the valence band (h^+_{VB}) that produces hydroxyl radicals (OH) and hydrogen ions (H^+). Lastly, the OH would react with pollutants and result in H_2O and CO_2 [9,10].

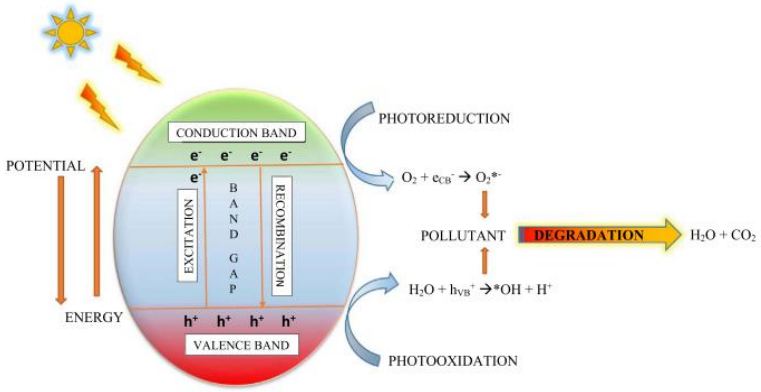


Figure 1. Basic principle of photocatalysis [9]

Many studies have been carried out to test a variety of light sources and mostly focused on the implementation of UV light because this light provides enough photons to generate electron hole pairs within the catalyst. Thus, it could perform efficiently in the production of radicals and the oxidative degradation of the toxic and dangerous pollutants [11]. Photocatalytic processes can use artificial UV lamps and sunlight as the radiation source in photocatalysis. Mostly used artificial UV lamps that were mercury lamps that can be divided into low pressure, medium pressure and high pressure. Moreover, sunlight also has been used in this reaction as nearly 4 to 5% of the sunlight that reaches the surface of earth is in the range of 300 to 400 nm. ZnS is powerful as a photocatalyst in UV range compared to visible range [12]. Furthermore, sunlight has its own limitation because of its graphical variation when compared with artificial UV lamps [13]. Munawaroh and co-author stated that zinc oxide/graphene oxide (ZnO/GO) had high adsorption capacity and GO addition made the band gap narrower, which prevented the recombination of electron and led to high electron transfer on the ZnO [14]. The photocatalytic activity of ZnO/GO is performed in different irradiation times which are 15, 30, 45 and 60 minutes and the maximum wavelength is 665 nm. Figure 3 shows that UV light is involved to activate the photocatalytic properties of the material to form radical species that lead to degradation of the methylene blue dye into green compounds. From Figure 2, it is proven that the longer the contact time, the more electrons would be excited which contribute to production of more h^+. Mechanisms (1) to (6) show the formation of h^+ which contributes to formation of hydroxyl radicals in the photocatalytic degradation. More production of h^+ would increase the photocatalytic degradation. The percent efficiency of degradation based on formula (7) in methylene blue with ZnO/GO 1:2 is 94.05% [14].

Excitation: Photon ($h\nu$) + Semiconductor $\rightarrow e^-_{CB} + h^+_{VB}$ (1)

Recombination: $e^- + h^+ \rightarrow$ energy (2)

Oxidation of H_2O: $H_2O + h^+_{VB} \rightarrow {}^{\bullet}OH + H^+$ (3)

Reduction of adsorbed O_2: $O_2 + e^- \rightarrow O_2^{\bullet-}$ (4)

Reaction with H^+: $O_2^{\bullet-} + H^+ \rightarrow {}^{\bullet}OOH$ (5)

Electrochemical reduction: ${}^{\bullet}OOH + {}^{\bullet}OOH \rightarrow H_2O_2 + O_2$ (6)

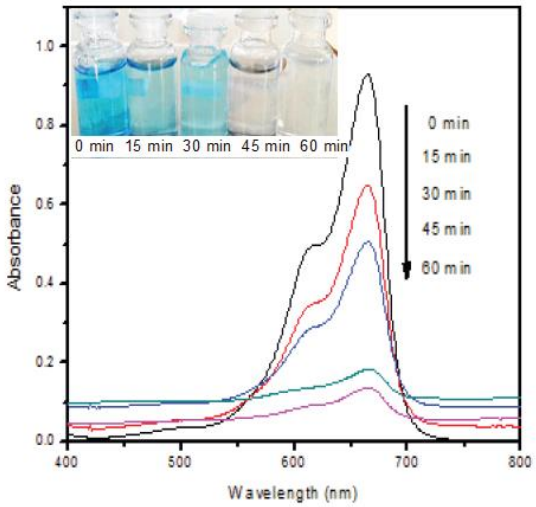


Figure 2. UV-vis spectra of methylene blue with ZnO/GO (1:2) and under UV illumination [14]

Preparation of zinc sulfide

In general, ZnS can be synthesised via various methods such as solution-phase reaction, hydrothermal, solvothermal, exfoliation, high pressure autoclave processes, physical vapour deposition (PVD) and chemical vapour deposition (CVD). ZnS can be easily synthesised with the aid of autoclave at high pressure and low temperature without the need of a catalyst [15]. At ambient conditions, ZnS possess two crystal structures which are zinc blend (cubic) and wurtzite (hexagonal), meanwhile at high pressure "rock salt" crystalline shape can be achieved but only in case of nanostructures of ZnS [15].

Hydrothermal method

Hydrothermal method refers to the heterogeneous reactions for synthesising inorganic materials in an aqueous media above ambient temperature and pressure which is used to obtain nanoparticles, generally at relatively high temperature which is around 200°C by using an autoclave reactor and high pressure. In order to get the desired size and shape of ZnS, a capping agent is applied to control the size and shape of ZnS such as surfactants, ligands, dendrimers and polymers [16]. In hydrothermal synthesis, this capping agent is used to control the nanometre size of ZnS. Thioglycolic acid (TGA) is a common capping agent that has been studied for synthesising ZnS. It is proven that ZnO/ZnS nanocable, ZnS/organic composite nanoribbons and ZnS nanotube arrays have been successfully synthesised by using TGA. In the previous study, TGA was used to prevent the chalcogenide nanocrystal accumulation which is known as stability agents. Thus, TGA is a perfect choice during the hydrothermal process as a capping agent for self-assembly and crystal growth of ZnS crystal to cluster. In this process, the temperature of 105°C is maintained during the autoclave for 7 hours. Based on the transmission electron microscopy (TEM) and selected area electron diffraction (SAED) in the range of 50 to 150 nm as shown in Figure 3, the morphology of ZnS crystal forms some loose spheres by accumulation of small particles. Most of the organic molecules are degraded because of the temperature that took place during the process. The ZnS nanocluster is formed at the final process due to only a part of the TGA molecule which is diffused into the ZnS nanoparticle. The SAED pattern also shows sharp rings of (1 1 1), (2 2 0) and (3 1 1) planes of cubic zinc blended ZnS that corresponded to the XRD study Figure. 4. The size of the nanocrystals based on the Scherrer formula ($D= 0.89\lambda/\beta \cos \theta$), estimated from the full width at half maxima (FWHM) of the (1 1 1) diffraction peak is about 4 nm for synthesised

nanoparticles which are much smaller than the spherical diameters. This indicates that the clusters are formed from nanocrystal mass assembly. It is fair to assume that the TGA-assisted hydrothermal process provides a great opportunity to scale-up other chalcogenides morphology preparation [17]. Based on a previous study, a composite of SnO_2/ZnS prepared by hydrothermal method at 180°C showed the highest photocatalytic activity to degrade RhB [18]. The photocatalytic degradation of 95% is reached at the 1 g/L SnO_2/ZnS dosage with 10 mg/L initial RhB concentration, 4.59 initial solution pH and 23°C. The photocatalytic degradation of the RhB really fitted to the first-order kinetic model and it is also showing the decrease of initial RhB concentration with the increase of SnO_2/ZnS dosage. The composited SnO_2/ZnS that are prepared by hydrothermal method also showed a stable performance during 5 runs of reuse [18].

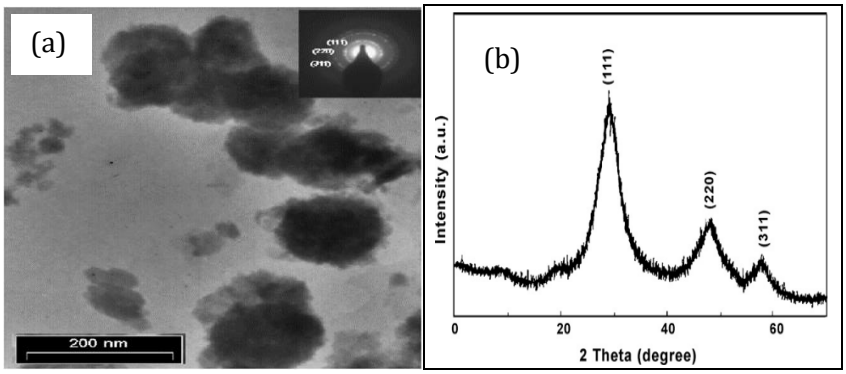


Figure 3. (a) TEM image of ZnS nanocluster; (b) Figure 4 XRD pattern of as-prepared ZnS nanocluster [17]

Solvothermal method

Solvothermal process refers to a heterogeneous reaction involving the thermal decomposition of metal complexes using the solvent mineraliser either by boiling the contents in an inert atmosphere or in a sealed vessel (autoclave). Solvothermal method possesses advantages including less energy consumption and simple and also some disadvantages including need for expensive autoclaves and Teflon liners in stainless steel, which can lead to safety problems during reaction processes and the impossibility of studying in-situ reactions due to their closed system [19]. Unlike hydrothermal route which needs a surfactant, toxic template or capping agent to control the size of ZnS morphology, solvothermal method is without surfactant and needs propylene glycol solvent at 140 °C for 12 hours to produce the ZnS nanoplates. The SEM image in Figure 4 (a) of ZnS exhibits flower-like morphology and a large amount of quasi hexagonal plates which were produced via solvothermal method. However, in the solvothermal method, the right choice of temperature is crucial. As can be seen in Figure 4 (b), higher temperature at 160 °C yielded non-uniform and amorphous nature of ZnS. Obviously, this condition via solvothermal technique did not favour the synthesis of ZnS. This is due to the decreasing crystallisation temperature which can be attributed to a slight increase in photocatalytic activity, hence temperatures higher than 140 °C mostly do not support this method [20]. Song and co-worker carried out the preparation of a ternary photocatalyst of zinc cadmium sulphide by this method which was synthesised at a maintained temperature of 120-140 °C for 3 hours [21]. The methylene blue (MB) was degraded by the photocatalytic activity of zinc cadmium sulphide. 0.4 g zinc cadmium sulphide photocatalyst was dispersed in 250 mL of MB solution. In this study, after a 1-hour reaction time, at 120 °C the photocatalytic activity showed the best photocatalytic activity compared to 140 and 130 °C as shown in Figure 5 below due to 120 °C being the lowest temperature so it is suitable for the solvothermal method.

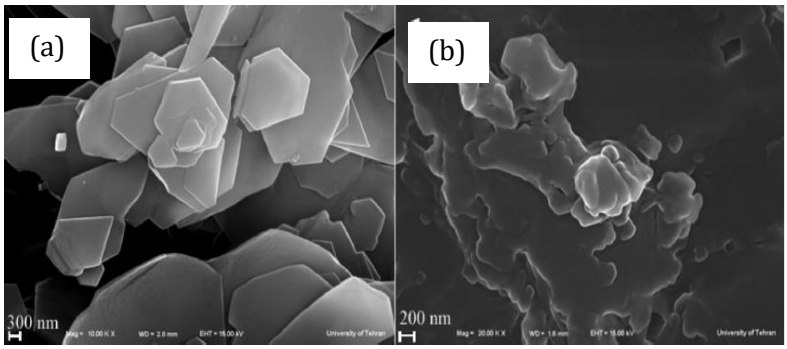


Figure 4. SEM image of as-synthesized product in propylene glycol for 12 hours: (a) 140 °C and (b) 160 °C [20]

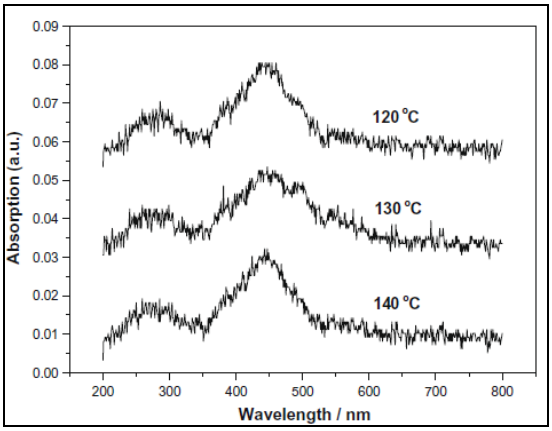


Figure 5. UV-vis absorbance spectra of sample treated at 120-140 °C [21]

Low temperature method

This method basically involves low temperature (below 100°C) by a chemical reaction that occurs between zinc ions and reduces sulphide ions in ethanol as a reaction medium. This method requires a strong reducing agent to have a better control reaction such as hydrazine hydrate to have better control to convert elemental sulphur (S_8) to reactive sulphide ions (S^{2-}) by in-situ reduction. The sulphide ions then react on impulse with zinc ions, since zinc chloride and elemental sulphur were used separately as sources of zinc and sulphur [22]. Low temperature method exhibited preferable characteristics as it is less toxic, less time consuming, low cost and needs low temperature without any solvent release, low waste and environmentally friendly [22]. The less time consumption can be observed when the reduction of S_8 into S^{2-} took place in a very short time. The reaction can be represented in Equation (7) [20].

Equation (7) showed a rapid process as it only takes a few seconds (30-40 seconds) of the elemental sulphur reduction to happen. The concentration of zinc before and after reaction was calculated to know the yield of the reaction by using an ICP-OES spectrometer. The reading of the ICP-OES spectrometer showed 99% consumption of zinc precursor in the reaction which means a very high conversion yield of the precursor to the final product was obtained. Study of the reaction time impact showed that longer reaction times lead to agglomeration of less particles to bigger ones. Hence, the reaction time should be adjusted to form the particles as soon as hydrazine hydrate has been added. Figure 6 (a) shows UV-Vis absorption spectra of ZnS

quantum dots at 60 °C with different reaction times of 2, 3, 5, 7 and 12 minutes which displayed that the size of ZnS quantum dots were almost the same and that longer time which was up to 60 minutes at 60 °C did not influenced the particle size with absorption peak at ~257 nm. Meanwhile, Figure 6 (b) shows UV-Vis absorption spectrum of ZnS quantum dots at 120 °C for 60 minutes. An absorption peak at 277 nm was observed which is red shifted as compared to the absorption peak at 60 ºC, displaying an increase in size [22]. The photocatalytic activity of ZnS synthesised by this method can be observed on the removal of MB with a photocatalyst of ZnS under UV irradiation. This study showed that ZnS succeeded in achieving removal efficiency of 75% during photocatalytic degradation of MB [23].

$$ZnCl_2 + \frac{1}{8S} + N_2H_2.H_2O \xrightarrow[C_3H_8O_2S]{C_2H_5OH,60\,^{\circ}C} ZnS + 2HCl + N_{2(g)}H_{2(g)} + H_2O \quad \textbf{(7)}$$

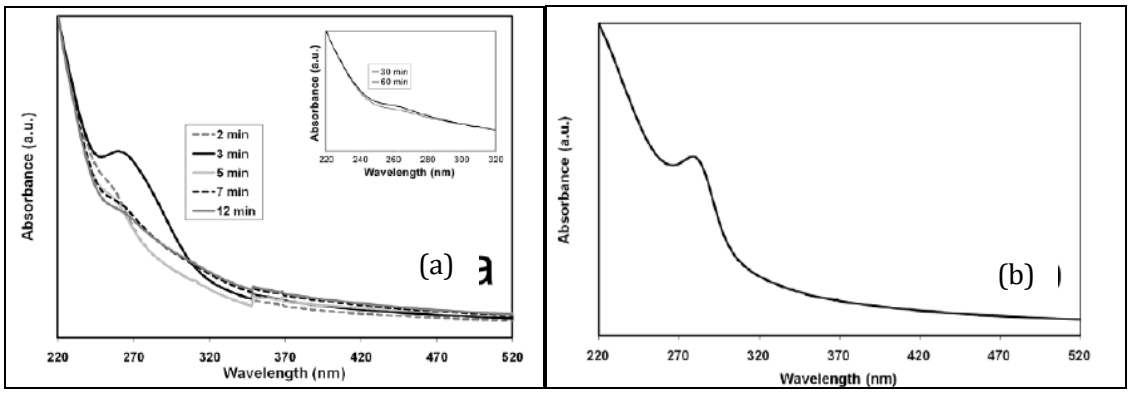


Figure 6. (a) UV-Vis absorption spectrum of ZnS quantum dots at 60 °C for reaction time 2, 3, 5, 7, 12 minutes (a) at 60 °C for reaction time 30 and 60 minutes (b) at 120 °C for 60 minutes [22]

Green synthesis method

Green synthesis method is a biological synthesis of nanoparticles that basically uses plants or plant extract which is low cost, nontoxic and environmental friendly method. A study on glucose was used as both stabilizer and capping agent while latex solution prepared from *Jatropha curcas* L. In the *Jatropha curcas* L there were curcacycline A (an octapeptide), curcain (an enzyme) and curcacyline B (a nanopeptide) equipped inside as a potential stabilizing and reducing agent [24,25]. Glucose is a monosaccharide that present in the plants with five hydroxyl groups are arranged in its own manners along its six-carbon backbone and it is renewable, natural, large quantity and biodegradable. Glucose is used in this method while zinc nitrate and sodium sulfide as zinc and sulphur source respectively. In this method, the resulting solution was heated at 70 °C up to 6 hours. The final product of this synthesis, can be observed in the Equation (8). The ZnS that obtained via this method, exhibited crystallinity peak at 28.38°, 47.73° and 56.50° as shown in Figure. 7. The peaks were assigned to the cubic of ZnS as (1 1 1), (2 2 0) and (3 1 1). The broad peaks in XRD indicated the formation of nanoparticles. Thus, it proved that ZnS nanoparticles succesfully synthesized by green method by using glucose as capping agent [24].

This method can be observed in its photocatalytic activity in a study by Kannan et al. (2020) involving ZnS that had been synthesised using plant extract of *Tridax procumbens* (T:ZnS). Biosynthesised T:ZnS (40 mL) nanoparticles displayed high surface area which was 131.84 m^2/g and also exhibited larger pore size which was 12.15 nm. This high surface area was able to promote more active sites, hence increasing the photocatalytic ability to degrade MB achieved 98% of degradation efficiency under visible light irradiation.

$$Zn(NO_3)_2 + Na_2S \xrightarrow{Glucose} ZnS + 2NaNO_3 \quad (8)$$

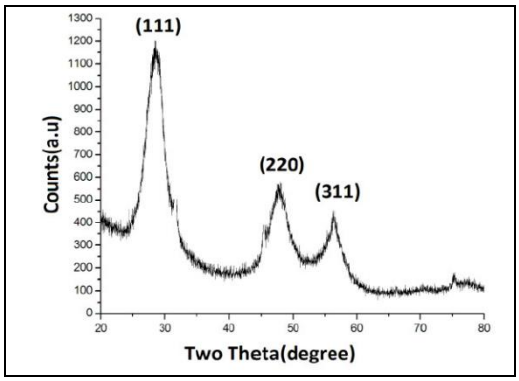


Figure 7. XRD spectra of ZnS nanoparticles [23]

Solid-state reaction method

Solid state reaction method is a simple reaction for the preparation of ZnS nanorods. This method utilises simple techniques such as melting or grinding together the starting materials or simply applying heat to a mixture of starting materials and also without any metal catalyst, solvent or templates. The nanoparticles were prepared by one-step, typically solid-state reaction of zinc chloride and sodium sulphide as zinc and sulphide sources, respectively which will be ground with mortar and pestle at ambient temperature in sodium chloride flux. This method, however, needs high temperatures because it involves precursors to synthesise nanotubes by using a furnace at 800 °C for 2 hours for the heat treatment sample. Figure 8 shows XRD spectra of final nanoparticle ZnS nanorods fabricated by annealing precursor ZnS nanoparticle in sodium chloride flux. The synthesised ZnS nanorods have changed from cubic to hexagonal structure via solid state reaction method [27].

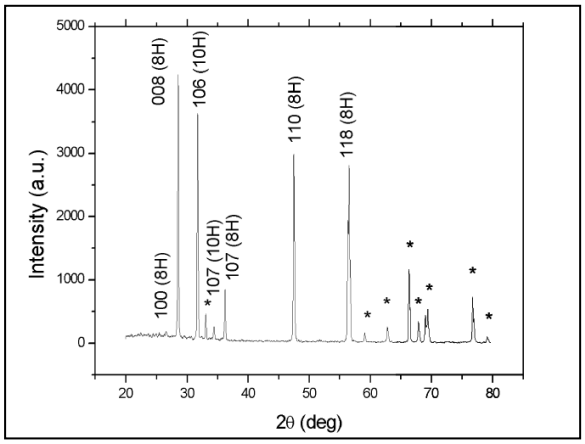


Figure 8. XRD spectra of final nanoparticle ZnS nanorods fabricated by annealing precursor ZnS nanoparticle in sodium chloride [27]

The photocatalytic performance is known to be dependent on the crystallinity, morphology and surface area that are able to enhance the recombination of photogenerated electron-hole pairs. Jothibas et al. (2018) showed the photocatalytic activity of ZnS doped with nickel (Ni) that was synthesised by this method. The ZnS doped Ni was used to degrade the MB. It proved the MB concentration decreases in the presence of ZnS doped Ni due to destruction of the homo and hetero-poly aromatic ring present in the MB or the fast degradation of the dye [27].

Microwave assisted synthesis method

Microwave (MW) assisted synthesis is a heating method that uses ionic liquids (ILs) as MW absorbing medium to synthesise the highly crystalline ZnS quantum dots (QDs). Imidazolium or phosphonium cations together with many types of anions ranging from simple anions including halides to more complex ones included bis(trifluoromethanesulphonyl) amide based, are two types of ionic liquids that were used in this method. The QDs that were synthesised as the final product were less than 5 nm in size and of wurtzite ZnS type. MW irradiation basically is a heating method where the dielectric heating mechanism involves bipolar polarisation and ionic conduction that allows for faster reactions with higher yields and higher purities without high vacuum requirements [22]. ILs are considered as friendly environmental media that can be replaced with other volatile and toxic organic solvent. It is also exhibiting some properties of high polarity, high thermal stability, high ionic conductivity and a good solvent for both electrolyte and organic compounds. Hence MW assisted with IL method that produced via 'green' synthesis route to produce the nanoparticles [23]. The microwave-assisted synthesis method to produce ZnS nanoballs with an average diameter of 41.9 nm was composited with graphene nanosheets (GNS) [29]. These ZnS nanoballs are made up of many small self-assembled ZnS crystals with an average size of 3 nm. 0.20 g of ZnS-GNS composite was used to degrade the MB, resulting in the intensity of the adsorption peaks of MB which gradually diminished with increasing exposure time and finally disappeared after about 32 minutes. This showed a complete degradation of MB as no new absorption peaks appeared in the visible and UV region.

Zinc sulfide as photocatalyst in photodegradation of organic pollutant

Overall, from the syntheses listed above, they show that photocatalytic performance of photocatalysts can be influenced by their crystallinity, morphology, size and surface area. Morphology-controlled synthesis are increasing in popularity because of the structure that decides the characteristics. Different sizes, morphology and structure of materials exhibited different properties. Scale quantisation of particles with semiconductors resulted in dramatic shifts of other essential properties of the materials. Firstly, the quantisation of the scale affects the electronics characteristics of the semiconductor particle, with ultra-small crystallites made up of a few molecular units maintaining their subtle HOMOs (Highest Occupied Molecular Orbitals) and LUMOs (Lowest Unoccupied Orbital Molecular Orbitals). Next, chemical and physical properties which are dedicated to electronic properties of the semiconductor really depend on the size of the nanoparticles. The band gap of the semiconductor becomes larger as the particle size decreases and is related to an absorption shift at shorter wavelengths hence, the level of valence band is shifted to lower energy while conduction band are strongly shifted to higher energies. To summarise, Table 1 represents comparable methods of ZnS preparation, properties and their degradation efficiency towards degradation of pollutants.

On the other hand, many methods have been developed to remove organic pollutants including photodegradation with usage of ZnS as semiconductor/photocatalyst. Among the semiconductors/photocatalysts mentioned above, degradation efficiency of ZnS also can be enhanced as in binary and ternary photocatalysts.

Table 1. Methods of preparation, properties, and their degradation efficiency

Methods of Preparation	Particle Size and Shape	Pollutants	Source of Light	Degradation Efficiency	References
Hydrothermal	Clearly observed lattice fringes indicate that the particles are crystalline.	Methyl Orange (MO)	UV lamp	70% in 120 min	[30]
Solvothermal	The shape and size are uniform and it is observed that all the nanorods are well dispersed.	Rhodamine B	UV lamp	98% in 90 minutes	[31]
Solid-state reaction	The orbital composition of well-defined particles, which has spherical shapes	MO	Visible	88% in 75 minutes	[32]
Green synthesis	Revealed the crystal structures and obvious atomic planes for single particles .	Phenanthrene	Visible	82% in 90 minutes	[33]
Microwave assisted	Looked like agglomerated spherical clusters with particle size	4-chlorophenol	UV lamp	100%	[34]

Binary photocatalyst

Binary photocatalyst of ZnS is when ZnS is composited with another filler for example graphene. This composite (ZnS-graphene) can result in new properties of photocatalysts. The photocatalytic activity of ZnS-graphene was observed by degrading methylene blue (MB) in water [29]. This study used a graphene nanosheet and the UV-Vis spectrum in the range of 300 to 800 nm is given in Figure 9. The characteristic absorption peak of methylene blue solution at 663 nm was selected as the parameter monitored to detect the methylene blue concentration. Figure 13 shows the evolution of absorption spectra of MB in the presence of 0.20 g ZnS-graphene composites. It was found that the intensity of the absorption peaks aligned directly to MB which gradually declined with increasing exposure time and finally vanished after about 32 minutes. There were no new absorption peaks pop up in the visible and ultraviolet region, showing the complete degradation of MB. In addition, the photocatalytic activity of ZnS-graphene can be observed to degrade 4-nitrophenol (4-NP) [34]. The declining of absorption peak intensity of nitrophenolate ion with ZnS-graphene was recorded over time under simulated light to observe the photocatalytic activity of the composite toward reduction of 4-NP.

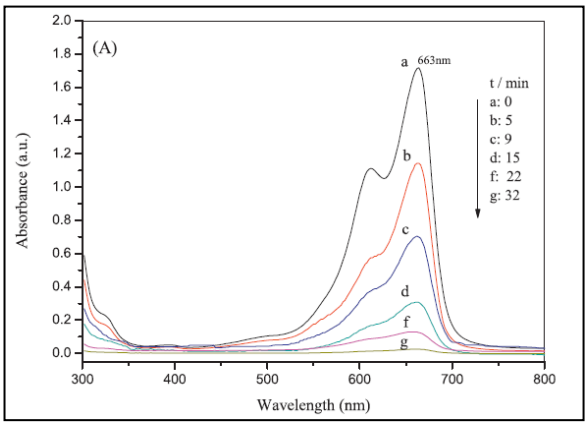


Figure 9. Absorption spectra of a solution of MB with ZnS-graphene [29]

The reduction efficiency of ZnS-graphene and ZnS was compared under simulated solar light illumination as indicated in Figure 10 (a) and (b) respectively. The time used for illumination was 70 minutes to achieve 87% of reduction efficiency with the composite while it was only 34% with single ZnS under similar experimental conditions. Hence, based on formula (10) of reduction rate constant, k shows the results of pseudo-first order reduction kinetics of 4-NP where the k of ZnS is 6×10^{-3} min^{-1} while ZnS-graphene composite is 30×10^{-3} min^{-1}. This shows that ZnS-graphene composite results in better efficiency compared to ZnS and 5 times higher k than ZnS because of its synergistic effect between reduced graphene oxide and ZnS where graphene is responsible for an efficient photo-induced charge separation and transportation [35]. Then, the photo-induced electrons generated in the ZnS nanorod high-band gap pass from its conduction bands to the 4-NP LUMO level through the graphene sheets and reduce the 4-NP to 4-aminophenol [35].

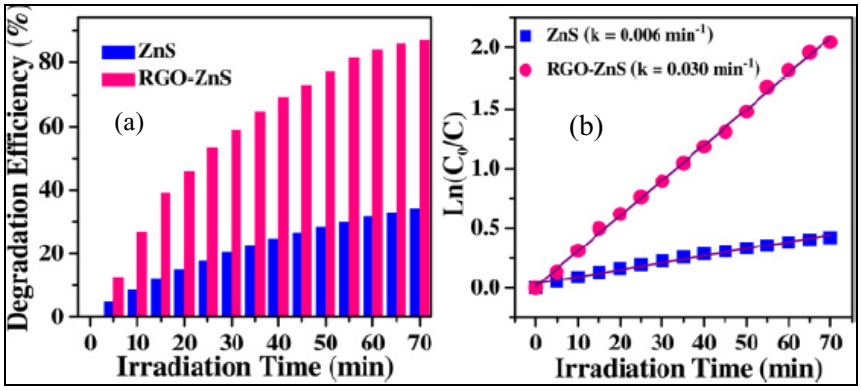


Figure 10. (a) The comparison of the reduction efficiency versus irradiation time over ZnS and ZnS-graphene (b) Plot of In (C_0/C) for the photocatalysis of 4-NP solution with ZnS and ZnS-graphene composite [35]

Ternary photocatalyst

Ternary photocatalyst is a photocatalyst that has a three-system photocatalysis; for example, reduced graphene oxide-ZnS-TiO_2 (rGO-ZnS-TiO_2). The photocatalytic activity of ternary photocatalysts of rGO-ZnS-TiO_2 nanocomposite can be observed on its application for crystal violet dye (CV) removal [36]. This combination is proven to be an effective photocatalyst for the treatment of wastewater. Through this study, the result showed that almost 97% CV dye was removed by adsorption and photodegradation at temperature of 35 °C with initial dye concentration of 50 ppm and nanocomposite amount of 0.4 g/L. The study was carried out with varied loadings of catalyst to decide the optimal amount of rGO-ZnS-TiO_2 nanocomposite prepared with the aid of ultrasonic irradiation. Based on Figure 11, the overall photocatalytic degradations are 94.83%, 97.02% and 96.30% obtained for 0.3 g/L, 0.4 g/L and 0.5 g/L of rGO-ZnS-TiO_2 nanocomposite respectively. The results also showed that the quantity of nanocomposite increased from 0.3 g/L to 0.4 g/L. The degradation of CV was also increased from 94.83% to 97.02% independently and continuous increase in the loading of rGO-ZnS-TiO_2 nanocomposite at 0.5 g/L exhibited a marginal decline in the degradation, which was meant to be at 96.30%. rGO-ZnS-TiO_2 nanoparticles displayed strong adsorption abilities and the excessive adsorption reduced the photocatalytic activity. Hence, the distribution of impudent loaded nanocomposite will hinder the UV light irradiation and the restriction can result in an efficient usage of light resulting in declining photocatalytic degradation of CV dye. So, the result concluded that the optimal dose of rGO-ZnS-TiO_2 is 0.4 g/L with the aid of ultrasonic illumination to obtain effective degradation of CV dye [36].

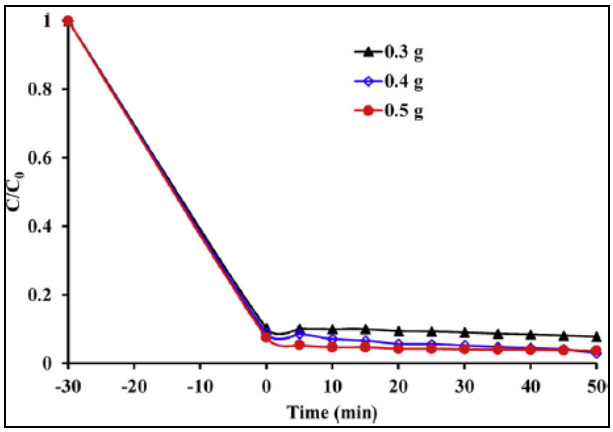


Figure 11. The effect of catalyst loading on degradation of CV dye [36]

Table 2. Comparison between binary and ternary ZnS composites in photocatalytic degradation

Types of ZnS Photocatalyst	Pollutants	Source of Light	Degradation Efficiency	References
Binary				
ZnS-graphene	methylene blue (MB)	UV light	98%	[29]
RGO-ZnS	4-nitrophenol	Solar Light	87%	[35]
Cadmium-ZnS	Methyl Orange	Visible light	90%	[32]
ZnS layers of ZnS(en)x complex	Chromium IV	Hg lamp	99%	[37]
Ternary				
rGO-ZnS-TiO_2	crystal violet dye	UV light	97%	[36]
ZnS–TiO_2/RGO	Methylene blue	Visible light	90%	[38]
ZnO/reduced graphene oxide (rGO)/polyaniline (PANI)	Methyl Orange	Visible Light	100%	[39]
ZnO-ZnS@Pani	2-chlorophenol	Visible Light	87%	[40]
Ag_2S–ZnS loaded on cellulose	Rhodamine B	Visible light	95%	[41]

Conclusion

Based on the overall review towards the application of ZnS, it can be concluded that ZnS can be successfully composited with conducting polymers and other photocatalysts. ZnS was able to be prepared through various preparations and methods resulting in different sizes and morphologies based on their SEM and TEM images. It is also proven that different sizes and morphologies of ZnS would result in different reactions of ZnS towards photocatalytic studies. The smaller the size of ZnS, the better the photocatalytic degradation of organic pollutants. Moreover, ZnS can also act as a photocatalyst in different forms including single semiconductor, binary photocatalyst and ternary photocatalyst. Ternary photocatalysts proved to be the better photocatalytic as three media compositions increased the photocatalytic behaviour of ZnS. This is because ternary photocatalysts improved the electric properties of the photocatalyst, hence improving the photocatalytic degradation of organic pollutants. Last but not least, it can be proven on the basis of the analysis that ZnS exhibited a strong photocatalytic activity to degrade organic contaminants such as organic dye and nitrophenols. Future studies can explore whether ZnS is able to act as a photocatalyst which is a composite with conducting polymer. Conducting polymer is widely used in applications such as sensors because of its characteristics including ease of synthesis, low density and conducting properties. Conducting polymers show potential as it can greatly increase conductivity has the advantages of conventional organic polymers including strength, plasticity, toughness and flexibility. It is believed that composited photocatalysts with conducting polymer increase the effectiveness of degradation because of the increasing appropriate surface of the photocatalyst.

References

1. Dehghanifard, E., Jafari, A. J., Kalantary, R. R., Mahvi, A. H., Faramarzi, M. A. and Esrafili, A. (2013). Biodegradation of 2, 4-dinitrophenol with laccase immobilized on nano-porous silica beads. *Iranian Journal of Environmental Health Science and Engineering*, 10(1): 25.

2. Anjum, M., Oves, M., Kumar, R. and Barakat, M. A. (2017). Fabrication of ZnO-ZnS@ polyaniline nanohybrid for enhanced photocatalytic degradation of 2-chlorophenol and microbial contaminants in wastewater. *International Biodeterioration and Biodegradation*, 119: 66-77.
3. Ayodhya, D. and Veerabhadram, G. (2018). A review on recent advances in photodegradation of dyes using doped and heterojunction based semiconductor metal sulfide nanostructures for environmental protection. *Materials Today Energy*, 9: 83-113.
4. Salah, N., Hameed, A., Aslam, M., Babkair, S. S., and Bahabri, F. S. (2016). Photocatalytic activity of V doped ZnO nanoparticles thin films for the removal of 2-chlorophenol from the aquatic environment under natural sunlight exposure. *Journal of Environmental Management*, 177: 53-64.
5. Das, M. and Sarkar, D. (2017). One-pot synthesis of zinc oxide-polyaniline nanocomposite for fabrication of efficient room temperature ammonia gas sensor. *Ceramics International*, 43(14): 11123-11131.
6. Allahyeran and Mehrizad (2017). Comparison between different d-dimer cutoff values to assess the individual risk of recurrent venous thromboembolism: Analysis of results obtained in the DULCIS study. *International Journal of Laboratory Hematology* 38(1): 42-49.
7. Lai, K., Wei, W., Yingtao, Z., Meng, G., Ying, D. and Baibiao, H. (2012). Effects of oxygen vacancy and n-doping on the electronic and photocatalytic properties of Bi_2MO_6 (M=Mo, W). *Journal of Solid State Chemistry* 187:103-108.
8. Goswami, M., Sahoo, S., Meikap, A. K. and Ghosh, R. (2011). Characterization, optical and dc electrical properties of polyaniline-zinc sulphide nanocomposite. In *International Conference on Nanoscience, Engineering and Technology*, 2011: 314-318.
9. Bora, L. V. and Mewada, R. K. (2017). Visible/solar light active photocatalysts for organic effluent treatment: Fundamentals, mechanisms and parametric review. *Renewable and Sustainable Energy Reviews,* 76: 1393-1421.
10. Byrne, C., Subramanian, G. and Pillai, S. C. (2018). Recent advances in photocatalysis for environmental applications. *Journal of Environmental Chemical Engineering*, 6(3): 3531-3555.
11. Al-Hamdi, Abdullah, M., Uwe, R. and Mika, S. (2017). Tin dioxide as a photocatalyst for water treatment: A review. *Process Safety and Environmental Protection* 107:190-205.
12. Mahvelati-Shamsabadi, T. and E. K. Goharshadi. (2017). Photostability and visible-light-driven photoactivity enhancement of hierarchical ZnS nanoparticles: The role of embedment of stable defect sites on the catalyst surface with the assistant of ultrasonic waves. *Ultrasonics Sonochemistry*, 34: 78-89.
13. Umar, M. and Aziz, H. A. (2013). Photocatalytic degradation of organic pollutants in water. *Organic Pollutants-Monitoring, Risk and Treatment*, 8: 196-197.
14. Munawaroh, H., Sari, P. L., Wahyuningsih, S. and Ramelan, A. H. (2018) The photocatalytic degradation of methylene blue using graphene oxide (GO)/ZnO nanodrums. *In AIP Conference Proceedings*, 2014: p. 020119.
15. Majhi, M., Choudhary, R. B., and Maji, P. (2017). HCl protonated polymeric PANI-ZnS nanocomposites and measurement of their robust dielectric, optical and thermal performance. *Optik*, 136: 181-191.
16. Varanda, L. C., de Souza, C. G. S., Perecin, C. J., de Moraes, D. A., de Queiróz, D. F., Neves, H. R. and da Silva, T. L. (2019). Inorganic and organic–inorganic composite nanoparticles with potential biomedical applications: Synthesis challenges for enhanced performance. In *Materials for Biomedical Engineering*: pp. 47-99.
17. Salavati-Niasari, M., Fatemeh, D. and Mehdi, M. (2009). Synthesis and characterization of ZnS nanoclusters via hydrothermal processing from [Bis(Salicylidene)Zinc(II)]. *Journal of Alloys and Compounds* 470(1–2): 502-506.

18. Hu, L., Feiyan, C., Pengfei, H., Lianpei, Z. and Xing, H. (2016). Hydrothermal synthesis of SnO2/ZnS nanocomposite as a photocatalyst for degradation of rhodamine b under simulated and natural sunlight. *Journal of Molecular Catalysis A: Chemical*, 411: 203-213.
19. Lee, G. J. and Wu, J. J. (2017). Recent developments in ZnS photocatalysts from synthesis to photocatalytic applications -A review. *Powder Technology*, 318: 8-22.
20. Shakouri-Arani, M. and Salavati-Niasari, M. (2014). Synthesis and characterization of wurtzite ZnS nanoplates through simple solvothermal method with a novel approach. *Journal of Industrial and Engineering Chemistry,* 20(5): 3179-3185.
21. Song, L., Zhang, S., Chen, B., Ge, J. and Jia, X. (2010). Fabrication of ternary zinc cadmium sulfide photocatalysts with highly visible-light photocatalytic activity. *Catalysis Communications*, 11(5): 387-390.
22. Shahid, R., Toprak, M., Soliman, H. and Muhammed, M. (2012). Low temperature synthesis of cubic phase zinc sulfide quantum dots. *Open Chemistry*, 10(1): 54-58.
23. Guo, J., Khan, S., Cho, S. H., and Kim, J. (2019). Preparation and immobilization of zinc sulfide (ZnS) nanoparticles on polyvinylidene fluoride pellets for photocatalytic degradation of methylene blue in wastewater. *Applied Surface Science*, 473: 425-432.
24. Senapati, U. S., Jha, D. K. and Sarkar D. (2013). Green synthesis and characterization of ZnS nanoparticles. *Research Journal of Physical Sciences,*1(7): 2320-4796.
25. Hudlikar, M., Shreeram, J., Mayur, D. and Kisan, K. (2012). Latex-mediated synthesis of ZnS nanoparticles: Green synthesis approach. *Journal of Nanoparticle Research,* 14(5): 865.
26. Kannan, S., Subiramaniyam, N. P. and Sathishkumar, M. (2020). A novel green synthesis approach for improved photocatalytic activity and antibacterial properties of zinc sulfide nanoparticles using plant extract of *Acalypha indica and Tridax procumbens*. *Journal of Materials Science: Materials in Electronics*, 31(12): 9846-9859.
27. Lan, C., Kunquan, H., Wenzhong, W. and Guanghou, W. (2003). Synthesis of ZnS nanorods by annealing precursor ZnS nanoparticles in NaCl flux. *Solid State Communications,* 125(9): 455-58.
28. Jothibas, M., Manoharan, C., Jeyakumar, S. J., Praveen, P., Punithavathy, I. K. and Richard, J. P. (2018). Synthesis and enhanced photocatalytic property of Ni doped ZnS nanoparticles. *Solar Energy*, 159: 434-443.
29. Hu, H., Wang, X., Liu, F., Wang, J. and Xu, C. (2011). Rapid microwave-assisted synthesis of graphene nanosheets–zinc sulfide nanocomposites: Optical and photocatalytic properties. *Synthetic Metals*, 161(5-6): 404-410.
30. Boulkroune, R., Sebais, M., Messai, Y., Bourzami, R., Schmutz, M., Blanck, C., ... and Boudine, B. (2019). Hydrothermal synthesis of strontium-doped ZnS nanoparticles: structural, electronic and photocatalytic investigations. *Bulletin of Materials Science*, 42(5): 1-8.
31. Chen, Y., Yin, R. H. and Wu, Q. S. (2012). Solvothermal synthesis of well-disperse ZnS nanorods with efficient photocatalytic properties. *Journal of Nanomaterials*, 2012: 560310.
32. Suganya, S., Jothibas, M. and Jeyakumar, S. J. (2019). Solid state synthesis of cadmium doped ZnS with excellent photocatalytic activity and enhanced visible light emission. *Journal of Materials Science: Materials in Electronics*, 30(8): 7916-7927.
33. Abbasi, M., Rafique, U., Murtaza, G. and Ashraf, M. A. (2018). Synthesis, characterisation and photocatalytic performance of ZnS coupled Ag2S nanoparticles: A remediation model for environmental pollutants. *Arabian Journal of Chemistry*, 11(6): 827-837.
34. Wang, W., Lee, G. J., Wang, P., Qiao, Z., Liu, N. and Wu, J. J. (2020). Microwave synthesis of metal-doped ZnS photocatalysts and applications on degrading 4-chlorophenol using heterogeneous photocatalytic ozonation process. *Separation and Purification Technology*, 237: 116469.

35. Ibrahim, S. K., Chakrabarty, S., Ghosh, S. and Pal, T. (2017). Reduced graphene oxide–zinc sulfide composite for solar light responsive photo current generation and photocatalytic 4-nitrophenol reduction. *ChemistrySelect*, 2(1): 537-545.
36. Kale, D. P., Deshmukh, S. P., Shirsath, S. R. and Bhanvase, B. A. (2020). Sonochemical preparation of multifunctional rGO-ZnS-TiO_2 ternary nanocomposite and its application for CV dye removal. *Optik*, 208: 164532.
37. Hernández-Gordillo, A., García-Mendoza, C., Alvarez-Lemus, M. A. and Gómez, R. (2015). Photocatalytic reduction of Cr(VI) by using stacked ZnS layers of ZnS (en) x complex. *Journal of Environmental Chemical Engineering*, 3(4): 3048-3054.
38. Qin, Y. L., Zhao, W. W., Sun, Z., Liu, X. Y., Shi, G. L., Liu, Z. Y., ... and Ma, Z. Y. (2019). Photocatalytic and adsorption property of ZnS–TiO_2/RGO ternary composites for methylene blue degradation. *Adsorption Science & Technology*, 37(9-10): 764-776.
39. Wu, H., Lin, S., Chen, C., Liang, W., Liu, X. and Yang, H. (2016). A new ZnO/rGO/polyaniline ternary nanocomposite as photocatalyst with improved photocatalytic activity. *Materials Research Bulletin*, 83: 434-441.
40. Anjum, M., Oves, M., Kumar, R. and Barakat, M. A. (2017). Fabrication of ZnO-ZnS@ polyaniline nanohybrid for enhanced photocatalytic degradation of 2-chlorophenol and microbial contaminants in wastewater. *International Biodeterioration & Biodegradation*, 119: 66-77.
41. Kumar, T. K. M. and Kumar, S. K. (2019). Visible-light-induced degradation of rhodamine B by nanosized Ag_2S-ZnS loaded on cellulose. *Photochemical & Photobiological Sciences*, 18(1): 148-154.

Malaysian Journal of Analytical Sciences (MJAS)
Published by Malaysian Analytical Sciences Society

PREPARATION OF EXTRACTED MAGNETITE FROM AN INDUSTRIAL WASTE MILL MODIFIED BY CETYL TRIMETHYL AMMONIUM BROMIDE FOR CADMIUM ION REMOVAL FROM AQUEOUS SOLUTION

(Penyediaan Magnetit daripada Sisa Buangan Sisik Besi yang Dimodifikasikan oleh Setil Trimetil Ammonium Bromida untuk Menyerap Kadmium Ion daripada Larutan Akues)

Nur Asyikin Ahmad Nazri[1,2]* , Raba'ah Syahidah Azis[2,3] , Hasfalina Che Man[4], Ismayadi Ismail[2]

[1]*Centre of Foundation Studies, Cawangan Selangor,*
Universiti Teknologi MARA, 43800 Dengkil, Selangor, Malaysia
[2]*Material Synthesis and Characterization Laboratory (MSCL), Institute of Advanced Technology (ITMA)*
[3]*Department of Physics, Faculty of Science*
[4]*Department of Biological and Agricultural Engineering, Faculty of Engineering*
Universiti Putra Malaysia, 43400 Serdang, Selangor, Malaysia

**Corresponding author:* asyikin2750@uitm.edu.my

Received: 9 September 2021; Accepted: 18 December 2021; Published: 28 April 2022

Abstract

This work, using a batch study, revealed the performance of modified magnetite millscales with a cationic surfactant [cetyl trimethyl ammonium bromide (CTAB)] (Fe_3O_4/CTAB MNS) in cadmium ion removal from aqueous solution. The self-assembly method was employed to modify Fe_3O_4 with CTAB. As prepared Fe_3O_4 limited the modification method to *ex situ*. Therefore, a heterocoagulation method was used to self-assemble CTAB on Fe_3O_4. The prepared magnetic nanosorbents (MNSs) were used in batch adsorption to optimize cadmium adsorption. In addition, characterization with Fourier transform infrared spectroscopy (FTIR) and transmission electron microscopy (TEM) revealed new characteristics of that modified Fe_3O_4 that contributed to the enhancement of the adsorption efficiency (Q) to reach 21.6 mg/g. The higher removal percentage shown by Fe_3O_4/CTAB MNS was 89%, which confirmed the successful modification. Therefore, Fe_3O_4 modified with CTAB has higher potential to be used as magnetic nanosorbent owing to lower cost of production with compatible adsorption capacity.

Keywords: stabilized magnetite, magnetic nanosorbents, cadmium solution, cation polymer, cetyl trimethyl ammonium bromide

Abstrak

Kajian ini mendedahkan prestasi skala magnetit yang diubah suai dengan surfaktan kationik (setil trimetil ammonium bromida (CTAB)) (Fe_3O_4 / CTAB), digunakan sebagai penyingkiran ion kadmium dari larutan akues melalui kajian kumpulan. Kaedah pemasangan diri digunakan untuk mengubah Fe_3O_4 dengan CTAB. Fe_3O_4 yang telah disiapkan telah membatasi kaedah modifikasi menjadi *ex situ*. Oleh itu, kaedah heterokoagulasi digunakan untuk memasang CTAB pada Fe_3O_4. Penjerap nano magnetik yang disiapkan (MNS) digunakan dalam penjerapan kumpulan untuk mengoptimumkan penjerapan kadmium. Selain itu, pencirian dengan spektroskopi infra merah transformasi Fourier (FTIR), dan mikroskopi elektron transmisi (TEM) telah

mengungkapkan ciri-ciri baru Fe_3O_4 yang dimodifikasi yang menyumbang kepada peningkatan kecekapan penjerapan (Q) menjadi 21.6 mg/g. Peratusan penyingkiran yang lebih tinggi yang ditunjukkan oleh Fe_3O_4 / CTAB MNS adalah 89% yang membuktikan pengubahsuaian berjaya. Oleh itu, dapat disimpulkan bahawa modifikasi dengan CTAB berpotensi lebih tinggi untuk digunakan sebagai penjerap nano magnetik kerana melibatkan kos pengeluaran yang lebih rendah dengan kapasiti penjerapan yang serasi.

Kata kunci: magnetit stabil, penjerap nano magnetik, larutan kadmium, polimer kation, setil trimetil ammonium bromida

Introduction

Contamination of water is a serious global issue that must be addressed. Contaminated water greatly affects the human well-being. Even if people do not directly drink the contaminated water, it may still cause harm to seafood through the spread of contaminants. Cadmium is a nonessential metal with a high exchange factor. Zinc deficiency increases the risk of Cd poisoning. Zinc acts as an antidote to the toxic effects of Cd. The use of foods and grains (developed in soil polluted by superphosphate compost and sewage slime), the use of refined food sources (exposed to cadmium at specific locations such as cadmium coating on iron and copper), and the consumption of plastics have contributed to an increase in zinc deficiency. Workers at the production line of battery anodes and semiconductors are particularly vulnerable to Cd poisoning. [1].

Cd is a heavy metal; it is a highly harmful industrial and environmental pollutant. It is not biodegradable and accumulates throughout the food chain as a result of plant uptake in polluted soils, which poses a serious health risk to humans. In Malaysia, the maximum allowed Cd concentration in drinking water is 0.005 mg/L. Cd toxicity has been reported by many researchers [2, 3, 4]. Any significant level of Cd in the body causes rapid poisoning and liver damage. Renal tubule failure is the cause of kidney disease [5]. Cd is also harmful to endocrine organs, especially the pituitary gland. Cd-containing compounds are strong carcinogens [6]. According to Hotz et al. [7], there is substantial evidence regarding the carcinogenicity of Cd and Cd compounds in humans. Renal dysfunction, bone degeneration, liver damage, and blood damage have all been linked to chronic exposure to high levels of Cd [5-7].

Ion exchange, membrane filtration, chemical reduction and precipitation, adsorption on activated carbon, nanotechnology treatments, electrochemical removal, and advanced oxidation processes are some of the traditional treatment techniques for removing heavy metal contaminants from the environment or wastewater effluents [4, 8-10]. Unfortunately, many of these traditional techniques have significant drawbacks such as low selectivity, high cost, partial removal, high energy consumption, or the production of large amounts of toxic waste. As a result, the demand for safe, less expensive, and more efficient technologies to remove heavy metals from polluted water has prompted research into low-cost alternatives to commercially available methods [10].

Currently, adsorption is widely accepted as a viable and cost-effective approach for heavy metal wastewater treatment. The adsorption process is versatile in terms of design and operation, and it typically produces high-quality treated effluent. Adsorbents can also be renewed using an appropriate desorption procedure because adsorption is sometimes reversible. Thus, extensive research was conducted to identify the best adsorbents that are low-cost, mass-produced in large quantities, and have a simple and rapid separation process, ensuring that this technology can replace the traditional method of removing heavy metals in wastewater treatment [6, 9].

Owing to their unique features, nanometer-sized materials have recently attracted considerable interest among mainstream researchers. These materials have been used in various areas including biotechnology, design, biomedical science, natural science, and materials science. The use of nanoparticles (NPs) as

effective adsorbentsfor heavy metals removal is gaining popularity among scientists [10]. Compared to micrometer-sized particles, NPs have a considerably larger surface area to volume ratio and a shorter diffusion path, which results in high extraction limit, fast extraction of elements, and high extraction efficiency.

Mill scale waste is a by-product of steel production that occurs during the hot rolling process. The annual output exceeds a million tonnes, and it may contribute to ground contamination [11]. Thus, repurposing mill scale in various applications may help to reduce waste and transform it into a useful agent. Mill scale contains 50% of wurtzite (FeO), 10% of hematite (Fe_2O_3), and 40% of magnetite (Fe_3O_4) [12]. Fe_3O_4 is a metal oxide that behaves as an amphoteric solid, allowing protonation and deprotonation on the surface to produce surface charge. This property is interesting for studying the adsorption mechanism of heavy metals on Fe_3O_4 because Fe_3O_4 easily reacts with the surrounding particles. Therefore, each year [13-16], several synthetic approaches for extracting magnetite from mill scales have been published. Furthermore, magnetite nanoparticles are receiving more attention owing to their superior magnetic properties and high specific surface area. To extract high purity magnetite from mill scale waste, Azis et al. developed a magnetic separation process. Specifically, 1 T of external magnetic field has been used for the extraction [12-14].

High-energy ball milling (HEBM) is a straightforward approach for size reduction. This approach decreases the size of particles from micrometer to nanometer size. However, nano-sized magnetite is unstable and readily oxidizes to form a new composite that does not exhibit the unique high magnetization behavior. Furthermore, because magnetite has a stronger magnetic force, the agglomeration is higher among the particles [11-15].

Therefore, the modification of the surface process may help to reduce the agglomeration problems and the unstable state of Fe_3O_4 NPs. CTAB is a cationic polymer that can self-assemble with other composites [16,17]. Previously, CTAB-modified Fe_3O_4 NPs have been used in removing dye. Faraji et al. believed that CTAB was essential in the dye adsorption mechanism. Therefore, they added CTAB into the dye solution, and CTAB was expected to coat Fe_3O_4 during the batch adsorption experiment; finally, the particles were separated together using an external magnetic field [18].

In this work, Fe_3O_4 was magnetically extracted from mill scale waste and underwent HEBM to become nano-sized. Then, the prepared Fe_3O_4 was coated with CTAB using an ultrasonication bath. The obtained product was used in batch adsorption to remove Cd ions from an aqueous solution. An equilibrium study was performed to evaluate the relevance of using the obtained material at an industrial scale. Thus, the obtained adsorption capacity of the particles, which was enhanced after coating with CTAB, indicates the potential of using the obtained material in removing heavy metals.

Materials and Methods

Sample preparation (adsorbent)

The first step of extraction was to remove the impurities from raw millscales collected at a steel factory in Malaysia. The manual removal of impurities (e.g., stones, sand, dust, or pieces of plastic) that may contaminate the samples was also performed. Then, approximately 100 g of MS flakes was crushed using conventional milling (Pascal Engineering, UK) for 24 h under dry conditions, 700 rpm speed, and 10:1 BRP. The first separation method was impurity magnetic separation (IMS) used to extract the magnetic particles from the RM. The iron oxides (IO) powder was placed inside a glass tube (with a stopper at the bottom) with deionized water (DI) (at room temperature of 22-24 °C) with the presence of a 1 T external field, as shown in Figures 1 and 2. Then, the tube was manually shaken for 10–15 min. Separation II: The Curie Temperature Separation Technique (CTST) was then used to remove stronger magnetic components from the magnetic powder. Separations I and II of waste mill scales were carried out in the same way as previously reported by Azis et al. [12]. CTST's magnetite (Fe_3O_4)

output was dried in an oven at 120°C for 24 h. The magnetite powder was processed for 8 h on a SPEX 8000D milling machine with a 10:1 ball-to-powder (BPR) ratio.

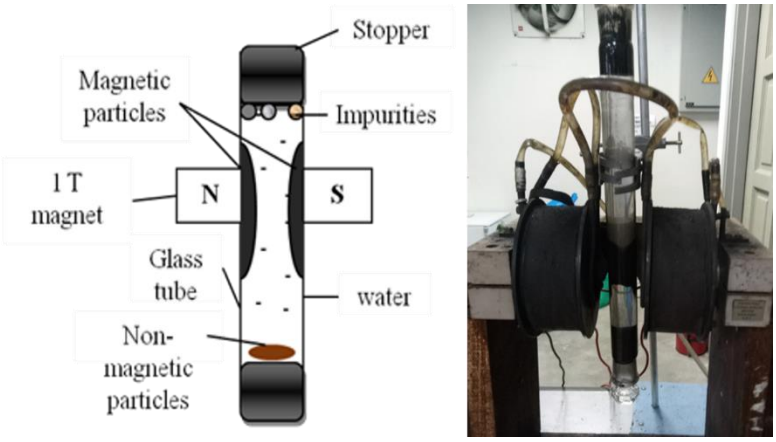


Figure 1. Set up for impurity magnetic separation

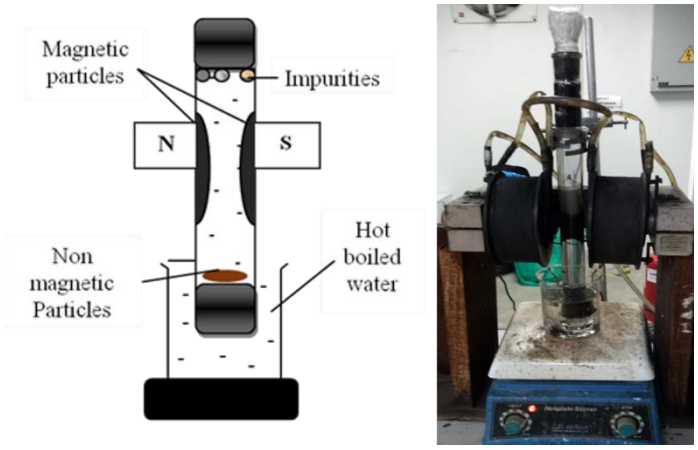


Figure 2. Set up for the curie temperature separation technique

Fe_3O_4/CTAB magnetic nanosorbents

CTAB with a 0.02 M concentration was prepared by mixing the CTAB powder with deionized water and stirred for 30 min in an ultrasonication bath. Then, 20 ml of CTAB solution at a concentration of 0.20 M was mixed with 1.0 g of magnetite extracted from millscales. After 30 min of mixing, an external magnetic field was applied to the mixture, and the collected magnetite coated with CTAB was dried in an oven for 24 h at 60 °C. A summary of the modification method is shown in Figure 3. Next, agitation by sonication in an ultrasonic bath for 20 min was performed. The pH to perform this was at optimum for the CTAB, which has a higher positivity and the highest negativity potential for MNPs (via zeta potential analysis). The pH was then adjusted by using NaOH and nitric acid using the titration method. This step was performed to increase the dispersity of Fe_3O_4 NPs in the CTAB. The Fe_3O_4/CTAB was then magnetically separated using an external magnetic field

to separate the modified magnetic NPs from the residue, as shown in Figure 3. The modified magnetic NPs were collected and then rinsed twice before being dried overnight in the oven at 60 °C. The dried samples were then ground using a mortar to obtain a fine powder of modified magnetic NPs. The surface modification of magnetic NPs using CTAB is summarized in Figure 3, the method was adjusted from previous works [16, 18, 19].

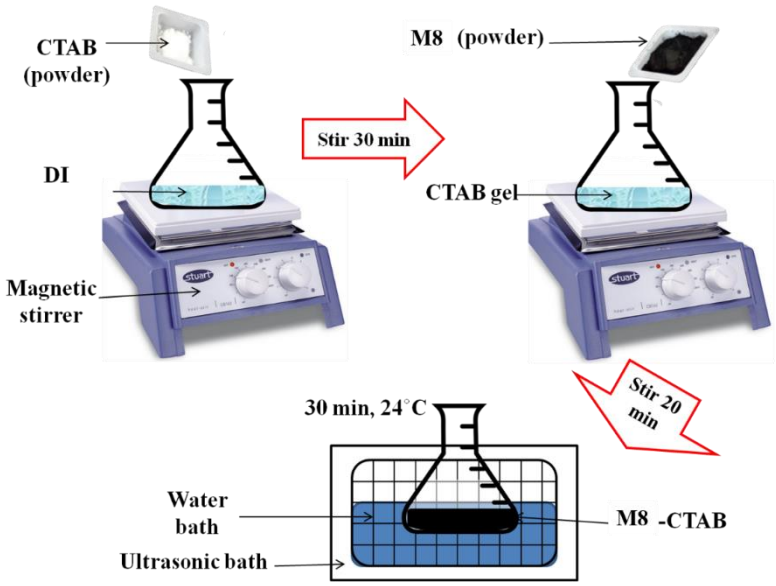


Figure 3. Summarized preparation steps of modified MNPs with CTAB

Adsorbate

All the compounds used to prepare the reagent solutions were of analytical reagent grade. The stock solution of cadmium nitrate ($Cd(NO_3)_2$) (99%, Sigma-Aldrich, UK) (3 mg/L) was prepared by dissolving a weighed quantity of the respective $Cd(NO_3)_2$ in deionized water. The concentration of the metal solution and pH used in this work were 3 mg/L with pH 7, respectively. The pH of the solution was adjusted by using sodium hydroxide (NaOH) and nitric acid (HNO_3).

Batch adsorption experiment

The 100 mL of Cd solution was mixed with 10 mg of Fe_3O_4 nanoparticle adsorbent and placed in a vibrator bath (variable speed reciprocal vibrator (model HY-8)) with a fixed 160 rpm for 5, 10, 15, 20, 25, 30, 35, and 40 min of contact time. All adsorption tests were performed in a vibrator at room temperature (22-25 °C) using accurately weighed amounts of adsorbents in a covered bottle with adsorbate solutions of specific concentrations. The pH of the solution was adjusted from 1 to 10. The adsorption capacity at any time, Q_t (mg g^{-1}), was calculated according to the following Equation 1:

$$Q_t = \frac{C_o - C_t}{m} V \quad (1)$$

where C_o and C_t (mgL/1) are the initial and residual Cd ions concentrations at any time (min), respectively. The volume of Cd ion solution was V (mL), and the mass of dry adsorbent was m (mg). Equation 2 was used to calculate the adsorption capacity at equilibrium:

$$Q_e = \frac{C_o - C_e}{m} V \quad (2)$$

Removal efficiency and adsorption capacity

The removal percentage of metal ions refers to the percentage of metal ions removed from the initial metal concentration solutions. Equation 3 was used to calculate the removal efficiency of Cd^{2+} from the aqueous solution.

$$Cd\ \%Removal = \frac{C_o - C_e}{C_o} \times 100\% \quad (3)$$

Sample characterization

Structural and phase composition

A JEM JEOL 2100 HR transmission electron microscope was used to examine the sample morphology, particle size, and atom arrangement (HR-TEM). Spectroscopic analysis using the infrared FTIR spectrometer was performed by recording infrared spectra (200-4000 cm^{-1}) (Thermo Nicolet, Model Nicolet 6700). Atomic adsorption spectroscopy (AAS) is a technique for determining the concentration of heavy metals in a solution.

Results and Discussion

Morphology analysis

Figure 4a shows the HR-TEM images, which show that aggregation occurred between the Fe_3O_4 nanoparticles that were a range of 5-20 nm in size. The particle sizes increased after coated with CTAB. The result is in agreement with previous works [21, 18]. The nanoparticles aggregated with higher dispersity, indicating good connectivity between the grains due to the higher magnetic forces and subjected to the modification process. The agglomeration was reduced after coated with CTAB [17]. Figure 4b shows images of Fe_3O_4 and Fe_3O_4/CTAB nanosorbents with a scale of 20 nm. Table 1 represent the average value of Fe_3O_4 and Fe_3O_4/CTAB MNS. The average size of the particles was calculated by using Image J. In total, 200 particles were used to determine the average particles. Clearly, the modified Fe_3O_4 was a larger size due to the presence of the CTAB layer on the particles. However, this result was in contrast with the previous publication, considering agglomerations [16-19]. The smaller size is due to the measurement of the real sizes of the particles without the occurrence of agglomeration.

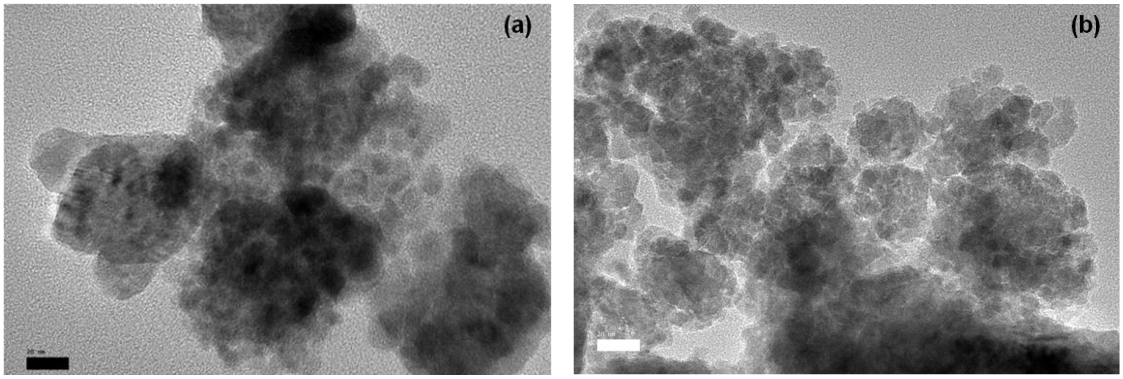


Figure 4. Fe_3O_4 extracted from (a) millscales waste and (b) Fe_3O_4/CTAB

Table 1. HR-TEM particle sizes

Adsorbent	**HR-TEM Particle Size, d_{TEM} (nm)**
Fe_3O_4	13.10
Fe_3O_4/CTAB	15.26

Phase analysis

Figure 5 shows the XRD spectrum of Fe_3O_4, and Fe_3O_4/CTAB MNS. As shown, diffraction peaks of all samples after HEBM completely correspond to standard pattern characteristic peaks of the magnetite hexagonal inverse spinel structure (JCPDS: 98-005-9302) 220 (30.1), 113 (35.45), 004 (43.07), 333 (56.97), 044 (62.47). As can be seen from the spectra, the main peaks which correspond to hkl (113) were observed to be broader as the milling time increased. The spectrum after modified with CTAB not showing any phase changes indicated that the modification process preserve the phase. In addition, it proved that the core shell of the MNS is still Fe_3O_4. This finding is in agreement with the previous report [18].

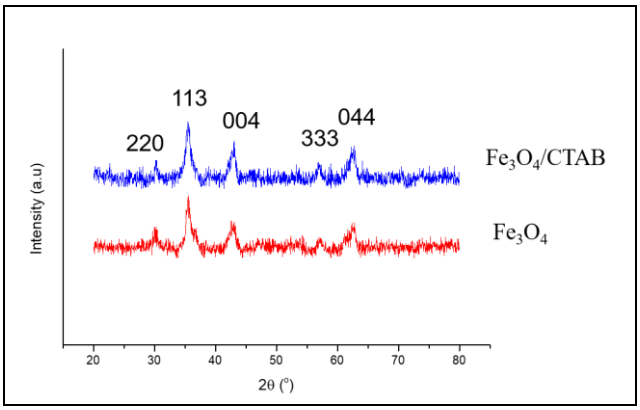


Figure 5. XRD spectrum of Fe_3O_4, and Fe_3O_4/CTAB MNS

Optical analysis

Figure 6 shows the FTIR spectrum of Fe_3O_4, Fe_3O_4/CTAB, and pure CTAB. CTAB's IR spectrum (Figure 6) contains a band at 3420 cm^{-1}, which could be attributed to the ammonium moiety's vibrations. Two distinct CH bands vibrations of the $–CH_2$ group in CTAB are responsible for the peaks at 2918 and 2848 cm^{-1}. The asymmetric and symmetric stretching vibrations of $N^+–CH_3$ are represented by the bands at 1630 and 1467 cm^{-1}, respectively, while the out-of-plane –CH vibration of CH_3 is represented by the band at 960 cm^{-1}. Br^- could be represented by the band at 720 cm^{-1}. The signal at 566 cm^{-1} in the FTIR spectrum of Fe_3O_4/CTAB MNS (Figure 5) reflects Fe-O of Fe_3O_4. The electrostatic interaction between Fe_3O_4 surface hydroxyl groups and the ammonium moiety in CTAB (OH....N^+) could account for the bandwidth at 3430 cm^{-1} [16-18].

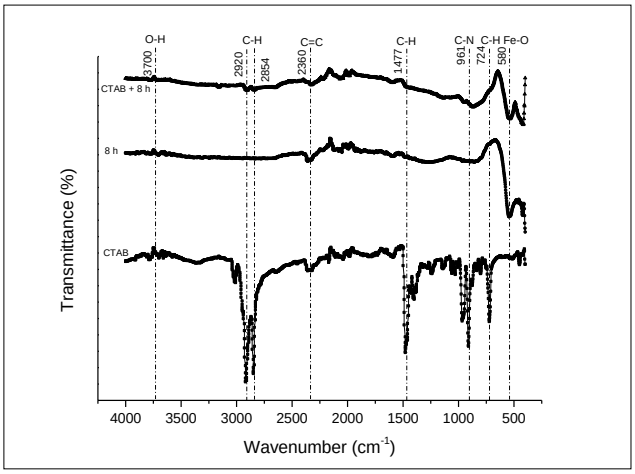


Figure 6. FTIR spectrum of Fe_3O_4 extracted from millscale waste and Fe_3O_4/CTAB MNS

Figure 7 shows magnetic behavior of the magnetic nanosorbents (MNS). The M-H curve indicated that both MNS are ferromagnetic materials with 50 and 28 emu/g. In addition, magnetic hysteresis loops measured at room temperature. The magnetization values observed in nanostructure materials are smaller than the corresponding bulk materials, assuming that is no changes in ionic configurations occurred. The reduction and lack of saturation after that are likely related to the smaller particle size and high surface areas, which could lead to some spin canting [12].

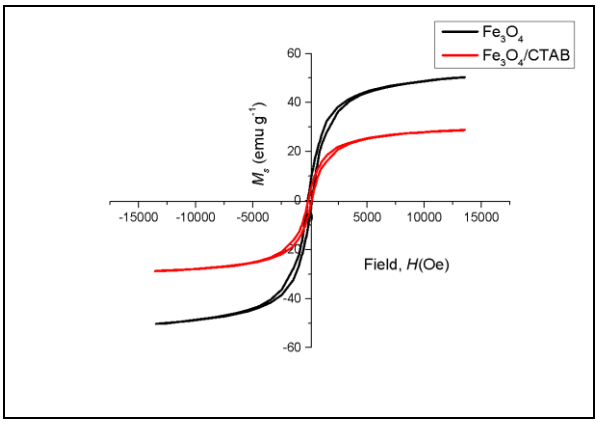


Figure 7. M-H hysteresis of Fe_3O_4 extracted from millscale waste and Fe_3O_4/CTAB MNS

Figure 8 shows that the formation of vesicular Fe_3O_4/CTAB. The coating showed self-assembly when the pH was 7. At that pH, CTAB had a higher positivity; meanwhile, Fe_3O_4 showed a higher negative surface charge. Therefore, it electrostatically self-assembled to form a vesicle [16]. The formation of the vesicle provided new surface charge for the nanoparticles. The new surface charge caused the repulsive force to increase. This is visible in the HR-TEM images showing that nanoparticles with higher dispersity formed. However, when more than a bilayer micelle already formed, the excess CTAB reacted on the surface, and the hydrophobic side formed a new layer. Therefore, when we added more CTAB, it did not increase the surface area; in fact, the surface area likely decreased [22].

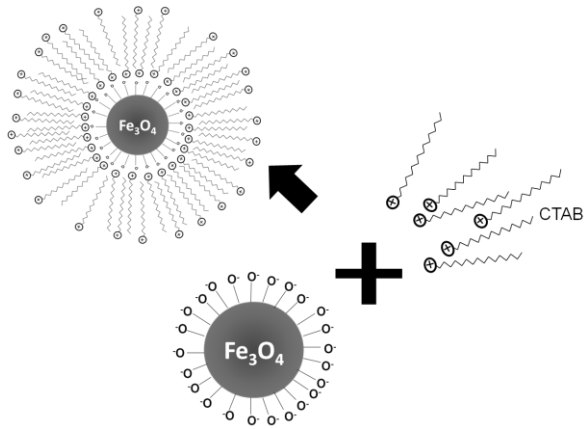


Figure 8. Schematic mechanism of the coating process of Fe_3O_4/CTAB MNS

Adsorption equilibrium studies

Effect of contact time

The influence of contact time on the adsorption capacity of Cd ions on Fe_3O_4/CTAB is shown in Figure 9. For the adsorption of Cd ions, the adsorption amount, Q_t, grew rapidly at first and then reached equilibrium in approximately 10 to 15 min. The increase in driving force produced by the concentration gradient of cations in solution and the presence of a considerable number of active sites on the surface of Fe_3O_4/CTAB MNS could be attributed to the fast adsorption rate in the incipient stage [13]. In the adsorption of Cd ions, a contact duration of 15 min was adequate to achieve equilibrium for Fe_3O_4/CTAB MNS. The adsorption capacity of Fe_3O_4 is 10.01 mg/g; meanwhile, that of Fe_3O_4/CTAB MNS is 21.6 mg/g.

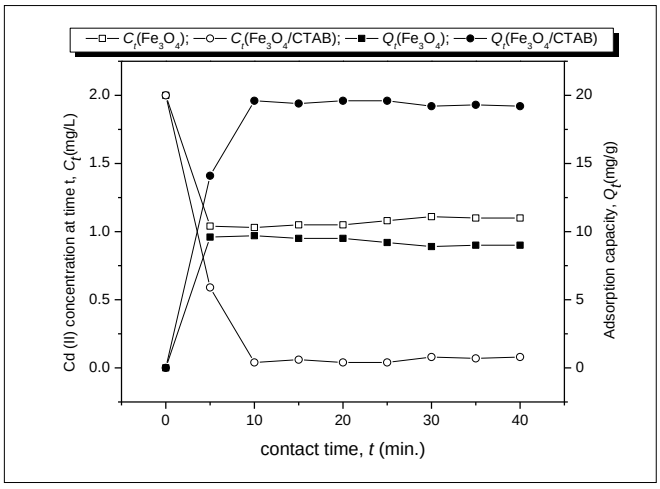


Figure 9. Effect of contact time on the adsorption capacity and concentration at equilibrium of Fe_3O_4 and Fe_3O_4/CTAB MNS

Effect of solution pH

According to the findings of a previous paper [14], adsorption can occur at various pH values. The pH setting would aid in the optimal uptake of Cd ions. As a result, the influence of solution pH on Cd ion adsorption onto Fe_3O_4/CTAB was investigated in the pH range of 1 to 10, as shown in Figure 8. For both modified and unmodified MNS, no adsorption was detected at pH values of 1 and 2, while half Cd ion absorption was recorded at pH 3 (>50%). Despite this, the adsorption capacity of the solution gradually increased from 3 to 6 and plateaued between pH 6 and 10. The ion exchange was responsible for the rapid increase in adsorption before pH 6. As a result, chemisorption, mainly ion exchange, is used exclusively for adsorption. The increase in adsorption after pH 6 could be due to electrostatic repulsion between H_3O^+ ions and cationic Cd ions, which cause Cd ions to be attracted to the Fe_3O_4/CTAB's negative surface charge. Van der Waal forces create an increase in the amount of Cd ions on a solid's surface (including dipole-dipole, dipole-induced dipole, London forces, and possibly hydrogen bonding). The increase can be explained as shown in Figure 6, where active hydroxyls can be found on the adsorbent surface based on FTIR data. These findings corroborate the intensity change in the IR spectra, as shown in Figure 10 [19]. As a result, the Q was highest at pH 9 for Fe_3O_4/CTAB MNS with 20.19 mg/g; meanwhile, 10.03 mg/g of Cd was removed by Fe_3O_4 MNS.

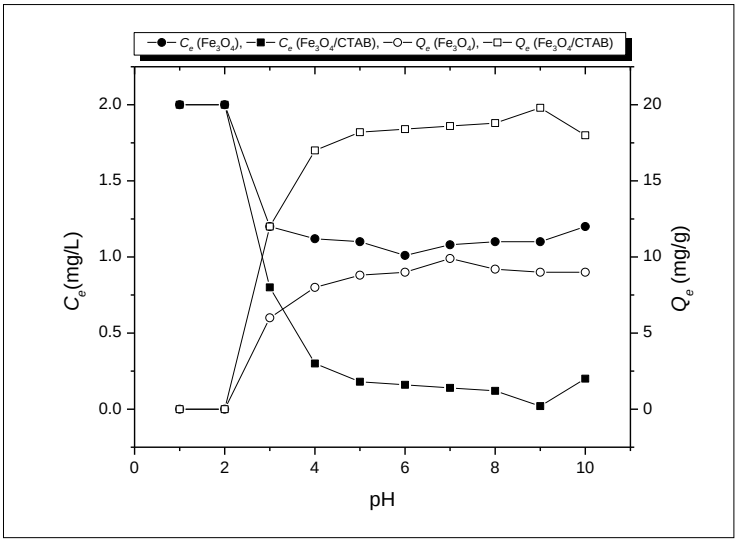


Figure 10. Effect of pH on the adsorption capacity and concentration at equilibrium of Fe_3O_4 and Fe_3O_4/CTAB MNS

Effect of initial Cd^{2+} concentration

One of the criteria utilized to examine the equilibrium of magnetic nano-adsorbents is initial concentration. The initial metal ion concentration serves as a driving factor for breaking through the mass transfer barrier between the adsorbent and the adsorbate medium. The

Fe_3O_4/CTAB MNS was first studied for its ability to remove metal ions from aqueous solutions. For the different beginning concentrations, the solution concentrations were 1, 2, 3, 4, and 5 mg/L, with an adsorbent dosage of 10 mg as the constant, as shown in Figure 11. For model Cd ions solutions with starting concentrations of 1 to 5 mg/L, the removal percentage approached 95%. As a result, increasing the concentration of Cd ions reduced the efficiency of Cd ion removal slightly. Furthermore, once equilibrium is reached, it will no longer be able to adsorb the other ions. This same pattern was discovered in a few other published studies [21, 22, 23].

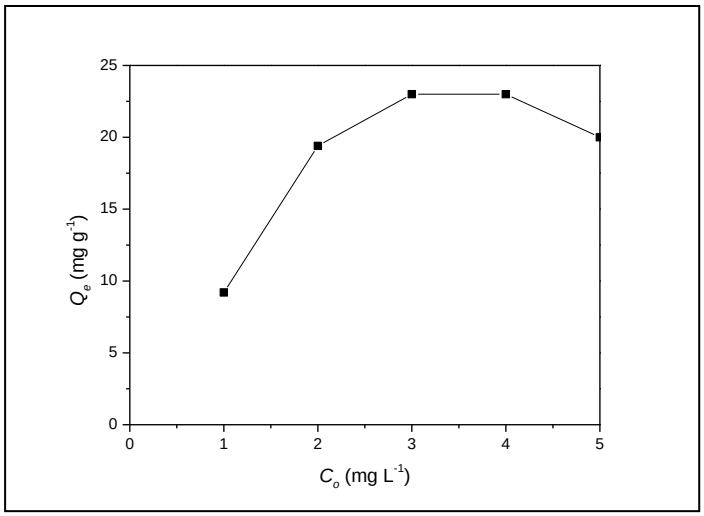


Figure 11. Effect of initial concentration on the adsorption capacity of the adsorption of Cd by using Fe_3O_4/CTAB

Conclusion

In this study, Fe_3O_4/CTAB MNS was prepared via the self-assembly method. The confirmation of success was supported by the characterization via FTIR and HR-TEM images before and after coating. Then, the Fe_3O_4/CTAB MNS was used as an adsorbent for removal of Cd ions from aqueous solution. The Fe_3O_4/CTAB MNS showed excellent performance in removing Cd ions from aqueous solution, which was evaluated by the equilibrium studied. The affecting parameters were studied, and the results showed that the presence of CTAB significantly affected the removal efficiency of the Cd ions. Due to the higher dispersity and magnetically assisted separability of the Fe_3O_4/CTAB MNS, high adsorption capacities could be obtained in a very short time. The reported data should be useful for the design and fabrication of an economically viable treatment process using batch or stirred tank reactors for Cd ion adsorption. This work involved a valuable contribution where the usage of millscales successfully lowered the production cost of the MNS.

Acknowledgement

This work was supported by Universiti Putra Malaysia Grants (Putra Impact Grants (UPM/700-/2/GPPI/2017/954160) and Putra Initiative Grants (GP-IPS/2017/9580600). Thanks to Falcon for proofing this manuscript.

References

1. Mahmood, Q., Asif, M., Shaheen, S., Hayat, M. T. and Ali, S. (2019). Cadmium contamination in water and soil. In *Cadmium toxicity and tolerance in plants*. Academic Press: pp. 141-161.
2. Pyrzynska, K. (2019). Removal of cadmium from wastewaters with low-cost adsorbents. *Journal of Environmental Chemical Engineering*, 7(1): 102795.
3. Ciesielczyk, F., Bartczak, P. and Jesionowski, T. (2016). Removal of cadmium (II) and lead (II) ions from model aqueous solutions using sol–gel-derived inorganic oxide adsorbent. *Adsorption*, 22(4): 445-458.
4. Ali, A. H. (2013). Comparative study on removal of cadmium (II) from simulated wastewater by adsorption onto GAC, DB, and PR. *Desalination and Water Treatment*, 51(28-30): 5547-5558.
5. Farhan, A. S. and Jasim, S. T. (2020). Cadmium toxicity and some target organs: A review. *Al-Anbar Journal of Veterinary Sciences*, 13(2): 17-26.
6. Riaz, U., Aslam, A., uz Zaman, Q., Javeid, S., Gul, R., Iqbal, S., ... and Jamil, M. (2021). Cadmium contamination, bioavailability, uptake mechanism and remediation strategies in soil-plant-environment system: a critical review. *Current Analytical Chemistry*, 17(1): 49-60.
7. Järup, L. and Åkesson, A. (2009). Current status of cadmium as an environmental health problem. *Toxicology and Applied Pharmacology*, 238(3): 201-208.
8. Cui, L., Chen, T., Yin, C., Yan, J., Ippolito, J. A. and Hussain, Q. (2019). Mechanism of adsorption of cadmium and lead ions by iron-activated biochar. *BioResources*, 14(1): 842-857.
9. Carolin, C. F., Kumar, P. S., Saravanan, A., Joshiba, G. J. and Naushad, M. (2017). Efficient techniques for the removal of toxic heavy metals from aquatic environment: A review. *Journal of Environmental Chemical Engineering*, *5*(3): 2782-2799.
10. Dubey, S., Banerjee, S., Upadhyay, S. N. and Sharma, Y. C. (2017). Application of common nano-materials for removal of selected metallic species from water and wastewaters: A critical review. *Journal of Molecular Liquids*, 240: 656-677.
11. Gaballah, N. M., Zikry, A. F., Khalifa, M. G., Farag, A. B., El-Hussiny, N. A. and Shalabi, M. E. H. (2013). Production of iron from mill scale industrial waste via hydrogen. *Open Journal of Inorganic Non-metallic Materials*, 3(3): 6.
12. Hashim, M., Saiden, N. M., Daud, N. and Shahrani, N. M. M. (2015). Study the iron environments of the steel waste product and its possible potential applications in ferrites. In *Advanced Materials Research*, 1109: 295-299.
13. Shahid, M. K., Phearom, S. and Choi, Y. G. (2018). Synthesis of magnetite from raw mill scale and its application for arsenate adsorption from contaminated water. *Chemosphere*, 203: 90-95.
14. Shahid, M. K., Phearom, S. and Choi, Y. G. (2019). Adsorption of arsenic (V) on magnetite-enriched particles separated from the mill scale. *Environmental Earth Sciences*, 78(3): 1-11.
15. Hosseinzadeh, M., Seyyed Ebrahimi, S. A., Raygan, S. and Masoudpanah, S. M. (2016). Removal of cadmium and lead ions from aqueous solution by nanocrystalline magnetite through mechanochemical activation. *Journal of Ultrafine Grained and Nanostructured Materials*, 49(2): 72-79.
16. Elfeky, S. A., Mahmoud, S. E. and Youssef, A. F. (2017). Applications of CTAB modified magnetic nanoparticles for removal of chromium (VI) from contaminated water. *Journal of Advanced Research*, *8*(4): 435-443.
17. Saksornchai, E., Kavinchan, J., Thongtem, S. and Thongtem, T. (2018). Simple wet-chemical synthesis of superparamagnetic CTAB-modified magnetite nanoparticles using as adsorbents for anionic dye Congo red removal. *Materials Letters*, 213: 138-142.
18. Faraji, M., Yamini, Y., Tahmasebi, E., Saleh, A. and Nourmohammadian, F. (2010). Cetyltrimethylammonium bromide-coated magnetite nanoparticles as highly efficient adsorbent for rapid removal of reactive dyes from the textile companies' wastewaters. *Journal of the Iranian Chemical Society*, 7(2): S130-S144.

19. Elfeky, S. A., Mahmoud, S. E. and Youssef, A. F. (2017). Applications of CTAB modified magnetic nanoparticles for removal of chromium (VI) from contaminated water. *Journal of Advanced Research*, 8(4): 435-443.
20. Chaki, S. H., Malek, T. J., Chaudhary, M. D., Tailor, J. P. and Deshpande, M. P. (2015). Magnetite Fe_3O_4 nanoparticles synthesis by wet chemical reduction and their characterization. *Advances in Natural Sciences: Nanoscience and Nanotechnology*, 6(3): 035009.
21. Xu, W., Liu, Z., Fang, J., Zhou, G., Hong, X., Wu, S., ... and Cen, C. (2013). CTAB-assisted hydrothermal synthesis of $Bi_2Sn_2O_7$ photocatalyst and its highly efficient degradation of organic dye under visible-light irradiation. *International Journal of Photoenergy*, 2013: 234806.
22. Nikoobakht, B., & El-Sayed, M. A. (2001). Evidence for bilayer assembly of cationic surfactants on the surface of gold nanorods. *Langmuir*, 17(20): 6368-6374.
23. Ehrampoush, M. H., Miria, M., Salmani, M. H., & Mahvi, A. H. (2015). Cadmium removal from aqueous solution by green synthesis iron oxide nanoparticles with tangerine peel extract. *Journal of Environmental Health Science and Engineering*, 13(1): 1-7.
24. Taleb, K., Markovski, J., Veličković, Z., Rusmirović, J., Rančić, M., Pavlović, V and Marinković, A. (2019). Arsenic removal by magnetite-loaded amino modified nano/microcellulose adsorbents: Effect of functionalization and media size. *Arabian Journal of Chemistry*, 12(8): 4675-4693.
25. Aydın, H., Yerlikaya, Ç. and Uzan, S. (2012). Equilibrium and kinetic studies of copper (II) ion uptake by modified wheat shells. *Desalination and Water Treatment*, 44(1-3): 296-305.
26. Hao, Y. M., Man, C. and Hu, Z. B. (2010). Effective removal of Cu (II) ions from aqueous solution by amino-functionalized magnetic nanoparticles. *Journal of Hazardous Materials*, 184(1-3): 392-399.
27. Cantu, Y. (2017). Remediation of trivalent and hexavalent chromium ions from aqueous solutions using titanium dioxide polymorphs. The University of Texas Rio Grande Valley: pp. 1576-1580.

Malaysian Journal of Analytical Sciences (MJAS)
Published by Malaysian Analytical Sciences Society

THERMAL DECOMPOSITION OF CALCIUM CARBONATE IN CHICKEN EGGSHELLS: STUDY ON TEMPERATURE AND CONTACT TIME

(Penguraian Kalsium Karbonat dalam Kulit Telur Ayam: Kajian Mengenai Suhu dan Masa)

Nadia Razali[1], Nurriswin Jumadi[1,2]*, Adlin Yasmin Jalani[1], Nurhanim Zulaikha Kamarulzaman[1], Khairul Faizal Pa'ee[3]

[1]Section of Environmental Engineering Technology
[2]Section of Process Engineering Technology
[3]Section of Food Engineering Technology
Universiti Kuala Lumpur – MICET, 78000 Alor Gajah, Melaka, Malaysia
[4]Kolej Komuniti Jelebu,
71600 Kuala Klawang, Negeri Sembilan, Malaysia

**Corresponding author: nurriswin@s.unikl.edu.my*

Received: 13 September 2021; Accepted: 3 February 2022; Published: 28 April 2022

Abstract

Within the context of a circular economy, the recycling or valorisation of eggshells, which are typically discarded in landfills, represents an opportunity. The primary compound in eggshells is calcium carbonate ($CaCO_3$), which can be decomposed into calcium oxide (CaO) by calcination. This study examined the calcination conditions (temperature and contact time) for the optimum $CaCO_3$ decomposition rate. The eggshell samples were pre-treated to eliminate dirt and unnecessary biological substance, ground into powder and sieved. The primary physical and chemical characteristics of eggshell powder were studied, including colour changes, mass loss, bulk density, moisture content, pH, thermal properties, and identification of chemical bonds and compounds in a molecule. This study evaluated the physical and chemical properties of the synthesised $CaCO_3$ from eggshells, moisture content, bulk density, pH, FTIR, and XRD. The results showed significant differences in the samples' colour transition at various temperatures and contact times based on the physical observation. The TGA analysis showed that eggshell powder decomposed at a temperature range of 600–900 °C. The FTIR results reported that for the calcine samples, the grey powder consists of $CaCO_3$, while the solid white powder consists of metal oxide content. Similar seven diffraction peaks were observed in the XRD analysis for calcination at 900 °C and industrial CaO (32.25, 37.41, 53.92, 64.18, 67.41, 79.70, and 88.58). The eggshell powder calcined at the temperature of 900 °C and contact time of 3 h was identified as an ideal condition for the decomposition of raw eggshell powder based on FTIR and XRD analyses. Both results showed that CaO corresponded to the wavelength spectrum and diffraction analysis of the sample.

Keywords: calcium carbonate, calcium oxide, eggshell, calcination

Abstrak

Dalam konteks ekonomi kitaran, terdapat peluang untuk mengitar semula kulit telur yang biasanya dibuang di tempat pembuangan sampah. Sebatian utama dalam kulit telur ialah kalsium karbonat dan ia boleh diuraikan kepada kalsium oksida melalui proses pengkalsinan. Kajian ini dilakukan untuk mengkaji keadaan kalsinasi (suhu dan masa pembakaran) yang sesuai

bagi kadar penguraian kalsium karbonat yang optimum. Sampel kulit telur diproses terlebih dahulu untuk membuang kotoran dan sisa biologi yang tidak diperlukan dan seterusnya dikisar menjadi serbuk serta diayak. Ciri-ciri fizikal dan kimia utama serbuk kulit telur seperti perubahan warna, kehilangan jisim, ketumpatan, kandungan lembapan, pH, sifat terma, dan mengenal pasti ikatan kimia dan sebatian dalam molekul telah dikaji. Untuk mengkaji ciri-ciri fizikal dan kimia sintesis kalsium karbonat daripada kulit telur, ujian kandungan lembapan, ketumpatan pukal, pH, FTIR, and XRD dilaksanakan. Daripada pemerhatian fizikal, hasil menunjukkan terdapat perbezaan dalam perubahan warna sampel pada pelbagai suhu dan masa pembakaran. Analisis TGA menunjukkan serbuk kulit telur terurai pada julat suhu 600°C hingga 900°C. Hasil FTIR melaporkan bahawa warna kelabu sampel terkalsin terdiri daripada kalsium karbonat sementara serbuk putih terdiri daripada kandungan oksida logam. Terdapat tujuh puncak difraksi yang serupa yang dilaporkan dalam analisis XRD untuk kalsinasi pada suhu 900 °C dan kalsium oksida (32.25, 37.41, 53.92, 64.18, 67.41, 79.70, dan 88.58). Pengkalsinan serbuk kulit telur pada suhu 900 °C selama 3 jam dikenal pasti sebagai keadaan yang sesuai untuk penguraian serbuk kulit telur mentah berdasarkan analisis FTIR dan XRD. Kedua-dua hasil menunjukkan terdapat kalsium oksida berdasarkan spektrum gelombang dan analisis difraksi sampel.

Kata kunci: kalsium karbonat, kalsium oksida, kulit telur, kalsinasi

Introduction

Poultry egg is a cost-effective food source due to its high protein and nutritional content [1]. The egg from a chicken or hen (Gallus gallus domesticus, Linnaeus, 1758) is now a global mass-production industry. Quail, duck, goose, turkey, and ostrich eggs are popular choices. Both white and yellow yolks contain aqua, protein, glucose, fat, and ash, but the proportions of these components differ in every egg breed [2]. Essential lipids, proteins, minerals, and low-calorie sources are also found in eggs. Egg products are utilised in various food industrial applications, including thickening, binding, leavening, glazing, and garnishing [3]. A three-layered structure makes up an eggshell: cuticle, spongeous, and lamellar layers. The cuticle layer is the outermost layer, mainly made up of proteins. Protein fibres coupled to calcium carbonate ($CaCO_3$) crystals form a matrix made up of spongey and lamellar layers. $CaCO_3$ accounts for 94% of the eggshell, followed by calcium phosphate (1%), magnesium carbonate (1%), and organic matter (4%) [4]. The eggshell and albumen are two thin eggshell membranes primarily of collagen, alkynes, alkanes, amines, protein amides, and carboxylic acids [5].

Approximately 8 million tons of eggshell wastes are produced annually worldwide [6]. Meanwhile, in Malaysia, 70,686 tons of eggshell waste are produced by various industries [7]. Eggshell waste is listed in the European Union regulation as hazardous waste, and this regulation leads to elevated costs of disposal management [8-11]. In America, companies spend millions of dollars annually to dispose of eggshells in landfills, and the capacity is reached by the fillings [12]. The majority of eggshells are usually disposed to landfills without being treated as eggshells are considered unusable and have no commercial value [13]. However, there have been many studies utilising eggshells in various applications, such as agricultural green chemicals [13, 14, 15], a low-cost catalyst for biodiesel production [16], biofilter in wastewater treatment [17], construction materials [18, 19, 20], biomedical [21], health supplements [22], and craft [23, 24]. [25] studied the effects of eggshell powder as a supplementary material to produce recycled paper.

Various researchers have studied calcined eggshell powder (CESP) waste as a source of calcium oxide (CaO). [26] studied calcined eggshells as a catalyst in biodiesel production, [27] reported the characterisation of nano-CaO based on eggshell waste, [28] studied the CaO sorbents from chicken eggshells for enhanced carbon dioxide (CO_2) capture, [29] utilised calcined eggshells to formulate mortar for building restoration, [30] studied the effects of calcined eggshells as biomaterials for the preparation of linear low-density polyethene, [31] examined the effects of calcined eggshell catalyst in the transesterification of waste cooking oil, and [32] identified the thermoluminescence properties of CaO powder obtained from chicken eggshells.

The calcination process can decompose $CaCO_3$ to CaO. Calcination is a technique for extracting volatile

chemicals from solids by heating them to a high temperature, oxidising a portion of the mass, or making them brittle [33]. Calcination is frequently thought of as a purifying method. $CaCO_3$ is calcined using two methods: combustion with CO_2/oxygen gas (O_2) or steam [34]. The process produces a completely decomposed substance depending on the temperature selected. $CaCO_3$ completely decomposed at the temperature range of 500–900 °C [35]. Research by [36] identified that seashell calcination at the temperature of 800 °C produced a higher amount of CaO based on Fourier transform infrared (FTIR) spectroscopy, scanning electron microscopy (SEM), energy-dispersive X-ray spectroscopy (EDX), and thermal gravimetric analysis (TGA) tests. Although seashells and eggshells are made of $CaCO_3$, their structure is different. It can be seen through their surface morphology. According to [37], the SEM image for seashell (cockle) is platy-shaped. On the other hand, the eggshell is porous and fibril [38]. Furthermore, based on the TGA result, the thermal decomposition of ESP and seashell varied. [39] established that the decomposition of raw eggshell powder (RESP) was in the range of 600–850 °C, while according to [40], the decomposition of cockle was in the range of 500–700 °C. [41] indicated that calcination was highly dependent on temperature, heating rate, and particle size. [39] identified no significant differences in the weight variation of eggshell powder samples during calcination. It was observed that the optimum operating conditions for the decomposition of $CaCO_3$ samples were 900 °C with a heating rate of 20 °C/min and particle size of 0.3 mm. Therefore, it is established that the best temperature for $CaCO_3$ calcination is 800 °C and above.

Researchers have recently studied CaO derived from eggshells for new green chemistry and catalyst by reducing dependence on limestone. However, variations in calcination temperatures and contact hours have been reported. Therefore, this study aimed at finding the ideal conditions in the calcination process for converting $CaCO_3$ from chicken eggshells to CaO. The experiments were conducted based on two parameters: contact time (h) and temperature (°C). The primary physical and chemical characteristics of eggshell powder were studied, including colour changes, mass loss, bulk density, moisture content, pH value, thermal properties, and identification of chemical bonds and compounds in a molecule.

Materials and Methods

Raw materials

Chicken eggshells were collected from local food truck vendors. The eggshells were instantly washed with gentle soap and tap water after being collected as preparation for cleaning treatment. The eggshells were boiled for 30 min [42]. This process is vital to avoid biological contamination and decaying of the eggshells. Next, the eggshells were cleaned by running tap water, air-dried for 24 h at room temperature, and stored in a dark-coloured container [43, 44]. The chicken eggshell samples were ground using an electrical powder grinder (SY-25) 2,000 W to obtain RESP. Then, the RESP was sieved with a 500-µm mesh to eliminate granular sizes. Figure 1 shows the pre-treated eggshells and ground eggshell powder.



Pre-treated eggshells Raw eggshell powder

Figure 1. Preparation of chicken eggshells samples

Material's thermal stability and the fraction of volatile components - Thermogravimetric analysis

TGA was performed using a Shimadzu TGA-50 thermobalance. In this study, approximately 8 g of eggshell powder was heated at 50–950 °C in a nitrogen atmosphere with a flow rate of 20 mL/min and a heating rate of 25 °C/min [45].

Calcination of chicken eggshell

The eggshell powder samples were placed in closed porcelain crucibles and calcined in a chamber furnace (Carbolite ELF 11/14B) according to the eight experiment sets as shown in Table 1. Two parameters were varied to examine the calcination process (i.e., temperature (°C) and contact time (h)) with a constant weight RESP (i.e., 20 g). Each calcination protocol was done in triplicates. To avoid a reaction with moisture and atmospheric air, the CESP was stored in flasks and placed atop a desiccator after calcination [46].

Table 1. Calcination parameters

No.	Sample Code	Parameter	
		Temperature (ºC)	Contact Time (hour)
1	CESP $T_{600\text{-}3}$	600	3
2	CESP $T_{600\text{-}4}$	600	4
3	CESP $T_{700\text{-}3}$	700	3
4	CESP $T_{700\text{-}4}$	700	4
5	CESP $T_{800\text{-}3}$	800	3
6	CESP $T_{800\text{-}4}$	800	4
7	CESP $T_{900\text{-}3}$	900	3
8	CESP $T_{900\text{-}4}$	900	4

Results and Discussion

Thermogravimetric analysis

TGA is carried out to determine the thermal stability of a material and its fraction of volatile components by monitoring the weight change that occurs as a sample is heated at a constant rate. Based on Figure 2, four reaction steps occurred in this experiment.

The first step showed that 1.13% mass decreased at midpoint 84.23 °C. The temperature range at step 1 can be considered as eliminating moisture of the sample. [48] supported this statement, stating that biomass drying is conducted in the range of 40–200 °C. Referring to [49], the slight decrease of mass in the second step was due to the decomposition of organic matter in the range of 200–600 °C. The RESP started to decompose from $CaCO_3$ to CaO and released CO_2 at 600 °C and ended at 850 °C in step 3. A slight mass loss in step 4 at 950 °C can be referred to as the end of the reaction.

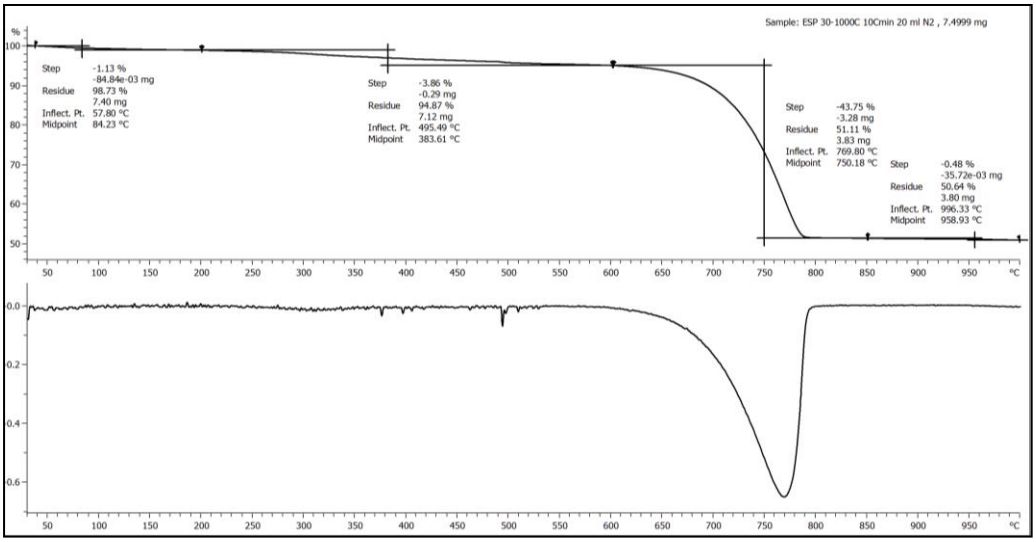


Figure 2. Thermogravimetric analysis of RESP

Calcination process

Calcination is the process of decomposing $CaCO_3$ by burning the compound at high temperatures. The catalysts were completely decomposed at the temperature range of 500–900 °C [39]. The optimum temperature for the calcination of $CaCO_3$ from cockle shell was 900 °C for 2 h with a particle size of 0.3 mm under inert conditions [41]. [13] supported this statement and reported that the suitable temperature and time for complete decomposition in the calcination of $CaCO_3$ from duck eggshells were 900 °C and 1 h, respectively. [50] and [40] argued that calcite fully decomposed to form CaO at 800 °C. Based on these studies, three conditions may affect the calcination process. In this study, CaO is derived from eggshell powder, as shown in Equation 3.

$$CaCO_{3(s)} \rightarrow CaO_{(s)} + CO_{2(g)} \quad (3)$$

The primary characteristics of CESP were studied and recorded, including physical observation (colour changes), moisture content, bulk density, and average mass loss. Based on the TGA result in Figure 2, the RESP decomposed in the temperature range of 600–850 °C. Therefore, the range of calcination temperature in this study was chosen from 600 °C to 900 °C. By referring to Table 2, as the temperature increases, the bulk density value decreases, and consequently, the mass loss increases. From the result, it shows that calcination temperature affected the reduction in mass for eggshell powder. Different colour changes were observed between uncalcined and calcined samples. The colour of the uncalcined eggshell is light brown based on its original colour. In comparison, a perfect CESP should be solid white. Based on the result, low calcination temperatures produced dark or grey colour, whereas at high calcination temperatures, solid white colour was obtained. More metal oxide (solid white powder) was produced for higher calcination temperatures. [51] stated that the higher temperature would produce a higher amount of metal oxide and the colour would become whiter. [41] established the optimum temperature of 900 °C for $CaCO_3$ decomposition. High temperatures are required for CESP to produce perfect CaO. The dark powder obtained at low temperatures indicates that eggshell powder has not completely decomposed.

Compared to other manipulated variables, the samples calcined at different contact times showed a massive percentage of mass loss. This could be explained by the longer calcination duration, which resulted in greater mass loss [52]. The colour transition for different contact times is presented in Table 2. Even though the samples of eggshell powder were calcined at the same temperature and weight, the calcination result was

affected by the contact time. The formation of dark grey powder at low contact time was due to a lack of heat distribution. The grey powder at the inner part of the sample showed that the heat was not well distributed to the whole part of the sample. Therefore, increasing the calcination period is one of the significant ways to improve the formation of metal oxide. [13] stated that higher temperature and longer calcination time produced better CaO quality.

Moisture loss occurred during calcination, which corresponds to the loss of water and/or gas of the eggshell powder. In this study, the moisture loss percentages of CESP in all conditions were too insignificant, and therefore, could be ignored. [54] stated that the decomposition of volatile materials (e.g., water and organic matter) occurred in the temperature range of 30–400 °C. There were no changes in the acidity of RESP and dark powder. Meanwhile, the acidity for solid white powder changed to alkali. Therefore, if the amount of dark powder is more significant than solid white powder, the sample can be considered as $CaCO_3$.

The bulk density values of eggshell powder calcined with different parameters are tabulated in Table 2. The solid white powder of CESP $T_{900\text{-}3}$ and CESP $T_{900\text{-}4}$ showed a softer and more refined texture. [13] reported that calcination at 900 °C for 1 h reduced the particle size of the samples. According to Equation 2, density is inversely proportional to volume. The bulk density decreased as the particle size increased [53]. The volume depends on the particle size of the samples.

The pH of RESP changed to alkali when it was calcined at high temperatures. The alkalinity value increased as the temperature and contact time increased. The samples of $CESP_{700\text{-}4}$ to $CESP_{900\text{-}4}$ showed an alkaline pH value of 12.70–13.26, indicating the presence of CaO. The result is correlated with previous findings, where the calcination temperature of 700 °C produced sufficient CaO and achieved the critical value of an alkaline solution [54].

Table 2. Calcination of ESP with different parameters

Sample	Physical Observation	Mass Loss (%)	Moisture Content (%)	Bulk Density (g/ml)	pH
Uncalcined		N/A	0.451	2.47	7.00
CESP $T_{600\text{-}3}$		0.84	N/A	1.38	9.36
CESP $T_{600\text{-}4}$		0.83	N/A	1.41	10.84
CESP $T_{700\text{-}3}$		1.13	N/A	1.36	11.64

Table 2 (cont'd). Calcination of ESP with different parameters

Sample	Physical Observation	Mass Loss (%)	Moisture Content (%)	Bulk Density (g/ml)	pH
CESP T_{700-4}		0.98	N/A	1.33	12.70
CESP T_{800-3}		2.19	N/A	1.38	12.67
CESP T_{800-4}		2.99	N/A	1.33	12.85
CESP T_{900-3}		11.00	N/A	3.00	12.96
CESP T_{900-4}		11.43	N/A	3.33	13.26

Compounds identification

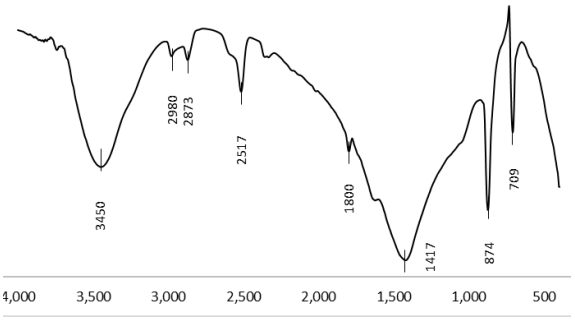
The FTIR analysis can be divided into three broad regions. The first region is from 4000 cm^{-1} to 3000 cm^{-1}, which represents hydrogen bonding. The second region, which is from 3000 cm^{-1} to 1500 cm^{-1}, shows functional groups. Meanwhile, the third region reveals the existence of biominerals. Based on physical observation and pH values in Table 2, chemical characterisation was conducted for the selected samples of CESP T_{700-4}, CESP T_{800-3}, CESP T_{800-4}, CESP T_{900-3}, and CESP T_{900-4}. Sufficient CaO content produced from the calcination of eggshells will make the pH value reach the critical value of 12.7 [56]. Therefore, the FTIR analysis identifies the functional groups present in the eggshells calcined at 900 °C with different contact times.

Figure 3 below presents the FTIR spectra for CESP at various temperatures and contact times. Small sharp peaks were detected at 874 cm^{-1} and 1417 cm^{-1} for CESP T_{700-3}, CESP T_{700-4}, CESP T_{800-3}, and CESP T_{800-4}. The bands at both wavelength indicated $CaCO_3$ in the tested samples [55,56]. Another strong peak was observed at 2516 cm^{-1} due to the presence of $CaCO_3$ [57]. According to [7], the observable peaks in the range of 713–875 cm^{-1} can be associated with the presence of $CaCO_3$. The observation by [58] for the band at 1430 cm^{-1} was attributed to the stretching vibration of $CaCO_3$. Meanwhile, the bands at 875 cm^{-1} and 715 cm^{-1} strongly corresponded to $CaCO_3$ [59]. The lowest band represents the weak band to indicate $CaCO_3$.

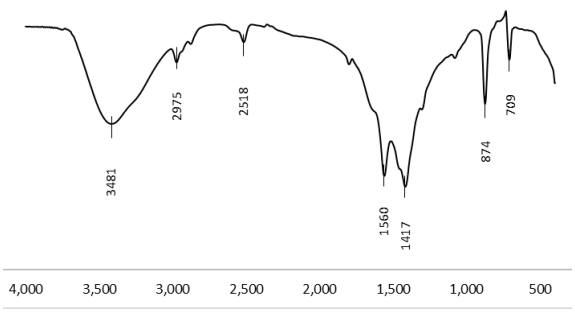
Sharp peaks were observed at 707 cm^{-1} and 709 cm^{-1}. The wavenumber increased as the transmittance increased intensely at the peak of 874 cm^{-1}. Both peaks are associated with in-plane deformation and out-plane deformation modes of eggshell powder in the presence of $CaCO_3$, as described by [7]. The sharp, strong band detected at 1560 cm^{-1} is attributed to the oxidation process [60].

An amine group was present at the band of 1055 cm^{-1}. According to [61], the presence of the functional groups of amines and amides was observed due to the chemical composition of fibrous proteins. As referred to [62], CESP $T_{900\text{-}3}$ showed a medium-sized peak at 1052 cm^{-1} corresponding to the stretching of both C-O in the C-OH bond. The peaks at 1424 cm^{-1} and 1422 cm^{-1} indicated the presence of OH bonding. The existence of hydroxide might be due to exposure to the atmosphere during calcination [63]. Another significant peak was detected at 2361 cm^{-1} in regard to the presence of O=C=O bonds. The presence of O=C=O bonds indicated the carbonation of CaO, as shown in Equation 4 [64].

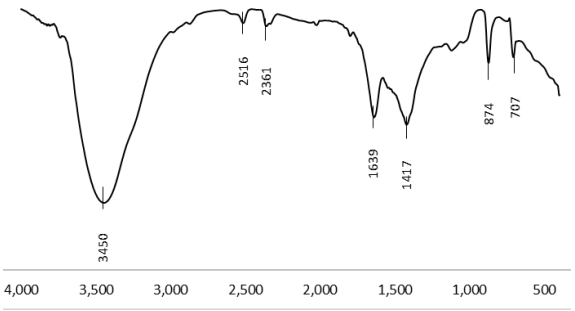
$$Ca(OH)^2 + CO_2 \rightarrow CaCO_3 + H_2O \quad (4)$$



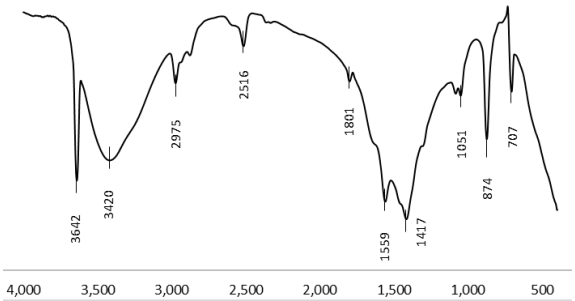
(a) CESP $T_{700\text{-}3}$



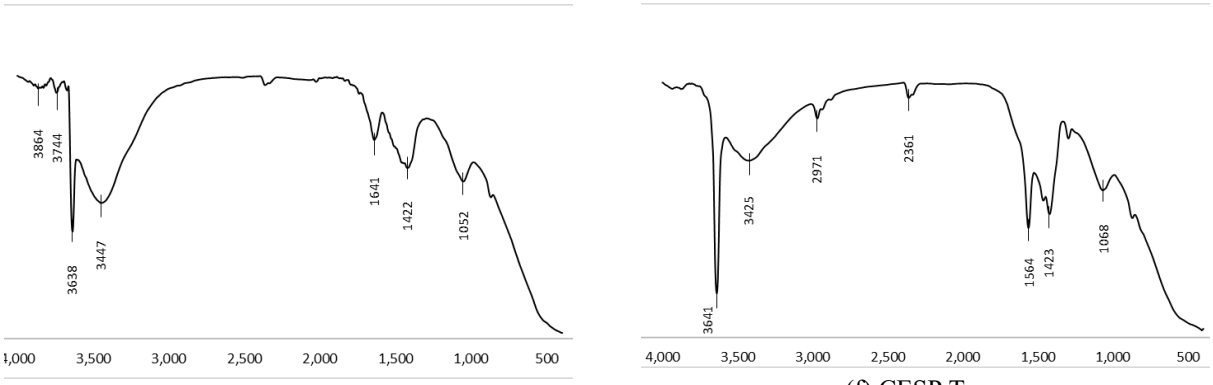
(b) CESP $T_{700\text{-}4}$



(c) CESP $T_{800\text{-}3}$



(d) CESP $T_{800\text{-}4}$



(e) CESP $T_{900\text{-}3}$ (f) CESP $T_{900\text{-}4}$

Figure 3. The FTIR spectra for CESP at different contact times and temperatures

The XRD analysis was carried out to identify CaO in CESP at different temperatures. Figure 4 illustrates the results of XRD analysis for RESP and CESP at 900 °C (CESP $T_{900\text{-}3}$), 700 °C (CESP $T_{700\text{-}3}$), and industrial CaO as a reference. The intensity of $CaCO_3$ showed the primary compound of RESP. The diffraction showed both distinct components of CaO and $CaCO_3$ for CESP $T_{700\text{-}3}$. Thus, the intensity of $CaCO_3$ decreased compared to RESP. At 700 °C, incomplete decomposition of $CaCO_3$ occurred, based on the diffraction pattern (c). A similar study by [53] claimed that CaO was absent at 700 °C. CESP $T_{700\text{-}3}$ showed a different peak pattern of CaO than CESP $T_{900\text{-}3}$ and industrial CaO. Meanwhile, CESP $T_{900\text{-}3}$ showed seven diffraction peaks similar to the diffraction peaks of industrial CaO. The simplified XRD analysis is shown in Table 3.

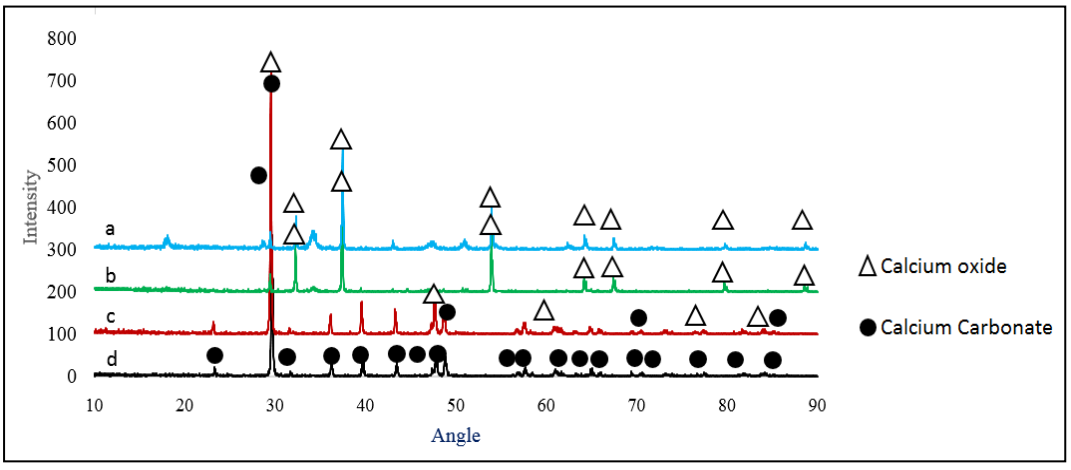


Figure 4. XRD patterns of a) industrial CaO, b) CESP $T_{900\text{-}3}$, c) CESP $T_{700\text{-}3}$, and d) RESP

Table 3. X-ray diffraction results for CaO and $CaCO_3$ from synthesised eggshell powder

Sample	Compound	Angle (2θ)						
CESP $T_{700\text{-}3}$	$CaCO_3$	28.78	47.25	62.73	71.79	84.88	-	-
	CaO	29.52	47.67	60.84	77.45	84.02	-	-
CESP $T_{900\text{-}3}$	CaO	32.25	37.41	53.92	64.18	67.41	79.70	88.58
Industrial CaO	CaO	32.33	37.45	56.97	64.24	67.47	79.78	88.66

Conclusion

Different calcination temperatures and contact times were applied in the calcination of eggshell waste to decompose $CaCO_3$ into CaO. Based on physical inspection, higher temperature and increased contact time produced white powder, which was later identified as CaO. Among the studied calcination conditions, the best conditions were the temperature of 900 °C and the contact time of 3 h. The CaO synthesized from eggshells can be used in various applications, such as in the laboratory (gas absorber), construction (lime putty and cement production), soil stabiliser, medicinal purposes, and others. Hence, it is believed that calcined chicken eggshells can be an alternative source of CaO to reduce the dependency on limestone resources.

Acknowledgement

An industrial research fund partially supported this research under the MRT-SSP-V208-Second Tier ICP Agreement 2019 (Grant Number: ICP/MTDC/2019). We would like to thank our colleagues from Universiti Kuala Lumpur – MICET and Universiti Teknikal Melaka Malaysia, who provided insight and expertise that greatly assisted the research.

References

1. Miranda, J.M., Anton, X., Redondo-Valbuena, C., Roca-Saavedra, P., Rodriguez, J.A. and Lamas, A. (2015). Egg and egg-derived foods: Effects on human health and use as functional foods. *Nutrients*, 7: 706-729.
2. Godbert, S.R., Guyot, N. and Nys, Y. (2019). The golden egg: Nutritional value, bioactivities, and emerging benefits for human health. *Nutrients*, 11(684): 1-26.
3. Laca, A., Paredes, B., Rendueles, M. and Díaz, M. (2014). Egg yolk granules: Separation, Characteristics, and Applications in The Food Industry. *LWT - Food Science and Technology*, 59(1): 1-5.
4. Rivera, E.M., Araiza, M., Brostow, W., Castano, V.M., Diaz-Estrada, J.R., Hernandez, R. and Rodriguez, J.R. (1999). Synthesis of hydroxyapatite from eggshells. *Materials Letter*, 41: 128-134.
5. Park, S., Choi, K.S., Lee, D., Kim, D., Lim, K.T., Lee, K.H., Seonwoo, H. and Kim. J. (2016). Eggshell membrane: Review and impact on engineering. *Biosystem Engineering*, 151: 446-463.
6. De Angelis, G., Medeghini, L., Conte, A.M. and Mignardi, S. (2017). Recycling of eggshell waste into low-cost adsorbents for Ni removal from wastewater. *Journal of Cleaner Production*, 164: 1497-1506.
7. Carvalho, J., Araujo, J. and Castro, F. (2011). Alternative low-cost adsorbent for water and wastewater decontamination derived from eggshell waste: an overview. *Waste Biomass Valor,* 2: 157-167.
8. Laca, A., Laca, A. and Díaz, M. (2017). Eggshell waste as catalyst: A review. *Journal of Environmental Management,* 197: 351-359.
9. Quina, M., Soares, M.A. and Quinta, F.R. (2017). Applications of industrial eggshells as a valuable anthropogenic resource. *Resources Conservation and Recycling*, 123: 176-186.
10. Ummartyotin S. and Manuspiya, H. (2018). A critical review of eggshell waste: An effective source of hydroxyapatite as photocatalyst. *Journal of Metals, Materials, and Minerals*, 28(1): 124-135.

11. Sonenklar, C. (1999). Famous for Egg Waste. The PennState news. The Pennsylvania State University. https://news.psu.edu/story/140891/ 1999/09/01/research/famous-egg-waste. [Access online 1 September 1999]
12. Arabhosseini, A. and Faridi, H. (2018). Application of eggshell wastes as valuable and utilizable products: A review. *Resource Agriculture Engineering*, 64: 104-114.
13. Tangboriboon, N., Kunanuruksapong, R. and Sirivat, A. (2012). Preparation and properties of calcium oxide from eggshells via calcination. *Materials Science-Poland*, 30(4): 313-322.
14. Ok, Y.S., Lee, S.S., Jeon, WT., Oh, S.E., Usman, A.R.A. and Moon, D.H. (2011). Application of eggshell waste for the immobilization of cadmium and lead in contaminated soil. *Environ Geochem Health* 33: 31-39.
15. Yasar, F. (2019). Biodiesel production via waste eggshell as a low-cost heterogeneous catalyst: Its effects on some critical fuel properties and comparison with CaO. *Fuel*, 255(1): 115828 .
16. Bashir, A.S.M. and Manusamy, Y. (2015). Characterization of raw eggshell powder (ESP) as a good bio filler. *Journal of Engineering Research and Technology,* 2(1): 56-60.
17. Ahmad, R., Rohim, R. and Ibrahim, N. (2015). Properties of waste eggshell as calcium oxide catalyst *Applied Mechanics and Materials,* 754: 171-175.
18. Karthick, J., Jeyanthi, R. and Petchiyammal, M. (2014). Experimental study on usage of egg shell as partial replacement for sand in concrete. *International Journal of Advanced Research in Education Technology,* 1(1): 7-10.
19. Gabol, N.A., Memon, F.A., Jawaduddin, M. and Zardari, Z.H. (2019). Analysis of eggshell powder as a partial replacing material in concrete. *International Journal of Modern Research in Engineering & Management,* 2(9): 22-31.
20. Razali, N., Azizan, M.A., Pa'ee, K.F., Razali, N. and Jumadi, N. (2020). Preliminary studies on calcinated chicken eggshells as fine aggregates replacement in conventional concrete. *Materials Today: Proceedings*, 31(1): 354-359.
21. Abdulrahman, I., Tijani, H.I., Mohammed, B.A., Saidu, H., Yusuf, H., Jibrin, M.N. and Mohammed, S. (2014). From garbage to biomaterials: An overview on eggshell-based hydroxyapatite. *Journal of Materials*, 2014: 1-6.
22. Bartter, J., Diffey, H., Yeung, Y.H., O'Leary, F., Häsler, B., Maulaga, W. and Alders, R. (2018). Use of chicken eggshell to improve dietary calcium intake in rural sub-saharan Africa. *Maternal & Child Nutrition*, 14(3): 1-10.
23. Hitchcock, R.K. (2012). Ostrich eggshell jewelry manufacturing and use of ostrich products among San and Bakgalagadi in the Kalahari. *Botswana Notes and Records*, 44: 93-105.
24. Zoran. A. (2018). The ostrich eggshell beads craft of the Ju/'hoansi: A reflection on modern craft theories. *Craft Research*, 9(2): 229-253.
25. Abdullah, M., Soo, K. Y., Raofuddin, D.N.A, Sukor, M.Z., Roslan, A., Ilyas, S.M.M. and Yasin, M.H. (2018). An evaluation of eggshell waste/waste paper mechanical properties as composite paper. *International Journal of Engineering & Technology*, 7: 239-241.
26. Sulaiman S., and Talha N.S. (2018) Technique to produce catalyst from egg shell and coconut waste for biodiesel production. In: Amid A., Sulaiman S., Jimat D., Azmin N. (eds) *Multifaceted Protocol in Biotechnology*.
27. Mosaddegh, E. and Hassankhani, A. (2014). Preparation and characterization of nano-cao based on eggshell waste: Novel and green catalytic approach to a highly efficient synthesis of pyrano[4,3-b] pyrans. *Chinese Journal Catalyst,* 35: 351-356.
28. Sacia, E.R., Ramkumar, S., Phalak, N. and Fan, L.S. (2013). Synthesis and regeneration of sustainable CaO sorbents from chicken eggshells for enhanced carbon dioxide capture. *ACS Sustainable Chemical Engineering*, 1: 903-909.
29. Beck, K., Brunetaud, X., Mertz, J.D. and Al-Mukhtar, M. (2010). The use of eggshell lime and tuffeau powder to formulate an appropriate mortar for restoration purposes. *Geological Society London Special Publications,* 331(1): 137-145.
30. Jirimali, H.D., Chaudhari, B.C., Khanderay, J.C., Joshi, S.A., Singh, V., Patil, A.M. and Gite, V.V. (2018). Waste eggshell-derived calcium oxide and nanohydroxyapatite biomaterials for the preparation of LLDPE polymer nanocomposite and their thermomechanical study. *Polym-Plast Technology Engineering,* 57: 804-811.
31. Tan, Y.H., Abdullah, M.O., Nolasco-Hipolito, C. and Zauzi, N.S.A. (2017). Application of RSM and Taguchi methods for optimizing the transesterification of waste cooking oil catalyzed by a solid ostrich and chicken-eggshell derived CaO. *Renew Energy*, 114(Part B): 437-447.

32. Nagabhushana, K.R., Lokesha, H.S., Reddy, S.S., Prakash, D., Veerabhadraswamy, M., Bhagyalakshmi, H. and Jayaramaiah, J.R. (2017). Thermoluminescence properties of CaO powder obtained from chicken eggshells. *Radiation Physics Chemistry,* 138: 54-59.
33. Britannica, T. Editors of Encyclopedia. Calcination. Encyclopedia Britannica. Retrieved Oct 04, 2016, from https://www.britannica.com/technology/calcination. [Access online 4 October 2016].
34. Lin. S., Kiga. T., Wang. Y. and Nakayama. K. (2011). Energy analysis of $CaCO_3$ calcination with CO_2 capture. *Energy Procedia,* 4: 356-361.
35. Al-Fatesh, A.S.A. and Fakeeha, A.H. (2012). Effects of calcination and activation temperature on dry reforming catalysts. *Journal of Saudi Chemical Society,* 16: 55-61.
36. Nordin, N., Hamzah, Z., Hashim, O., Kasim, F.H., and Abdullah, R. (2015). Effect of temperature in calcination process of seashells. *Malaysian Journal of Analytical Sciences*, 19(1): 65-70.
37. Dampang, S., Purwanti, E., Destyorini, F., Kurniawan, S. B. K., Abdullah, S. R. S. and Imron, M. (2021). Analysis of optimum temperature and calcination time in the production of CaO using seashells waste as $CaCO_3$ source. *Journal of Ecological Engineering,* 22(5): 221–228.
38. Aina, S., Plessis, B. D., Mjimba, V. and Brink, H. (2021). Eggshell valorization: Membrane removal, calcium oxide synthesis, and biochemical compound recovery towards cleaner productions. *Biointerface Research in Applied Chemistry,* 12(5): 5870-5883.
39. Razali, N., Musa, F. A. M., Jumadi, N. and Jalani, A. Y. (2021). Production of calcium oxide from eggshell: Study on calcination temperature, raw weight and contact time. *RSU International Research Conference,* 2021: 624-637.
40. Hussein, A. I., Ab-Ghani, Z., Mat, A. N. C., Ab-Ghani, N. A., Husein, A. and Rahman, I. A. (2021). Synthesis and characterization of spherical calcium carbonate nanoparticles derived from cockle shells. *Applied Science,* 10: 7170.
41. Mohamad, S.F.S, Mohamad, S. and Jemaat, Z. (2016). Study of calcination condition on decomposition of calcium carbonate in waste cockle shell to calcium oxide using thermal gravimetric analysis. ARPN *Journal of Engineering and Applied Sciences,* 11(16): 9917-9921.
42. Islam, K.N., Bakar, M.Z.B.A., Ali, M.E., Hussein, M.Z.B., Noordin, M.M., Loqman, M.Y., Miah, G., Wahid, H. and Hashim, U. (2013). A novel method for the synthesis of calcium carbonate (aragonite) nanoparticles from cockle shells. *Powder Technology*, 235: 70-75.
43. Ali, M. and Badawy W. Z. (2017). Utilization of eggshells by-product as a mineral source for fortification of bread strips. *Journal of Food and Dairy Sciences,* 8(11): 455-459.
44. Oulego, P., Laca, A., Calvo, S. and Díaz, M. (2019). Eggshell-supported catalysts for the advanced oxidation treatment of humic acid polluted wastewaters. *Water,* 12(100): 1-18.
45. Yahya, N., Tahir, S.M. and Rosli, N.H.M. (2019). Green eggshell/polypropylene biocomposite. *International Journal of Recent Technology and Engineering,* 8: 2277-3878.
46. Castro, L.D.S., Barañano, A.G., Pinheiro, C.J.G.L, Menini, L. and Pinheiro, P.F. (2019). Biodiesel production from cotton oil using heterogeneous CaO catalysts from eggshells prepared at different calcination temperatures. *Green Process Synthesis*, 8: 235-244.
47. Gatea, A.A., Kouzani, A.Z., Kaynak, A., Khoo, S.Y., Norton, M. and Gates, W. (2018). Soil bulk density estimation methods: A review. *Pedosphere,* 28(4): 581-596.
48. Jewiarz, M., Wrobel, M., Mudryk, K. and Szufa, S. (2020). Impact of the drying temperature and grinding technique on biomass grindability. *Energies,* 13(3392): 1-22.
49. Queirós, M.V.A., Bezerra, M.N. and Feitosa, J.P.A. (2017). Composite superabsorbent hydrogel of acrylic copolymer and eggshell: Effect of biofiller addition. *Journal Brazillian Chemical Society,* 2017: 1-9.
50. Loy, C.W., Matori, K.A., Way F.L., Schmid, S., Zainuddin, N., Wahab, Z.A., Alassan, Z.N. and Zaid, M.H.M. (2016). Effects of calcination on the crystallography and nonbiogenic aragonite formation of ark clamshells under ambient conditions. *Advances in Materials Science and Engineering.* 2016: 1-8.
51. Mohadi, R., Anggraini, K., Riyanti F. and Lesbani, A. (2016). Preparation of calcium oxide (CaO) from chicken eggshells. *Sriwijaya Journal of Environment*, 1(2): 32-35.
52. Krähenbühl, M., Etter, B. and Udert, K.M. (2015). Pre-treated magnesite as a source of low-cost magnesium for producing. *Science of The Total Environment,* 542: 1155-1161.

53. Zhang, S. (2015). Relationship between particle size distribution and porosity in dump leaching. Thesis of Doctor of Philosophy. The University of British Columbia.
54. Shao, W.C., and Dong, Y.W. (2020). A study on physicochemical properties and formaldehyde adsorption and degradation of purifying air quality by modified biocalcium. *International Journal of Environmental Science and Development,* 7(11): 327-335.
55. Rujitanapanich, S., Kumpapan, P. and Wanjanoi, P. (2014). Synthesis of hydroxyapatite from oyster shell via precipitation. *Energy Procedia*, 56: 112-117.
56. Yao, C., Xie, A., Shen, Y., Zhu, J. and Li, T. (2013). Green synthesis of calcium carbonate with unusual morphologies in the presence of fruit extracts. *Journal Chilean Chemical Society,* 58(4): 2235-2238.
57. Daskalakis, M.I., Magoulas, A., Kotoulas, G., Catsikis, I., Bakolas, A., Karageorgis, A.P., Mavridou, A., Doulia, D., Rigas, F. (2013). Pseudomonas, pantoea and cupriavidus isolates induce calcium carbonate precipitation for biorestoration of ornamental stone. *Journal of Applied Microbiology,* 115: 409-423.
58. Veerasingam, S. and Venkatachalapathy, R. (2014). Estimation of carbonate concentration and characterization of marine sediment by fourier transmission infrared spectroscopy. *Infrared Physics and Technology,* 66: 136-140.
59. Reyes, J., Gutiérrez, R., Centeno, G., Treviño, D., Bartolo, P., Quintana, P., Azamar, J.A., and Pérez, T. (2008). Chemical characterization of Crusts Formed in Mortars of Historical Buildings in San Francisco de Campeche City, Mexico. *Historical Mortars Conference,* 2008: pp. 1-11.
60. Pardo, F.N., Barrera, G.M., Hernández, A.L.M., Castaño, V.M., Armenta, J.L.R., Rodríguez, F.M. and Santos C.V. (2013). Effects on the thermo-mechanical and crystallinity properties of nylon 6,6 electrospun fibres reinforced with one dimensional (1d) and two-dimensional (2d) carbon. *Materials,* 8: 3494-3513.
61. Tsai, T.Y., Coumar, M.S., Hsu, T., Hsieh, H.P., Chien, C.H., Chen, C.T., Chang, C.N., Lo, Y.K., Wu, S.H., Huang, C.Y., Huang, Y.W., Wang, M.H., Wu, H.Y., Lee, H.J., Chen, X., Chao, Y.S., and Jiaang, W. (2006). Substituted pyrrolidine-2,4-dicarboxylic acid amides as potent dipeptidyl peptidase IV inhibitors. *Bioorganic & Medicinal Chemistry Letters.* 16(12): 3268-3272.
62. Nandiyanto, A.B.D., Oktiani, R. and Ragadhita, R. (2019). How to read and Interpret FTIR spectroscope of organic material. *Indonesian Journal of Science & Technology,* 4(1): 97-118.
63. Zaman, T., Mostari, M. S., Mahmood, M. A. and Rahman, M. S. (2018). Evolution and characterization of eggshell as a potential candidate of raw material. *CerâMica,* 64(370): 236-241.
64. Habte, L., Khan, M.D., Shiferaw, N., Farooq, A., Lee, M.H., Jung, S.H. and Ahn, J.W. (2020). Synthesis, characterization, and mechanism study of green aragonite crystals from waste biomaterials as a calcium supplement. *Sustainability*, 12(5062): 1-10.

Malaysian Journal of Analytical Sciences (MJAS)
Published by Malaysian Analytical Sciences Society

DEVELOPMENT AND OPTIMIZATION OF A RAPID RESOLUTION LIQUID CHROMATOGRAPHY METHOD FOR CYANIDIN-3-O-GLUCOSIDE IN RAT PLASMA

(Pembangunan dan Pengoptimuman Kaedah Kromatografi Cecair Resolusi Pantas untuk Sianidin-3-O-Glukosida Klorida di dalam Plasma Tikus)

Nadiratul Asyikin Sauji[1], Wan Amir Nizam Wan Ahmad[1], Liza Nordin[2], Ruzilawati Abu Bakar[3]*

[1]Biomedicine Program, School of Health Sciences
[2]Department of Physiology, School of Medical Sciences
[3]Department of Pharmacology, School of Medical Sciences
Universiti Sains Malaysia, 16150 Kubang Kerian, Kelantan, Malaysia

**Corresponding authors: ruzila@usm.my*

Received: 16 January 2022; Accepted: 15 March 2022; Published: 28 April 2022

Abstract

The growing interest in anthocyanins in plants has brought about the importance of investigating their pharmacological properties. Sensitive and specific analytical methods are required to accurately analyze the anthocyanins present in samples. One of the anthocyanins found in plants is cyanidin-3-O-glucoside. The objective of this study was to develop and optimize a rapid resolution liquid chromatography (RRLC) method for cyanidin-3-O-glucoside determination in rat plasma. Spectrophotometric analysis was performed to determine the best ultraviolet (UV) absorbance wavelength. Liquid-liquid extraction (LLE) and solid-phase extraction (SPE) methods were compared to determine the best extraction method for cyanidin-3-O-glucoside in rat plasma samples. The effects of varying the type and proportion of organic solvents, the type and concentration of buffer solutions, flow rates, column temperatures, and UV wavelengths were examined. The optimized chromatographic method for RRLC analysis of cyanidin-3-O-glucoside was a mobile phase composition of 0.1% trifluoroacetic acid aqueous solution and acetonitrile in a ratio of 81:19, respectively, with a 0.5 mL/min flow rate, at 30°C column temperature and 525 nm detection wavelength. SPE was our choice of final extraction method. Our findings revealed that the optimized RRLC method can be used to determine cyanidin-3-O-glucoside in rat plasma.

Keywords: rapid resolution liquid chromatography, method development, cyanidin-3-o-glucoside, rat plasma

Abstrak

Kajian antosianin dalam rosel yang semakin meluas mengetengahkan kepentingan analisis sebatian tersebut untuk mengkaji ciri-ciri farmakologinya. Kaedah analisis yang sensitif dan spesifik diperlukan untuk menganalisis antosianin yang terdapat dalam sampel dengan tepat. Salah satu antosianin yang terdapat dalam tumbuhan ialah sianidin-3-O-glukosida. Objektif kajian ini adalah untuk membangunkan dan mengoptimumkan kaedah kromatografi cecair resolusi pantas (RRLC) untuk sianidin-3-O-glukosida di dalam plasma tikus. Analisis spektrofotometri dilakukan untuk memilih penyerapan ultraungu yang terbaik. Kaedah pengekstrakan cecair-cecair (LLE) dan pengekstrakan fasa pepejal (SPE) juga dijalankan untuk menilai kaedah pengekstrakan

terbaik bagi antosianin daripada sampel plasma tikus. Kesan mempelbagaikan jenis dan peratusan pelarut organik, jenis dan kepekatan larutan penimbal, kadar aliran fasa bergerak, suhu turus dan panjang gelombang pengesan ultraungu telah diuji. Kaedah pengoptimuman kromatografi menunjukkan komposisi fasa bergerak bagi larutan akueus asid trifluoroasettik 0.1% dan asetonitril dalam nisbah 81:19, dengan kadar aliran 0.5 mL/min, pada suhu turus 30°C dan panjang gelombang pengesanan 525 nm adalah sesuai untuk analisis sianidin-3-O-glukosida. Kaedah SPE dipilih sebagai kaedah pengekstrakan terbaik kerana ia menghasilkan puncak kromatogram yang lebih baik berbanding kaedah LLE. Kesimpulannya, kaedah RRLC yang dibangunkan dalam kajian ini boleh digunakan untuk menentukan sianidin-3-O-glukosida dalam plasma tikus.

Kata kunci: kromatografi cecair resolusi pantas, pembangunan kaedah, sianidin-3-O-glukosida, plasma tikus

Introduction

Anthocyanins are polyphenolic pigments that belong to the flavonoid group and are present in the vacuolar sap of the epidermal tissues of flowers and fruits [1, 2]. These compounds are responsible for various colors of plant organs, such as fruits, flowers, and leaves, and they are also present in vegetables [1]. One of the anthocyanins found in plants is cyanidin-3-O-glucoside [3]. The ever-increasing evidence about anthocyanins has drawn many researchers to investigate more about these plant flavonoids. The increasing importance of elucidating their health -promoting properties has raised the need for specific tasks for their determination methods.

The development of a combined extraction method—spectrophotometric and chromatographic methods is regarded as having the most significant impact on the analysis of anthocyanins [3, 4]. Although liquid chromatography has been the most employed technique to identify or quantify anthocyanins [5], an advanced and improved method of high-performance liquid chromatography (HPLC), such as rapid resolution liquid chromatography (RRLC), is currently applied in anthocyanin research, as it offers better separation and identification of specific components of anthocyanins. Therefore, the objective of this study was to develop and optimize an RRLC method for cyanidin-3-O-glucoside in rat plasma. Spectrophotometric analysis was performed to determine the appropriate UV absorbance. Both liquid-liquid extraction (LLE) and solid-phase extraction (SPE) methods were performed to determine the best extraction method for cyanidin-3-O-glucoside chloride in the rat plasma sample. We tested the effects of varying the type and percentage of organic solvents, the type and concentration of buffer solutions, flow rates, and column temperatures.

Materials and Methods

Chromatographic equipment

The chromatographic system and machine consisted of the Agilent Technologies 1200 Series system consisted of a binary pump, an autosampler, thermostat column compartment, variable wavelength detector and a vacuum degasser (Agilent Technologies, Santa Clara, California, USA). The analytical column was Agilent Reverse Phase EC-C18 (4.6 x 150 mm I. D, particle size 2.7 µm) (Agilent Technologies, Santa Clara, California, USA). The guard column was Agilent Reverse Phase EC-C18 2.7 µm (4.6 x 5 mm) (Agilent Technologies, Santa Clara, California, USA).

Chemicals and reagents

All chemicals were HPLC grade. Acetonitrile (ACN), 5-sulfosalicylic acid dihydrate, ethyl acetate, methyl tert-butyl ether (MTBE), methanol (MeOH), formic acid (CH_2O_2), phosphoric acid (H_3PO_4), hydrochloric acid (HCL) and trifluoroacetic acid (TFA) were from Merck® (Darmstadt, Germany). Diethyl ether was from Fisher Chemical (Massachusetts, USA).

Drug standard and internal standard

The drug standard, cyanidin-3-O-glucoside chloride was purchased from ChemFaces (catalogue no. CFN99740) (CAS no. 7084-24-4). The internal standard, cyanidin-3,5-O-diglucoside chloride was also purchased from ChemFaces (catalogue no. CFN92138) (CAS no. 2611-67-8).

Standard stock solutions of cyanidin-3-O-glucoside chloride (100 µg/ml) and internal standard, cyanidin-3,5-O-diglucoside chloride (100 µg/ml) were prepared by dissolving 1 mg of each compound in 10 ml MeOH, respectively. The solutions were then stored at -20°C in clear vials and were protected from light with aluminum foils. The working cyanidin-3-O-glucoside chloride and internal standard solutions were prepared fresh daily by diluting the stock solutions with the mobile phase. The concentration of working solution for internal standard and cyanidin-3-O-glucoside chloride used for the optimization of chromatographic conditions were 250 ng/ml and 500 ng/ml, respectively.

Preparation of plasma standard and samples

The rats used in this study were approved by the USM Institutional Animal Care and Use Committee (USM IACUC) [USM/IACUC/2019/(118)(1000)] and supplied by the Animal Research and Service Centre (ARASC), Health Campus, USM Kelantan, Malaysia. Rats' blood was collected and stored in heparin blood tubes before being centrifuged to separate the plasma. Then, the rat plasma was stored at -80 °C within 8 hours of collection.

The fresh-frozen rat plasma was allowed to thaw naturally on the bench at room temperature for approximately 45-60 minutes. It was then vortexed for a few seconds to ensure uniform distribution. The plasma standard was prepared in the same ratio with different volumes for each extraction method.

Spectrophotometry analysis

The spectrophotometric analysis of cyanidin-3-O-glucoside chloride and the internal standard were performed on a Cary 100 UV-visible spectrophotometer. Dilutions of aliquots of standard stock solution (100 ug/mL) of both cyanidin-3-O-glucoside chloride and internal standard were carried out with 0.1% HCL in 75% MeOH to reach the concentration range 10 ug/mL and 50 ug/mL. The wavelength of range 300 to 700 nm was selected for the quantitation of cyanidin-3-O-glucoside chloride and internal standard.

Optimization of chromatographic conditions

We followed the RRLC optimisation guideline provided by Agilent Technologies to equilibrate the column and detector with 10 column volumes of the mobile phase prior to use (1 – 5 mL) depending on column size [6]. The approximate time to equilibrate the instrument was 20 minutes to 45 minutes or until the pressure pump reading was stabilized. The column of RRLC should be equilibrated each time before use and need to be performed when run for the new solvent of different mobile phases. The pressure pump was maintained at 147 bar during the equilibration process. The effect of varying the type and percentage of organic solvents, type and concentration of buffer solutions, flow rates, column temperatures and ultraviolet wavelengths were tested.

Optimization of extraction methods

Liquid-liquid extraction (LLE) and solid-phase extraction (SPE) methods were carried out to decide which extraction method is more suitable to be used in extracting the cyanidin-3-O-glucoside chloride from rat plasma. The method which demonstrated the best extraction results of cyanidin-3-O-glucoside chloride and internal standard would be chosen for further testing.

Liquid-liquid extraction

The LLE method was performed by referring to a study conducted by Banaszewski et al. [7]. In this method, 50 µL of working cyanidin-3-O-glucoside chloride and internal standard solutions were added to the 500 µL of rat plasma. The freshly prepared plasma standard was then acidified to pH 2 with CH_2O_2 because anthocyanin is more stable at low pH and then extracted with 1.5 mL of ACN. The sample was then centrifuged at 10,000 rpm for 15 minutes at a temperature of 4 °C. After that, they were re-extracted with 1.5 mL MeOH. The extracts were then pooled and the supernatants were collected. Then, the supernatants underwent an evaporation process in the pre-heated water bath at 35 °C, in vacuo using a vacuum pump. Next, they were reconstituted in 250 µL of mobile phase and centrifuged at 10,000 rpm for 30 minutes at 4 °C. Lastly, the samples were transferred to the amber vials and immediately analyzed by RRLC. We also

compared different extraction solvents to extract the anthocyanin from plasma such as diethyl ether, ethyl acetate and MTBE using the same procedure.

Solid-phase extraction

The SPE method was carried out by referring to a study conducted by Harada et al. [8]. The cartridge was firstly conditioned, by washing with 1 to 2 mL of MeOH and then equilibrated with the same volume of 0.1% TFA aqueous solution. The plasma standards were prepared by mixing 200 µL of cyanidin and internal standard working solutions of selected concentrations into 2 mL of the thawed plasma, followed by vortexing the solution for 5 seconds. Then, the plasma standard was subsequently mixed with 2 mL of 0.1% TFA aqueous solution and 100 µL of 20% sulfosalicylic acid aqueous solution. After that, it was vortex-mixed and centrifuged at 4000 x g for 20 minutes at 4 °C. The supernatant then was further treated in the conditioned and equilibrated Sep-Pak C18 cartridge. Next, the cartridge was rinsed with 2 mL of 0.1% TFA solution and subsequently purged with air. The dried cartridge was then eluted with 2 mL of MeOH and evaporated to dryness using a vacuum pump at a temperature below 40 °C (35 - 37°C). The resultant dry residue then was dissolved in 50 µL of 0.1% TFA aqueous solution. Afterwards, it was centrifuged at 6000 rpm for 15 minutes at 10 °C using an Ultrafree®-MC centrifugal filter (Merck, Germany). Lastly, the solution was subjected to RRLC for analysis.

Results and Discussion

Spectrophotometry analysis

The UV absorbances of cyanidin-3-O-glucoside chloride and cyanidin-3,5-O-diglucoside chloride were measured using a Cary 100 UV-visible spectrophotometer (Varian, California, USA). Spectrophotometry analysis of both cyanidin-3-O-glucoside chloride and cyanidin-3,5-O-diglucoside chloride showed that the maximum absorption was 524 nm, as shown in Figure 1. Thus, UV absorbance was used throughout the study.

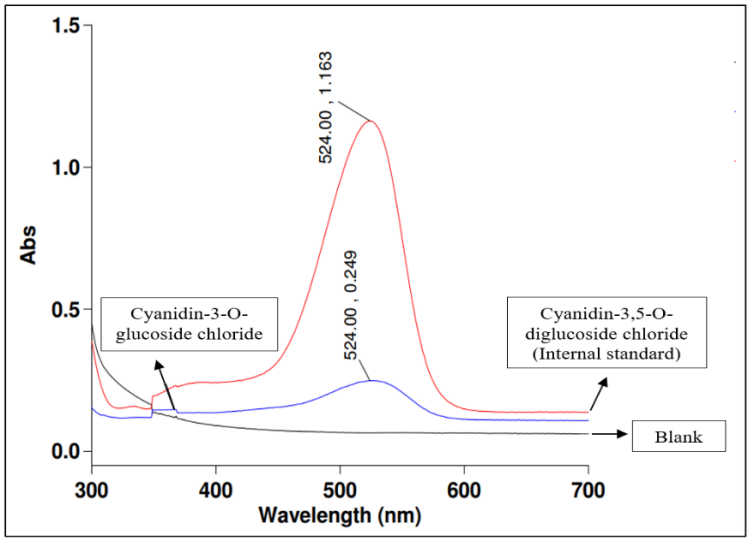


Figure 1. Spectrophotometry of the blank sample, cyanidin-3-O-glucoside chloride and cyanidin-3,5-O-diglucoside chloride (internal standard)

Absorption spectroscopy, especially UV-Vis spectroscopy, has been extensively utilized to identify anthocyanins and has revealed a lot about the structural properties and identification of these molecules [9]. From the results, the absorption peak of both cyanidin-O-glucoside chloride and the internal standard emerged at a wavelength of 524 nm. Using UV-Vis spectroscopy, absorption peaks emerged at

wavelengths of 266 nm and 530 nm, indicating that the extract contains anthocyanin compounds [10]. UV-Vis spectrophotometer demonstrated that absorption at an absorption maxima (λ_{max}) 536 nm was the specification of anthocyanins [11]. A typical UV-Vis spectrum of anthocyanin exhibits two basic absorbance clusters [9]. The first one is at 260–280 nm (UV area) and the second at 490–550 nm (VIS region) (visible region), in which the λ_{max} in the visible range is typically measured at 510–520 nm. The typical absorption bands of anthocyanins are in the 490 to 550 nm region of the visible spectra [12].

Optimization of chromatographic conditions: Type and concentration buffer solutions

Three different buffer solutions were investigated: 5% CH_2O_2 aqueous solution, 1% H_3PO_4 aqueous solution, and 0.1% TFA aqueous solution with acetonitrile (ACN) as the organic solvent. Each of the solvents was prepared with different concentrations according to the manufacturer's datasheet, as well as based on respective previous studies [8, 13]. The column temperature, mobile phase flow rate, and wavelength signal were kept constant. Among the three buffer solutions, the mobile phase of 0.1% TFA aqueous solution and ACN showed faster retention time and good peak shapes, with the least peak tailing. Thus, this combination of solvents was selected.

One of the factors that affects the retention of substances in RRLC is the mobile phase composition [14]. Buffers are usually used in mobile phases to hold and adjust the pH constant. The pH of the mobile phase is kept constant because it is always freshly prepared before RRLC analysis. The acid is used to improve the chromatographic peak shape and to provide a source of protons in reversed-phase LC/MS [15]. In this method, we also utilized isocratic elution, as it offers greater simplicity, lower cost, simpler instrumentation, and no need for column re-equilibration between consecutive injections [16].

The percentage of organic solvents

We investigated three ratios of TFA:ACN: 90%:10%, 85%:15%, and 81%:19%. The column temperature, wavelength signal, and mobile phase flow rate were kept constant. The ratio combination was determined based on the previous literature on anthocyanins [8]. Among the three ratios tested, only the 81%:19% composition showed the presence of peaks. The chromatograms of the other two ratios did not generate any peaks, possibly due to differences in the percentage of ACN used. The higher the percentage of acetonitrile, the faster the retention time for anthocyanins. Hence, the 81%:19% TFA:CAN combination was chosen because it also exhibited a faster retention time and good peak shapes.

Optimization of type of organic solvents

The selection of proper organic solvents is also important for retaining substances in RRLC. The two organic solvents tested, ACN and MeOH, are the most commonly used solvents in RRLC. We tested ACN and MeOH in combination with a 0.1% TFA aqueous solution. The column temperature, mobile phase flow rate, wavelength signal, and percentage of organic solvent in the mobile phase were kept constant.

The results showed that using ACN as an organic solvent generated peaks in the chromatogram, while there was no peak when MeOH was used. This could be due to the elution strength of the organic solvents. ACN has a higher elution strength than MeOH [17]. Thus, at the same percentage of organic solvent in the mobile phase, which was 19% for ACN and MeOH, we observed shorter retention times for the analytes with ACN than with MeOH. ACN has a lower viscosity than MeOH [18]. Hence, with increasing column temperature, the pressure also tends to decrease as the viscosity of the solvent decreases. ACN is also often used because of its low UV cut-off wavelength, which is lower than that of MeOH (190 nm and 205 nm for ACN and MeOH, respectively) [19]. Thus, ACN was chosen for further investigation, as the chromatogram showed peaks of cyanidin-3-O-glucoside chloride and an internal standard .

Optimization of flow rates

Another chromatographic parameter that affects chromatographic separation is the flow rate. Three different mobile phase flow rates 0.5, 0.8, and 1.0 ml/min were investigated. The percentage of organic

solvent in the mobile phase, column temperature, and injection volume were kept constant. An increase in the flow rate will decrease the retention factor, thereby resulting in rapid analysis [20]. A flow rate of 0.5 mL/min was chosen, as it displayed a good retention time of about 4 min, good area counts, and good peak shape. Although the peaks at other flow rates were generated at a shorter retention time, they were not chosen, as the increase in the flow rate caused a reduction in the peak area. Increased flow rates may shorten retention time, but they may contribute to band broadening and a decrease in the column's efficiency [20].

Optimization of column temperatures

One of the important chromatographic conditions is column temperature, as it is an important variable in LC separation [21]. The column temperature was optimized at three different temperatures: 30, 35, and 40°C. The percentage of organic solvent in the mobile phase, wavelength signal, and mobile phase flow rate were kept constant. The column temperature of 30°C was chosen because it gave the best peak area ratio, as recommended by the manufacturer.

Higher column temperatures can affect column pressure due to their effect on lowering mobile phase viscosities. Thus, a desirable lower systemic pressure will be produced. This, in return, allows a lower linear velocity for the chromatographic system and thus produces a sharper peak [22]. In this study, although column temperatures of 35 and 40°C generated shorter retention times, the column temperature of 30°C was selected because it also gave fast retention time and better peak shape without compromising the peak area. Further, a lower column temperature is preferable to sustaining the stability of cyanidin, as a higher temperature would result in a faster degradation rate of anthocyanins [23]. High temperatures could also be detrimental to the column's packing when used over a prolonged time [22].

Final chromatographic conditions

We performed the detection of cyanidin-3-O-glucoside chloride and internal standard cyanidin-3,5-O-diglucoside chloride at 525 nm with the ratio of mobile phase at 81:19 (0.1% TFA:ACN) (v/v). The mobile phase flow rate was set at 0.5 ml/min. The column temperature was set at 30°C. Using the column chromatographic conditions described above, the average retention times for cyanidin-3-O-glucoside chloride and cyanidin-3,5-O-diglucoside chloride were 4.4 min and 3.2 min, respectively , with a total run time of 10 min and a stop time of 5 min (Figure 2).

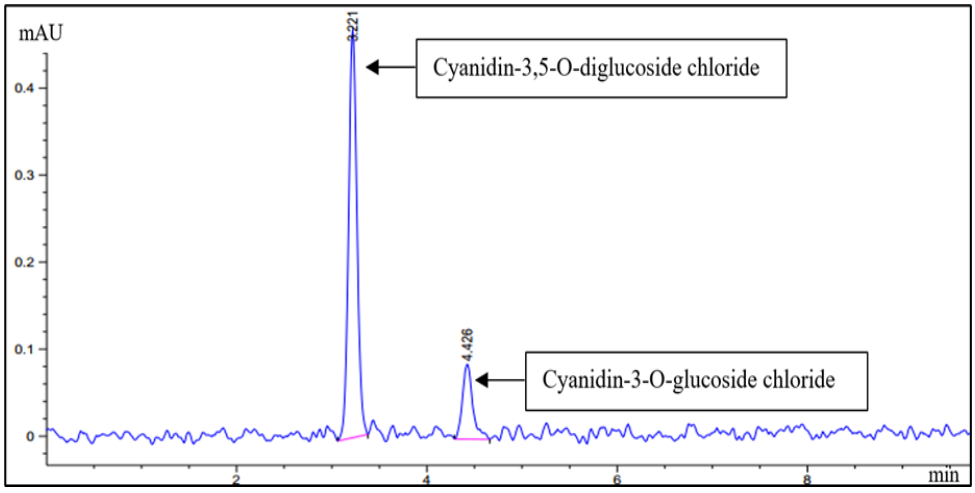


Figure 2. Chromatograms of standard solutions of cyanidin-3-O-glucoside chloride (3.221 min) and the internal standard, cyanidin-3,5-O-diglucoside chloride (4.426 min)

Optimization of liquid-liquid extraction method

The optimized chromatographic condition was applied for the analysis of plasma samples using the LLE method.

Effect of using different extracting solvents

The percentage recoveries of compounds extracted using different solvents were calculated (Table 1). The acetonitrile was chosen as the extracting solvent because both the percentage recoveries of analyte and internal standard were higher than those of the other solvents. The internal standard was used in this test to aid in quantification of analytes (anthocyanin) and improve the accuracy and precision of the method. Internal standard is used to compare the peak area of target analytes to the peak area of internal standard to obtain the peak area ratio.

Table 1. Percentage recoveries of cyanidin-3-O-glucoside chloride and cyanidin-3,5-O-diglucoside chloride by liquid-liquid extraction method when different extracting solvents were used

Solvent	Recovery for cyanidin-3-O-glucoside chloride (%)	Recovery for cyanidin-3,5-O-diglucoside chloride (%)
Acetonitrile (ACN)	72.85	119.05
Diethyl ether (Et_2O)	No peak seen	No peak seen
Ethyl acetate (EtAc)	66.72	38.85
Methyl tert-butyl ether (MTBE)	110.46	44.85

Optimization of solid-phase extraction method

The optimized chromatographic conditions were also applied for the analysis of the plasma samples using SPE.

Selection of final extraction method

The chromatograms of cyanidin-3-O-glucoside chloride for both the LLE and SPE methods were analyzed at concentrations of 500 ng/mL and 1000 ng/mL respectively. The recovery percentage of cyanidin-3-O-glucoside chloride from LLE was slightly better than that of SPE (72.85% and 68.36%, respectively). However, the chromatogram generated from the SPE method demonstrated better peak shapes for cyanidin-3-O-glucoside chloride and the internal standard compared to the chromatogram of the LLE method. In addition, the chromatogram of the SPE method showed less peak tailing compared to the LLE method. The chromatogram of the SPE method also exhibited similar retention times for cyanidin-O-glucoside chloride and internal standard prior to extraction. Hence, we chose SPE as the final extraction method, as it yielded more favorable results than LLE in the extraction cyanidin-O-glucoside chloride in rat plasma based on the results of RRLC analysis (Figure 3).

Extraction is a critical step in sample preparation, as the presence of endogenous impurities in biological fluids might cause interference in anthocyanin analysis. SPE and LLE are among the extraction methods used for anthocyanins, with increasing selectivity or specificity and improved recoveries and reproducibility [24]. In this experiment, we performed both methods to determine the most suitable extraction method for cyanidin-3-O-glucoside chloride.

LLE offers an advantage as an extraction method, in that the technique is relatively cheaper than SPE. However, this method requires costly and hazardous organic solvents, which are undesirable for health and disposal reasons [25]. LLE also requires a lengthy analysis period, which can give rise to the possible degradation of anthocyanins. By contrast, SPE techniques can overcome many of the problems associated with LLE, such as incomplete phase

separations, less-than-quantitative recoveries, and the use and disposal of large and expensive quantities of organic solvents [25]. The only drawback of the SPE compared to the LLE technique is that the cost of the equipment required for SPE is higher than for LLE. Another advantage of SPE is that this technique can be used not only in preparing liquid samples and extracting semi-volatile or non-volatile analytes but also for solids that are pre-extracted into solvents [25].

From our results, although the percentage recoveries of anthocyanin from the LLE method were slightly better than those from the SPE method, we also considered other factors. The chromatographic peak shapes obtained with the SPE method were better than those obtained with LLE. An optimum chromatographic peak shape is important to ensure more accurate quantitation of analytes. Abnormal peak shapes, such as peak tailing, generate imprecise results. The chromatograms of SPE displayed lesser peak tailing than those of LLE. Peak tailing is one of the common chromatographic peak shape distortions [26], which can occur for several reasons, including the purity of the packing material, a quality that can influence the peak shape [27]. Contaminants in the material can enhance secondary interactions, which lead to peak tailing. Thus, using an extraction method that employs a sample cleanup procedure will offer better results [26]. Here, the SPE method involved a filtration step that used an Ultrafree-MC 0.45 µm filter unit before RRLC analysis. Therefore, given its chromatogram results and advantages compared to LLE, the SPE method was adopted as the extraction method in this study.

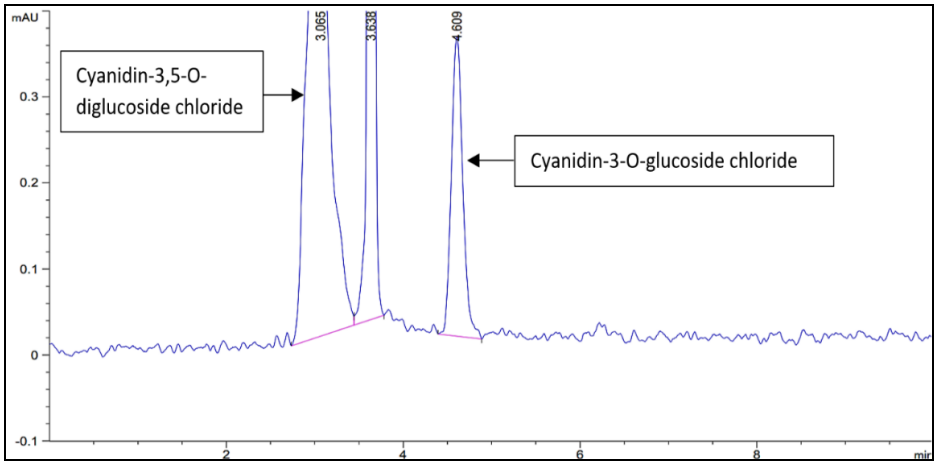


Figure 3. Chromatogram of cyanidin-3-O-glucoside chloride (4.609 min) and internal standard, cyanidin-3,5-O-diglucoside chloride (3.065 min) at concentration 1000 ng/mL following SPE method

Conclusion

We successfully determined cyanidin-3-O-glucoside chloride in rat plasma using RRLC analysis. The spectrophotometry analysis showed that the maximal absorbance of the compound was in the absorption range reported in the previous literature. The optimization of chromatographic conditions demonstrated that the mobile phase composition of 0.1% TFA aqueous solution and ACN in the ratio of 81:19%, respectively, with a flow rate of 0.5 ml/min, at 30°C column temperature and detection wavelength of 525 nm, were suitable for RRLC analysis of cyanidin-3-O-glucoside chloride. SPE was selected as the final extraction method for cyanidin-3-O-glucoside chloride and its internal standard.

Acknowledgement

The research was financially supported by the Ministry of Agriculture's Herbal Research Grant

Scheme (HRGS) (project: NH1015S020; 304.PPSK.6150169.K123).

References

1. Wallace, T. C. and Giusti, M. M. (2015). Anthocyanins. *Advances in Nutrition*, 6(5): 619-622.
2. Passeri, V., Koes, R. and Quattrocchio, F. (2016). New challenges for the design of high value plant products: stabilization of anthocyanins in plant vacuoles. *Front Plant Science*, 7: 1-9.
3. Riaz, G. and Chopra, R. (2018). A review on phytochemistry and therapeutic uses of *Hibiscus sabdariffa L*. *Biomedicine & Pharmacotherapy*, 102: 575-586.
4. Rubinskiene, M., Jasutiene, I., Venskutonis, P. R. and Viskelis, P. (2005). HPLC determination of the composition and stability of blackcurrant anthocyanins. *Journal of Chromatographic Science*, 43(9): 478-482.
5. Hapsari, B. W., Manikharda and Setyaningsih, W. (2021). Methodologies in the analysis of phenolic compounds in roselle (*Hibiscus sabdariffa L.*): Composition, biological activity, and beneficial effects on human health. *Horticulturae*, 7(2): 1-36.
6. Angelika, G.-H., Frank, M., & Gotenfels, C. (2009). Agilent 1200 series rapid resolution LC and rapid resolution LC/MS optimization guide. Access from https://www.agilent.com/cs/library/usermanuals/public/1200SeriesRRLC-Optimize Guide_ebook.pdf. [Access online 11 July 2021].
7. Banaszewski, K., Park, E., Edirisinghe, I., Cappozzo, J. C. and Burton-Freeman, B. M. (2013). A pilot study to investigate bioavailability of strawberry anthocyanins and characterize postprandial plasma polyphenols absorption patterns by Q-TOF LC/MS in humans. *Journal of Berry Research*, 3(2): 113-126.
8. Harada, K., Kano, M., Takayanagi, T., Yamakawa, O. and Ishikawa, F. (2004). Absorption of acylated anthocyanins in rats and humans after ingesting an extract of *Ipomoea batatas* purple sweet potato tuber. *Bioscience, Biotechnology and Biochemistry*, 68(7): 1500-1507.
9. Saha, S., Singh, J., Paul, A., Sarkar, R., Khan, Z. and Banerjee, K. (2021). Anthocyanin profiling using UV-Vis spectroscopy and liquid chromatography mass spectrometry. *Journal of AOAC International*, 103 (1): 23-39.
10. Dwilistiani, D., Darwis, D. and Santoni, A. (2015). Characterization of cyanidin 3-(6-acetylglucoside)-5-(3"-coumaryl-6"- malonylglucoside) compound from cinnamon bud leaves (*Cinnamomum burmanni* (Ness & T. Ness) Blume) by HPLC-DAD-ESI-MS. *Journal of Chemical and Pharmaceutical Research*, 7 (47): 519-523.
11. Nuryanti, S., Matsjeh, S., Anwar, C. and Raharjo, T. J. (2012). Isolation anthocyanin from roselle petals (*Hibiscus sabdariffa L*) and the effect of light on the stability. *Indonesian Journal of Chemistry*, 12(2): 167-171.
12. Prior, R. L. and Wu, X. (2012). Analysis methods of anthocyanins. In Z. Xu & L. R. Howard (Eds.), *Analysis of Antioxidant-Rich Phytochemicals*, John Wiley & Sons, New Jersey: pp. 149-180.
13. Durst, R. W. and Wrolstad, R. E. (2005). Separation and characterization of anthocyanins by HPLC. In *Current Protocols in Food Analytical Chemistry*, John Wiley & Sons, New Jersey: pp. 33-45.
14. Deineka, V. I., Deineka, L. A. and Saenko, I. I. (2015). Regularities of anthocyanins retention in RP HPLC for "water–acetonitrile–phosphoric acid" mobile phases. *Journal of Analytical Methods in Chemistry*, 2015 (2015): 1-6.
15. Guzzetta, A. (2001). Reverse phase HPLC basics for LC/MS. Access from http:// www.ionsource.com/tutorial/chromatography/ rphplc.htm. [Access online 18 July 2021].
16. Ukić, Š., Rogošić, M., Novak, M., Šimović, E., Tišler, V. and Bolanča, T. (2013). Optimization of IC separation based on isocratic-to-gradient retention modeling in combination with sequential searching or evolutionary algorithm. *Journal of Analytical Methods in Chemistry*, 2013 (1): 1-11.
17. Gilar, M., Jaworski, A. and McDonald, T. S. (2014). Solvent selectivity and strength in reversed-phase liquid chromatography separation of peptides. *Journal of Chromatography A*, 1337(1): 140-146.

18. Chua, Y. A., Abdullah, W. Z., Yusof, Z. and Gan, S. H. (2019). Validation of HPLC and liquid-liquid extraction methods for warfarin detection in human plasma and its application to a pharmacokinetics study. *ASM Science Journal*, 12(2019): 1-10.
19. Yabré, M., Ferey, L., Somé, I. T. and Gaudin, K. (2018). Greening reversed-phase liquid chromatography methods using alternative solvents for pharmaceutical analysis. *Molecules : A Journal of Synthetic Chemistry and Natural Product Chemistry*, 23(5): 1065-1089.
20. Afsah-Hejri, L., Jinap, S., Arzandeh, S. and Mirhosseini, H. (2011). Optimization of HPLC conditions for quantitative analysis of aflatoxins in contaminated peanut. *Food Control*, 22(3–4): 381-388.
21. Dolan, J. W. (2002). The importance of temperature. *LC GC Europe*, 20(6): 524-530.
22. Chua, Y. A., Abdullah, W. Z. and Gan, S. H. (2012). Development of a high-performance liquid chromatography method for warfarin detection in human plasma. *Turkish Journal of Medical Sciences*, 42 (5): 930-941.
23. Liu, Y., Liu, Y., Tao, C., Liu, M., Pan, Y. and Lv, Z. (2018). Effect of temperature and pH on stability of anthocyanin obtained from blueberry. *Journal of Food Measurement and Characterization*, 12(3): 1744- 1753.
24. Martín, J., Navas, M. J., Jiménez-Moreno, A. M. and Asuero, A. G. (2017). Anthocyanin pigments: Importance, sample preparation and extraction. In M. Soto-Hernandez, M. Palma-Tenango and M. R. Garcia-Mateos (Eds.), *Phenolic Compounds - Natural Sources, Importance and Applications*, Intech Open, London: pp. 117-152.
25. Garcia-Salas, P., Morales-Soto, A., Segura-Carretero, A. and Fernández-Gutiérrez, A. (2010). Phenolic-Compound-extraction systems for fruit and vegetable samples. *Molecules*, 15(12): 8813-8826.
26. Crawford Scientific. (2017). Peak tailing in HPLC. Access from https://www.crawfordscientific.com/chromatography-blog/post/peak-tailing-in-hplc. [Access online 19 July 2021].
27. Denoulet, B. (2020). The perfect peak shape: Five solutions to peak tailing problems. Access from https://www.barts-blog.net/the-perfect-peak-shape-five-solutions-to-peak-tailing-problems/.[Access online 19 July 2021].

Malaysian Journal of Analytical Sciences (MJAS)
Published by Malaysian Analytical Sciences Society

CHEMICAL CHARACTERISATION OF BIOCHAR FROM OIL PALM FROND FOR PALM OIL MILL SECONDARY EFFLUENT TREATMENT

Analisis Sifat Kimia Biochar Daripada Pelepah Kelapa Sawit Untuk Rawatan Air Sisa Sekunder Kilang Pemprosesan Kelapa Sawit

Nadia Razali and Nurhanim Zulaikha Kamarulzaman*

Section of Environmental and Polymer Engineering Technology,
Malaysian Institute of Chemical and Bioengineering Technology (MICET,
Universiti Kuala Limpur, 78000 Alor Gajah, Melaka, Malaysia

**Corresponding author: nurhanim.kamarulzaman@s.unikl.edu.my*

Received: 15 September 2021; Accepted: 3 February 2022; Published: 28 April 2022

Abstract

The oil palm frond (OPF) biomass contains chemical characteristics, which makes it a potential alternative adsorbent in wastewater treatment applications. In this study, the OPF sample was produced as biochar by using a top-lit updraft (TLUD) gasifier. The maximum temperature of this process was 750ºC and it yielded 20% w/w of biochar. The Brunauer–Emmett–Teller (BET) surface area for the OPF biochar was 248.08 m^2/g with an average pore size of 4.3 nm and categorised as mesoporous adsorbent. The OPF biochar had a high carbon content of more than 70%, which was desirable for the alternative adsorbent. It was discovered that the aromatic ring and aliphatic functional group was detected in the biochar based on the Fourier Transform Infrared (FTIR) analysis which was commonly found in biochar produced at temperatures above 500°C. Based on the result obtained from the adsorption test, the OPT biochar could provide a maximum removal of 64.65% of COD, with an initial COD of 3960 mg/L. This study has found that the OPF biochar is suitable to be used as an alternative adsorbent for wastewater applications.

Keywords: biochar, oil palm frond, adsorption, palm oil mill effluent

Abstrak

Pelepah kelapa sawit (OPF) mempunyai sifat kimia yang berpotensi sebagai bahan penjerap alternatif dalam aplikasi rawatan air sisa. Dalam kajian ini, sampel OPF digunakan sebagai bahan mentah untuk menghasilkan biochar dengan menggunakan *gasifier top-lit updraft* (TLUD). Suhu maksimum process ini adalah 750ºC dan 20% *w/w* biochar telah dihasilkan. Luas permukaan Brunauer–Emmett–Teller (BET) untuk biochar OPF adalah 248.08 m^2/g dengan ukuran purata saiz pori 4.3 nm dan diketagorikan sebagai penjerap mesoporos. Biochar OPF mempunyai kandungan karbon yang tinggi melebihi daripada 70%, yang merupakan ciri-ciri yang dikehendaki untuk penjerap alternatif. Berdasarkan analisis spektroskopi inframerah transformasi Fourier (FTIR), kumpulan organik alifatik dan cincin aromatik dikesan didalam bahan ini. Kumpulan organik ini biasanya ditemui dalam biochar yang dihasilkan pada suhu melebihi 500°C. Berdasarkan hasil kajian yang diperolehi daripada ujian penjerapan, biochar OPT mampu memberikan menyingkirkan 64.65% COD daripada air sisa kilang kelapa sawit yang mempunyai COD awal sebanyak 3650 mg/L. Kajian ini mendapati bahawa biochar OPF wajar digunakan sebagai penjerap altenatif untuk rawatan sisa pepejal.

Kata kunci: biochar, pelepah kelapa sawit, penjerapan, sisa efluen kilang kelapa sawit

Introduction

Crude palm oil (CPO), palm kernel oil (PKO), and palm kernel cake (PKC) are the primary interests in palm oil industry. In 2020, there were 5.87 million hectares of palm oil plantations in Malaysia. The production of crude palm oil (CPO) in the same year was 19.14 million tonnes [1]. A total of 80 million tonnes of biomass are generated annually in Malaysia, with the majority from the palm oil industry [2, 3]. Biomass generated by the palm oil industry are mainly produced from the harvesting of fresh fruit bunch (FFB) at the plantation, and the processing of FFB in mills. These biomasses include mesocarp fibre (MF), empty fruit bunch (EFB), palm shell (PS), oil palm fronds (OPF), oil palm leaflet (OPL), oil palm trunk (OPT), and palm mill effluent (POME). The presence of wastes creates a disposal problem, which requires the implementation of a robust management strategy.

POME is one of the wastes generated from the palm oil industry. POME is brownish wastewater generated from the processing of FFB; it has a high amount of organic contaminants and requires proper treatment before it can be discharged into any water body. Anaerobic and aerobic digestion treatments are the common treatments used to remove the organic contaminants in the wastewater, but both treatments are not sufficient to comply with the standard set by the Department of Environment (DOE) Malaysia, as shown in Table 1 [4]. The final discharge of POME from the biological treatment or palm oil secondary effluent (POMSE) usually remains high in chemical oxygen demand (COD) and biochemical oxygen demand (BOD), with an average of 800 mg/L and 200 mg/L respectively. Furthermore, it is also dark in colour, which is higher than the standard set by the DOE [5]. This is due to the presence of lignin, carotene, humic acids and other organic compounds that are recalcitrant to biological treatments [6]. Another treatment that should be implemented to polish the biologically treated POME, ensuring that it complies with environmental legislation, is the adsorption technique, a technology that can be applied to biologically treat POME as a polishing method. The key benefits of this technology are that it is easy to design, and it has a minimal initial investment. Natural resources such as biomass, silica, and zeolite can be used to make the adsorbent [7, 8].

Table 1. Environmental Quality (Industrial Effluent) Regulation 2009

Parameter	Unit	Standard	
		A	B
COD	mg/L	80	200
BOD_5	mg/L	20	50
Colour	ADMI	100	200
TSS	mg/L	50	100

The biomass from this industry has the potentials to be converted into valuable products. The potentials include using OPT as building materials, OPF as the precursor for ethanol production, OPS as an aggregate in lightweight cement, MF as a growing media for tissue culture, POME as a substrate for methane generation, and OPL and EFB as mulch in plantation [3, 9]. Some biomass, such as PKS and EFB, have critical functions as fuel sources for mills and to maintain soil conditions [10, 11]. However, there is still a significant amount of biomass that are unutilised, and measures should be taken to improve its functionalities. In recent years, there is an increasing amount of literature on the conversion of palm oil biomass into biochar. Biochar is a carbon-rich material produced from the thermochemical process. The pyrolysis process is the common thermochemical process utilised to produce biochar. However, scarce attention has been paid to gasification as a thermochemical process to produce biochar.

Gasification is defined as a thermochemical process to convert carbonaceous feedstock into syngas (a mixture of hydrogen, carbon dioxide, and methane), tar, and

biochar at high temperatures (≥ 500°C) in oxygen-deficit conditions [12, 13]. So far, this method has only been applied for the generation of energy [14]. Most of the literature on the gasification process only focus on the optimisation of process parameters and the quality of gas produced from this process [15, 16]. The solid product of gasification, i.e., biochar, receives less attention. In general, biochar is known as an effective carbon sequestration strategy due to its recalcitrant properties. Therefore, biochar produced from the gasification process might have the same potentials as biochar produced from other thermochemical processes, i.e., fast pyrolysis, and hydrothermal process. The characteristics of biochar are dependent on the properties of biomass, the conditions of the process, and the type of reactor used for the thermochemical process.

Most literature on biochar are more focused on carbon sequestration and soil conditioner. The potential of biochar is not only limited to carbon sequestration and soil application, but it also has the potential to be used in other applications especially in water application. However, there are limited studies done on the application of biochar in water and wastewater treatment. In a study on the application of biochar as an alternative adsorbent, Huggins et al. [17] found that biochar from the gasification process could reduce phosphate, COD, and nitrogen ammonia in brewery wastewater. Kearn et al. [18] proved that biochar produced from the gasification process could remove trace organic contaminants from drinking water. Similarly, Kaetzl et al. [19] found that biochar was found to reduce both organic and inorganic contaminants from a municipal wastewater. Overall, many studies highlighted that biochar was effective in eliminating organic and inorganic pollutants from water and wastewater [16-23] This could be due to the high porosity of biochar or the presence of other chemical species that aids the adsorption process [12, 25].

The utilisation of biochar produced from the gasification process in wastewater application is an interesting topic to be studied. This paper will focus on biochar produced from gasification by using top-lit updraft (TLUD) gasifier and oil palm frond (OPF), which were used as the raw materials in this study. The characteristics of the biochar and its performance to treat biologically treated POME will be evaluated.

Materials and Methods

Source and preparation of biomass

The raw material used in this study was oil palm frond (OPF). The OPF was obtained from a local plantation located in Tampin, Negeri Sembilan. Figure 1 shows the structure of OPF. The structure of the OPF consists of the top section, middle section, and basal. Only the basal part of the frond was used in this study as it was easier for real-life application. The OPF was chopped using a mechanical chopper with the particle size ranging from 1–4 mm and rinsed with tap water to remove any impurities. The OPF was then dried in a vacuum oven for 24 hours to avoid rotting.

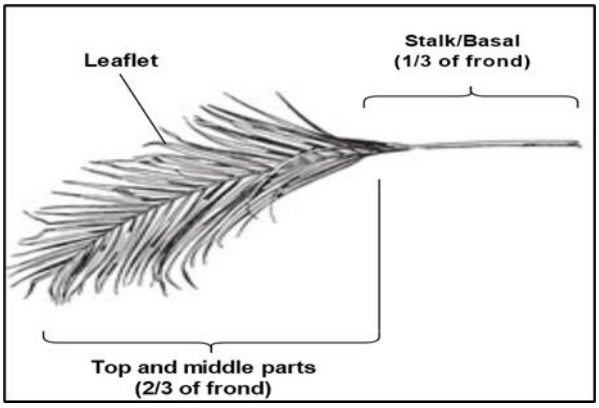


Figure 1. Structure of OPF

Gasification of oil palm frond

The top-lit updraft gasifier (TLUD) was used to produce OPF biochar, as illustrated in Figure 2. Before the gasification process, the raw OPF was sieved to ensure that the particle of the OPF was uniformed. The uniformity of the size of feedstock was vital to ensure that the feedstock was fully charred, and to achieve a good airflow through the reactor body. The dried OPF was weighed before it was filled into the gasifier. The dried OPF was then placed into the gasifier about ¾ of the reactor body (approximately 600 g of dried OPF). A small piece of paper or wood was used as rekindling. The kindling was lighted, and it would burn strongly.

The fan of the gasifier was turned on to provide air to assist the gasification process. The temperature of the process was monitored for quality control and assurance. The dried OPF was burnt from top to bottom until a bluish flame was formed. The blue flame was an indicator that the OPF was fully gasifier. The fan was then turned off and the gasifier was allowed to cool. The OPF biochar was then sprayed with some water to remove any ash and fine. The biochar was cooled until it was cool enough for handling.

The OPF biochar produced was weighted and the percentage of yield of the biochar was calculated using Equation 1.

$$\%\text{Yield} = \frac{W_1 - W_2}{W_1} \times 100 \quad (1)$$

where W_1 is a weight of biomass and W_2 is a weight of biochar.

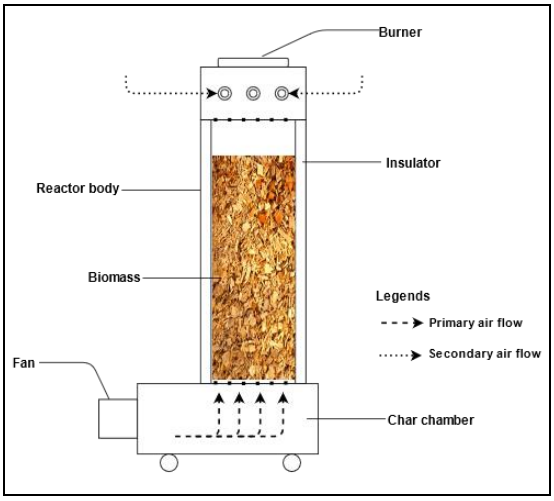


Figure 2. TLUD gasifier

Characterisation of OPF

pH of biochar

pH is an indicator of the acidity and basicity of the biochar. The pH of biochar can be a good indicator to understand the oxygen complexes and functional groups on the surface of biochar. The OPF biochar was soaked in the deionised water (ratio of 1:25% wt./v solid to water ratio) for one hour with agitation [26]. The pH of the slurry was then tested with a pH meter (Mettler Toledo).

Proximate analysis and ultimate analysis of raw material and biochar

There were three components of proximate analysis which were moisture content, ash content, and volatile matter. The proximate analysis of raw OPF was done using National Renewable Energy Laboratory (NREL) method for all three analyses. On the other hand, the proximate analysis of biochar was done using the ASTM method (ASTM D2867-09, ASTM D5832-98, and ASTM D2866-04).

The ultimate analysis of both raw OPF and OPF biochar was carried out using a CHNS analyser. This analysis was done to quantify the content of carbon, hydrogen, nitrogen, and sulphur in both samples. All four elements were analysed simultaneously.

Scanning electron microscopy analysis and Brunauer–Emmett–Teller surface area analysis

Scanning electron microscopy (SEM) analysis of raw OPF and OPF biochar was carried out using Scanning Electron Microscope SEM (FEI Quanta 450). BET analysis was used to determine the surface area of biochar in this study. The BET analysis was conducted using a BET Surface analyser (Micromeritic) with N_2 gas adsorption at 77 K in relative pressure from 0.05 to 0.2. The samples were degassed for 2 hours at 200 ºC.

Fourier transform infrared analysis

FTIR analysis was done to determine the functional groups of the biochar. This analysis is vital to gain an understanding of the chemical characteristic of biochar and the adsorption mechanism of biochar. Before conducting the FTIR analysis, the OPF biochar was ground into powder and dried in an oven overnight to remove any residual moisture in the biochar. The sample was then mixed with potassium bromide (KBr) with a ratio of 1:2000 (1 part sample: 2000-part KBr). The mixture was then pressed into a pellet form by using a hydraulic presser. The pellet was finally analysed using the FTIR analyser (Nicolet 5700, FTIR, Thermo Fisher Scientific, and Waltham, MA, USA).

Adsorption test

The batch adsorption test was conducted to determine the applicability of OPF biochar as an adsorbent for wastewater treatment. The adsorbate used in this study was palm oil mill secondary effluent (POMSE). POMSE is the effluent generated after the biological treatment of POME. It is high in chemical oxygen demand. (COD). Method No.8006 was used to measure the COD of POMSE before and after treatment. The measurement of COD was conducted using the APHA potassium dichromate method. The measurement was carried out in HACH COD high range vials by using DR900 spectrophotometer and HACH COD reactor (Model: 45600).

Next, the batch adsorption test was conducted using 100 ml of POMSE. The OPF biochar was added to the conical flask containing 100 ml of POMSE. The mixture of the OPF biochar and POMSE was then shaken for 24 hours at 150 rpm using an incubator shaker. The samples were withdrawn at a fixed time interval. The adsorbent was separated from samples by filtration. The filtrates were then analysed for COD. The number of COD adsorbed per unit mass of the adsorbent (qe) was calculated according to the following Equation 2 and the adsorption yield was calculated by using Equation 3.

$$q_e=(C_0-C)\times\frac{V}{m} \quad (2)$$

$$\%\text{COD removal} = \frac{C_0-C}{C_0}\times 100 \quad (3)$$

where, q_e is the number of COD adsorbed per gram of adsorbent (mg/g); C_0 and C are the initial and final COD concentrations (mg/L), respectively; V is the volume of POMSE (L); and m is the mass of biochar (g).

Results and Discussion

Gasification of OPF

The main products of the gasification process usually consist of syngas, bio-oil, and biochar. The quantity biochar product derived from the gasification process is usually lower compared to other types of thermochemical processes such as pyrolysis, hydrothermal and torrefaction. For this study, the yield of OPF biochar was 20%. The same yield of biochar was obtained by Nsamba et al.[26] using the same gasification system. The biochar obtained from the gasification process is usually lower than other thermochemical processes i.e., fast pyrolysis because of the partial oxidation of carbon into carbon monoxide and other flue gasses [27, 28]. Other than partial oxidation of carbon in the biomass, the release of volatile matter from the polymeric backbone of carbonaceous feedstock also contributed to the yield of the biochar. Apart from that, the temperature of the gasification that is usually ≥ 500 °C is good to produce high porosity biochar [29, 30]. In this study, the range of maximum temperature of the gasification process for OPF biochar was 750 °C by controlling the speed of the fan that improved the air supply. Studies on the effect of temperature on the properties of biochar in past studies found that the surface area of the biochar was increased as the temperature of the thermochemical increased [31, 32]. Increasing the surface area of the biochar contributed to better performance of biochar as an adsorbent as it can remove more pollutants from wastewater. This trend can be seen in earlier studies using orange peel biochar for removal of cadmium from aqueous solution; maximum removal of cadmium was obtained when the orange peel biochar was produced at a temperature of 700 °C, which was then used as an adsorbent [33]. Other studies showed a similar trend in the removal of chromium from aqueous solution [34, 35]. These findings suggest that gasification biochar has the potential to be used as an adsorbent.

Characterisation of OPF biochar

pH of biochar

The pH for OPF biochar in this study is alkaline (pH=8) which is similar to the literature where most biochar is best produced at temperatures higher than 400 °C [29, 30, 36, 37]. The alkaline pH of OPT biochar is correlated to the presence of basic functional groups on the surface of biochar, as shown in Figure 4. Generally, raw biomass has a high number of acidic functional groups. Figure 4 illustrates the presence of acidic functional group in the raw OPF that corresponded to the carboxylic acid functional group. However, the band of the functional group diminished

after the gasification process. The reduction of the acidic functional groups was aligned to the reduction of volatile matter of biomass as the temperature of the process increased.

Apart from the reduction of acidic functional groups, the alkalinity of OPF biochar was contributed by the formation of the aromatic and aliphatic functional group. The peak of the functional groups can be seen at the band of 1200–1600 cm^{-1}. The same findings can be seen in a study conducted by Usman et al. [38] on the production of biochar from the date palm waste. Other studies had established that the pH of biochar increased when the temperature of thermochemical increased [38-40]. The presence of alkaline metal contributed to the alkalinity of biochar [12, 42].

Proximate analysis and ultimate analysis

Table 2 shows the proximate analysis and ultimate analysis for both raw material and biochar. Generally, the value of each component changed after the gasification process. Table 2 shows that the volatile matter decreased sharply from 86.49% in raw OPF to 15.57%. This was due to the conversion of volatile matter into more condensed aromatic structures and/or may burn out which might help in the development of the porous structure of biochar [43]. The raw OPF had high volatile matter (86.49%), which was a good indicator that the biomass is suitable to be used as a feedstock for the thermochemical process. The percentage of volatile matter obtained in this study is closed to those obtained from other studies [11, 31, 11, 31].

Ash content is a vital indicator to determine the suitability of the biomass as feedstock for the thermochemical process. The ash content of the raw OPF in this study is 0.92%, which aligned with previous studies [11, 31, 44]. The ash content of the biochar is higher than the raw OPF due to the accumulation of inorganic material in the biomass after the volatilisation of carbon, oxygen, and hydrogen [45]. The fixed carbon content is significantly increased from 12.59% in raw OPF to 68.34% in OPF biochar. The ash content of OPF biochar is 13 times greater than raw OPF; similar trend can be observed in other studies [28, 36, 38, 46].

Table 2 provides the Carbon (C), Hydrogen (H), Nitrogen (N), Sulphur (S) and Oxygen (O) content of both raw OPF and OPF biochar. The C and N content of the OPF biochar was significantly higher compared to its original biomass. On the other hand, the O and H content of the biochar is lower than its original biomass. This may be due to the breakdown of carbon and functional groups of the biomass during the gasification which led to the formation of aromatic functional groups [47]. The O/C and H/C ratio of the biochar is found to be lower than the biomass, which indicated the formation of aromatic functional and reduction of hydrophilicity of the biochar [47], [48].

Table 2. Proximate analysis and ultimate analysis

Proximate Analysis (%w/w)	**Raw OPF**	**OPF Biochar**
Moisture content	9.95	3.71
Ash content	0.92	12.38
Volatile matter	86.49	15.57
Fixed carbon	12.59	68.34
Ultimate analysis (%w/w)		
Carbon (C)	41.87	76.97

Table 3 (cont'd). Proximate analysis and ultimate analysis

Proximate Analysis (%w/w)	**Raw OPF**	**OPF Biochar**
Hydrogen (H)	6.00	2.50
Nitrogen (N)	0.33	0.76
Sulphur (S)	0.70	0.39
Oxygen (O)	51.10	19.38
O/C ratio	0.92	0.19
H/C ratio	1.72	0.39
pH	-	8
Porous characteristics		
BET surface area, m^2/g	-	248.08
Pore Volume, cm^2/g	-	0.23
Average pore size, nm	-	4.3

Scanning electron microscopy analysis and Brunauer–Emmett–Teller surface area analysis

SEM analysis was performed to analyse the morphology of raw biomass and biochar. Figure 3 shows the morphology of raw material and biochar. Figure 3 demonstrates a significant change in the surface of OPF and OPL before and after the gasification process. In Figure 3 (a), the surface of OPF is very rough and less pore is visible whereas in Figure 3 (b) the surface of the OPF biochar is smoother than raw OPF. More pores were visible for OPF biochar. The formation of pores in the biochar are caused by the release of volatile matter, decomposition of cellulose and hemicellulose, which resulted in the complex structure of biochar with multiple diameters of pore [47, 49].

BET and BJH analysis were done on the OPF biochar to analyse its surface area and characteristics of pores. Table 2 provides the BET surface area, pore volume and average pore size of OPF biochar. The BET surface area of OPT biochar was 248.08 m^2/g with an average pore size of 4.3 nm. The OPF biochar can be classified in the mesopore category as the average pore size of OPF biochar fell within the range of 2–50 nm. When compared to other studies, the surface area and pore volume of OPF biochar found to be higher than other studies which, on average pores, are lower than 150 m^2/g [44, 50, 51]. Compared to commercial activated carbon (AC), the AC has a larger surface area and smaller average pore size which leads to high affinity to low molecular weight compound but is less efficient in the removal of high molecular weight compound. The high molecular weight compounds are commonly present in wastewater after biological treatments as refractory pollutants. A study conducted by An et al. [52] proved that a mesoporous lignite adsorbent was effective in removing refractory pollutants from biologically treated coal gasification wastewater. The result of this study is aligned to the findings from other studies using the same type of wastewater, similar to the research by Gai et al. [53] and Xu et al. [54]. The OPF biochar appears to have the potential to be used as alternative adsorbent to improve the characteristics of biologically treated wastewater.

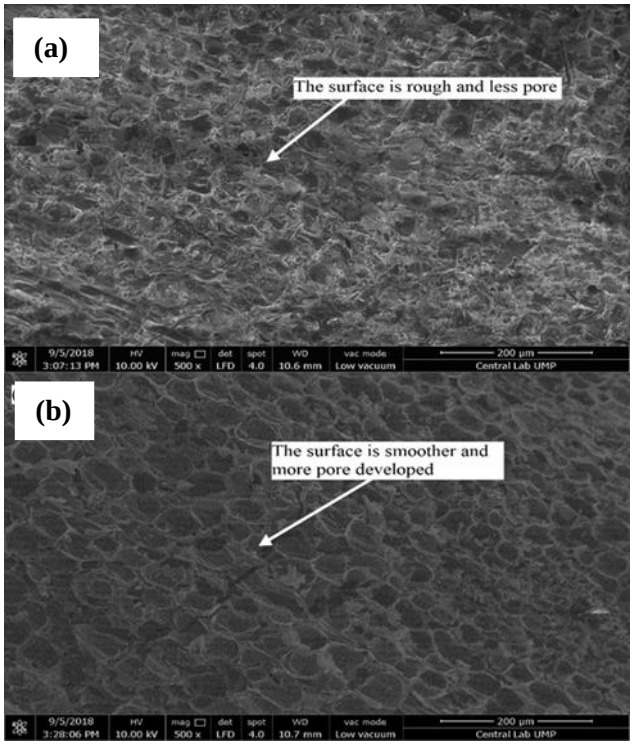


Figure 3. (a) raw OPF (b) OPF biochar

Fourier transform infrared analysis

FTIR analysis was done to determine the functional group of the biochar's. Figure 4 compares the FTIR spectra of both raw materials and biochar produced in the gasification process. Overall, the spectra between raw OPF and OPF biochar is different. In Figure 4, the peak between 3200-3600 cm^{-1} corresponded to the –OH group with stretch vibration and carboxylic acid functional group. The presence of broad –OH in the raw OPF which attributed to the moisture content and hydroxyl functional group found in lignin, hemicellulose, and cellulose [54], [55]. The intensity of the peak decreased after the gasification process. The reduction of the intensity of the peak indicated that the removal of moisture and volatile matter contributed to the porous structure of the biochar [39], [56].

There is a peak within the band of 2800-3000 cm^{-1} which corresponded to the saturated aliphatic C–H functional group. This functional group is associated with the methylene functional group in cellulose [54, 56]. The peak within the band of 1700-1800 cm^{-1} represents the C=O acetyl group associated with the ester functional group in hemicellulose [55, 57]. This band diminished after the gasification process due to the integration of cellulose and hemicellulose. There are some peaks within the band of 1600-1700 cm^{-1} in both biomass and biochar. These bands correlated with the carboxylic acid functional group. However, the peaks diminished after the gasification process is aligned with the alkaline pH of the biochar.

The intensity of the peak within the band of 1500-1600 cm^{-1} is abated. The peaks within this band correlated to the aromatic hydrocarbon functional group of lignin

C-C stretching vibration in the aromatic ring [55, 56]. The peaks within the band of 1000-1500 cm^{-1} corresponded to the aliphatic and aromatic functional groups. The intensity of the peaks was reduced in the OPF biochar. This might be due to the partial decomposition of lignin in the raw biomass. The presence of aromatic aliphatic functional groups in the biochar will provide the active sites to assist the adsorption process and contributes to the hydrophobicity of the biochar. This can be seen in the study conducted by Liu et al. [57] on the role of functional groups in the adsorption of bisphenol A (BPA) on activated carbon. The study revealed that the modified AC provided 10% higher removal of BPA compared to commercial AC. This was due to the decrease of acidic functional groups in the modified AC and stronger hydrophobicity than commercial AC which leads to better BPA adsorption and more water molecule exchange, which aligns with the findings by Sidik et al. [58] on the OPL adsorbent with enhanced hydrophobicity.

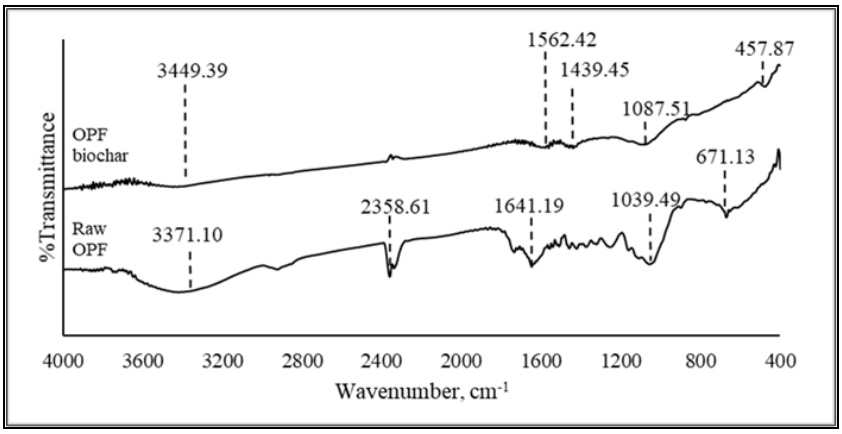


Figure 4. FTIR spectra of raw OPF and OPF biochar

Adsorption test

The wastewater used in this study was palm oil secondary effluent (POMSE) obtained from a local palm mill in Selangor. The POMSE is the effluent generated from the biological treatment of raw POME and it was still high in COD. This is a common problem faced by palm oil mill operators [59]. The high COD in the POMSE was contributed by the presence of macromolecules, such as fulvic acid and humic acid [60]. The initial concentration of COD is 3960 mg/L and the experiment was conducted in batch modes. Figure 5 and Figure 6 show the reduction of COD from POMSE by using OPF biochar as an adsorbent. As shown in Figure 5, there is a significant reduction of COD from POMSE. After 30 minutes of contact time with OPF biochar, the COD of POMSE is reduced from 3960 mg/L to 2100 mg/L. The COD of POMSE continuously reduced as the contact time with the OPF biochar increased.

From Figure 6, the maximum removal of COD is 64%, in which it is achieved after 24 hours of contact time. When compared to other studies, the biochar produced in this study can provide better removal of pollutants than other alternative adsorbent which on average can only provide 55% removal of pollutants [44]. Other than that, the performance of the OPF biochar in this study was comparable to the coconut-based activated carbon produced in the study conducted by Parveen et al. [61]. After 24 hours of contact time, the removal of COD from POMSE is constant. This is due to the unavailability of active adsorption sites on the OPF biochar [62], [63]. By comparing to the research conducted by Razali et al. [64] using oil palm trunk (OPT) biochar, the OPF biochar provided better removal of COD than OPT biochar. This might be due to the differences in characteristics of the biochar. In comparison, the surface area of the OPF biochar is

higher than the OPT biochar. Other than the surface area, the OPF biochar has a higher pore volume compared to OPT biochar which is in line with the surface area of the biochar.

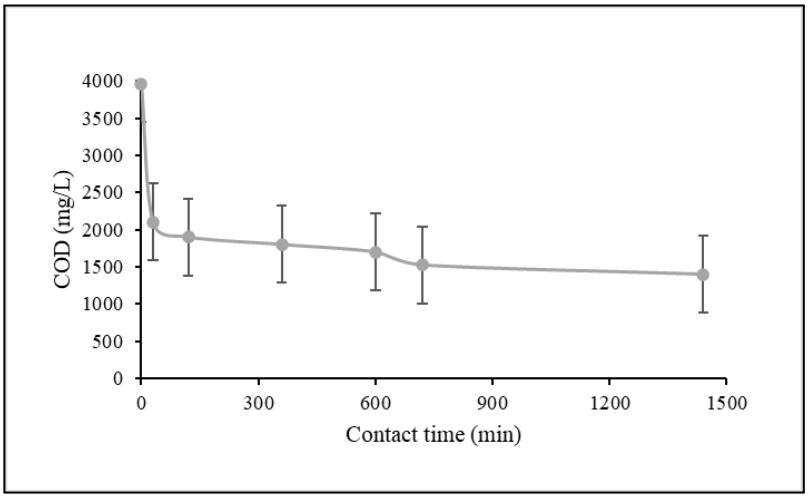


Figure 5. COD removal POMSE

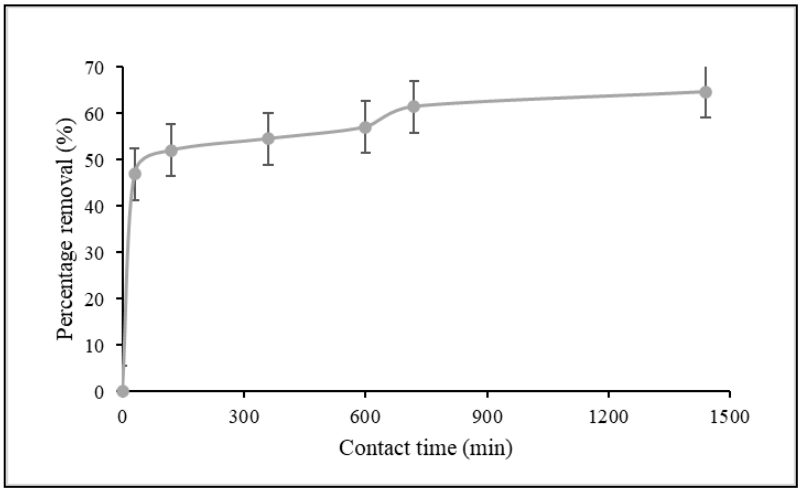


Figure 6. Percentage removal of COD from POMSE

Conclusion

The gasification process proves that other valuable and functional products (biochar) can be produced by using OPF, which is currently used as mulching and fertiliser. This study discovered that gasification biochar that was specifically produced from raw OPF has the potential to be used as adsorbents in wastewater application treatment. The biochar from the gasification process can be used as soil conditioning and in wastewater treatment as an adsorbent due to its unique characteristic, low moisture content, low ash content and high fixed carbon content. The OPF biochar produced from this study has a large surface area and high total pore volume which can be potentially used as alternative adsorbent in the adsorption process. The high carbon content and the

presence of carbonyl compound and aromatic rings in the biochar provide active sites that aid the adsorption process. It was proven that OPF biochar can provide more than 50% removal of pollutants from the wastewater tested in this study compared to other biochar produced in other studies.

A further study should be done on the application of biochar as an adsorbent for wastewater application. Further research on the factors and the kinetic of adsorption using this gasification biochar should be conducted to gain more understanding on the mechanism involved in the adsorption process by using gasification biochar.

Acknowledgement

This research is supported by Short Term Grant - STRG (Grant no. STRG/NBR/STR16034) from Universiti Kuala Lumpur.

References

1. Ghulam Kadir, A. P. (2020). Overview of the malaysian oil palm industry 2020. In Malaysian Palm Oil Board website. Access from https://www.mpob.gov. [Accessed Jun. 14, 2021].
2. Tan, Z. Y. (2020). Green technology: Time to Tap Biomass. The Edge Markets. https://www.theedgemarkets.com/article/green-technology-time-tap-biomass [Accessed Jun. 14, 2021].
3. Zwart, R. (2013). Sustainability in the cultivation of oil palm –issues and prospects for the industry. *Journal of Oil Palm and the Environment*, 4(5): 41-62.
4. Malaysian Department of Environment (2009). Environmental quality (industrial effluent) regulations 2009. In Environmental Quality Act 1974 (pp. 4010–4059). Access from https://www.doe.gov.my/portalv1/wpcontent/uploads/2015/01/Environmental_Quality_Industrial_Effluent_Regulations_2009_-_P.U.A_ 434-2009.pdf.
5. Zainuri, N. Z., Hairom, N. H. H., Sidik, D. A. B., Desa, A. L., Misdan, N., Yusof, N. and Mohammad, A. W. (2018). Palm oil mill secondary effluent (POMSE) treatment via photocatalysis process in presence of ZnO-PEG nanoparticles. *Journal of Water Process Engineering*, 26:10-16.
6. Zahrim, A. Y., Nasimah, A. and Hilal, N. (2014). Pollutants analysis during conventional palm oil mill effluent (POME) ponding system and decolourisation of anaerobically treated POME via calcium lactate-polyacrylamide. *Journal of Water Process Engineering*, 2014: 159-165.
7. Ngeno, E. C., Orata, F., Baraza, L. D., Shikuku, V. O. and Kimosop, S. J. (2016). Adsorption of caffeine and ciprofloxacin onto pyrolitically derived water hyacinth biochar: isothermal, kinetic and thermodynamic studies. *Journal of Chemistry and Chemical Engineering*, 10(4): 185-194.
8. Sia, Y. Y., Tan, I. A. W. and Abdullah, M. O. (2017). Adsorption of colour, TSS and COD from palm oil mill effluent (POME) using acid-washed coconut shell activated carbon: Kinetic and mechanism studies. *MATEC Web of Conferences*, 87:1-7.
9. Chin, M. J., Poh, P. E., Tey, B. T., Chan, E. S. and Chin, K. L. (2013). Biogas from palm oil mill effluent (POME): Opportunities and challenges from Malaysia's perspective. *Renewable and Sustainable Energy Reviews*, 26: 717-726.
10. Mukherjee, I. and Sovacool, B. K. (2014). Palm oil-based biofuels and sustainability in Southeast Asia: A review of Indonesia, Malaysia, And Thailand. *Renewable and Sustainable Energy Reviews*, 37: 1-12.
11. Umar, M. S., Jennings, P. and Urmee, T. (2013). Strengthening the palm oil biomass renewable energy industry in Malaysia. *Renewable Energy*, 60; 107-115.
12. Hansen, V., Müller-Stöver, D., Ahrenfeldt, J., Holm, J. K., Henriksen, U. B. and Hauggaard-Nielsen, H. (2015). Gasification biochar as a valuable by-product for carbon sequestration and soil amendment. *Biomass and Bioenergy*, 72: 300-308.
13. Shen, Y. (2015). Chars as carbonaceous adsorbents/catalysts for tar elimination during biomass pyrolysis or gasification. *Renewable and Sustainable Energy Reviews*, 43: 281-295.

14. Hosseini, S. E., Wahid, M. A. and Ganjehkaviri, A. (2015). An overview of renewable hydrogen production from thermochemical process of oil palm solid waste in Malaysia. *Energy Conversion and Management*, 94: 415-429.
15. Anukam, A., Mamphweli, S., Reddy, P., Meyer, E. and Okoh, O. (2016). Pre-processing of sugarcane bagasse for gasification in a downdraft biomass gasifier system: A comprehensive review. *Renewable and Sustainable Energy Reviews*, 66: 775-801.
16. Couto, N., Rouboa, A., Silva, V., Monteiro, E. and Bouziane, K. (2013). Influence of the biomass gasification processes on the final composition of syngas. *Energy Procedia*, 36:596-606.
17. Huggins, T. M., Haeger, A., Biffinger, J. C. and Ren, Z. J. (2016). Granular biochar compared with activated carbon for wastewater treatment and resource recovery. *Water Research*, 94: 225-232
18. Kearns, J., Anh, M. T. L., Reents, N. W., Shimabuku, K. K., Mahoney, R. B., Summers, R. S. and Knappe, D. R. U. (2014). Trace organic contaminant removal from drinking water using local char. *37th WEDC International Conference*, 2014: pp. 1-6.
19. Kaetzl, K., Lübken, M., Uzun, G., Gehring, T., Nettmann, E., Stenchly, K. and Wichern, M. (2019). On-farm wastewater treatment using biochar from local agro residues reduces pathogens from irrigation water for safer food production in developing countries. *Science of the Total Environment*, 682: 601-610.
20. Thompson, K. A., Shimabuku, K. K., Kearns, J. P., Knappe, D. R. U., Summers, R. S. and Cook, S. M. (2016). Environmental comparison of biochar and activated carbon for tertiary wastewater treatment. *Environmental Science & Technology*, 50(20): 11253-11262.
21. Zhang, F., Wang, X., Yin, D., Peng, B., Tan, C., Liu, Y., Tan, X. and Wu, S. (2015). Efficiency and mechanisms of Cd removal from aqueous solution by biochar derived from water hyacinth (*Eichornia crassipes*). *Journal of Environmental Management*, 153: 68-73.
22. Han, R., Wang, Y., Zhoa, X., Wang, Y., Xie, F., Cheng, J. and Tang, Mi. (2009). Adsorption of methylene blue by phoenix tree leaf powder in a fixed-bed column: Experiments and prediction of breakthrough curves. *Desalination*, 245(1–3): 284-297.
23. Enaime, G., Baçaoui, A., Yaacoubi, A. and Lübken, M. (2020). Biochar for wastewater treatment—conversion technologies and applications. *Applied Sciences*, 10: 1-29.
24. Wang, X., Guo, Z., Hu, Z. and Zhang, J. (2020). Recent advances in biochar application for water and wastewater treatment: A review. *PeerJ*, 8: 1-34.
25. Oliveira, F. R., Patel, A. K., Jaisi, D. P., Adhikari, S., Lu, H. and Khanal, S. K. (2017). Environmental application of biochar: Current status and perspectives. *Bioresource Technology*, 246: 110-122.
26. Nsamba, H. K., Hale, S. E., Cornelissen, G. and Bachmann, R. T. (2014). Improved gasification of rice husks for optimized biochar production in a top lit updraft gasifier. *Journal of Sustainable Bioenergy Systems*, 4: 225-242.
27. James, R. A. M., Yuan, W. and Boyette, M. D. (2016). The effect of biomass physical properties on top-lit updraft gasification of woodchips. *Energies*, 9(4): 1-13.
28. You, S., Ok, Y. S., Chen, S. S., Tsang, D. C. W., Kwon, E. E., Lee, J. and Wang, C. H. (2017). A critical review on sustainable biochar system through gasification: energy and environmental applications. *Bioresource Technology*, 246: 242-253.
29. Mohan, D., Sarswat, A., Sik, Y. and Pittman, C. U. (2014). Organic and inorganic contaminants removal from water with biochar, a renewable, low cost and sustainable adsorbent – a critical review. *Bioresource Technology*, 160: 191-202.
30. Ahmad, M., Rajapaksha, A. U., Lim, J. E., Zhang, M., Bolan, N., Mohan, D., Vithanage, M., Lee, S. S. and Sik Ok, Y. (2014). Biochar as a sorbent for contaminant management in soil and water: A review. *Chemosphere*, 99: 19-33.
31. Rahman, A. A., Abdullah, N. and Sulaiman, F. (2014). Temperature effect on the characterization of pyrolysis products from oil palm fronds. *Advances in Energy Engineering*, 2: 14-21.

32. Sun, Y., Gao, B., Yao, Y., Fang, J., Zhang, M., Zhou, Y., Chen, H. and Yang, L. (2014). Effects of feedstock type, production method, and pyrolysis temperature on biochar and hydrochar properties. *Chemical Engineering Journal*, 240: 574-578.
33. Tran, H. and Yuan, C. (2016). Effect of pyrolyisis temperatures and times in adsorption of cadmium onto orange peel derived biochar. *Waste Management & Research*, 34(2): 129-138.
34. Tan, X., Liu, Y., Zeng, G., Wang, X., Hu, X. and Gu, Y. (2015). Application of biochar for the removal of pollutants from aqueous solutions. *Chemosphere*, 125: 70-85.
35. Mojiri, A., Ziyang, L., Tajuddin, R. M., Farraji, H. and Alifar, N. (2016). Co-treatment of landfill leachate and municipal wastewater using the ZELIAC/Zeolite constructed wetland system. *Journal of Environmental Management*, 166: 124-130.
36. Lam, S. S., Liew, R. K., Cheng, C. K., Rasit, N., Ooi, C. K., Ma, N. L., Ng, J. H., Lam, W. H., Chong, C. T. and Chase, H. A. (2018). Pyrolysis production of fruit peel biochar for potential use in treatment of palm oil mill effluent. *Journal of Environmental Management*, 213: 400-408.
37. Angın, D. (2012). Effect of pyrolysis temperature and heating rate on biochar obtained from pyrolysis of safflower seed press cake. *Bioresource Technology*, 128: 593–597.
38. Usman, A. R. A., Abduljabbar, A., Vithanage, M., Ok, Y. S., Ahmad, M., Ahmad, M., Elfaki, J., Abdulazeem, S. S., & Al-Wabel, M. I. (2015). Biochar Production from Date Palm Waste: Charring Temperature Induced Changes in Composition and Surface Chemistry. *Journal of Analytical and Applied Pyrolysis*, 115: 392-400.
39. Mahmood, W. M. F. W., Ariffin, M. A., Harun, Z., Ishak, N. A. I., Ghani, J. A. and Rahman, M. N. A. (2014). Characterisation and potential use of biochar from gasified oil palm wastes. *Journal of Engineering Science and Technology*, 45-54.
40. Suárez-Hernández, L., Ardila-A, A. N. and Barrera-Zapata, R. (2017). Morphological And physicochemical characterization of biochar produced by gasification of selected forestry species. *Revista Facultad de Ingeniería*, 26(46): 123-130.
41. Feng, D., Zhao, Y., Zhang, Y., Sun, S. and Gao, J. (2018). Steam gasification of sawdust biochar influenced by chemical speciation of alkali and alkaline earth metallic species. *Energies*, 11(1): 205.
42. Shen, Y. (2015). Chars as carbonaceous adsorbents/catalysts for tar elimination during biomass pyrolysis or gasification. *Renewable and Sustainable Energy Reviews*, 43: 281-295.
43. Park, J., Hung, I., Gan, Z., Rojas, O. J., Lim, K. H. and Park, S. (2013). Activated carbon from biochar: influence of its physicochemical properties on the sorption characteristics of phenanthrene. *Bioresource Technology*, 149: 383-389.
44. Liew, R. K., Nam, W. L., Chong, M. Y., Phang, X. Y., Su, M. H., Yek, P. N. Y., Ma, N. L., Cheng, C. K., Chong, C. T. and Lam, S. S. (2017). Oil palm waste: An abundant and promising feedstock for microwave pyrolysis conversion into good quality biochar with potential multi-applications. *Process Safety and Environmental Protection*, 2017: 1-13.
45. Parveen, S., Kaman, D., Ai, I., Tan, W., Lik, L. and Lim, P. (2016). Palm oil mill effluent treatment using coconut shell – based activated carbon: adsorption equilibrium and isotherm. *MATEC Conference ENCON*, 2016: 1-6.
46. Majedi, Y., Alhilali, E., al Nehayan, M., Rashed, A., Ali, S. S., Al Rawashdeh, N., Thiemann, T. and Soliman, A. (2014). Treatment of dye-loaded wastewater with activated carbon from date palm leaf wastes. *World Sustainability Forum*, 2014: 1-12.
47. Abdulsalam, M., Man, H. C., Yunos, K. F., Abidin, Z. Z., Idris, A. I. and Hamzah, M. H. (2020). Augmented yeast-extract and diary-waste for enhancing bio-decolourization of palm oil mill effluent using activated sludge. *Journal of Water Process Engineering*, 36: 1-12.
48. Razali, N. and Kamarulzaman, N. Z. (2020). Chemical characterizations of biochar from palm oil trunk for palm oil mill effluent (POME) treatment. *Materials Today: Proceedings*, 31(1): 191-197.

49. Domingues, R. R., Trugilho, P. F., Silva, C. A., de Melo, I. C. N. A., Melo, L. C. A., Magriotis, Z. M. and Sánchez-Monedero, M. A. (2017). Properties of biochar derived from wood and high-nutrient biomasses with the aim of agronomic and environmental benefits. *PLoS ONE*, 12(5): 1-19.
50. Klasson, K. T. (2017). Biochar characterization and a method for estimating biochar quality from proximate analysis results. *Biomass and Bioenergy*, 96: 50-58.
51. Wijitkosum, S. and Jiwnok, P. (2019). Elemental composition of biochar obtained from agricultural waste for soil amendment and carbon sequestration. *Applied Sciences*, 9(19): 3980.
52. Wei, L., Huang, Y., Huang, L., Li, Y., Huang, Q., Xu, G., Müller, K., Wang, H., Ok, Y. S. and Liu, Z. (2020). The ratio of H/C is a useful parameter to predict adsorption of the herbicide metolachlor to biochars. *Environmental Research*, 184: 109324.
53. Griffith, S. M., Banowetz, G. M. and Gady, D. (2013). Chemical characterization of chars developed from thermochemical treatment of Kentucky bluegrass seed screenings. *Chemosphere*, 92(10): 1275-1279.
54. Ibrahim, I., Hassan, M. A., Abd-Aziz, S., Shirai, Y., Andou, Y., Othman, M. R., Ali, A. A. M. and Zakaria, M. R. (2017). Reduction of residual pollutants from biologically treated palm oil mill effluent final discharge by steam activated bioadsorbent from oil palm biomass. *Journal of Cleaner Production*, 141: 122-127.
55. Cibati, A., Foereid, B., Bissessur, A. and Hapca, S. (2017). Assessment of miscanthus × giganteus derived biochar as copper and zinc adsorbent: study of the effect of pyrolysis temperature, pH and hydrogen peroxide modification. *Journal of Cleaner Production*, 162: 1285-1296.
56. An, H., Liu, Z., Cao, X., Teng, J., Miao, W., Liu, J., Li, R. and Li, P. (2017). Mesoporous lignite-coke as an effective adsorbent for coal gasification wastewater treatment. *Environmental Science: Water Research & Technology*, 3(1): 169-174.
57. Gai, H., Guo, K., Xiao, M., Zhang, N., Li, Z., Lv, Z. and Song, H. (2018). Ordered mesoporous carbons as highly efficient absorbent for coal gasification wastewater – a real case study based on the inner Mongolia autonomous coal gasification wastewater. *Chemical Engineering Journal*, 341: 471-482.
58. Xu, L., Wang, J., Zhang, X., Hou, D. and Yu, Y. (2015). Development of a novel integrated membrane system incorporated with an activated coke adsorption unit for advanced coal gasification wastewater treatment. *Colloids and Surfaces A: Physicochemical and Engineering Aspects*, 484: 99-107.
59. Lamaming, J., Hashim, R., Sulaiman, O., Peng Leh, C., Sugimoto, T. and Nordin, A. (2015). Cellulose nanocrystals isolated from oil palm trunk. *Carbohydrate Polymers*, 127: 202-208.
60. Jahi, N., Ling, S., Othaman, R. and Ramli, S. (2015). Modification of oil palm plantation wastes as oil adsorbent for palm oil mill effluent (POME). *Malaysian Journal of Analytical Sciences*, 19: 31-40.
61. Liu, G., Li, X. and Campos, L. C. (2017). Role of the functional groups in the adsorption of bisphenol a onto activated carbon: Thermal modification and mechanism. *Journal of Water Supply: Research and Technology-Aqua*, 66(2): 105-115.
62. Sidik, S. M., Jalil, A. A., Triwahyono, S., Adam, S. H., Satar, M. A. H. and Hameed, B. H. (2012). Modified oil palm leaves adsorbent with enhanced hydrophobicity for crude oil removal. *Chemical Engineering Journal*, 203: 9-18.
63. Zainal, N. Ha., Jalani, N. F., Mamat, R. and Astimar, A. A. (2017). A review on the development of palm oil mill effluent (POME) final discharge polishing treatments. *Journal of Oil Palm Research*, 29(4): 528-540.
64. Bhalla, B., Saini, M. S. and Jha, M. K. (2013). Effect of Age and Seasonal Variations on Leachate Characteristics of Municipal Solid Waste Landfill. *International Journal of Research in Engineering and Technology*, 2(8): 223-232.

Malaysian Journal of Analytical Sciences (MJAS)
Published by Malaysian Analytical Sciences Society

ADSORPTION OF METHYLENE BLUE FROM AQUEOUS SOLUTIONS BY ACTIVATED CARBON PREPARED FROM BANANA TRUNK USING ZINC CHLORIDE ACTIVATION

(Penjerapan Metilena Biru daripada Larutan Akueus oleh Karbon Teraktif yang Disediakan dari Batang Pisang secara Pengaktifan Zink Klorida)

Zaidi Ab Ghani[1]*, Muhammad Taufiq Hafizuddin R. Azemi[1], Mohd Hafiz Yaacob[1], Noor Hafizah Uyup[1], Lee Sin Ang[1], Nor Azliza Akbar[2]

[1]Faculty of Applied Science,
Universiti Teknologi MARA Cawangan Perlis, 02600 Arau Perlis, Malaysia.
[2]School of Civil Engineering, College of Engineering,
Universiti Teknologi MARA Cawangan Pulau Pinang, 13500 Permatang Pauh, Pulau Pinang, Malaysia

**Corresponding author: zaidi433@uitm.edu.my*

Received: 10 September 2021; Accepted: 18 December 2021; Published: 28 April 2022

Abstract

In this study, the banana trunk-derived activated carbon (BTAC) used was prepared via zinc chloride ($ZnCl_2$) activation. BTAC is used as an adsorbent to remove methylene blue (MB) from the aqueous solutions. The BET surface area, total pore volume and pore diameters of the BTAC were 1329.5 m^2/g, 1.16 cm^3/g and 3.8 nm, respectively. The effect of adsorbent dosage, initial concentration, contact time and solution pH were studied in batch experiments. The experimental data were analyzed by Langmuir, Freundlich, Temkin, and Dubinin-Radushkevich (D-R) adsorption isotherms model. Data analysis study via RMSE and χ^2 analyses suggested that Temkin isotherm model was the best fitted with the adsorption of MB on BTAC. The maximum monolayer adsorption of MB onto BTAC was calculated to be 217 mg/g. Kinetic parameters were evaluated based on pseudo-first-order (PFO), pseudo-second-order (PSO) and Weber–Morris intraparticle diffusion (IPD) kinetic models. The regression results showed that a PSO model is more accurately representing the adsorption kinetics. While the plot of q_t versus $t^{1/2}$ for the IPD model represented multi-linearity and proved that the adsorption processes occurred more than one step. Thermodynamics parameters were determined between temperatures of 25 to 40 °C. The $\Delta G°$ and $\Delta H°$ values were negative and the overall adsorption process was determined as spontaneous and exothermic. While the positive value of $\Delta S°$ proposed good affinity of the MB molecules toward the BTAC. The results from this study suggested that BTAC could be a viable adsorbent in managing higher concentrations of dyes from water and wastewater.

Keywords: adsorption, activated carbon, methylene blue, isotherm, kinetic

Abstrak

Dalam kajian ini, karbon teraktif daripada batang pisang (BTAC) yang digunakan telah disediakan melalui pengaktifan zink klorida ($ZnCl_2$). BTAC telah digunakan sebagai penjerap untuk menyingkirkan metilena biru (MB) daripada larutan akueus. Keluasan permukakaan BET, jumlah isipadu dan diameter liang pori bagi BTAC masing-masing adalah 1329.5 m^2/g, 1.16 cm^3/g

dan 3.8 nm. Kesan dos penjerap, kepekatan permulaan, masa kontak dan pH larutan dilakukan secara eksperimen kelompok. Data ekperimen telah dianalisa menggunakan model Langmuir, Freundlich, Temkin dan Dubinin–Radushkevich. Analisa data kajian melalui RMSE dan χ^2 mencadangkan bahawa model isoterma Temkin adalah yang paling sesuai dengan penjerapan MB pada BTAC. Penjerapan lapisan-mono maksima MB kepada BTAC dikira sebagai 217 mg/g. Parameter kinetik telah dinilai berdasarkan model kinetik pseudo-pertama (PFO), pseudo-kedua (PSO) dan resapan intrazarah (IPD) Weber–Morris. Hasil regresi menunjukkan bahawa model PSO lebih tepat mewakili kinetik penjerapan. Sementara plot q_t melawan $t^{1/2}$ untuk model IPD menunjukkan garisan linear yang pelbagai dan membuktikan bahawa proses penjerapan berlaku lebih daripada satu langkah. Parameter termodinamik telah ditentukan di antara suhu 25 hingga 40 °C. Nilai ΔG° dan ΔH° adalah negatif, maka keseluruhan proses penjerapan telah ditentukan sebagai spontan dan eksotermik. Sementara itu, nilai positif bagi ΔS° mencadangkan bahawa pertalian yang baik diantara molekul MB terhadap BTAC. Keputusan dari kajian ini mencadangkan bahawa BTAC mampu menjadi penjerap yang berkesan dalam menguruskan kepekatan pewarna yang lebih tinggi dari air dan air sisa.

Kata kunci: penjerapan, karbon teraktif, metilena biru, isoterma, kinetik

Introduction

Wastewater effluent that contains dyes is a typical and one of the major causes of environmental pollution. The presence of dyes in the industries effluent poses the most prominent problem since they are toxic and the recalcitrant nature of dyes [1]. Typical biological wastewater treatment plants cannot eliminate toxic pollutants such as dyes since they were purposely designed for organic and nutrient removal. Methylene blue (MB) is an example of dye that is commonly used in industry. MB is a heterocyclic aromatic chemical compound. Thus, MB is highly toxic, carcinogenic and its degradation process is difficult [2]. Therefore, MB containing effluent must be treated appropriately before discharge. Previously, various advanced oxidation methods have been introduced to treat dyes polluted water, such as ozonation [3], photocatalyst [4] and electrochemical treatment [5]. However, oxidation or degradation of dyes might contribute to the secondary pollutants. The other methods that have been employed include reverse osmosis [6], coagulation-flocculation [7], membrane filtration [8], ion exchange[9] and adsorption [10]. Among these methods, adsorption is a well-known and applicable method of removing dyes contaminant water. In addition, the adsorption process has emerged as a cost-effective, efficient, and environmentally friendly method of dye removal [11].

Recently, there are a variety of absorbents have been introduced to treat dyes such as bio-composite [12], nanoparticles [13], graphene oxide [14], forest wastes [15], polystyrene foam [16] agriculture waste [17]. Based on the current scenario, activated carbon (AC) is the best adsorbent to treat textile effluent. Previously, the preparation of AC by using low-cost precursor from agriculture waste such as dates stone [18], ashitaba waste [19], banana peel [20], almond and walnut shells [21] have been employed extensively as a new precursor in the production of AC. Most of the mentioned researchers claimed that abundance and continuous availability of the agriculture biomass are the key motivation of their precursor selection. In addition, the treatment and reuse of agriculture waste should be implemented efficiently to obtain its valorization and achieve sustainable waste management [22].

In Malaysia, biomass derived from agriculture such as banana plantation is gaining increasing attention. Banana widely planted in tropical country such as Malaysia, thus it is not surprising that it is the major biomass source. Instead of burning and disposing naturally as an organic fertilizer, a better way would be converting them into AC. Thus, this study used banana trunk as a precursor to prepare AC. During preparation of AC via chemical activation, the lignocellulosic precursor is treated primarily with a chemical agent, such as H_3PO_4, H_2SO_4, HNO_3, NaOH, KOH, or $ZnCl_2$. According to Lewoyehu [23], during the activation with $ZnCl_2$ the cellulosic material will be degraded, results in charring and aromatization of the carbon skeleton and creation of the pore structure. Hence,

produced AC with high surface area and good adsorption capacity.

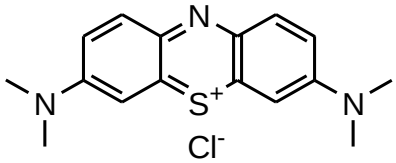
However, in order to treat water-containing dye via adsorption requires a deeper understanding especially on the effectiveness of the adsorbent towards the adsorbate. Therefore, the objective of the present work is to introduce BTAC as an adsorbent and to examine its effectiveness in removing MB from aqueous solutions. The effect of adsorbent dosage, initial concentration, contact time and solution pH were studied in batch experiments. The experimental were analyzed by Langmuir, Freundlich, Temkin, and Dubinin-Radushkevich (D-R) adsorption isotherms model. Kinetic parameters, rate constants, equilibrium adsorption capacities, and related correlation coefficients were evaluated based on pseudo-first-order (PFO), pseudo-second-order (PSO) and Weber–Morris intraparticle diffusion (IPD) kinetic models. Thermodynamics parameters such as ΔG°, ΔH°, and ΔS° have also were evaluated.

Materials and Methods

Materials

In this study, the adsorbent used was BTAC with particle size <215 um, which was obtained from our previous study [24]. The BTAC was prepared from the banana trunk and activated with $ZnCl_2$ at a temperature of 640 °C. All the chemicals used in this study were of analytical reagent grade unless otherwise stated. The adsorbate used is a cationic dye, namely methylene blue (Sigma Aldrich, Germany). The physicochemical information of BTAC and MB were shown in Table 1. MB adsorption data was used to obtain adsorption isotherms, kinetic and thermodynamic study. Stock solution of MB (1000 mg/L = 1000 ppm) was prepared by dissolving 1 g of MB into 1 L distilled water. The stock solution was further diluted with distilled water to obtain the desired concentrations of MB in the range of 75 to 125 mg/L.

Table 1. Physicochemical information of BTAC and MB[20]

Banana trunk derived activated carbon (BTAC)			
Textural properties		**Ultimate analysis (wt.% dry basis)**	
BET surface area (m^2/g)	1329.5	Carbon (wt%)	84.1
Mesopore surface area (m^2/g)	1152.6	Hydrogen (wt%)	2.1
Micropore surface area (m^2/g)	176.9	Nitrogen (wt%)	3.7
Total pore volume (cm^3/g)	1.16	Sulfur (wt%)	0.2
Pore diameter (nm)	3.83	Oxygen (wt%)	9.9
Physicochemical properties		**Proximate analysis (wt.% dry basis)**	
Bulk density (g/cm^3)	0.6	Volatile matter (wt%)	25.1
Iodine number (mg/g)	819.03	Fixed carbon (wt%)	74.7
pH_{pzc}	3.7	Ash (wt%)	0.2
Methylene blue (MB)			
 Structure formula of MB		Commercial name	Methylene blue
		Chemical name	Methylthioninium chloride
		Empirical formula	$C_{16}H_{18}ClN_3S$
		Molar mass	319.85 g/mol
		CAS number	61-73-4
		λ_{max}	664 nm

Batch adsorption study

The batch adsorption procedure was utilized to investigate the uptake of MB from aqueous solution onto BTAC. For the effect of adsorbent dosage, various dosage of BTAC ranging from 0.01 to 0.13 g was added into 250 mL Erlenmeyer flasks containing 100 mL of 150 mg/L MB concentration. The influence of initial concentration was explored using seven different concentrations from 50 to 150 mg/L MB solution. While the effect of contact time was determined from initial until equilibrium contact time is reached (5 to 360 min). The solution pH was varied from 5.0 to 8.0 with constant another adsorption parameter. The samples were then shaken at isothermal temperature (25 ±2 °C) at 125 rpm in an incubator shaker. Each experiment was conducted with two replications. Then, the samples were taken out and filtered through a 0.45 µm nylon membrane before analysis to minimize the adsorbent's interference. After that, the filtered solutions were analyzed for MB uptake analysis by UV-visible spectrophotometer at 664 nm, which is the maximum absorption peak of MB. The adsorption capacity of MB in the aqueous solution was calculated by using Eq. (1) as follows:

$$q_e = [(C_o - C_e)V] / M \quad (1)$$

where C_e (mg/L) and C_o (mg/L) respectively represent the equilibrium and initial concentration of adsorbate, adsorbent mass is denoted by M (g), and solution volume is V (L). The isotherm parameters of the Langmuir and Freundlich, Temkin and Dubinin-Radushkevich models were investigated using batch experimental adsorption data at various C_o studied. For the kinetic studies, the experiments were carried out similarly as described above. Approximately 2 mL of MB solution was withdrawn at specific time intervals using a plastic syringe. The MB concentration in the liquid phase (C_t, mg/g) was analysed as a function of contact time (t). The adsorption capacity (q_e) was calculated using Eq. (2):

$$q_t = [(C_o - C_t)V] / M \quad (2)$$

where q_t is the amount of MB adsorbed per unit weight of adsorbent at any time t (mg/g); C_o and C_t are the initial and liquid-phase concentrations of the adsorbate solution at any time t (mg/L), respectively; V is the volume of the solution (L); and M is the weight of the sorbent used (g).

The thermodynamic studies were performed similarly as adsorption equilibrium study. The adsorption temperatures were varied from 25, 30, 35 and 40 °C (±2 °C). These experiments were carried out in incubator shaker at shaking rate of 125 rpm. The BTAC dosage and MB concentration was fixed at 0.05 g and 125 mg/L, respectively. The adsorption capacity of MB in the aqueous solutions was calculated by using Eq. (1). All isotherm, kinetic and thermodynamic studies were fitted with the experimental data using their linear equations which were shown in Table 2.

Table 2. The equations of isotherm, kinetic and thermodynamic studies

Parameters	Equation		Nomenclature
Langmuir	$C_e/q_e = 1/K_L q_m + C_e/q_m$; $R_L = 1/(1 + K_L C_o)$	(3)	q_e = amount adsorbate quilibrium (mg/g) q_t = amount adsorbate retained at time (mg/g) q_m = monolayer adsorption capacity (mg/g) t = time (min) k_1 = PFO rate constant (1/min) k_2 = PSO rate constant (g/mg.min) k_{ID} = IPD rate constant (mg/g/min$^{0.5}$) C_i = thickness of the boundary layer (mg/g)
Freundlich	$\ln(q_e) = \ln(K_F) + 1/n \ln(C_e)$	(4)	
Temkin	$q_e = B \ln(K_T) + B \ln(C_e)$; $B = RT/b_T$	(5)	
Dubinin-Radushkevich	$\ln(q_e) = \ln(q_s) - \beta\varepsilon^2$; $\varepsilon = RT \ln[1 + 1/C_e]$; $E = 1/\sqrt{2\beta}$	(6)	
Pseudo first order (PFO)	$\ln(q_e - q_t) = \ln(q_e) - k_1 t$	(7)	
Pseudo second order (PSO)	$t/q_t = (1/k_2 q_e^2) + (1/q_e)t$	(8)	
Intraparticle diffusion (IPD)	$q_t = k_{ID} t^{0.5} + C_i$	(9)	
Thermodynamic	$\ln K_D = -\Delta G°/RT$; $\ln K_D = (\Delta S°/R) - (\Delta H°/RT)$; $\Delta G° = \Delta H° - T\Delta S°$	(10)	

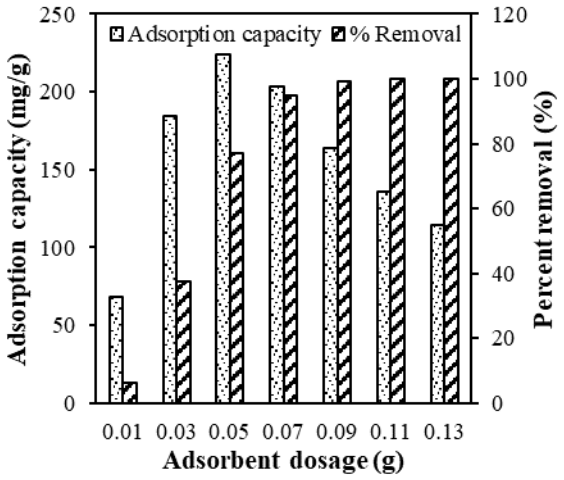
Results and Discussion

Effect of adsorption parameters on MB removal

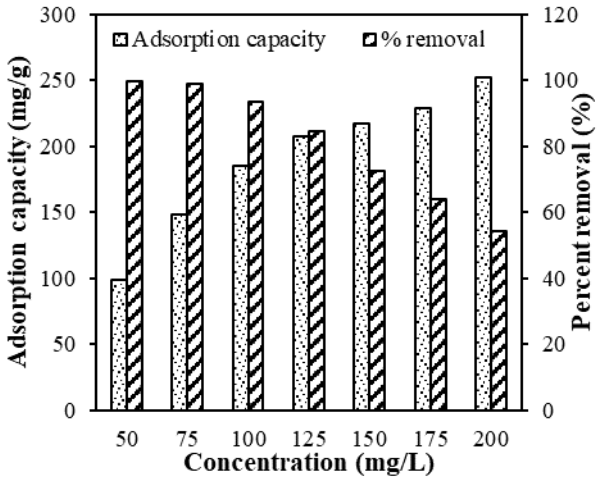
In this study, the preliminary experiments to explore the effect of several adsorption parameters were done by batch adsorption technique. For batch adsorption, the BTAC is mixed with the MB solution in an agitated vessel for specific time. The effects of adsorbent dosage, initial concentration, contact time and solution pH on adsorption efficiency were presented and described in the following subsections.

Effect of adsorbent dosage

Adsorbent dosage is an important parameter that affects the adsorption performance. This parameter is essential to observe the maximum adsorption with the minimum promising amount of adsorbent [25]. The effect of adsorbent dosage was studied by added different adsorbent dosage (0.01 to 0.13 g) into 100 mL of 150 mg/L MB concentrations under. Figure 1(a) shows the adsorption capacity and percentage removal of MB as a function of the BTAC dose. Adsorption capacity and percent removal of MB increased sharply as the BTAC dose increased from 0.01 to 0.05 g. However, an opposite trend was observed with the additional increased of BTAC dosage beyond 0.05 g. It was noticed that the adsorption capacity of MB start to reduce gradually from 224 to 115 mg/g. Similar trend reduction of adsorption capacity with additional increased in adsorbent dosage were observed by Xue, et al. [19], Muniyandi, et al. [10] and Fan, et al. [26]. While the percentage removal was further increased and reached approximately 100% and did not show any significant MB removal as the BTAC dosage beyond 0.09 g. The opposite relationship between adsorbent dosage and removal of the MB was explained by the existence of a greater number of available sorption sites on adsorbent surface as described by Saif Ur Rehman, et al. [27]. They claimed that the concentration of adsorbate is fixed against an increasing adsorbent dose. Thus, the MB per unit mass of BTAC decreased leaving a number of active sites uncovered at high dosage, subsequently leads to a low adsorption capacity. Hence, considering minimal dosage with the highest adsorption capacity, 0.05 g BTAC dosage was selected as the optimum adsorbent dosage and used for subsequent experiments to study the influence of initial concentration, contact time and solution pH.



(a)



(b)

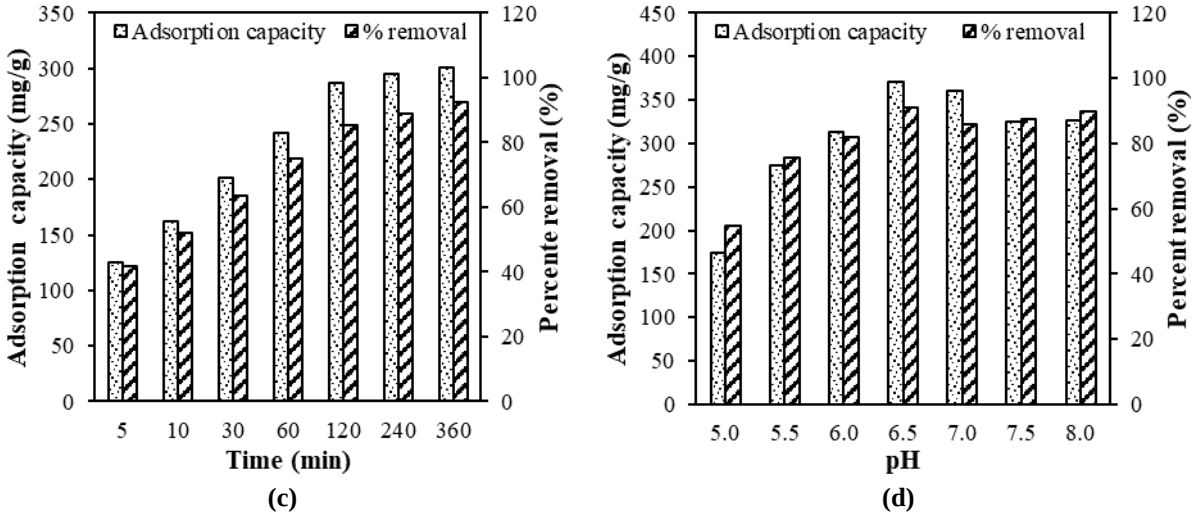


Figure 1. (a) effect of adsorbent dosage (b) effect of initial concentration, (c) effect of contact time and (d) effect of solution pH on the adsorption of MB dye

Effect of initial adsorbate concentration

Initial adsorbate concentration is another important parameter for adsorption study. Figure 1(b) shows an opposite trend of the adsorption capacity and percentage removal of MB as a function of initial MB concentration. Similar observation was reported previously for MB removal by using different type of adsorbent including modified lignocellulosic materials [28]. As per Figure 1(b), the adsorption capacity increased from 98 to 252 mg/g when the initial MB concentration increased from 50 to 200 mg/L. Higher adsorption capacity at high initial concentration is due to the generation of significant driving forces caused by a pressure gradient as explained by Benhouria et al. [29]. However, the percent MB removal gradually decreased from 99 to 54% for a similar increase in MB concentration. This observation related to the at low concentration [30]. This results clearly indicated that the adsorption process is highly dependent on the initial concentration of the solution. Based on the results, MB concentration of 125 mg/L was selected as an optimum concentration as the adsorption capacity was 207 mg/L with the percent removal of 83%, located in the middle of the graph. Thus, this initial concentration was adopted for the next experiment.

Effect of contact time

The influence of contact time (5 to 360 min) on adsorption capacity and MB percent removal is presented in Figure 1(c). Both adsorption capacity and percent removal increased as the function of contact time. When the contact time was approximately 360 min (6 h), the adsorption efficiency reached 92% with 301 mg/g adsorption capacity. It was noticed that the adsorptive removal of MB underwent two stages. During the first stage (within 60 min), the adsorption of MB increased quickly, followed by a slow adsorption stage during which adsorption capacity increased gradually. No further changed observed after 360 min which can be related to adsorption process reached the state of adsorbent–adsorbate equilibrium. This findings suggesting that high attraction existed between MB and the surface of the BTAC and the MB adsorption occurred mainly on the surface at the beginning as described by Li et al. [31]. However, with further extended the contact time, limited surface-active sites were accessible. Therefore, only a minor increase in the adsorption capacity and MB percent removal were observed and this finding mostly due to internal surface adsorption Maneerung et al. [32]. This finding suggested that significant contact time was needed for the adsorbate to diffuse into adsorption sites surface and internal pores of the adsorbent as mentioned by

Jawad et al. [33]. As no further improvement in term of adsorption capacity and MB percent removal were noticed after 360 min, therefore it was determined as an equilibrium contact time between MB and BTAC and was used as a contact time for isotherm study.

Effect of solution pH

The effect of pH on the removal of MB has been investigated. Solution pH was a key factor affecting ionic dyes (anionic or cationic) adsorption because the pH primarily influenced the surface charge on the adsorbent [34]. The adsorption experiment of MB onto BTAC was performed in 5.0 to 8.0 pH range, at controlled temperature of 30 °C for 360 min. Figure 1(d) shows the adsorption capacity and removal efficiency of MB by BTAC under different pH. It was notice that the adsorption capacity was lowest at pH 5.0 (174 mg/g) and the maximum adsorption capacity of the dye was achieved at pH 6.5 (371 mg/g). Similar trend was observed for percentage removal of MB. At the lowest pH (at pH 5.0) the MB removal efficiency was less than 60%. It showed that lower pH does not favour the uptake of cationic dye from the system and leads to electrostatic repulsion. This can be explained as dissolving MB in water results in having positively charged ions in the solution, thereby the positively charged surface of the adsorbent tends toward competing with the adsorption of the MB [35]. However, when the pH increased to 6.5, the MB removal efficiency increased up to 91% due to the decrease in electrostatic repulsion between the positively charged MB and the surface of the BTAC. While with further increase of pH to 7.0, removal efficiency reduced to 85% and no significant changes noticed as the pH increased from 7.0 to 8.0. According to Banerjee and Chattopadhyaya [36], change in pH affects the adsorptive process through the dissociation of functional groups on the adsorbent surface that tends to shift in equilibrium characteristics of the adsorption process. The present findings were supported by earlier reteaches who have reported the removal of MB onto waste carpets derived AC [34] and . Thus, the solution pH of 6.5 was selected as the optimum conditions for adsorption of MB on the surface of the investigated adsorbents.

Isotherm study

In order to study the adsorption behavior of MB in detail, the data for equilibrium adsorption isotherms were fitted into several isotherm models such as Langmuir, Freundlich, Temkin and Dubinin-Raduskevich. The parameters obtained in the isotherm equation and a determination coefficient (R^2) were listed in Table 3. According to the linear regression (R^2) analysis method, it was observed that the values of the correlation coefficients were slightly high (≥ 0.9300). Thus, it showed that the results fit these four models very well. Based on the value of R^2, the Langmuir isotherm model was the best fit with the adsorption equilibrium data with R^2=0.9998. However, according to Misran et al. [2], R^2 is not adequate to depict the applicability of the models to the experimental data. Hence, a comparison was exhibited between the calculated adsorption capacities at equilibrium (q_e) from the applied models and the experimental values. Further analysis of the isotherm data based on root-mean-square error (RMSE) and chi-square (χ^2) analysis showed that the Temkin isotherm model given the lowest values for RMSE and χ^2 analyses. Therefore, Temkin isotherm model was selected as the best fits with the adsorption of MB onto BTAC since it demonstrates better agreement with the experimental data.

Based on the Langmuir isotherm model on the linear Eq. (3), the isotherm parameters, K_L and maximum adsorption capacity, q_m can be determined from the slope of the plot C_e/q_e vs. C_e. In the conditions studied, the maximum adsorption capacity at monolayer coverage (q_m) was 217.4 mg/g. While the calculated R_L values for the selected range of concentration studied were in the range of 0.0045 to 0.0133. These values were greater than zero showing favorable adsorption of MB onto BTAC. Previous study, Ezechi et al. [37] and Fan et al. [26] claimed that for favorable adsorption, $0 < R_L < 1$; unfavorable adsorption, $R_L > 1$; linear adsorption, $R_L = 1$; and adsorption process is irreversible if $R_L = 0$. For the Freundlich isotherm model, the values of n and K_F can be calculated from the plot of ln q_e vs. ln C_e using Eq. (4). Based on the equation, the values of n and K_F were 6.9396 and 134.8

L/g, respectively, with R^2 =0.9797. Temkin isotherm represents the quantity of heat needed for the adsorption by one layer of adsorbate on the surface of the adsorbent [38]. Temkin isotherm constants were determined from the slope and intercept from the plot q_e vs. ln C_e based on the linear Eq. (5). The value of the Temkin constant (B) was calculated to be 22.13 J/mol. The value of B was greater than 1 indicates an exothermic process [39]. While b_T and K_T were calculated to be 111.9 mg/L and 569.2 L/g, respectively. The positive value of b_T proved that the adsorption process was exothermic [35]. Ahmad et al. [40] also observed comparable results for the adsorption study of synthetic dyes removal using pomegranate peel AC. The Dubinin-Radushkevich adsorption isotherm is generally applied to express the adsorption mechanism with a Gaussian energy distribution onto a heterogeneous surface. Based on the Eq. (6), the theoretical saturation adsorption capacity (q_s) and k_{ad} values were calculated to be 172.2 mg/g and 4×10^{-8} mol^2/J^2, respectively. While the value of adsorption energy (E) was determined as 3.53 kJ/mol. The value of E was noticed less than 8 kJ/mol implying that removal of MB by BTAC involves physical adsorption as reported by Xue, et al. [19]. Magnitude of E is useful for estimating the mechanism of the adsorption reaction [38]. Based on the result, it can be concluded that strong physical interactions are the driving force of MB adsorption onto BTAC, an assumption supported as well by the great value of saturation adsorption capacity.

The q_m value of MB onto BTAC was then compared with the adsorption capacities of ACs as prepared by various agriculture waste as listed in Table 4. This comparison data clarified that the BTAC is a highly effective adsorbent due to its high surface area and good adsorption capacity for MB dye removal from aqueous solution.

Table 3. Langmuir, Freundlich, Temkin and Dubinin–Radushkevich constants for MB adsorption

Langmuir		**Freundlich**		**Temkin**		**Dubinin-Radushkevich**	
q_m (mg/g)	217.4	n	6.9396	B (J/mol)	22.13	q_s (mg/g)	197.2
K_L (L/mg)	1.4838	K_F (L/g)	134.8	b_T (mg/L) K_T (L/g)	111.9 569.2	k_{ad} (mol^2/J^2) E (kJ/mol)	4.0×10^{-8} 3.53
R^2	0.9998	R^2	0.9797	R^2	0.9671	R^2	0.9304
RMSE	23.22	RMSE	11.60	RMSE	7.72	RMSE	14.48
χ^2	37.72	χ^2	4.58	χ^2	2.27	χ^2	5.74

Table 4. Comparison of MB adsorption capacities by different activated carbon materials

Raw Materials	**Surface Area (m^2/g)**	**MB q_m (mg/g)**	**References**
Banana trunk	1329.5	217.0	This study
Ashitaba biomass	1505.4	323.5	[19]
Sugarcane bagasse	709.3	136.5	[33]
Mangosteen peel	1832.0	871.5	[41]
Myristica fragrans shell	1462.0	346.8	[22]
Fox nutshell shell	2869	249.8	[42]

Kinetic study

In this study, pseudo-first order (PFO) and pseudo-second order (PSO) were used to examine the experimental adsorption data, such as the examination of the controlling mechanisms of the adsorption process (chemical reaction, diffusion control, and mass transfer). The parameter data of the PFO and PSO can be determined from the slope and intercept of plot ln ($q_e - q_t$) against t and plot t/q_t against t by the linear Eq. (7) and (8), respectively. The parameters obtained in the PFO and PSO equations, together with their R^2 and $q_{e,cal}$ is listed in Table 3. It was found that the plots ln ($q_e - q_t$) against t (Figure 2(a)) give a less linear relationship and subsequently contribute to the low R^2 values. In addition, the experimental and calculated values of q_e showed a significant difference. These results indicate that the experimental data do not agree with PFO kinetic model.

On the other hand, plot t/q_t against t (Figure 2(b)) showed a linear relationship. The R^2 value (~0.999) for the PSO kinetic model was relatively higher than the PFO. Moreover, the $q_{e,cal}$ values derived from the PSO model were slightly close to the $q_{e,exp}$ value. Thus, these results suggest that the PSO model provided a good correlation for the adsorption of MB onto BTAC. Most previous studies also report PSO kinetics for adsorption, such as the adsorption of MB onto forest wastes [15], methyl orange onto pumpkin seed powder [43], and adsorption of reactive orange by iron oxide nanospheres [44]. The PSO kinetic model also verified that the chemisorption was the rate-controlling step over the whole adsorption process [45].

The IPD model was also tested because the PFO and PSO kinetic models cannot identify a diffusion mechanism [46]. Intraparticle models parameters (k_{ID} and C) were calculated from the slope and intercept of plot q_t vs. $t^{1/2}$ and summarized in Table 5. As shown in Figure 2(c), plots of q_t vs. $t^{1/2}$ present multi-linearity, thus indicating that more than one step occurs during the adsorption of MB onto BTAC. Similar patterns have also been obtained by Kumar and Jena [42] and Bedin et al. [47] . According to Shin and Kim [46], the first portion is the fast adsorption or external surface adsorption stage, where adsorbate (MB molecules) migrates through the solution to the exterior surface of the adsorbent (BTAC) particles (Stage I). This portion was attributed to bulk diffusion. The second portion is the gradual adsorption stage, where MB molecules move within the particles (Stage II). This portion is due to intraparticle diffusion. The third portion is the final equilibrium stage, where the MB molecules are adsorbed at sites on the interior surface of BTAC (Stage III). Moreover, the observed multi-linearity also suggests that intraparticle diffusion is not the rate-limiting step [48]. It was observed from Table 5, the value of k_{ID1} and k_{ID2} increase with increasing MB concentration from 75 to 125 mg/L. In addition, at constant MB concentration, the values of k_{ID1} were found larger than k_{ID2}. In other words, the adsorption was rapidly at the initial stage and became slower beyond this stage and no more adsorption occurred when achieving the equilibrium. The magnitude in the C_1 pattern with the changes of adsorbate concentrations was not clearly observed. However, at the second stage, C_2 values were noticed to decrease as the adsorbate concentration increase. The reason behind this due that higher adsorbent dosage will weaker the boundary layer effect.

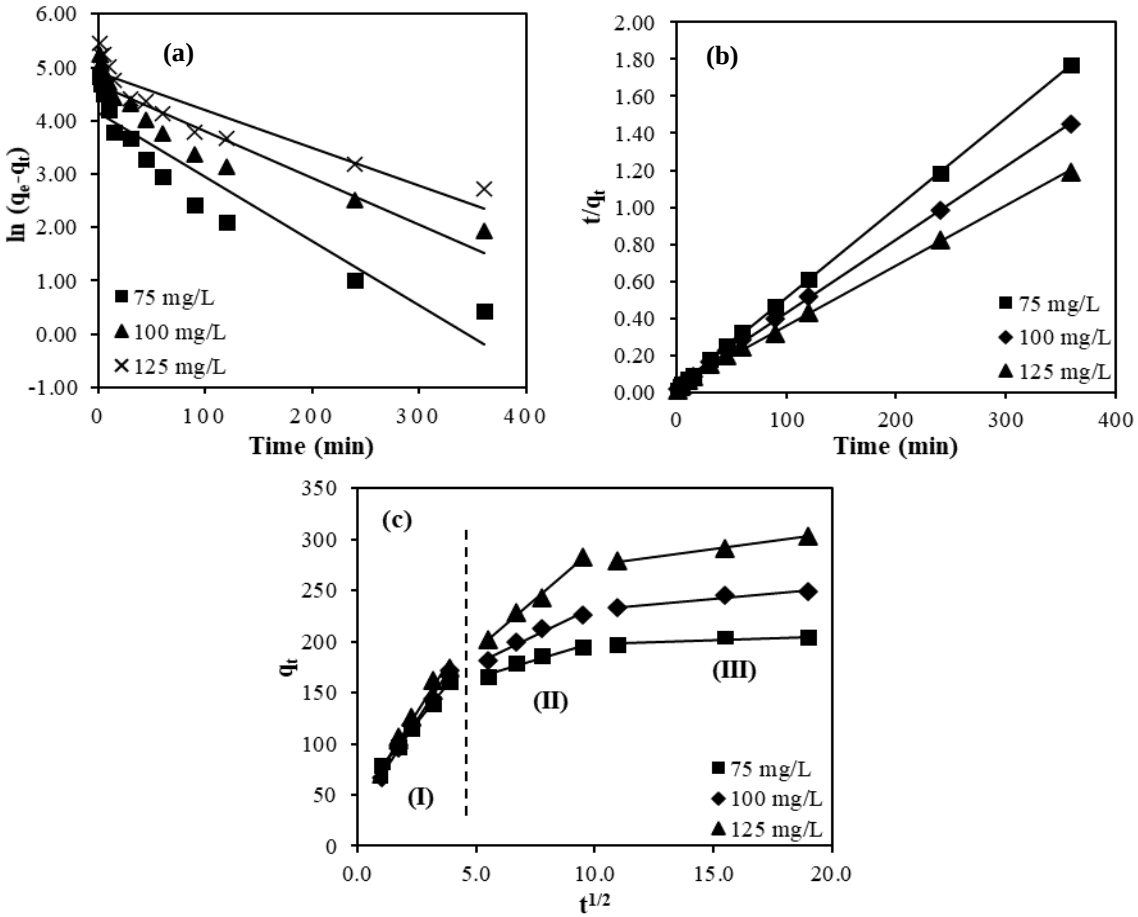


Figure 2. (a) PFO, (b) FSO and (c) IPD model for the adsorption of MB onto BTAC

Table 5. PFO, FSO and IPD parameters for adsorption of MB onto BTAC

Concentration (mg/L)	$q_{e,exp}$ (mg/g)	Kinetic Model					
		Pseudo First Order			Pseudo Second Order		
		$q_{e,cal}$ (mg/g)	k_1 (1/min)	R^2	$q_{e,cal}$ (mg/g)	k_2 (g/mg.min)	R^2
75	205.4	62.8	0.0121	0.8841	208.3	0.0010	0.9998
100	255.8	106.5	0.0087	0.8740	250.0	0.0005	0.9992
125	316.2	135.4	0.0071	0.8345	312.5	0.0003	0.9984

Concentration (mg/L)	Intra-Particle Diffusion Model					
	k_{ID1} (mg/g.min$^{0.5}$)	C_1 (mg/g)	R^2	k_{ID2} (mg/g.min$^{0.5}$)	C_2 (mg/g)	R^2
75	28.722	49.421	0.9978	5.515	139.9	0.9565
100	35.816	33.619	0.9936	9.192	136.3	0.9710
125	36.448	40.151	0.9767	19.173	98.0	0.9957

Thermodynamic study

The slope and the intercept of the plots of ln K_D versus 1/T using the Van't Hoff plot (figure not shown) are used to determine the ΔH° and ΔS° values. From the values of ΔH° and ΔS°, ΔG° can be calculated using Eq. 10. According to the data presented in Table 6, Gibbs free energy (ΔG°) values for MB were in between -25.83 and -26.34 kJ/mol as the temperature rose from 25 to 40 °C. These negative ΔG° values indicate that spontaneous sorption takes place. In addition, the value of ΔG° was observed to increase (less negative) with decreasing temperature, suggesting rapid and more spontaneous adsorption at lower temperatures. In addition, the calculated ΔH° value was -15.57 kJ/mol. The negative value of ΔH° for the adsorption process indicates that the adsorption was an exothermic process [15]. Furthermore, these results indicate weak attraction forces between the adsorbate and the BTAC. The low value of ΔH° (less than 40 kJ/mol) implies loose bonding between the adsorbate molecules and the adsorbent surface. In the case of entropy (ΔS°), it was found to be 33.87 J/mol.K. The positive value of ΔS° resulted from the increased randomness due to the adsorption of MB, which suggested good affinity of the solute molecules toward the BTAC and increased randomness at the solid-solution interface during the fixation of MB molecules on the active site of the BTAC. A similar finding was also reported by Alver et al. [12] for the adsorption of methylene blue on magnetic alginate/rice husk bio-composite.

Table 6. Thermodynamic study for adsorption of MB

Temperature °C	k_{ad} (L/g)	ΔG° (kJ/mol)	ΔH° (kJ/mol)	ΔS° (J/mol.K)
25	28.48	-25.83	-15.57	33.87
30	25.51	-26.00		
35	23.54	-26.17		
40	21.16	-26.34		

Conclusion

The present investigation revealed that BTAC is a promising adsorbent to remove MB from aqueous solutions. The equilibrium data fitted well to Langmuir, Freundlich, Temkin and Dubinin-Radushkevich isotherm models. Based on error analysis study via RMSE and χ^2 analyses, Temkin isotherm model was the best fitted with the adsorption of MB on BTAC. Maximum monolayer adsorption based on Langmuir was calculated to be 217.4 mg/g. Thermodynamic parameters such as free energy changes (ΔG°), enthalpy (ΔH°) and entropy (ΔS°) were evaluated between temperatures of 25 °C and 40 °C. The ΔG° was noticed progressively decrease from -25.83 to -26.34 kJ/mol as the temperature increase. The ΔH° and ΔS° values were found to be -15.57 kJ/mol and 33.87 J/mol.K respectively. The results showed that the overall adsorption process was exothermic and spontaneous. The findings from this study suggested that BTAC could be a viable adsorbent in managing higher dye problems associated with textiles industries effluent.

Acknowledgement

This work was supported by Universiti Teknologi MARA (UiTM). Great appreciation goes to the Ministry of Higher Education (MOHE) and members of ASTeRN research interest group for providing support throughout the completion of this research.

References

1. Amran, F. and Zaini, M. A. A. (2021). Sodium hydroxide-activated Casuarina empty fruit: Isotherm, kinetics and thermodynamics of methylene blue and congo red adsorption. *Environmental Technology & Innovation*, 23: 101727.

2. Misran, E., Bani, O., Situmeang, E. M. and Purba, A. S. (2022). Banana stem based activated carbon as a low-cost adsorbent for methylene blue removal: Isotherm, kinetics, and reusability. *Alexandria Engineering Journal*, 61(3): 1946-1955.
3. Wu, J. and Upreti, S. R. (2015). Continuous ozonation of methylene blue in water. *Journal of Water Process Engineering*, 8: 142-150.
4. Hoang, N. T. T., Tran, A. T. K., Hoang, M. H., Nguyen, T. T. H. and Bui, X. T. (2021). Synergistic effect of TiO_2/chitosan/glycerol photocatalyst on color and COD removal from a dyeing and textile secondary effluent. *Environmental Technology & Innovation*, 21: 101255.
5. Singh, J. and Dhaliwal, A. S. (2022). Electrochemical and photocatalytic degradation of methylene blue by using rGO/AgNWs nanocomposite synthesized by electroplating on stainless steel. *Journal of Physics and Chemistry of Solids*, 160: 110358.
6. Sahinkaya, E., Sahin, A., Yurtsever, A. and Kitis, M. (2018). Concentrate minimization and water recovery enhancement using pellet precipitator in a reverse osmosis process treating textile wastewater. *Journal of Environmental Management*, 222: 420-427.
7. Dotto, J., Fagundes-Klen, M. R., Veit, M. T., Palacio, S. M. and Bergamasco, R. (2019). Performance of different coagulants in the coagulation/flocculation process of textile wastewater. *Journal of Cleaner Production*, 208: 656-665.
8. Gnanasekaran, G., Sudhakaran, M. S. P., Kulmatova, D., Han, J., Arthanareeswaran, G., Jwa, E. and Mok, Y. S. (2021). Efficient removal of anionic, cationic textile dyes and salt mixture using a novel CS/MIL-100 (Fe) based nanofiltration membrane. *Chemosphere*, 284: 131244.
9. Sinha, A. K., Sasmal, A. K., Pal, A., Pal, D. and Pal, T. (2021). Ammonium phosphomolybdate $[(NH_4)_3PMo_{12}O_{40}]$ an inorganic ion exchanger for environmental application for purification of dye contaminant wastewater. *Journal of Photochemistry and Photobiology A: Chemistry*, 418: 113427.
10. Muniyandi, M. and Govindaraj, P. (2021). Potential removal of Methylene Blue dye from synthetic textile effluent using activated carbon derived from Palmyra (Palm) shell. *Materials Today: Proceedings*, 47: 299-311.
11. De Gisi, S., Lofrano, G., Grassi, M. and Notarnicola, M. (2016). Characteristics and adsorption capacities of low-cost sorbents for wastewater treatment: a review. *Sustainable Materials and Technologies*, 9: 10-40.
12. Alver, E., Metin, A. Ü. and Brouers, F. (2020). Methylene blue adsorption on magnetic alginate/rice husk bio-composite. *International Journal of Biological Macromolecules*, 154: 104-113.
13. Rohaizad, A., Shahabuddin, S., Shahid, M. M., Rashid, N. M., Hir, Z. A. M., Ramly, M. M., ... and Aspanut, Z. (2020). Green synthesis of silver nanoparticles from *Catharanthus roseus* dried bark extract deposited on graphene oxide for effective adsorption of methylene blue dye. *Journal of Environmental Chemical Engineering*, 8(4): 103955.
14. Arabpour, A., Dan, S. and Hashemipour, H. (2021). Preparation and optimization of novel graphene oxide and adsorption isotherm study of methylene blue. *Arabian Journal of Chemistry*, 14(3): 103003.
15. Gemici, B. T., Ozel, H. U. and Ozel, H. B. (2021). Removal of methylene blue onto forest wastes: Adsorption isotherms, kinetics and thermodynamic analysis. *Environmental Technology & Innovation*, 22: 101501.
16. Li, W., Xie, Z., Xue, S., Ye, H., Liu, M., Shi, W. and Liu, Y. (2021). Studies on the adsorption of dyes, Methylene blue, Safranin T, and Malachite green onto Polystyrene foam. *Separation and Purification Technology*, 276: 119435.
17. Meili, L., Lins, P. V. S., Costa, M. T., Almeida, R. L., Abud, A. K. S., Soletti, J. I., ... and Erto, A. (2019). Adsorption of methylene blue on agroindustrial wastes: experimental investigation and phenomenological modelling. *Progress in Biophysics and Molecular Biology*, 141: 60-71.

18. Shamsabadi, A. S., Bazarganipour, M. and Tavanai, H. (2021). An investigation on the pore characteristics of dates stone based microwave activated carbon nanostructures. *Diamond and Related Materials*, 120: 108662.
19. Xue, H., Wang, X., Xu, Q., Dhaouadi, F., Sellaoui, L., Seliem, M. K., ... and Li, Q. (2022). Adsorption of methylene blue from aqueous solution on activated carbons and composite prepared from an agricultural waste biomass: A comparative study by experimental and advanced modeling analysis. *Chemical Engineering Journal*, 430: 132801.
20. Khairiah, K., Frida, E., Sebayang, K., Sinuhaji, P. and Humaidi, S. (2021). Data on characterization, model, and adsorption rate of banana peel activated carbon (Musa Acuminata) for adsorbents of various heavy metals (Mn, Pb, Zn, Fe). *Data in Brief*, 39: 107611.
21. Salem, S., Teimouri, Z. and Salem, A. (2020). Fabrication of magnetic activated carbon by carbothermal functionalization of agriculture waste via microwave-assisted technique for cationic dye adsorption. *Advanced Powder Technology*, 31(10): 4301-4309.
22. Mariana, M., Mistar, E. M., Alfatah, T. and Supardan, M. D. (2021). High-porous activated carbon derived from *Myristica fragrans* shell using one-step KOH activation for methylene blue adsorption. *Bioresource Technology Reports*, 16: 100845.
23. Lewoyehu, M. (2021). Comprehensive review on synthesis and application of activated carbon from agricultural residues for the remediation of venomous pollutants in wastewater. *Journal of Analytical and Applied Pyrolysis*, 159: 105279.
24. Ab Ghani, Z., Yusoff, M. S., Zaman, N. Q., Zamri, M. F. M. A. and Andas, J. (2017). Optimization of preparation conditions for activated carbon from banana pseudo-stem using response surface methodology on removal of color and COD from landfill leachate. *Waste Management*, 62: 177-187.
25. Olu-Owolabi, B. I., Diagboya, P. N. and Ebaddan, W. C. (2012). Mechanism of Pb^{2+} removal from aqueous solution using a nonliving moss biomass. *Chemical Engineering Journal*, 195: 270-275.
26. Fan, S., Wang, Y., Wang, Z., Tang, J., Tang, J. and Li, X. (2017). Removal of methylene blue from aqueous solution by sewage sludge-derived biochar: Adsorption kinetics, equilibrium, thermodynamics and mechanism. *Journal of Environmental Chemical Engineering*, *5*(1): 601-611.
27. Saif Ur Rehman, M., Kim, I., Rashid, N., Adeel Umer, M., Sajid, M. and Han, J. I. (2016). Adsorption of brilliant green dye on biochar prepared from lignocellulosic bioethanol plant waste. *CLEAN–Soil, Air, Water*, 44(1): 55-62.
28. Manna, S., Roy, D., Saha, P., Gopakumar, D. and Thomas, S. (2017). Rapid methylene blue adsorption using modified lignocellulosic materials. *Process Safety and Environmental Protection*, *107*, 346-356.
29. Benhouria, A., Islam, M. A., Zaghouane-Boudiaf, H., Boutahala, M. and Hameed, B. H. (2015). Calcium alginate–bentonite–activated carbon composite beads as highly effective adsorbent for methylene blue. *Chemical Engineering Journal*, 270: 621-630.
30. Pathania, D., Sharma, S. and Singh, P. (2017). Removal of methylene blue by adsorption onto activated carbon developed from *Ficus carica* bast. *Arabian Journal of Chemistry*, 10: S1445-S1451.
31. Li, Z., Wang, G., Zhai, K., He, C., Li, Q. and Guo, P. (2018). Methylene blue adsorption from aqueous solution by loofah sponge-based porous carbons. *Colloids and Surfaces A: Physicochemical and Engineering Aspects*, 538: 28-35.
32. Maneerung, T., Liew, J., Dai, Y., Kawi, S., Chong, C. and Wang, C. H. (2016). Activated carbon derived from carbon residue from biomass gasification and its application for dye adsorption: kinetics, isotherms and thermodynamic studies. *Bioresource technology*, 200: 350-359.

33. Jawad, A. H., Abdulhameed, A. S., Bahrudin, N. N., Hum, N. N. M. F., Surip, S. N., Syed-Hassan, S. S. A., .. and Sabar, S. (2021). Microporous activated carbon developed from KOH activated biomass waste: surface mechanistic study of methylene blue dye adsorption. *Water Science and Technology*, 84(8): 1858-1872.
34. Hassan, A. F. and Elhadidy, H. (2017). Production of activated carbons from waste carpets and its application in methylene blue adsorption: Kinetic and thermodynamic studies. *Journal of Environmental Chemical Engineering*, *5*(1): 955-963.
35. Miraboutalebi, S. M., Nikouzad, S. K., Peydayesh, M., Allahgholi, N., Vafajoo, L. and McKay, G. (2017). Methylene blue adsorption via maize silk powder: Kinetic, equilibrium, thermodynamic studies and residual error analysis. *Process Safety and Environmental Protection*, 106: 191-202.
36. Banerjee, S. and Chattopadhyaya, M. C. (2017). Adsorption characteristics for the removal of a toxic dye, tartrazine from aqueous solutions by a low cost agricultural by-product. *Arabian Journal of Chemistry*, 10: S1629-S1638.
37. Ezechi, E. H., bin Mohamed Kutty, S. R., Malakahmad, A. and Isa, M. H. (2015). Characterization and optimization of effluent dye removal using a new low cost adsorbent: Equilibrium, kinetics and thermodynamic study. *Process Safety and Environmental Protection*, 98: 16-32.
38. Abbas, M. and Trari, M. (2015). Kinetic, equilibrium and thermodynamic study on the removal of Congo Red from aqueous solutions by adsorption onto apricot stone. *Process Safety and Environmental Protection*, 98: 424-436.
39. Nnadozie, E. C. and Ajibade, P. A. (2020). Adsorption, kinetic and mechanistic studies of Pb (II) and Cr (VI) ions using APTES functionalized magnetic biochar. *Microporous and Mesoporous Materials*, 309: 110573.
40. Ahmad, M. A., Puad, N. A. A. and Bello, O. S. (2014). Kinetic, equilibrium and thermodynamic studies of synthetic dye removal using pomegranate peel activated carbon prepared by microwave-induced KOH activation. *Water Resources and industry*, 6: 18-35.
41. Zhang, Z., Xu, L., Liu, Y., Feng, R., Zou, T., Zhang, Y., ... and Zhou, P. (2021). Efficient removal of methylene blue using the mesoporous activated carbon obtained from mangosteen peel wastes: Kinetic, equilibrium, and thermodynamic studies. *Microporous and Mesoporous Materials*, 315: 110904.
42. Kumar, A. and Jena, H. M. (2016). Removal of methylene blue and phenol onto prepared activated carbon from Fox nutshell by chemical activation in batch and fixed-bed column. *Journal of Cleaner Production*, 137: 1246-1259.
43. Subbaiah, M. V. and Kim, D. S. (2016). Adsorption of methyl orange from aqueous solution by aminated pumpkin seed powder: Kinetics, isotherms, and thermodynamic studies. *Ecotoxicology and Environmental Safety*, 128: 109-117.
44. Khosravi, M. and Azizian, S. (2014). Adsorption of anionic dyes from aqueous solution by iron oxide nanospheres. *Journal of Industrial and Engineering Chemistry*, 20(4): 2561-2567.
45. Zhu, C. S., Wang, L. P. and Chen, W. B. (2009). Removal of Cu (II) from aqueous solution by agricultural by-product: peanut hull. *Journal of Hazardous Materials*, 168(2-3): 739-746.
46. Shin, H. S. and Kim, J. H. (2016). Isotherm, kinetic and thermodynamic characteristics of adsorption of paclitaxel onto Diaion HP-20. *Process Biochemistry*, 51(7): 917-924.
47. Bedin, K. C., Martins, A. C., Cazetta, A. L., Pezoti, O. and Almeida, V. C. (2016). KOH-activated carbon prepared from sucrose spherical carbon: Adsorption equilibrium, kinetic and thermodynamic studies for Methylene Blue removal. *Chemical Engineering Journal*, 286: 476-484.
48. Ghani, Z. A., Yusoff, M. S., Zaman, N. Q., Andas, J. and Aziz, H. A. (2017). Adsorptive removal of dissolved organic matter (DOM) in landfill leachate by iron oxide nanoparticles (FeONPs). *AIP Conference Proceedings*, 1892: 040016.

Malaysian Journal of Analytical Sciences (MJAS)
Published by Malaysian Analytical Sciences Society

INITIATIVES IN UTILIZING NATURAL REAGENTS AND NATURAL MATERIALS FOR CHEMICAL ANALYSIS: TALENT AND CHALLENGE FOR ASEAN IN NEW NORMAL CHEMICAL ANALYSIS

(Inisiatif dalam Penggunaan Reagen Semulajadi dan Bahan Semulajadi bagi Analisis Kimia: Bakat dan Cabaran untuk ASEAN dalam Analisis Kimia Norma Baru)

Kanokwan Kiwfo[1,2], Pei Meng Woi[3]*, Chalermpong Saenjum[1,2,4], Treethip Sukkho[1,2,4], Kate Grudpan[1,2,5]

[1]Center of Excellence for Innovation in Analytical Science and Technology
[2]Cluster of Excellence on Biodiversity-based Economic and Society (B.BES-CMU)
Chiang Mai University, Chiang Mai 50200, Thailand
[3]Chemistry Department,
Faculty of Science, Universiti Malaya, 50603 Kuala Lumpur, Malaysia
[4]Pharmaceutical Sciences, Faculty of Pharmacy
[5]Department of Chemistry, Faculty of Science
Chiang Mai University, Chiang Mai 50200, Thailand

**Corresponding author: pmwoi@um.edu.my*

Received: 19 September 2021; Accepted: 28 November 2021; Published: 28 April 2022

Abstract

This review explores the contributions of natural resources with diverse disciplines which offers the insights into the design of greener chemical analysis. The discussion was focused on the published works in our group where a diverse range of natural reagents used in the determination of various environmental analytes has been highlighted, aiming to discuss the initiatives and applicability of the usage of alternative natural reagents and substitute synthetic methods in optimizing analytical processes, which in turn would lead to cost-effective and time-efficient in handling analytes assay. By exploring the potential of natural reagents, the sustainability in green chemical analysis could be promised in coming near future, especially in convincing for the talent and challenge for ASEAN in this new normal chemical analysis.

Keywords: green analytical chemistry, natural reagent, natural material, local wisdom, sustainable chemistry

Abstrak

Ulasan ini membincangkan sumbangan reagen semula jadi dalam pelbagai disiplin ilmu yang dapat memberikan gambaran mengenai analisis kimia hijau. Perbincangan in fokus kepada penerbitan yang telah diterbitkan oleh kumpulan kami di mana beberapa jenis reagen semula jadi yang digunakan dalam penentuan pelbagai analit persekitaran akan diutamakan, bagi membincangkan inisiatif dan penerapan penggunaan reagen semulajadi alternatif dan kaedah sintetik gantian dalam mengoptimumkan proses analisis, supaya analisis dapat dikendalikan secara kos efektif dan cekap masa. Dengan menerokai potensi reagen semula jadi, kesinambungan dalam analisis kimia hijau akan dapat dijanjikan dalam masa terdekat terutamanya dapat memberikan keyakinan dalam bakat dan cabaran di ASEAN dari segi analisis kimia di norma baru ini.

Kata kunci: kimia analisis hijau, reagen semula jadi, bahan semula jadi, kebijaksaan tempatan, kimia kelestarian

Introduction

Green chemistry concept was first devised in the early of 1990s, which is practically about 30 years ago [1, 2]. This concept is laid on the foundation of twelve principles for green chemistry which can be described as ecological approaches in molecules and materials making, reactions, and processes that are meant to provide a safer human health with the effort in minimizing or removing the use and production of harmful constituents. Evolving from here, green analytical chemistry has adopted the green chemistry's twelve principles to focus on the development of analytical methodologies and techniques with greater commitment in preservation of the environment and safety of operators. These two concepts, the green chemistry, and the green analytical chemistry, are closely associated with sustainable chemistry, which is the scientific notion that strive for efficiency improvement in natural resources utilization as to fulfill the human needs and requirement for chemical products and services. Sustainable chemistry encompasses the design, manufacture and use of efficient, effective, and more environmentally benign and friendly on chemical products and processes. This also serves the United Nations Sustainable Development Goals (UN SDGs) on the universal call to act in protecting the planet by integrating balance in between development involving social, economic, and environmental sustainability [3].

Having said that, a global consensus on how to assess and appraise the greenness of an analytical method has not yet been achieved, but several green metric tools have been proposed towards this goal [4]. Apart from the development in experimental techniques and instrumentation designs, which both are crucial for quality improvements in chemical analyses; efforts and attempts are being made to reduce or minimizing the undesirable impact of chemical analyses on the environment, and to enable sustainable development principles being embedded and implemented within analytical laboratories. As shown in Figure 1, the current trend in analytical practices is depending on high-performance instruments which emphasize on sensitivity, selectivity, and precision. Such laboratory design and set-up always required skillful human resource, and utilize enormous amounts of chemicals, solvents, as well as energy [5]. The similar practice was applied in almost all academia institutions in developed countries as well as for the laboratories setting in industry, where most of them rely on high-end instruments to generate most of the analytical information which applicable for process control, or environmental conditions assessment and evaluation [6]. Nevertheless, despite the capability of such designed-laboratories, there is an urgent need for simple indicator-type sensors in market that able to offer adequate precision and specificity, easy to handle thus do not require trained personnel, and while during operation, little or no waste generation thanks to volume minimization, which in return consume negligible amounts of energy or none, and still capable to obtain chemical information from the point-of-care, including on-site process analysis for the widest use. Such sensor characteristics would also link to cost-effective operation.

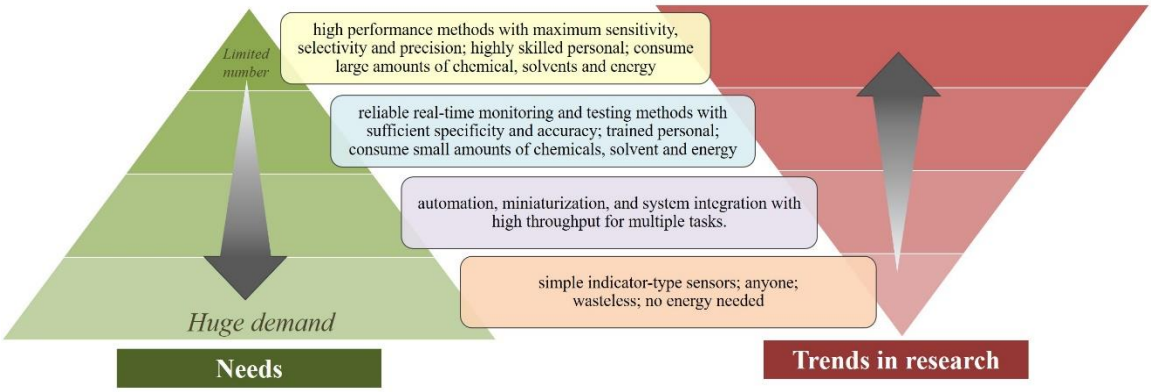


Figure 1. Comparison of the needs and trends in analytical chemistry. Reproduced with adaptation from [5]

Thus, one of the purposes of green analytical chemistry is to discover alternative reagents or substitutive synthetic methods which can reduce or minimize the usage of hazardous or poisonous chemicals. This suggestion may at first seem to be counteract to one of the best adhered principles of analytical chemistry, in which typically reagents of the highest purity grade are accounted for minimization of reagent blanks and impurities interferences. Nevertheless, in some cases there may be the possibility in replacing or substituting this highly purified reagents (which contributing to the costing in analysis) without compromising or bargaining the success of the assay determination. Under the typical condition of analytical experiments, a reagent is normally required in a small amount, or a crude extract which contains the essential active reagent are sufficient to get the analysis done. This is where the use of such natural reagents is highly desirable attributed to its simplicity in their preparation as well as the inherent or zero energy and chemical waste prevention. The ASEAN countries including Thailand and Malaysia are rich in natural resources. Utilizing a variety of natural resources existing in this region for health, chemicals, nutrient tests, and as natural dyes have been exercised as one of local wisdoms. Such wisdoms have long been employed in local peoples for improvement of life quality, for example using the fermented tea leaf like *Miang* as health supplement and snacks [7], which in return becomes the major source of income and tourism activities for one of the village in northern Thailand. Natural dyeing craftsmanship in textile industry has been kept alive thanks to discovery of various extracts from local plant such as mangosteen tree (*Garcinia dulcis*) [8] which offers bright yellow color, indigo leaves (*Indigofera tinctoria*) which contributes the blue color and coconut barks which attributed to pinkish brown color [9]. A team of chemists, focusing on the development of green chemical analysis techniques, has adapted the wisdoms in modern chemical analyses. In many parts of Thailand alone, there has been some regional handling of guava leaves as the sign or as an indicator towards the presence of iron in ground water. The appearance of darker color of water upon contacts with the guava leaves helps local villagers in making some decisions (or "screening test", as for today term), such as whether the water is suitable for cloth washing, due to the strain that tends to deposited on the cloth, attributed to the iron presence in the water source; or it can lead to pre-treatment decisions such as applying alum into the ground water prior consumed for drinking or cooking use. This example of local wisdom has never been published nor any scientific explanation is available until Settheeworrarit et al. reported the investigation of natural guava (*Psidium guajava L.*, Myrtaceae family) leaf extract as an alternative natural indicator for quantification of iron using the flow injection technique [10]. This is just one of the many examples which showcase on how the natural resources can work perfectly in applying chemical analysis in such green analytical approach.

From the Scopus database, trends in research works based on keywords "natural reagent" in "chemistry" have shown an increasing pattern as displays in Figure 2. This indicates an encouraging direction among analytical chemist in effort towards green analytical chemistry which adopted natural reagents as the active materials in performing assay testing. It is worth to notice that scientific articles contribution from our group are sharing the similar development. Different examples of the use of natural reagents for derivatization have been published as indicated by the used database. Natural reagents are consisted of extracts from various sources including the vegetables, plant-based, bacteria, or animals that required minimal treatment (extraction process) and among them, natural compounds contained in plants were able to distinguish themselves as the imperative key to green analytical chemistry initiatives.

Herein in this review, we have pin-pointed the published works done on natural reagents and materials, particularly in green analytical chemistry by our group to discuss its scientific potential as part of the ASEAN consortium efforts. The scope of discussion was designed to fortify the geographical advantages in this southern Asia region where each country is sharing the similar bioresources that could be explored further in various scientific exploration as well as collaboration and networking. One of the advantages of the reported works here is that it could help in shorten the needs of screening a vast range of natural compounds, hence open the opportunity to adopt the similar plant species for further exploration. A diverse range of natural reagents used for the determination of various environmental analytes has been highlighted, aiming to critically discussed the initiatives and applicability of the use of such alternative reagents and alternative synthetic methods in optimizing analytical processes, as a way to provide the required information in a manner that is environmentally friendly, prioritize sustainability with the least possible consumption of materials, energy, and generating less or zero waste along the way.

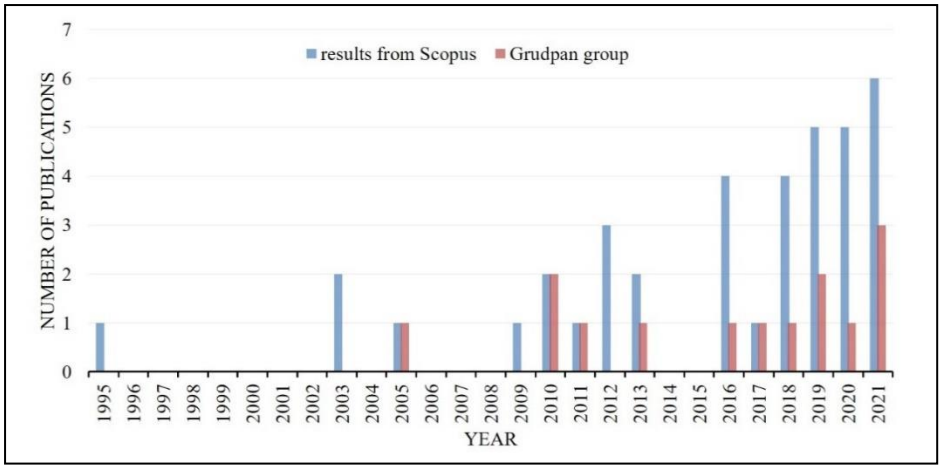


Figure 2. Number of publications obtained from Scopus database using the keywords of "natural reagent" (■) in chemistry and with "Grudpan" (■) (searched on 31 August 2021)

Natural reagents used in chemical analysis

Table 1 represents some natural reagents extracts which can be found in plants that grew in ASEAN countries. The tropical forests in this region offer a unique natural heritage which has been evolved for over a hundred million years, resulting in rich flora and fauna with spectacular biodiversity. Currently, these are in much demand due to their efficacy, safety, and minimal side effects. Sample treatment which involves both the extraction of the analytes and the purification of the sample extract obtained, is still considered the bottleneck of the entire analytical procedure, despite

much progress on automation and miniaturization has been accomplished. It is still the most labor-intensive and time-consuming analytical step, accounting for 60–80% of the total analysis time. These steps can affect both, the accuracy and precision, and green analytical features of analytical methods. Extraction of plant materials can be done by various conventional and nonconventional extraction procedures including maceration, infusion, percolation, digestion, decoction, Soxhlet extraction, ultrasound-assisted extraction, turbo-extraction, countercurrent extraction, microwave-assisted extraction, ultrasound extraction, supercritical fluid extraction, solid-phase extraction, and column chromatography. Considering the aforementioned information, it is easy to imagine that substantial efforts have been made in recent years to simplify the overall sample preparation steps and to tailor it to the green analytical chemistry principles. Major efforts of scientists have been devoted to miniaturization of the extraction device; development of new sorbent materials with advanced properties; reduction and replacement or elimination of toxic and hazardous organic solvents; reduction of sample volume and extraction time, and maximizing extraction efficiency and selectivity, among others. The natural reagents reported here can be obtained in a greener approach of extraction which only involving the use of water and ethanol as the organic solvent. The extracted chemical species have shelf-life of up for weeks provided with proper storage in fridge, thus allowing repeatability of experiments easily without restriction in chemical stocks.

Based on previous reported works, the chemical species which are active to certain analytes are listed. These active compounds are operating on the principle of colorimetric, where upon interacts with target analyte, the color changes will provide information on types of analytes as well as its concentration range, by performing the image analyzing via open source (free) color applications such as ImageJ and Color Grab. It should be noticed that for an analyte detection, the coloration visualization may be attributed to presence of different ligands from the reagents active compounds that forming chelation or binding with the analyte itself. This explains the versatility of various active compounds as they may obtain from different plants as of same species or family, yet capable to provide the equal analyte quantification. For instance, the anthocyanins species that active towards acidity measurement, can be obtained from butterfly pea, orchid and beetroot [11, 12]; iron can be quantified using phenolic compounds from green tea and guava leave [13, 14]. It is then of interest to explore which local plants would be use of in each analyte detection. By combining the efforts and intellectual of analytical chemists, natural products expertise, biologist, computational modeling, along with the advantages of ASEAN geographical, many plant species as natural reagents could be explored further. Such strategy one day may offer benefits in the possibility where we would be on self-reliance in using the reagents from the bioresources in our region, and with less dependent from the big chemical companies, thus affording the cost-effective in handling analytes assay; and time-efficiency where chemical delays arise from delivery would no longer be an issue.

Despite the detection limits and linear ranges are probably constrained by higher blank values originating from the reagents themselves, and the limitation of the detection systems used, yet the assay determination in analytical chemistry does not restrict to maximum sensitivity, rather to the applicability towards the targeted detection range. The trend of having high precision and sensitivity which restricted to advance instrument and highly trained personnel is not able to support the demand in analytical testing especially in those resources-limited countries. While most of these examples focus on agricultural, clinical or wastewater samples, which have higher analyte concentrations, the use of natural reagents for trace analytical purposes, e.g., in environmental waters, are possible to accomplish when the enhanced analytical control of flow injection-based or sequential injection analysis is utilized in combination with intrinsically sensitive detection methods such as chemiluminescence. Thus, when applied with recognition of their limitations, natural reagents, especially when used in combination with flow-based systems, can offer an alternative approach to sustainable and greener analytical measurement.

Table 1. Natural regents obtained from plants used in chemical analysis

Analyte	Active Species	Common Name	Scientific Name	Ref.	Photo of the Plant	Availability
Acidity and iron	Anthocyanins	Butterfly pea flower	*Clitoria ternatea* L.	[11]		Introduced into: Cambodia, Laos, Myanmar, Thailand, Vietnam, Brunei Darussalam, Philippines, Singapore, Indonesia, commercial hybrid
	Anthocyanins	Orchid flower	*Dendrobium* Sonia			Commercial hybrid
	Anthocyanins	Beet root	*Beta vulgaris subsp. Vulgaris*			Introduced into: Vietnam, Thailand
	Phenolic compounds	Tea	*Camellia sinensis* (L.) Kuntze			Native to: Laos, Myanmar, Thailand, Vietnam Introduced into: Cambodia
Acidity	Anthocyanins	Butterfly pea flower	*Clitoria ternatea* L.	[12]		Introduced into: Cambodia, Laos, Myanmar, Thailand, Vietnam, Brunei Darussalam, Philippines, Singapore, Indonesia, commercial hybrid

Table 1 (cont'd). Natural regents obtained from plants used in chemical analysis

Analyte	Active Species	Common Name	Scientific Name	Ref.	Photo of the Plant	Availability
Benzoyl peroxide	β-carotene compound	Pumpkin	*Cucurbita moschata* Duchesne	[15]		Introduced into: Thailand, Myanmar, Vietnam, Indonesia
Aluminum	Polyphenolic compounds	Indian almond leaf	*Terminalia catappa* L.	[16]		Native to: Cambodia, Myanmar, Philippines, Thailand, Vietnam, Brunei Darussalam, Indonesia, Malaysia, Singapore
Aluminum	Homo-isoflavonoid compounds	Heartwood of Indian radwwod/ Sappan tree	*Caesalpinia sappan* L.	[17]		Native to: Cambodia, Laos, Myanmar, Thailand, Vietnam Introduced into: Brunei Darussalam, Indonesia, Malaysia, Philippines, Singapore
Copper and acidity	Starch	Rice	*Oryza sativa* L.	[18]		Introduced into: Brunei Darussalam, Cambodia, Indonesia, Laos, Myanmar, Malaysia, Philippines, Singapore, Vietnam, Thailand
	Anthocyanins	Butterfly pea flower	*Clitoria ternatea* L.			Introduced into: Cambodia, Laos, Myanmar, Thailand, Vietnam, Brunei Darussalam, Philippines, Singapore, Indonesia, commercial hybrid

Table 1 (cont'd). Natural regents obtained from plants used in chemical analysis

Analyte	Active Species	Common Name	Scientific Name	Ref.	Photo of the Plant	Availability
Iron	Polyphenolic compounds	Guava leaf	*Psidium guajava* L.	[10]		Introduced into: Brunei Darussalam, Malaysia, Thailand, Singapore, Indonesia
Iron	Polyphenolic compounds	Green tea	*Camellia sinensis* (L.) Kuntze	[13]		Native to: Laos, Myanmar, Thailand, Vietnam Introduced into: Cambodia
Iron	Phenolic compounds	Guava leaves	*Psidium guajava* L.	[14]		Introduced into: Brunei Darussalam, Malaysia, Thailand, Singapore, Indonesia,
Iron	Phenolic compounds	Pomegranate Peels	*Punica granatum* L.	[19]		Introduced into: Laos, Thailand, Vietnam
Iron	Mimosine	Leucaena leaf	*Leucaena leucocephala* (Lam.) de Wit	[20]		Introduced into: Cambodia, Indonesia, Laos, Philippines, Thailand, Vietnam
Iron	Phenolic compounds	Betel nut	*Areca catechu* L.	[21]		Native to: Philippines Introduced into: Cambodia, Laos, Thailand, Vietnam, Malaysia, Brunei Darussalam, Indonesia

Table 1 (cont'd). Natural regents obtained from plants used in chemical analysis

Analyte	Active Species	Common Name	Scientific Name	Ref.	Photo of the Plant	Availability
Nitrite	Phenolic compounds	*Miang*	*Camellia sinensis* var. *assamica* (J.W.Mast.) Kitam.	[22]		Native to: Laos, Myanmar, Thailand, Vietnam

Natural reagents for green analytical procedures

Pertaining to the effective experimental measurement stage, greener analytical procedures and experimental setup are inherent to automated flow-based instrument setup, owing to their capability in reducing the consumption and needs of reagent and solvent and to the possibility of incorporating decontamination of wastes on-line. The development of flow-analysis-based techniques best suited in realizing such ideology. The flow analysis approach offers a feasible means of employing natural reagents for green chemical analysis.

Guava leaf extract is one of the widely studied natural reagent where its chemical compounds may serve as whitening essence, anti-bacterial, anti-pigmentation, and in diabetes prevention. Besides, guava leaf extract is an alternative natural compound used to identify ferrous (Fe^{2+}) metal through flow injection method. In one of the reported works by Hartwell and her co-workers, by using a simple flow injection system, the scientific explanation behind the use of guava leaf extract as an alternative reagent to quantify iron(II) in water samples has been revealed. Chemical and physical properties of the extract, including its stability and ability to form chelation complexes with iron(II) and (III), respectively, spectroscopic characteristics, the appropriate solvent medium used for extraction, and its potential to be used for quantification of iron in water samples were tabulated in detail. Minimization on guava leaf extract consumption was achieved via using the modified reverse flow injection manifold with two lines, where the reagent was injected into the buffer solution which was later mixed with the flow of sample solution. Such in-situ design displayed a better sensitivity and detection limit as compared to the conventional flow system. This is presumably attributed to higher amount and a concentrated iron solution are being introduced via pumping as compared to injection along the line. [10]

Some of the works discussed as follows, although were not registered in the above search (Table 1), they engaged with the deployment of natural reagent. A simple simultaneous quantification of two metals-iron and manganese in ground water via sequential injection spectrophotometry was reported by utilizing the astilbin crude which extracted from *Smilax china L. root*. This natural reagent can be found easily in one of those common plants that grown in many tropics and subtropics worldwide. The extraction was done with methanol solvent at room temperature and the solid astilbin was obtained after evaporation and recrystallization steps. By dissolving the natural reagent with buffer solution, the mixtures were sequentially aspirated into the holding coil and the reactions with iron(III), manganese(II) and astilbin which took place in the flow cell was monitored by measuring absorbance change at the visible light wavelength. The applicability and simplicity setup which demonstrated in this work indicates that the proposed system and the easily obtained reagent are useful for ground water analysis. [23].

A simple and cost-effective analytical device for determination of ammonia which based on gas pervaporation and diffusion method is proposed [24]. This user-friendly device is consisted of a well microplate as a donor chamber and the butterfly pea flower extract was applied as natural indicator. The

butterfly pea flower which having an intense blue color flower is easily grown in the ASEAN region. In this reported work, the flower extract was immobilized on the paper as the acceptor sensor. The anthocyanin color pigments from this flower extract are strongly influenced by the degree of acidity upon contact which changed the structure of the pigment and displaying color changes accordingly to different pH values. Using the reagent immobilization method on paper allows the microliter-scale solution handling. Such principle can reduce the consumption of reagent and the analyte itself. On the reported work, the sample preparation started by converting the ammonium ion into ammonia by using the solution in alkalinity range. The next procedure is allowing the ammonia gas pervaporation and diffusion across the PTFE membrane into the natural indicator which has been pre-immobilized on the filter paper. The colorimetric change (color appearance) on the paper was then detected by either a smartphone camera or naked eye which offer the quantitative or semi-quantitative analysis, respectively. Such simple paper sensor was successfully applied for real samples in ammonia detection that are widely found in the swine farming wastewater and chemical fertilizer samples. On top of that, the developed ammonia sensor could concurrently perform triplicate runs of 18 samples in just 15 minutes, which in return can generate 72 samples in one-hour timeframe. This proposed device with pervaporation and diffusion method offers on-site assay and green chemical analysis with relatively high throughput while at the same time display the example of cost-efficiency.

Several extracts from natural sources- vegetables and plant-based, namely carrots, leaves and flowers of peacock plants (*Caesalpinia pulcherrima*) were acquired through maceration and boiling procedures by using ethanol and water as solvents. Such extracts are being tested to detect lead(II), the poison heavy metal which mainly found in agriculture or industrial ecosystem. After performing the screening using the reagents which have been prepared, the researchers from Indonesia discovered those which can form complexes between ligand compounds of plant extract with lead(II), via the observation of color change, were only the flowers of the peacock plant (*Caesalpinia pulcherrima*). As such, the sequential injection analysis (SIA) system for determination of lead(II) in this work by employing the peacock flower extract as the natural reagent was developed. The discovery of using such natural reagent offers the advantages, once again, cost-effective and feasibility due to the easily available plant itself, inexpensive experimental setup, environmentally friendly, and the reagent can form the stable complex with the target lead ion [25].

In the recent published work, phenolic species of the guava leaf extract was used as natural reagent which responsible for chelation with the ferrous metal ions and leads to color formation. Such observation serves as a detection tool for the small and portable paper-based analytical devices (PADs) which can operate without any complicate supporting equipment, thus it is well-suited for point of care applications in places especially where budget is limited. The novel PAD reported here has been fabricated using a home-based printer with the design that able to complete replication test of iron analysis via a single run which in turn offers the versatility of having standards for calibration and duplicate or triplicate of sample analysis; concurrently under one analysis. Calibration plot in the concentration range from 0 to 20 ppm iron(III) was plotted based on the gray color intensity against iron concentration [26].

Natural materials used in chemical analysis

Various natural materials have been proposed for the use in chemical analysis, as represented in Table 2. They serve as platforms in colorimetric assays, in combining with the use of information technology (IT) devices including smartphone, webcam camera, and scanner, or via naked eyes, to perform the images analysis as the mode of detection. Such arrangements offer the benefits, such as easily accessible to local available materials, biodegradable, portable in terms of smartphones, and with simple fabrication (using home-based printer to complete the process). All the listed pros eventually will lead to cost-effective and user-friendly analytical applications.

Table 2. Natural materials used in chemical analysis

Material	**Analyte**	**Reagent**	**Detection Principle**	**Detection Device**	**Advantages**	**Ref.**
Paper	Ammonium	Alkaline solution and butterfly pea flower extract	Gas pervaporation, diffusion method and acid –base equilibrium	Smartphone	High sample through put, local available materials, biodegradable materials, portable	[24]
Paper and cotton cloth	Acidity	Red maple leaf extract	Acid-base equilibrium	Smartphone	Local available materials, biodegradable materials, portable	[27]
Paper	Iron, phosphate, water hardness	Iron: 1,10-phenanthroline/guava leaf extract phosphate: molybdenum blue water hardness: Eriochrome black T and EDTA	Iron: complex formation reaction phosphate: complex formation reaction water hardness: complexometric titration	Smartphone	Replication analysis of a sample within a single run, local available materials, biodegradable materials, portable	[26]
Cotton thread	Anionic surfactant	Methylene blue	Ion association	Smartphone	Local available materials, biodegradable materials, portable	[28]
Cotton thread	Total phenolic content and antioxidant capacity	Total phenolic content: Folin-ciocalteu antioxidant capacity : 2, 2-diphenyl-1-picryhydrazyl (DPPH)	Redox reaction	Smartphone	Local available materials, biodegradable materials, portable	[29]

Table 2 (cont'd). Natural materials used in chemical analysis

Material	Analyte	Reagent	Detection Principle	Detection Device	Advantages	Ref.
Noodle	Acidity and copper	Acidity: bromothymol blue/ butterfly pea flower extract copper: starch and potassium iodide	Acidity: acid-base equilibrium copper: redox reaction and complex formation	Webcam camera/ scanner	Local available materials, biodegradable materials, self-indicating platform	[18]
Kaolin clay	Acidity	Phenolphthalein/ thymol blue/ butterfly pea flower extract	Acid-base titration	Naked eye	Reusable, local available, materials, biodegradable materials	[12]

Natural reagents with synthetic materials

From the green analytical perspective, new analytical tools can be obtained via modification or combination of conventional molecules with synthetic materials and forming a kind of hybrid system. Such tactics set off a promising strategic way in getting synergistic and additive effect achieved from either the natural reagents or the synthetic materials. In the work reported by Rujiwatra et al., [22] *miang* (*Camellia sinensis var. assamica*) leaves from northern Thailand are being fermented and blended with silver (Ag) nanoparticles (NPs) which can be applied as colorimetric agents for nitrite determination. The working principle behind this work is depends on employing *p*-aminobenzoic acid as aiding reagent, and a camera phone as a detector to capture the color changes upon interaction of Ag-*miang* NPs with the target analyte. As an effort to design the synthesis route become more environmentally benign, crude water extracts of *miang* leaves, which are abundantly available locally throughout the year in two forms, i.e., non-fermented and fermented *miang*, were used as natural reagents. Unique color of AgNPs can be obtained via controlling the morphology and sizes of AgNPs itself. Thus, the Ag-*miang* nanocomposites in turn providing the rapid, simple, and selective tool for the determination of nitrite.

On another reported work by Rujiwatra et al., [30], the team has demonstrated a sustainable way of reducing the waste generation, which in turn offers the potential in minimizing the impact on the environment. Such approach is achieved via the consumption of crude water extract from the ground longan (*Dimocarpus longan Lour*) seeds industry in northern Thailand, which annually discarded in large amount. This untreated wastewater was being used as the natural reagent, serving as the starting material for the green synthesis of ZnO photocatalyst. By using the simple and rapid microwave synthesis, phytochemicals from longan seeds such as flavonoids, catechins, vitamins, proteins, and sugars can be employed as either the capping or reducing agents, or both at same time which driven the ZnO nanoparticles synthesis. Such green synthesis of ZnO nanoparticles can be employed further for wastewater treatment of the local textile dyeing industry and contributing to the circular economy in the region.

Natural reagents in new normal chemistry education

Covid-19 has deeply affected the education sector globally as it forced many schools and colleges to remain closed temporarily. For most science students, their hands-on experience working as a real scientist in school and university laboratory are limited during this lockdown period, whereas in some region, certain students are inaccessible to fully stocked and supported teaching lab owing to limited funding. Despite such scenarios have created many problems; one can harness it as an opportunity for profound changes in our practical education approach that will align our teaching laboratories with those where we conduct our research, by adopting green chemistry principles to the practice of science education lab work. We live in a golden age of easy-to-access instrumentation thanks to smartphones which can be used as detector in chemical analysis. The difficulties of having to set up a measurement almost from scratch, without technicians to prepare equipment and solutions, could help inculcate a spirit of improvisation. By combining these factors, lab-at-home teaching is ready in action. Some of the examples using natural reagents extracted from plants as alternative low-cost tools in teaching chemical analysis, especially in school laboratories that ought to operate within a stiff budget. In some of the universities in Thailand, the ready-to-use natural reagents were introduced in the academic year of 2019 in science and pharmaceutical science courses. They were also employed in lab-at-home sessions and E-workshops. One of the examples was using the natural reagent kit for iron assay in water quality testing which adapted from Thai local wisdom using guava leaves. The kit was equipped with dry guava leaf powder that served as natural reagent in the assay, iron(III) standard and buffer solutions, sample vials, 96-wells microplate as reaction platform and a manual. The camera from smartphone was used as the detector to monitor the difference in color intensity of the reaction product which attributed by the reaction in between iron(III) and phenolic compounds in the natural reagent. Students from six different universities have received the kit via postage during the pandemic lock-down period and had benefits from this lab-at-home practice [31]. The initiative of using modern green chemical analysis in the online classroom setting received great feedback from teachers and learners as the chemicals involved utilized locally available bioresource as the natural reagent for green analysis in chemistry education which supports the sustainable education in Thailand. The method is now being employed by an increasing number of institutions. The team has demonstrated that their experience in conducting this green analytical research can be incorporated into the new normal style of teaching [32].

Challenges in natural reagents application

Natural reagents hold great promise for addressing global humanitarian needs including the goals of sustainable development. The sources of natural reagents and their applications are numerous, yet they are still largely an untapped resource. Use of natural reagents as a source of greener and cheaper reagents for a range of analytical tasks should not be seen as an option just for the developing world, but as something that is equally applicable worldwide. Opportunity should be valued when a natural reagent can be legitimately substituted for a purified or synthetic material, without compromising the viability or quality of the analytical process. Despite not explored here, there is also great potential to utilize food grade or domestic chemicals in a range of analytical procedures, again without prejudice to analytical quality. However, most current developments are not immediately translatable to outside-the-lab scenarios which differ in terms of resource-accessible and resource-limited aspects. Resource-accessible settings include scenarios whereby technology is deployed with essentially unlimited access to resources and experienced personnel. Resource-limited settings refer to situations marked by limited or no access to resources and expertise, which unfortunately most part of ASEAN fall in this category. Such challenges necessitate the time constraints in accessing commercially available chemicals especially when dealing with the long duration of waiting period for procurement. The increasing prices of reagent grade chemicals may restrict the accessibility as well. For instance, when students extract an indicator from plant tissue, and applied in an acid base titration or extracting the acid phosphatase from potatoes and used in the study of

enzyme behavior and kinetics, costing of such experiments can be varied by 30 times as compared to procuring of 50 units acid phosphatase from a major US supplier which costs about $60 dollar with ca. $2 for a sack of potatoes. Students studying such fundamental analytical and biochemical behavior would gain an appreciation for the important role of natural product chemistry.

Conclusion

This mini review discusses the simple natural reagents and natural materials which were developed from a century-old local knowledge in the rural area, and through the combining with today technology, such phenomenon contributes to green chemistry, principally in green analytical chemistry aspect, leading to sustainable chemistry which could serves many goals of the United Nation Sustainable Development Goals (UN SDGs). Research of such direction has gained of interest as indicated by the increasing trends in publications. ASEAN is rich in bioresources, there are talent and challenges in development of utilizing natural reagents and natural materials for chemical analysis in new normal chemical analysis. To meet the talent and challenge, works across disciplines with networking would enhance the targets. Apart from analytical scientists, researchers in the other fields including, natural product, computational chemistry, chemometrics, other fields of chemistry, computer scientists etc. should work together. The work would reflect: Local issue- Global impact- Sustainable world.

Acknowledgement

The authors would like to thank the Thailand Research Fund (TRF) Distinguished Research Professor Award Grant (DPG6080002) and indirect support by Alexander von Humboldt Foundation (K. Grupdan); Universiti Malaya for RU SATU Grant ST022-2020 (P.M. Woi); Chiang Mai University (through Center of Excellence on Innovation in Analytical Science and Technology (I-ANALY-S-T), Cluster of Excellence on Biodiversity-based Economics and Society (B.BES-CMU) and postdoctoral fellowship grant (K. Kiwfo).

References

1. Anastas, P. and Eghbali, N. (2010). Green chemistry: principles and practice. *Chemical Society Reviews*, 39(1): 301-312.
2. Abdussalam-Mohammed, W., Qasem Ali, A. and Errayes, A. O. (2020). Green Chemistry: principles, applications, and disadvantages. *Chemical Methodologies*, 4(4): 408-423.
3. OECD (2021). Sustainable chemistry. Access from https://www.oecd.org/chemicalsafety/risk-management/sustainablechemistry.htm [Retrieved 13 September 2021].
4. Gamal, M., Naguib, I. A., Panda, D. S. and Abdallah, F. F. (2021). Comparative study of four greenness assessment tools for selection of greenest analytical method for assay of hyoscine N-butyl bromide. *Analytical Methods*, 13(3): 369-380.
5. Koel, M. (2016). Do we need green analytical chemistry?. *Green Chemistry*, 18(4): 923-931.
6. Chang, F., Zhang, X., Zhan, G., Duan, Y. and Zhang, S. (2021). Review of methods for sustainability assessment of chemical engineering processes. *Industrial & Engineering Chemistry Research*, 60(1): 52-66.
7. Chinwong, D., Charaj, P., Panitsupakamol, P., Chankaew, T., Chinwong, S. and Saenjum, C. (2021). Local wisdom of miang lifestyle and community for sustainable development in Northern Thailand. *Sustainability*, 13: 7381.
8. Lim, T. K. (2012). Garcinia dulcis. In edible medicinal and non-medicinal plants: fruits. Springer Netherlands: pp. 35-40.
9. Purnama, H., Hidayati, N., Safitri, D. S. and Rahmawati, S. (2017). Effect of initial treatment in the preparation of natural indigo dye from Indigofera tinctoria. *AIP Conference Proceedings*, 1855(1): 020022.
10. Settheeworrarit, T., Hartwell, S. K., Lapanatnoppakhun, S., Jakmunee, J., Christian, G. D. and Grudpan, K. (2005). Exploiting guava leaf extract as an alternative natural reagent for flow injection determination of iron. *Talanta*, 68(2): 262-26.

11. Grudpan, K., Hartwell, S. K., Wongwilai, W., Grudpan, S. and Lapanantnoppakhun, S. (2011). Exploiting green analytical procedures for acidity and iron assays employing flow analysis with simple natural reagent extracts. *Talanta*, 84(5): 1396-1400.
12. Kanna, M., Somnam, S., Wongwilai, W. and Grudpan, K. (2019). Towards green titration: Batchwise titration with reusable solid sorbed indicators. *Analytical Sciences*, 35(3): 347-350.
13. Pinyou, P., Kradtap Hartwell, S., Jakmunee, J., Lapanantnoppakhun, S. and Grudpan, K. (2010). Flow Injection determination of iron ions with green tea extracts as a natural chromogenic reagent. *Analytical Sciences*, 26(5): 619-623.
14. Siriangkhawut, W., Ponhong, K. and Grudpan, K. (2019). A green colorimetric method using guava leaves extract for quality control of iron content in pharmaceutical formulations. *Malaysian Journal of Analytical Sciences*, 23(4): 595-603.
15. Supharoek, S.-A., Ponhong, K. and Grudpan, K. (2017). A green analytical method for benzoyl peroxide determination by a sequential injection spectrophotometry using natural reagent extracts from pumpkin. *Talanta*, *171*, 236-241.
16. analytical methodology using indian almond (*Terminalia Catappa L.*) leaf extract for Insain, P., Khonyoung, S., Sooksamiti, P., Lapanantnoppakhun, S., Jakmunee, J., Grudpan, K., Zajicek, K. and Kradtap Hartwell, S. (2013). Green determination of aluminum ion in waste water from ceramic factories. *Analytical Sciences*, *29*(6): 655-659.
17. Siriangkhawut, W., Khanhuathon, Y., Chantiratikul, P., Ponhong, K. and Grudpan, K. (2016). A green sequential injection spectrophotometric approach using natural reagent extracts from heartwood of *Ceasalpinia sappan Linn*. for Determination of Aluminium. *Analytical Sciences*, 32(3): 329-336.
18. Kiwfo, K., Wongwilai, W., Paengnakorn, P., Boonmapa, S., Sateanchok, S. and Grudpan, K. (2018). Noodle based analytical devices for cost effective green chemical analysis. *Talanta*, 181: 1-5.
19. Siriangkhawut, W., Didpinrum, P., Khanhuathon, Y., Ponhong, K. and Grudpan, K. (2020). Small-scale ultrasound-assisted extraction of phenolics from pomegranate peels and their application as a natural reagent for the colorimetric assay of iron. *Analytical Letters*, 53(6): 887-904.
20. Kotchabhakdi, N., Seanjum, C., Kiwfo, K. and Grudpan, K. (2021). A simple extract of Leucaena leucocephala (Lam.) de Wit leaf containing mimosine as a natural color reagent for iron determination. *Microchemical Journal*, 162: 105860.
21. Weerasuk, B., Supharoek, S.-a., Grudpan, K. and Ponhong, K. (2021). Exploiting crude betel nut (*Areca catechu* Linn.) extracted solution as a natural reagent with sequential injection spectrophotometry for iron analysis in rice samples. *Journal of the Iranian Chemical Society*, 19: 741-751.
22. Tapala, W., Chankaew, C., Grudpan, K. and Rujiwatra, A. (2021). Silver-miang nanocomposites: A green, rapid and simple approach for selective determination of nitrite in water and meat samples. *Microchemical Journal*, 162: 105879.
23. Ganranoo, L., Chokchaisiri, R. and Grudpan, K. (2019). Simple simultaneous determination of iron and manganese by sequential injection spectrophotometry using astilbin extracted from Smilax china L. root. *Talanta*, 191: 307-312.
24. Jaikang, P., Paengnakorn, P. and Grudpan, K. (2020). Simple colorimetric ammonium assay employing well microplate with gas pervaporation and diffusion for natural indicator immobilized paper sensor via smartphone detection. *Microchemical Journal*, 152: 104283.
25. Sabarudin, A. and Indrayani, D. O. (2019). Sequential Injection analysis for determination of lead(II) using extract of *Caesalpinia pulcherrima* as a natural reagent. *IOP Conference Series. Materials Science and Engineering*, 546(3): 032027.

26. Kiwfo, K., Woi, P. M., Saenjum, C. and Grudpan, K. (2022). New designs of paper based analytical devices (PADs) for completing replication analysis of a sample within a single run by employing smartphone. *Talanta*, 236: 122848.
27. Kiwfo, K., Wongwilai, W., Sakai, T. N. T., Murakami, H.P. P., Phojuang, K., Kotchabhakdi, N. and Grudpan, K. (2020). Simple natural material based microfluidic platforms with a smartphone detection employing natural reagent for acidity assay. *Journal Flow Injection Analysis*, *37*(1): 9-12.
28. Sateanchok, S., Wongwilai, W., Kiwfo, K. and Grudpan, K. (2016). The assay of anionic surfactant employing thread based analytical device with mobile phone. *Journal Flow Injection Analysis*, 33(1): 5-7.
29. Sateanchok, S., Wangkarn, S., Saenjum, C. and Grudpan, K. (2018). A cost-effective assay for antioxidant using simple cotton thread combining paper based device with mobile phone detection. *Talanta*, 177: 171-175.
30. Chankaew, C., Tapala, W., Grudpan, K. and Rujiwatra, A. (2019). Microwave synthesis of ZnO nanoparticles using longan seeds biowaste and their efficiencies in photocatalytic decolorization of organic dyes. *Environmental Sciene Pollution Research International*, 26(17): 17548-17554.
31. Kiwfo, K., Yeerum, C., Issarangkura Na Ayutthaya, P., Kesonkan, K., Suteerapataranon, S., Panitsupakamol, P., Chinwong, D., Paengnakorn, P., Chinwong, S., Kotchabhakdi, N., Saenjum, C., Vongboot, M. and Grudpan, K. (2021). Sustainable Education with local-wisdom based natural reagent for green chemical analysis with a smart device: experiences in Thailand. *Sustainability*, 13(20): 11147.
32. Center, C. C. A. R. (2021). CMU researcher creates green innovation in chemical analysis from century-old wisdom of the Fang people. Access from https://www.cmu.ac.th/en/article/7b2719e8-86bc-4d0c-9205-9b4a40647597

Malaysian Journal of Analytical Sciences (MJAS)
Published by Malaysian Analytical Sciences Society

OPTIMISATION OF THE EXTRACTION METHOD OF RED *Christia vespertilionis* LEAVES TO YIELD BIOACTIVE PHYTOCHEMICAL AS MONITORED BY GAS CHROMATOGRAPHY-MASS SPECTROMETRY

(Pengoptimuman Kaedah Pengekstrakan Pada Daun Merah *Christia vespertilionis* untuk Menentukan Fotokimia Bioaktif Melalui Kromatografi Gas-Spektrometri Jisim)

Izzah Farhah Zambari[1], Sitti Rahma Abdul Hafid[2], Nur Airina Muhamad[1]*

[1]*Institute of Biological Sciences, Faculty of Science, Universiti Malaya, 50603 Kuala Lumpur, Malaysia.*
[2]*Nutrition Unit, Product Development and Advisory Services Division, Malaysian Palm Oil Board, 43000 Kajang, Selangor, Malaysia.*

**Corresponding author: nurairina@um.edu.my*

Received: 31 August 2021; Accepted: 30 December 2021; Published: 28 April 2022

Abstract

Christia vespertilionis (L. f.) Bakh. f. is well-known for treating various contagious diseases. This plant has been recognised among researchers and locals to have anti-inflammatory properties and has thus become popular for treating cancer. Two types of *C. vespertilionis* are acknowledged which are green and red. The green *C. vespertilionis* has been widely studied by many researchers, however just a few have studied the red type. This study was carried out to optimise the extraction method of red *C. vespertilionis* leaves by different extraction techniques (maceration and Soxhlet extraction) and solvents (methanol and ethanol) to yield bioactive phytochemicals using gas chromatography-mass spectrometry (GC-MS). The components were identified through GC-MS via comparisons as guided by the National Institute of Standards and Technology Mass Spectral Library 2011 (NIST 11, version 2.0g). According to the four (4) samples of red *C. vespertilionis* leaves using maceration of methanol (RMM), maceration of ethanol (RME), Soxhlet extraction of methanol (RSM), and Soxhlet extraction of ethanol (RSE), seventy-one (71) bioactive phytochemicals were identified. Eleven (11) major bioactive phytochemicals (abundance of > 4%) were identified namely, acetic acid, butyl ester; 1-butanol, 3-methyl-, acetate; heptanoic acid, propyl ester; hexanoic acid, 3-oxo-, ethyl ester; phenol, 3,5-bis(1,1-dimethylethyl)-; 1-octadecene; 4-O-methylmannose; .alpha.-d-mannofuranoside, methyl; 2-undecene, 9-methyl-, (E)-; n-hexadecanoic acid; and 1-octadecanol. Only seven (7) out of eleven (11) compounds were reported to have biological activities. Among those samples, RSM was the most effective using correlation coefficient between abundance (%) and retention time (minute(s)) with a significant difference at $P < 0.05$.

Keywords: *Christia vespertilionis*, gas chromatography-mass spectrometry, phytochemicals, maceration, Soxhlet extraction

Abstrak

Christia vespertilionis (L. f.) Bakh. f. dikenali secara meluas dalam merawat pelbagai penyakit berjangkit. Tumbuhan ini diakui di kalangan penyelidik dan penduduk tempatan tentang kelebihannya sebagai salah satu ubat tradisional yang mempunyai sifat

anti-radang serta digunakan secara meluas dalam merawat barah. Terdapat dua jenis *C. vespertilionis* iaitu jenis hijau dan merah. *C. vespertilionis* hijau telah banyak dikaji oleh penyelidik dan hanya sedikit yang dikaji untuk jenis merah. Kajian ini dijalankan untuk mengoptimumkan kaedah pengekstrakan daun *C. vespertilionis* merah dengan teknik pengekstrakan yang berbeza (pengekstrakan maserasi dan Soxhlet) dan pelarut (metanol dan etanol) untuk menentukan fitokimia bioaktif melalui kromatografi gas-spektrometri jisim (GC-MS). Komponen tersebut dikenal pasti melalui GC-MS dengan membuat perbandingan dari data rujukan Institut Piawaian dan Teknologi Nasional 2011 (NIST11-MS, version 2.0g). Berdasarkan 4 sampel daun merah *C. vespertilionis* melalui maserasi metanol (RMM), maserasi etanol (RME), pengekstrakan Soxhlet methanol (RSM) dan pengekstrakan Soxhlet etanol (RSE), tujuh puluh satu (71) sebatian fitokimia dikenal pasti. Sebelas (11) sebatian fitokimia utama (> 4 % kawasan puncak) juga dikenalpasti seperti asid asetik, butil ester; 1-butanol, 3-metil-, asetat; asid heptanoik, propil ester; asid heksanoik, 3-okso-, etil ester; fenol, 3,5-bis (1,1-dimetiletil)-; 1-oktadekena; 4-O-metilmanos; .alpha.-d-manofurosida, metil; 2-undekena, 9-metil-, (E)-; asid n-heksadekanoik dan 1-oktadekanol. Hanya tujuh (7) daripada sebelas (11) sebatian yang dilaporkan mempunyai aktiviti biologi. Di antara sampel tersebut, RSM adalah yang paling berkesan dengan menggunakan pekali korelasi antara kebanyakan (%) dan masa pengekalan (min) dengan perbezaan yang signifikan pada $P < 0.05$.

Kata kunci: *Christia vespertilionis*, kromatografi gas-spektrometri jisim, fitokimia, maserasi, pengekstrakan Soxhlet

Introduction

Christia vespertilionis (L. f.) Bakh. f. is a family of Fabaceae that is known as butterfly wing because of its shape, which is similar to that of a butterfly wing. This plant possesses the ability to cure several diseases due to it having various biological activities such as anti-cancer, anti-inflammatory, anti-proliferative and anti-plasmodial properties [1, 2, 3]. In Malaysia, *C. vespertilionis* leaves are consumed by cancer patients and have gained great popularity among Malaysians, including researchers who are keen to explore and discover the real potential of this plant.

C. vespertilionis is known to potentially exhibit various bioactive secondary compounds that can be used in food and pharmaceutical areas [4]. Previous studies revealed the presence of bioactive secondary compounds in *C. vespertilionis* such as alkaloid, phenol, fatty acid, triterpene and alcohol [2]. The aerial part of *C. vespertilionis* is revealed to contain corynoxidine and palmitine [2]. *C. vespertilionis* also possesses great anti-proliferative activities in MTC cells and is excellent in anti-plasmodial activities using aqueous-methanol extracts [1,2]. Other studies showed that *C. vespertilionis* extract has a high inhibition on cancer cells such as human medullary thyroid carcinoma and human intestinal neuroendocrine tumours [5]. In addition, *C. vespertilionis* exhibits moderately as an anti-malaria which is against the 3D7 malaria parasite and literally can be used for malaria treatment [6].

Today, people have developed high interest in traditional plants, as a substitute for synthetic drugs. Plant comes from nature and safe to use. It is also low cost and has less negative side effects [7]. However, the World Health Organization (WHO) has noted that inappropriate practices of using traditional plants for treatment can have dangerous effects. Therefore, further study is necessary to ascertain the efficacy and safety of plants for human consumption. While many studies of *C. vespertilionis* have been conducted, there is no study available on bioactive phytochemicals of red *C. vespertilionis* leaves using gas chromatography-mass spectrometry (GC-MS). GC-MS is one of the techniques that separates individual compounds in the form of a mass spectrum and measurement of the abundance of chromatography [8]. Identification of compounds in GC-MS is achieved by comparing mass spectrum of sample with the reference National Institute of Standards and Technology Mass Spectral Library 2011 (NIST11-MS) based on matching system.

Prior to that, before GC-MS, red *C. vespertilionis* leaves need to undergo extraction to separate the target products from the raw materials. Currently, solvent extraction is widely used in natural plants and herb medicines. Selection of solvent is also a crucial part for solvent extraction. The solvent with a shorter differences of polarity value to the polarity of the solute, is expected to perform better. As regarding the technique of extraction, there are two commonly used methods namely as maceration and Soxhlet extraction.

These methods were most of the time given acceptable results, however Soxhlet can be time-consuming although requires a small amount of sample compared to maceration. Therefore, this research aims to optimise the extraction method of red *C. vespertilionis* leaves in different extraction techniques (maceration and Soxhlet extraction) and solvents (methanol and ethanol) to yield bioactive phytochemicals using GC-MS.

Materials and Methods

Plant material

Red *C. vespertilionis* was collected from Floranika Nursery Sungai Buloh, Selangor (Malaysia), located at a latitude and longitude of 3° 13' 6.7764" N, 101° 34' 18.1704" E, respectively. The voucher specimen was authenticated by Dr Yong Kien Thai from Plant Taxonomy, Rimba Ilmu, University of Malaya. The voucher specimen of red *C. vespertilionis* (KLU 50025) was placed at the herbarium of the University of Malaya, and left to air-dry for 7 to 8 days. Leaves were ground with a blender to obtain coarse powder for extraction and were kept in a closed jar until further use.

Maceration

1 g of dried leaves powder of red *C. vespertilionis* was immersed into a 100 ml of methanol, MeOH (Merck, Germany), and absolute ethanol, EtOH (VWR Chemicals, American) in a 250 ml conical flask, separately. The samples were left in a water bath at 40 °C for 48 hours. The extracts were filtered and evaporated with rotary evaporator at 45 °C until they were concentrated. The extracts were filtered again to remove any solid particles and kept tightly closed in a microcentrifuge tube at 4 °C until further use.

Soxhlet extraction

1 g of dried leaves powder of red *C. vespertilionis* was extracted with 200 ml of MeOH (Merck, Germany), and absolute EtOH (VWR Chemicals, American) using a Soxhlet apparatus, separately. The samples were left in a water bath at 40 °C for 48 hours. The extracts were filtered and evaporated using a rotary evaporator at 45 °C until they were concentrated. The extracts were filtered again to remove any solid particles and kept tightly closed in a microcentrifuge tube at 4 °C until further use.

Gas chromatography-mass spectrometry analysis

Samples were diluted to 500 ppm with the respective solvents into 1.5 ml vials. The GC-MS analysis was done at the IPPP Central Laboratory Facilities, University Malaya, Kuala Lumpur, Malaysia. Model of GCMS-QP2010 Ultra (Shimadzu, Tokyo, Japan) was used for the GC-MS analysis. This model is a single quadrupole gas chromatograph-mass spectrometer that produces stable and affordable analyses for complex compounds. 0.5 µl of the sample was auto-injected into the system. The system was supplied with a capillary column of RTX5MS with length x diameter of 30.0 m × 0.25 mm and a 0.25 µm of thickness. The injection temperature was set to 200 °C which possessed a splitless injection mode. The initial temperature was 50 °C (3 minutes) with an accelerating rate of 10 °C (1 minute) to 300 °C (10 minutes). Helium gas was used with 47.8 cm/second of linear velocity. Electron ionisation (EI) mode at 70 eV with a spectral range of 35 m/z-500 m/z was performed for mass spectra results. The ion source temperature was fixed at 150 °C and the interface temperature was at 230 °C with a solvent cut-off time of 3 minutes. The start time was set at 3.0 minutes and the final time was adjusted at 33 minutes. The total flow programmed was 21.6 ml/minute with a column flow of 1.69 ml/minute. The compounds were determined based on the interpretation of mass spectrum with standard reference spectral using the National Institute of Standards and Technology Mass Spectral Library 2011 (NIST11) version 2.0g databases.

Statistical analysis

The correlation between abundance and retention time of the sample was determined using GraphPad Prism 8.0.2, where Pearson's correlation coefficient test was conducted and the difference was considered statistically significant when $P < 0.05$. Chemical structure drawing was applied on the website: https://chemwriter.com/.

Results and Discussion

GC-MS chromatogram and bioactive phytochemicals

GC-MS is important to identify bioactive phytochemicals in a complex compound using a technique of separation in a GC system and measuring on a mass spectrometer that comes with an electron ionisation (EI) ion source. There are two electron ionisation (EI) main spectrum library: main and replicate with a total of 212,961 and 30,932 mass spectra, respectively. NIST11-MS library has a total of 346,757 retention index for 70,835 compounds that were extracted based on column type, column class, data type and program type [9]. Through GC-MS analysis showed seventy-one (71) phytochemicals from four (4) samples that consist of major and minor compounds. Major compounds consisted of an abundance larger than 4% [10] as shown in Table 3. The conditions of the samples were shown in Table 1.

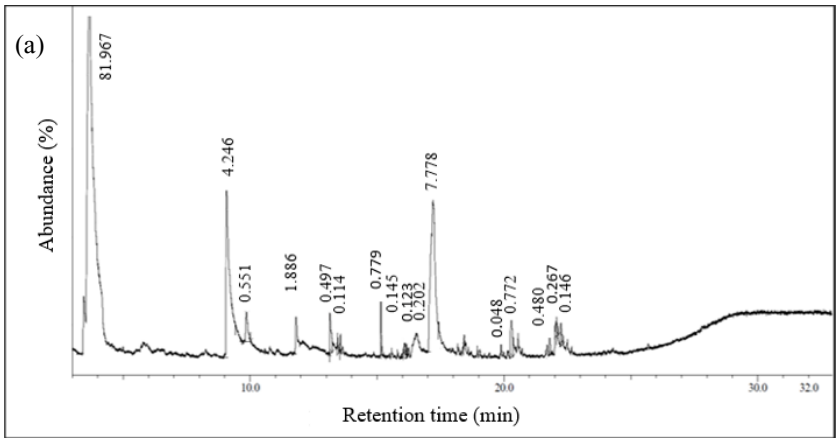
Bioactive phytochemicals of the samples were presented in Table 2 and the GC-MS chromatogram of the abundance of samples shown in Figure 1. GC-MS analysis for RMM resulted in a total of sixteen (16) peaks (according to Figure 1(a) and Table 2). There are three (3) major compounds, namely: acetic acid, butyl ester (81.967%); 1-butanol, 3-methyl-, acetate (4.246%) and 4-O-methylmannose (7.778%). RME resulted in a total of thirty (30) peaks (according to Figure 1(b) and Table 2). There were seven (7) major compounds, namely: 1-butanol, 3-methyl-, acetate (27.414%); heptanoic acid, propyl ester (5.700%); phenol, 3,5-bis(1,1-dimethylethyl)- (6.232%); 1-octadecene (6.079%); .alpha.-d-mannofuranoside, methyl (10.247%); 2-undecene, 9-methyl-, (E)- (5.505%) and 1-octadecanol (4.152%).

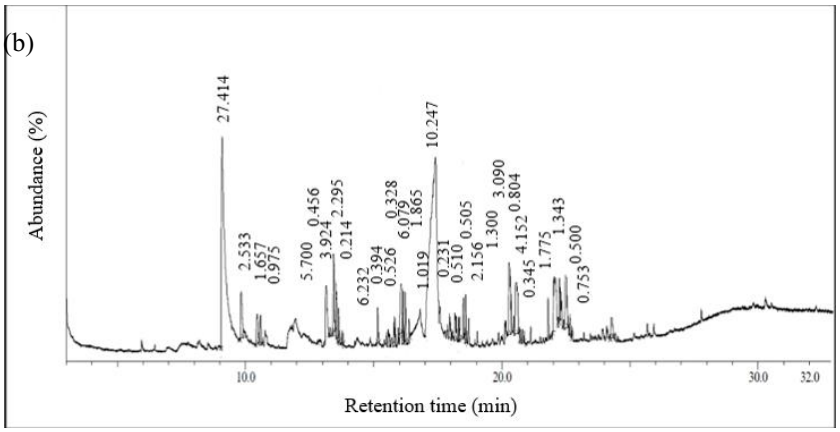
Furthermore, RSM resulted in a total of thirty-three (33) peaks (according to Figure 1(c) and Table 2). Five (5) major compounds were identified, namely: acetic acid, butyl ester (11.655%); 1-butanol, 3-methyl-, acetate (31.037%); hexanoic acid, 3-oxo-, ethyl ester (5.549%); 4-O-methylmannose (21.491%) and n-hexadecanoic acid (4.465%). Lastly, RSE resulted in a total of thirty-seven (37) peaks (according to Figure 1(d) and Table 2). Four (4) major compounds comprised: 1-butanol, 3-methyl-, acetate (6.414%); phenol, 3,5-bis(1,1-dimethylethyl)- (5.950%); 4-O-methylmannose (4.085%) and n-hexadecanoic acid (8.733%).

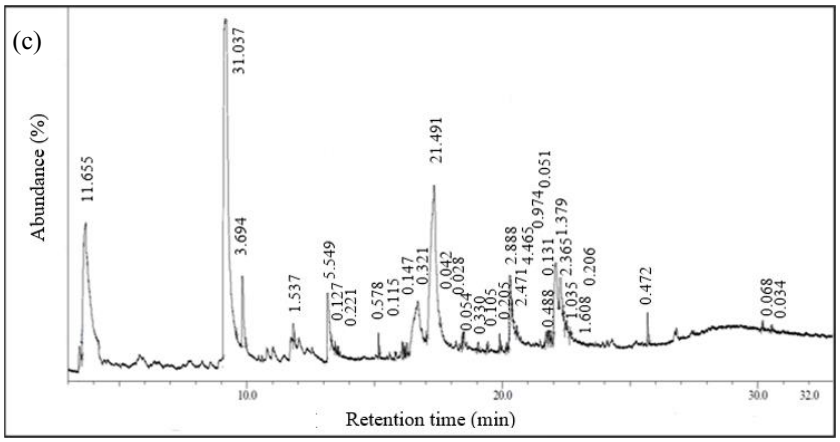
Previous study found other major compounds on red *C. vespertilionis* leaves extract such as 10-undecenoic acid (5.00%), 6-methylheptyl-2-propenoate (4.96%), 2-(2-benzothiazolylthio)-1-(3,5-dimethylpyrazolyl)-ethanone (2.70%), tetrahydro-2-methyl-thiophene (61.77%) and phytol (8.59%) [11]. Another study also found that *C. vespertilionis* leaves methanolic extract exhibited hexadecanoic acid (4.87 %), 9,12,15-octadecatrienoic acid (7.82%), phytol (6.97%), 2-propenoic acid (8.75%) and cyclododecane (7.04%) [12]. These previous study outcomes also can be found in Table 2 such as 9,12,15-octadecatrienoic acid, phytol and hexadecanoic acid.

Table 1. Conditions of samples

Plant	Technique	Solvent	Sample Code	Temperature (°C)	Time (hours)
Red *C. vespertilionis*	Maceration	MeOH	RMM	40	48
		EtOH	RME		
	Soxhlet extraction	MeOH	RSM	< 64.7	5
		EtOH	RSE	< 78.37	


(a)
Abundance (%)
81.967
4.246
0.551
1.886
0.497
0.114
0.779
0.145
0.123
0.202
7.778
0.048
0.772
0.480
0.267
0.146
10.0
20.0
30.0
32.0
Retention time (min)


(b)
Abundance (%)
27.414
2.533
1.657
0.975
5.700
0.456
3.924
2.295
0.214
6.232
0.394
0.526
0.328
6.078
1.865
1.019
10.247
0.231
0.510
0.505
2.156
1.300
3.090
0.804
4.152
0.345
1.775
1.343
0.500
0.753
10.0
20.0
30.0
32.0
Retention time (min)


(c)
Abundance (%)
11.655
31.037
3.694
1.537
5.549
0.127
0.221
0.578
0.115
0.147
0.321
21.491
0.042
0.028
0.054
0.330
0.105
0.205
2.888
2.471
4.465
0.974
0.051
0.488
0.131
2.365
1.379
1.035
1.608
0.206
0.472
0.068
0.034
10.0
20.0
30.0
32.0
Retention time (min)

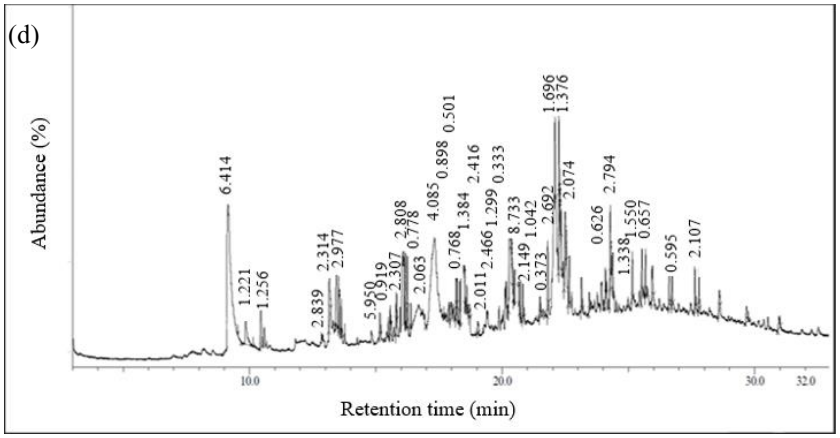


Figure 1. GC-MS chromatogram abundance (%) versus retention time (min) of a) red *C. vespertilionis* methanolic leaves extract in maceration (RMM); b) red *C. vespertilionis* ethanolic leaves extract in maceration (RME); c) red *C. vespertilionis* methanolic leaves extract in Soxhlet extraction (RSM); d) red *C. vespertilionis* ethanolic leaves extract in Soxhlet extraction (RSE)

Table 2. Phytochemicals compounds found in red *C. vespertilionis* leaves based on abundance and retention time

	Bioactive Phytochemicals	**Retention Time (min)**	**Abundance (%)**			
			Maceration		**Soxhlet**	
			MeOH (RMM)	**EtOH (RME)**	**MeOH (RSM)**	**EtOH (RSE)**
1	Acetic acid, butyl ester	3.683	81.967	-	11.655	-
2	1-butanol, 3-methyl-, acetate	9.179	4.246	27.414	31.037	6.414
3	4H-pyran-4-one, 2,3-dihydro-3,5-dihydroxy-6-methyl-	9.815	0.551	2.533	3.694	1.221
4	1-dodecene	10.459	-	-	-	1.256
5	3-tetradecene, (Z)-	10.461	-	1.657	-	-
6	Dodecane	10.590	-	0.975	-	-
7	1,3-diisobutyrin, trimethylsilyl	11.817	1.886	-	1.537	-
8	Heptanoic acid, propyl ester	13.140	0.497	5.700	-	-
9	Hexanoic acid, 3-oxo-, ethyl ester	13.160	-	0.456	5.549	2.839
10	1-tridecene	13.446	0.114	3.924	-	-
11	1-tetradecene	13.449	-	-	0.127	2.314
12	Tetradecane	13.555	-	2.295	0.221	2.977
13	Cyclotetradecane	13.775	-	0.214	-	-
14	Phenol, 3,5-bis(1,1-dimethylethyl)-	15.150	0.779	6.232	0.578	5.950
15	2-hexyl-1-octanol	15.570	-	0.394	-	-
16	1-octanol, 2-butyl-	15.801	-	0.526	-	-
17	1-hexadecene	16.072	0.145	0.328	-	-

Table 2 (cont'd). Phytochemicals compounds found in red *C. vespertilionis* leaves based on abundance and retention time

	Bioactive Phytochemicals	Retention Time (min)	Abundance (%)			
			Maceration		Soxhlet	
			MeOH (RMM)	EtOH (RME)	MeOH (RSM)	EtOH (RSE)
18	1-octadecene	16.077	-	6.079	-	0.919
19	1-heptadecene	16.079	-	-	0.115	2.307
20	Pentadecane	16.162	0.123	1.865	-	-
21	Nonadecane	16.167	-	-	-	2.808
22	Hexadecane	16.170	0.202	-	0.147	-
23	Dichloroacetic acid, 4-hexadecyl ester	16.253	-	-	-	0.778
24	2-undecene, 3-methyl-, (Z)-	16.254	-	1.019	-	2.063
25	1,2-benzenedicarboxylic acid, mono(2-ethylhexyl) ester	16.269	-	-	0.321	-
26	4-O-methylmannose	17.404	7.778	-	21.491	4.085
27	.alpha.-d-mannofuranoside, methyl	17.421	-	10.247	-	-
28	1-hexanol, 5-methyl-2-(1-methylethyl)-	17.958	-	0.231	-	-
29	Cyclohexane, 2-butyl-1,1,3-trimethyl-	18.173	-	-	-	0.898
30	1-decanol, 2-hexyl-	18.176	-	0.510	0.042	0.501
31	1-pentadecene, 2-methyl-	18.214	-	-	-	0.768
32	Cyclopropane, 1-methyl-1-(1-methylethyl)-2-nonyl-	18.400	-	-	-	1.384
33	2-undecene, 9-methyl-, (E)-	18.430	-	5.505	-	-
34	1-heneicosanol	18.431	-	2.156	-	2.416
35	4,5-heptadien-2-ol, 3,3,6-trimethyl-	18.435	-	-	0.028	-
36	n-heneicosane	18.501	-	-	-	2.011
37	Undecane, 3-methylene-	18.594	-	-	-	2.466
38	Tridecane, 3-methylene-	18.595	-	1.300	-	1.299
39	2-pentadecanone, 6,10,14-trimethyl-	19.039	-	-	0.054	0.333
40	1,2-benzenedicarboxylic acid, bis(2-methylpropyl) ester	19.392	-	-	0.330	-
41	Hexadecanoic acid, methyl ester	19.895	-	-	0.105	-
42	Heptacosanoic acid, methyl ester	19.900	-	-	0.205	-
43	1-eicosanol	20.282	-	-	2.888	-
44	Methyl di-tert-butylhydroxyhydrocinnamate	20.284	-	-	2.471	-
45	n-hexadecanoic acid	20.291	0.772	3.090	4.465	8.733
46	Dibutyl phthalate	20.392	-	-	0.974	-
47	Octacosanol	20.558	-	0.804	-	2.149
48	1-octadecanol	20.561	0.048	4.152	-	-
49	3-eicosene, (E)-	20.562	-	-	0.051	-

Table 2 (cont'd). Phytochemicals compounds found in red *C. vespertilionis* leaves based on abundance and retention time

	Bioactive Phytochemicals	Retention Time (min)	Abundance (%)			
			Maceration		Soxhlet	
			MeOH (RMM)	EtOH (RME)	MeOH (RSM)	EtOH (RSE)
50	Heneicosane, 11-(1-ethylpropyl)-	20.607	-	-	-	1.042
51	1-docosene	20.816	-	0.345	-	-
52	1-tetradecanol	21.502	-	-	-	0.373
53	Phytol	21.798	0.480	1.775	0.488	
54	1,1,1,3,5,7,7,7-octamethyl-3,5-bis-(trimethylsiloxy)-tetrasiloxane	21.808	-	-	-	2.692
55	Methyl 9-methyltetradecanoate	21.901	-	-	0.131	-
56	9,12,15-octadecatrienoic acid, methyl ester, (Z,Z,Z)-	22.090	-	-	1.379	-
57	9,12,15-octadecatrienoic acid, (Z,Z,Z)-	22.092	0.267	1.343	2.365	1.696
58	Tetradecyl trifluoroacetate	22.253	-	-	1.035	-
59	Octadecanoic acid	22.255	0.146	0.500	1.608	1.376
60	1-tetracosanol	22.498	-	-	-	2.074
61	2,4-pentadien-1-ol, 3-pentyl-, (2Z)-	22.659	-	-	0.206	-
62	9-(3,3-dimethyloxiran-2-yl)-2,7-dimethylnona-2,6-dien-1-ol	22.660	-	0.753	-	-
63	1-dodecanol, 2-octyl-	24.091	-	-	-	0.626
64	Heptasiloxane, hexadecamethyl-	24.377	-	-	-	2.794
65	Hexacosane	25.151	-	-	-	1.338
66	Diisooctyl phthalate	25.679	-	-	0.472	1.550
67	Docosane	25.954	-	-	-	0.657
68	Eicosane	26.730	-	-	-	0.595
69	Squalene	27.788	-	-	-	2.107
70	Cholesta-4,6-dien-3-ol, (3.beta.)-	30.174	-	-	0.068	-
71	.alpha.-tocopheryl acetate	30.522	-	-	0.034	-
	Quantity of identified compound		16	30	33	37

Optimisation of extraction

Correlation was used between abundance and retention time of the sample in GC-MS for all compounds found. Maceration using MeOH (RMM) was significantly high at $P < 0.011$ (Figure 2). When using EtOH (RME), the significant difference was at $P < 0.049$. In Soxhlet, the significant difference was high in MeOH (RSM) with $P < 0.009$ and there was no significant difference in (RSE) which was at $P < 0.104$. The smaller the P value, the more significant it is. A total of seventy-one (71) abundance were analysed for each sample. The results indicated that significant difference between abundance and retention time increased when using Soxhlet extraction particularly in MeOH.

Extraction methods using different solvents play an important role to exhibit bioactive phytochemicals. Based on Figure 2, abundances of compounds are exhibited more when using Soxhlet extraction and MeOH. A previous study stated that the polarity of MeOH could be the reason for the high exhibition of

compounds [13]. Other study stated that using MeOH produces high bioactive phytochemicals particularly compounds that cure inflammation which is extracted from the branches of *S. buxifolia* [14]. It was also revealed that MeOH is a solvent that is more effective in extracting secondary metabolite compounds from *M. viridis* than any other plants in the Lamiaceae family [15].

The technique of extraction is also one of the factors that contribute to the effectiveness of bioactive phytochemicals attribution. Based on Figure 2, more compounds were exhibited using Soxhlet extraction as compared to maceration. Soxhlet extraction offered more efficiency and was less time-consuming as compared to maceration. Other researches obtained similar results in *Nepeta leucophylla* and *Potentilla atrosanguinea* aerial parts when using Soxhlet extraction where it exhibited significantly higher, and attained maximum percentage yields than maceration [4, 16]. Therefore, for red *C. vespertilionis* leaves, Soxhlet extraction obtained highest compounds attribution as compared to the maceration technique. Overall, red *C. vespertilionis* leaves work efficiently using Soxhlet extraction and MeOH as a solvent.

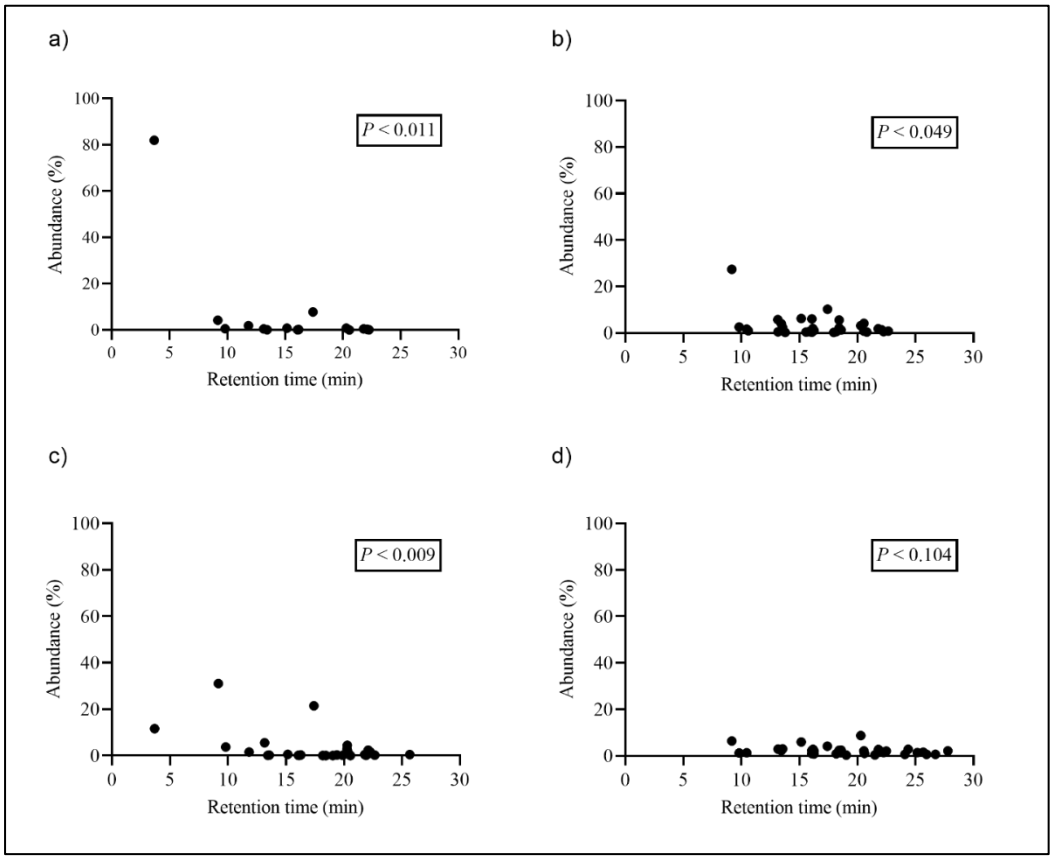


Figure 2. Correlation between abundance (%) versus retention time (min) of a) RMM b) RME c) RSM and d) RSE

Major bioactive phytochemicals

Four (4) samples (RMM, RME, RSM and RSE) of *C. vespertilionis* leaves extract, detected seventy-one (71) bioactive phytochemicals, which consisted of major and minor compounds using GC-MS, as presented in Table 2. The abundance presented for each sample is shown in Figure 1. Through this analysis, it was found that eleven (11) major compounds achieved higher than

4 % of the abundance from all of samples as presented in Table 3.

The eleven (11) major bioactive phytochemicals were acetic acid, butyl ester (81.967%), 1-butanol, 3-methyl-, acetate (31.037%), heptanoic acid, propyl ester (5.700%), hexanoic acid, 3-oxo-, ethyl ester (5.549%), phenol, 3,5-bis(1,1-dimethylethyl)- (6.232%), 1-octadecene (6.079%), 4-O-methylmannose (21.491%), .alpha.-d-mannofuranoside, methyl (10.247%), 2-undecene, 9-methyl-, (E)- (5.505 %), n-hexadecanoic acid (8.733%), and 1-octadecanol (4.152%).

The n-hexadecanoic acid and 1-octadecanol possessed anti-inflammatory activities [17,18]. The antimicrobial agent was revealed by 1-butanol, 3-methyl-, acetate, [19]. Ethyl acetate root extract of *C. vespertilionis* showed the highest total phenolic content that is responsible for good anti-inflammatory and anti-microbial properties [20,21]. Meanwhile, 1-octadecene possessed anti-cancer property [22, 23]. Based on the previous study, *C. vespertilionis* extract has viability against various cell lines such as WRL68 (normal liver), CRL 2522 (fibroblast), HepG2 (liver carcinoma), MCF-7 (breast cancer) and HaCaT (keratinocyte) with the IC50 values of 1.93, 1.51, 1.63, 1.74 and 1.22 mg/ml, respectively [24]. Four (4) compounds had antibacterial activities that included n-hexadecanoic acid, 4-O-methylmannose, 1-octadecene and phenol, 3,5-bis(1,1-dimethylethyl)- [23, 24, 26-30].

Most of the compounds possessed anti-oxidants, including 1-octadecanol, n-hexadecanoic acid and 1-octadecene [18, 23, 26, 31]. *C. vespertilionis* ethyl acetate: methanol extract has significantly exhibited the highest DPPH scavenging activity with the IC50 value of 0.549 ± 0.02 mg/mL [32]. Acetic acid, butyl ester was the most abundant compounds that is beneficial as an antifungal and antitumour [33]. *C. vespertilionis* inhibited tumour growth and increase survival time of mice induced with S180 AND H22 tumour cells [34]. Another known compound was phenol, 3,5-bis(1,1-dimethylethyl)- which acts as an antiseptic, disinfectant and flavourant [24, 29]. No biological activity was reported for heptanoic acid, propyl ester; hexanoic acid, 3-oxo-, ethyl ester; .alpha.-d-mannofuranoside, methyl and 2-undecene, 9-methyl-, (E)-. Therefore, only seven (7) out of eleven (11) major compounds were reported their biological activities.

Table 3. Major bioactive phytochemicals of red *C. vespertilionis* leaves

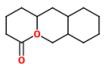
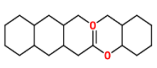
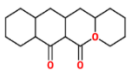
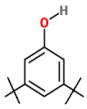
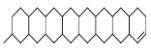
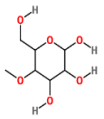
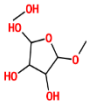
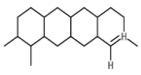
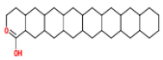
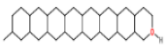
	Name of Compound/ Chemical Classes	Rt (Min)	Abundance (%) Maceration		Soxhlet		Formula	MW	Structure	Biological Properties
			MeOH (RMM)	EtOH (RME)	MeOH (RSM)	EtOH (RSE)				
1	Acetic acid, butyl ester (Carboxylic acid ester)	3.683	+ 81.967	-	+ 11.655	-	$C_{16}H_{12}O_2$	116		Antifungal, Antitumor [33]
2	1-butanol, 3-methyl-, acetate (Carboxylic acid ester)	9.179	+ 4.246	+ 27.414	+ 31.037	+ 6.414	$C_7H_{14}O_2$	130		Antimicrobia [19]
3	Heptanoic acid, propyl ester (fatty acid ester)	13.140	-	+ 5.700	-	-	$C_{10}H_{20}O_2$	172		No activity reported

Table 3 (cont'd). Major bioactive phytochemicals of red *C. vespertilionis* leaves

	Name of Compound/ Chemical Classes	Rt (Min)	Abundance (%) Maceration		Soxhlet		Formula	MW	Structure	Biological Properties
			MeOH (RMM)	EtOH (RME)	MeOH (RSM)	EtOH (RSE)				
4	Hexanoic acid, 3-oxo-, ethyl ester (fatty acid ester)	13.160	-	-	+ 5.549	-	$C_8H_{14}O_3$	158		No activity reported
5	Phenol, 3,5-bis(1,1-dimethylethyl)- (phenolic ester)	15.150	-	+ 6.232	-	+ 5.950	$C_{14}H_{22}O$	206		Antiseptic, disinfectant, flavouring, antibacterial [24,29]
6	1-octadecene (Alkene hydrocarbon)	16.077	-	+ 6.079	-	-	$C_{18}H_{36}$	252		Antibacterialal, antioxidant, anticancer [22, 23, 26]
7	4-O-methylmannose (aliphatic ether alcohol)	17.404	+ 7.778	-	+ 21.491	+ 4.085	$C_7H_{14}O_6$	194		Antibacterial [27, 28]
8	alpha.-d-mannofuranoside, methyl (methyl mannoside)	17.421	-	+ 10.247	-	-	$C_7H_{14}O_6$	194		No activity reported
9	2-undecene, 9-methyl-, (E)- (hydrocarbon)	18.430	-	+ 5.505	-	-	$C_{12}H_{24}$	168		No activity reported
10	n-hexadecanoic acid (fatty acid)	20.291	-	-	+ 4.465	+ 8.733	$C_{16}H_{32}O_2$	256		Anti-inflammatory, antibacterial, antioxidant [17, 30, 31].
11	1-octadecanol (fatty alcohol)	20.561	-	+ 4.152	-	-	$C_{18}H_{38}O$	270.5		Anti-inflammatory, antioxidant [18].
	Total of major compounds		3	7	5	4				

Conclusion

This study revealed that red *C. vespertilionis* leaves have various bioactive compounds that has high potential to treat diseases. Red *C. vespertilionis* leaves possessed biological activities of anti-inflammatory, antitumour, anticancer, antibacterial, antimicrobial, antioxidant and antifungal properties. The compounds were greatly exhibited from Soxhlet extraction and MeOH as a solvent. Conclusively, this study achieved success in identifying bioactive phytochemicals of red *C. vespertilionis* leaves in different techniques and solvents. Further study needs to be done to isolate bioactive phytochemicals and investigate its biological activities. A comparison to green *C. vespertilionis* needs to be analysed to observe the differences in terms of bioactive phytochemicals and biological activities.

Acknowledgement

The authors are thankful to the University of Malaya for the financial support on the research project through Research University of Faculty Programme Grant Scheme (GPF006B-2018). Appreciation to Institute of Biological Sciences and Infra Analysis Laboratory for the opportunity to use laboratories and infrastructures to perform this research.

References

1. Nguyen-Pouplin, J., Tran, H., Phan, T. A., Dolecek, C., Farrar, J., Tran, T. H., Caron, P., Bodo, B. and Grellier, P. (2007). Antimalarial and cytotoxic activities of ethnopharmacologically selected medicinal plants from South Vietnam. Journal Ethnopharmacology, 109: 417-427.
2. Hofer, D., Schwach, G., Tabrizi-Wizsy, N.G., Sadjak, A., Sturm, S., Stuppner, H. and Pfragner, R. (2013). *Christia vespertilionis* plant extracts as novel antiproliferative agent against human neuroendocrine tumor cells. *Oncology Reports,* 6(29): 2219-2226.
3. Osman, M. S., Ghani, Z. A., Ismail, N. F., Razak, N. A., Jaapar, J. and Ariff, M. A. (2017). Qualitative comparison of active compounds between red and green *Mariposa Christia vespertillonis* leaves extracts. *AIP Conference Proceedings,* 1885(020282): 1-6.
4. Sharma, A. and Cannoo, D.S. (2016). Effect of extraction solvents/techniques on polyphenolic contents and antioxidant potential of the aerial parts of *Nepeta leucophylla* and the analysis of their phytoconstituents using RP-HPLC-DAD and GC-MS. *RSC Advance,* 6: 78151-78160.
5. Bunawan, H., Bunawan, S. N. and Baharum, S. N. (2015). The red butterfly wing (*Christia vespertilionis*): A promising cancer cure in Malaysia. *International Journal of Pharmacy and Pharmaceutical Sciences* 7(8): 1.
6. Mohd Yasin, Z. N., Zakaria, M. A., Nik Mat Zin, N. N. I., Ibrahim, N., Mohamad, F. S., Mat Desa, W. N. S., Sul'ain, M. D. and Abu Bakar, N. (2020). Biological activities and GCMS analysis of the methanolic extract of *Christia vespertilionis* (L.F.) Bakh. F. leaves. *Asian Journal of Medicine and Biomedicine* 4(1): 1-11.
7. Haida, Z. and Hakiman, M. (2019). A review of therapeutics potentials of *Clinacanthus nutans* as source for alternative medicines. *Sains Malaysiana,* 48(12): 2683-2691.
8. Yusufzai, S. K., Khan, M. S., Hanry, E. L., Rafatullah, M. and Elison, B. (2019). GC-MS analysis of chemical constituents and *in vitro* antioxidant activity of the organic extracts from the stem of *Bridelia stipularis*. *Sains Malaysiana,* 48(5): 999-1009.
9. NIST/NIH/EPA Mass Spectral Library, Standard Reference Database 1, NIST 11. (2011). Standard Reference Data Program, National Institute of Standards and Technology. Gaithersburg, MD, USA.
10. Abd Rahim, E. N. A., Ismail, A., Omar, M. N., Rahmat, U. N. and Wan Ahmad, W. A. N. (2018). GC-MS analysis of phytochemical compounds in *Syzygium polyanthum* leaves extracted using ultrasound-assisted method. *Pharmacognosy Journal,* 10(1): 110-119.

11. Mohd Yasin, Z. N., Zakaria, M. A., Nik Mat Zin, N. N.I., Ibrahim, N., Mohamad, F. S., Mat Desa, W. N. S., Sul'ain, M. D. and Abu Bakar, N. (2020). Biological activities and chemical compositions of the methanol extract of *Christia vespertilionis* leaves. *Asian Journal of Medicine and Biomedicine* 4(2): 78-88.
12. Sidek, M. M., Ismail, N. Z., Zain, N. N. M. and Arsad, H. (2019). Cytotoxicity activity of *Christia vespertilionis* leaves extracts against Hela cells and the detection of compounds by GC-MS. *Journal of Biological & Scientific Opinion,* 7(6): 71-78.
13. Gami, B. and Parabia, F. (2011). Screening of methanol & acetone extract for antimicrobial activity of some medicinal plants species of Indian folklore. *International Journal Research Pharmaceutical Sciences,* 2(1): 69-75.
14. Truong, D-H., Nguyen, D-H., Ta, N.T.A., Bui, A.V., Do, T.H. and Nguyen, H.C. (2019). Evaluation of the use of different solvents for phytochemical constituents, antioxidants, and in vitro anti-inflammatory activities of *Severinia buxifolia*. *Journal of Food Quality*, 2019: 8178294.
15. Karunaratne, U. K. P. R. and Karunaratne, M. M. S. C. (2012). Evaluation of methanol, ethanol and acetone extracts of four plant species as repellents against *Callosobruchus maculatus* (Fab.). *Vidyodaya Journal of Science* 17: 1-8.
16. Kalia, K., Sharma, K., Singh, H.P. and Singh, B. (2008). Effects of extraction methods on phenolic contents and antioxidant activity in aerial parts of *Potentilla atrosanguinea* L. and quantification of its phenolic constituents by RP-HPLC. *Journal Agriculture Food Chemistry,* 56: 10129-10134.
17. Aparna, V., Dileep, K. V., Mandal, P. K., Karthe, P., Sadasivan, C. and Haridas, M. (2012). Antiinflammatory property of n-hexadecanoic acid: Structural evidence and kinetic assessment. *Chemical Biology Drug Design,* 80(3): 434-439.
18. Singab, A. N., El-Taher, E. M. M., Elgindi, M. R and Kassem, M-S. (2015). *Phoenix roebelenii* O'Brien DNA profiling, bioactive constituents, antioxidant and hepatoprotective activities. *Asian Pacific Journal Tropical Disease,* 5(7): 552-558.
19. Mitchell, A. M., Strobel, G. A., Moore, E., Robison, R. and Sears, J. (2010). Volatile antimicrobials from *Muscodor crispans*, A novel endophytic fungus. *Microbiology,* 156: 270-277.
20. Chew, Y. L., Chan, E. W. L., Tan, P. L., Lim, Y. Y., Stanslas, J. and Goh, J. K. (2011). Assessment of phytochemical content, polyphenolic composition, antioxidant and antibacterial activities of Leguminosae medicinal plants in Peninsular Malaysia. *BMC complementary and Alternative Medicine,* 11(1): 12.
21. Lee, J. J., Yazan, L. S., Kassim, N. K., Che Abdullah, C. A., Esa, N., Lim, P. C. and Tan, D.C. (2020). Cytotoxic activity of *Christia vespertilionis* root and leaf extracts and fractions against breast cancer cell lines. *Molecules,* 25(2610):1-18.
22. Lee, Y. S., Kang, M. H., Cho, S. Y. and Jeong, C. S. (2007). Effects of constituents of *Amomum xanthioides* on gastritis in rats and on growth of gastric cancer cells. *Achieve Pharmaceutical Research,* 30(4): 436-443.
23. Belakhdar, G., Benjouad, A. and Abdennebi, E.H. (2015). Determination of some bioactive chemical constituents from *Thesium humile* Vahl. *Journal Materials Environmental Sciences,* 6(10): 2778-2783.
24. Duke J. (2002). American Agricultural Research Service-Phytochemical & Ethnobotanical Database. Available at: *http://www.ars-grin.gov/duke/index.html* [accessed on 09 December 2019].
25. Mutalib, N. A. and Latip, N. A. (2019). Synergistic interactions between *Christia vespertilionis* leaves extract and chemotherapy drug cyclophosphamide on WRL-68 Cell Line. *Asian Journal of Pharmaceutical Research and Development*, 7(3): 109-113.
26. Mishra, P. M. and Sree, A. (2007). Antibacterial activity and GCMS analysis of the extract of leaves of *Finlaysonia obovata* (a mangrove plant). *Asian Journal Plant Sciences,* 6(1): 168-172.

27. Kumar, P. R. Z. A. and Bhaskar, A. (2012). Phytochemical evaluation by GC-MS and *in vitro* antioxidant activity of *Punica granatum* fruit rind extract. *Journal of Chemical and Pharmaceutical Research,* 4(6): 2869-2873.
28. Suman, T., Chakkaravarthi, K. and Elangomathavan, R. (2013). Phyto-chemical profiling of *Cleistanthus collinus* leaf extracts using GC-MS analysis. *Research Journal Pharmaceutical and Technology,* 6(11): 1173-1177.
29. Igwe, K. K., Okafor, P. N. and Ijeh, I. I. (2015). GC-MS analysis of phytocomponents in *Vernonia amygdalina. Del* leaves and its contractile potential in mammary tissue in female albino Wistar rats. *Journal of Agriculture and Veterinary Science,* 8(11): 25-30.
30. Johannes, E., Litaay, M. and Syahribulan. (2016). The bioactivity of hexadecanoic acid compound isolated from hydroid *Aglaophenia cupressina* lamoureoux as antibacterial agent against *Salmonella* typhi. *International Journal Biological Medicinal Research,* 7(2): 5469-5472.
31. Gavamukulya, Y., Abou-Elella, F., Wamunyokoli, F. and El-Shemy, H. A. (2015). GC-MS analysis of bioactive phytochemicals present in ethanolic extracts of leaves of *Annona muricata*: A further evidence for its medicinal diversity. *Pharmacognosy Journal*, 7(5): 300-304.
32. Shukri, N. S. S. M., Perumal, V., Balan, T., Murugesu, S., Khatib, A., Saleh, M. S. M, Hin, L.W., Darus, K. A., Zailani, I.A. and Zahidi, F. A. H. M. (2019). The screening of antioxidant activities and FTIR analysis of *Christia vespertilionis* leaves extracts. *International Journal of Research in Pharmaceutical Sciences*, 10(1): 1713.
33. Guo, L., Wu, J., Han, T., Cao, T., Rahman, K. and Qin, L. (2008). Chemical composition, antifungal and antitumor properties of ether extracts of *Scapania verrucosa* Heeg. and its endophytic fungus *Chaetomium fusiforme*. *Molecules,* 13: 2114-2125.
34. Wu, X. Y., Tang, A. C. and Lu, Q. Y. (2012). Study on antitumor effect of the extract from *Christia vespertilionis in vivo*. *Chinese Journal of Experimental Traditional Medical Formulae*, 8: 202-204.

Malaysian Journal of Analytical Sciences (MJAS)
Published by Malaysian Analytical Sciences Society

ESSENTIAL MINERALS AND HEAVY METALS ANALYSIS OF PENANG ASSAM LAKSA USING ATOMIC ABSORPTION SPECTROMETRY, FLOW INJECTION MERCURY SYSTEM, AND INDUCTIVELY COUPLED PLASMA OPTICAL EMISSION SPECTROMETRY

(Analisis Mineral Penting dan Logam Berat Asam Laksa Pulau Pinang Menggunakan Spektrometri Penyerapan Atom dn Spektrometri Pancaran Optik Induktif Gabungan Plasma)

Phang Hui Lee[1,2], Koo Pooi Ling[2], Lim Gin Keat[2]*, Oo Chuan Wei[2], Tan Kean Chye[3]

[1]Jabatan Perubatan Forensik,
Hospital Pulau Pinang,
1, Jalan Tull, George Town, 10450 George Town, Pulau Pinang, Malaysia
[2]School of Chemical Sciences,
Universiti Sains Malaysia, 11800 USM, Penang, Malaysia
[3]Department of Family Medicine,
RCSI and UCD Malaysia Campus,
4, Jalan Sepoy Lines, 10450 George Town, Pulau Pinang, Malaysia

**Corresponding author: limgk@usm.my*

Received: 9 November 2021; Accepted: 10 February 2022; Published: 28 April 2022

Abstract

Penang Assam Laksa is a sour, fish-based soup popular in Malaysian street food. The content of heavy metals (Cd, Hg, and Pb) as well as essential minerals (Fe, Ca, Na, and K) in ready-to-eat Penang Assam Laksa food samples collected from five stalls over three different days was determined using flame atomic absorption spectrometry (FAAS), a Flow Injection Mercury System (FIMS), and inductively coupled plasma optical emission spectrometry (ICP-OES) after a wet-digestion procedure. Statistical analyses such as Student's *t*-test and an inter-day precision study were conducted on the obtained results. The wet-digestion procedure was found to be effective, with recoveries above 85%. Meanwhile, an inconsistency in element content was observed for food samples collected on different days. Based on Student's *t*-test, both FAAS and ICP-OES were suitable for detecting and quantifying heavy metals and essential minerals in the food samples.

Keywords: Penang Assam Laksa, heavy metal, essential minerals, street food

Abstrak

Asam Laksa Pulau Pinang adalah sup masam yang berasaskan ikan. Kandungan logam berat (Cd, Hg, Pb) serta mineral penting (Fe, Ca, Na, K) dalam Asam Laksa Pulau Pinang (makanan sedia dimakan) yang dikumpul dari lima gerai terpilih pada tiga hari berbeza telah ditentukan menggunakan FAAS (spektrometri penyerapan atom nyalaan), FIMS (sistem merkuri suntikan aliran) dan ICP-OES (spektrometri pancaran optik induktif gabungan plasma) selepas prosedur pencernaan basah. Analisis statistik seperti *Ujian-t* pelajar dan kajian ketepatan antara hari telah dijalankan ke atas keputusan yang diperolehi. Prosedur pencernaan

basah didapati merupakan kaedah yang berkesan dalam mencerna sampel makanan dengan pemulihan lebih daripada 85%. Sementara itu, ketidakselarasan kandungan unsur diperhatikan daripada sampel makanan yang dikumpul pada hari yang berbeza. Berdasarkan *Ujian-t* pelajar, kedua-dua FAAS dan ICP-OES sesuai untuk pengesanan dan penentuan logam berat dan mineral penting dalam sampel makanan.

Kata kunci: Asam Laksa Pulau Pinang, logam berat, mineral penting, makanan jalanan

Introduction

Food is a fundamental requirement for sustaining life. The rapid acceleration of the human population has led to the creation of various kinds of foods, including street foods, which are defined as ready-to-eat foods and beverages that are prepared and/or sold by street vendors [1]. Generally, street foods are rich in macro- and micro-nutrients. Macro-nutrients such as carbohydrates, fats, and proteins are needed in relatively large amounts, as they provide energy to the human body, while micro-nutrients in food comprise vitamins and inorganic minerals such as calcium (Ca), potassium (K), and iron (Fe). Essential minerals are present in small quantities but play significant roles in human biology, especially as catalysts for enzymatic activities [2-5]. For example, sodium (Na) and K are common electrolytes that drive the transmission of signals along nerves as well as maintain water balance, while Fe is a principal component in hemoglobin production, which is responsible for oxygen transportation [6-8] in blood. Either inadequate or excessive intake of essential minerals will adversely affect human health. Hypocalcemia, also known as low blood calcium levels may result in tetany, whereas hypercalcemia may lead to kidney-stone formation (nephrolithiasis) [7].

Street foods can readily become contaminated with heavy metals such as cadmium (Cd), lead (Pb), and mercury (Hg) due to environmental pollution, which is all the more common in modern times [9]. Heavy metals are substances that occur naturally and are often present in the environment at trace levels [10]. Heavy metals have caused widespread concern due to their tendency to accumulate in selective human tissues (liver, brain, and kidney) and not decay over time. These characteristics will eventually lead to various types of disorders, such as peripheral neuropathy and different cancers9. Previous studies have shown that humans are exposed to heavy metals via the ingestion of contaminated food and beverages [3, 9, 10]. Hence, is has become necessary to perform food analysis in order to assess food quality and safety.

Food analysis is a challenging task in analytical chemistry; the presence of heavy metals and essential minerals in trace quantities, as well as the complex nature of food matrices, have only increased its difficulty. Proper and efficient sample preparation followed by a highly sensitive instrumental analysis is often required to obtain quality element-content data in food [11]. There are numerous types of sample digestion methods that have been successfully employed in determining element content in diverse food samples. Dry-ashing and wet-digestion procedures are well established methods, and their efficiency has been reported in previous studies. Dry ashing is known to be effective in digesting organic materials in food samples, but it is time-consuming and prone to losses due to volatilization and/or retention problems [9, 12, 13]. Wet digestion is relatively simple, rapid, and inexpensive compared to dry ashing. This procedure benefits from small sample quantities and greater flexibility, as the sample weight and digestion conditions can be changed accordingly.

In recent years, numerous analytical techniques have been developed for determining element content in food samples. These techniques include neutron activation analysis (NAA), voltammetry, atomic absorption spectrometry (AAS), inductively coupled plasma optical emission spectrometry (ICP-OES), and inductively coupled plasma mass spectrometry (ICP-MS) [4, 9, 10, 14, 15, 16]. Among these techniques, AAS (including flame atomic absorption spectrometry, FAAS, and graphite furnace atomic absorption spectrometry, GFAAS), ICP-OES, and ICP-MS [4, 15] are well established as mainstays in food analysis

because of their rapidity and effectiveness in detecting and quantifying elements in samples at extremely low concentrations [4, 10, 11, 16]. In addition, flow injection analysis (FIA) using devices such as the Flow Injection Mercury System (FIMS) is also employed, as it combines the advantages of flow injection and atomic absorption measurement into a compact Hg analyzer [17].

In Malaysia, Penang is well known as a food paradise due to its wide variety of street foods. These foods reflect the multicultural makeup of the state, which has citizens of Chinese, Malay, and Indian descent. One of the most famous Penang street foods is Penang Assam Laksa, which is a broth made of shredded fish (*Kembung* fish or mackerel) and finely sliced vegetables [cucumber, onions, red chilies, pineapples, lettuce, fresh mint, and torch ginger (in Malay: *bunga kantan*)][18]. An increased interest in street foods has led to public concern about their safety and quality, owing to their socioeconomic importance as well as nutritional value. However, there is a paucity of proper studies and data on this kind of fresh, ready-to-eat food, as most studies focus on raw, uncooked foods or commercialized food products. Thus, there is a need to perform a proper scientific study to obtain a general picture of the nutritional content of Penang Assam Laksa. Such information can help prove the safety of the food and increase confidence among consumers.

This study mainly aimed to detect the essential minerals (Ca, Fe, Na, and K) and heavy metals (Hg, Cd, and Pb) in Penang Assam Laksa by using FAAS, FIMS, and ICP-OES. The safety of the food was further assessed by comparing the element content obtained from collected food samples to the permissible levels stated in Malaysia Food Act 1983 and Food Regulations 1985 [19], as well as the recommended dietary allowance (RDA) from U.S. Dietary Guideline 2010 [18]. Finally, a simple comparative study was performed to evaluate the agreement between the results provided by these two different groups of techniques.

Materials and Methods

Chemicals and Standards

Concentrated nitric acid (HNO_3, 65%, Merck, USA) and hydrogen peroxide (H_2O_2, 35%, Hmbg, India) were purchased from local chemical suppliers. Commercial 1000-ppm standard stock solutions (Perkin Elmer Laboratory preparation, USA) containing elements of interest were used to prepare working standard solutions, all of which were freshly prepared prior to analysis. Ultrapure water was produced by a Milli-Q System (Millipore, Bedford, MA, USA) and used for solution preparation as well as sample digestion.

Sample Collection and Handling

Fifteen food samples (Penang Assam Laksa) were purchased from five selected areas throughout Penang Island on three different days, all of which were cooked and ready-to-eat. Upon purchasing, the solid ingredients (sliced vegetables and noodles) and the broth of the samples were packed separately with leak-proof nylon bags. During sample preparation, the solid ingredients were soaked in the broth and left for 20 min. After that, the mixture was filtered, and the broth was collected for further treatment.

Wet Digestion of Samples

The wet-digestion procedure performed in this work was adopted from a study by Salau and Hassan [5]. Three 5-mL aliquots of previously filtered broth samples were transferred to three conical flasks. Ten mL of HNO_3 was added to the sample and left overnight (24 h) in a fume hood. The following day, further digestion was carried out by adding a mixture of HNO_3 and H_2O_2. Details about the procedure and its steps are summarized in Table 1. The solutions were filtered with white filter papers (WHATMAN, qualitative filter papers, 125-mm diameter) and then re-filtered with a syringe filter. Then, the filtered solutions were diluted with ultrapure water to 100 mL and transferred into polyethylene sample bottles and kept in a refrigerator.

Table 1. Wet digestion procedure for samples

Step	Ultrapure water added (mL)	HNO_3 added (mL)	H_2O_2 added (mL)	Heating (°C)	Time (min)
1	-	10	-	-	Overnight
2	-	5	2	100	30
3	-	10	4	100	30
4	30	5	2	100	30
5	30	10	2	100	20

Recovery Study

Standard solutions containing the elements of interest were prepared at three different concentrations: 6.00, 8.00, and 10.00 ppm, except for those of Hg, which were prepared at 0.10, 0.15, and 0.20 ppm. Five-mL samples of the prepared food were spiked with 0.5 mL of the standard solutions. The spiked samples were prepared in triplicate at each concentration. Simultaneously, unspiked blank solutions containing 5 mL of food sample and 0.5 mL of ultrapure water were prepared as well. These spiked and unspiked samples then went through the digestion procedure as described above before subsequent instrumental analysis.

Instrumental Analysis

A Perkin Elmer AAnalyst 400, a Perkin Elmer FIMS 100, and a Perkin Elmer Optima 8000 were used for FASS, FIMS, and ICP-OES analyses of the target elements, respectively. All the instruments were equipped with WinLab 32 computer software for data acquisition. For every target element, calibration was performed prior to instrumental analysis. The calibration curves for all elements were plotted as absorbance intensity against concentration in ppm (with the exception of ppb for Hg analysis) using Microsoft Excel, and correlation coefficients, R^2, for all curves were determined. Working standard solutions of certain concentrations were prepared accordingly by diluting the 1000-ppm standard stock solutions. The standard stock solutions were drawn by using micropipette. Samples collected on Days 1 and 2 were run on instruments at the same time, while samples collected on Day 3 were run separately with a new calibration cycle. The concentrations of the working standards for each element remained unchanged for the first and second runs.

Statistical Analysis

Student's *t*-test was performed by means of Excel in order to determine whether the two methods (FAAS/FIMS and ICP-OES) gave significantly different results. Meanwhile, an inter-day precision study was conducted for the samples collected on different days by expressing the repeatability in terms of relative standard deviation (RSD).

Results and Discussion

Recovery and Efficiency of Wet Digestion Procedure

The accuracy and efficiency of the wet digestion procedure performed on the spiked samples at three different concentration levels were evaluated in triplicate. The average recovery (%) of all target elements is presented in Table 2, which shows that the recoveries for all the target elements were satisfactory - more than 85% of the elements were recovered from the spiked samples. In FAAS, the highest digestion efficiency was achieved for Cd at 96.1%, whereas Pb exhibited the lowest efficiency at 86.3%. In contrast, Hg exhibited the highest average recovery percentage in ICP-OES (94.5%). Based on this recovery assay, the efficiency of the digestion procedure used in this work was confirmed.

Table 2. Average recovery for all targeted elements

Elements	Average Recovery (%)	
	FAAS/FIMS	ICP-OES
Hg	91.6	94.5
Cd	96.1	85.8
Pb	86.3	91.7
Fe	94.0	90.3
Ca	91.7	91.1
Na	93.5	93.5
K	94.1	86.9

Instrumental Analysis of Studied Foods

Linearity of Analysis: Every elemental analysis carried out via FAAS, FIMS, and ICP-OES consisted of two calibration cycles, as the food samples were run in two batches. All the calibration curves exhibited linearity, with R^2 values greater than 0.99, except for Hg via ICP-OES, as well as K and Na via FAAS, which gave slightly lower R^2 values. As an overall observation, all the calibration curves demonstrated a linear response within a particular range. It was noted that both calibration cycles for the elements generated different regression equations and R^2 values, but these differences were quite small and negligible, as they did not possess any significant meaning.

Detection of Essential Minerals in Studied Food Samples: The mineral-content ranges of the food samples were compared to the RDA for minerals according to U.S. Dietary Guideline 2010, as shown in Table 3. Since the RDA values stated in the guideline are in units of mg/day, for ease of comparison, an assumption was made wherein the mineral content presented in the Tables 3 and 4 under this section is normalized as that in 250-mL samples. Adequate Fe intake is crucial to prevent anaemia [2]. It was noted that the order of Fe content for each sample collected at different locations showed the same pattern for the three different collection days. The highest detected Fe content was 1.98 mg/L by FAAS and 1.51 mg/L ICP-OES. According to U.S. Dietary Guideline 2010 [8], adult females and males are recommended to take approximately 18.00 mg and 8.00 mg of Fe per day, respectively. In general, all the studied food samples were considered to have adequate levels of Fe for an adult male older than 19 years. However, the Fe content was insufficient for an adult female because they experience the Fe losses associated with physiological processes (menstruation) [8].

Calcium is the most abundant cation in the human body. According to U.S. Dietary Guideline 2010 [8], an adult is recommended to take 1.00×10^3 mg of Ca daily as an upper intake level (UL). From Table 3, the highest detected Ca content was 3.25×10^2 mg/L (FAAS) and 2.61×10^2 mg/L (ICP-OES). The high Ca content in the studied food samples was most probably due to mackerel, the main ingredient of the food samples, since it was reported in a previous study that mackerel contains high levels of Ca, ranging from 1.60×10^3 to 1.80×10^3 mg/L [20]. All the studied food samples were considered to have adequate Ca levels for an adult older than 19 years.

For Na, adequate intake (AI) levels are used instead of RDA, since the latter could not be determined. The determined Na concentration of all the studied food samples approached the AI level and was less than the UL. The highest Na levels were 1.23×10^3 mg/L (FAAS) and 1.44×10^3 mg/L (ICP-OES). The Na content in the studied food samples was most likely due to salt (sodium chloride), which is added to enhance taste. Based on the obtained results, the

studied food samples were considered to have adequate Na levels. However, the consumption of Penang Assam Laksa is advised to be reduced in order to avoid excessive Na intake.

Potassium is important for building muscle as well as metabolizing proteins and carbohydrates [8]. The highest concentration of K was detected at 1.52×10^3 mg/L and 6.67×10^2 mg/L for FAAS and ICP-OES, respectively. The AI level for K established by U.S. Dietary Guideline 2010 is approximately 4.70×10^3 mg/day; all the studied samples were considered to have sufficient K, most likely because of the mackerel - the main ingredient of the broth [21].

Table 3. Ranges of Fe, Ca, Na, and K contents in the studied food samples detected by FAAS and ICP-OES (assuming 250 mL of broth per serving unit)

Element	Range of Concentration Detected (mg/L)		Recommended Dietary Allowance
	FAAS	ICP-OES	
Fe	5.48×10^{-1} to 1.98	5.57×10^{-1} to 1.51	18.00 mg per day (female above 19 y.o.) 8.00 mg per day (male above 19 y.o.)
Ca	3.96×10 to 3.25×10^2	1.18×10^2 to 2.61×10^2	1.00×10^3 mg per day (male and female above 19 y.o.) Adequate Intakes
Na	7.32×10^2 to 1.23×10^3	6.87×10^2 to 1.44×10^3	1.50×10^3 mg per day (male and female above 19 y.o.)
K	1.92×10^2 to 1.52×10^3	1.44×10^2 to 6.67×10^2	4.70×10^3 mg per day (male and female above 19 y.o.)

*All values are expressed as a mean in ppm or mg/L

* y.o. = years old

* Recommended dietary allowance and adequate intakes (Source: US DA & US DHS 2010)[8]

Detection of Heavy-Metal Contents in Studied Food Samples: The concentration of heavy metals detected in all food samples was tabulated and compared to the permissible levels stated in Malaysia Food Act 1983 and Food Regulations 1985 [19], as seen in Table 4.

Cadmium affects cell proliferation, differentiation, and apoptosis; it also inhibits both cellular respiration and oxidative phosphorylation at low concentrations [22]. In this study, Cd was not detectable via ICP-OES for all samples, while it was detectable via FAAS. This observation does not lead to the conclusion that the samples were free of Cd. Instead, the results only suggest that Cd was undetectable in ICP-OES, as FAAS was able to give readings. Basically, the Cd content in the studied food samples ranged from 7.80×10^{-2} to 2.85×10^{-1} mg/L (in FAAS determination). This concentration level was relatively low and did not exceed the permissible level stated in Malaysia Food Act 1983 and Food Regulations 1985 [19], which is 1.00 mg/L.

The FIMS used in this study was a dedicated Hg system coupled with a high-sensitivity Hg detector [17]. This instrument was designed purposely for Hg quantification with an extremely low detection limit (as suggested by the user manual of the instrument) of less than 5.00×10^{-6} mg/L, as compared to the much higher 5.10×10^{-3} mg/L for ICP-OES. In other words, ICP-OES is not sensitive enough to detect Hg at trace

levels; thus, it yielded no readings or measurements in this study. The Hg detected in most of the food samples was present at trace amounts ranging from 9.00×10^{-4} to 8.10×10^{-3} mg/L, lower than the permissible level of 5.00×10^{-2} mg/L as stated in Malaysian Food Act 1985 [12]. Meanwhile, Hg was undetectable in a few samples.

The Pb levels in the food samples were significantly higher than those of Cd and Hg. According to Malaysia Food Act 1983 and Food Regulations 1985 [19], the permissible level of Pb in food is 2.00 mg/L. Unfortunately, the majority of the samples contained excessive Pb levels, which possibly originated from the raw ingredients used to prepare the foods, such as fish, spices, and vegetables. This finding is of great concern, as Pb was classified as a "human carcinogen" by International Agency for Research on Cancer (IARC) in 1993 [23]. Excessive Pb intake can cause severe brain and kidney damage. Moreover, a high intake of (or exposure to) Pb may cause miscarriages in pregnant women [10, 24].

Table 4. Ranges of Cd, Hg, and Pb contents in the studied food samples detected by FAAS/FIMS and ICP-OES (assuming 250 mL of broth per serving unit)

Elements	Range of Concentration Detected (mg/L)		Permissible Level in Malaysia
	FAAS/FIMS	ICP-OES	
Cd	7.80×10^{-2} to 2.85×10^{-1}	n.d.	1.00 mg/L
Hg	9.00×10^{-4} to 8.10×10^{-3}	n.d.	5.00×10^{-2} mg/L
Pb	2.87 to 5.26	1.27 to 5.04	2.0 mg/L

*All values are expressed as a mean in ppm or mg/L

*n.d = non-detectable

*Permissible Level in Malaysia (Source: Malaysia Food Act 1983 and Food Regulations 1985, 2017 [19]

Statistical Testing

Student's *t*-test: The results provided (Table 5) by the two types of analytical instruments, FAAS/FIMS and ICP-OES, were compared using Student's *t*-test. There was no significant difference (at a confidence level of 95%) in the results of essential minerals as determined by FAAS and ICP-OES. However, there was a significant difference found in the heavy-metal results. This indicated that both FAAS and ICP-OES were suitable for the detection and quantification of essential minerals in food samples. For heavy metals, both analytical instruments failed to show a good correlation between the obtained results. Perhaps this was associated with the trace levels of heavy metals in the food samples and the sensitivities of the instruments. Thus, the suitability of an instrument in detecting and quantifying heavy metals in food samples is dependent upon its detection limit.

Table 5. Summary of Student's *t*-test for all targeted elements

Elements	*t*-calculated	*t*-critical	Result
Fe	1.24		No Significant difference
Ca	1.67		No Significant difference
Na	1.91		No Significant difference
K	1.25	2.15	No Significant difference
Cd	11.2		Significant difference
Hg	3.18		Significant difference
Pb	8.11		Significant difference

*Student's *t*-test performed at a 95% confidence interval

Inter-day Precision Study

An inter-day precision study was performed in order to assess the consistency of the determined content of minerals and heavy metals in the studied food samples. Sample collection was repeated on three different days at selected locations. The precision of repeatability is expressed as %RSD. In general, the acceptable level for %RSD is less than 10%[8]. Overall, almost all the elements exhibited a %RSD value above 10%, which suggests the inconsistency of the content of heavy metals and minerals for samples collected on different days. The variability of the element content is most likely a result of the ingredients comprising the food samples. However, it is difficult to ascertain the exact cause for such variation, as there are a wide variety of factors involved.

Conclusion

The heavy metals (Cd, Hg, and Pb) and essential minerals (Fe, Ca, Na, and K) present in Penang Assam Laksa collected from different areas were successfully characterized by using both FAAS/FIMS and ICP-OES. Cadmium and mercury were detected in Penang Assam Laksa at trace levels, whereas lead was found at levels higher than those permitted by Malaysian Food Act 1983 and Food Regulations 1985. Most of the Penang Assam Laksa contained adequate levels of iron, calcium, potassium, and sodium. As determined by Student's *t*-test, both FAAS and ICP-OES can be satisfactorily used in the detection and quantification of minerals, while an inter-day precision test showed variability of the element content in food samples collected on different days. Moreover, the wet-digestion procedure was efficient and suitable for digesting the food samples. In general, this work represents the first scientific study on the element content in Penang Assam Laksa, one of the most famous street foods in Penang. However, the findings stated above cannot be generalized to all Penang Assam Laksa samples, as this study just focused on five selected locations. Instead, this work serves as valuable direction for other researchers in the field. Further studies are needed in order to provide a full picture of the nutritional content in Penang Assam Laksa.

Acknowledgments

The authors would like to acknowledge participating local hawker stalls for supporting this research.

References

1. Food and Agriculture Organization. (1997). Street Foods: Report of an FAO technical meeting on street foods. Calcutta, India: Food and Agriculture Organization.
2. Tuzen, M., and Soylak, M. (2007). Evaluation of trace element contents in canned foods marketed from Turkey. *Food Chemistry*, 102(4): 1089-1095.
3. Damastuti E., Syahfitri W. Y. N., Santoso M. and Lestiani D. D. (2012). Assessment of trace element daily intake based on consumption rate of foodstuffs in Bandung City. *Atom Indonesia*, 38(1): 29-34.

4. Jignesh, S., Vineeta, K., Abhay, S. and Vilasrao, K. (2012). Analytical methods for estimation of metals. *International Journal of Research in Pharmacy and Chemistry*, 2(1): 146-163.
5. Salau, R. B. and Hassan, M. N. (2014). Evaluation and analysis of dietary essential mineral micronutrients in selected Malaysian foods using FAAS and ICP-MS. *Modern Applied Science*, 8(6): 103-111.
6. World Health Organization (1996). Trace elements in health and nutrition. Geneva: WHO.
7. Tee, E. S. and Rodolfo, F. F. (2005). Recommended dietary allowances: Homogenization in Southeast Asia. International Life Sciences Institute, Southeast Region (ILSI SEA Region).
8. U.S. Department of Agriculture and U.S. Department of Human Services. (2010). Dietary Guidelines for Americans. 7th Edition. Washington, DC.
9. Zukowska, J. and Biziuk, M. (2008). Methodological evaluation of method for dietary heavy metal intake. *Journal of Food Science*, 73(2): 1-9.
10. Das, S. K., Grewal, A. S. and Banerjee, M. (2011). A brief review: Heavy metal and their analysis. *International Journal of Pharmaceutical Sciences Review and Research,* 11(1): 13-18.
11. Korn, M. D. G. A., Morte, E. S. D. B., Santos, D. C. M. B. D., Castro, J. T., Barbosa, J. T. P., Teixeira, A. P., Fernandes, A. P., Welz, B., Santos, W. P. C. D., Santos, E. B. G. N. D. and Korn, M. (2008). Sample preparation for determination of metals in food samples using spectroanalytical methods – A review. *Applied Spectroscopy Reviews*, 43(2): 67-92.
12. Tuzen, M., Sari, H., Narin, I. and Soylak, M. (2004). Comparison of microwave, dry and wet digestion procedures for the determination of trace metal contents in spice samples produced in Turkey. *Journal of Food and Drug Analysis*, 12(3): 254-258.
13. Momen, A. A., Georage, A. Z., Anthemidis, A. N. and Stratis, J. A. (2006). Investigation of four digestion procedures for multi-element determination of toxic and nutrient elements in legumes by inductively coupled plasma-optical emission spectrometry. *Analytica Chimica Acta*, 565(1): 81-88.
14. Kira, C. S. and Maihara, V. A. (2007). Determination of major and minor elements in dairy products through inductively coupled plasma optical emission spectrometry after wet partial digestion and neutron activation analysis. *Food Chemistry,* 100(1): 390-395.
15. Luo, Y., Zhang, B., Chen, M., Wang, J., Zhang, X., Gao, W. Y. and Huang, J. F. (2010). Rapid and simultaneous determination of essential minerals and trace elements in human milk by improved flame atomic absorption spectroscopy (FAAS) with microwave digestion. *Journal of Agricultural and Food Chemistry,* 58(17): 9396-9400.
16. Boutakhrit, K., Crisci, M., Bolle, F. and Loca, J. V. (2011). Comparison of four analytical techniques based on atomic spectrometry for the determination of total tin in canned foodstuffs. *Food Additives and Contaminants,* 28(2): 1-18.
17. Perkin Elmer (2011). Exceptional performance for challenging mercury analyses. Perkinelmer, Inc.
18. Khor, S. (2015). Penang Laksa isn't the only laksa out there. You need to try them all. like really. SAYS. https://says.com/my/lifestyle/let-s-talk-about-laksa. [Access online 27 March 2020].
19. Malaysia Food Act 1983 and Food Regulations 1985 (2017). Warta Kerajaan Malaysia. Kuala Lumpur: Ministry of Health Malaysia.
20. Yuvarani, T., Anuradha, V., and Praveena, A. (2013). Analysis of antioxidants, minerals and vitamins composition between male and female Indian mackerel – Rastrelliger Kanagurta. *International Journal of Food, Agriculture and Veterinary Sciences*, 3(1): 76-81.
21. Nurnadia, A. A., Azrina, A., Amin, I., Mohd Yunus, A. S. and Mohd Izuan, E. H. (2013). Mineral contents of selected marine fish and shellfish from the west coast of Peninsular Malaysia. *International Food Research Journal,* 20(1): 431-437.
22. Mehrdad, R. R., Mehravar, R. R., Sohrab, K. and Ali, A. M. (2017). Cadmium toxicity and treatment: An update. *Caspian Journal of Internal Medicine,* 8(3): 135-145.

23. Salama, A. K., and Radwan, M. A. (2005). Heavy metals (Cd, Pb) and trace elements (Cu, Zn) contents in some foodstuffs from the Egyptian market. *Journal of Agricultural Sciences*, 17(1): 34-42.

24. Jarup, L. (2003). Hazards of heavy metal contamination. *British Medical Bulletin*, 68: 167-182.

Malaysian Journal of Analytical Sciences Vol 26 No 3 2022

Articles 9-20 are selected papers from the "Symposium on Fuel Cell and Hydrogen Technology (SFCHT2021), 26-27 October 2021; organized by the Fuel Cell Institute (SELFUEL), Universiti Kebangsaan Malaysia & The Malaysian Association of Hydrogen Energy (MAHE)."

Guest Editor: Mahendra Rao Somalu

		Page
1.	PHYTOCHEMICALS AND ANTIOXIDANT ACTIVITY OF ULTRASOUND-ASSISTED AVOCADO SEED EXTRACT (Fitokimia dan Aktiviti Antioksidan Ekstrak Biji Avokado Berbantukan Ultrabunyi) *Chin Xuan Tan, Renee Chin, Seok Tyug Tan, Seok Shin Tan*	439
2.	A COMPARISON OF CHEMICAL COMPOSITIONS IN KELULUT HONEY FROM DIFFERENT REGIONS (Perbandingan Komposisi Kimia dalam Madu Kelulut dari Kawasan Berbeza) *Hasnah Haron, Ruzita A Talib, Ponnusami Subramaniam, Zainorain Natasha Zainal Arifen, Muhammad Ibrahim*	447
3.	QUANTITATIVE STRUCTURE-ACTIVITY RELATIONSHIP (QSAR) STUDY OF NEWLY SYNTHESIZED CARBONYL THIOUREA DERIVATIVES ON *Acanthamoeba* sp. (Kajian Kuantitatif Hubungan Struktur-Aktiviti (QSAR) Terhadap Terbitan Karbonil Tiourea Hasilan Sintesis Baru Terhadap *Acanthamoeba* sp.) *Maizatul Akma Ibrahim, Nor Hafizah Zakaria, Mohd Sukeri Mohd Yusof*	457
4.	IMPROVING THE MORPHOLOGICAL, THERMAL, AND ACOUSTICS PROPERTIES OF POLYURETHANE-UREA BIOFOAM USING INDUSTRIAL PLYWOOD SAWDUST WASTE (Meningkatkan Morfologi, Termal dan Sifat Akustik Busa Poliuretan-Urea Menggunakan Sisa Habuk Papan Kayu Lapis) *Herlina Nofitasari, Ari Handono Ramelan, Mohammad Masykuri*	478
5.	SYNTHESIS OF GREEN-RENEWABLE BIOLUBRICANT BASE STOCK FROM MALAYSIAN PALM OIL (Sintesis Stok Asas Biopelincir Hijau-Diperbaharui daripada Minyak Sawit Malaysia) *Nurazira Mohd Nor and Jumat Salimon*	492
6.	THE REMOVAL OF BISPHENOL-A FROM SYNTHETIC WASTEWATER USING THIN-FILM COMPOSITE MEMBRANE (Penyingkiran Bisfenol A daripada Sisa Air Sintetik Mengunakan Membran Lapisan Komposit Nipis) *Taofiq Damilare Aiyelabegan , Siti Nur Alwani Shafie, Shafiq Mohd Hizam, Nik Abdul Hadi Nordin*	507
7.	CONSTRUCTING Ni-DOPED ZnO/GO HETEROSTUCTURES FOR ENHANCED SUNLIGHT-TRIGGERED DEGRADATION OF METHYLENE BLUE DYE (Pembinaan Heterostruktur Ni-Didop dengan ZnO/GO untuk Meningkatkan Degradasi Pewarna Metilina Biru di Bawah Sinar Matahari) *Hartini Ahmad Rafaie, Nur Shafiza Ismail, Syazni Hanun Nur Ili Dedy Dasiano, Muhd Firdaus Kasim, Nurul Infaza Talalah Ramli, Zul Adlan Mohd Hir, Mohomad Hafiz Mamat*	520
8.	BIOSORPTION CAPACITY OF HEAVY METAL LEAD (Pb(II)) USING DRY SEAWEED *Eucheuma denticulatum* (Kapasiti Biojerapan Logam Berat Plumbum (Pb(II)) Mengunakan Rumpai Laut Kering *Eucheuma denticulatum*)	532

Hamad Maalim Sharif, Yahya Makame, Mohammed Ali Sheikh, Hasrizal Shaari, Rokiah Suriadi

9. SYNTHESIS OF ZnO ON 3D GRAPHENE/NICKEL FOAM FOR PHOTOELECTROCHEMICAL WATER SPLITTING 546
(Sintesis ZnO pada 3D Grafin/Busa Nikel untuk Pembelahan Molekul Air Secara Fotoelektrokimia)
Nur Rabiatul Adawiyah Mohd Shah, Rozan Mohamad Yunus, Nurul Nabila Rosman, Wai Yin Wong, Khuzaimah Arifin, Lorna Jeffery Minggu

10. THE EFFECT OF MEMBRANE THICKNESS ON THE PERFORMANCE OF PASSIVE DIRECT ETHANOL FUEL CELLS USING A POLY VINYL ALCOHOL/GRAPHENE OXIDE COMPOSITE MEMBRANE 554
(Kesan Ketebalan Membran Terhadap Prestasi Sel Fuel Etanol Langsung Pasif Menggunakan Membran Komposit Alkohol Polivinil/Grafin Oksida)
Zulfirdaus Zakaria

11. EFFECT OF pH IN THE SYNTHESIS OF GOLD-COPPER NANOPARTICLES SUPPORTED ON ANODIC ALUMINIUM OXIDE AS CATALYST FOR THE REDUCTION OF *p*-NITROPHENOL 562
(Kesan pH dalam Sintesis Emas-Kuprum (Au-Cu) Partikel Nano Disokong pada Anodik Aluminium Oksida Sebagai Mangkin bagi Penurunan *p*-Nitrofenol)
Norizwan Nordin, Hanani Yazid, Nor Azira Irma Muhammad, Abdul Mutalib Md Jani

12. POTENTIAL OF TEXTILE WASTE AS NITROGEN DOPED POROUS CARBON FOR OXYGEN REDUCTION REACTION 571
(Potensi Sisa Tekstil Sebagai Karbon Poros Terdop Nitrogen Berliang untuk Tindak Balas Penurunan Oksigen)
Suhaila Mohd Sauid, Siti Kartom Kamarudin, Loh Kee Shyuan

13. PHOTOCATALYTIC HYDROGEN GENERATION FROM WATER BY TiO_2/Co_3O_4 COMPOSITE PHOTOCATALYSIS 581
(Penjanaan Hidrogen Fotokatalitik dari Molekul Air Mengunakan Komposi Fotomangkin TiO_2/Co_3O_4)
Siti Nurul Falaein Moridon, Dian Anggraini, Khuzaimah Arifin, Lorna Jeffery Minggu, Mohammad B. Kassim

14. THE THERMAL STABILITY AND PRELIMINARY PERFORMANCE OF SODIUM ALGINATE AND POLYVINYL ALCOHOL-BASED MEMBRANE IN DMFC: MONTMORILLONITE AS A FILLER 589
(Kestabilan Haba dan Prestasi Awal Membran Berasaskan Natrium Alginat dan Polivinil Alkohol untuk DMFC: Montmorillonit sebagai Pengisi)
Maryam Taufiq Musa and Norazuwana Shaari

15. FORMULATION AND CHARACTERISATION OF LSCF/YSZ-SDC AND LSCF/YSZ-SDCC DUAL COMPOSITE CATHODES FOR INTERMEDIATE-TEMPERATURE SOLID OXIDE FUEL CELL 600
(Formulasi dan Ciri Dwi-Komposit Katod LSCF/YSZ-SDC dan LSCF/YSZ-SDC Karbonat untuk Sel Bahan Api Oksida Pepejal Bersuhu Pertengahan)
Nurul Farhana Abdul Rahman, Umira Asyikin Yusop, Yohannes Nyambong Lowrance, Hamimah Abd. Rahman, Mohd Azham Azmi, Shahruddin Mahzan, Azzura Ismail

16. PtRu SUPPORTED ON POROUS 3D TITANIUM DIOXIDE-GRAPHENE AEROGEL AS A POTENTIAL ELECTROCATALYST FOR DIRECT METHANOL FUEL CELLS 613
(PtRu disokong pada 3D Titanium Dioksida-Grafin Aerogel Berliang Sebagai Potensi Elektromangkin untuk Sel Bahan Bakar Metanol Langsung)
Siti Hasanah Osman, Siti Kartom Kamarudin, Sahriah Basri, Nabila A. Karim

17. A REVIEW ON PREPARATION, MODIFICATION AND FUNDAMENTAL PROPERTIES OF SPEEK NANOCOMPOSITE PEM FOR DIRECT METHANOL FUEL CELL APPLICATIONS 622
(Satu Ulasan tentang Penyediaan, Pengubahsuaian dan Ciri Asas Komposit Nano Membran Elektrolit Polimer SPEEK untuk Aplikasi Sel Bahan Api)
Nor Fatina Raduwan and Norazuwana Shaari

18. PHYSICAL AND ELECTROCHEMICAL CHARACTERISTICS OF $LiCo_{0.6}Sr_{0.4O2}$ CATHODE INK FOR INTERMEDIATE-LOW TEMPERATURE SOLID OXIDE FUEL CELL
(Pencirian Fizikal dan Elektrokimia Terhadap Dakwat Katod $LiCo_{0.6}Sr_{0.4O2}$ bagi Sel Bahan Api Oksida Pepejal Bersuhu Sederhana Rendah)
Nur Nadhihah Mohd Tahir, Nurul Akidah Baharuddin, Wan Nor Anasuhah Wan Yusoff, Azreen Junaida Abd Aziz, Mahendra Rao Somalu, Andanastuti Muchtar 640

19. TITLECHEMICAL OXYGEN DEMAND AND TURBIDITY REMOVAL OF LANDFILL LEACHATE USING ELECTROCOAGULATION TECHNIQUE WITH Al ELECTRODE
(Penyingkiran Permintaan Oksigen Kimia dan Kekeruhan daripada Larut Resap Tapak Pelupusan dengan Menggunakan Elektrod Al)
Norilhamiah Yahya, M. Firdaus Mamat, Suhaini Mamat, Nabila A. Karim 652

20. ENHANCING THE OXYGEN REDUCTION REACTION OF LOW-PLATINUM AND NON-PLATINUM CATALYSTS FOR FUEL CELL APPLICATIONS
(Peningkatan Tindak Balas Penurunan Oksigen Mangkin Platinum Bermuatan Rendah dan Bebas Platinum Untuk Aplikasi Sel Bahan Api)
Kazi Rumanna Rahman, Kuan Ying Kok, Nor Azillah Fatimah Othman, Wai Yin Wong, Kean Long Lim 664

Malaysian Journal of Analytical Sciences (MJAS)
Published by Malaysian Analytical Sciences Society

PHYTOCHEMICALS AND ANTIOXIDANT ACTIVITY OF ULTRASOUND-ASSISTED AVOCADO SEED EXTRACT

(Fitokimia dan Aktiviti Antioksidan Ekstrak Biji Avokado Berbantukan Ultrabunyi)

Chin Xuan Tan[1]*, Renee Chin[1], Seok Tyug Tan[2], Seok Shin Tan[3]

[1]*Department of Allied Health Sciences, Faculty of Science,*
Universiti Tunku Abdul Rahman, Jalan Universiti Bandar Barat 31900, Kampar Perak, Malaysia
[2]*Department of Healthcare Professional, Faculty of Health and Life Sciences,*
Management and Science University, University Drive, Off Persiaran Olahraga, Seksyen 13, 40100 Shah Alam, Selangor, Malaysia
[3]*Jeffrey Cheah School of Medicine and Health Sciences,*
Monash University Malaysia, Bandar Sunway, Selangor, Malaysia

**Corresponding author: tancx@utar.edu.my*

Received: 13 February 2022; Accepted: 14 March 2022; Published: 27 June 2022

Abstract

Avocado seed is the residue from direct food consumption and fruit processing industry, which is rich in phytochemicals. Ultrasound-assisted extraction (UAE) has been proposed as a cost-effective technique to recover the phytochemicals from plant fractions. Sonication time is one of the parameters that may influence the quantity and quality of phytochemicals isolated from the plant fractions when using UAE. Hence, this study aimed to investigate the effect of different sonication times (0, 20, 40 and 60 min) used in the UAE on the phytochemicals and antioxidant capacity of methanolic avocado seed extract. Results indicated the total phenolic, flavonoid and anthocyanin content of the seed extracts were in the range of 31.90-41.62 mg GAE/100 g, 8.25-12.51 mg RE/100 g, and 8.02-24.57 mg CGE/100 g, respectively. UAE for 60 mins generated the significant highest (p<0.05) amount of phenolic, flavonoid and anthocyanin content. Based on the antioxidant capacity tests, UAE for 60 mins resulted in the highest antioxidant activity.

Keywords: avocado seed, sonication time, phytochemicals, ultrasound-assisted extraction

Abstrak

Biji alpukat merupakan bahan sisa daripada penggunaan secara langsung dan/atau industri pemprosesan buah-buahan, yang kaya dengan fitokimia. Pengekstrakan berbantukan ultrabunyi (UAE) merupakan kos efektif teknologi untuk mengisolasi fitokimia daripada sumber tumbuh-tumbuhan. Dalam kaedah UAE, masa sonikasi adalah salah satu faktor yang mempengaruhi kuantiti dan kualiti fitokimia yang diisolasi daripada sumber tumbuh-tumbuhan. Kajian ini bertujuan untuk analisa kesan masa sonikasi yang berbeza (0, 20, 40 dan 60 minit) dalam UAE terhadap fitokimia dan kapasiti antioksidan ekstrak biji alpukat metanol. Hasil kajian menunjukkan jumlah kandungan fenolik, flavonoid dan antosianin dalam ekstrak biji alpukat adalah dalam lingkungan 31.90-41.62 mg GAE/100 g, 8.25-12.51 mg RE/100 g dan 8.02-24.57 mg CGE/100 g. Penggunaan masa sonikasi 60 minit dalam UAE dapat menghasilkan kandungan fenolik, flavonoid dan antosianin yang paling signifikan banyak (p <0.05). Berdasarkan

ujian kapasiti antioksidan, pengunaan masa sonikasi 60 minit dalam UAE dapat menghasilkan aktiviti antioksidan yang paling tinggi.

Kata kunci: biji alpukat, masa sonikasi, fitokimia, pengekstrakan berbantukan ultrabunyi

Introduction

Avocado, also known as *Persea americana* Mill. or alligator pear, is a tropical and subtropical fruit that has been gaining increasing worldwide demand in recent years due to its relevant nutritional values and health benefits. There are over 100 varieties of avocado fruits have been recorded in the database of California Avocado Society [1]. Hass variety avocado is one of the most widely sought for commercialization [2]. A major portion of Hass avocado is constituted by the pulp (65%) whereas the seed (20%) and peel (15%) make up the rest [3].

Avocado fruits have been primarily used for human consumption, and to a lesser extent, as raw material in the pharmaceutical and cosmetic industries [4]. However, only the pulp of avocado is valued for commercial usance while other fruit fractions such as the seed and peel are considered obsolete and usually throw away as waste products. Hass avocado seed is ovoid shaped with a length of 5 to 6.4 cm. The ivory-colored avocado seed is covered with a thin, brown-colored seed coat that adheres to the flesh cavity when ripe [5].

Proximate analysis done by Saavedra [6] revealed that the Hass avocado seed contained 52.7% of moisture, 2.51% of protein, 1.15% of ash, 1.11% of lipids, and 42.5% of nitrogen-free extract. The seed was also rich in phytochemicals such as phenolic acids, flavonoids and condensed tannins [7]. Based on current findings with regards to the biological effects of avocado seed extracts, they are known to have various ethnopharmacological properties for health-related conditions including anti-cancer, anti-inflammatory, anti-diabetic, anti-hypertensive, hypercholesterolemic, anti-microbial and the application in dermatological [8]. Hence, there has been a growing interest in the extraction of phytochemicals from avocado seeds to be utilized in the food and pharmaceutical industries.

Techniques such as maceration, infusion, heat extraction, enzyme-assisted extraction and Soxhlet extraction are commonly used to extract bioactive compounds from plants [9]. These techniques, however, have numerous limitations including the requirement of high extraction times, solvents and/or temperatures. Although advanced techniques like supercritical fluid extraction, microwave-assisted extraction and accelerated solvent extraction have demonstrated their efficiency in the recovery of phytochemicals, but these techniques are complex in operation and/or not cost-effective.

Ultrasound-assisted extraction (UAE) has been noted as one of the most effective techniques for the isolation of phytochemicals from plant materials [1, 9]. It utilizes acoustic waves to induce cavitation force to disrupt the plant cell wall, consequently enhancing the extraction rate of phytochemicals. Sonication time, solvent composition, sonication temperature, solid-solvent ratio and sonication frequency are the parameters that may influence the quantity and quality of phytochemicals isolated from the plant materials when using UAE [1, 9]. Among these parameters, sonication time was reported to have the greatest influence on the quality of plant extracts [10].

Industrial processing of avocado fruits produces a large number of seeds as wastes. Exploiting the phytochemicals of avocado seed waste may lead to new products and add value to the food industry. Therefore, this study aimed to investigate the effect of different sonication times on the UAE of phytochemicals and antioxidant activity of avocado seed extract.

Materials and Methods

Sample preparation

Hass variety avocado fruits were purchased from a local retailer in 2019. The fruits were kept at room temperature (25 ± 5°C) until ripe. Ripe avocado fruit,

as indicated by changes in peel color (from green to purplish-black) and gentle pressure felt when held in the palm, were manually separated into seed, peel, and pulp. The outer coat layer of the seed was peeled off before being cut into slices with an average thickness of 5 mm [6], followed by drying in a lab-scale freeze dryer (Liobras L101, Brazil). The lyophilized seeds were milled into fine powder by using an electrical blender (Panasonic MX-799S, Malaysia) and sieved through a 250 µm stainless steel sieve. The powdered sample was kept in an air-tight container at -5°C until use.

Chemicals and reagents

Analytical reagent grade of methanol, glacial acetic acid, hydrochloric acid (37%) was purchased from Fisher Scientific (Massachusetts, U.S.). Folin-Ciocalteu reagent, sodium carbonate, gallic acid, sodium nitrite, aluminium chloride hexahydrate, sodium hydroxide, rutin, 2,4,6-Tripyridyl-S-triazine (TPTZ), 2,2-diphenyl-1-picrylhydrazyl (DPPH), iron (III) chloride and iron (II) sulphate were purchased from Sigma–Aldrich (St. Louis, USA).

Ultrasound-assisted extraction

Approximately 1 g of avocado seed powder was mixed with 15 mL of 80% methanol in a 50 mL dark reagent bottle. The mixture was subjected to different sonication times (0, 20, 40 and 60 mins) in an ultrasonic bath [Elmasonic 100 H, Germany; 37 kHz ultrasonic frequency; 600 W ultrasonic output power; 11.8″ x 9.4″ x 5.9″ (L x W x H) internal dimensions] operated at a constant temperature of 30°C. Extraction time and ultrasonic temperature were regulated from the panel of the instrument. A centrifuge set at 4,000 rpm for 10 mins at room temperature was used to separate the methanolic seed extract from the powdered sediment. The extract was then transferred into a dark bottle using a pipette and kept at 4°C until use.

Phytochemicals

Determination of total phenolic content

The TPC was determined by the Folin-Ciocalteu method described by Tan and Azrina [11]. Briefly, 600 µL of methanolic seed extract was diluted with the same amount of distilled water in a test tube and subsequently added with 300 µL of 1 N Folin-Ciocalteu reagent and 600 µL of 2.0% Sodium carbonate. The mixture was incubated in the dark for 30 min. The absorbance was measured at 750 nm using a spectrophotometer (DLAB Scientific SP V1000, China) against a blank. A standard curve was plotted by using different gallic acid concentrations (0.20, 0.70 and 0.90 mg/mL) for TPC calculation. The results were expressed as mg gallic acid equivalent (GAE) per 100 g of samples on the basis of fresh weight (mg GAE/100 g).

Determination of total flavonoid content

The TFC was determined by the aluminium chloride colorimetric method described by Sharma and Agarwal [12]. Exactly 100 µL of methanolic seed extract was pipetted into a test tube containing 4 mL of distilled water and 0.15 mL of 5% sodium nitrite solution. After 6 min of incubation at room temperature, 0.15 mL of 10% aluminium chloride solution, 2 mL of 4% sodium hydroxide solution and 0.2 mL of distilled water were added into the mixture and vortexed. The mixture was allowed to stand for 15 mins. The absorbance was recorded at 510 nm using a spectrophotometer (DLAB Scientific SP V1000, China) against a blank. A standard curve was plotted by using different rutin concentrations (7.0, 9.0, 11.0, 13.0 and 15.0 mg/mL) for TFC calculation. The results were expressed as mg rutin equivalent (RE) per 100 g of samples on the basis of fresh weight (mg RE/100 g).

Determination of total anthocyanin content

The TAC was determined according to the method of Granato et al. [13]. Exactly 1000 µL of methanolic seed extract was pipetted into a 25 mL volumetric flask and diluted with distilled water to volume. The absorbance of the mixture was measured at 535 nm using a spectrophotometer (DLAB Scientific SP V1000, China) against a blank. The results were expressed as mg cyanidin-3-glucoside equivalent (CGE) per 100 g of samples on the basis of fresh weight (mg CGE/100 g).

Antioxidant activity

Determination of ferric ion reducing antioxidant power

The FRAP was determined according to the method of Bagheri et al. [14]. Freshly prepared FRAP reagent was obtained by mixing 2.5 mL of 10 mM TPTZ in 40 mM hydrochloric acid, 2.5 mL of 20 mM ferric chloride solution and 24 mL of 300 mM acetate buffer (pH 3.6). Then, 40 µL of methanolic seed extract was pipetted into 1.2 mL of the FRAP reagent and incubated at 37°C for 10 mins. The absorbance of the mixture was measured at 593 nm using a spectrophotometer (DLAB Scientific SP V1000, China) against a blank. A standard curve was plotted by using different concentrations of iron (II) sulfate solution (0.01, 0.03 and 0.06 mg/mL) for FRAP calculation. The results were expressed as mmol Fe^{2+} per kg of samples on the basis of fresh weight (mmol Fe^{2+}/kg).

Determination of DPPH radical scavenging activity

The DPPH radical scavenging activity was determined according to the method of Ghafoor et al. [15]. Briefly, 0.25 mL of methanolic seed extract was mixed with 2 mL of 30 mg/L freshly prepared DPPH solution in methanol. The mixture was vigorously shaken and incubated at room temperature for 5 mins. A decline in absorbance was measured at 517 nm using a spectrophotometer (DLAB Scientific SP V1000, China) against a blank. Pure methanol was used as a negative control. The results were expressed as the percentage of antiradical activity (AA) of the extract on DPPH radicals relative to the control.

Statistical analysis

Statistical analyses were performed using IBM SPSS Statistic 26.0 for Windows (SPSS Inc., Chicago, USA). Data was summarized and expressed as mean ± standard deviation. Mean value refers to three analytical replicates. Comparison of mean differences among different sonication times (0, 20, 40 and 60 mins) was conducted using a one-way analysis of variance accompanied by Tukey's post hoc analysis. The association between bioactive compounds and antioxidant capacity was evaluated using Pearson correlation test. Statistical significance was set at $p < 0.05$.

Results and Discussion

Total phenolic, flavonoid and anthocyanin content

Various extraction media (methanol, ethanol, butanol, chloroform, ethyl acetate and water) have been utilized to extract the bioactive compounds from different fractions of fruits, either in pure form or in diluted form. In the present study, 80% methanol was selected as the media to prepare avocado seed extract. This is because 80% methanol has been deemed as a common medium to isolate the lipophilic and hydrophilic bioactive compounds of plant fractions [16].

The TPC, TFC and TAC of methanolic seed extracts sonicated at different times (0-60 mins) are shown in Table 1. Generally, increased sonication time enhanced the extraction of phenolics, flavonoids and anthocyanins from the avocado seed. This could be associated with the cavitation force produced by ultrasonic waves, which disrupt the integrity of plant cell walls and aid in the release of phytochemicals [9].

Phenolic compounds are secondary products produced by the metabolism of plants. They are widely recognized to have antioxidant characteristics, which could provide protection against oxidation induced by metal cations [7]. Avocado seed has been proposed as a potential food waste product for phenolic extraction [17]. It has been reported that the medicinal properties of avocado seed are attributed by its high phenolic compounds. As reported by Bahru et al. [18], the phenolic content of avocado seed (64%) was higher than its peel (23%) and pulp (13%). The TPC of methanolic seed extracts obtained from different sonication times was in the range of 31.90 to 41.62 mg GAE/100 g (Table 1). Application of UAE for 60 mins significantly increased ($p < 0.05$) the yield of phenolic content for 30%, as compared with the control without UAE at 0 min. Previously, the TPC of non-ultrasound assisted avocado seed extracts obtained from 70% methanol and 80% methanol were reported to be 2.92 mg GAE/100 g and 0.09-0.13 mg catechin equivalent (CE)/100 g, respectively [19, 20]. These values were much lower than the present study, possibly due to the different experimental protocols used in TPC analysis. As stated by Singh et al. [21], there are no standard method to determine phenolic compounds of plant seed

extracts and the parameters used (e.g. solute to solvent ratio, particle size of the seed samples and agitation rate) in the preparation of seed extract could affect the yield of TPC.

Flavonoid compounds are secondary metabolites corresponding to phenolics and are one of the most studied bioactive compounds due to their diverse benefits in human health. The TFC is analyzed based on color change due to the reaction between aluminium chloride and flavonoid compounds in the methanolic seed extract. Previous study reported the TFC of water and ethanolic avocado seed extract were 3.72 and 4.96 mg RE/100 mL, respectively [22]. These values were comparable with the results of the present study. In Table 1, application of UAE for 60 mins significantly increased (p <0.05) the yield of flavonoid content for 52%, as compared with the control without UAE at 0 min. A similar observation was reported by Ramić et al. [23], in which the TFC of ethanolic chokeberries extract was highest when sonicated for 60 min.

Anthocyanins are naturally occurring pigments that belong to the group of flavonoids. The flavylium cation form of anthocyanins requires a sufficiently acidic medium to maintain its stability, but not to the extent that can cause acyl moieties in acylated anthocyanins to be hydrolyzed [24]. It is difficult to achieve optimal protocol of extraction due to the diversity of anthocyanins structure and their sensitivity to heat, metal complexes, pH, and co-pigmentation. Hence, this study utilizes a method that quantifies TAC without requiring the use of chemical standards to plot a calibration curve. In Table 1, the application of UAE for 60 mins significantly increased (p <0.05) the yield of anthocyanin content for 102%, as compared with the control without UAE at 0 min. This may be due to the simultaneous enhancement of fragmentation and hydration from acoustic cavitation of UAE improves the mass transfer of anthocyanin compounds into the extraction solvent [9]. There has been limited data on the anthocyanin content of avocado seed extract documented thus far. Our current study demonstrated the effectiveness of UAE application in enhancing the yield of anthocyanin in avocado seed extract. Further study on quantifying the individual anthocyanin compound of avocado seed extract following UAE of 60 mins could be conducted.

Table 1. Phenolic, flavonoid and anthocyanin content of methanolic avocado seed extract

Sonication Time (mins)	TPC (mg GAE/100 g)	TFC (mg RE/100 g)	TAC (mg CGE/100 g)
0	31.90 ± 0.09[a]	8.25 ± 0.03[a]	8.02 ± 0.38[a]
20	32.20 ± 0.09[b]	8.74 ± 0.01[b]	16.04 ± 0.38[b]
40	32.26 ± 0.09[b]	8.81 ± 0.02[c]	21.26 ± 0.22[c]
60	41.62 ± 0.09[c]	12.51 ± 0.02[d]	24.57 ± 1.59[d]

Mean values in the same column with different letters are significantly different at p <0.05

FRAP and DPPH radical scavenging activity

Antioxidant capacity of methanolic seed extract from UAE was determined using two different antioxidant capacity assays and the finding results are shown in Table 2. Both FRAP and DPPH assays involved scavenging free radicals through electron transfer mechanism. As can be seen in both antioxidant capacity methods used, application of UAE at 60 mins had the highest antioxidant capacity, followed by 40 and 20 mins, while the control had the lowest antioxidant capacity. This shows the longest sonication time, the highest antioxidant activity in the methanolic seed extract. A similar observation was reported by Gómez et al. [25]. Their study demonstrated that the antioxidant activity of ethanolic avocado seed extract, as measured by oxygen radical antioxidant capacity assay, was the highest (158.77 mg Trolox Equivalents/g) when the longest sonication time (55 mins) was used during UAE.

Table 2. Antioxidant activities of methanolic avocado seed extract

Sonication Time (mins)	FRAP (mmol Fe^{2+}/kg)	DPPH (%)
0	0.72 ± 0.00^{a}	28.20 ± 1.42^{a}
20	0.96 ± 0.00^{b}	36.54 ± 0.83^{b}
40	1.19 ± 0.02^{b}	83.47 ± 0.19^{c}
60	1.72 ± 0.00^{c}	84.96 ± 1.20^{c}

Mean values in the same column with different letters are significantly different at $p < 0.05$

Correlation between phytochemicals and antioxidant activity

Correlation between phytochemicals (TPC, TFC and TAC) and antioxidant activities (FRAP and DPPH) are shown in Table 3. Positive correlation ($p < 0.05$) was found between total phenolic, flavonoid and anthocyanin content and antioxidant activity measured by FRAP and DPPH, indicating these phytochemicals contribute high antioxidant activity in the extract. This observation is in agreement with Wang et al. [26], who reported the high antioxidant capacity in Hass avocado seed extract was due to the high concentration of flavonoid and phenolic content. Sonication time is a significant factor that influences the extraction of plant phytochemicals and their antioxidant activity. This may be contributed by the cavitation effect of the ultrasound improved the fragmentation, swelling, hydration and pore production of the plant tissue matrix where the phytochemicals are to be isolated [27]. This will enhance the exposure of the phytochemicals and the extraction medium and help their release into the solvent, thereby increasing the antioxidant activity.

Table 3. Correlation between phytochemicals and antioxidant activity of methanolic avocado seed extract

	TPC	TFC	TAC	FRAP	DPPH
TPC	1	0.995**	0.675*	0.908**	0.609*
TFC		1	0.738**	0.940**	0.657*
TAC			1	0.916**	0.916**
FRAP				1	0.859**
DPPH					1

** Correlation was significant at $p < 0.01$

* Correlation was significant at $p < 0.05$

Conclusion

Avocado seed is the by-product of direct food consumption and food processing industry which could be further utilized to develop nutraceutical products. The TPC, TFC and TAC of methanolic seed extract were in the range of 31.90-41.62 mg GAE/100 g, 8.25-12.51 mg RE/100 g and 8.02-24.57 mg CGE/100 g, respectively. All phytochemicals and antioxidant activity demonstrated a positive and significant correlation. Efficacy of the UAE in terms of sonication time was demonstrated in this study. Sonication for 60 mins leads to the highest extraction yield of phenolic, flavonoids and anthocyanin content in methanolic seed extract. Further study to quantify the individual bioactive compound of avocado seed extract following UAE application of 60 mins could be carried out.

Acknowledgement

The authors would like to acknowledge Faculty of Science, Universiti Tunku Abdul Rahman, Kampar campus for providing the research facilities.

References

1. Tan, C. X., Tan, S. S. and Tan, S. T. (2017). Influence of geographical origins on the physicochemical properties of Hass avocado oil. *Journal American Oil Chemical Society,* 94:1431-1437
2. Zafar, T. and Sidhu, J. S. (2011). Avocado: production, quality, and major processed products. In: Handb. Veg. Veg. Process. Blackwell Publishing Ltd., New Jersey, United States: pp 525-543.
3. Costagli, G. and Betti, M. (2015). Avocado oil extraction processes: method for cold-pressed high-quality edible oil production versus traditional production. *Journal Agriculture Engineering,* 46:115.
4. Duarte, P. F., Chaves, M. A., Borges, C. D. and Mendonça, C. R. B. (2016). Avocado: characteristics, health benefits and uses. *Ciência Rural,* 46:747-754
5. Abraham, J. D., Abraham, J. and Takrama, J. F. (2018). Morphological characteristics of avocado (*Persea americana* Mill.) in Ghana. *African Journal Plant Sciences,* 12: 88-97.
6. Saavedra, J., Córdova, A., Navarro, R., Díaz-Calderón, P., Fuentealba, C., Astudillo-Castro, C., Toledo, L., Enrione, J. and Galvez L. (2017). Industrial avocado waste: Functional compounds preservation by convective drying process. *Journal Food Engineering,* 198: 81-90.
7. Segovia, F. J., Hidalgo, G. I., Villasante, J., Ramis, X. and Almajano, M. P. (2018). Avocado seed: A comparative study of antioxidant content and capacity in protecting oil models from oxidation. *Molecules* 23:1-14.
8. Dabas, D., Shegog, R. M., Ziegler, G. R. and Lambert, J. D. (2013). Avocado (*Persea americana*) seed as a source of bioactive phytochemicals. *Current Pharmaceutical Design,* 19: 6133-6140.
9. Fadimu, G. J., Ghafoor, K., Babiker, E. E., Al-Juhaimi, F., Abdulraheem, R. A., Adenekan, M. K. (2020) Ultrasound-assisted process for optimal recovery of phenolic compounds from watermelon (*Citrullus lanatus*) seed and peel. *Journal Food Measure Characterization,* 14:1784-1793.
10. Zhang, Q. W., Lin, L. G. and Ye, W. C. (2018). Techniques for extraction and isolation of natural products: A comprehensive review. *China Medicine,* 13: 1-26.
11. Tan, C. X. and Azrina, A. (2017). Dietary fiber and total phenolic content of selected raw and cooked beans and its combinations. *International Food Research Journal,* 24:1863-1868
12. Sharma, V. and Agarwal, A. (2015). Physicochemical and antioxidant assays of methanol and hydromethanol extract of ariel parts of *Indigofera tinctoria* Linn. *Indian Journal Pharmaceutical Sciences,* 77: 729-734.
13. Granato, D., Santos, J. S., Maciel, L. G. and Nunes, D. S. (2016). Chemical perspective and criticism on selected analytical methods used to estimate the total content of phenolic compounds in food matrices. *TrAC Trends Analytical Chemistry*, 80: 266-279.
14. Bagheri, E., Hajiaghaalipour, F., Nyamathulla, S. and Salehen, N. A. (2018). The apoptotic effects of Brucea javanica fruit extract against HT29 cells associated with p53 upregulation and inhibition of NF-κB translocation. *Drug Design Development Theraphy,* 12: 657-671.
15. Ghafoor, K., Al-Juhaimi, F. Y. and Choi, Y. H. (2012) Supercritical fluid extraction of phenolic compounds and antioxidants from grape (*Vitis labrusca* B.) seeds. *Plant Foods Human Nutrition,* 67:407-414
16. Saenjum, C., Pattananandecha, T. and Nakagawa, K. (2020). Detection of antioxidant phytochemicals isolated from Camellia japonica seeds using HPLC and EPR imaging. *Antioxidants,* 9:1-14
17. Segovia, F. J., Corral-Pérez, J. J. and Almajano, M. P. (2016) Avocado seed: Modeling extraction of bioactive compounds. *Industrial Crops Production,* 85:213-220.

18. Bahru, T. B., Tadele, Z. H. and Ajebe, E. G. (2019). A review on avocado seed: Functionality, composition, antioxidant and antimicrobial properties. *Chemical Science International Journal,* 27:1–10.
19. Pahua-Ramos, M. E, Ortiz-Moreno, A., Chamorro-Cevallos, G., Hernández-Navarro, M. D., Garduño-Siciliano, L., Necoechea-Mondragón, H. and Hernández-Ortega, M. (2012). Hypolipidemic effect of avocado (*Persea americana* Mill) seed in a hypercholesterolemic mouse model. *Plant Foods Human Nutrition,* 67:10-16.
20. Kosińska, A., Karama,ć M., Estrella, I., Hernández, T., Bartolomé, B. and Dykes, G. A. (2012). Phenolic compound profiles and antioxidant capacity of *Persea americana* Mill. peels and seeds of two varieties. *Journal Agriculture Food Chemistry,* 60: 4613-4619.
21. Singh, B., Singh, J. P., Kaur, A. and Singh, N. (2017). Phenolic composition and antioxidant potential of grain legume seeds: A review. *Food Research International,* 101:1-16.
22. Noorul, H., Mujahid, M., Khalid, M., Vartika, S., Nesar, A., Zafar, K. and Zohrameena, S. (2017). Physico-phytochemical analysis and estimation of total phenolic, flavonoids and proanthocyanidin content of *Persea americana* (avocado) seed extracts. *World Journal Pharmceutical Sciences,* 5:70-77.
23. Ramić, M., Vidović, S., Zeković, Z., Vladić, J., Cvejin, A. and Pavlić, B. (2015). Modeling and optimization of ultrasound-assisted extraction of polyphenolic compounds from *Aronia melanocarpa* by-products from filter-tea factory. *Ultrasonic Sonochemistry,* 23:360-368.
24. Martín, J., Navas, M. J., Jiménez-Moreno, A. M. and Asuero, A. G. (2017). Anthocyanin pigments: Importance, sample preparation and extraction. In: Phenolic Compd. sources, importance Appl. IntechOpen, London, UK, pp 117-152.
25. Gómez, F. S., Peirósánchez, S., Iradi, M. G. G., Azman, N. A. M. and Almajano, M. P. (2014). Avocado seeds: Extraction optimization and possible use as antioxidant in food. *Antioxidants*, 3:439-454.
26. Wang, W., Bostic, T. R. and Gu, L (2010). Antioxidant capacities, procyanidins and pigments in avocados of different strains and cultivars. *Food Chemistry,* 122: 1193-1198.
27. Kumar, K., Srivastav, S. and Sharanagat, V. S. (2021). Ultrasound assisted extraction (UAE) of bioactive compounds from fruit and vegetable processing by-products: A review. *Ultrasonic Sonochemisty,* 70:105325.

Malaysian Journal of Analytical Sciences (MJAS)
Published by Malaysian Analytical Sciences Society

A COMPARISON OF CHEMICAL COMPOSITIONS IN *KELULUT* HONEY FROM DIFFERENT REGIONS

(Perbandingan Komposisi Kimia dalam Madu Kelulut dari Kawasan Berbeza)

Hasnah Haron[1]*, Ruzita A Talib[1], Ponnusami Subramaniam[2], Zainorain Natasha Zainal Arifen[1], Muhammad Ibrahim[3]

[1]Nutritional Sciences Programme, Faculty of Health Sciences
[2]Health Psychology Programme, Faculty of Health Sciences
Universiti Kebangsaan Malaysia, 50300, Kuala Lumpur, Malaysia
[3]Department of Nutrition Sciences, Kuliyyah of Allied Health Sciences,
International Islamic University Malaysia, Jalan Istana, Bandar Indera Mahkota, 25200, Kuantan, Pahang, Malaysia

**Corresponding author: hasnaharon@ukm.edu.my*

Received: 1 December 2021; Accepted: 24 March 2022; Published: 27 June 2022

Abstract

Kelulut honey (KH) is honey produced by stingless bees (Trigona spp.) found in Malaysia. This study investigated the difference inherent in the chemical composition of kelulut honey collected from the east coast, and the central and northern regions of Peninsular Malaysia. Total sugar content, individual sugar content, total phenolics, total flavonoids, ascorbic acid, ascorbic acid equivalent antioxidant content (AEAC), and proline content were determined. Sugar analysis revealed that kelulut honey contained 62.33-79.53 g/100g of total sugar, with maltose as the predominant sugar (15.85-37.74 g/100g), followed by fructose (9.91-53.64 g/100g), glucose (10.96-25.04 g/100g), and sucrose (0.54-3.48 g/100g). The results indicate that total flavonoids (78.95±0.70 mg QE/kg) and phenolics (1149.48±40.52 mg GAE/kg) were the highest in honey from the east coast region. The proline and ascorbic acid content were less likely to be affected by geographical factors. Kelulut honey possesses a unique sugar profile that may contribute to its unique taste. In conclusion, the geographical and floral origin of honey are the two most important factors that fundamentally affect the physical-chemical properties of honey samples.

Keywords: chemical, compositions, kelulut, honey, region

Abstrak

Madu kelulut (KH) ialah madu yang dihasilkan oleh lebah tidak bersengat (Trigona spp.) yang terdapat di Malaysia. Kajian ini menyelidik perbezaan komposisi madu kelulut yang dikumpul dari pantai timur, tengah dan utara Semenanjung Malaysia. Jumlah dan gula individu, jumlah fenolik, jumlah flavonoid, asid askorbik, asid askorbik kandungan antioksidan setara (AEAC) dan kandungan prolin telah ditentukan. Analisis kandungan gula menunjukkan bahawa madu kelulut mengandungi 62.33-79.53 g/100g jumlah gula dengan maltosa sebagai gula utama (15.85-37.74 g/100g), diikuti oleh fruktosa (9.91-53.64 g/100g), glukosa (10.96-25. 100g) dan sukrosa (0.54-3.48 g/100g). Jumlah flavonoid (78.95±0.70 mg QE/kg) dan fenolik (1149.48±40.52 mg GAE/kg) adalah tertinggi dalam madu dari pantai timur. Prolin dan asid askorbik adalah kurang berkemungkinan dipengaruhi oleh faktor geografi. Madu kelulut mempunyai profil gula yang unik yang mungkin menyumbang kepada rasa unik madu

kelulut. Secara kesimpulannya, geografi dan floral madu adalah dua parameter kualiti penting yang pada asasnya mempengaruhi sifat fizikal-kimia sampel madu.

Kata kunci: kimia, komposisi, kelulut, madu, kawasan

Introduction

Honey is a natural food consisting of about 200 different compounds including sugars, phenolics, amino acids, enzymes, organic acids, and aromatic compounds. Honey composition varies by bee species, nectar source, and geographic origin [1]. Honey is not only known for its nutritional benefit, but also as traditional medicine due to its healing properties. It has been proven that honey exert antioxidant, anti-inflammatory, anti-bacterial and anti-mutagenic properties. The antioxidant activity assay for any product is based on the capability of the compounds to inhibit oxidation. The DPPH and FRAP assays are typically chosen because they are simple and rapid methods for assessing a honey sample's antioxidant capacity. These two assays are based on different principles, and thus may be used to screen compounds that have different antioxidant mechanisms. Recently, there is an increase in the Malaysian consumer demand for honey, especially for health maintenance and promotion purposes. There has been a surge of interest in honey's capacity as an antioxidant and its protective effects on the brain and other organs [2]. *Kelulut* honey is produced by the stingless bees that are indigenous to Malaysia. A local study reported that a low dose of *Kelulut* honey taken orally could improve wound healing rate in epidermal keratinocyte *in vitro* wound healing model [3]. It has also been reported to have a potential in preventing damage to sperm and testes in diabetic rats [4]. *Kelulut* honey is a multifloral honey which does not have any predominant pollen present in it. The nutritional profile and composition of this honey is still understudied. Over the decades, research on Malaysian honey production has been focused on *Apis* spp. which left a gap to be bridged by research work on *kelulut* honey. The effect of different botanical and geographical environment on honey chemical composition could be studied by comparing the honey of a particular type produced in different localities. Previous studies indicated that the nectar source can affect the antioxidant content and the antibacterial and radical scavenging activities of the honey [5]. Bioactive compounds from the plant are secreted into the nectar, thereby impacting the quality of honey and its medicinal properties that are very dependent on its bioactive composition. The present study was undertaken to study the compositional variations of *kelulut* honey collected from different locations in peninsular Malaysia.

Materials and Methods

Sample collection

Kelulut honey from *Heterotrigona itama* species were collected from three peninsular Malaysia regions, namely the east coast region, the northern region, and the central region. The honey samples were collected from each region in two different batches. Each batch were analyzed in triplicates, and the results were expressed as an average ± standard deviation of six replicates from samples collected in two batches.

Individual and total sugar analysis using HPLC

The composition of individual sugars in *kelulut* honey samples was determined using high performance liquid chromatography (HPLC) [6]. About 1 g of honey sample was weighed and loaded into a 50 mL centrifuge tube. 25 mL of 50:50 acetonitrile/deionized water was added into the tube. The sample was then filtered using a 0.45 μM nylon filter. The purified sugar extract was analyzed using a HPLC Waters model 2707 with an XBridge Amide column (250 x 4.6mm, 3.5μM) coupled with Water RI-2414 refractive index detector. The mobile phase was acetonitrile/deionized water (75:25). The injection volume was 20 μL with flow rate of 1.0 mL/min. The retention time for each sugar was determined by comparing with a known standard sugar solution consisting of fructose, glucose, sucrose, and maltose with a concentration of 0.5 g/10 mL. The composition of the individual sugar was calculated using Empower 2 software.

Total sugar content using chemical analysis

Total sugar content in *kelulut* honey were also determined using the phenol-sulphuric acid method [7]. This analysis was performed in this study because honey also contains a small amount of oligosaccharides that the HPLC method could not detect. For this analysis, 0.1 g of honey sample was diluted 100-fold and the solution was homogenized, 1 mL of the new solution was 20-fold diluted. A 2 mL aliquot of the honey solution was combined with 1 mL of 5% aqueous phenol solution in a test tube. 5 mL of concentrated sulphuric acid was then added rapidly to the mixture. The mixture was allowed to stand for 10 min and subsequently vortexed for 30 seconds. The test tube was then placed in a water bath at room temperature for 20 minutes for color development. The absorbance was then recorded on a spectrophotometer (Secomam, France) at 490 nm. Glucose solutions 0f 0.0-0.1 g/L were used as standard.

Total phenolic content

The Folin-Ciocalteu assay [8] was used to determine the total phenolic content in *kelulut* honey. 0.5 mL of the 10% honey solution was mixed with 2.5 mL of 0.2 N Folin-Ciocalteu reagent, and the mixture was left to stand for 5 minutes. Then, 2 mL of 7.5% sodium carbonate solution was added. The mixture was allowed to stand at room temperature for 2 hours. The absorbance of the mixture was then measured at 760 nm using spectrophotometer (Secomam, France) against methanol as blank. Gallic acid (50-200 mg/L) was used to produce standard curve (R^2 = 0.987). The total phenolic content was expressed in mg of gallic acid equivalent (GAE)/kg honey.

Total flavonoid content

The total flavonoid content in the honey samples was analyzed using the method described by Zhishen et al. [9]. A 1 mL volume of 20% honey was mixed with 4 mL of distilled water and 0.3 mL of sodium nitrite. After 5 minutes, 0.3 mL of 10% aluminum chloride was added followed by 2 mL of 1 M sodium hydroxide six minutes later. The volume was made up to 10 mL by distilled water, and the mixture was shaken thoroughly. The absorbance was read using spectrophotometer (Secomam, France) at 510 nm wavelength. A standard curve was plotted using a quercetin solution with concentrations ranging between 25 - 100 µg/mL (R^2 = 0.987). The results were expressed as mg quercetin equivalent (QE)/kg honey.

Proline content

The proline content in the honey sample was determined using the method described by Bogdanov et al. [10]. A 0.5 mL sample of honey (0.05 g/mL) was mixed with 1 mL of formic acid (80%) and 1 mL of ninhydrin solution (3% in ethylene glycol monomethylether). The mixture was shaken vigorously for 15 minutes. The mixture was incubated in a boiling water bath for 14 minutes before being transferred to a 70 ºC water bath for 10 minutes. A 5 mL 50% propanol-water solution was added, and the mixture was allowed to cool for 45 minutes. Its absorbance at 510 nm was measured. Water was used as the blank and a 0.032 mg/mL proline solution was used as the standard. Proline content (mg/kg) was calculated as follow:

$$Proline = \frac{E_s}{E_a} X \frac{E_1}{E_2} X80 \quad (1)$$

where E_s is the absorbance of the sample solution; E_a is the absorbance of the proline solution; E_1 is the concentration of proline in mg used for the standard; E_2 is the weight of honey in g; 80 is the dilution factor.

Ascorbic acid content determination

The honey sample (100 mg) was extracted with 10 mL of metaphosphoric acid for 45 minutes at room temperature and the mixture was filtered through a filter paper. About 1 mL of the filtrate was mixed with 9 mL of 2,6-dichlorophenolindophenol and the absorbance was determined at 515 nm within 30 min. L-ascorbic acid (0.02-0.12 mg/mL) was used as standard [11].

Ascorbic acid equivalent antioxidant content

AEAC was performed according to the procedure described by Meda et al. [12]. A 0.75 mL samples of honey in methanol (0.04 g/mL) was mixed with 1.5 mL of 0.02 mg/mL methanolic DPPH radical solution. The mixture was left for 15 minutes at room temperature before its absorbance was measured using a spectrophotometer (Secomam, France) at 517 nm. The

blank sample was prepared from a mixture of 0.75 mL of honey solution and 1.5 mL of methanol.

Carotenoid content

The measurement of carotenoid in *kelulut* honey was performed based on the method described by Ferreira et al. [11]. A 100 mg honey sample was shaken with a 4:6 ratio mixture of acetone and hexane for 1 minute. The mixture was filtered with filter paper and the absorbance of the filtrate was measured using a spectrophotometer (Secomam, France) at 454 nm, 505 nm, and 663 nm. The content of β-carotene inside the sample was calculated using the equation $0.216A_{663} - 0.304A_{505} + 0.452A_{453}$ while the lycopene content was calculated using the equation $-0.0458A_{663} + 0.372\ A_{505} - 0.0806\ A_{453}$. The total carotenoid content is defined as the sum of β-carotene and lycopene, and all measurements were expressed in mg/100mL.

Anti-oxidative activities

The DPPH radical scavenging capacity of *kelulut* honey was investigated using the procedure described Ferreira et al. [11]. Approximately 0.5 mL of the 0.2 g/mL honey extract was mixed with 2.7 mL of methanolic 0.024 mg/mL DPPH radical solution. The mixture was vigorously shaken and incubated for 15 minutes, then its absorbance was measured at 517 nm. IC_{50} was defined as the concentration of a substance that would scavenge 50% of DPPH radicals, which means that a lower IC_{50} value corresponds to a stronger antioxidant property. The FRAP assay was performed using the procedure described by Benzie & Strain [13]. A 200 µL sample of 0.1 g/mL honey was mixed with 1.5 mL of the FRAP reagent prepared from acetate buffer (300 mM/L), 2,4,6-tris(2-pyridyl)-*s*-triazine (TPTZ) solution (10 mM in 40 mM/L HCl), and ferric chloride ($FeCl_3.6H_2O$) (20mM) in the ratio of 10:1:1. The mixture was pre-warmed at 37 °C for 4 minutes before its absorbance was measured at 593 nm using a spectrophotometer (Secomam, France). Ferrous sulfate ($FeSO_4.7H_2O$) solutions with concentrations between 250-1000 µM/L was used to construct the standard curve (R^2=0.991). The FRAP values were expressed as µM Fe (II) per kg honey.

Data analysis

IBM SPSS version 23 was employed for the statistical analyses. ANOVA with Tukey's Honest Significant Difference (HSD) test was used for the comparisons of the chemical compositions of *kelulut* honey from three different zones. Pearson correlation was used to establish correlation between bioactive compounds and anti-oxidative activities. The significant level was set as α=0.05.

Results and Discussion

The compositional analysis revealed that the *kelulut* honey samples from *Trigona* spp. Collected in this study contained fructose and glucose at the concentrations of 9.91-27.33 g/100g and 10.96-25.04 g/100g, respectively (Table 1). Maltose was the predominant sugar of *kelulut* honey from the east coast and central regions of Peninsular Malaysia. The total sugar content of *kelulut* honey was 62.3-79.53 g/100g. The honey also contained oligosaccharides as the minor sugar constituents. In this study, the oligosaccharide content of *kelulut* honey was estimated by subtracting the individual sugars analyzed using HPLC from the total sugars analyzed using the phenol-sulphuric acid method. The results showed that *kelulut* honey contained 3.84-14.68 g/100g of oligosaccharides.

The total phenolic content of the *kelulut* honey samples collected in the present study was in the range of 530.28-1166.77 mg GAE/kg while the total flavonoid content was in the range of 48.82-79.02 mg QE/kg (Table 2). *Kelulu*t honey samples collected from the east coast region contained the highest level of carotenoids at 1.52 ± 0.17 mg lycopene/kg and 3.09 ± 0.25 mg β-carotene/kg. The total carotenoid content of *kelulut* honey samples in this study ranged between 2.22-4.61 mg carotenoids/kg. The proline content of *kelulut* honey in the present study was 277.76-291.89 mg/kg. The ascorbic acid content of the *kelulut* honey was within the range of 75.71-95.85 mg/kg. The central region *kelulut* honey had a significantly higher (p<0.05) ascorbic acid content compared to the east coast and northern *kelulut* honey. Meanwhile, the AEAC of *kelulut* honey was 78.10-146.48 mg/kg. Ascorbic acid in the *kelulut* honey contributed 65.44-96.94% to AEAC.

Table 1. Types of sugar in *kelulut* honey

Sugars	**East Coast Region Honey (n=6)**	**Northern Region Honey (n=6)**	**Central Region Honey (n=6)**
Total sugars (g/ 100g)	62.33 ± 10.33^{a}	79.53 ± 13.22^{b}	64.28 ± 19.63^{ab}
Maltose (g/100g)	22.80 ± 1.74^{a}	15.85 ± 0.05^{b}	37.74 ± 8.57^{c}
Fructose (g/100g)	10.41 ± 0.18^{a}	27.33 ± 0.15^{b}	9.91 ± 3.99^{a}
Glucose (g/100g)	10.96 ± 0.18^{a}	25.04 ± 0.14^{b}	11.98 ± 1.68^{a}
Sucrose (g/100g)	3.48 ± 0.65^{a}	0.54 ± 0.01^{b}	0.81 ± 0.22^{c}

Total sugar was obtained from phenol-sulphuric acid method while individual sugars were analyzed using HPLC. Different superscripts across the same row indicates significant difference (p <0.05).

Table 2. Phenolic, flavonoid, proline, ascorbic acid content and AEAC of *kelulut* honey

Parameters	**East Coast Region Honey (n=6)**	**Northern Region Honey (n=6)**	**Central Region Honey (n=6)**
TPC (mg GAE/kg)	1166.77 ± 47.85^{a}	728.42 ± 58.06^{b}	530.28 ± 30.31^{c}
TFC (mg QE/kg)	7902 ± 0.59^{a}	48.82 ± 0.67^{b}	55.38 ± 0.37^{b}
AEAC (mg/kg)	146.48 ± 6.43^{a}	78.10 ± 3.75^{b}	96.92 ± 1.31^{c}
Ascorbic acid content (mg/kg)	95.85 ± 13.48^{a}	75.71 ± 12.69^{a}	92.79 ± 0.75^{a}
Proline (mg/kg)	277.76 ± 19.75^{ab}	291.89 ± 3.46^{a}	284.82 ± 10.72^{b}
Lycopene (mg/kg)	1.52 ± 0.17^{a}	0.64 ± 0.08^{b}	0.76 ± 0.08^{c}
β-carotene (mg/kg)	3.09 ± 0.25^{a}	1.58 ± 0.14^{b}	1.57 ± 0.05^{b}
IC_{50} (DPPH radical scavenging) (mg/mL)	15.17 ± 1.02^{a}	28.47 ± 2.03^{b}	24.27 ± 2.68^{c}
FRAP (μM Fe (II)/ kg)	7481.08 ± 57.57^{a}	4122.97 ± 424.44^{b}	3633.78 ± 127.21^{c}

Different superscripts across the same row indicates significant difference (p <0.05)

The DPPH and FRAP assays were chosen because they are simple and rapid methods for assessing the antioxidant capacity of honey. The FRAP assay measures the ferric-reducing capacity of antioxidants, whereas the DPPH assay measures the ability of antioxidants to scavenge the DPPH radical. These two assays are based on different principles, and thus may be used to screen compounds that have different antioxidant mechanisms. *Kelulut* honey exhibited IC_{50} values in the range of 15.17-28.46 mg/mL. The honey collected from the east coast region showed the strongest DPPH radical scavenging activity with the lowest IC_{50} value of 15.17 ±1.02 mg/mL. The reducing power of *kelulut* honey assessed using FRAP was outlined in the order of east coast region *kelulut* honey > northern region *kelulut* honey > central region *kelulut* honey. The FRAP values were in the range of 3633.78-7481.08 μM Fe (II)/ kg.

The IC_{50} of the honey samples had a significant inverse correlation (p<0.01) with their bioactive compound compositions, namely total phenolics, total flavonoids, lycopene, β-carotene, ascorbic acid, and AEAC (Table 3). Their FRAP also had a significant and inverse

correlation ($p<0.01$) with their bioactive compound compositions, namely total phenolics, total flavonoids, lycopene, β-carotene and AEAC. The IC_{50} and FRAP had a strong inverse correlation ($r=-0.868$, $p<0.01$). The correlation matrix indicated the importance of the bioactive constituents of honey to its anti-oxidative capacity. The total phenolic content of a honey sample was negatively correlated with its IC_{50} value ($r^2 = -0.789$; $p<0.05$) and positively correlated with the FRAP value ($r^2 = 0.970$; $p<0.05$). In addition, a significant negative correlation was found between the honey sample's ascorbic acid composition and its IC_{50} value ($r^2 = -0.545$; $p<0.05$) and a positive correlation was found between its ascorbic acid composition and its lycopene value ($r^2 = 0.634$; $p<0.01$). These correlations between the bioactive compound content and the antioxidant activity of the extracts suggest that phenolic compounds are primarily responsible for the antioxidant activity of the honey samples as measured in the DPPH and FRAP assays.

Table 3. Correlation matrix of antioxidant content and anti-oxidative activities

	TPC	**TFC**	**IC_{50}**	**FRAP**	**Lycopene**	**β-carotene**	**Ascorbic Acid**	**AEAC**
TPC	1							
TFC	0.989**	1						
IC_{50}	-0.789**	-0.751**	1					
FRAP	0.970**	0.965**	-0.868**	1				
Lycopene	0.883**	0.861**	-0.895**	0.911**	1			
β-carotene	0.932**	0.924**	-0.868**	0.951**	0.987**	1		
Ascorbic Acid	0.228	0.172	-0.545**	0.323	0.634*	0.527	1	
AEAC	0.812**	0.813**	-0.948**	0.909**	0.932**	0.926**	0.557	1

TPC- total phenolic content; TFC- total flavonoid content; **Significant correlation at $p<0.05$; *Significant correlation at $p<0.01$

The fructose and glucose content of the *kelulut* honey samples gathered in this study were lower than those reported in the literature. Honey produced by stingless bees in the semi-arid region of Northeastern Brazil [14] has fructose as its predominant sugar (50.0-59.2 g/100g), followed by glucose (37.7-45.7 g/100g) and sucrose (0.7-3.9 g/100g). Ecuadorian stingless bee honey contained similar amounts of glucose (25.5 g/100g) and fructose (25.2 g/100g) with a smaller amount of sucrose (3.72 g/100g) [15]. Biluca et al. [16] also reported that the stingless bee honey from Santa Catarina, Brazil, contained 8.21-31.3 g glucose/100g and 30.4-46.1 g fructose/100g, while the honey from *Trigona fuscipennis* contained 36.22 g fructose /100g and 20.4 g glucose /100g. The amount of glucose and fructose measured were in accordance with the Malaysian Standard specification on kelulut stingless honey (MS 2683:2017), which dictates that it contains less than 7.5% sucrose and less than 85% fructose. The high concentration of sugar in honey combined with an acidic pH (3-5) do retard the growth of bacteria in honey [17].

The maltose content of the honey samples collected in the current study exceeded the limit set by the Malaysian Standard on kelulut stingless honey (MS 2683:2017), which dictated that the maltose content should be less than 9.5%. However, the current findings were in line with a recent study conducted by Chuttong et al. [18] which reported that Thai stingless bee honey contained 41 g maltose /100g, 17 g fructose/100g, 14 g glucose/100g and 1.2 g

sucrose/100g. An earlier study [19] also reported the *Trigona* honey, specifically of *Frieseomelita aff varia,* contained maltose as the predominant sugar (32.3%), followed by fructose (24.2%), glucose (18.1%), and sucrose (0.2%). The total sugar in our study were higher than those reported for Thai stingless bee honey (55±21 g/100g) [18]. The total sugar content of the *kelulut* honey in the current study was within the range of total sugars reported for Brazilian stingless monofloral honey (62.7-71.2 g/100g) [14]. The sucrose content (0.54-3.48 g/100g) obtained in this study was within the limit set by Codex Alimentarius (2001) [20] which is less than 5g/100g. *Kelulut* honey has a different sugar profile compared to the typical *Apis* spp. honey that contains fructose and glucose as the predominant sugar. This sugar profile in kelulut honey may contribute to its distinct flavor. Previous studies indicated that honey contains the oligosaccharides nigerose (1.11±2.81%), turanose (0.78±2.03%), maltotriose (0.24±1.03%), melezitose (0.21±0.37%) and raffinose (0.10±0.25%) that may also be present in *kelulut* honey.

Phenolic compounds play a role in countering the damage that oxidative stress incurs on the body. Having these active compounds makes the stingless bee honey valuable for medicinal purpose [21]. The vast difference in the phenolic content of the honey samples collected from the three different regions may be attributed to the differing bee species that produce those honey. A study showed the honey samples collected from three stingless bee species, namely *Geniotrigona thoracica*, *Heterotrigona itama,* and *Heterotrigona erythrogastra,* had significant differences in their phenolic content, which were 99.04 ± 5.14, 67.86 ± 7.40, 44.72 ± 6.50 mg/mL, respectively [22]. Apart from the different species of bees, geographical and botanical origins could explain the variation of phenolics content in stingless bee honey. Biluca et al. [16] reported that various stingless bee honey samples contained 10.3-98.0 mg GAE/100g phenolics while Silva et al. [23] reported a range of 1.1-1.3 mg GAE/g of phenolics found in stingless bee honey.

Furthermore, the total flavonoid content of *kelulut honey* were in fair agreement with results reported by Chan et al. [24], in which *Trigona* spp. honey from Malaysia contained 44.60-79.13 mg QE/kg. Tuksitha et al. [22] reported a higher flavonoids range (12.41-17.67 mg/mL) for stingless bee from Borneo. Previous study reported that various kinds of Hungarian honey contained 252-2283 mg proline /kg [23]. The value obtained in this study was within the range. The protein content of floral honey is 1.0-1.5% and the amino acid content is 1.0% of the total protein in honey. Proline is the main amino acid present in honey, constituting 50-85% of the total amino acids [23]. The proline content of honey decreases at a constant rate during storage; thus, it acts as an indicator of ripeness [23]. The minimum value of 180 mg/kg of proline is accepted for pure honey [26]. The value of ascorbic acid obtained in this study was lower than those obtained in Portuguese honey (140.01-145.80 mg/kg [11] and Algerian honey (159.70±0.78 mg/kg). A previous study [27] reported that Algerian honey contained 0.30-1.01 mg carotenoids/ 100 g.

A more recent study reported that floral honey from Tunisia contained 1.16-4.72 mg carotenoids/kg [28]. The carotenoid content of the *kelulut* honey samples collected from the three regions were significantly different (p <0.05), indicating the influence of geography on carotenoid content. Environmental factors and the changing seasons also contribute to the carotenoid content in honey [28]. The ascorbic acid content measured in this study was lower than those measured in Portuguese honey (140.01-145.80 mg/kg) [11] and Algerian honey (159.70±0.78 mg/kg). The value of AEAC in the present study was lower than those reported from other countries such as India (15.1-29.5 mg AEAC/100g) [29] and Bangladesh (18.4-34.1 mg AEAC/100g) [30].

The values of IC_{50} obtained in this study agreed well with the results reported for Tunisian floral honey which had a range of IC_{50} values from 11.08 mg/mL to 93.26 mg/mL [28]. Omani honey had higher IC_{50} values which were 25.1 mg/mL, 49.3 mg/mL, 144.5 mg/mL as the average values for Sumer, Sidr, and multifloral honey, respectively [31]. Our results were

higher than those of Brazilian honey (3.17-8.79 mg/mL) [32]. Despite the differences, we should acknowledge the inter-laboratory differences of these studies. Silva et al. [23] and Biluca et al. [16] reported that stingless bee honey had between 10.6-12.9 mg ascorbic acid equivalent/100g and 1.46-18.5 mg ascorbic acid equivalent/100g, respectively as the concentration needed to scavenge DPPH radicals. Recently, Tuksitha et al. [22] reported that stingless bee honey from Sarawak, Malaysia, contained 25.78-50.66 μM Fe (II)/100g. Compared to that, the samples collected in this study had stronger reducing activities. Our results were in fair agreement with the FRAP values of Polish honey 0.6-5.7 mM Fe (II)/kg honey [33] and stingless bee honey reported by Biluca et al. [16] in the ranged of 61.1-624 μM Fe (II)/100g.

Conclusion

Kelulut honey contains maltose as its predominant sugar and a relatively low amount of sucrose. *Kelulut* honey contains bioactive compounds namely phenolics and flavonoids, the compositions of which were significantly affected by the honey's botanical and geographical origin. Honey from the east coast region contained the highest amount of phenolics and flavonoids. Proline and ascorbic acid were not correlated with geographical factor.

Acknowledgement

This study was funded by Universiti Kebangsaan Malaysia research grant GUP-056-2014.

References

1. Escuredo, O., Míguez, M., Fernández-González, M., and Seijo, M. C. (2013). Nutritional value and antioxidant activity of honeys produced in a european atlantic area. *Food Chemistry,* 138: 851-856.
2. Arrifin, N. A. (2018). Determination of minerals in commercial honeys using atomic absorption spectrometry and inductively couple plasma-optical emission spectrometry. Thesis of Bachelor's Degree, Universiti Teknologi Mara.
3. Abid, N., Shiplu, R. C., Aminuddin, S. and Ruszymah, H. I. (2018). Low dose kelulut honey improves human keratinocyte viability, proliferation, and wound healing. *Regenerative Research,* 7(1):143.
4. Budin, S. B., Jubaidi, F. F., Azam, S. N. F. M. N., Yusof, N. L. M., Taib, I. S. and Mohamed, J. (2017). Kelulut honey supplementation prevents sperm and testicular oxidative damage in streptozotocin-induced diabetic rats. *Jurnal Teknologi*, 79(3).
5. Kaškonienė, V. and Venskutonis, P. R. (2010). Floral markers in honey of various botanical and geographic origins: a review. *Comprehensive reviews in food science and food safety,* 9(6): 620-634.
6. Wills, R. B. H., Balmer, N. and Greenfield, H. (1980). Composition of Australian foods. 2. Methods of analysis. *Food Technology in Australia*, 32(4): 198-204.
7. Dubois, M., Gilles, K. A., Hamilton, J. K., Rebers, P. T. and Smith, F. (1956). Colorimetric method for determination of sugars and related substances. *Analytical chemistry,* 28(3): 350-356.
8. Singleton, V. L., Orthofer, R. and Lamuela-Raventos, R. M. (1999). Analysis of total phenols and other oxidation substrates and antioxidants by means of Folin–Ciocalteu reagent. *Methods in Enzymology,* 299: 152-178.
9. Zhishen, J., Mengcheng, T. and Jianming, W. (1999). The determination of flavonoid contents in mulberry and their scavenging effects on superoxide radicals. *Food chemistry*, 64(4): 555-559.
10. Bogdanov, S., Lullmann, C., Mossel, B.L., D'arcy, B.R., Russmann, H., Vorwohl, G., Oddo, L., Sabatini, A.G., Marcazzan, G.L., Piro, R. and Flamini, C. (1999). Honey quality, methods of analysis and international regulatory standards: review of the work of the international honey commission. *Mitt Lebensmittelunters Hyg,* 90: 108-125.
11. Ferreira, I. C., Aires, E., Barreira, J. C., and Estevinho, L. M. (2009). Antioxidant activity of Portuguese honey samples: different contributions of the entire honey and phenolic extract. *Food Chemistry*, 114(4): 1438-1443.

12. Meda, A., Lamien, C. E., Romito, M., Millogo, J. and Nacoulma, O. G. (2005). Determination of the total phenolic, flavonoid and proline contents in burkina fasan honey, as well as their radical scavenging activity. *Food chemistry,* 91(3): 571-577.
13. Benzie, I. F., and Strain, J. J. (1999). Ferric reducing/antioxidant power assay: Direct measure of total antioxidant activity of biological fluids and modified version for simultaneous measurement of total antioxidant power and ascorbic acid concentration. *Methods in Enzymology,* 299: 15-27.
14. de Sousa, J. M. B., de Souza, E. L., Marques, G., de Toledo Benassi, M., Gullón, B., Pintado, M. M., and Magnani, M. (2016). Sugar profile, physicochemical and sensory aspects of monofloral honeys produced by different stingless bee species in Brazilian semi-arid region. *LWT-Food Science and Technology*, 65: 645-651.
15. Guerrini, A., Bruni, R., Maietti, S., Poli, F., Rossi, D., Paganetto, G., Muzzoli, M., Scalvenzi, L. and Sacchetti, G. (2009). Ecuadorian stingless bee (Meliponinae) honey: A chemical and functional profile of an ancient health product. *Food Chemistry*, 114(4): 1413-1420.
16. Biluca, F. C., Braghini, F., Gonzaga, L. V., Costa, A. C. O. and Fett, R. (2016). Physicochemical profiles, minerals and bioactive compounds of stingless bee honey (Meliponinae). *Journal of Food Composition and Analysis*, 50: 61-69.
17. Lia, A. S., Muhammad, A. I., Nik, M. S. and Fareed S. (2017). Pemencilan dan pengenalpastian bakteria daripada madu kelulut (*Trigona sp.*). *Undergraduate Research Journal for Biomolecular Sciences and Biotechnology*, 1: 151-157.
18. Chuttong, B., Chanbang, Y., Sringarm, K. and Burgett, M. (2016). Physicochemical profiles of stingless bee (Apidae: Meliponini) honey from South East Asia (Thailand). *Food chemistry,* 192: 149-155.
19. Bogdanov, S., Vit, P. and Kilchenmann, V. (1996). Sugar profiles and conductivity of stingless bee honeys from Venezuela. *Apidologie*, 27(6): 445-450.
20. Codex Alimentarius (2001). Revised codex standard for honey. Codex Standard 12(2001): 1982.
21. Yaacob, M., Rajab N.F., Shahar, S. and Sharif, R. (2018). Stingless bee honey and its potential value: A systematic review. *Food Research*, 2550-2166.
22. Tuksitha, L., Chen, Y. L. S., Chen, Y. L., Wong, K. Y. and Peng, C. C. (2018). Antioxidant and antibacterial capacity of stingless bee honey from Borneo (Sarawak). *Journal of Asia-Pacific Entomology*, 21(2): 563- 570.
23. Silva, T. M. S., dos Santos, F. P., Evangelista-Rodrigues, A., da Silva, E. M. S., da Silva, G. S., de Novais, J. S. and Camara, C. A. (2013). Phenolic compounds, melissopalynological, physicochemical analysis and antioxidant activity of Jandaíra (*Melipona subnitida*) honey. *Journal of Food Composition and Analysis*, 29 (1): 10-18.
24. Chan, B. K., Haron, H., Talib, R. A. and Subramaniam, P. (2017). Physical properties, antioxidant content and anti-oxidative activities of Malaysian stingless kelulut (Trigona spp.) honey. *Journal of Agricultural Science,* 9(13): 32.
25. Czipa, N., Borbély, M. and Győri, Z. (2012). Proline content of different honey types. *Acta Alimentaria,* 41 (1): 26-32.
26. Hermosín, I., Chicon, R. M. and Cabezudo, M. D. (2003). Free amino acid composition and botanical origin of honey. *Food Chemistry*, 83(2): 263-268.
27. Mouhoubi-Tafinine, Z., Ouchemoukh, S., & Tamendjari, A. (2016). Antioxidant activity of some Algerian honey and propolis. *Industrial Crops and Products,* 88: 85-90.
28. Boussaid, A., Chouaibi, M., Rezig, L., Hellal, R., Donsì, F., Ferrari, G. and Hamdi, S. (2018). Physicochemical and bioactive properties of six honey samples from various floral origins from tunisia. *Arabian Journal of Chemistry*, 11(2): 265-274.
29. Saxena, S., Gautam, S. and Sharma, A. (2010). Physical, biochemical and antioxidant properties of some indian honeys. *Food Chemistry,* 118(2): 391-397.

30. Islam, A., Khalil, I., Islam, N., Moniruzzaman, M., Mottalib, A., Sulaiman, S. A. and Gan, S. H. (2012). Physicochemical and antioxidant properties of Bangladeshi honeys stored for more than one year. *BMC Complementary and Alternative Medicine*, 12(1): 1.
31. Al-Farsi, M., Al-Amri, A., Al-Hadhrami, A. and Al-Belushi, S. (2018). Color, flavonoids, phenolics and antioxidants of Omani honey. *Heliyon,* 4(10): e00874.
32. Pontis, J. A., Costa, L. A. M. A. D., Silva, S. J. R. D. and Flach, A. (2014). Color, phenolic and flavonoid content, and antioxidant activity of honey from Roraima, Brazil. *Food Science and Technology,* 34(1): 69-73.
33. Kuś, P. M., Congiu, F., Teper, D., Sroka, Z., Jerković, I. and Tuberoso, C. I. G. (2014). Antioxidant activity, color characteristics, total phenol content and general HPLC fingerprints of six Polish unifloral honey types. *LWT-Food Science and Technology*, 55(1): 124-130.

Malaysian Journal of Analytical Sciences (MJAS)
Published by Malaysian Analytical Sciences Society

QUANTITATIVE STRUCTURE-ACTIVITY RELATIONSHIP (QSAR) STUDY OF NEWLY SYNTHESIZED CARBONYL THIOUREA DERIVATIVES ON *Acanthamoeba* sp.

(Kajian Kuantitatif Hubungan Struktur-Aktiviti (QSAR) Terhadap Terbitan Karbonil Tiourea Hasilan Sintesis Baru Terhadap *Acanthamoeba* sp.)

Maizatul Akma Ibrahim[1]*, Nor Hafizah Zakaria[1], Mohd Sukeri Mohd Yusof[2]

[1]*Department of Plant Science, Kulliyyah of Science,*
International Islamic University Malaysia, Bandar Indera Mahkota, 25200 Kuantan, Pahang, Malaysia
[2]*Faculty of Science and Marine Environment,*
Universiti Malaysia Terengganu, 21030 Kuala Nerus, Terengganu, Malaysia.

**Corresponding author: maizatulakma@iium.edu.my*

Received: 3 December 2021; Accepted: 23 March 2022; Published: 27 June 2022

Abstract

This research aims to build a mathematical quantitative structure-activity relationship (QSAR) model, which could relate the relationship between newly-synthesized carbonyl thiourea derivatives with their anti-amoebic activities. Therefore, in this study, inhibition concentration of 50% cells population (IC_{50}) was evaluated for 44 carbonyl thiourea derivatives on pathogenic *Acanthamoeba* sp. (Hospital Kuala Lumpur isolate). QSAR analysis was conducted using the obtained IC_{50} data with additional 4 thiourea compounds of the same group from our previous work by applying three linear regression techniques namely stepwise-MLR, GA-MLR, and GA-PLS. Results showed that these thiourea derivatives are positively active against the tested *Acanthamoeba* sp. with IC_{50} values ranging from 2.56 to 7.81 µg/mL. From the evaluation of the obtained models, the GA-PLS technique is found to be the best model due to its best predictive ability. The final equation of GA-PLS model gave good statistical output with values of r^2 = 0.827, r^2_{cv} = 0.682 *RMSEC*=0.047, *RMSECV*=0.064, and r^2_{test} =0.790 and *RMSEP*=0.051. Y-randomization test has confirmed that the model did not occur from the chance of correlation with r^2 = 0.015-0.372. Small residual with values less than 0.25 from the prediction in the test set proves the robustness of the model. The information generated from this study will provide an insight into designing a new lead compound from carbonyl thiourea containing highly potential anti-amoebic properties.

Keywords: thiourea derivatives, *Acanthamoeba* sp., IC_{50}, anti-amoebic activity, QSAR models

Abstrak

Kajian ini mensasarkan pembinaan model matematik kuantitatif hubungan struktur-aktiviti (QSAR) yang memberi hubungkait antara terhadap terbitan karbonil tiourea hasilan sintesis baru dengan aktiviti anti-amebik. Oleh itu, kepekatan penghambatan 50% populasi sel (IC_{50}) dikaji ke atas 44 sebatian karbonil tiourea terhadap *Acanthamoeba* sp. (Hospital Kuala Lumpur isolat) berstatus patogenik. Analisa hubungan struktur-aktiviti kuantitatif dijalankan menggunakan data IC_{50} yang diperolehi bersama 4 sebatian tambahan kumpulan sama dari hasil kerja kami sebelum ini, dengan mengaplikasi tiga teknik regresi linear, iaitu

stepwise-MLR, GA-MLR dan GA-PLS dijalankan. Hasil kajian menunjukkan bahawa sebatian tiourea ini aktif secara positif terhadap *Acanthamoeba* sp.yang diuji dengan nilai IC_{50} antara 2.56 hingga 7.81 μg/mL. Penilaian terhadap semua model QSAR yang dibina dalam kajian ini menunjukkan teknik GA-PLS adalah model yang terbaik kerana kemampuan ramalannya yang terbaik. Persamaan akhir untuk model GA-PLS menunjukkan output statistik yang baik dengan nilai r^2 = 0.827, r^2_{cv} = 0.682, *RMSEC* = 0.047, *RMSECV* = 0.064, r^2_{test} = 0.790 dan *RMSEP* = 0.051. Ujian perawakan-y mengesahkan bahawa model tersebut tidak terhasil secara kebetulan dengan r^2 = 0.015-0.372. Baki kecil dengan nilai kurang dari 0.25 dari ramalan set ujian membuktikan kekuatan model tersebut. Data terbina dari kajian ini akan memberi maklumat untuk mencipta sebatian penting baru dari tiourea karbonil yang mempunyai aktiviti anti-amebik yang berpotensi tinggi.

Kata kunci: tiourea terbitan, *Acanthamoeba* sp., IC_{50}, aktiviti anti-amebik, model QSAR

Introduction

Acanthamoeba is a pathogenic protozoan that is ubiquitously found in the environment. It can cause *Acanthamoeba* keratitis, which commonly occurs in contact lens users [1]. There are several antimicrobial agents such as chlorhexidine gluconate and polyhexamethylene biguanide that have been used to treat the disease but according to Vontobel et al. [2], both agents do not readily penetrate the cornea of the eyes, which require months of topical administration, making them ineffective for keratitis treatment. Reports showed resistance of *Acanthamoeba* towards these antiseptics, especially during the later stage of infection, which makes it difficult to be treated [3]. Therefore, the development of new potential antiamoebic agents is demanded to overcome these problems. Thiourea, an organosulfur compound has been reported to contain diverse biomedical benefits such as antibacterial, anticancer, antifungal, anti-inflammatory, antithyroid, herbicidal, and antitubercular properties [4, 5, 6]. Naz et al. evaluated the antibacterial activity of thiourea derivatives and found that these compounds significantly inhibited several pathogenic bacteria including *E. faecalis*, *P. aeruginosa*, *S. typhi*, and *K. pneumoniae* [7]. In another study, Keche and Kemble also reported the antimicrobial activity of novel thiourea compounds against several selected bacteria and fungi and they revealed that these compounds have promising antimicrobial activity [8]. Nevertheless, there is still lacking literature regarding the anti-amoebic properties of thiourea derivatives on *Acanthamoeba*. Therefore, a cytotoxicity test was conducted in this study to determine the lC_{50} values for the newly synthesized thiourea derivatives on *Acanthamoeba*.

A QSAR study was applied to analyze the molecular structures of the synthesized compounds to correlate with their anti-amoebic activities and allow for the effects of compounds of interest to be predicted [9]. In this study, QSAR methods were used to quantitatively study the relationship between the presented synthesized carbonyl thiourea analogs with their anti-amoebic activity. The approach applied multiple linear regression (MLR) and partial least square (PLS) to build the QSAR equation models. Conventional stepwise methods and genetic algorithm (GA) were employed to choose the best descriptors subset in the model development. Internal and external validations were carried out to evaluate the robustness of the generated models. From the information gained in this study, optimized thiourea-based compounds that work best against pathogenic *Acanthamoeba* could be predicted and developed as new agents to treat *Acanthamoeba* keratitis.

Materials and Methods

In this study, a set of carbonyls thiourea derivatives consisting of 40 compounds were synthesized and characterized at the Faculty of Science and Marine Environment, Universiti Malaysia Terengganu. These synthesized thiourea derivatives were confirmed by spectral studies of Fourier Transformation Infrared (FT-IR) spectroscopy and ^{1}H and ^{13}C Nuclear Magnetic Resonance (NMR). The preparation of M1–M44 compounds is based on the synthesis method of the previous study with additions of compounds

labeled as M7, M8, M25, and M26 attained from the same work [10]. The other synthesized thiourea and their molecular weights are listed in Table 1.

Table 1. Molecular structures of the newly-synthesized carbonyl thiourea derivatives

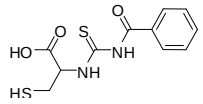
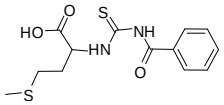
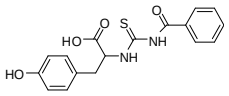
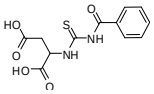
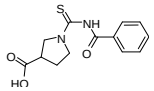
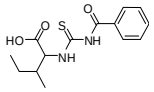
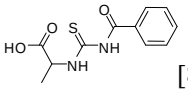
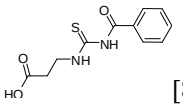
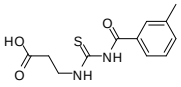
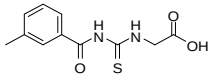
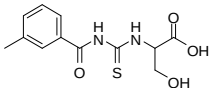
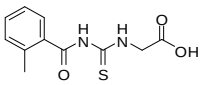
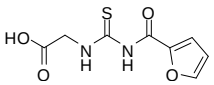
Code	Chemical Name	Molecular Weight	Structure
M1	2-(3-benzoyl thioureido)-3-mercapto propanoic acid	284.35	
M2	2-(3-benzoyl thioureido)-4-(methylthio)butanoic acid	312.41	
M3	2-(3-benzoyl thioureido)-3-(4-hydroxyphenyl)propanoic acid	344.38	
M4	2-(3-benzoyl thioureido)succinic acid	296.30	
M5	1-(benzoyl carbamothioyl) pyrrolodine-3-carboxyl acid	278.33	
M6	2-(3-benzoyl thioureido)-3-methyl pentanoic acid	294.37	
M7	2-(3-benzoyl thioureido)propanoic acid	252.29	 [8]
M8	3-(3-benzoyl thioureido)propanoic acid	252.29	 [8]
M9	3-[3-(3-methylbenzoyl) thioureido] propanoic acid	266.32	
M10	2-[3-(3-methylbenzoyl) thioureido] acetic acid	252.29	
M11	3-hydroxy-2-[3-(3-methylbenzoyl) thioureido]propanoic acid	282.32	
M12	2-[3-(2-methylbenzoyl)thioureido] acetic acid	252.29	
M13	2-(3-furan-2-carbonyl thioureido) acetic acid	228.23	

Table 1 (cont'd). Molecular structures of the newly-synthesized carbonyl thiourea derivatives

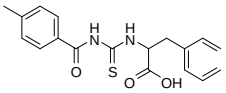
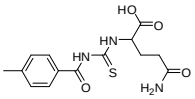
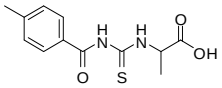
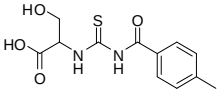
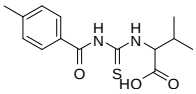
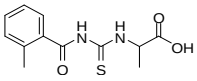
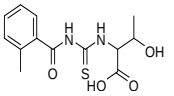
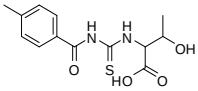
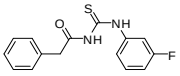
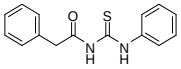
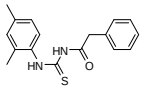
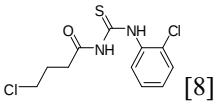
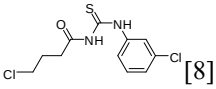
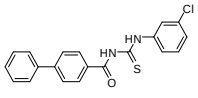
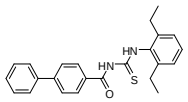
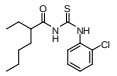
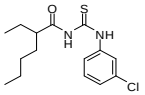
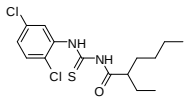
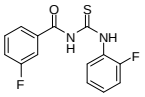
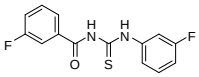
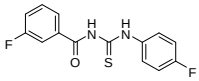
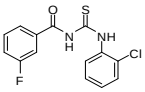
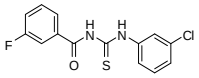
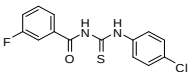
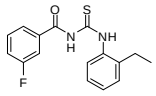
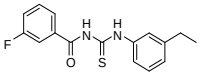
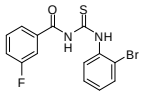
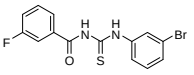
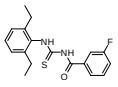
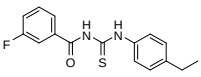
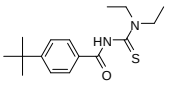
Code	Chemical Name	Molecular Weight	Structure
M14	2-[3-(4-methylbenzoyl) thioureido]-3-phenylpropanoic acid	342.41	
M15	5-amino-2-[3-(4-methylbenzoyl) thioureido]-5-oxopentanoic acid	323.37	
M16	2-[3-(4-methylbenzoyl) thioureido] propanoic acid	266.32	
M17	3-hydroxy-2-[3-(4-methylbenzoyl) thioureido]propanoic acid	282.32	
M18	3-methyl-2-[3-(4-methylbenzoyl) thioureido]butanoic acid	294.37	
M19	2-[3-(2-methylbenzoyl) thioureido] propanoic acid	266.32	
M20	3-hydroxy-2-[3-(2-methylbenzoyl) thioureido]butanoic acid	296.34	
M21	3-hydroxy-2-[3-(4-methylbenzoyl) thioureido]butanoic acid	296.34	
M22	*N*-(3-fluorophenyl)-*N'*-phenylacetyl thiourea	288.34	
M23	*N*-phenyl-*N'*-phenylacetyl thiourea	270.35	
M24	*N*-(2,4-dimethylphenyl)-*N'*-phenyl acetylthiourea	298.40	
M25	*N*-(2-chlorophenyl)-*N'*-(4-chlorobutanoyl) thiourea	291.20	 [8]
M26	*N*-(3-chlorophenyl)-*N'*-(4-chlorobutanoyl) thiourea	291.20	 [8]
M27	*N*-(3-chlorophenyl)-*N'*-(biphenyl-4-yl) carbamoyl thiourea	366.86	

Table 1 (cont'd). Molecular structures of the newly-synthesized carbonyl thiourea derivatives

Code	Chemical Name	Molecular Weight	Structure
M28	*N*-(2,6-diethylphenyl)-N'-(biphenyl-4-yl)carbamoyl thiourea	388.53	
M29	*N*-(2-chlorophenyl)-*N'*-(2-ethyl hexanoyl) thiourea	312.86	
M30	*N*-(3-chlorophenyl)-*N'*-(2-ethyl hexanoyl) thiourea	312.86	
M31	*N*-(2,5-dichlorophenyl)-*N'*-(2-ethyl hexanoyl) thiourea	347.40	
M32	*N*-(3-fluorobenzoyl)-*N'*-(2-fluoro phenyl) thiourea	292.30	
M33	*N*-(3-fluorobenzoyl)-*N'*-(3-fluoro phenyl) thiourea	292.30	
M34	*N*-(3-fluorobenzoyl)-*N'*-(4-fluoro phenyl) thiourea	292.30	
M35	*N*-(3-fluorobenzoyl)-*N'*-(2-chloro phenyl) thiourea	308.76	
M36	*N*-(3-fluorobenzoyl)-*N'*-(3-chloro phenyl) thiourea	308.76	
M37	*N*-(3-fluorobenzoyl)-*N'*-(4-chloro phenyl) thiourea	308.76	
M38	*N*-(3-fluorobenzoyl)-*N'*-(2-ethyl phenyl) thiourea	302.37	
M39	*N*-(3-fluorobenzoyl)-*N'*-(3-ethyl phenyl) thiourea	302.37	
M40	*N*-(3-fluorobenzoyl)-*N'*-(2-bromo phenyl) thiourea	353.21	
M41	*N*-(3-fluorobenzoyl)-*N'*-(3-bromo phenyl) thiourea	353.21	
M42	*N*-(3-fluorobenzoyl)-*N'*-(2,6-diethyl phenyl) thiourea	330.42	
M43	*N*-(3-fluorobenzoyl)-*N'*-(4-ethyl phenyl)thiourea	302.37	
M44	*N*-(4-*tert*-butylbenzoyl)-*N'*-diethyl phenyl thiourea	292.44	

Determination of IC_{50} values

Thiourea derivatives were prepared and chlorhexidine gluconate (Raza Manufacturing, Malaysia) was used as the positive control whereas 10^4 cells/mL of healthy *Acanthamoeba* sp. without any treatment was used as the negative control [10]. The plates were incubated at 30°C for 72 hours. After incubation, the staining process was performed using the eosin dye method [11]. The absorbance was measured at 490 nm using an ELISA plate reader (Tecan, Australia). The readings were plotted in GraphPad Prism software (version 5.03) (San Diego, USA) to give a non-linear sigmoidal dose-response curve in which the cytotoxicity study was expressed as 50% cytotoxic dose (IC_{50}). T-test (SPSS, version 11.5, USA) was used to compare mean values between untreated and treated cultures, and $p < 0.05$ is considered statistically significant.

Data set selection for QSAR study

The data set that contains thiourea derivatives with anti-amoebic activity is shown in Table 2. The IC_{50} values in the molar (M) unit were converted to pIC_{50} for the convenience of computational work. The data were divided into training and test set. The training set is comprised of 30 thiourea compounds while the test set consisted of the remaining 14 compounds. Compound M7 was later removed from the data set as it was detected to be an outlier throughout the model building by all selected methods of stepwise multiple linear regression (stepwise-MLR), genetic algorithm multiple linear regression (GA-MLR), and genetic algorithm partial least square (GA-PLS).

Table 2. Functional groups of carbonyl thiourea analogs with their anti-amoebic activity

Code	R_1	R_2	IC_{50} (μM)	pIC_{50} (M)
M1	$C_4H_8O_2S$	C_8H_8O	9.00	5.05
M2	$C_6H_{12}O_2S$	C_8H_8O	8.63	5.06
M3	$C_{10}H_{12}O_3$	C_8H_8O	9.65	5.02
M4	$C_5H_8O_4$	C_8H_8O	13.35	4.87
M5	$C_5H_{10}O_2$	C_8H_8O	11.06	4.96
M6	$C_7H_{14}O_2$	C_8H_8O	13.24	4.88
M7	$C_4H_8O_2$	C_8H_8O	10.85	4.97
M8	$C_4H_8O_2$	C_8H_8O	11.59	4.94
M9	$C_4H_8O_2$	$C_9H_{10}O$	19.26	4.72
M10	$C_9H_{10}O$	$C_3H_6O_2$	22.35	4.65
M11	$C_9H_{10}O$	$C_4H_8O_3$	18.52	4.73
M12	$C_9H_{10}O$	$C_3H_6O_2$	19.58	4.71
M13	$C_3H_6O_2$	$C_6H_6O_2$	20.16	4.70
M14	$C_9H_{10}O$	$C_{10}H_{12}O_2$	14.47	4.84
M15	$C_9H_{10}O$	$C_6H_{11}NO_3$	17.04	4.80
M16	$C_9H_{10}O$	$C_4H_8O_2$	21.79	4.66
M17	$C_9H_{10}O$	$C_4H_8O_3$	18.75	4.73
M18	$C_9H_{10}O$	$C_6H_{12}O_2$	17.20	4.76
M19	$C_9H_{10}O$	$C_4H_8O_2$	19.95	4.70
M20	$C_9H_{10}O$	$C_5H_{10}O_3$	15.58	4.81
M21	$C_9H_{10}O$	$C_5H_{10}O_3$	16.18	4.79

Table 2 (cont'd). Functional groups of carbonyl thiourea analogs with their anti-amoebic activity

Code	R_1	R_2	IC_{50} (µM)	pIC_{50} (M)
M22	$C_9H_{10}O$	C_7H_7F	14.65	4.83
M23	$C_9H_{10}O$	C_7H_8	19.47	4.71
M24	$C_9H_{10}O$	C_9H_{12}	19.80	4.70
M25	C_5H_9ClO	C_7H_7Cl	23.84	4.62
M26	C_5H_9ClO	C_7H_7Cl	26.81	4.57
M27	$C_{14}H_{12}O$	C_7H_7Cl	16.31	4.79
M28	$C_{14}H_{12}O$	$C_{11}H_{16}$	14.14	4.85
M29	$C_9H_{18}O$	C_7H_7Cl	20.93	4.68
M30	$C_9H_{18}O$	C_7H_7Cl	21.52	4.67
M31	$C_9H_{18}O$	$C_7H_6Cl_2$	18.62	4.73
M32	C_8H_7FO	C_7H_7F	23.46	4.63
M33	C_8H_7FO	C_7H_7F	22.28	4.65
M34	C_8H_7FO	C_7H_7F	20.91	4.68
M35	C_8H_7FO	C_7H_7Cl	20.78	4.68
M36	C_8H_7FO	C_7H_7Cl	20.23	4.69
M37	C_8H_7FO	C_7H_7Cl	20.03	4.70
M38	C_8H_7FO	C_9H_{12}	19.74	4.70
M39	C_8H_7FO	C_9H_{12}	19.29	4.72
M40	C_8H_7FO	C_7H_7Br	18.41	4.74
M41	C_8H_7FO	C_7H_7Br	17.98	4.75
M42	C_8H_7FO	$C_{11}H_{16}$	19.02	4.72
M43	C_8H_7FO	C_9H_{12}	20.93	4.68
M44	$C_{12}H_{16}O$	C_5H_{12}	21.55	4.67

Structure entry and molecular modeling

Structure entry and molecular modeling were first carried out by acquiring a three-dimensional (3D) representation of the thiourea derivative molecules. The compounds' two-dimensional (2D) molecular structures were generated using ChemDraw Ultra (version 10.0). The structures were then converted to 3D structures using Chem3D Ultra 10.0. The 3D molecules of thiourea compounds were analyzed with the MM2 method and MOPAC (Chem3D Ultra 10.0) at default settings to acquire stable molecular structures with the lowest energy.

Descriptors generation

A total of 1661 molecular descriptors of optimized thiourea molecules were computed with DRAGON software (version 5.2). In this analysis, only 0D, 1D, and 2D descriptors were used while the 3D descriptors were excluded since molecular structures of the compounds were not uniformly aligned.

Feature selection

The descriptors that did not contain relevant information for the model development were eliminated from the set. The next step was to find the best subset from the remaining descriptors. Stepwise multiple regression and Genetic Algorithm (GA) were used in this step using MATLAB version 7.6.0 (The Mathworks Inc.) software with PLS Toolbox version 5.2.2 (Eigenvector Research Inc.). Meanwhile, Genetic Algorithm GUI [genalg] function was used for GA selection.

Model development

For the model development, routines were performed in MATLAB with PLS Toolbox whereby MLR and PLS analyses were applied. The approaches for modeling utilize integrated stepwise with MLR (stepwise-MLR), GA with MLR (GA-MLR) and GA with PLS (GA-PLS). Statistical significance of the final model was characterized by the squared correlation coefficient, r^2, root mean square error of calibration, *RMSEC*, and root mean square error of cross validation, *RMSECV*. The obtained outputs were converted [regcon] to equation models. The regression coefficient in the equation indicates the significance of an individual descriptor. A plot of predicted versus experimental activity was evaluated to examine the goodness of fit for the generated models. A plot of residuals versus predicted values was used to detect outliers in the data set.

Model validation

The model validation process was also conducted by MATLAB with the PLS toolbox. Both internal and external validations were conducted in this study. Cross-validation by the leave-one-out (LOO) method was applied to provide a rigorous internal check on the built models. This validation process was accomplished by validating the models from their statistical outputs of cross validated squared correlation coefficient r^2_{cv}, squared correlation coefficient of test set, r^2_{test} and root mean square error of prediction, *RMSEP*. Data scrambling technique by the y-randomization test was performed to ensure that the constructed models were not the result of mere chance correlations. On the other hand, external validation was also performed involving the prediction of activity for compounds from the test set.

Results and Discussion

Inhibition concentration for half of cells population (IC_{50} values)

Thiourea derivatives that exhibited the best anti-amoebic activity were 2-(3-benzoylthioureido)-3-mercaptopropanoic acid and 2-(3-benzoylthioureido)-4-(methylthio)butanoic acid labeled as M1 and M2, respectively. These two thiourea compounds showed the lowest IC_{50} value suggesting that they provide the best intrinsic anti-amoebic activity. These two compounds are amino acid types of derivatives that could be recognized by the presence of hydroxyl (-COOH) with an amine group in the molecule. In general, all derivatives of amino acid groups in this study showed lower IC_{50} values compared to other compounds in the series. This indicates that amino acids could enhance the activity of the thiourea derivatives. Xu et al. [12] supported this finding by highlighting that in general, amino acid derivatives of the compounds could exhibit a variety of biological properties. Meanwhile, Hauck et al. [13] emphasized that amino acid derivatives in the compounds contribute to a hydrophilic moiety, which gives high selectivity toward receptors. Ibrahim et al. [8] that came out with thiourea derivatives labeled as M7, M8, M25, and M26 also suggested that the mechanism of action for the proposed thiourea derivatives toward the protozoan parasite *Acanthamoeba* should focus on the hydrophobicity of thiourea molecules to explain their actions. The suggested drug-receptors for the compounds' main target in the amoeba cells are the transport proteins that are distributed throughout the cell membrane.

Chlorhexidine gluconate was used as a positive control as it is a general biocidal effective against a wide variety of microorganisms [14]. The chlorhexidine-treated amoeba in the experiment exhibited a slightly lower IC_{50} of 6.30 ± 0.49 μM. From the T-test analysis, absorbance readings from the untreated and treated cells showed statistical significance (p <0.05). Thiourea in its basic structure has one sulfur atom. A sulfur atom has six valence electrons, and its electronic configuration is similar to oxygen [15]. Most sulfur-containing organics exhibit a low order of toxicity. However, their toxicity may be enhanced by substitution in the molecules. Patnaik [16] explained that an -SH group attached to a benzene ring imparts greater toxicity to the molecule than that attached to an alkyl group. Therefore, the thiourea derivatives were synthesized with at least one benzene ring as an attachment in this study with an attempt to increase their activity on the tested cells.

Table 3. IC_{50} values of 45 carbonyl thiourea derivatives compound on *Acanthamoeba* sp.

Code	Chemical Name	IC_{50} µg/mL
M1	2-(3-benzoylthioureido)-3-mercaptopropanoic acid	2.56 ± 0.46
M2	2-(3-benzoylthioureido)-4-(methylthio)butanoic acid	2.70 ± 0.27
M3	2-(3-benzoylthioureido)-3-(4-hydroxyphenyl)propanoic acid	3.32 ± 0.18
M4	2-(3-benzoylthioureido)succinic acid	3.96 ± 0.26
M5	1-(benzoylcarbamothioyl)pyrrolodine-3-carboxyl acid	3.08 ± 0.34
M6	2-(3-benzoylthioureido)-3-methylpentanoic acid	3.90 ± 0.20
M7	2-(3-benzoylthioureido)propanoic acid	2.74 ± 0.42
M8	3-(3-benzoylthioureido)propanoic acid	2.92 ± 0.24
M9	3-[3-(3-methylbenzoyl)thioureido]propanoic acid	5.13 ± 0.59
M10	2-[3-(3-methylbenzoyl)thioureido]acetic acid	5.64 ± 0.63
M11	3-hydroxy-2-[3-(3-methylbenzoyl)thioureido]propanoic acid	5.23 ± 0.41
M12	2-[3-(2-methylbenzoyl)thioureido]acetic acid	4.94 ± 0.20
M13	2-(3-furan-2-carbonylthioureido) acetic acid	4.60 ± 0.61
M14	2-[3-(4-methylbenzoyl)thioureido]-3-phenylpropanoic acid	4.95 ± 0.49
M15	5-amino-2-[3-(4-methylbenzoyl)thioureido]-5-oxopentanoic acid	5.51 ± 0.47
M16	2-[3-(4-methylbenzoyl)thioureido]propanoic acid	5.80 ± 0.20
M17	3-hydroxy-2-[3-(4-methylbenzoyl)thioureido]propanoic acid	5.29 ± 0.10
M18	3-methyl-2-[3-(4-methylbenzoyl)thioureido]butanoic acid	5.06 ± 0.40
M19	2-[3-(2-methylbenzoyl)thioureido]propanoic acid	5.31 ± 0.22
M20	3-hydroxy-2-[3-(2-methylbenzoyl)thioureido]butanoic acid	4.62 ± 0.43
M21	3-hydroxy-2-[3-(4-methylbenzoyl)thioureido]butanoic acid	4.80 ± 0.48
M22	*N*-(3-fluorophenyl)-*N'*-phenylacetylthiourea	4.23 ± 0.95
M23	*N*-phenyl-*N'*-phenylacetylthiourea	5.26 ± 0.55
M24	*N*-(2,4-dimethylphenyl)-*N'*-phenylacetylthiourea	5.91 ± 0.51
M25	*N*-(2-chlorophenyl)-*N'*-(4-chlorobutanoyl)thiourea	6.94 ± 0.79
M26	*N*-(3-chlorophenyl)-*N'*-(4-chlorobutanoyl)thiourea	7.81 ± 0.34
M27	*N*-(3-chlorophenyl)-*N'*-(biphenyl-4-yl)carbamoylthiourea	5.98 ± 0.79
M28	*N*-(2,6-diethylpehnyl)-N'-(biphenyl-4-yl)carbamoylthiourea	5.49 ± 0.38
M29	*N*-(2-chlorophenyl)-*N'*-(2-ethylhexanoyl)thiourea	6.55 ± 0.56
M30	*N*-(2-chlorophenyl)-*N'*-(2-ethylhexanoyl)thiourea	6.73 ± 0.30
M31	*N*-(2,5-dichlorophenyl)-*N'*-(2-ethylhexanoyl)thiourea	6.47 ± 0.70
M32	*N*-(3-fluorobenzoyl)-*N'*-(2-fluorophenyl)thiourea	6.86 ± 0.36
M33	*N*-(3-fluorobenzoyl)-*N'*-(3-fluorophenyl)thiourea	6.51 ± 0.27
M34	*N*-(3-fluorobenzoyl)-*N'*-(4-fluorophenyl)thiourea	6.11 ± 0.17
M35	*N*-(3-fluorobenzoyl)-*N'*-(2-chlorophenyl)thiourea	6.42 ± 0.28
M36	*N*-(3-fluorobenzoyl)-*N'*-(3-chlorophenyl)thiourea	6.25 ± 0.35
M37	*N*-(3-fluorobenzoyl)-*N'*-(4-chlorophenyl)thiourea	6.18 ± 0.32
M38	*N*-(3-fluorobenzoyl)-*N'*-(2-ethylphenyl)thiourea	5.97 ± 0.63
M39	*N*-(3-fluorobenzoyl)-*N'*-(3-ethylphenyl)thiourea	5.83 ± 0.49
M40	*N*-(3-fluorobenzoyl)-*N'*-(2-bromophenyl)thiourea	6.50 ± 0.52
M41	*N*-(3-fluorobenzoyl)-*N'*-(3-bromophenyl)thiourea	6.35 ± 0.71
M42	*N*-(3-fluorobenzoyl)-*N'*-(2,6-diethylphenyl)thiourea	6.29 ± 0.21

Table 3 (cont'd). IC_{50} values of 45 carbonyl thiourea derivatives compound on *Acanthamoeba* sp.

Code	Chemical Name	IC_{50} µg/mL
M43	*N*-(3-fluorobenzoyl)-*N'*-(4-ethylphenyl)thiourea	6.33 ± 0.44
M44	*N*-(4-*tert*-butylbenzoyl)-*N'*-diethylphenylthiourea	6.30 ± 0.59
M45	*N*-(3-fluorobenzoyl)-*N'*-(2-chlorophenyl)thiourea	6.42 ± 0.28

QSAR study

QSAR utilizes linear regression of statistical analysis to build mathematical equation models, which could elucidate the relationship for molecular structures of the compounds with their potential biological activities. QSAR will also help to create a preliminary hypothesis regarding the mechanism of action by investigating the compounds on a particular biological system. Through this approach, it is assumed that the compounds that fit in a QSAR model are acting with the same mechanism of action [17].

Development of QSAR model by stepwise-multiple linear regression (stepwise-MLR) analysis

In order to build a QSAR model, feature selection was primarily conducted to discard unnecessary variables from the pool of 202 descriptors. Stepwise multiple regression chose 7 descriptors that fit best with the equation model, which were MATS1m, GATS5m, GATS3e, ESpm01d, ESpm05d, JGI1, and JG12. To avoid the overfitting problem, the proportion of the descriptors to the compound was maintained in a 5:1 ratio of the thumb rule. The descriptors set were maintained to contain five or fewer variables that contain the best information to represent the model. This was done by single exclusion practice of each variable from the selected obtained descriptors. The variables were tested for their significance by removing each one of them and their predictive power was tested each time by using the proposed model. From this technique, two variables, GATS5m and GATS3e, were found to be insignificant for the model and were removed. From the verification by correlation matrix, a high degree of correlation was found between descriptor ESpm01d and ESpm05d with a value of > 0.8. ESpm05d was chosen from the two since it was more significant by giving a statistically better model with higher predictive ability. The regression model was constructed with four descriptors namely MATS1m, ESpm05d, JGI1, and JGI2. According to Hadanu et al. [18], the best model could be selected based on the value of correlation coefficient (r), squared correlation coefficient (r^2), Standard Error of Estimation (SE), degree of freedom (F) or Predictive Residual Sum of Square (PRESS). Frimayanti et al. [19] proposed that the accepted value range for QSAR models is $r^2 > 0.6$ and $r^2_{cv} > 0.5$. The final statistical output for the generated model of stepwise-MLR is shown in Table 4.

Table 4. Statistics for a model developed using the stepwise-MLR method

Statistical Output	Value
r^2	0.732
r^2_{cv}	0.522
RMSEC	0.058
RMSECV	0.080

r^2 = squared correlation coefficient;
r^2_{cv} = cross validated squared correlation coefficient;
RMSEC= root mean square error of calibration;
RMSECV= root mean square error of cross validation

Based on the statistical evaluation, high r^2 and r^2_{cv} values with very low *RMSEC* and *RMSECV* indicate that the constructed model is statistically robust to predict the activity of other compounds outside the training set. This statistical outcome shows that the model is capable to elucidate 73.2% of the variance in anti-amoebic activity.

The final QSAR equation model given by the stepwise-MLR method is shown in Equation 1.

The generated regression model shows the order of significance for used descriptors is as follow: ESpm05d > JGI1 > MATS1m > JGI2. The observed and calculated or predicted activity by using this model was compared and it showed that the predicted pIC_{50} values did not greatly differ from the pIC_{50} values obtained from the ex periments with residual values less than 0.95. The observed values are in the range of 4.57 to 5.05 M while the predicted values range from 5.50 to 5.54 M.

$$pIC_{50} = - 0.0145*MATS1m + 0.1013* ESpm05d - 0.0733*JGI1 - 0.0090*JGI2 + 4.7592 \quad (1)$$

Validation of QSAR regression model from stepwise multiple linear regression (stepwise-MLR)

The statistical output of model validation is shown in Table 5. It proves that the developed model has a high predictive ability. It was given that r^2_{test} was 0.739, which is above 0.5 with an *RMSEP* value of 0.062, which is low enough for roots mean square error of prediction.

The built of the QSAR models must be properly validated prior to use for interpreting and predicting biological responses of non-investigated compounds. Qin et al. [20] emphasized the importance of vigorous validation of QSAR models despite the high fitting accuracy for the training set and apparent mechanistic appeal. The model equation was later used to predict thiourea analogs' anti-amoebic activity in the test set data. The comparison showed that the observed values are in the range of 4.63 to 5.05 M. Meanwhile, the range of the predicted values was 5.49 to 5.56 M. The residuals obtained gave values less than 0.90. This indicates the robustness and high predictive power of the built model. The robustness of a QSAR model should be also validated by a y-randomization test to ensure that the statistical output in the original model, which gave high r^2 and r^2_{cv} values, were not merely from a chance correlation or structural dependency of the training set. If a true QSAR relationship existed with the real dependent variable, the results for the *y*-random runs should be very low [21]. Y-randomization test was run 20 times and gave r^2 values between 0.052 to 0.233, which shows low r^2 and r^2_{test} (Table 6). Thus, it is concluded that the generated model by stepwise-MLR was not obtained from a random chance of correlation.

Table 5. Statistics of prediction for stepwise-MLR model

Statistical Output	Value
r^2_{test}	0.739
RMSEP	0.062

r^2_{test} = correlation coefficient of test;
RMSEP = root mean square error of prediction

Table 6. Y- randomization test of stepwise-MLR model

Iteration	r^2	r^2_{test}	Iteration	r^2	r^2_{test}
1	0.055	0.016	11	0.181	0.052
2	0.180	0.010	12	0.248	0.034
3	0.143	0.083	13	0.152	0.007
4	0.059	0.007	14	0.147	0.042
5	0.089	0.146	15	0.089	0.334
6	0.182	0.011	16	0.060	0.015
7	0.055	0.034	17	0.110	0.233
8	0.052	0.006	18	0.233	0.004
9	0.129	0.115	19	0.082	0.025
10	0.182	0.003	20	0.141	0.001

r^2 = squared correlation coefficient;
r^2_{test} = correlation coefficient of test

Development of QSAR model by genetic algorithm multiple linear regression (GA-MLR) analysis

The regression model was constructed with five descriptors namely RBN, MATS2m, EEig07x, JGI1, and N-070. The correlation matrix was investigated to detect highly correlated variables that would be less important for the model, which detected 135 that represents ESpm05d to be highly correlated with 198, representing N-070 by giving a value higher than 0.80 from the correlation matrix. The analysis was executed again to find out which variable was more significant than others by removing each of them from the model. The final analysis concluded that N-070 was more significant compared to ESpm05d and, therefore, it was included in the model. The statistical output of the final model is shown in Table 7. Statistical result of the constructed GA-MLR model shows a high r^2 value that concludes the equation could explain 84.8% of the variance in the compounds' activity. Meanwhile, r^2_{cv} is also quite high with a value of 0.767. *RMSEC* and *RMSECV* obtained are very low with values of 0.044 and 0.055, respectively. The statistical output shows that the GA-MLR method was a good technique to obtain a good model. This result also proves that the hybrid GA-MLR approach produced a better QSAR model compared to the stepwise-MLR method for this study.

The final QSAR equation model of the GA-MLR method is elaborated in Equation 2 in which it shows a significant order of the five selected variables as follows; N-070 > MATS2m > JGI1 > EEig07x > RBN. The variables of MATS2m, JGI1, and N-070 were shown to work reversibly with pIC_{50} while RBN and EEig07x both worked positively with pIC_{50}. The predicted pIC_{50} values were compared to the experimental data. The data revealed that the predicted values ranging from 4.93 to 5.21 M and the experimental values ranging from 4.57 to 5.05 M. Low residual values in the range of less than 0.55 from the activity prediction proves that the constructed model was robust.

$$pIC_{50} = 0.0301*RBN - 0.0576*MATS2m + 0.0445*EEig07x - 0.0529*JGI1 - 0.0896*N\text{-}070 + 4.7602 \quad (2)$$

Table 7. Statistics for the model developed using GA-MLR method

Statistical Output	Value
r^2	0.848
r^2_{cv}	0.767
RMSEC	0.044
RMSECV	0.055

r^2 = squared correlation coefficient;
r^2_{cv} = cross validated squared correlation coefficient;
RMSEC= root mean square error of calibration;
RMSECV= root mean square error of cross validation

Validation of QSAR regression model from genetic algorithm multiple linear regression (GA-MLR)

The statistical result in Table 8 confirms the robustness of the generated GA-MLR model with acceptable values of r^2_{test} and *RMSEP*. Tropsha et al. [22] suggested that a proposed QSAR model is considered predictive if it satisfies the condition of $r^2_{test} > 0.6$. The predicted pIC_{50} values were compared to the experimental data. The predicted values ranged from 4.92 to 5.20 M and the experimental values ranged from 4.63 to 5.06 M. The residuals gave values less than 0.45 suggesting that the model is robust and has high predictive power.

Validation by y-randomization was run 20 times and the test showed that the squared correlation coefficient, r^2 were in the range of 0.004 to 0.300 (Table 9). The difference between randomized models compared to the original GA-MLR statistical representation was significant. Therefore, this proves that chance correlation was negligible in the model development.

Table 8. Statistics of prediction for GA-MLR model

Statistical Output	Value
r^2_{test}	0.777
RMSEP	0.057

r^2_{test} = correlation coefficient of test;
RMSEP= root mean square error of prediction

Table 9. Y- randomization test of GA-MLR model

Iteration	r^2	r^2_{test}	Iteration	r^2	r^2_{test}
1	0.151	0.008	11	0.227	0.457
2	0.047	0.240	12	0.176	0.288
3	0.233	0.099	13	0.226	0.064
4	0.130	0.113	14	0.127	0.122
5	0.046	0.066	15	0.212	0.126

Table 9 (cont'd). Y- randomization test of GA-MLR model

Iteration	r^2	r^2_{test}	Iteration	r^2	r^2_{test}
6	0.167	0.015	16	0.218	0.045
7	0.087	0.051	17	0.083	0.081
8	0.176	0.002	18	0.230	0.010
9	0.068	0.143	19	0.215	0.001
10	0.300	0.002	20	0.004	0.195

r^2 = squared correlation coefficient;
r^2_{test} = correlation coefficient of test

Development of QSAR model by genetic algorithm partial least square (GA-PLS) analysis

The third method of QSAR in this study applied GA in combination with the PLS technique. The selected variables used MATS2m, MATS3m, EEig09d, JGI6, and N-070. The correlation matrix of the selected variables showed that no higher correlation than 0.8 for the variables was used hence this explains the consistency to be used in the model. The statistical output for the GA-PLS model is shown in Table 10. The statistical result proves the reliability of the built QSAR model from GA-PLS regression with squared correlation coefficient, r^2 of 0.827 and cross-validated, r^2_{cv} of 0.682. This result is in accordance with a study by Edraki et al. [23] in QSAR analysis of 3,5-bis (arylidene)-4-piperidone derivatives in cytotoxicity models. The statistical output using the GA-PLS model revealed the r^2 of 0.86 and r^2_{cv} of 0.66. The model also gave low root mean square error values for *RMSEC* and *RMSECV*.

Table 10. Statistics for the model developed using the GA-PLS method

Statistical Output	Value
r^2	0.827
r^2_{cv}	0.682
RMSEC	0.047
RMSECV	0.064

r^2 = squared correlation coefficient;
r^2_{cv} = cross validated squared correlation coefficient;
RMSEC= root mean square error of calibration;
RMSECV= root mean square error of cross validation.

This statistical output of the model proves to be able to explain 82.7% of the variance in the experimental activity and r^2_{cv}, which manifests good predictive ability. The best combination of a selected variable by the GA-PLS method is illustrated in Equation 3.

The order of variables are as follows; EEig09d > N-070 > JGI6 > MATS2m > MATS3m in which this QSAR model was used to predict the activity of compounds in the training set. The values of calculated compared to observe activity. The predicted values were in the range of 4.72 to 4.82 M and the experimental values were in the range of 4.63 to 5.06 M. The residuals observed were compared to the predicted values, which were less than 0.25. This explains the robustness of the model. However, the predictive ability of the model was further evaluated in external validation to ensure that the QSAR model also has a good predictive ability for compounds that were not included in the training set.

$$pIC_{50} = -0.0457*MATS2m + 0.0242*MATS3m + 0.0638*EEig09d - 0.0511*JGI6 - 0.0609*N\text{-}070 + 4.7554 \quad (3)$$

Validation of QSAR regression model from genetic algorithm partial least square (GA-PLS)

The result gave good statistical output with r^2_{test} and *RMSEP* of 0.790 and 0.051, respectively (Table 10). The robustness of the GA-PLS QSAR model was also assessed through its predictive power for the comparison of the observed to predicted activity. The predicted values were in the range of 4.72 to 4.82 M while the experimental values were in the range of 4.57 to 5.05 M. Small residual with values less than 0.25 proved the robustness of the equation model, which could be used to predict other compounds that were not included in the model development. The test of y-randomization was run 20 times and confirmed that the model does not occur merely by random chance correlation of statistics since it gave low squared correlation coefficients, r^2 in the range of 0.015-0.372 (Table 11).

Table 10. Statistics of prediction for GA-PLS method

Statistical Output	Value
r^2_{test}	0.790
RMSEP	0.051

r^2_{test} = correlation coefficient of test;
RMSEP = root mean square error of prediction

Table 11. Y- randomization test of GA-PLS model

Iteration	r^2	r^2_{test}	Iteration	r^2	r^2_{test}
1	0.078	0.006	11	0.087	0.085
2	0.350	0.158	12	0.055	0.007
3	0.123	0.001	13	0.118	0.008
4	0.084	0.088	14	0.172	0.007
5	0.015	0.004	15	0.210	0.003
6	0.136	0.183	16	0.167	0.090
7	0.026	0.021	17	0.120	0.077
8	0.066	0.021	18	0.148	0.088
9	0.372	0.148	19	0.079	0.001
10	0.074	0.010	20	0.041	0.016

r^2 = squared correlation coefficient;
r^2_{test} = correlation coefficient of test

Comparisons of constructed QSAR models

QSAR mathematical models from three different techniques namely stepwise-MLR, GA-MLR, and GA-PLS were evaluated and compared (Table 12). A genetic algorithm (GA) is a well-suited approach to the problem of variable selection and optimization. GA performs its optimization by comparing root-mean-square error of cross validation, *RMSECV* of proposed

models as the measure of fitness [24]. The hybrid approach (GA-MLR) which combines GA with MLR may be useful in the derivation of highly predictive and interpretable QSAR models [17]. Therefore, this approach, as well as the conventional stepwise-MLR technique, was applied in this study. The method of stepwise-MLR gave four selected variables that are well fitted in the equation model. The model gave good statistical output with high r^2 and r^2_{cv} and low *RMSEC* and *RMSECV*. This indicates that the constructed model has good fitness and is robust. On the other hand, the model obtained from the GA-MLR method contains five descriptors and produced a statistically better model compared to the stepwise-MLR. This showed that GA-MLR is a good technique to obtain a better QSAR model in this study. However, the weaknesses of using the MLR technique are that the data are often crude, imprecise, and strongly collinear. These imply that this traditional regression technique, which assumes the selected descriptors to be exact and 100% relevant and independent of each other, will not always work well. Thus, in situations where many strongly collinear descriptors and biological responses operate together, data analytical methods, other than the classical MLR techniques, must be used [25].

Table 12. Summary of constructed models

	Stepwise-MLR	**GA-MLR**	**GA-PLS**
Statistical output:			
r^2	0.732	0.848	0.827
r^2_{cv}	0.522	0.767	0.682
RMSEC	0.058	0.044	0.047
RMSECV	0.080	0.055	0.064
r^2_{test}	0.739	0.777	0.790
RMSEP	0.062	0.057	0.051
Y-random (r^2)	0.055-0.248	0.004-0.300	0.015-0.372
No. of descriptors	4	5	5
Residual in train. set	$\leq$ 0.93	$\leq$ 0.54	$\leq$ 0.23
Residual in test set	$\leq$ 0.87	$\leq$ 0.42	$\leq$ 0.24
Descriptors:			
1	MATS1m	RBN	MATS2m
2	ESpm05d	MATS2m	MATS3m
3	JGI1	EEig07x	EEig09d
4	JGI2	JGI1	JGI6
5	-	N-070	N-070

r^2 = squared correlation coefficient;
r^2_{test} = correlation coefficient of test;
r^2_{cv} = cross validated squared correlation coefficient;
RMSEC= root mean square error of calibration;
RMSECV= root mean square error of cross validation

PLS is well suited to overcome overfitting and multicollinearity problems. It has been used to alleviate the effect of multicollinearity and to prevent overfitting by reducing the dimension size [tran 26]. This approach has also successfully come out with a statistically robust model of five variables that were better compared to the model developed from stepwise MLR and GA-MLR techniques based on the predictive ability. PLS also gave much lower residual values in both training and the test set with < 0.23 and < 0.24, respectively compared to the MLR models that gave higher residual values from their prediction. The descriptors or variables, which demonstrate to be important, are those that have been used more than once from the three approaches. It is suggested that these variables namely JGI1, MATS2m, and N-070 are found to be the influential factors and contributors in the models' development for this study and could possibly have a significant role in modulating the anti-amoebic activity for the thiourea derivative compounds. These variables are in the groups of topological charge indices, 2D-autocorrelations, and atom centered fragments.

GA, MLR, and PLS were also implemented by many authors in their studies for prediction in high-dimensional linear regressions [27,28]. GA is suitable to solve optimization and variable selection problems while MLR yields models that are simpler and easier to interpret compared to PLS because these methods perform regression on latent variables that do not have physical meaning [28]. Due to the co-linearity problem in MLR analysis, one may remove the collinear descriptors before MLR model development. MLR equations can describe the structure-activity relationships but some information will be discarded in the MLR analysis. On the other hand, factor analysis–based methods such as PLS regression can handle the collinear descriptors and, therefore, PLS analysis provides a better analysis with a highly predictive QSAR model [29]. In a previous study, the QSAR model built using PLS and GA-MLR methods showed a remarkable coefficient of determination (r^2) in predicting the anticholinergic side effects of drugs in lower urinary tract infection (PLS: R^2=0.808 and GA-MLR: R^2 =0.804) [26]. A series of 3-hydroxypyridine-4-one and 3-hydroxypyran-4-one derivatives were subjected to QSAR methods using factor analysis-based multiple linear regression (FA-MLR), principal component regression (PCR), and partial least squares combined with genetic algorithm for variable selection (GA-PLS). The result revealed that GA-PLS showed the most significant QSAR model with 96% and 91% predicted variances in the pIC_{50} data (compounds tested against *S. aureus*) [28]. The studies proved that GA-PLS is a reliable QSAR model in predicting the biological activities of chemical compounds based on mathematical and statistical relations.

Descriptors interpretation

In this study, all applied approaches offered a few similar descriptors or variables for the equations, which are JGI1, MATS2m, and N-070. The finding suggests that they might be the most influential descriptors that contribute to the QSAR models and provide a significant role in the anti-amoebic activity for the thiourea derivatives. Meanwhile, the selected and best QSAR model, which was obtained from the GA-PLS technique, gave 5 variables that include EEig09d, N-070, JGI6, MATS2m, and MATS3m. These variables belong to 2D autocorrelation (Moran autocorrelation - lag2/weighted, and -lag3/weighted by atomic masses), edge adjacency indices (Eigenvalue 09 from edge adjacency matrix weighted by dipole moments), topological charge indices (mean topological charge index of order 6), and atom-centered fragment class (Ar-NH-Al). According to Speck-Planche et al. [30], atom-centered fragments are simple molecular descriptors that are defined as the number of specific atom types in a molecule. They are calculated from molecular composition and atom connectivities. Each type of atom in the molecule is described in terms of its neighboring atoms. The atom-centered fragment descriptors have been demonstrated to be very useful descriptors and have been employed in previous QSAR studies. Meanwhile, Viswanadha et al. [31] reported that these atom-centered fragments descriptors provide important information about hydrophobic and dispersive interactions, which are involved in biological processes such as transport and distribution of compounds through cells membrane, as well as the information about the compound's receptor

interactions. From the variables that have been selected in the model of this study, it could be concluded that the atom-centered fragment plays a major role in providing the information on the thiourea molecules' preliminary penetration into *Acanthamoeba* through the cells membrane.

On the other hand, another representative descriptor or variable selected in the generated model of this study is topological structural descriptors, which are a representation of a molecular structure that arises from the chemical identity of each atom. In this study, two Moran autocorrelation descriptors were used in the GA-PLS model. These descriptors describe hydrophobicity scale, average flexibility index, polarizability parameter, the free energy of amino acid solution in water, residue accessible surface area, amino acid residue volume, steric parameters, and relative mutability [32]. In the meantime, physical interpretation of Burden eigenvalues and topological charge indices is difficult because they condense a large amount of structural and property information into a single number [33]. However, these descriptors have been extensively used in medicinal chemistry [34]. Todeschini and Consonni [35] reviewed that due to the relevancy and complexity of amino acid chains and macromolecules, some descriptors were defined to represent amino acid chains and sequences of amino acids. Amino acid properties were modeled for example by connectivity indices, substituent descriptors, charge descriptors, and principal properties. Raychaudury et al. [36] used a topological descriptor to characterize the size and shape of the side chains in the amino acids, which was based on a graph-theoretical approach applied to root weighted molecular graphs with hydrogen included. Substantially, it was relevant with the result obtained from analysis in this study that concentrated on topological descriptors in the model since the thiourea compound series contained 21 amino acids of the side chain of the molecules. Todeschini et al. [37] explained the interpretability of descriptors whereby it is important to take into account that model response is frequently the result of a series of complex biological or physicochemical mechanisms. Therefore, it is very difficult and reductionist to ascribe to the mechanistic meaning of the selected molecular descriptors in a QSAR model. Furthermore, it must also be highlighted that in multivariate models, even though the interpretation of a singular molecular descriptor can be certainly useful, it is only the combination of a selected set of descriptors that is able to model the studied biological end-point. It was also stressed that in QSAR modeling, attention should be focused on the model quality through its predictive ability.

Conclusion

QSAR models were constructed from the obtained IC_{50} values of 44 carbonyl thiourea analogues toward *Acanthamoeba* sp. (HKL isolate) ranging from 2.56 to 7.81 μg/mL. Linear regression techniques, stepwise-MLR, GA-MLR, and GA-PLS were applied to build the best QSAR model to correlate the compounds with their anti-amoebic activity. Three equation models were successfully generated with the hybrid GA-PLS approach that gave the best output with a statistically robust model of five variables. Thus, this GA-PLS QSAR model could be applied in the future for the development of a new lead compound based on carbonyl thiourea with optimized anti-amoebic activity to design a new anti-amoebic agent for A*canthamoeba* keratitis disease.

Acknowledgement

The authors would like to acknowledge and thank International Islamic University Malaysia (IIUM), Universiti Malaysia Terengganu (UMT), and Universiti Teknologi Malaysia (UTM) for providing the space and facilities to conduct this work. This paper is especially dedicated to the research team, Professor Dr. Nakisah Mat Amin and Professor Mohamed Noor Hasan, who has retired from UMT and UTM.

References

1. Kang, H., Sohn, H. J Park, A. Y. et al. (2021). Establishment of an *Acanthamoeba* keratitis mouse model confirmed by amoebic DNA amplification. *Scientific Report,* 11: 4183.

2. Vontobel, S. F, Abad-Villar, E. M., Kaufmann, C., Zinkernagel, A. S., Hauser, P. C. et al. (2015). Corneal Penetration of Polyhexamethylene Biguanide and Chlorhexidine Digluconate. *Journal of Clinical and Experimental Ophthalmology,* 6: 430.
3. Turner, N. A., Russell, A. D., Furr, J. R. and Lloyd, D. (2000). Emergence of resistance to biocides during differentiation of Acanthamoeba castellanii. *Journal of Antimicrobial Chemotherapy*, 46: 27-34.
4. Lorenzo-Morales, J., Khan, N. A. and Walochnik, J. (2015). An update on Acanthamoeba keratitis: diagnosis, pathogenesis and treatment. *Parasite*, 22: 10.
5. Chen, S., Wu, G. and Zeng, H. (2005). Preparation of high antimicrobial activity chitosan-Ag^{+} complex. *Carbohydrate Polymers,* 60: 33-38.
6. Alcolea, V., Plano, D., Karelia, D. N., Palop, J. A., Amin, S., Sanmartín, C. *et al.* (2016). Novel seleno- and thio-urea derivatives with potent in vitro activities against several cancer cell lines. *European Journal of Medical Chemistry*, 113: 134-144.
7. Sadeghian-Rizi, S., Sakhteman, A. and Hassanzadeh, F. (2016). A quantitative structure-activity relationship (QSAR) study of some diaryl urea derivatives of B-RAF inhibitors. *Research in Pharmaceutical Sciences*, 11(6): 445-453.
8. Naz, S., Zahoor, M., Umar, M., Alghamdi, S., Sahibzada, M. and UlBari, W. (2020). Synthesis, characterization, and pharmacological evaluation of thiourea derivatives. *Open Chemistry*, 18(1): 764-777.
9. Keche, A. P. and Kamble, V. M. (2019). Synthesis and anti-inflammatory and antimicrobial activities of some novel 2-methylquinazolin-4(3H)-one derivatives bearing urea, thiourea and sulphonamide functionalities, *Arabian Journal of Chemistry*, 12(7): 1522-1531.
10. Asadollahi-Baboli, M. and Dehnavi, S. (2018). Docking and QSAR analysis of tetracyclic oxindole derivatives as α-glucosidase inhibitors. *Computational Biology and Chemistry*, 76: 283-292.
11. Ibrahim, M. A., Yusof, M. S. and Amin, N. M. (2014). Anti-amoebic properties of carbonyl thiourea derivatives. *Molecules*, 19(4): 5191-5204.
12. Wiji Prasetyaningrum, P., Bahtiar, A. and Hayun, H. (2018). Synthesis and cytotoxicity evaluation of novel asymmetrical mono-carbonyl analogs of Curcumin (AMACs) against Vero, HeLa, and MCF7 Cell Lines. *Scientia Pharmaceutica*, 86(2): 25.
13. Xu, Q., Deng, H., Li, X. and Quan, Z. S. (2021). Application of amino acids in the structural modification of natural products: A review. *Frontiers in Chemistry,* 9: 650569.
14. Hauck, M., Jürgens, S. R. and Leuschner, C. (2010). Effect of amino acid moieties on metal binding in pulvinic acid derivatives and ecological implications for lichens producing these compounds. *The Bryologist*, 113(1): 1-7.
15. Ahmadi, S. and Habibpour, E. (2017). Application of GA-MLR for QSAR modeling of the arylthioindole class of tubulin polymerization inhibitors as anticancer agents. *Anticancer Agents in Medical Chemistry*, 17(4): 552-565.
16. Rahman, F. U., Bibi, M., Khan, E., Shah, A. B., Muhammad, M., Tahir, M. N., Shahzad, A., Ullah, F., Zahoor, M., Alamery, S. et al. (2021). Thiourea derivatives, simple in structure but efficient enzyme inhibitors and mercury sensors. *Molecules,* 26: 4506.
17. Patnaik, P. (2007). A comprehensive guide to the hazardous properties of chemical substances: Thiourea. Wiley-Interscience, Hoboken, New Jersey: pp. 904.
18. Saxena, A. K. and Prathipati, P. (2003). Comparison of MLR, PLS and GA-MLR in QSAR analysis. *SAR QSAR Environmental Research*, 14(5-6): 433-445.
19. Hadanu, R., Mastjeh, S., Mustofa, J., Sholikhah, E. N., Wijayanti, M. A. and Tahir, I. (2007). Quantitative structure-activity relationship analysis (QSAR) of antimalarial 1,10-phenanthroline derivatives compounds. *Indonesian Journal of Chemistry*, 7(1): 72-77.

20. Frimayanti, N., Yam, M. L., Lee, H. B., Othman, R., Zain, S. M. and Rahman, N. A. (2011). Validation of quantitative structure-activity relationship (QSAR) model for photosensitizer activity prediction. *International Journal of Molecular Sciences*, 12(12), 8626–8644.
21. Qin, L., Zhang, X., Chen, Y., Mo, L., Zeng, H. and Liang, Y. (2017). Predictive QSAR Models for the toxicity of disinfection byproducts. *Molecules***,** 22(10): 1671.
22. Ravichandran, V., Mourya, V. K. and Agrawal, R. K. (2009). Prediction of anti-HIV activity of phenyl ethyl thiourea (PET) derivatives: QSAR approach. *Digest Journal of Nanomaterials and Biostructures,* 4: 213-221.
23. Tropsha, A., Gramatica, P. and Gombar, V. K. (2003). The importance of being earnest: validation is the absolute essential for successful application and interpretation of QSPR Models. *QSAR and Combinatorial Science*, 22: 69-77.
24. Edraki, N., Das, U., Hemateenejad, B., Dimmock, J. R. and Miri, R. (2016). Comparative QSAR analysis of 3,5-bis (arylidene)-4-piperidone derivatives: The development of predictive cytotoxicity models. *Iranian Journal of Pharmaceutical Research,*15(2): 425-437.
25. Katoch, S., Chauhan, S. S. and Kumar, V. (2021). A review on genetic algorithm: past, present, and future. *Multimedia Tools Application,* 80**:** 8091–8126.
26. Filzmoser, P., Gschwandtner, M. and Todorov, V. (2012). Review of sparse methods in regression and classification with application to chemometrics. *Journal of Chemometrics*, 26: 42-51.
27. Tran, T. N., Afanador, N. L., Buydens, L. M. C. and Blanchet, L. (2014). Interpretation of variable importance in partial least squares with significance multi-variate correlation (sMC). *Chemometrics and Intelligent Laboratory System,* 138: 153-160.
28. Yuyama, M., Ito, T., Arai, Y., Kadowaki, Y., Iiyama, N. et al., (2020). Risk prediction method for anticholinergic action using auto-quantitative structure–activity relationship and docking study with molecular operating environment. *Chemical and Pharmaceutical Bulletin*, 68(8): 773-778.
29. Sabet, R. and Fassihi, A. (2008). QSAR study of antimicrobial 3-hydroxypyridine-4-one and 3-hydroxypyran-4-one derivatives using different chemometric tools. *International Journal of Molecular Sciences*, *9*(12): 2407-2423.
30. Deeb, O., Hemmateenejad, B, Jaber, A., Garduno-Juarez, R., Miri, R. (2007). Effects of the electronic and physicochemical parameters on the carcinogenecis activity of some sulfa drug using QSAR analysis based on genetic-MLR & genetic-PLS. Chemosphere, 67: 2122-2130.
31. Speck-Planche, A., Kleandrova, V.V., Luan, M.F., and Cordeiro, N.D.S. (2011). Fragment-based QSAR model toward the selection of versatile anti-sarcoma leads. *European Journal of Medicinal Chemistry*, 46: 5910-5916.
32. Viswanadhan, V. N., Reddy, M. R., Bacquet, R. J. and Erion, M. D. (1993). Assessment of methods used for predicting lipophilicity: application to nucleosides and nucleoside bases. *Journal of Computational Chemistry,* 14: 1019-1026.
33. Horne, D. S. (1988). Prediction of protein helix content from an autocorrelation analysis of sequence hydrophobicities. *Biopolymers,* 27: 451-477.
34. Helguera, A.M., Natália, M., Cordeiro, D.S., González, M.P., Pérez, M.A.C., Ruiz, R.M., and Castillo, Y.P. (2007). QSAR modeling for predicting carcinogenic potency of nitroso-compounds using 0D-2D molecular descriptors. *11th International Electronic Conference on Synthetic Organic Chemistry*, 1-30 November 2007.
35. Jain, H.K., and Agrawal, R.K. (2006). QSAR analysis of indomethacin derivatives as selective COX–2 inhibitors. *Internet Electronic Journal of Molecular Design*, 5: 224-236.
36. Todeschini, R., and Consonni, V. 2000. Handbook of Molecular Descriptors: Methods and Principles in Medicinal Chemistry. Volume 11, pp. 11. Weinheim: Wiley-VCH.

37. Raychaudhury, C., Banerjee, A., Bag, P., and Roy, S. (1999). Topological shape and size of peptides: Identification of potential allele specific helper T cell antigenic sites. *Journal of Chemical Information and Computer Sciences,* 39(2): 248-254.
38. Todeschini, R., Consonni, V., and Gramatica, P. (2009). Chemometrics in QSAR. In: Brown S, Tauler R, Walczak R. eds. Comprehensive Chemometrics: Chemical and biochemical analysis, pp. 129-172. Oxford: Elsevier.

Malaysian Journal of Analytical Sciences (MJAS)
Published by Malaysian Analytical Sciences Society

IMPROVING THE MORPHOLOGICAL, THERMAL, AND ACOUSTICS PROPERTIES OF POLYURETHANE-UREA BIOFOAM USING INDUSTRIAL PLYWOOD SAWDUST WASTE

(Meningkatkan Morfologi, Termal dan Sifat Akustik Busa Poliuretan-Urea Menggunakan Sisa Habuk Papan Kayu Lapis)

Herlina Nofitasari[1]*, Ari Handono Ramelan[2], Mohammad Masykuri[3]

[1]Master's Degree Program in Environmental Science
[2]Faculty of Mathematics and Natural Sciences
[3]Faculty of Teacher Training and Education
Universitas Sebelas Maret, Surakarta 57126, Indonesia

**Corresponding author: henosa25@gmail.com*

Received: 29 December 2021; Accepted: 27 February 2022; Published: 27 June 2022

Abstract

Majority of the polyurethane–urea (PUU) foam is made from petroleum raw materials. Concerns regarding the loss of petroleum resources promote the environmentally sustainable manufacture of foam. The production of PUU foam synthesis from natural materials and waste composites was then developed. The PUU/industrial plywood sawdust waste (IPSW) biofoam was synthesized from a mixture of polyethylene glycol (PEG), methylene diisocyanate (MDI), ethylenediamine (EDA), maleic anhydrate (MAH), and IPSW by using a one-shot method. 5% IPSW was applied to the composition of the synthesized biofoam and the MDI ratio was increased. Fourier Transform Infrared Spectroscopy (FTIR) was used to identify functional groups of biofoam. The pore morphology of the biofoam was observed with Microscope Camera and Scanning Electron Microscopy (SEM), the thermal ability was measured with Thermogravimetric Analysis (TGA), and the sound absorption ability was measured by using a two-microphone impedance tube according to the ASTM E-1050 standard. Based on FTIR spectra identification, the biofoam contains OH, CH, CO, and NH chemical groups. The results reveal that the PUU/IPSW biofoam had intermediate macropore morphology (closed and open cells), thermal resistance above 120^{o}C, and potential materials as sound-absorbing. The improvement in the biofoam properties upon the addition of organic filler shows that the biofoam is promotable as renewable material. This study suggests better formulation design to enhance the biofoam property performance.

Keywords: acoustics, polyurethane-urea foam, sawdust, scanning electron microscopy, thermogravimetric analysis

Abstrak

Kebanyakan busa poliuretan-urea (PUU) diperbuat daripada bahan mentah petroleum. Kebimbangan mengenai kehilangan sumber petroleum menggalakkan pembuatan busa yang mampan secara alam sekitar. Penghasilan sintesis busa PUU daripada bahan alam dan komposit sisa telah dibangunkan. Busa PUU telah disintesis daripada campuran polietilen glikol (PEG), metilen diisosianat (MDI), etilen diamin (EDA), maleat anhidrat (MAH), dan sisa habuk papan industri kayu lapis (IPSW) dengan menggunakan kaedah satu pukulan. Lima peratus IPSW telah digunakan pada komposisi biofoam tersintesis dan nisbah MDI

telah meningkat. Spektroskopi Infra-Merah Transformasi Fourier (FTIR) digunakan untuk mengenal pasti struktur biofoam. Morfologi liang biofoam diperhatikan menggunakan mikroskop kamera dan SEM, TGA untuk pengukuran haba, dan keupayaan biofoam untuk menyerap bunyi diukur menggunakan tabung impedansi dua mikrofon mengikuti standar ASTM E-1050. Berdasarkan pengenalpastian spektrum FTIR, biofoam mengandungi kumpulan kimia OH, CH, CO, dan NH. Keputusan menunjukkan bahawa biofoam PUU/IPSW mempunyai morfologi makropori perantaraan (sel tertutup dan sel terbuka), rintangan haba melebihi 120 ^{o}C, dan berpotensi menjadi bahan penyerapan bunyi. Kemajuan kinerja ketika ditambahkan pengisi organik menunjukkan bahawa ini dapat dipromosikan sebagai bahan terbarukan. Studi ini menyarankan agar membuat formulasi yang lebih baik untuk meningkatkan prestasinya.

Kata kunci: akustik, busa poliuretan-urea, habuk papan, mikroskopi imbasan elektron, analisis termogravimetrik

Introduction

Population growth and rapid transportation progress have led to environmental problems in the community, including noise pollution. The effects are severe for those who have been exposed, both physically and mentally. This condition can be regulated by using sound-absorbing materials. There are two types of sound-absorbing materials: resonant and porous sound-absorbing materials. The morphology of the latter is made up of channels, gaps, and holes that allow sound waves to pass through [1-3].

Foam is a porous material that can be used to absorb sound. The foam production is synthesized from diols and polyols i.e. polyurethane chemical compounds [2, 4]. Polyurethanes are widely used for other applications such as paints, jacket coatings, elastomers, insulators, elastic fibers, and leather equipment. Polyurethane production and demand projections rose through 2020 [5]. The production of polyurethane foam is incompatible with sustainable development because it uses petroleum as raw material. Therefore, it is necessary to find alternative raw materials that are less harmful to the environment.

Renewable polyol modification is developed in the production of polyurethane by using biomass as raw material through oxypropylation or acid liquefaction process. The production of bio-polyol using oxypropylation method includes the use of palm oil, *Sapium sabiferum* oil, castor oil, soybean oil, grapeseed oil, sunflower oil, tung oil and canola oil. The current bio-polyol production process using liquefaction acid is derived from eucalyptus and pine woods, bamboo, Cellulose nanofibrils, Yaupon holly (*Ilex vomitoria*), sugar-cane bagasse, bagasse, and jute fiber. Both processes can produce environmentally friendly polyurethane foam raw materials [4-8].

In addition to bio-polyols, the use of isocyanate alternatives such as Non-isocyanate polyurethane (NIPU), which is derived from mimose tannins [9], lysine, sorbitol, vegetable oils, and other sources, is another way to keep polyurethane foam production sustainable. Recycling polyurethane foam [4] and integrating natural waste materials into the production process are also green choices. Natural fiber blends of various concentrations and thicknesses in polyurethane foam composites have varied sound absorption capabilities [10]. The addition of *Shorea leprosa* wood fibers to the polyurethane foam affects its acoustic performance [11]. Production of biofoam from polyurethane-urea blends with various concentration of industrial plywood sawdust has a good sound absorption coefficient [12].

It was reported that polyurethane foam composites containing nanosilica and nanosilica solution at an optimum level of 2 wt.% had a negative impact on foam cell morphology, and the TGA test results for rigid polyurethane foam composites containing 1 wt.% nanosilica solution had poor thermal resistance [13]. As compared to foams without the addition of halloysite nanocomposites, rigid polyurethane foam with palm oil as raw material and halloysite nanocomposite had stable thermal resistance, and SEM results showed a smooth cell surface structure and larger cell size [2]. Polyurethane foam synthesized with clove composites (*Syzygium aromaticum*) at various concentrations had rheological behavior, cellular

structure, and further mechanical & thermal performance of the modified material [8].

The other research studied polyurethane foam with addition of diatomite and hydroxyapatite. The thermal degradation of diatomite porous polyurethane foam biocomposites was lower than that of hydroxyapatite porous polyurethane foam biocomposites. Diatomite and hydroxyapatite increase the surface area of the polyurethane foam and harden the pores [14]. Rigid foam made by combining non-isocyanate polyurethane (NIPU) tannins with addictive glutaraldehyde and citric acid had the same morphology, called Open-Cell, but the number of cell wall pores decreased as glutaraldehyde was added, while citric acid increased the number of foam cells. The thermal resistance of the NIPU foam in all compositions was the same except for the composition of 2 grams of hexamine and 6 grams of citric acid which was higher at a temperature of 790 ^{o}C and a residue of 18.7% [9].

This research described the synthesis of polyurethane-urea (PUU) biofoam with industrial plywood sawdust waste composites (IPSW). The PUU/IPSW biofoam was synthesized by adding a chain extender in the form of ethylene diamine (EDA), coupling agent in the form of maleic anhydrate (MAH), and industrial plywood sawdust waste as filler. The chain extender is a low molecule containing an amine group at the end that plays a major role in polymer morphology. The addition of a chain extender and diisocyanate provided a wide range of hard segment characteristics and the physical performance of polyurethane. The morphological structures were characterized by SEM and Microscope Camera. Meanwhile, thermal ability was analyzed by TGA, and acoustics test was conducted through impedance tube.

Materials and Methods

Materials

The materials used to synthesize the PUU/IPSW biofoam were chemical compounds and biomass. The chemical compounds included polyethylene glycol (PEG) 400 (Polyol), 4.4'-diphenylmethane diisocyanate (4.4'-MDI), ethylenediamine (EDA), and maleic anhydrate (MAH) while the biomass was in the form of industrial plywood sawdust waste (IPSW). The detail of various compositions of the PUU/IPSW biofoam are shown in Table 1.

Sample preparation

The biofoam was synthesized by using a one-shot method. This method worked by combining all of the ingredients until they were fully homogeneous, as detailed in Figure 1. First, the polyol and diisocyanate were mixed and stirred. Then, the chain extender (EDA), the coupling agent (MAH), and the IPSW filler were added. The composition of the ingredients was calculated by the mass ratio. The samples were coded as BP0, BP1, BP2, BP3, BP4, and BP5 for the PUU/IPSW biofoam with 0%, 1%, 2%, 3% , 4%, and 5% IPSW respectively with a ratio of PEG:MDI (1:1), and BP1.5 for the PUU/IPSW biofoam of 5% with a ratio of PEG:MDI (1:1.5).

Table 1. Variation of the PUU/IPSW biofoam composition

Samples	PEG (g)	MDI (g)	EDA 0.1% (g) (w/w)	MAH 0.01% (g) (w/w)	Waste % (g) (w/w)
BP0	15	15	0.3	0.03	0
BP1	15	15	0.3	0.03	0,31
BP2	15	15	0,3	0.03	0,62
BP3	15	15	0,3	0.03	0,94
BP4	15	15	0,3	0.03	1,26
BP5	15	15	0,3	0.03	1,6
BP1,5	15	22,5	0.3	0.03	1,6

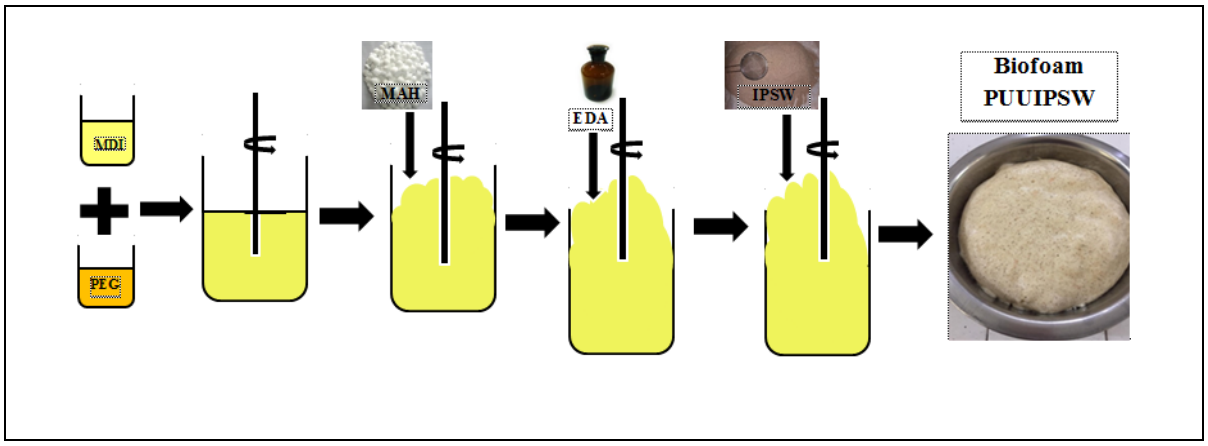


Figure 1. Procedural scheme for the PUU/IPSW biofoam synthesis

Microscope camera

The biofoam pore morphology in was observed by using a Nikon Eclipse 80i microscope camera for 10x magnification. The resulted pore distribution was calculated by using Image J software. The pore distribution data were analyzed by using OriginLab software.

Scanning Electron Microscopy

The morphological properties of biofoam cells were observed by using Scanning Electron Microscopy (SEM) Phenom ProX. the PUU/IPSW biofoam samples were ground into powders and then plated with gold and subjected to 10kV voltage. Prior to the test, the samples' surfaces were gold-plated in order to have conductive properties and to be detectable by the SEM detector Phenom ProX secondary electron detector (SED).

Fourier transform infrared spectroscopy

The PUU/IPSW biofoam chemical structure was analyzed with FTIR spectroscopy by using KBr pellet technique with measurements at 3500-400 cm^{-1} wavenumber.

Thermogravimetric analysis

The PUU/IPSW biofoam was subjected to TGA to obtain its thermal resistance with the TGA DSC 200 of Seiko SSC 5200H at a temperature of 25-600 (°C) with a heating rate of 10°C/minute.

Impedance tube testing

The PUU/IPSW biofoam sound-proofing ability was measured with an acoustic test that followed the ASTM E-1050 standard. The biofoam samples were shaped into a 28mm-diameter circle. Two microphone techniques and automated frequency analysis systems were used to quantify the effect of normal sound absorption coefficient and precise normal acoustic impedance comparisons of materials, with frequencies ranging from 0 to 6400 (Hz) [10, 11,15].

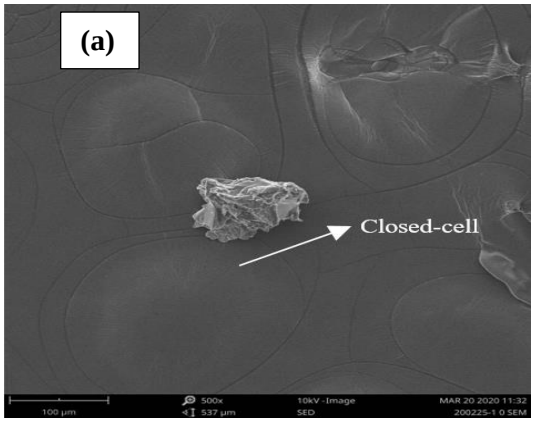
Results and Discussion

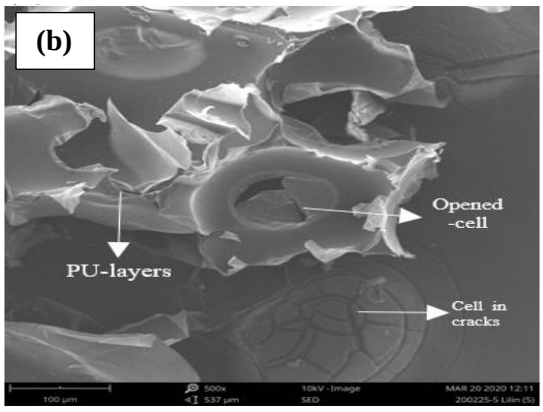
Cell morphology

Two microscopes, SEM for 500x magnification (Figure 2) and Microscope Camera for 10x magnification (Figure 3), were used to examine the biofoam pore morphology. Three samples, namely BP0, BP5, and BP1.5 were observed on SEM as representative treatments. The results show that majority of the pores formed were macropores since the size was found to be more than 50µm. Three types of biofoam morphology were then determined: 1) open-celled, meaning that the biofoam pores were found to have interconnecting holes between each other; 2) closed-celled, meaning that the biofoam pores were found to not have interconnecting holes between each other; and 3) intermediate-celled, meaning that the biofoam pores were found in a combination of the two. BP0 was found to be closed-celled, with circular to oval shape when it expanded. BP5 was found to be

intermediate-celled with oval shape [3]. Other microstructures were observed in PU layers. BP1.5 had closed-celled microstructure with polygonal shape. It had another microstructure, namely interconnecting hole. According the SEM images, filler addition influenced the biofoam morphology. It was observed that the filler could make a closed-celled sample to be an open-celled one, since it filled the biofoam matrices. Meanwhile, the effect of filler addition to MDI ratio enhancement was found to be not significant. The SEM image results were smooth, demonstrating MAH's ability to act as a coupling agent. The smoothest the sample captured by SEM causes the role of MAH which can relate the filler and the biofoam matrices. Therefore, the surface of samples seemed smooth.

The structure of the cavities and pores created during the polymerization process and the cell size were determined by the gelling and blowing reactions. If the cavity pressure is greater than the wall strength, biofoam with an open-celled structure may be created. At low channel flow rates, the cavity wall thickness retains hardness. However, if the hardening process is completed before the open pore formation, some open pores can form. Closed cells will remain if the cavity wall hardens completely before fracturing [2, 16, 17]. With the addition of filler, the pore distribution continued to reduce in size (Figure 3). It was identified that sample BP0 had the highest pore distribution with pore size in the range of 250-300 µm, while Samples BP1, BP3, BP4, BP5, and BP1.5 had pore sizes in the range of 100-150 µm. Meanwhile, Sample BP2 had pore distribution with pore size in the range of 150-200 µm. The factor which caused different sizes of pore distribution might occur when the minimum biofoam synthesis period and stirring velocity were not fulfilled. It was suggested that foaming under this kind of condition impacted the cell sizes of Sample BP2. This demonstrated that the presence of filler had a direct impact on the morphological properties and distribution. The biofoam mechanical and thermal efficiency depended on these factors [8].





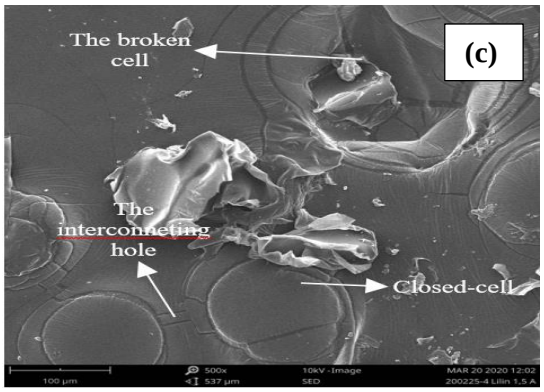
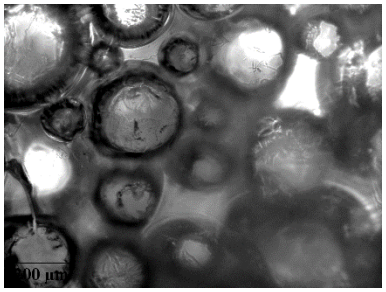
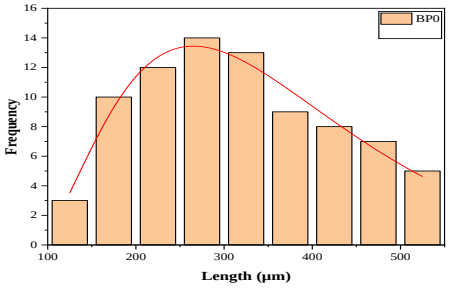


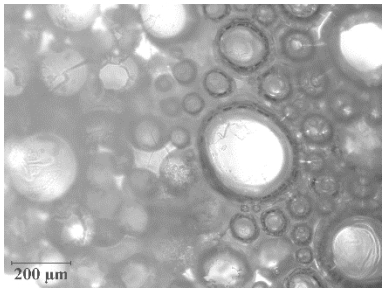
Figure 2. SEM images from the PUU/IPSW biofoam samples of (a) BP0, (b) BP5, and (c) BP1.5.



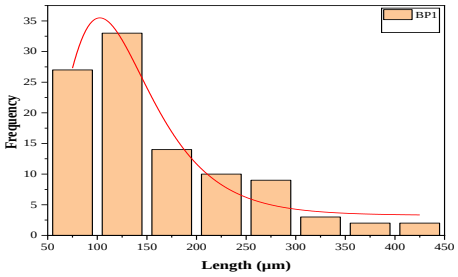
(BP0)



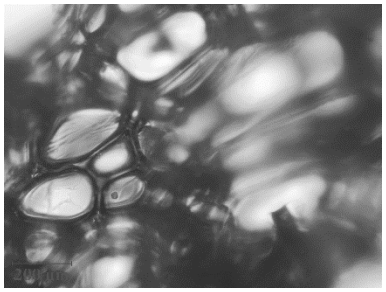
(BP0)



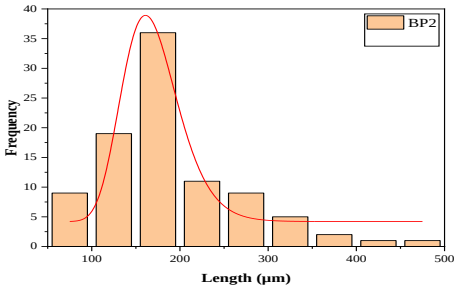
(BP1)



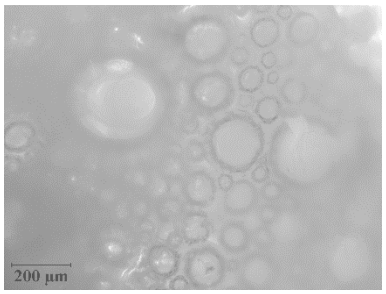
(BP1)



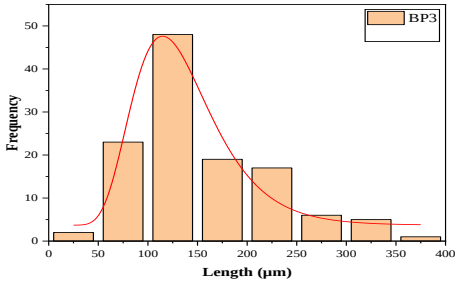
(BP2)



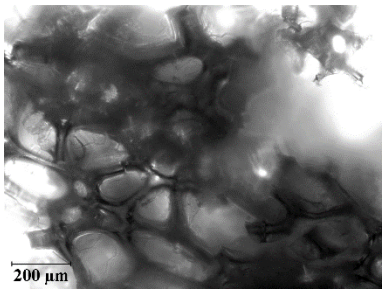
(BP2)



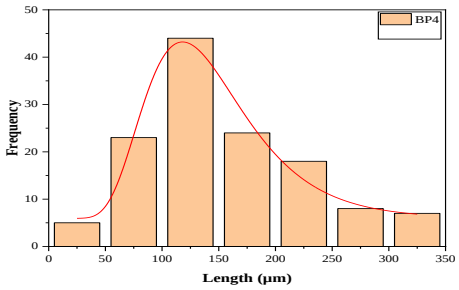
(BP3)



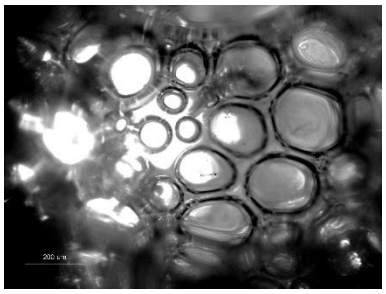
(BP3)



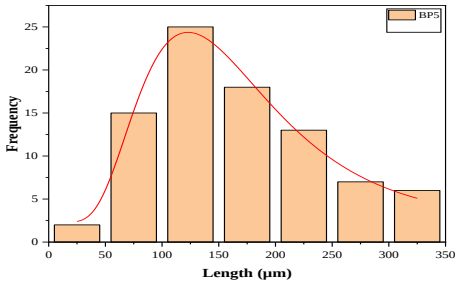
(BP4)



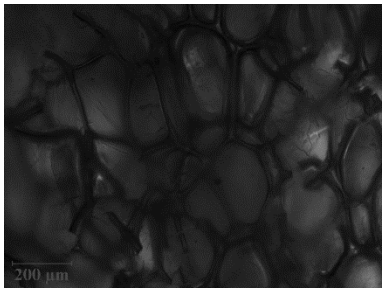
(BP4)



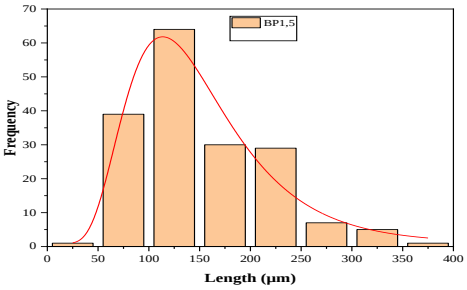
(BP5)



(BP5)



(BP1.5)



(BP1.5)

Figure 3. The PUU/IPSW biofoam microscope camera profile and pore distribution curves

Chemical structure

Urethane and urea are two forms of carbonyl groups formed by hydrogen bonds [18]. The PUU biofoam is derived from polyol and diisocyanate raw materials. Samples of MDI, PEG, BP0, and BP5 were observed to understand the PUU/IPSW biofoam chemical reaction. According to the absorption observed in the FTIR spectra, the -NH functional group was found in the wavenumber range of 3808-3308 cm^{-1} with broad intensity. This covered Samples BP0 (3516 cm^{-1}) and BP5 (3527 cm^{-1}). Samples BP0 (3382 cm^{-1}), MDI (3384 cm^{-1}) and BP5 (3382 cm^{-1}) belonged to -OH functional group found in the wavenumber range 3422-3314 cm^{-1}. The absorption peak of the PUU biofoam formed shifted to a lower wavenumber, suggesting a looser bond [13, 19]. Methylene functional group was detected at the absorption peak wavenumbers of 2972 cm^{-1} and 2971 cm^{-1} which was the -CH asymmetric stretching vibration of CH_3 [9, 19].

The absence of an isocyanate functional group absorption band at wavenumbers 2270-2250 cm^{-1} suggested that the isocyanate reacted properly with polyol (Figure 4). The first explanation is that due to the steric disturbance molecule, the -OH functional group interacted with the -NCO group. Another explanation is that the –NCO functional group interacted with the –OH group in the air, which was caused by humidity [6, 20]. The characteristics of amide III and C = O (-RNHCOO- / urethane linkage) functional groups in the absorption bands of 1230 cm^{-1} and 1077 cm^{-1} suggested that the PUU biofoam was successfully formed and chemically bonded [6, 19, 21]. In addition, another absorption peak was detected, namely the aromatic group C-C/C = C stretching modes in the wavenumber range 1600-1607 cm^{-1} [22]. The properties of EDA as a chain extender contributed to the PUU biofoam's hard segment character, which can be detected when the biofoam is heated or cooled. When PUU biofoam is heated to a specific temperature, it has a peak intensity –H bonded urethane C = O groups while urea groups decrease. This also applies if it is cooled to a temperature of 120-30 (°C) so that the peak intensity of -H bonded urethane C=O groups increases while the peak intensity of free urethane C=O decreases [18]. More information is presented inTable 2.

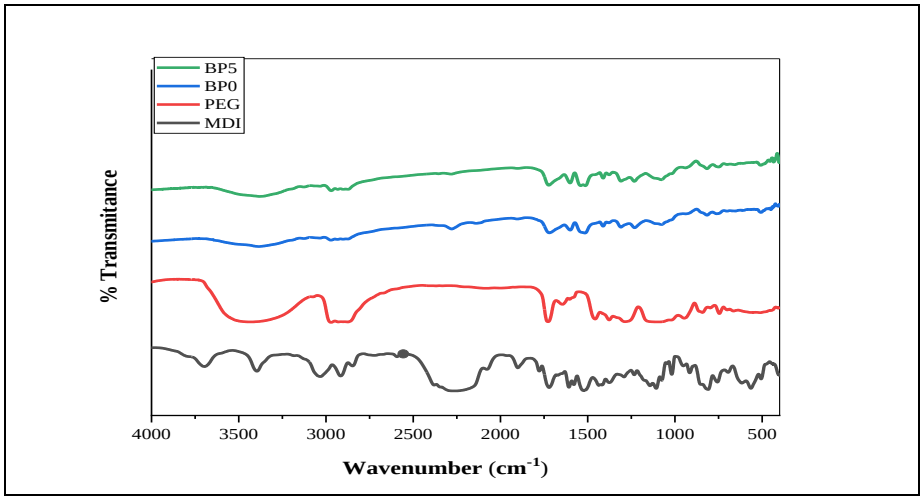


Figure 4. FTIR spectra of BP0, PEG, and MDI

Table 2. Peaks of FTIR spectra of BP0, PEG, and MDI

Wavenumber (cm^{-1})				Wavenumber Range (cm^{-1})	Functional Groups
MDI	**PEG**	**BP0**	**BP5**		
-		3516	3527	3808-3308	The stretching vibration of -NH
3384	-	3382	3382	3422-3314	-OH stretching modes from hydroxy groups
-	2972	2972	2971	3000-2970	-CH asymmetric stretching vibration CH_3 (methylene groups)
2257	-	-	-	2270-2250	-NCO- (isocyanate asymmetric stretching)
1720	-	1719	1724	1724-1705	Disorder H-bonded (C=O)OC in urethane
-	1644	1638	1635	1648-1627	Order H-bonded urea C=O
1607	1602	1600	1600	1615-1580	Aromatic C-C/C=C Stretching Modes
1233	-	1230	1230	1257-1222	υC-N+ δN-H (Amide III)
1075	-	1077	1075	1083-1070	H-Bonded (C=O)OC in urethane

TGA analysis

Thermogravimetric Analysis (TGA) is used to calculate the effect of filler addition (industrial plywood sawdust waste) and the ratio of MDI to its thermal performance, while DTG is a derivative of its mass loss. Samples BP0, BP5, and BP1.5 were observed because they were representatives to the treatment. Figure 5 and Table 3 show the results of the TG and DTG tests. Temperature characteristics were divided into T_{Onset} and T_{max}. T_{Onset} was the degradation of temperature when the mass loss was 5%, while T_{max} was the maximum degradation temperature of all samples [6]. All samples had T_{max} which was divided into three stages. Before the samples were degraded at the T_{Onset} temperature in the initial stage, there was a small degradation below 100ºC which was the degradation of moisture, solvent light organic molecules, and impurities from the biofoam [23]. The T_{Onsets} of the three samples were all above 120 ºC, with BP1.5 having the highest value of 130 ºC. The first and second stages of degradation occurred at temperatures of 190-209 (ºC) and 294-295 (ºC) respectively, and involved the decomposition of polymer urethane bonds [7, 13, 21]. The last degradation that occurred was the soft segment decomposition of the MDI biofoam at a temperature above 500ºC. This stage involved combustion and aromatic oxidation [7, 24], as well as the degradation of lignin (industrial plywood sawdust) and other molecules that were difficult to separate from the previous stage [21, 25]. Furthermore, the DTG curve (Figure 5) shows that the greatest mass loss occurred at 294 ºC which was the hard segment decomposition stage while the temperature above 525 ºC was the soft segment decomposition stage.

Figures 5(a)-(c) show the TGA results. It was found that BP0, or the biofoam without the addition of waste or MDI ratio, had better thermal resistance. This is because its thermal degradation profile showed that mass loss generally occurred at higher temperature compared to BP1 and BP1.5 (Figure 5 (a)). When biofoam filler was added, it is suggested that two things might have occurred: 1) the organic filler might contain a small amount of water residue as a result of the formation of urea bonds which increases the activation energy for thermal degradation [8], or 2) the addition of filler improved strength by giving the part a hard segment character, which increased thermal resistance [23]. Based on the results found, it should be the result that led to the second reason but this research showed that BP0 had highest thermal conductivity. It means that the filler-free biofoam had good thermal resistance. Another factor that caused a decrease in thermal performance was the uneven distribution of the filler in the polymer matrix which affected density. Besides, the TGA results were also influenced by pore

morphology. The modified biofoam's high pores and open cavities hastened the degradation process, thus reducing the thermal efficiency of the substance being analyzed [8].

DSC analysis was used to measure the change in mass of the heat-treated samples. TGA cannot normally detect physical changes in polymer structures such as glass transition, crystallization, or melting, but these can be determined through DSC [23]. The DSC analysis (Figure 5) reveals that none of the biofoam samples had endothermic melting peaks. This could be caused by a physical changeover of the polymer, or the density from melting at a fast cooling rate to a glassy amorphous state or impure samples. Samples B5 and BP1.5 had a single exothermic peak at 522 °C and 538 °C respectively, while Sample BP0 had two exothermic peaks at 539 °C and 551 °C.

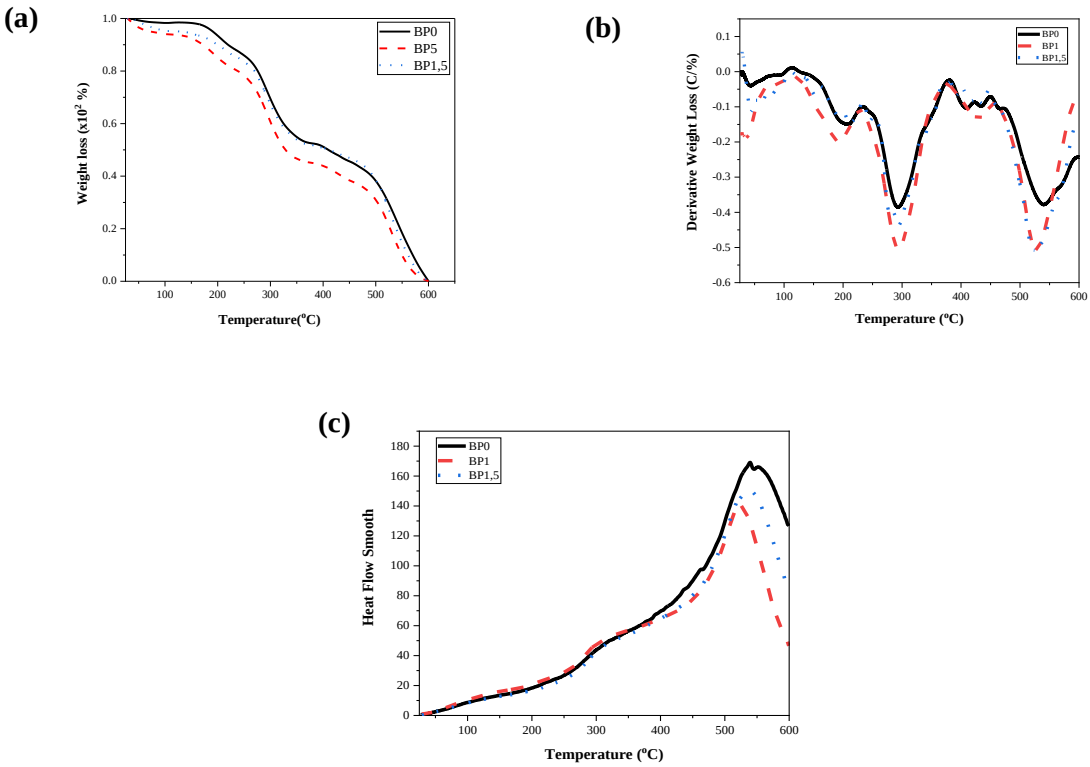


Figure 5. TGA (a), DTGA (b), and DSC (c) of the PUU/IPSW biofoam

Table 3. The sections of thermal degradation on the PUU/IPSW biofoam

Sample Codes	T_{onset} (°C)	(Stages) T_{max} (°C)			Residual Mass 600 °C (%)
		I	II	III	
BP0	126	206	294	539	37.29
BP5	130	190	295	528	23.00
BP1.5	130	209	294	527	33.48

Sound absorption coefficient

The sound absorption coefficient (α) for all samples is shown in Figure 6. The three samples (BP0, BP4, and BP1.5) were measured in the wavenumber range of 0-6400 (Hz) with two microphone impedance tubes and with similar sample thickness of 1.5 cm. Sample BP4 was selected as the representative to the treatment for 1:1 ratio, and the addition of IPSW with highest SAC compared to the other samples. The detailed information regarding SAC for all samples can be found in previous publication [12]. The results showed that BP4 had the highest sound absorption, with a value of 0.69 at 3864 Hz, followed by BP0 with a value of 0.65 at 4552 Hz, and BP1.5 with a value 0.45 at 4760 Hz. All samples showed the best acoustic performance at high frequencies above 3800 Hz. Based on these results, it was found that BP4 had the best acoustic performance, showing that that of BP0 and BP1.5 was not optimal. The addition of filler to the synthesis of polyurethane foam can enhance sound absorption [10, 11]. But this did not apply to the PUU/IPSW biofoam sample with IPSW of above 4% [12] and did not enhance MDI ratio. Several other factors influenced the biofoam sample ability to absorb sound which are explained in the following.

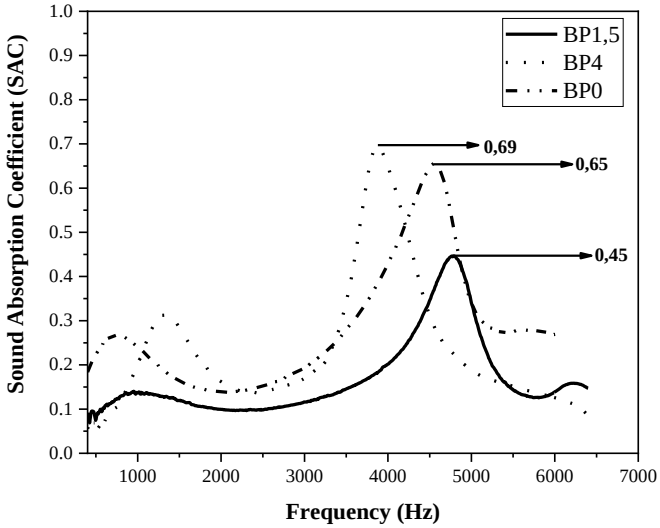


Figure 6. The PUU/IPSW biofoam sound absorption coefficient

Effect of texture, pore morphology, and density

Sound-absorbing foam will have a high SAC value if it has the following material characteristics [20, 25, 26]:

1. Flexible foam texture
2. Open-celled microstructure
3. Small-sized pores in large numbers
4. Higher density (not measured in this research)

The synthesized PUU/IPSW biofoam had the characteristics of semirigid texture, intermediate microstructure, smaller pore size, and higher SAC value than the control biofoam. This can be caused by other influencing factors such as the characteristics of the pores. Even if the size is small and numerous, it may not meet aspects such as structure and pore characteristics of sound-absorbing materials, including those mentioned below [17].

1. The material contains several pores and holes, all of which are small and uniform in size
2. The pores and holes must be connected.
3. The pores and holes inside the material must connect with the outer surface.

Effect of filler addition

The biofoam filler used, called IPSW, was measured by 30 mesh size. The filler had an impact on pore size in such a way that biofoam with added filler had smaller pores than those without filler addition. The smaller pore size was closely related to improved sound absorption mechanism. It is suggested that smaller pores allowed sound waves to dissipate sound energy and dampened it as they move through the sound-absorbing material. Therefore, smaller pores in large numbers allowed more sound wave to collide with the cell wall, lengthening the reflection & bending portion and causing more energy to be absorbed, resulting in higher SAC [10, 15, 20, 27]. The smaller pore size in the synthesized biofoam is shown in Figure 3. The existence of other factors that predominantly affect sound absorption such as the unfulfilled criteria for pores as sound absorbers had resulted in the reduced acoustic performance of the PUU/IPSW biofoam. However, if adjusted and designed with a better formula, the PUU/IPSW biofoam had a great potential as a noise-absorbing material with wide range frequency.

Effect of MDI ratio enhancement

Isocyanate (MDI) is composed of hard segment. Enhancing the MDI ratio can reduce SAC, as shown in Sample BP1.5. Biofoam with added MDI ratio had leaning rigid texture. The texture rigidity was caused by the closed-celled microstructure. Another factor which could make the biofoam texture rigid was chain extender [19, 20].

Conclusion

The PUU/IPSW biofoam was successfully synthesized after its functional groups (–NH, -OH, -CH, -CO and C-C) were identified in the FTIR spectra. Addition of filler and increase in MDI affect pore morphology, thermal resistance, and acoustic performance. Samples BP0 and BP1.5 of the synthesized biofoam had close-celled microstructure morphological type while Sample BP5 had intermediate-celled type. All samples had thermal resistance above 120 ^{o}C. Sample BP4 had the highest SAC with the value of 0.69. The acoustic output was poor, resulting in lower-frequency SAC when tested. However, if adjusted and designed with a better formula, PUU/IPSW biofoam can absorb sound at wide-range frequency. Lastly, filler addition could enhance the biofoam property performance. Therefore, IPSW is promotable as an organic filler for renewable material.

Acknowledgement

The authors thank Rosid Eka Mustofa for assisting with the OriginLab analysis, Iklima Maharani for directing the sample preparation stages, Safira C for laboratory access to the Microscope Camera tool, and all SEM, TGA, FTIR, and Acoustic laboratory test equipment operators who tested all samples in this research.

References

1. Aditya, V. T., Masykuri, M. and Setyono, P. (2019). Analysis of noise in the green open space Putri Kaca Mayang, Pekanbaru City. *AIP Conference Proceedings: International Conference on Biology and Applied Science (ICOBAS)*, 2019.040020.
2. Cao, L., Fu, Q., Si, Y., Ding, B. and Yu, J. (2018). Porous material for sound absorption. *Composites Communications*, 10(2018): 25-35.
3. Rojo-Gomez, R., Alameda, L., Rodriguez, A., Calderon, V. and Guiterrez-Gonzalez, S. (2019). Characterization of polyuretane foam waste for reuse in eco-efficient building materials. *Polymers*, 11: 359.
4. Gama, N.V., Ferreira, A. and Timmons, A. B. (2018). Polyurethane foams: Past, present and future. *Materials*, 11(10) : 1-35.
5. Akindoyo, J. O., Beg, M. D. H., Ghazali, S., Islam, M. R., Jeyaratman, N. and Yufaraj, A. R. (2016). Polyurethane types, synthesis and applications- a review. *Royal Society of Chemistry*, 6(1) : 114453-114482.
6. Alis, A., Majid, R. A., and Mohammad, Z. (2019). Morphologies and thermal properties of palm-oil based rigid polyurethane/halloysite nanocomposite foam. *Chemical Engineering Transactions*, 72(2019): 415-420.

7. Bundjali, B., Masykuri, M., Hartanti, F. W. and Arcana, I. M. (2018). Poly (urethane-urea) synthesized from 9-ethoxy-1, 10-octadecanediol obtained by modification of palm oil oleic acid. *Journal of Mathematics and Fundamental Sciences*, 50(1): 13-27.
8. Czlonka, S., Strakowska, A., Strzelec, K., Kairyte, A., and Kremensas, A. (2020). Bio-based polyurethane composite foams improved mechanical, termal, and antibacterial properties. *Materials*, 13(1):1-20.
9. Chen, X., Xi, X., Pizzi, A., Fredon, E., Zhou, X., Li, J., Gerardin, C. and Du, G. (2020). Preparation and characterization of condensed tannin non-isocynate polyurethane (NIPU) rigid foams by ambient temperature blowing. *Polymers*, 12(4):1-20.
10. Azahari, M. S. M., Rus, A. Z. M., Kormin, S. and Zaliran, M. T. (2017). Acoustic properties of polymer foam composites blended with different percentage loadings of natural fiber. *IOP Conferences Series: Materials Science and Engineering*, 244(2017):1-6.
11. Azahari, M. S. M., Rus, A. Z. M., Kormin, S. and Zaliran, M. T. (2018). An acoustic study of *Shorea leprosula* wood fiber filled polyurethane composite foam. *Malaysian Journal of Analytical Science*, 22(6): 1031-1039.
12. Nofitasari, H., Masykuri, M. and Ramelan, A. H. (2020). Reducing room noise using polyurethane-urea biofoam/industrial plywood sawdust waste (PUU/IPSW). *AIP Conferences Proceedings: International Conference on Science and Applied Science*, 2296(2020): 020061-020066.
13. Czlonka, S., Strakowska, A., Strzelec, K., Kairyte, A., and Vaitkus, S. (2019). Composites of rigid polyurethane foams and silica powder filler enhanced with ionic liquid. *Polymer Testing*, 75(2019) : 12-25.
14. Mustafov, S. D., Sen, F. and Seydibeyoglu, M. O. (2020). Preparation and characterization of diatomite and hidroxyapatite reinforced porous polyurethane foam biocomposites. *Scientific Reports*, 1(2020): 1-9.
15. Rus, A. Z. M. and Shafizah, S. (2015). Acoustic behavior of polymer foam composite of *Shorea leprosula* after UV-irradiation exposure *International Journal Mechanical Aerospace, Industry Mechatronics*, 9(2015) :188-192.
16. Sung, G., Kim, S. K., Kim, J. W. and Kim, J. H. (2016). Effect of isocyanate molecular structures in fabricating flexible polyurethane foams on sound absorption behavior, *Polymer Test*, 53(2016): 156-164.
17. Zhao, C., Wang, P., Wang, L. and Liu, D. (2014). Reducing railway noise with porous sound-absorbing concrete slabs. *Advance Material Science Engineering*, 2014: 1-11.
18. Kayalvizhi, M., Vakees, E., Suresh, J. and Arun, A. (2019). Poly(urethane-urea) based on functionalized polystyrene with HMDI: Synthesis and characterization. *Arabian Journal of Chemistry*, 12(8) : 2484-2491.
19. Jiang, L., Ren, Z., Zhao, W., Liu, W., Liu, H. and Zhu, C. (2018). Synthesis and structure/properties characterizations of four polyurethane model hard segments. *The Royal Society Open Science*, 5(7): 1-11.
20. Tiuc, A. E., Vasile, O., Usca, A-D., Gabor, T. and Vermesan, H. (2014). The analysis of factors that influnce the sound absorption coefficient in porous materials. *Romanian Journal of Acoustics and Vibration*, 11 (2):105-108.
21. Zhao, X., Qi, Y., Li, K. and Zhang, Z. (2019). Hydrogen bonds and FTIR peaks of polyether polyurethane-urea. *Key Engineering Materials*, 815(2019):151-156.
22. Bayu, A., Nandiyanto, D., Oktiani, R. dan Ragadhita, R. (2019). How to read and interpret FTIR spectroscope of organic material. *Indonesian Journal of Science and Technology*, 4(1): 97-118.
23. Ng, H. M., Omar, F. S., Saidi, N. M. and Kasi, R. (2018). *Encyclopedia of Polymers Science and Technology*. Jhon Waley Sons Inc, New York: pp. 1-29.

24. Kripluks, M., Cabulis, U., Ivdre, A., Kuranska, M., Zileniewska, M. and Auguscik, M. (2016). Mechanical and thermal properties of high-density rigid polyurethane foams from renewable resources. *Journal Renewable Material*, 4(1): 86-100.
25. Huang, X.Y., Hoop, C. F., Peng, X. P., Xie, J. L., Qi, J. Q., Jiang, Y. Z., Xiao, H. and Nie, S. X. (2018). Thermal stability analysis of polyurethane foams made from microwave liquefaction bio-polyols with and without solid residue. *BioResources*, 13(2): 3346-3361.
26. Amares, S., Sujatmika, E., Hong, T. W., Durairaj, R. and Hamid, H. S. H. B. (2017). A review: characteristic of noise absorption material. *IOP Conferences Series: Journal of Physics: Conferences Series*, 908(2017): 012005.
27. Hassan, N. N. M. and Rus, A. Z. M. (2016). Influences of thickness and fabric for sound absorption of biopolymer composite. *Applied Mechanics and Materials*, 393(1): 102-107.

Malaysian Journal of Analytical Sciences (MJAS)
Published by Malaysian Analytical Sciences Society

SYNTHESIS OF GREEN-RENEWABLE BIOLUBRICANT BASE STOCK FROM MALAYSIAN PALM OIL

(Sintesis Stok Asas Biopelincir Hijau-Diperbaharui daripada Minyak Sawit Malaysia)

Nurazira Mohd Nor[1]* and Jumat Salimon[2]

[1]MaterOleo Research Group,
Faculty of Applied Sciences,
Universiti Teknologi MARA, Cawangan Negeri Sembilan, Kampus Kuala Pilah, 72000 Kuala Pilah, Negeri Sembilan, Malaysia
[2]Department of Chemical Sciences, Faculty of Science and Technology,
Universiti Kebangsaan Malaysia, 43600 UKM Bangi, Selangor, Malaysia

**Corresponding author: nurazira@uitm.edu.my*

Received: 20 August 2021; Accepted: 3 February 2022; Published: 27 June 2022

Abstract

Palm oil has become one of the potential renewable resources in biolubricant application. However, the direct application of palm oil as a biolubricant is restricted due to its low oxidative stability and poor low temperature properties. These drawbacks can be overcome by molecule structural redesign through chemical modification process. Palm oil (PO) was modified via epoxidation, ring opening and esterification process. The epoxidized palm oil (EPO) was prepared by using an *in-situ* performic acid catalyst. Then, EPO was ring-opened using oleic acid in the presence of *p*-toluenesulfonic acid (PTSA) as a catalyst and further esterification with oleic acid using sulfuric acid as catalyst. The molecular structure confirmation of modified palm oils was proven through the oxirane oxygen content (OOC) value, iodin value, hydroxyl value, Fourier transformation infra-red (FTIR), proton and carbon nuclear magnetic resonance (^{1}H-NMR and ^{13}C-NMR) spectroscopy analysis. Results showed that the conversion of PO into EPO has improved its oxidative stability (190 °C). While, the esterification process has resulted in branching and bending in the molecule structure of the final product (palm oil dioleate, PODO), which improved its pour point (-10 °C), flash point (315 °C) and viscosity index (146). These make PODO suitable to be used in biolubricant application.

Keywords: biolubricant, epoxidation, esterification, ring opening, palm oil

Abstrak

Minyak sawit merupakan salah satu sumber yang boleh diperbaharui yang berpotensi dalam penghasilan biopelincir. Walaubagaimanapun, penggunaan secara terus minyak sawit sebagai biopelincir adalah terhad disebabkan oleh kestabilan oksidatif yang rendah dan sifat suhu rendah yang lemah. Kelemahan ini boleh diatasi dengan ubahsuai struktur molekul melalui proses pengubahsuaian kimia. Minyak sawit (PO) diubahsuai melalui proses pengepoksidaan, pembukaan gelang dan pengesteran. Minyak sawit terepoksida (EPO) dihasilkan menggunakan mangkin asid performik yang dijana secara in-situ. Seterusnya, EPO ditindakbalaskan melalui pembukaan gelang menggunakan asid oleik dengan kehadiran p-toluena asid sulfonik (PTSA) sebagai mangkin dan diikuti dengan pengesteran dengan asid oleik dengan menggunakan mangkin asid sulfurik. Pengecaman struktur molekul minyak sawit terubahsuai dibuktikan melalui nilai kandungan oksigen oksiran, nilai iodin, nilai

hidroksil, spektroskopi infra-merah transformasi Fourier (FTIR), proton dan karbon nuklear magnetik resonans (^{1}H-NMR dan ^{13}C-NMR). Keputusan menunjukkan penukaran PO kepada EPO telah memperbaiki nilai kestabilan oksidatifnya (190 °C). Manakala proses pengesteran telah menghasilkan struktur molekul yang bercabang dan bengkok bagi hasil akhir (dioleate minyak sawit, PODO) dan telah memperbaiki nilai takat tuang (-10 °C), takat kilat (315 °C) dan indeks kelikatan (146). Ini menjadikan PODO sesuai untuk digunakan dalam aplikasi biopelincir.

Kata kunci: biopelincir, pengepoksidaan, pengesteran, pembukaan gelang, minyak sawit

Introduction

Currently, there are wide ranges of base oils used in lubricant application, which include mineral oils, synthetic oils, re-refined oils and plant oils. Among these, mineral oils are the most commonly used [1]. However, mineral oils pose a constant threat to ecology and vast ground water reserves due to their inherent toxicity and non-biodegradable nature [1, 2]. The reduction of petroleum oil resources and increasing greenhouse gas emissions also provide a clear picture of the importance of the move towards sustainable development [3]. The use of renewable sources in the industry is vital to ensure sustainable development.

Plant oils are found to be the best alternative source to replace mineral oils in the production of biolubricant because they are renewable raw materials, biodegradable, non-toxic and environmentally friendly. Plant oil itself exhibits good lubrication properties with high viscosity index [4]. Biolubricants hold great potential for environmental conservation as an alternative lubricant. The global market size for biolubricants was USD 2.20 billion in 2019 and is projected to reach USD 2.46 billion by 2025, at a compound annual growth rate (CAGR) of 4.1% between 2020 and 2025 [5]. Stringent regulations and the growing acceptance among end-users are projected to drive the biolubricants market [5].

However, plant oils have several drawbacks that will restrict their direct application in the lubricant industries such as low oxidative stability [6, 7] and poor low temperature properties [3, 8]. The low oxidative stability is due to the presence of bis-allylic protons in plant oil's structure which are highly susceptible to free radical attack and therefore undergo oxidative degradation to form polar oxy compounds [9-13]. The rate of the oxidation process can be attributed to the number of unsaturated fatty acids present in its composition [10,14]. Meanwhile, poor low temperature properties include cloudiness, precipitation, poor flowability and solidification at relatively high temperatures [8, 15]. The poor low temperature properties also will limit its use at a low operating temperature [6].

The oxidative stability and poor low temperature drawbacks that occur in the plant oils can be overcome by molecule structural redesign through chemical modifications. The presence of the double bonds and their reactivity have allowed the functional addition reactions into the unsaturated fatty acids. The epoxidation process is one of the most important functionalization reactions of the double bond to other stable functional groups to improve the plant oil's oxidative stability [6, 16, 17]. The epoxidation of plant oil using peracids is one of the most important steps and a useful modification process toward the double bonds because the epoxides are reactive intermediates that can be converted to other functional groups through ring-opening reactions [18]. Plant oils with high content of unsaturated fatty acid are used to produce high epoxy functionality materials [19]. Epoxidized plant oils products from the epoxidation process can be used as high-temperature lubricants [20], plasticizers [21] and high temperature coating materials [22].

Meanwhile, the modification that can be used to improve poor low temperature properties of plant oil is ring opening and esterification reactions. The oxirane ring opening by acidic or alkaline catalyzed reaction with suitable reagent provides interesting polyfunctional compounds [15, 23], whereas reducing structural uniformity of the oil by attaching alkyl side chains would improve the low-temperature

performance [15, 24]. The branching group which resulted from ring opening reaction will interfere with the formation of macro-crystalline structures during low-temperature applications and provide enhanced fluidity to plant oils. These modified plant oils with chain branching were reported to have the superior performance of the physicochemical properties and are promising as biolubricants [25]. Products obtained from ring opening can be used as low-temperature lubricants [20].

Palm oil which is abundantly available all over Malaysia become one of the potential plant oils that can be used as biolubricant base stock [26, 27]. In this paper, the modification of palm oil molecule structure to produce a base stock oil for lubricant application as shown in Figure 1 is reported. Palm oil contains a high percentage of unsaturated fatty acid (49.4%) [28], which serves as good starting material for the epoxidation process. Palm oil was converted into epoxidized palm oil followed by the ring opening and esterification reactions with oleic acid to enhance the lubrication properties. The structure of products was confirmed by FTIR and NMR spectroscopy. Physicochemical properties of products were examined by using several tests such as oxidative stability, pour point, flash point and viscosity index.

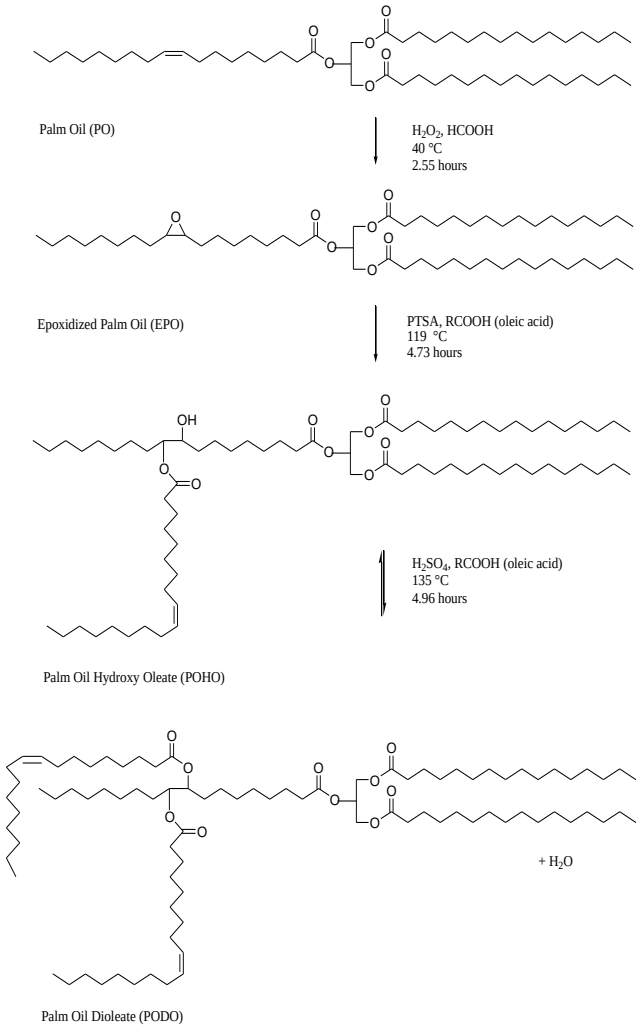


Figure 1. The schematic reaction for the modification of palm oil

Materials and Methods

Materials

Palm oil was obtained from Jomalina Refinery, Teluk Panglima Garang, Selangor, Malaysia. Formic acid (88%) was obtained from Fisher Scientific and hydrogen peroxide (30%) from Merck. Oleic acid (90%) was purchased from Sigma Aldrich. Ethyl acetate, toluene, sodium hydrogen carbonate and sodium chloride were purchased from Systerm.

Chemical modification processes

The epoxidation process was carried out based on the optimum conditions reported by Nurazira et al. [27]; mole ratio of PO: HCOOH: H_2O_2 (1:5.91:3.6), reaction temperature of 40 °C and reaction time of 2.55 hours. Next, the ring opening process was carried out based on the optimum conditions reported by Nurazira et al. [29]; mole ratio of EPO: oleic acid (1:3), reaction temperature of 119 °C, reaction time of 4.73 hours and 1.02% of *p*-toluenesulfonic acid (PTSA). The next esterification was carried out by using a mole ratio of POHO and oleic acid at 1:3, reaction temperature of 135 °C, reaction time of 4.96 hours and 1.86% of sulphuric acid.

Characterization of modified palm oils

The unsaturation of oil was determined by iodine value (IV) test using the Wijs method [30]. Oxirane oxygen content (OOC) value was determined by direct method using hydrobromic acid solution in glacial acetic acid (AOCS Cd 9-57) [31]. Hydroxyl value (HV) was performed according to analysis method (AOCS Tx 1a-66) [31]. The structure of modified oils was confirmed by using Fourier Transformation Infra-red (FTIR), proton and carbon Nuclear Magnetic Resonance (^{1}H-NMR and ^{13}C-NMR). FTIR spectra were recorded on a Perkin Elmer Infrared Spectrophotometer in the range of 400-4000 cm^{-1}. ^{1}H and ^{13}C NMR were recorded on JEOL-ECP 400 spectrometer (400 MHz ^{1}H/100.61 MHz ^{13}C) using $CDCl_3$ as a solvent.

Physicochemical properties tests of modified palm oils

The American Society for Testing Materials standards such as ASTM D-6186, ASTM D-5853, ASTM D-92 and ASTM D-2270 were used to measure oxidative stability, pour point, flash point and viscosity index [32]. The oxidative stability test was conducted using Differential Scanning Calorimetry (DSC). 1.5 mg of sample was placed into an aluminum pan with a pinhole cover to allow interaction between ester product and oxygen gas which acts as reaction gas. Then, aluminum pan was put into DSC and heated for 20 minutes up to temperatures of 250 °C by using nitrogen gas. Onset temperature was recorded to determine the oxidative stability.

In the pour point test, the sample was filled into a U-shaped glass tube until it reached a height of 4 cm. The thermometer was placed at one end of the U-shaped tube and both ends of the U-shaped tube was covered with parafilm. The U-shaped tube containing the sample was placed in the refrigerator (minimum temperature -80 °C) for 24 hours to ensure that the sample froze completely. After being left overnight, the U tube was removed and flipped upside down. The lowest temperature at which movement of the sample was observed was recorded as the pour point.

For flash point testing, 2 mL of sample was placed in a crucible and heated on a heating plate. A thermometer with a maximum reading temperature of 360 °C was placed on the sample to measure the sample's temperature. The temperature was rapidly increased at first and then at a slow constant rate as the flash point was approached. The lowest temperature at which the vapors above the surface of the liquid ignited was taken as the flash point.

For the viscosity index test, the Rheometer Anton Paar (Physica MCR 301 model) was used to measure the viscosity and viscosity index of the tested sample. The diameter used for both samples was 0.051 mm. Samples was tested at 40 °C and 100 °C [32]. The sample viscosity index was calculated based on the formula below:

$$\text{Viscosity index} = (L-U)/(L-H)\times 100$$

where: U= oil's kinematic viscosity at 40 °C, L and H = values based on the oil's kinematic viscosity at 100 °C.

Results and Discussion

Palm oil is golden yellow and exists in the semi-solid form at room temperature. The liquid fraction contains unsaturated triacylglycerol (TAG), whereas the solid fraction contains more saturated TAG. The epoxidation process is more likely to occur at unsaturated TAG.

In epoxidation reaction, hydrogen peroxide acts as an oxygen donor, while formic acid acts as an oxygen carrier and gets regenerated once the epoxidation reaction takes place [33]. Formic acid also takes part in the overall reaction as a catalyst in the formation of the oxirane ring and as a reactant in the hydrolysis of the oxirane ring. To attain the maximum oxirane oxygen content, the level of the formic acid should be such that these two effects are balanced [34,35]. Figure 2 shows the mechanism of the epoxidation reaction.

The results for the epoxidation of palm oil are shown in Table 1. The average percentage yield of epoxidation was 86% (w/w). The epoxi dation process can be monitored through the IV and OOC values. The IV should be as small as possible after epoxidation, while OOC should be as large as possible. There was a difference between the IV before and after epoxidation. The initial IV of palm oil before epoxidation was 57.8 m/g, while the IV obtained for EPO after epoxidation was low approaching zero (0.09 mg/g). EPO showed a high OOC value which was 3.46% with 99.43% of relative conversion oxirane (RCO). The theoretical value of OOC was 3.49%. It means almost all unsaturated fatty acids in PO were successfully epoxidized and converted to oxirane rings to produce EPO.

Many nucleophilic reagents are known to add to an oxirane ring, resulting in ring opening. The ester branching groups produced from oxirane ring opening based esterification reactions are effective for attaining the desired molecular spacing. Most of the oxirane ring groups were opened and converted into ester bonds in the molecule with the hydroxyl group [26, 36]. The modified plant oils with chain branching were reported to have superior performance properties and are promising as biodegradable lubricants [26,36,37]. Figure 3 shows the mechanism of ring opening reaction.

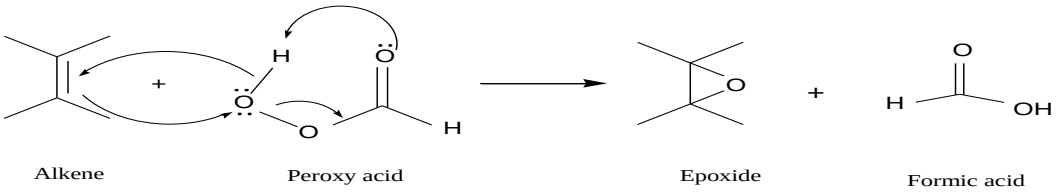


Figure 2. The mechanism of the epoxidation reaction

Table 1. Analysis results for modified palm oils

Compound	PO	EPO	POHO	PODO
Yield (%)	-	86	84	80
Iodine value (mg/g)	57.8	0.09	59.4	109.8
OOC value (%)	-	3.46	0.041	-
RCO (%)	-	99.43	-	-
Hydroxyl value (mgKOH/g)	19	23	118.7	25.4

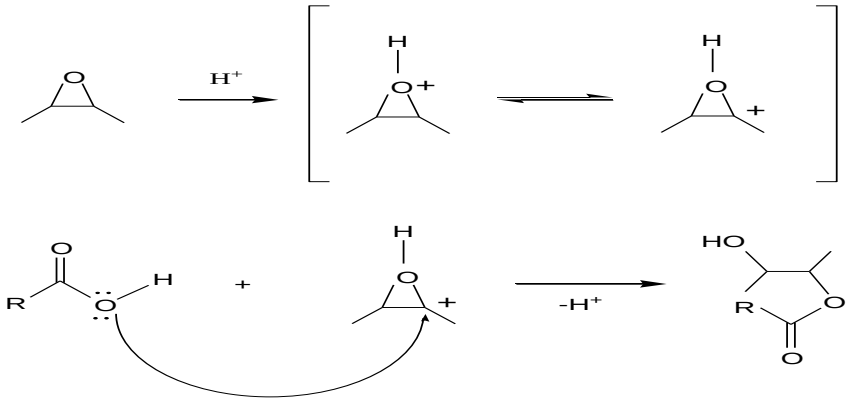


Figure 3. The mechanism of the ring opening reaction

This study reports the oxirane ring opening reaction of epoxidized palm oil (EPO) by the nucleophilic addition of oleic acid (OA) in the presence of homogenous acid catalysts which was *p*-toluenesulfonic acid (PTSA). PTSA was preferred to be used in the reactions due to the maximum yield of epoxy ring opening and no evidence of any side reaction occurred during the reaction [38]. The nucleophilic attack by the fatty acid molecule which was oleic acid on the oxirane ring of epoxidized palm oil (EPO) in the presence of PTSA as catalyst resulted in the ring opened product: palm oil hydroxy oleate (POHO).

The results for the ring opening process are shown in Table 1. The average percentage yield of ring opening was 84% (w/w). The ring opening process can be monitored through IV, HV and OOC values. The OOC value should be as small as possible. This is because the reduction of OOC value is proportional to the number of epoxides opened. OOC value obtained after ring opening process was low approaching zero (0.041%). It showed that the entire epoxide ring was successfully opened during the ring opening reaction with the oleic acid to produce POHO. The entire epoxide ring had been successfully converted to hydroxyl oleate ester functional groups. This can be evidenced by the increase of IV and HV of the product. The addition of the olefin which exists from the oleate acyl group had increased the IV of POHO to 59.4 mg/g. There was also an increase in HV from 23 mg KOH/g to 118.7 mg KOH/g after the ring opening process. Further esterification of POHO with oleic acid produced the final product: palm oil dioleate (PODO). The average percentage yield of the final esterification process was 80% (w/w). There was a decrease in HV of PODO to 25.4 mgKOH/g and an increase of IV (109.8 mg/g) after esterification. It means that the hydroxyl group of POHO was reacted with oleic acid to produce the oleate acyl group.

FTIR spectra

The presence of functional groups in all modified oils was identified by using FTIR spectroscopy. Figure 4 shows the FTIR spectra of PO, EPO, POHO and PODO. The disappearance of the double bond functional group peak at 3005 cm^{-1} which was initially present in the PO spectrum indicated the conversion of the double bond to the epoxy group. It can be proven by the presence of a C-O-C oxirane peak at 843 cm^{-1} in the EPO spectrum. Pavia et al. [39] reported the presence of epoxy group can be monitored at wavenumber range of 815-950 cm^{-1} which agrees well for this study.

The disappearance of the epoxide peak showed that the entire oxirane ring had been successfully converted to hydroxyl oleate ester functional groups during the ring opening reaction with oleic acid. This is evidenced by the increase of peaks intensity of the hydroxyl (OH) functional group at 3463 cm^{-1} and C=O stretching at 1740 cm^{-1} in the POHO spectrum. A significant change in the ring opening process also can be evidenced by

the existence of the C=C olefin peak of the oleate acyl group at 3003 cm^{-1} in the POHO spectrum. The final esterification product (PODO) was evidenced by the reduction of the peak intensity of the hydroxyl group in the PODO spectrum.

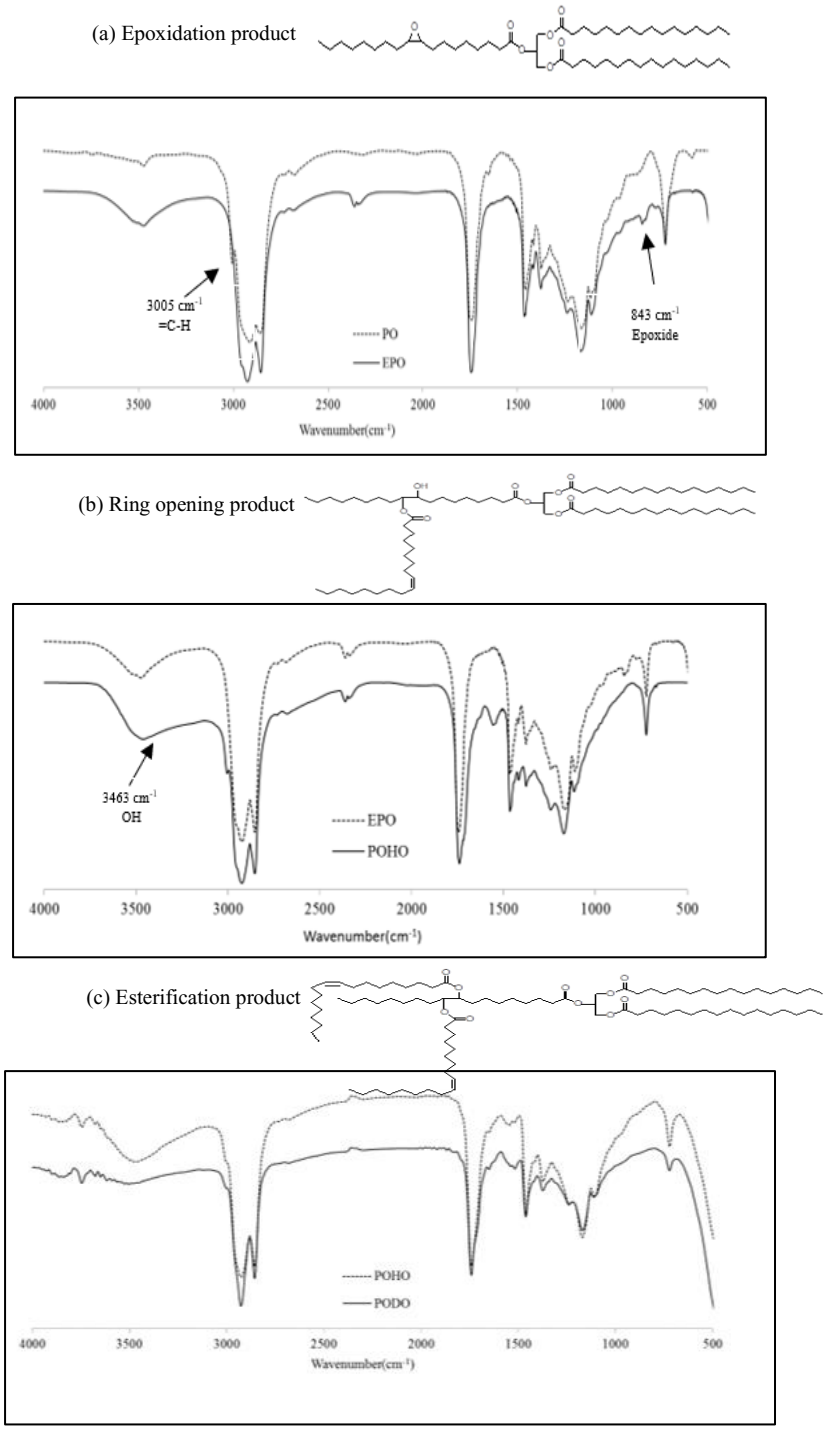
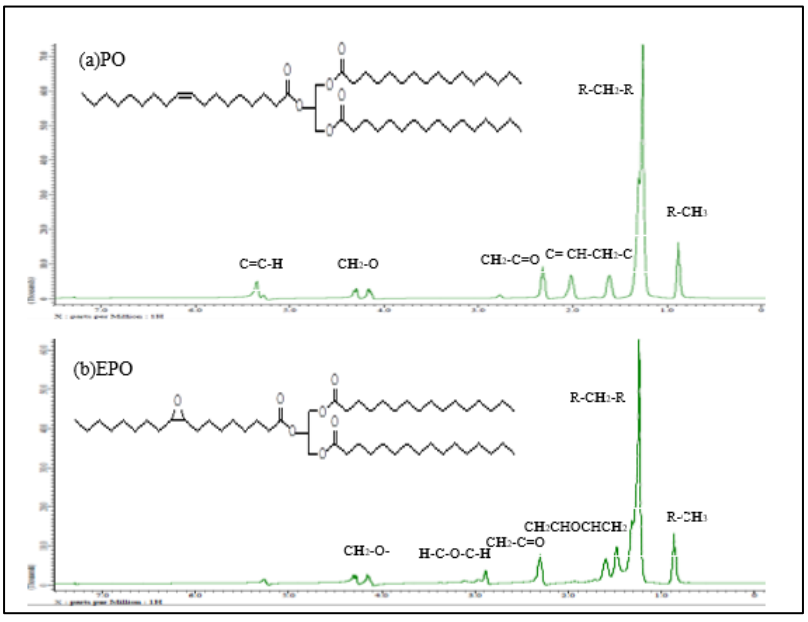


Figure 4. FTIR spectra of (a) epoxidation; (b) ring opening; (c) esterification products

NMR spectra

Figure 5 shows ^{1}H NMR spectra of PO, EPO, POHO and PODO and Table 2 shows the chemical shift for all products. The epoxidation process (EPO) can be proven by the disappearance of olefin proton at 5.34 ppm (C=C-H) and allylic proton at 2.0-2.05 ppm (C=C-C-H), which initially were present in the PO spectrum. They were replaced by the existence of a peak signal at 2.89 ppm, which corresponds to the proton of oxirane ring (CHOCH) and a peak signal at 1.49 ppm that represents epoxy proton (CH_2-CHOCH-CH_2) in the EPO spectrum. The result of ring opening reaction can be confirmed by the disappearance of peak signal of oxirane ring proton (CHOCH) in the POHO spectrum. Peak signal for olefin proton and allylic proton can be detected at 5.30-5.36 ppm (C=C-H) and 1.97-2.09 ppm (C=C-C-H) in the POHO spectrum. The final product showed that there was a disappearance of the C-O-H peak signal (C-O-H) in the PODO spectrum.

Figure 6 shows ^{13}C NMR spectra of PO, EPO, POHO and PODO and Table 3 shows the chemical shift for all products. The peaks at 127.85- 130.17 ppm in the PO spectrum represented the double bond (C=C). Conversion of the double bond to oxirane ring can be proven by the disappearance of double bond peak and existence of carbon atom of epoxy (C-O) at 54.19-57.22 ppm in EPO spectrum. The results of ring opening reaction can be evidenced by the disappearance of epoxy carbon, the existence of carbon olefin (C=C) at 129.60-129.97 ppm and also the existence of peak signal at 73.50 ppm, which represents the carbon next to the hydroxyl group (HC-OH) in POHO spectrum. The final product showed that there was a disappearance of the HC-OH signal peak in the PODO spectrum.



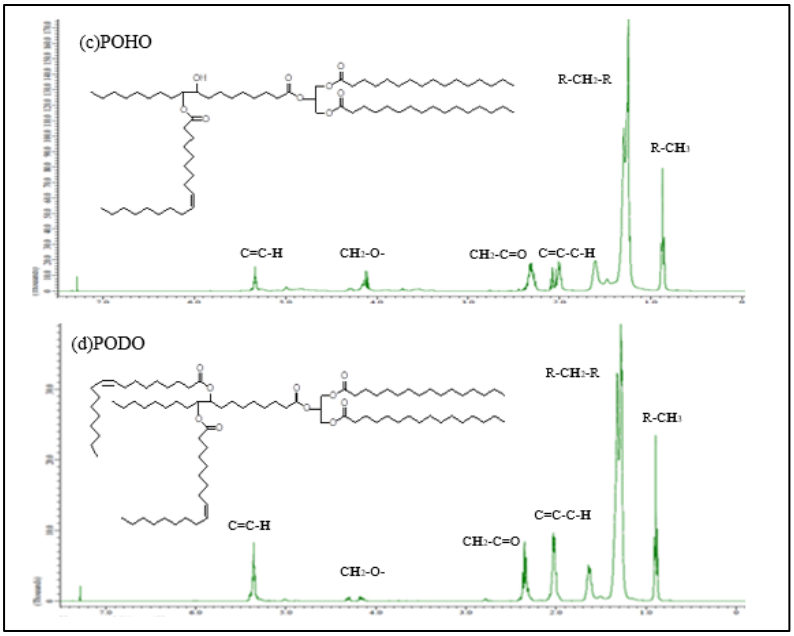


Figure 5. ^{1}H NMR spectra of (a) PO; (b) EPO; (c) POHO and (d) PODO

Table 2. The chemical shifts for ^{1}H NMR PO, EPO, POHO and PODO spectra

Compound	**Chemical Shift, ppm**	**Chemical Shift, ppm (Reference[36])**	**Remarks**
PO	5.34	4.5-6.5	C=C-H
	2.00 - 2.05	1.6-2.6	C=C-C-H
EPO	2.89	2.5-3.5	CHOCH
POHO	5.30-5.36	4.5-6.5	C=C-H
	1.97-2.09	1.6-2.6	C=C-C-H
	4.99	0.5-5.0	C-O-H
PODO	5.34-5.37	4.5-6.5	C=C-H
	2.00-2.07	1.6-2.6	C=C-C-H

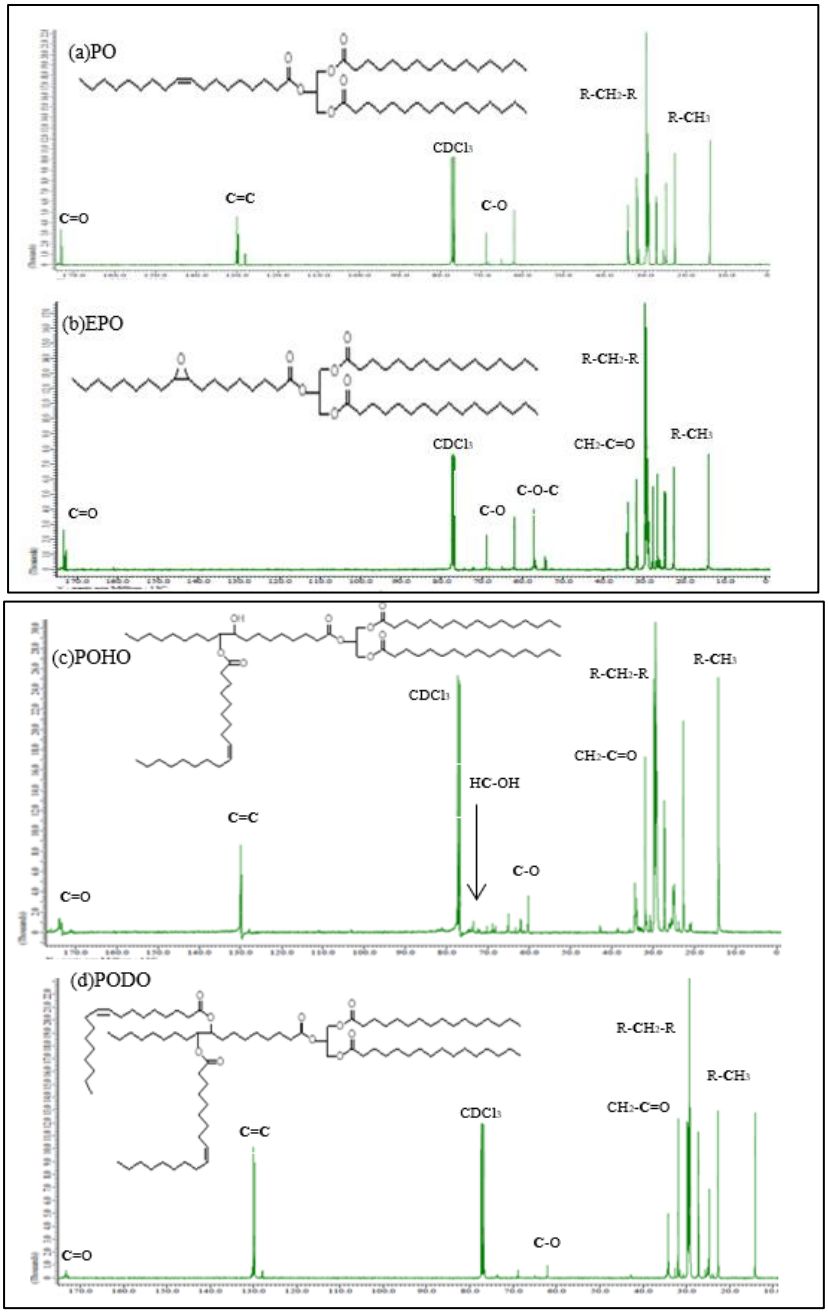


Figure 6. ^{13}C NMR spectra of (a) PO; (b) EPO; (c) POHO and (d) PODO

Table 3. The chemical shifts for ^{13}C NMR PO, EPO, POHO and PODO spectra

Compound	Chemical Shift, ppm	Chemical Shift, ppm (Reference[36])	Remarks
PO	127.85- 130.17	100-150	C=C
EPO	54.19-57.22	56.9-58.5	C-O-C
POHO	129.60-129.97	100-150	C=C
	60.18-63.30	40-80	C-O
PODO	127.88-130.16	100-150	C=C

Physicochemical properties

There were several tests conducted to determine the physicochemical properties of the modified oils. The physicochemical properties results obtained are shown in Table 4. The ability of a substance to resist oxidative degradation is an important property of biolubricant. Oxidative stability is determined by the onset temperature (OT) using Differential Scanning Calorimetry (DSC). OT is the temperature at which the occurrence of a sharp increase in the rate of oxidation of the sample. Higher onset temperature indicates that the lubricant has high oxidation stability [6]. Based on the DSC analysis, there was an improvement in oxidative stability for EPO (190 °C) compared to PO (181 °C). It was due to the conversion of the double bond group to the epoxy group which will reduce the active site of oxidation and make it less susceptible to radical attack. However, POHO and PODO showed low oxidative stability due to increasing double bond content and carbon chain, which will increase the potential active site for the oxidation process.

Table 4. Physicochemical properties of PO, EPO, POHO, PODO and commercial lubricants (100A and 100B)

Compound	PO	EPO	POHO	PODO	100A[a]	100B[b]
Oxidative stability (°C)	181	190	170	157	n/a	n/a
Pour point (°C)	7	18	-8	-10	-19	-27
Kinematic viscosity (40 °C)	56.97	97.72	616.46	83.45	96	96.7
Kinematic viscosity (100 °C)	9.24	14.56	60.73	15.30	10.9	11
Viscosity index (VI)	130	133	125	146	97	100
Flash point (°C)	240	255	295	315	276	254
ISO viscosity grade	46	100	680	100	100	100

a:100A: Denicol Compressor Oil ISO VG 100 [41],
b: SubsTech Hydraulic Oil ISO 100 [42]

Pour point is one of the important quality parameters to determine cold flow or low temperature properties of the lubricant. The cold flow properties of plant oils are extremely poor and these limit their use at low operating temperatures especially as automotive and industrial fluids. Plant oils tend to form

macrocrystalline structures at low temperatures through uniform self-stacking of the linear triacylglycerol molecules. The macrocrystals restrict the easy flow of the system due to the loss of kinetic energy of individual molecules during self-stacking [6, 15, 40]. PODO has the lowest pour point (-10 °C) compared to other products due to the branched carbon chain and bent structure. It makes it more restricted to self-stacking and more hollows in the structure, thus easier for it to flow, which contributed to the lowest pour point. In general, the presence of a branching group at the end of the molecule will disrupt this stacking process and create a steric barrier around the individual molecules and inhibit crystallization [18]. This will result in the formation of microcrystalline structures rather than macro structures. At lower temperatures, the microcrystalline structures can easily tumble and glide over one another resulting in better fluidity of the total matrix [6], resulting in a lower pour point. Moreover, the disappearance of the hydroxyl group in PODO esters means that no hydrogen bonds exist in the molecule, which causes the molecules to be less sticky to each other and to move freely around.

Viscosity also becomes one of the important quality parameters for lubricating oils. The efficiency of the biolubricant in reducing friction and wear is greatly influenced by its viscosity. The viscosity of PO is lower than EPO due to the existence of a double bond, which provides the lubricating properties of liquids by degrees of unsaturation. POHO has a higher viscosity due to the presence of intermolecular hydrogen bonding from the hydroxyl group resulted from the ring opening reaction. The hydroxyl group gives a higher polarity that influences the viscosity of the oil, in which more polar molecule of oil, the higher the viscosity [40]. In general, the hydroxyl group will form a bond between molecules and cause lubricating oil to become more viscous. After the final esterification process, the viscosity of PODO decreased due to the disappearance of the hydroxyl group. The viscosity of PODO was in the medium range, which was 83.45 centistokes (cSt) at 40 °C and decreasing to 15.30 cSt at 100 °C. It shows the viscosity of biolubricant decreases as temperature increases. The least viscous biolubricant which still forces the two moving surfaces apart is desired. If the biolubricant is too viscous, it will require a large amount of energy to move and if is too thin, the surfaces will rub and friction will increase [6]. The viscosity index highlights how the viscosity of biolubricant changes with variations in temperature [6]. PODO showed the highest viscosity index (146) compared to other products. It shows the viscosity of PODO is less affected by temperature changes and does not drastically change when the temperature varies. This is a good indicator and it is suitable for use at a large temperature range.

The flash point is often used as a descriptive characteristic of fuel oil and it is also used to describe oils that are not used as fuels such as a lubricant. Flash point refers to both flammable oils and combustible oils. The oils with a flash point of less than 43 °C are flammable, while those having a flash point above this temperature are combustible. Biolubricant which has a low flash point value is considered to have been contaminated by volatile and usually requires special precautions when handling these biolubricant [6]. PODO showed the highest flash point (315 °C) compared to other products. It is due to the increasing carbon number which causes an increasing molecular weight that gives a higher flash point. In addition, PODO also has a big branched molecular structure which requires more energy to burn. This will increase the flash point of PODO. A high flash point is important to ensure that the lubricant is not burned in the engine during its operation.

Table 4 also shows a comparison of lubrication properties between the biolubricant base stock produced (PODO) with commercial lubricants in the market. The selected commercial lubricants are ISO VG 100 grade lubricants, namely Denicol Compressor Oil (100A) [41] and SubsTech Hydraulic Oil (100B) [42]. Based on the comparison made, PODO has a higher viscosity index compared to 100A and 100B lubricants. The pour point value of PODO is also lower than 100A and 100B lubricant. In addition, PODO also recorded much higher flash point value than 100A and 100B lubricants.

Conclusion

The chemically modified palm oils showed improvement in physicochemical properties. The epoxidized palm oil (EPO) has the highest oxidative stability due to the reduction of double bond content, while the final esterification product, palm oil dioleate (PODO) has the lowest pour point due to the greater ability of the branched chain esters to disrupt crystalline formation. A bigger, bending, branching and hollow structure makes the molecule less compact, thus improve the lubricity of the lubricant. PODO also showed the highest viscosity index and flash point due to the big branched molecular structure. This makes PODO as plausible to be used as a biolubricant with better lubrication properties.

Acknowledgement

The authors gratefully acknowledge Universiti Kebangsaan Malaysia for financial support under research grant GUP-2016-012 and GUP-2016-058. The authors also thank the Ministry of Education, Malaysia for providing scholarship support (MyPhD) for the author.

References

1. Salimon, J. and Salih, N. (2009). Oleic acid diesters: Synthesis, characterization and low temperature properties. *European Journal of Scientific Research*, 32(2): 216-222.
2. Farhoosh, R., Einafshar, S. and Sharayei, P. (2009). The effect of commercial refining steps on the rancidity measures of soybean and canola oils. *Food Chemistry,* 115: 933-938.
3. Erhan, S. Z. and Asadauskas, S. (2000). Lubricant basestocks from vegetable oils. *Industrial Crops and Products,* 11: 277-282.
4. Nirmal, V. P. and Dineshbabu, D. (2015). Performance and emission of *Pongamia pinnata* oil as a lubricant in diesel engine. *International Journal of Innovative Research in Science, Engineering and Technology*, 4(2): 75.
5. Salih, N. and Salimon, J. (2021). A review on eco-friendly green biolubricants from renewable and sustainable plant oil sources. *Biointerface Research in Applied Chemistry*, 11(5): 13303-13327.
6. Salimon, J., Salih, N. and Yousif, E. (2011). Chemically modified biolubricant basestocks from epoxidized oleic acid: Improved low temperature properties and oxidative stability. *Journal of Saudi Chemical Society*, 15: 195-201.
7. Wu, X., Zhang, X., Yang, S., Chen, H. and Wang, D. (2000). The study of epoxidized rapeseed oil used as a potential biodegradable lubricant. *Journal of the American Oil Chemist Society,* 77: 561-563.
8. Salimon, J. and Salih, N. (2010). Modification of epoxidized ricinoleic acid for biolubricant base oil with improved flash and pour points. *Asian Journal of Chemistry*, 22(7): 5468-5476.
9. Adhvaryu, A., Liu, Z. and Erhan, S. Z. (2005). Synthesis of novel alkoxylated triacylglycerols and their lubricant base oil properties. *Industrial Crops and Products*, 21:113-119.
10. Borugadda, V. B. and Goud, V. V. (2015). Response surface methodology for optimization of biolubricant basestock synthesis from high free fatty acids castor oil. *Energy Science & Engineering,* 3(4): 371-383.
11. Erhan, S. Z., Sharma, B.K. and Perez, J. M. (2006). Oxidation and low temperature stability of vegetable oil-based lubricants. *Industrial Crops and Products,* 24: 292-299.
12. Sharma, B. K., Perez, J. M. and Erhan, S. Z. (2007). Soybean oil-based lubricants: A search for synergistic antioxidants. *Energy Fuel*s, 21: 2408-2414.
13. Singh, C. P. and Chhibber, V. K. (2013). Chemical modification in karanja oil for biolubricant industrial applications. *Journal Drug Delivery Therapeutic*s, 3:117-122.
14. Borugadda, V. B. and Goud, V. V. (2013). Comparative studies of thermal, oxidative and low temperature properties of waste cooking oil and castor oil. *Journal Renewable Sustainable Energy,* 5: 063104.
15. Salimon, J. and Salih, N. (2009). Substituted esters of octadecanoic acid as potential biolubricants. *European Journal of Scientific Research*, 31(2): 273 – 227.
16. Moser, B. R. and Erhan, S. Z. (2007). Preparation and evaluation of a series of α-hydroxy ethers from 9, 10-epoxystreates. *European Journal Lipid Science Technology,* 109: 206-213

17. Salimon, J., Ahmed, W. A., Salih, N., Yarmo, M. A. and Derawi, D. (2015). Lubricity and tribological properties of dicarboxylic acids and oleyl alcohol based esters. *Sains Malaysiana,* 44(3): 405-412.
18. Wang, R. and Schuman, T. P. (2013). Vegetable oil-derived epoxy monomers and polymer blends: A comparative study with review. *eXPRESS Polymer Letters,* 7(3):272–292.
19. Meyer, P. P., Techaphattana, N., Manundawee, S., Sangkeaw, S., Junlakan, W. and Tongurai, C. (2008). Epoxidation of soybean oil and jatropha oil. *Thammasat International Journal Science Technology*, 13: 1-5.
20. Lathi, P. S. and Mattiasson, B. (2007). Green approach for the preparation of biodegradable lubricant base stock from epoxidised vegetable oil. *Applied Catalysis B: Environmental*, 69: 207-212.
21. Joseph, R., Madhusoodhanan, K. N., Alex, R., Varghese, S., George, K. E. and Kuriakose, B. (2014). Studies on epoxidised rubber seed oil as secondary plasticiser/stabiliser for polyvinyl chloride. *Plastics Rubber and Composites,* 33(5): 217-222.
22. Derawi, D. and Salimon, J. (2016). Sintesis sebatian hidroksi-eter minyak sawit olein. *Sains Malaysiana,* 45(5): 817-823.
23. Yunus, R., Razi, A. F., Iyuke T. L. and Idris, A. (2003). Preparation and characterization of trimethylolpropane esters from palm kernel oil methyl esters. *Journal of Oil Palm Research*, 15(2):42-49.
24. Sharma, B. K., Doll, K. M. and Erhan, S. Z. (2008). Ester hydroxy derivatives of methyl oleate: tribological, oxidation and low temperature properties. *Bioresource Technology*, 99: 7333-7340.
25. Salimon, J., Abdullah, B. M., Yusop, R. M., Salih, N. and Yousif, E. (2013). Synthesis and optimization ring opening of monoepoxide linoleic acid using *p*-toluenesulfonic acid. *SpringerPlus*, 2: 429.
26. Nor, M. N., Derawi, D. and Salimon, J. (2017). Chemical modification of epoxidized palm oil for biolubricant application. *Malaysian Journal of Analytical Sciences*, 21(6):1423-1431.
27. Nor, M. N., Derawi, D. and Salimon, J. (2018). The optimization of RBD palm oil epoxidation process using D-optimal design. *Sains Malaysiana*, 47(7):1359-1367.
28. Njoku, P. C., Egbukole, M. O. and Enenebeaku, C. K. (2010). Physio-chemical characteristics and dietary metal levels of oil from *Elaeis guineensis* species. *Pakistan Journal of Nutrition,* 9(2):137-140.
29. Nor, M. N., Salih, N. and Salimon, J. (2021). Optimization of the ring opening of epoxidized palm oil using D-optimal design. *Asian Journal of Chemistry*, 33(1):67-75.
30. Kuntom, A., Lin, S. W., Ai, T. Y., Idris, N. A., Yusof, M., Sue, T. T. and Ibrahim, N. A. (2004). MPOB test methods: A compendium of test on palm oil products, palm kernel products, fatty acids, food related products and others. MPOB, Bangi.
31. A.O.C.S. (1998). *Official Methods and Recommended Practices of AOCS*, AOCS, Illionis.
32. Nadkarni, R. A. (2007). Guide to ASTM test methods for the analysis of petroleum products and lubricants. ASTM International, West Conshohocken
33. Mungroo, R., Pradhan, N. C, Goud, V. V. and Dalai, A. K. (2008). Epoxidation of canola oil with hydrogen peroxide catalyzed by acidic ion exchange resin. *Journal of the American Oil Chemist Society*, 85:887-896.
34. Goud, V.V., Patwardhan, A.V. and Pradhan, N. C. (2006). Studies on the epoxidation of mahua oil (*Madhumica indica*) by hydrogen peroxide. *Bioresource Technology*, 97:1365-1371.
35. Goud, V.V., Patwardhan, A.V., Dinda, S. and Pradhan, N. C. (2007) Kinetics of epoxidation of *Jatropha* oil with peroxyacetic and peroxyformic acid catalysed by acidic ion exchange resin. *Chemical Engineering Science*, 62: 4065-4076.
36. Baumann, H., Buehler, M., Fochem, H., Hirsinger, F., Zoebelein, H. and Falbe, J. (1988). Natural fats and oils – renewable raw materials for the chemical industry. *Angewandte Chemie*, 27(1): 41-62.

37. Hwang, H. S. and Erhan, S. Z. (2001). Modification of epoxidized soybean oil for lubricant formulation with improved oxidative stability and low pour point. *Journal of the American Oil Chemist Society*, 78(12): 1179-1184.
38. Salimon, J., Abdullah, B. M., Yusop, R. M., Salih, N. and Yousif, E. (2013). Synthesis and optimization ring opening of monoepoxide linoleic acid using *p*-toluenesulfonic acid. *SpringerPlus*, 2: 429.
39. Pavia, D. L., Lampman, G. M., Kriz, G. S. and Vyvyan, J. R. (2009). Introduction of spectroscopy, Fourth edition. Cengage Learning, United States: pp. 51-52
40. Sharma, A., Adhvaryu, A., Liu, Z. and Erhan, S. Z. (2006). Chemical modification of vegetable oils for lubricant applications. *Journal of the American Oil Chemist Society*, 83:129-136.
41. Denicol Motor Oils N.V (2020). Denicol compressor oil. Access from https://pdf4pro.com/view/compressor-oil-iso-vg-32-46-68-100-150-denicol-5786bc.html. [Access online 25 December 2020].
42. SubsTech: Substances and Technologies (2012). SubsTech hydraulic oil. Access from http://www.substech. com /dokuwiki/doku.php? id=hydraulic_oil_iso_100 .[Access online 25 December 2020].

Malaysian Journal of Analytical Sciences (MJAS)
Published by Malaysian Analytical Sciences Society

THE REMOVAL OF BISPHENOL-A FROM SYNTHETIC WASTEWATER USING THIN-FILM COMPOSITE MEMBRANE

(Penyingkiran Bisfenol A daripada Sisa Air Sintetik Mengunakan Membran Lapisan Komposit Nipis)

Taofiq Damilare Aiyelabegan , Siti Nur Alwani Shafie, Shafiq Mohd Hizam, Nik Abdul Hadi Nordin*

Department of Chemical Engineering,
Universiti Teknologi PETRONAS, 32610 Seri Iskandar, Perak, Malaysia

**Corresponding author: nahadi.sapiaa@utp.edu.my*

Received: 22 August 2021; Accepted: 24 March 2022; Published: 27 June 2022

Abstract

In this study, the removal performance of bisphenol A (BPA) from synthetic wastewater using the forward osmosis method was compared between polyamide thin film composite membrane (PA -TFC) and polysulfone (PSf) membrane substrate. The thin-film composite membrane was prepared by using flat polysulfone (PSf) sheets as membrane substrate through in-situ interfacial polymerization technique. To generate the thin film surface on the PSf substrate, M-phenylenediamine (MPD) and 1,3,5-benzene trichloride (TMC) were utilized as monomers in aqueous and organic solutions, respectively. The BPA retention efficiency of the PSf and TFC membranes was examined and compared accordingly. The membranes were characterized by using atomic force microscopy (AFM), field emission scanning electron microscope (FESEM), Fourier transform infrared spectroscopy (FTIR), and contact angle analysis. The fabricated thin film on the PSf substrate membrane has enhanced its hydrophilicity which aids in wastewater treatment by increasing the membrane's water flow rate. A synthetic BPA wastewater solution of 100 mgL-1 was prepared to evaluate the performance of the membrane. Based on the finding of this study, the PSf substrate and PA -TFC membrane yielded 25% and 91% of BPA removal from the feed solution, respectively.

Keywords: bisphenol-a, polyamide, thin-film composite membrane, forward osmosis

Abstrak

Dalam kajian ini, penyingkiran bisfenol A (BPA) dari air sisa sintetik disiasat menggunakan membran filem komposit nipis poliamida (PA -TFC) dan dibandingkan dengan substrat membran polisulfon (PSf) menggunakan proses osmosis hadapan. Membran TFC diperbuat melalui teknik pempolimeran dengan menggunakan permukaan PSf sebagai substrat membran. M-fenildiamina (MPD) dan 1,3,5-benzena triklorida (TMC) digunakan sebagai monomer dalam larutan berair dan organik untuk menghasilkan permukaan filem nipis pada substrat PSf. Penyingkiran BPA melalui membran PSf dan TFC disiasat dan dibandingkan. Setiap membran dicirikan dengan mikroskopi tekanan atom (AFM), mikroskopi imbasan elektron pancaran medan (FESEM), spektroskopi inframerah transformasi Fourier (FTIR) dan analisa sudut sentuhan. Lapisan filem nipis yang dihasilkan pada membran substrat PSf meningkatkan daya hidrofiliknya, yang membantu dalam rawatan air sisa dengan meningkatkan kadar pengeluaran air. 100 ppm larutan sisa air BPA sintetik disediakan untuk menguji prestasi membran. Dari data yang diperoleh dari kajian ini, substrat PSf dan membran PA -TFC menghasilkan 25% dan 91% penurasan BPA dari sisa tersebut.

Kata kunci: bisfenol a, poliamida, membran filem komposit nipis, osmosis hadapan

Introduction

The rapid growth and development of modern industries have led to serious environmental issues nowadays. The threats posed by organic micropollutants especially pharmaceutically active and endocrine-disrupting compounds have been of great concern over the previous years. Numerous studies have been performed on investigating their removal mechanism from the wastewater [1]. These compounds are highly related to the effluents of industrial sectors such as pharmaceutical, plastic, dye and textiles, oil refineries, and petrochemical industries [2]. Industrial wastewater treatment plant (WWTP) effluent is an important source of these compounds, as these micropollutants are hardly removed by the conventional treatment processes [3, 4]. Thus, advanced membrane treatment of WWTP effluents to remove these pollutants could be an effective approach to reduce their presence in the ecosystem and thus contribute to mitigating the environmental risk.

Bisphenol-A (BPA) is an endocrine disruptor that is commonly utilized in the manufacturing of polycarbonate, epoxy resins, dental composites, and medical equipment [5]. This organic pollutant has huge potential to cause serious health hazards to humans, wildlife, and the ecosystem even at low concentrations [6, 7]. Structurally, BPA consists of phenolic and hydroxyl groups in combination with an aromatic ring. BPA has a molecular weight of 228 g/mol and shows relatively low solubility in water with the range of 120-300mg/L at 25 ^{o}C [8]. However, its solubility increases if dissolved in polar organic solvents or aqueous solutions with alkaline concentrations. The total daily intake (TDI) of BPA has been regulated at 50µg/kg/day, while the oral reference dosage for BPA has been set at 100 µg/L as the maximum allowable concentration in drinking water according to the United States Environmental Protection Agency [9].

BPA can cause adverse health effects because it is an endocrine disruptor that binds to receptors in living organisms [38]. BPA acts as a hormone receptor blocker for various hormones and interferes with their activity which leads to damage to the human body. For instance, it acts as an antiestrogen by competing with endogenous E and inhibiting its estrogenic response [10]. Previous laboratory studies reported that this compound may also bind directly to the sex hormone receptors (androgen receptors) and inhibit the activity of endogenous androgen [11]. These hormone-inhibiting effects may lead to fertility problems such as decreased sperm quality, polycystic ovary syndrome, and sex hormone concentrations. Increases in chronic diseases such as type 2 diabetes, obesity, cardiovascular disease, prostate, and breast cancer have been linked to early exposure to BPA [12]. In addition, there is a high probability that maternal exposure to BPA can cause postnatal abnormalities in DNA methylation status, disrupting the expression of some particular genes and the epigenetic programming of gene expression during child development [13]. Due to their widespread dispersion in the environment and continuous usage in industry, it is critical to develop new treatment techniques for their degradation, detoxification, and removal in wastewater effluents.

Concentrative processes such as absorption, ozonation, and Fenton have effectively removed the major microbial contaminants and chemicals from wastewater treatment facilities. However, the application of these techniques for the removal of endocrine disruptors is restricted [14, 15, 16]. In addition, due to stringent water quality requirements, it is becoming increasingly important to remove BPA from water sources, even if it presents in extremely low concentrations. Pressure-driven membrane separation methods such as reverse osmosis (RO), nanofiltration (NF), ultrafiltration (UF), and microfiltration (MF) in pore sizes ascending order, have been demonstrated to be effective in removing BPA from wastewater and producing high-quality water from WWTP secondary effluent [17]. According to Schrotter et al., membrane technology has been utilized to treat approximately 60 million m^3 of water per day, with RO being the most widely used membrane process for wastewater treatment. Meanwhile, microfiltration and ultrafiltration have a combined average capacity of 20 million m^3 per day, accounting for 60% of total drinking water production [17].

Unlike chemical oxidation and biodegradation, membrane filtration does not utilize chemicals or

generate by-products/new metabolites, making it more suitable for treating drinking water due to its environmentally friendly's characteristic [17]. The membrane process uses a variety of mechanisms to remove micropollutants from wastewater. For example, BPA removal in NF and RO is performed by sieving and electrostatic interactions, while the removal mechanism in MF and UF is generally based on the adsorption process [18, 19]. When compared to traditional techniques, the employment of membrane separation processes has numerous advantages: low energy cost, easy operational control, no use of chemicals, and compact structure with possible material recovery [20].

Zhao et al. examined the removal of BPA using a commercial UF hollow fibre membrane at a dosage of 1000 µg/L. Due to the large pore size of the UF membrane (0.04 microns), the BPA removal efficiency was found to be < 5%. The removal approach applied the adsorption mechanism of the membrane rather than the size exclusion technique [21]. The UF-Koch membrane was tested for the removal performance of BPA at the concentration of 1µM. This membrane showed significant retention efficiency of BPA (> 40%), which was attributed to the adsorption process on the membrane surface [22]. Bing-Zhi et al. [2010] investigated the removal of BPA from wastewater using a commercial MF membrane. They found that this membrane showed poor BPA retention performance, with the removal rate decreasing from 95% to 20% at the end of the filtration process as the membrane got saturated with BPA [23].

Yuskel et al. observed that the RO and NF membranes performed well when tested for removing BPA from synthetic wastewater at a concentration of 50 mg/L with an operating pressure of 10 bar. The NF membranes made of compressed and loose polyamide were used in the experiment. A polyamide and cellulose acetate RO membrane was also tested. The dense RO and NF membranes demonstrated excellent BPA removal (> 98%), while the loose NF membrane demonstrated much lower rejection (80%), and the cellulose acetate RO membrane demonstrated low rejection of BPA of 10-40%, which was attributed to BPA adsorption on the membrane surface [24]. These technologies, however, fall short because they are particularly susceptible to membrane fouling, have large pore sizes (MF and UF), and rely on high pressure to work [17].

Forward osmosis (FO) is an alternative membrane filtration process that has been utilized in recent decades for desalination, wastewater treatment, and production of high-quality water. The FO method uses the osmotic differential pressure between the draw and feed solutions to reject the trace organic pollutants. [25]. This process has a great advantage over the conventional membrane filtration process as it does not require the application of hydraulic pressure to operate, and fouling propensity is minimal due to the generation of osmotic pressure from the concentrated draw solution [26]. Even when fouling occurs, it can easily be reversed and controlled via chemical, physical, or physiochemical cleanings unlike the RO and NF methods [27, 28].

Presently, there have been advancements in the type of membranes fabricated using interfacial polymerization (IP) that can be used with the forward osmosis process, such as the thin film composite and thin film nano-composite membranes. these membranes are controlled by the osmotic pressure of water and are usually utilized in the wastewater separation and desalination processes in pharmaceuticals and chemical industries [29]. TFC membranes are believed to be a viable method for eliminating tiny organic contaminants such as BPA from industrial and pharmaceutical effluents since they are modified to have smaller pore sizes as compared to RO, NF, and UF membranes. Nowadays, TFC membranes made from modifying a thin-film layer of aromatic polyamide on a porous membrane substrate are employed in wastewater treatment operations [30, 31]. The greater retention of feed solution components, along with an increase in permeate flow has led to their widespread adoption. TFC membranes can remove heavy metals, organic micropollutants such as pharmaceuticals, endocrine disruptors, and pesticides from wastewater [17]. In general, polyamide membranes have been reported in the literature that they performed better than cellulose acetate-based membranes in rejecting organic micropollutants. This is because they have lower pressure requirements and operate under more flexible settings [32].

Thus, the goal of this study is to determine if employing a thin-film composite membrane to remove BPA from pharmaceutical effluent is more feasible and efficient than using conventional polysulfone substrates. The interfacial polymerization method was used to fabricate the TFC membrane on the polysulfone membrane substrate layer. Both membranes' efficiency in removing BPA from the synthetic wastewater was compared in this study.

Materials and Methods

Materials and reagents

Bisphenol A (BPA), polysulfone (PSf), polyvinylpyrrolidone (PVP), N-methyl-2-pyrrolidinone (NMP), M-phenylenediamine (MPD), 1,3,5-benzenecarbon trichloride (TMC) were procured from Sigma Aldrich Chemicals Company. These materials were all of the analytical grades and were used exactly as they were received. All of the experiments were conducted using distilled water.

Forward osmosis membrane fabrication: Membrane substrate preparation (Psf substrate)

The wet phase inversion method was used to prepare the PSf membrane substrate. Firstly, a dope solution with the composition of PSf/NMP/PVP (wt.%) = (15/82/3) was prepared. The NMP was then dissolved in PSf pellets, and PVP was added as an additive to increase the porosity of the membrane substrate. The casting solution was continuously stirred until the polysulfone pellets were completely dissolved in the solution. The dock solution was then poured on the glass surface with a 200µm casting rod. The casted membrane on the glass surface was instantly submerged in a water bath for the wet phase inversion. The generated PSf support membrane was kept in distilled water before use.

Thin-film composite membrane fabrication

The thin-film polyamide layer was fabricated by using the interfacial polymerization method as shown in Figure 1. Two solutions were prepared: an aqueous solution comprising of 2 wt.% MPD in distilled water and an organic solution comprising of 0.05 wt.% TMC dissolved in heptane. The PSf membrane substrate was immersed in the MPD solution for 3 minutes. After that, a thin-film polyamide layer was formed by carefully pouring the TMC solution on top of the membrane for 3 minutes. The generated Polyamide Thin-Film Composite (PA-TFC) membranes were stored in distilled water and kept at room temperature before use.

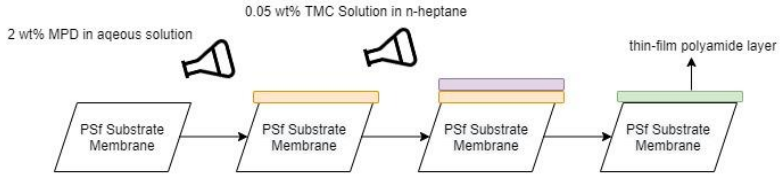


Figure 1. Preparation of polyamide TFC layer via interfacial polymerization method

Characterization of the PA-TFC FO membrane: Morphological Analysis

The morphological structures including top surface and cross-section of the PSf substrate and PA -TFC membrane were examined using field emission scanning electron microscopy (FESEM, Zeiss, supra 55VP, 12-2,000,000x). The samples were then further examined using a Zeiss Supra V55 microscope.

Contact angle analysis

The contact angle of the membranes was measured at room temperature with a GSPJ-360 goniometer and distilled water was used as the measuring liquid. When water was dropped onto the membrane's surface, the CA was instantaneously calculated and recorded. To reduce experimental errors, 10 measurements were conducted at random points on the membrane surface, and the average CA was calculated.

Fourier-transform infrared spectroscopy

An infrared spectroscope (Perkin Elmer, Frontier 01) with a range of 550-4000 cm^{-1} was used to investigate the chemical changes on the membrane surface before and after the TFC treatment. FTIR spectroscopy was used to detect the active polyamide layer as well as other functional groups.

Atomic force microscopy analysis

The surface roughness of the membrane was measured using an AFM (Hitachi AFM500II). The membrane samples were cut into sections of 5 cm × 5 cm. The samples were then mounted on the device for AFM investigation using a metal block.

Preparation of the Synthetic Wastewater and Determination of the PA-TFC Performance

Due to BPA's insolubility in water, a working feed solution with a concentration of 100 mgL^{-1} was prepared by dissolving the prescribed amount of BPA in a small amount of methanol before it was introduced to the experimental feed solution. The solution was then stirred at 120 ºC with a magnetic stirrer until the BPA particles were completed dissolved. The draw solution consisted of 4M NaCl. The active layer of the membrane was positioned toward the feed solution.

The forward osmosis experiment was conducted according to the setup as shown in Figure 2. The initial quantities of the feed and draw solutions were 500 and 800 mL, respectively. The draw and feed solutions were interacting directly with each other through the membrane module. The temperature of both solutions was maintained at room temperature. Membrane orientation was kept on AL-FS mode to mitigate the fouling effect [14]. The feed and draw solutions were recirculated in co-current mode to the membrane module at 200 mL/min using a BT600M dual-channel pump. The feed solution was placed on a precision balance (Huazhi Scientific Instrument HZK-3102) to record the weight variations associated with the water flux calculation. The precision weight balance was linked to a computer for data logging via the Serial-Port-to-Keyboard software provided by Huazhi Scientific Instrument. The samples were taken at predetermined intervals, and the concentrations of the feed and draw solutions were measured using a UV-Vis spectrophotometer. Each of the experiments was conducted twice in order to ascertain the accuracy and precision of the results.

Water permeation flux, J_w *in* L/m^2h was calculated using the change in weight of the feed solution over time and the membrane area, A_m(m^2) as shown in equation (1):

$$J_w = \frac{\Delta w}{A_m \Delta t} \quad (1)$$

Δw = The recorded weight change of the feed solution, and Δt(h) = Experimental test time

Equation (2) is used to calculate BPA rejection in the FO process

$$R\ (\%) = \frac{(C_i - C_f)}{C_f} \times 100\% \quad (2)$$

where, R = The rejection percentage of BPA, C_i = Concentration of BPA in the feed solution at the start of the experiment (mg/L), and C_f = Final concentration of BPA in the draw solution after the experiment (mg/L).

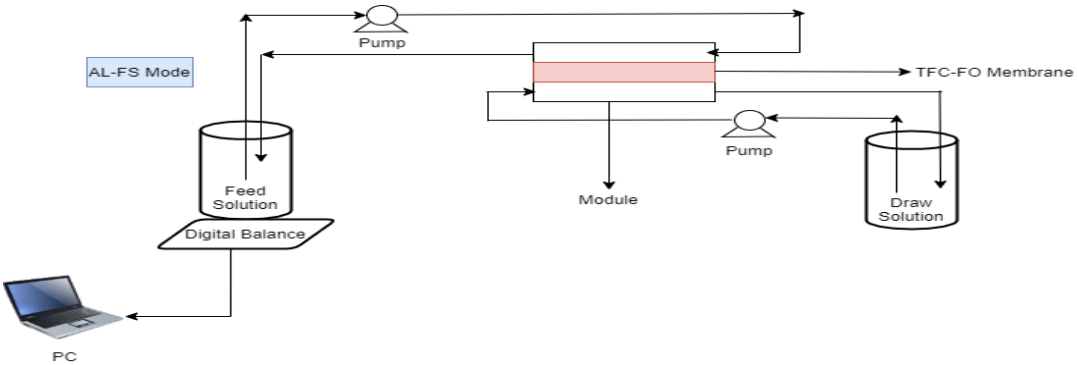


Figure 2. Illustration diagram of the forward osmosis setup (AL-FS mode)

Results and Discussion

Morphological analysis (FESEM)

The morphological structures of the surface and cross-section of the PA-TFC membrane were examined using FESEM (Zeiss, supra 55VP). In addition, the FESEM images were used to confirm the presence of the selective layer (PA layer) on top of the PSF membrane substrate. As depicted in Figure 3a, the thin polyamide layer can be seen on top of the PSf membrane substrate, which contains dense and porous layers. The denser layer of the membrane was found on top of the porous support layer, and it was believed to be a polyamide thin-film layer formed via interfacial polymerization. This morphological evidence indicates that the membrane's rejection capability is improving while its permeability is decreasing [33]. According to Khorshidi et al., one disadvantage of the denser layer of the membrane is the low water flow, and the only option to address this issue is for the dense layer to be extremely thin. The PA selective layer as depicted in Figure 3a was estimated to be roughly 4.4µm thick, which is sufficient because the typical thickness of PA thin film is around 200nm. The thickness of the PA layer is proportional to the concentration of TMC, which best explains the formation of the PA layer because low TMC concentrations were used in the preparation of the membrane (0.05%) [30].

There is a difference in the membrane surface appearance between the PSf and PA-TFC membranes, as shown by the FESEM surface images in Figures 3(b) and 3(c). The PSf substrate has a smooth and porous surface, but the PA-TFC membrane has a ridge-and-valley structure that results in a rough surface texture, as shown in Figure 3(b). The PSf membrane substrate has a porous structure with long finger-like pores formed under a thin sponge-like layer, making it excellent for FO membranes to minimize the structural parameters. The polyamide layer produced in this study has a ridge-valley structure, which is typical of TFC polyamide membranes prepared with the monomers MPD and TMC [34]. Miao et al. found that the ridge-and-valley structure is a significant indicator of the formation of the polyamide layer on the PSf membrane [35].

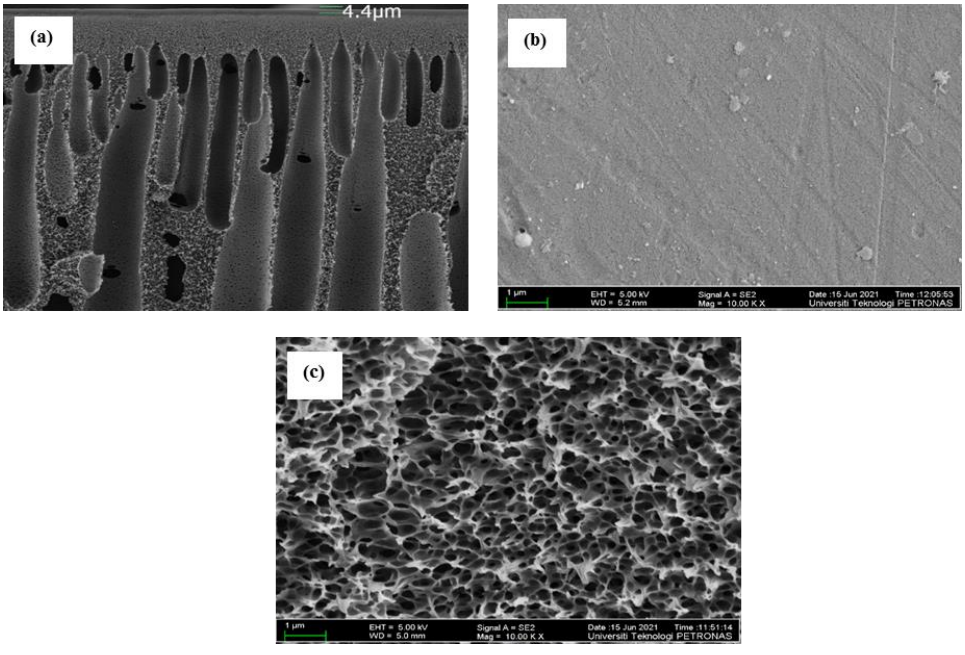


Figure 3. FESEM top surface morphologies of (a) cross section images of the PA-TFC membrane, surface images of (b) Polysulfone substrate and (c) Polyamide-TFC membrane

Fourier-transform infrared spectroscopy studies

The top surface of the modified PA-TFC membrane and Polysulfone substrate layer was analyzed using FTIR to examine the chemical compositions. Figure 4 shows the IR spectra of the Polysulfone and PA-TFC membrane. The transmittance peak at wavelengths of 1150 cm-1 (O-S-O stretching), 1243 cm-1 (C-O-C stretching) and 1106 cm-1 (S=O stretching) are the characteristics of sulfone group. Also, the absorption at 1013 and 833 cm-1 are assigned to the C-H stretching of the polysulfone aromatic rings. The peaks at 1605, 1538, 1486, 1247, 997 and 750 cm-1 are attributed to C=O of the amide linkage, O-H bending of the carboxylic acid, C-H bending, C-N stretching, C=O stretching and C-Cl stretching, respectively. These observations indicate the formation of polyamide layer on the polysulfone substrate. The absorbance at 3320 cm-1 suggests the N-H stretching of the amine functional group, indicating that the polyamide structure was formed through the interfacial polymerization of MPD and TMC [36].

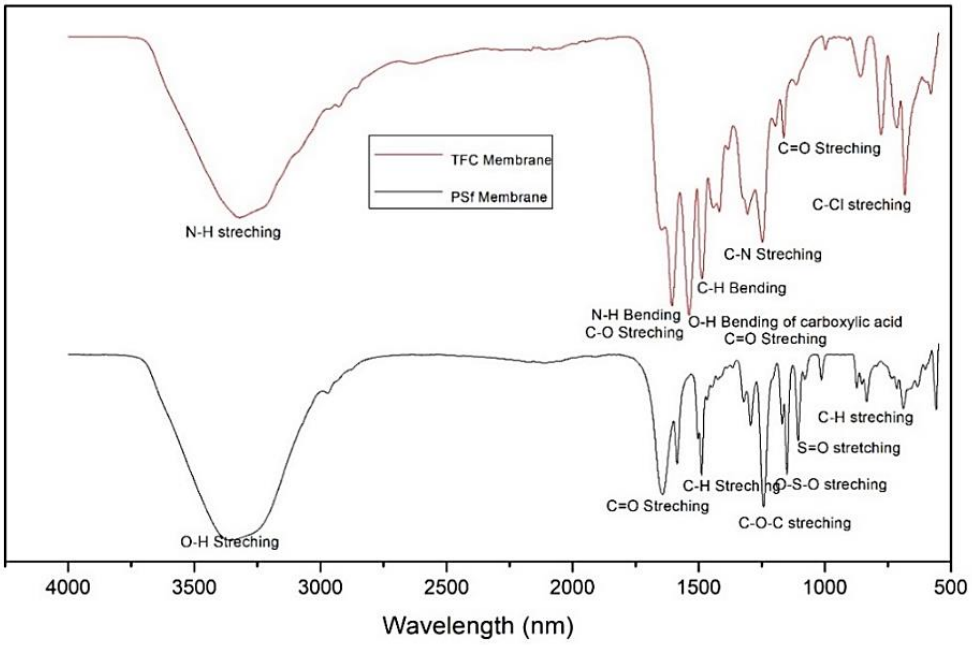


Figure 4. FTIR Spectra of PA-TFC and PSf membranes

Atomic force microscopy

The AFM was utilized to examine the surface morphology of polyamide layer (Figure 5). The three-dimensional images show the PSf substrate and the coated TFC-PA membrane via interfacial polymerization with different top surface roughness. The PSf membrane has a smooth surface with a root mean square (RMS) value of 4.5nm while the TFC-PA membrane has a higher root mean square value of 20.76 nm with increased surface roughness. This is because the polyamide layer was effectively polymerized over the porous PSf substrate layer [37]. The polymerization of the PA layer results in increased ridge-and-valley microstructure, raising the surface roughness value to 20.76nm. The increased surface roughness of the TFC membrane was also attributable to nodules generated on its surface as a result of MPD and TMC interaction. The advantage of having a higher surface roughness on the TFC membrane is that it will have a larger surface area for water to interact, resulting in a higher water flux performance for the membrane [38]. Morgan's theory states that the membrane roughness is related to the heterogeneity of different reactions between the amide and diacid chloride reactions following the initial formation of the Polyamide film [39].

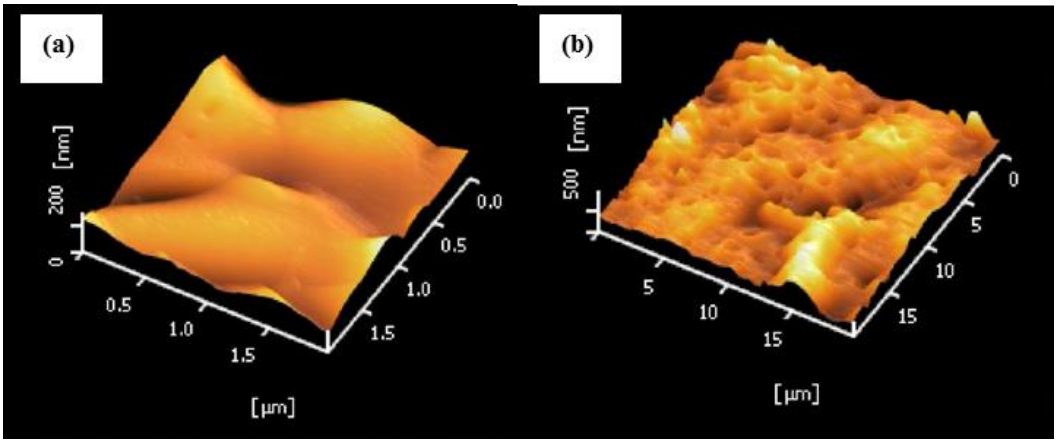


Figure 5. AFM surface morphology of (a) Polysulfone membrane substrate and (b) the thin-film composite membrane

Contact angle test

The contact angle of a membrane is one of its most important physical characteristics since it reveals its hydrophilicity and fouling susceptibility. An ideal membrane should be hydrophilic with high water flow rate and low fouling properties. The contact angle of the PSf substrate and the TFC membrane was assessed using a goniometer to determine their hydrophilicity. Figure 6 shows that the average contact angle for both membranes was less than 90^{o}, which indicates its hydrophilicity. The hydrophilicity of the TFC membrane (36.04^{o}) is higher than that of the PSf membrane (65.57^{o}), indicating that more amide groups are generated on the TFC membrane surface. TFC membranes have lower contact angle values because the polyamide layer structure contains strong polar amide functional groups that are hydrophilic in nature [40]. The presence of the pendant carboxylic acid groups inside the main chain has contributed to the increased hydrophilicity of the TFC membrane [33]. The TFC membrane thickened as the interfacial polymerization reaction time increased, contributing to its dense structure. This also explains why the contact angle of TFC membrane is decreasing [34].

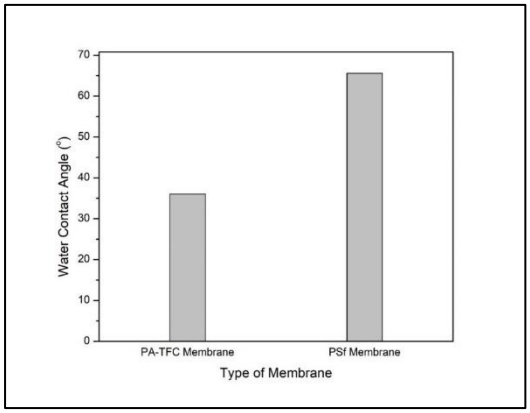


Figure 6. Comparison of contact angle values between PA-TFC and PSf membranes

Water permeability flux

The water flux change between TFC and PSf membrane was examined (Figure 7). Permeate flow is known to be highly related to membrane pore size, hence the increase in water flux in PSf substrate was expected. TFC membranes have a low water flux because of their dense structure, which obstructs water flow and hence reduces the water flux value across the membrane [29]. In addition, it is worth noting that a denser active layer offers better rejection and lower fouling propensity [41].

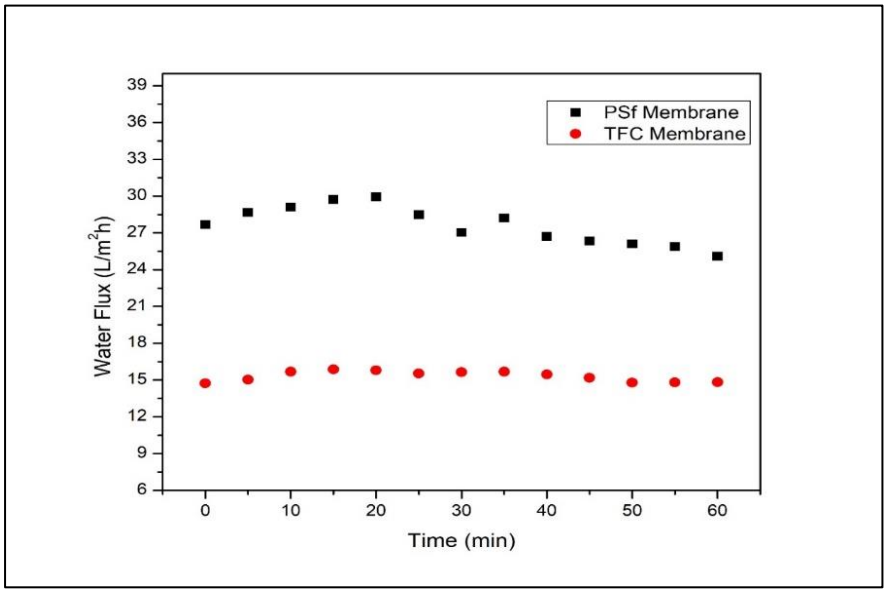


Figure 7. Water flux of FO with the model solution and pure water as feed (experimental conditions: AL-FS, 4M NaCl as DS

BPA removal

The retention of BPA was investigated utilizing both the PA-TFC and PSf membranes, and the results were compared accordingly. Figure 8 demonstrates that the overall rejection of BPA was within the range of 91% with the membrane orientation mode at AL-FS, whereas the PSf membrane yielded a rejection of 25%. The thin-film active layer produced on the membrane substrate was predicted to increase the retention capacity of TFC forward osmosis membrane. The thin-film layer which has a higher ridge-and-valley microstructure, entraps the BPA at the active layer. BPA rejection of more than 90% suggested that its pore size is substantially smaller than BPA particle size, which explains the high removal from the feed solution. The dense top coating of the TFC membrane was believed to have contributed to the significant BPA rejection due to its excellent substance retention properties [29, 34]. The result shows that the thin-film composite membrane fabricated through the IPIS method can be used to remove BPA from industrial and pharmaceutical wastewaters.

In terms of the forward osmosis rejection efficiency of BPA, the result from this study is slightly higher than the values reported by Zhu et al. (approx. 80%) [42], Hancock et al. (approx. 70%) [43] and Linares et al. (approx. 49%) [44]. These above-mentioned studies were basically carried out using the cellulose triacetate forward osmosis membranes. The interfacial polymerization of the polyamide layer on the polysulfone substrate could improve the BPA rejection by FO according to the findings of this study and comparisons with earlier research. This modification will enhance hydrophilicity, increase substance rejection from feed solution, and maintain the highest possible flow rates [29].

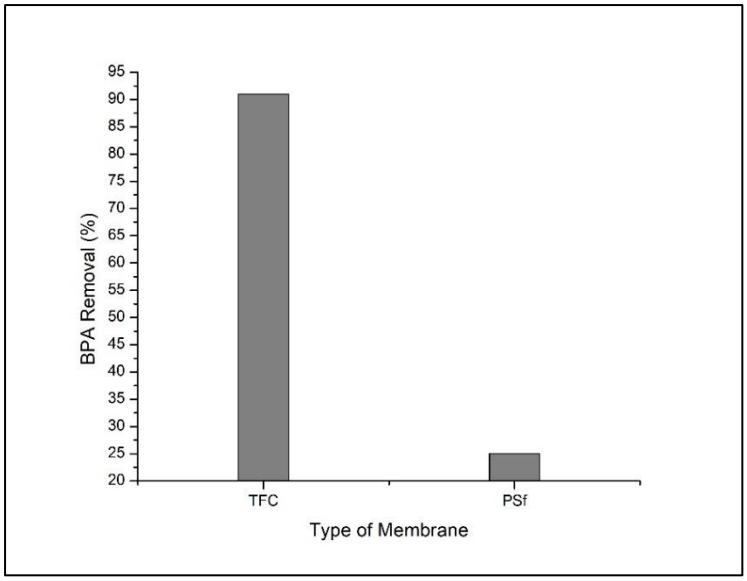


Figure 8. Rejection of BPA by PA-TFC and PSf membrane

Conclusion

This study assessed the effectiveness of a successfully fabricated PA-TFC membrane on a polysulfone membrane substrate using the interfacial polymerization method. Both membranes were examined and compared for their retention performance of bisphenol-A from a synthetic wastewater solution of 100mg/L using the forward osmosis process. The polyamide-based membrane performed well with a retention efficiency of 91%, whereas the polysulfone membrane retained just approximately 25%. The performance results of both membranes indicate that the fabricated membrane appears to be more promising and provides greater BPA retention than the polysulfone membrane substrate using the forward osmosis technique. It can be used to treat pharmaceutical and industrial wastewaters, which primarily contain small organic pollutants like phenols that are difficult to remove using other conventional or membrane treatment processes.

Acknowledgement

This research work was supported by the Yayasan Universiti Teknologi PETRONAS (Grant No: 015MD0-056) research grant. In addition, the authors thankfully acknowledge the support from the Centralized Analytical Lab (CAL) and the technical assistance offered by the Chemical Engineering Department throughout the experimental work.

References

1. Li, J., Liu, Q., Liu, Y. and Xie, J. (2017). Development of electro-active forward osmosis membranes to remove phenolic compounds and reject salts. *Environmental Science: Water Research & Technology*, 3(1): 139-146.
2. Silva, C. P., Otero, M. and Esteves, V. (2012). Processes for the elimination of estrogenic steroid hormones from water: A review. *Environmental Pollution*, 165: 38-58.
3. Xiao, M., Zhou, J., Tan, Y., Zhang, A., Xia, Y. and Ji, L. (2006). Treatment of highly-concentrated phenol wastewater with an extractive membrane reactor using silicone rubber. *Desalination*, 195(1-3): 281-293.

4. Mohammadi, S., Kargari, A., Sanaeepur, H., Abbassian, K., Najafi, A. and Mofarrah, E. (2015). Phenol removal from industrial wastewaters: a short review. *Desalination and Water Treatment*, 53(8): 2215-2234.
5. Huang, Y. Q., Wong, C. K. C., Zheng, J. S., Bouwman, H., Barra, R., Wahlström, B., Neretin, L., & Wong, M. H. (2012). Bisphenol A (BPA) in China: A review of sources, environmental levels, and potential human health impacts. *Environment International*, 42: 91-99.
6. Kumar, A., Gupta, K., Tomer, V., Kaur, A., & Kumar, V. (2018). Bisphenols as human health hazard: A systematic review on potent sources, route of exposure, harmful effects and safe alternatives. *Toxicology International*, *25*(1): 78–-92.
7. Katibi, K. K., Yunos, K. F., Man, H. C., Aris, A. Z., Mohd Nor, M. Z. and Azis, R. S. (2021). Recent advances in the rejection of endocrine-disrupting compounds from water using membrane and membrane bioreactor technologies: A review. *Polymers*, 13(3): 392.
8. Tsai, W. T. (2006). Human health risk on environmental exposure to bisphenol-A: A review. *Journal of Environmental Science and Health - Part C Environmental Carcinogenesis and Ecotoxicology Reviews*, *24*(2), 225-255.
9. Rubin, B. S. (2011). Bisphenol A: An endocrine disruptor with widespread exposure and multiple effects. *Journal of Steroid Biochemistry and Molecular Biology*, 127(1–2): 27-34.
10. Viñas, R., Jeng, Y. J. and Watson, C. S. (2012). Non-genomic effects of xenoestrogen mixtures. *International Journal of Environmental Research and Public Health*, 9(8): 2694-2714.
11. Zoeller, R. T., & Belcher, S. M. (2007). In vitro molecular mechanisms of bisphenol A action. *Reproductive Toxicology*, 24(2): 178-198.
12. Rochester, J. R. (2013). Bisphenol A and human health: A review of the literature. *Reproductive Toxicology*, 42: 132-155.
13. Kundakovic, M. and Champagne, F. A. (2011). Epigenetic perspective on the developmental effects of bisphenol A. *Brain, Behavior, and Immunity*, 25(6): 1084-1093.
14. Chen, H. W., Liang, C. H., Wu, Z. M., Chang, E. E., Lin, T. F., Chiang, P. C. and Wang, G. S. (2013). Occurrence and assessment of treatment efficiency of nonylphenol, octylphenol and bisphenol-A in drinking water in Taiwan. *Science of the Total Environment*, 449: 20-28.
15. Kleywegt, S., Pileggi, V., Yang, P., Hao, C., Zhao, X., Rocks, C., Thach, S., Cheung, P. and Whitehead, B. (2011). Pharmaceuticals, hormones and bisphenol A in untreated source and finished drinking water in Ontario, Canada - Occurrence and treatment efficiency. *Science of the Total Environment*, 409(8): 1481-1488.
16. Sodré, F. F., Locatelli, M. A. F. and Jardim, W. F. (2010). Occurrence of emerging contaminants in Brazilian drinking waters: A sewage-to-tap issue. *Water, Air, and Soil Pollution*, 206(1–4): 57-67.
17. Muhamad, M. S., Salim, M. R., Lau, W. J. and Yusop, Z. (2016). A review on bisphenol A occurrences, health effects and treatment process via membrane technology for drinking water. *Environmental Science and Pollution Research*, 23(12): 11549-11567.
18. Yüksel, S., Kabay, N. and Yüksel, M. (2013). Removal of bisphenol A (BPA) from water by various nanofiltration (NF) and reverse osmosis (RO) membranes. *Journal of Hazardous Materials*, 263: 307-310.
19. Mehwish, N., Kausar, A. and Siddiq, M. (2014). Advances in Polymer-based Nanostructured Membranes for Water Treatment. *Polymer - Plastics Technology and Engineering*, 53(12): 1290-1316.
20. Kim, I. C. And Lee, K. H. (2003). Effect of various additives on pore size of polysulfone membrane by phase-inversion process. *Journal of Applied Polymer Science*, 89(9): 2562-2566.
21. Zhao, F. B., Tang, C. C., Liu, X. Y., Shi, F. J., Song, X. R., Tian, Y. and Li, Z. S. (2015). Transportation characteristics of bisphenol A on ultrafiltration membrane with low molecule weight cut-off. *Desalination*, 362: 18-25.

22. Heo, J., Flora, J. R. V., Her, N., Park, Y. G., Cho, J., Son, A. and Yoon, Y. (2012). Removal of bisphenol A and 17β-estradiol in single walled carbon nanotubes-ultrafiltration (SWNTs-UF) membrane systems. *Separation and Purification Technology*, 90: 39-52.
23. Bing-zhi, D., Hua-qiang, C., Lin, W., Sheng-ji, X. and Nai-yun, G. (2010). The removal of bisphenol A by hollow fiber microfiltration membrane. *Desalination*, 250(2): 693-697.
24. Yüksel, S., Kabay, N. and Yüksel, M. (2013). Removal of bisphenol A (BPA) from water by various nanofiltration (NF) and reverse osmosis (RO) membranes. *Journal of Hazardous Materials*, 263: 307-310.
25. Lutchmiah, K., Verliefde, A. R. D., Roest, K., Rietveld, L. C. and Cornelissen, E. R. (2014). Forward osmosis for application in wastewater treatment: A review. *Water Research*, 58: 179-197.
26. Cartinella, J. L., Cath, T. Y., Flynn, M. T., Miller, G. C., Hunter, K. W. and Childress, A. E. (2006). Removal of natural steroid hormones from wastewater using membrane contactor processes. *Environmental Science and Technology*, 40(23): 7381-7386.
27. Lee, S., Boo, C., Elimelech, M. and Hong, S. (2010). Comparison of fouling behavior in forward osmosis (FO) and reverse osmosis (RO). *Journal of Membrane Science*, 365(1-2): 34-39.
28. Mi, B. and Elimelech, M. (2010). Organic fouling of forward osmosis membranes: Fouling reversibility and cleaning without chemical reagents. *Journal of Membrane Science*, 348(1-2): 337-345.
29. Adamczak, M., Kamińska, G. and Bohdziewicz, J. (2019). Preparation of polymer membranes by in situ interfacial polymerization. *International Journal of Polymer Science*, 2019: 6217924.
30. Khorshidi, B., Thundat, T., Fleck, B. A. and Sadrzadeh, M. (2016). A novel approach toward fabrication of high performance thin film composite polyamide membranes. *Scientific Reports*, 6(1): 1-10.
31. Al-Hobaib, A. S., El Ghoul, J., Ghiloufi, I. and El Mir, L. (2016). Synthesis and characterization of polyamide thin-film nanocomposite membrane reached by aluminum doped ZnO nanoparticles. *Materials Science in Semiconductor Processing*, 42: 111-114.
32. Mehwish, N., Kausar, A. and Siddiq, M. (2014). Advances in polymer-based nanostructured membranes for water treatment. *Polymer - Plastics Technology and Engineering*, 53(12): 1290-1316.
33. Wei, J., Qiu, C., Tang, C. Y., Wang, R. and Fane, A. G. (2011). Synthesis and characterization of flat-sheet thin film composite forward osmosis membranes. *Journal of Membrane Science*, 372(1–2): 292–302.
34. Syahida Mat Anan, N., Jaafar, J., Sato, S. and Mohamud, R. (2021). Titanium dioxide incorporated polyamide thin film composite photocatalytic membrane for bisphenol a removal. *IOP Conference Series: Materials Science and Engineering*, 1142(1): 012015.
35. Miao, L., Jiang, T., Lin, S., Jin, T., Hu, J., Zhang, M. and Liu, G. (2020). Asymmetric forward osmosis membranes from p-aramid nanofibers. *Materials & Design*, 191: 108591.
36. El-Arnaouty, M. B., Abdel Ghaffar, A. M., Eid, M., Aboulfotouh, M. E., Taher, N. H. and Soliman, E.-S. (2018). Nano-modification of polyamide thin film composite reverse osmosis membranes by radiation grafting. *Journal of Radiation Research and Applied Sciences*, 11(3): 204-216.
37. Park, H. M., Takaba, H., & Lee, Y. T. (2020). Preparation and characterization of TFC NF membrane with improved acid resistance behavior. *Journal of Membrane Science*, 616: 118620.
38. Song, X., Qi, S., Tang, C. Y. and Gao, C. (2017). Ultra-thin, multi-layered polyamide membranes: Synthesis and characterization. *Journal of Membrane Science*, 540: 10-18.
39. Morgan, P. W. and Kwolek, S. L. (1996). Interfacial polycondensation. II. Fundamentals of polymer formation at liquid interfaces. *Journal of Polymer Science Part A: Polymer Chemistry*, 40(137): 299-327.
40. Rajaeian, B., Rahimpour, A., Tade, M. O. and Liu, S. (2013). Fabrication and characterization of polyamide thin film nanocomposite (TFN) nanofiltration membrane impregnated with TiO_2 nanoparticles. *Desalination*, 313: 176-188.

41. McGinnis, R. L., Hancock, N. T., Nowosielski-Slepowron, M. S. and McGurgan, G. D. (2013). Pilot demonstration of the NH_3/CO_2 forward osmosis desalination process on high salinity brines. *Desalination*, 312: 67-74.
42. Zhu, H. and Li, W. (2013). Bisphenol A removal from synthetic municipal wastewater by a bioreactor coupled with either a forward osmotic membrane or a microfiltration membrane unit. *Frontiers of Environmental Science and Engineering*, 7(2): 294-300.
43. Hancock, N. T., Xu, P., Heil, D. M., Bellona, C. and Cath, T. Y. (2011). Comprehensive bench- and pilot-scale investigation of trace organic compounds rejection by forward osmosis. *Environmental Science and Technology*, 45(19): 8483-8490.
44. Valladares Linares, R., Yangali-Quintanilla, V., Li, Z. and Amy, G. (2011). Rejection of micropollutants by clean and fouled forward osmosis membrane. *Water Research*, 45(20): 6737-6744.

Malaysian Journal of Analytical Sciences (MJAS)
Published by Malaysian Analytical Sciences Society

CONSTRUCTING NI-DOPED ZnO/GO HETEROSTUCTURES FOR ENHANCED SUNLIGHT-TRIGGERED DEGRADATION OF METHYLENE BLUE DYE

(Pembinaan Heterostruktur Ni-Didop dengan ZnO/GO untuk Meningkatkan Degradasi Pewarna Metilina Biru di Bawah Sinar Matahari)

Hartini Ahmad Rafaie[1,5]*, Nur Shafiza Ismail[1], Syazni Hanun Nur Ili Dedy Dasiano[2,4], Muhd Firdaus Kasim[3], Nurul Infaza Talalah Ramli[1], Zul Adlan Mohd Hir[1], Mohomad Hafiz Mamat[4]

[1]Faculty of Applied Science,
Universiti Teknologi MARA Pahang, 26400 Bandar Tun Abdul Razak Jengka, Pahang, Malaysia
[2]Faculty of Applied Sciences
[3]Center for Nanomaterials Research, Institute of Science
[4]NANO-Electronic Centre, Faculty of Electrical Engineering
Universiti Teknologi MARA, 40450 Shah Alam, Selangor, Malaysia
[5]Centre of Foundation Studies,
Universiti Teknologi MARA, Selangor Branch, Dengkil Campus, 43800 Dengkil, Selangor, Malaysia

**Corresponding author: hartinirafaie@uitm.edu.my*

Received: 15 November 2021 ; Accepted: 3 February 2022 ; Published: 27 June 2022

Abstract

Chemical pollutants emitted by the textile industry are a major source of water contamination, resulting in dangerous diseases and most of the effluent treatment techniques are relatively ineffective. As a result, metal oxide-based photocatalysts emerged as a viable alternative to the already existing dye treatment methods. The current work focused on the synthesis and characterization of Ni-doped ZnO/GO heterostructures and evaluation of its photoactivity under sunlight irradiation. The nanocomposite was prepared via a simple mixing approach, by varying the weight ratio of graphene oxide (GO) ranging from 0.1 to 0.4 g prior to the incorporation into Ni-doped ZnO surfaces. The X-ray diffraction analysis revealed that Ni and GO were successfully incorporated into the wurtzite-structure of ZnO nanocomposites. FESEM images showed a uniformed particle with the average size of about 100-500 nm for all samples. The photocatalytic activity was assessed by monitoring the degradation of methylene blue (MB) dye under direct sunlight irradiation. Ni-doped ZnO/$GO_{0.1}$ nanocomposite exhibited the greatest degradation performance by degrading 94% MB. The highest degradation rate constant of 0.0250 min^{-1} was obtained within 120 minutes of reaction time. The current study is easy, effective, and compatible; hence it can be employed in the future to treat textile dye wastewater.

Keywords: graphene oxide, methylene blue, nickel, photodegradation, sunlight

Abstrak

Bahan pencemar kimia yang dikeluarkan oleh industri tekstil merupakan sumber utama pencemaran air, mengakibatkan penyakit berbahaya dan kebanyakan kaedah rawatan sisa bahan buangan yang dicipta masih tidak berkesan sepenuhnya. Justeru,

fotomangkin berasaskan logam oksida dihasilkan sebagai alternatif yang berdaya maju bagi kaedah rawatan pewarna sedia ada. Penumpuan kepada sintesis dan pencirian yang mudah bagi heterostruktur ZnO/GO yang didopkan dengan Ni dan penilaian fotoaktivitinya di bawah cahaya matahari. Nanokomposit disediakan melalui kaedah campuran yang ringkas dengan mengubah nisbah berat grafin oksida (GO) diantara 0.1 hingga 0.4 g sebelum dimasukkan ke dalam permukaan ZnO berdop Ni. Analisis pembelauan sinar-X mendedahkan bahawa Ni dan GO telah berjaya dimasukkan ke dalam struktur ZnO. Imej FESEM menunjukkan partikel seragam dengan saiz purata diantara 100-500 nm untuk semua sampel. Aktiviti fotokatalitik dinilai dengan memantau degradasi pewarna metilina biru (MB) di bawah penyinaran cahaya matahari secara lansung. Nanokomposit $ZnO/GO_{0.1}$ berdop Ni mempamerkan prestasi degradasi yang paling tinggi dengan nilai peratus degradasi 94% MB. Pemalar kadar degradasi tertinggi ialah 0.0250 min^{-1} diperolehi dalam masa 120 minit masa tindak balas. Kajian ini didapati mudah, berkesan dan sesuai, justeru ia boleh digunakan pada masa hadapan untuk merawat sisa buangan pewarna dari industri tekstil.

Kata kunci: grafin oksida, metilina biru, nikel, fotodegradasi, cahaya matahari

Introduction

In the past decades, contamination of freshwater resources with a large amount of dyes has been widely reported, mainly due to the rapid industrialization. They are employed in textile, paper, foods, cosmetics, pharmaceuticals, and printing industries [1]. The dyes are believed to have found their way entering the groundwater through dyeing process, leaching from various dye industries, and inappropriate discharge of untreated dye effluents [2, 3]. Human exposures to dyes occurred through consumption of food, water, air inhalation and direct contact with body and skin. This exposures hence have affected the human health and aquatic lives due to their toxicity [4, 5]. It is therefore essential to use promising treatment strategies, aiming to restore the quality of contaminated water by ensuring the sustainability of the environments with economically viable approach.

Presently, photocatalytic advanced oxidation processes (AOPs) have been studied extensively for water restoration, mainly due to its favorable degradation activity toward recalcitrant organic pollutants as compared to conventional water treatment approaches [6, 7]. The method highlights on the use of semiconductor oxides as the catalyst assisted with UV or solar irradiation during the process. It is a cost-effective method in such a way that it operates at/near ambient temperature and pressure for the *in-situ* production of reactive radical species such as •OH and $•O_2^-$ on the surface of the photocatalyst [8]. The process aims for the mineralization of the contaminants to harmless inorganic by-products, water, and carbon dioxide through a series of redox reaction [9]. Of various semiconductor metal oxides, zinc oxide (ZnO) is most likely to be of the highest interest and regarded as an ideal catalyst due to its exceptional capability such as wide and direct bandgap semiconductor materials, higher photocatalytic efficiency, ability to absorb over a larger fraction of the UV or solar spectrum, non-toxic, low cost and environmentally sustainable [10–13].

Nonetheless, ZnO has their own limitation such as lower reusability and adsorption ability, wide band gap energy (3.37 eV) which can only be fully utilized under UV ($\lambda < 387$ nm) [14]. It is well-established that solar light consists of merely ~4% UV, so it is not very effective for large band gap materials. Also, rapid charge recombination is believed to be a major loss for the photoexcited charge carriers and a critical factor that limits the photo-efficiency for wide band gap photocatalyst [15–17]. To overcome these drawbacks, the construction of heterojunctions by coupling ZnO with suitable band potentials materials has been revealed to be an efficient strategy to simultaneously improve its photoactivity and photostability. Researchers found that modifying ZnO surface by doping with metal such as nickel (Ni) could extend the light absorption range towards visible region [18]. In this respect, Tawale et al. [19] investigated different microstructural and photoluminescence performance of bare ZnO, Ni doped ZnO and Cr doped ZnO. The result revealed that the Ni-doped ZnO nanostructures had the stronger PL intensity compared to Cr doped and undoped ZnO nanostructures. Apparently, high quality and good physicochemical properties will enhance the photocatalytic properties.

Wang et al. [18] reported on the recyclable photocatalyst based on flower-like nickel zinc ferrite nanoparticles/ZnO (NZF/ZnO) using a hydrothermal method. It was found that the samples prepared using 2.0 wt.%, 4.0 wt.% and 6.0 wt.% NZF nanoparticles exhibit better degradation performance towards rhodamine B (RhB) with increasing amounts of NZF, and 6.0 wt.% NZF has the best photocatalytic activity under visible irradiation. This result may come from the fact that the sample grown with 6.0 wt.% NZF has a smaller diameter and a larger surface area. Moreover, the much higher photocatalytic performance comes from the charge separation effect due to the band alignment between NZF and ZnO.

Combination of semiconductor oxide on carbonaceous materials such as graphene oxide is also attractive to improve the charge separation efficiency for enhanced photoactivity. This is due to the fascinating properties of GO such as high adsorption capacity, high electron mobility, large surface area and high thermal conductivity [4, 20–23]. This can be seen from the research conducted by Wu and Wang [24], where they conducted a study on the preparation of graphene oxide/hexagonal flower-like ZnO (GO/ZnO) micro/nanoparticles through hydrothermal method. It was found that the degradation percentage of rhodamine (RhB) dye reached 90.8% in 60 min, which was much higher than pure ZnO. The micro/nanostructure of GO/ZnO significantly improved the photocatalytic ability compared to pure ZnO. Kherabadi and his co-workers [4] reported on the synthesis, physicochemical properties and performance of three-dimensional (3D) Ag/ZnO/graphene as photocatalyst using a combined hydrothermal-photo deposition method. The dye degradation under both UV and visible light irradiation exhibited an enhanced photoactivity in comparison to ZnO/graphene and graphene alone. The deposition of Ag nanoparticles onto the surface of ZnO/graphene enhanced the photocatalytic efficiency due to the electron capturing properties.

In this research, an attempt has been made to synthesize Ni-doped ZnO/GO nanocomposites using a simple mixing approach. The morphological, structural properties, and photocatalytic activities of the nanocomposites were also investigated utilizing methylene blue (MB) dye as the probe molecule. Attempts has made to investigate the influence of variation GO weight ratio to Ni-doped ZnO on its performance as photocatalyst. The resultant nanocomposite photocatalyst certainly tends to harvest direct sunlight absorption effectively for photoexcited electron-holes formation, enhance the interfacial charge migration and hold better photostability during the photocatalytic reaction. The growth of Ni-doped ZnO/GO provides a simple, environmentally friendly and cost saving approach.

Materials and Methods

Materials

Commercial zinc oxide powder (ZnO, purity > 99%), Graphene oxide powder (GO, purity > 99%), nickel powder (Ni, purity > 99%), and methylene blue dye were purchased from Merck (Selangor, Malaysia). All chemicals and reagents were used as received and no purification step was performed. Deionized water was utilized throughout the synthesis and other experimental process.

Synthesis of Ni-doped ZnO/GO nanocomposites

In this work, a simple mixing approach was employed to prepare the heterostructures photocatalyst. Firstly, 0.5 g of Ni and 9.5 g of ZnO powder were mixed in a 100 mL of deionized water under continuous magnetic stirring for 30 min. After that, GO was added into the mixture and the amount was varied from 0.1 to 0.4 g. The amount of Ni and ZnO powder was kept constant throughout the process. The mixed solution went through an ultrasonic agitation using a sonicator (Powersonic 405) at a power of 350 W with a 40 KHz working frequency for 60 min. Following that, the mixtures solution was continuously stirred with a heating temperature of 60°C for 1 h on magnetic stirrer. Subsequently, the obtained Ni-doped ZnO/GO catalysts in the form of a fine powder were filtered, washed several times with deionized water and dried at 300°C for 1 h, yielding a greyish powder. The samples were labelled as ZnO/Ni, ZnO/Ni/$GO_{0.1}$, ZnO/Ni/$GO_{0.2}$, ZnO/Ni/$GO_{0.3}$, and ZnO/Ni/$GO_{0.4}$ accordingly. The morphology of the Ni-doped ZnO/GO nanocomposites was examined using a field emission scanning electron

microscopy (JEOL JSM-7600F). X-ray diffraction patterns were obtained by PANalytical X'pert Pro powder diffraction equipment at room temperature (Cu Kα radiations of λ =1.5418 Å) between 2θ range of 10–90° with a scanning speed of 2°/min. Following that, the Ni-doped ZnO/GO samples then underwent photocatalytic degradation measurement.

Photocatalytic degradation study

The photocatalytic degradation of the Ni-doped ZnO/GO nanocomposites were evaluated using methylene blue (MB) dye on each interval under direct sunlight irradiation as shown in Figure 1. In a typical procedure, 10 mg of photocatalyst was dispersed in 100 mL of 10 mg/L of MB aqueous solution for every run. Prior to irradiation, the suspension was magnetically stirred for 30 min under dark condition to reach the adsorption/desorption equilibrium. Following that, the suspensions were subsequently exposed to sunlight irradiation under continuous stirring for 120 min. At predetermined time intervals, an aliquot of 5 mL of sample was extracted out and the residual concentration was monitored using UV-vis spectrophotometer at λ_{max} = 664 nm. The percentage of degradation of MB was calculated using equation (1). All the photocatalytic degradation experiments were carried out under similar condition on a sunny day from 12.00 to 2 pm, in the month of Mac where the temperature was T= (34±2) ºC at Bandar Tun Abdul Razak Jengka, Pahang.

$$\text{Percentage of degradation (\%)} = (C_o - C_t)/C_o * 100 \quad (1)$$

where C_0 is the concentration of MB before irradiation, while C_t is the concentration of MB at time 't'.

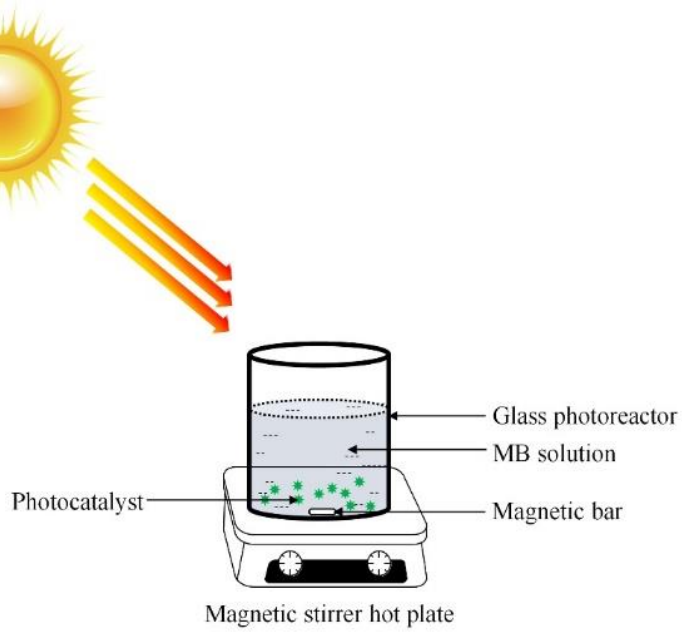


Figure 1. Illustration of the degradation process of Ni-doped ZnO/GO nanocomposites against MB under sunlight irradiation

Results and Discussion

X-ray diffraction pattern analysis

The crystalline phases of the pure and nanocomposites samples were analyzed by XRD, and the corresponding diffraction patterns are shown in Figure 2. Typically, all the diffraction peaks of pure ZnO (Figure 2a) are indexed according to the standard reference of hexagonal ZnO wurtzite structure (JCPDS No. 36-1451). The diffraction peaks at 2θ of 31.8°, 34.4°, 36.4°, 47.6°, 62.9°, 66.6°, 67.9° and 69.2° were respectively

assigned to the (100), (002), (101), (102), (103), (112) and (201), and were consistent with hexagonal zincite structure of pure ZnO [25, 26].

Meanwhile, Figure 2b shows the pattern for the peak of Ni obtained at 44.59° and 51.97° that corresponded to the (111) and (200) crystal faces of Ni standard pattern (JCPDS No. 04-0850) [27]. GO powder exhibits a diffraction peak at 26° corresponding to the (002) plane as can be seen in Fig. 2c. Interestingly, the presence of ZnO wurtzite structure with a very small peak of Ni were identified in the Ni-doped ZnO sample (Figure 2d). The existing of small Ni peak might be due to very small doping content of Ni element. All samples of Ni-doped ZnO/GO displayed the characteristic peaks belonging to ZnO (Figure 2e–h). However, the characteristic peak of Ni and GO was not observed in the XRD patterns possibly because of the low Ni and GO content (0.1 to 0.4 g), which is below the detection range of the XRD instrument. Also, no shift was observed in the position of ZnO diffraction peaks as compared to pure ZnO, proving that the native crystalline structure of ZnO had been maintained after the preparation of the hybrid heterostructure materials. The XRD analysis also revealed that the Ni and GO were incorporated into the wurtzite structure of ZnO crystal as there was no impurity or secondary phases existed in the pattern for all Ni-doped ZnO/GO samples.

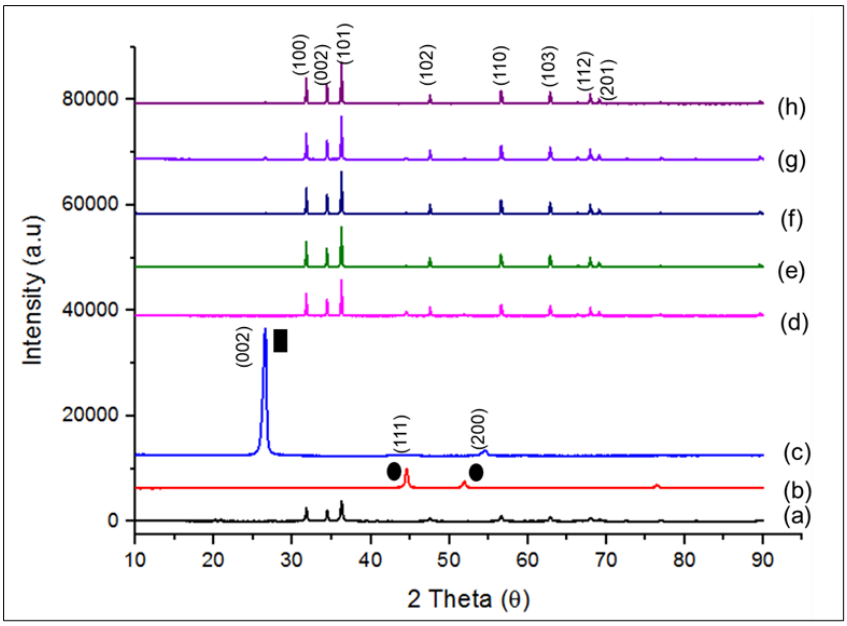


Figure 2. X-ray diffraction patterns of (a) pure ZnO, (b) pure Ni, (c) GO, (d) Ni-doped ZnO, and (e-h) Ni-doped $ZnO/GO_{0.1-0.4}$. (GO and Ni labelled as black square and circle in the graph respectively)

Surface morphological and structural analysis

The surface morphological and structural of pure ZnO, Ni-doped ZnO and Ni-doped $ZnO/GO_{0.1-0.4}$ nanocomposites were characterized by FESEM analysis (Figure 3). It could clearly be seen that similar structure particles with average size of about 100–500 nm was observed for pure ZnO, Ni-doped ZnO and Ni-doped $ZnO/GO_{0.1-0.4}$ nanocomposites. The incorporation of nickel and GO were not visible in the FESEM images. Nonetheless, the overall shapes for all samples composed of rod-like and cubic-like structures.

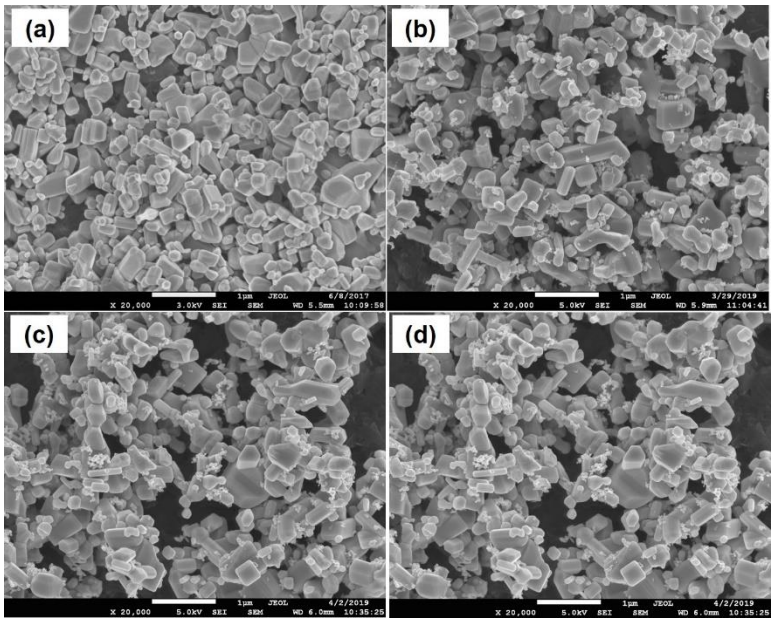


Figure 3. Selected FESEM images for (a) pure ZnO, (b) Ni-doped ZnO, (c) Ni-doped ZnO/$GO_{0.1}$, and (d) Ni-doped ZnO/$GO_{0.4}$

Evaluation of photocatalytic activity

Photocatalytic measurement of Ni-doped ZnO/GO nanocomposites photocatalyst in the removal of MB based on UV-vis spectra is depicted in Figure 4. The overall results revealed that the maximum absorption of MB at 664 nm decreased gradually as a function of time in the presence of different photocatalysts.

All the degradation behaviours were analysed and extrapolated in the following graph as presented in Figure 5. As depicted in the insert of Figure 5, no change was observed in the first 30 min before being exposed to sunlight for photodegradation of MB using ZnO/Ni/$GO_{0.1}$ catalyst because the MB was adsorbed on the surface of catalyst which led to an unchanged concentration and this unable the degradation of MB under dark condition. The photolysis of MB also seems negligible, indicating the stability of MB under sunlight. This is supported from our previous findings where the photolysis of MB under UV light was also insignificant even though UV contains high photon energy (shorter wavelength) as compared to sunlight (longer wavelength) [28]. The photocatalytic activity of pure ZnO reached almost 80% percentage of degradation against MB in aqueous phase. In contrast, the addition of Ni onto the ZnO surface did not improve the degradation efficiency since the percentage obtained was reduced to 15%. The addition of small amount of Ni to the ZnO might contribute to the decreasing of the percentage of degradation. Some researchers had found that the existence of Ni acted as a co-catalyst that reduced the over-potential of electrons at conduction band of ZnO which gave negative effect by lowering the degradation efficiency of ZnO itself. Previously, it was reported that there is high tendency for the occurrence of NiO (as a secondary phase) alongside Ni/ZnO on the catalyst surface which might impose undesirable defects and hence acted as a barrier to light absorption [29]. The transitions of metal ions substituted into the ZnO lattice also act as a recombination centre for electron-hole pairs and subsequently, producing lower percentage of degradation [30]. However, the incorporation of GO (0.1 g) into the samples shows a significant change in photocatalytic activity as compared to pure ZnO and Ni-doped ZnO samples with percentage obtained was around 95%. This was ascribed to the increase in the active sites and enhanced electron mobility which was responsible for the MB degradation.

The photocatalytic enhancement is also attributed by the strong and synergistic interaction between Ni/ZnO and GO in which the GO itself acts as an electron trapping site. The active sites here is referring to the GO surfaces which contain oxygenated functional groups (such as C=O, OH, etc.) that help in enhancing the electron mobility. Graphene itself is known to have superior charge carrier mobility properties (2×10^5 cm^2 V^{-1} s^{-1}) which allow for better electron transfer [31]. Theoretically, when ZnO is receiving the photon energy, the electrons (e^-) excited from the valence band (VB) to the conduction band (CB), leaving positive holes (h^+) behind. These excited electrons are then migrated to the Ni atom and GO sheet and subsequently avoiding the recombination behaviour through effective separation of electron-hole pairs. In this view, more charge carriers are produced from series of redox reactions with subsequent reactive oxidative species (such as •OH and $•O_2^-$) for efficient MB degradation [31]. The recombination could not be avoided if the electrons fall back to the valence band and no photocatalytic reaction could be observed. Thus, an appropriate amount of GO played a crucial role to facilitate the electron transfer and to support ZnO for effective electron mobility and separation of photogenerated charges. The percentage of degradation however decreased significantly at a higher GO content (0.2–0.4 g) due to the agglomeration of the nanocomposites which reduced the surface area and light absorption capacity of the photocatalysts. The percentage obtained for those nanocomposites with varied concentrations of GO displayed were almost comparable to each other.

Even though GO serves as an electron acceptor and mediator for an efficient carrier mobility [32], the presented results also suggested that, different GO content that was incorporated to the Ni-doped ZnO samples significantly affected the degradation efficiency. It might be due to the hindrance of actives sites by excess molecules that simultaneously prevented the light to reach and maximumly absorb the number of dye molecules on the photocatalyst surface. The light scattering and low penetration of light towards the catalyst surface decreased the effective irradiation for the reaction to progress [33]. This phenomenon further reduced the generation of photoexcited electron-hole pairs which leads to the decreased in the photocatalytic performances. This statement is in a good agreement with You et al. in which the decrease in the photocatalytic performance might be due to an excessive presence of GO content which resulted in agglomeration of particles. Hence, the photodegradation rate became more saturated. Furthermore, the higher content of GO in the catalyst lattice could cause a "shielding effect" that might shade the light and limited the light absorption capacity of the photocatalyst [34].

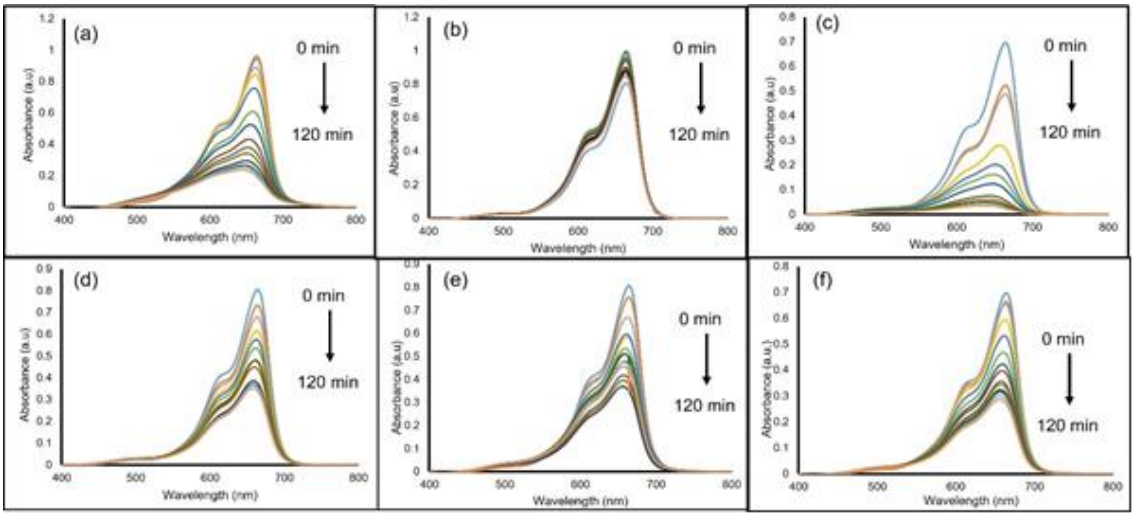


Figure 4. UV–vis absorbance spectra as a function of time for the degradation of MB using (a) pure ZnO, (b) Ni-doped ZnO, and (c – f) Ni-doped ZnO/$GO_{0.1–0.4}$ nanocomposites

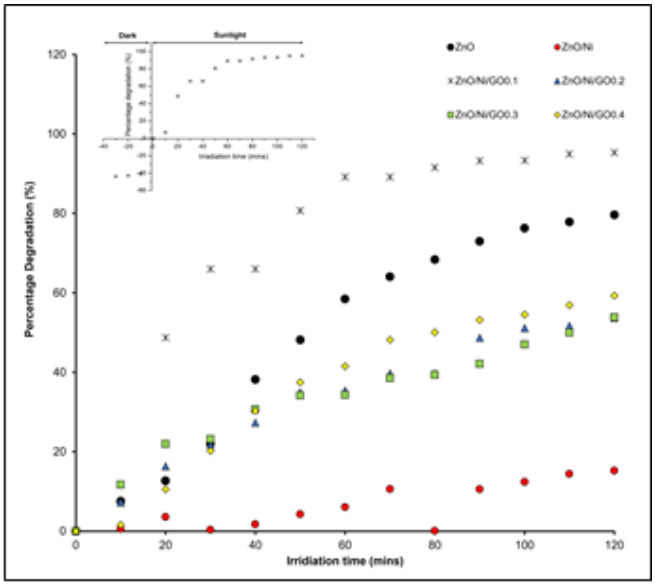


Figure 5. Percentage of degradation of MB under sunlight irradiation in the presence of different photocatalysts and the insert shows the photodegradation of MB under dark and sunlight irradiation using ZnO/Ni/$GO_{0.1}$ catalyst

Further analysis on the kinetic of MB disappearance had been carried out by plotting a first order decay plot of the characteristic of MB absorption peak. The experimental data were fitted based on the Langmuir–Hinshelwood (L–H) kinetic model as expressed by equations (2) and (3), hence the rate constant, *k* of the photocatalyst can be evaluated and quantified.

$$r = dC/dt = kC \quad (2)$$

where *r* and *k* represent the pseudo first-order reaction rate and rate constant, respectively. The equation can be rewritten as

$$\ln (C/C_o) = -kt \quad (3)$$

The pseudo first-order rate constant was determined from the slope of the plot of -ln (Co/Ct) versus irradiation time, t as illustrated in Figure 6. Linear plots were observed (with R^2 values higher than 0.9) which attested that photodegradation of MB obeyed pseudo-first order kinetics. The calculated pseudo-first order rate constant and corresponding R^2 values are presented in Table 1.

The results showed that the Ni-doped ZnO/$GO_{0.1}$ exhibited the highest *k* value of 0.025 min^{-1} compared to other samples which were found to be 0.0138, 0.0013, 0.070, 0.066 and 0.0081 min^{-1} for pure ZnO, Ni-doped ZnO, Ni-doped ZnO/$GO_{0.2}$, Ni-doped ZnO/$GO_{0.3}$, and Ni-doped ZnO/$GO_{0.4}$, respectively. As depicted in Table 1, the incorporation of GO into the Ni-doped ZnO composite influenced the photocatalytic performance as ZnO/Ni/$GO_{0.1}$ nanocomposite exhibited the highest percentage degradation of MB under direct sunlight. It can be suggested that Ni-doped ZnO/$GO_{0.1}$ should be regarded as the best photocatalyst as compared to pure ZnO and other samples. Nevertheless, the incorporation of excess amount of GO to ZnO did not give a significant trend of photodegradation performance due to the hindrance of actives sites by excess molecules that simultaneously prevents the light to reach and maximumly absorbed on the photocatalyst surface. The light scattering and low penetration of light towards the catalyst surface decreasing the effective irradiation for the reaction to progress [9].

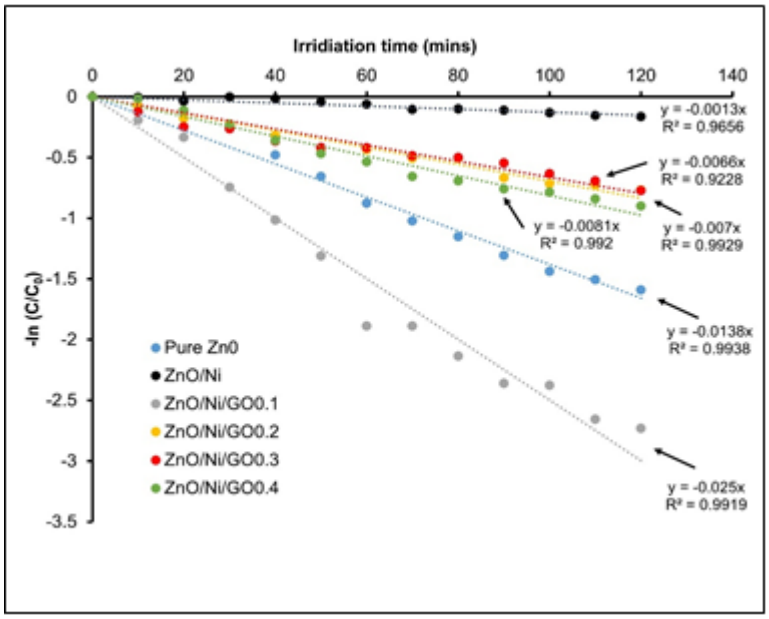


Figure 6. Plots of -ln (C/Co) versus irradiation time for the kinetic of disappearance of MB in the presence of different photocatalysts

Table 1. Photodegradation activities of MB using pure ZnO, Ni-doped ZnO, and Ni-doped ZnO/GO nanocomposites at different GO contents under sunlight irradiation

Sample	Percentage Degradation (%)	Photodegradation Rate Constant, k (min^{-1})	R^2 Value
Pure ZnO	79.64	0.0138	0.9808
ZnO/Ni	15.24	0.0013	0.9102
ZnO/Ni/$GO_{0.1}$	95.33	0.0250	0.9705
ZnO/Ni/$GO_{0.2}$	53.68	0.0070	0.9710
ZnO/Ni/$GO_{0.3}$	53.83	0.0066	0.9228
ZnO/Ni/$GO_{0.4}$	59.32	0.0081	0.9717

Conclusion

In this study, the XRD analysis revealed that the Ni and GO were successfully incorporated into the wurtzite structure of ZnO crystal as there were no impurity or secondary phases existed in the XRD pattern for sample Ni-doped ZnO/$GO_{0.1–0.4}$ nanocomposites. Other than that, it also showed the absence of Ni peak in the nanocomposite samples and this might be due to very small doping content of Ni element. The FESEM images with average size of about 100–500 nm was observed for pure ZnO, Ni-doped ZnO, Ni-doped ZnO/$GO_{0.1}$ and Ni-doped ZnO/$GO_{0.4}$ nanocomposites. Moreover, the morphological characteristics for all prepared samples composed of rod-like and cubic-like structures. The Ni-doped ZnO/$GO_{0.1}$ nanocomposite exhibited the best photocatalytic degradation of MB under direct sunlight within 120 min of reaction with percentage of degradation reaching 93.49% and photodegradation rate constant, k value of 0.0250 min^{-1} as compared to other samples. Overall, this research suggests a viable method

for improving the photocatalytic activity of ZnO-based photocatalysts, and it has promising implications for environmental issues.

Acknowledgement

This research is supported by FRGS-RACER: 600-RMI/FRGS/RACER 5/3 (041/2019). The authors fully acknowledged Ministry of Higher Education (MOHE) and Universiti Teknologi MARA Pahang for the approved fund which makes this important research viable and effective.

References

1. Jeyasubramanian, K., Hikku, G. S. and Sharma, R. K. (2015). Photo-catalytic degradation of methyl violet dye using zinc oxide nano particles prepared by a novel precipitation method and its anti-bacterial activities. *Journal of Water Process Engineering*, 8: 35-44.
2. Subbaiah, M. V. and Kim, D. S. (2016). Adsorption of methyl orange from aqueous solution by aminated pumpkin seed powder: Kinetics, isotherms, and thermodynamic studies. *Ecotoxicology and environmental safety*, 128:109-117.
3. Peter, A., Mihaly-Cozmuta, A., Nicula, C., Mihaly-Cozmuta, L., Jastrzębska, A., Olszyna, A. and Baia, L. (2017). UV light-assisted degradation of methyl orange, methylene blue, phenol, salicylic acid, and rhodamine B: photolysis versus photocatalyis. *Water, Air, & Soil Pollution*, 228(1): 1-12.
4. Kheirabadi, M., Samadi, M., Asadian, E., Zhou, Y., Dong, C., Zhang, J. and Moshfegh, A. Z. (2019). Well-designed Ag/ZnO/3D graphene structure for dye removal: Adsorption, photocatalysis and physical separation capabilities. *Journal of Colloid and Interface Science*, 537: 66-78.
5. Jothibas, M., Manoharan, C., Jeyakumar, S. J., Praveen, P., Punithavathy, I. K. and Richard, J. P. (2018). Synthesis and enhanced photocatalytic property of Ni doped ZnS nanoparticles. *Solar Energy*, 159: 434-443.
6. Rafaie, H. A., Nor, R. M., Azmina, M. S., Ramli, N. I. T. and Mohamed, R. (2017). Decoration of ZnO microstructures with Ag nanoparticles enhanced the catalytic photodegradation of methylene blue dye. *Journal of Environmental Chemical Engineering*, *5*(4): 3963-3972.
7. Syazwani, O. N., Mohd Hir, Z. A., Mukhair, H., Mastuli, M. S. and Abdullah, A. H. (2019). Designing visible-light-driven photocatalyst of Ag_3PO_4/CeO_2 for enhanced photocatalytic activity under low light irradiation. *Journal of Materials Science: Materials in Electronics*, 30(1): 415-423.
8. Asghar, A., Raman, A. A. A. and Daud, W. M. A. W. (2015). Advanced oxidation processes for in-situ production of hydrogen peroxide/hydroxyl radical for textile wastewater treatment: a review. *Journal of Cleaner Production*, 87: 826-838.
9. Mohd Hir, Z. A., Abdullah, A. H., Zainal, Z. and Lim, H. N. (2017). Photoactive hybrid film photocatalyst of polyethersulfone-ZnO for the degradation of methyl orange dye: Kinetic study and operational parameters. *Catalysts*, 7(11): 313.
10. Khaki, M. R. D., Shafeeyan, M. S., Raman, A. A. A. and Daud, W. M. A. W. (2017). Application of doped photocatalysts for organic pollutant degradation-A review. *Journal of Environmental Management*, 198: 78-94.
11. Bora, L. V. and Mewada, R. K. (2017). Visible/solar light active photocatalysts for organic effluent treatment: Fundamentals, mechanisms and parametric review. *Renewable and Sustainable Energy Reviews,* 76: 1393-1421.
12. Ahmed, S. N. and Haider, W. (2018). Heterogeneous photocatalysis and its potential applications in water and wastewater treatment: a review. *Nanotechnology,* 29(34): 342001.
13. Wang, P., Wu, D., Ao, Y., Wang, C. and Hou, J. (2016). ZnO nanorod arrays co-loaded with Au nanoparticles and reduced graphene oxide: Synthesis, characterization and photocatalytic application. *Colloids and Surfaces A: Physicochemical and Engineering Aspects,* 492: 71-78.

14. Zhu, P., Duan, M., Wang, R., Xu, J., Zou, P. and Jia, H. (2020). Facile synthesis of ZnO/GO/Ag_3PO_4 heterojunction photocatalyst with excellent photodegradation activity for tetracycline hydrochloride under visible light. *Colloids and Surfaces A: Physicochemical and Engineering Aspects,* 602: 125118.
15. Upadhyay, G. K., Rajput, J. K., Pathak, T. K., Kumar, V. and Purohit, L. P. (2019). Synthesis of ZnO: TiO_2 nanocomposites for photocatalyst application in visible light. *Vacuum,* 160: 154-163.
16. Muñoz-Fernandez, L., Sierra-Fernández, A., Milošević, O. and Rabanal, M. E. (2016). Solvothermal synthesis of Ag/ZnO and Pt/ZnO nanocomposites and comparison of their photocatalytic behaviors on dyes degradation. *Advanced Powder Technology,* 27(3): 983-993.
17. Xie, M., Zhang, D., Wang, Y. and Zhao, Y. (2020). Facile fabrication of ZnO nanorods modified with RGO for enhanced photodecomposition of dyes. *Colloids and Surfaces A: Physicochemical and Engineering Aspects,* 603: 125247.
18. Wang, W., Li, N., Hong, K., Guo, H., Ding, R. and Xia, Z. (2019). Z-scheme recyclable photocatalysts based on flower-like nickel zinc ferrite nanoparticles/ZnO nanorods: enhanced activity under UV and visible irradiation. *Journal of Alloys and Compounds*, 777: 1108-1114.
19. Tawale, J. S., Kumar, A., Swati, G., Haranath, D., Dhoble, S. J. and Srivastava, A. K. (2018). Microstructural evolution and photoluminescence performanance of nickel and chromium doped ZnO nanostructures. *Materials Chemistry and Physics*, 205: 9-15.
20. Gao, P., Ng, K. and Sun, D. D. (2013). Sulfonated graphene oxide–ZnO–Ag photocatalyst for fast photodegradation and disinfection under visible light. *Journal of Hazardous Materials,* 262: 826-835.
21. Ahmad, M., Ahmed, E., Hong, Z. L., Khalid, N. R., Ahmed, W. and Elhissi, A. (2013). Graphene–Ag/ZnO nanocomposites as high performance photocatalysts under visible light irradiation. *Journal of Alloys and Compounds,* 577: 717-727.
22. Haghshenas, S. S. P., Nemati, A., Simchi, A. and Kim, C. U. (2019). Dispute in photocatalytic and photoluminescence behavior in ZnO/graphene oxide core-shell nanoparticles. *Materials Letters,* 240: 117-120.
23. Moussa, H., Girot, E., Mozet, K., Alem, H., Medjahdi, G. and Schneider, R. (2016). ZnO rods/reduced graphene oxide composites prepared via a solvothermal reaction for efficient sunlight-driven photocatalysis. *Applied Catalysis B: Environmental,* 185: 11-21.
24. Wu, Z. and Wang, L. (2019). Graphene oxide (GO) doping hexagonal flower-like ZnO as potential enhancer of photocatalytic ability. *Materials Letters,* 234: 287-290.
25. Długosz, O., Szostak, K., Krupiński, M. and Banach, M. (2021). Synthesis of Fe_3O_4/ZnO nanoparticles and their application for the photodegradation of anionic and cationic dyes. *International Journal of Environmental Science and Technology,* 18(3): 561-574.
26. Huszla, K., Wysokowski, M., Zgoła-Grześkowiak, A., Staszak, M., Janczarek, M., Jesionowski, T. and Wyrwas, B. (2022). UV-light photocatalytic degradation of non-ionic surfactants using ZnO nanoparticles. *International Journal of Environmental Science and Technology,* 19(1): 173-188.
27. Li, J., Li, P., Li, J., Tian, Z. and Yu, F. (2019). Highly-dispersed Ni-NiO nanoparticles anchored on an SiO_2 support for an enhanced CO methanation performance. *Catalysts,* 9(6): 506.
28. Rafaie, H. A., Embong, N. A., Ramli, N. I., Mohamed, R. and Kasim, M. F. (2018). Synthesis of ZnO microstructure decorated with ag nanoparticles at different annealing temperature and their photocatalytic activity. *Recent Innovations in Chemical Engineering (Formerly Recent Patents on Chemical Engineering)*, 11(3): 192-200.
29. Behnood, R. and Sodeifian, G. (2020). Synthesis of N doped-CQDs/Ni doped-ZnO nanocomposites for visible light photodegradation of organic pollutants. *Journal of Environmental Chemical Engineering,* 8(4), 103821.

30. Yin, Q., Qiao, R., Li, Z., Zhang, X. L. and Zhu, L. (2015). Hierarchical nanostructures of nickel-doped zinc oxide: Morphology controlled synthesis and enhanced visible-light photocatalytic activity. *Journal of Alloys and Compounds,* 618: 318-325.
31. Julkapli, N. M. and Bagheri, S. (2015). Graphene supported heterogeneous catalysts: an overview. *International Journal of Hydrogen Energy,* 40(2): 948-979.
32. Ahmad, M., Ahmed, E., Ahmed, W., Elhissi, A., Hong, Z. L. and Khalid, N. R. (2014). Enhancing visible light responsive photocatalytic activity by decorating Mn-doped ZnO nanoparticles on graphene. *Ceramics International,* 40(7): 10085-10097.
33. Qin, J., Zhang, X., Xue, Y., Kittiwattanothai, N., Kongsittikul, P., Rodthongkum, N. and Liu, R. (2014). A facile synthesis of nanorods of ZnO/graphene oxide composites with enhanced photocatalytic activity. *Applied Surface Science,* 321: 226-232.
34. Tju, H., Shabrany, H., Taufik, A. and Saleh, R. (2017). Degradation of methylene blue (MB) using ZnO/CeO2/nanographene platelets (NGP) photocatalyst: Effect of various concentration of NGP. In *AIP Conference Proceedings,* 1862: p. 030037.

Malaysian Journal of Analytical Sciences (MJAS)
Published by Malaysian Analytical Sciences Society

BIOSORPTION CAPACITY OF HEAVY METAL LEAD (Pb(II)) USING DRY SEAWEED *Eucheuma denticulatum*

(Kapasiti Biojerapan Logam Berat Plumbum (Pb(II)) Mengunakan Rumpai Laut Kering *Eucheuma denticulatum*)

Hamad Maalim Sharif [1], Yahya Makame [2], Mohammed Ali Sheikh [3], Hasrizal Shaari [1,4]*, Rokiah Suriadi[1], Fatin Izzati Minhat[4]

[1]*Institute of Oceanography and Environment, Universiti Malaysia Terengganu, 21030, Kuala Nerus, Terengganu, Malaysia*
[2]*Chemistry Department, School of Natural and Applied Sciences, University of Dar es Salaam, P.O. Box 35065, Dar es Salaam, Tanzania*
[3]*School of Natural and Social Sciences, The State University of Zanzibar, P. O. Box 146, Zanzibar, Tanzania*
[4]*Faculty of Science and Marine Environment, Universiti Malaysia Terengganu, 21030, Kuala Nerus, Terengganu, Malaysia*

**Corresponding author: riz@umt.edu.my*

Received: 29 October 2021; Accepted: 27 February 2022 ; Published: 27 June 2022

Abstract

The seaweed industry plays a significant socio-economic role in tropical coastal communities. This study presents the biosorption behaviour of Pb(II) aqueous solution onto seaweed *E. denticulatum*. The impact of pH contact time, the initial concentration of the metals, and the adsorption activities were studied. The findings demonstrated that the Pb(II) uptake rate rose with increased concentration and contact time. The Pb(II) uptake reached saturation at 1000 mg/L after 120 min at room temperature. Pb(II) biosorption onto *Eucheuma denticulatum* fitted well to the Langmuir isotherm, with a maximum adsorption capacity (q_{max}) of 416.67 mg/g. The results suggest that this type of seaweed, *E. denticulatum*, is an effective biosorbent for removing Pb (II) and may control toxic metal pollution in tropical aquatic ecosystems.

Keywords: biosorption, *Eucheuma denticulatum*, heavy metals, Langmuir and Freundlich models

Abstrak

Industri rumpai laut memainkan peranan sosio-ekonomi yang sangat penting bagi masyarakat pesisir pantai tropika. Kajian ini menunjukkan tingkah laku biojerapan larutan akues Pb(II) ke atas *Eucheuma denticulatum*. Pengaruh hubungan masa pH, kepekatan awal logam, dan kajian penjerapan-penyerapan telah dilakukan. Hasil kajian menunjukkan bahawa kadar pengambilan Pb(II) meningkat dengan peningkatan kepekatan dan masa hubungan. Pengambilan Pb(II) mencapai titik tepu pada 1000 mg/L setelah 120 minit pada suhu bilik. Biojerapan Pb(II) ke atas *E. denticulatum* dipasang dengan baik pada isoterm Langmuir dengan kapasiti penjerapan maksimum (q_{max}) 416.67 mg/g. Hasilnya menunjukkan bahawa rumpai laut *E. denticulatum* adalah biopenjerap yang berkesan untuk menghilangkan Pb(II) dan mungkin boleh digunakan untuk mengawal pencemaran logam toksik di ekosistem perairan tropika.

Kata kunci: biojerapan, *Eucheuma denticulatum*, logam berat, model Langmuir dan Freundlich

Introduction

Heavy metal pollution is a serious concern due to its profound impact, even at small concentrations. It is caused by enhanced industrialisation and human activities that release various contaminants into the environment [1, 2, 3]. Heavy metals are considered among the most toxic groups reaching the food chain via waste disposal in water bodies and on land [4]. Therefore, eliminating heavy metal ions in wastewater is crucial for public health protection. The conventional methods for treating toxic metals are expensive and difficult to manage. Some methods lead to ineffective metals removal, restricted tolerance to pH change, slight metal selectivity, and the generation of toxic by-product waste that must be appropriately disposed of [5]. Attention has focused on heavy metals biosorption using various biological materials as this enables a higher metal binding capacity than chemical-based methods [6, 7].

Biosorption is a subtraction technique directed at contaminants or pollutants through inactive biomass, which allows the contaminants to be passively concentrated and bound to their cellular structure. Several absorbent materials have previously been used, including algae [8], fungi [9], bacteria [10], seaweeds [11], and some higher plants [12]. Several studies have assessed the efficiency of using different biosorbent materials for treating heavy metals in wastewater. For example, Tabaraki et al. [13] assessed the efficiency of brown seaweed on Pb(II) ions biosorption. At optimal conditions, they found the maximum seaweed uptake for the Pb(II) ions uptake to be 195±3.3 mg/g. The study of peanut shell efficacy on Pb^{2+} ions was carried out by Taşar et al. [14], and 39 mg/g was the maximum uptake obtained. The biosorption capacities of olive mill solid (OMS) and olive stone (OS) on Pb^{2+} ions uptake were examined by Blázquez et al. [15] in batch experiments under varied temperatures. The results revealed that the maximum Pb uptake was 6.57 mg/g on OS and 23.69 mg/g on OMS at 25 ºC. Gerola et al. [16] investigated the biosorption capacity of the residue of passionfruit skin onto Pb^{2+} ions and found that the maximum biosorption capacity was 204 mg/g at pH 4 for 170 min. Senthilkumar et al. [17] evaluated the biosorption functions of ten (10) different seaweed species on Pb^{2+} ions uptake under varied pH environments. The brown seaweed *Turbinaria Conoides* displayed optimal Pb^{2+} ions uptake of 439.4 mg/g at pH 4.5 and a temperature of 30 ºC. The work of Abdel-Aty et al. [18] presented the applicability of Blue-Green Alga *Anabaena Sphaerica* as a biosorbent of Cd^{2+} and Pb^{2+} ions from aqueous solutions. The ideal biosorption capacity was 111.1 mg/g and 121.95 mg/g, respectively, at peak conditions. The adsorption capacities of Macroalgae *Eucheuma Spinosum*, *Padina Minor*, and *Sargassum Crasifollum* were assessed by Putri [19] for their Pb^{2+} biosorption. The maximum biosorption capacity (55.56 mg/g) was demonstrated by *Sargassum Crasifollum*, followed by *Padina Minor* (40.00 mg/g), while the lowest (32.26 mg/g) was demonstrated by *Eucheuma Spinosum*. Studies on Pb^{2+} ions adsorption from aqueous solutions using raw and chemically modified green freshwater algae (*Scenedesmus Obliquus*) were conducted by Abdel Ghafar et al. [20]. The modified biomass was found to have higher biosorption capacity (207.2 mg/g) compared to raw biomass (112.0 mg/g). Therefore, algae have proven to be a more efficient and promising biosorbent to use for heavy metal removal from wastewater. The biosorption method is comparatively inexpensive and it offers elevated efficiency in terms of metal removal, as well as minimum chemical and/or biological sludge production, among others [21].

Algae biosorbent materials are gaining significant attention due to their abundance in the oceanic environment, relative easiness to process, and high accumulated ability of metal content. Algal-like seaweed is sufficient to facilitate a complex solid-liquid separation process, thus making seaweed a suitable form of biomass for heavy metal biosorption in the marine environment [22]. Seaweeds are marine algae found in coastal areas. The red algae *Eucheuma cottonii* and

Eucheuma denticulatum are grown in eastern Africa's tropical coastal regions [23, 24]. The seaweed industry in Tanzania employs more than 30,000 people [25]. Approximately 5,000 tons of dry seaweed are exported annually from Tanzania [25]. The high production of seaweed in Tanzania has motivated the authors to propose this substance as a potential biosorption material.

Heavy metal pollution has recently gained scientific attention due to its ubiquity in marine and coastal ecosystems [26]. Heavy metals' pathways into the human body are through food, water, and air. They are absorbed through the skin or by exposure from various agricultural, manufacturing, pharmaceutical, and urbanisation activities. Lead (Pb) is among the heavy metals proving to be the most serious toxic contaminant in Tanzania [27, 28, 29].

Previous studies have demonstrated the high metal-binding abilities of brown and green seaweeds [30, 31, 32]. However, there is a lack of data on the heavy metal biosorption by red seaweed species (*E. denticulatum*) in Tanzania. Therefore, this study discusses the biosorption behaviour of Pb(II) solution onto *E. denticulatum*. The findings from this study on *E. denticulatum* as a potential biosorption material of toxic metals have extensive consequences for the economy and health of farmers engaged in seaweed aquaculture in the coastal areas of Tanzania.

Materials and Methods

Study area

This study was conducted in three locations (Unguja Ukuu, Tumbe, and Kiungoni) along the coastal areas of Zanzibar. Tumbe and Kiungoni are located in the northern part of Pemba Island (Figure 1), while Unguja Ukuu is situated in the southern part of Unguja island (Figure 2). Seaweed farming is mainly found in these areas. Fresh seaweed *E. denticulatum* samples were cleaned carefully on-site with ocean water to eliminate impurities.

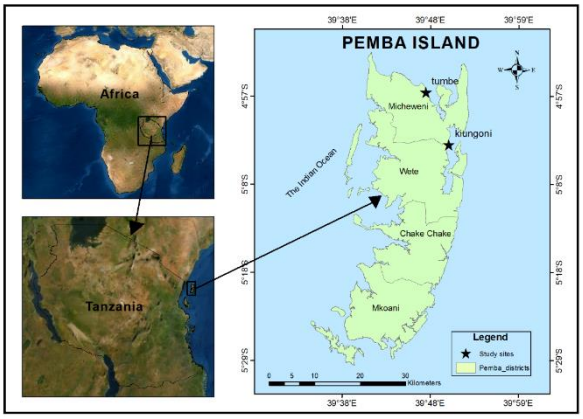


Figure 1. The sampling areas in the Pemba Island coastal region

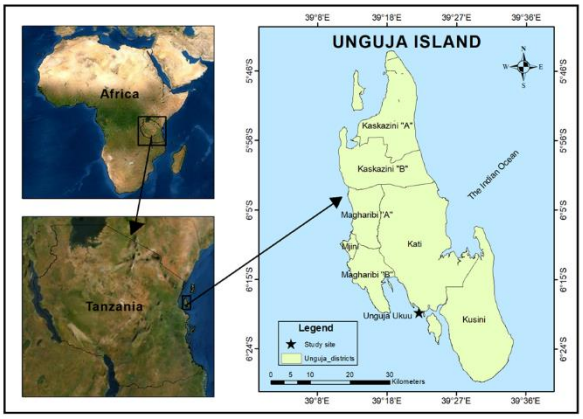


Figure 2. The sampling area in the Unguja Island coastal region

Sample preparation

The seaweed samples were washed with tap water, before being washed again with deionised water to eradicate salts and particulate matter from the surface of samples. The samples were then air-dried for 48 hours and then oven-drying at 80 ℃ for 24 hrs. The dried samples were ground into a homogeneous powder using a laboratory blender and stored in a desiccator before the biosorption experiments were conducted.

Pb(II) ions solution preparation

Pb(II) ions stock solution was prepared by dissolving 1.60g of Pb $(NO)_3$ in 1000 ml of deionised water. The different concentrations of Pb(II) solutions (50, 100, 250, 500, 1000, 1500, and 2000 mg/L were prepared by diluting the stock solution. The initial pH of the standard solutions was adjusted to the desired value by adding 0.1 M HCl or 0.1 M NaOH. The analytical grade of chemicals from Merck was used in this study. The concentrations of the standard solutions of 0.20, 1.00, 2.00, 7.00, 10.00, and 20.00 mg/L were precisely prepared.

Preliminary concentration of Pb(II) in *E. Denticulatum*

The initial Pb(II) ions levels were determined using a modified version of the methods devised by Luis et al. [33] and Rubio et al. [34]. Next, 25 g of *E. denticulatum* was oven-dried at 70 ℃ for 12 hours. Then, the sample was burned in a furnace at 550 ℃ for 20 hours to remove the organic matter. The ash of the sample was digested in 2 mL of HNO_3 (v/v) for 18 hours. The digested solution was filtered with a filter paper (Whatman no 2) and transferred into a 50 mL test tube. The solution was meshed up to 30 mL with deionised water. The atomic absorption spectrometer (AAS) Thermo Scientific model iCE 3300 was used to determine the Pb(II) ion concentrations.

Batch biosorption experiments

The batch biosorption experiments were established using a magnetic stirrer (120 - 180 min) at 120 rpm in a 250 mL beaker. Next, 50 mL of the standard solution was introduced into the beaker and biosorbent was added appropriately. The different parameters were organised as follows: solution pH (2-8), contact time (0-150 minutes), initial Pb(II) ion concentration (50-2000 mg/L). The Pb (II) ion biosorption characteristics were evaluated using a biomass weight of 0.5 g. The solution was separated using a Whatman filter paper No 2 or centrifuging and decanting.

Optimum pH for Pb(II) biosorption

The Pb(II) biosorption optimum pH was established by adding 50 mL solutions of 50 mg/L Pb (II) ions into a 100 mL centrifuge tube with 0.5 g of dry seaweed. The samples, which were of varying pH (2.0 to 8.0), were adjusted using 0.1 M NaOH or 0.1 M HNO_3 [35]. The mixtures were stirred for 180 minutes with a magnetic stirrer at room temperature. The supernatant was collected after centrifuging the mixture using the Gallen Kamp Centrifuge 200 at the lowest rate for 10 minutes. The AAS was used to determine the Pb(II) ion concentration in the supernatant. The analysis of each sample was performed in a duplication setting.

Optimum contact time for Pb(II) adsorption

The optimum contact time for Pb(II) adsorption was determined at optimum pH by adding 0.5 g biomass to 50 mL of the 50 mg/L metal solution. The mixture was stirred for 180 min using a magnetic stirrer at moderate speed at room temperature. At 5, 10, 30, 60, 120, and 180 min, the samples were removed, centrifuged, decanted. The supernatant was collected and stored for AAS analysis. The samples were prepared in duplicate.

The effect of Pb(II) ion concentration on biosorption

The effect of Pb(II) ion concentration on biosorption was investigated by mixing 0.5 g of seaweed and 50 mL of solutions of known concentrations at room temperature. The Pb(II) ion concentration levels were 50, 100, 250, 500, 1000, 1500, and 2000 mg/L. The solution mixture was corrected to the required pH with HNO_3 or NaOH solution before it was stirred with a magnetic stirrer at moderate speed and room temperature for 120 minutes. The samples were decanted using a Gallen Kamp Centrifuge 200 centrifuge for 20 minutes. The supernatants were then kept in centrifuge tubes and determined using the Atomic Absorption Spectrometer (AAS). This process was performed in duplicate.

Biosorption models

The Langmuir and Freundlich isotherm models were used to calculate Pb(II) biosorption from the aqueous solutions. The following is a linearised Langmuir equation [36]:

$$\frac{1}{q} = \frac{1}{q_{max}} + \frac{1}{b.q_{max}C_f} \quad (1)$$

where q_{max} is the Langmuir adsorption capacity (mg/g) and b is the adsorption energy (l/mg). The intercept and slope from the 1/q Vs $1/C_f$ graph were used to calculate q_{max} and b.

The following equation represents the Freundlich isotherm linear form [37]:

$$\log q = logK + \frac{1}{n}\, logC_f \quad (2)$$

where *K* is the Freundlich constant correlated to adsorption capacity, and *n* is the adsorption intensity. Furthermore, the separation factor R_L describes the essential characteristics of the Langmuir isotherm [38]:

$$R_L = \frac{1}{1+bq_{max}} \quad (3)$$

Kinetic adsorption study

Adsorption kinetics is a significant aspect of biosorption studies since it presents valuable information concerning adsorption mechanisms and allows the investigation of the controlling biosorption mechanism. The assessment of Pb^{2+} ions adsorption kinetics onto *E denticulatum* was conducted using pseudo-first-order and pseudo-second-order kinetics. The pseudo-first-order equation was devised by Febrianto et al. [39]

$$\log(q_e - q_t) = \log q_e - \frac{k_1\, t}{2.303} \quad (4)$$

where q_e and q_t (mg/g) are the equilibrium and time t, respectively, of the adsorption capacities. k_1 (min^{-1}) is the pseudo-first-order adsorption rate constant. The linear correlation of $\log(q_e - q_t)$versus t implies that the reaction fits with the pseudo-first-order reaction. The slope and the model's intercept, respectively, give k_1 and q_e.

According to Ho and Ofomaja [40], the pseudo-second-order reaction is expressed as:

$$\frac{t}{q_t} = \frac{1}{k_2 q_e^2} + \frac{t}{q_e} \quad (5)$$

where k_2 (g $mg^{-1}min^{-1}$) is the rate constant for the pseudo-second-order adsorption model. The linear relationship from the $\frac{t}{q_t}$ versus t plot gives the values of q_e and k_2 from the slope and intercept, respectively.

Results and Discussion

The initial levels of Pb(II) in seaweed

The initial concentration of Pb (II) detected in *E. denticulatum* was 0.084 µg/g. The results indicate that only trace amounts of Pb(II) were present in the *E. denticulatum* samples. The lead levels in Zanzibar's coastal areas range from 228 to 1150 ppm [41]. It was surmised that the trace value might be attributed to the anthropogenic sources and/or the natural background value.

Optimum pH for the biosorption of Pb(II)

The solution pH plays a vital role in controlling the metal ions biosorption of metal ions from aqueous solutions [42]. The findings presented in Figure 3 indicate that the removal of Pb(II) was low in an acidic medium (pH < 4). As pH increased, the metal uptake also increased until pH 4. Afterwards (beyond pH > 4), it showed a rapid decline. At low pH, the biosorption capacity was low due to the competition for binding sites on the biomass surface between the H^+ ions and the metal ions [43, 44]. Therefore, repulsive forces between the metal ions and the protonated biomass cell wall prevent the metal ions from approaching the cell wall [38]. However, as pH increased, the concentration of H^+ ions declined. The biomass became more negatively charged, resulting in the electrostatic attraction of the positive charge metal ions. Therefore, biosorption rose to its maximum point [45, 46, 47] before the precipitation of metal hydroxides occurred at higher pH due to the high OH^- ion concentration. This resulted in a decline in uptake capacity [48] and the electrostatic repulsion between the negatively charged anionic species in the solution [49]. This study revealed that the adsorption rate of Pb(II) ions was optimum at pH 4 and with a concentration of 4.7 mg/g. Therefore, the findings suggest that pH 4 is the most effective pH to use for Pb (II) biosorption, based on the range investigated (Figure 3).

Various biosorption studies employing algal biomass have demonstrated similar results (that pH 4 is the optimum pH). These include the works by Yipmantin et al. [50] using *Chondracanthus* (red alga); Lee and Park, [51] using brown seaweeds; and Nessim et al. [52] using *Ulva fasciata*, green seaweed and *Sargassum sp*., brown seaweed.

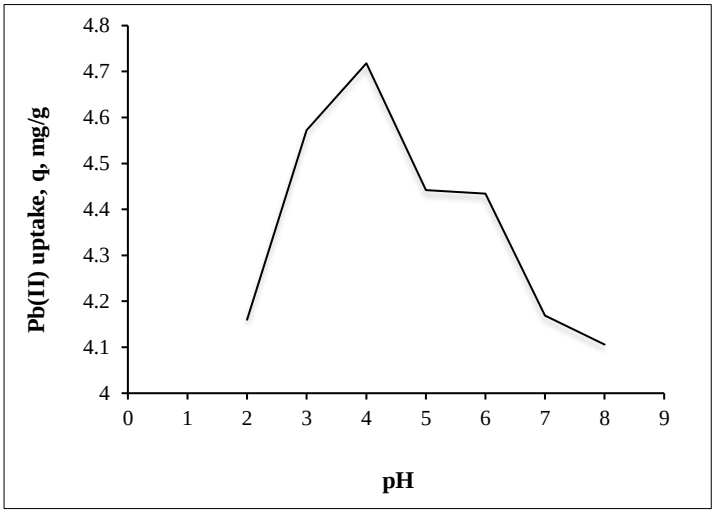


Figure 3. Variation of Pb(II) uptake of *E. denticulatum* with pH

Optimum contact time for Pb(II) biosorption

The metal ions biosorption in aqueous solutions is highly influenced by contact time, as shown in Figure 4. The results from this research study demonstrated that Pb(II) uptake onto *E. denticulatum* increased with longer contact times. Initially, during the first 20 minutes, there was a rapid Pb (II) uptake and a gradual increase until equilibrium at 120 minutes. Meanwhile, no further changes in biosorption were noticed beyond 120 minutes. Thus, 120 minutes can be considered the ideal contact time in other biosorption experiments.

The sharp increase in biosorption during the early stage was likely due to the high solute concentration gradient [53] and the availability of vacant active sites on the biomass surface. Thus, the adsorption of metal ions took place on these sites [54, 55]. In the subsequent stages, the metal removal declined because the active sites were gradually occupied [56] and there was difficulty occupying the residual binding spots due to the forces between the solid and bulk phases [57, 58].

Several biosorption studies have demonstrated that metal ions adsorption employing algal biomass attained maximum adsorption in the interval between 60 and 120 min. These include the works of Ibrahim, [59] using *Corallina mediterranea, Galaxaura oblongata, Jania rubens*, and *Pterocladia capillacea* (red macroalgae); Ozudogru, [60] using *Padina pavonica* (brown algae); and Abdel-Aty et al. [18] using *Anabaena sphaerica* (freshwater alga).

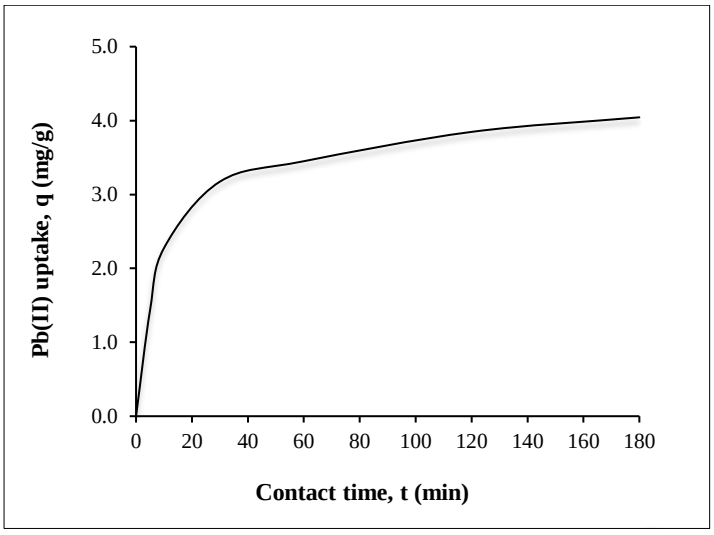


Figure 4. Effect of contact time on Pb(II) adsorption

Effect of initial metal ion concentration on Pb(II) biosorption

The initial metal ion concentration highly affects the biosorption capacity due to a substantial driving force that eliminates the resistance of all the metal ions between the aqueous and solid phases [61]. The present study demonstrated a rapid increase in Pb(II) biosorption with increased metal ion concentration until 1000mg/L, as shown in Figure 5. The metal uptake increased slowly, implying that the biomass had approached the saturation point [62].

The increased Pb(II) uptake during the early stage might be due to the enhanced driving force of metal ions into the biomass surface and the presence of abundant binding spots on the biosorbent surface areas [63, 64]. Consequently, when the Pb(II) ion concentration increases further, the active sites are overburdened by the ions, thereby preventing further metal ions adsorption [64, 65]. Thus, the metal uptake was enhanced with an increase in the initial levels of Pb(II) ions, reaching saturation when Pb(II) concentration attained a threshold value.

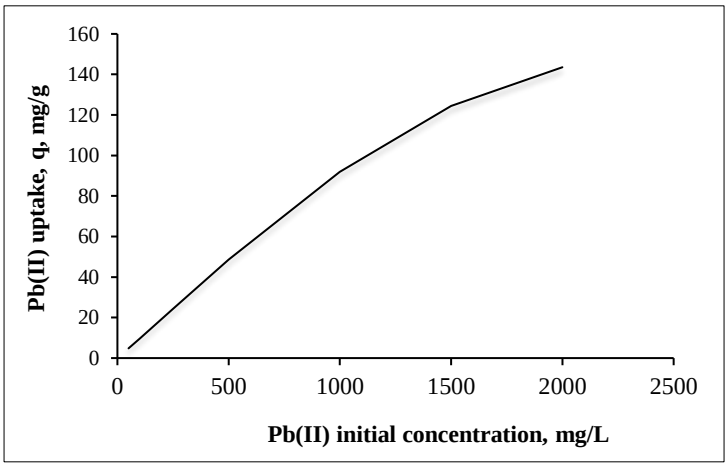


Figure 5. Effect of initial Pb (II) concentration on Pb(II) biosorption onto *E. denticula*

Biosorption models

The Freundlich and Langmuir models are isotherm models used to present the relation between equilibrium metal biosorption (q) and final concentration (C_f) at equilibrium [66]. Both adsorption models were used to measure the relationship between the Pb (II) uptake capability (*q*) and equilibrium concentration (C_f). The constants and correlation coefficients of the adsorption models employed were determined from the respective adsorption isotherms (Table 1). It was found that the Langmuir model (R^2 = 0.9935) fitted well, compared with the Freundlich model (R^2 = 0.9534). The high Langmuir correlation coefficient suggests the conformity of the P(II) adsorption to the model, implying the existence of monolayer adsorption conditions in the Pb (II) – *E. denticulatum* system [67].

The maximum Langmuir monolayer Pb(II) uptake capacity (q_m) and the Langmuir constant (b) isotherm were 175.13 mg/g and 0.01476 l/mg, respectively, implying the high uptake of Pb(II) by the biomass, which might have been due to its low capability of forming complex [68]. The presence of carboxylate polysaccharides in seaweed promotes the binding of cations with large ionic areas [69]. Moreover, the range of the Pb(II) ions separation factor, R_L = 0.2789, fell between 0 and 1 ($0 < R_L < 1$), implying that Pb(II) adsorption is favourable at all the concentrations studied [70].

The slopes and intercepts from the linear graphs (Figures 6 and 7) were used to compute the Langmuir and Freundlich isotherm constants, and the results are summarised in Table 1.

The magnitude of the Freundlich constant *K* suggests the high adsorption capacity of Pb(II) ions on *E. denticulatum***.** The value of n = 1.67 (n > 1) indicates that under the given experimental conditions, the heterogeneity of the biomass surface and the metal ions were adequately and intensively adsorbed by the dried seaweed *E. denticulatum.*

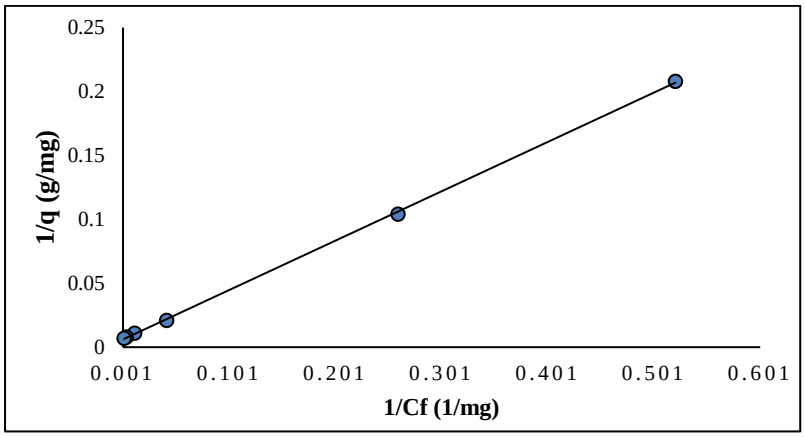


Figure 6. Langmuir isotherm for Pb (II) biosorption by *E. denticulatum*

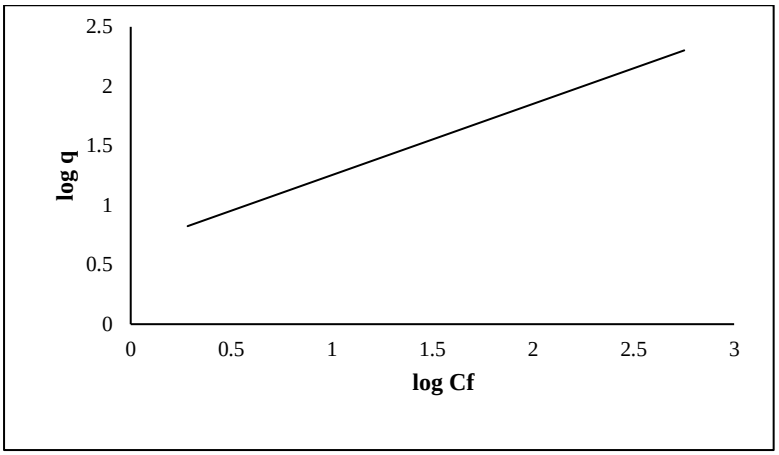


Figure 7. Linearised Freundlich isotherm for Pb(II) biosorption by *E. denticulatum*

Table 1. The Langmuir and Freundlich parameters and correlation coefficients for the biosorption of Pb (II) onto *E. denticulatum*

Metal	**Langmuir Isotherm Parameters**			**Freundlich Isotherm Parameters**			
	q_{max}, mg/g	*b*, l/mg	R^2	*K*, mg/g	1/*n*	*n*	R^2
Pb	175.13	0.01476	0.9991	4.517	0.632	1.67	0.9272

Kinetic studies

The Pb^{2+} ions adsorption rate onto *E.denticulatum* was estimated for contact times ranging from (0 – 180) min. The experimental data were interpreted using pseudo-first-order and pseudo-second-order kinetic models. The kinetic parameters and regression coefficients were obtained from their corresponding linear graphs (Figures 8 (a) and (b)) and these are summarised in Table 2. The $\log(q_e - q_t)$ Vs. t plot gives an approximate line, and the rate constant (k_1) and q_e can be estimated from the slope and the intercept, respectively. The k_1, q_e, and R^2 are shown in Table 2. Even though the plot is linear and the R^2 is 0.911, the value of q_e does not agree with the experimental q_e value (4.044). Therefore, Pb(II) adsorption does not follow pseudo-first-order kinetics.

The pseudo-second-order kinetic model was employed to find a more trustworthy Pb (II) adsorption kinetics description. The results from the $\frac{t}{q_t}$ Vs. t plot indicates that the pseudo-second-order kinetic model fits the metal adsorption experiment. The regression coefficient (R^2) was 0.998, and the q_e equals 4.3802 mg/g, which is close to the experimental q_e (4.044mg/g).

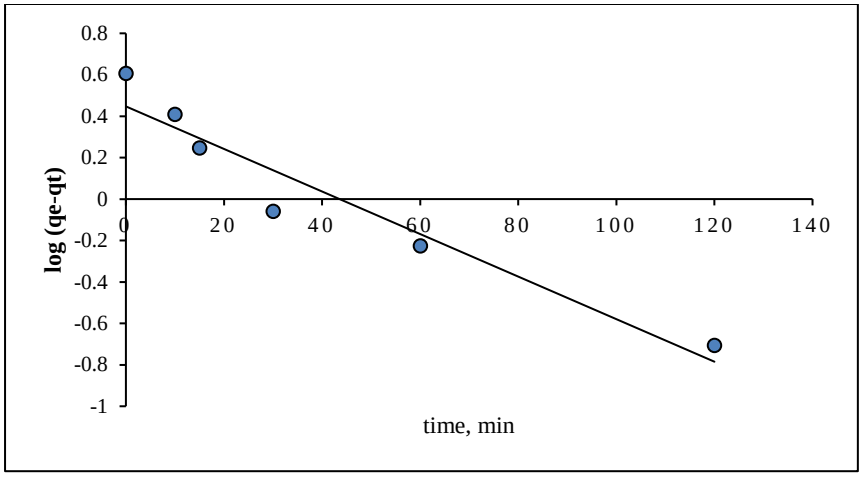


Figure 8(a). Pseudo-first-order for Pb(II) adsorption kinetics onto *E. denticulatum*

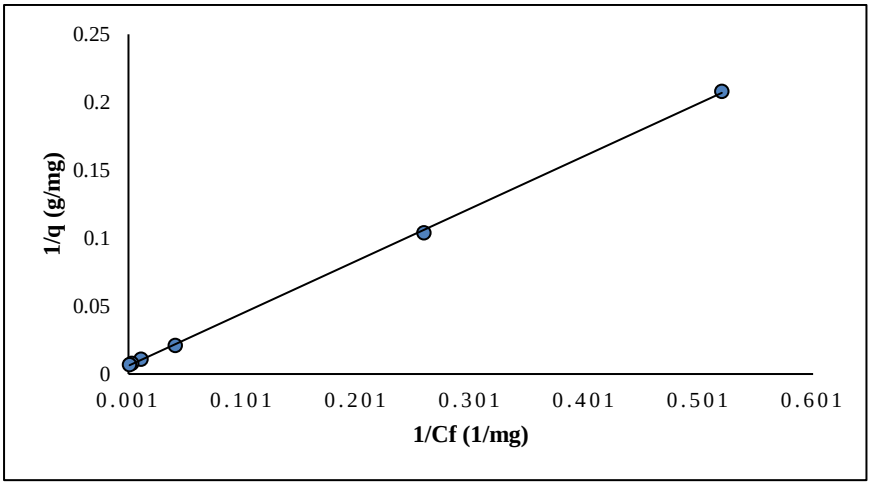


Figure 8(b). Pseudo-second-order for Pb(II) adsorption kinetics onto *E. denticulatum*

Table 2. The pseudo-first-order and pseudo-second-order kinetics parameters and correlation coefficients for the Pb (II) adsorption kinetics onto *E. denticulatum*

Pseudo-first-order kinetics			**Pseudo-second-order kinetics**		
K_1 (min^{-1})	qe (mg g^{-1})	R^2	K_2 (g $mg^{-1}min^{-1}$)	q_e (mg g^{-1})	R^2
20.0237	2.801	0.911	0.0148	4.3802	0.998

Conclusion

The present study demonstrated that the seaweed *E. denticulatum* was an effective biosorbent of Pb^{2+} from aqueous solutions. The availability of biomass and its cost-effectiveness are additional benefits that make it a potential biosorbent for treating heavy metals in the marine environment. The impact of processing constraints - including pH, metal ion concentrations, and

absorption period - significantly affected the equilibrium process. The Pb^{2+} uptake increased with the increase in metal ion concentration. It was also ascertained that the metal uptake increased with the rise in pH until pH 4; thereafter, the metal uptake began to decline. The Langmuir model might better represent the adsorption isotherms compared to the Freundlich model. According to these findings, the seaweed *E. denticulatum* can be considered a potential biosorbent for removing heavy metal from marine and coastal areas due to its high biosorption capability.

Acknowledgements

The authors of this paper are thankful to the Institute of Oceanography and Environment (INOS) and the State University of Zanzibar (SUZA) for their support.

References

1. Asnani, P. U. and Zurbrugg, C. (2007). Improving municipal solid waste management in India: A sourcebook for policymakers and practitioners. World Bank Publications.
2. Tian, H. Z., Lu, L., Cheng, K., Hao, J. M., Zhao, D., Wang, Y., Jia, W. X. and Qiu, P. P. (2012). Anthropogenic atmospheric nickel emissions and its distribution characteristics in China. *Science of the Total Environment*, 417–418: 148-157.
3. Yoon, J., Cao, X., Zhou, Q. and Ma, L. Q. (2006). Accumulation of Pb, Cu, and Zn in native plants growing on a contaminated Florida site. *Science of the Total Environment*, 368(2–3): 456-464.
4. Dixit, R., Wasiullah, Malaviya, D., Pandiyan, K., Singh, U. B., Sahu, A., Shukla, R., Singh, B. P., Rai, J. P., Sharma, P. K., Lade, H. and Paul, D. (2015). Bioremediation of heavy metals from soil and aquatic environment: An overview of principles and criteria of fundamental processes. *Sustainability (Switzerland)*, 7(2): 2189-2212.
5. Das, N. (2005). Heavy metals biosorption by mushrooms. *Indian Journal of Natural Products and Resources*, 4(6): 454-459.
6. Volesky, B. (2007). Biosorption and me. *Water Research*, 41(18): 4017-4029.
7. Zeraatkar, A. K., Ahmadzadeh, H., Talebi, A. F., Moheimani, N. R. and McHenry, M. P. (2016). Potential use of algae for heavy metal bioremediation, a critical review. *Journal of Environmental Management*, 181: 817–831.
8. Mousavi, S. A., Almasi, A., Navazeshkh, F. and Falahi, F. (2019). Biosorption of lead from aqueous solutions by algae biomass: Optimization and modeling. *Desalination and Water Treatment*, 148: 229-237.
9. Dwivedi, S., Mishra, A. and Saini, D. (2012). Removal of heavy metals in liquid media through fungi isolated from waste water. *International Journal of Science and Research*, 1: 2319-7064.
10. Vijayaraghavan, K. and Yun, Y. S. (2008). Bacterial biosorbents and biosorption. *Biotechnology Advances*, 26(3): 266-291.
11. Elangovan, R., Philip, L. and Chandraraj, K. (2008). Biosorption of chromium species by aquatic weeds: Kinetics and mechanism studies. *Journal of Hazardous Materials*, 152(1): 100-112.
12. Rahman, H. U., Shakirullah, M., Ahmad, I., Shah, S. and Shah, A. A. (2005). Removal of copper (II) ions from aqueous medium by sawdust of wood. In *Journal of the Chemical Society of Pakistan*, 27(3): 233-238.
13. Tabaraki, R., Nateghi, A. and Ahmady-Asbchin, S. (2014). Biosorption of lead (II) ions on *Sargassum ilicifolium*: Application of response surface methodology. *International Biodeterioration and Biodegradation*, 93: 145-152.
14. Taşar, Ş., Kaya, F. and Özer, A. (2014). Biosorption of lead(II) ions from aqueous solution by peanut shells: Equilibrium, thermodynamic and kinetic studies. *Journal of Environmental Chemical Engineering*, 2(2): 1018-1026.
15. Blázquez, G., Calero, M., Hernáinz, F., Tenorio, G. and Martín-Lara, M. A. (2010). Equilibrium biosorption of lead(II) from aqueous solutions by solid waste from olive-oil production. *Chemical Engineering Journal*, 160(2): 615-622.
16. Gerola, G. P., Boas, N. V., Caetano, J., Tarley, C. R. T., Gonçalves, A. C. and Dragunski, D. C. (2013). Utilization of passion fruit skin by-product as lead(II) ion biosorbent. *Water, Air, and Soil Pollution*, 224(2): 1-11.

17. Senthilkumar, R., Vijayaraghavan, K., Thilakavathi, M., Iyer, P. V. R. and Velan, M. (2007). Application of seaweeds for the removal of lead from aqueous solution. *Biochemical Engineering Journal*, 33(3): 211-216.
18. Abdel -Aty, A. M., Ammar, N. S., Abdel Ghafar, H. H. and Ali, R. K. (2013). Biosorption of cadmium and lead from aqueous solution by freshwater alga *Anabaena sphaerica* biomass. *Journal of Advanced Research*, 4(4): 367-374.
19. Putri, L. S.(2016). Biosorption of lead using macroalgae *Eucheuma spinosum*, *Padina minor*, and *Sargassum crassifolium* in an aqueous solution. *Asian Journal of Applied Sciences*, 4: 520-525.
20. Abdel Ghafar, H. H., Abdel-Aty, A. M., Ammar, N. S. and Embaby, M. A. (2014). Lead biosorption from aqueous solution by raw and chemically modified green freshwater algae *Scenedesmus obliquus*. *Desalination and Water Treatment*, 52(40–42): 7906-7914. https://doi.org/10.1080/19443994.2013.856345
21. Shrestha, R., Ban, S., Devkota, S., Sharma, S., Joshi, R., Tiwari, A. P., Kim, H. Y. and Joshi, M. K. (2021). Technological trends in heavy metals removal from industrial wastewater: A review. *Journal of Environmental Chemical Engineering*, 9(4): 105688.
22. Pan, Y., Wernberg, T., de Bettignies, T., Holmer, M., Li, K., Wu, J., Lin, F., Yu, Y., Xu, J., Zhou, C., Huang, Z. and Xiao, X. (2018). Screening of seaweeds in the East China Sea as potential bio-monitors of heavy metals. *Environmental Science and Pollution Research*, 25(17): 16640-16651. https://doi.org/10.1007/s11356-018-1612-3.
23. Valderrama, D., Cai, J., Hishamunda, N., Ridler, N., Neish, I. C., Hurtado, A. Q., Msuya, F. E., Krishnan, M., Narayanakumar, R., Kronen, M., Robledo, D., Gasca-Leyva, E. and Fraga, J. (2015). The economics of Kappaphycus seaweed cultivation in developing countries: A comparative analysis of farming systems. *Aquaculture Economics and Management*, 19(2): 251-277.
24. Rönnbäck, P., Bryceson, I. and Kautsky, N. (2002). Coastal aquaculture development in eastern Africa and the western Indian Ocean: Prospects and problems for food security and local economies. *Ambio*, 31(7–8): 537-542.
25. TWAS. (2004). *TWAS newsletter*. pp. 1–84.
26. Vijayaraghavan, K., Raj Jegan, J., Palanivelu, K. and Velan, M. (2004). Copper removal from aqueous solution by marine green alga *Ulva reticulata*. *Electronic Journal of Biotechnology*, 7(1): 47-54.
27. Chove, B. E., Ballegu, W. R. and Chove, L. M. (2006). Copper and lead levels in two popular leafy vegetables grown around Morogoro Municipality, Tanzania. *Tanzania Health Research Bulletin*, 8(1): 37-40.
28. Mwegoha, W. J. S. and Kihampa, C. (2010). Heavy metal contamination in agricultural soils and water in Dar es Salaam city, Tanzania. *African Journal of Environmental Science and Technology*, 4(11): 763-769.
29. Shemdoe, R. S. (2010). Heavy metal concentrations in soils and leachates of Mtoni dumpsite bordering the Indian Ocean in Dar es salaam, Tanzania. *Scientific Research and Essays*, 5(16): 2143-2147.
30. Awasthi, M. K., Guo, D., Awasthi, S. K., Wang, Q., Chen, H., Liu, T., Duan, Y., Soundari, P. G. and Zhang, Z. (2020). Recent advances in phytoremediation of toxic metals from contaminated sites: A road map to a safer environment. *Bioremediation of Industrial Waste for Environmental Safety*, 2: 77-112.
31. Diniz, V. and Volesky, B. (2005). Biosorption of La, Eu, and Yb using Sargassum biomass. *Water Research*, 39(1): 239-247.
32. Nirmal Kumar, J. I., Oommen, C. and Kumar, R. N. (2009). Biosorption of heavy metals from aqueous solution by green marine macroalgae from Okha Port, Gulf of Kutch, India. *American Eurasian Journal Agriculture and Environmental Sciences*, 6(3): 317-323.
33. Luis, G., Rubio, C., Gutiérrez, Á. J., González-Weller, D., Revert, C. and Hardisson, A. (2014). Evaluation of metals in several varieties of sweet potatoes (*Ipomoea batatas* L.): Comparative study. *Environmental Monitoring and Assessment*, 186(1): 433-440.

34. Rubio, C., Lucas, J. R. D., Gutiérrez, A. J., Glez-Weller, D., Pérez Marrero, B., Caballero, J. M., Revert, C. and Hardisson, A. (2012). Evaluation of metal concentrations in mentha herbal teas (*Mentha piperita, Mentha pulegium* and Mentha species) by inductively coupled plasma spectrometry. *Journal of Pharmaceutical and Biomedical Analysis,* 71: 11-17.
35. Vieira, D. M., Da Costa, A. C. A., Henriques, C. A., Cardoso, V. L. and De França, F. P. (2007). Biosorption of lead by the brown seaweed *Sargassum filipendula* - Batch and continuous pilot studies. *Electronic Journal of Biotechnology,* 10(3): 368-375. https://doi.org/10.2225/vol10-issue3-fulltext-3
36. Dąbrowski, A. (2001). Adsorption - From theory to practice. *Advances in Colloid and Interface Science,* 93(1–3): 135-224.
37. Yang, C. hai. (1998). Statistical mechanical study on the Freundlich isotherm equation. *Journal of Colloid and Interface Science,* 208(2): 379-387.
38. Hall, K. R., Eagleton, L. C., Acrivos, A. and Vermeulen, T. (1966). Pore- and solid diffusion kinetics in fixed-bed adsorption under constant pattern conditions. *Industrial and Engineering Chemistry Fundamentals,* 5(2): 212-223. https://doi.org/10.1021/i160018a011
39. Febrianto, J., Kosasih, A. N., Sunarso, J., Ju, Y. H., Indraswati, N. and Ismadji, S. (2009). Equilibrium and kinetic studies in adsorption of heavy metals using biosorbent: a summary of recent studies. *Journal Of Hazardous Materials,* 162(2-3): 616-645.
40. Ho, Y. S. and Ofomaja, A. E. (2006). Pseudo-second-order model for lead ion sorption from aqueous solutions onto palm kernel fiber. *Journal of Hazardous Materials,* 129(1–3): 137-142.
41. Sheikh, M. A., Noah, N. M., Tsuha, K. and Oomori, T. (2007). Occurrence of tributyltin compounds and characteristics of heavy metals. *International Journal of Environmental Science and Technology,* 4(1): 49-59.
42. Yoonaiwong, W., Kaewsarn, P. and Reanprayoon, P. (2011). Biosorption of lead and cadmium ions by non-living aquatic macrophyte, *Utricularia aurea*. *Sustainable Environment Research,* 21(6): 369-374.
43. Oyedepo, T. A. (2011). Biosorption of lead (II) and copper (II) metal ions on *Calotropis procera* (Ait.). *Science Journal of Purel & Applied Chemistry,* 2011: 1-7.
44. Vilar, V. J. P., Botelho, C. M. S. and Boaventura, R. A. R. (2008). Copper removal by algae Gelidium, agar extraction algal waste and granulated algal waste: Kinetics and equilibrium. *Bioresource Technology,* 99(4): 750-762.
45. Ali Redha, A. (2020). Removal of heavy metals from aqueous media by biosorption. *Arab Journal of Basic and Applied Sciences,* 27(1): 183-193.
46. Murphy, V., Hughes, H. and McLoughlin, P. (2007). Cu(II) binding by dried biomass of red, green, and brown macroalgae. *Water Research*, 41(4): 731-740.
47. Vilar, V. J. P., Botelho, C. M. S. and Boaventura, R. A. R. (2008b). Lead uptake by algae Gelidium and composite material particles in a packed bed column. *Chemical Engineering Journal*, 144(3): 420-430.
48. Farooq, U., Kozinski, J. A., Khan, M. A. and Athar, M. (2010). Biosorption of heavy metal ions using wheat-based biosorbents - A review of the recent literature. *Bioresource Technology*, 101(14): 5043-5053.
49. Escudero, C., Fiol, N., Villaescusa, I. and Bollinger, J. C. (2009). Arsenic removal by a waste metal hydroxide entrapped into calcium alginate beads. *Journal of Hazardous Materials,* 164(2–3), 533–541.
50. Yipmantin, A., Maldonado, H. J., Ly, M., Taulemesse, J. M. and Guibal, E. (2011). Pb(II) and Cd(II) biosorption on *Chondracanthus chamissoi* (a red alga). *Journal of Hazardous Materials,* 185(2–3): 922-929.
51. Lee, S. H., & Park, C. H. (2012). Biosorption of heavy metal ions by brown seaweeds from the southern coast of Korea. *Biotechnology and Bioprocess Engineering*, 17(4): 853-861.
52. Nessim, R. B., Bassiouny, A. R., Zaki, H. R., Moawad, M. N. and Kandeel, K. M. (2011). Biosorption of lead and cadmium using marine algae. *Chemistry and Ecology,* 27(6): 579-594.

53. Akpomie, K. G., Ezeofor, C. C., Olikagu, C. S., Odewole, O. A. and Ezeorah, C. J. (2018). Abstraction and regeneration potential of temperature-enhanced rice husk montmorillonite combo for oil spill. *Environmental Science and Pollution Research*, 25(34): 34711-34719.
54. Aroua, M. K., Leong, S. P. P., Teo, L. Y., Yin, C. Y. and Daud, W. M. A. W. (2008). Real-time determination of the kinetics of lead(II) adsorption onto palm shell-based activated carbon using an ion-selective electrode. *Bioresource Technology*, 99(13): 5786-5792.
55. Wu, Y., Zhang, S., Guo, X. and Huang, H. (2008). Adsorption of chromium(III) on lignin. *Bioresource Technology*, 99(16): 7709-7715.
56. Bishnoi, N. R. and Pant, A. (2004). Biosorption of copper from an aqueous solution using algal biomass. *Journal of Scientific and Industrial Research*, 63: 813-816.
57. Wang, G., Zhang, S., Yao, P., Chen, Y., Xu, X., Li, T. and Gong, G. (2018). Removal of Pb(II) from aqueous solutions by *Phytolacca americana* L. biomass as a low-cost biosorbent. *Arabian Journal of Chemistry*, 11(1): 99-110.
58. Ghasemi, M., Naushad, M., Ghasemi, N. and Khosravi-fard, Y. (2014). Adsorption of Pb(II) from aqueous solution using new adsorbents prepared from agricultural waste: Adsorption isotherm and kinetic studies. *Journal of Industrial and Engineering Chemistry*, 20(4): 2193-2199.
59. Ibrahim, W. M. (2011). Biosorption of heavy metal ions from an aqueous solution by red macroalgae. *Journal of Hazardous Materials*, 192(3): 1827-1835.
60. Ozudogru, Y. (2017). Biosorption of Cu (II) and Pb (ii) ions by using marine brown algae *Padina pavonica*. *Fresenius Environmental Bulletin*, 22: 3725-3729.
61. Arshadi, M., Amiri, M. J. and Mousavi, S. (2014). Kinetic, equilibrium, and thermodynamic investigations of Ni(II), Cd(II), Cu(II), and Co(II) adsorption on barley straw ash. *Water Resources and Industry*, 6: 1-17.
62. Naiya, T. K., Bhattacharya, A. K., Mandal, S. and Das, S. K. (2009). The sorption of lead(II) ions on rice husk ash. *Journal of Hazardous Materials*, 163(2–3): 1254-1264.
63. Meitei, M. D. and Prasad, M. N. V. (2014). Adsorption of Cu(II), Mn(II), and Zn(II) by *Spirodela polyrhiza* (L.) Schleiden: Equilibrium, kinetic and thermodynamic studies. *Ecological Engineering*, 71: 308-317.
64. Al-Homaidan, A. A., Al-Houri, H. J., Al-Hazzani, A. A., Elgaaly, G. and Moubayed, N. M. S. (2014). Biosorption of copper ions from aqueous solutions by Spirulina platensis biomass. *Arabian Journal of Chemistry*, *7*(1): 57-62.
65. Onwuka, J. C., Ajibola, V. O., Kagbu, J. A. and Manji, A. J. (2011). Biosorption of Cr(VI) and Co(II) ions from synthetic wastewater using dead biomass of freshwater green algae *Cosmarium panamense*. *Archives of Applied Science Research*, 3(6): 191-207.
66. Ashraf, M. A., Mahmood, K., Wajid, A., Maah, M. J. and Yusoff, I. (2011). Study of low-cost biosorbent for biosorption of heavy metals. In *Proceedings of the International Conference on Food Engineering and Biotechnology*, 9: pp. 60-68.
67. Ayawei, N., Ekubo, A. T., Wankasi, D. and Dikio, E. D. (2015). Adsorption of congo red by Ni/Al-CO_3: Equilibrium, thermodynamic and kinetic studies. *Oriental Journal of Chemistry*, 31(3): 1307-1318.
68. Lasheen, M. R., Ammar, N. S. and Ibrahim, H. S. (2012). Adsorption/desorption of Cd(II), Cu(II), and Pb(II) using chemically modified orange peel: Equilibrium and kinetic studies. *Solid-State Sciences*, 14(2): 202-210.
69. Yalçın, S. (2014). The mechanism of heavy metal biosorption on green marine macroalga *Enteromorpha linza*. *CLEAN–Soil, Air, Water*, 42(3): 251-259.
70. Weber, T. W. and Chakravorti, R. K. (1974). Pore and solid diffusion models for fixed-bed adsorbers. *AIChE Journal*, 20(2): 228-238.

Malaysian Journal of Analytical Sciences (MJAS)
Published by Malaysian Analytical Sciences Society

SYNTHESIS OF ZnO ON 3D GRAPHENE/NICKEL FOAM FOR PHOTOELECTROCHEMICAL WATER SPLITTING

(Sintesis ZnO pada 3D Grafin/Busa Nikel untuk Pembelahan Molekul Air Secara Fotoelektrokimia)

Nur Rabiatul Adawiyah Mohd Shah, Rozan Mohamad Yunus*, Nurul Nabila Rosman, Wai Yin Wong, Khuzaimah Arifin, Lorna Jeffery Minggu

Fuel Cell Institute,
Universiti Kebangsaan Malaysia, 43600 UKM Bangi, Selangor, Malaysia

**Corresponding author: rozanyunus@ukm.edu.my*

Received: 13 December 2021; Accepted: 27 February 2022; Published: 27 June 2022

Abstract

Photoelectrochemical (PEC) water splitting is a promising method that involves a direct route to produce green hydrogen (H_2). An efficient semiconductor photoelectrode that has a suitable band gap between the valence and conduction band is stable in an aqueous solution and cost-effective. Efficient charge transfer and outstanding light absorption are required to achieve enhanced PEC water splitting performance. However, the wide band gap of current photoelectrode such as zinc oxide (ZnO) limits their ability to transport electron, causing photogenerated electron–hole pair recombination and poor PEC performance. This study aims to design an efficient photoelectrode by incorporating a three-dimensional (3D) graphene with ZnO, where 3D graphene serves as a co-catalyst/support to enhance the photocatalytic activity of ZnO. The 3D graphene was first synthesized on nickel foam (Ni-foam) via chemical vapor deposition method with the flow of argon, H_2, and methane gas flow in a quartz tube, followed by the growth of ZnO via a hydrothermal method at 150 °C and 200 °C. FESEM, EDX and Raman confirmed the successful growth of ZnO on 3D graphene/Ni-foam. The flower-like ZnO was observed by FESEM after the hydrothermal method, and the highest photocurrent density was measured at 150 °C (108.2 mA cm^{-2}). Therefore, flower-like ZnO flower-like on 3D graphene/Ni-foam can be used as an efficient semiconductor photoelectrode in PEC water splitting.

Keywords: 3D graphene, zinc oxide, photoelectrode, photoelectrochemical water splitting

Abstrak

Pembelahan molekul air secara fotoelektrokimia (PEC) merupakan kaedah yang menggunakan laluan yang mudah untuk menghasilkan hidrogen (H_2). Fotoelektrod semikonduktor yang cekap mempunyai jurang jalur yang sesuai antara jalur valensi dan konduksi, stabil dalam larutan berair dan kos yang rendah. Pemindahan cas yang cekap dan penyerapan cahaya yang baik diperlukan untuk mencapai prestasi pembelahan molekul air PEC yang tinggi. Walau bagaimanapun, jurang jalur fotoelektrod yang lebar seperti zink oksida (ZnO) menghadkan kebolehannya untuk pengangkutan elektron, menyebabkan penggabungan semula lubang–elektron terjana dan prestasi PEC yang rendah. Kajian ini bertujuan untuk merekacipta fotoelektrod yang cekap dengan menggabungkan tiga-dimensi (3D) grafin dengan ZnO, di mana 3D grafin bertindak sebagai pemangkin bersama/sokongan untuk meningkatkan aktiviti fotokatalitik ZnO. 3D grafin disintesis pada busa nikel (busa-Ni) melalui kaedah pemendapan wap kimia dengan aliran gas argon, H_2 dan metana dalam tiub kuarza, diikuti dengan pertumbuhan ZnO melalui kaedah hidrotherma pada

150 °C and 200 °C. FESEM, EDX dan Raman mengesahkan pertumbuhan ZnO pada 3D grafin/busa-Ni. Pertumbuhan ZnO seperti bunga dapat dilihat dengan alat FESEM selepas melalui kaedah hidrotherma dan ketumpatan foto arus yang tinggi diukur pada suhu 150 °C (108.2 mA cm^{-2}). Oleh itu, ZnO berbentuk seperti bunga pada 3D grafin/busa-Ni boleh digunakan untuk fotoelektrod semikondutor yang cekap dalam pembelahan air secara PEC.

Kata kunci: 3D grafin, zink oksida, fotoelektrod, pembelahan molekul air secara fotoelektrokimia.

Introduction

Photoelectrochemical (PEC) water splitting is a potential technology that involves a direct route using sunlight and water to produce green hydrogen (H_2) for a variety of applications [1, 2]. Water is a primary source of H_2, and the consumption and cycle of H_2 are in a continuous loop. In addition, as compared to a photovoltaic-electrolysis system, the PEC system is simple and space saving with fewer components [3]. However, current solar-to-hydrogen (STH) efficiencies of the PEC system, 16.2% produced by a multijunction semiconductor, are insufficient compared with existing technologies. Thus, continuous, high-efficiency, and sustainable photocatalytic H_2 evolution from water without the assistance of electron donors with STH values greater than 10% is necessary [4–6].

In general, semiconductor materials with an appropriate band gap are often used as photoelectrode for light absorption in the PEC system. Nevertheless, not all semiconductors fulfill the band gap requirements for overall water splitting, which require the conduction band (CB) to be more negative than the reduction potential of water to produce H_2 and the valence band to be more positive than the oxidation potential of water to produce oxygen [7, 8]. The wide band gap of current photoelectrode, such as zinc oxide (ZnO), which is approximately 3.37 eV, inhibits the ability to transport electrons, resulting in the recombination of photogenerated electron–hole pairs [9–11]. Hence, three-dimensional (3D) graphene with a high surface area, high conductivity, and fast charge carrier transport as a co-catalyst/support can overcome the limitations of ZnO by extending the light absorption range and improving charge separation and transportation properties [12, 13].

In this work, 3D graphene was synthesized on nickel foam (Ni-foam) using chemical vapor deposition (CVD) method, followed by hydrothermal method to synthesize ZnO on 3D graphene/Ni-foam by using two different reaction temperature (150 °C and 200 °C) for 2 hours (Figure 1). The photocatalytic performance of 3D graphene/Ni-foam hierarchical flower-like ZnO exhibits a large surface area that can increase the charge separation efficiency, resulting in excellent photocatalytic performance.

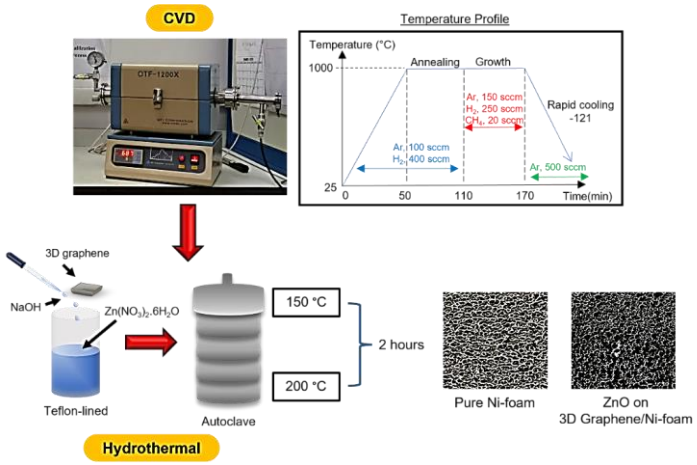


Figure 1. Schematic illustration for preparation of ZnO on 3D graphene/Ni-foam

Materials and Methods

Preparation of three-dimensional (3D) graphene

The nickel foam (Ni-foam; 1.5 cm x 1.5 cm x 0.16 cm, Brand TOB) was used as a template to grow graphene via chemical vapor deposition (CVD) method. Acetone, ethanol, and deionized water were used during ultrasonic cleaning and dried using nitrogen blow. Then, the Ni-foam was placed in the center of the quartz tube and heated up to 1000 °C for 50 min at 20 °C/min. The temperature was maintained for another 60 min with argon (Ar, 100 sccm) and H_2/Ar (400 sccm) gas flow. For 60 min of growth time, methane (CH_4) with 20 sccm gas flow was introduced as the carbon source. The sample is rapidly cooled to room temperature.

Synthesis of 3D Graphene/ZnO on nickel foam (Ni-foam)

Zinc nitrate hexahydrate ($Zn(NO_3)_2.6H_2O$), sodium hydroxide (NaOH) from Sigma-Aldrich, and deionized water were used throughout the experiment. 0.5 M $Zn(NO_3)_2.6H_2O$ solutions were prepared in 30 mL deionized water under stirring for 30 min. Simultaneously, 5 M NaOH solutions were prepared in 30 mL deionized water under stirring for the same duration. $Zn(NO_3)_2.6H_2O$ solution was transferred to a sealed Teflon-lined stainless-steel autoclave. Next, 3 drops of NaOH solution were added to the former solution to change the pH of the reactants, and the 3D graphene/Ni-foam was immersed into the reaction before being kept in a box furnace at 150 °C and 200 °C for 2 hours. Finally, the autoclave was taken outside, and the as-sample were dried for 2 hours at 80 °C.

Characterization techniques

Raman analysis was conducted using DXR2xi, Thermo Scientific, to confirm the presence of graphene on Ni foam. The morphology of the samples was examined by field emission scanning electron microscopy (FESEM) and energy dispersive X-ray (EDX) analysis to confirm the existence of graphene and ZnO (Carl Zeiss/GeminiSEM 500).

Photocatalytic measurements

UV-Vis Spectroscopy (Perkin Elmer/Lambda 35) was used to evaluate the band gap energy for ZnO on 3D graphene/Ni-foam at 150 °C and 200 °C for 2 hours. A three-electrode system was used to study the photocurrent of the as-samples, where the working electrode is ZnO on 3D graphene/Ni-foam, the counter electrode is Pt wire, and the reference electrode is Ag/AgCl (3.0 M KCl). A 0.5 M sulfuric acid (H_2SO_4) aqueous solution was used as the electrolyte, and it was purged with nitrogen before testing. 100 mW cm^{-2} Xe lamp was used as the light source, and the area of the ZnO on 3D graphene/Ni-foam exposed to light was 1.5 cm^2.

Result and Discussion

Typically, 3D graphene can be synthesized by using CVD method based on the previous study [14]. FESEM was used to study the physical and structural characteristics of the resulting 3D graphene/Ni-foam, ZnO on 3D graphene/Ni-foam, and ZnO nanoparticles, as shown in Figure 2(a). Combining 3D graphene with metal oxide like ZnO can enhance the PEC performance through shifting the band gap energy, lowering electron–hole pair recombination, increasing charge separation efficiency, and producing smaller particle size with larger surface area [15]. Figure 2(b – c) shows the FESEM image of pristine graphene taken after the CVD growth. Two different color contrasts were observed on the image where the dark contrast corresponds to graphene, which will be validated through Raman and EDX analysis. The hydrothermal method was then performed to develop ZnO on 3D graphene/Ni-foam at 150 °C and 200 °C. The morphological images of flower-like ZnO on 3D graphene/Ni-foam in Figure 2(d – e) demonstrate a high coverage area of ZnO on 3D graphene/Ni-foam. During the hydrothermal process, ZnO nanoparticles were formed (Figure 2(f – g)), and the presence of graphene influenced the growth of hierarchical flower-like ZnO structures. The mechanism of flower-like ZnO was well explained in previous study [16].

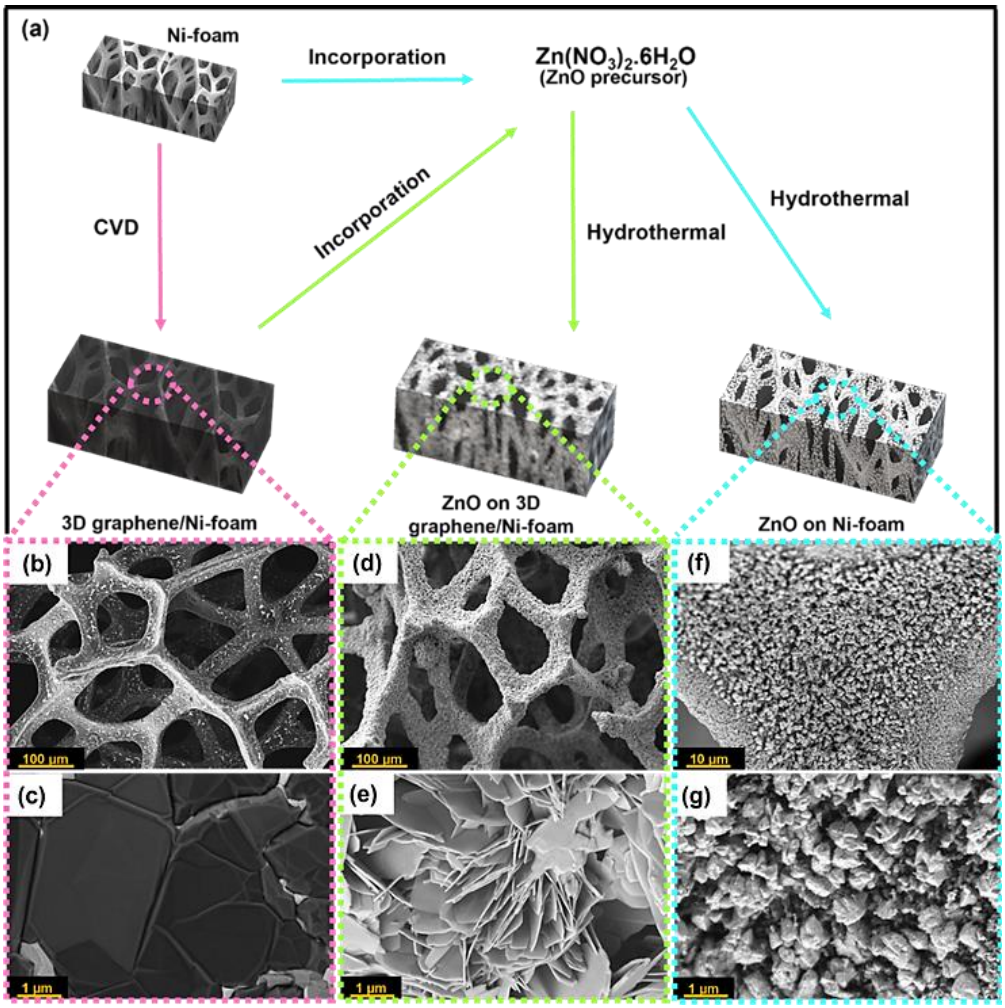


Figure 2. (a) Schematic illustration of the prepared sample. FESEM image of (b – c) 3D graphene/Ni-foam, (d – e) ZnO on 3D graphene/Ni-foam, and (f – g) ZnO on Ni-foam at the low and high magnification, respectively.

Raman spectra for 3D graphene/Ni-foam (Figure 3(a)) were determined. Two graphene fingerprint peaks, including G and 2D bands at ~1581 and ~2700 cm^{-1}, respectively, were observed (Figure 3(b)). The graphene is successfully growth with high quality as there is no D band (~1350 cm^{-1}) observed, in which the D band corresponds to the disorder and defect in graphene [17]. Thus, a sample at low temperature (150 °C) was selected to confirm the successful growth of ZnO using EDX mapping due to the good coverage and flower-like structure of ZnO. As shown in Figure 3(c – d), the existence of carbon (C), zinc (Zn), oxygen (O) and nickel (Ni) indicates the successful growth of ZnO using the hydrothermal method.

Photocatalysts with a narrow band gap can harvest visible light and generate excellent efficiency in photocatalytic applications. The reflectance spectra and Kubelka-Munk plot were used to determine the band gap energy for pure Ni-foam, 3D graphene/Ni-foam and ZnO on 3D graphene/Ni-foam at 150 °C and 200 °C at 2 hours, respectively. Figure 4(a) shows a significance

decrease around 380 nm. This decrease is related to the electron transitions occurring the optical band gap. The Kubelka-Munk function was used to convert the UV-Vis reflectance spectrum to measure the precise value of the band gap. As a result, the band gap energy of pure Ni-foam and 3D graphene/Ni-foam are E_g= 3.217 eV and ZnO on 3D graphene/Ni-foam at 150 °C and 200 °C for 2 hours are E_g= 3.218 eV, respectively (Figure 4(b)). There are no significance changes of band gap energy with the introduction of ZnO. However, the presence of ZnO enhances the photocatalytic performance, where the highest photocurrent density is achieved with ZnO on 3D graphene/Ni-foam at 150 °C, approximately 108.2 mA cm^{-2} (Figure 4(c)). Considering that the coverage of ZnO for 150 °C is larger than that for 200 °C, the structure of ZnO starts to agglomerate with the increase of temperature to 200 °C, thereby decreasing the surface area and resulting in a low photocurrent density [18]. In addition, the electron transfer rate of reaction for all samples is evaluated. Electrochemical impedance spectroscopic (EIS) analysis (Figure 4(d)) demonstrates that ZnO on 3D graphene/Ni-foam at 150 °C has the smallest arc radius of a semicircle, implying that the sample experienced faster interfacial electron charge transfer. This finding could be explained by the porous structure of 3D graphene, which has a large surface area, excellent mechanical and electrical properties, good electron transport, and electron–hole separation, making them suitable for PEC applications [7,8,14]. As shown in Table 1, ZnO on 3D graphene/Ni foam shows higher photocurrent density as compared with other conventional methods and materials for PEC water splitting.

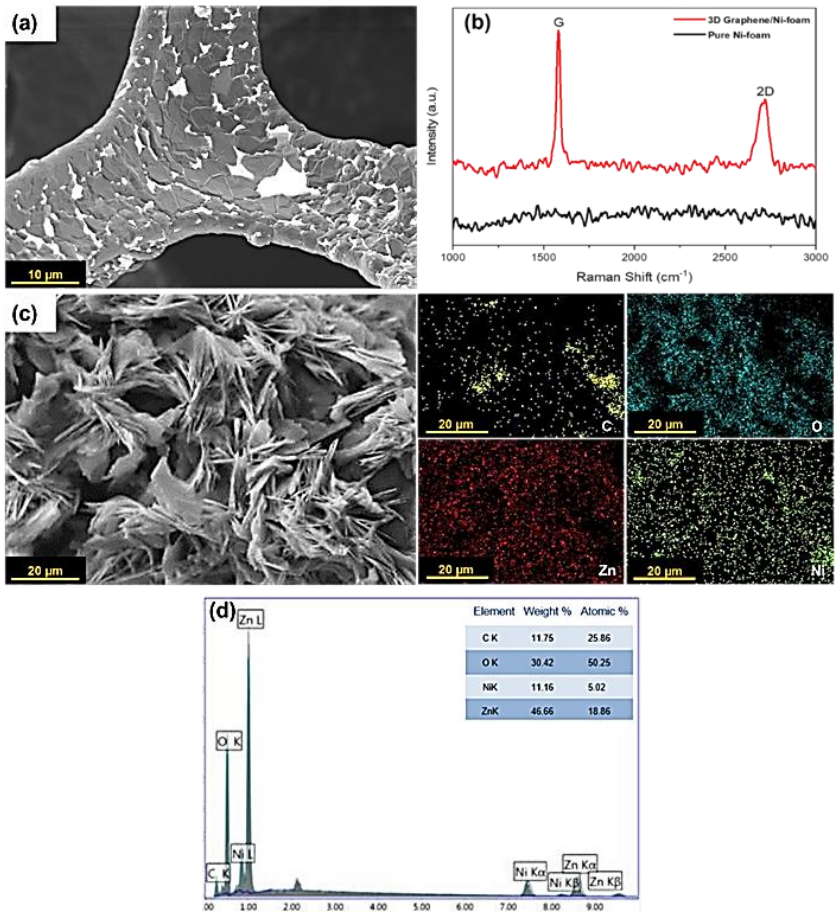


Figure 3. (a) FESEM image and (b) Raman spectra of 3D graphene/Ni-foam. EDX (c) mapping and (d) analysis of

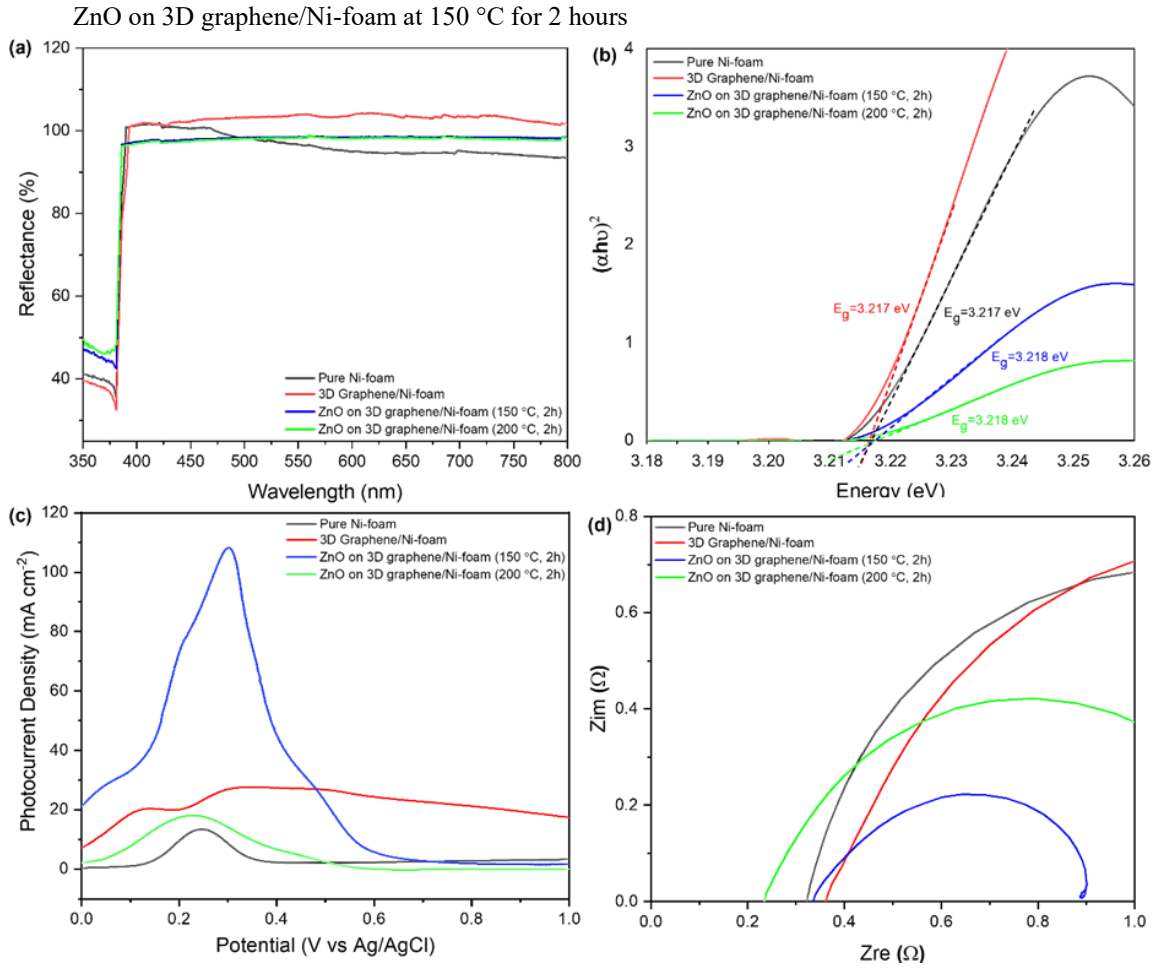


Figure 4. (a) Diffuse reflectance spectra, (b) Kubelka-Munk plot, (c) Photocurrent density at 0.0 – 1.0 V vs Ag/AgCl and (d) EIS analysis using Nyquist plot for pure Ni-foam, 3D graphene/Ni-foam, ZnO on 3D graphene/Ni-foam at 150 °C and 200 °C for 2 hours

Table 1. PEC performance of modified ZnO using various methods

Materials	**Methods**	**Structures of ZnO**	**Photocurrent Densities (mA cm^{-2})**	**Reference**
ZnO on 3D graphene/Ni-foam	CVD and hydrothermal	Flower-like	108.2 at 0 – 1.0 V vs Ag/AgCl	This work
ZnO-C@Ni-foam	Hydrothermal	Mixed of nanorods and flower-like	100 at 0 – 0.9 V vs Ag/AgCl	[19]
ZnO@Ni-foam	Hydrothermal	Mixed of nanorods and flower-like	30 at 0 – 0.9 V vs Ag/AgCl	[19]
ZnO/rGO foam	One-step hydrothermal	Nanorods	0.27 at 1.0 V vs Ag/AgCl	[20]

Figure 5 illustrates a possible mechanism for efficient electron transport in ZnO on 3D graphene/Ni-foam based on the results of the PEC test. When sunlight illuminates ZnO on 3D graphene/Ni-foam, electrons in the VB of ZnO are excited to jump to the CB using 3D graphene/Ni-foam as a co-catalyst/support. Hydrogen was produced on the surface of ZnO and 3D graphene/Ni-foam. The incorporation of 3D graphene/Ni-foam provides a good electron transport channel in the ZnO on 3D graphene/Ni-foam structure.

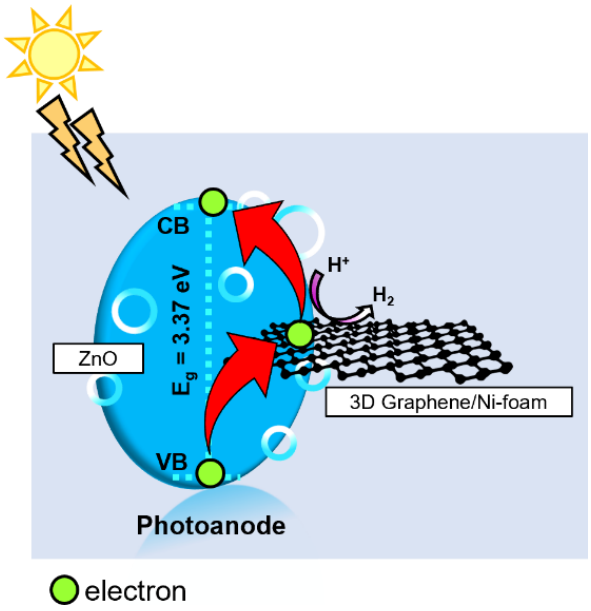


Figure 5. Schematic illustration of PEC water splitting using ZnO on 3D graphene/Ni-foam.

Conclusion

ZnO on 3D graphene/Ni-foam was successfully synthesized by a two-step approach, CVD and hydrothermal methods. The highest photocurrent density was achieved at 150 °C for 2 hours (108.2 mA cm^{-2}). Therefore, a photoelectrode with a high surface area, which provides more active sites, can enhance the photocatalytic performance by increasing charge separation efficiency. Thus, ZnO on 3D graphene/Ni-foam could be a potential photoelectrode for PEC water splitting.

Acknowledgement

This work is funded by Ministry of Higher Education (MOHE) and Universiti Kebangsaan Malaysia (UKM) through FRGS/1/2019/STG07/UKM/02/2 and DIP-2019-020, respectively. The authors would also like to express their gratitude to all UKM staff and technicians who contributed to this study, especially from the Fuel Cell Institute and Faculty of Science and Technology.

References

1. Li, Y. and Tsang, S. C. E. (2020). Recent progress and strategies for enhancing photocatalytic water splitting. *Mater. Today Sustain.*, 9: 100032.
2. Li, X., Zhao, L., Yu, J., Liu, X., Zhang, X., Liu, H. and Zhou, W. (2020). Water splitting: From electrode to green energy system. *Nano-Micro Letters*, Springer Singapore 12.
3. Dias, P. and Mendes, A. (2018). Hydrogen production from photoelectrochemical water splitting. In encyclopedia of sustainability science and technology (Meyers, R. A., ed.). Springer New York, New York: pp 1-52.

4. Cao, S., Piao, L. and Chen, X. (2020). Emerging photocatalysts for hydrogen evolution. *Trends Chemistry*, Elsevier Inc. 2: pp. 57-70.
5. Hisatomi, T. and Domen, K. (2019). Reaction systems for solar hydrogen production via water splitting with particulate semiconductor photocatalysts. *Nature Catalyst*, 2: 387-399.
6. Young, J. L., Steiner, M. A., Döscher, H., France, R. M., Turner, J. A. and Deutsch, T. G. (2017). Direct solar-to-hydrogen conversion via inverted metamorphic multi-junction semiconductor architectures. *Nature Energy*, 2: 1-8.
7. Kuang, P., Sayed, M., Fan, J., Cheng, B. and Yu, J. (2020). 3D graphene-based H_2-production photocatalyst and electrocatalyst. *Advance Energy Materials*, 10: 1-53.
8. Mohd Shah, N. R. A., Mohamad Yunus, R., Rosman, N. N., Wong, W. Y., Arifin, K. and Jeffery Minggu, L. (2021). Current progress on 3D graphene-based photocatalysts: From synthesis to photocatalytic hydrogen production. *International Journal Hydrogen Energy*, 46: 9324-9340.
9. Gowtham, M., Chandrasekar, S., Mohanraj, C. and Senthil Kumar, N. (2020). Morphology dependent photocatalytic activity of ZnO nanostructures-A short review. *NanoNEXT*, 1: 30-38.
10. Baruah, S. and Dutta, J. (2009). Hydrothermal growth of ZnO nanostructures. *Science Technology Advance Materials*, 10: 013001.
11. Vaseem, M., Umar, A. and Hahn, Y. (2010). ZnO nanoparticles: Growth, properties, and applications. *Metal Oxide Nanostructures Their Applications*, 5: 1-36.
12. Singh, P., Shandilya, P., Raizada, P., Sudhaik, A., Rahmani-Sani, A. and Hosseini-Bandegharaei, A. (2020). Review on various strategies for enhancing photocatalytic activity of graphene based nanocomposites for water purification. *Arabian Journal Chemistry*, 13: 3498-3520.
13. Gao, C., Zhong, K., Fang, X., Fang, D., Zhao, H., Wang, D., Li, B., Zhai, Y., Chu, X. and Li, J. (2021). Brief review of photocatalysis and photoresponse properties of ZnO–graphene nanocomposites. *Energies*, 14: 6403.
14. Mohd Shah, N. R. A., Rosman, N. N., Wong, W. Y., Arifin, K., Jeffery Minggu, L. and Mohamad Yunus, R. (2021). Effect of annealing time on chemical vapor deposition growth of 3D graphene for photoelectrochemical water splitting. *Material Today Proceeding,* 57(3): 1215-1219.
15. Ong, C. B., Ng, L. Y. and Mohammad, A. W. (2018). A review of ZnO nanoparticles as solar photocatalysts: Synthesis, mechanisms and applications. *Renewable Sustainable Energy Review*, 81: 536–551.
16. Mohamed, M. A., M. Zain, M. F., Jeffery Minggu, L., Kassim, M. B., Jaafar, J., Saidina Amin, N. A., Mastuli, M. S., Wu, H., Wong, R. J. and Ng, Y. H. (2019). Bio-inspired hierarchical hetero-architectures of in-situ C-doped g-C3N4 grafted on C, N co-doped ZnO micro-flowers with booming solar photocatalytic activity. *Journal Industry Engineering Chemistry*, 77: 393-407.
17. Wang, W. X., Zhang, S. C., Xing, Y. L., Wang, S. B. and Ren, Y. B. (2016). The closed-environment CVD method for preparing three-dimensional defect controllable graphene foam with a conductive interconnected network for lithium-ion battery applications. *RSC Advance,* 6: 75414-75419.
18. Ghorbani, M., Abdizadeh, H., Taheri, M. and Golobostanfard, M. R. (2018). Enhanced photoelectrochemical water splitting in hierarchical porous ZnO/Reduced graphene oxide nanocomposite synthesized by sol-gel method. *Int. J. Hydrogen Energy*, 43, 7754–7763.
19. Gadisa, B. T., Baye, A. F., Appiah-Ntiamoah, R. and Kim, H. (2021). ZnO@Ni foam photoelectrode modified with heteroatom doped graphitic carbon for enhanced photoelectrochemical water splitting under solar light. *International Journal Hydrogen Energy*, 46: 2075-2085.
20. Men, X., Chen, H., Chang, K., Fang, X., Wu, C., Qin, W. and Yin, S. (2016). Three-dimensional free-standing ZnO/graphene composite foam for photocurrent generation and photocatalytic activity. *Applied Catalyst B Environment*, 187: 367-374.

Malaysian Journal of Analytical Sciences (MJAS)
Published by Malaysian Analytical Sciences Society

THE EFFECT OF MEMBRANE THICKNESS ON THE PERFORMANCE OF PASSIVE DIRECT ETHANOL FUEL CELLS USING A POLY VINYL ALCOHOL/GRAPHENE OXIDE COMPOSITE MEMBRANE

(Kesan Ketebalan Membran Terhadap Prestasi Sel Fuel Etanol Langsung Pasif Menggunakan Membran Komposit Alkohol Polivinil/Grafin Oksida)

Zulfirdaus Zakaria*

Fuel Cell Institute,
Universiti Kebangsaan Malaysia, 43600 UKM Bangi, Selangor, Malaysia

**Corresponding author: zulfirdaus@ukm.edu.my*

Received: 27 November 2021; Accepted: 3 February 2022; Published: 27 June 2022

Abstract

Ethanol is a renewable fuel because it can be produced from a variety of production sources that are non-toxic and environmentally friendly. Thus, the consumption of passive direct ethanol fuel cells (DEFCs) as a power supply for portable devices is intriguing and potentially marketable in the future. Unfortunately, one constraint in the application of passive DEFCs is the lack of a Nafion membrane replacement. The Nafion membrane is expensive and has high ethanol permeability. We previously synthesised a crosslinked poly vinyl alcohol/graphene oxide (PVA/GO) composite membrane for passive DEFCs using low-cost polymer materials and successfully achieved low ethanol permeability. Furthermore, the characterization and performance of a crosslinked PVA/GO composite membrane outperformed that of the Nafion membrane. In the passive DEFCs, the optimal membrane thickness is a critical parameter that influences the membrane and single-cell performance. This experimental study attempted to examine the effect of a crosslinked PVA/GO composite membrane thickness on proton conductivity, ethanol permeability, membrane selectivity, and single-cell performance. The passive DEFCs achieved a maximum performance of 7.54 mW cm^{-2} at 60 °C by using a crosslinked PVA/GO composite membrane with a membrane thickness of 0.24 mm.

Keywords: polymer electrolyte membrane, membrane thickness, passive direct ethanol fuel cells, poly (vinyl)/graphene oxide

Abstrak

Etanol merupakan bahan api yang boleh diperbaharui kerana ia boleh dihasilkan daripada pelbagai sumber pengeluaran, tidak toksik, dan mesra alam. Oleh itu, penggunaan sel fuel etanol langsung pasif (DEFCs) sebagai bekalan kuasa untuk peranti mudah alih adalah menarik dan berpotensi untuk dipasarkan pada masa hadapan. Walau bagaimanapun, satu kekangan terhadap penggunaan DEFCs pasif adalah ketiadaan penggantian membran Nafion. Membran Nafion adalah mahal dan mempunyai kebolehtelapan etanol yang tinggi. Sebelum ini, kami telah mensintesis membran komposit alkohol polivinil/grafin oksida (PVA/GO) terpaut silang untuk DEFC pasif menggunakan bahan polimer berkos rendah dan berjaya mencapai kebolehtelapan etanol yang rendah. Tambahan lagi, pencirian dan prestasi membran komposit PVA/GO silang mengatasi prestasi membran Nafion. Dalam DEFCs pasif, ketebalan membran optimum ialah parameter kritikal yang mempengaruhi prestasi membran dan sel tunggal. Kajian eksperimen ini cuba untuk mengkaji kesan ketebalan membran komposit PVA/GO terpaut silang terhadap kekonduksian

proton, kebolehtelapan etanol, selektiviti membran, dan prestasi sel tunggal. DEFC pasif telah memperoleh prestasi maksimum 7.54 mW cm^{-2} pada 60 °C melalui penggunaan membran komposit PVA/GO bersilang dengan ketebalan membran 0.24 mm.

Kata kunci: membran elektrolit polimer, ketebalan membrane, sel bahan api etanol langsung pasif, alkohol polivinil/grafin oksida

Introduction

High reliance on fossil fuel consumption tends to increase greenhouse gas emissions, resulting in impending climate change. Furthermore, as fossil fuel sources deplete, researchers and industry are attempting to boost the use of renewable fuels such as fuel cells. Fuel cells of many forms have been investigated, including proton exchange membrane fuel cells (PEMFCs), direct alcohol fuel cells (DAFCs), and solid oxide fuel cells (SOFCs). According to the fuel cell design, each type of fuel cell has a specific application based on the physical fuel condition and type of electrolyte used [1]. For example, direct ethanol fuel cells (DEFCs) are commonly utilised for portable device applications such as electrical and electronic devices due to the fact that these fuel cell systems can be manufactured on a small micrometre scale. Although methanol is more commonly used in the systems of DAFCs for portable device applications, there are numerous advantages to using ethanol in fuel cell systems over methanol. Ethanol is a low-cost, less-toxic, naturally existing, green, and renewable fuel that can be easily manufactured through the fermentation process [2]. Besides, the energy density of ethanol (i.e., 8.00 kW h kg^{-1}) is higher than that of methanol (i.e., 6.09 kW h kg^{-1}). Furthermore, ethanol is safe for human consumption (i.e., used in medicine). Thus, ethanol is easier to handle for the processes of storage, transfer, and management [3].

Passive DEFCs are appropriate for small portable device applications due to the unavailability of an external component required. For example, this fuel cell system does not require an external fuel pump or air blower to supply the fuel and oxidant needed for energy generation [4]. Passive DEFCs can be operated in the single-cell mode with a polymer electrolyte membrane (PEM) located in the centre cell and a pair of electrodes, as presented in Figure 1. PEM is a critical component that influences the overall performance of passive DEFCs. To achieve excellent long-term operating conditions for fuel cells, PEM should exhibit high chemical and mechanical stability, high proton conductivity, and low ethanol permeability to obtain high membrane selectivity [5]. Unfortunately, the conventional membrane that is widely used in fuel cell systems, which is a perfluorinated sulfonic acid electrolyte membrane (Nafion membrane, manufactured by DuPont), has significant ethanol permeability and leads to rapid ethanol crossover. As a result, the performance of the cell is degraded and damaged on the cathode side [6].

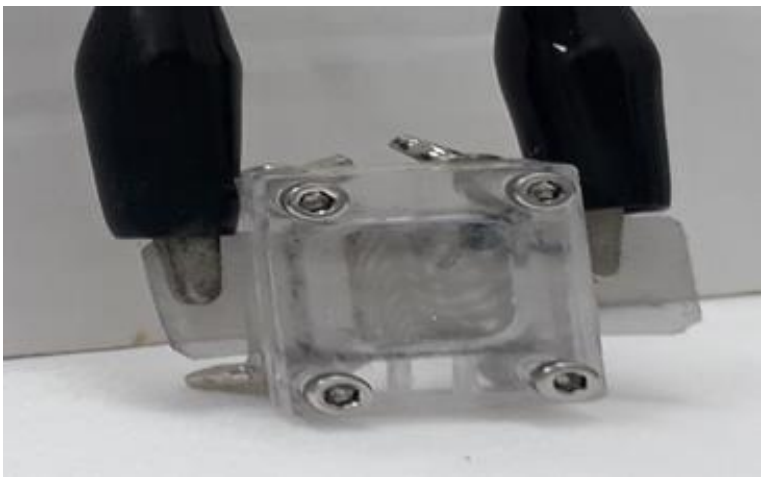


Figure 1. DIY single-cell passive DEFCs

The thickness of the membrane has a considerable effect on the membrane properties and performance of the fuel cell. Numerous studies have examined the influence of membrane thickness on fuel cell performance [7, 8]. For example, Sudaroli et al. [9] tested two distinct types of Nafion membranes with varying membrane thicknesses for fuel cell applications, Nafion 117 and Nafion 1110. According to Sudaroli et al. [9], that thicker membranes substantially decrease fuel crossover and improve single-cell efficiency. While raising the membrane thickness is efficient at decreasing fuel crossover, it has a detrimental effect on the polymeric membrane's conductivity qualities. Thus, the optimal membrane thickness is necessary to achieve the appropriate conductivity-fuel crossover balance [10].

Previously, the performance of a crosslinked poly vinyl alcohol/graphene oxide (PVA/GO) composite membrane in the use of passive DEFCs has been described. Compared to the Nafion membrane, the crosslinked PVA/GO composite membrane has a 15 wt.% loading of GO and demonstrated low ethanol permeability and good membrane selectivity [11]. In this study, the effect of the membrane thickness of a crosslinked PVA/GO composite membrane was studied to enhance the cell performance of passive DEFCs. In order to achieve the optimal membrane thickness for the crosslinked PVA/GO composite membrane, several evaluations were performed, including membrane composite self-performance and performance on single-cell passive DEFCs.

Materials and Methods

All chemicals and procedures for fabricating the membranes used in this study were previously described in our prior study utilising the simple casting solution method [11]. The GO loading was maintained at 15% by weight throughout this research. Additionally, the membrane thickness was modified according to the volume of the solution created, resulting in four distinct membrane thicknesses (i.e., 0.16 mm, 0.20 mm, 0.24 mm, and 0.28 mm). The membrane self-performance was evaluated for proton conductivity, ethanol permeability, and membrane selectivity with various membrane thicknesses. Next, the performance of single-cell passive DEFCs was measured with different membrane thicknesses of crosslinked QPVA/GO composite membranes. The cell condition was constant with 4 mg cm^{-2} of Pt/Ru catalyst (i.e., anode), 2 mg cm^{-2} of Pt catalyst (i.e., cathode), and 2 cm^2 of active cell area at 30 °C. The technical and calculation information followed the details of the experiment from our previous work [11].

Results and Discussion

The self-performance of a crosslinked QPVA/GO composite membrane, comprising proton conductivity, ethanol permeability, and membrane selectivity, is shown in Table 1. According to the self-performance results, lowering the membrane thickness substantially boosted proton conductivity. This indicated that decreasing the membrane thickness reduced the ohmic resistance slightly and shortened the proton pathway. As a result, proton transfer within the PEM was rapid. The mechanism of proton conductivity inside the crosslinked PVA/GO composite membranes is depicted in Figure 2. The proton is mostly diffused via the vehicle and hopping mechanisms. Thus, the thin membrane thickness is generated during the proton transfer process, which is accelerated due to the resistance effect, resulting in lower resistance and a shorter diffusion pathway [12].

Table 1. Self–performance of a crosslinked PVA/GO composite membrane with varying membrane thicknesses

Membrane thickness (mm)	σ, × 10^{-3} S cm^{-1}	ρ, × 10^{-7} cm^2 s^{-1}	Membrane selectivity, × 10^4 S s cm^{-3}
0.16	11.3	2.34	4.829
0.20	9.5	1.78	5.337
0.24	8.4	1.51	5.562
0.28	7.6	1.46	5.241

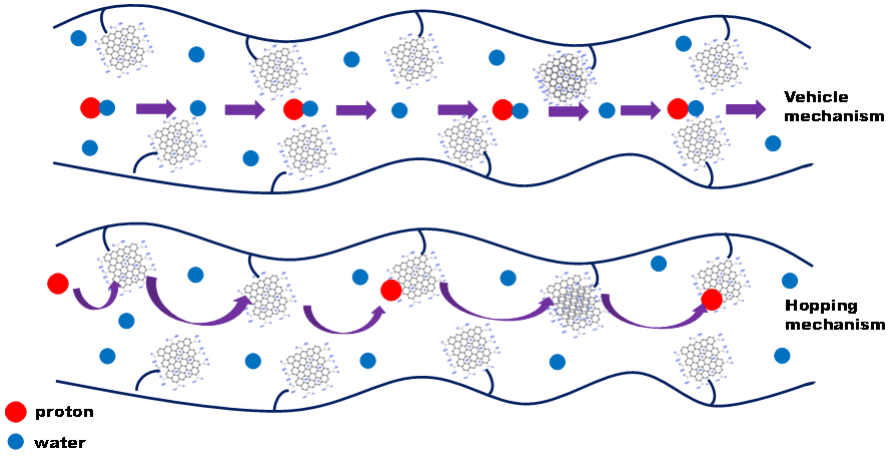


Figure 2. The mechanism of proton conductivity within the crosslinked PVA/GO composite membranes

Unfortunately, the thin membrane thickness allowed for high ethanol permeability to occur quickly due to the reduction of obstacle regions within the matrix polymer. Based on Table 1, the increasing membrane thickness is beneficial for the ethanol barrier because the fuel movement becomes more difficult to penetrate the three-dimensional matrix polymer structure between PVA, GO, and crosslinking interaction [13]. However, the proton conductivity is sacrificed due to the large membrane thickness. As a result, determining the optimal membrane thickness is critical for balancing both the membrane's self-performance and the membrane's performance. Thus, membrane selectivity is a precise metric that demonstrates the optimal membrane thickness, which balances proton conductivity and ethanol permeability [14]. According to Table 1, the maximum membrane selectivity is 5.562 $\times$ 10^4 S s cm^{-3} for a crosslinked QPVA/GO composite membrane with a membrane thickness of 0.24 mm. This indicated that the optimum membrane thickness is 0.24 mm and that the higher power density should be shown during the single-cell performance.

Overall, all membrane thicknesses have good results in terms of proton conductivity in the range of $\sim 10^{-3}$ S cm^{-1} and ethanol permeability in the range of $\sim 10^{-7}$ cm^2 s^{-1}. As illustrated in Figure 3, the characterization of a crosslinked PVA/GO composite membrane demonstrated suitable morphologies and structures for usage as a PEM in applying passive DEFCs. Figure 1 presents our previous characterization results, which include the analyses of FTIR, XRD, and FESEM [11]. As illustrated in Figure 3(a), the modification of PVA with GO and a crosslinked agent resulted in the presence of numerous oxygenic functional groups necessary for the hopping mechanism and the retention of water in the vehicle mechanism for proton transfer within the PEM. The crystalline and amorphous structures of a crosslinked PVA/GO composite membrane are then balanced to enhance the self-performance of the membrane, particularly in terms of proton conductivity and ethanol permeability, as shown in Figure 3(b). Besides, the dense morphology of a crosslinked PVA/GO composite membrane that was successfully synthesised as presented in Figures 3(c) and 3(d) has contributed to the critical function of managing the issue of ethanol crossover [15, 16].

All the different membrane thicknesses of a crosslinked PVA/GO composite membrane were evaluated in single-cell passive DEFCs with 2 M ethanol. Figure 4 shows the cell voltage and power density performance for all samples. The result has proven that the highest membrane selectivity with 0.24 mm membrane thickness obtained the highest power density with 5.71 mW cm^{-2}. Besides, the open cell voltage of 0.24 mm membrane thickness produced a maximum voltage of 0.85 V. This indicates that the minimum ethanol crossover was obtained with the optimal membrane

thickness [17]. Furthermore, the high proton conductivity of a crosslinked PVA/GO composite membrane enhanced the electrochemical properties that rapidly transferred the proton within the matrix polymer. As a result, the redox reaction occurred smoothly and produced high cell voltage and power density [18]. Hence, the optimal membrane thickness of a crosslinked PVA/GO composite membrane for this study was 0.24 mm.

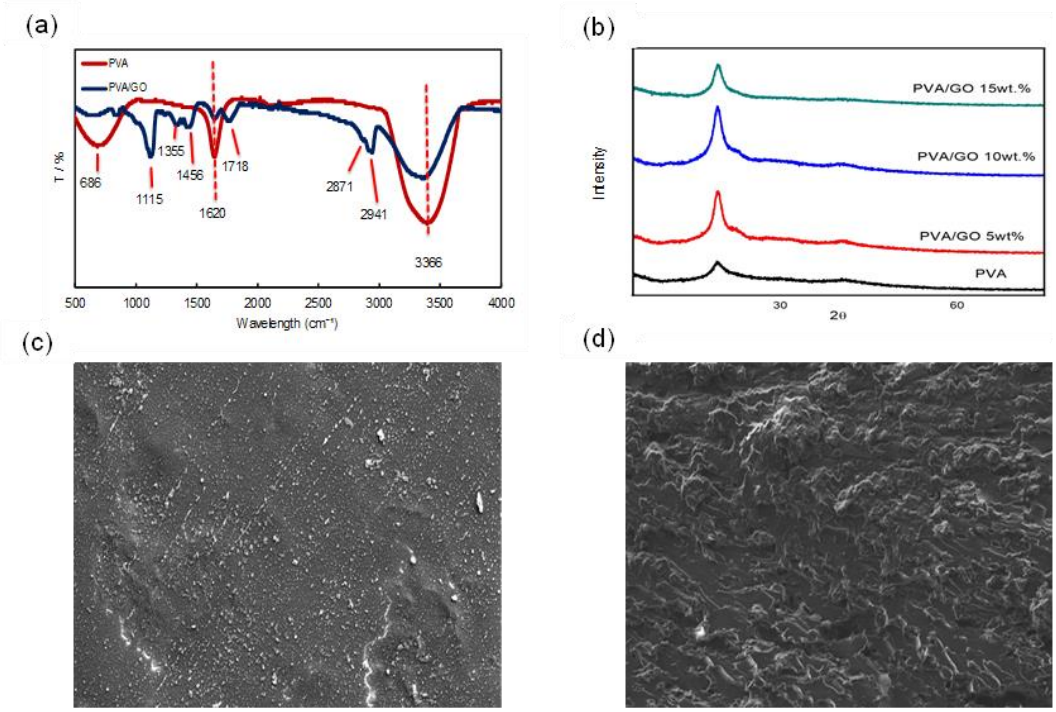


Figure 3. (a) FTIR analysis of a crosslinked PVA/GO composite membrane; (b) XRD analysis of membranes; FESEM analysis of membrane; (c) surface; (d) cross-section [11]

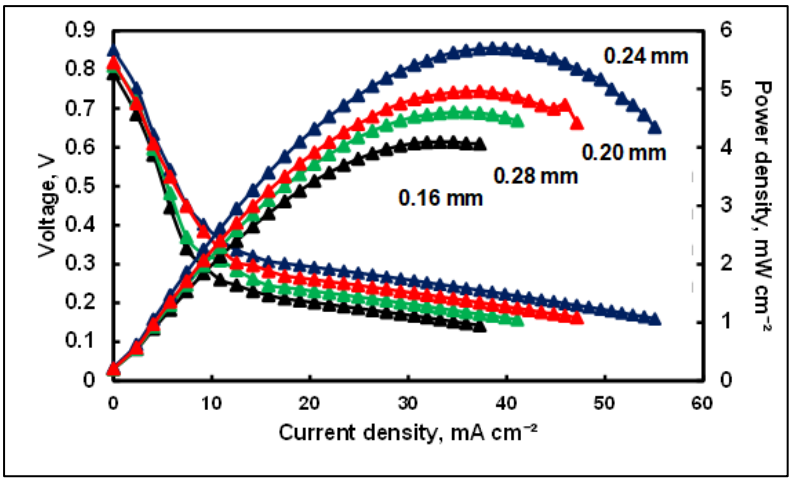


Figure 4. Cell voltage and power density of a crosslinked PVA/GO composite membrane in the passive DEFCs by varying the membrane thickness.

Finally, the optimal membrane thickness was determined using various ethanol concentrations in order to improve the cell performance of single-cell passive DEFCs using a crosslinked PVA/GO composite membrane. Three ethanol concentration values were used with the constant parameters of catalyst loading and cell operating temperature. Figure 3 presents the effect of varying ethanol concentrations, ranging from 2 M ethanol to 6 M ethanol. Obviously, the maximum power density of passive DEFCs utilising a crosslinked PVA/GO composite membrane increased from 5.71 mW cm^{-2} to 7.04 mW cm^{-2} when the ethanol concentration was changed from 2 M to 4 M. This indicates that a fuel concentration of 4 M of ethanol is a good fuel concentration to consume that can significantly improve the electrochemical activity for this investigation and boost the attainment of current density. In fact, the increment in ethanol concentration will result in a high density of ethanol molecules that can be converted to energy during the oxidation reaction at the anode [19, 20]. Unfortunately, the increment level of ethanol concentration has a limited level. Thus, this study provided a significant discovery for fuel limitation concentration. As shown in Figure 5, when 6 M ethanol was applied in passive DEFCs, the power density of a crosslinked PVA/GO composite membrane significantly decreased, going from 7.04 mW cm^{-2} to 4.45 mW cm^{-2}. This indicates that the high ethanol concentration caused the ethanol crossover to occur quickly due to the high density of ethanol molecules present at the anode. As a result, the ethanol osmotic state within the cell and ethanol transfer significantly occurred due to the different ethanol concentration conditions between the anode side and cathode side. Thus, ethanol transfers to the cathode side from the anode side through a crosslinked PVA/GO composite membrane without being affected by the oxidation process. Furthermore, this circumstance may result in both a potential problem on the cathode side and a reduction in cell performance [21, 22]. As a result, the ideal ethanol concentration was set at 4 M for this study in order to boost the performance of a crosslinked PVA/GO composite membrane in passive DEFCs.

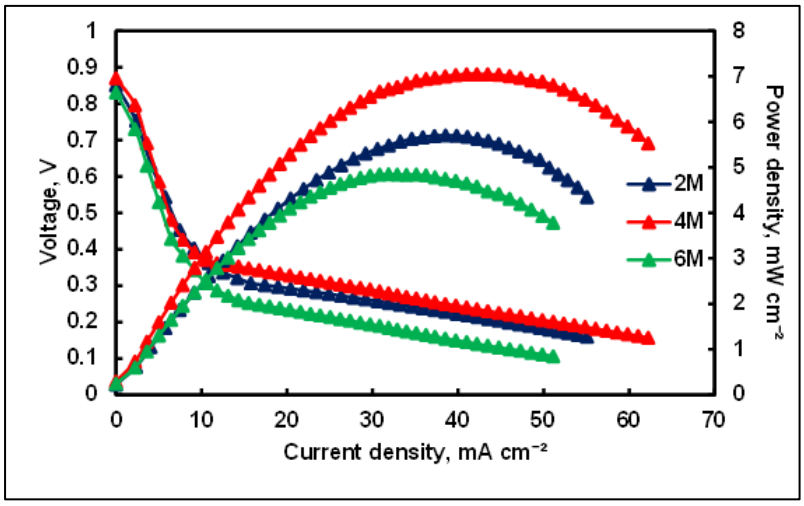


Figure 5. Cell voltage and power density of a crosslinked PVA/GO composite membrane in the passive DEFCs with optimum membrane thickness by varying the ethanol concentration

Conclusion

A simple casting solution method managed to synthesise a crosslinked PVA/GO composite membrane with good morphology and characterization. Furthermore, the thermal, mechanical, and chemical stability of this membrane has been demonstrated in our previous study, as has the excellent performance of single-cell passive DEFCs. In this study, the membrane thickness of a crosslinked PVA/GO composite membrane was manipulated to improve the cell performance of this membrane in passive DEFCs. The 0.24 mm membrane thickness demonstrated good membrane selectivity with 5.562 104 S s cm^{-3}. Thus, 0.24 mm was obtained as an optimal membrane thickness that effectively balanced

the crucial parameters of a PEM (i.e., proton conductivity and ethanol permeability). At 30 °C, the power density of single-cell passive DEFCs using a crosslinked PVA/GO composite membrane was 7.04 mW cm^{-2} at an optimal ethanol concentration of 4 M. In conclusion, the membrane thickness of a PEM significantly influences the performance of passive DEFCs.

Acknowledgement

The authors gladly acknowledge their gratitude to the University of Kebangsaan Malaysia for providing this research with financial support under the Dana Modal Insan grant.

References

1. Zakaria, Z., Kamarudin, S. K., Abd Wahid, K. A. and Hassan, S. H. A. (2021). The progress of fuel cell for Malaysian residential consumption: Energy status and prospects to introduction as a renewable power generation system. *Renewable and Sustainable Energy Reviews,* 144: 110984.
2. Akhairi, M. A. F. and Kamarudin, S. K. (2016). Catalysts in direct ethanol fuel cell (DEFC): An overview. *International Journal of Hydrogen Energy,* 41(7): 4214-4228.
3. Zakaria, Z., Kamarudin, S. K. and Timmiati, S. N. (2016). Membranes for direct ethanol fuel cells: an overview. *Applied Energy,* 163: 334-342.
4. Abdullah, S., Kamarudin, S. K., Hasran, U. A., Masdar, M. S. and Daud, W. R. W. (2015). Development of a conceptual design model of a direct ethanol fuel cell (DEFC). *International Journal of Hydrogen Energy*, 40(35): 11943-11948.
5. Ying, Y. P., Kamarudin, S. K. and Masdar, M. S. (2018). Silica-related membranes in fuel cell applications: An overview. *International Journal of Hydrogen Energy*, 43(33): 16068-16084.
6. Kamarudin, M. Z. F., Kamarudin, S. K., Masdar, M. S. and Daud, W. R. W. (2013). Direct ethanol fuel cells. *International Journal of Hydrogen Energy,* 38(22): 9438-9453.
7. Liu, J. G., Zhao, T. S., Liang, Z. X. and Chen, R. (2006). Effect of membrane thickness on the performance and efficiency of passive direct methanol fuel cells. *Journal of Power Sources,* 153(1): 61-67.
8. Kienitz, B. (2021). Optimizing polymer electrolyte membrane thickness to maximize fuel cell vehicle range. *International Journal of Hydrogen Energy,* 46(19): 11176-11182.
9. Sudaroli, B. M. and Kolar, A. K. (2016). An experimental study on the effect of membrane thickness and PTFE (polytetrafluoroethylene) loading on methanol crossover in direct methanol fuel cell. *Energy,* 98: 204-214.
10. Shaari, N., Zakaria, Z. and Kamarudin, S. K. (2019). The optimization performance of cross-linked sodium alginate polymer electrolyte bio-membranes in passive direct methanol/ethanol fuel cells. *International Journal of Energy Research,* 43(14): 8275-8285.
11. Zakaria, Z., Kamarudin, S. K., Timmiati, S. N. and Masdar, M. S. (2019). New composite membrane poly (vinyl alcohol)/graphene oxide for direct ethanol–proton exchange membrane fuel cell. J*ournal of Applied Polymer Science,* 136(2): 46928.
12. Hren, M., Hribernik, S., Gorgieva, S., Motealleh, A., Eqtesadi, S., Wendellbo, R. and Božič, M. (2021). Chitosan-Mg $(OH)_2$ based composite membrane containing nitrogen doped GO for direct ethanol fuel cell. *Cellulose,* 28(3): 1599-1616.
13. Pereira, J. P., Falcão, D. S., Oliveira, V. B. and Pinto, A. M. F. R. (2014). Performance of a passive direct ethanol fuel cell. J*ournal of Power Sources,* 256: 14-19.
14. Jiang, X., Sun, Y., Zhang, H. and Hou, L. (2018). Preparation and characterization of quaternized poly (vinyl alcohol)/chitosan/MoS_2 composite anion exchange membranes with high selectivity. *Carbohydrate Polymers,* 180: 96-103.
15. Taufiq Musa, M., Shaari, N. and Kamarudin, S. K. (2021). Carbon nanotube, graphene oxide and montmorillonite as conductive fillers in polymer electrolyte membrane for fuel cell: an overview. *International Journal of Energy Research,* 45(2): 1309-1346.

16. Shaari, N. and Kamarudin, S. K. (2017). Characterization studies of sodium alginate/sulfonated graphene oxide based polymer electrolyte membrane for direct methanol fuel cell. *Malaysian Journal of Analytical Sciences*, 21(1), 113-118.
17. Hamid, N. S., Kamarudin, S. K. and Karim, N. A. (2021). Potential of Nafion/eggshell composite membrane for application in direct methanol fuel cell. *International Journal of Energy Research*, *45*(2), 2245-2264.
18. Thiam, H. S., Daud, W. R. W., Kamarudin, S. K., Mohamad, A. B., Kadhum, A. A. H., Loh, K. S. and Majlan, E. H. (2013). Nafion/Pd–SiO_2 nanofiber composite membranes for direct methanol fuel cell applications. *International Journal of Hydrogen Energy,* 38(22): 9474-9483.
19. Yang, C. C., Chiu, S. J., Chien, W. C. and Chiu, S. S. (2010). Quaternized poly (vinyl alcohol)/alumina composite polymer membranes for alkaline direct methanol fuel cells. *Journal of Power Sources,* 195(8): 2212-2219.
20. An, L. and Zhao, T. S. (2011). Performance of an alkaline-acid direct ethanol fuel cell. *International Journal of Hydrogen Energy,* 36(16): 9994-9999.
21. Seweryn, J. and Lewera, A. (2014). High selectivity of ethanol electrooxidation to carbon dioxide on platinum nanoparticles in low temperature polymer electrolyte membrane direct ethanol fuel cell. *Applied Catalysis B: Environmental,* 144: 129-134.
22. An, L., Zhao, T. S., Chen, R. and Wu, Q. X. (2011). A novel direct ethanol fuel cell with high power density. *Journal of power sources*, 196(15): 6219-6222.

Malaysian Journal of Analytical Sciences (MJAS)
Published by Malaysian Analytical Sciences Society

EFFECT OF pH IN THE SYNTHESIS OF GOLD-COPPER NANOPARTICLES SUPPORTED ON ANODIC ALUMINIUM OXIDE AS CATALYST FOR THE REDUCTION OF *p*-NITROPHENOL

(Kesan pH dalam Sintesis Emas-Kuprum (Au-Cu) Partikel Nano Disokong pada Anodik Aluminium Oksida Sebagai Mangkin bagi Penurunan *p*-Nitrofenol)

Norizwan Nordin[1], Hanani Yazid[1,2], Nor Azira Irma Muhammad[2], Abdul Mutalib Md Jani[3]*

[1]Faculty of Applied Sciences,
Universiti Teknologi MARA, 40450 Shah Alam, Selangor, Malaysia
[2]Faculty of Applied Sciences,
Universiti Teknologi MARA, Perlis Branch, Arau Campus, 02600 Arau, Perlis, Malaysia
[3]Faculty of Applied Sciences,
Universiti Teknologi MARA, Perak Branch, Tapah Campus, 35400 Tapah Road, Perak, Malaysia

**Corresponding author: abdmutalib@uitm.edu.my*

Received: 9 December 2021; Accepted: 6 March 2022; Published: 27 June 2022

Abstract

Gold–copper (Au–Cu) bimetallic catalysts were prepared through chemical reduction with Cu and Au precursors at the pH of 3, 5, 7 and 9 and hexadecylamine as the capping agent to produce Au–Cu bimetallic nanoparticles (Au–Cu NPs). The colloidal Au–Cu NPs were then grafted onto an anodic aluminium oxide (AAO) support through spin coating. The AAO support was fabricated via a two-step anodization method at 80 V by using oxalic acid as the electrolyte. The Au–Cu/AAO catalysts were characterized through field emission scanning electron microscopy–energy dispersive X-ray spectroscopy, Fourier transform infrared spectroscopy and inductive coupled plasma–optical emission spectroscopy. The catalytic activities of the Au–Cu bimetallic catalysts in the reduction of *p*-nitrophenol (*p*-NP) were evaluated. Results showed that the rate constant (k) varied in accordance with the pH of the Au precursor. The highest k value of 4.6×10^{-3} s^{-1} was obtained with the Au–Cu catalyst prepared at pH 7. The better performance of the investigated bimetallic catalyst than that of the monometallic Au and Cu catalysts demonstrated the promotional role of the second metal in the reduction of *p*-NP.

Keywords: Au–Cu NPs, pH, anodic aluminium oxide

Abstrak

Pemangkin dwilogam Au-Cu dengan prekursor Au pH 3, 5, 7 dan 9 disediakan dengan menggunakan prekursor Cu secara kaedah penurunan kimia dengan heksadesilamin (HDA) sebagai agen penutup untuk penghasilan nanopartikel Au-Cu (NP Au-Cu). Dwilogam NP Au-Cu telah dicantumkan pada sokongan anodik aluminium oxida (AAO) melalui kaedah salutan putaran. Sokongan AAO telah difabrikasi pada 80 V menggunakan asid oksalik sebagai elektrolit melalui kaedah anodisasi dua langkah. Pemangkin Au-Cu/AAO dicirikan oleh mikroskopi elektron pengimbasan pelepasan medan-spektroskopi sinar-X penyerakan tenaga (FESEM-EDX), spektroskopi inframerah transformasi fourier (FTIR) dan spektroskopi pelepasan plasma-optik berganding induktif (ICP-OES). Penurunan *p*-nitrofenol digunakan untuk menilai aktiviti pemangkin bimetal Au-Cu. Keputusan

menunjukkan bahawa pemalar kadar, (*k*) adalah berbeza bergantung kepada pH prekursor. Nilai *k* tertinggi iaitu 4.6 x 10^{-3} s^{-1} telah diperolehi daripada pemangkin Au-Cu yang disediakan pada pH 7. Daripada kajian ini, pemangkin dwilogam menunjukkan prestasi yang lebih baik berbanding pemangkin Au dan Cu logam mono, menunjukkan peranan promosi logam kedua ke arah penurunan *p*-nitrophenol.

Kata kunci: NP Au-Cu, pH, anodik aluminium oksida

Introduction

Gold nanoparticles (Au NPs) are small particles with diameters that range from 1 nm to 100 nm and unique optical and electronic properties. Au NPs can be easily dispersed in water to form colloidal Au, which offers many benefits for various applications. Au NPs are an excellent catalyst for the selective oxidation or hydrogenation of organic substrates. In recent years, interest in using Au NPs as catalysts for the reduction of p-nitrophenol (*p*-NP) and p-nitroaniline (*p*-NA) has grown [1-2]. Au NPs have been extensively researched as monometallic or bimetallic NPs. The performance of monometallic Au NPs is limited by particle size and manufacturing technique, but these constraints can be overcome by adding a second metal [3-6]. Au NPs mixed with other transition metals such Au-Pt, Au-Cu, Au-Pd, and Au-Ag have higher catalytic activity than monometallic Au NPs. It is highlighted that Au-Cu NPs are an excellent bimetallic alloy because they are more resistant to oxidation thus have a longer catalytic lifetime [5]. The characteristic of the NPs is highly dependent on their preparation condition such as pH, capping agent and precursor concentration.

However, the Au-Cu NPs tend to agglomerate on their own [6-15]. This can be prevented by introducing the support materials such as metal oxides to stabilize and disperse the Au-Cu NPs. Anodic aluminium oxide (AAO) was chosen as the support as it offers several advantages, such as (i) high surface area and porous structure; the reactants get easy access to the active catalytic site [16-17], (ii) prevent agglomeration of Au-Cu NPs, and (iii) this supported catalyst can easily be separated from the reaction mixture at the end of the reaction by simple filtration.

p-NP is a common pollutant that originates from agricultural, pharmaceutical and petrochemical industries; it is highly carcinogenic and tends to persist in water and soil [2,18]. *p*-NP causes the irritation and inflammation of the eyes, skin and respiratory tract. The delayed reaction of *p*-NP in the blood of people exposed to this compound causes methemoglobinemia. The symptoms of methemoglobinemia include cyanosis, confusion and unconsciousness. Therefore, this compound has prompted the development of a wide range of analytical devices by researchers for its determination and eventual removal from contaminated sites. The reduction of *p*-NP can be monitored easily by using a UV-Vis spectrophotometer at 400 nm. Therefore, in this work, we proposed the preparation of Au–Cu NPs with a Au precursor at different pH values via chemical reduction followed by immobilization on an AAO membrane through spin coating. The activities of these Au–Cu/AAO catalysts were then tested in *p*-NP reduction. *p*-NP is a pollutant that is commonly found in most water bodies; it can be upcycled for use in the production of analgesics, such as paracetamol, through reduction into p-aminophenol [1,6].

Materials and Methods

Preparation of Au-Cu NPs

The bimetallic Au-Cu NPs were synthesized based on the chemical reduction technique. An aqueous solution of $CuCl_2 \cdot 2H_2O$ (50 mM) was mixed with 0.3 mL $HAuCl_4 \cdot 3H_2O$ (50 mM) of various pH of 3, 5, 7, and 9 by using 0.5 M NaOH. The molar ratio of the Au to Cu is 2.5 to 1. The mixture was then added with 0.28 mL of glucose (0.5 M) in a glass vial containing the hexadecylamine (HDA) solution of 22.5 mg in 2 mL distilled water [3]. The vial was magnetically stirred at room temperature overnight followed by heating treatment at 100 ^{o}C for 10 mins. After the vial was cooled in an ice bath, 15 mg of HDA was added and the vial was heated again till colour changes observed.

The samples are denoted as Au-Cu pH3, Au-Cu pH5, Au-Cu pH7 and Au-Cu pH9.

Fabrication of AAO membrane

A 99.99% purity aluminium foil with a thickness of approximately 0.1 mm was cut into (2 cm x 2 cm) pieces, and an AAO membrane was formed on the aluminium foil using a two-step electrochemical anodization procedure that was previously reported [1,16]. The AAO was manufactured in multiple phases. The aluminium foils were cleaned and degreased in the first phase by sonication in acetone for 15 mins. The aluminium foils were then submerged in a chemical polishing solution (15 mL HNO_3 and 85 mL H_3PO_4) for 1 min at 70 °C. Then, using 0.3 M oxalic acid as the electrolyte, the initial anodization was performed for 1 minute at 5 °C with a constant voltage of 80 V. The anodic layer was then removed by immersing the foil for roughly 2 hours in a solution of 1.5 wt.% chromic and 6 wt% phosphoric acids. Next, the second anodization procedure was carried out for 2 hours in the conditions described above. Finally, a solution of 5% $CuCl_2.2H_2O$ and 15% HCl was used to dissolve the aluminium foils and obtain AAO membrane. The constructed AAO membrane was cleaned multiple times with generous volumes of ethanol and DI water and stored in the desiccator until further used.

Immobilization of Au-Cu NPs on AAO

The previously prepared Au-Cu NPs solution was deposited on both sides of the AAO by spin-coating at 1000 rpm for 30 s. Subsequently, the AAO was subjected to calcination at 400 °C for 4 hours at a rate of 10 °C/min. The immobilized Au-Cu NPs are denoted as Au-Cu/AAO pH3, Au-Cu/AAO pH 5, Au-Cu/AAO pH 7 and Au-Cu/AAO pH 9 correspond to the Au-Cu NPs prepared at pH 3, 5, 7, and 9, respectively.

Reduction of *p*-Nitrophenol

The *p*-NP solution was prepared by dissolving solid by *p*-NP (99%, Sigma Aldrich) in distilled water. In a cuvette, 1 mg of Au-Cu/AAO catalyst was added to a solution of $NaBH_4$ (1.5×10^{-2} M, 1.5 mL) and *p*-NP (0.05×10^{-2} M, 1.5 mL). The absorbance of the *p*-NP solution was determined at 1-minute intervals using a UV–vis spectrophotometer (Lambda 25, Perkin Elmer) set at 399 nm. At room temperature and pressure, the catalytic reduction was carried out. Depending on the catalyst, the total reaction time for complete reduction of *p*-NP would take 5 to 10 mins. Pseudo-first-order kinetics was used to get the value of the rate constant (*k*) as described by Yazid et al. [6].

Characterization

Characterization of the catalysts by Fourier Transform Infrared Spectroscopy was used to assess the surface functionalities of the produced samples (FTIR; Spectrum, Perkin Elmer). Meanwhile, the surface morphology was observed via Field Emission Scanning Electron Microscopy (FESEM: FEI Nova Nanosem 450). The elements of Au and Cu loading on the AAO membrane were determined by using an Inductive Couple Plasma-Optical Emission Spectrometer (ICP-OES: Optima 8000, Perkin Elmer).

Results and Discussion

Immobilization of Au-Cu NPs on the AAO

Figure 1 shows the photograph of AAO and Au-Cu/AAO. The change of color from yellow to light purple indicates the successful deposition of Au on AAO. The calcination process will vaporize any organic material from the previous steps and leave just the metal and metal oxide species which are Au-Cu NPs and AAO membrane. The calcination step also ensures that the Au-Cu NPs are covalently bonded to the -OH group on the AAO membrane [1,6]. This strong covalent bond prevents aggregation of the particles thus improving their catalytic performance. The spin-coating method provides homogenous distribution of the NPs on the AAO membrane. It is to note that all catalysts prepared at pH 3 to 9 show the same appearance to the naked eyes (Figure 1).

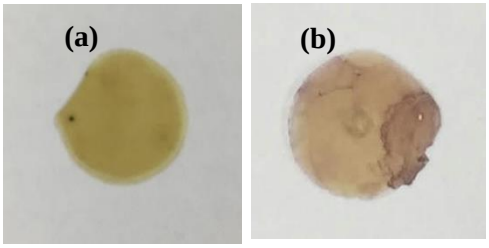


Figure 1. Photograph of (a) bare AAO (b) Au-Cu/AAO pH3

The FTIR spectra of the bare AAO (bAAO) and Au-Cu/AAO are presented in Figure 2. Some changes of peaks intensity, particularly O–H vibrations, confirm the attachment of the Au-Cu NPs on the surface of the AAO [7]. The O–H peak in bAAO at 3210 cm^{-1} is very sharp when compared to Au-Cu/AAO O-H peak at 3195 cm^{-1}. Even though the FTIR instrumentation was unable to detect the presence of gold and copper in the compound, it could be inferred through the observed peak shifting for O-H from 3210 cm^{-1} to 3195 cm^{-1}.

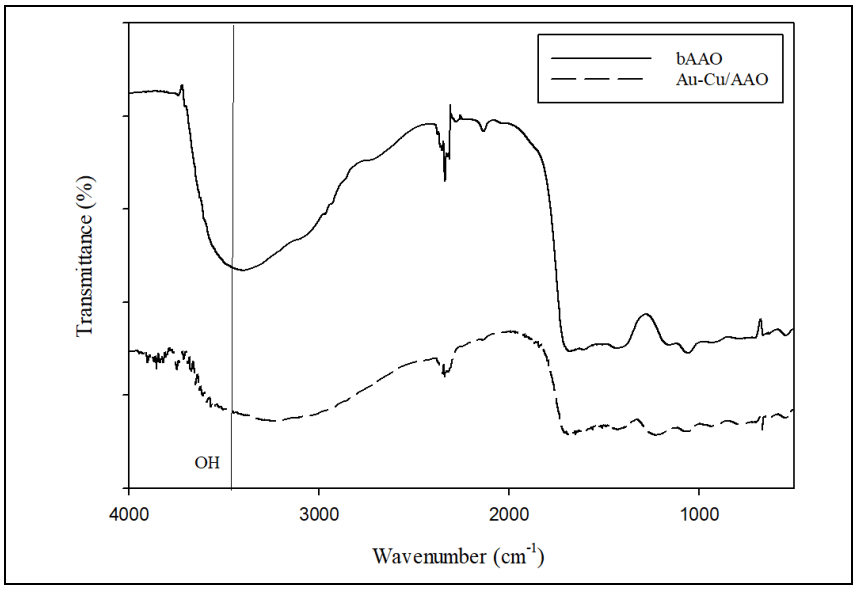


Figure 2. FTIR spectra of bAAO and Au-Cu/AAO

Figure 3 shows FESEM images of synthesized Au-Cu/AAO at pH3 to pH9. FESEM images taken from the top indicated the creation of a hexagonally aligned AAO structure via electrochemical anodization, with typical pore sizes of 100-110 nm. The pores are non-intercrossing and cylindrical in shape resulting in a high surface area. The nanostructure of the as-prepared AAO has a considerable effect on the accessibility (flow) of liquid reactants on both sites of the porous support. A good flow for the reactant to reach the active site is vital for efficient catalytic performance. It is worth noting that exact control of the AAO structure's size and interpore spacing may be accomplished by adjusting the anodization conditions and electrolyte concentration, respectively [16].

The adjustment of pH of the Au precursor has resulted in different sizes and arrangements of the NPs. On Au-Cu/AAO pH3 the size of the NPs is between 113.75 ± 85.20 nm and the NPs are clustered together as shown in Figure 3(a). Whereas, Au-Cu/AAO pH5 and pH7 demonstrated a mix of clustered and individual arrangement of the NPs with a size of 61.54 ± 96.55 nm and 32.33 ± 22.75 nm, respectively. An individually disperse NPs was shown by Au-Cu/AAO pH9 with a size of 34.33 ± 56.47 nm. Noting that the adjustment of pH of the precursor will result in various arrangement and sizes. Table 1 summarizes the characteristic of Au-Cu NPs as observed from FESEM images.

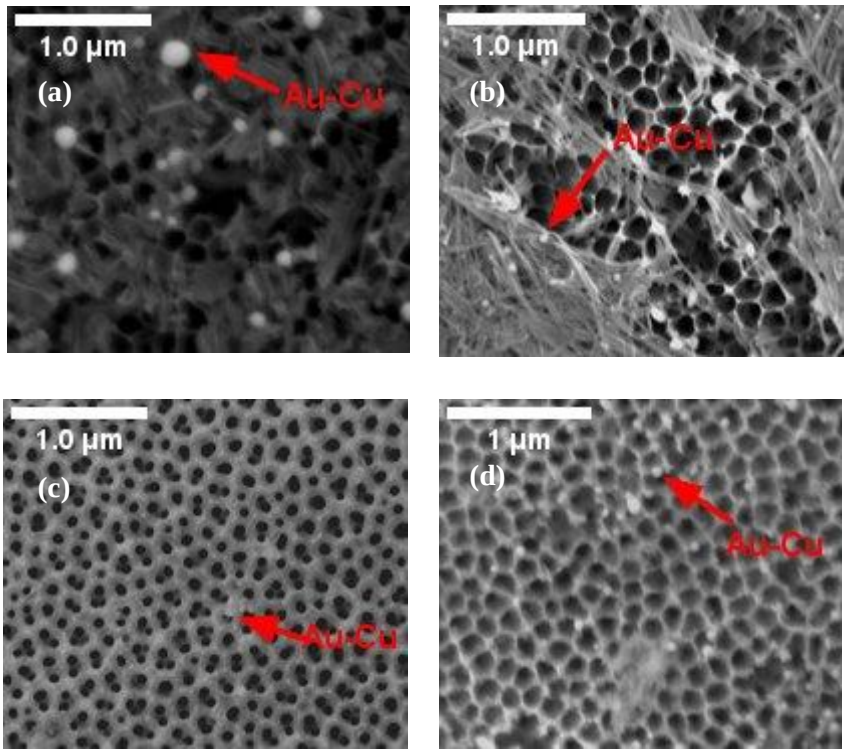


Figure 3. FESEM images of Au-Cu/AAO at different pH of (a) 3 (b) 5 (c) 7 and (d) 9

Table 1. Summary of the characteristic of Au-Cu NPs observed from FESEM images

Catalyst	Diameter Size (nm)	Distribution
Au-Cu/AAO pH3	113.75 ± 85.20	Clustered
Au-Cu/AAO pH5	61.54 ± 96.55	Mix of Clustered and Individual Dispersal
Au-Cu/AAO pH7	32.33 ± 22.75	Mix of Clustered and Individual Dispersal
Au-Cu/AAO pH9	34.33 ± 56.47	Individually Disperse

The Au-Cu pH 7 was selected for an area scan using EDX analysis (Figure 4). Figure 4(a) shows the area viewed using FESEM. Figure 4(b) depicts only large Au NPs can be detected. Small Au NPs and Cu NPs were also present but cannot be monitored clearly as seen in Figure 4(b) and (c). In contrast, the Al species from the support AAO can be seen clearly. The production of small and highly dispersed NPs on the AAO membrane resulted in reading below the EDX detection limit for small Au and Cu species. The presence of Cu species will be proved when using ICP-OES.

Based on the ICP-OES results presented in Figure 5, the Au to Cu molar ratio were determined to be 1.4: 1, 1.7:1, 2.27:1 and 1.59:1 for the Au-Cu/AAO pH3, pH5, pH7 and pH9 samples, respectively. The Au-Cu/AAO pH 7 is the closest mol to mol ratio from the experimental value of the precursor used which is 2.5 Au to 1 Cu. These results suggest that the deprotonation of the hydroxyl groups at high pH leads to the accumulation of negative charge on the surface of the Au NPs [1,18].

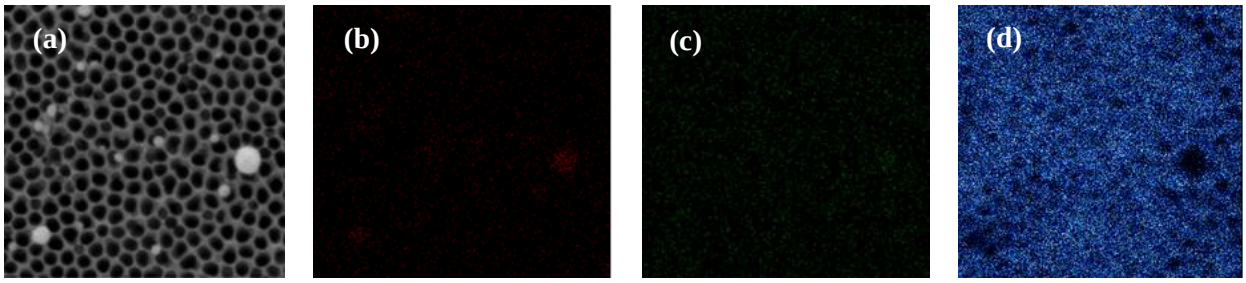
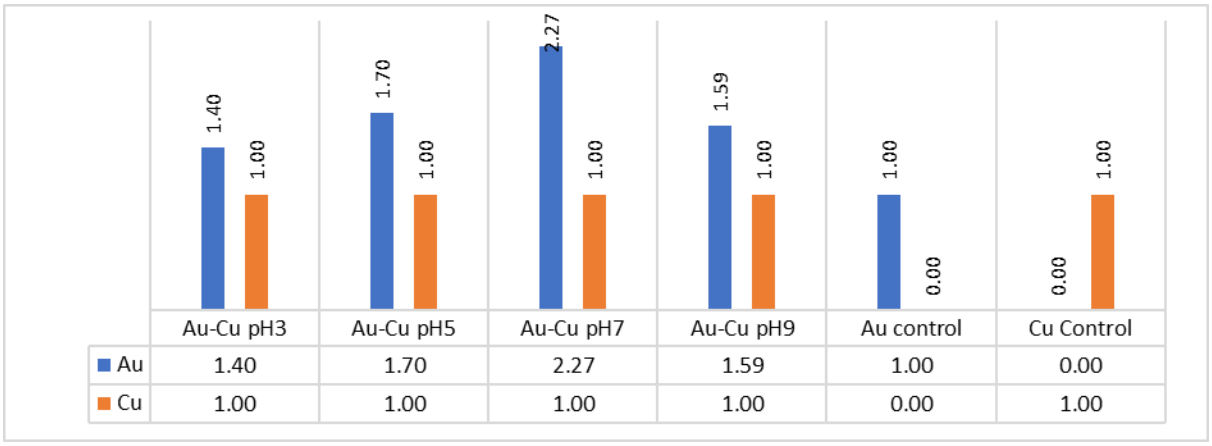


Figure 4. The Au-Cu/AAO pH 7(a) FESEM image and corresponding elemental EDX mapping of (b) Au (c) Cu and (d) Al



	Au-Cu pH3	Au-Cu pH5	Au-Cu pH7	Au-Cu pH9	Au control	Cu Control
Au	1.40	1.70	2.27	1.59	1.00	0.00
Cu	1.00	1.00	1.00	1.00	0.00	1.00

Figure 5. ICP-OES detection of Au to Cu molar ratio

Catalytic performance

The efficacy of the prepared Au-Cu/AAO catalysts were tested by catalytic reduction of *p*-NP to *p*-AP. The *p*-NP solution exhibited a high absorption peak at 317 nm under neutral or acidic conditions, but the addition of $NaBH_4$ increased the alkalinity of the solution, resulting in the creation of *p*-nitrophenolate ions and shifting the absorption peak to 400 nm [2,6]. The appearance and growth of a new peak at 300 nm corresponds to the formation of the product *p*-AP as shown in Figure 6 [1, 6, 18]. The gradual decrease in absorbance at 399 nm with time indicates that the nitro group has been reduced, while the appearance and growth of a new peak at 300 nm corresponds to the formation of the product *p*-AP [6,18]. The dark yellow colour of *p*-NP decreases with the formation of the *p*-AP, and bubbles are produced by $NaBH_4$ converting water to H_2 gas. Because the concentration of $NaBH_4$ in this reaction system far exceeds that of *p*-NP, its concentration remains constant throughout the reaction. The rate constant (*k*) for the reaction was calculated using pseudo-first order kinetics in the case of *p*-NP [6]. The absorbance at 400 nm remains constant over time in the absence of a catalyst, demonstrating that the reduction does not occur. Figure 6 depicts the gradual production of *p*-AP; two isosbestic spots are visible at 280 and 312 nm, implying that the conversion reaction is carried out by the two main species [1, 6].

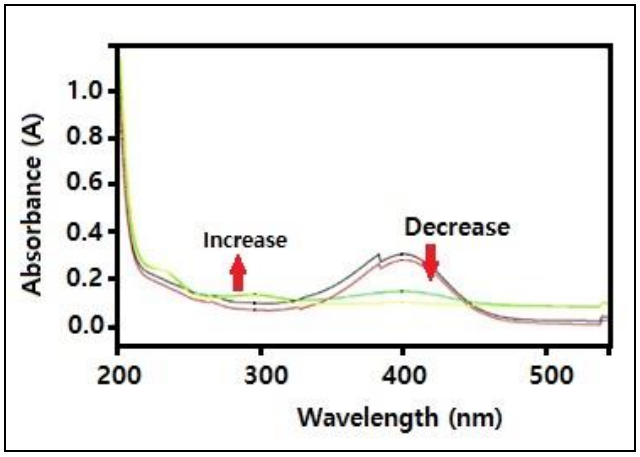


Figure 6: UV-Vis spectra of *p*-NP over time for Au-Cu/AAO pH 7

For all the studies, the graph of $\ln(C/C_o)$ vs reaction time is linear (Figure 7), showing that the catalytic reaction followed first-order kinetics. The Au-Cu/AAO pH3, pH, pH7 and pH9 samples were found to have *k* values of 4×10^{-4} s^{-1}, 2×10^{-3} s^{-1}, 4.6×10^{-3} s^{-1}, and 6×10^{-4} s^{-1}, respectively. A greater *k* value means that *p*-NP is reduced more quickly [1,6,18]. The Au control catalyst had the lowest *k* value, while Cu control had no reaction at all. These findings show that the presence of Cu had an impact in enhancing the catalytic activity of Au NPs in the reduction of *p*-NP. As previously stated, the Au-Cu/AAO pH7 catalyst possesses smaller Au NPs with a uniform distribution of clustering and individual NPs, resulting a good impact on catalytic activity. A neutral pH leads to the formation of small and a mix of individual and clustered dispersal arrangements. The various size and arrangement of Au-Cu NPs generated by grafting the NPs onto the AAO is responsible for the various *k*-values. Even though Cu shows zero catalytic activity the presence of it being with Au has increased the catalytic activity of Au when comparing Au control. Table 2 summarizes the *k*-values of all the prepared catalysts for the reduction of *p*-NP. The results indicate that the adjustment of Au precursor at pH 7 and synthesizing it with Cu has a good effect on the catalytic activity.

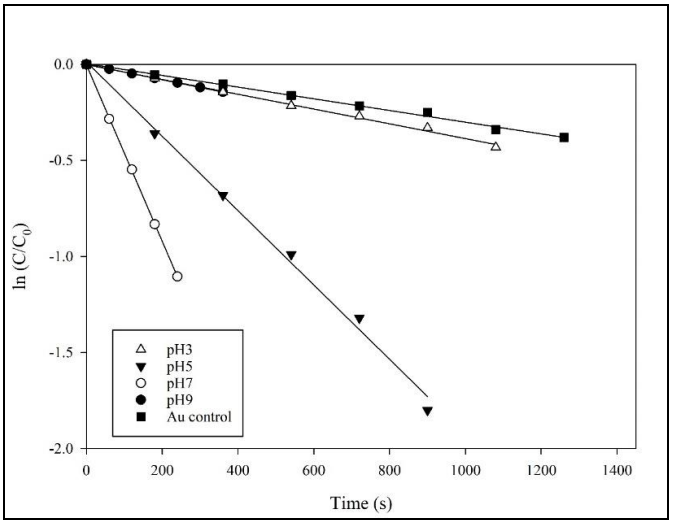


Figure 7. Plot of ln (C/C_o) versus time (min) for the catalysts Au-Cu/AAO

Table 2. Rate of reaction (*k*) of the catalysts

Catalyst	***k*-value (s^{-1})**
Au-Cu/AAO pH3	4.00×10^{-4}
Au-Cu/AAO pH5	2.00×10^{-3}
Au-Cu/AAO pH7	4.60×10^{-3}
Au-Cu/AAO pH9	6.00×10^{-4}
Au/AAO pH7 control	3.00×10^{-4}
Cu/AAO control	no reduction

Conclusion

All synthesized Au-Cu/AAOs were characterized by FESEM-EDX, FTIR, and ICP-OES. The adjustment of pH for the Au precursor during the preparation method has resulted in different Au size and arrangements. The highest activity of 4.6×10^{-3} s^{-1} was obtained for Au-Cu/AAO prepared at pH 7. Furthermore, this bimetallic catalyst exhibited higher catalytic activity than monometallic Au/AAO and Cu/AAO. Further work is underway to extend this concept by using Au NPs at pH 7 with other metals (X) to make another Au-X/AAO catalyst that can be easily recovered from liquid-phase catalytic reactions.

Acknowledgment

We would like to thank Universiti Teknologi MARA (UiTM) for providing generous internal financial support under DPPD grant: 600-TNCPI 5/3/DDN (09) (003/2020) in conducting this study and providing all the facilities.

References

1. Ahmad Zulkifli, F. W., Yazid, H. and Jani, A. M. M. (2021). Immobilization of carbon nanotubes decorated gold nanoparticles on anodized aluminium oxide (Au-CNTs-AAO) membrane for enhanced catalytic performance. *Materials Chemistry and Physics*, 264: 124445.
2. Behera, M., Tiwari, N., Basu, A., Rekha Mishra, S., Banerjee, S., Chakrabortty, S. and Tripathy, S. K. (2021). Maghemite/ZnO nanocomposites: A highly efficient, reusable and non-noble metal catalyst for reduction of 4-nitrophenol. *Advanced Powder Technology*, 32(8): 2905-2915.
3. He, R., Wang, Y.-C., Wang, X., Wang, Z., Liu, G., Zhou, W., Wen, L., Li, Q., Wang, X., Chen, X., Zeng, J. and Hou, J. G. (2014). Facile synthesis of pentacle gold–copper alloy nanocrystals and their plasmonic and catalytic properties. *Nature Communications*, 5: 1-10.
4. Heiligtag, F. J. and Niederberger, M. (2013). The fascinating world of nanoparticle research. *Materials Today*, 16: 262-271.
5. Odenbrand, C. U. I., Blanco, J., Avila, P. and Knapp, C. (1999). Lean NOx reduction in real diesel exhaust with copper and platinum titania based monolithic catalysts. *Applied Catalysis B: Environmental*, 23: 37-44.
6. Yazid, H., Adnan, R., Farrukh, M. A. and Hamid, S. A. (2011). Synthesis of Au/Al_2O_3 nanocatalyst and its application in the reduction of p-Nitrophenol. *Journal of the Chinese Chemical Society*, 58(5): 593-601.
7. Rout, L., Kumar, A., Dhaka, R. S., Reddy, G. N., Giri, S. and Dash, P. (2017). Bimetallic Au-Cu alloy nanoparticles on reduced graphene oxide support: Synthesis, catalytic activity and investigation of synergistic effect by DFT analysis. *Applied Catalysis A: General*, 538: 107-122.
8. Sobczak, I. and Wolski, Ł. (2015). Au–Cu on Nb_2O_5 and Nb/MCF supports – Surface properties and catalytic activity in glycerol and methanol oxidation. *Catalysis Today*, 254: 72-82.

9. Sharma, G., Kumar, A., Sharma, S., Naushad, M., Prakash Dwivedi, R., Al Othman, Z. A. and Mola, G. T. (2017). Novel development of nanoparticles to bimetallic nanoparticles and their composites: A review. *Journal of King Saud University-Science.* 31(2): 257-269.
10. Zeng, S., Yong, K. T., Roy, I., Dinh, X. Q., Yu, X. and Luan, F. (2011). A review on functionalized gold nanoparticles for biosensing applications. *Plasmonics*, 6(3): 491-506.
11. Rocha Rocha, M. Cortez Valadez, A. R. Hernandez Martinez, R. Gamez Cor-rales, R. A. Alvarez, R. Brito Hurtado, M. and Flores Acosta, (2019). Green synthesis of Ag-Cu nanoalloys using opuntia ficus-indica, *Journal of Electronic Material, 46*: 802-807.
12. Kumar, V., Singh, D. K., Mohan, S., Bano, D., Gundampati, R. K. and Hasan, S. H. (2017). Green synthesis of silver nanoparticle for the selective and sensitive colorimetric detection of mercury (II) ion. *Journal of Photochemistry and Photobiology B: Biology*, 168: 67-77.
13. Chen, H. J., Shao, L., Li, Q. and Wang, J. F. (2013). Gold nanorods and their plasmonic properties, *Chemical Society Reviews*, 42: 2679-2724.
14. Brust, M. and Kiely, C. J. (2002). Some recent advances in nanostructure preparation from gold and silver particles: a short topical review, *Colloids Surf. A, Physicochemical and Engineering Aspect 202* 175-186.
15. Seo, M. H., Choi, S. M., Seo, J. K., Noh, S. H., Kim, W. B., & Han, B. (2013). The graphene-supported palladium and palladium–yttrium nanoparticles for the oxygen reduction and ethanol oxidation reactions: Experimental measurement and computational validation. *Applied Catalysis B, Environmental*, 129: 163-171.
16. Habiballah, A. S., Jani, A. M. M., Mahmud, A. H., Osman, N. and Radiman, S. (2016). Facile synthesis of Ba0.5Sr0.5Co0.8Fe0.2O3-δ (BSCF) perovskite nanowires by templating from nanoporous anodic aluminium oxide membranes. *Materials Chemistry and Physics*, 177: 371-378.
17. Chung, C. K., Tsai, C. H., Hsu, C. R., Kuo, E. H., Chen, Y. and Chung, I. C. (2017). Impurity and temperature enhanced growth behaviour of anodic aluminium oxide from AA5052 Al-Mg alloy using hybrid pulse anodization at room temperature. *Corrosion Science*, 125: 40-47.
18. Nordin, N., Noor, N. M., Wahab, N. A. A., Yazid, H. and Jani, A. M. (2020). Preparation of bimetallic catalyst: gold-copper (Au-Cu) nanoparticles for catalytic reduction of p-nitrophenol. *IOP Conference Series: Materials Science and Engineering*, 957(1): 012036.

Malaysian Journal of Analytical Sciences (MJAS)
Published by Malaysian Analytical Sciences Society

POTENTIAL OF TEXTILE WASTE AS NITROGEN DOPED POROUS CARBON FOR OXYGEN REDUCTION REACTION

(Potensi Sisa Tekstil Sebagai Karbon Poros Terdop Nitrogen Berliang untuk Tindak Balas Penurunan Oksigen)

Suhaila Mohd Sauid[1, 3], Siti Kartom Kamarudin[1,2]*, Loh Kee Shyuan[1]

[1]*Fuel Cell Institute*
[2]*Department of Chemical and Process Engineering, Faculty of Engineering and Built Environment*
Universiti Kebangsaan Malaysia, 43600 UKM Bangi, Selangor, Malaysia
[3]*School of Chemical Engineering, College of Engineering*
Universiti Teknologi MARA, 40450 Shah Alam, Selangor, Malaysia

**Corresponding author: ctie@ukm.edu.my*

Received: 13 December 2021; Accepted: 27 February 2022; Published: 27 June 2022

Abstract

Transforming waste into usable materials can protect and conserve the environment, thereby reducing the dependence on landfills, limiting the use of natural resources, and decreasing the carbon footprint. Every year, millions of tons of textile waste are sent to landfills primarily from discarded clothing. Therefore, this waste is worthwhile to convert into functional carbon product. Herein, textile waste from used clothing was converted into nitrogen-doped porous carbons (TNPC) by simple chemical activation followed by carbonisation. Urea and calcium chloride ($CaCl_2$) served as nitrogen precursor and pore forming agent, respectively. The surface area and porosity of the prepared TNPCs were affected by the activation temperature. The optimal sample (TNPC900) activated at 900 °C exhibited a large surface area (496 m^2 g^{-1}) with appropriate porosity and a reasonable amount of nitrogen doped. Remarkably, the resultant TNPC900 catalyst tested as the electrode material for oxygen reduction reaction in 0.1 M KOH exhibited an outstanding positive onset potential of 0.94 V vs. RHE. TNCP900 catalyst also demonstrated superior stability and tolerance to methanol than Pt/C. Overall, this study showed that the conversion of textile waste through a simple synthesis technique into electrocatalyst could offer a sustainable alternative to Pt for potential applications in fuel cell and energy-storage technology.

Keywords: textile waste, nitrogen-doped porous carbon, oxygen reduction reaction, metal-free catalyst

Abstrak

Mengubah sisa menjadi bahan yang boleh digunakan dapat melindungi dan memulihara alam sekitar sekaligus dapat mengurangkan kebergantungan pada tapak pelupusan sampah, mengehadkan penggunaan sumber semula jadi, dan mengurangkan jejak karbon. Setiap tahun, jutaan ton sisa tekstil dihantar ke tapak pelupusan sampah terutama dari pakaian terpakai. Oleh itu, menukar sisa ini menjadi produk karbon berfungsi adalah usaha yang berbaloi. Di sini, sisa tekstil daripada pakaian terpakai telah ditukar kepada karbon berliang terdop nitrogen (TNPC) dengan pengaktifan kimia mudah diikuti dengan langkah karbonisasi. Urea dan kalsium klorida ($CaCl_2$) bertindak masing-masing sebagai bahan sumber nitrogen dan ejen pembentukan liang. Keluasan permukaan dan keliangan TNPC yang disediakan telah dipengaruhi oleh suhu pengaktifan.

Sampel optimum (TNPC900) diaktifkan pada 900 ° C mempamerkan keluasan permukaan yang besar (496 m^2 g^{-1}) dengan keliangan dan jumlah nitrogen terdop yang sesuai. Mangkin TNPC900 yang diuji sebagai bahan elektrod untuk tindak balas penurunan oksigen (ORR) di dalam larutan 0.1 M KOH menunjukkan potensi permulaan positif yang luar biasa iaitu 0.94 V vs RHE. Selain itu, mangkin TNCP900 menunjukkan kestabilan dan toleransi yang unggul terhadap metanol daripada mangkin Pt/C. Oleh itu, kajian ini menunjukkan bahawa penukaran sisa tekstil menggunakan teknik sintesis yang mudah menjadi elektmangkin dapat menawarkan alternatif Pt yang mampan untuk aplikasi di dalam sel bahan api dan teknologi penyimpanan tenaga.

Kata kunci: sisa tekstil, karbon poros terdop nitrogen, tindak balas penurunan oksigen, mangkin bebas metal

Introduction

The growing demand of green and efficient energy has driven the exploration for new technologies because of the depletion of fossil fuels and major environmental problems associated with the usage of conventional energy sources. Fuel cells are a competitive energy device for supplying energy with promising efficiency and negligible emission levels through electrochemical reactions into electricity [1]. However, the sluggish oxygen reduction reaction (ORR) at the cathode significantly affects the overall fuel-cell performance and thus requires an efficient catalyst to accelerate the ORR. The scarce platinum (Pt) and its alloy are extensively used as ORR catalysts, but their high price, low stability, and susceptibility to methanol crossover hinder its large-scale application [2, 3]. Extensive researches have been performed for Pt alternatives that are more cost effective and sustainable with high ORR activity [4]. Metal-free nitrogen-doped carbon materials exhibit massive potential as a substitute to costly Pt-based catalysts, where it demonstrates good ORR electrocatalytic activity and durability, even in acidic electrolytes [5, 6]. Furthermore, owing to the absence of metals, these catalysts could significantly reduce the cathode cost [7].

In recent years, biomass-derived nitrogen-doped carbon materials have prompted fascination and huge consideration in various energy-related applications [8]. Since 2010, many types of biomass such as animal and plant biomass, starch, cellulose derivatives, sugar, microorganisms such as fungi and yeast, and human and industrial waste have been converted into nitrogen-doped carbon for ORR [9, 10]. Biomass materials are used because of their adequate source of carbon, relatively low cost, readily available around the world, and environment friendliness [11, 12]. In particular, the transformation of waste biomass into nitrogen-doped carbon materials reduces the use of natural resources and thus lowers the carbon footprint, eventually leading to less dependence on landfills. Over the past 15 years, the manufacture and use of textile have increased twofold owing to cheaper production cost, more efficient operation, and increasing demand caused by the fast changing fashion industry [13]. Inevitably, more textile waste is created when more textiles are produced. In the U.S only, 11.3 million tonnes of textiles are disposed in landfills, and only 14.7% (2.5 million tonnes) of the total textiles waste generated is being recycled [14]. The reason for the small amount of textiles being recycled is the complexity of segregating the blended fabric materials [15]. Therefore, the conversion of textiles waste into other usable novel materials is worth exploring.

In the present work, we developed metal-free nitrogen-doped porous carbon for ORR from discarded clothing. Urea and calcium chloride were used as nitrogen source and pore-forming agent, respectively, during synthesis. Different pyrolysis temperatures were used to explore temperature's effect on the surface characteristics and electrochemical performance of the electrocatalyst. The obtained nitrogen-doped carbon showed a comparable electrocatalytic activity to that of Pt/C, with superior stability and tolerance to methanol.

Materials and Methods

Preparation of nitrogen-doped porous carbon

TNPCs were fabricated following a previously reported procedure [16]. Typically, small textile cuts of polyester blend fabrics were impregnated in solution containing calcium chloride and urea for 12 h. Then, it

was dried at 80 °C for another 12 h prior to pyrolysis at the desired temperature (800, 900, and 1000 °C) for 1 h in N_2 environment. After cooling to room temperature, the pyrolysis products were ground using pestle and mortar into fine powder and then acid etched in 3 M HCl to remove any unstable elements. Multiple rinsing with distilled water was conducted until the eluent reached neutral pH before finally drying at 105 °C overnight. The prepared sample was denoted according to its pyrolysis temperature, i.e., TNPC800, TNPC900, and TNPC1000 for 800, 900, and 1000 °C, respectively.

Surface characterisation

The surface morphology of the TNPCs was examined by scanning electron microscopy (SEM; CARL ZEISS EVO MA 10). The Brunauer–Emmett–Teller (BET) surface area and porosity of TNPCs were determined from nitrogen adsorption–desorption isotherms evaluated by a Micromeritics 3 Flex instrument. The surface element and binding energy of the prepared TNPCs were analysed by X-ray photoelectron spectroscopy (XPS) by using an Axis Ultra DLD system (Kratos) with a monochromic Al/K-Alpha X-ray source. Background correction were performed for all peaks with carbon peaks (284.8 eV).

Electrochemical characterisation

Electrochemical tests were performed using an Autolab PGSTAT128N potentiostat (Metrohm-Autolab) with a rotating ring-disk electrode (RRDE). A typical three-electrode system comprising a platinum rod, 5 mm-diameter glassy carbon, and Ag/AgCl electrodes serving as counter, working, and reference electrodes, respectively, were used. The catalyst ink was prepared by dispersing 4 mg of catalyst powder in the mixture of deionised water, ethanol, and 5wt% Nafion solution. ORR measurements were conducted by cyclic voltammetry (CV) in N_2- and O_2-saturated 0.1 M KOH solution at a scan rate of 25 mV s^{-1}, whereas linear scan voltammetry (LSV) was performed at a sweeping rate of 5 mV s^{-1} from 100 to 1600 rotation speeds. CV and LSV were swept within the same potential range from 0.2 V to -0.9 V vs. Ag/AgCl. For comparison, 20wt% Pt/C with the same catalyst loading was used in the electrochemical measurement. Kinetic current density (j_K) was calculated according to equation (1) where j, j_K, and j_L are the measured, kinetic current, and the diffusion-limiting current densities, respectively.

$$j_K = \frac{j \cdot j_L}{j_L - j} \quad (1)$$

The electron-transfer number (n) was calculated from the Koutecky–Levich (K-L) equations (2) [17].

$$\frac{1}{j} = \frac{1}{j_K} + \frac{1}{j_L} = \frac{1}{B}\omega^{-1/2} + \frac{1}{j_K} \quad (2)$$

where ω is defined as the angular velocity (rad s^{-1}), and the proportionality coefficient B is defined as equation (3) [17].

$$B = 0.62D^{2/3}\nu^{-1/6}nFC^{*} \quad (3)$$

where D is the diffusion coefficient of O_2 in 0.1 M KOH (1.9×10^{-5} cm^2 s^{-1}), ν is the kinematic viscosity of the electrolyte (0.01 cm^2 s^{-1}), F is the Faraday constant (96485C mol^{-1}), and C^* is the concentration of O_2 in 0.1 M KOH (1.2×10^{-6} mol cm^{-3}) [18]. Electron-transfer numbers (n) and H_2O_2 (%) yield were calculated from the RRDE curves using equations (4) and (5), respectively [19].

$$n_{RRDE} = 4 \times \frac{i_d}{i_d + i_r/N_c} \quad (4)$$

$$H_2O_2\ (\%) = 200 \times \frac{i_r/N_C}{i_d + i_r/N_c} \quad (5)$$

where i_r is the ring current, i_d is the disk current, and N_c is the disk-current collection efficiency of ring electrode. (N_c= 0.256). For stability test, we compared the LSV curves of before and after a continuous 1000 CV cycle of 100 mV s^{-1} scan rate in O_2-saturated 0.1 M KOH of TNPC and Pt/C. The ring potential was set at 1.4 V vs. RHE during the RRDE measurement, which was within the recommended potential window of inducing H_2O_2 oxidation to O_2 [17].

Results and Discussion

Surface characterisation of TNPCs

The SEM images of TNPC800, TNPC900, and TNPC1000 are shown in Figure 1, respectively. All three samples had pore-like morphology on the TNPC surface. For TNPC800 and TNPC900, the pores were

more visible and had depth (Figures 1a and 1b, respectively), whereas the pores on TNPC1000 were larger and seemed shallower as if the pores had collapsed (Figure 1c). This finding indicated that the development of pore structures on TNPCs was affected by pyrolysis temperature. An electrocatalyst with porous structure is desirable as it could accommodate abundant active sites and transport channels for ions [20, 21].

N_2 adsorption–desorption isotherm was used to determine the porosity properties of the TNPC samples. As shown in Figure 1(d), all TNPCs demonstrated type-IV isotherm curves with a clear hysteresis loop (parallel adsorption and desorption branches) at $P/P_o \approx 0.45–1.0$, signifying the existence of mesopores in all samples [22]. Furthermore, the BJH pore-size distribution plot (Figure 1d inset) also confirmed that all samples contained mesopores within their distribution. The surface areas calculated based on BET for all TNPCs are listed in Table 1. TNPC900 had the largest surface area of 495.97 m^2 g^{-1} and the highest pore volume within the range of the pyrolysis temperature studied. Furthermore, the surface area increased with increased temperature from 800 °C to 900 °C but significantly dropped when the pyrolysis temperature was 1000 °C with decreased surface area to 207.76 m^2 g^{-1}. The pore volume also followed the same trend as the surface area. However, the ratio of S_{meso}/S_{micro} increased with increased pyrolysis temperature. This finding indicated that with increased temperature to 1000 °C, the micropore structures collapsed and created larger pores. Consequently, the surface area decreased, as supported by the higher average pore size obtained at 1000 °C. The increase in pore diameter well agreed with the morphology observed by SEM. Given that ORR occurs at the interfacial/surface of a catalyst, the micro- and mesoporous structure of a catalyst with high surface area and pore volume can serve as abundant active sites influencing the mass-transport properties and diffusion of the electrolyte [23, 24]. Therefore, the porosity structure of these TNPCs is expected to affect ORR performance.

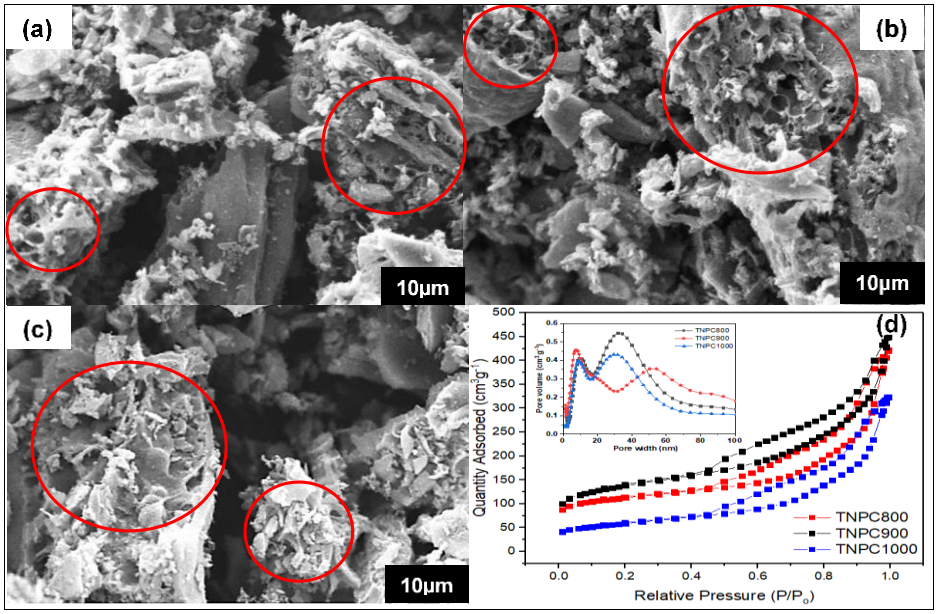


Figure 1. SEM images of (a) TNPC800, (b) TNPC900, (c) TNPC1000 (1k magnification respectively), and (d) N_2 adsorption–desorption isotherms of TNPCs (inset, corresponding pore-size distribution)

N_2 adsorption-desorption isotherm was used to determine the porosity properties of the TNPC samples. As shown in Figure 1 (d), all TNPCs demonstrate type IV isotherm curves with a clear hysteresis loop (parallel adsorption and desorption branches) at P/P_o ~0.45 – 1.0, signify the existence of mesopores in all samples [22]. Furthermore, the BJH pore size distribution plot (Figure 1d inset) also corroborates that all samples contain mesopores within their distribution. The surface area calculated based on Brunauer-Emmett-Teller (BET) for all TNPCs are tabulated in Table 1. As we can see, TNPC900 has the largest surface area of 495.97 m^2 g^{-1} and the highest pore volume in the range of the pyrolysis temperature studied. Furthermore, the surface area enlarge as the temperature was increased from 800 to 900 °C but drop significantly when the temperature of pyrolysis was at 1000 °C as the surface area reduced to 207.76 m^2 g^{-1}. The pore volume also follows the same trend as surface area. However, the ratio of S_{meso}/S_{micro} increase with the increment in pyrolysis temperature. This might indicate that as the temperature raised to 1000 °C, the micropore structures had collapsed which creating larger pores thus decreasing the surface area and this is supported by the higher average pore size obtained at 1000 °C. The increase in pore diameter is in agreement with the morphology observed by SEM. Since ORR occur at the interfacial/surface of a catalyst, the micro- and mesoporous structure of a catalyst with high surface area and pore volume can serve as abundance active sites that influence the mass transport properties and diffusion of the electrolyte [23,24]. Therefore, it is expected that the porosity structure of these TNPCs will affect the ORR performance.

Table 1. Surface properties of TNPCs

Sample	S_{BET} (m^2 g^{-1})	S_{micro} (m^2 g^{-1})	S_{meso} (m^2 g^{-1})	S_{meso} / S_{micro} ratio	Pore Volume (cm^3 g^{-1})	Average Pore Size (nm)	C (at%)	N (at%)	O (at%)
TNPC800	416.1	235.55	180.55	0.43	0.64	6.12	92.96	3.54	2.88
TNPC900	495.97	214.77	281.20	0.57	0.67	5.43	91.85	2.80	3.99
TNPC1000	207.76	54.36	153.40	0.74	0.49	9.43	93.39	1.54	3.86

The surface compositions and bonding states of all samples were analysed by XPS. Figure 2(a) displays the survey scans of TNPC samples. C 1s, N 1s, and O 1s were identified at binding energies around 284, 400, and 532 eV. The presence of a small N 1s signal indicated that nitrogen was successfully doped into carbon. The estimated elemental content is listed in Table 1. The nitrogen content can be as high 3.54 at% for TNPC800 and as low as 1.54 at% for TNPC1000, indicating that increased temperature significantly affected nitrogen doping. High-resolution scans of N 1s were further performed to investigate its chemical structure and deconvoluted into three peaks, as exemplified in Figure 2(b). The peaks at 398.4, 400.0, and 401.5 eV corresponded with pyridinic-N, pyrrolic-N, and graphitic-N, respectively [25, 26]. Pyridinic-N is when two carbon atoms located at the edge of graphitic planes are bound to the nitrogen atom, whereas pyrrolic-N is the nitrogen atom incorporated into the pentagonal ring. Meanwhile, graphitic-N is when a nitrogen atom replaces a carbon atom and bonded with three carbon atoms in the graphene layer [27, 28]. As shown in Figure 2(c), pyridinic-N was the highest for TNPC900 followed by TNPC1000. Furthermore, the rise in temperature from 900 °C to 1000 °C reduced the contents of pyridinic-N slightly but significantly reduced pyrrolic-N. By contrast, the graphitic-N content rose to almost 50 at% at 1000 °C, which was attributed to the transformation of pyrrolic-N and fractional conversion of pyridinic-N into

graphitic-N from the condensation of graphite rings at 1000 °C [29]. Recent studies have reported that pyridinic-N and graphitic-N played important roles in enhancing ORR performance [30, 31]. Pyridinic-N provided active sites and facilitated the dominant 2e⁻ to 4e⁻ process in the ORR mechanism, whereas graphitic-N promoted the reduction of oxygen to hydrogen peroxide by adsorbing OOH intermediates through a 2e- pathway [32].

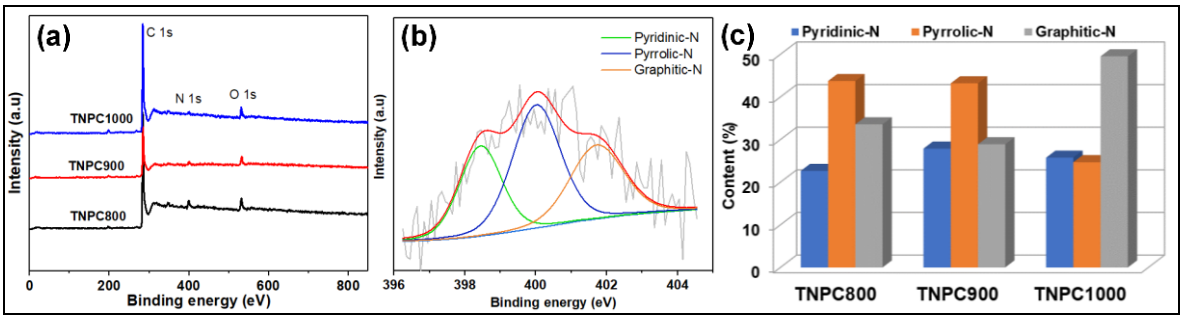


Figure 2. (a) XPS survey spectra; (b) high-resolution XPS of N 1s for TNPC900, and (c) content of nitrogen species of TNPC800, TNPC900, and TNPC1000

Electrochemical performance of TNPCs

To investigate the possible application of the prepared catalysts for fuel-cell or energy-storage systems, the electrochemical activity of TNPCs was evaluated using a three-electrode system. RRDE or a glassy carbon electrode was loaded with the as-prepared catalyst ink with 0.285 mg cm^{-2} loading. As shown in Figure 3 (a), all three catalysts showed no reduction peak observed in N_2-saturated 0.1 M KOH solution but obvious peaks in a solution of O_2 saturated with the same electrolyte, indicating that these TNPCs were catalytically active towards ORR. However, TNPC900 illustrated a stronger cathodic peak at 0.76 V vs. RHE, and it was more positive than TNPC800 and TNPC1000. Figure 3(b) shows the LSV plots for TNPCs and the commercial Pt/C (20wt%) at 1600 rpm in O_2-saturated electrolyte. Amongst the three TNPCs, TNPC900 had the highest ORR activity based on the most positive onset potential E_o and half-wave potential $E_{1/2}$ at 0.94 and 0.78 V vs. RHE, respectively. The E_o and $E_{1/2}$ of TNPC800 (0.92 and 0.74 V, respectively) and TNPC1000 (0.93 and 0.75 V, respectively) were more negative than those of TNPC900. The E_o of TNPC900 was slightly inferior to that of commercial Pt/C but comparable with values obtained in previous studies using a different biomass, such as coconut mesocarp [26], but higher than those of waste lotus seedpod [12] and cotton stalk [33]. The ORR activity of the TNPCs can also be assessed by their kinetic current densities (j_K) [34]. The j_K values at 0.8 V vs. RHE were in the order TNPC900 (1.82 mA cm^{-2}) > TNPC1000 (0.55 mA cm^{-2}) > TNPC800 (0.46 mA cm^{-2}), consistent with E_o and $E_{1/2}$.

To further investigate the kinetic information of ORR for TNPC900, LSV curves were collected at different rotating speeds from 100 rpm to 1600 rpm in O_2-saturated 0.1 M KOH solution (Figure 3(c)). With increased rotation, the limiting current density increased because of the shorter distance of diffusion [12]. The K-L plot (Figure 3(c) inset) illustrated a linear trend for the potential range of 0.2 V to 0.6 V vs. RHE, signifying similar electron-transfer number (3.5–3.8) around these potentials. The corresponding electron-transfer number calculated from the ring current and disk current of RRDE (3.55–3.73) curve also agreed with the K-L results (Figure 3d) suggesting a dominant 4e⁻ pathway in ORR for TNPC900 catalyst. Conversely, the electron-transfer number calculated for TNPC800 (3.35–3.53) and TNPC1000 (3.48–3.58) was slightly lower than that for TNPC900, indicating that ORR occurred through a combined 2e⁻ and 4e⁻ transfer pathway. The yield of H_2O_2 shown in Fig. 3d indicated lesser H_2O_2 formation on TNPC900, further validating

a higher catalytic efficiency of TNPC900 in 0.1 M KOH solution.

The superior ORR performance of TNPC900 may be largely influenced by the highest surface area, proper ratio of mesopores over micropores, and the role of pyridinic-N. Given that pyridinic-N served as the active sites for the adsorption and dissociation of oxygen [35], TNPC900 exhibited superior ORR activities than the other TNPCs. However, despite TNPC800 having a slightly lower surface area than TNPC900 and the highest nitrogen content (Table 1), its effect was not as important to ORR as the E_o and $E_{1/2}$ were the lowest for TNPC800. This finding may be due to the higher proportion of micropores (56.6%) dominating the effect to ORR because the restricted active sites such as micropores were difficult to be wet by liquid electrolyte [36]. This finding was further supported by the higher ORR characteristics of TNPC1000 that even though the surface area and the nitrogen content were the least (Table 1), the larger proportion of mesopores was assumed to facilitate a better ORR activity than TNPC800.

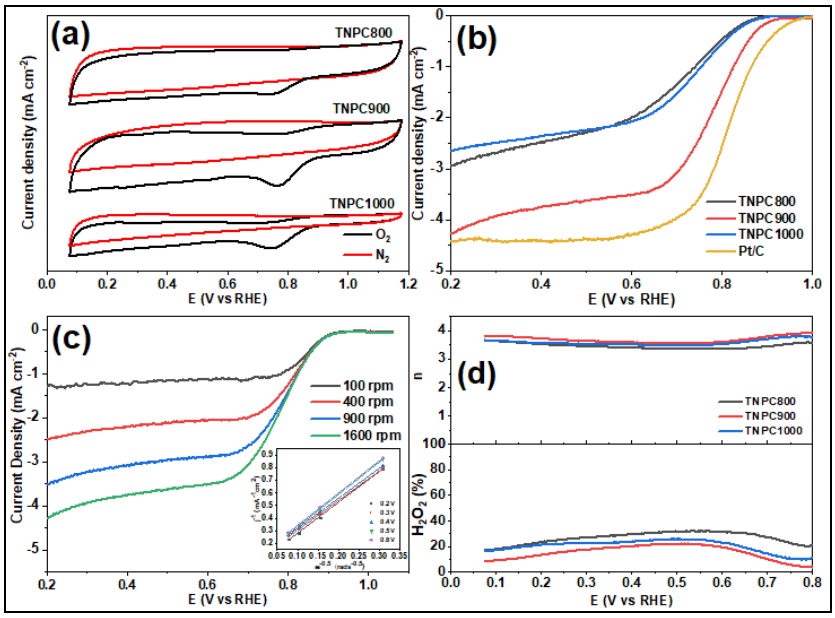


Figure 3. (a) CV curves of TNPCs in N_2- or O_2-saturated 0.1 M KOH solution. (b) LSV of samples and Pt/C. (c) LSV of TNPC900 at different rotation speeds (inset, K-L plots of TNPC at 0.2 V to 0.6 V vs. RHE). (d) Plots of number of electron transfer; n and H_2O_2 yield of TNPC900 calculated from RRDE currents

Stability of TNPC900

To evaluate the durability of TNPC900, stability test particularly CV was performed in O_2-saturated 0.1 M KOH at a scan rate of 100 mV s^{-1}. After 1000 potential cycles, the E_o and $E_{1/2}$ of TNPC900 remained unchanged (Figure 4a), whereas a significant negative shift was observed for Pt/C (Figure 4(a) inset) under the same condition. Pt/C also experienced 11% loss of the limiting current density. These results indicated TNPC900 had a relatively better stability than Pt/C under alkaline condition. TNPC900 also showed good tolerance to methanol (Figure 4(b)) as the CV curve was similar before and after adding 3 M methanol. Conversely, a visible oxidation peak emerged for Pt/C (Figure 4(b) inset), which was typical owing to the higher selectivity of Pt for methanol oxidation reaction than ORR [37]. Therefore, the superior stability and methanol tolerance of TNPC900 over Pt/C signified possible application in direct methanol fuel-cell application.

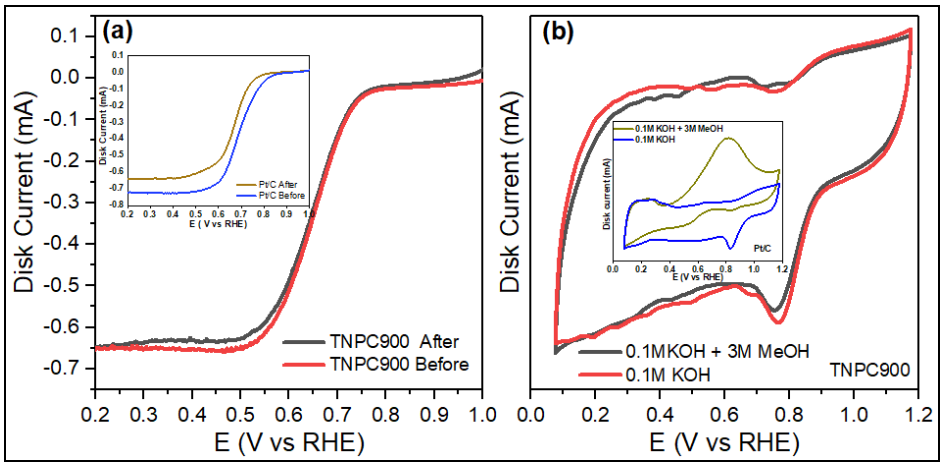


Figure 4. (a) LSV plots for TNPC900 (inset: Pt/C) before and after 1000 CV cycle in O_2-saturated 0.1 M KOH. (b) CV curves for TNPC900 (inset: Pt/C) before and after 3 M methanol addition

Conclusion

We successfully fabricated nitrogen-doped porous carbon from textile waste through chemical activation and pyrolysis. Calcium chloride-induced pore formation and urea served as the nitrogen precursor. Different pyrolysis temperatures (from 800 °C to 1000 °C) impacted the surface characteristics and ORR performance of the TNPCs produced. Among the TNPCs prepared, TNPC900 catalyst exhibited the highest ORR activity with the least H_2O_2 formation. The excellent electrocatalytic activity may be attributed to the collusion of high surface area, proper ratio of mesopores and micropores, and high pyridinic-N. Although ORR performance was slightly inferior to that of Pt/C, TNPC900 is a good potential Pt substitute because of its abundantly available resource and simple production method. TNPC900 also showed better stability and methanol immunity than commercial Pt/C catalyst, making it potentially suitable for direct methanol fuel-cell application.

Acknowledgement

This work is financially supported by the Ministry of Higher Education of Malaysia: TRGS/1/2018/UKM/01/6/2 and Universiti Kebangsaan Malaysia: DIP-2019-021.

References

1. Steele, B. C. H. and Heinzel, A. (2001). Materials for fuel-cell technologies. *Nature*, 414(6861): 345-352.
2. Wang, Y., Li, J. and Wei, Z. (2018). Transition-metal-oxide-based catalysts for the oxygen reduction reaction. *Journal of Materials Chemistry A*, 6(18): 8194-8209.
3. Karim, N. A. and Kamarudin, S. K. (2013). An overview on non-platinum cathode catalysts for direct methanol fuel cell. *Applied Energy*, 103(9): 212-220.
4. Wu, Z., Song, M., Wang, J. and Liu, X. (2018). Recent progress in nitrogen-doped metal-free electrocatalysts for oxygen reduction reaction. *Catalysts*, 8(5): 196.
5. Guo, D., Shibuya, R., Akiba, C., Saji, S., Kondo, T. and Nakamura, J. (2016). Active sites of nitrogen-doped carbon materials for oxygen reduction reaction clarified using model catalysts. *Science*, 351(6271): 361-365.
6. Li, J., Wang, S., Ren, Y., Ren, Z., Qiu, Y. and Yu, J. (2014). Nitrogen-doped activated carbon with micrometer-scale channels derived from luffa sponge fibers as electrocatalysts for oxygen reduction reaction with high stability in acidic media. *Electrochimica Acta*, 149: 56-64.

7. Quílez-Bermejo, J., Morallón, E. and Cazorla-Amorós, D. (2020). Metal-free heteroatom-doped carbon-based catalysts for ORR. A critical assessment about the role of heteroatoms. *Carbon*, 165: 434-454.
8. Gao, Z., Zhang, Y., Song, N. and Li, X. (2017). Biomass-derived renewable carbon materials for electrochemical energy storage. *Materials Research Letters*, 5(2): 69-88.
9. Borghei, M., Lehtonen, J., Liu, L. and Rojas, O. J. (2018). Advanced biomass-derived electrocatalysts for the oxygen reduction reaction. *Advanced Materials*, 30(24): 1703691.
10. Kaur, P., Verma, G. and Sekhon, S. S. (2019). Biomass derived hierarchical porous carbon materials as oxygen reduction reaction electrocatalysts in fuel cells. *Progress in Materials Science*, 102: 1-71.
11. Zhou, H., Zhang, J., Zhu, J., Liu, Z., Zhang, C. and Mu, S. (2016). A self-template and KOH activation co-coupling strategy to synthesize ultrahigh surface area nitrogen-doped porous graphene for oxygen reduction. *RSC Advances*, 6(77): 73292-73300.
12. Zheng, B., Wang, J., Pan, Z., Wang, X., Liu, S., Ding, S. and Lang, L. (2020). An efficient metal-free catalyst derived from waste lotus seedpod for oxygen reduction reaction. *Journal of Porous Materials*, 27(3): 637-646.
13. Polajnar Horvat, K. and Šrimpf Vendramin, K. (2021). Issues surrounding behavior towards discarded textiles and garments in Ljubljana. *Sustainability (Switzerland)*, 13(11): 1-11.
14. USEPA (2019). Textiles: Material-specific data. Available from https://www.epa.gov/facts-and-figures-about-materials-waste-and-recycling/textiles-material-specific-data#TextilesOverview. [Accessed online: 16-Dec-2019].
15. Ramamoorthy, S. K., Skrifvars, M., Alagar, R. and Akhtar, N. (2018). End-of-life textiles as reinforcements in biocomposites. *Journal of Polymers and the Environment*, 26(2): 487-498.
16. Sauid, S. M., Kamarudin, S. K., Karim, N. A. and Shyuan, L. K. (2021). Superior stability and methanol tolerance of a metal-free nitrogen-doped hierarchical porous carbon electrocatalyst derived from textile waste. *Journal of Materials Research and Technology*, 11: 1834-1846.
17. Ge, X., Sumboja, A., Wuu, D., An, T., Li, B., Goh, F. W. T., … and Liu, Z. (2015). Oxygen reduction in alkaline media: from mechanisms to recent advances of catalysts. *ACS Catalysis*, *5*(8): 4643-4667.
18. Ratso, S., Kruusenberg, I., Käärik, M., Kook, M., Saar, R., Kanninen, P., … and Tammeveski, K. (2017). Transition metal-nitrogen co-doped carbide-derived carbon catalysts for oxygen reduction reaction in alkaline direct methanol fuel cell. *Applied Catalysis B: Environmental*, 219: 276-286.
19. Zhou, R., Zheng, Y., Jaroniec, M. and Qiao, S. Z. (2016). Determination of the electron transfer number for the oxygen reduction reaction: From theory to experiment. *ACS Catalysis*, 6(7): 4720-4728.
20. Tang, J., Wang, Y., Zhao, W., Zeng, R. J., Liu, T. and Zhou, S. (2019). Biomass-derived hierarchical honeycomb-like porous carbon tube catalyst for the metal-free oxygen reduction reaction. *Journal of Electroanalytical Chemistry*, 847: 113230.
21. Shi, J., Lin, N., Lin, H. B., Yang, J. and Zhang, W. L. (2020). A N-doped rice husk-based porous carbon as an electrocatalyst for the oxygen reduction reaction. *Xinxing Tan Cailiao/New Carbon Materials*, 35(4): 401-409.
22. Thommes, M., Smarsly, B., Groenewolt, M., Ravikovitch, P. I. and Neimark, A. V. (2006). Adsorption hysteresis of nitrogen and argon in pore networks and characterization of novel micro- and mesoporous silicas. *Langmuir*, 22(2): 756-764.
23. Jiang, M., Yu, X., Yang, H. and Chen, S. (2020). Optimization strategies of preparation of biomass-derived carbon electrocatalyst for boosting oxygen reduction reaction: A minireview. *Catalysts*, 10(12): 1-17.

24. Mao, X., Cao, Z., Yin, Y., Wang, Z., Dong, H. and Yang, S. (2018). Direct synthesis of nitrogen and phosphorus co-doped hierarchical porous carbon networks with biological materials as efficient electrocatalysts for oxygen reduction reaction. *International Journal of Hydrogen Energy*, 43(22): 10341-10350.
25. Zhao, Q., Ma, Q., Pan, F., Wang, Z., Yang, B., Zhang, J. and Zhang, J. (2016). Facile synthesis of nitrogen-doped carbon nanosheets as metal-free catalyst with excellent oxygen reduction performance in alkaline and acidic media. *Journal of Solid State Electrochemistry*, 20(5): 1469-1479.
26. Zhang, W., Qi, J., Bai, P., Wang, H. and Xu, L. (2019). High-level nitrogen-doped, micro/mesoporous carbon as an efficient metal-free electrocatalyst for the oxygen reduction reaction: Optimizing the reaction surface area by a solvent-free mechanochemical method. *New Journal of Chemistry*, 43(27): 10878-10886.
27. Lazar, P., Mach, R. and Otyepka, M. (2019). Spectroscopic fingerprints of graphitic, pyrrolic, pyridinic, and chemisorbed nitrogen in N-doped graphene. *Journal of Physical Chemistry C*, 123(16): 10695-10702.
28. Zainul Abidin, A. F., Loh, K. S., Wong, W. Y. and Mohamad, A. B. (2019). Nitrogen-doped carbon xerogels catalyst for oxygen reduction reaction: Improved structural and catalytic activity by enhancing nitrogen species and cobalt insertion. *International Journal of Hydrogen Energy*, 44(54): 28789-28802.
29. Sharifi, T., Hu, G., Jia, X. and Wågberg, T. (2012). Formation of active sites for oxygen reduction reactions by transformation of nitrogen functionalities in nitrogen-doped carbon nanotubes. *ACS Nano*, 6(10): 8904-8912.
30. Liu, R., Zhang, H., Liu, S., Zhang, X., Wu, T., Ge, X., … and Wang, G. (2016). Shrimp-shell derived carbon nanodots as carbon and nitrogen sources to fabricate three-dimensional N-doped porous carbon electrocatalysts for the oxygen reduction reaction. *Physical Chemistry Chemical Physics*, 18(5): 4095-4101.
31. Zheng, F. Y., Li, R., Ge, S., Xu, W. R. and Zhang, Y. (2020). Nitrogen and phosphorus co-doped carbon networks derived from shrimp shells as an efficient oxygen reduction catalyst for microbial fuel cells. *Journal of Power Sources*, 446: 227356.
32. Lai, L., Potts, J. R., Zhan, D., Wang, L., Poh, C. K., Tang, C. and Ruoff, R. S. (2012). Exploration of the active center structure of nitrogen-doped graphene-based catalysts for oxygen reduction reaction. *Energy and Environmental Science*, *5*(7): 7936-7942.
33. Xu, S. S., Qiu, S. W., Yuan, Z. Y., Ren, T. Z. and Bandosz, T. J. (2019). Nitrogen-containing activated carbon of improved electrochemical performance derived from cotton stalks using indirect chemical activation. *Journal of Colloid and Interface Science*, 540: 285-294.
34. Akula, S. and Sahu, A. K. (2019). Heteroatoms co-doping (N, F) to the porous carbon derived from spent coffee grounds as an effective catalyst for oxygen reduction reaction in polymer electrolyte fuel cells. *Journal of The Electrochemical Society*, 166(2): F93-F101.
35. Li, D., Fan, Y., Yuan, H., Deng, L., Yang, J., Chen, Y. and Luo, B. (2020). Renewable and metal-free carbon derived from aquatic scindapsus affording meso–microporosity, large interface, and enriched pyridinic-N for efficient oxygen reduction reaction catalysis. *Energy & Fuels*, 34(10): 13089-13095.
36. Fan, Z., Li, J., Zhou, Y., Fu, Q., Yang, W., Zhu, X. and Liao, Q. (2017). A green, cheap, high-performance carbonaceous catalyst derived from *Chlorella pyrenoidosa* for oxygen reduction reaction in microbial fuel cells. *International Journal of Hydrogen Energy*, 42(45): 27657-27665.
37. Cao, C., Wei, L., Zhai, Q., Wang, G. and Shen, J. (2017). Biomass-derived nitrogen and boron dual-doped hollow carbon tube as cost-effective and stable synergistic catalyst for oxygen electroreduction. *Electrochimica Acta*, 249: 328-336.

Malaysian Journal of Analytical Sciences (MJAS)
Published by Malaysian Analytical Sciences Society

PHOTOCATALYTIC HYDROGEN GENERATION FROM WATER BY TiO_2/Co_3O_4 COMPOSITE PHOTOCATALYSIS

(Penjanaan Hidrogen Fotokatalitik dari Molekul Air Mengunakan Komposi Fotomangkin TiO_2/Co_3O_4)

Siti Nurul Falaein Moridon[1], Dian Anggraini[2], Khuzaimah Arifin[1]*, Lorna Jeffery Minggu[1], Mohammad B. Kassim[1,3]

[1]*Fuel Cell Institute,*
Universiti Kebangsaan Malaysia, 43600 UKM Bangi, Selangor, Malaysia
[2]*Department of Chemistry, Faculty of Mathematic and Natural Science,*
Universitas Riau,Kampus Binawidya, Km 12.5 Simpang Baru, Pekan baru, Riau, Indonesia,
[3]*Faculty of Science and Technology,*
Universiti Kebangsaan Malaysia, 43600 UKM Bangi, Selangor, Malaysia

**Corresponding author: khuzaim@ukm.edu.my*

Received: 28 November 2021; Accepted: 6 March 2022; Published: 27 June 2022

Abstract

Titanium dioxide (TiO_2) is one of the most studied materials as photocatalyst of water splitting for hydrogen generation. However, TiO_2 has a large band gap of around 3.2 eV, limits its absorption energy to visible light, and the photoexcitation products, such as electron and hole, are recombined rapidly. One method to overcome this problem is by creating a composite heterojunction with other semiconductor materials. In this study, the photocatalytic hydrogen generation of water splitting by TiO_2/Co_3O_4 composite photocatalyst was evaluated. The composite was prepared through hydrothermal synthesis assisted by ball mill crushing, and the powder was annealed at 550 °C. The percentage of Co_3O_4 loading on the TiO_2 varied at 0.5% w/w (TC-05), 1% w/w (TC-1), and 2% w/w (TC-2) to study the suitable amount of Co_3O_4. The surface morphology of the composites was investigated through field emission scanning electron microscopy (FESEM) analyses. Results showed that nanosphere and cubic–shaped morphologies were obtained. For the hydrogen performance analysis, two different conditions of photocatalytic hydrogen generation, which are in pure water and water with addition of 10 vol% of methanol solution as the sacrificial reagent, were measured by using a hydrogen sensor (UNISENSE). TC-1 showed the highest hydrogen production in the pure water, which is 6.75 μmol h^{-1} g^{-1} compared with others. The addition of 10% methanol enhanced the hydrogen production by three times compared with pure water (20.22 μmol h^{-1} g^{-1}. The superior heterojunction of TiO_2 and Co_3O_4 performance can be used in practical applications to enhance the photocatalytic properties of TiO_2.

Keywords: cobalt oxide, hydrogen production, PEC, titanium dioxide

Abstrak

Titanium dioksida (TiO_2) adalah salah satu bahan yang paling banyak dikaji sebagai fotomangkin pembelahan molekul air untuk penjanaan hidrogen. Walau bagaimanapun, TiO_2 mempunyai jurang jalur yang besar sekitar 3.2 eV, yang mengehadkan tenaga

penyerapannya kepada cahaya nampak, dan hasil fotopengujaan, iaitu, elektron dan lubang mengakibatkan bergabung semula dengan cepat. Salah satu cara untuk mengatasi masalah tersebut ialah dengan mencipta gabungan komposit dengan bahan semikonduktor lain. Dalam kajian ini, untuk penjanaan hidrogen bagi pembelahan molekul air fotomangkin gabungan komposit TiO_2/Co_3O_4 telah dinilai. Kaedah sintesis hidroterma dibantu oleh proses penghancuran penggilingan bebola yang digunakan untuk menyediakan komposit berikutan penyepuhlindapan serbuk pada 550 °C. Peratusan pengabungan Co_3O_4 pada TiO_2 telah divariasi pada 0.5% w/w (TC-05), 1% w/w (TC-1), dan 2% w/w (TC-2) untuk mengkaji kadar Co_3O_4 yang sesuai. Morfologi permukaan komposit telah disiasat menggunakan analisis FESEM. Berdasarkan FESEM menunjukkan nanosfera dan berbentuk kubik. Untuk analisis prestasi hidrogen, dua keadaan berbeza penjanaan hidrogen fotokatalitik iaitu dalam air tulen dan air ditambah 10 vol % larutan metanol sebagai reagen, dan telah diukur menggunakan sensor hidrogen (UNISENSE). Hasilnya, TC-1 menunjukkan pengeluaran hidrogen tertinggi dalam air tulen iaitu 6.75 μmol h^{-1} g^{-1} berbanding yang lain. Penambahan 10% metanol meningkatkan pengeluaran hidrogen 3 kali lebih tinggi berbanding dengan air tulen 20.22 μmol h^{-1} g^{-1}. Gabungan komposit TiO_2 dan Co_3O_4 boleh digunakan dalam aplikasi praktikal meningkatkan sifat fotomangkin TiO_2.

Kata kunci: kobalt oksida, pengeluaran hidrogen, PEC, titanium dioksida

Introduction

The growth in global population and quality of life has caused a remarkably increase in energy consumption, where fossil-based fuels are the primary energy contributors to date. Given the nonrenewable nature of fossil fuels, they will be depleted if humans do not undertake steps to safeguard these resources. Alternative fuels are necessary to fulfil future energy demands if fossil fuels are no longer available, particularly for the transportation sector, which consumes around 60% of global energy [1, 2]. Hydrogen was identified four decades ago as a fundamental element of a feasible future energy framework for giving safe, savvy, and ecologically harmless energy. The Energy Policy Act of 1992 classifies hydrogen as an alternative fuel. The ability to power fuel cells in zero-emission cars and the fuel cell's rapid filling time and high efficiency have sparked interest in hydrogen as an alternative transportation fuel. A fuel cell with an electric motor is two to three times more efficient than a gasoline-powered internal combustion engine. Internal combustion engines may use hydrogen as a fuel [3, 4].

The availability of H_2 has become a new barrier because it is not naturally accessible on earth. Hydrogen may be found in a variety of forms, including hydrocarbons, water molecules, and acid and base molecules. Thus, H_2 must be eliminated from all of the abovementioned sources [5]. Coal gasification, steam reforming of natural gas, cryogenic distillation, and water splitting are the methods used for producing commercial hydrogen [6]. Coal gasification and steam reforming of natural gas processes can produce significant quantities of hydrogen. However, these approaches need a strong and safe system due to the tremendous energy consumption (temperatures > 1000 °C) necessary to perform reactions [7]. Electricity generated from renewable energy sources, such as hydropower, wind power, and solar power, might be used to electrolyze water molecules. However, these procedures are inefficient and costly [8]. Photocatalytic water splitting technologies have gained considerable interest for producing green and sustainable hydrogen energy from water. The intrinsic features and architectures of semiconductor-based photocatalysts and photoelectrodes have a large influence on the efficiency of solar-to-hydrogen conversion in photocatalytic and/or PEC catalysis [9].

Titanium dioxide (TiO_2) became the most widely used photocatalyst in the 1970s when water splitting drew the attention of researchers. This condition is due to the low cost, chemical stability, Earth abundance, and nontoxicity of TiO_2. Unfortunately, the potential of TiO_2 is limited because of its high band gap width, poor conductivity, and problematic excited dissociation and electron transport. Thus, many studies have focused on improving the TiO_2's photocatalytic efficacy by changing its surface and microstructure, adding cocatalysts, and creating heterojunctions with metals or other semiconductors [10]. Engineered heterojunctions in photocatalysts were revealed to be a viable approach for increasing catalyst activity by allowing

photogenerated electron–hole pairs to be separated spatially. Co_3O_4 is a good choice for fabricating TiO_2-based hybrids for water splitting because Co_3O_4 is one of the most well-known p-type semiconductors, with incredible substance dependability, low solvency, and solid electrical, attractive, and reactant attributes. The cost-effectiveness and availability of Co-based chemicals may simplify large-scale applications [11-13]. Compared with the typical hydrogen electrode, Co_3O_4 has conduction band (CB) and valence band (VB) areas of 0.97 and 1.23 eV, respectively, thereby resulting in a p–n heterointersection with TiO_2. The performance of a combination of varying weight percent of TiO_2/Co_3O_4 thin films in PEC and photocatalytic water splitting was investigated in this work. TiO_2 P25 was used to make a heterojunction with Co_3O_4 by using a hydrothermal technique.

Materials and Methods

Materials

Cobalt nitrate hexahydrate Co $(NO_3)_2.6H_2O$ and TiO_2 P25 were obtained from Sigma-Aldrich. Urea (analytical grade), polyethylene glycol, and ethanol were purchased from Chem-Supply. All chemicals were used without further purification.

Preparation of TiO_2

Ethanol (1 mL) was mixed with 0.2 g of TiO_2 P25 and 0.05 g of polyethylene glycol, and the mixture was crushed. Blade coating was used to coat the slurry on the fluorine-doped tin oxide (FTO) surface at 0.5 mm thickness, which was then annealed at 500 °C for 2 h.

Synthesis of cobalt oxide

In accordance with prior research, cobalt oxide was produced by using a hydrothermal technique [11]. Cobalt nitrate hexahydrate (1.74 g) and urea (0.72 g) were dissolved in 50 mL deionized water. A stainless-steel autoclave was used to transfer the homogenous solution. The autoclave was placed in a furnace for 6 h at 100 °C. The autoclave was turned off and allowed to cool to ambient temperature. The sample was washed with deionized water before being dried in an oven. Cobalt oxide produced by hydrothermal technique was ball milled for 2 h before being mixed with TiO_2.

Synthesis of the composite heterojunction of TiO_2 and Co_3O_4 as a sample

TiO_2, Co_3O_4, polyethylene glycol, and ethanol were ball milled for 20 min, coated over the FTO surface, and annealed for 2 h at 550 °C. TC-05 (0.5% $Co_3O_4.TiO_2$), TC-1 (1% $Co_3O_4.TiO_2$), and TC-2 (2% $Co_3O_4.TiO_2$) were the three weight variants of TiO_2:Co_3O_4. The sample was characterized and used as a working electrode.

Characterization

A field emission scanning electron microscopy (FESEM) model of ZEISS MERLIN was used to examine the surface morphology with 10k magnification and signal A intense duo.

Electrochemical study

In a three-electrode setup with 0.5 M Na_2SO_4 electrolyte solution, linear sweep voltammetry (LSV) analysis was performed by using an Ametek Versastat 4 under a 100 mW/cm^2 xenon light. The working electrodes were TiO_2/Co_3O_4 thin films, the counter electrodes were platinum wires, and the reference electrodes were Ag/AgCl electrodes.

Photocatalytic H_2 generation measurements

The sample (100 mg) was weighed and placed in a reactor to conduct the photocatalytic H_2 generation measurements. The sample was added with 100 mL of sodium sulfate and placed under solar AM 1.3 illumination (100 mW cm^{-2}) using 75 W Xenon light at 500 nm bandwidth for 2 h, and hydrogen readings were taken every 20 min. The steps were repeated by adding methanol as scavenger, and the readings were taken. In this study, a hydrogen sensor was used to measure the hydrogen produced through a photochemical process.



Figure 1. Photoreactor set up for the photocatalytic H_2 generation measurements

Results and Discussion

Characterizations of catalysts

Figure 2 displays the FESEM images of the as-prepared (a) TiO_2 (b) TC-05, (c) TC-1, and (d) TC-2 samples. From Figure 2a, the TiO_2 shows well-defined nanocubic morphology, with the width of 1.011 µm. Figures 2b–c shows that the loaded Co_3O_4 is finely dispersed on the TiO_2 surface with a diameter of approximately 7.14 nm. Figure 2d shows that an obvious agglomeration occurs during the introduction of Co_3O_4 species. The result is mostly similar to a previous study [12]. However, the different weight percentages of composite heterojunction show different sizes of loaded Co_3O_4 [12].

LSV analysis was used to study the potential of the photocatalyst, and the overpotentials of TC-05, TC-1, and TC-2 were calculated. Figure 3a shows the photocurrent responses of (a) TiO_2, (b) TC-05, (c) TC-1, and (d) TC-2 samples. TC-1 had the highest photocurrent density (70 µA cm^{-2}) among the composites, implying that coating TiO_2 with Co_3O_4 nanoparticles (NPs) improved the photogeneration performance. However, the photocurrent decreased when the Co_3O_4 composites increased to 2 wt.%. This condition occurred because of the agglomeration of the photocatalyst, as shown in the FESEM image (Figure 2d). The agglomeration of the photocatalyst decreased the active site and surface area. EIS analysis was used to test the charge carrier transport capabilities of the composites (Figure 3b), The Nyquist plot of TC-1 was less than that of TC-05 and TC-2. This finding revealed that the TC-1 sample had the lowest electron migration resistance among the samples, indicating that it had a high photocatalytic hydrogen evolution reaction (HER) performance. These findings suggested that the TC-1 sample had the best charge detachment behavior of photogenerated carriers among the photocatalyst samples. The amount of active free radicals available for photocatalytic H_2 creation will rise if charge carrier separation was effective [14].

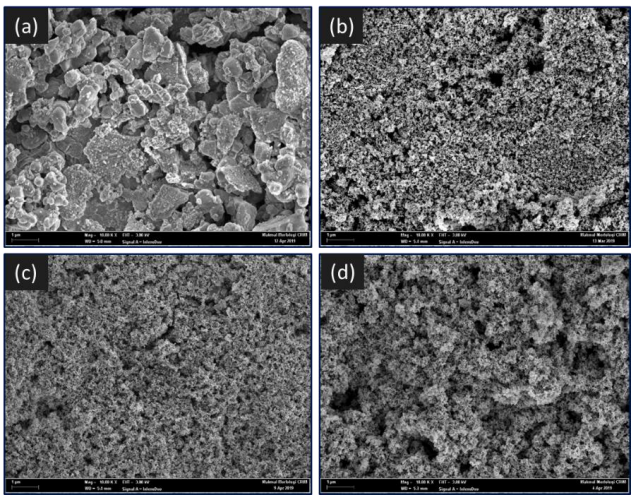


Figure 2. FESEM image of (a) TiO_2 (b) TC-05, (c) TC-1, and (d) TC-2

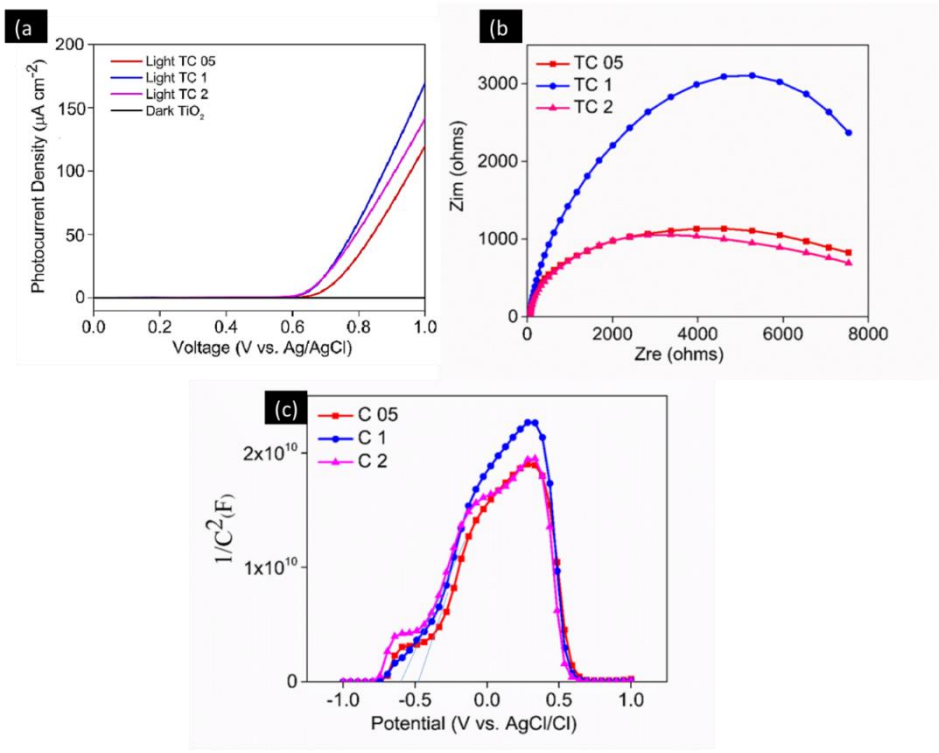


Figure 3. (a) Photocurrent density (b) Electrochemical impedance spectroscopy (EIS), and (c) Mott–Schottky plot of TC-05, TC-1 and TC-2

Photocatalytic hydrogen generation

The photocatalytic hydrogen evolution of the prepared samples was evaluated under artificial sunlight irradiation by using a hydrogen sensor. The photocatalytic hydrogen evolution was tested in two different solutions, and the results were compared. The first analysis (Figure 3a) was tested by using only pure water, and the second analysis (Figure 4b) was tested by using pure water with the addition of 10 vol% of methanol solution as the sacrificial reagent. The comparison of Figures 4a and b showed that the sample with methanol exhibited three times excellent photocatalytic hydrogen evolution as compared without methanol. As shown in Figures 4a and b, the TC-1 sample exhibited the highest H_2 advancement rate (6.75 μmol $g^{-1}h^{-1}$) in pure water and (20.22 μmol $g^{-1}h^{-1}$) in methanol among all the prearranged Co_3O_4/TiO_2 tests. The H_2 production in methanol is higher compared with pure water because methanol effectively separates the hole charges, and the hole–electron pair recombination is reduced [15]. The H_2 advancement rate of TC-2 diminished to 5.70 μmol $g^{-1}h^{-1}$ in pure water and 16.71 μmol $g^{-1}h^{-1}$ in methanol.

The photocatalytic HER of the proposed TiO_2/Co_3O_4 heterojunctions is shown in Figure 5 to analyze the composite heterojunction of TiO_2/Co_3O_4. A previous study [11] provided the specifics of the Co_3O_4 band structure. TiO_2 has a higher Fermi level than Co_3O_4 before they come into contact in the heterojunction. Negative charges migrated from TiO_2 to Co_3O_4 after the heterojunction because p-type Co_3O_4 NPs developed on the surface of n-type TiO_2. This condition caused the Fermi level alignment between TiO_2 and Co_3O_4, resulting in a *p–n* Co_3O_4/TiO_2 junction. According to Wang et al. (2022), a space charge region with a strong built-in electric field in the TiO_2 to Co_3O_4 direction occurs at the TiO_2/Co_3O_4 interface when the energy bands of TiO_2 and Co_3O_4 are bent up and down, resulting in a drift of the

photogenerated charge carrier for heat transfer until a balance thermal equilibrium is reached [16]. The charge transfer mechanism is shown in Figure 5. Under solar AM 1.3 illumination, photogenerated electrons migrated from TiO_2 and Co_3O_4 VBs to the corresponding CBs. The photogenerated electrons were guided from the p-type Co_3O_4 CB to the n-type TiO_2 CB by the induced built-in electric field, resulting in the spatial detachment of photogenerated electron–hole sets. Similarly, Co_3O_4 NPs filled in as a cocatalyst in this *p–n* Co_3O_4/TiO_2 intersection, assisting in expanding the charge partition. Therefore, more photogenerated electrons might focus on TiO_2, which can then be used in the water reduction cycle to produce H_2.

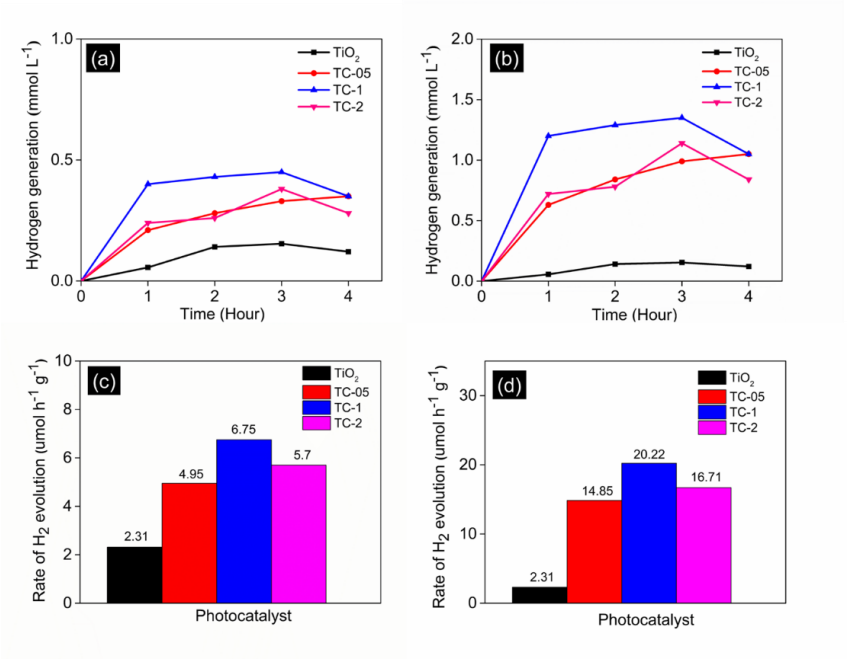


Figure 4. Photocatalytic hydrogen evolution of sample with (a) pure water (b) pure water and methanol, and hydrogen evolution rate of sample with (c) pure water and (d) pure water and methanol.

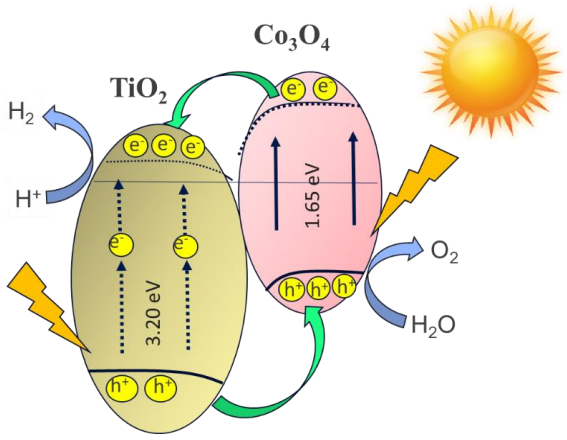


Figure 5. Schematic of the photocatalytic HER mechanism and photogenerated electron–hole separation route of Co_3O_4/TiO_2 *p–n* junction.

Conclusion

In this study, hydrothermal synthesis was used to efficiently construct a Co_3O_4/TiO_2 *p–n* heterojunction. With a photocatalytic H_2 development pace of 20.22 mol $g^{-1}h^{-1}$, the enhanced Co_3O_4/TiO_2 heterojunction had the best photocatalytic H_2 advancement rate. This study used the catalytic effect of Co_3O_4 to distinguish photogenerated electron–hole pairs. A unique Co_3O_4/TiO_2 contact interface and a *p–n* heterojunction was utilized for fast charge carrier transport pathways to enhance the photocatalytic performance. This study may help in the future development and production of *p–n* heterojunction photocatalyst with high visible light-driven energy conversion efficiency.

Acknowledgment

This work was supported by the Malaysia's Ministry of Education through the FRGS/1/2019/STG01/ UKM/03/2 research grant.

References

1. Acar, C. and Dincer, I. (2020). The potential role of hydrogen as a sustainable transportation fuel to combat global warming. *International Journal of Hydrogen Energy,* 45(5): 3396-3406.
2. Rath, B. N., Akram, V., Bal, D. P. and Mahalik, M. K. (2019). Do fossil fuel and renewable energy consumption affect total factor productivity growth? Evidence from cross-country data with policy insights. *Energy Policy,* 127: 186-199.
3. Griffiths, S., Sovacool, B. K., Kim, J., Bazilian, M. and Uratani, J. M. (2021). Industrial decarbonization via hydrogen: A critical and systematic review of developments, socio-technical systems and policy options. *Energy Research & Social Science,* 80: 102208.
4. Zhao, F., Mu, Z., Hao, H., Liu, Z., He, X., Victor Przesmitzki, S. and Ahmad Amer, A. (2020). Hydrogen fuel cell vehicle development in China: An industry chain perspective. *Energy Technology,* 8(11): 2000179.
5. Hosseini, S. E. and Wahid, M. A. (2020). Hydrogen from solar energy, a clean energy carrier from a sustainable source of energy. *International Journal of Energy Research,* 44(6): 4110-4131.
6. Mah, A. X. Y., Ho, W. S., Bong, C. P. C., Hassim, M. H., Liew, P. Y., Asli, U. A., ... and Chemmangattuvalappil, N. G. (2019). Review of hydrogen economy in Malaysia and its way forward. *International Journal of Hydrogen Energy,* 44(12): 5661-5675.
7. Ahmad, H., Kamarudin, S. K., Minggu, L. J. and Kassim, M. (2015). Hydrogen from photo-catalytic water splitting process: A review. *Renewable and Sustainable Energy Reviews,* 43: 99-610.
8. Acar, C. and Dincer, I. (2019). Review and evaluation of hydrogen production options for better environment. *Journal of Cleaner Production,* 218: 835-849.
9. Qureshy, A. M., Ahmed, M. and Dincer, I. (2019). Performance assessment study of photo-electro-chemical water-splitting reactor designs for hydrogen production. *International Journal of Hydrogen Energy,* 44(18): 9237-9247.
10. Arifin, K., Yunus, R. M., Minggu, L. J. and Kassim, M. B. (2021). Improvement of TiO_2 nanotubes for photoelectrochemical water splitting. *International Journal of Hydrogen Energy, 4*6(7): 4998-5024.
11. Moridon, S. N. F., Salehmin, M. I., Mohamed, M. A., Arifin, K., Minggu, L. J. and Kassim, M. B. (2019). Cobalt oxide as photocatalyst for water splitting: Temperature-dependent phase structures. *International Journal of Hydrogen Energy,* 44(47): 25495-25504.
12. Anggraini, D., Wardani, P. K., Agustina, M., Awaluddin, A.and Arifin, K. (2019). TiO_2/Co_3O_4 Composite as photoanode of photoelectrochemical water splitting. *In Journal of Physics: Conference Series*, 1351: 012032.
13. Moridon, S. N. F., Salehmin, M. N. I., Arifin, K., Minggu, L. J. and Kassim, M. B. (2021). Synthesis of cobalt oxide on FTO by hydrothermal method for photoelectrochemical water splitting application. *Applied Sciences,* 11(7): 3031.

14. Kumar, S.G. and Rao, K. K. (2017). Comparison of modification strategies towards enhanced charge carrier separation and photocatalytic degradation activity of metal oxide semiconductors (TiO_2, WO_3 and ZnO), *Applied Surface Science*, 2017: 391124-148.
15. Alenzi, N., Liao, W. S., Cremer, P. S., Sanchez-Torres, V., Wood, T. K., Ehlig-Economides, C. and Cheng, Z. (2010). Photoelectrochemical hydrogen production from water/methanol decomposition using Ag/TiO_2 nanocomposite thin films. *International Journal of Hydrogen Energy,* 35(21): 11768-11775.
16. Wang, L., Tang, G., Liu, S., Dong, H., Liu, Q., Sun, J. and Tang, H. (2022). Interfacial active-site-rich 0D Co_3O_4/1D TiO_2 pn heterojunction for enhanced photocatalytic hydrogen evolution. *Chemical Engineering Journal,* 428: 131338.

Malaysian Journal of Analytical Sciences (MJAS)
Published by Malaysian Analytical Sciences Society

THE THERMAL STABILITY AND PRELIMINARY PERFORMANCE OF SODIUM ALGINATE AND POLYVINYL ALCOHOL-BASED MEMBRANE IN DMFC: MONTMORILLONITE AS A FILLER

(Kestabilan Haba dan Prestasi Awal Membran Berasaskan Natrium Alginat dan Polivinil Alkohol untuk DMFC: Montmorillonit sebagai Pengisi)

Maryam Taufiq Musa and Norazuwana Shaari*

Fuel Cell Institute,
Universiti Kebangsaan Malaysia, Bangi,43600, Selangor, Malaysia

**Corresponding author: norazuwanashaari@ukm.edu.my*

Received: 15 December 2021; Accepted: 24 March 2022; Published: 27 June 2022

Abstract

Biopolymer-based membranes have emerged vastly in recent years for fuel cell applications. Polymer electrolyte membranes (PEM) have become a major component in DMFC stacks that have gone through many studies beforehand. An improvement has been made to PEM, especially using biopolymers like alginate based. Sodium alginate (SA) has significant characteristics such as being too hydrophilic, which is its biggest weakness as a PEM. Blending it with another polymer of polyvinyl alcohol (PVA) and adding a clay filler of montmorillonite (MMT) would be a great solution, in this work. From TGA-DSC analysis, SA/PVA-MMT achieved different thermal stability as the filler content differed. The glass transition temperature of the membrane had increased as the MMT content increased, at a maximum range of 240-260 °C at 15 wt.% of MMT content. The membrane's thermal stability ranking was then followed by 10 wt.% (250 °C) and 2 wt.% (240 °C) of filler content. The higher the glass transition temperature, the greater the thermal stability due to the greater mass loss after being exposed to a later heating. Meanwhile, for the proton conductivity test, a hybrid membrane of SA/PVA-MMT with SVM 20 (20 wt.% MMT) obtained the highest value of 8.0510 mS/cm, followed by SVM 10, SVM 2, SVM 15 and SVM 5 with values of 6.5025, 2.6429, 2.0332 and 1.6083 mS/cm respectively. Higher proton conductivity enables the potential of the hybrid to conduct electricity in DMFC. The lowest methanol uptake was shown by the membrane with 20 wt.% MMT content, with a value of 53.00%, followed by 15 wt.% (97.46%), 10 wt.% (121.59%), 5 wt.% (132.23%) and 2 wt.% (203.30%), respectively. Low methanol uptake of the membrane indicated that the DMFC stack could operate with high efficiency. This study showed that SA/PVA-MMT could be a promising choice of PEM with an optimum MMT content of 10 wt.% for a better performance produced by a cheaper hybridized membrane.

Keywords: alginate, polyvinyl alcohol, montmorillonite, copolymer membrane, thermal stability

Abstrak

Membran berasaskan biopolimer telah muncul secara meluas sejak kebelakangan tahun ini, dalam aplikasi sel fuel. Membran polimer elektrolit (PEM) telah menjadi komponen utama dalam tindanan DMFC, yang mana telah menjadi objek kajian berkali ganda sebelumnya. Satu penambahbaikan PEM telah dibuat khususnya menggunakan biopolimer alginat. Natrium Alginat (SA)

mempunyai sifat signifikan iaitu terlalu hidrofili, yang mana ianya merupakan kelemahan terbesar sebagai PEM. Di dalam kajian ini, Natrium alginat (SA) akan dicampur bersama polivinil alkohol (PVA) dan montmorillonit (MMT), sejenis pengisi berasaskan tanah liat. Campuran ini telah menghasilkan prestasi yang amat baik. Daripada analisis TGA-DSC, SA/PVA-MMT telah mencapai kestabilan haba yang berbeza apabila kandungan pengisi turut berbeza. Suhu peralihan kaca membran tersebut bertambah apabila kandungan MMT dalam sampel juga bertambah, pada 15 wt.% MMT, maksima julat suhu dicapai ialah 240-260 ℃. Kestabilan haba membran ini kemudiannya diikuti dengan 10 wt.% (250 ℃) dan 2 wt.% (240 ℃) konten pengisi. Semakin tinggi suhu peralihan kaca, semakin tinggi kestabilan haba membran disebabkan jisim mula berkurang banyak pada suhu pemanasan yang tinggi (lebih lewat). Manakala untuk kekonduksian proton, SVM 20 (20 wt.% MMT) mendapat nilai tertinggi iaitu, 8.0510 mS/cm, diikuti dengan SVM 10, SVM 2, SVM 15 dan SVM 5 dengan nilaian 6.5025, 2.6429, 2.0332 dan 1.6083 mS/cm masing-masing. Tingginya nilai kekonduksian proton, semakin besarlah potensi membran hibrid tersebut untuk mengalirkan elektrik dalam DMFC. Ambilan metanol terendah dibuktikan oleh SVM 20 (20 wt.% MMT) dengan nilaian 53.00%, diikuti dengan 15 wt.% (97.46%), 10 wt.% (121.59%), 5 wt.% (132.23%) dan 2 wt% (203.30%) masing-masing. Hasil ambilan metanol yang rendah menunjukkan tindanan DMFC boleh beroperasi pada tahap keberkesanan yang tinggi. Kajian ini menyimpulkan bahawa SA/PVA-MMT boleh menjadi pilihan PEM yang terbaik, dengan kandungan MMT optimum pada 10 wt% beserta kos yang rendah untuk prestasi yang lebih baik.

Kata kunci: alginat, polivinil alkohol, montmorillonit, membran dwipolimer, kestabilan haba

Introduction

A polymer electrolyte membrane (PEM) that contains additives is normally able to enhance performance when operating in a fuel cell system. There are many polymers, such as sulfonated poly(ether ether) ketone [1], polybenzimidazole [2], polyvinyl alcohol [3], sulfonated polyimide [4] and polyether sulfone [5], that have been utilized in previous studies to develop non-Nafion based membranes. These polymers are claimed to be capable of replacing Nafion owing to their polysaccharide backbone, which is able to act as both hydrophilic and hydrophobic domains. However, with the high production costs needed for polymer materials, an alternative innovation has been constructed, using biopolymers that are PEM-based.

Recent studies have discovered that chitosan [6], carrageenan [7] and alginate [8] are PEM-based. These biopolymers have the potential to conduct protons as they are mostly in an amorphous state. The highly amorphous condition of the materials resulted in high proton conductivity as there are more proton pathways in amorphous mediums [9]. Charradi et al. worked on SiO_2-montmorillonite filled membranes (9% content) for PEMFC and obtained 0.158 S/cm proton conductivity, which was higher than the pristine polymer at 120 ℃ and 100% relative humidity [10]. Sainul Abidin et al. achieved the highest proton conductivity of 0.0706 S/cm by using modified montmorillonite at 10 wt.% loading, under 70 ℃ conditions, using a polyimide based PEM [11]. Wang et al. synthesized chitosan-based PEM that was filled with solvent-free carbon nanotube fluids and was able to perform maximum proton conductivity at a value of 0.044 S/cm at 80 ℃ [12]. Since biopolymers are highly amorphous, by blending them with other semi-crystalline polymers such as PVA, the resulting membrane could have better flexibility and a firmer structure. Zakaria et al. and Yang et al. worked on PVA-based membranes, each achieving the highest proton conductivity of 0.0095 S/cm and 0.0368 S/cm respectively, both at 30 ℃ [13, 14]. Nevertheless, these works were unable to figure out the hidden potential of blending membrane composites of sodium alginate and polyvinyl alcohol together with an inorganic filler – montmorillonite. Montmorillonite is a clay-type filler, that contains silica tetrahedral, an octahedral layer of aluminum, and exchangeable cations like magnesium and potassium.

Montmorillonite (MMT) has been studied previously, modified with additional protons like H^+, Na^+, Mg^{2+} Ca^{2+} and K^+. Wu et al. achieved high proton conductivities at 38.5 mS/cm with balanced water uptake, 24.26% when developed cloisite sodium montmorillonite [15]. Wang et al. reported 5wt% of

MMT-PBI-O exhibited 0.5 mS/cm proton conductivities at 80 ℃ and losing weight easily (under TGA analysis) compared to pure PBI-O membrane [16]. This was because the insertion of MMT facilitates water absorption thus allowing proton channel formation; 5 wt.% was better than 3wt% MMT. When blending MMT with SPEEK polymer, the water uptake reached 35% which was lower than pure SPEEK, contributing to 0.057 S/cm of ionic conductivity at ambient condition, which was a good finding from Ata et al. [17].

These reports potentially bring up this study to show how MMT involvements can improve proton conductivity of polymer matrix besides its thermal stability could be maintained as well. To distinguish, additional polymer – PVA was included together with biopolymer sodium alginate for developing a novel hybrid membrane electrolyte for direct methanol fuel cell application. This work highlighted on membrane performance tests relating to the thermal degradation analysis.

Materials and Methods

The membranes comprising of sodium alginate, polyvinyl alcohol and montmorillonite as the hybridized membrane of SA/PVA-MMT, were simply named as SVM in this work. The variation of MMT loadings in each sample were differentiated as shown in Table 1.

Table 1. The notation for each sample

MMT Loadings (wt.%)	Notation
0	SV0
2	SVM2
5	SVM5
10	SVM10
15	SVM15
20	SVM20

Membrane preparation

The SVM blended solution was prepared using the solution casting method. Sodium alginate (SA, Acros Belgium) and polyvinyl alcohol (PVA, R & M Chemicals) were mixed together at a concentration ratio of 40:60. The SA and PVA solutions were prepared separately, then dispersed in deionized (DI) water, at 70 ℃ and 90 ℃ respectively. Both polymer solutions were mixed in a beaker and stirred for 1 hour, adding 1 mL of 10% glutaraldehyde (GA, Nacalai Tesque Japan) for internal crosslinking, dropwise, until homogenized. Then solutions of 2 wt.%, 5 wt.%, 10 wt.%, 15 wt.% and 20 wt.% Montmorillonite (MMT, Acros Belgium) were prepared in 5 mL DI water each, which were dispersed overnight at ambient temperature. The SA/PVA solutions and MMT solutions were blended altogether, stirring for 5 hours, to create a homogenized mixture. The mixture was then cast in a petri dish and dried for 12 hours at 60 ℃, followed by 1 hour at 80 ℃ using a box furnace (Carbolite chamber) to become a membrane film. The membrane film was externally crosslinked with 1.5 wt.% $CaCl_2$ and 10% GA by soaking it for 30 minutes under ambient conditions, before further testing.

Thermal analysis

The film samples were characterized using the Simultaneous Thermal Analyzer-Differential Scanning Calorimetry (STA-DSC), NETZSCH Proteos Software, to determine their thermal stability based on the glass transition temperature (T_g). The analysis was run under a nitrogen atmosphere, within the temperature range of 30-800 ℃, with a heating rate of 10 ℃/min.

Membrane performance tests

The membrane film was proceeded to the liquid uptake performance test and proton conductivity test. The membrane film was cut according to a 2 cm x 2 cm dimension for both water and methanol uptake. The film was weighed after 24 hours of being soaked in DI water and 10 % methanol for respective tests, which is denoted as W_{wet} (g). The films were weighed again after drying for 24 hours at room temperature, denoted as W_{dry} (g). The weights recorded were calculated using the liquid uptake equation formula (1) to obtain the percentage of water uptake and methanol uptake.

$$\frac{W_{wet}-W_{dry}}{W_{dry}} \times 100 \quad (1)$$

For proton conductivity testing, the membrane film (4 cm x 1 cm dimension) must be in a fully hydrated

state; it was immersed in DI water for an hour before being placed in a four-electrode conductivity cell that was connected to a potentiostat/galvanostat (WonATech) for 60 seconds, over a frequency range of 1 MHz–50 Hz. This potentiostat would produce a linear trend of voltage versus the current graph, producing a membrane resistance from the slope. The in-plane proton conductivity value (σ) can be calculated by using the in-plane proton conductivity equation (2) [5]:

$$\sigma = \frac{L}{RWT} \quad (2)$$

where L is the length of the film in cm, R is the average resistance (Ω), W is the film width (cm) and T is the thickness of the film (cm).

Results and Discussion

FESEM

For micrographs images, only four samples were observed, because the morphology analysis demand was required just to emphasized on the homogeneity of the surfaces as clay loadings increased – SV0, SVM5, SVM10, SVM20. These desired membranes were proven having carbon, oxygen and sodium elements as observed in EDX in Figure 1(c), (f), (i), (l). Figure 1 (a), (d), (g), (j) were the surface morphology of the membranes while Figure 1 (b), (e), (h), (k) were showing the cross sectional of the membranes. based on Figure 1 (a), which resembling SV0, the present surface image seemed to have pores, as well as could be seen in the cross-section image (Figure 1(b)). Too many porosities were undesirable because it creates channel for water absorption which then leading to excessive membrane swelling. When introduce a little amount of MMT, the surface image for SVM5 looked rougher than SV0, as illustrated in Figure 1(d). The cross-sectional image for SVM2 looked rougher as well, implying the successful intercalation of MMT, with proven EDX elemental peak based on the rising of Mg, Al, Si, K peaks. However, the declining peak of Na, was due to the well-blend of MMT with the polymer chain, interrupting the structure of polymer consisting Na.

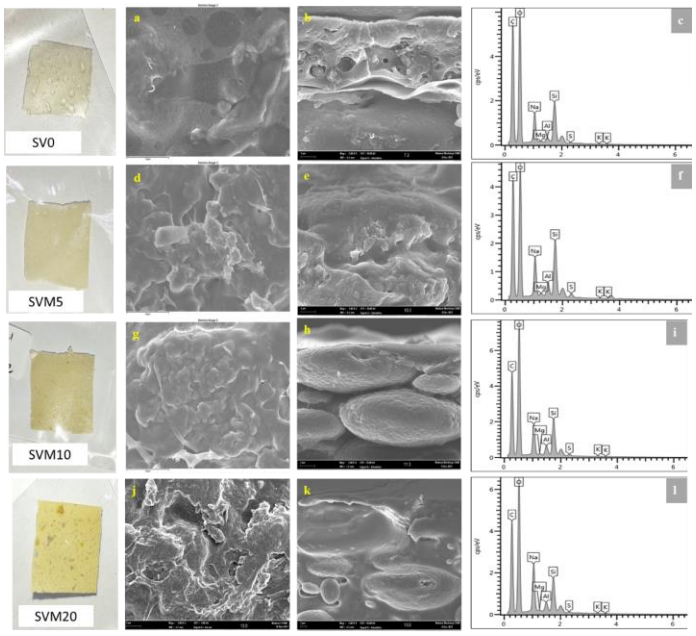


Figure 1. FESEM images of membrane samples, followed by the physical sample on the left-handside, surface images, cross-sectional images and elemental peaks EDX on the right-handside. SV0 (a, b, c), SVM5 (d, e, f), SVM10 (g, h, i) and SVM20 (j, k, l)

As MMT increased higher, SVM10 membrane surface looked much rougher and compact cross-sectional area as shown in Figure 1(g, h). This indicating that water molecules had fully evaporated from the polysaccharide matrix [18], as white tiny particle were visible in Figure 1(h) depicting the successful intercalation of MMT into the SA/PVA copolymer matrix. Nevertheless, the agglomeration presented in SVM20 because of excessive MMT addition resulting it to concentrate at one point, that further discussed in liquid uptake part.

TGA-DSC

For thermal stability analysis, only four samples were involved since we just insisted to compare the obvious trend among the expected significant MMT loadings in the membranes – SV0, SVM2, SVM10, SVM15. The membrane film obtained good thermal stability, with an increased temperature phase of degradation as MMT loadings increased. Referring to Figure 2, the polymer blend started to degrade at 220–240 ℃ and proved to be better than previous studies, which indicated that the first stage began at 80 ℃ [19] and 198 ℃ [20] with only PVA and SA. This first degradation phase was attributed to solvent evaporation [21]. By adding MMT, the membrane has a combination of amorphous and crystalline phases, making the degradation phases a bit slower. The polymer must have a semi-crystalline phase since high amorphous properties might result in a low strength structure of the film. The presence of semi-crystalline properties of the PVA could strengthen the interaction bond between the polymer chain and the filler bond. The interaction bond involved was a strong hydrogen bond, which is difficult to break apart. The weight loss of the membranes was around 50.4–55.2%, which began at a range of 259.8–263.5 ℃, which was dominated by SVM 15. In comparison, the second degradation phase of these MMT-filled membranes had slightly lower thermal stability than the SP/PVA membrane at 307 ℃ [19]. This was due to the presence of MMT, which has hydrophilic properties that cause it to easily degrade. The hydrophilicity enables the membrane to retain water molecules in the matrix, thus degrading at lower temperatures [20, 22]. However, the presence of PVA and MMT in a sodium alginate-based membrane was much better as this blended membrane took higher ranges of the third degradation phase (470–800 ℃) to fully depolymerize the polysaccharide backbone owing to the interfacial connections and improvised crystallinity.

The thermograms of DSC shown in Figure 3, indicating that the glass transition phase changed as MMT loading increased. The glass transition temperature increased from SV0 to SVM10 which was owing to the dipole interaction declining that happened within the homopolymers [23]. This is simultaneous phase to the TGA thermogram whereby the hybridized membranes facing phase changes to rubbery state at a later temperature as the clay fillers added. However, when reaching 15 wt.% of MMT in the hybridized membrane, the glass transition temperature decreased to complex peak value of 123.6 ℃, which could be seen overlapping peak with the control membrane, SV0 in the thermogram. This indicating that backbone polymers became soften at certain higher loading point. In relation to the water uptake performance, SVM15 absorb more water molecules than SVM10 by 10.84%, deducing it has voids for water binding. The voids presence turned up SVM15 membrane to be easily degraded and change phase. Therefore, SVM10 was much preferable type of membrane in this case because it possessed the greater thermal stability with peak value glass transition temperature at 196.7 ℃.

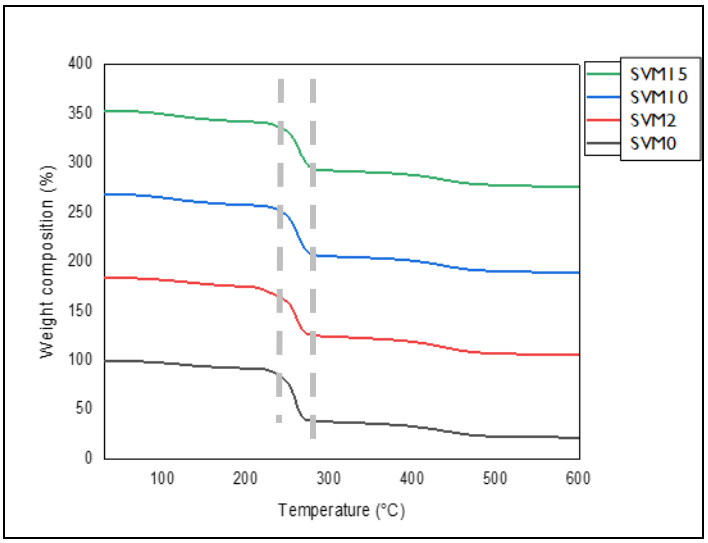


Figure 2. The thermogram of the membranes

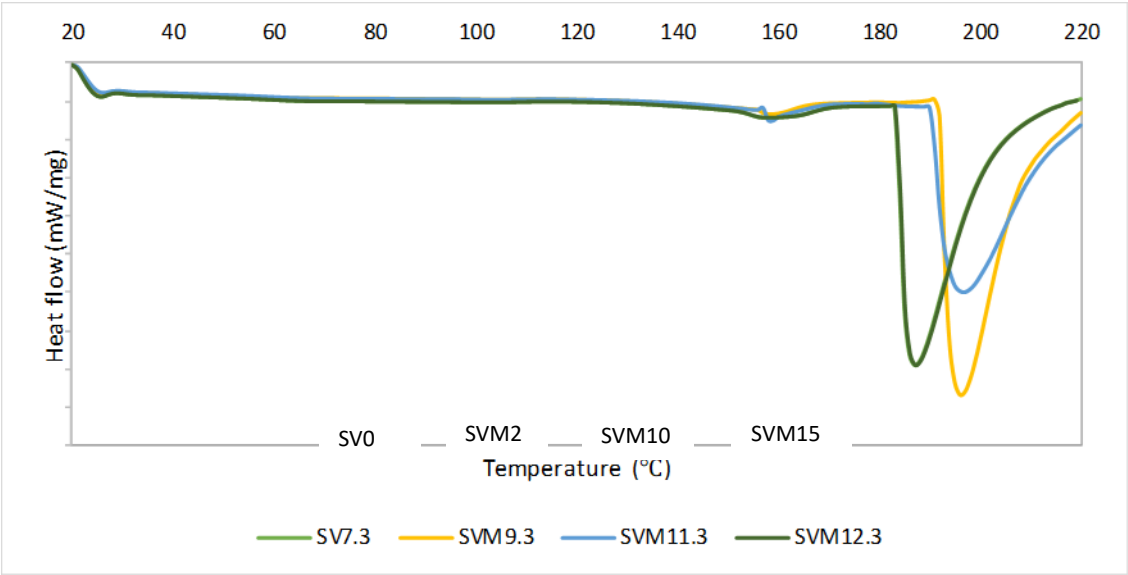


Figure 3. DSC thermogram of the membranes

Membrane performance tests

From Figure 4, the graph trend fluctuated as the MMT content increased. The maximum value of proton conductivity was achieved at 8.0510 mS/cm by using SVM20 (at 20 wt.% MMT loadings). During the conductivity testing, the prominent functional groups involved were H^+, H_3O^+ and ^-OH ions, where H^+ dissociated from the water molecules, hopping from one molecule to another. The insufficiency of single electrons causes the H^+ to react actively with the ^-OH free ions from the MMT, which also contributes to transporting the protons throughout the medium. The hydration state of the membrane was crucial as it would produce more H^+ to actively bind with lone pairs of electrons in H_2O, thus forming a highly reactive ion, H_3O^+. The cycle of transporting protons through

negatively charged ions was repeated simultaneously with the protons hopping. In this study, both mechanisms could potentially occur - the proton hopping mechanism, namely, the Grotthuss mechanism, and the proton being transported, namely the Vehicular mechanism [24]. As shown by SVM15, the existence of free volumes in the membrane decreased when a higher MMT filling was introduced, which resulted in difficulties for the protons to be transferred. The tendency of the proton conductivity to increase at 20 wt.% MMT was due to the presence of active sites at the MMT, which enabled the transport of the proton to pass through. The values were lower at SVM5 and SVM15, most probably caused by the activation of the inhibition properties of MMT when extra loading produced an aggregated effect on the membrane [25, 26].

For water uptake performance, according to Figure 5, the membrane began to reduce absorbing water at 2 wt.% MMT. Then, the trend started to decline again at 15 wt.% MMT after a slight increase at 10 wt.% MMT. The increment of water absorption was due to the introduction of MMT to the pure SAPVA membrane, slightly induced by the hydrophilicity of MMT, which provides a high water content to the membrane [22].

This hydrophilic property, owing to its oxygenated functional group (-OH) [27], through the abundance of water, creates a continuous transferring channel and facilitates ion movement [22]. These functional groups interact with each other (polymer and fillers) via strong hydrogen bonding or polar-polar interaction [27]. The lowest water uptake point was at 20 wt.% (SVM20), after 10 wt.% (SVM10) of MMT. The water uptake level dropped from 162.46% to a value of 129.65% at 10 wt.%, before it decreased even further to 74.89%, with the addition of SVM20.

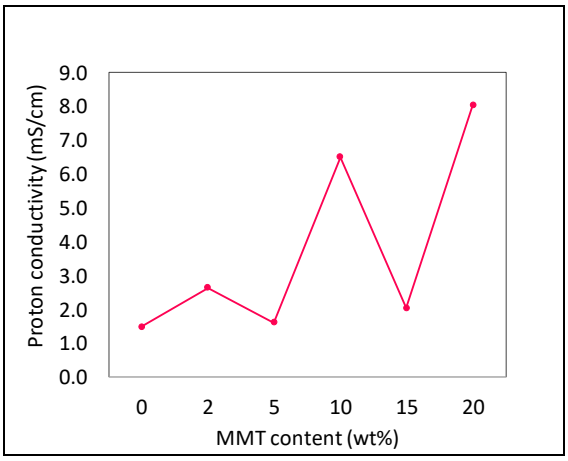


Figure 4. Proton conductivity for SVM2 (2 wt.%), SVM5 (5 wt.%), SVM10 (10 wt.%), SVM15 (15 wt.%) and SVM20 (20 wt.%)

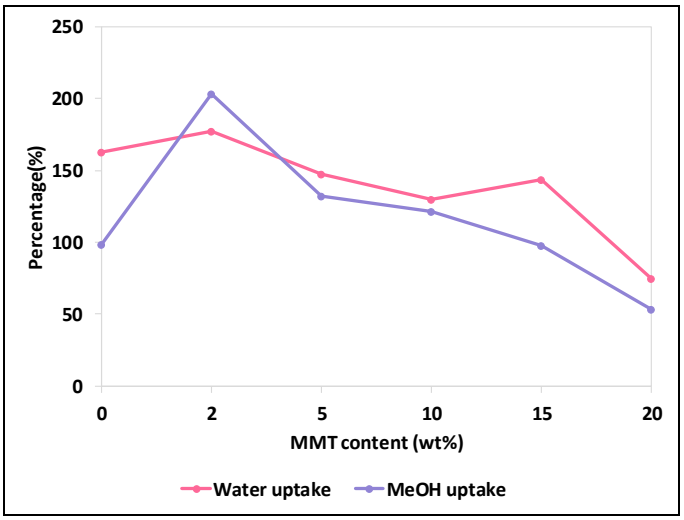


Figure 5. Water uptake and methanol uptake performances for SVM2-20

Table 2. The comparison of previous membrane hybridized studies

Membrane Composite	**Filler Loadings (wt.%)**	**Proton Conductivity (mS/cm)**	**References**
Pure SA	0	0.48	[18]
PVA/SA(6/4)	0	91.0	[19]
PVA/TiO_2	15	48.0	[28]
SA/TiO_2	25	17.3	[8]
SA/Alumina	15	13.0	[20]
PVA/MMT	10	36.8	[14]

The additional MMT filler had partially reduced the size of the ion channels because of agglomeration, hence blocking the absorption of water. Figure 6 and Figure 7 illustrate the plausible figures of how MMT filled up the polymers' matrix. The matrix inside the membranes was homogenously distributed, thus decreasing the free voids of the resultant matrix [27]. The mobility of the SA/PVA chains was reduced then, thus leading to a decrement of water content. Based on the experimental results as shown in Table 3 and Figure 5, the methanol uptake value dropped after reaching its peak at 2 wt.% MMT, from 203.30%, to 53% at 20 wt.% MMT. The explanation for methanol uptake was similar, since the graph trend also decreased as MMT loading increased. The same trend showed that there was good networking and bonding between the alginate polymer and MMT, which prevented fuel crossing [22].

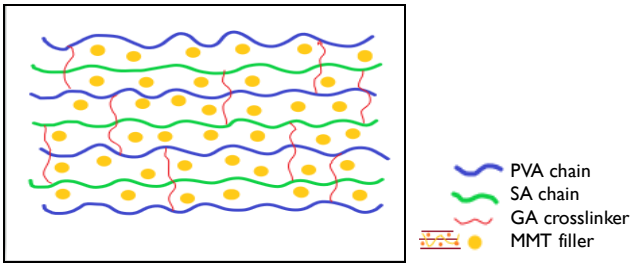


Figure 6. The plausible figures for blended SVM membranes [29]

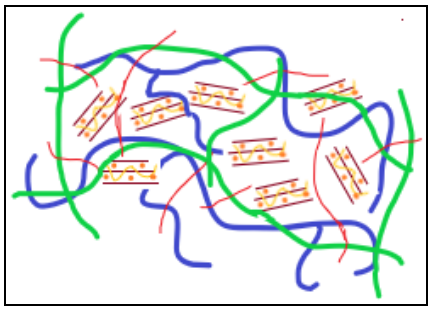


Figure 7. The another version of plausible figures [3]

Table 3. Proton conductivity and liquids uptake of the membranes according to the MMT loadings

Sample	MMT Loadings (wt.%)	Proton Conductivity (mS/cm)	Water Uptake (%)	Methanol Uptake (%)
SV 0	0.0	1.4828	162.46	98.55
SVM 2	2.0	2.6429	177.50	203.30
SVM 5	5.0	1.6083	147.10	132.23
SVM 10	10.0	6.5025	129.65	121.59
SVM 15	15.0	2.0332	143.70	97.46
SVM 20	20.0	8.0510	74.89	53.00

Conclusion

Sodium alginate-based membranes are biopolymers that have a high potential to be used in conducting protons. By blending it with semi-crystalline PVA, the membrane is more thermally stable when the depolymerization phase occurs at a higher temperature. The addition of the inorganic filler, MMT, to the PEM could have a more powerful impact in terms of the liquid uptake. The study proves that 10 wt.% of MMT is the most preferable to obtain a balanced water uptake and reduce methanol uptake, hence suggesting SVM10 as the best composite PEM with improved proton conductivity. Overall, further research might require functionalizing MMT or PVA to enhance the conductivity value in order to be the most promising alternative PEM.

Acknowledgement

The authors would like to give their heartiest gratitude to Universiti Kebangsaan Malaysia for the research funding received through GGPM-2019-002 that has financially supported this work.

References

1. R., Chirachanchai, S., Shishatskiy, S. and Nunes, S. P. (2008). Sulfonated montmorillonite/sulfonated poly(ether ether ketone) (SMMT/SPEEK) nanocomposite membrane for direct methanol fuel cells (DMFCs). *Journal of Membrane Science*, *323*(2), 337-346.
2. Singha, S., Koyilapu, R., Dana, K. and Jana, T. (2019). Polybenzimidazole-clay nanocomposite membrane for PEM fuel cell: Effect of organomodifier structure. *Polymer*, 167: 13-20.
3. Yang, C. C. (2011). Fabrication and characterization of poly(vinyl alcohol)/montmorillonite/ poly(styrene sulfonic acid) proton-conducting composite membranes for direct methanol fuel cells. *International Journal of Hydrogen Energy*, 36(7): 4419–4431.
4. You, P. Y., Kamarudin, S. K. and Masdar, M. S. (2019). Improved performance of sulfonated polyimide composite membranes with rice husk ash as a bio-filler for application in direct methanol fuel cells. *International Journal of Hydrogen Energy*, 44(3): 1857-1866.
5. Xing, D., He, G., Hou, Z., Ming, P. and Song, S. (2011). Preparation and characterization of a modified montmorillonite/sulfonated polyphenylether sulfone/PTFE composite membrane. *International Journal of Hydrogen Energy*, 36(3): 2177-2183.
6. Rosli, N. A. H., Loh, K. S., Wong, W. Y., Mohamad Yunus, R., Lee, T. K., Ahmad, A. and Chong, S. T. (2020). Review of chitosan-based polymers as proton exchange membranes and roles of chitosan-supported ionic liquids. *International Journal of Molecular Sciences*, 21(632): 1-52.
7. Mohy Eldin, M. S., Farag, H. A., Tamer, T. M., Konsowa, A. H. and Gouda, M. H. (2020). Development of novel iota carrageenan-g-polyvinyl alcohol polyelectrolyte membranes for direct methanol fuel cell application. *Polymer Bulletin*, 77(9), 4895-4916.
8. Shaari, N., Kamarudin, S. K. and Zakaria, Z. (2019). Potential of sodium alginate/titanium oxide biomembrane nanocomposite in DMFC application. *International Journal of Energy Research*, 43(14): 8057-8069.
9. Yang, C. C. and Lin, S. J. (2002). Preparation of composite alkaline polymer electrolyte. *Materials Letters*, *57*(4): 873-881.
10. Charradi, K., Ahmed, Z., Aranda, P. and Chtourou, R. (2019). Silica / montmorillonite nanoarchitectures and layered double hydroxide-SPEEK based composite membranes for fuel cells applications. *Applied Clay Science*, 174: 77-85.
11. Sainul Abidin, K., Kannan, R., Bahavan Palani, P. and Rajashabala, S. (2017). Role of structural modifications of montmorillonite , electrical properties effect , physical behavior of nanocomposite proton conducting membranes for direct methanol fuel cell applications. *Materials Science-Poland*, 35(4): 707-716.
12. Wang, J., Gong, C., Wen, S., Liu, H., Qin, C., Xiong, C. and Dong, L. (2018). Proton exchange membrane based on chitosan and solvent-free carbon nanotube fluids for fuel cells applications. *Carbohydrate Polymers*, 186: 200-207.
13. Zakaria, Z., Kamarudin, S. K., Timmiati, S. N. and Masdar, M. S. (2019). New composite membrane poly(vinyl alcohol)/graphene oxide for direct ethanol–proton exchange membrane fuel cell. *Journal of Applied Polymer Science*, 136(2): 1-13.
14. Yang, C. C. and Lee, Y. J. (2009). Preparation of the acidic PVA/MMT nanocomposite polymer membrane for the direct methanol fuel cell (DMFC). *Thin Solid Films*, 517(17): 4735-4740.
15. Wu, X.-W., Wu, N., Shi, C.-Q., Zheng, Z.-Y., Qi, H.-B. and Wang, Y.-F. (2016). Proton conductive montmorillonite-Nafion composite membranes for direct ethanol fuel cells. *Journal of Applied Surface Science*, 2016: 1-6.
16. Wang, F., Wang, D. and Zhu, H. (2018). Montmorillonite-polybenzimidazole inorganic-organic composite membrane with electric field-aligned proton transport channel for high temperature proton exchange membranes. *Polymer-Plastics Technology & Engineering*, 2018: 1-8.
17. Ata, K. C., Kadioglu, T., Turkmen, A. C., Celik, C. and Akay, R. G. (2020). Investigation of the effects of SPEEK and its clay composite membranes on the performance of direct borohydride fuel cell. *International Journal of*

Hydrogen Energy, 45(8): 5430-5437.

18. Shaari, N., Kamarudin, S. K., Basri, S., Shyuan, L. K., Masdar, M. S. and Nordin, D. (2018). Enhanced mechanical flexibility and performance of sodium alginate polymer electrolyte bio-membrane for application in direct methanol fuel cell. *Journal of Applied Polymer Science*, 135(37): 46666.
19. Yang, J. M., Wang, N. C. and Chiu, H. C. (2014). Preparation and characterization of poly(vinyl alcohol)/sodium alginate blended membrane for alkaline solid polymer electrolytes membrane. *Journal of Membrane Science*, 457: 139-148.
20. Shaari, N. and Kamarudin, S. K. (2020). Sodium alginate/alumina composite biomembrane preparation and performance in DMFC application. *Polymer Testing*, 81: 106183.
21. Yang, C. C., Lee, Y. J. and Yang, J. M. (2009). Direct methanol fuel cell (DMFC) based on PVA/MMT composite polymer membranes. *Journal of Power Sources*, 188(1): 30-37.
22. Shaari, N., Kamarudin, S. K., Basri, S., Shyuan, L. K., Masdar, M. S., & Nordin, D. (2018). Enhanced Proton Conductivity and Methanol Permeability Reduction via Sodium Alginate Electrolyte-Sulfonated Graphene Oxide Bio-membrane. *Nanoscale Research Letters*, 13(1): 1-16.
23. Hemalatha, R., Alagar, M., Selvasekarapandian, S., Sundaresan, B. and Moniha, V. (2019). Studies of proton conducting polymer electrolyte based on PVA, amino acid proline and NH_4SCN. *Journal of Science: Advanced Materials and Devices*, 4(1): 101-110.
24. Kreuer, K. D. (2001). On the development of proton conducting polymer membranes for hydrogen and methanol fuel cells. *Journal of Membrane Science*, 185: 29-39.
25. Radmanesh, F., Rijnaarts, T., Moheb, A., Sadeghi, M. and de Vos, W. M. (2019). Enhanced selectivity and performance of heterogeneous cation exchange membranes through addition of sulfonated and protonated Montmorillonite. *Journal of Colloid and Interface Science*, 533: 658-670.
26. Uddin, F. (2018). Montmorillonite: An introduction to properties and utilization. IntechOpen Web of Science, Pakistan: pp. 1-23.
27. Kakati, N., Maiti, J., Das, G., Lee, S. H. and Yoon, Y. S. (2015). An approach of balancing the ionic conductivity and mechanical properties of PVA based nanocomposite membrane for DMFC by various crosslinking agents with ionic liquid. *International Journal of Hydrogen Energy*, 40(22): 7114-7123.
28. Yang, C.-C., Chiu, S. J., Lee, K.-T., Chien, W.-C., Lin, C.-T. and Huang, C.-A. (2008). Study of poly(vinyl alcohol)/titanium oxide composite polymer membranes and their application on alkaline direct alcohol fuel cell. *Journal of Power Sources*, 184(1): 44-51.
29. Kamjornsupamitr, T., Sangthumchai, T., Saejueng, P., Sumranjit, J., Hunt, A. J. and Budsombat, S. (2021). Composite proton conducting membranes from chitosan, poly(vinyl alcohol) and sulfonic acid-functionalized silica nanoparticles. *International Journal of Hydrogen Energy*, 46(2): 2479-2490.

Malaysian Journal of Analytical Sciences (MJAS)
Published by Malaysian Analytical Sciences Society

FORMULATION AND CHARACTERISATION OF LSCF/YSZ-SDC AND LSCF/YSZ-SDCC DUAL COMPOSITE CATHODES FOR INTERMEDIATE-TEMPERATURE SOLID OXIDE FUEL CELL

(Formulasi dan Ciri Dwi-Komposit Katod LSCF/YSZ-SDC dan LSCF/YSZ-SDC Karbonat untuk Sel Bahan Api Oksida Pepejal Bersuhu Pertengahan)

Nurul Farhana Abdul Rahman, Umira Asyikin Yusop, Yohannes Nyambong Lowrance, Hamimah Abd. Rahman*, Mohd Azham Azmi, Shahruddin Mahzan, Azzura Ismail

Faculty of Mechanical and Manufacturing Engineering,
Universiti Tun Hussein Onn Malaysia, 86400 Parit Raja, Batu Pahat, Johor, Malaysia

**Corresponding author: hamimah@uthm.edu.my*

Received: 28 November 2021; Accepted: 27 February 2022; Published: 27 June 2022

Abstract

A cathode component solid oxide fuel cell (SOFC) is important in the manufacturing of the cells. This study evaluated two dual composite cathodes, namely, $(La_{0.6}Sr_{0.4})_{0.97}Co_{0.2}Fe_{0.8}O_3$ (LSCF)/$Y_{0.8}Zr_{0.92}O_{1.96}$ (YSZ)-$Sm_{0.2}Ce_{0.8}O_{1.9}$ (SDC) and LSCF/YSZ-SDC carbonate (SDCC). The dual composite cathodes with different compositions were developed through high-energy ball milling (HEBM) for the production of dual composite powder and screen-printing method for the fabrication of symmetrical cells. The properties of the dual composite cathodes were studied. Phase identification was carried out via X-ray diffractometry (XRD), and the electrochemical performance of the symmetrical cells was measured by impedance test. The physical morphologies of LSCF/YSZ-SDC and LSCF/YSZ-SDCC were slightly different. The XRD patterns of the LSCF/YSZ-SDC cathode powder showed no secondary peak, whereas the LSCF/YSZ-SDCC cathode powder had $SrCO_3$ as an impurity. Microstructure and powder homogeneity are considered essential in addition to the good formulation of the dual composite's cathodes. The particle sizes of LSCF/YSZ-SDC and LSCF/YSZ-SDCC as analyzed by ImageJ software were in the range of 130–160 nm. The printed cathode was investigated under heat treatment from 700 °C to 500 °C. The electrochemical performance of LSCF/YSZ-SDCC was slightly better compared with that of LSCF/YSZ-SDC because of the addition of the carbonate; however, the polarization resistance obtained did not meet the standard range. The electrochemical performance obtained from this study was not favorable because of severe problems, such as the technique applied during cell fabrication and the presence of impurity after the HEBM process.

Keywords: dual composite cathodes, intermediate temperature, screen printing, solid oxide fuel cell

Abstrak

Komponen katod untuk sel bahan api oksida pepejal (SOFC) adalah penting dalam pembuatan sel. Dalam kajian ini, penilaian katod komposit dwi (LSCF)/(YSZ)-(SDC) and (LSCF)/(YSZ)-Karbonat (SDCC) dibentangkan. Komposisi yang berbeza bagi katod komposit dwi telah dibangunkan melalui teknik pengisaran bebola tenaga tinggi untuk penghasilan serbuk komposit dwi dan kaedah percetakan skrin telah digunakan untuk fabrikasi sel simetri. Pencirian sifat katod komposit dwi telah dikaji. Pengenalpastian fasa melalui kaedah pembelauan sinaran-X telah dijalankan dan prestasi electrokimia sel simetri diukur dengan

menggunakan ujian impedans. Perbandingan antara morfologi fizikal LSCF/YSZ-SDC and LSCF/YSZ-SDCC menunjukkan sedikit perbezaan dengan penambahan karbonat. Corak sinar-X untuk komposit dwi campuran LSCF/YSZ-SDC katod serbuk tidak memaparkan puncak sekunder. Bagaimanapun, Komposit dwi campuran LSCF/YSZ-SDCC katod serbuk memaparkan kehadiran sebagai bendasing. Kehomogenan struktur mikro dan serbuk dianggap pentiing sebagai tambahan kepada perumusan katod dwi komposit yang baik. Purata saiz zarah purata bagi LSCF/YSZ-SDC and LSCF/YSZ-SDCC dwi komposit selepas dianalisis oleh perisian Image J didedahkan berada dalam julat antara 130-160. Filem bercetak katod telah disiasat di bawah suhu rawatan haba dari 700 ℃ hingga 500 ℃. Prestasi elektrokimia LSCF/YSZ-SDCC menunjukkan lebih baik sedikit berbanding LSCF/YSZ-SDC kerana penambahan karbonat namun keputusan yang diperoolehi tidak mencapai julat piawai rintangan polarisasi. Prestasi elektokimia yang diperoleh daripada kajian ini adalah tidak memberangsangkan kerana masalah yang teruk seperti teknik yang digunakan semasa fabrikasi sel dan kehadiran bendasing selepas proses HEBM.

Kata kunci: katod komposit dwi, suhu pertengahan, percetakan skrin, sel bahan api oksida pepejal

Introduction

Solid oxide fuel cells (SOFCs) are still highly investigated because they have the highest potential for future power-generating devices in fuel cell technology. The capability of SOFCs to convert chemical energy from hydrogen or versatile fuels, particularly hydrocarbon fuels, into electrical or thermal energy made SOFCs a potential renewable energy source. Recent developments in SOFCs have focused on limiting the operating temperature and selecting a stable material for SOFC components. Although many cathodes have been developed and studied in detail, dual composite cathodes are barely reported. Dual composite cathodes are introduced to create an ideal cathode microstructure that can help improve phase contiguity and interfacial coherence by selecting suitable materials as cathode components [1-4]. Several studies have development of dual composite cathode was investigated. According to Ko et al. [3], $(La_{0.6}Sr_{0.4})_{0.97}Co_{0.2}Fe_{0.8}O_3$ (LSM)-$Y_{0.8}Zr_{0.92}O_{1.96}$ (YSZ) composite cathodes struggle to achieve a high electrochemical performance because their effective surface area is small for electrocatalytic reactions. As a solution, an LSM/YSZ-YSZ dual composite cathode was created with LSM and YSZ particles conjugated together on YSZ-based particles. Based on the reported analysis, the LSM/YSZ-YSZ dual composite cathode had improved cathodic performance and also improved the durability of the cell by enhancing the phase contiguity and interfacial coherence between cells. Several dual composite cathodes were created for the further investigation of dual composite cathode materials. For example, LSM/YSZ-gadolinium-doped ceria (GDC), LSCF/YSZ-GDC and LSCF/GDC-YSZ were developed. The cell performances of these dual composite cathodes were investigated by comparing with a single composite cathode (LSCF-GDC), and the results showed that LSCF/GDC-YSZ had a lower polarization resistance (0.075 Ωcm^2) than LSCF-GDC (0.195 Ωcm^2) [3-4]. However, the operating temperatures of previously developed dual composite cathodes for SOFCs are high.

In this study, two new dual composite cathodes, namely, LSCF/YSZ-$Sm_{0.2}Ce_{0.8}O_{1.9}$ (SDC) and LSCF/YSZ-SDC carbonate (SDCC), were developed in an attempt to investigate their electrochemical performances in limited operating temperatures. Previous research developed and evaluated two different dual composite cathodes, namely, LSM/GDC-YSZ and LSCF/YSZ-GDC. The electrochemical performances of these cathodes were investigated at high operating temperatures [3-4]. In the present study, the operating temperature was limited to 700–500 °C. YSZ was added to the LSCF-SDC composite cathode as an electrolyte material because YSZ can help increase the performances of cell components [5]. Moreover, SDC was used instead of GDC in this research. Both doped ceria are good oxygen ion conductors [6], but SDC is preferred because of its excellent ionic conductivity, which is related to oxygen vacancy [6]. Samarium causes a remarkable increase in oxygen vacancies, which help increase ionic conductivity [6]. Additionally, incorporating carbonate salts (Li_2CO_3 and Na_2CO_3) can improve ionic conductivity [7]. For these reasons, two

new dual composite cathodes were developed and examined in this study.

The present work aimed to investigate the electrochemical performances of dual composite cathodes in an operating temperature between 700 °C and 500 °C. The dual composite cathodes were prepared by mixing LSCF with YSZ-SDC and YSZ-SDCC with different weight percentages. The symmetrical cells were prepared by screen printing method using LSCF/YSZ-SDC and LSCF/YSZ-SDCC as the inks. Moreover, the phase microstructure and electrochemical performances of the dual composite cathode symmetrical cells were evaluated in depth in this study.

Materials and Methods

Preparation and characterization of dual composite powders

YSZ-SDC and YSZ-SDCC composite powders were prepared using high-speed ball milling technique. SDCC electrolyte was prepared using low-speed ball milling method with 80 wt.% raw SDC powder (Kceracell, South Korea) mixed with 20 wt.% binary carbonates, which comprise 67 mol.% Li_2CO_3 and 33 mol.% Na_2CO_3 (Sigma Aldrich, USA) [7]. YSZ-SDC and YSZ-SDCC composite powders were prepared by mixing commercial YSZ powder (Kceracell, South Korea) with commercial SDC and SDCC electrolyte powders, respectively, via high-energy ball milling (HEBM) (Fritsch Pulveristte, Germany) at 550 rpm for 2 h in zirconia jars. Three different weight ratios (50 wt.%:50 wt.%, 60 wt.%:40 wt.% and 70 wt.%:30 wt.%) for YSZ-SDC and YSZ-SDCC were selected as inspired from a previous research [8]. The resultant YSZ-SDC and YSZ-SDCC wet mixtures were dried and calcined.

In the second step, a commercial LSCF powder (Kceracell, South Korea) was added into the obtained YSZ-SDC and YSZ-SDCC composite powders with a 50:50 ratio to form dual composite cathode powders. HEBM was applied to produce homogenous mixtures of the dual composite cathode powders. Lastly, both dual composite cathode powders were dried overnight and heat treated at 750 °C for 1 h [8]. Table 1 shows the compositions of the prepared composite powders and dual composite powders.

All the fabricated powders were characterized by X-ray diffractometry (XRD; D8 Advanced Bruker, Germany) to identify the crystalline phases and the formation of any secondary phases. Then, the microstructure and element composition distribution were characterized using field-emission scanning electron microscopy (FESEM) with electron-dispersive spectroscopy (EDS; JSM 6380-Jeol, Japan). The particle sizes of all the resultant powders were estimated through the ImageJ software using the micrographs obtained by FESEM.

Table 1. Weight ratio compositions of composite and dual composite powders

Composite Powder	Weight Ratio Composition (wt.%)	Dual Composite Powder	Designated samples	Weight Ratio Composition (wt.%)
YSZ-SDC	50:50	LSCF/YSZ-SDC	LYS1	50/50:40
YSZ-SDC	60:40	LSCF/YSZ-SDC	LYS2	50/60:40
YSZ-SDC	70:30	LSCF/YSZ-SDC	LYS3	50/70:30
YSZ-SDCC	50:50	LSCF/YSZ-SDCC	LYSC1	50/50:50
YSZ-SDCC	60:40	LSCF/YSZ-SDCC	LYSC2	50/60:40
YSZ-SDCC	70:30	LSCF/YSZ-SDCC	LYSC3	50/70:30

Electrical performance analysis of LSCF/YSZ-SDC and LSCF/YSZ-SDCC dual composite cathodes

The dual composite symmetrical cells (LSCF/YSZ-SDC//YSZ electrolyte//LSCF/YSZ-SDC and LSCF/YSZ-SDCC//YSZ electrolyte// SCF/YSZ-SDCC) were prepared for the evaluation of the electrical performances of the dual composite cathodes. YSZ electrolyte pellet was prepared using a uniaxial press (Bench Top 3851, Carver, USA). Commercial YSZ powder (0.5 g) was mixed with a drop of polyethylene glycol to produce 13 mm-thick YSZ pellets. LSCF/YSZ-SDC and LSCF/YSZ-SDCC were screen printed on both sides of the YSZ electrolyte pellet. The dual composite powder was merged with terpineol (solvent; Merck kGaA, Germany), ethyl cellulose (binder; Sigma Aldrich, USA) and oleic acid (dispersant; Sigma Aldrich, USA) to create the screen-printing ink [9]. All the chemicals were mixed and agitated for several hours in an agate mortar until the suitable ink viscosity was achieved. Samples of the dual composite cathode symmetrical cells were placed in alumina boats and sintered at 600 °C for 90 min at a heating rate of 5 °C/min using a furnace (PLF 130, Protherm, Turkey) [10]. The surface morphologies of the dual composite cathodes were examined by scanning electron microscopy (SEM; Jeol, Japan). The electrical performances of symmetrical cells were tested using AC impedance spectroscopy (Metroahm Autolab Potentiostat and Galvanostat) in the frequency range of 0.1–1 MHz and AC voltage amplitude of 500–700 °C. Figure 1 shows the schematic diagram for the dual composite cathode symmetrical cell with its characterization, which will be discussed later in this paper.

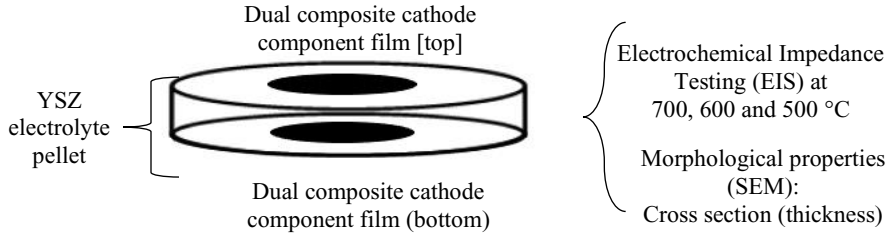


Figure 1. Schematic diagram of the dual composite cathode symmetrical cell

Results and Discussion

Characterization of dual composite powders

The XRD patterns of LSCF/YSZ-SDC and LSCF/YSZ-SDCC powders with different electrolytes and electrolyte contents (YSZ-SDC and YSZ-SDCC) are shown in Figures 2(a) and (b), respectively. Both dual composites cathodes were compared with commercial LSCF, YSZ, SDC and SDCC. As shown in Figure 2, only three primary phases of the standard peaks of LCSF perovskite (JCPDS No 01-089-5720), SDC (JCPDS No 01-075-0157) and YSZ (JCPDS No 00-030-1468) were detected. The carbonate (Li/Na) peaks in the SDCC composite shown in Figure 2(b) yielded the crystallite peak of the pure fluorite structure of SDC, which is equivalent to the pure SDC structure. This result indicates that carbonates form an amorphous form, whereas SDC forms a well-defined fluorite crystal structure [8]. The SDCC peak was similar to the SDC pattern, as the addition of binary carbonates did not affect the shape and size of the original structures of the SDC particles. Li_2CO_3 and Na_2CO_3 were in molten amorphous states because the calcination temperature was over their melting temperatures [10]. Secondary phases were detected in the LSCF/YSZ-SDCC dual composite. Figure 2(c) shows the enlarged XRD pattern of the secondary phase identified as strontium carbonate ($SrCO_3$, JCPDS No. 00-005-0418). According to Rahman et al. (2020), this phenomenon is normally due

to excessive power generated during the milling process of commercial LSCF powders, which caused the minor phase of $SrCO_3$ to form [11]. The formation of $SrCO_3$ impurity might be one of the reasons that caused the degradation of the electrochemical performances of the dual composite cathode cells owing to its incompatibility with the electrolyte material. A further analysis between the formation of impurities and the performances of dual composite cells need to be addressed more in the future.

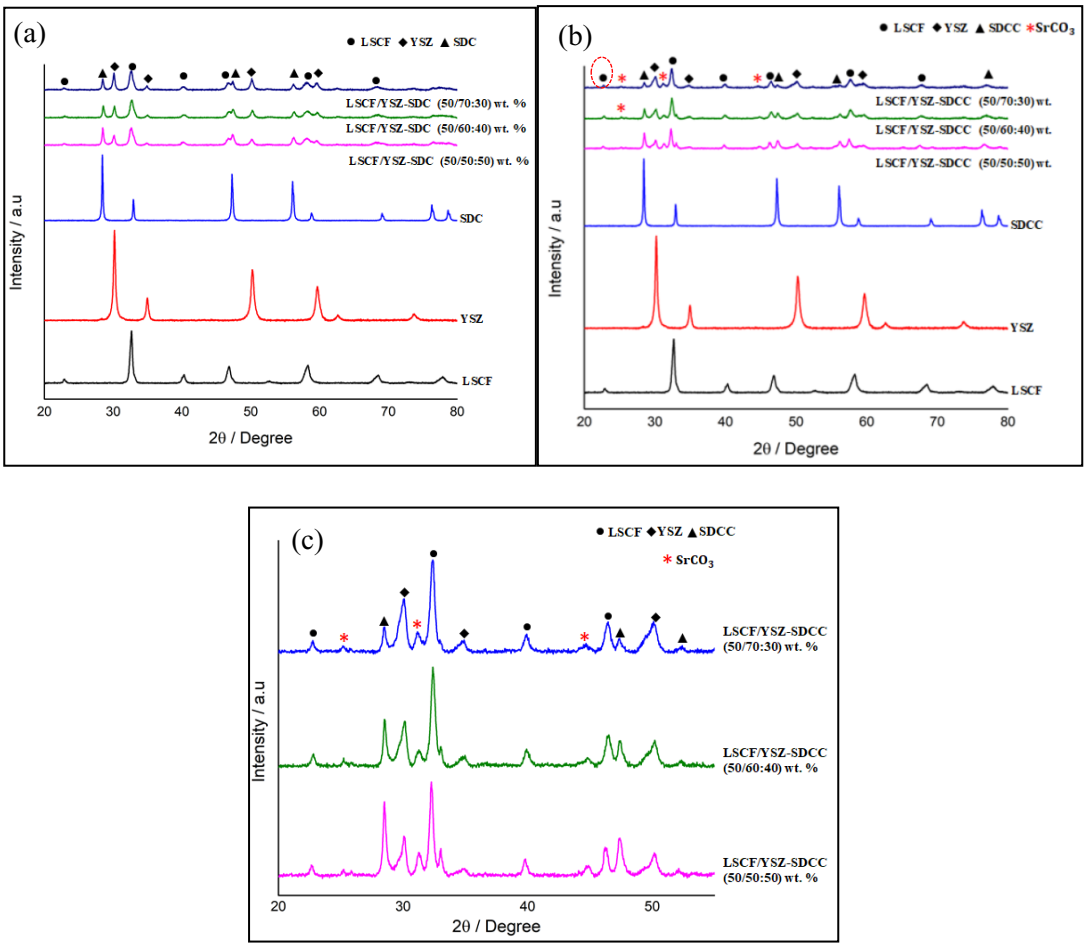


Figure 2. XRD patterns of (a) LSCF/YSZ-SDC and (b) LSCF/YSZ-SDCC dual composite cathode powders. (c) Peak enlargement for LSCF/YSZ-SDCC dual composite cathode powder

Microstructure analysis of dual composite cathode powders

The effect of various weight compositions (YSZ-SDC and YSZ-SDCC) on powder morphology after the incorporation with LSCF were further investigated via FESEM. Figures 3 and 4 show the FESEM micrographs of the LSCF/YSZ-SDC and LSCF/YSZ-SDCC dual composite cathodes. Well-distributed and fine particles were obtained in all dual composite cathode powders after HEBM. Fine particles in the range of 130–160 nm were observed. HEBM is a well-known technique used to synthesise nanocrystalline perovskites that exhibit an improvement in response ratios at low operating temperatures [12]. The particle sizes of the commercial

powders of LSCF,YSZ and SDC, as well as those of the developed dual composite cathodes, are tabulated in Table 2. LYSC1 (159 nm) had the largest particle size, followed by LYSC2 (145 nm) and LYSC3 (135 nm). Similarly, amongst the LSCF/YSZ-SDC dual composites, LYS1 (147 nm) displayed a slightly larger particle size compared with LYS2 (138 nm) and LYS3 (126 nm). The prepared LSCF/YSZ-SDC and LSCF/YSZ-SDCC dual composite powders had smaller particles compared with commercial LSCF, YSZ and SDC powders. The decrease in size can be affected by the calcination process, as the calcination temperature directly influences the parameters [14]. The decrease in the average particle size of the dual composite powders was expected because the milling process creates mechanical energy to breakdown the particles into smaller size and creates a uniform mixture of solid contents [15]. However, a slight agglomeration was seen in the LYS3 dual composite powders. This finding indicates that the composition 70YSZ:30SDC is not suitable for the development of dual composite cathodes. As a result, the total polarisation resistance of LYS3 was the highest amongst the compounds. Parwaiz et al. reported that the improper selection of a sample parameter will induce unwanted phase transformation and undesirable material properties [16].

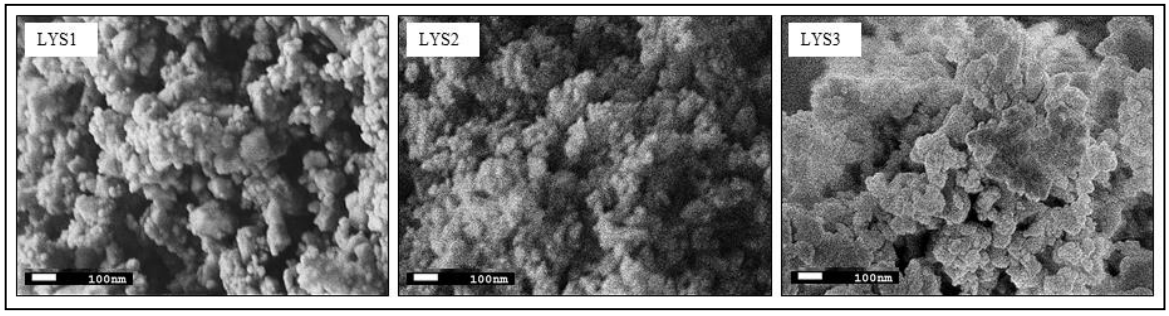


Figure 3. FESEM micrographs of the LSCF/YSZ-SDC dual composite cathode after HEBM and calcination at 50,000× magnification

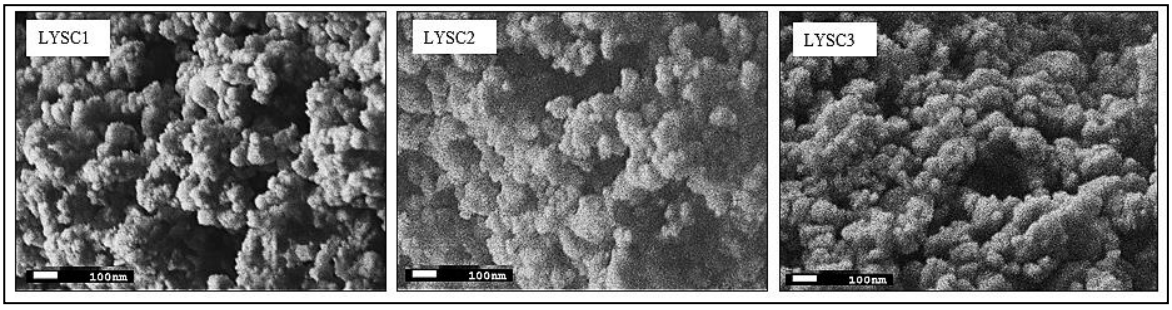


Figure 4. FESEM micrographs of the LSCF/YSZ-SDCC dual composite cathode after HEBM and calcination at 50,000× magnification

Table 2. Average particle sizes of the commercial and prepared dual composite powders

Powders	Average Particle Size (nm)
Commercial Powder LSCF	567
Commercial Powder YSZ	379
Commercial Powder SDC	130
Prepared LSCF/YSZ-SDC (50/50:50 wt.%)	147
Prepared LSCF/YSZ-SDC (50/60:40 wt.%)	138
Prepared LSCF/YSZ-SDC (50/70:3 0wt.%)	126
Prepared LSCF/YSZ-SDCC (50/50:50 wt.%)	159
Prepared LSCF/YSZ-SDCC (50/60:40 wt.%)	145
Prepared LSCF/YSZ-SDCC (50/70:30 wt.%)	135

Microstructure analysis of dual composite cathode symmetrical cells

The printed surfaces and cross-sections of the LSCF/YSZ-SDC and LSCF/YSZ-SDCC pellets were observed through SEM and EDS as illustrated in Figure 5, Figure 6 and Figure 7. Figure 5 shows the secondary (SE) SEM images of the printed surfaces of the dual composite cathodes in the same magnification. Small pores were seen in all LSCF/YSZ-SDCs, whereas large pores were detected in the LSCF/YSZ-SDCCs. This outcome was probably because the binary carbonate reached the melting point as the sintering temperature (600 °C) during the preparation of the symmetrical cells was fixed. In addition, the porosity of the cathode should lie in the range of 20%–40% to achieve a better electrochemical performance [17]. The estimated average porosity for both dual composite cathodes was determined using SEM. The maximum porosity percentages of all LSCF/YSZ-SDC and LSCF/YSZ-SDCC dual composite cathodes were kept within the acceptable range. Table 3 shows the estimated averages porosity for the different compositions of the dual composite cathodes. The morphology of the pellets showed a regular distribution; however, the addition of carbonate as the solid content increased the roughness of the printed surface. The addition of a solid content helps increase the surface roughness by improving the elastic properties of the screen-printing ink [18]. As shown in Figure 5, a small crack was observed on the surface of the printed cathode films in the LYS3 and LYSC3 dual composite cathodes. Carbonate degradation might have led to the cracking phenomenon. Besides, a weak adhesion to the surface of the substrate during the deposition of the printed material is perhaps one of the reasons that caused the cracking surface [19].

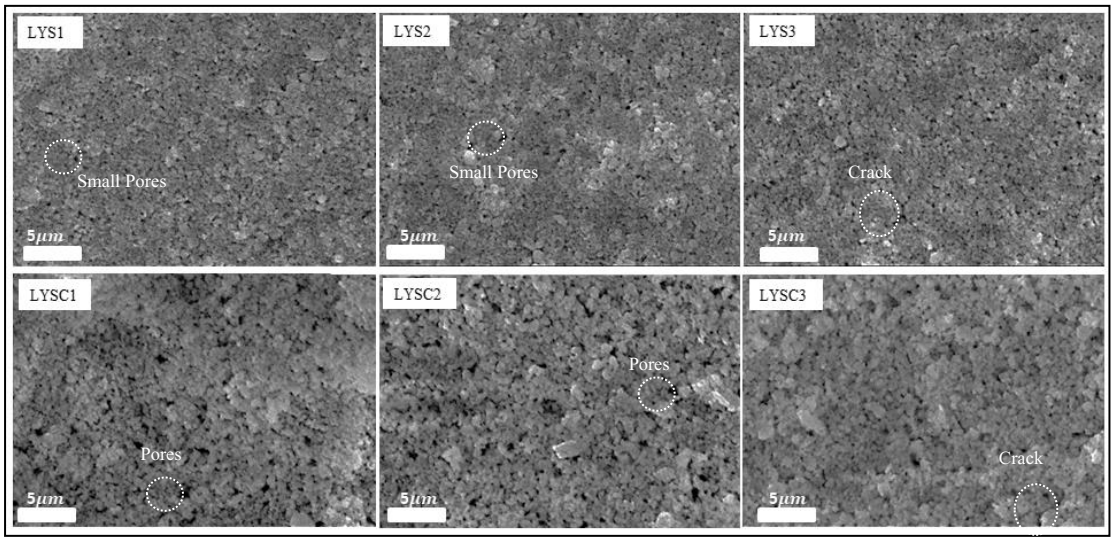


Figure 5. SEM micrographs for of the printed surfaces of (above) LSCF/YSZ-SDC and (below) LSCF/YSZ-SDCC at 10,000× magnification

Table 3. Average porosity of dual composite cathode symmetrical cells

Dual Composite Cathode	Average Porosity (%)		
	50/50:50	50/60:40	50/70:30
LSCF/YSZ-SDC	20.22	25.91	25.07
LSCF/YSZ-SDCC	23.85	26.29	25.86

Figure 6 and Figure 7 show the cross-section micrograph view and EDS spectra of LSCF/YSZ-SDC and LSCF/YSZ-SDCC dual composite cathode layer on YSZ electrolyte pellet by 10 times repetition using screen printing method. The EDS spectra presented all the elements consist of La, Sr, Co, Fe, Sm, Ce, Y, Zr, O and C from LSCF/YSZ-SDC dual composite cathode. Na element was detected from LSCF/YSZ-SDCC as the addition of the Na_2Co_3 carbonate existing in melting amorphous state however due to a very low energy characteristics radiation, element Li were not detected in EDS spectra analysis region

The screen-printing thickness of the dual composite cathode layer was uniform thickness for 10 times repetition for each layer. Table 4 shows the total thickness of each LSCF/YSZ-SDC and LSCF/YSZ-SDCC after the printing of 10 layers. The average thicknesses of the dual composite cathodes per printing are presented in Table 4. The thickest screen-printed layer was 45.6 μm for the LYSC3 composition. The thickness of the cathode layer using the LSCF/YSZ-SDCC ink seen wider compared with that of the LSCF/YSZ-SDC ink. The increase in thickness using the LSCF/YSZ-SDCC inks may be related to the improved elastic properties caused by the addition and increase in solid content [18]. The formulations for dual composite cathode ink are non-identical for each composition as the weight compositions (YSZ-SDC and YSZ-SDCC) are different. The powder volume of the final dual composite ink was <30 vol.% as suggested from a previous research to obtain good quality cathode inks [18]. Thus, the thickness of the screen-printing layer and the production of cathode inks are important as it can help improve cell performance [20].

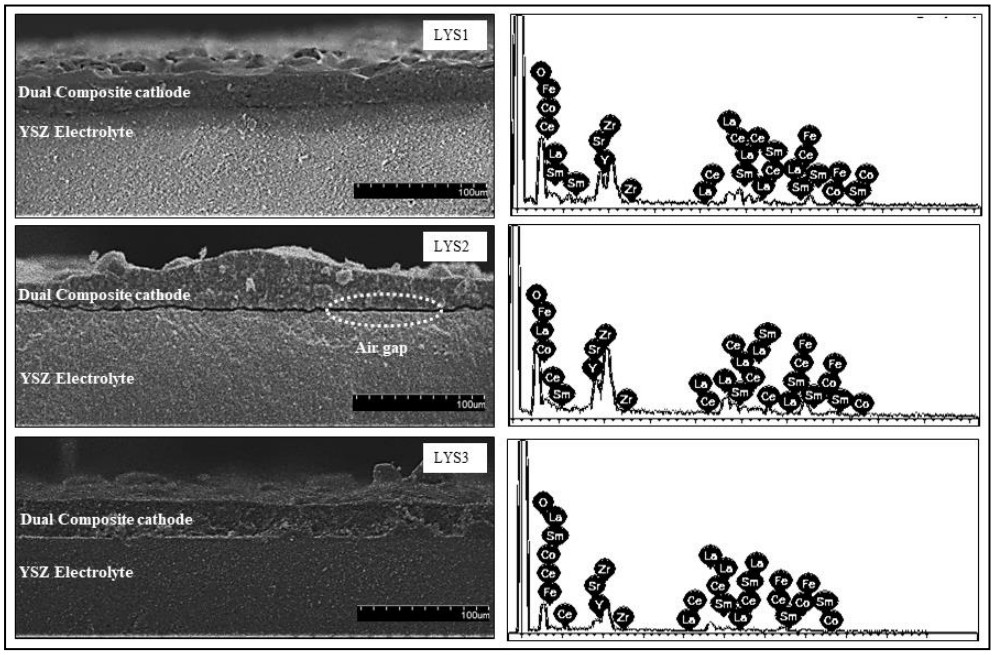


Figure 6. Cross-sectional micrographs and EDS spectra of screen-printed LSCF/YSZ-SDC cathode films

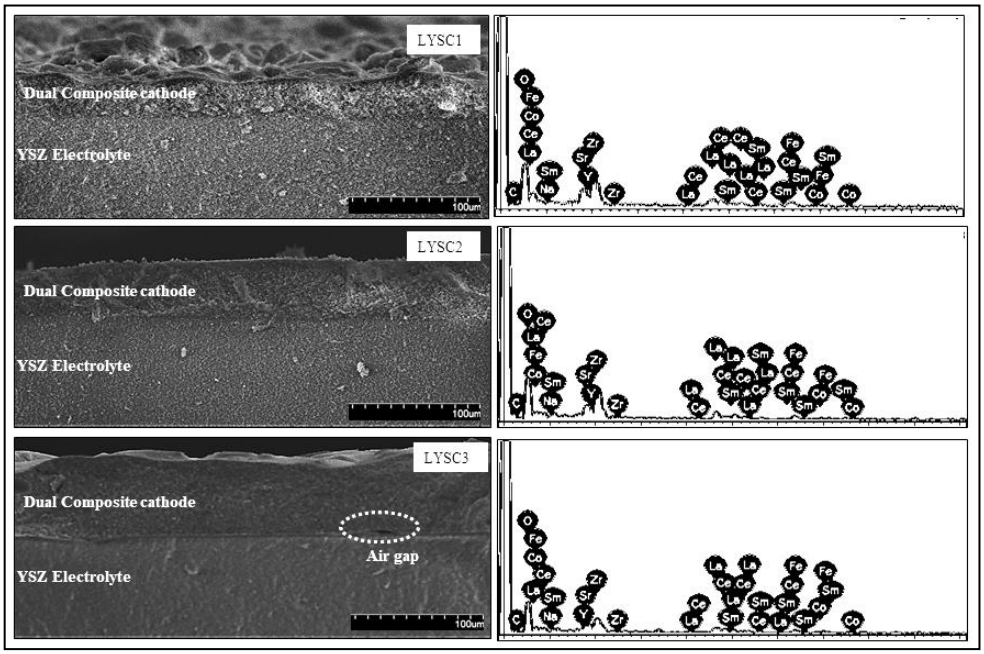


Figure 7. Cross-sectional micrographs and EDS spectra of screen-printed LSCF/YSZ-SDCC cathode films

Table 4. Screen printing thickness of the cathode layer

Dual Composite Cathode	Total Thickness (µm)	Average Thickness per Printing (µm)
LYS1	17.9	1.79
LYS2	16.3	1.63
LYS3	15.1	1.51
LYSC1	23.8	2.38
LYSC2	32.5	3.25
LYSC3	45.6	4.56

Electrochemical performance of the dual composite cathodes

The ionic conductivities of the symmetrical cells of LSCF/YSZ-SDC and LSCF/YSZ-SDCC were measured. Figures 8 and 9 show the impedance spectra of LSCF/YSZ-SDC and LSCF/YSZ-SDCC in an open circuit condition with a firing temperature from 700 °C to 500 °C in air. The impedance spectra were fitted, and the fitting results are shown in Table 5. The total polarization resistance of all cells showed a decrement with the increment in operating temperature (500–700 °C). In addition, the ionic conductivities of the dual composite cathodes were calculated using equation below.

Ionic conductivity formula:

$$\sigma = \frac{1}{\rho} = \left(\frac{1}{R}\right) x \left(\frac{A}{d}\right) \quad (1)$$

where: σ: Conductivity, d: Thickness of the sample (cm), R: Resistance (Ω), A: Effective area (cm^2), and ρ: Resistivity (Ωm).

LYS2 (0.080×10^{-5} S cm^{-1}) yielded the highest ionic conductivity for the LSCF/YSZ-SDC parameter, whereas LYSC1 (0.410×10^{-5} S cm^{-1}) attained the greatest ionic conductivity for the LSCF/YSZ-SDCC parameter. Both dual composite cathodes yielded the best ionic conductivity at 700 °C. LYSC1 (307 kΩ) showed the lowest polarization resistance, followed by LYSC2 (37.90 kΩ) and LYSC3 (39.20 kΩ), at 700 °C. Unfortunately, the recorded polarization resistance values were not favorable, as the resistance was too high, and the ionic conductivity was extremely low. Nonetheless, this finding proved that the conductivity and polarization resistance of LSCF/YSZ-SDCC was slightly better compared with those of the dual composite cathodes without the addition of binary carbonate. This finding was also coherent with the findings of previous research, which reported that binary carbonates are able to enhance the electrochemical performances. [11-12] .

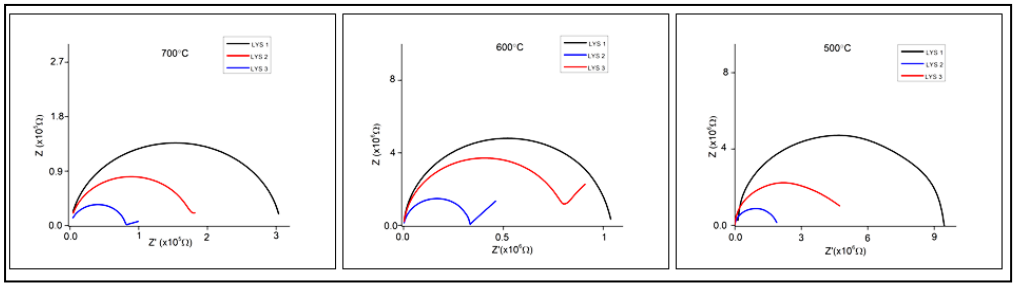


Figure 8. Impedance spectra of LSCF/YSZ-SDCC at 700, 600 and 500 °C

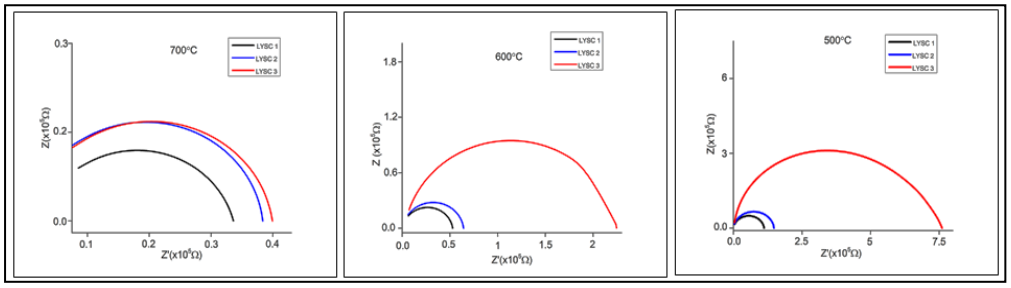


Figure 9. Impedance spectra of LSCF/YSZ-SDCCC at 700, 600 and 500 °C

Table 5. Polarization resistance and conductivity of the dual composite cathodes from 700 °C to 500 °C

Temperature	**Samples**	**Total Resistance, (R_{total}) [kΩ]**	**Conductivity, (σ) [$\times 10^{-5}$ S cm^{-1}]**
700 °C	LYS1	307.0	0.042
	LYS2	159.90	0.080
	LYS3	3.61×10^{3}	0.004
	LYSC1	31.10	0.410
	LYSC2	37.90	0.336
	LYSC3	39.20	0.325
600 °C	LYS1	1.04×10^{3}	0.012
	LYS2	666.0	0.019
	LYS3	8×10^{3}	0.0016
	LYSC1	52.50	0.2426
	LYSC2	63.60	0.2003
	LYSC3	222.0	0.0574
500 °C	LYS1	9.31×10^{3}	0.0014
	LYS2	6.39×10^{3}	0.0020
	LYS3	16.1×10^{3}	0.0008
	LYSC1	111.0	0.1148
	LYSC2	148.0	0.0861
	LYSC3	759.0	0.0168

The high ionic conductivity for excellent fuel cell performance at the intermediate- to low-temperature region is in the range of 0.01–1 S cm^{-1}[21]. The data gathered in this study show that the obtained ionic conductivity is not within the acceptable range. Some factors possibility affected the performances of the LSCF/YSZ-SDC and LSCF/YSZ-SDCC cells. The first factor was the selection of sintering temperature during the preparation of the symmetrical cells. The sintering temperature for a YSZ material is 1300–1600 °C;

therefore, 1400 °C was chosen as the sintering temperature for SOFC application [22]. In addition, selecting the appropriate temperature for a material is crucial, as high conductivity is achieved when the operating temperature is above the melting point of the material [23]. Besides the selection of sintering temperature, the development of symmetrical cells is considered one of the reasons for the low ionic conductivity. For example, during the cross-sectional analysis, the dual composite ink was not well screen printed on the surface of the YSZ pellet. This poor application may trap air between the cathode and electrolyte layers. During the printing process, parameters, including printing repetition layer, squeegee-related parameters, printing angle and forces exerted during the screen-printing process, influence the quality of the printed layer [20].

Conclusion

The current study presented the development of new dual composite cathodes, namely, LSCF/YSZ-SDC and LSCF/YSZ-SDC carbonate, for use in intermediate-temperature SOFC application. The main objective was to enhance the electrochemical performances of LSCF/YSZ-GDC and LSM/GDC-YSZ, which remains a challenge owing to the poor ionic conductivities of LSCF/YSZ-SDC and LSCF/YSZ-SDCC. However, this study proved that the addition of the Li/Na binary carbonate helped increase the ionic conductivity and showed a better electrochemical performance compare with LSCF/YSZ-SDC.

Acknowledgement

The research was supported by the Ministry of Higher Education of Malaysia through funding under the Fundamental Research Grant Scheme (FRGS/1/2020/TK0/UTHM/02/15) and partially funded by Universiti Tun Hussein Onn Malaysia under the Collaborative Research Grant (CRG K260) and Postgraduate Research Grant (GPPS H577).

References

1. Udomsilp, D., Thaler, F., Menzler, N. H., Bischof, C., de Haart, L. G. J., Opitz, A. K. and Bram, M.(2019). Dual-phase cathodes for metal-supported solid oxide fuel cells: Processing performance, durability. *Journal of the Electrochemical Society*, 166(8): F506.
2. Rahman, N. F. A., Rahman, H. A and Azmi, M. A. (2021). Perovskite-type oxide-based dual composite cathode for solid oxide fuel cells: A short review. *Solid State Phenomena*, 317: 417-425.
3. Ko, H. J., Myung, J. H., Hyun, S. H. and Chung, J. S. (2012). Synthesis of LSM–YSZ–GDC dual composite SOFC cathodes for high-performance power-generation systems. *Journal of Applied Electrochemistry*, 42(4): 209-215.
4. Ko, H. J., Myung, J. H., Lee, J. H., Hyun, S. H. and Chung, J. S. (2012). Synthesis and evaluation of $(La_{0.6}Sr_{0.4})(Co_{0.2}Fe_{0.8})O_3$ (LSCF)-$Y_{0.08}Zr_{0.92}O_{1.96}$ (YSZ)-$Gd_{0.1}Ce_{0.9}O_{2-\delta}$ (GDC) dual composite SOFC cathodes for high performance and durability. *International Journal of Hydrogen Energy*, 37(22): 17209-17216.
5. Railsback, J., Choi, S. H. and Barnett, S. A. (2019). Effectiveness of dense Gd-doped ceria barrier layers for (La,Sr)(Co,Fe)O_3 cathodes on Yttria-stabilized zirconia electrolytes. *Solid State Ionics*, 335: 74-81.
6. Fergus, J., Hui, R., Li, X., Wilkinson, D. P and Zhang, J. (2016). Solid oxide fuel cells: Materials properties and performance. CRC press.
7. Rahman, H. A., Ng, K. H., Ahmad, S., Taib, H., Mahzan, S., Salleh, S. M. and Muchtar, A. (2019, March). Influence of microstructure on the electrochemical behaviour of LSCF-SDCC. In *IOP Conference Series: Materials Science and Engineering*, 494(1): 012062.
8. Mohammad, S. F., Ahmad, S., Rahman, H. A. and Muchtar, A. (2019). Effect of SSC Loading on the microstructural stability SSC-SDCC composite cathode as new potential SOFC. *International Journal of Integrated Engineering*, 11(7): 162-168.
9. Somalu, M. R., Muchtar, A., Daud, W. R. W. and Brandon, N. P. (2017). Screen-printing inks for the fabrication of solid oxide fuel cell films: a review. *Renewable and Sustainable Energy Reviews*, 75: 426-439.

10. Huang, J., Gao, Z. and Mao, Z. (2010). Effects of salt composition on the electrical properties of samaria-doped ceria/carbonate composite electrolytes for low-temperature SOFCs. *International Journal of Hydrogen Energy*, 35(9): 4270-4275.
11. Abd Rahman, H., Agun, L., Hoa, N. K., Ahmad, S. and Nordin, N. A. (2020). Effects of binary (lithium/natrium)$_2$ carbonates on the phase and microstructural stability of LSCF-SDC for low temperature solid oxide fuel cells. *Sains Malaysiana*, 49(12): 3155-3167.
12. Mohammad, S. F., Ahmad, S., Rahman, H. A. and Muchtar, A. (2019). Effect of SSC loading on the microstructural stability SSC-SDCC composite cathode as new potential SOFC. *International Journal of Integrated Engineering*, 11(7): 162-168.
13. Ghasdi, M. and Alamdari, H. (2010). CO sensitive nanocrystalline $LaCoO_3$ perovskite sensor prepared by high energy ball milling. *Sensors and Actuators B: Chemical*, 148(2): 478-485.
14. Baharuddin, N. A., Abd Rahman, H., Muchtar, A., Sulong, A. B. and Abdullah, H. (2013). Development of lanthanum strontium cobalt ferrite composite cathodes for intermediate-to low-temperature solid oxide fuel cells. *Journal of Zhejiang University Science A*, 14(1): 11-24.
15. Gao, D., Zhao, J., Zhou, W., Ran, R. and Shao, Z. (2011). Influence of high-energy ball milling of the starting powder on the sintering; microstructure and oxygen permeability of $Ba_{0.5}Sr_{0.5}Fe_{0.5}O_{3-\delta}$ membranes. *Journal of Membrane Science*, 366(1-2): 203-211.
16. Parwaiz, S., Khan, M. M. and Pradhan, D. (2019). CeO_2-based nanocomposites: An advanced alternative to TiO_2 and ZnO in sunscreens. *Materials Express*, 9(3): 185-202.
17. Lu, X., Heenan, T. M., Bailey, J. J., Li, T., Li, K., Brett, D. J. and Shearing, P. R. (2017). Correlation between triple phase boundary and the microstructure of solid oxide fuel cell anodes: The role of composition, porosity and Ni densification. *Journal of Power Sources*, 365: 210-219.
18. Somalu, M. R., Muchtar, A., Daud, W. R. W. and Brandon, N. P. (2017). Screen-printing inks for the fabrication of solid oxide fuel cell films: a review. *Renewable and Sustainable Energy Reviews*, 75: 426-439.
19. Zhang, J. and Jung, Y. G. (2018). Advanced ceramic and metallic coating and thin film materials for energy and environmental applications Berlin: Springer: pp. 20.
20. Baharuddin, N. A., Abdul Rahman, N. F., Abd. Rahman, H., Somalu, M. R., Azmi, M. A. and Raharjo, J. (2020). Fabrication of high-quality electrode films for solid oxide fuel cell by screen printing: a review on important processing parameters. *International Journal of Energy Research*, 44(11): 8296-8313.
21. Chen, Y., Lin, Y., Zhang, Y., Wang, S., Su, D., Yang, Z. and Chen, F. (2014). Low temperature solid oxide fuel cells with hierarchically porous cathode nano-network. *Nano Energy*, 8: 25-33.
22. Talebi, T., Haji, M. and Raissi, B. (2010). Effect of sintering temperature on the microstructure, roughness and electrochemical impedance of electrophoretically deposited YSZ electrolyte for SOFCs. *International Journal of Hydrogen Energy*, 35(17): 9420-9426.
23. Ali, S. M., Muchtar, A., Sulong, A. B., Muhamad, N. and Majlan, E. H. (2013). Influence of sintering temperature on the power density of samarium-doped-ceria carbonate electrolyte composites for low-temperature solid oxide fuel cells. *Ceramics International*, 39(5): 5813-5820.

Malaysian Journal of Analytical Sciences (MJAS)
Published by Malaysian Analytical Sciences Society

PtRu SUPPORTED ON POROUS 3D TITANIUM DIOXIDE-GRAPHENE AEROGEL AS A POTENTIAL ELECTROCATALYST FOR DIRECT METHANOL FUEL CELLS

(PtRu disokong pada 3D Titanium Dioksida-Grafin Aerogel Berliang Sebagai Potensi Elektromangkin untuk Sel Bahan Bakar Metanol Langsung)

Siti Hasanah Osman[1]*, Siti Kartom Kamarudin[1,2], Sahriah Basri[1], Nabila A.Karim[1]

[1]*Fuel Cell Institute*
[2]*Department of Chemical and Process Engineering, Faculty of Engineering and Built Environment*
Universiti Kebangsaan Malaysia, 43600 UKM Bangi, Selangor, Malaysia

**Corresponding author: ctie@ukm.edu.my*

Received: 9 November 2021; Accepted: 27 February 2022; Published: 27 June 2022

Abstract

The catalyst support is typically implemented to improve the catalytic activity in direct methanol fuel cells (DMFCs). Thus, this study focused on the novel support of 3D hierarchical porous TiO_2-graphene aerogel which was established via a combination of hydrothermal method and freezing drying method. XRD, Raman spectra, and FESEM were used to study the PtRu/TiO_2-GA. The estimated particle size of PtRu/TiO_2-GA determined from the XRD analysis was less than composite TiO_2-GA. The existence of the carbon support material was confirmed by the Raman spectra in all generated samples. Within the electrocatalyst and TiO_2-GA, the ratio value of the D band to the G band (I_D/I_G) was not significantly different. The computed I_D/I_G values for TiO_2-GA and PtRu/TiO_2-GA electrocatalysts were 0.99 and 1.02, respectively. The best TiO_2-GA was doped with PtRu catalyst for the electrochemical test and DMFC performance based on FESEM characterization. PtRu/ TiO_2-GA exhibited better electrocatalytic activity, as well as improved PtRu usage efficiency stability and methanol oxidation reaction. Notably, the ECSA value was around 76.01 m^2g^{-1}, and the mass activity (957.15 $mAmg^{-1}$) was higher than commercial with the same loading (20%) PtRu/C (110.79 $mAmg^{-1}$). Interestingly after the 2000s, the current density of PtRu/TiO_2-GA was consistently higher than that of PtRu/C. The superior electrocatalytic performance of PtRu/TiO_2-GA towards methanol oxidation demonstrates its use in practical application as a promising anode material for DMFCs

Keywords: 3D titanium dioxide-graphene aerogel, platinum-ruthenium nanoparticles, electrocatalysis, methanol electro-oxidation

Abstrak

Sokongan mangkin biasanya dilaksanakan untuk meningkatkan aktiviti pemangkin dalam sel bahan api metanol langsung (SFML). Oleh itu, kajian ini memberi tumpuan kepada novel sokongan pada TiO_2-grafin aerogel berliang hierarki 3D telah ditubuhkan dengan gabungan kaedah hidroterma dan kaedah pengeringan beku. XRD, spektrum Raman dan FESEM digunakan untuk mengkaji PtRu/TiO_2-GA. Anggaran saiz zarah PtRu/TiO_2-GA yang ditentukan daripada analisis XRD adalah kurang daripada komposit TiO_2-GA. Kewujudan bahan sokongan karbon telah disahkan oleh spektrum Raman dalam semua sampel yang dihasilkan. Dalam elektromangkin dan TiO_2-GA, nilai nisbah jalur D kepada jalur G (I_D/I_G) tidak berbeza dengan ketara. Nilai

I_D/I_G yang dikira untuk elektromangkin TiO_2-GA dan PtRu/TiO_2-GA ialah 0.99 dan 1.02, masing-masing. TiO_2-GA terbaik akan didop dengan mangkin PtRu untuk ujian elektrokimia dan prestasi SFML berdasarkan pencirian FESEM. PtRu/ TiO_2-GA mempamerkan aktiviti elektrokatalitik yang lebih baik, serta peningkatan kestabilan kecekapan penggunaan PtRu dan tindak balas pengoksidaan metanol. Terutama, nilai ECSA adalah sekitar 76.01 m^2g^{-1}, aktiviti jisim (957.15 $mAmg^{-1}$) adalah lebih tinggi daripada komersial dengan pemuatan yang sama (20%) PtRu/C (110.79 $mAmg^{-1}$). Menariknya selepas minit ke-2000 saat, ketumpatan semasa PtRu/TiO_2-GA sentiasa lebih tinggi daripada PtRu/C. Prestasi elektrokatalitik unggul PtRu/TiO_2-GA terhadap pengoksidaan metanol boleh digunakan dalam aplikasi praktikal sebagai bahan anod yang menjanjikan untuk DMFC.

Kata kunci: 3D titanium dioksida-grafin aerogel, nanopartikel platinum-ruthenium, elektromangkin, elektro-pengoksidaan metanol

Introduction

Direct methanol fuel cells (DMFCs) have gained traction recently due to their technological advances through a variety of characteristics: low emissions, excellent energy conversion efficiency, liquid fuel handling convenience, and low operating temperature. These are the results of the increasing use of mobile devices and the prerequisite of affording sufficient energy and power for the application [1, 2]. The electrochemical reaction in a direct methanol fuel cell is represented as follows:

$CH_3OH + H_2O \rightarrow CO_2 + 6H^+ + 6e^-$
$E° = 0{:}016V$ (vs: SHE) (Anode reaction)

$3/2O_2 + 6H^+ + 6e^- \rightarrow 3H_2O$
$E° = 1{:}229V$ (vs: SHE) (Cathode reaction)

$CH_3OH + H_2O \rightarrow CO_2 + 6H^+ + 6e^-$
$E° = 1{:}245V$ (vs: SHE) (Overall reaction)

The need for highly active catalysts for the oxidation process of hydrogen-rich liquid fuels is one of the major driving forces behind the development of DMFC technology. The electrocatalyst selection is critical for DMFC because the quality of the reaction kinetics of catalyst influences current density and cell lifespan. Improved catalyst activity and durability can be achieved through the development of novel support materials or the use of innovative catalytic metals [3]. Due to their increased catalytic activity in the electrooxidation of methanol, platinum group metals (PGMs) are the most used anode catalysts in DMFCs [4-8]. Platinum is costly, thus finding a replacement catalyst will necessitate further research. The best catalyst for DMFCs right now is bimetallic platinum-ruthenium (PtRu). Pt loading can be lowered by reducing the electrocatalyst costs in DMFC using only the corresponding ratio of 1:1. Additionally, bimetallic Ru catalyst works in catalytic operations by eliminating carbon monoxide (CO) from the active site for HOR, where this catalyst can reduce CO poisoning [11, 12]. PtRu demonstrated a higher catalytic activity in the DMFC according to research by Bock et al. [4], and it was evident that the catalytic performance was significantly dependent on the distribution of Pt and Ru sites at the atomic level. However, the PtRu catalyst cannot solve the problem of low methanol oxidation. Further catalyst modifications are required to help the fuel cell sector.

The DMFC has been in progress for a decade with the creation of several catalyst-based solutions. Alternative support materials are stable and cost-effective, and they have been identified and developed with great effort [28–30]. Novel carbon supports, for example carbon nanotubes [5], mesoporous carbon [6], graphene [7], noncarbon materials, and nonconductive whiskers, due to their strong corrosion-resistance, have been explored as carbon alternatives. Graphene is the best candidate for catalyst support in fuel cells because of its chemical resistance, large and sufficient porosity, high conductivity, and diversity of topologies (network, aerogel, foam, etc.) [8, 9]. In general, the graphene aerogel (GA), which has a three-dimensional (3D) structure, has received a lot of attention due to its extensive macroporosity and multidimensional electron transport pathways, making it ideal for catalysis and energy storage devices [10, 11]. In the advancement of DMFCs, applying additional materials to the catalyst, including the formation of new hybrid catalysts, has become a trend [4–6]. However, issues such as

electronic and protonic functioning, poor catalytic activity, stability, and conductivity are still persistent.

The most used materials to improve the electrocatalysis of DMFCs are metal oxides. Titanium dioxide (TiO_2) is a type of inorganic substance, non-flammable, corrosion-resistant, and fundamentally stable. Furthermore, TiO_2 crystal structures are thermodynamically stable, contributing to the production of a composite material that is thermally and electrochemically stable [12]. Anatase stimulates charge carriers deeper within the bulk material, leading more in surface reactions and rising catalytic activity with time [13]. Additionally, when the TiO_2 metal oxide interacts with another component, the electrical behaviour of the materials improves as well. Instead of lowering CO oxidation potentials, this material can also support to increase oxidation activity [14]. The metal catalyst is supported by TiO_2, which impacts the reaction kinetics and mechanism [15]. TiO_2 has all the advantages recorded above and it can be used in a variety of industries. Despite these benefits, the low conductivity of material prevents it from being widely used in fuel cell applications.

Significant loading of a Pt catalyst on TiO_2 made from an electrically conductive substance like N-doped carbon, as well as the use of sub-stoichiometric TiO_2, is necessary to overcome this obstacle [16]. In 2018, Abdullah et al. [16] developed PtRu alloys on a nanofiber catalyst structure with metal oxide as the catalyst support; PtRu/TiO_2-embedded carbon nanofiber (CNF) (PtRu/TECNF) was designed by Ito et al. [17], and Ercelik et al. [18] demonstrated PtRu/ C-TiO_2 as an electrocatalyst in DMFC technology; the result indicated that the performance of this new composite electrocatalyst was superior to PtRu catalyst. The above-mentioned performance is due to the homogeneous dispersion of PtRu nanoparticles on the support material. Consequently, combining a powerful PtRu catalyst with a rational TiO_2 and graphene aerogel structure has unique properties and high surface area, it has developed as the latest support material, with the possibility to increase electrocatalytic activity in MOR.

Materials and Methods

Preparation of TiO_2-GA and electrocatalyst

TiO_2-GA was produced hydrothermally, then freeze-dried in a typical experiment. Firstly, 20 mg of TiO_2 were homogeneously disseminated into 10 mL of GO solution (2 mg/mL) using moderate ultrasonication for 2 hours. After that, the solution was placed in a 50mL of Teflon-lined autoclave and kept at 200°C for 12 hours. To make a TiO_2-GA composite, the produced TiO_2-graphene hydrogel was thoroughly rinsed with deionized water before being freeze-dried for 24 hours. The steps of TiO_2-GA production are depicted schematically in Figure 1.

For electrocatalyst synthesis, a microwave-assisted alcohol reduction approach was used. The optimal TiO_2-GA support doped with PtRu catalyst was chosen specifically for this study. On TiO_2-GA support, 20 wt.% Pt-Ru with an atomic ratio of 1:1 was loaded. To begin, Ethylene Glycol (EG) solutions were combined with ruthenium chloride precursors and chloroplatinic acid precursors, and were homogenized for 15 minutes. After that, the TiO_2-GA powder that had been produced was mixed into the cooperation precursor solutions and agitated for 30 minutes to ensure that everything was well mixed. After that, the pH of the solution was adjusted to 10 using a 1 M NaOH solution. In addition, the mixture was microwaved for 1 minute, and was left to accomplish the reduction process for 1 minute twice. Finally, before being dried in a 120 °C oven for 3 hours, the sample was filtered and rinsed a few times with ethanol and DI water to remove the impurities.

Characterizations

To prove crystallinity in the manufactured tests for characterization uses, X-ray Diffraction (XRD) is a powerful physical description method. Using a D8 Advance/Bruker, AXS Germany model, all fabricated tests were examined at 2θ from 5° to 100°. Moreover, the degree of graphitization was described using Raman spectrum analysis. The surface morphology and forms of the samples were explored using a Field Emission Scanning Electron Microscope (FESEM).

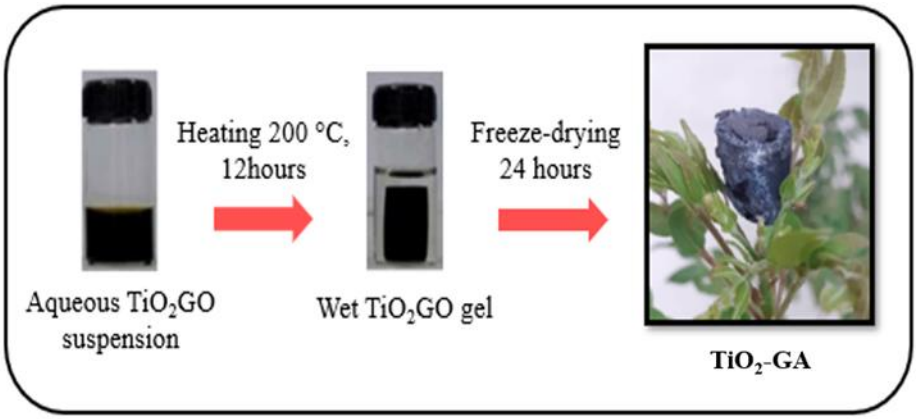


Figure 1. Design of the preparation of TiO_2-GA composite

Electrochemical characterization and performance test

In a 0.5 M H_2SO_4 the electrocatalyst performance was estimated by determining the electrochemical surface area, ECSA, cyclic voltammetry (CV), and catalyst stability measured with a chronoamperometry (CA) test. Three-electrode cell systems were used at room temperature: a working electrode with a glassy carbon electrode (3 mm Ø), reference electrodes noted as Ag/AgCl electrodes, and counter platinum-based electrode. Furthermore, 3 mg of electrocatalyst of PtRu/TiO_2-GA and commercial catalyst were dispersed in 150 mL DI water, 150 mL IPA, and 50 mL Nafion (5 wt.%) solution to make the electrocatalyst ink for the working electrode. On the glassy electrode, there was a catalyst loading of 0.0503 mg cm^{-2}. The CV was measured at a 50 mVs^{-1} scan rate with potentials ranging from -0.2 to 1.0 V vs. Ag/AgCl. Note that in this analysis, the potentials ranged from -0.2 to 1.0 V vs. Ag/AgCl, while CV was recorded at a 50 mVs^{-1} scan rate. The long- term performance of all electrocatalysts was assessed using chronoamperometry (CA) in the electrolyte solution at a potential of 0.6 V for 2000 s.

Results and Discussion

The crystal structure and pattern of the built catalyst support and electrocatalyst were investigated using XRD analysis. As a result, the TiO_2-GA support was synthesized by hydrothermal at 200 °C. The microwave-assisted alcohol reduction approach was used to make the PtRu/TiO_2-GA and PtRu/C marketable. The analysis of the diffraction peak for the associated sample and comparative samples of XRD pattern for PtRu/TiO_2-GA electrocatalyst is shown in Figure 2(a). Peaks at 25.3°, 37.8°, 48.0°, 53.9°, 55.1°, 62.7°, 68.8°, 70.3°, and 75.0° are indexed to (101), (004), (200), (105), (211), (204), (116), (220), and (215) crystal planes of TiO_2 anatase, respectively based on XRD examination for TiO_2-GA support sample [19, 20]. The TiO_2-GA hydrothermal at 200 °C was chosen as the best-produced TiO_2-GA and was doped with PtRu catalyst. The XRD results for the synthesized PtRu/TiO_2-GA showed the presence of all particles, PtRu, and C support. The Pt particles peaked at 39.7° (111), 46.2° (200), 67. 5° (220), and 81.3° (311). The diffraction peaks for Ru were 40.7° (111), 47° (200), 69° (220), and 83.7° (311). The structure of both metals was cubic, and in the electrocatalyst sample, high Bragg angles were detected in the range of 25°–60°, indicating that the catalyst possessed bimetallic or alloy interaction [21]. Additionally, the estimated crystallite size of PtRu was computed using Scherrer's equation, which revealed that PtRu/TiO_2-GA particles were smaller than PtRu/C particles [22]. As shown in Table 1, the particle size of Pt and Ru can also be predicted using the crystallite size. In general, smaller particles perform better in MOR electrocatalysis reactions than larger particles, since smaller catalyst particles contribute to a higher particle surface area. Furthermore, the smaller catalyst particle size may allow for a reduction in the use of Pt in electrocatalyst, as well as a reduction in the overall cost of DMFC production. The decreased size of PtRu particles found in the

electrocatalyst sample could potentially be due to the lower crystalline structure.

In terms of the chemical and structural information offered by the shift in wavelength of inelastically scattered radiation, the D and G bands were 1350 and 1590 cm^{-1}. The two separate peaks in the Raman spectra for the samples in Figure 2(b) indicated that the D band was linked to crystal boundary vibrations and the G band reflected perfect sp2 vibrations of graphitic crystals. From the Raman spectrum analysis, the intensity ratio of the D to G band (I_D/I_G) had a descending order: TiO_2-GA (1.02), PtRu/ TiO_2-GA (0.99) and PtRu/C (0.98). The band fluctuated depending on the relative intensity of the D and G bands on the type of graphite material, and it could be used to estimate the degree of graphitization. The I_D/I_G ratio observed in this work showed that the aerogel was successfully achieved after the catalyst was disseminated at TiO_2-GA [23], [24]. Ultimately, in the disintegrated region and structure of TiO_2-GA, the carbon layer in these electrocatalysis samples was not significantly different. The weak Raman shift bands at 152 cm^{-1} and 154 cm^{-1} were identified in TiO_2-GA and PtRu/TiO_2-GA, respectively, and were linked to unique characteristics of TiO_2 anatase [25].

FESEM was used to analyze the dispersion surface, morphologies, and sizes of PtRu/TiO_2-GA and PtRu/C produced using a microwave-assisted alcohol-reduction technique. PtRu/TiO_2-GA had a 3D-porous cellular structure, exhibiting constant porosity of sizes ranging from micrometres to sub micrometres as seen in Figure 3. Furthermore, the tight inspection revealed an evenly adorned PtRu nanoparticles in a 3D porous cellular structure, demonstrating a strong interaction among the PtRu-carbon building block. Interestingly, the PtRu/C images revealed that these carbon-supporting materials were spherical. [26]. The findings indicated that the samples were agglomerated with a diameter of 120-150 nm, which was available in the nanoscale range. The Van der Waals interaction surrounded by the particles could be causing the aggregation [27].

Table 1. Estimated crystallite size of TiO_2-GA and PtRu/TiO_2-GA on XRD analysis

Samples	XRD/Crystallite Size (nm)
TiO_2-GA	7.9
PtRu/TiO_2-GA	3.8
PtRu/C	3.9

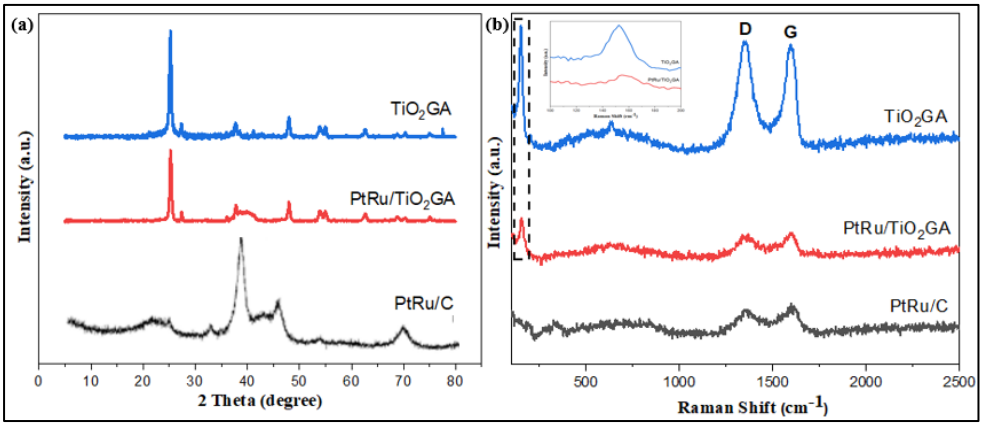


Figure 2. (a) XRD patterns of TiO_2-GA composite and PtRu/TiO_2-GA electrocatalyst (b) Raman spectra of TiO_2-GA composite and PtRu/TiO_2-GA electrocatalyst

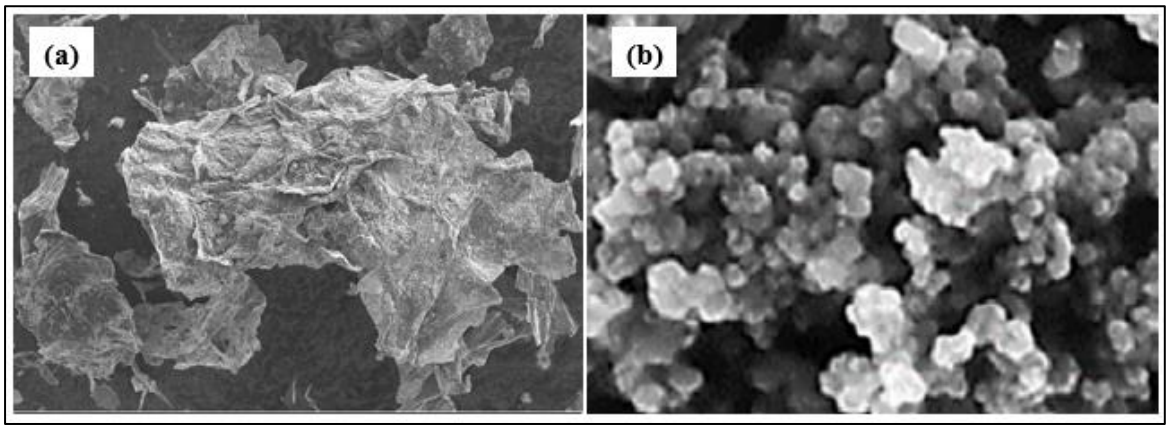


Figure 3. FESEM image of the prepared (a) PtRu/TiO_2-GA and (b) PtRu/C Electrocatalytic performance

In recent decades, DMFCs have been intensively explored and gained increasing attention in the electrooxidation by methanol. For the methanol oxidation in acid media, the electrochemical efficiency of the PtRu/TiO_2-GA catalyst has been explored. The PtRu/TiO_2-GA CV curves and PtRu/C catalysts in N_2 with 0.5M H_2SO_4 saturated solutions are displayed in Figure 4(a). In the area from -0.2 V to 1.0 V vs Ag/AgCl, both electrics demonstrated the characteristics of hydrogen adsorption-desorption. The ECSAs computed for PtRu/TiO_2-GA and PtRu/C amount was about 68.44 m^2 g^{-1} and 20.44 m^2 g^{-1}, respectively. The ECSA for PtRu/TiO_2-GA was 3 times that of PtRu/C and 30 % greater than that for commercial PtRu/C. This finding demonstrates that retaining a bimetallic 3D structure in TiO_2-GA helps to increase the ECSA of PtRu nanoparticles and improve catalyst utilization. This is owing to the differences in crystallite size between PtRu/TiO_2-GA and PtRu/C as shown in Table 1 from the XRD analysis: the PtRu/TiO_2-GA crystallite size for TiO_2-GA was the lowest and it had a superior ECSA value. Hence, the catalyst and reaction surface area can be increased by using the smallest crystallite size.

Figure 4(b) illustrates that the peak mass activity PtRu/TiO_2-GA is greater than PtRu/C. The CV values are indicated in Table 2 for the PtRu/TiO_2-GA and PtRu/C electrocatalyst. For PtRu/TiO_2-GA catalyst, the value for mass activity was 957.15 mA mg^{-1} PtRu, 12 times greater than that of the commercial PtRu/C catalyst. This reveals that the support for TiO_2-GA is a superior replacement for carbon catalyst support. Throughout the carbonization process, the aerogel mixture can boost the electrical and thermal leads of the catalyst [28].

In a composite electrocatalyst, using an aerogel structure can increase the overall surface area as well as the active reaction site on the surface of the electrocatalyst. An additional benefit is the high anatase TiO_2 composition, as determined by the XRD measurements. Anatase has a higher electrocatalytic activity than rutile TiO_2. Besides increasing peak current density, the metal-support interaction also shows a favourable effect, and the material combination of PtRu and TiO_2-GA is an effective electrocatalyst in DMFCs. The performance of PtRu/C is significantly poorer than that of PtRu agglomeration, where the ECSA value as well as the crystallite size as determined by XRD are emphasized. Such state reduces the possibility of the electrocatalyst surface to be an active site and lowers the performance of the electrocatalysts.

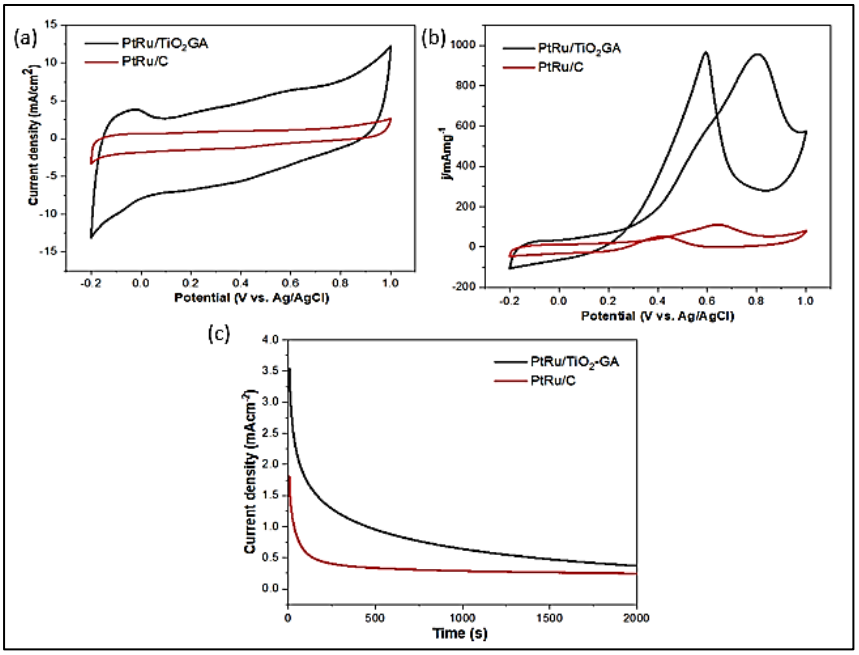


Figure 4. (a) CVs of PtRu/TiO_2-GA and PtRu/C in N_2 saturated 0.5 M H_2SO_4 solution at scan rate 50 mVs^{-1}, (b) CVs of PtRu/TiO_2-GA and PtRu/C in N_2 saturated 0.5 M H_2SO_4 solution containing 1 M CH_3OH at scan rate 50 mVs^{-1}, and (c) Chronoamperometric curves of H_2SO_4 in N_2 saturated containing 1 M CH_3OH

Table 2. Assessment of the performance outcomes with the previous research

Research	**Type of Catalyst**	**ECSA (m^2/g_{PtRu})**	**Mass ativity (mA/mg_{PtRu})**
This study	PtRu/TiO_2-GA	68.44	957.15
This study	PtRu/C	20.44	79.11
Abdullah et al. [16]	PtRu/TiO_2-CNF	10.4	345.64
Basri et al. [29]	PtRuNiFe/MWCNT	-	151.47
Ramli et al. [30]	PtRu/CNC	16.23	427.00

CA tests were carried out to verify the stability of electrocatalyst and endurance for long-term MOR performance in a 1M methanol solution containing 0.5 M H_2SO_4 for 2000 seconds. At 0.6 V, the potential was kept constant. The CA curves electrocatalysts for the PtRu/TiO_2-GA and PtRu/C are shown in Figure 4(c). The current density of electrocatalysts indicates a dramatic decline at the beginning of the experiment probably due to methanol oxidation mediation poisoning. The limiting current PtRu/TiO_2-GA was higher than PtRu/C across the entire duration, indicating better stability. The result demonstrated that the PtRu/TiO_2-GA catalyst showed higher stability than PtRu/C. Consequently, it is assumed that the synergistic effects of combining Pt and Ru help to reduce poisoning rates [16]. Hence, the 3D hierarchical porous TiO_2-graphene aerogel encapsulation structure is important in enhancing the durability. This unique structure can be extensively applicable to commercial catalytic products. It was also shown that TiO_2-GA as support was a better alternative to bimetallic support since the mesoporous

structure of TiO_2-GA could improve the total surface area on the electrocatalyst surface area.

Conclusion

The novel 3D hierarchical porous TiO_2-graphene aerogel (TiO_2-GA) was synthesized using hydrothermal technique and then freeze-dried before being used as a catalytic support for an anodic catalyst in the DMFC. Therefore, the catalytic activity of electrocatalyst was determined by comparing it to that of commercial PtRu/C. The maximal mass activity of the manufactured electrocatalyst PtRu/TiO_2-GA was 12 times that of the PtRu/C commercial electrocatalyst. The catalyst support of TiO_2 and the graphene aerogel catalyst structure resulted in the maximum catalytic activity. The reaction between the PtRu and TiO_2-GA catalysts at the metal-support interface serves to advance the characteristics of catalyst layers. Therefore, PtRu/TiO_2-GA is a viable choice for anode catalyst support in DMFCs.

Acknowledgement

The authors gratefully acknowledge the financial support for this work by The Ministry of Higher Education (MOHE) MALAYSIA and Universiti Kebangsaan Malaysia under Grant No: KKP/2020/UKM-UKM/3/1.

References

1. Rashidi, R., Dincer, I., Naterer, G. F. and Berg, P. (2009). Performance evaluation of direct methanol fuel cells for portable applications. *Journal of Power Sources,* 187(2): 509-516.
2. Achmad, F., Kamarudin, S. K., Daud, W. R. W. and Majlan, E. H. (2011). Passive direct methanol fuel cells for portable electronic devices. *Applied Energy,* 88(5): 1681-1689.
3. Zhao, L., Wang, Z. B., Li, J. L., Zhang, J. J., Sui, X. L. and Zhang, L. M. (2016). Hybrid of carbon-supported Pt nanoparticles and three dimensional graphene aerogel as high stable electrocatalyst for methanol electrooxidation. *Electrochimica Acta,* 189: 175-183.
4. Bock, C., Paquet, C., Couillard, M., Botton, G. A. and MacDougall, B. R. (2004). Size-selected synthesis of PtRu nano-catalysts: reaction and size control mechanism. *Journal of the American Chemical Society,* 126(25): 8028-8037.
5. Zhang, X., Ma, J., Yan, R., Cheng, W., Zheng, J. and Jin, B. (2021). Pt-Ru/polyaniline/carbon nanotube composites with three-layer tubular structure for efficient methanol oxidation. *Journal of Alloys and Compounds,* 867: 159017.
6. Li, W., Wang, Q., Wang, L., Fu, X. Z. and Luo, J. L. (2021). Mesoporous CeO_2–C hybrid spheres as efficient support for platinum nanoparticles towards methanol electrocatalytic oxidation. J*ournal of Rare Earths,* 39(6): 674-681.
7. Yang, Y., Guo, Y. F., Fu, C., Zhang, R. H., Zhan, W., Wang, P., ... & Zhou, X. W. (2021). In-situ loading synthesis of graphene supported PtCu nanocube and its high activity and stability for methanol oxidation reaction. *Journal of Colloid and Interface Science,* 595: 107-117.
8. Ren, X., Lv, Q., Liu, L., Liu, B., Wang, Y., Liu, A. and Wu, G. (2020). Current progress of Pt and Pt-based electrocatalysts used for fuel cells. *Sustainable Energy & Fuels,* 4(1): 15-30.
9. Karuppanan, K. K., Raghu, A. V., Panthalingal, M. K., Thiruvenkatam, V., Karthikeyan, P. and Pullithadathil, B. (2019). 3D-porous electrocatalytic foam based on Pt@ N-doped graphene for high performance and durable polymer electrolyte membrane fuel cells. *Sustainable Energy & Fuels,* 3(4): 996-1011.
10. Gorgolis, G. and Galiotis, C. (2017). Graphene aerogels: a review. *2D Materials,* 4(3): 032001.
11. Mao, J., Iocozzia, J., Huang, J., Meng, K., Lai, Y. and Lin, Z. (2018). Graphene aerogels for efficient energy storage and conversion. *Energy & Environmental Science,* 11(4): 772-799.
12. Siwińska-Stefańska, K. and Jesionowski, T. (2017). Advanced hybrid materials based on titanium dioxide for environmental and electrochemical applications. In Titanium Dioxide. IntechOpen.
13. Odling, G. and Robertson, N. (2015). Why is anatase a better photocatalyst than rutile? The importance of free hydroxyl radicals. *ChemSusChem,* 8(11): 1838-1840.

14. Dey, S. and Mehta, N. S. (2020). Synthesis and applications of titanium oxide catalysts for lower temperature CO oxidation. *Current Research in Green and Sustainable Chemistry,* 3: 10002.
15. Bagheri, S., Muhd Julkapli, N. and Bee Abd Hamid, S. (2014). Titanium dioxide as a catalyst support in heterogeneous catalysis. *The Scientific World Journal,* 2014: 727496.
16. Abdullah, N., Kamarudin, S. K. and Shyuan, L. K. (2018). Novel anodic catalyst support for direct methanol fuel cell: characterizations and single-cell performances. *Nanoscale Research Letters,* 13(1): 1-13.
17. Ito, Y., Takeuchi, T., Tsujiguchi, T., Abdelkareem, M. A. and Nakagawa, N. (2013). Ultrahigh methanol electro-oxidation activity of PtRu nanoparticles prepared on TiO_2-embedded carbon nanofiber support. *Journal of Power Sources,* 242: 280-288.
18. Ercelik, M., Ozden, A., Seker, E. and Colpan, C. O. (2017). Characterization and performance evaluation of PtRu/CTiO_2 anode electrocatalyst for DMFC applications. *International Journal of Hydrogen Energy,* 42(33): 21518-21529.
19. Liu, R., Guo, W., Sun, B., Pang, J., Pei, M. and Zhou, G. (2015). Composites of rutile TiO_2 nanorods loaded on graphene oxide nanosheet with enhanced electrochemical performance. *Electrochimica Acta,* 156: 274-282.
20. Xiang, C., Guo, R., Lan, J., Jiang, S., Wang, C., Du, Z. and Cheng, C. (2018). Self-assembling porous 3D titanium dioxide-reduced graphene oxide aerogel for the tunable absorption of oleic acid and RhodamineB dye. *Journal of Alloys and Compounds,* 735: 246-252.
21. Cordero-Borboa, A. E., Sterling-Black, E., Gómez-Cortés, A. and Vázquez-Zavala, A. (2003). X-ray diffraction evidence of the single solid solution character of bi-metallic Pt-Pd catalyst particles on an amorphous SiO_2 substrate. *Applied Surface Science,* 220(1-4): 169-174.
22. Vorokh, A. S. (2018). Scherrer formula: estimation of error in determining small nanoparticle size. *Nanosystem Physics Chemistry Mathematics*, pp. 364-369.
23. Stankovich, S., Dikin, D. A., Piner, R. D., Kohlhaas, K. A., Kleinhammes, A., Jia, Yue, W., SonBinh, T. N., and Ruoff, R. S. (2007). Synthesis of graphene-based nanosheets via chemical reduction of exfoliated graphite oxide. carbon, 45(7): 1558-1565.
24. Zhu, Y., Murali, S., Cai, W., Li, X., Suk, J. W., Potts, J. R. and Ruoff, R. S. (2010). Graphene and graphene oxide: synthesis, properties, and applications. *Advanced Materials,* 22(35): 3906-3924.
25. Li, Y., Cai, Q., Wang, L., Li, Q., Peng, X., Gao, B., … and Chu, P. K. (2016). Mesoporous TiO_2 nanocrystals/graphene as an efficient sulfur host material for high-performance lithium–sulfur batteries. *ACS Applied Materials & Interfaces,* 8(36): 23784-23792.
26. Norilhamiah, Y., Kamaruddin, S. K., Karim, N. A., Masdar, M. S. and Loh, K. S. (2017). Gliserol, P. E. (2017). Preliminary study on pd-based binary catalysts supported with carbon nanofiber for the electrooxidation of glycerol. *Malaysian Journal of Analytical Sciences,* 21(3): 700-708.
27. Ibrahim, S. A., Anwar, M. K., Ainuddin, A. R., Hariri, A., Rus, A. Z. M., Kamdi, Z., Yunos, M. Z., and Harun, Z. (2019). Synthesis and characterization of visible light active Fe-TiO_2 using hydrothermal method. *International Journal of Integrated Engineering,* 11(5): 80-85.
28. Shaari, N. and Kamarudin, S. K. (2019). Current status, opportunities, and challenges in fuel cell catalytic application of aerogels. *International Journal of Energy Research,* 43(7): 2447-2467.
29. Basri, S., Kamarudin, S. K., Daud, W. R. W., Yaakob, Z. and Kadhum, A. A. H. (2014). Novel anode catalyst for direct methanol fuel cells. *The Scientific World Journal,* 2014: 547604.
30. Ramli, Z. A., Kamarudin, S. K., Basri, S. and Zainoodin, A. M. (2020). The potential of novel carbon nanocages as a carbon support for an enhanced methanol electro - oxidation reaction in a direct methanol fuel cell. *International Journal of Energy Research,* 44(13): 10071-10086.

Malaysian Journal of Analytical Sciences (MJAS)
Published by Malaysian Analytical Sciences Society

A REVIEW ON PREPARATION, MODIFICATION AND FUNDAMENTAL PROPERTIES OF SPEEK NANOCOMPOSITE PEM FOR DIRECT METHANOL FUEL CELL APPLICATIONS

(Satu Ulasan tentang Penyediaan, Pengubahsuaian dan Ciri Asas Komposit Nano Membran Elektrolit Polimer SPEEK untuk Aplikasi Sel Bahan Api)

Nor Fatina Raduwan and Norazuwana Shaari*

Fuel Cell Institute,
Universiti Kebangsaan Malaysia, Bangi, 43600 Selangor, Malaysia

**Corresponding author: norazuwanashaari@ukm.edu.my*

Received: 14 December 2021; Accepted: 3 February 2022; Published: xx June 2022

Abstract

Various types of promising proton exchange membrane (PEM) are based on thermoplastics due to their excellent conductivity, good thermal and chemical stability, high durability as well as low fabrication and material cost. Sulfonated poly (ether ether ketone) or SPEEK is one of the examples of thermoplastic polymer that has been sulfonated to enhance its fundamental properties. These properties can be altered and improved through the fabrication process and modifications of the membranes. Thus, current researches on combining SPEEK with other polymers and inorganic particles through various fabrication methods are discussed in this review. The characterization of SPEEK-based membrane in terms of its water uptake, methanol permeability, proton conductivity, thermal and mechanical stability are also included in the discussion. The impact of membrane modifications on the fundamental properties and comparison of different membrane preparation methods are addressed. In addition, the advantages and drawbacks of modified membranes are summarized.

Keywords: SPEEK; polymer electrolyte membrane; fuel cell

Abstrak

Pelbagai jenis polimer elektrolit membran yang diyakini adalah daripada termoplastik disebabkan oleh kekonduksian yang cemerlang, kestabilan terma dan kimia yang baik, ketahanan yang tinggi dan kos bahan dan pembuatan yang rendah. Poli (eter eter keton) tersulfonat atau SPEEK adalah satu contoh polimer termoplastik yang telah disulfonasi untuk mempertingkatkan ciri asas seperti pengambilan air dan ketertelapan metanol yang rendah, meningkatkan kekonduksian proton dan mempunyai ketahanan dan kestabilan yang tinggi. Ciri-ciri ini boleh diubahsuai dan dipertingkat melalui proses fabrikasi dan pengubahsuaian ke atas membran. Oleh yang demikian, para penyelidik menggabungkan SPEEK dengan polimer jenis lain dan bahan tak organik melalui pelbagai cara fabrikasi telah dibincangkan dalam ulasan ini. Kesan daripada pengubahsuaian membrane k etas ciri-ciri asanya dan perbandingan cara penyediaan membrane turut dibincangkan. Seterusnya, kelebihan dan kekurangan membran terubahsuai turut diringkaskan.

Kata kunci: SPEEK, membran elektrolit polimer, sel fuel

Introduction

As of September 2021, the current world population is 7.9 billion, according to the most recent United Nations estimates as elaborated by Worldometer. It is estimated that the population will reach up to 10 billion in another 30 years [1]. In line with the increase in the world population, the demand for energy also increases. Conventional fossil fuels are the primary sources of power to meet the world's energy demands. However, the depletion of fossil fuel sources and the rise of environmental issues, i.e., global warming due to the excessive releases of greenhouse gases have shifted the interest into the environmentally sustainable energy research [2]. One of the alternative energies that can solve this issue is through the utilization of natural sources such as hydrogen.

Hydrogen is one of the most abundant elements in the universe. For instance, the sun consists mainly of hydrogen. While on earth, hydrogen combines with other elements either in liquid, gas, or solid form as it does not exist freely in nature. As it only exists in a compound form, specific processes are required to split and obtain hydrogen, such as reforming, hydrolysis, and electrolysis [3]. Hydrogen can be utilized in many applications such as petroleum refining and fertilizer production, and for the past decades it has been widely used in fuel cell to generate electricity.

Fuel cell technology

Fuel cell is an electrochemical device that converts fuel and oxidant into electricity [4]. Basically, hydrogen is supplied as fuel at the anode and oxygen (oxidant) at the cathode. At the cathode, oxygen is reduced, and oxygen ions are produced. These oxygen ions will pass through the electrolyte and move towards the anode. When reaching the anode, they react with the protons that are broken down from hydrogen [5]. Electrons that are obtained from hydrogen molecules travel at the outer circuit and generate electricity. The half-reactions of this process at both sides are shown by the following equation:

$$\text{Cathode} : \tfrac{1}{2} O_2 + 2H^+ + 2e^- \rightarrow H_2O \quad (1)$$

$$\text{Anode} : H_2 \rightarrow 2H^+ + 2e^- \quad (2)$$

$$\text{Overall reaction} : H_2 + \tfrac{1}{2} O_2 \rightarrow H_2O \quad (3)$$

As it generates electricity through an electrochemical reaction, the by-products from the reaction are basically water and heat, which do not contribute to the environmental pollution. In fact, the water can be reused in the system, and the heat that is generated can be recycled into another system, such as a water heater system. These reused and recycled processes eliminate energy wastes and yield high energy efficiency of fuel cells up to 90% [6]. Correspondingly, there are various types of fuel cells depending on the types of electrolytes that are used. They are further sub-categorized by the types of fuel (hydrogen, reforming hydrogen-rich fuels, i.e., methanol, ethanol, and hydrocarbon), and operating temperature- low temperature (LT), intermediate temperature (IT), high temperature (HT). For example, direct methanol fuel cell (DMFC) and direct ethanol fuel cell (DEFC), also known as direct liquid fuel cell (DLFC), are the extension study to the proton exchange membrane fuel cell (PEMFC). While for microbial fuel cell (MFC), some improvements are being made where glucose is employed on-non enzymatic noble metal electrode to overcome certain drawbacks of the conventional MFC, which is known as direct glucose fuel cell (DGFC). Whereas a direct borohydride fuel cell (DBFC) is a sub-category of an alkaline fuel cell (AFC), and the latest research has reported that the anionic exchange membrane fuel cell (AEMFC) possesses great potential in replacing the traditional liquid electrolyte AFC [7]. In SOFC, there are three sub-categories, which are differentiated by the range of operating temperature, i.e., LT-SOFC, IT-SOFC and HT-SOFC. Each temperature range requires different types of material to be used as electrolytes. All existing fuel cells and their characteristics, including the efficiency, are summarized in Table 1.

Table 1. Types of fuel cells and their characteristics

Electrolyte	Types of Fuel Cells	Sub-Category	Operating Temperature (°C)	Fuel/Oxidant	Efficiency (%)
Phosphate buffer	MFC	DGFC	25-30	Organic load/Oxygen	-
Alkaline solution	AFC	DBFC	50-90	Sodium or potassium borohydride/Oxygen or hydrogen peroxide	50-70
		AEMFC		Hydrogen/Oxygen	
Solid polymer membrane	PEMFC	DMFC DEFC	50-120	Methanol/Oxygen Ethanol/Oxygen	40-50
Acidic solution	PAFC		175-220	Hydrogen/Oxygen	40-45
Molten mixture	MCFC		600-650	Hydrogen/Oxygen	50-60
Ceramic oxides	SOFC	LT-SOFC IT-SOFC HT-SOFC	400-600 600-800 800-1000	Hydrogen or hydrocarbon/Oxygen	60-90

Among the types of fuel cells, DMFC which is the sub-category of PEMFC has been widely used in various applications- covering small-scale appliances to mobile usage such as transportation. These broad applications are due to the advantages of low operating temperature, which lead to rapid start-up and a long-life span. Besides that, the DMFC system yields high power density and through its compact design, provides superior transportation facilities compared to other existing fuel cells. Although it has a compact design, complex heat and water management are unavoidable. Also, it uses expensive materials as a catalyst, such as Platinum, Pt, and Palladium, Pd to speed up the chemical reaction, and Nafion® for membrane materials. However, owing to its vast advantages, DMFC has generated an interest among researchers to find a way to overcome the drawbacks.

Development of proton exchange membrane (PEM) for DMFC

DMFC is a type of fuel cell that uses methanol as fuel to replace hydrogen in a typical fuel cell. As methanol is a non-volatile liquid fuel, it does not easily evaporate into gas at room temperature. In fact, this type of fuel cell does not require any fuel processing equipment as the mixture of methanol and water are directly fed into the cell. Therefore, it is easy to store and handle compared to the volatile hydrogen gas. Other advantages of using methanol in fuel cell systems are the high energy density that is obtained; due to its abundant resources, the price of methanol is relatively cheap and affordable. The reactions that take place in both electrodes are as follows:

Anode : $CH_3OH + H_2O \rightarrow CO_2 + 6H^+ + 6e^-$ (4)

Cathode : $3/2\ O_2 + 6H^+ + 6e^- \rightarrow 3H_2O$ (5)

Accordingly, the overall cell reaction is

Overall : $3/2\ O_2 + CH_3OH \rightarrow CO_2 + 2H_2O$ (6)

One of the key components in fuel cells, especially for DMFC, is the proton exchange membrane (PEM). PEM is needed to complete the electrochemical reaction to fulfill the energy requirement in which it serves to transfer H^+ within itself from anode to cathode [8]. The high and outstanding PEM must meet specific criteria such as having good oxidative and hydrolytic stability, possessing high mechanical and thermal stability, and

yield a high proton conductivity as well as being cost effective in the fabrication of membrane electrode assembly (MEA). As it is located between the electrodes, the PEM must also have good barrier properties to avoid the mixing of fuel (methanol) from the anode and oxidant (oxygen) coming from the cathode. The permeability of the membrane is an unresolved issue that is still under ongoing research. The high permeability membrane or leakage of the MEA (consisting of PEM) can contribute to a serious methanol crossover issue, which eventually will deteriorate the performance of fuel cell. Therefore, a high durability membrane is needed to overcome this issue.

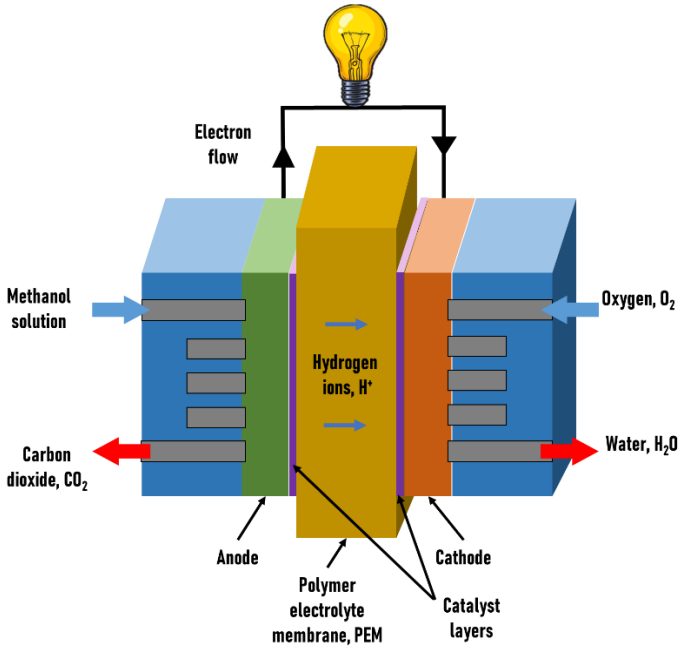


Figure 1. Working principle of DMFC

Table 2. Target requirement for an ideal PEM [9]

Criteria	**Target Requirement**
Proton conductivity	0.1 – 1 S cm^{-1}
Oxygen crossover	2 mA cm^{-2}
Fuel crossover	2 mA cm^{-2}
Electrical resistance	1000 Ω cm^{-2}
Durability	20,000 cycles
Chemical stability	More than 500 h

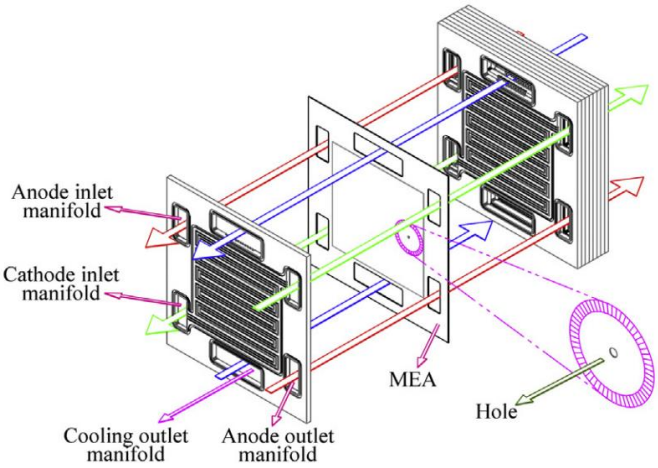


Figure 2. The leakage passing through the PEM [10]

Classification of polymeric membranes

Polymeric membranes can be classified into fluorinated and non-fluorinated polymers. Fluorocarbon-based ion-exchange membrane or Nafion® is the most common and readily available membrane in the market. Nafion® possesses unique structures that contribute to stability in terms of mechanical and chemical aspects as well as imparts high proton conductivity [11]. However, the presence of (approximately 4 nm) ionic clusters which are considerably large in size compared to methanol molecules, make them penetrate easily from anode to cathode. The methanol crossover is also being contributed by the separated nanophase of hydrophobic and hydrophilic domains of Nafion®. This methanol crossover will create a mixed potential that includes methanol and performance loss at cathode and anode, respectively. It will simultaneously affect the oxygen reduction reaction (ORR) and methanol oxidation reaction (MOR), which lead to a lower cathode potential and decrease in the cell voltage (as much as 0.15-0.2V)[12]. Besides that, electrocatalyst poisoning might occur at the cathode due to methanol oxidation from the crossover [13].

The ways to overcome these problems are (a) synthesizing new polymeric membranes (non-fluorinated polymers) such as poly ether sulfone (PES), polyphenyl sulfone (PPSU), poly benzimidazole (PBI)[14, 15], poly ether ether ketone (PEEK), polyvinyl alcohol (PVA)[16] and polyimide (PI); (b) sulfonation of aromatic polymers; and (c) incorporating the existing polymer membrane with other materials which are also known as filler. Filler can consist of inorganic particles such as titanium dioxide, iron titanate, zirconium phosphate, silica, heteropolyacid, and zeolites. The incorporation of this filler into the polymer produces a composite or hybrid membrane. This composite or hybrid membrane with control structure and outstanding properties for DMFC is attracting significant attention among researchers. This is proven by the number of papers that have been published in high-impact journals for the past ten years. Using the keywords search of 'composite membrane' or 'hybrid membrane' and 'direct methanol fuel cell' in the ScienceDirect website, the increasing trend of published papers that are related to the keywords is observed in Figure 3.

Due to the shortcomings and drawbacks of the perfluorosulfonic acid membrane as stated, non-fluorinated polymers, specifically poly arylene ether ether type-polymers such as PEEK, PES, PS, PI, PBI, and their derivatives have the potential to replace it. Besides having good thermal and mechanical stability, these alternative polymers also possess good cost-effective properties as well as high proton conductivity.

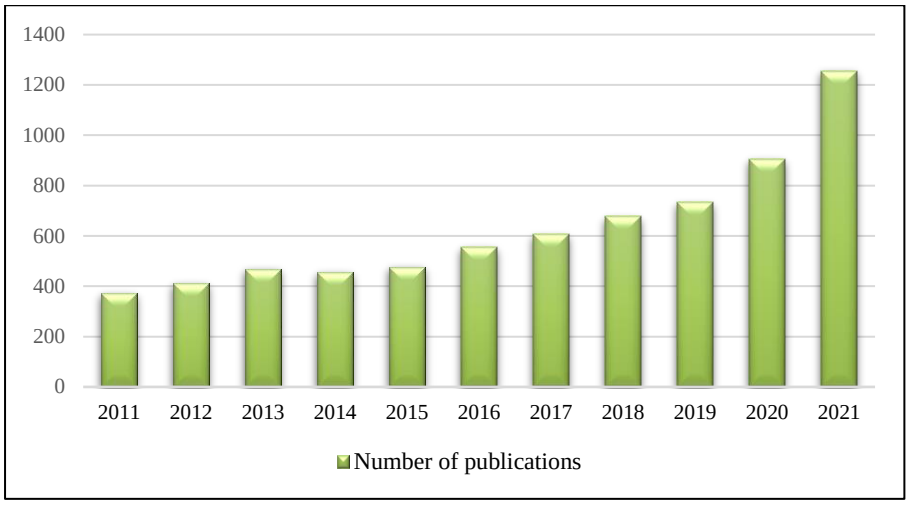


Figure 3. The trend of publication of composite membrane in high impact journals for the past 10 years

Sulfonated and modified PEEK as PEM

Polyether ether ketone or PEEK is a semi-crystalline thermoplastic polymer that belongs to the polyketone family of polymers (PEK, PEEK, PEEKK, PEKK, PEKEKK). Amongst them, PEEK is the most commonly used and produced in bulk production. The key properties of PEEK that make it widely used in various fields such as aerospace, automotive, electrical, and biomedical application are its good solvent resistance, dimensional stability, biocompatible, long life, and it exhibits exceptional mechanical properties [17, 18].

In order to improve the hydrophilicity and transportation of ions in PEEK material, sulfonation is carried out. Sulfonation is the process of either introducing sulfonic acid groups using sulfuric acid directly into the polymer chains as shown in Figure 4, by polymerizing functionalized sulfonated monomers or by grafting the sulfonic acid onto the aromatic backbone to produce random copolymers [9, 19]. However, the last method does not seem to be suggested as it leads to chemical degradation of the polymer chain [20].

The charged groups are important as they separate the protons from each other by water molecules and provide proton transport. Their addition depends on the substituents present in the ring [18]; substitution occurs on the aromatic ring between two ether (-O-) links. Many other polymers have also been sulfonated to enhance their properties in terms of wettability, water flux, perm selectivity, and solubility in solvents for processing. The solubility of PEEK enables it to be easily cast from organic solution and to eliminate complicated processes rather than when to fabricate perfluorosulfonic acid membranes. Other polymers, sulfonated polyarylene ether ketones (SPAEKs) with 60% of sulfonation degree, showed the best performance in terms of conductivity and methanol permeability [19].

At the same time, sulfonation also increased the proton conductivity of the polymer due to the improved hydrophilicity [21]. The proton conductivity is increased by increasing the degree of sulfonation. However, a higher sulfonation degree will increase the water uptake and raise another swelling issue. Swelling can make the membrane fragile, and changes of dimensions that lead to mechanical failures. Therefore, an optimum and moderate degree of sulfonation is crucial when undergoing the SPEEK sulfonation process. Based on the research by Li et al., it is advisable that for DMFC application, the degree of sulfonation for SPEEK is in the range of 30% to 60%. This is because too low a sulfonation degree will give poor conductivity. Otherwise, the polymers are highly swollen in methanol

water solution (1 M) when the degree of sulfonation is above 60% [22].

In the recent past, researchers have incorporated SPEEK with fillers to further enhance its properties, in addition to overcoming some limitations of having SPEEK alone as the membrane. This is due to the presence of significant numbers of dead-end channels in SPEEK limits, the conductivity thus affecting the overall performance [24]. Therefore, in order to not sacrifice the mechanical strength in the higher degree of sulfonation, fillers are added into an organic polymeric matrix.

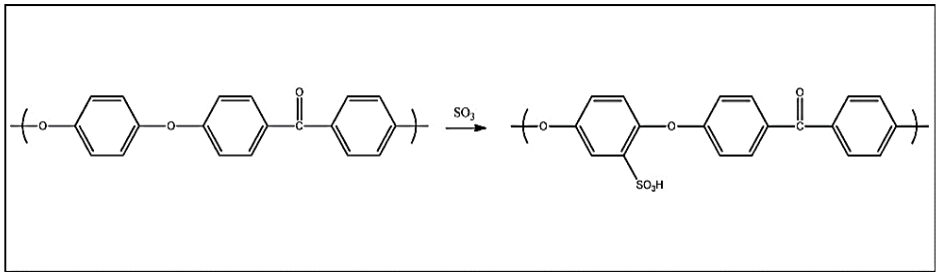


Figure 4. Process of PEEK sulfonation [23]

Preparation methods of composite PEM

As polymer SPEEK owns many of the dead channels, it limits the flow of effective ionic conductivity. These ionic conductive channels can be built by incorporating organic polymers with inorganic backbones. Different ways of incorporating them are illustrated in Figure 5. Organic-inorganic composite membrane can benefit in mechanical and thermal stability from inorganic backbone, while the organic polymer gives advantages in terms of chemical reactivity, ductility and flexibility of processing.

The composite of ionically conductive polymer and inorganic material can be varied, as shown in Figure 6. Usually, an inorganic precursor such as a monomer or oligomer is blended with a linear or network polymer matrix. The preparation methods of the nanocomposite materials include mixing or blending, *in-situ* polymerization or infiltration, and sol-gel.

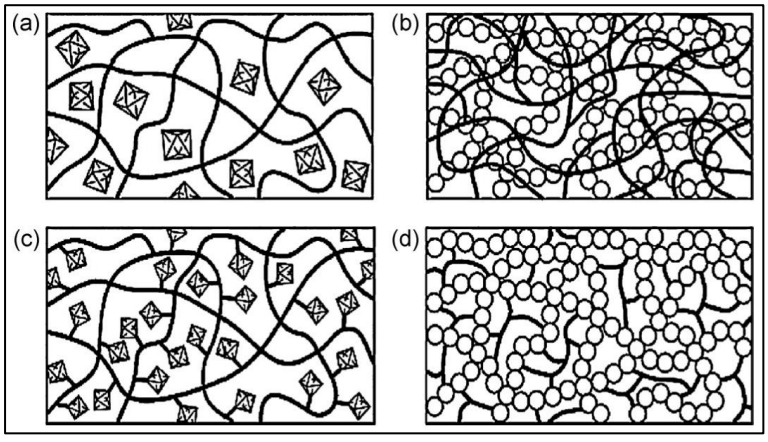


Figure 5. Different ways of incorporating the inorganic system in organic polymers: (a) inorganic moiety embedded into an organic polymer (b) interpenetrating networks with chemical bonds (c) inorganic groups incorporated by bonding to the backbone and (d) dual organic-inorganic hybrid polymer [25]

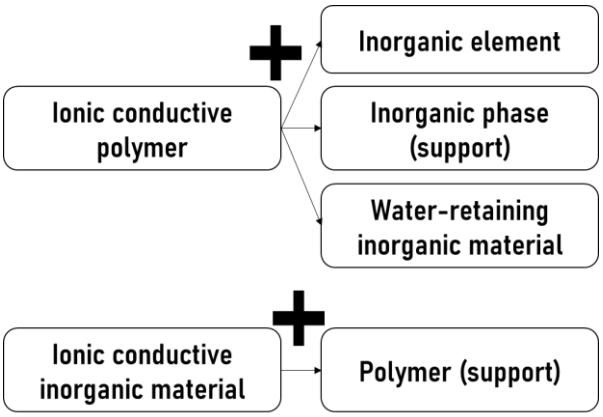


Figure 6. Different ways of organic-inorganic composite membranes arrangements [26]

Mixing or blending method.

The simplest method to prepare composite PEM is by direct mixing or blending of inorganic materials into the organic polymer matrix. There are two ways of blending the composite, which are melt blending and liquid-state blending. In both ways, it is important to ensure the desired composite components can be dispersed in a common solvent or melt at a high temperature.

Salarizadeh et al. [27] prepared blend nanocomposite SPEEK/perfluorosulfonic acid (PFSA)/barium strontium titanate (BST) membranes by dissolving SPEEK in N,N-dimethylacetamide (DMAC) followed by mixing with the BST dispersion and PFSA solution. The experimental procedure is shown in Figure 7.

Although melt blending is more common due to its efficiency and prevention from the dispersing of hazardous material into the environment, the filler agglomeration tends to occur when the inorganic nanoparticles are dispersed in polymer matrix. In order to overcome the limitation, the surface of the nanoparticles is being modified to produce nanostructural composites.

Composite of nanosilica and polymer is the common example of membrane that is prepared by solution blending due to its simplicity in preparation. This membrane is widely being researched for gas separation, pervaporation and PEM in fuel cell application [28].

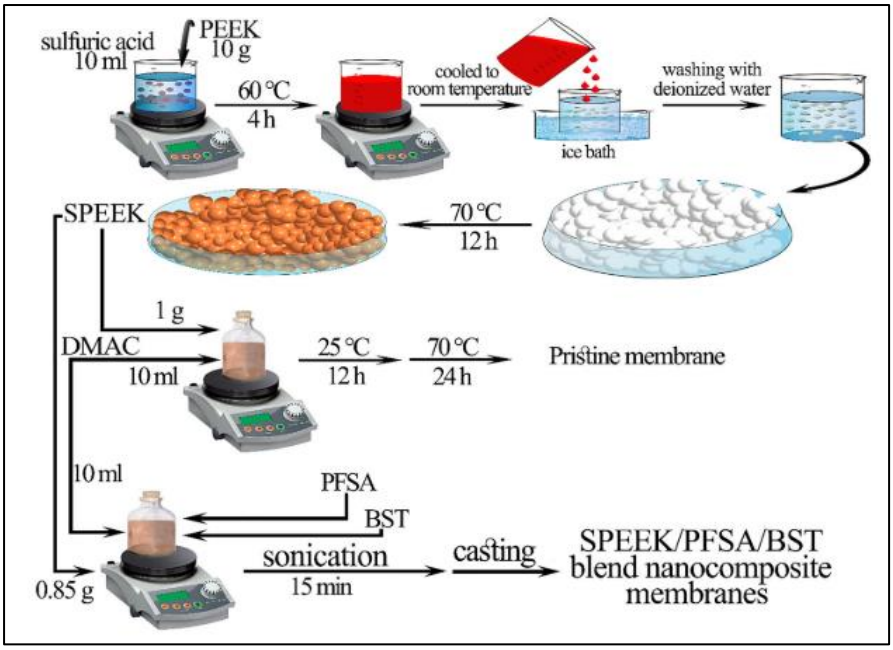


Figure 7. The steps involved in preparing the blend nanocomposite membrane SPEEK/PFSA/BST [29]

In-situ polymerization or infiltration method

In this method, inorganic nanoparticles are introduced in the polymer membrane to modify the transport properties. Firstly, the preformed membrane will be immersed in a solvent, allowing it to swell in order to increase the pore or void volume before the inorganic particle is doped or infiltrated. After the inorganic particle is infiltrated, the composite is cured by heat, radiation, or chemical grafting to gain covalent bonding inside the matrix. The drawback of this method is the leaching of inorganic materials from the membrane matrix [30].

Sol-gel method

This method is favorable as it is an environmentally friendly way and is conducted in low temperature. Briefly, sols are dispersions of colloidal particles in a liquid, while gels may be classified into four categories: (i) well-ordered lamellar structures of inorganics with organics (i.e., organopolysilsesquioxanes; (ii) covalent disordered polymeric networks; (iii) polymer networks formed through physical aggregation; (iv) disordered structures of inorganic and organic networks. There are two consecutive steps in sol–gel reactions, which are hydrolysis of metal alkoxides to produce hydroxyl groups and polycondensation of the hydroxyl groups to form a three-dimensional network. The process is started with solvents (low molecular weight) with alkoxide precursors $M(OR)_n$, (M is a network-forming element: Si, Ti, Zr, Al, B, etcetera, and R is an alkyl group (C_xH_{2x+1})) and water. Later, low molecular weight byproducts (alcohol or water) are produced during hydrolysis and condensation. They must be removed, resulting in shrinkage during the sol-gel process.

Modification of SPEEK membrane

Sulfonated PEEK is an organic thermoplastic polymer that possesses outstanding thermal and mechanical properties. As mentioned in the previous section, fillers are needed to overcome some of the drawbacks of SPEEK that can limit its potential to emerge as high-performance membrane. The introduction of nanostructures fillers can overcome the thermal and mechanical instability of SPEEK polymer. The inorganic materials as additives such as hygroscopic oxides (silicon oxide, zirconium oxide, titanium dioxide, iron-titanates, zeolites, and boron phosphate), solid acids and heteropolyacids (HPAs), clay, graphene oxide (GO), carbon nanotubes (CNTs), fullerene and perovskite oxides have shown improved performance for SPEEK membrane [31–33]. Besides overcoming the instability in thermal and mechanical properties, the modifications to SPEEK membrane through inorganic filler also improve methanol permeability in DMFC.

Zhang et al. [34] synthesized nanocomposite membrane by incorporating sulfonated hallyosite nanotubes (SHNTs) into the SPEEK matrix. The well-dispersed SHNTs in the SPEEK matrix bring advantages in terms of the thermal and mechanical stabilities of the membrane. Besides that, the water uptake, ionic exchange capacity, and proton conductivity have been improved tremendously due to the construction of ionic channels that are interconnected by the SHNTs in the SPEEK matrix. Figure 8 shows the improved proton pathways that will allow efficient proton transfer and lead to the enhancement of proton conductivity.

Bagheri et al. [35] prepared SPEEK, sulfonated poly (vinilidinfluoride-co-hexaflourpropylen) (SPVDF-co-HFP), and lanthanum chromite ($LaCrO_3$) as nanocomposite blend membrane using solvent casting method. The increasing in proton conductivity is observed at the nanoparticle content of 1.5 wt.%, and the addition of 1.5 wt.% $LaCrO_3$ nanoparticles managed to make this membrane as effective barrier against methanol permeation. Figure 9 shows the performance of the composite membrane with different content.

Later, Salarizadeh et al. [29] prepared another blend nanocomposite membrane of SPEEK with two different types of additives, namely perfluorosulfonic acid (PFSA) and $Ba_{0.9}Sr_{0.1}TiO_3$ (BST) doped-perovskite nanoparticles. The addition of both additives has indicated that proton conductivity is improved while methanol permeability is decreased compared to pristine SPEEK membrane. The increase in proton conductivity is contributed by the high specific surface area of perovskite nanoparticles

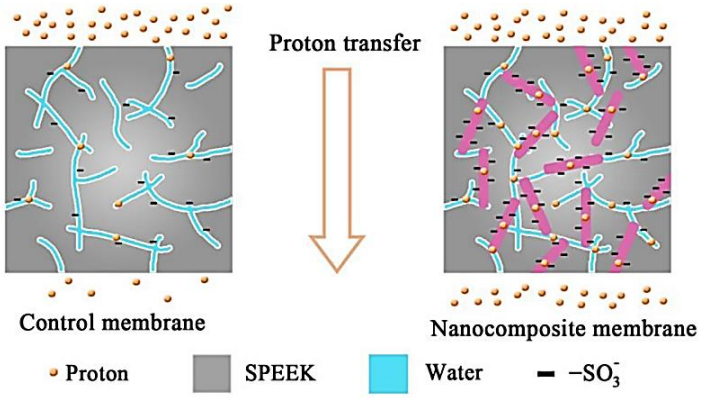


Figure 8. SHNTs interconnect the ionic channels within SPEEK matrix via -SO_3H groups [34]

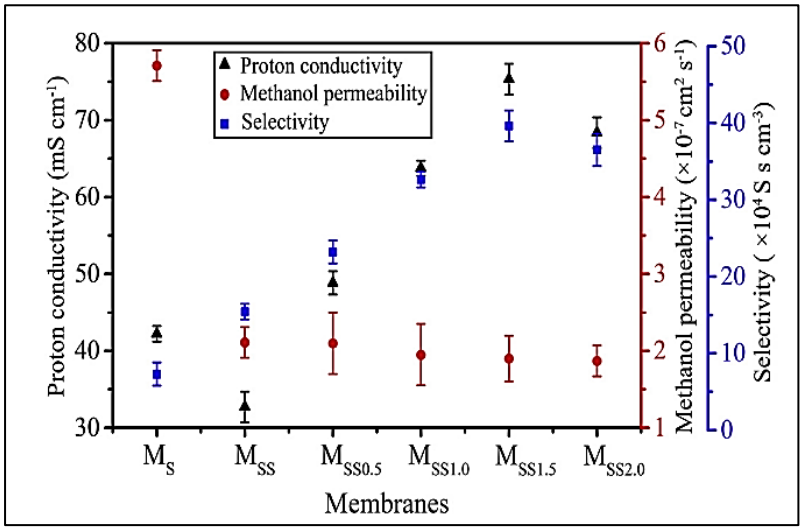


Figure 9. Comparison of different content with the performance of prepared membrane [35]

Table 3. Influence on membrane performances during the SPEEK modification

Composite	Improvement	Ref.
SPEEK/SnO_2/sBH	Water retention properties increase, which consequently enhance the ionic conductivity of the composite membrane. Methanol diffusion channels decrease and demonstrate the high power density as well as excellent durability	[36]
SPEEK/QDs/CS	Enhanced through-plane conductivity and decreased transfer anisotropy	[37]
sPEEK/sGNR-sGQD	Improved physico-chemical properties resulting in enhanced electrochemical selectivity. Significant enhancement in DMFC performance and better durability can be observed	[38]
SPEEK/CNFs	Improved mechanical strength and water uptake of the composite membranes and low methanol permeability	[39]
SPEEK/PVA/TEOS	The proton transport and fuel cells performance increased	[40]
SPEEK/PFSA/BST	Improved proton conductivity and methanol barrier. Enhanced mechanical stability	[29]

Properties of SPEEK composite membrane

Water uptake, swelling ratio, ion-exchange capacity, mechanical properties

The water uptake (WU) and membrane swelling (SW) are essential parameters in DMFC application as they directly affect the proton conductivity and mechanical stability of the membrane. Controlling the WU of the membrane is quite necessary for high WU can lead to mechanical and dimensional stability while low WU decreases the proton transferring rate within the membrane. They are calculated from the following equations:

$$WU\ (\%) = \frac{m_{wet} - m_{dry}}{m_{dry}} \times 100 \quad (7)$$

$$SW\ (\%) = \frac{L_{wet} - L_{dry}}{L_{dry}} \times 100 \quad (8)$$

To determine the water uptake (WU) and membrane swelling (SW), the membranes are dried and then their weights (M_{dry}) and the thickness (L_{dry}) are measured. After that, they are soaked in deionized water. Finally, the surface water of membranes is blotted with a clean paper, and immediately weights (M_{wet}) and thickness (L_{wet}) of membranes are measured.

The ion-exchange capacity (IEC) value is defined as the molar number of fixed sulfonate sites per gram polymer. It is decided by the concentration of exchangeable ions in membranes and determined by an acid-base titration method[41]. It is very closely related to water uptake as increasing the water uptake will increase the value of IEC. The value of IEC was calculated based on the following formula:

$$IEC = \frac{(N_{NaOH} \times V_{NaOH})}{mass_{dry}} \times 100\ \% \quad (9)$$

The dried membrane is soaked in a saturated NaCl solution for a certain time and later is titrated with a NaOH solution using phenolphthalein as an indicator. The N_{NaOH} is the concentration of NaOH solution, while V_{NaOH} is the volume of NaOH solution consumed. The mechanical properties of the membrane are investigated using a universal tensile testing machine. It is evaluated with tensile stress-strain tests. Typically, the value of Young's modulus is calculated from the slope of the initial linear part of the stress-strain curve. The maximum stress value of the entire curve was taken as the tensile strength [42].

Thermal and chemical stability

The thermal stability of the membrane is measured by its degradation of decomposition at a specific temperature. The membrane that has a good thermal stability should withstand a required temperature for a longer time before it degrades or decomposes [43]. It is usually investigated by a thermogravimetric analyzer (TGA) where the weight loss of the samples is determined.

The thermal stability study of the composite membrane SPEEK with inorganic additive, clay and electrospun fibers is carried out by Awang et al. [43]. The thermogravimetric analysis indicated that SPEEK with added inorganic filler (i.e., Cloisite) gives a higher degradation temperature compared to pristine SPEEK. It shows that the composite organic-inorganic membrane is thermally stable, especially when the amounts of Cloisite is increased as shown in Figure 10. The Cloisite acts as a mass transport barrier and insulator against the colatile compound when the heat is applied [44].

The chemical stability of the membrane is usually being tested by Fenton's reagent. The experiment subjects the membrane to a very large excess of hydroxyl radicals between 60 and 80 °C to assess chemical durability. The reagent is made when ferrous sulfate is dissolved in hydrogen peroxide (H_2O_2) aqueous solution. This is to mimic the real situation during DMFC operation where H_2O_2 is formed at the cathode side due to the partial reduction of O_2 and the iron ion (Fe^{2+}) that is formed from the corrosion of the iron back plate. The migration of Fe^{2+} to the cathode side will react with H_2O_2 and produces a free radical similar to the Fenton reagent. Then the prepared membrane is immersed in the reagent under stirring at a specific temperature. Carbon dioxide (CO_2) will be produced as a by-product when free radicals react with organic polymer. As CO_2 gas forms bubbles, the membrane structures tend to break if they cannot withstand the bubbles' pressure. Oxidative stability of the membrane is recorded by the time the membrane begins to break [35].

From the chemical stability test conducted by Salleh et al. [45] on composite membrane SPEEK/Cloisite/ triaminopyrimidine (SP/CL/TAP), it is proven that the presence of inorganic particles in nanocomposite membrane increased its resistance towards radical attack. The nanocomposite membrane can maintain its weight up to 48 hours. From the FESEM image, as shown in Figure 10, the surface deformation of SP/CL/TAP membrane started to occur after being exposed to Fenton reagent solution for 24h (Figure 11(h)).

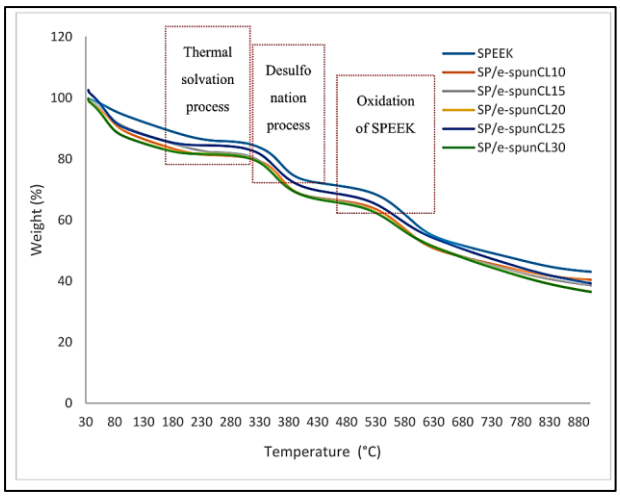


Figure 10. TGA of the SPEEK and composite SPEEK membrane with different amounts of Cloisite [43].

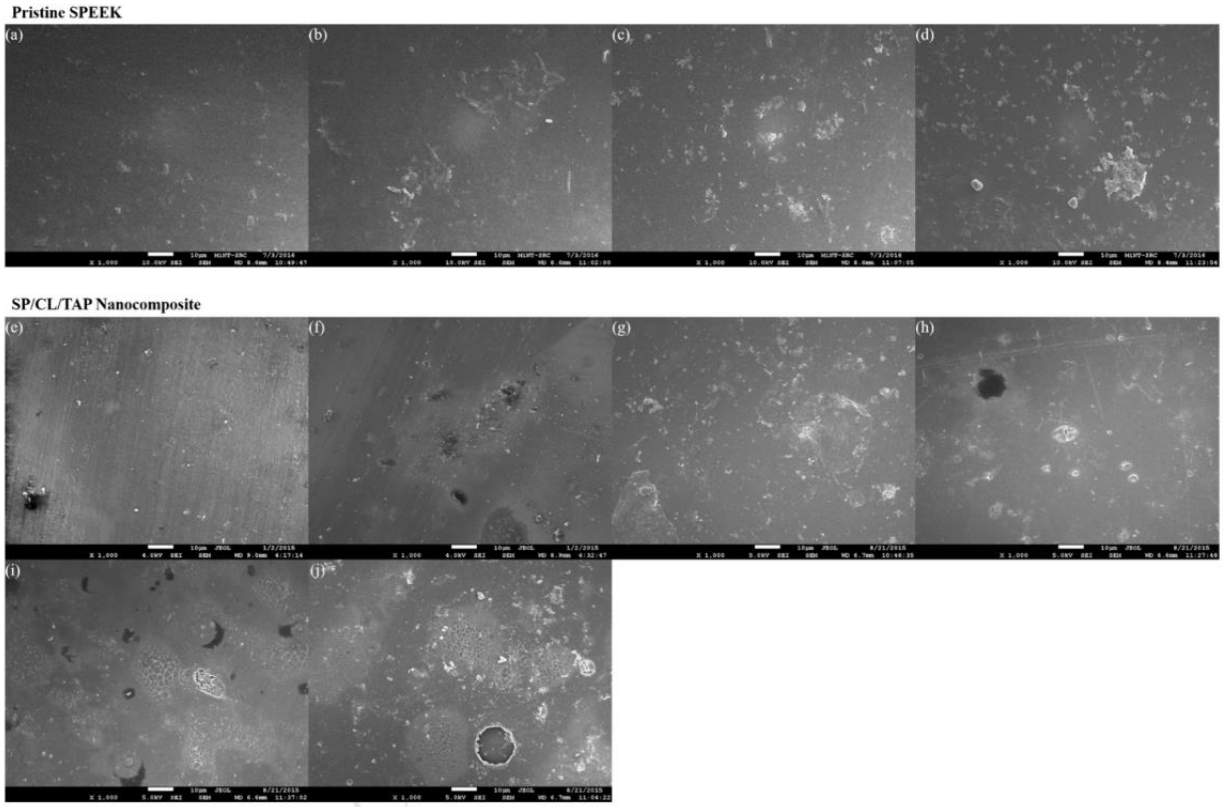


Figure 11. FESEM micrographs of pristine SPEEK and nanocomposite membrane SP/CL/TAP surface before (a,e) and after exposed to Fenton reagent solution for 6h (b,f), 12h (c,g) and 24h (d,h), 48h (i) and 96h (j) [45]

Methanol permeability

The methanol permeability (P, cm^2 s^{-1}) can be determined by different techniques such as potentiometry, gas chromatography technique (GC), and densimetry method. Each and every technique have its respective advantages and drawbacks, as summarized in Table 4. These three different experimental methods, however, provided very comparable results.

The cell was separated into two equal-sized compartments by a membrane. The compartment in the left side was filled with methanol solution while the compartment in the right was filled with deionized water and both part had equal volume. The prepared membranes with certain areas are located vertically between the two compartments after keeping them in deionized water. The schematic experimental set-up is illustrated in Figure 12 [46]. As there is a methanol concentration gradient between these two parts, methanol can diffuse from the left to the right compartment, and methanol permeability was measured as a function of time. It is calculated from the following equation:

$$C_R(t) = \frac{A\,P}{L\,V_R} C_L(t - t_0) \quad (10)$$

where, C_L and C_R are the concentration of methanol in methanol and water compartment (mol L^{-1}) respectively; L is the thickness of the membranes (cm), A is the diffusion area (cm^2), and V_R is the volume of deionized water in water compartment (mL). Methanol concentration in the water compartment was examined with time using a density meter.

Table 4. Summary of different techniques used to measure methanol permeability

Techniques	Advantages	Drawbacks
Potentiometry	• Simplest method • Cheapest	• Limited for certain parameters • Absolute values of concentration at a given time cannot be measured • Time-consuming
Gas chromatography technique	• Highly precise	• Very expensive
Densimetry	• Most efficient in terms of accuracy, simplicity, experimental time, and cost	-

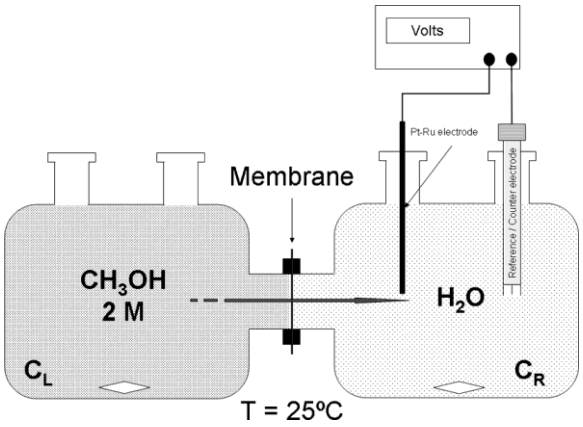


Figure 12. Schematic diagram of experimental set up to determine methanol permeability across the membrane [46]

Proton conductivity

The electrochemical performance of the composite membrane is often indicated by the value of proton conductivity. The proton conductivity heavily relied on the degree of sulfonation, water uptake, and methanol permeation. A summary of fundamental properties that contributed to proton conductivity of SPEEK based membrane is tabulated in Table 5. The proton conductivity is determined from the following equation:

$$\sigma = L/RA \quad (11)$$

where, σ is the proton conductivity of the membrane (S cm^{-1}), L is the thickness of the membrane (cm), R is the resistance of the membrane (Ω), and A is the surface area of the two electrodes (cm^2).

Gong et al. [42] illustrated proton conduction in composite membrane SPEEK/BPO_4@CNT in Figure 13. The composite membrane has higher proton conductivity compared to the pure SPEEK membrane. It could be primarily attributed to the dissociation of the absorbed water molecules on the BPO_4. The fundamental properties that contribute to the performance of composite SPEEK-based membranes that have been discussed in the earlier section are summarized in Table 5.

Table 5. Summary of fundamental properties of composite membrane SPEEK

Composite SPEEK-Based Membrane	Water Uptake (%)	Methanol Permeability ($\times 10^{-7}$ $cm^2 s^{-1}$)	Proton Conductivity @RT (Scm^{-1})	Ref
SPEEK/SPVDF-co-HFP	~25	2.11	0.0327	[35]
SPEEK/SPVDF-co-HFP (0.5 wt.%)	~30	2.10	0.0488	
SPEEK/SPVDF-co-HFP (1.0 wt.%)	~35	1.95	0.0638	
SPEEK/SPVDF-co-HFP (1.5 wt.%)	41.23	1.90	0.0753	
SPEEK/SPVDF-co-HFP (2.0 wt.%)	~35	1.87	0.0684	
sPEEK	29.3	9.24 ± 0.02	0.0102	[38]
sPEEK/[1]sGNR (1.5 wt.%)	30.4	6.25 ± 0.28	0.0150	
sPEEK/sGNR-[2]sGQD (1.0 wt.%)	33.9	6.76 ± 0.20	0.0135	
sPEEK/sGNR-sGQD (1.5 wt.%)	37.1	4.35 ± 0.17	0.0195	
sPEEK/sGNR-sGQD (2.0 wt.%)	33.6	5.24 ± 0.17	0.0147	
[3]CS/[4]SP	52	-	0.158*	[37]
CS/SP/[5]PQD-10%	-	-	0.327*	
CS/SP/PQD-20%	-	-	0.375*	
CS/SP/PQD-30%	85	-	0.456*	
CS/SP/[6]GQD-20%	-	-	0.309*	
SPEEK/[7]BH	25.05	1.58	0.0570**	[36]
SPEEK/sBH (1 wt.%)	38.62	2.52	0.0586**	
SPEEK/sBH(3 wt.%)	45.01	2.90	0.0728**	
SPEEK/sBH (5 wt.%)	44.73	2.87	0.0618**	
SPEEK/SBH/SnO_2 (3 wt.%)	50.34	1.28	0.0920**	
SPEEK/[8]rGONR@TiO_2		-	1.78	[47]

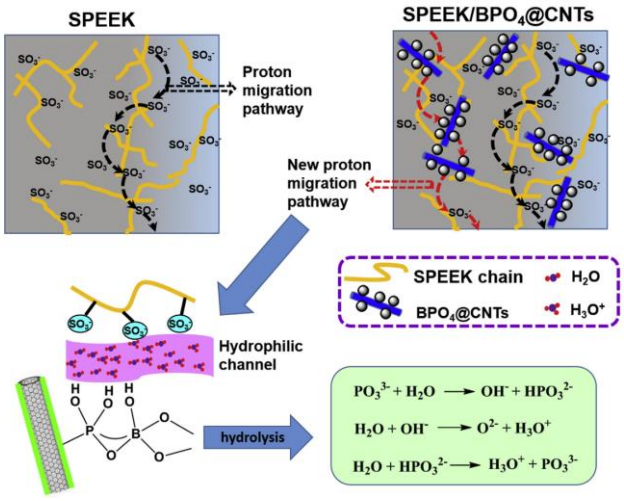


Figure 13. Schematic illustration of proton conduction in SPEEK and composite membrane SPEEK [42]

Future perspective and conclusions

The potential of composite SPEEK membrane as high-performance PEM is undeniable based on the past research. The properties such as water uptake and methanol permeation are closely linked to the performance of the membrane in terms of mechanical, thermal, chemical stability, and proton conductivity. With the results that have been obtained in literatures, the composite SPEEK membrane will be a strong competitor that has a big chance to replace the Nafion membrane. However, further investigations are needed i) to find optimum parameters and cost-effective methods in preparing the membrane , ii) to improve the distribution and proportion of inorganic particles in the polymer matrix , iii) to optimize the water uptake and methanol permeation in the membrane, iv) to produce a membrane that is suitable for higher temperature, humidity, and pressure.

In conclusion, the role of filler in improving the performance and properties of the SPEEK membrane is significant in comparison to the properties of either component in isolation.

References

1. Worldometer. (2021). Current World Population. Access from https://www.worldometers.info/world-population/ [Retrieved September 8, 2021]
2. Haiges, R., Wang, Y. D., Ghoshray, A. and Roskilly, A. P. (2017). Optimization of Malaysia's Power generation mix to meet the electricity demand by 2050. *Energy Procedia*, 142: 2844-2851.
3. Laguna-Bercero, M. A. (2012). Recent advances in high temperature electrolysis using solid oxide fuel cells: a review. *Journal of Power Sources*, 203: 4-16.
4. Dai, H., Jiang, B., Hu, X., Lin, X., Wei, X. and Pecht, M. (2020). Advanced battery management strategies for a sustainable energy future: multilayer design concepts and research trends. *Renewable and Sustainable Energy Reviews*, 8: 110480.
5. Bahru, R., Shaari, N. and Mohamed, M. A. (2020). Allotrope carbon materials in thermal interface materials and fuel cell applications: A review. *International Journal of Energy Research*, 44(4): 2471-2498.
6. Raduwan, N. F., Muchtar, A., Somalu, M. R., Baharuddin, N. A. and Muhammed Ali, S. A. (2018). Challenges in fabricating solid oxide fuel cell stacks for portable applications: A short review. *International Journal of Integrated Engineering*, 10(5): 80-86.
7. Ferriday, T. B. and Middleton, P. H. (2021). Alkaline fuel cell technology - a review. *International Journal of Hydrogen Energy*, 46(35): 18489-18510.
8. Junoh, H., Jaafar, J., Mohd Norddin, M. N. A., Ismail, A. F., Othman, M. H. D., Rahman, M. A., … and Ilbeygi, H. (2015). A review on the fabrication of electrospun polymer electrolyte membrane for direct methanol fuel cell. *Journal of Nanomaterials*, 4: 4.
9. Esmaeili, N., Gray, E. M. A. and Webb, C. J. (2019). Non-fluorinated polymer composite proton exchange membranes for fuel cell applications – a review. *ChemPhysChem*, 20(16): 2016-2053.
10. Asghari, S., Fouladi, B., Masaeli, N. and Imani, B. F. (2014). Leak diagnosis of polymer electrolyte membrane fuel cell stacks. *International Journal of Hydrogen Energy*, 39(27): 14980-14992.
11. Wu, H., Hou, W., Wang, J., Xiao, L. and Jiang, Z. (2010). Preparation and properties of hybrid direct methanol fuel cell membranes by embedding organophosphorylated titania submicrospheres into a chitosan polymer matrix. *Journal of Power Sources*, 195(13): 4104-4113.
12. Jiang, S. P., Liu, Z. and Tian, Z. Q. (2006). Layer-by-layer self-assembly of composite polyelectrolyte-nafion membranes for direct methanol fuel cells. *Advanced Materials*, 18(8): 1068-1072.
13. Kim, H. J., Kim, D. Y., Han, H. and Shul, Y. G. (2006). PtRu/C-Au/TiO_2 Electrocatalyst for a direct methanol fuel cell. *Journal of Power Sources*, 159: 484-490.

14. Taherkhani, Z., Abdollahi, M., Sharif, A. and Barati, S. (2021). Poly(benzimidazole)/ poly(vinylphosphonic acid) blend membranes with enhanced performance for high temperature polymer electrolyte membrane fuel cells. *Solid State Ionics*, 364: 115635.
15. Zarrin, H., Jiang, G., Lam, G. Y. Y., Fowler, M. and Chen, Z. (2014). High performance porous polybenzimidazole membrane for alkaline fuel cells. *International Journal of Hydrogen Energy*, 39(32): 18405-18415.
16. Herranz, D., Escudero-Cid, R., Montiel, M., Palacio, C., Fatás, E. and Ocón, P. (2018). Poly (vinyl alcohol) and poly (benzimidazole) blend membranes for high performance alkaline direct ethanol fuel cells. *Renewable Energy*, 127: 883-895.
17. Gao, X., Liu, Y. and Li, J. (2015). Review on modification of sulfonated poly (-ether-ether-ketone) membranes used as proton exchange membranes. *Medziagotyra*, 21(4): 574-582.
18. Yee, R. S. L., Zhang, K. and Ladewig, B. P. (2013). The effects of sulfonated poly(ether ether ketone) ion exchange preparation conditions on membrane properties. *Membranes*, 3(3): 182-195.
19. Xiang, Z., Zhao, X., Ge, J., Ma, S., Zhang, Y. and Na, H. (2016). Effect of sulfonation degree on performance of proton exchange membranes for direct methanol fuel cells. *Chemical Research in Chinese Universities*, 32(2): 291-295.
20. Hasani-Sadrabadi, M. M., Dashtimoghadam, E., Sarikhani, K., Majedi, F. S. and Khanbabaei, G. (2010). Electrochemical investigation of sulfonated poly(ether ether ketone)/clay nanocomposite membranes for moderate temperature fuel cell applications. *Journal of Power Sources*, 195(9): 2450-2456.
21. Chang, J. H., Park, J. H., Park, G. G., Kim, C. S. and Park, O. O. (2003). Proton-conducting composite membranes derived from sulfonated hydrocarbon and inorganic materials. *Journal of Power Sources*, 124(1): 18-25.
22. Li, L., Zhang, J. and Wang, Y. (2003). Sulfonated Poly(ether ether ketone) membranes for direct methanol fuel cell. *Journal of Membrane Science*, 226(1–2): 159-167.
23. Ata, K. C., Kadıoğlu, T., Türkmen, A. C., Çelik, C. and Akay, R. G. (2020). Investigation of the effects of SPEEK and its clay composite membranes on the performance of direct borohydride fuel cell. *International Journal of Hydrogen Energy*, 45(8): 5430-5437.
24. Rambabu, G. and Bhat, S. D. (2015). Sulfonated fullerene in SPEEK matrix and its impact on the membrane electrolyte properties in direct methanol fuel cells. *Electrochimica Acta*, 176: 657-669.
25. Kickelbick, G. (2003). Concepts for the incorporation of inorganic building blocks into organic polymers on a nanoscale. *Progress in Polymer Science*, 28(1): 83-114.
26. Peighambardoust, S. J., Rowshanzamir, S. and Amjadi, M. (2010). Review of the proton exchange membranes for fuel cell applications. *International Journal of Hydrogen Energy*, 35(17): 9349-9384.
27. Balazs, A. C., Emrick, T. and Russell, T. P. (2006). Nanoparticle polymer composites: Where two small worlds meet. *Science*, 314(5802): 1107-1110.
28. Zou, H., Wu, S. and Shen, J. (2008). Polymer/silica nanocomposites: Preparation, characterization, propertles, and applications. *Chemical Reviews*, 108(9): 3893-3957.
29. Salarizadeh, P., Bagheri, A., Beydaghi, H. and Hooshyari, K. (2019). Enhanced properties of SPEEK with incorporating of PFSA and barium strontium titanate nanoparticles for application in DMFCs. *International Journal of Energy Research*, 43(9): 4840-4853.
30. Tripathi, B. P. and Shahi, V. K. (2011). Organic-inorganic nanocomposite polymer electrolyte membranes for fuel cell applications. *Progress in Polymer Science (Oxford)*, 36(7): 945-979.
31. Wong, C. Y., Wong, W. Y., Ramya, K., Khalid, M., Loh, K. S., Daud, W. R. W., … and Kadhum, A. A. H. (2019). Additives in proton exchange membranes for low- and high-temperature fuel cell applications: A review. *International Journal of Hydrogen Energy*, 44(12): 6116-6135.

32. Rambabu, G., Bhat, S. D. and Figueiredo, F. M. L. (2019). Carbon nanocomposite membrane electrolytes for direct methanol fuel cells—a concise review. *Nanomaterials*, 9(9): 1292.
33. Taufiq Musa, M., Shaari, N. and Kamarudin, S. K. (2020). Carbon nanotube, graphene oxide and montmorillonite as conductive fillers in polymer electrolyte membrane for fuel cell: An overview. *International Journal of Energy Research*, 45(2): 1309-1346.
34. Zhang, H., Ma, C., Wang, J., Wang, X., Bai, H. and Liu, J. (2014). Enhancement of proton conductivity of polymer electrolyte membrane enabled by sulfonated nanotubes. *International Journal of Hydrogen Energy*, 39(2): 974-986.
35. Bagheri, A., Javanbakht, M., Hosseinabadi, P., Beydaghi, H. and Shabanikia, A. (2018). Preparation and characterization of SPEEK/SPVDF-Co-HFP/$LaCrO_3$ nanocomposite blend membranes for direct methanol fuel cells. *Polymer*, 138: 275-287.
36. Ranjani, M., Al-Sehemi, A. G., Pannipara, M., Aziz, M. A., Phang, S. M., Ng, F. L. and Kumar, G. G. (2020). SnO_2 nanocubes/bentonite modified SPEEK nanocomposite composite membrane for high performance and durable direct methanol fuel cells. *Solid State Ionics*, 353(3): 115318.
37. Li, P., Dang, J., Wu, W., Lin, J., Zhou, Z., Zhang, J. and Wang, J. (2020). Nanofiber composite membrane using quantum dot hybridized SPEEK nanofiber for efficient through-plane proton conduction. *Journal of Membrane Science*, 609(5): 118198.
38. Shukla, A., Dhanasekaran, P., Nagaraju, N., Bhat, S. D. and Pillai, V. K. (2019). A facile synthesis of graphene nanoribbon-quantum dot hybrids and their application for composite electrolyte membrane in direct methanol fuel cells. *Electrochimica Acta*, 297: 267-280.
39. Liu, X., Yang, Z., Zhang, Y., Li, C., Dong, J., Liu, Y. and Cheng, H. (2017). Electrospun multifunctional sulfonated carbon nanofibers for design and fabrication of SPEEK composite proton exchange membranes for direct methanol fuel cell application. *International Journal of Hydrogen Energy*, 42(15): 10275-10284.
40. Sahin, A. (2018). The development of SPEEK/PVA/TEOS blend membrane for proton exchange membrane fuel cells. *Electrochimica Acta*, *271*, 127–136.
41. Jiang, Z., Zhao, X. and Manthiram, A. (2013). Sulfonated poly(ether ether ketone) membranes with sulfonated graphene oxide fillers for direct methanol fuel cells. *International Journal of Hydrogen Energy*, *38*(14): 5875-5884.
42. Gong, C., Zheng, X., Liu, H., Wang, G., Cheng, F., Zheng, G., … and Tang, C. Y. (2016). A new strategy for designing high-performance sulfonated poly(ether ether ketone) polymer electrolyte membranes using inorganic proton conductor-functionalized carbon nanotubes. *Journal of Power Sources*, 325: 453-464.
43. Awang, N., Jaafar, J. and Ismail, A. F. (2018). Thermal stability and water content study of void-free electrospun SPEEK/cloisite membrane for direct methanol fuel cell application. *Polymers*, 10(2): 1-15.
44. Yamaguchi, T., Miyata, F. and Nakao, S. I. (2003). Pore-filling type polymer electrolyte membranes for a direct methanol fuel cell. *Journal of Membrane Science*, 214(2): 283-292.
45. Salleh, M. T., Jaafar, J., Mohamed, M. A., Norddin, M. N. A. M., Ismail, A. F., Othman, M. H. D., … and Salleh, W. N. W. (2017). Stability of SPEEK/Cloisite®/TAP nanocomposite membrane under fenton reagent condition for direct methanol fuel cell application. *Polymer Degradation and Stability*, 137: 83-99.
46. Mollá, S., Compañ, V., Lafuente, S. L. and Prats, J. (2011). On the methanol permeability through pristine Nafion® and /PVA membranes measured by different techniques. A comparison of methodologies. *Fuel Cells*, 11(6): 897-906.
47. Roy, T., Wanchoo, S. K. and Pal, K. (2020). Novel sulfonated poly (ether ether ketone)/rGNOR@TiO_2 nanohybrid membrane for proton exchange membrane fuel cells. *Solid State Ionics*, 349: 115296.

Malaysian Journal of Analytical Sciences (MJAS)
Published by Malaysian Analytical Sciences Society

PHYSICAL AND ELECTROCHEMICAL CHARACTERISTICS OF $LiCo_{0.6}Sr_{0.4}O_2$ CATHODE INK FOR INTERMEDIATE-LOW TEMPERATURE SOLID OXIDE FUEL CELL

(Pencirian Fizikal dan Elektrokimia Terhadap Dakwat Katod $LiCo_{0.6}Sr_{0.4}O_2$ bagi Sel Fuel Oksida Pepejal Bersuhu Sederhana Rendah)

Nur Nadhihah Mohd Tahir[1], Nurul Akidah Baharuddin[1]*, Wan Nor Anasuhah Wan Yusoff[1], Azreen Junaida Abd Aziz[1], Mahendra Rao Somalu[1], Andanastuti Muchtar[1,2]

[1]*Fuel Cell Institute*
[2]*Department of Mechanical and Manufacturing Engineering, Faculty of Engineering and Built Environment Universiti Kebangsaan Malaysia, 43600 UKM Bangi, Selangor, Malaysia*

**Corresponding author: akidah@ukm.edu.my*

Received: 30 November 2021; Accepted: 27 February 2022; Published: 27 June 2022

Abstract

Solid oxide fuel cell (SOFC) is a technology used to generate electricity with less emission. Selection of a suitable, compatible cathode material that will be used with the ionic and protonic electrolyte is crucial in achieving an excellent performance of intermediate-low temperature SOFC. $LiCo_{0.6}Sr_{0.4}O_2$ (LCSO) is stoichiometrically prepared via glycine nitrate combustion followed by ball milling and triple roll mill (TRM) machine to produce a homogeneous LCSO cathode ink. The prepared sample powder of LCSO is initially characterised by X-ray diffraction (XRD) and scanning electron microscope (SEM) fitted with energy-dispersive X-ray spectroscopy. The XRD demonstrated that the prepared LCSO powder calcined at 800 °C shows a phase structure of rhombic lattice and space group of R-3m. The prepared ink is then layered on both sides of the samarium-doped-ceria (SDC) electrolyte to produce LCSO | SDC | LCSO symmetrical cell. The prepared ink has varied gap sizes on the TRM machine. The electrochemical performance of electrochemical impedance spectroscopy reports that the best gap size is at 40 µm with the lowest polarisation resistance (R_p), of 8.32 Ω. In conclusion, this work confirms the importance of a high-quality lithium-based cathode ink in SOFC applications.

Keywords: solid oxide fuel cell, cathode, ink, lithium, triple roll mill

Abstrak

Sel fuel oksida pepejal (SOFC) boleh dikategorikan sebagai teknologi pembebasan karbon rendah dalam menjana tenaga elektik. Pemilihan bahan katod yang sesuai dan serasi untuk digunakan bersama dengan elektrolit ionik dan protonik adalah penting dalam mencapai prestasi SOFC bersuhu sederhana-rendah (IT-LT SOFC) yang baik. $LiCo_{0.6}Sr_{0.4}O_2$ (LCSO) telah disediakan mengikut stoikiometri menggunakan pembakaran glisin nitrat diikuti dengan pengisaran bebola dan pengisaran tiga penggelek untuk menghasilkan dakwat katod LCSO yang homogen. Serbuk sampel LCSO yang disediakan pada mulanya dicirikan menggunakan pembelauan sinar-X (XRD) dan mikroskop elektron pengimbasan (SEM) yang dipasang dengan spektroskopi sinar-X penyebaran tenaga (EDX). Hasil dapatan XRD menunjukkan kalsin serbuk katod LCSO yang disediakan pada 800 °C menunjukkan struktur

fasa kekisi Rhombo dan kumpulan ruang R-3m Dakwat yang disediakan kemudiannya disapukan pada kedua-dua belah elektrolit samarium terdop seria (SDC) untuk menghasilkan sel simetri LCSO | SDC | LCSO. Dakwat yang disediakan dipelbagaikan saiz celah mesin gulung tiga. Daripada prestasi elektrokimia spektroskopi impedans elektrokimia (EIS) melaporkan bahawa saiz celah terbaik adalah pada 40 µm dengan rintangan polarisasi terendah, R_p 8.32 Ω Kesimpulannya, kajian ini mengesahkan kepentingan dakwat katod berasaskan litium berkualiti tinggi dalam aplikasi SOFC.

Kata kunci: sel fuel oksida pepejal, katod, dakwat, litium, pengisar tiga penggelek

Introduction

Fuel cells are currently receiving great attention worldwide due to their claim of being the safest and cleanest technology [1]. A fuel cell can also be considered an efficient power generator due to lesser emission and a higher rate of energy conversion efficiency compared with conventional internal combustion engines. Lina et al. stated that a fuel cell is a clean power generator with less noise pollution [2]. Fuel cells have several types, and this work explains solid oxide fuel cell (SOFC) in detail. Nowadays, SOFC is well-known in the technological and industrial fields. The only identification that distinguishes SOFC from other types of fuel cells is that they operate at a high temperature, ranging from 400 °C to 1000 °C [3–5]. SOFC is an energy conversion device that can convert chemical energy derived from the fuel into electrical and thermal energy [6,7].

SOFC consists of three main components: anode, cathode and electrolyte. The anode and the cathode are known as an electrode–electrolyte layer that is sandwiched between the anode and cathode electrodes [8]. The schematic of the SOFC is shown in Figure 1.

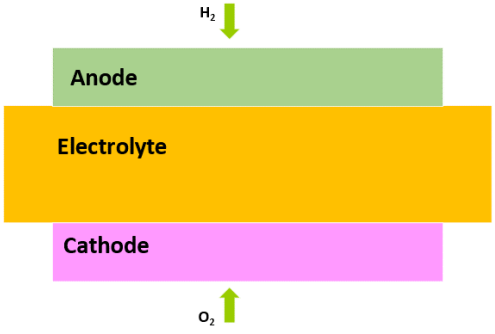


Figure 1. Schematic of SOFC

SOFC has a high energy efficiency when operating at a high temperature of 1000 °C [9, 10]. Studies show that SOFC can achieve an efficiency of 60%–65%. On the one hand, SOFC has been declared as the most promising power generation technology due to its variety of advantages. On the other hand, the high operating temperature which causes material degradation and an increase in manufacturing cost, also results in poor durability of SOFC and limits its application [11]. Accordingly, selection of an intermediate-low temperature is crucial to overcome these arising issues on high operating temperature. The temperature range of intermediate-low temperature is 400 °C–700 °C [12]. The operating cost of this device will be reduced by lowering its temperature, thereby enhancing its commercialisation. SOFC has two types of environments: oxide-conducting SOFC (O^{2-}-SOFC), which is the pioneer or conventional type, and proton-conducting SOFC (H^+-SOFC). Figure 2 (a) and (b) show the O^{2-}SOFC and H^+-SOFC, respectively.

Currently, the focus of SOFC development is on intermediate-low temperature SOFC (IT-LT SOFC). However, the high operating temperature of SOFC causes cell degradation issues. To overcome this problem, the operating temperature of SOFC should be reduced to 400-800 ℃. Existing materials that have been traditionally operated at elevated temperatures have poor electrochemical performance under this intermediate-low temperature environment. Accordingly, selection of a suitable and compatible cathode material is crucial for IT-LT SOFCs. Lithiated-based materials are one of the strong candidates for the cathode component of IT-LT SOFCs. The lithiated-based cathode has been widely used in many applications, such as batteries, electrochemical capacitors and O_2 metal batteries [13–22]. The lithiated-based material in SOFC provides a free moving lithium-

ion (Li^+) cation pathway [23]. The lithium-based cathode can be categorised as a triple ($H^+/O^{2-}/e^-$) conducting cathode material, indicating that it can allow those three conducting elements to pass through the cathode boundary or cathode active site [24]. Liu et al. stated that lithium cobaltite, $LiCoO_2$ is one of the promising lithiated-based materials to be used in SOFC applications with triple conducting mechanism capabilities [25,26]. Wan Yusof [27] reported that $LiCoO_2$ or lithium-based material shows a reasonable perspective in intermediate to low temperature for proton- and oxide-conducting SOFC applications [28]. Moreover, strontium (Sr) is widely used as a cathode dopant for most cathode materials to achieve high electrocatalytic activity, especially at the oxygen reduction reaction (ORR) that occurs only in the cathode [29]. Jamil et al. adopted a broad perspective, in which the existence of an Li compound may uplift oxygen concentration, especially at the grain boundary, resulting in high ionic conductivity [30]. Li^+ promotes proton transfer, which makes Li-based cathode materials viable for proton-conducting IT-LT SOFC. Improving the performance of this material requires an in-depth study of the powder and ink preparation aspects. Meanwhile, numerous studies have been conducted on the powder synthesis-related parameters. As previously discussed, a huge gap was observed on the ink production-related parameters. Hence, this study aims to produce a high-quality lithiated-based cathode ink ($LiCo_{0.6}Sr_{0.4}O_2$) by altering the gap size of roller in triple-roll mills and to characterize the physical properties and electrochemical performance of the cathode inks for IT-LT SOFC application. The high-quality cathode ink will be produced with a triple roll mill machine, which has been proven to be the optimum method for ink production.

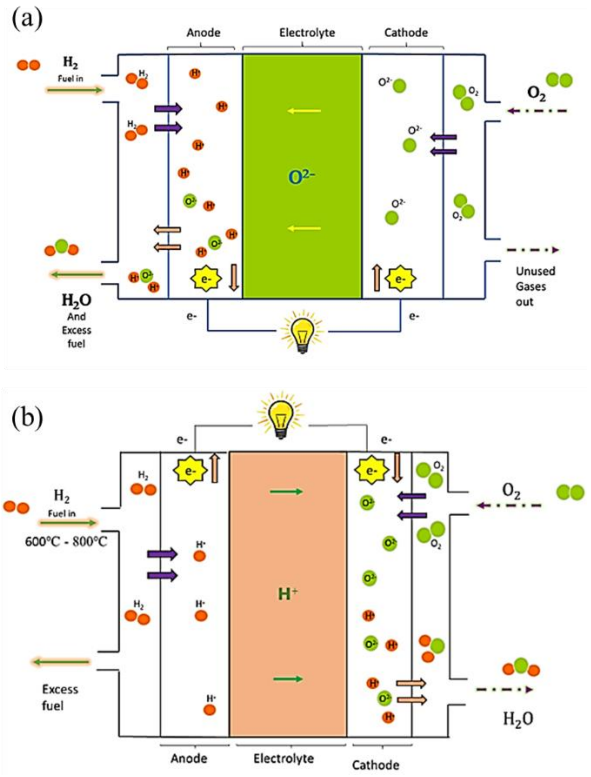


Figure 2. (a) O^{2-}SOFC and (b) H^+-SOFC

Materials and Methods

Preparation of cathode sample powder LiCoSrO

In this work, $LiCo_{0.6}Sr_{0.4}O_2$ precursor powders were produced through the glycine nitrate combustion method. The precursor materials were Lithium Nitrate ReagentPLus, $LiNO_3$ (Sigma Aldrich, Germany), Strontium Nitrate (ACS Reagent, >99%) $Sr(NO_3)_2$ (Sigma Aldrich, Germany) and Cobalt (II) Nitrate Hexahydrate Reagent Grade, 98%, $Co(NO_3)_2.6H_2O$ (Merck Chemicals, Germany). A stoichiometric amount of the precursor materials was dissolved in 100 mL deionised water and stirred for 40 min on a hotplate with a magnetic stirrer at room temperature. Afterwards, a calculated amount of glycine (Sigma–Aldrich, Germany) was added to the precursor material solution as fuel. The mixture was continuously stirred on the hotplate at room temperature for 18 h. Subsequently, the solution was continuously stirred whilst the temperature of the hotplate was slowly increased to between 250 °C to 300 °C to achieve the combustion of the materials and all the nitrates. Thereafter, the obtained black ash precursor powder was further dried at 120 °C for 12 h in

a drying oven. The raw powder was then ground using a mortar agate to obtain a fine, smooth powder. Finally, the dried fine precursor powder was calcined at 800 ℃ in a high-temperature furnace (Berkeley Scientific, USA) for 5 h holding time. The TGA graph of the previous study [27] on the same material shows that LCSO materials were decomposed at temperatures ranging from 700 – 1000 ℃. After the LCSO powder was calcined, it was subjected to X-ray diffraction (XRD) testing and scanning electron microscope (SEM) analysis for LCSO its characterisation.

Material characterisation

Wan Yusoff et al. [27] investigated the thermal decomposition behaviour of the LCSO powder in 2020, via thermogravimetric analysis/differential scanning calorimetry (TGA/DSC, SING Mettler Toledo, United States) to determine the optimal calcination temperature. The analysis was conducted on the LCSO precursor powder synthesised from room temperature to 1000 °C at a heating rate of 10 °C/min^{-1} under air with a flow rate of 50 mL/min^{-1}. Then, the precursor LCSO powder was further analysed via XRD (Bruker AXS D8 Advance, Germany) with a CuKα (λ = 0.15406 nm) radiation source to confirm its phase and structure. An X-ray diffractometer was operated at 40 kV and 40 mA, and fitted with a 1-D fast detector (Lynx-Eye). The XRD spectrum was recorded for 2θ ranging from 20° to 70° with a step size of 0.025°. The morphology of the LCSO particles was examined via SEM (Carl Zeiss EVO MA10, Germany). From the material characterisation, the optimal calcination temperature was selected to produce another batch of LCSO cathode powder, which was used to synthesise the LCSO cathode ink.

Ink preparation

The cathode ink was produced using several methods and techniques that have been utilized by other researchers. The common methods used for synthesizing the ink are triple roll mill (TRM) machine, ball milling and manual mixing (hands-on). The methods used by other researchers are summarised in Table 1.

Table 1. Summary of methods used to produce ink

Method	Element	Performance	Reference
Ball Milling	Iron and nitrogen dope carbide-derived carbon (SiCDC)	The grain size decreases from 1 μ to 200 nm.	Ratso et al. 2021[31]
	Multiwalled carbon nanotubes/epoxy suspensions	A better-quality texture of the material is produced.	Olowojoba et al. [32]
TRM Machine	Soda lime glass	Fast response and process can be broken down into phases. The particle size breakage yields a good result.	Böttcher et al. [33]
	$La_{0.6}Sr_{0.4}CoO_{3-\delta}$ (LSC)	High porosity and good electrochemical performance are achieved with a TRM machine.	Samat et al. [10]
Manual Mixing	$La_{0.6}Sr_{0.4}CoO_{3-\delta}$ (LSC)	The porosity is lower, and the value of ASR is higher compared with other methods.	Samat et al. [34]

Table 1 shows that using the TRM machine as the medium in synthesising the cathode is the best option because if the better quality and outstanding electrochemical performance. Several parameters in the ink production process are maintained variable during the research. Determining and varying the parameters is crucial to producing a high-quality cathode ink. Table 2 shows the parameters considered and previously studied. The parameters studied by the researchers include roller speed, frequency of rotation, roller gap size, ink thickness, feed rate and breakage behaviour.

Table 2. Parameter study related to the TRM machine

Parameter study related to the TRM	Reference
Roller gap size	Wan Yusoff et al. [27]
Roller speed and rotation frequency	Olowojoba et al. [32]
Roller speed, roller gap size, feed rate and breakage behaviour	Böttcher et al. [33]
Ink thickness	Samat et al. [34]
Roller speed and roller gap size	Somalu et al. [35]

TRM is essential in the production of homogenous screen-printing inks because it breaks down most particle agglomerates during milling. The difference in roller speeds produces shear stress between the rollers, which pull agglomerates apart when the material passes between the gaps. The working principle of the TRM machine is shown in Figure 3. The resulting shear rates between the gaps are provided in the following equation:

$$\text{Shear rate} = \frac{\Delta v}{x}, \quad (1)$$

Δv: speed difference, and x: gap between rollers.

The LCSO ink was prepared with EXAKT 50 I, Germany TRM machine in the SOFC Laboratory at Institute Fuel Cell UKM. The produced LCSO powder was ball-milled for 24 h with a 10-rpm rotating rate. The ink was prepared by using the right composition to produce a good-quality cathode ink. The ink composition is tabulated in Table 3. The postball milled LCSO powder was mixed with a vehicle buffer solution, dispersant and solvent. The premixed ink was manually ground before producing a smooth, fine ink with the TRM machine. Then, all the premixed ink was mixed well. The LCSO with various ink parameters were formed, and the parameters produced throughout this work are listed in Table 4.

Table 3. LCSO ink composition

Solid Content	Weigh (wt.%)
LCSO powder (ball milled)	67.33
Solvent (Terpineol)	29.98
Binder (Ethylcelulose N7 grade (0.25%–0.5 wt.%)	1.35
Dispersant (Hypermer KD15)	1.35

Table 4. LCSO ink parameter

Variable Parameter	Gap Size (μm)
1	g_1- 10
2	g_2- 20
3	g_3- 30
4	g_4- 40
5	g_5- 50

Fabrication of symmetrical cell LCSO|SDC|LCSO

The fabrication of symmetrical cell started with the production of an electrolyte pellet of $Sm_{0.2}Ce_{0.8}O_{1.9}$ (SDC). Then, the prepared LCSO cathode ink was layered on both sides of the electrolyte pellet. Prior to the half and symmetrical cell production for electrical conductivity and electrochemical impedance spectroscopy (EIS) analysis, the SDC powders (Sigma–Aldrich) were pressed into a coin-shaped structure to form an electrolyte substrate at 52 MPa. The SDC electrolyte was sintered at 1400 °C for 6 h. Then, the as-prepared cathode inks were screen printed two layers on one side (half-cell) and both sides (symmetrical cell) of the electrolyte surface with an active area, A, of 1 cm^2 prior to sintering at 800 °C for 2 h. The prepared symmetrical cell LCSO|SDC|LCSO is shown in Figure 3.

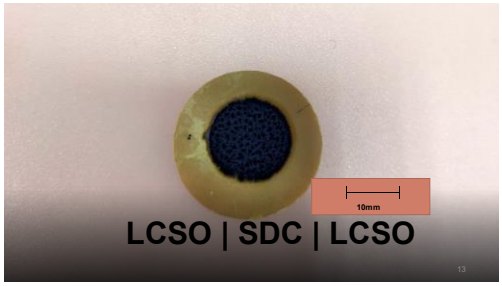


Figure 3. Prepared symmetrical cell LCSO|SDC|LCSO

Electrochemical analysis of the LCSO|SDC|LCSO symmetrical cell

The electrochemical performance was measured using EIS with a potentiostat (PGSTAT302 N, Metrohm Autolab, Netherlands) operating at 106–0.1 Hz with a sinusoidal voltage amplitude of 10 mV. Symmetrical cells were evaluated in the air at 500 °C–800 °C under typical IT-SOFC operating conditions, with a constant air flow rate of 0.2 $Lmin^{-1}$. EIS was performed on all symmetrical cells with a constant active area of 1 cm^2, and the data were processed with NOVA software (version 1.10) to determine the ASR values of the LCSO cathode.

Results and Discussion

Properties of prepared powder

The XRD spectrum of the as-synthesised powder cathode calcined at 800 °C and 900 °C for 5 h is shown in Figure 4. The data base cannot provide the full spectrum of LiCoSrO because this material is new. Accordingly, the XRD was compared with $LiCoO_2$ and $SrCO_3$. The calcined LCSO powders exhibited merely a single phase, as confirmed by the XRD measurement. The plotted results showed a peak almost similar to the reference $LiCoO_2$ with $SrCO_3$. All the prominent peaks in the XRD spectrum of the calcined powder were matched with the reference code PDF 00-050-0653 lithium cobalt oxide ($LiCoO_2$) of rhombic lattice structure and space group of R-3m and PDF 01-084-1778 strontium carbonate ($SrCO_3$) of orthorhombic lattice structure with space group of R-3m. Thus, the highest peaks were indexed to their Miller indices (hkl) of (111) and (104) for $LiCoO_2$ and $SrCO_3$, respectively.

The morphological analysis was conducted on the LCSO powders calcined at temperatures of 800 °C and 900 °C by SEM and EDX. The results for both microstructures are illustrated in Figures 5 and 6. The results show that the microgram has a random fragment structure, whereas EDX confirms that all the components of LCSO are in the cathode powders. The EDX graph in Figure 6 clearly shows that all the components of Li, cobalt (Co), strontium (Sr) and oxide (O_2) are present in the LCSO powder for both temperatures of calcined LCSO. However, the LCSO precursor powder calcined at a temperature of 800 °C shows less impurities than that calcined at 900 °C.

After analysing the calcined powder and producing a high-quality ink, the best composition was considered. Based on the LCSO ink composition in Table 3, the smooth, fine-texture ink was successfully produced using the in-house TRM machine. The produced LCSO cathode ink is shown in Figure 7.

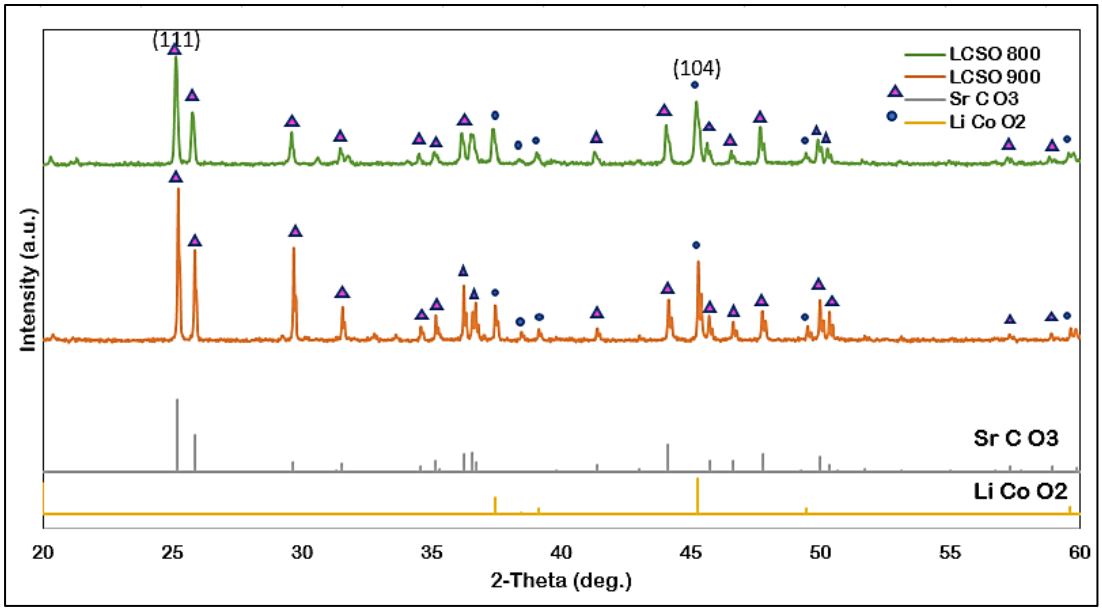


Figure 4. XRD spectrum obtained by this research

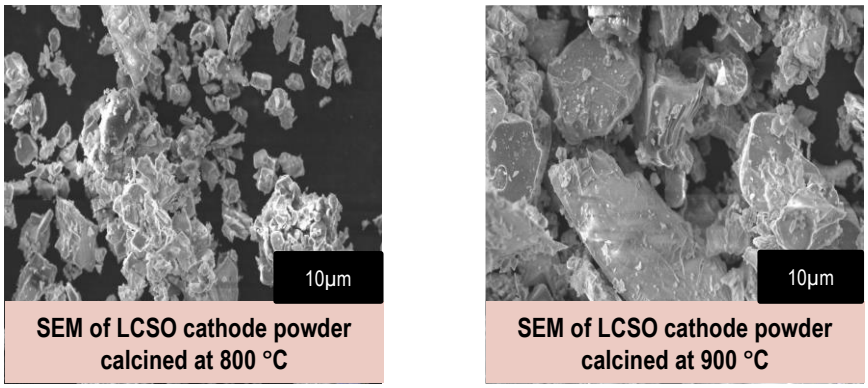


Figure 5. SEM of the LCSO powder calcined at temperatures of 800 °C and 900 °C

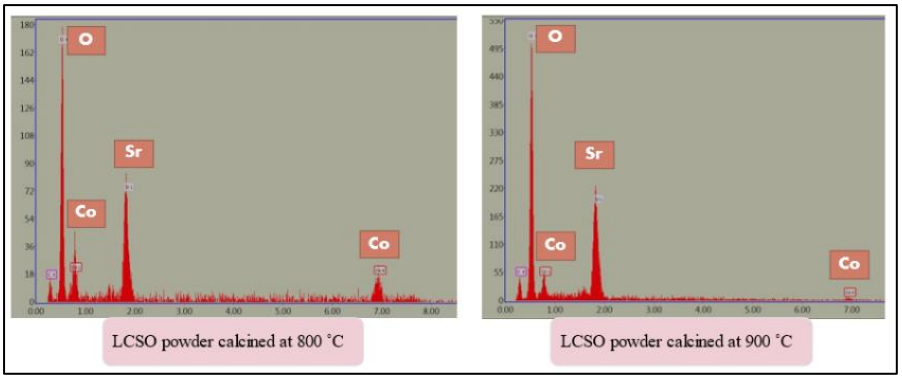


Figure 6. EDX analysis of the calcined LCSO powder

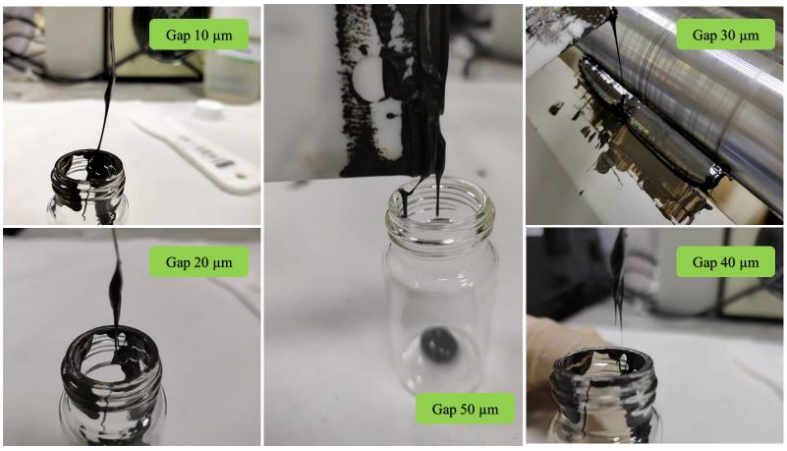
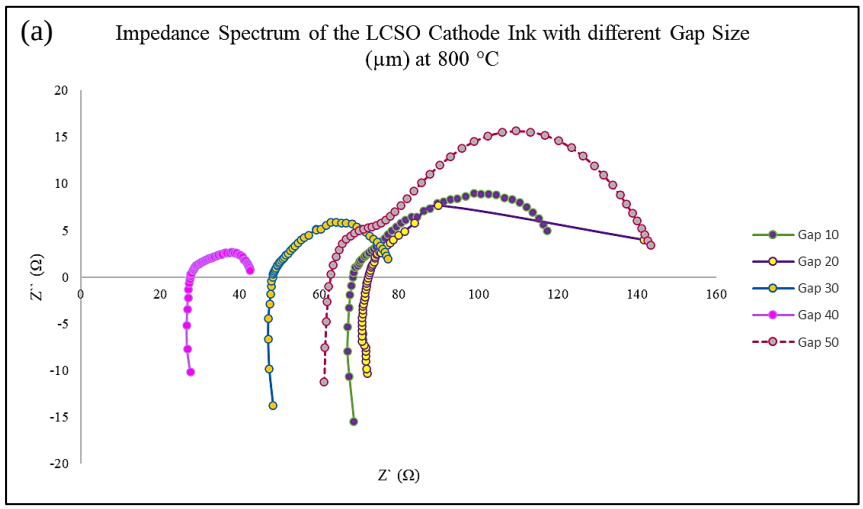


Figure 7. Produced LCSO cathode ink

Electrochemical performance analysis

Figure 8 shows the electrochemical impedance spectrum of the LCSO|SDC|LCSO symmetrical cells with different cathode ink parameters of the gap size of the TRM. The spectra are fitted via electrical circuit fitting composed of resistance (R) and constant phase element (CPE). Resistances and constant phase elements are illustrated by R_S, R_1, R_2, CPE_1 and CPE_2 for high- and low-frequency arcs. The impedance arc was analysed using an electric equivalent circuit, as shown in Figure 8(b). All the measured and calculated values of polarisation resistance and area specific resistance (ASR) at 800 °C of each symmetrical cell with different gap size are listed in Table 5. The impedance spectra in Figure 8(a) show that gap size of 40 µm is the lowest amongst the other gap sizes, and this is proven by the measured and calculated polarisation resistance, R_p, value in Table 5 that shows the gap sizes of 10, 20, 30, 40 and 50 µm of 32.35, 39.63, 17.07, 8.32 and 43.36 Ω, respectively. The LCSO cathode ink produced with the TRM shows that the best gap size is 40 µm with proven electrochemical performance of 8.32 Ω.



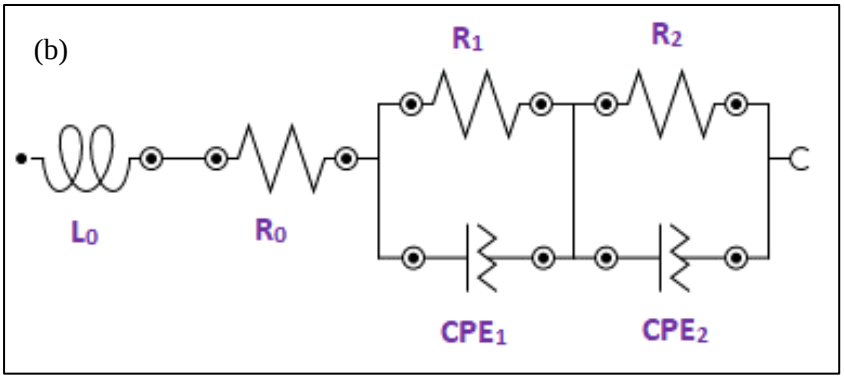


Figure 8. (a) Impedance spectra of the different gap sizes; (b) adopted an electrical equivalent circuit to analyse the impedance data

Table 5. Values of the polarisation resistance and ASR of LCSO|SDC|LCSO symmetrical cells of different gap sizes of the ink produced

Gap Size (μm)	Polarisation Resistance, Rp (Ω)	ASR at 800 °C (Ω cm^2)
10	32.35	16.175
20	39.63	19.815
30	17.07	8.535
40	8.32	4.160
50	43.36	21.680

Conclusion

The LCSO cathode ink is synthesised via glycine nitrate combustion. Subsequently, the cathode ink was produced using the TRM machine method, and the gap size of the TRM varied at 10, 20, 30, 40 and 50 μm. Amongst the different gap sizes, the best gap size is 40 μm with proven electrochemical performance of EIS with polarisation resistance, R_p value of 8.32 Ω and ASR of 4.160 Ωcm^2. This work benchmarks the attempt of a compatibility of an Li-based cathode ink in the application of IT-LT SOFCs. Moreover, this work is involved in and will compete in the production of a durable SOFC system to enhance its viability in actual applications. In the future, the production of the LCSO cathode ink under various IT-LT SOFC environments, such as proton conducting SOFC (H^+-SOFC) and oxide conducting SOFC (O^{2-}SOFC) will be conducted to find the optimal environment for LCSO cathode ink to work for.

Acknowledgement

The authors gratefully acknowledge the financial support provided by the Ministry of Higher Education, Malaysia and the funding support via the research sponsorship under Fundamental Research Grant Scheme grant number FRGS/1/2019/TK07/UKM/02/1 and Universiti Kebangsaan Malaysia through Research Grant DIP-2010-011.

References

1. Ali, S. M., Anwar, M., Abdalla, A. M., Somalu, M. R. and Muchtar, A. (2017). Ce0.80Sm0.10Ba0.05Er0. 05O2-δ multi-doped ceria electrolyte for intermediate temperature solid oxide fuel cells. *Ceramics International,* 43(1): 1265-1271.

2. Rashid, N. L. R. M., Samat, A. A., Jais, A. A., Somalu, M. R., Muchtar, A., Baharuddin, N. A. and Isahak, W. N. R. W. (2019). Review on zirconate-cerate-based electrolytes for proton-conducting solid oxide fuel cell. *Ceramics International,* 45(6): 6605-6615.
3. Baharuddin, N. A., Abdul Rahman, N. F., Abd. Rahman, H., Somalu, M. R., Azmi, M. A. and Raharjo, J. (2020). Fabrication of high-quality electrode films for solid oxide fuel cell by screen printing: a review on important processing parameters. *International Journal of Energy Research,* 44(11): 8296-8313.
4. Abd Aziz, A. J., Baharuddin, N. A., Somalu, M. R. and Muchtar, A. (2020). Review of composite cathodes for intermediate-temperature solid oxide fuel cell applications. *Ceramics International,* 46(15): 23314-23325.
5. Tahir, N. N. M., Baharuddin, N. A., Samat, A. A., Osman, N. and Somalu, M. R. (2022). A review on cathode materials for conventional and proton-conducting solid oxide fuel cells. *Journal of Alloys and Compounds,* 894: 162458.
6. Kim, M., Kim, D. H., Han, G. D., Choi, H. J., Choi, H. R. and Shim, J. H. (2020). Lanthanum strontium cobaltite-infiltrated lanthanum strontium cobalt ferrite cathodes fabricated by inkjet printing for high-performance solid oxide fuel cells. *Journal of Alloys and Compounds,* 843: 155806.
7. Rainwater, B. H., Liu, M. and Liu, M. (2012). A more efficient anode microstructure for SOFCs based on proton conductors. *International Journal of Hydrogen Energy,* 37(23): 18342-18348.
8. Dwivedi, S. (2020). Solid oxide fuel cell: Materials for anode, cathode and electrolyte. *International Journal of Hydrogen Energy,* 45(44): 23988-24013.
9. Rosli, A. Z., Somalu, M. R., Osman, N. and Hamid, N. A. (2021). Physical characterization of LSCF-NiO as cathode material for intermediate temperature solid oxide fuel cell (IT-SOFCs). *Materials Today: Proceedings,* 46:1895-1900.
10. Samat, A. A., Somalu, M. R., Muchtar, A. and Osman, N. (2019, June). Electrochemical performance of La0. 6Sr0. 4CoO3-δ cathode in air and wet air for BaCe0.54Zr0.36Y0.1O3-based proton-conducting solid oxide fuel cell. *In IOP Conference Series: Earth and Environmental Science*, 268(1): 012136.
11. Lv, H., Jin, Z., Peng, R., Liu, W. and Gong, Z. (2019). BaCoxFe0. 7-xZr0. 3O3-δ (0.2≤ x≤ 0.5) as cathode materials for proton-based SOFCs. *Ceramics International*, 45(18): 23948-23953.
12. Huan, D., Shi, N., Xie, Y., Li, X., Wang, W., Xue, S., ... and Lu, Y. (2020). Cathode materials for proton-conducting solid oxide fuel cells. *Intermediate Temperature Solid Oxide Fuel Cells*: pp. 263-314.
13. Le, S., Zhu, S., Zhu, X. and Sun, K. (2013). Densification of Sm0. 2Ce0.8O1.9 with the addition of lithium oxide as sintering aid. *Journal of Power Sources,* 222: 367-372.
14. Yuan, L. X., Wang, Z. H., Zhang, W. X., Hu, X. L., Chen, J. T., Huang, Y. H. and Goodenough, J. B. (2011). Development and challenges of $LiFePO_4$ cathode material for lithium-ion batteries. *Energy & Environmental Science,* 4(2): 269-284.
15. Hofmann, T., Westhoff, D., Feinauer, J., Andrä, H., Zausch, J., Schmidt, V. and Mueller, R. (2020). Electro-chemo-mechanical simulation for lithium ion batteries across the scales. *International Journal of Solids and Structures,* 184: 24-39.
16. Janowitz, K., Kah, M. and Wendt, H. (1999). Molten carbonate fuel cell research: Part I. Comparing cathodic oxygen reduction in lithium/potassium and lithium/sodium carbonate melts. *Electrochimica Acta,* 45(7): 1025-1037.
17. Accardo, G., Kim, G. S., Ham, H. C. and Yoon, S. P. (2019). Optimized lithium-doped ceramic electrolytes and their use in fabrication of an electrolyte-supported solid oxide fuel cell. *International Journal of Hydrogen Energy,* 44(23): 12138-12150.
18. Preethi, S., Abhiroop, M. and Babu, K. S. (2019). Low temperature densification by lithium co-doping and its effect on ionic conductivity of samarium doped ceria electrolyte. *Ceramics International,* 45(5): 5819-5828.

19. Kanthachan, J., Khamman, O., Intatha, U. and Eitssayeam, S. (2021). Effect of reducing calcination processing on structural and electrochemical properties of LiNi0.5Mn0.3Co0.2O2 cathode materials for lithium battery. *Materials Today: Proceedings,* 47: 3600-3603.
20. Hu, X., Qiang, W. and Huang, B. (2017). Surface layer design of cathode materials based on mechanical stability towards long cycle life for lithium secondary batteries. *Energy Storage Materials,* 8: 141-146.
21. Peng, Y., Tan, R., Ma, J., Li, Q., Wang, T. and Duan, X. (2019). Electrospun $Li_3V_2(PO_4)_3$ nanocubes/carbon nanofibers as free-standing cathodes for high-performance lithium-ion batteries. *Journal of Materials Chemistry A*, 7(24): 14681-14688.
22. Yan, R., Oschatz, M. and Wu, F. (2020). Towards stable lithium-sulfur battery cathodes by combining physical and chemical confinement of polysulfides in core-shell structured nitrogen-doped carbons. *Carbon,* 161, 162-168.
23. Zhang, L., Lan, R., Kraft, A., Wang, M. and Tao, S. (2010). Cost-effective solid oxide fuel cell prepared by single step co-press-firing process with lithiated NiO cathode. *Electrochemistry Communications,* 12(11): 1589-1592.
24. Hussain, S. and Yangping, L. (2020). Review of solid oxide fuel cell materials: Cathode, anode, and electrolyte. *Energy Transitions*, 4(2): 113-126.
25. Hou, J., Miao, L., Hui, J., Bi, L., Liu, W. and Irvine, J. T. (2018). A novel in situ diffusion strategy to fabricate high performance cathodes for low temperature proton-conducting solid oxide fuel cells. *Journal of Materials Chemistry A,* 6(22): 10411-10420.
26. Yuan, K., Yu, Y., Wu, Y., Ji, X., Xu, Z. and Shen, J. (2018). Plasma sprayed coatings for low-temperature SOFC and high temperature effects on Lix (Ni, Co) yO_2 catalyst layers. *International Journal of Hydrogen Energy,* 43(28): 12782-12788.
27. Wan Yusoff, W. N. A., Somalu, M. R., Baharuddin, N. A., Muchtar, A. and Wei, L. J. (2020). Enhanced performance of lithiated cathode materials of $LiCo0.6X0.4O_2$ (X= Mn, Sr, Zn) for proton-conducting solid oxide fuel cell applications. *International Journal of Energy Research,* 44(14): 11783-11793.
28. Yusoff, W. N. A. W., Norman, N. W., Samat, A. A., Somalu, M. R., Muchtar, A. and Baharuddin, N. A. (2019). Performance of $LiCo0.6Zn0.4O_2$ as a potential cathode material candidate for intermediate solid oxide fuel cell application. *In IOP Conference Series: Earth and Environmental Science*, 268(1): 012139.
29. Zhang, Y., Yang, G., Chen, G., Ran, R., Zhou, W. and Shao, Z. (2016). Evaluation of the CO_2 poisoning effect on a highly active cathode SrSc0.175Nb0.025Co0.8O3-δ in the oxygen reduction reaction. *ACS Applied Materials & Interfaces,* 8(5): 3003-3011.
30. Jamil, S. M., Othman, M. H. D., Rahman, M. A., Jaafar, J., Mohamed, M. A., Yusop, M. Z. M., ... and Tanemura, M. (2017). Dual-layer hollow fiber MT-SOFC using lithium doped CGO electrolyte fabricated via phase-inversion technique. *Solid State Ionics,* 304: 113-125.
31. Ratso, S., Zitolo, A., Käärik, M., Merisalu, M., Kikas, A., Kisand, V., ... and Tammeveski, K. (2021). Non-precious metal cathodes for anion exchange membrane fuel cells from ball-milled iron and nitrogen doped carbide-derived carbons. *Renewable Energy,* 167: 800-810.
32. Olowojoba, G., Sathyanarayana, S., Caglar, B., Kiss-Pataki, B., Mikonsaari, I., Hübner, C. and Elsner, P. (2013). Influence of process parameters on the morphology, rheological and dielectric properties of three-roll-milled multiwalled carbon nanotube/epoxy suspensions. *Polymer,* 54(1): 188-198.
33. Böttcher, A. C., Thon, C., Fragnière, G., Chagas, A., Schilde, C. and Kwade, A. (2021). Rigidly-mounted roll mill as breakage tester for characterizing fine particle breakage. *Powder Technology,* 383: 554-563.

34. Abdul, S. A., Yusoff, W. N. A. W., Baharuddin, N. A., Somalu, M. R., Muchtar, A. and Osman, N. (2018). Electrochemical performance of sol-gel derived La0.6S0.4CoO3-δ cathode material for proton-conducting fuel cell: A comparison between simple and advanced cell fabrication techniques. P*rocessing and Application of Ceramics,* 12(3): 277-286.
35. Somalu, M. R., Muchtar, A., Daud, W. R. W. and Brandon, N. P. (2017). Screen-printing inks for the fabrication of solid oxide fuel cell films: a review. *Renewable and Sustainable Energy Reviews,* 75: 426-439.
36. Sun, G., Yu, F. D., Zhao, C., Yu, R., Farnum, S., Shao, G., ... and Wang, Z. B. (2021). Decoupling the voltage hysteresis of Li-rich cathodes: electrochemical monitoring, modulation anionic redox chemistry and theoretical verifying. *Advanced Functional Materials,* 31(1): 2002643.

Malaysian Journal of Analytical Sciences (MJAS)
Published by Malaysian Analytical Sciences Society

CHEMICAL OXYGEN DEMAND AND TURBIDITY REMOVAL OF LANDFILL LEACHATE USING ELECTROCOAGULATION TECHNIQUE WITH Al ELECTRODE

(Penyingkiran Permintaan Oksigen Kimia dan Kekeruhan daripada Larut Resap Tapak Pelupusan dengan Menggunakan Elektrod Al)

Norilhamiah Yahya[1]*, M. Firdaus Mamat[1], Suhaini Mamat[1], Nabila A. Karim[2]

[1]Malaysian Institute of Chemical and Bioengineering Technology,
Universiti Kuala Lumpur, 78000 Alor Gajah, Malacca, Malaysia
[2]Fuel Cell Institute,
Universiti Kebangsaan Malaysia, 43600 Bangi, Malaysia

**Corresponding author: norilhamiah@unikl.edu.my*

Received: 2 December 2021; Accepted: 6 March 2022; Published: 27 June 2022

Abstract

The electrocoagulation process is classified as green technology to treat landfill leachates. A 16 full factorial experimental design evaluated and optimized the electrocoagulation method and compromised efficiency and operational costs. This study assessed three factors: operation time, voltage, and electrode size, to determine the most influencing parameters and describe the interaction between chemical oxygen demand (COD) and turbidity removal. Statistical analysis results using a half-normal plot demonstrated that all main factors significantly affected the removal efficiency of COD and turbidity. The Pareto chart reveals that the order of significance for COD and turbidity removal efficiency was voltage > operation time > electrode size> interaction between voltage and electrode. The best regression coefficients (R^2) were obtained for COD and turbidity, which reached 0.9597 and 0.9908, respectively, confirming that the predicted values complied with the experimental values. This implied the appropriateness of the employed regression model. The optimization process results showed that for maximizing the removal efficiency of COD and turbidity, the optimal level of operation time was 30 min, voltage 30 V and electrode 10 cm2 by using a batch reactor.

Keywords: electrocoagulation, landfill leachate, chemical oxygen demand, turbidity

Abstrak

Proses elektrokoagulasi diklasifikasikan sebagai teknologi hijau untuk merawat tapak pelupusan larut lesap. Reka bentuk eksperimen 16 faktorial penuh telah digunakan untuk menilai dan mengoptimumkan kaedah elektrokoagulasi dan untuk mencapai kompromi antara kecekapan dan kos operasi. Kajian ini menilai tiga faktor: masa operasi, voltan dan saiz elektrod untuk menentukan parameter yang paling mempengaruhi dan menerangkan interaksi antara parameter untuk permintaan oksigen kimia (COD) dan penyingkiran kekeruhan. Keputusan analisis statistik menggunakan plot separa normal menunjukkan bahawa semua faktor utama mempunyai kesan yang ketara ke atas kecekapan penyingkiran COD dan kekeruhan. Carta Pareto mendedahkan, untuk COD dan kecekapan penyingkiran kekeruhan, urutan kepentingan ialah voltan > masa operasi > saiz elektrod > interaksi antara voltan dan saiz elektrod.. Pekali regresi terbaik (R^2) diperoleh untuk COD dan kekeruhan mencapai nilai masing-masing

0.9597 dan 0.9908 mengesahkan bahawa nilai yang diramalkan adalah mematuhi nilai eksperimen yang membayangkan kesesuaian model regresi yang digunakan. Hasil proses pengoptimuman menunjukkan bahawa untuk memaksimumkan kecekapan penyingkiran COD dan kekeruhan, tahap masa operasi yang optimum adalah 30 minit, voltan 30 V dan elektrod 10 cm^2 dengan menggunakan reaktor batch.

Kata kunci: elektrokoagulasi, larut lesap tapak pelupusan, permintaan oksigen kimia, kekeruhan

Introduction

Malaysia produces about 42,672 metric tons of solid waste every day, and the value may be increased every year due to urbanization, increase in population, and per capita waste generation [1]. Generally, organic wastes constitute 40 – 60 % of the overall weight in most developing countries. Despite several advantages of landfilling, the resulting heavily polluted leachate has caused an urgent concern because landfilling is a widely used method for solid waste disposal. Various factors influence leachate quality and quantity, such as landfilling technique, seasonal weather variation, waste type and composition, and landfill structure [2]. Therefore, environmental specialists are determined to develop effective treatments for vast quantities of heavily polluted leachates.

The EC process is a process to form floc with the help of oxidized metal in wastewater, whereby it needs to be cleaned by the electro-dissolution anode [3]. EG can also be defined as a process of removing the suspended solids from wastewater by using electricity to neutralize the harmful particles through hydroxide complexes formation in water to gather the suspended solid, help bridge, bind, and strengthen floc sedimentation due to gravity force. This process collects the suspended solids in water without coagulants, and then coagulation occurs when a direct current is applied, thus capable of removing small particles and setting them into motion. Several factors that influence the EC process's efficiency are electrode types, the gap between electrodes, electrode size, the configuration of metals, current density, charge loading, pH value of the sample, the addition of supporting electrolyte, and operation time. The electrodes that are usually used are iron, aluminum, and stainless steel. This metal sheet pair is anode and cathode [4].

Nowadays, most treatment methods widely used worldwide to treat wastewater are physical-chemical and biological processes, but the treatment of leachates by using these methods is complex due to low biodegradability and high toxicity. The biological process is a method that uses natural methods that depend on microorganisms, nematodes, and tiny creatures. At the same time, physical-chemical processes require added synthetic substances [5]. For example, Castillo-Suárez [6] used peroxicoaguation and solar peroxicoagulation in a batch electrolytic reactor in the presence of solar ultraviolet light and studied three main parameters to treat the leachates, which are pH value, current density, and treatment time. The use of these three parameters gives the optimal value of biochemical oxygen and COD removed at 55.5% and 62.3%, respectively. Jang et. al [7] studied the effect of adding lithium manganese oxide and activated carbon electrodes in the electrochemical sorption of the lithium-ion battery leachate. The authors found that increased capacity, selectivity, and purity depended on the reaction time and applied current. The same parameters; time, and current density, were also studied by Galvão [8] in the EC process treatment. Five responses were recorded: ultraviolet absorbance, biological oxygen demand, COD, turbidity, and color, while the percentage values of removal when applied with 128 Am^{-2} for 90 min were 40%, 90%, 40%, 82%, and 82%, respectively. The removal efficiency was increased to a maximum by increasing the electrolysis time, leading to a constant rate. The number of generated metal hydroxides increased with the electrolysis time.

In this regard, a group of researchers used the EC process to remove cefazolin and COD from hospital wastewater [9]. The tests were performed in three specific voltages (15V, 30 V, 50 V) and periods (10 min, 30 min, 50 min). The result showed that the maximum

efficiency of contamination removal in 50 min was more than 92%. Chairunnisak et al. [10] reported that the electrocoagulation method resulted in the optimum COD reduction of 94.53% from operating time of 39.28 min, 20 V, and without electrolyte concentration. A study conducted by Amarine et al. [11] showed that the removal efficiency depended on the electrodes' applied voltage and immersed surface. This removal efficiency was 94.41% after 150 min, the electrical voltage of 30 V, and the immersed surface of 33.75 cm^2. Another research by Bajpai et al. [12] found that an optimum condition (14 V and 47 min) at a pH value of 7.35, which provided experimental removal efficiency (75.6% COD, 78.7% total dissolved solids, 93.4% turbidity, and 63.2% chloride).

There is in situ generation of coagulants by the dissolution of sacrificial anodes due to direct current flow. Different studies have proven that the aluminum electrode was the most effective and successful. Therefore, aluminum was used as the electrode material in this study. The anode produces metal cations after its oxidation process by applying direct current; this cation involves further reactions and produces different polymeric hydroxides of metal, similar to salts used in conventional coagulation.

The reactions when using aluminum electrodes can be summarized as follows;

.

Anode reactions:

$$Al(s) \rightarrow Al^{3+}_{(aq)} + 3e \quad (1)$$

$$Al^{3+}_{(aq)} + 3OH^- \rightarrow Al(OH)_3 \quad (2)$$

Alkaline reactions:

$$Al^{3+}_{aq} + 3H_2O \rightarrow Al(OH)_3 + 3H^+ \quad (3)$$

Acidic pH range

Cathode reactions leads to mainly hydrogen evolution:

$$3H_2O + 3e \leftrightarrow {}^3/_2\, H_2 \uparrow + OH^- \quad (4)$$

As seen in the above reactions, EC combines oxidation, flocculation and flotation. The EC occurs in three steps. In the first step, a coagulant is formed due to oxidation of the anode. In the second step, pollutants get destabilized, while in the last step, the destabilized matters get united and removed.

EC is an exceptional strategy for water and wastewater treatment. While the EC has been applied to different modern gushing, for example, nourishment businesses, tannery, mechanical shops (dissolvable oil), polymerization production, and wastewater material industry. Naje & Abbas [13] limited studies were carried out on the effective voltage, operation time and electrode side in the electrocoagulation process time in the COD and turbidity removal. Simple, affordable, and efficient leachate treatment systems are urgently needed in developing countries because most conventional technologies in industrialized nations are too expensive and complex. Rusdianasari et al. [14]. EC is a simple method to treat wastewater efficiently, and it seems to be a promising treatment method due to its high effectiveness, lower maintenance cost, less need for labor, and rapid achievement of results. In this study, statistical analysis via factorial design was used to investigate factors that influence the reduction of two primary contaminants in leachate, which were COD and turbidity.

Materials and Methods

Sample collection

A close landfill that was shut down for over five years was selected to collect the leachate samples. Even though the landfill was shut down, the leachate was still being produced in the landfill. The amount of leachate produced was 200 m^3 per day, while the volume of leachate discharged was 190 m^3. The grab sampling technique was used for collecting the samples. Samples were kept at a temperature of 4 °C in an icebox to preserve the original circumstances of the sample. The main characteristics of the studied leachate samples are shown in Table 1.

Table 1. Characteristics of the leachate sample used in this study

Parameters	Units	Value
Chemical Oxygen Demand (COD)	mg/L	675
Turbidity	NTU	705

Experimental set-up

The batch experimental was set up as the electrochemical unit, which consisted of an electrocoagulation cell, a DC power supply, and aluminum electrodes. In this study, EC cell was made from aluminum anodes, and cathodes with 2 cm spacing were placed vertically on the cell floor. The electrodes had dimensions of 5.65 cm × 13.9 cm, with a functional area of 28.76 cm^2 (anode). The stirrer was set at 100 rpm to maintain the composition and avoid flocs in the solution. The electrodes were soaked in 0.4 M of HCl (hydrochloric acid) for 10 min and then rinsed with deionized or distilled water to remove any organic proteins from the surface of the electrodes. The procedure started with an electrocoagulation cell cleaned with distilled water and dried using a dryer. The experiments were carried out in batches. In each experiment, a 500 ml leachate sample was filled into the electrochemical cell with the Al electrodes dipped into the sample at room temperature. The electrodes (anode and cathode) were clamped at the electrode stand. The circuit was completed by connecting wires to the electrodes (anode and cathode) and the DC power supply.

Analysis

The removal efficiency of COD and turbidity was determined according to the following formulas:

$$\text{COD}\ (\%) = \frac{\text{COD}o - \text{COD}t}{\text{COD}o} \times 100 \quad (5)$$

where COD_O and CODt are the chemical oxygen demand (COD) at time = 0 (initial) and at t (reaction time, t), respectively.

$$\text{Turbidity}\ (\%) = \frac{Co - Ct}{Co} \times 100 \quad (6)$$

where C_0 and C_t are turbidity registered (in NTU) at time t=0 (initial) and at t (reaction time), respectively.

Full factorial design of experiments

The three independent factors used in the full factorial design were the voltage, operation time, and electrode size. In contrast, the responses used were the removal percentage of COD and turbidity to achieve the optimum conditions in the experimental design method approach. The input factor variables with their range and levels are shown in Table 2. In this work, 16 experiments were run wholly, including the combination of all levels of other factors, and performed randomly to reduce experimental errors. As the output of factorial screening tests, the critical interactions between all variables were given. The model's validity is verified by analyzing values in the analysis of variance (ANOVA) table. The interactive statistical data analysis tool software in the analysis design was used to construct the model for factorial screening design.

Table 2. Factors and levels used in this experimental design

Parameter	Low Level (-)	High Level (+)
Operation Time (min)	10	30
Voltage (v)	10	30
Size of electrode (m^2)	10	30

Results and Discussion

The effect of the voltages

The initial concentration is one of the remarkable factors in the electrocoagulation process. The influence of this factor on the COD and turbidity removal efficiency is depicted in Figures 1(a) and 1(b). As demonstrated in both figures, the COD and turbidity removal efficiency increased by increasing the voltages for the electrocoagulation process from 5V to 30V. However, more voltage increments caused a descending trend in the removal efficiency. The descending trend can be attributed to the fact that there is a threshold limit for the elimination. The decaying of COD and turbidity removal efficiencies due to the increase in electrical power reduced the lifespan of the electrodes.

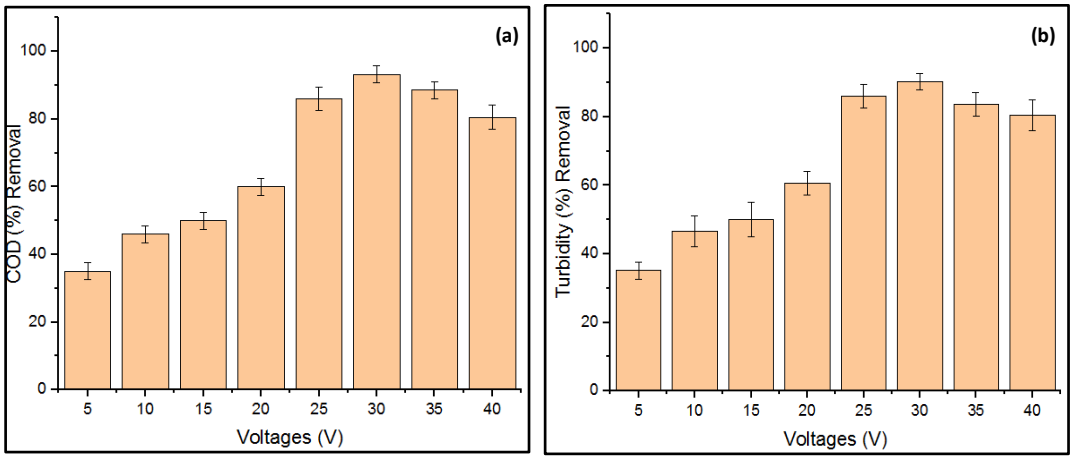


Figure 1. Removal percentages for (a) COD and (b) turbidity removal after 30 min of the mode of operation at different voltages

The effect of the operation time

Figure 2(a) and Figure 2(b) depict the effect of operating time on COD and turbidity removal efficiency. By changing the operating time from 5 min to 30 min, the removal percentages of COD and turbidity increased in the same trend of increment. In this process, EC involved two stages: destabilization and aggregation. The first stage is usually short, whereas the second stage is relatively long. Metal ions, as destabilization agents, are produced at the anode through electrochemical reactions. For 30 min, they indicated an increase in electrolysis duration and increased destabilization of colloidal particles. Both graphs demonstrated that the maximum efficiency of the EC process is obtained at a treatment time of 30 min, and a further increase in treatment time to 40 min did not result in any significant improvement in the removal efficiency of the studied parameters.

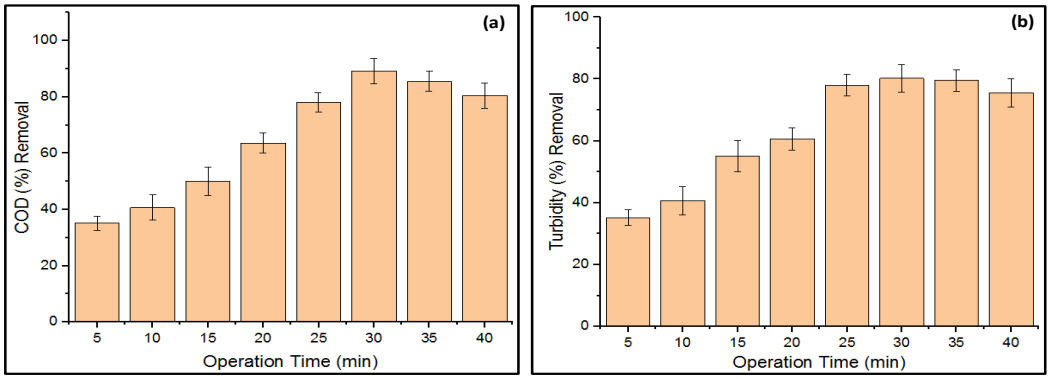


Figure 2. Removal percentages for (a) COD and (b) turbidity removal for 30 voltages for different operation time

The effect of the size of electrodes

Figures 3(a) and 3(b) shows that larger electrodes contribute to high COD and turbidity removal efficiencies. A larger surface area electrode has more area for this oxidation process. However, larger electrodes will incur higher costs and worsen portability. This study aims to preliminarily ascertain the effect of the electrode size on COD and turbidity removal and provide optimal electrode size for electrocoagulation

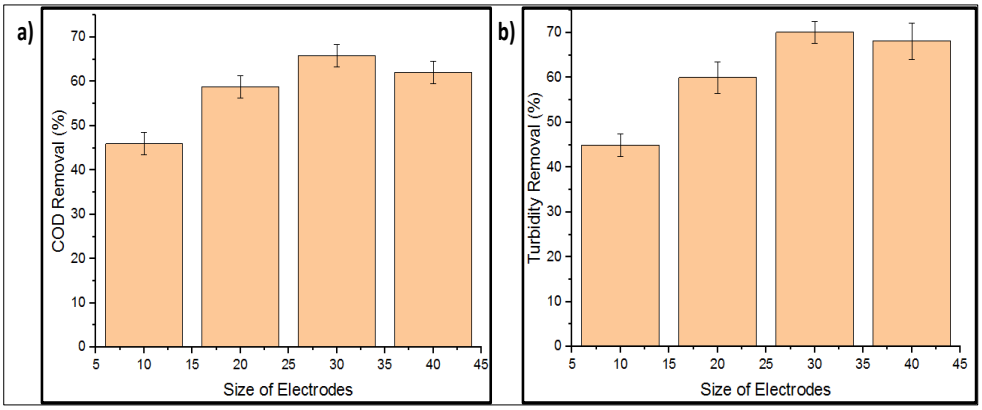


Figure 3. Removal percentages for (a) COD and (b) turbidity removal at the different sizes of electrodes for 30 min operation time and 40 volt

Statistical validity of the model

A matrix of full-factorial design from the two levels (24) is shown in Table 3. Each combination is experimentally carried out in a randomized sequence to meet the statistical requirement for independence of observations. As a result, two responses are examined in the leachate treatment: the COD and turbidity removal.

Table 3. The 3-factor full factorial design matrix and the response function

Exp	Factors			Removal Efficiencies	
	Operation Time	Voltage	Electrode Size	COD (mg/l)	Turbidity (NTU)
1	10	30	10	96	100
2	10	10	10	200	209
3	10	30	10	98	97
4	30	30	30	65	60
5	30	10	30	92	95
6	30	10	30	97	100
7	10	10	30	140	141
8	30	10	10	156	151
9	10	30	30	49	51
10	30	10	10	150	152
11	10	30	30	87	90
12	10	10	10	170	190
13	30	30	10	56	60
14	30	30	10	40	42
15	30	30	30	70	75
16	10	10	30	138	140

Analysis of variance (ANOVA)

Effect of variables on COD removal

The ANOVA for the correlative model development step is presented in Table 4 to describe the removal efficiency of COD as a function of the studied variables. It demonstrated that all the above factors are significant, and the (B) voltage is a highly remarkable variable. The ANOVA shows that the p-value for the model is less than 0.0001, and an F value of 27.22 is obtained for the model, demonstrating the significance of the developed correlation. Besides the main factors A, B, and C, which refer to the operation time, voltage, and electrode size, the model also suggested the interactions of AB, AC, BC, and ABC. Those interactions in the model are less than 0.05, except for the interactions of AB and AC. Nevertheless, these higher values of AB and AC did not affect the total p-value of the model.

Furthermore, the ANOVA table displays supplementary pieces of beneficial information. For instance, the quantity "R-squared" is defined as [15];

$$R^2 = \frac{\text{model sum of squares}}{\text{total sum of squares}} \quad (7)$$

The coefficient of determination (R^2), which shows proportional variation in the response explained by the independent variables in the linear regression model, is 0.9597, which means that the model could describe 95.97% of the variations in the response. The adjusted coefficient of determination (R^2adj) is 0.9244. The value of R^2, which is close to 1, revealed a significant linear relationship between the factors and response. There is a slight difference between R^2 and R^2adj values, which shows that some insignificant conditions (error) are included in the model. The final empirical models in terms of actual parameters are determined as follow

$$COD = +106.50 -15.75*A - 36.38 *B -14.25 *C +3.38 *AB +4.50 *AC + 11.88 *BC + 7.62*ABC \quad (8)$$

Table 4. ANOVA test for the removal of COD

Source	Sum of Squares	df	Mean Square	*F*-Value	*P*-Value	
Model	32081	7	4583	27.21901	<0.0001	significant
A-Operation time	3969	1	3969	23.57238	0.001	
B-Voltage	21170.25	1	21170.25	125.7327	<0.0001	
C-Size electrode	3249	1	3249	19.29621	0.002	
AB	182.25	1	182.25	1.082405	0.3286	
AC	324	1	324	1.924276	0.203	
BC	2256.25	1	2256.25	13.40015	0.0064	
ABC	930.25	1	930.25	5.52487	0.0466	
Pure Error	1347	8	168.375			
Cor Total	33428	15				
Model Summary						
s	R-sq		R-sq(Adj)		R-sq(Pre)	
12.98	95.97%		92.44%		83.88%	

Figure 4 depicts the half-normal plot and Pareto chart, which shows that the primary factors and interaction factors might positively or negatively affect electrocoagulation process COD and turbidity removal efficiencies. A half-normal plot (Figure 4a) shows that the non-significant ones fell along with a straight line normal distribution and centered near 0. Meanwhile, the essential factors contributed to COD removal efficiencies away from the straight line. Therefore, in order of significance, B (voltage), A (operation time), and C (size of the electrode) have the effects of the most critical factors in COD removal efficiency. Other

significant factors included interaction between (BC) voltage and size of electrodes and (ABC) interaction between three factors, which are operation time, voltage, and size of electrodes (ABC). Factors with the tallest bars significantly affected the process in the Pareto chart. As depicted in Figure 4b, the Pareto chart had two lines: Bonferroni (3.584) and t value limit lines (2.306). The factors with t values above the Bonferroni line are essential. Also, the factors with t values between the Bonferroni and t value lines are significant. However, those with t values below the t value-line are not remarkable.

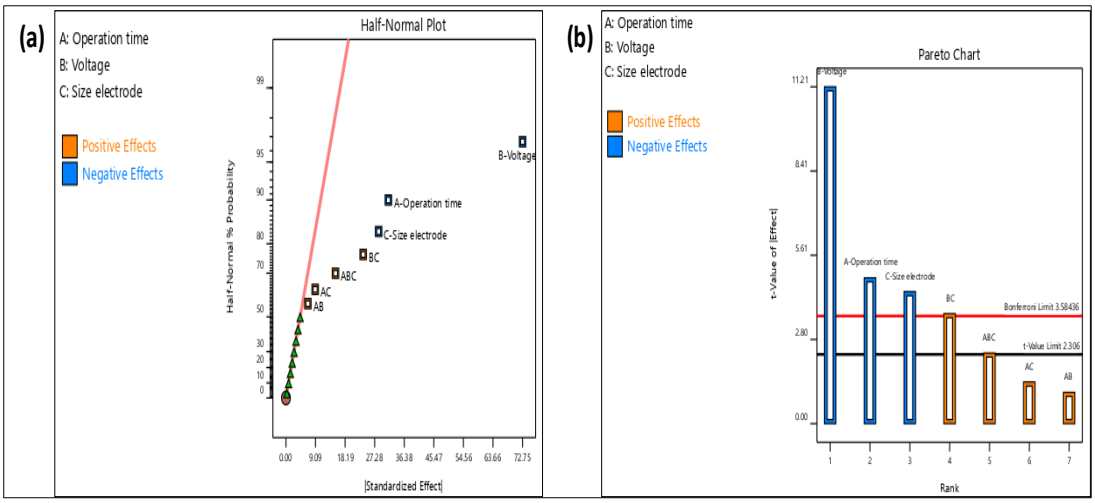


Figure 4. (a) Half-normal probability plot of the effects for the removal of COD and (b) standardized Pareto chart for COD

Effect of variables on turbidity removal

Table 5 shows the ANOVA test for the removal of turbidity. The models or variables with a *p*-value < 0.05 are considered significant with a 95% confidence level. Therefore, the result of ANOVA in Table 4 showed that all variables A, B, and C and the interactions of AB, AC, and BC are significant model terms in terms of turbidity, except for the ABC interaction. The model obtained a *p*-value of 0.0001, implying that the model is significant. The ANOVA result shows that the coefficient of determination, R^2, for the model was 0.9908, which means that the quality of the model is 99.08%. The adjusted R^2 for the model is 0.9522, which shows a good agreement between the results predicted by the regression design and experimental data. A reasonable agreement between the adjusted R^2 and predicted R^2 indicated an adequate model, as shown in Table 5. The final empirical models in terms of actual parameters are determined as follows,

$$\text{Turbidity} = +109.56 - 17.69 *A - 37.69 *B - 15.56*C + 5.06 *AB + 6.19 *AC + 12.69*BC + 4.94*ABC \quad (9)$$

Table 5. ANOVA test for the removal of turbidity

Source	Sum of Squares	df	Mean Square	*F*-Value	*P*-Value	
Model	35594.44	7	5084.92	32.98	< 0.0001	significant
A-Operation time	5005.56	1	5005.56	32.46	0.0005	
B-Voltage	22725.56	1	22725.56	147.39	< 0.0001	
C-Size electrode	3875.06	1	3875.06	25.13	0.0010	
AB	410.06	1	410.06	2.66	0.1416	
AC	612.56	1	612.56	3.97	0.0814	
BC	2575.56	1	2575.56	16.70	0.0035	
ABC	390.06	1	390.06	2.53	0.1504	
Pure Error	1233.50	8	154.19			
Cor Total	36827.94	15				
Model Summary						
s	R-sq		R-sq(Adj)		R-sq(Pre)	
12.42	96.65%		93.72%		86.60%	

The factorial design plot, including the half-normal plot and Pareto chart of effects, are shown in Figure 5. The half-normal probability plot of the effects in Figure 5a shows the absolute values of the estimated effects from the largest effect to the smallest effect. From this analysis, it could be observed that the largest effect on turbidity removal efficiencies that is well displaced in the plot was the AB interaction (operation time and voltage), followed by B (voltage), AC interaction (operation time and size of electrode), BC interaction (voltage and size of electrode), A (operation time) and (C) size of the electrode. The sequence of the significant main effects with respect to decreasing influence on turbidity removal is found to be AB > B > AC > BC > A > C > ABC. The half-normal plot of the effects indicated that the single factor has a negative effect. By increasing the level, there is a significant reduction in turbidity in landfill leachates - another quick way to screen the significant factors is by analyzing the Pareto chart of the estimated effects. The Pareto chart is generated and tabulated, as shown in Figure 5b, to validate the results obtained from the half-normal probability plot of effects in Figure 5a. Pareto chart analyses revealed that all factors and interaction factors are statistically significant, and none of them was below the limit of Benferroni (3.46).

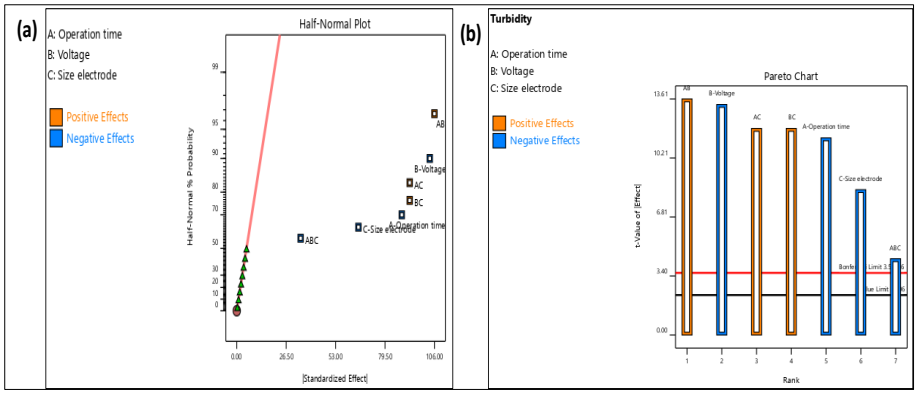


Figure 5. (a) Half-normal probability plot of the effects for the removal of turbidity and (b) standardized Pareto chart for turbidity

Model validation and multiple response optimization
An additional experiment is performed for each set of experiments to validate the models further. Optimized conditions and corresponding maximum COD removal are depicted using the ramp graph shown in Figure 6. Under the optimum conditions, three replicate experiments are conducted. The conditions with predicted and measured results are listed in Table 6. The table shows that the three responses are close to those estimated using factorial design. The model's validity is confirmed as the variation coefficients were around 5% for COD and turbidity removals. This method provided savings in terms of the time and size of electrodes.

Electrolysis time also significantly affects the efficiency of electrochemical coagulation methods in removing pollutants. It determines how much coagulant is produced and how much the cycle costs [16]. Increasing electrolysis time up to the optimum level increases pollutant removal efficiency but does not increase it beyond the optimum level. The fact is that the formation of coagulants at constant current voltage increases with an increase in electrolysis time, resulting in increased efficiency for removal [17]. The voltage applied to the electrodes is one of the most critical parameters that affect the efficiency and economy of the electrocoagulation cycle [18]. Figure 7 shows a sample of leachate landfill before and after the electrocoagulation process. A clear solution is obtained after using the electrocoagulation process by using parameters in this experime

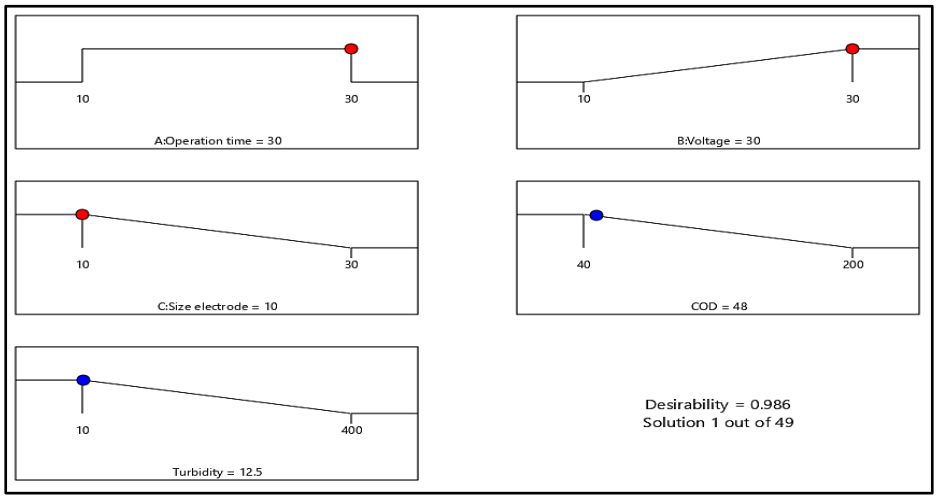


Figure 6. Suggestion value for optimization model

Table 6. Validation of the model

Removal Efficiencies	Factors			Predicted	Average Experimental Results
	Operation Time (min)	Voltage (V)	Electrode Size (m^2)		
COD (mg/l)	30	30	10	48.00	45.72
Turbidity (NTU)	30	30	10	12.5	11.87

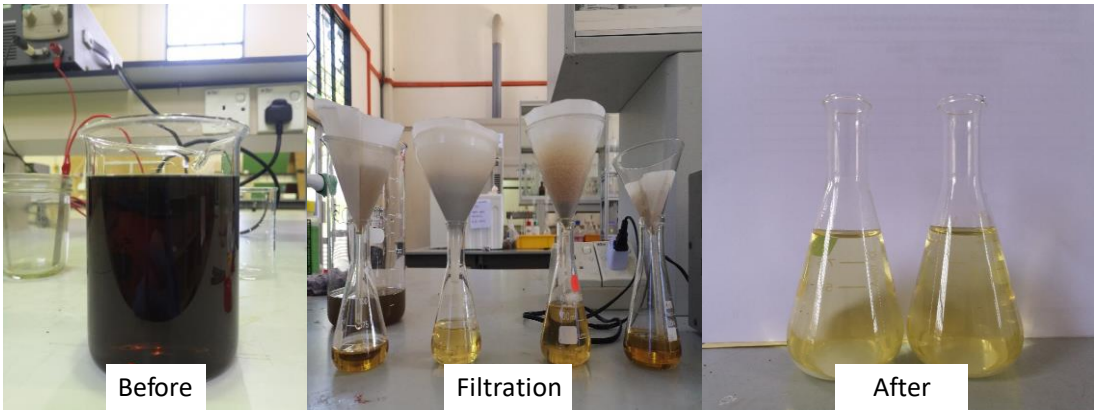


Figure 7. Sample leachate landfill before and after electrocoagulation

Conclusion

In this study, the FFD design of the experiment was used to observe the impact of voltage, operation time, and size of electrodes for the removal of COD and turbidity from landfill leachates by the electrocoagulation process. The screening experiment for the EC process was obtained by running 16 combinations of experiments provided by FFD design in the design of experiment software. The optimum condition was achieved by keeping the goal of operating time maximum, voltage maximum, size of electrode minimum, COD, and turbidity pollutant removal efficiencies in the "maximized" condition. The statistical analysis showed that the relevant p-value of each model was less than 0.001 (p-value < 0.001), indicating the corresponding significance of the model for all responses. The predicted values of COD and turbidity were 48 mg/l and 12.5 NTU, respectively. The maximum COD and turbidity removal experimental values were 45.72 mg/l and 11.87 NTU, respectively, at 30V, 30 min, and 10 cm electrode sizes. Therefore, this indicated that the electrocoagulation process gave good response for the treatment of leachate samples and agreed with the predicted values with less than 5% deviation.

Acknowledgments

The authors gratefully acknowledge the financial support for this work by Universiti Kebangsaan Malaysia under Grant GUP-2021-075.

References

1. Adhikari, B., Dahal, K. R. and Nath Khanal, S. (2014). A review of factors affecting the composition of municipal solid waste landfill leachate. *International Journal of Engineering Science and Innovative Technology*, 3(5): 273-281.
2. Hoai, S. T., Nguyen Lan, H., Thi Viet, N. T., Nguyen Hoang, G. and Kawamoto, K. (2021). Characterizing seasonal variation in landfill leachate using leachate pollution index (LPI) at nam son solid waste landfill in Hanoi, Vietnam. *Environments*, 8(3): 17.
3. Zailani, L. M. and Zin, N. S. M. (2018). Application of electrocoagulation in various wastewater and leachate treatment-A review. In I*OP Conference Series: Earth and Environmental Science*, 140(1): 012052.
4. Makde, K. N. and Hedaoo, M. N. (2018). Application of electrocoagulation in wastewater treatment: A general review. *International Research Journal of Engineering and Technology*, 5(12): 1567-1572.
5. Musa, M. A. and Idrus, S. (2021). Physical and biological treatment technologies of slaughterhouse wastewater: A review. *Sustainability*, 13(9): 4656.
6. Castillo-Suárez, L. A., Bruno-Severo, F., Lugo-Lugo, V., Esparza-Soto, M., Martínez-Miranda, V. and Linares-Hernández, I. (2018). Peroxicoagulation and solar peroxicoagulation for landfill leachate treatment using a Cu–Fe system. *Water, Air, & Soil Pollution*, 229(12): 1-17.

7. Jang, Y., Hou, C. H., Park, S., Kwon, K. and Chung, E. (2021). Direct electrochemical lithium recovery from acidic lithium-ion battery leachate using intercalation electrodes. *Resources, Conservation and Recycling*, 175: 105837.
8. Gatsios, E., Hahladakis, J. N. and Gidarakos, E. (2015). Optimization of electrocoagulation (EC) process for the purification of a real industrial wastewater from toxic metals. *Journal of Environmental Management*, 154: 117-127.
9. Pirsaheb, M., Mohamadisorkali, H., Hossaini, H., Hossini, H. and Makhdoumi, P. (2020). The hybrid system successfully to consisting of activated sludge and biofilter process from hospital wastewater: Ecotoxicological study. J*ournal of Environmental Management*, 276: 111098.
10. Chairunnisak, A., Arifin, B., Sofyan, H. and Lubis, M. R. (2018, March). Comparative study on the removal of COD from POME by electrocoagulation and electro-Fenton methods: Process optimization. *In IOP Conference Series: Materials Science and Engineering*, 334(1): 012026.
11. Amarine, M., Lekhlif, B., Sinan, M., El Rharras, A. and Echaabi, J. (2020). Treatment of nitrate-rich groundwater using electrocoagulation with aluminum anodes. *Groundwater for Sustainable Development*, 11: 100371.
12. Bajpai, M., Singh Katoch, S. and Singh, M. (2020). Optimization and economical study of electro-coagulation unit using CCD to treat real graywater and its reuse potential. *Environmental Science and Pollution Research*, 27(33): 42040-42050.
13. Naje, A. S. and Abbas, S. A. (2013). Electrocoagulation technology in wastewater treatment: a review of methods and applications. *Civil and Environmental Research*, 3(11): 29-42.
14. Rusdianasari, R., Taqwa, A., Jaksen, J. and Syakdani, A. (2017). Treatment of landfill leachate by electrocoagulation using aluminum electrodes. *In MATEC Web of Conferences*, 101: 02010.
15. Shadmehr, J., Mirsoleimani-azizi, S. M., Zeinali, S. and Setoodeh, P. (2019). Electrocoagulation process for propiconazole elimination from wastewater: experimental design for correlative modeling and optimization. *International Journal of Environmental Science and Technology*, 16(10): 5409-5420.
16. Akhter, F., Soomro, S. A., Siddique, M. and Ahmed, M. (2021). Pollutant Removal efficiency of electrocoagulation method from industrial wastewater: Comparison with other treatment methods and key operational parameters—a comparative study review. *Water, Air, & Soil Pollution*, 232(3): 1-13.
17. Mallesh, B. (2018). A review of electrocoagulation process for wastewater treatment. *International Journal Chemical Technology Research*, 11: 289-320.
18. Graça, N. S., Ribeiro, A. M. and Rodrigues, A. E. (2019). Removal of fluoride from water by a continuous electrocoagulation process. *Industrial & Engineering Chemistry Research*, 58(13): 5314-5321.

Malaysian Journal of Analytical Sciences (MJAS)
Published by Malaysian Analytical Sciences Society

ENHANCING THE OXYGEN REDUCTION REACTION OF LOW-PLATINUM AND NON-PLATINUM CATALYSTS FOR FUEL CELL APPLICATIONS

(Peningkatan Tindak Balas Penurunan Oksigen Mangkin Platinum Bermuatan Rendah dan Bebas Platinum Untuk Aplikasi Sel Bahan Api)

Kazi Rumanna Rahman[1], Kuan Ying Kok[2], Nor Azillah Fatimah Othman[3], Wai Yin Wong[1], Kean Long Lim[1]*

[1]*Fuel Cell Institute,*
Universiti Kebangsaan Malaysia, 43600 UKM Bangi, Selangor, Malaysia
[2] *Industrial Technology Division*
[3]*Radiation Processing Technology Division*
Malaysia Nuclear Agency, 43000, Kajang, Selangor, Malaysia

**Corresponding author email: kllim@ukm.edu.my*

Received: 13 December 2021; Accepted: 6 March 2022; Published: 27 June 2022

Abstract

Nowadays, research efforts are focused on developing low-Pt and non-Pt catalysts for ORR. The addition of Pt-group metal (PGM) in pure Pt to form Pt-PGM catalysts exhibits better ORR performance than pure PGM catalysts and Pt/C. More than 20 wt.% of Pt loading is required in Pt-PGM alloys for improving catalytic activity. Studies have also shown that the addition of transition metal (TM), which has a smaller atomic size, into PGM reduced the bond distance between two metallic atoms and geometric parameters, thus remarkably improving the catalytic stability and ORR activity. However, TM based catalysts should be supported on nitrogen-doped carbon with high surface area to attain high ORR activity. A large surface area and high electronic conductivity of carbon support also facilitate the ORR activity. Performances of alloy catalysts are directly related to their synthesis temperature and structural properties. Designing the core-shell combinations and controlling the shell thickness is one of the structural strategies in enhancing mass activity and durability. Lately, irradiation techniques are used to modify the physicochemical properties. Nevertheless, TM-based catalysts are usually stable in alkaline solutions but not in acidic solutions. This review focuses on the strategies to develop cost-effective catalysts from low-platinum and non-platinum catalysts with enhanced ORR activity.

Keywords: oxygen reduction reaction, platinum group metal alloys, transition metal catalysts, synthesis techniques

Abstrak

Pada masa kini, usaha penyelidikan tertumpu kepada pembangunan mangkin platinum (Pt) bermuatan rendah dan bebas platinum untuk tindak balas penurunan oksigen (ORR). Penambahan logam kumpulan Pt (PGM) dalam Pt tulen untuk membentuk Pt-PGM menunjukkan prestasi ORR yang lebih baik daripada prestasi mangkin PGM tulen dan Pt/C. Sebanyak lebih daripada 20 wt.% muatan Pt adalah diperlukan dalam aloi Pt-PGM untuk meningkatkan aktiviti pemangkinan. Kajian telah menunjukkan penambahan logam peralihan (TM) yang mempunyai saiz atom yang lebih kecil ke dalam PGM mengurangkan jarak antara dua atom logam dan parameter geometri sekali gus meningkatkan kestabilan pemangkinan dan aktiviti ORR. Namun demikian,

mangkin berasakan TM perlu disokong dengan karbon terdop nitrogen yang berpermukaan yang luas untuk mencapai aktiviti ORR yang tinggi. Penyokong karbon yang berpemukaan luas dan mempunyai kekonduksian elektronik yang tinggi juga memudahkan aktiviti ORR. Prestasi mangkin aloi adalah berkait langsung dengan suhu sintensi dan sifat strukturnya. Mereka bentuk gabungan teras-cangkerang dan mengawal ketebalan cangkerang adalah salah satu strategik penstrukturan dalam meningkatkan aktiviti jisim dan ketahanan. Akhir-akhir ini, teknik-teknik penyinaran digunakan ubah mengubahsuai sifat fizikokimia. Namun demikian, mangkin berasaskan TM biasanya stabil dalam larutan alkali tetapi tidak dalam larutan asid. Ulasan ini berfokus pada strategik untuk membangunkan magkin berkos efektif daripada mangkin Pt bermuatan rendah dan bebas platinum dengan aktitiviti ORR yang dipertingkatkan.

Kata kunci: tindak balas penurunan oksigen, logam aloi kumpulan platinum, mangkin logam peralihan, kaedah sintesis

Introduction

A fuel cell is an energy conversion device that converts chemical energy into electric energy through an oxidation reaction at the anode and a reduction reaction at the cathode. The cathode reaction, known as oxygen reduction reaction (ORR), is a fundamental reaction to various disciplines, such as energy conversion, material dissolution, or biology. The performance of fuel cells depends on the rate of ORR [1, 2]. Difficulties in O_2 adsorption, O-O bond cleavage and oxide removal are the main reasons for the sluggish reaction kinetics of ORR [3]. The state-of-the-art Pt/C (platinum/carbon black) catalyst and Pt-based alloy catalysts are used for the cathode reaction in aqueous electrolytes, and these catalysts are considered the best for ORR. All Pt or Pt-based catalysts still suffer from CO and S poisoning on Pt, loss of active surface area, corrosion of carbon support, low durability and limited supply, high cost, and use of a high amount of Pt [4–6]. So, non-Pt based catalysts with improved catalytic activity are required to overcome these limitations of Pt [7]. The main characteristic of an effective fuel cell catalyst is its capability to facilitate the rate of ORR [8]. Transition metal (TM) alloys, chalcogenides, carbides, nitrides, and metal-N4 macrocyclic compounds instead of Pt/C and PGM catalysts, are potential electrocatalysts for ORR [9]. Composition, particle size, crystallographic orientation, etc contribute to the enhancement in catalytic activity and d-band vacancy is considered as an important factor for enhancing catalytic behavior towards ORR. For developing a cost effective catalyst with improving ORR activity, the current research follows four different trends: 1) to reduce the wt% of Pt in alloy catalysts, 2) to develop the PGM free catalyst named M-N-C, where M for transition metal, nitrogen, and carbon, 3) to utilize the carbon with large surface area as catalyst support and 4) synthesis technique for designing cost-effective ORR cathode catalysts[10–13]. In the following section, we describe the general mechanism of ORR cathode in acidic and alkaline solutions, which gives a clear idea of the reaction paths.

General mechanism of ORR cathode

In general, anode and cathode reactions occur on a metal surface. The reaction that occurs at the cathode site is known as the ORR reaction. Usually, the ORR reaction is the limiting reaction step of the overall reaction because of its sluggish kinetic, hence it is essential to understand the ORR mechanisms to design an effective catalyst.

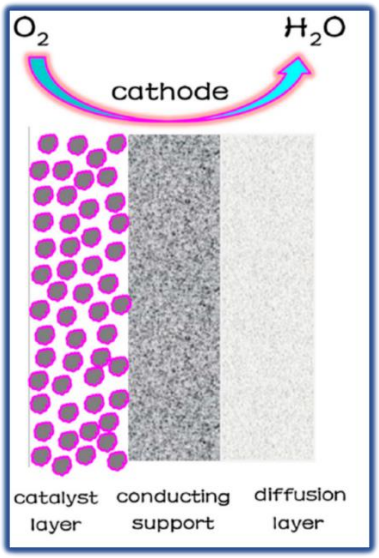


Figure 1. The structure of PEMFC cathode with catalyst layer [14]

The ORR mechanism involves a direct four-electron (4e-) or a series of two-electron (2e-) pathways. A one-step 4e- transfer mechanism is more efficient than a 2e-transfer mechanism. Thus, catalysts that facilitate the 4e- pathway reaction are more favorable. In the $4e^-$ transfer pathway, O_2 is converted into either H_2O (acidic medium) or OH^- (alkaline medium) on a single catalytic site. This process depends completely on the electrolytes [14–17].

In an acidic electrolyte, the $4e^-$ transfer pathway can be written as in Eq. (1):

$$O_2\,(g) + 4H^+\,(aq) + 4e^- \rightarrow 2H_2O(l) \quad (1)$$

and $2e^-$ transfer pathway can be expressed as Eqs. (2, 3, and 4):

$$O_2\,(g) + 2H^+\,(aq) + 2e^- \rightarrow H_2O_2\,(l) \quad (2)$$

H_2O_2 is produced in the intermediate step of the Eq.(2) pathway. H_2O_2 is finally reduced to water:

$$H_2O_2\,(aq) + 2H^+\,(aq) + 2e^- \rightarrow 2H_2O\,(l) \quad (3)$$

or is decomposed as follows:

$$H_2O_2(aq) + 2H(aq) + 2e^- \rightarrow 2H_2O(l) + O_2(g) \quad (4)$$

On the other hand, O_2 is converted into OH^- by $4e^-$ pathway, which is written as Eq. (5), and forms HO_2^- via $2e^-$ pathway in an alkaline medium,

$$O_2\,(g) + 2H_2O\,(aq) + 4e^- \rightarrow 4OH^-\,(l) \quad (5)$$

Eqs. (6,7 and 8) express the step of the $2e^-$ transfer pathway alkaline solutions.

$$O_2\,(g) + H_2O\,(aq) + 2e^- \rightarrow HO_2^-\,(l) + HO^- \quad (6)$$

Peroxide is also unstable

$$HO_2^-\,(aq) + H_2O\,(l) + 2e^- \rightarrow 3OH^-\,(aq) \quad (7)$$

and decomposes into the following:

$$2HO_2^-\,(aq) \rightarrow 2HO^-\,(aq) + O_2(g) \quad (8)$$

Pt-group alloy catalysts

Pt is the best monometallic catalyst for ORR in acidic and alkaline solutions. The fuel cell stack needs almost 80%–90% Pt, which increases the cost of the entire stack. Moreover, Pt has some drawbacks, such as CO poisoning, short life span, low durability, etc. So, the current research trend emphasizes reducing Pt use and the development of bimetallic and trimetallic alloy catalysts to overcome the stumbling block of Pt [18–20]. Some researchers used several noble metals like Pd, Ir, Rh, Ag, and Ru as cathode catalysts. All single noble metal catalysts followed the $4e^-$ pathway but exhibited lower catalytic activity than Pt. Improvement of catalytic activity depends on the optimization of particle size and shape, surface structure, support metal, and synthesis process [21]. It also revealed that combinations of two Pt-group metals can tune the ability of oxygen adsorption due to constructing a hetero-metal-metal bond by altering the electronic configurations. Coupled metals also generate a new active site. The mutual effect of changing electronic and geometric structure encourages a $4e^-$ reaction pathway towards ORR [17]. The d band vacancies which consider as important parameters increase due to the existence of Pt atom, d band vacancies boosted 2π electron donation from O_2 to the catalyst surface. Finally, O_2 reacted with donated electrons and protons to yield desirable H_2O molecules [22].

Due to the similar crystal structure of Pt, palladium-based catalysts have stimulated extensive concern among researchers [23]. Zhou et al. reported that Pt-Pd/C exhibited higher durability than commercial Pt/C as a cathode catalyst. They also concluded that particle size and electrochemical surface area (ECSA) loss are associated with durability, and larger particles are more stable in alkaline solution [24]. Wang et al. established the relationship between weight ratio and particle size. They reported that ORR activity was controlled by the size of Pt nanoparticles, and 30% of Pt-Pd/C exhibited remarkable performances, whereas the weight ratio of Pt: Pd was 1:1. The mass activity (MA) and the ECSA value of this Pt-Pd/C catalyst (MA= 0.488 mA μg^{-1} and ECSA=107.7 $m^2\,g^{-1}$) are four times and 1.69 times higher than those of commercial 10% Pt/C (MA=0.123 mA μg^{-1} and ECSA=63.6 $m^2\,g^{-1}$) in acidic solution[25, 26]. The ratio of Pt-Pd has a great impact on surface morphology and catalytic activity. In the presence of Pd, Pt-Pd/C exhibits larger ECSA, higher mass activity, and larger particle size.

The impact of Pt-Pd/C with different atomic ratios on the particle size, mass activity (MA), and ECSA values

are depicted in Figure 2. From the graph, it is clear that smaller particle size is expected for better ORR activities. A relationship is observed between ECSA and the particle size and ratio. Particle size shows an increasing trend with an increasing Pt: Pd in compositions, and ECSA shows a decreasing trend with the increasing Pt: Pd. A higher amount of Pd, i.e. above 1:2 (Pt: Pd), causes a lower dispersion rate, which is the key reason for the decrease in catalytic activity and mass activity [27]. Pd increases overall ORR performance, especially stability in both acidic and alkaline-aqueous electrolytes. A low particle dispersion rate still occurs if the ratio of Pt: Pd is more significant than 1:2. So, it is a major question of which ratio will be taken into consideration.

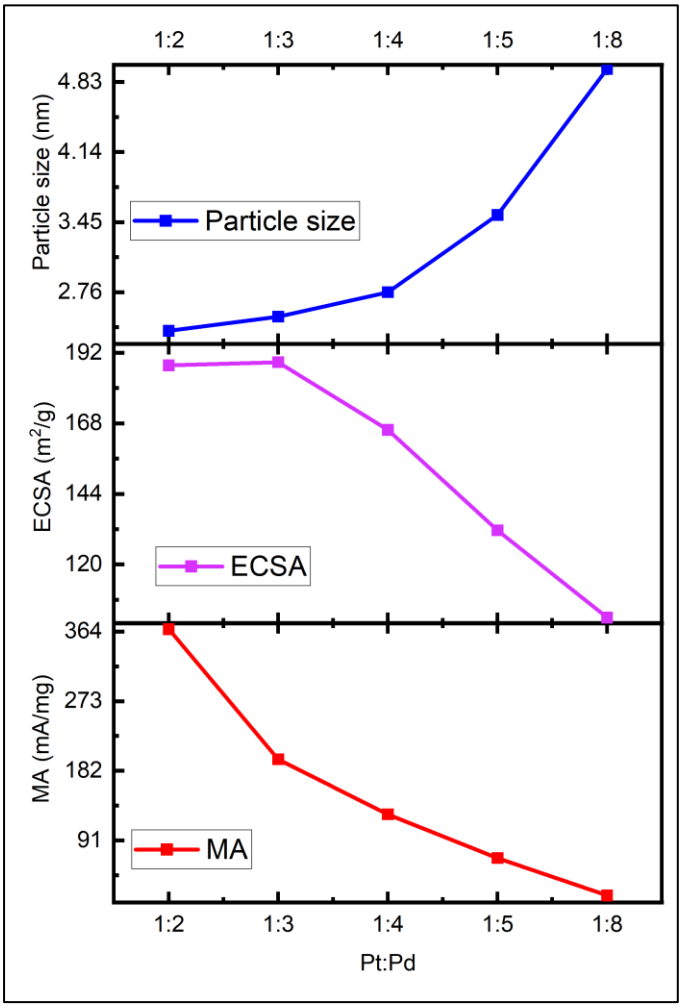


Figure 2. The Impact of Pt: Pd on particle size MA, and ECSA [27]

Ru is another alternative metal for reducing the use of Pt and improving catalytic activity. Small particles show better CO tolerance than large particles for Pt-Ru alloys. The Pt: Ru ratio of 1:1 exhibits an enhanced ORR activity, and the morphological change induces several active sites for CO oxidation, but the oxidation state of Ru is gradually decreased by increasing particle size [28]. In both types of electrolytes. Pt-Ru alloy exhibited better mass activity and stability than state of art Pt/C. Ru surface facilitates the break of O-O bond and

supports the proton transport at the same time. As a result, Pt nanoparticles exhibited enhanced ORR catalytic activity [29, 30]. The ECSA, mass activity, and Pt-Ru particle size vary with Pt atom in alloys[31]. According to the literature, the degree of alloying Pt-Ru strongly depends on the nature of the electrolyte. The particle size of the Pt-Ru catalyst decrease with increasing pH of solution[32]. The main drawback of Pt-Ru alloy is that it needs more Pt than Pt-Pd, and as a single metal catalyst, Ru/C exhibits lower catalytic activity compared with Pd/C, Ir/C, and Rh/C in acidic media [33].

In acidic solution, Pt-Pd/C and Pt-Ir/C both catalysts exhibited almost the same ECSA and both catalysts performed better than Pt/C. In terms of stability, Pt-Ir/C was better than Pt-Pd/C and Pt/C. Pt and Ir's nucleation helps to improve the durability and catalytic activity. Crystallite size could be able to tune the performance of Pt-Ir [34, 35]. The mass ratio is the most important factor for the Pt-Ir catalyst. The Pt-Ir/C (16:84) presents a larger ECSA value, which is 28.7 $m^2 g^{-1}$, and its mass activity is 373.3 mA mg_{pt}^{-1}, which is greater than Pt/C (ECSA=18.3 m^2 g^{-1} and MA=142.9 mA mg_{pt}^{-1}). However, Pt-Ir/C (4:96) and Pt/C possess the same ECSA value, but Pt-Ir/C (4:96) exhibits lower catalytic activity than Pt/C [36]. Like other Pt group metal alloys, Pt-Ir follows the 4e- pathway and exhibits improved ORR activity. Catalytic performances of this catalyst are strongly influenced by the synthesis technique, treatment temperature, catalyst support, and the presence of Pt [37].

Pt-Rh alloy also exhibits better durability than a single Pt catalyst. Rh itself does not participate in the activity of the catalyst, but the existence of Rh plays a crucial role[38]. Rh covers only 15%–20% of the surface because Pt suppresses it. Both metals possess a similar crystal structure and similar-sized cells. So, it is difficult to determine the active phase that belongs to Rh. A small amount of Rh is needed to make a Pt-Rh alloy and acts as a bimetallic catalyst[39]. Narayanamoorthy et al[40] reported that supportless Pt-Rh alloy is better than Pt-Rh catalyst with Vulcan carbon (VC) and Pt/C (CB). Supportless Pt-Rh (154.4 m^2g^{-1}) possesses a higher ECSA value than Pt-Rh/C (103.5 $m^2 g^{-1}$) and is 2.5 times higher than Pt-Rh/VC (61.76 m^2 g^{-1}). The cluster morphology depends on the availability of Pt surface[40]. Several studies concluded that smaller particle sizes presented larger ECSA, which exhibit higher mass activity and stability. All PGM alloys follow the $4e^-$ pathway and exhibit comparable catalytic activity in both electrolytes.

Making alloys with low-cost materials is a good strategy for reducing Pt use. TMs are the most acceptable metals for changing the electronic configuration in the cluster [41]. The addition of PGM increases the particle size, whereas Ag reduces the particle size due to its small diameter (<5 nm), facilitating ECSA and ORR activity. Many investigations have been performed on Ag to overcome the limitation of Pt/C [42]. The catalytic activity of Pt-Ag/rGO is slightly higher than that of Pt/C in acidic solution with a Pt: Ag ratio of 1:3.This catalyst exhibits a larger ECSA value (67.8 $m^2 g^{-1}$) than Pt/C (39.2 $m^2 g^{-1}$) [43]. Pt-M/C (M=Fe, Co, Ni) presents a larger particle size compared with Pt/C. The particle size of Pt-M/C is calculated to be 2.5 nm to 2.8 nm, whereas that of Pt/C is 2.1 nm when the ratio of Pt: M is 50:50. Pt-Fe/C (100 $m^2 g^{-1}$) exhibits the highest ECSA value among Pt-M/C, which is lower than 50 wt% of Pt/C (119 m^2 g^{-1}). All Pt-M/C show improved mass activity compared with Pt/C. The variable electron state of TM atoms induces a strong interaction between TM-O, which encourages the slower loss rate of ECSA than PGM [44, 45].

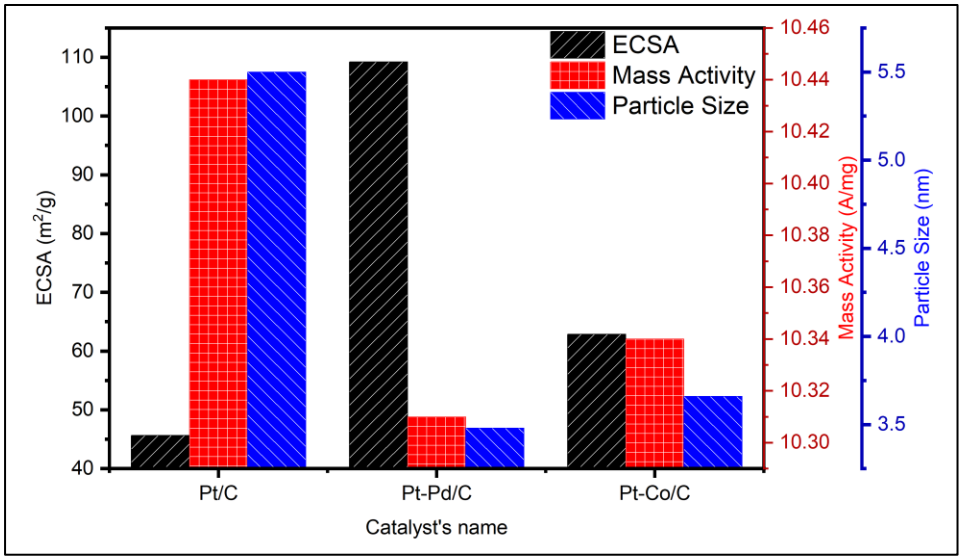


Figure 3. Effect of making alloy with platinum group metal (PGM) and transition metal (TM) [46]

From Figure 3, it has been seen that Pt-Pd/C increases the ECSA and decreases the particle size. On the other hand, Pt-Co/C reduces the ECSA, and particle size was a little larger than Pt-Pd/C. In the case of MA, TM exhibited better performance than PGM. Catalytic activity increased due to lattice compression, resulting from the downward shift of the d-band center of Pt and Pd. ORR activity showed a decreasing trend with an increasing amount of Co. Compare with Pt-Pd/C and Pt/C, Pt-Co/C showed better stability in acidic solution. However, it has been suffering from low stability while using in Toyota Mirai Fuel Cell Vehicles [46–49]. To overcome the stability problem, Pt-Fe/C is a good substitute for Pt/C. Fe can tune the electronic structure of Pt that enhanced the durability of Pt-Fe/C in an acid medium [50, 51]. PGM sites' surface activity has been influenced by the small atomic size of TM and the reduction in the PGM-TM bond, which serves better catalytic activities of PGM-TM alloys. The study revealed that the enhancement of ORR performance depends on the density of PGM [52].

According to literature, the observed improvement in catalytic activity reveals several issues that should be considered in future studies to develop a better catalyst, as follows: (i) increase in the resistance to particle sintering; (ii) surface roughening due to the removal of some alloying metal that increases the electrochemical surface area; and (iii) preferential crystal orientation [52–55]. High durability and catalyst activity are the keys to solving the current problem of Pt. PGM and PGM-TM alloy catalysts exhibit excellent activity and stability compared with traditional Pt/C catalysts. All types of mixed metal alloys are suitable substitutes for commercial Pt/C in alkaline electrolytes. In acidic electrolytes, these catalysts show poor performances without Pt in their composition. PGM-TM bond helps increase durability and stability, but a large amount of PGM is needed to exhibit better catalytic activity.

TM alloy catalysts for ORR

Many experimental studies proved that nitrogen-doped carbon support increases the concentrations of ORR active sites and stability by associating two adjacent carbon crystallites of TM catalyst; the configuration of TM active sites changes completely according to C-N species [56–58]. Here, we discuss some promising TM catalysts that exhibit improved ORR activity in the presence of N.

Fe-N-C has drawn much attention due to its catalytic performances. N coordinated Fe atom has been a highly active center for ORR [59]. Fe-N-C nanoparticles show outstanding stability in both acidic and alkaline

solutions. Only 0.5 wt% of the Fe-contained Fe-N-C catalyst possesses a high surface area (1501 m^2g^{-1}) and exhibits superior durability to Pt/C. Half wave potential ($E_{1/2}$) of Fe-N-C and commercial Pt/C is presented in Figure 4.

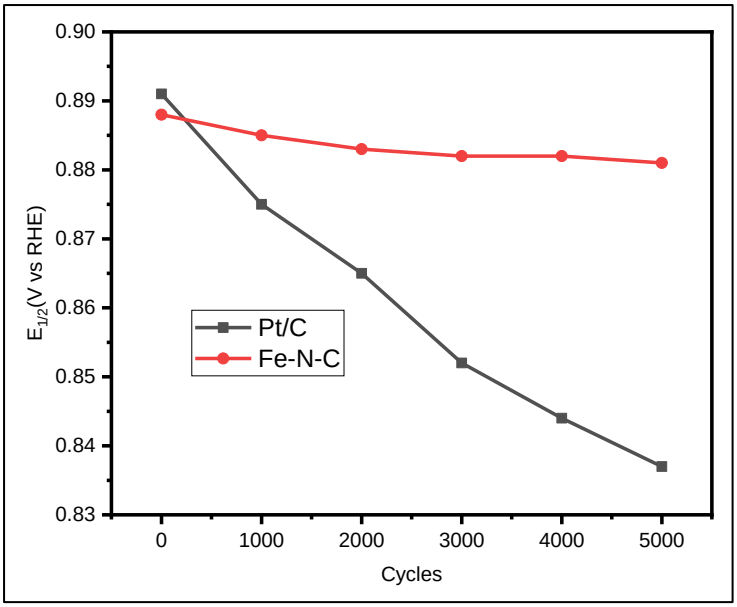


Figure 4. $E_{1/2}$ of Fe-N-C and Pt/C at every 1000 cycles in the durability test [60]

From Figure 4, it is clearly observed that after 5000 potential cycles, Fe-N-C remains unchanged whereas Pt/C gradually decreases under the same condition [60, 61]. The formation of Fe-N is powerfully demonstrated by carbon chemistry. Fe-N active sites are also an essential issue for ORR activity. The Fe-N/C/rGO (10% to 20% of Fe) exhibits improved ECSA and ORR activity, which are comparable with those of Pt/C and are higher in comparison with those of Fe-N/C/rGO (5%–10% of Fe), Fe-N/C, and Fe-N/rGO [62, 63]. Fe-N-based catalyst follows the $4e^-$ reaction pathway in both types of electrolytes. The weight percentage of Fe plays an important role in the composition. This percentage depends on the presence of inducing elements, such as N, P, and S [64]. The gap between the valence and conduction bands of Fe atom (-0.82 eV) enhances catalytic stability and a small amount of metal doping can increase conductivity, and durability [65]. Jiang et al reported that the binding energy of O_2 that presents in the Fe-N_x site helps the adsorption of O_2 on Fe-N_x sites, which promotes ORR activity of Fe-N-C. 20wt% to 35wt% ionomer concentration increases the ionic conductivity of the cathode site. Above 35 wt.% concentration, active sites gradually decrease. However, unsaturated Fe can change the charge density of N-doped carbon support and the central Fe atom in Fe-N_x. Some researchers replaced Fe with Co or Ni [66–68].

Co is the most widely used substitute and partial substitute metal in compositions due to its low price, high durability, and $4e^-$ reaction selectivity [69]. The Co-based catalyst exhibited superior stability to that of Fe. Like Fe, the bimetallic atom-doped Co catalyst shows better ORR performance by forming dual sites than a single metal Co catalyst. Double active sites facilitate electron transfer [70]. Partially substituted Co-Te/C (1:1.93) and Co-Se/C (1:1.25) are catalysts that follow the $4e^-$ reaction pathway in acidic solution, but the catalytic activity is not comparable with that of Pt/C [71]. Support metal has an impact on Co-based catalytic activity. Co_2P/NRC nanorods enhance durability and catalytic action to a level comparable to Pt/C in alkaline media [72]. The performance of the Co-N-C-based catalyst depends on the active site of Co-N_x and

nitrogen-containing functional groups and the effect of mutual interaction between Co-O-C and Co-N-C bond formations. Co-N/C catalyst follows the $4e^-$ reaction pathway and exhibits high durability and current density. High amounts of Co^{2+} oxidation states are associated with increasing ORR activity [41, 57, 73]. Co-Fe alloy is among the prominent non-PGM catalysts for ORR. It has been reported that charge redistribution between Fe-Co alloy and N-supported graphitic carbon-nanotube enhances the catalysts' behavior. The corrosion resistance and electronic conductivity increase with the amount of Co increase in alloy [74, 75].

Ni-based catalyst is another good alternative to most active Pt-group metal catalysts. Ni or Ni alloys are not easily oxidizable, and the Ni structure facilitates the transportation of ions and the charge conductivity[76]. N-doped Ni-Co and Fe-Ni catalysts showed comparable ORR performance with Pt/C and exhibited superior stability [77, 78]. The enhancement of catalytic activity completely depends on the mutual effect of Ni and the N-carbon metal's electronic structures. The edge N atom and the geometric effect of support metal regulate the electronic configuration of Ni [79, 80]. Ni-Mo catalyst showed the highest mass activity among Pt free catalysts used in the present time due to the high dispersion of Ni particles, and Mo facilitates mass activity[81]. In an alkaline aqueous solution, the N-C structure works as a support of the Ni nanoparticles and enhances the catalytic activity towards ORR [79].

As a 3d transition metal, Cu shows high electro-catalytic activity towards ORR due to its valence electron configuration, which is closest to Pt. It has a very strong complex ability to generate Cu-N bonds and exhibits the highest stability in an aqueous solution among 3d transition metals [82]. Cu metal works as an active component for ORR, and this metal is used for constituting active sites. Cu enlarges the surface area of the catalyst. Cu^{2+} ions have a great affinity to form a stable complex with N-based ligands. Cu-N interaction speeds up the peroxide reduction and oxygen activation [83, 84]. The CuFe/C (1.5wt.% Fe and 1.7 wt.% Cu) alloy catalyst and Pt/C (30%) exhibit the same catalytic activity. Fe^{3+}-N works as an active site for ORR, and Cu^{2+}/Cu^{+} plays the role of a redox mediator that shuttles the electron from the electrode to $FeN\text{-}O_2$ [85]. During ORR, the Fe atom in Cu alloy facilitates the desorption of oxygenated intermediates, which increases the rate of ORR kinetics. The electronic structure of catalyst metals has been changed by the interaction between the metal catalyst and the support metal. N particularly helps donate electrons to the O-O bond, thereby increasing stability [86]. Cu ascribes to high redox potentials, and the current densities of the d-orbital of Cu lead to a weaker O-O bond [87].

Among the transition metals, manganese oxides became the focus of research due to their variable oxidation states and high stability in alkaline media. Mn^{3+} species modifies the crystallinity, surface area, and pore size of catalysts [88]. Liu and co-workers identified the two types of Mn coordination, octahedral Mn^{4+} (i.e. partial d-orbital filling Mn) and pyramidal Mn^{3+} and Mn^{3+} coordination is essential for ORR activity [89]. The N-C structure helps reduce electron cloud densities on a carbon atom by inducing N. The active site of the Mn-N-C catalyst is the combined structure of N-C and Mn-N [90]. The covalency of the Mn-O bond is responsible for specific ORR activity and works as an electron transfer mediator to O. The existence of Mn^{3+} on the active site facilitates the ORR activity, whereas Mn^{4+} encourages the $4e^-$ reaction pathway [91].

However, TM based catalysts exhibit higher levels of ORR activity in alkaline media that indicate the exchange of electrons and the change of oxidation state during ORR, the exact role of TM is not clear[57]. Transition metals (TM) have been recognized as alternatives due to their high corrosion resistance and stabilities, electrical conductivities, and mechanical strengths. N-doped carbon-supported TM catalyst exhibits better ORR activity in alkaline solution. Formation of C-N increases the concentration of active sites.

Benefits of the carbon support

Carbon support helps increase the electronic behavior of catalysts and enhances ORR performance. ECSA, durability, reaction pathway, and electrical conductivity have been influenced by support materials [92]. Corrosion of metal is an important factor in fuel cell

operations. Carbon support metal helps overcome corrosion problems by making a strong bond between nanoparticles and support materials [93]. Carbon nanomaterials are considered good catalyst support due to their excellent properties, which ensure the following parameters: 1) high electrical conductivity; 2) large surface area; 3) strong interaction between support and catalyst; 4) high electrical stability under the fuel cell condition, and 5) low cost [94–96]. Large surface areas of support suppress the particle size. This criterion helps make a highly concentrated catalyst particle that increases the efficiency of the electrode by reducing embedded sites and shortening the reactant pathway [97, 98]. C(Carbon black) is widely used for commercial Pt catalysts. Poor durability and low catalyst metal utilization are the main weaknesses of C. GO (graphene oxide), rGO (reduced graphene oxide, MWCNT(multiwall carbon nanotube), and so on are considered a better substitute for C. [99, 100]. Nowadays, GO and rGO are widely used because of the partial transition from sp^2 to sp^3carbon atoms. Both GO and rGO derivatives of graphene are easy to produce on a large scale using graphene sheets, catalyst metal is located between pores, thereby reducing the aggregation of catalyst metals, and this behavior helps enhance catalyst efficiency [101, 102]. Studies revealed that in rGO, oxygen groups participate in the transfer of electrons, which causes the reduction of catalytic activity. Electric contact efficiency plays an important role between two catalyst particles. rGO has higher thermal stability than GO due to lower defect density [103, 104].

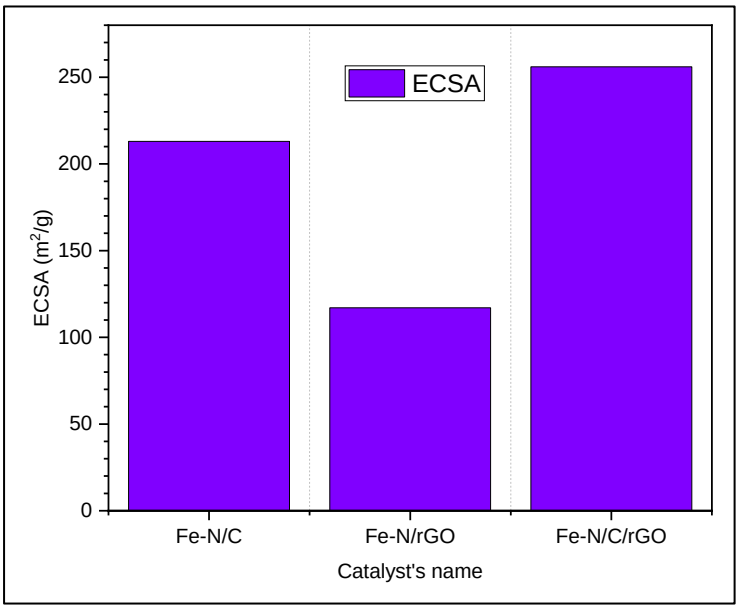


Figure 5. Effect of carbon support on ECSA [63]

It has been seen from Figure 5, ECSA of catalysts changes with the change of support metal, carbon black (C) supported Fe catalyst exhibited larger ECSA than reduced graphene oxide (rGO). Fe catalyst presented the largest ECSA while C and rGO were used together [63] Surface modification of the graphene sheet is conducted by inducing the heteroatom to boost the interaction with a metal catalyst; graphene aggregation is avoided by changing the interfacial properties [105]. The electrochemical activity of the non-PGM catalyst depends on the doped element (N, S, and P) that supports carbon. The edge plane sites contribute to the improvement of catalytic performances, and spin densities on adjoining carbon atoms induce different ORR sites [64, 106–109]. Based on the above discussion, we summarise the properties of different carbon forms in Table 1, that influence the ORR activity.

Table 1. Represents the ECSA, conductivity, advantages, and disadvantages of widely used carbon forms as support

Carbon Materials	**ECSA ($m^2 g^{-1}$)**	**Conductivity ($S\ cm^{-1}$)**	**Advantages**	**Disadvantages**	**Ref.**
Vulcan XC-72	250	2.77	The catalytic activity can be increased by surface modification and pre-heat treatment.	Low utilization of metal catalysts and poor durability.	[110, 111]
CNT	50-1000	200-900	Excellent electrochemical stability and high hydrophilicity produce better ORR reactions.	Highly sensitive to different gas and synthesis methods.	[52, 112, 113]
GO	2630	$\sim 10^4$	Easy to synthesis on an industrial scale and functionalized as well.	Catalytic properties change with changing synthesis tech.	[114–116]
Ordered porous carbon(OPC)	600-2800	3.28×10^{-4} - 2.2×10^{-3}	Stability increases with increasing annealing temperature	Electrochemical activities strongly depend on pore size and the diameter less than 10nm.	[117–120]
Graphene nanosheets (GNS)	56	10^3-10^4	Highly stable than MWCNT, SWCNT, CB, and GO	Highly sensitive to the synthesis process. During preparation, it losses many properties due to aggregate.	[98, 121, 122]

Promising synthesis technique for ORR catalysts

The synthesis condition influences the catalyst compositions and structure of active sites. Several strategies are used to establish a catalyst that is comparable to Pt/C in both acid and base solutions. Among the improvement techniques, pyrolysis and core-shell techniques are widely used for developing alloy catalysts. Most recently, the irradiation method utilizes for obtaining a higher degree of alloying.

Pyrolysis

Different types of metal alloys help reduce PGM use and help modify the surface structure and reactivity within alloying elements through the change of electronic and geometric structure [11, 111]. Alloying PGM with transition metals declines the OH adsorption due to the existence of PGM-TM bond distance in lattice contraction, which promotes higher ORR activity than pure PGM. The durability of PGM-TM alloys depends

on the degree of alloy homogeneity [52, 123]. Performances of alloy catalysts are directly related to pyrolysis treatment. The effect of pyrolysis temperature has been illustrated in Figure 6(a-f).

From the TEM image of FeCN/GN(graphene nanosheets), it is clear that below 700^{o} C, only a few FeCN particles have been observed, marked by the white circle in Figure 6(a) and 6(b) which were pyrolyzed at 500^{o} C and 600^{o} C respectively. Figure 6(d-f) represents FeCN samples that pyrolyzed at 800 ^{o}C, 900 ^{o}C, and 1000 ^{o}C respectively. FeCN particles were uniformly distributed on GN(graphene nanosheets) above 700 ^{o}C. Figure 6(c) represents the sample pyrolyzed at 700 ^{o}C. At 700 ^{o}C, FeCN/GN exhibited the highest electron transfer (3.94) and ORR activity in acidic solutions. In general, a pyrolysis temperature below 700 °C is not enough to induce stable and active ORR sites [112, 124, 125]. The formation of Fe-N_x active sites strongly depends on pyrolysis, which contributes to ORR activity. N atoms have been successfully united into a carbon matrix, and the proportion of N touches the maximum level at 900 ^{o}C [53,119]. The pyrolysis treatment approach helps increase the concentration of ORR sites by modifying the M-N_x/C structure. Heat treatment also controls metal-N bonding [76,120].

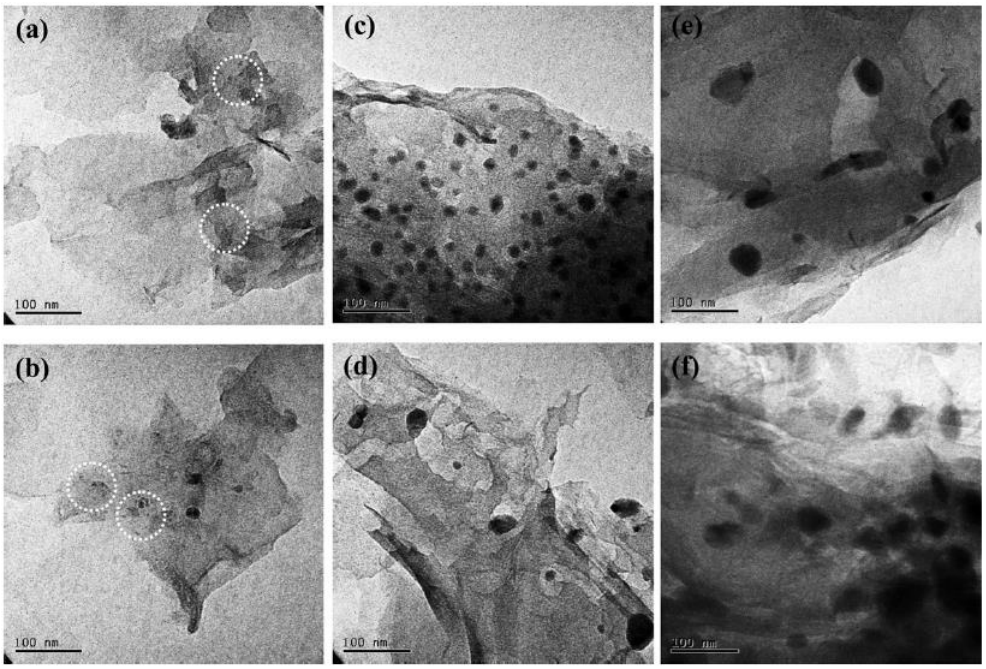


Figure 6. TEM image of FeCN/GN at 500 ^{o}C (a), 600 ^{o}C (b), 700 ^{o}C (c),800 ^{o}C (d), 900 ^{o}C (e), and 1000 ^{o}C (f) [124]

Core-shell structure

Mutual interaction of core metal and shell facilitates the mass activity and durability of ORR in both acidic and alkaline electrolytes. Generally, a core-shell-structured catalyst is designed by capturing the catalyst metal in carbon materials. This structure provides an exclusive electronic interaction between confined nanomaterials and carbon shells, thereby playing the main role in the enhancement of catalytic activity. Both single metal particles and metal alloy materials can serve as shells or core [105, 108]. This approach leads to a change in the d-band positions, which help provide higher activation energies. Ligand performances enhance catalytic activity and improve charge transfer [100]. Core materials and shell thickness are important factors for stability and ORR performance. Shell thickness helps with long term stability. The thickness of the shell screens the core interactivity, which improves catalytic stability [31, 115]. Gautam et al. reported that a shell material graphene nanosheets appears on behalf of electron collectors and tricks the core ion to form the existing active sites by providing high stability [116]. [116]

Irradiation technique

The irradiation process helps improve structural properties and chemical properties. γ-Irradiation helps reduce the oxygen functional group from the GO sheet and increases C=C bands. It also modifies the sp^2 character of C. Some work has been done using gamma irradiation. In the case of few-layered graphene materials, the O/C ratio exhibits a decreasing trend when γ-irradiation dose increases for GO and GONR (nanorod) [117]. A remarkable characteristic has been observed in preparing graphene aerogel (GA) from the GO sheet. GA shows more stability and has a honeycomb structure with a high C/O ratio after irradiation. No significant weight loss can be observed due to γ-irradiation.[118]. However, dose rate, total dose, type of solvent are important parameters for gamma irradiation induced synthesis technique. These parameters can be able to alter the size, chemical, and physical properties of the final product. Sharin and co-workers reported the reduction of GO has occurred when the cumulative dose was 35kGy. They utilized different amounts of irradiation dose,0, 5, 15, 20, and 35kGy on GO powders [119, 126, 127] In an aqueous solution (water/alcohol), Irradiation decompose the water molecules to hydroxyl radical, OH^-, hydrogen radical, and hydrated electron, H^* and e^- species. Alcohol removes the oxidative OH and converts it into reductive radicals.[121]. In the case of a heterogeneous catalyst, gamma irradiation changes the concentration of the active site of a catalyst surface, whereas electron beam irradiation induces a new active center by switching the chemical bond and creating defects on a catalyst surface [128]. Kakitani et al. reported that Pt-C bond formed during ion-beam irradiation (Ar^+). This bond changes the chemical state of Pt nanoparticles and carbon support that suppresses Pt oxidation and improves overall catalytic activity towards ORR [129]. After Ar^+ irradiation, carbon nanofiber-supported PtRu exhibits a lower crystal size (19.5 nm) due to the change in the valence state of support metal, whereas non-irradiated carbon nanofiber-supported PtRu shows a larger crystal size (20.1 nm) [130]. Proton irradiation leads to a break M (metal)-O bond by producing highly active radicals on the metal surface. During irradiation, the 2p orbital of O and the 3d orbital of metal merge, thereby reducing the bang gap, which increases the electronic conductivity and overall performance of the metal catalyst [131]. Ohkubo and co-workers suggested that the electron beam irradiation reduction method can synthesize both alloy and metal oxide on the carbon support simultaneously[132].

Conclusion

From the discussions, it is clear that all PGM alloys are comparable catalysts for ORR cathode in both acid and alkaline mediums, though 20%wt of Pt is needed for promising performance. Mixing PGM and transition metal is a good strategy for reducing the use of Pt. PGM-TM alloy catalysts also improve ORR activity and follow the $4e^-$ pathway in both types of solutions. However, 50wt% of PGM is required in the PGM-TM cluster for enhancing ORR activity. Most of the TM-based catalysts have been developed with the N supported carbon. N atom produces C-N sites that provide higher active site densities and mass transport. In the absence of the N atom, the TM-based catalysts are not comparable with commercial Pt/C and other PGM catalysts. N supported Fe, and Fe doped Co catalysts

work in acidic solutions, but it is not comparable with commercial Pt/C. All M-N-C (M= transition metal) exhibited better catalytic activity than Pt/C in alkaline solution. Choosing ideal carbon support can improve the catalytic activity of TM alloy in an acidic medium. The amount of nitrogen and carbon defects and metallic particles' existence are common factors for improving performance.

Alloy and pyrolysis are closely related to each other. Homogeneity of alloy catalysts depends on pyrolysis temperature. Core-shell is a popular technique for alloy catalysts. In this process, catalyst behaviour is associated with the mutual interaction between the core metal and the shell metal. Shell thickness also plays a hidden role to facilitates ORR. Nowadays, different types of irradiations have been taken a superior position in research.

Acknowledgment

This paper was completed with the financial assistance of Universiti Kebangsaan Malaysia (GUP-2018-041) and the International Atomic Energy Agency (R23130) and support of Fuel Cell Institute, UKM.

References

1. Rajapakse, R. M. G., Senarathna, K. G. C., Kondo, A., Jayawardena, P. S. and Shimomura, M. (2015). Extremely low-cost alternative for the oxygen reduction catalyst of fuel cell. *Advances in Automobile Engineering*, 4(1): 1.
2. Zhang, Y., Huang, N., Zhou, F., He, Q. and Zhan, S. (2018). Research on the oxygen reduction reaction (ORR) mechanism of g-C_3N_4 doped by Ag based on first-principles calculations. *Journal of the Chinese Chemical Society*, 65(12): 1431-1436.
3. She, Y., Chen, J., Zhang, C., Lu, Z., Ni, M., Sit, P. H. L. and Leung, M. K. H. (2017). Oxygen Reduction reaction mechanism of nitrogen-doped graphene derived from ionic liquid. *Energy Procedia*, 142: 1319-1326.
4. Hazarika, K. K., Goswami, C., Saikia, H., Borah, B. J. and Bharali, P. (2018). Cubic Mn_2O_3 nanoparticles on carbon as bifunctional electrocatalyst for oxygen reduction and oxygen evolution reactions. *Molecular Catalysis*, 451: 153-160.
5. Laurent-Brocq, M., Job, N., Eskenazi, D. and Pireaux, J. J. (2014). Pt/C catalyst for PEM fuel cells: Control of Pt nanoparticles characteristics through a novel plasma deposition method. *Applied Catalysis B: Environmental*, 147: 453-463.
6. Shao-Horn, Y., Sheng, W. C., Chen, S., Ferreira, P. J., Holby, E. F. and Morgan, D. (2007). Instability of supported platinum nanoparticles in low-temperature fuel cells. *Topics in Catalysis*, 46(3–4): 285–305.
7. Dombrovskis, J. K. and Palmqvist, A. E. C. (2016). Recent progress in synthesis, characterization and evaluation of non-precious metal catalysts for the oxygen reduction reaction. *Fuel Cells*, 16(1): 4-22.
8. Holton, O. and Stevenson, J. (2013). The role of platinum in proton exchange membrane fuel cells - Johnson Matthey technology review. *Platinum Metals Reviews*, 57(4): 259-271.
9. Mustain, W. E., Shrestha, S., Ashegi, S., Timbro, J., Lang, C. M. and Mustain, W. E. (2011). ORR and fuel cell performance of Pt supported on N-functionalized mesoporous carbon, *ECS Transactions*, 41(1): 1183.
10. Ghosh, S., Mondal, S. and Retna Raj, C. (2014). Carbon nanotube-supported dendritic Pt-on-Pd nanostructures: Growth mechanism and electrocatalytic activity towards oxygen reduction reaction. *Journal of Materials Chemistry A*, 2(7): 2233-2239.
11. Guha, A., Lu, W., Zawodzinski, T. A. and Schiraldi, D. A. (2007). Surface-modified carbons as platinum catalyst support for PEM fuel cells, *Carbon*, 45: 1506-1517.
12. Mun, Y., Lee, S., Kim, K., Kim, S., Lee, S., Han, J. W. and Lee, J. (2019). Versatile strategy for tuning ORR activity of a single Fe-N4 site by controlling electron-withdrawing/donating properties of a carbon plane. *Journal of the American Chemical Society*, 141(15): 6254-6262.
13. Kodali, M., Santoro, C., Serov, A., Kabir, S., Artyushkova, K., Matanovic, I. and Atanassov, P. (2017). Air breathing cathodes for microbial fuel cell using Mn-, Fe-, Co- and Ni-containing platinum group metal-free catalysts. *Electrochimica Acta*, 231: 115-124.

14. Song, M., Song, Y., Sha, W., Xu, B., Guo, J. and Wu, Y. (2020). Recent advances in non-precious transition metal/nitrogen-doped carbon for oxygen reduction electrocatalyst. *Catalysts*, 10(1): 141.
15. Mao, J., Liu, P., Du, C., Liang, D., Yan, J. and Song, W. (2019). Tailoring 2D MoS_2 heterointerfaces for promising oxygen reduction reaction electrocatalysis. *Journal of Materials Chemistry A*, 7(15): 8785-8789.
16. Ma, R., Lin, G., Zhou, Y., Liu, Q., Zhang, T., Shan, G. and Wang, J. (2019). A review of oxygen reduction mechanisms for metal-free carbon-based electrocatalysts. *NPJ Computational Materials*, *5*(1): 1-15.
17. Tang, Z., Wu, W. and Wang, K. (2018). Oxygen reduction reaction catalyzed by noble metal clusters. *Catalysts*, 8(2): 65.
18. Kim, J. Y., Oh, T. K., Shin, Y., Bonnett, J. and Weil, K. S. (2011). A novel non-platinum group electrocatalyst for PEM fuel cell application. *International Journal of Hydrogen Energy*, 36(7): 4557-4564.
19. Wang, B. (2005). Recent development of non-platinum catalysts for oxygen reduction reaction. *Journal of Power Sources*, 152(1–2): 1-15.
20. Sui, S., Wang, X., Zhou, X., Su, Y., Riffat, S. and Liu, C. J. (2017). A comprehensive review of Pt electrocatalysts for the oxygen reduction reaction: Nanostructure, activity, mechanism and carbon support in PEM fuel cells. *Journal of Materials Chemistry A*, 5(5): 1808-1825.
21. Raciti, D., Kubal, J., Ma, C., Barclay, M., Gonzalez, M., Chi, M. and Wang, C. (2016). Pt_3Re alloy nanoparticles as electrocatalysts for the oxygen reduction reaction. *Nano Energy*, 20: 202-211.
22. Hyun, K., Lee, J. H., Yoon, C. W. and Kwon, Y. (2013). The effect of platinum based bimetallic electrocatalysts on oxygen reduction reaction of proton exchange membrane fuel cells. *International Journal of Electrochemical Science*, 8(10): 11752-11767.
23. Tian, J., Wu, W., Tang, Z., Wu, Y., Burns, R., Tichnell, B. and Chen, S. (2018). Oxygen reduction reaction and hydrogen evolution reaction catalyzed by Pd–Ru nanoparticles encapsulated in porous carbon nanosheets. *Catalysts*, 8(8): 1-15.
24. Zhou, Z. M., Shao, Z. G., Qin, X. P., Chen, X. G., Wei, Z. D. and Yi, B. L. (2010). Durability study of Pt-Pd/C as PEMFC cathode catalyst. *International Journal of Hydrogen Energy*, 35(4): 1719-1726.
25. Wang, W., Wang, Z., Wang, J., Zhong, C. J. and Liu, C. J. (2017). Highly active and stable Pt–Pd Alloy catalysts synthesized by room-temperature electron reduction for oxygen reduction reaction. *Advanced Science*, 4(4): 1-9.
26. Yusof, M. S. M., Jalil, A. A., Ahmad, A., Triwahyono, S., Othman, M. H. D., Abdullah, T. A. T. and Nabgan, W. (2019). Effect of Pt–Pd/C coupled catalyst loading and polybenzimidazole ionomer binder on oxygen reduction reaction in high-temperature PEMFC. *International Journal of Hydrogen Energy*, 2019: 20760-20769.
27. Thanasilp, S. and Hunsom, M. (2011). Effect of Pt: Pd atomic ratio in Pt-Pd/C electrocatalyst-coated membrane on the electrocatalytic activity of ORR in PEM fuel cells. *Renewable Energy*, 36(6): 1795-1801.
28. Jackson, C., Conrad, O. and Levecque, P. (2017). Systematic study of Pt-Ru/C catalysts prepared by chemical deposition for direct methanol fuel cells. *Electrocatalysis*, 8(3): 224-234.
29. Huang, H., Zhu, J., Li, D., Shen, C., Li, M., Zhang, X. and Wu, Y. (2017). Pt nanoparticles grown on 3D RuO_2-modified graphene architectures for highly efficient methanol oxidation. *Journal of Materials Chemistry A*, 5(9): 4560-4567.
30. Yang, G., Sun, Y., Lv, P., Zhen, F., Cao, X., Chen, X. and Kong, X. (2016). Preparation of Pt–Ru/C as an oxygen-reduction electrocatalyst in microbial fuel cells for wastewater treatment. *Catalysts*, 6(10): 150.
31. Jackson, A., Strickler, A., Higgins, D. and Jaramillo, T. F. (2018). Engineering Ru@Pt core-shell catalysts for enhanced electrochemical oxygen reduction mass activity and stability. *Nanomaterials*, *8*(1): 38.
32. Tolmachev, Y. V. and Petrii, O. A. (2017). Pt–Ru electrocatalysts for fuel cells: developments in the last decade. *Journal of Solid State Electrochemistry*, 21(3): 613-639.

33. Durst, J., Simon, C., Hasché, F. and Gasteiger, H. A. (2015). Hydrogen oxidation and evolution reaction kinetics on carbon supported Pt, Ir, Rh, and Pd electrocatalysts in acidic media. *Journal of The Electrochemical Society*, 162(1): F190-F203.
34. Zeng, M., Wang, X. X., Tan, Z. H., Huang, X. X. and Wang, J. N. (2014). Remarkable durability of Pt-Ir alloy catalysts supported on graphitic carbon nanocages. *Journal of Power Sources*, 264: 272-281.
35. Zheng, H. B., An, L., Zheng, Y., Qu, C., Fang, Y., Liu, Q. and Dang, D. (2018). Tuning the catalytic activity of Ir@Pt nanoparticles through controlling ir core size on cathode performance for PEM fuel cell application. *Frontiers in Chemistry*, *6*(7): 1-7.
36. Fang, D., Tang, X., Yang, L., Xu, D., Zhang, H., Sun, S. and Yi, B. (2019). Facile synthesis of Pt-decorated Ir black as a bifunctional oxygen catalyst for oxygen reduction and evolution reactions. *Nanoscale*, 11(18): 9091-9102.
37. Zhu, J., Elnabawy, A. O., Lyu, Z., Xie, M., Murray, E. A., Chen, Z., Xia, Y. (2019). Facet-controlled Pt–Ir nanocrystals with substantially enhanced activity and durability towards oxygen reduction. *Materials Today*, 2019: 1-9.
38. Lin, C., Wu, G., Li, H., Geng, Y., Xie, G., Yang, J. and Jin, J. (2017). Rh nanoparticles supported on ultrathin carbon nanosheets for high-performance oxygen reduction reaction and catalytic hydrogenation. *Nanoscale*, 9(5): 1834-1839.
39. Paál, Z., Gyorffy, N., Wootsch, A., Tóth, L., Bakos, I., Szabó, S. and Schlögl, R. (2007). Preparation, physical characterization and catalytic properties of unsupported Pt-Rh catalyst. *Journal of Catalysis*, *250*(2): 254-263.
40. Narayanamoorthy, B., Datta, K. K. R., Eswaramoorthy, M. and Balaji, S. (2014). Self-stabilized Pt–Rh bimetallic nanoclusters as durable electrocatalysts for dioxygen reduction in PEM fuel cells. *RSC Advances*, 4(98): 55571-55579.
41. Goswami, C., Hazarika, K. K. and Bharali, P. (2018). Transition metal oxide nanocatalysts for oxygen reduction reaction. *Materials Science for Energy Technologies*, 1(2): 117–128.
42. Xin, L., Zhang, Z., Wang, Z., Qi, J. and Li, W. (2013). Carbon supported Ag nanoparticles as high performance cathode catalyst for H_2/O_2 anion exchange membrane fuel cell. *Frontiers in Chemistry*, 1: 16.
43. Esfandiari, A., Kazemeini, M. and Bastani, D. (2016). Synthesis, characterization and performance determination of an Ag@Pt/C electrocatalyst for the ORR in a PEM fuel cell. *International Journal of Hydrogen Energy*, 41(45): 20720-20730.
44. Chiwata, M., Yano, H., Ogawa, S., Watanabe, M., Iiyama, A. and Uchida, H. (2016). Oxygen reduction reaction activity of carbon-supported Pt-Fe, Pt-Co, and Pt-Ni alloys with stabilized Pt-skin layers. *Electrochemistry*, *84*(3), 133–137.
45. Li, W., Pan, Z., Huang, Z., Zhou, Q., Xu, Y., Wu, S., Hu, G. (2018). Pt nanoparticles supported on titanium iron nitride nanotubes prepared as a superior electrocatalysts for methanol electrooxidation. *International Journal of Hydrogen Energy*, 43(20): 9777-9786.
46. Termpornvithit, C., Chewasatn, N. and Hunsom, M. (2012). Stability of Pt-Co/C and Pt-Pd/C based oxygen reduction reaction electrocatalysts prepared at a low temperature by a combined impregnation and seeding process in PEM fuel cells. *Journal of Applied Electrochemistry*, 42(3): 169-178.
47. Cui, Y., Wu, Y., Wang, Z., Yao, X., Wei, Y., Kang, Y., Gan, L. (2020). Mitigating metal dissolution and redeposition of Pt-Co catalysts in PEM fuel cells: Impacts of structural ordering and particle size. *Journal of The Electrochemical Society*, 167(6): 064520.
48. Rohendi, D., Rachmat, A. and Syarif, N. (2018). Fabrication and characterization of Pt-Co/C catalyst for fuel cell electrode. *Journal of Physics: Conference Series*, 1095(1): 012007.
49. Singh, R. N. (2012). Preparation of bimetallic Pd-Co nanoparticles on graphene support for use as methanol tolerant oxygen reduction electrocatalysts. *Engineering, Technology & Applied Science Research*, *2*(6): 295-301.
50. Ramli, Z. A. C. and Kamarudin, S. K. (2018). Platinum-based catalysts on various carbon supports and conducting polymers for direct methanol fuel cell applications: a review. *Nanoscale Research Letters*, 13: 1-25.

51. Mechler, A. K., Sahraie, N. R., Armel, V., Zitolo, A., Sougrati, M. T., Schwämmlein, J. N. and Jaouen, F. (2018). Stabilization of iron-based fuel cell catalysts by non-catalytic platinum. *Journal of The Electrochemical Society*, 165(13): F1084–F1091.
52. Mohanraju, K. and Cindrella, L. (2014). Impact of alloying and lattice strain on ORR activity of Pt and Pd based ternary alloys with Fe and Co for proton exchange membrane fuel cell applications. *RSC Advances*, 4(23): 11939-11947.
53. Li, X. P., Xiang, X. D., Yang, H. Y., Wang, X. J., Tan, C. L. and Li, W. S. (2013). Hydrogen tungsten bronze-supported platinum as electrocatalyst for methanol oxidation. *Fuel Cells*, 13(2): 314-318.
54. Seselj, N., Engelbrekt, C. and Zhang, J. (2015). Graphene-supported platinum catalysts for fuel cells. *Science Bulletin*, 60(9): 864-876.
55. Lv, H., Li, D., Strmcnik, D., Paulikas, A. P., Markovic, N. M. and Stamenkovic, V. R. (2016). Recent advances in the design of tailored nanomaterials for efficient oxygen reduction reaction. *Nano Energy*, 29: 149-165.
56. Thippani, T., Mandal, S., Wang, G., Ramani, V. K. and Kothandaraman, R. (2016). Probing oxygen reduction and oxygen evolution reactions on bifunctional non-precious metal catalysts for metal-air batteries. *RSC Advances*, 6(75): 71122-71133.
57. Osgood, H., Devaguptapu, S. V., Xu, H., Cho, J. and Wu, G. (2016). Transition metal (Fe, Co, Ni, and Mn) oxides for oxygen reduction and evolution bifunctional catalysts in alkaline media. *Nano Today*, 11(5): 601-625.
58. Akbari, A., Amini, M., Tarassoli, A., Eftekhari-Sis, B., Ghasemian, N. and Jabbari, E. (2018). Transition metal oxide nanoparticles as efficient catalysts in oxidation reactions. *Nano-Structures and Nano-Objects*, 14: 19-48.
59. Ren, G., Gao, L., Teng, C., Li, Y., Yang, H., Shui, J. and Dai, L. (2018). Ancient Chemistry "pharaoh's Snakes" for Efficient Fe-/N-Doped Carbon Electrocatalysts. *ACS Applied Materials and Interfaces*, 10(13): 10778–10785.
60. Gu, L., Jiang, L., Li, X., Jin, J., Wang, J. and Sun, G. (2016). A Fe-N-C catalyst with highly dispersed iron in carbon for oxygen reduction reaction and its application in direct methanol fuel cells. *Cuihua Xuebao/Chinese Journal of Catalysis*, 37(4): 539-548.
61. Park, M., Lee, J., Hembram, K., Lee, K.-R., Han, S., Yoon, C. and Kim, J. (2016). Oxygen reduction electrocatalysts based on coupled iron nitride nanoparticles with nitrogen-doped carbon. *Catalysts*, 6(6): 86.
62. Rahman, K. R., Kok, K. Y., Wong, W. Y., Yang, H. and Lim, K. L. (2021). Effect of iron loading on the catalytic activity of Fe/N-doped reduced graphene oxide catalysts via irradiation. *Applied Sciences (Switzerland)*, 11(1): 1-10.
63. Xi, J., Wang, F., Mei, R., Gong, Z., Fan, X., Yang, H. and Luo, Z. (2016). Catalytic performance of a pyrolyzed graphene supported Fe-N-C composite and its application for acid direct methanol fuel cells. *RSC Advances*, 6(93): 90797-90805.
64. Meng, H., Chen, X., Gong, T., Liu, H., Liu, Y., Li, H. and Zhang, Y. (2019). N, P, S/Fe-codoped carbon derived from feculae bombycis as an efficient electrocatalyst for oxygen reduction reaction. *ChemCatChem*, 11(24): 6015-6021.
65. Basri, S. and Kamarudin, S. K. (2018). Nanocatalyst FeN_4/C molecular orbital behaviour for oxygen reduction reaction (ORR) in cathode direct methano fuel cell (DMFC). *Jurnal Kejuruteraan*, 1(2): 59-64.
66. Jiang, W. J., Gu, L., Li, L., Zhang, Y., Zhang, X., Zhang, L. J. and Wan, L. J. (2016). Understanding the high activity of Fe-N-C electrocatalysts in oxygen reduction: Fe/Fe_3C nanoparticles boost the activity of Fe-Nx. *Journal of the American Chemical Society*, 138(10): 3570-3578.
67. Hossen, M. M., Artyushkova, K., Atanassov, P. and Serov, A. (2018). Synthesis and characterization of high performing Fe-N-C catalyst for oxygen reduction reaction (ORR) in alkaline exchange membrane fuel cells. *Journal of Power Sources*, 375: 214-221.
68. Zhan, Y., Xie, F., Zhang, H., Lin, Z., Huang, J., Zhang, W. and Meng, H. (2018). Non noble metal catalyst for oxygen reduction reaction and its characterization by simulated fuel cell test. *Journal of The Electrochemical Society*, 165(15): J3008-J3015.

69. Kim, S., Park, H. and Li, O. L. (2020). Cobalt nanoparticles on plasma-controlled nitrogen-doped carbon as high-performance ORR electrocatalyst for primary Zn-Air battery. *Nanomaterials*, 10(2): 223.
70. Zang, J., Wang, F., Cheng, Q., Wang, G., Ma, L., Chen, C. and Yang, H. (2020). Cobalt/zinc dual-sites coordinated with nitrogen in nanofibers enabling efficient and durable oxygen reduction reaction in acidic fuel cells. *Journal of Materials Chemistry A*, 8(7): 3686-3691.
71. Grinberg, V. A., Mayorova, N. A., Pasynskii, A. A., Modestov, A. D., Shiryaev, A. A., Vysotskii, V. V. and Nogai, A. S. (2018). Nanostructured platinum-free catalysts of oxygen reduction based on metal chalcogenide cobalt clusters. *Russian Journal of Coordination Chemistry*, 44(10): 589-595.
72. Winey, K. I., Li, J., Doan-Nguyen, V. V. T., Murray, C. B., Su, D., Trigg, E. B. and Agarwal, R. (2015). Synthesis and X-ray characterization of cobalt phosphide (Co_2P) nanorods for the oxygen reduction reaction. *ACS Nano*, 9(8): 8108-8115.
73. Zhao, H., Xing, T., Li, L., Geng, X., Guo, K., Sun, C. and An, B. (2019). Synthesis of cobalt and nitrogen co-doped carbon nanotubes and its ORR activity as the catalyst used in hydrogen fuel cells. *International Journal of Hydrogen Energy*, 44(46): 25180-25187.
74. Liang, G., Huang, J., Li, J., Wu, Y., Huang, G., Jin, Y. Q., ... and Meng, H. (2020). Improving the catalytic performance of Co/N/C catalyst for oxygen reduction reaction by alloying with Fe. J*ournal of The Electrochemical Society*, 167(10), 104502.
75. An, L., Jiang, N., Li, B., Hua, S., Fu, Y., Liu, J. and Sun, Z. (2018). A highly active and durable iron/cobalt alloy catalyst encapsulated in N-doped graphitic carbon nanotubes for oxygen reduction reaction by a nanofibrous dicyandiamide template. *Journal of Materials Chemistry A*, 6(14): 5962-5970.
76. Liu, P., Ran, J., Xia, B., Xi, S., Gao, D. and Wang, J. (2020). Bifunctional oxygen electrocatalyst of mesoporous Ni/NiO nanosheets for flexible rechargeable Zn–Air batteries. *Nano-Micro Letters*, *12*(1), 1–12.
77. Hao, Y., Xu, Y., Liu, J. and Sun, X. (2017). Nickel-cobalt oxides supported on Co/N decorated graphene as an excellent bifunctional oxygen catalyst. *Journal of Materials Chemistry A*, 5(11): 5594-5600.
78. Trzešniewski, B. J., Diaz-Morales, O., Vermaas, D. A., Longo, A., Bras, W., Koper, M. T. M. and Smith, W. A. (2015). In situ observation of active oxygen species in Fe-containing Ni-based oxygen evolution catalysts: The effect of pH on electrochemical activity. *Journal of the American Chemical Society*, 137(48): 15112-15121.
79. Zhuang, Z., Giles, S. A., Zheng, J., Jenness, G. R., Caratzoulas, S., Vlachos, D. G. and Yan, Y. (2016). Nickel supported on nitrogen-doped carbon nanotubes as hydrogen oxidation reaction catalyst in alkaline electrolyte. *Nature Communications*, 7: 1–8.
80. Faubert, P., Kondov, I., Qazzazie, D., Yurchenko, O. and Müller, C. (2018). A non-noble Cr-Ni-based catalyst for the oxygen reduction reaction in alkaline polymer electrolyte fuel cells. *MRS Communications*, *8*(1): 160-167.
81. Kabir, S., Lemire, K., Artyushkova, K., Roy, A., Odgaard, M., Schlueter, D. and Serov, A. (2017). Platinum group metal-free NiMo hydrogen oxidation catalysts: High performance and durability in alkaline exchange membrane fuel cells. *Journal of Materials Chemistry A*, 5(46): 24433-24443.
82. Xie, X., Liu, J., Li, T., Song, Y. and Wang, F. (2018). Post-formation copper-nitrogen species on carbon black: their chemical structures and active sites for oxygen reduction reaction. *Chemistry - A European Journal*, *24*(39): 9968-9975.
83. Hamedi, M., Wigenius, J., Tai, F. I., Björk, P. and Aili, D. (2010). Polypeptide-guided assembly of conducting polymer nanocomposites. *Nanoscale*, 2(10): 2058-2061.
84. Kang, Y. S., Heo, Y., Kim, P. and Yoo, S. J. (2017). Preparation and characterization of Cu–N–C electrocatalysts for oxygen reduction reaction in alkaline anion exchange membrane fuel cells. *Journal of Industrial and Engineering Chemistry*, 52(3): 35-41.

85. He, Q., Yang, X., Ren, X., Koel, B. E., Ramaswamy, N., Mukerjee, S. and Kostecki, R. (2011). A novel CuFe-based catalyst for the oxygen reduction reaction in alkaline media. *Journal of Power Sources*, 196(18): 7404-7410.
86. 86. Qiao, Y., Ni, Y., Kong, F., Li, R., Zhang, C., Kong, A. and Shan, Y. (2019). Pyrolytic carbon-coated Cu-Fe alloy nanoparticles with high catalytic performance for oxygen electroreduction. *Chemistry - An Asian Journal*, 14(15): 2676-2684.
87. Cui, L., Cui, L., Li, Z., Zhang, J., Wang, H., Lu, S. and Xiang, Y. (2019). A copper single-atom catalyst towards efficient and durable oxygen reduction for fuel cells. *Journal of Materials Chemistry A*, 7(28): 16690-16695.
88. Mosa, I. M., Biswas, S., El-Sawy, A. M., Botu, V., Guild, C., Song, W. and Suib, S. L. (2015). Tunable mesoporous manganese oxide for high performance oxygen reduction and evolution reactions. *Journal of Materials Chemistry A*, 4(2): 620-631.
89. Liu, J., Yu, M., Wang, X., Wu, J., Wang, C., Zheng, L. and Wang, W. (2017). Investigation of high oxygen reduction reaction catalytic performance on Mn-based mullite $SmMn_2O_5$. *Journal of Materials Chemistry A*, 5(39): 20922-20931.
90. Zhang, R., Zhang, J., Ma, F., Wang, W. Y. and Li, R. F. (2014). Preparation of Mn-N-C catalyst and its electrocatalytic activity for the oxygen reduction reaction in alkaline medium. *Ranliao Huaxue Xuebao/Journal of Fuel Chemistry and Technology*, 42(4): 467-475.
91. Stoerzinger, K. A., Risch, M., Han, B. and Shao-Horn, Y. (2015). Recent insights into manganese oxides in catalyzing oxygen reduction kinetics. *ACS Catalysis*, 5(10): 6021-6031.
92. Shao, Y., Liu, J., Wang, Y. and Lin, Y. (2009). Novel catalyst support materials for PEM fuel cells: Current status and future prospects. *Journal of Materials Chemistry*, 19(1): 46-59.
93. Qin, C., Wang, J., Yang, D., Li, B. and Zhang, C. (2016). Proton exchange membrane fuel cell reversal: A review. *Catalysts*, *6*(12), 197.
94. Chong, S. T., Lee, T. K., Samad, S., Loh, K. S., Wong, W. Y., Wan Daud, W. R. and Sunarso, J. (2018). Carbon and non-carbon support materials for platinum-based catalysts in fuel cells. *International Journal of Hydrogen Energy*, 43(16): 7823-7854.
95. Devrim, Y., Arıca, E. D. and Albostan, A. (2018). Graphene based catalyst supports for high temperature PEM fuel cell application. *International Journal of Hydrogen Energy*, 43(26): 11820-11829.
96. Khan, A. S. A., Ahmed, R. and Mirza, M. L. (2010). Performance evaluation of platinum-based catalysts for the development of proton exchange membrane fuel cells. *Turkish Journal of Chemistry*, 34(2): 193-206.
97. Choi, S. M., Seo, M. H., Kim, H. J. and Kim, W. B. (2011). Synthesis of surface-functionalized graphene nanosheets with high Pt-loadings and their applications to methanol electrooxidation. *Carbon*, 49(3): 904-909.
98. Suda, Y., Ozaki, M., Tanoue, H. and Takikawa, H. (2013). Supporting PtRu catalysts on various types of carbon nanomaterials for fuel cell applications. *Journal of Physics: Conference Series*, 433(1): 012008.
99. Molina-García, M. A. and Rees, N. V. (2016). Effect of catalyst carbon supports on the oxygen reduction reaction in alkaline media: A comparative study. *RSC Advances*, 6(97): 94669-94681.
100. Esfandiari, A. and Kazemeini, M. (2018). Investigating electrochemical behaviors of Ag@Pt core–shell nanoparticles supported upon different carbon materials acting as PEMFC's cathodes. *Chemical Engineering Transactions*, 70: 2161-2166.
101. Minitha, C. R. and Rajendrakumar, R. T. (2013). Synthesis and characterization of reduced graphene oxide. *Advanced Materials Research*, 678: 56-60.
102. Kang, S. Y., Kim, H. J. and Chung, Y. H. (2018). Recent developments of nano-structured materials as the catalysts for oxygen reduction reaction. *Nano Convergence*, 5(1): 1-15.

103. Grigoriev, S. A., Fateev, V. N., Pushkarev, A. S., Pushkareva, I. V., Ivanova, N. A. and Kalinichenko, V. N., Wei, X. (2018). Reduced graphene oxide and its modifications as catalyst supports and catalyst layer modifiers for PEMFC. *Materials*, 11(8): 1405.
104. Alam, S. N., Sharma, N. and Kumar, L. (2017). Synthesis of graphene oxide (GO) by modified hummers method and its thermal reduction to obtain reduced graphene oxide (rGO). *Graphene*, 6(1): 118
105. Liu, J., Choi, H. J. and Meng, L. Y. (2018). A review of approaches for the design of high-performance metal/graphene electrocatalysts for fuel cell applications. *Journal of Industrial and Engineering Chemistry*, 64: 1-15.
106. Santoro, C., Serov, A., Stariha, L., Kodali, M., Gordon, J., Babanova, S. and Atanassov, P. (2016). Iron based catalysts from novel low-cost organic precursors for enhanced oxygen reduction reaction in neutral media microbial fuel cells. *Energy and Environmental Science*, 9(7): 2346-2353.
107. Soo, L. T., Loh, K. S., Mohamad, A. B., Daud, W. R. W. and Wong, W. Y. (2015). An overview of the electrochemical performance of modified graphene used as an electrocatalyst and as a catalyst support in fuel cells. *Applied Catalysis A: General*, 497: 198-210.
108. Xiao, M., Zhu, J., Feng, L., Liu, C. and Xing, W. (2015). Meso/macroporous nitrogen-doped carbon architectures with iron carbide encapsulated in graphitic layers as an efficient and robust catalyst for the oxygen reduction reaction in both acidic and alkaline solutions. *Advanced Materials*, 27(15): 2521-2527.
109. Liang, Y., Wang, H., Zhou, J., Li, Y., Wang, J., Regier, T. and Dai, H. (2012). Covalent hybrid of spinel manganese-cobalt oxide and graphene as advanced oxygen reduction electrocatalysts. *Journal of the American Chemical Society*, 134(7): 3517-3523.
110. Choi, H. J., Jung, S. M., Seo, J. M., Chang, D. W., Dai, L. and Baek, J. B. (2012). Graphene for energy conversion and storage in fuel cells and supercapacitors. *Nano Energy*, 1(4): 534-551.
111. Anastasopoulos, A., Blake, J. and Hayden, B. E. (2011). Non-noble intertransition binary metal alloy electrocatalyst for hydrogen oxidation and hydrogen evolution. *Journal of Physical Chemistry C*, 115(39): 19226-19230.
112. Osmieri, L. (2019). Transition metal–nitrogen–carbon (M–N–C) catalysts for oxygen reduction reaction. insights on synthesis and performance in polymer electrolyte fuel cells. *ChemEngineering*, 3(1): 16.
113. Li, L., Shen, S., Wei, G., Li, X., Yang, K., Feng, Q. and Zhang, J. (2019). A comprehensive investigation on pyrolyzed fe-n-c composites as highly efficient electrocatalyst toward the oxygen reduction reaction of PEMFCs. *ACS Applied Materials and Interfaces*, 11: 14126-14135.
114. Chen, Z., Higgins, D., Yu, A., Zhang, L. and Zhang, J. (2011). A review on non-precious metal electrocatalysts for PEM fuel cells. *Energy and Environmental Science*, 4(9): 3167-3192.
115. Ren, X., Lv, Q., Liu, L., Liu, B., Wang, Y., Liu, A. and Wu, G. (2019). Current progress of Pt and Pt-based electrocatalysts used for fuel cells. *Sustainable Energy and Fuels*, 4(1): 15-30.
116. Gautam, J., Huu Tuan, L., Kim, N. H., Van Hien, H., Thanh Tran, D., Lee, J. H. and Dinh Chuong, N. (2018). Emerging core-shell nanostructured catalysts of transition metal encapsulated by two-dimensional carbon materials for electrochemical applications. *Nano Today*, 22: 100-131.
117. Ansón-Casaos, A., Puértolas, J. A., Pascual, F. J., Hernández-Ferrer, J., Castell, P. and Benito, A. M., Martínez, M. T. (2014). The effect of gamma-irradiation on few-layered graphene materials. *Applied Surface Science*, 301: 264-272.
118. He, Y., Li, J., Li, L. and Li, J. (2016). Gamma-ray irradiation-induced reduction and self-assembly of graphene oxide into three-dimensional graphene aerogel. *Materials Letters*, 177(1): 76-79.
119. Abidin, Z., Muhamad, E., Ahmad Daud, N., Ibrahim, N., Chieng, B. and Talib, Z. (2017). Functionalizing graphene oxide with alkylamine by gamma-ray irradiation method. *Nanomaterials*, 7(6): 135.

120. Wang, W., Zhao, X., Shi, H., Liu, L., Deng, H., Xu, Z. and Miao, X. (2020). Shape inducer-free polygonal angle platinum nanoparticles in graphene oxide as oxygen reduction catalyst derived from gamma irradiation. *Journal of Colloid and Interface Science*, 575: 1-15.
121. Xu, Z., Chen, L., Zhou, B., Li, Y., Li, B., Niu, J. and Qian, X. (2013). Nano-structure and property transformations of carbon systems under γ-ray irradiation: A review. *RSC Advances*, 3(27): 10579-10597.
122. Park, H. Y., Yang, D. S., Bhattacharjya, D., Song, M. Y. and Yu, J. S. (2014). A highly efficient carbon-supported Pt electrocatalyst prepared by γ-irradiation for cathodic oxygen reduction. *International Journal of Hydrogen Energy*, 39(4): 1688-1697.
123. Meku, E., Du, C., Wang, Y. and Du, L. (2016). Impact of different synthesis methods on the electrocatalytic activity and stability of Pd-Fe/C nanoparticles for oxygen reduction reaction in fuel cells. *2016 International Conference on Engineering and Technology Innovations:* pp. 127-131.
124. Hung, T. F., Tu, M. H., Tsai, C. W., Chen, C. J., Liu, R. S., Liu, W. R. and Lo, M. Y. (2013). Influence of pyrolysis temperature on oxygen reduction reaction activity of carbon-incorporating iron nitride/nitrogen-doped graphene nanosheets catalyst. *International Journal of Hydrogen Energy*, 38(10): 3956-3962.
125. Jeon, M. K. and McGinn, P. J. (2012). Co-alloying effect of Co and Cr with Pt for oxygen electro-reduction reaction. *Electrochimica Acta*, *64*(3): 147-153.
126. Sharin, S., Rahman, I. A., Ahmad, A. F., Mohd, H. M. K., Mohamed, F., Radiman, S., … and Bastamam, I. S. A. (2015). Penurunan grafin oksida kepada grafin menggunakan sinar gama. *Malaysian Journal of Analytical Sciences*, 19(6): 1223-1228.
127. Li, Z., Yang, Y., Relefors, A., Kong, X., Siso, G. M., Wickman, B. and Soroka, I. L. (2021). Tuning morphology, composition and oxygen reduction reaction (ORR) catalytic performance of manganese oxide particles fabricated by γ-radiation induced synthesis. *Journal of Colloid and Interface Science*, 583: 71-79.
128. Mashentseva, A. A., Shlimas, D. I., Kozlovskiy, A. L., Zdorovets, M. V., Russakova, A. V., Kassymzhanov, M. and Borisenko, A. N. (2019). Electron beam induced enhancement of the catalytic properties of ion-track membranes supported copper nanotubes in the reaction of the P-nitrophenol reduction. *Catalysts*, 9(9): 737.
129. Kakitani, K., Kimata, T., Yamaki, T., Yamamoto, S., Shimoyama, I., Matsumura, D. and Terai, T. (2017). Activity enhancement of platinum nanoparticle catalysts on ion-beam-irradiated carbon support. *National Institutes for Quantum and Radiological Science and Technology*, 34: 2016-2018.
130. Nakagawa, N., Ishitobi, H., Abe, S., Kakinuma, M., Koshikawa, H., Yamamoto, S. and Yamaki, T. (2019). A novel method to enhance the catalytic activity of PtRu on the support using CeO_2 by high-energy ion-beam irradiation. *Catalysis Today*, 364: 118-124.
131. Choi, Y., Lim, D., Oh, E., Lim, C. and Baeck, S. H. (2019). Effect of proton irradiation on electrocatalytic properties of MnO_2 for oxygen reduction reaction. *Journal of Materials Chemistry A*, 7(19): 11659-11664.
132. Ohkubo, Y., Hamaguchi, Y., Seino, S., Nakagawa, T., Kageyama, S., Kugai, J. and Yamamoto, T. A. (2013). Preparation of carbon-supported PtCo nanoparticle catalysts for the oxygen reduction reaction in polymer electrolyte fuel cells by an electron-beam irradiation reduction method. *Journal of Materials Science*, 48(14): 5047-5054.

Malaysian Journal of Analytical Sciences Vol 26 No 4 2022

		Page
1.	SYNTHESIS, PHOTOPHYSICAL AND COMPUTATIONAL APPROACHES ON NONLINEAR OPTICAL (NLO) PROPERTIES OF NAPHTHALEN-1-YL ETHYNYLATED-CHALCONE DERIVATIVE (Sintesis, Pendekatan Fotofizik dan Pengkomputeran Terhadap Sifat Optik Tak Linear (NLO) bagi Terbitan Naftalen-1-il Teretinil-Kalkon) *Mas Mohammed, Wan M. Khairul, Rafizah Rahamathullah, Fazira Ilyana Abdul Razak, Suhaila Sapari*	684
2.	EVALUATION OF THE TOTAL FLAVONOID, PHENOLIC CONTENT, AND ANTIOXIDANT ACTIVITY IN SABAH SNAKE GRASS EXTRACTS (*Clinacanthus nutans* Lindau) (Penilaian Jumlah Kandungan Flavonoid, Fenolik dan Aktiviti Antioksida bagi Ekstrak Belalai Gajah (*Clinacanthus nutans* Lindau)) *Idham Zaharudie and Chong Shu Xian*	698
3.	FORMULATION OF HIGH-QUALITY UV-CURABLE COATING CONTAINING RENEWABLE REACTIVE DILUENTS FOR WOOD PROTECTION (Formulasi Salutan Awetan-UV Berkualiti Tinggi yang Mengandungi Diluen Reaktif yang Boleh Diperbaharui untuk Perlindungan Kayu) *Noraini Abd Ghani, Emilia Abdulmalek, Rajni Hatti-Kaul, Azren Aida Asmawi, Mohd Basyaruddin Abdul Rahman*	708
4.	DETERMINATION OF 3-MONOCHLOROPROPANE-1,2-DIOL (3-MCPD) ESTERS IN EDIBLE PLANT OILS BY INDIRECT ACIDIC TRANSESTERIFICATION METHODS AND THE BPX-5 (Penentuan Ester 3-Monokloroprapana-1,2-diol (3-MCPD) dalam Minyak Tumbuhan Boleh Dimakan dengan Kaedah Transesterifikasi Berasid Tidak Langsung dan Turus Kapilari BPX-5) *May Yee Wong, Huey Fang Teh, Sook Mei Khor*	718
5.	THE ANTIBACTERIAL, ANTIFUNGAL, ANTIOXIDANT POTENTIAL AND TOTAL PHENOLIC CONTENT OF MALAYSIAN ENDANGERED SPECIES *Coscinium fenestratum* FROM PAYA BUNGOR PAHANG (Potensi Sifat Antibakteria, Antikulat, Antioksida dan Jumlah Kandungan Fenolik *Cosinium fenestratum* Spesies Terancam Malaysia dari Paya Bungor Pahang) *Aiza Harun, Noorshilawati Abdul Aziz, Shaari Daud*	734
6.	EFFECTS OF PROCESSING PARAMETERS ON THE QUALITY AND PROPERTIES OF MANGO KERNEL FLOUR: A MINI-REVIEW (Kesan Pemprosesan Parameter Terhadap Kualiti dan Sifat Tepung Biji Mango: Ulasan Mini) *Amal Hanani Binti Zikri, Boon Yih Tien, Boon Yih Hui, Wang Kang Han*	742
7.	SYNTHETIC APPROACHES TOWARDS QUINOLACTACIN DERIVATIVES VIA DIELS-ALDER, ACYL MIGRATION AND MULTICOMPONENT REACTIONS (Pendekatan Sintesis Ke Arah Terbitan Quinolaktasin Melalui Tindak Balas Diels-Alder, Migrasi Asil dan Tindak Balas Pelbagai Komponen) *Ahmad Zahir Hafiz Ismail, Putri Nur Arina Mohd Arif, Nurul Syafiqah Rezali, Mohd Fazli Mohammat, Zurina Shaameri*	755

8. PHYTOCHEMICAL ANALYSIS OF *Muntingia calabura* Linn. AND ITS ANTIBACTERIAL PROPERTIES VIA IN VITRO EVALUATION 766
(Analisis Fitokimia *Muntingia calabura* Linn. dan Sifat-sifat Antibakteria Melalui Penilaian In Vitro)
Suhaidi Ariffin, Juita Zulkefli, Aqilah Muhammad Saleh

9. DETERMINATION OF RESIDUAL XYLAZINE BY GAS CHROMATOGRAPHY IN DRUG-SPIKED BEVERAGES FOR FORENSIC INVESTIGATION 774
(Penentuan Sisa Xilazin dengan Kromatografi Gas dalam Minuman Ditambah dengan Dadah bagi Penyiasatan Forensik)
Nabeesathul Sumayya Mohamed Sadiq, Way Koon Teoh, Kasrin Saisahas, Apichai Phoncai, Vanitha Kunalan, Noor Zuhartini Md Muslim, Warakorn Limbut, Kah Haw Chang, Ahmad Fahmi Lim Abdullah

10. MAGNETITE-GRAPHENE BASED NANOCOMPOSITES IN ELECTROCHEMISTRY: A BRIEF REVIEW ON THEIR APPLICATIONS 788
(Nanokomposit Magnetit-Grafin dalam Elektrokimia: Ulasan Ringkas dalam Aplikasinya)
Farhanini Yusoff, Karthi Suresh, Azleen Rashidah Mohd Rosli, Nur Ayunie Kamaruzaman, Noorashikin Md Saleh, Muggundha Raoov Ramachandran, Nur Nadhirah Mohamad Zain

11. A SIMPLE REAGENT-FREE METHOD FOR ANALYSIS OF THE ETHANOL CONTENT IN GASOHOL 808
(Kaedah Mudah Tanpa Reagen bagi Analisis Kandungan Etanol di dalam Gasohol)
Jutharut Pansombut, Phetlada Sunchayanukun, Sasithorn Muncharoen

12. PRELIMINARY STUDIES ON SUNLIGHT ASSISTED DEGRADATION OF 2-CHLOROPHENOL USING MoS_2/GO AS PHOTOCATALYST 819
(Kajian Awal Mengenai Cahaya Tampak Dituruti Penyusutan Sinaran 2-klorofenol Menggunakan MoS_2/GO Sebagai Pemangkin Cahaya)
Kavirajaa Pandian Sambasevam, Syara Syazliana Muhammad Rajab, Izyan Najwa Mohd Norsham, Siti Nor Atika Baharin

13. THE COMPATIBILITY OF JACKFRUIT SEED STARCH AND POLYVINYL ALCOHOL BLEND AS BIOPOLYMER ELECTROLYTE HOST 829
(Keserasian Kanji Biji Nangka dan Campuran Polivinil Alkohol sebagai Hos Elektrolit Biopolimer)
Raihan Ramli, Fairuzdzah Ahmad Lothfy, Asiah Mohd Nor, Ab Malik Marwan Ali

14. STRUCTURAL AND ELECTROCHEMICAL CHARACTERISATIONS OF LANTHANUM-BASED COBALT FERRITE AND BARIUM CERATE-ZIRCONATE OXIDES AS COMPOSITE CATHODE FOR PROTON CERAMIC FUEL CELL 838
(Pencirian Struktur dan Elektrokimia Lantanum Berasaskan Kobalt Ferum Oksida dan Barium Serat-Zirkonat Oksida Sebagai Komposit Katod untuk Aplikasi Sel Fuel Seramik Proton)
Nurul Izzati Abd Malek, Ismariza Ismail, Abdul Mutalib Md Jani, Mohd Hafiz Dzarfan Othman, Nafisah Osman

15. ASSESSMENT OF METALS IN SEDIMENT OF A MONSOON-DOMINATED REGION IN THE NORTHERN MALACCA STRAIT 845
(Penilaian Logam dalam Sedimen di Wilayah yang Didominasi Monsun di Utara Selat Melaka)
Mohamad Arif Che Abd Rahim, Shengfa Liu, Xuefa Shi, Che Abd Rahim Mohamed

16. APPLICATIONS OF NINHYDRIN: SPECTROPHOTOMETRIC DETERMINATION OF HYDRAZINE AND HYDROXYLAMINE 855
(Aplikasi Ninhidrin: Penentuan Spektrofotometri bagi Hidrazin dan Hidroksil Amina)
Khaled Elgendy, Mohamed Alaa Eldeen Elmosallamy, Mohamed Hassan, Hend Gamal

17. A BRIEF REVIEW ON CORROSION INHIBITION STUDY OF ORGANIC LIGAND: ELECTROCHEMICAL, MORPHOLOGY, AND ISOTHERM STUDIES 867
(Ulasan Ringkas Terhadap Kajian Perencatan Kakisan Ligan oleh Ligan Organik: Kajian Elektrokimia, Morfologi dan Isoterma)
Nur Nadia Dzulkifli, Nur Zalin Khaleda Razali, Norsanida Iswa Sahani, Sheikh Ahmad Izaddin Sheikh Mohd Ghazali, Dzeelfa Zainal Abidin, Asiah Abdullah, Nurazira Mohd Nor

18. POLYPHENOL-MEDIATED GREEN SYNTHESIS OF ZINC OXIDE AND THEIR ANTIBACTERIAL PROPERTIES: A NOVEL SIZE-CONTROLLED APPROACH 884
(Sintesis Hijau dengan Mediasi Polifenol dan Ciri Antibakteria Zink Oksida: Pendekatan Kawalan Saiz Baharu)
Neo Zhi Zing, Balkis A. Talip, Soon Chin Fhong, Ainun Rahmahwati Ainuddin, Hatijah Basri

19. APLIKASI KARBON TERAKTIF SEKAM PADI TERHADAP EFLUEN KILANG KELAPA SAWIT MENGGUNAKAN KAEDAH PENJERAPAN 902
(Application of Rice Husk Activated Carbon on Palm Oil Mill Effluent using Adsorption Method)
Mohamad Jani Saad, Chia Chin Hua, Sarani Zakaria, Mohd Shaiful Sajab

20. CHANGES OF FATTY ACID COMPOSITION IN SCLERACTINIAN CORAL, *Galaxea fascicularis* (LINNAEUS, 1767) BY ACUTE EXPOSURE OF IRGAROL-1051 914
(Perubahan Komposisi Asid Lemak dalam Karang Scleractinia, *Galaxea fascicularis* (LINNAEUS, 1976) oleh Pededahan Akut Irgarol-1051)
Hassan Rashid Ali, Che Din Mohd Safuan, Marinah Mohd Ariffin, Mohammed Ali Sheikh, Noor Azhar Mohamed Shazili, Aminudin Muhammad Afiq-Firdaus, Zainudin Bachok

Malaysian Journal of Analytical Sciences (MJAS)
Published by Malaysian Analytical Sciences Society

SYNTHESIS, PHOTOPHYSICAL AND COMPUTATIONAL APPROACHES ON NONLINEAR OPTICAL (NLO) PROPERTIES OF NAPHTHALEN-1-YL ETHYNYLATED-CHALCONE DERIVATIVE

(Sintesis, Pendekatan Fotofizik dan Pengkomputeran Terhadap Sifat Optik Tak Linear (NLO) bagi Terbitan Naftalen-1-il Teretinil-Kalkon)

Mas Mohammed[1], Wan M. Khairul[1]*, Rafizah Rahamathullah[2], Fazira Ilyana Abdul Razak[3], Suhaila Sapari[4]

[1]Faculty of Science and Marine Environment,
Universiti Malaysia Terengganu, 21030, Kuala Nerus, Terengganu, Malaysia
[2]Faculty of Engineering Technology,
Universiti Malaysia Perlis, Level 1, Blok S2, Kampus UniCITI Alam, Sungai Chuchuh, 02100, Perlis, Malaysia
[3]Department of Chemistry, Faculty of Science,
Universiti Teknologi Malaysia, 81310 UTM Johor Bahru, Johor, Malaysia
[4]Department of Chemical Sciences, Faculty Science and Technology,
Universiti Kebangsaan Malaysia, 43600 UKM Bangi, Selangor, Malaysia.

**Corresponding author: wmkhairul@umt.edu.my*

Received: 10 March 2022; Accepted: 23 April 2022; Published: 25 August 2022

Abstract

A new dual mixed moieties of acetylide (C≡C) and chalcone (-CO-CH=CH) system namely 3-(naphthalen-1-yl)-1-(4-(phenylethynyl)phenyl)-2-propen-1-one (**3NPP**) was successfully designed and synthesized via Claisen Schmidt condensation reaction. Spectroscopic characterization and thermal analysis were conducted via Infrared Spectroscopy (FTIR), ^{1}H and ^{13}C Nuclear Magnetic Resonance (NMR) and Thermogravimetric (TGA) analysis. Density functional theory (DFT) assessment with basis set of B3LYP/6-31G (d,p) was computed to investigate the energy level of HOMO and LUMO, charge transfer within the molecule by global chemical reactivity descriptors (GCRD), molecular electrostatic potentials (MEP) and hyperpolarizability analyses. The simulated calculation reveals that the HOMO-LUMO energy gap of **3NPP** exhibited at 3.51 eV and has demonstrated good agreement with experimental optical band gap (E_g^{opt}). Additionally, **3NPP** possesses high NLO response with total first hyperpolarizability (β_{tot}) of 420.51× 10^{-30} esu. The presence of π-conjugated acetylide groups has improved nonlinear optical property and potential for application in optoelectronic.

Keywords: ethynyl, chalcone, density functional theory, non-linear optics, first hyperpolarizability

Abstrak

Moiti dwi tercampur sistem asetilida (C≡C) dan kalkon (-CO-CH=CH) baharu yang diberi nama 3-(naftalen-1-il)-1-((4-feniletinil)fenil)-2-propen-1-on (**3NPP**) telah berjaya direkabentuk dan disintesis melalui tindak balas kondensasi Claisen Schmidt. Pencirian spektroskopi dan analisis terma telah dijalankan melalui spektroskopi inframerah (FTIR), ^{1}H dan ^{13}C Resonan Magnetik Nuklear (NMR) dan analisis termogravimetrik (TGA). Penilaian fungsi teori ketumpatan (DFT) dengan set asas

B3LYP/6-31G (d,p) telah dikira untuk mengkaji jurang tenaga bagi HOMO dan LUMO, pemindahan caj dalam sebatian melalui petunjuk kereaktifan kimia global (GCRD), potensi elektrostatik molekul (MEP) dan analisis hiperpolarisasi. Pengiraan simulasi menunjukkan jurang tenaga HOMO-LUMO **3NPP** memberikan nilai 3.51 eV dan ternyata menunjukkan nilai yang selari dengan jurang tenaga optik eksperimen (E_g^{opt}). Tambahan pula, **3NPP** mempunyai sifat NLO yang tinggi dengan jumlah hiperpolarisasi pertama (β_{tot}) sebanyak 420.51x 10^{-30} esu. Dengan kehadiran kumpulan asetilida π-terkonjugat telah meningkatkan sifat optik tak linear dan berpotensi untuk aplikasi optoelektronik.

Kata kunci: etinil, kalkon, fungsi teori ketumpatan, sifat optik tak linear, hiperpolarisasi pertama

Introduction

Recently, organic nonlinear optical (NLO) materials attracted enormous interest due to their promising applications in optical power limiting applications [1, 2], second harmonic generation (SHG) photonics and electro optic (EO) processes [3, 4]. The development of this material becomes a promising alternative approach due to their large nonlinear response, extremely fast switching time and convenient optimization routes through molecular engineering compared to the currently studied inorganic materials [5]. Among various NLO materials reported, chalcone derivatives exhibit excellent nonlinear optical (NLO) properties by having the combination of electron donor and acceptor group substituents on phenyl rings are used due to the delocalization of electron of the electron in π-conjugated system [5, 6, 7, 8]. Besides that, the process of delocalization of electron of the electron in π-conjugated leads to high electron density mobility which makes them the ideal candidates for NLO materials [9]. According to Arshad et al., Donor-π-Acceptor (D-π-A) systems are widely been used in information storage, optoelectronic, and also NLO applications. π-conjugated framework will act as the centre which gets appended by electron acceptor at one side and an electron donor group at the other side [10]. In previous study, many researchers had synthesized chalcone derivatives based on aromatic system with tuning the electron donating group (EDG) and electron withdrawing group (EWG) such as (E)-1-(4-ethylphenyl)-3-(4-(heptyloxy) phenyl) prop-2-en-1-one [11],(E)-N-(2-(3-(4-ethoxyphenyl)-1-(2-(phenyl sulfonylamine)phenyl)prop-2-en-1-one, (E)-3-(4-chlorophenyl)-1-(2-(phenylsulfonylamine)phenyl) prop-2-en-1-one and (E)-3-(4-bromophenyl)-1-(2-(phenylsulfonylamine)phenyl)prop-2-en-1-one [9]. These system were reported as the ideal candidates to be developed as NLO materials.

Within this interest, herein we present a work by introducing new chalcone-based system, 3-(naphthalen-1-yl)-1-(4-(phenylethynyl)phenyl)-2-propen-1-one (**3NPP**) with the combination of active extended conjugated acetylide system (C≡C) featuring D-π-A system. The focal point molecular candidates in this work are the extended conjugated system of acetylene (C≡C) and the chalcone system, which are made up of two distinct moieties that are used as active electronic components. Due to the extension of conjugation within the molecules aided by active donor and acceptor groups located at each terminal of the molecules, it is expected that the combination of these two systems in a single molecular framework will allow electrons to easily move through the conjugated framework from electron donor to electron acceptor group. It was designed and synthesized due to its structural simplicity and high reactivity, acetylene represents a versatile building block for organic synthesis, and its chemistry has evolved rapidly [12]. This molecule consists of π-electron which can facilitate the electron in the compound. The presence of π-conjugated polymer possessing electron-donating and electron-withdrawing groups exhibit low-lying charges transfer excited states and large second-order optical nonlinearities [13]. Besides, π-bridges and spacers, are important when tweaking NLO characteristics. The essential characteristics for a material to qualify as a good NLO material are red shifted absorption maxima, greater dipole moments, and thermal stabilities. Alkyne analogues have demonstrated blue shifted absorption maxima and worse thermal stabilities [14, 15]. In addition, the calculations were performed by using density functional theory (DFT) method to investigate

the physico-chemical properties of the designed molecule and can support experimental values. Furthermore, DFT calculation can be carried out to obtain the molecular orbitals, orbitals and electrostatic surface map [16]. In addition, DFT was used due to its great accuracy in reproducing the experimental values of molecular geometry, vibrational frequencies, atomic charges, dipole moment [17]. From the DFT calculation, NLO properties of **3NPP** can be described and compared to experimental values.

Materials and Methods

All chemicals, solvents, and reagents that were used in this work were 4-iodoacetophenone, phenylacetylene, 1-pyrenecarboxaldehyde, palladium(II) chloride, triphenylphosphine, sodium hydroxide, acetonitrile, triethylamine, tetrahydrofuran, hexane, dichloromethane, and ethanol were purchased from Acros Organics, Fisher Scientific, Merck, and Sigma Aldrich. They were used as received without further purification tasks carried out.

Characterization and Instrument

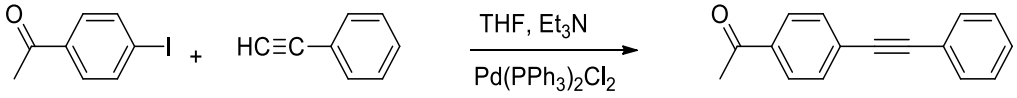
Fourier Transform-Infrared Spectrometer (ATR-FTIR) spectra were recorded using Perkin Elmer 100 spectrophotometer in the range of 4000-450 cm^{-1} spectral. The ^{1}H-NMR and ^{13}C-NMR spectroscopy analyses were conducted by using Bruker Avance III 400 MHz Spectrometer by using deuterated $CDCl_3$ as solvent. Next, the UV-Vis spectra were obtained using Spectrophotometer Shimadzu UV-1601PC in 1 cm^3 cuvette. Besides, Thermogravimetric analysis (TGA) was performed using Perkin-Elmer TGA analyzer from 30 ℃ to 900 ℃ at a heating rate of 10 ℃/min in the presence of a constant nitrogen flow.

Computational method

Frontier molecular orbitals (FMOs), global chemical reactivity descriptors (GCRD), and the NLO properties such as dipole moment, polarizability, and hyperpolarizability were carried out by density functional theory (DFT) using Gaussian 16 program package. All the images and graphs are visualized by Gauss view 6.0. The B3LYP functional was used with the 6-31G(d,p) basis set for the optimization of the structure. The basis set was chosen due to the calculated values by using B3LYP/6-31G(d,p) basis are considerably better agreement with the experimental which also includes the consideration of the polarization function supplied provided a lower error, more precise bond lengths [18].

Synthesis of precursor: 1-(4-(phenylethynyl)phenyl) ethanone (PPE)

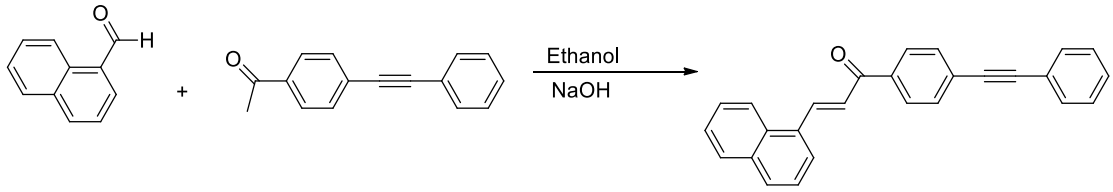
The experimental details regard to Sonogashira precursor, **PPE** has been reported before in previous literature [19]. Hence, in this study, some modification have been carried out in for the interest of this work. 4-iodoacetophenone (0.5 g, 2.03 mmol), phenylacetylene (0.23 mL, 2.03 mmol), $Pd(PPh_3)_2Cl_2$ (40 mg, 0.057 mmol), and triethylamine (7 mL) were dissolved in tetrahydrofuran (40 mL) in the two-necked 250 mL round bottom flask. The reaction was refluxed for approximately 14 hours. The progress of the reaction was monitored by using Thin Layer Chromatography (TLC) (hexane: ethyl acetate, 4:1). After the reaction was adjudged completion, the reaction was cooled to room temperature prior filtration. Then, the mixture was dried *in-vacuo* prior purification via column chromatography to afford off-white solid as a precursor (**PPE**). Yield; 50%. The synthetic pathway of precursor is shown in Scheme 1.



Scheme 1. Synthetic pathway for precursor, 1-(4-(phenylethynyl)phenyl)ethanone (**PPE**)

Synthesis of 3-(naphthalen-1-yl)-1-(4-(phenyl ethynyl)phenyl)-2-propen-1-one (3NPP)

The synthetic approach for the preparation of title compound (**3NPP**) is summarized in Scheme 2. 1-(4-(phenylethynyl)phenyl)ethanone (0.2 g, 0.908 mmol) was dissolved in ethanol (20 mL) in 250 mL two-necked round bottom flask. Then, 1-naphtaldehyde (0.12 mL, 0.908 mmol) was charged into the reaction while being stirred. Then, the mixture was left unattended for a few minutes in order to become homogeneous. Next, 20% sodium hydroxide solution (15 mL) was added into the mixture dropwise and the reaction was left with constant stirring for approximately 7 hours. The progress of the reaction was monitored by using thin-layer chromatography (TLC) (hexane: dichloromethane, 3:2). After the reaction has completed, the mixture was poured into the beaker containing several ice cubes. The mixture was left overnight for the precipitate formation. After that, it was filtered and dried at ambient environment. The crude product obtained was recrystallized from acetonitrile to obtain yellow solid as the title product (yield: 75%).



Scheme 2. Synthetic pathway for **3NPP**

Results and Discussion

Vibrational analysis

The FT-IR spectrum of **3NPP** is presented in Figure 1 within the range of 4000-450 cm^{-1}. Form the experimental data, there are five absorption bands of interest which represent the ν(CH) aromatic, ν(C≡C), ν(C=O), ν(C=C) aromatic and ν(C=C) ranging from weak to medium intensities. The absorption band for experimental stretching aromatic CH was observed at 3048 cm^{-1} and 2997 cm^{-1}. Meanwhile, the absorption band for C≡C was observed at 2361 cm^{-1} and 2342 cm^{-1} as the medium intensity peak. This peak appeared as a diminished absorption intensity of ν(C≡C) was observed due to the effect of the inter-stacking interaction and dipole moment of the molecule [13]. The medium and sharp band for carbonyl (C=O) appeared at 1655 cm^{-1} which is supported by Mobaraki and Hemmateenejad, 2011 which stated the peak of carbonyl (C=O) stretching can be found at the range of 1750-1600 cm^{-1} [20]. In **3NPP**, the presence of intermolecular hydrogen bonds and the conjugation of the carbonyl bond with the C=C bonds greatly decrease the carbonyl group's double bond nature, lowering the stretching frequency of C=O [21]. The absorption band of C=C stretching was observed at 1589 cm^{-1} which confirms the formation of chalcone compound [22] and C=C aromatic was found at 1570 cm^{-1}.

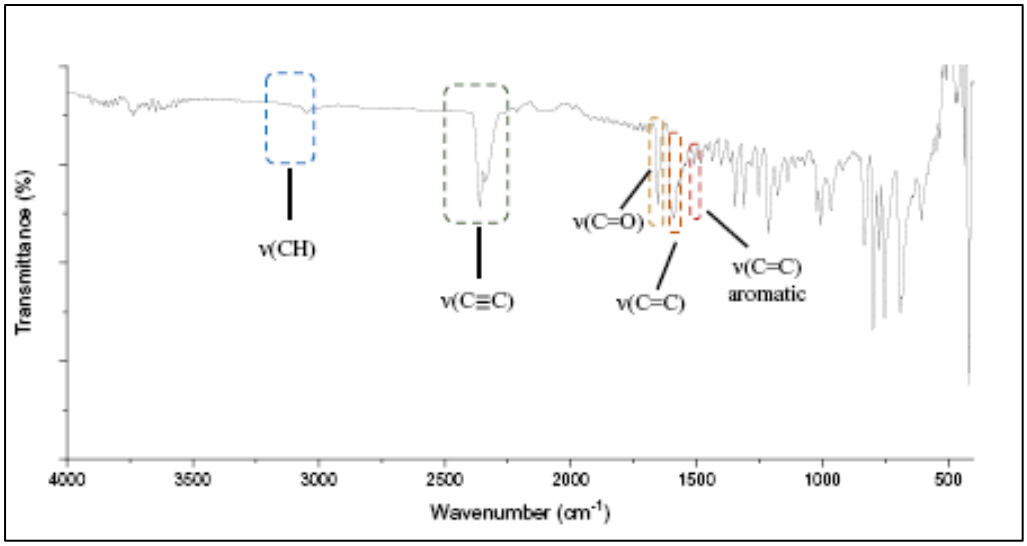


Figure 1. IR spectrum of **3NPP**

Optical properties

Electronic absorption spectrum of **3NPP** was recorded in the range of 200-600 nm in dichloromethane (DCM) solvent (c= 1×10^{-5} M). In the solution state, absorption maxima were recorded at 266 and 335 nm, which indicate π-π* and n-π* transitions. The value of maximum wavelength (λ_{max}) of absorption of **3NPP** was observed at 266 nm shows π-π* transition which assigned to arise from overlapping of phenyl ring and carbonyl (C=O) chromophore. Next, n-π* transition at the wavelength (λ_{max}) 335 nm shows the presence of carbonyl (C=O) moieties. Eq. 1 was used to calculate the optical energy band gap (E_g^{opt}), which was given in eV. According to the formula of $E_{gap} = hc/\lambda_{edge}$, the E_g value of **3NPP** is exhibited 2.92 eV.

$$E_g^{opt}(eV) = 1240 / \lambda_{edge} \quad (1)$$

The computed electronic absorption using time dependent-DFT approach employing B3LYP functional and 6-31G (d,p) basis set in solvent effect (dichloromethane) through Integral Equation Formalism Polarizable Continuum Model (IEF-PCM). The spectrum are shown in Figure 2. The electronic transition of the computed UV-Visible at 398 nm which attributed to HOMO to LUMO transition orbitals. This region shows n-π* and π-π* transition which attributed the to the excitation in the aromatic ring and the presence of carbonyl (C=O) moieties [23].

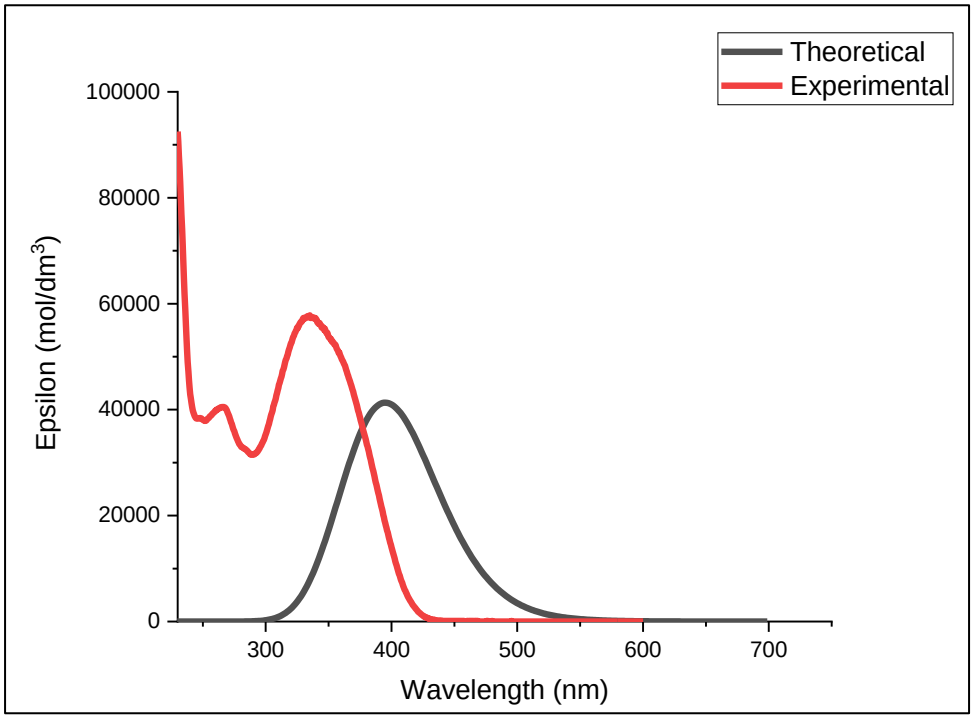


Figure 2. The UV-Visible spectrum of **3NPP**

NMR analysis

The title derivative of ethynylated-chalcone (**3NPP)** was identified by using nuclear magnetic resonance (NMR). The spectra of ^{1}H and ^{13}C NMR were recorded by using Bruker Advance III 400 spectrometer, deuterated chloroform ($CDCl_3$) is used as solvent, and trimethylsilane (TMS) was used as an internal standard. Moreover, the frequency that is used for both ^{1}H and ^{13}C NMR were 400.11 MHz and 100.61 MHz respectively. The spectra of ^{1}H and ^{13}C for **3NPP** are shown in Figure 3 and Figure 4. In ^{1}H spectrum, alkene moieties can be observed at δ_H 7.46-7.55 ppm (*J*-coupling=12 Hz) and δ_H 8.190 ppm (*J*-coupling=10 Hz) as doublet resonance multiplet due to the overlapping between the aromatic proton and doublet resonance which indicates the *E*-configuration of the synthesized compound. The strong coupling constants mostly represent the trans coupling of nearby protons, confirming the trans conformation with regard to the double bond [24]. Then, aromatic phenyls proton which can be observed at the range of δ_H 6.900 -8.650 ppm as multiplet and pseudo-doublet resonances which are supported by previous reported studies [6].

For the ^{13}C NMR, there are two signals appeared within the range of δ_C 87.79-91.72 ppm which represent the alkyne moieties where the splitting of these peaks were due to the influence of their non-symmetrical structure [20]. The aromatic phenyls carbons can be observed at δ_C 121.54-140.71 ppm. The peak resonated at δ_C 188.25 ppm corresponded to carbonyl (C=O) carbon atom. This is due to the formation of intramolecular hydrogen bonding and electronegativity effect of oxygen atom which pulled a certain number of electrons and deshielded the resonance to higher chemical shift [20].

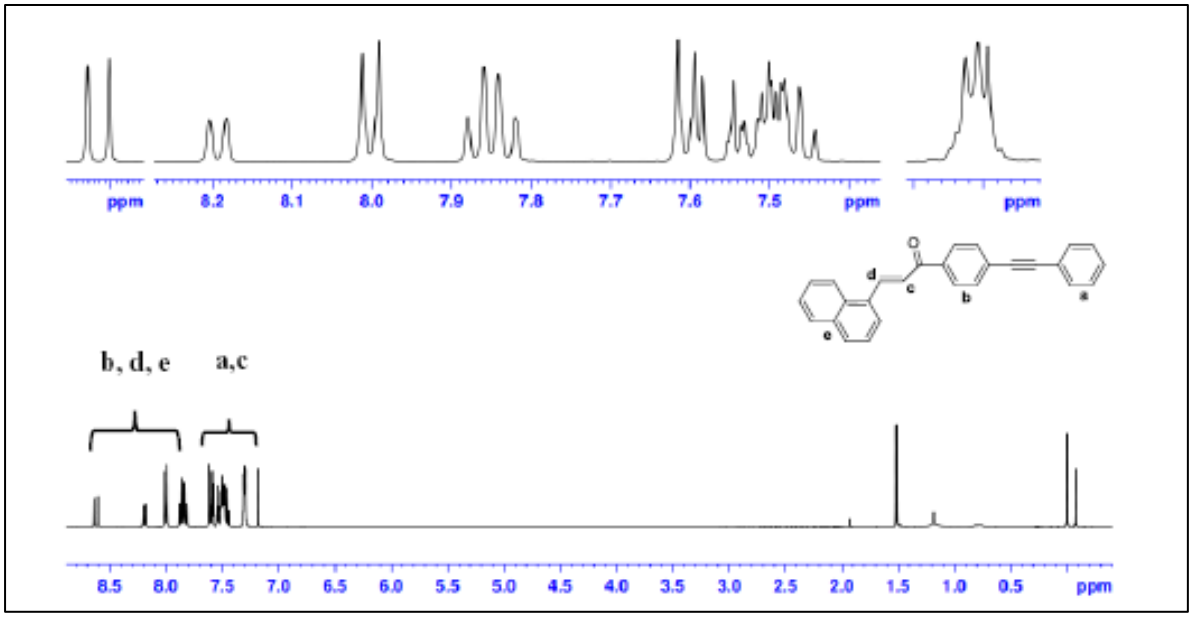


Figure 3. [1]H NMR spectrum of **3NPP**

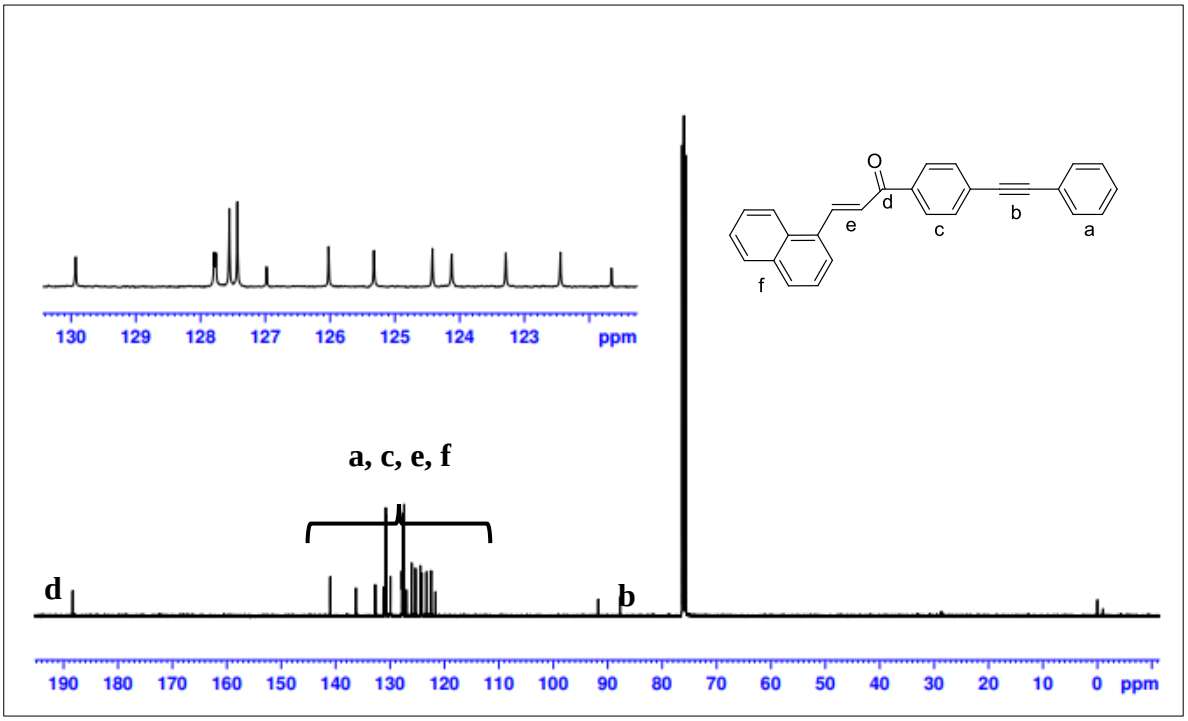


Figure 4. [13]C NMR spectrum of **3NPP**

Thermal analysis

The TGA and DTG thermogram of **3NPP** are shown in Figure 5. The TGA/DTG curve shows that the title compound started to degrade in two steps. For the first step, the degradation occurred at 273.81 ℃ which the onset temperature (T_{onset}) and ended at 539.93 ℃ which the offset temperature (T_{offset}) with an initial weight loss of 18.27%. Meanwhile, for the second step, the degradation occurred at 539.93 ℃ which the onset temperature (T_{onset}) and stop at 735.53 ℃ which was the offset temperature (T_{offset}) with the weight loss of 72.75%. The weight loss is due to the decomposition of compound to a gaseous state. The high thermal stability of the compound is suitable for NLO application [25].

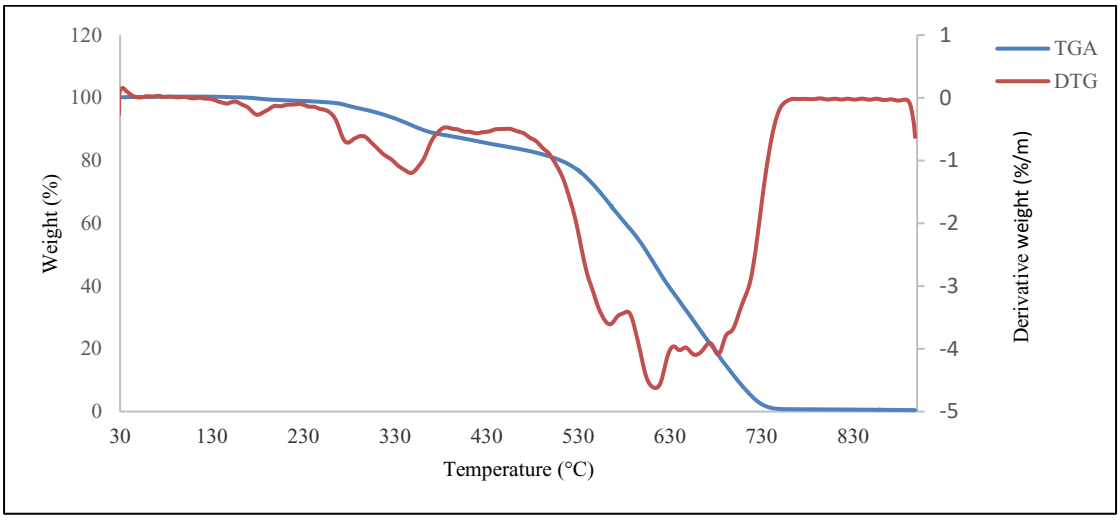


Figure 5. The TGA and DTG thermogram of **3NPP**

Frontier molecular orbitals

Frontier molecular orbitals (FMOs) are an important key role to understand the chemical stability of a molecule. The FMOs of **3NPP** was computed via TD-DFT with B3LYP/6-31G (d,p) as shown in Figure 6. The HOMO is the outermost orbital containing donor electron, while LUMO is the innermost orbital containing free places to accept electrons [16]. The HOMO is mainly concentrated on the chalcone structure and naphthalene substituent, which acts as electron donor groups. This is due to the existence of a greater electron density in the chalcone structure's naphthalene substituent. The LUMO is produced by the molecule's conjugated double bond, implying that the naphthalene substituent plays a role. Aromatic electrophile substitution reactions on chalcone structures and aromatic nucleophile substitution reactions on alkyne groups is facilitated by the naphtalene group. Furthermore, the inclusion of an alkyne group increases the title compound's intermolecular charge transfer (ICT). The energy gap for HOMO-LUMO of the synthesized molecules is relatively small which is 3.51 eV. The differences between theoretical and experimental results can be attributed to the fact that the experimental results were obtained in the solution phase, wherein various inter and intra molecule interactions can be observed within the solvent and solution. It could be attributed to a solvent phase of an isolated single molecule in theoretical calculations (using the stated software) [26]. It is found that the energy band gap relatively small than the previous chalcone compound [11]. This molecule is soft and the values of the energy bandgap is in the range of semiconducting materials which can exhibit good polarizability and non-linear optical (NLO) properties [11]. There are two electronic excitation energies were involved which are the electron transition from the ground state (S_0) to the excited state (S_n) and others information are depicted in Table 1.

Moreover, the global chemical reactivity descriptors (GCRD) are the technique to understand the chemical properties such as chemical hardness (η), chemical softness (S), chemical potential (μ), electronegativity (χ) and electrophilic index (u) = [$\mu^2/2\eta$]. The formula is derived from HOMO-LUMO energies, taking the HOMO energy as ionization potential (I) and LUMO as electron affinity (A) [27], and the data are tabulated in Table 2.

Chemical hardness (η) = [($E_{LUMO} - E_{HOMO}$)/2] (2)
Chemical softness (S) = [$1/2\eta$] (3)
Chemical potential (μ) = [($E_{HOMO} + E_{LUMO}$)/2] (4)
Electronegativity (χ) = [(I + A)/2] (5)
Electrophilic index (u) = [$\mu^2/2\eta$] (6)

From the calculation, it was found that **3NPP** is kinetically stable with the hardness value of 1.76 eV, chemical potential of -4.05 eV, chemical softness of 0.28 $e^{-1}V^{-1}$, electronegativity of 4.05 eV and electrophilic index of 4.66 eV suggesting that the title compound gives excellent chemical strength and stability properties.

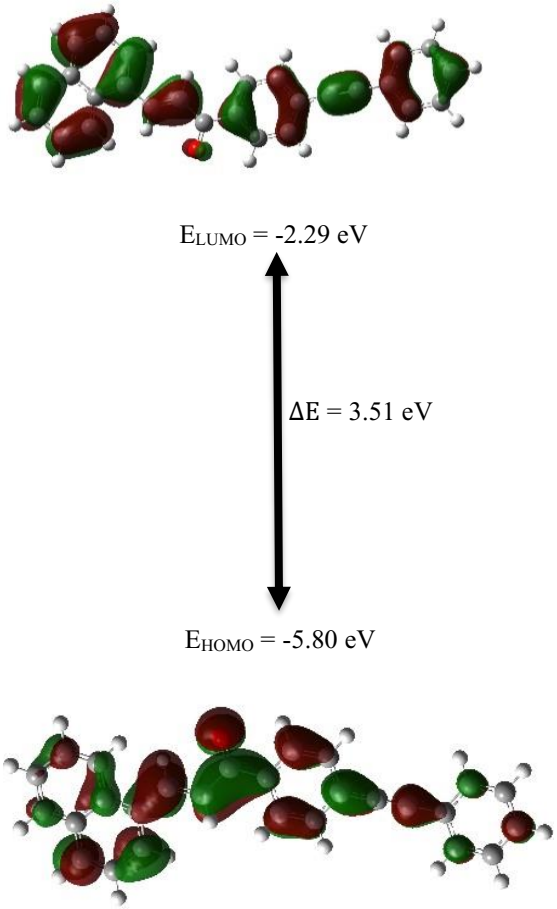


Figure 6. Molecular orbitals of **3NPP**

Table 1. Excitation energy, oscillator strength and major contribution of electronic transition

Molecule	Wavelength, λ (nm)	Excitation Energy (eV)	Oscillator Strength (f_o)	Assignments, Major Contributors (%)
3NPP	403	0.07	0.67	$S_0 \rightarrow S_n$ (62.45 %)

Table 2. Molecular orbitals energies of HOMO and LUMO (eV) and the global chemical reactivity descriptors (GCRD)

Molecule	E_{HOMO}	E_{LUMO}	ΔE (eV)	η (eV)	μ (eV)	S ($e^{-1}V^{-1}$)	χ (eV)	u (eV)
3NPP	-5.80	-2.29	3.51	1.76	-4.05	0.28	4.05	4.66

Molecular electrostatic potential analysis

The molecular electrostatic potential (MEP) analysis is computed by using DFT B3YLP/6-31G (d,p) level of theory. MEP as in Figure 7 gives important information regarding the reactive site of the molecule [28, 29], visualizing the size and shape of the molecule [30]. The reactivity of **3NPP** can be determined by predicting the nucleophile and electrophile site of the molecule. MEP surface gives the information of the charge distribution region of the molecule. In this 3D plot, the blue and brown regions indicate the positive and negative charge of **3NPP**. The blue region is spread over the hydrogen atom comprising the electrophilic sites meanwhile the red region is the nucleophilic site which contains oxygen atom [10]. For **3NPP**, the negative charges are more concentrated on the oxygen atom of the carbonyl (C=O) group in the range between -5.239×10^{-2} a.u (red) towards 5.239×10^{-2} a.u (blue) in the map because it represents a potential nucleophilic attack site. This indicates that the (C=O) oxygen atom is the most reactive spot for interacting with the nucleophile via an intermolecular hydrogen bond [6].

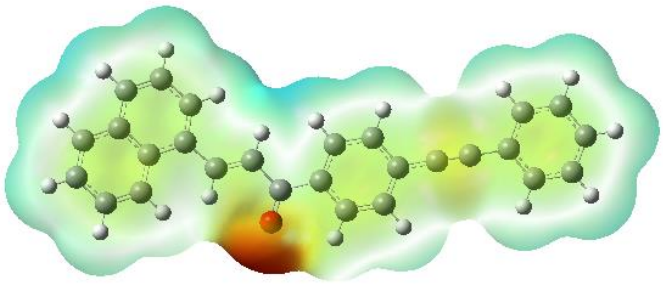


Figure 7. MEP surface for **3NPP**

Non-linear optical properties: DFT calculation

In the computational NLO studies, dynamic linear polarizabilities (α) and first hyperpolarizabilities (β) were calculated in order to examine the nonlinear optical (NLO) properties by using DFT method in the Gaussian 16 program. In addition, the isotropic polarizability ($<\alpha>$), anisotropic polarizability ($\Delta\alpha$), total beta (β_{tot}) of the first hyperpolarizability were calculated via DFT B3LYP/6-31G (d,p) and were calculated using the following equations [27, 31]. The Gaussian output file had ten hyperpolarizability tensors (β_{xxx}, β_{xyy}, β_{xzz}, β_{yyy}, β_{xxy}, β_{yzz}, β_{zzz}, β_{xxz}, β_{yyz}, β_{xyz}) and six linear polarizability tensors (α_{xx}, α_{yy}, α_{zz}, α_{xy}, α_{xz}, α_{yz})

correspondingly, in the x, y, and z directions [32]. The related parameters of **3NPP** are tabulated in Table 3.

The total dipole moment (μ_{tot}) was recorded at 2.93 which is higher than the previous chalcone compound [11]. The higher dipole moment will indicate the higher electron density which will lead to a greater charge transfer [33]. The higher the dipole moment, the higher the first polarizability will indicate the higher NLO properties [31]. Moreover, the isotropy polarizability ($<\alpha>$) of **3NPP** was found at 57.52×10^{-24} esu, while the anisotropy of polarizability ($\Delta\alpha$) was recorded at 86.81×10^{-24} esu. Furthermore, the 1st polarizability β_{tot} of **3NPP** was 420.51×10^{-30} esu. The higher value first polarizability due to the small HOMO-LUMO gap [25].

$$\mu_{tot} = (\mu_x^2 + \mu_y^2 + \mu_z^2)^{1/2} \quad (7)$$

$$<\alpha> = \frac{1}{3}(\alpha_{xx} + \alpha_{yy} + \alpha_{zz}) \quad (8)$$

$$\Delta\alpha = \frac{1}{\sqrt{2}}[(\alpha_{xx} - \alpha_{yy})^2 + (\alpha_{yy} - \alpha_{zz})^2 + (\alpha_{zz} - \alpha_{xx})^2 + 6(\alpha_{xy}^2 + \alpha_{xz}^2 + \alpha_{yz}^2)]^{1/2} \quad (9)$$

$$\beta_{tot} = (\beta_x^2 + \beta_y^2 + \beta_z^2)^{1/2} \quad (10)$$

$$\beta_{tot} = [(\beta_{xxx} + \beta_{xyy} + \beta_{xzz})^2 + (\beta_{yyy} + \beta_{yzz} + \beta_{yxx})^2 + (\beta_{zzz} + \beta_{zxx} + \beta_{zyy})^2]^{1/2} \quad (11)$$

Table 3. Dipole moment, polarizability, and the value of 1st order hyperpolarizability

Dipole moment (Debye)	**3NPP**
μ_{tot}	2.93
Polarizability, α ($\times 10^{-24}$ esu)	
α_{xx}	110.17
α_{yy}	18.40
α_{zz}	44.00
α_{xy}	-8.81
α_{xz}	11.67
α_{yz}	7.45
$< \alpha >$ ($\times 10^{-24}$) in esu	57.52
$\Delta\alpha$ ($\times 10^{-24}$) in esu	86.81
1st Hyperpolarizability, β ($\times 10^{-30}$ esu)	
β_{xxx}	-102.36
β_{xyy}	2.53
β_{xzz}	-9.28
β_x	-342.06
β_{yyy}	0.40
β_{xxy}	14.75
β_{yzz}	1.48
β_y	53.09
β_{zzz}	-1.18
β_{xxz}	-72.76
β_{yyz}	-9.46
β_z	238.75
β_{xyz}	8.90
β_{tot}	420.51

Conclusion

The new conjugated ethynylated based chalcone (**3NPP**) featuring D-π-A concept was designed and successfully synthesised as active non-linear optical (NLO) response. From the findings, the title compound of **3NPP** is thermally stable up to 320.60 ℃ with the weight loss of 91.02 % in two steps of degradation process. The introduction of acetylide moiety reveals the enhancement of stability of this system. The energy band gap of **3NPP** is 3.51 eV which is compatible to further this system for optoelectronics applications. According to the findings, this compound also could be used as a good NLO active material. The development of suitable electron transport materials for organic electronic devices can be aided by precise design, synthesis, and theoretical investigation of these compounds. Furthermore, the molecular electrostatic potential (MEP) also shows the reactive sites in this reaction. **3NPP** also has excellent NLO properties by DFT calculation with the value of β_{tot} =420.51× 10^{-30} esu and reveals good polarizability. From the preliminary outcome, further investigation on the similar molecular system can be applied as ideal and promising NLO material for the development of any optical application.

Acknowledgment

The authors would like to acknowledge Ministry of Higher Education, Malaysia for the financial support Fundamental Research Grant Scheme (FRGS 59515) (FRGS/1/2018/STG07/UMT/02/6), Faculty of Science, Universiti Teknologi Malaysia for NLO analysis, Institute Marine Biotechnology, UMT for NMR analysis and Faculty of Science and Marine Environment, Universiti Malaysia Terengganu for research facilities and supports.

References

1. Sankaraperumal, A., Shetty, A. N. and Karthikeyan, J. (2015). Structural characterization and nonlinear optical properties of 1-phenyl-3-(4-bis(2-chloroethyl)aminophenyl)-2-propen-1-one. *Journal of Structural Chemistry*, 56: 1398-1404.
2. Abegão, L. M. G., Fonseca, R. D., Santos, F. A., Souza, G. B., Barreiros, A. L. B. S., Barreiros, M. L., Alencar, M. A. R. C., Mendonca, C. R., Silva, D. L., Boni, L. D. and Rodrigues Jr, J. J. (2016). Second- and third-order nonlinear optical properties of unsubstitutedand mono-substituted chalcones. *Chemical Physical Letters*, 648: 91-96.
3. Shkir, M., Riscob, B. and Bhagavannarayana, G. (2012). Synthesis, growth, structural, spectroscopic, crystalline perfection, second harmonic generation (SHG) and thermal studies of 2-aminopyridinium picrate (2APP): A new nonlinear optical material. *Solid State Sciences*, 14(7): 773-776.
4. Liu, J., Ouyang, C., Huo, F., He, W. and Cao, A. (2020). Progress in the enhancement of electro-optic coefficients and orientation stability for organic second-order nonlinear optical materials. *Dyes and Pigments*, 181: 108509.
5. Prasad, A. A., Muthu, K., Meenatchi, V., Rajasekar, M., Agilandeshwari, R., Meena, K., Manonmoni, J. V. and Meenakshisundaram, S. P. (2015). Optical, vibrational, NBO, first-order molecular hyperpolarizability and hirshfeld surface analysis of a nonlinear optical chalcone. *Spectrochimica Acta Part A: Molecular and Biomolecular Spectroscopy*, 140: 311-327.
6. Ekbote, A., Patil, P. S., Maidur, S. R., Chia, T. S. and Quah, C. K. (2017). Structural, third-order optical nonlinearities and figures of merit of (e)-1-(3-substituted phenyl)-3-(4-fluorophenyl)prop-2-en-1-one under CW regime: New chalcone derivatives for optical limiting applications. *Dyes and Pigments*, 16: S0143-7208.
7. Zaini, M. F., Khairul, W. M., Arshad, S., Abdullah, M., Zainuri, D. A., Rahamathullah, R., Rosli, M. I., Aziz, M. S. A. and Razak, I. A. (2020). The structure-property studies and mechanism of optical limiting action of methyl 4-((4-aminophenyl)ethynyl)benzoate crystal under continuous wave laser excitation. *Optical Materials*, 107: 110087.
8. Ganapayya, B., Jayarama, A., Sankoli, R., Hathwar, V. R. and Dharmaprakash, S. M. (2012). Synthesis, growth, and characterization of a new NLO material 3-(2,3-Dimethoxyphenyl)-1-(pyridin-2-yl)prop-2-en-1-one. *Journal of Molecular Structure*, 1007: 175-178.

9. Patil, P. S., Gummagol, N. B., Ekbote, A., Wong, Q. A., Quah, C. K., Shkir, M., Maidur, S. R. and Rao, S. V. (2020). Structural and femtosecond third-order nonlinear optical properties of electron donor-acceptor substituted chalcones: an experimental and computational approach. *Journal of Molecular Structure*, 1219: 128523.
10. Custodio, J. M. F., Gotardo, F., Vaz, W. F., D'Oliveira, G. D. C., de Almeida, L. R., Fonseca, R. D., Cocca, L. H. Z., Perez, C. N., Oliver, A. G., de Boni, L. and Napolitano, H. B. (2020). Benzenesulfonyl incorporated chalcones: synthesis, structural and optical properties. *Journal of Molecular Structure*, 1208: 127845.
11. Arshad, M. N., Al-Dies, A, M., Asiri, A. M., Khalid, M., Birinji, A. S., Al-Amry, K. A. and Braga, A. A. C. (2017). Synthesis, crystal structures, spectroscopic and nonlinear optical properties of chalcone derivatives: a combined experimental and theoretical study. *Journal of Molecular Structure,* 1141: 124-156.
12. Daud, A. I., Khairul, W. M., Augustine, E., Arshad, S. and Razak, I. A. (2019). Synthesis, spectroscopic, structural elucidation, NLO characteristic and hirshfeld surface analysis of (e)-1-(4-ethylphenyl)-3-(4-(heptyloxy)phenyl)prop-2-en-1-one: a dual approach of experimental and DFT calculations. *Journal of Molecular Structure*, 1194: 124-137.
13. Voronin, V. V., Ledovskaya, M. S., Bogashenkov, A. S., Rodygin, K. S. and Ananikov, V. P. (2018). Acetylene in organic synthesis: recent progress and new uses. *Molecules*, 23: 2442.
14. Sakaguchi, T., Azuma, S. and Hashimoto, T. (2016). Metathesis polymerization of diphenylacetylenes possessing electron-donating and electron-withdrawing groups and emission properties of polymers. *Synthetic Metals*, 212: 174-179.
15. Moylan, C. R., Twieg, R. J., Lee, V.Y., Swanson, S. A., Betterton, K. M. and Miller, R. D. (1993). Nonlinear optical chromophores with large hyperpolarizabilities and enhanced thermal stabilities. *Journal of the American Chemical Society*, 115: 12599-12600.
16. Ghanavathar, C. W., Mishra, V. R. and Sekar, N. (2021). Review of NLO phoric azo dyes – developments in hyperpolarizabilities in last two decades. *Dyes and Pigments*, 191: 109367.
17. Teixeira, A. M. R., Santos, H. S., Bandeira, P. N., Juliao, M. S. S., Freire, P. T. C., Lima, V. N., Cruz, B. G., da Silva, P. T., Coutinho, H. D. M. and Sena Jr, D. M. (2019). Structural, spectroscopic and microbiological characterization of the chalcone 2e-1-(2′-hydroxy-3′,4′,6′-trimethoxyphenyl)-3-(phenyl)-prop-2-en-1-one derived from the natural product 2-hydroxy-3,4,6-trimethoxyacetophenone. *Journal of Molecular Structure*, 1179: 739-748.
18. Kosar, B. and Albayak, C. (2011). Spectroscopic investigations and quantum chemical computational study of (e)-4-methoxy-2-[(p-tolylimino)methyl]phenol. *Spectrochimica Acta Part A: Molecular and Biomolecular Spectroscopy*, 78: 160-167.
19. Boudhar, K., Debieche, M., Serhane, A. and Zeghdaoui, A. (2021). Crystal structure, raman spectroscopy study and quantum chemical DFT calculations of n-phenyl -3-para nitro phenyl isoxazolidine-5-carbonitrile. *Journal of Molecular Structure*, 1246: 131029.
20. Thorand, S. and Krause, N. (1998). Improved procedures for the palladium-catalyzed coupling of terminal alkynes with aryl bromides (sonogashira coupling). *Journal of Organic Chemistry*, 1998: 8551-8553.
21. Mobaraki, N. and Hemmateenejad, B. (2011). Structural characterization of carbonyl compounds by IR spectroscopy and chemometrics data analysis. *Chemometrics and Intelligent Laboratory Systems*, 109: 171-177.
22. John, J. S., Sajan, D., Narayana, C., Joy, N. and Philip, R. (2018). Theoretical and experimental approach to the investigation of hyperpolarizability and charge transfer characteristics of NLO active 2′,3,4,4′,5-pentamethoxy chalcone with silver atoms adsorbed. *Optical Materials*, 84: 409-421.

23. Prabu, S. R., Upadhyaya, V. and Jayarama, A. (2017). Synthesis, crystal structure and hirshfeld surface analysis of a novel chalcone derivative: (*2e*)-3-(2,3-dimethoxyphenyl)-1-(3-nitrophenyl) prop-2-en-1-one. *Chemical Data Collections*, 11-12: 199-210.
24. Khairul, W. M., Zuki, H. M., Hasan, M. F. A. and Daud, A. I. (2016). Pyridine acyl thiourea as ionophore for the detection of copper (II) in aqueous phase. *Procedia Chemistry*, 20: 105-114.
25. Kumar, P. C. R., Ravindrachary, V., Janardhana, K., Manjunath, H. R., Karegouda, P., Crasta, V. and Sridhar, M. A. (2011). Optical and structural properties of chalcone NLO single crystals. *Journal of Molecular Structure*, 1005: 1-7.
26. Naik, V. S., Patil, P. S., Gummagol, N. B., Wong, Q. A., Quah, C. K. and Jayanna, H. S. (2020). Structural, linear optical, second and third-order nonlinear optical properties of two halogenated chalcone derivatives containing thiophene moiety. *Chemical Physics Letters*, 761: 138051.
27. Pramod, A. G., Nadaf, Y. F. and Renuka, C. G. (2019). A combined experimental theoretical approach for energy gap determination, photophysical, photostable, optoelectronic, NLO, and organic light emitting diode (OLED) application: synthesized coumarin derivative. *Journal of Molecular Structure*, 1194: 271-283.
28. Maidur, S. R., Patil, P. S., Rao, S. V., Shkir, M. and Dharmaprakash, S. M. (2017). Experimental and computational studies on second- and third-order nonlinear optical properties of a novel D-p-A type chalcone derivative: 3-(4-methoxyphenyl)-1-(4-nitrophenyl) prop-2-en-1-one. *Optics and Laser technology*, 97: 219-228.
29. Zaini, M. F., Razak, I. A., Khairul, W. K. and Arshad, S. (2020). Structural, Hirshfeld and DFT studies of conjugated D–π–A carbazole chalcone crystal. *Crystallographic Communications*, E76: 387-391.
30. Barakat, A., Al-Majid, A. M., Soliman, S. M., Mabkhot, Y. N., Ali, M., Ghabbour, H. A., Fun, H-K. and Wadood, A. (2015). Structural and spectral investigations of the recently synthesized chalcone (*E*)-3-mesityl-1-(naphthalen-2-yl) prop-2-en-1-one, a potential chemotherapeutic agent. *Chemistry Central Journal*, 9: 35.
31. Anizaim, A. H., Arshad, S., Zaini, M. F., Abdullah, M., Zainuri, D. A. and Razak, I. A. (2019). Third order nonlinear optical properties of selected fluorinated chalcone derivatives. *Optical Materials*, 98: 109406.
32. Woon, P. S., Sapari, S., Matmin, J. and Razak, F. I. A. (2020). Computational studies on nonlinear optical properties of metal complexes containing azobenzene. *Malaysian Journal of Analytical Sciences*, 24: 719-726.
33. Khalid, M., Ali, A., Jawaria, R., Asghar, M. A., Asim, S., Khan, M. U., Hussain, R., ur Rehman, M. F., Ennis, C. J. and Akram, M. S. (2020). First principles study of electronic and nonlinear optical properties of A–D–π–A and D–A–D–π–A configured compounds containing novel quinoline–carbazole derivatives. *RSC Advances*, 10: 22273.
34. Bartashevich, E. and Tsirelson, V. (2013). Atomic dipole polarization in charge-transfer complexes with halogen bonding. *Physical Chemistry Chemical Physics*, 15: 2530-2538.

Malaysian Journal of Analytical Sciences (MJAS)
Published by Malaysian Analytical Sciences Society

EVALUATION OF THE TOTAL FLAVONOID, PHENOLIC CONTENT, AND ANTIOXIDANT ACTIVITY IN SABAH SNAKE GRASS EXTRACTS *(Clinacanthus nutans Lindau)*

(Penilaian Jumlah Kandungan Flavonoid, Fenolik dan Aktiviti Antioksida bagi Ekstrak Belalai Gajah *Clinacanthus nutans Lindau*)

Idham Zaharudie and Chong Shu Xian*

Faculty of Pharmacy,
SEGi University, No. 9, Jalan Teknologi, Taman Sains Selangor, Kota Damansara, PJU 5,
47810 Petaling Jaya, Selangor, Malaysia

**Corresponding author: chongshuxian@segi.edu.my*

Received: 3 March 2022; Accepted: 12 April 2022; Published: 25 August 2022

Abstract

Clinacanthus nutans Lindau (*C. nutans*) or locally known in Malaysia as the Sabah Snake Grass (SSG) contains phytochemicals such as flavonoids and phenolic acids. The leaves of the plant exhibit antioxidant, anti-inflammatory, and antiviral properties, thus, it was traditionally used to treat venomous injuries, rheumatism, and sprains throughout Asia. Previous studies of the antioxidative activity in *C. nutans* extracts have been carried out under different conditions or using different extraction methods, which may have resulted in a varied yield of antioxidative constituents. Thus, this study aimed to compare the total phenolic content (TPC), total flavonoid content (TFC), and antioxidative activity of *C. nutans* methanol, water, and hexane extracts using the traditional solvent extraction method. Results showed that the water extract contains the highest TPC value (3.66 ± 0.11 mg GAE/g) followed by methanol (2.84 ± 0.36 mg GAE/g) and hexane (0.13 ± 0.03 mg GAE/g). The TPC values of methanol and water extracts were significantly higher than hexane ($p < 0.05$). For TFC value, the methanol extract was the highest (1.91 ± 0.05 mg QE/g), followed by water extract (1.50 ± 0.01 mg QE/g) and hexane was not detected. The radical scavenging activity (RSA) decreased in the order of methanol > water > hexane extract. In conclusion, the study suggests that high phenolic and flavonoid contents in *C. nutans* extracts may be the key factor for it to act as an excellent source of natural antioxidants.

Keywords: Sabah snake grass, total phenolic content, total flavonoid content, radical scavenging activity

Abstrak

Clinacanthus nutans Lindau (C. nutans) atau lebih dikenali oleh penduduk tempatan di Malaysia sebagai belalai gajah mengandungi fitokimia seperti flavonoid dan asid fenolik. Dedaun tumbuhan berikut mempamerkan sifat-sifat seperti antioksida, anti radang, dan antivirus. Oleh itu, ia secara tradisionalnya digunakan di seluruh asia untuk merawat kecederaan berbisa, sakit sendi, dan seliuh. Kajian terdahulu mengenai aktiviti antioksida dalam ekstrak *C. nutans* menggunakan kaedah ekstrak yang berbeza atau dalam keadaan yang berbeza. Justeru, ini boleh menjana hasil kandungan antioksidan yang berbeza. Kajian ini betujuan membuat penilaian jumlah kandungan fenolik (TPC), flavonoid (TFC), dan aktiviti antioksida bagi ekstrak metanol, air, dan heksana daripada *C. nutans* dengan kaedah pengekstrakan pelarut tradisional. Keputusan menunjukkan bahawa ekstrak air

mengandungi kandungi TPC tertinggi (3.66 ± 0.11 mg GAE/g) diikuti metanol (2.84 ± 0.36 mg GAE/g) and heksana (0.13 ± 0.03 mg GAE/g). Bagi nilai TFC, ekstrak methanol adalah tertinggi (1.91 ± 0.05 mg QE/g), mingikuti ekstrak air (1.50 ± 0.01 mg QE/g) dan heksana (tidak dikesan). Nilai TPC ekstrak metanol dan air adalah jauh lebih tinggi daripada heksana ($p < 0.05$). Perencatan radikal bebas (RSA) bagi ekstrak dalam tertib menurun adalah seperti berikut; metanol > heksana > air. Konklusinya, kajian ini mencadangkan bahawa kandungan fenolik dan flavonoid yang tinggi dalam ekstrak *C. nutans* mungkin menjadi faktor utama untuk ia bertindak sebagai sumber antioksida semula jadi yang hebat.

Kata kunci: belalai gajah, jumlah kandungan flavonoid, jumlah kandungan fenolik, perencatan radikal bebas

Introduction

C. nutans, or commonly known as *Belalai Gajah* in Malaysia, is a small plant native to tropical Asian countries [1]. The leaves of the plant can be described as flat, opposite, and narrowly elliptic-oblong in shape and the mature part of the plant exhibits lower levels of phytochemicals, chlorophyll, ascorbic acid, and phenolic content in comparison to its younger counterparts [2]. The slightly curved stem that supports the leaves resembles the curvature of an elephant's trunk where the name *Belalai Gajah* was derived [3].

C. nutans is used in Thailand as a traditional antivenom therapy for venomous creatures like snakes, jellyfish, and scorpions [4], while native Singaporeans utilise the plant for detoxification purposes [5]. The plants' anti-inflammatory characteristics allow locals in China to utilise it as a treatment for rheumatism and sprains from injuries [6]. The extract of *C. nutans* has demonstrated antioxidant activity and protection against free radical-induced haemolysis [7], which allows the plant to be further developed as a natural antioxidant for human consumption [8]. The leaf of the plant also exhibits antiviral properties against the herpes simplex virus type-2 (HSV-2) [9]. Yet, more studies are needed to establish and comprehend the bioactive components and therapeutic characteristics of this plant due to its multiple and beneficial attributes [10].

An antioxidant is an agent that has the ability to greatly delay or prevent the oxidation of an oxidisable substance when it is introduced at low concentrations compared to the substance [11]. The antioxidant effect mainly results from phenolic compounds such phenolic acid, flavonoids, and phenolic diterpenes. These compounds have the capability to undergo redox reaction, which absorbs and neutralises free radicals through the suppression of singlet and triplet oxygen [12]. Studies have isolated various bioactive compounds in *C. nutans* which exhibit antioxidant activity such as polyphenols [13], ferulic acid, caffeic acid, protocatechuic acid, chlorogenic acid [14], phthalic acid [15] and gendarucin A [16]. Studies have reported that the ethanolic extract of the leaf exhibited higher antioxidative activity than the stem extract [16], yet the extract exhibited remarkably lower antioxidative activity than green tea extract [13]. A study demonstrated that crude chloroform extract possessed the highest antioxidant activity compared to crude methanol and aqueous extracts [15]. However, other have reported that the crude 80% aqueous methanol extract had the highest antioxidant activity compared to fractionation extracts [17]. In addition, the activity of a younger plant extract was found to be higher than the older plant, and the buds extract showed significant higher activity than the leaf extract [18].

Most of the previous literatures had employed the basic liquid extraction method to study the antioxidative properties of methanolic extract in *C. nutans* [19-22]. Nevertheless, the investigation of antioxidative properties for other extracts, such as water and hexane extracts, had either used liquid extraction at higher temperatures (70°C) [21] or fractionation extraction from the crude methanolic extract [20]. Antioxidants are heat sensitive and are prone to degradation after prolonged heating [23], which results in a lower yield of its constituents. In addition, different extraction methods may result in varied yields of antioxidative constituents [24]. Previous studies have no comparable data on the antioxidative activity of *C. nutans* crude extract using methanol, water, and hexane. This study was thus conducted to compare the TPC, TFC and antioxidant

activity of *C. nutans* using the basic liquid extraction method under room temperature.

Materials and Methods

Plant material

1 kg of *C. nutans* leaf was purchased from a herbal shop in Cheras, Kuala Lumpur. The authentication of the plant was confirmed by the Forest Research Institute Malaysia.

Extraction of *C. nutans*

The dried leaf of *C. nutans* was grinded into a fine powder with a blender. 100 g of fine plant powder was agitated in three different solvents (hexane, methanol, and distilled water) for 48 hours at room temperature. Each sample was filtered and concentrated by evaporation using a rotary evaporator at 60°C. The dried extracts were weighted and dissolved in methanol with the concentration of 0.1 g/mL and were stored at -20°C for further analysis.

Determination of TPC of *C. nutans* extracts

The Folin-Ciocalteu colorimetric method was used to quantify TPC. Gallic acid (GA) was used as the standard. The GA stock solution (50 µg/mL) was prepared in water and further dilution was made to achieve the calibration curve in the range of 1-40 µg/mL. 0.1 mL of each extract were placed into a volumetric flask and mixed with 0.2 mL of Folin-Ciocalteu phenol reagent and 1.5 mL of 6% Na_2CO_3 solution. The volume of the mixture was adjusted to 10 mL before incubation for 30 min in the dark. The absorbance of the mixture was then monitored and quantified against blank at 725 nm using a UV-visible spectrometer (Beckman Coulter DU730). The concentration of phenolic compounds was represented in microgram GA equivalent per gram of extract (mg GAE/g) [25], with the equation shown below:

$$\text{TPC} = \frac{[\text{Concentration of GA from calibration curve (µg/mL) x Volume of extract (mL)}]}{\text{Mass of plant extract (g)}} \quad (1)$$

Determination of TFC of *C. nutans* extracts

The aluminium colorimetric method was used to analyse the TFC [25]. Quercetin was used as the standard. The quercetin stock solution (50 µg/mL) was prepared in ethanol and further dilution was made to achieve the calibration curve in the range of 6.25-40 µg/mL. 50 µL of each three extracts were placed into a volumetric flask and mixed with 5 mL water, 0.6 mL $NaNO_3$, 0.5 mL $AlCl_3$, and 4 mL NaOH. The mixture was then incubated for 20 min in the dark. The absorbance of the mixture was then quantified at 415 nm using a UV-visible spectrometer. The concentration of flavonoid was represented in microgram quercetin equivalent per gram of extract (mg QE/g) [25], with the equation shown below:

$$\text{TFC} = \frac{[\text{Concentration of quercetin from calibration curve (µg/mL) x Volume of extract}]}{\text{Mass of plant extract (g)}} \quad (2)$$

Radical scavenging activity of *C. nutans* extracts: 2,2-diphenyl-1-picrylhydrazyl (DPPH) assay

An amount 60 µg/mL DPPH (Alfa Aesar, Lancashire, UK) stock was freshly prepared with ethanol. 10 µL of plant extracts were individually mixed with 3 mL of DPPH and incubated for 30 min. The absorbance values were recorded using a UV-vis spectrometer at 517 nm [25].

2,2'-azino-bis-(3-ethyl)benzothiazoline)-6-sulfonic acid diammonium salt (ABTS) radical cation scavenging assay

The ABTS assay was carried out as described by Rakholiya et al. [26]. 10 µL of plant extracts were individually mixed with 3 mL of ABTS radical cation solution and incubated for 40 min. The absorbance values were recorded using a UV-vis spectrometer at 734 nm.

The %RSA of DPPH and ABTS cation radical were quantified according to the equation shown below:

$$\%RSA = \frac{(\text{Absorbance of blank} - \text{Absorbance of sample}) \times 100\%}{\text{Absorbance of blank}} \quad (3)$$

Statistical analysis

The two-tailed t-test was used to analyse the differences between methanol, hexane, and water extracts of *C. nutans*, where $p < 0.05$ is considered statistically significant. Statistical calculation was performed using Microsoft Excel (Microsoft Office Professional Plus 2019, Washington, United States).

Results and Discussion

Extraction of *C. nutans*

The percentage yield for methanolic, hexane, and water extracts were obtained from 100 g of dried plant powder as shown in Table 1. Water extract had the highest percentage yield (8.09%) when compared to the methanolic extract (4.92%) and hexane extract (4.80%), which had the lowest percentage yield. The high yield in methanol was most likely due to the solubility of important components of SSG in methanol, such as the phenolic groups [27]. The polarity of the solvents used for extraction impacted the phenolic solubility [28]. Furthermore, water can enhance extraction efficiency [29] and this may result in the high recovery of phenolic compounds due to the high polarity in water.

Table 1. The net weight and percentage yield of *C. nutans* for methanol, hexane, and water extract

Solvent for Plant Extraction	Net Weight (g)	Yield (%)
Methanol	2.191	4.92
Hexane	2.400	4.80
Water	4.050	8.09

Total phenolic content

Phenolic acids, flavonoids, and tannins are considered the most important dietary phenolic components among several types of phenolic compounds [30]. Phenolic compounds especially phenols act as antioxidants, immunological boosters, anti-clotting agents, and hormone modulators by modifying the prostaglandin pathways which prevent platelets from clumping and have the capacity to inhibit particular enzymes that induce inflammation [31]. The Folin–Ciocalteu test is the current standardised technique to determine TPC in food or biological samples, which is based on the interaction of phenolic compounds with a colorimetric reagent that permits detection in a visible spectrum [32-33]. Gallic acid (GA) was used as the positive control in the quantification of TPC. The TPC of three extracts (methanol, water, and hexane) were yielded from the calibration curve [$y = 0.0389x - 0.0079$); $R^2 = 0.9901$] obtained from the GA concentrations in µg GAE/g expression (Figure 1), where y is sample absorbance at 750 nm while x is the concentration of TPC.

Figure 2 shows that the methanolic extract has the highest content of TPC (3.66 ± 0.11 mg GAE/g), followed by methanol extract (2.84 ± 0.04 mg GAE/g), while hexane extract had the lowest content of TPC (0.13 ± 0.03 mg GAE/g). The two-tailed t-test showed significant differences between the TPCs among the three extracts ($p < 0.05$). All TPC values obtained were lower than reported in literature. Fadhlin Baharuddin et al. [34] reported that the TPC of methanolic extract was 11.05-13.87 mg GAE/g when the temperature ranged from 30-55°C. Ismail et al. [17] reported that the TPC of aqueous and hexane extracts fractionated from the crude methanolic extract possessed 415.76 and 50.24 mg GAE/g, respectively. These inconsistent findings resulted from differences in method of extraction, parts

of plant, maturity of plant and storage of plant [35]. Nevertheless, our results agreed with previous study which showed that the water extract had the highest TPC and hexane extract had the lowest TPC [17].

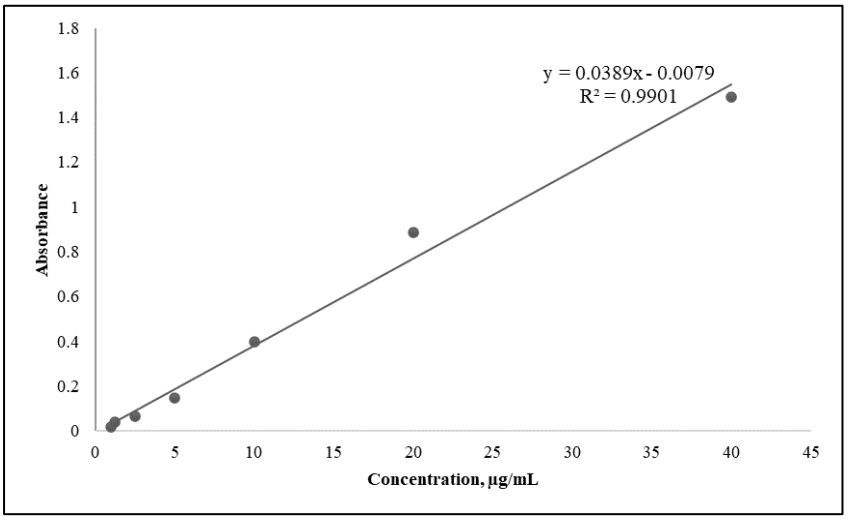


Figure 1. The calibration curve of the gallic acid standard solutions

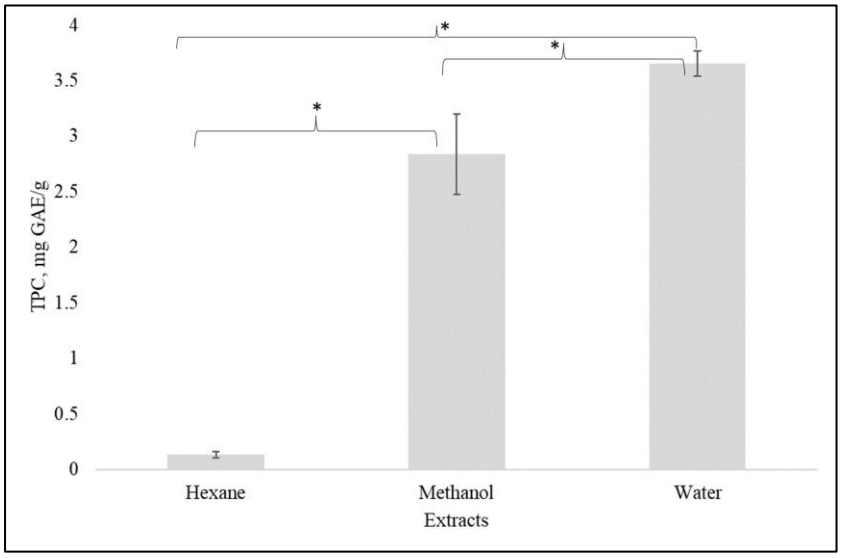


Figure 2. Mean total phenolic content for *C. nutans* hexane, methanol, and water extracts which were expressed as gallic acid equivalent (GAE). All experiments were performed in triplicates. Asterisk (*) indicates statistically significant at the level of $p < 0.05$ between the extracts

Total flavonoid content

Flavonoids are classified into different subclasses based on their composition, including flavanones, flavones, flavanols, and flavonols, with myricetin, kaempferol, and quercetin being the most common [36]. It is a water-soluble phytochemical compound which is obtained from essential plant phenolic with beneficial antimicrobial, anti-inflammatory, and antioxidant properties as well as the ability to inhibit oxidative cell damage and carcinogenesis [30]. Quercetin was used as the positive control in determining TFC. The TFC of three different extracts were yielded from the calibration curve [$y = 0.0824x - 0.2444$; $R^2 = 0.957$] obtained from the quercetin concentrations in µg QE/g as shown in Figure 3, where y is sample absorbance at 415 nm and x is the concentration of TFC. Figure 4 shows that the methanolic extract has the highest content of TFC (1.91 ± 0.05 mg QE/g), followed by the water extract (1.50 ± 0.01 mg QE/g); meanwhile, the hexane extract cannot be determined as the absorbance is below the limit of detection from the calibration curve. The two-tailed t-test showed significant differences in TFCs between the water and methanol extract ($p < 0.05$). Previous literature reported that the TFC of 80% methanolic extract of *C. nutans* was 4.31-7.32 mg QE/g, where the phenolics content of the plant was higher as the plant grew [19]. The variation in results may be due to many factors such as plant age [19] or different geographical distribution of the plant which affects the plant's metabolism [35]. Our findings showed that the TPC in methanolic and aqueous extract was remarkably higher than hexane extract, and this trend is also observed in previous literature where the water extract has the highest TPC and hexane extract has the lowest TFC [17].

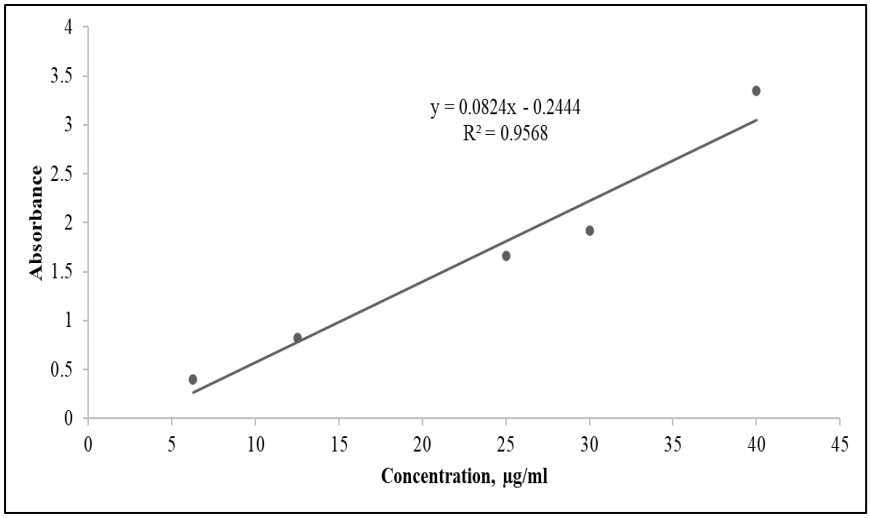


Figure 3. The calibration curve of the quercetin standard solution

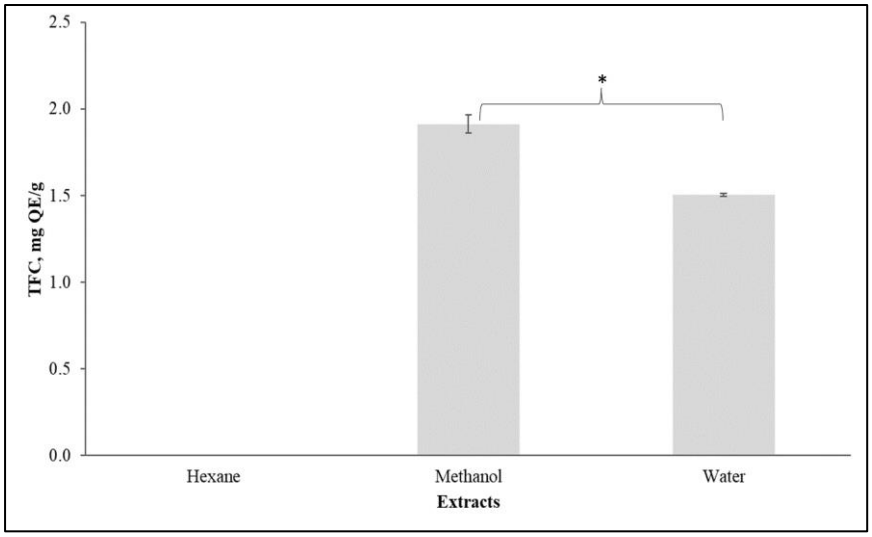


Figure 4. Mean total flavonoid content for *C. nutans* hexane, methanol and water extracts which were expressed as quercetin equivalent (QE). All experiments were performed in triplicates. Asterisk (*) indicates statistically significant at the level of $p < 0.05$ between the extracts

Radical scavenging activity - DPPH and ABTS assay

DPPH and ABTS assays are prominent surrogate markers to detect antioxidant capacity and evaluate potential substances behaving as free radical scavengers [37]. Table 2 shows that the DPPH and ABTS scavenging activity have the same trend, where the %RSA decreases in the order of methanolic > water > hexane extract. Our findings agree well with Ismail *et al*. [34] who reported that the methanolic crude extract exhibited the highest antioxidative activity and hexane fraction extract exhibited the lowest antioxidative activity.

Table 2. The %RSA of DPPH and ABTS cation radical for hexane, methanol and water extracts of *C. Nutans*

Plant Extract	%RSA	
	DPPH	ABTS
Hexane	16.04 ± 1.46	3.64 ± 0.48
Methanol	59.27 ± 0.86	99.94 ± 0.22
Water	53.40 ± 3.72	74.94 ± 2.04

Conclusion

C. Nutans was extracted using liquid extraction method under room temperature. The three types of solvents used for extraction are hexane, methanol and water. The TPC, TFC, and antioxidative activity were quantified using Folin-Ciocalteu assay, aluminium colorimetric method, DPPH, or ABTS assay, respectively. The value of TPC decreased in the following order: water > methanol > hexane, where the water extract (3.66 ± 0.11 mg GAE/g) was 1.3- and 28-folds higher than the methanol (2.84 ± 0.04 mg GAE/g) and hexane (0.13 ± 0.03 mg GAE/g) extracts, respectively. Meanwhile, the TFC value of methanol extract (1.91 ± 0.05 mg QE/g) was 1.3-fold higher than water extract (1.50 ± 0.01 mg

QE/g), however, the hexane extract was too low to be detected. Lastly, the DPPH and ABTS radical scavenging capability of the three extracts decreased in the following order: methanol > water > hexane. Methanol and water extracts displayed supreme antioxidative scavenging activity compared to hexane extract and this might be due to the high phenolic and flavonoid content. These results suggest that *C. nutans* extracts are a good source of natural antioxidants.

Acknowledgement

This research is supported by SEGi University, SEGiIRF/2014-15/FoP-4/29 research fund.

References

1. Intan, S., Mahiran, B., Kim, W., Siti, E., Hamid, R. and Maznah, I. (2015). In vitro antioxidant, cytotoxic and phytochemical studies of *Clinacanthus nutans Lindau* leaf extracts. *African Journal of Pharmacy and Pharmacology*, 9(34): 861-874.
2. Zulkipli, I., Rajabalaya, R., Idris, A., Sulaiman, N. and David, S. (2017). *Clinacanthus nutans*: A review on ethnomedicinal uses, chemical constituents and pharmacological properties. *Pharmaceutical Biology*, 55(1): 1093-1113.
3. Yahaya, R., Dash, G. K., Abdullah, M. S. and Mathews, A. (2015). *Clinacanthus nutans* (burm. F.) *Lindau*: An useful medicinal plant of south-east Asia, *International Journal of Pharmacognosy and Phytochemical Research*, 7(6): 1244-1250.
4. P'ng, X., Akowuah, G. and Chin, J. (2013). Evaluation of the sub–acute oral toxic effect of methanol extract of *Clinacanthus nutans* leaves in rats. *Journal of Acute Disease*, 2(1): 29-32.
5. Siew, Y., Zareisedehizadeh, S., Seetoh, W., Neo, S., Tan, C. and Koh, H. (2014). Ethnobotanical survey of usage of fresh medicinal plants in Singapore. *Journal of Ethnopharmacology*, 155(3): 1450-1466.
6. Globinmed.com (2021). GlobinMed – a unique interactive e-database with validated, up-to-date and comprehensive information on integrated medicine. http://www.globinmed.com/index.php?option=com_content&view=article&id=79320:clinacanthus-nutans-burmf-lindau&catid=199:safety-of-herbal&Itemid=139 [Accessed online 22 August 2021].
7. Pannangpetch, P., Laupattarakasem, P., Kukongviriyapan, V., Kukongviriyapan, U., Kongyingyoes, B. and Aromdee, C. (2007). Antioxidant activity and protective effect against oxidative hemolysis of *Clinacanthus nutans* (Burm.f) *Lindau*. S*ongklanakarin Journal of Science and Technology*, 29: 1-9.
8. Kong, H., Musa, K. and Abdullah Sani, N. (2016). *Clinacanthus nutans* (Belalai Gajah/Sabah Snake Grass): Antioxidant optimization on leaves and stems. AIP Conference Proceedings, 1784: 0300301-0300305.
9. Jayavasu, C., Dechatiwongse, T. and Balachandra, K. (1992). Virucidal activity of *Clinacanthus nutans Lindau* extracts against herpes simplex virus type-2: In vitro study. *Warasan Krom Witthayasat Kanphaet*, 34 (4): 153-158.
10. Ghasemzadeh, A., Nasiri, A., Jaafar, H., Baghdadi, A. and Ahmad, I. (2014) Changes in phytochemical synthesis, chalcone synthase activity and pharmaceutical qualities of Sabah snake grass (*Clinacanthus nutans L.*) in relation to plant age. *Molecules*, 19(11): 17632-17648.
11. Halliwell, B. (1990) How to characterize a biological antioxidant. *Free Radical Research Communications*, 9(1): 1-32.
12. Krauss, R., Eckel, R., Howard, B., Appel, L., Daniels, S., Deckelbaum, R. (2000). The american heart association dietary guidelines. *Circulation*, 102(18): 2284-2299.
13. Yuann, J. M. P., Wang, J. S., Jian, H. L., Lin, C. C. and Liang, J. Y. (2012). Effects of *Clinacanthus nutans* (Burm. f) *Lindau* leaf extracts on protection of plasmid DNA from riboflavin photoreaction. *MC-Transaction on Biotechnology*, 4: 45-58.
14. Sarega, N., Imam, M. U., Md Esa, N., Zawawi, N. and Ismail, M. (2016). Effects of phenolic-rich extracts of *Clinacanthus nutans* on high fat and high cholesterol diet-induced insulin resistance. *BMC Complementary and Alternative Medicine*, 16(1): 1-11.

15. Yong, Y. K., Tan, J. J., The, S. S., Mah, S. H., Ee, G. C. L., Chiong, H. S. and Ahmad, Z. (2013). *Clinacanthus nutans* extracts are antioxidant with antiproliferative effect on cultured human cancer cell lines. *Evidence-Based Complementary and Alternative Medicine*, 2013: 462751.
16. Khoo, L.W., Mediani, A., Zolkeflee, N. K. Z., Leong, S. W., Ismail, I. S., Khatib, A., Shaari, K. and Abas, F. (2015). Phytochemical diversity of *Clinacanthus nutans* extracts and their bioactivity correlations elucidated by NMR based metabolomics. *Phytochemistry Letters*, 14:123-133.
17. Ismail, N. Z., Md Toha, Z., Muhamad, M., Nik Mohamed Kamal, N. N. S., Mohamad Zain, N. N. and Arsad, H. (2020). Antioxidant effects, antiproliferative effects, and molecular docking of *Clinacanthus nutans* leaf extracts. *Molecules*, 25: 2067.
18. Ghasemzadeh, A., Nasiri, A., Jaafar, H. Z. E., Baghdadi, A. and Ahmad, I. (2014). Changes in phytochemical synthesis, chalcone synthase activity and pharmaceutical qualities of Sabah snake grass (*Clinacanthus nutans L.*) in relation to plant age. *Molecules*, 19: 17632-17648.
19. Abd Samat, N. M.A., Ahmad, S., Awang, Y., Bakar, R. A. H. and Hakiman, M. (2020). Alterations in herbage yield, antioxidant activities, phytochemical contents, and bioactive compounds of Sabah snake grass (*Clinacanthus Nutans L.*) with regards to harvesting age and harvesting frequency. *Molecules*, 25 (12): 2833.
20. Alam, M. A, Zaidul, I. S., Ghafoor, K., Sahena, F., Hakim, M. A., Rafii, M.Y., Abir, H.M., Bostanudin, M. F., Perumal, V. and Khatib, A. (2017). In vitro antioxidant and, α-glucosidase inhibitory activities and comprehensive metabolite profiling of methanol extract and its fractions from *Clinacanthus nutans*. *BMC Complementary and Alternative Medicine*, 17(1): 181.
21. Haron, N. H., Md Toha, Z., Abas, R., Hamdan, M. R., Azman, N., Khairuddean, M. and Arsad, H. (2019). In vitro cytotoxic activity of *Clinacanthus nutans* leaf extracts against HeLa cells. *Asian Pacific Journal of Cancer Prevention*, 20(2): 601-609.
22. Sarega, N., Imam, M. U., Ooi, D. J., Chan, K. W., Md Esa, N., Zawawi, N. and Ismail, M. (2016). Phenolic rich extract from *Clinacanthus nutans* attenuates hyperlipidemia-associated oxidative stress in rats. *Oxidative Medicine and Cellular Longevity*, 2016: 4137908.
23. Ioannou, I., Chekir, L. and Ghoul, M. (2020). Effect of heat treatment and light exposure on the antioxidant activity of flavonoids. *Processes*, 8: 1078.
24. Tushar, D., Sonal, S., Gajbhiye, N. A. and Satyanshu, K. (2017). Effect of extraction methods on yield, phytochemical constituents and antioxidant activity of *Withania somnifera*. *Arabian Journal of Chemistry*, 10(1): S1193-S1199.
25. Iqbal, E., Salim, K. and Lim, L. (2015). Phytochemical screening, total phenolics and antioxidant activities of bark and leaf extracts of *Goniothalamus velutinus* (airy shaw) from Brunei Darussalam, *Journal of King Saud University - Science*, 27(3): 224-232.
26. Rakholiya, K., Kaneria, M., Nagani, K., Patel, A. and Chanda, S. (2015). Comparative analysis and simultaneous quantification of antioxidant capacity of four terminalia species using various photometric assays. *World Journal of Pharmaceutical Research*, 4 (4): 1280-1296.
27. Ismail, H., Chan, K., Mariod, A. and Ismail, M. (2010). Phenolic content and antioxidant activity of cantaloupe (*Cucumis melo*) methanolic extracts. *Food Chemistry*, 119(2): 643-647.
28. Naczk, M. and Shahidi, F. (2006). Phenolics in cereals, fruits and vegetables: Occurrence, extraction and analysis. *Journal of Pharmaceutical and Biomedical Analysis*, 41(5): 1523-1542.
29. Hemwimon, S., Pavasant, P. and Shotipruk, A. (2007). Microwave-assisted extraction of antioxidative anthraquinones from roots of *Morinda citrifolia*. *Separation and Purification Technology*, 54(1): 44-50.
30. King, A. and Young, G. (1999). Characteristics and occurrence of phenolic phytochemicals. *Journal of the American Dietetic Association*, 99(2): 213-218.

31. Hussain, I., Ullah, R., Ullah, R., Khurram, M., Ullah, N., Abdul, B., Khan, F., Khattak, M., Zahoor, M., Khan, J. and Khan, D. N. (2011). Phytochemical analysis of selected medicinal plants. *African Journal of Biotechnology*, 10(38): 7487-7492.
32. Folin, O. and Ciocalteu, V. (1927). On tyrosine and tryptophane determinations in proteins. *Journal of Biological Chemistry*, 73(2): 627-650.
33. Robards, K. and Antolovich, M. (1997). Analytical chemistry of fruit bioflavonoids: a review. *The Analyst*, 122(2): 11R-34R.
34. Fadhlin Baharuddin, N. A., Mad Nordin, M. F., Morad, N. A., Aris, N. I. A. and Che Yunus, M. A. (2018). Total phenolic, flavonoid content and antioxidant activity of *Clinacanthus nutans* leaves by water-based ultrasonic assisted extraction. *Malaysian Journal of Analytical Sciences*, 22(4): 659-666.
35. Ho, S. Y., Cheong, B. E. and How, S. E. (2017). Evaluation of antioxidant activity of *Clinacanthus nutans* (Acanthaceae). *Short Communications in Biotechnology*, 4: 63-74.
36. Serafini, M., Peluso, I. and Raguzzini, A. (2010). Flavonoids as anti-inflammatory agents. *Proceedings of the Nutrition Society*, 69(3): 273-278.
37. Ilyasov, I. R., Beloborodov, V. L., Selivanova, I. A. and Terekhov, R. P. (2020). ABTS/PP decolorization assay of antioxidant capacity reaction pathways. *International Journal of Molecular Sciences*, 2020(21): 1131.

Malaysian Journal of Analytical Sciences (MJAS)
Published by Malaysian Analytical Sciences Society

FORMULATION OF HIGH-QUALITY UV-CURABLE COATING CONTAINING RENEWABLE REACTIVE DILUENTS FOR WOOD PROTECTION

(Formulasi Salutan Awetan-UV Berkualiti Tinggi yang Mengandungi Diluen Reaktif yang Boleh Diperbaharui untuk Perlindungan Kayu)

Noraini Abd Ghani[1,2,3], Emilia Abdulmalek[1,2], Rajni Hatti-Kaul[4], Azren Aida Asmawi[1,2], Mohd Basyaruddin Abdul Rahman[1,2]*

[1]*Integrated Chemical BioPhysics Research, Faculty of Science*
[2]*Department of Chemistry, Faculty of Science*
Universiti Putra Malaysia, 43400 UPM Serdang, Selangor, Malaysia
[3]*Department of Fundamental and Applied Sciences, Faculty of Science and Information Technology,*
Universiti Teknologi PETRONAS, 32610, Perak, Malaysia
[4]*Department of Biotechnology, Center for Chemistry and Chemical Engineering,*
Lund University, P.O. Box 124, SE-221 00 Lund, Sweden

**Corresponding author: basya@upm.edu.my*

Received: 29 November 2021; Accepted: 23 April 2022; Published: 25 August 2022

Abstract

Fine quality coating materials for a variety of surfaces using environmentally friendly substrates are continuously in demand. A large proportion of acrylate derivatives, which are toxic and hazardous, were found in most of the coating formulations. Many efforts have been done to replace acrylate derivatives with other materials derived from renewable resources. In this work, several formulations of wood coating containing different composition of epoxy acrylate and enzymatically synthesized epoxide from soybean oil or wax esters mixture of dioleyl adipate and 1,5-pentanediol diricinoleate were prepared. The formulations were subjected to performance evaluations including gel content, pendulum hardness, and surface test. Formulation 1 containing 85% epoxy acrylate and 15% epoxidation from soybean oil exhibited the highest gel content (79.5%), pendulum hardness (61.02%) and surface resistance to different types of liquid. Increase in surface resistance was observed using a formulation containing 85% epoxy acrylate and a mixture of 1,5-pentanediol diricinoleate and dioleyl adipate (1:1, w/w; 15%). Therefore, these reduced acrylate formulations showed good potential in the development of high-quality UV-curable wood coating.

Keywords: coating, acrylate, epoxide, ester, ricinoleate

Abstrak

Bahan salutan yang berkualiti untuk pelbagai permukaan menggunakan substrat mesra alam sentiasa mendapat permintaan. Sebilangan besar derivatif akrilat, yang beracun dan berbahaya, ditemui dalam kebanyakan rumusan salutan. Pelbagai usaha telah dilakukan untuk menggantikan derivatif akrilat dengan bahan lain yang diperoleh daripada sumber yang boleh diperbaharui. Dalam kajian ini, beberapa formulasi salutan kayu yang mengandungi komposisi epoksi akrilat dan epoksida yang disintesis secara

enzimatik daripada minyak kacang soya atau campuran ester lilin dioleil adipate dan 1,5-pentanediol dirisinoleate yang berbeza telah disediakan. Formulasi ini tertakluk kepada penilaian prestasi termasuk kandungan gel, kekerasan pendulum, dan ujian permukaan. Formulasi 1 yang mengandungi 85% epoksi akrilik dan 15% epoksida dari minyak kacang soya menunjukan kandungan gel (79.5%), kekerasan pendulum (61.02%) dan rintangan permukaan terhadap pelbagai jenis cecair yang tertinggi. Selain itu, peningkatan terhadap rintangan permukaan diperhatikan menggunakan formulasi yang mengandungi 85% epoksi akrilik dan campuran dioleil adipate dan 1,5-pentanediol dirisinoleate (1:1, w/w; 15%). Oleh itu, formulasi akrilat yang dikurangkan ini menunjukan potensi yang baik dalam pembangunan salutan kayu awetan-UV yang berkualiti tinggi.

Kata kunci: salutan, akrilat, epoksida, ester, risinoleate

Introduction

A protective coating is an essential layer of material that is applied to the surface of another material, especially wood-based products, to protect it against degradation and disintegration over time [1–3]. The coating must be stabilized from yellowing, cracking, blistering, and delaminating. The commonly used conventional solvent-based curing coatings are always susceptible to environmental pollution. High amounts of volatile organic compounds (VOCs) or hazardous air pollutants (HAPs) are emitted into the atmosphere during the curing process [4]. In recent years, advances in environmental awareness, economic view, energy preservation, and products performance have prompted a change from conventional to UV radiation curing method. A high number of tightly crosslinked polymer networks can be easily formed using the method, which improves coating properties including high gel content, hardness, and surface resistance [5–7].

In UV curable coatings formulation, the use of acrylate derivatives in the coating formulations is unavoidable as it is essential for polymerization during the curing process [3, 8, 9]. However, many health issues have been reported due to its toxicity [10, 11]. Epoxides derived from vegetable oils have been prospected to lead the changes in UV-curable coatings due to their biodegradability, high abundance, low toxicity, and triglyceride structures suitable for the preparation of major constituents of UV-curable coatings [12, 13]. Demengeot et al. has discovered that the crosslinking of epoxidized linseed and rapeseed oils without reactive diluents resulted in viscous formulations that were difficult to dry. The addition of reactive diluents, on the other hand, had greatly increased the film's hardness [14]. Besides, epoxidation of soybean oil (ESBO) with hydroxyethyl methacrylated maleate precursor had significantly improved in the coating properties when compared with the commercial product [13].

Liquid wax esters are also gaining industrial interest since they are non-hazardous, biodegradable, and have excellent tribological properties [15], thus being attractive in lubricants and coating applications. They consist of long-chain fatty acids and fatty alcohols with a chain length of 12 carbons or more. Liquid wax adipate esters such as dioleyl adipate can be enzymatically synthesized in a solvent-free system which offers a green benign process and great product selectivity [16]. Dioleyl adipate, which contains two double bonds, may have a significant effect on the radiation curing because the free radical would attack the bonds for polymerization to occur. It was reported that a coated thin film of formulation containing dioleyl adipate made from renewable raw materials can produce 90% polymerization and surface resistant performance of up to 4.5 N [17].

Hence, this study aimed to evaluate and validate the usage of epoxide (ESBO) or a mixture of esters (dioleyl adipate and 1,5-pentanediol diricinoleate) produced via enzymatic reaction in replacing acrylate derivatives for wood coating formulations. The products were then undergone ultraviolet (UV) radiation curing and their hardness and chemical resistance were tested to estimate their suitability as wood coatings.

Materials and Methods

Materials

Craynor 104D80 (mixture of EB600 and glyceryl propoxylated triacrylates, 60:40) used in this study was a gift from Akzo Nobel Industrial Coatings (Malmo, Sweden) while, Darocur 1173 was a gift from Malaysia Nuclear Agency (Selangor, Malaysia). Epoxidized Soybean Oil (ESBO) was a gift from Prof. Rajni Hatti-Kaul (Lund University, Sweden). Novozyme® 435 (immobilized *Candida antarctica* lipase B on macroporous acrylic resin, 10,000 propyl laurate units/g) was purchased from Novozymes A/S (Bagvaerd, Denmark). All chemicals and solvents used in this study were analytical grade and used without any further treatments unless otherwise stated.

Enzymatic Production of Esters

Dioleyl adipate was synthesized using an optimized method from a previous study [16]. Briefly, the synthesis was prepared in a 500 ml stirred tank reactor with a working volume of 350 ml. The reactor was equipped with a flat-blade disk turbine agitator, with a temperature control system (Julabo MB-13, Germany) and sampling ports. The enzymatic synthesis of dioleyl adipate was prepared by mixing oleyl alcohol and adipic acid in the reactor at a molar ratio of 5.3:1 and catalyzed by Novozym® 435. Meanwhile, 1,5-pentanediol diricinoleate was produced by reacting ricinoleic acid and 1,5-pentanediol with a molar ratio of 3:1 in a 1 L three-neck flask for a large-scale reaction. An amount of 3% Novozyme® was used in toluene solvent. The reaction was started at 65 °C with 200 rpm under 100 mmHg vacuum pressure for 9 hours. The percentage of fatty acid conversion during the esterification was then quantitated using Equation (1). The ester formed was expressed as equivalent to the conversion of the fatty acid. In addition, both products were confirmed by Fourier transform infrared (FTIR) analysis (Perkin-Elmer, Model 1650, United States).

$$\text{Percentage of conversion (\%)} = \frac{V_{\text{control}} - V_{\text{sample}}}{V_{\text{control}}} \times 100\% \quad (1)$$

where, $V_{control}$ is a volume of 0.1 M KOH needed to titrate the control, and V_{sample} is a volume of 0.1 M KOH needed to titrate the sample.

Formulation of wood coating

Oligomer (epoxy acrylate) and reactive diluents (ESBO and esters) were mixed in different proportions with continuous stirring to obtain a homogenous mixture for reduced acrylate wood coating formulations as summarized in Table 1. Formulations 1-8 were mixed with a 6% photoinitiator (Daracour1173) and applied onto paper plates of desired sizes using a bar coater with 150 μm thickness. The coated samples were irradiated using a UV curing conveyor system which is available at Akzo Nobel Surface Coatings, Malmö, Sweden. Even though formulations were aimed as wood surface coating, paper plates have been used as a standard to undergo further analysis after radiation. The formulation mixture was applied on a paper to determine the maximum curing rate by passing through a UV oven equipped with a 120 W/cm^2 mercury lamp. Performances of Formulations 1-8 on pendulum hardness, surface test and physical observation were evaluated according to the standard requirements.

Table 1. Epoxide and esters composition in reduced acrylate wood coating formulations

Formulation	Composition (%, w/w)			
	Epoxy Acrylate	Epoxidation Soybean Oil	1,5-Pentanediol Diricinoleate	Dioleyl Adipate
1	85	15	-	-
2	85	-	7.5	7.5
3	75	25	-	-
4	75	-	12.5	12.5
5	65	35	-	-
6	65	-	17.5	17.5
7	55	45	-	-
8	55	-	22.5	22.5

Gel content

Gel content was determined by measuring the weight loss of the sample after extraction using acetone for 10 hours at 60 °C [17]. Cured films for different UV radiation exposure were peeled off from the glass tile and weighed to obtain the initial weight. Then, the films were extracted using a Soxhlet extractor to remove unreacted materials inside the coating film. Finally, all cured films were dried in a vacuum and weighed to estimate the gel content. Higher gel content means more crosslinking took place. The amount of gel content was calculated using Equation (2).

Pendulum hardness

Two pendulum hardness methods including Köenig and Persoz can be used to measure the hardness of a coating. A Köenig pendulum hardness tester (Byk, Switzerland) was employed to monitor the surface hardness of the cured film during UV curing, where oscillation was counted between 6° and 3°[18]. After UV exposure, the pendulum hardness of the UV cured film surface was measured with respect to the pendulum oscillation time. The result is expressed as percentage hardness and calculated using Equation (3).

Surface resistance

Assessment of the surface resistance including mar and chemical resistance was evaluated according to EN 12720 (European Standard EN 12720: 1997 Furniture-Assessment of surface resistance to cold liquid) and was performed using Akzo Nobel Industrial Coatings, Malmö, Sweden. The high-speed mar tester was utilized to simulate the effect of fingernail mar at a computed velocity range from 0.3 m/s to 3.4 m/s in a consistent manner by controlling the speed and normal impact force across a coating surface as described by Anderson et al. [19]. The chemical resistance test was then conducted by exposing the cured film to different types of liquids including alcohol (1 hour), coffee (1 hour), water (24 hours), and grease (24 hours). Briefly, a filter paper was immersed in a liquid and was placed on the test surface and later was covered by an inverted glass basin. After a specified period, the paper was removed, and the surface was washed and dried. The surface was then examined for possible damages such as discoloration, changes in gloss or color, and blistering [4].

$$\text{Gel Content (\%)} = \frac{\text{Weight after extraction}}{\text{Initial Weight}} \times 100\% \quad (2)$$

$$\text{Pendulum Hardness (\%)} = \frac{\text{No. of oscillation for sample}}{\text{No. of oscillation for standard glass}} \times 100\% \quad (3)$$

Results and Discussion

Enzymatic production of esters

Direct enzymatic esterification of oleyl alcohol and adipic acid using the previously optimized method [16] was found to produce 95% conversion of dioleyl adipate in the reactor. The presence of ester was confirmed by the FTIR analysis. The FTIR analysis of dioleyl adipate was found to be similar as reported by Chaibakhsh et al. [16], where the absorption bands of C=O and C-O were observed in the region 1690-1794 cm^{-1} and 1162-1263 cm^{-1}, respectively. In addition, ricinoleic ester had also been enzymatically prepared using lipase to evade the problems of discoloration, odor, and high energy costs which usually occurred in high-temperature chemical processes [13,14]. Approximately 87% conversion of 1,5-pentanediol diricinoleate was successfully achieved after 9 hours of reaction. Figure 1 shows that ricinoleate ester had a higher absorption band at wavenumber 1733 cm^{-1} as compared to ricinoleic acid due to the transmittance percentage of C=O (carboxyl and ester group). A similar finding was reported by Ghoshray et al. on the enzymatic synthesis of ricinoleate ester with long-chain fatty alcohol by Lipozyme TM [22].

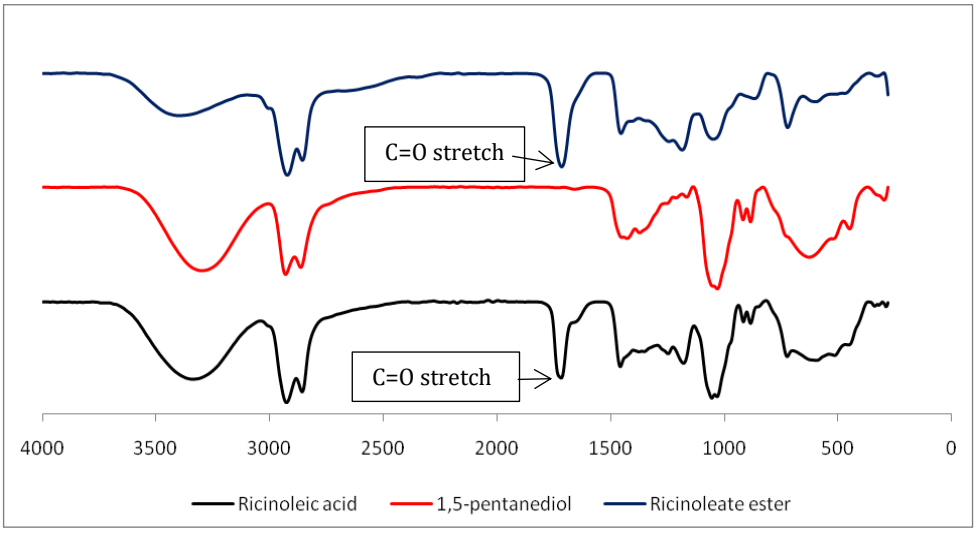


Figure 1. Infrared spectrum for ricinoleic acid, 1,5-pentanediol, and ricinoleate ester after enzymatic reaction using Novozyme® in toluene at 65 °C and 200 rpm stirring rate under 100 mmHg vacuum pressures for 9 hours.

Formulation of Wood Coating

Many researchers have reported on the development of UV-curable coating formulations. However, only a few studies on the production of high-quality UV-curable wood coatings with reduced epoxy acrylate using liquid wax esters as reactive diluents have been done. In this study, different percentages (15-45%) of epoxide (ESBO) or ester (mixture of dioleyl adipate and pentanediol ricinoleate) were used in the formulation. As shown in Table 2, the physical appearance of Formulation 1 and Formulation 2 showed a clear and transparent coating, which was similar to the commercial product containing high epoxy concentration. However, further reducing the epoxy concentration will lead to a transparent and opaque appearance on the glass plate.

Table 2. The physical appearance of coating formulations cured by UV light

Formulation	Amount of Epoxy Acrylate (%)	Physical Appearance After Radiation
Epoxidation of soybean oil		
1	85	Cured, transparent
3	75	Cured, translucent
5	65	Not cured
7	55	Not cured
Mixture of 1,5-pentanediol diricinoleate and dioleyl adipate (1:1, w/w)		
2	85	Cured, transparent
4	75	Cured, opaque
6	65	Cured, opaque
8	55	Cured, opaque

Gel content

Gel content estimation is an important property of any coating as it directly measures the degree of crosslinking, which decides the final properties of the coating [23]. Since the first pass under the ultraviolet light, the photoinitiators will break and produce active radicals. The radicals will then attack the unsaturated double bond of ESBO and wax esters in the formulation and start the crosslinking process. More crosslinking occurs if the process is repeated, resulting in a higher percentage of gel content. As shown in Figure 2, more than 69% of gel contents were found in Formulations 1-4, representing a well cross-linking behavior amongst the various constituents present in different formulations. It was found that as the proportion of epoxy acrylates in the formulations decreased, the gel content values of the film were found to gradually decrease. Formulation 1, which contained ESBO with a high oxirane number and the highest vinyl group from acrylates, had the highest gel content value (79.53%). It is known that oxirane and vinyl groups have a branching effect and can yield more crosslinking in the cured film as compared to double bonds and a hydroxyl group.

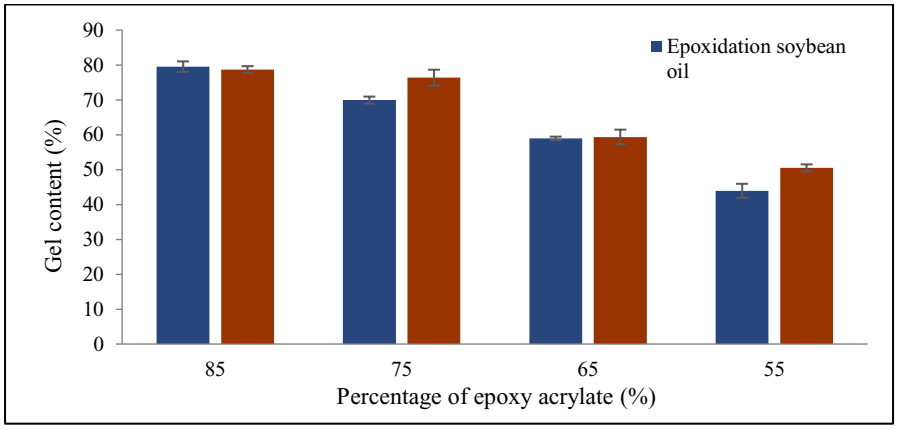


Figure 2. The effect of reduced-epoxy acrylate formulations containing epoxidation soybean oil (ESBO) and a mixture of 1,5-pentanediol diricinoleate and dioleyl adipate (1:1, w/w) on the gel content of coating cured by UV light

Pendulum hardness

One of the most important parameters to ensure scratch resistance in coating formulation is the pendulum hardness. Formulations 1-4 successfully dried in a single exposure to UV curing. Meanwhile, Formulations 5-8 required more UV exposure of up to six passes to completely dry. The formulation was then applied onto glass to test the pendulum hardness. The level of hardness varies depending on the final application, but a pendulum hardness of 40% can be considered as a minimum in many applications. The hardness of coating was found to increase in parallel with the number of passes under UV-light until maximum exposure was reached, at which the point of hardness value remained constant. The hardness percentage of Formulations 1-8 after being exposed to the UV-light until completely dry is shown in Table 3.

From the results obtained, it can be noticed that a higher percentage of reactive diluents including both epoxide and mixed esters in the coating formulation reduced stiffness. Besides, the hardness of Formulations 5 and Formulation 7 could not be measured due to the large amount of ESBO used and the formulations were difficult to dry completely. Formulations 1-3 meets the minimum hardness requirement, which is more than 40%. However, Formulation 1 and Formulation 3 containing 15% and 25% ESBO, respectively, showed greater hardness than Formulation 2 containing a mixture of 15% of pentanediol diricinoleate and dioleyl adipate. This is possibly due to the presence of oxirane ring and more double bonds in ESBO than diricinoleate and dioleyl adipate, which only having two double bonds for crosslinking [23].

Table 3. The percentage of pendulum hardness of coatings cured by UV light

Formulation	Amount of Epoxy Acrylate (%)	Pendulum Hardness (%)
Epoxidation of soybean oil		
1	85	61.02
3	75	44.63
5	65	Not applicable
7	55	Not applicable
Mixture of 1,5-pentanediol diricinoleate and dioleyl adipate (1:1, w/w)		
2	85	43.50
4	75	32.77
6	65	14.69
8	55	9.04

Surface resistance

The ability of a good drying and high-quality formulation was evaluated by fingernail mar and chemical resistance tests as tabulated in Table 4. The coating must endure marring stress and exposure to a wide range of chemicals with various acidity and basicity without staining and losing gloss. The results showed that both mar and chemical resistance performances were reduced as the amount of epoxy acrylate was decreased. No fingernail marring was produced in a formulation containing more than 75% epoxy acrylate. Therefore, only Formulations 1-4 were chosen for further evaluation in the chemical resistance test. The test was simulated by exposing the cured film to different types of liquids including alcohol, coffee, water, and grease. Formulation 2 exhibited excellent resistance towards all the tested liquids after being exposed for up to 24 hours. However, limited exposure to alcohol was observed in Formulation 1 as a slight variation in gloss was noticed after the exposure.

Therefore, formulation containing 85% epoxy acrylate and 15% mixture of pentanediol diricinoleate and dioleyl adipate was able to provide the best coating characteristics and possessed a potential for industrial application.

Table 4. The performance of formulations as wood coatings in mar and chemical resistance

Formulation (+ 6% Photoinitiator)	Fingernail Mar Resistance	Chemical Resistance			
		Alcohol	Coffee	Water	Grease
1	No fingernail marring	L	R	R	R
2	No fingernail marring	R	R	R	R
3	No fingernail marring	NR	R	R	R
4	No fingernail marring	NR	NR	NR	NR
5	Fingernail marring	NA	NA	NA	NA
6	Fingernail marring	NA	NA	NA	NA
7	Fingernail marring	NA	NA	NA	NA
8	Fingernail marring	NA	NA	NA	NA

R: recommended; L: limited exposure; NR: not recommended, NA: not available

Conclusion

This work proposed up to 15% reduction of epoxy acrylate by replacing it with enzymatically synthesized epoxide from soybean oil (ESBO) or wax esters mixture of dioleyl adipate and 1,5-pentanediol diricinoleate (1:1, w/w) to produce high-quality and transparent coating formulations. The reduced acrylate formulations were found to perform well in terms of pendulum hardness test and surface resistance. Moreover, the effect of irradiation doses on the gel content of coated film cured by UV light could reach almost 80%. Therefore, the enzymatically synthesized renewable monomers including ESBO and wax esters could be used as a potential reactive diluent in UV-curable wood coating to reduce the proportion of highly toxic acrylate products.

Acknowledgment

The authors gratefully acknowledge the Ministry of Science, Technology, and Innovation (MOSTI) with project number Science Fund 5450341 for its financial support. Our sincere thanks are also extended to Prof Rajni Hatti-Kaul Head Department of Biotechnology, Center for Chemistry and Chemical Engineering, and Cecillia Orellana-Coca for their outstanding assistance during the six-month research attachment at Lund University.

References

1. Andrady, A. L., Pandey, K. K. and Heikkilä, A. M. (2019). Interactive effects of solar UV radiation and climate change on material damage. *Photochemical and Photobiological Sciences*, 18(3): 804-825.
2. Paquet, C., Schmitt, T., Klemberg-Sapieha, J. E., Morin, J.-F. and Landry, V., (2020). Self-healing UV curable acrylate coatings for wood finishing system, part 1: Impact of the formulation on self-healing efficiency. *Coatings,* 10(8): 770.
3. Teacă, C. A., Roşu, D., Bodîrlău, R. and Roşu, L. (2013). Structural changes in wood under artificial UV light irradiation determined by FTIR spectroscopy and color measurements-a brief review, *BioResources*, 8(1): 1478-1507.
4. Ulker, O. C., Ulker, O. and Hiziroglu, S. (2021). Volatile organic compounds (VOCs) emitted from coated furniture units. *Coatings,*11(7): 806.

5. Suriano, R., Ciapponi, R., Griffini, G., Levi, M. and Turri, S. (2017). Fluorinated zirconia-based sol-gel hybrid coatings on polycarbonate with high durability and improved scratch resistance. *Surface Coatings Technology*, 311: 80-89.
6. Teaca, C. A., Tanasa, F. and Zanoaga, M. (2018). Multi-component polymer systems comprising wood as bio-based component and thermoplastic polymer matrices – an overview, *BioResources*, 13(2): 4728-4769.
7. Hang, Z., Yu, H., Lu, Y., Huai, X. and Luo, L. (2020). Effect of graphene carbon nitride on ultraviolet-curing coatings. *Materials*, 13(1): 153.
8. Pezzana, L., Malmström, E., Johansson, M. and Sangermano, M. (2021). UV-curable bio-based polymers derived from industrial pulp and paper processes. *Polymers,* 13(9): 1530.
9. Rosu, D., Bodîrlău, R., Teacă, C. A., Rosu, L. and Varganici, C. D. (2016). Epoxy and succinic anhydride functionalized soybean oil for wood protection against UV light action. *Journal Cleaner Production*, 112: 1175-1183.
10. LoPachin, R. M. and Gavin, T. (2014). Molecular mechanisms of aldehyde toxicity: a chemical perspective, *Chemical Research Toxicology*, 27(7): 1081-1091.
11. Gan, Y. and Jiang, X. (2014). Chapter 1: Photo-cured materials from vegetable oils, in green materials from plant oils. Royal Society of Chemistry, pp. 1–27.
12. Xia, C., Wang, L., Dong, Y., Zhang, S., Shi, S. Q., Cai, L. and Li, J. (2015). Soy protein isolate-based films cross-linked by epoxidized soybean oil. *RSC Advances*, 5(101): 82765-82771.
13. Wu, Q., Hu, Y., Tang, J., Zhang, J., Wang, C., Shang, Q., Feng, G., Liu, C., Zhou, Y. and Lei, W. (2018). High-performance soybean-oil-based epoxy acrylate resins: "Green" synthesis and application in UV-curable coatings. *ACS Sustainable Chemical Engineering*, 6(7): 8340-8349.
14. Demengeot, E.-A.-C., Baliutaviciene, I., Ostrauskaite, J., Augulis, L., Grazuleviciene, V., Rageliene, L., and Grazulevicius, J. V. (2010). Crosslinking of epoxidized natural oils with diepoxy reactive diluents. *Journal Applied Polymer Sciences*, 115(4): 2028-2038.
15. Abdul Rahman, M. B., Zaidan, U. H., Basri, M., Hussein, M. Z., Rahman, R. N. Z. R. A. and Salleh, A. B. (2008). Enzymatic synthesis of methyl adipate ester using lipase from Candida rugosa immobilised on Mg, Zn and Ni of layered double hydroxides (LDHs), *Journal Molecular Catalyst B Enzyme*, 50(1): 33-39.
16. Chaibakhsh, N., Abdul Rahman, M. B., Abd-Aziz, S., Basri, M., Salleh, A. B. and Rahman, R. N. Z. R. A. (2009). Optimized lipase-catalyzed synthesis of adipate ester in a solvent-free system, *Journal Industrial Microbiology Biotechnology*, 36(9): 1149-1155.
17. Abdul Rahman, M. B., Abdul Ghani, N., Salleh, N. G. N., Basri, M., Abdul Rahman, R. N. Z. and Salleh, A. B. (2010). Development of coating materials from liquid wax esters for wood top-based coating, *Journal Coatings Technology Research*, 8(2): 229-236.
18. Ma, X., Qiao, Z., Huang, Z. and Jing, X. (2013). The dependence of pendulum hardness on the thickness of acrylic coating. *Journal Coatings Technology Research*, 10(3): 433-439.
19. Anderson, J., Brown, M., Kan, C., Nanjundiah, K. and Kalihari, V. (2013). Quantitative method for evaluating fingernail induced mar damage of coatings. *Journal Coatings Technology Research*, 10(4): 579-588.
20. Ferrer, M., Cruces, M. A., Plou, F. J., Pastor, E., Fuentes, G., Bernabé, M., Parra, J. L. and Ballesteros, A. (2000). Chemical versus enzymatic catalysis for the regioselective synthesis of sucrose esters of fatty acids, *Studies Surface Science Catalyst*, 130: 509-514.
21. Kondamudi, N., and McDougal, O. M. (2019). Microwave-assisted synthesis and characterization of stearic acid sucrose ester: a bio-based surfactant. *Journal Surfactants Detergents*, 22(4): 721-729.
22. Ghoshray, S., Bhattacharya, D. K. (1992). Enzymatic preparation of ricinoleic acid esters of long-chain monohydric alcohols and properties of the esters. *Journal American Oil Chemical Society,* 69(1): 85-88.

23. Said, H. M., Nik Salleh, N. G., Alias, M. S. and El-Naggar, A. W. M. (2013). Synthesis and characterization of hard materials based on radiation cured bio-polymer and nanoparticles, *Journal Radiation Research Applied Sciences*, 6(2): 71-78.

Malaysian Journal of Analytical Sciences (MJAS)
Published by Malaysian Analytical Sciences Society

DETERMINATION OF 3-MONOCHLOROPROPANE-1,2-DIOL (3-MCPD) ESTERS IN EDIBLE PLANT OILS BY INDIRECT ACIDIC TRANSESTERIFICATION METHODS AND THE BPX-5 CAPILLARY COLUMN

(Penentuan Ester 3-Monokloroprapana-1,2-diol (3-MCPD) dalam Minyak Tumbuhan Boleh Dimakan dengan Kaedah Transesterifikasi Berasid Tidak Langsung dan Turus Kapilari BPX-5)

May Yee Wong[1, 2], Huey Fang Teh[3], Sook Mei Khor[1]*

[1]*Department of Chemistry, Faculty of Science, Universiti Malaya, 50603 Kuala Lumpur, Malaysia.*
[2]*Behn Meyer R&D Services Sdn. Bhd., 47600 Subang Jaya, Selangor, Malaysia.*
[3]*Sime Darby Plantation Technology Centre Sdn Bhd, 1st Floor, Block B, UPM-MTDC Technology Centre III, Universiti Putra Malaysia, Lebuh Silikon, 43400 Serdang, Selangor Darul Ehsan, Malaysia.*

**Corresponding author: naomikhor@um.edu.my*

Received: 19 Jan 2022; Accepted: 13 April 2022; Published: 25 August 2022

Abstract

3-monochloropropane-1,2-diol (3-MCPD) and its ester are categorized as food toxicants that formed during high-temperature processing of fat-based matrices. It has been classified as a possible human carcinogen (Group 2B) due to its potential to induce cancer in humans. This study investigated the level of 3-MCPD esters in palm oil and other edible plant oils available in the Malaysian market. The samples were analyzed using indirect methods involving acidic transesterification, then quantified by gas chromatography-mass spectrometry (GC-MS) equipped with BPX-5 capillary column using selected ion monitoring (SIM) mode. The method performance showed good recovery between 92.80% to 105.22% and good reproducibility with RSD of 4.18% to 5.63% for three different concentrations of spiked 3-MCPD. The limits of detection (LOD) and quantification (LOQ) were 0.11 mg kg^{-1} and 0.14 mg kg^{-1}, respectively. The highest concentrations of 3-MCPD esters were detected in refined palm oil, ranging from 2.29 to 4.10 mg kg^{-1}, while 3-MCPD esters in other edible plant oils varied from <LOQ to 3.75 mg kg^{-1}. The validated results are presented to attract policymakers' attention and achieve the goal of ensuring consumer rights while monitoring food safety and quality.

Keywords: 3-monochloropropane-1,2-diol, gas chromatography-mass spectrometry, edible plant oils, food safety, food control

Abstrak

3-monokloroprapana-1,2-diol (3-MCPD) dan esternya dikategorikan sebagai bahan toksik makanan yang terbentuk semasa pemprosesan bersuhu tinggi matriks berasaskan lemak. Ia telah diklasifikasikan sebagai karsinogen manusia yang berkemungkinan (Kumpulan 2B) kerana potensinya untuk menyebabkan kanser pada manusia. Kajian ini dijalankan untuk menyiasat tahap ester 3-MCPD dalam minyak sawit dan minyak tumbuhan boleh dimakan lain yang terdapat di pasaran Malaysia. Sampel dianalisis

menggunakan kaedah tidak langsung yang melibatkan transesterifikasi berasid, yang kemudiannya dikuantifikasi oleh kromatografi gas-spektrometri jisim (GC-MS) yang dilengkapi dengan turus kapilari BPX-5 menggunakan mod pemantauan ion (SIM) terpilih. Prestasi kaedah menunjukkan perolehan semula yang baik antara 92.80% hingga 105.22% dan juga kebolehulangan yang baik dengan RSD sebanyak 4.18% hingga 5.63% untuk tiga kepekatan berbeza 3-MCPD terpaku. Had pengesanan (LOD) dan kuantifikasi (LOQ) didapati masing-masing pada 0.11 mg kg^{-1} dan 0.14 mg kg^{-1}. Kepekatan tertinggi ester 3-MCPD dikesan dalam minyak sawit ditapis, antara 2.29 hingga 4.10 mg kg^{-1}, manakala ester 3-MCPD dalam minyak tumbuhan boleh dimakan lain berbeza daripada <LOQ hingga 3.75 mg kg^{-1}. Keputusan yang disahkan dibentangkan dengan harapan dapat menarik perhatian penggubal dasar dan mencapai matlamat untuk memastikan hak pengguna sambil memantau keselamatan dan kualiti makanan.

Kata kunci: 3-monokloropropana-1,2-diol, kromatografi gas-spektrometri jisim, minyak tumbuhan boleh dimakan, keselamatan makanan, kawalan makanan

Introduction

Edible plant oils, also known as vegetable oils, are extracted from seeds, fruits, nuts, legumes, and pulps of plants. They are mainly used in cooking to change the flavor, color, and fragrance of foods and provide diversified flavor and enrich the sense of satiety during the cooking process [1]. In 2019, the global market of vegetable oils was almost 203 million tons [1]. With the increasing demand for edible plant oils globally, their quality and safety have gained significant attention as they play an essential role in human dietary nutrition. Hence, oils undergo a refining process to enhance their stability and quality. Although unwanted impurities are removed from the oils, refining often originates new contaminants such as chloropropanols and glycidols that can cause additional health hazards to consumers [2].

3-monochloropropane-1,2-diol (3-MCPD) and its esters are a class of food processing contaminant that belongs to chloropropanols, a group of alcohols comprised of a 3-carbon backbone substituted with one or two chlorine atoms [3]. The formation of such contaminants is mainly due to the high-temperature processing of fat-based matrices [4, 5]. 3-MCPD was first identified in its free form by Velisek et al. in acid-hydrolyzed vegetable proteins (acid-HVP) used in soy sauce production, while its esterified (bound) form was then discovered in 1980 [6, 7]. Their occurrence existed in soy sauces and other flavoring materials and foodstuffs such as edible oils, heat-processed foods, cereal, meat products, infant formula, and even human breast milk [8-12].

Previous studies have reported that high 3-MCPD esters were found in refined edible oils, especially palm oils [10]. They were formed during the refining process of vegetable oils in the deodorization step at high temperatures exceeding 200 °C to remove free fatty acid contents in oils while giving a good color and odor [13]. The potential risks of such contaminants have raised immediate concern among the public since 3-MCPD esters can be metabolized to release free 3-MCPD in the human gastrointestinal system [14]. In addition, 3-MCPD has been categorized as a possible human carcinogen (Group 2B) by the International Agency for Research on Cancer (IARC) due to its potential to induce cancer in experimental animals [15]. Hence, it is vital to have a sensitive and robust method to determine the concentration of 3-MCPD in edible oils and fats.

The European Food Safety Authority (EFSA) published a scientific opinion in May 2016 based on a survey done by the Panel on Contaminants in Food Chain (CONTAM) regarding the issue of contaminants found in processed vegetable oils and foods. They stated that the highest levels of 3-MCPD esters were found in palm oil [16]. Previous literature reports indicated that refined palm oil contained the highest levels of 3-MCPD esters [10, 17]. Due to the rising concern about the 3-MCPD potential health risk to humans, the European Commission (EC) Scientific Committee on Food and the Joint FAO/WHO Expert Committee on Food Additives (JECFA) have set a maximum tolerable daily intake (TDI) of 2 μg kg^{-1} of body weight of 3-MCPD levels [18, 19]. Such food safety issues from 3-MCPD cause implications for major vegetable oil producers, especially Malaysia, with high palm oil production [20]. Furthermore, about 85% of global palm oil produced was used in food applications [21]. Therefore, it is of utmost importance to identify the 3-MCPD levels in various edible plant oils so that the researchers and

manufacturers can control and mitigate the occurrence and intensity of 3-MCPD esters formation to ensure the refined oils are safe and of the best quality for consumers [20].

Several analytical methods have been developed and published over the years to determine 3-MCPD esters in edible oils. Generally, there are two main approaches for detecting 3-MCPD esters in edible oils: the direct and indirect analysis methods. Direct methods involve the direct determination of individual MCPD esters using liquid chromatography coupled with time-of-flight mass spectrometry (LC-TOFMS) [22, 23]. This method has the advantage of being simple, requiring a minor degree of sample preparation without any additional steps of analyte transformation, is not time-consuming, and gives detailed information on the chemical structure of the esters [24]. However, it has not been widely used in routine analysis due to its high cost and the possibility of contamination of complex matrices on the instrument [24]. In contrast, indirect methods involve quantifying the total content of free 3-MCPD released from their esterified form mainly by using gas chromatography-mass spectrometry (GC-MS) [25]. Due to the detection of only a single analyte (free 3-MCPD) and the need for just a single internal standard, this method provides higher sensitivity for the quantification of 3-MCPD. It is more suitable for routine analysis [4]. Indirect methods follow similar protocols, which are the addition of an internal standard to the sample (either free or esterified form of 3-MCPD-d5) for quantification purposes, acid or alkaline transesterification to release free 3-MCPD from its esterified form, followed by neutralization and salting out, derivatization of the extracted 3-MCPD, extraction of the derivative, and finally GC-MS analysis [5].

This research aims to determine the levels of 3-MCPD esters in edible plant oils. The validated results are presented to attract policymakers' attention and ensure consumer rights while monitoring food safety and quality. Palm oil and other edible plant oils such as peanut oil, corn oil, sunflower oil, and olive oil were analyzed using a GC-MS equipped with a BPX-5 capillary column and selected ion monitoring (SIM) mode to determine and quantify the concentration of 3-MCPD esters. Because the performance of the BPX-5 column for detecting 3-MCPD esters has not been reported, its performance for the analysis of the target analyte was also a focus of this study. This research aimed to identify the concentration of 3-MCPD esters in two different local brands of unrefined and refined palm oil and two different brands of peanut oil, corn oil, sunflower oil, and olive oil available in the Malaysia market. The results obtained from the analysis were used to compare the levels of 3-MCPD esters among the edible plant oils and different brands for each type of oil sample.

Materials and Methods

Chemicals and samples

3-monochloropropane-1,2-diol (3-MCPD, 98%) was purchased from Sigma-Aldrich (St. Louis, MO, USA), while the internal standard deuterated 3-monochloropropane-1,2-diol (3-MCPD-d5, 98.7%) was purchased from Dr. Ehrenstorfer (Augsburg, Germany). Tetrahydrofuran (≥99.9%), sulfuric acid (H_2SO_4, 95-97%), methanol (≥99.8%), sodium sulfate (Na_2SO_4, ≥ 99.0%), sodium bicarbonate ($NaHCO_3$, ≥99.0%, and n-hexane (≥99.0%) were purchased from Merck (Selangor, Malaysia). Phenylboronic acid (PBA, ≥ 97.0%) was purchased from Sigma-Aldrich (St. Louis, MO, USA). All chemicals used were of analytical and LC grades.

Twelve edible oil samples were used to analyze 3-MCPD esters by the indirect method, including two different local brands of unrefined and refined palm oil, two different local brands of peanut oil, corn oil, sunflower oil, and olive oil, respectively. An extra virgin olive oil was used as a blank sample for method performance and validation. All the edible oil samples were obtained from local supermarkets and were stored at room temperature (25 °C) before analysis.

Preparation of reagents and standards solutions

Methanolic sulfuric acid solution (1.8%, v/v) used in acidic transesterification was prepared by dissolving 1.8 mL of sulfuric acid in 100 mL of methanol. The saturated solution of sodium bicarbonate was prepared by mixing 4.8 g of $NaHCO_3$ in 50 mL of ultra-pure water. In contrast, sodium sulfate solution (20%, w/v)

was prepared by dissolving 20 g of Na_2SO_4 in 100 mL of ultra-pure water. The derivatization agent, PBA solution (25%, w/v), was prepared by dissolving 1 g of PBA in 4 mL of acetone: water mixture (19:1, v/v).

The concentration of 1 mg mL^{-1} of 3-MCPD stock solution was prepared by weighing 10 mg (± 0.1 mg) of the 3-MCPD standard into a 10 mL volumetric flask and diluted to the mark with tetrahydrofuran. 10 µg mL^{-1} of 3-MCPD standard solution (S1) was prepared by pipetting 100 µL 3-MCPD stock solution into a 10 mL volumetric flask and filled up to the mark by diluting it with tetrahydrofuran. In comparison, 1 µg mL^{-1} of 3-MCPD standard solution (S2) was then prepared by pipetting 1 mL of 3-MCPD standard solution (S1) into a 10 mL volumetric flask and filled up to the mark by diluting it with tetrahydrofuran. Both S1 and S2 3-MCPD standard solutions were used for calibration purposes.

0.5 mg mL^{-1} of 3-MCPD-d5 stock solution was prepared by weighing 5 mg (± 0.1 mg) of 3-MCPD-d5 into a 10 mL volumetric flask and diluted to the mark with tetrahydrofuran. The working solution of 3-MCPD-d5 was used as the internal standard. It was prepared by pipetting 100 µL of its stock solution into a 10 mL volumetric flask and diluted to the mark with tetrahydrofuran to give a final concentration of 5 µg mL^{-1}. All the standard solutions prepared were stored at 4 °C for up to 3 months.

Determination of 3-MCPD esters using the indirect method

Analysis of 3-MCPD esters in edible oil samples was carried out using the indirect method of acidic transesterification by Zelinková et al. and Hrncirik et al. [5, 10]. 100 mg (± 5 mg) of oil sample was weighed in a clean glass tube, dissolved in 0.5 mL of tetrahydrofuran, and vortexed for 20 s. 80 µL of the internal standard solution, 3-MCPD-d5, was then added to the sample, followed by 1.8 mL of methanolic sulfuric acid solution (1.8%, v/v) vortexed for another 20 s. The tube was capped and incubated in a water bath at 40 °C for 16 hours. After the incubation period, 0.5 mL of a saturated aqueous sodium bicarbonate solution was added to the tube to stop the reaction and vortexed for 10 s. The organic solvents were evaporated to dryness at 55 °C by using a vacuum rotary evaporator.

Then, 2 mL of aqueous sodium sulfate solution (20%, v/v) was added to the mixture, followed by liquid-liquid extraction with n-hexane (2×2 mL) to remove the fatty acid methyl esters (FAMEs). FAMEs were removed by discarding the organic phase (upper layer) after phase separation. 250 µL of PBA derivatizing solution (25%, w/v, acetone/water, 19/1, v/v) was added to the aqueous extract. The tube was capped, sealed, vortexed for 15 s, and heated in a water bath at 80 °C for 20 min. After 20 min, the tube was allowed to cool to room temperature (25 °C). N-hexane (2×1 mL) was added, and the tube was vortexed for 30 s to extract the 3-MCPD-PBA derivative. The tube was allowed to stand for phase separation, and the supernatant (n-hexane) was transferred to a clean tube. A small amount of anhydrous sodium sulfate was added to the supernatant to remove any excess water. Finally, the supernatant was transferred to a sterile vial. 1 µL of the sample was injected and analyzed using GC-MS. The analysis was carried out in triplicate.

Gas chromatography-mass spectrometry analysis

Analyte detection was performed by a single quadrupole gas chromatography-mass spectrometer GCMS-QP2010 Plus equipped with an AOC-20i auto-injector from Shimadzu (Kyoto, Japan). 1 µL of the sample was introduced into the injector operating at 280 °C in splitless mode. The chromatographic separation was carried out on a bonded, poly(dimethylsiloxane) capillary column BPX-5 (SGE Analytical Science, 30 m length, 0.25 mm id, 0.25 µm film thickness). Helium (99.999%) was used as a carrier gas set at a constant flow of 1.2 mL min^{-1}. The column temperature was programmed at 60 °C for 1 min, which increased to 150 °C at the rate of 6 °C min^{-1} and held for another 2 min. The temperature was further increased to 280 °C at the rate of 10 °C min^{-1} and held constant for 5 min. The mass spectrometer was operated in electron ionization (EI) mode at 70 eV ionization energy. The MS transfer line temperature was maintained at 280 °C, while the ion source and quadrupole temperatures were at 250 °C and 150 °C, respectively. Qualitative analysis was carried out by running the mass spectrometer in a full-scan

mode over m/z 50 to 400 for peak confirmation. The quantitative analysis was performed by selected ion monitoring (SIM) mode to monitor characteristic ions at m/z 91, 147, and 196 for 3-MCPD derivatives, while for 3-MCPD-d5, the characteristic ions were at m/z 93, 150, and 201.

Method validation

A calibration curve was established by spiking a blank sample with eight different concentration levels of 3-MCPD. 100 mg (± 5 mg) of the blank sample (extra virgin olive oil), with no detection of the 3-MCPD esters, was spiked with different concentrations of the 3-MCPD standard. The concentrations of spiked 3-MCPD were 0.25, 0.5, 1.0, 2.0, 3.0, 4.0, 5.0, and 6.0 mg kg^{-1} of 3-MCPD per 100 mg of sample, respectively. The known amount of 3-MCPD-d5 internal standard (4.0 mg kg^{-1} per 100 mg of the sample) was also spiked before extraction based on the sample preparation procedure.

Recovery and repeatability were evaluated by selecting three different concentrations of 3-MCPD (low, medium, and high: 0.25, 3.0, and 6.0 mg kg^{-1}), prepared for six replicates (n = 6), and subjected to 3-MCPD analysis. Besides, within-laboratory reproducibility was also conducted by measuring three different concentrations of 3-MCPD (low, medium, and high: 0.25, 3.0, and 6.0 mg kg^{-1}), with six replicates for each concentration level (n = 6) for three consecutive days. Limit of detection (LOD) and limit of quantification (LOQ) were performed by preparing one lowest concentration of 3-MCPD and subjected to 3-MCPD analysis. The same concentration was then repeated ten times. LOD and LOQ were calculated as three- and ten-fold standard deviations of ten independent samples.

Statistical evaluation

The oil samples were analyzed in triplicate. General statistical evaluation was carried out using Microsoft Office Excel 365. The average of triplicate analyses was reported together with the standard deviation (± SD). Significant differences between the results obtained were examined using Student's t-test with a 95% confidence interval ($p < 0.05$).

Results and Discussion

3-MCPD-PBA derivative chromatogram

This study was conducted using the BPX-5 capillary column, which directly replaces the GC columns used by previous literature, such as HP-5MS and DB-5MS [13, 26, 27]. These columns have similar phases of (5%-phenyl)-methylpolysiloxane (non-polar) with very low bleed characteristics, making them ideal for GC-MS applications. The BPX-5 capillary column is a multi-purpose column that can be used for a wide range of applications and is suitable for almost 80% of routine GC analyses, such as ultra-trace analyses, hydrocarbons, pesticides, herbicides, and triglycerides. Nonetheless, the BPX-5 column has not been applied and reported to detect 3-MCPD-PBA derivatives. Although the BPX-5 and HP/DB-5MS columns have similar phases in general, the retention times of the target analytes with similar characteristic ions may be slightly different. Likewise, retention times also vary depending on the type of columns employed and the analysis method. Several factors such as column length, column temperature, oven temperature, or gas flow rate may influence the retention time of a target analyte even if similar phases of GC columns are used. For example, the retention times for both 3-MCPD esters and their deuterated form varied between 14.50 min to 17.17 min [13, 26, 27].

The gas chromatograms for both 3-MCPD esters and their deuterated form in the spiked blank samples are shown in Figure 1. The retention time of 3-MCPD-d5 was 17.08 min, while the retention time of 3-MCPD esters was 17.17 min. The EI mass spectra for the PBA derivative of 3-MCPD and 3-MCPD-d5 were also illustrated in Figure 2. SIM mode was used for GC-MS quantification, where m/z 147 and m/z 150 were served as the quantifier ions for 3-MCPD derivatives and 3-MCPD-d5, respectively. In addition, m/z 91 and 196 were used as the qualifier ions for 3-MCPD derivatives and m/z 93 and 201 for 3-MCPD-d5. Table 1 shows detailed information on the retention times and characteristic ions used for GC-MS analysis.

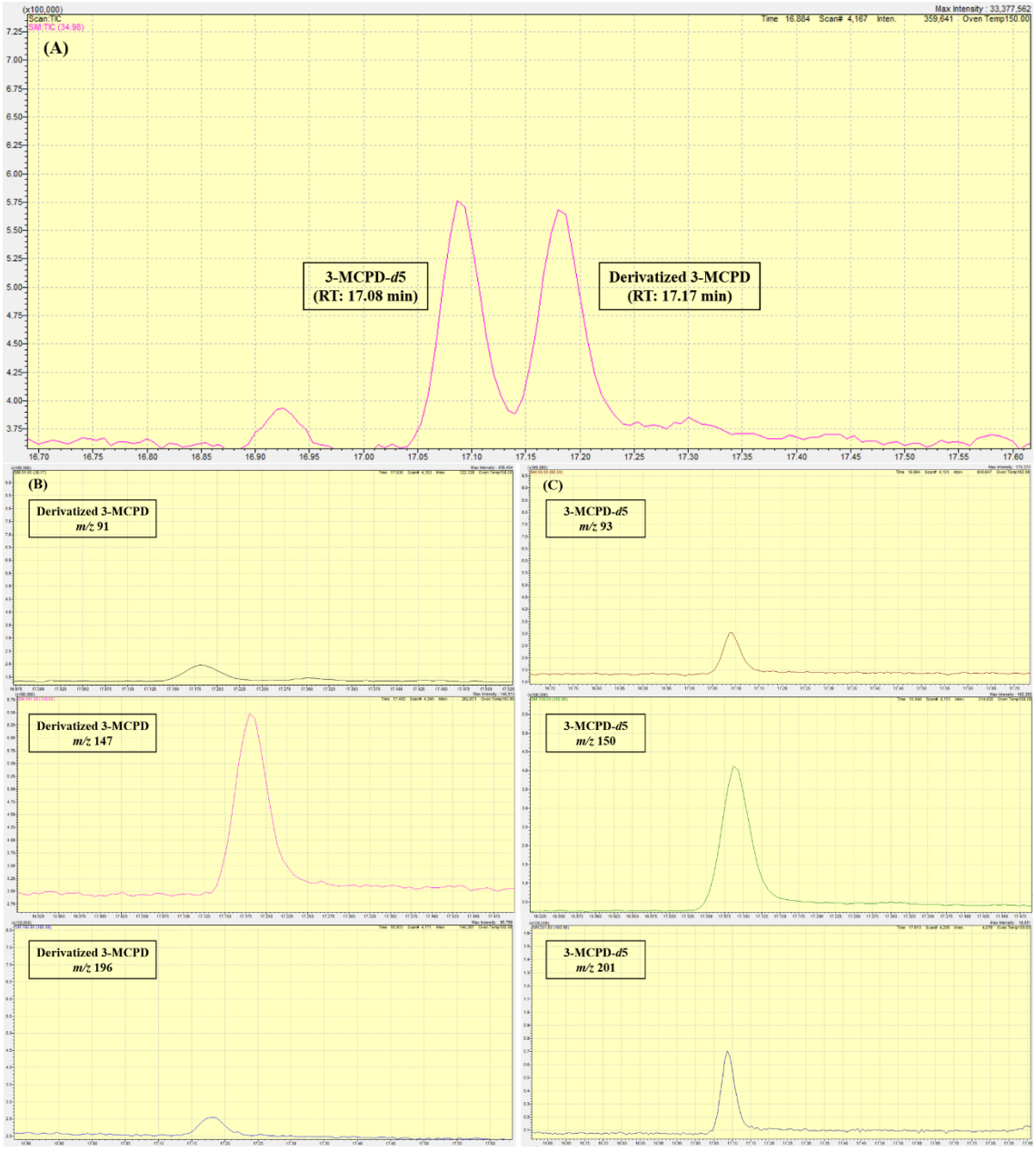


Figure 1. GC chromatograms of 3-MCPD esters and 3-MCPD-d5 in spiked blank samples (RT = retention time). (A) TIC of derivatized 3-MCPD, (B) SIM chromatogram of 3-MCPD esters, (C) SIM chromatogram of 3-MCPD-d5

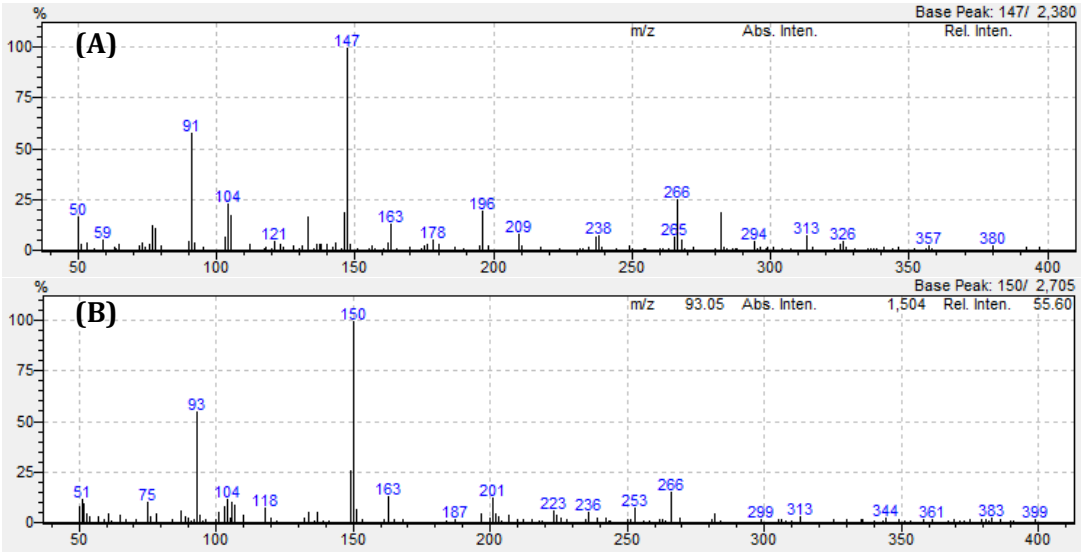


Figure 2. EI mass spectra for PBA derivatives of (A) 3-MCPD and (B) 3-MCPD-d5

Table 1. Retention times and characteristic ions used for SIM mode in GC-MS analysis

Analyte	Retention Time (min)	Quantifier Ion (m/z)	Qualifier Ion (m/z)
3-MCPD-d5	17.08	150	93 & 201
3-MCPD	17.17	147	91 & 196

Method validation

Method validation for the analysis of 3-MCPD esters using GC-MS was conducted about linearity, recovery, precision (repeatability and within-laboratory reproducibility), LOD, and LOQ. Linearity was evaluated using eight calibration points from 0.25 mg kg^{-1} to 6.0 mg kg^{-1} of the 3-MCPD standard. The calibration curve was constructed by plotting the response ratio of the 3-MCPD standard and 3-MCPD-d5 internal standard against the concentration of the 3-MCPD standard, as illustrated in Figure 3. The results showed a linear relationship between the concentration of 3-MCPD standards and the area ratio of 3-MCPD/3-MCPD-d5, with the linearity was verified at $r^2 \geqslant 0.99$. The calibration curve obtained shows that the area ratio of 3-MCPD/3-MCPD-d5 is directly proportional to the concentration of spiked 3-MCPD standards, which obeys Beer's law. The linear range is broad enough to cover the total concentration of 3-MCPD esters found in most edible oils.

In addition, method validation was also conducted based on the recovery test. The result in Table 2 shows the percentage recovery for three different concentrations of 3-MCPD, with the lowest recovery of 92.80% was obtained for the lowest concentration of 3-MCPD (0.25 mg kg^{-1}), while the highest concentration of 3-MCPD (6.0 mg kg^{-1}) recorded the highest recovery of 105.22%. Apart from the recovery determination, the intra-day and inter-day (intermediate) precision were also performed in this study to determine the repeatability and within-laboratory reproducibility of the method, respectively. The RSD percentage obtained for repeatability was 4.30%, 6.38%, and 5.01% for 3-MCPD levels of 0.25, 3.0, and 6.0 mg kg^{-1}, respectively (Table 2). On the other hand, the percentage of RSD

obtained for within-laboratory reproducibility was 5.63% for the lowest concentration (0.25 mg kg^{-1}), 5.32% for the intermediate concentration (3.0 mg kg^{-1}), and 4.18% for the highest concentration of 3-MCPD (6.0 mg kg^{-1}) (Table 2). The low RSD of the replicates showed the reliability of the data acquired by an indirect method and the usage of the BPX-5 column, which attest to satisfactory repeatability and reproducibility. The high accuracy, good repeatability, and reproducibility are crucial in method validation as these parameters build a degree of confidence in obtaining the results. For instance, the RSD values must show the degree of variation expected when the method was repeated several times under standard situations [28]. Any tedious repeats can be eliminated, resulting in better time management for subsequent analyses using the same procedure and settings.

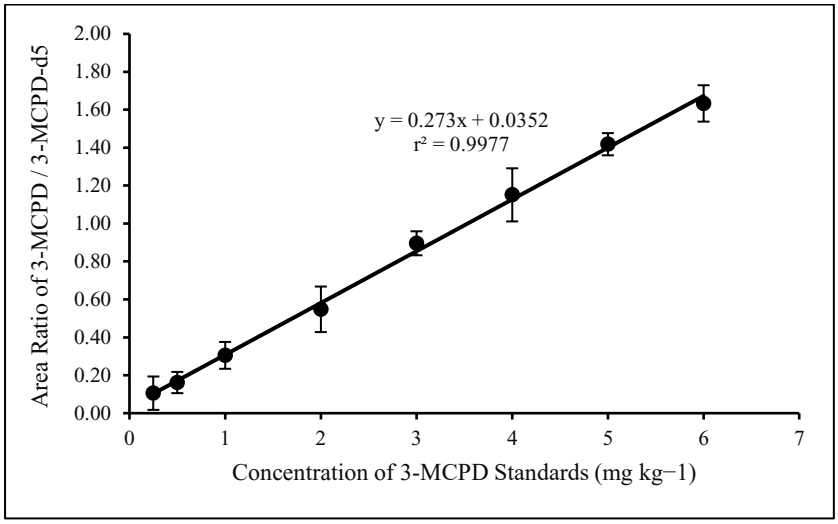


Figure 3. Calibration curve of 3-MCPD esters. Error bars are standard deviations obtained from the triplicate analysis

Table 2. Recovery and precision (repeatability and within-laboratory reproducibility) for 3-MCPD esters (n = number of replicates for each spike level)

Concentration of 3-MCPD (mg kg^{-1})	**% Recovery (n = 6)**	**RSD (%)**	
		Repeatability (n = 6)	**Within-Laboratory Reproducibility**
0.25	92.80 ± 4.21	4.30	5.63
3.0	104.65 ± 6.70	6.38	5.32
6.0	105.22 ± 5.28	5.01	4.18

According to the guidelines in EURACHEM, a blank sample containing no detectable or too low level of analyte might need to be spiked for specific analytical techniques such as chromatography to obtain a non-zero standard deviation [29]. In this study, the LOD and LOQ were estimated by calculating the mean and standard deviation of ten spiked blank samples (extra virgin olive oil) corresponding to the lowest point of the calibration curve. The calculated mean and standard deviation values were fitted into the following equations for the estimation of LOD and LOQ,

$$LOD \cong \bar{x}_{blank} + 3\ SD_{blank} \quad (1)$$

$$LOQ \cong \bar{x}_{blank} + 10\ SD_{blank} \quad (2)$$

where $\bar{x}_{blank}$ is the mean of the spiked blank sample and SD_{blank} is the standard deviation of the spiked blank sample. Hence, the LOD and LOQ of the method obtained in this study were 0.11 mg kg^{-1} and 0.14 mg kg^{-1}, respectively.

Table 3 compares the analytical performances of this study (validated method) to those of other indirect methods previously reported. Except for the slightly lower recovery reported by Abd. Razak et al., who employed the AOCS official method, all the procedures mentioned here exhibited good recovery (> 85%) and repeatability (RSD <10%). The linear range in this study was significantly more extensive than the AOCS official method and the method reported by Arisseto et al., which can determine a wide range of target analyte concentrations without excessive dilution. However, the LOQ was established at a minimum of 0.10 mg kg^{-1}, implying that none of the methods given are sensitive enough to detect 3-MCPD esters within the maximum tolerable limit of 0.002 mg kg^{-1} set by the Scientific Committee on Food (SCF) of the European Commission [18]. This suggests that all of the reported indirect methods (including direct HPLC methods) cannot reliably detect edible oil samples with low concentrations of 3-MCPD esters (below the maximum tolerable limit of 0.002 mg kg^{-1}). In other words, all indirect methods face the same challenges and have the same limitation. The detectable 3-MCPD esters in most edible oils are much greater than the maximum tolerable limit, even though the indirect method's LOD and LOQ are higher than the maximum tolerable limit of 0.002 mg kg^{-1}. In summary, this indirect method, combined with the BPX-5 capillary column, is suitable for routine analysis in practice.

Table 3. Comparison of the analytical performance of the current method with other indirect methods that have been reported

Methods	BfR Method 008 (Column: HP-5MS)	BfR Method 008 (Column: DB-5MS)	AOCS Official Method Cd 29a-13 (Column: HP-5MS)	Acid Cleavage	Acid Cleavage	Special Remark
Linear Range (mg kg^{-1})	0.25-6.00	0.25-6.00	0.08-2.39	0-4.00	0.25-6.00	Compared to the official AOCS method, this method has a wider linear range.
Recovery (%)	97.60-107.90	85.40-110.50	80.30-85.80	101.00-110.00	92.80-105.22	The recovery % range is narrower and closer to 100%.
Repeatability (RSD, %)	0.02-0.12 (n = 6)	4.18-4.79 (n = 8)	7.00-10.20 (n = 7)	4.40–8.40 (n = 6)	4.30-6.38 (n = 6)	This method outperforms the standard AOCS method in terms of precision.

Table 3 (cont'd). Comparison of the analytical performance of the current method with other indirect methods that have been reported

Methods	BfR Method 008 (Column: HP-5MS)	BfR Method 008 (Column: DB-5MS)	AOCS Official Method Cd 29a-13 (Column: HP-5MS)	Acid Cleavage	Acid Cleavage	Special Remark
Reproducibility (RSD, %)	NA	NA	NA	3.90-6.10 (n = 6)	4.18-5.63 (n = 6)	In real-world applications, this approach has proven to be reliable.
LOD (mg kg^{-1})	0.25	0.09	0.02	0.05	0.11	Despite having a greater LOD than the standard AOCS method, this method is reliable for quantifying the concentration of 3-MCPD esters in all edible oils examined.
LOQ (mg kg^{-1})	0.50	0.23	NA	0.10	0.14	In comparison to other studies, this approach has a decent LOQ.
Reference	[13]	[27]	[30]	[31]	This study	

[a]Column: VF-1MS; Temperature program: 60 °C held for 1 min, 6 °C min^{-1} to 190 °C, 20 °C min^{-1} to 280 °C, 280 °C held for 30 min
[b]Column: BPX-5; Temperature program: 60 °C held for 1 min, 6 °C min^{-1} to 150 °C, 150 °C held for 2 min, 10 °C min^{-1} to 280 °C, 280 °C held for 5 min
NA means not available

3-MCPD esters in edible plant oils

The indirect method with PBA as the derivatizing agent was applied in this study as it readily reacts with 3-MCPD to form a stable derivative 4-chloromethyl-2-phenyl-1,3,2-dioxaborolane. Due to its high selectivity and ability to extract with non-polar solvents such as n-hexane, PBA was suitable for the choice of derivatization agent for GC-MS analysis. In this study, a total of 12 edible plant oils available in local supermarkets were analyzed to detect their 3-MCPD esters content, with two different brands for each type of oil. The concentrations of 3-MCPD esters in these samples ranged from <LOQ to 4.10 mg kg^{-1}, as shown in Figure 4.

Since Malaysia is the second-largest producer of palm oil in the world, with approximately 85% of global palm oil produced was used in food applications, the levels of 3-MCPD esters in palm oil were studied in this research because once the validated results are reported in a scientific journal or a media article, it will draw the attention of policymakers. In short, it fulfills the objective of ensuring consumers' rights while monitoring food safety and quality. The concentration of

3-MCPD esters was compared among red palm oil and refined palm oil, in which refined palm oil comprised a higher concentration of 3-MCPD esters, ranging from 2.29 ± 0.09 to 4.10 ± 0.06 mg kg^{-1} when compared to red palm oil (0.41 ± 0.03 to 3.40 ± 0.25 mg kg^{-1}). Red palm oil is often referred to as unrefined palm oil, and it is dark red due to the high content of carotenoids. Thus, it is vital to perform deodorization at low temperatures to avoid the thermal destruction of carotenoids [32]. Conversely, refined palm oil is light yellow and odorless as it undergoes deodorization at a high temperature of around 250 °C to remove any FFA and volatile components [32]. Such a process led to the formation of high 3-MCPD esters levels in refined palm oil. As shown in Figure 4, a low concentration of 3-MCPD esters with a value of 0.41 ± 0.03 mg kg^{-1} was identified in red palm oil (brand B). However, the other brand of red palm oil (brand A) detected a high concentration of 3-MCPD esters with a value of 3.40 ± 0.25 mg kg^{-1}. This suggested that the oil extraction conditions, for instance, the red palm oil sample (brand A), may consist of a mixture of unrefined and refined oils that eventually led to the occurrence of 3-MCPD esters.

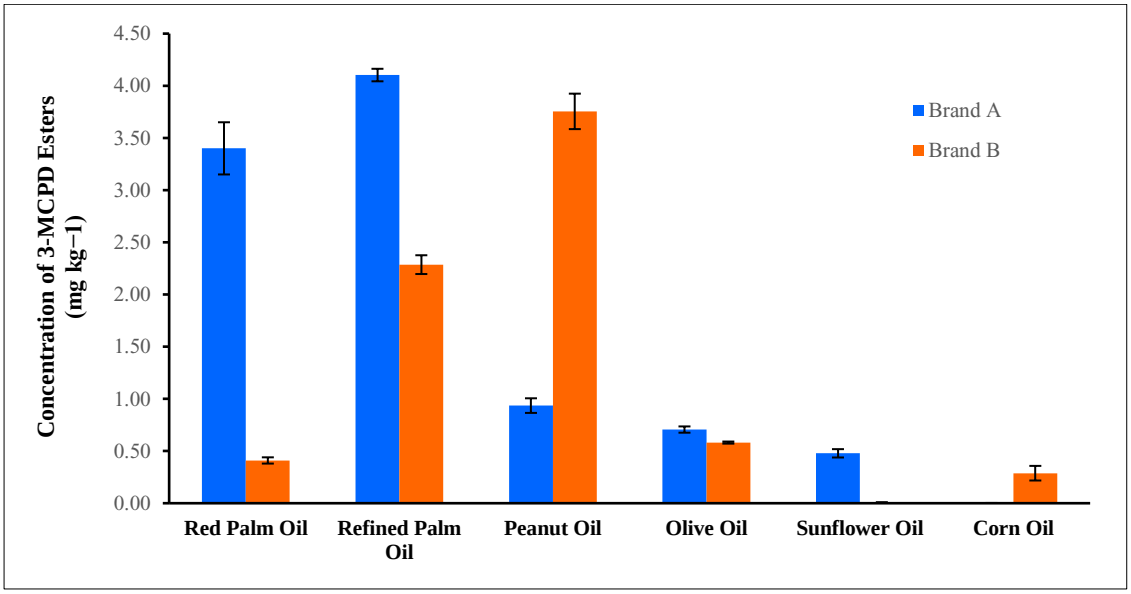


Figure 4. 3-MCPD esters levels determined in edible plant oils by indirect acidic transesterification methods and the BPX-5 capillary column, with two different brands for each type of oil

Besides palm oil, the other edible plant oils that consumers commonly used were also analyzed for the presence of 3-MCPD esters. Overall, olive oil, sunflower oil, and corn oil contained lower levels of 3-MCPD esters varied from <LOQ to 0.71 ± 0.03 mg kg^{-1}, a meanwhile higher concentration of 3-MCPD esters was found in refined palm oil and peanut oil, ranging from 0.94 ± 0.07 to 4.10 ± 0.06 mg kg^{-1} (Fig. 4). Sunflower oil and corn oil consisted of slightly lower concentrations of 3-MCPD esters (<LOQ to 0.48 ± 0.04 mg kg^{-1}) as compared to olive oil (0.58 ± 0.01 to 0.71 ± 0.03 mg kg^{-1}). Extra virgin olive oil was produced by physical pressing at low temperature (below 27 °C) without heating and therefore consisted of deficient levels of 3-MCPD esters [33]. In contrast, a higher temperature (150 °C) during deodorization involved in the production of refined olive oil resulted in higher content of 3-MCPD esters [33]. Since olive oil is a blend of both extra virgin olive oil and refined olive oil, thus it contains a higher concentration of 3-MCPD esters due

to the combination of unrefined and refined olive oil in various ratios. Such a trend of results confirmed the previous literature by Zelinková et al. (2006) that reported a higher concentration of 3-MCPD esters was detected in refined olive oil than that of sunflower oil and corn oil [10]. The highest concentration of 3-MCPD esters was found in refined palm oil (2.29 ± 0.09 to 4.10 ± 0.06 mg kg^{-1}), which was then followed by peanut oil (0.94 ± 0.07 to 3.75 ± 0.17 mg kg^{-1}). Peanut oil used in this study was a blended oil containing refined palm oil and peanut oil (as indicated on the product package and labeled). High deodorization temperature in the refining process further contributed to the formation of 3-MCPD esters in refined palm oil and peanut oil. Generally, refined fruits oil such as palm oil and olive oil generate higher levels of 3-MCPD esters than seed oils like sunflower oil and corn oil [10]. Palm oil derived from the mesocarp (pulp) of the fruit has a different composition from seed oils, which contain relatively high levels of potential precursors of 3-MCPD esters such as chloride ions and partial acylglycerols [34]. This eventually contributes to the high concentration of 3-MCPD esters in palm oil.

By comparing different brands for each type of oil sample, there is a significant variation in the concentration of 3-MCPD esters in all the oil samples, except olive oil (Figure 4). A significant difference was observed at a 95% confidence interval using Student's t-test with a p-value less than 0.05 between two different brands of oil samples, with red palm oil and peanut oil specifically, as shown in Figure 4. The reason for the significant variation in the concentration of 3-MCPD esters found between two different brands of red palm oil was explained previously. The same goes for peanut oil. The refining process involving bleaching and deodorization may be one of the factors that cause the differences in the 3-MCPD esters levels between the two different brands. It may also link to the preliminary heat treatment of seeds, such as roasting peanuts, which results in a variation of 3-MCPD esters among different peanut oil brands. For other types of oil samples, it isn't easy to justify these variations because the main precursors in the reaction and the actual mechanism of 3-MCPD esters formation were not completely understood. The formation of 3-MCPD esters during the production of edible oils might be due to the presence of chlorine as a donor. Plants took up chloride ions via the soil either by the natural occurrence or through the fertilizers, which then further metabolized into hydrophilic chloride substances that may generate hydrochloric acid upon high-temperature treatment, thereby leading to the occurrence of 3-MCPD esters [3]. Table 4 compares the trend of 3-MCPD esters levels in different types of plant edible oil samples from this study to those from previous studies. It should be noted that this study and earlier literature found that among the six types of edible oils, refined palm oil had the most significant level of 3-MCPD esters. In contrast, corn oil had the lowest 3-MCPD esters, regardless of where the edible oil samples originated. Except for the high concentration of 3-MCPD esters identified in this study due to the type of red palm oil used for analysis, the concentration range of 3-MCPD esters for unrefined or red palm oil is essentially similar. This investigation suggests that the BPX-5 capillary column utilized has good separation performance, comparable to previously published analysis trends, indicating that this column could be useful in identifying 3-MCPD esters in a variety of edible oils.

Several factors such as thermal treatment, the presence of precursors, or soil conditions might trigger the formation of 3-MCPD esters beyond the maximum tolerable limit. Since 3-MCPD is a type of food-borne toxicant, it is vital to analyze and detect the content of 3-MCPD esters in edible oils as they have been widely used in our everyday life. Consumers have the right to choose the healthiest plant edible oils to be consumed. Consequently, continue researching on all possible pathways for the formation and mitigation of 3-MCPD esters should be done by researchers to ensure that the processed plant-based oils consumed by consumers are safe while maintaining the best nutritious quality of oils.

Table 4. 3-MCPD esters in edible oils found in this study compared to previously reported indirect methods using acidic transesterification

Methods	3-MCPD Esters Concentration Range (mg kg^{-1})						Reference
	Unrefined/Red Palm Oil	Refined Palm Oil	Peanut Oil	Olive Oil	Sunflower Oil	Corn Oil	
Bfr method 008	<0.25-0.90	<0.25-5.80	2.45	NA	0.60	<0.25-0.35	[13]
AOCS official method Cd 29a-13	<1.00	1.00-3.00	1.00-3.00	1.00-3.00	<1.00	<1.00	[30]
Acid cleavage (column: EquityTM-1)	NA	NA	<0.10	<0.30-2.46	<0.30	0.37	[10]
Acid cleavage (column: VF-1MS)	<0.05-0.33	1.05-2.95	0.13-0.29	0.14-0.33	0.10-0.27	<0.05-1.12	[31]
Acid cleavage (column: BPX-5)	0.41-3.40	2.29-4.10	0.94-3.75	0.58-0.71	<LOQ-0.48	<LOQ-0.29	This study

NA means not available

Conclusion

An indirect method involving acidic transesterification was used to detect and quantify 3-MCPD esters in various edible plant oils. PBA was chosen as the derivatizing agent since it reacts specifically with 3-MCPD to form a stable non-polar cyclic derivative (4-chloromethyl-2-phenyl-1,3,2-dioxaborolane) extractable with n-hexane. The use of the BPX-5 capillary column in GC-MS analysis was a direct replacement for other GC capillary columns that have been primarily used in previous literature. This provides researchers with a promising alternate choice/method for detecting 3-MCPD esters in various edible plant oil samples. The method validation verified that a linear calibration curve with extra virgin olive oil as a blank sample and spiked with eight different concentrations of 3-MCPD standards was established with $r^2 \geq 0.99$. Besides, the applied indirect method also showed the percentage recovery of three different concentration levels of 3-MCPD fell from 92.80% to 105.22%, together with RSD of 4.30% to 6.38% and 4.18% to 5.63% for both repeatability and within-laboratory reproducibility, respectively. The LOD and LOQ of the method were identified at 0.11 mg kg^{-1} and 0.14 mg kg^{-1}, respectively. As a result, this indirect method showed good accuracy and repeatability for the analysis of 3-MCPD esters in all studied edible plant oils.

From the results obtained for a total of 12 edible plant oils, 3-MCPD esters were found to be the lowest in corn oil (<LOQ to 0.29 mg kg^{-1}) and highest in refined palm oil (2.29 to 4.10 mg kg^{-1}). Refined palm oil contained a higher concentration of 3-MCPD esters than red palm oil (unrefined palm oil) due to high temperature during the deodorization step, contributing to the formation of 3-MCPD esters. Different brands for each type of edible plant oil samples also showed significant variation in 3-MCPD esters levels. Several factors, such as the refining process and the crude oil's quality, may contribute to forming 3-MCPD esters in various plant oils. Since 3-MCPD is a type of process contaminant that induces possibly carcinogenic to humans, it is significant to have potential mitigation of 3-MCPD in oils for the safety of consumers. Improvement can be made by upgrading the current technology of the refining process, for example, by implementing a more flexible deodorizing technology that could be carried out at low temperature (<250 °C) so that the occurrence of 3-MCPD in edible plant oils can be permanently reduced or eliminated in the future, without tarnishing the premium quality of the edible plant oils.

Acknowledgment

This work was financially supported by the Fundamental Research Grant Scheme (FRGS) from the Ministry of Higher Education of Malaysia (MOHE) (FRGS/1/2019/STG01/UM/02/6). May Yee Wong would like to thank Behn Meyer R&D Services Sdn. Bhd. for providing the facilities needed to complete this project.

References

1. Zhou, Y., Zhao, W., Lai, Y., Zhang, B. and Zhang, D. (2020). Edible plant oil: Global status, health issues, and perspectives. *Frontiers in Plant Science*, 11: 1315.
2. Costa, H., Gonçalves Albuquerque, T. and Oliveira, M. (2018). 3-MCPD occurrence in vegetable oils: Impact on human nutrition and future challenges. *EC Nutrition,* 13: 455-469.
3. Stadler, R. H. (2015). Monochloropropane-1,2-diol esters (MCPDEs) and glycidyl esters (GEs): an update. *Current Opinion in Food Science*, 6:12-18.
4. Ermacora, A. and Hrncirik, K. (2012). Evaluation of an improved indirect method for the analysis of 3-MCPD esters based on acid transesterification. *Journal of Oil & Fat Industries*, 89:211-217.
5. Hrncirik, K., Zelinkova, Z. and Ermacora, A. (2011). Critical factors of indirect determination of 3-chloropropane-1,2-diol esters. *European Journal of Lipid Science and Technology*, 113: 361-367.
6. Velísek, J., Davídek, J., Hajslová, J., Kubelka, V., Janícek, G. and Mánková, B. (1978). Chlorohydrins in protein hydrolysates. *Z Lebensm Unters Forsch*, 167(4): 241-244.
7. Davídek, J., Vfiaek, J., Kubelka, V., Janîek, G. and `imicová, Z. (1980). Glycerol chlorohydrins and their esters as products of the hydrolysis of tripalmitin, tristearin and triolein with hydrochloric acid. *Zeitschrift für Lebensmittel-Untersuchung und Forschung*, 171:14-17.
8. Doležal, M., Chaloupská, M., Divinová, V., Svejkovská, B. and Velišek, J. (2005). Occurrence of 3-chloropropane-1,2-diol and its esters in coffee. *European Food Research and Technology*, 221(3):221-225.
9. Hamlet, C. and Sadd, P. A. (2004). Chloropropanols and their esters in cereal products. *Czech Journal of Food Sciences*, 22: 259-262.
10. Zelinková, Z., Svejkovská, B., Velíšek, J. and Doležal, M. (2006). Fatty acid esters of 3-chloropropane-1,2-diol in edible oils. *Food Additives & Contaminants*, 23(12):1290-1298.
11. Zelinková, Z., Doležal, M. and Velíšek, J. (2009). Occurrence of 3-chloropropane-1,2-diol fatty acid esters in infant and baby foods. *European Food Research and Technology*, 228(4):571-578.
12. Zelinková, Z., Novotný, O., Schůrek, J., Velíšek, J., Hajšlová, J. and Doležal, M. (2008). Occurrence of 3-MCPD fatty acid esters in human breast milk. *Food Additives & Contaminants: Part A*, 25(6): 669-676.
13. Abd. Razak, R. A., Kuntom, A., Siew, W. L., Ibrahim, N. A., Ramli, M. R., Hussein, R. and Nesaretnam K. (2012). Detection and monitoring of 3-monochloropropane-1,2-diol (3-MCPD) esters in cooking oils. *Food Control*, 25(1): 355-360.

14. Buhrke, T., Weißhaar, R. and Lampen, A. (2011). Absorption and metabolism of the food contaminant 3-chloro-1,2-propanediol (3-MCPD) and its fatty acid esters by human intestinal Caco-2 cells. *Archives of Toxicology*, 85(10):1201-1208.
15. IARC (2013). Some chemicals present in industrial and consumer products, food and drinking-water. *IARC Monograph Evaluation Carcinogenic Risks Human*, 101:9-549.
16. CONTAM (2016). Risks for human health related to the presence of 3- and 2-monochloropropanediol (MCPD), and their fatty acid esters, and glycidyl fatty acid esters in food. *EFSA Journal*, 14(5):e04426.
17. Kuhlmann, J. (2011). Determination of bound 2,3-epoxy-1-propanol (glycidol) and bound monochloropropanediol (MCPD) in refined oils. *European Journal of Lipid Science and Technology*, 113(3): 335-344.
18. Commission E (2001). Opinion of the Scientific Committee on Food on 3-Monochloro-propane-1, 2-diol (3-MCPD). European Commission Health & Consumer Protection Directorate-General, 2001: pp 1-5.
19. Joint FAOWHOECoFAM, Safety evaluation of certain food additives and contaminants / prepared by the fifty-seventh meeting of the Joint FAO/WHO Expert Committee on Food Additives (JECFA). 2002, World Health Organization: Geneva.
20. Arris, F. A., Thai, V. T. S., Manan, W. N. and Sajab, M. S. (2020). A revisit to the formation and mitigation of 3-chloropropane-1,2-diol in palm oil production. *Foods*, 9(12):1769.
21. May, C. Y. and Nesaretnam, K. (2014). Research advancements in palm oil nutrition. *European Journal of Lipid Science and Technology,* 116(10): 1301-1315.
22. Garballo-Rubio, A., Soto-Chinchilla, J., Moreno, A. and Zafra-Gómez, A. (2017). A novel method for the determination of glycidyl and 3-monochloropropanediol esters in fish oil by gas chromatography tandem mass spectrometry. *Talanta*, 165:267-273.
23. Haines, T. D., Adlaf, K. J., Pierceall, R. M., Lee, I., Venkitasubramanian, P. and Collison, M. W. (2011). Direct determination of MCPD fatty acid esters and glycidyl fatty acid esters in vegetable oils by LC–TOFMS. *Journal of the American Oil Chemists' Society*, 88(1):1-14.
24. Jędrkiewicz, R., Kupska, M., Głowacz, A., Gromadzka, J. and Namieśnik, J. (2016). 3-MCPD: A worldwide problem of food chemistry. *Critical Reviews in Food Science and Nutrition*, 56(14): 2268-2277.
25. Divinova, V., Svejkovska, B., Doležal, M. and Velisek, J. (2004). Determination of free and bound 3-chloropropane-1,2-diol by gas chromatography with mass spectrometric detection using deuterated 3-chloropropane-1,2-diol as internal standard. *Czech Journal Food Sciences*, 22: 182-189.
26. Samaras, V. G., Giri, A., Zelinkova, Z., Karasek, L., Buttinger, G. and Wenzl, T. (2016). Analytical method for the trace determination of esterified 3- and 2-monochloropropanediol and glycidyl fatty acid esters in various food matrices. *Journal of Chromatography A*, 1466: 136-147.
27. Wöhrlin, F., Fry, H. and Preiss-Weigert, A. (2011). Collaborative study for the determination of 3-MCPD fatty acid esters in edible fats and oils. second collaborative study—part I. Method validation and proficiency test. *Federal Institute for Risk Assessment*: pp. 83-99.
28. Veerasamy, R., Sivadasan, S., Karupiah, S. and Rajak, H. (2010). Validation of analytical methods - Strategies & importance. *International Journal of Pharmacy and Pharmaceutical Sciences*, 2: 18-22.
29. Bertil, M. and Örnemark. U. (2014). The fitness for purpose of analytical methods: A laboratory guide to method validation and related topics. A laboratory guide to method validation and related topics, LGC, Teddington, Middlesex, UK.
30. Cassiday, L. (2017). Red palm oil. *Inform*, 28(2): 7.
31. Hung, W-C., Peng, G-J., Tsai, W-J., Chang, M-H., Liao, C-D., Tseng, S-H., Kao, Y-M., Wang, D-Y. and Cheng, H-F. (2017). Identification of 3-MCPD esters to verify the adulteration of extra virgin olive oil. *Food Additives & Contaminants: Part B*, 10(3): 233-239.

32. Hamlet, C., Asuncion, L., Velisek, J., Doležal, M., Zelinkova, Z. and Crews, C. (2011). Formation and occurrence of esters of 3-chloropropane-1,2-diol (3-CPD) in foods: What we know and what we assume. *European Journal of Lipid Science and Technology*, 113: 279-303.
33. Abd. Razak, R. A., Ahmad Tarmizi, A. H., Abdul Hammid, A. N., Kuntom, A., Ismail, I. S. and Sanny, M. (2019). Verification and evaluation of monochloropropanediol (MCPD) esters and glycidyl esters in palm oil products of different regions in Malaysia. *Food Additives & Contaminants: Part A*, 36(11):1626-1636.
34. Arisseto, A., Marcolino, P. and Vicente, E. (2014). Determination of 3-monochloropropane-1,2-diol fatty acid esters in Brazilian vegetable oils and fats by an in-house validated method. *Food Additives & Contaminants. Part A, Chemistry, Analysis, Control, Exposure & Risk Assessment*, 31:1-8.

Malaysian Journal of Analytical Sciences (MJAS)
Published by Malaysian Analytical Sciences Society

THE ANTIBACTERIAL, ANTIFUNGAL, ANTIOXIDANT POTENTIAL AND TOTAL PHENOLIC CONTENT OF MALAYSIAN ENDANGERED SPECIES *Coscinium fenestratum* FROM PAYA BUNGOR PAHANG

(Potensi Sifat Antibakteria, Antikulat, Antioksida dan Jumlah Kandungan Fenolik *Cosinium fenestratum* Spesies Terancam Malaysia dari Paya Bungor Pahang)

Aiza Harun[1]*, Noorshilawati Abdul Aziz[2], Shaari Daud[1]

[1]*Faculty of Applied Sciences*
[2]*Faculty of Plantation and Agrotechnology*
Universiti Teknologi MARA Cawangan Pahang, 26400 Bandar Jengka, Pahang, Malaysia

**Corresponding author: aizaharun@uitm.edu.my*

Received: 21 January 2022; Accepted: 2 April 2022; Published: 25 August 2022

Abstract

Coscinium fenestratum (family: Menispermaceae), which is locally known as *akar sekunyit*, is one of the endangered species in Malaysia. *C. fenestratum* is wildly grown in the forest reserve, Paya Bungor, Pahang. This study aims to investigate the potential of *C. fenestratum* as an antibacterial, antifungal, and antioxidant agent as well as its total phenolic content. Four types of extracts were prepared from the consecutive soaking using hexane, dichloromethane (DCM), ethyl acetate (EA), and methanol. All types of extracts were assessed for their antibacterial and antifungal activities using the disc diffusion method against *Salmonella thypi* ATCC 10708, *Staphylococcus aureus* ATCC 43300, *Escherichia coli* UPMC 25922, *Candida albicans* ATCC 90028, and *Aspergillus brasiliensis* ATCC 16404. The potency of this species as an antioxidant agent was evaluated using semiquantitative staining dot blot assay against DPPH (2,2-diphenyl-1-picrylhydrazyl). The total phenolic content was assessed using the Folin-Ciocalteu method. The phytochemical screening for all types of extracts revealed the presence of alkaloid, terpenoid, phenolic, and saponin. All extracts with the concentration of 1,000 ppm demonstrated antibacterial and antifungal activities against *S. aureus* ATCC 43300 and *C. albicans* ATCC 90028 but none for the rest of the bacteria and fungi. The methanol extract was more active with a moderate inhibition zone. The semiquantitative staining dot blot assay against DPPH revealed that the lowest concentration of methanol extract for DPPH inhibition was at the concentration of 0.012 mg/ml, and the DCM extract showed that the DPPH inhibition was at 0.006 mg/ml. However, the methanol extract of *C. fenestratum* had a higher total phenolic content (TPC) with the value of 12.722 mg GAE/g sample compared to the DCM extract at 8.627 mg GAE/g sample. Hence, both methanol extract and DCM extract of *C. fenestratum* exhibited stimulating antimicrobial and antioxidant properties with potent phenolic content.

Keywords: *Coscinium fenestratum*, antibacterial, antifungal, akar sekunyit, antioxidant

Abstrak

Coscinium fenestratum (keluarga: Menispermaceae) yang dikenali sebagai akar sekunyit adalah salah satu spesies terancam di Malaysia iaitu Pahang dan ia tumbuh secara liar di hutan simpan Paya Bungor Pahang. Kajian ini bertujuan untuk menyiasat potensi *C. fenestratum* sebagai agen antibakteria, antikulat dan antioksidan serta jumlah kandungan fenolik. Empat jenis ekstrak

telah disediakan daripada rendaman berturut-turut menggunakan heksana, diklorometana (DCM), etil asetat dan metanol. Semua jenis ekstrak telah dinilai untuk aktiviti antibakteria dan antikulat menggunakan kaedah penyebaran cakera terhadap *Salmonella thypi* ATCC 10708, *Staphylococcus aureus* ATCC 43300, *Escherichia coli* UPMC 25922, *Candida albicans* ATCC 90028 dan *Aspergillus brasiliensis* ATCC 90028. Keupayaan spesies ini sebagai agen antioksida dinilai daripada ujian bintik-bintik pewarnaan semikuantitatif terhadap DPPH (2,2-difenil-1-pikrilhidrazil). Jumlah kandungan fenolik dinilai menggunakan kaedah Folin-Ciocalteu. Pemeriksaan fitokimia untuk semua jenis ekstrak mendedahkan kehadiran alkaloid, terpenoid, fenolik dan saponin. Semua ekstrak dengan kepekatan 1,000 ppm menunjukkan aktiviti antibakteria dan antikulat terhadap *S. aureus* ATCC 43300 dan *C. albicans* ATCC 90028, tetapi aktiviti itu tidak dapat dilihat untuk bakteria dan kulat yang lain. Ekstrak metanol didapati sebagai ekstrak yang lebih aktif dengan zon perencatan sederhana berbanding dengan ekstrak yang lain. Ujian bintik-bintik pewarnaan separa kuantitatif terhadap DPPH mendedahkan bahawa kepekatan terendah ekstrak metanol untuk perencatan DPPH adalah pada kepekatan 0.012 mg/ml dan ekstrak DCM menunjukkan perencatan DPPH pada 0.006 mg/ml. Walau bagaimanapun, ekstrak metanol *C. fenestratum* mempunyai jumlah kandungan fenolik yang lebih tinggi dengan nilai 12.722 mg sampel GAE/g berbanding ekstrak DCM pada 8.627 mg sampel GAE/g. Oleh itu, adalah disahkan bahawa kedua-dua ekstrak metanol dan ekstrak DCM *C. fenestratum* mempamerkan sifat antimikrob dan antioksida yang baik dan sederhana dengan kandungan fenolik yang memberangsangkan.

Kata kunci: *Coscinium fenestratum*, antibakteria, antikulat, akar sekunyit, antioksida

Introduction

Many medicinal plants have a high content of antioxidants such as vitamin C, vitamin E, polyphenols, and phytochemical substances of antimicrobial agents. Most antimicrobial plant compounds are identified as secondary metabolites that mainly originated from the family of terpenoid or phenolic. To date, herbal extracts are well-known for defeating various infectious diseases. Many plant species have been investigated for their effectiveness to combat microbes that cause disease but the investigation is still insufficient. Some medicinal plants are rich in natural antioxidants and have fewer side effects compared to synthetic antioxidants which can reduce the risk of certain diseases such as heart disease and cancer. It has been discovered that plant species with polyphenolic compounds enhance antioxidant activities [1]. The polyphenolic compounds react as a hydrogen donor or an electron donor to stabilise the toxic radical that causes harmful diseases.

Coscinium fenestratum belonged to the family Menispermaceae, is known as akar sekunyit in Malaysia, and has been vastly used as a traditional medicine to treat snake bites, lower blood sugar and blood cholesterol, and stabilise blood pressure [2]. It is reported that the stem of *C. fenestratum* is anti-inflammatory and antiseptic, has a bitter taste, and has a potential in pharmacological studies to exhibit antifungal, antibacterial, antifungal, and antiproliferative activities [3]. *C. fenestratum* is considered a critically endangered medicinal species as a result of its high demands in traditional practice. It is reported that the function of *C. fenestratum* ethanolic extract irradiated with a gamma ray acts as an antimicrobial agent and is outstanding against *Staphylococcus aureus* with the inhibition zone of 16.3-17.5 mm as well as the antioxidant activity [4]. However, the effect of gamma irradiation was insignificant to enhance the TPC of the crude extract. This study aims to evaluate the antimicrobial, antioxidant, and TPC of four crude extracts of *C. fenestratum* stem from Paya Bungor, Pahang, Malaysia.

Material and Methods

Plant material

The stems of *C. fenestratum* (Menispermaceae) were collected from Paya Bungor forest, Kuantan, Pahang. Fresh samples were cut into small pieces and air dried at room temperature. The small pieces of dry samples were grounded into powder using a grinder before proceeding to the extraction process.

Preparation of extracts from the stem of *C. fenestratum*

About 1kg of *C. fenestratum* stem was subjected to consecutive soaking with hexane, dichloromethane, ethyl acetate, and methanol to obtain four different types

of crude extracts. After three times of soaking in each solvent, the extracts were filtered and evaporated until they are dried using a rotary evaporator. The crude extracts were kept in the refrigerator before use.

Antibacterial and antifungal activity assay

The assay was conducted to evaluate the potency of *C. fenestratum*'s crude extracts against selected fungi and bacteria such as *Salmonella thypi* ATCC 10708, *Staphylococcus aureus* ATCC 43300, *Escherichia coli* UPMC 25922, *Candida albicans* ATCC 90028, and *Aspergillus brasiliensis* ATCC 16404. The sterile discs of all crude extracts with the concentration of 1,000 ppm were prepared for antibacterial and antifungal works and were used in the disc diffusion method. The antibacterial work of all crude extracts against *S. thypi*, *S. aureus*, and *E. coli* and the antifungal work against *C. albicans* and *A. brasiliensis* were slightly modified according to our previous study [5,6]. The positive standard discs were streptomycin and nystatin.

Thin layer chromatography analysis

The TLC method was conducted to screen phytochemicals such as alkaloid, phenolic compounds, and terpenoid. Spraying reagents such as the Dragendorff's solution, ferric chloride solution, and vanillin/H_2SO_4 were used to screen the presence of alkaloid, phenolic, and terpenoid, respectively [6].

Antioxidant activity

Semiquantitative DPPH staining dot blot assay

This method was modified from our previous work [7] and was conducted to measure the lowest concentration of *C. fenestratum*'s extracts to scavenge the free radical of DPPH by observing the formation of yellow spots against the purple background of the marked TLC plate. The extracts were two-fold serially diluted ranging from 100 mg/mL to 0.003 mg/mL. Then, 10µL of each prepared extract was dripped into the marked TLC plate and was allowed to dry for about 30 min under the fume hood. After completing the drying process, the TLC plate was carefully sprayed with 0.05% DPPH solution in methanol. The results were determined by observing the formation of yellow spots around the applied extracts. The yellow spot indicates the amount and nature of radical scavengers in the extracts. The experiment was also conducted for isolated compound alkaloid and ascorbic acid as the positive standard.

Total phenolic content (TPC)

About 5 mg of each extract or standard ascorbic acid was measured and diluted with 5 mL of suitable solvent to produce the final concentration of 1 mg/mL (1,000 ppm). Then, 0.5 mL of each extract was mixed with 2.5 mL Folin-Ciocalteu reagent (10 times dilution) and left for 2 min. Then, 2 mL of 7.5% w/v Na_2CO_3 solution was added to the mixture and incubated for 30 min. After reaching the incubation time, the absorbance of all samples was determined using UV-VIS Spectrometer (Secomam, France) at 765 nm [8]. The method was repeated for the standard solution of gallic acid (1000, 500, 250, 125, 62.5, 31.25 ppm). The blank was made with the same procedure without any extract or standard. The standard curve was plotted using the value absorbance of standard gallic acid solution.

Results and Discussion

Phytochemical analysis

The present study of the TLC phytochemicals screening test was conducted on four different types of extracts namely hexane, DCM, EA, and methanol extracts of the stem of *C. fenestratum.* The test revealed the presence of some medicinally active constituents in a TLC fingerprint of extracts. The common phytochemical constituents found were alkaloid, phenolic, terpenoid, and saponin in each extract of the stem of *C. fenestratum* as summarised in Table 1. DCM, EA, and methanol extracts were screened and contained the most phytochemicals. The hexane extract only showed the positive appearance of terpenoid compounds. The screening of these important phytochemicals is important as they are attributed to antimicrobial action and antioxidant activity. It was reported that the phenolic compounds of white cabbage have retarded lipid oxidation and microbial growth of foodborne pathogenic bacteria and fungi [9].

Figure 1 depicts some TLC fingerprints that screen the presence of alkaloid and phenolic in methanol extract and DCM extract. TLC A shows the obvious presence of alkaloid from the methanol extract compared to the alkaloid in the DCM extract in TLC D, which is

consistent with the previous finding [10, 11]. TLC B and TLC C of methanol extract show that alkaloid behaves as an antioxidant agent as the placement of alkaloid on TLC B is similar to the yellow spot of antioxidant on TLC C. TLC E and TLC F of DCM extract reveal the presence of antioxidative phenolic compounds. The observations of TLC D, TLC E, and TLC F of DCM extract show that alkaloid and phenolic compounds were also antioxidative.

Table 1. Phytochemicals in the stem of *C. fenestratum*

Types of extracts	**Phytochemicals**			
	Alkaloid	**Phenolic**	**Terpenoid**	**Saponin**
Hexane	x	x	√	x
DCM*	√	√	√	x
Ethyl acetate* (EA)	x	√	√	x
Methanol*	√	√	√	√

√ = present; x = not present; * = antioxidative; DCM: dichloromethane

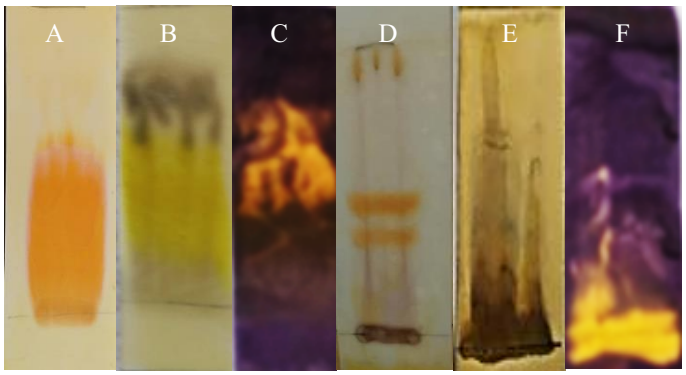


Figure 1. TLC fingerprint of alkaloid, phenolic, and antioxidant

A. The orange spot against the yellow background indicates the presence of alkaloid in the methanol extract after spraying with Dragendorff's reagent.
B. The black area indicates the presence of phenolic compounds in the methanol extract after spraying ferric chloride solution; The yellow area indicates the presence of alkaloid.
C. The yellow spot against the purple background indicates the presence of antioxidant in the methanol extract.
D. The orange spot against the yellow background indicates the presence of alkaloid in the DCM extract after spraying with Dragendorff's reagent.
E. The black spots indicate the presence of phenolic compounds in the DCM extract after spraying with ferric chloride solution
F. The yellow spot against the purple background indicates the presence of antioxidant in the DCM extract.

Antimicrobial activity of *C. fenestratum* stem

The results of antifungal and antibacterial activities in Table 2 indicate no inhibition zone towards *S. thypi*, *E. coli*, and *A. brasiliensis* for all crude extracts. All extracts were susceptible to *S. aureus* and *C. albicans* due to the use of a low concentration (1,000 ppm) of

extracts which causes no visible inhibition zone against *S. thypi*, *E. coli*, and *A. brasiliensis*. However, a previous study [12] revealed that the methanol extract attempted to inhibit the growth of *E. coli* moderately at the concentration of 150 mg/ml with the zone inhibition of 17 mm. This finding confirms that the extracts may have the capability to block the growth of all tested microbes at a higher concentration of more than 1,000 ppm. Among the extracts, the methanol extract was moderately inhibiting the growth of *C. albicans* and weakly inhibits *S. aureus* compared to other extracts. The richness of secondary metabolites mainly alkaloid in the methanol extract could be the main reason for the antimicrobial action. This scientific finding is also in line with other previous reports where alkaloid berberine from the stem of *C. fenestratum* was responsible for the antibacterial activity against several human pathogenic bacteria [10]. Alkaloid berberine also displayed remarkable antimicrobial activities against phytopathogenic fungi [12]. The current investigation [13] revealed that the methanol extract of *C. fenestratum* has promising antibacterial activity against the plant pathogen *Erwinia chrysanthemi* with an inhibition zone of about 19 mm. Thus, the result of *C. fenestratum* methanol extract which behaves as a potent antimicrobial agent is in the line with the previous research.

Table 2. Antibacterial and antifungal activities of *C. fenestratum*

Types of Extracts (1,000 ppm)/Standard	**Diameter of Inhibition Zone (mm)**				
	S. thypi	***S. aureus***	***E. coli***	***C. albicans***	***A. brasiliensis***
Hexane	-	+	-	+	-
DCM	-	+	-	+	-
EA	-	+	-	+	-
MeOH	-	+	-	++	-
Streptomycin	+++	+++	+++	-	-
Nystatin	-	-	-	+++	+++

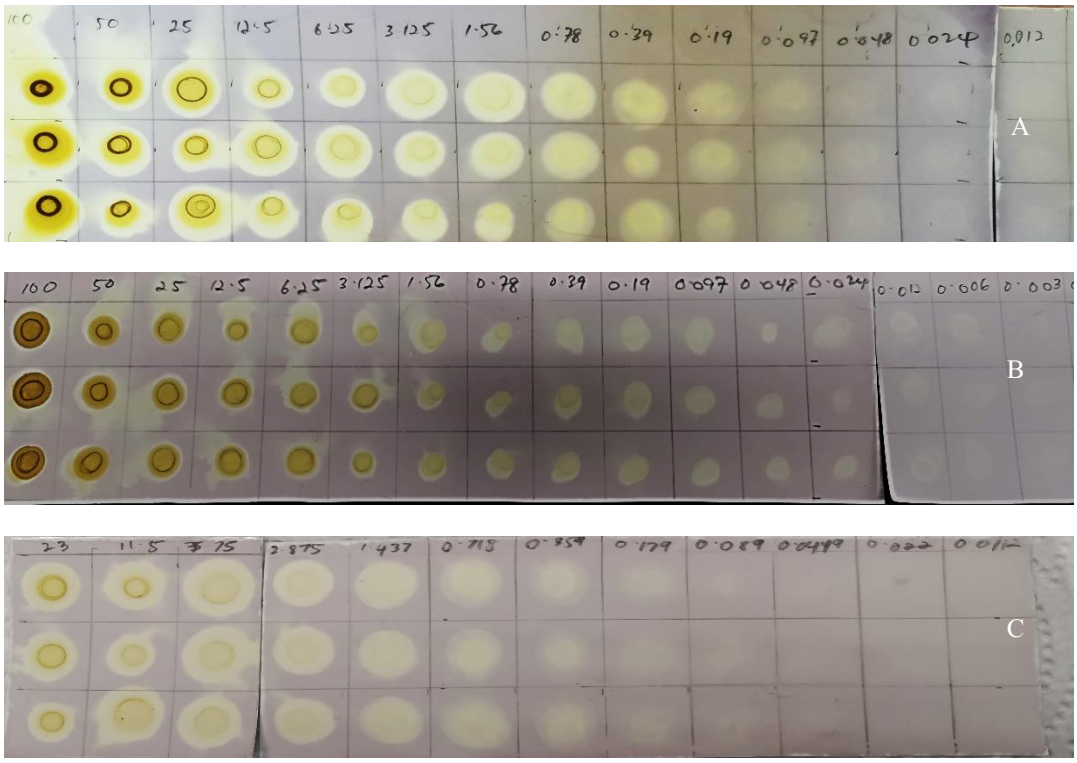
+++: strongly inhibited; ++: moderately inhibited; +: weakly inhibited; -: no inhibition zone; DCM: dichloromethane; MeOH: methanol; EA: ethyl acetate

Antioxidant activity and total phenolic content

DPPH dot blot assay is a semiquantitative antioxidant activity method that has been used on *C. fenestratum* by referring to its ability to reduce the DPPH – a stable free radical. The antioxidant activities of different concentrations (two-fold serially diluted) of methanol extract, DCM extract, EA, alkaloid, and ascorbic acid were evaluated through the observation of the appearance of yellow colour against the purple background on the marked TLC as illustrated in Figure 2. The hexane extract was not further evaluated for its antioxidant activity since it had been previously screened and did not display any trace of yellow colour indicating the presence of antioxidants. Table 3 shows the dot blot assay where both DCM extract and methanol extract have comparable values of their lowest concentration to scavenge DPPH radical at 0.006 mg/mL and 0.012 mg/mL, respectively. EA extract started to scavenge DPPH radical at the concentration of 0.089 mg/mL as the yellow spot first appeared at this concentration. The concentration where the yellow colour was firstly observed on the marked TLC is considered the lowest concentration of extracts that scavenged the DPPH radical as illustrated in Figure 2. The isolated compound alkaloid scavenged the DPPH radical at a slightly higher concentration of 0.625 mg/mL. In this case, any compounds or extracts that can scavenge DPPH radical at a lower concentration are said to function as a good scavenger. This result explains that the methanol extract and DCM extract were more antioxidative as they scavenged DPPH radical at a lower

concentration compared to the EA extract and isolated compound alkaloid.

The antioxidant activities of DCM and methanol extract might be attributable to the presence of phenolic compounds in both extracts. The presence of phenolic compounds was authenticated from the determination of TPC values using the Folin-Ciocalteu method. Table 3 shows the methanol extract of *C. fenestratum* that contained a larger TPC value of 12.722 mg GAE/g sample compared to the DCM with a TPC value of 8.627 mg GAE/g sample. The result is parallel with a previous study [9] that determined the TPC value of methanol extract of *C. fenestratum* in Western Ghats, India at 18.35 mg GAE/g sample. It was reported that the phytochemical phenolic compounds were the main cause of methanol extract of *Coscinium blumeanum* for having a moderate antioxidant activity with an EC_{50} value of 50.1 µg/mL [14]. However, the scavenging of DPPH radical by the EA extract at 0.089 mg/ml was not responsible for the presence of phenolic content as it had a negative value of TPC. The activity might be due to the presence of terpenoid as depicted in Table 1. The synergistic action between alkaloid, terpenoid, and phenolic in the DCM extract could cause the DCM extract to scavenge DPPH radical at a lower concentration compared to the methanol extract although it contains a lower TPC value compared to the methanol extract.



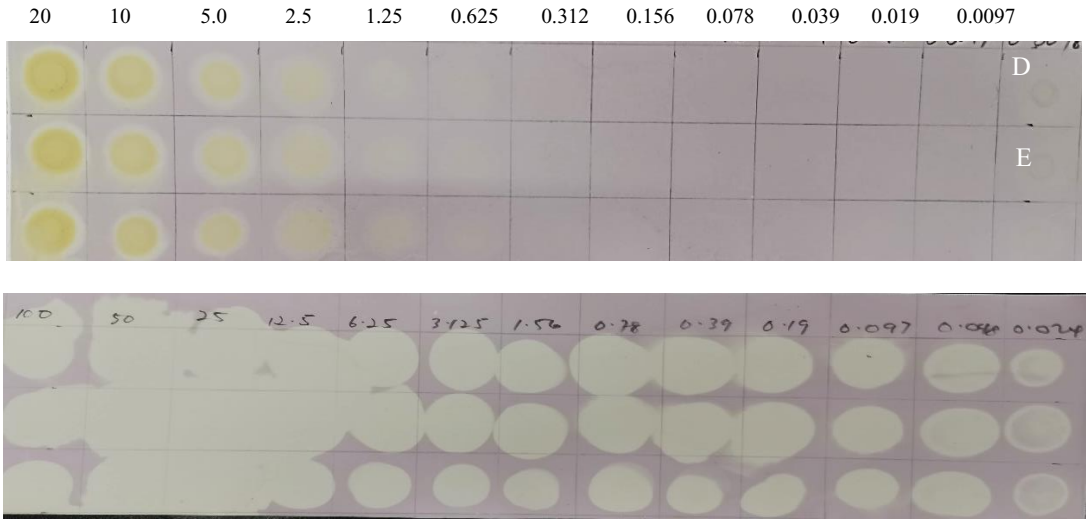


Figure 2. DPPH staining dot blot assay of *C. fenestratum* extracts, alkaloid, and standard ascorbic acid

A. DPPH staining of two-fold serial dilution of methanol extract
B. DPPH staining of two-fold serial dilution of DCM extract
C. DPPH staining of two-fold serial dilution of EA extract
D. DPPH staining of two-fold serial dilution of alkaloid from methanol extract
E. DPPH staining of two-fold serial dilution of standard ascorbic acid

Table 3. Semiquantitative antioxidant activity from DPPH staining dot blot assay and total phenolic content

Extract/Standard	**Lowest Concentration for DPPH Inhibition (mg/mL)**	**Total Phenolic Content, mg GAE/g sample**
Dichloromethane (DCM)	0.006	8.627
Ethyl acetate (EA)	0.089	negative
Methanol	0.012	12.722
Alkaloid (isolate from methanol extract)	0.625	negative
Standard ascorbic acid	< 0.006	693.416

Conclusion

We concluded that the methanol extract of *C. fenestratum* acts as a potent antibacterial and antifungal agent. The dichloromethane and methanol extracts scavenged the DPPH radical at the concentration of 0.006 mg/ml and 0.012 mg/ml, respectively. The highest TPC value among the extracts belonged to the methanol extract with a TPC value of 12.722 mg GAE/g sample. It is recommended that future work uses different concentrations of extracts tested on fungi that cause superficial skin disease and other bioactivity assays such cytotoxicity and anti-inflammatory and antiviral activities.

Acknowledgement

The author would like to express her warmest gratitude to Puan Nor Habibah Mohd Rosli, En. Mohd Zahir Ismail, and En. Mohd Rosdi Mat Tahir who were involved directly or indirectly in the completion of this research work.

References

1. Cook, N. C. and Samman, S. (1996). Flavonoids-chemistry, metabolism, cardioprotective effects, and dietary sources. *Nutritional Biochemistry*, 7: 66-76.
2. Rojsanga, P. and Gritsanapan, W.(2005). Variation of berberine content in *Coscinium fenestratum* stem in thailand market. *Mahidol University Journal of Pharmaceutical Sciences*, 32(3-4): 66-70.
3. Danapur, V., Haleshi, C. and Sringeswara A. N. (2020). Endangered medicinal plant *Coscinium fenestratum* (Gaertn.) Colebr. - A review. *Pharmacognosy Journal,* 12(5): 1077-1085
4. Eamsiri, J., Chookaew, S., Pewlong, W., Sajjabut, S. and Orpong, P. (2019). Effects of irradiation on antioxidant and antimicrobial activities of *Coscinium fenestratum* (Goetgh.) Colebr. *IOP Conf. Series: Journal of Physics*: Conf. Series 1285 (2019) 012006.
5. Harun, A., Mat So'ad, S.Z., Mohd Hassan, N. and Che Mohd Ramli, N.K. (2014). In-vitro antidermatophytic activity of methanolic fractions from *Entada spiralis* Ridl. stem bark and its bioautographic profile. *Pertanika Journal Science & Technology* 22(1): 113-121.
6. Daud, A. D., Azman, N. S., Alias, N. I. A., Syaifudin, N., Harun, A. and Abdul Aziz, N. (2021). Phytochemical and antibacterial properties on three medicinal plants for potent anti-soft rot agents. *Malaysian Journal of Analytical Sciences*, 25(1): 119-128.
7. Harun, A., Abdul Aziz, N., Mohd Azenan, N. S., Muhammad Kamarazzaman, N. F and Mat So'ad., S. Z. (2020). Antimicrobial efficacy, antioxidant profile and nine alternative active constituents from petroleum ether and ethyl acetate extract of *Entada spiralis*. *Malaysian Journal of Analytical Sciences*, 25(5): 707-718.
8. Siddiqui, N., Rauf, A., Latif, A. and Mahmood, Z.(2017). Spectrophotometric determination of the totalphenolic content, spectral and fluorescence study of the herbal Unani drug Gul-e Zoofa (Nepeta bracteata Benth). *Journal of Taibah University Medical Sciences,* 12(4): 360-363.
9. Rubab, M., Chelliah, R., Saravanakumar, K., Kim, J. R., Yoo, D., Wang, M. H. and Oh, D. H. (2020). Phytochemical characterization, and antioxidant and antimicrobial activities of white cabbage extract on the quality and shelf life of raw beef during refrigerated storage. Royal Society of Chemistry,10: 41430-41442.
10. Nair, G. M., Narasimhan, S., Shiburaj, S. and Abraham, T. K.(2005). Antibacterial effects of *Coscinium fenestratum*. *Fitoterapia*,76: 585-587.
11. Singburaudom, N. (2015). The alkaloid berberine isolated from *Coscinium fenestratum* is an inhibitor of phytopathogenic fungi. *Journal of Biopesticides,* 8(1):28-36.
12. Goveas, S.W. and Abraham, A. (2013). Evaluation of antimicrobial and antioxidant activity of stem and leaf extracts of *Coscinium fenestratum*. *Asian Journal of Pharmaceutical Clinical Research*, 6(3): 218-221.
13. Mohd Azli, N. A. N., Harun, A., Abdul Aziz, N. and Daud, S. (2021). Anti soft rot and antioxidant behaviour of nine medicinal plants from Paya Bungor, Pahang. *GADING Journal of Science and Technology*, 4(2): 20-26.
14. Keawpradub, N., Dej-adisai, S. and Yuenyongsawad., S. (2005). Antioxidant and cytotoxic activities of Thai medicinal plants named Khaminkhruea: *Arcangelisia flava, Coscinium blumeanum and Fibraurea tinctoria*. *Songklanakarin Journal of Science Technology*, 27(2): 455-467.

Malaysian Journal of Analytical Sciences (MJAS)
Published by Malaysian Analytical Sciences Society

EFFECTS OF PROCESSING PARAMETERS ON THE QUALITY AND PROPERTIES OF MANGO KERNEL FLOUR: A MINI-REVIEW

(Kesan Pemprosesan Parameter Terhadap Kualiti dan Sifat Tepung Biji Mango: Ulasan Mini)

Amal Hanani Binti Zikri[1], Boon Yih Tien[1,2]*, Boon Yih Hui[3], Wang Kang Han[4]

[1]Department of Food Science and Technology, Faculty of Applied Sciences
[2]Alliance of Research and Innovation for Food (ARIF)
Universiti Teknologi MARA, Kampus Kuala Pilah, 72000 Kuala Pilah,
Negeri Sembilan, Malaysia
[3]Research and Development Centre, KL-Kepong Oleomas Sdn. Bhd, Lot 1 & 2, Solok Waja 3, Bukit Raja Industrial Estate, 41710 Klang, Selangor, Malaysia
[4]Faculty of Applied Sciences,
UCSI University, UCSI Height, 56000 Cheras, Kuala Lumpur, Malaysia

**Corresponding author: boonyihtien@uitm.edu.my*

Received: 28 February 2022; Accepted: 23 April 2022; Published: 25 August 2022

Abstract

Mango (*Mangifera indica* Linn) is a popular tropical fruits that is widely available in the market. In order to reduce food waste, mango kernels are usually treated as waste mango kernel flour due to their nutritional composition and bioactive compounds. However, the processing method used during the production of mango kernel flour has lowered its nutritional value and affected the quality of the mango kernel flour. In addition, the anti-nutritional found in the mango kernel influences the flour's quality. Hence, this review provides an overview of the effect of processing parameters on the quality of mango kernel flour (in terms of nutritional, functional properties, and bioactive compounds) and the application of mango kernel flour in baking products. The findings proposed that the soaking, blanching, and drying processes have an impact on the nutritional value, functional properties, and bioactive compounds of mango kernel flour. Further investigation into optimising processing parameters is required to obtain high-quality mango kernel flour.

Keywords: mango kernel flour, soaking, blanching, nutritional composition, anti-nutrient

Abstrak

Mangga (*Mangifera indica* Linn) merupakan salah satu buah tropika yang terkenal di pasaran. Bagi mengurangkan sisa biji manga, biji mangga biasanya diproses menjadi tepung biji mangga kerana komposisi nutrisi dan sebatian bioaktifnya. Bagaimanapun, kaedah pemprosesan semasa penghasilan tepung biji manga telah mengurangkan nilai nutrisi dan mempengaruhi kualiti tepung biji mangga. Selain itu, anti-nutrien yang terdapat di dalam biji mangga juga mempengaruhi kualiti tepung. Oleh itu, ulasan ini memberikan gambaran keseluruhan kesan parameter pemprosesan ke atas kualiti tepung biji mangga (dari segi komposisi nutrisi, sifat fungsi dan sebatian bioaktif) dan penggunaan tepung biji mangga dalam produk bakeri. Hasil kajian menunjukkan bahawa proses rendaman, penceluran dan pengeringan adalah faktor yang mempengaruhi nilai nutrisi, sifat berfungsi dan sebatian bioaktif

dalam tepung biji mangga. Siasatan lanjut keatas pengoptimuman parameter pemprosesan diperlukan bagi mendapatkan tepung biji mangga yang berkualiti tinggi.

Kata kunci: tepung biji mangga, rendaman, blanching, komposisi nutrisi, anti-nutrien

Introduction

Mangifera indica Linn, or commonly known as mango, belongs to the family of Anacardiaceae. Mango is well grown in the tropical and subtropical regions [1]. The production of mango throughout the year is about 42 million tonnes [2], and it is considered the second most traded fruit globally after bananas [3]. Countries that largely produce mangoes are India, Mexico, Thailand, China, and Indonesia [4]. Among these countries, India is the largest producer of mango [5], whereas Mexico is the largest exporter of mango, as it exports about 287,771 tonnes per annum [6]. Generally, mangoes are rich in dietary fibre, carbohydrates, fats, protein, phenolic compounds and provide high energy. Those nutrients found are crucial for the growth development and health of well-being [7]. Besides that, mango is also known as a super fruit due to its functionality as a food and an ingredient in new food product development [8]. Since mango is one of the most widely produced tropical fruits in the world, the waste generated from its processing is massive. It is estimated that about 35% to 60% [6] of mango by-products such as seeds and kernels have been discarded as waste [9], subsequently causing environmental pollution. In line with the concept of waste to wealth, mango kernels (Figure 1) usually undergo further processing into raw materials or food sources, such as mango kernel flour (Figure 2). According to Shabeer et al. [10], mango kernels can be used to replace wheat flour in the composite flour technology for baked products. Nevertheless, the production processes of mango kernel flour, such as soaking, blanching, and drying are known to affect the quality of mango kernel flour. The presence of anti-nutrient components also restricted the application of mango seed kernels in the food industry. This review aims to provide an overview of their past and current perspectives. This review will cover the effect of processing parameters on the quality of mango kernel flour in terms of nutritional composition, functional properties, bioactive compounds, and their application in the food industry.



Figure 1. Mango kernel seed [11]



Figure 2. Processed mango kernel flour [11]

Overview of mango

Mangoes are grown in over 90 countries. According to the Food and Agriculture Organization (FAO), the harvested mangoes were over 28 million tonnes in 2014, accounting for 35% of global tropical fruit production. Asia accounts for around 77% of the worldwide mango supply, followed by the America and Africa, accounting for 13% and 9%, respectively. The Asian countries include India, China, Thailand, Indonesia, Pakistan, the Philippines, and Bangladesh. However, cultivation has extended to Mexico, Brazil, Madagascar, Tanzania, the Dominican Republic, Haiti, Brazil, and Australia [12]. Meanwhile, in Malaysia, mangoes are mostly found in northern regions such as Perlis, Kedah, and Northern Perak as they can thrive well under humid and dry conditions [13]. The most popular export mango cultivars are Kent, Tommy Atkins, Haden, and Keitt, which have a red blush and are fibreless, harder, and more suited for long-distance shipping compared to other cultivars [12]. Whereas in Malaysia, the famous

mango clones planted are 'Harumanis', 'Maha 65', 'Masmuda', 'Sala', 'Chok Anan', and 'Siam Panjang' [13]. Generally, mango has an oval shape covered with leathery skin that changes colour from green to yellow when ripe [14] (Figure 3). The ripening stage of mango can be identified by its colour and texture, as it will turn from green to reddish orange [15] or yellow when ripe [16]. Unripened mangoes are extremely popular in Asia, but ripe mangoes are mostly consumed in the West [17].

The term "beak" is used to describe the shape of the mango as it has the characteristic of a conical projection. Large and fleshy mango fruits can vary depending on their shape, size, colour, fibre content, flavour, and aroma [18]. Depending on the cultivar, mango seeds appeared hairy or fibrous on the surface of the single flat oblong [19]. According to Beyene and Araya [15], the weight of mangoes can be up to one kilogramme depending on the cultivars, and it takes about three to six months to fully mature. The mango seed makes up roughly 10-25% of the overall weight of the fruit, while the kernel makes up about 45–85% of the seed's weight, which is about 20% of the total weight of the fruit [19]. In addition, the size of a mango and its kernel followed by their nutritional value can be determined by the mango's type, climate, ripening stage, cultivation, region, or harvesting time [20]. Moreover, Asia has the highest consumption levels, followed by Latin America, Africa, and Australia [17].

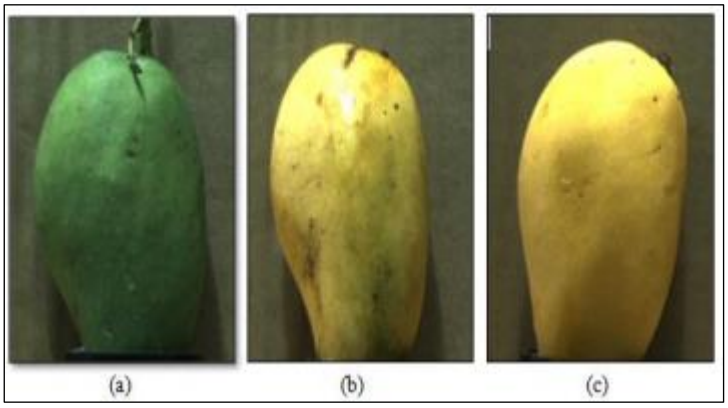


Figure 3. Different ripening stages of Chokanan mango: (a) Unripe fruit, (b) Yellowish-green peel, (c) Ripe fruit [14, 21]

Application of mango kernel flour in food industry

The demand for bakery products has increased the use of wheat flour [11, 22]. However, problems such as inadequate supply of wheat flour [23], higher cost, and geographical scarcity [11] have become the main factors in political and economic issues [23]. Therefore, a new alternative source of flour was introduced by converting mango kernels into mango kernel flour. Wheat flour can be substituted partially with mango kernel flour as composite flour due to its aesthetic chemical and functional properties. According to Das et al. [22], mango kernel flour can be a rich source of dietary minerals as the amount of ash in mango kernel flour (2.16%) is higher than in wheat flour (0.54%). Furthermore, the incorporation of mango kernel flour in the production of bakery products can lower the use of shortening agents as the fat content in mango kernel flour is 12 times higher than the fat content in wheat flour. Mango kernel flour has a lower swelling index compared to wheat flour, making the flour ideal and acceptable to be applied in extruded products such as noodles [22, 26]. Mango kernel flour and wheat flour had a crude fibre content of 1.16% and 0.42%, respectively. Because of its high fibre content, mango kernel flour can assist in improving digestion. On top of that, the amount of oil absorption capacity for mango

kernel flour (0.94 grams) is lower than wheat flour (1.26 grams) [22]. The capability of medium oil absorption by flour implies that it may be used to make bread items [26]. This is because oil functions as a flavour keeper and enhances mouthfeel; thus, flour's capacity to absorb oil is critical as it is also related to the occurrence of rancidity and storage stability [29].

Several studies have described the application of mango kernel flour in cake production as it consists of many nutritional compositions such as fat, energy, protein, calcium, potassium, and magnesium [11]. Aside from cakes, the addition of up to 25% mango kernel flour to wheat flour produced cookies with satisfactory sensory properties and improved the quality of cookies in terms of physical properties and colour [1]. Gumte et al. [24] concluded that 30% mango kernel flour is the optimum amount to be added in the biscuits production because the proximate composition of the whole biscuit is 2.56% moisture, 5.21% protein, 14.06% fat, 1.92% ash, and 74.68% carbohydrate. This indicates that adding mango kernel flour to biscuits can produce a product with nutraceutical properties and good sensory evaluation results. Moreover, adding 20% of defatted mango kernel flour to bread also increases the nutritional properties [25]. According to Lakshmi et al. [26], mango kernel flour has a good foaming capacity and is suitable to be used in the preparation of whipped topping, ice cream, frozen desserts, breads, and cakes. Overall, mango kernel flour seems to potentially minimise the use of wheat flour, which can be incorporated into different baking products such as cakes, cookies, biscuits, and bread.

Effect of processing parameters

Research gaps on the mango kernel flour

The processing parameters involved in the production of mango kernel flour include soaking, blanching, and drying steps. Table 1 shows various ranges of processing parameters result in different properties of mango kernel flour. The purpose of soaking is to soften the kernels and remove anti-nutrients [11]. Mango kernels are recommended not to soak for more than 24 hours as it will reduce the protein content due to protein solubilisation. Moreover, the ash level at 72 hours is the lowest, which might be attributed to mineral leaching from the kernel, particularly the more soluble ones [8]. This can be supported by Mwaurah et al. [3] as the soaking process needs to be minimised in order to get a high amount of protein and fat content. Meanwhile, Gumte et al. [27] concluded that the soaking time used is best at 18 to 20 hours, but different results were obtained when the kernel was soaked for only 30 minutes in another study conducted by Das et al. [22]. Therefore, a maximum of 24 hours of soaking time is recommended for processing mango kernel flour in order to ensure excellent nutritional status since, at this level, the reduction of anti-nutrients to an acceptable level and an insignificant decrease of minerals is assured [8].

Blanching aims to inactivate the polyphenol oxidase (PPO) enzyme in order to preserve the quality and increase the shelf life of the food during storage. However, blanching also induces chemical changes in fruit by reducing the phytochemical compounds and organoleptic properties. Based on Ojha et al. [28], blanching the mango kernel flour at 45°C for 2 minutes caused a reduction in water absorption capacity (131.67%) and oil absorption capacity (72.60%) as compared to untreated mango kernel flour, whereby the reported water absorption capacity and oil absorption capacity were 173.33% and 80.00%. In contrast to Florence et al. [29], blanched mango kernel flour has a higher water absorption capacity (230.75%) and oil absorption capacity (212.60%) as compared to unblanched mango kernel when the blanching parameter was set at 100°C for 10 minutes. This indicates that the blanching process has improved the functional properties of the mango kernel flour. Nevertheless, further research should be conducted to investigate the optimum parameters of the blanching process in producing high quality mango kernel flour.

Drying is one of the popular technological methods used to inactivate the enzymatic degradation and extraction of functional components [30]. For example, Uzombah et al. [8] demonstrated the effect of different drying temperatures on the quality of mango kernel flour at 65°C, 75°C, and 85°C for 24 hours. The results showed that the drying process affected the fat, protein, ash, and fibre content, in which the amount of nutrients decreased

with increased temperature. Ekorong et al. [30] reported that the effects of drying time and temperature play a role in the moisture content and total polyphenol of mango seed kernels. Figure 4 illustrates that the increment of drying temperature from 40℃ to 80℃ resulted in a reduction of moisture content of 13.1%, which is caused by the increase in permeability to vapour. For drying time, the moisture content of the mango seed kernels initially dropped from 23.20% w/w at 6 hours to a minimum of 9.30% w/w at 56 hours and then rose up to 10.30% w/w at 69 hours. This can be explained by the fact that when air contained the maximum amount of vapour possible, the vapour exerted a saturation vapour pressure because the quantity of water vapour present was less than the maximum, thus the air took up more moisture.

Meanwhile, the decrease in total polyphenol from 1.20 mg/g to 0.20 mg/g is due to the degradation of phenolic compounds at a higher temperature. Therefore, a drying step is needed to obtain the product in powder form and reduce the moisture content for better storage stability. Even though phenolic compounds are heat-sensitive, an increase in total polyphenols was detected as the drying duration increased. As shown in Figure 5, it began at 1.20 mg/g after 6 hours and increased to 1.38 mg/g after 69 hours. According to Ekorong et al. [30], this may be accounted for by the sum of the concentrations of the different phenolic acids in the free fraction, which increased significantly as the drying time increased. Subsequently, study on the optimum drying temperature and time is required to produce high-quality mango kernel flour.

Table 1. Different processing parameters of mango kernel flour

Author	Soaking Time (h)	Blanching Temperature (℃)	Blanching Time (min)	Drying Temperature (℃)	Drying Time (H)	Properties of Mango Kernel Flour
Florence et al. [29]	-	100	10	30	964	● Blanched mango kernel flour has higher water absorption capacity and oil absorption capacity as compared to unblanched mango kernel flour
Ojha et al. [28]	48	45	2	60	7	● Soaking and blanching reduced ash and fibre but increased protein, fat, and carbohydrate content ● Soaking and blanching caused a reduction in water absorption and oil absorption capacity ● Soaking and blanching reduced bioactive compounds (polyphenol, ascorbic acid, flavonoids, and tannin)
Das et al. [22]	0.5	-	-	65	16	● Functional properties: higher bulk density and water absorption capacity than wheat flour ● Nutritional value: higher ash, fibre, fat and energy content than wheat flour

Table 1 (cont'd). Different processing parameters of mango kernel flour

Author	Soaking Time (h)	Blanching Temperature (°C)	Blanching Time (min)	Drying Temperature (°C)	Drying Time (H)	Properties of Mango Kernel Flour
Uzombah et al. [8]	24, 48, 72	100	3	65,75, 85	24	• Soaking time affected the tannin, fibre, ash, and fat content • Dying temperature affect fat, protein, ash, and fibre • Drying and soaking increase the carbohydrate content
Gumte et al. [27]	18–20	-	1–2	60	5	• Reduced nutritional values: protein, ash, and fibre • Reduced tannin and flavonoids

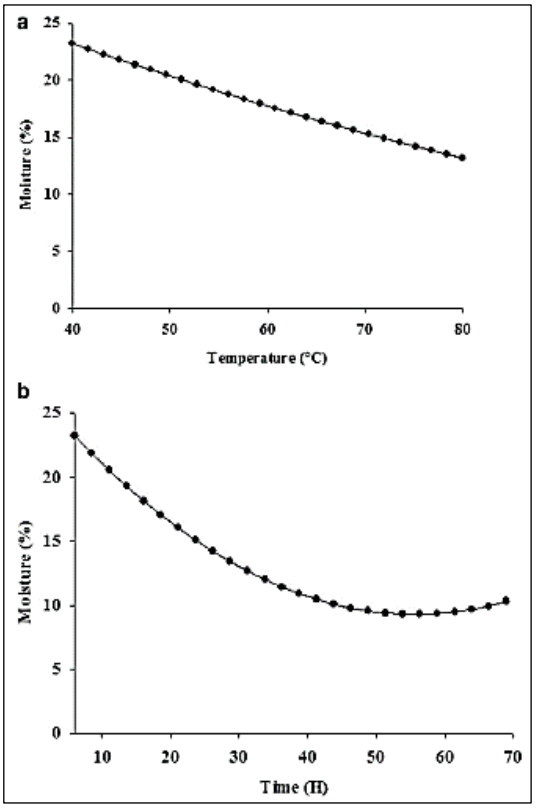


Figure 4. Effects of drying temperature and time on the moisture content of mango seed kernels [30]

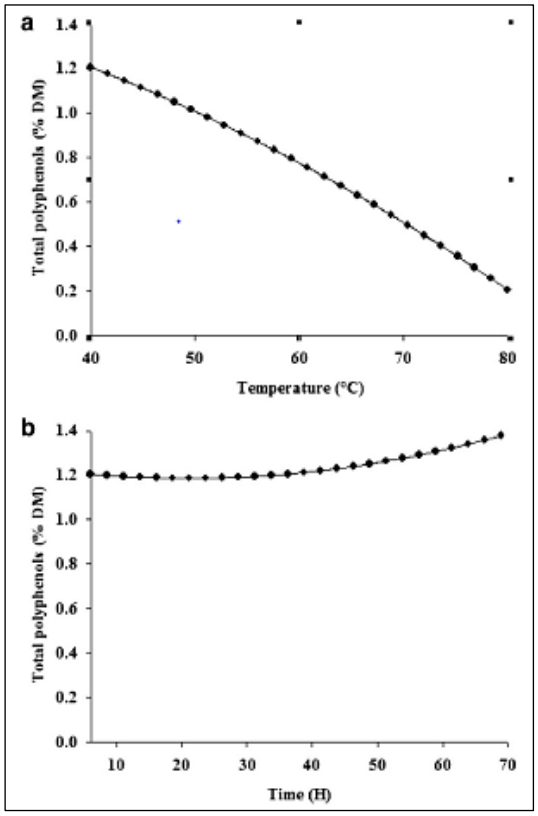


Figure 5. Effects of drying a) temperature and b) time on the total polyphenol content of mango seed kernels [30]

Nutritional composition

Mango kernel flour has shown that it is rich in carbohydrates, protein, and fat, which fit the nutrients that are needed in the human body. According to Mas'ud et al. [19], the nutritional compositions of mango kernel flour include moisture, carbohydrate, crude protein, total lipid, crude fibre, and ash content with their respective values of 9.20–9.60%, 36.20–39.30%, 5.20–6.60%, 6.00–7.20%, 2.20–2.50 %, and 2.90–5.50%, respectively. However, a few processing parameters have been identified to affect the quality of the produced mango kernel flour, including soaking, blanching, and drying time and temperature, as shown in Table 2. According to Uzombah et al. [8], soaking and drying parameters have affected the protein content. This is because of the protein denaturation and solubilisation at higher drying temperatures and longer soaking time. Besides that, Gumte et al. [27] also found the protein content of the raw mango kernel (10.02%) had slightly reduced after being processed into mango kernel flour (9.36%). Das et al. [22] deduced that an increase in drying temperature and time has prolonged the uptake of moisture, hence reducing the moisture content in mango kernel flour.

In addition to this, Sogi et al. [31] mentioned that drying temperature had affected the moisture content by increasing the vapour permeability, allowing the pore structure to remain open, hence decreasing the moisture content. Meanwhile, for fat content, Uzombah et al. [8] reported that an increase in drying temperature resulted in higher fat reduction, which is due to fat oxidation. In contrast to Ojha et al. [28], soaked mango kernel powder has higher fat content (10.17%) as compared to blanched (9.63%) and untreated mango kernel powder (9.53%). They proposed that the soaking process had resulted in the swelling of the kernel, thus increasing the fat content. Similarly, the ash and fibre content in mango kernel flour have also been reduced by the treatment of soaking and blanching due to the leaching loss of minerals [8], [28]. At the same time, soaking and drying have increased the carbohydrate content. This can be explained by the fact that soaking tends to reduce other components such as anti-nutrients that can form complexes with the nutrient. In contrast, increasing the drying temperature has accelerated the moisture removal process, increasing the carbohydrate content [8].

Table 2. Effects of processing parameters on the nutritional compositions of mango kernel flour

Nutritional Composition	Soaking	Blanching	Drying
Protein	• Longer soaking time solubilised the protein, hence reducing the protein content in mango kernel flour [8]	-	• Protein content in mango kernel flour is denatured at higher temperature [8]
Moisture	-	-	• The higher the drying temperature and time, the higher the uptake of moisture [22] • Drying temperature influenced the vapour permeability, thus affecting the moisture content [31]
Fat	• Soaking process caused the kernel to swell, thus increasing the fat content [28]	-	• Reduced the fat content in mango kernel flour through oxidation of fat at higher temperatures [8]

Table 2 (cont'd). Effects of processing parameters on the nutritional compositions of mango kernel flour

Nutritional Composition	Soaking	Blanching	Drying
Ash & Fibre	• Longer soaking time has reduced the amount of ash in mango kernel flour [8]	• Blanching process affected the ash and fibre content through leaching loss of minerals [28]	-
Carbohydrate	• Reduced other components that can form complexes with the nutrients, thus increasing the carbohydrate [8]	-	• Facilitated the concentration of carbohydrates by increasing the removal of moisture at higher temperatures [8]

Functional properties

Table 3 shows the effect of processing parameters on the functional properties of mango kernel flour, such as bulk density, oil absorption capacity, and swelling index. Das et al. [22] found that the bulk density in mango kernel flour is higher (0.63 g/mL) than wheat flour (0.58 g/mL). Based on Ojha et al. [28], the bulk density of mango kernel flour has increased after the treatment of soaking and blanching compared with untreated mango kernel flour. Sogi et al. [31] mentioned that higher amounts of bulk density might be due to excess tissue shrinkage during the drying process. This phenomenon indicates that processing parameters greatly influence the functional properties of mango kernel flour. The amount of oil absorption capacity is crucial in determining the product's sensory properties. This is because oil functions as a flavour keeper and enhances mouthfeel; thus, flour's capacity to absorb oil is critical [26]. Ojha et al. [28] showed that the oil absorption capacity of mango kernel flour has decreased after being soaked for 24 hours and blanched at 45℃ for 2 minutes, where the amount of oil absorption capacity for untreated mango kernel flour (80.00%) is higher than soaked mango kernel flour (60.00%) and blanched mango kernel flour (72.60%). The measurement of the swelling index is used to describe the gelatinisation of starches and flours [26].

Das et al. [22] demonstrated the soaking of mango kernels for 30 minutes and dried at 60–65℃ for 15–16 hours, and the obtained swelling index was 1.45 g/g. Surprisingly, the result is in contrast to Lakshmi et al. [26] as the swelling index for mango kernel flour obtained from three different types of mangoes (Neelam, Totapuri, and Alphonso) is 10.40 to 10.83 g/g in which the stone kernels were soaked for 48 hours and dried at 50℃ for 2 hours. In comparison with wheat flour, the swelling index is 3.54 g/g, while for durian seed flour, the swelling index is 8.03 g/g [32]. The lower amount of swelling index is due to the higher fat content in mango kernel flour, which resists starch gelatinisation [22]. Therefore, the processing parameters in mango kernel flour production should be optimised in order to enhance the functional properties of mango kernel flour and obtain high-quality mango kernel flour.

Table 3. Effects of processing parameters on the functional properties of mango kernel flour

Functional properties	Soaking	Blanching	Drying
Bulk density	• Increased the bulk density of soaked mango kernel flour compared to untreated mango kernel flour [28]	-	• Increased the amount of bulk density through the shrinkage of excess tissue [31]
Oil absorption capacity	• Decreased the amount of oil absorption capacity in soaked mango kernel flour (60.00%) compared to untreated mango kernel flour (80.00%) [28]	• Lowered the oil absorption capacity of blanched mango kernel flour (72.80%) compared to untreated mango kernel flour (80.00%) [28]	-
Swelling index	• The swelling index of mango kernel flour is 1.45 g/g when soaked for 30 minutes [22] • The swelling index of mango kernel flour is 10.40–10.83 g/g when soaked for 48 hours [26]	-	• The swelling index of mango kernel flour is 1.45 g/g when dried at 60–65°C for 15–16 hours [22] • The swelling index of mango kernel flour is 10.40–10.83 g/g when dried at 50°C for 2 hours [26]

Bioactive compounds

Generally, the processing parameters influence the amounts of bioactive compounds in mango kernel flour, such as ascorbic acid, tannin, polyphenol, and antioxidants (Table 4). According to Ojha et al. [28], the value of ascorbic acid present in blanched mango kernel powder is 112.00 mg/100 g, whereas in soaked mango kernel powder it is 119.33 mg/100 g. In contrast to Mas'ud et al. [19], the amount of ascorbic acid obtained in the mango kernel flour is 66.8 to 73.10 mg/100 g. The results are comparable with those of Sogi et al. [31] as the amount of ascorbic acid found in mango kernel powder is 61.22 to 74.48 mg/100 g. The researcher mentioned that the lower value of ascorbic acid is influenced by the thermal degradation and oxidation during the processing method. Tannin is one of the anti-nutritional substances found in raw mango kernel seed [33]. Besides reducing the availability of nutrients, tannin has astringent properties that contribute to the bitter principle and sour taste [27]. Thus, tannin needs to be removed before being applied in food or feed to reduce its toxic effect (about 75% of tannin in hydrolysable form). Soaking is an important step in this process because it promotes the leaching loss of anti-nutrients such as tannin from the mango seed kernel, but it should be done in less than 24 hours to avoid protein loss.

The total polyphenols found in mango seed kernel flour are 62.40 to 72.90 mg [19]. Nevertheless, Ojha et al. [28] stated that the polyphenols consisting of mango kernel flour had been significantly reduced through the process of soaking and blanching as the number of polyphenols recorded in untreated mango kernel powder (1630.00 mg/100 g) is higher than the soaked mango kernel powder (1573.33 mg/100 g) and blanched mango kernel powder (1553.33 mg/100 g). This reveals that the treatments of soaking for 24 hours and blanching at 45°C for 2 minutes have affected the amount of polyphenol. Besides that, drying time and temperature also influenced the polyphenol content since the degradation of phenolic compounds occurs at high temperatures [30]. The antioxidant present in mango seed kernels is the highest compared to other fruit seeds

such as jackfruit, avocado, and logan [34]. Unfortunately, the level of antioxidants found by Ojha et al. [28] in untreated mango kernel flour is 84.33%, which is higher than blanched mango kernel powder (68.33%) and soaked mango kernel powder (79.00%). This showed that the processing parameters of soaking for 24 hours and blanching at 45°C for 2 minutes have negatively affected the concentration of antioxidants exhibited by the mango kernel flour.

Table 4. Effects of processing parameters on bioactive compounds in the mango kernel flour

Bioactive compounds	Soaking	Blanching	Drying
Ascorbic acid	• Soaking process increased the amount of ascorbic acid in mango kernel flour [28]	• Blanched mango kernel flour has a lower amount of ascorbic acid compared to soaked mango kernel flour [28]	• The lower amount of ascorbic acid is affected by the thermal degradation and oxidation [31]
Tannin	• Soaking for less than 24 hours helps in the removal of antinutrients such as tannin.	-	-
Polyphenol	• Soaking for 24 hours affected the amount of polyphenol in soaked mango kernel flour compared to untreated mango kernel flour [28]	• Blanching at 45°C for 2 hours lowered the amount of polyphenols in blanched mango kernel flour compared to untreated mango kernel flour [28]	• Drying at a high temperature contributed to the degradation of phenolic compounds
Antioxidants	• Soaking for 24 hours has lowered the antioxidants in the soaked mango kernel (79.00%) compared to untreated mango kernel flour (83.44%) [28]	• Blanching at 45°C for 2 hours has reduced the antioxidants in blanched mango kernel (68.33%) compared to untreated mango kernel flour (83.44%) [28]	-

Challenges

Removal of tannin from mango seed kernel remains a big challenge in the production of mango kernel flour as it can negatively impact human health and reduce the bioavailability of nutrients. According to Bala et al. [35], soaking the mango seed kernel at 70–80°C removes the tannin significantly and effectively, but this treatment affects the protein content of the mango seed kernel. Besides that, processing activities have a different impact on the nutritional composition of the finished mango kernel product [3]. Thus, an optimum processing parameter for the production of mango kernel flour should be further investigated. On top of that, the palatability of mango kernel flour may be affected by the high tannin content. This is because tannin can impart a bitter taste and reduce the flour quality by discolouration [8]. Incorporating mango kernel flour up to or more than 50% is also undesirable in the food product. It can impart a bitter taste and cause the product to be slightly darker due to the high amount of total phenolic content. The properties of mango kernel flour in terms of nutritional, functional, and bioactive compounds have made it such a great deal, especially in the food industry. Hence, it is recommended to conduct a study on the specifications for safeguarding mango kernel flour against adulteration being commercialised

in the industry. Furthermore, it is suggested for the mango kernel flour to apply the mango kernel flour as a functional food ingredient [19]. In addition, turning mango kernels into a valuable product would also reduce the kernel waste and keep the environment clean.

Conclusion

In conclusion, the steps involved during the processing of mango kernel flour greatly influenced the quality of mango kernel flour in terms of its nutritional composition, functional properties, and bioactive compounds. This is because soaking and blanching lead to leaching loss of certain nutrients, bioactive compounds, and functional properties, but at the same time, they help reduce the anti-nutrients, which refer to tannin. Meanwhile, the drying process reduces the protein, fat, moisture, ash, and fibre but also helps to increase the carbohydrate content, resulting in a high energy value. The presence of bioactive compounds in mango kernel flour, such as polyphenol and ascorbic acid, exhibited therapeutic value, which is high in antioxidants and is beneficial to human health. The functional properties of mango kernel flour make it potentially useful as a functional ingredient in food products, especially in bakery products. Further research on the optimisation of each of the processing steps is required in order to obtain high-quality mango kernel flour.

Acknowledgement

The authors wish to acknowledge the Universiti Teknologi MARA (UiTM), Cawangan Negeri Sembilan, Kampus Kuala Pilah at Kuala Pilah, Negeri Sembilan, Malaysia, for supporting this study.

References

1. Awolu, O. O., Sudha, M. L. and Monohar, B. (2018). Influence of defatted mango kernel seed flour addition on the rheological characteristics and cookie making quality of wheat flour. *Food Science Nutrition,* 6(8): 2363-2373.
2. Ediriweera, M. K., Tennekoon, K. H. and Samarakoon, S. R. (2017). A review on ethnopharmacological applications, pharmacological activities, and bioactive compounds of *Mangifera indica* (mango). *Evidence-based Complementry Alternative Medicines,* 2017: 6949835.
3. Mwaurah, P. W., Kumar, S., Kumar, N., Panghal, A., Attkan, A. K., Singh, V. K. and Garg, M. K. (2020). Physicochemical characteristics, bioactive compounds and industrial applications of mango kernel and its products: A review. *Comprehensive Review Food Science Food Safety,* 19(5): 2421-2446.
4. Izli, N., İzli, G. and Taskin, O. (2017). Influence of different drying techniques on drying parameters of mango. *Food Science Technology,* 37(4): 604-612.
5. Masibo, M. and He, Q. (2009). Mango bioactive compounds and related nutraceutical properties-a review. *Food Review International,* 25(4): 346-370.
6. Torres-León, C., Rojas, R., Contreras-Esquivel, J. C., Serna-Cock, L., Belmares-Cerda, R. E. and Aguilar, C. N. (2016). Mango seed: functional and nutritional properties. *Trends Food Sci Technology*, 55(2016): 109-117.
7. Jahurul, M. H., Zaidul, I. S., Ghafoor, K., Al-Juhaimi, F. Y., Nyam, K. L., Norulaini, N. A. and Mohd Omar, A. K. (2015). Mango (*Mangifera indica l.*) by-products and their valuable components: a review. *Food Chemistry,* 183: 173-180.
8. Uzombah, T. A., Awonorin, S. O., Shittu, T. A. and Adewumi, B. A. (2019). Effect of processing parameters on the proximate and antinutritive properties of mango kernel flour processed for food applications. *Journal Food Processing Preservation,* 43(10): e14131.
9. Diarra, S. S. (2019). Potential of mango (*Mangifera indica L.*) seed kernel as a feed ingredient for poultry: a review. *Worlds Poultry Science Journal,* 70(2): 279-288.
10. Shabeer, M., Sultan, M. T., Abrar, M., Suffyan Saddique, M., Imran, M., Saad Hashmi, M. and Sibt-e-Abbas, M. (2016). Utilization of defatted mango kernel in wheat-based cereals products: Nutritional and functional properties. *International Journal Fruit Sciences,* 16(4): 444-460.
11. Yatnatti, S., Vijayalakshmi, D. and Chandru, R. (2014). Processing and nutritive value of mango seed kernel flour. *Current Research Nutrition Food Science Journal,* 2(3): 170-175.

12. Ram, R. A., Rahim, M. A. and Alam, M. S. (2020). Diagnosis and management of nutrient constraints in mango. *Fruit Crops*, 2020: 629-650.
13. Afiqah, A. N., Nulit, R., Hawa, Z. E. J. and Kusnan, M. (2014). Improving the yield of 'Chok Anan' (MA 224) mango with potassium nitrate foliar sprays. *International Journal Fruit Sciences,* 14(4): 416-423.
14. Okpala, L. C. and Gibson-Umeh, G. I. (2013). Physicochemical properties of mango seed flour. *Nigeria Food Journal,* 31(1): 23-27.
15. Beyene, G. and Araya, A. (2015). Review of mango (*Mangifera indica*) seed-kernel waste as a diet for poultry. *Journal Biology Agriculture Healthcare,* 5(11): 156-159.
16. Lauricella, M., Emanuele, S., Calvaruso, G., Giuliano, M. and D'Anneo, A. (2017). Multifaceted health benefits of *Mangifera indica l.*(mango): the inestimable value of orchards recently planted in Sicilian rural areas. *Nutrients,* 9(5): 525.
17. Matheyambath, A. C., Subramanian, J. and Paliyath, G. (2016). Mangoes. In *Encyclopedia of Food and Health*: pp. 641-645.
18. Elsheshetawy, H. E., Mossad, A., Elhelew, W. K. and Farina, V. (2016). Comparative study on the quality characteristics of some Egyptian mango cultivars used for food processing. *Annals Agriculture Sciences,* 61(1): 49-56.
19. Mas'ud, F., Rifai, A. and Sayuti, M. (2020). Mango seed kernel flour (*Mangifera indica*): nutrient composition and potential as food. *Malaysian Journal Nutrition,* 26(1): 101.
20. Patel, G. N. and Kheni, J. (2018). Mango seed kernel, a highly nutritious food, should we continue to trash or use? *Journal Pharmacognosy Phytochemistrt, 7*(4): 04-07.
21. Bejo, S. K. and Kamaruddin, S. (2014). Determination of Chokanan Mango sweetness (*'Mangifera indica'*) using non-destructive image processing technique. *Australian Journal Crop Sciences, 8*(4): 475.
22. Das, P. C., Khan, M. J., Rahman, M. S., Majumder, S. and Islam, M. N. (2019). Comparison of the physico-chemical and functional properties of mango kernel flour with wheat flour and development of mango kernel flour based composite cakes. *NFS Journal,* 17: 1-7.
23. Perez, I. C., Mu, T. H., Zhang, M. and Ji, L. L. (2017). Effect of heat treatment to sweet potato flour on dough properties and characteristics of sweet potato-wheat bread. *Food Science Technology International, 23*(8): 708-715.
24. Gumte, S., Taur, A., Sawate, A. and Kshirsagar, R. (2018). Effect of fortification of mango (*Mangifera indica*) kernel flour on nutritional, phytochemical and textural properties of biscuits. *Journal Pharmacognosy Phytochemistry, 7*(3): 1630-1637.
25. Amin, K., Akhtar, S. and Ismail, T. (2018). Nutritional and organoleptic evaluation of functional bread prepared from raw and processed defatted mango kernel flour. *Journal Food Processing Preservation,* 42(4): e13570.
26. Lakshmi, M., Preetha, R. and Usha, R. (2016). Mango (*Mangifera indica*) stone kernel flour-a novel food ingredient. *Malaysian Journal Nutrition,* 22(3): 461-467.
27. Gumte, S., Taur, A., Sawate, A. and Thorat, P. (2018). Effect of processing on proximate and phytochemical content of mango (*Mangifera indica*) kernel. *International Journal Chemical Studies,* 6(2): 3728-3733.
28. Ojha, P., Raut, S., Subedi, U. and Upadhaya, N. (2019). Study of nutritional, phytochemicals and functional properties of mango kernel powder. *Journal Food Science Technology Nepal,* 11: 32-38.
29. Florence, O. S., Abdoulaye, T., Tidiane, K., Rodrigue, K. N., Monon, K. and Rene, S. Y. (2020). Chemical composition, functional and antioxidant properties of mango seed kernel (Kent variety) flour grown in Korhogo (Ivory Coast). *International Journal Science Engineering Research,* 11(11) : 357-369.
30. Ekorong, F. J. A. A., Zomegni, G., Desobgo, S. C. Z. and Ndjouenkeu, R. (2015). Optimization of drying parameters for mango seed kernels using central composite design. *Bioresource Bioprocessing, 2*(1): 1-9.
31. Sogi, D. S., Siddiq, M., Greiby, I. and Dolan, K. D. (2013). Total phenolics, antioxidant activity, and functional properties of *'Tommy Atkins'* mango peel

32. and kernel as affected by drying methods. *Food Chemistry,* 141(3): 2649-2655.
33. Kumoro, A. C. and Hidayat, J. P. (2018). Functional and thermal properties of flour obtained from submerged fermentation of durian (*Durio Zibethinus Murr*.) seed chips using *Lactobacillus Plantarum*. *Potravinarstvo,* 12(1): 965.
34. Dakare, M. A., Ameh, D. A., Agbaji, A. S. and Atawodi, S. E. (2014). Chemical composition and antinutrient contents of yellow maize, raw and processed composite mango (*Mangifera indica*) seed kernel from Zaria, Kaduna State Nigeria. *International Journal Advance Research,* 2(7): 90-97.
35. Lebaka, V. R., Wee, Y.-J., Ye, W. and Korivi, M. (2021). Nutritional composition and bioactive compounds in three different parts of mango fruit. *International Journal Environmental Research Public Health,* 18(2): 741.
36. Bala, S., Ameh, D., Omage, J., Bugaje, S., Makeri, M., Dikko, H. and Usman, M. (2013). Influence of processing method on the nutrients and antinutrients content of kernels of three Nigerian local mango (*Mangifera indica L*.) varieties. *Journal Applied Agriculture Research, 5*(1): 203-213.

Malaysian Journal of Analytical Sciences (MJAS)
Published by Malaysian Analytical Sciences Society

SYNTHETIC APPROACHES TOWARDS QUINOLACTACIN DERIVATIVES VIA DIELS-ALDER, ACYL MIGRATION AND MULTICOMPONENT REACTIONS

(Pendekatan Sintesis Ke Arah Terbitan Quinolaktasin Melalui Tindak Balas Diels-Alder, Migrasi Asil dan Tindak Balas Pelbagai Komponen)

Ahmad Zahir Hafiz Ismail[1,2], Putri Nur Arina Mohd Arif [1,2], Nurul Syafiqah Rezali[3], Mohd Fazli Mohammat[2], Zurina Shaameri[2]*

[1]Organic Synthesis Laboratory, Institute of Science,
Universiti Teknologi MARA Puncak Alam, 43200 Bandar Puncak Alam, Selangor, Malaysia
[2]Faculty of Applied Sciences,
Universiti Teknologi MARA, 40450 Shah Alam, Selangor, Malaysia
[3]Chemical Sciences Programme,
School of Distance Education, Universiti Sains Malaysia, 11800 Penang, Malaysia

**Corresponding author: zurina@uitm.edu.my*

Received: 18 September 2021; Accepted: 27 February 2022; Published: 25 August 2022

Abstract

Quinolactacins are rare fungal alkaloids extracted from the culture broth of Penicillium species isolated from larvae mulberry pyralis (*Margonia pyloalis Welker*). The synthesis of the natural alkaloids has gained interests among many researchers due to its unique γ-lactam conjugated ring quinolone skeleton. Furthermore, the alkaloids are also proven to exhibited inhibitory activities against tumour necrosis factor (TNF) production. Synthesizing the alkaloids is initiated by forming the key pyrrolidine-2,4-dione intermediates *via* the acid-mediated Meldrum reaction and tetramic acid cyclisation of different amino acids. Subsequently, the diketo intermediates are reduced and eliminated to form hydroxy and enone analogues. The enone analogues are then reacted with an amine-substituted diene by aza Diels-Alder reaction to form the anticipated 4-pyridone-lactam moiety with different substitutions. Nonetheless, the availability of amine-substituted dienes is limited even though aza Diels-Alder reactions shorten the formation of the tricyclic compounds. Consequently, the present study synthesised quinolactacin derivatives through alternative routes, including acylating the key pyrrolidine-2,4-dione with 2-nitrobenzoyl chloride to obtain an acylated tetramic acid and hydrogenated and furnish the final quinolactacin derivatives. The derivatives were also procured through a multicomponent reaction of diethyl oxaloacetate salt with aldehydes and amines. The synthesised compounds were analysed and confirmed with proton and carbon nuclear magnetic resonance (^{1}H- and ^{13}C-NMR) and infrared (IR) spectroscopy.

Keywords: *Penicillium* sp., Diels-Alder, 2,4-pyrrolidinone, quinolactacin

Abstrak

Quinolaktasin adalah kulat alkaloid nadir yang terhasil daripada kultur kaldu Penicillium spesies, di ekstrak daripada larva piralis mulberi (*Marfonia pyloalis Welker*). Sintesis bahan alkaloid yang natural ini telah menarik minat ramai ahli penyelidik oleh kerana keunikan struktur quinolone di mana ianya konjugat bersama gegelang γ-lactam. Alkaloid ini telah dibuktikan bahawa ianya bersikap aktif terhadap aktiviti rencatan melawan penghasilan faktor tumor nekrosis (TNF). Sintesis ini bermula dengan bahantara pirolidina-2,4-dion melalui tindak balas asid Meldrum dan pengitaran asid tetramik dari variasi asid amino. Bahantara diketo pula akan melalui pengurangan berturutan dan tindak balas penyingkiran kumpulan hidroksi dan variasi enon. Variasi enon ini bertindak balas dengan diena amina gantian melalui reaksi aza Diels-Alder bagi menghasilkan sebatian 4-piridona-laktam dengan variasi gantian. Walaupun reaksi kimia aza Diels-Alder dapat membantu menghasilkan sebatian trisiklik dalam langkah yang pendek, tetapi variasi diena amina gentian juga adalah terhad. Oleh itu, sintesis bagi penghasilan variasi quinolaktasin dijalankan melalui cara alternatif di mana pirolidina-2,4-dion menjalani pengasilan dengan 2-nitrobenzoil klorida untuk menghasilkan tetramik asid terasilasi dan penghidrogenan bagi menghasilkan sebatian akhir quinolaktasin. Reaksi pelbagai komponen oleh garam dietil oxaloasetat bersama aldehid dan amina pula adalah alternatif lain bagi penghasilan variasi sebatian quinolaktasin. Semua sebatian di dalam kajian ini dianalisa dan disahkan menggunakan resonans magnet nucleus (^{1}H- dan ^{13}C-NMR) dan spektroskopi infra merah (IR).

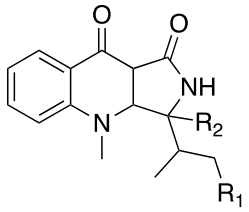
Kata kunci: *Penicillium* sp., diels-alder, 2,4-pirolidina, quinolaktasin

Introduction

The first quinolactacin was extracted from the fermented broth of Penicillium sp. EPF-6 extracted from mulberry pyralid larvae (*Margaronia pyloalis Welker*). Solvent extraction and chromatographic purification separated the quinolactacins from the culture medium. The substances were reported to behave as active inhibitors against tumour necrosis factor (TNF) produced by murine macrophages and macrophage-like J774.1 cells stimulated with LPS [1]. Consequently, numerous studies have attempted to synthesise the chemicals in the laboratory. Similarly, the current study described the synthesis of the quinolactacin derivatives.

To date, three different quinolactacins have been discovered by scientists, quinolactacins A, B, and C, differentiated by the alkyl groups at the C-5 position (see Figure 1). The quinolactacins were demonstrated to be weak antifungals against *Aspergillus niger* ATCC 9642 and inactive towards a range of bacteria, filamentous fungi, and yeasts [2]. Nonetheless, the substances are still gaining interest from researchers as they exhibit several biological activities.

The current study found other derivatives types, including quinolactacin H and quinolactacide. The current study also investigated pyrrolidine synthesis, as previous reports demonstrated that numerous pyrrolidine-type molecules were active antibacterial, antifungal, and anti-inflammatory agents [3]. Furthermore, pyrrolidine-2,4-dione or tetramic acid is the essential ring moiety required in the synthesis of quinolactacin.



Quinolactacin A : $R_1 = CH_3$, $R_2 = H$; Quinolactacin B : $R_1 = R_2 = H$; Quinolactacin C : $R_1 = CH_3$, $R_2 = OH$

Figure 1. The chemical structure of quinolactacins A, B, and C

Materials and Methods

The current study utilized Boc-Val-OH, *D*-valine, 2,2-dimethyl-1,3-dioxane-4,6-dione (Meldrum's acid), 4-dimethylaminopyridine (DMAP), *N,N'*-dicyclohexylcarbodiimide (DCC), 2-nitrobenzoylchloride, tetra-n-butylammonium fluoride (TBAF) in THF, sodium hydride (NaH), sodium borohydride ($NaBH_4$), acetic acid, sodium hydroxide (NaOH), di-*tert*-butyl dicarbonate (BOC_2O), aluminium chloride, *N*-benzylideneaniline, *trans*-1-methoxy-3-trimethylsilyloxy-buta-1,3-diene, 2,4-hexadiene, diphenyl ether, methanol, potassium bisulfate ($KHSO_4$), hexane, diethyl ether, ethyl acetate, tetrahydrofuran (THF), hydrochloric acid (HCl), potassium cyanonitrile

(KCN), *iso*butylraldehyde, formaldehyde, ammonia, aniline, 40% methylamine in water, formic acid diethyl oxaloacetate sodium salt, chloroform, dichloromethane, anhydrous magnesium sulphate, sodium chloride (NaCl), dioxane.

Synthesis of (*tert*-butoxycarbonyl)valine (1)

A solution of *D*-valine, (1.00 g, 8.51 mmol) in dioxane/water (2:1) (40 ml) and 1 M NaOH (8 ml) was stirred. Upon the formation of a homogenous mixture, the reaction mixture was cooled in an iced-water bath before adding the BOC_2O (3.73 g, 17.07 mmol). Then, the reaction mixture was left stirring overnight at room temperature. Progress of the reaction was monitored using TLC analysis. After the reaction completed, the undissolved materials were filtered and the filtrate was partially evaporated. The residue was cooled in an iced-water bath and diluted with ethyl acetate. The mixture was acidified to pH 2-3 with 1 M $KHSO_4$. The aqueous layer was extracted with ethyl acetate and the organic layer was washed with water and brine, dried with anhydrous magnesium sulphate and evaporated under reduced pressure to furnish the compound (*tert*-butoxycarbonyl)valine (**1)** 66 %. White solid, m.p 164-165ºC; 1H-NMR (400 MHz, CD_3OD) δ 3.97 (d, J = 5.5 Hz, 1H), 2.13-2.04 (m, 1H), 1.42 (s, 9H), 0.94 (d, J = 8.9 Hz, 6H); 13C-NMR (100 MHz, CH_3OD) δ 174.26, 157.20, 79.14, 59.02, 30.40, 27.37, 18.26, 16.85.

Synthesis of *tert*-butyl 2-isopropyl-3,5-dioxopyrrolidine-1-carboxylate (2)

To a solution of (*tert*-butoxycarbonyl)valine **(1)** (1.00 g, 4.60 mmol) Meldrum acid (0.66 g, 4.60 mmol), DMAP (0.79 g, 6.44 mmol) in dichloromethane (25 ml), DCC (1.14 g, 5.52 mmol) was added at room temperature. The resulting mixture was stirred for three hours at room temperature. Then the mixture was filtered and washed with ethyl acetate. The combined filtrates were diluted with cold ethyl acetate and were washed with 5% citric acid, water and brine, respectively. The organic layer was dried using anhydrous magnesium sulphate and evaporated under reduced pressure to give a yellow liquid which was dissolved in ethyl acetate and refluxed for one hour. The solvent was removed to furnish *tert*-butyl 2-isopropyl-3,5-dioxopyrrolidine-1-carboxylate, **(2)** 76 %. 1H-NMR (400 MHz, $CDCl_3$) δ 4.26 (d, J= 3.7 Hz, 1H), 3.10 (s, 2H), 2.38-2.28 (m, 1H), 1.52 (s, 9H), 1.09 (d, J= 7.3 Hz, 3H), 0.90 (d, J= 6.9 Hz, 3H); 13C-NMR (100 MHz, $CDCl_3$) δ 203.70, 168.08, 149.08, 84.34, 71.92, 44.2, 31.23, 28.33, 19.14,17.55.

Synthesis of *tert*-butyl-3-hydroxy-2-*iso*propyl-5-oxopyrrolidine-1-carboxylate (3)

In 10 ml chloroform, *tert*-butyl 2-isopropyl-3,5-dioxopyrrolidine-1-carboxylate **(2)** (0.35 g, 1.66 mmol) was dissolved. Then, acetic acid (0.10 ml, 1.66 mmol) and sodium borohydride (0.07 g, 1.82 mmol) were added into the reaction mixture. The resulting mixture was stirred at 0°C for one hour. After one hour, the mixture was continued to stir at room temperature for 8 hours. The progress of the reaction was monitored with TLC analysis. As the reaction completed, the solvent was removed under reduced pressure before being partitioned with ethyl acetate and sodium hydrogen carbonate for extraction. The organic layer was collected and dried over anhydrous magnesium sulphate and evaporated under reduced pressure to furnish the compound, *tert*-butyl-3-hydroxy-2-isopropyl-5-oxopyrrolidine-1-carboxylate, **(3)** 70 %. Yellow oil, 1H-NMR (400 MHz, CH_3OD) δ 4.65 (q, J = 8.5 Hz, 1H, CH), 4.08 (dd, J = 4.8 Hz, 1H), 2.19-2.37 (m, 1H), 1.49 (s, 9H), 1.05 (d, J = 7.3 Hz, 3H), 1.00 (d, J = 7.3 Hz, 3H); 13C-NMR (100 MHz, CH_3OD) δ 172.47, 150.30, 83.28, 66.82, 65.12, 40.66, 28.33, 28.01, 20.64, 18.82.

Synthesis of *tert*-butyl 2-*iso*propyl-5-oxo-2,5-dihydro-1H-pyrrole-1-carboxylate (4)

In a stirred solution of *tert*-butyl-3-hydroxy-2-*iso*propyl-5-oxopyrrolidine-1-carboxylate **(3)** (1.61 g, 6.64 mmol) in anhydrous THF (35 ml), DMAP (2.43 g, 19.91 mmol) and BOC_2O (4.34 g, 19.91 mmol) were added. The resulting mixture was continued to stir for 48 hours at room temperature. After the reaction completed, THF was removed under reduced pressure. Then, the residue was dissolved in 30 ml ethyl acetate. The mixture was then extracted twice with 1 N HCl, twice with $KHCO_3$ and brine. The organic layer was collected and dried over anhydrous magnesium sulphate and the solvent was removed under reduced pressure to furnish compound, *tert*-butyl 2-*iso*propyl-5-oxo-2,5-dihydro-1H-pyrrole-1-carboxylate, **(4)** 9 %. Yellow solid, m. p. 79-82ºC; 1H-NMR (400 MHz, $CDCl_3$) δ

7.20 (td, J = 2.1 Hz, 1H), 6.17 (td, J = 2.1 Hz, 1H), 4.36 (t, J = 1.8 Hz, 2H), 1.57 (s, 9H); 13-C NMR (100 MHz, $CDCl_3$) δ 169.64, 149.63, 147.91, 127.82, 82.90, 67.34, 28.93, 28.17, 19.56, 14.91.

Synthesis of *tert*-butyl 2-*iso*propyl-3-((2-nitrobenzoyl)oxy)-5-oxo-2,5-dihydro-1H-pyrrole-1-carboxylate (9)

To a stirred solution of *tert*-butyl 2-isopropyl-3,5-dioxopyrrolidine-1-carboxylate **(4)** (0.22 g, 0.93 mmol) and sodium hydride (0.08 g, 1.20 mmol) in anhydrous THF (10 ml), 2-nitrobenzoyl chloride (0.23 ml, 1.87 mmol) was added. The reaction mixture was stirred at room temperature for one hour. The solvent was removed, and the crude product was then purified by silica gel column chromatography with ethyl acetate/ petroleum ether, 1/1 to furnish compound *tert*-butyl 2-isopropyl-3-((2-nitrobenzoyl)oxy)-5-oxo-2,5-dihydro-1H-pyrrole-1-carboxylate, **(9)** 26 %. Brown oil, 1H-NMR (400 MHz, $CDCl_3$) δ 8.09-8.07 (m, 1H), 7.87-7.64 (m, 4H), 6.32 (d, J = 0.9 Hz, 1H), 4.53 (q, J = 1.2 Hz, 1H), 2.50-2.43 (m, 1H), 1.57-1.50 (m, 9H), 0.98 (d, J = 7.3 Hz, 3H), 0.87-0.83 (m, 3H); 13C-NMR (100 MHz, $CDCl_3$) δ 168.3, 165.6, 161.0, 149.3, 133.9, 133.1, 132.2, 130.0, 124.7, 109.2, 83.4, 77.4, 77.1, 76.8, 64.8, 29.6, 28.2, 18.6, 16.0.

Synthesis of *tert*-butyl 2-*iso*propyl-4-(2-nitrobenzoyl)-3,5-dioxopyrrolidine-1-carboxylate (10)

To a stirred solution of *tert*-butyl 2-*iso*propyl-3-((2-nitrobenzoyl)oxy)-5-oxo-2,5-dihydro-1H-pyrrole-1-carboxylate **(9)** (0.06 g, 0.17 mmol) and potassium cyanonitrile (0.01 g,0.19 mmol) in anhydrous acetonitrile (10 ml), trimethylamine (0.02 g, 0.19 mmol) was added. The reaction mixture was let to stir for 12 hours at room temperature. Then, the reaction mixture was acidified with 1 N HCl and extracted with diethyl ether. After washing the ether layer with aqueous sodium bicarbonate, the resulting aqueous phase was neutralized to pH 7, extracted with ether, dried, and concentrated to furnish the compound *tert*-butyl 2-*iso*propyl-4-(2-nitrobenzoyl)-3,5-dioxopyrrolidine-1-carboxylate, **(10)** 20%. Yellow oil, 1H-NMR (400 MHz, $CDCl_3$) δ 8.20-8.26 (1H), 7.47-7.83 (4H), 6.91-7.01 (1H), 4.50-4.54 (1H), 2.50-2.59 (1H), 1.48 (s, 9H), 1.13 (d, J = 6.9 Hz, 3H), 0.89 (d, J = 6.9 Hz, 3H); 13C-NMR (100 MHz, $CDCl_3$) δ 207.1, 193.8, 168.9, 149.3, 144.7, 135.4, 134.7, 134.0, 126.3, 123.8, 82.5, 75.2, 68.9, 28.4, 25.9, 19.0.

General synthesis of compounds 11a-c

A mixture of equimolar amount of diethyl oxaloacetate salt (10.00 g, 47.62 mmol), *iso*butyraldehyde (4.34 ml, 47.62 mmol) and 40% methylamine in water (4.12 ml, 47.62 mmol) in ethanol (100 ml) was refluxed for one hour. After cooling, the mixture was poured into ice water and acidified using concentrated hydrochloric acid. The precipitate formed was filtered and washed with water and diethyl ether to furnish compounds **11a-c**.

Ethyl 4-hydroxy-1-methyl-5-oxo-2,5-dihydro-1H-pyrrole-3-carboxylate, **11a**, 20 %. White solid, m.p 152-155ºC; 1H-NMR (400 MHz, $CDCl_3$) δ 8.95 (s, 1H), 4.30 (q, J = 7.2 Hz, 2H), 3.97 (s, 2H), 3.08 (s, 3H), 1.32 (t, J = 7.3 Hz, 3H); 13C-NMR (100 MHz, $CDCl_3$) δ 157.3, 107.6, 77.4, 77.1, 76.8, 61.2, 48.1, 30.1, 14.3.

Ethyl 4-hydroxy-2-isopropyl-1-methyl-5-oxo-2,5-dihydro-1H-pyrrole-3-carboxylate, **11b**, 54 %. Yellow solid, m.p 165-169ºC; 1H-NMR (400 MHz, $CDCl_3$) δ 4.36-4.26 (m, 2H), 4.08 (d, J = 1.8 Hz, 1H), 3.03 (s, 3H), 2.44-2.37 (m, 1H), 1.34-1.30 (m, 3H), 0.97 (d, J = 6.9 Hz, 3H), 0.83 (d, J = 6.9 Hz, 3H); 13C-NMR (100 MHz, $CDCl_3$) δ 165.8, 164.3, 158.6, 110.8, 82.4, 77.5, 77.1, 76.8, 64.1, 62.0, 61.3, 30.2, 30.1, 29.3, 19.6, 18.9, 16.5, 14.3, 13.9.

Ethyl 4-hydroxy-2-isopropyl-5-oxo-2,5-dihydro-1H-pyrrole-3-carboxylate, **11c**, 42 %. Yellow solid, m.p 161-164ºC; 1H-NMR (400 MHz, $CDCl_3$) δ 7.80 (s, 1H), 4.37-4.28 (m, 2H), 4.24 (q, J = 1.4 Hz, 1H), 2.43-2.34 (m, 1H), 1.34 (td, J = 7.3, 4.1 Hz, 3H), 1.10 (d, J = 7.3 Hz, 3H), 0.63 (d, J = 6.9 Hz, 3H); 13C-NMR (100 MHz, $CDCl_3$) δ 166.9, 166.0, 158.3, 113.2, 82.5, 77.4, 77.1, 76.8, 62.0, 61.3, 58.8, 30.2, 29.1, 20.5, 19.6, 14.3, 14.2, 14.1, 13.9

General synthesis of compounds 12a-c

To a solution of ethyl 4-hydroxy-1-methyl-5-oxo-2,5-dihydro-1H-pyrrole-3- carboxylate (2.00 g, 10.80 mmol) in ethanol (10 ml) was added formic acid (0.65 ml, 17.28 mmol) and aniline (1.28 ml, 12.96 mmol). The resulting mixture was heated to reflux for 12 hours. The mixture was cooled to room temperature and the product was separated as solid which was collected by filtration to furnish compounds **12a-c**.

Ethyl 1-methyl-5-oxo-4-(phenylamino)-2,5-dihydro-1H-pyrrole-3-carboxylate, **12a**, 72 %. Yellow solid, m.p 239-242^{o}C; 1H-NMR (400 MHz, $CDCl_3$) δ 8.02 (s, 1H), 7.28-7.07 (m, 5H), 4.15 (q, J = 7.0 Hz, 2H), 4.04 (s, 2H), 3.07 (s, 3H), 1.16 (t, J = 7.1 Hz, 3H); 13C-NMR (100 MHz, $CDCl_3$) δ 165.2, 164.8, 143.3, 138.8, 128.4, 124.4, 122.5, 103.7, 77.5, 77.2, 76.8, 60.2, 49.9, 30.0, 14.3.

Ethyl 2-isopropyl-1-methyl-5-oxo-4-(phenylamino)-2,5-dihydro-1H-pyrrole-3-carboxylate, **12b**, 51 %. Yellow solid, m.p 252-255^{o}C; 1H-NMR (400 MHz, $CDCl_3$) δ 8.06 (s, 1H), 7.28-7.24 (m, 2H), 7.10-7.06 (m, 3H), 4.16 (d, J = 1.8 Hz, 1H), 4.14-4.08 (m, 2H), 3.03 (s, 3H), 2.51-2.45 (m, 1H), 1.13 (t, J = 7.1 Hz, 3H), 1.06 (d, J = 7.3 Hz, 3H), 0.83 (d, J = 6.9 Hz, 3H); 13C-NMR (100 MHz, $CDCl_3$) δ 165.1, 143.5, 139.2, 128.5, 124.3, 122.4, 107.8, 77.4, 77.1, 76.8, 65.5, 60.2, 30.3, 29.8, 19.6, 16.0, 14.1.

Ethyl 2-isopropyl-5-oxo-4-(phenylamino)-2,5-dihydro-1H-pyrrole-3-carboxylate, **12c**, 45 %. Yellow solid, m.p 245-249^{o}C; 1H-NMR (400 MHz, $CDCl_3$) δ 8.11 (s, 0H), 7.28-7.06 (m, 1H), 4.28 (t, J = 1.5 Hz, 0H), 4.15 (qd, J = 7.2, 3.7 Hz, 0H), 2.49 (td, J = 7.0, 2.9 Hz, 0H), 1.57-1.80 (0H), 1.16 (t, J = 7.1 Hz, 1H), 1.07 (d, J = 7.3 Hz, 1H), 0.68 (d, J = 6.9 Hz, 1H); 13C-NMR (100 MHz, $CDCl_3$) δ 167.8, 165.2, 143.4, 139.1, 128.5, 124.2, 122.1, 110.5, 77.4, 77.1, 76.8, 60.3, 59.9, 29.4, 20.6, 14.2, 14.0.

General synthesis of compounds 13a-c

A solution of ethyl 1-methyl-5-oxo-4-(phenylamino)-2,5-dihydro-1H-pyrrole- 3-carboxylate (1.00 g, 3.84 mmol) in diphenyl ether (100 ml) was heated to reflux at 250°C under nitrogen for one hour. The resulting clear solution was cooled at room temperature and the product was separated as solid which was collected by filtration. The solid product was washed with petroleum ether to furnish compounds **13a-c**.

2-Methyl-1,4-dihydro-3H-pyrrolo[3,4-b]quinoline-3,9(2H)-dione, **13a**, 62 %. Yellow solid, m.p >320^{o}c; 1H-NMR (400 MHz, DMSO-D6) δ 8.14 (d, J = 8.2 Hz, 1H), 7.76 (d, J = 8.2 Hz, 1H), 7.67 (t, J = 7.5 Hz, 1H), 7.35 (t, J = 7.5 Hz, 1H), 4.31 (s, 2H), 3.08 (s, 3H); 13C-NMR (100 MHz, DMSO-D6) δ 132.7, 125.5, 124.1, 119.9, 49.1, 40.4, 40.2, 40.0, 39.8, 39.6, 39.4, 30.1.

1-*iso*propyl-2-methyl-1,4-dihydro-3H-pyrrolo[3,4-b]quinoline-3,9(2H)-dione, **13b**, 63 %. Yellow solid, m.p 278-283^{o}C; 1H-NMR (400 MHz, DMSO-D6) δ 8.12 (d, J = 8.2 Hz, 1H), 7.75-7.63 (m, 2H), 7.33 (t, J = 7.3 Hz, 1H), 4.52 (s, 1H), 3.03 (s, 3H), 2.62 (t, J = 6.9 Hz, 1H), 1.01-0.82 (m, 6H); 13C-NMR (100 MHz, DMSO-D6) δ 173.5, 141.6, 140.5, 132.7, 127.1, 125.8, 124.1, 122.3, 119.8, 65.7, 40.6, 40.4, 40.2, 40.0, 39.8, 39.6, 39.4, 29.8, 28.5, 18.7, 17.2.

1-*iso*propyl-1,4-dihydro-3H-pyrrolo[3,4-b]quinoline-3,9(2H)-dione, **13c**, 82 %. Yellow solid, m.p 286-296^{o}C; 1H-NMR (400 MHz, DMSO-D6) δ 9.22 (s, 1H), 8.12 (dd, J = 8.2, 0.9 Hz, 1H), 7.75 (d, J = 7.8 Hz, 1H), 7.68-7.64 (m, 1H), 7.35-7.31 (m, 1H), 4.50 (q, J = 1.4 Hz, 1H), 2.66-2.59 (m, 1H), 1.05 (d, J = 7.3 Hz, 3H), 0.46 (d, J = 6.9 Hz, 3H); 13C-NMR (100 MHz, DMSO-D6) δ 174.1, 166.4, 141.8, 140.7, 132.6, 126.9, 125.6, 124.2, 124.0, 119.9, 60.2, 28.4, 20.7, 14.8.

Results and Discussion

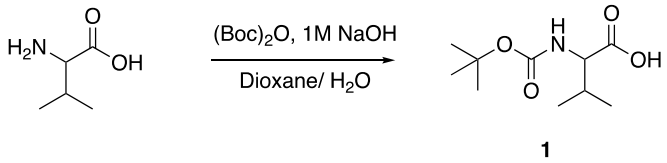
In the present study, the nitrogen atoms in amino acids were protected before synthesising the desired quinolactacins derivates. The step was performed as amino acids are good nucleophiles and bases, making the protection of the nitrogen atoms crucial. Moreover, protecting the atoms prevented any possible side reactions from occurring. The current study protected the nitrogen atoms with *tert*-butyloxycarbonyl (Boc), later deprotected by adding an acid or heating. Besides Boc anhydrides, several other protecting groups could also be employed, such as carbobenzyloxy (Cbz) and benzyl (Bn) groups.

The Boc anhydride was chosen as the protecting agent for the nitrogen atoms in the present investigation as it was commercially available. Moreover, Boc anhydride could be easily introduced under basic conditions and is easily removed under acidic conditions. Caplar and co-workers (2003) [4] protected the nitrogen atoms in the amino acid *D*-valine with Boc anhydride to synthesise amino alcohols. The *D*-valine was treated with 1 M NaOH as the base and dioxane/water as the solvent. Subsequently, Boc anhydride was added to produce the *N*-protected amino acid in a moderate yield of 66%. The protected *D*-valine was successfully synthesised following Caplar's procedure in the present study, as illustrated in Scheme 1.

Tetramic acid or 2,4-pyrrolinedione ring was synthesised post-*N*-protected amino acids production as the acid was the key ring moiety in the present study. According to the method reported by Ma, the tetramic acid was synthesised with Meldrum's acid, DMAP as the base, and DCC as the peptide coupling agent, in dichloromethane, the solvent (Scheme 2). The coupling agent, DCC, was added to activate the carbonyl group on the amino acid, making it more electrophilic for nucleophilic attacks that led to the amide bonds formation. Cyclisation occurred upon reflux in ethyl acetate, producing C-5 isopropyl substituted tetramic acid, compound 2.

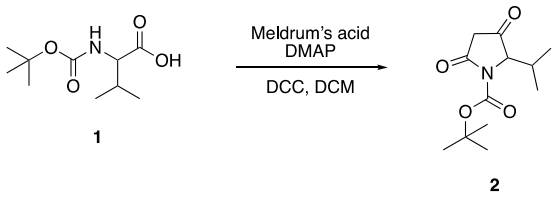
Spectral studies proved that the tetramic acid, compound 2, could tautomerise to its enol form depending on the solvents used. The observation was supported by the data from the 1H-NMR spectroscopy of the tetramic acid that employed deuterated solvents of different polarities, namely $CDCl_3$ as the less-polar solvent and CH_3OD as the more-polar solvent. The acid existed in both forms, keto and enol tautomers, when analysed with the less-polar solvent, $CDCl_3$. A total of 18 protons from the *tert*-butyloxycarbonyl substituents that belonged to the tautomers of the Boc groups and enol olefin protons were identified. Conversely, the tetramic acid was more stable in its keto form in the more-polar solvent as only one CH_2 at the C-3 position of the tetramic acid was present.

Compound 2 was converted to an enone to obtain the appropriate dienophile for the subsequent Diels-Alder reaction to form the desired quinolactacin derivatives. First, the carbonyl functionality of the pyrrolidine-2,4-dione at the C-4 position was reduced to a hydroxyl group and eliminated (Scheme 3). Subsequently, the pyrrolidine-2,4-dione was treated with $NaBH_4$ as the reducing agent and acetic acid in dichloromethane as the solvent to reduce the carbonyl group at the C-4 position. The $NaBH_4$ was selected as the reducing agent due to its selectivity, thus reducing only carbonyl-keto in the presence of other active functional groups. Finally, the hydroxyl pyrrolidinone was treated with Boc anhydride and NaOH to remove the hydroxyl group. The Boc group was introduced again to make the hydroxyl group a good leaving group during the elimination reaction, deriving enone, compound **4**, at a 9% yield.

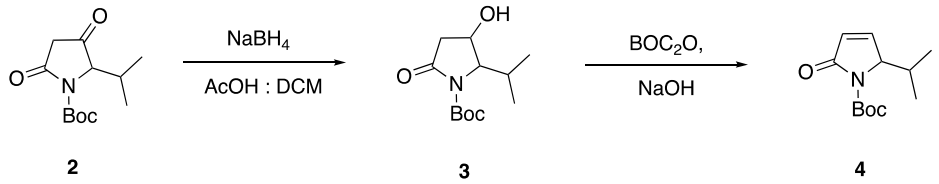


1

Scheme 1. The amine protection of *D*-valine



Scheme 2. The synthesis of tetramic acid, 2

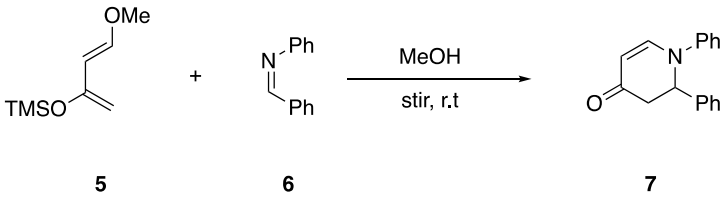


Scheme 3. The reduction and elimination reaction of the functional group at the C-4 position of compound 2

The Diels-Alder reaction was performed to synthesise the derivatives of quinolactacin. Studies on Diels-Alder reactions by Yuan et al. [5] and Jurcik [6], demonstrated that an aza Diels-Alder reaction was successfully performed between *N*-benzylidiene and Danishefsky's diene, as described in Scheme 4. The present study repeated a similar reaction, but the desired compound 8 was not obtained (Scheme 5). The unsuccessful attempt might be due to the different nature of the functional groups in the starting materials utilised in the current study.

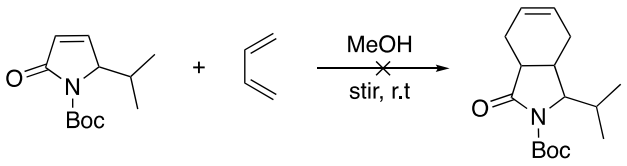
Enone, compound 4, was employed as the dienophile and was reacted with 2,4-hexadiene. Nonetheless, the reaction did not successfully yield the desired final product. The observation was due to the amide group in the enone, an electron-withdrawing group, and 2,4-hexadiene had a methyl group, an electron-donating group. Furthermore, Yuan and Jurcik demonstrated that Danishefsky's diene was rich in electrons with a trimethylsilyl group as the activating group. Consequently, future studies on the configuration, temperature, catalyst, and reaction conditions involving the diene should be done prior to reaction attempts.

Having failed to synthesise the derivatives of quinolactacin via the aza Diels-Alder reactions, an alternative route that involved acylation and hydrogenation reactions was attempted. The key substance, pyrrolidine-2,4-dione, was treated with 2-nitrobenzoyl chloride and sodium hydride as the base in anhydrous THF, as depicted in Scheme 6. The reaction was performed in an inert condition, a nitrogen (N_2) atmosphere, hence producing either the *O*-acylated or the *C*-acylated compounds. The observation could be explained based on the stability of the intermediate enolate formed during the reaction. The *O*-acylation reaction was favoured since the enol was likely to be more stable due to electron conjugation within the ring system.



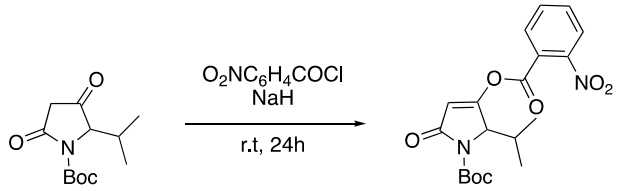
5 **6** **7**

Scheme 4. Aza Diels-Alder reaction [5, 6]



4 **8**

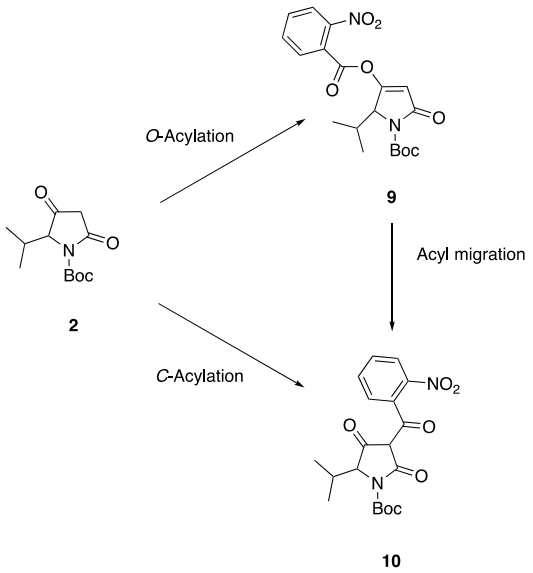
Scheme 5. The Diel-Alder of enone, 4



2 **9**

Scheme 6. The acylation of tetramic acid, 2

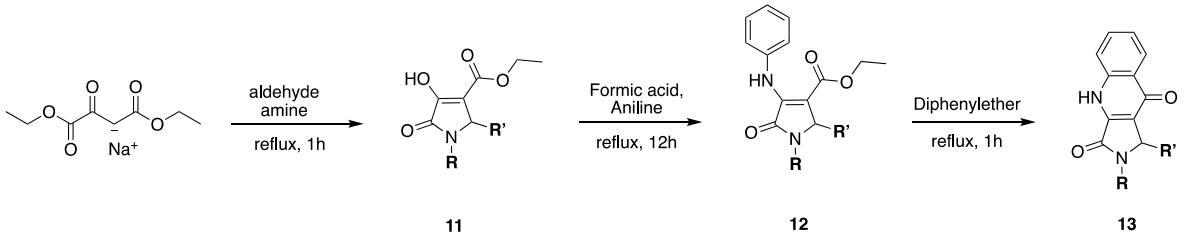
During the synthesis of quinolactacin derivatives, a hydrogenation reaction to convert the nitro functionality in the acylated compound to an amine is required to react the nucleophilic amine with the C-4 carbonyl ketone, yielding the quinolone-lactam ring moiety. Nevertheless, the acyl group must be at C-3 to produce the fused tricyclic system. Consequently, repositioning the acyl group from the *O*-enol position to the C-3 position was mandatory in the current study (Scheme 7).



Scheme 7. The *O*- and *C*-acylations of tetramic acid, 2

The *O*-acylated pyrrolidinone, compound 9, was treated with potassium cyanide for almost 12 hours to furnish the *C*-acylated pyrrolidinedione, compound 10, but in a low yield. Consequently, the present study conducted the hydrogenation reaction following the procedure described by Masaki (2006) [7]. Resultantly, the nitro functional group was reduced to an amine that spontaneously attacked the C-4 carbonyl ketone to form the quinolactacin ring moiety.

Studies on the synthesis of such derivatives via alternative ways have allowed the employment of a multicomponent reaction or a one-pot reaction, as illustrated in Scheme 8. The present study synthesised derivatives of quinolactacin through multicomponent reactions of diethyl oxaloacetate sodium salt, aldehydes, and amines in good yields. The C-5 substituted pyrrolidine-2,3-diones were reacted with formic acid and aniline and heated in diphenyl ether to yield derivatives of quinolactacin (Tables 1, 2, and 3). The synthetic route was focused on utilising pyrrolidine-2,3-dione as the key intermediate, which is different from those in Diels-Alder and synthetic acylation routes abovementioned.



Scheme 8. The synthesis of quinolactacin derivatives *via* a multicomponent reaction

Table 1. The yield percentage of compounds 11 a–c from the multicomponent reactions of diethyl oxaloacetate sodium salt, aldehydes, and amines

Entry	Aldehyde	Amine	Yield, %
11a	Formaldehyde	Methylamine	20
11b	Isobutyraldehyde	Methylamine	54
11c	Isobutyraldehyde	Ammonia	42

Table 2. The yield percentage of compounds 12 a–c from the insertion of aniline in ethanol

Entry	Yield, %
12a	72
12b	51
12c	45

Table 3. The yield percentage of compounds 13 a–c from cyclisation by refluxing in diphenyl ether

Entry	Yield, %
13a	62
13b	63
13c	82

Conclusion

The current study explored and attempted synthesising quinolactacin and its derivatives through several synthetic routes. The routes employed during the investigation involved numerous chemistry concepts, including intramolecular cyclisation, acylation, Diels-Alder, and hydrogenation reactions. Currently, the synthesis of quinolactacin via aza Diels-Alder reaction is being further studied. Consequently, the present study might be an essential reference for other researchers in procuring similar target compounds in the future.

Acknowledgement

The authors would like to thank the Organic Synthesis Laboratory, Institute of Science, Universiti Teknologi MARA (UiTM) and the Faculty of Applied Sciences, Universiti Teknologi MARA (UiTM) for their general support. This work was also financially supported by the Fundamental Research Grant Scheme (600-IRMI/FRGS 5/3 (110/2019)).

References

1. Sasaki, T., Takahashi, S., Uchida, K., Funayama, S., Kainosho, M. and Nakagawa, A. (2006). Biosynthesis of quinolactacin A, a TNF production inhibitor. *Journal of Antibiotics*, 59(7): 418-427.
2. Kakinuma, N., Iwai, H., Takahashi, S., Hamano, K., Yanagisawa, T., Nagai, K. and Nakagawa, A. (2000). Quinolactacins A, B and C. novel quinolone compounds from *Penicillium* sp. EPF-6. I. Taxonomy, production, isolation and biological properties. *The Journal of Antibiotics*, *53*(11): 1247-1251
3. Abe, M., Imai, T., Ishii, N., Usui, M., Okuda, T. and Oki, T. (2005). Quinolactacide, a new quinolone insecticide from *Penicillium citrinum* Thom F 1539. *Bioscience, Biotechnology and Biochemistry*, 69(6): 1202-1205.

4. Čaplar, V., Raza, Z., Katalenić, D. and Žinić, M. (2003). Syntheses of amino alcohols and chiral C2-symmetric bisoxazolines derived from O-alkylated R-4-hydroxyphenylglycine and S-tyrosine. *Croatica Chemica Acta*, 76(1): 23-36.
5. Yuan, Y., Li, X. and Ding, K. (2002). Acid-free aza diels-alder reaction of Danishefsky's diene with imines. *Organic Letters*, 4(19), 3309-3311.
6. Chemie, O. and Universit, T. (2005). Imidazolinium salts as catalysts for the aza-Diels–Alder reaction. *Organic & Biomolecular Chemistry,* 3(2):239-244.
7. Abe, M., Imai, T., Ishii, N. and Usui, M. (2006). Synthesis of quinolactacide via an acyl migration reaction and dehydrogenation with manganese dioxide, and its insecticidal activities. *Bioscience, Biotechnology and Biochemistry*, 70(1): 303-306.

Malaysian Journal of Analytical Sciences (MJAS)
Published by Malaysian Analytical Sciences Society

PHYTOCHEMICAL ANALYSIS OF *Muntingia calabura* Linn. AND ITS ANTIBACTERIAL PROPERTIES VIA *IN VITRO* EVALUATION

(Analisis Fitokimia *Muntingia calabura* Linn. dan Sifat-sifat Antibakteria Melalui Penilaian *In Vitro*)

Suhaidi Ariffin*, Juita Zulkefli, Aqilah Muhammad Saleh

Faculty of Applied Sciences,
Universiti Teknologi MARA Cawangan Negeri Sembilan, Kampus Kuala Pilah,
72000 Kuala Pilah, Negeri Sembilan, Malaysia

**Corresponding author: suhaidi@uitm.edu.my*

Received: 14 March 2022; Accepted: 27 April 2022; Published: 25 August 2022

Abstract

Muntingia calabura Linn. is one of the roadside trees that can easily be found in Malaysia. The *calabura* is the only species found in the genus Muntingia. The valuable bioactive compounds from this species had been documented, however, those originating from local are still considered scanty. This study was conducted to screen the phytochemicals presented, to identify the total phenolic content (TPC) and total flavonoid content (TFC), and to determine the antibacterial properties of both extracted ripe and unripe fruits. The extraction process was achieved by the successive maceration technique using three different solvents namely *n*-hexane, ethyl acetate, and methanol. The analysis of TPC and TFC was successfully done by Folin-Ciocalteu method and aluminium chloride colorimetric method respectively. A disc diffusion method had been employed to test the antibacterial effect. It was found that the percentage yield of methanol crude extract was the highest with 5.92% for unripe fruit and 8.66% for ripe fruit. Phytochemical screening of *M. calabura* L. extracts indicated the presence of flavonoids, phlobatannins, tannins, and glycosides for unripe fruit, and the ripe fruit extracts show the presence of alkaloids, flavonoids, tannins, and glycosides. The greatest TPC and TFC were observed in the methanol extract with 47.96 mg GAE/g (unripe), 94.43 mg GAE/g (ripe), and 99.74 mg QE/g (unripe), 35.38 mg QE/g (ripe) respectively. The *in vitro* antibacterial study of methanol and ethyl acetate extracts of the unripe fruit were active against all tested bacteria (*B. subtilis*, *S. aureus*, *E. coli*, and *K. pneumonia*). However, the ripe fruit extracts demonstrated no antibacterial activity. Thus, the findings remark the potential of these extracts especially the crude from methanol to obtain unique chemical compounds for drug discovery.

Keywords: fruit extracts, phytochemical, total phenolic content, total flavonoid content, antibacterial

Abstrak

Muntingia calabura Linn. merupakan antara pokok tepi jalan yang mudah didapati di Malaysia. *Calabura* adalah satu-satunya spesies yang terdapat dalam genus Muntingia. Sebatian bioaktif yang berharga daripada spesies ini telah didokumenkan, bagaimanapun, yang berasal dari tempatan masih dianggap sedikit. Kajian ini dijalankan untuk menyaring fitokimia yang dibentangkan, untuk mengenal pasti jumlah kandungan fenolik (TPC) dan jumlah kandungan flavonoid (TFC), dan untuk menentukan sifat antibakteria kedua-dua buah masak dan tidak masak yang diekstrak. Proses pengekstrakan dilakukan dengan teknik pemekatan berturut-turut menggunakan tiga pelarut berbeza iaitu *n*-heksana, etil asetat, dan metanol. Analisis TPC dan TFC

telah berjaya dilakukan dengan kaedah Folin-Ciocalteu dan kaedah kolorimetrik aluminium klorida. Kaedah penyebaran cakera telah digunakan untuk menguji kesan antibakteria. Didapati peratusan hasil ekstrak mentah metanol adalah yang tertinggi iaitu 5.92% bagi buah yang belum masak dan 8.66% bagi buah masak. Pemeriksaan fitokimia bagi ekstrak *M. calabura* L. menunjukkan kehadiran flavonoid, phlobatannin, tanin, dan glikosida untuk buah yang belum masak, dan ekstrak buah masak menunjukkan kehadiran alkaloid, flavonoid, tanin, dan glikosida. Nilai TPC dan TFC terbesar telah diperolehi daripada ekstrak metanol dengan 47.96 mg GAE/g (belum masak), 94.43 mg GAE/g (matang), dan 99.74 mg QE/g (belum masak), 35.38 mg QE/g (matang). Kajian antibakteria *in vitro* bagi ekstrak metanol dan etil asetat buah yang belum masak adalah aktif terhadap semua bakteria yang diuji (*B. subtilis*, *S. aureus*, *E. coli*, dan *K. pneumonia*). Walau bagaimanapun, ekstrak buah masak tidak menunjukkan aktiviti antibakteria. Oleh itu, hasil kajian menunjukkan ekstrak methanol terutamanya, mempunyai potensi yang besar untuk mendapatkan sebatian kimia yang unik bagi hasilan ubat.

Kata kunci: ekstrak buah-buahan, fitokimia, jumlah kandungan fenolik, jumlah kandungan flavonoid, antibakteria

Introduction

Nature gives everything to the prosperity of humankind since the ancient times and this includes the keys for the principal endeavour at the therapeutic intervention. In old-fashioned times, humans depend on the natural resources such as plants for the treatment of numerous diseases. Even in the modernized days, plant materials remain a crucial resource to treat illnesses, including infectious diseases [1]. Plant-derived natural products have consistently been an essential source of medicines for the treatment of numerous illnesses and have received extensive attention in the recent years [2]. Therefore, the plant is one of the most important sources for isolating active chemical compounds that contribute to many uses in combating diseases [3]. However, some medicinal plants are still concealed inside the plant and must be carefully analysed.

Muntingia calabura Linn. (*M. calabura* L.) locally known as "buah ceri" or "kerukup siam" is belongs to the family of Muntingiaceae. *M. calabura* L. is native to Central America but has been widely cultivated in many tropical climate countries, such as Brazil, China, India, the Philippines, as well as Malaysia due to its strong tolerance to soil and climate [4, 5]. Extensive literature search shows that *calabura* is the only species found in the genus Muntingia. *Calabura's* fruits (Figure 1) are very sweet and juicy if they are fully ripen. The sweetness of these ripe cherries is due to their high soluble solid content and low total titratable acidity [5]. Traditionally, the fruits of *calabura* are eaten fresh and sometimes cooked in tarts or made into jam [6]. However, this plant was reported to have many health benefits in curing illnesses [7] but the exploration of the fruit's part is very little.

From many reported studies, several compounds were successfully elucidated from each part of this plant including the leaf, root, bark, and fruit [7]. In addition, a few of the reported compounds were found active as antibacterial [9, 10, 11], antitumor [12], anti-inflammatory [13], antipyretic [14], antinociception [15], antiproliferative [16], and also antioxidant [4, 17]. It indicates that *calabura* is one of the potential plants to screen valuable active compounds for drug discovery. However, the study on this species from Malaysia is still limited due to the less reported data from local publications that can be obtained. Thus, this study will present the qualitative phytochemical screening on alkaloids, flavonoids, glycosides, phlobatannins, and tannins, reported the quantitative phytochemical analysis of total phenolic content (TPC), and total flavonoid content (TFC), as well as documented the antibacterial properties from both ripe and unripe of *M. calabura* L. fruit extracts.



Figure 1: The fruits of *M. calabura* L. [8]

Materials and Methods

Fruit samples

The ripe fruits of *M. calabura* L. were collected from Seremban, Negeri Sembilan, and the unripe fruits were collected from Kampung Jembatan Duyong, Melaka, Malaysia in October 2021.

Preparation of fruit extracts

Fresh fruits (ripe and unripe) of *M. calabura* L. were washed with tap water and were directly dried under the sun for one week. The dried fruits were ground into powder form by using a grinder. The extraction process proceeded successively by mixing 100 g of powdered fruits with *n*-hexane, followed by ethyl acetate and methanol (500 mL of each) for 72 hours at room temperature. The extract was filtered by using Whatman no. 1 filter paper and the filtrate was concentrated by using a rotary evaporator. Crude extracts were stored at 4 ℃ prior to phytochemical and *in vitro* antibacterial analyses [18].

Qualitative phytochemical screening

Phytochemical tests were carried out on each extract using the standard procedure [19, 20] to identify the presence of alkaloids [21], flavonoids, glycosides, phlobatannins [22], and tannins [23].

Determination of total phenolic content

Total phenolic content (TPC) in the fruit extracts was determined by using the Folin-Ciocalteu method as described by [24] with minor modifications. An amount of 10 mg of the extract was dissolved in 10 mL of methanol to yield a concentration of 1 mg/mL. To each extract, 0.5 mL of sample was added to 2.5 mL of 10% Folin-Ciocalteu's reagent. After 5 minutes, 2.5 mL of 7.5% Na_2CO_3 was added. The mixture was placed in the dark for 2 hours and the absorbance was measured at 725 nm by using UV-Vis Spectrophotometer. A similar procedure as described was repeated for the standard solution of gallic acid with different concentrations (6.25, 12.5, 25, 50, and 100 µg/mL), and the calibration curve was constructed. The concentration of phenolics (µg/mL) was obtained based on the calibration curve and the content of phenolic in the extract was expressed in terms of gallic acid equivalent (mg of gallic acid/g of extract), and methanol was used as blank.

Determination of total flavonoid content

Total flavonoid content (TFC) in the fruit extracts was determined by using the modified aluminium chloride colorimetric method [25]. An amount of 10 mg of the extract was dissolved in 10 mL of 80% ethanol (1 mg/mL). To each extract, 0.5 mL of sample was mixed with 1.5 mL of 95% ethanol, 0.1 mL of 10% aluminium chloride, 0.1 mL of 1 M potassium acetate, and 2.8 mL of distilled water. The mixture was incubated at room temperature for 30 minutes and the absorbance was measured at 425 nm by using UV-Vis Spectrophotometer. A similar step as described was repeated for the standard solution of quercetin with various concentrations (6.25, 12.5, 25, 50, and 100 µg/mL), and the calibration curve was constructed. The concentration of flavonoids (µg/mL) was obtained based on the calibration curve and the content of flavonoids in the extract was expressed in terms of quercetin equivalent (mg of quercetin/g of extract), and ethanol was used as blank.

Determination of antibacterial properties

Antibacterial assay of *M. calabura* L. fruit extracts was carried out based on the Clinical and Laboratory Standards Institute (CLSI) [26], and the disc diffusion method was used. The overnight bacterial culture (*Escherichia coli*, *Klebsiella pneumonia*, *Staphylococcus aureus*, and *Bacillus subtilis*) from nutrient broth (NB) was adjusted to the turbidity of 0.5 McFarland standard (1.5 X 10^8 CFU/mL). Afterward, 0.1 mL of bacterial culture was pipetted out onto the Muller-Hinton agar (MHA) and spread in a direction and evenly distributed. The dried-loaded extracts (20 µL with a concentration of 10 mg/mL) of disc paper (5.5 mm diameter) were transferred onto the seeded MHA medium and incubated at 37°C for 24 hours. Streptomycin (10 µg) and 10% DMSO were used as positive and negative control. The diameter of zone inhibition was measured and recorded.

Results and Discussion

Qualitative phytochemical screening

M. calabura L. extracts (*n*-hexane, ethyl acetate, and methanol) for both ripe and unripe fruits were first tested for a qualitative phytochemical screening to check the presence and absence of alkaloids, flavonoids, glycosides, tannins, and phlobatannins in which these constituents might be responsible for the antibacterial properties. The data displayed in Table 1 shows that *calabura's* fruit contained various phytochemicals. Flavonoids were detected in all extracts from both ripe and unripe fruits. Meanwhile, alkaloids and phlobatannins were found absent in all extracts from unripe and ripe fruits respectively. However, [21] reported the presence of alkaloids in both ripe and unripe *M. calabura* L. fruit extracts, but the study conducted and the sample collected was from India. For a local sample studied by [4], alkaloids were also reported absent but the sample was from *M. calabura* L. leaf extracts. Thus, abiotic factors such as soil, temperature, air, humidity, light, pH, salinity, minerals, and water may influence the accumulations of secondary metabolites [27, 28, 29].

Table 1. Detected phytochemical constituents in *M.calabura* L. fruit extracts

Constituents	Fruit Extracts					
	Ripe			Unripe		
	***n*-hexane**	**Ethyl Acetate**	**Methanol**	***n*-hexane**	**Ethyl Acetate**	**Methanol**
Alkaloids	-	+	+	-	-	-
Flavonoids	+	+	+	+	+	+
Glycosides	-	-	+	-	-	+
Tannins	-	+	+	-	+	+
Phlobatannins	-	-	-	-	+	+

'-' indicates absence; '+' indicates presence

Quantitative phytochemical analysis

The results of total phenolic content (TPC) and total flavonoid content (TFC) were summarized in Table 2. Among all extracts, methanol extract from both ripe and unripe fruits exhibited the highest TPC with 94.43 and 47.96 mg GAE/g respectively. In general, the more polar solvent influences the amount of TPC which gives a higher value. The 5-hydroxy-3,7,8-trimethoxyflavone compound is reported to contribute as a major phenolic compound [30] and [31, 32] revealed that this compound was elucidated from the fruits of *M. calabura* L. that have polar sites interaction (hydrogen bonds) with the solvent, which increased the solvation of compounds in the solvent.

Similarly, TFC was found highest in methanol extract with 35.38 and 99.74 mg QE/g in ripe and unripe fruits respectively. The TFC content is correlated with the preliminary phytochemical screening to prove that flavonoids are an important constituent in the *calabura* fruits and it is essential for future antioxidant study.

Table 2. The total phenolic and total flavonoid contents of different fruit extracts from *M. calabura* L.

Assay		Solvents Extraction		
		***n*-hexane**	**Ethyl Acetate**	**Methanol**
TPC (mg GAE/g extract)	Ripe	24.11	45.06	94.43
	Unripe	15.43	27.96	47.96
TFC (mg QE/g extract)	Ripe	4.08	22.97	35.38
	Unripe	42.70	61.59	99.74

This study proves that *M. calabura* L. fruit contains phytochemicals as an antibacterial agent. As shown in Table 3, methanolic fruit extract from the unripe sample gave the highest antibacterial effect against all tested bacteria compared to ethyl acetate extract and this is similar to the study reported by [21]. Moreover, the fruit extracts were more active against Gram-positive bacteria with zone inhibition of 14 mm and 12 mm for *S. aureus* and *B. subtilis* respectively. The Gram-negative cell wall is a multilayered structure and quite complex. It consists of an additional lipopolysaccharide layer called the outer membrane to make it more difficult for antibiotics to invade the cell wall [33]. However, none of the ripe sample extracts and extract from *n*-hexane exhibited antibacterial properties. Thus, the active compounds of this extract might have consisted of semi-polar to polar functional groups. Figure 2 displays the disc diffusion assay of *M. calabura* L. fruit extracts against tested bacteria.

Mahmood et al. [7] in their reviewed article had mentioned that various parts of the *M. calabura* L. plant were traditionally used to cure many illnesses. Several reported the antibacterial properties from the local sample used leave part [34, 35, 36]. The fruit part was only mentioned to be used as eaten fresh and cooked to make into jam. Therefore, the antibacterial result from this study can be used as a reference to support that *calabura* fruit also has potential active compounds to combat diseases.

Table 3. The inhibition zone value (mm) of *M. calabura* L. fruit extracts against tested bacteria

Extracts		Zone Inhibition Value (mm)			
		Tested Bacteria			
		Gram-negative		Gram-positive	
		E. coli	***K. pneumonia***	***S. aureus***	***B. subtilis***
n-hexane	Ripe	-	-	-	-
	Unripe				
Ethyl acetate	Ripe	-	-	-	-
	Unripe	6.17 ± 0.15	6.10 ± 0.10	7.13 ± 0.15	6.23 ± 0.21
Methanol	Ripe	-	-	-	-
	Unripe	10.10 ± 0.10	9.17 ± 0.15	14.17 ± 0.15	12.10 ± 0.10
Streptomycin	Ripe	17.00 ± 0.00	15.00 ± 0.00	19.00 ± 0.00	18.00 ± 0.00
	Unripe				
10% DMSO	Ripe	-	-	-	-
	Unripe				

The values are represented as mean ±, SD

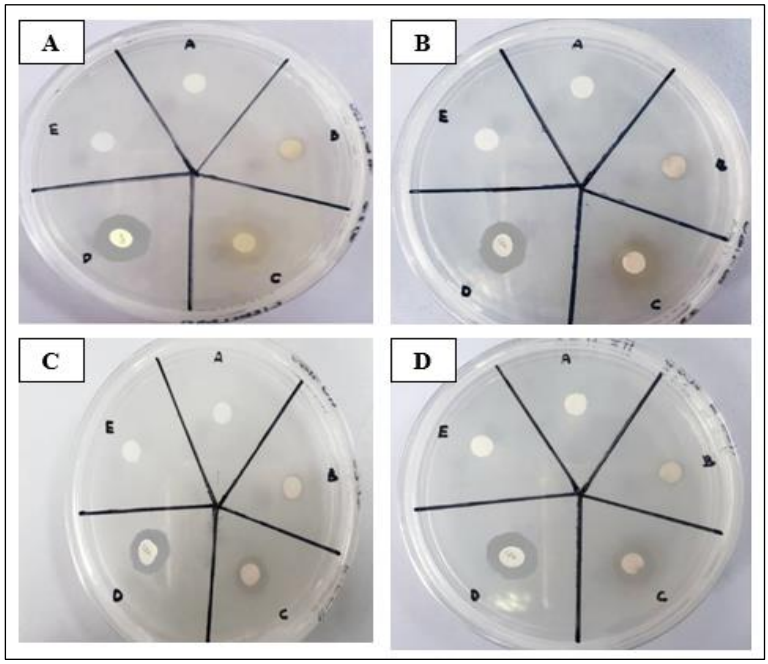


Figure 2. The zone inhibition observation of *M. calabura* L. extracts against *S. aureus* (A), *B. subtilis* (B), *K. pneumonia* (C), and *E. coli* (D) by disc diffusion method

Conclusion

M. calabura L. fruit extracts contain different phytochemical constituents including alkaloids, flavonoids, phlobatannins, tannins, and glycosides. The methanolic fruit extracts showed the highest TPC and TFC values from both ripe and unripe samples, and also exhibited the greatest antibacterial properties against all tested bacteria from the unripe sample. An antioxidant study is required to be performed since antibacterial and antioxidant studies serve as a basis for drug discovery.

Acknowledgment

The authors would like to thank UiTM Cawangan Negeri Sembilan, Kampus Kuala Pilah for providing facilities for this study.

References

1. Durai, M. V., Balamuniappan, G., Anandalakshmi, R., Geetha, S. and Senthil, N. (2016). Qualitative and quantitative analysis of phytochemicals in crude extract of big-leaf mahogany (*Swietenia macrophylla* King.). *International Journal of Herbal Medicine,* 4(6): 88-91.
2. Majumder, J. and Roy, S. (2017). Identification of quinones and coumarins in *Swietenia macrophylla* leaf. *Pharmaceutical Biology, 7*(6): 1-5.
3. Boy, H. I. A., Rutilla, A. J. H., Santos, K. A., Ty, A. M. T., Yu, A. I., Mahboob, T., Tangpoong, J. and Nissapatorn, V. (2019). Recommended medicinal plants as source of natural products: A review. *Digital Chinese Medicine,* 1(2): 131-142.
4. Pungot, N. H., Zainal Abidin, N. A. and Nazaharuddin, N. S. A. (2020). Potential of malaysian cherry leaves (*Muntingia calabura*) as an antioxidant agent. *Science Letters,* 14(2): 103-109.
5. Pereira, G. A., Arruda, H. S., de Morais, D. R., Eberlin, M. N. and Pastore, G. M. (2018). Carbohydrates, volatile and phenolic compounds composition, and antioxidant activity of *calabura* (*Muntingia calabura* L.) fruit. *Food Research International,* 10(8): 264-273.

6. Zakaria, Z. A., Mohd Nor Hazalin, N. A., Ghani, M. A., Hassan, M. H., Gopalan, H. K. and Sulaiman, M. R. (2007). Antinociceptive, anti-inflammatory and antipyretic effects of *Muntingia calabura* aqueous extract in animal models. *Journal of Natural Medicines,* 10(6): 443-448.
7. Mahmood, N. D., Nasir, N. L. M., Rofiee, M. S., Tohid, S. F. M., Ching, S. M., Teh, L. K., Salleh, M. Z., and Zakaria, Z. A. (2014). *Muntingia calabura*: A review of its traditional uses, chemical properties, and pharmacological observations. *Pharmaceutical Biology,* 52(12): 1598-1623.
8. Planting Man (2018). *Muntingia calabura - fruit garden*. Planting Man. Accessed from https://plantingman.com/muntingia-calabura-fruit-garden/. [Retrieved March 9, 2022].
9. Buhian, W. P. C., Rubio, R. O., Valle, D. L., and Martin-Puzon, J. J. (2016). Bioactive metabolite profiles and antimicrobial activity of ethanolic extracts from *Muntingia calabura* L. leaves and stems. *Asian Pacific Journal of Tropical Biomedicine*, 6(8): 682-685.
10. Fitri, G. D., Tistiana, H. and Radiati, L. E. (2017). Review study on antibacterial activity of cherry leaf (*Muntingia calabura*) against *Staphylococcus* spp. and *Salmonella* spp. The most causing disease in livestock. *Jurnal Ilmu-Ilmu Peternakan,* 27(2): 63-73.
11. Paramesha, M., Tg, T., Ck, R. and S, N. (2017). Bioprospecting of *Muntingia calabura*: Bioactive compounds and its antioxidant, antimicrobial and anthelmentic activity. *Innovare Journal of Sciences, 5*(5): 7-11.
12. Ragasa, C. Y., Tan, M. C. S., Chiong, I. D. and Shen, C. C. (2015). Chemical constituents of *Muntingia calabura* L. *Der Pharma Chemica, 7*(5): 136-141.
13. Ansori, A. N. M., Kharisma, V. D. and Solikhah, T. I. (2021). Medicinal properties of *Muntingia calabura* L.: A review. *Research Journal of Pharmacy and Technology*, 14(8): 4509-4512.
14. Sarojini, S., and Mounika, B. (2018). *Muntingia calabura* (Jamaica cherry): An overview. *PharmaTutor,* 6(11): 1-9.
15. Zakaria, Z. A., Mohd Sani, M. H., Abdul Kadir, A., Kek, T. L. and Salleh, M. Z. (2016). Antinociceptive effect of semi-purified petroleum ether partition of *Muntingia calabura* leaves. *Revista Brasileira de Farmacognosia*, 26: 408-419.
16. Rahmawati, A. N., Astirin, O. P. and Pangastuti, A. (2018). Intracellular antioxidant activity of *Muntingia calabura* leaves methanolic extract. *Nusantara Bioscience*, 10(4): 210-214.
17. Zakaria, Z. A., Mahmood, N. D., Omar, M. H., Taher, M. and Basir, R. (2019). Methanol extract of *Muntingia calabura* leaves attenuates CCl4-induced liver injury: Possible synergistic action of flavonoids and volatile bioactive compounds on endogenous defence system. *Pharmaceutical Biology,* 57(1): 335-344.
18. Mogollón, O. F. C., Gonzalez-Cuello, R. E. and López, J. S. G. (2018). In vitro antibacterial and antioxidant activity of *Muntingia calabura* fruits extract. *Contemporary Engineering Sciences,* 11(18): 881-890.
19. Rao, U. S. M., Mohd, K. S. and Abdurrazak, M. (2016). Phytochemical screening, total flavonoid and phenolic content assays of various solvent extracts of tepal of *Musa paradisiaca*. *Malaysian Journal of Analytical Science,* 20(5): 1181-1190.
20. Gul, R., Jan, S. U., Faridullah, S., Sherani, S. and Jahan, N. (2017). Preliminary phytochemical screening, quantitative analysis of alkaloids, and antioxidant activity of crude plant extracts from *Ephedra intermedia* indigenous to Balochistan. *The Scientific World Journal*, 2017: 5873648.
21. Singh, R., Iye, S., Prasad, S., DeshmukH, N., Gupta, U., Zanje, A., Patil, S. and Joshi, S. (2017). Phytochemical analysis of *Muntingia calabura* extracts possessing anti-microbial and anti-fouling activities. *International Journal of Pharmacognosy and Phytochemical Research,* 9(6): 826-832.
22. Shaikh, J. R., and Patil, M. (2020). Qualitative tests for preliminary phytochemical screening: An overview. *International Journal of Chemical Studies, 8*(2), 603–608.

23. Iswantini, D., Tuwalaid, B. and Trivadila. (2021). The potency of legetan warak (*Adenostemma lavenia*) and Kersen leaf (*Muntingia calabura*) extract as a candidate for chronic obstructive pulmonary disease (COPD) herbal medicine. *Proceedings of the 2nd International Conference on Science, Technology, and Modern Society,* 2020: 447-452.
24. Kabra, S. and Patel, S. (2018). Total phenolics and flavonoid content of the leaves of *Carica papaya* and *Syzygium cumini*. *World Journal of Pharmaceutical Research,* 7(14): 734-741.
25. Pertiwi, R. D., Suwaldi, Martien, R. and Setyowati, E. P. (2020). Radical scavenging activity and quercetin content of *Muntingia calabura* L. leaves extracted by various ethanol concentration. *Journal of Food and Pharmaceutical Sciences, 8*(1): 173-183.
26. CLSI GP02-A5. (2006). Laboratory documents: development and control; approved guideline-fifth edition. Accessed from https://webstoe.ansi.org/Standards/CLSI/CLSIGP02A5. [Retrieved December 24, 2020]
27. Ma, Z., Li, S., Zhang, M., Jiang, S. and Xiao, Y. (2010). Light intensity affects growth, photosynthetic capability, and total flavonoid accumulation of anoectochilus plants. *HortScience*, 45(6): 863-867.
28. Waqas, M. A., Kaya, C., Riaz, A., Farooq, M., Nawaz, I., Wilkes, A. and Li, Y. (2019). Potential mechanisms of abiotic stress tolerance in crop plants induced by thiourea. *Frontiers in Plant Science*, 10: 1336.
29. Li, Y., Kong, D., Fu, Y., Sussman, M. R. and Wu, H. (2020). The effect of developmental and environmental factors on secondary metabolites in medicinal plants. *Plant Physiology and Biochemistry*, 148: 80-89.
30. Yusof, M. M., Teh, L. K., Zakaria, Z. A. and Ahmat, N. (2011). Antinociceptive activity of the fractionated extracts of *Muntingia calabura*. *Planta Medicine*, 77: 21.
31. Babbar, N., Oberoi, H. S., Sandhu, S. K., and Bhargav, V. K. (2014). Influence of different solvents in extraction of phenolic compounds from vegetable residues and their evaluation as natural sources of antioxidants. *Journal of Food Science and Technology,* 51(10): 2568-2575.
32. Boeing, J. S., Barizão, É. O., e Silva, B. C., Montanher, P. F., de Cinque Almeida, V. and Visentainer, J. V. (2014). Evaluation of solvent effect on the extraction of phenolic compounds and antioxidant capacities from the berries: Application of principal component analysis. *Chemistry Central Journal,* 8(1): 1-9.
33. Miller, S. I. (2016). Antibiotic resistance and regulation of the gram-negative bacterial outer membrane barrier by host innate immune molecules. *MBio,* 7(5): 5-7.
34. Sufian, A. S., Ramasamy, K., Ahmat, N., Zakaria, Z. A. and Yusof, M. I. M. (2013). Isolation and identification of antibacterial and cytotoxic compounds from the leaves of *Muntingia calabura* L. *Journal of Ethnopharmacology*, 146: 198-204.
35. Zakaria, Z. A., Mat Jais, A. M., Mastura, M., Mat Jusoh, S. H., Mohamed, A. M., Mohd, N. S., ... and Sulaiman, M. R. (2007). *In vitro* antistaphylococcal activity of the extracts of several neglected plants in Malaysia. *International Journal of Pharmacology*, 3(5): 428-431.
36. Zakaria, Z. A. (2006). The *in vitro* antibacterial activity of *Muntingia calabura* extracts. *International Journal of Pharmacology*, *2*(3): 290-293.

Malaysian Journal of Analytical Sciences (MJAS)
Published by Malaysian Analytical Sciences Society

DETERMINATION OF RESIDUAL XYLAZINE BY GAS CHROMATOGRAPHY IN DRUG-SPIKED BEVERAGES FOR FORENSIC INVESTIGATION

(Penentuan Sisa Xilazin dengan Kromatografi Gas dalam Minuman Ditambah dengan Dadah bagi Penyiasatan Forensik)

Nabeesathul Sumayya Mohamed Sadiq[1], Way Koon Teoh[1], Kasrin Saisahas[1], Apichai Phoncai[2], Vanitha Kunalan[3], Noor Zuhartini Md Muslim[1], Warakorn Limbut[1,4,5], Kah Haw Chang[1], Ahmad Fahmi Lim Abdullah[1]*

[1]Forensic Science Programme, School of Health Sciences, Universiti Sains Malaysia, 16150 Kubang Kerian, Kelantan, Malaysia
[2]Division of Health and Applied Sciences, Faculty of Science, Prince of Songkla University, Hat Yai, Songkhla, 90112, Thailand
[3]Narcotics Division, Forensic Science Analysis Centre, Department of Chemistry, Jalan Sultan, 46661 Petaling Jaya, Selangor, Malaysia
[4]Center of Excellence for Trace Analysis and Biosensors (TAB-CoE)
[5]Center of Excellence for Innovation in Chemistry, Faculty of Science Prince of Songkla University, Hat Yai, Songkhla, 90112, Thailand

**Corresponding author: fahmilim@usm.my*

Received: 16 February 2022; Accepted: 15 June 2022; Published: 25 August 2022

Abstract

The utilization of xylazine, a veterinary drug, had recently been reported in drug facilitated crimes (DFC). Victims are incapacitated after consumption of drug-spiked beverages and subsequently exposed to the risk of robbery and sexual assault. In many instances, the suspected drug-spiked beverage samples are available at the scene but the concentration level of xylazine could be very low or restricted by its recoverable amount for forensic testing. To address challenges linked to samples with low or limited recoverable amounts, this study was aimed to establish a laboratory-based gas chromatography method by detecting and quantifying xylazine in drug-spiked beverage samples appearing in liquid, droplet, and dry forms. In this study, a gas chromatography-mass spectroscopy (GC-MS) method was optimized to detect the presence of xylazine, and a gas chromatography-flame ionization detector (GC-FID) method was validated for quantification of the substance. Subsequently, xylazine from four different beverage samples in three different physical forms, simulating the possible forensic settings; were recovered and determined. A validated GC method for the determination and quantification of xylazine within 15 minutes was reported. Limit of detection (LOD) and limit of quantitation (LOQ) were reported at 0.08 µg/mL and 0.26 µg/mL, respectively. Higher recoveries of xylazine were achieved from beverage samples in liquid form (77.2-97.3%) compared to droplet (50.8% – 80.0%) and dry samples (39.8% – 66.9%). This study evidenced that limited volume of leftover beverage samples, and even the dried samples; did not hinder the recovery of the targeted drug. To conclude, a gas chromatographic technique was successfully established for the determination of residual xylazine in drug-spiked beverages that can then provide valuable investigative technique to laboratory analysts and crime scene officers in DFC

investigations.

Keywords: forensic science, drug-facilitated crime, xylazine, gas chromatography, drug spiked beverage

Abstrak

Baru-baru ini, penggunaan xilazin, sejenis ubat haiwan, telah dilaporkan dalam jenayah disebabkan dadah (DFC). Mangsa menjadi lemah selepas meminum minuman yang ditambah dengan dadah dan seterusnya terdedah kepada risiko rompakan dan gangguan seksual. Dalam kebanyakan situasi, sampel minuman yang disyaki telah dimasukkan dadah boleh dijumpai di tempat kejadian tetapi tahap kepekatan xilazin berkemungkinan amat rendah atau dibatasi oleh jumlah yang boleh diperolehi semula untuk pengujian forensik. Untuk mengatasi cabaran dalam mengaitkan sampel yang berisipadu rendah atau mempunyai kebolehpulihan yang terhad, kajian ini bertujuan untuk membangunkan satu kaedah kromatografi gas yang berasaskan makmal dengan mengesan dan menentukan kuantiti xilazin dalam sampel minuman yang dimasukkan dadah yang wujud dalam keadaan cecair, titisan dan kering. Dalam kajian ini, satu kaedah kromatografi gas-spektrometri jisim (GC-MS) telah dioptimumkan untuk mengesan kehadiran xilazin dan satu kromatografi gas-pengesanan pengionan nyalaan (GC-FID) telah ditentu-sahkan untuk pengkuantitian sebatian tersebut. Seterusnya, xilazin daripada empat sampel minuman dalam tiga keadaan fizikal berlainan, menyerupai tetapan forensik yang berkemungkinan, telah diperolehi semula dan ditentukan. Satu kaedah GC yang sah bagi penentuan dan penentuan kuantiti xilazin dalam 15 minit telah dilaporkan. Had pengesanan (LOD) dan had pengkuantitian (LOQ) telah dilaporkan masing-masing pada 0.08 μg/mL and 0.26 μg/mL. Xilazin dapat diperoleh semula daripada sampel minuman dalam keadaan cecair dengan peratusan yang lebih tinggi (77.2-97.3%) berbanding dengan sampel titisan (50.8 – 80.0%) dan sampel kering (39.8 – 66.9%). Kajian ini membuktikan bahawa isipadu sampel minuman tertinggal yang terhad dan dalam keadaan kering tidak menghalang perolehan semula dadah yang disasarkan. Kesimpulannya, satu kaedah kromatografi gas telah berjaya dibangunkan untuk menentukan sisa-sisa xilazin dalam minuman yang dimasukkan dadah. Hal ini dapat membantu teknik penyiasatan kepada juruanalisis makmal dan pegawai tempat kejadian dalam penyiasatan DFC.

Kata kunci: sains forensik, jenayah disebabkan dadah, xilazin, kromatografi gas, minuman yang dimasukkan dadah

Introduction

Xylazine serves as relaxant, sedative, analgesic, and anti-hypertensive agent [1–3]. It is widely used in veterinary practice but is not approved by the Food and Drug Administration (FDA) for human use [3] due to its deleterious side effects such as bradycardia, hypotension, and possibly death [4, 5]. The substance is not scheduled as a controlled substance by the Drug Enforcement Administration (DEA) [6]. In South-East Asian countries, for instance, xylazine is accessible to certain groups of people, such as veterinary personnel and animal trainers under the Poison Act 1952 in Malaysia [7] whereas it is scheduled as a controlled substance in Thailand [8]. According to the FDA, the use of xylazine in "food-producing animals" is specifically not allowable in the United States of America; however, in Canada, United Kingdom, France, Germany, and Switzerland, xylazine can legally be used in food-producing animals [3, 9]. In fact, this substance is still accessible in the market, commonly in injectable solutions, such as Rompun®, Sedazine®, and Anased® [5].

Drug-facilitated crime (DFC) is a serious issue worldwide. It refers to crimes committed whenever victims of the crime are placed under the influence of drugs [10]. More specifically, drug-facilitated sexual assault (DFSA) occurs whenever sexual assault has been committed with a victim has been drugged by the rapist beforehand [11]. The victim had previously unknowingly consumed either a beverage or food that was spiked with drugs and sexual assault occurred without the knowledge, understanding, or consent of the victim due to the drug's affect. In other words, drugs originally designed for medicinal or veterinary use have been illegally used to incapacitate victims by exploiting the pharmacological effects of such drugs [12, 13]. Common examples include benzodiazepine [14-17], ketamine [14, 18] and gamma hydroxybutyrate (GHB) [19-20]. Recently, xylazine was also found in the list [21-25].

One way of DFC modus operandi is via drug-spiked beverages, whereby the beverages are allegedly produced by the unsolicited addition of drugs into them in drug-facilitated crimes, especially in robbery and rape

cases [26]. Recent cases reported drug-spiking incidents through the addition of xylazine into a victim's drink which alleged of sexual assault and robbery utilizing the sedative effects of xylazine [21]. Upon consumption of the spiked drinks, the victims would suffer intoxication with blurred vision, shortness of breath and vomiting before passing out shortly after [3,21]. In view of its potential abuse in DFC and DFSA, the searching of forensic evidence and successful detection of illicit drug contained in drug-spiked beverages is crucial for obtaining justice for victims.

Previous studies have suggested various instrumental techniques in detecting xylazine, for instance gas chromatography (GC) [27, 28], liquid chromatography [21, 28], thin layer chromatography [4] and electrochemical technique [29, 30]. These published articles and technical reports have undoubtedly provided significant contributions, mainly on the toxicology studies in human through the analysis of biological samples. Nonetheless, limited information could be retrieved from published works, particularly from the perspective of forensic related evidence, including the seizure of xylazine as an illicit drug or as an adulterant. The mass spectrometry detector was frequently employed in GC analysis of xylazine as a screening approach [21, 31]. In comparison to gas-chromatography-mass spectrometry (GC-MS), gas chromatography equipped with flame ionization detector (GC-FID) analysis can also serve as a reliable, sensitive, and reproducible method for trace analyses, depending on the structure and behavior of the analyte of interest [32]. When dealing with spiked drink samples, liquid-liquid extraction (LLE) was found to be the most common method applied in forensic drug analyses due to its low cost, comparably rapid and the procedures are easy to implement [33]. A portable electrochemical sensor was recently developed to provide quick, on-scene screening of xylazine in spiked drinks [34]. However, a laboratory-based technique would be crucial in supporting the forensic analysis for drug confirmation.

Additionally, the misuse of xylazine in DFC through the spiking of drug into beverages of victims is particularly serious that needs urgent actions from law enforcement agencies and testing laboratories. In certain cases, a victim claimed that his/her drink has been spiked with drugs, but the obtained sample had tested negative [35]. When dealing with biological samples, a false negative result could be reported due to delayed sample collection and detection [35]. Literature has reported the calculated plasma half-life of xylazine in human plasma was 4.9 hours [36]. As a victim suffers from an altered state of mind or other psychoactive effect upon intoxication, it would further increase the time elapsed between the occurrence of a crime and eventual forensic analysis, as well as pose challenges to rely solely on a witness's statement for legal recourse [37]. In such situation, alternative sample *i.e.,* consumed drinks, could be proposed as evidence to be collected from the glass left at crimes scenes.

Therefore, a study was designed to detect and quantify xylazine from beverages collected directly from drinking containers where the drug residues present might be at trace level. A GC technique was optimized and validated, taking into consideration that such an instrument is routinely used and available in most forensic laboratories. GC-MS was utilized to confirm the presence of xylazine, followed by GC-FID, used to quantitate xylazine that are found in spiked sample. Subsequently, the detection and quantification of xylazine in spiked beverages were investigated with the aid of LLE techniques. Other than appearing in liquid form, a glass or a cup suspected to have contained xylazine could be left with a few residual drops or even have dried off traces. As such, samples present in such states ought to be simulated and explored to maximize potential forms of evidence tracing in alleged DFC. It is hoped that this analytical method would aid in detecting the target drug in suspected spiked beverages to assist forensic investigation and to facilitate the tracing of suspects, while providing some insights to decide crime scene sampling decision by the crime scene officers.

Materials and Methods

Materials and chemicals

Dichloromethane (DCM) of GC grade was obtained from Merck (Whitehouse Station, NJ). Xylazine hydrochloride standard was purchased from U.S. Pharmacopeia (Rockville, MD). 2,2,2-triphenylacetophenone was used as an internal standard (IS), and certified reference material (CRM) standards of heroin, paracetamol, caffeine, codeine, morphine, 6-monoacetylmorphine and ketamine (≥99%); were obtained from the Department of Chemistry Malaysia. Analytical grade sodium hydroxide and anhydrous sodium sulphate were sourced from Merck (Whitehouse Station, NJ).

Ultrapure water (18.2 MΩ) was prepared in-house from a Millipore water purification system (Bedford, NY). Sample beverages (mineral water, carbonated drink, energy drink, and commercial fruit juice) were purchased from the local supermarket. The drinking glasses used in this study were obtained from a nearby kitchenware store.

Instrumentation

An Agilent 7890B GC system equipped with split/splitless injector and a 5977B Mass Spectrometer (MS) (Santa Clara, CA) was utilized to confirm the presence of xylazine. Chromatographic separation was achieved using a (5%-phenyl)-methylpolysiloxane (HP-5) capillary column (30 m × 0.32 μm i.d., 0.25 μm film thickness) purchased from Agilent Technologies (Santa Clara, CA). Purified helium gas (99.9% purity) was used as the carrier gas with a constant flow rate of 1 mL/min. The front inlet was set at 280°C. The oven temperature program began with an initial temperature of 170°C and held for 2 mins. The temperature was gradually increased to reach a temperature of 210°C at 20°C/min and subsequently ramped to 220°C at 3°C/min. It was further increased to 280°C at 50°C/min, and the final temperature was held for 6 mins. Data acquisition rate was set at 1.0 scan/sec and mass spectra were collected in scan mode from m/z 41 to m/z 500. The target compounds were studied, and the resultant peaks were identified using the NIST mass spectral library (Version 2.0) (National Institute of Standards and Technology, Gaithersbury, MD) and literature search.

An Agilent 7890A Gas Chromatographic system equipped with a split/splitless injector and a Flame Ionization Detector (FID) (Agilent Technologies, Santa Clara, CA) was used for quantification of xylazine. HP-5 capillary column with a splitless injection mode was used, and the purified nitrogen gas (99.9% purity) was utilized as the carrier gas at a constant flow rate of 1 mL/min. Liquid injection mode was performed at a constant inlet temperature (280°C). The initial oven temperature was set at 170°C with an equilibration time of 2 min. A temperature ramp of 20°C/min was selected to reach the maximum of 210°C and ramped to 220°C at 3°C/min. It was further increased to 280°C at 50°C/min and held for 6 mins. Hydrogen flow, air flow, and the make-up flow (purified nitrogen gas) were supplied to the detector at 30, 300, and 15 mL/min, respectively. A volume of 1 μL of standard solution or the extract from beverage samples were introduced into the injector port. Chemstation software (Rev. B.04.02, Agilent, Santa Clara, CA) was used for GC automation and data analysis. All standards and IS were identified by comparing the retention time.

Method validation

The xylazine stock solution with a concentration of 1 mg/mL was prepared in DCM. A 5 μg/mL internal standard was also prepared in DCM. Calibration standard solutions ranging from 5 μg/mL to 100 μg/mL were prepared independently by adding in a pre-determined volume of stock solution into volumetric flasks and diluting with DCM. Quality control (QC) solutions at three concentration levels, namely QC_{low}, QC_{medium}, and QC_{high}, were prepared at respective concentration levels of 15, 45, and 75 μg/mL using a separately prepared stock solution.

In this study, GC parameters were adjusted accordingly to establish chromatographic conditions with optimum results and good peak separation. Subsequently, the GC method was validated according to the criteria set by United Nations Office on Drugs and Crime (UNODC) [38]. Selectivity, linearity range, limit of detection and limit of quantitation, repeatability and reproducibility, and the accuracy of the analytical method were evaluated.

Sample extraction

Liquid-liquid extraction (LLE) procedure was performed prior to GC analysis. Briefly, a volume of 1 mL of beverage sample aliquot spiked with xylazine of definite concentration level was carefully transferred into a vial and adjusted to alkaline pH (pH ≈11) using 13% sodium hydroxide solution. The pH of liquid sample was pre-verified using pH litmus paper. Subsequently, the aliquot was extracted with 0.5 mL of DCM twice. Upon extraction, the extracted solution was combined, passed through anhydrous sodium sulphate, and evaporated carefully under a gentle stream of nitrogen gas. Lastly, the residue was reconstituted with 100 µL of 10 µg/mL internal standard solution.

Analysis of xylazine-spiked beverage samples

The recoveries of extraction from the four beverage samples were determined by assaying spiked samples in five replications at concentration levels of 15, 45, and 75 µg/mL. Beverages were chosen based on the range of possible household beverages that would commonly be encountered in drink spiking cases. The selected beverages represented a plain water, an energy drink, a carbonated drink, and a fruit-based drink. To simulate the real case scenario, three different settings of xylazine-spiked beverage samples were prepared.

Firstly, a beverage with remaining at least 2 mL in its volume can be encountered at a scene (spiked liquid samples). To simulate such a setting, the definite amount of xylazine standard was spiked into the respective beverage samples. Following, 1 mL of the spiked liquid beverages were subjected to LLE procedure.

Secondly, leftover of any beverages priorly spiked with xylazine can appear as droplets (spiked droplet samples). To simulate this case, 1 mL of each sample beverage carrying the respective concentration levels was separately sprayed into drinking glass and left for a three-hour duration. Note that such duration did not dry the residues but remained as droplet samples. Then 1 mL of the distilled water was used to rinse the inner surface of the drinking glasses. The rinsates were collected and subjected to LLE procedure.

Thirdly, a beverage sample suspected to have been spiked with drug can exist in completely dry form, either due to the complete consumption by an individual or because of the extended duration of exposure to room conditions (spiked dry samples). To simulate the third scenario, 1 mL of sample beverages with definite concentration of xylazine was sprayed into drinking glass and left overnight to dry undisturbed. Then, 1 mL of distilled water was used to rinse the inner side of the drinking glasses and the rinsate was subjected to LLE procedure.

All prepared samples were analyzed by the validated GC method. Recovery percentages of xylazine from each beverage appearing at three different scenarios were calculated, evaluated, and compared.

Results and Discussion

Through the analysis, it was found that the GC-FID method was selective toward paracetamol, PCM (5.61 min), caffeine, CF (7.02 min), ketamine, KET (7.32 min), xylazine, XYZ (8.23 min), codeine, CD (10.70 min), morphine, MP (11.11 min), 6-monoacetylmorphine, MM (11.74 min), heroin, HR (12.65 min) and 2,2,2-triphenylacetophenone, IS (13.48 min), as shown in Figure 1. The presence of xylazine was also confirmed using the GC-MS, and a mass spectrum which most abundant molecular peak of m/z appeared at 205.1 and 220.1 is demonstrated in Figure 2. Calibration curve of peak area ratio against concentration was plotted with an equation of $y = 0.205x - 0.0583$ with a correlation coefficient of 0.997, suggesting the direct proportional relationship with the concentration of the analyte. For the established method, LOD and LOQ were determined as 0.08 µg/mL and 0.26 µg/mL, respectively, allowing detection and quantification at low microgram levels. This analytical ability of achieving very low LOD and LOQ is important in forensic cases, especially in scenarios where the amount of xylazine available for detection might appear at trace level such as in spiked beverages.

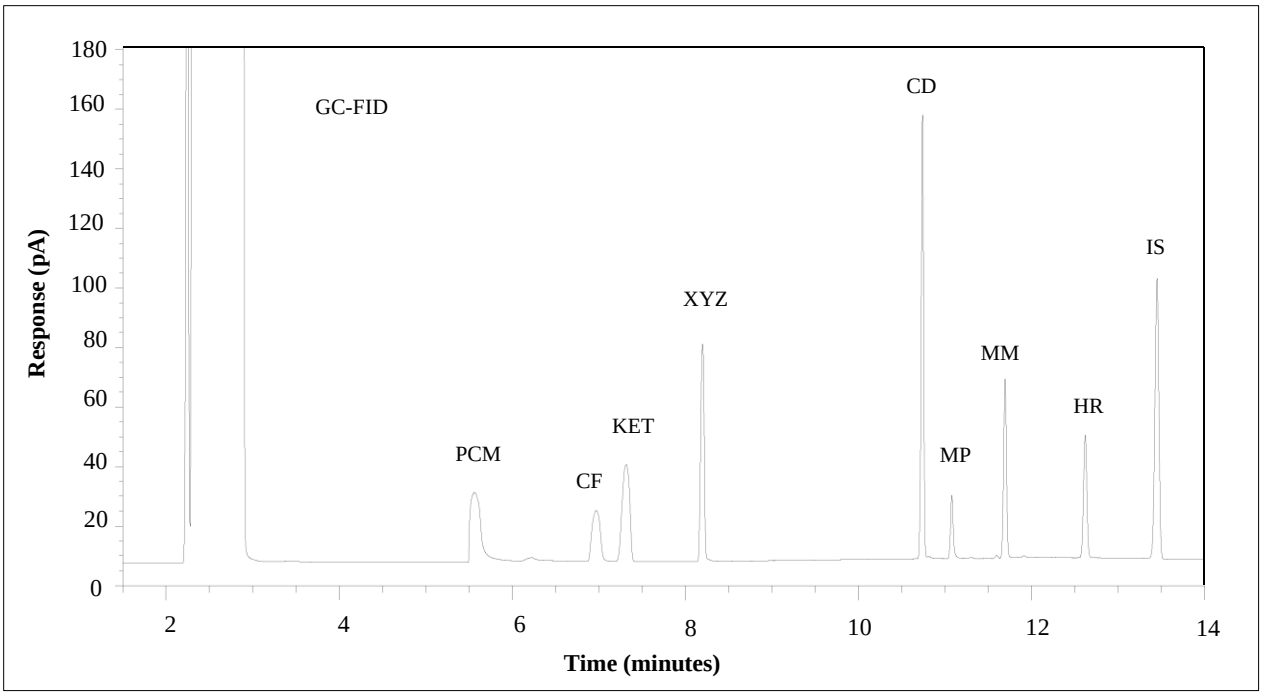


Figure 1. Chromatograms on the selectivity test of the developed method using GC-FID method.

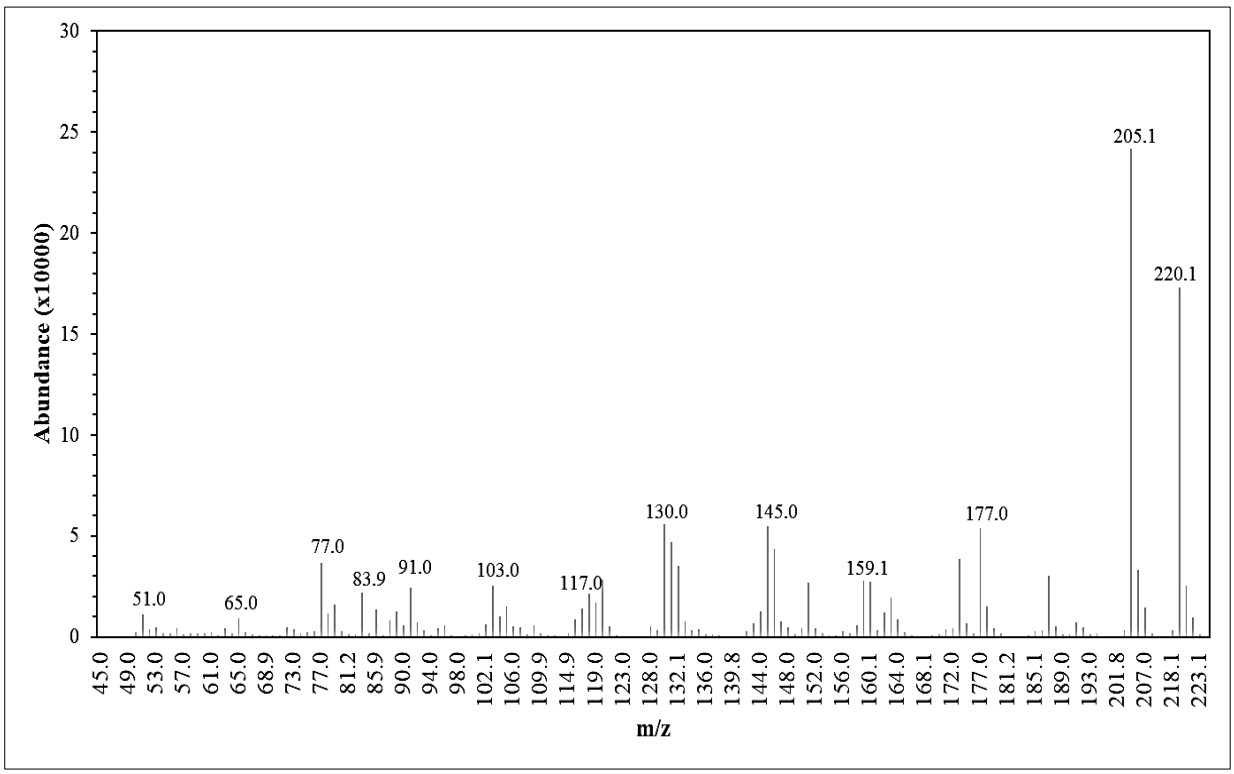
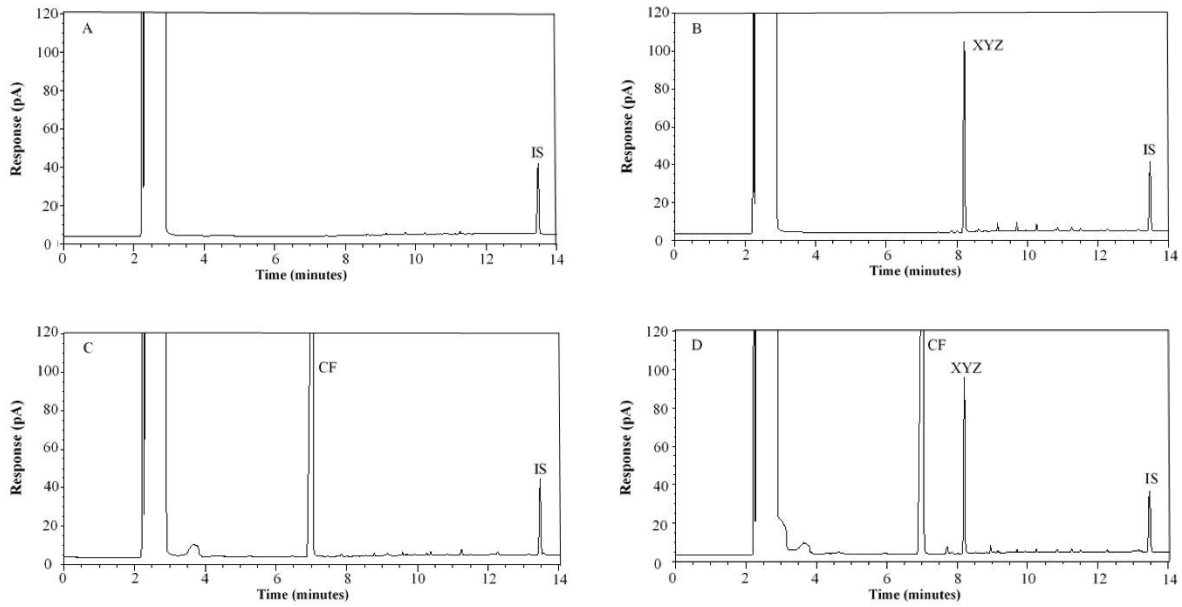


Figure 2. Mass spectrum of xylazine

This study showed good precision, where the intra-day precision reported RSD ranged from 0.5% to 0.7%, while the inter-day precision demonstrated a range of RSD between 1.6% and 3.9%. Repeatable and reproducible data were generated from multiple analyses of the same samples. For accuracy test, recoveries of xylazine from three different QC concentration levels were ranged between 97.3% to 100.7%, i.e., ± 5.0% of the pre-determined concentrations. The GC method proposed here met the intended scope of xylazine analysis, subsequently applied to test the recoveries of the targeted drug from various beverage samples.

Prior to sample analyses, beverage-negative controls, i.e., the extract of beverage-negative without addition of any drug; were run to determine possible matrix interference originating from the beverages. Figure 3 shows the representative chromatograms of beverages-negative controls and xylazine-spiked beverage samples. With the exception of mineral water, it was found that certain substances had been co-extracted, indicated by the presence of extraneous peaks in the chromatograms. Compounds extractable by the LLE procedure were detected, and the presence of caffeine peak was especially evident in both the chromatograms generated from the analyses of beverage-negative carbonated and energy drinks tested in this study. The composition contained in the fruit-based beverage also contributed to extraneous peaks in the chromatogram of beverage-negative control, thus, deserving further identification, perhaps through mass spectrometry, if the identities of these chemical substances are of concern, and they are beyond the scope of this current study.



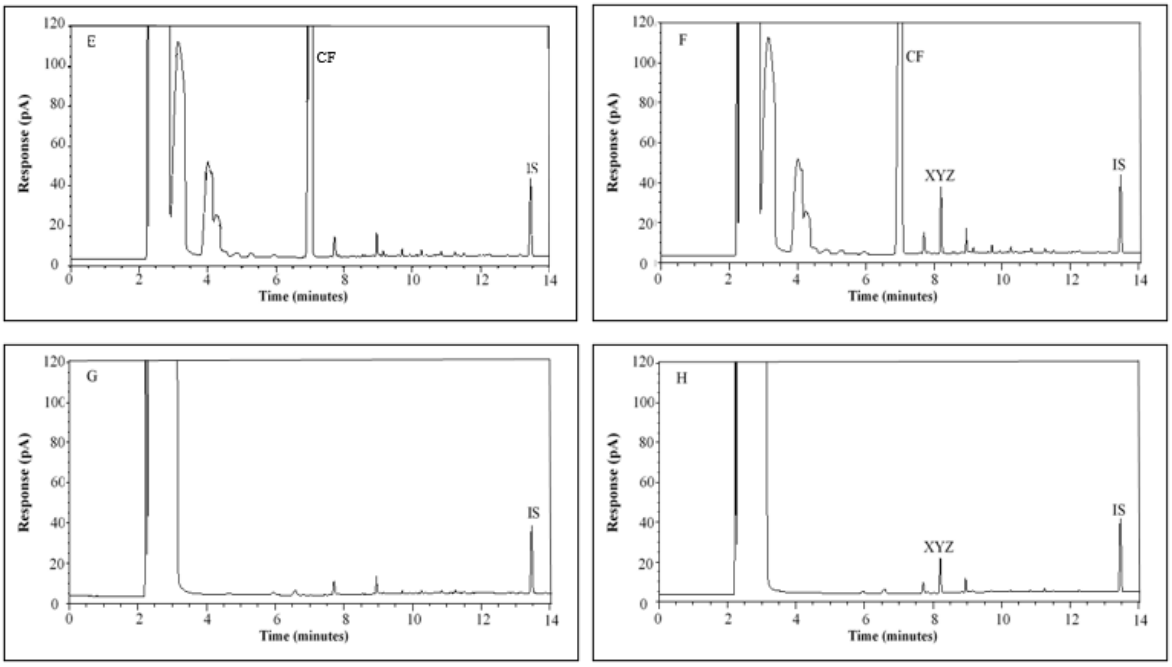


Figure 3. Representative chromatograms of negative control and spiked samples; (A-B) mineral water; (C-D) carbonated drink; (E-F) energy drink; (G-H) fruit-based drink

Although extraneous peaks originated from the beverages were noticed in their respective chromatographic outputs, all these peaks did not interfere the determination and quantification of xylazine as its peak was well-separated from the potential interferences. As a good laboratory practice, it is recommended that a beverage-negative control run is performed in every instance whenever the recovery of a target drug from any beverage is to be determined. This is to avoid obtaining a false positive result, especially in drug-spiked beverage samples.

Under the optimized LLE procedure, DCM was chosen as the extracting solvent due to its relatively good polarity that could increase the recovery efficiency [42]. Apart from that, multiple extraction could potentially increase the distribution coefficient of xylazine [43], while the xylazine was extracted upon basifying the aqueous sample to pH 11 in this study. As a basic drug, alkaline aqueous sample, in this case the beverage sample, allowed greater extraction of the analyte to the DCM layer [43]. It is noted that all drinks except mineral water were appeared acidic in their respective original forms. Therefore, all the solution were made basic for better recovery efficiencies.

Recoveries of xylazine were determined through the evaluation of the extraction efficiency from beverage samples appearing in liquid, droplet, and dry forms. Spiked levels of xylazine with respective mass of 1.5 µg, 4.5 µg and 7.5 µg were utilized, and Table 1 demonstrates the recovery percentages of the drug for each beverage samples.

Table 1. Recoveries (± RSD) of xylazine from the four different beverage

Beverage Sample	1.5 µg	4.5 µg	7.5 µg
Liquid form beverage sample			
Mineral Water	97.3 ± 0.9%	92.1 ± 1.7%	90.1 ± 2.8%
Carbonated drink	90.7 ± 5.7%	90.0 ± 3.2%	85.5 ± 2.1%
Fruit-based drink	87.8 ± 7.0%	82.0 ± 8.6%	77.2 ± 5.3%
Energy drink	89.8 ± 5.3%	84.1 ± 3.5%	82.2 ± 6.4%
Droplet beverage sample			
Mineral Water	71.9 ± 9.0%	80.0 ± 7.9%	75.5 ± 4.4%
Carbonated drink	69.8 ± 14.3%	72.0 ± 7.9%	75.9 ± 3.9%
Fruit-based drink	50.8 ± 5.3%	59.3 ± 9.9%	54.6 ± 11.6%
Energy drink	59.2 ± 16.7%	54.3 ± 15.9%	56.5 ± 12.1%
Dry beverage sample			
Mineral Water	60.8 ± 14.5%	56.1 ± 8.4%	60.5 ± 8.5%
Carbonated drink	57.7 ± 4.3%	58.3 ± 7.7%	66.9 ± 5.3%
Fruit-based drink	51.3 ± 16.2%	49.7 ± 11.6%	45.1 ± 11.3%
Energy drink	50.3 ± 10.2%	42.7 ± 8.9%	39.8 ± 12.4%

In this study, the percentages of xylazine successfully recovered from the liquid beverage samples ranged between 77.2% and 97.3%, depending on the beverages used as the substrates. Meanwhile, percentage recoveries were reported relatively lower in both droplet (50.8-80.0%) and dry samples (39.8-66.9%). In other words, the extraction procedure implemented in this study appeared to be more effective in recovering the target drug from a liquid beverage sample. Unlike liquid sample, both droplet and dry form of samples were highly subjected to variation as they were exposed to the surrounding environment. Perhaps, the variations might be greater in real case scenarios when samples have to be recovered from non-laboratory settings.

Through GC analysis, the amount of xylazine contained in a liquid beverage sample could be quantified with recoveries greater than 82%. It is noted that the recovery and detection of sedative-hypnotics from beverage samples using gas chromatographic method is not a new practice implemented by the forensic communities, especially for the determination of DFC. Research had also been carried out for the detection of various drugs in beverages, including benzodiazepines [14-17], ketamine [14, 18] and GHB [19, 20]. However, to the authors' knowledge, the current study was the first to investigate the determination of xylazine from spiked beverages, with the substance having similar effects as in the above-mentioned drugs on the victim after consumption.

Through the analyses, the composition of beverages could have interfered the extraction efficiencies in recovering the target drug [44, 45], in this case the xylazine. In this study, mineral water with the least matrix interference was found to allow better recoveries of the target drug from liquid samples, reporting at percentages greater than 90%. By comparison, substrates carrying greater matrix within their composition were reported with relatively lower recoveries but remained greater than 82%.

Literatures had suggested a wide range of recovery percentages from 70% and 110% based on the target

illicit drugs and beverages used under different experimental conditions [14, 15, 18, 20]. Whenever beverage samples with complex matrices were used, lower recoveries of the target were achieved as reported by Famiglini et al. [17] with only 47% – 59% of benzodiazepines were successfully recovered from milk-based alcoholic beverages. It is therefore important that a sample of unspiked beverage must be obtained by the crime scene officer and made available for the analyst to use as a control to determine the degree of matrix effect, and extractable percentage.

In real case scenarios, forensic evidence in liquid form might not be always available. There were instances where a few drops of the residual beverages were discovered within a glass or cup, particularly after a victim consumed a drink or after a beverage content was dispensed but has not completely dried up. Additionally, the drinking glass might have totally dried up with no leftover residue being evident due to time elapse, probably due to beyond-control delayed discovery of such forensic evidence. It is mentioned here that the previous published studies mainly focused on the recovery of target drug from liquid beverage samples [14-20]. Droplet and dry evidence should not be overlooked by the forensic investigator as advances in technology which enables the detection of drug traces, as evidenced in this current study, subsequently aiding in DFC investigation.

Nonetheless, the presence of xylazine could still be detected from the droplets and dry form of each beverage. As reported in Table 1, using trace residues of the analyte available for testing, at least 40% of the xylazine can be recovered and detected. It is important to emphasize that the recoveries from droplet and dry beverage samples could vary due to the existence of uncontrolled factors and physical loss in this study, perhaps the variations might be greater in real case scenarios. However, our experimental procedure had successfully allowed for the recovery of xylazine from the drinking glass, at least for positive detection regardless of the volume of its content.

Rinsing is a recommended technique for sampling of traces from a surface [46]. It is useful, particularly in the sampling of large surface area, hollowed area or any area that is hard to access. It was also noted that a sampling method must be comprehensive enough to quantify both soluble and insoluble residuals [46]. A previous study reported the applicability of rinsing procedure to recover illicit ketamine from spiked drinks [47]. Swabbing has also been proposed for sampling of trace surface residues; however, it might yield limited qualitative determination [48-51]. The FDA recommended swabbing procedure to recover the targeted compound from a surface [46] and this shall be further explored in future studies to maximize the recovery and increase the chance for detection, as well as to evidence comparison of suitable sampling strategies in real case scenarios.

This study demonstrated the possibility to detect and quantify trace xylazine from spiked-beverage samples, regardless of its physical forms. Apart from the intention in conducting DFC by criminals, smuggling activities of illicit drugs in adulterated beverages were also reported, deserving screening and testing for the presence of controlled or illegal substances [52]. Therefore, it is important to maximize the likelihood of positive detection, and the method established in this study had allowed the trace detection of 0.08 μg/mL xylazine under experimental parameters. Note that such detection limit was adequately good for the detection of xylazine in real case scenario as the amount of the drug in causing toxicity was reported to be in the range between 40 mg and 2400 mg [3,53]. The outcome of this study provided useful detection technology information and could be beneficial for forensic investigation, sample collection and forensic testing, even in cases with very limited residual samples.

Conclusion

In this study, a gas chromatographic technique was successfully established to determine xylazine in drug-spiked beverages. More than 40% of xylazine can be detected at trace concentration. With the requirement of small amount of beverage samples, the GC method offers valuable investigation clues. As DFC is a serious threat to vulnerable groups, the detection of targeted drug should be performed through an accurate and validated analytical technique. Herein, an appropriate extraction protocol to maximize the recovery of targeted

drugs is presented. The information provided in this study is also beneficial for crime scene investigation and scene sampling practices in cases involving DFC.

Acknowledgement

The authors thank the financial support from the Ministry of Science, Technology and Innovation, Malaysia via International Collaboration Fund (IF0618F1022) and Universiti Sains Malaysia via the USM RUI grant (1001/PPSK/8012322). Special thanks to Department of Chemistry Malaysia for providing logistics and technical assistance. Appreciation is also extended to Associate Professor Dr Geshina Ayu Mat Saat for her editorial assistance.

References

1. Spoerke, D. G., Hall, A. H., Grimes, M. J., Honea, B. N. and Rumack, B. H. (1986). Human overdose with the veterinary tranquilizer xylazine. *The American Journal of Emergency Medicine*, 4(3): 222-224.
2. Elejalde, J. I., Louis, C. J., Elcuaz, R. and Pinillos, M. A. (2003). Drug abuse with inhaled xylazine. *European Journal of Emergency Medicine*, 10(3): 252-253.
3. Ruiz-Colón, K., Chavez-Arias, C., Díaz-Alcalá, J. E. and Martínez, M. A. (2014). Xylazine intoxication in humans and its importance as an emerging adulterant in abused drugs: A comprehensive review of the literature. *Forensic Science International*, 240: 1-8.
4. Hoffmann, U., Meister, C. M., Golle, K. and Zschiesche, M. (2001). Severe intoxication with the veterinary tranquilizer xylazine in humans. *Journal of Analytical Toxicology*, 25(4): 245-249.
5. Zheng, X., Mi, X., Li, S. and Chen, G. (2013). Determination of xylazine and 2,6-xylidine in animal tissues by liquid chromatography-tandem mass spectrometry. *Journal of Food Science*, 78(6): T955-T959.
6. Drug Enforcement Administration (2020). List of scheduling actions, controlled substances and regulated chemicals – 2020. Access from https://www.gpo.gov/fdsys/. [Access online 29 September 2021].
7. Poison Act 1952 (2021). Accessed from https://www.pharmacy.gov.my/v2/en/documents/poisons-act-1952-and-regulations.html. [Access online 29 September 2021].
8. Asean Now (2013). Xylazine enlisted as controlled medicine in Thailand. Access from https://forum.thaivisa.com/topic/674890-xylazine-enlisted-as-controlled-medicine-in-thailand/. [Access online 29 September 2021].
9. Arthur, L. C., Martha, R-L., Paul, D. and Jim, E. R. (1997). Extra label uses of tranquilizer and general anesthetics. *Journal of the American Veterinary Medical Association*, 211(3): 302-304.
10. Pépin, G. (2014). The history of drug-facilitated crimes in France. Toxicological aspects of drug-facilitated crimes. Academic Press, New York: pp. 1-8.
11. Anderson, L. J., Flynn, A. and Pilgrim, J. L. (2017). A global epidemiological perspective on the toxicology of drug-facilitated sexual assault: a systematic review. *Journal of Forensic and Legal Medicine*, 47: 46-54.
12. Gharedaghi, F., Hassanian-Moghaddam, H., Akhgari, M., Zamani, N. and Taghadosinejad, F. (2018). Drug-facilitated crime caused by drinks or foods. *Egyptian Journal of Forensic Sciences*, 8(1): 4-10.
13. Tiemensma, M. and Davies, B. (2018). Investigating drug-facilitated sexual assault at a dedicated forensic centre in Cape Town, South Africa. *Forensic Science International*, 288: 115-122.
14. Acikkol, M., Mercan, S. and Karadayi, S. (2009). Simultaneous determination of benzodiazepines and ketamine from alcoholic and nonalcoholic beverages by GC-MS in drug facilitated crimes. *Chromatographia*, 70(7-8): 1295-1298.
15. Gautam, L., Sharratt, S. D. and Cole, M. D. (2014). Drug facilitated sexual assault: Detection and stability of benzodiazepines in spiked drinks using gas chromatography-mass spectrometry. *PLoS One*, 9(2): e89031

16. Ghobadi, M., Yamini, Y. and Ebrahimpour, B. (2014). SPE coupled with dispersive liquid–liquid microextraction followed by GC with flame ionization detection for the determination of ultra-trace amounts of benzodiazepines. *Journal of Separation Science*, 37: 287-294.
17. Famiglini, G., Capriotti, F., Palma, P., Termopoli, V. and Cappiello, A. (2015). The rapid measurement of benzodiazepines in a milk-based alcoholic beverage using QuEChERS extraction and GC-MS analysis. *Journal of Analytical Toxicology*, 39(4): 306 – 312.
18. Lee, K., Awang, Z., Kunalan, V., Chang, K. H. and Abdullah, A. F. L. (2016). Recovery of ketamine from ribena using liquid-liquid extraction followed by gas chromatography techniques recovery of ketamine from ribena using liquid-liquid extraction followed by gas chromatography techniques. *Malaysian Journal of Forensic Sciences*, 7(1): 32-37.
19. Meyers, J. E. and Almirall, J. R. (2005). Analysis of gamma-hydroxybutyric acid (GHB) in spiked water and beverage samples using solid phase microextraction (SPME) on fiber derivatization/gas chromatography-mass spectrometry (GC/MS). *Journal of Forensic Sciences*, 50(1): 1-6.
20. Meng, L., Chen, S., Zhu, B., Zhang, J., Mei, Y. Cao, J. and Zheng, K. (2020). Application of dispersive liquid-liquid microextraction and GC–MS/MS for the determination of GHB in beverages and hair. *Journal of Chromatography B*, 1144: 122058.
21. Krongvorakul, J., Auparakkitanon, S., Trakulsrichai, S., Sanguanwit, P., Sueajai, J., Noumjad, N. and Wananukul, W. (2018). Use of xylazine in drug-facilitated crimes. *Journal of Forensic Sciences*, 63(4): 1325-1330.
22. Andresen-Streichert, H., Iwersen-Bergmann, S., Mueller, A. and Anders, S. (2017). Attempted drug-facilitated sexual assault—xylazine intoxication in a child. *Journal of Forensic Sciences,* 62(1): 270-273.
23. Elena, C. (2016). Tech officer spiked poly lecturer's water with "love potion". https://www.straitstimes.com/singapore/courts-crime/tech-officer-spiked-poly-lecturers-water-with-love-potion. [Access online 15 October 2021].
24. Jeanous, J. (2019). Teen spiked stepfather's energy drinks with cow tranquilizers to be funny". https://metro.co.uk/2019/03/05/teen-spiked-stepfathers-energy-drinks-cow-tranquilizers-funny-8825490/. [Access online 15 October 2021].
25. The Star (2020). Thailand: Nonthaburi water-bottle spiking cases likely aimed at sexual assault, says police. https://www.thestar.com.my/aseanplus/aseanplus-news/2020/07/12/thailand-nonthaburi-water-bottle-spiking-cases-likely-aimed-at-sexual-assault-says-police. [Access online 15 October 2021].
26. Chan, K. W. and Ramli, S. H. (2018). Development of an in-house HPLC method for the analysis of ecstasy-laced beverages. *Egyptian Journal of Forensic Sciences*, 8(1): 18.
27. Barroso, M., Gallardo, E., Margalho, C., Devesa, N., Pimentel, J. and Vieira, D. N. (2007). Solid-phase extraction and gas chromatographic-mass spectrometric determination of the veterinary drug xylazine in human blood. *Journal of Analytical Toxicology*, 31(3): 165-169.
28. Meyer, G. M. J., Meyer, M. R., Mischo, B., Schofer, O. and Maurer, H. H. (2013). Case report of accidental poisoning with the tranquilizer xylazine and the anesthetic ketamine confirmed by qualitative and quantitative toxicological analysis using GC-MS and LC-MS. *Drug Testing and Analysis*, 5(9-10): 785-789.
29. Mendes, L. F., Souza e Silva, Â. R., Bacil, R. P., Serrano, S. H. P., Angnes, L. and Paixão, T. R. L. C. and de Araujo, W. R. (2019). Forensic electrochemistry: Electrochemical study and quantification of xylazine in pharmaceutical and urine samples. *Electrochimica Acta*, 295: 726-734.
30. El-Shal, M. A. and Hendawy, H. A. M. (2019). Highly sensitive voltammetric sensor using carbon nanotube and an ionic liquid composite electrode for xylazine hydrochloride. Analytical Sciences. 35 (2): 189–194.
31. Fiorentin, T. R., Logan, B. K., Martin, D. M., Browne, T. and Rieders, E. F. (2020). Assessment of a portable quadrupole-based gas chromatography mass spectrometry for seized drug analysis. *Forensic Science International*, 313: 110342.

32. Misra, B. B., Bassey, E. and Olivier, M. (2019). Comparison of a GC-orbitrap-MS with parallel GC-FID capabilities for metabolomics of human serum. *BioRxiv*, 2019: 740795.
33. Kim, J., Choi, K., & Chung, D. (2012). Sample Preparation for Capillary Electrophoretic Applications. *Electrophoresis,* 30(16):2905-2911
34. Saisahas, K., Soleh, A., Promsuwan, K., Phonchai, A., Mohamed Sadiq, N. S., Teoh, W. K. Chang, K. H., Abdullah, A. F. L. and Limbut, W. (2021). A portable electrochemical sensor for detection of the veterinary drug xylazine in beverage samples. *Journal of Pharmaceutical and Biomedical Analysis*, 198: 113958.
35. Hughes, H., Peters, R., Davies, G. and Griffiths, K. (2007). A study of patients presenting to an emergency department having had a "spiked drink". *Emergency Medicine Journal*, 24(2): 89-91.
36. Hoffmann, U., Meister, C., Golle, K. and Zschiesche, M. (2001). Severe intoxication with the veterinary tranquilizer xylazine in humans. *Journal of Analytical Toxicology*, 25(4): 245-249.
37. Birkler, R. I., Telving, R., Ingemann-Hansen, O., Charles, A. V., Johannsen, M. and Andreasen, M. F. (2012). Screening analysis for medicinal drugs and drugs of abuse in whole blood using ultra-performance liquid chromatography time-of-flight mass spectrometry (UPLC-TOF-MS)-toxicological findings in cases of alleged sexual assault. *Forensic Science International*, 222(1-3): 154-161.
38. United Nations Office on Drugs and Crime (2009). Guidance for the validation of analytical methodology and calibration of equipment used for testing of illicit drugs in seized materials and biological specimens a commitment to quality and continuous improvement. Vienna: United Nations Office on Drugs and Crime.
39. Wong, S. C., Curtis, J. A. and Wingert, W. E. (2008). Concurrent detection of heroin, fentanyl, and xylazine in seven drug-related deaths reported from the Philadelphia medical examiner's office. *Journal of Forensic Sciences*, 53(2): 495-498.
40. Forrester, M. B. (2016). Xylazine exposures reported to Texas poison centers. *Journal of Emergency Medicine*, 51(4): 389-393.
41. Tobias, S., Shapiro, A. M., Wu, H. and Ti, L. (2020). Xylazine identified in the unregulated drug supply in British Columbia, Canada. *Canadian Journal of Addiction*, 11(3): 28-32.
42. Mashayekhi, H. A., Rezaee, M. and Khalilian, F. (2014). Solid-phase extraction followed by dispersive liquid-liquid microextraction for the sensitive determination of ecstasy compounds and amphetamines in biological samples. *Bulletin of the Chemical Society of Ethiopia*, 28(3): 339-348.
43. Cairns, D. (2012). Essentials of pharmaceutical chemistry. Pharmaceutical Press
44. Sarin, R. K., Sharma, G. P., Varshney, K. M. and Rasool, S. N. (1998). Determination of diazepam in cold drinks by high-performance thin-layer chromatography. *Journal of Chromatography A,* 822(2): 332-335.
45. Webb, R., Doble, P. and Dawson, M. (2007). A rapid CZE method for the analysis of benzodiazepines in spiked beverages. *Electrophoresis*, 28(19): 3553-3565.
46. United State Food and Drug Administration (2021). Validation of cleaning processes (7/93). https://www.fda.gov/validation-cleaning-processes-793. [Access online 15 October 2021].
47. Albright, J. A., Stevens, S. A. and Beussman, D. J. (2012). Detecting ketamine in beverage residues: Application in date rape detection. *Drug Testing and Analysis*, 4(5): 337-341.
48. D'Aloise, P. and Chen, H. (2012). Rapid determination of flunitrazepam in alcoholic beverages by desorption electrospray ionization-mass spectrometry. *Science and Justice*, 52(1): 2-8.
49. Lygrisse, J., Lapp, M., Witherspoon, K., Van Stipdonk, M. J. (2009). Detection and quantification of ketamine HCl in alcohol/water matrices using ESI-MS and LC-ESI-MS. *In Proceedings: 5th Annual Symposium: Graduate Research and Scholarly Projects:* p. 48-49.
50. Norma Esmeraldo, G. I. (2011). Qualitative analysis of sodium gamma-hydroxybutyric acid (GHB) residue from plastic and glass containers using FTIR-ATR. Thesis of Master Degree, University of California, Darvis.

51. Øiestad, E. L., Karinen, R., Christophersen, A. S., Vindenes, V. and Bachs, L. (2014). Analyses of beverage remains in drug rape cases revealing drug residues - the possibility of contamination from drug concentrated oral fluid or oral cavity contained tablets. *Journal of Forensic Sciences*, 59(1): 208-210.
52. Xie, R. F., Lu, Z. Q., Chai, Y. F., Wang, X. H., Li, H. F. and Gu, J. Y. (2018). Rapid determination of heroin in adulterated commercial beverage in drug transportation cases. *Chinese Journal of Analytical Chemistry*, 46(10): e1880-e1886.
53. Mittleman, R. E., Hearn, W. L. and Hime, G. W. (1998). Xylazine toxicity—literature review and report of two cases. *Journal of Forensic Sciences*, 43(2): 400-402.

Malaysian Journal of Analytical Sciences (MJAS)
Published by Malaysian Analytical Sciences Society

MAGNETITE-GRAPHENE BASED NANOCOMPOSITES IN ELECTROCHEMISTRY: A BRIEF REVIEW ON THEIR APPLICATIONS

(Nanokomposit Magnetit-Grafin dalam Elektrokimia: Ulasan Ringkas dalam Aplikasinya)

Farhanini Yusoff[1]*, Karthi Suresh[1,5], Azleen Rashidah Mohd Rosli[1], Nur Ayunie Kamaruzaman[1], Noorashikin Md Saleh[2], Muggundha Raoov Ramachandran[3], Nur Nadhirah Mohamad Zain[4]

[1]Faculty of Science and Marine Environment,
Universiti Malaysia Terengganu, 21030 Kuala Terengganu, Terengganu, Malaysia.
[2]Department of Chemical and Process Engineering,
Universiti Kebangsaan Malaysia, 43600 Bangi, Selangor, Malaysia
[3]Chemistry Department, Faculty of Science,
University of Malaya, 50603 Kuala Lumpur, Malaysia.
[4]Advanced Medical & Dental Institute,
Universiti Sains Malaysia, Bertam 13200 Kepala Batas, Pulau Pinang Malaysia.
[5]Adcertech Sdn Bhd,
Plot 2,Taman Meru Industrial Estate, Jelapang, 30020 Ipoh, Perak, Malaysia.

**Corresponding author: farhanini@umt.edu.my*

Received: 5 January 2022; Accepted: 22 March 2022; Published: 25 August 2022

Abstract

Magnetite incorporates graphene or its derivatives, graphene oxide, or reduced graphene oxide, has received significant attention for its superior features, such as unique structure and large surface area with great number of active sites. The nanocomposite is priorly used in biosensors and biomedical for drug study. Many researchers currently opt for the nanocomposite in various electrochemistry applications as the first-rate material for said applicative fields due to its environmental-friendly nature and inexpensive production cost. This paper reviews the advantages of magnetic graphene-based material and its applications. The scope of this review is to highlight important justifications of electrochemical applications. A comprehensive discussion of the nanocomposite's physical and electrochemical properties, as well as its stability and reusability, are presented.

Keywords: magnetite, graphene, electrochemical, eco-friendly, electrode

Abstract

Magnetit digabungkan dengan grafin atau produk derivasinya, seperti grafin oksida atau grafin oksida terturun mendapat kajian meluas kerana ciri unik komposit tersebut, misalnya kawasan permukaan yang luas dengan bilangan tapak aktif yang amat banyak. Pada asalnya, nanokomposit tersebut digunakan dalam bidang biosensor dan biomedik untuk terutamanya dalam kajian dadah. Kini, ramai penyelidik memilih nanokomposit ini dan mengaplikasikannya sebagai bahan utama dalam pelbagai bidang elektrokimia atas dasar mesra alam dan kos penghasilan yang murah. Dalam kertas kajian ini, kelebihan nanokomposit dan penggunaan dalam bidang elektrokimia diulas. Skop ulasan memberi penghujahan yang penting tentang bidang elektrokimia. Di

samping itu, ciri-ciri fizikal dan elektrokimia nanokomposit tersebut dibincangkan secara mendalam selain daripada kestabilan dan kebolehgunaan semula bahan tersebut.

Keywords: magnetit, grafin, elektrokimia, mesra alam, elektrod

Introduction

Technological advancements in electrochemistry have gained remarkable growth over past decades recently for their constant developed applications. Electrochemical technique is predominantly an efficient and alternative solution to conventional spectroscopic and chromatographic techniques. It offers rapid analysis, low cost, selective sensitivity, and user portability while being environmentally friendly. To further improve the electrochemical technology, electrocatalysis was introduced, which attracted significant attention from researchers globally as an establishment since the new hybrid approach was introduced. Moreover, the typical unmodified electrode such as bare carbon electrode or bare gold electrode has a chemically fouling nature, poor chemical stability, low mechanical strength, and tend to agglomerate on its own [1, 2].

Graphene is known as one of the most interesting materials in the research field for its exclusive characteristics and potential applications in various fields [3]. It is as discrete as one carbon atom in size but still carries a greater surface area, twice larger than ordinary activated carbon [4, 5]. It has a honeycomb lattice arrangement, a primitive building block for other carbon allotropes, such as 0D fullerenes, 1D carbon nanotubes, and 3D graphite. The composite has the capacity to adsorb an assortment of aromatic biomolecules via p–p stacking interaction and electrostatic interaction, making them optimal materials for forming biosensors and loading drugs [6]. Graphene is further refined into graphene oxide for enhanced properties, such as boosted surface area and reactive sites from the addition of oxides functional groups. Hydrophilicity and high dispersibility of graphene make it popular in removing water pollutants; however, it is difficult to be separated from aqueous solutions [7].

Graphene oxide (GO) is a resultant of graphene sheet embellished with oxygen (-OH) functional groups to great negative charge density and hydrophilic character. Typically, GO is a natural insulator, where it has lured sizeable interest for its prospective applications as an electrically insulating material in electronics and can be applied as an adsorbent. Nevertheless, it could be a conductive material through adequate exposure to reducing agents such as hydrazine hydrate or sodium borohydride, reducing and defecting its sites to make it active [8]. It is a prime component in the field of chemistry because of its high surface area with many functional groups around the plane. The high surface area subsequently supports the oxygen reduction reaction [9, 10]. The existence of functional groups on the GO plane produces a high negative charge density, larger surface area, and hydrophilic character.

Diminishing the oxygen-based functional groups in sheets of graphene oxide by in-situ reduction produces reduced graphene oxide (rGO). It is a better choice of using rGO as compared to GO in the aspect of electrochemistry. The reduced oxygen in GO sheets promptly increases Π-Π interaction by increasing sp^2 carbons [11, 12]. With these properties, a study was conducted to foresee the strong interaction between graphene and nanoparticles, especially with magnetic properties, which resulted in a salient potential with exclusive and enhanced functionalities useful in several applications [13].

Magnetic nanoparticle (MNP) utilised in electrochemical activities is known for its decent theoretical value, inexpensive production, and environmentally friendly. Together with magnetic properties, it has metallic properties that can conduct good electricity. Iron oxide nanoparticles, scientifically known as magnetite, are the utmost explored metal-based magnetic nanoparticles up to date. It turns to superparamagnetic once the ferrite particles become smaller than 128 nm. This averts self-agglomeration since they display their magnetic behaviour only when an external magnetic field is implemented [14]. However, inferior cycling stability, vulnerability to air oxidation, and agglomeration caused by imbalanced electron transfer occur easily. Therefore, merging of

magnetite with carbon related materials, especially graphene (for its unique properties) into a nanocomposite was researched [15]. This technically increased the surface area and performed better electrochemical reactions when utilised in applications. With current findings, the nanocomposite can be further utilised for various applications, such as in big energy production plants. This changes the current perspective in the energy production field. More than 51% of global energy production is produced from non-renewable energy resources, to an option of renewable energy source that saves cost [16, 17].

The integration of magnetite-graphene plays a pivotal role in the electrochemical efficiency of a cell, other than to ensure the excellency of characteristics and longevity of nanocomposite while possessing better stability in terms of thermal and conditioning. This is based on the increase of electrical conductivity [18]. Generally, the development of magnetite-graphene nanocomposite begins with the synthesis of graphene oxide via modified Hummers' method [19] followed by the synthesis of MNP using a facile one-pot method or chemical induction method. This combination has been used in various fields such as biosensors, data storage, bioseparation, targeted drug delivery, coating from corrosion, and energy production [20]. The nanocomposite showed a great response in the biomedical field through excellent detection capability in sensor application, which proves to be an optimal substrate for surface immobilisation. This characteristic can be further explored and enhanced in targeted detection apart from the biomedical field, such as water pollution sensors.

Applications of Magnetic Graphene Nanocomposite Batteries

Batteries, the handy energy storage material is a common material in daily life. It can be categorised into three types which are lithium-ion battery (LIB), sodium-ion battery (SIB), and lithium/sulphur-ion battery (LSIB) [21-23]. Among these, LIB is more preferably used for its exclusive features such as high energy density, high voltage, lightweight, and long life-cycle. The first LIB was introduced in 1991 by Sony Inc., and extensively used as handily and portable power source for electric and electronic devices [24]. This type of battery also has attracted attention in aerospace application as well as in military-based devices. As for the working principle of rechargeable batteries, it contains two electrodes, an anode (negative electrode) and a cathode (positive electrode). The cathode, as the lower capacity electrode, determines the overall capacity of a battery. Different types and structures of the separator component have been introduced. It primarily serves to physically separate the electrodes to prevent shorting while providing porosity for lithium-ion flow during charge and discharge [25]. In the discharging process of LIB, lithium-ion moves from the negative electrode to the positive electrode through an electrolyte and vice versa during the charging process. The process of ion movement is illustrated in Figure 1. Generally, the positive electrode in LIB is an intercalated lithium compound, while various materials have been developed for the negative electrode to increase the properties of the lithium-ion battery [26].

Magnetite developed into one of the promising active materials for anode of LIB due to the highest theoretical capacities (926 mAh/g) [27], which shows that Fe_3O_4 can react with eight lithium ions per formula unit compared to the currently used graphite anode with 372 mAh/g of capacity [28]. Apart from that, magnetite also possesses higher conductivity ($\sigma = 2 \times 104\ Sm^{-1}$) than most of other metal oxides [29] due to its magnetic properties [30]. However, a stand-alone magnetite nanoparticle is not significant for the Li-ion batteries' application due to its poor cyclic performance and rate capability, which causes aggregation of the composite and fluctuation of volume during the insertion or the extraction process of Li-ion. Furthermore, this anode exhibits intrinsic large electrochemical polarisation upon cycling, which reduces the system's 'round trip efficiency' and electrochemical reversibility. This is primarily due to poor electronic and ionic conductivities of Fe_3O_4 and slow solid-state diffusion of Li ions in this anode [31]. The low conductivity of composite also may lead to a rapid degradation process.

To add on, the combination of graphene with magnetite boosts the electrical properties and increases surface area, leading to exceptional thermal conductivity (~5000

W/mK). The extremely high values of thermal conductivity suggests that graphene can outperform carbon nanotubes (CNTs) in heat conduction. 2D nanosheets structure of graphene constitutes abundant active sites and accessible surfaces where it enables energy storage materials to achieve high power and energy density [32]. It is supported that the theoretical capacity of graphene (744 mAh/g) is twice as much as that of graphite because graphene can accommodate two Li-ions, instead of one for graphite, in each hexagonal loop of carbon (Li_2C_6). Thus, incorporating magnetite with graphene can overcome the aggregation of magnetite nanoparticles as the high surface area (2620 m^2/g) graphene will help the nanosized magnetite bind to its nanosheets. The large-volume variation of magnetite during the discharge-charge process also can be mitigated through the high surface area graphene [33]. The strategies of coating the magnetite nanoparticles to graphene enhance the electronic conductivity and boost the conversion yield as the metal integration of the magnetite possess an excellent magnetic property. Based on Huang et al. [34] combination of magnetite and graphene leading to the high Fe_3O_4 loading and outstanding cycling stability (83 per cent retention of the initial reversible capacity after 40 cycles) generated by the volume buffering effect of graphene sheets, the discharge capacity was increased to 750.0 mAh/g. This improved Fe_3O_4/graphene composite with improved performance could have a promising future in lithium-ion battery applications [35].

According to Kai Zhu et al. [36], it was observed that there was no capacity loss and better cycling stability of the improved batteries using nanocomposite. The discharge/charge rate of the battery increased while the Coulombic efficiency reached more than 95%. The nanocomposite supported short diffusion between electron transfer which indicated the enhanced conductivity of the battery. Previous works using various magnetite-graphene nanocomposites and their derivatives nanocomposites on lithium-ion batteries are tabulated in Table 1.

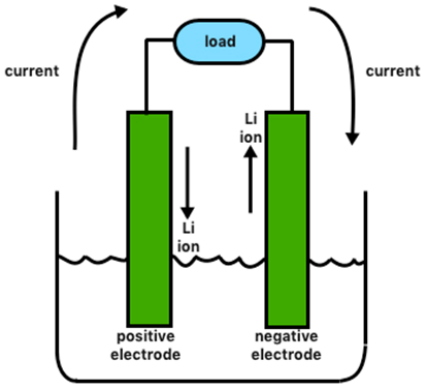


Figure 1. Discharging process of lithium-ion in lithium-ion battery

Table 1. Comparison of fabricated graphene-magnetite for lithium-ion battery application

Anode Materials	**Current Density (mAg^{-1})**	**Discharge Capacity ($mAhg^{-1}$)**	**Reversible Capacity ($mAhg^{-1}$)**	**Coulombic Efficiency (%)**	**Refs.**
Tight anchoring Fe_3O_4/Graphene	50	1133	1045	100	[30]
Gelatin-functionalized graphene decorated with iron oxide	100	1096	924	99	[36]
Fe_3O_4/Gr nanoparticles	-	920	-	96	[21]
Fe_3O_4/trigol reduced graphene	100	1880	1024	91	[37]
N-doped carbon coated Fe_3O_4	-	1173	800	99	[38]
3D hierarchical Fe_3O_4/Graphene	92.5	1114	609	92.5	[20]
Reduced graphene oxide@ nitrogen doped carbon	-	409.4	-	100	[26]
Fe_2O_3/rGO	1000	-	1242	97	[39]

Fuel cell

Fuel cell has been a source of energy generation for the past few decades. It has been recognised as the most efficient substitute for fossil fuels [44]. Sir William Robert Grove invented the first fuel cell by developing a wet-cell battery that depended on the electrochemical reaction that split water into hydrogen (H^+) and oxygen (O^-) ions. Since then, many other types of fuel cells have been invented and applied as a source of energy which contributes less pollution compared to other methods. Commonly used fuel cells include alkaline fuel cells, solid oxide fuel cells, microfluidic fuel cell, proton exchange membrane fuel cell, microbial fuel cell, and many more [45, 46]. The concept of fuel cell is the movement of electrons from cathode to anode. In general, hydrogen atoms enter a fuel cell at the anode, stripped of their electrons by a chemical reaction. The hydrogen atoms become "ionised," or electrically charged. Negatively charged electrons carry electricity across wires, allowing work to be done. The DC output of the fuel cell must be channelled via a conversion device called an inverter if alternating current (AC) is required. The cathode is where oxygen enters the fuel cell and then combines with electrons returning from the electrical circuit and hydrogen ions that have gone through the electrolyte from the anode in some cell types (like the one seen above). In other types of cells, oxygen picks up electrons and then travels through the electrolyte to reach the cell membrane. The best part of the fuel cell is that it is a renewable energy resource, easy to be constructed, and environmentally friendly, where no mass land destruction needs to be done to build platforms for other renewable resources such as windmills and hydro turbines. Fuel cell does not stop working as long as fuels (e.g., hydrogen, which is often used) and oxidants are supplied to the anodic chamber and cathodic chamber. The hydrogen oxidises at the anode where the reaction is called hydrogen evolution reaction (HER). At the same time, the oxygen is being reduced at the cathode, and the reaction is known as oxygen reduction reaction (ORR).

ORR at the cathode proceeds proceeds mainly through two pathways: indirect two-electron reduction (equation 1 and 2) and direct four-electron reduction (equation 3). The four-electron reaction is preferable because it does not produce peroxide species in the reaction as the reactivity of H_2O_2 is relatively higher than the stability of H_2O produced in the direct reaction [47]. The direct reaction also has higher operating potential and current efficiency as compared to the indirect reaction. But in general terms, hydrogen atoms enter a fuel cell at the anode, where a chemical reaction strips them off their electrons. The hydrogen atoms are "ionised" and carries a positive electrical charge. The negatively charged electrons provide the current through wires to do work. If alternating current (AC) is needed, the DC output of the fuel cell must be routed through a conversion device called an inverter. Oxygen enters the fuel cell at the cathode. In some cell types (like the one illustrated above), it combines with electrons returning from the electrical circuit and hydrogen ions that have travelled through the electrolyte from the anode. In other cell types, oxygen picks up electrons and then travels through the electrolyte to the anode, where it combines with hydrogen ions. The electrolyte plays a key role. It must permit only the appropriate ions to pass between the anode and cathode. If free electrons or other substances travel through the electrolyte, they will disrupt the chemical reaction whether they combine at anode or cathode, together with hydrogen and oxygen form water, which drains from the cell. As long as a fuel cell is supplied with hydrogen and oxygen, it will generate electricity.

$$O_2 + 2H^+ + 2e^- \rightarrow H_2O_2 \quad (1)$$

$$H_2O_2 + 2H^+ + 2e^- \rightarrow 2H_2O \quad (2)$$

$$O_2 + 4H^+ + 4e^- \rightarrow 2H_2O \quad (3)$$

The overall performance of the fuel cell is mainly dependable on the electrode applied. Therefore, the exceptional material such as graphene is opted as the appropriate electrode for fuel cell. Noticeable high electrical conductivity features of graphene aids to smoothen the flow of ions and charge transportation in the fuel cell. Graphene's sp2 hexagonal lattice structure exhibits a high specific area which contributes to high capacitance value in the fuel cell and can be easily used as electrode for both application of HER and ORR [48, 12]. Graphene also possesses a high carrier mobility

with a value of $2x10^{-5}$ $cm^2/V/s$, high mechanical strength, high transparency (~97.7%), and is also thermochemically stable.

The highly abundant iron oxide is acknowledged as a low-cost material to replace the conventional Pt electrode which make it one of the main reasons of usage in fuel cell application. Iron oxide possess excellent magnetic properties and high selectivity towards the oxygen reduction reaction [49, 50]. However, during the synthesis process of iron oxide, the composite tends to agglomerate due to uncontrollable growth of magnetite ion thus resulting in depleting performance in ORR and HER. In order to prevent such problem, use of carbonised materials as support to magnetite are very convenient. The incorporation of graphene with iron oxide will decrease the agglomeration of iron oxide. The efficient catalytic activity can also be achieved through the positive synergistic coupling effect between graphene and magnetite particles. Table 2 below shown the reaction pathway of composite in ORR.

Table 2. Reaction pathway of composite in ORR

Composites	Reaction Pathway	ORR Potential (V)	Reaction Kinetics	Refs.
α-Fe_2O_3/GO	3.2 to 3.4	-0.3 to -0.5	-	[51,52]
Fe_2O_3/ carbon	3.6	-	-	[53]
$FeO_{1.4}$/N-C	3.1-3.3	-0.056	-0.40 to -0.55	[54]
Fe_3O_4/N-Gas	4	-0.19	-0.19 to -1.2	[55]
Fe_3O_4/N-GSs	2	-0.26	-0.26 to -0.62	[55]
Fe_3O_4/N-CB	2	-0.24	-0.24 to -0.60	[55]
Fe_3O_4-CNx-Lys	3.4-3.6	-0.25	-0.25 to -0.45	[56]

Corrosion

Corrosion is a natural process that converts a refined metal into a more chemically stable form, and the process is well-known for the gradual destruction of materials by chemical and electrochemical reactions with the environment as the corrosive medium. Protection from corrosion is important to prevent structural and material damage. Corrosion also poses a threat towards public health and safety. Many types of organic-based coatings have been used to reduce corrosion of metal surfaces, as such epoxy coatings. However, these coatings only protect the top layer of the metal surface and are permeable to corrosive electrolytes' exposure. Hence, corrosion does occur underneath the epoxy coating [57]. To add on, the epoxy coating was attached to the applied surface through hydrogen bonding, where the stability reduces by time and is vulnerable to wet conditions. Shielding effect of the corrosion coatings is essential as its function is to block the contact between the substrate interface with the corrosive medium such as oxygens or sulfates and impede the diffusion of the corrosive medium to the protected metals through the anti-corrosion coatings [58]. This shielding effect can be increased by a uniform distribution of the anti-corrosive materials [59].

The high dispersibility and ultra-thin two-dimensional structure of graphene formed a barrier and increased the shielding effect. Apart from that, graphene has also become one of the promising corrosion protection due to its characteristics, which is impermeable to almost all molecules and ions [56]. It is believed that graphene is a revolutionary material in the field of corrosion protection because, as corrosion protection pigments, graphene is able to simultaneously improve the wear resistance, barrier properties, thermal conductivity, mechanical properties, and thermal stability of polymeric coatings [60]. The uniform dispersion and

orientation of graphene parallel to the metal surface make it one of the promising materials for anti-corrosion coatings [61]. Graphene also retains a high adhesion force to enhance the bonding strength between the corrosion protecting coatings with the metals as a strong bonding force material able to hinder the accumulation of oxygen and sulphates at the metals interface and disrupt the corrosion process. A remarkable conductivity of graphene also helps to improve the cathodic protection effect of zinc-rich coatings on metal which an active zinc powder was used to formed corrosion couple with the protected metal interface.

The strength of corrosion protective layer against corrosive medium is determined by the angle of anti-corrosion materials with the substrate interface. A narrower angle of the materials with substrate will toughen the barrier of corrosion protective layer [62]. Thus, only graphene parallel to the surface obeys the shielding effect theory; meanwhile, the graphene perpendicular to the substrate interface did not provide the shielding effect. Therefore, a magnetic field-induced orientated alignment of magnetic graphene was introduced by loading magnetite onto the graphene surface. The magnetised graphene was movable under the action of the external magnetic field. It could also be horizontally aligned in the epoxy resin by the magnetic torque applied to the magnetic graphene sheet by the horizontal magnetic field, as shown in Figure 2 [63]. Moreover, the integration of magnetics with graphene is helpful as the magnetic effect increases the stability of the layer on the surface of metal applied [64].

Numerous works on magnetite graphene as a corrosion protective layer have been published in the past few years. One of the works demonstrated by Nayak *et al.,* deployed a graphene coated Ni film with effectiveness up to post annealing of 500 ^{0}C. Another study found that the use of graphene-coated Cu (111) surface, confirms that no corrosion is detected after the annealing process. Meanwhile, Anisur et al., stated a CVD graphene growth on nickel has improved corrosion resistance to 700 kΩcm^2 with the absence of hydrogen during the graphene growth process. Besides that, Fronczak et al., investigated the corrosion resistance of carbon-encapsulated iron nanoparticles with the use of nitric acid as corrosion agent. as it releases a large amount of Fe and exhibits a high corrosion resistance and high effectiveness up to post-annealing of 450-500 ^{0}C [65-67]. In addition, graphene-coated Cu and graphene-coated Cu/Ni alloy foil by CVD under heating for four at 200 °C in laboratory air, and immersing into a solution of 30% hydrogen peroxide, up to 45 minutes showed no changes to the surfaces. In contrast, bare Cu/Ni turned a dark shade of brown onto its surface [68]. It is shown that the presence of graphene in transition metal can act as anti-corrosive and protect the surface from damage. However, there is a challenge in this field, where the existence of defects may ruin all the advantages of graphene films acting as corrosion inhibitor. Table 3 illustrates the corrosion potential among the previous research on magnetite and graphene-based.

Table 3. Corrosion Potential (E_{corr}) Values obtained from potentiodynamic polarisation test

Composite	**Conditions**	**E_{corr} (mv)**	**I_{corr} (μA cm−1)**	**C_R (mm/year)**	**Refs.**
Bare carbon steel	In 3.5% NaCl	−530.89	95.0	1.103	[69]
Fe_3O_4	In 3.5% NaCl	−559.45	46.7	0.542	[69]
Fe_3O_4/PANI	In 3.5% NaCl	−598.69	3.0	0.035	[69]
Ni	In 3.5% NaCl	−481.0	6.138	2.605	[70]
Ni-GO1	In 3.5% NaCl	-424.0	4.845	2.055	[70]
Magnetite NPs (blank)	In 1M HCl, 30°C	−558.2	1.13	-	[71]
Magnetite NPs (0.1%)	In 1M HCl, 30°C	−588.6	0.021	-	[71]

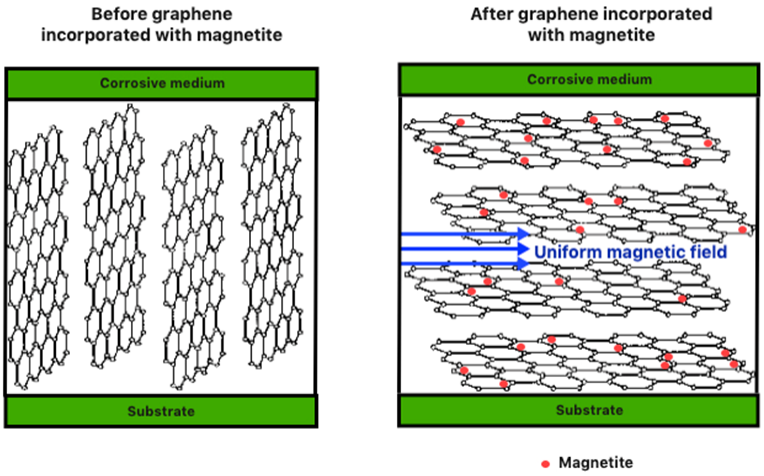


Figure 2. Perpendicular distribution of graphene without magnetite and parallel orientation of magnetite graphene in uniform magnetic field

Sensor

Electrochemical sensors work on the basis that an electrical current travels through a sensing electrode as a result of an electrochemical reaction that occurs at the surface of a sensing electrode coated with a catalyst, such as platinum. An electrochemical sensor consists of a metallic anode and a metallic cathode that are submerged in an electrolytic solution (such as H_2SO_4) to allow ion movement between the two electrodes. Electrochemical sensors typically have two or three-electrode designs with a membrane for gas transport. The electrical current is proportional to the hydrogen concentration, which may be monitored to determine the gas concentration [74]. An electrochemical sensor detects and analyses a specific compound by measuring the chemical signals produced from the electrochemical system and converting them into digital signals or well-known as chemical signals. These signals can be measured by analysing the current, potential, and conductance changes being emitted from the system [75]. The response obtained in the electrochemical sensor is due to the interaction between the electron transfer of the analyte in the electrolyte and the electricity being applied to the electrochemical system based on potentiometric, amperometric, voltammetric or conductivity measurements. The two most common electrochemical sensor configurations are amperometric and potentiometric sensors. Amperometric sensors work with a constant applied voltage, and the sensor signal is current. In contrast, potentiometric sensors work with zero current, and the sensor signal is the potential difference between the sensing electrode and a reference electrode [74]. The attraction of applying electrochemical sensors is based on their high sensitivity, good selectivity, cost-effectiveness compared to the conventional method, nature-friendly, simple pre-treatment process and fast analytical period [15].

In the application of electrochemical sensors, it is crucial to have excellent electron transfer properties to promote the ability of some enzymes and exceptional catalytic behaviour towards small biomolecules; and graphene with outstanding electron mobility (200,000 $cm^2V^{-1}s^{-1}$ at electron density ~$2x10^{11}$ cm^{-2}) can fulfil this critical requirement [76]. Graphene also possesses a less weighty graphene chemical sensor that is wearable and operates at normal atmospheric pressure and room temperature, making it cost-effective and low environmental impacts material [79].

Meanwhile, magnetite based-electrochemical sensors have shown to be an excellent choice for highly sensitive sensing with a linear range of several orders of magnitude [79]. Magnetite possesses distinguished properties which one could benefit from. However, it suffers from agglomeration due to its high surface energy and poor conductivity. Therefore, incorporating

magnetite and graphene will enhance the conductivities of magnetite nanoparticles, reduce the agglomeration, improve the effective surface area and accelerate the rate of electron transfer across the electrode surface. This will eventually promote the sensitivity and stability of the analytical response [77, 78]. Table 4 outlines the graphene-magnetite modified electrode in electrochemical sensor application.

Table 4. Graphene-magnetite modified electrode in electrochemical sensor

Electrode	Analyte	Detection Method	Detection Limit	Linear Range	Refs.
C-rGO/Fe_3O_4	Dopamine	CA	7.00 nM	0.01 – 100.55 μM	[80]
Fe_3O_4/r-GO	Dopamine	DPV	0.08 μM	0.40 – 3.50 μM	[81]
Fe_3O_4/r-GO	H_2O_2	CV	6.00 nM	0.02-19.00 μM	[81]
CR-GO	H_2O_2	CV	0.05 μM	0.05 – 1500 μM	[82]
Fe_3O_4-Au/HRP	H_2O_2	CV	12.00 μM	0.02 – 2.50 mM	[83]
Fe_3O_4/GO	Prostate Specific Antigen (PSA)	Amperometric	15 fg/mL	0.1 – 1000 nM	[84]
Fe_3O_4/GO	Prostate Specific Membrane Antigen (PSMA)	Amperometric	4.8 fg/mL	1 – 10000 nM	[84]
Fe_3O_4/r-GO	NADH	CV	0.40 μM	15.00-190.00 μM	[81]
CR-GO	NADH	CV	10.00 μM	40.00-800.00 μM	[82]

Super-capacitor

As a type of electrochemical energy storage device, supercapacitors have received considerable attention because of their high-power density, fast charging/discharging rate, long cycle life, and low equivalent series resistance. A supercapacitor is ideal for numerous applications such as portable devices, electric vehicles, and flexible electronic devices [85]. Many parts make up a supercapacitor, including current collectors, electrodes, electrolytes, and separators. The separator's function is similar to that of the battery's separator. It isolates the two electrodes, allowing ions to travel through while preventing a short circuit between them. The basic principle of supercapacitor energy storage is to store electrical energy via an electric double-layer capacitance generated by charge separation at the electrolyte-bath solution interface [86]. Depending on the charge storage mechanisms, supercapacitors are divided into two main categories, including electrical double-layer capacitors (EDLC), which are based on the charge storage mechanism at the electrode/ electrolyte interface [87] and pseudocapacitance that relies on fast and reversible redox reaction that occurs at the surface of active materials [88, 89]. Electrostatic double-layer capacitors (EDLCs) use carbon electrodes or derivatives electrode-electrolyte (non-faradaic process) [90], while electrochemical pseudocapacitors use metal oxide or conducting polymer electrodes, reversible redox reaction (faradaic process) [91] with a high amount of electrochemical pseudocapacitance additional to the double-layer capacitance. By extending the electrode–electrolyte contact with nanomaterials with large specific area, the EDLC contribution can be boosted even more [92].

The distinctive properties of graphene will enhance the flexibility of the electrode and provide maximum adhesion with minimal distance between the electrode and electrolyte interface; thus, the charge-storage mechanism will eventually be more efficient [93]. However, to further improve the performance of supercapacitor, a nanosized transition metal oxide

incorporated with carbonous material is one of the promising solutions.

The incorporation of magnetite with graphene reduces the aggregation of Fe_3O_4 nanoparticles as the native magnetite is found to be low conductive. Thus the capacity of magnetite-based supercapacitors is easily faded [96]. To overcome this problem, most of the Fe_3O_4 nanoparticles will be attached onto the surface of graphene therefore, the immobilisation of the magnetite particles on the surface of graphene would eventually lower the intensity of the aggregation as graphene had high conductivity and more electrochemical stability. Magnetite-graphene composite considerable as excellent electroactive materials as the composite being composed of 30 Fe_3O_4/r-GO bilayers which reported from Wang *et al.*,., 2014 being synthesised through a layer-by-layer self-assembly method on silicon or indium tin oxide (ITO) substrate and it provides the capacitance, C_s of 151 Fg^{-1} at 0.9 Ag^{-1} [97]. Another work reported by Wang *et al.*,., 2014 provide a capacitance, C_s of 220.1 Fg^{-1} at 0.5 Ag^{-1} by the production of magnetite-graphene via hydrothermal reaction method [98]. Table 5 displays different composites of magnetite graphene used as supercapacitors. Moreover, Table 6 below illustrates advantages, disadvantages and challenges in each application, batteries, fuel cell, corrosion, sensor and supercapacitors

Table 5. Different composites of magnetite graphene used as supercapacitor

Electrode Materials	**Current Collector**	**Electrolyte**	**Highest Specific Capacitance (Fg^{-1})**	**Current Density (Ag^{-1})**	**Refs.**
Multilayer rGO	Au-sputtered	PVA/H_3PO_4	247.3	0.176	[99]
Graphene hydrogel	Au-coated PI	PVA/H_2SO_4	186.0	1.000	[100]
CNT-graphene/Fe_3O_4 nPs	Au-coated PET	Filter paper/Na_2SO_4	200.4	1.000	[101]
Hollow Carbon Sphere/Fe_3O_4	Stainless steel	5M LiCl	193	1.000	[102]
Fe_3O_4/C core shell microsphere	-	1M KOH	110.8	0.500	[103]

Table 6. Summary of advantages, disadvantages and challenges between applications

Applications	**Advantages**	**Disadvantages**	**Challenges**	**Ref.**
Batteries	High electrical conductivity, big Li^+ storage capacity, greater reversible capacity, high-rate performance, and cyclic stability.	Large surface area of rGO tends to restack, causing passivated solid electrolyte interface (SEI) film forms and irreversible electrolyte consumptions, resulting in capacity fading and low Coulombic efficiencies	Fabricating three-dimensional (3D) rGO or porous rGO to reduce agglomerations of graphene sheets and increase the active surface area, resulting in fast diffusion	[40-43]
Fuel cell	Surface of the electrocatalyst will not be inactivated prematurely. The catalyst is easy to recycle, which saves money and protects the environment	Graphene sheets tend to restack due to the attractive forces between graphene sheets, leading to a decrease in the availability of active sites	The choice of carrier material is key to the activity, selectivity, durability and cost-effectiveness of a catalyst.	[43]
Corrosion	Preventing the transport of corrosive or oxidative species toward the underlying substrate without notably altering its thermal conductivity and optical properties	Poor adhesion of graphene-based coatings to the most engineering metals	Graphene-based coatings produced directly on metallic surfaces do not improve corrosion protection	[72, 73]
Sensors	High sensitive sensing with a linear range magnitude nanoparticles can be highly dispersed on its surface, and the charge transfer at the interface of these hybrid materials can provide a synergistic effect	Decreasing interfering species' non-specific adsorption, and (3) maintaining the sensor's repeatability and stability in complicated actual matrices	Sensitive to temperature and, therefore, the sensors typically are internally temperature compensated greater the exposure to the target gas, the shorter the life span	[79, 80]

Table 6 (cont'd). Summary of advantages, disadvantages and challenges between applications

Applications	Advantages	Disadvantages	Challenges	Ref.
Super Capacitors	Can be coupled to generate hybrid nanostructures with EDLC and pseudocapacitive capabilities. Adding Fe_3O_4 to the anode boosted both the power output and the anodic capacitance	Poor electrochemical stability and had low conductivity	Limitations in transferring capacitive (F) performance values to bigger scales or commercial devices that retain the desirable properties of EDL SCs that outperform the current supercapacitor generation	[40-43]

Stability and Reusability

The stability and reusability of the magnetite graphene nanocomposite are important aspects to be considered to avoid any loss of cost and energy. The magnetite graphene composite seems to be potential material to supplement the techniques in use due to particular characteristics such as selectivity, low building and storage cost, miniaturising potential, easy automaticity, and simple to build and portable apparatus.

For example, work using batteries application as described by Li et al. revealed that the capacity of the magnetite graphene composite was ~434 $mAhg^{-1}$ after 50 cycles which is still 61% of the initial capacity (709.6 $mAhg^{-1}$) [105]. Another work presented by Zhou et al., uses graphene wrapped Fe_3O_4 nanoparticles for anode materials in applying lithium-ion batteries. The charge capacity of the magnetite graphene remained at 950 $mAhg^{-1}$ from the initial capacity even after the 85^{th} cycle which demonstrates the improvement of cycling stability of the composite. The Coulombic efficiency of the magnetite graphene after the second cycle remained close to 100% until the 30^{th} cycle. The magnetite graphene composite is also reported to exhibit an outstanding cyclic ability where it retains 91% of its initial capacity after 100 cycles when tested at a higher current density of 700 $mAhg^{-1}$ [106].

Based on the work conducted by Guo et al., which used magnetite modified graphene for oxygen reduction reaction (ORR) of fuel cell application, the composites exhibited outstanding stability and a four-electron transfer pathway, suggesting the direct reduction of oxygen to water. The nanocomposite decorated graphene also displayed superior oxygen reduction reaction activity with a half-wave potential of 0.85 V and 0.97 V of the onset potential, where the value is higher than the commercial 20 wt% Pt/C electrode [107].

On top of that, Vinodha et al. also used magnetite graphene as an electrode modifier for detection of hydrazine, The stability of Fe_3O_4-rGO were determined through the stability curves of the composite/GCE between the potential of negative 1 (-1) to positive 1 (+1) at a scan rate of 0.05 Vs^{-1} in 0.1M PBS solution. The composites reached their stable form at 30th cycle after continuous cycle. The redox peak current density decreased evenly before the 30th cycle. Once the magnetite graphene composite reaches its stable form, the stability of the composite remains until the 35^{th} cycle. The reproducibility and reusability properties remained 95.16% from the original detection limit after a gap of 20 days of analysis [108, 109-111].

Long term stability of magnetite graphene composite also has been reported by Ghasemi et al., which used the

composite for supercapacitors application. The composite being tested for 500 cycles by repeating the charge/discharge test, and during the first 100 cycles, it is being observed that it is only a slight increase, and the composite remains 87% of the initial capacitance after 500 cycles and only 3% decay in the capacitance [89,111-113].

Future Perspectives

Magnetite nanoparticles decorated on graphene sheets require comprehensive understanding both theoretically and experimentally. To improve this aspect, researchers are encouraged to use advanced physical characterisation techniques to deeply comprehend the control of the iron oxide nanoparticles' shape, size, crystallinity, distribution, and phase composition onto the graphene sheets. It is recommended to study the electrocatalytic efficiency of the nanocomposite towards ORR that can be further analysed using RDE and RRDE voltammetry techniques, where exposure to hydrodynamic effect and kinetic parameter will be obtained. The synthesis and production of high-quality graphene sheets also need extra attention. The in-situ production may lead to several defects and low purity of product as the core is graphene before magnetite is embedded into the sheets. Small-scale consumption of the nanocomposite in the electrochemical field can be enhanced into big-scale production, which can be used in energy generation plants as a primary source of renewable energy. The appropriate storage of Fe_3O_4/rGO is vital to avoid any contamination towards the sample or oxidation process to maghemite or hematite. The nanocomposite can be used extensively in other fields other than energy production, such as biomedical imaging, wastewater treatment, or water pollution removal. The properties of the nanocomposite might boost and give better-targeted yield throughout applications. Magnetic graphene can be further studied for its usage in human body for bone regeneration surgery treatment. The nanocomposite can be further modified with the addition of different, non-metallic nanoparticles to prolong the lifetime of the nanocomposite and give an increase in surface area and added exceptional properties.

Conclusion

Most of the process to synthesise magnetic graphene oxide is environmentally friendly, obeying the green chemistry rule. Graphene oxide is used as a unique and excellent material in the research field. Magnetic compound integration into GO strengthens the nanocomposite with more active sites and a larger surface area. A various alternative has been found recently to overcome the dependency of fossil fuels that will deplete sooner in the current rate of usage. Fuel cell is the brainchild of scientists who have a more excellent prospect in future; however, not favoured due to high costs due to the requirement of expensive materials such as platinum for generation of energy. Small scale energy production such as batteries improved its efficiency by the usage of magnetite graphene oxide nanocomposite. In corrosion, the nanocomposite layer proved to be better in protecting metal surfaces. Use of magnetite graphene oxide nanocomposite also improvises any gadgets and instruments applied. The simple method of production that obeys the green chemistry rules makes the production of the nanocomposite is safer and can be done at low cost. This is important as it is beneficial to industries and developing countries to cut-cost of energy production mainly. The material would be the most applied compound in wider fields in the future.

Acknowledgement

The authors are grateful to the Ministry of Higher Education Fundamental Research Grant Scheme (FRGS/1/2021/STG04/UMT/02/1) and Universiti Malaysia Terengganu for financial support and providing facilities for undertaking this research.

References

1. Ramachandran, R., Chen, T. W., Chen, S. M., Baskar, T., Kannan, R., Elumalai, P., ... and Dinakaran, K. (2019). A review of the advanced developments of electrochemical sensors for the detection of toxic and bioactive molecules. *Inorganic Chemistry Frontier*, *6*(12): 3418-3439.
2. Wang, G., Chen, J., Ding, Y., Cai, P., Yi, L., Li, Y., and Dai, L. (2021). Electrocatalysis for CO_2 conversion: from fundamentals to value-added products. *Chemical Society Reviews*, 50(8): 4993-5061.

3. Khan, W., Singh, A. K., Naseem, S., Husain, S., Shoeb, M. and Nadeem, M. (2018). Synthesis and magnetic dispersibility of magnetite decorated reduced graphene oxide. *Nano-structures & Nano-objects*, 16: 180-184.
4. Jin, C., Feng, G., Linghu, W., Zhang, L., Shen, R., Hu, J., ... and Sheng, J. (2018). Decontamination performance of magnetic graphene oxide towards nickel ions and its underlying mechanism investigation by XAFS. *Journal Molecular Liquids*, 258: 48-56.
5. Li, S., Duan, Y., Teng, Y., Fan, N. and Huo, Y. (2019). MOF-derived tremelliform Co_3O_4/NiO/Mn_2O_3 with excellent capacitive performance. *Applied Surface Sciences*, 478: 247-254.
6. Yuan, R., Yuan, J., Wu, Y., Chen, L., Zhou, H. and Chen, J. (2017). Efficient synthesis of graphene oxide and the mechanisms of oxidation and exfoliation. *Applied Surface Sciences*, 416: 868-877.
7. Lakshmi, K. B., Kumar, K. A., Reddy, J. V. and Sugunamma, V. (2019). Influence of nonlinear radiation and cross diffusion on MHD flow of Casson and Walters-B nanofluids past a variable thickness sheet. *Journal Nanofluids*, *8*(1): 73-83.
8. Jiao, X., Zhang, L., Qiu, Y. and Guan, J. (2017). Comparison of the adsorption of cationic blue onto graphene oxides prepared from natural graphites with different graphitisation degrees. *Colloids and Surface A: Physicochemical and Eng. Aspects*, 529: 292-301.
9. D'Souza, A., Yoon, J. H., Beaman, H., Gosavi, P., Lengyel-Zhand, Z., Sternisha, A. and Makhlynets, O. V. (2020). Nine-residue peptide self-assembles in the presence of silver to produce a self-healing, cytocompatible, antimicrobial hydrogel. *ACS Applied Materials & Interfaces*, 12(14): 17091-17099.
10. Ansari, M. O., Gauthaman, K., Essa, A., Bencherif, S. A. and Memic, A. (2019). Graphene and graphene-based materials in biomedical applications. *Current Medical Chemistry,* 26(38): 6834-6850.
11. Smith, A. T., LaChance, A. M., Zeng, S. and Sun, L. (2019). Synthesis, properties, and applications of graphene oxide/reduced graphene oxide and their nanocomposites. *Nano Materials Sciences,* 1(1): 31-47.
12. Suresh, K. and Yusoff, F. (2020). Thermal stability and porosity of reduced graphene oxide/zinc oxide nanoparticles and their capacity as a potential oxygen reduction electrocatalyst. *Malaysian Journal Analytical Sciences*, 24(3): 405-412.
13. Hussain, S., Kongi, N., Treshchalov, A., Kahro, T., Rähn, M., Merisalu, M., ... and Tammeveski, K. (2021). Enhanced oxygen reduction reaction activity and durability of Pt nanoparticles deposited on graphene-coated alumina nanofibres. *Nanoscale Advances*, 3(8): 2261-2268.
14. Park, S. K., Sure, J., Vishnu, D., Jo, S. J., Lee, W. C., Ahmad, I. A. and Kim, H. K. (2021). Nano-Fe_3O_4/carbon nanotubes composites by one-pot microwave solvothermal method for supercapacitor applications. *Energies*, 14(10): 2908.
15. He, B. and Li, J. (2019). A sensitive electrochemical sensor based on reduced graphene oxide/Fe_3O_4 nanorod composites for detection of nitrofurantoin and its metabolite. *Analytical Methods*, 11(11): 1427-1435.
16. Sammaiah, A., Huang, W. and Wang, X. (2018). Synthesis of magnetic Fe_3O_4/graphene oxide nanocomposites and their tribological properties under magnetic field. *Materials Research Express*, 5(10): 105006.
17. Banerjee, P., Chakrabarty, S., Thapa, R., & Das, G. P. (2017). Exploring the catalytic activity of pristine T6 [100] surface for oxygen reduction reaction: A first-principles study. *Applied Surface Science*, 418: 56-63.
18. Carmona-Carmona, A. J., Palomino-Ovando, M. A., Hernández-Cristobal, O., Sánchez-Mora, E. and Toledo-Solano, M. (2017). Synthesis and characterization of magnetic opal/Fe_3O_4 colloidal crystal. *Journal of Crystal Growth*, 462: 6-11.

19. Narayanaswamy, V., Obaidat, I. M., Kamzin, A. S., Latiyan, S., Jain, S., Kumar, H., ... and Issa, B. (2019). Synthesis of graphene oxide-Fe_3O_4 based nanocomposites using the mechanochemical method and in vitro magnetic hyperthermia. *International Journal of Molecular Sciences*, 20(13): 3368.
20. Manna, R. and Srivastava, S. K. (2021). Reduced graphene oxide/Fe_3O_4/polyaniline ternary composites as a superior microwave absorber in the shielding of electromagnetic pollution. *ACS omega*, 6(13): 9164-9175.
21. Venkataprasad, G., Reddy, T. M., Narayana, A. L., Hussain, O. M., Shaikshavali, P., Gopal, T. V. and Gopal, P. (2019). A facile synthesis of Fe_3O_4-Gr nanocomposite and its effective use as electrochemical sensor for the determination of dopamine and as anode material in lithium ion batteries. *Sensors and Actuators A: Physical*, *293*, 87-100.
22. Wang, L., Wei, Z., Mao, M., Wang, H., Li, Y. and Ma, J. (2019). Metal oxide/graphene composite anode materials for sodium-ion batteries. *Energy Storage Materials,* 16: 434-454.
23. Shobukawa, H., Alvarado, J., Yang, Y. and Meng, Y. S. (2017). Electrochemical performance and interfacial investigation on Si composite anode for lithium ion batteries in full cell. *Journal of Power Sources*, 359: 173-181.
24. Costa, C.M., Lee, Y.-H., Kim, J.-H., Lee, S.-Y. and Lanceros-Méndez, S. (2019). Recent advances on separator membranes for lithium-ion battery applications: from porous membranes to solid electrolytes. *Energy Storage Materials*, 22: 346-375.
25. Park, C. M., Heo, J., Wang, D., Su, C. and Yoon, Y. (2018). Heterogeneous activation of persulfate by reduced graphene oxide–elemental silver/magnetite nanohybrids for the oxidative degradation of pharmaceuticals and endocrine disrupting compounds in water. *Applied Catalysis B: Environmental*, 225: 91-99.
26. Tian, H., Liu, H., Yang, T., Veder, J.P., Wang, G., Hu, M., Wang, S., Jaroniec, M. and Liu, J. (2017). Fabrication of core-shell, yolk-shell and hollow Fe_3O_4@carbon microboxes for high-performance lithium-ion batteries. *Materials Chemistry Frontiers*, 1: 823-830.
27. Wang, Z., Xing, B., Zeng, H., Huang, G., Liu, X., Guo, H., Zhang, C., Cao, Y. and Chen, Z. (2021). Space-confined carbonisation strategy for synthesis of carbon nanosheets from glucose and coal tar pitch for high-performance lithium-ion batteries. *Applied Surface Sciences*, 547: 149228.
28. Li, R., Zhang, F., Du, C. and Liu, J. (2012). Synthesis of Fe_3O_4@SnO_2 core – shell nanorod film and its application as a thin-film supercapacitor electrode. *Chemical Communication*, 48: 5010-5012.
29. Meng, Y., Liu, X., Xiao, M., Hu, Q., Li, Y., Li, R., ... and Zhu, F. (2019). Reduced graphene oxide@ nitrogen doped carbon with enhanced electrochemical performance in lithium ion batteries. *Electrochimica Acta*, 309: 228-233.
30. Martha, S.K., Nanda, J., Zhou, H., Idrobo, J.C., Dudney, N.J., Pannala, S., Dai, S., Wang, J. and Braun, P.V. (2014). Electrode architectures for high capacity multivalent conversion compounds: iron (II and III) fluoride. *RSC Advances,* 4: 6730-6737.
31. Yoon, D., Hwang, J., Chang, W. and Kim, J. (2017). Uniform one-pot anchoring of Fe_3O_4 to defective reduced graphene oxide for enhanced lithium storage. *Chemical Engineering Journal*, 317: 890-900.
32. Wang, Y., Jin, Y., Zhao, C., Pan, E. and Jia, M. (2018). 3D graphene aerogel wrapped 3D flower-like Fe_3O_4 as a long stable and high rate anode material for lithium ion batteries. *Journal of Electroanalytical Chemistry*, 830: 106-115.
33. Huang, X., Zhou, X., Qian, K., Zhao, D., Liu, Z. and Yu, C. (2012). A magnetite nanocrystal/graphene composite as high performance anode for lithium-ion batteries. *Journal of Alloys and Compounds,* 514: 76-80.
34. Tian, H., Zhang, C., Wang, Q., Miao, J., Zhang, Y., Li, X., ... and Chen, Y. (2021). SiO_2 aerogel@ carbon nanotube anchored on graphene sheet as anode material for lithium ion battery. *Journal of Materials Science: Materials in Electronics*, 32(9): 11478-11488.

35. Zhu, K., Zhang, Y., Qiu, H., Meng, Y., Gao, Y., Meng, X., ... and Wei, Y. (2016). Hierarchical Fe_3O_4 microsphere/reduced graphene oxide composites as a capable anode for lithium-ion batteries with remarkable cycling performance. *Journal of Alloys and Compounds*, 675: 399-406.
36. Lee, S. H., Kotal, M., Oh, J. H., Sennu, P., Park, S. H., Lee, Y. S. and Oh, I. K. (2017). Nanohole-structured, iron oxide-decorated and gelatin-functionalised graphene for high rate and high capacity Li-Ion anode. *Carbon*, 119: 355-364.
37. Mhamane, D., Aravindan, V., Taneja, D., Suryawanshi, A., Game, O., Srinivasan, M. and Ogale, S. (2016). Graphene based nanocomposites for alloy (SnO_2), and conversion (Fe_3O_4) type efficient anodes for Li-ion battery applications. *Composites Science and Technology*, 130: 88-95.
38. Shen, X., Liu, H., Cheng, X. B., Yan, C. and Huang, J. Q. (2018). Beyond lithium ion batteries: Higher energy density battery systems based on lithium metal anodes. *Energy Storage Materials*, 12: 161-175.
39. Meng, Y., Liu, X., Xiao M., Hu, Q., Li, Y., Li, R., Ke, X., Ren, G. and Zhu, F. (2019). Reduced graphene oxide@nitrogen doped carbon with enhanced electrochemical performance in lithium ion batteries. *Electrochimica Acta*, 309: 228-233.
40. Hameed, M.U., Akram, M.Y., Ali, G., Hafeez, M., Altaf, F., Ahmed, A., Shahida, S. and Bocchetta, P. (2021). Facile preparation of Fe_3O_4 nanoparticles/reduced graphene oxide composite as an efficient anode material for lithium-ion batteries. *Coatings,* 2021: 11836.
41. Su, F. Y., Tang, R. and He, Y. B. (2017). Graphene conductive additives for lithium ion batteries: Origin, progress and prospect. *Chinese Science Bulletin*, 62: 3743-3756.
42. Xiang Y, Xin L, Hu J, Li C, Qi J, Hou Y, Wei X. (2021). Advances in the applications of graphene-based nanocomposites in clean energy materials. *Crystals*, 11(1):47.
43. Lee, J. G., Joshi, B. N., Lee, J. H., Kim, T. G., Kim, D. Y., Al-Deyab, S. S., ... and Yoon, S. S. (2017). Stable high-capacity lithium ion battery anodes produced by supersonic spray deposition of hematite nanoparticles and self-healing reduced graphene oxide. *Electrochimica Acta*, 228: 604-610.
44. Abdalla, A. M., Hossain, S., Azad, A. T., Petra, P. M. I., Begum, F., Eriksson, S. G. and Azad, A. K. (2018). Nanomaterials for solid oxide fuel cells: A review. *Renewable and Sustainable Energy Reviews*, *82*: 353-368.
45. Zhang, W., Chen, J., Li, X., Zhang, J., Li, Y., Zhao, Y., ... and Jin, X. (2020). Cuprum metal-organic-framework and polyacrylonitrile-derived Cu-NC electrocatalyst for application in zinc-air batteries. *Nano*, 15(01): 2050012.
46. Kumar, S. R., Wang, J. J., Wu, Y. S., Yang, C. C. and Lue, S. J. (2020). Synergistic role of graphene oxide-magnetite nanofillers contribution on ionic conductivity and permeability for polybenzimidazole membrane electrolytes. *Journal of Power Sources*, 445: 227293.
47. Papiya, F., Nandy, A., Mondal, S. and Kundu, P. P. (2017). Co/Al_2O_3-rGO nanocomposite as cathode electrocatalyst for superior oxygen reduction in microbial fuel cell applications: The effect of nanocomposite composition. *Electrochimica Acta*, 254: 1-13.
48. Santoro, C., Arbizzani, C., Erable, B. and Ieropoulos, I. (2017). Microbial fuel cells: From fundamentals to applications. A review. *Journal of Power Sources*, 356: 225-244.
49. Li, S., Pan, W., Wang, S., Meng, X., Jiang, C. and Irvine, J. T. (2017). Electrochemical performance of different carbon fuels on a hybrid direct carbon fuel cell. *International Journal of Hydrogen Energy*, 42(25): 16279-16287.
50. Goswami, C., Hazarika, K. K. and Bharali, P. (2018). Transition metal oxide nanocatalysts for oxygen reduction reaction. *Materials Science for Energy Technologies*, 1(2): 117-128.
51. Liu, X. and Hu, X. (2016). Iron oxide/oxyhydroxide decorated graphene oxides for oxygen reduction reaction catalysis: a comparison study *RSC Advance, 6*: 29848.

52. Hof, F., Liu, M., Valenti, G., Picheau, E., Paolucci, F. and Pénicaud, A. (2019). Size control of nanographene supported iron oxide nanoparticles enhances their electrocatalytic performance for the oxygen reduction and oxygen evolution reactions. *The Journal of Physical Chemistry C*, 123(34): 20774-20780.
53. Ma, Y., Wang, H., Key, J., Linkov, V., Ji, S., Mao, X., Wang, Q. and Wang, R. (2014). Ultrafine iron oxide nanoparticles supported on N-doped carbon black as an oxygen reduction reaction catalyst. *International Journal of Hydrogen Energy,* 39(27): 14777-14782.
54. Wu, Z.-S., Yang, S., Sun, Y., Parvez, K., Feng, X. and Müllen, K. (2012). 3D nitrogen-doped graphene aerogel-supported Fe_3O_4 nanoparticles as efficient electrocatalysts for the oxygen reduction reaction. *Journal of the American Chemical Society,* 134(22): 9082-9085.
55. Sun, W., Wu, T., Wang, L., Yang, Z., Zhua, T., Dong, C. and Liu, G. (2019). The role of graphene loading on the corrosion-promotion activity of graphene/epoxy nanocomposite coatings. *Composites Part B: Engineering,* 173: 106916
56. Karunagaran, R., Coghlan, C., Tung, T. T., Kabiri, S., Tran, D. N., Doonan, C. J. and Losic, D. (2017). Study of iron oxide nanoparticle phases in graphene aerogels for oxygen reduction reaction. *New Journal of Chemistry*, 41(24): 15180-15186.
57. Duan, Z. (2019). Application of graphene in metal corrosion protection. *IOP Conference Series: Materials Science Engineering,* 493: 012020.
58. Parhizkar, N., Ramezanzadeh, B. and Shahrabi, T. (2018). Corrosion protection and adhesion properties of the epoxy coating applied on the steel substrate pre-treated by a sol-gel based silane coating filled with amino and isocyanate silane functionalised graphene oxide nanosheets. *Applied Surface Sciences,* 439: 45-59.
59. Chen, S., Brown, L., Levendorf, M., Cai, W., Ju, S.-Y., Edgeworth, J., Li, X., Magnuson, C. W., Velamakanni, A., Piner, R. D., Kang, J., Park, J. and Runoff, R.S. (2011). Oxidation resistance of graphene-coated Cu and Cu/Ni alloy. *ACS Nano,* 5(2): 1321-1327.
60. Ding, R., Chen, S., Zhou, N., Zheng, Y., Li, B. J., Gui, T. J., ... and Tian, H. W. (2019). The diffusion-dynamical and electrochemical effect mechanism of oriented magnetic graphene on zinc-rich coatings and the electrodynamics and quantum mechanics mechanism of electron conduction in graphene zinc-rich coatings. *Journal of Alloys and Compounds*, 784: 756-768.
61. Zhang, L., Wu, H., Zheng, Z., He, H., Wei, M. and Huang, X. (2019). Fabrication of graphene oxide/multi-walled carbon nanotube/urushiol formaldehyde polymer composite coatings and evaluation of their physico-mechanical properties and corrosion resistance. *Progress in Organic Coatings*, 127: 131-139.
62. Yu, F., Camilli, L., Wang, T., Mackenzie, D. M., Curioni, M., Akid, R. and Bøggild, P. (2018). Complete long-term corrosion protection with chemical vapor deposited graphene. *Carbon*, 132: 78-84.
63. Bouanis, F. Z., Moutoussammy, P., Florea, I., Dominique, N., Chaussadent, T. and Pribat, D. (2019). Graphene nanoplatelets coating for corrosion protection of aluminum substrates. *Corrosion*, *75*(7): 799-808.
64. Necolau, M. I. and Pandele, A. M. (2020). Recent advances in graphene oxide-based anti-corrosive coatings: An overview. *Coatings*, 10(12): 1149.
65. Nayak, P. K., Hsu, C. J., Wang, S. C., Sung, J. C. and Huang, J. L. (2013). Graphene coated Ni films: a protective coating. *Thin Solid Films*, 529: 312-316.
66. Anisur, M. R., Banerjee, P. C., Easton, C. D. and Raman, R. S. (2018). Controlling hydrogen environment and cooling during CVD graphene growth on nickel for improved corrosion resistance. *Carbon*, 127: 131-140.
67. Chen, S., Brown, L., Levendorf, M., Cai, W., Ju, S.-Y., Edgeworth, J., Li, X., Magnuson, C.W., Velamakanni, A., Piner, R.D., Kang, J., Park, J. and Runoff, R.S. (2011). Oxidation resistance of graphene-coated Cu and Cu/Ni alloy. *ACS Nano,* 5(2): 1321-1327.

68. Bagherzadeh, M., Haddadi, H. and Iranpour, M. (2016). Electrochemical evaluation and surface study of magnetite/PANI nanocomposite for carbon steel protection in 3.5% NaCl. *Progress in Organic Coatings,* 101: 149-160
69. Sai, K. Jyotheender and Srivastava, C. (2019). Ni-graphene oxide composite coatings: Optimum graphene oxide for enhanced corrosion resistance. *Composites Part B: Engineering,* 175: 107145.
70. Khamis, E. A., Hamdy, A. and Morsi, R.E. (2018). Magnetite nanoparticles/polyvinyl pyrrolidone stabilised system for corrosion inhibition of carbon steel. *Egyptian Journal of Petroleum*, 27(4): 919-926
71. Bohdan, K., Maria A A. F. Nuno, F. F. S., Farzin, M., Alexandre, F. F. C. Kiryl, Y., António J. S. S. F. Adriana, B., Bruno, F., Rui, S., João, T. and Florinda M. C. (2021). A critical review on the production and application of graphene and graphene-based materials in anti-corrosion coatings. *Critical Reviews in Solid State and Materials Sciences,* 47(3): 309-355.
72. Mahmoudi, M., Raeissi, K., Karimzadeh, F. and Golozar, M. A.(2019). A study on corrosion behavior of graphene oxide coating produced on stainless steel by electrophoretic deposition. *Surface and Coatings Technology*, 372: 327-342,
73. Manjavacas, G., & Nieto, B. (2016). Hydrogen sensors and detectors. In *Compendium of Hydrogen Energy* (pp. 215-234). Woodhead Publishing.
74. Fronczak, M., Łabędź, O., Kaszuwara, W. and Bystrzejewski, M. (2018). Corrosion resistance studies of carbon-encapsulated iron nanoparticles. *Journal of Materials Science*, 53(5): 3805-3816.
75. Nag, A., Mitra, A. and Mukhopadhyay, S. C. (2018). Graphene and its sensor-based applications: A review. *Sensors and Actuators A: Physical*, 270: 177-194.
76. Agnihotri, A. S., Varghese, A. and Nidhin, M. (2021). Transition metal oxides in electrochemical and bio sensing: A state-of-art review. *Applied Surface Science Advances*, 4: 100072.
77. Yusoff, F., Rosli, A. R. and Ghadimi, H. (2021). Synthesis and characterisation of gold nanoparticles/poly3,4-ethylene-dioxythiophene/reduced-graphene oxide for electrochemical detection of dopamine. *Journal of Electrochemical Society*, 168(2): 026509.
78. Ladmakhi, H. B., Chekin, F., Fathi, S. and Raoof, J. B. (2020). Electrochemical sensor based on magnetite graphene oxide/ordered mesoporous carbon hybrid to detection of allopurinol in clinical samples. *Talanta,* 211: 120759.
79. Rosli, A. R. M., Yusoff, F., Loh, S. H., Yusoff, H. M., Jamil, M. M. A. and Shamsudin, S. H. (2021). Simultaneous electrochemical detection of ascorbic acid, dopamine, and uric acid at magnetic nanoparticles/reduced graphene oxide modified electrode. *Jurnal Teknologi*, 83(3): 85-92.
80. Salamon, J., Sathishkumar, Y., Ramachandran, K., Lee, Y. S., Yoo, D. J. and Kim, A. R. (2015). One-pot synthesis of magnetite nanorods/graphene composites and its catalytic activity toward electrochemical detection of dopamine. *Biosensors and Bioelectronics*, 64: 269-276.
81. Teymourian, H., Salimi, A. and Khezrian, S. (2013). Fe_3O_4 magnetic nanoparticles/reduced graphene oxide nanosheets as a novel electrochemical and bioeletrochemical sensing platform. *Biosensors and Bioelectronics*, 49: 1-8.
82. Shao, Y., Wang, J., Wu, H., Liu, J., Aksay, I. A. and Lin, Y. (2010). Graphene based electrochemical sensors and biosensors: a review. *Electroanalysis: An International Journal Devoted to Fundamental and Practical Aspects of Electroanalysis,* 22(10): 1027-1036.
83. Xin, Y., Fu-bing, X., Hong-wei, L., Feng, W., Di-zhao, C. and Zhao-yang, W. (2013). A novel H_2O_2 biosensor based on Fe_3O_4–Au magnetic nanoparticles coated horseradish peroxidase and graphene sheets–Nafion film modified screen-printed carbon electrode. *Electrochimica Acta,* 109: 750-755.
84. Sharafeldin, M., Bishop, G. W., Bhakta, S., El-Sawy, A., Suib, S. L. and Rusling, J. F. (2017). Fe_3O_4 nanoparticles on graphene oxide sheets for isolation and ultrasensitive amperometric detection of cancer biomarker proteins. *Biosensors and Bioelectronics*, 91: 359-366.
85. Häggström, Fredrik; Delsing, Jerker. (2018). IoT Energy Storage – A Forecast". *Energy Harvesting and Systems.* 5 (3–4): 43-51

86. Xu, B., Zheng, M., Tang, H., Chen, Z., Chi, Y., Wang, L., ... and Pang, H. (2019). Iron oxide-based nanomaterials for supercapacitors. *Nanotechnology*, *30*(20), 204002.
87. Ghanbari, R., Shabestari, M. E., Kalali, E. N., Hu, Y. and Ghorbani, S. R. (2021). Iron (II and III) Oxides/reduced graphene oxide/polypyrrole ternary nanocomposite as electrochemical supercapacitor electrode. *Journal of The Electrochemical Society*, 168(3): 030543.
88. Ghasemi, S., Hosseini, S. R. and Kazemi, Z. (2018). Electrophoretic preparation of graphene-iron oxide nanocomposite as an efficient Pt-free counter electrode for dye-sensitised solar cell. *Journal of Solid State Electrochemistry*, 22(1): 245-253.
89. Sharma, P. and Bhatti, T.S. (2010). A review on electrochemical double-layer capacitors. *Energy Conversion Management,* 51(12): 2901-2912
90. Fleischmann, S., Mitchell, J. B., Wang, R., Zhan, C., Jiang, D. E., Presser, V. and Augustyn, V. (2020). Pseudocapacitance: from fundamental understanding to high power energy storage materials. *Chemical Reviews,* 120(2020): 6738-6782.
91. Wang, G., Zhang, L. and Zhang, J. (2012). A review of electrode materials for electrochemical supercapacitors. *Chemical Society Reviews,* 41(2): 797-828.
92. Geng, L., Gao, Z. and Deng, Q. (2018). Electrochemical performance of iron oxide nanoflakes on carbon cloth under an external magnetic field. *Metals*, 8(11): 939.
93. Peng, X., Yu, H., Ai, L., Li, N. and Wang, X. (2013). Time behavior and capacitance analysis of nano-Fe_3O_4 added microbial fuel cells. *Bioresource Technology,* 2013: 144689-114692.
94. Peng, X., Yu, H., Wang, X., Zhou, Q., Zhang, S., Geng, L., ... and Cai, Z. (2012). Enhanced performance and capacitance behavior of anode by rolling Fe_3O_4 into activated carbon in microbial fuel cells. *Bioresource Technology,* 121: 450-453.
95. Azhar, A., Yamauchi, Y., Allah, A. E., Alothman, Z. A., Badjah, A. Y., Naushad, M., ... and Zakaria, M. B. (2019). Nanoporous iron oxide/carbon composites through in-situ deposition of prussian blue nanoparticles on graphene oxide nanosheets and subsequent thermal treatment for supercapacitor applications. *Nanomaterials*, 9(5): 776.
96. Xia, X. H., Chao, D. L., Zhang, Y. Q., Shen, Z. X. and Fan, H. J. (2014). Three-dimensional graphene and their integrated electrodes. *Nano Today*, 9(6): 785-807.
97. Wang, Q., Jiao, L., Du, H., Wang, Y. and Yuan, H. (2014). Fe_3O_4 nanoparticles grown on graphene as advanced electrode materials for supercapacitors. *Journal of Power Sources*, 245: 101-106.
98. Yoo, J. J., Balakrishnan, K., Huang, J., Meunier, V., Sumpter, B. G., Srivastava, A., ... and Ajayan, P. M. (2011). Ultrathin planar graphene supercapacitors. *Nano Letters*, 11(4): 1423-1427.
99. Papandrea, B., Xu, X., Xu, Y., Chen, C. Y., Lin, Z., Wang, G., ... and Duan, X. (2016). Three-dimensional graphene framework with ultra-high sulfur content for a robust lithium–sulfur battery. *Nano Research*, 9(1): 240-248.
100. Kuila, T., Mishra, A. K., Khanra, P., Kim, N. H. and Lee, J. H. (2013). Recent advances in the efficient reduction of graphene oxide and its application as energy storage electrode materials. *Nanoscale*, *5*(1): 52-71.
101. Shi, X., Zhang, S., Chen, X., Tang, T. and Mijowska, E. (2017). Effect of iron oxide impregnated in hollow carbon sphere as symmetric supercapacitors. *Journal of Alloys and Compounds*, 726: 466-473.
102. Pu, J., Shen, L., Zhu, S., Wang, J., Zhang, W. and Wang, Z. (2014). Fe_3O_4@ C core–shell microspheres: synthesis, characterisation, and application as supercapacitor electrodes. *Journal of Solid State Electrochemistry*, 18(4): 1067-1076.
103. Horn, M., Gupta, B., MacLeod, J., Liu, J. and Motta N. (2019). Graphene-based supercapacitor electrodes: Addressing challenges in mechanisms and materials. *Current Opinion in Green and Sustainable Chemistry,* 17: 42-48.
104. Li, X., Huang, X., Liu, D., Wang, X., Song, S., Zhou, L. and Zhang, H. (2011). Synthesis of 3D hierarchical Fe_3O_4/graphene composites with high lithium storage capacity and for controlled drug delivery. *The Journal of Physical Chemistry C*, 115(44): 21567-21573.

105. Zhou, M., Zhai, Y. and Dong, S. (2009). Electrochemical sensing and biosensing platform based on chemically reduced graphene oxide. *Analytical Chemistry*, 81(14): 5603-5613.
106. Gu, D., Zhou, Y., Ma, R., Wang, F., Liu, Q. and Wang, J. (2018). Facile synthesis of N-doped graphene-like carbon nanoflakes as efficient and stable electrocatalysts for the oxygen reduction reaction. *Nano-Micro Letters*, 10(2): 1-12.
107. Vinodha, G., Shima, P. D. and Cindrella, L. (2019). Mesoporous magnetite nanoparticle-decorated graphene oxide nanosheets for efficient electrochemical detection of hydrazine. *Journal of Materials Science*, 54(5): 4073-4088.
108. Khairul, W. M., and Yusoff, F. (2019). Synthesis and characterisation of poly (3, 4-ethylenedioxythiophene) functionalised graphene with gold nanoparticles as a potential oxygen reduction electrocatalyst. *Journal of Solid State Chemistry*, 275: 30-37.
109. Rosli, A. R., Loh, S. H. and Yusoff, F. (2019). Synthesis and characterisation of magnetic Fe_3O_4/reduced graphene oxide and its application in determination of dopamine. *Asian Journal of Chemistry*, 31(12): 2785-2792.
110. Yusoff, F., Suresh, K. and Khairul, W. M. (2021). Synthesis and characterisation of reduced graphene oxide/iron oxide/silicon dioxide ($rGO/Fe_3O_4/SiO_2$) nanocomposite as a potential cathode catalyst. *Journal of Physics and Chemistry of Solids*, 2021: 110551.
111. Yusoff, F., Suresh, K., Khairul, W. M. and Noorashikin, M. S. (2021). Electrocatalytic reduction of oxygen on reduced graphene oxide/iron oxide (rGO/Fe_3O_4) composite electrode. *Russian Journal of Physical Chemistry A*, *95*(4): 834-842.
112. Yusoff, F. and Suresh, K. (2021). Performance of reduced graphene oxide/iron (iii) oxide/silica dioxide (rGO/Fe_3O_4). *Sains Malaysiana*, 50(7): 2017-2024.
113. Yusoff, F., Suresh, K. and Noorashikin, M. S. (2020). Synthesis and characterisation of reduced graphene oxide-iron oxide nanocomposite as a potential fuel cell electrocatalyst. In *IOP Conference Series: Earth and Environmental Science*, 463: p. 012078.

Malaysian Journal of Analytical Sciences (MJAS)
Published by Malaysian Analytical Sciences Society

A SIMPLE REAGENT-FREE METHOD FOR ANALYSIS OF THE ETHANOL CONTENT IN GASOHOL

(Kaedah Mudah Tanpa Reagen bagi Analisis Kandungan Etanol di dalam Gasohol)

Jutharut Pansombut, Phetlada Sunchayanukun, Sasithorn Muncharoen*

Department of Chemistry, Faculty of Science,
Burapha University, Chonburi 20130, Thailand

**Corresponding author: Muncharoen@go.buu.ac.th*

Received: 29 December 2021; Accepted: 27 April 2022; Published: 25 August 2022

Abstract

A simple, convenient, economical and especially environmentally friendly method for ethanol analysis in gasohol was developed. The ethanol was extracted from gasohol by water based on 'like dissolved like' principle and then determined by simply weighing the water ethanol mixture using an analytical balance as a detector. The parameters that effect on the extraction such as extraction device, extraction ratio and sample volume were investigated. The results showed the correlation coefficient was 0.9976 for linear ranges 3-100% (v/v). Since this correlation coefficient was nearly 1 the relationship between ethanol content in gasohol and weigh of extracted water was linear. The limit of detection (LOD) and the limit of quantitation (LOQ) were 1.4% (v/v) and 4.6% (v/v), respectively. The percentage recovery (%Recovery) was 88-111%. The proposed method was successfully applied for determination of ethanol content in some gasohol products produced in Thailand and validated by gas chromatographic method (GC). The results obtained from the developed method was not significantly different from the GC at 95% confidence level (t_{stat} = 2.41, t_{crit} = 2.78).

Keywords: a reagent-less method, ethanol analysis, gasohol, analytical balance, green analytical method

Abstrak

Kaedah mudah, meyakinkan, ekonomik dan mesra alam bagi analisis etanol di dalam gasohol telah dibangunkan. Etanol yang diekstrak dari gasohol oleh pelarut air berasaskan prinsip larutan suka pelarut dan kemudian ditentukan melalui timbangan campuran air dan methanol menggunakan penimbang analitikal sebagai pengesan. Parameter yang memberi kesan terhadap pengekstrakan seperti alat pengesktrakan, nisbah pengekstrakan dan isipadu sampel telah dikaji. Keputusan menunjukkan pekali korelasi ialah 0.9976 untuk julat kelinearan 3-100% (v/v). Nilai pekali korelasi yang menghampiri 1 menjelaskan hubungan linear antara kandungan etanol dalam gasohol dan berat pelarut air yang diekstrak. Had pengesanan (LOD) dan had pengkuantitian (LOQ) masing -masing ialah 1.4% (v/v) dan 4.6% (v/v). Peratus perolehan semula ialah 88-111%. Kaedah yang dicadang telah Berjaya digunapakai bagi penentuan kandungan etanol di dalam beberapa produk gasohol di Thailand dan ditentusahkan melalui kaedah gas kromatografi (GC). Keputusan yang diperolehi tidak menghasilkan perbezaan secara signifikan pada aras keyakinan (t_{stat} = 2.41, t_{crit} = 2.78).

Kata kunci: kaedah tanpa reagen, analisis etanol, gasohol, penimbang analitikal, kaedah analisis hijau

Introduction

Today gasohol is used as an alternative energy source and is very popular in many countries around the world, for example America, Canada, Brazil, Kenya, Paraguay, Spain, Sweden, Australia and China. In Thailand there are attempts bring to use gasohol as a supplement or replacement fuel instead of crude oil because of several advantages including being more environmentally friendly [1-3]. Gasohol usually consists of a mixture of gasoline (fossil fuel) and purified ethanol (99.0-99.5% purity) in various proportions. Generally, ethanol or ethyl alcohol can be produced from natural raw materials such as sugar cane and cassava. Inferences can supply and growing up in a short time [4-7]. Then the gasohol is not only used as a green fuel for people around the world, but it can help agriculturalists' revenue around the world also. Especially Thailand, it is an agricultural land. Due to foreseeing of the Royal Majesty the King Rama 9, the gasohol was occurred in 1985 by the Royal Development project. Then, the gasohol in Thailand has started at that time and has developed continuously to this day [8-10]

The different percentages of ethanol which are added into gasoline, are by the E-number, for instance E10 contains 10% (v/v) purified ethanol and 90% (v/v) gasoline. The advantages of ethanol blending with gasoline base-fuel include decreasing toxic combustion products, reduced price, increasing agriculture and boosting the octane number of the fuel. It is important that the ethanol content be monitored to control the quality of the fuel [11, 12].

Since, the quality of gasohol depends on the amount of ethanol added to the gasoline, the determination of ethanol in fuel ethanol is important to the oil and petroleum industry. There are many methods available to investigate the ethanol content in fuel including those based on chromatography, spectroscopy and electrochemistry. For example, chromatographic methods; gas chromatography (GC) is used as a standard method for determination of ether and alcohols in gasoline (ASTMD 4815-03) [13] and a liquid chromatography method was reported by Zinbo in 1984 [14] for the determination of C1-C3 alcohols in gasoline and alcohol blends using a mixed mode of size-exclusion and adsorption liquid chromatography (LC). In 2018, Morine et al., described the determination of ethanol in gasoline by high performance liquid chromatography (HPLC) [15]. In addition, GC was also used for determination of alcohols in other samples such as groundwater and surface water [16]. Spectroscopic methods; one of spectroscopy for ethanol analysis in fuel gas was infra-red spectroscopy (IR) [17, 18]. In 1981, Battiste et al. presented the measurement of ethanol concentration in a series of gasohol using IR-reflectance detection [17]. In 2003, Mendes et al. exhibited Fourier Transforms (FT)-near infra-red and FT-Raman spectrometry to analyze the ethanol content in fuels and beverages [18]. Flow based methods have also been used for analysis of ethanol in fuel [1, 19, 20]. Electrochemical method such as voltammetry [21, 22] and amperometry [23, 24] are often chosen for ethanol analysis. However, all the above methods require chemical reagents, sophisticated instruments and operators with special expertise. At the present time "green analytical methods" have become widely popular.

The main objectives of these methods are reduction of environmentally harmful chemicals and the harm caused using chemicals. The reagent-less method is one of the green analytical method. It is widely popular in various fields. The ultimate aim is to develop reagentless analytical strategies in this case for determination of the ethanol content in gasohol. The method is based on ethanol extraction from gasohol into distilled water and simply weighting the extract using an analytical balance .

Materials and Methods

Reagents and chemicals

An analytical balance Model RC 250 S (Scientific Promotion CO., LTD) and 10 mL syringe with metal lure lock (Mira) were used in the "reagent-free" analytical method. A UV-Visible Spectrophotometer model HP 8453 (Hewlett Packard CO., LTD) was used for the extraction efficiency study. A gas chromatograph (GC) model HP 6890 (Hewlett Packard CO., LTD) was used as the standard calibration method for ethanol.

Analytical procedure

The "reagent-free" method for analysis of ethanol in

gasohol fuels was as follows: 3 mL of distilled water and then 1 mL of gasohol or based fuel was withdrawn into a 10 mL graduated syringe. The needle of syringe was inverted with the needle up and the solution was mixed well by pulling the plunger in and out for 2 min. The syringe was placed with the needle down and left united the water and oil layers separated. The extracted bottom water/ethanol layer was transferred into a vial for weighing using an analytical balance. Finally, the weight was analyzed to determine the amount of ethanol in gasohol. The schematic diagram of this extraction is shown in Figure 1 Additionally, the ethanol content analyzed by the proposed method were compared to that obtained by the standard GC method [25], [26].

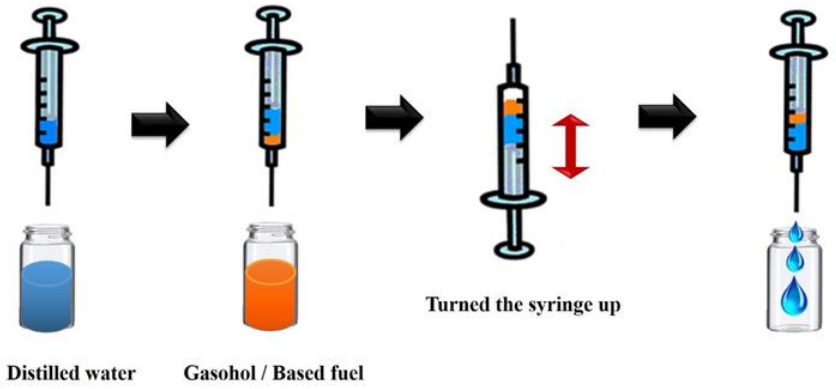


Figure 1. The schematic diagram of the 1st method that proposed for ethanol extraction from gasohol.

Optimization of the extraction device

The devices for extraction of the ethanol from gasohol studied here were burette, glass vial, modified burette and syringe with metal lure lock as shown in the Figure 2. These were used for extraction of standard gasohol fuel with various concentrations of ethanol content of 0, 10, 20, 40 and 60*%v/v.* The extraction procedure using these various devices was done according to topic 2.3. The extraction ratio used in this study was 1:2 (gasohol: distilled water) for plotting the calibration. The calibrations were plotted between the extracted water weight (y-axis) and concentrations of standard gasohol (x-axis) using different extraction devices.

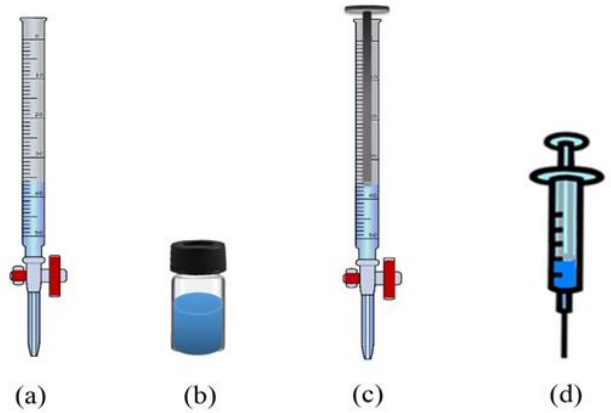


Figure 2. The devices used for the study of ethanol extraction from gasohol (a) commercial burette (b) glass vial (c) modified burette and (d) syringe.

Extraction ratio and sample volume

According to the experiment procedure (Analytical procedure), the ratio of gasohol fuel and distilled water was varied among 1:1, 1:2 and 1:3. In this study, the sample volume of 1 mL was used for varying these ratios. For sample volume study, the optimum ratio was used in this investigation varying the sample volumes of 0.6, 1.0 and 2.0 mL, respectively. Both studies, the comparisons of absorbance between the extracted ethanol and standard ethanol in water were studied using the regression line method as criterion.

Results and Discussion

Extraction device

These devices: burette, glass vial, modified burette and syringe with metal lure lock were used for the optimized extraction device study. The linearity, sensitivity and correlation coefficient (r^2) were considered as criterion for the suitability of the extraction device. As shown in the Table 1, the sensitivities, which were slopes of the linear equations, were almost identical (0.0143-0.0149). However, the correlation coefficient (r^2) created from the syringe was the closet to 1 (0.9896), while r^2 for the glass vial was slightly lower (0.9619) probably because of the many transfers step involved. Thus, the vial method was found to be less suitable as an ethanol extraction device. Considering the relative standard deviation (%RSD), the results illustrated that the highest value and subordinate values were burette, vial, modified burette and syringe, respectively (Table 1). This indicated that both the modified burette and syringe exhibited good precision. Nevertheless, considering convenience, controlling the volume of distilled water or gasohol using the modified burette was more difficult than the syringe. Consequently, the syringe with a metal lure lock was chosen as the most appropriate extraction device for extraction of ethanol.

Table 1. Linear equation, correlation coefficient, relative standard deviation (%RSD) of all studied extraction devices: burette, glass vial, modified burette and syringe

Extraction device	Linear equation	Correlation coefficient (r^2)	%RSD (n= 3)
Burette	y = 0.0145x - 0.0144	0.9778	1.8
Glass vial	y = 0.0149x - 0.0285	0.9619	0.9
Modified burette	y = 0.0147x + 0.0650	0.9823	0.7
Syringe	y = 0.0143x + 0.1336	0.9896	0.6

Optimization of the extraction condition: Extraction sequence

The extraction sequence was studied by different series of gasohol and distilled water. Here, the sequence of extraction was divided to 3 sets: (i) suction of 4.0 mL distilled water and then 2.0 mL standard gasohol (ii) suction of 2.0 mL standard gasohol and then 4.0 mL distilled water (iii) the series of 2.0 distilled water, 1.0 mL standard gasohol, 2.0 distilled water and finally 1.0 mL standard. The criteria sensitivity and relative standard deviation (%RSD) were used to compare the methods. The results shown in Table 1, found that the 3rd method gave the highest sensitivity due to the higher surface contact between the gasohol and water. However, it was found that this method also gave a poor method precision (the highest %RSD). It may because of difficult control of the capacitance of these solutions. The 2nd method gave the lowest slope of linearity range (sensitivity) compared to other methods, perhaps due to the easier evaporation of ethanol in gasohol. In the 1st method, the distilled water was pulled first and the gasohol was sucked later. Ethanol in the gasohol could be more easily trapped in the distilled water than in the 2nd set. It may be reason of the sensitivity of the 2nd one showed the higher value (slope of linearity). In addition, the precision in the 1st set was greater than the 2nd method (%RSD = 0.7467 and 1.0237 for the 1st and the 2nd sets, respectively). Consequently, the 1st method was selected for the extraction of ethanol content in gasohol for further work.

The ratio of gasohol and distilled water

In this study, the ratio of gasohol fuel and distilled water was varied among 1:1, 1:2 and 1:3. The absorbance of extracted ethanol results was compared to these of standard ethanol in water using the regression line method is shown in Figure 3. As a compromise between the correlation coefficient (r^2) and extraction percentage for these ratios (Table 2), a ratio of 1:3 was chosen for further work (Figure 3).

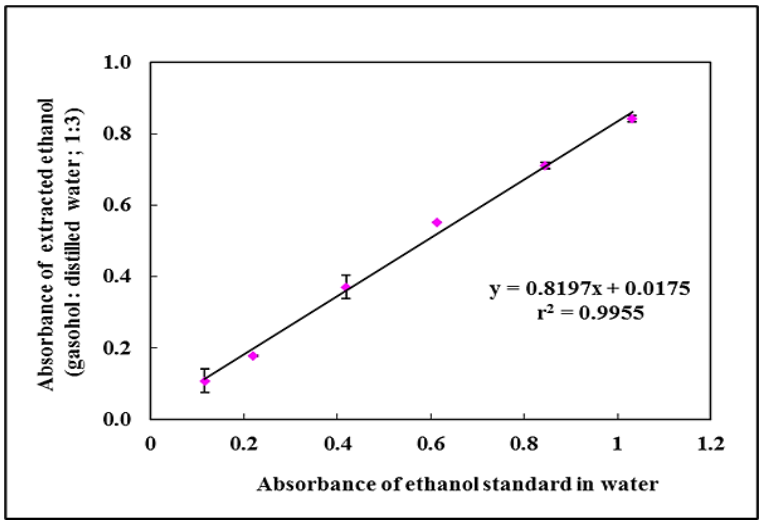


Figure 3. The plot of absorbance of extracted ethanol in water (from gasohol) and standard ethanol (the regression line method)

Table 2. Linear equations, correlation coefficient (r^2) and extraction percentage of standard ethanol for the extraction at various ratios of samples (gasohol) and distilled water

Ratio of extraction	Linear equation	Correlation coefficient (r^2)	Percentage extraction of extracted ethanol at various concentrations (%*v/v*)					
			10	20	40	60	80	100
1 : 1	y = 0.0177x + 0.0264	0.9964	71	72	62	53	52	50
1 : 2	y = 0.0178x - 0.0612	0.9976	85	86	60	76	76	72
1 : 3	y = 0.0175x - 0.0273	0.9958	94	82	89	90	84	82

Volume of gasohol and distilled water for 1:3 ratio extraction

The volume of standard gasohol and extractant (distilled water) at 1:3 extraction ratio was studied. The volume (mL) of gasohol : distilled water was 0.6: 1.8; 1.0: 3.0; 2.0: 6.0 mL, respectively. The standard gasohol concentrations of ethanol content of 0, 10, 20, 40, 60 and 100 %*v/v* were studied for construction of calibration plots. The results (Figure 4) showed that the ratio of 2.0 mL gasohol : 6.0 mL distilled water gave the highest

sensitivity and r^2. Thus, the volume of standard gasohol fuel and distilled water of 2.0 : 6.0 mL was selected for all subsequent experiments. Finally, the optimized extraction conditions for the 'reagent-free' method were in Table 3.

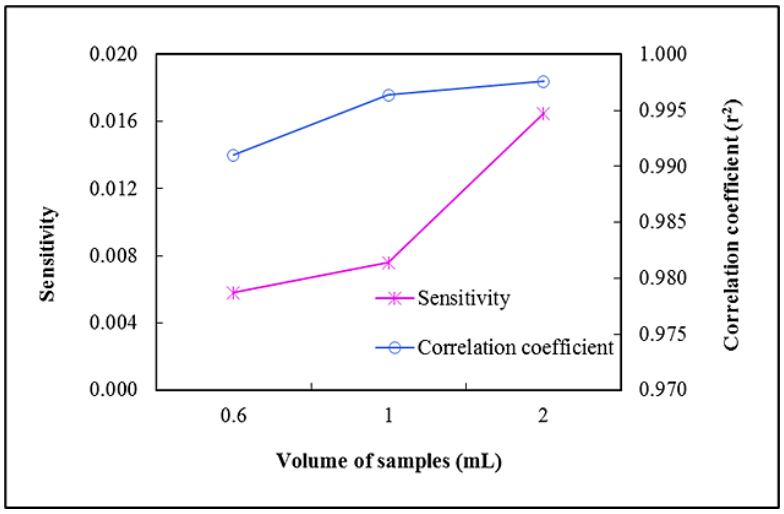


Figure 4. The relation plots of sensitivities (pink line) and correlation coefficient (r^2) (blue line) of the extraction method with ratio of sample or gasohol : distilled water of 1:3 with sample volumes

Table 3. Optimization of experimental parameters for extraction of ethanol in gasohol

Parameter	**Studied Condition**	**Selected Condition**
Extraction sequence	1st method (the distilled water was pulled first, and the gasohol was sucked later). 2nd method (the gasohol was pulled first, and the distilled water was sucked later). 3rd method (switching the distilled water and gasohol).	1st method
The ratio of gasohol and distilled water	1 : 1 1 : 2 1 : 3	1 : 3
Volume of gasohol and distilled water for 1:3 ratio extraction (mL)	0.6 : 1.8 1.0 : 3.0 2.0 : 6.0	2.0 : 6.0

Analytical performance: Linearity range

The capability of the proposed method for ethanol analysis was investigated using 'reagent-free' method. This method showed the two linearity ranges of 3-100 %*v/v* with r^2 of 0.9976 as shown in Figure 5.

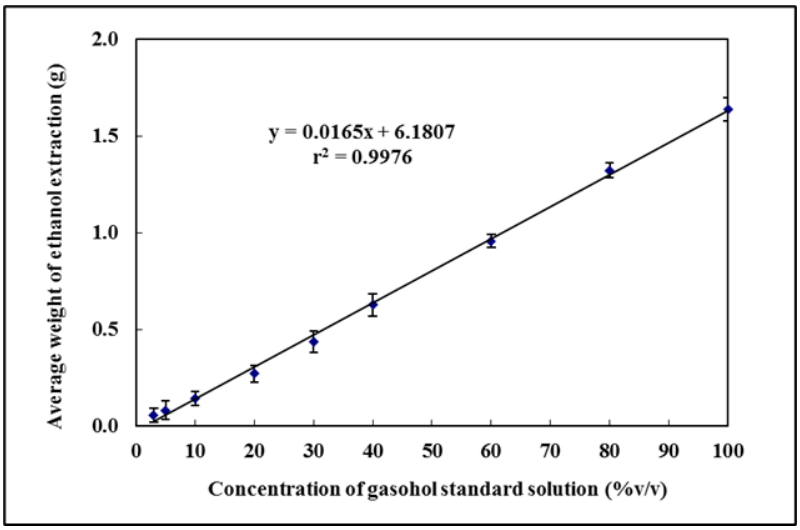


Figure 5. The calibration plots from the 'reagent-free' method corresponding to different concentrations of ethanol in the range of 3 to 100 %*v/v*

Limit of detection (LOD) and limit of quantitation (LOQ)

The LOD was 1.4 %*v/v* while the LOQ was 4.6 %*v/v* (Table 4), these were calculated by 3SD/slope and 10SD/slope, respectively. SD is the standard deviation of a series of replicate analyses and the slope is the gradient of the calibration curve.

Table 4. Analytical parameters for determination of ethanol in gasohol using 'reagent-free' method

Parameter	Optimized Value
Linearity range (%*v/v*)	3 - 100
Linear equations:	y = 0.0165x + 6.1807 (r^2= 0.9976)
LOD (%*v/v*)	1.4
LOQ (%*v/v*)	4.6
% RSD (n=10)	<1
% Recovery	88.0 -111

Repeatability

The precision of the method or repeatability is represented by the relative standard deviation (%RSD). For concentrations of standard gasohol were 10 and 20%*v/v*, the %RSD of the weight were less than 1% for 10 replicate analyses (Table 5). This indicated that the proposed 'reagent-free' method provided a good precision for determination of ethanol in gasohol fuel.

Table 5. Relative standard deviation (%RSD) for precision study of the proposed method

Ethanol Concentration (%*v/v*)	**Average Weight of Extracted Ethanol (g)***	**Relative Standard Deviation (%RSD)**
10	6.3688 ± 0.0466	0.73
20	6.4977 ± 0.0610	0.94

Note * n = 10

Recovery percentage

To test the accuracy of the ethanol analysis in gasohol fuel the standard addition method with the reagent-free method was used to evaluate as the recovery percentage. Normally gasohol fuel (10% *v/v*) called E10, is found at fuel service stations in Thailand. Thus, different brands of E10 were used in this study. The recoveries achieved for the samples spiked with various concentrations of ethanol were in the range of 88 -111% as shown in Table 6. This indicated that the proposed method was reliable for determination of ethanol in real samples.

Table 6. Recovery percentage for determination of ethanol in gasohol samples using the developed method

Sample	**Concentration of Ethanol (%*v/v*)**				**Recovery (%)**
	Added	**Found (mean ± SD; n = 3)**			
A	-	9.1	±	0.0106	
	5	13.6	±	0.0173	89.8
B	-	9.8	±	0.0091	
	5	15.3	±	0.0116	111
C	-	8.9	±	0.0093	
	5	14.3	±	0.0076	108
D	-	9.3	±	0.0214	
	5	13.7	±	0.0138	87.6
E	-	19.8	±	0.0084	
	5	25.7	±	0.0168	117

Sample analysis

The determination of the ethanol content in gasohol fuel (real samples) was achieved using the external standard method. The results obtained using this method agreed with the data from gas-chromatography (GC) for all samples as shown in Table 7. The paired *t*-test [27] showed that the ethanol contents in real samples determined by the reagent-free methods were not significantly different from the contents given by gas-chromatography the at the 95% confidence level (t_{stat} = 2.41, t_{crit} = 2.78). This showed that the developed method was accurate and reliable for determination of ethanol in gasohol

Table 7. Validation of the 'reagent-free method' by comparison the results with the standard gas chromatography

Sample	Type Of Gasohol	The Proposed Method	Standard Method (Gas-Chromatography: GC)
A	E10	9.3 ± 0.1	10.7 ± 0.1
B	E10	10.7 ± 0.6	10.2 ± 0.1
C	E10	10.0 ± 0.6	11.3 ± 0.2
D	E10	9.2 ± 1.5	10.0 ± 0.1
E	E20	19.5 ± 0.6	20.8 ± 0.3

Note: E10 is 10% *v/v* and E20 is 10% *v/v* of ethanol added in based fuel. Sample A-E were purchased from the gas stations in Chonburi province of Thailand

Conclusion

A reagent-free method was developed and applied to the analysis of ethanol content in gasohol fuel. The proposed experimental process uses no chemicals including using syringes in the experimental procedure that are commonly available is easy. Especially, other experimental devices are simple and economical. The responses of the method were found to be linear in the range of 3-100 %*v/v* of ethanol, Additionally, a comparison of the accurate values given by the gas chromatographic method and the proposed method revealed that there is no significant difference between the two methods. This suggests that the proposed method is valid alternative for determination of ethanol in fuel. Additionally, another application of the proposed method is in education especially quantitative analysis. Due to simple equipment non-toxicity and easy to operation.

Acknowledgement

This work was financially supported by the Research Grants from Burapha University and Government Budget Grant (B.E. 2562) through the National Research Council of Thailand (Grant no. 57.2/2562). We would like to enunciate thank to Miss Chinanan Sauguanboonyapong for undertaking the GC experiments. Additionally, we would like to thank the Faculty of Science, Burapha University for providing in English proofreading service for academic manuscripts. We express thanks to Dr. Ronald Beckett for useful suggestions on the manuscript.

References

1. Muncharoen, S., Sitanurak, J., Tiyapongpattana, W., Choengchan, N., Ratanawimarnwong, N., Motomizu, S., Wilairat, P. and Nacapricha, D. (2009). Quality control of gasohol using a micro-unit for membraneless gas diffusion. *Microchimica Acta*, 164(1): 203-210.
2. Alhadeff, E. M., Salgado, A. M., Pekeira, N. and Valdman, B. (2004). Development and application of an integrated system for monitoring ethanol content of fuels. *Applied Biochemistry and Biotechnology - Part A Enzyme Engineering and Biotechnology*, 113(1-3): 125-136.
3. Zinbo, M. (1984). Determination of one-carbon to three-carbon alcohols and water in gasoline/alcohol blends by liquid chromatography. *Analytical Chemistry,* 56(2): 244-247.
4. Silalertruksa, T., Gheewala, S. H. and Pongpat, P. (2015). Sustainability assessment of sugarcane biorefinery and molasses ethanol production in Thailand using eco-efficiency indicator. *Applied Energy*, 160(1): 603-609.
5. Gani, M. (2018). Production of bioethanol from sugarcane bagasse using saccharomyces production of bioethanol from sugarcane bagasse using *Saccharomyces cerevisiae. Journal of Basic & Applied Mycology (Egypt),* 22(1): 1-8.

6. Ajibola, F. O., Edema, M. O. and Oyewole, O. B. (2012). Enzymatic production of ethanol from cassava starch using two strains of *Saccharomyces cerevisiae. Nigerian Food Journal*, 30(2): 114-121.
7. Adeleye, T. M., Kareem, S. O., Mobolaji, O., Atanda, O. and Adeogun, A. I. (2020). Ethanol production from cassava starch by protoplast fusants of *Wickerhamomyces anomalus* and *Galactomyces candidum. Egyptian Journal of Basic and Applied Sciences*, 7(1): 67-81.
8. Yoosin, S. and Sorapipatana, C. (2007). A study of ethanol production cost for gasoline substitution in thailand and its competitiveness. *Science and Technology Asia*, 12(l): 69-80.
9. Mungkalasiri, W. and Pan-in, B. (2018). Optimization of bioethanol production from raw sugar in Thailand. *Science and Technology Asia*, 23(1): 57-66.
10. Thailand industry outlook (2021-2023). Ethanol Industry. https://www.krungsri.com/en/research/industry /industry-outlook/Energy-Utilities/Ethanol/IO/io-ethanol-21. [Access Online 10 September 2021].
11. Journal, B., Belincanta, J. and Alchorne, J. A. (2016). The brazilian experience with ethanol fuel: aspects of production, use, quality and distribution logistics. *Brazilian Journal of Chemical Engineering,* 33(4): 1091-1102.
12. Santos, A. P. F.d., Silva, K. K. D., Borges, G. A., and d'Avila, L. A. (2020). Fuel quality monitoring by color detection. In L.-W. Zeng and S.-L. Cao (Eds.), Color Detection. IntechOpen: pp. 1-22.
13. Drews, A. W. (1998). In manual on hydrocarbon analysis, 6th edition, standard test method for determination of MTBE, ETBE, TAME, DIPE, tertiary-amyl alcohol and C1 to C4 Alcohols in gasoline by gas chromatography. Blatimore: pp. 73-738.
14. Zinbo, M. (2020). Determination of methanol in gasoline and ethanol fuels by high-performance liquid chromatography. *Journal of the Brazilian Chemical Society*, 31(5): 1055-1063.
15. Morine, L., Pereira, A., Ignácio, D., Mattos, M. De, Gimenes, C., Souza, D., França, D., Andrade, D. and Antonio, L. (2018). Determination of ethanol in gasoline by high-performance liquid chromatography. *Fuel,* 212: 236-239.
16. Cassada, D. A., Zhang, Y., Snow, D. D. and Spalding, R. F. (2000). Trace analysis of ethanol, MTBE, and related oxygenate compounds in water using solid-phase microextraction and gas chromatography/mass spectrometry. *Analytical Chemistry,* 72(19): 4654-4658.
17. Battiste, D. R., Fry, E., Ted, B., and Perkin-elmer, T. (1981). Determination of ethanol in gasohol by infrared spectrometry. *Analytical Chemistry*, 53(1): 1096-1099.
18. Mendes, L. S., Oliveira, F. C. C., Suarez, P. A. Z. and Rubim, J. C. (2003). Determination of ethanol in fuel ethanol and beverages by Fourier transform (FT) -near infrared and FT-Raman spectrometries. *Analtica Chimica Acta,* 493(2): 219-231.
19. Alhadeff, E. M., Salgado, A. M., Pereira, N. and Valdman, B. (2005). A sequential enzymatic microreactor system for ethanol detection of gasohol mixtures. I*n Twenty-Sixth Symposium on Biotechnology for Fuels and Chemicals*, pp. 361-371.
20. Alhadeff, E. M., Salgado, A. M., Cos, O., Pereira, N. and Valero, F. (2007). Enzymatic microreactors for the determination of ethanol by an automatic sequential injection analysis system. *Applied Biochemistry And Biotechnology,* 137(1): 17-25.
21. Pereira, P. F., Sousa, R. M. F., Munoz, R. A. A. and Richter, E. M. (2013). Simultaneous determination of ethanol and methanol in fuel ethanol using cyclic voltammetry. *Fuel*, 103: 725-729.
22. Cardoso, J. L., and Bertotti, M. (2007). The use of a copper microelectrode to measure the ethanol content in gasohol samples. *Fuel,* 86(7-8): 1185-1191.
23. Tomassetti, M., Capesciotti, G. S., Angeloni, R. and Martini, E. (2016). Bioethanol in biofuels checked by an amperometric organic phase enzyme electrode (OPEE) working in " substrate antagonism " format. *Sensors,* 16(9): 1-10.
24. Campanella, L., Capesciotti, G. S., Gatta, T., and Tomassetti, M. (2010). An innovative organic phase enzyme electrode (OPEE) for the determination of ethanol in leadless petrols. *Sensors and Actuators: B. Chemical*, 147(1): 78-86.

25. Leary, J. J. (1983). A quantitative gas chromatographic ethanol determination: a contemporary analytical experiment. *Journal of Chemical Education*, 60(8): 675.
26. Hönig, V., Táborský, J., Orsák, M. and Ilves, R. (2015). Using gas chromatography to determine the amount of alcohols in diesel fuels. *Agronomy Research*, 13(5): 1234-1240.
27. Miller, J.N., and Miller, J. (2010). Statistics and Chemometrics for analytical chemistry, 6th edition. Ashford Colour Press Ltd., Gosport: pp. 43-45.

Malaysian Journal of Analytical Sciences (MJAS)
Published by Malaysian Analytical Sciences Society

PRELIMINARY STUDIES ON SUNLIGHT ASSISTED DEGRADATION OF 2-CHLOROPHENOL USING MoS_2/GO AS PHOTOCATALYST

(Kajian Awal Mengenai Cahaya Tampak Dituruti Penyusutan Sinaran 2-klorofenol Menggunakan MoS_2/GO Sebagai Pemangkin Cahaya)

Kavirajaa Pandian Sambasevam, Syara Syazliana Muhammad Rajab, Izyan Najwa Mohd Norsham, Siti Nor Atika Baharin*

Advanced Material for Environmental Remediation (AMER) Research Group, Faculty of Applied Sciences, University Teknologi MARA, Cawangan Negeri Sembilan, Kampus Kuala Pilah, 72000, Kuala Pilah, Negeri Sembilan, Malaysia

**Corresponding author: atikabaharin@uitm.edu.my*

Received: 14 September 2021; Accepted: 24 March 2022; Published: 25 August 2022

Abstract

This study highlighted preliminary studies on photodegradation of 2-chlorophenol using MoS_2/rGO photocatalyst with different weight ratios under sunlight irradiation. The 2-chlorophenol is known as one of the most dangerous pollutant due to its hazardous properties of mutagenicity, carcinogenicity and eco-pollutant. The MoS_2/rGO photocatalysts were synthesized using the hydrothermal method and used for the degradation of 2-chlorophenol under solar light irradiation. Three different compositions of MoS_2/rGO (1%, 5% and 15%) were synthesized with different weight ratio of MoS_2. The composites material of MoS_2, GO and MoS_2/rGO was characterized by FTIR and XRD indicating successful formation of MoS_2/rGO composites. The photodegradation of the 10 ppm of 2-chlorophenol were observed under the exposure of sunlight for 180 minutes and analyzed using UV-VIS to measure percent degradation of 2-chlorophenol. 1% MoS_2/rGO has been chosen as the composite to degrade 2-chlorophenol due to having the highest percent degradation of 51.41% among other photocatalysts.

Keywords: graphene oxide, molybdenum disulfide, photocatalytic degradation, semiconductor photocatalyst, solar irradiation

Abstrak

Kajian in menekankan kajian awal mengenai fotodegradasi 2-klorofenol dengan menggunakan berat ratio pemangkin cahaya MoS_2/rGO yang berlainan dibawah radiasi matahari. 2-klorofenol dikenali sebagai salah satu bahan pencemar yang mempunyai ciri-ciri merbahaya seperti mutagenisiti, karsinogenik dan eko-pencemar. Komposit MoS2/rGO telah disintesis menggunakan kaedah hidroterma. Kaedah fotokatalisis yang menggunakan MoS_2/rGO sebagai pemangkin cahaya untuk merosotkan 2-klorofenol dibawah sinaran matahari. Tiga komposisi MoS_2/rGO yang berlainan (1%, 5% and 15%) telah disintesis menggunakan nisbah berat MoS_2 yang berbeza. Bahan komposit MoS_2, GO dan MoS_2/rGO yang dicirikan menggunakan FTIR dan XRD telah menunjukkan hasil jaya pembentukan komposit MoS_2/rGO dengan jayanya. Penyusutan sinaran oleh 10 ppm 2-klorofenol telah diperhatikan dibawah sinaran matahari selama 180 minit telah dianalisiskan dengan UV-VIS untuk mengukur peratus penyusutan sinaran 2-klorofenol. 1% MoS2/rGO telah dipilih untuk merosotkan 2-klorofenol kerana mempunyai peratusan penyosotan yang tinggi iaitu 51.41%.

Kata kunci: grafena oksida, molibdenum disulfida, degradasi fotokatalitik, pemangkin cahaya semikonduktor, penyinaran suria

Introduction

2-chlorophenol is one of the chemical groups derives from chlorophenol that were made by electrophilic halogenation of phenol with chlorine. It is widely known as one of the most priority pollutants by the US Environmental Protection Agency and World Health Organization (WHO) based on its properties of strong odor, mutagenicity, carcinogenicity and eco-persistent [1]. It is highly toxic and difficult to degrade due to its high thermal and chemical stability [2]. Even with its hazardous characteristics, it is largely used in industrial and commercial scales such as plastic, pesticide, textile, steel, pharmaceutical, iron, paper and wood preserving that were reported to be a major source of chlorophenol compound found in the wastewater [3]. It can affect organisms when it released to the environment. Thus, many studies have been made to eliminate it such as biodegradation, adsorption and Fenton-like advanced oxidation processes. However, due to utilization of extra oxidants, vigorous conditions and intensive energy input, studies are made to search for sustainable technology to degrade 2-chlorophenol. Hence, to overcome the environment issues, solar-driven photocatalysis method is being used to eliminate the contaminant in the wastewater, ground water and rivers.

Photocatalysis is known as one of the advanced oxidation processes which is a method of removing contaminants concerning wastewater effluents. Photocatalysis is a technique to degrade pollutant by using photocatalyst to utilize photogenerated carriers such as electrons and holes in order to start the redox reaction for the conversion of solar to chemical energy [4]. Photocatalysis is one of the advanced treatment technologies to degrade contaminant by using radicals produced from transition-metal oxide photocatalysts involving UV irradiation. To promote indirect hole oxidation, the electron-hole pairs are generated on the photocatalyst surface and the valence band edge of photocatalysts must be better of the oxidation potential of hydroxyl radical, •OH [5].

Table 1 examines the different types of photocatalyst materials for degradation of 2-chlorophenol.

Table 1. Degradation of 2-chlorophenol using photocatalytic degradation

Photocatalyst	Source of Light	Degradation Time	Percentage Degradation	References
Ru/TiO_2	UV light	180 minutes	50%	[6]
Cu doped $BiFeO_3$ and Ba-Cu co-doped $BiFeO_3$	Visible light	70 minutes	98% and 100%	[7]
C_3N_4/TiO_2-NTs in pH of 9 and 12	UV/ Visible light	180 minutes	25.02% and 70.25%	[8]
ZnO-ZnS@PANI	Visible light	240 minutes	89%	[9]
5% Ag-TiO_2	UV light	150 minutes	74%	[10]

Meanwhile, photocatalyst is material that absorbs light energy to facilitate chemical reaction. Semiconductor photocatalyst uses light energy to get desirable chemical transformation through reduction-oxidation (redox) reaction. The photocatalytic semiconductors are commonly used for wastewater treatment, surfaces with self-cleaning and antifogging properties, purification of outdoor air, indoor air deodorization and cancer therapy [11]. It uses suitable band gap to produce strong visible light response with a high photocatalytic presentation, non-toxicity, good thermal, inexpensive and have chemical stability [12].

Graphene is a 2-D structure of hexagonal carbon atom in the sp^2 hybrid orbital that is widely used in electrochemical energy storage, optical and optoelectronics bioengineering due to its outstanding electrical, optical, thermal and mechanical properties. Graphene and its derivatives consist of large surface area, thermal conductivity and carrier mobility. Thus, it has the high potential in energy sensors and microelectronic devices. Integration of GO with other semiconductor can effectively improve the structural stability of the composites and enhance the photocatalytic activity by hindering the recombination of photo-generated carrier. Moreover, GO-based composite can alleviate the serious agglomeration of nanoparticles to a certain extent [13, 14] . Graphene is also known as electron cocatalyst that can improve hydrogen performance of photocatalysts due to its excellent of conductivity [15]. It also has capacity for adsorption of organic pollutants and potential mechanical strength and electrical conductivity [16]. GO can give productive route for highly dispersive, band tunable and few-layer structured of graphene-based materials thus it acts as supportive material for photocatalyst semiconductor [17].

MoS_2 is a 2-D layered n-type semiconductor and has narrow bandgap of 1.20 eV for its few layers where each layers have gap value of 1.90 eV. Thus, it has large specific surface area complex edge structure and abundant unsaturated active sites. It has high thermal stability and strong absorption in visible spectrum region. MoS_2 have limitations as it has limit in energy storage and photocatalytic properties due to high recombination rate of photo-generated electron hole pairs, low energy density and poor electronic conductivity. Combining with other metal oxide nanostructures, it can improve the disadvantages of MoS_2 such as GO can enhance its photocatalytic performances [18, 19]. This can be explained by transfer of photo-generated electrons from MoS_2 conduction band to the graphene [20]. When the band gap of MoS_2 increases due to quantum confinement effects of MoS_2, it will change the redox potential of MoS_2 thus photo-generated electron can be easily migrate [21]. Therefore, this research focusses on preliminary studies on the ability of MoS_2-GO photocatalyst to degrade 2-chlorophenol from aqueous solution under sunlight.

Materials and Methods

Materials

2-chlorophenol, sulphuric acid (H_2SO_4), sodium nitrate ($NaNO_3$), graphite powder, hydrogen peroxide (H_2O_2), hydrochloric acid (HCl), sodium molybdate dihydrate ($Na_2MoO_4.2H_2O$), thiourea (H_2NCSNH_2) were purchased from Merck Sdn. Bhd. Finally, deionized water was supplied from Purite machine model Fusion system (United Kingdom) that has ultrapure water 18.2 M Ω at a flow rate of 48 L/hr.

Synthesis of GO

Graphene oxide was prepared by using modified Hummers method from pure graphite powder. Solution of 23 mL sulphuric acid, H_2SO_4, 0.5 g of sodium nitrate, $NaNO_3$ and 1.0 g of graphite powder were mixed. The solution was stirred for an hour in ice bath until it becomes dark green solution. The solution was stirred for another 4 hours after being removed from the ice bath where the solution turned into dark grey solution. The solution was transferred into a water bath and the temperature was raised to 35˚C and stirred for 30 minutes. The solution was added 250 mL of deionized water and was stirred for another 15 minutes while heated up to 70˚C then added dropwise of 10 mL of hydrogen peroxide, H_2O_2. Cool the solution as there will be exothermic reaction occurs. The solution was centrifuged three times at 3000rpm for 10 minutes and the supernatant drained, and the residual was washed HCl to obtain GO solution. The GO solution was dried

the using the oven at ˚C for 24 hours to gain powdered form of GO [22].

Synthesis of MoS_2

Molybdenum disulfide, MoS_2 was synthesized by using hydrothermal method. Firstly, 3.0 g sodium molybdate dihydrate, $Na_2MoO_4.2H_2O$, 3.8 g of thiourea, H_2NCSNH_2, 80 mL of deionized water were mixed and stirred for 30 minutes. 10 mL of 1M HCl was added to the solution and transferred into 100 mL Teflon stainless steel autoclave and heated in the oven at 120˚C for 24 hours. The solution was kept in the room temperature to let it cooled before centrifuged three times and washed with deionized water. The solution was dried in the oven at 70˚C for 24 hours [23].

Synthesis of MoS_2/GO

The solution was prepared by using ex-situ and hydrothermal method by adding 0.001 g of molybdenum disulfide, MoS_2 and 20 mL of deionized water were mixed and sonicated for 30 minutes. Another solution was prepared of 0.1 g of graphene oxide, GO and added with 20 mL of deionized water before sonicated for 30 minutes. Both solutions were added together and sonicate for another 30 minutes before transferred into the Teflon stainless steel and dry in the oven overnight at 120˚C. Centrifuged and washed the solution with deionized water three times after cooling at room temperature and dried the product at 80˚C for 24 hours [24].

Characterisations

Perkin Elmer Fourier Transform model 100 was used to identify the functional group of the sample by producing infrared absorption spectrum in the range 600-4000 cm^{-1}. Ultraviolet-visible spectroscopy solid Perkin Elmer model was used to measure light absorbance of the sample at the wavelength range of 200 to 500 nm. The model Oxford Instruments of X-ray Diffractometer (XRD) was used to determine the crystallographic structure of composites.

Degradation of 2-Chlorophenol by using MoS_2/ GO

The composites undergo screening process to determine the optimum sorbent for the extraction of 2-chlorophenol by exposing under the sunlight for 3 hours. 20 mL of 10 ppm of 2-chlorophenol was added to 10 mg photocatalyst. The degradation of 2-chlorophenol was measured using UV-visible in wavelength between 230 nm to 500 nm. Degradation percentage of 2-chlorophenol was determined by using the formula:

Degradation of 2-chlorophenol(%)

$$= \frac{Ao - A}{Ao} \times 100 \qquad (1)$$

where A_o is an initial absorption of 2-chlorophenol and A is an absorption of 2-chlorophenol at sampling time after the degradation process [25]. The natural sunlight photocatalysis was measured from April to May 2021 (Wednesday to Friday) at (2° 47' 20.3892" N, 102° 13' 4.6992" E) in Kuala Pilah, Negeri Sembilan Malaysia, (10AM- 1PM). The daily solar irradiance could reach 4.21–5.56 $kWhm^{-2}$ [26].

Results and Discussion

Figure 1 below show IR spectra of the representative composites within the range of 650 to 4000 cm^{-1}. The broad peak at 3353.94 cm^{-1} in Figure 1 represented the hydroxyl group stretching vibration of graphene oxide composite. Besides, there is also C=O stretch of carboxylic acid at 1737.46 cm^{-1}. The peak at 1163.52 cm^{-1} and 1042.35 cm^{-1} assigned to C-O-C, epoxy and C-O stretch. Next, the peak at 1588.21 cm^{-1} were corresponding to the C=C aromatic stretch group. The peaks at 862.28 cm^{-1} that were observed at the MoS2 composite corresponds to the Mo-O bond. [24]. FTIR spectroscopy in Figure 1 confirms the presence of MoS_2 and GO which indicates successful preparation of MoS_2/GO in the experiment. Moreover, there are band shifts and intensified of the spectra for different concentration of the 1%, 5% and 15% MoS_2/GO composites.

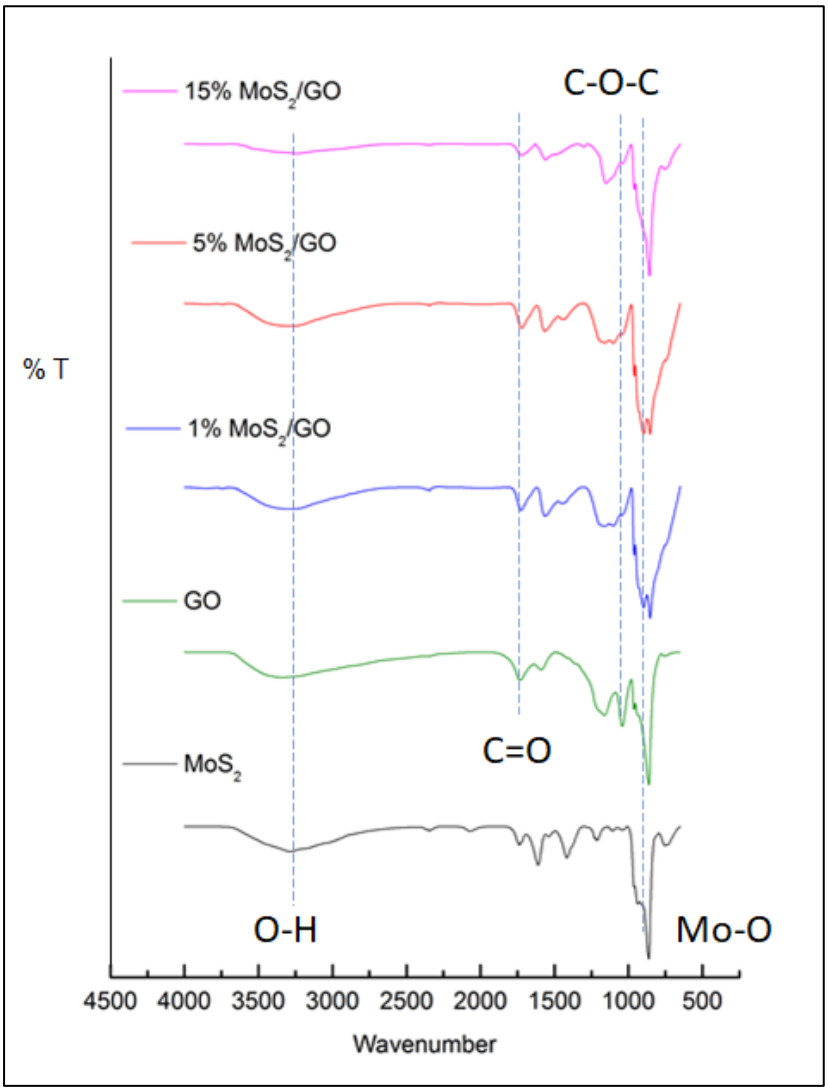


Figure 1. FTIR spectrum of MoS_2, GO and MoS_2/GO composites (1%, 5% and 15%)

Figure 2 shows diffractogram of MoS_2, GO and MoS_2/GO composites (1%, 5% and 15%). Based on the figure, the diffraction peak of GO can be seen at 2^{θ} = 24.92˚ indicating interplanar space of the GO sheet (001) [25]. MoS_2 also showed peak corresponding to (100) plane at 2^{θ} = 32.65˚ which successfully appeared at all of the mass ratio of MoS_2/GO (1%, 5% and 15%)[27][28]. Thus, it confirmed that GO and MoS_2 composites were successfully integrated.

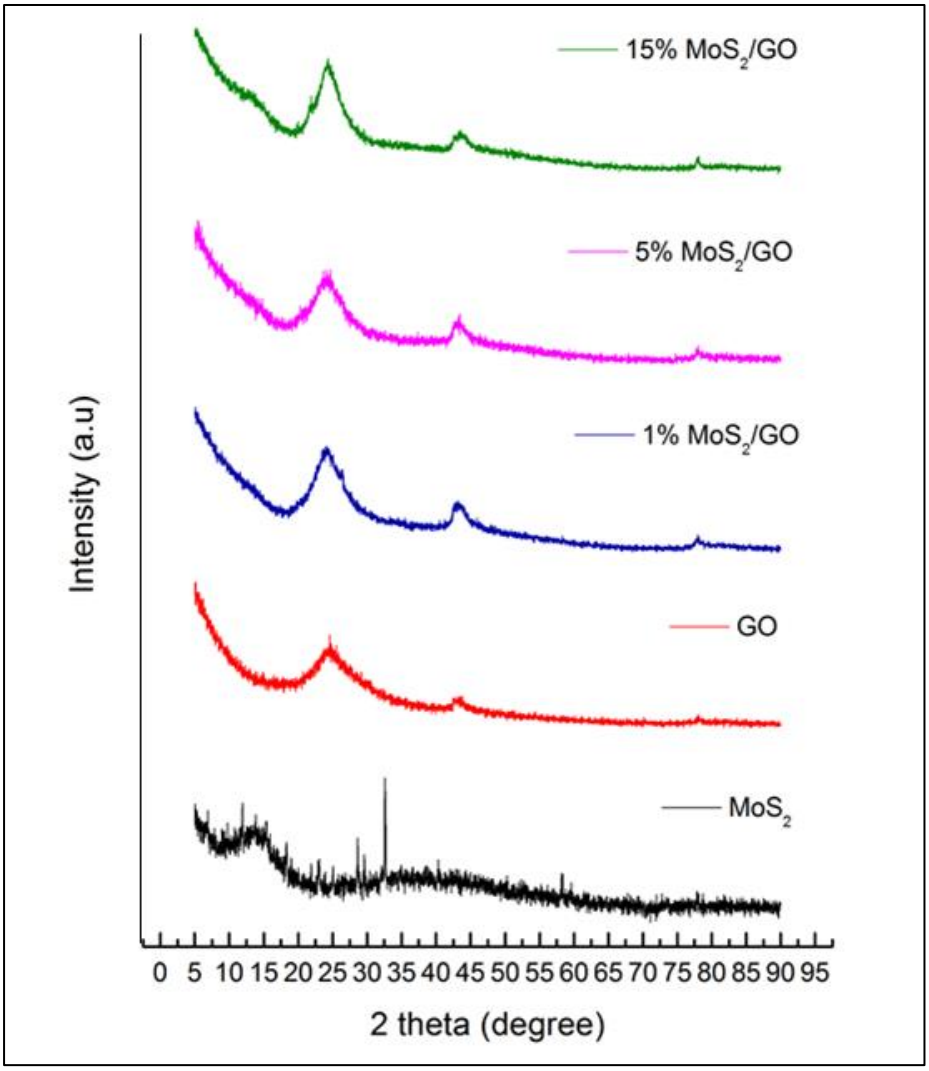


Figure 2. XRD patterns of MoS_2, GO, MoS_2/GO composite (1%, 5% and 15%)

Figure 3 reveals the photodegradation of 2-chlorophenol under sunlight using MoS_2, GO, MoS_2/GO composite (1%, 5% and 15%) photocatalyst. Successful photodegradation was monitored by decreasing in the intensity of absorbance with time irradiation. Hence, 1% MoS_2/GO proved for having lowest absorbance of 0.086 Abs. Based on the Figure 3, the MoS_2 showed an increase in absorption at 0.198 Abs of the visible light in the range of ~275 nm due to the absorption of MoS_2 in the 2-chlorophenol pollutant as it hinders complete usage of sunlight for charge carrier generation due to having wider band gap and have low mobility preventing charge transfer [29]. Moreover, rapid recombination of photogenerated electron hole pairs can decline its photocatalytic activities and poor dispersion happened when the nanomaterials are accumulated [30]. Meanwhile, Figure 4 presents the degradation percentage of all composites where the highest percent degradation is 51.41% for 1% MoS_2/GO composite due to the compatibility between graphene and MoS_2 as it enhanced the catalytic activities of amorphous producing highly efficient hydrogen production under visible light irradiation [31].

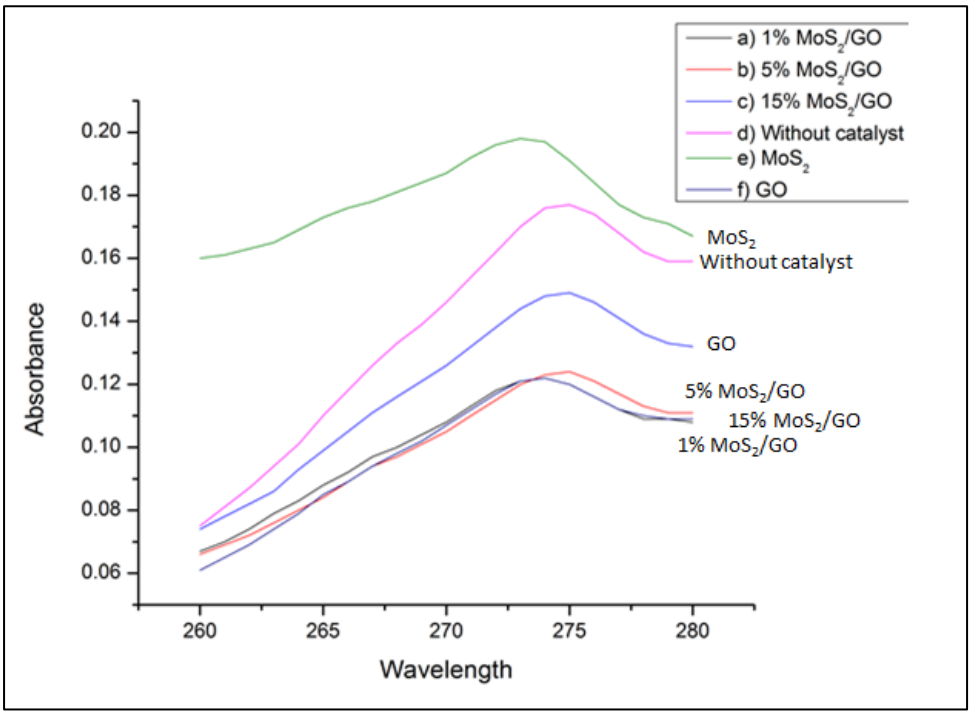


Figure 3. Different absorbance for different catalyst for 3 hours

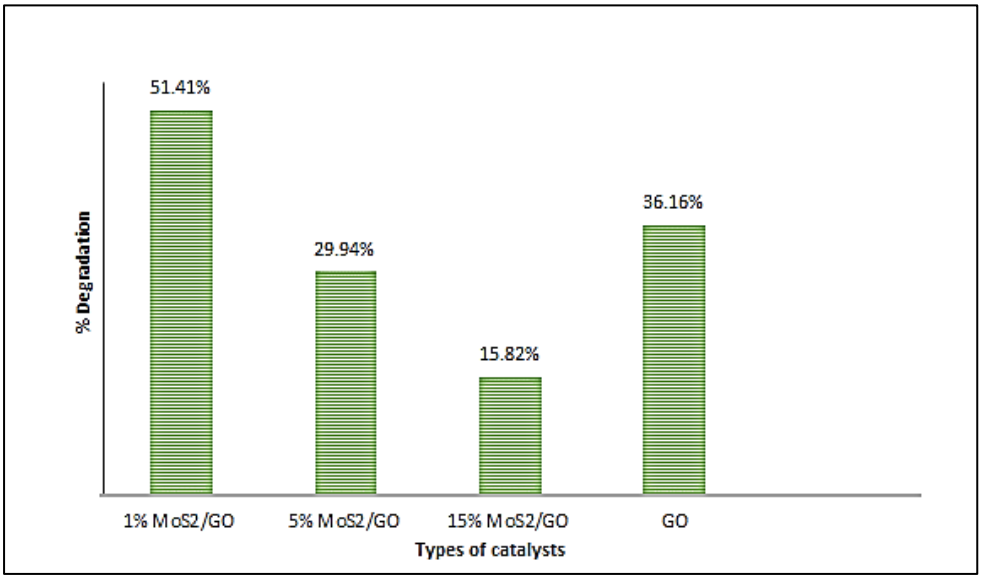


Figure 4. Degradation percentage of 2-chlorophenol for different catalysts under sunlight

Conclusion

MoS_2/GO composites were successfully prepared using ex-situ and hydrothermal method. This can be seen from the analyses of the FTIR, UV-Vis and XRD which confirmed the functional group and incorporated of MoS_2 and GO composites. From the findings, all of the

composites prepared have the potential in degrading 2-chlorophenol under sunlight assisted degradation. 1% MoS_2/GO was revealed as the best composite to degrade 2-chlorophenol with the percentage degradation of 51.41%. Further optimization and controlled experiments can be done to tackle the most prominent condition for 2-chlorophenol to degrade with sunlight as the main source of light to achieve highest degradation percentage within a short time.

Acknowledgement

We acknowledge the financial support of the Ministry of Higher Education for Fundamental Research Grant (FRGS/1/2018/STG01/UITM/02/1). We also acknowledge School of Chemistry and Environment in the Faculty of Applied Science at UiTM Negeri Sembilan, Kuala Pilah Campus for the facilities that have been provided for the research.

References

1. Li, K., Fang, X., Fu, Z., Yang, Y., Nabi, I., Feng, Y., Bacha, A. U. R. and Zhang, L. (2020). Boosting photocatalytic chlorophenols remediation with addition of sulfite and mechanism investigation by *in-situ* DRIFTs. *Journal of Hazardous Materials*, 398: 123007.
2. Lei, M., Gao, Q., Zhou, K., Gogoi, P., Liu, J., Wang, J., Song, H., Wang, S. and Liu, X. (2021). Catalytic degradation and mineralization mechanism of 4-chlorophenol oxidized by phosphomolybdic acid/H_2O_2. *Separation and Purification Technology*, 257: 117933.
3. Garba, Z. N., Zhou, W., Lawan, I., Xiao, W., Zhang, M., Wang, L., Chen, L. and Yuan, Z. (2019). An overview of chlorophenols as contaminants and their removal from wastewater by adsorption: A review. *Journal of Environmental Management*, 241: 59-75.
4. Han, Z., Fei, J., Li, J., Deng, Y., Lv, M., Zhao, J., Wang, C. and Zhao, X. (2020). Enhanced dye-sensitized photocatalysis for water purification by an alveoli-like bilayer Janus membrane. *Chemical Engineering Journal*, 407: 127214.
5. Abada, B., Alivio, T. E. G., Shao, Y., O'Loughlin, T. E., Klemashevich, C., Banerjee, S., Jayaraman, A., and Chu, K. H. (2018). Photodegradation of fluorotelomer carboxylic 5:3 acid and perfluorooctanoic acid using zinc oxide. *Environmental Pollution*, 243: 637-644.
6. Elsalamony, R. A. and Mahmoud, S. A. (2017). Preparation of nanostructured ruthenium doped titania for the photocatalytic degradation of 2-chlorophenol under visible light. *Arabian Journal of Chemistry*, 10(2): 194-205.
7. Soltani, T. and Lee, B. K. (2017). Enhanced formation of sulfate radicals by metal-doped $BiFeO_3$ under visible light for improving photo-Fenton catalytic degradation of 2-chlorophenol. *Chemical Engineering Journal*, 313: 1258-1268.
8. Barakat, M. A., Kumar, R. and Eniola, J. O. (2021). Adsorption and photocatalytic scavenging of 2-chlorophenol using carbon nitride-titania nanotubes based nanocomposite: Experimental data, kinetics and mechanism. *Data in Brief*, 34: 106664.
9. Anjum, M., Oves, M., Kumar, R. and Barakat, M. A. (2017). Fabrication of ZnO-ZnS@polyaniline nanohybrid for enhanced photocatalytic degradation of 2-chlorophenol and microbial contaminants in wastewater. *International Biodeterioration and Biodegradation*, 119: 66-77.
10. Onkani, S. P., Diagboya, P. N., Mtunzi, F. M., Klink, M. J., Olu-Owolabi, B. I. and Pakade, V. (2020). Comparative study of the photocatalytic degradation of 2–chlorophenol under UV irradiation using pristine and Ag-doped species of TiO_2, ZnO and ZnS photocatalysts. *Journal of Environmental Management*, 260: 110145.
11. Rueda-Marquez, J. J., Levchuk, I., Fernández Ibañez, P. and Sillanpää, M. (2020). A critical review on application of photocatalysis for toxicity reduction of real wastewaters. *Journal of Cleaner Production*, 258: 120694
12. Prasad, C., Liu, Q., Tang, H., Yuvaraja, G., Long, J., Rammohan, A. and Zyryanov, G. V. (2020). An overview of graphene oxide supported semiconductors based photocatalysts: Properties, synthesis and photocatalytic applications. *Journal of Molecular Liquids*, 297: 111826.

13. Chen, Y., Zhai, B. and Liang, Y. (2019). Enhanced degradation performance of organic dyes removal by semiconductor/MOF/graphene oxide composites under visible light irradiation. *Diamond and Related Materials*, 98: 107508.
14. Kamalam, M. B. R., Inbanathan, S. S. R. and Sethuraman, K. (2018). Enhanced photo catalytic activity of graphene oxide /MoO_3 nanocomposites in the degradation of Victoria Blue Dye under visible light irradiation. *Applied Surface Science*, 449: 685-696.
15. Cao, Y., Wang, P., Fan, J. and Yu, H. (2021). Covalently functionalized graphene by thiourea for enhancing H_2-evolution performance of TiO_2 photocatalyst. *Ceramics International*, 47(1): 654-661.
16. El-Fawal, E. M., Younis, S. A. and Zaki, T. (2020). Designing $AgFeO_2$-graphene/$Cu_2(BTC)_3$ MOF heterojunction photocatalysts for enhanced treatment of pharmaceutical wastewater under sunlight. *Journal of Photochemistry and Photobiology A: Chemistry*, 401: 112746.
17. Long, D., Peng, J., Liu, H., Feng, Z., Chen, L., Chen, X. and Lu, M. (2020). Graphene oxide discarded solution for high surface area photocatalyst. *Solar Energy Materials and Solar Cells*, 209: 110446.
18. Asaithambi, S., Sakthivel, P., Karuppaiah, M., Balamurugan, K., Yuvakkumar, R., Thambidurai, M. and Ravi, G. (2021). Synthesis and characterization of various transition metals doped SnO_2@MoS_2 composites for supercapacitor and photocatalytic applications. *Journal of Alloys and Compounds*, 853: 157060.
19. Yu-Cheng, C. and Yu-Wen, L. (2020). MoS_2@SnO_2 core-shell sub-microspheres for high efficient visible-light photodegradation and photocatalytic hydrogen production. *Materials Research Bulletin*, 129: 110902.
20. Zhao, Y., Zhang, X., Wang, C., Zhao, Y., Zhou, H., Li, J. and Jin, H. B. (2017). The synthesis of hierarchical nanostructured MoS_2 /Graphene composites with enhanced visible-light photo-degradation property. *Applied Surface Science*, 412: 207-213.
21. Rani, A., Singh, K., Patel, A. S., Chakraborti, A., Kumar, S., Ghosh, K. and Sharma, P. (2020). Visible light driven photocatalysis of organic dyes using SnO_2 decorated MoS_2 nanocomposites. *Chemical Physics Letters*, 738: 136874.
22. Zaaba, N. I., Foo, K. L., Hashim, U., Tan, S. J., Liu, W. W. and Voon, C. H. (2017). Synthesis of graphene oxide using modified hummers method: solvent influence. *Procedia Engineering*, 184: 469-477.
23. Gopalakrishnan, K., Sultan, S., Govindaraj, A. and Rao, C. N. R. (2015). Supercapacitors based on composites of PANI with nanosheets of nitrogen-doped RGO, $BC_{1.5}N$, MoS_2 and WS_2. *Nano Energy*, 12: 52-58.
24. Song, Y., Cao, K., Li, W., Ma, C., Qiao, X., Li, H. and Hong, C. (2020). Optimal film thickness of rGO/MoS_2 @ polyaniline nanosheets of 3D arrays for carcinoembryonic antigen high sensitivity detection. *Microchemical Journal*, 155: 104694.
25. Hanafi, N. N., Sambasevam, K. P., Arifutzzaman, A., Rahman, S. and Baharin, S. N. A. (2020). Solar-driven degradation of 2-chlorophenol using PANI/GO as photocatalyst. *Orbital*, 12(4): 205-212.
26. Pawson, S. (n.d.). Weatherspark.com. Average Weather in April in Kuala Pilah, Malaysia - Weather Spark. https://weatherspark.com/m/114181/4/Average-Weather-in-April-in-Kuala-Pilah-Malaysia.
27. Phung, H. N. T., Truong, N. D., Duong, P. A. and Tuan Hung, L. V. (2018). Influence of MoS_2 deposition time on the photocatalytic activity of MoS_2/ V, N co-doped TiO_2 heterostructure thin film in the visible light region. *Current Applied Physics*, 18(6): 737-743.
28. Chao, J., Yang, L., Zhang, H., Liu, J., Hu, R. and Zhu, M. (2020). Engineering layer structure of MoS_2/polyaniline/graphene nanocomposites to achieve fast and reversible lithium storage for high energy density aqueous lithium-ion capacitors. *Journal of Power Sources*, 450: 227680

29. Beura, R., Pachaiappan, R. and Paramasivam, T. (2021). Photocatalytic degradation studies of organic dyes over novel Ag-loaded ZnO-graphene hybrid nanocomposites. *Journal of Physics and Chemistry of Solids*, 148: 109689.
30. Saha, S., Chaudhary, N., Mittal, H., Gupta, G. and Khanuja, M. (2019). Inorganic–organic nanohybrid of MoS_2-PANI for advanced photocatalytic application. *International Nano Letters*, 9(2): 127-139.
31. Sha, C., Lu, B., Mao, H., Cheng, J., Pan, X., Lu, J. and Ye, Z. (2016). 3D ternary nanocomposites of molybdenum disulfide/polyaniline/reduced graphene oxide aerogel for high performance supercapacitors. *Carbon*, 99: 26-34.

Malaysian Journal of Analytical Sciences (MJAS)
Published by Malaysian Analytical Sciences Society

THE COMPATIBILITY OF JACKFRUIT SEED STARCH AND POLYVINYL ALCOHOL BLEND AS BIOPOLYMER ELECTROLYTE HOST

(Keserasian Kanji Biji Nangka dan Campuran Polivinil Alkohol sebagai Hos Elektrolit Biopolimer)

Raihan Ramli[1], Fairuzdzah Ahmad Lothfy[1]*, Asiah Mohd Nor[2], Ab Malik Marwan Ali[2]

[1]Faculty of Applied Science,
Universiti Teknologi MARA Pahang, 26400 Bandar Tun Abdul Razak Jengka, Pahang, Malaysia
[2]Faculty of Applied Science,
Universiti Teknologi MARA, 40450 Shah Alam, Selangor, Malaysia

**Corresponding author: fairuzdzah@uitm.edu.my*

Received: 29 March 2022; Accepted: 3 July 2022; Published: 25 August 2022

Abstract

Biopolymer electrolytes have a lot of potential for future electrochemical device developments because of their environmentally-friendly features. In general, the structural characteristics of the biopolymer host play the most crucial impact in determining electrolyte conductivity. However, the semi crystallinity structure of biopolymer hosts caused the reduction of electrolyte conductivity. As a result, in this study, the structural characteristics of the biomaterial have been modified by blending jackfruit seed starch (JSS) and polyvinyl alcohol (PVA) to obtain the optimal composition of the blend that is compatible to be employed as a biopolymer electrolyte host. The jackfruit seed starch and polyvinyl alcohol were blended with various compositions using th e solution casting technique. The purpose of this study is to look into the amorphousness, functional groups, and morphology of J SS with PVA blend and determine the compatibility of JSS with PVA blend as a polymer electrolyte host. The best compatible bl end composition is JSS-PVA with a 1:1 ratio, which has the highest degree of amorphosity and the highest percentage of hydroge n bonding contact, C=O stretching, and C-O vibrations. Scanning electron microscopy investigation confirms the results, indicati ng that the blend is evenly dispersed.

Keywords: **j**ackfruit seed starch, polyvinyl alcohol, biopolymer electrolyte host, amorphous

Abstrak

Elektrolit biopolimer mempunyai banyak potensi untuk perkembangan peranti elektrokimia masa depan kerana ciri-ciri mesra alamnya. Secara umumnya, ciri-ciri struktur hos biopolimer memainkan peranan yang paling penting dalam menentukan kekonduksian elektrolit. Walau bagaimanapun, struktur separa kristal perumah biopolimer menyebabkan pengurangan dalam kekonduksian elektrolit. Hasilnya, dalam kajian ini, ciri-ciri struktur biomaterial telah diubahsuai dengan mencampurkan kanji biji nangka (JSS) dan polivinil alkohol (PVA) untuk mendapatkan komposisi optimum campuran yang serasi untuk digunakan sebagai hos elektrolit biopolimer. Kanji biji nangka dan polivinil alkohol diadun dengan pelbagai komposisi menggunakan teknik 'solution casting'. Ia bertujuan untuk melihat sifat amorfousness, kumpulan berfungsi, dan morfologi JSS dengan campuran PVA dan menentukan keserasian JSS dengan campuran PVA sebagai hos elektrolit polimer. Komposisi campuran serasi terbaik ialah JSS-PVA dengan nisbah 1:1, yang mempunyai tahap amorphositi tertinggi dan peratusan tertinggi hubungan ikatan hidrogen, regangan

C=O, dan getaran C-O. Mengimbas penyiasatan mikroskopi elektron mengesahkan hasilnya, menunjukkan bahawa campuran itu tersebar sama rata.

Kata kunci: kanji biji nangka, polivinil alkohol, perumah elektrolit biopolimer, amorphous

Introduction

Polymer electrolytes (PEs) are generally described as linear macromolecular chains containing a large charge. It is also utilized in solar cells, batteries, and supercapacitors, among other electrochemical devices [1, 2]. PE has recently piqued researchers' interest because of its promising features, which can be employed as a powerful platform for achieving high efficiency in the energy storage device. Recently, most of commercialized PE was prepared with non-biodegradable materials that are harmful to the environment and humans. This is due to most of the PE using petroleum-based polymers in the production of PEs. Petroleum-based polymer have limitations such as being expensive, depleting petroleum supplies, and causing environmental issues.

Biopolymer is a polymer host that has advantages since it eliminates the need for petroleum as a material source. In general, the choice of polymer host is an essential issue in the development of PEs [2]. Based on the previous studies, the choice of polymer host depends on two factors. Firstly, the presence of polar (functional) groups with adequate electron donor power to establish coordination with cations. For example, by having high concentration of polar groups (containing electron donors: O, NH, CN, F). Secondly, a low impediment to bond rotation [2]. Aside from that, the polymer host must be highly amorphous. It may occur due to increase in ionic diffusivity, as ions can move freely due to the low energy barrier. Furthermore, an amorphous polymer has a flexible backbone, which can increase local chain mobility. As a result, the segmental motion of a polymer can improve the electrolyte's transportation property [2]. Other researchers also found that selection of a polymer host is determined by factors such as the presence of atoms or groups of atoms with sufficient electron donor capacity to form coordination bonds with cations, a low barrier to bond rotations, allowing for easy segmental motion of the polymer chain, and a suitable distance between coordinating centers, which allows for the formation of multiple intra-polymer ion bonds [3].

To replace the petroleum-based material, the structural properties of jackfruit seed starch were investigated to determine its compatibility as a polymer electrolyte host. In Malaysia, the average weight of a jackfruit ranges from 3.5 kg to 10 kg, with the largest edible fruit weighing up to 35 kg, and the source is abundant [4]. Seeds can account for up to 10% to 15% of the total weight of the fruit [5]. Jackfruit seed starch has a high amylose content (24-32%) and a high polar group [6]. Previous studies indicate that the functional properties of jackfruit seed starch, which have C=O and C-O-C bonding which suggest that they can be used as a polymer electrolyte host [7, 8, 9]. It demonstrates that jackfruit seed starch contained an electron donor and met one of the requirements of the polymer host. However, no research has been conducted on the percentage of C=O and C-O-C bonding functional groups. As a result, the percentage of these functional groups was measured in this study.

Semi-crystalline properties are found in some of the native starch polymers. The previous researchers discovered that the sample's ionic conductivity is low due to its crystalline structure after synthesizing PEs by reacting poly(ethylene oxide) (PEO) with a salt such as lithium iodide (LiI) [10]. PVA also has semi-crystallinity structure, by blending PVA with another polymer, it might reduce the crystallinity properties. The previous researchers found that blending PVA with pure cornstarch and chitosan can reduce the crystallinity peak [11, 12]. The chain structure promotes the formation of interchain "tunnels" through which the desired ion can bounce between coordination sites while the counterion travels down the polymer chain [13]. These tunnels constrain the movement of anion and cation in crystalline PEs due to their highly ordered crystalline domains that are selective for an ion and exclude its counterion, allowing for separation [10]. The conductivity of amorphous polymers is higher due to

their amorphous properties, which allow for significant chain movement because ion coordination is transitory, enhancing ion mobility [14]. Ion transport is triggered in the amorphous phase by local mobility of polymer chain segments, which creates new coordination sites into which the ions can then travel [10]. While the crystallinity can restrict the movement of ions. It has been well reported that the ion transport occurs mainly in the amorphous region rather than the crystalline region, but the polymers host materials that used in PEs are often semi-crystalline. To summarize, the movements of ions in the amorphous phase allow ionic conductivity.

Thus, in this research, synthetic polymers such as PVA were blended with jackfruit seed starch to modify the polymer's structural properties and achieve the optimal state of amorphosity [15]. According to previous study, PVA is used because it has excellent charge storage properties, optical properties, and high dielectric strength. Fahmy et al. stated that PVA has a carbon chain backbone that is connected with hydroxyl groups [16]. Due to hydroxyl groups, or OH groups, are a source of hydrogen bonding, they aid in the formation of polymer blends or polymer complexes. Chen et al. investigated varied features of PVA/chitosan blends at different ratios and discovered that chitosan, as a natural polymer which can reduce the PVA crystallinity [17].

As a result, the primary goal of this study is to investigate the amorphousness, functional groups, and morphology of JSS with PVA blend to ensure that these properties are compatible as potential polymer electrolyte hosts.

Materials and Methods

Materials

JSS used in this experiment was purchased from the jackfruit merchant in Bandar Pusat Jengka, Pahang. The chemicals used were PVA and glycerol from R & M Chemicals, UK. 0.1 M sodium hydroxide (NaOH) and 0.1 M hydrochloric acid (HCl) were also used and were purchased from Sigma-Aldrich, USA.

Preparation of jackfruit seed starch and polyvinyl alcohol blend

The samples were prepared by using solution casting method. Different compositions of JSS and PVA were used as represented in Table 1. Firstly, the PVA solution was prepared by dissolving PVA into distilled water. The solution was heated at 100 ℃ for 30 minutes. While the PVA was being diluted, the JSS mixture were prepared by using double boiled method. JSS was mixed with distilled water before adding 1.5 mL of glycerol, HCl and NaOH. The mixture was stirred at 90 ℃ for 20 minutes. Then, the PVA solution was added into the mixture and it was stirred continuously for 30 minutes at 100 ℃ until the homogenous gel-like mixture was formed. After being homogenous, it was poured into a petri dish and dried for 48 hours at room temperature. Next, the dried films were peeled from the petri dish and was cut according to the characterization method used.

Table 1. Composition of JSS and PVA

Sample	JSS (%)	PVA (%)
S1	0	100
S2	30	70
S3	50	50
S4	70	30
S5	100	0

Characterization

The Fourier-transform infrared spectral analysis of functional groups for the bioplastic films was carried out by Perkin Elmer FTIR Model 2000 spectrometer in a range of 500-4000 cm^{-1} at a resolution of 4 cm^{-1}. The surface analysis of the bioplastic films was carried out

by using Scanning Electron Microscopy (SEM, Vega 3, Tescan Analytics, France). The morphological structure of the bioplastic films was obtained at a voltage of 20 kV (magnification of 1000x). The X-ray diffraction patterns of the films was characterized by X'Pert PRO MPD diffractometer (PANalytical, UK). It operated at 36 kV (20 mA) and the scanning range was 5°-90° in the scale of the angle 2θ.

Results and Discussion

Fourier-transform infrared spectral analysis

The FTIR spectra for JSS and PVA blend are shown in Figure 1. The strong and wide absorption band at 3300 cm^{-1} indicates that the blend has the stretching vibration of OH groups [18]. The possible functional groups for this peak are the hydroxyl group and H-bonded OH stretch. The available hydroxyl groups on the starch chains cause the formation of the peak at 3300 cm^{-1} [19]. The absorption band is also present in the PVA film, indicating that there are many water hydroxyl groups in the film, which are the same as those studied by El-Sawy and his colleagues [20]. The major OH groups that appear in all samples at 3300 cm^{-1}, indicate that there is an interaction between different –OH groups in the JSS and PVA blends for the other four samples. The intensity of S1 becomes lower with additional JSS into the blend due to the intensity of pure JSS, which is S5 that is the lowest. In other words, the FTIR spectra pattern for JSS and PVA blends seems to overlap compared to a single polymer component.

The peaks that occurred at 2900 to 2950 cm^{-1} were attributed to C=H asymmetric stretching vibration [21]. Then, the peak at 1650 cm^{-1} was caused by C=O stretch [22]. This peak belongs to PVA. Next, the peak at 1040 cm^{-1} was attributed to C-O vibration of C-O-C groups [18]. The bands at 1000–1200 cm^{-1} were ascribed to the C-O stretching vibration. The changes occurred of the peak intensity of C-O in C-O-C groups by blending JSS and PVA. The highest intensity was obtained at S3. It shows that the S3 has the highest C-O in C-O-C groups. Then, the peak for S3 slightly shifted to the left, from 1040 cm^{-1} to 1029 cm^{-1}, indicating that strong hydrogen bonding interactions occurred between starch and PVA components. Both JSS and PVA have a lot of OH and C-O groups, which might help them establish hydrogen bonds and increase their compatibility [18]. The absorption peaks have also changed and shifted at 1400 cm^{-1} to 1450 cm^{-1}. The peak for PVA appeared at 1400 cm^{-1}, but when there was the presence of JSS, the peak shifted to 1450 cm^{-1}. The shift indicates that there is a weak interaction caused by C-O bonds that occurred during the solution blending and casting process [8]. The FTIR spectra for the JSS and PVA blend films showed the same pattern with the FTIR spectra for PVA film which is S1. From Figure 1, there is no major change that occurred in the functional group due to the JSS and PVA that is homogenously blended. Changes in the characteristic spectra peaks alter the physical blends versus chemical interactions when two components are blended [23]. Based on the previous studies, if the shape and location of the characteristic peak for the blend films is similar to PVA, the interaction among the PVA molecules is dominant and stronger compared to the JSS-PVA molecules and JSS-JSS molecules [20].

The percentage area under the graph for each stretch was summarized in Table 2. The peak at 1040 cm^{-1} for S3 has the highest percentage area under the graph. Having a higher percentage area under the graph for the C=O and C-O-C region is important in PEs because it is related to the conductivity of the PEs. Having a higher percentage area in those regions means that it has higher conductivity compared to the other blend films [24].

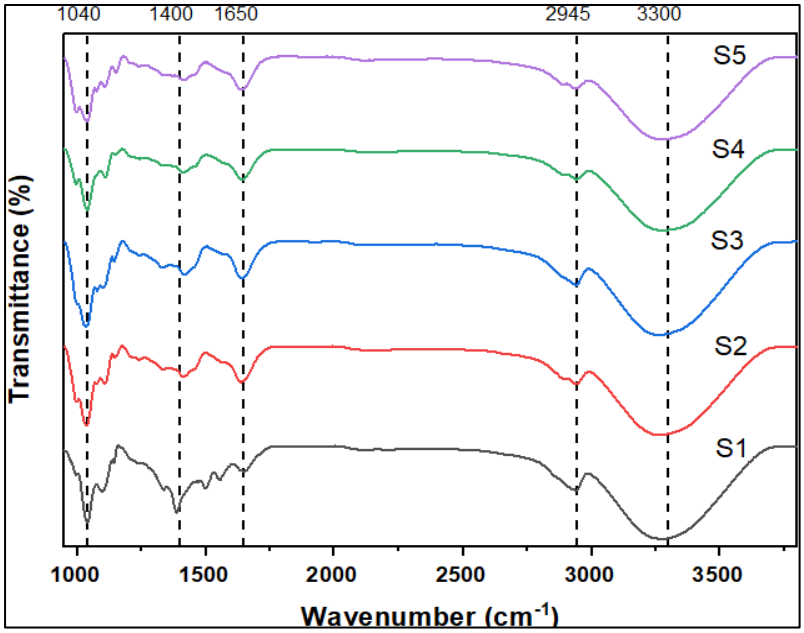


Figure 1. FTIR spectra of polymer blend with different composition of JSS and PVA blend

Table 2. Percentage area under the graph for each stretch

Sample	Percentage Area Under the Graph (%)				
	1040 (cm^{-1})	1400 (cm^{-1})	1650 (cm^{-1})	2945 (cm^{-1})	3300 (cm^{-1})
S1	9.99	14.27	6.30	6.98	62.45
S2	10.55	16.52	5.44	5.96	61.52
S3	14.26	8.00	4.47	7.09	66.18
S4	9.66	6.05	4.99	5.69	73.61
S5	12.25	6.05	5.25	5.90	70.60

Scanning electron microscope testing

The morphological structure of JSS and PVA blend films was analysed by SEM at magnification of 1000x (Figure 2). A homogenous structure was analysed for all of the samples. The surface of S1, which is an unfilled PVA film, had a smooth and clear surface as shown in Figure 2a. JSS is present in semi-round shaped granules and PVA is completely dissolved in the blend. The previous researchers also observed the semi-round shaped granules at a magnification of 1000x [25]. Then, a few other researchers also found that the presence of granules belong to the starch which is JSS [6, 11, 26]. Figure 2b, 2c, and 2d show that the JSS and PVA is evenly distributed and there is no formation of voids. The interface between those two materials in the blend was indistinct, which indicates the strong interaction between starch and PVA components. As indicated in the FTIR section, there is a strong hydrogen bonding formed between JSS and PVA, and it could improve the compatibility effectively [18]. The surface of S2 in Figure 2b shows a clear, semi-round shaped granules of JSS due to the fact that the amount of JSS in the blend is less than PVA. The JSS is evenly blended in the PVA matrix. As the amount of JSS added into the blend increases, the shape of the JSS in the blend can barely

be seen as the JSS becomes more compact and the blend films become smoother and homogenous.

The smoothness of the blend films represents the amorphous phase of the electrolyte films [27]. As the amorphous surface in PEs increases, the conductivity will also increase. This is because the ions can move freely when a smooth surface PE is formed [28]. As a result, the conductivity is improved. For S5 with only JSS in the blend film, the surface of the blend film looks a little rough without the presence of PVA. Based on the previous research, blend films with the presence of PVA will appear a lot smoother compared to those without it [29]. The previous research also indicates that a rough surface morphology in the electrolyte film reflects a semi-crystalline phase, which reduces the film's ionic conductivity [28]. From the morphological structure obtained, S3 with 50:50 of JSS and PVA demonstrated the optimum interaction between JSS and PVA compared to the other films with different compositions of JSS and PVA. Figure 2c reveals that the starch granules are well dispersed, homogenous, and have a smoother surface compared to other blend films. It can be concluded that S3 has the best conductivity based on the smoothness of the blend film.

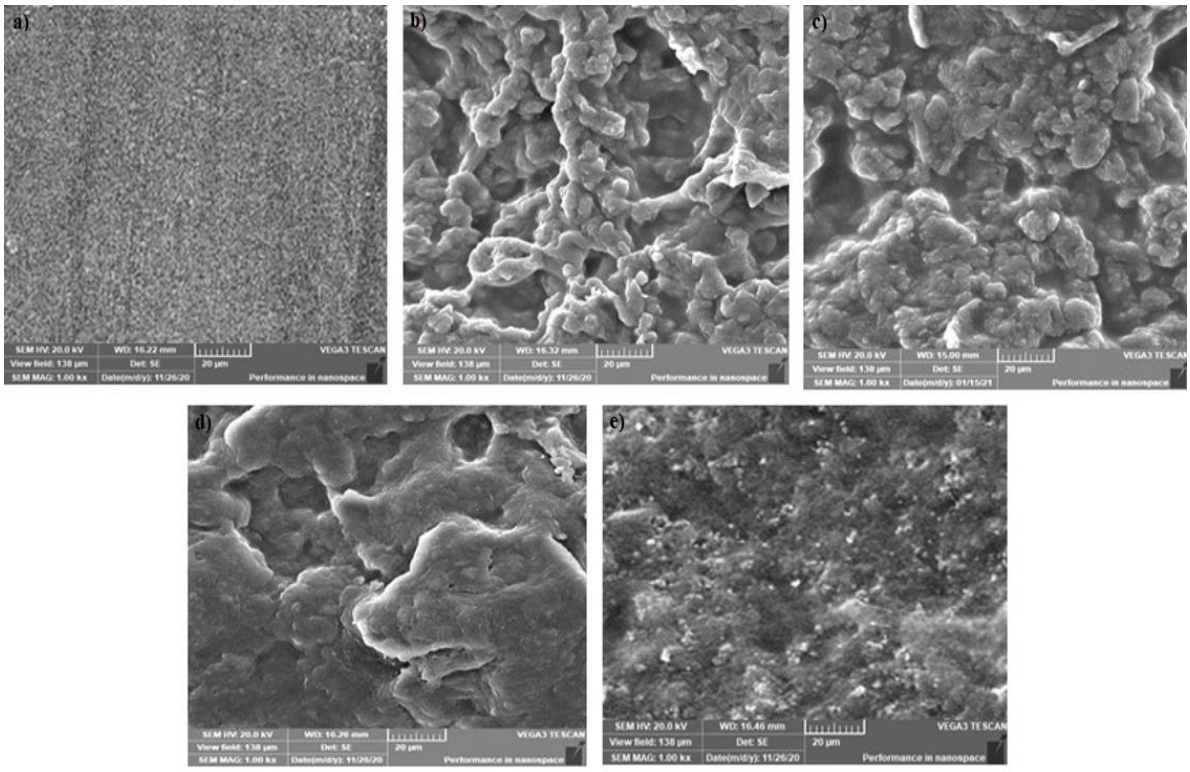


Figure 2. Surface morphology of different composition of JSS: (a) S1; (b) S2; (c) S3; (d) S4; (e) S5

X-ray powder diffraction testing

The XRD pattern for five samples with different compositions of JSS and PVA was presented in Figure 3 in the range 13° to 30°. Based on the figure, broad peak has been observed at 19.7° for all samples. This peak is related to the PVA phase where it is in a partially crystalline structure. The broad diffraction peak indicates that the crystallite is very small [4]. The position of the broad peaks for amorphous is normally within the range of 15° to 30°, implying that the broad peaks at 19.7° exhibit amorphous properties [30]. In Figure 3, the broadness for S2 and S3 increased while the intensity decreased. However, the intensity for S4 increased as the broadness increased. The increase in the broadness of the peak portrays the amorphous nature in the samples [31]. The previous researchers reported that

the amorphousness in the system is related to the height of the peak and the degree of crystallinity of the system [31]. Thus, S3 is the sample that has the highest amorphous nature compared to the other samples as it has a broad diffraction peak with low intensity. It can be proven based on the value of percent crystallinity in Table 3, where S3 has the lowest percent crystallinity compared to other samples. This is compatible with the SEM analysis where S3 has the optimum interaction between JSS and PVA compared to other films.

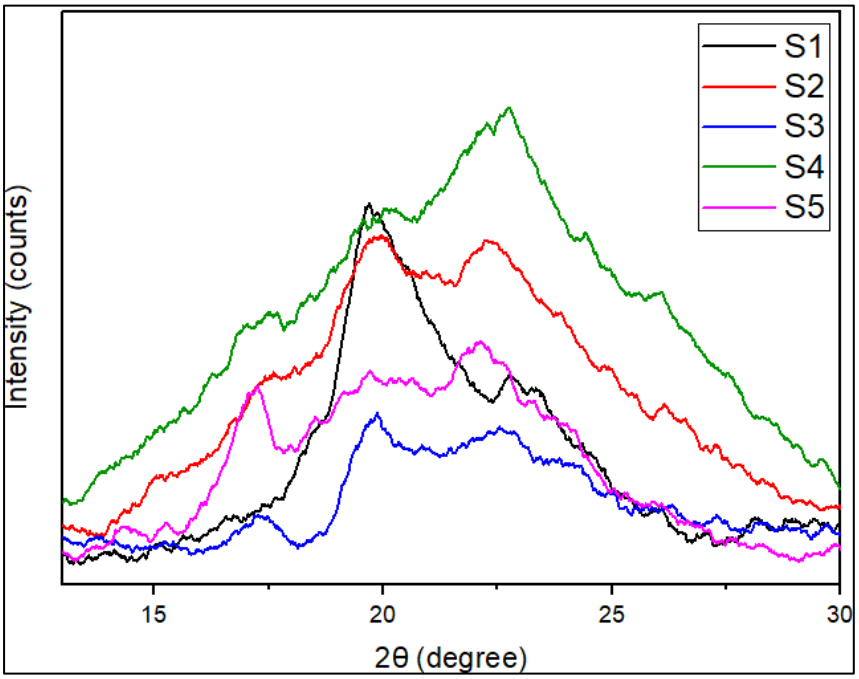


Figure 3. XRD analysis at 20° for polymer blend with different composition of JSS

Table 3. Percent crystallinity for each sample

Sample	Percent Crystallinity (%)
S1	84.04
S2	88.35
S3	41.82
S4	81.87
S5	74.55

Conclusion

The blend of JSS and PVA with different compositions was prepared via the solution casting method and their properties were investigated. From this study, it shows that the JSS and PVA have good compatibility and can be effectively reinforced together. Based on the FTIR analysis, the blend has a hydrogen bonding interaction and also have C=O stretching and C-O vibrations. Then, from SEM and XRD analysis, S3 has the most amorphous structure which then leads to high ionic conductivity. Thus, this study suggests that JSS and PVA are suitable to be used as PEs.

Acknowledgement

The authors acknowledge Universiti Teknologi MARA (UiTM) for a research grant FRGS (Grant No. 600-IRMI/FRGS 5/3 (267/2019)) and Faculty of Applied Science UiTM Jengka, Pahang for providing research facilities.

References

1. Hallinan, D. T. and Balsara, N. P. (2013). Polymer electrolytes. *Annual Review of Materials Research*, 43: 503-525.
2. Aziz, S. B., Woo, T. J., Kadir, M. F. Z. and Ahmed, H. M. (2018). A conceptual review on polymer electrolytes and ion transport models. *Journal of Science: Advanced Materials and Devices*, 3(1): 1-17.
3. Gurusiddappa, J., Madhuri, W., Padma Suvarna, R. and Priya Dasan, K. (2016). Studies on the morphology and conductivity of PEO/$LiClO_4$. *Materials Today: Proceedings*, 3(6): 1451-1459.
4. Theivasanthi, T. and Alagar, M. (2013). An insight analysis of nano sized powder of jackfruit seed. *Nano Biomedicine and Engineering*, 3(3): 2-3.
5. Tulyathan, V., Tananuwong, K., Songjinda, P. and Jaiboon, N. (2002). Some physicochemical properties of jackfruit (*Artocarpus heterophyllus* Lam) seed flour and starch. *ScienceAsia*, 28: 37-41.
6. Santana, R. F., Bonomo, R. C. F., Gandolfi, O. R. R., Rodrigues, L. B., Santos, L. S., dos Santos Pires, A. C., de Oliveira, C. P., da Costa Ilhéu Fontan, R. and Veloso, C. M. (2018). Characterization of starch-based bioplastics from jackfruit seed plasticized with glycerol. *Journal of Food Science and Technology*, 55(1): 278-286.
7. Lothfy, F. A., Haron, M. F. and Rafaie, H. A. (2018). Fabrication and characterization of jackfruit seed powder and polyvinyl alcohol blend as biodegradable plastic. *Journal of Polymer Science and Technology*, 3(2): 1-5.
8. Lestari, R. A. S., Kasmiyatun, M., Dermawan, K., Aini, A. N., Riyati, N. and Putri, F. R. (2020). Bioplastic from jackfruit seeds and rice. *IOP Conference Series: Materials Science and Engineering*, *835*(1).
9. Lin, Z., Guo, X., Wang, Z., Wang, B., He, S., Dell, L. A. O., Huang, J., Li, H., Yu, H. and Chen, L. (2020). Nano energy a wide-temperature superior ionic conductive polymer electrolyte for lithium metal battery. *Nano Energy*, *73*(3): 104786.
10. Gadjourova, Z., Andreev, Y. G., Tunstall, D. P. and Bruce, P. G. (2001). Ionic conductivity in crystalline polymer electrolytes. *Nature*, 412(6846): 520-523.
11. Zou, G. X., Jin, P. Q. and Xin, L. Z. (2008). Extruded starch/PVA composites: Water resistance, thermal properties, and morphology. *Journal of Elastomers and Plastics*, 40(4): 303-316.
12. Aziz, S. B., Marf, A. S., Dannoun, E. M. A., Brza, M. A. and Abdullah, R. M. (2020). The study of the degree of crystallinity, electrical equivalent circuit, and dielectric properties of polyvinyl alcohol (PVA)-based biopolymer electrolytes. *Polymers*, 12(10): 1-17.
13. Long, L., Wang, S., Xiao, M. and Meng, Y. (2016). Polymer electrolytes for lithium polymer batteries. *Journal of Materials Chemistry A*, 4(26): 10038-10039.
14. Hagfeldt, A., Boschloo, G., Sun, L., Kloo, L. and Pettersson, H. (2010). *Dye-Sensitized Solar Cells*. 6595–6663.
15. Aslam, M., Kalyar, M. A. and Raza, Z. A. (2018). Polyvinyl alcohol: A review of research status and use of polyvinyl alcohol based nanocomposites. *Polymer Engineering and Science*, 58(12): 2119-2132.
16. Fahmy, T., Sarhan, A. and Elqahtani, Z. M. (2020). Structural and optical characterization of thiourea-poly (vinyl alcohol) composites. *International Journal of Engineering Research and Technology*, 13(3): 454-461.
17. Chen, S. H., Tsao, C. T., Chang, C. H., Lai, Y. T., Wu, M. F., Liu, Z. W., ... and Hsieh, K. H. (2013). Synthesis and characterization of reinforced poly (ethylene glycol)/chitosan hydrogel as wound dressing materials. *Macromolecular Materials and Engineering*, 298(4): 429-438.
18. Tian, H., Yan, J., Rajulu, A. V., Xiang, A. and Luo, X. (2017). Fabrication and properties of polyvinyl alcohol/starch blend films: Effect of composition and humidity. *International Journal of Biological Macromolecules*, 96: 518-523.

19. Retnowati, D. S., Ratnawati, R. and Purbasari, A. (2015). A biodegradable film from jackfruit (*Artocarpus heterophyllus*) and durian (*Durio zibethinus*) seed flours. *Scientific Study and Research: Chemistry and Chemical Engineering, Biotechnology, Food Industry*, 16(4): 395-404.
20. Ooi, Z. X., Ismail, H. and Teoh, Y. P. (2018). Characterization and properties of biodegradable polymer film composites based on polyvinyl alcohol and tropical fruit waste flour. In *Natural Fibre Reinforced Vinyl Ester and Vinyl Polymer Composites*. Elsevier Ltd.
21. Jayakumar, A., Heera, K. V., Sumi, T. S., Joseph, M., Mathew, S., Praveen, G., ... and Radhakrishnan, E. K. (2019). Starch-PVA composite films with zinc-oxide nanoparticles and phytochemicals as intelligent pH sensing wraps for food packaging application. *International Journal of Biological Macromolecules,* 136: 395-403.
22. Nandiyanto, A. B. D., Oktiani, R. and Ragadhita, R. (2019). How to read and interpret FTIR spectroscope of organic material. *Indonesian Journal of Science and Technology*, 4(1): 97-118.
23. Sarebanha, S., & Farhan, A. (2018). Eco-friendly composite films based on polyvinyl alcohol and jackfruit waste flour. *Journal of Packaging Technology and Research*, 2(3): 181-190.
24. Arof, A. K., Amirudin, S., Yusof, S. Z. and Noor, I. M. (2014). A method based on impedance spectroscopy to determine transport properties of polymer electrolytes. *Physical Chemistry Chemical Physics*, 16(5): 1856-1867.
25. Kane, S. N., Mishra, A. and Dutta, A. K. (2016). Preface: International Conference on Recent Trends in Physics (ICRTP 2016). *Journal of Physics: Conference Series*, 755(1): 6.
26. Sarifuddin, N., Shahrim, N. A., Rani, N. N. S. A., Zaki, H. H. M. and Azhar, A. Z. A. (2018). Preparation and characterization of jackfruit seed starch/poly (vinyl alcohol) (PVA) blend film. *IOP Conference Series: Materials Science and Engineering*, 290(1): 012065.
27. Hamsan, M. H., Nofal, M. M., Aziz, S. B., Brza, M. A., & Dannoun, E. M. A. (2021). Plasticized polymer blend electrolyte based on chitosan for energy storage application: structural, circuit modeling, morphological and electrochemical properties. *Polymers,* 13(8): 1233.
28. Yap, Y. L., You, A. H., Teo, L. L. and Hanapei, H. (2013). Inorganic filler sizes effect on ionic conductivity in polyethylene oxide (PEO) composite polymer electrolyte. *International Journal of Electrochemical Science*, *8*(2): 2154-2163.
29. Janik, W., Wojtala, A., Pietruszka, A., Dudek, G. and Sabura, E. (2021). Environmentally friendly melt-processed chitosan/starch composites modified with pva and lignin. *Polymers,* 13(16): 2685.
30. Liew, C. W. and Ramesh, S. (2015). Electrical, structural, thermal and electrochemical properties of corn starch-based biopolymer electrolytes. *Carbohydrate Polymers*, 124: 222-228.
31. Hema, M., Selvasekarapandian, S., Arunkumar, D., Sakunthala, A. and Nithya, H. (2009). FTIR, XRD and ac impedance spectroscopic study on PVA based polymer electrolyte doped with NH_4X (X = Cl, Br, I). *Journal of Non-Crystalline Solids*, 355(2): 84-90.

Malaysian Journal of Analytical Sciences (MJAS)
Published by Malaysian Analytical Sciences Society

STRUCTURAL AND ELECTROCHEMICAL CHARACTERISATIONS OF LANTHANUM-BASED COBALT FERRITE AND BARIUM CERATE-ZIRCONATE OXIDES AS COMPOSITE CATHODE FOR PROTON CERAMIC FUEL CELL

(Pencirian Struktur dan Elektrokimia Lantanum Berasaskan Kobalt Ferum Oksida dan Barium Serat-Zirkonat Oksida Sebagai Komposit Katod untuk Aplikasi Sel Fuel Seramik Proton)

Nurul Izzati Abd Malek[1], Ismariza Ismail[2], Abdul Mutalib Md Jani[3], Mohd Hafiz Dzarfan Othman[4], Nafisah Osman[1,5]*

[1]Proton Conducting Fuel Cell Research Group, Faculty of Applied Sciences, Universiti Teknologi MARA, 40450 Shah Alam, Selangor, Malaysia
[2]Faculty of Engineering Technology, Universiti Malaysia Perlis, 02100 Padang Besar, Perlis, Malaysia
[3]Faculty of Applied Sciences, Universiti Teknologi MARA, 35400 Tapah Road, Tapah, Perak, Malaysia
[4]Advanced Membrane Technology Research Centre (AMTEC), School of Chemical & Energy Engineering, Faculty of Engineering, Universiti Teknologi Malaysia, 81310 UTM Skudai, Johor, Malaysia
[5]Faculty of Applied Sciences, Universiti Teknologi MARA Perlis, 02600 Arau, Perlis, Malaysia

[*]Corresponding author: fisha@uitm.edu.my

Received: 12 September 2021; Accepted: 12 July 2022; Published: 25 August 2022

Abstract

This study investigated the composite cathode of $LaSrCoFeO_3$-$BaCeZrYO_3$ (LSCF-BCZY) in a ratio of 7 : 3. A 13-mm symmetrical half-cell was fabricated using the dry pressing and spin-coating techniques to yield the configuration of LSCF-BCZY|BCZY|LSCF-BCZY. The phase of the sample was verified using the X-Ray Diffraction (XRD) spectroscopy. The electrochemical and microstructure of the half-cell were characterized using the Electrochemical Impedance Spectroscopy and Scanning Electron Microscopy (SEM), respectively. The XRD analysis showed that the single-phase structure of LSCF and BCZY was still preserved at the calcination temperature of 900 ºC. The half-cell demonstrated a thermally activated trend in a humidified atmosphere with area-specific resistance values of 0.25, 0.33, 1.02, 1.64, and 5.75 Ω.cm^2 at temperatures of 800, 750, 700, 650, and 600 ºC, respectively. The SEM image revealed that the 10-µm LSCF-BCZY layer was well-adhered on the dense BCZY electrolyte surface. This synthesised LSCF-BCZY in the ratio of 7 : 3 demonstrated excellent characteristics as a composite cathode for PCFCs.

Keywords: composite cathode, single phase, spin coating, proton ceramic fuel cells

Abstrak

Dalam kajian ini, komposit katod daripada $LaSrCoFeO_3$-$BaCeZrYO_3$ (LSCF-BCZY) dengan nisbah 7 : 3 dipilih disebabkan kelebihanya berbanding dengan LSCF tulen. Teknik penekanan kering dan saduran berpusing telah digunakan untuk menghasilkan 13-mm sel separa simetri dengan konfigurasi iaitu LSCF-BCZY|BCZY|LSCF-BCZY. Pembentukan fasa sampel telah disahkan oleh pembelauan sinar-X (XRD). Sifat elektrokimia dan struktur mikro daripada sel separa simetri masing-masing telah diciri menggunakan spektroskopi impedans elektrokimia (EIS) dan pengimbasan mikroskop elektron (SEM). Pada suhu kalsinan 900 ^oC, komponen LSCF dan BCZY tidak menunjukkan sebarang perubahan dan berfasa tunggal seperti dibuktikan melalui analisis XRD. Sel ini menunjukkan kecenderungan aktif secara terma, yang disahkan melalui pengukuran EIS dalam atmosfera lembap dengan kawasan rintangan khusus (ASR) masing-masing iaitu 0.25, 0.33, 1.02 , 1.64, dan 5.75 $\Omega.cm^2$ pada suhu 800, 750, 700, 650 dan 600 ^oC. Gambar SEM menunjukkan bahawa lapisan 10 μm LSCF-BCZY melekat dengan baik pada permukaan elektrolit padat BCZY. Maka, penghasilan LSCF-BCZY dengan nisbah 7 : 3 menunjukkan ciri-ciri yang terbaik sebagai katod komposit bagi aplikasi PCFC.

Kata kunci: katod komposit, fasa tunggal, saduran berpusing, sistem sel fuel seramik proton

Introduction

A Proton Ceramic Fuel Cell (PCFC) is a green device that converts chemical energy to electrical energy with heat and water as by-products for a high-power generation system. However, a high cathode polarisation resistance (R_p) reduces the overall cell system performance substantially, particularly at the intermediate temperature range of 500 to 800 ^oC [1]. The rising trend in R_p is related to the lack of a surface-active site for the oxygen reduction process (ORR) at the triple-phase boundary (TPB) that connects the electrolyte, cathode, and gas phase. Thus, selecting the best materials for the cathode component is crucial for the PCFC system because materials will exhibit different characteristics when coupled with other materials or operating at elevated temperatures. In this respect, pure $LaSrCoFeO_3$ (LSCF) is a well-known cathode material for PCFCs because it contains more excellent ionic and electronic charge carrier species than traditional cathodes [2]. However, because LSCF has a limited number of TPB sites, various methods or materials have been suggested to increase the TPB length [3, 4]. One of the suggested methods is the use of a composite cathode for integrating proton conductors, mixed electronic-ionic conductors, or a catalytic layer [5].

For PCFCs, a composite cathode is produced by mixing materials of the cathode and proton conductor electrolyte for high-kinetic ORR. The electrical conductivity of the composite cathode increased about two times higher than the pure cathode [6 - 8]. However, an excessive amount (> 50%) of protonic species in the mixed ionic-electronic conductor MIEC cathodes caused water loading across the bulk cathode, reducing the overall performance of the fuel cell [9, 10]. Meanwhile, protonic species based on cerate-zirconate oxides exhibited high conductivity; they were chemically stable and compatible with LSCF cathodes [11]. Recently, adding some protonic species, for example, doped-barium cerate zirconate oxide, into the LSCF cathode using chemical approaches lengthened the TPB [12].

In general, a symmetrical half-cell is fabricated for electrochemical studies to evaluate the behaviour of the composite cathode. The half-cell requires the optimised electrolyte substrate and cathode thin-film design. The electrolyte substrate is dry-pressed at the desired pressure and sintered at high temperatures to obtain the dense pellet. The cell is subjected to electrochemical impedance spectroscopy (EIS) measurement to study the material behaviour and performance. A suitable equivalent circuit for EIS spectra is introduced to fit the EIS spectrum via a fitting procedure. Information or data gained is used to calculate capacitance, arc summit frequency, and area-specific resistance (ASR) of the half-cell as a function of temperature. The Adler Lane Steel (ALS) model is used to extract the associated response in the EIS spectrum.

In this study, $BaCeZrYO_3$(BCZY) was chosen as a proton-conducting medium to form the composite cathode of LSCF-BCZY. The structural and electrochemical properties of the prepared cathode were further analysed and characterised.

Materials and Methods

The $LaSrCoFeO_3$ cathode powder was produced using a modified sol-gel process in which all the metal nitrate salts in the universal solvent were dissolved, followed by adding citric acid and ethylenediaminetetraacetic acid (EDTA). Upon alkalinising the mixture to pH 9 with ammonium hydroxide, ethylene glycol was added, and the brownish gel produced was calcined for five hours at 900 ºC. The single-phased BCZY powder and the high relative density pellet (97.1%) were prepared as previously described [13]. The LSCF and BCZY powders were mixed in the ratio of 7: 3 weight percent (wt%) to form the LSCF-BCZY composite cathode. The composite powder was transformed into cathode slurry and spin-coated on both sites of the BCZY pellet under optimised conditions (2,000 rpm for 30 s). The half-cell with the configuration of LSCF-BCZY|BCZY|LSCF-BCZY was sintered at 600 ºC for one hour and 900 ºC for three hours.

The prepared powder and half-cell were characterised using X-ray diffraction (XRD) spectroscopy, EIS, and scanning electron microscopy (SEM). For XRD, the LSCF-BCZY powder was radiated with Cu-K_α at the ambient temperature at the wavelength of 1.5406 Å using 8.04 keV (PANalytical X'Pert PRO MRD PW 3040). The scanning was set at the rate of 0.02 s^{-1} to collect the two thetas from 20º to 80º. The XRD data was analyzed with X'Pert HighScore Plus software (version 5.1, Malvern Panalytical) and compared to the Joint Committee on Powder Diffraction Standard (JCPDS) card number 089-1268 for LCSF and 01-089-2485 for BCZY. The perovskite phases were calculated using the Swarts and Shrout equation. Meanwhile, the symmetrical half-cell was passed through wet air at the flow rate of 90 mL/min, and the electrochemical parameter was measured between 1 MHz and 10 MHz with amplitude voltages ranging from 3 to 5 mV at 600 – 800 ºC using the electrochemical workstation ZIVE SP2 (ZIVE LAB WonATech). An equivalent circuit of L_s-R_s(R1Q1)-(R2Q2) was used for the impedance spectrum analysis using the test station (ZIVE ZMAN™ 2.4). Values of capacitance, arc summit frequency, and polarisation resistance were calculated for each temperature using the equations reported in another study [14]. The raw and fitted data were re-plotted using the software Origin 2019b. After electrochemical testing, the morphology of pellets was evaluated using SEM with energy dispersive X-ray (EDX). The software ImageJ was used to measure the porosity of the SEM image.

Results and Discussion

Figure 1 shows the XRD pattern of LSCF-BCZY composite cathode powder upon calcination at 900 ºC. All diffraction peaks agreed with JCPDS-card no. (LSCF ID: 01-089-1268) and (BCZY ID: 01-089-2485) with orthorhombic and cubic structures, respectively. More than 90% of the single perovskite phase was formed for both LSCF and BCZY, indicating that these materials maintained their phases after the heat treatment at 900 °C. The prominent peaks were indexed using Miller Indices (hkl) reflected plane as follows: (110), (020), (202), (220), (132), (224), and (332) for LSCF, and (110), (200), (211), (220), and (222) for BCZY. The lattice constants of LSCF and BCZY were calculated using the software Mathcad 14.0 (Mathsoft). Table 1 shows the lattice constants of LSCF and BCZY, and they agreed with the reference data. These values were consistent with the finding of another study [15] for LSCF-BCZY treated at 1,000 ºC.

Figure 2 shows the Nyquist impedance plot of the fabricated half-cell in humidified air at temperatures ranging from 600 to 800 ºC. As the temperature increased, the impedance spectrum became smaller in size, obeying the thermally activated behaviour, as expected by Arrhenius's Law [16]. The arcs were resolved using an equivalent circuit (the inset of Figure 2). The first arc, represented by R_1Q_1, was referred to as an electronic charge transfer that occurred at the cathode surface. The second arc, R_2Q_2, was associated with the ionic charge transfer reaction at the cathode-electrolyte interphase. The calculated capacitance ranged from 10^{-2} - 10^{-4} for the R_1Q_1 circuit and 4 x 10^{-5} - 10^{-7} for the R_2Q_2 circuit [5], denoting the respective cathode process. Also, the arc summit frequency confirmed the presence of these two arcs in the middle and low-frequency regions. ASR values of 0.25, 0.33, 1.02, 1.64, and 5.75 Ω.cm^2 were obtained between 800 and 600 ºC at intervals of 50 ºC. ASR values of the pure LSCF increased by about one time

higher than modified samples (800 – 600 ºC: 1.06, 1.13, 3.13, and 6.50 Ω.cm^2). Compared to the pure LSCF, the reduction of ASR values for LSCF-BCZY suggested that the use of composite cathode could potentially enhance the performance of PCFC.

Figure 3 shows the SEM images of the fractured cross-section and cathode surface of the LSCF-BCZY|BCZY|LSCF-BCZY symmetrical half-cell after the electrochemical measurement. There was no sign of crack and delamination in the cell, indicating a good adhesion between a 10-µm LSCF layer and a dense electrolyte that promoted a low contact resistance [15]. The cathode surface showed a well dispersed and homogenised microstructure with a porosity of 32%. This amount was sufficient to allow better oxygen diffusion through the cathode material as the required porosity ranged from 20% to 40% [16]. Good adhesion between LSCF-BCZY cathode and BCZY electrolyte as well as the homogenised microstructure of the LSCF layer reduced the resistance of cathode bulk, leading to fast surface oxygen ion diffusion [5, 17].

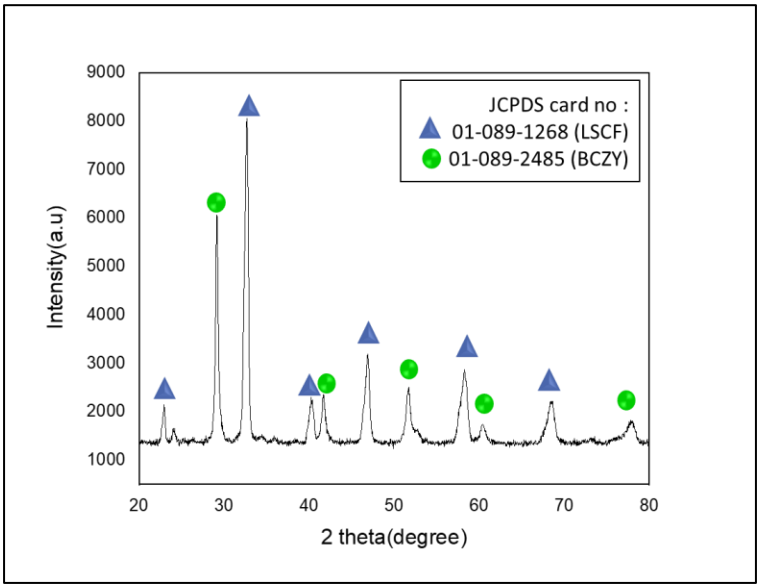


Figure 1. XRD pattern of the LSCF-BCZY composite cathode after calcined at T = 900ºC.

Table 1. Lattice parameter of the LSCF and BCZY taken from JCPDS-card and calculated ones using Mathcad 14 software

Sample ID	**Lattice Parameter/Å (JCPDS-card)**	**Lattice Parameter/Å (Mathcad 14 software)**
LSCF (Orthorombic)	a = 5.475	a = 5.471
	b = 5.536	b = 5.482
	c = 7.848	c = 7.900
BCZY (Cubic)	a = 4.3436	a = 4.335

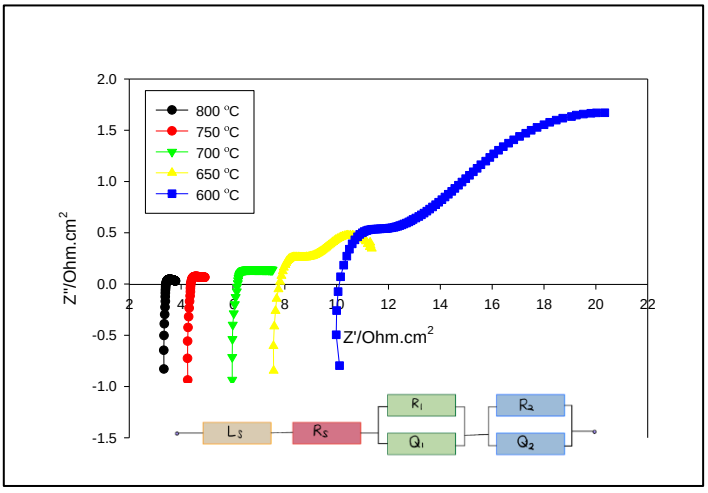


Figure 2. The EIS spectrum of LSCF-BCZY|BCZY|LSCF-BCZY under humidified air at the temperature in the range of 600 °C to 800 °C (Inset is the used equivalent circuit to resolve the associated responses)

Table 2. The calculated values of capacitance, arc summit frequencies and R_p and ASR for the LSCF-BCZY|BCZY|LSCF-BCZY

Temperature (°C)	**Capacitance, C (Fcm^2)**	**Arc summit frequency, f° (Hz)**	**Polarization Resistance, R_p (Ωcm^2)**	**Area specific resistance, ASR (Ωcm^2)**
800	C_1: 3.08x10^{-5}	$f°_1$: 1.09x10^4	R_1: 0.080	0.250
	C_2: 2.58x10^{-2}	$f°_2$: 2.67x10^3	R_2: 0.420	
			R_p: 0.500	
750	C_1: 2.39x10^{-5}	$f°_1$: 5.35x10^6	R_1: 0.075	0.332
	C_2: 7.86x10^{-1}	$f°_2$: 4.89x10^3	R_2: 0.589	
			R_p: 0.664	

Table 2 (cont'd). The calculated values of capacitance, arc summit frequencies and R_p and ASR for the LSCF-BCZY|BCZY|LSCF-BCZY

Temperature (°C)	Capacitance, C (Fcm^2)	Arc summit frequency, f° (Hz)	Polarization Resistance, R_p (Ωcm^2)	Area specific resistance, ASR (Ωcm^2)
700	C_1: 1.02x10^{-5} C_2: 2.40x10^{-1}	f°$_1$: 3.37x10^5 f°$_2$: 1.67x10^2	R_1: 0.750 R_2: 1.290 R_p: 2.040	1.020
650	C_1: 3.11x10^{-6} C_2: 1.79x10^{-2}	f°$_1$: 2.81x10^4 f°$_2$: 3.16x10^2	R_1: 0.800 R_2: 2.478 R_p: 3.278	1.639
600	C_1: 8.46x10^{-5} C_2: 1.79x10^{-2}	f°$_1$: 2.14x10^4 f°$_2$: 5.35x10^2	R_1: 2.100 R_2: 9.400 R_p: 11.500	5.750

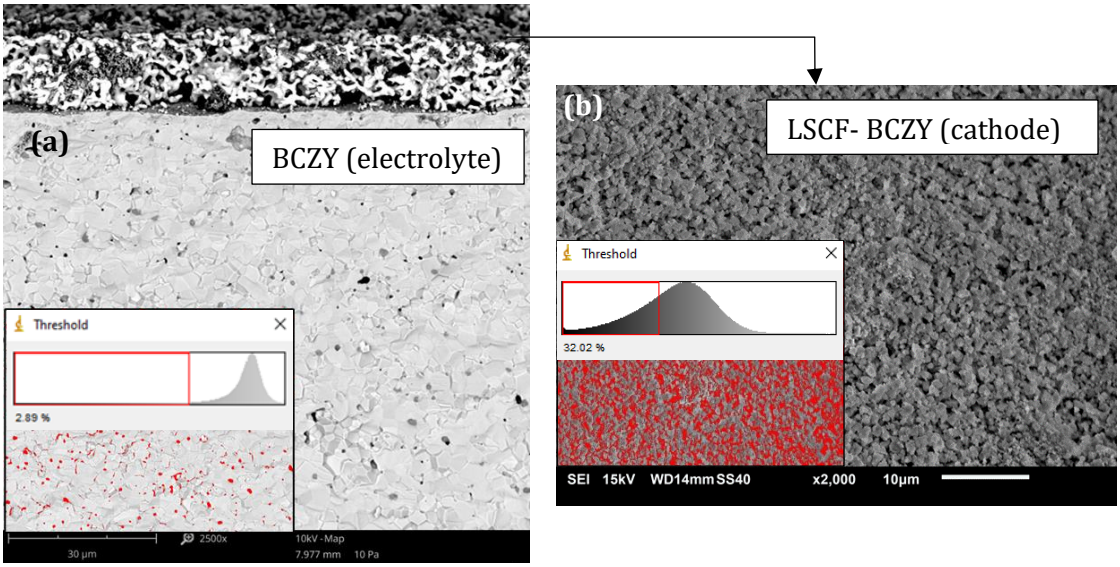


Figure 3. SEM images of the LSCF-BCZY|BCZY|LSCF-BCZY after electrochemical measurement (a) cross section and (b) top view of the cell

Conclusion

The LSCF and BCZY powders were prepared by the sol-gel method using metals nitrate salts. Both compounds maintained their respective phase even after they were simultaneously calcined at 900 °C. ASR values at the intermediate temperatures of 800 to 600 °C with the composite cathode half-cell were 0.25, 0.33, 1.02, 1.64, and 5.75 Ω.cm^2. After the electrochemical testing, the morphology of the well-distributed cells remained unchanged, i.e., with no delamination and porosity optimised. The use of the LSCF-BCZY composite cathode reduced the polarization resistance of the fabricated cell substantially, suggesting that it might have great potential for PCFC application.

Acknowledgement

We acknowledged Strategic Research Partnership Grant UiTM-UTM (100-RMC 5/3/SRP GOV(002/2021)) for the sponsorship and UiTM for the facilities.

References

1. He, W., Yuan, R. H., Dong, F. F., Wu, X. L. and Ni, M. (2017). High performance of protonic solid oxide fuel cell with $BaCo_{0.7}Fe_{0.22}Sc_{0.08}O_{3-\delta}$ electrode. *International Journal of Hydrogen Energy,* 42(39): 25021-25025.
2. Chen, J., Li, J., Jia, L., Moussa, I., Chi, B., Pu, J. and Li, J. (2019). A novel layered perovskite Nd $(Ba_{0.4}Sr_{0.4}Ca_{0.2})$ $Co_{1.6}Fe_{0.4}O_{5+\delta}$ as cathode for proton-conducting solid oxide fuel cells. *Journal of Power Sources,* 428: 13-19.
3. Fang, X., Zhu, J. and Lin, Z. (2018). Effects of electrode composition and thickness on the mechanical performance of a solid oxide fuel cell. *Energies,* 11(7): 1735.
4. Osman, N., Ismail, I., Samat, A. A. and Md Jani, A. M. (2016). Reactivity study of $LaSrCoFeO_3$-Ba (Ce, Zr) O_3 composite cathode material. *In Materials Science Forum,* 846: pp. 58-62.
5. Ismail, I., Osman, N. and Jani, A. M. M. (2018). Evaluation of $La_{0.6}Sr_{0.4}Co_{0.2}Fe_{0.8}O_{3-\delta}$ as a potential cathode for proton-conducting solid oxide fuel cell. *Sains Malaysiana,* 47(2): 387-391.
6. Matsui, T., Kunimoto, N., Manriki, K., Miyazaki, K., Kamiuchi, N., Muroyama, H. and Eguchi, K., 2021. Oxygen reduction reaction over (Ba, $Sr)_6RE_2Co_4O15$–$Ba(Ce,Pr,Y)O_3$ composite cathodes for proton-conducting ceramic fuel cells. *Journal of Materials Chemistry* A, 9(27): 15199 15206.
7. Loureiro, F. J., Ramasamy, D., Mikhalev, S. M., Shaula, A. L., Macedo, D. A. and Fagg, D. P. (2021). $La_4Ni_3O_{10}$±δ–$BaCe0.9Y0.1O_3$-δ cathodes f or proton ceramic fuel cells; short-circuiting analys is using BaCe0. 9Y0. 1O3-δ symmetric cells. *International Journal of Hydrogen Energy*, 46(25): 13594-13605.
8. Song, Y., Chen, Y., Wang, W., Zhou, C., Zhong, Y ., Yang, G., ... and Shao, Z. (2019). Self-assembled triple-conducting nanocomposite as a superior protonic ceramic fuel cell cathode. *Joule*, *3*(11): 28 42-2853.
9. Shao, L., Si, F., Fu, X. Z. and Luo, J. L. (2018). Stable $SrCo0.7Fe0.2Zr0.1O_3$-δ cathode material for proton conducting solid oxide fuel cell reactors. *International Journal of Hydrogen Energy*, *43*(15): 7511-7514.
10. Zhu, H., Ricote, S., Duan, C., O'Hayre, R. P., Tsvetkov, D. S. and Kee, R. J. (2018). Defect incorporation and transport within dense $BaZr_{0.8}Y_{0.2}O_{3-\delta}$ (BZY_{20}) proton-conducting membranes. *Journal of The Electrochemical Society,* 165(9): F581.
11. Osman, N., Senari, S. M. and Md Jani, A. M. (2020). Characterization of NiO-BCZY as composite anode prepared by a one-step sol-gel method. *Malaysian Journal of Fundamental and Applied Sciences,* 16(4): 450–452.
12. Miao, L., Hou, J., Gong, Z., Jin, Z. and Liu, W. (2019). A high-performance cobalt-free Ruddlesden-Popper phase cathode $La_{1.2}Sr_{0.8}Ni_{0.6}Fe_{0.4}O_{4+\delta}$ for low temperature proton-conducting solid oxide fuel cells. *International Journal of Hydrogen Energy,* 44(14): 7531-7537.
13. Mohsin, M., Yousaf, A., Raza, R. and Zia, R. (2019). Highly conducting perovskite structured (M-$SrCoFe-O_{3-\delta}$, M= Ce, Ba) cathode for solid oxide fuel cell. *Journal of Alloys and Compounds,* 791: 248-254.
14. Lee, S., Park, S., Wee, S., woo Baek, H. and Shin, D. (2018). One-dimensional structured $La_{0.6}Sr_{0.4}Co_{0.2}Fe_{0.8}O_{3-\delta}$-$BaCe_{0.5}Zr_{0.35}Y_{0.15}O_{3-\delta}$ composite cathode for protonic ceramic fuel cells. *Solid State Ionics,* 320: 347-352.
15. Osman, N., Ismail, I., Samat, A. A. and Md Jani, A. M. (2016). Reactivity study of $LaSrCoFeO_3$-Ba (Ce, Zr)O_3 composite cathode material. *In Materials Science Forum,* 486: 58-62.
16. Kuroha, T., Yamauchi, K., Mikami, Y., Tsuji, Y., Niina, Y., Shudo, M., ... and Okuyama, Y. (2020). Effect of added Ni on defect structure and proton transport properties of indium-doped barium zirconate. *International Journal of Hydrogen Energy,* 45(4): 3123-3131.
17. Baek, S.-W., J. Bae, and Y.-S. Yoo, Cathode reaction mechanism of porous-structured $Sm0.5Sr0.5CoO_3$−δ and $Sm0.5Sr0.5CoO_3$−δ/ Sm0.2Ce0.8O1.9 for solid oxide fuel cells. *Journal of Power Sources,*193(2): 431-440.

Malaysian Journal of Analytical Sciences (MJAS)
Published by Malaysian Analytical Sciences Society

ASSESSMENT OF METALS IN SEDIMENT OF A MONSOON-DOMINATED REGION IN THE NORTHERN MALACCA STRAIT

(Penilaian Logam dalam Sedimen di Wilayah yang Didominasi Monsun di Utara Selat Melaka)

Mohamad Arif Che Abd Rahim[1], Shengfa Liu[2,3], Xuefa Shi[2,3], Che Abd Rahim Mohamed[1]*

[1]*Faculty of Science and Technology,*
Universiti Kebangsaan Malaysia, 43600 UKM Bangi, Selangor, Malaysia
[2]*Key Laboratory of Marine Geology and Metallogeny,*
First Institute of Oceanography, Ministry of Natural Resources, Qingdao, China
[3]*Laboratory for Marine Geology,*
Qingdao National Laboratory for Marine Science and Technology, Qingdao, China

**Corresponding author: carmohd@ukm.edu.my*

Received: 23 March 2022; Accepted: 18 May 2022; Published: 25 August 2022

Abstract

Fluctuation levels of geochemical elements, sediment texture and nutrients were analysed from five surface sediments taken from the northern Malacca Straits. These samples were obtained during the RV Discovery Scientific cruises in September 2017 and April 2018, to assess pollution sources during monsoonal events. The results show a high output of clay and silt, revealing that the monsoonal season and cross-shelf inputs affect textural sediment. On the other hand, fluctuations in geochemical concentrations are due to industrialisation and urbanisation along the Malacca Straits, contributed by the local drainage basin. The presence of the monsoon also affects the diffusivity and absorption between the water-sediment interfaces, leading to constant fluctuation along the straits. Principal Component Analysis (PCA) of the association between the geochemical elements, sediment texture and nutrients reveal hydrological factors, mobility and accumulation through the sediment interface.

Keywords: weathering, pollution, monsoon, sediment, Malacca Strait

Abstrak

Tahap kepekatan unsur geokimia, tekstur sedimen dan nutrien telah dianalisis daripada lima sedimen permukaan yang diambil dari kawasan utara Selat Melaka. Sampel ini diperoleh semasa pelayaran RV Discovery Scientific pada September 2017 dan April 2018 untuk menilai sumber pencemaran semasa peristiwa monsun. Keputusan menunjukkan keluaran lempung dan kelodak yang lebih tinggi, menunjukkan bahawa musim monsun dan input rentas pelantar mempengaruhi sedimen tekstur. Sebaliknya, fluktuasi kepekatan geokimia adalah disebabkan oleh kawasan perindustrian dan pembandaran di sepanjang Selat Melaka, disumbangkan oleh lembangan saliran tempatan. Kehadiran monsun juga menjejaskan resapan dan penyerapan antara antara muka air-mendapan, yang membawa kepada fluktuasi yang berterusan di sepanjang selat. Analisis Komponen Utama (PCA) perkaitan antara unsur geokimia tekstur sedimen dan nutrien mendedahkan faktor hidrologi, mobiliti dan pengumpulan melalui antara muka sedimen.

Kata kunci: luluhawa, pencemaran, monsun, sedimen, Selat Melaka

Introduction

The Malacca Strait is located between the west coast of the Malaysian Peninsular and the east coast of Sumatra Island, and is connected with the Strait of Singapore at its south-eastern end. There are also smaller straits, such as the Johor Strait, Bengkali Strait and Rupat Strait. Together, these straits play an important role in international shipping routes linking the Indian Ocean to the Pacific Ocean [1]. The tropical climate in the Malacca Strait results in an annual precipitation of 3000 mm yr^{-1} [2], leading to severe weathering on the adjacent peninsular. The tides and currents present in the Malacca Straits are mainly semi-diurnal, following the monsoonal current as the main force around the surrounding coast [3]. Low to medium high turbidity has been recorded, with transparency ranging from 10 to 30 m. Primary productivity is influenced geographically but is constant throughout the whole year. Shallower water along the coastlines leads to vertical mixing and nutrient inputs from drainage basins adjacent to the Malacca Straits [4].

A high volume of annual precipitation (3000 mm yr^{-1}) also leads to severe terrestrial weathering towards the straits, resulting in elevated sediment discharge [5]. On the west coast of the Malaysian Peninsular, a number of discharged sediment sources are the result of physical and chemical weathering [6], with most of the weathered material originating from igneous rock. The granitic rock present in the Malaysian Peninsular originates from the Central and Western Belts, for which the primary source are the Titiwangsa Ranges [7, 8]. According to Shoieb et al. [9], the Sibumasu Terrane, which comprises the Malaysian Peninsula's Western Belt, was derived from the North West Australian Gondwana margin within the late Cambrian-Early Permian period. Therefore, the discharged weathered sedimentary rock material is Palaeozoic shale. An earlier study by Zakariah et al. [10] on the sustainability of the Kuala Muda basin located in the Kedah River, revealed a large quantity of granitic-bearing rocks, most of it originating from the Bintang Range granites. In Penang and Langkawi Island, the formation of the bedrock surrounding both islands originated from the Quaternary deposits, where most of the discharge was feldspar and plagioclase [11, 12]. This has resulted in the constant supply of igneous rock towards the Malacca Straits. In term of temporal influences, the Malacca Strait is affected by monsoonal seasons, where the northeast monsoon prevails from November to March and the southwest monsoon runs from May to September. In essence, the energy generated by the monsoonal season leads to corresponding changes in sea currents through eddies and cyclonic and anti-cyclonic events, thus altering the sinking processes in the Malacca Strait [13]. These monsoonal seasons also affect hydrological processes in the straits, leading to the distribution of weathered material around the coast.

The Malacca Strait is abundant in natural resources and many socio-economic activities related to metal processes and consumption, such as industrial and residential activities which are concentrated in this area, resulting in an increased contaminants load, due to rapid urbanisation and increased population density [14]. Urban development and industrialisation over the previous decade have raised major environmental issues. Pollutants in rivers are a severe problem in many rapidly growing cities, owing to the fact that water quality and sanitary infrastructure do not keep up with population and city expansion, particularly in developing countries. Human activities such as sand mining, land reclamation, deforestation, landfill leachate and urban water runoff are common anthropogenic problems of environmental concern [15]. Contaminants are deposited in aquatic environments as a result of physical erosion, chemical weathering and soil leaching [16]. Furthermore, monsoon-induced events (i.e., storms, flash floods and landslides) can be devastating in mountainous tropical environments, causing severe soil erosion with both on-site and downstream repercussions. When combined with anthropogenic inputs, these result in severe damage to the local population. These hazards also elevate geochemical concentrations and sedimentation.

Sediment is a major source of concern when it comes to environmental quality because of its importance in monitoring the health of both humans and the ecosystem. The importance of sediment is evidenced by its constant deposition of many sources of contamination, leading to bioaccumulation and

bioassimilation in aquatic life, through source and sink processes. In theory, the high level of pollution surrounding the Malacca Straits is the result of natural and anthropogenic inputs, backed with monsoonal seasons, enhancing its concentration under physical and hydrological processes. The objective of this study is to identify the source of geochemical elements within the Malacca Straits, while assessing several factors influencing these geochemical elements. This paper examines pollution concentrations in the Malacca Strait and the prominent factors affecting geochemical elements along the straits.

Materials and Methods

During the UKM-FIO Scientific cruise in August 2017 and May 2018, five surface sediment samples were collected using a Veen Van Grab, at locations on the western coast of the Malaysia Peninsular (Figure 1 and Figure 2). Water depth in the study area ranged from 15.5 m to 67.8 m (Table 1). The sediment samples in this study were taken using a plastic scoop, rather than a metal scoop, to prevent cross contamination. They were stored in zipped polyethylene bags and frozen below 15°C on-board, before being shipped back to National University of Malaysia (UKM).

Sediment textural analysis was carried out, according to the method by Miller and Miller [17, 18]. Calgon solution was used, as proposed by Kaur and Fanourakis [19]. The 4 g bulk sample was mixed in a 50 ml centrifuge tube with 4.2% Calgon solution for better separation into clay, sand and silt layers. The sample was then mixed and sonicated for 15 to 30 minutes, for dispersion. The sample was centrifuged at 770 rpm for 3.3 minutes, for the clay to settle. The clay was then removed at 2.5 cm below the centrifuge tube meniscus level. Silt was obtained via wet sieving at 45 μm and the total amount of sand was calculated via the subtraction of total clay and silt [20].

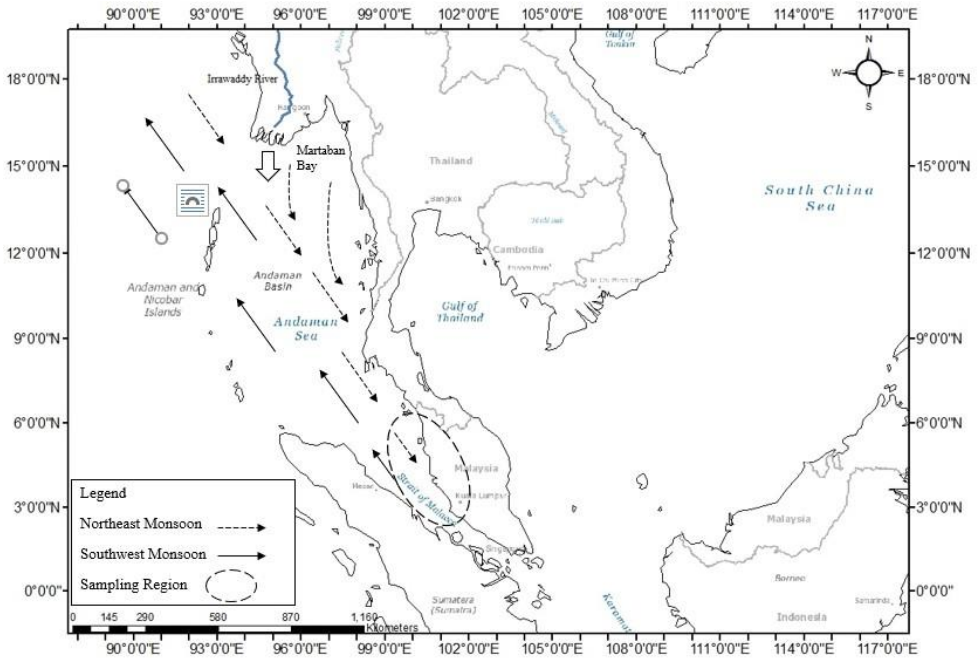


Figure 1. The area of sampling in Northern Malacca Straits affected by monsoonal season (Data source: [23])

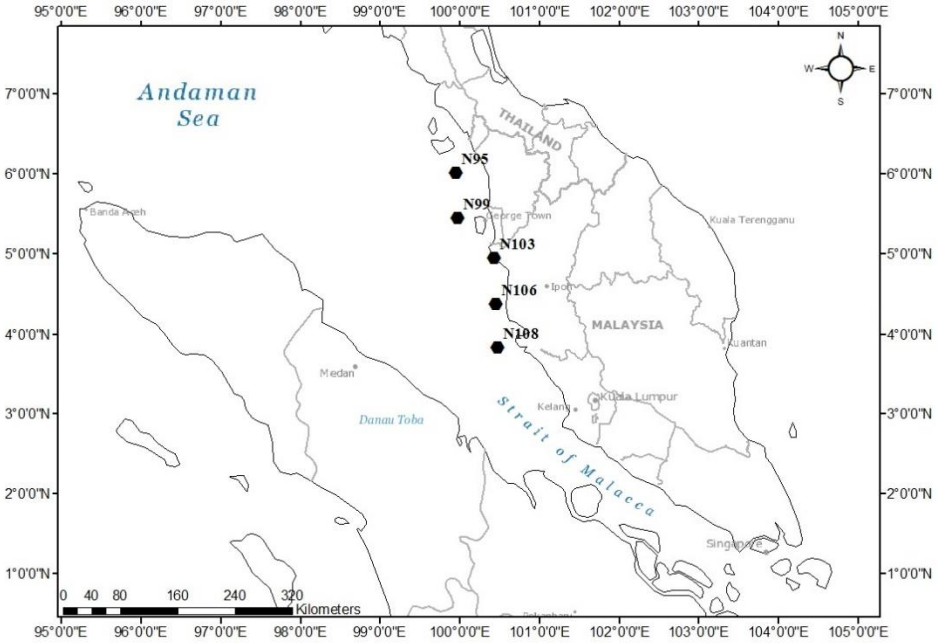


Figure 2. Sampling station in the Malacca Straits

Table 1. Sampling stations along the Malacca Straits

Station	Longitude	Latitude	Sampling Date	Depth (m)
N95	99.9606	6.0069	1/5/2018	39.5
N99	99.9811	5.4428	2/5/2018	40.8
N103	100.44	4.9433	2/5/2018	15.5
N106	100.4561	4.3733	2/5/2018	22.0
N108	100.4828	3.8247	2/5/2018	67.8

Geochemical element analysis was conducted, following the methods in Rahim et al. [16]. In summary, the dry and homogenised sediment was used and mixed with a mixture of 10 mL nitric acid (HNO_3), 5 mL perchloric acid ($HClO_4$) and 1 mL hydrofluoric acid (HF) for 2 h in a Teflon beaker at 120°C. With the acquisition of three replicates for each sample, the concentration of Al, Fe, Ti, Mn, Mg and Cr were determined using Inductively Coupled Plasma Mass Spectrometry (ICP-MS). Standard reference material (NIST 1633b) was used for the five replicates, to assess the yield and effectiveness of the established methods. The yield obtained was between 88% and 92%, with an average result of 13.54 ± 0.1% for Al, 7.00 ± 0.03% for Fe, 0.71 ± 0.02% for Ti, 0.43 ± 0.04% for Mg,118.55 ± 1.1 µg/g for Mn and 174.41 ± 1.3 µg/g for Cr.

For organic matter (OM) and calcium carbonate ($CaCO_3$) content, the loss of ignition (LOI) method was used, as suggested by Santisteban et al. [21]. The dried, finely ground and homogenised sediment was weighed accordingly and treated with high combustion heat for 4 hours at 550°C in a furnace. After heating, the sample was cooled down in the desiccator and weighed again.

The same sample was then treated for 2 hours at 950°C, for $CaCO_3$ determination.

Results and Discussion

The data in Table 2 shows that the average percentage was 10.93% for clay, 37.99% for silt and 51.08% for sand, while OM and $CaCO_3$ averaged 5.87% and 9.51%, respectively, along the Malacca Strait. There was an average difference of OM (5.41%) and $CaCO_3$ (9.51%) between stations N95 and N108, where station N95 dominated with a higher value for OM and $CaCO_3$. In the meantime, the difference between N95 and N108 was apparent in the sediment, where a higher value of silt was present in N95, while N108 secured a higher value for clay and sand content in its sediment. This suggests that constant remobilisation acts on surface sediments and that this occurred at station N108. The constant discharge of particulates due to anthropogenic inputs and frequent precipitation from the nearby drainage basin, lead to the dominance of clay and sand at station N108 [22]. According to Ramaswamy et al. [23], sediment discharge from the Irrawaddy River, due to the continuous weathering of igneous rock, leads to accumulation within the Irrawaddy Delta. In addition, the severity of the monsoonal seasons has an effect on the Andaman Sea, extending to the Gulf of Martaban. Hence, the tides, waves and the Ekman transport generates a net motion via the monsoonal season, causing mass migration of suspended particulates towards station N95, before sinking to the bottom.

In nutrient distribution along the Malacca Strait, the average OM and $CaCO_3$ acquired was 5.87 ± 0.12% and 9.51 ± 0.28%, respectively. There is a difference in OM (5.41%) and $CaCO_3$ (8.24%) content between stations N95 and N108, due to the exposure of the neighbouring shelf, where hydrological changes affect the total distribution along the Malacca Strait. There are higher OM and $CaCO_3$ contents at N95, compared to N108, due to hydrological factors taking place within the Malacca Straits. According to [24], the general circulation of the Malacca Strait was affected by monsoonal seasons, producing ebb tides which, in turn, affected the sediment composition present in the Malacca Straits. The presence of the monsoonal season affects seabed sediment as the major sink, where the rate of removal is higher, in accordance with diffusion rates in the seabed sediment [25]. Similar to composition differences in textural sediments, the monsoonal season affects the coast where the reworking process on the seabed sediment is present, leading to the constant production of nutrients along the station.

Table 2. Physio-chemical characteristics of sediment in the Malacca Straits

Station	Clay (%)	Silt (%)	Sand (%)	OM (%)	$CaCO_3$ (%)
N95	7.23	21.98	70.79	8.53 ± 0.11	14.42 ± 0.34
N99	11.30	15.09	73.61	6.73 ± 0.02	10.02 ± 0.19
N103	13.24	65.70	21.06	4.24 ± 0.2	3.9 ± 0.47
N106	11.44	83.43	5.12	7.63 ± 0.2	6.68 ± 0.13
N108	11.41	3.77	84.81	3.12 ± 0.19	6.18 ± 0.45

The geochemical elements shown in Table 3 reveal that the average concentration for each element is 5.00 ± 0.5 % (Al), 2.88 ± 0.34 %(Fe), 0.23 ± 0.03 % (Ti), 51.41 ± 0.9 µg/g (Zn), 94.56 ± 6.4 µg/g (Cr), 526.08 ± 41.95 µg/g (Mn), and 1.92 ± 0.18 % (Mg). Following the acquired concentrations above, several elements show a difference in concentration compared to the paper by Shaari et al. [26], where higher levels of Fe and Zn were apparent, with respective differences of 44% and 10% on the east coast, compared to the west coast of the Malaysian Peninsular. This suggests continuous inputs from several sources, i.e., the Gulf of Thailand, the Western Pacific and the Natuna Straits. The weathering rate is more apparent as the monsoonal season elevates the precipitation rate, leading to a higher discharge rate. Furthermore, the industrialisation occurring along both river channels also contributes to the increase in geochemical elements. Low geochemical element

concentrations, compared to Shaari et al. [26], are due to the bathymetry of the Malacca Straits, which promotes the diurnal prevailing tides within its semi-enclosed straits, which, in turn, contributes to the mobilisation and dilution of geochemical elements [24,27]. Cross-shelf inputs towards the semi-enclosed coast also affects the total geochemical elements being supplied to the east coast of the Malaysian Peninsular [28]. The cross-shelf input via the Western Pacific, which mobilises via the longshore currents of the Vietnamese coast through the Luzon Strait and through the southern South China Sea (sSCS), coupled with periodic monsoonal seasons, lead to the fluctuations of geochemical elements on the east coast of the Malaysian Peninsular [29].

Table 3. Concentration of geochemical elements in the Malacca Straits

Station	Al (%)	Fe (%)	Ti (%)	Zn (µg/g)	Cr (µg/g)	Mn (µg/g)	Mg (%)
N95	6.09 ± 0.29	3.01 ± 0.31	0.19 ± 0.02	55.09 ± 1.09	121.46 ± 6.25	371.62 ± 20.18	3.01 ± 0.12
N99	5.51 ± 0.24	2.68 ± 0.19	0.23 ± 0.02	46.05 ± 0.6	85.08 ± 5.07	319.86 ± 26.62	2.10 ± 0.10
N103	6.40 ± 0.96	3.00 ± 0.58	0.28 ± 0.05	59.78 ± 1.05	91.78 ± 9.77	564.96 ± 89.81	1.81 ± 0.32
N106	8.11 ± 1.56	3.75 ± 0.95	0.27 ± 0.06	73.09 ± 1.11	128.35 ± 5.97	598.15 ± 91.47	2.44 ± 0.46
N108	3.31 ± 0.09	1.48 ± 0.03	0.13 ± 0.01	52.57 ± 1.26	39.42 ± 2.07	505.40 ± 2.52	1.59 ± 0.06

On the west coast, the prominent contributor is the Andaman Sea, with its origins in the Bay of Bengal and Martaban Bay. Martaban Bay is the drainage basin for the Irrawaddy River and the Bay of Bengal is the drainage basin for the Ganges River, contributing most of the geochemical elements into the sea. Depth differences on the west coast may affect the bottom current trajectory, leading to a difference in the up-welling and down-welling dynamics. This results in less transport in deeper water, leading to a lower rate of remobilisation of seabed sediment. According to Väli et al. [30], the difference in dynamic uplift due to water depth suggests a larger difference in nutrient transport, leading to lower nutrient content in shallower coastal waters due to constant remobilisation. Furthermore, the difference in topography may lead to a lower current output, due to convergence at the northern Malacca Strait. Haditiar et al. [31] stated that the Malacca Strait facilitates a small water mass exchange between the Andaman Sea and the Malacca Strait, compared to the east coast of the Malaysian Peninsular, under the influence of monsoon, resulting in a smaller transport dynamic between the coasts.

To assess environment quality at the sampling stations, principal component analysis (PCA) was used to assess the significance of sediment contamination levels to aquatic ecosystem and environmental management. It also provides more quantification of dataset regarding geochemical elements in sediments and its controlling factors. The results of the PCA are presented in Table 4 for two principal components. The analysis shows that about 54 % of the total variation is explained by the first principal component, followed by 38% for the second principal component.

The first PCA is defined by the hydrological process that results in the accumulation preserved in silts, which, in turn, becomes a depository for Al, Fe, Ti, Cr, Mn and Zn (Table 4). Constant remobilisation of surficial sediment in the Malacca Strait may occur due to difference in the depths of the straits, leading to severe fluctuations in coastal transport dynamics, thus affecting the silt fraction and geochemical content in the sediment [30]. The absorbent nature of Fe-Mn oxyhydroxides combined with silt, would lead to sorption of most of the geochemical elements into the silt, leading to higher affinity, as well as through oxidation and reduction [32]. Fe-Mn acts as a scavenger in coastal environments where the co-precipitation process occurs, leading to the strong enrichment of geochemical elements [33]. On the other hand, the presence of Al, with respect to the silt fraction in seabed sediment, suggests the presence of feldspar and plagioclase, since both of the minerals are

the main constituents in the sediment surrounding the Malaysian Peninsular due to weathering [34,35]. Furthermore, weathering effects in the natural environment lead to the conversion of common zinc species into a soluble form, which is then discharged into the aquatic environment and supplies the sediment in the Malacca Straits [36].

Table 4. Principal component loadings against variables in the Malacca Straits

	Component	
	1	2
Clay	0.265	-0.893
Silt	0.985	-0.166
Sand	-0.976	0.218
Al	0.941	0.316
Fe	0.897	0.412
Ti	0.868	-0.063
Mg	0.285	0.943
Cr	0.759	0.649
Mn	0.619	-0.635
Zn	0.873	-0.101
OM	0.374	0.91
$CaCO_3$	-0.307	0.952

Extraction Method: Principal Component Analysis
Rotation Method: Varimax with Kaiser Normalisation

The second PCA is defined by mobility, where clay acts as a carrier for geochemical elements and OM. A high negative value for clay represents the removal of the clay as the main carrier for nutrients and geochemical elements. This can be seen in Table 4, where a lower clay gradient is apparent with respect to nutrients (i.e., OM and $CaCO_3$). According to Pitt et al. [37], lower clay content represents the elevated infiltration of nutrients in the sediments, hence increasing the availability of nutrients within the sediments. Furthermore, Bobrowsky and Marker [38] also suggest that the association of Mg, Cr and Zn (Table 4) forms a dispersive clay, rather than ordinary clay; dispersive clay is easily flocculated in water and very erodible [39]. This characteristic explains why there is elevated Mg and Cr but less Mn, as the dispersity process prohibits clay from forming into fine-sized clumps. Furthermore, Mg and Cr are known pollutants within the marine ecosystem, where higher levels of water hardness are contributed by Mg, while toxicity and persistent Cr could bioaccumulate in aquatic environments. According to Ismail et al. [40], a medium to high level of chromium was detected due to various industrialisation and shipping activities adjacent to the coast. Similar connections were present when Idriss [41] stated that the Juru River contributed to elevated Cr levels, due to frequent land reclamation surrounding its deltaic region and deforestation within Penang Island, leading to mobilisation along the Juru River.

Conclusion

Sediment in the Malacca Strait faces elevated geochemical elements from natural and anthropogenic inputs. Cross-shelf inputs contribute towards the distribution and differences in concentrations along the Malacca Strait. Furthermore, the Malacca Strait is subject to physical and hydrological factors which lead to fluctuations in geochemical element distribution. In

addition, local drainage basins channel pollutants from natural sources (via weathering) and through anthropogenic sources (via deforestation and land reclamation).

Acknowledgements

The authors would like to thank the First Institute of Oceanography (FIO) and the People's Republic of China, for providing the research grant (ST-2016-005) through the Universiti Kebangsaan Malaysia (UKM). We also thank the Ministry of Science Technology & Innovation (MOSTI) of Malaysia and the Universiti Malaysia Terengganu and Universiti Kebangsaan Malaysia, for their support during sampling. Lastly, we thank the laboratory members, for being an excellent research group, and the staff of the Department of Earth Sciences & Environment, Faculty of Science and Technology, Universiti Kebangsaan Malaysia, for their help during sampling.

References

1. Thia-Eng, A., Gorre, I. R. L., Ross, S. A., Bernad, S. R., Gervacio, B. and Ebarvia, C. (2000). The Malacca straits. *Marine Pollution Bulletin*, 41: 160-178.
2. Liu, Z., Wang, H., Hantoro, W.S., Sathiamurthy, E., Colin, C., Zhao, Y. and Li, J. (2012). Climatic and tectonic controls on chemical weathering in tropical Southeast Asia (Malay Peninsula, Borneo, and Sumatra). *Chemical Geology*, 291: 1-12.
3. Haditiar, Y., Putri, M.R., Ismail, N., Muchlisin, Z.A., Ikhwan, M. and Rizal, S. (2020). Numerical study of tides in the Malacca Strait with a 3-D model. *Heliyon*, 6(9): e04828.
4. Tan, C.K., Ishizaka, J., Matsumura, S., Yusoff, F.M., and Mohamed, M.I.H. (2006). Seasonal variability of SeaWiFS chlorophyll a in the Malacca Straits in relation to Asian monsoon. *Continental Shelf Research*, 26(2): 168-178.
5. Fujita, M., Kimura, F. and Yoshizaki, M. (2010). Morning precipitation peak over the strait of Malacca under a calm condition. *Monthly Weather Review*, 138(4): 1474-1486.
6. Amin, M. Z. M., Shaaban, A. J., Ercan, A., Ishida, K., Kavvas, M. L., Chen, Z. Q. and Jang, S. (2017). Future climate change impact assessment of watershed scale hydrologic processes in Peninsular Malaysia by a regional climate model coupled with a physically-based hydrology modelo. *Science of the Total Environment*, 575: 12-22.
7. Yusoff, A. H., and Mohamed, C. A. R. (2016). Mini review uranium-thorium decay series in the marine environment of the Southern South China Sea. *Journal of Geology & Geophysics*, 5(03): 1-9.
8. Schwartz, M. O., Rajah, S. S., Askury, A. K., Putthapiban, P. and Djaswadi, S. (1995). The Southeast Asian tin belt. *Earth Science Reviews*, 38(2–4): 95-293.
9. Shoieb, M. A., Sum, C. W., Ismail, M. S., and Tsegab, H. (2019). Geological characteristic of the Kroh formation in the upper Perak shales, western Peninsula Malaysia. *International Journal of Advanced and Applied Sciences*, 6(2): 102-106.
10. Zakariah, M. N. A., Roslan, N., Sulaiman, N., Lee, S. C. H., Hamzah, U., Noh, K. A. M. and Lestari, W. (2021). Gravity analysis for subsurface characterization and depth estimation of Muda River basin, Kedah, Peninsular Malaysia. *Applied Sciences*, 11(14): 6363.
11. Abdul Hamid, F. A. Z., Abu Bakar, A. F., Ng, T. F., Ghani, A. A. and Mohamad Zulkifley, M. T. (2019). Distribution and contamination assessment of potentially harmful elements (As, Pb, Ni, Cd) in top soil of Penang Island, Malaysia. *Environmental Earth Sciences*, 78(21): 1-13.
12. Khandaker, M. U., Asaduzzaman, K., Sulaiman, A. F. Bin, Bradley, D. A. and Isinkaye, M.O. (2018). Elevated concentrations of naturally occurring radionuclides in heavy mineral-rich beach sands of Langkawi Island, Malaysia. *Marine Pollution Bulletin*, 127 (12): 654-663.
13. Aboobacker, V. M. (2017). Wave energy resource assessment for eastern Bay of Bengal and Malacca Strait. *Renewable Energy*, 114 (3): 72-84.
14. Redzwan, G., Halim, H. A., Alias, S. A. and Rahman, M. M. (2014). Assessment of heavy metal contamination at west and east coastal area of Peninsular Malaysia. *Malaysian Journal of Science*, 33 (1): 23-31.

15. Saili, N. A. B. and Mohamed, C. A. R. (2021). Natural radioactivity of ^{210}Pb in mussels at the semi-enclosed water of the johor strait, malaysia through statistical approach. *Malaysian Journal of Analytical Sciences*, 25(1): 166-183.
16. Rahim, M. A. C. A., Aproi, A. A., Shi, X., Liu, S., Ali, M. M., Yaacob, W. Z. W. and Mohamed, C. A. R. (2019). Distribution of chromium and gallium in the total suspended solid and surface sediments of sungai kelantan, kelantan, Malaysia. *Sains Malaysiana*, 48(11): 2343-2353.
17. Miller, W. P. and Miller, D. M. (1987). A micro-pipette method for soil mechanical analysis. *Communications in Soil Science and Plant Analysis*, 18(1): 1-15.
18. Miller, W. P. (1993). A micro-pipette method for water dispersible clay. *Communications in Soil Science and Plant Analysis*, 24 (19–20): 2531-2544.
19. Kaur, A. and Fanourakis, G. C. (2018). Effect of sodium carbonate concentration in calgon on hydrometer analysis results. *Periodica Polytechnica Civil Engineering*, 62(4): 866-872.
20. Gray, J. E. and Riehle, J. R. (1998). Geologic Studies in Alaska by the US Geological Survey 1998: 200.
21. Santisteban, J. I., Mediavilla, R., López-Pamo, E., Dabrio, C.J., Blanca Ruiz Zapata, M., José Gil García, M., Castaño, S. and Martínez-Alfaro, P. E. (2004). Loss on ignition: a qualitative or quantitative method for organic matter and carbonate mineral content in sediments? *Journal of Paleolimnology*, 32(3): 287-299.
22. Othman, S. Z., Adlan, M. N., and Selamat, M. R. (2015). A study on the potential of riverbank filtration for the removal of color, iron, turbidity and *E. Coli* in Sungai Perak, Kota Lama Kiri, Kuala Kangsar, Perak, Malaysia. *Jurnal Teknologi*, 74(11): 83-91.
23. Ramaswamy, V., Rao, P. S., Rao, K. H., Thwin, S., Rao, N. S. and Raiker, V. (2004). Tidal influence on suspended sediment distribution and dispersal in the northern Andaman Sea and Gulf of Martaban. *Marine Geology*, 208(1): 33-42.
24. Rizal, S., Damm, P., Wahid, M. A., Sündermann, J., Ilhamsyah, Y., Iskandar, T. and Muhammad (2012). General circulation in the Malacca Strait and Andaman Sea: A numerical model study. *American Journal of Environmental Sciences*, 8(5): 479-488.
25. Mohamed, K. N., Godon, E., Adnan, N. A., Rahim, Q. A., Liew, C., Abidin, A. I. Z. and Zainuddin, M. F. (2019). Study of dissolved nutrient condition at pulau perhentian, Terengganu. *Pertanika Journal of Science and Technology*, 27(2): 601-617.
26. Shaari, H., Mohamad Azmi, S. N. H., Sultan, K., Bidai, J. and Mohamad, Y. (2015). Spatial distribution of selected heavy metals in surface sediments of the EEZ of the East Coast of Peninsular Malaysia. *International Journal of Oceanography*, 2015(5): 1-10.
27. Rezai, H., Yusoff, F. M., Kawamura, A., Arshad, A. and Othman, B. H. R. (2003). Zooplankton biomass in the Straits of Malacca. *Indian Journal of Marine Sciences*, 32(3): 222-225.
28. Kok, P. H., Mohd Akhir, M. F., Tangang, F. and Husain, M. L. (2017). Spatiotemporal trends in the southwest monsoon wind-driven upwelling in the southwestern part of the South China Sea. *PLOS ONE*, 12(2): e0171979.
29. Schroeder, A., Wiesner, M. G. and Liu, Z. (2015). Fluxes of clay minerals in the South China Sea. *Earth and Planetary Science Letters*, 430: 30-42.
30. Väli, G., Zhurbas, V., Laanemets, J. and Elken, J. (2011). Simulation of nutrient transport from different depths during an upwelling event in the Gulf of Finland. *Oceanologia*, 53(1-TI): 431-448.
31. Haditiar, Y., Putri, M. R., Ismail, N., Muchlisin, Z. A. and Rizal, S. (2019). Numerical simulation of currents and volume transport in the Malacca Strait and part of South China Sea. *Engineering Journal*, 23(6): 129-143.
32. Batista, A. H., Melo, V. F., Gilkes, R. and Roberts, M. (2018). Identification of heavy metals in crystals of sand and silt fractions of soils by scanning electron microscopy (SEM EDS/WD-EPMA). *Revista Brasileira de Ciencia do Solo*, 42: 1-16.
33. Singh, S.K. and Subramanian, V. (1984). Hydrous fe and mn oxides — scavengers of heavy metals in the aquatic environment. *Critical Reviews in Environmental Control*, 14(1): 33-90.

34. Taylor, K. G. and Macquaker, J. H. S. (2014). Diagenetic alterations in a silt- and clay-rich mudstone succession: an example from the Upper Cretaceous Mancos Shale of Utah, USA. *Clay Minerals*, 49(2): 213-227.
35. Raj, J. K. (2021). Soil moisture retention characteristics of saprock from the weathering profile over a biotite-muscovite granite in Peninsular Malaysia. *Warta Geologi*, 47(3): 217-225.
36. Yap, C. K. and Pang, B. H. (2011). Assessment of Cu, Pb, and Zn contamination in sediment of north western Peninsular Malaysia by using sediment quality values and different geochemical indices. *Environmental Monitoring and Assessment*, 183(1–4): 23-39.
37. Pitt, R., Lantrip, J. and O'Connor, T. P. (2004). Infiltration through disturbed urban soils. *Joint Conference on Water Resource Engineering and Water Resources Planning and Management 2000: Building Partnerships*: p. 104.
38. Bobrowsky, P. T. and Marker, B. (2018). *Encyclopedia of Engineering Geology*, Springer International Publishing AG, Cham, Switzerland.
39. Zorluer, I., Icaga, Y., Yurtcu, S. and Tosun, H. (2010). Application of a fuzzy rule-based method for the determination of clay dispersibility. *Geoderma*, 160(2): 189-196.
40. Ismail, A., Toriman, M. E., Juahir, H., Zain, S. M., Habir, N. L. A., Retnam, A., Kamaruddin, M. K. A., Umar, R., and Azid, A. (2016). Spatial assessment and source identification of heavy metals pollution in surface water using several chemometric techniques. *Marine Pollution Bulletin*, 106(1–2): 292-300.
41. Idriss, A. A. (2012). Concentration of selected heavy metals in water of the Juru River, Penang, Malaysia. *African Journal of Biotechnology*, 11(33): 8234-8240.

Malaysian Journal of Analytical Sciences (MJAS)
Published by Malaysian Analytical Sciences Society

APPLICATIONS OF NINHYDRIN: SPECTROPHOTOMETRIC DETERMINATION OF HYDRAZINE AND HYDROXYLAMINE

(Aplikasi Ninhidrin: Penentuan Spektrofotometri bagi Hidrazin dan Hidroksil Amina)

Khaled Elgendy*, Mohamed Alaa Eldeen Elmosallamy, Mohamed Hassan, Hend Gamal

Department of Chemistry, Faculty of Science,
Zagazig University, Egypt

**Corresponding author: elgendykh64@gmail.com*

Received: 15 September 2021; Accepted: 18 May 2022; Published: 25 August 2022

Abstract

A rapid, accurate, and sensitive spectrophotometric method for the determination of micro amounts of hydroxylamine and hydrazine is described. The proposed method is based on the interaction of ninhydrin with the amino group of hydroxylamine and hydrazine. Hydroxylamine reacted with ninhydrin as a chromogenic reagent in phosphate buffer at pH 9.14, forming a violet complex with a maximum absorbance at 375 nm after heating for 10 min at 70 °C. Hydrazine reacted with ninhydrin upon heating for 10 min at 85 °C in the presence of phosphate buffer (pH 9), giving a red-brown complex with a maximum absorbance at 425 nm. The optimum conditions affecting the method, such as pH and buffer, sequence of addition, time, temperature, organic solvent, and surfactant, were studied. The complexes of ninhydrin with hydroxylamine and hydrazine were formed in a molar ratio of 1:2. The hydroxylamine–ninhydrin and hydrazine–ninhydrin complexes obeyed Beer's law in a concentration range of 0.033-3.3 and 0.130-3.25 µg mL^{-1}, respectively. Molar absorptivity and Sandell's sensitivity were 0.21508×10^2 L mol^{-1} cm^{-1} and 1.53 µg cm^{-2}, respectively, for hydroxylamine and 0.8583×10^2 L mol^{-1} cm^{-1} and 1.51 µg cm^{-2}, respectively, for hydrazine. The limit of detection and quantification was calculated. The interference effect of various foreign ions and substances was also studied. The proposed method was applied for the determination of micro amounts of hydroxylamine in urine and tap water and hydrazine in tap water.

Keywords: spectrophotometric method, ninhydrin, hydroxylamine, hydrazine, urine

Abstrak

Kaedah spektrofotometri yang cepat, tepat dan sensitif untuk penentuan jumlah mikro hidroksilamin dan hidrazin diterangkan. Kaedah yang dicadangkan adalah berdasarkan interaksi ninhidrin dengan kumpulan amino yang terdapat dalam hidroksilamin dan hidrazin. Hidroksilamin bertindak balas dengan ninhidrin sebagai reagen kromogenik dalam medium beralkali pada pH = 9.14 menggunakan penimbal fosfat membentuk kompleks ungu dengan penyerapan maksimum pada 375 nm selepas dipanaskan selama 10 minit pada 70 °C. Hidrazin bertindak balas dengan ninhidrin apabila dipanaskan selama 10 minit pada 85 °C dengan kehadiran penimbal fosfat (pH = 9) memberikan kompleks merah-coklat dengan penyerapan maksimum pada 425 nm. Keadaan optimum yang mempengaruhi kaedah dikaji seperti pH dan penimbal, jujukan penambahan, masa, suhu, pelarut organik, dan surfaktan. Dua kompleks yang terbentuk bagi ninhidrin dengan hidroksilamin dan hidrazin terbentuk dengan nisbah molar (1:2). Kompleks hidroksilamin–ninhidrin dan hidrazin–ninhidrin mematuhi hukum Beer dalam julat kepekatan 0.033-3.3 dan 0.130-3.25 µg mL^{-1}, masing-masing. Penyerapan molar dan kepekaan Sandell masing-masing ialah 0.21508×10^2 L mol^{-1} cm^{-1} dan 1.53 µg cm^{-2}, untuk hidroksilamin dan 0.8583×10^2 L mol^{-1} cm^{-1} dan 1.51 µg cm^{-2} masing-masing, untuk hidrazin. Had

pengesanan dan kuantifikasi telah dikira. Kesan gangguan pelbagai ion dan bahan asing turut dikaji. Kaedah yang dicadangkan digunakan untuk penentuan jumlah mikro hidroksilamin dalam air kencing dan air paip dan hidrazin dalam air paip

Kata kunci: kaedah spektrofotometri, ninhidrin, hidroksilamin, hidrazin, urin

Introduction

Ninhydrin (2,2-dihydroxyindane-1, 3-dione), a white solid soluble in ethanol and acetone, is generally used to determine ammonia or primary and secondary amines via the formation of Ruhemann's purple as a result of the interaction ninhydrin with these free amines. Ninhydrin has been applied in various spectrophotometric methods for the determination of famotidine in drug formulations [1], cobalt [2], amino acids, peptides, and proteins in agricultural and biomedical fields [3], trace cyanide [4], neomycin sulfate [5], gabapentin [6], and amlodipine besylate [7] in pharmaceutical forms, and glyphosate [8] and ammonia [9].

Hydroxylamine is produced during nitrification and anaerobic ammonium oxidation, which are both essential microbial processes in the nitrogen cycle [10-11]. Hydroxylamine is frequently used as a starting material for the production of pharmaceutical intermediates and drugs [12]; however, hydroxylamine is a well-known mutagen that is toxic to humans, animals, and plants [13], even at low concentration [12]. Many methods have been developed for the determination of hydroxylamine, including spectrophotometry, gas chromatography (GC), and voltammetry methods. For instance, a spectrophotometric method for the determination of hydroxylamine involves its oxidation to nitrite by using sodium arsenate in alkaline conditions. Then the diazo coupling reaction between *p*-nitroaniline and *N*-(1-naphthyl) ethylenediamine dihydrochloride is used to determine the amount of nitrite produced [14]. The use of ferric ammonium sulfate as an oxidant and 1,10-phenanthroline as a chromogenic agent was reported for the determination of the concentration of hydroxylamine in biological wastewater treatment processes [15]. Meanwhile, an indirect spectrophotometric determination of hydroxylamine based on its reaction with iodate was also reported [16]. Another hydroxylamine determination method based on its oxidation to nitrite uses *N, N*-dimethyl aniline and *p*-nitroaniline accompanied by micelle-mediated extraction of the produced azo dye for nitrite determination [17]. As examples of GC and voltammetry methods, the conversion of hydroxylamine to nitrous oxide (N_2O) allows for the GC indirect determination of hydroxylamine [18], and a carbon-paste electrode modified with TiO_2 nanoparticles and quinizarine was reported for the voltammetric determination of hydroxylamine [19].

Hydrazine is an important inorganic base of formula N_2H_4, which is a colorless and flammable liquid highly toxic and dangerously unstable in solution [20]. There are a variety of spectrophotometric methods for the determination of hydrazine such as the condensation of veratraldehyde with hydrazine in acidic medium [21]. Hydrazine can be also determined by reducing ferric ion to ferrous ion, which then reacts with 2,2'-bipyridyl at 60 °C to form a stable red-pink complex [22]. Other method for detecting hydrazine is based on its inhibitory effect on the oxidation of Victoria Blue 4- R by $KBrO_3$ [23]. Moreover, hydrazine can be detected using the Firordt method, which consists in its preliminary derivatization with 5-nitro-2-furaldehyde [24]. A flow injection spectrometric method for the determination of hydrazine consists of its reaction with *p*-dimethylamino-benzaldehyde to produce aldazine [25]. The chemical structures of hydroxylamine, hydrazine, and ninhydrin are shown in Figure 1(a, b), respectively.

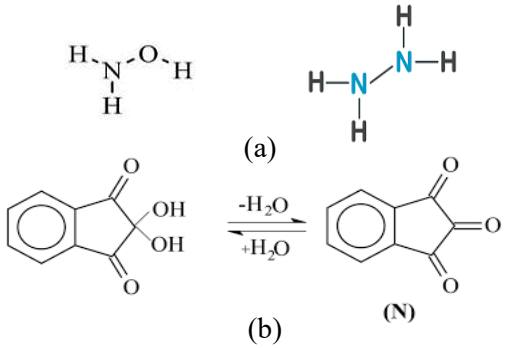


Figure 1. (a) Chemical structure of hydroxylamine and hydrazine, (b) ninhydrin

Materials and Methods

Reagents and solutions

All the chemicals and solvents utilized were of analytical grade and were used without further purification. The materials used were of the highest quality. Ninhydrin (purity 99.00%) was obtained from BDH Company. Hydroxylamine (purity 99.00%) and hydrazine sulfate (purity 99.00%) were obtained from Sigma-Aldrich. Ethanol (purity 99.99%) was obtained from Elnaser Company, Egypt. Ninhydrin stock solutions (1×10^{-2} M) were prepared by dissolving 0.20 g of ninhydrin in 100 mL ethanol 96%. Hydroxylamine stock solutions (1×10^{-2} M) were prepared by dissolving 0.033 g hydroxylamine in appropriate quantities of distilled water, followed by dilution to 100 mL in a measuring flask. A hydrazine sulfate (1×10^{-2} M) solution was prepared by adding 0.13 g in a 100 mL measuring flask and diluting up to the mark with distilled water.

Instrumentation

A UV/VIS double beam spectrophotometer (T80 Spectrophotometer, PG instruments Ltd. Company, United Kingdom) was used to measure the absorbance using matched quartz cells with a path length of 10 mm and a width of 2 mm. An Adwa pH meter, model AD 1030, from Romania was used to determine the pH change.

Buffers

Different types of buffers were prepared according to standard methods, including acetate buffer (pH 3.5-6) universal buffer (pH 1.81-11.98) [26], borate buffer (pH 7.6-10) [27], citrate buffer (pH 3-6), phosphate buffer (pH 7-11) and acetate buffer (pH 3.5-6) [28].

Surfactant solutions

Different surfactants such as anionic sodium laurate sulfate (SLS), nonionic Triton-X 100, and cationic cetyl trimethyl ammonium bromide (CTAB) were prepared at a concentration of 1×10^{-2} M by dissolving the appropriate amounts in 100 mL of deionized water and used without further purification.

General procedure

In a 10 mL measuring flask, 2.00 mL of hydroxylamine (1×10^{-2} M) or 1.00 mL hydrazine (1×10^{-2} M) was added, followed by 2.00 mL of ninhydrin (1×10^{-2} M), and 2.00 mL of phosphate buffer at pH 9.14 for hydroxylamine and at pH 9 for hydrazine. The measuring flask was heated in a water bath for 10 min at 70 °C for hydroxylamine but at 85 °C for hydrazine, and the absorbance was then measured by scanning the wavelength from 200 to 700 nm against a blank reagent containing 2.00 mL of both ninhydrin and phosphate buffer and 6.00 mL of distilled water.

Beer's law

Aliquots of hydroxylamine in a concentration range of 0.033-3.3 μg mL^{-1} and hydrazine in a concentration range of 0.0130-3.25 μg mL^{-1} hydrazine were transferred into a series of 10 mL measuring flasks containing 2.00 mL of phosphate buffer at pH 9.14 and 9 for hydroxylamine and hydrazine, respectively, and 2.00 mL of ninhydrin was then added. The absorbance was recorded at 375 and 425 nm for hydroxylamine and hydrazine, respectively. The calibration graph was obtained by plotting the absorbance against the concentration of the studied materials in μg mL^{-1}.

Applications of hydroxylamine and hydrazine: Spectrophotometric determination of hydroxylamine and hydrazine in tap water

Tap water (250 mL) was heated gently until the volume was reduced to 25 mL. In two 10 mL volumetric flasks, 2.00 mL of concentrated tap water was added, followed by 2.00 mL of ninhydrin (1×10^{-2} M) and 2.00 mL of phosphate buffer at pH 9.14 for hydroxylamine and pH 9 for hydrazine, and the mixture was heated in a water bath for 10 min at 70 °C for hydroxylamine and at 85 °C for hydrazine. The absorbance was measured against the blank solution.

Spectrophotometric determination of hydroxylamine in urine

A urine sample was obtained from two patients, i.e., an adult man (32 years old) and a woman (24 years old), who did not suffer from kidney problems. 50 mL of urine sample was concentrated to 7 mL by gentle heating and then filtrated. The filtrate (0.5 mL), 2.00 mL of ninhydrin (1×10^{-2} M) and 2.00 mL of phosphate buffer (pH 9.14) were placed in a 10 mL measuring flask using a microburette. The measuring flask was heated in a water bath for 10 min at 70 °C, and the absorbance was measured against the blank at 375 nm.

Results and Discussion

Absorption curve

Ninhydrin was used as a new spectrophotometric reagent for the determination of hydroxylamine and hydrazine sulfate on the basis of the reaction of ninhydrin with the amino group of the studied compounds, which produced a violet complex with hydroxylamine and a red-brown complex with hydrazine showing maximum absorbance at 375 and 425 nm, respectively, as shown in the absorption curve depicted in Figure 2**.**

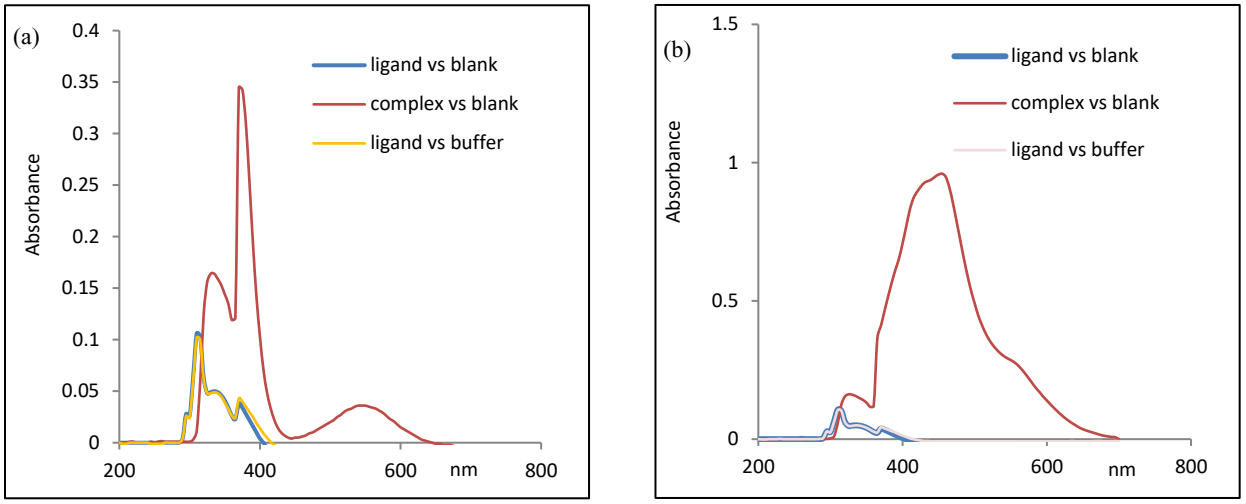


Figure 2. Absorption curves for the complexes of ninhydrin with (a) hydroxylamine and (b) hydrazine

Effect of pH and buffer solutions

The influence of pH on the formation of complexes between ninhydrin and hydroxylamine or hydrazine was studied in a pH range of 1.26–11 using 0.1 M NaOH and 0.1 M HCl solutions. The pH required for complete complex formation ranged between 9 and 11. To adjust the pH, the influence of different buffer solutions (universal, phosphate, and borate buffers) was studied. The maximum absorbance and color Intensity of the complex was attained using the phosphate buffer at pH 9.14 for hydroxylamine and at pH 9 for hydrazine, and 2.00 mL of phosphate buffer gave the maximum absorbance. Figure 3 illustrates the results.

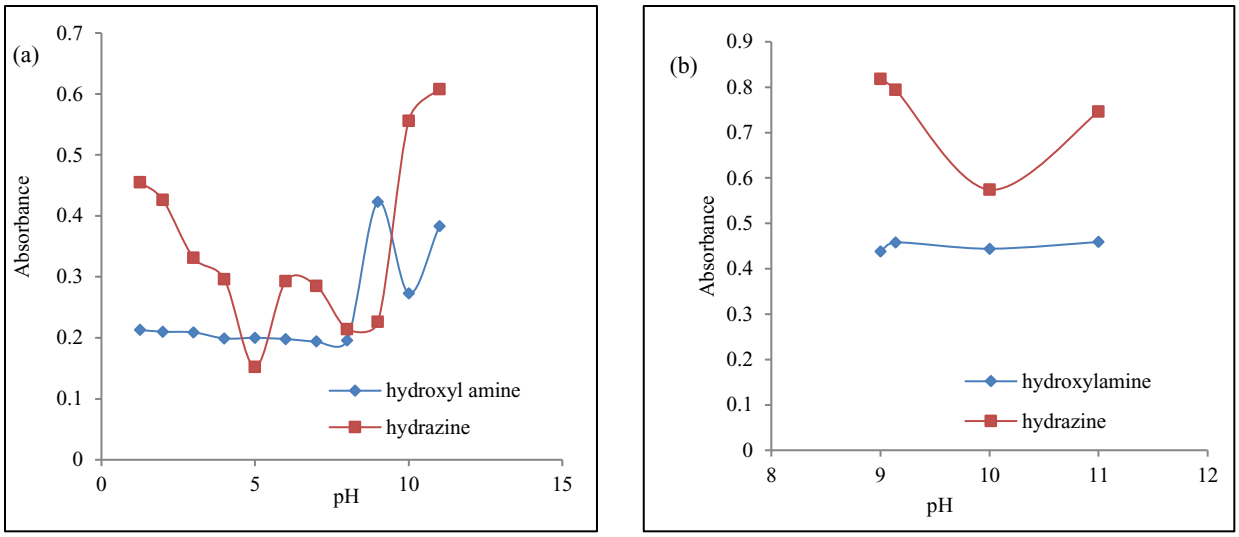


Figure 3. Effect of (a) pH and (b) phosphate buffer on the formation of hydroxylamine and hydrazine complexes with ninhydrin

Influence of the sequence of addition

To determine the optimum sequence of addition, the absorbance of different samples prepared by changing the order of addition of hydroxylamine or hydrazine, ninhydrin, and phosphate buffer was recorded. The total volume of the samples was 10 mL which comprised about 2.00 mL of hydroxylamine or hydrazine, 2.00 mL of ninhydrin, 2.00 mL of phosphate buffer, and 4.00 mL of distilled water. The results showed that the most suitable sequence of addition was hydroxylamine or hydrazine – buffer – ninhydrin, as shown in Table 1.

Table 1. Effect of the sequence of addition on hydroxylamine and hydrazine with ninhydrin

Sequence of addition	Absorbance of Hydroxylamine	Absorbance of Hydrazine
Hydrazine or hydroxylamine + ninhydrin + buffer	0.414	0.835
Hydrazine or hydroxylamine + buffer + ninhydrin	0.422	0.838
Buffer + ninhydrin + hydrazine or hydroxylamine	0.420	0.816
Ninhydrin + buffer + hydrazine or hydroxylamine	0.394	0.822

Effect of time

The effect of time on the color intensity of the ninhydrin complexes was studied by measuring the absorbance of the colored solution at different times (2 to 120 min). The results showed that the absorbance of both complexes reached its maximum at two min time and then decreased slightly with time, which indicates that time had no significant effect on the absorbance of the produced complexes, as shown in Figure 4.

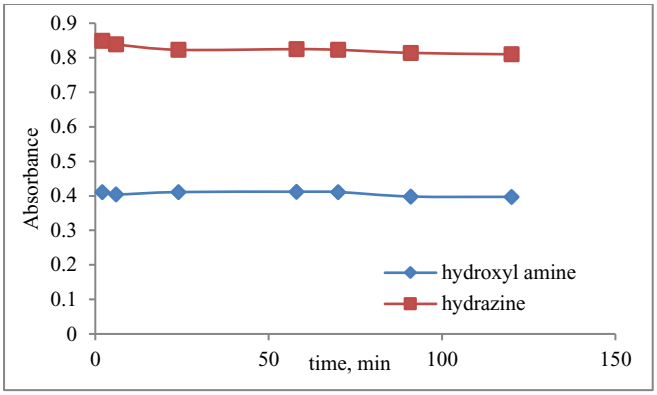


Figure 4. Effect of time on the hydroxylamine and hydrazine complexes with ninhydrin

Effect of temperature

Different samples were prepared by heating in a water bath at different temperatures to investigate the effect of temperature on the hydroxylamine and hydrazine complexes with ninhydrin, and the maximum absorbance was measured against the blank. The results showed that the hydroxylamine complex reached its maximum absorbance at 70 °C, whereas that of the hydrazine complex was observed at 85 °C (Figure 5).

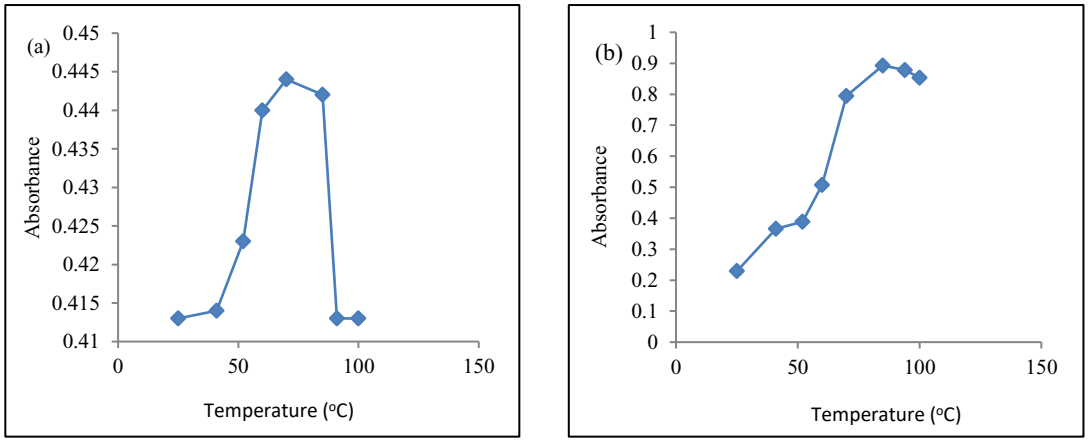


Figure 5. Effect of temperature on the ninhydrin complexes with (a) hydroxylamine and (b) hydrazine

Effect of the addition of an organic solvent

To evaluate the effect of the addition of an organic solvent, 2.00 mL of various organic solvents were added to the prepared samples and the absorbance was measured against the blank. The results depicted in Figure 6 shows that ethanol, ethylene glycol, and glycerin shifted the absorbance to higher values in the case of the complex with hydroxylamine, whereas the addition of the organic solvents decreased the absorbance of the hydrazine complex.

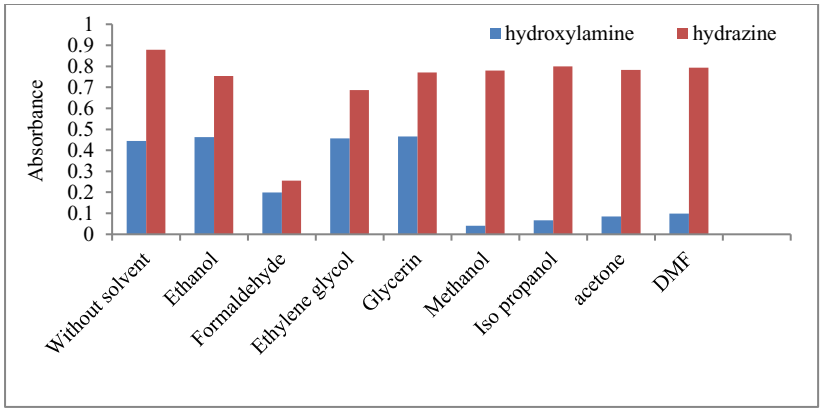


Figure 6. Effect of organic solvent on hydroxylamine and hydrazine complex with ninhydrin

Effect of surfactant

To study the effect of a surfactant on the formed complex, 1.00 mL of cationic surfactant (CTAB), nonionic surfactant (Triton X-100), and anionic surfactant (SLS) was added to a sample solution containing 1.00 mL of hydroxylamine or hydrazine (1×10^{-2} M), 2.00 mL of ninhydrin (1×10^{-2} M), and 2.00 mL of phosphate buffer at pH 9.14 or 9. Then, the absorbance was measured versus the blank. As shown in Table 2 and Figure 7, the presence of the three surfactants decreased the absorbance.

Table 2. Effect of surfactants on the hydroxylamine and hydrazine complexes with ninhydrin

Surfactant	**Absorbance of Hydroxylamine**	**Absorbance of Hydrazine**
Without surfactant	0.444	0.878
SLS	0.136	0.792
Triton X-100	0.040	0.765
CTAB	0.099	0.758

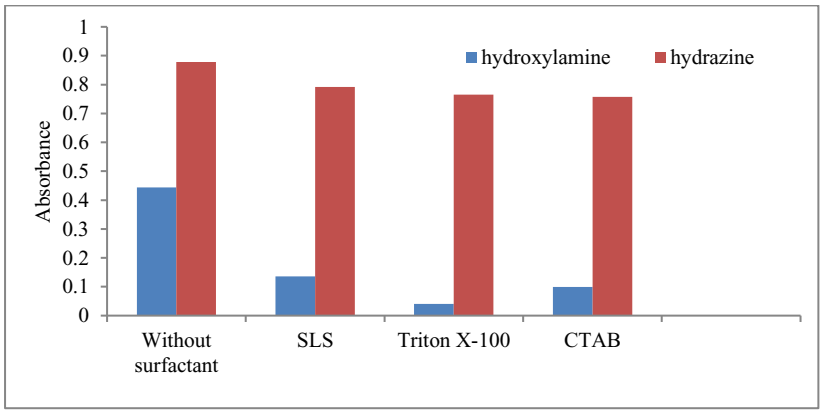


Figure 7. Effect of surfactants on the hydroxylamine and hydrazine complexes with ninhydrin

Determination of the stoichiometric ratio: The molar ratio method

To determine the precise stoichiometry of the complexes formed between hydroxylamine or hydrazine and ninhydrin, a series of solutions were prepared by varying the amount of 1×10^{-2} M solution of ninhydrin from 1.00 to 5.00 mL while keeping the amount of hydroxylamine or hydrazine sulfate constant (2.00 mL of 1×10^{-2} M solution). The absorbance of the samples was then measured and plotted against the molar ratio [ninhydrin] / [hydroxylamine or hydrazine sulfate] [29], as shown in Figure 8 revealing that the complexes were formed in a molar ratio of 1:2.

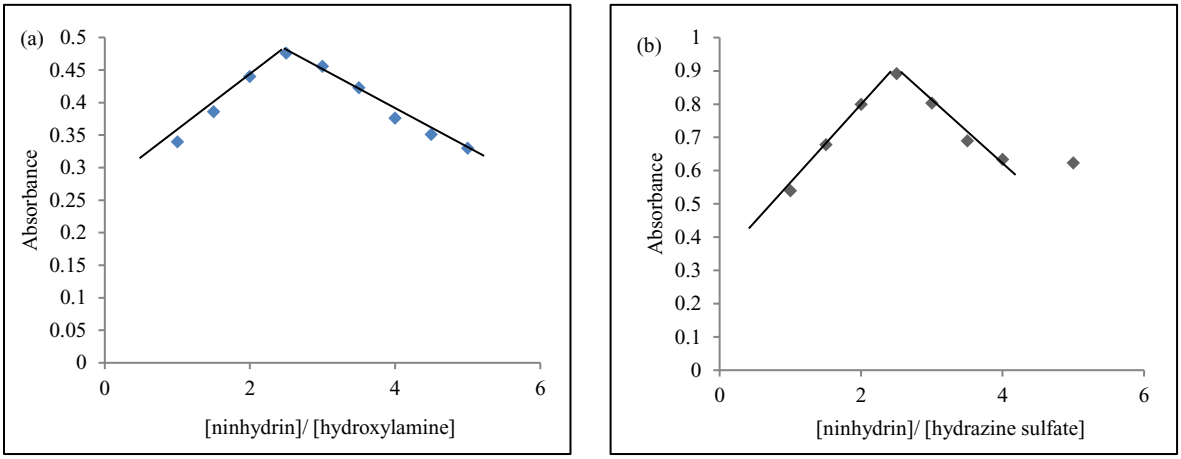


Figure 8. Effect of molar ratio of ninhydrin complexes with (a) hydroxylamine and (b) hydrazine

The continuous variation method

A series of solutions were prepared by combining an equimolar amount of hydroxylamine or hydrazine with 1×10^{-2} M ninhydrin in various proportions (0.10–0.90 mL) while keeping the total molar concentration constant, and the absorbance was measured and plotted against the mole fraction [30], as shown in Figure 9.

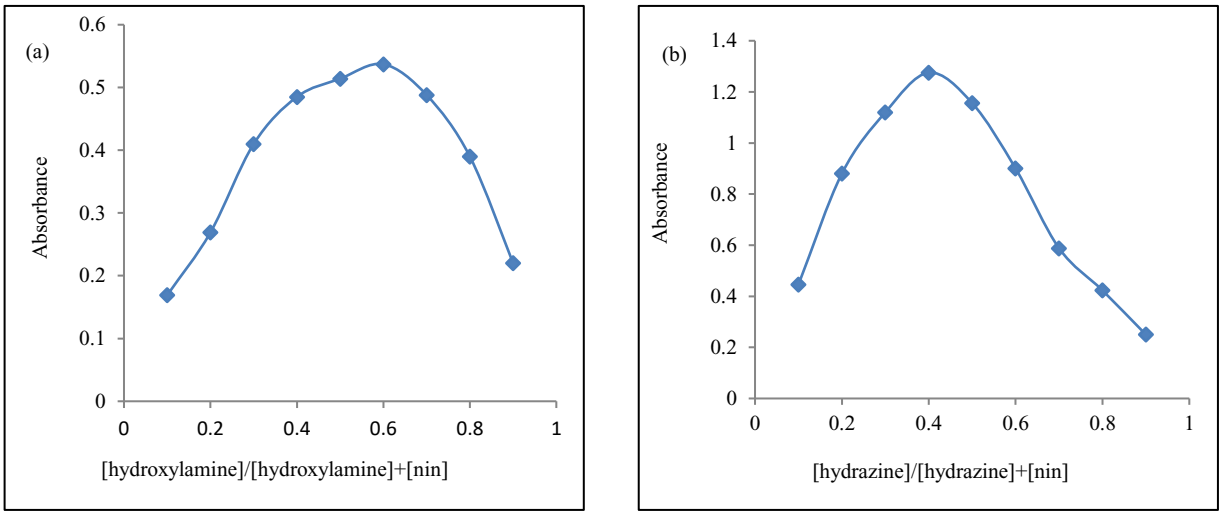


Figure 9. Continuous variation of the ninhydrin complexes with (a) hydroxylamine and (b) hydrazine

Calibration curve (Beer's law)

To determine whether Beer's law was obeyed in the present system, several solutions were prepared by varying the concentration of hydroxylamine and hydrazine while maintaining the concentration of ninhydrin constant at 1×10^{-2} M. The results depicted in Figure 10 show that Beer's law was obeyed in the concentration range 0.033-3.3µg mL^{-1} for hydroxylamine and 0.130-3.25 µg mL^{-1} for hydrazine.

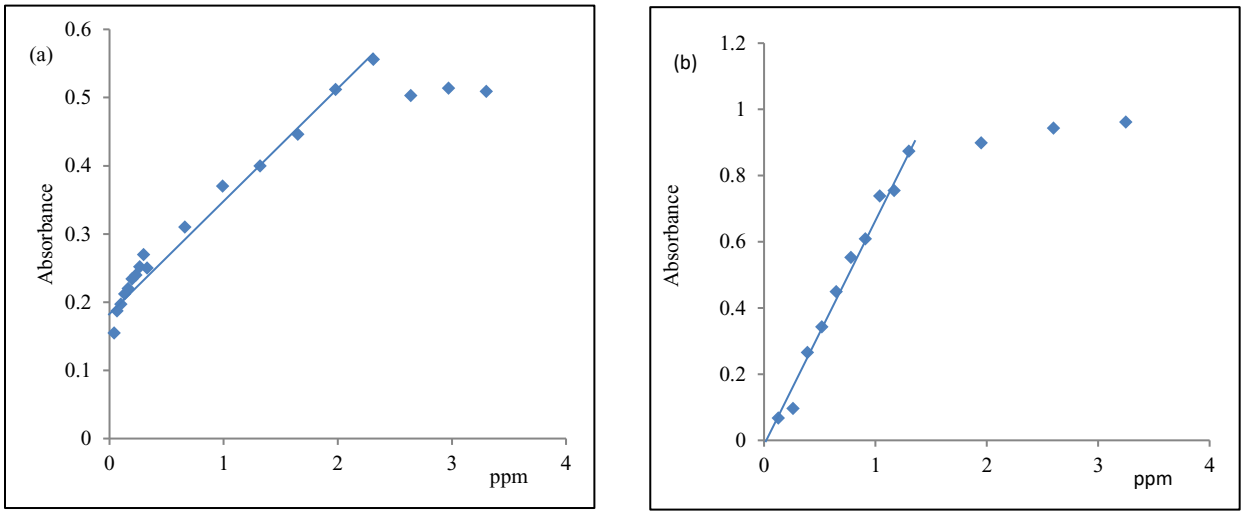


Figure 10. Calibration curves of the ninhydrin complexes with (a) hydroxylamine and (b) hydrazine

Effect of interferences

A variety of interfering materials such as thiourea, urea, ascorbic acid, sodium nitrate, ammonium sulfate, sodium nitrite, fructose, trisodium citrate, sodium benzoate, magnesium sulfate, and hydroxide ammonia at a concentration of 1×10^{-1} M were added to 1×10^{-2} M of hydroxylamine or hydrazine to study their interference effect. The results showed that sodium nitrite and hydroxide ammonia caused interference with hydroxylamine and magnesium sulfate caused interference with hydrazine.

Statistical treatment

Seven measurements were conducted for concentrations of 0.33 and 0.91 µg mL^{-1} of hydroxylamine and hydrazine sulfate, respectively, under the optimum conditions to evaluate the reproducibility of the method. Table 3 summarizes a series of statistical parameters, such as standard deviation, molar absorptivity, Sandell's sensitivity, Student's t-test, correlation coefficient, limit of detection, and limit of quantification. The results indicate that the proposed method exhibited excellent linearity, high sensitivity, and good accuracy and precision. Analytical properties such as pH and buffer, time, temperature, and Beer's law are also listed in Table 3.

Table 3. Statistical treatment and analytical properties for the determination of hydroxylamine and hydrazine using ninhydrin as a chromogenic reagent in the presence of phosphate buffer

Parameter	Hydroxylamine	Hydrazine
Molar absorptivity L mol^{-1} cm^{-1}	0.21508×10^2	0.8583×10^2
Standard deviation (SD)	0.003134	0.004887
(RSD %)	0.930246	0.53136
Standard error of the mean (SE)	0.0011845	0.001847
Student t-test	5.487	5.25144
Intercept	0.2075	0.2477
Correlation coefficient	0.9427	0.8572
Slope	0.11466	0.289801
Limit of detection (µg / mL)	0.09019	0.0556488
Limit of quantification (µg / mL)	0.27331	0.168632
Complex color	Violet	Reddish-brown
Beer's law range (mg mL^{-1})	(0.033─3.3)	(0.130─3.25)
pH and buffer	Phosphate (pH 9.14)	Phosphate (pH 9)
Time (min)	2	2
Temperature °C	70	85

Applications of hydroxylamine and hydrazine

The suggested method was used to determine hydroxylamine in urine, hydroxylamine and hydrazine in tap water. The results in a Table 4 were in good agreement with the recommended method, indicating that the proposed method could be used.

Table 4. Determination of hydroxylamine and hydrazine in urine and tap water

Sample	Taken (mg)	Found (mg)	Recommended Method	% Recovery	% RSD
Hydroxylamine in urine	2.1	2.202	2.04	99.998	0.0022
Hydroxylamine in tap water	0.32	0.31	0.317	99.9999	0.00007
Hydrazine sulfate in tap water	0.25	0.27	0.24	99.9997	0.0003

Recommended method according to Watt [31] and Frear [32]

Conclusion

A simple, accurate, cost-effective, and sensitive method for the determination of microamounts of hydroxylamine and hydrazine has been demonstrated. The method is based on the use of ninhydrin as a chromogenic reagent, which reacts with the amino group of the substrates. The color of the formed complex between ninhydrin and hydroxylamine or hydrazine remains stable for a long time. The use of organic solvents or high temperature is not required. However, some foreign substances interfere with hydroxylamine and hydrazine, leading to a decrease or increase in the absorbance. The feasibility of the method for determining hydroxylamine and hydrazine sulfate in real samples, i.e., tap water and urine, is demonstrated.

References

1. Rahman, N. and Kashif, M. (2003). Application of ninhydrin to spectrophotometric determination of famotidine in drug formulations. *Il Farmaco*, 58(10): 1045-1050.
2. Mahmood, K., Wattoo, F. H., Wattoo, M. H. S., Imran, M., Asad, M. J., Tirmizi, S. A. and Wadood, A. (2012). Spectrophotometric estimation of cobalt with ninhydrin. *Saudi Journal of Biological Sciences*, 19(2): 247-250.
3. Friedman, M. (2004). Applications of the ninhydrin reaction for analysis of amino acids, peptides, and proteins to agricultural and biomedical sciences. *Journal of Agriculture and Food Chemistry*, 52(3): 3854-3806.
4. Surleva, A., Zaharia, M., Ion, L., Gradinaru, R. V., Drochioiu, G. and Mangalagiu, I. (2013). Ninhydrin-based spectrophotometric assays of trace cyanide. *Acta Chemica Iasi*, 21: 57-70.
5. Alsamarrai, K. F., Al-Abbasi, M. A. and Alsamarrai, E. T. (2019). Spectrophotometric determination of neomycin sulphate in tablets form via reaction with ninhydrin reagent. *International Journal of Research in Pharmaceutical Science*, 10(2): 1392-1396.
6. Siddiquia, F. A., Araynea, M. S., Sultanab, N., Qureshia, F., Mirzaa, A. Z., Zuberia, M. H., Bahadura, S. S., Afridia, N. S., Shamshadb, H. and Rehman, N. (2010). Spectrophotometric determination of gabapentin in pharmaceutical formulations using ninhydrin and π-acceptors. *European Journal of Medicinal Chemistry*, 45: 2761-2767.
7. Rahman, N. and Azmi, S. N. H. (2001). Spectrophotometric method for the determination of amlodipine besylate with ninhydrin in drug formulations. *Il Farmaco*, 56: 731-735.
8. Bhaskara, B. L. and Nagaraja, P. (2006). Direct sensitive spectrophotometric determination of glyphosate by using ninhydrin as a chromogenic reagent in formulations and environmental water samples. *Helvetica Chimica Acta*, 89: 2686-2693.
9. Baker, H. M. and Alzboon, K. F. (2015). Spectrophotometric determination of ammonia using ninhydrin assay and kinetic studies. *European Journal of Chemistry*, 6(2): 135-140.
10. Arp, D. J., Stein, L. Y. (2003). Metabolism of inorganic N compounds by ammonia-oxidizing bacteria. *Critical Reviews* in *Biochemistry* and *Molecular Biology*, 38(6): 471-495.
11. Jetten, M. S. M. (2001). New pathways for ammonia conversion in soil and aquatic systems. *Plant and Soil*, 230: 9-19.
12. Guzowski Jr, J. P., Golanoski, C. and Montgomery, E. R. (2003). A gas chromatographic method for the indirect determination of hydroxylamine in pharmaceutical preparations, conversion into nitrous oxide. *Journal of Pharmaceutical and Biomedical Analysis*, 33(5): 963-974.
13. Smith, R. P., and Layne, W. R. (1969). A comparison of the lethal effects of nitrite and hydroxylamine in the mouse. *Journal of Pharmacology and Experimental Therapeutics*, 165: 30-35.
14. Deepa, B., Balasubramanian, N. and Nagaraja, K. S. (2004). Spectrophotometric determination of hydroxylamine and its derivatives in pharmaceuticals. *Chemical and Pharmaceutical Bulletin*, 52(12): 1473-1475.
15. Hu, B., Tian, X. L., Shi, W. N., Zhao, J. Q., Wu, P. and Mei, S. T. (2018). Spectrophotometric determination of hydroxylamine in biological wastewater treatment processes. *International Journal of Environmental Science and Technology*, 15: 323-332.
16. Afkhami, A., Madrakian, T. and Maleki, A. (2006). Indirect kinetic spectrophotometric determination of hydroxylamine based on its reaction with iodate. *Analytical Sciences*, 22: 329-331.
17. Afkhami, A., Madrakian, T. and Maleki, A. (2005). Spectrophotometric determination of hydroxylamine and nitrite in mixture in water and biological samples after micelle-mediated extraction. *Analytical Biochemistry*, 347: 162-164.
18. Guzowski, J. P., Golanoski, C. and Montgomery, E. R. (2003). A gas chromatographic method for the indirect determination of hydroxylamine in pharmaceutical preparations, conversion into nitrous oxide. *Journal of Pharmaceutical and Biomedical Analysis*, 33(5): 963-974.

19. Ardakani, M. M., Beitollahi, H., Taleat, Z. and Naeimi, H. (2010). Voltammetric determination of hydroxylamine at the surface of a quinizarine/TiO_2 nanoparticles-modified carbon paste electrode. *Analytical Methods*, 2: 1764-1769.
20. Reddy, A. V. B., Venugopal, N. and Madhavi, G. (2014). A selective and sensitive LC-MS/MS method for the simultaneous determination of two potential genotoxic impurities in celecoxib. *Journal of Analytical Science and Technology*, 5(18): 1-8.
21. Kaveeshwar, R. and Gupta, V. K. (1992). A new spectrophotometric method for the determination of hydrazine in environmental samples. *Fresenius Journal of Analytical Chemistry*, 344: 114-117.
22. Majeed, S. Y. and Bashir, W. A. (2019). Spectrophotometric determination of hydrazine sulphate using Fe (ii)-2,2'-bipyridyl-application to various water samples. *The Eurasia Proceedings of Science, Technology, Engineering and Mathematics*, 7: 23-32.
23. Mitic, V. D., Nikolic, S. D. and Jovanovic, V. P. S. (2010). Kinetic spectrophotometric determination of hydrazine. *Central European Journal of Chemistry*, 8(3): 559-565.
24. Kosyakov, D. S., Amosov, A. S., Ul'yanovskii, N. V., Ladesov, A. V., Khabarov, Yu. G. and Shpigun, O. A. (2017). Spectrophotometric determination of hydrazine, methylhydrazine, and 1, 1–dimethylhydrazine with preliminary derivatization by 5–nitro-2–furaldehyde. *Journal of Analytical Chemistry*, 2: 171-177.
25. Yu, L., Zhang, X. and Yu, L. (2012). Flow injection spectrophotometric determination of hydrazine in environmental water samples. *Advanced Materials Research*, 396–398: 130-133.
26. Britton, H. T. S. (1952). Hydrogen ions, 4th edition, Chapman and Hall, 28: pp. 359-364.
27. Bower and Bates (1955). pH values of the Clark and Lubs buffer solutions at 25 °C. *Journal of Research of the National Bureau of Standards*, 55: 197-202.
28. Lurie, J. U. (1978); Handbook of Analytical Chemistry, 2nd edition, Mir Publishers, Moscow.
29. Yoe, J. H. and Jones, A. L. (1944); Colorimetric determination of Fe with disodium 1, 2-dihydroxybenzene-3, 5-disulfonate, *Industrial Engineering Chemistry*, 16: 111-118.
30. Job, P. (1928). Formation and stability of inorganic complexes in solution, *Analytical Chemistry,* 9: 113-119.
31. Watt, G. W. and Chirsp, J. D. (1952). Spectrophotometric method for determination of hydrazine, *Analytical Chemistry*, 24(12): 2006-2008.
32. Frear, D. S. and Burrell, R. C. (1955). Spectrophotometric method for determining hydroxylamine reductase in higher plants. *Analytical Chemistry*, 27(10): 1664-1665.

Malaysian Journal of Analytical Sciences (MJAS)
Published by Malaysian Analytical Sciences Society

A BRIEF REVIEW ON CORROSION INHIBITION STUDY OF ORGANIC LIGAND: ELECTROCHEMICAL, MORPHOLOGY, AND ISOTHERM STUDIES

(Ulasan Ringkas Terhadap Kajian Perencatan Kakisan Ligan oleh Ligan Organik: Kajian Elektrokimia, Morfologi dan Isoterma)

Nur Nadia Dzulkifli[1,3]*, Nur Zalin Khaleda Razali[3], Norsanida Iswa Sahani[3], Sheikh Ahmad Izaddin Sheikh Mohd Ghazali[1,3], Dzeelfa Zainal Abidin[2], Asiah Abdullah[1,3], Nurazira Mohd Nor[1,3]

[1]Material, Inorganic, and Oleochemistry (MaterInOleo) Research Group, Faculty of Applied Sciences
[2]Academy of Language Studies
[3]School of Chemistry and Environment, Faculty of Applied Sciences
Universiti Teknologi MARA Cawangan Negeri Sembilan, Kampus Kuala Pilah, Pekan Parit Tinggi, 72000 Kuala Pilah, Negeri Sembilan, Malaysia

**Corresponding author: nurnadia@uitm.edu.my*

Received: 10 February 2022; Accepted: 2 April 2022; Published: 25 August 2022

Abstract

Over the past decade, the corrosion inhibition of organic ligands has been extensively studied in numerous experiments in acid media. The number of published papers related to corrosion inhibition studies of organic ligands has been rising exponentially. The organic ligands have high inhibitive properties due to their capability to adsorb on the surface of metal by forming a protective layer. Having lone pair electrons (S, N, O) and multiple bonds (π bonds) allow them to adsorb on the surface of metals efficiently. However, there is very limited and less comprehensive information on the characterization of corrosion inhibition performance of organic ligands on the surface of metals. Therefore, this review paper provides a comprehensive review on the corrosion inhibition performance through various characterization methods, which are the electrochemical method [Electrochemical Impedance Spectroscopy (EIS), Polarization], Scanning Electron Microscope (SEM) with Energy Dispersive X-ray (EDX), and Langmuir Isotherm, which are thoroughly discussed herein.

Keywords: electrochemical impedance spectroscopy, polarization, scanning electron microscope with energy dispersive X-ray; Langmuir isotherm

Abstrak

Sepanjang dekad yang lalu, perencatan kakisan ligan organik di dalam media berasid telah diuji di dalam eksperimen secara meluas dalam banyak eksperimen dalam media asid. Bilangan makalah yang diterbitkan berkaitan dengan kajian perencatan kakisan ligan organik telah meningkat secara eksponen. Ligan organik mempunyai sifat perencat yang tinggi kerana keupayaannya untuk menjerap pada permukaan logam dengan membentuk lapisan pelindung. Mempunyai pasangan elektron tunggal (S, N, O) dan ikatan berganda (ikatan π) membolehkan ligan organik menjerap pada permukaan logam dengan berkesan. Walau bagaimanapun, terdapat maklumat yang sangat terhad dan kurang komprehensif mengenai pencirian prestasi perencatan kakisan ligan organik

pada permukaan logam. Oleh itu, kertas kajian ini menyediakan ulasan kajian secara menyeluruh tentang pencirian prestasi perencatan kakisan melalui pelbagai kaedah pencirian seperti kaedah elektrokimia [Spectroskopi Impedan Elektrokimia (EIS), Polarisasi], Mikroskop Elektron Pengimbas (SEM) dengan Sinar-X Serakan Tenaga (EDX), dan Isoterma Langmuir dan telah dibincangkan dengan teliti di sini.

Kata kunci: spektroskopi impedan elektrokimia, polarisasi, mikroskop elektron pengimbas dengan sinar-X serakan tenaga, isoterma Langmuir

Introduction

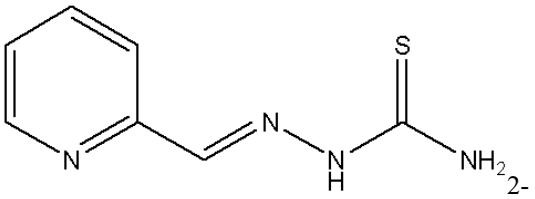
Corrosion is the term used for the natural oxidation of metal. Corrosion is also prescribed as the electrochemical corrosion or deterioration of metals and alloys in the presence of an environment [1-2]. When metals and alloys are unprotected in an acidic environment, they corrode rapidly. When metals come into contact with inorganic acids, pits and cracks formation on the surface causes machinery and equipment to fail [3-4]. Organic and inorganic compounds are the two major classes of corrosion inhibitors. Inorganic corrosion inhibitors are legislation restricted due to their potential for toxicity and pollution, while organic inhibitors are the most common means of preventing metal corrosion in harsh environments [5-6]. The organic inhibitor, when introduced in small amounts to the environment where a metal would corrode, results in lessened oxidization of the metal [7-9]. By adsorbing on the metal surface and generating an obstacle that inhibits the metal active sites, the organic inhibitor improves mild steel's resistance to corrosive media [10]. Organic ligands having π bonds, C=N, and lone electron pairs (S, O, N) would produce high inhibitive characteristics because they can enhance effective adsorption by covalent bonding with metal atoms' unoccupied *d*-orbitals [11-13]. Khaled et al. proclaimed that the S and N atoms have been shown to have the capability to form stable complexes that are closely arranged in the coordination sphere of metal ions [14]. Inhibitor molecules adsorb on metal surfaces, forming thin films that prevents corrosion by 'insulating' the metal from the corrosive electrolyte and altering the processes as well as the kinetics of corrosion reactions [15]. The organic corrosion inhibitor can be adsorbed on the metallic substrate through physical or chemical adsorption [16]. Multiple electrochemical and physical characterization techniques were used to deduce the nature of adsorption and evaluate the inhibitor's corrosion inhibition efficacy.

This review presents the electrochemical techniques, Electrochemical Impedance Spectroscopy (EIS) and Polarization, which have been used to evaluate the efficacy of organic compounds as corrosion inhibits on the surface of metal. Besides, the adsorption behavior of the inhibitors was also thoroughly reviewed through EDX and isotherm characterization.

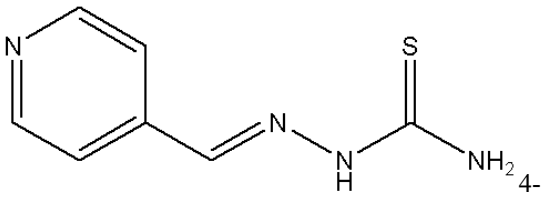
Corrosion Inhibition Performance Studies

Electrochemical impedance spectroscopy

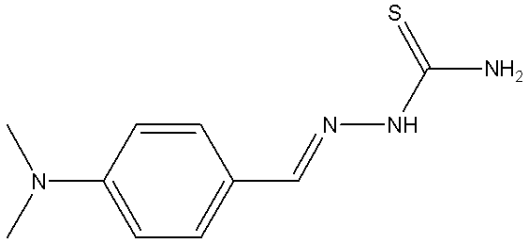
EIS is a common method for exploring organic-coated metals because it is a quick and easy approach to figure out the protective characteristics of organic inhibitors on metal surfaces [17]. Besides, Nikooa et al., proclaimed that EIS is a valuable tool for learning more about the corrosion inhibition characteristic of organic inhibitors and their mechanism of protection [18]. Corrosion inhibitors, 2-pyridinecarboxaldehyde thiosemicarbazone (2-PCT), 4-pyridinecarboxaldehyde thiosemicarbazone (4-PCT) [19], 4-(*N*,*N*-dimethylamino)benzaldehyde thiosemicarbazone (DMABT) [28] and {[(Benzylsulfanyl)carbonothioyl] amino} acetic acid (BDTC), {[(Propylsulfanyl) carbonothioyl] amino} acetic acid (PDTC) [18] structures, as shown in Figure 1, are examples that are used for the discussion.



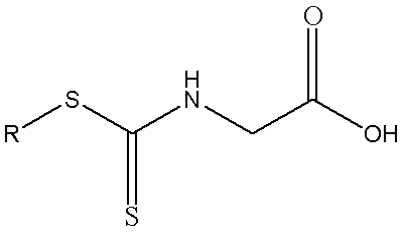
pyridinecarboxaldehyde (2-PCT)



pyridinecarboxaldehyde (4-PCT)



DMBAT



R = benzyl (BDTC)

R = propyl (PDTC)

{[(Benzylsulfanyl)carbonothioyl]amino} acetic acid (BDTC):

{[(Propylsulfanyl)carbonothioyl]amino} acetic acid (PDTC):

Figure 1. Structures of 2-PCT, 4-PCT, DMBAT, BDTC, and PDTC

There was a single depressed semicircle as shown in Figure 2 in all of the impedance spectra acquired for DBMAT, which consisted of two loops, one capacitive loop at a higher frequency and an inductive loop at a lower frequency. It indicated that the electrochemical solid/liquid barrier has a non-ideal capacitive behavior [20-21]. The non-homogeneity or crack (roughness) of the metal surface results in a depressed semicircle, which is attributed to frequency dispersion [22-23]. In addition, the "dispersing effect" of the depressed semicircle is a phenomenon that is commonly linked to surface roughness, chemical inhomogeneity, inhibitor adsorption, and the degree of poly crystallinity [24-26]. The existence of roughness and non-homogeneity on the metal surface because of the formation of corrosive chemicals and metal oxides might alter the density of active sites on the surface. The semicircle-shaped Nyquist plots signify the development of a barrier on the surface and a charge transfer process that is principally responsible for metal corrosion [27]. Mourya et al. revealed that in an acid media, the DMABT [28] created a single semicircle with its center below the real axis (x-axis), indicating the existence of a single charge-transfer process during the metal dissolution [28-29]. Overall, the impedances spectra showed that the diameters of imperfect semicircles steadily increase as the inhibitor concentration rises, implying that the inhibitor molecules can prevent metal dissolution in acidic conditions and so improve corrosion resistance [18, 30]. Increased surface coverage of inhibitive molecules on the surface of metal can be linked to increased capacitive loop diameters [19, 31].

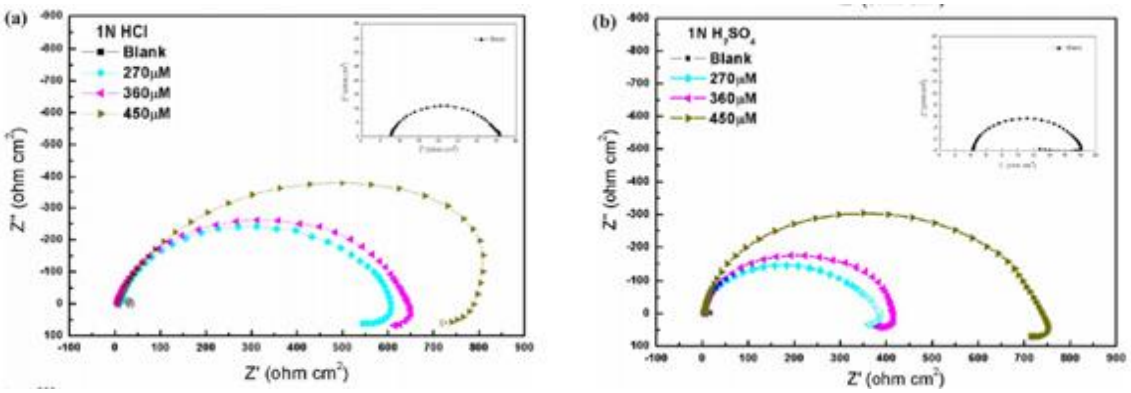


Figure 2. Nyquist plots of the corrosion of mild steel in acidic media absence and existence diverse concentrations of DMABT at 298 K: (a) 1N HCl; (b) 1N H_2SO_4 [28]

In general, the impedance curve contains three patterns, which are the high, medium, and low frequency capacitive loops. The impedance spectra possess a large capacitive loop at high frequencies, followed by a smaller inductive loop at low frequencies. The charge transfer of the corrosion process and double-layer behavior is frequently correlated with the high-frequency capacitive loop. The relaxation process of the adsorbed intermediates regulating the anodic process could be the reason for the low inductive loop induced by the adsorption of inhibitors or Cl^-_{ads} and H^+_{ads} from HCl on the electrode surface [28, 32-33]. Additionally, the layer stabilization consequences of the corrosion action on the electrode surface, involving inhibitor molecules and their reactive products, are most likely responsible for the inductive behavior at low frequencies [32]. It could also be the outcome of passivated surface re-dissolution. The medium capacitive loop is linked to the adsorption of corrosion inhibitors on the metal surface, which increases as the inhibitor 's concentration increases [32]. Mourya et al. reported that in the absence and existence of an inhibitor, the form of the curve in the two electrolytes remained unchanged [28]. This signifies that the addition of an inhibitor has no effect on the corrosion mechanism [34].

The intercept complements electrolyte resistance (R_s), solution resistance at the higher frequency end, and electrolyte resolution (R_s) + charge transfer resistance (R_{ct}) at the lower frequency end. The charge transfer resistance is R_{ct}, which is the contrast between these two quantities. R_{ct} is a measure of electron transfer over a surface that is inversely proportional to the corrosion rate [35]. Corrosion reactions that are strongly charged transfer-controlled and have impedance characteristics could be demonstrated using a simple and frequently used equivalent circuit consisting of a double layer capacitance, R_{ct}, and R_s. Instead of a pure double layer capacitance, a constant phase element, CPE, is used in the circuit compared to the capacitor, providing a more definite fit as shown in Figure 3 [36-37].

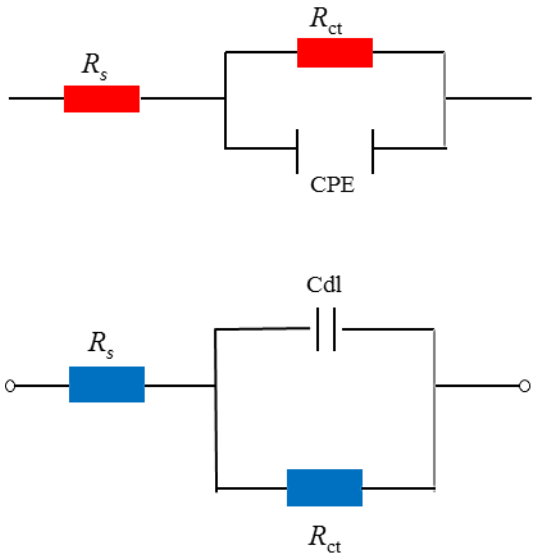


Figure 3. Equivalent circuit used to suit the EIS data of mild steel in 1N HCl consisting of diverse concentrations of inhibitors [36]

The CPE incorporates the component C_{dl} and the coefficient of exponential value of CPE α, which explains physical processes such as surface roughness, inhibitor adsorption, and the development of porous layers [38-39]. A few studies reported that the C_{dl} values dropped when the concentration of various inhibitors increased and deduced that inhibitor molecules were deposited on the steel surface [36, 40-41]. In addition, lower C_{dl} values possibly be induced by a decrease in local dielectric constant and an increment in electrical double layer thickness [42-44]. The Helmholtz model can be used to explain the decreasing C_{dl} values [45]:

$$C_{\mathrm{dl}} = \frac{\varepsilon\varepsilon_0}{\delta} S, \tag{1}$$

Where, ε = the dielectric constant of the medium, ε_0 = the vacuum permittivity, S = the electrode area, and δ = the thickness of the protective layer.

Most studies proclaimed that with the increase of inhibitor concentrations, the R_{ct} values increased. The increase in charge transfer resistance could be ascribed to the creation of a protective layer on the metal/solution interface [46-48]. The CPE's impedance function is denoted by the expression [19, 49]:

$$Z_{\mathrm{CPE}} = Y_0^{-1}(j\omega)^{-n} \tag{2}$$

where, Y_0 = a proportional factor, ω = the angular frequency, n = a deviation parameter ($-1 \leq n \leq +1$); n shows phase shift that is the degree of surface in-homogeneity, and n = 0, the CPE represents a pure resistor, f or n = 1 an inductor and for n = +1, a pure capacitor.

The values of the double layer capacitance (Q_{dl}), and inhibition effectiveness (η) are computed as follows:

$$Q_{\mathrm{dl}} = \mathrm{Y}_0(\omega_m^{''})^{n-1} \tag{3}$$

where, ω" = the angular frequency at the maximum value of the imaginary part of the impedance spectrum, and a constant phase angle element (CPE) Q_{dl} is used to define the C_{dl}.

According to the Helmholtz model [50], the Q_{dl} can be computed as follows:

$$Q_{\mathrm{dl}} = \frac{\varepsilon^0\varepsilon}{d}\mathrm{S} \tag{4}$$

where, d = the thickness of the protective layer, ε° is the permittivity of the air, and ε = the local dielectric constant, and S is the electrode surface area.

$$\eta = \frac{R_{ct} - R_{ct}^0}{R_{ct}} \times 100\% \tag{5}$$

R_{ct} = polarization resistance values observed in the presence of the inhibitor molecule, and R_{ct}° = polarization resistance values observed in the presence and absence of the inhibitor molecule [51].

Xu et al. reported that the values of R_{ct} rose dramatically and values of Q_{dl} decreased when the inhibitor concentration rose [19]. A reduction in Q_{dl} denotes a lowering in the local dielectric constant or a buildup in the electrical double layer thickness. As a result, the addition of 2-PCT and 4-PCT to the electrode surface may adsorb on the electrode surface by exchanging water molecules. The R_{ct} value in the blank solutions without the inhibitor is comparatively low due to the high conductivity of the HCl solution.

According to the phase angle graphs shown in Figure 1, more negative phase angle readings were observed when the concentration of corrosion inhibitors was increased in 1.0M HCl, and showed better inhibitive activity due to more inhibitor molecules adsorbed on the metal surface at higher concentrations. Adsorption of inhibitors results in increased surface smoothness [33]. Furthermore, the broadening of the curves is observed, confirming the buildup of the inhibitor molecule on the mild steel surface [52]. Nikooa et al. reported the uninhibited HCl solution exhibits a phase angle of -54.6° at 63 Hz, which increases to a maximum of -72.6 at 398 Hz for BDTC and -71.4 at 316 Hz for PDTC [18]. It can be supported by the presence of π electrons in the aromatic ring of BDTC. In comparison to the PDTC, the BDTC's more planar structure provides better interaction and coverage on the metal surface.

As a conclusion from the EIS study, corrosion inhibitors are effective on metal surfaces in an acid solution, as demonstrated by the results. The inclusion of electronegativity atoms such N and S, which are active centers of adsorption, could explain the greater inhibitory effectiveness. These groups increase electron density on the adsorption centers in inhibitor compounds, enabling smoother electron transfer between the functional group and the metal. The adsorption of inhibitors on the metal surface increases the R_{ct} because of the formation of a protective layer. Indirectly, Q_{dl} and local dielectric values decrease because of the increasing electrical double layer. An increment of surface coverage on the metal surface by corrosion inhibitors might be due to the lessening of water molecules and other ions. Besides, the impedance behavior of the metal surface was significantly altered when the inhibitor was added, and the diameter of the semicircle produced in the Nyquist plots was subsequently enlarged in the presence of inhibitors.

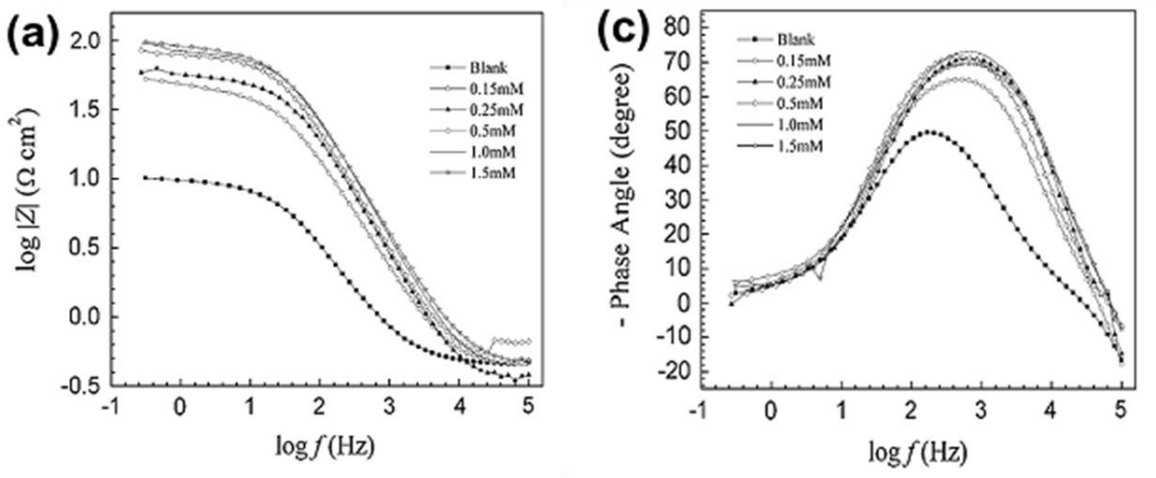


Figure 4. The Bode and Phase Angle plots for mild steel in 1.0M HCl solutions absence and existence diverse concentrations of inhibitors at 30ºC: (a and c) 2-PCT [19]

Polarization plot

The shift in potential induced by concentration changes the environment, surrounding the electrode surface is known as concentration polarization. The voltage difference between the anode and the cathode, as well as the resistance of the corrosion cell, affects the rate of corrosion (or current density). The current flow is present in all corrosive reactions, and it changes the potential of the metal surfaces involved. Tafel curves were used to compute corrosion potentials (E_{corr}) and corrosion current densities (I_{corr}) [53]. The anodic reaction of corrosion occurs when metal ions from the metal surface flow into the solution or electrolyte, and the cathodic reaction occurs when hydrogen ions are discharged to form hydrogen gas or a reduction of dissolved oxygen in acidic solutions [54]. Cao stated that if the E_{corr} of the inhibitor-containing solution is almost equivalent to the uninhibited solution, it can be deduced that the inhibition effect is mediated by adsorption inhibitive species obstructing the surface of the metal electrode geometrically [55].

The addition of the Thiophene derivative as a corrosion inhibitor reduces the corrosion rate dramatically, lowering current densities by modifying both the anodic and cathodic Tafel curves [56]. Both anodic and cathodic reactions are impeded by this pattern, with the suppression effect becoming stronger as the inhibitor concentration rises. It is plausible that this is due to the inhibitors' adsorption at the active sites on the surface.

The mechanisms of anodic reaction in acid are shown below:

The process of Fe dissolution pathways in HCl [57]:

$$\begin{aligned} &Fe + Cl^- \longrightarrow (FeCl^-)_{ads} \\ &(FeCl^-)_{ads} \longrightarrow (FeCl^-)_{ads} + e \\ &(FeCl)_{ads} \longrightarrow FeCl + e \\ &FeCl^+ + e \longrightarrow Fe^{2+} + Cl^- \end{aligned} \quad (6)$$

According to the mechanism depicted below, the iron electrodissolution in H_2SO_4 solvent is mostly dependent on the intermediate adsorption of $FeOH_{ads}$:

$$\begin{aligned} &Fe + H_2O \longrightarrow Fe.H_2O_{ads} \\ &FeH_2O_{ads} \longrightarrow FeOH_{ads} + H^+ + e \\ &FeOH_{ads} \longrightarrow FeOH^+ + e \\ &FeOH^+ + H^+ \longrightarrow Fe^{2+} + 2e \end{aligned} \quad (7)$$

As a conclusion, Okafor and Zheng described that the anodic dissolution of iron in an H_2SO_4 solution is mostly reliant on the adsorbed intermediate $(FeOH)_{ads}$, whereas in an HCl solution, Shukla and Quraishi stated that it is mostly reliant on $(FeCl)_{ads}$ [58-59]. The corrosion inhibitors mechanism in the acid solution can be described as:

Anodic oxidation in H_2SO_4 [60]:

$$\begin{aligned} &Fe.H_2O_{ads} + Inh \longrightarrow FeOH_{ads}^- + H^+ + Inh \\ &Fe.H_2O_{ads} + Inh \longrightarrow Fe.Inh_{ads} + H_2O \\ &FeOH_{ads}^- \longrightarrow FeOH_{ads} + e \text{ (rate-determining step)} \\ &Fe.Inh_{ads} \longrightarrow Fe.Inh_{ads}^+ + e \\ &FeOH_{ads} + Fe.Inh_{ads}^+ \longrightarrow FeOH^+ + Fe.Inh_{ads} \\ &FeOH^+ + H^+ \longrightarrow Fe^{2+} + H_2O \end{aligned} \quad (8)$$

Anodic oxidation in HCl [60]:

$$\begin{aligned} &(FeCl^-)_{ads} + InhH^+ \longrightarrow (FeCl^-InhH^+)_{ads} \\ &(FeCl^-)_{ads} + InhH^+ \longrightarrow (Fe.InhH^+)_{ads} + Cl^- \end{aligned} \quad (9)$$

The adsorption of H^+_{Inh} onto the adsorbed $FeCl^-$ present at the metal/electrolyte interface causes the I_{corr} values to drop at varied inhibitor concentrations. In the presence of corrosion inhibitor, the cathodic reaction process can be computed as follows:

$$\begin{aligned} &Fe + H^+ + e \longrightarrow (FeH)_{ads} \\ &Fe + (InhH^+) + e \longrightarrow (Fe.InhH)_{ads} \\ &(FeH)_{ads} + (FeH)_{ads} \longrightarrow Fe + H_2 \end{aligned} \quad (10)$$

The corrosion inhibitory effectiveness (Tafel) of compounds is computed using the following formula [61-62]:

$$\eta \text{Tafel } (\%) = \frac{I_{corr} - I_{corr(i)}}{I_{corr}} \times 100 \quad (11)$$

where, i_{corr} = corrosion current densities in the absence of inhibitors, and $i_{corr(inh)}$ = corrosion current densities in the absence and in the presence of inhibitors

$$\eta(\%) = \left(\frac{R_{ct} - R_{ct}^0}{R_{ct}}\right) \times 100 \quad (12)$$

where, R_{ct} = charge transfer resistance in the presence of the inhibitor, and R^0_{ct} = charge transfer resistance in the absence of the inhibitor [63].

Figure 5 shows that the E_{corr} of the corrosion inhibitors are shifted to a more negative side and the E_{corr} displacement is less than 85 mV. As a result of this finding, corrosion inhibitors were classified as mixed-type inhibitors, with cathodic polarization being the most prevalent. A reduction in the rate of anodic metal dissolution as well as a delay in the cathodic hydrogen evolution reaction reflect the inhibitors' mixed inhibitory nature [54, 68-69]. If the difference in corrosion between the inhibitor and the blank exceeded 85 mV, the inhibitor was categorized as cathodic or anodic [64-65]. As shown in Figure 6, when the inhibitors were added to the corrosive solutions, the E_{corr} values changed in a more positive manner than when they were absent. The inhibitors' corrosion potentials have shifted to the positive side and the E_{corr} displacement was less than 85 mV, indicating that they behave as mixed-type inhibitors with an anodic reaction-predominant effect. Besides, the corrosion inhibitor can be deduced by $ß_a$ and $ß_c$ values. Sahin et al. and Nazir et al. reported that $ß_c$ values are higher than $ß_a$ in different concentrations. It can be concluded that the inhibitor is predominantly cathodic in nature, as supported by the polarization curve and E_{corr} values [66-67]. The parallel cathodic current–potential curves as shown in Figure 5 implies that the addition of this inhibitor has no effect

on hydrogen evolution and that hydrogen evolution is controlled by activation. Fathabadi et al., deduced that the charge-transfer mechanism is primarily responsible for the reduction of H^+ ions on the metal surface [70]. The observation can be elucidated by the fact that the metal surface has been covered with adsorbed corrosion inhibitor molecules, which has suppressed the corrosion process. This indicates that the presence of the inhibitor has no effect on the reduction pathway, and so the hydrogen evolution is retarded by the inhibitor's surface blocking effect [71-72].

The shape of polarization curves with and without the corrosion inhibitor is identical for most corrosion inhibition performance studies in the acid media. The occurrence explained that the addition of corrosion inhibitors had no impact on the corrosion mechanism of metal dissolving in acid solution, and the inhibitory impact of these inhibitors was due to the covering of inhibitor molecules at the active sites to limit their exposure to the acidic environment [73].

The inhibitor molecule attaches to the mild steel surface and blocks the anodic reaction's available reaction sites [74-75]. With increasing inhibitor concentrations, the surface coverage increases. At varying inhibitor concentrations, the surface coverage, θ of the inhibitor was estimated using the equation:

$$\theta = \frac{i_{corr} - i_{corr(inh)}}{i_{corr}} \quad (13)$$

where; i_{corr} = corrosion current densities in the absence of inhibitors, and $i_{corr(inh)}$ = corrosion current densities in the presence of inhibitors.

Therefore, the inhibition effectiveness can be computed using:

$$\eta(\%) = \theta \times 100 \quad (14)$$

The rise in polarization resistance in the presence of the inhibitor supports the development of a non-conducting physical barrier of compound on the metal surface, leading to an increase in corrosion inhibiting effectiveness. Besides, the formation of a plateau at anodic polarization refers to a passivation process that arises after oxygen evolution [76]. Desorption potential is described as a sudden increase in current density with increasing potential, as evidenced by the flat region on the anodic curve. The simultaneous adsorption of inhibitor molecules on the metal surface and desorption of inhibitor molecules due to the metal's dissolution in corrosive media can explain these phenomena. The desorption rate of the inhibitor is greater than its adsorption rate in this circumstance, resulting in an increase in the corrosion current as the potential increment [77-78].

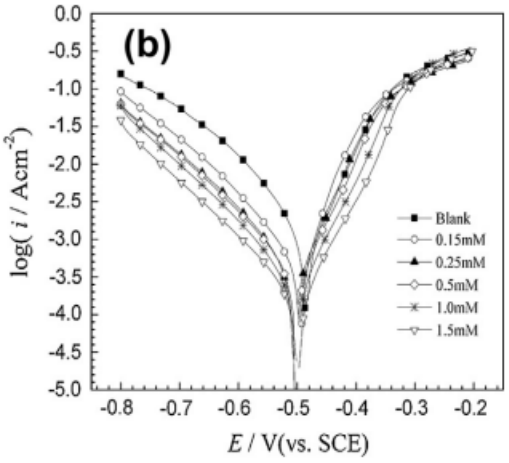


Figure 5. Potentiodynamic polarization curves for mild steel in the absence and presence of diverse concentrations of inhibitors in 1.0 M HCl: (a) 2-PCT, (b) 4-PCTat30ºC [19]

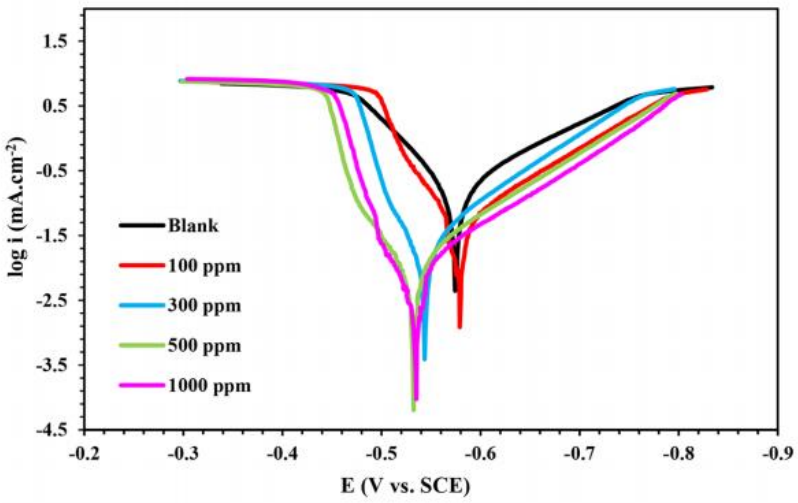


Figure 6. Potentiodynamic polarization curves for CRS in the presence and absence of diverse concentrations of the inhibitor at room temperature in 0.5 M HCl: (a) BDTC [18]

Scanning electron microscope-energy dispersive X-ray

SEM is used to scrutinize the morphology of mild steel surfaces before and after their immersion in acid solution. While EDX is used to confirm the creation of the protective coating owing to inhibitor adsorption on the surface of mild steel [79-80]. EDX spectra displayed the presence of N, S, P (corrosion inhibitors) and decreased composition of Fe on the metal surface as a proof of protective layer formation [81-82]. This increased inhibitory efficacy was presumably due to a strong interaction between the ($-NH_2$) and (=S) groups classified as electronegative atoms in the inhibitors' molecular structures and the metal surface, which blocks the active sites of adsorption. According to a few studies, the availability of free electron pairs, heteroatoms, and π orbitals permits the corrosion inhibitor to have a significant inhibitory performance, resulting in the blocking of active sites and, as a result, a reduction in corrosion rate [83]. Therefore, it improves the metal surface roughness (smoothness) and reduce the pits [84-85]. The development of iron oxide on the metal surface causes a peak of O to be extremely high in an uninhibited hydrochloride solution [86-87]. Whereas, due to the adsorption of the BDTC molecules, the oxidation of CRS on the surface is reduced, showing that there is less oxidation of CRS on the surface. The surface of uninhibited metal is severely eroded, and due to the Cl^--induced attack, a surface deep hole can be seen at greater resolutions [88] Besides, the corroded metal showed an uneven, pit-shaped pattern and the formation of crystal gain corrosion products [89]. Al-Amiery et al. deduced that because the surface was dried before SEM scanning, the cracks in the film are attributable to surface dehydration [90]. The electrochemical analysis correlates well with these findings.

Adsorption isotherm

Adsorption isotherms are commonly used to indicate the efficacy of organic adsorbent type inhibitors and are crucial in understanding how organic electrochemical reactions occur. The adsorption behavior of inhibitors can be depicted using two different types of interactions: physisorption and chemisorption. The adsorption of organic inhibitor molecules from an aqueous solution onto a metal surface has the following equilibrium equation:

$$Org_{(sol)} + xH_2O_{(ads)} \longrightarrow Org_{(ads)} + xH_2O_{(sol)} \quad (15)$$

From the equation, it can be deduced that the adsorption of corrosion inhibitors (organic compounds) was

complemented by the desorption of H_2O molecules from the metal surface [91-92]. Langmuir, Temkin, and Frumkin isotherms, which characterizes the relationship between surface coverage, θ and concentration of corrosion inhibitor, are the most utilized adsorption isotherms using weight loss data. Ozkir et al. surmised that an adsorption isotherm can reveal a lot about how corrosion inhibitors interact with the metal surface [93].

The following attempts were made to suit θ values to Langmuir, Frumkin, Freundlich, and Temkin isotherms [94-96]:

$$\text{Langmuir: } \frac{C}{\theta} = \frac{1}{K} + C \tag{16}$$

$$\text{Frumkin: } \frac{\theta}{1-\theta}\exp(-2f\theta) = KC \tag{17}$$

$$\text{Temkin: } \exp(f\theta) = KC \tag{18}$$

where; θ = surface coverage, K = the adsorption-desorption equilibrium constant or adsorptive equilibrium constant ($Lmol^{-1}$), C = inhibitor concentration ($molL^{-1}$), and f = factor of energetic inhomogeneity.

$$\theta = \frac{w_0 - w_i}{w_0} \tag{19}$$

$$\theta = \frac{i_{\mathbf{corr}} - i_{corr}^{inh}}{i_{\mathbf{corr}}} \tag{20}$$

$$\theta = \frac{R_{ct} - R_{ct}^0}{R_{ct}} \tag{21}$$

where, w_0= weight loss of metal in the blank, w_i = weight loss of metal in the inhibitor solution, i_{corr} = current density of metal in the blank, i^{inh}_{corr} = current density of metal in the inhibitor solution, R_{ct} = charge transfer resistance in the blank, and R_{ct}°= charge transfer resistance in the inhibitor solution [36, 97, 98].

The isotherm that significantly suited the experimental data was determined using the correlation coefficient (R^2). Mostly, the corrosion inhibition studies of organic compounds' weight losses values were fitted with Langmuir Isotherm. The Langmuir equation is based on the presumption that the adsorption is monolayer, that all active sites have a consistent distribution of energy levels, and that adsorbed molecules do not interact with each other [99-100] Its phenomenon is supported if the R^2 value is close to 1 or unity [101] The intercepts of the straight lines were used to compute the values of k_{ads} from the graphs of C/θ versus C or log(θ/1-θ) versus log C. The high K_{ads} value demonstrates the inhibitor's high adsorption capacity on metal surfaces. Additionally, increasing the temperature reduced the value of k_{ads}, indicating that increasing the solution temperature generates more agitation, and consequently, the desorption of some inhibitor molecules from the metal surface [102-103] The following equation can be applied to estimate the standard free energy of inhibitor adsorption using the value of k_{ads} [104]:

$$\Delta G_{ads}^0 = -\mathrm{RTln}55.5\mathrm{k}_{\mathbf{ads}} \tag{22}$$

where, 55.5 = molar concentration of water, R = universal gas constant (8.314 $JK^{-1}mol^{-1}$), T = temperature (K), and ΔG°_{ads} = Gibbs free energy of adsorption.

The negative value of G°_{ads} suggests that the process is spontaneous, implying that the inhibitor molecules are efficiently adsorbed on the mild steel surface [105]. Yurt et al. stated that the presence of electrostatic interactions between charged molecules and metal surface charges are indicated by the magnitude of ΔG°_{ads} smaller than 20 $kJmol^{-1}$ (physisorption) [106]. When ΔG°_{ads} is more than 40 $kJmol^{-1}$, it suggests that electrons from the inhibitor molecules are shared or transferred to the metal surface, forming a coordinate type of bond (chemisorption) [107-109]. The ΔG°_{ads} values are in the range of -20 to -40 $kJmol^{-1}$, showing that both chemisorption and physisorption are involved in the adsorption process [110-111]. Adsorption initiates electrostatic interactions between water molecules and metal surfaces, followed by chemical interactions between the metal surface and the adsorbate (inhibitor). Zhang et al. reported that if the value of ΔG°_{ads} is in between -20 to -40 $kJmol^{-1}$,but near to -40 $kJmol^{-1}$,then it can be concluded that the inhibitor is a combination of chemisorption and physisorption which is predominantly chemisorption [112]. Therefore, if the ΔG°_{ads} is near to -20 $kJmol^{-1}$, it is predominantly physisorption.

Conclusion

In this review paper, different techniques were discussed that will help researchers explain the phenomenon and mechanism that have occurred on the metal surface after the adsorption of the inhibitor. The type of adsorption of inhibitors on the metal surface can be deduced using electrochemical techniques (EIS and polarization), SEM-EDX, and Langmuir isotherm.

Acknowledgement

The authors would like to thank Universiti Teknologi MARA Negeri Sembilan Branch, Kuala Pilah campus, for all the support given throughout the process of producing this paper.

References

1. Damborenea, J. de., Conde, A. and Arenas, M. A. (2014). Chapter 3: 3 - Corrosion inhibition with rare earth metal compounds in aqueous solutions. Rare Earth-Based Corrosion Inhibitors. Woodhead Publishing Series in Metals and Surface Engineering. Elsevier.
2. Amitha, R. B. E. and Basu, B. B. J. (2012). Green inhibitors for corrosion protection of metals and alloys: an overview. *International Journal of Corrosion,* 2012: 1-15.
3. Kumar, H. and Yadav, V. (2021). Highly efficient and eco-friendly acid corrosion inhibitor for mild steel: Experimental and theoretical study. *Journal of Molecular Liquid,* 335: 1-16.
4. Danaee, I., Bahramipanah, N., Moradi, S. and Nikmanesh, S. (2016). Impedance spectroscopy studies on corrosion inhibition behavior of synthesized *n*,*n*'-bis(2,4-dihydroxyhydroxybenzaldehyde)-1,3-propandiimine for API-5L-X65 steel in HCl solution. *Journal of Electrochemical Science and Technology,* 7(2): 153-160.
5. Thoume, A., Elmakssoudi, A., Benmessaoud, L. D., Benzbiria, N., Benhiba, F., Dakir, M., Zahouily, M., Zarrouk, A., Azzi, M. and Zertoubi, M. (2020). Amino acid structure analog as a corrosion inhibitor of carbon steel in 0.5 M H_2SO_4: Electrochemical, synergistic effect and theoretical studies. *Chemical Data Collections,* 30: 1-18.
6. Dehghani, A., Mostafatabar, A. H., Bahlakeh, G., Ramezanzadeh, B. and Ramezanzadeh, M. (2020). Detailed-level computer modeling explorations complemented with comprehensive experimental studies of Quercetin as a highly effective inhibitor for acid-induced steel corrosion. *Journal of Molecular Liquid,* 309: 1-51.
7. Beytur, M., Irak, Z. T., Manap, S. and Yuksek, H. (2019). Synthesis, characterization and theoretical determination of corrosion inhibitor activities of some new 4,5-dihydro-1H-1,2,4-Triazol-5-one derivatives. *Heliyon,* 5: 1-8.
8. Ozkir, D. (2019). A newly synthesized schiff base derived from condensation reaction of 2,5-dichloroaniline and benzaldehyde: Its applicability through molecular interaction on mild steel as an acidic corrosion inhibitor by using electrochemical techniques. *Journal of Electrochemical Science and Technology,* 10(1): 37-54.
9. Marinescu, M. (2019). Recent advances in the use of benzimidazoles as corrosion inhibitors. *BMC Chemistry,* 13(136): 1-21.
10. Jamil, D. M., Al-Okbi, A. K., Al-Baghdadi, S. B., Al-Amiery, A. A., Kadhim, A., Gaaz, T. S., Kadhum, A. A. H. and Mohamad, A. B. (2018). Experimental and theoretical studies of Schiff bases as corrosion inhibitors. *Chemistry Central Journal,* 12(7): 1-9.
11. Padash, R., Rahimi-Nasrabadi, M., Rad, A. S., Sobhani-Nasab, A., Jesionowski, T. and Ehrlich, H. (2019). A theoretical study of two novel Schiff bases as inhibitors of carbon steel corrosion in acidic medium. *Applied Physic A,* 125(78): 1-11.
12. Keles, H., Emir, D. M. and Keles, M. (2015). A comparative study of the corrosion inhibition of low carbon steel in HCl solution by an imine compound and its cobalt complex. *Corrosion Science,* 101: 19-31.
13. Lgaz, H., Salghi, R., Jodeh, S. and Hammout, B. (2017). Effect of clozapine on inhibition of mild steel corrosion in 1.0 M HCl medium. *Journal of Molecular Liquid,* 225: 271-280.

14. Khaled, K. F., Samardzija, K. B. and Hackerman, N. (2006). Cobalt(III) complexes of macrocyclic-bidentate type as a new group of corrosion inhibitors for iron in perchloric acid. *Corrosion Science*, 48: 3014-3034.
15. Abdallah, M., Gad, E., Sobhi, M., Al-Fahemi, J. H. and Alfakeer, M. (2019). Performance of tramadol drug as a safe inhibitor for aluminum corrosion in 1.0M HCl solution and understanding mechanism of inhibition using DFT. *Egyptian Journal of Petroleum,* 28(2): 173-181.
16. Boughoues, Y., Benamira, M., Messaadia, L., Bouider, N. and Abdelaziz, S. (2020). Experimental and theoretical investigations of four amine derivatives as effective corrosion inhibitors for mild steel in HCl medium. *RSC Advances,* 10: 24145-24158.
17. Ferreira, E. S., Giancomelli, C., Giacomelli, F. C. and Spinelli, A. (2004). Evaluation of the inhibitor effect of L-ascorbic acid on the corrosion of mild steel. *Materials Chemistry and Physics,* 83(1): 129-134.
18. Nikoo, S. Z., Shockravi, A., Ghartavol, H. M., Halimehjani, A. Z., Ostadrahimi, M., Mirhosseini, S. M., Behzadi, H. and Ghorbani, M. (2020). A study of Glycine-based dithiocarbamates as effective corrosion inhibitors for cold rolled carbon steel in HCl solutions. *Surfaces and Interfaces,* 21: 1-67.
19. Xu, B., Yang, W., Liu, Y., Yin, X., Gong, W. and Chen, Y. (2014). Experimental and theoretical evaluation of two pyridine carboxaldehyde thiosemicarbazone compounds as corrosion inhibitors for mild steel in hydrochloric acid solution. *Corrosion Science,* 78: 260-268.
20. Mahgoub, F. M., Abdel-Nabey, B. A. and El-Samadisy, Y. A. (2010). Adopting a multipurpose inhibitor to control corrosion of ferrous alloys in cooling water systems. *Materials Chemistry and Physics,* 120(1): 104-108.
21. Geoffrey, B., Dang, D. N., Stephanie, M. and Sebastien, T. (2014). Analysis of the non-ideal capacitive behaviour for high impedance organic coatings. *Progress in Organic Coatings,* 77(12): 2045-2053.
22. Aouniti, A., Elmsellema, H., Tighadouini, S., Elazzouzi, M., Radi, S., Chetouani, A., Hammouti, B. and Zarrouk, A. (2016). Schiff's base derived from 2-acetyl thiophene as corrosion inhibitor of steel in acidic medium. *Journal of Taibah University for Science,* 10: 774-785.
23. Prajila, M., Ammal, P. R. and Abraham, J. (2018). Comparative studies on the corrosion inhibition characteristics of three different triazine based Schiff's bases, HMMT, DHMMT and MHMMT. *Egyptian Journal of Petroleum*, 27(4): 467-475.
24. Chetouani, A., Medjahed, K., Benabadji, K. E., Hammouti, B., Kertit, S. and Mansri, A. (2003). Poly(4-vinylpyridine isopentyl bromide) as inhibitor for corrosion of pure iron in molar sulphuric acid. *Progress in Organic Coatings,* 46(4): 312-316.
25. Aby, P., Joby, T. K., Vinod, P. R. and Shaju, K. S. (2012). 3-Formylindole-4-aminobenzoic Acid: A potential corrosion inhibitor for mild steel and copper in hydrochloric acid media. *ISRN Corrosion,* 2012: 1-10.
26. Okonkwo, P. C., Sliem, M. H., Shakoor, R. A., Mohamed, A. M. A. and Abdullah, A. M. (2017). Effect of temperature on the corrosion behavior of API X120 pipeline steel in H_2S environment. *Journal of Materials Engineering and Performance,* 26: 3775-3783.
27. Aytac, A., Ozmen, U. and Kabasakaloglu, A. (2005). Investigation of some Schiff bases as acidic corrosion of alloy AA3102. *Materials Chemistry and Physics,* 89(1): 176-181.
28. Mourya, P., Banerjee, S., Rastogi, R. B. and Singh, M. M. (2013). Inhibition of mild steel corrosion in hydrochloric and sulfuric acid media using a thiosemicarbazone derivative. *Industrial & Engineering Chemistry Research,* 52(36): 12733-12747.
29. Elias, E. E., Henry, U. N. and Damian, C. O. (2018). Synthesis and characterization of Schiff bases NBBA, MNBA and CNBA. *Heliyon*, 4(7): 1-25.

30. Jiyaul, H., Ansari, K. R., Vandana, S., Quraishi, M. A. and Obot, I. B. (2017). Pyrimidine derivatives as novel acidizing corrosion inhibitors for N80 steel useful for petroleum industry: A combined experimental and theoretical approach. *Journal of Industrial and Engineering Chemistry,* 49: 176-188.
31. Solmaz, R., Kardas, G., Çulha, M., Yazici, B. and Erbil, M. (2008). Investigation of adsorption and inhibitive effect of 2-mercaptothiazoline on corrosion of mild steel in hydrochloric acid media. *Electrochimica Acta,* 53(20): 5941-5952.
32. Khaled, K. F. (2010). Electrochemical behavior of nickel in nitric acid and its corrosion inhibition using some thiosemicarbazone derivatives. *Electrochimica Acta,* 55: 5375-5383.
33. Bhawna, C., Ashish, K. S., Sanjeeve, T., Balaram, P., Hassane, L., Ill-Min, C., Ranjana, J. and Eno, E. E. (2020). Comparative investigation of corrosion-mitigating behavior of thiadiazole-derived bis-schiff bases for mild steel in acid medium: experimental, theoretical, and surface study. *ACS Omega,* 5: 13503-13520.
34. El Basiony, N. M., Amr, E., Nady, H., Migahed, M. A. and Zaki, E. G. (2019). Adsorption characteristics and inhibition effect of two Schiff base compounds on corrosion of mild steel in 0.5 M HCl solution: experimental, DFT studies, and Monte Carlo simulation. *RSC Advances,* 9: 10473-10485.
35. Jacob, K. S. and Geetha, P. (2010). Corrosion inhibition of mild steel in hydrochloric acid solution by Schiff base furoin thiosemicarbazone. *Corrosion Science,* 52: 224-228.
36. Idouhli, R., Ousidi, A. N., Koumya, Y., Abouelfida, A., Benyaich, A., Auhmani, A. and Moulay, Y. A. I. (2018). Electrochemical studies of monoterpenic thiosemicarbazones as corrosion inhibitor for steel in 1 M HCl. *International Journal of Corrosion,* 2018: 1-15.
37. Manilal, M., Sourav, K. S., Prabhas, B., Naresh, C. M., Harish, H. and Priyabrata, B. (2020). Corrosion inhibition property of azomethine functionalized triazole derivatives in 1 $molL^{-1}$ HCl medium for mild steel: Experimental and theoretical exploration. *Journal of Molecular Liquid,* 313: 1-15.
38. Muthukrishnan, P., Prakash, P., Jeyaprabha, B. and Shankar, K. (2019). Stigmasterol extracted from *Ficus hispida* leaves as a green inhibitor for the mild steel corrosion in 1M HCl solution. *Arabian Journal of Chemistry,* 12(8): 3345-3356.
39. Ammal, P. R., Prajila, M. and Abraham, J. (2018). Physicochemical studies on the inhibitive properties of a 1,2,4-triazole Schiff's base, HMATD, on the corrosion of mild steel in hydrochloric acid. *Egyptian Journal of Petroleum,* 27: 307-317.
40. Chitra, S., Parameswari, K. and Selvaraj, A. (2010). Dianiline Schiff bases as inhibitors of mild steel corrosion in acid media. *International Journal of Electrochemical Science,* 5: 1675-1697.
41. Ilhem, K., Tahar, D., Djamel, D., Saifi, I., Lakhdar, S. and Salah, C. (2021). Synthesis, characterization and anti-corrosion properties of two new Schiff bases derived from diamino diphenyl ether on carbon steel X48 in 1M HCl. *Journal of Adhesion Science and Technology,* 35(6): 1-31.
42. Shirin, S., Sarmin, H., Jahan, B. G., Parviz, N. and Alireza, S. (2019). Synthesis, experimental, quantum chemical and molecular dynamics study of carbon steel corrosion inhibition effect of two Schiff bases in HCl solution. *Journal of Molecular Liquid,* 285: 626-639.
43. Deng, X. and Li, X. X. (2014). Hydroxymethyl urea and 1,3-bis(hydroxymethyl) urea as corrosion inhibitors for steel in HCl solution. *Corrosion Science,* 80: 276-289.
44. Uzma, N., Zareen, A., Naveed, Z. A. and Faiz, U. S. (2019). Experimental and theoretical insights into the corrosion inhibition activity of novel Schiff bases for aluminum alloy in acidic medium. *RSC Advances,* 9: 36455-36470.
45. Khadraoui, A., Khelifa, M. H., Razika, M., Kamel, H., Tidu, A., Azari, Z., Ime, B. O. and Zarrouk, A. (2016). Extraction, characterization and anti-corrosion activity of *Mentha pulegium* oil: Weight loss, electrochemical, thermodynamic and surface studies. *Journal of Molecular Liquid,* 216: 724-731.

46. Nimmy, K., Joby, T. K., Vinod, P. R. and Shaju, K. S. (2014). Electrochemical impedance spectroscopy and potentiodynamic polarization analysis on anticorrosive activity of thiophene-2-carbaldehyde derivative in acid medium. *Indian Journal of Materials Science,* 2014: 1-6.
47. Hamdani, N. E., Fdil, R., Tourabi, M., Jama, C. and Bentiss, F. (2015). Alkaloids extract of *Retama monosperma* (L.) Boiss. seeds used as novel eco-friendly inhibitor for carbon steel corrosion in 1 M HCl solution: Electrochemical and surface studies. *Applied Surface Science,* 357: 1294-1305.
48. Turuvekere, K. C., Kikkeri, N. S. M. and Harmesh, C. T. (2015). Thermodynamic, electrochemical and quantum chemical evaluation of some triazole Schiff bases as mild steel corrosion inhibitors in acid media. *Journal of Molecular Liquid,* 211: 1026-1038.
49. Ragi, K., Joby, T. K., Vinod, P. R., Sini, V. C. and Binsi, M. P. (2019). Synthesis, cyclic voltammetric, electrochemical, and gravimetric corrosion inhibition investigations of schiff base derived from 5,5-dimethyl-1,3-cyclohexanedione and 2-aminophenol on mild steel in 1 M HCl and 0.5 M H_2SO_4. *International Journal of Electrochemistry,* 2019: 1-13.
50. Weihua, L., Qiao, H., Changling, P. and Baorong, H. (2007). Experimental and theoretical investigation of the adsorption behaviour of new triazole derivatives as inhibitors for mild steel corrosion in acid media. *Electrochimica Acta,* 52(22): 6386-6394.
51. Ifzan, A., Aamer, S., Pervaiz, A. C., Syeda, A. S., Muhammad, N. A. and Muhammad, S. (2020). Bis-Schiff bases of 2,2′-dibromobenzidine as efficient corrosion inhibitors for mild steel in acidic medium. *RSC Advances,* 10: 4499-4511.
52. Yadav, M., Kumar, S., Sinha, R. R. and Kumar, S. (2014). Experimental and theoretical studies on synthesized compounds as corrosion inhibitor for mild steel in hydrochloric acid solution. *Journal of Dispersion Science and Technology,* 35: 1751-1763.
53. Poorqasemi, E., Abootalebi, O., Peikari, M. and Haqdar, F. (2009). Investigating accuracy of the Tafel extrapolation method in HCl solutions. *Corrosion Science,* 51: 1043-1054.
54. Sam, J., Jeevana, R., Aravindakshan, K. K. and Abraham, J. (2017). Corrosion inhibition of mild steel by *n*(4)-substituted thiosemicarbazone in hydrochloric acid media. *Egyptian Journal of Petroleum,* 26: 405-412.
55. Cao, C. (1996). On electrochemical techniques for interface inhibitor research. *Corrosion Science,* 38 (12): 2073-2082.
56. Zachariah, P. M., Keerthi, R., Cyril, A., Bincy, J. and Sam, J. (2020). Corrosion inhibition of mild steel using poly (2-ethyl -2-oxazoline) in 0.1M HCl solution. *Heliyon,* 6(11): 1-8.
57. Poornima, T., Nayak, J. and Shetty, A. N. (2012). Effect of diacetyl monoxime thiosemicarbazone on the corrosion of aged 18 Ni 250 grade maraging steel in sulphuric acid solution. *Journal of Metallurgy,* 2012: 1-13.
58. Okafor, P. C. and Zheng, Y. (2009). Synergistic inhibition behaviour of methylbenzyl quaternary imidazoline derivative and iodide ions on mild steel in H_2SO_4 solutions. *Corrosion Science,* 51: 850-859.
59. Shukla, S. K. and Quraishi, M. A. (2010). The effects of pharmaceutically active compound doxycycline on the corrosion of mild steel in hydrochloric acid solution. *Corrosion Science,* 52: 314-321.
60. Okafor, P. C., Ikpi, M. E., Uwah, I. E., Ebenso, E. E., Ekpe, U. J. and Umoren, S. A. (2008). Inhibitory action of *Phyllanthus amarus* extracts on the corrosion of mild steel in acidic media. *Corrosion Science,* 50 (8): 2310-2317.
61. Kassim, K., Kamal, N. K. M. and Fadzil, A. H. (2016). Synthesis, characterization and electrochemical studies of 4-methoxybenzoylthiourea derivatives. *Malaysian Journal of Analytical Sciences,* 20(6): 1311-1317.
62. Verma, C., Olasunkanmi, L. O., Obot, I. O., Ebenso, E. E. and Quraishi, M. A. (2016). 5-Arylpyrimido-[4,5-b] quinoline-diones as new and sustainable corrosion inhibitors for mild steel in 1 M HCl: a combined experimental and theoretical approach. *RSC Advances,* 6(19): 15639-15654.

63. Sourav, K. S., Alokdut, D., Pritam, G., Dipankar, S. and Priyabrata, B. (2016). Novel Schiff-base molecules as efficient corrosion inhibitors for mild steel surface in 1 M HCl medium: experimental and theoretical approach. *Physical Chemistry Chemical Physics,* 18(27): 17898-17911.
64. Fouda, A. S., El-Desoky, H. S., Abdel-Galeil, M. A. and Dina, M. (2021). Niclosamide and dichlorphenamide: new and effective corrosion inhibitors for carbon steel in 1M HCl solution. *SN Applied Sciences,* 3(287): 1-20.
65. Ghulamullah, K., Wan, J. B., Salim, N. K., Pervaiz, A., Ladan, M., Ahmed, S. M., Khan, G. M., Rehman, M. A. and Mohamad Badry, A. B. (2017). Electrochemical investigation on the corrosion inhibition of mild steel by Quinazoline Schiff base compounds in hydrochloric acid solution. *Journal of Colloid and Interface Science,* 502: 134-145.
66. Sahin, M., Bilgic, S. and Yilmaz, H. (2002). The inhibition effects of some cyclic nitrogen compounds on the corrosion of the steel in NaCl mediums. *Applied Surface Science,* 195(1-4): 1-7.
67. Nazir, U., Akhter, Z., Janjua, N. K., Asghar, M. A., Kanwal, S., Butt, T. M., Sani, A., Liaqat, F., Hussain, R. and Shah, F. U. (2020). Biferrocenyl Schiff bases as efficient corrosion inhibitors for an aluminium alloy in HCl solution: a combined experimental and theoretical study. *RSC Advances,* 10: 7585-7599.
68. Prabakaran, M., Kim, S. H., Hemapriya, V., Gopiraman, M., Kim, I. S. and Chung, I. M. (2016). Rhus vernicifua as a green corrosion inhibitor for mild steel in 1 M H_2SO_4. *RSC Advances,* 6(62): 57144-57153.
69. Goulart, C. M., Esteves-Souza, A., Martinez-Huitle, C. A., Rodrigues, C. J. F., Maciel, M. A. M. and Echevarria, A. (2013). Experimental and theoretical evaluation of semicarbazones and thiosemicarbazones as organic corrosion inhibitors. *Corrosion Science,* 67: 281-291.
70. Fathabadi, H. E., Ghorbani, M. and Ghartavol, H. M. (2021). Corrosion inhibition of mild steel with tolyltriazole. *Materials Research,* 24(4): 1-16.
71. Ehteshamzadeh, M., Jafari, A. H., Naderi, E. and Hosseini, M. G. (2009). Effect of carbon steel microstructures and molecular structure of two new Schiff base compounds on inhibition performance in 1 M HCl solution by EIS. *Materials Chemistry and Physics,* 113(2-3): 986-993.
72. Govindaraju, K. M., Gopi, D. and Kavitha, L. (2009). Inhibiting effects of 4-amino-antipyrine based schiff base derivatives on the corrosion of mild steel in hydrochloric acid. *Journal of Applied Electrochemistry,* 39: 2345-2352.
73. Satapathy, A. K., Gunasekaran, G., Sahoo, S. C., Amit, K. and Rodrigues, P. V. (2009). Corrosion inhibition by *Justicia gendarussa* plant extract in hydrochloric acid solution. *Corrosion Science,* 51(12): 2848-2856.
74. Ebenso, E. E., Arslan, T., Kandemirli, F., Caner, N. and Love, I. (2010). Quantum chemical studies of some rhodanine azosulpha drugs as corrosion inhibitors for mild steel in acidic medium. *International Journal of Quantum Chemistry,* 110(5): 1003-1018.
75. Solmaz, R. (2010). Investigation of the inhibition effect of 5-((E)-4-phenylbuta-1,3-dienylideneamino)-1,3,4-thiadiazole-2-thiol Schiff base on mild steel corrosion in hydrochloric acid. *Corrosion Science,* 52 (10): 3321-3330.
76. Masahiko, T., Kazushige, I., Yoichi, W., Motohiro, A. and Motomasa, F. (2009). Study of polarization curve measurement method for type 304 stainless steel in BWR high temperature-high purity water. *Journal of Nuclear Science and Technology,* 46(2): 132-141.
77. Chakravarthy, M. P., Mohana, K. N. and Pradeep Kumar, C. B. (2014). Behaviour of nicotinamide derivatives on mild steel in hydrochloric acid solution. *International Journal of Industrial Chemistry,* 5 (19): 1-21.
78. Lorenz, W. J. and Mansfeld, F. (1982). Determination of corrosion rates by electrochemical DC and AC methods. *Corrosion Science,* 21(9-10): 647-672.
79. Youcef, B., Fatiha, B. and Saida, K. (2021). A new corrosion inhibitor for steel rebar in concrete: Synthesis, electrochemical and theoretical studies. *Journal of Molecular Structure,* 1225: 1-17.

80. Abdelghani, M., Lakhdar, S., Abdelkader, H., Ilhem, K. and Embarek, B. (2021). Synthesis, density functional theory study, molecular dynamics simulation and anti-corrosion performance of two benzidine Schiff bases. *Journal of Molecular Structure,* 1235: 1-15.
81. Merah, S., Larabi, L., Abderrahim, O. and Harek, Y. (2017). Study of corrosion inhibition of C38 steel in 1 M HCl solution by polyethyleneiminemethylene phosphonic acid. *International Journal of Industrial Chemistry,* 8: 263-272.
82. Xifeng, Y., Feng, L. and Weiwei, Z. (2019). 4-(Pyridin-4-yl) thiazol-2-amine as an efficient non-toxic inhibitor for mild steel in hydrochloric acid solutions. *RSC Advances,* 9**:** 10454-10464.
83. Laabaissi, T., Benhiba, F., Missioui, M., Rouifi, Z., Rbaa, M., Oudda, H., Ramli, Y., Guenbour, A., Warad, I. and Zarrouk, A. (2020). Coupling of chemical, electrochemical and theoretical approach to study the corrosion inhibition of mild steel by new quinoxaline compounds in 1 M HCl. *Heliyon,* 6(5): 1-15.
84. Quy, H. D., Tran, D. and Nam, P. C. (2021). A Study of 1-benzyl-3-phenyl-2-thiourea as an effective steel corrosion inhibitor in 1.0 M HCl Solution. *Journal of Chemistry,* 2021: 1-14.
85. Parul, D., Quraishi, M. A. and Obot, I. B. (2018). A combined electrochemical and theoretical study of pyridine-based Schiff bases as novel corrosion inhibitors for mild steel in hydrochloric acid medium. *Journal of Chemical Sciences,* 130(8): 1-19.
86. Kumari, P. P., Shetty, P. and Rao, S. A. (2017). Electrochemical measurements for the corrosion inhibition of mild steel in 1 M hydrochloric acid by using an aromatic hydrazide derivative. *Arabian Journal of Chemistry,*10(5): 653-663.
87. Maryam, C., Abdelkarim, C., Hassane, L., Rachid, S., Santosh, L. G., Bhat, K. S., Riadh, M., Ismat, H. A., Mohammad, I. K., Hiroki, S. and Ill-Min, C. (2020). Synthesis and corrosion inhibition evaluation of a new schiff base hydrazone for mild steel corrosion in HCl medium: electrochemical, DFT, and molecular dynamics simulations studies. *Journal of Adhesion Science and Technology,* 34(12): 1283-1314.
88. Zhenzhen, Z., Min, S., Yiming, J., Li, L. and Jin, L. (2016). Effect of tin on the corrosion resistance of 16 Cr ferritic stainless steel in acidic solution and chloride-containing media. *International Journal of Electrochemical Science,* 11: 3963-3975.
89. Zesheng, C., Zheng, L., Kun-Huan, H., Guo-Cheng, H., Yiju, L., Jiaxing, H. and Xianmei, W. (2021). Two diamine Schiff base as a corrosion inhibitor for carbon steel in sulfuric acid solution: Electrochemical assessment and theoretical calculation. *International Journal of Electrochemical Science,* 16: 1-21.
90. Al-Amiery, A. A., Kassim, F. A., Kadhum, A. A. H. and Mohamad, A. B. (2016). Synthesis and characterization of a novel eco-friendly corrosion inhibition for mild steel in 1 M hydrochloric acid. *Scientific Reports,* 6: 1-13.
91. Negm, N. A., Kandile, N. G., Badr, E. A. and Mohammed, M. A. (2012). Gravimetric and electrochemical evaluation of environmentally friendly nonionic corrosion inhibitors for carbon steel in 1 M HCl. *Corrosion Science,* 65: 94-103.
92. Narvaez, L., Cano, E. and Bastidas, D. M. (2005). 3-Hydroxybenzoic acid as AISI 316L stainless steel corrosion inhibitor in a H_2SO_4–HF–H_2O_2 pickling solution. *Journal of Applied Electrochemistry,* 35: 499-506.
93. Ozkır, D., Kayakırılmaz, K., Bayol, E., Gürten, A. A. and Kandemirli, F. (2012). The inhibition effect of Azure A on mild steel in 1 M HCl. A complete study: Adsorption, temperature, duration and quantum chemical aspects. *Corrosion Science,* 56: 143-152.
94. Agrawal, R. and Namboodhiri, T. K. G. (1990). The inhibition of sulphuric acid corrosion of 410 stainless steel by thioureas. *Corrosion Science,* 30(1): 37-52.
95. Zhao, T. P. and Mu, G. N. (1999). The adsorption and corrosion inhibition of anion surfactants on aluminium surface in hydrochloric acid. *Corrosion Science,* 41: 1937-1944.

96. Yaro, A. S., Khadom, A. A. and Ibraheem, H. F. (2011). Peach juice as an anticorrosion inhibitor of mild steel. *Anti-Corrosion Methods and Materials,* 58(3): 116-124.
97. Hegazy, M. A., Hasan, A. M., Emara, M. M., Bakr, M. F. and Youssef, A. H. (2012). Evaluating four synthesized Schiff bases as corrosion inhibitors on the carbon steel in 1 M hydrochloric acid. *Corrosion Science,* 65: 67-76.
98. Goulart, C. M., Esteves-Souza, A., Martinez-Huitle, C. A., Rodrigues, C. J. F., Maciel, M. A. M. and Echevarria, A. (2013). Experimental and theoretical evaluation of semicarbazones and thiosemicarbazones as organic corrosion inhibitors. *Corrosion Science,* 67 (3): 281-291.
99. Muthukrishnan, P., Jeyaprabha, B. and Prakash, P. (2017). Adsorption and corrosion inhibiting behavior of *Lannea coromandelica* leaf extract on mild steel corrosion. *Arabian Journal of Chemistry,* 10: 2343-2354.
100. Adewuyi, A., Gopfert, A. and Wolf, T. (2014). Succinyl amide gemini surfactant from *Adenopus breviforus* seed oil: A potential corrosion inhibitor of mild steel in acidic medium. *Industrial Crops and Products,* 52: 439-449.
101. Ji, G., Shukla, S. K., Dwivedi, P., Sundaram, S. and Ebenso, E. E. (2012). Green *Capsicum annuum* fruit extract for inhibition of mild steel corrosion in hydrochloric acid solution. *International Journal of Electrochemical Science,* 7: 12146-12158.
102. Gopiraman, M., Selvakumaran, N., Kesavan, D. and Karvembu, R. (2012). Adsorption and corrosion inhibition behaviour of N-(phenylcarbamothioyl) benzamide on mild steel in acidic medium. *Progress in Organic Coatings,* 73 (1): 104-111.
103. Ahamad, I., Prasad, R. and Quraishi, M. A. (2010). Inhibition of mild steel corrosion in acid solution by Pheniramine drug: experimental and theoretical study. *Corrosion Science,* 52 (9): 3033-3041.
104. Fazayel, A. S., Khorasani, M. and Sarabi, A. A. (2018). The effect of functionalized polycarboxylate structures as corrosion inhibitors in a simulated concrete pore solution. *Applied Surface Science,* 441: 895-913.
105. Singh, A. K. and Quraishi, M. A. (2010). Inhibiting Effects of 5-Substituted Isatin-Based Mannich Bases on the Corrosion of Mild Steel in Hydrochloric Acid Solution. *Journal of Applied Electrochemistry,* 40 (7): 1293-1306.
106. Yurt, A., Bereket, G., Kivrak, A., Balaban, A. and Erk, B. (2005). Effect of Schiff bases containing pyridyl group as corrosion inhibitors for low carbon steel in 0.1 M HCl. *Journal of. Applied Electrochemistry,* 35: 1025-1032.
107. Saliyan, V. R. and Adhikari, A. V. (2008). Quinolin-5-ylmethylene-3-{[8-(trifluoromethyl)quinolin-4-yl] thio}propanohydrazide as an effective inhibitor of mild steel corrosion in HCl solution. *Corrosion Science,* 50 (1): 55-61.
108. Deyab, M. A. (2015). Egyptian licorice extract as a green corrosion inhibitor for copper in hydrochloric acid solution. *Journal of Industrial and Engineering Chemistry,* 22: 384-389.
109. Abd El-Lateef, H. M., Abu-Dief, A. M., Abdel-Rahman, L. H., Sanudo, E. C. and Aliaga-Alcalde, N. (2015). Electrochemical and theoretical quantum approaches on the inhibition of C1018 carbon steel corrosion in acidic medium containing chloride using some newly synthesized phenolic Schiff bases compounds. *Journal of Electroanalytical Chemistry,* 743: 120-133.
110. Sigircik, G., Tuken, T. and Erbil, M. (2015). Inhibition effectiveness of aminobenzonitrile compounds on steel surface. *Applied Surface Science,* 324: 232-239.
111. Kowsari, E., Payami, M., Amini, R., Ramezanzadeh, B. and Javanbakht, M. (2014). Task-specific ionic liquid as a new green inhibitor of mild steel corrosion. *Applied Surface Science,* 289: 478-486.
112. Zhang, H. H., Qin, C. K., Chen, Y. and Zhang, Z. (2019) Inhibition behaviour of mild steel by three new benzaldehyde thiosemicarbazone derivatives in 0.5 M H_2SO_4: Experimental and computational study. *Royal Society Open Science,* 6(8): 1-19.

Malaysian Journal of Analytical Sciences (MJAS)
Published by Malaysian Analytical Sciences Society

POLYPHENOL-MEDIATED GREEN SYNTHESIS OF ZINC OXIDE AND THEIR ANTIBACTERIAL PROPERTIES: A NOVEL SIZE-CONTROLLED APPROACH

(Sintesis Hijau dengan Mediasi Polifenol dan Ciri Antibakteria Zink Oksida: Pendekatan Kawalan Saiz Baharu)

Neo Zhi Zing[1], Balkis A. Talip[1]*, Soon Chin Fhong[2], Ainun Rahmahwati Ainuddin[3], Hatijah Basri[1]

[1]Faculty of Applied Sciences and Technology,
[2]Microelectronics and Nanotechnology-Shamsuddin Research Centre, Faculty of Electrical and Electronics Engineering
[3]Nano Structure and Surface Modification (NANOSURF), Faculty of Mechanical Engineering and Manufacturing
Universiti Tun Hussein Onn Malaysia, 86400 Parit Raja, Batu Pahat, Johor, Malaysia

**Corresponding author: balkis@uthm.edu.my*

Received: 15 March 2022 ; Accepted: 18 May 2022 ; Published: 25 August 2022

Abstract

The concept of feasibility in green synthesis of zinc oxide (ZnO) nanoparticles has been discussed in many studies. However, size control using volume of plant extracts undermines the process upscaling potential. This study is aimed at improving the repeatability and reproducibility of green synthesis of ZnO by controlling total phenolic content of plant extracts. Leaf extracts of *Camellia sinensis*, *Manilkara zapota* and *Elaeis guineensis* were incorporated at gallic acid equivalent of 100 mgg^{-1} to synthesize ZnO. The phytochemical profile of plant extracts and physical properties of ZnO were determined. In addition, antibacterial activity of ZnO against *Escherichia coli* and *Staphylococcus aureus* was examined. Consistency in particle sizes of ZnO has justified the feasibility of using total phenolic content for size control. Under neutral pH, role of phytochemicals as chelating agents predominated. Under basic condition, complex phytochemicals demonstrated structure-directing effect on ZnO microparticles. The antibacterial strength of ZnO has been reduced by 16 times with reduction in particle size. Meanwhile, the incorporation of phytochemicals enhanced antibacterial activity of ZnO by fourfold. This study proposed that particle size and morphology of ZnO could be controlled through manipulation of total phenolic content of plant extracts and the reaction pH of green synthesis.

Keywords: green synthesis, polyphenol, zinc oxide, size control

Abstrak

Konsep dalam kebolehlaksanaan proses sintesis hijau terhadap nanopartikel zink oksida (ZnO) telah diperjelaskan dalam pelbagai kajian. Namun begitu, kawalan saiz menggunakan isipadu ekstrak tumbuhan menjejaskan potensi dalam meningkatkan skala proses. Kajian ini bertujuan untuk meningkatkan kebolehulangan sintesis hijau ZnO dengan mengawal jumlah kandungan fenolik ekstrak tumbuhan yang digabungkan. Ekstrak daun *Camellia sinensis*, *Manilkara zapota* dan *Elaeis guineensis* telah dicampurkan pada persamaan asid gallik sebanyak 100 mgg^{-1} untuk menghasilkan ZnO. Profil fitokimia ekstrak tumbuhan dan sifat fizikal ZnO telah ditentukan. Di samping itu, aktiviti antibakteria ZnO terhadap *Escherichia coli* dan *Staphylococcus aureus* telah diperiksa. Ketekalan dalam saiz partikel ZnO menjustifikasikan kebolehlaksaan penggunaan jumlah kandungan fenolik untuk kawalan saiz

dalam sintesis hijau. Di bawah pH neutral, peranan fitokimia sebagai agen pengkelat berdominasi. Di bawah keadaan alkali, fitokimia kompleks menunjukkan kesan pengarahan struktur pada mikropartikel ZnO. Kekuatan antibakteria ZnO berkurangan sebanyak 16 kali ganda dengan pengurangan saiz partikel. Sementara itu, penggunaan fitokimia dalam proses sintesis telah meningkatkan aktiviti antibakteria ZnO sebanyak 4 kali ganda. Kajian ini mencadangkan bahawa saiz partikel dan morfologi ZnO boleh dikawal melalui manipulasi jumlah kandungan fenolik ekstrak tumbuhan dan pH tindak balas sintesis hijau.

Kata kunci: sintesis hijau, polifenol, zink oksida, kawalan saiz

Introduction

Nanotechnology is an extensively researched field with an anticipated global market share of approximately 55 million dollars by 2022 [1]. Nanomaterials are categorized depending on their compositions, which includes carbon, organic, inorganic, and composite compounds [2]. Metal oxide nanoparticles fall under composite-based nanomaterials. Metal oxide nanoparticles are synthesized in the laboratory via physical and chemical methods [3,4]. However, the upscaling of two methods suffers from the limitations due to the need for sophisticated technology, high-energy consumption, and the use of toxic chemicals [5]. Recent trends in nano synthesis reveal a growing interest in the utilization of biological materials to react with metal precursors under regulated conditions [6, 7]. The terms "green synthesis" and "biosynthesis" are used interchangeably to describe the synthesis of nanoparticles using biological components derived from bacteria, fungi, algae, and plants [4]. Green synthesis that utilizes plant extracts as the bioreductants is a sustainable route since phytochemicals can be extracted from any plant parts [8]. Due to the essential starting materials which are metal precursors, plant extracts, and water, green synthesis of metal oxide nanoparticles are both cost-effective and environmentally friendly [3, 4]. Apart from being reducing and chelating agents, phytochemicals can act as capping agents to regulate the morphology and particle size of nanoparticles [3, 4].

Zinc oxide (ZnO) nanoparticles have gained attention for a wide range of applications due to their distinctive physical and chemical properties. They have been described as a photocatalytic adsorbent for water treatment, gas sensors, solar cells, and an active component in cosmetics [9]. Meanwhile, the biocidal action of ZnO nanoparticles against harmful microbes has piqued the interest of researchers in commercializing them as preservatives and biocidal products [10, 11]. The versatility of ZnO nanoparticles has prompted the development of a green synthetic pathway that incorporates different plant extracts. However, the incorporation of plant extracts is expressed in weight, volume, or percentage, with no quantitative information on the phytochemicals present in the reaction. Xu et al. [12] emphasized that plant extract concentration is one of the major manipulating factors in the green synthesis of ZnO nanoparticles. Even though a trend was observed in which the size of nanoparticles decreased as the concentration of plant extract used increased, the method was not replicable because the unit employed to express the incorporation of plant extract was empirical. Lack of information in reaction mechanisms also limit the effort in advancing green synthesis. It is ideal for controlling the biologically active compounds present in the extracts. Polyphenols are the most prevalent phytochemicals in the plant kingdom [13]. They are regarded as a marker group for the quality evaluation of medicinal plants due to their significant roles in the biological activity of extracts [14]. In fact, a study has been carried out to determine the roles of isolated phenolic acids in the green synthesis of metal nanoparticles [15].

This work is fundamental research undertaken with the goal of improving the repeatability and reproducibility of green synthesis for ZnO size control. This study was also intended to elucidate the reaction mechanisms of the green synthesis of ZnO.

Materials and Methods

Materials

Commercial *Camellia sinensis* (black tea leaves) were purchased from local market while leaves of *Manilkara zapota* (sapodilla) and *Elaies guineensis* (oil palm) were obtained from local plantation. Folin-Ciocalteu (FC) reagent, sodium carbonate (Na_2CO_3), benzene, ammonia solution, methanol, aluminium chloride

($AlCl_3$), chloroform, sulphuric acid (H_2SO_4), and zinc oxide (ZnO) were bought from Merck (Darmstadt, Germany). Gallic acid, sodium hydroxide (NaOH), zinc nitrate hexahydrate [$Zn(NO_3)_2.6H_2O$], and resazurin sodium salt were purchased from Sigma-Aldrich Co. (St. Louis, MO, USA). Wagner's solution was purchased from Avondale Laboratories (Banbury, England). Meanwhile, hydrochloric acid (HCl) and ferric chloride ($FeCl_3$) were obtained from QRëC (Selangor, Malaysia) and R&M Chemicals (Selangor, Malaysia) respectively.

Bacterial culture of *Escherichia coli* ATCC 8739 and *Staphylococcus aureus* ATCC 25923 were purchased from Remel Europe (Dartford, England). The McFarland Standard was supplied by ThermoFisher Scientific (Massachusetts, USA). Mueller Hinton Broth (MHB) and Mueller Hinton Agar (MHA) were from Condalab (Madrid, Spain). Meanwhile, oxacillin sodium salt monohydrate and ampicillin sodium salt were obtained from HiMedia Laboratories (Mumbai, India).

Aqueous extraction of phytochemicals

Commercial black tea leaves were used as-is. Fresh *chikoo* leaves and oil palm leaves were cleaned with tap water and dried overnight in convection oven at 65 ˚C (UFE500, Memmert GmbH + Co.KG, Germany). Dried plant leaves were ground using kitchen blender. Aqueous extraction method of Mercado-Mercado et al. [16] was employed with modification. Samples were decocted in deionized water through double boil method at 85 ˚C for 15 min. The decoction ratio was 1 part ground leaves to 10 parts deionized water. Decocted samples were filtered through muslin cloth. Then, the aqueous extracts were centrifuged at 1,500 rpm for 1 min at room temperature (Centrifuge 5804 R, Eppendorf, Germany). The aqueous extracts were filtered through Whatman No. 1 filter paper. Then, the crude plant extracts were dried in convection oven at 65 ˚C (UFE500). Dried crude plant extracts were ground into fine powder using pestle and mortar. Sample codes for the crude plant extracts were BTLE (black tea leaf extract), CLE (*chikoo* leaf extract) and OPLE (oil palm leaf extract).

Determination of total phenolic content

Folin-Ciocalteu assay was performed with reference to method of Dudonné et al. [17]. The reaction began by mixing 400 µL aqueous sample solution with 2.0 mL of FC reagent (diluted to 10-fold in deionized water). After 5 minutes, 1.6 mL of 7.5% Na_2CO_3 solution was added into the mixture and mixed thoroughly. The mixture was allowed to react for 1 h at room temperature. Absorbance value was measured at 765 nm using UV-Vis spectrophotometer (Spectrophotometer T60 U, PG Instruments Ltd., UK). All tests were performed at triplicates. The calibration curve was plotted using aqueous solution of gallic acid.

Identification of organic compounds

The organic compounds present in crude plant extracts were identified using Attenuated Total Reflection - Fourier transform infrared (ATR-FTIR) spectroscope (Spectrum Two, Perkin Elmer, USA). The FTIR spectra of the extracts were examined by placing powder of crude plant extract directly onto the crystal plate of ATR-FTIR spectroscope. The measurement was taken in the range of 4000-400 cm^{-1} with a resolution of 4 cm^{-1}.

Screening for phytochemicals

Aqueous solutions of BTLE, CLE and OPLE were prepared at concentration of 1 $mgmL^{-1}$ for the screening of phytochemicals. The aqueous plant extracts were screened for the presence of alkaloids, anthraquinones, flavonoids, saponins, steroids, tannins, and terpenoids.

Wagner's test was used to determine the presence of alkaloids. Few drops of Wagner's solution were added to the aqueous plant extracts. Formation of brown precipitate indicated the presence of alkaloid [18]. The presence of anthraquinones was tested by adding 10 mL benzene to 5 mL aqueous plant extracts. Then, 10 mL 10% ammonia solution was added to the mixture. The mixture was shaken vigorously. Presence of anthraquinones was indicated by pink, violet or red colour solution [19].

The presence of flavonoids was examined with Shinoda's test, aluminium chloride test and alkaline reagent test. In Shinoda's test, 4 mL aqueous plant

extract was mixed with 1.5 mL 50% methanol. Magnesium metal was added to the mixture followed by the addition of few drops of fuming HCl. Changes of colour of mixture to red indicated the presence of flavonoids [20]. In aluminium chloride test, 5 mL aqueous plant extract was added with 1 mL 1% $AlCl_3$ solution. The solution was shaken vigorously. Presence of yellow precipitates indicated presence of flavonoids [21]. Meanwhile, alkaline reagent test was performed by mixing 2 mL 2.0% NaOH solution with aqueous plant extract. In the presence of flavonoids, concentrated yellow solution would turn colourless with addition of 2 drops of 2 M HCl [19].

The presence of saponins in plant extracts was examined using method of El Aziz et al. [22] with modifications. Five millilitres (5 mL) aqueous plant extract was vortexed for 2 min. Presence of saponins was confirmed by persistent appearance of foam lasting for at least 15 min. Salkowski's test was performed to confirm the presence of steroids. Two millilitres (2 mL) chloroform and 2 mL concentrated H_2SO_4 were added to 5 mL aqueous plant extract. Red colouration in lower chloroform layer indicated presence of steroids [19]. Presence of tannins was indicated by greenish black colouration formed from reaction between 5 mL aqueous plant extract and 1 mL 5% $FeCl_3$ solution [23]. Screening for the presence of terpenoids commenced by mixing 2.5 mL aqueous plant extract with 2.5 mL chloroform. The mixture was evaporated to dryness. Then, 3 mL concentrated H_2SO_4 was added and boiled for 10 min. A grey solution would form in the presence of terpenoids [21].

Synthesis of ZnO

Synthesis method of Top et al. [24] was adapted with modification. The combinations of reaction mixture and sample codes are summarized in Table 1.

Table 1. Combinations of reaction mixture and sample codes of zinc oxide

Reaction Mixture	Molar Ratio of $Zn(NO_3)_2.6H_2O$ to NaOH	Sample Codes of ZnO with Reference to Incorporated Crude Plant Extract		
		BTLE	CLE	OPLE
B	1.0 : 2.0	$ZnO_{BTLE(B)}$	$ZnO_{CLE(B)}$	$ZnO_{OPLE(B)}$
C	1.0 : 1.8	$ZnO_{BTLE(C)}$	$ZnO_{CLE(C)}$	$ZnO_{OPLE(C)}$
D	1.0 : 1.6	$ZnO_{BTLE(D)}$	$ZnO_{CLE(D)}$	$ZnO_{OPLE(D)}$
E	1.0 : 1.4	$ZnO_{BTLE(E)}$	$ZnO_{CLE(E)}$	$ZnO_{OPLE(E)}$
F	1.0 : 1.2	$ZnO_{BTLE(F)}$	$ZnO_{CLE(F)}$	$ZnO_{OPLE(F)}$
G	1.0 : 1.0	$ZnO_{BTLE(G)}$	$ZnO_{CLE(G)}$	$ZnO_{OPLE(G)}$
Control sample				
A	1.0 : 2.0		$ZnO_{control(A)}$	
H	1.0 : 1.0		$ZnO_{control(H)}$	

The pH of reaction mixture was measured using pH meter (pH 700, Eutech Instrument, USA). The concentration of crude plant extracts employed for green synthesis was computed from volume of gallic acid equivalent (GAE) based on the results of total phenolic content (TPC) obtained prior to synthesis. All crude plant extracts were added at 100 mg GAE g^{-1}. The reaction mixtures were incubated in incubator shaker at 60 ˚C for 1 hour with constant agitation (KS 4000 i control, IKA, Germany). After 1 hour, the precipitates were collected through centrifugation followed by twice washing with deionized water (Centrifuge 5804 R). The collected precipitates were dried in convection oven at 60 ˚C for 24 hours (UFE500). Calcination was

conducted at 500 ˚C for 3 hours (ELF 11/14 Chamber Furnace, Carbolite Gero, UK). Each synthesis pathway was performed in triplicates. Representative samples were prepared for further analysis.

Determination of minimum inhibitory concentration and minimum bactericidal concentration

The viability of *E. coli* and *S. aureus* under exposure to different concentrations of ZnO was determined through Resazurin Cell Viability Test using method by He et al. [25] with modification. Bacterial culture was grown in MHB and incubated in incubator shaker at 37 ˚C for 24 hours with constant agitation (KS 4000 i control). The overnight bacterial cells were suspended in sterilized 0.9 % saline solution and adjusted to 2.0 McFarland Standard and 3.0 McFarland Standard for *S. aureus* and *E. coli* respectively.

Samples of ZnO were suspended in sterilized distilled water at concentration of 8 $mgmL^{-1}$. The suspension was mixed thoroughly with vortex mixer for 1 min (MX-S, Dragon Laboratory Instruments Ltd., China). The samples of ZnO were deployed with twofold dilution at starting concentration of 8 $mgmL^{-1}$ for *S. aureus* and 16 $mgmL^{-1}$ for *E. coli*. To each well containing 100 µL ZnO suspension, 100 µL bacterial suspension and 20 µL 0.02% resazurin solution were added. Positive control (without ZnO samples) and negative control (without bacterial suspension) were included in each plate. The 96 well microtiter plate was incubated at 37 ˚C for 24 hours (INB500, Memmert GmbH + Co.KG, Germany). To compare effectiveness of ZnO samples and commercial antibiotics against the tested strains of bacteria, Resazurin Cell Viability Test was performed by employing ampicillin and oxacillin at starting concentration of 8 $mgmL^{-1}$ under the same protocol.

Colour changes were observed and recorded after incubation period. The lowest concentration of ZnO samples that inhibited visible growth of microorganisms after overnight incubation was considered the minimum inhibitory concentration (MIC). A loopful of aliquot from the MIC well was transferred and streaked on MHA. The streak plates were incubated at 37 ˚C for 24 hours. Viability of bacterial cells was observed after 24 hours for the determination of bactericidal or bacteriostatic properties at MIC of ZnO samples. All tests were conducted at triplicates.

Statistical analysis

The results of replicated tests were expressed as mean value with standard deviations. Comparison between means of independent groups was analysed by one-way analysis of variance (ANOVA) followed by Tukey's honestly significant difference (HSD) post hoc test ($p<0.05$). Correlation analysis was performed using Pearson's correlation coefficient (R) in bivariate linear correlations ($p<0.01$). All statistical analysis was computed using IBM SPSS Statistics 22.0.

Results and Discussion

Morphology, particle size and elemental composition of ZnO

The designed pathways resulted in the synthesis of nano- and microsized zinc oxide (ZnO). In the current study, ZnO particles smaller than 100 nm were referred to as ZnO nanoparticles, while those larger than this size limit were defined as ZnO microparticles. Table 2 summarizes the particle sizes of ZnO obtained from the study. Morphologies of ZnO nanoparticles and ZnO with defined microstructures are shown in Figure 1. Elemental analysis validated the purity of all samples.

Reaction mixtures E, F, and G with the incorporation of CLE and OPLE and reaction mixture G with the incorporation of BTLE were capable of producing ZnO nanoparticles. The irregularly shaped nano- and micro-particles agglomerated into microstructures with no defined morphology as the molar ratio of $Zn(NO_3)_2$ to NaOH increased. Zinc oxide microparticles in the shape of microflower were obtained using the reaction mixtures control(A), BTLE(B), and CLE(B), while ZnO in the shape of spheroid microstructure was obtained from reaction mixture OPLE(B). It is important to highlight that the morphologies and size ranges of $ZnO_{control(A)}$ and $ZnO_{control(H)}$ are similar to those of their respective green synthesis counterparts.

The particle sizes of ZnO decreased within the crude plant extract group in response to a reduction in the molar ratio of $Zn(NO_3)_2$ to NaOH and a simultaneous increase in the ratio of plant extracts used at a

concentration of 100 mg GAE g^{-1}. Likewise, standard errors, which represent the range of particle size distribution, decreased along with the trend. However, the sample of $ZnO_{CLE(G)}$ contained a heterogeneous mixture of nanoparticles and microparticles. As the condition was an isolated case that was not observed in other samples produced under the same conditions ($ZnO_{BTLE(G)}$, $ZnO_{OPLE(G)}$, $ZnO_{control(H)}$), particle size measurements were only performed on nanoparticles that were not arranged into microstructures.

Table 2. Particle sizes and morphologies of zinc oxide

Reaction Mixture	**Shape and Morphology**	**Particle Size, nm**		
		ZnO_{BTLE}	**ZnO_{CLE}**	**ZnO_{OPLE}**
B	Microflower (ZnO_{BTLE} and ZnO_{CLE}); spheroid (ZnO_{OPLE})	Length: 838.97 ± 195.97[a]; width: 608.80 ± 112.67[a]	Length: 1736.63 ± 405.47[b]; width: 885.43 ± 196.06[b]	Length: 943.30 ± 118.61[a]; width: 719.53 ± 176.59[a]
C	Agglomerated microparticles	214.02 ± 39.69[a]	317.68 ± 48.30[b]	217.40 ± 42.99[a]
D	Agglomerated microparticles	159.30 ± 46.92[a]	239.72 ± 48.63[b]	154.92 ± 42.59[a]
E	Agglomerated microparticles	149.33 ± 32.00[a]	92.55 ± 23.89[b]	81.15 ± 26.17[b]
F	Agglomerated microparticles	121.80 ± 32.02[a]	71.22 ± 21.65[b]	80.62 ± 27.37[b]
G	Nanoparticles	70.77 ± 21.74[a]	41.87 ± 15.52[b]	63.80 ± 21.33[a]
A	Microflower	Length: 1193.30 ± 193.31; width: 700.47 ± 145.09		
H	Nanoparticles	81.17 ± 21.02		
Analytical grade ZnO	Nanorods	Length: 196.80 ± 79.93; width: 81.20 ± 29.65		

[a,b] denote significant difference for data within row ($p<0.05$)

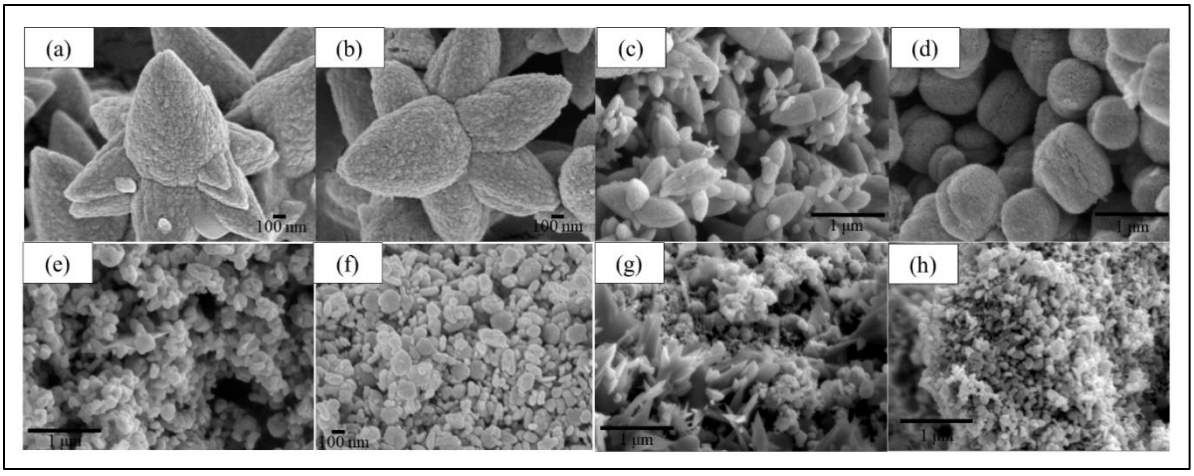


Figure 1. FESEM images of ZnO observed under magnification of 50,000x (a) $ZnO_{control(A)}$, (b) $ZnO_{BTLE(B)}$, (c) $ZnO_{CLE(B)}$, (d) $ZnO_{OPLE(B)}$, (e) $ZnO_{control(H)}$, (f) $ZnO_{BTLE(G)}$, (g) $ZnO_{CLE(G)}$, (h) $ZnO_{OPLE(G)}$

Meanwhile, particle sizes of ZnO were found to differ significantly (p <0.05) across the group of crude plant extracts. However, a statistically significant linear relationship with the trend in particle size reduction was observed for ZnO synthesized with the incorporation of crude extracts of black tea and oil palm leave (p <0.01). A positive linear relationship with a strong magnitude of association was observed (r=0.997). It is deduced that there is a potential in using the total phenolic content of plant extracts for size control of ZnO through the proposed pathway when different plant extracts are employed.

Moreover, the particle sizes of representative samples from the triplicate synthesis procedure showed no significant difference (p >0.05), implying that the synthesis pathway is repeatable. The designed protocol is feasible for size control in order to achieve consistency in the particle size of ZnO.

Phytochemical analysis of the crude plant extracts

The total phenolic content (TPC) of crude plant extracts differed significantly (p <0.05), with CLE containing the highest phenolic compounds (1.07 ± 0.13 mg GAE g^{-1}), followed by BTLE (0.87 ± 0.09 mg GAE g^{-1}) and OPLE (0.37 ± 0.10 mg GAE g^{-1}). During the green synthesis incorporation, significant differences in TPC of crude plant extracts had translated to significant weight differences. The OPLE was incorporated at the highest weight per volume.

A broad band recorded between 3650 and 3250 cm^{-1}, accompanied by the absorption bands between 1600 and 1300 cm^{-1} and 1200 and 1000 cm^{-1} indicated the presence of hydrogen bonds [26]. Grasel et al. [27] reported that bands in 3500 to 3100 cm^{-1} resulted from hydroxyl (–OH) group stretching, were common characteristics of polyphenolic compounds. The aromatic ring stretching group frequency was determined to be between 1615 and 1580 cm^{-1} [26, 28]. Absorption peaks around 2970-2950 cm^{-1} and 2880-2860 cm^{-1} were evidences of saturated aliphatic groups [28]. All tested plant extracts showed absorption peaks in the specified wavenumbers ranges except for alkanes (Figure 2). The spectra provided pieces of evidence for the presence of phenolic compounds with –OH and –COOH side chains in the samples.

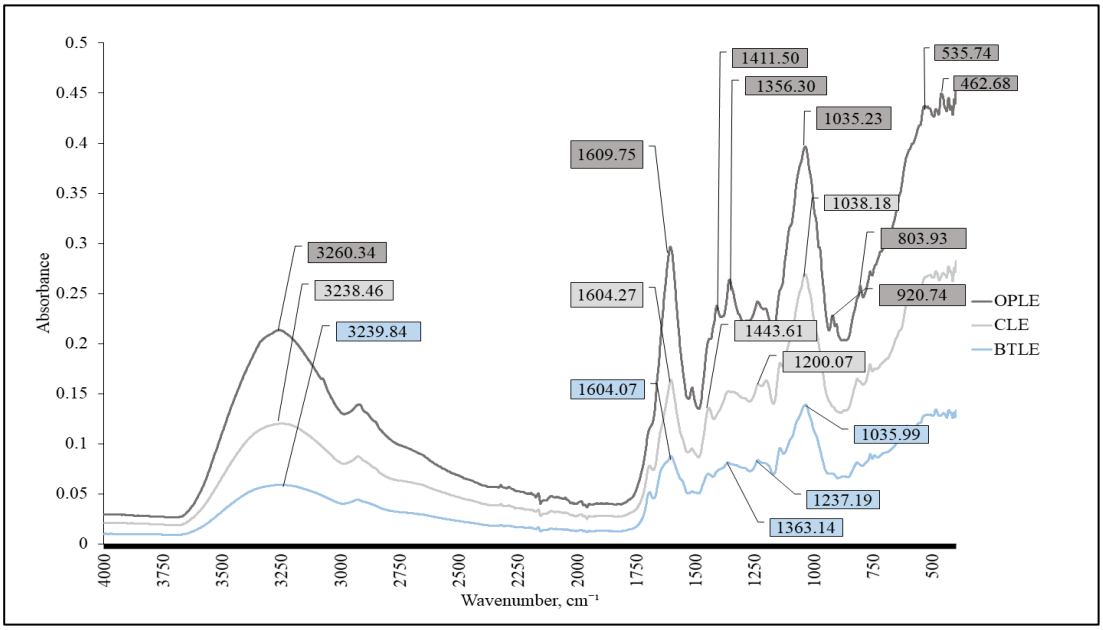


Figure 2. The crude plant extracts were composed primarily of phenolic compounds. OPLE registered the most number of peaks in the IR spectra. It is inferred to be composed of relatively more complex organic compounds compared to CLE and OPLE

Phytochemicals of OPLE were speculated to be larger organic molecules compared to those of BTLE and CLE. The presence of amine groups (C-N) were only observed in OPLE samples at 920.74 cm^{-1} and 535.74 cm^{-1}. Moreover, absorption bands less than 1000 cm^{-1} were only observed in OPLE. Bands at around 750-500 cm^{-1} were associated with alkenes =C-H bending [29]. The alkane C-C bending vibrations were manifested as absorption peak below 500 cm^{-1} [29]. In addition, the presence of absorption bands at wavenumbers less than 1000 cm^{-1} was claimed to be an indicator for the presence of isoprenoid [30,31]. The presence of isoprenoid in OPLE was speculated.

The phytochemical composition of plant extracts is summarized in Table 3. Oil palm leaf extract was the only crude plant extract that was screened positive for alkaloids. In addition, the absorption peaks at wavenumber 920.74 and 535.74 cm^{-1}, which were assigned to N-CH_3 symmetric stretching and C-N-CH_3 deformation of alkaloids [32], were observed in IR spectrum of OPLE. Although the IR fingerprint for isoprenoid was only observed in OPLE's IR spectrum, saponins, which is a form of polar isoprenoids, were found to be present in all crude extracts.

By combining the observations from the Folin-Ciocalteu assay and FTIR analyses, it was determined that all plant extracts were primarily composed of phenolic compounds. Overall, in comparison to both BTLE and CLE, OPLE contains relatively more complex phytochemicals, made up of phenolic compounds with hydroxyl, carboxyl, and amine groups. The complexity of phytochemicals in OPLE had contributed to the inconsistency in process output, in terms of morphologies of ZnO, across different crude plant extracts.

Table 3. Phytochemical compounds present in aqueous plant extracts

Phytochemical Compounds	**Type of Aqueous Plant Extract**		
	BTLE	**CLE**	**OPLE**
Alkaloids	-	-	+
Anthraquinones	-	-	-
Flavonoids			
- Shinoda' test	-	-	-
- Aluminium chloride test	-	-	-
- Alkaline reagent test	-	-	-
Saponins	+	+	+
Steroids	+	+	-
Tannins	+	+	+
Terpenoids	+	-	+

+ denotes present, - denotes absent

Effects of pH and concentration of plant extracts on the formation of ZnO

The pH of reaction mixtures did not differ significantly when the molar ratio of $Zn(NO_3)_2$ to NaOH was changed from 1.0:1.0 to 1.0:1.8 (p >0.05). The pH of the reaction mixtures was determined to be neutral (Table 4). However, significant difference was observed when the molar ratio of the reaction mixture was raised to 1.0:2.0 (p <0.05), where the pH increased to 11.44. It is worth noting that despite bearing no pH difference, a trend of particle size reduction was observed from reaction mixtures C to G. The trend was attributed to the additive effect of phytochemical capping properties, in addition to the size reduction effect of reaction pH

Table 4. The pH of reaction mixtures

Molar ratio of $Zn(NO_3)_2$ to NaOH	**pH**
1.0 : 2.0	11.44 ± 0.25^a
1.0 : 1.8	7.59 ± 0.24^b
1.0 : 1.6	7.46 ± 0.02^b
1.0 : 1.4	7.34 ± 0.03^b
1.0 : 1.2	7.23 ± 0.01^b
1.0 : 1.0	7.16 ± 0.03^b

[a,b] denote significant difference (p <0.05)

Studies showed that the degree of organization of ZnO nanoparticles increases with an increase in pH of reaction mixture [33, 34]. Meanwhile, studies in green synthesis of ZnO nanoparticles revealed that increasing the pH resulted in particle size increment despite the acclaimed function of plant extracts as capping agents [35-37].

The observations necessitate the answers to the following questions, 'Is the addition of base necessary in green synthesis?', 'Would the addition of base negate the effect or alter the role of plant extracts?' and 'What is the advantage of ZnO produced through green synthesis over the one produced through direct reaction between $Zn(NO_3)_2$ and NaOH when both exhibit the same morphology?'.

Proposed mechanisms for the green synthesis of ZnO nanoparticles

Plant extracts are widely accepted to act as reducing agents in green synthesis [38,39]. In the current work, no precipitation was observed when $Zn(NO_3)_2$ and plant extracts were used as the only process inputs. In fact, precipitation was observed upon mixing of NaOH and $Zn(NO_3)_2$ in the absence of phytochemicals. Additionally, it was observed that precipitates bearing the color of the incorporated plant extracts were produced following the addition of NaOH. Fine white ZnO powder was produced after calcination.

A review of recent studies reveals that all three pathways illustrated in Figure 3 are employed and classified as green synthesis. Pal et al. [7], Suresh et al. [38] and Sharmila et al. [40] implemented pathway B to produce ZnO nanoparticles, while Matinise et al. [41] adopted pathway C. Meanwhile, pathway A involves the addition of NaOH as an alkalizing agent or precipitating agent [42-44]. To elucidate the reaction mechanism, emphasis was made on the nature of divalent zinc (Zn^{2+}) ions and phytochemicals. Divalent zinc ion acts as an intermediate Lewis acid, which can interact with a wide range of ligand bases to form Zn complexes with up to six coordination numbers [45,46,47]. The nature of zinc relies on the redox potential and pH values, where it exists as hydrated zinc complexes in acidic conditions and as zinc hydroxo complexes in alkaline conditions [46].

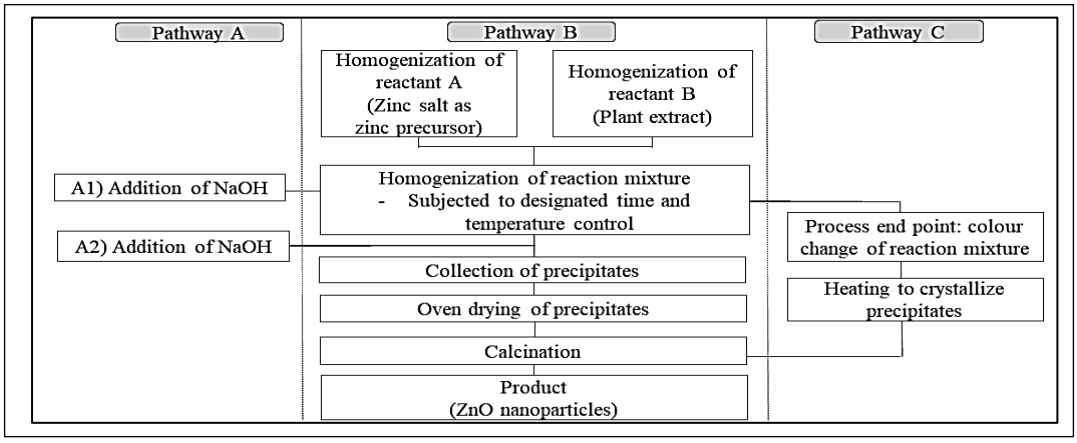


Figure 3. NaOH acts as alkalizing agent in pathway A1 and precipitating agent in pathway A2. Process endpoints of pathway A1, A2 and B are indicated by precipitation of zinc salts while that of pathway C is indicated by colour changes of reaction mixture.

Zinc oxide nanoparticles are formed in pathways B and C through the complexation of zinc with phytochemicals. The organic compounds are vaporized by calcining the zinc complexes. Based on the reaction mechanism, it is more precise to classify the phytochemicals as chelating agents rather than reducing agents. Since the mechanisms do not involve the nucleation and growth of ZnO particles, the nanoparticles produced should be smaller in size. However, the complexity of phytochemicals limits the repeatability of the pathway. Fluctuation in phytochemical quality would have a substantial impact on process yield and overall process duration.

Despite having a similar process flow with pathway B, pathway A2 requires the addition of NaOH at the end of synthesis. The acidity value (pKa) of the complex is determined by the acid-base properties of the ligand, where strong binding results in an increment of pKa [46]. A stable complex would precipitate at higher pH. The addition of NaOH is essential for the precipitation of Zn complexes after being subjected to a specific time and temperature control.

Present study employed pathway A1, which involved adding NaOH to the one-pot mixture of Zn precursor and plant extracts. The reducing properties of phytochemicals depend on their antioxidative activities. An antioxidant compound exhibits its properties via the hydrogen atom transfer (HAT) reaction and transfer reaction of a single electron (SET) [48]. Cited as reducing agents, the phytochemicals are favorable for their electron transfer tendency that would result in the formation of Lewis bases for Zn complexation. As per this study, deprotonated plant phenolic compounds were targeted as the main driving force in the formation of ZnO nanoparticles.

Depending on their pKa, phenolic compounds in liquid media exist as either weak acids or weak bases. Generally, the pKa of phenolic compounds lies between pH 8 and pH 10 [49]. When the pH of the surrounding falls below 8, the phenolic compounds exist as weak acids. Without the help of an alkalizing agent, a range of activation energies must be overcome for the –OH group of phenolic compounds to deprotonate. In present work, the addition of NaOH is crucial to accelerate the green synthesis of ZnO nanoparticles by aiding in phytochemical deprotonation.

In addition to assisting deprotonation of phytochemicals, an increase in reaction pH promotes the deprotonation of hydrated zinc complexes. This condition has a substantial effect on predominant species and the roles of phytochemicals. According to Krężel et al. [46], the deprotonation of hydrated zinc complexes begins at pH 7.8, and zinc hydroxo complexes predominate when the pH of the solution surpasses 8. The reaction ends at pH 11.8, with the final product being $[Zn(OH)_4]^{2-}$ complex [46]. Equations 1 – 4 represent the progression of hydrolysis and deprotonation.

$$[Zn(H_2O)_6]^{2+} + H_2O \rightleftharpoons [Zn(H_2O)_5(OH)]^{+} + H_3O^{+} \quad (1)$$

$$[Zn(H_2O)_5(OH)]^{+} + H_2O \rightleftharpoons [Zn(H_2O)_4(OH)_2] + H_3O^{+} \quad (2)$$

$$[Zn(H_2O)_4(OH)_2] + H_2O \rightleftharpoons [Zn(H_2O)_3(OH)_3]^{-} + H_3O^{+} \quad (3)$$

$$[Zn(H_2O)_3(OH)_3]^{-} + H_2O \rightleftharpoons [Zn(OH)_4]^{2-} + 2H_2O + H_3O^{+} \quad (4)$$

According to Krężel et al. [46], the precipitation of the uncharged $[Zn(H_2O)_4(OH)_2]$ results in the formation of an amorphous $Zn(OH)_2$ and five distinct types of $Zn(OH)_2$ crystals. The crystal forms of $Zn(OH)_2$ are unstable [46, 50], and their decomposition leads to the formation of ZnO nuclei. Meanwhile, $[Zn(OH)_4]^{2-}$ serves as growth template for the growth of ZnO nuclei in addition to decomposing into ZnO.

The pH profile of the reaction mixture reveals that the formation of ZnO nuclei occurs through the outlined mechanisms, with reaction mixtures A and B producing unstable $[Zn(OH)_4]^{2-}$ while reaction mixtures C, D, E, F, and G producing unstable $Zn(OH)_2$ crystals. According to LaMer's mechanism, this phase is critical for size control of ZnO nanoparticles since a high nucleation rate during a protracted reaction will result in the formation

of larger particles. This is evidenced by the fact that the particle sizes of ZnO generated from reaction mixtures A and B were larger than those of the other reaction mixtures. This reaction mechanism explained the effect of pH and NaOH concentration on the particle size of ZnO.

The roles of phytochemicals in green synthesis are inferred to be dependent on the reaction pH and the dominant species in the reaction mixture. In present study, the roles of phenolic compounds were defined with reference to particle sizes of green synthesized ZnO. When NaOH is added to the one-pot mixture, the role of phytochemicals as ligand bases for the formation of zinc complexes is expected to be diminished, while their role as capping agents, which stabilize the ZnO nuclei, becomes prominent under basic conditions. Nevertheless, increasing the pH of the solution would aid in the deprotonation of phenolic compounds [49]. Phenoxide ions could interact with the Zn hydroxo complexes to achieve ligand substitution. However, the role of phytochemicals as capping agents was more significant in this investigation, as demonstrated by the morphological differences between $ZnO_{control(A)}$ and $ZnO_{OPLE(B)}$. Meanwhile, when the concentration of NaOH used was relatively low, the involvement of phytochemicals as ligand bases for the formation of zinc complexes predominated in pathway A1. The condition was demonstrated by the decrement in particle sizes of ZnO as reaction pH was reduced. It is important to note that the addition of NaOH in pathway A1 does not negate the function of phytochemicals since deprotonation of phytochemicals is required for subsequent reactions.

In present study, phytochemicals and hydrated zinc complexes competed for NaOH to achieve deprotonation. Under basic conditions, the moiety rich in $[Zn(OH)_4]^{2-}$ complex ions will facilitate the growth of ZnO along the [0001] direction [50, 51]. In the meantime, the deprotonated phytochemicals with negative charges will be drawn to the Zn polar plane [0001], as well. A high concentration of $[Zn(OH)_4]^{2-}$ led to anisotropic growth and thus the formation of ZnO microflowers. As the concentration of $[Zn(OH)_4]^{2-}$ complex ions decreased, the adsorption of deprotonated phytochemicals on Zn polar plane became dominant.

The structure-directing effect of OPLE, as demonstrated by $ZnO_{OPLE(B)}$, could be attributed to its phytochemical complexity. It is speculated that the higher dosage of OPLE, which exhibited lower TPC, contributed to a higher content of amphiphilic phytochemicals in the aqueous plant extracts of green synthesis. This condition resulted in the isotropic growth of ZnO owing to the uniform adsorption by the phytochemicals.

Previously, the terms 'reducing agent', 'chelating agent', 'capping agent', and ‘structure-directing agent' were used interchangeably, and the definitions were ambiguous. Deprotonated phytochemical, which is a form of ligand base, is structurally a chelating agent when it interacts with either zinc hydroxo complexes or ZnO nuclei in the green synthesis. In the event that Zn complexes are formed, deprotonated phytochemicals shall be referred to as chelating agents; meanwhile, when deprotonated phytochemicals interact with ZnO nuclei to achieve electrostatic stabilization, they shall be defined as capping agents for precision. A structure-directing agent, on the other hand, possesses a structure-directing effect to control the growth of the nanoparticles [52]. It is illustrated in Figure 4 that nucleation and growth of ZnO nanoparticles occur via pathways A1 and A2, whereas the formation of Zn complexes occurs via pathways C and B.

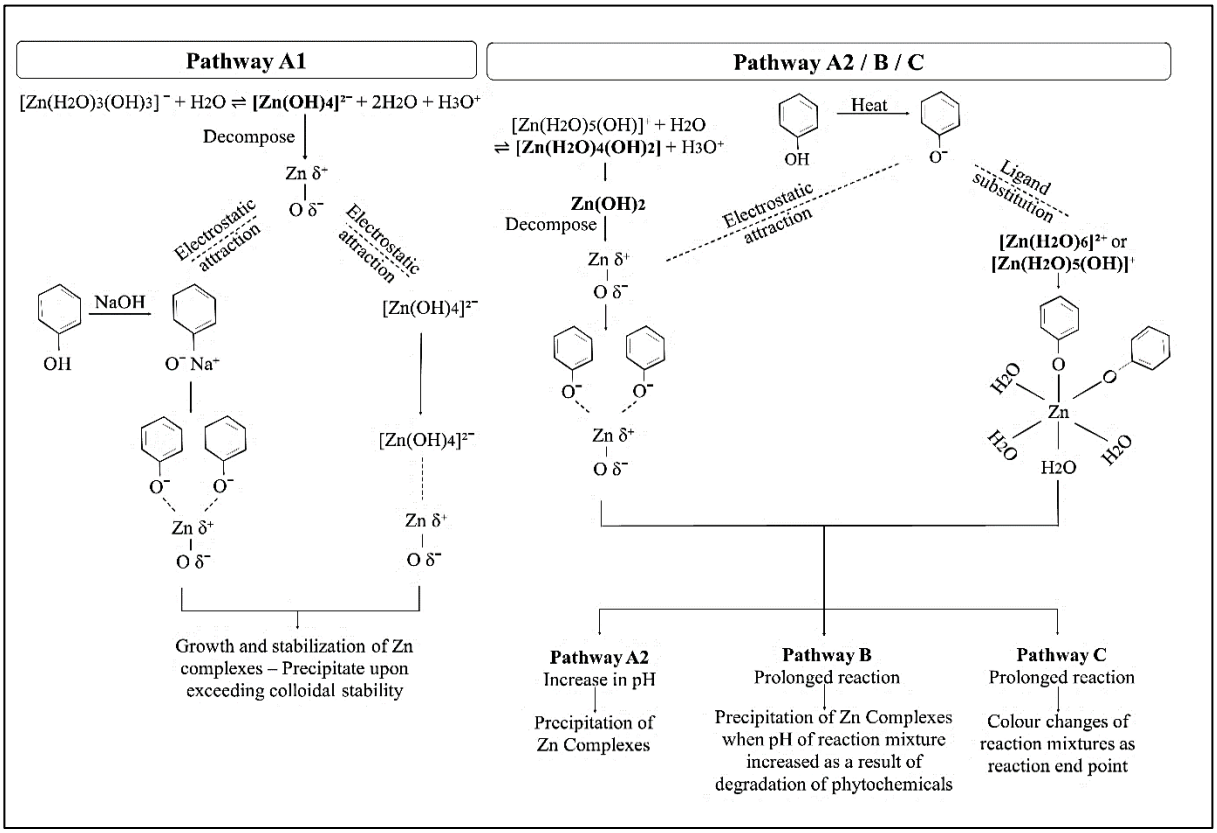


Figure 4. Deprotonated phytochemicals act primarily as capping agent when $[Zn(OH)_4]^{2-}$ is the predominant species while their roles as chelating agent are more prominent at neutral pH where Zn complexes are the predominant species.

Antibacterial strength of the green synthesized ZnO

Antibacterial activity of ZnO samples against *Staphylococcus aureus and Escherichia coli* was examined. There was a lack of antibacterial action against the latter. The minimum inhibitory concentration (MIC) of ZnO samples against *S. aureus* decreased with increasing ZnO particle size (Table 5). However, a slight dip was observed from $ZnO_{CLE(E)}$ to $ZnO_{CLE(F)}$. The condition was attributed to the colloidal stability of ZnO, which was dependent on the interplay of particle sizes and surface properties. It is worth noting that the antibacterial strength of ZnO synthesized through the incorporation of plant extracts ($ZnO_{BTLE(B)}$, $ZnO_{CLE(B)}$, and $ZnO_{OPLE(B)}$) were superior to that of $ZnO_{control(A)}$. In addition, the ZnO microstructures exhibited stronger antibacterial effects against *S. aureus* when compared to ampicillin and oxacillin. The two antibiotics showed no antibacterial activity when deployed at the same starting concentrations of 8 $mgmL^{-1}$ under the same experimental setup.

Table 5. Minimum inhibitory concentration of zinc oxide samples against *Staphylococcus aureus*

Reaction mixture	Minimum inhibitory concentration, mgmL^{-1}		
	ZnO_{BTLE}	**ZnO_{CLE}**	**ZnO_{OPLE}**
B	0.0313*	0.1250	0.1250*
C	0.2500*	0.2500	0.2500
D	1.0000	0.2500*	0.5000
E	1.0000	1.0000*	1.0000*
F	1.0000*	0.5000	2.0000*
G	2.0000	2.0000	2.0000*
A (control)		0.5000*	
Analytical grade ZnO		0.0625*	
Oxacillin		not effective	
Ampicillin		not effective	

*denotes minimum bactericidal concentration of ZnO samples

The antibacterial strength of ZnO microstructures had improved by at least fourfold when plant extracts were incorporated. Despite having similar morphologies, $ZnO_{BTLE(B)}$ and $ZnO_{CLE(B)}$ exhibited enhanced antibacterial effects against *S. aureus* than $ZnO_{control(A)}$. The capping of phytochemicals on the ZnO microstructures are speculated to have an additive effect on their antibacterial properties. However, no organic compounds were observed in the FTIR spectra of ZnO samples. This condition might be related to the method sensitivity, where particle size of samples negatively affected penetration depth of the IR light and intensity of bands the spectra [53].

Theoretically, the decrement in particle size would essentially enhance the antibacterial strength of nanoparticles since smaller particles have higher surface energy to aid in dissolution [54,55,56]. Raghupathi et al. [57] and Naqvi et al. [58] discovered the inversed relationship between particle size of ZnO and antibacterial activity against *S. aureus*. Contradictory to the theory, present studies found that the antibacterial strength against *S. aureus* reduced with a decrement in particle sizes, whereas ZnO with defined microstructures exhibited better antibacterial strength. It is speculated that the dissolution properties of nanoparticles might have contributed to the condition.

The dissolution of nanoparticles is affected by the chemistry of the administered condition, which includes ionic strength, pH, and temperature of the medium [59, 60]. The presence of dissolved organic matters would improve the colloidal stability of nanoparticles, which in turn reduces the rate of agglomeration [60, 61]. In the current investigation, however, ZnO samples and bacteria were suspended in sterile distilled water and 0.9 % saline. Peng et al. [60] reported that presence of inorganic ions would disrupt the electrostatic stability of nanoparticles. The presence of inorganic ions is speculated to be the factor contributing to the lack of ZnO nanoparticles' antibacterial action in present study.

The attack mechanisms of ZnO nanoparticles were theorized to be through the formation of ROS, cell internalization of abrasive ZnO, and the release of Zn^{2+} [9,62]. Despite being deployed at higher starting concentrations (16 mgmL^{-1}), ZnO samples and antibiotics had no antibacterial effect against *E. coli*. Meanwhile, Jin et al. [63] discovered that the UV irradiated spherical ZnO nanoparticles at 0.05 mgmL^{-1} had a remarkable activity against *E. coli*. The ZnO samples were used without any prior treatment in the present study. The absence of antibacterial activity against *E. coli* might be attributed to the incompatibility of attack mechanisms.

Based on these observations, it is postulated that the morphology of ZnO played a substantial role in its antibacterial properties against *S. aureus*. The abrasiveness and defined surface morphology of ZnO microstructures contribute to their improved antibacterial properties when compared to ZnO nanoparticles under the given experimental conditions. Meanwhile, the lack of antibacterial activity against *E. coli* might be due to the concentration-dependent effect of ZnO. Besides, the physical properties of ZnO microstructures and nanoparticles employed in this work are speculated to be incompatible with the target site of the tested strain of *E. coli*, making them incapable of exhibiting antibacterial activity.

Conclusion

The designed pathway is stable and repeatable for the green synthesis of ZnO nano- and micro- particles. Manipulation of total phenolic content is a feasible method to control concentration of incorporated plant extracts. The proposed synthesis pathway is feasible for size control of ZnO. Green synthesis is accelerated by the addition of NaOH where it assists deprotonation of phytochemicals to commence Zn chelation. Reaction pH influenced the roles of phytochemicals. The role of deprotonated phytochemicals as capping agent, which possesses structure-directing effect, is prominent under basic condition. Meanwhile, their role as chelating agent, which enhances particle size reduction, is prominent under neutral condition. In addition, it was deduced that the morphology of ZnO played a more substantial role in determining its antibacterial strength compared to particle size. In addition to quantitative phenolic profile, future studies are recommended to establish the interrelation between qualitative phytochemical profile of plant extracts and particle size of ZnO produced to improve universality of the green synthesis pathway.

Acknowledgement

This project is funded by the Ministry of Education Malaysia under the Consortium Research Grant Scheme (KKP) or KPM-special grant RMK10 with a reference number of KKP Vot No. K343. The authors would also like to thank Ministry of Higher Education Malaysia (MOHE) through Fundamental Research Grant Scheme (FRGS/1/2019/TK07/UTHM/02/1) and Universiti Tun Hussein Onn Malaysia which provide Graduate Research Grant Scheme (GPPS) under grant code H630 for sponsoring this work.

References

1. Inshakova, E. and Inshakov, O. (2017). World market for nanomaterials: structure and trends. *MATEC Web of Conferences,* 129: 02013.
2. Jeevanandam, J., Barhoum, A., Chan, Y. S., Dufresne, A. and Danquah, M. K. (2018). Review on nanoparticles and nanostructured materials: history, sources, toxicity and regulations. *Beilstein Journal of Nanotechnology,* 9: 1050-1074.
3. Singh, J., Dutta, T., Kim, K., Rawat, M., Samddar, P. and Kumar, P. (2018). 'Green' synthesis of metals and their oxide nanoparticles: applications for environmental remediation. *Journal of Nanobiotechnology,* 16: 84.
4. Zikalala, N., Matshetshe, K., Parani, S. and Oluwafemi, O. S. (2018). Biosynthesis protocols for colloidal metal oxide nanoparticles. *Nano-Struct. Nano-Objects,* 16: 288-299.
5. Kharissova, O. V., Kharisov, B. I., González, C. M. O., Méndez, Y. P. and López, I. (2019). Greener synthesis of chemical compounds and materials. *Royal Society Open Sciences,* 6: 191378.
6. Rodríguez-León, E., Rodríguez-Vázquez, B. E., Martínez-Higuera, A., Rodríguez-Beas, C., Larios-Rodríguez, E., Navarro, R. E., López-Esparza, R. and Iñiguez-Palomares, R. A. (2019). Synthesis of gold nanoparticles using *Mimosa tenuiflora* extract, assessments of cytotoxicity, cellular uptake, and catalysis. *Nanoscale Research Letters,* 14: 334.
7. Pal, S., Pal, K., Mukherjee, S., Bera, D., Karmakar, P. and Sukhen, D. (2020). Green cardamom mediated phytosynthesis of ZnO NPs and validation of its antibacterial and anticancerous potential. *Materials Research Express,* 7: 015068.

8. Soni, V., Raizada, P., Singh, P., Cuong, H. N., Rangabhashiyam, S., Saini, A., Saini, R. V., Le, Q. V., Nadda, A. K., Le, T. and Nguyen, V. (2021). Sustainable and green trends in using plant extracts for the synthesis of biogenic metal nanoparticles toward environmental and pharmaceutical advances: a review. *Environmental Research,* 202: 111622.
9. Siddiqi, K. S., Ur Rahman, A., Tajuddin and Husen, A. (2018). Properties of zinc oxide nanoparticles and their activity against microbes. *Nanoscale Research Letters,* 13(1): 141.
10. Pasquet, J., Chevalier, Y., Pelletier, J., Couval, E., Bouvier, D. A and Bolzinger, M. (2014). The contribution of zinc ions to the antimicrobial activity of zinc oxide. *Colloids Surface A Physicochemical Engineering Aspects,* 457: 263-274.
11. Król, A., Pomastowski, P., Rafińska, K., Railean-Plugaru, V. and Buszewski, B. (2017). Zinc oxide nanoparticles: synthesis, antiseptic activity and toxicity mechanism. *Advance Colloid Interface Sciences,* 249: 37-52.
12. Xu, J., Huang, Y., Zhu, S., Abbes, N., Jing, X. and Zhang, L. (2021). A review of the green synthesis of ZnO nanoparticles using plant extracts and their prospects for application in antibacterial textiles. *Journal Engineering Fibers Fabrication,* 16: 1-14.
13. Câmara, J. S., Albuquerque, B. R., Aguiar, J., Corrêa, R. C. G., Gonçalves, J. L., Granato, D., Pereira, J. A. M., Barros, L. and Ferreira, I. C. F. R. (2020). Food bioactive compounds and emerging techniques for their extraction: polyphenols as a case study. *Foods (Basel, Switzerland),* 10(1): 37.
14. Belščak-Cvitanović, A., Valinger, D., Benković, M, Tušek, A. J., Jurina, T., Komes, D. and Kljusurić, J. G. (2017). Integrated approach for bioactive quality evaluation of medicinal plant extracts using HPLC-DAD, spectrophotometric, near infrared spectroscopy and chemometric techniques. *International Journal Food Production,* 20(3): 1-18.
15. Almini, S. M. and Akbari, A. (2019). Metal nanoparticles synthesis through natural phenolic acids. *IET Nanobiotechnology,* 13(8): 771-777.
16. Mercado-Mercado, G., Blancas-Benitez, F. J., Velderrain-Rodríguez, G. R., Montalvo-González, E., González-Aguilar, G. A., Alvarez-Parrilla, E. and Sáyago-Ayerdi, S. G. (2015). Bioaccessibility of polyphenols released and associated to dietary fibre in calyces and decoction residues of Roselle (*Hibiscus sabdariffa* L.). *Journal Functional Foods,* 18: 171-181.
17. Dudonné, S., Vitrac, X., Coutière, P., Woillez, M. and Mérillon, J. (2009). Comparative study of antioxidant properties and total phenolic content of 30 plant extracts of industrial interest using DPPH, ABTS, FRAP, SOD, and ORAC assays. *Journal Agriculture Food Chemistry,* 57: 1768-1774.
18. Iqbal, E., Salim, K. A. and Lim, L. B. L. (2015). Phytochemical screening, total phenolics and antioxidant activities of bark and leaf extracts of *Goniothalamus velutinus* (Airy Shaw) from Brunei Darussalam. *Journal King Saud University Sciences,* 27: 224-232.
19. Gul, R., Jan, S. U., Faridullah, S., Sherani, S. and Jahan, N. (2017). Preliminary phytochemical screening, quantitative analysis of alkaloids, and antioxidant activity of crude plant extracts from *Ephedra intermedia* indigenous to Balochistan. *Science World Journal,* 2017: 5873648.
20. Aiyegoro, O. A. and Okoh, A. I. (2010). Preliminary phytochemical screening and *In vitro* antioxidant activities of the aqueous extract of *Helichrysum longifolium* DC. *BMC Complementary Alternative Medicine,* 10: 21.
21. Ukoha, P. O., Cemaluk, E. A. C., Nnamdi, O. L. and Madus, E. P. (2011). Tannins and other phytochemicals of the *Samanaea saman* pods and their antimicrobial activities. *African Journal Pure Applied Chemstry,* 5(8): 237-244.
22. El Aziz, M. M. A., Ashour, A. S. and Melad, A. S. G. (2019). A review on saponins from medicinal plants: chemistry, isolation, and determination. *Journal Nanomedicine Research,* 7(4): 282-288.
23. Shukla, S., Mehta, A. and Bajpai, V. K. (2013). Phytochemical screening and anthelmintic and antifungal activities of leaf extracts of *Stevia rebaudiana*. *Journal of Biologically Active Products from Nature,* 3(1): 56-63.

24. Top, A. and Çetinkaya, H. (2015). Zinc oxide and zinc hydroxide formation via aqueous precipitation: effect of the preparation route and lysozyme addition. *Materials Chemical Physics*, 167: 77-87.
25. He, Y., Ingudam, S., Reed, S., Gehring, A., Strobaugh, Jr. T. P. and Irwin, P. (2016). Study on the mechanism of antibacterial action of magnesium oxide nanoparticles against foodborne pathogens. *Journal Nanobiotechnology*, 14: 54.
26. Nandiyanto, A. B. D., Oktiani, R. and Ragadhita, R. (2019). How to read and interpret FTIR spectroscope of organic material. *Indonesian Journal Science Technology*, 4(1): 97-118.
27. Grasel, F. d. S., Ferrão, M. F. and Wolf, C. R. (2016). Development of methodology for identification the nature of the polyphenolic extracts by FTIR associated with multivariate analysis. *Spectrochimica Acta A Molecular Biomolecular Spectroscopy*, 153: 94-101.
28. Coates, J. (2006). Interpretation of infrared spectra, A practical approach. in R. A. Meyers and M. L. McKelvy (Ed.). *Encyclopedia of Analytical Chemistry*. Wiley, New York: pp. 10815-10837.
29. Santos, D. I., Correia, M. J. N., Mateus, M. M., Saraiva, J. A., Vicente, A. A. and Moldão, M. (2019). Fourier transform infrared (FT-IR) spectroscopy as a possible rapid tool to evaluate abiotic stress effects on pineapple by-products. *Applied Science*, 9: 4141.
30. Caunii, A., Pribac, G., Grozea, I., Gaitin, D. and Samfira, I. (2012). Design of optimal solvent for extraction of bio-active ingredients from six varieties of *Medicago sativa*. *Chemical Central Journal*, 6: 123.
31. Thummajitsakul, S., Samaikam, S., Tacha, S. and Silprasit, K. (2020). Study of FTIR spectroscopy, total phenolic content, antioxidant activity and anti-amylase activity of extracts and different tea forms of *Garcinia schomburgkiana* leaves. *LWT*, 134: 110005.
32. Baranska, M. and Schulz, H. (2009). Determination of alkaloids through infrared and Raman spectroscopy. in Cordell, G. A. (Ed.). *The Alkaloids: Chemistry and Biology*. Elsevier Inc., Netherlands: pp. 217-255.
33. Wahab, R., Kim, Y. and Shin, H. (2009). Synthesis, characterization and effect of pH variation on zinc oxide nanostructures. *Materials Transaction*, 50(8): 2092-2097.
34. Rayerfrancis, A., Bhargav, P. B., Ahmed, N., Chandra, B. and Dhara, S. (2015). Effect of pH on the morphology of ZnO nanostructures and its influence on structural and optic properties. *Physica B Condensation Matters*, 457: 96-102.
35. Rafaie, H. A., Samat, N. and Nor, R. M. (2014). Effect of pH on the growth of zinc oxide nanorods using *Citrus aurantifolia* extracts. *Materials Letters*, 137: 297-299.
36. Padalia, H., Moteriya, P. and Chanda, S. (2018). Synergistic antimicrobial and cytotoxic potential of zinc oxide nanoparticles synthesized using *Cassia auriculata* leaf extract. *BioNanoScience*, 8: 196-206.
37. Mohammadi, F. M. and Ghasemi, N. (2018). Influence of temperature and concentration on biosynthesis and characterization of zinc oxide nanoparticles using *cherry* extract. *Journal Nanostructure Chemistry*, 8: 93-102.
38. Suresh, J., Pradheesh, G., Alexramani, V., Sundrarajan, M. and Hong, S. I. (2018). Green synthesis and characterization of zinc oxide nanoparticles using insulin plant (*Costus pictus D. Don)* and investigation of its antimicrobial as well as anticancer activities. *Advance Nature Sciences: Nanoscience, Nanotechnology*, 9: 015008.
39. Umar, H., Kavaz, D. and Rizaner, N. (2019). Biosynthesis of zinc oxide nanoparticles using *Albizia lebbeck* stem bark, and evaluation of its antimicrobial, antioxidant, and cytotoxic activities on human breast cancer cell lines. *International Journal Nanomedicine*, 14: 87-100.
40. Sharmila, G., Thirumarimurugan, M. and Muthukumaran, C. (2019). Green synthesis of ZnO nanoparticles using *Tecoma castanifolia* leaf extract: characterization and evaluation of its antioxidant, bactericidal and anticancer activities. *Microchemical Journal*, 145: 578-587.

41. Matinise, N., Fuku, X. G., Kaviyarasu, K., Mayedwa, N. and Maaza, M. (2017). ZnO nanoparticles via *Moringa oleifera* green synthesis: physical properties & mechanism of formation. *Applied Surface Sciences,* 406: 339-347.
42. Fakhari, S., Jamzad, M. and Fard, H. K. (2019). Green synthesis of zinc oxide nanoparticles: a comparison. *Green Chemistry Letters Review*, 12(1): 19-24.
43. Liu, Y. C., Li, J., Ahn, J., Pu, J., Rupa, E. J., Huo, Y. and Yang, D. C. (2020). Biosynthesis of zinc oxide nanoparticles by one-pot green synthesis using fruit extract of *Amomum longiligulare* and its activity as a photocatalyst. *Optik*, 218: 165245.
44. Chakraborty, S., Farida, J. J., Simon, R., Kasthuri, S. and Mary, N. L. (2020). *Averrhoe carrambola* fruit extract assisted green synthesis of ZnO nanoparticles for the photodegradation of congo red dye. *Surface Interfaces,* 19: 100488.
45. Díaz, N., Suárez, D. and Merz, Jr. K. M. (2000). Hydration of zinc ions: theoretical study of $[Zn(H_2O)_4](H_2O)_8^{2+}$ and $[Zn(H_2O)_6](H_2O)_6^{2+}$. *Chemistry Physics Letters,* 326: 288-292.
46. Krężel, A. and Maret, W. (2016). The biological inorganic chemistry of zinc ions. *Archive Biochemical Biophysics,* 611: 3-19.
47. Soldatavić, T. (2018). Mechanism of interactions of zinc(II) and copper(II) complexes with small biomolecules. *IntechOpen*: pp. 79472.
48. Santos-Sánchez, N. F., Salas-Coronado, R., Villanueva-Cañongo, C. and Hernández-Carlos, B. (2019). Antioxidant compounds and their antioxidant mechanisms. *IntechOpen*: 85270.
49. Sobiesiak, M. (2017). Chemical structure of phenols and its consequence for sorption processes. *IntechOpen*: 66537.
50. Wang, M., Zhou, Y., Zhang, Y., Hahn, S. H. and Kim, E. J. (2011). From $Zn(OH)_2$ to ZnO: a study on the mechanism of phase transformation. *CrystEngComm,* 13: 6024-6026.
51. Zhu, Y. F., Fan, D. H., Dong, Y. W. and Zhou, G. H. (2014). Morphology-controllable ZnO nanostructures: ethanol-assisted synthesis, growth mechanism and solar cell applications. *Superlattices Microstructure,* 74*:* 261-272.
52. Javed, R., Zia, M., Naz, S., Aisida, S. O., Ain, N. U. and Ao, Q. (2020). Role of capping agents in the application of nanoparticles in biomedicine and environmental remediation: recent trends and future prospects. *Journal Nanobiotechnology,* 18: 172.
53. Udvardi, B., Kovács, I. J., Fancsik, T., Kónya, P., Bátori, M., Stercel, F., Falus G. and Szalai, Z. (2017). Effects of particle size on the attenuated total reflection spectrum of minerals. *Applied Spectroscopy,* 71(6): 1157-1168.
54. Peng, X., Palma, S., Fisher, N. S. and Wong, S. S. (2011). Effect of morphology of ZnO nanostructures on their toxicity to marine algae. *Aquatic Toxicology,* 102: 186-196.
55. Lallo da Silva, B., Abuçafy, M. P., Berbel Manaia, E., Oshiro Junior, J. A., Chiari-Andréo, B. G., Pietro, R. and Chiavacci, L. A. (2019). Relationship between structure and antimicrobial activity of zinc oxide nanoparticles: an overview. *International Journal Nanomedicine*, 14: 9395-9410.
56. Jin, S. and Jin, H. (2021). Antimicrobial activity of zinc oxide nano/microparticles and their combinations against pathogenic microorganisms for biomedical applications: from physicochemical characteristics to pharmacological aspects. *Nanomaterials (Basel, Switzerland),* 11(2): 263.
57. Raghupathi, K. R., Koodali, R. T. and Manna, A. C. (2011). Size-dependent bacterial growth inhibition and mechanism of antibacterial activity of zinc oxide nanoparticles. *Langmuir*, 27: 4020-4028.
58. Naqvi, Q., Kanwal, A., Qaseem, S., Naeem, M., Ali, S. R., Shaffique, M. and Maqbool, M. (2019). Size-dependent inhibition of bacterial growth by chemically engineered spherical ZnO nanoparticles. *Journal Biology Physics*, 45(2): 147-159.
59. Misra, S. K., Dybowska, A., Berhanu, D., Luoma, S. N. and Valsami-Jones, E. (2012). The complexity of nanoparticle dissolution and its importance in nanotoxicological studies. *Science Total Environment,* 438: 225-232.

60. Peng, Y., Tsai, Y., Hsiung, C., Lin, Y. and Shih, Y. (2017). Influence of water chemistry on the environmental behaviors of commercial ZnO nanoparticles in various water and wastewater samples. *Journal Hazardous Materials,* 322: 348-356.
61. Zhang, Y., Chen, Y., Westerhoff, P. and Crittenden, J. (2009). Impact of natural organic matter and divalent cations on the stability of aqueous nanoparticles. *Water Research*, 43: 4249-4257.
62. Dimapilis, E. A. S., Hsu, C., Mendoza, R. M. O. and Lu, M. (2018). Zinc oxide nanoparticles for water disinfection. *Sustainable Environmental Research,* 28: 47-56.
63. Jin, S., Jin, J., Hwang, W. and Hong, S. W. (2019). Photocatalytic antibacterial application of zinc oxide nanoparticles and self-assembled networks under dual UV irradiation for enhanced disinfection. *International Journal Nanomedicine,* 14: 1737-1751.

Malaysian Journal of Analytical Sciences (MJAS)
Published by Malaysian Analytical Sciences Society

APLIKASI KARBON TERAKTIF SEKAM PADI TERHADAP EFLUEN KILANG KELAPA SAWIT MENGGUNAKAN KAEDAH PENJERAPAN

(Application of Rice Husk Activated Carbon on Palm Oil Mill Effluent using Adsorption Method)

Mohamad Jani Saad[1]*, Chia Chin Hua[2], Sarani Zakaria[2], Mohd Shaiful Sajab[3]

[1]Pusat Penyelidikan Kejuruteraan,
Institut Penyelidikan dan Kemajuan Pertanian Malaysian (MARDI), Persiaran Mardi-UPM, 43400 Serdang Selangor, Malaysia
[2]Fakulti Sains dan Teknologi
[3]Fakulti Kejuruteraan
Universiti Kebangsaan Malaysia, 43600 UKM Bangi, Selangor, Malaysia

**Pengarang utama: jani@mardi.gov.my*

Received: 16 November 2021; Accepted: 27 February 2022 ; Published: 25 August 2022

Abstrak

Karbon aktif sekam padi (RHAC) dihasilkan dan digunakan untuk menghilangkan warna pewarna organik dan efluen kilang kelapa sawit (POME) melalui proses penjerapan. Sekam padi dikarbonisasi dan diaktifkan menggunakan kalium hidroksida (KOH) dan natrium hidroksida (NaOH) untuk menghasilkan karbon aktif. Sifat karbon aktif (AC) dikaji melalui analisis permukaan dan morfologi. Penjanaan semula bahan penjerap dengan proses penjerapan/penyaherapan menunjukkan bahawa AC dapat dijana semula hingga lima kitaran sementara masih memberikan maksimum 67.26% kapasiti penjerapan pada regenerasi pertama dan serendah 2.72% kapasiti penjerapan pada regenerasi kelima. RHAC juga digunakan untuk perawatan POME untuk penyahwarnaan dan pengurangan jumlah karbon organik (TOC) dan permintaan oksigen kimia (COD). Kajian ini menunjukkan bahawa RHAC berpotensi digunakan sebagai bahan penjerap untuk menghilangkan pelbagai jenis cas positif bahan terjerap dan POME dari larutan berair.

Kata kunci: karbon aktif, sekam padi, penjerapan, karbonisasi, efluen kilang kelapa sawit

Abstract

Rice husk activated carbon (RHAC) is produced and used to remove the color of organic dyes and palm oil mill effluents (POME) through an adsorption process. Rice husk is carbonized and activated using potassium hydroxide (KOH) and sodium hydroxide (NaOH) to produce activated carbon. The properties of activated carbon (AC) were studied through surface and morphological analysis. Adsorbent regeneration by adsorption/absorption process showed that AC could be regenerated for up to five cycles while still providing a maximum of 67.26% adsorption capacity on the first regeneration and as low as 2.72% adsorption capacity on the fifth regeneration. RHAC is also used for POME treatment for discoloration and reduction of total organic carbon (TOC) and chemical oxygen demand (COD). This study shows that RHAC has the potential to be used as an adsorbent to remove various types of positive charge adsorbate and POME from aqueous solutions.

Keywords: activated carbon, rice husk, adsorption, carbonization, palm oil mill effluents

Pendahuluan

Pemprosesan minyak sawit menghasilkan dua jenis produk sampingan, iaitu biojisim pepejal dan enapcemar cecair atau dipanggil POME. Setiap tan pemprosesan buah kelapa sawit, 5.5% biji minyak, 13.5% serat mesocap dan 23.4% tandan buah kelapa sawit dihasilkan sebagai sisa biojisim pepejal. Selain itu kira-kira 67% POME juga dihasilkan [1]. POME dihasilkan dari 3 aktiviti pembuatan iaitu pensterilan (0.2-0.25 tan per tan buah kelapa sawit), pencerahan (0.4-0.45 tan per tan buah kelapa sawit) dan hidroklon (0.03-0.05 tan per tan buah kelapa sawit) pada nisbah 6:15:1 [2].

Ciri-ciri POME bergantung pada kualiti buah kelapa sawit dan aktiviti pembuatan di kilang kelapa sawit. POME adalah cecair pekat, likat dan warna keperangan yang terdiri daripada 95-96% air, 0.6-0.7% minyak dan 4-5% pepejal. Ia juga mempunyai nilai BOD (> 18 000 mg/L) dan COD (> 45 000 mg/L), yang dikeringkan pada suhu 80-90 °C pada pH berasid. POME mengandungi nitrogen, organik, fosforus, dan sisa selulosa yang merupakan campuran karbohidrat dan minyak. Kandungan organik yang tinggi dalam POME disumbangkan oleh beberapa gula seperti xilosa, glukosa, galaktosa dan mannos [3]. POME juga terdiri daripada sejumlah nutrien seperti nitrogen, kalium, magnesium, kalsium, kromium, tembaga dan zat besi [4]. POME bukan bahan cemar yang berbahaya kerana tidak ada bahan kimia yang dimasukkan semasa pemprosesan buah kelapa sawit, ia mengandungi sumber nutrien yang baik, namun POME yang tidak dirawat mempengaruhi alam sekitar kerana kandungan organik dan nutriennya menyebabkan pengurangan kandungan oksigen dalam sistem akuatik [5]. Terdapat beberapa kaedah untuk merawat POME iaitu teknologi membran [6, 7], pembekuan/flokulasi [8, 9], proses pengoksidaan [10] serta penjerapan menggunakan arang teraktif (AC) [11, 12, 13].

Amalan biasa dalam rawatan POME adalah melalui sistem kolam, yang memerlukan kawasan tanah yang besar dan masa pendedahan yang lama [13]. Sebagai tambahan, POME yang dirawat masih mengandungi tahap pencemaran yang tinggi kerana keberkesanan kaedah rawatan sedemikian yang rendah. Oleh itu, penjerapan sering digunakan untuk merawat POME yang dirawat sebelum dialirkan ke sungai. Terdapat beberapa kajian mengenai penggunaan bahan penjerap AC dari biojisim dalam merawat POME seperti yang ditunjukkan dalam Jadual 1.

Jadual 1. Penjerapan POME menggunakan penjerap AC

Bahan	Kaedah Ujian	Efisensi (%)	Rujukan
AC tempurung kelapa	TSS, COD dan warna POME	TSS (39), COD (66), warna (61)	[13]
Gentian kelapa sawit	COD dan SS POME	SS (80), COD (70)	[14]
AC kulit pisang	TSS, BOD, warna	TSS (96), BOD (100), warna (95)	[15]
AC komersial	COD dan TSS	COD (73.08), TSS (98.33)	[16]
AC tempurung kelapa sawit	SS	71.26	[17]

AC cenderung untuk berinteraksi dengan zarah bukan polar pada bahan yang terjerap dalam larutan hidrofobik. Zarah hidrofobik mempunyai kecenderungan untuk berinteraksi dengan zarah yang serupa berbanding dengan titisan minyak. Proses ini mengakibatkan pemutusan ikatan hidrogen antara zarah air. Begitu juga, bahan penjerap hidrofilik boleh berkesan untuk pengurangan larutan polar dalam air sisa. Gabungan zarah hidrofilik mempunyai interaksi termodinamik yang lebih baik daripada interaksi dengan zat hidrofobik seperti minyak. Tahap zarah hidrofobik atau hidrofilik ditentukan oleh ketegangan permukaan bahan dalam fasa berair dan gabungan bahan penjerap sangat berkesan untuk pengurangan air buangan berkekuatan tinggi yang mengandungi larutan polar dan bukan polar [18]. POME juga dianalisis oleh jumlah

karbon organik (TOC) dan permintaan oksigen kimia (COD). TOC bertujuan untuk menentukan jumlah karbon yang terdapat dalam bahan organik. TOC adalah penentu kualiti air yang tidak spesifik. Manakala COD dapat menentukan jumlah oksigen yang dimakan oleh tindak balas dalam larutan yang dikaji.

Penjanaan semula bahan penjerap (AC) mampu mengurangkan kos penghasilan bahan penjerap setelah bahan terjerap dapat dikeluarkan. Walaupun begitu, potensi penjanaan semula bahan penjerap adalah salah satu sifat khas bahan penjerap. Keupayaan penjerapan dan kecekapan bahan yang dijerap adalah antara kelebihannya. Didapati bahawa dengan bertambahnya kitaran regenerasi maka kapasiti penjerapan penjerap akan menurun. Penjanaan semula AC memerlukan prosedur khusus untuk mengeluarkan molekul bahan yang terjerap dari permukaan AC. Terdapat tiga kaedah regenerasi utama untuk AC iaitu termal, kimia dan biologi [19-23]. Setiap kaedah mempunyai batasannya iaitu tenaga haba yang tinggi, kehilangan karbon, penggunaan bahan kimia mahal dan masa. Penjanaan semula bahan penjerap setelah tepu dilakukan dengan proses penjerapan. Kajian penjerapan diperlukan untuk pemulihan bahan yang dijerap dan untuk memahami mekanisme penjerapan. Proses penjerapan dilakukan dengan mencampurkan penjerap tepu dengan bahan nyahjerap (NaOH, HCl, CH_3COOH, C_3H_6O, C_2H_5OH) untuk penyingkiran bahan yang dijerap dan dipisahkan dengan penapisan [24-27]. Pewarna yang dijerap dapat dinyahjerap dengan menggunakan air neutral, pewarna dijerap dengan penjerap melalui ikatan yang lemah. Sekiranya pewarna dapat dijerap dengan asid sulfurik atau air alkali, penjerapan pewarna melalui pertukaran ion. Penggunaan pelarut organik seperti aseton atau asid asetik untuk menjerap, pewarna telah dijerap melalui penjerapan kimia. Manakala dengan asid mineral seperti HCl, pewarna telah dijerap melalui penjerapan fizikal [28].

Bahan dan Kaedah

Penyediaan sekam padi

Sekam padi diambil dari sawah di Sekinchan, Selangor, Malaysia. Ia dibersihkan dengan air untuk menghilangkan kotoran dan dikeringkan di dalam oven pada suhu 105 °C selama semalaman.

Penyediaan AC sekam padi

Sekam padi diprolisis pada suhu 400 °C selama 4 jam untuk menghasilkan arang sekam padi (RHC). Kemudian, RHC diayak untuk memperolehi saiz 60 mesh. RHC direndam dengan larutan KOH (13M) pada nisbah 1:4 (RHC: KOH) selama 24 jam. Ia ditapis dan dikeringkan dengan oven pada suhu 105 °C semalaman. Proses pengaktifan dilakukan di dalam relau tiub dengan aliran gas nitrogen (100 mL/min) selama 2 jam pada suhu 850 °C. Sampel disejukkan dan dicuci dengan larutan asid hidroklorik (HCl) (1 M) dan air deionisasi sehingga pH 6 hingga 7 diperoleh. Proses yang sama seperti dilakukan bagi NaOH. Sampel diberi label sebagai RHC (arang sekam padi), RHACK (rawatan dengan KOH) dan RHACNa (rawatan dengan NaOH).

Pencirian AC

Luas permukaan sampel RHC, RHACK, dan RHACNa dikaji dengan menggunakan analisis penjerapan-penyaherapan N2 (Micromeritics ASAP, 2010) kemudian diikuti oleh piawai penjerapan-penjerapan nitrogen pada 77 K. Sifat morfologi permukaan sampel diperolehi dengan menggunakan mikroskopi elektron imbasan (SEM) model FEI Quanta 400.

Kajian perubahan warna, COD dan TOC POME

Efluen industri kelapa sawit (POME) diperoleh dari kilang kelapa sawit KPSB di Gua Musang, Kelantan, Malaysia. Sifat POME yang asal adalah seperti di Jadual 2. POME pertama kali disaring kotoran dan enapan dan disimpan di dalam peti sejuk sebelum menjalani analisis perubahan warna dengan AC. POME (pH 8.5) dilakukan analisis penyahwarnaan (Persamaan 1) menggunakan kaedah Platinum-Cobalt (Pt-Co) yang dianalisis oleh Spectrophotometer (HACH DR 3900) pada panjang gelombang 450 nm. Analisis dilakukan dengan 100 mL POME diaduk dengan bahan penjerap AC pada 0.1 g, 0.4 g dan 0.6 g dan nilai Pt-Co POME diambil pada selang waktu yang ditetapkan sehingga titik keseimbangan penjerapan warna POME tercapai. Nilai perubahan dikira seperti Persamaan 1. Analisis permintaan oksigen kimia (COD) dan jumlah karbon organik (TOC) masing-masing mengikuti kaedah 5220D dan kaedah TNT yang dianalisis dengan instrumen HACH DRB 200.

$$\text{Perubahan warna (\%)} = \frac{C_0 - Ce}{(C_0)} \text{ x } 100 \quad (1)$$

di mana C_0 dan C_e masing-masing adalah nilai perubahan warna awal dan akhir POME.

Jadual 2. Sifat POME yang asal

Parameter	Nilai
pH	9.5
DO (mg/L)	7.32
BOD5 (mg/L)	11.5
COD (mg/L)	280
SS (mg/L)	17
Warna(Pt-Co)	888
NH_3-N (mg/L)	0.5
Minyak & Gris (mg/L)	5
TOC (mg/L)	96

Kajian penjerapan dan penjanaan semula AC

Larutan metilena biru (MB) dengan kepekatan 450 mg/L disediakan untuk proses kajian penjerapan dan penyaherapan MB dengan sampel RHACK dan RHACNa. Serbuk AC seberat 0.05 g diaduk bersama 50 mL larutan MB pada pengaduk magnet pada 300 rpm selama semalaman. Kepekatan larutan MB sebelum dan selepas proses penjerapan diperoleh menggunakan spektrofotometer UV. Serbuk AC yang telah melalui proses penjerapan disaring dari larutan MB dan dibilas dengan air suling untuk membersihkan sisa larutan MB di permukaan AC. Proses penyaherapan dengan kaedah kimia dilakukan dengan merendam AC dalam larutan agen penyaherapan (3 M) selama 3 jam. Tiga jenis agen penyaherapan adalah aseton (CH_3H_6O), asid asetik ($C_2H_4O_2$) (kedua-duanya adalah pelarut organik) dan asid sulfurik (H_2SO_4) (pelarut bukan organik). Nilai kepekatan larutan yang dijerap diambil dengan spektrofotometer UV. AC ditapis dan dibilas dengan air suling sebelum dikeringkan semalaman di dalam ketuhar pada suhu 60 °C. Proses di atas diulang untuk penjanaan semula seterusnya hingga lima kitaran. Nilai peratusan penjerapan bahan yang dijerap diperoleh berdasarkan Persamaan 2.

$$\text{Peratusan penjerapan bahan dijerap} = \frac{A}{B} \text{ x } 100\% \quad (2)$$

di mana A ialah kepekatan larutan penjerapan (mg/L), B adalah kepekatan larutan bahan dijerap (mg/L).

Keputusan dan Perbincangan

Analisis permukaan

Jadual 3 menunjukkan sampel RHACK dan RHACNa mempunyai nilai luas permukaan yang tinggi masing-masing pada 1131.73 m^2/g dan 429.82 m^2/g dibandingkan dengan RHC pada 0.23 m^2/g. Peranan kenaikan suhu membantu meningkatkan pembentukan liang pada struktur karbon. Hasil ini mungkin didorong oleh kesan pemanasan dalaman dan pembukaan liang [29]. KOH sebagai agen pengaktif telah bertindak balas dengan pusat reaktif bahan karbon seperti karbon tidak berstruktur, karbon dengan heteroatom dan karbon di sisi grafin menghasilkan liang baru dan melebarkan yang sedia ada, ia meningkat dengan peningkatan kehadiran KOH [30]. Jumlah keseluruhan liang AC telah meningkat dengan peningkatan suhu pengaktifan. Sebagai contoh, isipadu liang RHC pada 0.0026 cm^3/g meningkat menjadi 0.76 cm^3/g untuk RHACK dan RHACNa pada 0.29 cm^3/g. Peningkatan luas permukaan menyumbang kepada peningkatan jumlah liang berukuran meso [31]. Saiz liang RHACK dan RHACNa masing-masing adalah 2.67 nm dan 2.69 nm. Fenomena ini menunjukkan bahawa liang-liang berukuran antara 2-50 nm, iaitu bersaiz meso. Menurut IUPAC 1972, ukuran liang boleh dikelaskan kepada tiga jenis iaitu liang mikro (di bawah 2 nm), liang meso (2-50 nm) dan liang makro (lebih dari 50 nm) [32].

Jadual 3. Keputusan analisa permukaan

Sampel	Luas Permukaan (m^2/g)	Isipadu Liang (cm^3/g)	Saiz Liang (nm)
RHC	0.23	0.0026	4.42
RHACK	1131.73	0.76	2.67
RHACNa	429.82	0.29	2.69

Nilai luas permukaan RHACK adalah 1131.73 m^2/g berbanding RHACNa 429.82 m^2/g. Didapati bahawa KOH bertindak sebagai agen pengaktifan yang lebih baik daripada NaOH. Ia menyebabkan pembentukan liang dan isipadu liang dan seterusnya menghasilkan karbon berliang dengan luas permukaan yang lebih tinggi [33]. Peningkatan keliangan didapati berkaitan dengan kation alkali agen pengaktif mengikut urutan: Li <Na <K <Rb <Cs, dalam hal ini KOH mempunyai lebih banyak kation alkali daripada NaOH, oleh itu KOH lebih banyak bertindak balas dengan karbon dan menghasilkan lebih liang [34]. Tindak balas kimia antara alkali hidroksida dan karbon berlaku semasa proses pengaktifan seperti dalam Persamaan 3, 4 dan 5 [35].

$$4KOH + C \rightarrow K_2CO_3 + K_2O + 2H_2 \quad (3)$$

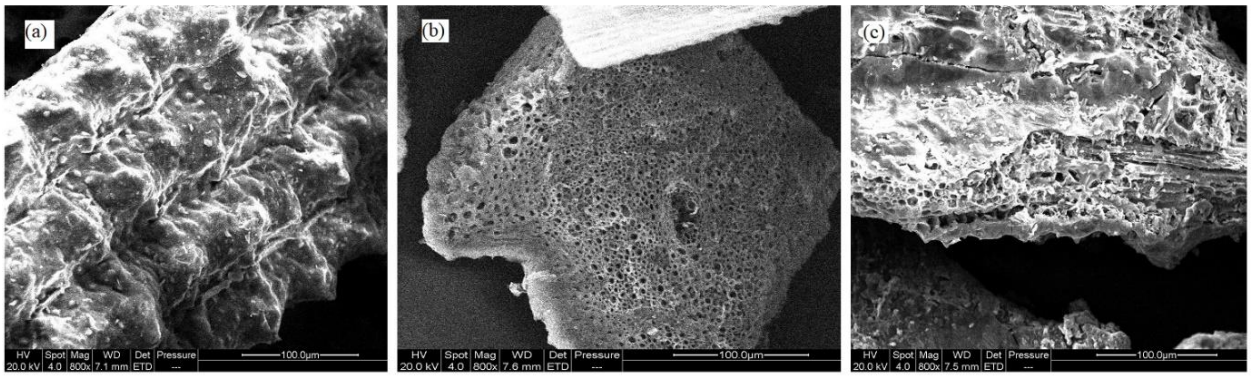
$$2K_2O + C \rightarrow 4K + CO_2 \quad (4)$$

$$K_2CO_3 + 2C \rightarrow 2K + 3CO \quad (5)$$

Proses pengaktifan menghasilkan gas hidrogen, karbonat dan kalium (K atau K_2O). Logam kalium dikeluarkan semasa proses pembasuhan dan K_2CO_3 terurai semasa proses pengaktifan dan gas CO_2 dihasilkan. Tindak balas antara agen pengaktif dan karbon menyebabkan penguraian organik meruap dan membentuk permukaan liang pada permukaan sampel AC. Proses gasifikasi semasa pengaktifan menggunakan agen pengaktifan yang sesuai sangat penting dalam proses pembentukan liang [36].

Mikroskopi elektron pengimbasan

Rajah 1(a) menunjukkan mikrograf SEM RHC yang nampaknya hampir tidak mempunyai liang di permukaannya. Pembentukan struktur liang yang dihasilkan daripada pengaktifan KOH dan NaOH masing-masing ditunjukkan pada Rajah 1(b) dan 1(c). Pengaktifan kimia menghasilkan struktur karbon berliang di permukaan. Hasil yang serupa juga dilaporkan oleh para penyelidik yang lain di mana kesan pengaktifan telah menambah liang-laing pada permukaan AC [30, 37, 38].



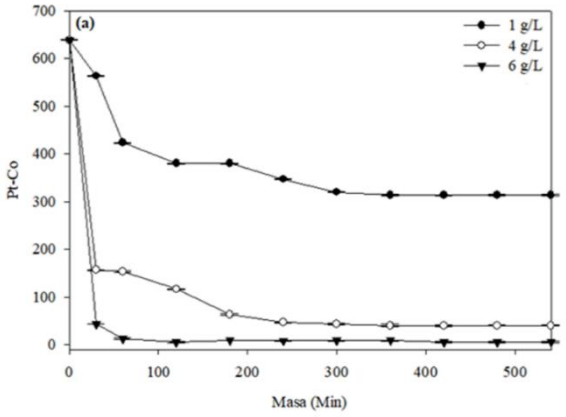
Rajah 1. SEM (a) RHC, (b) RHACK dan (c) RHACN

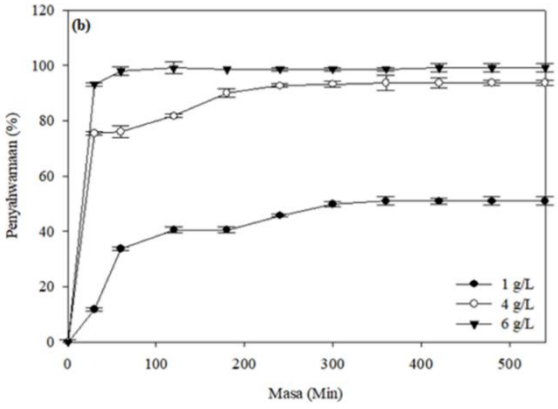
Analisis perubahan warna POME: Kesan bahan penjerap

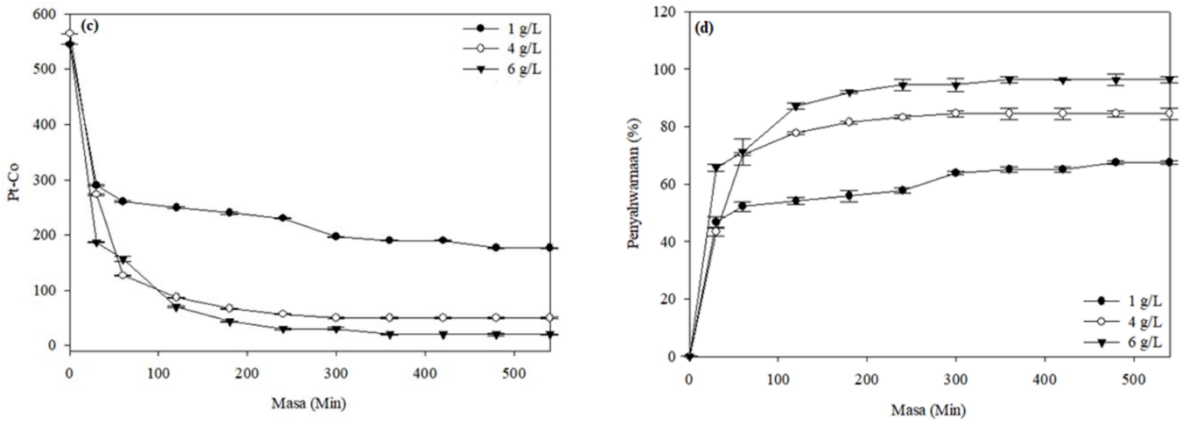
Rajah 2 menunjukkan kesan RHACK dan RHACNa sebagai bahan penjerap terhadap peratusan penyahwarnaan POME. Peningkatan bahan penjerap telah mengurangkan peratusan warna POME. Sebanyak 50.94% (313 Pt-Co) warna POME dikurangkan dengan menggunakan bahan penjerap RHACK pada 1 g/L. Peratusan penyahwarnaan POME terus meningkat sebanyak 93.22% (43 Pt-Co) kepada 99.11% (13 Pt-Co) kerana bahan penjerap RHACK meningkat dari 4 g/L menjadi 6 g/L seperti yang ditunjukkan dalam Rajah 2(a) dan (b). Seterusnya, pola yang sama turut diperhatikan bagi sampel RHACNa yang menunjukkan peningkatan peratusan penyahwarnaan POME 67.56% (177 Pt-Co) pada 4 g/L, 84.49% (50 Pt-Co) pada 6 g/L dan 96.33% (20 Pt-Co) pada 10 g/L seperti dalam Rajah 2(c) dan (d). Pada peringkat pertama, penjerapan meningkat dengan cepat, menunjukkan bahawa terdapat luas permukaan aktif bahan penjerap AC. Hasil peningkatan bahan penjerap menyebabkan peningkatan peratusan penyahwarnaan POME di mana ia sejajar dengan laporan penyelidik sebelumnya [12, 39]. Keadaan ini akhirnya menunjukkan graf mendatar setelah mencapai keseimbangan, mungkin disebabkan oleh lapisan pencemar mono-organik yang menutupi permukaan bahan penjerap [40]. Secara amnya, bahan penjerap pada kadar 0.4 g dalam 100 mL POME mencukupi untuk menyahwarnakan POME.

Didapati bahawa kadar penyahwarnaan meningkat seiring dengan masa dan bahan penjerap [41], di mana daripada analisis didapati kadar penjerapan seimbang berlaku setelah 420 minit (1 g/L) untuk sampel RHACK. Keseimbangan meningkat dengan cepat untuk bahan penjerap 4 g/L pada 60 minit dan 30 minit untuk 6 g/L. RHACNa memberikan keseimbangan selepas 300 minit untuk bahan penjerap 4 g/L dan 6 g/L, sementara bahan penjerap 10 g/L berlaku selepas 60 minit. Para penyelidik sebelum ini telah melaporkan hasil yang serupa pada kadar penyahwarnaan dan kesan bahan penjerap AC dalam eksperimen penyahwarnaan POME menggunakan AC [11, 13, 42].

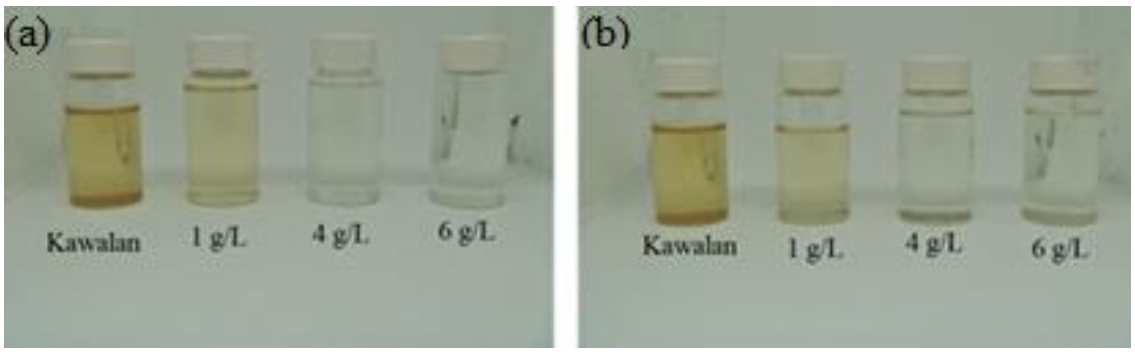
Secara umum, sampel AC-KOH menunjukkan peratusan penyahwarnaan yang lebih baik daripada AC-NaOH. Kemungkinan besar disebabkan oleh faktor luas permukaan yang lebih tinggi yang terbentuk di permukaan sampel yang membolehkan bahan organik tercemar mengisinya. Ini disokong oleh gambar-gambar pada Rajah 3(a) di mana kecerahan warna larutan sampel RHACK terbentuk lebih cepat yakni pada 4 g/L berbanding 6 g/L daripada sampel AC-NaOH pada Rajah 3(b).







Rajah 2. Graf warna (Pt-Co) dan peratus penyahwarnaan RHACK (a) dan (b) serta RHACNa (c) dan (d)



Rajah 3. POME selepas dinyahwarna oleh (a) RHACK, (b) RHACNa

COD dan TOC

Jadual 4 adalah hasil analisis keperluan oksigen kimia (COD) dan jumlah karbon organik (TOC) terhadap POME sebelum dan selepas eksperimen penjerapan dengan 0.4 g sampel bahan penjerap sampel RHACK dan RHACNa. Keempat-empat sampel AC berjaya menurunkan peratusan COD dari serendah 69.57% hingga setinggi 72.82%. Ini mungkin kerana AC mampu menjerap bahan cemar organik pada permukaan aktif. Hasil ujian TOC juga menunjukkan penurunan nilai TOC setelah proses penjerapan POME dengan AC. Peratusan kehilangan nilai TOC antara 87.62% hingga 95.24%. AC mampu mengurangkan kandungan bahan organik yang tercemar dengan mengurangkan kandungan karbon dan oksigen POME. Terdapat penyelidik yang berjaya mengurangkan COD POME sebanyak 89.60% dan NH_3-N 75.61% dengan menggunakan AC sebagai bahan penjerap [18]. Pengurangan COD dan TOC berlaku semasa proses penjerapan di mana kawasan utama untuk penjerapan berlaku di permukaan luar AC. Sekiranya penjerapan berlaku di permukaan dalaman liang maka proses penjerapan memerlukan lebih lama [42].

Kajian sebelum ini mendapati bahawa AC pada 10 g/L telah menyebabkan penurunan COD dan SS secara drastik [43]. Penemuan ini selari dengan keputusan kajian sebelumnya di mana AC terbukti dapat mengurangkan karbon organik terlarut (DOC) [44]. AC mengurangkan bahan organik melalui ukuran liang yang sangat halus semasa proses penjerapan. Sebagai bahan penjerap, AC mempunyai luas permukaan berliang untuk memerangkap molekul organik yang menyumbang kepada penurunan kepekatan BOD dan

COD [45]. Oleh itu, AC boleh digunakan sebagai langkah rawatan awal yang membawa kepada pengurangan bahan penyumbatan/pembekuan dan penyingkiran organik yang lebih baik [44].

Jadual 4. Keputusan COD dan TOC

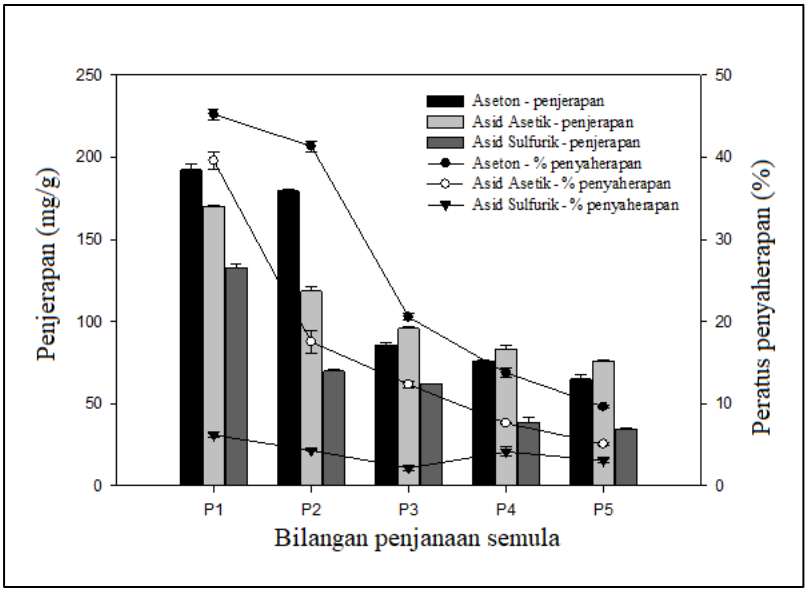
Sampel	COD (mg/L)	COD (%)	TOC (mg/L)	TOC (%)
POME (kawalan)	401	-	105	-
RHACK	122	69.57	5	95.24
RHACNa	109	72.82	13	87.62

Penjanaan semula dengan kaedah kimia terhadap AC-MB: Kesan agen penyaherapan

Hasil penjerapan dan peratusan penyaherapan untuk RHACK pada Rajah 4 mendapati bahawa peningkatan bilangan penjanaan semula telah mengurangkan kapasiti penjerapan dan peratusan penyaherapan sampel. Kecekapan penyaherapan AC oleh agen penyaherapan yang berbeza menghasilkan nilai yang berbeza. Peratusan penyaherapan MB pada RHACK (Rajah 4) dengan agen penyaherapan aseton tertinggi pada 45.22-9.63% dan penjerapan 192.30-65.14 mg/g untuk lima penjanaan semula, diikuti oleh asid asetik pada 39.58-5.10% dan penjerapan 170.28-76.14 mg/g, sementara asid sulfurik terendah adalah 6.18-2.18% dan penjerapan 132.86-34.56 mg/g. Hasil kajian menunjukkan bahawa agen penyaherapan pelarut organik, iaitu aseton dan asid asetik, lebih menyaherap daripada pelarut bukan organik asid sulfurik pada RHAC-MB. Pewarna yang terjerap dapat dinyaherap menggunakan air neutral, maka pewarna tersebut terjerap dengan bahan penjerap melalui ikatan lemah. Jika dapat dinyaherap pewarna dengan asid sulfurik atau air alkali, maka pewarna melakukan penjerapan melalui pertukaran ion. Penggunaan pelarut organik seperti aseton atau asid asetik untuk menyaherap pewarna telah terjerap melalui kimia jerapan. Manakala jika ternyaherap dengan asid mineral seperti HCl, maka pewarna telah dijerap melalui jerapan fizikal [28]. Ini menunjukkan jerapan kimia merupakan mekanisma penjerapan AC-MB.

Faktor berat molekul agen penyaherapan cenderung mempengaruhi hasilnya. Berat molekul agen penyaherapan lebih kecil daripada bahan yang dijerap (MB) akan memberikan pemindahan fizikal (pelarutan) molekul MB oleh molekul agen penyaherapan [46]. Aseton mempunyai berat molekul yang lebih kecil 58 g/mol diikuti oleh asid asetik (60 g/mol) dan asid sulfurik (98 g/mol) berbanding dengan MB 319.86 g/mol cenderung menghasilkan peratusan penyaherapan yang lebih baik oleh aseton daripada asid asetik dan asid sulfurik.

Sebilangan besar pelarut organik mempunyai kumpulan hidrofobik ((-CH_3, -CH_2CH_3) dan hidrofilik (-OH, -CN, = O). Pelarut organik mempunyai kumpulan hidrofobik seperti kumpulan metil ((-CH_3) yang akan dijerap pada kumpulan hidrofobik aromatik struktur karbon, sementara kumpulan hidrofilik berinteraksi dengan kumpulan fungsi bahan penjerap. Hal ini kerana kumpulan metil lebih berkait rapat dengan kumpulan hidrofobik karbon, ada kekuatan pendorong untuk molekul MB tidak aktif daripada AC-MB yang diisi [47]. Aseton mempunyai kumpulan metil yang lebih besar yang memudahkan proses penyaherapan. Kumpulan hidrofobik agen penyaherapan akan lebih terjerap daripada kumpulan hidrofilik dengan bahagian hidrofobik AC, yang seterusnya membentuk dorongan kepada proses penyaherapan molekul bahan yang dijerap [48].



Rajah 4. Keputusan penjerapan dan peratus penyaherapan RHACK pada analisa penjanaan semula

Kesimpulan

Peningkatan bahan penjerap AC mengakibatkan peningkatan peratusan perubahan warna POME. Secara amnya, bahan penjerap pada kadar 0.4 g dan masa 60 min mampu menyahwarnakan POME. RHACK menunjukkan peratusan penyahwarnaan yang lebih baik daripada RHACNa kerana faktor luas permukaan liang. Sampel AC dapat menurunkan COD 69.57-72.82% kerana kemampuan AC menyerap bahan cemar organik. Nilai TOC diturunkan kepada 87.62-95.24% kesan AC yang dapat mengurangkan kehadiran C dan O dalam kandungan bahan organik POME. Kajian lima pusingan penjanaan semula analisa penjerapan-penyaherapan MB-AC mendapati bahawa penyaherapan menggunakan aseton menghasilkan peratusan penjerapan dan penyaherapan terbaik untuk sampel RHACK berbanding dengan menggunakan asid asetik dan asid sulfurik. Pelarut organik lebih cekap dalam proses penyaherapan pewarna kationik pada RHACK daripada pelarut bukan organik. Pengaruh jenis pelarut/agen penyaherapan adalah faktor penyebab kepada kebolehnyaherapan AC-MB. Sebagai perbandingan untuk ketiga-tiga jenis agen penyaherapan, aseton menghasilkan peratusan penyaherapan MB yang lebih tinggi diikuti oleh asid asetik dan asid sulfurik. Faktor berat molekul dan kumpulan hidrofobik pada agen penyaherapan mungkin antara sebab aseton lebih baik.

Penghargaan

Penulis ingin mengucapkan penghargaan dan ucapan terima kasih kepada pihak MARDI dan UKM kerana masing-masing telah menyediakan bantuan kewangan dan peralatan makmal semasa kajian ini dilakukan.

Rujukan

1. Eleanor, S., Abel, R., Soh, Loh, K. and Abu Bakar, N. (2018). Bio-based products from palm oil mill effluent. *Palm Oil Engineering Bulletin* 127: 25-31.
2. Ma, A. N. (1999). The planters, Kuala Lumpur innovations in management of palm oil mill effluent. Palm Oil research Institute of Malaysia (PORIM).
3. Singh, R.P., Ibrahim, M.H., Esa, N. and Iliyana, M.S. (2010). Composting of waste from palm oil mill: a sustainable waste management practice. *Reviews in Environmental Science and Biotechnology* 9(4): 331-344.

4. Ohimain, E. I., Seiyaboh, E. I., Izah, S. C., Oghenegueke, E. V. and Perewarebo, G.T. (2012). Some selected physico-chemical and heavy metal properties of palm oil mill effluents. *Greener Journal of Physical Sciences* 2(4): 131-137.
5. Kamyab, H., Tin Lee, C., Md Din, M. F., Ponraj, M., Mohamad, S. E. and Sohrabi, M. (2014). Effects of nitrogen source on enhancing growth conditions of green algae to produce higher lipid. *Desalination and Water Treatment* 52(19-21): 3579-3584.
6. Amosa, M. K. (2017). Towards sustainable membrane filtration of palm oil mill effluent: Analysis of fouling phenomena from a hybrid PAC-UF process. *Applied Water Science,* 7(6): 3365-3375.
7. Ghani, M.S.H., Haan, T.Y., Lun, A.W., Mohammad, A.W., Ngteni, R. and Yusof, K.M.M. (2018). Fouling assessment of tertiary palm oil mill effluent (POME) membrane treatment for water reclamation. *Journal of Water Reuse and Desalination* 8(3): 412-423.
8. Poh, P. E., Ong, W. Y. J., Lau, E. V. and Chong, M. N. (2014). Investigation on micro-bubble flotation and coagulation for the treatment of anaerobically treated palm oil mill effluent (POME). *Journal of Environmental Chemical Engineering* 2(2): 1174-1181.
9. Zahrim, A.Y., Dexter, Z. D., Joseph, C. G. and Hilal, N. (2017). Effective coagulation-flocculation treatment of highly polluted palm oil mill biogas plant wastewater using dual coagulants: decolourisation, kinetics and phytotoxicity studies. *Journal of Water Process Engineering* 16: 258-269.
10. Ng, K. H., Lee, C. H., Khan, M. R. and Cheng, C. K. (2016). Photocatalytic degradation of recalcitrant POME waste by using silver doped titania: Photokinetics and scavenging studies. *Chemical Engineering Journal* 286: 282-290.
11. Abdulsalam, M., Hasfalina, C. M., Mohamed, H. A., Abd Karim, S. F. and Faiez, M. S. (2018). Microwave irradiated coconut shell-activated carbon for decolourisation of palm oil mill effluent (POME). *Food Research* 2(6): 526-534.
12. Alkhatib, M. F., Mamun, A. A. and Akbar, I. (2015). Application of response surface methodology (RSM) for optimization of color removal from POME by granular activated carbon. *International Journal of Environmental Science and Technology* 12(4): 1295-1302.
13. Kaman, S. P. D., Tan, I. A. W. and Lim, L. L. P. (2017). Palm oil mill effluent treatment using coconut shell – based activated carbon: Adsorption equilibrium and isotherm. *MATEC Web of Conferences* 87: 03009.
14. Ibrahim, I., Hassan, M. A., Abd-Aziz, S., Shirai, Y., Andou, Y., Othman, M. R., Ali, A. A. M., Zakaria, M. R. (2017). Reduction of residual pollutants from biologically treated palm oil mill effluent final discharge by steam activated bioadsorbent from oil palm biomass. *Journal Cleaner Production* 141: 122- 127.
15. Mohammed, R. R. and Chong, M. F. (2014). Treatment and decolorization of biologically treated palm oil mill effluent (POME) using banana peel as novel biosorbent. *Journal of Environmental Management* 132: 237-249.
16. Parthasarathy, S., Mohammed, R.R., Fong, C.M., Gomes, R.L., Manickam, S. 2016. A novel hybrid approach of activated carbon and ultrasound cavitation for intensification of palm oil mill effluent (POME) polishing. *Journal Cleaner Production* 112: 1218-1226.
17. Azmi, N. S. and Yunos, K. F. M. (2014). Wastewater treatment of oil palm mill effluent (POME) by ultrafiltration membrane separation technique coupled with adsorption treatment as pre-treatment. A*griculture and Agricultural Science Procedia* 2: 257-264.
18. Adeleke, A. R. O., Latiff, A. A. A., Daud, Z., Ridzuan, B., Daud, M. (2016). Remediation of raw wastewater of palm oil mill using activated cow bone powder through batch adsorption. *Key Engineering Materials* 705: 380-384.
19. Shah, I. K., Pre, P., Alappat, B. J. (2013). Steam regeneration of adsorbents: an experimental and technical review. *Chemical Science Transaction* 2(4): 1078-1088.

20. Foo, K.Y. and Hameed, B. H. (2012). A cost effective method for regeneration of durian shell and jackfruit peel activated carbons by microwave irradiation. *Chemical Engineering Journal,* 193-194: 404-409.
21. Sanyiirek, N. K. and Yönten, V. (2018). The desorption of methyl orange on active carbon by *Vitu vinifera* L. and the effect of temperature to this system. *International Conference on Physical Chemistry and Functioned Materials* 19-21 June 2018, Firat University, Elazig Turkey.
22. Yu, M., Jianli, Y., Wang, L. 2017. CO_2 - activated porous carbon derived from cattail biomass for removal of malachite green dye and application as super capacitors. *Chemical Engineering Journal* 317: 493-502.
23. Regti, A., Laamari, M. R., Stiriba, S. E. and El Haddad, M. (2017). Potential use of activated carbon derived from Persea species under alkaline conditions for removing cationic dye from wastewaters. *Journal Associate Arab University Basic Appllied Sci*ence 24: 10-18.
24. Salleh, M. A. M., Mahmoud, D. K., Karim, W. A. W. A. and Idris, A. (2011). Cationic and anionic dye adsorption by agricultural solid wastes: a comprehensive review. *Desalination* 280(1-3): 1-13.
25. Berenguer, R., Marco-Lozar, J. P., Quijada, C., Cazorla-Amoros, D. and Morallon, E. (2010). Comparison among chemical, thermal and electrochemical regeneration of phenol-saturated activated carbon. *Energy Fuels,* 24: 3366-3372.
26. He, X., Male, K. B., Nesterenko, P. N., Brabazon, D., Paull, B. (2013). Adsorption and desorption of methylene blue on porous carbon monoliths and nanocrystalline cellulose. *Applied Materials & Interfaces* 5: 8796-8304.
27. Lata, S., Singh, P. K., Samadder, S. R. (2014). Regeneration of adsorbents and recovery of heavy metals: a review. *International Journal of Environment Science Technology* 12: 1461-1478.
28. Bharathi, K. S. and Ramesh, S. T. (2013). Removal of dyes using agricultural waste as low-cost adsorbents: a review. *Appllied Water Science* 3: 773-790.
29. Foo, K. Y. and Hameed, B. H. (2011). Utilization of rice husks as a feedstock for preparation of activated carbon by microwave induced KOH and K_2CO_3 activation. *Bioresource Technology* 102(20): 9814-9817.
30. Zhang, F., Li, G. D. and Chen, J. S. (2008). Effects of raw material texture and activation manner on surface area of porous carbons derived from biomass resources. *Journal of Colloid and Interface Science* 327(1): 108-114.
31. Sricharoenchaikul, V., Pechyen, C., Aht-Ong, D. and Atong, D. (2008). Preparation and characterization of activated carbon from the pyrolysis of physic nut (*Jatropha curcas* L.) waste. *Energy and Fuels* 22(1): 31-37.
32. Lu, C., Pan, L. and Zhu, B. (2015). Study the static adsorption/desorption of formaldehyde on activated carbon. *International Forum on Energy, Environment Science and Materials,* 2015: 943-947.
33. Lillo-Ródenas, M. A., Lozano-Castelló, D., Cazorla-Amorós, D. and Linares-Solano, A. (2001). Preparation of activated carbons from Spanish anthracite - II. Activation by NaOH. *Carbon* 39(5): 751-759.
34. Guo, Y., Yu, K., Wang, Z. and Xu, H. (2003). Effects of activation conditions on preparation of porous carbon from rice husk. *Carbon,* 41(8): 1645-1648.
35. Chunlan, L., Shaoping, X., Yixiong, G., Shuqin, L. and Changhou, L. (2005). Effect of pre-carbonization of petroleum cokes on chemical activation process with KOH. *Carbon* 43(11): 2295-2301.
36. Muniandy, L., Adam, F., Mohamed, A. R. and Ng, E. P. (2014). The synthesis and characterization of high purity mixed microporous/mesoporous activated carbon from rice husk using chemical activation with NaOH and KOH. *Microporous and Mesoporous Materials* 197: 316-323.
37. Pandey, B. D., Saima, H. K. and Chattree, A. (2015). Preparation and characterization of activated carbon derived from rice husk by NaOH activation. *International Journal of Mathematics and Physical Sciences Research*, 3(2): 158-164.

38. Cheenmatchaya, A. and Kungwankunakorn, S. (2014). Preparation of activated carbon derived from rice husk by simple carbonization and chemical activation for using as gasoline adsorbent. *International Journal of Environmental Science and Development* 5(2): 171-175.
39. Gobi, K. and Vadivelu, V. M. (2013). By-products of palm oil mill effluent treatment plant - a step towards sustainability. *Renewable and Sustainable Energy Review* 28: 788-803.
40. Mohammed, R. R. (2013). Decolorisation of biologically treated palm oil mill effluent (POME) using adsorption technique. *International Refereed Journal of Engineering and Science,* 2(10): 01-11.
41. Mohammed, R. R. and Chong, M. F. (2014). Treatment and decolorization of biologically treated palm oil mill effluent (POME) using banana peel as novel biosorbent. *Journal of Environmental Management,* 132: 237-249.
42. AremuMuyibi, S., Tajari, T., Jami, M. S. and KoladeAmosa, M. (2014). Removal of organics from treated palm oil mill effluent (POME) using powdered activated carbon (PAC). *Advances in Environmental Biology,* 8(3): 590-595.
43. Othman, M. R., Hassan, M. A., Shirai, Y., Baharuddin, A. S., Ali, A. A. M. and Idris J. (2013). Treatment of effluents from palm oil mill process to achieve river water quality for reuse as recycled water in a zero emission system. *Journal of Cleaner Production* 67: 58-61.
44. Siebdrath, N., Ziskind, G. and Gitis, V. (2012). Cleaning secondary effluents with organoclays and activated carbon. *Journal Chemical Technology and Biotechnol*ogy 87: 51-57.
45. Idris, J., MdSom, A., Musa, M., Ku Hamid, K. H., Husen, R. and MuhdRodhi, M. N. (2013). Dragon fruit foliage plant-based coagulant for treatment of concentrated latex effluent: comparison of treatment with ferric sulfate. *Journal of Chemistry* 38: 1-7.
46. Lu, P. J., Lin, H. C., Yu, W. T. and Chern, J. M. (2011). Chemical regeneration of activated carbon used for dye adsorption. *Journal of the Taiwan Institute of Chemical Engineer*s 42: 305-311.
47. Gerard, C. and Örjan, G. (2005). Prediction of large variation in biota to sediment accumulation factors due to concentration dependent black carbon adsorption of planar hydrophobic organic compounds. *Environmental Toxicology & Chemistry* 24(3): 495-498.
48. Xing, X., Qu, H., Shao, R., Wang, Q. and Xie, H. (2017). Mechanism and kinetics of dye desorption from dye-loaded carbon (XC-72) with alcohol-water system as desorbent. *Water Science & Technology,* 76(5): 1243-1250.

Malaysian Journal of Analytical Sciences (MJAS)
Published by Malaysian Analytical Sciences Society

CHANGES OF FATTY ACID COMPOSITION IN SCLERACTINIAN CORAL, *Galaxea fascicularis* (LINNAEUS, 1767) BY ACUTE EXPOSURE OF IRGAROL-1051

(Perubahan Komposisi Asid Lemak dalam Karang Scleractinia, *Galaxea fascicularis* (LINNAEUS, 1976) oleh Pededahan Akut Irgarol-1051)

Hassan Rashid Ali[1], Che Din Mohd Safuan[2], Marinah Mohd Ariffin[3], Mohammed Ali Sheikh[1], Noor Azhar Mohamed Shazili[2], Aminudin Muhammad Afiq-Firdaus[2], Zainudin Bachok[2]*

[1]*Tropical Research Centre for Oceanography, Environment and Natural Resources, The State University of Zanzibar, P. O. Box 146, Zanzibar-Tanzania*
[2]*Institute of Oceanography and Environment*
[3]*Faculty of Science and Marine and Environment*
University Malaysia Terengganu, 21030 Kuala Nerus, Terengganu, Malaysia

**Corresponding author: zainudinb@umt.edu.my*

Received: 20 February 2022; Accepted: 18 May 2022; Published: 25 August 2022

Abstract

Antifouling biocide such as Irgarol 1051 has been widely used as a replacement of tributyl tin (TBT). In Malaysia, we reported the level of Irgarol in coastal water up to 2021ng/L. This raises concern because high dosage of chemical pollutant in the seawater can affect the marine organisms. This study therefore, examined the effect of Irgarol 1051 on fatty acids composition of reef building coral *Galaxea fascicularis*, collected in Pulau Bidong, Malaysia. The corals were exposed to different doses of Irgarol 1051 under short term exposure (96 hrs) and the fatty acid compositions of the coral tissues were determined using the gas chromatography technique. The findings revealed no clear different (p >0.05) among untreated samples (fresh and control) and both were dominated by polyunsaturated fatty acids (PUFA), followed by saturated fatty acids (SAFA) and monounsaturated fatty acids (MUFA). In contrast, the treated samples of *G. fascicularis* (20, 100 and 500 µg/L) were significant different (p <0.05) where both SAFA and PUFA were significantly lowered than untreated samples especially at the samples exposed to higher dose of Irgarol 1051 (100 and 500 µg/L). As the level of dose increased, SAFA such as 16:0 and unsaturated fatty acid from ω3 and ω6 series were largely affected by the toxicology effect of the Irgarol 1051. The results indicate that Irgarol 1051 significantly affecting the health of the corals even at the lowest dose of Irgarol 1051 applied in this study. It is suggested that the antifouling biocide may have implication on metabolisms of the corals.

Keywords: booster biocides, antifouling chemicals, fatty acids, hard coral, coral reefs

Abstrak

Biosid anti-kotoran seperti Irgarol 1051 telah digunakan secara meluas sebagai pengganti kepada tributil tin (TBT). Di Malaysia, kami telah melaporkan tahap Irgarol di perairan pantai mencapai setinggi 2021ng/L. Ini menimbulkan kebimbangan kerana dos bahan pencemar kimia yang tinggi dalam air laut boleh menjejaskan organisma marin. Oleh itu, kajian ini mengkaji kesan Irgarol

1051 pada komposisi asid lemak di dalam karang keras *Galaxea fascicularis*. Pendedahan jangka pendek (96 jam) telah dilakukan ke atas spesis karang ini dengan menggunakan kepekatan Irgarol yang berbeza dan komposisi asid lemak didalam tisu karang ditentukan dengan menggunakan teknik gas kromatografi. Hasil kajian mendapati tiada perubahan yang ketara pada karang yang tidak terdedah dengan Irgarol (sampel segar dan kawalan) dan kedua-duanya mempunyai kandungan asid lemak yang didominasi oleh asid lemak poli tidak tepu (PUFA), diikuti dengan asid lemak tepu (SAFA) serta asid lemak mono tidak tepu (MUFA). Sebaliknya, terdapat perbezaan yang ketara antara sampel karang yang tededah dengan kepekatan berbeza Irgarol (20, 100 and 500 µg/L) dimana komposisi SAFA dan PUFA lebih rendah berbanding sampel segar dan kawalan, terutamanya pada sampel yang terdedah pada kepekatan Irgarol 1051 yang tinggi. SAFA seperti 16:0 dan asid lemak tidak tepu dari kumpulan ω3 dan ω6 adalah antara asid lemak yang sangat terkesan terhadap pendedahan pada bahan kimia ini. Dapatan kajian juga menunjukkan, Irgarol 1051 sangat mempengaruhi kesihatan karang walaupun hanya terdedah pada dos yang rendah. Ini menunjukkan bahawa terdapat implikasi pada metabolisma karang apabila terdedah kepada bahan kimia ini.

Kata kunci: biosid penggalak, bahan kimia anti-kotoran, asid lemak, karang keras, terumbu karang

Introduction

Booster biocide such as Irgarol 1051 is categorized as priority hazardous substance by the European commission [1] but is used in worldwide as a means to control the fouling on boats and ships. The research to date has tended to report a contamination by alternative biocides Irgarol 1051 in coastal water of Malaysian peninsular [2] as well as in sediments and mussels around Malaysian coast [3]. Despite their increased use worldwide, far too little attention has been paid to the fate, toxicity and persistence of this booster biocide Irgarol as well as their potential risks on marine ecosystems [4]. The toxicity of this booster biocide on marine organisms, especially those from tropical and subtropical regions are still largely unknown, as most available and relevant toxicity data were generated with temperate species [5]. As a consequence, coral reefs around the world are facing a number of threats of the toxic chemical's inputs from terrestrial such as domestic activities, agricultural, and industrial [6, 7]. For example, in Japan, it was reported that, development activities such as road building, farming, and modification of drainage systems have increased runoff of red soil in coral reefs which have negative impact to coral reef ecosystems [4, 8]. Toxic chemical substances are contributing to the destruction of coral reef ecosystems. Research by Knutson et al. [9] revealed a potential effect of Irgarol 1051 on coral larvae which significantly reduce the larvae settlement even at low dose of Irgarol 1051 (100ng/l). However, in Malaysia most of the pollutant's studies have been focused on heavy metals either in ports, marinas and islands; but attention has not been paid to the distribution and impacts of antifouling chemicals (*e.g.,* Irgarol) in this region. Recently, we reported the effects of Irgarol on fatty acid of Asian sea-bass, *Lates calcarifer* in Malaysia [10] but still there is a significant gap on research information regarding to the toxicity of new antifouling chemicals such as Irgarol in relation with the health of coral reef organisms worldwide.

Comparatively few studies have dealt with the effects of new antifouling Irgarol in particular on different coral reef organism in aquatic systems. Furthermore, the studies that have dealt with the effects of Irgarol on lake or river bacteria, have seldom examined these effects on the composition of these communities [11] or have analysed the whole microbial communities or the whole plankton [12] without testing the direct effects of these pollutants on marine organisms using fatty acid as an indicator. Hence, the direct effects of Irgarol and many other pesticides on natural aquatic organisms are poorly known. Understanding the effects of Irgarol and other pesticides on coral reef is of interest, given that the alteration of marine communities might affect their ecosystem function. Therefore, this study was carried out to determine the fatty acid profile of fresh sample (control) and compared with those short term exposed *Galaxea fascicularis* in different doses of Irgarol to realize environmental causing damages to these vital marine natural resources.

Materials and Methods

Experimental design

Fresh corals (*Galaxea fascicularis*) were taken from Pulau Bidong, Terengganu, Malaysia (5°37′N 103°4′E). The corals were acclimatized for 2 weeks in well aerated holding polyethylene tanks (500 L), containing natural seawater with a salinity of 30 ppt, under a natural

photoperiod 12 h:12 h (light: dark) cycle. The water in the tank was passed through a 1-mm filter, treated with UV-sterilized and refilled daily. For the purpose of the experiment, the coral was not fed at all.

A stock solution of 1000 mg/l Irgarol (Sigma-Aldrich) was prepared by using acetone and the working concentrations were made up by spiking the required concentrations to the sea water (volume= 3000 mL). *Galaxea fascicularis* were acclimatized for two weeks in the laboratory before the acute exposure tests to Irgarol for 96 hrs [13] as shown in Figure 1. Water quality characteristics were measured daily: dissolved oxygen (DO) 7.2±0.5 mg/L, and pH 7.69±0.2, but the temperature was automatically controlled to 27 ^{0}C using cooling chiller throughout the whole experiment duration. After the two weeks acclimatization period, corals were transferred into different experimental tanks containing three litres of water and exposed to test concentrations of 0 (T1), 20 µg/L (T2), 100 µg/L (T3), and 500 µg/L (T4) of Irgarol in three replicates for 96h. Samples in control the control tank was kept for the sake of comparison. After four days (96hrs), the tissue of the coral was removed by using water pick and taken to the laboratory for fatty acid analysis.

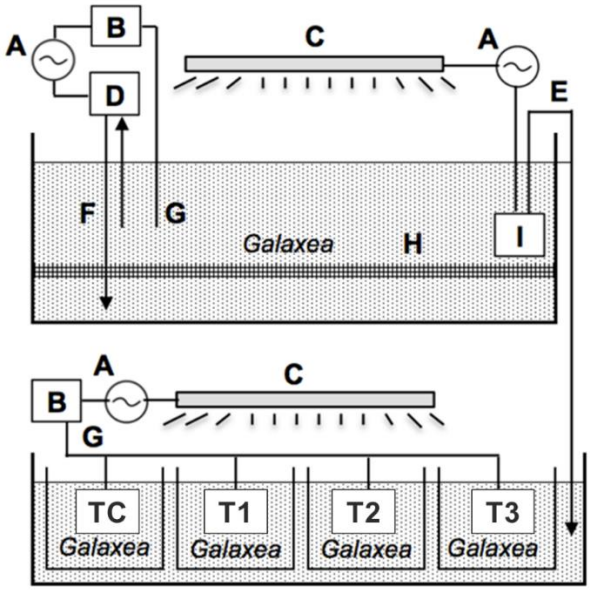


Figure 1. Schematic diagram of acclimation tank (top) and experiment tanks (bottom) during exposure experiment of Irgarol on the corals *Galaxea fascicularis*. A, power supply; B, aeration compressor; C, lamp; D, water chiller; E, outflow water; F, inflow and outflow chiller water; G, aeration tubes; H, filter; I, water pump. T1 to T3 are Irgarol test concentrations of 20 µg/L, 100 µg/L, and 500 µg/L, respectively while TC as control.

Sample preparation

Fatty acid methyl ester extraction

Tissues of *Galaxea fascicularis* were taken as samples for fatty acid composition analysis. The one step method [14] was used in this experiment to combine extraction and esterification processes in a single tube. Three replicates of each tissue samples (200-300 mg) were mixed with 4 mL of hexane and 1 mL (1 mg/mL) of internal standard (analytical standard of nonadecanoic acid, C19:0, Sigma-Aldrich) solution in a 50 mL centrifuge tube. After adding 2 mL of 14% BF_3 in methanol and a magnetic stirring bar, the head space of tube was flushed with nitrogen gas and then closed tightly with a Teflon-lined screw-cap. The capped tube was heated on a hot plate at 100 °C for 120 min under continuous stirring. After cooling to room temperature, 1 mL of hexane was added followed by 2 mL of distilled water. The tube was then shaken vigorously for 1 min

and centrifuged for 3 min at 2500 rpm. Of the two phases which formed, the upper phase was hexane layer containing the FAMEs. Finally, ~1–2 ml of the hexane layer was transferred using a Pasteur pipette into a clean sample vial prior to for injection for the GC-FID FAME analysis. Fatty acid concentrations (CFA, mg/g of dry sample) were calculated by comparing the peak area of fatty acid in the sample with the peak area of internal standard as follows:

$$C_{FA} = {}^{A_S}/_{A_{IS}} \times {}^{C_{IS}}/_{W_S} \quad (1)$$

where; A_S = peak area of fatty acid in the sample in chromatogram, A_{IS}= peak area of internal standard in chromatogram, C_{IS} = concentration of internal standard (mg), and W_S = weight of sample (g).

Qualitatively (as a percentage), composition of individual fatty acids was calculated by comparing the peak area of each fatty acid with the total peak area of all fatty acids in the sample.

Gas chromatography conditions

The FAMEs were separated and quantified using a gas chromatography equipped with flame ionization detector, GC-FID (GC = Agilent Technologies 6890N, FID = Agilent 5973 MSD). Separation was performed with an FFAP-polar capillary column (30 m×0.32 mm internal diameter, 0.25 μm film thickness) in split-less mode. Hydrogen was used as a carrier gas. The inlet temperature is 250 °C. After injection at 60 °C, the oven temperature was raised to 150 °C at a rate 40 °C min^{-1}, then to 230 °C at 3 °C min^{-1}, and finally held constant for 30 min. The flame ionization was held at 240 °C. FAME peaks were identified by comparing their retention times with those of authentic standards (Supelco Inc.). Fatty acids were designated as an n:pωx, where n is the number of carbon atoms in the aliphatic chain, p is the number of double bonds and x is the position of the first double bond from the terminal methyl group. The analytical precision for samples was generally <5% for total amounts and major components of FAMEs.

Statistical analysis

Differences among the mean value of fatty acid compositions (ΣSAFA, ΣMUFA, ΣPUFA and fatty acid components) were examined by Generalize Linear Model (GLM) which involves the Multivariate Analysis of Variance (MANOVA). The null hypotheses of 'no difference between treatments' were tested and significant levels less than 0.05 (p <0.05) indicated significant differences for the test treatment. Any significance differences between the treatment samples were further tested via multiple comparison using Bonferroni post-hoc test. Prior to the analysis, data were tested for homogeneity of variances (Leven's test) and the normality of the data (Shapiro–Wilk's test). Statistical analysis was performed using IBM SPSS statistic software.

Results and Discussion

Major fatty acid composition

There was a significant different on the composition of ΣSAFA [$F_{(4,10)} = 39.965$, $p < 0.001$], ΣMUFA [$F_{(4,10)} = 81.811$, $p < 0.001$] and ΣPUFA [$F_{(4,10)} = 30.449$, $p < 0.001$] among the treatment samples. As shown in Figure 2, lower composition of ΣSAFA, ΣMUFA and ΣPUFA were found in the samples exposed with Irgarol 1051. Pairwise test revealed no clear different ($p > 0.05$) between fresh, control and T1 in ΣSAFA composition but significantly different (p <0.05) with the samples exposed to 100 μg/L (T2) and 500 μg/L (T3) Irgarol 1051. Both ΣMUFA and ΣPUFA were not significantly differ ($p > 0.05$) between fresh and control but the composition in the samples exposed to Irgarol 1051 do not follow the trend. Higher composition of ΣMUFA was found in T1 and T2 with palmitoleic acid (16:1) highly contribute to the MUFA composition while ΣPUFA significantly lowered as compared to fresh and control samples.

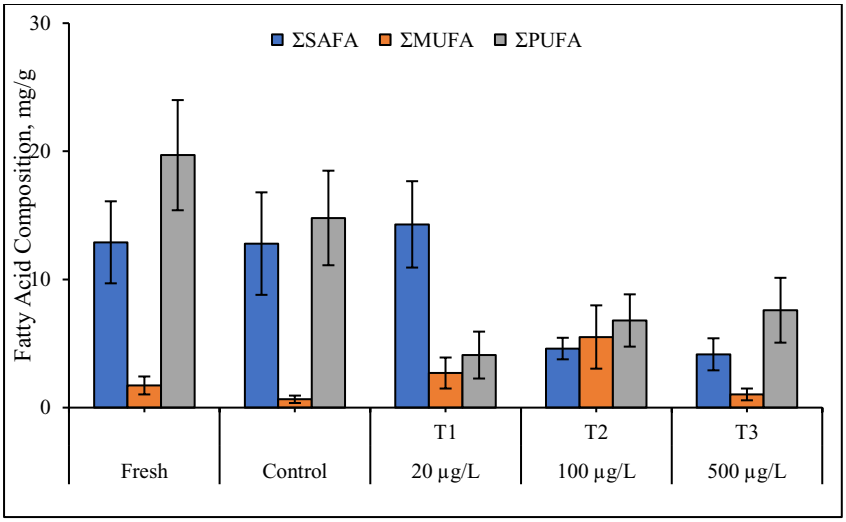


Figure 2. Composition (mg/g) dry weight of SAFA, MUFA, PUFA and total fatty acid in tissue samples of *Galaxea fascicularis* after 96hrs acute exposure test of Irgarol 1051. Values are means with standard deviation (n=3)

Fatty acid components

There was a statistically significant difference in the composition of C14:0 [F (4,10) = 6.101, p = 0.009], C16:0 [F (4,10) = 34.282, p <0.001] and other SAFA [F (4,10) = 46.661, p <0.001] among the treatment samples. Based on post-hoc test, the composition of C16:0 was found significantly lower (p <0.05) in the samples expose to 20 µg/L,100 µg/L and 500 µg/L Irgarol as compared to fresh and control sample, whereby no clear differences (p > 0.05) were found between fresh and control. As shown in Figure 3, the fatty acid compositions of 16:0 was largely affected when the samples were exposed to100 µ/g and 500 µ/g Irgarol. No clear trend was found in the composition of 14:0 and In this study, four PUFA components comprised of omega-6 and omega-3 fatty acids namely γ-Linolenic acid (18:3ω6), α-linolenic acid (18:3ω3 or ALA), eicosatrienoic acid (20:3n3) and eicosapentaenoic acid (20:5ω3 or EPA) were examined. The composition of 18:3ω6 [F (4,10) = 89.997, p < 0.001], 18:3ω3 [F (4,10) = 19.808, p <0.001], 20:3n3 [F (4,10) = 17.364, p <0.001] and 20:5ω3 [F (4,10) = 56.966, p <0.001] were significantly different among the treatment samples. No clear differences (p > 0.05) were found between fresh, and control as indicated by pairwise test but significantly lowered in the samples exposed to 20 µg/L/g ,100 µg/L and 500 µg/L Irgarol (Figure 4).

This study revealed the effect of different concentrations of Irgarol on fatty acid composition in the tissue of *G. fascicularis*. The present findings demonstrate that Irgarol 1051 affecting the health of corals due to changes of fatty acids composition of *G. fascicularis* and may have implications on metabolisms of the corals. Lower fatty acid composition of ΣSAFA and ΣPUFA was observed in the tissue of *G. fascicularis* especially when exposed to high concentration (100 µg/L and 500 µg/L) of Irgarol. Previously, similar trend was also found in a study using Asian sea-bass *Lates calcarifer* where lower ΣSAFA and ΣPUFA was found in the samples exposed to 10%, 30% and 50% of the 96 hrs LC50 = 0.535 mg/ml of triazine herbicides Irgarol 1051 as compared to fresh and control [10]. In contrast, toxicity test of Irgarol 1051 to hard coral *Fungia fungites* revealed that ΣSAFA, ΣPUFA and ΣMUFA were reduced in a as the dose of Irgarol 1051 increased [15]. The inconsistency of fatty acid composition between different species of hard corals can be related to their species-specific and dietary of the species [16, 17].

Lower ΣSAFA is largely associated with the lower composition of palmitic acid (16:0) when the samples exposed to Irgarol 1051 especially at higher doses (100 µ/g and 500 µ/g). Generally, the high content of palmitic acid is commonly found in healthy corals and can reach 50% of the total FA composition [15-17]. Toxicity test

of metal cadmium to marine macroalgae, *Ulva lactuca* revealed that reduction in palmitic acid can be due to an active desaturation process of fatty acid for the production of unsaturated fatty acid such as linoleic (18:2ω6) and linolenic acid (18:3ω6) [18]. However, in the present study, there was no evidence to support the biosynthesis process because some of the PUFAs such as linolenic acid was below the detectable limit.

Among the unsaturated fatty acid, ΣPUFA are largely affected by Irgarol 1051 as compared to ΣMUFA which significantly higher in control and fresh samples. ΣMUFA shows inconsistent trend as compared to fresh and control samples. Perhaps, the MUFA is the intermediate fatty acid in biosynthesis of fatty acid pathway for the conversion from SAFA to PUFA following the contemporary concept [16]. Hence, extensive change in both SAFA and PUFA possibly affecting the inconsistent of ΣMUFA composition. The ΣMUFA having the least composition in fresh and control samples, which is commonly observed in a healthy coral and could remain the low in the samples under stress condition by Irgarol 1051 [10, 15]. In contrast, high composition of ΣMUFA was found in the samples exposed to 100 µ/g of Irgarol 1051 where only palmitoleic acid (16:1) was detected in the GC-FID where the rest of MUFA components were below the detectable limit. High level of ΣMUFA than ΣSAFA possibly due to the active conversion of SAFA to unsaturated fatty acid which leading to high content of ΣMUFA and ΣPUFA in T2 samples [17].

Presently, ΣPUFA was largely affected and significantly lower in all tested samples as compared to fresh and control samples even at lower dosage of Irgarol 1051. It is known that unsaturated fatty acid such as PUFA is highly susceptible to oxidative stress [20]. There is an increasing interest in oxidative stress in the context of chemical stress in marine organisms [21-23]. In corals, cellular mechanism underlying the bleaching is tightly coupled with the accumulation of toxic reactive oxygen species (ROS) which is naturally counterbalance with other SAFA as indicated by the post-hoc test (Figure 3). antioxidant enzymes [24]. A study on acute exposure of Irgarol 1051 on branching coral *Madracis mirabilis* proven that the chemical toxicity greatly enhances the intracellular formation of toxic ROS which compromise by oxidative defence capacity [23]. However, under certain condition, coral will utilize their energy reserve as a barrier or as a repair system against the oxidative stress when the antioxidant enzymes cannot cope with excessive production of ROS [20]. It is well proven that the depletion of PUFA composition after the loss of symbiont can be associated with oxidative stress [20, 25, 26]. Additionally, all PUFA components from the n-3 (18:3ω3, 20:3ω3 and 20:5n3) and n-6 (18:3ω6) were significantly affected by Irgarol 1051. According to Okuyama et al. [27], the long-chain n-3 series such as the EPA (20:5ω3) which has an antioxidative effect are likely to function as a primary protective barrier against the oxidative stress caused by the accumulation of ROS. Among the PUFAs, the 18:3ω6 and 20:5ω3 are known as a fatty acid biomarker for the symbiotic algae [10, 16, 28]. Irgarol is highly toxic and powerful inhibitor to the symbiotic algae in coral because this antifouling chemical is used to prevent the growth of algae [30]. Symbiotic algae provide up to 90% of photosynthetically fixed carbon to corals including fatty acids which is an important nutrient for daily energy requirement of their host [28, 30]. Study on *Seriatopora histrix* [29] and *Acropora tenuis* [31] exposed to Irgarol 1051 revealed that the Irgarol 1051 able to inhibit the PSII that involve with the photosynthesis process in the symbiotic algae. Moreover, it is known that some of the fatty acids especially PUFA were translocated from symbiotic algae to coral [20, 26, 17], hence, lower composition of PUFA in the present samples exposed by Irgarol 1051 is partly associated with the disruption of the photosynthetically fixed carbon production by the symbiotic algae.

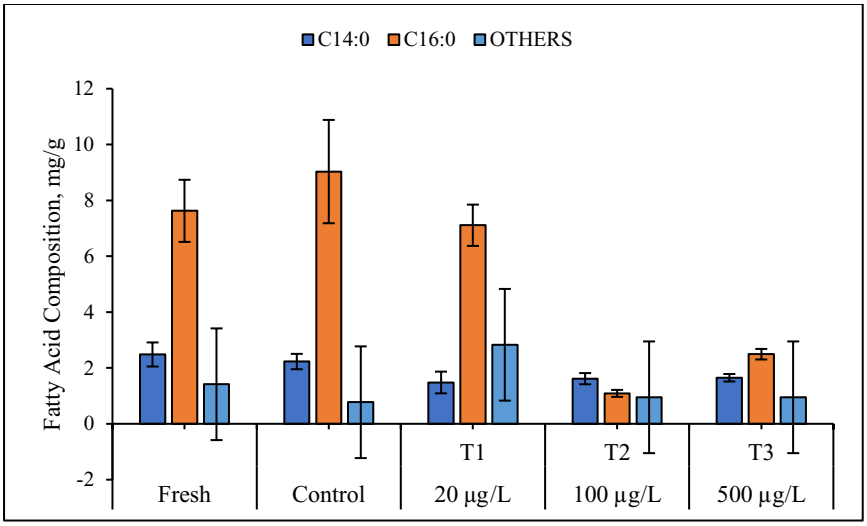


Figure 3. Composition (mg/g) dry weight of SAFA components namely myristic acid (14:0), palmitic acid (16:0) and other components of SAFA (total) in tissue samples of *Galaxea fascicularis* after 96hrs acute exposure test of Irgarol. Values are means with standard deviation (n=3)

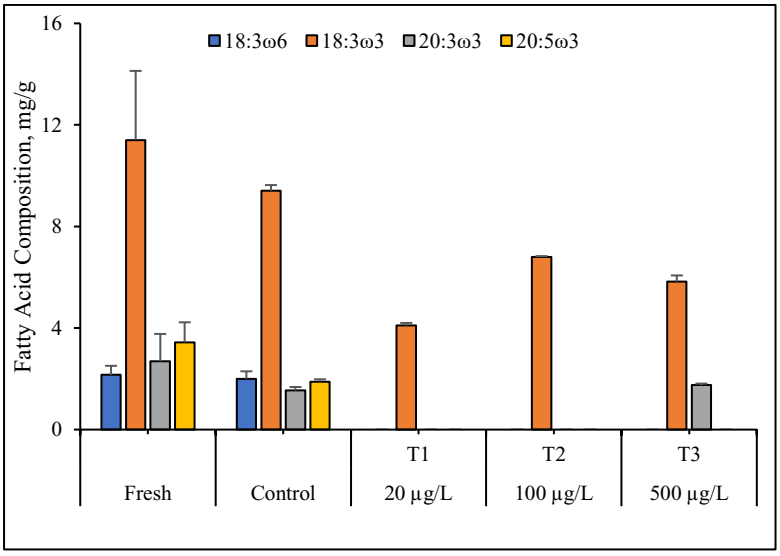


Figure 4. Composition (mg/g) dry weight of PUFA components namely γ-linolenic acid (18:3ω6), α-linolenic acid (18:3ω3), eicosatrienoic acid (20:3n3) and eicosapentaenoic acid (20:5ω3) in tissue samples of *Galaxea fascicularis* after 96hrs acute exposure test of Irgarol. Values are means with standard deviation (n=3)

Conclusion

This paper explains the toxicological responses of *Galaxea fascicularis* upon acute exposure to different concentrations of Irgarol in laboratory experiments. It can be concluded that; acute exposure to *Galaxea fascicularis* (96 hours) to different concentrations of Irgarol 1051 had shown significant impact to the fatty acid compositions of this organism. Moreover, fresh and control samples of *Galaxea fascicularis* were dominated by PUFA followed by SAFA and then MUFA which significantly different trend with the treated samples. It is proven that the Irgarol have affecting the fatty acids composition of the reef-building coral even exposed at the low levels of this biocide. As hard corals are the main reef-builder, further research is required to understand the ecotoxicological effect of Irgarol to their metabolism to comprehend the consequences of this antifouling chemicals to the health of coral reefs ecosystem.

Acknowledgement

We sincerely acknowledge the Ministry of Higher Education of Malaysia (MoHE) for providing fund to support conducting this study using Fundamental Research Grant Scheme (FRGS/1/2011/STWN/ UMT/02/3) and Higher Institution Centers of Excellence (HICoE, 66928) program. We also acknowledge University of Malaysia Terengganu (UMT) special Institute of Oceanography and Environment (INOS), School of Marine and Environmental Sciences (FSSM), and The State University of Zanzibar (SUZA) for their support in conducting this research.

References

1. Malato, S., Blanco, J., Cáceres, J., Fernández-Alba, A. R., Agüera, A. and Rodríguez, A. (2002). Photocatalytic treatment of water-soluble pesticides by photo-Fenton and TiO_2 using solar energy. *Catalysis Today,* 76(2-4): 209-220.
2. Ali, H. R., Arifin, M. M., Sheikh, M. A., Mohamed Shazili, N. A. and Bachok, Z. (2013). Occurrence and distribution of antifouling biocide Irgarol-1051 in coastal waters of Peninsular Malaysia. *Marine Pollution Bulletin,* 70(1-2): 253-257.
3. Harino, H., Arai, T., Ohji, M., Ismail, A. and Miyazaki, N. (2009). Contamination profiles of antifouling biocides in selected coastal regions of Malaysia. *Archives of Environmental Contamination and Toxicology,* 56(3): 468-478.
4. Sheikh, M. A., Higuchi, T., Fujimura, H., Imo, T. S., Miyagi, T. and Oomori, T. (2009). Contamination and impacts of new antifouling biocide Irgarol-1051 on subtropical coral reef waters. *International Journal of Environmental Science and Technology,* 6(3): 353-358.
5. Bao, V. W. W., Leung, K. M. Y., Qiu, J. W. and Lam, M. H. W. (2011). Acute toxicities of five commonly used antifouling booster biocides to selected subtropical and cosmopolitan marine species. *Marine Pollution Bulletin,* 62(5): 1147-1151.
6. West, K. and Van Woesik, R. (2001). Spatial and temporal variance of river discharge on Okinawa (Japan): Inferring the temporal impact on adjacent coral reefs. *Marine Pollution Bulletin,* 42(10): 864-872.
7. Kitada, Y., Kawahata, H., Suzuki, A. and Oomori, T. (2008). Distribution of pesticides and bisphenol a in sediments collected from rivers adjacent to coral reefs. *Applied Catalysis B: Environmental,* 82(3-4): 163-168.
8. Omija, T. (2004). Corals and Coral Reefs, In Coral Reefs of Japan. Ministry of Environment and Japanese Coral Reef Society, Tokyo, pp. 64–68.
9. Knutson, S., Downs, C. A. and Richmond, R. H. (2012). Concentrations of Irgarol in selected marinas of Oahu, Hawaii and effects on settlement of coral larval. *Ecotoxicology,* 21(1): 1-8.
10. Ali, H. R., Arifin, M. M., Sheikh, M. A., Mohamed Shazili, N. A. and Bachok, Z. (2015). Toxicological studies of Irgarol-1051 and its effects on fatty acid composition of Asian sea-bass, *Lates calcarifer. Regional Studies in Marine Science,* 2: 171-176.
11. Cragg, B. A. and Fry, J. C. (1984). The use of microcosms to simulate field experiments to determine the effects of herbicides on aquatic bacteria. *Journal General Microbiology,* 130: 2309-2316.

12. Sumpono Perotti, P., Belan, A., Forestier, C., Lavedrine, B. and Bohatier, J. (2003). Effect of diuron on aquatic bacteria in laboratory-scale wastewater treatment ponds with special reference to Aeromonas species studied by colony hybridization. *Chemosphere,* 50: 445-455.
13. American Public Health Association (1995). Standard method for the examination of water and wastewater, nineteenth edition. Washington, DC.
14. Abdulkadir, S. and Tsuchiya, M. (2008). One-step method for quantitative and qualitative analysis of fatty acids in marine animal samples. *Journal of Experimental Marine Biology and Ecology,* 354(1): 1-8.
15. Bachok, Z., Arifin, M. M., Sheikh, M. A., Mohamed Shazili, N. A. and Ali, H. R. (2016). Effects of Irgarol -1051 on fatty acid profile of solitary corals, *Fungia fungites* after acute exposure. *Malaysian Journal of Analytical Sciences,* 20(4): 697-703.
16. Imbs, A. B., Demidkova, D. A., Latypov, Y. Y. and Pham, L. Q. (2007). Application of fatty acids for chemotaxonomy of reef-building corals. *Lipids,* 42: 1035-1046.
17. Imbs, A. B., Yakovleva, I. M., Latyshev, N. A. and Pham, L. Q. (2010). Biosynthesis of polyunsaturated fatty acids in zooxanthellae and polyps of corals. *Russian Journal of Marine Biology,* 36(6): 452-457.
18. Harland, A. D., Navarro, J. C., Spencer Davies, P. and Fixter, L.M. (1993). Lipids of some Caribbean and Red Sea corals: total lipid, wax esters, triglycerides and fatty acids. *Marine Biology,* 117: 113-117.
19. Kumar, M., Kumari, P., Gupta, V., Anisha, P. A., Reddy, C. R. K. and Jha, B. (2010). Differential responses to cadmium induced oxidative stress in marine macroalga *Ulva lactuca* (Ulvales, Chlorophyta). *Biometals* 23: 315-325.
20. Mohd Safuan, C. D., Samshuri, M. A., Jaafar, S. N. T., Tan, H. C. and Bachok, Z. (2021). Physiological response of shallow-water hard coral *Acropora digitifera* to heat stress via fatty acid composition. *Frontiers in Marine Science,* 2021: 1187.
21. Filimonova, V., Goncalves, F., Marques, J. C., De Troch, M. and Goncalves, A. M. (2016). Fatty acid profiling as bioindicator of chemical stress in marine organisms: a review. *Ecological Indicators,* 67: 657-672.
22. Regoli, F. and Giuliani, M. E. (2014). Oxidative pathways of chemical toxicity and oxidative stress biomarkers in marine organisms. *Marine Environmental Research,* 93: 106-117.
23. Downs, C. and Downs, A. (2007). Preliminary examination of short-term cellular toxicological responses of the coral *Madracis mirabilis* to acute Irgarol 1051 exposure. *Archives of Environmental Contamination and Toxicology*, 52(1): 47-57.
24. Baird, A. H., Bhagooli, R., Ralph, P. J. and Takahashi, S. (2008). Coral bleaching: the role of the host. *Trends in Ecology & Evolution,* 24(1): 16-20.
25. Rodríguez-Troncoso, A. P., Carpizo-Ituarte, E. and Cupul-Magaña, A. L. (2016). Physiological response to high temperature in the Tropical Eastern Pacific coral *Pocillopora verrucosa*. *Marine Ecology,* 37(5): 1168-1175.
26. Imbs, A. B. and Yakovleva, I. M. (2012). Dynamics of lipid and fatty acid composition of shallow-water corals under thermal stress: an experimental approach. *Coral Reefs,* 31(1): 41-53.
27. Okuyama, H., Orikasa, Y. and Nishida, T. (2008). Significance of antioxidative functions of eicosapentaenoic and docosahexaenoic acids in marine microorganisms. *Applied and Environmental Microbiology,* 74(3): 570-574.
28. Papina, M., Meziane, T. and Van Woesik, R. (2003). Symbiotic zooxanthellae provide the host-coral Montipora digitata with polyunsaturated fatty acids. *Comparative Biochemistry and Physiology Part B: Biochemistry and Molecular Biology,* 135(3): 533-537.
29. Jones, R. J. and Kerswell, A. P. (2003). Phytotoxicity of Photosystem II (PSII) herbicides to coral. *Marine Ecology Progress Series,* 261: 149-159.
30. Teece, M. A., Estes, B., Gelsleichter, and E., Lirman, D. (2011). Heterotrophic and autotrophic assimilation of fatty acids by two scleractinian corals, *Montastraea faveolata* and *Porites astreoides*. *Limnology and Oceanography,* 56(4): 1285-1296.

31. Kamei, M., Takayama, K., Ishibashi, H., Takeuchi, I. (2020). Effects of ecologically relevant concentrations of Irgarol 1051 in tropical to subtropical coastal seawater on hermatypic coral *Acropora tenuis* and its symbiotic dinoflagellates. *Marine Pollution Bulletin*, 150: 110734.

Malaysian Journal of Analytical Sciences Vol 26 No 5 2022

Articles 15-19 are selected papers from the "8th International Conference on Solid State Science and Technology (8th ICSSST 2021), 1-3 November 2021; organized by the Universiti Teknologi MARA Perlis & Malaysian Solid State Science and Technology Society (MASS)."

Guest Editor: Dalina Samsudin

1. SYNTHESIS, ELECTROCHEMICAL ANALYSIS AND DFT CALCULATION OF NEW ALKOXYLATED-CHALCONE AS SEMICONDUCTOR MATERIAL 924
(Sintesis, Analisis Elektrokimia dan Pengiraan DFT bagi Alkoksi-Kalkon Sebagai Bahan Semikonduktor)
Syaharil Saidin, Wan M. Khairul, Rafizah Rahamathullah

2. STRUCTURAL AND CONDUCTIVITY STUDIES OF CHOLINE CHLORIDEBASED DEEP EUTECTIC SOLVENT AS A POTENTIAL ELECTROLYTE IN LITHIUM-ION BATTERIES 936
(Kajian Struktur dan Kekonduksian Pelarut Eutektik Dalam Berasaskan Kolina Klorida yang Berpotensi sebagai Elektrolit dalam Bateri Ion Litium)
Intan Qhuzairin Zaharuddin, Nabilah Akemal Muhd Zailani, Khuzaimah Nazir, Rizana Yusof, Mohd Azlan Mohd Ishak

3. THE EFFECTS OF SOAKING TIME ON THE QUALITY AND PROPERTIES OF DURIAN (*Durio zibethinus*) SEED GUM: A MINI REVIEW 944
(Kesan Masa Rendaman Terhadap Kualiti Dan Sifat Gam Biji Durian (*Durio zibethinus*): Ulasan Mini)
Nurul Izzati Ramli, Boon Yih Tien, Boon Yih Hui, Wang Kang Han

4. DISPERSIVE MICRO-SOLID-PHASE EXTRACTION (D-μ-SPE) WITH POLYPYRROLE-GRAPHENE OXIDE (PPY-GO) NANOCOMPOSITE SORBENT FOR THE DETERMINATION OF TETRACYCLINE ANTIBIOTICS IN WATER SAMPLES 953
(Pengekstrakan Fasa-Pepejal-Mikro Secara Serakan (D-μ-SPE) menggunakan Polipirol-Grafin Oksida (Ppy-GO) Penjerap Nanokomposit bagi Penentuan Antibiotik Tetrasiklin dalam Sampel Air)
Nurzaimah Zaini, Nor Suhaila Mohamad Hanapi, Wan Nazihah Wan Ibrahim, Rozita Osman, Sazlinda Kamaruzaman, Noorfatimah Yahaya, Ahmad Lutfi Anis

5. ADSORPTION AND MOLECULAR DOCKING STUDY OF BISPHENOL A USING REUSABLE ZIF- 8 (ZN) METAL-ORGANIC FRAMEWORKS IN AN AQUEOUS SOLUTION 965
(Penjerapan dan Kajian Penambatan Molekul Bisfenol A Menggunakan Kerangka Logam-Organik ZIF-8 (Zn) yang boleh Digunakan Semula dalam Larutan Air)
Afzan Mahmad, Teh Ubaidah Noh, Maizatul Shima Shaharun, Zakariyya Uba Zango

6. MICROBIAL DEGRADATION OF PALM OIL IN NATURAL SEAWATER AND IDENTIFICATION OF OIL DEGRADING BACTERIAL CONSORTIUM 976
(Degradasi Mikrob Minyak Sawit dalam Air Laut Semula Jadi dan Pengenalpastian Konsortium Bakteria Pendegradasi Minyak)
Arularasu Muthaliar Tamothran, Sree Selva Kumar Ganesen, Hing Lee Siang, Sabiqah Tuan Anuar, Razmah Ghazali, Kesaven Bhubalan

7. SYNTHESIS AND CHARACTERIZATION OF NEOPENTYLGLYCOL ESTER AS BIOLUBRICANT BASE STOCK FROM PALM OIL FATTY ACIDS 989
(Sintesis dan Pencirian Ester Neopentilglikol Sebagai Stok Asas Biopelincir daripada Asid Lemak Minyak Sawit)
Nurazira Mohd Nor and Jumat Salimon

8. SPECTROPHOTOMETRIC METHODS FOR DETERMINING TROLOX EQUIVALENT ANTIOXIDANT CAPACITIES OF TEA THROUGH DIFFERENT *In Vitro* ASSAYS 999
(Kaedah Spektrofotometrik bagi Penentuan Trolox Kapasiti Antioksida Teh Melalui Pelbagai Ujian *In Vitro)*
Le-Thi Anh-Dao, Do Minh-Huy, Nguyen Thanh-Nho, Nguyen Quoc-Duy, Nguyen-Thi Thanh-Dieu, Le Nhon-Duc, Nguyen Quang-Hieu, Nguyen Cong-Hau

9. ASSESSMENT ON THE CURRENT QUALITY AND IDENTITY CHARACTERISTICS OF MALAYSIAN PALM SUPEROLEIN 1011
(Penilaian Kualiti dan Ciri Identiti Semasa Superolein Sawit Malaysia)
Najwa Sulaiman, Yeoh Chee Beng, Farah Khuwailah Ahmad Bustamam, Elina Hishamuddin

10. BIOTEMPLATED BISMUTH FERRITE ($BiFeO_3$) NANOCATALYST FOR THE PHOTODEGRADATION OF OFLOXACIN BY SOLAR LIGHT UNDER THE INFLUENCE OF OPERATIONAL PARAMETERS 1023
(Templat Bio Bismut Ferit ($BiFeO_3$) Nanopemangkin untuk Fotodegradasi Ofloxacin Menggunakan Cahaya Suria Dibawah Pengaruh Parameter Operasi)
Ahmad Fadhil Rithwan, Muhammad Alif Abdul Khani, Noor Haida Mohd Kaus, Rohana Adnan, Sirikanjana Thongmee, Siti Fairus Mohd Yusoff, Takaomi Kobayashi, Mohd Amirul Ramlan

11. AN ANALYSIS OF DOG FAT IN BEEF MEATBALLS USING FOURIERTRANSFORM INFRARED SPECTROPHOTOMETRY COMBINED WITH CHEMOMETRICS 1037
(Analisis Lemak Anjing dalam Bakso Melalui Kaedah Spektrometri Inframerah Transformasi Fourier Gabungan Bersama Kemometri)
Laela Hayu Nurani, Any Guntarti, Achmad Rizaldy, Citra Ariani Edityaningrum, Nina Salamah, Lalu Muhammad Irham, Dzulfikar Muhammad Aditama, Abdul Rohman

12. RECENT DEVELOPMENT ON THE SYNTHESIS OF THIOUREA DERIVATIVES AND EFFECT OF SUBSTITUENTS ON THE ANTICANCER ACTIVITY: A SHORT REVIEW 1047
(Perkembangan Terkini Sintesis Sebatian Terbitan Tiourea dan Kesan Kumpulan Penukargantian Terhadap Aktiviti Antikanser: Ulasan Ringkas)
Norashikin Roslan, Noraslinda Muhamad Bunnori, Khairul Bariyyah Abdul Halim, Karimah Kassim,Mohd Fadhlizil Fasihi Mohd Aluwi, Nurziana Ngah

13. OPTIMIZATION OF MICROWAVE-ASSISTED EXTRACTION OF PHENOLIC COMPOUNDS FROM *Eleusine indica* USING RESPONSE SURFACE METHODOLOGY 1070
(Pengoptimuman Pengekstrakan Berbantu Gelombang Mikro bagi Sebatian Fenolik dari *Eleusine indica* Mengunakan Kaedah Gerak Balas Permukaan)
Angelica A. Angeles-Macalalad, Bryan John A. Magoling, Jennielyn C. De Chavez, Love Angel H. Flores, Alona B. Intac

14. EVALUATION OF PHYSICOCHEMICAL PROFILE, MULTI ELEMENTAL COMPOSITION AND ANTIOXIDANT PROPERTY OF *Heterotrigona itama* FROM NORTHERN REGION IN MALAYSIA 1082
Penilaian Profil Fizikokimia, Komposisi Berbilang Unsur dan Sifat Antioksidan *Heterotrigona itama* Dari Wilayah Utara Di Malaysia
Amira Syafiqah Jamaludin, Mardiana Saaid, Ganapaty Manickavasagam, Ho Boon Han, Norsyafiah Muhamad Faizal, Rozita Osman

15. CONVERTING WASTE CHICKEN BONES INTO HETEROGENEOUS CATALYST FOR BIODIESEL SYNTHESIS FROM WASTE COOKING OIL 1102
(Pertukaran Sisa Tulang Ayam kepada Mangkin Hetrogen Bagi Penghasilan Biodiesel dari Minyak Masak Terpakai)
Jeyashelly Andas and Nur Fazira Elyana Jusoh

16. POLYMER-FREE TRANSFER OF GRAPHENE-BASED MATERIAL DERIVED FROM COOKING PALM OIL BY CHEMICAL VAPOUR DEPOSITION TECHNIQUE 1112
(Pemindahan Bebas Polimer bagi Bahan Berasaskan Grafin yang Disintesis dari Minyak Masak Kelapa Sawit Menggunakan Teknik Pemendapan Wap Kimia)
Azzafeerah Mahyuddin, Abd. Khamim Ismail, Muhammad Firdaus Omar, Ainul Hakimah Karim

17. CHARACTERIZATION AND TENSILE PROPERTIES OF POLYLACTIC ACID BIOCOMPOSITE FILLED MICROCRYSTALLINE CELLULOSE EXTRACTED FROM KENAF 1123
(Ciri-Ciri Dan Sifat Tensil Poli(Asid Laktik) Biokomposit yang Diisi Selulosa Mikrohablur yang Diekstrak daripada Kenaf)
Norhazirah Azhar, Adzrie Baharudin, Zuliahani Ahmad, Rozyanty Rahman, Luqman Musa, Siti Nor Din, Nor Mazlina Abdul Wahab

18. MORPHOLOGICAL STUDIES OF SILICON CARBIDE THIN FILM DEPOSITED BY VERY HIGH FREQUENCY - PLASMA ENHANCED CHEMICAL VAPOUR DEPOSITION THROUGH GAS DILUTION ADJUSTMENT 1135
(Kajian Morfologi Filem Nipis Silikon Karbida Yang Dimendapkan oleh Frekuensi Sangat Tinggi - Pemendapan Wap Kimia Dipertingkatkan Plasma dengan Melaraskan Pencairan Gas)
Zainur Atika Ibrahim, Muhammad Firdaus Omar, Abd Khamim Ismail

19. DFT STUDY ON STRUCTURAL PROPERTIES, DENSITY OF STATES AND BAND STRUCTURE OF MONOLAYER & BILAYER GRAPHENE 1142
(Kajian Teori Tentang Sifat Struktur, Ketumpatan Keadaan dan Struktur Jalur Grafin Lapisan Tunggal dan Dwi Lapisan)
Nurhafizah Md Disa, Henna Malakar, Nurhayati Abdullah

Malaysian Journal of Analytical Sciences (MJAS)
Published by Malaysian Analytical Sciences Society

SYNTHESIS, ELECTROCHEMICAL ANALYSIS AND DFT CALCULATION OF NEW ALKOXYLATED-CHALCONE AS SEMICONDUCTOR MATERIAL

(Sintesis, Analisis Elektrokimia dan Pengiraan DFT bagi Alkoksi-Kalkon Sebagai Bahan Semikonduktor)

Syaharil Saidin[1], Wan M. Khairul[1*], Rafizah Rahamathullah[2]

[1]Faculty of Science and Marine Environment,
Universiti Malaysia Terengganu, 21030, Kuala Nerus, Terengganu, Malaysia
[2]Faculty of Engineering Technology,
Universiti Malaysia Perlis,
Level 1, Block S2, UniCITI Alam Kampus, Sungai Chuchuh, Padang Besar, 02100 Perlis, Malaysia

[*]Corresponding author: wmkhairul@umt.edu.my

Received: 13 March 2022; Accepted: 18 May 2022; Published: 30 October 2022

Abstract

A new alkoxylated-chalcone derivative displaying donor(D)-π-acceptor(A) system was successfully synthesized via Claisen-Schmidt condensation to be integrated as organic semiconductor material. The correlation between electronic, optical properties, electrochemical and DFT calculation of the designated system were assessed in thorough. This alkoxylated-chalcone (**OCT-CHAL**) reveals an absorption band at λ_{max} 312 nm with molar coefficient of *ca.* 10^5 L mol^{-1} cm^{-1} which corresponding to π-π* transition. The optical band gap gives the value of 3.40 eV which shows good agreement with the value of energy level between HOMO and LUMO for theoretical calculation. Meanwhile, this derivative also reveals good thermal stability up to 200 ℃ with total mass loss at 97 %. In turn, the electrochemical behaviour of **OCT-CHAL** was investigated and exhibited redox potential with the values of 2.40 V for oxidation potential while the reduction potential exhibited at value of -1.72 V as quasi-reversible reduction. From the outcome, the existence of conjugation effect on chalcone moiety with ideal relation between the experimental and theoretical approach provides good support of being a potential candidate in organic semiconductor material for advance material application.

Keywords: alkoxy, chalcone, bandgap, DFT, electrochemistry

Abstrak

Terbitan alkoksi-kalkon baharu yang memaparkan sistem penderma(D)-π-penerima(D) telah berjaya disintesis melalui kaedah kondensasi Claisen-Schmidt untuk diintegrasikan sebagai bahan organik semikonduktor. Perkaitan antara elektronik, sifat optik, elektrokimia dan pengiraan DFT bagi sistem yang direkabentuk telah dinilai secara menyeluruh. Alkoksi-kalkon (**OCT-CHAL**) ini menunjukkan jalur serapan pada λ_{mak} 312 nm dengan pekali molar 10^5 L mol^{-1} cm^{-1} yang selari dengan peralihan π-π*. Nilai jurang jalur optik memberikan nilai 3.40 eV yang mana keputusannya menunjukkan nilai yang selari dengan nilai aras tenaga antara HOMO dan LUMO bagi pengiraan teori. Sementara itu, terbitan ini juga menunjukkan kestabilan terma yang baik sehingga 200 ˚C dengan jumlah jisim yang hilang sebanyak 97 %. Selanjutnya sifat elektrokimia bagi **OCT-CHAL** telah dikaji dan

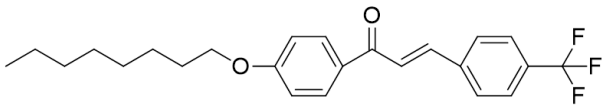
menunjukkan keupayaan redoks dengan nilai 2.40 V untuk potensi pengoksidaan manakala potensi penurunan adalah pada nilai -1.72 V sebagai penurunan kuasi-terbalik. Daripada keputusan yang diperolehi, kehadiran kesan konjugasi pada moiti kalkon dengan hubungan yang baik antara kaedah eksperimen dan teori memberikan sokongan yang baik untuk menjadi calon berpotensi dalam bahan organik semikonduktor bagi aplikasi bahan termaju.

Kata kunci: alkoksi, kalkon, jurang jalur, DFT, Elektrokimia

Introduction

In recent years, the development of organic semiconductor has been extensively explored due to its electronic delocalization in π-orbital system in optimizing the efficiencies of various application in electrical and optoelectronic application [1]. The materials have been extensively studied as a small molecule and polymer and mostly comprised of carbon and hydrogen atom in their molecular structure where the mobility of electron transfer is occurred within the molecule. Considering to the ability in transferring electron, chalcone backbone has been introduced as an organic material which fulfilled this criterion [2,3]. Chalcone, known as 1,3-diphenyl-2-propen-1-one is a molecule that consists of two phenyl rings with α, β-unsaturated ketone (C=C-C=O) moiety in their molecular build-up has attracted considerable attention among researchers due to its electronic properties according to the presence of π-conjugated system in their molecular backbone [4]. Generally, a conjugated system would generate a cloud of delocalized electron merging by π-electron system which enables the flowing of electron along the molecular framework thus activates its potential as charge carrier mobility [5]. Meanwhile, chalcone is considered as a molecule with high charge transfer mobility as it exhibits intramolecular charge transfer (ICT) properties and is known as considerably highly emissive molecule as reported previously [6]. However, the elections of substituents towards the terminals of the phenyl rings would determine their contribution as good charge transfer ability [7], and appropriate selection of these substituents lead to the development of application such as in optoelectronics particularly in potential non-linear optical interests [8].

In this context, the chalcone based compound is introduced with the attachment of ideal substituents to develop a molecule with donor-π-acceptor (D-π-A) system in enhancing the ICT properties of the molecule [9]. The introduction of alkoxy chain towards chalcone based molecule was believed in lowering the energy band gap due to the steric bulkiness of the compound [10], thus enables it to lie in typical band gap range of semiconducting materials. Various physicochemical evaluations were accomplished via cyclic voltammetry (CV) technique in order to study their electrochemical properties and behaviour to establish their potentiality as semiconducting materials. As part of our studies in this area, a model molecule of new alkoxylated-based chalcone derivative namely, 1-(4-octoxyphenyl)-3-[4-(trifluoromethyl)phenyl]prop-2-en-1-one **(OCT-CHAL)** featuring D-π-A system presented in Figure 1 was successfully designed, synthesized and demonstrated as a semiconducting material as reported herein.



OCT-CHAL

Figure 1. Molecular structure of **OCT-CHAL** derivative

Materials and Methods

4-hydroxyacetophenone, 1-bromooctane, potassium carbonate, 4-trifluoromethylbenzaldehyde, hexane, dimethylformamide (DMF), hexane, ethyl-acetate,

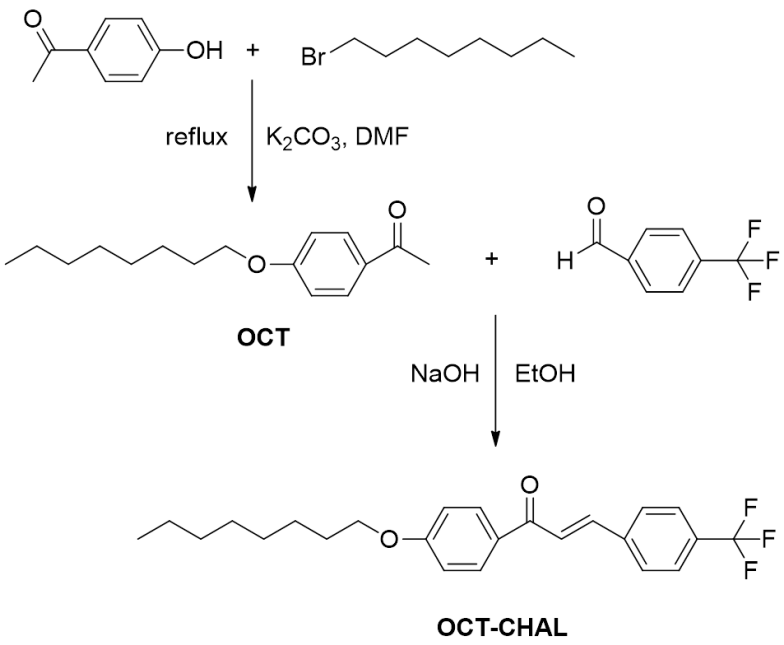
sodium hydroxide (NaOH), anhydrous hydrochloric acid (HCl), sodium sulphate and silica gel blue were commercially purchased form standard commercial suppliers namely Sigma Aldrich, Merck, Fisher Scientific and R&M Chemical without any further purification procedures were performed. The reaction was carried out under ambient atmosphere with no special condition including air or mixture exclusion.

Instrumentations

The infrared (IR) spectra were recorded by using Perkin Elmer Spectrum 100 Fourier Transform Infrared Spectrophotometer via Attenuated Total Reflection (ATR) in the spectral range of 4000 cm^{-1}-400 cm^{-1}. Whilst, ^{1}H and ^{13}C nuclear magnetic resonance (NMR) were determined by Bruker Avance III 400 spectrometer ^{1}H (400MHz) and ^{13}C (100.61MHz) by using deuterated chloroform ($CDCl_3$) acting as a solvent and tetramethylsilane (TMS) as an internal standard of δ_H (0-15 ppm) and δ_C (0-200 ppm) respectively. CH elemental analysis was carried out via Vario EL Cube Elemental Analyzer to determine the percentage weight of the elements of carbon and hydrogen presence in the synthesized compound. The UV-Vis spectroscopy spectrum was observed by using Spectrophotometer Shimadzu UV-1800 PC in 1 cm^3 quartz cuvette in dichloromethane solution with concentration of 1×10^{-5} M in the spectra range of 200–500 nm for absorbance analysis. The optimized molecular structure was obtained via density functional theory (DFT) calculation using ab initio quantum mechanical software of Gaussian 09 with correlation functional of B3LYP with basis set of 6-31G (d, p). Then, the excitation energies and correlation absorption wavelength were calculated through TD-DFT quantum mechanical calculation to obtain the energy level of HOMO-LUMO energy transition. The thermal stability was recorded via Perkin Elmer TGA Analyzer from 30 ℃ to 900 ℃ with heating rate of 10 ℃/min in the of presence nitrogen gas with flow rate of 10 mL/min. The electrochemistry was performed via AUTOLAB PGSTAT101 model potentiostat driven by NOVA 2.1 software which comprises three-electrode cell system which are working electrode (glassy carbon electrode), counter electrode (platinum wire) and reference electrode (Ag/AgCl). This experimental work-up were carried out in dichloromethane solution containing 0.1 M of tetrabutylammonium hexafluorophosphate $[NBu_4]PF_6$ as a supporting electrolyte with sample concentration of 1×10^{-3} M.

Synthetic approach

The synthesis work consists of two major parts which was the formation of 4-octyloxyacetophenone **(OCT)** as a precursor and the formation of 1-(4-octoxyphenyl)-3-[4-(trifluoromethyl)phenyl]prop-2-en-1-one **(OCT-CHAL)** as a targeted compound which were synthesized via Williamson ether synthesis and Claisen-Schmidt condensation respectively as shown in Scheme 1.



Scheme 1. Synthetic pathway for preparation of **OCT-CHAL** derivative

Synthesis of precursor: 4-octyloxyacetophenone (OCT)

Precursor of **OCT** was reported by previous literature [11], however some modifications in the experimental set-up were carried out in this study. The preparation of **OCT** was prepared by the mixture of 4-hydroxyacetophenone (1.0 g, 7.3 mmol), 1-bromooctane (1.41 g, 7.3 mmol) and potassium carbonate (3.02 g, 21.9 mmol) that were charged in 250 ml of two-necked round bottom flask. The mixture was treated with 40 ml of dimethylformamide (DMF) and was put at reflux with constant stirring for approximately 24 hours. After adjudged completion by thin layer chromatography, (TLC) (hexane: ethyl acetate; 4:1), the mixture was cooled down to room temperature and then was filtered and extracted with hexane and distilled water. The organic layer fraction obtained then was separated and washed with 1 M of aqueous NaOH (25 ml) and then with 1 M of aqueous HCl (25 ml). The organic layer obtained was dried over sodium sulphate, Na_2SO_4 and was dried *in vacuo*. (yellow viscous liquid; yield: 1.25 g, 69 %). IR (cm^{-1}): 2926.01 (*ν*C-H alkanes), 2856.58 (*ν*C-H alkane CH_2), 1676.14 (*ν*C=O), 1598.99 (*ν*C=C), 1465.90 (*ν*CH_2 bend), 1357.89 (*ν*CH_3 bend), 1251.80 (*ν*C-O carbonyl group), 1170.79 (*ν*C-O ether), 835.18 (*ν*C-H aromatic OOP). ^{1}H NMR (400 MHz, $CDCl_3$) δ: 7.85 (pseudo-d, 2H, J = 8.8 Hz, Ar-H), 6.85 (pseudo-d, 2H, J = 9.2 Hz, Ar-H), 3.98 (t, 3H, J = 13.2 Hz, O-CH_2), 2.50 (s, 2H, H_3C-C=O), 1.75 (m, 2H, -CH_2), 1.45 (m, 2H, -CH_2), 1.25 (m, 9H, -CH_2), 0.85 (t, 3H, J = 14 Hz, -CH_3). ^{13}C NMR (100.61 MHz, $CDCl_3$) δ: 195.83, 162.11, 129.56, 129.05, 113.10, 67.24, 30.77, 28.29, 28.19, 28.07, 25.31, 24.95, 21.63, 13.08.

Synthesis of 1-(4-octoxyphenyl)-3-[4-(trifluoromethyl)phenyl]prop-2-en-1-one (OCT-CHAL)

The preparation of **OCT-CHAL** derived from the reaction of **OCT** (0.14 g, 0.8 mmol) and 4-trifluoromethylbenzaldehyde (0.2 g, 0.8 mmol) that both were charged in 250 ml of two-necked round bottom flask. The mixture was treated with 30 ml of ethanolic solution and then 20 % of NaOH was added dropwise to the mixture until the precipitate was formed under constant stirring for approximately 24 hours. When adjudged completion by thin layer chromatography, (TLC) (hexane: dichloromethane; 3:2), the mixture was

poured into icy water and the cooled mixture was filtered and washed with distilled water. The precipitate collected was dried over silica gel blue before recrystallized from methanol, CH_3OH (off-white crystalline solid, 0.2 g, 55 %). IR (cm^{-1}): 2921.24 (*ν*C-H alkanes), 2855.66 (*ν*C-H alkane CH_2), 1664.60 (*ν*C=O ketone), 1601.91 (*ν*C=C alkene), 1573.94 (*ν*C=C aromatic), 1470.75 (*ν*CH_2 bend), 1391.65 (*ν*CH_3 bend), 1328.01 (*ν*C-X fluoride), 1169.85 (*ν*C-O ether), 830.19 (*ν*C-H aromatic OOP). ^{1}H NMR (400.11 MHz, $CDCl_3$) δ: 7.95 (pseudo-d, 2H, J = 8.8 Hz, Ar-H), 7.72 (d, 1H, 16 Hz, HC=CH), 7.65 (pseudo-d, 2H, 8.4 Hz, Ar-H), 7.60 (pseudo-d, 2H, 8.4 Hz, Ar-H), 7.55 (d, 1H, 16 Hz, HC=CH), 6.90 (pseudo-d, 2H, J = 9.2 Hz, Ar-H), 3.95 (t, 2H, J = 13.2 Hz, -OCH_3), 1.75 (m, 2H, -CH_2), 1.35 (m, 2H, -CH_2), 1.20 (m, 9H, -CH_2), 0.85 (t, 3H, J = 10 Hz, -CH_3). ^{13}C NMR (100.61 MHz, $CDCl_3$) δ: 187.14, 162.36, 140.76 130.17, 129.44, 127.38, 124.86, 124.82, 123.16, 113.41, 67.35, 30.78, 28.30, 28.19, 28.08, 24.97, 21.63, 13.07.

Results and Discussion

Infrared spectroscopy analysis

The spectral data of **OCT-CHAL** were recorded and analysed spectroscopically. In IR spectrum of chalcone derivative as depicted in Figure 2, it revealed all the expected bands of interest *ν*(C-H alkanes), *ν*(C-H alkanes, -CH_2), *ν*(C=O), *ν*(C=C aromatic) and *ν*(C=C alkenes). The medium intensity at 2921.24 cm^{-1} and 2855.66 cm^{-1} were corresponded to vibrational of *ν*(C-H alkanes). The sharp peak of IR band was observed at 1664.60 cm^{-1} and 1601.91 cm^{-1} which assigned to *ν*(C=O) and *ν*(C=C) with good agreement to previous researchers [12]. The medium intensity at 1573.94 cm^{-1} shows the vibrations of *ν*(C=C aromatic) while strong band at 1328.01 cm^{-1} corresponded to *ν*(C-X fluoride), in which the absorption of its wavenumber increase with increment of force constant from C-F bonds due to the inductive effect between C-F bond and fluorine that are attracted by fluorine electrons [13], and the vibrational of *ν*(C-O) ether revealed at 1169.85 cm^{-1}.

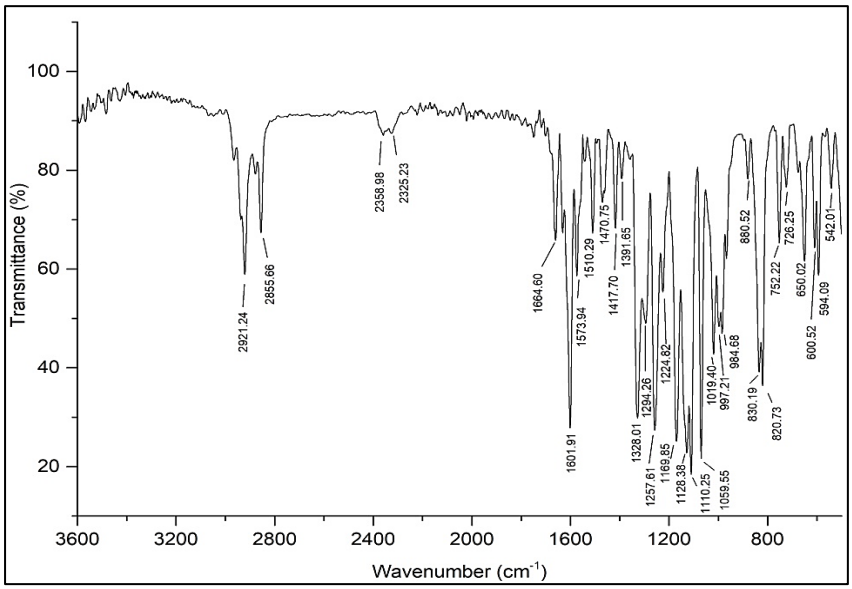


Figure 2. IR spectrum of **OCT-CHAL**

^{1}H and ^{13}C nuclear magnetic resonance analysis

In ^{1}H NMR, it revealed a pseudo-doublet resonance in the range of δ_H 7.95-6.90 ppm due to aromatic protons of para-substitution at the aromatic rings. A doublet resonance can be found at δ_H 7.72 ppm and δ_H 7.55 ppm while triplet resonance at δ_H 3.95 ppm was observed as OCH_2 due to the deshielding effect of the nearby oxygen atom which is more electronegative. Multiplet overlapping resonances lies on δ_H 1.75- 1.20 ppm while triplet resonance was recorded at shielded position δ_H

0.85 ppm. Figure 3 shows the spectrum of ^{1}H NMR for **OCT-CHAL**.

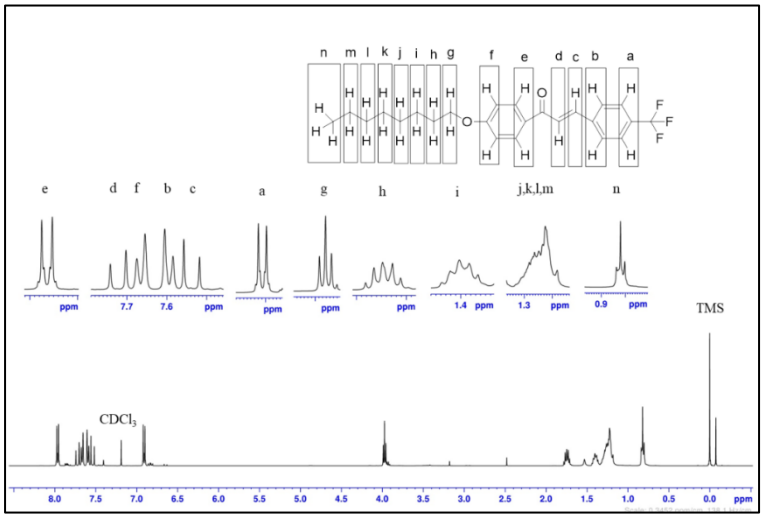


Figure 3. ^{1}H NMR spectrum of **OCT-CHAL**

The ^{13}C NMR spectrum of **OCT-CHAL** is represented in Figure 4. The C=O was identified as singlet resonance at δ_C 187.14 ppm according to deshielding effect due to the presence of nearby oxygen atom in which this trend of chemical shift position was also observed in prior reported literature [14]. Meanwhile, the aromatic carbons were recorded in the range of δ_C 162.36- 113.41 ppm. Two vinylic resonances were observed at δ_C 140.76 ppm and δ_C 123.16 ppm referring to the carbon splitting of α and β unsaturated carbons respectively due to their unsymmetrical nature within the molecular structure.

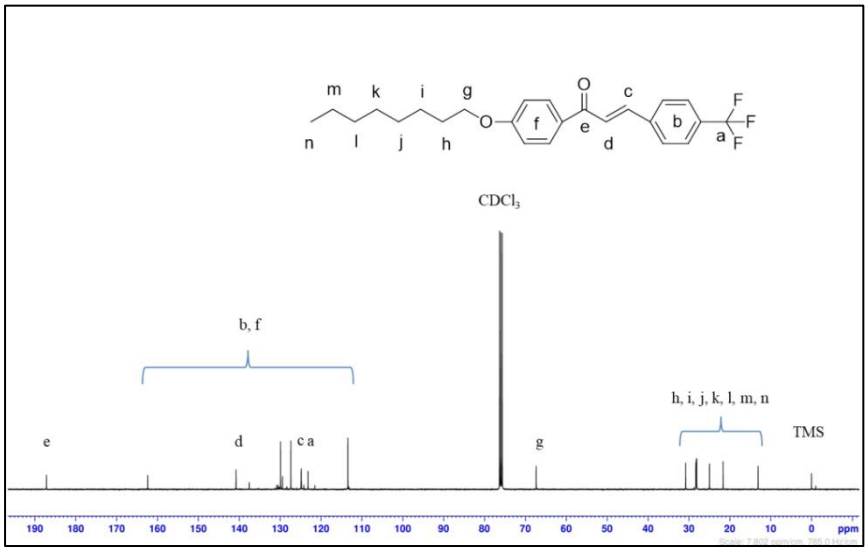


Figure 4. ^{13}C NMR spectrum of **OCT-CHAL**

Optical properties

In electronic transition of **OCT-CHAL**, it revealed π→π* transition attributed by C=O chromophore which lies in the range of 240 nm to 245 nm where the transition is shifted to longer wavelength due to the interaction of π-conjugation of carbonyl and phenyl rings. The strong absorption band between 280 nm to 330 nm can be contributed by π→π* and n→π* transitions that may correspond to C=C and C-O chromophores [8, 15]. The experimental spectrum of **OCT-CHAL** as depicted in Figure 5 (a) enables the calculation of optical band gap of this compound by referring to the formula of [E_g^{opt}= hc/ λ_{offset} (365 nm) eV]. The calculated optical band gap for **OCT-CHAL** is 3.40 eV. Comparatively, this finding has a good agreement with the values of theoretical energy band gap. The theoretical and optical band gap values are slightly different as the optical band gap are influenced by the type of solute-solvent interaction, where the solvent polarity would determine the level of ground state and excited state energy which then lead to bathochromic shift of optical spectrum. Whilst, the estimation of theoretical energy band gap was used has lowered solvatochromism in their calculation [16]. Moreover, the differences of theoretical and optical energy band gap values are also occurred due to the exciton energy binding [9], which stated that the different amount of energy band gap in the range from 0.45 eV to 1.0 eV.

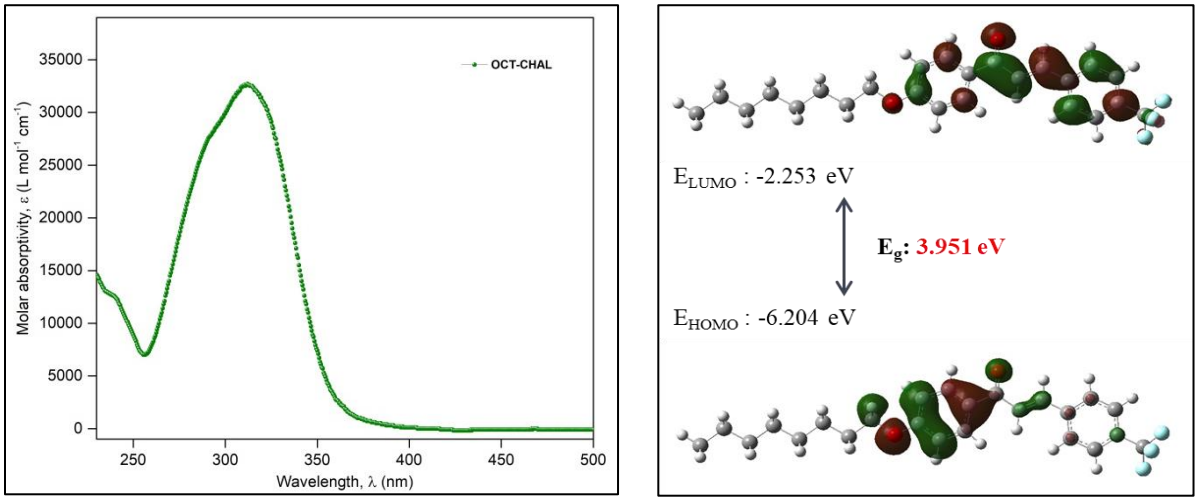


Figure 5. (a) UV-Vis spectrum of **OCT-CHAL** recorded in dichloromethane solution and (b) energy separation between HOMO-LUMO of **OCT-CHAL**

Computational calculations using time dependent density functional theory (TD-DFT) method with basis set of B3LYP-631G (d, p) was optimized from molecular structure of **OCT-CHAL** for further investigation of energy separation between the highest occupied molecular orbitals (HOMO) and lowest unoccupied molecular orbitals (LUMO). The energy separation between HOMO-LUMO energy level as depicted in Figure 5 (b). In **OCT-CHAL**, HOMO orbital density was located on electron donating alkoxy substituents while its LUMO coefficient was concentrated over enone and vinyl-substituted aryl group [17].

Molecular electrostatic potential

The molecular electrostatic potential (MEP) was performed to evaluate the molecular interaction of **OCT-CHAL**. MEP shows three-dimensional charge distributions of the molecules in which provide some information regarding to electron acceptor as well as electron donator which is displayed by colour as depicted in Figure 6. On MEP mapped surface, red area represents nucleophilic region which is rich of electron while blue area represents electrophilic region that poor

of electron and green area is zero potential as it is the halfway interaction of red and blue region. The evaluation of this potential region is necessary in estimate the intermolecular and intramolecular hydrogen bonds of the molecules [17].

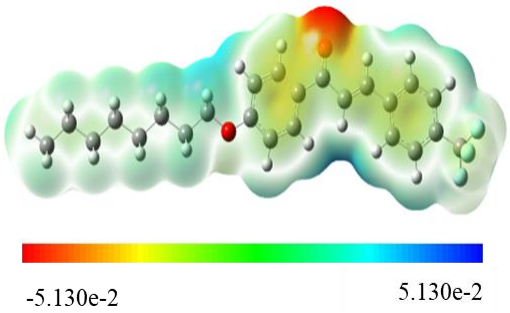


Figure 6. MEP mapped surface of **OCT-CHAL**

Global chemical reactivity descriptors

The differential global chemical reactivity descriptors (GCRD) were calculated by the evaluation of HOMO and LUMO energy level which reveal their ability as electron donor and acceptor in the compound. HOMO indicates to ionization energy (IP) while LUMO indicates to electron affinity (EA) where these findings determine the chemical properties of the molecule in term of chemical hardness (η), chemical softness (S), electronegativity (χ), chemical potential (μ) and electrophilic index (ω) as tabulated in Table 1. In addition, the calculation of HOMO-LUMO energy band gap determine the reactivity and stability of the molecule where the large optical energy band gap corresponding to less reactive and more stable and vice versa [15]. The stated parameters were used in measure the stabilities energy and reactivity of a molecule and the calculation of their quantum mechanical stabilities were calculated by equation as reported by previous literature [18, 19].

The calculation of Chemical hardness, [$\eta = (IP\text{-}EA) / 2$];
The Chemical Softness of the molecules evaluated as, [$S = 1 / 2\eta$];
The electronegativity of the molecule estimated as, [$\chi = (IP+EA) / 2$];
The chemical potential of the molecules calculated as, [$\mu = -\chi$];
The value of electrophilic index, [$\omega = \mu^2 / 2\eta$]

Table 1. Chemical properties of **OCT-CHAL** via GCRD calculation

Parameter	[DFT-B3LYP/6–31G (d, p)]
E_{HOMO} (eV)	-6.204
E_{LUMO} (eV)	-2.253
ΔE (eV)	3.951
Ionization potential I (eV)	6.204
Electron affinity EA (eV)	2.253
Chemical hardness η (eV)	1.976
Chemical Softness S (eV^{-1})	0.253
Electronegativity χ (eV)	4.229
Chemical potential μ (eV)	-4.229
Electrophilic index ω (eV)	4.525

Thermal studies

Thermal stability of **OCT-CHAL** was determined by thermogravimetric analyzer (TGA) where the molecule is stable up to 200 ℃ with two stages of major mass loss in the degradation process as shown in Figure 7. By observing the thermogram, the first degradation was occurred at around 201.47 ℃ (T_{onset}) and ended at 420.38 ℃ whilst second degradation was taken place at around 499.46 ℃ and ended at 570.16 ℃ with total mass loss of 97 %. Hence, the targeted alkoxylated-chalcone system of **OCT-CHAL** exhibits thermal stability at satisfactory temperature and gives good indication for the fabrication of thin film to be applied in any potential advanced materials application.

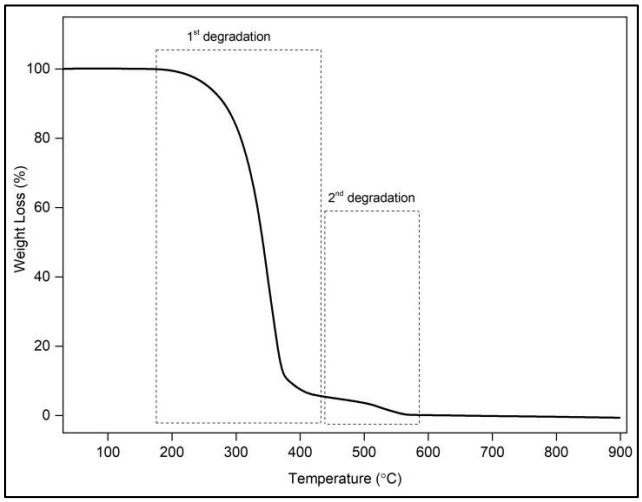


Figure 7. TGA of **OCT-CHAL**

Electrochemical properties

Cyclic Voltammetry (CV) analyzer was used in the evaluation of redox potential (oxidation and reduction) of **OCT-CHAL**. The measurement was carried out in dichloromethane solution with the presence of 0.1 M of tetrabutylammonium hexafluorophosphate, $[NBu_4]$ PF_6 acting as supporting electrolyte in the potential range of -3.0 V to 3.0 V as shown in Figure 8. From the cyclic voltammogram, the oxidation potential took place around 2.40 V at anodic peak which corresponding to oxidation of chalcone derivative due to the absorption of chalcone and/or oxidation of product occurred on the electrode surface [20]. The reduction of C=O may be corresponding to the peak revealed in the range of -1.30 V to -2.0 V with quasi-reversible reduction [21] and the process of quasi-reversibility reduction was determined by the calculation of energy separation between cathodic peak potential (E_{pa}= -1.55 V) with anodic peak potential which are (E_{pc}= -1.72 V). In addition, Ilhan and his team have confirmed this classification by evaluating the ratio of anodic peak current-to-cathodic peak current that are almost unity [22], with the values of (ΔE_p= 0.17 V).

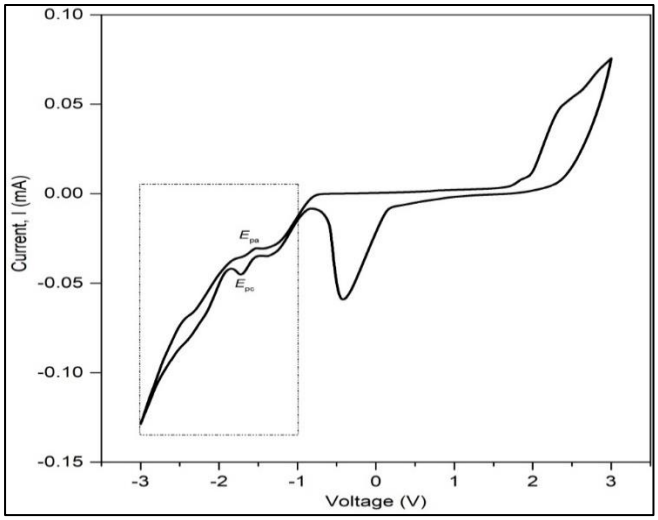


Figure 8. Cyclic voltammogram of **OCT-CHAL** in DCM/ 0.1 $[NBu_4]PF_6$ with scan rate of 0.03 Vs^{-1}

Conclusion

A new alkoxylated-chalcone derivative featuring donor (D)-π-Acceptor (A) system has been successfully designed and synthesized via Claisen-Schmidt condensation. The semiconductor property of **OCT-CHAL** was investigated via optoelectronic using UV-Vis spectroscopy and DFT calculation. The preliminary result reveals that this derivative exhibited an optical band gap of 3.40 eV which showed good relationship between the experimental and theoretical data. The simulated data from frontier molecular orbitals (FMO) analysis, chemical reactivity and molecular electrostatic potential (MEP) also demonstrated that this chalcone based with alkoxy substituent significantly gives good HOMO-LUMO gap which lies in the range of organic semiconducting material. Hence, from this finding, **OCT-CHAL** has proven to exhibit favourable properties for advanced material applications in the near future.

Acknowledgement

The authors would like to thank the financial support from Minister of Higher Education (MOHE) for Fundamental Research Grant (FRGS59515), FRGS/1/2018/STG07/UMT/02/6 as well as Faculty of Science and Marine Environment, Faculty of Ocean Engineering and Institute of Marine Biotechnology (IMB), Universiti Malaysia Terengganu for facilities and research aids.

References

1. Chen, F. C. (2018). Organic semiconductors. Encyclopedia of Modern Optics, Elsevier: pp. 220-231.
2. Fayed, T. A. (2006). A novel chalcone-analogue as an optical sensor based on ground and excited states intramolecular charge transfer: A combined experimental and theoretical study. *Chemical Physics*, 324 (2-3): 631-638.
3. Bangal, P. R., Lahiri, S., Kar, S. and Chakravorti, S. (1996). Vibronic interaction and photophysics of chalcone derivatives. *Journal of Luminescence*, 69(1): 49-56.
4. Kagatikar, S. and Sunil, D. (2021). Aggregation induced emission of chalcones. *Chemical Papers*, 75(12): 6147-6156.
5. Coskun, D., Gunduz, B. and Coskun, M. F. (2019). Synthesis, characterization and significant optoelectronic parameters of 1-(7-methoxy-1-benzofuran-2-yl) substituted chalcone derivatives. *Journal of Molecular Structure*, 1178: 261-267.
6. Nappi, C., Romeo, F. and Sarnelli, E. (2020). Electronic properties of one-dimensional pentacene crystals. *Nano Express*, 1 (3): 030002.

7. da Costa, R. G., Farias, F. R., Maqueira, L., Castanho, C., Carneiro, L. S., Almeida, J., Buarque, C., Aucélio, R. and Limberger, J. (2019). Synthesis, photophysical and electrochemical properties of novel D-π-D and D-π-A triphenylamino-chalcones and β-arylchalcones. *Journal of the Brazilian Chemical Society*, 30(1): 81-89.
8. Lee, S. T., Khairul, W. M., Lee, O. J., Rahamathullah, R., Daud, A. I., KuBulat, K. H., Sapari, S., Razak, F. I. A. and Krishnan, G. (2021). Electronic, reactivity and third order nonlinear optical properties of thermally-stable push-pull chalcones for optoelectronic interest: experimental and DFT assessments. *Journal of Physics and Chemistry of Solids*, 159: 110276.
9. Makhlouf, M. M., Radwan, A. S. and Ghazal, B. (2018). Experimental and DFT insights into molecular structure and optical properties of new chalcones as promising photosensitizers towards solar cell applications. *Applied Surface Science*, 452: 337-351.
10. Namal, I., Ozelcaglayan, A. C., Udum, Y. A. and Toppare, L. (2013). Synthesis and electrochemical characterization of fluorene and benzimidazole containing novel conjugated polymers: Effect of alkyl chain length on electrochemical properties. *European Polymer Journal*, 49(10): 3181-3187.
11. Nam, S. W., Kang, S. H. and Chang, J. Y. (2007). Synthesis and photopolymerization of photoreactive mesogens based on chalcone. *Macromolecular Research*, 15(1): 74-81.
12. Tay, M. G., Tiong, M. H., Chia, Y. Y., Kuan, S. H. C. and Liu, Z. Q. (2016). A way to improve luminescent efficiency of bis-chalcone derivatives. *Journal of Chemistry*, 2016: 3608137.
13. Kumar, R., Kumar, A., Deval, V., Gupta, A., Tandon, P., Patil, P. S., Desmukh, P., Chaturvedi, D. and Watve, J. G. (2017). Molecular structure, spectroscopic (FT-IR, FT Raman, UV, NMR and THz) investigation and hyperpolarizability studies of 3-(2-Chloro-6-fluorophenyl)-1-(2-thienyl) prop-2-en-1-one. *Journal of Molecular Structure*, 1129: 292-304.
14. Rahamathullah, R. and Khairul, W. M. (2017). Evaluation on the electrochemically deposited alkoxy thiourea as liquid crystalline semiconductor film. *Applied Surface Science*, 424: 45-51.
15. Veeramanikandan, S., Sherine, H. B., Dhandapani, A. and Subashchandrabose, S. (2019). Synthesis, solid state structure, Hirshfeld surface, nonlinear optics and DFT studies on novel bischalcone derivative. *Journal of Molecular Structure*, 1180: 798-811.
16. Castro, G. T., Filippa, M. A., Sancho, M. I., Gasull, E. I. and Almandoz, M. C. (2020) Solvent effect on the solubility and absorption spectra of meloxicam: experimental and theoretical calculations. *Physics and Chemistry of Liquids*, 58(3): 337-348.
17. Ustabaş, R., Süleymanoğlu, N., Özdemir, N., Kahriman, N., Bektaş, E. and Ünver, Y. (2020). New chalcone derivative: Synthesis, characterization, computational studies and antioxidant activity. *Letters in Organic Chemistry*, 17 (1): 46-53.
18. Shruthi, C., Ravindrachary, V., Guruswamy, B., Prasad, D. J., Goveas, J., Kumara, K. and Lokanath, N. K. (2021). Molecular structure, Hirshfeld surface and density functional theoretical analysis of a NLO active chalcone derivative single crystal-A quantum chemical approach. *Journal of Molecular Structure*, 1228: 129739.
19. Kumar, R., Kumar, A., Deval, V., Gupta, A., Tandon, P., Patil, P. S., Deshmukh, P., Chaturvedi, D. and Watve, J. G. (2017). Molecular structure, spectroscopic (FT-IR, FT Raman, UV, NMR and THz) investigation and hyperpolarizability studies of 3-(2-Chloro-6-fluorophenyl)-1-(2-thienyl) prop-2-en-1-one. *Journal of Molecular Structure*, 1129: 292-304.
20. Naik, K. M. and Nandibewoor, S. T. (2012). Electrochemical behavior of chalcone at a glassy carbon electrode and its analytical applications. *American Journal of Analytical Chemistry*, 3(9): 656-663.

21. Baggio, R., Brovelli, F., Moreno, Y., Pinto, M. and Soto-Delgado, J. (2016). Structural, electrochemical and theoretical study of a new chalcone derivative containing 3-thiophene rings. *Journal of Molecular Structure*, 1123: 1-7.
22. Ilhan, S., Temel, H., Yilmaz, I. and Sekerci, M. (2007). Synthesis, structural characterization and electrochemical studies of new macrocyclic Schiff base containing pyridine head and its metal complexes. *Journal of Organometallic Chemistry*, 692 (18): 3855-3865.

Malaysian Journal of Analytical Sciences (MJAS)
Published by Malaysian Analytical Sciences Society

STRUCTURAL AND CONDUCTIVITY STUDIES OF CHOLINE CHLORIDE-BASED DEEP EUTECTIC SOLVENT AS A POTENTIAL ELECTROLYTE IN LITHIUM-ION BATTERIES

(Kajian Struktur dan Kekonduksian Pelarut Eutektik Dalam Berasaskan Kolina Klorida yang Berpotensi sebagai Elektrolit dalam Bateri Ion Litium)

Intan Qhuzairin Zaharuddin, Nabilah Akemal Muhd Zailani*, Khuzaimah Nazir, Rizana Yusof, Mohd Azlan Mohd Ishak

Fakulti Sains Gunaan,
Universiti Teknologi MARA, Cawangan Perlis, Kampus Arau, 02600 Arau, Perlis, Malaysia

**Corresponding author: nabilahakemal@uitm.edu.my*

Received: 14 February 2022; Accepted: 18 August 2022 ; Published: 30 October 2022

Abstract

Utilizing volatile and flammable electrolytes in lithium-ion batteries has become a primary concern worldwide. Consequently, a safer high-performance electrolytes approach is required to solve the issue. In this circumstance, deep eutectic solvent (DES) might be the best option to substitute the harmful conventional liquid electrolytes. The present study explores the potential of ternary DES, which comprises choline chloride (ChCl), 1,4-butanediol (1,4-BD), and lithium triflate (LiTf), as an electrolyte in lithium-ion batteries. The structural and conductivity of ChCl/1,4-BD at 1:1, 1:2; and 1:3 mole ratios and ChCl/1,4-BD/LiTf at 2.5, 5, and 10 wt.% LiTf systems were investigated. The ChCl/1,4-BD at 1:1 ratio (DES1:1) recorded the highest ionic conductivity of 2.41 mS cm^{-1}, which resulted from the least amount of hydrogen bonds between ChCl and 1,4-BD. Subsequently, the DES1:1 was doped with different percentages of LiTf. The highest ionic conductivity, 2.56 mS cm^{-1}, was obtained from the ChCl/1,4-BD/2.5 wt.% LiTf system. The elevated ionic conductivity was attributable to the high amount of mobile lithium ions available due to fewer hydrogen bonds formed between the ChCl/1,4-BD and LiTf. Conclusively, the highly conducting ChCl/1,4-BD/2.5 wt.% LiTf demonstrated the best potential for application in lithium-ion batteries.

Keywords: deep eutectic solvents, liquid electrolytes, lithium salts, ionic conductivity

Abstrak

Penggunaan elektrolit yang mudah meruap dan terbakar dalam bateri ion litium merupakan isu utama di seluruh dunia. Oleh itu, elektrolit yang berprestasi tinggi dengan pendekatan yang lebih selamat diperlukan bagi menyelesaikan isu ini. Dalam keadaan ini, pelarut eutektik dalam (DES) dilihat sebagai alternatif terbaik untuk menggantikan cecair elektrolit konvensional yang berbahaya. Kajian ini meneroka potensi DES ternari yang terdiri daripada kolina klorida (ChCl), 1,4-butanadiol (1,4-BD) dan litium triflat (LiTf) sebagai elektrolit hijau dalam bateri ion litium. Struktur dan kekonduksian bagi sistem dengan 1:1, 1:2; dan 1:3 nisbah mol ChCl/1,4-BD dan ChCl/1,4-BD/LiTf dengan 2.5, 5, 10 wt.% LiTf telah dikaji. Sistem ChCl/1,4-BD dengan 1:1 nisbah mol (DES1:1) telah menunjukkan kekonduksian ionik paling tinggi, iaitu 2.41 mS cm^{-1}, yang terhasil daripada interaksi ikatan hidrogen yang rendah antara ChCl dengan 1,4-BD. Seterusnya, DES1:1 telah ditambah dengan LiTf pada peratusan yang berbeza.

Kekonduksian ionik yang tertinggi, iaitu 2.56 mS cm^{-1}, telah diperoleh sistem ChCl/1,4-BD/2.5 wt.% LiTf. Kekonduksian yang tinggi ini disumbangkan oleh kehadiran ion litium bebas yang tinggi hasil daripada kurang interaksi ikatan hidrogen antara ChCl/1,4-BD dengan LiTf. Kesimpulannya, ChCl/1,4-BD/2.5 wt.% LiTf dengan kekonduksian yang tinggi menunjukkan potensi terbaik untuk digunakan dalam bateri ion litium.

Kata kunci: pelarut eutektik dalam, cecair elektrolit, garam litium, kekonduksian ionik

Introduction

The rapid increase in the world population and economic power has escalated energy demand. Accordingly, exceptionally efficient, stable, and ecologically benign energy storage systems are highly desired. Lithium-ion batteries are one of the most widely studied devices for energy storage as they possess great energy density and thermal stability and are less expensive than other types of batteries [1, 2]. Moreover, the application of lithium-ion batteries is not limited to mobile phones, they are also employed in medical and aerospace instruments [3]. Nevertheless, the conventional liquid electrolytes of lithium-ion batteries comprise flammable and volatile organic solvents [4] that result in issues such as leakages, corrosion, and even explosions.

The utilization of ionic liquids (IL)-based liquid electrolytes has been extensively investigated [4, 5]. The IL provides superior safety attributes to liquid electrolytes as it possesses distinctive physical properties, such as non-flammable, low melting point and volatility, and high thermal stability [6]. Nonetheless, deep eutectic solvents (DES) have been reported to exhibit more desirable properties, including cost-effectiveness, high biodegradability, and very low toxicity, despite sharing similar physicochemical properties with IL (non-flammable, low volatility, high thermal stability) [4, 7].

The DES is obtainable from the self-association of hydrogen bond acceptor (HBA) and hydrogen bond donor (HBD) via a simple heating technique [8]. Consequently, its biodegradability is contributed by their natural HBA (choline chloride (ChCl), phosphonium salts) and HBD (carboxylic acid, urea, renewable polyols, amines, amides, carbohydrates) contents. The DES consisted of N-methylacetamide (MAc) and different lithium salts (lithium bis[(trifluoromethyl)sulfonyl]) imide (LiTFSI) and lithium hexafluorophosphate ($LiPF_6$) has been reported as potential electrolytes for lithium-ion batteries. Nevertheless, liquid-state-electrolytes were not obtainable when the Li molar fraction was over 0.35, hence limiting the ionic conductivity to only 1 mS cm^{-1} [9]. The finding led to the development of ternary DES, such as ChCl/ethylene glycol/$LiPF_6$, that remains in a liquid state even at a 0.5 Li molar fraction, hence bearing higher ionic conductivity of 7.95 mS cm^{-1}. Nonetheless, the $LiPF_6$ exhibited low thermal decomposition temperature [10,11], thus deteriorating when subjected to high temperatures.

The lithium triflate (LiTf) has been demonstrated to possess higher thermal stability than $LiPF_6$ [11]. Consequently, the current study investigated a DES ternary system comprising a choline chloride (ChCl), 1,4-butanediol (1,4-BD), and LiTf mixture. The most optimum ChCl to1,4-BD mole ratio (1:1, 1:2; or 1:3) as the solvent for LiTf was first investigated. The study then doped the ChCl/1,4-BD with different weight percentages of LiTf (2.5, 5, and 10 wt.%). The structural and conductivity assessments of the systems were conducted with Fourier Transform Infrared Spectroscopy (FTIR) and conductivity meter, respectively.

Materials and Methods

Preparation of DES

The chemical components DES, 99% ChCl (Acros Organic), > 99% 1,4-butanediol (Sigma), and 99% LiTf (Sigma) were employed in the present study without further purification. Three ChCl/1,4-BD mixtures at 1:1, 1:2, and 1:3 mole ratios, labelled as DES1:1, DES1:2, and DES1:3, respectively, were mixed and heated at 80℃ while stirring until dissolution. Subsequently, LiTf with different weight percentages, 2.5, 5, and 10 wt.%, were dissolved in the highest conducting ChCl/1,4-BD while stirring and were designated as LE2.5, LE5, and

LE10, respectively. All the samples were kept in a desiccator before being characterized.

Fourier Transform Infrared Spectroscopy

The FTIR spectra of the samples evaluated in this study were recorded with a Perkin Elmer spectroscope at room temperature. First, the samples were dropped directly onto the crystal before measurements were obtained under the transmittance mode over the 4000-600 cm^{-1} frequency range with 4 cm^{-1} resolutions and 16 scans. Peak deconvolution was carried out with the Origin 8.1 software, in which the Gaussian function was employed to resolve overlapping bands. Prior to the deconvolution process, baseline corrections were conducted.

Conductivity meter

A conductivity meter (HANNA Instruments) was utilized to measure the ionic conductivities of the samples in the current study. The samples were placed in 50 ml beakers and the conductivity meter was dipped into each solution. The assessment was performed at room temperature and the ionic conductivities were recorded three times for each sample.

Result and Discussion

Preparation of the ChCl/1,4-BD mixture

The present study successfully obtained the homogenous liquid mixtures of ChCl/1,4-BD at varying mole ratios. Furthermore, the mixtures remained in their liquid conditions even at room temperature.

Structural analyses of the ChCl/1,4-BD

Figure 1 displays the FTIR spectra for the ChCl, 1,4-BD and the ChCl/1,4-BD mixtures at different mole ratios. The FTIR peaks representing ChCl were observed at 3222, 1480, and 1349 cm^{-1} due to OH stretching and CH_2 and CH_3 bending, respectively [12]. The FTIR spectra of the 1,4-BD appeared at 3292, 1169, and 1428 cm^{-1}, which denoted the O-H and C-O stretching and CH_2 bending, respectively [13]. The O-H stretching peak of the 1,4-BD also shifted to a higher wavenumber, from 3292 to 3297, 3298, and 3293 cm^{-1}, in the DES1:1, DES1:2 and DES1:3 samples, respectively. The observations confirmed the hydrogen bonding interactions between ChCl and 1,4-BD in the binary DES obtained. The peak intensities of the solutions were also reduced.

The decrease in the peak intensity of O-H stretching with the increasing amount of 1,4-BD indicated the diminished free O-H stretching in the system. The phenomenon might be due to the formation of hydrogen bonding interactions between the O-H···O-H and O-H···Cl in the ChCl/1,4-BD mixtures, as illustrated in Figure 2. The interaction between ChCl and 1,4-BD could also be further confirmed by the upshift in the CH_2 bending of 1,4-BD from 1428 to 1441, 1442, and 1448 cm^{-1} in the DES1:1, DES1:2, and DES1:3, respectively. The trends observed in this study agreed with a previous investigation on the formation of citric acid monohydrate-ChCl based DES [12].

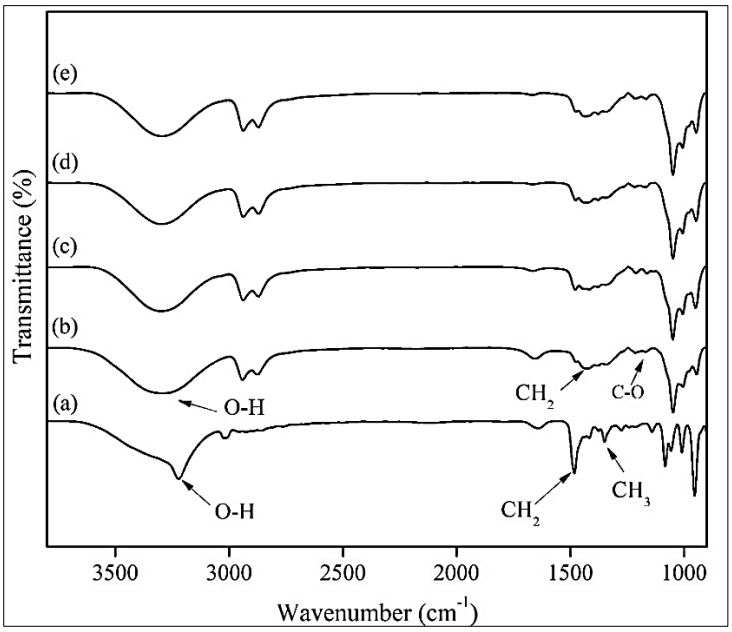


Figure 1. The FTIR spectra of (a) ChCl, (b) 1,4-BD, (c) DES1:1, (d) DES1:2, and (e) DES1:3

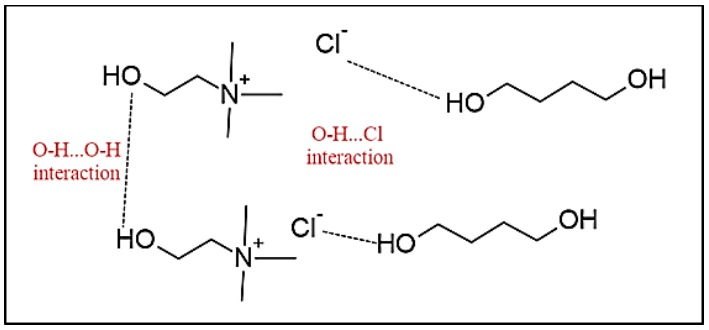


Figure 2. The possible hydrogen bonding interactions in ChCl/1,4-BD

Wang and co-workers [14] reported that the amount of hydrogen bonding interactions in ChCl-polyol DES could be further confirmed by the deconvolution and band-fitting of the broad O-H stretching peak between the 3700–3100 cm^{-1} region. Accordingly, the deconvolution and band fitting of DES1:1, DES1:2, and DES1:3 samples were conducted and is illustrated in Figure 3. Three types of O-H peaks were present at ~3400, ~3300, and ~3200 cm^{-1}, which corresponded to the free O-H stretching and inter- and intramolecular O-H⋯O-H and O-H⋯Cl stretching, respectively. As the amount of 1,4-BD increased, the amount of free O-H stretching decreased. The observations were due to the elevated inter- and intramolecular O-H⋯O-H and O-H⋯Cl interactions in the ChCl/1,4-BD mixtures.

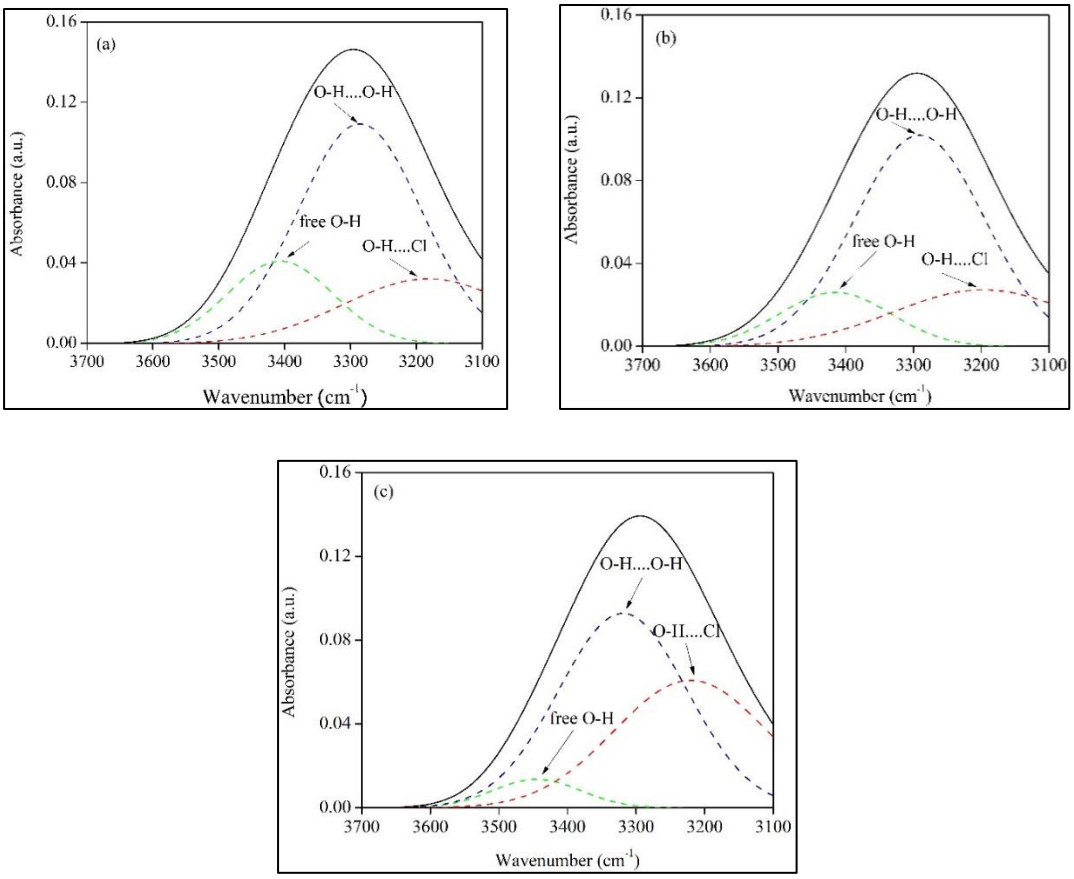


Figure 3. The deconvolution and band fitting of the FTIR spectra from 3700–3100 cm^{-1} of the (a) DES1:1, (b) DES1:2, and (c) DES1:3 samples

Conductivity assessments of the ChCl/1,4-BD

Table 1 lists the ionic conductivity values of the varying mole ratios of ChCl/1,4BD produced in the current study. The highest ionic conductivity, 2.41 mS cm^{-1}, was recorded by the DES1:1, however, the value decreased with higher 1,4-BD in the DES1:2 and DES1:3 systems. The observations resulted from elevated hydrogen bonds confirmed in the FTIR analysis. Furthermore, the presence of an excessive amount of 1,4-BD alkyl chain in the ChCl/1,4-BD mixture might also contribute to the diminished ionic conductivity of the samples.

The HBD alkyl chain structure has been reported to affect the ionic conductivity of DES [6]. As the amount of 1,4-BD was increased, an excessive amount of alkyl chain was produced in the ChCl/1,4-BD system, resulting in higher van der Waals interactions within the ChCl/1,4-BD. Consequently, the mobility of the ions was lowered, hence decreasing the ionic conductivity of the system. Similar observations were reported by Zhang and co-workers [5].

The ionic conductivity values of the DES1:1 was slightly higher if compared to other DES systems such as ChCl/EG (1.79 mS cm^{-1}) [15] and TBABr/EG (0.53 mS cm^{-1}) [6]. The findings were attributable to the non-excessive hydrogen bonds formed between HBA and HBD, which would ease the movement of lithium ions. Hence, the ChCl/1,4-BD at a 1:1 mole ratio was the optimal solvent selection for dissolving LiTf in the present study.

Table 1. The ionic conductivities of the ChCl/1,4BD systems

System	Ionic conductivity (Mean ± SD, mS cm^{-1})
DES1:1	2.41 ± 0.27
DES1:2	1.34 ± 0.44
DES1:3	0.92 ± 0.12

Preparation of the ChCl/1,4-BD/LiTf

In the current study, homogenous liquid mixtures of ChCl/1,4-BD/LiTf with different LiTf weight percentages were successfully obtained. Furthermore, the mixtures remained as liquids even at room temperature.

Structural evaluations of the ChCl/1,4-BD/LiTf

Figure 4 demonstrates the FTIR spectra for the DES1:1 with LiTf LE2.5, LE5, and LE10. The SO_3 and CF_3 stretching peaks were recorded at 1265 and 1182 cm^{-1}, respectively, for pure LiTf. Upon incorporation of LiTf into the ChCl/1,4-BD system, the SO_3 and CF_3 stretching peaks of LiTf were observed, hence confirming the miscibility of LiTf in ChCl/1,4-BD [16]. The O-H stretching peaks of the DES1:1 shifted to higher wavenumbers, from 3297 to 3303, 3301, and 3335 cm^{-1}, respectively, in the LE2.5, LE5, and LE10 systems. Moreover, the peak intensities were diminished.

Meanwhile, the peak intensities of the SO_3 and CF_3 stretching of LiTf were recorded to increase with higher amounts of LiTf. The findings indicated that interactions between the LiTf anions and the hydrogen from the DES hydroxyl groups occurred, as demonstrated in Figure 5. Furthermore, the decreased peak intensity of the OH stretching in the samples indicated that more hydrogen bonding between the LiTf and ChCl/I,4-BD transpired as the percentage of the LiTf added was increased. Dhingra and co-workers also reported similar results in the study of ChCl/urea/lithium chloride DES [4].

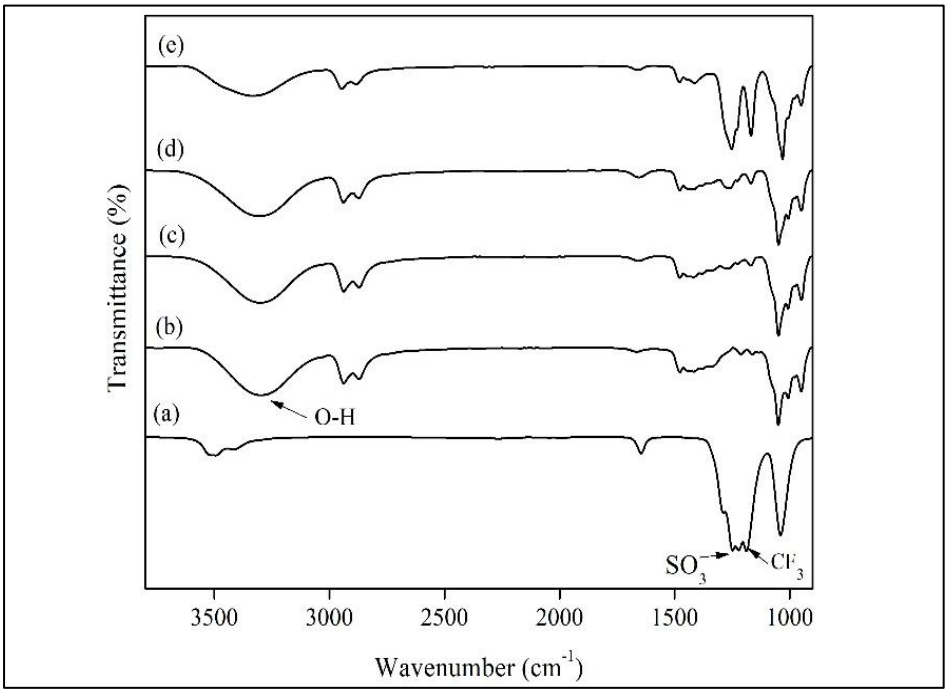


Figure 4. The FTIR spectra of the (a) LiTf, (b) DES1:1, (c) LE2.5, (d) LE5, and (e) LE10

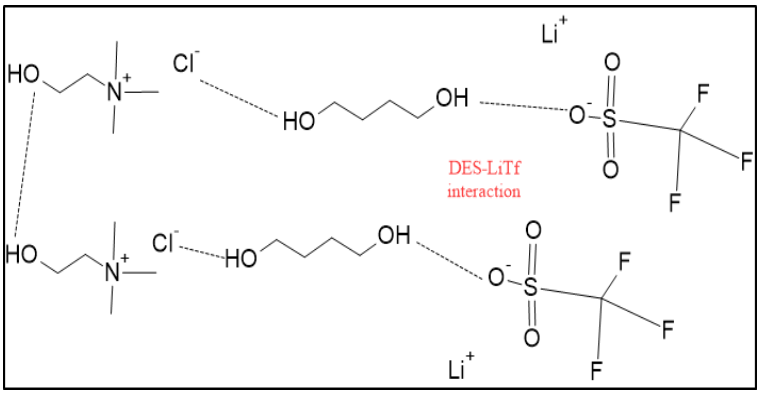


Figure 5. Possible hydrogen bonding interactions in the ChCl/1,4-BD/LiTf samples

Conductivity studies of the ChCl/1,4-BD/LiTf

Table 2 lists the ionic conductivity of the ChCl/1,4-BD/LiTf systems manufactured in the present study. The conductivity of the system increased from 2.41 to 2.56 mS cm^{-1} as 2.5 wt.% of LiTf was added into the ChCl/1,4-BD. The ionic conductivity increment was attributable to the free mobility of the lithium ions in the DES mixtures, which resulted from the formation of hydrogen bonds between the anions in the salt and DES that was confirmed with FTIR.

The amount of mobile lithium ions has been demonstrated to affect the ionic conductivity of DES systems [16]. Nevertheless, as the addition of LiTf in the current study was increased to 5 and 10 wt.%, the conductivity reduced to 1.84 mS cm^{-1} and 0.65 mS cm^{-1}, respectively. The observations might be due to the formation of more hydrogen bonds that eventually prevented lithium ions from moving freely. Nonetheless, the highest conductivity value obtained in the present study was comparable to other ternary DES systems comprising EG/ChCl/ $LiPF_6$ (7.95 mS cm^{-1}) [7].

Table 2. Ionic Conductivity for ChCl/1,4-BD/LiTf System

System	Ionic conductivity (Mean ± SD, mS cm^{-1})
LE2.5	2.56 ± 0.12
LE5	1.84 ± 0.26
LE10	0.65 ± 0.17

Conclusion

An increased 1,4-BD amount would lead to more hydrogen bonding formation, hence reducing the free mobility of ions and conductivity of ChCl/1,4BD systems. In the present study, the optimal ChCl/1,4-BD to dissolve LiTf was recorded at a 1:1 mole ratio as the solution contained non-excessive hydrogen bonds, thus easing lithium-ion movements. Moreover, adding 2.5 wt.% of LiTf to the ChCl/1,4-BD mixture resulted in the highest number of mobile ions, contributing to its conductivity, 2.56 mS cm^{-1}, which was the highest. Conclusively, ternary DES consisting of a 1:1 mole ratio of ChCl/1,4-BD and 2.5% LiTf exhibited the optimal potential of being applied in lithium-ion batteries.

Acknowledgement

The authors would like to acknowledge Faculty of Applied Sciences, UiTM Perlis branch for supporting this research. Financial support by Dana Pembudayaan Penyelidikan Dalaman (DPPD) (600-TNCPI 5/3/DDN (09) (018/2020)) is highly acknowledged.

References

1. Chen, T., Jin, Y., Lv, H., Yang, A., Liu, M., Chen, B., Xie, Y. and Chen, Q. (2020). Applications of Lithium-Ion Batteries in Grid-Scale Energy Storage Systems. *Transactions of Tianjin University*, 26(3): 208-217.
2. Liu, K., Liu, Y., Lin, D., Pei, A. and Cui, Y. (2018). Materials for lithium-ion battery safety. *Science Advances*, 4(6): eaas9820.
3. Zubi, G., Dufo-López, R., Carvalho, M. and Pasaoglu, G. (2018). The lithium-ion battery: State of the art and future perspectives. *Renewable and Sustainable Energy Reviews*: 89: 292-308.
4. Dhingra, D., Bhawna and Pandey, S. (2018). Effect of lithium chloride on the density and dynamic viscosity of choline chloride / urea deep eutectic solvent in the temperature range (303.15-358.15)K. *The Journal of Chemical Thermodynamics*, 130: 166-172.
5. Zhang, Q., Vigier, K. D. O., Royer, S. and Jerome, F. (2012). Deep eutectic solvents: syntheses, properties and applications. *The Royal Society of Chemistry*, 41(21): 7108-7146.
6. Yusof, R., Abdulmalek, E., Sirat, K. and Rahman, M. B. A. (2014). Tetrabutylammonium bromide (TBABr)-Based deep eutectic solvents (DESs) and their physical properties. *Molecules*, 19(6): 8011-8026.
7. Millia, L., Dall'Asta, V., Ferrara, C., Berbenni, V., Quartarone, E., Perna, F. M., Capriati, V. and Mustarelli, P. (2018). Bio-inspired choline chloride-based deep eutectic solvents as electrolytes in for lithium-ion batteries. *Solid State Ionics*, 323: 44-48.
8. Tomé, L. I. N., Baião, V., Silva, W. and Brett, C. M. A. (2018). Deep eutectic solvents for the production and application of new materials. *Applied Materials Today*, 10: 30-50.
9. Boisset, A., Menne, S., Jacquemin, J., Balducci, A. and Anouti, M. (2013). Deep eutectic solvents based on N-methylacetamide and a lithium salt as suitable electrolytes for lithium-ion batteries. *Physical Chemistry Chemical Physics*, 15(46): 20054-20063.
10. Tomaszewska, A., Chu, Z., Feng, X., O'Kane, S., Liu, X., Chen, J., Ji, C., Endler, E., Li, R., Liu, L., Li, Y., Zheng, S., Vetterlein, S., Gao, M., Du, J., Parkes, M., Ouyang, M., Marinescu, M., Offer, G. and Wu, B. (2019). Lithium-ion battery fast charging: A review. *e-Transportation*, 1: 100011.
11. Wang, Q., Jiang, L., Yu, Y. and Sun, J. (2019). Progress of enhancing the safety of lithium ion battery from the electrolyte aspect. *Nano Energy*, 55: 93-114.
12. Shafie, M., Yusof, R. and Gan, C. (2019). Synthesis of citric acid monohydrate-choline chloride based deep eutectic solvents (DES) and characterization of their physicochemical properties. *Journal of Molecular Liquids*, 288: 111081.
13. Jesus, A. J. L., Rosado, M. T. S., Reva, I., Fausto, R., Eusébio, M. E. S. and Redinha, J. S. (2008). Structure of Isolated 1 , 4-Butanediol : Combination of MP2 calculations, NBO analysis, and matrix-isolation infrared spectroscopy. *The Journal of Physical Chemistry A*, 112(20): 4669-4678.
14. Wang, H., Liu, S., Zhao, Y., Wang, J. and Yu, Z. (2019). Insights into the hydrogen bond interactions in deep eutectic solvents composed of choline chloride and polyols. *ACS Sustainable Chemistry & Engineering*, 7: 7760-7767.
15. Zhong, M., Fang, Q., Wu, Y., Ying, X. and Jie, Z. (2020). An alternative electrolyte of deep eutectic solvent by choline chloride and ethylene glycol for wide temperature range supercapacitors. *Journal of Power Sources*, 452: 227847.
16. Dinh, T. T. A., Huynh, T. T. K., Le, L. T. M., Truong, T. T. T., Nguyen, O. H., Tran, K. T. T., Tran, M. V, Tran, P. H., Kaveevivitchai, W. and Le, P. M. L. (2020). Deep eutectic solvent based on lithium bis [(tri fluoromethyl) sulfonyl] imide (LiTFSI) and 2,2,2- trifluoroacetamide (TFA) as a promising electrolyte for a high voltage lithium-ion battery with a $LiMn_2O_4$ cathode. *ACS Omega*, 5(37): 23843-23853.

Malaysian Journal of Analytical Sciences (MJAS)
Published by Malaysian Analytical Sciences Society

THE EFFECTS OF SOAKING TIME ON THE QUALITY AND PROPERTIES OF DURIAN (*Durio zibethinus*) SEED GUM: A MINI REVIEW

(Kesan Masa Rendaman Terhadap Kualiti Dan Sifat Gam Biji Durian (*Durio zibethinus*): Ulasan Mini)

Nurul I'zzati Ramli[1], Boon Yih Tien[1,2*], Boon Yih Hui[3], Wang Kang Han[4]

[1]Department of Food Science and Technology,
Faculty of Applied Sciences, Universiti Teknologi MARA Cawangan Negeri Sembilan, Kampus Kuala Pilah,
72000 Kuala Pilah, Negeri Sembilan, Malaysia
[2]Alliance of Research and Innovation for Food (ARIF),*
Universiti Teknologi MARA Cawangan Negeri Sembilan, Kampus Kuala Pilah,
72000 Kuala Pilah, Negeri Sembilan, Malaysia
[3]Research and Development Centre, KL-Kepong Oleomas Sdn. Bhd,
Lot 1 & 2, Solok Waja 3, Bukit Raja Industrial Estate, 41710 Klang, Selangor, Malaysia
[4]Faculty of Applied Sciences,
UCSI University, UCSI Height, 56000 Cheras, Kuala Lumpur, Malaysia.

**Corresponding author: boonyihtien@uitm.edu.my*

Received: 28 February 2022; Accepted: 19 May 2022; Published: 30 October 2022

Abstract

Durian (*Durio zibethinus*) is one of the most notorious fruits in the world, especially in Southeast Asian countries. It is well-known as the "King of Fruits" due to its rich flavour and large size. The unique taste of durian has created its own global demand, which continues to increase despite its unpleasant odour. However, only one-third of the entire durian is consumable, while the seeds and husks are ordinarily disposed of as waste. The seed waste can be potentially converted into value-added products such as seed gum. The high content of carbohydrates and starch in the seeds makes them suitable for use as biopolymers. A natural hydrocolloid can be obtained from durian seeds through a chemical extraction process. This review provides an overview of the effects of different extraction parameters on the physicochemical and functional properties of durian seed gum and discusses the potential application of durian seeds as a food gum. The physical and chemical properties of durian seed gum highly depend on the further extraction parameters and processing of the gum. The findings showed that the soaking process has a greater impact on the quality of the gum produced compared to the concentration of acid used in terms of solubility and water-holding capacity. The physicochemical properties of durian seed gum are comparable to those of commercial food gum, but its anti-nutrient content and sensory evaluation in food products must be further investigated to ensure its safety before consumption.

Keywords: seed waste, chemical extraction, durian seed gum, physicochemical properties

Abstrak

Durian (*Durio zibethinus*) adalah salah satu buah-buahan yang terkenal di negara-negara Asia Tenggara. Durian dikenali sebagai "Raja Buah" kerana ciri-cirinya yang kaya dengan rasa dan mempunyai saiz yang besar. Keenakan dan rasanya yang unik menyebabkan durian telah meraih permintaan yang tinggi di peringkat global walaupun mempunyai bau yang kurang menyenangkan. Walau bagaimanapun, hanya satu pertiga daripada keseluruhan buah durian yang dapat dimakan, iaitu bahagian isinya, manakala biji dan kulitnya biasanya dibuang sebagai sisa kerana dipercayai tiada nilai komersial. Biji durian berpotensi tinggi untuk diolah menjadi produk nilai tambah seperti gam makanan kerana mengandungi karbohidrat dan kanji yang tinggi. Objektif kajian ini adalah untuk menilai pengaruh perbezaan parameter pengekstrakan terhadap sifat fiziko-kimia serta fungsi gam biji durian dan menilai potensi penggunaan biji durian sebagai penstabil makanan. Ciri-ciri fizikal dan kimia gam biji durian bergantung pada parameter pengekstrakan dan pemprosesan yang lebih lanjut. Hasil kajian menunjukkan bahawa proses rendaman mempunyai kesan yang lebih besar terhadap kualiti gam yang dihasilkan dibandingkan dengan kepekatan asid yang digunakan dari segi kelarutan dan kapasiti pengekalan air. Ciri-ciri fiziko-kimia gam biji durian adalah setanding dengan gam makanan yang terdapat di pasaran, tetapi kandungan anti-nutrien dan penilaian berderia dalam produk makanan perlu dikaji dengan lebih mendalam untuk memastikan keselamatannya sebelum digunakan dalam pemakanan.

Kata kunci: sisa biji benih, pengekstrakan kimia, gam biji durian, sifat fizikokimia

Introduction

Durian (*Durio zibethinus*) belongs to the Bombacaceae family and is the most popular seasonal fruit in Southeast Asia, especially Thailand, Malaysia, the Philippines, and Indonesia. In 2019, the national production of durian increased tremendously due to its great demand on the global stage, such as China, Vietnam, Singapore, and the United States [1]. During the breakdown of the COVID-19 pandemic, between March and May 2020, the reported sales of durian in Malaysia had reached one tonne per day [2]. However, only one-third of the entire durian is consumable, while the seeds (20–25%) and the husk are ordinarily disposed of. For example, the Philippines, a country in Southeast Asia, faces a problem with the large amount of durian waste produced every year. According to Ana et al., about 40% of durian husks, including 25% of durian seeds (21,880), are considered waste in the Philippines annually [3]. Furthermore, in the first half of 2018, around 4000 tonnes of durian seeds were discarded in Singapore [4]. Subsequently, extensive research has been conducted on the growth of value-added products to reduce the wastage from the inconsumable part of durian. Mirhosseini and Amid stated that the unused durian seeds have great potential to be produced as value-added goods, such as flour and stabilisers, as they contain a high amount of carbohydrates, fibre, and vitamins [5].

Generally, durian seed gum can be obtained through a chemical extraction process as it produces a higher quality of gum compared to the aqueous extraction process. This is because the aqueous extraction process produces gum with a higher moisture content, which indirectly affects the shelf life of the gum produced. The difference in extraction parameters, such as soaking time, soaking temperature, and decolourisation time, was reported to have affected the physicochemical properties of the gum produced. Meanwhile, purification methods also affect the functional characteristics of durian seed gum [6]. Although there has been plenty of research conducted globally on the production and application of durian seed gum, much improvement is still required for a larger yield and better properties of the gum.

Based on current knowledge, the effects of acetic acid concentration and soaking time on the physicochemical properties of durian seed gum have not been fully investigated. Therefore, the present study aims to review the effects of acetic acid concentration and soaking time, especially on the physicochemical and functional properties of durian seed gum, and to explore the potential application of durian seeds as food gum. This study also intends to provide an overview and future perspective on the use of durian seeds in resolving the global food waste issue faced by Asian countries over the years. Converting food waste into useful products not only helps to reduce agricultural waste, but also helps to minimise environmental pollution [7].

Overview of food gum

Food gum, also referred to as natural hydrocolloid, is commonly used in food manufacturing as thickeners, gelling agents, stabilisers, coating agents, and packaging film. Gum is a complex polysaccharide that can be obtained from various sources, such as seaweed extract (e.g., agar), the endosperm of plant seeds (e.g., guar gum), and bacteria (e.g., xanthan gum). According to Clemens and Pressman, food gum consists of carbohydrates with a large number of hydroxyl groups, resulting in hydrophilic characteristics [8]. Therefore, food gums are highly water-soluble due to their polymers that form a cross-linked network by trapping and immobilising water in a viscoelastic, flow-resistant structure. One of the common functional properties of hydrocolloid is their thickening properties, which determine the viscosity of the gum produced. According to Phillips and Williams, the viscosity of the gum is significantly influenced by the molecular mass of the polymer [9]. The higher the molecular mass, the more viscous the gum produced. The next functional properties of food gum are emulsification properties. Golkar et al. reported that the emulsification properties of food gum are affected by its interfacial activity, which stabilises and forms oil droplets in emulsions [10].

Other functional properties of food gum are hydration and solubilisation. All polysaccharides have sections in their solid state where the chain segments or molecules are disordered and unorganised. As a result, these amorphous regions have a large number of unfulfilled hydrogen bonding spots that can easily hydrate [9]. Polysaccharides that are entirely dry have a slow but extremely significant affinity for water. When a soluble polysaccharide is immersed in water, the numerous water molecules directly enter amorphous regions and attach to accessible polymer sites. Subsequently, the number of other inter-polysaccharide linkages can be minimised. The inter-polysaccharide bonds are broken down by kinetic action and result in the full solubility of the polysaccharide chain.

Generally, polysaccharides can be found in four common structures: linear, single-branch, substituted linear, and branch-on-branch [1]. Figure 1 shows the different types of polysaccharide polymer structures. Glicksman stated that the solution of branched polysaccharides is more stable than the solution of a linear molecule [1]. The solution with branched molecules remains homogenous for a long period of time due to its high affinity for water and good adhesive properties. Durian seed gum exemplifies good adhesive properties as it is composed of branched molecules [5].

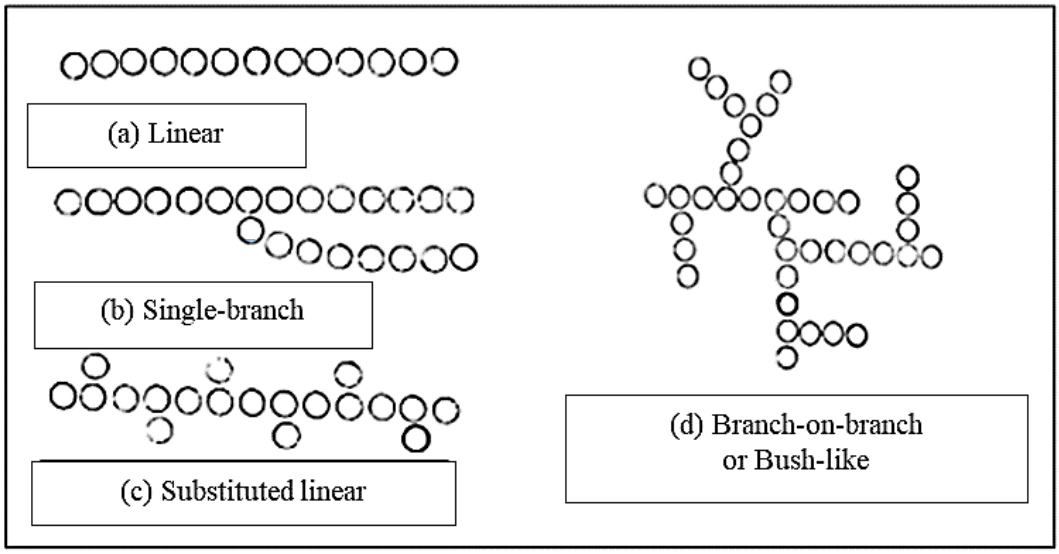


Figure 1. The types of polysaccharide polymer structures [1]

Potential application of durian seeds as food gum

The durian seed contains a high level of polysaccharides suitable for being used as gum for thickening and gelling properties [11]. The protein content of durian seeds is estimated to be 3.40%, the moisture content to be 54.90%, the starch content to be 18.92%, and the fat content to be 1.32% [12]. Amin et al. studied the composition of durian seed gum for the dehulled and whole durian seed flour. The study found that the entire durian seed flour contains 6.0% protein, 0.4% fat, 3.1% ash, 10.1% crude fibre, 73.9% carbohydrates, and 6.0% water [13]. Meanwhile, dehulled durian seed flour contains 0.4% fat, 3.8% ash, 7.6% protein, 4.8% crude fibre, 76.8% carbohydrates, and 6.6% water. The high carbohydrate content in both types of durian seed flour makes them suitable to undergo further processing due to their excellent thickening properties. Amin et al. stated that the durian seed gum is stable at pH levels between 2.0 and 10.0. This pH is similar to the pH of xanthan gum (2.0 to 12.0) and further supports their application in a wide range of products [13].

In addition to this, the three primary sugars in durian seed gum are rhamnose, D-galactose, and glucose. Amin et al. found that the ratio of these sugars (i.e., glucose, rhamnose, and D-galactose) is 9:3:1, respectively [13]. The primary component in the formation of gum in durian seeds is L-rhamnose, which is also known as C-5 polysaccharide. When rhamnose sugar comes into contact with water, polysaccharides form a structure to prevent water molecules from joining. As a result, a thicker gel is formed after the detraction of water molecules by C-5 polysaccharide [14]. Therefore, the presence of sugar in the polysaccharide is important in enhancing the rheological properties of the gum, which are dependent on the soaking and purification process [15]. Moreover, the durian seed gum is comparable to guar gum in terms of colour, solubility, water, and oil-holding capacity [2]. The study revealed that the solubility of durian seed gum is higher than that of guar gum due to its active interaction between protein and monosaccharide fractions. Apparently, the colour of durian seed gum is slightly darker compared to the colour of guar gum (Figure 2), but it is acceptable.

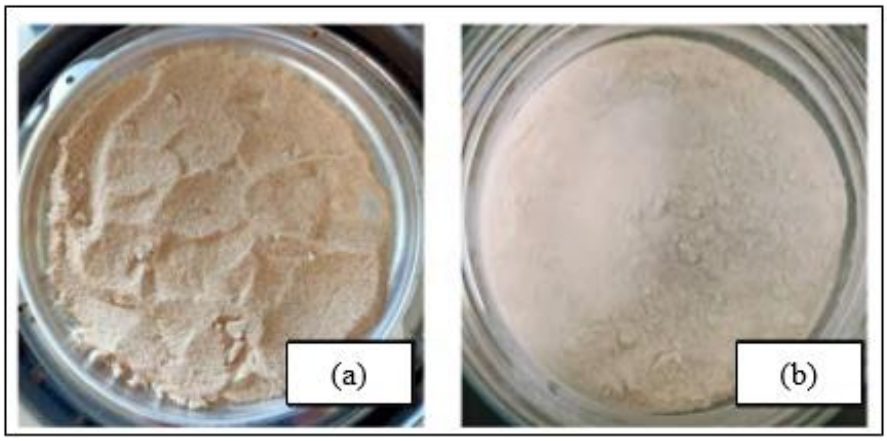


Figure 2. (a) Durian seed gum; (b) guar gum [2]

In another study, Cornelia et al. described that the use of durian seed gum as an emulsifier in vegan mayonnaise results in the same texture as commercial vegan mayonnaise [11]. Furthermore, there is no significant cream helps to improve the consistency and texture of the ice cream. This is proven when the overrun of the ice cream at a low concentration (0.1%) of durian seed gum difference in terms of aroma in vegan mayonnaise made from durian seed gum. The application of durian seed gum in ice cream was investigated by Sawasdikarn et al. and found that the use of durian seed gum in sherbet ice was higher (30.26%) compared to the overrun of ice cream without any durian seed gum (25.36%) [16].

Effects of extraction parameters on the properties of durian seed gum

The processing steps involved in producing durian seed gum include extraction and purification phases. As shown in Table 1, different researchers have used different ranges of extraction parameters (soaking time, soaking temperature, decolouring time, and concentration of acid and pH). Sompie et al. reported that prolonging the soaking time in the presence of heat during the extraction process opens up the bonds of gelation molecules, thus resulting in a higher yield [17]. This finding is supported by Veira et al. that a temperature of 60°C produced a high yield of flaxseed gum [18].

Besides that, the hydration properties of the gum also depend on the water-holding capacity (WHC), solubility, and swelling capacity [5]. The interaction of soaking time and soaking temperature represents the most significant effect on the WHC of the gum as compared to the decolourisation process. The WHC of gum is determined by the conformational structure, pore size, and capillary of the molecule that are associated with the hydration molecule with polar compound and hydrophilic interaction [19]. According to Mirhosseini and Amid, gum extracted below 85°C with an alkaline pH has a higher WHC [6]. Besides, the interaction of soaking time and soaking temperature represents the most significant effect on the WHC of the gum compared to the decolourisation process. This is because the swelling properties of the gum generally depend on the ratio between the solvent and matrix, soaking time, and soaking temperature. The longer soaking time results in lower WHC properties because it has a poor affinity for absorbing water. Therefore, a shorter soaking process is required as it leads to a smaller pore size of the gum and thus increases the WHC. In contrast to the WHC, the lower soaking temperature and longer decolourisation produce a gum with a higher oil-holding capacity (OHC). High OHC is associated with a hydrophobic character and the presence of non-polar amino acids. According to Mirhosseini and Amid, purified gum has lower OHC than crude gum due to the presence of hydrophobic fractions and non-polar side chains in the crude durian seed gum that may bind the hydrocarbon units of oil [6].

Generally, gum exhibits high solubility and relatively low viscosity. Sompie et al. reported that the presence of heat during the soaking process may help in forming gum with higher viscosity properties, but eventually reduces them at higher temperatures [17]. According to Viera et al., the soaking process at 60 °C is sufficient to produce gum with a high viscosity. This is because the heat opens up the bonds between molecules and free-flowing liquids that are initially trapped inside the structure, thus forming a viscous gel [18].

Besides that, the solubility of a polymer in a solution depends on the size and weight of molecules as well as the concentration of the polymer in the solution. A study found that gum soaked for 4 to 8 hours has low solubility properties [5], but the finding is contradictory. A study conducted by Akdowa et al. found that the gum undergoes a one-to-three-hour soaking process to have better solubility properties [20], while the study by Batal and Hasib reported that one hour of the soaking process is sufficient to produce gum with high solubility properties [21]. The study found that the longer the soaking process, the larger the particle size of gum. Figure 3 shows a simple illustration of the effects of soaking time on the particle size of gum produced. A shorter soaking process results in a smaller particle size due to the lower absorption of insoluble matter into the final extract.

According to Mirhosseini and Amid, gum with high impurities and larger molecules has lower solubility properties [5]. This is because coarser and larger particles require a longer time to be dissolved due to the longer time required to penetrate water into the sample matrix. Therefore, the soaking time is crucial in producing a high-quality durian seed gum as it helps to reduce the protein content, ash content, and insoluble impurities. Generally, a shorter soaking process is preferable as it results in the presence of small gum particles and better solubility of gum.

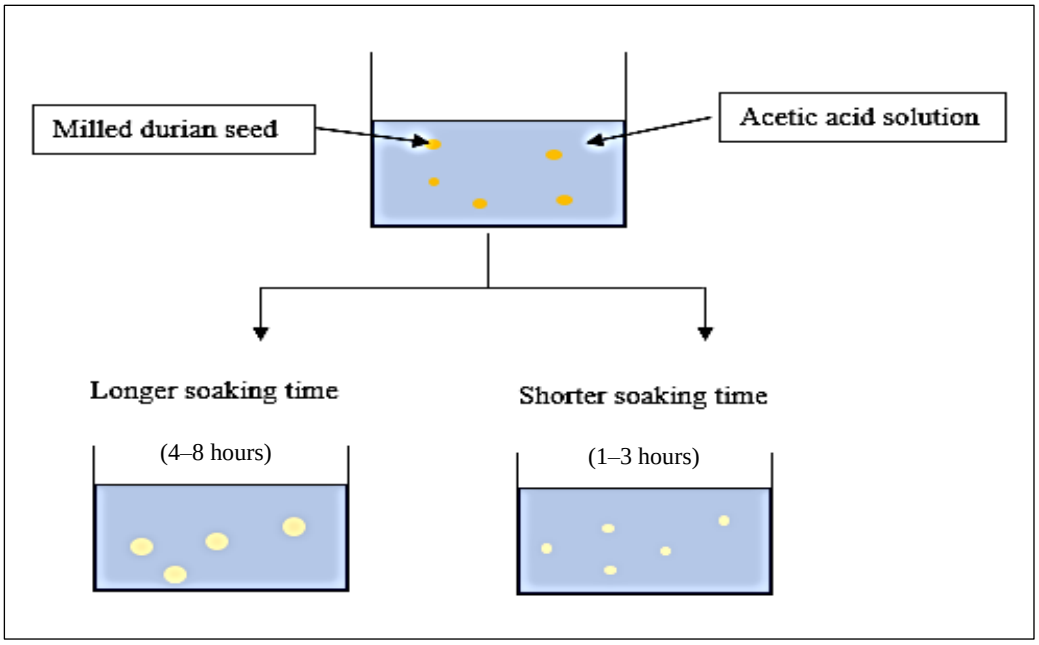


Figure 3. Illustration on the effects of soaking time on the particle size of gum produced

Apart from that, protein content in gum is also a known factor in affecting the purity of the gum. Gum with large amounts of protein is more flexible and has good adsorption capacity at the interface. Therefore, the protein content of the gum is highly critical toward achieving a good emulsifier property. According to Sompie et al., the acid concentration used during extraction influences the protein content of the gum produced [17]. The study showed that 4% of acid is good for producing gum with excellent emulsifying properties. Meanwhile, a high concentration of acid used reduces the viscosity of the gum due to the destruction of protein structures (hydrolysation of the peptide bond). Another work by Akdowa et al., which employed 1% of acetic acid, was also able to produce viscous gum coupled with a proper soaking process during the chemical extraction [20]. The suitable range of acetic acid concentration is between 1% and 4%, because at these concentrations, the peptide bond in the molecules cannot be broken down. Thus, high viscosity gum can be produced. However, a 1% concentration of acetic acid is preferable as it is less acidic and toxic.

Table 1. Different ranges of extraction parameters for durian seed gum.

Ref.	Parameters					Findings / Properties of Gum Obtained
	Temperature (℃)	Soaking Time (hr)	Decolouring Time (hr)	Concentration of Acid (%)	pH	
[5]	25℃ – 55℃	4 hrs – 8 hrs	1 hr – 3 hrs	1%	N/A	• Low solubility and WHC properties • Soaking time should be considered as the most critical extraction variable
[17]	50℃ – 60℃	N/A	N/A	2% – 6%	N/A	• Strong gel strength • Higher concentration causes a decrease in viscosity • Optimum condition: 4% of acetic acid at 55℃
[20]	N/A	1 hr – 3 hrs	N/A	1%	4 – 10	• Good solubility properties • Optimum condition: 1 hour; pH 7
[21]	70℃ – 100℃	20 mins – 60 mins	N/A	1%	N/A	• Maximum yield of gum • Optimum condition: 95℃ for 60 minutes

Challenges of durian seeds as food gum

Despite the merits of durian seeds as food gum, some challenges still arise. First, the amount of anti-nutrients in durian-derived seed gum is higher compared to that of other types of gum. According to Marina et al., the amount of anti-nutrients such as tannins, saponins, phytates, and oxalates was 232.19±4.92 mg/100g, 60.22±1.27 mg/100g, 181.32±4.46 mg/100g, and 105.55±13.07 mg/100g, respectively, after the durian seed underwent the boiling process [22]. These values were much higher than the amounts found in acacia seeds and karaya (3.0 mg/100g and 3.5 mg/100g) [4].

Next, food products require more durian seed gum than other commercial gums. For example, vegan mayonnaise requires at least 4% of durian seed gum to achieve a preferable texture [11]. Apart from that, additional usage of other commercial gums such as Arabic gum or xanthan gum is required if the concentration of durian seed gum used is lower than 4%. As a result, if manufacturers are forced to double or triple the quantities of stabilisers used in their products, production costs may rise. Besides that, research on the sensory properties of food using durian seed gum is less reported and lacking. To date, there have only been two available studies that focused on mayonnaise [11] and ice cream [16]. Inadequate sources of information are a limitation for further studies on the application of durian seed gum as a potential food ingredient.

Finally, the nature of the durian's growth, which belongs to the seasonal fruit category, might be a drawback to its continuous production. Commonly, the fruiting season of durian in Malaysia is from June to July. In order to ensure the availability of durian seed gum, the seeds must be handled with extra care during the fruiting season. Improper storage of the seeds may result in the loss of viability, which may reduce their moisture content and their overall quality [23].

Conclusion

To sum up, the soaking process has a significant impact on the properties of durian seed gum compared to the concentration of acid used during the extraction process. This is because the soaking time affects the quantity of impurities present in the gum and the particle size of the gum extracted, which have a direct impact on the solubility and water-holding capacity of the gum. Nevertheless, the selection of the extraction parameters depends on the purpose of the extracted gum. If the physicochemical and functional properties of the gum are targeted, a soaking time of 1 to 2 hours is sufficient. Meanwhile, a longer soaking time is needed if the gum yield is targeted. The ideal range of soaking temperatures is between 55°C and 95°C. Further research on anti-nutrient content and sensory evaluation of durian seed gum in food products is needed for safety purposes. It is also beneficial to analyse the nanoparticles of durian seed gum to improve its solubility, thus producing food gum of better quality.

Acknowledgement

The authors wish to acknowledge the Universiti Teknologi MARA (UiTM), Cawangan Negeri Sembilan, Kampus Kuala Pilah at Kuala Pilah, Negeri Sembilan, Malaysia, for supporting this study.

References

1. Glicksman, M. (2020). *Food Hydrocolloid* (1st ed.). CRC Press Publisher.
2. Syamila, M., Hikmah, A.R., Zaiton, H. and Radhiah, O. (2020). Comparative study on the absorption and solubility properties of durian seed gum and commercial guar gum. Retrieved from https://oarep.usim.edu.my/jspui/handle/123456789/6888.
3. Ana, M.E., Carmen, S., María, L.E., Berta, E., Sandra, E. and Cristian, S. (2004). Extraction methods and some physical properties of mesquite (*Prosopis chilensis (Mol) Stuntz*) seed gum. *Journal of the Science of Food and Agriculture,* 84(12): 1487-1492.
4. Hamdani, A. M., Wani, I. A., Bhat, N. A. and Masoodi, F. A. (2018). Chemical composition, total phenolic content, antioxidant and antinutritional characterisation of exudate gums. *Food BioScience*, 23: 67-74.
5. Mirhosseini, H. and Amid, B.T. (2012). Effect of different drying techniques on flowability characteristics and chemical properties of natural carbohydrate-protein gum from durian fruit seed. *Chemistry Central Journal*, 2013: 7
6. Mirhosseini, H. and Amid, B. T. (2012). Influence of chemical extraction conditions on the physicochemical and functional properties of polysaccharide gum from durian (*Durio zibethinus*) seed. *Molecules,* 17(6) : 6465-6480.
7. Khalaf, A., Desa, S. and Baharum, S. (2019). Overview of selected native seeds in agricultural wastes and its properties. *Medico-legal Update,* 19(2): 324-330.
8. Clemens, R. and Pressman, P. (2017). Food gums: An overview. *Nutrition Today,* 52(1): 41-43.
9. Phillips, G. and Williams, P. (2020). *Handbook of Hydrocolloids* (3rd ed.). Woodhead Publishing.
10. Golkar, A., Taghavi, S. M. and Dehnavi, F. A. (2018). The emulsifying properties of Persian gum (*Amygdalus scoparia Spach*) as compared with gum Arabic. *International Journal of Food Properties*, 21(1): 416-436.
11. Cornelia, M., Siratantri, T. and Prawita, R. (2015). The utilization of extract durian (*Durio zibethinus L.*) seed gum as an emulsifier in vegan mayonnaise. *Procedia Food Science,* 3: 1-18.
12. Srianta, I., Hedrawan, B., Kusumawati, N. and Blanc, P. J. (2012). Study on durian seed as a new substrate for angkak production. *International Food Research Journal,* 19(3): 941-945.
13. Amin, A. M., Ahmad, A. S., Yin, Y., Yahya, N. and Ibrahim, N. (2007). Extraction, purification, and characterization of durian (*Durio zibethinus*) seed gum. *Food Hydrocolloids,* 21(2): 273-279.
14. Navaratne, S. B and Nawarathne, N. H. N. T. (2014). Determination of suitability of durian seed gum extract (*Durio zebethinus*) in replacing of xanthan gum in fruit nectar. *International Journal of Scientific Engineering and Research,* 2(2): 86-89.

15. Amid, B., Mirhosseini, H. and Kostadinovic, S. (2012). Chemical composition and molecular structure of polysaccharide-protein biopolymer from *Durio zibethinus* seed: extraction and purification process. *Chemistry Central Journal*, 6: 117.
16. Sawasdikarn, J., Nilanon, W. and Suwannarat, Y. (2017). Characterization of gum from durian seed an application in ice cream. *International Journal of Agricultural Technology*, 13(7): 2661-2667.
17. Sompie, M., Surtijono, S. E., Pontoh, J. H. W., and Lontaan, N. N. (2015). The effects of acetic acid concentration and extraction temperature on physical and chemical properties of pigskin gelatin. *Procedia Food Science*, 3: 383-388.
18. Vieira, J. M., Mantovani, R. A., Raposo, M. F. J., Coimbra, M. A., Vicente, A. A. and Cunha, R. L. (2019). Effect of extraction temperature on rheological behavior and antioxidant capacity of flaxseed gum. *Carbohydrate Polymers*, 213: 217-227.
19. Shad, M. A., Nawaz, H., Hussain, M. and Yousuf, B. (2011). Proximate composition and functional properties of rhizomes of lotus (*Nelumbo nucifera*) from Punjab, Pakistan. *Pakistan Journal of Botany*, 43: 895-904.
20. Akdowa, E. P., Boudjeko, T., Woguia, A. L. and Njintang N. Y. (2014). Optimization of variables for aqueous extraction of gum from grewia mollis powder. *Journal of Polymers*, 2014: 1-10.
21. Batal, H. E. and Hasib, A. (2013). Optimization of extraction process of carob bean gum purified from carob seeds by response surface methodology. *Chemical and Process Engineering Research*, 12: 1-8
22. Marina, Z., Noriham, A., Noorlaila, A. and Azmi, M. N. (2016). Influence of thermal processing on chemical composition and antinutritional factors of durian (*Durio zibethinus*) seed. Retrieved from https://ir.uitm.edu.my/id/eprint/26756/.
23. Selvi, D. T. and Saraswathy, S. (2017). Seed viability, seed deterioration and seed quality improvements in stored onion seeds: A review. *Journal of Horticultural Science and Biotechnology*, 93(1): 1-7.

Malaysian Journal of Analytical Sciences (MJAS)
Published by Malaysian Analytical Sciences Society

DISPERSIVE MICRO-SOLID-PHASE EXTRACTION (D-µ-SPE) WITH POLYPYRROLE-GRAPHENE OXIDE (PPY-GO) NANOCOMPOSITE SORBENT FOR THE DETERMINATION OF TETRACYCLINE ANTIBIOTICS IN WATER SAMPLES

(Pengekstrakan Fasa-Pepejal-Mikro Secara Serakan (D-µ-SPE) menggunakan Polipirol-Grafin Oksida (Ppy-GO) Penjerap Nanokomposit bagi Penentuan Antibiotik Tetrasiklin dalam Sampel Air)

Nurzaimah Zaini[1], Nor Suhaila Mohamad Hanapi[1]*, Wan Nazihah Wan Ibrahim[1], Rozita Osman[1], Sazlinda Kamaruzaman[2], Noorfatimah Yahaya[3], Ahmad Lutfi Anis[4]

[1]Faculty of Applied Sciences,
Universiti Teknologi MARA, 40450 Shah Alam, Selangor, Malaysia
[2]Department of Chemistry,
Faculty of Science, Universiti Putra Malaysia, Serdang, Selangor, Malaysia
[3]Integrative Medicine Cluster, Advanced Medical and Dental Institute (AMDI),
Universiti Sains Malaysia, 13200 Bertam Kepala Batas, Penang, Malaysia
[4]Faculty of Applied Sciences,
Universiti Teknologi MARA, 94300 Kota Samarahan, Sarawak, Malaysia

**Corresponding author: norsuhaila979@uitm.edu.my*

Received: 18 May 2022; Accepted: 21 July 2022; Published: 30 October 2022

Abstract

Dispersive micro-solid-phase extraction (D-µ-SPE) method using polypyrrole-graphene oxide (PPy-GO) nanocomposite sorbent has been developed for the extraction and pre-concentration of tetracycline antibiotics (TCs) residues, namely oxytetracycline (OTC), tetracycline (TC), chlortetracycline (CTC), demeclocycline (DMC) and doxycycline (DOC) in water samples prior to high-performance liquid chromatography-ultraviolet/diode array detector (HPLC-UV/DAD). The PPy-GO nanocomposite was prepared by *in situ* oxidative chemical polymerization. The effects of sample pH, a mass of sorbent, desorption solvent, extraction time and desorption time on the extraction of analytes were evaluated and optimized. Under the optimum conditions, the method demonstrated good linearity (R^2=0.9989-0.9995) over a concentration range of 10-1000 µg L^{-1}. The limit of detection (LOD) was in the range of 4.9-8.7 µg L^{-1} with satisfactory relative recoveries (80 – 105 %) and a good relative standard deviation (RSD) of ⩽ 2.3 % (n = 3) was obtained. The method was successfully applied to river water and tap water samples. Results obtained using the developed method were compared with results previously reported using other SPE-based methods.

Keywords: tetracycline antibiotics, PPy-GO, dispersive micro-solid-phase extraction, liquid chromatography, water samples

Abstrak

Kaedah pengekstrakan fasa-pepejal-mikro secara serakan (D-µ-SPE) menggunakan penjerap nanokomposit polipirol- grafin oksida (PPy-GO) telah dibangunkan untuk pengekstrakan dan pra-pemekatan sisa antibiotik tetrasiklin (TCs), iaitu oksitetrasiklin (OTC), tetrasiklin (TC), klortetrasiklin (CTC), demeklosiklin (DMC) dan doksisiklin (DOC) di dalam sampel air sebelum kromatografi cecair berprestasi tinggi-pengesan tatasusunan ultraungu/diod (HPLC-UV/DAD). Nanokomposit PPy-GO telah disediakan melalui pempolimeran oksidatif kimia *in situ*. Kesan pH sampel, jisim penjerap, pelarut nyahjerapan, masa pengekstrakan dan masa nyahjerapan pada pengekstrakan analit telah dinilai dan dioptimumkan. Di bawah keadaan optimum, kaedah menunjukkan kelinearan yang baik (R^2=0.9989-0.9995) dalam julat kepekatan 10-1000 µg L^{-1}. Had pengesanan (LOD) adalah dalam julat 4.9-8.7 µg L^{-1} dengan pemulihan relatif yang memuaskan (80-105%) dan sisihan piawai relatif (RSD) yang baik sebanyak ≤ 2.3% (n = 3) telah diperoleh. Kaedah tersebut berjaya diaplikasikan pada sampel air sungai dan air paip. Keputusan yang diperoleh menggunakan kaedah yang dibangunkan dibandingkan dengan keputusan yang dilaporkan sebelum ini menggunakan kaedah berasaskan SPE yang lain.

Kata kunci: antibiotik tetrasiklin, Ppy-GO, pengekstrakan fasa-pepejal-mikro secara dispersif, kromatografi cecair, sampel air

Introduction

The discovery of antibiotics in the 1940s has witnessed traditional medicine and herbal therapies being replaced by a more effective remedy for treating bacterial infections [1-2]. Since then, antibiotics have become essential in medicine and are critical components of the modern healthcare systems. Tetracycline, for example, is a group of broad-spectrum antibiotics active against several Gram-positive and Gram-negative bacteria [3]. Since their discovery, tetracycline antibiotics have played a prominent role in veterinary and human medicine, specifically for treating and preventing microbial infections and as additives in animal feed [4]. Although the role of antibiotics in fighting harmful bacteria cannot be neglected, the mishandling of antibiotics can adversely affect public health.

Tetracycline antibiotics (Figure 1) can be discharged from industrial production, animal foodstuff and human medicine into rivers and local groundwater [5]. The occurrence of these antibiotic residues in water samples in high concentrations will cause harmful effects on public health, including allergic reactions in humans, liver damage, accumulative toxicity, yellowing of teeth, the transfer of drug-resistant bacteria from food to humans, and gastrointestinal disturbance [6]. There is also growing concerned that antimicrobials are affecting water quality because they can accelerate the evolution of antimicrobial-resistant bacteria [7]. Hence, it is critical to develop reliable analytical methods for routine monitoring of tetracycline in the environment. The method should be rapid, precise, economical, less time-consuming, and environmentally friendly.

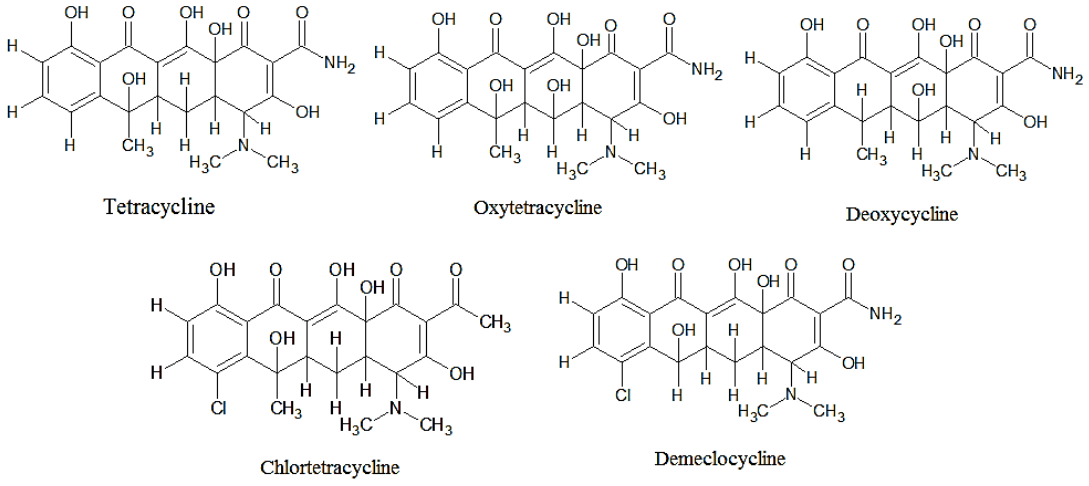


Figure 1. Chemical structure of some commonly used tetracycline antibiotics

In recent years, numerous analytical methods have been developed for the detection of tetracycline in complex environmental matrices such as swine wastewater and manure [8, 9], livestock tissues [10], milk [11], honey [12], and soils [13]. Several extraction techniques have been reported mainly for the extraction and pre-concentration of tetracycline antibiotics in aqueous matrices. These include solid-phase extraction (SPE) [14], solid-phase microextraction (SPME) [15], liquid-liquid extraction [16] and pressurized liquid extraction [17].

SPE is the most common sample isolation and pre-concentration technique for the extraction of pharmaceuticals, including tetracycline in water samples [18]. Yang et al. [19] developed an analytical method for the determination of 11 tetracyclines using solid-phase extraction and liquid chromatography-electrospray ionization tandem mass spectrometry in the influent and effluent of domestic wastewater. Dzomba et al. [20] have reported a comparative study of ultrasonic coupling to the modern SPE method, such as tandem solid-phase extraction (TSPE), dispersive solid-phase extraction (DSPE) and matrix solid-phase dispersion (MSPD) for the extraction of tetracycline in river water.

Trapping media in SPE have aroused increasing interest in research on sample preparation as they have a key role in obtaining high clean-up and enrichment efficiency for trace analysis in complex matrices. In recent years, there have been many successful works on the use of varieties of commercialized sorbent materials for an efficient SPE technique [21]. Apart from commercially available sorbents, researchers are devoted and have been passionate on developing new sorbents to enhance the extraction process. In the past few decades, various type of solid sorbent has been developed for the determination of environmental decontamination, including carbon-based [22], molecularly imprinted polymers [23], nano-fibres [24] and carbon nanotubes [25].

Graphene has been extensively employed in a wide range of applications since its discovery by Novoselov et al. in 2004 [26]. Graphene oxide performs well as sorbent, with high porosity, chemical stability, unique surface structure, large specific surface area and hydrophilicity due to its richness in oxygenated groups [27]. However, because they tend to agglomerate easily due to the strong Van der Waals interaction between molecules and have low selectivity, their usage as extraction sorbent is restricted [28]. To address the aforementioned issues, varieties of graphene-based composite materials have recently been developed. Polypyrrole-graphene oxide (Ppy-GO) composites have been utilized as supercapacitor electrodes and biosensors due to their remarkable electrical and optical properties [29-30]. Nonetheless, the efficacy of PPy-GO as sorbent has not been explored much, especially in the detection of pharmaceutical residues in complex matrices.

Hence, this research aimed to investigate the use of PPy-GO as a promising material for the determination of tetracycline antibiotics in water samples with the aid of D-μ-SPE, which is believed to be a simple, rapid, selective and efficient alternative method compared to the traditional SPE.

Materials and Methods

Chemicals and materials

Five (5) tetracycline antibiotics, namely oxytetracycline (OTC), tetracycline (TC), demeclocycline (DMC), chlortetracycline (CTC), and doxycycline (DC) with purity assay in range of 98-101% were purchased from Sigma-Aldrich. Acetonitrile (ACN), methanol (MeOH), formic acid (of HPLC grade), sodium hydroxide (NaOH) and hydrochloric acid (HCl) were purchased from Merck (Darmstadt, Germany). Pyrrole monomer and ferric chloride crystal ($FeCl_3.6H_2O$, 99.0%) were procured from Xian, China. Graphene oxide powder and methane sulfonic acid (MSA) were purchased from Sigma-Aldrich (St. Louis, USA). Ultrapure water was produced by Barnstead Nanopure (Thermo Scientific).

Preparation of standard and sample solutions

The individual stock solutions of OTC, TC, DMC, CTC, and DOC were prepared separately in HPLC grade methanol to a final concentration of 1000 mg L^{-1}. All standard solutions were stored in amber glass bottles at 4 °C when not in use. A series of working standard solutions were prepared in methanol by dilution before

analysis to prevent the decomposition of analytes. Tap water samples were collected from a laboratory in Universiti Teknologi MARA (UiTM) Shah Alam, Selangor, Malaysia, while river water samples were collected from Hulu Langat, Selangor, Malaysia. The collected samples were filtered through 0.45 µm nylon filter paper to remove any suspended particles. Samples were kept in polyethene bottles pre-cleaned with acetone and stored at 4 ºC prior to the analysis process. For accuracy and precision studies, the river and tap water samples (10 mL, pH 3) were spiked with the standard mixture of five tetracycline antibiotics to give a final concentration of 1 mg L^{-1} for each analyte.

Preparation of PPy-GO nanocomposite material

The method of synthesis was adapted from literature [31]. The synthesis of PPy-GO nanocomposite material was prepared by in situ chemical polymerization of pyrrole. About 0.05 g GO was dispersed in distilled water and sonicated to form a 2 mg mL^{-1} homogeneous suspension. Then, 25 µL pyrrole monomer was slowly added to the yellowish-brown GO solution under ultrasonication for 40 min. Approximately 0.3 g $FeCl_3.6H_2O$ was dissolved in 10 mL distilled water, introduced into the mixture dropwise and followed by ultrasonication for another 0.5 h. After that, the black-colored PPy-GO composites were collected by centrifugation and washed with distilled water and ethanol several times, followed by vacuum drying at 45 ºC for 12 h.

Dispersive micro-solid-phase extraction procedure by using PPy-GO nanocomposite material

The extraction method of D-µ-SPE was adopted from Othman et al. [32]. About 50 mg of PPy-GO nanocomposite material was dispersed into the aqueous sample (10 mL, pH 3). The mixture was vigorously stirred with a magnetic stirrer to trap the analytes for 15 min. Subsequently, the PPy-GO nanocomposite material was isolated from the solution by centrifugation (4000 r min^{-1}, for 5 min). The supernatant was discarded. About 1 mL of desorption solvent was added, and then the mixture was sonicated for 10 min to desorb the analytes. The mixture was then centrifuged at 4000 rpm for 5 min. The solvent was collected and evaporated until dry under a soft stream of nitrogen gas. Finally, 10 µL of the extract was injected into the HPLC system for analysis. The workflow of this method is illustrated in Figure 2. The PPy-GO nanocomposite material can be reused several times after washing with 2 mL of methanol and water, respectively. Several optimization parameters for D-µ-SPE were optimized by changing one variable at a time.

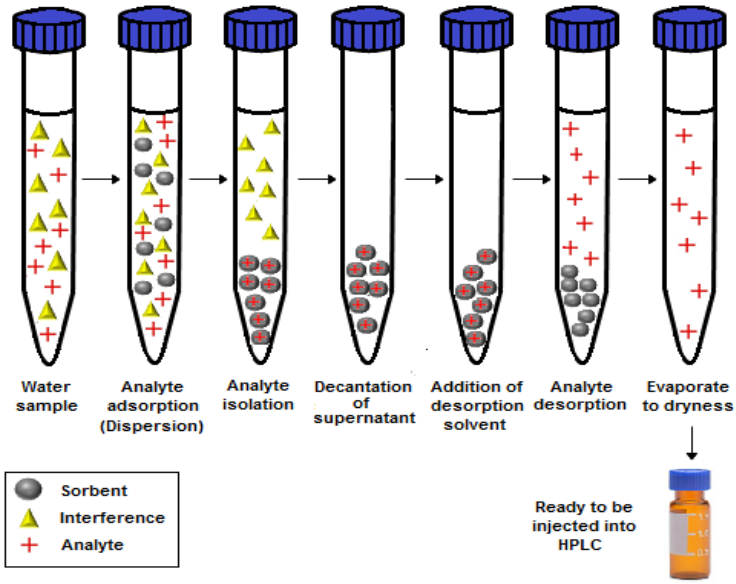


Figure 2. Dispersive micro-solid-phase extraction (D-µ-SPE) procedure by using Ppy-GO as sorbent

Chromatographic conditions

All analyses were performed using an automated high-performance liquid chromatography (HPLC) Dionex Ultimate 3000 (Sunnyvale, CA, USA) system, using an Acclaim Polar Advantage II (5 µm, 120 Å, 4.6×150 mm) (Dionex USA) as the analytical column. A gradient elution consisting of acetonitrile, methanol and formic acid was applied. The flow rate was programmed at 1 mL min^{-1}. For initialization of the LC analysis, the chromatographic system was cleaned and stabilized for 1 h. The quantification of TCs was performed by measuring the peak area of the chromatogram. TCs were detected using an ultraviolet/diode array detector (UV/DAD) at a selected wavelength of 270 nm.

Validation of the analytical method

The extraction method was assessed for linearity (R^2), the limit of detection (LOD), the limit of quantification (LOQ), precision (% RSD), and accuracy (% relative recovery) prior to sample analysis. Linearity was measured by plotting the calibration curve of five (5) different concentration levels for the standard mixture of TCs. The same calibration graph was used for the determination of LOD and LOQ. Method precision was measured using three (3) different extractions of the calibration standard at the lowest concentration.

Results and Discussion

Optimization of extraction parameter

The oxytetracycline (OTC), tetracycline (TC), demeclocycline (DMC), chlortetracycline (CTC), and doxycycline (DC) were selected as model analytes in this study as they are among the most commonly used TCs. To determine the optimum conditions for the extraction of TCs from aqueous samples, many parameters that can affect the extraction efficiency were investigated, namely the extraction time, desorption time, sample pH, extraction solvent and mass of sorbent. The optimization was carried out using one variable at a time while other parameters were kept constant. Optimization was carried out using deionized water samples spiked with each TC to give a final concentration of 1 mg L^{-1} in 10 mL of water samples. About 1 mL of acetonitrile was used as the desorption solvent. Triplicate extractions were carried out for each parameter optimized in this study.

Effect of sample pH on the extraction of TCs

The experiment was carried out by varying the pH value of the spiked sample solution from pH 3 to pH 11 to determine the effect of sample pH on the extraction of TCs. It was observed that the peak area slightly increased with increasing pH from pH 3 to pH 7 and highest at pH 7. This is shown in Figure 3(a). The peak area starts to decrease after pH 7.

The effect of sample pH on the adsorption of analytes can be explained based on its amphoteric characteristics under varied pH conditions [33]. Tetracycline is an amphoteric compound with various ionizable functional groups and will form different ionic species in an aqueous solution at different pHs. Thus, in the analysis of TCs, pH adjustment is a very crucial step [34]. TCs have three pKa values ($pKa_1 \approx 3$, $pKa_2 \approx 7$, $pKa_3 \approx 9$) [35].

Throughout the range of pH, tetracycline occurs as cationic in strong acid solution approximately at pH 3, zwitterionic at pH 4 to 7.7 and anionic at pH > 7.7 [36]. The adsorption of TCs onto Ppy-GO nanocomposite sorbent is strongly affected by either the acidity or basicity of the sorbent surface and the tetracycline speciation. At pH 4 - 7.7, TCs are mainly in their molecular form and are less protonated. Meanwhile, the sorbent surface had an increasing negative charge. Hence, the TCs exhibited increasing hydrophobicity with increasing pH, resulting in better adsorption on the sorbent. From the experiment carried out, the extraction of TCs was observed to be highest at pH 7. After pH 7, the adsorption became less efficient due to the electrostatic repulsion between anionic TCs and the negatively charged sorbent surface. Therefore, pH 7 was selected as the pH value used in subsequent experiments.

Effect of extraction time

The influence of extraction time on the peak area of analytes was studied in the range of 5 to 25 min. The effect of contact time between sorbent and analytes is shown in Figure 3(b). It was observed that the adsorption capacity of TCs rapidly increased from 5 to 15 min of extraction time. The highest extraction efficiency was obtained after 15 min of extraction time.

After 15 min, the adsorption of analytes became practically constant. This could be due to the long duration of extraction time, whereby all the active sites on the surface area of sorbent were fully saturated with the analyte as time progressed [37]. Therefore, 15 min was selected as the optimal extraction time and was used in further experiments.

Effect of desorption time

The effect of desorption time was studied in the range of 5-25 min of sonication. The sonication method was used for the desorption solvent to desorb TCs from the PPy-GO sorbent as this technique is suitable to be applied for reversible adsorption [38]. The maximum desorption time for the analytes was achieved within 10 min of sonication (Figure 3(c)). However, beyond 10 min of sonication, the peak area of analytes was constant. This was probably due to the analytes being fully desorbed from the sorbent into the desorption solvent. Therefore, a desorption time of 10 min of sonication was chosen for subsequent experiments.

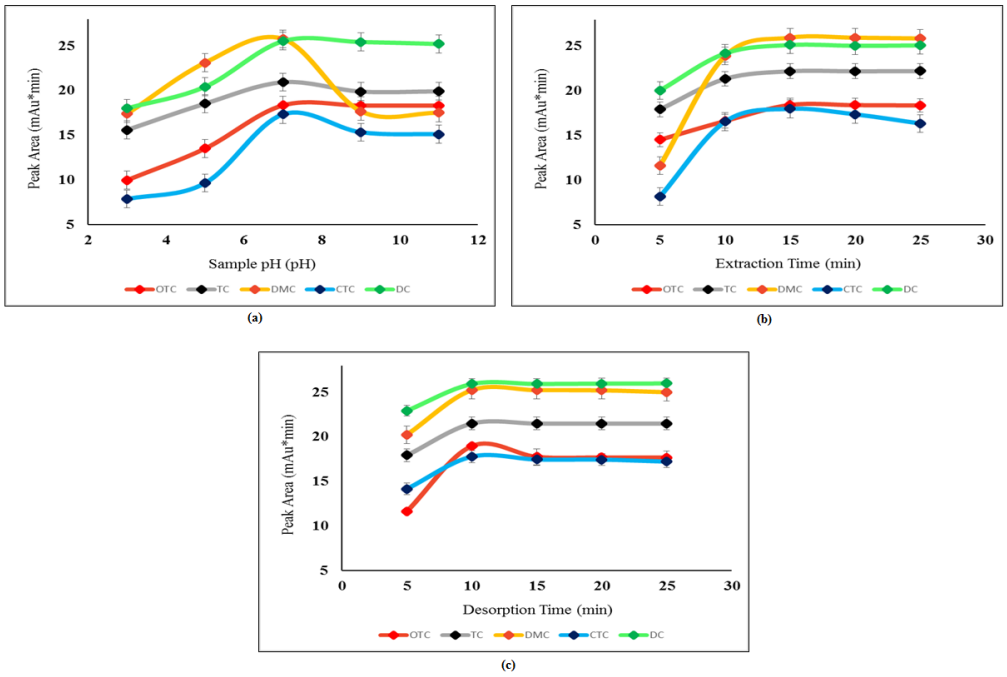


Figure 3. Optimization for the extraction performance of PPy-GO using D-μ-SPE. (a) Effect of sample pH, (b) extraction time and (c) desorption time on PPy-GO-D-μ-SPE of TCs in water samples. (Error bars represent standard deviations of results, n = 3)

Effect of desorption solvent

A complete back extraction process depends on the time of sonication and the strength of the desorption solvent [39]. The selection of a suitable organic solvent is crucial to ensure the complete elution of trapped analytes from the surface of the PPy-GO nanocomposite. In this study, the influence of different types of organic solvents was investigated to enhance the recovery of analytes. The solvents used in this study were acetone, acetonitrile, ethanol, and methanol, according to the increasing order of polarity. The experimental results depicted in Figure 4(a) demonstrate that the use of acetone as a desorption solvent yielded the lowest recovery and was therefore not sufficiently powerful for desorption of the targeted TCs. The data also showed that the best efficiency (expressed as peak area) was obtained when methanol was used as a desorption solvent. This can be related to its polar characteristic. Methanol has a stronger hydrogen bond and dipole-dipole intermolecular interactions with the targeted TCs, thus enabling effective desorption of TCs from the sorbent surface. Therefore, methanol was

selected as the desorption solvent in all subsequent experiments.

Effect of mass of sorbent

For the optimization of the mass of sorbent, about 5 mg to 100 mg of PPy-GO powder was used. The result showed that the lowest proposed mass of sorbent (5 mg) produced the lowest peak area (Figure 4(b)). On the other hand, 50 mg of sorbent gave the highest peak area of analytes. No significant increase in the peak area was observed with a further increase in sorbent mass. This was probably due to all the analytes having been fully adsorbed by the sorbent while there were still a lot of active sites available for surface adsorption [40].

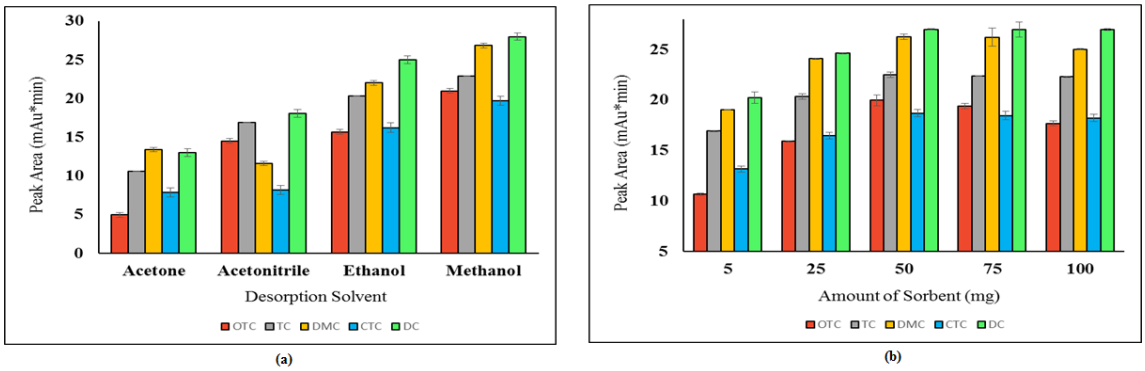


Figure 4. Optimization for the extraction performance of PPy-GO using D-μ-SPE. (a) Desorption solvent and (b) sorbent amount on PPy-GO-D-μ-SPE of TCs in water samples. (Error bars represent standard deviations of results, n = 3).

Optimum extraction conditions

The final adopted PPy-GO-D-μ-SPE conditions were: sample pH, pH 7; extraction time, 15 min; desorption time, 10 min; desorption solvent, methanol; sorbent mass, 50 mg. Hence, these optimum extraction conditions were applied for subsequent studies.

Reusability of sorbent

The reusability of the sorbent was tested by rinsing the sorbent five times with 2 mL methanol with sonication after each extraction. Then, the sorbent was dried at 60 °C for 1 hour before further use in the next D-μ-SPE procedure. The result showed that the sorbent could be conveniently reused up to fifteen times without any significant loss in the extraction recovery (> 80%) for TCs before the recovery starts to decrease slowly. This was probably due to the loss of carboxyl groups from the surface of the sorbent after repeated use.

Method validation and analytical performance of D-μ-SPE

The optimization of D-μ-SPE was then validated for relative recoveries, sample calibration and LOD. From the linearity range of 10-1000 μg $L^{-1,}$ good linearity was obtained for the four analytes, where the coefficients of determination (R^2) were in the range of 0.9989-0.9995. The LODs and LOQs were calculated at a signal-to-noise ratio of 3, and the results were in the range of 4.9 - 8.7 μg L^{-1} for LODs. The precision of the method was measured by the relative standard deviation (RSD), and the results obtained were between 1.4-3.0 %. Table 1 shows the validation data for D-μ-SPE of TCs from water samples.

Table 1. Quantitative results of DSPE-LC of TCs in tap and river water samples

Sample	Analyte	Linear Range (μg L^{-1})	Coefficient of Determination (R^2)	LOD (μg L^{-1})	RSD (%, n = 3)
Tap water	OTC	10-1000	0.9991	8.6	2.5
	TC	10-1000	0.9994	5.6	1.4
	DMC	10-1000	0.9992	8.1	3.0
	CTC	10-1000	0.9995	7.4	2.0
	DC	10-1000	0.9990	5.9	1.9
River water	OTC	10-1000	0.9992	8.7	2.3
	TC	10-1000	0.9989	4.9	2.0
	DMC	10-1000	0.9993	8.6	2.1
	CTC	10-1000	0.9995	7.4	1.6
	DC	10-1000	0.9991	6.6	2.2

Application of D-μ-SPE on river and tap water samples

The developed PPy-GO-D-μ-SPE method was successfully applied to river and tap water samples. Relative recovery studies were conducted by spiking the water samples to give a final concentration of 50 and 500 μg L^{-1}. The results are presented in Table 2. It shows that good relative recoveries were obtained in the range of 80% to 105%. The results suggest that dispersive micro-solid-phase extraction is an efficient technique for extracting drugs in aqueous matrices. Figure 5 shows HPLC chromatograms of the OTC, TC, DMC, CTC and DC in river and tap water samples.

Table 2. Relative recovery studies of DSPE-LC of TCs from different spiked water samples (n = 3)

Analyte	Spiked concentration (μg L^{-1})	Tap water		River water	
		Relative Recovery (%)	RSD (%)	Relative Recovery (%)	RSD (%)
OTC	50	95	4.8	98	2.3
	500	103	3.9	98	0.8
TC	50	99	0.4	85	1.9
	500	100	0.9	88	1.1
DMC	50	97	1.2	102	1.8
	500	99	3.9	95	0.8
CTC	50	80	0.9	100	1.2
	500	105	1.0	98	0.2
DC	50	101	1.3	80	1.8
	500	99	0.1	94	2.0

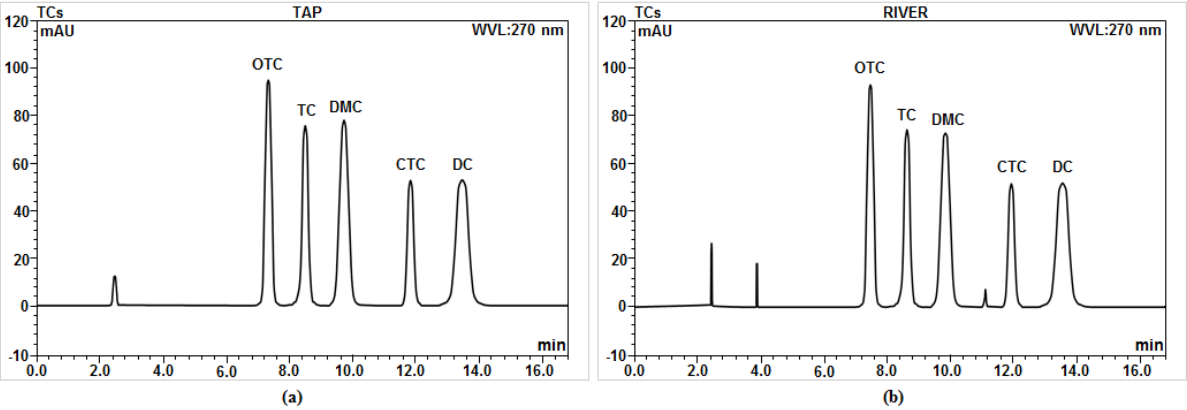


Figure 5. HPLC chromatogram of five tetracycline antibiotics spiked in (a) tap water samples and (b) river water samples

Comparison with other reported methods

The efficiency of the proposed D-μ-SPE method for TCs was compared with other reported methods in terms of analysis method, extraction sorbent, linear range and LODs. The comparative results are summarized in Table 3. As can be seen, the method developed in this study achieved a comparable LOD with other prior reported methods, which also used graphene-based nanocomposite. Furthermore, compared with other developed nanocomposite sorbents, Ppy-GO is easy to prepare and can be reused fifteen times. On the other hand, extraction of tetracycline using conventional SPE involves high consumption of organic solvents and sorbents, which is laborious, somewhat costly, and time-consuming [44]. On the other hand, D-μ-SPE only requires a small amount of organic solvent and sorbent for every single analysis. In addition, since D-μ-SPE requires simple devices such as a sonicator and centrifuge, it can be considered relatively inexpensive, simple, rapid and suitable for routine analyses.

Table 3. Comparison of Ppy-GO-D-μ-SPE with other published methods for the determination of TCs.

Analysis Method	Sorbent	Type of Sample	Linear Range (μg L^{-1})	LOD (μg L^{-1})	Recoveries (%)	Ref.
μ-SPE- HPLC-UV	PET-GO nano-fiber	Honey	10–5000	15.3	89–94	[24]
MSPE-DLLME	Fe_3O_4@SiO_2@GO-β-CD	Milk, Water	10–200	1.8–2.9	71-122	[41]
SPE-HPLC	Graphene	Milk	20–1000	10-20	82-104	[42]
MSPE- UPLC–TUV	Fe_3O_4@SiO_2@FeO	Tap, river	0.133–333	0.027-0.107	91-105	[43]
D-μ-SPE-HPLC-UV	Ppy-GO	Tap, river	10-1000	4.9-8.7	80-105	This work

μ-SPE- HPLC-UV: micro-solid-phase extraction high-performance liquid chromatography
MSPE-DLLME: magnetic solid-phase extraction dispersive liquid-liquid microextraction
SPE-HPLC: solid-phase extraction high-performance liquid chromatography
MSPE-UPLC-TUV: magnetic solid-phase extraction ultra-performance liquid chromatography tunable ultra-violet
D-μ-SPE-HPLC-UV: dispersive micro solid-phase extraction high-performance liquid chromatography ultra-violet

Conclusion

This paper reports the use of polypyrrole incorporated with graphene oxide for the extraction of tetracycline antibiotics using dispersive micro solid-phase extraction combined with HPLC-UV/DAD. Several parameters were optimized in the D-μ-SPE method. The optimum

parameters were used to analyse real samples for successful extraction of oxytetracycline, tetracycline, demeclocycline, chlortetracycline, and doxycycline from river and water samples. Good linearities were achieved for the analytes with coefficients of determination R^2, in the range of 0.9989-0.9995. The method was successfully applied to the analysis of river and tap water samples, with good relative recoveries in the 80-105 % range. Compared with other previously reported methods that employed graphene-based nanocomposites, the D-μ-SPE method proved to be a simple, sensitive, selective and green extraction method that could potentially be used in the chemical laboratory for routine analysis of water samples.

Acknowledgement

The authors would like to thank Universiti Teknologi MARA for facilitation and the Ministry of Higher Education Malaysia for financial support through research grant number 600-RMC/MyRA 5/3/LESTARI (059/2020).

References

1. Tam, V. C., Suen, R., Treuting, P. M., Armando, A., Lucarelli, R., Gorrochotegui-Escalante, N., Diercks, A. H., Quehenberger, O., Dennis, E. A., Aderem, A. and Gold, E. S. (2020). PPARα exacerbates necroptosis, leading to increased mortality in postinfluenza bacterial superinfection. *Proceedings of the National Academy of Sciences*, 117(27): 15789-15798.
2. Aminov, R. I. (2010). A brief history of the antibiotic era: lessons learned and challenges for the future. *Frontiers in Microbiology*, 1: 134.
3. Tsai, W. H., Huang, T. C., Huang, J. J., Hsue, Y. H. and Chuang, H. Y. (2009). Dispersive solid-phase microextraction method for sample extraction in the analysis of four tetracyclines in water and milk samples by high-performance liquid chromatography with diode-array detection. *Journal of Chromatography A*, 1216 (12): 2263 - 2269.
4. Chopra, I. and Roberts, M. (2001). Tetracycline antibiotics: mode of action, applications, molecular biology, and epidemiology of bacterial resistance. *Microbiology and Molecular Biology Reviews*, 65(2): 232-260.
5. Chang, X., Meyer, M. T., Liu, X., Zhao, Q., Chen, H., Chen, J. A., Qiu, Z., Yang, L., Cao, J. and Shu, W. (2010). Determination of antibiotics in sewage from hospitals, nursery and slaughter house, wastewater treatment plant and source water in Chongqing region of Three Gorge Reservoir in China. *Environmental Pollution*, 158(5): 1444-1450.
6. Xu, J. J., An, M., Yang, R., Tan, Z., Hao, J., Cao, J., Peng, L.Q. and Cao, W. (2016). Determination of tetracycline antibiotic residues in honey and milk by miniaturized solid-phase extraction using chitosan-modified graphitized multiwalled carbon nanotubes. *Journal of Agricultural and Food Chemistry*, 64(12): 2647 - 2654.
7. Choi, K. J., Kim, S. G., Kim, C. W. and Kim, S. H. (2007). Determination of antibiotic compounds in water by on-line SPE-LC/MSD. *Chemosphere*, 66(6): 977-984.
8. Wang, Z., Wang, X., Tian, H., Wei, Q., Liu, B., Bao, G., Liao, M., Peng, J., Huang, X. and Wang, L. (2019). High through-put determination of 28 veterinary antibiotic residues in swine wastewater by one-step dispersive solid phase extraction sample cleanup coupled with ultra-performance liquid chromatography-tandem mass spectrometry. *Chemosphere*, 230: 337-346.
9. Zhi, S., Zhou, J., Liu, H., Wu, H., Zhang, Z., Ding, Y. and Zhang, K. (2020). Simultaneous extraction and determination of 45 veterinary antibiotics in swine manure by liquid chromatography-tandem mass spectrometry. *Journal of Chromatography B*, 1154: 122286.
10. Araby, E., Nada, H. G., Abou El-Nour, S. A. and Hammad, A. (2020). Detection of tetracycline and streptomycin in beef tissues using Charm II, isolation of relevant resistant bacteria and control their resistance by gamma radiation. *BMC Microbiology*, 20(1): 1-11.
11. Saleh, H., Elhenawee, M., Hussien, E. M., Ahmed, N. and Ibrahim, A. E. (2021). Validation of HPLC-UV multi-residue method for the simultaneous determination of tetracycline, oxytetracycline, spiramycin and neospiramycin in raw milk. *Food Analytical Methods*, 14(1): 36-43.

12. Galyautdinova, G. G., Egorov, V. I., Saifutdinov, A. M., Rakhmetova, E. R., Malanev, A. V., Aleyev, D. V., Smolentsev, S.Y. and Semenov, E. I. (2020). Detection of tetracycline antibiotics in honey using high-performance liquid chromatography. *International Journal of Research in Pharmaceutical Sciences*, 11 (1): 311-314.
13. Ma, Z., Liu, J., Li, H., Zhang, W., Williams, M. A., Gao, Y., Gudda, F.O., Lu, C., Yang, B. and Waigi, M. G. (2019). A fast and easily parallelizable biosensor method for measuring extractable tetracyclines in soils. *Environmental Science & Technology*, 54(2): 758-767.
14. Feng, Y., Wei, C., Zhang, W., Liu, Y., Li, Z., Hu, H., Xue, J. and Davis, M. (2016). A simple and economic method for simultaneous determination of 11 antibiotics in manure by solid-phase extraction and high-performance liquid chromatography. *Journal of Soils and Sediments*, 16(9): 2242-2251.
15. Sereshti, H., Karami, F., Nouri, N. and Farahani, A. (2021). Electrochemically controlled solid phase microextraction based on a conductive polyaniline‐graphene oxide nanocomposite for extraction of tetracyclines in milk and water. *Journal of the Science of Food and Agriculture*, 101(6): 2304-2311.
16. Desmarchelier, A., Anizan, S., Minh Tien, M., Savoy, M. C. and Bion, C. (2018). Determination of five tetracyclines and their epimers by LC-MS/MS based on a liquid-liquid extraction with low temperature partitioning. *Food Additives & Contaminants: Part A*, 35(4): 687-695.
17. Andreu, V., Vazquez-Roig, P., Blasco, C. and Picó, Y. (2009). Determination of tetracycline residues in soil by pressurized liquid extraction and liquid chromatography tandem mass spectrometry. *Analytical and Bioanalytical Chemistry*, 394(5): 1329-1339.
18. Sadutto, D. and Picó, Y. (2020). Sample preparation to determine pharmaceutical and personal care products in an all-water matrix: solid phase extraction. *Molecules*, 25(21): 5204.
19. Yang, S., Cha, J. and Carlson, K. (2005). Simultaneous extraction and analysis of 11 tetracycline and sulfonamide antibiotics in influent and effluent domestic wastewater by solid-phase extraction and liquid chromatography-electrospray ionization tandem mass spectrometry. *Journal of Chromatography A*, 1097 (1-2): 40-53.
20. Dzomba, P., Kugara, J. and Zaranyika, M. F. (2015). Extraction of tetracycline antimicrobials from river water and sediment: a comparative study of three solid phase extraction methods. *African Journal of Pharmacy and Pharmacology*, 9(19): 523-531.
21. Azzouz, A., Kailasa, S. K., Lee, S. S., Rascón, A. J., Ballesteros, E., Zhang, M. and Kim, K. H. (2018). Review of nanomaterials as sorbents in solid-phase extraction for environmental samples. *TrAC Trends in Analytical Chemistry*, 108: 347-369.
22. Yu, H., Zhang, B., Bulin, C., Li, R. and Xing, R. (2016). High-efficient synthesis of graphene oxide based on improved Hummers method. *Scientific reports*, 6(1): 1-7.
23. Caro, E., Marce, R. M., Cormack, P. A. G., Sherrington, D. C. and Borrull, F. (2005). Synthesis and application of an oxytetracycline imprinted polymer for the solid-phase extraction of tetracycline antibiotics. *Analytica Chimica Acta*, 552(1-2): 81-86.
24. Arabsorkhi, B. and Sereshti, H. (2018). Determination of tetracycline and cefotaxime residues in honey by micro-solid phase extraction based on electrospun nanofibers coupled with HPLC. *Microchemical Journal*, 140: 241-247.
25. Niu, H., Cai, Y., Shi, Y., Wei, F., Liu, J., Mou, S. and Jiang, G. (2007). Evaluation of carbon nanotubes as a solid-phase extraction adsorbent for the extraction of cephalosporins antibiotics, sulfonamides and phenolic compounds from aqueous solution. *Analytica Chimica Acta*, 594(1): 81-92.
26. Novoselov, K. S., Geim, A. K., Morozov, S. V., Jiang, D. E., Zhang, Y., Dubonos, S. V., Jiang, D.E., Zhang, Y., Dubonos, S.V., Grigorieva, I.V. and Firsov, A. A. (2004). Electric field effect in atomically thin carbon films. *Science*, 306 (5696): 666-669.
27. Hartono, T., Wang, S., Ma, Q. and Zhu, Z. (2009). Layer structured graphite oxide as a novel adsorbent for humic acid removal from aqueous solution. *Journal of Colloid and Interface Science*, 333(1): 114-119.

28. Guo, R., Jiao, T., Li, R., Chen, Y., Guo, W., Zhang, L., Zhou, J., Zhang, Q. and Peng, Q. (2018). Sandwiched Fe_3O_4/carboxylate graphene oxide nanostructures constructed by layer-by-layer assembly for highly efficient and magnetically recyclable dye removal. *ACS Sustainable Chemistry & Engineering*, 6(1): 1279-1288.
29. Xue, J., Sun, Q., Zhang, Y., Mao, W., Li, F. and Yin, C. (2020). Preparation of a polypyrrole/graphene oxide composite electrode by electrochemical codeposition for capacitor deionization. *ACS Omega*, 5(19): 10995-11004.
30. Demirkan, B., Bozkurt, S., Cellat, K., Arıkan, K., Yılmaz, M., Şavk, A., Çalımlı, M.H., Nas, M.S., Atalar, M.N., Alma, M.H. and Sen, F. (2020). Palladium supported on polypyrrole/reduced graphene oxide nanoparticles for simultaneous biosensing application of ascorbic acid, dopamine, and uric acid. *Scientific Reports*, 10 (1): 1-10.
31. Sheng, Q., Liu, D. and Zheng, J. (2016). NiCo alloy nanoparticles anchored on polypyrrole/reduced graphene oxide nanocomposites for nonenzymatic glucose sensing. *New Journal of Chemistry*, 40(8): 6658-6665.
32. Othman, N. Z., Hanapi, N. S. M., Ibrahim, W. N. W. and Saleh, S. H. (2020). Alginate incorporated multi-walled carbon nanotubes as dispersive micro solid phase extraction sorbent for selective and efficient separation of acidic drugs in water samples. *Nature Environment & Pollution Technology*, 19(3): 1155-1162.
33. Tong, L., Li, P., Wang, Y. and Zhu, K. (2009). Analysis of veterinary antibiotic residues in swine wastewater and environmental water samples using optimized SPE-LC/MS/MS. *Chemosphere*, 74(8): 1090-1097.
34. Seifrtova, M., Novakova, L., Lino, C., Pena, A. and Solich, P. (2009). An overview of analytical methodologies for the determination of antibiotics in environmental waters. *Analytica Chimica Acta*, 649 (2): 158-179.
35. Qiang, Z. and Adams, C. (2004). Potentiometric determination of acid dissociation constants (pKa) for human and veterinary antibiotics. *Water Research*, 38(12): 2874-2890.
36. Sassman, S. A. and Lee, L. S. (2005). Sorption of three tetracyclines by several soils: assessing the role of pH and cation exchange. *Environmental Science & Technology*, 39(19): 7452-7459.
37. Azouaoua, N., Belmedanib, M., Mokaddema, H. and Sadaoui, Z. (2013). Adsorption of lead from aqueous solution onto untreated orange barks. *Chemical Engineering Transactions*, 2013: 32.
38. Loh, S. H., Sanagi, M. M., Ibrahim, W. A. W. and Hasan, M. N. (2013). Multi-walled carbon nanotube-impregnated agarose film microextraction of polycyclic aromatic hydrocarbons in green tea beverage. *Talanta*, 106: 200-205.
39. Talebpour, Z., Taraji, M. and Adib, N. (2012). Stir bar sorptive extraction and high performance liquid chromatographic determination of carvedilol in human serum using two different polymeric phases and an ionic liquid as desorption solvent. *Journal of Chromatography A*, 1236: 1-6.
40. Ghati, S. K. (2017). Removal of chlorpyrifos (dursban) pesticide from aqueous solutions using barley husks. *Ibn Al-Haitham Journal for Pure and Applied Science*, 29(3): 54-68.
41. Al-Afy, N., Sereshti, H., Hijazi, A. and Nodeh, H. R. (2018). Determination of three tetracyclines in bovine milk using magnetic solid phase extraction in tandem with dispersive liquid-liquid microextraction coupled with HPLC. *Journal of Chromatography B*, 1092: 480-488.
42. Wu, X. J., Wang, G. N., Yang, K., Liu, H. Z. and Wang, J. P. (2017). Determination of tetracyclines in milk by graphene-based solid-phase extraction and high-performance liquid chromatography. *Analytical Letters*, 50(4): 641-650.
43. Lian, L., Lv, J., Wang, X. and Lou, D. (2018). Magnetic solid–phase extraction of tetracyclines using ferrous oxide coated magnetic silica microspheres from water samples. *Journal of Chromatography A*, 1534: 1-9.
44. Wilkowska, A. and Biziuk, M. (2011). Determination of pesticide residues in food matrices using the QuEChERS methodology. *Food Chemistry*, 125(3): 803-812.

Malaysian Journal of Analytical Sciences (MJAS)
Published by Malaysian Analytical Sciences Society

ADSORPTION AND MOLECULAR DOCKING STUDY OF BISPHENOL A USING REUSABLE ZIF–8 (ZN) METAL–ORGANIC FRAMEWORKS IN AN AQUEOUS SOLUTION

(Penjerapan dan Kajian Penambatan Molekul Bisfenol A Menggunakan Kerangka Logam–Organik ZIF–8 (Zn) yang boleh Digunakan Semula dalam Larutan Air)

Afzan Mahmad[1, 3], Teh Ubaidah Noh[2], Maizatul Shima Shaharun[3*], Zakariyya Uba Zango[4]

[1]*Laboratory Department,*
Universiti Kuala Lumpur, Royal College of Medicine Perak, Malaysia
[2]*Institute of Bioproduct Development, Universiti Teknologi Malaysia, Malaysia*
[3]*Fundamental and Applied Sciences Department,*
Universiti Teknologi PETRONAS, Seri Iskandar, Perak, Malaysia
[4]*Department of Chemistry, Al-Qalam University, Katsina, Nigeria*

[*]*Corresponding author: maizats@utp.edu.my*

Received: 24 May 2022; Accepted: 18 July 2022; Published: 30 October 2022

Abstract

Bisphenol A (BPA) is a derivative of phenol that has been identified as a pollutant in water. This work aimed to evaluate the experimental and molecular docking findings on the adsorption of BPA using porous material metal–organic frameworks (MOFs) of zeolitic imidazolate frameworks (ZIF–8 (Zn)). The commercial ZIF–8 (Zn) was characterized by field emission scanning electron microscopy (FESEM), scanning electron microscopy (SEM), and energy dispersive X–ray (EDX). The surface morphology of ZIF–8 (Zn) showed cubic particles and zinc components (18.70 %) detected by EDX. The adsorption of endocrine–disruptive chemicals of BPA was performed by batch adsorption experiments and measured using ultraviolet–visible (UV–Vis) spectrophotometry. ZIF–8 (Zn) was shown to achieve adsorption at BPA dosage (0.4 g), and pH 6 (25 ^{o}C) with high BPA removal (98.84%). Molecular docking simulation represented that BPA was bound to ZIF–8 (Zn) via the inner pores. The mechanism interaction of BPA and ZIF–8 (Zn) was via van der Waals interaction. The adsorption of BPA onto ZIF–8 (Zn) fitted the Langmuir isotherm and the pseudo–second–order model. The possible regeneration and reusability of ZIF–8 (Zn) show good suitability for reusable adsorbent in BPA adsorption application from environmental water.

Keywords: bisphenol A, adsorption, ZIF–8, water pollutants, metal–organic frameworks

Abstrak

Bisfenol A (BPA) adalah terbitan fenol yang telah dikenal pasti sebagai bahan pencemar di dalam air. Kerja kajian ini bertujuan untuk menilai ekperimen dan kajian penambatan molekul pada penjerapan BPA menggunakan kerangka kerja logam–organik (MOFs) bahan berliang iaitu kerangka besi zeolitik imidazolat (ZIF–8 (Zn)). ZIF–8 (Zn) secara komersil dicirikan oleh mikroskopi electron imbasan pancaran medan (FESEM), mikroskopi electron elektron imbasan (SEM), dan sinar–X serakan tenaga (EDX). Morfologi permukaan ZIF–8 (Zn) oleh EDX menunjukkan zarah padu partikel kubik dan komponen zink (18.70 %) dikesan oleh

EDX. Penjerapan BPA yang mengganggu bahan kimia endokrin telah dilakukan oleh secara eksperimen penjerapan kelompok dan diukur menggunakan spektrofotometer ultraungu tampak (UV–Vis). ZIF–8 (Zn) yang ditunjukkan mencapai penjerapan pada dos BPA (0.4 g), pH 6 (25 ºC) dengan penyingkiran BPA yang tinggi (98.84%). Simulasi penambatan molekul menunjukkan bahawa BPA terikat kepada ZIF–8 (Zn) melalui liang dalam. Mekanisma BPA dan ZIF–8 (Zn) adalah melalui interaksi van der Waals. Penjerapan BPA ke atas ZIF–8 (Zn) adalah sepadan dengan model Langmuir dan pseudo–tertib–kedua. Kemungkinan penjanaan dan kebolehgunaan semula untuk ZIF–8 (Zn) menunjukkan kesesuaian yang baik untuk bahan penjerap yang boleh diguna semula dalam aplikasi penjerapan BPA daripada air persekitaran.

Kata kunci: bisfenol A, penjerapan, ZIF–8, pencemaran air, kerangka besi logam–organik

Introduction

Toxic organic compound contamination of water has remained an issue for ecosystems. Endocrine–disrupting compounds of bisphenol A (BPA) and bisphenol S (BPS) have been frequently detected in industrial and environmental water [1]. BPA is widely used in the manufacturing of storage containers, such as plastics [1], water supply pipes [2], reusable water bottles [3–5], and food containers [6–7]. A phenolic molecule with two phenol moieties [8], low vapor pressure, moderate water solubility, and low volatility [9] are some of the characteristics of BPA. BPA is a solid at room temperature and very toxic to aquatic life at concentrations of 1,000 to 10,000 mg/L in freshwater [10–11].

Multiple wastewater treatment strategies have been shown to effectively remove BPA from water [8–10]. Adsorption is one of the promising techniques to remove organic and inorganic pollutants from wastewater [8]. The most commonly used adsorbent is activated carbon and multi–walled carbon nanotubes at both laboratory and industrial scales. However, it has several disadvantages, such as problems with hydrophilic substances, the selective performance of the carbon used, high cost, and the need for complexing agents [2]. Thus, an alternative reusable adsorbent has been proposed to treat BPA wastewater so that the discharged water can comply with environmental regulations.

Metal–organic frameworks (MOFs) are suggested as one of the most advanced materials that can effectively remove toxic pollutants from wastewater. MOFs are organic–inorganic hybrid crystalline porous substances with positively charged metal ions next to organic linker molecules [12]. The compounds offer many advantages, such as ultra–porous structure for the surface area [13], high pore volume [14], uniform particle size [15–18], good thermal and chemical stability [19], and the flexibility of geometrical structures to impart different shapes for the frameworks [10]. These advantages of MOFs have the potential for effective BPA adsorption in wastewater. ZIFs, or zeolitic imidazolate frameworks, are a subclass of MOFs that are primarily composed of tetrahedrally coordinated transition metals such as cobalt, zinc, and imidazolate linkers. They are assembled through the process of self–assembly. With the strong and small bonds of the metal ions–imidazolate, ZIFs are associated with great characteristics as universal adsorbents for adsorption of BPA [19].

According to the findings that were published by Peng et al. [20], the elimination of BPA by employing chitosan–modified zeolite (Ch–Z) in the absence and presence of sodium cholate (NaC) was examined. It was discovered that the elimination of BPA by adsorption onto Ch–Z with NaC was over nine times higher than when there was no NaC present in the experiment. The research conducted by Genc et al. [21] utilized surfactant–modified natural zeolite to remove BPA from aqueous solutions. The robust design technique developed was applied in order to maximize the adsorption of BPA, and the maximum adsorption capacity was reported to be 6.90 mg/g. The adsorption of BPA by modified zeolites containing cetyltrimethyl ammonium bromide (CTAB) and cetylpyridinium bromide (CPB) was investigated by Wang et al. [22]. The most effective modified zeolite for the removal of BPA was found to be one that combined 10% CTAB with pre-treated zeolite and was carried out at a temperature of 25℃ for thirty-six hours. Other research found that the ZIF-8@SBA-15 adsorbent, which was made by modifying the ZIF-8 coating layers using the

coordination method, has a maximum adsorption capacity of 123.4 mg/g for 200 mg/L BPA. More than a twofold increase in adsorption capacity was seen with the ZIF-8@SBA-15 adsorbent, and an almost twentyfold increase in adsorption rate constant was observed [23]. Synthetic zeolite with a NaX structural type was modified with cyclodextrin (CD) in the study conducted by Bandura et al. [24] to improve the adsorption of BPA from aqueous solutions. The adsorption of BPA was consistent with a monolayer model, and it suggested the creation of host–guest complexes along with hydrogen bond formation. The highest adsorption capabilities for the removal of BPA were measured at 32.7 mg/g. According to the adsorption behavior of ZIFs, they can function as an effective adsorbent for the removal of BPA from aqueous media.

In this work, ZIF–8 (Zn) was chosen as the adsorbent in this investigation of the BPA removal from an aqueous solution. There has been no previously published work for ZIF–8 (Zn) utilizing ultraviolet–visible (UV–Vis) spectroscopy that studied regeneration and reusability. The reusable ZIF–8 (Zn) may help in the development of a green adsorbent that will offer a high yield whilst having very low operational expenses. The batch adsorption experiments were measured using scanning electron microscopy (SEM), energy–dispersive X–ray spectroscopy (EDX), field emission scanning electron microscopy (FESEM), and UV–Vis spectrophotometer for absorbance measurement. The effects of parameters were studied for effective BPA adsorption. The thermodynamics, kinetics, and isotherm of the process were also determined, and possible mechanisms step and molecular docking for the BPA adsorption were proposed. By considering reusable adsorbent, ZIF–8 (Zn) could reduce the maintenance cost and be environmentally friendly in the removal of BPA.

Materials and Methods

Chemicals Reagents

The chemicals used in this experiment were analytical grade and had no purification before use. BPA analytical standard (> 99% purity), and Basolite Z1200@ZIF–8 (Zn) (99% purity) was obtained from Sigma–Aldrich (USA). Sodium hydroxide (NaOH), and hydrochloric acid (HCl) were obtained from Avantis Laboratory, Malaysia.

Characterization of ZIF–8 (Zn)

The surface morphology of ZIF–8 (Zn) was determined using FESEM–EDX (Zeiss Supra 55 VP, the United Kingdom). Meanwhile, the equipment was operated at 200 kV and the samples were sputtered–coated with Au metal. EDX was conducted to detect the elemental composition of the ZIF–8 (Zn).

Batch adsorption studies

The experiments were carried out using ZIF–8 (Zn) that was added to 200 mL of BPA solutions. Fig. S1 represents typical calibration curves for the BPA solution. The conical flasks were sealed and placed in a shaker and mixed using an orbital shaker (Daihan Scientific, China). The samples were withdrawn at a certain time interval using a syringe and the residual BPA concentration was analyzed spectrophotometrically by observing the absorbance at the maximum wavelength of absorption (276 nm) using a UV–vis spectrophotometer (Shimadzu, UV–1800). The parameters that affect the adsorption, such as the MOF dosage, temperature, and pH were systematically studied using one parameter at a time (OFAT).

The % BPA removal is stated by the formula below [17]:

$$\%R = \frac{C_o - C_e}{C_o} \times 100\% \quad (1)$$

And the BPA quantity adsorbed at a time (q_t) and equilibrium (q_e) is calculated as:

$$q_t = \frac{(C_o - C_t)V}{w} \quad (2)$$

$$q_e = \frac{(C_o - C_e)V}{w} \quad (3)$$

where C_t is the equilibrium concentration of the BPA (mg/L), C_o is the initial BPA concentration (mg/L), V is the volume of the water (L) and w is the mass of BPA (g).

The adsorption isotherms for BPA were obtained via adsorption for 60 minutes, which is sufficient for

equilibrium. The effect of the ZIF–8 (Zn) dosage (0.05–0.4 g) was investigated and maintained at 90 mg/L. For BPA adsorption under a range of pH (2–12), the pH of the BPA solution (90 mg/L) with 0.4 g of ZIF–8 (Zn) was adjusted, before adsorption, by using 0.10 M HCl or 0.10 M NaOH solution. The effect of changing the BPA removal temperature was also investigated at temperatures ranging from 25 to 45 °C. The results obtained from the effect of adsorption temperatures were used to analyse the thermodynamic values using $\Delta G^{\theta} = -RTInK_C$ where ΔG^{θ} (kJ/mol) is the change in Gibbs free energy, R is gas constant, T is the temperature (K) and K_C is a ratio of the amount of BPA adsorbed onto the ZIF–8 (Zn) to the concentration of BPA at equilibrium. The equation explains the extent of the spontaneity of the removal process.

For thermodynamic calculation, the value Kc represents the distribution coefficient, which refers to the ratio of the amount of BPA adsorbed onto the MOFs (C_{ads}) to the concentration of BPA at equilibrium (C_e). Equation 4 can also be rewritten as [17]:

$$InK_C = \frac{\Delta H^{\theta}}{R} - \frac{\Delta S^{\theta}}{RT} \quad (4)$$

where ΔH^{θ} (kJ/mol) is the enthalpy change and ΔS^{θ} ($Jmol^{-1}K^{-1}$) is the entropy change of the adsorption process.

The regeneration and reusability of ZIF–8 (Zn) was also investigated. Using 100 mL of ethanol solution, the ZIF–8 (Zn) was regenerated by discharging the filtrate and washing the leftover particles away. Following that, the MOFs were vacuum dried at 100 ° C for 3 hours. For stability studies, the samples were stored in a desiccator and remained unaltered during the long–term storage.

Molecular docking simulation

The molecular docking study of the 1:1 ratio of BPA with ZIF–8 (Zn) molecules was conducted using AutoDock Tools version 1.5.6. The docking process was studied by the macromolecule (ZIF–8 (Zn)) and ligand (BPA) into the system. After that, the Autogrid tool in the AutoDock program was used to generate a grid box of 120 × 120 × 120 Å cubic with 0.375 Å spacing points. It was installed wider than ZIF–8 (Zn) and attached to the middle of ZIF–8 (Zn) molecules to verify that the box encompassed the whole surface of ZIF–8 (Zn). Cambridge Crystallographic Data Centre (CCDC) and ChemTube3D (University of Liverpool, ChemTube3D) [25] were also used to achieve the crystallographic parameter of one unit cell of ZIF–8 (Zn). BPA's original structure was obtained via the Automated Topology Builder (ATB) service [25], and it was then optimized that use the DFT technique at the B3LYP/631G* level of theory. The BPA compounds were then presented into the cavity of ZIF–8's macromolecular receptor (Zn). To estimate the potential dock framework of BPA with ZIF–8 (Zn) complex and evaluate the binding energy (ΔG_{bind}), the Lamarckian genetic algorithm (LGA) has been used [17].

$$\Delta G_{bind} = \Delta G_{VDW} + \Delta G_{electrostatic} + \Delta G_{H°bond} + \Delta G_{desolv} + \Delta G_{tor} \quad (5)$$

ΔG_{VDW} represents van der Waal energy, $\Delta G_{H°bond}$ represents hydrogen bonding energy, $\Delta G_{electrostatic}$ refers to electrostatic energy, ΔG_{tor} is torsional free energy and ΔG_{desolv} represents desolvation energy.

Results and Discussion

ZIF–8 (Zn) Characterization

The surface morphology of ZIF–8 (Zn) was determined by FESEM analysis, as depicted in Figure 1(a). From the FESEM images, it is observed that the external surfaces of ZIF–8 (Zn) are relatively smooth with fine pores in a cubic structure (yellow arrows). The particle size of ZIF–8 (Zn) was estimated in the range of 219.2 to 572.1 nm which showed a smaller particle size that could contribute to the high surface area. The porosity of ZIF–8 (Zn) was described by the nitrogen (N_2) adsorption–desorption analysis. ZIF–8 (Zn) showed good BET surface area and pore volume, as highlighted in Mahmad et al. [26] studies, which are the characteristics of a highly porous material. It shows the typical nature of porous materials with ZIF–8 (Zn) having a surface area and pore volume of 1299 m^2/g and 0.6 m^3/g,

respectively. ZIF–8 (Zn) showed a high BET surface area due to the flexible amine group pendants [17]. The pore size of the ZIF–8 (Zn) was determined using Barrett–Joyner–Halenda (BJH) analysis as shown in Fig. 1 (d). Also, the surface elemental composition from the EDX analysis of ZIF–8 (Zn) (Figure 1(b)) proved that the surface elemental compositions consisted of carbon (45.55 %), nitrogen (30.34 %), oxygen (5.41 %), and zinc (18.70 %).

In addition, the ZIF–8 (Zn) with good chemical, thermal, and moisture stability was synthesized and characterized. The ZIF–8 (Zn) is described by the cubic–like particles, indicating the good stability of the MOFs as emphasized in the works of literature [17–18]. To further ascertain the stability of the adsorbents for the *in vivo* application, the ZIF–8 (Zn) had aged in a strong acidic condition (pH 1) for a period of one week. However, the SEM analysis has shown no defect in the structural morphology of the ZIF–8 (Zn) as shown by the images in Fig. 1 (c). The detail on the good stability of the ZIF–8 (Zn) is in the same agreement as previously reported by Molavi et al. [27] and Oveisi et al. [28].

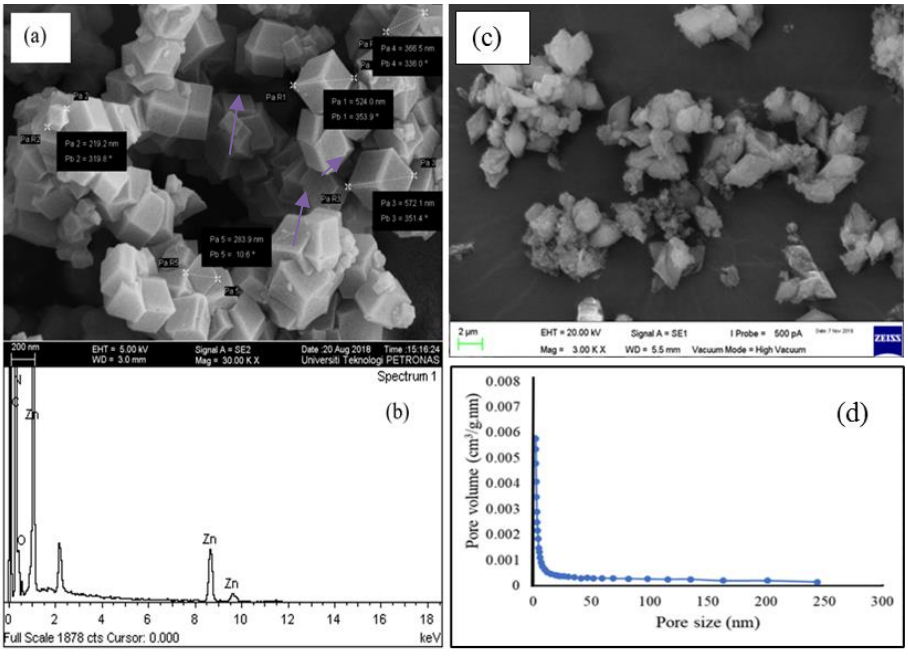


Figure 1. (a) FESEM and (c) SEM images at 30,000× magnification, (b) EDX spectra, and (d) the image of the pore size distribution of ZIF–8 (Zn)

BPA adsorption study

The effect of different dosages of ZIF–8 (Zn) on BPA adsorption was analyzed and the data are shown in Figure 2(a). ZIF–8 (Zn) achieved the highest percentage of BPA removal (98.84 %) at a 0.4 g dosage, which is exactly equivalent to the work done by Zango et al. [17–18]. The mass transfer increased as the dosage of ZIF–8 (Zn) increased, which was determined based on the increase in BPA adsorption capacity. This is because increasing the ZIF–8 (Zn) dosage, increases the number of active pore sites on the surface of ZIF–8 (Zn) for BPA adsorption to occur [29]. At higher dosage, BPA molecules acquired higher equilibrium adsorption capacity due to the increase in the diffusion gradient as the driving force for adsorption [30].

As the pH increased, the removal percentage of BPA decreased (Figure 2 (b)). At the acidic phase, the optimum removal of BPA was 94.68% (pH 6) using ZIF–8 (Zn). Fundamentally, pH affects the electrostatic attraction between ZIF–8 and BPA molecules in an aqueous solution. Based on the results, the adsorption

between ZIF–8 (Zn) and BPA molecules is promoted in an acidic medium. The H^+ ions in the BPA solution are present in an acidic medium, which produced positively charged BPA [17–18]. The BPA removal increased in the presence of acids compared to bases because the negative charge of ZIF–8 (Zn) increases as pH decreases [17]. Hence, there is more electrostatic attraction between ZIF–8 (Zn) and BPA molecules, leading to higher BPA uptake.

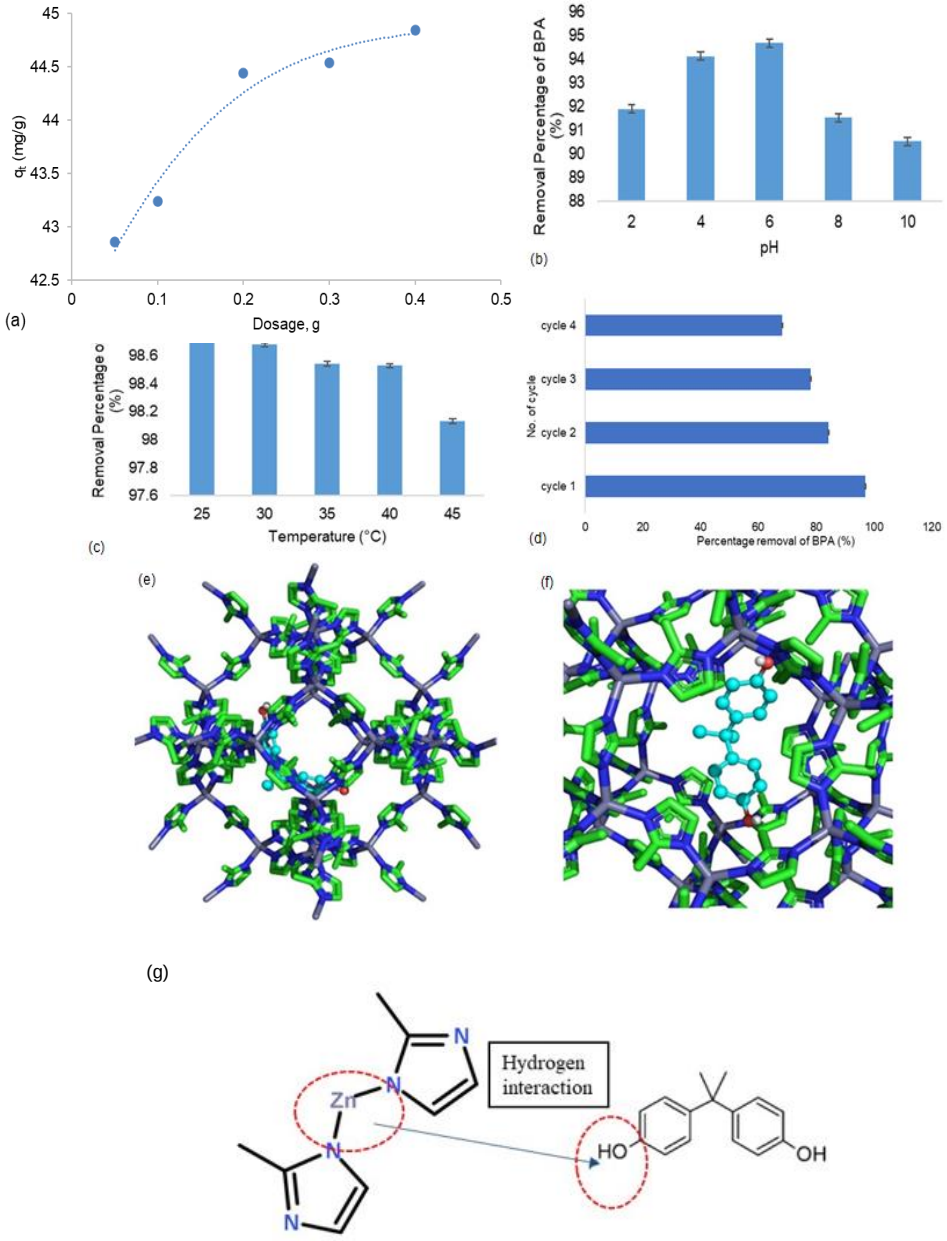


Figure 2. The graph for effect of (a) dosage, (b) pH, (c) temperature, (d) reusability for BPA adsorption onto ZIF–8 (Zn), molecular structure of (e) ZIF–8 (Zn)(BPA) (full view), (f) ZIF–8 (Zn)(BPA) (zoom view) and (g) possible mechanism of ZIF–8 (Zn)(BPA). BPA was colored light blue.

On the other hand, the removal efficiency for ZIF–8 (Zn) at a particular temperature is presented in Figure 1(c). A decrease in the removal percentage of BPA was recorded at accumulated temperatures. As the temperature rises, the mass transfer rate from the bulk solution to the boundary layer near ZIF–8 (Zn) decreases. The increased BPA solubility reveals a lower tendency to the surface of ZIF–8 (Zn) [17–18]. To determine the thermodynamics of the adsorption, Van't Hoff equation was applied and the corresponding enthalpy (ΔH^{θ}), Gibbs free energy (ΔG^{θ}), and entropy changes (ΔS^{θ}) were deduced [17–18] (Table 1). The ΔG^{θ} values were reported to be negative and decreased at high temperatures, indicating a spontaneous and unfavorable nature of the process as the temperature increases [17–18]. The ΔH^{θ} value was 9.957 kJ/mol for ZIF–8 (Zn). This further shows the exothermic and endothermic nature of the BPA adsorption. The rate of diffusion of ZIF–8 (Zn) molecules through the external boundary layers and interior pores of ZIF–8 (Zn) increased as the temperature rises, representing an endothermic adsorption mechanism. The value of ΔS^{θ} was 0.0142 J/mol/K for ZIF–8 (Zn), which showed a high degree of randomness in the ZIF–8 (Zn) adsorption system. In addition, according to Mahmad et al. [26], the adsorption of BPA onto ZIF–8 (Zn) fitted the Langmuir isotherm and the pseudo–second–order model.

Table 1. Thermodynamic parameters for the adsorption of BPA onto ZIF–8 (Zn)

Temp (°C)	ΔG^{θ}(kJ/mol)	ΔH^{θ}(kJ/mol)	ΔS^{θ}(J/mol/K)
25	−14.241		
30	−14.222		
35	−14.424	9.957	0.0142
40	−14.852		
45	−14.632		

After the batch adsorption tests, the regeneration and reusability of ZIF–8 (Zn) demonstrate remarkable potential as adsorbents for BPA removal. The BPA removal percentage obtained by ZIF–8 (Zn) in the 4th cycle was 68.2% (Figure 1 (d)). This finding shows that ZIF–8 (Zn) has good reusability features with good removal performance [17–18]. Zango et al. [17] reported that MOF has the possibility to be regenerated and reused until the 5th cycle with a good percentage of pollutant removal. A significant *p*–value is vital for determining the fit of the model. In other words, a *p*–value < 0.05 indicates the significance of the model for the regression analysis under the influence of independent variables. The temperature and dosage of ZIF–8 (Zn) were considered significant for BPA adsorption. Thus, these values proved that the alternative hypothesis is accepted and there is a difference between the means of the parameters. Meanwhile, the pH of ZIF–8 (Zn) was not statistically significant. This shows that the null hypothesis is accepted and there is no difference between the means of the parameters.

Molecular docking of adsorption of BPA onto ZIF–8 (Zn)

Docking simulation was also performed to analyze the molecular interaction for the BPA removal onto ZIF–8 (Zn). The binding conformers for the complex formation are shown in Figure 1 (e–f) for ZIF–8 (Zn). It was observed that BPA molecules prefer to bind with the internal pores of ZIF–8 (Zn) due to their smaller size [17–18]. The stability of the docking conformers is determined by the binding energy of the inclusion complex formed. It represents the strength and stability of the interaction of ZIF–8 (Zn) with BPA. The result of molecular docking for the interaction of ZIF–8 (Zn) with

BPA was supported by the calculated equilibrium adsorption capacities obtained from the contact time optimization studies with ZIF–8 (Zn) adsorption, where the q_e value was 43.82 ±0.17 mg/g [31]. The BPA adsorption onto ZIF–8 (Zn) exhibited the ΔG_{bind} of −4.21 kcal mol^{-1} [31]. The docking findings follow a pattern that is comparable to that seen in the experimental data collected for the adsorption capacity of ZIF–8 (Zn). More stable physisorption interaction is associated with lower free energy values [32], as opposed to higher free energy values. ZIF–8 (Zn) models were established with BPA and also exhibit van der Waals interactions with the adsorbing contaminants. Table 2 lists the van der Waals as well as electrostatic energies associated with the inclusion complexes, as well as the values of interaction energies. The distance of the hydrogen bond was reported as 3.6 Å. However, the hydrogen bond of ZIF–8 (Zn) was insignificant due to the large average distance (more than 3 Å) from the experimentally determined geometry, which can be due to wrong orientation or displacement (Figure 2 (g)) [32–33]. Hence, due to the lowest ΔG_{bind}, ZIF–8 (Zn) was predicted to have van der Waals interaction with BPA in adsorption studies. Thus, the information obtained from the docking simulation is relevant.

Table 2. The interaction energy of ZIF–8 (Zn) with BPA inclusion complex obtained from molecular docking simulation

Interaction Energy (kcal/mol)					
$\Delta G_{binding}$	$\Delta G_{\text{vdw + HBond + desolv}}$	ΔG_{elec}	ΔG_{total}	$\Delta G_{unbound}$	ΔG_{tor}
−4.21	−5.38	−0.02	−0.50	−0.50	+1.19

Comparison with other adsorbents

Table 3 shows the key features of adsorbents for the removal of BPA from wastewater that have been reported. Based on the reported studies, it is clear that ZIF–8 (Zn) has a higher BPA removal percentage (% R = 98.84 %). The optimum contact time was also rapid (30 minutes) [26], and the ZIF–8 (Zn) was reported with good reusability and regeneration. In contrast to the adsorbents given in Table 3, the listed adsorbents have not undergone any studies on their potential to be regenerated and reused. Because ZIF–8 (Zn) has the capacity to regenerate itself and is reusable, it has the potential to reduce costs, has a high level of efficiency, and is kind to the environment. Despite this, when compared to the other adsorbents, the ZIF–8 (Zn) demonstrated the shortest amount of time necessary for the adsorption of BPA to attain the optimal result. When compared to the other adsorbents, the surface area of ZIF–8 (Zn) was reported as having the greatest value; as a result, ZIF–8 (Zn) has a high potential for future research into the maximum adsorption capacity based on the impact of a high concentration of BPA. As a result of these findings, ZIF–8 (Zn) has the possibility to be a future alternative reusable adsorbent for the removal of BPA.

Table 3. Comparison of reported adsorbents with MOFs used for BPA removal

Adsorbents	Surface Area (m^2/g)	Maximum Adsorption Capacity (mg/g)	Initial Concentration, Solid/Liquid Ratio	Isotherm Models	Kinetic Models	Removal of BPA (%R)	Equilibrium Time	References
Commercial powdered activated carbon	1027	307.00	5–70 mg/L, 10 mg/100 mL	Langmuir	Ps2	>99.00	>90 min	[34]
Palygorskite–montmorillonite	1777	77.30	0.01–10 mg/L, 3 g/25 mL	Langmuir	–	–	>48 hours	[35]
CTAB–modified zeolite	–	37.85	0–200 mg/L, 1 g/L	Freundlich	Ps2	–	–	[22]
Chitosan–modified zeolite (Ch–Z) in the absence and presence of sodium cholate (NaC)	–	77.82	100 µmol/L, 1 g/L, 1.68 mmol/L	Freundlich	Ps2	78.00	<9–10 hours	[20]
Surfactant–modified natural zeolite	–	6.90	10–100 mg/L, 0.25 g/50 mL	Temkin	Ps2	–	30 min	[21]
ZIF–8@SBA–15	722	123.40	200 mg/L	–	Ps2	–	2 min	[23]
Zeolite from fly ash modified with β–cyclodextrin	166	32.70	0.5 g/L	Langmuir	Ps2	–	90 min	[24]
This work ZIF–8 (Zn)	1299	43.81 ± 0.17	90 mg/L, 0.4 g	Langmuir	Ps2	98.84	30 min	[26]

* Ps2=pseudo–second order

Conclusion

The BPA removal onto the commercial ZIF–8 (Zn) has been studied. The high BPA removal percentage was successfully achieved with ZIF–8 (Zn). For the regeneration and reusability studies of ZIF–8 (Zn) for BPA adsorption, the removal percentage achieved 68.2% in the 4th cycle. The van der Waals interaction could occur in the adsorption of BPA, as determined using molecular docking simulation. The Langmuir isotherm and the pseudo–second order model were also compatible with the findings. Molecular docking simulation predicted better interaction between ZIF–8 (Zn) and BPA molecules, which agreed well with the experimental findings. Based on the comparison of previously used adsorbents, ZIF–8 (Zn) was shown to be superior in terms of rapid equilibration (30 min), highest BPA removal, and reusable features. Thus, ZIF–8 (Zn) as a future reusable adsorbent can achieve good results in the removal of BPA from wastewater.

Acknowledgment

This work was sponsored by a grant provided through the Financial Aid from Universiti Teknologi PETRONAS (UTP) and the Ministry of Higher Education Malaysia, FRGS No: FRGS/1/2011/SG/UTP/02/13. The authors acknowledge the use of the facilities within the UTP Centralized Analytical Laboratory (CAL).

References

1. Bhatnagar, A. and Anastopoulos, I. (2017). Adsorptive removal of bisphenol A (BPA) from aqueous solution: a review. *Chemosphere*, 168: 885-902.
2. Min Park, J. and Hwa Jhung, S. (2020). A remarkable adsorbent for removal of bisphenol S from water: aminated metal–organic framework, MIL–101–NH_2. *Chemical Engineering Journal*, 2020:125224.

3. Ohore, O. E. and Songhe, Z. (2019). Endocrine disrupting effects of bisphenol A exposure and recent advances on its removal by water treatment systems. A review. *Scientific African*, 5: e00135.
4. Goldinger, D. M., Demierre, A. L., Zoller, O., Rupp, H., Reinhard, H. and Magnin, R. (2015). Endocrine activity of alternatives to BPA found in thermal paper in Switzerland. *Regulatory Toxicology and Pharmacology*, 71: 453-462.
5. Banaderakhshan, R., Kemp, P., Breul, L., Steinbichl, P., Hartmann, C. and Fürhacker, M. (2022). Bisphenol A and its alternatives in Austrian thermal paper receipts, and the migration from reusable plastic drinking bottles into water and artificial saliva using UHPLC–MS/MS. *Chemosphere*, 286: 131842.
6. Ginter–Kramarczyk, D., Zembrzuska, J., Kruszelnicka, I., Zając–Woźnialis, A. and Ciślak, M. (2020). Influence of temperature on the quantity of bisphenol A in bottled drinking water. *International Journal of Environmental Research and Public Health*. 19(9): 5710.
7. Ali, M., Jaghbir, M., Salam, M., Al–Kadamany, G., Damsees, R. and Al–Rawashdeh, N. (2018). Testing baby bottles for the presence of residual and migrated bisphenol A. *Environmental Monitoring & Assessment*, 191(1): 1-7.
8. Abraham, A. and Chakraborty, P. (2020) A review on sources and health impacts of bisphenol A. *Reviews on Environmental Health*, 35(2): 201-210.
9. Han, C. and Hong, Y. C. (2016). Bisphenol A, hypertension, and cardiovascular diseases: epidemiological, laboratory, and clinical trial evidence. *Current hypertension reports*, 18:1-11.
10. Singh, N. (2016). Exposure to bisphenol–A through excess use of polymer, with environmental toxicity. *International Journal of Scientific Research in Science, Engineering, and Technology*, 2: 454-457.
11 Adamakis, I. S., Malea, P. and Panteris, E. (2018). The effects of bisphenol A on the seagrass *Cymodocea nodosa*: Leaf elongation impairment and cytoskeleton disturbance. *Ecotoxicology and Environmental Safety*,157: 431-440.
12. Pettamanna, A., Raghav, D. and Nair, R. H. (2020). Hepatic toxicity in *Etroplus suratensis* (Bloch 1790): An economically important edible fish in Vembanad fresh water Lake, Kerala, India. *Bulletin of Environmental Contamination and Toxicology*, 105(4): 565-571.
13. Samanidou, V. F. and Deliyanni, E. A. (2020). Metal organic frameworks: Synthesis and application. *Molecules*, 25(4): 960.
14. Tibbetts, I. and Kostakis, G. E. (2020). Recent bio–advances in metal–organic frameworks. *Molecules*, 25(6): 1291.
15. Wang, L. C., Ni, X. J., Cao, Y. H. and Cao, G. Q. (2018). Adsorption behavior of bisphenol A on CTAB–modified graphite. *Applied Surface Science*, 428: 165-170.
16. Hoseinpour, V. and Shariatinia, Z. (2021). Applications of zeolitic imidazolate framework-8 (ZIF-8) in bone tissue engineering: A review. *Tissue and Cell*, 72: 101588.
17. Zango, Z. U., Sambudi, N. S., Jumbri, K., Ramli, A., Hanif Abu Bakar N. H., Saad B., Rozaini, M. N. H., Isiyaka, H. A., Osman, A. M., and Sulieman, A. (2020). An overview and evaluation of highly porous adsorbent materials for polycyclic aromatic hydrocarbons and phenols removal from wastewater. *Water*, 2020: 1-40.
18. Zango, Z. U., Sambudi, N. S., Jumbri, K., Ramli, A., Hanif Abu Bakar, N. H., Saad, B., Rozaini, M. N. H., Isiyaka, H. A., Osman, A. M. and Sulieman, A. (2020). A critical review on metal–organic frameworks and their composites as advanced materials for adsorption and photocatalytic degradation of emerging organic pollutants from wastewater. *Polymers,* 12: 264.
19. Ighalo, J. O., Rangabhashiyam, S., Adeyanju, C. A., Ogunniyi, S., Adeniyi, A. G. and Igwegbe, C. A. (2022). Zeolitic Imidazolate Frameworks (ZIFs) for aqueous phase adsorption – A review. *Journal of Industrial and Engineering Chemistry*, 105: 34-48.
20. Peng, S., Hao, K., Han, F., Tang, Z., Niu, B., Zhang, X. and Hong, S. (2015). Enhanced removal of bisphenol–AF onto chitosan–modified zeolite by sodium cholate in aqueous solutions. *Carbohydrate Polymers*, 130: 364-371.

21. Genç, N., Kılıçoğlu, Ö. and Narci, A. O. (2016). Removal of bisphenol A aqueous solution using surfactant–modified natural zeolite: Taguchi's experimental design, adsorption kinetic, equilibrium, and thermodynamic study. *Environmental Technology*, 38(4): 424-432.
22. Wang, H., Gao, J., Liu, W., Zhang, M. and Guo, M. (2016). Recovery of metal–doped zinc ferrite from zinc–containing electric arc furnace dust: Process development and examination of elemental migration. *Hydrometallurgy*, 166: 1-8.
23. Peng, J., Li, Y., Sun, X., Huang, C., Jin, J., Wang, J. and Chen, J. (2019). controlled manipulation of metal–organic framework layers to nanometer precision inside large mesochannels of ordered mesoporous silica for enhanced removal of bisphenol A from water. *ACS Applied Materials & Interfaces*, 11(4): 4328-4337.
24. Bandura, L., Białoszewska, M., Malinowski, S. and Franus, W. (2021). Adsorptive performance of fly ash–derived zeolite modified by β–cyclodextrin for ibuprofen, bisphenol A and caffeine removal from aqueous solutions–equilibrium and kinetic study. *Applied Surface Science*, 56: 150160.
25. Mahmad A., Shaharun M., Noh T. U., Zango Z. U. and Faisal M. (2022). Experimental and molecular modelling approach for rapid adsorption of bisphenol A using Zr and Fe–based metal–organic frameworks. *Inorganic Chemistry Communication*. 142(2022): 109604.
26. Mahmad, A., Shaharun, M. S., Zango, Z. U., Noh, T. U. and Saad, B. (2021). Adsorptive removal of bisphenol a using zeolitic imidazolate framework (ZIF–8). In: Abdul Karim, S. A., Abd Shukur, M. F., Fai Kait, C., Soleimani, H., Sakidin, H. (eds) *Proceedings of the 6th International Conference on Fundamental and Applied Sciences.* Springer Proceedings in Complexity. Springer, Singapore.
27. Molavi, H., Hakimian, A., Shojaei, A. and Raeiszadeh, M. (2018). Selective dye adsorption by highly water stable metal–organic framework: long term stability analysis in aqueous media. *Applied Surface Science*, 445: 424–436.
28. Oveisi, M., Mahmoodi, N. M. and Asli, M. A. (2019). Facile and green synthesis of metal–organic framework/inorganic nanofiber using electrospinning for recyclable visible–light photocatalysis. *Journal of Cleaner Production,* 222: 669-684.
29. Yu, L., Cheng, J., Yang, H., Lv, J., Wang, P., Li, J. R. and Su, X. (2021). Simultaneous adsorption and determination of bisphenol compounds in water medium with a Zr(IV)–based metal–organic framework. *Microchimica Acta*, 188(3): 83.
30. Zango, Z. U., Sambudi N. S., Jumbri, K., Abu Bakar, N. H., Abdullah, N. A. F., Negim, E. S. M. and Saad, B. (2020). Experimental and molecular docking model studies for the adsorption of polycyclic aromatic hydrocarbons onto UiO−66 (Zr) and NH_2−UiO−66 (Zr) metal−organic frameworks. *Chemical Engineering Science*, 220: 115608.
31. Groom, C. R., Bruno, I. J., Lightfoot, M. P. and Ward, S. C. (2016). The Cambridge structural database. *Acta Crystallographica Section* B, 72: 171-179.
32. Zango, Z. U., Bakar, N. H. H. A., Sambudi, N. S., Jumbri, K., Abdullah, N. A. F., Kadir, E. A. and Saad, B. (2020). Adsorption of chrysene in aqueous solution onto MIL-88 (Fe) and NH2-MIL-88 (Fe) metal-organic frameworks: Kinetics, isotherms, thermodynamics and docking simulation studies. *Journal of Environmental Chemical Engineering*, 8(2): 103544.
33. Xiang, Y., Yan, H., Zheng, B., Faheem, A., Chen, W. and Hu, Y. (2021). *E. coli@* UiO−67 composites as a recyclable adsorbent for bisphenol A removal. *Chemosphere*, 270: 128672.
34. Libbrecht, W., Vandaele, K., De Buysser, K., Verberckmoes, A., Thybaut, J., Poelman, H., Van Der Voort, P. (2015). Tuning the pore geometry of ordered mesoporous carbons for enhanced adsorption of bisphenol A. *Materials,* 8(4): 1652-1665.
35. Berhane, T. M., Levy, J., Krekeler, M. P. S., and Danielson, N. D. (2016). Adsorption of bisphenol A and ciprofloxacin by palygorskite–montmorillonite: Effect of granule size, solution chemistry, and temperature. *Applied Clay Science*, 132-133: 518-527.

Malaysian Journal of Analytical Sciences (MJAS)
Published by Malaysian Analytical Sciences Society

MICROBIAL DEGRADATION OF PALM OIL IN NATURAL SEAWATER AND IDENTIFICATION OF OIL DEGRADING BACTERIAL CONSORTIUM

(Degradasi Mikrob Minyak Sawit dalam Air Laut Semula Jadi dan Pengenalpastian Konsortium Bakteria Pendegradasi Minyak)

Arularasu Muthaliar Tamothran[1,2], Sree Selva Kumar Ganesen[1], Hing Lee Siang[1], Sabiqah Tuan Anuar[1], Razmah Ghazali[2], Kesaven Bhubalan[1,2,3]*

[1]*Faculty of Science and Marine Environment,*
Universiti Malaysia Terengganu, 21030 Kuala Nerus, Terengganu, Malaysia
[2]*Malaysian Palm Oil Board (MPOB),*
Persiaran Institusi, Bandar Baru Bangi, 43000 Kajang Selangor, Malaysia
[3]*Institute of Marine Biotechnology (IMB),*
Universiti Malaysia Terengganu, 21030 Kuala Nerus, Terengganu, Malaysia

**Corresponding author: kesaven@umt.edu.my*

Received: 15 March 2022; Accepted: 3 July 2022; Published: 30 October 2022

Abstract

Palm oil industry is among the most important commodities industry in Malaysia where Malaysia dominates 39% and 44% of global palm oil production and exports respectively. Most of the palm oil exports to various countries are done via sea-shipping which increases the risk towards marine pollution in form of oil spillage from vessels. Microbial degradation studies are important in establishing baseline data which is instrumental for mitigation planning and policy making. Degradation of palm oil derivatives was investigated using natural seawater collected from Klang Port and isolated bacteria *Pseudomonas aeruginosa* UMTKB-5 based on modified shake flask method as described by OECD Guidelines for Testing Chemicals, OECD TG 306 (Biodegradability in Seawater). Analytical method for determination of CPO and CPKO degradation comprises of measurement of dissolved organic carbon (DOC), colony forming unit (CFU), bacterial diversity using 16S rDNA gene based metagenomic analysis, and fatty acid measurements. Degradation of CPO and CPKO in seawater collected from Klang Port show increase in bacterial population which peaked in day 7 and 21 before declining indicating that palm oil is being used as substrate for bacterial growth in tandem with degradation which is aided by lipase enzyme produced by selected bacteria. Similar growth pattern observed in *P. aeruginosa* UKTKB-5 cultivated sample. DOC removal in sample showed negative value showing that carbon input from CPO and CPKO degradation is higher than consumption by bacteria. Fatty acid measurement shows changes in composition where bacterial degradation and utilisation of oil. The metagenomic analysis revealed diverse bacteria population in the different sampling locations and four lipase-producing bacterial strains were isolated at the end of the biodegradation experiment. The study has shown the biodegradability of palm oil in seawater and able to provide baseline data to understand and formulate the action plan in the event of spill in marine environment.

Keywords: palm oil, bacteria diversity, microbial degradation, fatty acids

Abstrak

Industri minyak sawit adalah antara industri komoditi terpenting di Malaysia di mana Malaysia menguasai 39% dan 44% pengeluaran dan eksport minyak sawit secara global masing-masing. Kebanyakan eksport minyak sawit ke pelbagai negara dilakukan melalui perkapalan laut yang meningkatkan risiko pencemaran marin dalam bentuk tumpahan minyak dari kapal. Kajian degradasi mikrob yang mampan adalah penting dalam mengesahkan data asas yang memainkan peranan penting untuk perancangan mitigasi dan pembuatan dasar dan polisi. Degradasi minyak sawit tidak ditapis (CPO) dan minyak isirong sawit tidak ditapis (CPKO) dalam air laut semula jadi yang dikumpul dari Pelabuhan Klang and bakteria *Pseudomonas aeruginosa* UMTKB-5 telah dikaji menggunakan kaedah kelalang goncang yang diubah suai seperti yang diterangkan oleh garis panduan OECD untuk pengujian bahan kimia, OECD TG 306 (kebolehbiodegradan dalam air laut). Analisa process degradasi CPO and CPKO melibatkan pengukuran karbon organik terlarut (DOC), kiraan unit pembentuk koloni (CFU), analisis metagenomik berasaskan gen 16S rDNA untuk kepelbagaian bakteria, dan perubahan acid lemak bebas. Keputusan menunjukkan peningkatan dalam kiraan CFU apabila bilangan hari meningkat dan kiraan CFU berada pada tahap tertinggi pada hari ke-7 dan 21 sebelum menurun. Situasi ini menunjukkan penggunaan minyak sawit sebagai substrat oleh bakteria. Peningkatan populasi bakteria yang sama ditunjukkan oleh bakteri *P. aeruginosa* UMTKB-5. Perubahan nilai penyingkiran DOC kepada nilai negatif mendedahkan kemasukan karbon melalui process degradasi CPO and CPKO pada tahap yang melebihi penggunaan oleh bakteria. Perubahan komposisi asid lemak penggunaan substrat oleh bakteria. Analisis metagenomik mendedahkan populasi bakteria yang pelbagai di lokasi persampelan yang berbeza dan lebih daripada empat strain bakteria telah diasingkan pada akhir eksperimen biodegradasi. Strain positif juga diuji untuk aktiviti lipolitik. Kajian ini telah mendedahkan kebolehbiodegradasian minyak sawit dalam air laut dan dijangka dapat membekalkan maklumat asas kepada pihak berkuasa berkaitan minyak sawit, pengangkutan dan agensi alam sekitar untuk memahami dan merangka pelan tindakan sekiranya berlaku tumpahan dalam persekitaran marin.

Kata kunci: minyak sawit, kepelbagaian bakteria, bakteria pendegradasi, asid lemak

Introduction

The demand for vegetable oil for food and as alternative fuel has fuelled the rapid production of oilseed [1]. The vegetable oil production is estimated to be around 187 million tonnes for 2016/2017 and is expected to grow to 195 million tonnes in the following year [2]. Four types of vegetable oil namely palm oil, soyabean oil, rapeseed oil and sunflower oil dominated the global vegetable oil market [1,3]. The major vegetable oil produced are palm oil (PO) and palm kernel oil (PKO) which accounts for 70.3 million tonnes (37.6%) of global production and followed by soybean oil where 55 million tonnes (30%) are produced [1].

The major producer of PO and PKO are Indonesia and Malaysia where nearly 86.5% of oil is produced. Malaysia is the second largest producer of palm oil where it accounts for 39% of global palm oil production and 44% of exports [4]. The oil palm tree *Elaeis guineensis* of tenera (thin shelled) variety is commonly planted in Malaysia due to its high oil yield [5]. Oil palm of tenera variety has higher palm oil content where it yields about four to five tonnes of crude palm oil (CPO) and one ton of crude palm kernel oil (CPKO) per hectare per year which made it as suitable planting material for commercialisation approach.

Significant portions of export and import activities of palm oil and its derivatives are conducted via sea shipping [6]. Malaysia exports palm oil to countries such as People's Republic of China, European Union, India, and United States via sea-shipping through major ports such as Johor Port, Klang Port, and Sandakan Port. This mode of transportation has led to pollution of marine environment where spillage of palm oil and its derivatives has occurred. There are several reported incidents of palm oil, and the most recent incident is the oil spill that occurred in Chinese waters where 9000 tonnes of palm stearin spilled from vessel collision [7] as well as dumping of palm oil by ships at the North Sea, Great Britain [8]. Vegetable oil spill incidents can negatively impact the exposed ecosystem where exposed organisms suffer oxygen depletion, toxicity effects, and smothering of surface-dwelling organisms causing fatal effects.

The United States Environmental Protection Agency (USEPA) has classified environmental impact of

vegetable oil spill as similar to hydrocarbon oil spills [9]. However, there are limited studies on the degradation of vegetable oil especially palm oil in marine environment. A study into natural palm oil degradation process and the role microbes play in the degradation process is necessary to understand the potential short and long-term impact of vegetable oil spills. This study aims to investigate the utilisation of different palm oil derivates by naturally occurring bacteria and cultivated marine bacteria to assess the degradability of oil via assessment of bacterial population, carbon removal, and fatty acid profile.

Materials and Methods

Degradation of crude palm oil and crude palm kernel oil using natural seawater: Study area

The sampling site chosen for natural seawater collection was Klang Port where the sample was collected at the coordinates for Site A: 2.999119°N, 101.379022°E and Site B: 3.004477°N, 101.354947°E (Figure 1). The seawater was collected based on the methods by American Public Health Association (APHA) [10]. Furthermore, the physical parameters such were measured and recorded *in situ* using portable Hydrolab Quanta Multiprobe meter. The sample was stored in ice until further analysis.

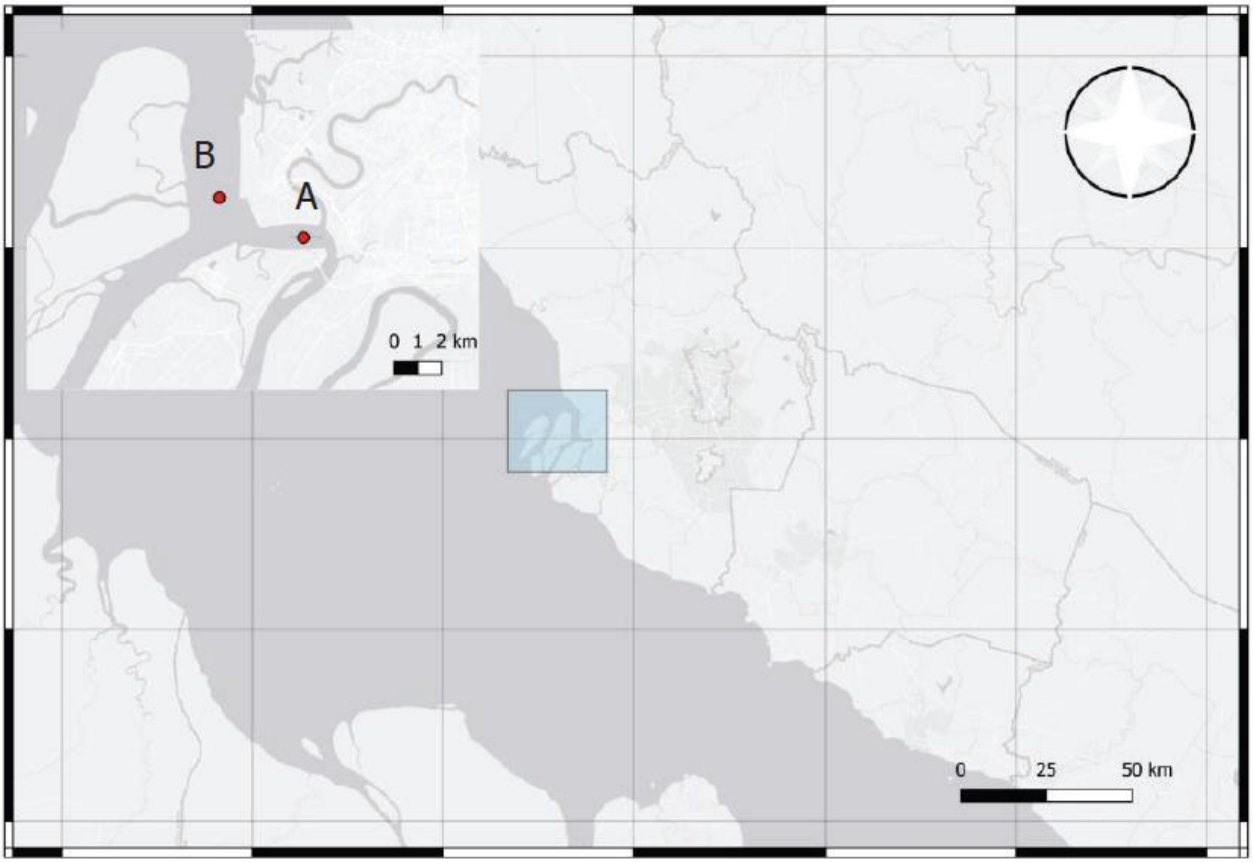


Figure 1. Map indicating the seawater sampling location at Klang Port, Selangor

Degradation of palm oil

The degradation of crude palm oil (CPO) and crude palm kernel oil (CPKO) that were obtained courtesy of MPOB were investigated using OECD Guidelines for Testing Chemicals, OECD TG 306: Biodegradability in Seawater with some modifications [11]. Shaken flask culture method was used in this study. The seawater was enriched with 1 mL litre^{-1} of each mineral nutrients that were prepared according to OECD guideline. The degradation study included blank, which is enriched

seawater without any test substance, test substance at two loading rate (1 g L^{-1} and 10 g L^{-1}) and aniline as reference substance. The degradation study was carried out for a period of 42 days at room temperature and was incubated at 150 rpm using Protech Orbital Shaker 721 ambient shaker. Samples were taken at selected interval for colony forming unit (CFU) determination using Zobell Marine Agar 2216 (HiMedia, India) and dissolved organic carbon (DOC) measurement. Furthermore, formation of floating and precipitate particles, oil droplets and dispersion were observed. Experiment was conducted in triplicates.

Determination of DOC

The DOC levels in culture medium were determined on samples from day 0, 7, 14, 21 and 28. The collected water samples were filtered using 0.45-µm polyether sulfone syringe filter (Sartorius, Germany) [12]. The DOC was measured using high-temperature catalytic oxidation (HTCO) method with a Shimadzu TOC-L & SSM 5000A (Shimadzu, Japan) total organic carbon equipped with non-dispersive infrared gas analyser (NDIR) detector [13]. The sample were acidified to pH then the samples were then sparged for 5 min before being analysed. Calibration of the instrument was done using freshly prepared standards [14]. Based on the DOC data obtained, degradation value was calculated based on formula provided in the guidelines [11].

Identification of bacterial consortium

The bacterial population of water sample before and after cultivation period were identified. The water sample collected during sampling was outsourced to Apical Scientific Sdn. Bhd. immediately after sample for metagenomic assessment of bacterial population. Meanwhile, phenotypically different bacterial colonies obtained at the end of degradation experiment was identified using 16S rDNA sequencing. Polymerase chain reaction (PCR) amplification was performed under the conditions: 3 min initial denaturation at 95°C; 34 cycles of denaturation (30 s at 95°C), annealing (45 s at 55°C) and extension (90 s at 72°C); and final extension at 72°C for 5 min [15,16]. The primer sets used were 63F (5'-CAGGCCTAACACATGCAAGTC-3') and 1389R (5'-ACGGGCGGTGTGTACAAG-3') [15,16]. The PCR products were sent to Apical Scientific Sdn. Bhd. for purification and sequencing. The obtained sequences obtained were compared with Basic Local Alignment Search Tool (BLAST) databases using Standard Nucleotide BLAST (BLASTn) to identify the bacteria.

Degradation of crude palm oil and crude palm kernel oil using natural seawater: Bacterial strain and utilisation test

P. aeruginosa UMTKB-5 (GenBank accession number: KT194193.1) was obtained from the culture collection of Institute of Marine Biotechnology, Universiti Malaysia Terengganu (Terengganu, Malaysia) [17]. The strain was isolated from marine sediment of Pulau Bidong. The strain was maintained on Zobell Marine Agar 2216 (HiMedia, India). The utilisation test was conducted using modified OECD TG 306 method based on previous study [15]. Test substance which are aniline, CPO, CPKO refined bleached and deodorised palm oil (RBDPO) and refined, bleached and deodorised palm olein (RBDPL) were added at concentration of 1 g L^{-1} into 100 mL working volume of artificial seawater. The utilisation study was carried out for a period of 8 days at room temperature and was incubated at 150 rpm using Protech Orbital Shaker 721 ambient shaker. The utilisation of different palm oil derivatives by *P. aeruginosa* UMTKB-5 was determined by CFU count determination, residual oil measurement, emulsification test [18] and free fatty acid determination.

Residual oil measurement

The residual oil was extracted using 30 mL of hexane on the culture broth [10,19]. The mixture was shaken vigorously, and 5 mL of hexane layer is transferred onto pre-weighted container and air-dried until complete evaporation of hexane before weighing.

Fatty acid determination via gas chromatography-flame ionisation detector (GC-FID)

The acid-catalysed ethylation of sample was done according to a methodology described by Anuar et al. [20] and some modifications based on Bhubalan et al. [15]. Total 1 mg of sample was mixed with 1% H2SO4 (1 mL) in a test tube. The mixture was then added into 2 mL of methanol followed by 1 mL of toluene (C_8H_8) before leaving the mixtures overnight at 50°C. Then the

samples were washed with 5 mL of 5% sodium chloride (NaCl) in distilled water using pipette. After washing, 5 mL of hexane was used to extract the fatty acid methyl ester (FAME). The extraction was performed twice to ensure all the FAMEs were extracted. The hexane layer was washed using 2 mL of 2% NaHCO3 solution and dried with anhydrous sodium sulphate (Na_2SO_4). Prior to GC analysis, samples were weighed and diluted with hexane. The GC-FID parameter setting is done according to previous study as reported by Bhubalan et al [15].

Results and Discussion

Degradation of CPO and CPKO using natural seawater collected from Klang Port

Based on Figure 2, it can be noted that, the bacterial counts were increasing over the 42 day of experiment excluding the sudden drop at day 14. The colony count with aniline (AR, BR) as test substance dropped sharply from day 28 compared to other test substances. Table 1 shows the degradation of test substances in percentage of DOC removal where 70% DOC removal is needed for a substance to be concluded to have potential biodegradation ability in marine environment. Based on the results obtained, only aniline (1 g L^{-1}) [AR, BR] achieved more than 70% DOC removal. The CPO (1 g L^{-1}) [A1C1 B1C1] CPO (10 g L^{-1}) [A1C2, B1C2], CPKO (1 g L^{-1}) [A2C1, B2C1] and CPKO (10 g L^{-1}) [A2C2, B2C2] showed a negative trajectory on regards of DOC removal which is an interesting observation.

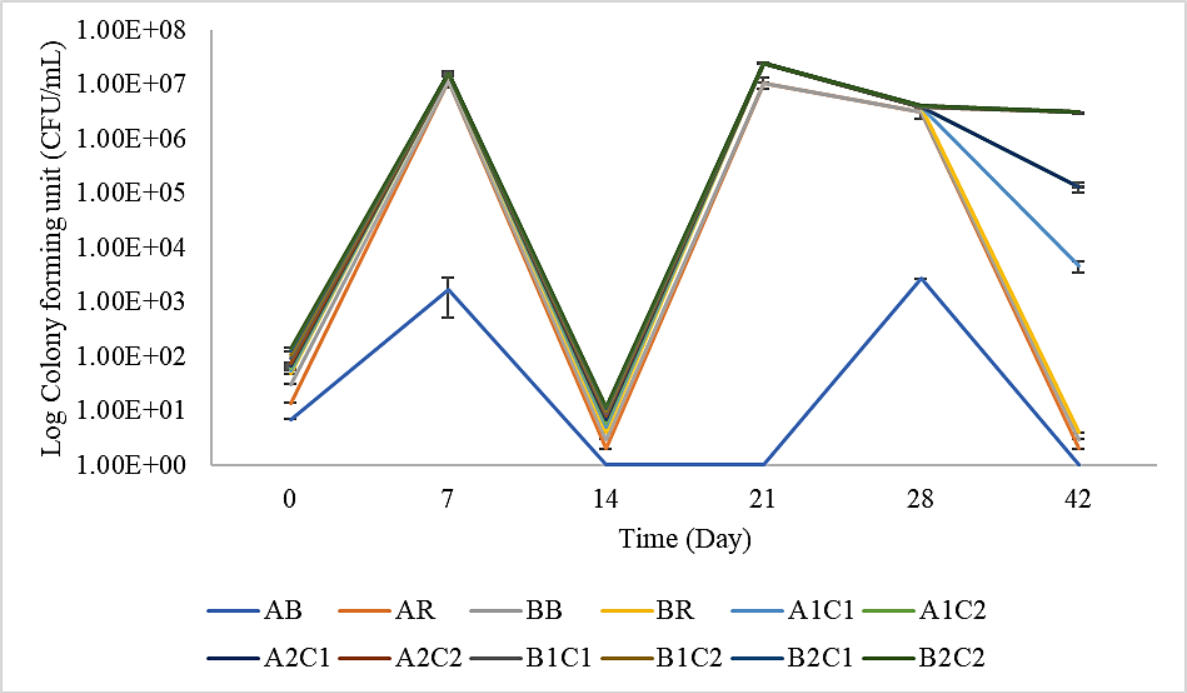


Figure 2. CFU (log CFU/mL) count of bacteria in test substance over 42-day period

Table 1. Degradation in percentage DOC removal of test substance over test period

Sample ID	7	14	21	28	42
AR	98.086	99.322	97.881	97.820	100.335
A1C1	-5510.538	-1874.647	-1999.754	-1170.653	-310.645
A1C2	-4821.903	-981.477	-2801.420	-3299.845	-3794.894
A2C1	-1529.398	-1008.931	-2196.576	-2628.693	-8420.959
A2C2	-218.753	-926.742	-751.751	-1828.224	-1877.354
BR	99.446	98.960	98.054	98.886	99.154
B1C1	-168.624	-1010.523	-579.506	-1026.525	-1960.295
B1C2	-32.329	-7303.336	-12856.814	-4824.614	-6293.079
B2C1	-929.503	-5407.807	-2223.564	-3737.025	-2781.695
B2C2	-41.934	-988.270	-810.753	-1815.315	-3089.373

The metagenomic results of bacterial population at the start of the experiment shows a diverse bacterial population compared to the bacteria isolated at the end of 42 days of experiment (Figure 3). The genus of isolated bacteria was present in the metagenomic results indicating their presence in the beginning of the experiment. A total of four phenotypically different bacteria were isolated. Table 2 shows the nucleotide BLAST results of these bacteria. The isolated bacteria were *Microbacterium* sp. 1204, *Vibrio fluvialis* NCTC 11327, *Oceanobacter* sp., and *Thalassospira profundimaris* WP0211.

Table 2. BLAST matches against NCBI-database of 16S rRNA sequences obtained from bacterial sequences

Bacterial Isolate	Accession No.	Identification Result	Similarity (%)	Query Cover (%)
N	NR_149816.1	*Microbacterium* sp. 1204	97.85%	92%
J	NR_118443.1	*Vibrio fluvialis* NCTC 11327	98.70%	100%
P	NR_113758.1	*Oceanobacter* sp.	92.78%	92%
O	NR_042766.1	*Thalassospira profundimaris* WP0211	97.36%	95%

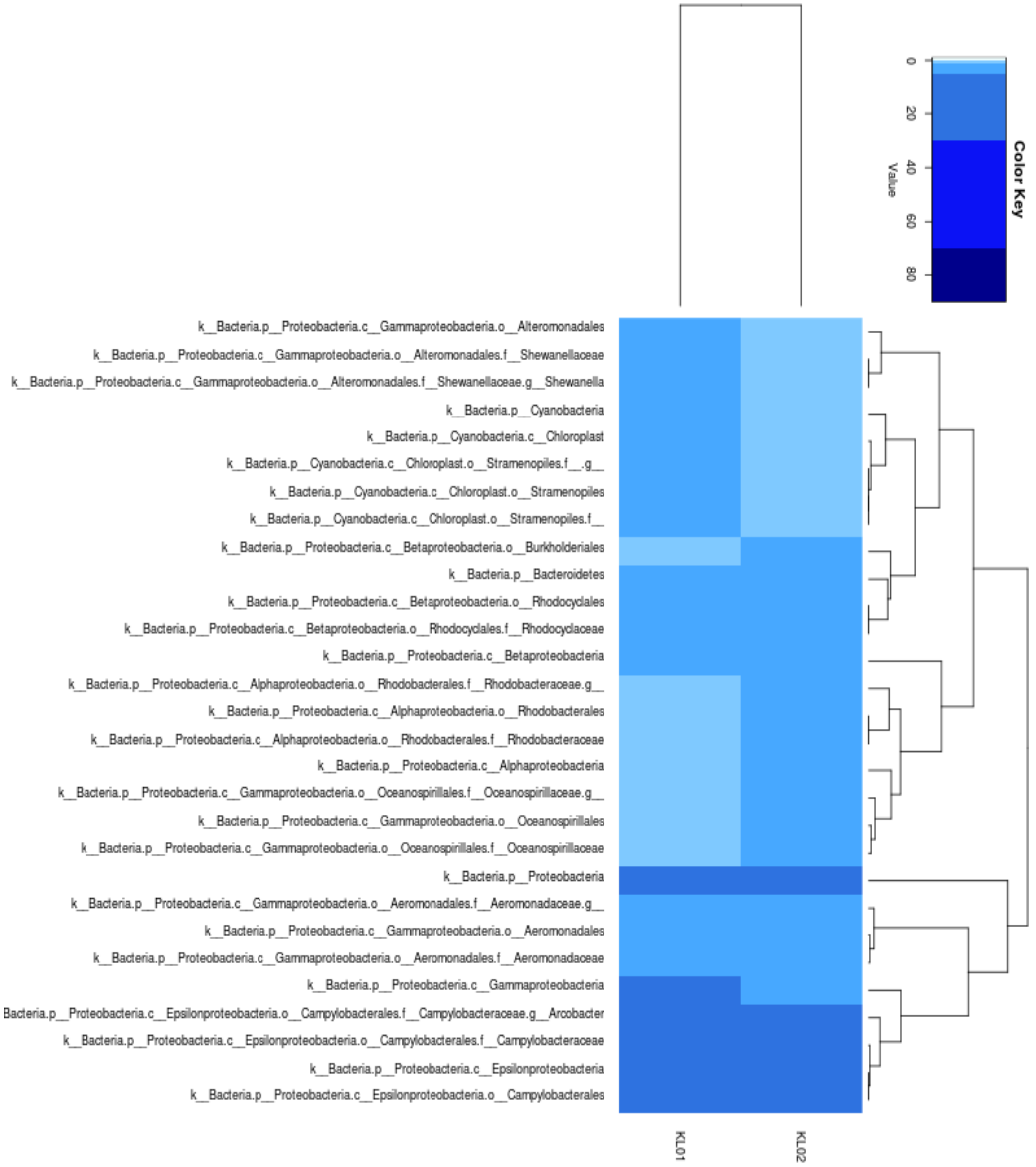


Figure 3. Metagenomic result of bacterial population at genus level of water sample collected at Klang Port

Degradation of palm oil and its derivatives using cultivated marine bacteria *P. aeruginosa* UMTKB-5

Figure 4 shows the CFU (log CFU/mL) count of *P. aeruginosa* UMTKB-5 supplemented with different substrate. The bacterial growth generally increased from day 0 to day 4 but decreased at day 8. The CPO and CPKO were the only two carbon substrates showing highest log CFU/mL on Day 4 (9.426 ± 0.6703 and 9.434 ± 0.7358, respectively) but by comparing Day 0 log CFU/mL between CPO and CPKO, it was clear that bacteria showed more growth in CPO to achieve similar log CFU/mL to CPKO at Day 4. The RBDPO and RBDPL had very little bacterial growth where log CFU/mL at Day 4 was 8.236 ± 0.2386 and 8.297 ± 0.9197 respectively.

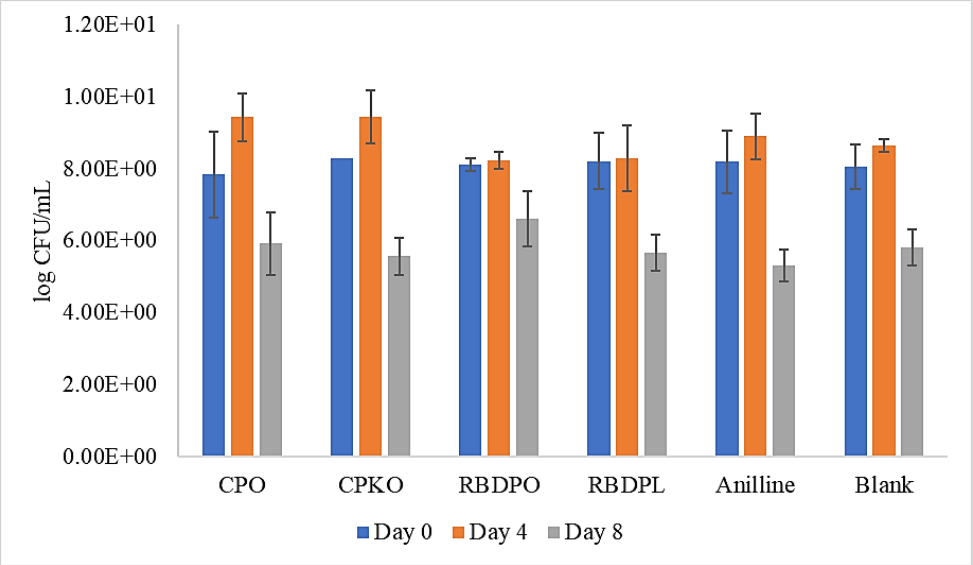


Figure 4. CFU count of *P. aeruginosa* UMTKB-5 cultured in test substances for Day 0, 4 and 8

Based on Figure 5, it can be noted that all the palm oil substrates tested were utilised. However, among all the substrate CPO was utilised the most where 83.37% of CPO initial weight added is lost. CPKO had the most of amount of residual oil remaining (69.3%) indicating lesser utilisation by *P. aeruginosa* UMTKB-5.

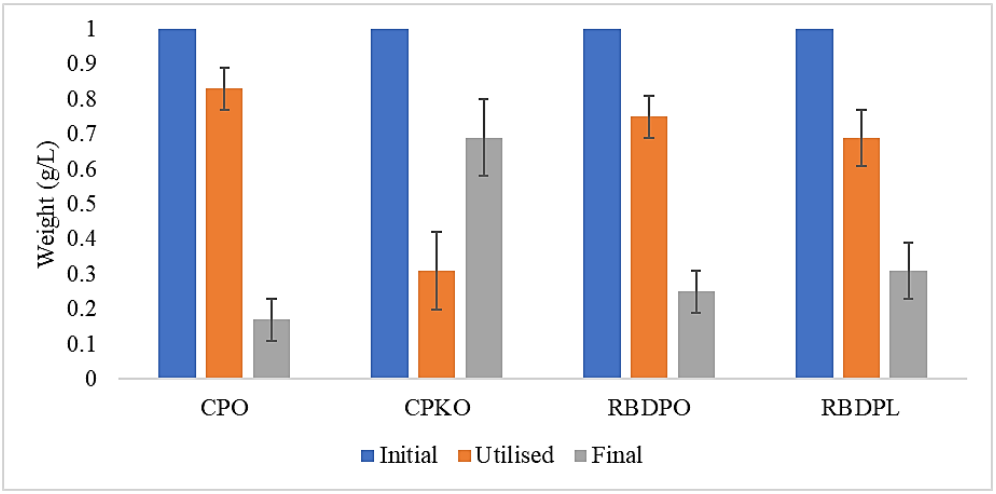


Figure 5. Residual oil measurement of carbon substrate left after the eight-day utilisation

Palmitic acid (C16:0) was detected in all the carbon substrate (Figure 6). Meanwhile, capric acid (C10:0), caprylic acid (C8:0) and caproic acid (C6:0) was found exclusively in CPKO. Palmitic acid in RBDPO and RBDPL were not detected after the utilisation. Concentration of palmitic acid in CPO decreased by 21.6%. Capric acid in CPKO was observed only before utilisation. After the 8-day incubation, both caprylic acid and caproic acid showed a decrease in concentration (37.1% and 6.98%, respectively).

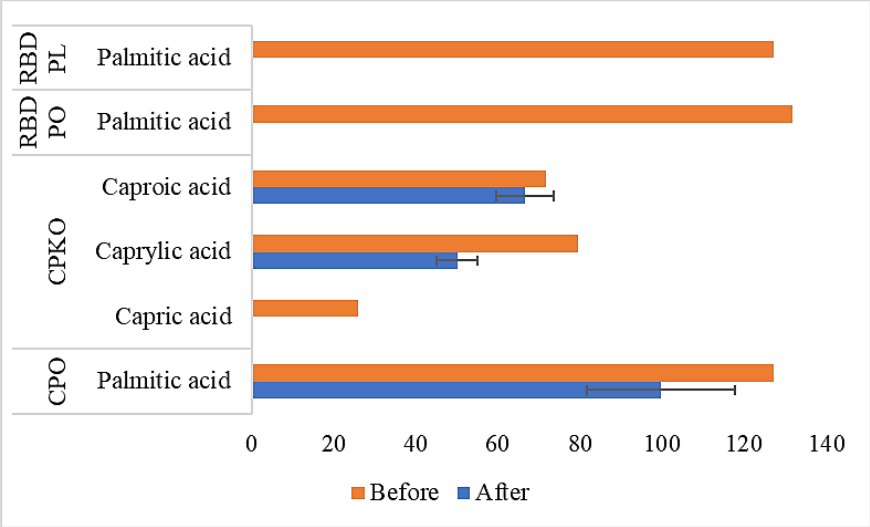


Figure 6. Fatty acid composition of all carbon substrates before and after utilisation by *P. aeruginosa* UMTKB-5

All the culture broth where palm oil derivatives supplemented as carbon substrate to *P. aeruginosa* UMTKB-5 able to exhibit emulsification activity (Figure 7). The CPO containing culture broth was able to exhibit emulsification activity at day 1,4 and 8. However, CPKO, RBDPL and RBDPO containing culture broth was able to exhibit emulsification activity only once. Furthermore, at day 4, RBDPL exhibited the highest emulsification index (E24) [12.28 ± 1.75%] compared to other palm oil derivatives tested.

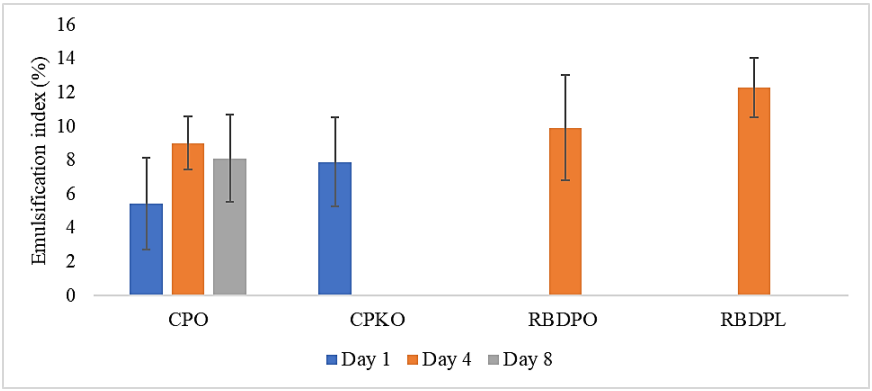


Figure 7. Emulsification index (E24) of selected carbon substrates test substances for Day 1, 4 and 8

Vegetable oil spill in the marine environment has been reported as early as 1975 where palm oil and coconut spilled near coral reef area of Fanning Atoll, Kiribati [21]. Since then, more incidents of vegetable oil spill have been reported and their environmental impacts were investigated. Mudge reported that vegetable oil spilled in the marine environment could pose lethal and sub-lethal effects towards organisms [22]. However, Mudge further reported that naturally occurring marine bacteria can degrade the vegetable oil whilst being in an unpolymerized state [22].

The assessment of ex-situ degradation of CPO and CPKO using Klang Port water showed some interesting

results where the bacterial count increased over the 42 days of experiment but the DOC removal (%) showing a negative trend. This modified experimental design based on OECD TG 306 method was intended to observe the degradation pattern in cases of large amount of oil spill where 1 g L^{-1} and 10 g L^{-1} of test substance was supplemented instead of 5 to 40 mg L^{-1} range proposed by the OECD method [11]. However, the fluctuations in DOC removal rate (%) along with bacterial counts indicates that there is utilisation of CPO and CPKO as carbon substrate and degradation of those palm oil is occurring. Despite not achieving 70% of DOC removal as set by OECD guideline, the negative result does not indicate that the substance is non-biodegradable but a more sophisticated confirmatory is needed [23].

The research by Al-Darbi et al. studied the biodegradation of natural oils namely canola oil, mustard oil, and olive oil in seawater [24]. In regard to the bacterial counts, they reported similar observation where bacterial counted increased over time in oil contaminated samples. However, the bacterial counts differed based on the type of oil tested. Canola oil had the highest bacterial count (500 000 CFU/mL) in fortified seawater at day 15 compared to other oil type. Thus, they concluded that canola oil degraded easily followed by mustard, cod and olive oil. The structure of oil in terms of length of carbon chain and number and location of double bond influences the degradation process [24].

Formation of white and yellow particles were noticed during the degradation study. According to Al-Darbi and colleagues [24], the white particles are saponified oil that reacted with sodium, potassium and calcium that are present in seawater to produce fatty acid salts. Similar observations are made by previous studies when seawater interacted with sunflower oil, canola oil and palm olein to form solid white polymer [15,24,25]. Furthermore, Mudge added that polymerised oils will reduce the natural biodegradation rate [22].

The presence of the isolated bacteria before and after the 42 days of experimentation shows their ability of survive, utilise CPO and CPKO as carbon substrate and to degrade them. Different bacteria species of the same genus were obtained in this study as from study conducted by Bhubalan et al., where *Vibrio fluvialis* was isolated in this study while *V. harveyi* and *V. alginolyticus* was isolated by Bhubalan et al. [15]. Variation and concentration of microbial communities due to origin of water sample influences the biodegradation process as presence of competent degrader is essential [23,26].

P. aeruginosa UMTKB-5 is a rhamnolipid biosurfactant-producing bacteria that was isolated from marine sediment. Previously, different *P. aeruginosa* strains were reported being able to utilise palm oil as substrate for growth and to produce biosurfactant. Palm oil were supplemented as carbon source for *P. aeruginosa* IFO3924 and *P. aeruginosa* A41 to produce rhamnolipid [27,28]. The ability of biosurfactant-producing bacteria is crucial is bioremediation effort of oil spill. Rhamnolipid application can be useful in degradation of oil due to their emulsifying property. In the presence of biosurfactant the rate of biodegradation of organic compounds is increased due to increased solubility [29]. The increased solubility enables microorganisms to be more accessible to the compounds. In the utilisation study of different palm oil derivatives by *P. aeruginosa* UMTKB-5, the increased bacterial counts were reflected by the reduced residual oil obtained at the end of day 8 of experiment as well as the emulsification index (E_{24}) value obtained. Furthermore, the changes in the concentration of fatty acid (ppm) composition indicates the utilisation of palm oil by *P. aeruginosa* UMTKB-5.

The utilisation of palm oil derivatives by bacteria as carbon substrate fuelled the population growth. Studies by Bhubalan et al. [15] along with Al-Darbi et al. [24] reported the similar trends where the bacterial counts increased over time when supplemented with RDB palm olein and canola oil respectively. However, the bioremediation of oil spill using biosurfactant producing bacteria is more focused on hydrocarbon-based oil spill [29]. The summary of findings of this study and other comparable literature is summarised in Table 3 below.

Table 3. Summary of research findings and comparison with other literature

Oil Type	Findings	Reference
CPO and CPKO	• Bacterial population increased over 42 days with population number peaking on day 7 and 21. • Increase in DOC level thorough input of carbon from bacterial degradation of oil.	This study
CPO, CPKO, RBDPO, RBDPL	• Degradation by rhamnolipid-producing bacteria increased the bacterial population. • Presence of rhamnolipid increased the degradation process and decrease in fatty acid concentration indicted the utilisation of palm oil as substrate by bacteria.	
Canola Oil, Mustard Oil, Olive Oil	• Increase in bacterial population in oil exposed seawater with population count highest on day 15. • Chemical structure of oil influences the degradability of oil with shorter chain oil more susceptible to degradation. • Formation of white and yellow particles that are saponified oil due to polymerisation.	[24]
RBD Palm Olein	• Growth of bacterial population in oil exposed sample. • Decreased in fatty acid composition of palmitic acid (C16:0), stearic acid (C18:0) and oleic acid (C18:1)	[15]
Palm oil (commercial product)	• *P. aeruginosa* IFO3924 utilised palm oil for bacterial growth and synthesis of rhamnolipid.	[27]
Palm oil	• Rhamnolipid production by *P. aeruginosa* A41 by utilisation of palm oil as carbon feedstock.	[28]

This study serves as preliminary study into the potential application of biosurfactant in bioremediation of vegetable oil thus more detailed study in needed.

Conclusion

As the increasing demand for palm oil increases the potential risk of spillage occurring in the marine environment, there is a need to understand the degradation potential of the palm oil. This study shows that naturally occurring marine bacteria can utilise different palm oil derivatives as substrates for growth and subsequently degrade them. Furthermore, the isolated bacteria were able to survive for an extended period in palm oil enriched environment indicating their potential as degrader. *P. aeruginosa* UMTKB-5 a biosurfactant-producing oil-degrading bacteria is able to exhibit emulsifying activity in palm oil-exposed water as well as using palm oil as carbon substrate. The emulsifying property could be helpful in bioremediation of oily contamination. However, it is important to investigate the optimum method of deployment.

Acknowledgement

This study was supported by Fundamental Research Grant Scheme [FRGS] [FRGS/1/2017/WAB09/UMT/02/2] awarded by Ministry of Higher Education, Malaysia. The authors would like to acknowledge MPOB for providing the palm oil that was used in this study. Furthermore, we would like to thank Jabatan Laut for providing us support in accessing the port area. The authors thank Tan Suet May Amelia for proofreading and formatting the manuscript.

References

1. El-Hamidi, M. and Zaher, F. A. (2018). Production of vegetable oils in the world and in Egypt: An overview. *Bulletin of the National Research Centre*, 42(1): 19.
2. USDA. (2017). United States Department of Agriculture. Accessed at www.fas.usda.gov [Access date March 01, 2022].

3. Purba, H. J., Sinaga, B. M., Novianti, T. and Kustiari, R. (2018). The impact of changes in external factors on the world vegetable oil market. *International Journal of Economics and Financial Issues*, 8(6): 176.
4. MPOB. (2017). *Pocketbook of Oil Palm Statistics.* Malaysia, Malaysian Palm Oil Board.
5. Sambanthamurthi, R., Sundram, K. and Tan, Y. A. (2000). Chemistry and biochemistry of palm oil. *Progress in Lipid Research*, 39(6): 507-558.
6. Bucas, G., and Saliot, A. (2002). Sea transport of animal and vegetable oils and its environmental consequences. *Marine Pollution Bulletin*, 44(12): 1388-1396.
7. South China Morning Post (2017). Japanese-owned tanker and Singapore container ship identified as vessels in collision leading to palm oil spill. Accessed from http://www.scmp.com/news/hong-kong/health-environment/article/2106702/japanese-owned-tanker-and-singapore-container-ship [Access date March 01, 2022].
8. The Telegraph. (2018). Ships dumping noxious palm oil off British coast without legal consequences. Accessed from https://www.telegraph.co.uk/news/2018/02/03/ships-dumping-noxious-palm-oil-british-coast-without-legal-consequences [Access date March 01, 2022].
9. USEPA. (2015). Emergency response, oil spills prevention and preparedness regulations - vegetable oils and animal fats. Accessed from http://www.epa.gov/emergency-response/vegetable-oils-and-animal-fats [Access date March 01, 2022].
10. APHA. (1999). Standard Methods of Water and Wastewater. Washington D.C., USA, American Public Health Association.
11. OECD. (1992). Test No. 306: Biodegradability in seawater. Paris, OECD Publishing. Accessed date March 01, 2022]
12. Karanfil, T., Erdogan, I. and Schlautman, M. A. (2003). Selecting filter membranes for measuring DOC and UV254. *Journal - American Water Works Association*, 95(3): 86-100.
13. Suratman, S., Zan, N. H. C., Aziz, A. A. and Tahir, N. M. (2017). Spatial and seasonal variations of organic carbon-based nutrients in Setiu wetland, Malaysia. *Sains Malaysiana*, 46(6): 859-865.
14. Suratman, S., Weston, K., Jickells, T. and Fernand, L. (2009). Spatial and seasonal changes of dissolved and particulate organic C in the North Sea. *Hydrobiologia*, 628(1): 13-25.
15. Bhubalan, K., Hui-Wan, R. A. C., Renganathan, P., Tamothran, A. M., Ganesen, S. S. K. and Ghazali, R. (2019). Bacterial degradation of palm olein in seawater and identification of some cultivable strains. *Malaysian Applied Biology*, 48(1): 1-7.
16. Hongoh, Y., Yuzawa, H., Ohkuma, M. and Kudo, T. (2003). Evaluation of primers and PCR conditions for the analysis of 16S rRNA genes from a natural environment. *FEMS Microbiology Letters*, 221(2): 299-304.
17. Azran, M. F. M., Fazielawanie, N., Saidin, J., Wahid, E. and Bhubalan, K. (2014). Bioconversion of cane sugar refinery by-products into rhamnolipid by marine *Pseudomonas aeruginosa*. *Proceedings of International Conference on Beneficial Microbes*, 2014: 259-262.
18. Shahaliyan, F., Safahieh, A. and Abyar, H. (2015). Evaluation of emulsification index in marine bacteria *Pseudomonas* sp. and *Bacillus* sp. *Arabian Journal for Science and Engineering*, 40(7): 1849-1854.
19. Bhubalan, K., Rathi, D. N., Abe, H., Iwata, T. and Sudesh, K. (2010). Improved synthesis of P (3HB-*co*-3HV-*co*-3HHx) terpolymers by mutant *Cupriavidus necator* using the PHA synthase gene of *Chromobacterium* sp. USM2 with high affinity towards 3HV. *Polymer Degradation and Stability*, 95(8): 1436-1442.
20. Anuar, S. T., Mugo, S. M. and Curtis, J. M. (2015). A flow-through enzymatic microreactor for the rapid conversion of triacylglycerols into fatty acid ethyl ester and fatty acid methyl ester derivatives for GC analysis. *Analytical Methods*, 7(14): 5898-5906.
21. Russell, D. J. and Carlson, B. A. (1978). Edible-oil pollution on Fanning Island. *Pacific Science*, 32(1): 1-15.
22. Mudge, S. M. (1995). Deleterious effects from accidental spillages of vegetable oils. *Spill Science & Technology Bulletin*, 2(2-3): 187-191.

23. Ott, A., Martin, T. J., Whale, G. F., Snape, J. R., Rowles, B., Galay-Burgos, M. and Davenport, R. J. (2019). Improving the biodegradability in seawater test (OECD 306). *Science of the Total Environment*, 666: 399-404.
24. Al-Darbi, M. M., Saeed, N. O., Islam, M. R. and Lee, K. (2005). Biodegradation of natural oils in seawater. *Energy sources*, 27(1-2): 19-34.
25. Mudge, S. M., Salgado, M. A. and East, J. (1993). Preliminary investigations into sunflower oil contamination following the wreck of the MV Kimya. *Marine Pollution Bulletin*, 26(1): 40-44.
26. Thouand, G., Friant, P., Bois, F., Cartier, A., Maul, A. and Block, J. C. (1995). Bacterial inoculum density and probability of para-nitrophenol biodegradability test response. *Ecotoxicology and Environmental Safety*, 30(3): 274-282.
27. Marsudi, S., Unno, H. and Hori, K. (2008). Palm oil utilization for the simultaneous production of polyhydroxyalkanoates and rhamnolipids by *Pseudomonas aeruginosa*. *Applied Microbiology and Biotechnology*, 78(6): 955-961.
28. Thaniyavarn, J., Chongchin, A., Wanitsuksombut, N., Thaniyavarn, S., Pinphanichakarn, P., Leepipatpiboon, N., Morikawa, M. and Kanaya, S. (2006). Biosurfactant production by *Pseudomonas aeruginosa* A41 using palm oil as carbon source. *The Journal of General and Applied Microbiology*, 52(4): 215-222.
29. Karlapudi, A. P., Venkateswarulu, T. C., Tammineedi, J., Kanumuri, L., Ravuru, B. K., Dirisala, V. and Kodali, V. P. (2018). Role of biosurfactants in bioremediation of oil pollution - A review. *Petroleum*, 4(3): 241-249.

Malaysian Journal of Analytical Sciences (MJAS)
Published by Malaysian Analytical Sciences Society

SYNTHESIS AND CHARACTERIZATION OF NEOPENTYLGLYCOL ESTER AS BIOLUBRICANT BASE STOCK FROM PALM OIL FATTY ACIDS

(Sintesis dan Pencirian Ester Neopentilglikol Sebagai Stok Asas Biopelincir daripada Asid Lemak Minyak Sawit)

Nurazira Mohd Nor[1]* and Jumat Salimon[2]

[1]*MaterOleo Research Group, Faculty of Applied Sciences,*
Universiti Teknologi MARA, Cawangan Negeri Sembilan,
Kampus Kuala Pilah, 72000 Kuala Pilah, Negeri Sembilan, Malaysia

[2]*Department of Chemical Sciences,*
Faculty of Science and Technology,
Universiti Kebangsaan Malaysia, 43600 Bangi, Selangor, Malaysia

[*]*Corresponding author: nurazira@uitm.edu.my*

Received: 17 May 2022; Accepted: 6 August 2022; Published: 30 October 2022

Abstract

Palm oil is one of the potential renewable resources in biolubricant production. However, the direct application of palm oil as a biolubricant base stock is restricted due to some performance limitations such as low oxidative stability. It is due to the presence of oxidation active site β-hydrogen in a glycerol backbone structure. This oxidative drawback can be overcome by molecule structural redesign through a chemical modification process such as esterification with polyhydric alcohol. The esterification of palm oil fatty acids (POFAs) with neopentylglycol (NPG) was carried out in a mole ratio of 2:1, 1% of sulphuric acid, reaction temperature of 145 °C and reaction time of 4.56 hours. Gas Chromatography equipped with a Flame Ionization Detector (GC-FID) was used to determine the ester composition in Neopentylglycol Diester (NPGDE). The structure of NPGDE was confirmed by Fourier Transformation Infra-Red (FTIR), proton and carbon Nuclear Magnetic Resonance (^{1}H-NMR and ^{13}C-NMR) spectroscopy. Results showed that the percentage yield of NPGDE was 90% and NPGDE existed in liquid form at room temperature. NPGDE was successfully synthesised with 100% composition of diesters. The existence of the ester functional group is evidenced by FTIR at 1738 cm^{-1}, the chemical shift of ^{1}H NMR at 2.29-2.33 ppm and ^{13}C NMR at 173.71 ppm. Physicochemical properties analysis showed that NPGDE has oxidative stability at 184 °C, pour point at 10 °C, flash point at 235 °C and 160-viscosity index which makes NPGDE plausible to be used in lubrication applications.

Keywords: esterification, neopentylglycol, oxidative stability, palm oil fatty acids

Abstrak

Minyak sawit merupakan salah satu sumber boleh diperbaharui yang berpotensi untuk digunakan dalam penghasilan biopelincir. Walau bagaimanapun, penggunaan minyak sawit secara terus sebagai stok asas biopelincir adalah terhad disebabkan oleh had prestasi seperti kestabilan oksidatif yang rendah. Ini disebabkan oleh kehadiran tapak aktif pengoksidaan β-hidrogen dalam struktur

tulang belakang gliserol. Kelemahan oksidatif ini boleh diatasi dengan melakukan ubahsuai struktur molekul melalui proses pengubahsuaian kimia seperti pengesteran dengan alkohol polihidrik. Pengesteran asid lemak minyak sawit (POFAs) dengan neopentilglikol (NPG) telah dijalankan pada nisbah mol 2:1, 1% asid sulfurik, suhu tindak balas 145 °C dan masa tindak balas 4.56 jam. Kromatografi gas dengan pengesan nyala pengionan (GC-FID) digunakan untuk menentukan komposisi ester dalam Diester Neopentilglikol (NPGDE). Struktur NPGDE disahkan dengan menggunakan spektroskopi infra-merah transformasi Fourier (FTIR), resonans magnetik nuklear proton dan karbon (^{1}H-NMR dan ^{13}C-NMR). Keputusan menunjukkan bahawa peratusan hasil NPGDE ialah 90% dan NPGDE wujud dalam bentuk cecair pada suhu bilik. NPGDE telah berjaya disintesis dengan 100% komposisi diester. Kehadiran kumpulan berfungsi ester dibuktikan melalui FTIR pada 1738 cm^{-1}, anjakan kimia ^{1}H NMR pada 2.29-2.33 ppm dan ^{13}C NMR pada 173.71 ppm. Analisis sifat fizikokimia menunjukkan bahawa NPGDE mempunyai kestabilan oksidatif pada 184 °C, takat tuang pada 10 °C, takat kilat pada 235 °C dan indeks kelikatan 160 yang menjadikan NPGDE sesuai untuk digunakan dalam aplikasi pelinciran.

Kata kunci: pengesteran, neopentilglikol, kestabilan oksidatif, asid lemak minyak sawit

Introduction

In the field of lubricants, there are wide ranges of lubricant base oils used which include mineral oils, synthetic oils, re-refined oils and plant oils. Among these, mineral oils are the most commonly used [1]. Mineral oil is stable, readily available and exists in a wider range of viscosities [2]. However, they pose a constant threat to ecology and vast groundwater reserves due to their inherent toxicity and non-biodegradable nature [1, 3]. The reduction of petroleum oil resources and increasing greenhouse gas emissions give a clear picture of the importance of the move towards sustainable development [4]. The use of renewable sources in the industry is vital to ensure sustainable development. These include studies on plant oils as feedstock in the manufacture of products for daily use.

Plant oils are not only renewable resources but also cheaper, biodegradable and non-toxic, unlike conventional mineral-based oils [1, 5]. As a lubricant, they also exhibit excellent lubricity and high viscosity index, which are being more closely examined as base stock for lubricants and functional fluids [6-8]. Biolubricants hold great potential for environmental conservation as an alternative lubricant. The global market size for biolubricants was USD 2.20 billion in 2019 and is projected to reach USD 2.46 billion by 2025, at a compound annual growth rate (CAGR) of 4.1% between 2020 and 2025 [9, 10]. Stringent regulations and the growing acceptance among end-users are projected to drive the biolubricants market [9, 10].

However, plant oils have some drawbacks such as poor thermal and oxidative stability which restrict their direct application as a lubricant [2, 8, 11, 12]. It is because of the existence of oxidation active sites β-hydrogen in glycerol backbone structure and double bonds in the unsaturated fatty acid structure that will make palm oil becomes easily damaged at high temperature. The β-hydrogen is easily removed from triacylglycerol molecules and it will form acid and olefin (unsaturated compounds). The resulting unsaturated compounds will undergo polymerization and will cause the formation of precipitate that will increase the viscosity of plant oil [13].

Chemical modification of plant oils becomes one of the attractive ways to solve these problems by replacing glycerol with polyhydric alcohols such as neopentylglycol (NPG), trimethylolpropane (TMP) and pentaerythritol (PE) through esterification. The advantage of using polyhydric alcohol is the absence of β-hydrogen which enhances the thermal and oxidative stability of the lubricant at high temperatures [14-16]. Recently, palm oil which is abundantly available all over Malaysia become one of the potential plant oils that can be used as biolubricant base stock [17, 18]. There are many studies reported on the production of biolubricant from palm oil and polyhydric alcohols.

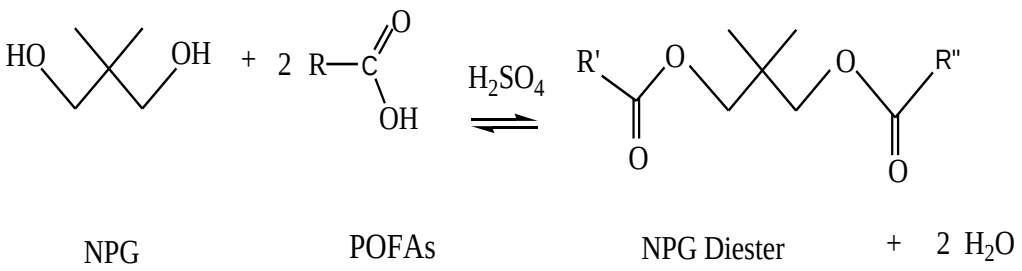
The production of biolubricant via transesterification of palm oil methyl ester (POME) with trimethylolpropane (TMP) was reported by Yunus et al. [19]. TMP is polyhydric alcohol that has three hydroxyl groups. The transesterification of POME and TMP was carried out in a mole ratio of 3.9:1, a reaction temperature of 120 °C, a reaction time of 1 hour, 20 mbar of pressure and 0.8%

of sodium methoxide catalyst has successfully produced 98% palm oil TMP triesters. Sulaiman et al. [20] also reported the optimization of transesterification of POME and TMP. The optimum conditions obtained were a 3.8:1 mole ratio, a reaction temperature of 120 °C, a reaction time of 2 hours, 20 mbar of pressure and 0.9% of sodium methoxide catalyst. At these optimum conditions, 86% of palm oil TMP triesters were successfully synthesised. In 2013, Salih et al. [21] reported the esterification between palm kernel oil fatty acids (PKOs) with TMP in a mole ratio of 4:1, a reaction temperature of 150 °C, a reaction time of 5 hours and 1% of sulphuric acid as catalyst. Results showed that a 68% yield of TMP ester was successfully synthesised with good lubrication properties such as high flash point (over 300 °C), low pour point (3 °C) and high viscosity index (157).

In 2014, Aziz et al. [22] reported the production of biolubricant through transesterification between POME and pentaerythritol (PE). PE is polyhydric alcohol with four hydroxyl groups. The transesterification process was carried out in a mole ratio of 4.5:1, reaction temperature of 158 °C, reaction time of 1 hour and 1.19% of sodium methoxide catalyst. The transesterification has produced a 40% yield of PE ester which has a flash point at 302 °C and 12.7 cSt viscosity at 100 °C.

Other than TMP and PE, there was also a study using neopentylglycol (NPG) in the production of biolubricant. NPG is a polyhydric alcohol with two hydroxyl groups. Synthesis of neopentylglycol (NPG) ester was reported by Vanitah et al. [23]. Synthesis of NPG ester was carried out via esterification of NPG and oleic acid in a mole ratio of 1:2, reaction temperature of 130 °C, reaction time of 4 hours and 2% sulphuric acid as catalyst. Results showed that an 80% yield of NPG ester was successfully synthesised with oxidative stability at 177 °C, high flash point (200 °C), low pour point (-44 °C) and high viscosity index (227).

In this study, the esterification of palm oil fatty acids (POFAs) with NPG to produce NPG Diester (NPGDE) as shown in Figure 1 is reported. Fatty acid composition of POFAs and NPGDE, as well as ester composition in NPGDE, were analysed by GC-FID, while the structure of NPGDE was confirmed by FTIR and NMR spectroscopy. Physicochemical properties of NPGDE were examined by using several tests such as oxidative stability, pour point, flash point and viscosity index.



R= Mixed palm oil fatty acids (myristic, stearic, palmitic, oleic and linoleic acid)

Figure 1. Esterification of palm oil fatty acids (POFAs) with neopentylglycol

Materials and Methods

Materials

Palm oil was obtained from Jomalina Refinery, Teluk Panglima Garang, Selangor, Malaysia. Neopentylglycol was purchased from Sigma Aldrich. Sulphuric acid, toluene, ethyl acetate, sodium bicarbonate, sodium chloride, sodium sulphate, hydrochloric acid, n-hexane, potassium hydroxide and ethanol were purchased from Systerm.

Hydrolysis of palm oil

The hydrolysis process was conducted by mixing 50 g of palm oil with alkaline ethanol and heated at 60 °C for 2 hours [24]. Then, the mixture was washed with 150 mL of 6N hydrochloric acid, 200 mL of distilled water

and 100 mL of *n*-hexane. The washing process was continued with 100 mL of hexane followed by 50 mL of distilled water until the pH became neutral. The product, palm oil fatty acids (POFAs), was kept overnight by adding anhydrous sodium sulphate. The product was filtered by Whatmann No. 1 filter paper and the solvent used was isolated by rotary evaporator at 70 °C. The product (POFAs) was analysed using GC-FID.

Esterification of POFAs and NPG

The esterification process was conducted by mixing POFAs and NPG at a 2:1 molar ratio. 1% of sulphuric acid and 100 mL toluene were added to the mixture and then heated at 145 °C for 4.56 hours. The product, NPG Diester (NPGDE) was neutralised with sodium hydrogen carbonate solution, sodium chloride solution and ethyl acetate. The product was kept overnight by adding anhydrous sodium sulphate. The product was filtered by Whatmann No. 1 filter paper and the solvent used was isolated by a rotary evaporator at 70 °C. The NPGDE was analysed using Gas Chromatography equipped with a Flame Ionization Detector (GC-FID), Fourier Transformation Infra-Red (FTIR), and proton and carbon Nuclear Magnetic Resonance (^{1}H-NMR and ^{13}C-NMR).

Fatty acid composition analysis

Fatty acid composition of palm oil, POFAs and NPGDE were analysed using GC-FID (column BPX-70). Fatty acid methyl esters (FAMEs) were prepared using two methods: acid-catalysed for POFAs and base-catalysed for palm oil and NPGDE. For acid-catalysed, 1 g of POFAs was weighed into a 250 mL three-neck round bottom flask equipped with a mechanical stirrer, thermometer and reflux condenser. 3.75 mL methanol was added with 0.75 mL reagent mixture (5 mL methanol and 1.25 mL concentrated hydrochloric acid (36.5%)), followed by 0.75 mL of toluene. The mixture was heated at 65 °C for 1.5 hours. The mixture was transferred into a separation funnel. 7.5 mL of hexane and 5 mL of distilled water were added to the mixture. The mixture was allowed to stand to separate two layers. The upper layer was slowly collected and dried using anhydrous sodium sulphate overnight. The sample was filtered and injected into GC for analysis. For base-catalysed, FAME was prepared by mixing 0.1 mL of the palm oil or NPGDE with 1 mL of hexane. 1 mL of sodium methoxide solution (1.55 g NaOH and 50 mL of methanol) was added to the solution and the solution was stirred vigorously using a Vortex stirrer for 10 seconds. The solution was allowed to stand for 10 minutes to separate the clear solution of FAMEs from the cloudy aqueous layer. The upper FAMEs layer was slowly collected and injected into GC for analysis.

NPGDE analysis

Ester composition in NPGDE was determined using GC-FID (column DB-5HT). The sample was prepared by mixing 0.3 µL of NPGDE with 1mL of ethyl acetate. The structure of NPGDE was confirmed using FTIR and NMR analysis. FTIR spectra were recorded on a Perkin Elmer Infrared Spectrophotometer in the range of 500-4000cm^{-1}. ^{1}H and ^{13}C NMR were recorded on JEOL-ECP 400 spectrometer (400 MHz ^{1}H/100.61 MHz^{13}C) using $CDCl_3$ as solvent.

Physicochemical properties tests of NPGDE

The American Society for Testing Materials standards such as ASTM D-6186, ASTM D-5853, ASTM D-92 and ASTM D-2270 were used to measure oxidative stability, pour point, flash point and viscosity index [25]. The oxidative stability test was conducted using Differential Scanning Calorimetry (DSC). 1.5 mg of NPGDE was placed into an aluminium pan with a pinhole cover to allow interaction between ester product and oxygen gas which acted as a reaction gas. Then, the aluminium pan was put into DSC and heated for 20 minutes up to temperatures of 250 °C by using nitrogen gas. Onset temperature was recorded to determine oxidative stability.

In the pour point test, the NPGDE was filled into a U-shaped glass tube until it reached a height of 4 cm. The thermometer was placed at one end of the U-shaped tube and both ends of the U-shaped tube were covered with parafilm. The U-shaped tube containing the sample was placed in the refrigerator (minimum temperature -80 °C) for 24 hours to ensure that the sample froze completely. After being left overnight, the U tube was removed and flipped upside down. The lowest temperature at which movement of the sample was observed was recorded as the pour point.

For flash point testing, 2 mL of NPGDE was placed in a crucible and heated on a heating plate. A thermometer with a maximum reading temperature of 360 °C was placed on the sample to measure the sample's temperature. The temperature was rapidly increased at first and then at a slow constant rate as the flash point was approached. The lowest temperature at which the vapours above the surface of the liquid ignited was taken as the flash point.

For the viscosity index test, the Rheometer Anton Paar (Physica MCR 301 model) was used to measure the viscosity and viscosity index of NPGDE. The diameter used was 0.051 mm. The viscosity of NPGDE was tested at 40 °C and 100 °C. The NPGDE viscosity index was calculated based on the formula below:

$$\text{Viscosity index} = (L-U)/(L-H)\times 100 \quad (1)$$

Where: U = oil's kinematic viscosity at 40 °C. L and H = values based on the oil's kinematic viscosity at 100 °C.

Results and Discussion

Palm oil is golden yellow and exists in the semi-solid form at room temperature. The hydrolysis process has successfully separated 95% of the fatty acids from the glycerol backbone. Figure 2 shows a GC-FID chromatogram of fatty acid compositions in palm oil (a-before hydrolysis) and POFAs (b-after hydrolysis). The percentage composition of fatty acids has been simplified in Table 1. The major fatty acids in POFAs were oleic acid with 43.5%, followed by palmitic acid (42.5%), linoleic acid (9.5%), stearic acid (3.7%) and myristic acid (0.8%). The fatty acid composition of both samples is approximately close to the value of the fatty acid composition of palm oil reported by Chowdhury et al. [26].

The esterification process between POFAs and NPG has successfully produced a 90% yield of NPGDE. Fatty acid compositions in NPGDE are shown in Figure 2(c) and the percentage composition of fatty acids also has been simplified in Table 1. The GC result showed that NPGDE contains 54.2% of saturated fatty acid and 45.8% unsaturated fatty acid. It means that saturated fatty acid which has a straight-chain structure has a higher tendency to react with NPG compared to the bent structure of unsaturated fatty acid due to less steric hindrance.

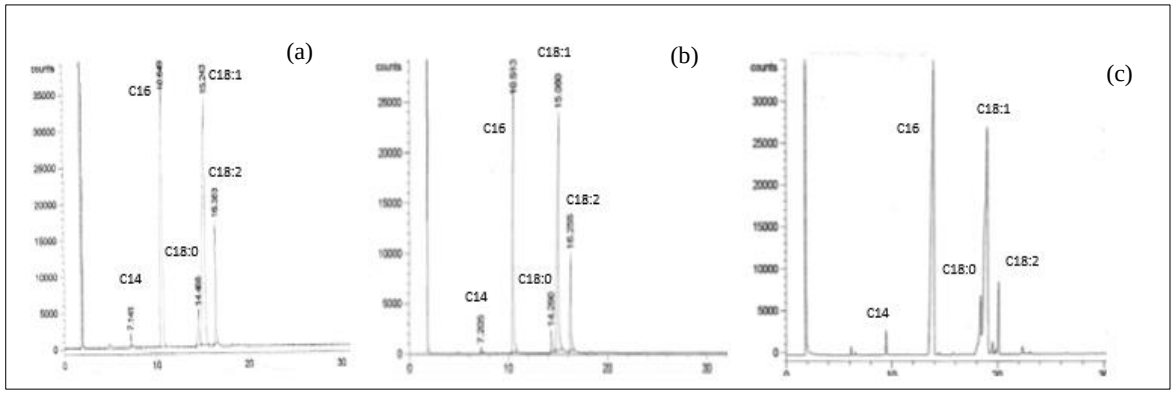


Figure 2. GC-FID chromatogram a) palm oil; b) POFAs; c) NPGDE

Table 1. Fatty acid composition (percentage) of palm oil, POFAs and NPGDE

Fatty Acid Composition	Palm Oil	POFAs	NPGDE	Reference [26]
Myristic acid (C14)	0.6	0.8	1	1.23
Palmitic acid (C16)	41.9	42.5	47	41.78
Stearic acid (C18)	3.6	3.7	6.2	3.39
Oleic acid (C18:1)	44.8	43.5	41.4	41.9
Linoleic acid (C18:2)	9.1	9.5	4.4	11.03

The percentage of ester composition was also determined by GC-FID as shown in Figure 3. In esterification, two types of esters will be produced which are monoesters and diesters. Monoesters will be formed as intermediate products towards the completion of the reaction producing NPGDE diesters. Figure 3 shows that 100% of diesters were produced in NPGDE. It means all hydroxyl groups in NPG were successfully esterified with POFAs. This result was supported by the low hydroxyl value of NPGDE which was 24.68 mgKOH/g compared to the hydroxyl value of NPG which was 1075 mgKOH/g.

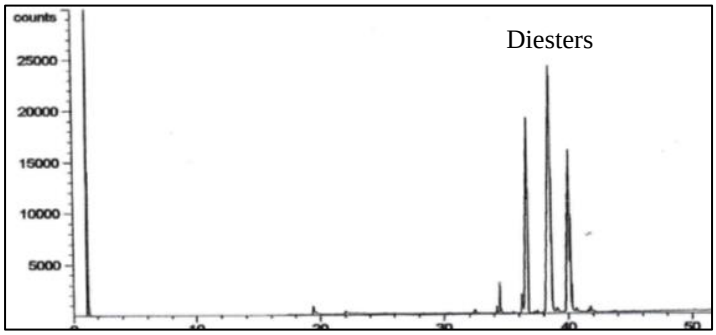


Figure 3. GC-FID chromatogram of NPGDE

FTIR analysis

The formation of ester was confirmed by FTIR analysis. The comparison between FTIR spectra of POFAs (before esterification) and NPGDE (after esterification) is shown in Figure 4. In the FTIR spectrum of NPGDE, there are appearances of the stretching of the C=O ester peak at 1738 cm^{-1} and the stretching of the C-O ester peak at 1161 cm^{-1} and 1241 cm^{-1}. On the other hand, the FTIR spectrum of POFAs shows the stretching of the C=O group of carboxylic acid at 1696 cm^{-1} and the stretching of C-O carboxylic acid at 1291 cm^{-1} and 1247 cm^{-1}. The shift in wavenumbers for both spectra showed that POFAs have been successfully esterified with NPG to form NPGDE. In addition, the -OH peak which initially exists in the POFAs spectrum (2400-3400 cm^{-1}) is no longer visible in the NPGDE spectrum.

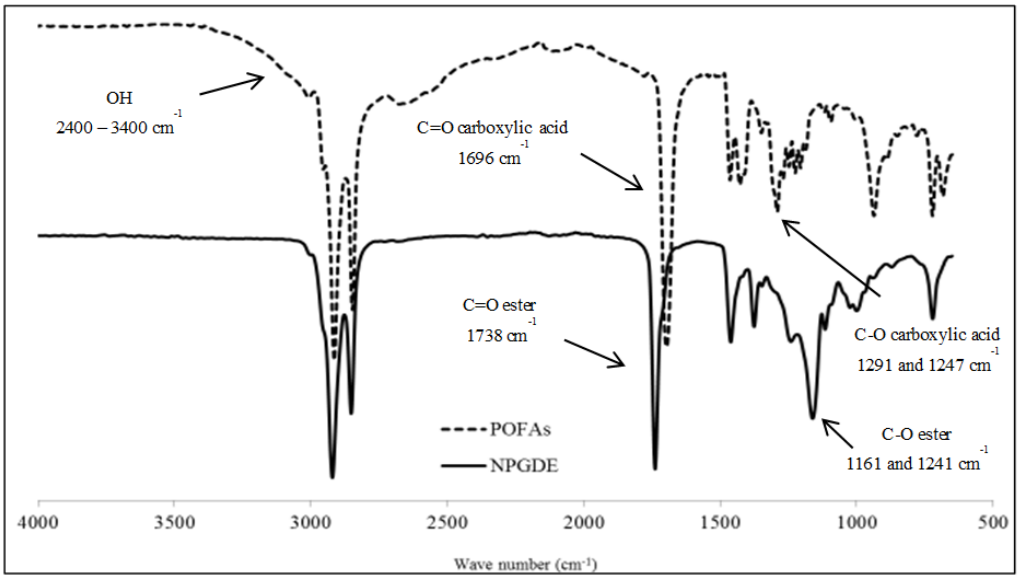


Figure 4. FTIR spectra of POFAs and NPGDE

NMR spectroscopy

NPGDE structure was also analysed using NMR spectroscopy. Figure 5 shows the ^{1}H NMR spectrum of NPGDE. In the ester structure, there are two types of protons which are the proton of C**H**$_2$-O and the proton of C**H**$_2$-C=O. The proton of C**H**$_2$-O for NPGDE was detected at 3.88 ppm and the proton of C**H**$_2$C=O was detected at 2.29-2.33 ppm. These values are in agreement with the reference which is a chemical shift for proton C**H**$_2$-O is 3.5- 4.8 ppm, while the chemical shift for proton C**H**$_2$C=O is at 2.1- 2.5 [27]. NPGDE consists of a mixture of acyl groups such as myristate, palmitate, stearate, oleate and linoleate. The presence of unsaturated fatty acids was determined by the identification of the alkene group. In the alkene group, there are two types of protons which are protons of double bond (-C=C-**H**) at chemical shift 4.5-6.5 ppm and proton of methylene group which bound to double bond (-C=C-C-**H**) at chemical shift 1.6-2.6 ppm [25]. Figure 5 shows the existence of both protons at chemical shifts 5.32-5.37 ppm (-C=C-**H**) and 1.95-2.03 ppm (-C=C-C-**H**). This spectrum also shows there is no signal detected for the hydroxyl group which means all hydroxyl groups have reacted with fatty acids.

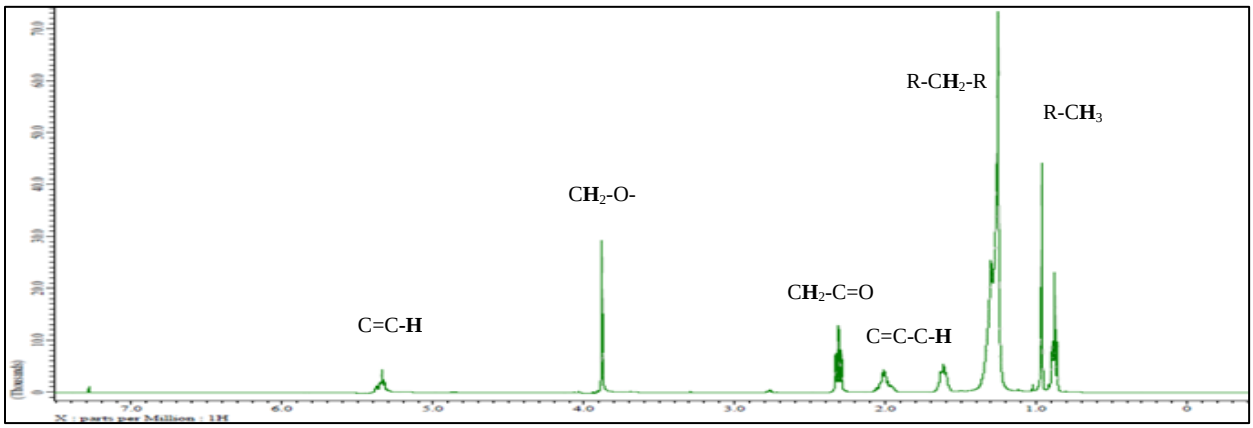


Figure 5. ^{1}H NMR spectrum of NPGDE

Figure 6 shows the ^{13}C NMR spectrum of NPGDE. The existence of ester carbon carbonyl (**C**=O) in NPGDE was detected at a chemical shift of 173.71 ppm. This value was in agreement with Pavia et al. [27] who showed that the chemical shift for carbon carbonyl ester (**C**=O) was in the range of 155-185 ppm. The signal peak for carbon **C**-O which bound fatty acid to NPG was detected at a chemical shift of 68.96 ppm. The presence of both carbons indicates the presence of an ester bond between POFAs and NPG which forms NPGDE. The quaternary carbon for NPGDE $(CH_3)_2$-**C**-$(CH_2OCOR)_2$ was detected at 34.59 ppm and this value was in agreement with the reference which was 20-60 ppm [27]. The alkene group (**C**=**C**) in NPGDE was detected at chemical shift 127.87-130.51ppm and this value was in agreement with the reference which was 100-150 ppm [27]. This spectrum also shows there is no signal detected for the hydroxyl group.

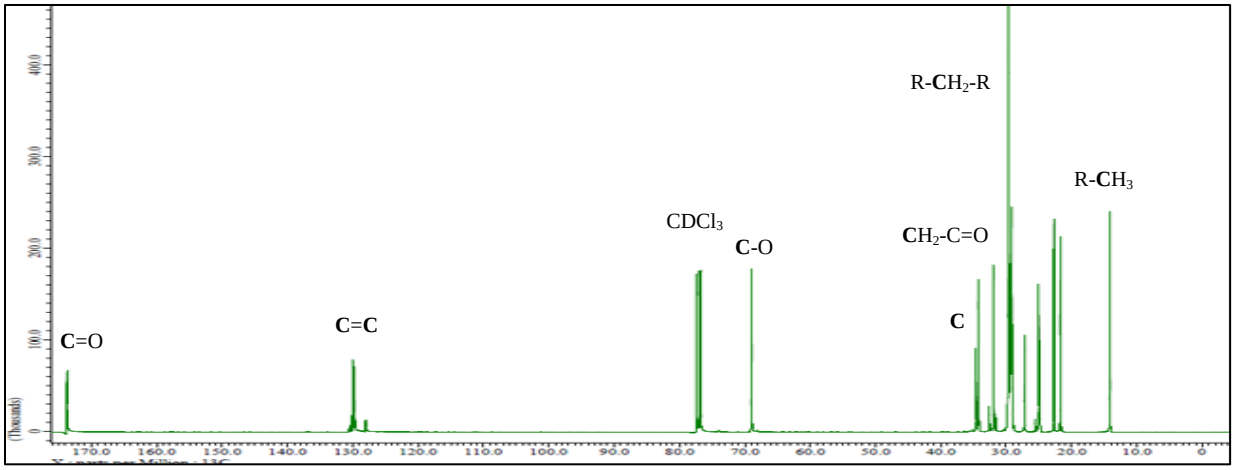


Figure 6. ^{13}C NMR spectrum of NPGDE

Physicochemical properties of NPGDE

The quality of biolubricant depends on various physicochemical properties such as oxidative stability, pour point, flash point, viscosity and viscosity index. Modification of the oil structure has influenced the properties of biolubricant. The physicochemical properties results obtained are shown in Table 2.

The ability of a substance to resist oxidative degradation is an important property of biolubricant. NPGDE was analysed using Differential Scanning Calorimetry (DSC) to measure its oxidative stability by determination of onset temperature (OT). A higher onset temperature indicates that the lubricant has high oxidation stability [2]. In this study, NPGDE possesses good oxidative stability with a high onset temperature at 184 °C. It is due to its high percentage of saturated fatty acid (54.2%). Reduction of unsaturated fatty acid will reduce oxidation active site; thus it will make NPGDE more stable in high temperatures.

Pour point is one of the important quality parameters to determine the cold flow properties of the lubricant. NPGDE has a high pour point (10 °C) due to the high saturated fatty acid content. High saturated fatty acids content has caused lubricant tends to form macrocrystalline structures through uniform precipitation at low temperatures. Flash point is often used as a descriptive characteristic of fuel oil and it is also used to describe oils that are not used as fuels such as a lubricant. NPGDE ester showed a high flash point at 235 °C. A high flash point value is important to ensure that the biolubricant is not burned in the engine during its operation [2].

Viscosity has also become one of the most important quality parameters for lubricating oils. The efficiency of the biolubricant in reducing friction and wear is greatly influenced by its viscosity. The least viscous biolubricant which still forces the two moving surfaces apart is desired. If the biolubricant is too viscous, it will require a large amount of energy to move and if is too thin, the surfaces will rub each other and friction will increase [2]. The viscosity of NPGDE was in the medium range which was 50.07 centistokes (cSt) at 40 °C and decreased to 11.47 cSt at 100 °C. The viscosity of oils decreases as temperature increases [2]. The viscosity index highlights how the viscosity of biolubricant changes with variations in temperature [2]. NPGDE has high viscosity index which is 160 compared to palm oil (130). It shows the viscosity of NPGDE is less affected by temperature changes and does not drastically change when the temperature varies. This is a good indicator and suggests its suitability for use in a large temperature range.

Table 2 also shows a comparison of lubrication properties between the biolubricant base stock produced (NPGDE) with commercial lubricants in the market. The selected commercial lubricants are ISO VG 100 grade lubricants, namely Denicol Compressor Oil

(100A) [28] and SubsTech Hydraulic Oil (100B) [29]. Based on the comparison made, NPGDE has a higher viscosity index compared to 100A and 100B lubricants.

Table 2. Physicochemical properties of palm oil and NPGDE.

Physicochemical properties	Palm oil	NPGDE	100A[a]	100B[b]
Oxidative stability (°C)	181	184	n/a	n/a
Pour point (°C)	7	10	-19	-27
Flash point (°C)	240	235	276	254
Kinematic viscosity at 40 °C	56.97	50.07	96	96.7
Kinematic viscosity at 100 °C	9.24	11.47	10.9	11
Viscosity index (VI)	130	160	97	100
ISO viscosity grade	46	46	100	100

a: 100A: Denicol Compressor Oil ISO VG 100 [28], b: SubsTech Hydraulic Oil ISO 100 [29]

Conclusion

Neopentylglycol Diester (NPGDE) was successfully synthesised from palm oil fatty acids and neopentylglycol with 90% of yield and 100% of diesters composition. NPGDE showed good lubrication properties which are having high oxidative stability and high viscosity index compared to palm oil. The removal of β-hydrogen in palm oil and replacing polyhydric alcohol in NPGDE has successfully increased the lubricity properties. This makes NPGDE plausible to be used as a biolubricant.

Acknowledgement

The authors would like to acknowledge Universiti Kebangsaan Malaysia for the financial support under research grants GUP-2016-012 and GUP-2016-058. The authors also thank the Ministry of Education Malaysia for providing scholarship support (MyPHD) for the author.

References

1. Salimon, J. and Salih, N. (2009). Oleic Acid Diesters: Synthesis, characterization and low temperature properties. *European Journal of Scientific Research*, 32(2): 216-222.
2. Salimon, J., Salih, N. and Yousif, E. (2011). Chemically modified biolubricant basestocks from epoxidized oleic acid: Improved low temperature properties and oxidative stability. *Journal of Saudi Chemical Society*, 15: 195-201.
3 Farhoosh, R., Einafshar, S. and Sharayei, P. (2009). The effect of commercial refining steps on the rancidity measures of soybean and canola oils. *Food Chemistry*, 115: 933-938.
4. Erhan, S. Z. and Asadauskas, S. (2000). Lubricant basestocks from vegetable oils. *Industrial Crops and Products,*11: 277-282.
5. Cerretani, L., Bendini, A., Estrada, M. T. R., Vittadini, E. and Chiavaro, E. (2009). Microwave heating of different commercial categories of olive oil: Part I. Effect on chemical oxidative stability indices and phenolic compounds. *Food Chemistry,* 115:1381-1388.
6. Moser, B. R., Sharma, B. K., Doll, K. M. and Erhan, S. Z. (2007). Diesters from oleic acid: Synthesis, low temperature properties and oxidative stability. *Journal of the American Oil Chemists' Society,* 84: 675-680.
7. Salimon, J. and Salih, N. (2009). Substituted esters of octadecanoic acid as potential biolubricants. *European Journal of Scientific Research*, 31(2): 273-279.
8. Nirmal, V. P. and Dineshbabu, D. (2015). Performance and emission of *pongamia pinnata* oil as a lubricant in diesel engine. *International Journal of Innovative Research in Science, Engineering and Technology*, 4(2):435-441.
9. Salih, N. and Salimon, J. (2021). A review on eco-friendly green biolubricants from renewable and sustainable plant oil sources. *Biointerface Research in Applied Chemistry*, 11(5): 13303-13327.

10. Nor, N. M. and Salimon, J. (2022). Synthesis of green- renewable biolubricant base stock from Malaysia palm oil. *Malaysian Journal of Analytical Sciences,* 26(3): 492-506
11. Masood, H., Yunus, R., Choong, T. S. Y., Rashid, U. and Yap, Y. H. T. (2012). Synthesis and characterization of calcium methoxide as heterogeneous catalyst for trimethylolpropane esters conversion reaction. *Applied Catalyst A: General*, 425-426: 184-290.
12. Wu, X., Zhang, X., Yang, S., Chen, H. and Wang, D. (2000). The study of epoxidized rapeseed oil used as a potential biodegradable lubricant. *Journal of the American Oil Chemists Society*, 77: 561-563.
13. Fox, N. J. and Stachowiak, G. W. (2007). Vegetable oil-based lubricants-a review of oxidation. *Journal of Tribology International*, 40: 1035-1046.
14. Leung, D. Y. C, Wu, X. and Leung, M. K. M. (2010). A review of biodiesel production using catalyzed transesterification. *Applied Energy*, 87:1083-1095.
15. Sripada, P. K., Sharma, R. V. and Dalai, A, K. (2013). Comparative study of tribological properties of trimethylolpropane-based biolubricant derived from methyl oleate and canola biodiesel. *Industrial Crops and Products*, 50: 95-103.
16. Wilson, B. (1998). Lubricants and functional fluids from renewable sources. *Industrial Lubrication and Tribology*, 50: 6-15.
17. Nor, M. N., Derawi, D. and Salimon, J. (2017). Chemical modification of epoxidized palm oil for biolubricant application. *Malaysian Journal of Analytical Sciences*, 21(6): 1423-1431.
18. Nor, M. N., Derawi, D. and Salimon, J. (2018). The optimization of RBD palm oil epoxidation process using d-optimal design. *Sains Malaysiana*, 47(7):1359-1367.
19. Yunus, R., FakhrulRazi, T. L., OoiI, S. E., Iyuke. and A. Idris. (2003). Development of optimum synthesis method for transesterification of palm oil methyl esters and trimethylolpropane to environmentally acceptable palm oil based lubricants. *Journal of Oil Palm Research*, 15: 35-41.
20. Sulaiman, S. Z., Chuah, A. L. and Fakhru`I-Razi, A. (2007). Batch production of trimetylolpropane ester from palm oil as lubricant base stock. *Journal of Applied Sciences*, 7: 2002-2005.
21. Salih, N., Salimon, J. and Jantan, F. N. (2013). Synthesis and characterization of palm kernel oil based trimethylolpropane ester. *Asian Journal of Chemistry*, 25(17): 9751-9754.
22. Aziz, N. A. M., Yunus, R., Rashid, U. and Syam, A. M. (2014). Application of response surface methodology (RSM) for optimizing the palm-based pentaerythritol ester synthesis. *Industrial Crops and Products*, 62: 305-312.
23. Rajaendran, V., Salimon, J. and Yusop, R. M. (2016). Synthesis and characterization of epoxidized neopentylglycol dioleate as an intermediate of biolubricant. *Malaysian Journal of Analytical Sciences*, 20(6): 1329-1337.
24. Nor, M. N., Derawi, D. and Salimon, J. (2019). Esterification and evaluation of palm oil as biolubricant base stock. *Malaysian Journal of Chemistry*, 21(2): 28-35.
25. Nadkarni, R. A. (2007). Guide to ASTM test methods for the analysis of petroleum products and lubricants. ASTM International, West Conshohocken
26. Chowdhury, K., Banu, L .A., Khan, S. and Latif, A. (2007). Studies on the fatty acid composition of edible oil. *Bangladesh Journal of Scientific and Industrial Research*, 42(3): 311-316.
27. Pavia, D. L., Lampman, G. M. and Kriz, G. S. (2010). Introduction to Spectroscopy, 4th edition United States, Thomson Learcning, Inc,
28. Denicol Motor Oils N.V (2020). Denicol compressor oil. https://pdf4pro.com/view/compressor-oil-iso-vg-32-46-68-100-150-denicol-5786bc.html. [Access online 25 December 2020].
29. SubsTech: Substances and Technologies (2012). SubsTech hydraulic oil. http://www.substech.com/dokuwiki/doku.php?id=hydraulic_oil_iso_100. [Access online 25 December 2020].

Malaysian Journal of Analytical Sciences (MJAS)
Published by Malaysian Analytical Sciences Society

SPECTROPHOTOMETRIC METHODS FOR DETERMINING TROLOX EQUIVALENT ANTIOXIDANT CAPACITIES OF TEA THROUGH DIFFERENT *In Vitro* ASSAYS

(Kaedah Spektrofotometrik bagi Penentuan Trolox Kapasiti Antioksida Teh Melalui Pelbagai Ujian *In Vitro*)

Le-Thi Anh-Dao[1], Do Minh-Huy[1], Nguyen Thanh-Nho[1], Nguyen Quoc-Duy[1], Nguyen-Thi Thanh-Dieu[1], Le Nhon-Duc[2], Nguyen Quang-Hieu[1], Nguyen Cong-Hau[1*]

[1]Faculty of Environmental and Food Engineering, Nguyen Tat Thanh University, Ho Chi Minh City, Vietnam
[2]Warrantek Joint Stock Company-Testing Center, Can Tho City, Vietnam

[*]Corresponding author: nchau@ntt.edu.vn

Received: 14 April 2022; Accepted: 11 June 2022; Published: 30 October 2022

Abstract

Tea (*Camellia sinensis*) is among the most popular non-alcoholic beverages consumed daily in the world due to its unique taste and flavor. Tea leaves and their products have obtained significant attention because of their high antioxidant capacities. In this study, the analytical methods based on the molecular absorption spectrophotometric principle were evaluated for determining the Trolox equivalent antioxidant capacities (TEACs), including 2,2'-Azino-bis(3-ethylbenzothiazoline-6-sulphonic acid) (ABTS) radical scavenging activity, ferric reducing antioxidant power (FRAP), and cupric reducing antioxidant capacity (CUPRAC) in several commercial dried tea products originated from Lam Dong Province (Vietnam). Double liquid extraction in a water bath at 70 ℃ (10 min for each extraction cycle) was employed to obtain the extracts for further colorimetric reactions. The results demonstrate low limits of detection and quantification (12.3-37.3 µmol TE/L, 9.9-30.1 µmol TE/L, and 11.8-35.7 µmol TE/L for ABTS, FRAP, and CUPRAC, respectively), wide working ranges (100-700 µmol TE/L), favorable repeatability (RSD_r of 1.03-1.52%), reproducibility (RSD_R of 1.26-1.55%), and acceptable recoveries (98.0-101%) according to Appendix F of AOAC (2016). The Shewhart charts were also constructed based on the UV-Vis 1800 Shimadzu (Japan) from 21 separate working days to control the accuracy and precision of the analytical results. For tea products in Lam Dong, the TEACs of all samples in the descending order were determined as green tea > oolong tea > black tea, which could be mainly due to the differences in the oxidation levels during the fermentation. In addition, strong correlation was recorded for pairs of FRAP-CUPRAC (R^2 = 0.8579), ABTS-FRAP (R^2 = 0.8453), and ABTS-CUPRAC (R^2 = 0.710).

Keywords: tea, antioxidant capacities, 2,2'-Azino-bis(3-ethylbenzothiazoline)-6-sulphonic acid radical scavenging activity, ferric reducing antioxidant power, cupric reducing antioxidant capacity

Abstrak

Teh (*Camellia sinensis*) merupakan minuman tak beralkohol popular yang diambil setiap hari di seluruh dunia kerana keunikkan rasanya. Daun teh dan produknya mendapat perhatian penting kerana mempunyai kapasiti antioksida yang tinggi. Dalam kajian

ini, kaedah analisis berasaskan prinsip spektrofotometrik serapan molekul telah dinilai bagi penentuan kapasiti antioksida setara Trolox (TEACs), termasuk cerakin pemerangkapan radikal 2,2'-Azino-bis(3-etilbenzothiazolin-6-asid sulfonik) (ABTS), kuasa antioksida penurunan ferik (FRAP) dan kapasiti antioksida penurunan kuprik (CUPRAC) di dalam pelbagai produk teh komersial berasal dari wilayah Lam Dong (Vietnam). Pengekstrakan cecair cecair di dalam rendaman air pada suhu 70 °C (10 min bagi setiap kitaran pengekstrakan) telah dibangunkan bagi tujuan memperolehi hasil ekstrak sebelum tindak balas kolorimetrik. Hasil menunjukkan had pengesanan dan pengkuantitian rendah (12.3-37.3 µmol TE/L, 9.9-30.1 µmol TE/L,dan 11.8-35.7 µmol TE/L masing-masing bagi ABTS, FRAP, dan CUPRAC), julat kelinearan (100-700 µmol TE/L), kebolehulangan (RSD_r of 1.03-1.52%), kebolehasilan semula (RSD_R of 1.26-1.55%), dan perolehan semula (98.0-101%) berdasarkan Appendix F AOAC (2016). Carta Shewhart telah dibangunkan berdasarkan UV-Vis 1800 Shimadzu (Jepun) dari 21 hari bekerja berbeza bagi mengawal ketepatan dan kejituan hasil analisis. Bagi produk teh Lam Dong, nilai TEACs semua sampel di susun tertib menurun iaitu teh hijau > teh oolong > teh hitam, disebabkan oleh perbezaan tahap pengoksidaan semasa penapaian. Tambahan lagi, hubungkait yang kuat direkodkan bagi pasangan FRAP-CUPRAC (R^2 = 0.8579), ABTS-FRAP (R^2 = 0.8453), dan ABTS-CUPRAC (R^2 = 0.710).

Kata kunci: teh, keupayaan antioksida, ,2'-Azino-bis(3-etilbenzothiazolin-6-asid sulfonik), kuasa antioksida penurunan ferik, kapasiti antioksida penurunan kuprik

Introduction

Antioxidants are known as any substances capable of slowing or preventing the oxidation of easily oxidized components [1]. In addition, they have been commonly used in food production to limit the deterioration in food quality and maintain nutritional values, in which the antioxidants can slow lipid oxidation by inhibiting the initial free radical formation or preventing the generation of free radicals [2]. Plants and food products containing high contents of antioxidants perform great biological benefits since they are reported to have the ability to protect the animals' and humans' bodies against oxidizing agents, such as reactive oxygen, nitrogen, and chlorine species [3]. Dietary antioxidants generally belong to the family of phenolic and polyphenolic compounds. The phenolic compounds occurring in foods are in the phenylpropanoid (C6-C3) family and are also the derivatives of cinnamic acid. The condensation of C6–C3 compounds through the participation of malonyl coenzyme A leads to the formation of chalcones, which can then cyclize under acidic conditions to produce flavonoids and isoflavonoids. The antioxidant activity of flavonoids is significantly dependent on the number and position of hydroxyl groups in the molecule structures [2]. In tea leaves and their products, the antioxidant activity is mainly due to the combination of aromatic rings and hydroxyl groups incorporating their chemical structures, thereby binding and neutralizing lipid free radicals basically by these hydroxyl groups. The antioxidant compounds in tea, including catechins, inhibit the formation of lipid peroxides by binding lipid alkoxyl radicals. Such activity depends on the structure of the molecules, and the number and position of the hydroxyl groups in the molecule. Specifically, the –OH groups at the 3'-, 4'-, and 5'- positions in the B-ring of flavonoids would increase the value of the measured antioxidant capacities. Sample matrices containing the vast majority of simple phenolic compounds with only one hydroxyl group exhibit lower antioxidant activity [4, 5]. The catechin compounds in green tea also exhibit antioxidant capacities through the inhibition of pro-oxidant enzymes and the formation of antioxidant enzymes. The antioxidant capacities generally show a general trend as follows: green tea > oolong tea > black tea [2].

Food contains macronutrients such as carbohydrates, proteins, and lipids as well as trace elements such as minerals and vitamins. These components with the potential to interact with antioxidant compounds are present at various concentrations in the sample matrices and performed different activity behaviors. Therefore, the antioxidant capacities of food products obtained from a single chemical reaction mechanism do not provide adequate information due to the diversity of the chemical compositions in different samples, which may influence the results [2, 6, 7]. Moreover, there have been no officially published standardized methods for determining the antioxidant capacities of any food in general, and tea products in specific. Thus, there are discrepancies in the extraction and analytical methods presented in different papers. The performance of the analytical method in determining the antioxidant capacities based on different mechanisms of chemical

reaction in a specific food product should be evaluated to be applied in routine analysis and research activities. The determination of antioxidant capacities based on molecular absorption spectrophotometry is considered as one of the most effective approaches to assess and compare the general information about the antioxidant activity in various foods and drinks. Particularly, the changes in antioxidant capacities can occur when foods undergo processing and storage periods [2, 7, 8]. However, the antioxidant activity should be interpreted specifically based on the chemical nature of the applied methods and the chemical compositions of the analyzed samples. The chemical nature of the method used is determined based on the types of reagents used and the reaction mechanisms between the agents and the antioxidant components present in the sample matrices. The antioxidant activity was evaluated by various methods, both in vitro and/or in vivo. Based on the chemical nature of the in vitro process, the methods for the determination of antioxidant activity can be classified into different mechanisms such as single electron transfer (SET), hydrogen atom transfer (hydrogen atom transfer-HAT), and association mechanisms. The single-electron transfer methods are known as the most popular method, which is based on free radical scavenging reaction, ferric reducing antioxidant power (FRAP) [7], 2,2-diphenyl-1-picrylhydrazyl radical (DPPH) radical neutralizing/scavenging activity [9], 2,2'-Azino-bis(3-ethylbenzothiazoline-6-sulphonic acid) (ABTS) free radical neutralizing/scavenging activity [5], cupric-reducing antioxidant capacity (CUPRAC) [7]. For tea leaves and their products, most of the published studies have focused on 1 and/or 2 determination assays to assess antioxidant capacities. The combination of two or more assays assists to perform a more adequate reflection of the antioxidant activity behavior [10, 11].

The objectives of this current study are to evaluate the performance of the analytical method for determining the Trolox equivalent antioxidant capacities (TEACs) via three different in vitro assays, namely ABTS, FRAP, and CUPRAC in dried tea products. The evaluation included the estimation of the limit of detection and quantification (LOD and LOQ), the establishment of calibration curves, the assessment of repeatability (intra-day precision) and reproducibility (inter-day precision), method accuracy through the recovery test, and the construction of the quality control charts. Then, the analytical methods were applied for the determination and assessment of TEACs of several commercial dried tea products belonging to different types of green, oolong, and black teas originating from Lam Dong Province, one of the prominent tea plantation regions located in the South of the Vietnam.

Materials and Methods

Sampling and pretreatment

To evaluate the analytical methods for determining the Trolox equivalent antioxidant capacities (TEACs) based on the three different assays of ABTS, FRAP, and CUPRAC in dried tea products. The commercial black tea product, called "investigated sample", was used to carry out the analytical method evaluation. Then, the evaluated methods were applied to 15 commercial dried tea products collected from the local supermarkets in Ho Chi Minh City (Vietnam). The tea products belong to three different types of green, oolong, and black tea, representing the non-fermented, partially fermented, and fully fermented tea types, respectively. As displayed on the tea product labels, these products originated from Lam Dong Province, one of the prominent tea plantation regions in the southern part of Vietnam. The tea products were packed in non-permeable bags (250 g per bag) and sealed under a vacuum. The purchased samples were transferred to the laboratory in Ho Chi Minh City and stored at −10 ℃ until pre-treatment and further use. The tea samples underwent a pre-treatment procedure [12] which involved homogenization in the for determination of TEACs. The homogenized tea samples were put in non-permeable bags sealed under a vacuum, stored at 25 ℃ with 70% humidity, away from direct sunlight.

Extracts were obtained from the well-homogenized tea products via the extraction procedure performed in ISO 14502-1:2005 [13] with some modifications. Shortly, 0.2 ($\pm$0.001) g of dried tea product was subjected to solid-liquid extraction using the 7:3 v/v mixture of methanol ($\geq$ 99.9%, Merck, Germany) and deionized water (MeOH:DIW) as the extraction solvent. The extraction was carried out in duplicate within 20 min (i.e., 10.00 mL solvent and 10 min for each extraction

cycle) at 70 ℃ in a water bath. All extracts were collected and transferred to a 50-mL volumetric flask. The extraction solvent with a ratio of MeOH:DIW (7:3 v/v) was used to generate the calibration mark. The extracts were then filtered through a 0.45 µm PTFE membrane, and further diluted 20 times by DIW before being subjected to colorimetric assays and spectrophotometric measurement on the UV-Vis 1800 Shimadzu (Japan).

ABTS assay

For the ABTS free radical scavenging activity, the reagent of 2,2'-Azino-bis(3-ethylbenzothiazoline-6-sulphonic acid) or ABTS (≥ 98%, Merck, Germany) was used and the assay was carried out according to the method reported by Abdullahi et al. [14]. The ABTS radical cation was generated through the reaction between aqueous stock solutions of ABTS and $K_2S_2O_8$ for 12 to 16 hours in the dark at the ambient temperature to reach the final concentrations of 7.0 mmol/L and 2.45 mmol/L, respectively. Before use, the ABTS stock solution was diluted using acetate buffer solution of pH = 4.5 (0.3 mol/L) to obtain an absorbance of 0.74 ± 0.03 at 734 nm (working ABTS solution). In the presence of Trolox as the standard or an antioxidant in the sample matrices that are capable of giving hydrogen, the nitrogen atoms can quench the hydrogen atom in the ABTS reagent, resulting in the decolorization of the reaction solutions [15, 16]. In this current study, 200 µL of the diluted tea extract was mixed with 4000 µL of working ABTS solution. The mixture was shaken gently and protected from direct light for 7 minutes. The absorbance was measured at 734 nm for quantification purposes.

FRAP assay

The ferric reducing antioxidant power or FRAP was utilized to evaluate the reducing ability of the antioxidants present in dried tea products. The FRAP procedure was carried out according to the publication of Pellegrini et al. [7], which is based on the reduction reaction of Fe^{3+}–TPTZ (2,4,6-tris(2-pyridyl)-1,3,5-triazine, ≥ 98%, Merck, Germany) with antioxidant compounds in the sample matrices, forming Fe^{2+}–TPTZ. Briefly, a volume of 100 µL of the diluted tea extract was reacted with 3900 µL of working FRAP solution, comprising 300 mmol/L sodium acetate-acetic acid buffer of pH = 3.6, 10 mmol/L TPTZ solution, and 20 mmol/L ferric chloride solution at a volume ratio of 10:1:1. The binding of Fe^{2+} to the ligands from the reduction reaction creates a color of deeply intense navy blue, which absorption values at 593 nm were measured to determine the concentrations of antioxidants that correlates with the amount of iron reduced [7].

CUPRAC assay

For the analysis of cupric reducing antioxidant capacity or CUPRAC of tea products, the tea extract was mixed with $CuCl_2$ and neocuproine (Nc, ≥ 98%, Merck, Germany) working solutions, in which Cu(II) was reduced to Cu(I) through the action of electron-donating antioxidants. The procedure was briefly described as follows: 4.00 mL of the diluted tea extract was mixed with 1.00 mL of 10^{-2} mol/L $CuCl_2$; 1.00 mL of 7.5×10^{-3} mol/L neocuproine was diluted in ethanol; and 1.00 mL ammonium acetate buffer (pH = 7.0) was prepared by dissolving 19.27 g ammonium acetate in 250 mL DIW. After 1 hour of reaction, the absorbance was measured at 450 nm for the quantification of antioxidants that wer present in the tea products [7].

Analytical method evaluation

Trolox (6-hydroxy-2,5,7,8-tetramethylchroman-2-carboxylic acid, 97%, Merck, Germany) was used as the standard for all criteria of interest. The quantification was carried out according to the calibration curves, which were established based on the linear relationship (y = ax + b) between the analyte concentrations (µmol TE/L) and the respective absorption. The calibration curves of FRAP and CUPRAC (reducing power) were constructed based on the linear relationship between the Trolox concentrations and the absorption signal of each standard solution after subtracting the signal of the blank solution ($Abs_{std} - Abs_{blk}$). For ABTS (radical scavenging activity), the calibration curve was built up according to the linear relationship between the Trolox concentrations and the values derived from the subtraction of absorbances (Abs) between the blank solution (blk) as the control sample and the signal of each standard (std) point ($Abs_{blk} - Abs_{std}$). The bias values for each standard point of the calibration curves

(calculated in percentage) were calculated by the equation 1 [17]:

$$\text{bias } (\%) = \frac{C_{cal.} - C_{std}}{C_{std}} \times 100 \quad (1)$$

where $C_{cal.}$ and C_{std} stand for the concentration of the standard solutions calculated from the established calibration curves and from the practical preparation (concentration values used to establish the calibration curves), respectively.

The limit of detection (LOD) and quantification (LOQ) of the analytical methods was estimated by simultaneously analyzing 11 separate blank solutions (containing only the extraction solvents and colorimetric reagents). Next, the estimated average concentrations ($\bar{x}$) and their standard deviation value (SD) were calculated to apply in the following relationships [18]:

$$LOD = \bar{x} + 3SD \text{ and } LOQ = 3LOD \quad (2)$$

The black tea (as the "investigated sample") was used for the repeatability assessment (intra-day precision) within one day (six replicates, n = 6) and reproducibility assessment (inter-day precision) for three separate days (six replicates per day) through the calculation of relative standard deviations, RSD_r and RSD_R, respectively, at the significance level of 0.05. In addition, the standard solution was spiked into this sample at three different levels ($0.5C_x$, $1C_x$, and $1.5C_x$, where C_x is the estimated analyte concentration in the investigated sample for the recovery test to evaluate the method accuracy.

The Shewhart charts were constructed for quality control by analyzing the investigated sample in successive runs along with "warning" and "action" limits employed to detect the arisen problems in different measurements on the UV-Vis 1800 Shimadzu (Japan) [18].

The evaluated analytical methods for determining ABTS, FRAP, and CUPRAC were applied to the collected dried tea products (performed in dried weight). All the analytical data were carried out in triplicate and analyzed by Microsoft Office Excel 2016 (version 16.54, Microsoft 365 Subscription), expressed as mean value ± standard deviation (SD). For potential correlation assessment of the measurements, the correlation analysis was performed using the statistical package software of SPSS (version 23).

Results and discussion

Calibration curves

Trolox, a derivative of vitamin E, is the most commonly used chemical standard for quantifying the antioxidant capacities from different sample matrices, including the reducing power, e.g., FRAP and CUPRAC, and free radical scavenging ability, e.g., ABTS. In addition, Trolox is soluble in polar solvents [19], thus compatible with the extraction solvent used in this study, i.e., 70% v/v MeOH in DIW.

For the analysis of ABTS, FRAP, and CUPRAC in dried tea products, the calibration curves were established for quantification purposes. Table 1 shows the parameters of the established calibration curves, which performed the goodness of linearity ($R^2 > 0.995$) according to the Appendix F of AOAC (2016) [20]. The working ranges for all TEAC detection methods were wide (from 100 to 700 µmol TE/L), which was suitable for different tea types with varying analyte concentrations, prepared through the same sample preparation procedure and dilution factor. The bias values obtained from all standard points were from 0.010 to 14.2% (Table 1), which are in agreement with the recommended value (< 15%) published in "Method validation for chemical and microbiological analysis" published by Vietnam National Institute for Food Control [17].

Table 1. Parameters of the calibration curves

	ABTS	FRAP	CUPRAC
Working range (μmol TE/L)	100-700	100-700	100-700
Slope (a)	0.0009	0.0011	0.0011
Intercept (b)	−0.0111	0.0113	0.0127
R^2	0.9985	0.9982	0.9979
Bias range (%)	0.20-10.5	0.010-14.2	0.42-9.6

Limit of detection and quantification

The results in Table 2 indicate that the LODs and LOQs of ABTS, FRAP, and CUPRAC (LOD-LOQ) were low (in the range from 9.9 to 37.3 μmol TE/L) compared to the remarkably high concentrations of antioxidants (up to thousands of μmol TE/g dried weight) in tea products due to the rich phenolic contents [21-25]. Therefore, the obtained LOD and LOQ values were suitable for tea matrices, and it is not necessary to lower these values for analytical method development.

Table 2. LODs, LOQs, intra-day precision (RSD_r), inter-day precision (RSD_R), and recoveries

Criteria	LOD (μmol TE/L)	LOQ (μmol TE/L)	RSD_r (%)	RSD_R (%)	Recovery (%)		
					$0.5C_x$	$1C_x$	$1.5C_x$
ABTS	12.3	37.3	1.37	1.48	99.3-99.6	98.7-99.8	99.7-101
FRAP	9.9	30.1	1.03	1.26	98.7-98.9	99.6-100	99.1-99.9
CUPRAC	11.8	35.7	1.52	1.55	98.0-100	98.5-99.5	98.9-99.6

Repeatability and reproducibility

In this current study, the precision (intra- and inter-day) of the analytical methods for TEACs was evaluated through the repeatability and reproducibility tests. The results in Table 2 indicate the favorable repeatability (RSD_r from 1.03 to 1.52%) regarding the Appendix F of AOAC (2016) [20]. The calculation of one-way ANOVA was carried out to evaluate the reproducibility in three separate working days (6 replicates/day) at the confidence level of 95%. The results of RSD_R ranged from 1.26 to 1.55%, consistent with the requirements of AOAC (2016) [20] for the analyte concentrations of 10-100% in Appendix F.

Recovery test

In this study, the accuracy of the analytical methods for ABTS, FRAP, and CUPRAC was assessed by the recovery test. Typically, the Trolox standard solution was spiked into the investigated sample in different concentrations, i.e., $0.5C_x$, $1C_x$, and $1.5C_x$, where C_x is the estimated analyte concentration of the corresponding investigated sample. The results in Table 2 demonstrate the high recoveries (98.0-101% for all spiked samples), favorable to the requirements of AOAC (2016) [20] for method validation in Appendix F. The analytical methods can be applied for the quantification of the antioxidant capacities of dried tea products with proper precision and accuracy. The extraction was performed once to obtain the sample liquids for the measurement of ABTS, FRAP, and CUPRAC, as well as for better comparison and assessment. Moreover, the analytical methods are simple, inexpensive, and suitable for both research and routine analysis of tea products and potentially, tea-related matrices.

Shewhart quality control chart

To control the sensitivity and stability of the analytical system, the Shewhart quality control charts were constructed based on the analysis of the investigated sample (black tea) within 21 days. The black tea product, representing the fully fermented tea type, was used to generate the quality control chart to ensure consistent results under proper preservation conditions during the analysis period. In this situation, the investigated black tea sample plays the role of quality control or QC sample. Figure 1 demonstrates the Shewhart charts for ABTS, FRAP, and CUPRAC, including the mean concentration (C_{mean}) and warning values listed as upper warning limit

(UWL), lower warning limit (LWL), upper action limit (UAL), and lower action limit (LAL). These limits were calculated following the principles of ± 2SD and ± 3SD (SD: standard deviations of three replicates within one day) for warning and action limits, respectively. For each working day, the QC sample can be analyzed to examine the stability and robustness of the measurement system, in which the analyzed results of the QC sample should be between the LWL and UWL to ensure the accuracy of the analytical results [18]. However, during the analytical period, there could be a different emerging situation that needs to be solved based on the QC results. Typically, the analysis should be temporarily stopped and the obtained results and the measurement system need to be carefully checked if one of the following situations happens: (i) any QC results that are beyond the range of LAL-UAL, (ii) the values of more than two in three continuous QC samples are beyond the range of LWL-UWL, (iii) the QC results tend to be located at the same side of the mean line, which it is not acceptable if more than nine continuous points are located at the same side (above or under the mean line), and (iv) the QC results has the tendency to increase or decrease, which it is not acceptable if there are six continuous points tend to go up or down [26]. The results in Figure 1 indicate that the measurement system was stable, i.e., all the values of UAL, UWL, LWL, and LAL were close to C_{mean}, the obtained results are in the range of LWL-UWL and none of the nine continuous points were located at the same side of the mean line. Therefore, the evaluated analytical method meets the proper stability, and robustness for long-term analysis and could be applied in the analysis of dried tea products both for research activities and routine approaches. Moreover, tea products belonging to other types and different geographical origins could be analyzed for their TEACs by employing the evaluated analytical methods due to the favorable adaptability of the operating conditions for diverse tea matrices.

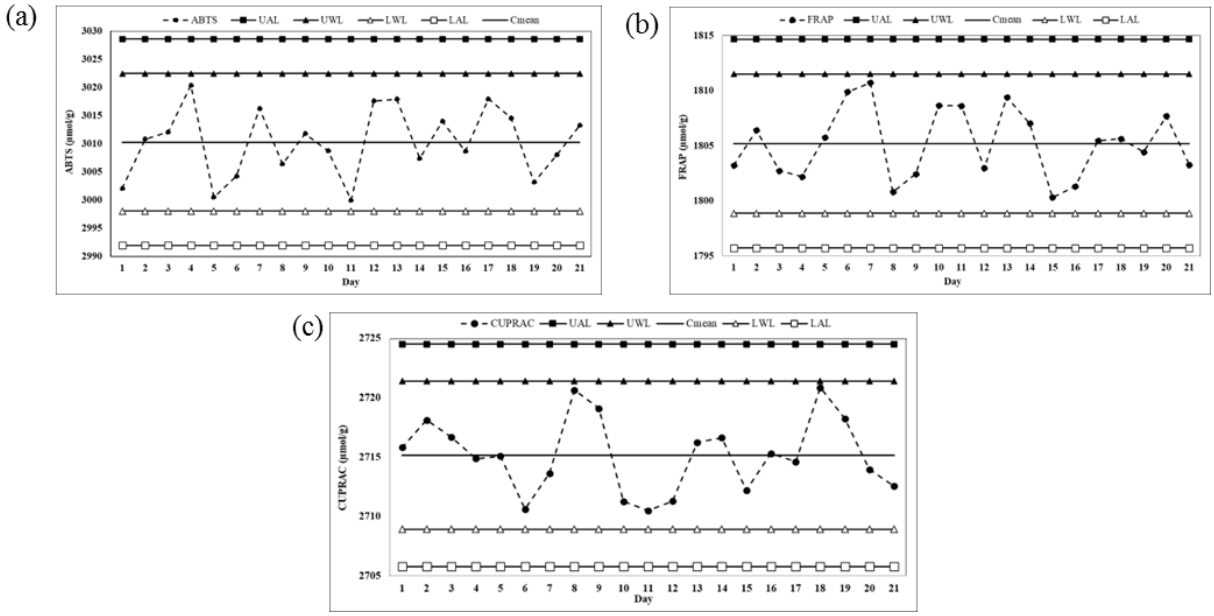


Figure 1. Quality control charts of (a) ABTS, (b) FRAP, and (c) CUPRAC

Application of the evaluated analytical methods for dried tea products

The evaluated analytical methods were applied to determine ABTS, FRAP, and CUPRAC in several commercial dried tea products originating from Lam Dong Province (Vietnam). The results in Figure 2 indicate the TEACs of the tea products in descending order: green tea > oolong tea > black tea. For ABTS, Green-05 and Black-05 exhibited the highest (4006 ± 31 μmol TE/g) and lowest values (3593 ± 41 μmol TE/g), respectively. A similar observation for ABTS in dried tea products was published in Carloni et al. [23], which

reported the highest ABTS values for green tea samples, followed by white and black tea products. Another study by Qian et al. [27] employed a liquid chromatography system coupled with a reaction compartment containing the ABTS reagents after the column, which also demonstrated an ABTS radical scavenging activity of different tea products in descending order: green tea > oolong tea > black tea. Generally, green tea products exhibit significant antioxidant capacities due to the high contents of phenolic and flavonoid compounds [2, 28-30]. The antioxidant capacities of black and dark tea products may be decreased by the activity of polyphenol oxidase enzymes and bacteria during the fermentation period, which could lead to the degradation of simple catechins and other phenolic compounds, as well as formation of more complicated dimers and/or polymers [31-33]. These large molecular compounds could be less reactive with the ABTS reagents, leading to lower ABTS readings [8, 27]. Moreover, the oxidation of catechins to produce the theaflavins during fermentation may also contribute to the intense color and characteristic flavor of oolong and black tea [34, 35].

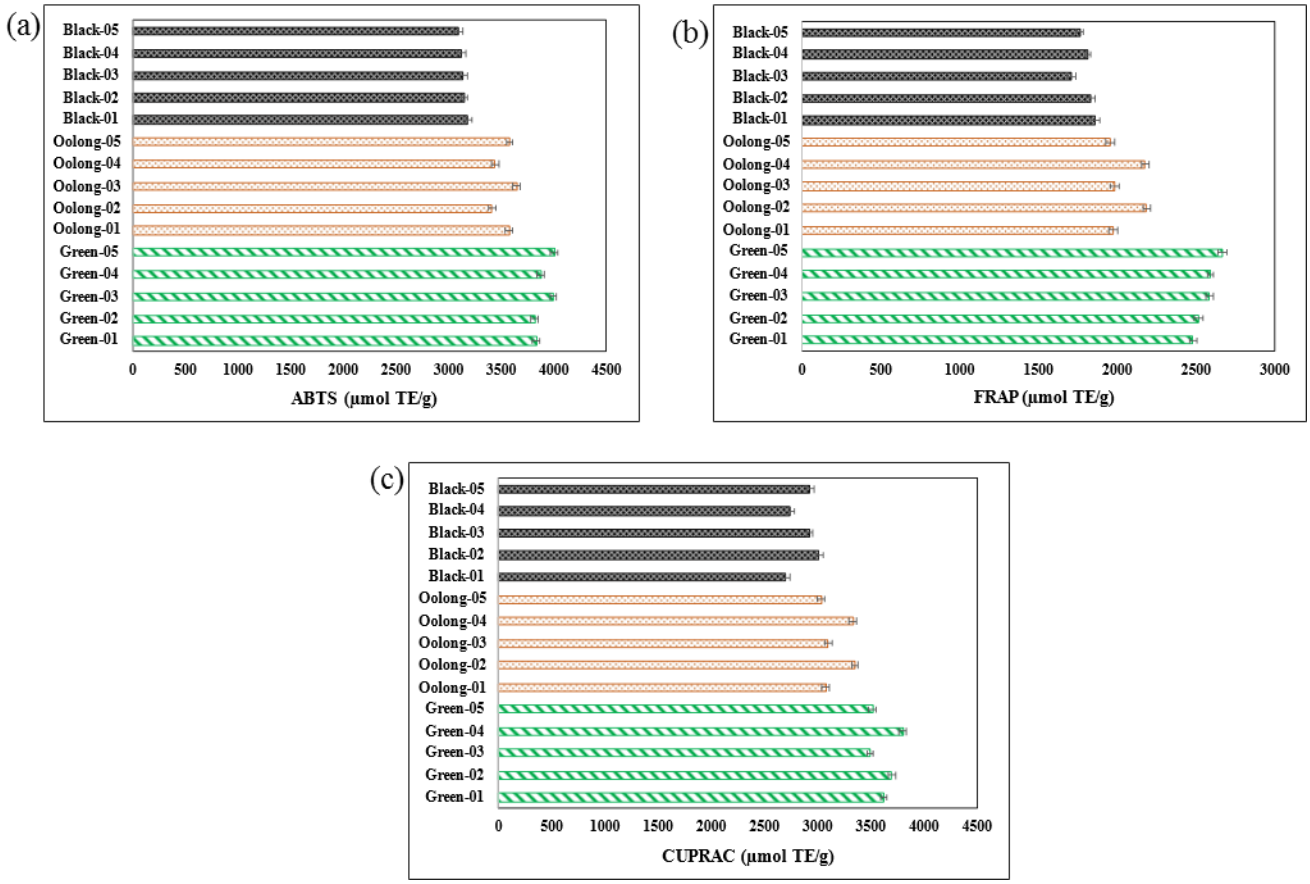


Figure 2. Trolox equivalent antioxidant capacities: (a) ATBS, (b) FRAP, and (c) CUPRAC

The TEACs of the dried tea products in CUPRAC analysis were higher than that of FRAP (2701 ± 35 to 3805 ± 35 μmol TE/g *vs.* 1708 ± 26 to 2668 ± 29 μmol TE/g). However, among the three types of tea, both FRAP and CUPRAC produced results that were similar to that of ABTS. This was supported by the strong correlation obtained (Figure 3) (R^2 = 0.8579, 0.8453, and 0.710 for pairs of FRAP-CUPRAC, ABTS-FRAP, and ABTS-CUPRAC, respectively). Similar results were observed in the publications of Zhao et al. [8] and Lee et al. [36]. As mentioned before, oxidation during fermentation could change the chemical compositions of tea, especially compounds with antioxidant properties, through decomposition, dimerization, and

polymerization, forming complex compounds with larger molecular weight [31-33]. The formation of these new compounds is likely to degrade the reactivity by the transition metal reduction mechanism. This was supported by the FRAP and CUPRAC values of the tea products in descending order green tea > oolong tea > black tea (FRAP: 2479 ± 24 to 2668 ± 29 µmol TE/g > 1956 ± 25 to 2187 ± 21 µmol TE/g > 1708 ± 26 to 1860 ± 27 µmol TE/g, respectively, and CUPRAC: 3494 ± 34 to 3805 ± 35 µmol TE/g > 3033 ± 40 to 3363 ± 31 µmol TE/g > 2701 ± 35 to 3017 ± 32 µmol TE/g, respectively), which also indicates the oxidation during the fermentation has certain effects on the TEACs by the transition metal reduction mechanisms [8, 22].

Generally, the variabilities in TEACs between samples of the same species or different species can also be contributed by the variations in raw materials, i.e., fresh tea leaves, due to the different plantation of origin, soil type, altitude, cultivation condition, quality of tea leaves, processing procedure, preservation method, and growing condition of tea plants [22, 37-39].

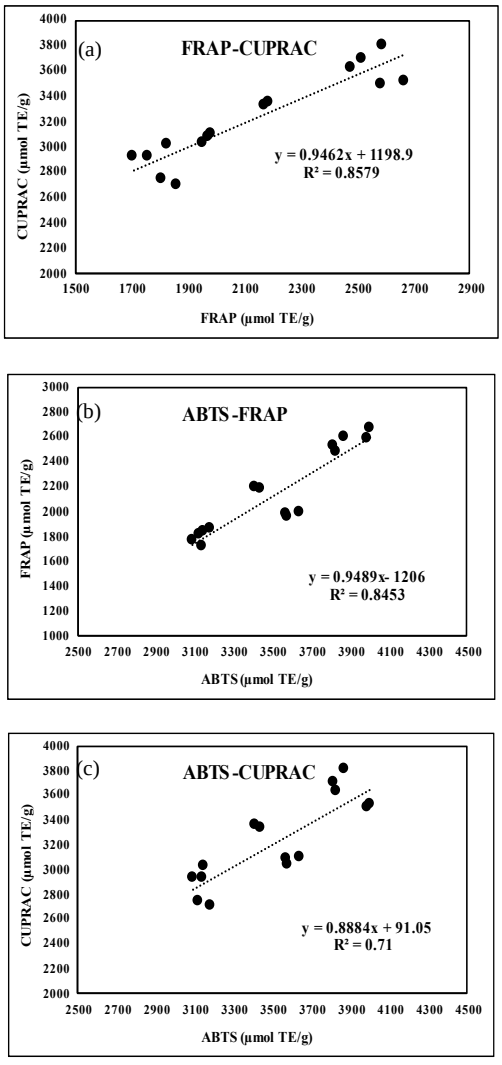


Figure 3. Correlation between (a) FRAP and CUPRAC, (b) ABTS and FRAP, and (c) ABTS and CUPRAC

Conclusion

This study evaluated the molecular absorption spectrophotometric methods for the determination of Trolox equivalent antioxidant capacities (TEACs) through different chemical reactions or in vitro assays. The reactions investigated for determination of TEACs were classified into two mechanisms: radical scavenging activity of ABTS and transition metal reduction via FRAP and CUPRAC. The performance analysis of the analytical method demonstrated low LODs and LOQs compared to the concentrations of antioxidants in dried tea products. The working ranges were wide (from 100 to 700 µmol TE/L), which is compatible with different types of tea matrices prepare through the same sample preparation procedure and dilution factor. The established calibration curves demonstrated the goodness of linearity ($R^2 > 0.995$). The repeatability, reproducibility, and recovery were favorable according to Appendix F of AOAC (2016). The Shewhart charts were constructed to control the analytical results achieved from the UV-Vis 1800 spectrophotometer (Shimadzu, Japan) on different working days. The analytical methods were then applied to several purchased dried tea products, i.e., green, oolong, and black teas, which demonstrated the variabilities in TEACs of the three tea types according to the differences in the processing period. The discrepancies in the result could be due to the increasing oxidation levels from green to oolong and black teas during the fermentation. This study contributes to food areas in terms of the determination and assessment of antioxidant capacities in tea and other tea-related products.

To broaden this study and better assess the tea products, more dried tea samples from various tea plantations should be collected. Additionally, the chemical profiles could be analyzed to adequately support the determined antioxidant capacity behaviors of different tea samples. The changes in TEACs due to the processing demonstrate the potential use of these TEACs as the contributing variables for grouping or discrimination of tea products, particularly in the case of samples in large quantity.

Acknowledgment

The authors would like to express the gratitude and appreciation to Nguyen Tat Thanh University for the assistance and support throughout this study.

References

1. Halliwell, B. (1999). Food-derived antioxidants. Evaluating their importance in food and in vivo. *Food Science and Agricultural Chemistry*, 1(2): 67-109.
2. Namal Senanayake, S.P.J. (2013). Green tea extract: Chemistry, antioxidant properties and food applications – A review. *Journal of Functional Foods*, 5(4): 1529-1541.
3. Ohigashi, H., Osawa, T., Terao, J., Watanabe, S. and Yoshikawa, T. (2013). Food factors for cancer prevention, Springer Science & Business Media.
4. Heim, K.E., Tagliaferro, A.R. and Bobilya, D.J. (2002). Flavonoid antioxidants: chemistry, metabolism and structure-activity relationships. *The Journal of Nutritional Biochemistry*, 13(10): 572-584.
5. Kopjar, M., Tadić, M. and Piližota, V. (2015). Phenol content and antioxidant activity of green, yellow and black tea leaves. *Chemical and Biological Technologies in Agriculture*, 2 (1): 1-6.
6. Frankel, E. N. and Meyer, A. S. (2000). The problems of using one dimensional methods to evaluate multifunctional food and biological antioxidants. *Journal of the Science of Food and Agriculture,* 80(13): 1925-1941.
7. Pellegrini, N., Serafini, M., Colombi, B., Del Rio, D., Salvatore, S., Bianchi, M. and Brighenti, F. (2003). Total antioxidant capacity of plant foods, beverages and oils consumed in Italy assessed by three different in vitro assays. *The Journal of Nutrition*, 133(9): 2812-2819.
8. Jayasekera, S., Molan, A.L., Garg, M. and Moughan, P.J. (2011). Variation in antioxidant potential and total polyphenol content of fresh and fully-fermented Sri Lankan tea. *Food Chemistry*, 125 (2): 536-541.
9. Lachman, J., Šulc, M. and Schilla, M. (2007). Comparison of the total antioxidant status of Bohemian wines during the wine-making process. *Food Chemistry*, 103 (3): 802-807.

10. Anh-Dao, L.-T., Nhon-Duc, L., Cong-Hau, N. and Thanh-Nho, N. (2021). Variability of total polyphenol contents in ground coffee products and their antioxidant capacities through different reaction mechanisms. *Biointerface Research in Applied Chemistry*, 12(4): 4857-4870.
11. ISO 1572 (1980). Tea-Preparation of ground sample of known dry matter content.
12. ISO 14502-1 (2005). Determination of substances characteristic of green and black tea.
13. Marc, F., Davin, A., Deglène-Benbrahim, L., Ferrand, C., Baccaunaud, M. and Fritsch, P. (2004). Studies of several analytical methods for antioxidant potential evaluation in food, *Medecine Sciences: M/S*. 20(4): 458-463.
14. Abdullahi, A.D., Kodchasee, P., Unban, K., Pattananandecha, T., Saenjum, C., Kanpiengjai, A., Shetty, K. and Khanongnuch, C. (2021). Comparison of phenolic contents and scavenging activities of miang extracts derived from filamentous and non-filamentous fungi-based fermentation processes. *Antioxidants*, 10(7): 1144.
15. Munteanu, I. G. and Apetrei, C. (2021). Analytical methods used in determining antioxidant activity: A review. *International Journal of Molecular Sciences*, 22(7): 3380.
16. Son, T. C., Da, P. X., Dao, L. T. H. and Trung, N. T. (2010). Method validation in chemical and microbiological analyses, National Institute for Food Control (Vietnamese).
17. Ellison, S.L., Barwick, V. J. and Farrant, T. J. D. (2009). Practical statistics for the analytical scientist: a bench guide, Royal Society of Chemistry.
18. Hrabárová, E., Valachová, K., Rapta, P. and Šoltés, L. (2010). An alternative standard for Trolox-equivalent antioxidant-capacity estimation based on thiol antioxidants. Comparative 2, 2'-Azinobis [3-ethylbenzothiazoline-6-sulfonic acid] decolorization and rotational viscometry study regarding hyaluronan degradation. *Chemistry & Biodiversity*, 7(9): 2191-2200.
19. Yashin, A., Yashin, Y. and Nemzer, B. (2011). Determination of antioxidant activity in tea extracts, and their total antioxidant content. *American Journal of Biomedical Sciences*, 3(4): 322-335.
20. Shannon, E., Jaiswal, A. K. and Abu-Ghannam, N. (2018). Polyphenolic content and antioxidant capacity of white, green, black, and herbal teas: a kinetic study. *Food Research*, 2(1): 1-11.
21. Carloni, P., Tiano, L., Padella, L., Bacchetti, T., Customu, C., Kay, A. and Damiani, E. (2013). Antioxidant activity of white, green and black tea obtained from the same tea cultivar. *Food Research International*, 53 (2): 900-908.
22. Zhang, C., Suen, C.L.-C., Yang, C. and Quek, S.Y. (2018). Antioxidant capacity and major polyphenol composition of teas as affected by geographical location, plantation elevation and leaf grade. *Food Chemistry*, 244: 109-119.
23. Chan, E.W.C., Lim, Y.Y. and Chew, Y.L. (2007). Antioxidant activity of *Camellia sinensis* leaves and tea from a lowland plantation in Malaysia. *Food Chemistry*, 102(4): 1214-1222.
24. Appendix F of AOAC (2016). Guidelines for Standard Method Performance Requirements.
25. ISO 8258 (1991). Shewhart control charts.
26. Qian, Z.-M., Fang, B.-W., Chen, H.-M., Li, C.-H., Huang, Q., Chen, L., Li, W.-J. and Li, D.-Q. (2020). Online liquid microextraction coupled with HPLC-ABTS for rapid screening of natural antioxidants: Case study of three different teas. *Journal of Chromatographic Science*, 58(9): 875-879.
27. Maizura, M., Aminah, A. and Wan Aida, W. (2011). Total phenolic content and antioxidant activity of kesum (*Polygonum minus*), ginger (*Zingiber officinale*) and turmeric (*Curcuma longa*) extract. *International Food Research Journal*, 18(2): 526-531.
28. Azlim Almey, A., Ahmed Jalal Khan, C., Syed Zahir, I., Mustapha Suleiman, K., Aisyah, M. and Kamarul Rahim, K. (2010). Total phenolic content and primary antioxidant activity of methanolic and ethanolic extracts of aromatic plants' leaves. *International Food Research Journal*, 17(4): 1077-1083.

29. Cong-Hau, N., Anh-Dao, L.-T., Nhon-Duc, L. and Thanh-Nho, N. (2021). Spectrophotometric determination of total flavonoid contents in tea products and their liquors under various brewing conditions. *Malaysian Journal of Analytical Science,* 25(5): 740-750.
30. Atoui, A. K., Mansouri, A., Boskou, G. and Kefalas, P. (2005). Tea and herbal infusions: their antioxidant activity and phenolic profile. *Food Chemistry*, 89(1): 27-36.
31. Izzreen, N.Q. and Mohd Fadzelly, A. (2013). Phytochemicals and antioxidant properties of different parts of *Camellia sinensis* leaves from Sabah Tea Plantation in Sabah, Malaysia. *International Food Research Journal*, 20(1): 307-312.
32. Rusak, G., Komes, D., Likić, S., Horžić, D. and Kovač, M. (2008). Phenolic content and antioxidative capacity of green and white tea extracts depending on extraction conditions and the solvent used. *Food Chemistry*, 110(4): 852-858.
33. Harbowy, M.E., Balentine, D.A., Davies, A.P. and Cai, Y. (1997). Tea chemistry. *Critical Reviews in Plant Sciences*, 16(5): 415-480.
34. Graham, H.N. (1992). Green tea composition, consumption, and polyphenol chemistry. *Preventive Medicine*, 21(3): 334-350.
35. Zhao, C.-N., Tang, G.-Y., Cao, S.-Y., Xu, X.-Y., Gan, R.-Y., Liu, Q., Mao, Q.-Q., Shang, A. and Li, H.-B. (2019). Phenolic profiles and antioxidant activities of 30 tea infusions from green, black, oolong, white, yellow and dark teas. *Antioxidants*, 8(7): 215.
36. Zielinski, A. A. F., Haminiuk, C. W. I., Alberti, A., Nogueira, A., Demiate, I. M. and Granato, D. (2014). A comparative study of the phenolic compounds and the in vitro antioxidant activity of different Brazilian teas using multivariate statistical techniques. *Food Research International*, 60: 246-254.
37. Imran, A., Butt, M. S., Sharif, M. K. and Sultan, J. I. (2013). Chemical profiling of black tea polyphenols. *Pakistan Journal of Nutrition*, 12(3): 261-267.
38. Lee, J.-E., Lee, B.-J., Chung, J.-O., Kim, H.-N., Kim, E.-H., Jung, S., Lee, H., Lee, S.-J. and Hong, Y.-S. (2015). Metabolomic unveiling of a diverse range of green tea (*Camellia sinensis*) metabolites dependent on geography. *Food Chemistry*, 174: 452-459.
39. Pacheco-Coello, F., Peraza-Marrero, M., Orosco-Vargas, C., Ramirez-Azuaje, D. and Pinto-Catari, I. (2020). Determination of total phenolic compounds and evaluation of the antioxidant activity of commercial and artisanal green tea traded in Maracay, Venezuela. *Revista Boliviana de Química*, 37(1): 28-33.

Malaysian Journal of Analytical Sciences (MJAS)
Published by Malaysian Analytical Sciences Society

ASSESSMENT ON THE CURRENT QUALITY AND IDENTITY CHARACTERISTICS OF MALAYSIAN PALM SUPEROLEIN

(Penilaian Kualiti dan Ciri Identiti Semasa Superolein Sawit Malaysia)

Najwa Sulaiman*, Yeoh Chee Beng, Farah Khuwailah Ahmad Bustamam, Elina Hishamuddin

Malaysian Palm Oil Board,
6 Persiaran Institusi, Bandar Baru Bangi, 43000 Kajang, Selangor, Malaysia

**Corresponding author: najwa.sulaiman@mpob.gov.my*

Received: 19 May 2022; Accepted: 19 July 2022; Published: 30 October 2022

Abstract

An experimental investigation was conducted to assess the current quality and identity characteristics of palm superolein (PSO) produced in Malaysia. A total of 44 PSO samples were collected from several palm oil refineries and ports in Malaysia and were tested for several important indices for characterization of PSO, *i.e.,* iodine value, fatty acids composition, triacylglycerols composition, refractive index, apparent density, relative density, slip melting point, peroxide value, impurities content, moisture content, free fatty acids content, unsaponifiable matter and saponification value. Generally, the quality of PSO was within the specification listed in Codex CXS 210-1999, with slight variations compared to the previous assessment conducted two decades ago. Most prominent variations were observed for refractive index and apparent density of PSO in which the experimental temperature was changed to 40 °C, and a new set of range values were obtained. The findings from this current quality assessment have provided significant data for the revision of the international food standard, as well as the Malaysian national standard for PSO, to accurately reflect the present quality of PSO for consumer health protection, hence removing any barriers to the international trading of PSO.

Keywords: assessment, Malaysia, palm superolein, quality, standard

Abstrak

Satu kajian eksperimen telah dijalankan untuk menilai kualiti dan ciri identiti semasa superolein sawit (PSO) yang dihasilkan di Malaysia. Sebanyak 44 sampel PSO yang diperoleh dari beberapa kilang penapisan minyak sawit dan pelabuhan di Malaysia telah diuji untuk beberapa indeks penting bagi pencirian PSO seperti nilai iodin, komposisi asid lemak, komposisi triasilgliserol, indeks biasan, ketumpatan ketara, ketumpatan relatif, takat lebur gelincir, nilai peroksida, bendasing, kelembapan, asid lemak bebas, bahan tak tersaponinan dan nilai penyabunan. Secara amnya, kualiti PSO menepati spesifikasi yang disenaraikan dalam Codex CXS 210-1999, dengan sedikit perbezaan berbanding penilaian yang telah dijalankan dua dekad yang lalu. Perbezaan ketara dilihat pada indeks biasan dan ketumpatan ketara PSO di mana suhu eksperimen telah diubah kepada 40 °C, dan satu nilai julat baru diperoleh. Hasil penemuan daripada penilaian kualiti ini telah menyediakan data yang signifikan bagi semakan semula piawaian makanan antarabangsa, dan juga piawaian kebangsaan Malaysia bagi PSO, bagi memberikan gambaran yang tepat berkenaan kualiti semasa PSO untuk penjagaan kesihatan pengguna, seterusnya menghapuskan sebarang halangan dalam perdagangan antarabangsa PSO.

Kata kunci: penilaian, Malaysia, superolein sawit, kualiti, piawai

Introduction

Oil palm (*Elaeis guineensis*) is a special crop as two types of oils are produced from the palm fruits, *i.e.*, crude palm oil (CPO) from the fleshy mesocarp, and crude palm kernel oil from the kernel [1]. Palm oil is ranked as the most consumed edible oils with 75.45 million metric tonnes of world edible oil consumption [2]. In 2020, export revenue for palm oil products increased to RM 73.25 billion due to higher export prices of palm oil [3], whereby the export volume of PSO to various destinations in the world was 67,408 tonnes worth RM 226.02 million [4]. PSO is widely consumed as cooking oil due to its high stability during frying and less tendency for cloudiness at low temperature [5].

CPO is the first product obtained during the milling of fresh fruit bunches. Native peoples in African countries consume CPO, the unrefined form of palm oil which is high in carotenes and vitamin E contents [6], albeit most people would consume it in the refined form. A further refining process turns CPO into refined palm oil, which is then subjected to fractionation to yield a more edible form of palm oil. Palm oil fractionation is an industrial process to separate liquid and solid phases of palm oil, yielding palm olein (liquid phase) and palm stearin (solid phase), with distinctive physico-chemical characteristics. Fractionation mainly involves crystallization at low temperature, and filtration to separate the two phases [7].

It has become a new interest in the market for high value added or special cuts products, *i.e.*, high iodine value (IV) olein or PSO, which is manufactured through multiple stages of fractionation as shown in Figure 1 [8]. High IV olein of 64 to 66 can even be produced through a single step fractionation, although multiple stages are often required. This special cut product is tailored to cater palm olein with higher stability towards cloudiness at low temperature settings, through the removal of saturated triacylglycerols from the olein fraction.

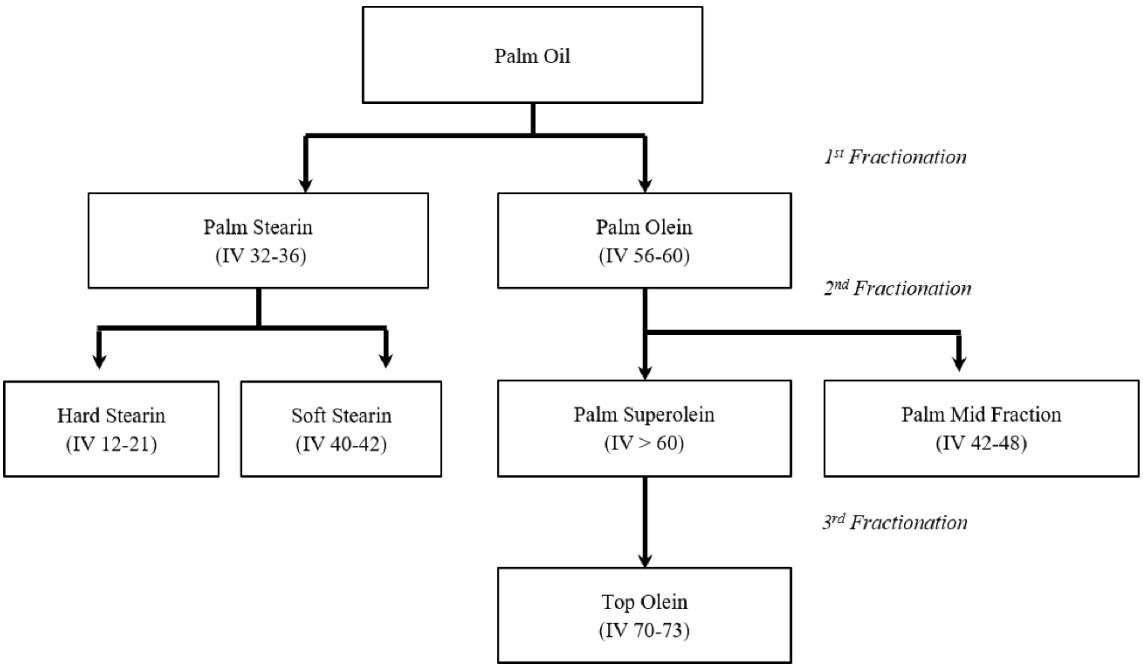


Figure 1. Multiple stages of fractionation in palm oil

PSO is the liquid fraction derived from palm oil produced through a specified controlled crystallization process to achieve a desirable IV of 60 and above [9]. It is produced by single or double fractionation. Although less demanded, it is one of the higher value fractions of palm oil. PSO has the ability to withstand colder temperatures, hence it has better resistance to clouding. It also has better clarity and stability. Generally, PSO appears transparent with light yellow in colour. Apart from being used as cooking and frying oils, it is also used for blending with polyunsaturated oils produced in temperate countries [10].

Parameters such as free fatty acids content, peroxide value and moisture content are among the important factors in determining the quality of the oil produced, and subsequently puts a price on the oil [11, 12]. Global trading of palm oil products is based on quality specifications set by international and national standards bodies. The standard specification documents commonly referred to includes Codex Alimentarius International Food Standards and Malaysian Standards. Trading specifications may also be practiced on a "willing buyer, willing seller" basis [13]. These standards are introduced to harmonise and establish uniformly accepted criteria for a certain product. The important quality parameters specified in Codex CXS 210-1999 are listed in Table 1 [9, 10].

Table 1. General characteristics of palm superolein

Parameter	**1995 Palm Superolein Assessment** [10] **(n = 32)**		**Codex CXS 210-1999** [9]
	Range	**Mean ± Standard Deviation**	
Refractive Index, RI (nD, 30 °C)	1.4631 – 1.4641	1.4634 ± 0.0003	1.459 – 1.460 (@ 40 °C)
Apparent Density, AD (g mL^{-1}, 30 °C)	0.9042 – 0.9054	0.9046 ± 0.0003	0.886 – 0.900 (@ 40 °C)
Iodine Value, IV (Wijs)	60.1 – 67.5	61.9 ± 2.15	≥ 60
Saponification Value (mg KOH g^{-1} oil)	181 -191	187 ± 3.18	180 – 205
Slip Melting Point, SMP (°C)	12.9 – 16.6	15.1 ± 0.91	-
Cloud Point (°C)	2.8 – 5.7	4.4 ± 0.71	-
Unsaponifiable Matter (%)	0.31 – 0.42	0.38 ± 0.03	≤ 13

Periodic assessments of the quality attributes of palm oil products assist in providing current information for revision of the standards, to reflect current production quality among palm oil producing companies. The previous and only published assessment on the characteristics of PSO was reported by Tang et al. [10] and presented limited information on the general characteristics and compositions of PSO (Table 1).

In view of the requirement for an up-to-date study on PSO quality, the objective of this article is to present the outcome of an assessment on the quality of Malaysian PSO for better understanding and evaluation of its current quality and identity characteristics for future improvement of the fractionation technology. The findings from this assessment were used for the revision of the Codex CXS 210-1999 Standard for Named Vegetable Oils and Malaysian Standard 1762:2004 – Palm Superolein Specifications. This round of assessment was believed to be timely as the last round of national assessment was conducted more than 25 years ago.

Materials and Methods

Sample collection

In the present study, a total of 44 refined, bleached and deodorized (RBD) PSO samples were collected from several palm oil refineries and ports in Peninsular Malaysia, Sabah and Sarawak in 2016, 2018 and 2019. One kilogram of sample was collected into a one litre opaque bottle, on a monthly basis, or whenever there was a PSO production at the refinery as PSO is usually manufactured upon request from the buyer. The samples were stored in a cool (~5 °C), dry place prior to analysis.

Chemicals and reagents

All chemical reagents and solvents used were analytical grade and high-performance liquid chromatography (HPLC) grade, and were purchased from Sigma-Aldrich, Michigan, USA.

Sample preparation

PSO samples collected were thoroughly shaken to ensure complete homogeneity according to the method described in MPOB Test Method p1.2 [14].

Physico-chemical parameters testing

The samples were subjected to physico-chemical characteristics evaluation which included iodine value, fatty acids composition, triacylglycerols composition, refractive index, apparent density, relative density, slip melting point, peroxide value, impurities content, moisture content, free fatty acids content, unsaponifiable matter and saponification value. The method of analyses was based on MPOB Test Methods, AOCS Official Methods and ISO Standard Methods. All measurements were done in triplicate, unless stated otherwise.

Free fatty acids (FFA) content

FFA content was determined according to the titration procedure based on AOCS Official Method Ca 5a-40 [15]. About 20 g of PSO sample was dissolved in neutralized *iso*-propanol and the free acids were titrated with 0.1 M sodium hydroxide solution (standardised with potassium hydrogen phthalate before usage). Phenolphthalein was added as an indicator to observe and to detect the endpoint. The endpoint is determined at the appearance of the first permanent pink colour which persists for 30 s. FFA analysis was carried out in duplicate and expressed as percentage of palmitic acid as it is the major fatty acid in palm oil.

Iodine value (IV)

The IV was analysed using the Wijs method based on the procedure described in ISO 3961 [16]. This method involved the dissolution of about 0.4 g PSO sample in a mixture of *iso*-octane and cyclohexane (1:1), and the subsequent addition of Wijs solution. The mixture was then incubated for 60 min, followed by the addition of potassium iodide (10 %) solution and 100 mL deionized water. The mixture was titrated with 0.1 M thiosulphate solution (standardised before usage) until the endpoint was reached. A blank solution was determined concurrently. Potentiometric measurement of the IV was carried out using an automated titration system T90 (Mettler Toledo, Switzerland), and the mean value of duplicate analysis was determined.

Refractive index (RI)

The RI was determined using refractometer Abbemat 300 (Anton Paar, Austria) at the temperature of 40 °C according to the method described in ISO 6320 [17]. The refractometer was calibrated daily against deionised water. A sufficient amount of PSO sample was dropped onto the measuring prism for the RI determination. The RI was determined in duplicate analysis.

Apparent density (AD)

The AD was determined at the temperature of 40 °C, using Densitometer DMA 4500M (Anton Paar, Austria), based on the method in ISO 18301 [18]. A heating element was attached to the densitometer to ensure that the samples remained melted and homogenised during the measurement. The densitometer was calibrated against air for every measurement. Duplicate analysis was carried out.

Relative density (RD)

The RD at 40 °C was determined by calculation using equation 1:

$$Relative\ density\ = \frac{Density\ of\ PSO}{0.9982} \quad (1)$$

where the density of PSO can be obtained during the measurement of apparent density and the value 0.9982 is the density of ultrapure water at 20 °C.

Moisture content

Moisture content was measured using the Karl Fischer volumetric moisture analyser (Mettler Toledo, Switzerland) according to the procedure described in ISO 8534 [19]. Samples were introduced into the flask containing Aqualine™ Complete 5 reagent (Fischer Scientific, USA). The fat content was titrated against an iodine solution and sulfur dioxide was oxidised by

iodine in the presence of water. The moisture content was measured in duplicate analysis.

Impurities content

Impurities content was determined using an oven method based on ISO 663 [20]. The sample was first filtered by using Whatman glass fibre filter paper, followed by washing with petroleum ether for several times. The filter paper with the filtrate was then heated in the oven at 103 °C for 2 h. The residue weight was measured and calculated as the impurities content in the percentage of mass fraction. The mean of duplicate analysis was reported as the impurities content.

Peroxide value (PV)

Analysis of PV was carried out using the titration technique and the potentiometric endpoint determination was based on the procedure described in ISO 27107 [21]. 5 g of PSO sample was dissolved in 50 mL acetic acid: iso-octane (3:2). Next, approximately 0.5 mL of saturated potassium iodide solution was added into the mixture and gently stirred for 1 min, followed by the addition of 30 mL deionized water. The mixture was then titrated with 0.01 M sodium thiosulphate ($Na_2S_2O_3$) solution until the endpoint was reached. The mean value of duplicate analysis was determined as the PV.

Slip melting point (SMP)

The measurement of SMP was carried out following procedures described in AOCS Official Method Cc 3-25 [22]. The sample was placed in a tube and solidified in the freezer, before heat was applied to the tube containing the sample. The sample was heated until the fat rose in the tube and the temperature at which the sample rose was recorded as the slip melting point. The measurement of SMP was carried out in triplicate.

Saponification value (SV)

The SV was analysed by titration of excess potassium hydroxide with hydrochloric acid solution, as described in ISO 3657 [23]. Approximately 2 g of sample was first mixed with 25 mL ethanolic potassium hydroxide solution and refluxed for 60 min. About 0.5 to 1.0 mL phenolphthalein indicator was added into the hot solution. The mixture was then titrated with hydrochloric acid until the pink colour of the indicator disappeared. A blank measurement was also carried out. The mean of two determinations was taken as the SV and expressed as a whole number.

Unsaponifiable matter

The unsaponifiable matter was determined following the method in ISO 3596 [24]. About 5 g of PSO was refluxed with 50 mL of potassium hydroxide solution for 1 h. The mixture was then cooled, and 100 mL of water was added and mixed well. The solution was then extracted several times with diethyl ether. Each time, the organic layer was collected and washed twice with 40 mL portions of water and once with 40 mL potassium hydroxide solution, and neutralised with 40 mL of water. The solution was evaporated at 103 °C for 15 min, allowed to cool and weighed until constant mass was obtained. The unsaponifiable matter was analysed in duplicate and the mean value was expressed as the result in percentage mass.

Fatty acids composition (FAC)

The FAC in the oil sample was measured as their corresponding methyl esters (FAME) based on the method described in ISO 12966 - Part 2 [25]. About 0.2 mL methanolic sodium methoxide was added to 0.05 g of dissolved oil sample for transmethylation to take place. After 5 min, approximately 1 mL of sodium chloride solution was added. The clear upper phase of methyl esters was carefully pipetted out and approximately 0.5 g of sodium hydrogen sulfate was added into the solution. The FAME was analysed using an Agilent GC 7890A series equipped with a flame ionization detector and a fused silica capillary column SP™ 2560 (100 m × 0.25 mm film thickness). The oven temperature was initiated at 120 °C and increased to 240 °C at 4 °C min^{-1}, then maintained for 7 min at 240 °C. Hydrogen gas was used as the carrier gas with a flow rate of 1 mL min^{-1}. The injection volume was 1 µL. The analysis was carried out in triplicate. FAC is expressed as percentage of respective fatty acids.

Triacylglycerols composition (TAG)

Quantification of TAG was carried out based on AOCS Official Method Ce 5b-89 [26] and Ce 5c-93 [27]. About 1 µL of samples dissolved in acetone was injected into

an Acquity UPLC® BEH C18 column (Waters Corp., Milford, Massachusetts, USA), with particle size of 1.7 µm, id 2.1 mm × 150 mm length, maintained at 30 °C. Isocratic elution using a mixture of acetone and acetonitrile (63.5:36.5) was carried out at a flow rate of 0.25 mL min^{-1} with a total runtime of 30 min. The detection of TAG was performed by refractive index and the TAG was quantified using the peak area normalisation method. The analysis was carried out in triplicate.

Statistical analysis

All statistical analyses were performed using Microsoft Excel 2013 (Microsoft Corporation, Redmond, WA). The linear correlation between selected quality parameters was assessed by Pearson's correlation coefficient using Minitab 19 (Minitab LLC, Pennsylvania, USA). All numerical data were expressed as the mean ± standard deviation (SD).

Results and Discussion

Physico-chemical characterisation of PSO

From the 44 samples of PSO analysed, the relevant quality control parameters such as RI, AD, IV, moisture and impurities (M&I), SMP, FFA, SV and unsaponifiable matter were found to be within the limits set by Codex CXS 210-1999 for PSO. Results are presented in Table 2 in terms of mean, standard deviation and range observed.

Table 2. Mean value with standard deviations and range of physicochemical characteristics of palm superolein

Parameter	2016/19 Palm Superolein Assessment (n = 44)			
	Mean	Standard Deviation	Min	Max
Refractive Index, RI (nD, 40 °C)	1.45933	0.00023	1.45898	1.45974
Apparent Density, AD (g mL^{-1}, 40 °C)	0.89785	0.00027	0.89720	0.89839
Iodine Value, IV (g I_2/100 g oil)	62.3	1.6	59.5	65.2
Moisture & Impurities, M&I (%)	0.05	0.01	0.02	0.08
Slip Melting Point, SMP (°C)	15.3	1.3	12.9	16.8
Free Fatty Acid, FFA (%)	0.08	0.04	0.02	0.14
Saponification Value (mg KOH g^{-1} oil)	201	10.6	181	217
Unsaponifiable Matter (%)	0.37	0.27	0.14	1.06
Peroxide Value (meq O_2 kg^{-1})	2.08	1.22	0.92	5.88

Determination of M&I contents in PSO is one of the quality requirements specified in the Malaysian Standard (MS) 1762 – Palm Superolein Specification [28]. The maximum M&I content allowed for PSO is 0.10%. The current assessment revealed that the PSO analysed had lower M&I (0.05%) than the maximum allowable limit, with a range of between 0.02% and 0.08%. Refined products should have lower amount of M&I than the crude palm oil as the crude palm oil was first subjected to drying process prior to the refining process. This step is important to avoid further hydrolysis reaction of the oil which will facilitate the increase in the FFA content of the oil [29].

FFA is commonly used as an early indicator of the quality and the acceptability of palm oil or any edible oil. It is one of the most important key quality parameters in the trading of oils and fats as it is a product of triacylglycerols hydrolytic degradation [13]. The Palm Oil Refiners Association of Malaysia (PORAM) standard specifications for RBD palm olein listed FFA as 0.1% maximum. The samples showed an average FFA content of 0.08% varying between 0.02% and 0.14%, of which were within the PORAM specifications. These ranges are acceptable as PSO is considered stable and less susceptible to hydrolytic reaction as high amount of moisture and FFA was significantly removed during the refining process [1].

PV is a parameter reflecting the degree of deterioration of palm oil products exposed to atmospheric oxygen [30]. From the PSO samples analysed, PV varied widely

from as low as 0.92 meq O_2 kg^{-1} to 5.88 meq O_2 kg^{-1}. This was probably due to the gap in time of production at the refinery as well as the time of analysis of the samples [31]. Although there was a wide variation of PV in the PSO samples, these values were acceptable by Codex which specifies PV up to 10 meq O_2 kg^{-1} for refined oils [9]. Moreover, PV is known to be unstable due to the fact that the hydroperoxides of the unsaturated fatty acids resulting from lipid oxidation are very unstable, and degrade into various volatile and non-volatile components [32]. This trend of PV instability may also be attributed to the rapid degradation of the hydroperoxides to secondary oxidation products, *i.e*., ketones, aldehydes.

RI is the measure of light ray bend angle when it goes through oil into air. It is highly dependent on the temperature it is measured, which usually is the temperature at which the oil is completely liquid [33]. It is typically used for the determination of purity together with other identity parameters. Tang et al. [10] reported that RI of PSO was in the range of 1.4631 and 1.4641, analysed at 30 °C. However, the values were not comparable to the values specified in the Codex CXS 210-1999 as the experimental temperature was not standardised to 40 °C. The recent Codex Committee of Fats and Oils in 2019 had endorsed a new range value at 40 °C. The PSO samples analysed at 40 °C had a mean value of 1.45933, with a narrow range from 1.45898 to 1.45974. This range is acceptable by Codex as it fell between the RI values of 1.459 to 1.460 as specified in Codex CXS 210-1999 [9]. RI is a physical characteristic associated to the structural property of the oil [34]. Hence, the more liquid the oil is, the higher the RI. It is important to note that the RI increases as the length of carbon chain and number of double bonds (unsaturation) of the fatty acid of the triacylglycerol increases [35], whereby the angle of refraction is reduced, and hence giving higher RI [36]. The values of RI may also be affected by oxidation and polymerisation processes [34, 37].

PSO is traded on a weight basis, but in fact measured in volume. The AD of PSO is an essential parameter for the weight determination in the cargo during shipment [10]. A similar case as in RI was observed for AD, whereby a new range value at experimental temperature of 40 °C was set at 0.886 to 0.900. In the present assessment, the AD measured at 40 °C was between 0.89720 and 0.89839 which fell within the values specified in Codex CXS 210-1999 [9]. It is important for the experimental temperature to be appropriate for testing of both RI and AD in which the oil samples are completely melted, as well as to harmonise with the reference methods recognised internationally such as ISO standard methods. The use of linear least square fit to correlate the function of RI and AD with IV, together with temperature was reported by Liew et al. [38]. Notably, both RI and AD were found to be linearly decreasing with temperature (30 to 80 °C), and linearly dependent on the IV of the oil. IV is a degree of the unsaturation of the fatty acids in the triacylglycerols. The high IV of PSO (>60) is contributed by the monounsaturated fatty acids (MUFA) and polyunsaturated fatty acids (PUFA) groups [39].

As PSO has higher IV compared to single-fractionated palm olein, it has better characteristics in terms of oil clarity, stability, and is less likely to turn cloudy [40]. Cloudiness of normal palm olein is often observed in low temperature settings during transportation and storage, as well as in cold weather [41]. This is a result of diacylglycerols (DAG) crystallisation. Although it does not affect the oil quality itself, it is always preferable by consumers to have a non-cloudy oil. Thus, the practice of blending palm olein with other soft oils, and double fractionating palm olein into PSO is applied to obtain a clearer oil. The control of the fractionation process is important to obtain a good quality product, more importantly palm olein of higher IV [42]. Optimising crystallisation temperature influences the yield and the quality of PSO. This advancement in fractionation technology has produced better quality PSO, as more solid fraction is refrained from passing through the membrane filter press, giving higher IV and improved chemical and physical properties of PSO.

PSO contains a high amount of unsaturated fatty acids (MUFA and PUFA) and the major fatty acids in PSO are mainly oleic acid (47%), palmitic acid (35%) and linoleic acid (14%) [40, 43]. Table 3 shows the FAC of PSO analysed in the current assessment. The FAC was

found to be within the range as reported in the previous articles and assessment [10, 40, 43], with oleic acid having the highest mean percentage (45.8%), followed by palmitic acid (35.7%) and linoleic acid (12.6%). The high content of unsaturated fatty acids in PSO makes it the most liquid form of palm oil products.

Table 3. Fatty acids composition of palm superolein

Fatty Acid (Weight Percent as Methyl Ester)	**2016/19 Palm Superolein Assessment (n = 44)**		**Codex CXS 210-1999** [9]
	Mean (%)	**Range (%)**	**Range (%)**
Lauric acid, C12:0	0.3	0.2 - 0.6	0.1 – 0.5
Myristic acid, C14:0	1.0	1.0 - 1.2	0.5 – 1.5
Palmitic acid, C16:0	35.7	32.5 – 38.0	30.0 – 39.0
Palmitoleic acid, C16:1	0.2	0.1 - 0.3	*ND – 0.5
Stearic acid, C18:0	3.7	3.5 - 4.2	2.8 – 4.5
Oleic acid, C18:1	45.8	43.9 – 48.7	43.0 – 49.5
Linoleic acid, C18:2	12.6	11.1 – 13.7	10.5 – 15.0
Linolenic acid, C18:3	0.3	0.2 - 0.3	0.2 – 1.0
Arachidic acid, C20:0	0.3	0.1 - 0.4	ND – 0.4

*ND: not detected

The TAG composition of PSO is listed in Table 4. In general, PSO contains mostly TAG (91%) and DAG (9%) [43]. In this study, the PSO samples analysed showed slightly higher TAG (92.51%) and lower DAG (7.49%). PSO contains more triunsaturated and monosaturated TAG, and less trisaturated TAG, hence the greater IV. Additionally, the much lower trisaturated TAG content in PSO contributed to its resistance towards cloudiness. With regards to the correlation of TAG composition with IV, the function of TAG composition by HPLC analysis to predict the IV of the oil was reported by Haryati et al. [44]. The IV was estimated from the regression model mainly on the peak areas of the disaturated, trisaturated and triunsaturated TAGs.

The SMP is the temperature at which a fat change from solid to liquid phase. It is dependent on the FAC of the oil. The average SMP observed from the PSO analysed was 15.3 °C, with range values between 12.9 °C and 16.9 °C. These values were similar to those reported by Tang et al. [10], and they also reported that PSO with high IV had lower SMP as a result of complex composition of the PSO itself which is a mixture of various species of acylglycerols.

The SV is used to measure the types of acylglycerols in the oil by measuring alkali-reactive groups in the oil. A higher SV indicates low-molecular weight triacylglycerols of edible fats and oils. The range observed for SV was 181 to 217 mg KOH g^{-1}, a slightly wider range compared to the previous assessment in 1995. This range conformed to the lower limit of SV (180 mg KOH g^{-1}) in Codex CXS 210, and slightly exceeded the upper limit of 205 mg KOH g^{-1}. Low SV for PSO is attributable to the high amount of long chain fatty acids, *i.e.* oleic and linoleic acids in the composition of PSO.

The unsaponifiable matter is the fraction of substances in the PSO after saponification, which is not volatile at 103 °C that includes sterols, higher hydrocarbons and alcohols, aliphatic and terpenic alcohols, and foreign matter extracted by diethyl ether [45]. An average value of 0.37% of unsaponifiable matter was observed for PSO. Palm oil is classified as a vegetable oil having low unsaponifiable matter of less than 1.2% [46]. The previous study [46] also stated that sterols are the predominant unsaponifiable matter in most oils. In palm oil, Codex CXS 210-1999 listed β-sitosterol, campesterol and stigmasterol as the three main sterols found in PSO. Tocopherols and tocotrienols fractions are also abundant in palm oil products, in the range of 400 to 1400 mg kg^{-1} [9]. These minor components are highly useful in food applications as well as play a significant role in both human and animal nutrition.

Table 4. Acylglycerol composition of palm superolein

	2016/19 Palm Superolein Assessment (n = 44)	
Glycerol	**Mean (%)**	**Range (%)**
DAG	7.49	6.20 – 10.44
Triunsaturated TAG		
*OLL	0.63	0.52 – 0.88
OLO	2.38	2.04 – 2.67
OOO	5.36	4.55 – 6.37
Monosaturated TAG		
PLL	3.27	2.66 – 3.68
PLO	12.40	10.84 – 13.94
POO	31.18	28.73 – 35.25
SOO	3.12	2.71 – 3.55
Disaturated TAG		
MLP	0.71	0.61 – 0.79
PLP	11.22	10.13 – 12.14
POP	18.30	12.54 – 22.99
POS	3.31	2.42 – 4.11
SOS	0.43	0.29 – 0.56
Trisaturated TAG		
MPP	0.10	0.03 – 0.93
PPP	0.13	0.06 – 0.51

*O – oleic; L – linoleic; P – palmitic; S – stearic; M – myristic

Correlation analysis of selected quality and identity parameters

The linear relationship for IV, RI, AD, FFA and moisture of the PSO samples was assessed using Pearson correlation. The correlation results shown in Table 5 demonstrates a positive relationship for RI-IV, AD-IV and FFA-moisture. A very strong positive correlation was observed for AD-IV with *p*-value of 0.000 (p <0.05), indicating the highly significant correlations. A similar observation was noted for FFA-moisture and this is expected as FFA is highly influenced by moisture content in the oil. Correlations between RI-AD and RI-IV were somewhat insignificant (p >0.05). More data are required to confirm and to derive conclusive correlations between each parameter.

Table 5. Correlation of selected parameters in PSO quality performance

Parameter	**Pearson Correlation Coefficient**	***p*-value**
RI-AD	-0.011	0.944
RI-IV	0.012	0.939
AD-IV	0.843	0.000
FFA-Moisture	0.538	0.012

Conclusion

The present study concludes that the physical characteristics and the chemical compositions of PSO have experienced slight variations over the last two decades, particularly in its RI and AD. This shift suggests that the current advancement in the

fractionation technology has produced better quality PSO for its various uses in the food industry. The overall quality performance of PSO was satisfactory and largely conformed to Codex CXS 210-1999. Periodic evaluation of PSO has helped in understanding the current situation of PSO produced in Malaysia in terms of its quality and the setting of realistic and achievable targets in the quality specification. These new sets of quality data will be used in the revision of guidelines for the identity characteristics of PSO in MS 1762:2004, Palm Superolein - Specification.

Acknowledgement

The authors thank the Director General of MPOB for the permission to publish the research findings. Heartfelt thanks to the technical assistance from the Analytical Research Laboratory of Product Development and Advisory Services Division and Analytical Testing Services Laboratory of Advance Oleochemical Technology Division.

References

1. Tan, C. H., Ghazali, H. M., Ainie, K., Tan, C. P. and Ariffin, A. A. (2009). Extraction and physicochemical properties of low free fatty acid crude palm oil. *Food Chemistry*, 113: 645-650.
2. Statista (2020). Consumption of vegetable oils worldwide from 2013/14 to 2021/2022, by oil type. https://www.statista.com/statistics/263937/vegetable-oils-global-consumption/ [Access online 15 September 2021].
3. Parveez, G. K. A., Tarmizi, A. H. A., Sundram, S., Loh, S. K., Ong-Abdullah, M., Kosheela Devi, P. P., Mohamed Saleh, K., Mohd Ishak, S. and Zainab, I. (2021). Oil palm economic performance in Malaysia and R&D progress in 2020. *Journal of Oil Palm Research*, 33(2): 181-214.
4. Malaysian Palm Oil Board (MPOB) (2020). Malaysian Oil Palm Statistics 2020. MPOB, Malaysia: pp. 75.
5. Pande, G., Akoh, C. C. and Lai, O. M. (2012). Palm Oil: Production, Processing, Characterization and Uses. AOCS Press, USA: pp. 576-577.
6. Palm Oil World (2020). Nutrition benefits. http://www.palmoilworld.org/nutrition.html [Access online 23 November 2020].
7. Gee, P.T. (2007). Analytical characteristics of crude and refined palm oil and fractions. *European Journal of Lipid Science and Technology*, 109: 373-379.
8. Gibon, V. (2012). Palm oil: Production, processing, characterization and uses. AOCS Press, USA: pp. 364-365.
9. Food and Agriculture Organization of the United Nations and World Health Organization. Codex Alimentarius International Food Standards - CODEX Standard for Named Vegetable Oils Codex CXS 210-1999 [Access online 15 September 2021].
10. Tang, T. S., Chong, C. L., Yusoff, M. S. A. and Ab Gapor, M. T. (1995). Characteristics of superolein from the fractionation of palm oil. *PORIM Technology*, 17: 1-9.
11. Endo, Y. (2018). Analytical methods to evaluate the quality of edible fats and oils: The JOCS standard methods for analysis of fats, oils and related materials (2013) and advanced methods. *Journal of Oleo Science*, 67(1): 1-10.
12. Decker, E., Elias, R., McClements, J.D. (2010). Oxidation in foods and beverages and antioxidant applications. Elsevier, Amsterdam: pp. 432.
13. Chong, C. L. (2012). Palm Oil: Production, Processing, Characterization and Uses. AOCS Press, USA: pp. 445.
14. Malaysian Palm Oil Board (2004). MPOB Test Methods: A compendium of test on palm oil products, palm kernel products, fatty acids, food related products and others. MPOB, Malaysia: pp. 153-155.
15. American Oil Chemists' Society (AOCS) (2017). Official methods and recommended practices of the AOCS, 7th ed. AOCS Press, USA: Method Ca 5a-40.
16. International Organization for Standardization (ISO) (2018). ISO 3961. Animal and vegetable fats and oils - Determination of iodine value. ISO, Switzerland.
17. International Organization for Standardization (ISO) (2017). ISO 6320. Animal and vegetable fats and oils - Determination of refractive index. ISO, Switzerland

18. International Organization for Standardization (ISO) (2014). ISO 18301. Animal and vegetable fats and oils - Determination of conventional mass per volume (litre weight in air) - Oscillating U-tube method. ISO, Switzerland.
19. International Organization for Standardization (ISO) (2017). ISO 8534. Animal and vegetable fats and oils - Determination of water content - Karl Fischer method (pyridine free). ISO, Switzerland.
20. International Organization for Standardization (ISO) (2017). ISO 663. Animal and vegetable fats and oils - Determination of insoluble impurities content. ISO, Switzerland.
21. International Organization for Standardization (ISO) (2008). ISO 27107. Animal and vegetable fats and oils - Determination of peroxide value - Potentiometric end-point determination. ISO, Switzerland.
22. American Oil Chemists' Society (AOCS) (2017). Official methods and recommended practices of the AOCS, 7th ed. AOCS Press, USA: Method Cc 3-25.
23. International Organization for Standardization (ISO) (2020). ISO 3657. Animal and vegetable fats and oils - Determination of saponification value. ISO, Switzerland.
24. International Organization for Standardization (ISO) (2000). ISO 3596. Animal and vegetable fats and oils - Determination of unsaponifiable matter - Method using diethyl ether extraction. ISO, Switzerland.
25. International Organization for Standardization (ISO) (2017). ISO 12966-2. Animal and vegetable fats and oils - Gas chromatography of fatty acid methyl esters - Part 2: Preparation of methyl esters of fatty acids. ISO, Switzerland.
26. American Oil Chemists' Society (AOCS) (2017). Official methods and recommended practices of the AOCS, 7th ed. AOCS Press, USA: Method Ce 5b-89.
27. American Oil Chemists' Society (AOCS) (2017). Official methods and recommended practices of the AOCS, 7th ed. AOCS Press, USA: Method Ce 5c-93.
28. Malaysian Standard (2004). MS 1762. Palm Superolein – Specification. ICS: 67.200.10. Department of Standards, Malaysia.
29. Sherine, S. M. A.E. and Basma, M. M. E. (2020). Precision Agriculture Technologies for Food Security and Sustainability. 1st Ed. USA, IGI Global: pp. 437.
30. Frankel, E. N. (2012). Lipid Oxidation. Woodhead Publishing Limited, USA: pp. 104.
31. Almeida, D. T., Viana. T. V., Costa, M. M., Silv,a C. S. and Feitosa, S. (2019). Effects of different storage conditions on the oxidative stability of crude and refined palm oil, olein and stearin (*Elaeis guineensis*). *Food Science and Technology,* 39(1): 211-217.
32. Kaleem, A., Aziz, S., Iqtedar, M., Abdullah, R., Aftab, M., Rashid, R., Shakoori, F. R. and Naz, S. (2015). Investigating changes and effect of peroxide values in cooking oils subject to light and heat. *FUUAST Journal of Biology,* 5(2): 191-196.
33. Hishamuddin, E., Sulaiman, N., Ahmad Bustamam, F. K. and Yeoh, C. B. (2020). Recent updates on the Codex standard for named vegetable oils (CXS 210-1999) in relation to palm oil and palm kernel oil. *Palm Oil Developments,* 72: 34-41.
34. Godswill, A. C., Omagwula, I. O., Victory, I. S. and Gonzaga, A. I. (2018). Effects of repeated deep-frying on refractive index and peroxide value of selected vegetable oils. *International Journal of Advanced Academic Research,* 4 (4): 106-119.
35. Al Majidi, M. I. H. and Bader, A. T. (2015). Physicochemical characteristics of some imported edible vegetable oils in Iraq. *Research Journal of Pharmaceutical, Biological and Chemical Science, 6(5): 488-494.*
36. Imoisi, O. B., Ukhun, M. E., Ezoguan, V. O. and Osemwegie, Q. E. (2018). Fatty acid profiles, correlation of iodine value, refractive index of heated, unheated palm kernel oil and palm olein. *Journal of Chemical Society of Nigeria*, 43 (4): 745-751.
37. Patterson, H. B. W. (2009). Bleaching and Purifying Fats and Oils: Theory and Practice. AOCS Press, USA: pp. 18.

38. Liew, K. Y., Latiff, N. A., Nordin, M. R. and Seng, C. E. (1995). Densities and refractive indices of hydrogenated palm olein and fractionated palm oil. *Elaeis*, 7(2): 159-164.
39. Hashem, H. A., Nasser, E. A., Ghareeb, A. A. and Adel, G. A. (2018). Industrial scale production of palm super olein using modified and innovative dry fractionation technique. *Egyptian Journal of Chemistry*, 61: 1-11.
40. Malaysian Palm Oil Board (MPOB) (2009). Pocketbook of Palm Oil Uses. MPOB, Malaysia: pp. 23.
41. Idris, N. A., Jamaludin, R. and Hassan, H. (2003). Process to prevent and delay clouding in palm olein. *US Patent* No. 20030068426 A1.
42. Che Man, Y. B., Haryati, T., Ghazali, H. M. and Asbi, B. A. (1999). Composition and thermal profile of crude palm oil and its products. *Journal of the American Oil Chemists' Society,* 76(2): 237-242.
43. Goon, D. E., Siti Hamimah, S. A. K., Ab Latip, N., Ab Rahim, S. and Mazlan, M. (2019). Palm oil in lipid-based formulations and drug delivery systems. *Biomolecules,* 9(2): 64.
44. Haryati, T., Che Man, Y. B., Ghazali, H. M., Asbi, B. A. and Buana, L. (1998). Determination of iodine value of palm oil based on triglyceride composition. *Journal of the American Oil Chemists' Society,* 75(7): 789-792.
45. Malaysian Palm Oil Board (2004). MPOB test methods: A compendium of test on palm oil products, palm kernel products, fatty acids, food related products and others. MPOB, Malaysia: pp. 198-203.
46. Rao, B. S. N. (2001). Nonglyceride components of edible oils and fats. 1. Chemistry and distribution. *Food and Nutrition Bulletin*, 22(1): 81-86.

Malaysian Journal of Analytical Sciences (MJAS)
Published by Malaysian Analytical Sciences Society

BIOTEMPLATED BISMUTH FERRITE ($BiFeO_3$) NANOCATALYST FOR THE PHOTODEGRADATION OF OFLOXACIN BY SOLAR LIGHT UNDER THE INFLUENCE OF OPERATIONAL PARAMETERS

(Templat Bio Bismut Ferit ($BiFeO_3$) Nanopemangkin untuk Fotodegradasi Ofloxacin Menggunakan Cahaya Suria Dibawah Pengaruh Parameter Operasi)

Ahmad Fadhil Rithwan[1], Muhammad Alif Abdul Khani[1], Noor Haida Mohd Kaus[1]*, Rohana Adnan[1], Sirikanjana Thongmee[2], Siti Fairus Mohd Yusoff[3], Takaomi Kobayashi[4], Mohd Amirul Ramlan[5]

[1] School of Chemical Sciences,
Universiti Sains Malaysia, 11800, Pulau Pinang, Malaysia
[2]Physics Department,
Faculty of Science, Kasetsart University, Bangkok 10900, Thailand
[3] Department of Chemical Sciences,
Faculty of Science and Technology, Universiti Kebangsaan Malaysia,
Bangi 43600, Selangor, Malaysia
[4]Department of Materials Science and Technology,
Nagaoka University of Technology Nagaoka, Japan
[5]Department of Polytechnic & Community Colleges Education,
Ministry of Higher Education, Persiaran Perdana, Presint 4, Putrajaya 62100, Malaysia

**Corresponding author: noorhaida@usm.my*

Received: 2 March 2022; Accepted: 3 July 2022; Published: 30 October2022

Abstract

Bismuth ferrite ($BiFeO_3$) has been demonstrated to be one of the most efficient perovskite-based photocatalysts for pollutant degradation under direct sunlight. The focus of this research was to study the photocatalytic activity of $BiFeO_3$ in relation to the degradation of the antibiotic ofloxacin. Different operational parameters for the optimized system were determined, such as photocatalyst dosage (0.05 g L^{-1} to 0.50 g L^{-1}), pollutant concentration (2.5 mg L^{-1} to 20 mg L^{-1}), reaction duration (2 hours), pH of solution (pH 2 to pH 12), and the effect of hydrogen peroxide, H_2O_2 as an oxidant (0.1 M to 0.7 M). X-ray Diffraction (XRD), Scanning Electron Microscope-Energy Dispersive X-ray (SEM-EDX), and Fourier Transform Infrared Spectroscopy (FTIR) analyses all corroborated that the rhombohedral $BiFeO_3$ has a high purity and large surface area. The most efficient condition for all selected parameters was 0.07 g L^{-1} $BiFeO_3$ at pH 8 in 10 mg L^{-1} of ofloxacin and the addition of 0.3 M H_2O_2 with 70.1% degradation and the total organic carbon left in the solution was 9.36%. The reaction obeyed pseudo-first order kinetics with R^2 value obtained is 0.9399, with decreasing *k* values as the initial concentration increased. This demonstrated that the system performed best at low concentrations. This discovery paves the way for future research into the operational parameters that contribute to the photocatalyst efficacy in removing antibiotics as a pollutant.

Keywords: photocatalysis, photofunctional material, ofloxacin, visible light source, bismuth ferrite

Abstrak

Ferit bismut, $BiFeO_3$ terbukti sebagai salah satu daripada fotopemangkin berasaskan perovskit terbaik untuk degradasi pelbagai pencemar di bawah cahaya matahari langsung. Kajian ini dijalankan untuk mempelajari prestasi fotoaktiviti $BiFeO_3$ terhadap degradasi antibiotik ofloxacin. Parameter operasi yang berbeza telah ditentukan untuk sistem yang dioptimumkan termasuk dos fotopemangkin (0.05 g L^{-1} hingga 0.50 g L^{-1}), kepekatan bahan cemar (2.5 mg L^{-1} hingga 20 mg L^{-1}), masa tindak balas (2 jam), pH (pH 2 hingga pH 12), dan kesan hidrogen peroksida (H_2O_2) sebagai agen pengoksidaan (0.1 M hingga 0.7 M). Keputusan analisis pembelauan sinar-x (XRD), spektroskopi inframerah-transformasi Fourier (FT-IR) dan mikroskop elektron imbasan-spektroskopi sinar-x penyebaran tenaga (SEM-EDX) mengesahkan ketulenan tinggi $BiFeO_3$ rombohedral yang telah dihasilkan dengan luas permukaan yang tinggi. Keadaan yang paling berkesan untuk semua parameter terpilih adalah dos $BiFeO_3$ 0.07 g L^{-1} pada pH 8 di dalam 10 mg L^{-1} ofloxacin dengan penambahan 0.3 M H_2O_2 yang menghasilkan degradasi ofloxacin sebanyak 70.1% dan jumlah kesuluruhan karbon yang tinggal didalam larutan adalah sebanyak 9.36 %. Tindak balas ini tergolong di dalam urutan kinetik pseudo-pertama dengan nilai R^2 tercapai sebanyak 0.9399, dengan nilai *k* menurun apabila kepekatan awal meningkat. Ini menunjukkan bahawa sistem ini adalah lebih efisyen pada kepekatan yang rendah. Penemuan ini telah membuka satu kajian berpotensi ke arah penerokaan faktor yang meningkatkan kecekapan fotopemangkin bagi penyingkiran pencemar antibiotik.

Kata kunci: fotopemangkinan, bahan fotofungsian, ofloxacin, sumber cahaya boleh lihat, bismut ferit

Introduction

Urbanization and industrialization have a detrimental effect on many countries water sources. Textile industries, hospitals, farms, and residences may discharge a variety of contaminants, including dyes [1], heavy metals [2], pesticides [3], and antibiotics [4]. Antibiotics can be classified as an emerging contaminant since their concentration in water bodies has increased over the years due to increases in utilization rates in the human and livestock sectors [5]. According to Ambrosetti et al. [6], antibiotics may exist in the environment as parent molecules, breakdown products, and they are partially metabolites in nature. Moreover, these antibiotic wastes are reported to be bioaccumulated, bio-transformed, and deposited in the solid and aqueous phases [7], thus increased the antibiotic persistence in the environment.

A fluoroquinolone antibiotic called ofloxacin (OFL) has been utilized for treating bacterial infections of the skin, lungs, and urinary tract [8]. Fluoroquinolones may be discovered in amounts ranging from 18.28 ng L^{-1} to 6,058 µg L^{-1} in hospital, wastewater, and slaughterhouse effluent. These range of values exceeded the values recommended by The World Health Organization (WHO) guideline that should be less than 100 µg L^{-1}. Although several reports claimed that the measured concentration of ofloxacin in water bodies is lower than the limit, its presence is still a severe problem that should be eliminated. Researchers have been working on developing methods to eradicate this contaminant using adsorption [9], biosorption [10], or photocatalysis [11] methods. Nonetheless, photocatalysis remains as one of the best strategies for antibiotic degradation as it is cost-effective and generates little waste. Conventional photocatalysts, such as TiO_2 and ZnO, have significant drawbacks, including a restricted response to visible light irradiation as a result of their large band gap energies of 3.2 eV and 3.3 eV, respectively [12,13]. As a result, research on alternatives has been conducted to overcome the restrictions.

Soltani et al. [14] discovered that bismuth ferrite ($BiFeO_3$) has a band gap of 2.17 eV, which is narrow and is theoretically suitable for the operation employing visible light irradiation. $BiFeO_3$ enhanced magnetic and optical characteristics, as well as its increased oxidizing capacity, has made it a viable photocatalyst [15]. This material exists in three common phases: perovskite ($BiFeO_3$), mullite ($Bi_2Fe_4O_9$), and sillenite ($Bi_{25}FeO_{40}$), each with slightly different photocatalytic performance [16]. Previously, Yang et al. [17] used a sillenite phase of $BiFeO_3$ in the degradation of levofloxacin, and the photocatalytic activity was exceptional. Zahra et al. [18] also employed $BiFeO_3$ for tetracycline breakdown and demonstrated substantial potential under visible light irradiation.

The initial concentration of pollutants, photocatalyst dosage, pH solution, and irradiation time are examples of the important operational parameters in the photocatalytic reaction. As Wang et al. [19] reported, the removal efficiency increases with increasing catalyst dosage until it reaches the optimum dosage and start to decline as the dosage further increase. The turbidity of the solution caused the reduction in the photon penetration through the solution. In their work, Hapeshi et al. [20] stated that the removal efficiency of ofloxacin started to decrease from 100 % to 88 % as the initial concentration increased from 10 mg L^{-1} to 20 mg L^{-1}. Besides, Hu et al. [16] also reported that the solution pH could affect the photocatalytic degradation of bisphenol A due to the alteration of the surface charge in different pH conditions.

The morphological, optical, and other features of the produced perovskite $BiFeO_3$ were studied in this work. Also, the influence of the operating settings on the ofloxacin photocatalytic degradation by $BiFeO_3$ was investigated under the illumination of sunlight.

Materials and Methods

Bismuth nitrate pentahydrate ($Bi(NO_3)_3.5H_2O$), iron nanohydrate ($Fe(NO_3)_3.9H_2O$), *kappa*-carrageenan, and ofloxacin were all purchased from Sigma-Aldrich with more than 99 % purity. Meanwhile, sodium hydroxide (NaOH) pellets, sodium nitrate ($NaNO_3$), ethanol (99.7%), and hydrochloric acid (HCl) (37%) were supplied from R&M Chemicals.

Synthesis of perovskite bismuth ferrite (BFO)

$BiFeO_3$ nanoparticles were synthesised utilising the sol-gel technique with bio-templating, as proposed by Satar et al. [21]. An amount 2.80 g bismuth nitrate pentahydrate ($Bi(NO_3)_3.5H_2O$) was first dissolved in 50 mL deionized water. The aforementioned solution was then mixed with 4.04 g of iron (III) nitrate nonahydrate ($Fe(NO_3)_3.9H_2O$). In 100 mL of deionized water, 1.00 g of *kappa*-carrageenan powder (1%) was dissolved completely. Following that, 40 mL of 1%-carrageenan solution and 10 mL of Bi and Fe salts solution were mixed and agitated with a magnetic stirrer. Using 1.0 M NaOH solution, the pH of the combination was adjusted to pH 10. The resultant sol was dried in an oven at 80 °C overnight after 2 hours of stirring. In the muffle furnace, the dried gel was calcined for 2 hours at 550 °C. Subsequently, the powder was rinsed multiple times with deionized water and ethanol prior drying at 80 °C for 2 hours.

Characterization of perovskite bismuth ferrite (BFO)

The X-Ray Diffraction (XRD) pattern of $BiFeO_3$ nanoparticles was obtained using a PANalytical X'Pert PRO with graphite monochromator and Cu K radiation ($\lambda = 1.5406$) in the range of 10 - 80°. The morphology and chemical composition of $BiFeO_3$ nanoparticles before and after photocatalytic activity were examined utilizing scanning electron microscopy (SEM, FEI-QUANTA FEG 650) and an Energy Dispersive X-Ray spectroscopy (EDX) microanalyzer (INCA X, Oxford Instruments). The band gap of $BiFeO_3$ was estimated using the reflectance percentage (%R) acquired from the UV-vis diffraction reflectance (UV-DRS) spectrophotometer (LAMBDA 25). The functional group present in $BiFeO_3$ was identified using Perkin Elmer's System 2000 IR in the wavenumber range 4000 – 400 cm^{-1}. Through nitrogen adsorption (BET analyser), the surface features and porosity of $BiFeO_3$ were investigated using the Micromeritics ASAP 2020 Surface Area and Porosity analyzer. Finally, the removal of total organic carbon (TOC) was assessed using a TOC analyzer (Shimadzu TOC-L).

Degradation of ofloxacin under direct sunlight

The photocatalytic activities of $BiFeO_3$ nanoparticles were investigated using the degradation of ofloxacin (OFL) solution in the presence of sunlight. This study was carried out between March and August 2021, from 11 a.m. to 3 p.m. Typically, 100 mL of 10 mg L^{-1} OFL solution (unadjusted pH) was placed into a beaker followed by adding catalyst (10 mg, that corresponds to 0.1 g L^{-1}). First, the solution was magnetically agitated for 30 minutes in the dark to produce adsorption-desorption equilibrium. The solution was then exposed to sunlight for 2 hours. Sampling was performed by withdrawing 5 mL of the solution at 20-minute intervals and filtering with 0.22-micron filters before been analyzed at 288 nm using UV-vis spectrophotometer (Shimadzu UV-2600). A control experiment was done

by using the same procedure but without the presence of photocatalyst. A calculation by using the following equation was made to obtain the percentage removal of OFL solution:

$$Removal\ (\%) = \left(1 - \frac{C_t}{C_o}\right) \times 100 \quad (1)$$

Based on the above equation, removal (%) represents the percentage removal of OFL in the experiments. C_t and C_o represent the concentration of OFL at the given time and the initial concentration of OFL, respectively. The effect of catalyst dosage in the experiment was carried out by varying the dosage at 0.05, 0.07, 0.09, 0.3, and 0.5 g L^{-1}. For the effect of pH, 0.1 M NaOH and 0.1 M HCl were used to alter the pH to obtain pH 2, 4, 6, 8, 10, and 12. In the initial concentration of the OFL solution, the concentration used are 2.5, 5, 10, 15, and 20 mg L^{-1} and finally, 0.1, 0.3, 0.5, and 0.7 M H_2O_2 were used to study the effect of hydrogen peroxide in the photocatalytic degradation OFL by $BiFeO_3$ photocatalyst. For each parameter, the test was repeated thrice to achieve an average value.

Results and discussion

Structural and morphological analysis of $BiFeO_3$

$BiFeO_3$ had been successfully synthesized by using the sol-gel method with kappa-carrageenan as a bio template as shown in Figure 1. The chains of κ-carrageenan performed cross-linking to give the protective layers and stabilize the Fe^{3+} and Bi^{3+} ions. As the pH of the mixture increases, κ-carrageenan self-capped the ions and this localized area became the nucleation and growth sites of the $BiFeO_3$ particles. The calcination process did the elimination of κ-carrageenan and the structure of $BiFeO_3$ remained. Figure 2 depicts SEM micrographs and EDX spectra of $BiFeO_3$ nanoparticles before and after photocatalytic degradation. Figure 2(a) shows the morphology of unused $BiFeO_3$ as distorted rhombohedral structure and homogeneously distributed. The average particle size calculated by J-image software, is 90 nm as in agreement with previous method. The SEM micrograph for the employed $BiFeO_3$ in Figure 2(b) confirmed that no substantial changes could be noticed, although average particle sizes increase to more or less than 170 nm. This could be due to $BiFeO_3$ agglomeration after being utilized in photocatalytic activity. The presence of elements such as Bi, Fe, and O in the sample was demonstrated by EDX and the absence of additional elements verified the samples purity. The XRD pattern of synthesized $BiFeO_3$ was demonstrated in Figure 3(a). The catalyst exhibited diffraction peaks at 2θ = 22.48°, 32.12°, 39.56°, 45.89°, 51.67°, 57.12°, and 67.18°, which corresponded to pure rhombohedral phase $BiFeO_3$ Miller's indices of (0 1 2), (1 1 0), (0 2 4), (1 1 6), (3 0 0), and (2 2 0). This pattern is in agreement to the standard perovskite $BiFeO_3$ data (JCPDS card No. 01-073-0548). The predominant peak that could be assigned was (1 0 1), and no corresponding impurity peak was observed, implying that the $BiFeO_3$ nanoparticles produced were pure and exhibited a highly crystalline distorted rhombohedral structure.

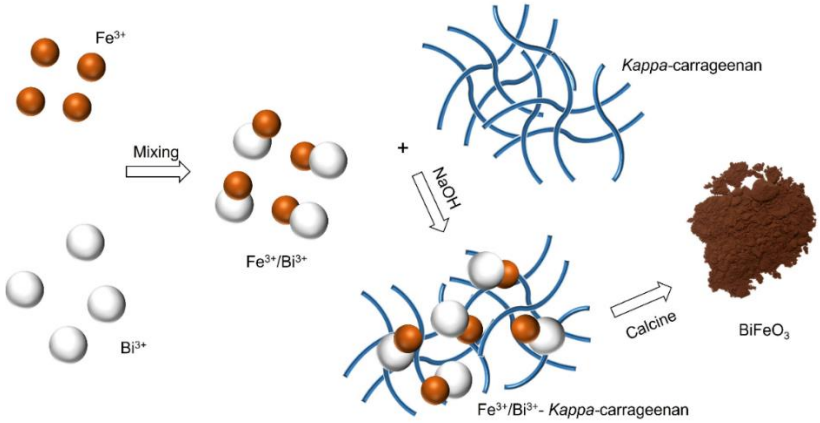


Figure 1. The possible mechanism of utilization of κ-carrageenan as the biotemplate in the synthesis of $BiFeO_3$ nanoparticles

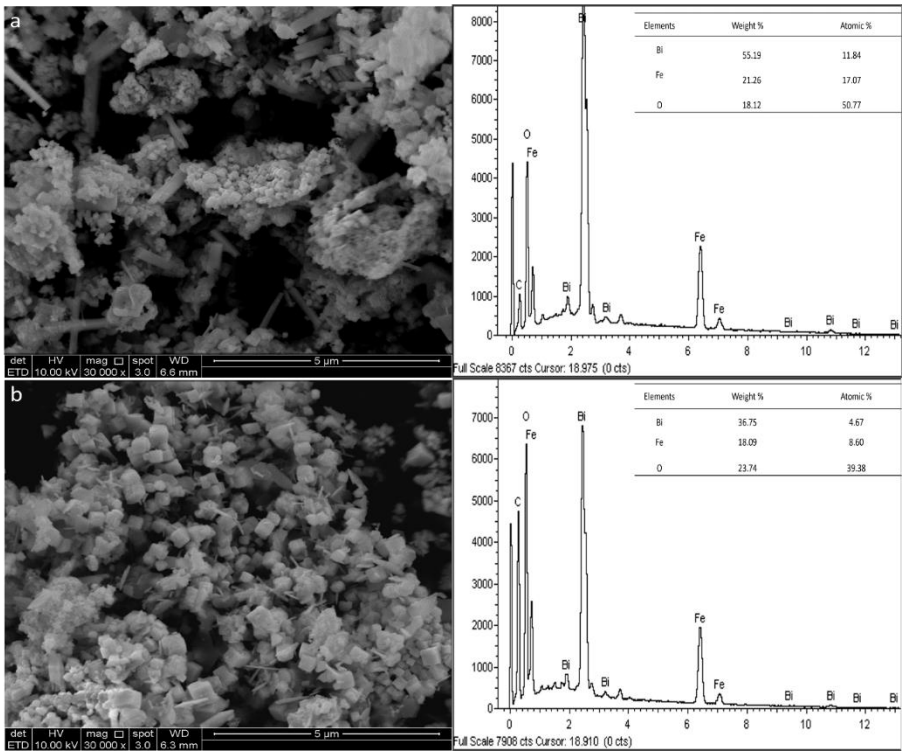


Figure 2. The SEM images of (a) $BiFeO_3$ photocatalyst, and (b) $BiFeO_3$ photocatalyst (used) and their elemental composition

Analysis of the N_2 sorption isotherm

Brunauer, Emmett, and Teller (BET) nitrogen adsorption analysis was used to determine the N_2 sorption isotherm, pore size, pore volume and surface area of $BiFeO_3$. Based on Figure 3(b), the isotherm obtained suggested that $BiFeO_3$ has Type IV and H3 hysteresis loop classification, implying that the sample was primarily composed of mesopores [22] typically range from 2 nm to 50 nm. The presence of plate-like particles in the sample, which aggregated to create slit-shaped pores, is indicated by the H3 hysteresis loop [23]. Figure 3(c) displays pore distribution model (PSD) based on Barrett-Joyner-Halenda (BJH) theory, with pore diameters ranging from 8 nm to 98 nm, confirming the material has mesoporous pores. The PSD plot demonstrated that the pore size and pore volume of $BiFeO_3$ were 31.94 nm and 0.041 $cm^3\ g^{-1}$, respectively, and the surface area obtained was 4.67 $m^2\ g^{-1}$. The porosity features are essential because they can be associated with the adsorption-desorption process of pollutant molecules to the photocatalyst prior to degradation by the photocatalysis process.

BFO optical analysis

The photocatalyst optical properties aid in determining their band gap energy, which is connected to the UV-absorption edge. The UV-vis diffraction reflectance spectra of the synthesized $BiFeO_3$ photocatalyst are depicted in Figure 3(d), and it exhibits substantial absorption of light in the visible light spectrum. Kubelka-Munk theory formula was used to determine the band gap energy of $BiFeO_3$. The corresponding band gap energy can be ascertained from the extrapolated tangent line in the plot of squared Kubelka-Munk functions, $F(R)^2$ vs photon energy of $E=h\nu$. The band gap energy obtained for the as-prepared $BiFeO_3$ is 2.04 eV, which is less than 2.10 eV found in previous investigations by Huo et al. [24]. The decrease in band gap energy could be caused by the lattice strain effect in $BiFeO_3$, which is correlated to particle size reduction. As a result, $BiFeO_3$ nanoparticles were demonstrated to

be responsive to visible light and can be employed for the photodegradation of contaminants under visible light.

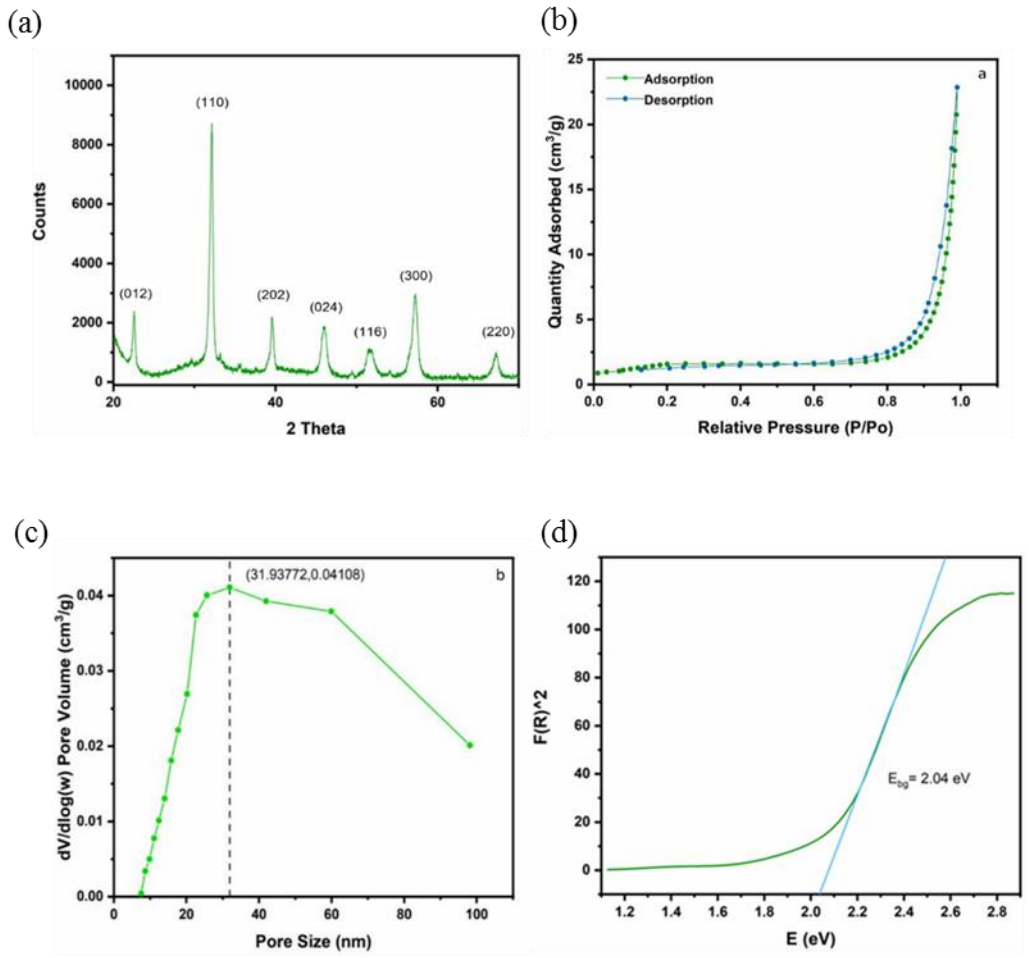


Figure 3. The (a) XRD pattern, (b) nitrogen linear adsorption, (c) pore size distribution and (d) bandgap energy of synthesized $BiFeO_3$ nanoparticles

BFO FTIR spectra

FT-IR spectroscopy analysis was utilized to validate the presence of functional groups in the synthesized perovskite $BiFeO_3$. Figure 4(a) reveals a broad and strong absorption band between 3000 cm^{-1} and 3500 cm^{-1} that can be referred to as stretching vibrations of the O-H group, while the bending vibrations mode of water can be detected at 1625 cm^{-1}. Bending vibrations of Fe-O and Bi-O may be observed at the sharp peak at 568 cm^{-1} and 457 cm^{-1}, respectively. These absorptions corresponded to the features of the octahedral FeO_6 group found in perovskite compounds like $BiFeO_3$.

Figure 4(b) depicts the FTIR spectrum of $BiFeO_3$ employed in the photocatalytic degradation of ofloxacin. There were slight changes observed, such as the shape of stretching vibrations of O-H group to a medium broad absorption band and the loss of nitrate groups at 875 cm^{-1}. However, some absorption bands, particularly the Fe-O and Bi-O bending vibrations of $BiFeO_3$ nanoparticles, were successfully preserved. As a result, this proves that $BiFeO_3$ is a stable catalyst that is not damaged by the contaminants.

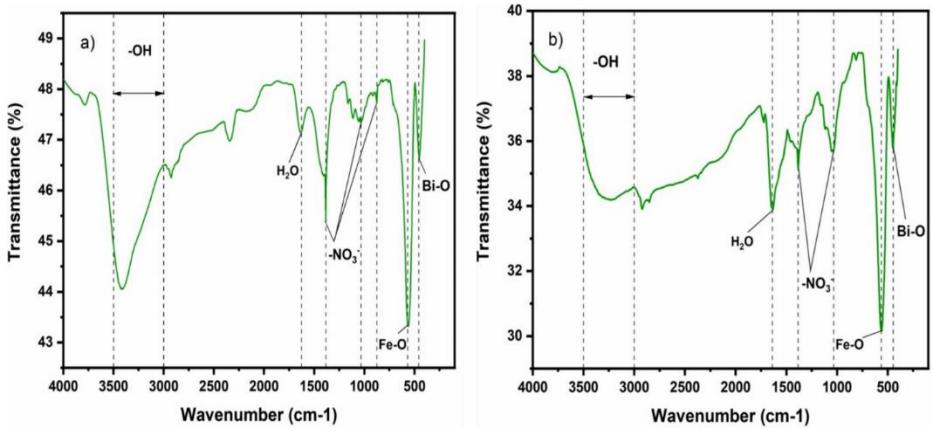


Figure 4. FTIR spectra of $BiFeO_3$ (a) before and (b) after photocatalytic reactions

Point of zero charge (PZC)

At a specific pH level, the point of zero charge (PZC) is a state in which there is no net charge on the surface of the molecules [25]. As illustrated in Figure 5(a), the point of zero charge (pH_{pzc}) pH value can be detected at the x-intercept of the plotted curve between the difference of final and initial pH and initial pH of the solution. $BiFeO_3$ pH_{pzc} value was 7.75, which is in the neutral region. When the pH value was less than pH_{pzc}, the presence of the positive charge on the surface of the $BiFeO_3$ can be observed. Whereas, at the pH value above pH_{pzc}, the presence of negative charge can be observed on the surface of the photocatalyst. The electrostatic interaction between the photocatalyst and pollutant molecules can be linked to the effect of pH on the photodegradation efficiency of $BiFeO_3$.

Degradation of ofloxacin by photocatalysis: Catalyst dosage

The degradation of ofloxacin in the control experiment gave a non-significance result, thus the research was continued with the operational parameter studies. The influence of catalyst dosage was studied by changing the $BiFeO_3$ dosage from 0.05 g L^{-1} to 0.50 g L^{-1} in a solution of 20 mg L^{-1} of ofloxacin without adjusting the pH level. This investigation is necessary to ascertain the best amount of catalyst to be utilized in order to maximize the photocatalyst's potential. Table 1 and Figure 5(b) illustrate the effect, which were tabulated and plotted respectively. As the dosage increased from 0.05 g L^{-1} to 0.07 g L^{-1}, the degradation efficiency of $BiFeO_3$ was raised from 29.32 % to 34.96 %. The behaviour can be elucidated by the fact that as the catalyst dosage increases, the number of active sites in the photocatalyst increases, which is closely proportional to the number of radicals produced during the degradation of ofloxacin [26]. However, as the catalyst dosage is continuously increased from 0.09 g L^{-1} to 0.50 g L^{-1}, the degrading performance began to decline from 32.93 % to 23.47 %. When the amount of catalyst used exceeded the optimum dose, the turbidity of the solution increased, and photocatalyst particle agglomeration occurred in the solution, affecting the light penetration and reducing the photocatalytic activity of $BiFeO_3$ [14]. Photooxidation kinetics of ofloxacin depended on $BiFeO_3$ loading and it was discovered that the rates increased as the $BiFeO_3$ loading increased until a certain limit and then the rates started to decrease back to a constant value. Therefore, an optimum $BiFeO_3$ dosage added is important to prevent the unnecessary excess catalyst and to ensure total absorption of light photons for efficient photo mineralization. According to the findings, the best catalyst dosage in the experiment was 0.07 g L^{-1}, with a removal rate of 35% in 120 minutes under sunshine exposure.

Table 1. The removal efficiency of OFL at different $BiFeO_3$ dosage with respect to time. (Condition: 20 mg L^{-1} OFL with unadjusted pH and 120 min irradiation under sunlight)

BFO Dosage (g L^{-1})	% Removal of OFL		
	Dark (30 mins)	1 hour	2 hours
0.05	0.32	14.21	29.32
0.07	0.26	14.87	34.96
0.09	0.65	17.82	32.93
0.30	3.20	18.08	31.70
0.50	2.56	11.16	23.47

The pH of the ofloxacin solution

The photocatalytic activity of the photocatalyst has been found to be directly connected to the pH of the pollutants, which has an important influence on the degradation performance. The pH change may modify the electrical double layer of the catalyst and pollutant interface, affecting the adsorption-desorption processes and the separation of the carrier charges in catalyst particles. Ofloxacin, according to Crespo-Alonso et al. [27], is an amphoteric molecule that exists as an anion at pKa 8.22 and a cation at pKa 6.05 while exists as a zwitterion between these pKa values. The pH value of the 20 mg L^{-1} ofloxacin solution with a catalyst dosage of 0.07 g L^{-1} was done by adjusting the pH of solution from pH 2 to pH 12. The removal efficiency of ofloxacin increases from 16.84 % to 36.70 % as the pH decreases from 12 to 8, as tabulated in Table 2 and plotted in Figure 5(c). Then, as the pH value dropped to 6, the performance declined to 21.01 %. As the $BiFeO_3$ is within the acidic region at pH 2, its photocatalytic performance decreases significantly, with a very low value of 0.84 %. This suggests that the breakdown of ofloxacin in the acidic medium is unfavourable. At pH 2 and pH 4, the surface charge of $BiFeO_3$ is positive, and ofloxacin exists as a cation at these pH levels. As a result, electrostatic repulsion between the photocatalyst and pollutant molecules arises, resulting in a decrease in degradation efficiency. Nevertheless, the photocatalytic performances also declined in the strong alkaline region as the surface charge of $BiFeO_3$ is negative and ofloxacin exists in its anionic state as its structure undergoes deprotonation, which caused the repulsion between ofloxacin and $BiFeO_3$ molecules. These suggest that the breakdown of ofloxacin in the strong acidic and alkaline medium are unfavourable [28]. Therefore, the optimum pH value was obtained at pH 8 as the removal effectiveness was the highest, with 36.70 % removal. The $BiFeO_3$ surface exhibited anionic behaviour at pH 8, and ofloxacin occurred in a zwitterionic state with both positive and negative charges. As a result, electrostatic interaction between the $BiFeO_3$ surface and ofloxacin molecules might occur, thereby improving the removal efficiency of the antibiotic. The study proved that pH value variation could affect the adsorption of ofloxacin on the surface of $BiFeO_3$ and its photodegradation efficiency.

Table 2. The removal efficiency of OFL at different pH with respect to time(Condition: 0.07 g L^{-1} $BiFeO_3$, 20 mg L^{-1} OFL and 120 min irradiation under sunlight)

Solution pH	% Removal of OFL		
	Dark (30 mins)	1 hour	2 hours
2	0.14	2.82	0.84
4	3.35	4.59	3.79
6	1.58	11.05	21.01
8	5.93	22.10	36.70
10	1.24	16.59	29.19
12	9.89	13.63	16.84

Initial concentration of ofloxacin solution

The initial concentration study was done by using different concentrations of ofloxacin from 2.5 mg L^{-1} to 20 mg L^{-1} with the 0.07 g L^{-1} catalyst dosage and in pH 8 medium. Generally, the initial concentration study was conducted to identify the optimum concentration for the photocatalyst to carry out the photocatalysis optimally. Table 3 and Figure 5(d) show that as the initial concentration of ofloxacin increases from 2.5 mg L^{-1} to 10 mg L^{-1}, the degradation efficiency of ofloxacin also increases steadily from 37.00 % to 46.13 %. The optimum initial concentration in the study was 10 mg L^{-1} due to the highest removal efficiency. The removal efficiency decreased to 37.52 % and 36.78 %, respectively, when the starting concentration rose to 15 mg L^{-1} and 20 mg L^{-1}. This can be explained as the higher the concentration of ofloxacin, the higher the number of ofloxacin molecules in the medium. Therefore, a greater amount of light being absorbed by the ofloxacin molecules and reduced the photo flux from hitting the photocatalyst surface. Besides, the competition between the ofloxacin molecules might increase because of higher amount of pollutant molecules compared to the amount of available active sites on the photocatalyst [29]. It may be deduced that a high initial concentration of ofloxacin will reduce its removal effectiveness.

Table 3. The removal efficiency of OFL at different initial concentration with respect to time. (Condition: 0.07 g L^{-1} $BiFeO_3$, OFL solutions with pH 8 and 120-min irradiation under sunlight)

Concentration OFL (mg L^{-1})	% Removal of OFL		
	Dark (30 mins)	1 hour	2 hours
2.5	1.72	30.77	37.00
5.0	6.40	27.34	41.79
10.0	6.10	30.14	46.13
15.0	5.03	22.54	37.52
20.0	5.42	22.44	36.78

Effect of hydrogen peroxide addition

The final parameter in this work is the influence of the addition of hydrogen peroxide (H_2O_2) to the extent of the photocatalysis reaction. The study on the effect of H_2O_2 addition was carried out by adding a different concentration of H_2O_2 from 0.1 M to 0.7 M in 10 mg L^{-1} of ofloxacin solution at a pH level of 8 with 0.07 g L^{-1} catalyst dosage. As shown in Table 4 and Figure 5(e), the removal efficiency drastically increases as the concentration of hydrogen peroxide introduced

increases from 0.1 M to 0.3 M with an efficiency of 56.68 % to 70.10%, respectively. However, as the concentration of H_2O_2 kept on increasing, only a small amount of increment can be observed in the removal efficiency being the highest of 72.42 % with 0.7 M of H_2O_2. The trend that can be seen from the study may cause by the increased number of radicals generated from the breakdown of hydrogen peroxide through the reduction of it at the conduction band and decomposition by the illumination of sunlight. As the concentration of H_2O_2 increases beyond 0.3 M, the generation of radicals may achieve saturation as the removal efficiency only slightly increases. The purpose of this study was to utilize the lowest possible concentration of H_2O_2 used with excellent removal efficiency as in low concentrations of H_2O_2, more efficient is the production of hydroxyl radicals and inhibition of charge carrier recombination. Besides, the solution may sometimes experience oxygen starvation because of slow oxygen mass transfer or oxygen consumption. The addition of H_2O_2 can help to achieve a sufficient oxygen supply and modify the $BiFeO_3$ surface, however high concentration of it could act as photoproduced holes scavenger. Therefore, the optimum concentration of H_2O_2 used in the study was 0.3 M. The results proved that the introduction of hydrogen peroxide with minimal concentration could successfully boost the photocatalytic degradation of ofloxacin by $BiFeO_3$.

Table 4. The removal efficiency of OFL at different concentration H_2O_2 used with respect to time. (Condition: 0.07 g L^{-1} $BiFeO_3$, 10 mg L^{-1} OFL with pH 8 and 120-min irradiation under sunlight).

Concentration H_2O_2 (M)	**% Removal of OFL**		
	Dark (30 mins)	**1 hour**	**2 hours**
0.1	13.42	44.75	56.68
0.3	7.46	31.32	70.10
0.5	13.04	59.39	70.97
0.7	10.14	59.39	72.42

Kinetic model and total organic carbon (TOC) removal

The Langmuir-Hinshelwood (LH) model was used to investigate the reaction kinetics for the photocatalytic degradation of ofloxacin. The model has usually been utilized for the heterogeneous photocatalytic degradation in various types of pollutants and simplified to pseudo-first order expression [16]. Figure 5(f) shows the plotted LH model and the data obtained are tabulated in Table 5. The LH equation had been simplified into a pseudo-first order kinetic model equation as follows:

$$ln\frac{C_t}{C_o} = kt \quad (2)$$

where, C_o and C_t are the initial concentration of ofloxacin and concentration of ofloxacin at the time, t, respectively. k is the degradation rate constant and t is the irradiation time. k value can be obtained directly from the slope of the plot between ln C_o/C_t versus irradiation time. Based on the plotted graph and its square of correlation coefficient (0.9399), r^2, it can be concluded that the reaction followed pseudo-first order kinetic and fitted the model perfectly and k value obtained from the graph was 0.0084 min^{-1}.

Next, total organic carbon (TOC) removal is an important study and can be used to identify the total carbon content of the organic pollution in the water bodies after being treated [30]. From the plot in Figure 6(a), after exposure to sunlight for 120 mins, 65.99% of ofloxacin has been degraded by $BiFeO_3$. On the contrary, as shown in Figure 6(b), the total organic content (TOC) in the solution has been significantly removed and left with only 9.36%. The great efficiency of mineralization shows that $BiFeO_3$ is an excellent photocatalyst to be applied in wastewater treatment.

Table 5. The rate constant and correlation factor of LH kinetic model for OFL antibiotic. (Condition: 0.07 g L^{-1} $BiFeO_3$, 0.3 M H_2O_2 added, 10 mg L^{-1} OFL with pH 8 and 120-min irradiation under sunlight)

	Langmuir- Hinshelwood Kinetic Model	
OFL	**K_{LH} (min^{-1})**	**R^2**
	0.0084	0.9399

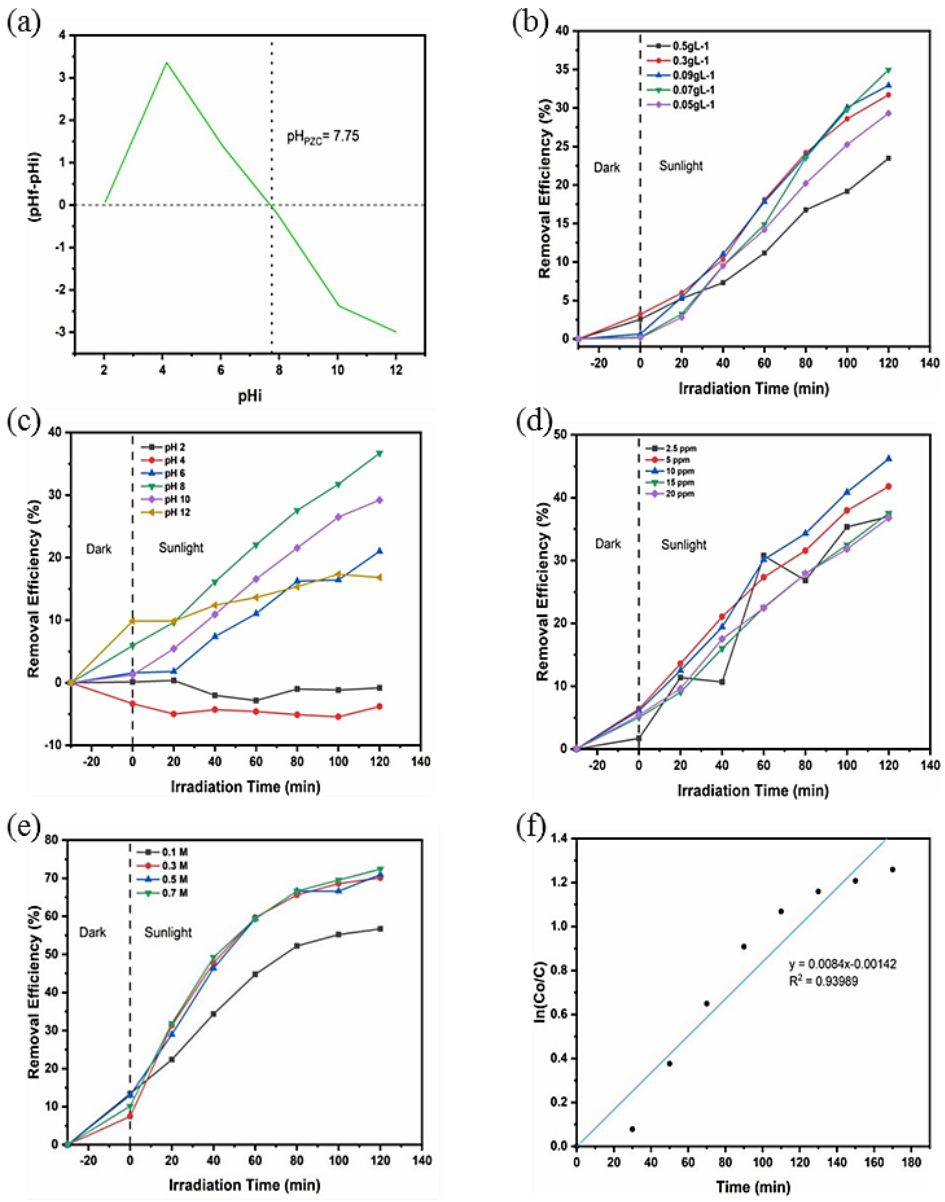


Figure 5. (a) pHpzc of $BiFeO_3$, the removal efficiency of OFL under different (b) $BiFeO_3$ dosage (c) pH of solution, (d) initial concentration (e) H_2O_2 model for OFL degradation using $BiFeO_3$ versus irradiation time and (f) Langmuir-Hinshelwood kinetic model

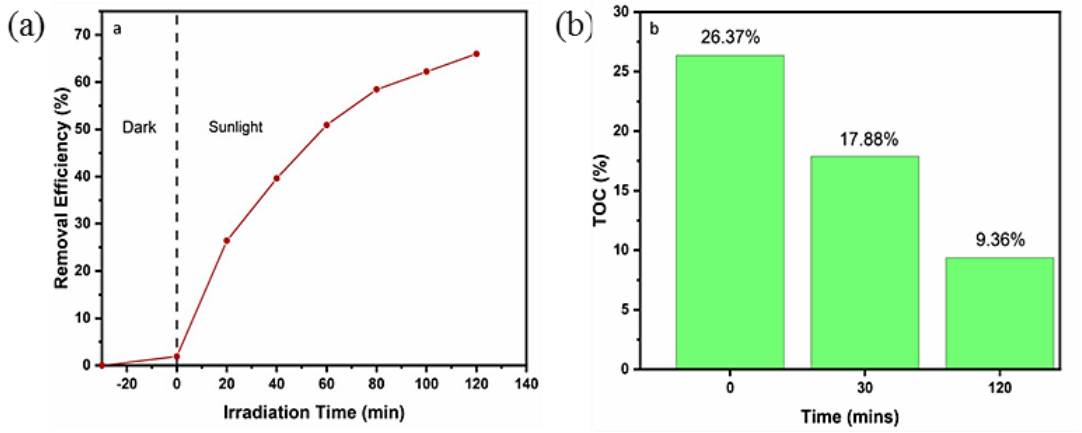


Figure 6. The (a) removal efficiency of OFL for TOC analysis and (b) depletion in TOC value of OFL solution with respect to time (Condition: 0.07 g L^{-1} $BiFeO_3$, 0.3 M H_2O_2 added, 10 mg L^{-1} OFL with pH 8 and 120-min irradiation under sunlight)

Conclusion

In conclusion, a facile $BiFeO_3$ photocatalyst was synthesized effectively using the bio-templated sol-gel approach. The purity of the photocatalyst, as well as significant chemical and physical properties, were investigated using various experimental characterizations. $BiFeO_3$ has been shown to have important properties, such as a narrow band gap energy of 2.04 eV with a surface area of 4.67 m^2 g^{-1}. Photocatalysis in the presence of $BiFeO_3$ has been proven to have an excellent property to eliminate ofloxacin with 70.1 % removal efficiency under optimum conditions. The effect of the parameters was controversial in some cases; thus, it is required to further study the nature of the pollutant to be degraded, and on types of photocatalyst to be utilized in the photodegradation. The kinetic study was conducted and found that the reaction is in good agreement with Langmuir-Hinshelwood kinetic model. The TOC analysis showed a great mineralization of ofloxacin. The knowledge of photocatalytic activity and its operational parameters could provide a better understanding for the elimination of pollutants, especially antibiotics.

Acknowledgement

The author gratefully acknowledges financial assistance from the Ministry of Higher Education (MOHE) under the Fundamental Research Grant Scheme (FRGS) [FRGS/1/2019/STG07/USM/02/7]. The author also acknowledges School of Chemical Sciences, Centre for Global Archaeological Research, School of Physics, USM and Nagaoka University of Technology, Japan for the research facilities.

Reference

1. Siddique, M., Khan, N. M., & Saeed, M. (2019). Photocatalytic activity of bismuth ferrite nanoparticles synthesized via sol-gel route. *Zeitschrift Fur Physikalische Chemie*, 233(5): 595-607.
2. Huang, Q., Liu, Y., Cai, T. and Xia, X. (2019). Simultaneous removal of heavy metal ions and organic pollutant by BiOBr/Ti3C2 nanocomposite. *Journal of Photochemistry and Photobiology A: Chemistry*, 375(December 2018): 201-208.
3. Boruah, P. K. and Das, M. R. (2020). Dual responsive magnetic Fe_3O_4-TiO_2/graphene nanocomposite as an artificial nanozyme for the colorimetric detection and photodegradation of pesticide in an aqueous medium. *Journal of Hazardous Materials*, 385: 121516.
4. Sharma, P., Kumar, N., Chauhan, R., Singh, V., Srivastava, V. C. and Bhatnagar, R. (2020). Growth of hierarchical ZnO nano flower on large functionalized rGO sheet for superior photocatalytic mineralization of antibiotic. *Chemical Engineering Journal*, 392: 123746.

5. Van Boeckel, T. P., Gandra, S., Ashok, A., Caudron, Q., Grenfell, B. T., Levin, S. A. and Laxminarayan, R. (2014). Global antibiotic consumption 2000 to 2010: An analysis of national pharmaceutical sales data. *The Lancet Infectious Diseases*, 14(8): 742-750.
6. Ambrosetti, B., Campanella, L. and Palmisano, R. (2015). Degradation of antibiotics in aqueous solution by photocatalytic process: Comparing the efficiency in the use of ZnO or TiO_2. *Journal of Environmental Science and Engineering A,* 4(6): 273-281.
7. Manzetti, S. and Ghisi, R. (2014). The environmental release and fate of antibiotics. *Marine Pollution Bulletin*, 79(1–2): 7-15.
8. Huang, J., Cao, J., Ding, Y., Hu, Y., Cen, Y. and Tang, H. (2018). Variable-valence metals catalyzed solid $NaBiO_3$ nanosheets for oxidative degradation of norfloxacin, ofloxacin and ciprofloxacin: Efficiency and mechanism. *Chemosphere,* 205: 531-539.
9. Wang, J., Tsuzuki, T., Tang, B., Hou, X., Sun, L. and Wang, X. (2012). Reduced graphene oxide/ZnO composite: Reusable adsorbent for pollutant management. *ACS Applied Materials and Interfaces, 4(6),* 3084-3090.
10. Nurchi, V. M., Crespo-Alonso, M., Pilo, M. I., Spano, N., Sanna, G. and Toniolo, R. (2019). Sorption of ofloxacin and chrysoidine by grape stalk. A representative case of biomass removal of emerging pollutants from wastewater. *Arabian Journal of Chemistry,* 12(7): 1141-1147.
11. Bhatia, V., Ray, A. K. and Dhir, A. (2016). Enhanced photocatalytic degradation of ofloxacin by co-doped titanium dioxide under solar irradiation. *Separation and Purification Technology,* 161: 1-7.
12. Dai, J. F., Xian, T., Di, L. J. and Yang, H. (2013). Preparation of $BiFeO_3$ -graphene nanocomposites and their enhanced photocatalytic activities. *Journal of Nanomaterials,* 2013: 1155.
13. Moussa, H., Girot, E., Mozet, K., Alem, H., Medjahdi, G. and Schneider, R. (2016). ZnO rods/reduced graphene oxide composites prepared via a solvothermal reaction for efficient sunlight-driven photocatalysis. *Applied Catalysis B: Environmental,* 185: 11-21.
14. Soltani, T. and Entezari, M. H. (2013). Photolysis and photocatalysis of methylene blue by ferrite bismuth nanoparticles under sunlight irradiation. *Journal of Molecular Catalysis A: Chemical,* 377(3): 197-203.
15. Gómez-Pastora, J., Dominguez, S., Bringas, E., Rivero, M. J., Ortiz, I. and Dionysiou, D. D. (2017). Review and perspectives on the use of magnetic nanophotocatalysts (MNPCs) in water treatment. *Chemical Engineering Journal,* 310: 407-427.
16. Hu, Z. T., Liu, J., Yan, X., Oh, W. Da and Lim, T. T. (2015). Low-temperature synthesis of graphene/$Bi_2Fe_4O_9$ composite for synergistic adsorption-photocatalytic degradation of hydrophobic pollutant under solar irradiation. *Chemical Engineering Journal,* 262: 1022-1032.
17. Liu, Y., Guo, H., Zhang, Y., Tang, W., Cheng, X. and Li, W. (2018). Heterogeneous activation of peroxymonosulfate by sillenite $Bi_{25}FeO_{40}$: Singlet oxygen generation and degradation for aquatic levofloxacin. *Chemical Engineering Journal,* 343(February): 128-137.
18. Rouhani, Z., Karimi-Sabet, J., Mehdipourghazi, M., Hadi, A. and Dastbaz, A. (2019). Response surface optimization of hydrothermal synthesis of Bismuth ferrite nanoparticles under supercritical water conditions: Application for photocatalytic degradation of Tetracycline. *Environmental Nanotechnology, Monitoring and Management,* 11: 100198.
19. Wang, X., Wan, X., Xu, X. and Chen X. (2014). Facile fabrication of highly efficient AgI/ZnO heterojunction and its application of methylene blue and rhodamine B solutions degradation under natural sunlight. *Applied Surface Sciences,* 321:10-8.
20. Hapeshi, E., Achilleos, A., Vasquez, M. I., Michael, C., Xekoukoulotakis, N. P., Mantzavinos, D. (2014). Drugs degrading photocatalytically: Kinetics and mechanisms of ofloxacin and atenolol removal on titania suspensions. *Water Research,* 44(6):1737-1746.

21. Satar, N. S. A., Aziz, A. W., Yaakob, M. K., Yahya, M. Z. A., Hassan, O. H., Kudin, T. I. T. and Kaus, N. H. M. (2016). Experimental and first-principles investigations of lattice strain effect on electronic and optical properties of biotemplated $BiFeO_3$ nanoparticles. *Journal of Physical Chemistry C*, 120(45): 26012-26020.
22. Lowell, S., Shields, J. E., Thomas., M. A. (2004). Characterization of porous solids and powders: surface area, pore size and density. *Molecularly Imprinted Materials: Science and Technology*, 127(40): 14118-14120.
23. Sing, K. S. W., Everett, D. H., Haul, R. A. W., Moscou, L., Pierotti, R. A., Rouquerol, J., & Siemieniewska, T. (1985). Reporting physisorption data for gas/solid systems with special reference to the determination of surface area and porosity. *Pure and Applied Chemistry*, 57(4): 603-619.
24. Huo, Y., Jin, Y. and Zhang, Y. (2010). Citric acid assisted solvothermal synthesis of $BiFeO_3$ microspheres with high visible-light photocatalytic activity. *Journal of Molecular Catalysis A: Chemical*, 331(1–2): 15-20.
25. Fiol, N. and Villaescusa, I. (2009). Determination of sorbent point zero charge: Usefulness in sorption studies. *Environmental Chemistry Letters*, 7(1): 79-84.
26. Xu, H. Y., Wu, L. C., Zhao, H., Jin, L. G. and Qi, S. Y. (2015). Synergic effect between adsorption and photocatalysis of metal-free g-C_3N_4 derived from different precursors. *PLoS One*, 10(11): 1-20.
27. Crespo-Alonso, M., Nurchi, V. M., Biesuz, R., Alberti, G., Spano, N., Pilo, M. I., & Sanna, G. (2013). Biomass against emerging pollution in wastewater: Ability of cork for the removal of ofloxacin from aqueous solutions at different pH. Journal of Environmental Chemical Engineering, 1(4), 1199–1204.
28. Peres, M. S., Maniero, M. G. and Guimarães, J. R. (2015). Photocatalytic degradation of ofloxacin and evaluation of the residual antimicrobial activity. *Photochemical Photobiological Sciences*;14(3):556-562.
29. Senasu, T., Chankhanittha, T., Hemavibool, K. and Nanan, S. (2021). Visible-light-responsive photocatalyst based on ZnO/CdS nanocomposite for photodegradation of reactive red azo dye and ofloxacin antibiotic. *Materials Science in Semiconductor Processing*, 123: 105558.
30. Lescano, M. R., Lopez, A. O., Romero, R. L. and Zalazar, C. S. (2021). Degradation of chlorpyrifos formulation in water by the UV/H_2O_2 process: Lumped kinetic modelling of total organic carbon removal. *Journal of Photochemistry and Photobiology A: Chemistry*, 404: 112924.

Malaysian Journal of Analytical Sciences (MJAS)
Published by Malaysian Analytical Sciences Society

AN ANALYSIS OF DOG FAT IN BEEF MEATBALLS USING FOURIER-TRANSFORM INFRARED SPECTROPHOTOMETRY COMBINED WITH CHEMOMETRICS

(Analisis Lemak Anjing dalam Bakso Melalui Kaedah Spektrometri Inframerah Transformasi Fourier Gabungan Bersama Kemometri)

Laela Hayu Nurani[1,2*], Any Guntarti[1,2], Achmad Rizaldy[1], Citra Ariani Edityaningrum[1], Nina Salamah[1,2], Lalu Muhammad Irham[1], Dzulfikar Muhammad Aditama[1], Abdul Rohman[3,4]

[1]Faculty of Pharmacy,
Universitas Ahmad Dahlan Yogyakarta 55164, Indonesia
[2]Ahmad Dahlan Halal Center,
Universitas Ahmad Dahlan Yogyakarta 55164, Indonesia
[3]Center of Excellence, Institute for Halal Industry and Systems,
Universitas Gadjah Mada, Yogyakarta 55281, Indonesia
[4]Faculty of Pharmacy,
Universitas Gadjah Mada, Yogyakarta 55281, Indonesia

**Corresponding author: laela.farmasi@pharm.uad.ac.id*

Received: 30 March 2022; Accepted: 6 August 2022; Published: 30 October 2022

Abstract

Bakso is a meatball made from beef and is very popular among Indonesians. However, the increasing number of cases of counterfeits and mixing of this meatball with dog meat in the city of Yogyakarta has caused significant unrest in several communities, especially Muslims. This study aimed to detect the fat content of dog meat in meatballs circulating in the city of Yogyakarta with an analysis using a combination of the FTIR method and the chemometric PCA. This research was designed with the making of a variety of meatballs consisting of 25 grams of beef and dog meat in calibrated samples of 0%, 20%, 40%, 60%, 80%, 90%, and 100%, as well as other ingredients, such as flour, garlic, and spices, as much as 5% of the meat weight. Three of the calibrated samples were validated and extracted with a Soxhlet extractor using the n-hexane solvent. The extracted fat was further analyzed by FTIR and processed with the Minitab19 software. The results showed that the wavenumbers ranged from 1,750 to 800 cm^{-1}, producing various peak intensities as well as, with the PLS calibration equation $y = 0.998206x + 0.999929$, an R^2 value of 0.9982, an RMSEC of 1.37%, an RMSEP of 1.19%, and an RMSECV of 2.32%. Furthermore, the dog and beef fats were successfully classified using the multivariate PCA. In conclusion, the analysis results showed that the FTIR spectrophotometric method combined with chemometrics was effective at classifying dog fat from other animal fats. Meanwhile, the analysis results showed that 2 out of 3 samples contained other meat contaminants.

Keywords: dog meat, meatball, Fourier transform infrared, principle component analysis, partial least squares

Abstrak

Makanan bakso yang diperbuat menggunakan daging lembu sangat popular di kalangan masyarakat Indonesia. Bagaimanapun, kes pemalsuan dan pencampuran daging lembu dengan daging anjing dalam pembuatan bakso yang berleluasa di bandar Yogjakarta telah menimbulkan keresahan yang ketara dalam sesetengah masyarakat khususnya di kalangan umat Islam. Kajian ini bertujuan untuk mengesan kandungan lemak anjing dalam daging bakso yang beredar di bandar Yogjakarta dengan menggunakan analisis gabungan kaedah FTIR dan kemometri PCA. Kajian ini direka bentuk dengan membuat variasi daging bakso yang terdiri daripada 25 gram daging lembu dan kandungan daging anjing yang telah ditetapkan kepada 0, 20, 40, 60, 80, 90 dan 100%, serta bahan-bahan lain seperti tepung, bawang putih dan perasa sebanyak 5% daripada berat daging. Tiga sampel yang telah ditetapkan diekstrak dengan Soxhlet menggunakan n-heksana sebagai pelarut. Lemak yang diekstrak kemudiannya dianalisis oleh FTIR dan diproses dengan perisian Minitab19. Keputusan menunjukkan julat gelombang antara 1750 hingga 800 cm-1 menghasilkan keamatan puncak yang berbeza-beza dan persamaan PLS y = 0.998206x + 0.9999929, nilai R^2 = 0.9982, RMSEC 1.37%, RMSEP 1.37%, RMSEP 1.52%. Tambahan pula, lemak anjing dan daging lembu berjaya dikelaskan menggunakan analisis PCA multivariate. Kesimpulannya, hasil analisis menunjukkan kaedah spektrofotometri FTIR yang digabungkan dengan kimometrik berkesan dalam mengklasifikasikan lemak anjing daripada haiwan lain. Sementara itu, analisis menunjukkan 2 daripada 3 sampel mengandungi bahan cemar daripada daging yang lain.

Kata kunci: bakso, daging anjing, inframerah transformasi Fourier, analisis komponen utama, kuasa dua terkecil separa

Introduction

According to Sahih Hadith Muslim no. 1933 *"The eating of all fanged beasts of prey is unlawful."* Additionally, Sahih Hadith Bukhari no. 3314 and Sahih Hadith Muslim no. 1198 state, *"There are five (harmful) things upon whose killer there is no sin whether he is in a state of ihram or otherwise: rats, scorpions, crows, kites, and voracious dogs (Kalb aqur)"*. In this regard, halal is a food requirement and is a mandatory provision for Muslims [1]. Therefore, food is said to be halal if there is no evidence forbidding it; however, it can also become haram if it is not good for consumption [2].

The Muslim community forbids the consumption of dog meat. However, dog meat adulteration in food products including buns, sausages, shredded meat, and meatballs has recently gained notice. This become quite profitable due to the trade-in of wild dog meat in several countries, which is carried out at low prices [3]. Furthermore, considering that the price of beef is more expensive compared to other varieties of meat, some traders have tried to minimize the cost of meatball production by mixing beef with other kinds of meat during the manufacturing process. This act is now considered to be an effective solution to reduce the production price of meatballs [4]. According to news reported by IDN Times Jogja published on January 13, 2020, dozens of dogs are slaughtered daily at various slaughterhouses in Bantul, Yogyakarta, Indonesia, to be served as dishes. In this regard, it is feared that there are meatball traders who produce counterfeits by mixing beef with dog meat, and this has become very detrimental to the consumers, especially Muslim consumers who have been prohibited by the Islamic belief from the consumption of dog meat.

Several approaches are being used to detect and measure the fat content of dog meat and pork derivatives in food products. The first approach is to determine the ratio of several chemical constituents of the products and ensure that this ratio is constant. Secondly, it is to look for certain markers on food products, both in the form of chemical contents and morphological components that can prove the presence of pork derivatives in the food. Lastly, it is conducted in a physico-chemical analysis [5]. Subsequently, analytical methods have been developed for the analysis of non-halal products in raw materials and food products. These methods include Fourier-transform infrared (FTIR) spectrophotometry [6], chromatography [7], and differential scanning calorimetry (DSC) [8]. Furthermore, DNA-based methods such as polymerase chain reaction [9] and analysis methods based on odor identification (electronic nose) [10] are also used for the analysis.

FTIR was not able to distinguish dog fat from beef fat because they have peaks with the same wave number related to the functional groups of the compounds. The FTIR results differed in the peak intensity of each peak, but it is difficult to see the difference visually. The feasibility of FTIR spectroscopy in combination with

multivariate partial least squares (PLS) calibration was used for the quantitative analysis of dog meat in a binary mixture of beef in meatball formulations. The chemometric principal component analysis (PCA) was used for the classification of dog meat and beef meatballs [26-28].

Therefore, this research aimed to determine the presence of dog meat in meatball products with the partial least squares (PLS) model. The classification of dog fat and chicken fat was performed using a principal component analysis (PCA) with the FTIR method [11].

Materials and Methods

Materials

The main materials used in this research were reference meatballs made from a mixture of beef obtained from Gedong Kuning Market, Rejowinangun, Kotagede District, Yogyakarta City, Special Region of Yogyakarta, Indonesia. Likewise, the dog meat ingredients were obtained from Jombor Lor, Mlati District, Sleman Regency, Special Region of Yogyakarta. The flour, as well as seasonings, was made in varying degrees of concentrations. In addition, the market sample beef meatballs were obtained by random selection of 3, out of the several meatball traders in various parts of Yogyakarta City, namely Timoho, Balirejo, and Glagahsari Streets, Special Region of Yogyakarta, Indonesia, and these samples were taken in October 2020. The solvents used in this research were technical n-hexane (Merck®) and Na_2SO_4 (Merck®). Research method (workflow analysis) is as shown in Figure 1.

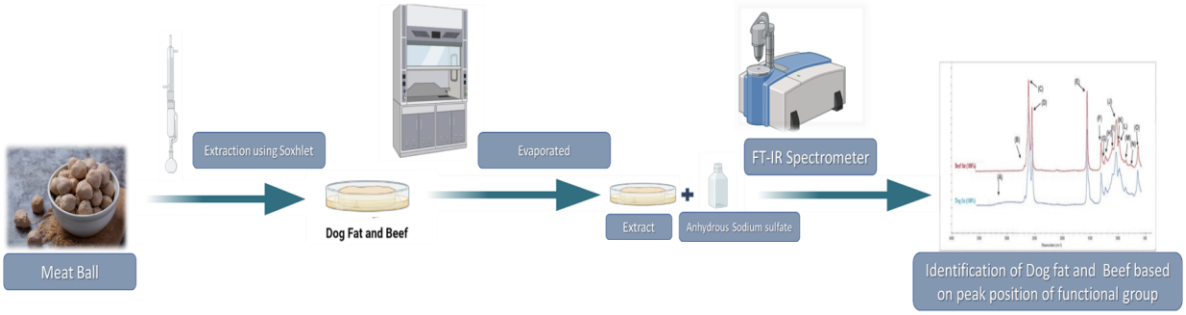


Figure 1. Workflow analysis of dog fat in beef meatballs using a Fourier-transform infrared spectrophotometer combined with chemometrics

Identification of dog species

Identification of dog species was carried out in the Laboratory of Animal Systematics, Faculty of Biology, Gadjah Mada University, Yogyakarta.

Table 1. Variations in concentration of beef and dog meatball samples

Concentration (%)	Beef (grams)	Dog Meat (grams)
Cow 100	25	-
Dog 20	20	5
Dog 40	15	10
Dog 60	10	15
Dog 80	5	20
Dog 90	2.50	22.50
Dog 100	-	25

Meatballs production with variations in concentration

The meat ingredients were mashed, and additional ingredients such as tapioca flour and spices, including shallots, garlic, ginger, and finely ground pepper, were added. The samples made in various concentrations can

be seen in Table 1. Meatballs were made by grinding beef and dog meat separately, consisting of 25 grams of meat. In addition, variations in concentration of dog meat in the beef meatballs made were: 0%, 20%, 40%, 60%, 80%, 90%, and 100% [12].

Fat extraction in meatballs

The meatballs were weighed according to the concentration made (Table 1), mashed, and extracted with a Soxhlet apparatus. Additionally, the solvent used was n-hexane, which was extracted for 4-7 hours at 70 °C. The extract was then added with anhydrous Na_2SO_4, which evaporated in a fume hood. The viscous extract was analyzed using an FTIR spectrophotometer [12].

Sample analysis with FTIR

The fat samples were analyzed using FTIR spectrophotometry. This analysis was carried out at a frequency of 4,000–650 cm^{-1}. Following this, the samples were dropped onto an ATR crystal at a controlled temperature (25 °C), and measurements were carried out on 32 scans at a resolution of 4 cm^{-1} [13].

Statistical data analysis

The qualitative and quantitative statistical analysis of FTIR spectrophotometric test results on meatball samples combined with PLS and PCA multivariate chemometric calibration with the Minitab 19 software on a computer device was carried out. The partial least squares (PLS) method was used to determine the linearity. A Microsoft Excel 2010 software worksheet was also used to relate the actual sample to the predicted sample concentrations. The accuracy of the PLS model was evaluated by the coefficient of determination (R^2), while that of the data analysis method was assessed using the root mean square error of cross-validation (RMSECV) and the root mean square error of prediction (RMSEP). The formula used to obtain the RMSECV (equation 1):

$$\text{RMSECV} = \sqrt{\frac{\sum_{i=1}^{n}(\hat{x}i - xi)^2}{n}},$$

where $\hat{x}i$ is the actual value of meatballs, xi is the value calculated from cross-validation of meatballs, and n is the number of calibrations or validation samples [14]. Meanwhile, the formula used to obtain the RMSEP (equation 2):

$$\text{RMSEP} = \sqrt{\frac{\sum_{i=1}^{n}(\hat{y}i - yi)^2}{n}},$$

where $\hat{y}i$ is the actual value of meatballs, xi is the predictive value of meatballs, and n is the number of calibrations or validation samples [4].

Results and Discussion

Identification of dog species used as sample

The identification of dog species was conducted using pictures of several parts of the animal's body, such as the face, tail, legs, and ears, and pictures of the combined parts as a whole body [15]. The identification results indicated that the type of dog used was the mutt otherwise known as a local dog with the Latin name *Canis lupus familiaris*. The mutt is a dog species characterized by a skull with a relatively elongated snout and teeth adapted for eating meat. This dog species is generally not intentionally bred by humans but survives in areas where humans live, such as streets, cities, and villages [16].

Meatball fat extraction

The fat content in the meatballs was extracted using the Soxhlet extraction method. Similarly, a non-polar solvent such as n-hexane can also be used to extract fat. The extraction process was carried out at a temperature of about 70 °C, which corresponds to the boiling point of n-hexane [17]. For optimal extraction, this process was conducted for approximately 5 hours. Subsequently, whether the extraction process had been optimized was demonstrated by the turn of the color of n-hexane into dripping clear like its original color. Lastly, the addition of sufficient anhydrous Na_2SO_4 was intended for binding to the water molecules that may still be contained in the n-hexane as the presence of water in fat may interfere with the response of the FTIR spectrum [18].

Based on Figure 2(a), the FTIR spectra obtained were in the wavenumber range 4,000-600 cm^{-1}. It can be seen that there is no significant difference between the beef and dog meatball fat spectra because the main components of both fats, which are triglycerides, are the same, and both are regarded as animal fats. Therefore, it was deemed necessary to carry out a further analysis with the chemometric PCA to distinguish the intensity of infrared absorption peaks, which are more varied, making it easier to classify the beef and dog meatball fat

spectra. The descriptions of the absorption peaks and the identified functional groups are summarized in Table 2. From Table 2, the beef and dog fat shared a similarity in functional fat groups. Carbonyl, CH, and CO groups appeared on the FTIR spectrogram. The difference in the variations of such functional groups can be seen with the chemometric PCA [29].

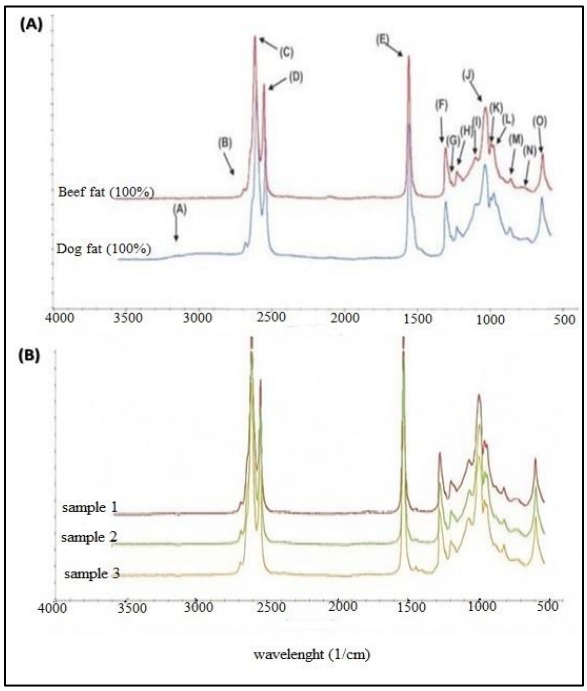


Figure 2. (a) Difference in the spectra of 100% beef meatball fat and 100% dog meatball fat and (**b**) the FTIR spectra of market beef meatball samples

Table 2. Identification of functional groups and vibrational types of the FTIR spectra of dog and beef fats

Peak Position (cm^{-1})		Functional Groups	Vibration Type	Intensity
Dog	**Beef**			
3,283	-	O-H	Stretching	Medium
3,007	3,003	C=C-H (cis)	Stretching	Medium
2,921	2,921	C-H(CH_3)	Asymmetric stretching	Strong
2,852	2,852	C-H(CH_2)	Asymmetric stretching	Strong
1,744	1,743	C=O (ester)	Stretching	Strong
1,461	1,462	C-H (CH_2)	Bend scissoring	Strong
1,418	1,417	C=C-H (cis)	Bend (rocking)	Strong
1,376	1,376	C-H (CH_2)	Bend Symmetrical	Strong
1,230	1,236	C-O (ester)	Stretching	Medium
1,160	1,159	C-O (ester)	Stretching	Medium
1,115	1,097	C-O (ester)	Stretching	Medium
968	965	C=C-H (trans)	Bend out	Medium
839	889	C=C-H (trans)	Bend out	Medium
721	721	C=C-H (cis)	Bend out	Strong

Wavenumber optimization as PLS calibration model

The results of the quantitative analysis which was carried out in the fingerprint area of the FTIR spectra to show a distinctive difference in the intensity of the absorption was significant and became the target for selecting the optimization wavenumbers [19]. The selection of these wavenumbers was intended for a calibration model that produces an R^2 value that is close to 1 and the smallest RMSEC [11]. The wavenumbers selected ranged from 1,750 to 800 cm^{-1}.

Additionally, the results of the optimization of the calibration model showed an optimal range of wavenumbers from 800 to 1,750 cm^{-1} with the equation y = 0.99820x + 0.99992. Moreover, the resulting coefficient of determination (R^2) was 0.99820 (Figure 3), with an RMSEC value of 1.464435%. The optimization results obtained indicated the accuracy between the predicted value and the actual value, which was 99.82%. The random error value also indicated an error in the sample prediction from the calibration model equation with an RMSEP value of 1.52% and an RMSECV of 2.329%.

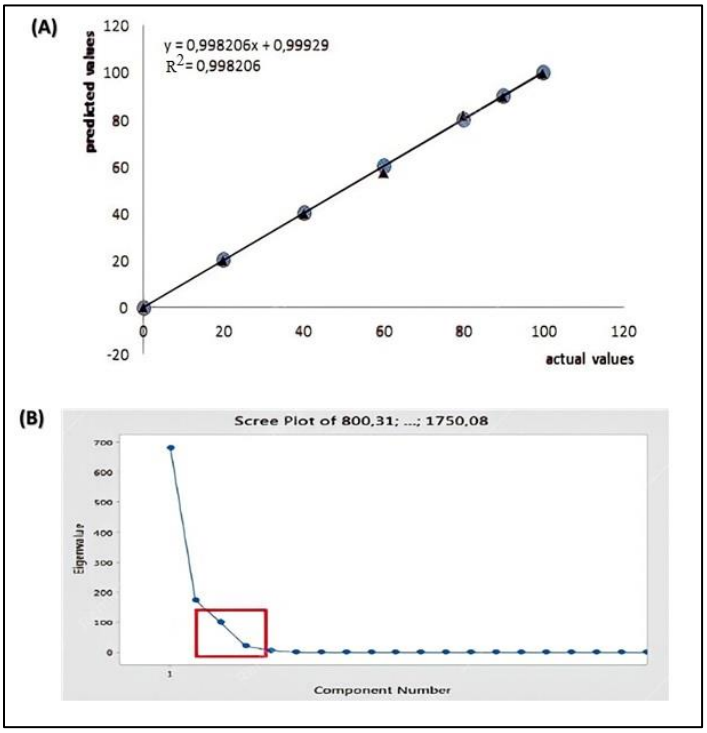


Figure 3. (a) The concentration variation of dog and beef fat resulted using the PLS data calibration model (0–100%) and (b) screen plot of the relationship between eigenvalues and PC results from the PCA

Pattern recognition analysis with the principal component analysis (PCA)

The PCA was performed using an absorbance data set of dog and beef fats, in addition to market samples, in the 1,750–800 cm^{-1} area, which was the fingerprint area. From this frequency range, information on which frequency contributes more to the PCA model will be obtained, and with the market samples, a clear separation between dog and beef fats will be provided. The PCA was performed with the help of Minitab19 and was integrated with Microsoft Excel 2010 [25]. The chemometric PCA was selected for grouping the variables of each sample used. With the variable of fatty acids of each group of samples, the proximity of chemical properties will be known.

Scree plot

The selection of the number of main components (PC) was one of the aspects that contributed to the success of the PCA results. In addition, the choice of the number of PCs in the PCA could be determined from the eigenvalues generated by each of the main components.

Therefore, the number of PCs gained was relevant for explaining the initial information from PC data with eigenvalues > 1 [20].

Furthermore, the eigenvalue is used to describe a large number of variations and is said to be part of the total variation that can be explained by each PC. Based on Figure 3 (b), PC1 with an eigenvalue of 683.35 was able to explain 69.3% of the variance in the initial variable. Meanwhile, PC2 with an eigenvalue of 174.06 was able to explain 87.0% of the variance, PC3 with an eigenvalue of 99.76 was able to explain 97.1% of the variance, and PC4 with an eigenvalue of 21.17 was able to explain 99.2% of the variance, which was part of the elbow, where there was a significant decrease in eigenvalues. Of the first 4 PCs, 99.2% of data variance was included and was relevant to explain the characteristics of the alert variable and the information contained [21].

Score plot

The PCA analysis was performed by the comparison of components after entering spectral data of 100% dog and beef fats. The analysis was then carried out by replication to ensure that the principal components were separated from other components using an optimized wavenumber [22]. The separation and grouping of the two score plots are presented in Figure 4 (a).

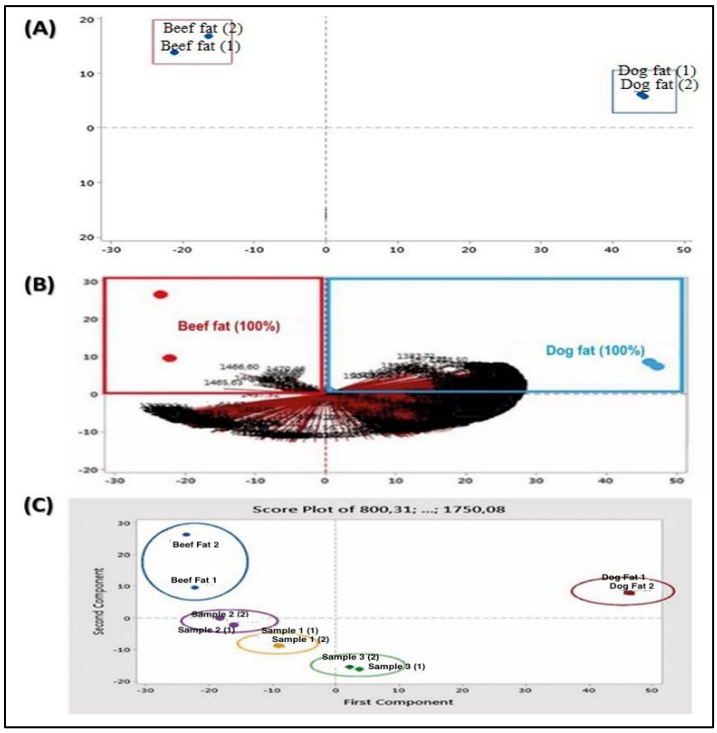


Figure 4. (a) Score plot PCA results in 100% dog fat and 100% beef fat. Note: red (beef fat) and blue (dog fat), (b) biplot of 100% dog fat and 100% beef fat, and (c) the score plot result of the PCA market sample, 100% dog, and 100% beef

Figure 4 (a) shows the results of the PCA analysis of two samples occupying different quadrants. Sample A (red) consisted of 2 beef tallows which were separated by 100% and had similar properties as a result of the close distance between the two fat plots which were also within the same quadrant, while sample B (blue) consisted of two 100% dog fat data which were found in different quadrants and at a great distance from sample A. Additionally, the two samples in the biplot were shown to be sticking together. Hence, the closer the distance between the two plots, the more the fat similarities. Meanwhile, the farther apart the plots, the lesser the similarities between the fats. From this, it can be seen that sample A and sample B were well separated because they are in different quadrants [23].

Figure 4 (b) shows that 100% beef fat (red) and 100% dog fat (blue) both had special variables. The beef fat was in the same quadrant with several variables, including 1,348.96–1,360.53 cm^{-1}; 1,453.10 cm^{-1}; 1,456.96 cm^{-1}; 1,457.92 cm^{-1}; 1,465.63 cm^{-1}; 1,466.60 cm^{-1}; and 1,470.46 cm^{-1}. Based on this, it can be said that the wave numbers 1,348.96–1,360.53 cm^{-1}; 1,453.10 cm^{-1}; 1,456.96 cm^{-1}; 1,457.92 cm^{-1}; 1,465.63 cm^{-1}; 1,466.60 cm^{-1}; and 1,470.46 cm^{-1} are therefore characteristic of the beef fat.

Comparatively, the results of the dog fat were in the same quadrant with many variables, including 800.31–1,430.92 cm^{-1}; 1,475.28–1,487.81 cm^{-1}; and 1,520.60–1,727.91 cm^{-1}. Hence, it indicates that these wavenumber variables are characteristic of dog fat because they were all in the same quadrant.

Analysis of beef meatball samples circulating in Yogyakarta City

The grouping contained in the score plot of dog and beef fats has explained that the two samples were perfectly separated and were in different quadrants; hence, they can be applied to the market samples. The samples of market beef meatballs analyzed were 3 meatballs obtained from 3 different places in Yogyakarta city. The results of the spectra were then analyzed by the PCA together with a reference sample of 100% beef and dog fats at the wavenumber of the optimization results to determine the presence of dog meat adulteration in the market sample. The results of the FTIR spectra of the three samples are presented in Figure 2 (b).

At first glance, the spectra of the market samples looked the same, but the three fat spectra had different intensities for each wavenumber, especially in the fingerprint area. To further confirm the difference in the intensity of the three spectra, the score plot was used as shown in Figure 4 (c). The results of the PCA on the FTIR spectra of 100% dog and beef fats, with the three market samples, are shown in the score plot, with the five fats being in separate quadrants. None of the three market samples had proximity to both dog and beef fat standards.

Furthermore, all market sample plots were in different quadrants from the standard % dog fat plot, indicating that both plots did not share a similarity. The result of this research therefore showed that the three meatball samples were not adulterated with dog meat. However, of the three market sample plots, only number 2 was in the same quadrant as the 100% beef fat plot. This shows that sample 2 had similar characteristics with beef fat. The further the plots of sample 1 and sample 3 from the 100% beef fat plot, the greater the difference in characteristics. In Figure 4 (C), the two samples (1 and 3) were most likely not pure beef and were likely to contain other types of meat contamination, which can be proven by further research.

Conclusion

The quantitative analysis of dog fat using PLS chemometrics resulted in optimization of wavenumbers in the range 1,750-800 cm^{-1} with the calibration model equation $y = 0.998206x + 0.99992$, which was quite accurate with a predicted value of 99.82% of the actual value. Furthermore, a coefficient of determination (R^2) of 0.998, an RMSEC of 1.46%, an RMSEP of 1.52%, and an RMSECV of 2.32% were obtained. In this regard, it can be concluded that the meatball samples in the market did not contain dog fat, but they were suspected to contain other types of fat.

Acknowledgements

The authors would like to thank UAD Professorship Program (with a letter of agreement for the implementation of the Professorship Program Number: R3/3/SP-UAD/II/2022) for providing funds for this publication.

References

1. Mursyidi, A. (2013). The role of chemical analysis in the halal authentication of food and pharmaceutical products. *Journal of Food and Pharmaceutical Sciences*, 1(1): 1-4.
2. Regenstein, J. M., Chaudry, M. M. Regenstein, C. E. (2003). The kosher and halal food laws. *Comprehensive Reviews in Food Science and Food Safety*, 2(3): 111-127.
3. Rahman, M. M., Ali, M. E., Abd Hamid, S. B., Mustafa, S., Hashim, U. and Hanapi, U. K. (2014). Polymerase chain reaction assay targeting cytochrome b gene for the detection of dog meat adulteration in meatball formulation. *Meat Science*, 97(4): 404-409.

4. Rahmania, H. (2014). *Analisis Daging Tikus Dalam Bakso Sapi Menggunakan Metode Spektroskopi Inframerah yang Dikombinasikan dengan Kemometrika*. Fakultas Farmasi Universitas Gajah Mada.
5. Cordella, C., Moussa, I., Martel, A.-C., Sbirrazzuoli, N. and Lizzani-Cuvelier, L. (2002). Recent developments in food characterization and adulteration detection: Technique-oriented perspectives. *Journal of Agricultural and Food Chemistry*, 50(7): 1751-1764.
6. Guntarti, A, Martono, S., Yuswanto, A. and Rohman, A. (2015). FTIR spectroscopy in combination with chemometrics for analysis of wild boar meat in meatball formulation. *Asian Journal of Biochemistry*, 10(4): 165-172.
7. Rohman, Abdul, Man, Y. B. C. and Noviana, E. (2013). Analysis of emulsifier in food using chromatographic techniques. *Journal of Food and Pharmaceutical Sciences*, 1(3): 54-59.
8. Tan, C. P. and Man, Y. B. C. (2012). Analysis of adible oils differential scanning calorimetry, in: Adolf, RO (Ed.), Advance in Lipid Methodology. Oily Press Lipid Library Series. Woodhead Publishing.
9. Guntarti, Any, Rohman, A., Martono, S. and Yuswanto, A. (2017). Authentication of wild boar meat in meatball formulation using differential scanning calorimetry and chemometrics. *Journal of Food and Pharmaceutical Sciences*, 5(1): 8-12.
10. Marina, A. M., Che Man, Y. B. and Amin, I. (2010). Use of the SAW sensor electronic nose for detecting the adulteration of virgin coconut oil with RBD palm kernel olein. *Journal of the American Oil Chemists' Society*, 87(3): 263-270.
11. Rohman, A. (2012). Pengembangan dan Analisis Produk Halal, Pusat Penelitian Produk Halal. Laboratorium Penelitian dan Pengujian Terpadu (LPPT) UGM.
12. Guntarti, A. (2018). Fourier-transform infrared spectroscopy combined with chemometrics for detection of pork in beef meatball formulation. *International Journal of Green Pharmacy*, 12(03): 153-157.
13. Guntarti, Any, and Prativi, S. R. (2017). Application method of Fourier transform infrared (FTIR) combined with chemometrics for analysis of rat meat (*Rattus diardi*) in meatballs beef. *Pharmaciana,* 7(2): 133-140.
14. Bucchianico, A. D. (t.t.). Coefficient of determinations (R^2), encyclopedia of statistics in quality and reliability. John Willey & Sons.
15. Hausman, G. J., Bergen, W. G., Etherton, T. D. and Smith, S. B. (2018). The history of adipocyte and adipose tissue research in meat animals. *Journal of animal science*, 96(2): 473-486.
16. Boyko, A. R., Boyko, R. H., Boyko, C. M., Parker, H. G., Castelhano, M., Corey, L., Degenhardt, J. D., Auton, A., Hedimbi, M. and Kityo, R. (2009). Complex population structure in African village dogs and its implications for inferring dog domestication history. *Proceedings of the National Academy of Sciences*, 106(33): 13903-13908.
17. Lobb, K. and Chow, C. K. (2007). Fatty Acid Classification and Nomenclature. CRC Press.
18. Rohman, A, Arsanti, L., Erwanto, Y. and Pranoto, Y. (2016). The use of vibrational spectroscopy and chemometrics in the analysis of pig derivatives for halal authentication. *International Food Research Journal*, 23(5): 1839-1848.
19. Saadah, M. (2012). Kombinasi metode spektroskopi inframerah dan kemometrika untuk analisis lemak babi (lard) dalam sediaan lotion. Fakultas Farmasi Universitas Gadjah Mada.
20. Lumakso, F. A. and Rohman, A. (2014). Autentikasi minyak buah alpukat (*Persea americana* Mill.) dari minyak kedelai dan minyak biji anggur menggunakan kombinasi teknik spektroskopi inframerah dan analisis multivariat. Universitas Gadjah Mada.
21. Miller, J. and Miller, J. (2010). Statistics and chemometrics for analytical chemistry. Sixth edition. Vol. 6th Pearson Education Limited.
22. Rohman, A and Che Man, Y. B. (2012). Analysis of pig derivatives for halal authentication studies. *Food Reviews International*, 28(1): 97-112.
23. Roggo, Y., Chalus, P., Maurer, L., Lema-Martinez, C., Edmond, A. and Jent, N. (2007). A review of near infrared spectroscopy and chemometrics in pharmaceutical technologies. *Journal of Pharmaceutical And Biomedical Analysis*, 44(3): 683-700.
24. Guntarti, A. and Abidin, M. A. Z. (2018). Dog fat analysis in chicken meatbun using FTIR (Fourier Transform Infrared) with chemometric combination. *Media Farmasi*, 15: 34-42.

25. Johnsen, L. G., Skou, P. B., Khakimov, B., & Bro, R. (2017). Gas chromatography–mass spectrometry data processing made easy. *Journal of Chromatography A*, 1503: 57-64.

Malaysian Journal of Analytical Sciences (MJAS)
Published by Malaysian Analytical Sciences Society

RECENT DEVELOPMENT ON THE SYNTHESIS OF THIOUREA DERIVATIVES AND EFFECT OF SUBSTITUENTS ON THE ANTICANCER ACTIVITY: A SHORT REVIEW

(Perkembangan Terkini Sintesis Sebatian Terbitan Tiourea dan Kesan Kumpulan Penukargantian Terhadap Aktiviti Antikanser: Ulasan Ringkas)

Norashikin Roslan[1,5], Noraslinda Muhamad Bunnori[2,5], Khairul Bariyyah Abdul Halim[2,5], Karimah Kassim[3], Mohd Fadhlizil Fasihi Mohd Aluwi[4], Nurziana Ngah[1,6*]

[1]*Department of Chemistry,*
Kulliyah of Science, International Islamic University Malaysia, Kuantan Campus,
Bandar Indera Mahkota, 25200 Kuantan, Pahang, Malaysia
[2]*Department of Biotechnology,*
Kulliyah of Science, International Islamic University Malaysia, Kuantan Campus,
Bandar Indera Mahkota, 25200 Kuantan, Pahang, Malaysia
[3]*Institute of Sciences,*
Universiti Teknologi MARA Shah Alam, 40450 Shah Alam, Selangor, Malaysia
[4]*Faculty of Industrial Sciences and Technology,*
Universiti Malaysia Pahang, Gambang, 26300 Kuantan, Pahang, Malaysia
[5]*Research Unit for Bioinoformatic & Computional (RUBIC),*
Kulliyyah of Science, International Islamic University Malaysia, Kuantan Campus,
Bandar Indera Mahkota, 25200 Kuantan, Pahang, Malaysia
[6] *Synthetic and Functional Material Research Group,*
Department of Chemistry,
Kulliyyah of Science, International Islamic University Malaysia, Kuantan Campus,
Bandar Indera Mahkota, 25200 Kuantan, Pahang, Malaysia

**Corresponding author: nurziana@iium.edu.my*

Received: 1 June 2022; Accepted: 18 August 2022; Published: 30 October 2022

Abstract

Thiourea is a carbon, hydrogen, sulphur, and nitrogen-based organic molecule. The thiourea group has been improved by replacing various substituents for its hydrogen atoms at the nitrogen terminal, resulting in a wide range of biological activities, especially on anticancer properties. Despite the fact that thiourea derivatives have remarkable anticancer potential, finding a novel anticancer agent that is both safe and selective remains a challenge. This paper summarizes recent research on thiourea compounds that can be used to treat malignant cell lines. Several synthesis methods and the effects of substituents as well as their anticancer therapeutic potential in a variety of healthy and malignant cell lines are discussed. As a result, it is envisaged that this review will guide the design and synthesis of new thiourea derivatives in the future for the development of highly effective and selective anticancer

drugs.

Keywords: thiourea derivatives, synthesis method, anticancer activity, substituents

Abstrak

Tiourea merupakan sebatian organik yang mempunyai atom karbon, hidrogen, sulfur dan nitrogen. Modifikasi sebatian organik tiourea ini dengan menggantikan atom hidrogen pada terminal nitrogen dengan pelbagai kumpulan penukargantian yang terpilih telah menghasilkan sebatian yang mempunyai pelbagai aktiviti biologi. Salah satu daripada aktiviti biologinya adalah sebagai agen antikanser. Meskipun sebatian terbitan tiourea ini dilaporkan mempunyai aktiviti antikanser yang signifikan, namun masih terdapat cabaran untuk mencari sebatian terbitan tiourea baru yang selamat dan bersifat selektif. Kertas ini meringkaskan kajian terkini mengenai sebatian terbitan tiourea yang boleh diaplikasi untuk kajian merawat sel kanser. Pelbagai kaedah sintesis, kesan kumpulan penukargantian serta potensi sebatian ke atas pelbagai jenis sel termasuk sel sihat dan malignan telah dibincangkan. Ulasan ringkas ini dapat memberi panduan untuk meningkatkan kemajuan dalam mencipta dan mensintesis sebatian antikanser baru yang berkesan dan selektif berasaskan tiourea.

Kata kunci: terbitan tiourea, kaedah sintesis, aktiviti antikanser, kesan kumpulan penukargantian

Introduction

The incidence and mortality of cancer-related diseases are quickly growing year after year, with 19.3 million new cases and 10 million deaths reported in 2020. Despite the availability of advanced treatments including immunotherapy, radiotherapy and chemotherapy, the number of cancer cases has not decreased in the last 30 years [1]. This pattern was linked to acquired resistance, rapid mutability as well as bad effects that occurred for a year after taking current anticancer drugs [2, 3]. Therefore, finding a new anticancer drug that is efficient and safe is crucial to solving the alarming issue. The anticancer properties of thiourea derivatives are undeniable. Besides that, they also play an important role in a wide range of biological activities such as anti-thyroid [4], anti-bacterial [5], anti-inflammatory [6], anti-malaria [7], antioxidant [5], antihypertensive [8], anti-viral [9] and anticancer [10].

The discovery of 5-fluorouracil (5-FU), sorafenib, and tenovin medicines spurred substantial research into thiourea derivatives as potential anticancer therapies (Figure 1). A compound of 5-FU, cyclic fluorinated urea has been used to treat colorectal cancer [11] and other solid tumours (gastrointestinal tract, pancreas, ovary, liver, brain, and breast) for over 50 years, whereas Sorafenib is a diaryl urea-containing compound that has been clinically tested for lung, breast, colon, ovarian, pancreatic, and gastric cancer. Meanwhile, tenovin with thiourea-based compounds exerted inhibitation towards the colon, prostate, gastric and lung cancer [12, 13].

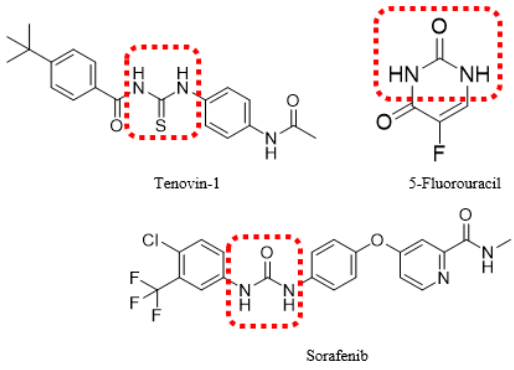


Figure 1. Thio(urea) scaffold-containing anticancer chemotherapeutics [12, 13]

Over the years, many reports have been published on the synthesis of thiourea derivatives and their evaluation as anticancer agents along with the structure-activity relationships (SAR). The nature and different types of substitutions on nitrogen atoms of thiourea moiety considerably boosted the anticancer activity and determined whether the thiourea was mono-substituted, di-substituted or multi-substituted [14]. However, the substitution of one hydrogen atom at each thiourea nitrogen atom with desirable moieties dominates the structural pattern of thiourea derivatives as an active chemical [14, 15]. It is concluded that coupling the thiourea scaffold with other substituents results in

pharmacophore molecules which are extremely good anticancer agents [15, 5, 6]. The derivatives were reported to demonstrate potent cytotoxic activities against a series of cancer cells including breast [16], lung [17], renal [18], colon [5], prostate [19], liver [20] and ovarian [18] cancers. These have sparked an interest in expanding the research by synthesising novel thiourea compounds as possible anticancer drugs. Thus, the present review aims to summarize the recent development in thiourea derivatives in terms of the synthesis pathway, anticancer activities as well as the effect of substituents on the anticancer activities.

Chemistry of thiourea

Thiourea or thiocarbamide moiety is the first urea analogue which was synthesized for the first time by Marceli Nencki, a Polish scientist [21]. It is defined by the substitution of a sulfur atom for the oxygen atom. A lot of research articles are focused on thiourea scaffold as anticancer chemotherapeutics than urea moiety because of their remarkable polarity, reactivity, and efficient process of preparation [22]. A sulfur atom has a large size and is less electronegative resulting in the electrons being more polarizable as well as a stronger nucleophile for better reactivity than an oxygen atom [23]. Thiourea is considered an important group in drug design due to its extensive biological properties [22]. The thiourea scaffold serves as an excellent building block in constructing anticancer molecules with the presence of C=S regarded as an excellent acceptor, while thiourea N-H moiety is a favourable hydrogen bond donor. This dual nature of thiourea functionality is crucial in the drug's aqueous solubility and permeability [24]. The unique feature of thiourea moiety with desirable electron-rich characteristics is beneficial for thiourea derivatives which allows them to easily bind with a variety of enzymes and receptors in biological systems. Moreover, these interactions play a key role in the stability of ligand-receptor interactions subsequently, inhibiting the progression of cancer [25].

Thiourea (Figure 2a) compound is a needle-like glossy crystal with a colourless to pale yellow, bitter-tasting and ammonia-like odour. Thiourea is slightly soluble in cold water and soluble in hot water with a boiling point of 150-160 ºC [17]. Figure 2b shows the resonance forms of thiourea in which the amphoteric character of thiourea is demonstrated by its resonance, which indicates electrophilic attack at the C-1 position; nucleophilic attack at either N-1 or N-2. Meanwhile, the tautomerization at H-atom that is attached to either N-1 or N-2 position would form two pairs of isomers namely thione and thiol (Figure 2c).

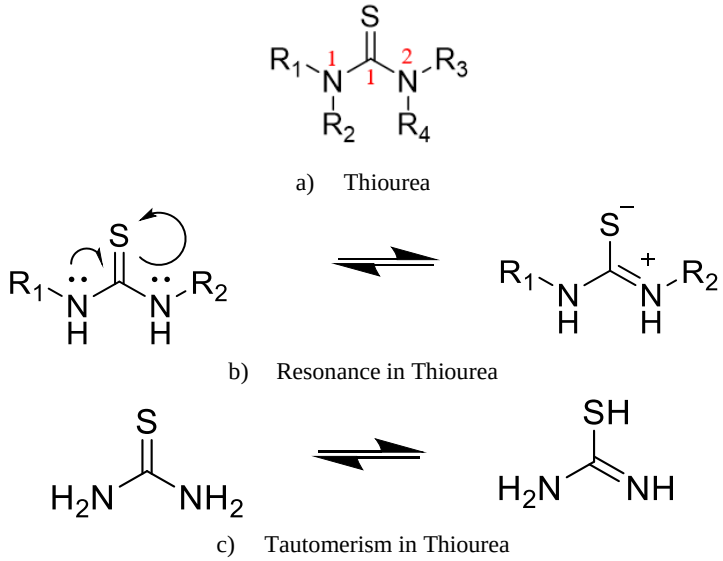


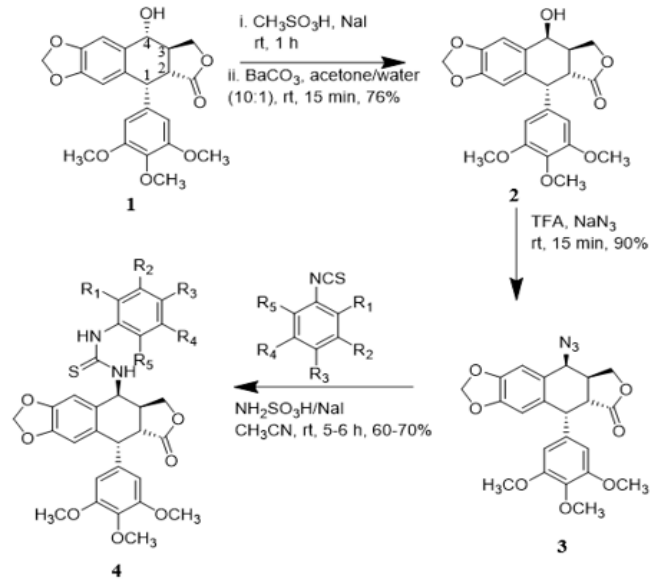
Figure 2. Thiourea scaffold showing numbering (a), resonance (b) and tautomerism (c)

Thiourea is a chemically interesting compound over the years due to its planar and flexible structure which exhibits greater π-electron delocalisation which also would enhance the binding ability to a variety of proteins in the biological system. The thiourea moiety is easily protonated under acidic conditions and interact with important amino acid residues on cancer cells such as carboxyl and phosphate groups, thus enhancing the anticancer activities [26].

Synthesis pathway of thiourea derivatives and their anticancer activities

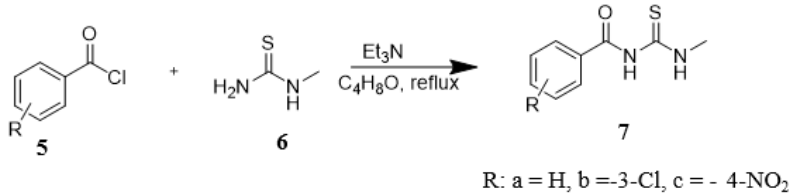
A lot of research on the thiourea moiety is currently ongoing to identify novel lead compounds to combat various cancers. The thiourea pharmacophore (-HN-C(=S)-NH-) is important in designing novel anticancer chemotherapeutics which leads to further development through structural modification. This pharmacophore acquires specific binding sites such as the hydrogen binding area thus increasing the binding affinity of the ligand-protein complex. The presence of C=S and N-H functional groups on thiourea which represents weak hydrogen bond acceptor as well as hydrogen bond donor respectively would significantly enhance the blocking of the enzymatic activity and simultaneously be a potent anticancer agent.

A novel of podophyllotoxin–thiourea derivatives (Scheme 1) were synthesized and evaluated for their in vitro cytotoxicity against A549 (human lung cancer), MDA MB-231 (human breast carcinoma), DU-145 (human prostate cancer), LNCaP (androgen-sensitive human prostate adenocarcinoma) and HGC- 27 (human gastric carcinoma) cell lines by MTT assays [27]. The synthesis strategy of podophyllotoxin–thiourea congeners **4a–u** was successfully performed by reaction with various isothiocyanates in the presence of NH_2SO_3H and NaI from 4ß-azido intermediate **(3)** and 4ß-deoxy-epipodophyllotoxin **(2)**. Among the compounds synthesized, compound **4a** was found to be effective in the DU-145 cell line compared to etoposide (standard drug) with half-maximal inhibitory concentration (IC_{50}) values less than 10 µM which is the range of 0.50-7.89µM. These compounds were further assayed for cytotoxicity on normal human prostate cell line (RWPE-1) and were shown as safe to be used. The introduction of bulky groups at the C-4 position at the podophyllotoxin thiourea derivative (**4**) significantly aids the antitumor activity [28]. The *N*-substituted benzene thiourea derivatives at the C-4 position showed that R_3 substituent (**4**) was significant for anticancer activity. For example, the presence of a small group such as methoxy **(4a)** increases the electron density and activates the ring. However, a bulky substituent at the R_3 position of the phenyl ring resulted in no cytotoxic activity.



Scheme 1. Synthesis of novel podophyllotoxin-thiourea congeners

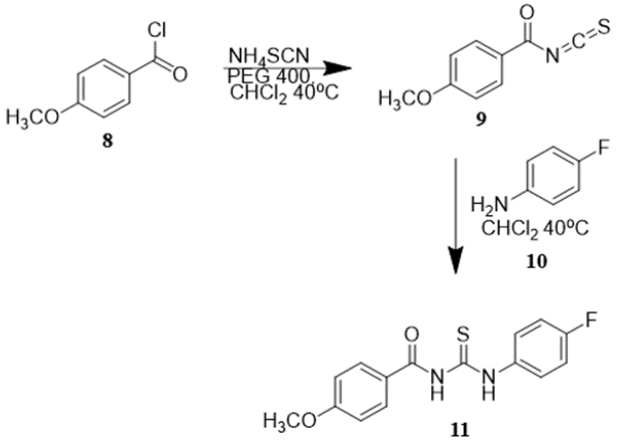
The 1-benzoyl-3-methyl thiourea derivatives were designed with different substitutions at *meta* and *para* positions on the phenyl ring of 1-benzoyl-3-methyl thiourea [29]. The compounds **7a-c** were synthesized from the reaction of starting material *N*-methylthiourea **(6)** with several ring-substituted benzoyl chlorides **(5)** (Scheme 2). The standard MTT assay was used to assess in vitro cytotoxicity against cervical cancer cell lines (HeLa). All of the compounds had higher cytotoxicity, with IC_{50} values ranging from 160 to 383µg/mL, than hydroxyurea (HU) as a reference drug, which had an IC_{50} of 428 µg/mL. It is revealed that the presence of benzoyl and methyl group on thiourea would increase the resonance within the compounds thus improving the compound stability and enhancing cytotoxic activity. The nitro substituents on the *para*-position **(7c)** had the highest activity, making it more active than HU. The electron-withdrawing group (EWG) substitutions such as chloro at the *meta*-position and nitro at the *para*-position of the aromatic ring improve the lipophilicity of molecules and are responsible for increased cytotoxicity [29]. The strong EWG would withdraw electrons through a π-bond due to the overlap of a *p* orbital on the substituent with a *p* orbital on the aromatic ring and stabilized by the electron-donating group (EDG) from methyl by resonance. Meanwhile, the absence of a sidechain on benzoyl showed the lowest activity among the synthesized compounds **(7a)**. These findings suggest that 1-benzoyl-3-methylthiourea derivatives could be used as anticancer agents in HeLa cells.



Scheme 2. Synthesis reaction of the 1-benzoyl-3-methylthioureas

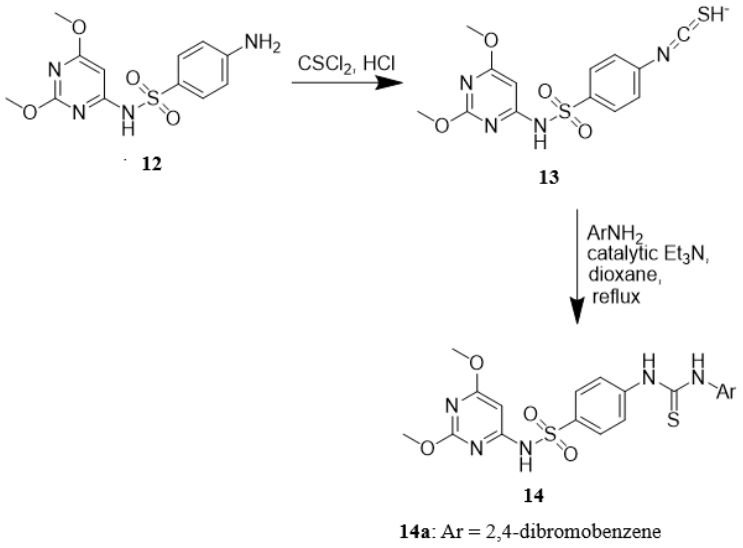
Encouraged by the outstanding anticancer activity from the presence of EWG as substituents at phenyl rings, the effect of EDG on the phenyl ring was also studied. The EDG group has been introduced to the

phenyl ring of benzoyl moiety linked thiourea in a compound of *N*-4-methoxybenzoyl-*N'*-(4-fluorophenyl)thiourea **(11)** and tested against HeLa cell line and compared with HU as a standard drug [30]. Scheme 3 shows that the compound was synthesized by the reaction of 4-methoxybenzoyl chloride **(8)** with ammonium thiocyanate to give an intermediate compound namely 4-methoxybenzoylisothiocyanate (**9**). Further reaction of **(9)** with 4-fluoroaniline **(10)** yielded the desired compound. The MTT results displayed that the compound has a lower inhibitory concentration IC_{50} value (0.720 ± 0.07 mM) which is more potent than HU (16.535 ± 2.092 mM). The presence of *p*-methoxy on benzoyl moiety and *p*-fluoro on phenyl ring enhanced the cytotoxic activity due to the lipophilic, electronic and steric properties. The methoxy (EDG) is a strongly activating group with the electron donor which imparts the resonance effect whereas fluorine (EWG) deactivates the ring by withdrawing the electron of the ring and stabilizing the compound. Thus, the combination of EWG and EDG in a thiourea compound potentially enhanced anticancer properties.



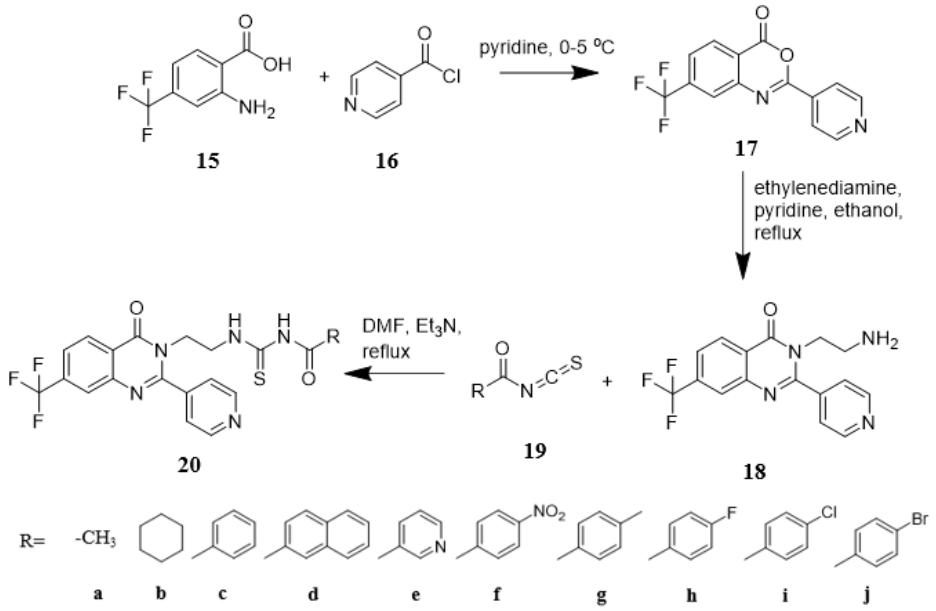
Scheme 3. Synthesis of *N*-methoxybenzoyl-*N'*-(4-fluorophenyl)thiourea derivatives

Subsequently, several novel thiourea derivatives bearing sulfonamide were synthesized and screened against HepG2, MCF-7, Caco-2, HCT-116, PC-3 cancer cell lines and Vero-B normal cell line [6]. The compounds were synthesized from the starting compound *N*-(2,6-dimethoxypyrimidin-4-yl)-4-isothiocyanatobenzenesulfonamide **(13)** as represented in Scheme 4. Among the compounds synthesized, compound **14a** which contains 2,4-dibromobenzene as a substituent exhibited broad selective cytotoxicity against cancer cells HepG2, MCF-7, Caco-2, and PC-3 with IC_{50} values 19.3, 20.5, 15.08 15.6 µg/ml respectively. This compound is a potent anticancer agent which might be due to the substitution of EWG (bromine atom) at *ortho* and *para* positions which activates the benzene ring through inductive effect, thus enhancing the anticancer properties.



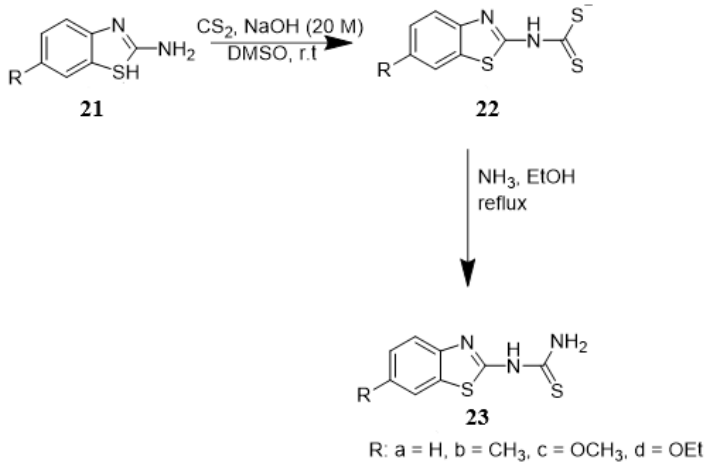
Scheme 4. Synthesis thioureas derivatives bearing a sulfonamide moiety

Another series is the novel 7-trifluoromethyl-2-pyridylquinazolin-4(3H)-one-based acyl thiourea derivatives **(20a-j)** as potential antiproliferative agents. The compounds were synthesized and tested for cytotoxicity in both cancerous human ovarian cancer (SK-OV-3), cervical cancer (HeLa), renal cancer (Caki-2) as well as noncancerous human umbilical vein endothelial cell (HUVEC) cell lines [18]. From the MTT bioassay results, the fluorine substitution on the benzoyl group was the most advantageous compared to other EWG due to the high electronegativity, highest carbon-fluorine bond strength, and smallest atomic radius (50 pm) as well as increased hydrophobic properties [31]. Compounds containing halogen atoms have higher potency overall. The presence of nicotinoyl and acetyl as the substituents contributed more to electron delocalization in the compound resulting in outstanding efficacy, whereas the absence of any functional or donor group on the benzoyl ring resulted in inert compounds. In addition, the conjugation bonds contributed by the quinazoline group in substituted thiourea derivatives correlated to the increase of lipophilic properties which is a salient feature for inhibition of DNA replication thus leading to the increased antiproliferative activity. However, all compounds showed desirable cytotoxicity towards the noncancerous cell line. It was discovered that modifying the substituent at the thiourea linkage gave different cytotoxic potentials to specific cell lines as summarized in Scheme 5. Specifically, thiourea-bearing quinazoline compounds with 4-fluorophenyl functionality **(20h)** and pyridyl moieties **(20e)** showed encouraging anticancer effects and could be used as a platform to design further chemotherapeutic agents.



Scheme 5. Synthesis of acyl thiourea derivatives of 7-trifluoromethyl-2-pyridylquinazolin-4(3H)-one

A new series of benzothiazole thiourea derivatives (**23a-d**) were tested for anticancer activity on human breast cancer cells (MCF-7), human cervix epithelial carcinoma (HeLa), human colon cancer cell line (HT-29), human leukaemia cell line (K-562), and mouse neuroblastoma cell line (Neuro-2a) [5]. The derivatives were prepared by the treatment of substituted 2-amino benzothiazole **(21)** with carbon disulfide and the ammonolysis of intermediate **(22)** in ethanol under reflux conditions as shown in Scheme 6. The compounds showed weakly to moderately cytotoxic activity with IC_{50} values ranging from 0.39 µM and up to 200 µM. Compound **23d** exhibited the most potent cytotoxic activity which was roughly four times more effective than cisplatin against the two cancer cell lines MCF-7 and HT-29, as depicted in Table 1. The synthesized compounds showed no cytotoxic effects on normal cells (L-929). The highest cytotoxicity of compound **23d** reflects the higher EDG nature of the ethoxy group and its steric effect. Therefore, combining benzothiazole and thiourea moieties might contribute to the improvement of the antiproliferation action.



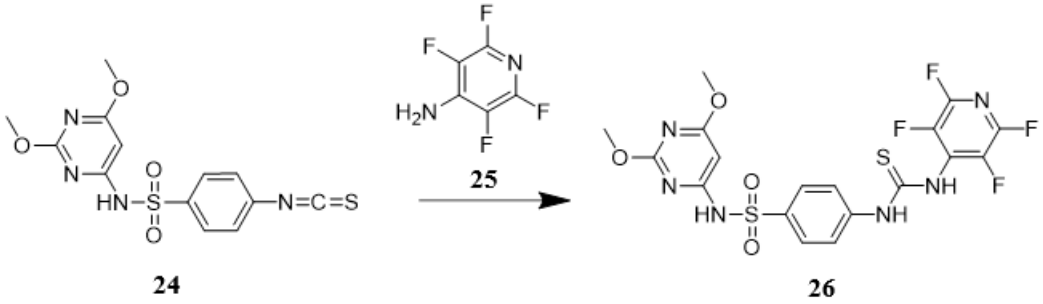
Scheme 6. General synthesis of the benzothiazole thiourea derivatives

Table 1. Cytotoxic activities of compounds (**23a–d**) against MCF-7, HeLa, HT-29, K-562, and Neuro-2a cancer cell lines

	Cell Lines (μM)					
Compound	**MCF-7**	**HeLa**	**HT-29**	**K-562**	**Neuro-2a**	**L-929**
23a	8.55	21.7	8.1	69.7	57.4	134.1
23b	11.9	47.3	14.8	85.3	235.3	135.0
23c	12.8	45.2	15.0	98.1	200.5	230.7
23d	6.72	4.97	3.90	40.5	22.7	107.6
Cisplatin	6.25	0.39	16.2	25.8	211.0	0.7

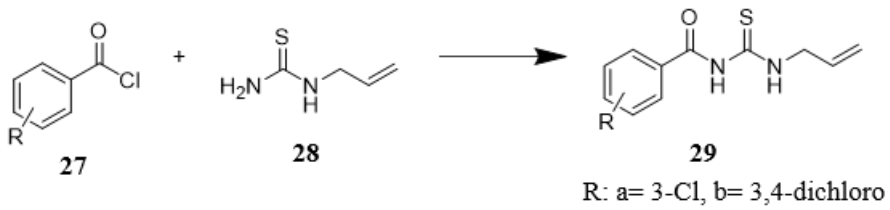
* The agent with IC_{50} > 100 μM is considered to be inactive

Inspired by the activity profile of a previous report [6] on thiourea-based sulfonamide derivatives, a new compound was developed namely *N*-(2,6-dimethoxypyrimidin-4-yl)-4-(3-(arylthioureido)benzenesulfonamides derivatives [20]. The desired compound was synthesized and tested for antiproliferative activity. The reaction scheme is depicted in Scheme 7. The antiproliferative assay showed that compound **(26)** with more EWG (fluorine atom) substituted to phenyl ring showed broad selective cytotoxicity against HepG2, MCF-7, Caco-2, and PC-3 cancer cells with IC_{50} values ranging from 15.08 μg/mL to 20.5 μg/mL. This compound also exhibited no cytotoxicity toward healthy cells (Vero-B). This work is in line with the previous study [6,20,29,18,15] which stated that EWG attached to phenyl ring bearing thiourea moiety would enhance the anticancer activity.



Scheme 7. Synthesis of thiourea derivatives bearing sulfonamides 26

Besides, two novel compounds namely *N*-(allylcarbamothioyl)-3-chlorobenzamide (**29a**) and *N*-(allylcarbamothioyl)-3,4-dichlorobenzamide **(29b)** were synthesized by reacting ally thiourea **(28)** and *N*-benzoyl chloride **(27)** as presented in Scheme 8 [15]. The compounds that have a different number of chlorine atoms on the phenyl ring were screened for cytotoxicity study on human breast cancer cell lines (T47D) using the MTT assay. This study concluded that an extra chlorine atom in compound **29b** contributed to higher cytotoxicity activity than compound **29a** and standard drug 5-FU with IC_{50} values of 86 μg/mL, 128 μg/mL and 213 μg/mL, respectively. The increased number of chlorine (EWG) would reduce the electron density and deactivate the ring but was stabilized by the presence of ally thiourea. Thus, the effect of the allyl group, as well as more EWG on thiourea structure, showed a substantial increase in antiproliferative activity as the conjugation makes the compounds more stable.



Scheme 8. Synthesis thiourea derivatives **29a-b**

Next, potent anticancer drugs were synthesized featuring the novel 4-*tert*-butylbenzoyl-3-allylthiourea framework and screened against MCF-7 cells overexpressed by HER-2 (MCF-7/HER-2) [32]. From the results of the MTT assay, compound **30** showed the best antiproliferative activity in comparison with positive control HU **(31)** with IC_{50} values of 0.15±6.48 mM and 2.01±1.05 mM, respectively (Figure 3). The *tert*-butyl functional group is EDG which will activate the *para* position of the phenyl ring due to more electron donation from C-H subsequently increasing compound conjugation. Thus, this study confirmed that a compound with allyl group and EDG is significantly cytotoxic and has the potential to be developed as a breast anticancer agent with HER-2 overexpression.

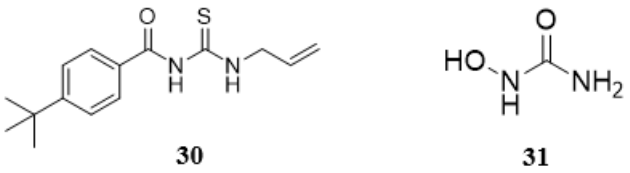
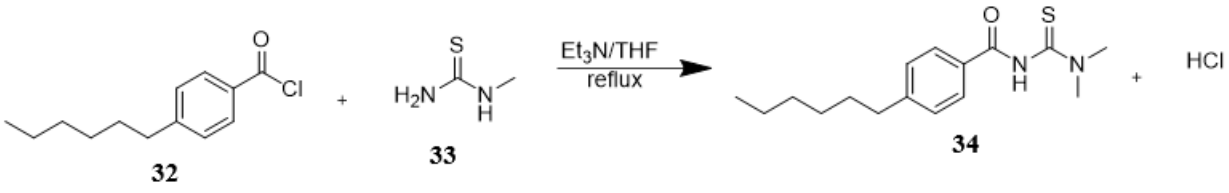


Figure 3. Structure of 4-t-butylbenzoyl-3-allylthiourea (30) and hydroxyurea (31)

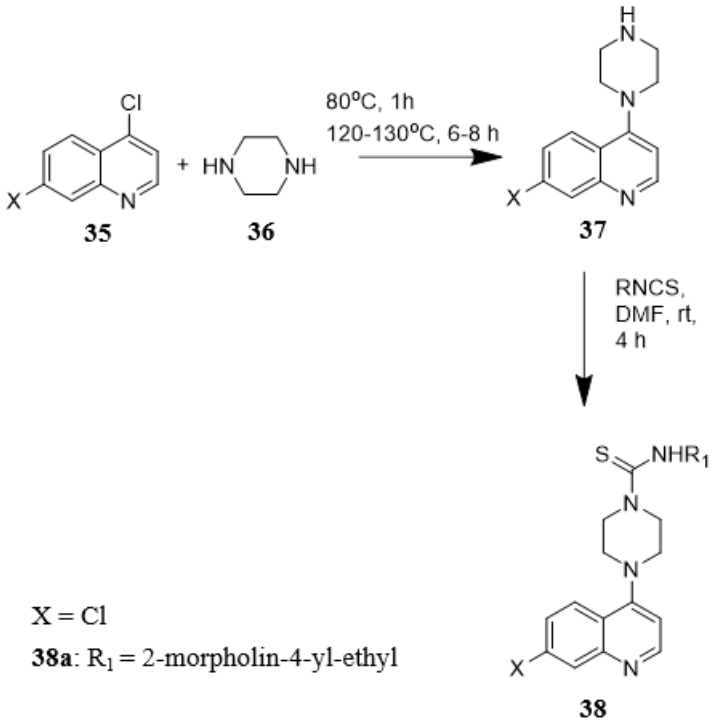
A new potent compound was discovered by reacting 4-hexylbenzoyl chloride **(32)** and *N*-methylthiourea **(33)** as shown in Scheme 9 [33]. The compound 1-(4-hexylbenzoyl)-3-methylthiourea **(34)** displayed significant anticancer activity against four cancer cell lines as compared to the control (hydroxyurea). This compound revealed low IC_{50} values; HeLa = 412 µM (5632 µM), MCF-7 = 390 µM (2829 µM), WiDr = 433 µM (1803 µM), and T47D = 179 µM (1803 µM). The incorporation of *n*-heptane aliphatic substituent would enhance the activity due to the increased lipophilic as well as pharmacokinetic properties. However, replacing the aliphatic chain with a tricyclic aliphatic reduces anticancer activity.



Scheme 9. The reaction between 4-hexyl benzoyl chloride with *N*-methylthiourea

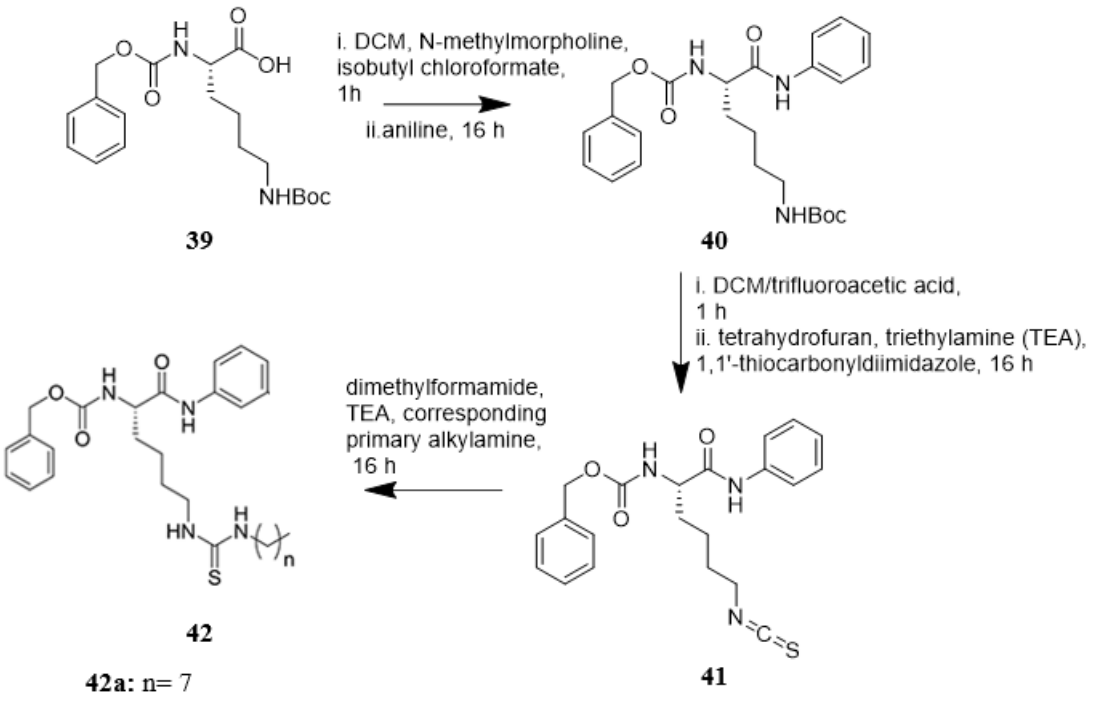
A new compound 4-piperazinylquinoline derived thioureas (Scheme 10) was developed and examined for their antiproliferative activity on three human breast tumour cell lines (MDA-MB231, MDA-MB468, and MCF7) as well as two non-cancer breast epithelial cell lines (184B5 and MCF10A) [16]. Among the novel compounds synthesized, compound **38a** namely (4-(7-chloro-quinoline-4-yl)-piperazine-1-carbothioic acid

(2-morpholine-4-yl-ethyl)-amide) showed significantly improved antigrowth/antiproliferative activity against breast cancer cells; MDA-MB231, MDA-MB468 and MCF7 with IC_{50} values ranging from 3.0 to 4.6 µM which is 7 to 11-fold selective to cancer cells and non-toxic to non-cancer cells. Attachment of quinoline, piperazine and morpholine on thiourea significantly enhanced antiproliferative activity with the cytotoxicity value 7 to11-fold higher in cancer than in noncancerous cells. This might be due to the heterocyclic compounds possessing hydrogen bond donor-acceptor capability which subsequently would enhance the lipophilic properties [34,35,36].



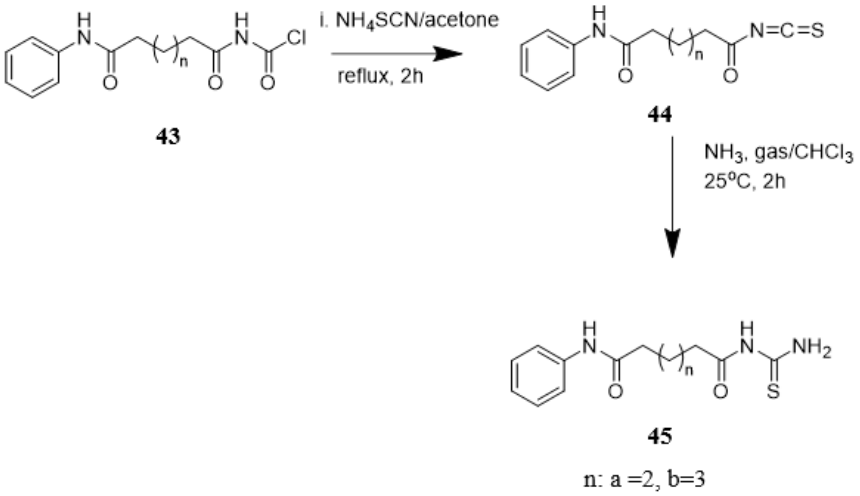
Scheme 10. Synthesis of 4-piperazinyl quinoline derived thiourea

Sirtuin 2 (SIRT 2) is an enzyme that is responsible for tumour suppressors in general, although knocking it down or inhibiting it has a broad anticancer effect in human breast cancer cell lines through boosting c-Myc degradation [37]. A novel lysine-derived thioureas as SIRT2 inhibitors were synthesized against MCF7 (breast cancer), MDA-MB-468 (breast cancer), MDA-MB-231(breast cancer), BxPC-3 (pancreatic cancer), NCI-H23 (lung cancer), A549 (lung cancer), SW948 (colorectal cancer), HCT116 (colorectal cancer), and CCD841 CoN (colon cell) [38]. The chemical reaction to synthesize the compounds is shown in Scheme 11. In comparison to thioamide-type inhibitor (reference drug), compound **42a** was highly selective and demonstrated broad cytotoxicity amongst cancer cell lines, specifically, human colorectal cancer cell line HCT116 with half-maximal growth inhibitory (GI_{50}) values of ~7 µM. None of the inhibitors was toxic to noncancerous HME1 epithelial cells.



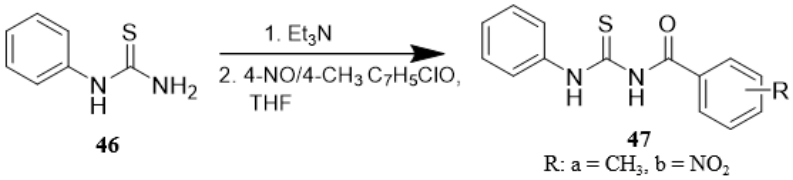
Scheme 11. Synthesis of Thiourea derivatives with varying chain lengths

Other novel compounds that were discovered are namely *N*-adipoyl monoanilide thiourea **(45a)** and *N*-pimeloyl monoanilide thiourea **(45b)** as histone deacetylase (HDAC) inhibitors [39]. Generally, HDAC is important to regulate epigenetic or non-epigenetic, as well as in cancer cell death, apoptosis, and cell cycle arrest [40]. The compounds were synthesized as shown in Scheme 12. Both compounds showed better inhibition against human colon adenocarcinoma (HRT-18) and mouse hepatoblastoma (HC-04) cells with a low cytotoxic effect on normal human breast cells (HBL-100) through MTT assay. It was also found that compound **45b** had higher antiproliferative activity than compound **45a** against the tested cancer cells with IC_{50} values of 21.44 µM and 24.12 µM and 27.37 µM and 30.42 µM, respectively against HC-04 and HRT-18 cell lines. The increased chain of carbon would increase the lipophilicity of the compound and subsequently enhance the cytotoxicity [41].



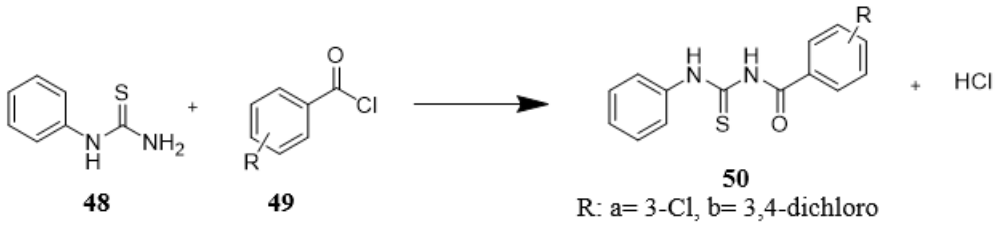
Scheme 12. Synthesis of the target compounds (45a-b)

Two compounds of *N*-(phenylcarbamothyoil) benzamide derivatives **(47)** were synthesized by reacting *N*-phenylthiourea, triethylamine **(46)**, and 4-nitro/4-methylbenzoyl chloride as presented in Scheme 13 [42]. This study investigated the effect of electronic and lipophilic substitution on anticancer activity. Compound **47b** with a strong electronic effect of 4-NO_2 (σ = 0.78) is more potent with lower IC_{50} values compared to compound **47a** with a strong lipophilic effect of 4-CH_3 (π =0.56) with IC_{50} values of 0.12±0.014 and 1.08±0.013 mM, respectively. The effect of the EWG is stronger than the EDG. Overall, the tested compounds have better activity than HU (4.58 ±0.019 mM) and are non-toxic to healthy Vero cells. The study suggested that *N*-(phenylcarbamothyoil) benzamide derivatives compound has a stronger electronic effect than lipophilic effect.



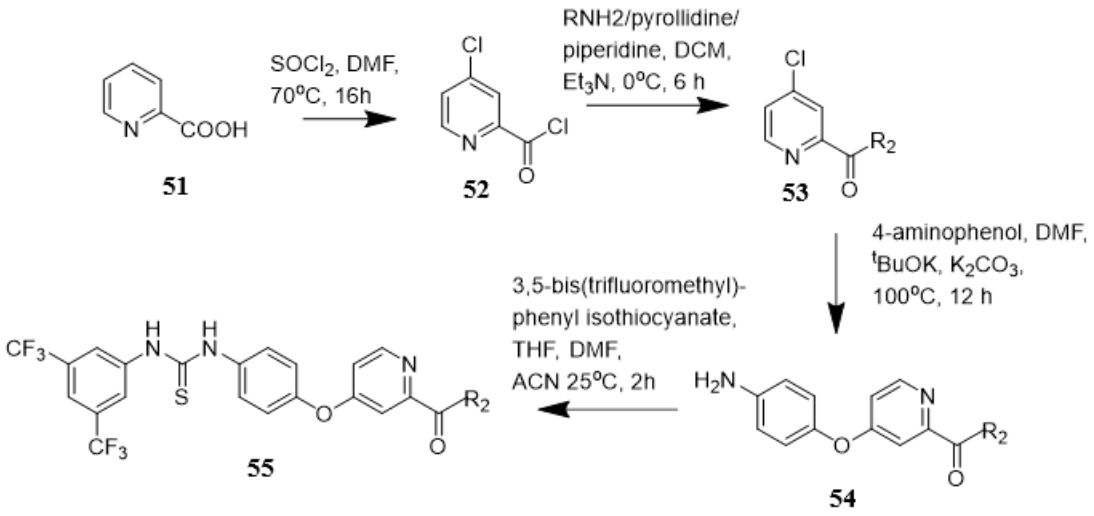
Scheme 13. Synthesis of *N*-(phenylcarbamothyoil) benzamide derivatives

In response to the strong EWG effect in cytotoxicity, another two compounds of *N*-benzoyl-*N'*-phenylthiourea derivatives were designed, namely *N*-(3-chloro)benzoyl-*N'*-phenylthiourea **(50a)** and N-(3,4-dichloro) benzoyl-*N'*-phenylthiourea **(50b)** [43]. The test compounds were synthesized from *N*-phenylthiourea (**48**) with benzoyl chloride derivatives (**49)** via acyl nucleophilic substitution reactions as represented in Scheme 14. A cytotoxicity study obtained from the MTT assay showed that **50a** has a higher cytotoxic effect than **50b** with IC_{50} values of 0.43 mM and 0.85 mM respectively. Overall, all compounds showed better anticancer activity compared with HU (IC_{50} = 4.58 mM). The activities of these two novel compounds were projected to be cell-targeted because they were harmful to cancer cells but not to Vero normal cells.



Scheme 14. Synthesis of *N*-benzoyl-*N'*-phenylthiourea or *N*-(phenylcarbamothioyl)-benzamide derivatives

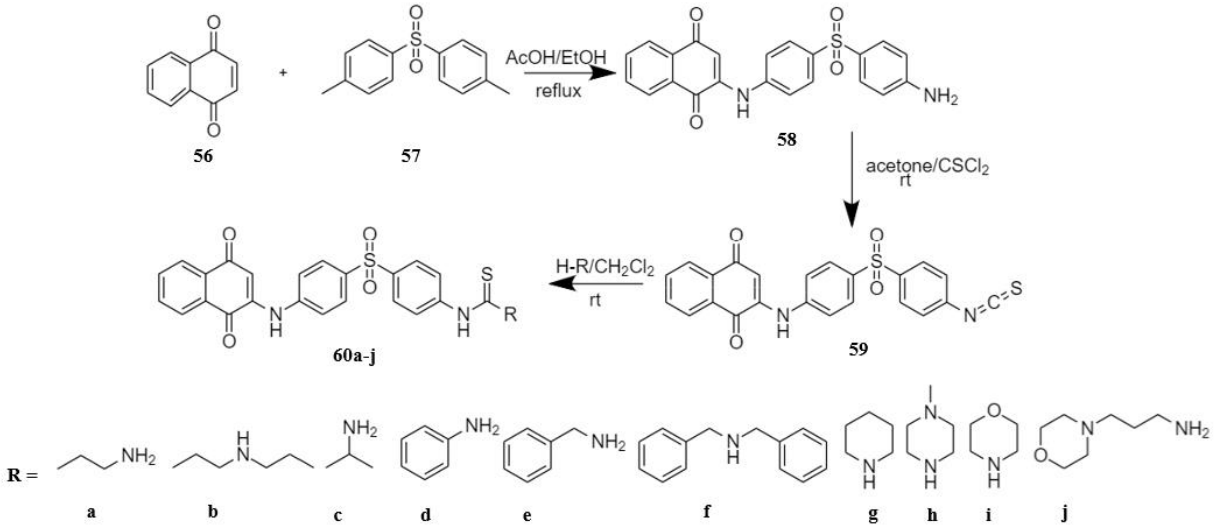
The synthesis of a series of novel thiourea derivatives containing 3,5-bis(trifluoromethyl)phenyl moiety (R_1) at terminal thiourea and phenylamino (R_2) at the terminal acyl position is shown in Scheme 15 [44]. Compound (**55a)** showed the best cytotoxicity against seven cancer cell lines: NCI-H460, Colo-205, HCT116, MDA-MB-231, MCF-7, HEpG2 and PLC/PRF/5 with IC_{50} values of 1.86, 9.92, 6.42, 8.21, 9.19, 6.21 and 7.82µM, respectively. Compound **55a** was found to be most potent with higher antiproliferative activities than Sorafenib and has excellent activity against normal cell HUVEC (IC_{50}: 2.81µM). When 3,5-bis(trifluorophenyl) was replaced with a nitro group (**55b**), good antiproliferative activity was observed. Meanwhile, none and weak activities were reported for unsubstituted (**55c**) and EDG substituent ring **(55d**) on phenyl ring respectively.



Scheme 15. Synthesis novel thiourea derivatives **55a-d**

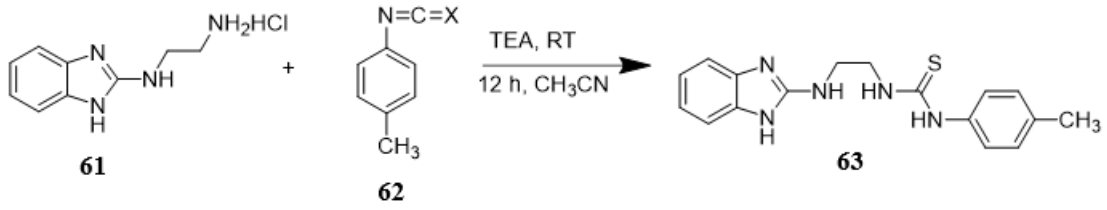
Another novel thiourea compounds that are potent anticancer chemotherapeutic are thiourea bearing dapsone-naphthoquinone derivatives [45]. The synthesis pathways of the desired compounds **(60a-j)** are illustrated in Scheme 16. The reaction between 1,4-naphthoquinone **(56)** and dapsone **(57)** produces 2-[4-(4-aminobenzenesulfonyl)-phenylamino]-[1,4]naphthoquinone **(58)**. The 2-[4-(4-isothiocyanato-benzenesulfonyl)-phenylamino]-[1,4]naphthoquinone **(59)** was obtained by adding thiophosgene to the **(58)** suspension in acetone. Finally, the synthesis of thiourea derivatives **(60a-j)** was completed by adding primary or secondary amines to the isothiocyanato intermediate **(59)**. The most effective compound was found to be a thiourea derivative containing *N*-methyl piperazine (**60h**) with an IC_{50} of 5.8±0.55 µM against chronic

myelogenous leukaemia (CML) (K562 cell lines). The anticancer action of thiourea derivatives was diminished by increasing the inhibitory effect of nucleophile steric hindrance. The anticancer activity of compounds **(60d–f)** containing phenyl, benzyl, and dibenzyl amines, respectively is significantly reduced. The anticancer activity of compounds **(60g-j)** revealed that adding N-CH_3 group to the thiourea skeleton considerably increased the anticancer activity of **60h**, with an IC_{50} of 5.8±0.55 µM. Furthermore, the anticancer activity of **60h** was 5.2 times more active than the carbon-substituted compound 60g (IC_{50}=30.37±2.21 µM) and 5 times more active than the oxygen-substituted compound **60i** (IC_{50}=29.06±2 µM).



Scheme 16. Preparation of the aimed compound (**60a–j**)

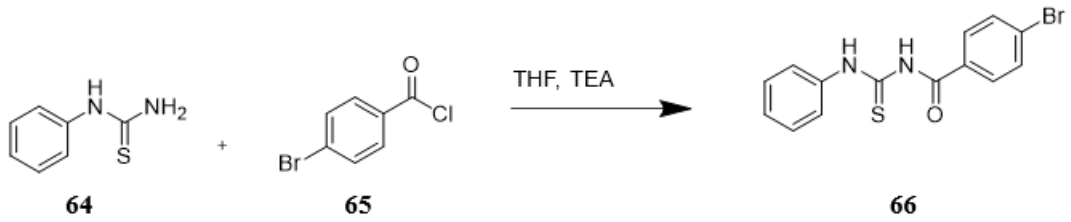
A new thiourea benzimidazole derivatives were synthesized, as outlined in Scheme 17 [47]. The cytotoxic activity of the compounds was assessed in human breast cancer cell lines viz MDA-MB-231 and MCF-7. The compound 1-(2-(1*H*-benzo[d]imidazol-2-yl-amino)ethyl)-3-*p*-tolylthiourea **(63)** was found with higher activity in MCF-7 with IC_{50} values of 25.8 µM, as compared with MDA- MB-231 cells (54.3µM). It was revealed that benzimidazole is connected to thiourea moiety through ethylenediamine linker contributed to the anticancer activity due to its resonance structure. These findings could lead to the development of novel thiourea benzimidazole compounds with significant anticancer properties.



Scheme 17. Synthesis thiourea benzimidazole derivatives **63**

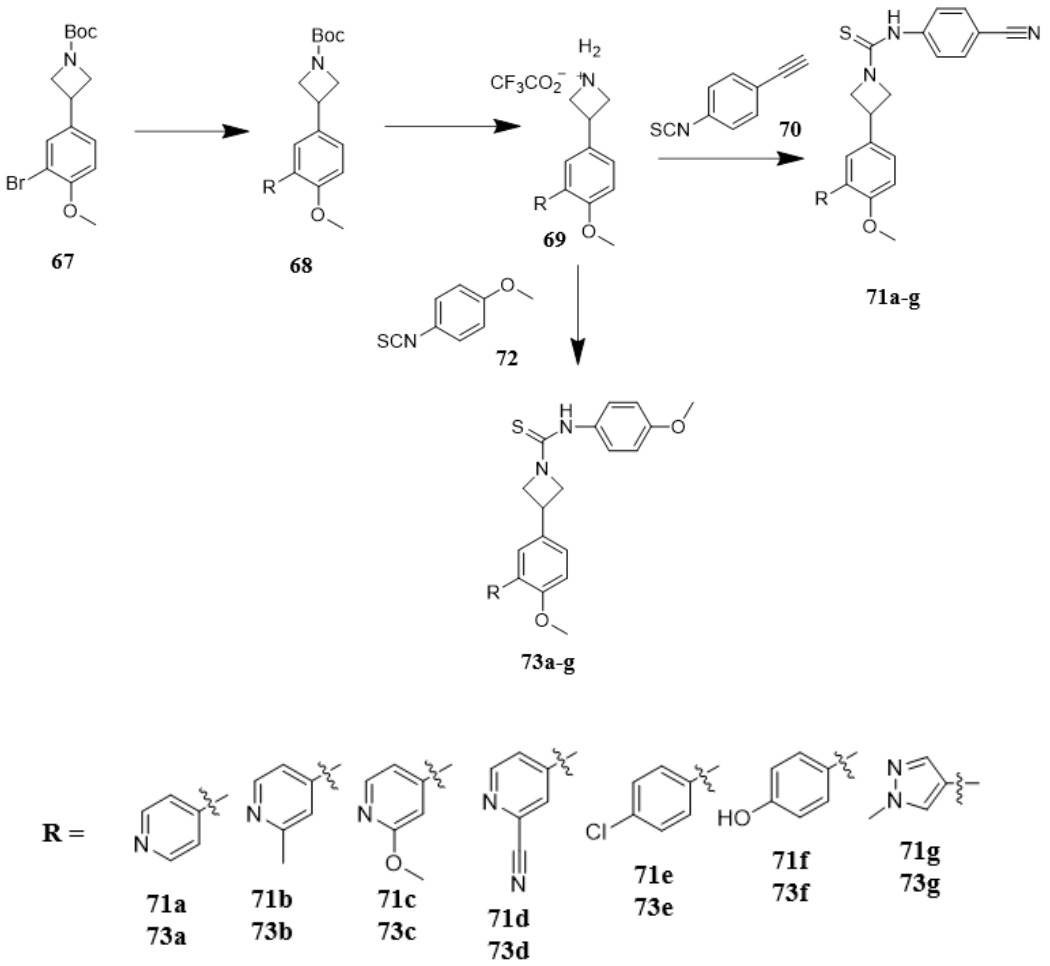
Next, a potent compound was revealed namely *N*-(4-bromo)-benzoyl-*N'*-phenylthiourea **(66)** [47]. The compound was synthesized by reaction of N-phenylthiourea **(64)** and 4-bromobenzoyl chloride **(65)** through acyl nucleophilic substitution as depicted in Scheme 18. In vitro cytotoxicity assay was carried out on HER2-positive primary breast cancer cells and produced IC_{50} values of 0.54 mM, lower than standard

drug hydroxyurea with an IC_{50} value of 11.61mM. This finding is correlated to the previous study [42] which confirmed that the inductive effect of EWG showed greater cytotoxicity than the lipophilic effect of EDG. Thus, the substituent of EWG for benzoyl ring of thiourea is important and could be further developed as an anticancer candidate for HER2-positive breast cancer.



Scheme 18. Synthesis of *N*-(4- bromo)-benzoyl-*N*'-phenylthiourea **66**

Other than that, a novel series of compounds were developed with thiourea-azetidine hybrid **(71a-g)** and **(73a-g)** [48]. The synthesis pathway of these compounds is illustrated in Scheme 19. All compounds were evaluated for their in vitro anticancer activity against various human cancer cell lines viz; lung (A549), prostate (PC3), breast (MCF7), liver (HepG2), colon (HCT116), ovarian (SKOV3), skin (A431), brain (U251), and kidney (786-O). With medium effective dose (EC_{50}) values of 0.25, 0.6, 0.03, and 0.03 µM, the compound of 3-(4-methoxy-3-(2-methoxypyridin-4-yl)phenyl)-*N*-(4-methoxyphenyl)azetidine-1-carbothioamide **(73c)** was shown to be the most potent member against PC3, U251, A431, and 786-O cancer cell lines, respectively, and demonstrated more potency than doxorubicin. In the A431 cell line, the median effective concentration (EC_{50}) values for compounds **73a-g** ranged from 0.03 to 12.55 µM. For A431 and 786-O cell lines, compound 3-(4-methoxy-3-(pyridin4-yl)phenyl)-N-(4-methoxyphenyl)azetidine-1-carbothioamide **(73a)** was shown to be highly effective, with EC_{50} values of 0.77 and 0.73 µM, respectively. All of the substances have a good to moderate level of toxicity. The study revealed that thiourea derivatives containing EDG (–OCH_3) on the phenyl ring and pyridine **(73a)**, substituted pyridine derivatives **(73b-d)** and substituted pyrazole derivative **(73g)**, respectively were found to be the most potent than compounds with substituted pyridine **(71a-d)** and pyrazole heterocycle derivatives **(71g)**, which contained EWG (–CN, in place of –OCH_3). In their series, the compound with *p*–chloro substitution and EWG (–CN) on the phenyl ring **(71e)** was found to have significantly higher activity against HepG2 and HCT-116 cell lines than phenyl derivatives with EDG (*p*-OH) **(71f)**. Out of nine cancer cell lines studied, the derivatives with EDG on both sides (–OH and –OCH_3) **(73f)** showed good to moderate activity on cell lines of A431, A549, HepG2, and HCT-116. Thus, this study confirmed that EDG substituent would enhance the cytotoxic activity.



Scheme 19. The synthesis of thiourea-azetidine derivatives (71a-g and 73a-g)

Another study is the synthesis and evaluation of several thioureas and benzylidine moieties as carbonic anhydrase-II (CA-II) inhibitors [49]. The CA-II enzyme is important to catalyse the reversible hydration of carbon dioxide, which results in the creation of bicarbonate and proton. The inhibition of this enzyme is used as a biomarker and therapeutic target in the treatment of leukaemia, cystic fibrosis, glaucoma, and epilepsy [50]. Within this study, several thiourea derivatives and compound **84** of the benzylidene series showed outstanding inhibitory activity against CA. The cytotoxic evaluation against 3T3 cell lines (Mouse Fibro-blast) using MTT assay exhibited prominent inhibition activity with IC_{50} values ranging from 1.90 ± 1.30 to 25.90 ± 2.05 µM compared to standard inhibitor acetazolamide (IC50 = 0.13 ± 0.05). Meanwhile, benzylidene derivatives showed weak inhibition potential with IC_{50} values in the range of 52.68 ± 0.47 to 348.57 ± 3.32 µM. Also, the study reported that *N*-(trifluoromethyl) benzoyl moiety in thiourea is important for CA II inhibition. The structures of thiourea derivatives are shown in Figure 4. It was revealed that compound **(82)**, with ethoxy substituents (EDG) on the N-phenyl ring, significantly enhance the potency of the compound with an IC_{50} value of 1.90 µM. The presence of EDG increased the electron density and activate the ring. Unsubstituted *N*-phenyl ring **(80)** showed a slight decrease in anticancer activity. However, the presence of EWG such as F, CN, NO_2 and Br group on the *N*-

phenyl ring for compounds (**74-83)** suppresses the activity with IC_{50} values ranging from 4.40 ± 1.80 µM to 25.90 ± 2.05 µM. On the other hand, the presence of furylmethylene ring increased the potency of compound **84**. Overall, it is indicated that EDG on the benzene ring of thiourea derivatives and benzylidene have significantly enhanced the anticancer activity.

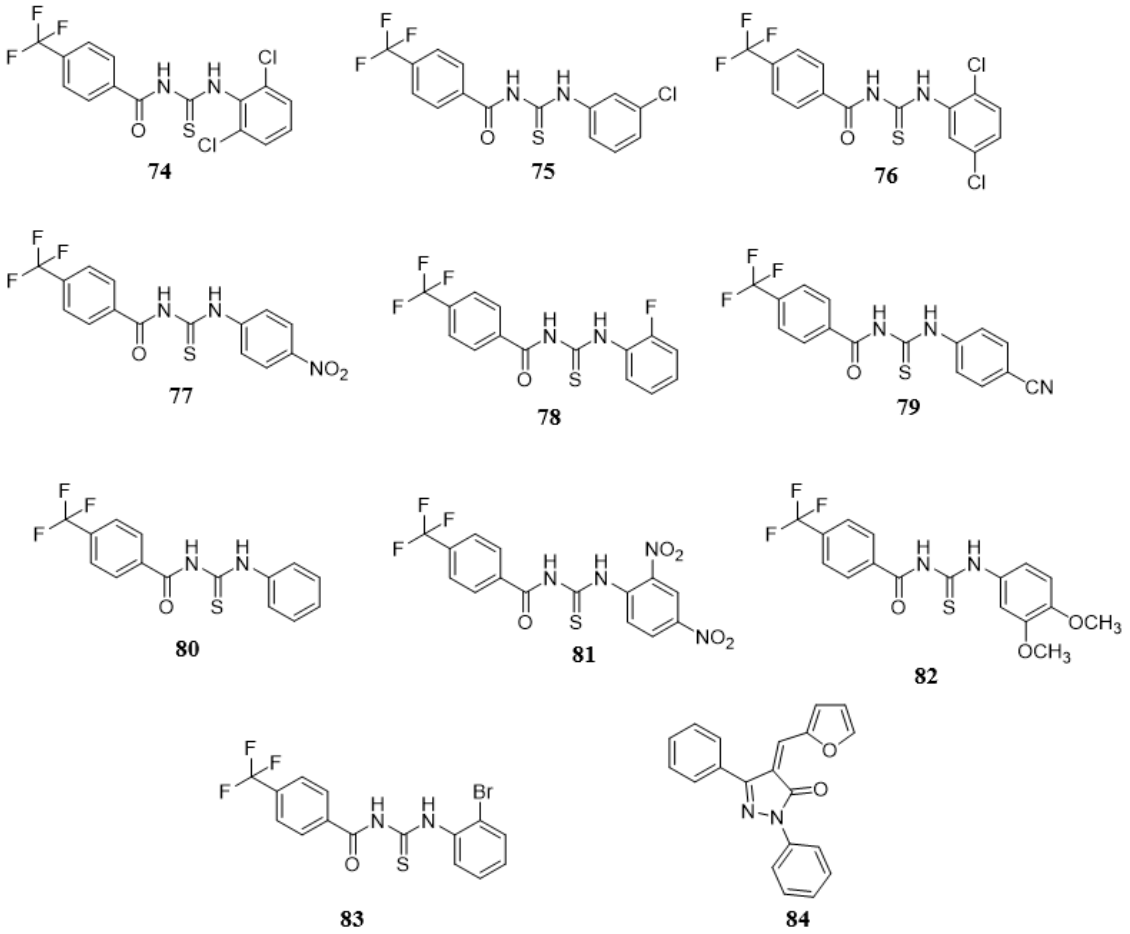
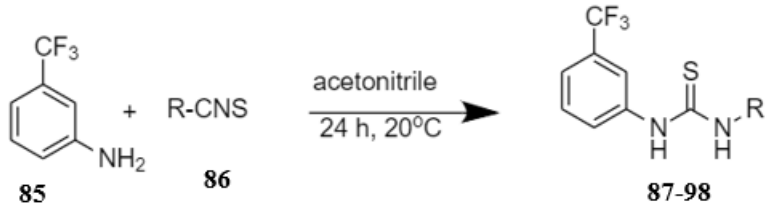


Figure 4. Structure of thiourea derivatives **74-84**

The potent *N*-(trifluoromethyl) benzoyl moiety linked to thiourea potential for anticancer activity led to the synthesis of 1,3-disubstituted thioureas **(87-98)** [12]. The synthesis pathway of these compounds involves a single-step reaction of 3-(trifluoromethyl)aniline **(85)** with various isothiocyanates **(86)**, belonging to a group of dihalogenophenyl **(87-90)**, halogenomethylphenyl **(91-92)**, alkylphenyl **(96)**, or monophenyl-substituted **(91–95)** derivatives (Scheme 20). Then, the cytotoxicity of the compounds was investigated against four human carcinoma cell lines, such as SW480 (primary colon cancer), SW620 (metastatic colon cancer), PC3 (metastatic prostate cancer), and K-562 (chronic myelogenous leukaemia), as well as against the normal cell line HaCaT (immortalized human keratinocytes), the IC_{50} values are summarized in Table 2. This study summarized the increasing impact of cytotoxicity according to the terminal benzene moiety functionalities as follows: 4-bromo- **(97)** < 2-(trifluoromethyl)- **(93)** < 2-methyl-5-chloro- **(92)** < 4-cyano- **(96)** < 2-methyl-3-chloro- **(91)** < 2,3-dichloro- **(90)** << 2,4-dichloro- **(89)** < 4-chloro- **(95)** < 3-chloro-4- fluoro- **(87)** < 4-(trifluoromethyl)- **(94)** < 3,4-dichloro- **(88)**. Dihalogenophenyl

derivatives **(87-90)**, compounds **94- 95** were the most active among the series towards all tumour cell lines with $IC_{50} \leq 10$ µM. The most promising drug candidates **(87-90, 94, 95)** were weakly cytotoxic towards normal HaCaT cell lines. Meanwhile, the introduction of the unsubstituted alkylphenyl group **(98)** to the thiourea branch dramatically decreased the compound's bioactivity. The structural modifications of the thiourea terminal moieties indicated the dihalogenophenyl derivative **(88)**, followed by its isomer **(89)** and para-substituted analogue **(94)**, as the most effective in cancer treatment. Therefore, this study highlighted the significance of EWG substituent in enhancing anticancer activity.



85 **86** **87-98**

87, R= 3-Cl, 4-F-Ph **90**, R= 2-Cl, 3-Cl-Ph **93**, R= 2-CF_3-Ph **96**, R= 4-CN-Ph
88, R =3-Cl, 4-Cl-Ph **91**, R =2-CH_3, 3-Cl-Ph **94**, R =4-CF_3-Ph **97**, R =4-Br-Ph
89, R = 2-Cl, 4-Cl-Ph **92**, R = 2-CH_3, 5-Cl-Ph **95**, R = 4-Cl-Ph **98**, R = -CH_2CH_2-Ph

Scheme 20. Synthesis procedure for 3-(trifluoromethyl)phenylthiourea derivatives **87-98**.

Table 2. Cytotoxic activity (IC_{50}, µM) of the studied compounds estimated by the MTT assay

No.	R	Cancer Cells				Normal Cells
		SW480	SW620	PC-3	K-562	HaCaT
87	3-Cl,4-F-Ph	12.7	9.4	53.6	6.8	43.6
88	3-Cl,4-Cl-Ph	9.0	1.5	31.7	6.3	24.7
89	2-Cl,4-Cl-Ph	30.1	5.8	13.7	54.3	52.1
90	2-Cl,3-Cl-Ph	22.5	14.0	10.5	35.9	13.9
91	2-CH_3, 3-Cl-Ph	7.3	23.2	51.8	52.5	55.6
92	2-CH_3, 5-Cl-Ph	15.6	22.1	65.9	40.3	14.5
93	2-CF_3-Ph	>100	30.1	17.1	76.5	65.7
94	4-CF_3-Ph	8.9	7.6	6.9	54.8	41.3
95	4-Cl-Ph	38.1	6.7	22.6	10.2	71.5
96	4-CN-Ph	20.6	18.7	66.2	12.9	50.1
97	4-Br-Ph	41.5	16.2	76.6	74.2	17.2
98	-CH_3CH_3-Ph	25.3	38.2	26.7	23.8	55.4
Cisplatin	-	10.4	6.7	13.2	8.2	6.3

Conclusion

This review summarizes the recently synthesized thiourea compounds and their anticancer activities. It shows that thiourea moiety is important in discovering potent, effective and safer drugs to treat cancer. As described above, there were numerous synthesis pathways to prepare the thiourea derivatives. Based on the evaluation of thiourea derivatives as an anticancer agent, modification of thiourea moiety with suitable substituents at N1 and N2 improved the cytotoxicity properties of the compounds. The study also indicates that the substituent containing electron donating and electron withdrawing groups play an excellent role in improving anticancer activities. Even though most of these reported compounds are in clinical trials, the urgent need for further derivation and cytotoxicity studies will provide an opportunity for managing therapeutic values more efficiently and with greater efficacy. In short, the thiourea derivatives scaffold is a valuable candidate in the design and development of novel compounds that warrants further investigation with a clinical trial.

Acknowledgement

We thank Universiti Malaysia Pahang (UMP) for funding the project under UMP-IIUM-UiTM Sustainable Research Collaboration 2020 (project vot: SRCG20-007-0007). Also, International Islamic University Malaysia (IIUM) for providing the facilities to conduct the research.

References

1. Sung, H., Ferlay, J., Siegel, R. L., Laversanne, M., Soerjomataram, I., Jemal, A. and Bray, F. (2021). Global Cancer Statistics 2020: GLOBOCAN Estimates of Incidence and Mortality Worldwide for 36 Cancers in 185 Aountries. *CA: A cancer Journal for Clinicians*, 71(3): 209-249.
2. Mansoori, B., Mohammadi, A., Davudian, S., Shirjang, S. and Baradaran, B. (2017). The different mechanisms of cancer drug resistance: A brief review. *Advanced Pharmaceutical Bulletin*, 7(3): 339.
3. Levitzki, A. and Klein, S. (2019). My journey from tyrosine phosphorylation inhibitors to targeted immune therapy as strategies to combat cancer. *Proceedings of the National Academy of Sciences*, 116(24): 11579-11586.
4. Kirishnamaline, G., Magdaline, J. D., Chithambarathanu, T., Aruldhas, D. and Anuf, A. R. (2021). Theoretical investigation of structure, anticancer activity and molecular docking of thiourea derivatives. *Journal of Molecular Structure*, 1225: 129118.
5. Eshkil, F., Eshghi, H., Saljooghi, A., Bakavoli, M. and Rahimizadeh, M. (2017). Benzothiazole thiourea derivatives as anticancer agents: design, synthesis, and biological screening. *Russian Journal of Bioorganic Chemistry*, 43(5): 576-582.
6. Ghorab, M., SA El-Gaby, M., S Alsaid, M., AMM Elshaier, Y., M Soliman, A., F El-Senduny, F., ... and YA Sherif, A. (2017). Novel thiourea derivatives bearing sulfonamide moiety as anticancer agents through COX-2 inhibition. *Anti-Cancer Agents in Medicinal Chemistry (Formerly Current Medicinal Chemistry-Anti-Cancer Agents)*, 17(10): 1411-1425.
7. Guria, T., Roy, P. and Maity, T. K. (2018). Synthesis, pharmacological evaluation and ligand-protein interaction study of hybrid urea and thiourea derivatives as antihyperglycemic agents. *International Research Journal of Pharmacy*, 9(5): 36-44.
8. Türk, S., Tok, F., Erdoğan, Ö., Çevik, Ö., Tok, T. T., Koçyiğit-Kaymakçıoğlu, B. and Karakuş, S. (2020). Synthesis, anticancer evaluation and in silico ADMET studies on urea/thiourea derivatives from gabapentin. *Phosphorus, Sulfur, and Silicon and the Related Elements*, 196(4): 382-388.
9. Ghorab, M. M., Alsaid, M. S., Al-Dosary, M. S., Nissan, Y. M. and Attia, S. M. (2016). Design, synthesis and anticancer activity of some novel thioureido-benzenesulfonamides incorporated biologically active moieties. *Chemistry Central Journal*, 10(1): 1-13.
10. Kumar, V. and Chimni, S. S. (2015). Recent developments on thiourea based anticancer chemotherapeutics. *Anticancer Agents in Medicinal Chemistry*, 15(2): 163-175.

11. Sethy, C. and Kundu, C. N. (2021). 5-Fluorouracil (5-FU) resistance and the new strategy to enhance the sensitivity against cancer: Implication of DNA repair inhibition. *Biomedicine & Pharmacotherapy*, 137: 111285.
12. Strzyga-Łach, P., Chrzanowska, A., Podsadni, K. and Bielenica, A. (2021). Investigation of the Mechanisms of cytotoxic activity of 1, 3-disubstituted thiourea derivatives. *Pharmaceuticals*, 14(11): 1097.
13. Lee, B. B., Kim, Y., Kim, D., Cho, E. Y., Han, J., Kim, H. K., ... and Kim, D. H. (2019). Metformin and Tenovin-6 synergistically induce apoptosis through LKB1-independent SIRT1 down-regulation in non-small cell lung cancer cells. *Journal of Cellular and Molecular Medicine*, *23*(4): 2872-2889.
14. Shakeel, A., Altaf, A. A., Qureshi, A. M. and Badshah, A. (2016). Thiourea derivatives in drug design and medicinal chemistry: a short review. *Journal Drug Design Medicine Chemistry*, 2(1): 10.
15. Widiandani, T. and Hardjono, S. (2017). Docking and cytotoxicity test on human breast cancer cell line (T47d) of *n*-(allylcarbamothioyl)-3-chlorobenzamide and *n*-(allylcarbamothioyl)-3, 4-dichlorobenzamide. *Research Journal of Pharmaceutical, Biological and Chemical Sciences*, 8(2): 1909-1914.
16. Viswas, R. S., Pundir, S. and Lee, H. (2019). Design and synthesis of 4-piperazinyl quinoline derived urea/thioureas for anti-breast cancer activity by a hybrid pharmacophore approach. *Journal of Enzyme Inhibition and Medicinal Chemistry*, 34(1): 620-630.
17. Liu, J., Liao, P., Hu, J., Zhu, H., Wang, Y., Li, Y., ... and He, B. (2017). Synthesis and antitumor activities of chiral dipeptide thioureas containing an alpha-aminophosphonate moiety. *Molecules*, 22(2): 238.
18. Mistry, B. M., Shin, H. S., Pandurangan, M. and Patel, R. V. (2017). Synthesis of acyl thiourea derivatives of 7-trifluoromethyl-2-pyridylquinazolin-4-(3*h*)-one as anticancer agents. *Journal of Chemical Research*, 41(10): 598-602.
19. Kulabaş, N., Özakpınar, Ö. B., Özsavcı, D., Leyssen, P., Neyts, J. and Küçükgüzel, İ. (2017). Synthesis, characterization and biological evaluation of thioureas, acylthioureas and 4-thiazolidinones as anticancer and antiviral agents. *Marmara Pharmaceutical Journal*, 21(2): 371-384.
20. Ghorab, M. M., Alsaid, M. S., El-Gaby, M. S., Elaasser, M. M. and Nissan, Y. M. (2017). Antimicrobial and anticancer activity of some novel fluorinated thiourea derivatives carrying sulfonamide moieties: synthesis, biological evaluation and molecular docking. *Chemistry Central Journal*, 11(1): 1-14.
21. Ronchetti, R., Moroni, G., Carotti, A., Gioiello, A. and Camaioni, E. (2021). Recent advances in urea-and thiourea-containing compounds: Focus on innovative approaches in medicinal chemistry and organic synthesis. *RSC Medicinal Chemistry*, 12(7): 1046-1064.
22. Francioso, A., Baseggio Conrado, A., Mosca, L. and Fontana, M. (2020). Chemistry and biochemistry of sulfur natural compounds: Key intermediates of metabolism and redox biology. *Oxidative Medicine and Cellular Longevity*, 2020: 8294158
23. Olson, K. R. (2020). Are reactive sulfur species the new reactive oxygen species? *Antioxidants & Redox Signaling*, 33(16): 1125-1142.
24. Ghosh, A. K. and Brindisi, M. (2019). Urea derivatives in modern drug discovery and medicinal chemistry. *Journal of Medicinal Chemistry*, 63(6): 2751-2788.
25. Vologzhanina, A. V., Ushakov, I. E. and Korlyukov, A. A. (2020). Intermolecular interactions in crystal structures of imatinib-containing compounds. *International Journal of Molecular Sciences*, 21(23): 8970.
26. Abd Halim, A. N. and Ngaini, Z. (2016). Synthesis and bacteriostatic activities of bis(thiourea) derivatives with variable chain length. *Journal of Chemistry*, 2016: 2739832

27. Shankaraiah, N., Kumar, N. P., Amula, S. B., Nekkanti, S., Jeengar, M. K., Naidu, V. G. M., ... and Kamal, A. (2015). One-pot synthesis of podophyllotoxin–thiourea congeners by employing NH_2SO_3H/NaI: Anticancer activity, DNA topoisomerase-II inhibition, and Apoptosis inducing agents. *Bioorganic & Medicinal Chemistry Letters*, 25(19): 4239-4244.
28. Cheng, W. H., Shang, H., Niu, C., Zhang, Z. H., Zhang, L. M., Chen, H. and Zou, Z. M. (2015). Synthesis and evaluation of new podophyllotoxin derivatives with *in-vitro* anticancer activity. *Molecules*, 20(7): 12266-12279.
29. Miftah, A. M. and Tjahjono, D. H. (2015). Synthesis and *in-vitro* cytotoxicity of 1-benzoyl-3-methyl thiourea derivatives. *Procedia Chemistry*, 17: 157-161.
30. Nasyanka, A. L. (2017). Docking, synthesis, and cytotoxic activity of *n*-4-methoxybenzoyl-*n'*-(4-fluorophenyl)thiourea on HeLa cell line. *Thai Journal of Pharmaceutical Sciences*, 41(3): 99-102.
31. Casa, S. and Henary, M. (2021). Synthesis and applications of selected fluorine-containing fluorophores. *Molecules*, 26(4): 1160.
32. Widiandani, T. and Meiyanto, E. (2018). Docking and antiproliferative effect of 4-*tert*-butylbenzoyl-3-allylthiourea on MCF-7 breast cancer cells with/without HER-2 overexpression. In *Proceedings of International Conference on Applied Pharmaceutical Sciences*, 2018: 3461444.
33. Ruswanto, R., Mardianingrum, R., Lestari, T., Nofianti, T. and Siswandono, S. (2018). 1-(4-Hexylbenzoyl)-3-methylthiourea. *Molbank*, (3): 2-6.
34. Jain, S., Chandra, V., Jain, P. K., Pathak, K., Pathak, D. and Vaidya, A. (2019). Comprehensive review on current developments of quinoline-based anticancer agents. *Arabian Journal of Chemistry*, 12(8): 4920-4946.
35. Martins, P., Jesus, J., Santos, S., Raposo, L. R., Roma-Rodrigues, C., Baptista, P. V. and Fernandes, A. R. (2015). Heterocyclic Anticancer Compounds: Recent Advances and the Paradigm Shift Towards the Use of Nanomedicine's Tool Box. *Molecules*, 20(9): 16852-16891.
36. Shekarkhand, M., Zare, K., Monajjemi, M., Tazikeh-Lemeski, E. and Sayadian, M. (2022). Computational study of heterocyclic anticancer compounds through NBO method. *Nexo Revista Científica*, 35(01): 367-381.
37. Nielsen, A. L., Rajabi, N., Kudo, N., Lundø, K., Moreno-Yruela, C., Bæk, M., ... and Olsen, C. A. (2021). Mechanism-based Inhibitors of SIRT2: Structure–activity relationship, X-ray structures, target engagement, regulation of α-tubulin acetylation and inhibition of breast cancer cell migration. *RSC Chemical Biology*, *2*(2): 612-626.
38. Farooqi, A. S., Hong, J. Y., Cao, J., Lu, X., Price, I. R., Zhao, Q., ... and Lin, H. (2019). Novel Lysine-based thioureas as mechanism-based inhibitors of Sirtuin 2 (SIRT2) With anticancer activity in a colorectal cancer murine model. *Journal of Medicinal Chemistry*, 62(8): 4131-4141.
39. Al-Amily, D. H. and Hassan Mohammed, M. (2019). Design, Synthesis, and docking study of acyl thiourea derivatives as possible histone deacetylase inhibitors with a novel zinc binding group. *Scientia Pharmaceutica*, 87(4): 28.
40. Ho, T. C., Chan, A. H., and Ganesan, A. (2020). Thirty Years of HDAC Inhibitors: 2020 Insight and Hindsight. *Journal of Medicinal Chemistry*, 63(21): 12460-12484.
41. Fatima, T., Haque, R. A., Razali, M. R., Ahmad, A., Asif, M., Khadeer Ahamed, M. B. and Abdul Majid, A. M. S. (2017). Effect of lipophilicity of wingtip groups on the anticancer potential of mono *n*-heterocyclic carbene silver (I) complexes: Synthesis, crystal structures and *in-vitro* anticancer study. *Applied Organometallic Chemistry*, 31(10): e3735
42. Kesuma, D., Nasyanka, A. L., Rudyanto, M., Purwanto, B. T. and Sumartha, I. G. A. (2020). A prospective modification structure: The effect of lipophilic and electronic properties of *n*-(phenylcarbamothyoil) benzamide derivatives on cytotoxic activity by in silico and in vitro assay with T47d cells. *Rasayan Journal of Chemistry*, 13(3): 1914-1918.

43. Kesuma, D., Purwanto, B. T. and Rudyanto, M. (2019). Synthesis and anticancer evaluation of *n*-benzoyl-*n'*-phenyltiourea derivatives againts human breast cancer cells (T47D). *Journal of Chinese Pharmaceutical Sciences*, 29(2): 123-129.
44. Bai, W., Ji, J., Huang, Q. and Wei, W. (2020). Synthesis and evaluation of new thiourea derivatives as antitumor and antiangiogenic agents. *Tetrahedron Letters*, 61(40): 152366.
45. Alimohammadi, A., Mostafavi, H. and Mahdavi, M. (2020). Thiourea derivatives based on the dapsone-naphthoquinone hybrid as anticancer and antimicrobial agents: *In-vitro* screening and molecular docking studies. *ChemistrySelect*, 5(2): 847-852.
46. Siddig, L. A., Khasawneh, M. A., Samadi, A., Saadeh, H., Abutaha, N. and Wadaan, M. A. (2021). Synthesis of novel thiourea-/urea-benzimidazole derivatives as anticancer agents. *Open Chemistry*, 19(1): 1062-1073.
47. Kirtishanti, A., Siswandono, S. and Sudiana, I. K. (2021). Synthesis and cytotoxic activity of *n*-(4-bromo)-benzoyl-*n'*-phenylthiourea and 4-(*tert*-butyl)-*n*-benzoylurea on primary cells of HER2-positive breast cancer. *Research Journal of Pharmacy and Technology*, 14(3): 1195-1200.
48. Parmar, D. R., Soni, J. Y., Guduru, R., Rayani, R. H., Kusurkar, R. V., Vala, A. G., ... and Battula, S. (2021). Discovery of new anticancer thiourea-azetidine hybrids: Design, synthesis, *in-vitro* antiproliferative, SAR, *In-silico* molecular docking against VEGFR-2, ADMET, Toxicity, and DFT studies. *Bioorganic Chemistry*, 115: 105206.
49. Qaiser, S., Mubarak, M. S., Ashraf, S., Saleem, M., Ul-Haq, Z., Safdar, M., ... and Maalik, A. (2021). Benzilydene and thiourea derivatives as new classes of carbonic anhydrase inhibitors: An *In-vitro* and molecular docking study. *Medicinal Chemistry Research*, 30(3): 552-563.
50. Khan, A., Khan, M., Halim, S. A., Khan, Z. A., Shafiq, Z. and Al-Harrasi, A. (2020). Quinazolinones as competitive inhibitors of carbonic anhydrase-ii (human and bovine): Synthesis, in-vitro, in-silico, selectivity, and kinetics studies. *Frontiers in Chemistry*, 2020: 1113.

Malaysian Journal of Analytical Sciences (MJAS)
Published by Malaysian Analytical Sciences Society

OPTIMIZATION OF MICROWAVE-ASSISTED EXTRACTION OF PHENOLIC COMPOUNDS FROM *Eleusine indica* USING RESPONSE SURFACE METHODOLOGY

(Pengoptimuman Pengekstrakan Berbantu Gelombang Mikro bagi Sebatian Fenolik dari *Eleusine indica* Mengunakan Kaedah Gerak Balas Permukaan)

Angelica A. Angeles-Macalalad, Bryan John A. Magoling*, Jennielyn C. De Chavez, Love Angel H. Flores, Alona B. Intac

Department of Chemistry,
College of Arts and Sciences,
*Batangas State University-Pablo Borbon, Rizal Avenue, Batangas City, 4200 Philippine*s

**Corresponding author: bryanmagoling@gmail.com*

Received: 28 February 2022; Accepted: 19 May 2022; Published: 30 October 2022

Abstract

Eleusine indica belongs to the Pocaceae family and is abundantly found in many tropical countries. Because of its anti-malarial, antioxidant, anti-viral, and antidiabetic properties, among many others, studies are being aimed on developing time and cost-effective methods that could efficiently extract its active components. This study focused on the optimization of the microwave-assisted extraction (MAE) of phenolic contents from *E. indica*. A response surface methodology (RSM) using a Box-Behnken design (BBD) of experiment was employed to determine the optimized condition for the extraction method. The extraction was performed with three varying factors (ethanol concentration, microwave power, and irradiation time) and one response (total phenolic content or TPC). A maximum TPC of 74.81 ± 5.22 GAE mg/g was obtained through MAE, using 57.23% (v/v) ethanol with microwave irradiation of 217.77 W for 4.53 minutes. The optimized condition had an extraction yield of 11.62 ± 1.97%. The ethanolic *E. indica* extract obtained using the optimum condition contained mostly of triterpenes, saponins and glycosides; and moderately of flavonoids and tannins.

Keywords: *Eleusine indica*, microwave-assisted extraction, phenolic compound extraction, response surface methodology

Abstrak

Eleusine indica dari keluarga Pocaceae dan ia sering dijumpai di negara tropika. Oleh kerana sifatnya anti-malaria, antioksida, anti-viral dan antidiabetik, banyak kajian dijalankan bangi membangunkan kaedah yang berkesan dari aspek masa dan kos bagi tujuan pengkestrakan komponen aktif. Kajian ini memberi tumpuan kepada pengoptimuman pengekstrakan berbantu gelombang mikro (MAE) bagi kandungan fenolik dari *E. indica*. Kaedah gerak balas permukaan (RSM) mengunakan reka bentuk eksperimen Box-Behnken telah dibangunkan bagi penentuan keadaan optimum kaedah pengekstrakan. Pengekstrakan telah dijalankan Bersama tiga faktor (kepekatan etanol, kuasa gelombang mikro, dan masa penyinaran) dan satu respons (jumlah kandungan fenolik atau TPC). Nilai maksimum TPC ialah 74.81 ± 5.22 GAE mg/g diperolehi melalui MAE, mengunakan 57.23% (v/v) etanol bersama

217.77 W penyinaran gelombang mikro selama 4.53 minit. Keadaan optimum telah menghasilkan ekstrak 11.62 ± 1.97%. Ekstrak etanolik *E. indica* mengunakan keadaan optimum mengandungi triterpen, saponin dan glikosida, dan flavonoid dan tannin.

Kata kunci: *Eleusine indica*, pengekstrakan berbantu gelombang mikro, pengekstrakan sebatian fenolik, kaedaj gerak balas permukaan

Introduction

For many years, plants with medicinal properties have been widely used as sources of traditional medicines to treat various disease and illnesses. Since then, immense efforts have been put into the study and optimization of extracting active components from plants in the aim of increasing their medicinal potencies and applications. Plants are rich in many natural products, such as secondary metabolites, which possess valuable pharmacological activities. These secondary metabolites include phenols, phenolic glycosides, flavonoids, cyanogenic glycosides, saponins, unsaturated lactones, and glucosinolates [1]. Phenolic compounds have been found to have anti-inflammatory [2], anti-mutagenic [3] and antimicrobial activities [4]; exhibit chemoprotective [5]; and inhibit nitric oxide production [6]. Recent reports have found high phenolic compounds in *Eleusine indica* [4, 7, 8].

E. indica (also known as goose grass) is an invasive annual weed which is native in tropical and subtropical regions. It has been used as a traditional medicine for treating diarrhea and malaria [9]. It has also shown anthelmintic [10], antioxidant [4], anti-viral [11] and antidiabetic [12] properties. The crude chloroform and methanolic extracts of *E. indica* were reported to contain tannins, flavonoids, and alkaloids which exhibited anti-fungal and antibacterial activities against *Enterobacter aerogenes*, *Escherichia coli, Klebsiella agerogenes, Proteins vulgaris, Pseudomonas aerogenes, Staphylococcus aureus*, and unspecified *Streptococcus* and *Bacillus* species [13].

The phenolic compound extraction from *E. indica* is commonly performed using a conventional maceration method, which may involve different solvent systems (water, methanol, ethanol, ethyl acetate, or hexane) [14]. However, this extraction technique consumes high amounts of solvent, requires long extraction times, and impose a high risk of degrading the heat-labile constituents in the sample. To resolve these drawbacks, increasing studies are being done aiming to develop more efficient extraction techniques. Of these methods, the microwave-assisted extraction (MAE) shows one with the highest potentials. The application of MAE does not only reduce the amount of solvent and extraction time needed; it also improves the extraction yield with minimal degradation of bioactive compounds in the sample [15]. The amounts of phenolic compounds extracted from pineapple peelings using conventional (Soxhlet) and microwave-assisted methods have been compared and it was found that at a similar sample-to-solvent (ethanol) ratio, MAE required 6-fold less time to extract around 7-fold more phenolic content compared to Soxhlet method [16]. Further, the overall operational cost of microwave-assisted processes is estimated to be lower than those using conventional heating in terms of energy consumption and the overall process turnover time [17]. Hence, the use MAE could be a good alternative for extracting phenolic compounds in medicinal plants.

Few reports are available on the extraction of total phenolic compounds (TPC) from *E. indica*. These studies either used cold maceration [4], decoction [8], or ultrasonication [7] in their extraction procedures. The main factors affecting MAE efficiency include sample particle size, pre-leaching time, microwave power, extraction temperature, solvent to solid ratio, solvent composition, and extraction time/cycles [18].

For studying a process with multiple variables, an experimental design that can generate optimum conditions from a minimum number of experiments is highly desired. Response surface methodology (RSM) is a useful technique for studying the effects of important factors, unaccompanied or in combination with the involved processes [19]. It is also capable of generating a mathematical model of the possible interrelationship among the tested variables. Compared to other designs of experiments for RSM, such as Central Composite Design (CCD), the Box-Behnken Design (BBD)

requires fewer design points to study processes with a minimum of three levels and allows for studying processes with extreme ranges.

Achieving higher yields using safer and better extraction method (considering economic, environmental and practical dimensions) for the phenolic content extraction in *E. indica* using MAE presents many economic and medicinal potentials. Therefore, this study aimed to determine the optimum condition for the microwave-assisted extraction of phenolic compounds from *E. indica*, at varying ethanol concentrations, microwave power and microwave irradiation time using RSM with a BBD experimental design.

Materials and Methods

Chemicals and reagents

The Folin-Ciocalteu reagent, sodium carbonate (Na_2CO_3), hydrochloric acid (HCl), sulfuric acid (H_2SO_4), and acetic acid were purchased from Sigma-Aldrich (St. Louis, Mo). Gallic acid and ethanol were purchased from ATR Trading System (Metro Manila, PH). All other chemicals and reagents used in this study were analytical grade.

Sample collection

The *Eleusine indica* plants were collected from Barangay Dalig, Batangas City, Philippines. The samples were authenticated at the Bureau of Plant Industry, Department of Agriculture, Manila, Philippines with the certificate number of PLT-ID-CRPSD-0833-18.

Sample preparation

The collected plant samples were rinsed with tap water followed by distilled water to remove dirt from the surface. They were air-dried in a well-ventilated area at room temperature until a constant weight difference of ± 0.001 kg was obtained. The dried samples were crushed using an Astron BL153 food processor, and then sieved using a size 30 mesh screen. The sieved samples were transferred into air-tight glass containers and stored in room temperature for further analyses.

Microwave-assisted extraction of phenolic contents

Preliminary experiments were carried out to determine the working ranges of individual parameters, prior the RSM experiments. Ethanol was chosen as the solvent for the microwave-assisted extraction (MAE) process since it has been reported to extract higher concentrations of phenolic compounds compared to water, methanol, and acetone [16, 20, 21]. The determined parameter ranges for the MAE of the TPC from *E. indica* were investigated and optimized using a response surface methodology (RSM), following a BBD of experiment.

In here, the three selected variables (ethanol concentration, microwave power, and irradiation time) were varied at either a low, medium, or high level (coded as -1, 0, and +1, respectively). The measured TPC from each extraction experiment served as the responses. These responses were then used to generate a mathematical model for the process. The design matrix used in this study is summarized in Table 1.

Table 1. Independent variables and their coded levels for the Box-Behnken Design (BBD) of experiment

Factors	Code	Unit	Coded Variable Levels		
			-1	0	1
Ethanol concentration	A	% v/v	20	40	60
Microwave power	B	Watt (W)	210	350	490
Microwave irradiation time	C	minute (min)	4	7	10

The extraction process was performed based on the study of Pan *et al*. with some modifications on the pre-setting procedure [22]. Preliminary experiments were carried out to test and determine the working ranges of individual parameters (i.e., sample-to-solvent ratio, pre-leaching time, solvent concentration, microwave power, and irradiation time) for the phenolics extraction process. The three parameters with the highest individual effects on the phenolic extraction yield were then selected and their individual and combined interactions were studied further using RSM.

Prior to microwave treatment, the air-dried *E. indica* samples were subjected to a pre-leaching step by soaking them in varied concentrations (20, 40, or 60% v/v) of ethanol (20 mL/g dried sample) for 90 minutes. Using a MWX203 BL Whirlpool microwave oven (with eleven discreet MW power level settings ranging from 0 to 700 W), the mixtures were then exposed to varying microwave power levels (210, 350, or 490 W) for either 4, 7, or 10 minutes. After microwave treatment, the sample mixtures were cooled to room temperature, then filtered through a Whatman No. 1 filter paper (Whatman, Maidstone, Kent, UK). The filtrates were transferred into volumetric flasks and were diluted to a final volume of 100 mL.

***E. indica* extract sample preparation**

The TPC of the ethanolic *E. indica* extracts were determined using the Folin-Ciocalteu method [23]. In brief, 1 mL of each extract was transferred into a volumetric flask, followed by the addition of 5 mL of the Folin-Ciocalteu reagent and 4 mL of Na_2CO_3 solution, respectively. The solutions were mixed and then incubated (away from light) for 1 hour at room temperature, prior to absorbance read-out.

Gallic acid standard preparation

A 1 mL volume of each standard solution was transferred into a volumetric flask, followed by the addition of 5 mL of the Folin-Ciocalteu's phenol reagent and 4 mL of Na_2CO_3 solution, respectively. The solutions were mixed and then incubated (away from light) for 1 hour at room temperature, prior to absorbance read-out.

Spectroscopic analysis of standard and sample solutions

The absorbance of each of the prepared standard and sample solutions was measured at 760 nm using a UV-2700 UV-Vis spectrophotometer (Shimadzu Corporation, Kyoto, Japan). The TPC in each of the original sample solutions were computed using the generated standard calibration curve equation and were expressed as the milligram of gallic acid equivalent (GAE) per gram of dried *E. indica* sample, as shown in the equation 1:

$$TPC = C1\ (V/w) \quad (1)$$

TPC is total phenolic content expressed as GAE (mg/g); C1 is the GAE concentration in the sample (mg/mL); V is the volume of extract in mL; and w is the weight of the initial dried plant sample used (g).

Extraction process optimization and validation

The optimization of the microwave-assisted extraction of phenolic compounds from *E. indica* was carried out using the Design- Expert® v10.0.8 (Stat-Ease Inc., Minneapolis, MN, USA) software. An analysis of variance (ANOVA) was applied to test the validity of the generated model. The adequacy of the fitted model was determined by evaluating the lack of fit and the coefficient of determination (R^2). The model's Fisher variation ratio (F-value), probability value (Prob > F), and adequate precision (AP) were also evaluated to test for its significance and adequacy.

Extraction yield of the optimized MAE

To obtain the dried *E. indica* extract, the ethanolic extract was concentrated using a rotary vacuum evaporator (Buchi rotavapor R-205) set at 280 rpm for 15 min. at 40°C. The extraction yield was calculated using equation 2 [24]:

$$\text{Extraction yield (\%)} = (\text{mass of dried extract / mass of } \textit{E. indica}) \times 100 \quad (2)$$

Phytochemical screening

Standard procedures for the phytochemical screening of the *E. indica* extract obtained from the optimized MAE condition were performed to identify and estimate the presence of its chemical constituents such as alkaloid, flavonoid, saponin, triterpenoid, steroid, tannins, and glycosides [25].

Test for Sterols (Liebermann-Burchard Test). About 1 g of the sample was dissolved in 2 mL of acetic acid. The soluble portion was collected and was kept on ice. One to two drops of H_2SO_4 was then added to the solution. The development of color from violet to blue or bluish-green indicates the presences of steroidal rings.

Test for Triterpenoids (Salkowski Test). A 0.5 g of sample was mixed in 2 mL of chloroform. Then, 3 mL of concentrated H_2SO_4 as dropwise added to the mixture. The development of a reddish-brown color indicates the presence of triterpenoids.

Test for Flavonoids (Shinoda Test). Magnesium ribbon fragments were mixed with 2 g of the sample. Then, a few drops of concentrated HCl were added. The development of a pink to red color indicates the presence of flavanoids.

Test for Saponins (Froth Test). Hot distilled water was used to dissolve 5 g of sample and the mixture was then filtered. The filtrate was vigorously shaken. The formation of a persistent froth that lasts at least 15 minutes indicates the presence of saponins.

Test for Glycosides (Fehling's Test). Hot distilled water (5 mL) was used to dissolve 1 g of sample and the mixture was then filtered. Into each of two test tubes, 2 mL of the filtrate was added. In the first test tube, 1 mL of HCl was added; nothing was added to the second test tube (control). Both of the tubes were placed in a water bath at 100ºC for 5 minutes, then cooled to room temperature. Anhydrous sodium carbonate was added to neutralize the sample until there was no more effervescence. To each test tube, 1 mL of freshly mixed Fehling's A and B (1:1) was added. The test tubes were then placed in a water bath at 100ºC for 2 mins. The formation of the brick red precipitate indicates the presence of glycosides.

Test for Tannins (Ferric Chloride Test). The dried extract was dissolved in hot water then filtered. Few drops of 5% ferric chloride solution were added. A dark green or bluish-black color indicates the presence of tannins.

Results and Discussion

Microwave-assisted extraction parameters and responses

A total of fifteen experiments were performed to generate a response surface model (RSM) for the extraction of phenolic contents in *E. indica* at varying ethanol concentration, microwave power, and microwave irradiation time. The experimental factors used in this study and their responses are listed in Table 2. Each value is the mean of triplicate analysis. The results from the experiment revealed TPC varying from 16.82±1.3 to 74.81±3.9 GAE mg/g.

Table 2. Experimental factors and their responses for the MAE of TPC from *E. indica*

Standard Number	Run Number	A: Ethanol Concentration (% v/v)	B: Microwave Power (W)	C: Irradiation Time (min)	TPC [a] (GAE mg/g)
1	2	20	210	7	25.67 ± 1.5
2	4	60	210	7	60.05 ± 3.6
3	12	20	490	7	35.20 ± 3.7
4	13	60	490	7	25.41 ± 1.8
5	11	20	350	4	34.53 ± 4.1
6	10	60	350	4	62.67 ± 1.4
7	3	20	350	10	25.55 ± 1.5
8	15	60	350	10	16.82 ± 1.3
9	7	40	210	4	74.81 ± 3.9
10	9	40	490	4	58.80 ± 4.5
11	8	40	210	10	30.93 ± 2.1
12	6	40	490	10	29.23 ± 1.8
13	5	40	350	7	44.46 ± 3.3
14	14	40	350	7	44.11 ± 2.1
15	1	40	350	7	41.80 ± 2.5

[a] TPC values are expressed as mean ± standard deviation (SD), calculated from three independent experiments.

Optimization of the MAE of phenolic compounds in *E. indica* using RSM

The responses obtained from the batch microwave-assisted extraction experiments, with respect to the variables used, were fitted with the second-order polynomial equation 3:

$$Y = b_o + \sum_{i=1}^{k} b_i X_i + \sum_{i=1}^{k} b_{ii} X_i^2 + \sum_{i=1}^{k-1} \sum_{j=i+1}^{k} b_{ij} X_i X_j + e_i \quad (3)$$

where Y is the predicted response, b_o is the constant coefficient, bi is the linear coefficient, b_{ij} is the interaction coefficient, b_{ii} is the quadratic coefficient, Xi and X_j are the coded values of the AC activation factors, and e_i is the error.

As shown in Table 3, an analysis of variance (ANOVA) was performed to determine which model-order best fit the responses for the process in study. The acceptability of the model was evaluated based on correlation coefficient (R^2) and standard deviation. The model fitting revealed that the microwave-assisted extraction of phenolic compounds in *E. indica* best followed a second-order response surface model.

Table 3. ANOVA of the quadratic model of MAE of TPC from *E. indica*

Source	Sum of Squares	df	Mean Square	*F*-value	*p*-value	Remark[a]
Model	3872.59	9	430.29	37.29	0.0005	sig.
A - Ethanol Conc.	242.11	1	242.11	20.98	0.0059	sig.
B - MW Power	229.26	1	229.26	19.87	0.0067	sig.
C - Irradiation Time	2056.96	1	2056.96	178.24	< 0.0001	sig.
AB	487.67	1	487.67	42.26	0.0013	sig.
AC	340.11	1	340.11	29.47	0.0029	sig.
BC	51.16	1	51.16	4.43	0.0891	not.sig.
A^2	385.08	1	385.08	33.37	0.0022	sig.
B^2	41.14	1	41.14	3.57	0.1176	not sig.
C^2	10.04	1	10.04	0.87	0.3937	not sig.
Residual	57.70	5	11.54			
Lack of Fit	53.50	3	17.83	8.49	0.1071	not sig.
Pure Error	4.20	2	2.10			
Standard deviation = 4.43				R^2 = 0.9600		
Coefficient of variance = 10.90				Adjusted R^2 = 0.9300		
Adequate precision = 17.077				Predicted R^2 = 0.8631		

[a] sig. = significant; not sig. = not significant

A high correlation coefficient value of 0.9600 was obtained in the present study, indicating that only 4.00% of the total variation is unexplained by the generated model.

The ANOVA results for the quadratic response surface model for TPC extraction gave an F-value of 37.29 and a corresponding probability > F that is less than 0.05, validating that the model is significant. For the model terms, probability factor (prob > F) values less than 0.05 are considered significant. In this work, model terms *A*, *B*, *C*, *AB*, *AC*, and A^2 were significant while *BC*, B^2 and C^2 were insignificant terms. To improve the model's efficiency, insignificant model terms were excluded from the study.

Adequate precision (AP) describes the ratio between signal and noise and is used to decide whether the

predicted model can be utilized to move along the design space [26]. The obtained AP ratio of 17.077 that is higher than the desired value of 4 suggested that the model presented in this work is efficient to predict TPC of the extract, within the established set of parameters.

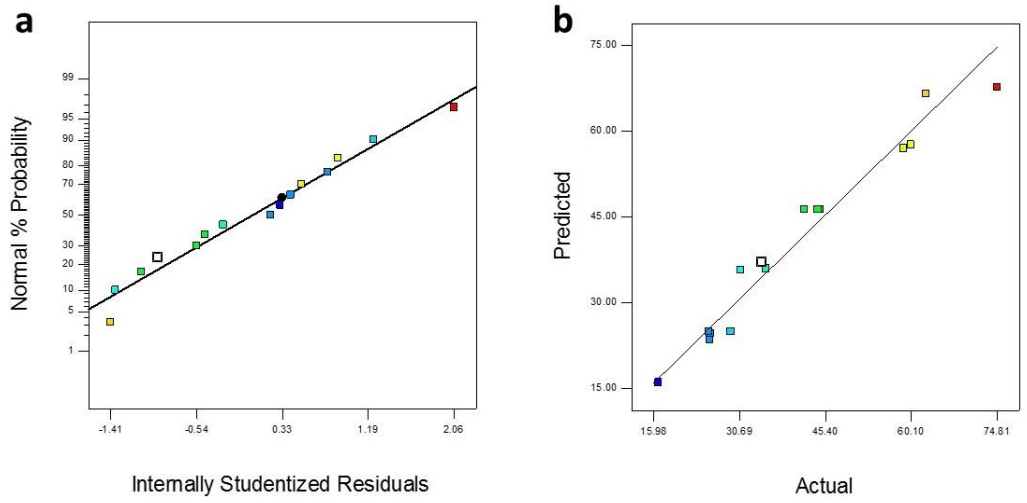


Figure 1. Plots of the (a) normal probability versus studentized residuals and the (b) predicted versus actual values for the MAE of TPC from *E. indica*

The normal probability plot of the studentized residuals for TPC extraction is illustrated in Fig. 1a. The linear plot illustrated adequate standard distribution, with minor scattering, between the residuals and the experimental points. Fig. 1b revealed good agreement between the experimentally-obtained and the model-generated responses. This indicated that the data generated by the model were valid and may represent that of the real system.

The final regression model, in terms of the coded factors for total phenolic content (TPC), is expressed in equation 4:

$$\text{TPC (GAE mg/g)} = 46.31 + 5.50A - 5.35B - 16.03C - 11.04AB - 9.22AC - 10.57A^2 \quad (4)$$

where TPC is total phenolic content expressed as GAE (mg/g), *A* is the ethanol concentration (% v/v), *B* is the MW irradiation power (210 to 490 W), and *C* is the MW irradiation time (4 to 10 min).

On the other hand, the final regression model, in terms of the actual factors for the total phenolic content (TPC), is expressed equation 5:

$$\text{TPC (GAE mg/g)} = -54.41274 + 4.84476(\text{ethanol conc.}) + 0.11950(\text{MW Power}) + 0.80238(\text{MW irradiation time}) - 3.94342\text{x}10^{-3}\,(\text{ethanol conc.})\,(\text{MW Power}) - 0.15368(\text{ethanol conc.})\,(\text{MW irradiation time}) - 0.02642(\text{ethanol conc.})^2 \quad (5)$$

Both equations 4 and 5 can be used for predicting the TPC yields along the design space. However, only the coded coefficients are proportional to the observed effect since the intercept in coded values is in the center of the design. In the actual values, the intercept usually lies far from the design space. The coefficients in terms

of actual factors account for differences in the factor ranges which may not be directly interpreted. Eq. 4 presents the relative effects of the model terms toward the TPC yield. Specifically, it could be observed that irradiation time exhibits the largest effect toward the TPC yield of the MAE process, while microwave power presented a comparable magnitude but contrasting effect as that of ethanol concentration.

The optimum extraction condition was established using Design-Expert® v10.0.8 (Stat-Ease Inc., Minneapolis, MN, USA) software. In the software optimization step, the goal for each operational condition (ethanol concentration, microwave power, and irradiation time) was set to be 'within' range while the response (TPC) was set as 'maximum' to achieve the highest possible yield. The highest predicted TPC was obtained at 52.23% v/v of ethanol, with microwave irradiation of 217.77 W for 4.53 min. with a predicted TPC of 75.22 GAE mg/g.

To further illustrate the relationships among parameters, ethanol concentration, microwave power input and irradiation time, toward the responses predicted by the model, three-dimensional (3D) surface response plots were generated, as shown in Figure 1.

In the plots shown in Figure 2, one variable was kept constant at the optimum value, while the two remaining parameters were varied within their experimental ranges. Figure 2a shows the 3D response surface plots of the combined effects of the ethanol concentration and microwave power, while the irradiation time was kept at the optimum value of 4.53 minutes. The predicted TPC in the *E. indica* extract showed an increasing trend with increasing ethanol concentration of up to 57.23%. Beyond this point, the TPC levels started to plateau which indicated that higher concentrations of the solvent had minimal effect on the TPC extraction. On the other hand, a decreasing trend in TPC yield was observed beyond the established optimum MW power around 218 W.

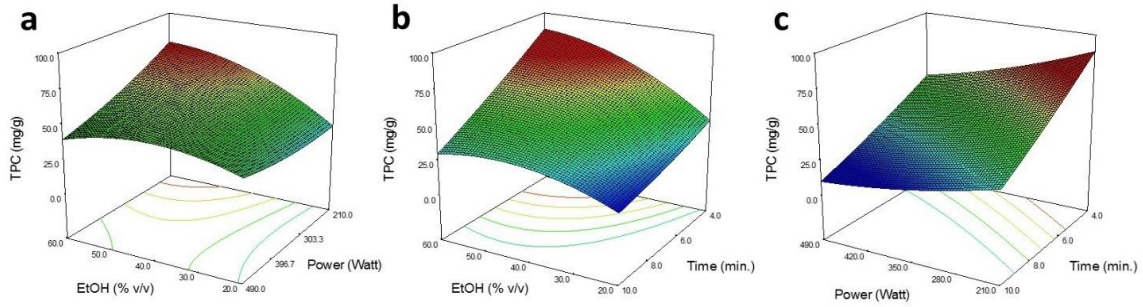


Figure 2. 3D response surface plots showing the predicted total phenolic content in the *E indica* extract as a function of (a) microwave power and ethanol concentration; (b) microwave irradiation time and ethanol concentration; and (c) irradiation time and microwave power.

Figure 2b shows the effect of the contact between ethanol concentration and microwave irradiation time on the TPC of *E. indica* when microwave power is fixed at 217.77 W. Increasing the ethanol concentration up to its optimum level showed positive correlation with the TPC in the extract, while a decreasing trend in TPC was observed as the irradiation time was increased above the optimum level of around 4.5 mins.

Figure 2c demonstrates the contact between microwave power and irradiation time on the TPC value at a fixed ethanol concentration of 57.23%. The 3D plot showed that the TPC level was at its highest when both parameters were set near their lowest levels.

Experimental validation of the predicted TPC from the optimized MAE condition

The predicted TPC in the *E. indica* extract obtained using the optimized MAE condition was validated by comparing experimentally obtained TPC values with the predicted TPC value. Table 4 shows the comparison of the experimental and the predicted TPC in the *E. indica* extracts obtained from the optimized MAE condition.

Table 4. Experimental validation of the predicted TPC obtained from optimized MAE condition

Optimized MAE Condition			Experimental TPC (GAE mg/g)	Mean Exp. TPC ± s.d. (GAE mg/g)	Predicted TPC (GAE mg/g)	% Error
Ethanol Conc. (% v/v)	MW Power (W)	Irradiation Time (min.)				
57.23	217.77	4.53	71.00 72.72 80.75	74.81 ± 5.23	75.22	0.541

As shown in Table 4, the obtained experimental TPC value of 74.81 ± 5.23 GAE mg/g was in close agreement with the predicted TPC of 75.22 GAE mg/g. A computed relative percent error of 0.541% between the predicted and obtained experimental value was observed. This validated the reliability of the generated predictive model and the goodness-of-fit with the experimental results.

Extraction yield of the *E. indica* extract obtained using the optimized MAE condition

Table 5 shows the extraction yield of the ethanolic *E. indica* extracts obtained using the determined optimum MAE condition. The mean extraction yield was determined to be 11.62 ± 1.96%.

Table 5. Extraction yield of the ethanolic *E. indica* extract obtained using the optimized MAE condition

Sample	Extraction Yield (%)
Trial 1	10.85
Trial 2	10.16
Trial 3	13.86
Mean ± s.d.	11.62 ± 1.96

Qualitative determination of phytochemicals in the *E. indica* extract

Based on Table 6, the ethanolic *E. indica* extract obtained using the optimized microwave-assisted extraction condition showed was abundant in triterpenes, saponins and glycosides. On the other hand, moderate amounts of flavonoids and tannins were observed. Sterols were not detected in the extract.

Table 6. Phytochemicals present in the *E. indica* extract obtained using the optimized MAE condition

Secondary Metabolite	Presence [a]
Sterols	(-)
Triterpenes	(+++)
Flavonoids	(++)
Saponins	(+++)
Glycosides	(+++)
Tannins	(++)

[a] presence is reported as either (-) absent, (+) traces, (++) moderate, or (+++) abundant

In this paper, the microwave-assisted procedure for the extraction of phenolic contents in *E. indica* was optimized, aiming to maximize TPC extraction yield while minimizing both the processing time and solvent consumption. The established optimized condition yields high amounts of extracted TPC, at a quicker processing time compared to conventional maceration methods.

In the predictive model equation, irradiation time showed to have the largest effect toward the TPC yield of the MAE process, while microwave power presented a contrasting effect as that of ethanol concentration. In the MAE of TPC from pomegranates, it was observed that more phenolics could be extracted using 50% ethanol than 70% [27]. It was associated with the fact that both the dielectric constant and dielectric loss factor of water are higher than those of ethanol. Under the same microwave power, the solvent with a fair ratio of ethanol and water may absorb more thermal energy enough to increase diffusion of phenolics. Based on the 3D response models (Figures 2a-c), the amount of TPC extracted from the sample start to decrease when the sample was exposed to higher microwave power for longer periods of time.

Introduction to microwave energy could strengthen the molecular interaction between the electromagnetic field and sample and improve the efficiency of the extraction process [28]. However, the observed decrease in TPC yield when the sample is exposed to MW levels that are beyond the established optimum could be caused by degradation of the desired phenolic compounds at higher levels of microwave power. Similar observations were seen in the findings of Peng et al. and Zheng et al. [29, 30].

While the nature of solvents used for MAE greatly contributes toward extraction efficiency, polar solvents such ethanol and water can get rapidly heated as they become exposed to too high levels of microwaves, resulting to the degradation of thermo labile phenolics and/or coextraction of other unwanted compounds in the sample [31]. More so, exposure to too much MW energy input for an excessive period could cause the sample mixture's temperature to extremely and abruptly elevate, initiating the rapid break down of the plant matrix. Hence, the MW power input and irradiation time must be maintained at the optimum level to achieve a selective MAE process and avoid solute degradation due to abrupt cell bursting from pressure buildup [32].

The optimum MW power level and irradiation time established for the MAE of TPC in *E. indica* both lie near the lower ends of the studied ranges. While this could indicate a possibility that the method may still be further optimized by exploring lower levels of MW power and shorter irradiation times, it was not done in this present study because of a limitation in the MW irradiation mechanism of the commercial microwave oven used.

The ethanolic *E. indica* extract obtained in this work contained different phenolic compounds such as triterpenes, saponins, glycosides, flavonoids, and tannins which are comparable to the finding in the study of *E. indica* by Morah and Otuk [13]. Phenolic compounds have been identified to exhibit many medicinal properties. The current optimized procedure was able to extract high amounts of secondary metabolites from *E. indica*, which can be further processed and used for medicinal applications.

Conclusion

The optimization of microwave-assisted extraction (MAE) of phenolic contents from *E. indica* was investigated in this present work. A second-order regression model for predicting the total phenolic contents (TPC) at varying ethanol concentration, MW irradiation power, and MW irradiation time was developed, with a high R^2 value of 0.9600. The diagnostic plots for the generated model demonstrated good agreement between the predicted and experimentally–obtained TPC extraction, proving the validity of the predictive model. Analysis of the 3D response plots derived from the model revealed interactions among the three parameters. Optimization was carried out using RSM following BBD with three variables. The optimized conditions for the MAE of TPC was successfully established through initial contact of dried *E. indica* samples to 57.23% v/v ethanol, followed by MW irradiation at 217.77 W for 4.53 min.

This resulted to the TPC yield of 74.81 ± 5.23 GAE mg/g. By optimizing the ethanol concentration, microwave power, and irradiation time for MAE, we were able to extract high amounts of phenolic compounds from *E. indica* in a short processing time. The obtained extract in this work contained abundant amounts of important secondary metabolites that could be further processed and used for medicinal applications.

Acknowledgments

The authors would like to extend their gratitude to Mr. Russel Jimenez for his technical assistance during the conduct of this study.

References

1. Quiroga, E., Sampietro, A. and Vattuone, M. (2001). Screening antifungal activities of selected medicinal plants. *Journal of Ethnopharmacology*, 74: 89-96.
2. Zhang, H. (2016). Dietary polyphenols, oxidative stress and antioxidant and anti-inflammatory effects. *Current Opinion in Food Science*, 8: 33-42.
3. Nile, S., Park, S. W. (2013). Edible Berries: Bioactive components and their effect on human health. Nutrition. Burbank, Los Angeles County, California, 30.
4. Al-Zubairi, A., Abdul, A., Abdelwahab, S. I., Peng, C. Y. P., Mohan, S. and Elhassan, M. M. (2011). *Eleucine indica Possesses Antioxidant, Antibacterial and Cytotoxic Properties*. Evidence-based Complementary and Alternative Medicine. eCAM. p. 965370.
5. Deng, H. and Dai, J. (2009). Preparation and characterization of activated carbon from cotton stalk by microwave assisted chemical activation—application in methylene blue adsorption from aqueous solution. *Journal of Hazardous Materials*, 166(2-3): 1514-1521.
6. Del Rio, D., Borges, G. and Crozier, A. (2010). Berry flavonoids and phenolics: Bioavailability and evidence of protective effects. *British Journal of Nutrition*, 3: S67-90.
7. Chitindingu, K., Chitindingu, J. J., Benhura, M. A. N., Marume, A., Mutingwende, I., Bhebhe, M. and Muchuweti, M. (2012). Antioxidant capacity of bioactive compounds extracted from selected wild and domesticated cereals of Zimbabwe. *African Journal of Biochemistry Research*, 6: 62-68.
8. Iqbal, M. and Gnanaraj, C. (2012). *Eleusine indica L*. possesses antioxidant activity and precludes carbon tetrachloride (CCl_4)-mediated oxidative hepatic damage in rats. *Environmental Health and Preventive Medicine*, 17(4): 307-315.
9. Okokon, J. (2010). Antiplasmodial and antidiabetic activities of *Eleusine indica*. *International Journal of Drug Development and Research*, 2: 493-500.
10. Gruyal, G. (2014). Ethnomedicinal plants used by residents in Northern Surigao del Sur, Philippines. *Natural Products Chemistry & Research*, 20142-4.
11. Iberahim, R., Yaacob, A. and Ibrahim, N. (2015). Phytochemistry, cytotoxicity and antiviral activity of *Eleusine indica* (sambau). *Proceedings of the Universiti Kebangsaan Malaysia, Faculty of Science and Technology 2015 Postgraduate Colloquium*, 030013-01-030013-04.
12. Kore K. J., Shete R. V. and Desai N. V. (2011). Anti-arthritic activity of hydroalcoholic extract of *Lawsonia Innermis*. *International Journal of Drug Development and Research*, 3: 217-224.
13. Morah F. and Otuk M. (2015). Antimicrobial and antihelmintic activity of *Eleusine indica*. *Acta Scientiae et Intellectus*, 1(4): 28-32.
14. Ignat I, Volf I, Popa V. (2011). A critical review of methods for characterisation of polyphenolic compounds in fruits and vegetables. *Food Chemistry*, 126(4): 1821-1835.
15. Wang, L. (2006). Recent advances in extraction of nutraceuticals from plants. *Trends in Food Science & Technology*, 17(6): 300-312.
16. Nor Halaliza A. and Zulkifly A. (2017). Microwave-assisted extraction of phenolic compound from pineapple skins: The optimum operating condition and comparison with Soxhlet extraction. *Malaysian Journal of Analytical Sciences*, 21(3): 690-699.
17. Kan, X., Zhang, J., Tong, Y. W. and Wang C. H. (2018). Overall evaluation of microwave-assisted alkali pretreatment for enhancement of biomethane production from brewers' spent grain. *Energy Conversion and Management*, 158: 315-326.

18. Eskilsson C. and Björklund E. (2001). Analytical-scale microwave-assisted extraction. *Journal of Chromatography*, 902: 227-250.
19. Lundstedt, T., Seifert, E., Abramo, L., Thelin, B., Nystrom, A., Pettersen, J. and Bergman, R. (1998). Experimental design and optimization. *Chemometrics and Intelligent Laboratory Systems*, 42(1): 3-40.
20. Koffi, E., Sea T., Dodehe, Y., and Soro, S. (2010). Effect of solvent type on extraction of polyphenols from twenty-three ivorian plants. *Journal Animal Plant Sciences*, 5: 550-558.
21. Randika, S., Nilushi, N., Pathmalal, M., Lanka, U., Dhanushka, U. and Nilmini, L. (2021). Effects of extraction solvents on phytochemical screening, cytotoxicity and anti-obesity activities of selected Sri Lankan medicinal plants. *Pharmacognosy Research*, 13(4): 246-256.
22. Pan, X, Niu, G. and Liu, H. (2003). Microwave-assisted extraction of tea polyphenols and tea caffeine from green tea leaves. *Chemical Engineering and Processing: Process Intensification*, 42(2): 129-133.
23. Rezaei, S., Rezaei, K., Haghighi, M. and Labbafi M. (2013). Solvent and solvent to sample ratio as main parameters in the microwave-assisted extraction of polyphenolic compounds from apple pomace. *Food Science and Biotechnology*, 22(5): 1-6.
24. Zhang, S. Q., Bi, H. M. and Liu, C. J. (2007). Extraction of bio-active components from *Rhodiola sachalinensis* under ultrahigh hydrostatic pressure. *Separation and Purification Technology*, 57(2): 277-282.
25. Trease, G. E. and Evans, W. C. (2002). A text book of pharmacognosy, 15th edition. London: Academic press.
26. Magoling, B. J. A. and Macalalad, A. A. (2017). Optimization and response surface modelling of activated carbon production from mahogany fruit husk for removal of chromium (VI) from aqueous solution. *BioResources*, 12: 3001-3016.
27. Kaderides, K., Papaoikonomou, L., Serafim, M. and Goula, A. (2019). Microwave-assisted extraction of phenolics from pomegranate peels: Optimization, kinetics, and comparison with ultrasounds extraction. *Chemical Engineering & Processing: Process Intensification*, 137: 1-11.
28. Shang, A., Luo, M., Gan, R. Y., Xu, X., Xia, Y., Liu, Y. and Li, H. B. (2020). Effects of microwave-assisted extraction conditions on antioxidant capacity of sweet tea (*Lithocarpus polystachyus Rehd*.). *Antioxidants*, 9(8): 678.
29. Peng, F., Cheng, C., Xie, Y. and Yang, Y. (2015). Optimization of microwave-assisted extraction of phenolic compounds from "Anli" pear (*Pyrus ussuriensis* Maxim). *Food Science and Technology Research*, 21(3): 463-471.
30. Zheng, X., Xu, X., Liu, C., Sun, Y., Lin, Z. and Liu, H. (2013). Extraction characteristics and optimal parameters of anthocyanin from blueberry powder under microwave-assisted extraction conditions. *Separation and Purification Technology*, 104: 17-25.
31. Akhtar, I., Javad, S., Yousaf, Z., Igbal, S. and Jabeen, K. (2019). Microwave assisted extraction of phytochemicals an efficient and modern approach for botanicals and pharmaceuticals. *Pakistan Journal Pharmaceutical Sciences*, 32(1): 223-230.
32. Mandal, V., Mohan, Y. and Hemalatha, S. (2007). Microwave assisted extraction – an innovative and promising extraction tool for medicinal plant research. *Pharmacognosy Reviews*, 1(1): 7-18.

Malaysian Journal of Analytical Sciences (MJAS)
Published by Malaysian Analytical Sciences Society

EVALUATION OF PHYSICOCHEMICAL PROFILE, MULTI ELEMENTAL COMPOSITION AND ANTIOXIDANT PROPERTY OF *Heterotrigona itama* FROM NORTHERN REGION IN MALAYSIA

(Penilaian Profil Fizikokimia, Komposisi Berbilang Unsur dan Sifat Antioksidan *Heterotrigona itama* Dari Wilayah Utara Di Malaysia)

Amira Syafiqah Jamaludin[1], Mardiana Saaid[1]*, Ganapaty Manickavasagam[1], Ho Boon Han[1], Norsyafiah Muhamad Faizal[1], Rozita Osman[2]

[1]School of Chemical Sciences,
Universiti Sains Malaysia, 11800 USM, Pulau Pinang, Malaysia
[2]Faculty of Applied Sciences,
Universiti Teknologi MARA, 40450 Shah Alam, Selangor, Malaysia

**Corresponding author: mardiana@usm.my*

Received: 25 March 2022; Accepted: 19 July 2022; Published: 30 October 2022

Abstract

Studies on physical and chemical compositions of stingless bee honey from northern region in Malaysia are still limited. Therefore, this study evaluates the physicochemical profile [pH, free acidity, ash content, total dissolved solids (TDS) and 5-hydroxymethylfurfural (5-HMF)], multi-elemental composition and antioxidant property of fresh stingless bee honey of *Heterotrigona itama*. Twenty honey samples were collected from the Northern regions (Kedah and Penang) of Malaysia. The results revealed that the values for pH, free acidity, ash content, and TDS were pH 3.01-3.43, 65.42-184.66 meq/kg, 0.07-0.61 g/100g, and 258.83-365.67 ppm, respectively. The concentration of 5-HMF in the honey samples elevated from not detected (fresh) to a maximum of 214.38 mg/kg (after 6- and 15-months storage). For multi-elemental composition, potassium was the highest concentration (16.13-1623.75 mg/kg) followed by calcium (36.23-272.5 mg/kg), sodium (31.25-148.25 mg/kg), aluminum (25.35-62.25 mg/L) and magnesium (11.14-179.75 mg/kg). Iron (< 0.02-41.55 mg/kg), copper (< 0.05-23.15 mg/kg), manganese (< 0.02-13.85 m/kg) and zinc (< 0.01-4.63 mg/kg) were found in low concentrations. Arsenic, lead, nickel, barium, cadmium and chromium were found in lower concentrations than the limit of detection, which indicates no contamination or environmental pollution on the studied areas. The total phenolic content (TPC) of the samples was 95.0-364.9 mg GAE/100g, showed relevant amounts of antioxidant properties, suggesting a source of natural antioxidants. In conclusion, the ash content, pH, and 5-HMF of fresh honey samples were compliant with the limit set by the Malaysian Standards. The 5-HMF concentration of all the honey samples after prolonged storage for six months exceeded the permitted range, which indicates that the honey samples deteriorated. Therefore, it is advised to consume the honey in less than six months.

Keywords: Stingless bee honey, *Heterotrigona itama*, northern Malaysia, physicochemical properties, multi-element

Abstrak

Kajian tentang komposisi fizikal dan kimia madu lebah tanpa sengat dari wilayah utara di Malaysia masih terhad. Oleh itu, kajian ini menilai profil fizikokimia (pH, keasidan bebas, kandungan abu, jumlah pepejal terlarut (TDS) dan 5-hidroksimetilfurfural (5-HMF)), komposisi pelbagai unsur dan sifat antioksidan madu lebah tanpa sengat segar iaitu *Heterotrigona itama*. Dua puluh sampel madu telah dikumpul dari wilayah Utara (Kedah dan Pulau Pinang) Malaysia. Keputusan menunjukkan bahawa nilai pH, keasidan bebas, kandungan abu, dan TDS masing-masing adalah pH 3.01-3.43, 65.42-184.66 meq/kg, 0.07-0.61 g/100g dan 258.83-365.67 ppm. Kepekatan 5-HMF dalam sampel madu adalah daripada tidak dikesan (segar) kepada maksimum 214.38 mg/kg (selepas penyimpanan 6 dan 15 bulan). Bagi komposisi berbilang unsur, kalium adalah berkepekatan tertinggi (16.13-1623.75 mg/kg) diikuti kalsium (36.23-272.5 mg/kg), natrium (31.25-148.25 mg/kg), aluminium (25.35-62.25 mg/L) dan magnesium (11.14-179.75 mg/kg). Besi (< 0.02-41.55 mg/kg), kuprum (< 0.05-23.15 mg/kg), mangan (< 0.02-13.85 m/ kg) dan zink (< 0.01-4.63 mg/kg) didapati dalam kepekatan rendah. Arsenik, plumbum, nikel, barium, kadmium dan kromium didapati mempunyai kepekatan lebih rendah daripada had pengesanan yang menunjukkan tiada pencemaran atau pencemaran alam sekitar di kawasan yang dikaji. TPC sampel ialah 95.0-364.9 mg GAE/100g, menunjukkan jumlah sifat antioksidan yang relevan, mencadangkan sumber antioksidan semulajadi. Kesimpulannya, kandungan abu, pH, dan 5-HMF sampel madu segar adalah mematuhi had yang ditetapkan oleh Piawaian Malaysia. Kepekatan 5-HMF bagi semua sampel madu selepas penyimpanan berpanjangan selama 6 bulan telah melebihi julat yang dibenarkan, menunjukkan sampel madu semakin merosot. Oleh itu, adalah dinasihatkan untuk mengambil madu kurang daripada 6 bulan.

Kata kunci: madu lebah tanpa sengat, *Heterotrigona itama*, utara Malaysia, sifat fizikokimia, pelbagai unsur

Introduction

Honeybees are categorized into two main groups: sting bees and stingless bees [1]. The name of the respective groups indicates the presence of sting on the bees. Stingless bees live in forests that have warm and humid conditions [2]. Hence, they can be found in Australia, Africa, Southeast Asia, and South America [3]. The honey produced by stingless bees is known as stingless bee honey. Other than honey, stingless bees are able to produce propolis, royal jelly, pollen, and beeswax. There are about 600 species with 56 genera of stingless bee honey identified worldwide [4]. In Malaysia, there are 33 species of stingless bee from the genus of *Trigona* and *Melipona* such as *Heterotrigona itama*, *Tetrigona apicallis*, *Geniotrigona thoracica*, *Lepidotrigona terminata*, and *Trigona binghami* [5, 6]. On the other hand, as the species of stingless bee vary, the chemical and physical compositions of stingless bee honey also change. Besides the bees' species, there are other factors that influence the compositions of honey such as botanical origin, extraction season, number of nectar source(s), and geographical origin [7].

Stingless bee honey mainly contains sugars (fructose and glucose), water and minor constituents of vitamins, enzymes, amino acids, minerals, and phenolic compounds (flavonoids and phenolic acids) [8]. In conjunction with the constituents of honey, there has been growing interest in the potential use of local and overseas stingless bee honeys for the food, pharmaceutical, and cosmetic industries in recent years [9, 10]. Therefore, the nutritional, therapeutic, and medical benefits as well as biological properties of stingless bee honey have been studied all over the world. Even though there are studies about the Malaysian stingless bee honey, they are limited to stingless bee honey from the northeast and southern end of Peninsular Malaysia [11, 12]. Therefore, this study is vital as it covers the investigation of various physical and chemical compositions of the Malaysian stingless bee honey belonging to *Heterotrigona itama* species from the northern region of Peninsular Malaysia. The physical and chemical compositions were physicochemical properties, total phenolic content, multi-elemental composition, and 5-hydroxymethylfurfural (5-HMF) content. These parameters have been chosen for this study because they have their respective significance as briefly discussed below. The investigated parameters were compared to the Malaysian Standard for stingless bee honey (Table 1) established by the Department of Standards Malaysia, in line with the international standards established by the Codex Alimentarius Commission and European Council Directive with the advice of the International Honey Commission [13, 14].

Table 1. Malaysian Standard for stingless bee honey

Parameter	Malaysian Standard
Moisture (g/100g)	Max 35
Sum of fructose and glucose (g/100g)	Max 35
Sucrose (g/100g)	Max 7.5
Maltose (g/100g)	Max 9.5
Free acidity (meq/100g)	Not applicable
Ash content (g/100g)	Max 1.0
5-HMF (mg/kg)	Max 30
Diastase activity	Not applicable
pH	2.5-3.8
Presence of plant phenolics	Present

In this study, there are four physicochemical properties that were investigated (pH, free acidity, total dissolved solids, ash). Stingless bee honey is naturally acidic; its acidity helps to minimize the growth of bacteria which can improve honey shelf life [15]. The acidity of stingless bee honey is caused by the presence of organic acids, for example, formic acid, oxalic acid, acetic acid, tartaric acid, etc. [5]. On the other hand, when the storage period of honey increases, the acidity of honey also increases due to the fermentation process which converts alcohol into organic acid [16]. Thus, the degree of deterioration of stingless bee honey can be investigated by measuring their pH and free acidity [17]. By measuring the total dissolved solids of stingless bee honey, the total content of inorganic and organic elements can be associated [18]. The ash content analysis of stingless bee honey indicates the total inorganic elements, including sodium, potassium, magnesium, calcium, iron, zinc, manganese, chromium, copper, and aluminum in the samples [19]. In short, all these four properties are well-known criteria for the determination and evaluation of stingless bee honey quality [20].

Polyphenols are one of the most abundant and extensively dispersed chemical groups in plants since the nectar is obtained from blossoms of plants and hence it contains polyphenols too [21]. The common polyphenol compounds in stingless bee honey are flavonoids and simple phenolic derivatives [22]. According to the Malaysian Standards, the presence of phenolic compounds shows the good quality of stingless bee honey [13]. The higher the total phenolic content, the higher the quality of the honey [23]. By determining the total phenolic content of honey, the antioxidant properties of honey can be identified [24]. This is because the total phenolic content has a strong correlation with redox and antioxidant capacities [25]. Other than TPC assay, there are a few other tests normally used to determine the antioxidant properties of the honey which are the DPPH, β-carotene linoleic acid emulsion method, and iron reduction power [26, 27, 28].

Minerals in the honey are particularly important since the mineral contents are dependent on the plant uptake from the soil that the source of the nectar-bearing plant is located and the environment where the bees will collect the nectar for the production of the honey [29]. Furthermore, the content of heavy metals in honey is an indicator of surrounding environmental pollution [30]. As honeybees interact with water, soil, air, and plants located within a particular radius from beehives, pollutants will consequently be brought by honeybees into beehives [31].

During the manufacturing and storage process of foods that are rich in sugar, the chemical alteration of carbohydrates can occur [32]. The chemical alteration of carbohydrates will be triggered if the food is in acidic condition; thus, the formation of furfural compounds via the dehydration process of carbohydrates in honey is unavoidable [32]. Furfurals are organic compounds; and

the common furfural compounds found in foodstuffs are 5-hydroxymethylfurfural (5-HMF), 2-furfural (2-FAL), 2-furfurol (2-FOL), 5-methylfurfural (5-MF), and 2-acetylfuran (2-AF) [33]. The concentration of 5-HMF is used as a quality indicator of heat processing and freshness of various foodstuffs such as sauces, honey, oils, jams, vegetable products, and fruit-based products [32]. This is because its concentrations tend to elevate during the heating process or long storage period [34]. There are several studies that reported that 5-HMF can be detrimental to human bodies and health due to its cytotoxicity, carcinogenicity, and mutagenicity [35].

Materials and Methods

Chemicals and reagents

All the chemicals and reagents used were of analytical grade. Methanol was purchased from Merck (Darmstadt, Germany). Methanol HPLC grade was purchased from Elite Advanced Material (EAM) (Selangor, Malaysia). Hydrochloric acid (HCl) (37%), nitric acid (HNO_3) (65%), sodium hydroxide (NaOH) pellets, and sodium carbonate were from QRëC (Asia) Sdn. Bhd.; gallic acid was from Fluka (Buchs, Switzerland); and Folin-Ciocalteu's phenol reagent (2N), and 5-HMF standard were from Sigma-Aldrich (St. Louis, MO, USA). Quality control standard 7A elements, 5% HNO_3/trace tartaric acid/trace HF: K (1,000 mg/L); Ag (50 mg/L); Al, B, Ba, Na (100 mg/L); and Si (500 mg/L) in 5% HNO_3/trHF; and quality control standard TruQ™ms, 5% HNO_3/trace tartaric acid/trace HF (1,000 mg/L): As, Be, Ca, Cd, Co, Cr, Cu, Fe, Li, Mg, Mn, Mo, Ni, Pb, Sb, Se, Sr, Ti, Tl, V, and Zn in 5% HNO_3 were purchased from PerkinElmer (USA). Ultrapure water used in the experiments was purified using a Direct-Q®RƐT Direct-Q UV-R water purification system (Millipore, MA, USA).

Honey samples

Twenty honey samples of *Heterotrigona itama* were obtained directly from the beekeepers in Penang and Kedah, Malaysia. Their geographical origins are listed in Table 2. The evaluation of physicochemical profile (pH, free acidity, ash content, TDS, 5-HMF), multi-elemental composition, and antioxidant property were only carried out using the fresh honey samples. The honey samples were stored in the dark at room temperature for six and fifteen months to figure out the consequence of storage duration on the concentration only for 5-HMF.

Table 2. The stingless bee honey species and geographical origins

Honey Sample ID	Geographical Origin
1	Kampung Pondok Upih, Balik Pulau, Per
2	Kampung Pondok Upih, Balik Pulau, Penang
3	Kampung Pondok Upih, Balik Pulau, Penang
4	Kampung Pondok Upih, Balik Pulau, Penang
5	Bukit Berapit, Bukit Mertajam, Penang
6	Kubang Hulu, Bukit Mertajam, Penang
7	Jitra, Kedah
8	Merbok, Kedah
9	Merbok, Kedah
10	Merbok, Kedah
11	Merbok, Kedah
12	Merbok, Kedah
13	Merbok, Kedah
14	Sungai Petani, Kedah
15	Sungai Petani, Kedah
16	Sungai Petani, Kedah
17	Sik, Kedah
18	Sik, Kedah
19	Sik, Kedah
20	Sik, Kedah

Preparation of gallic acid standard solutions

Approximately 0.11 g of gallic acid was dissolved in ultrapure water in a 100 mL volumetric flask to produce a stock solution. Then, the stock solution was further diluted to a series of concentrations between 100-1,000 mg/L and marked as standard solutions prior to UV-Vis analysis. A control sample with a concentration of 0.5 mg/L was also prepared to ensure the analysis is properly performed to obtain reliable results.

Preparation of 5-HMF standard and honey sample solutions

Roughly 2,000 mg/L of stock solution was prepared by dissolving 50 mg of 5-HMF with ultrapure water in a 25 mL volumetric flask. The standard solutions (0.05, 0.5, 25, 50 mg/L) were freshly prepared to construct a calibration curve. The calibration curve was obtained by plotting the peak area against the concentrations. The preparation of honey sample was performed according to Moniruzzaman et al.'s study, with slight modification [18]. One gram of honey sample was diluted to 10 mL with ultrapure water. The solution was filtered through a 0.45 μm nylon membrane filter prior to injection into the HPLC.

Multi-elemental analysis

One gram of honey sample was mixed with 10 mL HNO_3 (65%), and the mixture was heated using a hot plate until it was nearly dry. The sample was then diluted to 50 mL with ultrapure water and analyzed using ICP-OES. The following 15 elements were determined using ICP-OES: Ca, K, Na, Ba, Mg, Cd, Cr, Cu, Fe, Ni, Pb, Zn, As, Mn, and Al.

pH analysis

The pH of the honey sample was analyzed based on AOAC Official Method 962.19 (2005) [36]. Two grams of honey sample was dissolved in 15 mL of distilled water, and the pH was measured using a pH meter (Oakton® pH 700 Benchtop). The pH meter was calibrated with a standard buffer solution of pH 1, 4, and 7 prior to the pH determination.

Free acidity

Free acidity was performed according to AOAC Official method 962.19 (2005) [36]. The titrimetric method was used to determine the free acidity of the honey sample. One gram of honey sample was dissolved in 7.5 mL of distilled water. Then, the solution was titrated with 0.1 M NaOH until the pH reached 8.0, and the amount of NaOH used was recorded. Free acidity was expressed as milliequivalent acid per kg of honey (meq/kg).

Ash content

Ash content was measured according to AOAC methods 920.181 (2006) [37]. The crucible was washed with 10% concentrated HCl, rinsed with distilled water, and dried in an oven at 100 ^{o}C for one hour. Then, the crucible was cooled down to room temperature and weighed. Next, 2.5 g of honey sample was weighed in the crucible and heated at 500 ^{o}C in the furnace for two hours. The sample was then cooled and reweighed. The ash content was calculated using the formula below:

$$\text{Ash content (\%)} = (Z - X / Y - X) \times 100 \quad (1)$$

Where X is a weight of empty crucible in g, Y is a sample before ashing + weight of crucible in g, and Z is a after complete ashing, weight of crucible + ash in g

Total dissolved solids

The total dissolved solids were determined by weighing 5 g of honey sample and diluted with 50 mL of distilled water, and measured using conductometer.

Antioxidant property

The Folin-Ciocalteu method based on Gul and Pehlivan [38] was used to determine the total phenolic compound (TPC). Briefly, 1 g of honey sample was dissolved in 5 mL methanol and filtered through Whatman No 1 filter paper. Forty microliter of this solution was mixed with 2.4 mL of ultrapure water and 200 μL of non-diluted Folin-Ciocalteu reagents for three minutes. Then, 0.6 mL of Na_2CO_3 (20%) was added to this mixture, and the mixture was incubated in the dark for two hours at room temperature. The incubated samples were used for TPC determination by using UV-Vis spectrometer. Ultrapure water was used as a blank and reference in UV-Vis analysis. Each sample was scanned at a wavelength of 244.4 nm for one minute. Gallic acid (100-1,000 mg/L) was used to plot a standard calibration curve. The maximum absorbance of the samples and the gallic acid

standards were determined through scanning at a range of 200 nm to 1,100 nm. The TPC was expressed as mg gallic acid equivalents (GAE) per 100 g of honey and calculated using the equation below:

$$\text{TPC (mg } GAE/100g) = \frac{C_{GA}\ x\ V\ x\ DF}{weight\ of\ honey\ sample\ (g)} \quad (2)$$

Where C_{GA} is the concentration of gallic acid from the curve (mg/L), V is the volume of honey sample solution (L), and DF is the dilution factor.

The evaluation of physicochemical profile (pH, free acidity, ash content, TDS, 5-HMF), multi-elemental composition, and antioxidant property were carried out in triplicates.

Instrumentation: UV-Vis spectrophotometer

Lambda 35 UV-Vis Spectrometer used for the TPC determination was from PerkinElmer (Singapore). Oakton® pH 700 Benchtop (USA) pH meter was used to evaluate free acidity and pH measurement. Alpha 800 conductometer was used for the determination of total dissolved solid, while WiseTherm furnace was used for the determination of ash content.

High performance liquid chromatography

Quantitative analysis of 5-HMF was carried out using HPLC unit (Shimadzu, Tokyo, Japan) consisting of a pump (LC-10AT), UV-Vis detector (SPD 10A), injector, and 20 µL sample loops. The HPLC analytical column was an Inertsil ODS C18 column (150 mm, 4.6 mm i.d., 10 µm particle size). Isocratic elution was performed using methanol-water (10:90, v/v) at a flow rate of 1 mL/min and the detector was monitored at a wavelength of 285 nm. The injection volume was 20 µL. The 5-HMF concentrations in the honey samples were calculated by comparing the peak area with the standard solutions after correcting the dilution of the honey samples.

ICP-OES

The ICP-OES used was an Axial Viewed Perkin Elmer Optima 8000 ICP-OES equipped with a Meinherd nebulizer, a cyclonic spray chamber, and ICP Winlab software data system.

HPLC instrumental validation

The instrumental validation (linear range, linearity, precision, limit of detection and quantification, and recovery) in this study is based on the ICH Guidelines [39].

Results and Discussion

HPLC instrumental validation

The instrumental validation for the analysis 5-HMF using HPLC was performed by determining the linear range, linearity, precision, limit of detection (LOD), limit of quantification (LOQ), and recovery. The results are summarized in Table 3.

Table 3. Analytical characteristics of the HPLC method

Parameter	Value
Linear range (mg/L)	0.05-50
Linear equation	y = 493900x + 370074
Correlation coefficient (R^2)	0.9992
Limit of detection (LOD) (µg/L)	0.32
Limit of quantification (LOQ) (µg/L)	0.96
Intra-day precision (% RSD)	0.05-2.70
Inter-day precision (% RSD)	1.38-3.97
Recovery (%)	96.8-99.4

Linear range and linearity

The linearity of the calibration curve of 5-HMF was determined by injecting five standard solution concentrations in the range of 0.05 mg/L to 50 mg/L. The linear regression was obtained by plotting the peak area against the concentration of standard solutions. Good linearity with R^2 of 0.9992 was obtained between the peak area and analyte concentrations.

Precision

The precision of the method was assessed by injecting five times each of the standard solutions (0.05, 5, and 50 mg/L) on the same day (intra-day) and over seven days (inter-day), respectively. Good precision of both intra-day (0.05 to 2.70%) and inter-day (1.38 to 3.97%) was found.

Limit of detection and quantification

The LOD and LOQ values were calculated by dividing the standard deviation of the lowest concentration of 5-HMF (0.05 mg/L) to the slope of regression equation and multiplying the result by 3 and 9, respectively. The LOD and LOQ for 5-HMF were 0.32 mg/L and 0.96 mg/L, respectively.

Recovery

Recovery studies were carried out by spiking two concentrations (0.05 and 5 mg/L) of 5-HMF standards to the honey samples. The data obtained were compared with the blank sample, and the percent recoveries were calculated for both spiked samples. Satisfactory recoveries were obtained (96.8-99.4%).

ICP-OES instrumental validation

The instrumental validation for multi-element analysis using ICP-OES was performed by determining the R^2 of the calibration curve, LOD, and LOQ. Results are summarized in Table 4.

Table 4. Analytical characteristics of the ICP-OES

Element	Range of Calibration Curve (mg/L)	Correlation Coefficient (R^2)	LOD (mg/L)	LOQ (mg/L)
Ca	1-5	0.9996	0.03	0.10
Cd	1-5	0.9991	0.01	0.03
Cr	1-5	0.9990	0.04	0.11
Cu	1-5	0.9998	0.05	0.16
Fe	1-5	0.9993	0.02	0.06
Mg	1-5	0.9992	0.02	0.06
Ni	1-5	0.9994	0.03	0.09
Pb	1-5	0.9996	0.02	0.05
Zn	1-5	0.9993	0.01	0.02
As	1-5	0.9993	0.02	0.07
Mn	1-5	0.9993	0.02	0.07
Al	1-5	0.9820	0.13	0.39
K	5-25	0.9983	0.20	0.59
Na	0.5-2.5	0.9977	0.02	0.05
Ba	0.5-2.5	0.9962	0.01	0.02

Linearity

The linearity of the ICP-OES analysis was determined by injecting five standard concentrations as stated in Table 4. The linear regression of multi-element was obtained by plotting the mean intensity of standard solutions against the concentration of standard solutions. All elements have good linearity with R^2 between 0.9820-0.9998.

Limit of detection and quantification

The LODs and LOQs for all elements were in the range of 0.01 to 0.20 mg/L and 0.02 to 0.59 mg/L, respectively.

Physicochemical properties of stingless bee honey

Table 5 shows the results of the selected physicochemical property of pH, free acidity, ash content, and total dissolved solids. All the measurements were determined in triplicates.

Table 5. Physicochemical properties of the stingless bee honey

Sample	pH	Free Acidity (meq/kg)	Ash Content (g/100g)	Total Dissolved Solid (ppm)	TPC (mg GAE/100 g)
1	3.16 ± 0.09	150.01 ± 21.20	0.21 ± 0.01	289.83 ± 29.51	226.5 ± 8.5
2	3.43 ± 0.07	162.64 ± 24.55	0.61 ± 0.10	519.83 ± 66.46	304.2 ± 9.9
3	3.24 ± 0.08	184.66 ± 14.62	0.20 ± 0.05	277.00 ± 6.08	202.4 ± 8.6
4	3.21 ± 0.03	151.23 ± 12.40	0.25 ± 0.02	322.33 ± 5.53	262.3 ± 8.0
5	3.18 ± 0.04	103.54 ± 9.13	0.25 ± 0.10	308.82 ± 113.11	265.1 ± 2.2
6	3.01 ± 0.17	99.08 ± 8.37	0.07 ± 0.06	313.83 ± 7.01	172.1 ± 0.5
7	3.01 ± 0.38	161.04 ± 12.66	0.18 ± 0.04	267.17 ± 11.73	177.0 ± 9.7
8	3.29 ± 0.05	160.84 ± 20.01	0.42 ± 0.06	362.33 ± 45.74	272.5 ± 5.0
9	3.29 ± 0.11	178.46 ± 16.32	0.33 ± 0.01	312.17 ± 15.00	322.3 ± 7.0
10	3.28 ± 0.14	93.07 ± 9.80	0.40 ± 0.11	303.33 ± 17.21	135.0 ± 4.9
11	3.23 ± 0.13	154.71 ± 7.48	0.21 ± 0.06	275.00 ± 17.32	95.0 ± 0.3
12	3.32 ± 0.11	145.48 ± 6.40	0.46 ± 0.18	330.33 ± 22.67	212.9 ± 2.2
13	3.18 ± 0.14	123.88 ± 1.59	0.20 ± 0.02	302.83 ± 29.75	327.6 ± 9.4
14	3.26 ± 0.14	129.07 ± 29.60	0.24 ± 0.20	320.50 ± 56.25	204.7 ± 4.9
15	3.27 ± 0.13	120.54 ± 6.31	0.20 ± 0.04	333.83 ± 25.97	115.4 ± 6.5
16	3.22 ± 0.12	85.59 ± 6.24	n.c.o.	302.00 ± 55.33	364.9 ± 4.8
17	3.28 ± 0.03	65.42 ± 13.53	n.c.o.	282.67 ± 24.19	210.6 ± 1.5
18	3.22 ± 0.11	114.07 ± 1.32	n.c.o.	258.83 ± 57.93	n.c.o.
19	3.29 ± 0.16	149.57 ± 14.75	n.c.o.	365.67 ± 36.43	n.c.o.
20	3.18 ± 0.14	96.02 ± 5.62	n.c.o.	315.00±33.06	n.c.o.

n.c.o. refer as not carried out

pH analysis

All of the honey samples analyzed in this study were found to be acidic with a range of 3.01 to 3.43 (Table 5). The range of the pH was compliant with the Malaysian Standards for stingless bee honey (pH 2.5-3.8). The pH values obtained from the current study were almost similar to the finding of other regions in Malaysia (pH 2.92-3.71) (Table 6). However, based on the previous study by Selvaraju et al. [40], they found a sample in Penang that has a pH (pH 4.03) higher than the maximum value stated by the Malaysian Standards. The findings proved that despite the different geographical and

botanical sources of the honey samples, their pH was almost within the same range and had no significant difference ($p > 0.05$). This was confirmed by running the pH reading of 20 samples in One-Way ANOVA Test, and the p-value was 0.4028. The result might suggest that stingless bee honey has a similar range of pH regardless of their origin [11]. As reported by Moniruzzaman et al. [41], the high acidity of the honey is caused by the fermentation of sugar into organic acid, which is responsible for honey flavor and stability against microbial spoilage. A low pH value also indicates that the stingless bee honey is more acidic and has more hydrogen ions, which are involved in the formation of other compounds in the honey [11].

Table 6. Physicochemical properties of stingless bee honey produced by *Heterotrigona itama* at different regions in Malaysia

Location	**pH**	**Free Acidity (meq/kg)**	**Ash (g/100g)**	**Total Dissolved Solids**	**TPC (mg GAE/100g)**	**Ref.**
Pahang	3.71		0.41			[42]
Kedah	3.71		0.23			
Selangor	3.29		0.22			
Johor	3.24-3.42		0.15-0.67		357.1 - 520.8	[29]
Melaka	3.27-3.36		0.18-0.47			
Perak	3.26	136.8	0.08			[43]
Kelantan	2.93		0.27			[11]
Terengganu	2.92		0.53			
Kedah			0.39		228.1-235.3	[44]
Johor			0.29			
Melaka	3.18	176.3		74.9 °Brix		[5]
Johor	3.27	107.5		74.7 °Brix		
Pahang	3.00	246.3		73.9 °Brix		
Penang	4.03					[40]
Kedah	3.22					
Pahang	3.17					[45]
Sarawak	2.92-3.58		0.29 %			[46]
Penang Kedah Kelantan Terengganu Selangor Negeri Sembilan Melaka	3.17	220.6	0.28 %	0.28%		[47]
Sarawak Selangor Johor Kedah	2.86-3.42	17.0-336.2	0.05-0.15 %		251.1-541.8	[48]
Penang	3.01-3.43	99.08-184.66	0.07-0.61	277.00-519.83	95.0-364.9	Present study
Kedah	3.01-3.32	65.42-178.46	0.18-0.46	258.83-365.67	95.0-364.9	

Free acidity

The free acidity of the honey samples was ranged from 65.42 to 184.66 meq/kg (Table 5). The values detected were in a similar range with the previous studies from other regions in Malaysia (Table 6), except for the sample studied by Shamsudin et al. [5] and Zawawi et al. [48] which contained a relatively higher free acidity value (246.3 and 336.2 meq/kg, respectively). The Malaysian Standards did not set a limit for the free acidity in stingless bee honey. Based on the Codex Alimentarius, the free acidity of honey shall not exceed 50 meq/kg. The free acidity of the samples studied were significantly high and did not comply with the Codex standard of honey. Free acidity is a quality parameter related to honey fermentation of sugars to organic acids which depends on the nectar of different floras [43, 49, 50]. Therefore, it can be concluded that the high fermentation of sugars creates the organic acids in the stingless bee honey.

Ash content

The ash content is depending on the amount of minerals present in the honey. The higher the value of ash content, the greater the amount of mineral present in the nectar. The percentage of the ash was measured based on the remaining inorganic residue found after the incineration of the honey sample [46]. The ash content obtained from this study was between 0.07 and 0.61 g/100g. However, analysis on samples 16 to 20 have not carried out due to the constraint of instruments. Nonetheless, for samples 1 to 15, the ash content obtained was aligned with the Malaysian Standards (max 1.0 g/100g). The values were also similar to the previous studies from other regions in Malaysia (0.08-0.47 g/100g) (Table 6) which also complied with the Malaysian Standards.

Total dissolved solids

The total dissolved solids are related to the moisture and sugar content in the honey. In general, honey with high total dissolved solids possesses high sugar content and low moisture content [5]. The total dissolved solids from this study were in the range of 258.83 to 365.67 ppm, except for sample 2 which had a very high value (519.83 ppm). The high value of total dissolved solids of sample 2 is probably due to the high content of organic and inorganic substances, mainly sugars such as glucose and fructose [51]. In other words, the probability of the honey being adulterated with syrup or honeybees which have been fed with sugar syrup is high. From the previous studies, only Moniruzzaman et al. [51] reported the total dissolved solids of Malaysian stingless bee honeys in ppm unit, whereas Shamsudin et al. [5] and Ng et al. [52] reported the total dissolved solids in percent °Brix. In order to record the total dissolved solids in percent °Brix, a digital refractometer is used. The total dissolved solids of Malaysian stingless bee honey from Moniruzzaman et al. [51] ranged from 138.00 to 395.00 ppm.

TPC analysis

The gallic standard solutions and all the samples were scanned from the wavelength of 200 nm to 1100 nm by using UV-Vis spectrometer in order to determine the maximum absorbance. The maximum wavelength was roughly scanned at 244.4 nm for the standard solutions and the sample solutions against the blank solution.

From Table 5, the TPC values varied from 95.0 mg GAE/100 g to 364.9 mg GAE/100 g. The highest TPC was found in sample 16, while the lowest TPC was found in sample 11. However, the TPC found by Abu Bakar et al. [29] (Table 6) showed higher TPC values which were between 357.14 and 520.83 mg GAE/100 g. As the TPC assay is able to identify the total amount of phenolic content in the samples, a high TPC value indicates a greater amount of phenolic content. When the amount of phenolic content of honey is greater, then honey will have better redox properties which leads to higher antioxidant activity.

Analysis of 5-HMF

The concentration of 5-HMF in the honey samples was quantified based on the external standard method using the calibration curve. The standard calibration curve of 5-HMF was constructed using four different concentrations which included 0.05, 1, 10, 50 mg/L of the standard solutions. The baseline separation for 5-HMF was achieved in less than four minutes under the stated experimental conditions.

5-HMF is known as the best indicator for the freshness and quality of the honey which provides information on

degradation, adulteration, and deterioration of the honey [53]. The honey samples used in this study were obtained freshly from the local beekeepers in Kedah and Penang, Malaysia in December 2019. The concentration of 5-HMF present in the fresh honey samples was analyzed after receiving the honey samples from the beekeepers. From the analysis, only honey sample 10 contained a very low concentration (0.31 ± 0.01 mg/kg) of 5-HMF, while the other 19 honey samples were not detected (Table 7). The results obtained from the previous study by our research group are congruent with other studies of different regions and countries where the 5-HMF was not detected or present in a very little amount in fresh stingless bee honey samples (Table 8).

To investigate the consequence of prolonged storage on the concentration of 5-HMF, the honey samples were stored for six months in the dark at room temperature. The honey samples were kept at room temperature to stimulate the common practice that honey is normally stored at room temperature. Besides, the honey samples were stored in the dark in order to prevent excess heat from sunlight; otherwise, the temperature of the honey samples would increase when exposed to sunlight. The increase in temperature of the honey samples would lead to an escalation in the concentration of 5-HMF which will affect the results of the study [54]. After storage for six months, the honey samples were analyzed in July 2020, and the concentrations of 5-HMF were found to have increased to the range of 48.18 ± 1.11 to 192.99 ± 10.39 mg/kg (Table 7). These values exceeded the maximum allowed limit of both Codex Alimentarius Standard (80 mg/kg) and the Malaysian Standard (30 mg/kg). Sample 6 showed a significantly higher concentration of 5-HMF, which might have been influence by the floral source of the honey [53].

Table 7. Concentrations of 5-HMF in honey samples of fresh and different storage durations

Sample	Concentration of 5-HMF (mg/kg)		
	December 2019 (Fresh)	**July 2020 (6 months storage)**	**May 2021 (15 months storage)**
1	N.D.	70.84 ± 0.23	65.10 ± 3.11
2	N.D.	56.20 ± 0.06	38.71 ± 0.91
3	N.D.	49.95 ± 2.13	45.98 ± 1.41
4	N.D.	52.26 ± 0.68	62.45 ± 0.74
5	N.D.	72.97 ± 0.51	75.82 ± 0.65
6	N.D.	192.99 ± 10.39	214.38 ± 4.03
7	N.D.	55.77 ± 5.24	56.31 ± 1.81
8	N.D.	61.95 ± 4.96	44.95 ± 0.65
9	N.D.	73.25 ± 0.34	66.04 ± 2.50
10	0.31 ± 0.01	81.29 ± 0.94	74.29 ± 2.32
11	N.D.	92.10 ± 1.33	54.72 ± 1.28
12	N.D.	57.48 ± 1.01	74.07 ± 1.49
13	N.D.	78.32 ± 0.08	91.00 ± 2.87
14	N.D.	68.50 ± 0.59	79.52 ± 0.59
15	N.D.	48.18 ± 1.11	95.33 ± 2.12
16	N.D.	61.39 ± 0.25	127.36 ± 5.43
17	N.D.	66.10 ± 1.96	117.85 ± 0.02
18	N.D.	61.97 ± 0.54	56.74 ± 2.28
19	N.D.	109.05 ± 1.46	64.01 ± 1.85
20	N.D.	62.76 ± 0.62	80.59 ± 2.87

N.D. refer to not detected

Table 8. Concentration of 5-HMF in fresh stingless bee honey of different regions and countries

Region/Country	Concentration of 5-HMF (mg/kg)	Ref.
Guatemala	N.D.	[55]
Australia	0.4 – 2.1	[56]
Thailand	0.25 – 1.89	[57]
Thailand	2.2 – 68.8	[58]
Brazil	N.D.	[59]
Pakistan	14.54 – 37.09	[60]
Brazil	17.81 – 34.62	[61]
Colombia	N.D.	[62]
Kelantan	3.42 ± 1.03	[11]
Terengganu	0.080 ± 0.16	[11]
Pahang	74.3 – 85.9	[63]
Pahang	0.07 ± 0.06	[5]
Malacca	0.05 ± 0.02	[5]
Johor	N.D.	[5]
Kelantan	0.42 – 0.95	[64]
Johor	0.02 – 48.68	[12]
Sarawak	0.21 – 0.48	[46]
Pahang	N.D.	[45]
Sarawak	0.11 – 0.91	[65]

N.D. refer to not detected

The honey samples were then kept for another nine months in the dark at room temperature in order to study the consequence of prolonged storage on the concentration of 5-HMF. The honey samples were analyzed in May 2021, and the results obtained are presented in Table 9. It was observed that all the honey samples contained a high concentration of 5-HMF. The concentration of 5-HMF present in the honey samples were ranging from 38.71 ± 0.91 to 214.38 ± 4.03 mg/kg. This situation shows that the honey samples have violated the allowed limit for the concentration of 5-HMF in the Malaysian Standard and Codex Alimentarius Standard. Thus, this indicates that the honey samples have deteriorated.

Malaysia is a tropical country where the climate is warm and humid all year round [66]. Thus, the concentration of 5-HMF in the honey originating from Malaysia should not exceed 80 mg/kg according to the Codex Alimentarius Standard. The results demonstrate that all the honey samples were within the maximum allowed limit of 5-HMF established by the Codex Alimentarius Standard, except for honey samples 6, 13, 15, 16, 17, and 20. Therefore, this indicates that honey samples 6, 13, 15, 16, 17, and 20 have deteriorated after prolonged storage of another nine months and are not suitable to be consumed.

On the other hand, it was found that the 5-HMF concentration in the honey samples determined in May 2021 fluctuated as compared to the honey samples determined in July 2020. It was noticed that the 5-HMF concentration in some of the honey samples increased, while some decreased. The concentration of 5-HMF increased for honey samples 4, 5, 6, 7, 12, 13, 14, 15, 16, 17, and 20 after prolonged storage. The escalation in the concentration of 5-HMF in the honey samples after prolonged storage is consistent with other earlier studies [54, 58].

The escalation in the concentration of 5-HMF in the honey samples is due to the degradation of the glucose

and fructose under acidic conditions [67, 68]. The longer the duration of storage for the honey samples, the more glucose and fructose are converted to 5-HMF, as stingless bee honey is acidic in nature. Hence, this situation would lead to a higher concentration of 5-HMF [33]. The high concentration of 5-HMF in the honey samples indicates that the honey samples degraded due to prolonged storage. As a result, the high concentration of 5-HMF in the honey samples would decrease the commercial value of the honey.

For honey samples 1, 2, 3, 8, 9, 10, 11, 18, and 19, it was found that the concentration of 5-HMF decreased after prolonged storage. However, large decrease in the concentration of 5-HMF was noticed for honey samples 11 and 19. The concentration of 5-HMF decreased to half when compared with the value quantified in July 2020. The concentration of 5-HMF's decrease in the honey samples could be due to the augmentation of complex processes which favor the decomposition of 5-HMF, whereby it will reduce the formation of 5-HMF [69].

Besides, the concentration of 5-HMF's decrease in the honey samples could also be due to the decomposition of 5-HMF from other products in the diluted honey samples, specifically for the diluted honey samples stored at room temperature. This is proven by the study of Wunderlin et al. [70] whereby the decrease in the 5-HMF band at 284 nm had a simultaneous increase of a new band at 252 nm. Thus, they suggested that the sample solutions containing 5-HMF should be stored in the dark at temperatures ranging from 4 to 8 °C before the sample solutions are analysed. Wunderlin et al. [70] also suggested that the analysis of 5-HMF should be made within six hours after sample preparation in order to prevent the decomposition of 5-HMF in sample solutions.

Furthermore, fructose is known to have a protective effect on the decomposition of 5-HMF [70]. The decomposition of 5-HMF is significant in honey samples without fructose. Therefore, the decrease in 5-HMF observed in a few honey samples in this study could be explained by the lesser amount of fructose in the honey samples which reduces the protective effect of fructose on the decomposition of 5-HMF. This eventually led to the decomposition of 5-HMF in the honey samples. As observed in this study, the 5-HMF concentration in some of the honey samples reduced after prolonged storage in the dark at room temperature for another nine months.

Multi-elemental composition

For the multi-elemental analysis, it was found that the highest concentration of elements was potassium (Table 9). Sample 2 exhibited a very high concentration of potassium (1,623.75 mg/kg), while sample 6 exhibited a very low concentration of potassium (16.13 mg/kg). By excluding these two samples, the average concentration range of potassium was 255.40 mg/kg to 915.50 mg/kg. Calcium, sodium, and aluminum were present in moderate concentrations in the honey with an average concentration range of 36.23 to 272.5 mg/kg, 31.25 to 148.25 mg/kg, and 25.35 to 62.25 mg/kg, respectively. For magnesium, the average range of concentration was 11.14 to 78.38 mg/kg, excluding one sample from Penang (sample 2) that had a relatively high concentration (179.75 mg/kg).

Table 9. Elemental analysis of honey samples (n=2, mean±SD) (mg/kg)

Sample	Element					
	K	Na	Al	Ca	Mg	Fe
1	469.63 ± 34.64	94.88 ± 0.03	176.25 ± 0.02	125.50 ± 0.01	43.88 ± 0.02	2.90 ± 0.00
2	1623.75 ± 0.22	148.25 ± 0.02	79.50 ± 0.01	205.75 ± 0.01	179.75 ± 0.02	4.28 ± 0.00
3	426.50 ± 28.82	95.13 ± 1.24	463.50 ± 0.08	191.00 ± 0.02	60.25 ± 1.66	6.05 ± 0.00
4	425.75 ± 0.06	77.44 ± 4.00	450.00 ± 0.06	178.75 ± 0.01	41.00 ± 0.01	3.73 ± 0.00
5	478.31± 36.33	140.00 ± 0.00	662.25 ± 0.06	272.50 ± 0.01	58.00 ± 0.01	5.53 ± 0.00
6	16.13 ± 0.00	76.94 ± 4.33	114.53 ± 0.02	36.23 ± 0.01	11.14 ± 0.37	3.35 ± 0.00

7	532.69 ± 42.69	113.50 ± 0.02	229.00 ± 0.02	234.90 ± 0.06	78.38 ± 0.03	7.68 ± 0.00
8	612.25 ± 0.06	74.75 ± 0.01	227.00 ± 0.01	129.50 ± 0.01	70.73 ± 0.04	1.65 ± 0.00
9	588.00 ± 14.85	105.75 ± 0.00	103.85 ± 0.06	139.50 ± 0.06	23.63 ± 0.02	1.60 ± 0.00
10	512.00 ± 16.26	112.93 ± 4.07	112.75 ± 0.02	163.95 ± 6.01	65.18 ± 1.66	41.55 ± 0.01
11	474.45 ± 38.25	79.75 ± 0.02	137.65 ± 0.03	81.90 ± 0.02	34.88 ± 2.65	< 0.02
12	376.25 ± 0.07	87.70 ± 0.01	73.50 ± 0.04	79.50 ± 0.02	28.25 ± 0.00	< 0.02
13	351.65 ± 0.15	31.25 ± 0.01	42.35 ± 0.01	52.05 ± 0.01	34.25 ± 0.01	< 0.02
14	560.63 ± 14.67	108.625 ± 0.01	67.13 ± 0.05	144.69 ± 4.33	23.41 + 0.44	1.10 ± 0.00
15	410.75 ± 0.06	107.31 ± 5.75	109.98 ± 7.88	136.15 ± 7.11	21.40 ± 1.13	1.15 ± 0.00
16	612.75 ± 2.48	129.75 ± 0.01	101.48 ± 0.07	154.18 ± 5.69	34.08 ± 0.11	1.00 ± 0.00
17	915.50 ± 0.11	150.13 ± 11.84	270.58 ± 1.24	166.13 ± 5.20	44.15 ± 0.02	1.45 ± 0.21
18	489.48 ± 10.15	102.00 ± 0.02	209.35 ± 0.04	159.18 ± 5.48	34.95 ± 0.92	1.70 ± 0.00
19	594.50 ± 0.06	86.25 ± 0.02	136.50 ± 0.03	121.05 ± 0.07	22.05 ± 0.00	4.50 ± 0.00
20	255.40 ± 0.06	47.75 ± 0.03	25.35 ± 0.01	78.95 ± 0.04	22.00 ± 0.01	< 0.02

Elements found in low concentrations were iron (< 0.02 to 41.55 mg/kg), copper (< 0.05 to 23.15 mg/kg), manganese (< 0.02 to 13.85 mg/kg), and zinc (< 0.01 to 4.63 mg/kg) (Table 10). The concentration of heavy metals such as arsenic, lead, nickel, barium, cadmium, and chromium were found lower than the LODs values (Table 4). The differences in the multi-element concentrations of the same honey species collected from different locations might be due to the type of soil in which the nectar of the flower was located [71].

Table 10. Elemental analysis of honey samples (n=2, mean±SD) (mg/kg)

Sample	Element								
	Cu	**Zn**	**Mn**	**As**	**Pb**	**Ni**	**Ba**	**Cd**	**Cr**
1	6.28 ± 0.00	1.95 ± 0.00	1.43 ± 0.00	< 0.02	< 0.02	< 0.03	< 0.01	< 0.01	< 0.04
2	20.85 ± 0.01	1.43 ± 0.00	5.90 ± 0.11	< 0.02	< 0.02	< 0.03	< 0.01	< 0.01	< 0.04
3	13.83 ± 0.01	1.70 ± 0.00	1.70 ± 0.00	< 0.02	< 0.02	< 0.03	< 0.01	< 0.01	< 0.04
4	14.45 ± 0.01	1.33 ± 0.00	< 0.02	< 0.02	< 0.02	< 0.03	< 0.01	< 0.01	< 0.04
5	12.05 ± 0.01	2.03 ± 0.00	0.80 ± 0.00	< 0.02	< 0.02	< 0.03	< 0.01	< 0.01	< 0.04
6	8.85 ± 0.01	0.70 ± 0.00	< 0.02	< 0.02	< 0.02	< 0.03	< 0.01	< 0.01	< 0.04
7	10.80 ± 0.00	4.63 ± 0.00	2.55 ± 0.00	< 0.02	< 0.02	< 0.03	< 0.01	< 0.01	< 0.04
8	23.15 ± 0.01	2.25 ± 0.00	2.63 ± 0.00	< 0.02	< 0.02	< 0.03	< 0.01	< 0.01	< 0.04
9	19.88 ± 0.02	1.40 ± 0.00	2.90 ± 0.04	< 0.02	< 0.02	< 0.03	< 0.01	< 0.01	< 0.04
10	< 0.05	1.05 ± 0.00	1.15 ± 0.07	< 0.02	< 0.02	< 0.03	< 0.01	< 0.01	< 0.04
11	< 0.05	< 0.01	< 0.02	< 0.02	< 0.02	< 0.03	< 0.01	< 0.01	< 0.04
12	< 0.05	< 0.01	< 0.02	< 0.02	< 0.02	< 0.03	< 0.01	< 0.01	< 0.04
13	< 0.05	< 0.01	4.25 ± 0.00	< 0.02	< 0.02	< 0.03	< 0.01	< 0.01	< 0.04
14	7.80 ± 0.00	2.09 ± 0.09	2.73 ± 0.00	< 0.02	< 0.02	< 0.03	< 0.01	< 0.01	< 0.04
15	11.30 ± 0.32	1.08 ± 0.00	< 0.02	< 0.02	< 0.02	< 0.03	< 0.01	< 0.01	< 0.04
16	< 0.05	3.50 ± 0.00	1.90 ± 0.00	< 0.02	< 0.02	< 0.03	< 0.01	< 0.01	< 0.04
17	< 0.05	< 0.01	13.85 ± 0.00	< 0.02	< 0.02	< 0.03	< 0.01	< 0.01	< 0.04
18	< 0.05	2.10 ± 0.00	< 0.02	< 0.02	< 0.02	< 0.03	< 0.01	< 0.01	< 0.04
19	< 0.05	< 0.01	< 0.02	< 0.02	< 0.02	< 0.03	< 0.01	< 0.01	< 0.04
20	< 0.05	< 0.01	< 0.02	< 0.02	< 0.02	< 0.03	< 0.01	< 0.01	< 0.04

Our findings for this species were similar to the values from the study performed by Abu Bakar et al. [29] in Melaka and Johor. The concentrations found for potassium, calcium, magnesium, and zinc were 236.33 to 701.33 mg/kg, 51.83 to 292.67 mg/kg, 18.53 to 50.30 mg/kg, and 4.37 to 5.33 mg/kg, respectively. Another study by Cheng et al. [72] in Selangor, Johor, Terengganu, and Sabah found that the concentrations of potassium, sodium, calcium, magnesium, iron, and zinc were 484.11 mg/L to 761.22 mg/L, 381.47 mg/L to 589.46 mg/L, 141.22 mg/L to 205.98 mg/L, 14.56 mg/L to 41.06 mg/L, 5.98 mg/L to 7.81 mg/L, and 1.02 mg/L to 3.03 mg/L, respectively. They also found that the concentrations of arsenic, lead, and cadmium were below the LODs.

From this study, the highest concentration of potassium was 1623.75 mg/L and the lowest was 16.13 mg/L. The daily recommended intake (Recommended Daily Allowance, RDA) of calcium is based on age, sex, and physio-pathological conditions, generally ranging from 1,000 to 1,200 mg [73]. The World Health Organization (WHO) recommends a potassium daily intake of more than 3,500 mg and a sodium daily intake of less than 2,000 mg [74]. The concentration obtained for these three elements was below the maximum daily intake, therefore it is safe for daily consumption for nutritional values. The concentration of the toxic elements was below the LOD. In terms of food safety, the multi-elemental profile, especially on the toxic elements in the honeys, gave information on the environmental conditions of the harvesting region. Based on the results obtained, our study indicated that there is neither contamination nor environmental pollution in the studied areas.

Conclusion

In this study, the Malaysian stingless bee honey which originated from a particular bee species (*Heterotrigona itama*) from the northern region of Malaysia (Kedah and Penang) was successfully investigated for its physicochemical profile, multi-elemental composition, and antioxidant activity. The antioxidant activity of honey was studied by evaluating their TPC. The pH, free acidity, ash content, total dissolved solids, minerals, and TPC were studied for the fresh honey samples only; whereas the 5-HMF content was investigated for fresh samples, after 6 and 15 months. The findings of ash content, pH, and TPC of all the honey samples were compliant with the advised limit set by Malaysian Standards and previous studies. The free acidity of all the samples and total dissolved solids of sample 2 exceeded the permitted range. The concentration of minerals was observed that their concentration is below the advised daily intake. At the same time, it was observed that the concentration of toxic elements is below the LOD; thus, it is safe to consume these honey samples. The 5-HMF content of all the fresh honey samples was not detected, except sample 10 (0.32 mg/kg). Although 5-HMF was detected in fresh sample 10, it is still low and within the permitted range by Malaysian Standards. Unfortunately, the 5-HMF content of all the honey samples (after 6 and 15 months) exceeded the permitted range. Therefore, it is advised to consume the honey in less than six months. Alternatively, a new study regarding the 5-HMF content of honey samples stored at 4 °C (refrigerator) for different storage periods has to be carried out in order to visualize the change pattern of 5-HMF content in honey. Additionally, the new study has to include the influence of storage period on the physicochemical profile and antioxidant activity of honey, so that the correlation of the parameters can be studied too.

Acknowledgement

The authors are grateful for the financial support of the Short Term Grant (304/PKIMIA/6315099) provided by Universiti Sains Malaysia and the facilities at School of Chemical Sciences, Universiti Sains Malaysia.

References

1. Nordin, A., Omar, N., Sainik, N. Q. A. V., Chowdhury, S. R., Omar, E., Saim, A. and Idrus, R. (2018). Low dose stingless bee honey increases viability of human dermal fibroblasts that could potentially promote wound healing. *Wound Medicine*, 23: 22-27.
2. Lourenço, C. T., Carvalho, S. M., Malaspina, O. and Nocelli, R. C. F. (2012). Oral toxicity of fipronil insecticide against the stingless bee *Melipona scutellaris* (Latreille, 1811). *Bulletin of Environmental Contamination and Toxicology*,

89(4): 921-924.

3. Rao, P. V., Krishnan, K. T., Salleh, N. and Gan, S. H. (2016). Biological and therapeutic effects of honey produced by honey bees and stingless bees: A comparative review. *Revista Brasileira de Farmacognosia*, 26(5): 657-664.
4. Bilandžić, N., Tlak Gajger, I., Kosanović, M., Čalopek, B., Sedak, M., Solomun Kolanović, B., Varenina, I., Luburić, Đ. B., Varga, I. and Đokić, M. (2017). Essential and toxic element concentrations in monofloral honeys from southern Croatia. *Food Chemistry*, 234: 245-253.
5. Shamsudin, S., Selamat, J., Sanny, M., Abd. Razak, S. B., Jambari, N. N., Mian, Z. and Khatib, A. (2019). Influence of origins and bee species on physicochemical, antioxidant properties and botanical discrimination of stingless bee honey. *International Journal of Food Properties*, 22(1): 238-263.
6. Biluca, F. C., Braghini, F., Gonzaga, L. V., Costa, A. C. O. and Fett, R. (2016). Physicochemical profiles, minerals and bioactive compounds of stingless bee honey (Meliponinae). *Journal of Food Composition and Analysis*, 50: 61-69.
7. Karabagias, I. K., Badeka, A. V., Kontakos, S., Karabournioti, S. and Kontominas, M. G. (2014). Botanical discrimination of Greek unifloral honeys with physico-chemical and chemometric analyses. *Food Chemistry*, 165: 181-190.
8. Solayman, M., Islam, M. A., Paul, S., Ali, Y., Khalil, M. I., Alam, N. and Gan, S. H. (2016). Physicochemical properties, minerals, trace elements, and heavy metals in honey of different origins: A comprehensive review. *Comprehensive Reviews in Food Science and Food Safety*, 15(1): 219-233.
9. Jalil, M. A. A., Kasmuri, A. R. and Hadi, H. (2017). Stingless bee honey, the natural wound healer: A review. *Skin Pharmacology and Physiology*, 30(2): 66-75.
10. Ediriweera, E. R. H. S. S. and Premarathna, N. Y. S. (2018). Medicinal and cosmetic uses of bee's honey – A review. *An International Quarterly Journal of Research in Ayurveda*, 33(2): 178-182.
11. Fatima, I.J., Mohd Hilmi, A.B., Salwani, I. and Lavaniya, M. (2018). Physicochemical characteristics of Malaysian stingless bee honey from Trigona species. *International Medical Journal Malaysia*, 17 (Special Issue): 187-191.
12. Ya'akob, H., Norhisham, N.F., Mohamed, M., Sadek, N. and Endrini, S. (2019). Evaluation of physicochemical properties of Trigona sp . stingless bee honey from various districts of Johor. *Jurnal Kejuruteraan*, 2(1): 59-67.
13. Department of Standards Malaysia (2017). *Kelulut (Stingless bee) honey - Specification*.
14. Bogdanov, S. and Martin, P. (2002). Honey authenticity : A review. Swiss Bee Research Centre: pp 20.
15. Prica, N., Baloš, M. Ž, Jakšić, S., Mihaljev, Ž., Kartalović, B., Babić, J. and Savić, S. (2015). Moisture and acidity as indicators of the quality of honey originating from Vojvodina region. *Archives of Veterinary Medicine*, 7(2): 99-109.
16. Ananias, K. R., de Melo, A. A. M. and de Moura, C. J. (2013). Analysis of moisture content, acidity and contamination by yeast and molds in *Apis mellifera* L. honey from central Brazil. *Brazilian Journal of Microbiology*, 44(3): 679-683.
17. Salazar, L. N., Freitas, A. B. B. de, Luz, M. V. da, Bersch, P. and Salazar, R. F. dos S. (2017). Physicochemical characterization of honey from different regions in Rio Grande Do Sul State labeled with different inspection service stamps. *Ciência e Natura*, 39(3): 656.
18. Moniruzzaman, M., Sulaiman, S. A., Khalil, M. I. and Gan, S. H. (2013). Evaluation of physicochemical and antioxidant properties of sourwood and other Malaysian honeys: A comparison with manuka honey. *Chemistry Central Journal*, *7*(1): 1-12.
19. Ng, W.-J., Sit, N.-W., Ooi, P.A.-C., Ee, K.-Y. and Lim, T.-M. (2021). Botanical origin differentiation of Malaysian stingless bee honey produced by *Heterotrigona itama* and *Geniotrigona thoracica* using chemometrics. *Molecules*, 26: 7628.

20. Vit, P., Rodríguez-Malaver, A., Roubik, D. W., Moreno, E., Almeida, B. S., Sancho, M. T., Fernández-Muiño, M., Almeida-Anacleto, D., Carlos, L. M., Gil, F., González, C., Aguilera, G. and Nieves, B. (2009). Expanded parameters to assess the quality of honey from Venezuelan bees (*Apis melllifera*). *Journal of ApiProduct and ApiMedical Science*, 1(3): 72-81.
21. Al-Farsi, M., Al-Amri, A., Al-Hadhrami, A. and Al-Belushi, S. (2018). Color, flavonoids, phenolics and antioxidants of Omani honey. *Heliyon*, 4(10): e00874.
22. Abbas, M., Saeed, F., Anjum, F. M., Afzaal, M., Tufail, T., Bashir, M. S., Ishtiaq, A., Hussain, S. and Suleria, H. A. R. (2017). Natural polyphenols: An overview. *International Journal of Food Properties*, 20(8): 1689-1699.
23. Alves, A., Ramos, A., Gonçalves, M. M., Bernardo, M. and Mendes, B. (2013). Antioxidant activity, quality parameters and mineral content of Portuguese monofloral honeys. *Journal of Food Composition and Analysis*, 30(2): 130-138.
24. Noreen, H., Semmar, N., Farman, M. and McCullagh, J. S. O. (2017). Measurement of total phenolic content and antioxidant activity of aerial parts of medicinal plant Coronopus didymus. *Asian Pacific Journal of Tropical Medicine*, 10(8): 792-801.
25. Oliveira, A. M. D. F., Pinheiro, L. S., Pereira, C. K. S., Matias, W. N., Gomes, R. A., Chaves, O. S., de Souza, M. de F. V., de Almeida, R. N. and de Assis, T. S. (2012). Total phenolic content and antioxidant activity of some malvaceae family species. *Antioxidants*, 1(1): 33-43.
26. Bendini, A., Cerretani, L., Pizzolante, L., Toschi, T. G., Guzzo, F., Ceoldo, S., Marconi, A. M., Andreetta, F. and Levi, M. (2006). Phenol content related to antioxidant and antimicrobial activities of Passiflora spp. extracts. *European Food Research and Technology*, 223(1): 102-109.
27. Wong, C. C., Li, H. Bin, Cheng, K. W. & Chen, F. (2006). A systematic survey of antioxidant activity of 30 Chinese medicinal plants using the ferric reducing antioxidant power assay. *Food Chemistry*, 97(4): 705–711.
28. Dawidowicz, A. L. and Olszowy, M. (2010). Influence of some experimental variables and matrix components in the determination of antioxidant properties by β-carotene bleaching assay: Experiments with BHT used as standard antioxidant. *European Food Research and Technology*, 231(6): 835-840.
29. Abu Bakar, M. F., Sanusi, S. B., Abu Bakar, F. I., Cong, O. J. and Mian, Z. (2017). Physicochemical and antioxidant potential of raw unprocessed honey from malaysian stingless bees. *Pakistan Journal of Nutrition*, 16(11): 888-894.
30. Bargańska, Z.,Ɫebioda, M. and Namieśnik, J. (2016). Honey bees and their products: Bioindicators of environmental contamination. *Critical Reviews in Environmental Science and Technology*, 46(3): 235-248.
31. Naggar, Y. Al, Brinkmann, M., Sayes, C. M., Al-Kahtani, S. N., Dar, S. A., El-Seedi, H. R., Grünewald, B. and Giesy, J. P. (2021). Are honey bees at risk from microplastics? *Toxics*, 9(5): 1-8.
32. Abu-Siada, A., Lai, S. P. and Islam, S. M. (2012). A novel fuzzy-logic approach for furan estimation in transformer oil. *IEEE Transactions on Power Delivery*, 27(2): 469-474.
33. Shapla, U. M., Solayman, M., Alam, N., Khalil, M. I. and Gan, S. H. (2018). 5-Hydroxymethylfurfural (HMF) levels in honey and other food products: effects on bees and human health. *Chemistry Central Journal*, 12(1): 1-18.
34. Foo Yong, W., Makahleh, A., Al-Azzam, K. M., Yahaya, N., Saad, B. and Sulaiman, S. A. (2012). Micellar electrokinetic chromatography method for the simultaneous determination of furanic compounds in honey and vegetable oils. *Talanta*, 97: 23-31.
35. Choudhary, A., Kumar, V., Kumar, S., Majid, I., Aggarwal, P. and Suri, S. (2021). 5-hydroxymethylfurfural (HMF) formation, occurrence and potential health concerns: Recent developments. *Toxin Reviews*, 40(4): 545-561.

36. AOAC (2005). Official methods of analysis of AOAC international, 17th Edition.; Association of Analytical Chemists: Gaithersburg, MD, USA.
37. AOAC (2006). Official methods of analysis. 18th Edition, Association of Official Analytical Chemists, Gaithersburgs, Gaithersburg, MD, USA.
38. Gul, A. and Pehlivan, T. (2018). Antioxidant activities of some monofloral honey types produced across Turkey. *Saudi Journal of Biological Sciences*, 25: 1056-1065.
39. ICH Harmonised Tripartite guideline. Validation of analytical procedures: Text and methodology Q2(R1).
40. Selvaraju, K., Vikram, P., Jan M. S., Krishnan, K. T. and Mohammed, A. (2019), Melissopalynological, physicochemical and antioxidant properties of honey from West Coast of Malaysia. *Journal of Food Science and Technology*, 56(5): 2508-2521.
41. Moniruzzaman, M., Khalil, M. I., Sulaiman, S. A. and Siew H. G. (2013). Physicochemical and antioxidant properties of Malaysian honeys produced by *Apis cerana, Apis dorsata* and *Apis mellifera*. *BMC Complementary and Alternative Medicine*, 13: 43.
42. Boon, K.C., Haron, H., Talib, R.A. and Subramaniam, P. (2017). Physical properties, antioxidant content and anti-oxidative activities of Malaysian stingless Kelulut (*Trigona* spp.) honey. *Journal of Agricultural Science*, 9: 32-40.
43. Kek, S. P., Chin, N. L., Yusof, Y. A., Tan, S. W., Suan, L., Kek, S. P. and Chin, N. L. (2017). Classification of entomological origin of honey based on its physicochemical and antioxidant properties. *International Journal of Food Properties*, 20: S2723-S2738.
44. Ranneh, Y., Alia, F., Zarei, M., Md Akimb, A., Abd Hamid, H. and Khazaai, H. (2018). Malaysian stingless bee and tualang honeys: A comparative characterization of total antioxidant capacity and phenolic profile using liquid chromatography-mass spectrometry. *LWT-Food Science and Technology*, 89: 1-9.
45. Salim, S. N. M., Ramakreshnan, L., Fong, C. S., Wahab, R. A. and Rasad, M. S. B. A. (2019). In-vitro cytotoxicity of Trigona itama honey against human lung adenocarcinoma epithelial cell line (A549). *European Journal of Integrative Medicine*, 30(4): 100955.
46. Wong, P., Ling, HS., Chung, KC., Yau, T. M. S. and Gindi, S. R. A. (2019). Chemical analysis on the honey of Heterotrigona itama and Tetrigona binghami from Sarawak, Malaysia. *Sains Malaysia*, 48(8): 1635-1642.
47. Ismail, N. F., Maulidiani, M., Omar, S., Zulkifli, M. F., Radzi, M. N. F. M., Ismail, N., Jusoh, A. Z., Roowi, S., Wooi M. Y., Rudiyanto, R. and Ismail, W. I. W. (2021). Classification of stingless bee honey based on species, dehumidification process and geographical origins using physicochemical and ATR-FTIR chemometric approach. *Journal of Food Composition and Analysis*, 104: 104126.
48. Zawawi, N., Jiali Z., Hungerford, N. L., Yates, H. S.A., Webber, D. C., Farrell, M., Tinggi, U., Bhandari, B. and Fletcher M. T. (2022). Unique physicochemical properties and rare reducing sugar trehalulose mandate new international regulation for stingless bee honey. *Food Chemistry*, 373:131566.
49. Silva, T. M. S., dos Santos, F. P., Evangelista-Rodrigues, A., da Silva, E. M. S., da Silva, G. S., de Novais, J. S., dos Santos, F. de A. R. and Camara, C. A. (2013). Phenolic compounds, melissopalynological, physicochemical analysis and antioxidant activity of Jandaíra (*Melipona subnitida*) honey. *Journal of Food Composition and Analysis*, 29(1): 10-18.
50. da Silva, P.M., Gauche, C., Gonzaga, L.V., Costa, A.C.O. and Fett, R. (2016) Honey: Chemical composition, stability and authenticity. *Food Chemistry*, 196: 309-323.
51. Moniruzzaman, M., Chowdhury, M. A., Rahman, M. A., Sulaiman, S. A. and Gan, S. H. (2014). Determination of mineral, trace element, and pesticide levels in honey samples originating from different regions of Malaysia compared to Manuka Honey. *BioMed Research International*, 2014: 359890.
52. Ng, W. J., Sit, N. W., Ooi, P. A.-C., Ee, K. Y. and Lim, T. M. (2021). Botanical origin differentiation of Malaysian stingless bee honey produced by

Heterotrigona itama and *Geniotrigona thoracica* using chemometrics. *Molecules*, 26(24): 7628.

53. Gomes, T., Feás, X., Iglesias, A. and Estevinho, L. M. (2011). Study of organic honey from the northeast of Portugal. *Molecules*, 16(7): 5374-5386.
54. Biluca, Fabíola C., Della Betta, F., De Oliveira, G. P., Pereira, L. M., Gonzaga, L. V., Costa, A. C. O. and Fett, R. (2014). 5-HMF and carbohydrates content in stingless bee honey by CE before and after thermal treatment. *Food Chemistry*, 159(12): 244-249.
55. Vit, P., Roubik, D. W. and Pedro, S. R. M. (2012). Pot-Honey: A legacy of stingless bees. Springer.
56. Oddo, L. P., Heard, T. A., Rodríguez-Malaver, A., Pérez, R. A., Fernández-Muiño, M., Sancho, M. T., Sesta, G., Lusco, L. and Vit, P. (2008). Composition and antioxidant activity of *Trigona carbonaria* honey from Australia. *Journal of Medicinal Food*, 11(4): 789-794.
57. Suntiparapop, K., Prapaipong, P. and Chantawannakul, P. (2012). Chemical and biological properties of honey from Thai stingless bee (*Tetragonula leaviceps*). *Journal of Apicultural Research*, 51(1): 45-52.
58. Chuttong, B., Chanbang, Y., Sringarm, K. and Burgett, M. (2015). Efectos del almacenamiento a largo plazo en la miel de abejas sin aguijón (Hymenoptera: Meliponini: Apidae). *Journal of Apicultural Research*, 54(5): 441-451.
59. de Sousa, J. M. B., de Souza, E. L., Marques, G., Benassi, M. de T., Gullón, B., Pintado, M. M. and Magnani, M. (2016). Sugar profile, physicochemical and sensory aspects of monofloral honeys produced by different stingless bee species in Brazilian semi-arid region. *LWT - Food Science and Technology*, 65: 645-651.
60. Ahmed, M., Shafiq, M. I., Khaleeq, A., Huma, R., Qadir, M. A., Khalid, A., Ali, A. & Samad, A. (2016). Physiochemical, biochemical, minerals content analysis, and antioxidant potential of national and international honeys in Pakistan. *Journal of Chemistry*, 2016: 8072305.
61. Lemos, M. S., Venturieri, G. C., Dantas Filho, H. A. & Dantas, K. G. F. (2018). Evaluación de los parámetros físico-químicos y constituyentes inorgánicos de mieles de la región amazónica. *Journal of Apicultural Research*, 57(1): 135-144.
62. Cardona, Y., Torres, A. and Hoffmann, W. (2019). Colombian stingless bee honeys characterized by multivariate analysis of physicochemical properties. *Apidologie*, 50(6): 881-892.
63. Julika, W. N., Ajit, A., Sulaiman, A. Z. and Naila, A. (2019). Physicochemical and microbiological analysis of stingless bees honey collected from local market in Malaysia. *Indonesian Journal of Chemistry*, 19(2): 522-530.
64. Omar, S., Enchang, F. K., Nazri, M. U. I. A., Ismail, M. M. and Ismail, W. I. W. (2019). Physicochemical profiles of honey harvested from four major species of stingless bee (Kelulut) in North East Peninsular of Malaysia. *Malaysian Applied Biology*, 48(1): 111-116.
65. Wong, P., Hii, S. L., Koh, C. C., Moh, T. S. Y., Gindi, S. R. and Wong, W. P. M. (2020). Physicochemical and proximate analysis of Heterotrigona itama honey from inland and coastal regions of Sarawak. *ASM Science Journal*, 13(4): 36-44.
66. Jamaludin, N., Mohammed, N. I., Khamidi, M. F. and Wahab, S. N. A. (2015). Thermal comfort of residential building in Malaysia at different micro-climates. *Procedia - Social and Behavioral Sciences*, 170: 613-623.
67. Capuano, E. and Fogliano, V. (2011). Acrylamide and 5-hydroxymethylfurfural (HMF): A review on metabolism, toxicity, occurrence in food and mitigation strategies. *LWT - Food Science and Technology*, 44(4): 793-810.
68. Ruoff, K., Luginbühl, W., Bogdanov, S., Bosset, J. O., Estermann, B., Ziolko, T., Kheradmandan, S. and Amadò, R. (2007). Quantitative determination of physical and chemical measurands in honey by near-infrared spectrometry. *European Food Research and Technology*, 225(3–4): 415-423.
69. Kędzierska-Matysek, M., Florek, M., Wolanciuk, A. and Skałecki, P. (2016). Effect of freezing and room temperatures storage for 18 months on quality of raw rapeseed honey (*Brassica napus*). *Journal of Food Science and Technology*, 53(8): 3349-3355.

70. Wunderlin, D. A., Pesce, S. F., Amé, M. V. and Faye, P. F. (1998). Decomposition of hydroxymethylfurfural in solution and protective effect of fructose. *Journal of Agricultural and Food Chemistry*, 46(5): 1855-1863.
71. Vanhanen, L. P., Emmertz, A. and Savage, G. P. (2011). Mineral analysis of mono-floral New Zealand honey. *Food Chemistry*, 128(1): 236-240.
72. Cheng, M.Z.S.Z., Ismail, M., Chan, K. W., Ooi, D. J., Ismail, N., Zawawi, N., Lila, M. A. M. and Esa, N. M. (2019). Comparison of sugar content, mineral elements and antioxidant properties of Heterotrigona itama honey from suburban and forest in Malaysia. *Malaysian Journal of Medicine and Health Sciences*, 15(SP1): 104-112.
73. Muscariello, R., Rendina, D., Giannettino, R., Ippolito, S., Romano, O., Coretti, F., De Vita S., Martino, M., Sepe, C., Nuzzo, V. and ASL NA1 GP Network Researchers (2021). Calcium daily intake and the efficacy of a training intervention on optimizing calcium supplementation therapy: A clinical audit. *Nutrition, Metabolism & Cardiovascular Diseases*, 31: 354-360.
74. World Health Organization (2012). Guideline: sodium intake for adults and children. Geneva, Switzerland.

Malaysian Journal of Analytical Sciences (MJAS)
Published by Malaysian Analytical Sciences Society

CONVERTING WASTE CHICKEN BONES INTO HETEROGENEOUS CATALYST FOR BIODIESEL SYNTHESIS FROM WASTE COOKING OIL

(Pertukaran Sisa Tulang Ayam kepada Mangkin Hetrogen Bagi Penghasilan Biodiesel dari Minyak Masak Terpakai)

Jeyashelly Andas* and Nur Fazira Elyana Jusoh

Faculty of Applied Sciences,
Universiti Teknologi MARA, Cawangan Perlis, Kampus Arau, Perlis, Malaysia

**Corresponding author: drshelly@uitm.edu.my*

Received: 16 November 2021; Accepted: 5 February 2022; Published: 30 October 2022

Abstract

Depletion of non-renewable energy sources such as petroleum has triggered researchers to design a green catalyst for the synthesis of biodiesel. Thus, in this study, chicken bones were subjected to calcination-hydration-dehydration treatment to obtain a catalyst of high activity for the production of biodiesel from waste cooking oil (WCO). The physicochemical properties of the synthesized catalysts were analyzed by Fourier Transform Infrared Spectroscopy (FTIR) and N_2 adsorption-desorption. The catalyst prepared via calcination-hydration-dehydration treatment (C900-600) exhibited improved surface area (SBET, 71.14 m^2g^{-1}) and BJH pore diameter of 31.03 nm, in comparison with chicken bone derived catalyst calcined at 900 ˚C (C900) and commercial CaO with 31.72 m^2g^{-1}, 29.35 nm and 2.21 m^2g^{-1}, 15.98 nm, respectively. After 45 min, the activity of 5 wt.% catalysts in the transesterification of WCO with 1:15 oil to methanol ratio at 65 °C, increased as the following trend: C900-600 (92.15%) > C900 (80.63%) > commercial CaO (73.30%). C900-600 was truly a stable and reused catalyst, sustaining its activity of 87.00% even after five consecutive cycles. This research undoubtedly promises a cheap utilization of waste chicken bones for the conversion of WCO into renewable energy sources.

Keywords: waste chicken bones, biodiesel, waste cooking oil, acid value, reusability

Abstrak

Kekurangan sumber tenaga yang tidak boleh diperbaharui seperti petroleum telah mendorong para penyelidik untuk menghasilkan mangkin hijau untuk sintesis biodiesel. Maka, dalam penyelidikan ini, sisa tulang ayam telah dirawat menggunakan kalsinasi-hidrasi-dehidrasi untuk menghasilkan mangkin yang aktif dalam penghasilan biodiesel dari minyak masak terpakai. Ciri fizikokimia mangkin telah dianalisis menggunakan Spektroskopi Inframerah Transformasi Fourier (FTIR) dan N_2 penjerapan-penyahjerapan. Mangkin yang disediakan menggunakan rawatan kalsinasi-hidrasi-dehidrasi (C900-600)menunjukkan peningkatan luas permukaan BET (SBET, 71.14 m^2g^{-1}) dan diameter liang BJH; 31.03 nm, dibandingkan dengan mangkin dari sisa tulang ayam yang dikalsinasi pada suhu 900 ˚C (C900) dan CaO komersial dengan masing-masing merekodkan 31.72 m^2g^{-1}, 29.35 nm dan 2.21 m^2g^{-1}, 15.98 nm. Selepas 45 min, aktiviti mangkin (5% berat) dalam transesterifikasi minyak masak terpakai dengan nisbah minyak dan metanol 1:15 pada 65 °C meningkat berdasarkan tren berikut: C900-600 (92.15%)> C900 (80.63%)> CaO komersial (73.30%). C900-600 merupakan mangkin yang stabil dan boleh digunapakai, mengekalkan aktivitinya sebanyak 87.00% walaupun

setelah lima kekerapan dikitar semula. Penyelidikan ini pasti menjanjikan penggunaan sisa tulang ayam yang murah untuk penukaran minyak masak terpakai menjadi sumber tenaga yang boleh diperbaharui.

Kata kunci: sisa tulang ayam, biodiesel, minyak masak terpakai, nilai asid, kitar semula

Introduction

Growing depletion of non-renewable reserves, sickening environmental issues, and health concerns arising from petroleum-based diesel has positioned biodiesel as an alternative green energy fuel owing to its remarkable properties such as cleaner emission, non-hazard, and offers rapid biodegradability [1]. In biodiesel synthesis, feedstock contributes to 70% to 95% of the overall production cost [2]. This worrying situation draws the attention of global researches to utilise relatively cheap and easily available non-edible oil such as waste cooking oil (WCO). Asian countries, including Malaysia, produce nearly 40,000 tonnes of WCO per annum [3] and it is usually collected from households, fried food outlets, and restaurants [4]. Biodiesel price could be significantly reduced to 50% upon converting WCO into biodiesel [5] and this appears as the best practice to recycle WCO, which will otherwise end-up in palatable water and pose a substantial threat to the environment.

Nowadays, turning waste materials into a catalyst is the most viable way to address the production of biodiesel at a commercial scale. Solid base catalysts involving natural wastes, such as egg shell [6-9], chicken bone [2,10], fusion chicken and fish bone [11], ostrich bone [12], and scallop shell [13], are some of the potential CaO sources for transesterification reaction. For example, Borah et al. [9] have synthesised biodiesel from WCO using Zn doped egg shell derived CaO nanocatalyst that registered a maximum FAME yield of 96.74% after 4 h reaction. Nevertheless, great loss in the activity during the fifth recycle (64.49%) was reported, probably resulting from the leached active Zn species into the reaction medium. Similarly, a longer reaction duration of 5 h was required to reach 100% biodiesel yield over egg shell derived catalyst in the transesterification of WCO [6]. In another work, Dehkordi and Ghasemi [14] demonstrated excellent activity of ZrO_2 CaO in catalysing WCO into 92.1% biodiesel at only 2 h. However, the catalysis requires large catalyst dosage of 10 wt.% and 30 mole excess of methanol. Waste oyster shell employed as a sustainable base heterogeneous catalyst, yielded 87.3% of FAME after 3 h reaction in the presence of 9:1 methanol/WCO molar ratio and 6 wt.% catalyst [15]. However, no reusability study was reported in this work.

Malaysians consume nearly 50 kg of chicken per capita per year, making it rank first and third in Asia and in the world, respectively [16]. With this huge production, large numbers of chicken by-products such as chicken bone are generated and dumped in landfills, ending in poor solid waste management. Chicken bones are made up of organic and inorganic components with 65% (hydroxyapatite), 25 wt.% of protein, and the remaining % of water [17]. They have a high potential to be converted into a value-added product such as CaO based catalyst. However, very scarce studies were focused on chicken bone as a catalyst for biodiesel synthesis. For example, in 2015, Farooq et al. [2] discovered the efficiency of chicken bone as a base catalyst in the triglyceride conversion of WCO and registered a maximum biodiesel yield of 89.33% at optimised reaction conditions of 4 h, methanol to oil molar ratio of 15:1, reaction temperature of 65 °C, and 5 wt.% of catalyst loading.

The performance of Fe impregnated CaO derived chicken bone catalyst was documented by Hantoro Satraidi et al. [18]. The catalyst afforded a biodiesel yield of 22% after 3 h reaction time, with 6:1 of methanol:WCO. In a recent study by AlSharifi and Znad [10], lithium based chicken bone composite converted 96.6% of canola oil into biodiesel after 3 h. In this regard, the world's biodiesel present demand has triggered the search for an active heterogeneous catalyst that offers high yield and excellent properties. As such, in this present work, waste chicken bone was subjected to the calcination-hydration-dehydration technique to enhance the surface area that apparently affects the biodiesel yield. Little literature has shown the importance of the calcination-hydration-dehydration route. For example, CaO derived waste clamshell

prepared via calcination-hydration-dehydration treatment resulted in an enhanced surface area and basicity that greatly affected the biodiesel production from WCO [19]. Similarly, Niju and co-workers [7] reported an improved catalysis of egg shell based CaO catalyst synthesised by the calcination-hydration-dehydration route in the biodiesel synthesis (94.52%) from waste frying oil compared with commercial CaO that gave only 67.57%.

Hence, a lack of publication on the synthesis of CaO derived waste chicken bone catalyst by calcination-hydration-dehydration has encouraged us to prepare a preliminary characterisation of the catalyst using Fourier Transform Infrared Spectroscopy (FTIR) and N_2 sorption analysis. The catalysts were further evaluated in the synthesis of biodiesel from WCO and promised a green conversion of waste materials into value-added products.

Materials and Methods

Raw materials and reagents

The chicken bones and waste cooking oil (WCO) were collected from the cafeteria in Universiti Teknologi MARA (UiTM) Perlis, Malaysia. The chemicals used were CaO (HmbG), 99% anhydrous methanol (HmbG), 98% H_2SO_4 (QREC), sodium sulphate, potassium hydroxide (HmbG chemical), toluene (QREC Asia), phenolphthalein indicator (HmbG), and *n*-hexane (QREC). All the chemicals were used as procured.

Preparation of chicken bone

300 g of waste chicken bones were weighed and boiled in water for 1 h to remove adhering excess tissue and fats. Later, the boiled bones were thoroughly washed with copious amount of water to eliminate meat and other soft tissues [20], and allowed to dry at 110 ℃ for 2 h. The dried bones were crushed into small pieces and subsequently ground using a hammer mill into powder of < 2 mm particle size [21]. Finally, the sample was stored in a closed container to prevent moisture content changes.

Preparation of C900 and C900-600 catalyst

100 g of the powdered sample was placed in a crucible and heated at 900 ℃ for 4 h to obtain hydroxyapatites (HAP). The sample was designated as C900. To prepare C900-600, C900 was refluxed in water at 60 ℃ for 6 h and subsequently filtered and oven dried at 120 ℃ for 24 h [22]. Later, calcination was performed at 600 ℃ for 3 h. This stage allows the conversion of the hydroxide form into an oxide form [22]. For comparison, the commercial CaO catalyst was used.

Catalyst characterisation

The FTIR spectra of the catalysts were collected on a Thermo Electron Corporation Nicolet 380 spectrophotometer at wavenumber ranging from 4000 to 400 cm^{-1} with a resolution of 5 cm^{-1}. In prior analysis, the pellet was prepared with 1:10 w/w KBr:Sample. The surface area (S_{BET}) and BJH pore size distribution were obtained by means of N_2 adsorption-desorption (Micromeritics Instrument Corporation model ASAP 2000) after degassing for 12 h.

Treatment of WCO

The collected WCO was filtered to remove food residues and washed with hot distilled water. Later, it was treated with anhydrous Na_2SO_4 to remove any water content. The molecular weight of fatty acid in oil was determined by GC/MS (Agilent Technologies 6980N).

Acid value (AV) and free fatty acid (FFA) determination

Acid number refers to the quantity of KOH required to titrate 1 g of FFA in sample to its neutral point [23]. The acid number was evaluated according to standard testing procedure ASTM D664 as reported by Corro et al. [24] Briefly, 3 g of WCO was dissolved in 150 mL containing an equal volume of toluene and isopropanol. Then, 1to 2 drops of phenolphthalein were added into the prepared solution and titrated with 0.1 N KOH solution until the colour changed from light yellow to pink. The AV and FFA for feedstock and esterification product were determined as in equations (1) and (2), respectively.

$$Acid\ value\ (AV)\ =\ 56.1\ x\ \frac{M(A-B)}{W} \quad (1)$$

$$FFA\ (\%\ as\ palmitic)\ =\ \frac{A\ x\ M\ x\ 25.6}{W} \quad (2)$$

where M - KOH Concentration (N), A – Volume of KOH

volume required to reach the neutral point (mL), *B* - the volume corresponding to the blank titration (mL), and *W* - Sample weight (g).

Catalytic transesterification and biodiesel production

A two-step transesterification reaction consisting of acid transesterification to reduce the FFA content followed by base transesterification was carried out. Acid transesterification was done following the method by Tan et al. [25], however, with slight modification. In brief, WCO was heated to 110 ℃ overnight to reduce the viscosity. In a 250 mL flask, 50 mL of methanol and 0.1 mL concentrated H_2SO_4 were stirred; and later, 100 mL WCO (preheated at 65 ℃) was transferred and the mixture was stirred at 65 ℃ for 1 h.

Base transesterification and FAME analysis

In a typical run, 5 wt.% of catalyst was added into a three-neck round bottom flask containing 1:15 Oil/MeOH and equipped with a condenser. The reaction was performed at 65 ℃ with continuous stirring (250 rpm) for 1 h. Afterwards, the pre-treated WCO was transferred into the round bottom flask and the reaction was continued for 45 min. Later, the catalyst was filtered off and the reaction mixture containing biodiesel and glycerol at the upper and lower layer, respectively, was allowed to stand in a separating funnel for 24 h, with prior washing using hot distilled water. The water content in biodiesel phase was removed with sodium sulphate. Product composition in biodiesel was identified by GC/MS (Agilent Technologies 6890N, carrier gas: He) with the following temperature program: initial oven temperature of 383 K; ramp of 283 K/min, holding time of 2 min; intermediate temperature of 473 K; final ramp of 278 K/min; and final temperature of 553 K for 9 min. The % conversion was calculated based on equation (3) [24].

$$\%\ Conversion\ = \frac{AV1-AV2}{AV1}\ x\ 100\% \quad (3)$$

where, *AV1*–acid value of raw materials, *AV2*–acid value of transesterification product

Catalyst reusability

Upon completion of each experiment, the spent catalyst was separated from the reaction mixture by centrifugation and washed with *n*-hexane and subsequently subjected to heating at 600 ˚C for 2 h [2]. The recovered catalyst was reused in the transesterification reaction at similar reaction conditions for five consecutive runs.

Results and Discussion

FTIR spectral studies

The FTIR spectra of uncalcined chicken bone, C900, and C900-600 are compared in Figure 1. Broad band at ~ 3419 to 3438 cm^{-1} for all the samples represents the stretching vibration of the hydroxyl group (OH) on the surface, which is often associated with the -OH group of $Ca(OH)_2$ [25].

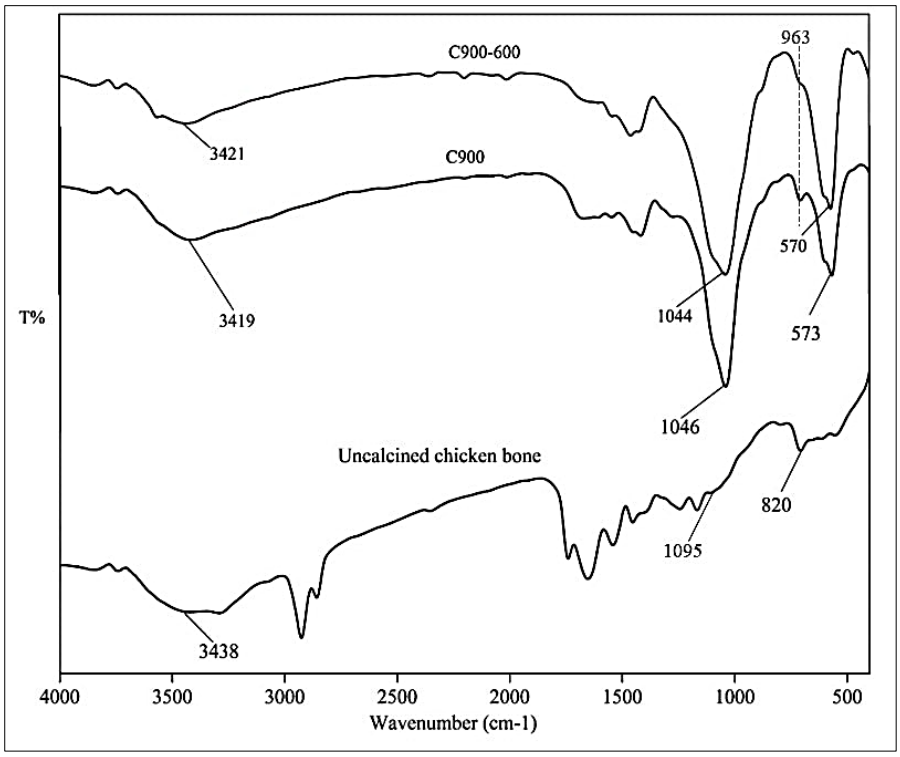


Figure 1. FTIR spectra of the samples

However, the interesting observation to be noted from Figure 1 is the existence of sharp peaks at 1044 to 1095 cm^{-1} and 570 to 573 cm^{-1} for both C900 and C900-600 that evidenced the presence of PO_4^{3-} group, and reflects the O-P-O bonds in calcium phosphate [21]. In addition, the shoulder peak at ~963 cm^{-1} for C900 and C900-600 belongs to PO_4^{3-} that resembles asymmetric stretching vibrations of P–O [24]. According to Corro et al. [24], the peaks at ~3400, 1036 to 1091, and 956 cm^{-1} evidenced the characteristic peaks of hydroxyapatite, which are undoubtedly shown by the calcined samples. Notably, the peaks are more intense for C900-600 compared with C900. This resembles the effectiveness of hydration-dehydration treatment on the chicken bone sample. On the contrary, the IR pattern of uncalcined chicken bone is almost similar to the spectra reported for uncalcined egg shell by Tan et al. [25]. In addition, the shoulder band detected at 820 cm^{-1} for the uncalcined chicken bone is due to CO_3^{2-} [21] and similar vibrations appeared at 1400 to 1500cm^{-1} for all the samples [26].

Textural properties

The S_{BET} and BJH pore diameter of C900-600, C900, and commercial CaO measured from N_2 adsorption-desorption analysis are summarised in Table 1.

Table 1. S_{BET} and BJH pore diameter of C900-600, C900, and commercial CaO

Sample	S_{BET} (m^2/g)	BJH pore diameter (nm)
C900-600	71.14	31.03
C900	31.72	29.35
Commercial CaO	2.21	15.98

According to IUPAC classification, the pore diameters of the synthesised catalysts are classified as mesopores (2 to 50 nm) and accordingly, mesoporous material is most suitable to be used as a catalyst since it allows the diffusion of larger molecules or reactants compared with micropores. It is worth reporting the higher S_{BET} and BJH pore diameter of C900-600 and C900 catalysts than the commercial CaO. To add, the synthesised catalysts in the present work showed greater S_{BET} than the lithium-based chicken bone catalyst prepared by AlSharfi and Znad [10]. The hydration-dehydration treatment significantly improved the surface area and pore diameter of the C900-600 catalyst as shown in Table 1. During dehydration, the removal of attached water molecules from the catalyst lattice might have led to a higher surface area by breaking the crystallite into smaller sizes.

N_2 adsorption-desorption isotherms of the catalysts are compared in Figure 2. Both C900 and C900-600 exhibited Type IV characteristics of mesoporous materials with H1 hysteresis loops, often associated with uniform pores. On contrary, commercial CaO showed a sigmoid type with almost no closure at $P/P_o = 0$ [27].

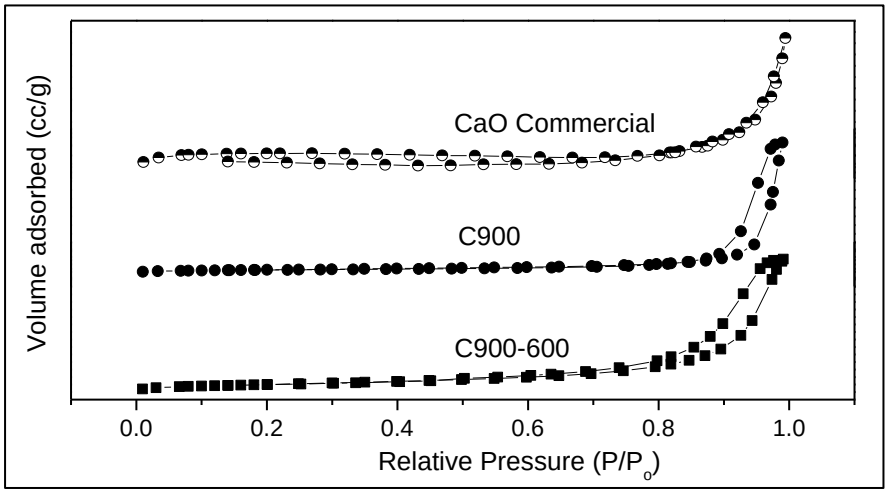


Figure 2. The N_2 adsorption-desorption isotherms of the catalysts

This characteristic is related with materials that have tendencies to swell [27]. Referring Figure 2, the broadening of the hysteresis loop of C900-600 compared to C900 is attributed to its larger pore diameter as evidenced in Table 1.

Production of biodiesel from WCO

The transesterification activity of the catalyst is compared in Table 2. C900-600 gave the maximum conversion of FFA to FAME (92.15%) compared with other catalysts.

Table 2. The activity of the catalysts in the transesterification of WCO

Sample	Acid Value (mg KOH/g)		Biodiesel Conversion (%)
	Initial	After	
C900-600	1.91	0.15	92.15
C900	1.91	0.37	80.63
Commercial CaO	1.91	0.51	73.30

Reaction conditions: Catalyst dosage: 5 wt.%; temperature: 65 °C; Methanol: WCO molar ratio: 15:1; time: 45 min

Higher catalysis of C900-600 can be inferred to its larger surface area and wider BJH pore diameter. Heterogeneous catalysis works on the principle of adsorption of reactants on surface. Thus, theoretically, larger surface area provides greater adsorption sites for the reactants to adsorb and react, which later influences the rate of reaction. In addition, the wider pore diameter of C900-600 eased the diffusion and accessibility of WCO and methanol deep into the active sites, actively participating in the reaction. Higher intensity of functional groups as evidenced through IR studies, have also aided the activity of C900-600 compared with C900. In addition, based on ASTM D-6751 and EN 14214 standards of biodiesel, the transesterification products registered using C900-600 and C900 catalysts were less than 0.5 mg KOH/g, which indicated the perfect fuel for automobiles [28].

Composition of biodiesel

The composition of FAME catalysed by C900-600 is shown in Figure 3 and summarised in Table 3.

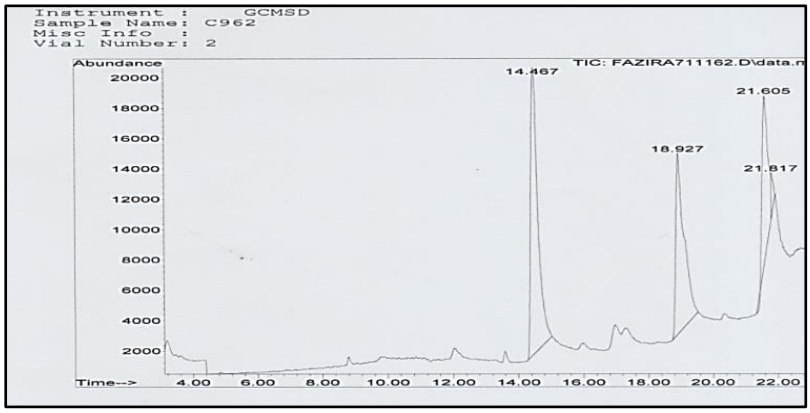


Figure 3. GC-MS profile of the biodiesel synthesised by C900-600

The major FAMEs identified in the synthesised biodiesel are as listed in Table 3. The findings are in accordance with Girish et al. [29], who evaluated the activity of clam shell catalyst in the conversion of waste frying oil.

Table 3. Methyl esters composition of the synthesised biodiesel

Retention Time (min)	Name of Compound	Molecular Formula	Molecular Weight (g/mol)
14.47	Dodecanoic acid methyl ester	$C_{13}H_{26}O_2$	214
18.93	10-Octadecadienoic acid methyl ester	$C_{19}H_{36}O_2$	296
21.61	Docosanoic acid methyl ester	$C_{23}H_{46}O_2$	354

Reusability of C900-600

The key characteristic of a heterogeneous catalyst is the ability to be reused with insignificant loss during the reusability. Figure 4 resembles the trend in the activity of C900-600 after five consecutive runs.

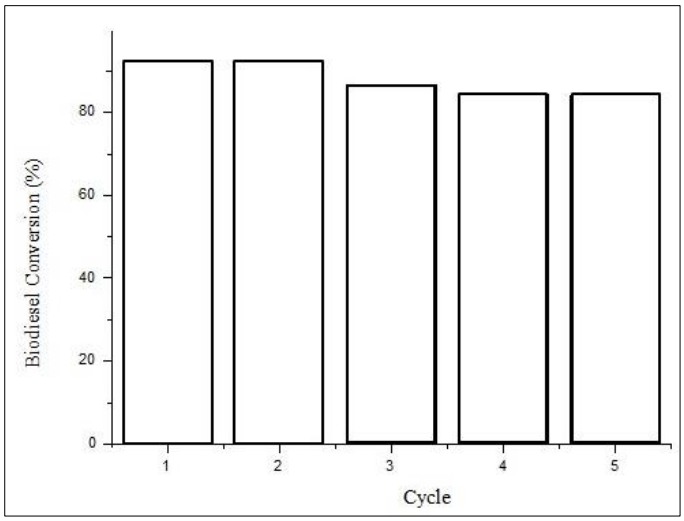


Figure 4. Regeneration activity of C900-600

C900-600 retained its activity up to the second cycle (92.12%), which indicated the high stability of the C900-600 catalyst. However, a slight reduction in the activity was experienced during the third (88.20%) and 87.00% for the subsequent runs. The lowering in the biodiesel conversion could be due to the attachment of unreacted reactants or products at the active sites that might have blocked the active sites and hindered the participation of the catalyst. The findings from this present work correlates well with several studies [7, 22] that demonstrated that the catalyst prepared from calcination-hydration-dehydration treatment can be reused for several runs compared with without treatment.

Conclusion

Heterogeneous CaO catalyst derived from waste chicken bone was synthesised using an improved hydration-dehydration method to cater to the drawbacks of lower surface area and poor activity of reported catalysts for biodiesel synthesis. Enhanced surface area and improved textural properties of C900-600 were the deciding factors for the better catalysis of C900-600 compared with C900. The preliminary characterisation proved the existence of hydroxyapatite, which are the active species for transesterification. However, the strength of basicity of C900-600 and C900 needs to be studied in the future for better insight into the effect of the hydration-dehydration treatment on the catalysis. To conclude, this research has successfully produced an active and recyclable catalyst for the sustainable production of biofuel within 45 min, employing 5 wt.% catalyst at 65 ℃ with insignificant loss of biodiesel after five regeneration studies, comparable to reported literature.

Acknowledgement

J. Andas acknowledges Universiti Teknologi MARA Perlis for providing financial assistance for the completion of the work.

References

1. Vasić, K., Hojnik Podrepšek, G., Knez, Ž. and Leitgeb, M. (2020). Biodiesel production using solid acid catalysts based on metal oxides. *Catalysts*, 10(2): 237.
2. Farooq, M., Ramli, A. and Naeem, A. (2015). Biodiesel production from low FFA waste cooking oil using heterogeneous catalyst derived from chicken bones. *Renewable Energy*, 76: 362-368.
3. Zik, N. A. F. A., Sulaiman, S. and Jamal, P. (2020). Biodiesel production from waste cooking oil using calcium oxide/nanocrystal cellulose/polyvinyl alcohol catalyst in a packed bed reactor. *Renewable Energy*, 155: 267-277.

4. AbuKhadra, M. R., Basyouny, M. G., El-Sherbeeny, A. M., El-Meligy, M. A., and Abd Elatty, E. (2020). Transesterification of commercial waste cooking oil into biodiesel over innovative alkali trapped zeolite nanocomposite as green and environmental catalysts. *Sustainable Chemistry and Pharmacy*, 17: 100289.
5. Pauline, J. M. N., Sivaramakrishnan, R., Pugazhen dhi, A., Anbarasan, T. and Achary, A. (2021). Trans esterification kinetics of waste cooking oil and its d iesel engine performance. *Fuel*, 285: 119108.
6. Navajas, A., Issariyakul, T., Arzamendi, G., Gandía, L. M. and Dalai, A. K. (2013). Development of eggshell derived catalyst for transesterification of used cooking oil for biodiesel production. Asia-*Pacific Journal of Chemical Engineering*, 8(5): 742-748.
7. Niju, S., Meera, K. M., Begum, S. and Anantharaman, N. (2014). Modification of egg shell and its application in biodiesel production. *Journal of Saudi Chemical Society*, 18(5): 702-706.
8. Mansir, N., Teo, S. H., Ibrahim, M. L. and Hin, T. Y. Y. (2017). Synthesis and application of waste egg shell derived CaO supported W-Mo mixed oxide catalysts for FAME production from waste cooking oil: Effect of stoichiometry. *Energy Conversion and Management*, 151: 216-226.
9. Borah, M. J., Das, A., Das, V., Bhuyan, N. and Deka, D. (2019). Transesterification of waste cooking oil for biodiesel production catalyzed by Zn substituted waste egg shell derived CaO nanocatalyst. *Fuel*, 242: 345-354.
10. AlSharifi, M. and Znad, H. (2019). Development of a lithium-based chicken bone (Li-Cb) composite as an efficient catalyst for biodiesel production. *Renewable Energy*, 136: 856-864.
11. Tan, Y. H., Abdullah, M. O., Kansedo, J., Mubarak, N. M., San Chan, Y. and Nolasco-Hipolito, C. (2019). Biodiesel production from used cooking oil using green solid catalyst derived from calcined fusion waste chicken and fish bones. *Renewable Energy*, 139: 696-70.
12. Khan, H. M., Iqbal, T., Ali, C. H., Javaid, A., and Cheema, I. I. (2020). Sustainable biodiesel production from waste cooking oil utilizing waste ostrich (Struthio camelus) bones derived heterogeneous catalyst. *Fuel*, 277: 118091.
13. Sirisomboonchai, S., Abuduwayiti, M., Guan, G., Samart, C., Abliz, S., Hao, X. and Abudula, A. (2015). Biodiesel production from waste cooking oil using calcined scallop shell as catalyst. *Energy Conversion and Management*, 95: 242-247.
14. Dehkordi, A. M., and Ghasemi, M. (2012). Transesterification of waste cooking oil to biodiesel using Ca and Zr mixed oxides as heterogeneous base catalysts. *Fuel Processing Technology*, 97: 45-51.
15. Lin, Y. C., Amesho, K. T., Chen, C. E., Cheng, P. C. and Chou, F. C. (2020). A cleaner process for green biodiesel synthesis from waste cooking oil using recycled waste oyster shells as a sustainable base heterogeneous catalyst under the microwave heating system. *Sustainable Chemistry and Pharmacy*, 17: 100310.
16. Carmelo Firlito (2020). The poultry industry and its supply chain in Malaysia: Challenges from the Covid-19 Emergency. [Access online 7 September 2021].
17. Hanny, A., Islam, M. R., Sumdani, M. G. and Rashidi, N. M. (2019). The effects of sintering on the properties of epoxy composites reinforced with chicken bone-based hydroxyapatites. *Polymer Testing*, 78: 105987.
18. Satraidi, H., Prasetyaningrum, A., Ningrum, A. S. and Dewi, R. O. N. (2019). Development of heterogeneous catalyst from chicken bone and catalytic testing for biodiesel with simultaneous processing. In *IOP Conference Series: Materials Science and Engineering*, 509(1): 012125.
19. Asikin-Mijan, N., Lee, H. V. and Taufiq-Yap, Y. H. (2015). Synthesis and catalytic activity of hydration–dehydration treated clamshell derived CaO for biodiesel production. *Chemical Engineering Research and Design*, 102: 368-377.

20. Khoo, W., Nor, F. M., Ardhyananta, H. and Kurniawan, D. (2015). Preparation of natural hydroxyapatite from bovine femur bones using calcination at various temperatures. *Procedia Manufacturing*, 2: 196-201.Obadiah, A., Swaroopa, G. A., Kumar, S. V., Jeganathan, K. R. and Ramasubbu, A. (2012). Biodiesel production from palm oil using calcined waste animal bone as catalyst. *Bioresource Technology*, 116: 512-516.
21. Yoosuk, B., Udomsap, P., Puttasawat, B. and Krasae, P. (2010). Modification of calcite by hydration–dehydration method for heterogeneous biodiesel production process: The effects of water on properties and activity. *Chemical Engineering Journal*, 162(1): 135-141.
22. Pan, Y., Alam, M. A., Wang, Z., Wu, J., Zhang, Y. and Yuan, Z. (2016). Enhanced esterification of oleic acid and methanol by deep eutectic solvent assisted Amberlyst heterogeneous catalyst. *Bioresource Technology*, 220: 543-548.
23. Corro, G., Sánchez, N., Pal, U. and Bañuelos, F. (2016). Biodiesel production from waste frying oil using waste animal bone and solar heat. *Waste Management*, 47: 105-113.
24. Tan, Y. H., Abdullah, M. O., Nolasco-Hipolito, C. and Taufiq-Yap, Y. H. (2015). Waste ostrich-and chicken-eggshells as heterogeneous base catalyst for biodiesel production from used cooking oil: Catalyst characterization and biodiesel yield performance. *Applied Energy*, 160: 58-70.
25. AlSharifi, M., and Znad, H. (2020). Transesterification of waste canola oil by lithium/zinc composite supported on waste chicken bone as an effective catalyst. *Renewable Energy*, 151, 740-749.
26. Adam, F., Andas, J., & Rahman, I. A. (2010). A study on the oxidation of phenol by heterogeneous iron silica catalyst. *Chemical Engineering Journal*, *165*(2), 658-667.
27. Aworanti, O. A., Ajani, A. O., Agarry, S. E., Babatunde, K. A., & Akinwumi, O. D. (2019). Evaluation of process parameters for biodiesel production from vegetable and palm waste frying oils using a homogeneous catalyst. *International Journal of Energy Engineering*, *9*(2), 25-35.
28. Girish, N., Niju, S. P., Begum, K. M. M. S., & Anantharaman, N. (2013). Utilization of a cost-effective solid catalyst derived from natural white bivalve clam shell for transesterification of waste frying oil. *Fuel*, 111: 653-658.

Malaysian Journal of Analytical Sciences (MJAS)
Published by Malaysian Analytical Sciences Society

POLYMER-FREE TRANSFER OF GRAPHENE-BASED MATERIAL DERIVED FROM COOKING PALM OIL BY CHEMICAL VAPOUR DEPOSITION TECHNIQUE

(Pemindahan Bebas Polimer bagi Bahan Berasaskan Grafin yang Disintesis dari Minyak Masak Kelapa Sawit Menggunakan Teknik Pemendapan Wap Kimia)

Azzafeerah Mahyuddin[1,2*], Abd. Khamim Ismail[1], Muhammad Firdaus Omar[1], Ainul Hakimah Karim[3]

[1]Department of Physics,
Faculty of Science, Universiti Teknologi Malaysia, 81310 Johor, Malaysia
[2]Department of Quality Engineering,
Universiti Kuala Lumpur, Malaysian Institute of Industrial Technology,
Persiaran Sinaran Ilmu, Bandar Seri Alam, 81750 Johor, Malaysia.
[3]Department of Instrumentation and Control Engineering,
Universiti Kuala Lumpur, Malaysian Institute of Industrial Technology,
Persiaran Sinaran Ilmu, Bandar Seri Alam, 81750 Johor, Malaysia.

[*]Corresponding author: azzafeerah@unikl.edu.my

Received: 17 December 2021; Accepted: 10 March 2022; Published: 30 October 2022

Abstract

Chemical vapour deposition (CVD) of cooking palm oil precursors with a nickel (Ni) catalyst is an established method to produce graphene-based materials. Nonetheless, transferring the graphene sheets from the substrate surface to a selected target substrate presents a major challenge. The utilisation of well-known poly (methyl methacrylate) (PMMA)-assisted graphene transfer promotes defects, impurities, folds, and wrinkles in the graphene sheets, thus affecting its properties. Consequently, the present study demonstrated a polymer-free graphene sheets transfer technique on a Ni substrate derived from cooking palm oil. A dropwise hexane layer substituted the PMMA supporting layer during the etching process to remove the Ni substrate. The quality of the graphene sheet was investigated with optical microscopy by employing a Leica DM1750 M microscope, scanning electron microscopy (SEM) with a Hitachi S-3400N, and Raman spectroscopy utilising a UniDRON automated microscope Raman mapping system with 514 nm laser excitation. Resultantly, macroscopically clean and crack-free graphene sheets were was obtained. Furthermore, the technique was less complicated than the PMMA-assisted transfer technique. The Raman spectra of the polymer-free method also revealed visible graphene peaks, which was absent in the PMMA-transferred samples.

Keywords: graphene, chemical vapour deposition, polymer-free transfer

Abstrak

Kaedah pemendapan wap kimia (CVD) yang menggunakan minyak masak kelapa sawit sebagai prekursor serta nikel sebagai pemangkin dalam proses sintesis bahan berasaskan grafin merupakan teknik yang telah lama dikenali. Namun, cabaran utama dalam menggunakan teknik CVD ini ialah proses pemindahan helaian grafin dari permukaan substrat asal ke substrat baru. Salah

satu kaedah pemindahan yang sering digunakan ialah kaedah pemindahan poli (metil-metakrilat) (PMMA) iaitu sejenis polimer yang akan menyebabkan helaian grafin mengalami kerosakan seperti kotor, berlipat dan berkedut. Oleh yang demikian, kajian ini akan menampilkan suatu teknik pemindahan grafin yang bebas polimer, disintesis di atas substrat nikel menggunakan minyak masak kelapa sawit. Lapisan heksana digunakan sebagai pengganti lapisan PMMA semasa proses penghakisan substrat nikel. Kualiti helaian grafin daripada hasil proses pemindahan ini dikaji menggunakan mikroskop optik (Leica DM1750 M), mikroskop pengimbasan elektron (SEM) dari Hitachi S-3400N dan spektroskopi Raman (system pemetaan mikroskop automatik Raman UniDRON dengan pengujaan laser 514 nm). Dapatan menunjukkan bahawa kaedah ini dapat menghasilkan helaian grafin yang bersih, tidak koyak serta pemprosesan yang tidak rumit berbanding teknik PMMA. Kaedah bebas polimer ini juga dapat menerbitkan puncak grafen menggunakan spektroskopi Raman berbanding kaedah pemindahan PMMA.

Kata kunci: grafin, kaedah pemendapan wap kimia, pemindahan bebas polimer

Introduction

Graphene is a two-dimensional (2D) substance comprising sp^2 carbon atoms in a gigantic aromatic structure [1]. The extraordinary performance of graphene in electrical [2], mechanical [3], and chemical [4] applications are promising, but previous studies revealed several gaps and shortcomings of the material. For instance, high-quality large-area graphene is not defect-free. Generally, graphene is synthesised through various methods, including mechanical, liquid, and chemical exfoliations, thermal decomposition of silicon carbide, chemical synthesis, and chemical vapour deposition (CVD). Among the techniques, CVD has been investigated as an alternative method to overcome inherent limitations in manufacturing large-area graphene with uniform thickness, high crystallinity, and fewer defects [5,6]. Traditional CVD techniques employ purified gaseous precursors, which are expensive, explosive, and require high-temperature growth, and accordingly, carbon waste has become a substitute precursor to synthesising functional carbonaceous material, such as graphene. The capability to fabricate graphene from such economic precursors would be cost-effective and sustainable for practical applications [7].

Recent studies have investigated the utilisation of several renewable natural carbon precursor sources for graphene production, namely camphor [8], reed (grass family) [9], cookies, chocolate, grass, roaches, dog faeces [10], and rice husks [11]. Numerous research reported employing cooking oil to manufacture graphene [12–14]. Most graphene growth via the CVD technique implement a post-grow polymer transfer from the surface catalyst onto the target substrate. The method introduces a complicated process in which a thin polymer layer is deposited on a graphene sheet that acts as a support to remove the metallic substrate by wet etching. The procedure induces defects, wrinkles, impurities, cracks, and stubborn polymer residues [15], which might obstruct the performance of graphene in subsequent applications [16, 17]. The graphene must be free to appreciate its extraordinary properties fully. Consequently, alternative routes of transfer methods such as polymer-free techniques are being explored to resolve the contamination problems [18, 19].

The main objective of the current work was to investigate a polymer-free method for improving the graphene transfer process synthesised from cooking palm oil through the CVD technique. The polymer-free approach employed hexane as a low-viscosity liquid organic layer, which would be very beneficial to stabilise and safeguard the graphene-based sheet generated during the metal substrate wet etching. The present study utilised hexane as the organic layer as it lacks heteroatoms and aromatic groups and is very volatile. Essentially, hexane could serve as a more efficient alternative to the polymer layer deposited on the graphene sheets in most currently practised transfer methods. A comparison study with the poly (methyl methacrylate) (PMMA) transfer method was also performed.

Materials and Methods

The CVD graphene growth

The graphene-based films in the present study were synthesised in a conventional CVD system equipped with a vacuum and argon (Ar) gas purging system. First, nickel (Ni) sheets were cut into 1 cm × 1 cm pieces and subjected to a specific cleaning protocol. Subsequently,

the Ni pieces were loaded into a CVD chamber to eliminate organic contaminations, impurities, and oil to increase the adhesion of the fabricated films on the substrate. The cleaning process began with an ultrasonic bath in ethanol for 10 minutes, followed by rinsing with distilled water. The metal sheets were then cleaned in isopropyl alcohol (IPA) for ten minutes, washed with distilled water, and blown dry with nitrogen (N_2) gas.

Graphene growth was conducted in a conventional thermal CVD furnace with a quartz tube. Two alumina boats were positioned in the heating region of the tube furnace. One boat was filled with a millilitre of cooking palm oil precursor, while the other contained several pieces of Ni sheets. The boat filled with the cooking palm oil precursor was covered with aluminium foil with tiny holes to avoid oil spillage during the heating process. The ends of the quartz tube were sealed. The air and impurities in the tubes were evacuated with a vacuum pump prior to purging with Argon (Ar) gas. The evacuation and Ar purging processes took approximately 30 minutes.

At this point, both boats filled with cooking palm oil and Ni sheets were present during the evacuation process. Subsequently, while the reaction tubes were in the Ar environment, the furnace temperature was raised to 400 ℃ at a 30 ℃ min^{-1} rate. The temperature was maintained for five minutes, during which the cooking palm oil was expected to reach its vaporisation point and flow towards the Ni sheets to start the graphene-based material growth. Subsequently, the furnace was switched off, and the sample was cooled to room temperature. After the effective thermal decomposition mechanism, carbon (C) from the vapourised cooking palm oil was anticipated to disperse evenly on the heated substrate surface.

Polymer-free graphene transfer

Sandpaper mechanical polishing was utilised to eliminate graphene-based material films on the backside of the Ni sheet. The sample was then subjected to metal etching. The graphene-based/Ni was gently placed onto the surface of 0.1 M iron (III) chloride [($FeCl_3$), System ≥ 98%] aqueous solution. Subsequently, the sample was floated (graphene-based side up) atop $FeCl_3$ solution (10 mL) for approximately a few seconds before a layer of hexane (Merck, ≤ 100%) was gently added to the top with a dropper. The hexane layer ensured that the graphene was not torn due to the surface tension associated with the etchant solution.

The Ni etching occurred in the $FeCl_3$ solution for approximately five hours, with the graphene-based sheet layer remaining trapped at the hexane and $FeCl_3$ aqueous solution interface. After etching, only the graphene sheet remained floating between the hexane and $FeCl_3$ solution, whereas the Ni sheet had fully submerged to the bottom of the etchant solution. The graphene sheet was then scooped out with a clean glass slide that was cleaned in a hot acetone bath for 10 minutes, methanol for 5 minutes, and rinsed with distilled water.

The sheet was transferred to a hexane/water interface at one to one ratio. The step was conducted to remove any remaining salt particles and debris from the back of the graphene layer. The graphene sheet was removed with a glass slide and let dry at room temperature after several hours. Fundamentally, the lack of heteroatoms and aromatic groups and volatility and rapid evaporation of hexane enabled the vapourisation and removal of hexane residues at room temperature.

The standard poly (methylmethacrylate) (PMMA) transfer method was performed on a sample set for comparison purposes. According to previous works, the polymer films were designed to protect graphene, which is fragile and could break. The solid support also helps reduce graphene wrinkles from the thermal expansion coefficient between the metal substrate and graphene.

A PMMA layer was spin-coated onto the surface of the graphene/Ni sheet at 1200 rpm for 30 s. Subsequently, the layer was annealed at 80℃ for 15 min to cure it, followed by etching in $FeCl_3$ to eliminate the Ni sheet. After an appropriate etching time, a clean glass slide was employed to scoop out the PMMA/graphene sheet. The sheet was rinsed with distilled water and baked at 60℃ for five minutes. The step was necessary to enhance contact adhesion and eliminate trapped water.

The second layer of PMMA was spin-coated on top of

the PMMA/graphene sheet and let dry at room temperature. Subsequently, the PMMA layer was washed with acetone and rinsed with distilled water. Finally, the graphene sheet was transferred to a clean glass substrate. The second PMMA layer was developed to reduce cracks in the transferred graphene [20]. Without the second layer of PMMA, tension might be imposed, resulting in large cracks on the graphene after the transfer process.

Sample characterisation

Evaluation of the initial quality of the graphene-based sheet was performed through optical microscopy by employing a material analysis microscope Leica DM1750 M. The surface morphology was assessed utilising scanning electron microscopy (SEM) (Hitachi S-3400N). Raman spectroscopy was conducted with UniDRON Automated Microscope Raman mapping system equipped with 514 nm laser excitation.

Results and Discussion

Optical microscopy

Optical microscopy analysed the coverage and distribution of the graphene-based films prior- and post-transfer process. Figure 1 displays the optical images of the graphene-based films on the Ni sheets after the CVD furnace growth process. Yellow, brown, purple, and grey layers covered the Ni sheet entirely. Similar results were reported by [12] as the colour might be the initial information of the graphene-based film structure.

The samples were subjected to two graphene transfer processes following the growth process, the PMMA and polymer-free transfers. Figure 2 illustrates the optical microscopy images of the graphene-based films after being polymer-free transferred on the glass substrate. A complete graphene-based film was obtained after transfer. The films exhibited colourful patterns dominated by grey and yellow. Some brownish colour from $FeCl_3$ residue was observed in the optical images, which was reported commonly occurring in transfer-free methods [21]. The phenomenon might arise from the graphene/Ni sample not correctly floated on the etching solution and correctly trapped in the hexane/ $FeCl_3$ solution interface. Moreover, the "soft support" from the hexane solution might be contaminated with the $FeCl_3$ etching solution.

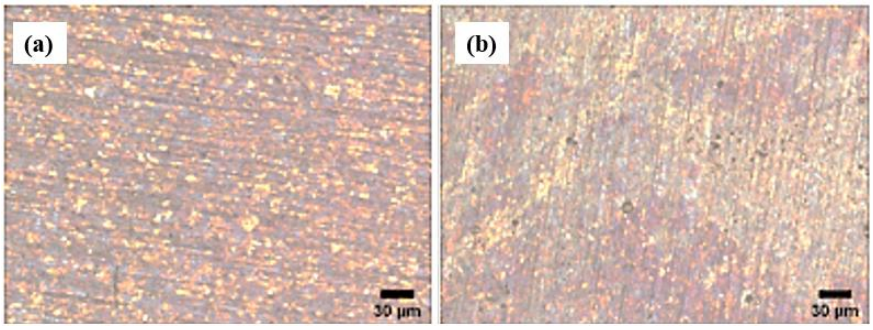


Figure 1. The optical images of two sample pieces of the graphene-based structure on Ni sheet grown at 400 °C

Due to cracks, the graphene-based films transferred with the PMMA technique demonstrated poor film quality. Additionally, some parts of the films were folded during the transfer process. The PMMA transfer process is often intricate, and the free-standing graphene could be broken due to surface tension as it dries [21]. Furthermore, some films failed to attach to the glass substrates, tended to break away, and immediately produced cracks when acetone dissolved the PMMA layer.

Trapped water between the PMMA and graphene and glass substrate throughout the transfer procedure might lead to folded layers and wrinkles. Consequently, the polymer-free transfer method offered a better option for transferring graphene-based films onto the desired substrate. Nonetheless, improvements to minimise the residues might be necessary for future works.

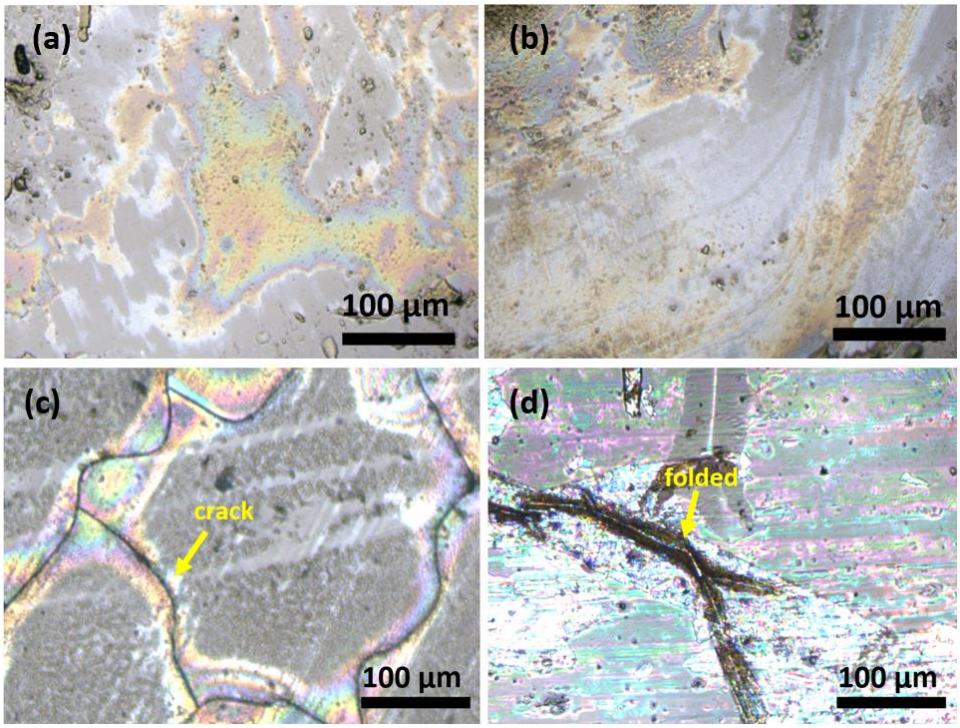


Figure 2. The optical images of the polymer transfer-free samples, denoted (a) and (b), and the PMMA transfer samples, represented by (c) and (d)

Scanning electron microscopy

The graphene films transfer is a crucial process that could affect the quality and performance of graphene in devices. Consequently, SEM was employed to record the surface morphology of the graphene films post-transfer onto the glass substrate. The measurements would further confirm the optical analysis results. Figure 3 exhibits the two specific spots focused on for the SEM assessment.

The PMMA transferred film sample observed suffered folded films and was heavily contaminated with PMMA residue. Although acetone wash was performed several times during the transfer process, the films still contained the residue. Meanwhile, the polymer-free transfer sample demonstrated a much cleaner and smoother surface. The low viscosity of the hexane layer on top of an aqueous etchant layer stabilised and safeguarded the free-standing graphene layer created during the Ni wet etch and water rinse.

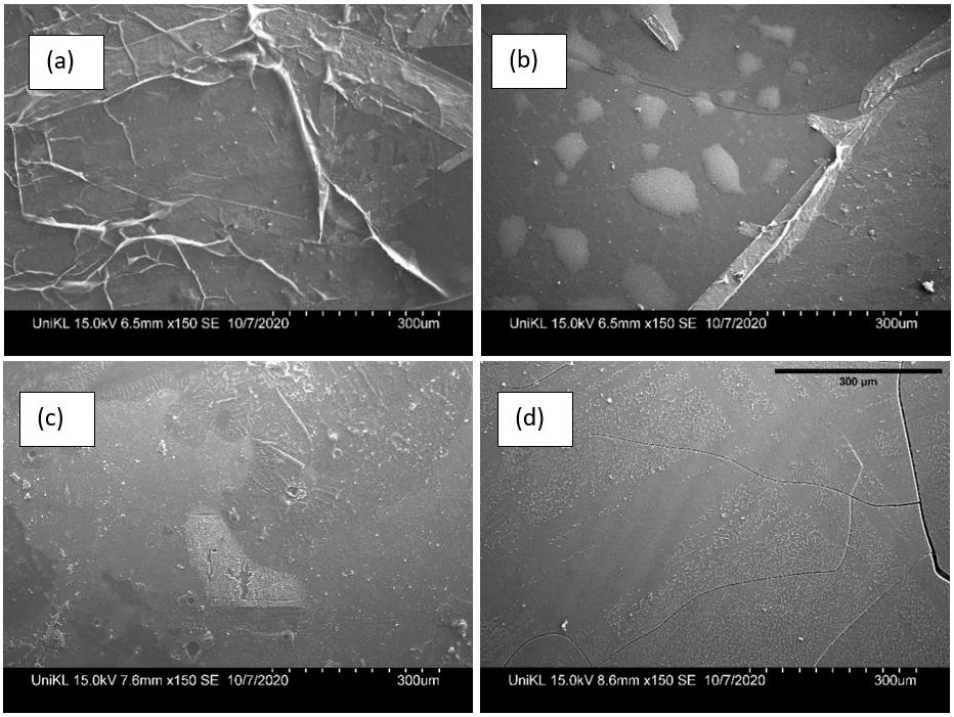


Figure 3. The SEM images of the graphene-based materials (a) and (b) after PMMA and (c) and (d) polymer-free transferred

Fundamentally, the hexane layer substituted the polymer layers currently employed in most graphene transfer procedures. The hexane layer prevented the graphene films from breaking due to the surface tension of the etching solution. The lack of heteroatoms and aromatic groups and high volatility of hexane resulted in no debris left on the graphene surface when transferred to the preferred substrate [19].

Raman spectroscopy

Raman analyses were performed on both samples to examine the synthesised graphene-based films. Figure 4 displays the Raman spectra of the films after being transferred onto the glass substrate utilising two different methods. No graphene structure was formed on the PMMA transfer samples and only PMMA peaks were detected (represented by pink dots). The observation might be due to the PMMA films not being fully dissolved with acetone. The films transferred with the polymer-free method exhibited two peaks that correlated to the D and G bands. The D band was observed at ~1348 cm^{-1}, while the G band was located at ~1543 cm^{-1}. For the sample analysed, the D and G bands demonstrated broad peaks, with no 2D peak, implying that the sample was a graphene oxide (GO) film. A previous study reported similar GO Raman spectra [22].

The D band peak was attributed to the structural defects and disorder of the graphite surfaces [23]. The G band was associated with the radial C-C stretching of the sp^2 bonded carbon [23]. Furthermore, the intensity of the D band peak to the intensity of the G band peak (I_D/I_G) ratio provided details on the defect density of the graphic structure. The I_D/I_G ratio for the GO sample was 0.99. The ratio would be helpful in future studies on the growth kinetics of the films. Shah et al. stated that as the rate of I_D/I_G decreased, the defects in the films were reduced, resulting from nucleation and the joining of the individual nucleation islands [24].

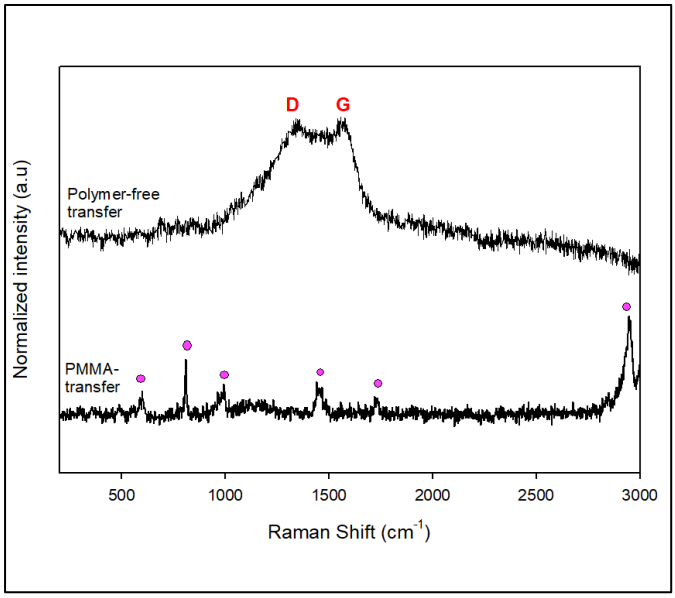


Figure 4. The Raman spectra of the PMMA transferred (bottom) and (above) polymer-free transferred samples

The multiple Raman spectra of four spots on the polymer-free transferred samples are displayed in Figure 5. Two peaks were detected at ~1354 cm^{-1} and ~1540 $cm^{-1,}$ respectively, thus corresponding to D and G peaks. No 2D peak (theoretically at 2670 cm^{-1}) was detected at any spot. Incomplete graphene film formation was observed at spots 1 and 2, which might be due to the lack of energy required for graphene formation to detach and transform the precursor material (hydrocarbon species).

Notably, the low growth temperature of 400°C was insufficient to decompose carbon feedstock from cooking palm oil. Nevertheless, the results might be fundamental in designing a CVD experimental setup. A similar situation was observed in soybean oils-graphene [25]. In the initial stages of the annealing process, the long carbon chains in the soybean oil precursor were thermally detached into methyl and ethyl gaseous carbon atoms. As the growth temperature was increased to 800°C, the carbon-building units began detaching into carbon atoms and dissolve into the Ni bulk. The short duration of the annealing process would then promote carbon atom dissolution in the Ni substrate. In particular, excessive precursor material preceded an oversaturation of deposited carbon in the bulk of the Ni and crystallised the graphite on the Ni surfaces.

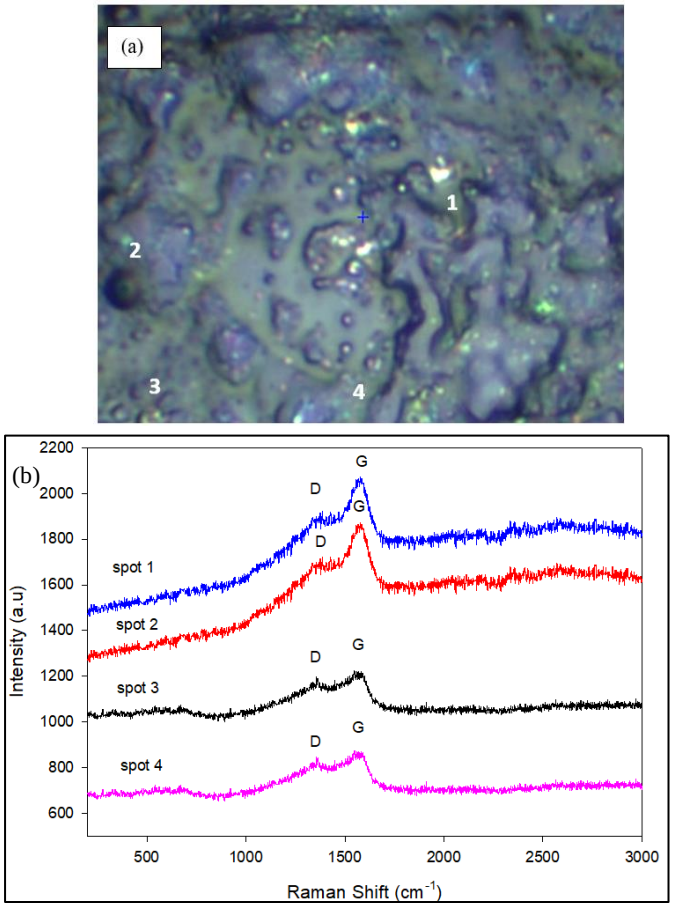


Figure 5. The (a) Four Raman mapping spots and (b) multiple Raman spectrum of the graphene films on a glass substrate of the polymer-free transferred sample

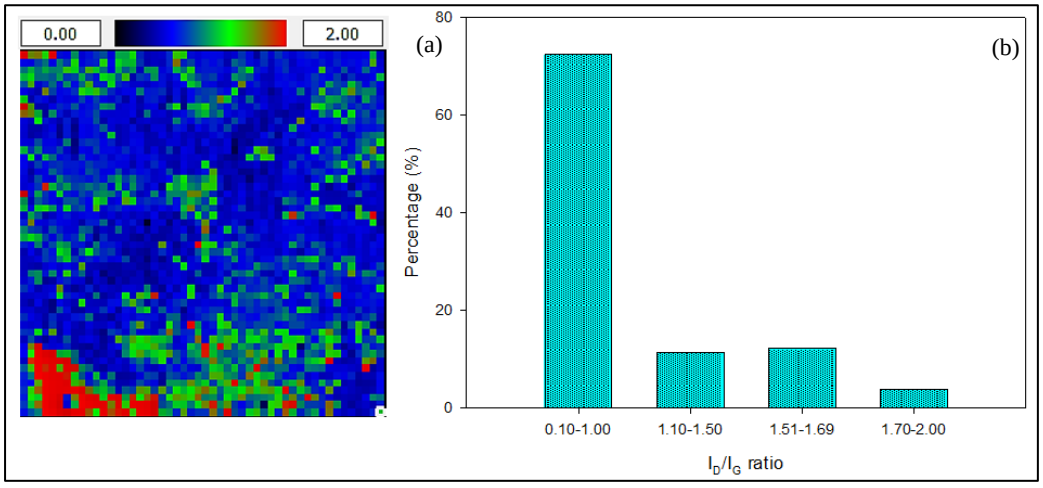


Figure 6. The (a) Raman mapping image of the graphene films on a glass substrate with I_D/I_G ratio within a 2 µm × 2 µm area and (b) histograms of the I_D/I_G ratio intensity percentages

Based on the Raman mapping of the I_D/I_G ratio and the intensity of the GO sample in Figure 6, the grown film was not uniformly distributed on the substrate. The non-uniform colour distribution provided fundamental knowledge of the substrate. The current study employed Ni polycrystalline sheet that was not subjected to polishing and etching treatment. The Ni surfaces in the carbon/polycrystalline Ni combination was densely populated by grain boundaries, particularly interplane grain boundaries, allowing carbon to accumulate throughout the segregation phase. Meanwhile, the single-crystalline surface on Ni (111) was very smooth, with almost no grain boundaries, allowing uniform carbon segregation, forming single-layer graphenes [26].

Histograms derived from the Raman mapping indicated the I_D/I_G ratio percentages. The ratio was divided into four groups, which corresponded to the most prominent family colours in the Raman mapping image, such as blue, dark green, light green, and red. Resultantly, the blue pixels were accounted for a ratio of less than 1.00, while the light green pixels had a 1.10–1.50 ratio, the dark green pixels exhibited a 1.51–1.69 ratio, and the red pixels was at a 1.70–2.00 ratio.

The counted pixels were presented in a histogram as a function of percentage. From the histogram, 70% of the I_D/I_G ratio was denominated by a ratio of less than 1.00. Meanwhile, 12, 11, and 3% corresponded to 1.51–1.69, 1.10–1.50, and 1.70–2.00 ratios, respectively. A high I_D/I_G ratio value corresponded to the high value of defects and disorders in the films [27]. Since 70% of the sample exhibited a ratio of less than 1.00, the film probably has a low value of defect and disorder. Consequently, hexane-assisted transfer promoted a clean graphene layer which might have enhanced the fundamental studies of graphene transfer.

Conclusion

The current study has successfully demonstrated an efficient polymer-free method to transfer graphene-based material sheets onto a substrate. The method was polymer contamination- and wrinkle-free. Compared to the PMMA transfer technique, the polymer-free method was easier to implement and less complicated. A significant advantage of hexane, contradictory to PMMA, was a smaller molecule with its high volatility, simplifying elimination from the graphene. The Raman studies demonstrated fundamental information in developing high-quality graphene-based material for future applications.

Acknowledgement

The authors would like to extend their gratitude to the Ministry of Higher Education for supporting the study under the FRGS, Registration Proposal No: FRGS/1/2019/STG07/UTM/02/17 (Vot no: R.J130000.7854.5F236). The work was also funded by the short-term research grant (str19062) from Universiti Kuala Lumpur-Malaysian Institute of Industrial Technology (UNIKL MITEC).

References

1. Novoselov, K. S., Geim, A. K., Morozov, S. V., Jiang, D. E., Zhang, Y., Dubonos, S. V., ... and Firsov, A. A. (2004). Electric field effect in atomically thin carbon films. *Science,* 306(5696): 666-669.
2. Avouris, P. (2010). Graphene: Electronic and photonic properties and devices. *Nano Letters*, 10(11): 4285-4294
3. Lee, C., Wei, X., Kysar, J.W., and Hone, J. (2008). Measurement of the elastic properties and intrinsic strength of monolayer graphene. *Science*, 321(5887): 385-388.
4. Paulus, G. L. C., Wang, Q. H. and Strano, M. S. (2013). Covalent electron transfer chemistry of graphene with diazonium salts. *Accounts of Chemical Research*, 46(1): 160-170.
5. Muñoz, R. and Gómez-Aleixandre, C. (2013). Review of CVD synthesis of graphene. *Chemical Vapor Deposition*, 19: 297-322
6. Yan, Z., Peng, Z. and Tour, J. M. (2014). Chemical vapor deposition of graphene single crystals. *Accounts of Chemical Research*, 47(4): 1327-1337
7. Kwon, S.-J., Seo, H.-K., Ahn, S. and Lee, T.-W. (2019). Value-added recycling of inexpensive carbon sources to graphene and carbon nanotubes. *Advanced Sustainable Systems*, 3(1): 1800016.

8. Aryal, H. R., Adhikari, S., Uchida, H., Wakita, K. and Umeno, M. (2016). Few layers isolated graphene domains grown on copper foils by microwave surface wave plasma CVD using camphor as a precursor. *2D Materials*, 3(1): 011009.
9. Rahbar Shamskar, K., Rashidi, A., Aberoomand Azar, P., Yousefi, M. and Baniyaghoob, S. (2019). Synthesis of graphene by in situ catalytic chemical vapor deposition of reed as a carbon source for VOC adsorption. *Environmental Science and Pollution Research*, 26(4): 3643-3650.
10. Ruan, G., Sun, Z., Peng, Z., and Tour, J. M. (2011). Growth of graphene from food, insects, and waste. *ACS Nano*, 5 (9): 7601-7607
11. Wang, Z., Yu, J., Zhang, X., Li, N., Liu, B., Li, Y., ... and Sun, L. (2016). Large-scale and controllable synthesis of graphene quantum dots from rice husk biomass: a comprehensive utilization strategy. *ACS Applied Materials & Interfaces*, 8(2): 1434-1439.
12. Rahman, S. F. A., Mahmood, M. R. and Hashim, A. M. (2014). Growth of graphene on nickel using a natural carbon source by thermal chemical vapor deposition. *Sains Malaysiana*, 43(8): 1205-1211.
13. Salifairus, M. J., Abd Hamid, S. B., Soga, T., Alrokayan, S. A., Khan, H. A. and Rusop, M. (2016). Structural and optical properties of graphene from green carbon source via thermal chemical vapor deposition. *Journal of Materials Research*, 31(13): 1947-1956.
14. Maarof, S., Ali, A. A. and Hashim, A. M. (2019). Synthesis of large-area single-layer graphene using refined cooking palm oil on copper substrate by spray injector-assisted CVD. *Nanoscale Research Letters*, 14(1): 143.
15. Chen, Y., Gong, X. and Gai, J. (2016). Progress and challenges in transfer of large-area graphene films. *Advanced Science*, 3(8): 1500343
16. Ng, J., Jones, T., Martinez-Velis, I., Wang, A., Hopkins, J. and Xie, Y. H. (2020). Effects of polymer residue on the pull-in of suspended graphene. *Journal of Vacuum Science & Technology B, Nanotechnology and Microelectronics: Materials, Processing, Measurement, and Phenomena*, 38(2): 023001.
17. Stehle, Y. Y., Voylov, D., Vlassiouk, I. V., Lassiter, M. G., Park, J., Sharma, J. K. ... and Polizos, G. (2017). Effect of polymer residues on the electrical properties of large-area graphene–hexagonal boron nitride planar heterostructures. *Nanotechnology*, 28(28): 285601.
18. Belyaeva, L. A., Fu, W., Arjmandi-Tash, H. and Schneider, G. F. (2016). Molecular caging of graphene with cyclohexane: transfer and electrical transport. *ACS Central Science*, 2 (12): 904-909.
19. Zhang, G., Güell, A. G., Kirkman, P. M., Lazenby, R. A., Miller, T. S. and Unwin, P. R. (2016). Versatile polymer-free graphene transfer method and applications. *ACS Applied Materials & Interfaces*, 8(12): 8008-8016.
20. Li, X., Zhu, Y., Cai, W., Borysiak, M., Han, B., Chen, D., ... and Ruoff, R. S. (2009). Transfer of large-area graphene films for high-performance transparent conductive electrodes. *Nano Letters*, 9(12): 4359-4363.
21. Suk, J. W., Kitt, A., Magnuson, C. W., Hao, Y., Ahmed, S., An, J., ... and Ruoff, R. S. (2011). Transfer of CVD-grown monolayer graphene onto arbitrary substrates. *ACS Nano*, *5*(9): 6916-6924.
22. Marcano, D. C., Kosynkin, D. V., Berlin, J. M., Sinitskii, A., Sun, Z., Slesarev, A., ... and Tour, J. M. (2010). Improved synthesis of graphene oxide. *ACS Nano*, 4(8): 4806-4814.
23. Kudin, K. N., Ozbas, B., Schniepp, H. C., Prud'Homme, R. K., Aksay, I. A. and Car, R. (2008). Raman spectra of graphite oxide and functionalized graphene sheets. *Nano Letters,* 8(1): 36-41.
24. Shah, J., Lopez-Mercado, J., Carreon, M. G., Lopez-Miranda, A. and Carreon, M. L. (2018). Plasma synthesis of graphene from mango peel. *ACS Omega,* 3(1): 455-463.
25. Seo, D. H., Pineda, S., Fang, J., Gozukara, Y., Yick, S., Bendavid, A., ... and Ostrikov, K. K. (2017). Single-step ambient-air synthesis of graphene from renewable precursors as electrochemical genosensor. *Nature Communications,* 8(1): 1-9.
26. Zhang, Y., Gomez, L., Ishikawa, F. N., Madaria, A., Ryu, K., Wang, C., ... and Zhou, C. (2010). Comparison of graphene growth on single-crystalline and polycrystalline Ni by chemical vapor deposition. *The Journal of Physical Chemistry Letters*, 1(20): 3101-3107.

27. Khalid, A., Mohamed, M. A., and Umar, A. A. (2017). Graphene growth at low temperatures using RF-plasma enhanced chemical vapour deposition. *Sains Malaysiana*, 46 (7): 1111-1117.

Malaysian Journal of Analytical Sciences (MJAS)
Published by Malaysian Analytical Sciences Society

CHARACTERIZATION AND TENSILE PROPERTIES OF POLYLACTIC ACID BIOCOMPOSITE FILLED MICROCRYSTALLINE CELLULOSE EXTRACTED FROM KENAF

(Ciri-Ciri Dan Sifat Tensil Poli(Asid Laktik) Biokomposit yang Diisi Selulosa Mikrohablur yang Diekstrak daripada Kenaf)

Norhazirah Azhar [1], Adzrie Baharudin[2], Zuliahani Ahmad[2,3 *], Rozyanty Rahman[3,4], Luqman Musa[3,4], Siti Nor Din[2], Nor Mazlina Abdul Wahab[2]

[1]Malaysian Nuclear Agency, Bangi, 43000 Kajang Selangor
[2]Department of Polymer Technology,
Faculty of Applied Sciences
Universiti Teknologi MARA, 02600 Arau, Perlis, Malaysia
[3]Advanced Polymer Group,
Center of Excellence Geopolymer & Department of Polymer Technology (CEGeoGTech),
Universiti Malaysia Perlis, 02600 Perlis, Malaysia
[4] Faculty of Chemical Engineering & Technology,
Universiti Malaysia Perlis, Kompleks Pusat Pengajian Taman Muhibah, 02600 Perlis, Malaysia

[*]Corresponding author: zuliahani@uitm.edu.my

Received: 17 November 2021; Accepted: 24 March 2022; Published: 30 October2022

Abstract

Microcrystalline cellulose (MCC) was successfully extracted from kenaf bast fiber plant (*Hibiscus cannabinus* L.) and incorporated into PLA biocomposite. The kenaf bast fiber undergone alkali treatment and bleaching prior to acid hydrolysis using 1M HNO_3 in obtaining MCC. Several characterizations on isolated MCC and PLA/MCC biocomposite conducted such as Fourier-transform infrared (FT-IR) spectroscopy and crystallinity index. Further characterization was made on the PLA/MCC biocomposite to study its mechanical and physical properties. FT-IR spectral indicated the successive elimination of non-cellulosic constituents in MCC. Differential scanning calorimetry (DSC) analysis revealed the percentage of crystalline region in the MCC obtained from kenaf bast fiber is higher at 88.53, making it suitable to be used as reinforcement filler in PLA biocomposite. Whilst tensile testing on various loading of PLA/MCC composites showed increment in tensile strength and elastic modulus but decrement in percent elongation. The optimum parameters were found at 9% MCC loading at 18.7 MPa in tensile strength attributed to well mixing of PLA and MCC and 88.53 crystallinity index. The potential application of PLA/MCC biocomposite to be used as food packaging.

Keywords: biocomposite, kenaf, microcrystalline cellulose, polylactic acid

Abstrak

Selulosa mikrohablur (MCC) berjaya diekstrak daripada tumbuhan gentian kulit kenaf (*Hibiscus cannabinus* L.) dan dimasukkan ke dalam biokomposit PLA. Gentian kulit kenaf menjalani rawatan alkali dan pelunturan sebelum dihidrolisis asid menggunakan

1M HNO_3 dalam mendapatkan MCC. Beberapa pencirian pada biokomposit MCC dan PLA/MCC terpencil dijalankan seperti Fourier-transform infrared (FT-IR) dan indeks kehabluran. Pencirian lanjut dibuat pada biokomposit PLA/MCC untuk mengkaji sifat mekanikal dan fizikalnya. Spektrum FT-IR menunjukkan penghapusan berturut-turut juzuk bukan selulosa dalam MCC. Analisis kalorimetri pengimbasan pembezaan (DSC) menunjukkan peratusan kawasan kristal dalam MCC yang diperoleh daripada gentian kulit kenaf adalah lebih tinggi iaitu 88.53, menjadikannya sesuai digunakan sebagai pengisi tetulang dalam biokomposit PLA. Manakala ujian tegangan ke atas pelbagai pemuatan komposit PLA/MCC menunjukkan peningkatan dalam kekuatan tegangan dan modulus keanjalan tetapi penyusutan dalam peratus pemanjangan. Parameter optimum didapati pada 9% pemuatan MCC pada 18.7 MPa dalam kekuatan tegangan yang dikaitkan dengan pencampuran telaga PLA dan MCC dan indeks sistaliniti 88.53. Potensi penggunaan biokomposit PLA adalah untuk digunakan dalam pembungkusan makanan.

Kata kunci: biokomposit, kenaf, selulosa mikrohablur, poli(asid laktik)

Introduction

Poly lactic acid (PLA) is biodegradable and renewable thermoplastic polyesters and one of commercially developed polyester from natural source [1]. It is eco-friendly due to its compostable, biodegradable and consumes carbon dioxide during the production. These advantages make PLA an alternative for other petrochemical-based polymers which mostly non-biodegradable. However, there are many limitations of PLA such as low thermal stability, low impact strength, brittleness and poor elongation. Hence, it is only applicable to products that do not require high performance such as disposable cups, cutlery, plastic bags and food packaging materials [1, 2]. Due to these limitations, many research and studies were done to improve both mechanical and physical properties of composite. Extensive study on the blending between PLA and other biodegradable polymer with reinforcing fillers either natural or even manmade has been carried out. Nano clay, natural fibers, cellulose whiskers and Microcrystalline cellulose (MCC) are among reinforcing filler used in composite preparation. Rice husk, oil palm biomass, kenaf and rice straw are among fibers used as reinforcing filler in composite preparation [2, 3].

MCC is a refined wood pulp which derived from cellulose which appears as inert white crystalline powder with no odor and also tasteless [1]. It is generally applied in composite, pharmaceutical, cosmetics, and food industries. Properties of MCC such as its high crystallinity, stiffness, water insolubility, renewability and biodegradability make them an excellent component for various manufacturing purpose. MCC commonly can be obtained from various woody plants and cotton. However, other new potential sources of MCC such as from kenaf, rice husk, oil palm biomass, rice straw and other plant wastes were investigated since the common woody plants and cotton sources make the production costly. It is believed the lignocelluloses contain cellulose (40-55%), hemicellulose (25-50%) and lignin (10-40%) suitable in obtaining the MCC [4]. Enzymatic, mineral acid or microorganism's hydrolysis are among methods used to isolate MCC. Nevertheless, due to high-cost method and lower crystallinity production of MCC using enzymatic hydrolysis becomes less preferable [5]. Previous researchers found that MCC extracted from various sources through acid hydrolysis process has potential to be used in biocomposite preparation [6].

Kenaf or scientifically known as Hibiscus cannabinus L [7] is a common wild plant found in tropical and subtropical countries such as in Asia and Africa. Kenaf is preferred for industrial purposes as an abundantly available renewable annual fiber crop. It is mainly used as high protein animal feed, building materials, in textiles, fuel and also in the composite preparation [7]. This lignocellulosic fiber plant made up of hemicelluloses, lignin and pectin which help cellulose fibrils to be attached together. Presence of both long outer bast (about 25-40%) that provides high quality pulp and inner short core fiber (about 60-75%) of low-quality pulp makes a unique property in kenaf. Research done by Abdul Khalil et al., [8] found that kenaf core fiber contain higher lignin and holocellulose whilst its bast fibers have higher in α-cellulose and ash content. Recently, many researches were done on extraction of microcrystalline cellulose and cellulose nanocrystals from kenaf bast fibers. The potential end usage of biocomposite obtained is in food packaging since it is

biodegradable and food grade PLA. Many biodegradable polymers such as starch, chitosan, polylactic acid (PLA), and chitin commonly used in food packaging. This is due to their low-cost, flexible and see-through properties [8, 9].

Therefore, this study is focusing on the incorporation of MCC extracted from kenaf fiber in PLA biocomposite since less information recorded on usage of kenaf as one of MCC resources. MCC was characterized to determine its morphology using Scanning Electron Microscope (SEM), determination of degree of crystallinity using Differential Scanning Calorimetry (DSC) and Fourier Transform Infrared (FTIR) to identify the molecular bonds exists. The PLA/MCC (kenaf) biocomposite produced undergone characterization using FTIR and tensile mechanical test to determine its tensile strength, elongation at break, and elastic modulus.

Materials and Methods

PLA was obtained from Toray Malaysia while kenaf was collected from Lembaga Kenaf Malaysia in Kelantan. Analytical grade of sodium hydroxide, NaOH (QRec, 99%) and Sodium hypochlorite, NaOCl (QRec, 5%) was used for alkali treatment and bleaching agents respectively whereas 1M HNO_3 was used in acid hydrolysis process. Chloroform was used to dissolve the PLA for solvent casting method.

Extraction of Microcrystalline Cellulose from Kenaf

10 g of dried kenaf was refluxed with 300 mL of NaOH at 80°C for 1 hour and 30 minutes. After alkali treatment, the kenaf pulp was refluxed at 30°C for 18 minutes using 350 mL of 5% sodium hypochlorite (NaOCl). Again, the solution was refluxed in 83 mL of 1M HNO_3 at 80°C for 30 minutes via mechanical stirring. Then the obtained mixture was filtered, washed several times with distilled water and dried at 105°C in oven until constant weight was achieved [2].

Characterization of MCC (Kenaf)

Functional group that presents in MCC was identified using Perkin Elmer FTIR spectrometer 1650 within wave number range of 4000 cm^{-1} to 400 cm^{-1}. As for DSC measurements, approximately 8-10 mg of MCC sample was run through Perkin Elmer Instruments Pyris DSC to determine its crystalline percentage using rate 5 min at 5°C and heated at rate of 10°C/min until 250°C The percent of crystalline region in the MCC was calculated using Equation 1. T_m was determined from the second scan cycle on the melting peak temperature. Scanning Electron Microscopy (SEM) was conducted via Hitachi Regulus 8220 in Universiti Sains Malaysia to analyse the morphological properties of the selected samples.

$$\text{Percent crystallinity, } X_c = (\Delta Hm \text{ (Treated)})/((\Delta H°m \text{ (Untreated)}) \times 100\% \quad (1)$$

Where, ΔH_m is the MCC obtained after acid hydrolysis (treated kenaf) while $\Delta H°_m$ is the untreated kenaf.

Preparation of PLA/MCC composite

Ten g of PLA was added into 100 mL chloroform to obtain 10% w/v solution in water bath at 60 °C for 2 hours until PLA was completely dissolved. Different amount of MCC (0, 1, 3, 5, 7 and 9 wt.%) was added into 10% w/v solution of PLA and sonicated for 5 minutes to ensure homogenous mixing. Then, casted on glass plates with dimension of 16 cm x 13 cm x 0.5 cm and left to dry at room temperature in 24 hours for complete removal of chloroform.

Characterization and mechanical testing of PLA/MCC biocomposite

The functional groups present in PLA/MCC was identified using Perkin Elmer FTIR spectrometer 1650 within wave number range of 4000 cm^{-1} to 400 cm^{-1}. Tensile testing was carried out using ASTM D882 type V standard test method using Instron Tensile Tester with 5 replicates for each formulation.

Water absorption test for PLA/MCC biocomposite.

ASTM D570 standard test method was used to determine the water absorption properties of PLA/MCC biocomposite. Five replicates of each composite with dimension of 1 cm x 3 cm were made using Equation 2.

Percent water absorption = ([Wet weight - Dry weight])/ (Dry weight) x 100 (2)

Results and Discussion

Fourier transform infrared (FTIR) analysis on isolated MCC

The FTIR spectral obtained were shown in Figure 1. The broad absorption band in at 3409 and 3407 cm^{-1} for untreated kenaf and MCC respectively indicate the presence of –OH group. The –OH groups of untreated kenaf slightly shifted toward lower wavelength after the treatment. This is probably due to weakening of hydrogen bonding in cellulose during acid hydrolysis process [10]. Absorption peaks at 2922 cm^{-1} for untreated kenaf and 2896 cm^{-1} for the MCC is related to CH_2 stretching frequency. The peaks that appeared due to water absorption between 1637 until 1654 cm^{-1} indicates the water presence in the sample [10]. Previous research by Rosa et al. [10] stated that bending modes of water molecules arise due to great interaction between water and cellulose molecules. On the other hand, peaks that appeared within 1035 to 1112 cm^{-1} are due to C-O stretching vibration within the ring of anhydroglucose in cellulose [11, 12]. The absorption peak presents at 1739 cm^{-1} for untreated kenaf is in line with Abdul Khalil et al. [8] and approximate to 1735cm^{-1} [13]. This signifies the presence of C=O stretching vibration of carbonyl group and acetyl group in the hemicelluloses [8]. Whilst for MCC, the absent peak for the C=O stretching indicates a complete removal of hemicelluloses during alkali treatment. The peak at 1424 cm^{-1} in untreated kenaf indicates the presence of lignin (1509-1609 cm^{-1}) whereas it is absent from MCC spectrum proves that lignin had been completely extracted out of the MCC [10].

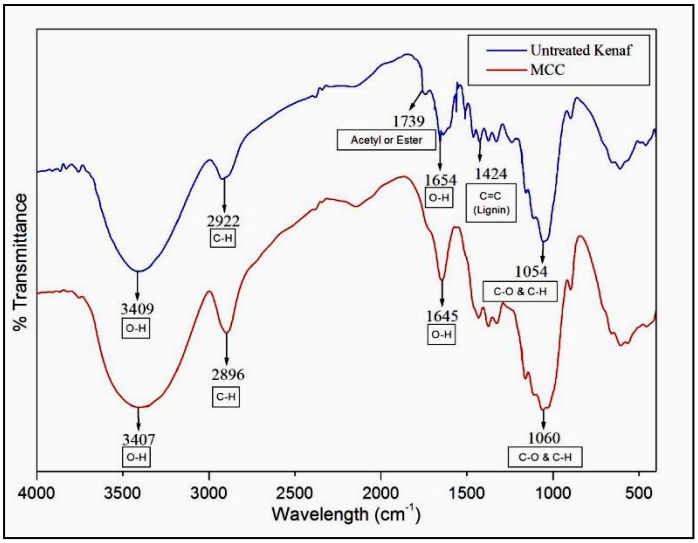


Figure 1. FT-IR spectroscopy for untreated kenaf and MCC from kenaf

FT-IR analysis was performed on pure PLA and PLA/MCC biocomposite in order to determine their interaction and phase behavior. Figure 2 shows the typical FT-IR spectra obtained. The characteristics peak for pure PLA is shown in Figure 2(a). The –OH stretching vibration is apparent at 3316-3843 cm^{-1}while the band observed in between 2850-3000 cm^{-1} is the asymmetric stretching of C-H. The peaks that attributes to C=O stretching vibration of carbonyl appears at 1630-1820 cm^{-1}. Peak that appears in between 1450-1475 cm^{-1} resulted from C-H bending of the -CH_3 group. The C-C bonding of alkane appears at 820-871 cm^{-1} almost similar with peak at 871 cm^{-1} by Haafiz *et* al. [9].

Whilst, PLA/MCC spectra for 1, 3, 5, 7 and 9 wt. % MCC is shown in the same Figure 2. From analysis, there is no new peak present upon gradual addition of MCC into PLA matrix. Haafiz et al. [9] suggest that the

interaction between PLA matrix and MCC most probably involve only physical interaction instead of chemical. Relatively small peaks of pure PLA for –OH stretching and bending that appear at 3200-3400 cm^{-1} gradually absent upon increasing MCC content. Identical result was described by Haafiz et al. [9] in PLA/MCC biocomposite extracted from rice husk.

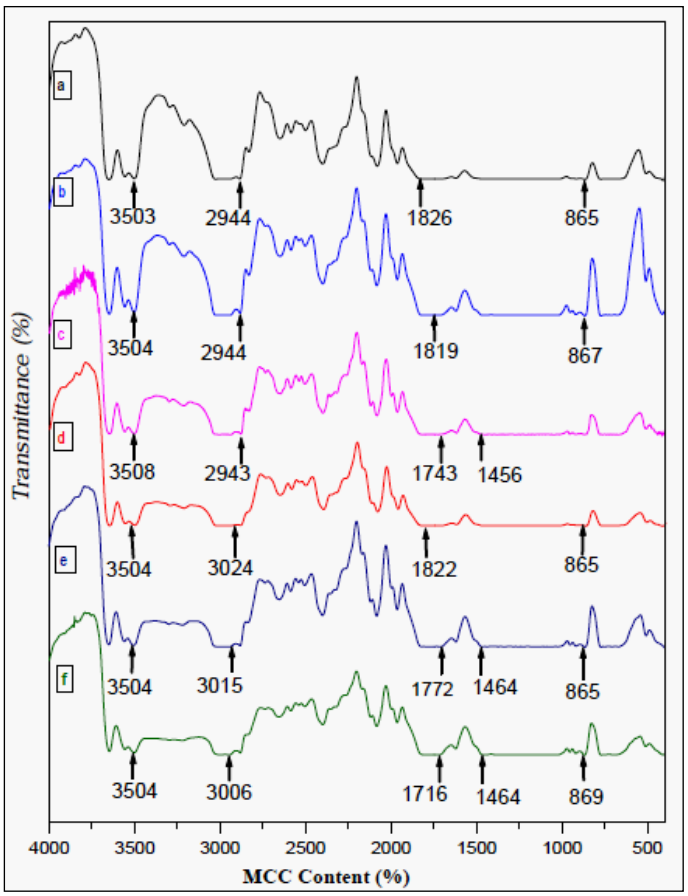


Figure 2. FT-IR spectroscopy for (a) PLA and PLA/MCC composite with different MCC loadings ((b) 1%, (c) 3%, (d) 5%, (e) 7% and (f) 9%)

Differential scanning calorimetry analysis on isolated MCC

Table 1 indicates some thermal characteristics obtained for kenaf, PLA, PLA/MCC. It is shown that melting enthalpies (ΔH_m) obtained for both untreated kenaf bast fiber and MCC extracted from kenaf is 492.38 and 435.89 J/g respectively. The T_m for PLA/MCC composite of 1, 3, 5, 7 and 9 wt. % MCC is in between 152-153°C which is not very different with T_m for pure PLA (152.9°C) due to MCC having nucleating effect on PLA [2]. The degradation of PLA composite lowers its melting point since the length of molecular chains is reduced [14]. It is believed the addition of chemical additives to enhance the PLA for other purpose especially in manufacturing industries decreased the melting point. The percent crystallinity was measured according to formula in Equation. 1. The percentage for crystalline region in MCC calculated is 88.53%. The effect of higher crystallinity in MCC obtained is manifested in increment of tensile and young modulus properties. This indicated physical crosslinking taken place and hindered the mobility of polymer matrix. It is believed highly crystalline MCC acted as nucleating agents and restricted the mobility of the polymer chains

by arranging the crystal lattice structure [1]. The results are in good agreement with SEM images Figure 3(b) showing rough surfaces found at 9 wt.% of PLA/MCC. This is in agreement with Nur Aimi et al. reported that higher crystallinity of the fiber improves the mechanical properties of the composites [15].

Table 1. DSC Characteristic of kenaf, MCC, PLA and PLA/MCC biocomposite

Characteristics	Kenaf	MCC	PLA	PLA/MCC (9%)
Melting Temperature T_m(0c)	80.38	74.83	168	153
Glass transition Temperature T_g(0c)	45	55	58	63

Scanning electron microscope image analysis

Fracture surfaces of pure PLA and PLA/MCC composite for 9 wt.% were analyzed using SEM to investigate the morphology of microcrystalline cellulose embedded in the PLA matrix. Smooth fracture surface can be observed on the pure PLA as shown in Figure 3(a) which can be categorized as ductile fracture due to amorphous property of PLA itself. Whilst, uneven fracture shown for both composite filled MCC (Figure 3b). Smooth fracture surface can be observed on the pure PLA as shown in Figure 3a. Mukherjee et al. [16] suggested that uneven fracture of composites possibly take place after the addition of MCC cause a significant deformation on PLA matrix as compared. It is also indicating that more force is needed to fail the samples during testing.

Through observation, the diameter of 5 and 9 wt.% MCC content measured is approximately 25.55 μm and 17.69 μm respectively (Figure 3(c) and (d)) and there is no significant filler agglomeration observed. This is the evidence of good interaction between MCC and the PLA matrix that helps to reinforce the composite as it manifested in tensile strength and modulus. In addition, only a little irregularity in the MCC shape found in both samples which is a good feature for filler. According to Yussuf et al. [17], the irregularities shape of filler in polymer matrix lowers the mechanical strength of the composite because it reduces the ability of filler to transfer the applied stress from the polymer matrix [16]. Since the size of MCC is small enough to lower the irregularities shape in the composite, mechanical properties of the PLA/MCC composite are enhanced.

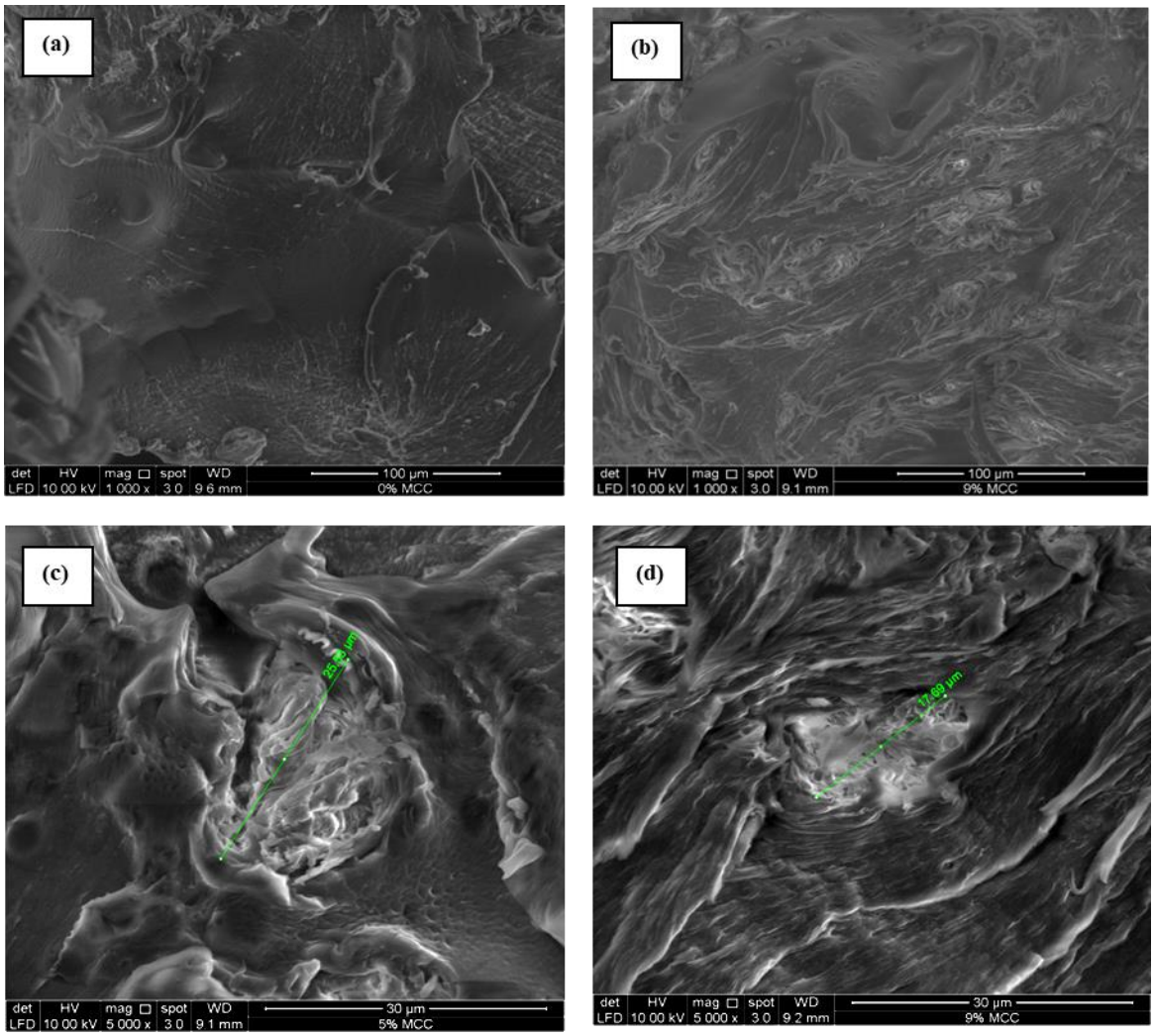


Figure 3. (a) Scanning electron micrographs of fractured surface of pure PLA at 1000, (b) 9 wt.% PLA/MCC at 1000x, (c) 5 wt.% PLA/MCC biocomposite at 5000x, and (d) 9 wt.% PLA/MCC biocomposite at 5000x

Tensile properties of PLA/MCC (kenaf) biocomposite

The tensile strength of PLA/MCC blends is higher than that of pure PLA as shown in Figure 4. For 1 and 3 wt. % composites, slight increment of tensile strength can be observed compared to the pure PLA. Whereas, at 5 to 9 wt.% MCC contents in PLA composite shows higher tensile strength which is 1.2 to 1.4-fold greater than the pure PLA due to good dispersion between MCC and PLA resulting in good interaction between them. Previous study by Haafiz et. al. indicates that MCC have higher tendency to agglomerate which makes it interact and distributed poorly in PLA matrix [9]. As proven by analysis under SEM, no significant agglomeration observed in all the composites thus it can be suggested that the interaction and distribution of MCC in the PLA matrix is good. Furthermore, it can be seen from the SEM fractography there is good interaction between PLA and MCC. This is because of the MCC possess a high aspect ratio giving way to better interaction and finally increased the tensile strength. Figure 5 illustrate the result for elastic modulus. PLA/MCC blends of 1, 3 and 5 wt.% MCC in PLA show improvement compared to the pure PLA with order of 217.94, 226.83 and 236.52 MPa correspondingly. Nevertheless, as MCC contents increased more than 5 wt.%, the elastic modulus

maintained at average value approximately at 237 MPa. According to Haafiz et al. the increasing of MCC loading may be attributed by common filler/polymer features such as increasing rigidity effect, hydrogen bonding and also the percentage of crystalline region in the filler [9].

On contrary, PLA/MCC blend shows a gradual reduction for percent elongation when more MCC added as shown in Figure 6. The values then retained between 39 to 40% elongation for 5, 7 and 9 wt.% MCC loading with average of 3.2-fold lower than pure PLA. This might due to properties of MCC itself which possess strong hydrophilic properties compared to PLA that slightly hydrophilic cause poor interfacial adhesion between them [14]. Stiffening action by MCC may cause the restriction on chain movement of PLA molecules during testing [17]. In contrast, PLA/MCC blend shows a gradual reduction for percent elongation when more MCC added as shown in Figure 6. The values then retained between 39 to 40% elongation for 5, 7 and 9 wt.% MCC loading with average of 3.2-fold lower than pure PLA. This might due to properties of MCC itself which possess strong hydrophilic properties compared to PLA that slightly hydrophilic cause poor interfacial adhesion between them [12]. Stiffening action by MCC may cause the restriction on chain movement of PLA molecules during testing [15].

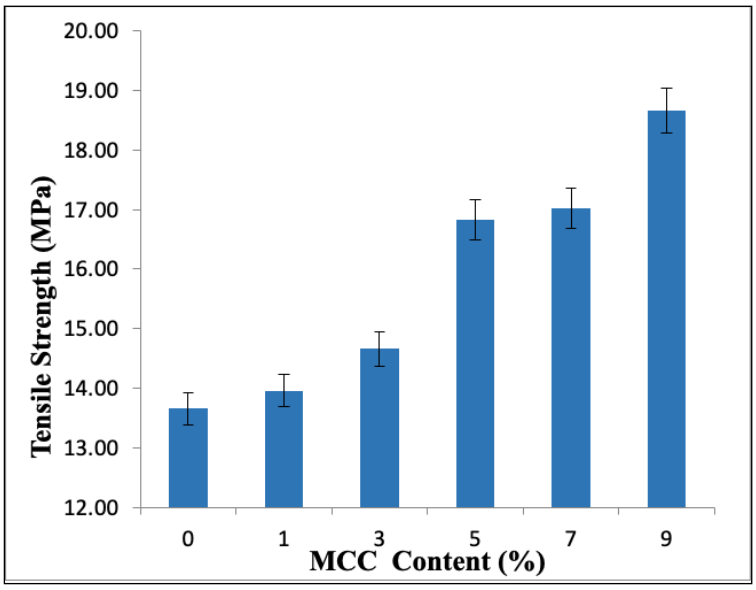


Figure 4. The effect of MCC content on the Tensile strength of PLA biocomposite

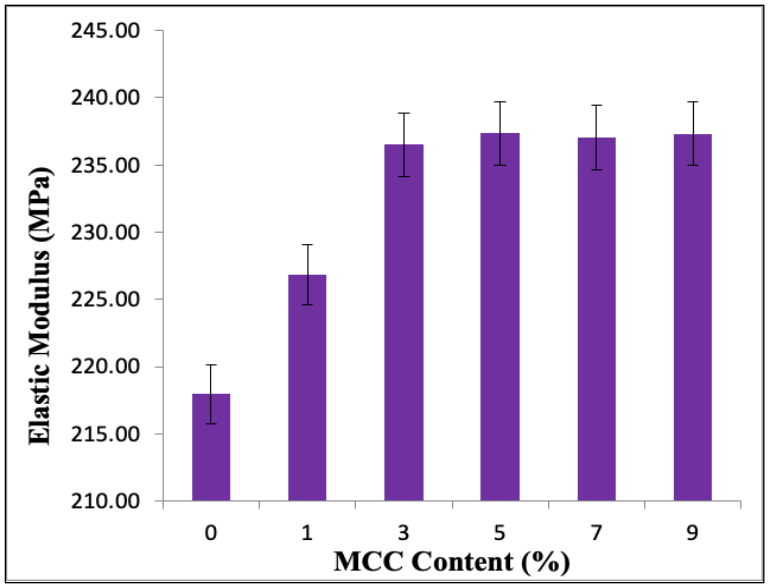


Figure 5. The effect of MCC content on the tensile modulus of PLA biocomposite

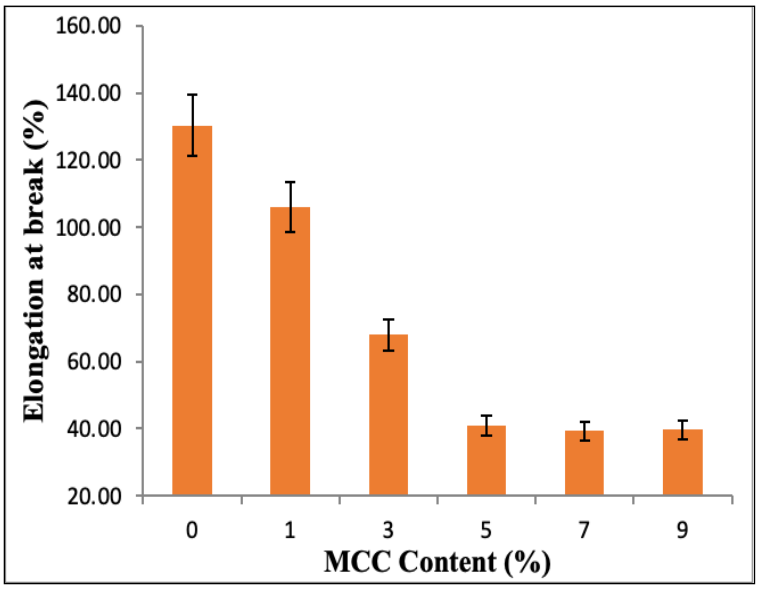


Figure 6. The effect of MCC content on the elongation at break of PLA biocomposite

Water immersion testing

The percentage of water absorption and thickness swelling of PLA/MCC composites increases upon MCC addition as shown in Figure 7 and 8. However, the water absorption does not linearly increase and might due to dispersion of MCC in the matrix not good enough for some of the composite. For an example the percentage of water absorption for 1% MCC is closer to pure PLA compared to 3 wt. % MCC. Based on the result obtained, it shows significant increment in the water absorption and thickness swelling with the increasing of MCC content after 1 % loading. It gives a better picture that

addition of MCC in the composite will help to boost the degradation of PLA since water is one of the important aspects in hydrolysis process as mentioned by Rocca-Smith et al. [18]. The process is the hydrolysis induced by water penetration and diffusion is where the penetration water into the PLA is driving force the biodegradability of the PLA [19]. From the result obtained also show that pure PLA have low water absorption capability. So that beside the mechanical improvement, addition of MCC into the PLA also can contributed to the degradability of the material which significantly important aspect as bio-based thermoplastic.

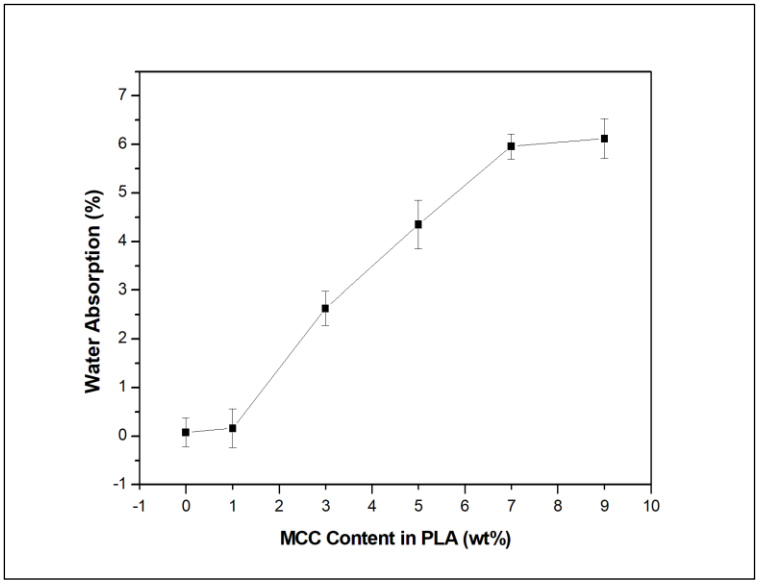


Figure 7. Water absorption of various MMC PLA biocomposite

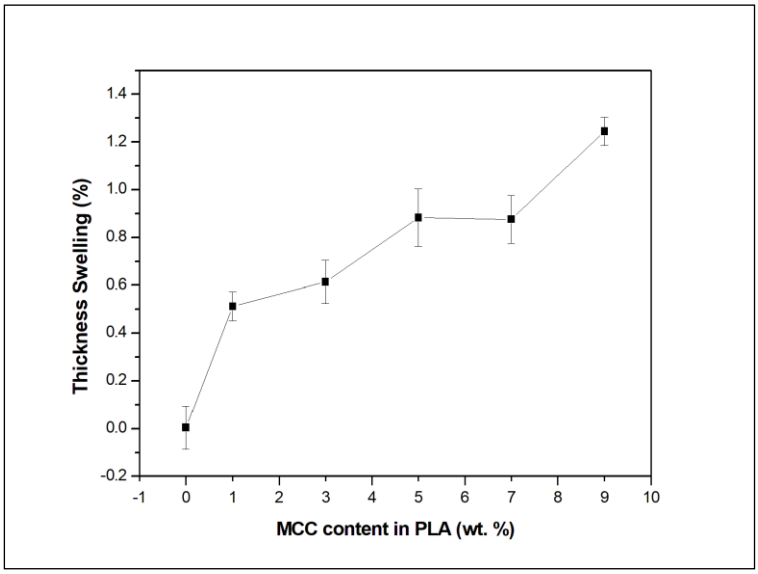


Figure 8. Thickness Swelling of Various MMC PLA Biocomposite

Conclusion

The finding from the research shows that MCC from kenaf bast fiber has been successfully isolated and characterized. The uniqueness of the research is the combination of MCC isolated from kenaf and PLA in biocomposite preparation since it possesses the biodegradability and renewability properties. In addition, Cellulose was purified using general chemical treatments which are alkali treatment and bleaching. The alkali treatment was used to remove hemicelluloses whilst bleaching was done for delignification purpose. Extraction of MCC from the treated kenaf fiber was done via acid hydrolysis 1M HNO_3. Characterization using FT-IR spectrum obtained for both kenaf and MCC proved a successful elimination of hemicelluloses and lignin from MCC. The analysis under DSC shows that percent crystallinity of MCC is high which validated that acid hydrolysis does not alter the crystal structure of cellulose in the kenaf fiber. The isolation of MCC from kenaf by means of acid hydrolysis is sufficient to produce high crystalline MCC. PLA/MCC biocomposite was successfully fabricated with addition of 1, 3, 5, 7, and 9 wt.% MCC through solvent casting technique. FTIR spectra of showed insignificant changes in the peak position of PLA/MCC biocomposite suggest that PLA matrix and MCC only physically interacted. Mechanical properties of PLA/MCC biocomposite proved an increasing tensile strength and elastic modulus due to stiffening action of MCC upon increasing MCC content. Conversely, elongation at break decreased when MCC content increased. This caused by brittleness property of crystalline region in MCC causing subsequent restriction on the biocomposite chain movement. Observation under SEM revealed a good dispersion of MCC in PLA matrix which gave reason for the increasing in tensile strength of the biocomposite. Physical test was done upon PLA/MCC to determine the water absorption properties of the biocomposite. Upon addition of MCC, water absorption of the composite showed increment as MCC content added due to hydrophilic properties of MCC which important for degradability of PLA. Thus, it can be concluded that addition of 1 to 9 wt. % MCC into PLA matrix gave significant effect.

Acknowledgement

The author would like to thank Faculty of Applied Sciences (FSG), Universiti Teknologi MARA (UiTM) Perlis for providing the facilities and laboratory materials used in this research project.

References

1. Bhasney, S. M., Kumar, A. and Katiyar, V. (2020). Microcrystalline cellulose, polylactic acid and polypropylene biocomposites and its morphological, mechanical, thermal and rheological properties. *Composites Part B: Engineering*, 184: 107717.
2. Bhasney, S. M., Bhagabati, P., Kumar, A. and Katiyar, V. (2019). Morphology and crystalline characteristics of polylactic acid [PLA]/linear low-density polyethylene [LLDPE]/microcrystalline cellulose [MCC] fiber composite. *Composites Science and Technology*, 171: 54-61.
3. Zuliahani, A., Nurul Nadhirah, R., Rozyanty, A. R., Nawawi, W. I. and Nor Hanani, A. B. (2016). Crystallinity, tapping and bulk density of microcrystalline cellulose (MCC) isolated from rice husk (RH). In *Applied Mechanics and Materials*, 835: 272-276.
4. Sadalage, P. S. and Pawar, K. D. (2021). Production of microcrystalline cellulose and bacterial nanocellulose through biological valorization of lignocellulosic biomass wastes. *Journal of Cleaner Production*, 327: 129462.
5. Nampoothiri, K. M., Nair, N. R. and John, R. P. (2010). An overview of the recent developments in polylactide (PLA) research. *Bioresource technology*, 101(22): 8493-8501.
6. Adel, A. M., Abd El-Wahab, Z. H., Ibrahim, A. A. and Al-Shemy, M. T. (2011). Characterization of microcrystalline cellulose prepared from lignocellulosic materials. Part II: Physicochemical properties. *Carbohydrate Polymers*, 83(2): 676-687.
7. Ahmad, Z., Roziaizan, N. N., Rahman, R., Mohamad, A. F. and Ismail, W. I. N. W. (2016). Isolation and characterization of microcrystalline cellulose (MCC) from rice husk (RH). In *MATEC Web of Conferences*, 47: p. 05013.

8. Khalil, H. A., Yusra, A. I., Bhat, A. H. and Jawaid, M. (2010). Cell wall ultrastructure, anatomy, lignin distribution, and chemical composition of Malaysian cultivated kenaf fiber. *Industrial Crops and Products*, 31(1): 113-121.
9. Haafiz, M. M., Eichhorn, S. J., Hassan, A. and Jawaid, M. (2013). Isolation and characterization of microcrystalline cellulose from oil palm biomass residue. *Carbohydrate polymers*, 93(2): 628-634.
10. Radzi, M. K. F. M., Muhamad, N., Akhtar, M. N., Razak, Z. and Foudzi, F. M. (2018). The effect of kenaf filler reinforcement on the mechanical and physical properties of injection moulded polypropylene composites. *Sains Malaysiana*, 47(2): 367-376.
11. Sun, X., Lu, C., Liu, Y., Zhang, W. and Zhang, X. (2014). Melt-processed poly (vinyl alcohol) composites filled with microcrystalline cellulose from waste cotton fabrics. *Carbohydrate Polymers*, 101: 642-649.
12. Rosa, S. M., Rehman, N., de Miranda, M. I. G., Nachtigall, S. M. and Bica, C. I. (2012). Chlorine-free extraction of cellulose from rice husk and whisker isolation. *Carbohydrate Polymers*, 87(2): 1131-1138.
13. Chaiwutthinan, P., Pimpan, V., Chuayjuljit, S. and Leejarkpai, T. (2015). Biodegradable plastics prepared from poly (lactic acid), poly (butylene succinate) and microcrystalline cellulose extracted from waste-cotton fabric with a chain extender. *Journal of Polymers and the Environment*, 23(1): 114-125.
14. Ibrahim, M. M., El-Zawawy, W. K., Jüttke, Y., Koschella, A. and Heinze, T. (2013). Cellulose and microcrystalline cellulose from rice straw and banana plant waste: preparation and characterization. *Cellulose*, 20(5): 2403-2416.
15. Aimi, M. N., Anuar, H., Maizirwan, M., Sapuan, S. M., Wahit, M. U. and Zakaria, S. (2015). Preparation of durian skin nanofibre (DSNF) and its effect on the properties of polylactic acid (PLA) biocomposites. *Sains Malaysiana*, 44(11): 1551-1559.
16. Mukherjee, T., Sani, M., Kao, N., Gupta, R. K., Quazi, N. and Bhattacharya, S. (2013). Improved dispersion of cellulose microcrystals in polylactic acid (PLA) based composites applying surface acetylation. *Chemical Engineering Science*, 101: 655-662.
17. Yussuf, A. A., Massoumi, I. and Hassan, A. (2010). Comparison of polylactic acid/kenaf and polylactic acid/rise husk composites: the influence of the natural fibers on the mechanical, thermal and biodegradability properties. *Journal of Polymers and the Environment*, 18(3): 422-429.
18. Rocca-Smith, J. R., Whyte, O., Brachais, C. H., Champion, D., Piasente, F., Marcuzzo, E., ... & Karbowiak, T. (2017). Beyond biodegradability of poly (lactic acid): physical and chemical stability in humid environments. *ACS Sustainable Chemistry & Engineering*, *5*(3): 2751-2762.
19. Wan, L., Zhou, S. and Zhang, Y. (2019). Parallel advances in improving mechanical properties and accelerating degradation to polylactic acid. *International Journal of Biological Macromolecules*, 125: 1093-1102.

Malaysian Journal of Analytical Sciences (MJAS)
Published by Malaysian Analytical Sciences Society

MORPHOLOGICAL STUDIES OF SILICON CARBIDE THIN FILM DEPOSITED BY VERY HIGH FREQUENCY – PLASMA ENHANCED CHEMICAL VAPOUR DEPOSITION THROUGH GAS DILUTION ADJUSTMENT

(Kajian Morfologi Filem Nipis Silikon Karbida Yang Dimendapkan oleh Frekuensi Sangat Tinggi – Pemendapan Wap Kimia Dipertingkatkan Plasma dengan Melaraskan Pencairan Gas)

Zainur Atika Ibrahim, Muhammad Firdaus Omar*, Abd Khamim Ismail

Department of Physics, Faculty of Sciences,
Universiti Teknologi Malaysia, 81310 Skudai, Johor Bahru, Malaysia

**Corresponding author: firdausomar@utm.my*

Received: 15 December 2021; Accepted: 27 March 2022; Published: 30 October 2022

Abstract

Dilution of gas was deployed to investigate the surface morphology and the surface topography of Silicon Carbide (SiC) film deposited using Very High Frequency – Plasma Enhanced Chemical Vapour Deposition (VHF-PECVD) technique. The deposition process of SiC thin film was performed with 150 MHz excitation frequency and 20 W radio frequency (RF) power. The argon and hydrogen carrier gas dilution was set to 5 sccm. Silane (SiH_4) and methane (CH_4) functioned as precursor gases and their flow rates were fixed at 2 and 8 sccm, respectively. Direct observations revealed that the surface morphology of deposited nanostructured-silicon carbide (ns-SiC) films in all samples had layer-island structure with varied island density and size formation above the critical layer thickness. Next, surface topography and roughness of the deposited SiC films were examined using Atomic Force Microscopy (AFM) in non-contact mode. As a result, all samples displayed different roughness, surface topography structure, and average grain diameter.

Keywords: silicon carbide, plasma enhanced chemical vapour deposition, dilution gas

Abstrak

Pencairan gas digunakan untuk menyiasat morfologi permukaan dan topografi permukaan filem silikon karbida (SiC) yang dimendap menggunakan kaedah Frekuensi Sangat Tinggi – Pemendapan Wap Kimia Dipertingkatkan Plasma (VHF-PECVD). VHF-PECVD dikendalikan menggunakan frekuensi pengujaan 150 MHz pada kuasa gelombang radio (RF) 20 W. Sementara itu, pencairan gas pembawa argon dan hidrogen ditetapkan kepada 5 sccm. Gas pendahulu silane (SiH_4) dan metana (CH_4) masing-masing ditetapkan pada 2 dan 8 sccm. Pemerhatian langsung mendedahkan bahawa morfologi filem nanostruktur-silikon karbida (ns-SiC) yang dideposit dalam semua sampel mempamer sktruktur lapisan-pulau dengan ketumpatan pulau yang berbeza dan pembentukan saiz di atas ketebalan lapisan kritikal. Topografi permukaan dan kekasaran filem SiC yang dimendap diperiksa dengan Mikroskopi Daya Atom (AFM) dalam mod bukan sentuhan. Hasil kajian menunjukkan bahawa semua sampel mempunyai kekasaran struktur topografi permukaan dan diameter butiran purata yang berbeza.

.

Kata kunci: silikon karbida, pemendapan wap kimia dipertingkatkan plasma, gas pencairan

Introduction

Nanoscience and nanomaterial are the fastest growing research areas to date since the introduction to nanotechnology by Richard Feynman [1]. Material properties improve when the material is reduced to nanoscale [2-7]. The cutting-edge trend of nanomaterial applications includes electronic devices for extreme environments such as high temperature, high corrosion, high nuclear radiation, and high electromagnetic radiation - the importance of using unique material as resource in extreme conditions. Silicon carbide (SiC) is a relatively new semiconductor material that has been gaining popularity in high-frequency and high-power applications. Since several decades ago, SiC has been identified as a potential material for use in extreme conditions due to its mechanical properties, chemical inertness, thermal stability, high oxidation resistance, high hardness, large band gap, and relatively lightweight [1, 8-11]. In fact, SiC has a crucial role in some optoelectronic device applications [11-13], including light-emitting diodes (LEDs), electroluminescent devices [14], and thermoelectric cooling (TEC) devices [15]. Nevertheless, low-quality material has hindered the development of high-quality devices [16].

Several methods that can be used to synthesise SiC thin films are hot wall chemical vapour deposition (HWCVD), plasma enhanced CVD (PECVD), electron cyclotron resonance CVD (ECR-CVD), magnetron sputtering, pulsed laser deposition (PLD), ion implantation, and molecular beam epitaxy (MBE) [8, 17]. Many studies revealed that high-quality thin films and nanostructured-SiC (ns-SiC) can be produced using higher radio frequency (RF) PECVD at lower temperature. Notably, PECVD with RF exceeding 13.56 MHz is classified as very high frequency (VHF-PECVD) [19].

The VHF-PECVD technique was employed in this study at 150 MHz plasma excitation frequency to deposit SiC film. The effect of dilution gas on SiC film was examined and characterised by using FTIR spectroscopy, FESEM, and AFM. Notably, high excitation frequency of PECVD has some advantages over conventional PECVD, including higher deposition rate, less defect and better-quality films, higher electron density, lower plasma potential, and lower impact of ion bombardment when compared to conventional PECVD [19]. However, no study has assessed SiC film synthesised with RF-PECVD at a frequency exceeding 100 MHz with SiH_4 and CH_4 precursors at low temperature. The ns-SiC thin film should successfully grow using VHF-PECVD at the said excitation frequency.

Materials and Methods

First, Si [100] substrates were thoroughly cleaned with ethanol and followed by organic cleaning in ultrasonic bath for 10 minutes. Next, the substrates were immersed in acetone for 10 minutes in ultrasonic bath. To remove the remaining contaminant particles, the substrates were submerged in 50% sulphuric acid (H_2SO_4) before another ultrasonic bath for 10 minutes. The oxide layer on the substrate surface was stripped off by immersing in 50% fluoric acid (HF). Finally, the substrates were rinsed with deionised (DI) water and blow-dried with N_2 gas. The substrates were then ready to be placed in the process chamber.

The substrates were labelled as samples A, B, and C. Sample A was diluted with the mixture of argon and hydrogen gases, while sample B was diluted only with hydrogen gas, and sample C without dilution of gas mixture. Substrate temperature, RF power, deposition time, and SiH_4 flow rate were fixed at 400 °C, 20 W, 15 minutes, and 2 sccm, respectively, for all samples A-C. The growth parameters for samples A-C are summarised in Table 1.

Table 1. Gas dilution growth parameter

Sample	Power (W)	Temperature (°C)	Argon Flow Rate (sccm)	Hydrogen (sccm)	Silane Flow Rate (sccm)	Methane Flow Rate (sccm)	Deposition Time (min)
A			5	5			
B	20	400	-	5	2	8	15
C			-	-			

Results and Discussion

Both chemical composition and bonding structure of Si C thin film samples were verified using IR spectroscop y. This technique has been vastly used to qualitatively a ssess the type of chemical bonding present in thin film materials, including a-Si:H, a-SiO_2, a-SiNx:H, a-SiCx: H, and a-C:H. In fact, IR spectroscopy is used to quanti tatively determine the concentration of terminal hydrog en bonds (Si-H, C-H, O-H, & N-H) and network bonds (Si-C, Si-O, Si-N, P-O, & B-O) present in thin film mat erials.

Figure 1 illustrates the IR spectrum for samples A-C in two regions ranging from 650 to 1500 cm^{-1} and 1800 to 3000 cm^{-1}. The sharp peaks observed at 1500-1800 cm^{-1} range are attributed to O-H water vapour vibration in t he air during the measurement [20, 25]. Moreover, sign als of the deposited thin film were noted at 650-1500 c m^{-1} and 1800-3000 cm^{-1}, in comparison to the blank Si wafer.

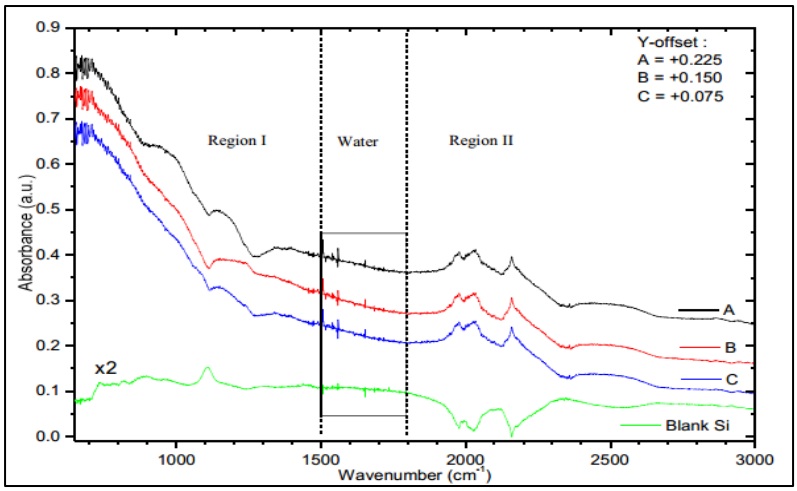


Figure 1. Comparison of IR spectrum between Si wafer and samples A-C

Spectra in regions (I) and (II) revealed the following vibrational bands: absorption band at ~ 650-1000 cm^{-1} is correlated to Si-C stretching [18, 21, 26-28]. The band at ~ 1000-1150 cm^{-1} is ascribed to Si-O-Si asymmetry and symmetry stretching vibration band or Si-CH_2-Si wagging mode [18, 21, 26, 28]. At ~ 1000 cm^{-1}, the band corresponds to Si-CH_n bending mode [24, 27]. In most samples, lower intensity absorption bands in the range of 1200-1500 cm^{-1} were detected. A shoulder at ~ 1250 cm^{-1} is linked with Si-CH_3 stretching mode [26] or Si-CH_n wagging mode [24]. The symmetry and asymmetry C-H_n bending and stretching modes are associated with ~ 1250-1500 cm^{-1} and 2700-3000 cm^{-1} bands, respectively [20-22, 26-27]. The Si-H_n stretching mode is assigned to the band from ~ 1850 cm^{-1} to 2300 cm^{-1} [21]. The small sharp peak at ~ 2350 cm^{-1} is attributed to CO_2 in the atmosphere [24, 27]. All the peaks verified that all the deposited thin film samples possessed Si-C

network bonds.

Scanning electron microscopy

Figures 2 (a-c) illustrate the overall surface morphology of the thin films, with inset images zooming in on the flat region for samples A-C respectively. Next, Figures 2 (i-iii) portray the cross-sectional morphology for samples A-C respectively. In sample A, the thin film had the largest island diameter at less than 1 µm and the film thickness was roughly ~ 397 nm. The island diameter in sample B was similar to that of sample A. However, the size exceeded 1 µm when agglomeration occurred among the islands. Sample B had thinner film thickness than sample A at 337 nm. Without argon gas during deposition, the density of island nucleation displayed an increase in sample B, when compared to sample A. Meanwhile, sample C showed the highest density of island nucleation above the film surface after attaining critical thickness. Notably, island formation increased in sample B and island density was higher in sample C. Therefore, dilution gas was proven effective to reduce the C-H network, which is ascribed to the high dissociation of methane on the films [23]. The film thickness values obtained from FESEM were 397 nm, 337 nm, and 357 nm for samples A-C respectively.

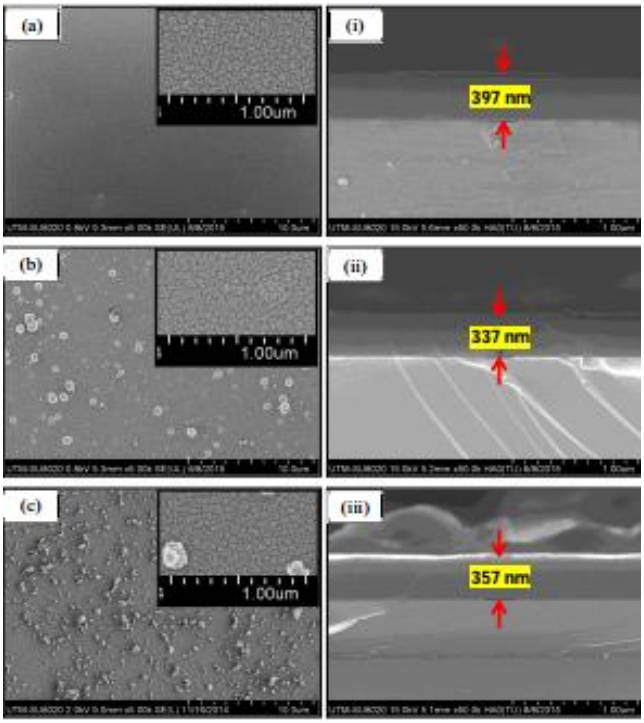


Figure 2. FESEM images of surface morphology ((a), (b), & (c)) and cross-sectional view ((i), (ii), & (iii)) of SiC films grown with different types of gas carriers for samples A, B, and C, respectively

Atomic force microscopy

Figure 3 shows high resolution surface topography of AFM images for samples A-C represented in root-mean-square roughness (R_{rms}). Sample B had smoother surface with R_{rms} of 0.798 nm, when compared to samples A and C with R_{rms} values of 1.505 nm and 1.599 nm, respectively. Dilution gas influenced the formation of different grain structure shapes, including triangular base pyramid [29, 31], square plateaus [30, 32], and semi-square plateaus for samples A-C respectively. This result is ascribed to the phase transition from amorphous to crystalline phase when hydrogen and argon were added during the deposition process [23]. Upon comparing the R_{rms} values of samples A and B, higher surface roughness in sample A is attributed to the effect of argon ion bombardment on film surface, although the

deposition pressure in sample A was lower than that of sample B. Hydrogen ions that existed in sample B deposition process could have less ion bombardment effect due to high electronegativity of H ion to have reaction in gas space with other reactants, when compared to the behaviour of argon ions as inert gas naturally. The mean diameter value of triangular pyramid island was ~ 81 nm and sample B showed well definite square plateaus of ~ 120 nm wide (based). For sample C, it had no perfect square plateau shape of each grain and the average wide of grain was ~ 140 nm.

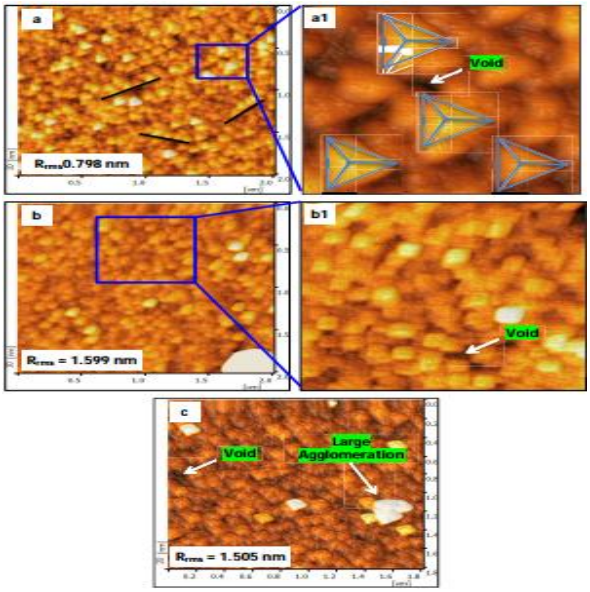


Figure 3. AFM images of the surface topography of SiC films grown with different types of gas carriers for samples A, B, and C represented by (a & a1), (b & b1), and (c), respectively

Conclusion

In conclusion, the surface morphology of the deposited ns-SiC films revealed a layer-island structure with varied island density and size formation above the critical layer thickness in all samples. Both surface topography and roughness of the deposited SiC films were assessed using non-contact AFM mode. The results revealed that all samples had different roughness, surface topography structure, and average grain diameter. Thin film deposited with dilution gas had a very smooth surface with the lowest R_{rms} value of 0.798 nm. Notably, dilution gas had affected the formation of different grain structure shapes. Nonetheless, the role of argon gas in changing the grain structure from square plateaus to triangular base pyramid demands further investigation.

Acknowledgement

The authors gratefully acknowledge the financial supported by Universiti Teknologi Malaysia, under Collaborative Research Grant National (CRG) (Vot no: R.J130000.7354.4B523) and UTM-TDR, Registration Proposal No: PY/2018/03249 (Vot no: Q.J130000. 3554.06G21). We are thankful to Physics Department, Faculty of Sciences, Universiti Teknologi Malaysia and Ibnu Sina Institute for providing the experimental facilities.

References

1. Bandyopadhyay, A. K. (2008). Nano Materials. New Age International (P) Ltd, New Delhi.
2. Tritt, T. M. and Subramanian, M. A. (2006). Thermoelectric materials, phenomena, and applications: a bird's eye view. *MRS Bulletin*, 31(3): 188-198.

3. J. J. and Wang, J. N. (2007). An approach to the synthesis of silicon carbide nanowires by simple thermal evaporation of ferrocene onto silicon wafers. *European Journal of Inorganic Chemistry*, 2007 (25): 4006-4010.
4. Huczko, A., Bystrzejewski, M., Lange, H., Fabianowska, A., Cudziło, S., Panas, A. and Szala, M. (2005). Combustion synthesis as a novel method for production of 1-D SiC nanostructures. *The Journal of Physical Chemistry B*, 109(34): 16244-16251.
5. Huczko, A., Lange, H., Bystrzejewski, M., Rűmmeli, M. H., Gemming, T., & Cudziło, S. (2005). Studies on spontaneous formation of 1D nanocrystals of silicon carbide. *Crystal Research and Technology: Journal of Experimental and Industrial Crystallography*, 40(4-5): 334-339.
6. Hamashita, D., Miyajima, S. and Konagai, M. (2012). Preparation of Al-doped hydrogenated nanocrystalline cubic silicon carbide by VHF-PECVD for heterojunction emitter of n-type crystalline silicon solar cells. *Solar Energy Materials and Solar Cells*, 107: 46-50.
7. Zhou, W., Zhang, Y., Niu, X., & Min, G. (2008). One-dimensional SiC nanostructures: Synthesis and properties. In *One-Dimensional Nanostructures* (pp. 17-59). Springer, New York, NY.
8. Kamble, M. M., Waman, V. S., Mayabadi, A. H., Ghosh, S. S., Gabhale, B. B., Rondiya, S. R., ... and Jadkar, S. R. (2014). Hydrogenated silicon carbide thin films prepared with high deposition rate by hot wire chemical vapor deposition method. *Journal of Coatings*, 2014: 1-11.
9. Pearton, S. J. and Ren, F. (2013). Wide bandgap semiconductor one-dimensional nanostructures for applications in nanoelectronics and nanosensors. *Nanomaterials and Nanotechnology*, 3: 1-15.
10. Neudeck, P. G. (2007). SiC technology. in The VLSI Handbook, 2nd ed. CRC Press, Boca Raton, Florida: pp. 5.1-5.34.
11. Harris G. L. (1995). Properties of silicon carbide. INSPEC, The Institution of Electrical Engineers, London, United Kingdom: pp. 3-9.
12. Palmour, J. W., Edmond, J. A., Kong, H. S. and Carter Jr, C. H. (1993). 6H-silicon carbide devices and applications. *Physica B: Condensed Matter*, 185(1-4): 461-465.
13. Sheng, S., Spencer, M. G., Tang, X., Zhou, P., Wongchotigul, K., Taylor, C. and Harris, G. L. (1997). An investigation of 3C-SiC photoconductive power switching devices. *Materials Science and Engineering: B*, 46(1-3): 147-151.
14. Saddow S. and Agarwal A. (2004). Advances in silicon carbide processing and applications. Artech House, Inc., Boston, London.
15. Zorman, C. A. and Parro, R. J. (2008). Micro-and nanomechanical structures for silicon carbide MEMS and NEMS. *Physica Status Solidi (b)*, 245(7): 1404-1424.
16. Willander, M., Friesel, M., Wahab, Q. U. and Straumal, B. (2006). Silicon carbide and diamond for high temperature device applications. *Journal of Materials Science: Materials in Electronics*, 17(1): 1-25.
17. Avram, M., Avram, A., Bragaru, A., Chen, B., Poenar, D. P., & Iliescu, C. (2010, October). Low stress PECVD amorphous silicon carbide for MEMS applications. In *CAS 2010 Proceedings (International Semiconductor Conference,* 1: pp. 239-242.
18. Künle, M., Hartel, A., Löper, P., Janz, S. and Eibl, O. Nanostructure and phase formation in annealed a-Si1-xCx: H thin films for advanced silicon solar cells. *21st Workshop on Quantum Solar Energy Conversion (QUANTSOL)*: pp. 1-4.
19. Hamidinezhad, H., Wahab, Y. and Othaman, Z. (2011). Ultra-sharp pointed tip Si nanowires produced by very high frequency plasma enhanced chemical vapor deposition via VLS mechanism. *Journal of Materials Science*, 46(15), 5085-5089.
20. Socrates G. (2004). Infrared and raman characteristic group frequencies: Tables and charts. 3rd edition. John Wiley & Son Ltd.
21. King, S. W., French, M., Bielefeld, J. and Lanford, W. A. (2011). Fourier transform infrared spectroscopy investigation of chemical bonding in low-k a-SiC: H thin films. *Journal of Non-*

Crystalline Solids, *357*(15), 2970-2983.

22. Gates, S. M., Neumayer, D. A., Sherwood, M. H., Grill, A., Wang, X. and Sankarapandian, M. (2007). Preparation and structure of porous dielectrics by plasma enhanced chemical vapor deposition. *Journal of Applied Physics*, 101(9): 094103-1-094103-8.
23. Gradmann, R., Loeper, P., Künle, M., Rothfelder, M., Janz, S., Hermle, M and Glunz, S. (2011). Si and SiC nanocrystals in an amorphous SiC matrix: Formation and electrical properties. *Physica Status Solidi C*, 8(3): 831-834.
24. Kim, Y. T., Yoon, S. G., Kim, H., Suh, S. J., Jang, G. E., & Yoon, D. H. (2005). Crystallization of a-Si: h and a-SiC: h thin films deposited by PECVD. *Journal of Ceramic Processing & Research*, 6(4): 294-297.
25. Chen, E., Du, G., Zhang, Y., Qin, X., Lai, H. and Shi, W. (2014). RF-PECVD deposition and optical properties of hydrogenated amorphous silicon carbide thin films. *Ceramics International*, 40(7): 9791-9797.
26. Kuznetsov V. L. and Butenko Y. V. (2006). Diamond phase transitions at nanoscale in ultrananocrystalline diamond: Synthesis, properties and applications. William Andrew Publishing, New York: pp. 405-475.
27. Lin, Z., Guo, Y., Song, C., Song, J., Wang, X., Zhang, Y., ... and Huang, X. (2015). Influence of the oxygen content in obtaining tunable and strong photoluminescence from low-temperature grown silicon oxycarbide films. *Journal of Alloys and Compounds*, 633: 153-156.
28. Peri, B., Borah, B. and Dash, R. K. (2015). Effect of RF power and gas flow ratio on the growth and morphology of the PECVD SiC thin film s for MEMS applications. *Bulletin of Materials Science*, 38(4): 1105-1112.
29. El Khalfi, A. I., Ech-chamikh, E. M., Ijdiyaou, Y., Azizan, M., Essafti, A., Nkhaili, L. and Outzourhit, A. (2014). Infrared and Raman study of amorphous silicon carbide thin films deposited by radiofrequency cosputtering. *Spectroscopy Letters*, 47(5): 392-396.
30. ElGazzar, H., Abdel-Rahman, E., Salem, H. G. and Nassar, F. (2010). Preparation and characterizations of amorphous nanostructured SiC thin films by low energy pulsed laser deposition. *Applied Surface Science*, 256(7): 2056-2060.
31. Bosi, M., Attolini, G., Negri, M., Frigeri, C., Buffagni, E., Ferrari, C., ... and Verucchi, R. (2013). Optimization of a buffer layer for cubic silicon carbide growth on silicon substrates. *Journal of Crystal Growth*, 383: 84-94.
32. Radmilovic, V., Dahmen, U., Gao, D., Stoldt, C. R., Carraro, C. and Maboudian, R. (2007). Formation of< 111> fiber texture in β-SiC films deposited on Si (100) substrates. *Diamond and Related Materials*, 16(1): 74-80.
33. Wu, X. L., Gu, Y., Xiong, S. J., Zhu, J. M., Huang, G. S., Bao, X. M. and Siu, G. G. (2003). Self-organized growth and optical emission of silicon-based nanoscale β-SiC quantum dots. *Journal of Applied Physics*, 94(8): 5247-5251.

Malaysian Journal of Analytical Sciences (MJAS)
Published by Malaysian Analytical Sciences Society

DFT STUDY ON STRUCTURAL PROPERTIES, DENSITY OF STATES AND BAND STRUCTURE OF MONOLAYER & BILAYER GRAPHENE

(Kajian Teori Tentang Sifat Struktur, Ketumpatan Keadaan dan Struktur Jalur Grafin Lapisan Tunggal dan Dwi Lapisan)

Nurhafizah Md Disa*, Henna Malakar, Nurhayati Abdullah

School of Physics,
Universiti Sains Malaysia, 11800 USM Gelugor, Penang, Malaysia

**Corresponding author: mdnurhafizah@usm.my*

Received: 16 November 2021; Accepted: 27 February 2022; Published: 30 October 2022

Abstract

This two-dimensional (2-D) carbon structure, known as graphene, has tremendous potential due to its unique properties. This research intends to identify the existing knowledge gap because of the lack of substantial studies and prior comparisons in bilayer graphene and bring to light any pertinent differences between monolayer and bilayer graphene in this field. So, a density functional theory (DFT) study was done using a Quantum Espresso package for analysing the structural properties of mono- and bi-layer graphene. Generalised gradient approximation (GGA) under Perdew-Burke-Ernzerhof (PBE) of the DFT study and pseudopotential method was employed in this research. The monolayer and bilayer graphene have successfully predicted the bandgap and the Density of states (DOS), proving the zero-gap semiconductor tag. Furthermore, the band structure of the monolayer graphene illustrated a toroidal like shape, whereas the bilayer graphene projected a hyperbolic type of band-structure. The hybridisation of graphene was identified as sp^2 in which the bilayer graphene consumed more time for the orbital hybridisation compared to that of the monolayer. Therefore, this study is able to obtain the band gap vale for monolayer and bilayer graphene and provide a detail studies related to bilayer graphene beneficial for semiconductor applications.

Keywords: density functional theory, graphene, quantum espresso, structural properties, bandgap

Abstrak

Struktur karbon dua dimensi (2-D) ini, yang dikenali sebagai grafin, berpotensi besar kerana sifatnya yang unik. Penyelidikan ini mengatasi ketiadaan pengetahuan yang ada kerana kekurangan nilai teori yang signifikan dalam struktur jalur dwi lapisan dan perbandingan yang jelas dari lapisan tunggal dan lapisan dwi grafin dalam kajian sebelumnya. Oleh itu, kajian teori fungsi ketumpatan (DFT) dilakukan menggunakan pakej espresso kuantum untuk menganalisis sifat struktur grafin lapisan tunggal dan lapisan dwi. Kaedah gradien umum (GGA) di bawah Perdew-Burke-Ernzerhof (PBE) kajian DFT dan kaedah pseudopotensial digunakan dalam penyelidikan ini. Struktur jalur dan ketumpatan telah berjaya diramalkan oleh kajian grafin lapisan tunggal dan lapisan dwi, yang membuktikan tanda semikonduktor jurang sifar. Tambahan pula, struktur pita bentuk yang digambarkan untuk grafin lapisan tunggal adalah toroidal manakala grafin dwi lapisan mengunjurkan jenis struktur pita hiperbolik. Hibridisasi grafin dikenal pasti sebagai sp^2 di mana grafin dwi lapisan menggunakan lebih banyak masa untuk hibridisasi orbit berbanding dengan grafin lapisan tunggal. Oleh itu, kajian ini dapat memperoleh nilai jurang jalur untuk grafin lapisan tunggal dan dwi lapisan serta menyediakan kajian terperinci berkaitan grafin dwilapisan yang bermanfaat untuk aplikasi semikonduktor.

Kata kunci: teori fungsi ketumpatan, grafin, espresso kuantum, sifat struktur, jurang jalur

Introduction

Carbon-based materials have advanced at a breakneck pace over the last few decades, particularly in the previous decade. For instance, carbon nanotubes, carbon nanofibers, graphene and carbon sponges [1] are carbon-based materials. The fullerene discovery, the carbon nanotubes, and the graphene have dramatically increased the variety of carbon-based materials available to researchers. The critical experiments of Novoselov and Geim in isolating graphene and identifying its basic properties sparked a surge in interest in graphene [2]. Graphene, as mentioned previously, is a carbon nanomaterial of zero-bandgap [3–4], a planar two-dimensional (2-D) hexagonal lattice [5-14], and sp2 bonded carbon atom [8, 15-17]. These carbon atoms are bound to the of their neighbours in the graphene lattice by σ bonds. The particles in the lattice each have a π orbital [18], which helps form an independent electron network. Graphene has strong electrical conductivity[5, 6, 8, 10-12, 14, 16, 19, 20], because of freedom of the π electrons in 2-D plane of a graphene sheet.

Electron transfer occurs at room temperature and below, resulting in low resistance and high conductivity due to the material's unique band structure [21]. It is said that a two-dimensional (2-D) sheet of crystals is entirely stable, as it is slightly wavy rather than flat. The high-expanded surface area [4, 5, 7, 16, 21-22], electrical conductivity [5, 6, 8, 10-12, 14, 16, 19-20], high-velocity and high absorption rate[23] of graphene add to each other to yield a lot of these properties. To top it all of this, it also has exceptional electrical properties such as low noise and high mobility [5, 7, 9, 21, 24-25]. Great attention has recently been directed toward electronic devices such as biosensors [6, 7, 12, 15], radio frequency (RF) transistors [6], and flexible displays. Aside from this, graphene has a wide range of possible uses in photonics, electronics, optical, and photonic technologies such as electrochemical energy storage [3]. Due to its unique physical properties, monolayer and bilayer graphene-based quantum electronic devices are in-demand today [26]. DFT is very accurate in predicting atomic structures, properties and phonon spectrums [27]. Several interpretations of good accordance between DFT simulations and observational study demonstrate that DFT is highly appropriate and precise for infinitesimal investigations of physics and chemistry. Knowledge of density of states and electronic bandgap is valuable when modelling materials for energy applications, such as graphene.

The experimental value of monolayer graphene from the study of Jeon et al. is reported to be 0.2eV [28]. Zhang and Quhe et al. have found the experimental value of band gap for bilayer graphene and is said to be 0.25eV [29-30]. To investigate the properties of a finite-size graphene sheet, Banerjee et al. experimented with various possible defects and edge effects and used software such as MOLDEN and GAMESS-US [31]. However, this software can be used for generating the molecular and electronic structure only, unlike Quantum Espresso that can calculate the structural and other electrical properties of graphene. Besides, Abbood and co-workers [32] used Gaussian 09 package to study electronic and electrical graphene sheets. Gaussian software utilises local basis functions rather than plane-wave to compute them, so it is more challenging to find basis functions.

In a study done by Geng and co-workers, DFT calculations using CASTEP software was utilised to evaluate the DFT aspects of the interface between graphene and ZnO [33]. Zhu and co-workers also used CASTEP software to study the electronic properties of nano-structural ZnO [34]. Although CASTEP can be used as one of the DFT studies, it has drawbacks at the price as it is licensed software, unlike Quantum Espresso (QE), an open-source code. QE is an open-source quantum mechanical software package with high performance capable of supporting various applications at the nanoscale level, including the design of materials, structural optimisation, and the simulation of atomic electronic structures, all based on DFT theory. The past research proves that Quantum Espresso is the best for studying and analysing the properties of graphene sheets among the other software. Pashangpour and co-workers also used Quantum Espresso to investigate the structural and electronic properties while adhering to Density Functional Theory (DFT) [35]. However, his study has not discovered the value of the bandgap for monolayer and bilayer graphene (AA or AB stacking).

Investing substantial time over the years has taken place to enhance the Quantum Espresso distribution by advancing computational methods, theoretical studies, and property calculations and improving interoperability with external codes [36]. High performance was one of the main motivations behind the Quantum Espresso

project's inception [37]. Past research proves that Quantum Espresso is the best for studying and analysing the properties of graphene sheets among the other software. However, detailed studies of monolayer and bilayer graphene are not discovered using Quantum Espresso. Therefore, this research attempts to do detailed studies on monolayer and bilayer graphene using the DFT study with the Quantum Espresso package.

Computational Details

Density Functional Theory (DFT) [38-44] and the generalised gradient approximation (GGA) known as Perdew-Burke-Ernzerhof (PBE) were used in the PWSCF code to obtain the first-principles calculations. The input files are created using PW Graphical User Interface (GUI) in Quantum Espresso software package under Linux 64-bit. Kohn Sham orbitals are expanded in a plane-wave basis set. Norm-conserving (NC) and ultra-soft (US) forms make up most of the pseudopotentials used in plane-wave electronic structure codes. Thus, this allows for a much lower cut-off in the basis set, which results in a much better cut-off, faster computational efficiency and increased accuracy. Fermi-distribution smoothing was performed using a Monkhorst & Pack (10 × 10 × 1) particular point grid used to perform Brillouin zone integrations, using Gaussian smearing technique with a smearing width of 0.01 Rydberg (Ry).

For monolayer graphene, the energy cut-off (80Ry) and the charge density (320Ry) are set, while for bilayer graphene, these values are 40Ry and 225Ry, respectively. With the ultra-soft pseudopotential of bilayer graphene, using lower cut-off energy is preferable. Variable cell relaxation calculation was done to obtain the optimised cell lattice vectors by introducing Broyden-Fletcher-Goldfarb-Shanno (BFGS) algorithm as the type of ion dynamics. Relaxation calculation was also performed to get the optimised atomic coordinates essential for other following calculations. Burai Software, a GUI for Quantum Espresso (QE) was used to obtain the unit cell and lattice structure of monolayer and bilayer graphene.

K points were chosen to be *automatic* for Self-Consistent Field (SCF) and non-SCF calculations, whereas k points were set to 'crystal_b' for band calculations. To calculate the density of states (DOS) calculation, grids of (24 × 24 × 1) and (11 × 11 × 3) for monolayer and bilayer graphene, respectively, were used using non-self-consistent field type. The number of bands was set to be 8 for monolayer graphene whereas 16 for bilayer graphene. Another feature of Brillouin zone is that they have been fine-tuned to obtain band structure. XCRYSDEN was used to find paths along the primitive Brillouin zone using k-path selection. After locating symmetrical points on the selection set, the symmetrical points are used for the band calculation. The selected high symmetrical points are tabulated in Table 1 and Table 2 for monolayer and bilayer graphene, respectively. The Quantum Espresso software package computed the bandgap, highest occupied molecular orbital (HOMO), lowest unoccupied molecular orbital (LUMO), and Fermi energy. In order to obtain information about the orbitals, the projected band structure calculation was done.

Table 1. Coordinates values for Brillouin zone (Monolayer)

Coordinates	x-	y-	z-
K	0.33	0.33	0
L	0	0	0
M	0.5	0	0

Table 2. Coordinates values for Brillouin zone (Bilayer)

Coordinates	x-	y-	z-
A	0	0	0
H	0.67	0	0
K	0.67	0	0
L	0.5	0.29	0.14
M	0.5	0.29	0

Result and Discussion

Structural properties

Monolayer and bilayer graphene atomic geometries are optimized as the initial step. This type of calculation is done so that other analysis uses these optimized atomic coordinates, which is beneficial for less or defect-free structure and structural optimization. The bond length between C-C is 1.4214Å which is in excellent agreement with the experimental value of bond length 1.42 Å [45], and the bond angle of C-C-C is 120°. The unit cell and hexagonal lattice structure in 2-D and 3-D viewed in XCRYSDEN for monolayer graphene and bilayer graphene are illustrated in Figure 1 and Figure 2, respectively. The unit cell of monolayer graphene contains two carbon atoms, whereas four carbon atoms are reported to be for bilayer graphene with a lattice constant of 2.467 Å. The AB bilayer is 3.35 Å apart, which is in the range of interlayer distance by past researchers [46-47]. In addition, the shape of the unit cell of monolayer and bilayer graphene is said to be in a lozenge shape. The lattice structure of the monolayer can be seen to be as a single layer of atoms with the axis of direction given in Figure 1(b) & (d). Therefore, these structures are proven accordingly as monolayer graphene, which is in excellent agreement with the experimental design [48]. The lattice structure of the bilayer can be seen to be stacked up as double or two layers of atoms with the axis of direction given in Figure 2(b) & (d). Therefore, these structures are verified accordingly as bilayer graphene, which is in excellent agreement with the experimental design [49]. In AB bilayer graphene, half of the carbon atoms in the upper layer are located above the centres of the lower-layer hexagons. AB bilayer graphene is the most stable [50], and it has a wide range of applications because of its stable characteristics.

The charge density of graphene is visualized under Visualization for Electronic & Structural Analysis (VESTA) software illustrated in Figure 3. Color in the 4 edges of this figure refers to electrostatic potential, where green represents positive charge and orange represents negative charge. The arrow in Figure 3 indicates the yellow color in the unit cell, indicating graphene's charge density. The charge distribution is equally transmitted in the graphene unit cell, implying a minimal structure defect. The output file details are tabulated in Table 3, in which the input file of PP.X was used for data analysis and plotting purposes. The space group of the graphene is P1, where P indicates primitive lattice type and the symbol P 1 refers to triclinic Bravais lattice. The lattice constant is in excellent agreement with the theoretical value of 2.47 Å [42]. The grid size was changed from a smooth grid of (10 x 10 x 1) to a denser grid of (27 x 27 x 216) to view the charge density. Dense grids of k-points are needed for periodic structures.

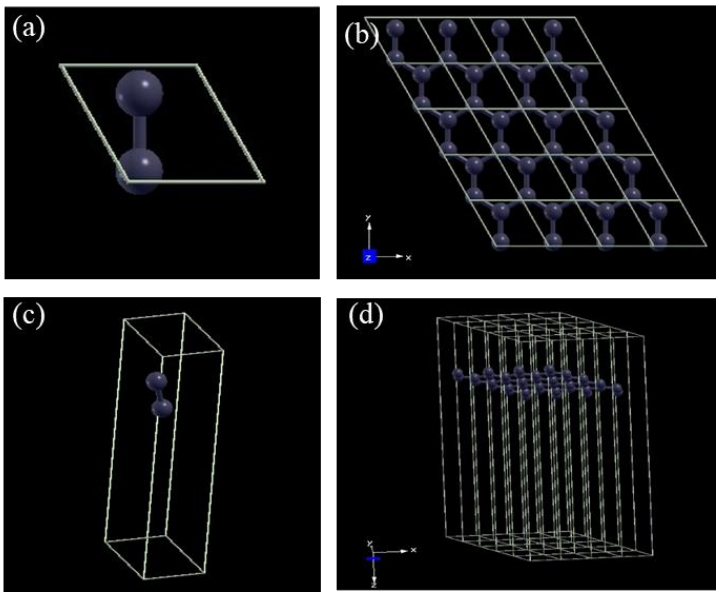


Figure 1. Monolayer graphene unit cell (a) 2-D (c) 3-D (b) and lattice structure (b) 2-D (d) 3-D

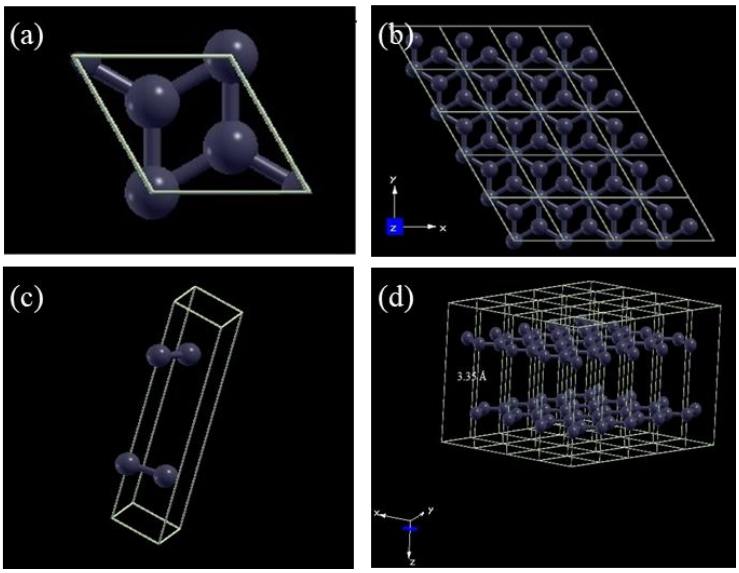


Figure 2. Bilayer graphene unit cell (a) 2-D (c) 3-D (b) and lattice structure (b) 2-D (d) 3-D]

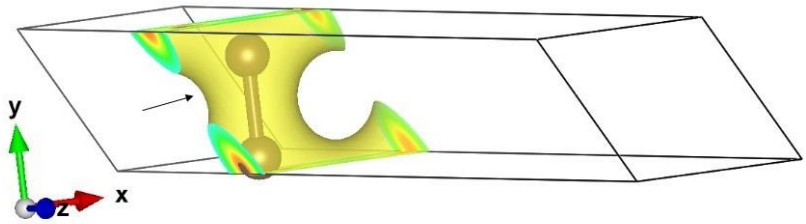


Figure 3. Charge density of graphene

Table 3. Structural details of the unit cell of graphene

Space Group	Lattice Constant, Å	Bond Length, Å	Angle	Grid Size ($x \times y \times z$)	Volume, Å^3
P1	A = 2.4674 A = 2.4674 C = 20.000	1.4214	$\alpha = 90.0°$ $\beta = 90.0°$ $\gamma = 120.0°$	27 × 27 × 216	104.1362

Electronic properties (density of states)

The density of states represents the number of electron states per unit volume per unit energy. In DOS calculation, the type of calculation used was non-SCF. The solution field minimizes the density charge functional until a predefined limit in the energy difference between two consecutive steps. The non-SCF analysis used a denser grid (24 × 24 × 1) for monolayer graphene and a grid (11 × 11 × 3) for bilayer graphene. Grid size here indicates the lattice size. *nbnd* is specified in this type of calculation, and it represents the number of bands where electron value 8 and 16 is included for monolayer and bilayer graphene respectively. The Brillouin zone is divided into a tetrahedron. The energies of the corners of each tetrahedron are used to calculate the eigen energies. These values are then interpolated to obtain the overall eigen energy. It follows the trapezoidal rule for approximating the integral of single-variable functions, making the tetrahedron method similar. Therefore, the type of occupation was

set to '*tetrahedra*' as this is applicable for accuracy in non-SCF calculation. Figure 4 and Figure 5 illustrate the density of states (DOS) for mono- and bi-layer graphene.

The Fermi energy was set to zero in the axis. It can be interpreted from those figures, the DOS is near 0, around the energy of 0. Since the cones are connected at an infinitely small point with no range or extent in the E-k space of band structure, the density of states is 0 for both monolayer and bilayer graphene. Therefore, there are no states at this point, so DOS is zero. In other words, we can say that the DOS of graphene increases linearly with energy. The bilayer graphene also shows zero DOS because layers' stacking (AB) is through planes and not edges in this study. Figure 6 shows the shapes formed by the bonds between carbon atoms (edge stacking pattern).

AB stacking of bilayer used in this research is of one structure only, which is zigzag pattern similar to plane AB stacking. The AB stacking of bilayer through armchair or zigzag nanoribbons (narrow strips of graphene) has specific DOS and bandgap because it depends on the edge orientation. This value is due to the stacking of layers through edges which can modify the electronic properties of graphene. For instance, in the armchair pattern, the bandgap is dependent on the nanoribbon width, unlike the zigzag pattern. The zigzag structure supports localized states [51-52], resulting in covalent bond formation, bonding and anti-bonding states. Moreover, the zigzag pattern, similar to plane AB stacking, possesses metallic behavior regardless of graphene nanoribbon width [53]. Consequently, the DOS and band gap is still zero for the zigzag pattern. To study the edge stacking in bilayer graphene, LDA should be used. However, GGA was used in this study instead of LDA because GGA gives a minor error and is more accurate in illustrating structural or electronic properties. LDA underestimate the bond length and over-bind, which causes a more significant interatomic force constant (IFC) to be generated [54].

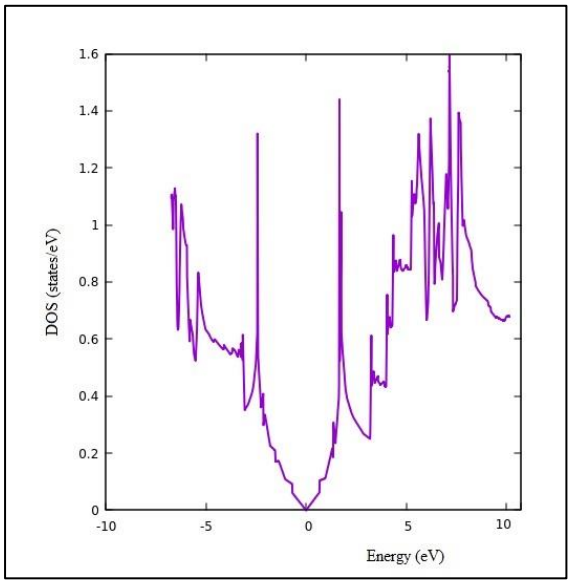


Figure 4. Charge density of graphene

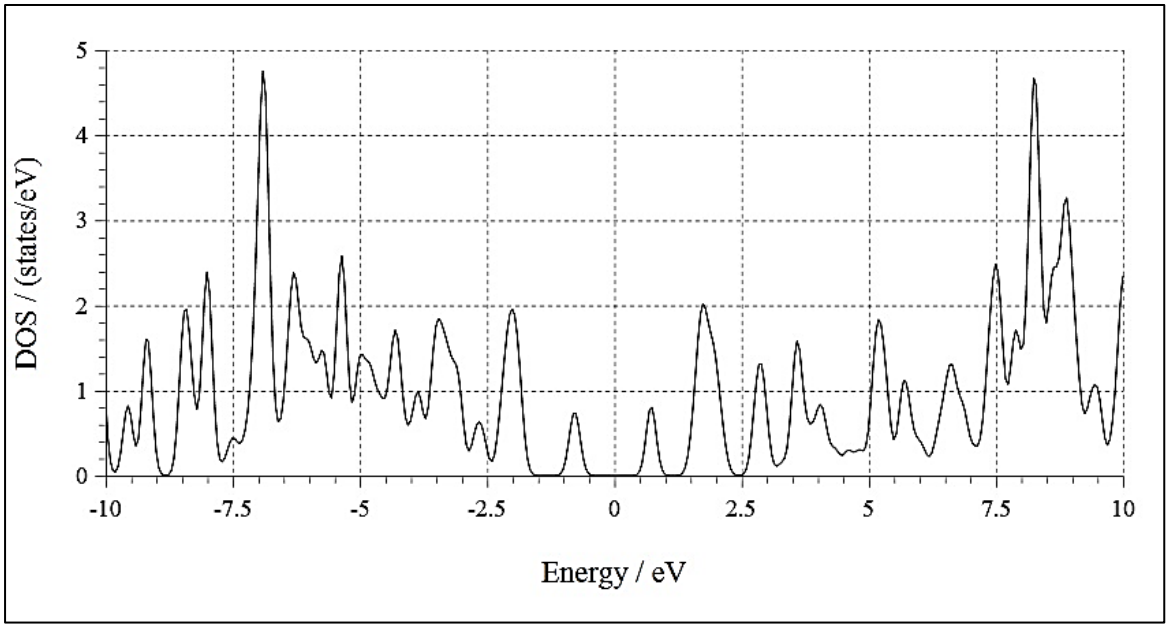


Figure 5. Density of states (DOS) of bilayer graphene

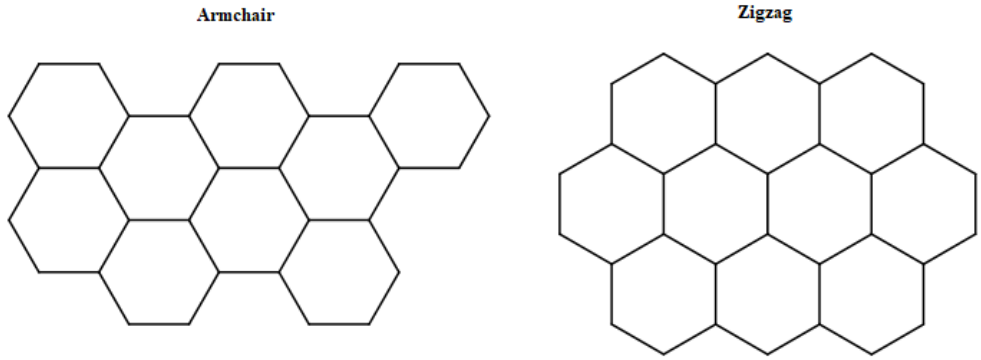


Figure 6. Shapes formed by the bonds between carbon atoms (edge stacking pattern)

***Electronic* properties (projected band structure)**

The results obtained from the projected band structure are illustrated in Figure 7 for monolayer graphene and Fig. 8 for bilayer graphene, respectively. Two and four atoms were specified for monolayer and bilayer graphene, respectively, based on their unit cell. Therefore, the monolayer has eight atomic states, and the bilayer has sixteen atomic states.

a) $l = 0$ indicates the s orbital
b) $l = 1$ refers to the p orbital
c) $m = -1, 0, 1$ refers to the magnetic quantum number (p_x , p_y , p_z)

The results projected in Figure 7 and Figure 8 concludes that graphene has s and 2p orbitals. The total charge in Figure 8 and Figure 10 for monolayer and bilayer graphene recorded 4.0497 and 3.9553, which gives a value of 4.0 when rounded off to one decimal place. This total charge here represents the number of valence electrons. The spilling parameter setting represents what percentage of the total density is not projected by these schematics. As the spilling parameter gets closer to zero, the representation is more accurate. Therefore, both mono- and bi-layer graphene recorded a value of 0.01, which is in excellent agreement with the accuracy range. Carbon with 6 electrons has $1s^2$, $2s^2$, $2p^2$ ground-state electron configuration, whereby two is in the inner shell, and four are in the outer shell. In graphene, each carbon atom is connected to three other carbon atoms on the two-dimensional plane, leaving one outer shell electron available for chemical bonding. Carbon atoms in graphene have sp^2 hybridized, which means the mixture of a single 2s orbital with two 2p orbitals. The diagram in Figure 9 is the representation of sp^2 hybridization with 120º spacing. Therefore, the orbitals (2s, $2p_x$, $2p_y$) results in trigonal planar (120º apart) structure with the formation of σ bond between carbon atoms. Because of this arrangement, the hexagonal structure of graphene was formed. Carbon's robust lattice structure is due to the σ bond. Since the Pauli principle is in effect, these bands have a filled shell. A valence band is therefore formed. $p_z$orbital covalently bound to carbon atoms occurs along the graphene plane [55]. This $p_z$orbital constitutes the π bond. When joining together, the π bonds form the π band (bonding) and π^* bands (anti-bonding). The π band is half-filled since every p orbital contains one extra electron and is not doped [50]. Most graphene's remarkable electronic properties are credited to these bands because they have a half-filled band that enables free-moving electrons. Because bilayers are hybrids between s orbitals and p_z orbitals, the hybridization is more time-consuming than for monolayer graphene. Therefore, the hybridization for bilayer graphene is more complicated than monolayer graphene.

Besides, the highest occupied molecular orbital (HOMO) and lowest unoccupied molecular orbital (LUMO) can provide information on the chemical stability [56–58]. The gap between the highest energy HOMO and LUMO orbitals is where most likely excited states can be found. Therefore, it is crucial to know the energy gap. Conjugated π orbital systems allow for the transfer of energy more freely within a molecule, helping to keep it stable. Better molecular stability is associated with higher HOMO-LUMO gaps. Monolayer and bilayer graphene have recorded values of 2.034eV and 1.877eV, respectively, for (HOMO - LUMO) gap. Consequently, monolayer graphene is more stable molecularly in this study. HOMO – LUMO gap value from theoretical study reported to be in range of 2.2eV to 3.1eV for graphene quantum dot [59]. However, there's no value reported in experimental study for monolayer and bilayer graphene.

(a)

```
state #   1: atom   1 (C  ), wfc  1 (l=0 m= 1)
state #   2: atom   1 (C  ), wfc  2 (l=1 m= 1)
state #   3: atom   1 (C  ), wfc  2 (l=1 m= 0)
state #   4: atom   1 (C  ), wfc  2 (l=1 m= -1)
state #   5: atom   2 (C  ), wfc  1 (l=0 m= 1)
state #   6: atom   2 (C  ), wfc  2 (l=1 m= 1)
state #   7: atom   2 (C  ), wfc  2 (l=1 m= 0)
state #   8: atom   2 (C  ), wfc  2 (l=1 m= -1)
```

(b)

```
Lowdin Charges:

     Atom #   1: total charge =   4.0497, s =  0.8933,
     Atom #   1: total charge =   4.0497, p =  3.1564, pz=  1.0799, px=  1.0458, py=  1.0307,
     Atom #   2: total charge =   4.0497, s =  0.8933,
     Atom #   2: total charge =   4.0497, p =  3.1564, pz=  1.0799, px=  1.0458, py=  1.0307,
     Spilling Parameter:  0.0124
```

Figure 7. Monolayer graphene (a) atomic states (b) lowdin charges

(a)

```
state #   1: atom   1 (C  ), wfc  1 (l=0 m= 1)
state #   2: atom   1 (C  ), wfc  2 (l=1 m= 1)
state #   3: atom   1 (C  ), wfc  2 (l=1 m= 0)
state #   4: atom   1 (C  ), wfc  2 (l=1 m= -1)
state #   5: atom   2 (C  ), wfc  1 (l=0 m= 1)
state #   6: atom   2 (C  ), wfc  2 (l=1 m= 1)
state #   7: atom   2 (C  ), wfc  2 (l=1 m= 0)
state #   8: atom   2 (C  ), wfc  2 (l=1 m= -1)
state #   9: atom   3 (C  ), wfc  1 (l=0 m= 1)
state #  10: atom   3 (C  ), wfc  2 (l=1 m= 1)
state #  11: atom   3 (C  ), wfc  2 (l=1 m= 0)
state #  12: atom   3 (C  ), wfc  2 (l=1 m= -1)
state #  13: atom   4 (C  ), wfc  1 (l=0 m= 1)
state #  14: atom   4 (C  ), wfc  2 (l=1 m= 1)
state #  15: atom   4 (C  ), wfc  2 (l=1 m= 0)
state #  16: atom   4 (C  ), wfc  2 (l=1 m= -1)
```

(b)

```
Lowdin Charges:

     Atom #   1: total charge =   3.9553, s =  0.9179,
     Atom #   1: total charge =   3.9553, p =  3.0374, pz=  0.9879, px=  1.0247, py=  1.0247,
     Atom #   2: total charge =   3.9553, s =  0.9179,
     Atom #   2: total charge =   3.9553, p =  3.0374, pz=  0.9879, px=  1.0247, py=  1.0247,
     Atom #   3: total charge =   3.9565, s =  0.9180,
     Atom #   3: total charge =   3.9565, p =  3.0385, pz=  0.9888, px=  1.0248, py=  1.0248,
     Atom #   4: total charge =   3.9565, s =  0.9180,
     Atom #   4: total charge =   3.9565, p =  3.0385, pz=  0.9888, px=  1.0248, py=  1.0248,
     Spilling Parameter:   0.0110
```

Figure 8. Bilayer graphene (a) atomic states (b) lowdin charges

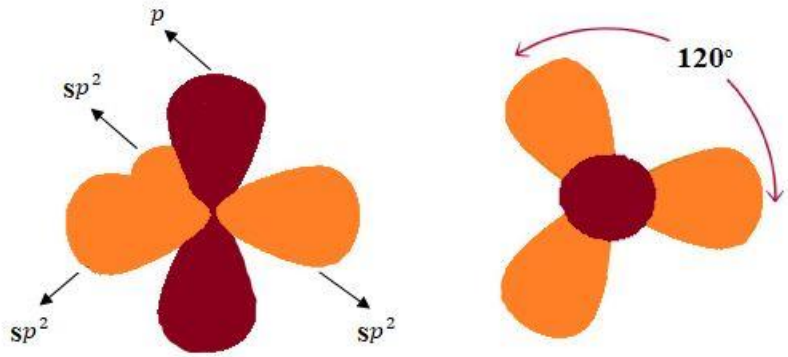


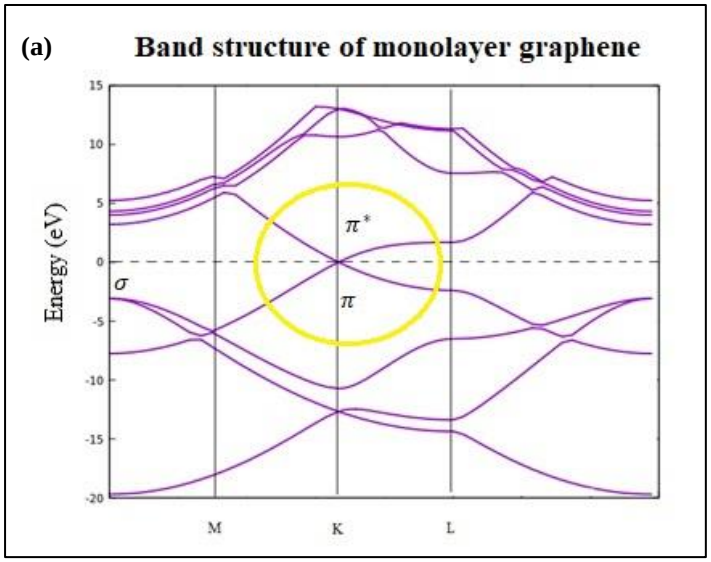
Figure 9. sp^2 hybridization of carbon in graphene b.) trigonal planar with 120º apart

Electronic properties (band structure)

Figure 10 illustrates band structure for monolayer and bilayer graphene obtained from the band calculation explained in methodology. The band structure where two cones touching at the Dirac point is presented in Figure 11. The dispersion of the bands can be visualized from the result as two cones that intersect at the Dirac point. Electron and holes are expected to have the same properties at the Dirac point. The orthogonal π and π^* do not interact, so the crossing of band-structure is possible. The yellow circle in Figure 10 shows the intersection of the valence band (VB) and conduction band (CB) clearer. Results show that graphene is a zero-gap semiconductor because the VB and CB intersect at the Dirac point. Graphene's zero bandgap originates from the carbon-rich environment of the unit cell. In short, electron flow can happen at the top of the VB without any external stimulus, so electrons from the VB can flow into the CB at lower energy.

Graphene's outstanding electrical properties are due to its use of zero-mass, low-energy carriers that behave as relativistic Dirac fermions [55]. An independent energy-independent group velocity is seen in the low energy excitations of graphene's linear dispersion, meaning zero effective mass. Moreover, being massless allows an electron to quickly move within the graphene, which means graphene has high electron mobility. The difference in band structure for both monolayer and bilayer graphene is that monolayer graphene has a toroidal-like shape and exhibits a band state density that approaches zero at the Dirac point. Besides, the density of states rises exponentially from zero energy with bilayer graphene, showing a hyperbolic band structure. Gapless band structure in AB-stacked bilayer graphene results in massive Dirac quasi-particles classified as Dirac Fermions in monolayer graphene [53].

Electron transfer from VB to CB is vital for current to flow. Therefore, electrical conductivity is heavily influenced by the bandgap of the material. In the absence of a semiconducting bandgap, semiconducting materials are impossible. This absence means that applications where graphene performs well, such as high-frequency analogue electronics and transparent conductive films, will be compromised. While silicon-based electronics dimensional scaling is approaching its limit, graphene semiconducting with a sizable bandgap might become the next generation's silicon alternative. Even though symmetry is commonly associated with geometry, it can also be disrupted through stacking two graphene layers in a Bernal stacking (AB stacking) [60]. Bilayer graphene sheets have two valence and conduction bands since they contain four atoms in a unit cell. Bilayer structure offers a new stacking order to fine-tune the electronic properties because of weak interlayer van der Waals interactions (forces). Consequently, modifying bilayer stacked graphene is suitable for fine-tunable electronic circuits or field-effect transistor (FET) applications. Bilayer graphene has been extremely promising since doping or an external electric field could open the energy gap [42,50]. Furthermore, applying external voltage and strain to bilayer graphene can increase the electron's mass [53].



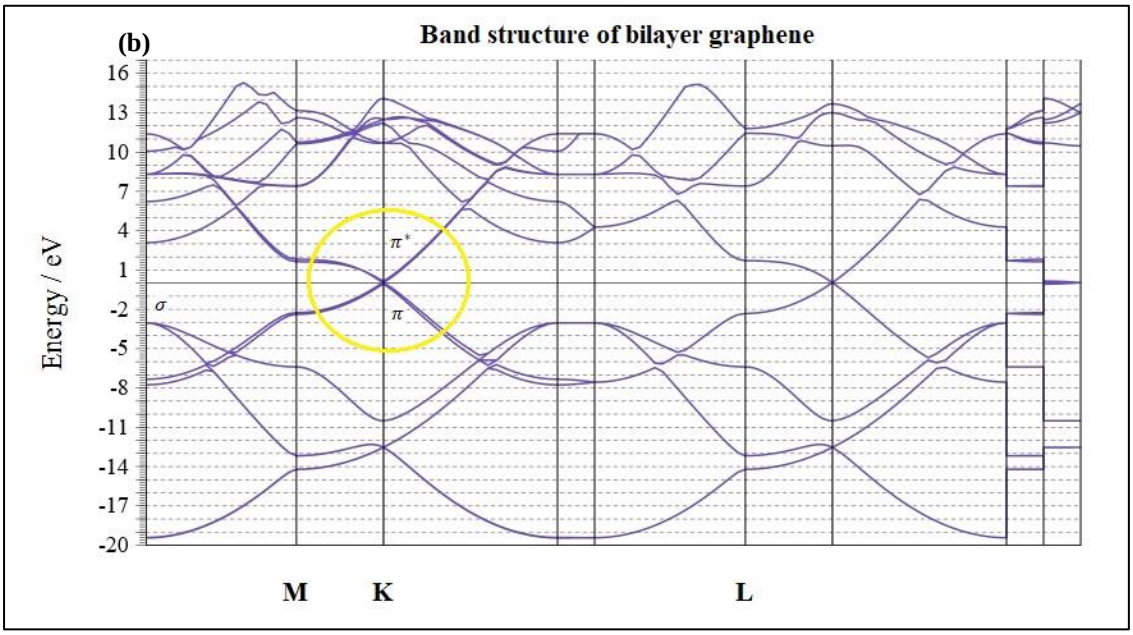


Figure 10. Band structure of (a) monolayer graphene (b) bilayer graphene

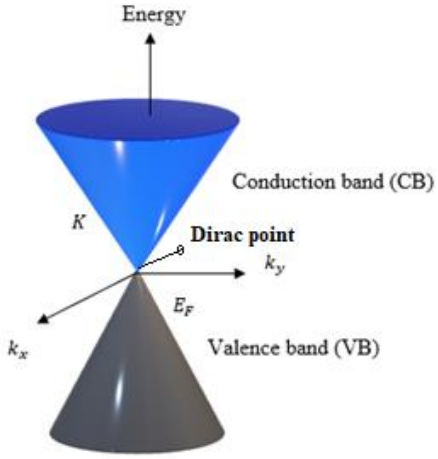


Figure 11. Dirac point band-structure of graphene

Conclusion

The Density Functional Theory (DFT) study involved a detailed theoretical investigation of monolayer and bilayer. Ultrasoft and norm-conserving pseudopotentials approaches were used in the calculations. Therefore, both Brillouin zone sampling parameters (10 × 10 × 1, k-point) and plane-wave monolayer and bilayer graphene parameters (320eV and 225eV, respectively) were optimized. The results of this study were computed using the open-source Quantum Espresso software package that incorporates the electronic structure software. Using the Broyden-Fletcher-Goldfarb-Shanno (BFGS) force and energy minimization method, monolayer and bilayer graphene were calculated to have a stable geometry. Graphene's very stable lattice and unit cell structure were discerned and observed using XCRYSDEN. The density of states and band gap have been calculated using the band calculation for ground-state properties. In both cases of graphene, zero DOS and 0eV for bandgap were recorded. Using this information, proving the properties of zero-gap semiconductor tags for graphene has been made possible. The shape of the band structure for monolayer graphene differs from bilayer graphene. sp^2 hybridization of graphene is the same for monolayer and bilayer graphene but more time consuming for bilayer. Monolayer graphene is more stable molecularly than bilayer graphene due to having a larger (HOMO – LUMO) gap. Therefore, it is reasonable to assume that results given by Quantum Espresso are reliable, given that the software has proven accurate in both electronic and structural analyses. At times, the absence of a zero-bandgap semiconductor material can hinder the use of electronic and optical devices. Expanding the study to AB stacked bilayer offers tremendous potential for application in devices due to its ability to tune the bandgap. The usage of graphene should not be restricted because it is a promising material. Stacking bilayer graphene with armchair and zigzag edges results in a bandgap value different from the bandgap obtained in this study. This subject is essential and requires more study from a theoretical and experimental perspective.

Acknowledgement

This work is funded by Short Term Grant with Project Code: 304/PFIZIK/6315241 for the financial supports, Research University Grant (RUI), USM (Grant code:1001/PFIZIK/8011113), and Fundamental Research Grant Scheme (FRGS) (Grant code: 203.PFIZIK.6711771).

References

1. Abbood, H. I. and Jabour, H. S. (2017). Theoretical study of electronic and electrical properties of pure and doped graphene sheets. *International Journal of Advanced Engineering Research and Science*, 4(7): 124-127.

2. Arrigoni, M. and Madsen, G. K. H. (2018). Comparing the performance of LDA and GGA functionals in predicting the lattice thermal conductivity of semiconductor materials: the case of AlAs. *Computational Materials Science*, 156: 354-360.
3. Banerjee, S. and Bhattacharyya, D. (2008). Electronic properties of nano-graphene sheets calculated using quantum chemical DFT. *Computational Materials Science*, 44(1): 41-45.
4. Bas, S. Z., Ozmen, M. and Yildiz, S. (2017). Electrochemical H_2O_2 sensor based on graphene oxide-iron oxide nanoparticles composite. *7th International Conference Nanomaterials: Application & Properties,* pp. 04NB05-1.
5. Castro, E. V, Peres, N. M. R., Santos, J. M. B. L. dos, Guinea, F. and Neto, A. H. C. (2008). Bilayer graphene: gap tunability and edge properties. *Journal of Physics: Conference Series*, 129: 012002.
6. Chaitanya Sagar, T. and Chinthapenta, V. (2018). Lower and upper bound estimates of material properties of pristine graphene: Using quantum espresso. *Advances in Structural Integrity* (pp. 253–265). Springer Singapore.
7. Chu, K.-L., Wang, Z.-B., Zhou, J.-J. and Jiang, H. (2017). Transport properties in monolayer–bilayer–monolayer graphene planar junctions. *Chinese Physics B*, 26(6): 067202.
8. Cooper, D. R., D'Anjou, B., Ghattamaneni, N., Harack, B., Hilke, M., Horth, A., Majlis, N., Massicotte, M., Vandsburger, L., Whiteway, E. and Yu, V. (2012). Experimental review of graphene. *ISRN Condensed Matter Physics*, 2012: 1-56.
9. Cruz-Silva, E., Jia, X., Terrones, H., Sumpter, B. G., Terrones, M., Dresselhaus, M. S. and Meunier, V. (2013). Edge–Edge Interactions in Stacked Graphene Nanoplatelets. *ACS Nano*, *7*(3): 2834-2841.
10. Dai, X. S., Shen, T. and Liu, H. C. (2019). DFT study on electronic and optical properties of graphene modified by phosphorus. *Materials Research Express*, *6*(8): 085635.
11. Dinh Le, T.-S., An, J. and Kim, Y.-J. (2017). Femtosecond laser direct writing of graphene oxide film on polydimethylsiloxane (PDMS) for flexible and stretchable electronics. *Conference on Lasers and Electro-Optics Pacific Rim (CLEO-PR)*, 2017: 1-4.
12. Freitas, R. R. Q., Rivelino, R., Mota, F. de B. and de Castilho, C. M. C. (2011). DFT Studies of the Interactions of a Graphene Layer with Small Water Aggregates. *The Journal of Physical Chemistry A*, 115(44): 12348-12356.
13. Gao, H. and Liu, Z. (2017). DFT study of NO adsorption on pristine graphene. *RSC Advances*, 7(22): 13082-13091.
14. Geng, W., Zhao, X., Liu, H. and Yao, X. (2013). Influence of interface structure on the properties of ZnO/graphene composites: A theoretical study by density functional theory calculations. *The Journal of Physical Chemistry C*, 117(20): 10536-10544.
15. Giannozzi, P., Baroni, S., Bonini, N., Calandra, M., Car, R., Cavazzoni, C., Ceresoli, D., Chiarotti, G. L., Cococcioni, M., Dabo, I., Dal Corso, A., de Gironcoli, S., Fabris, S., Fratesi, G., Gebauer, R., Gerstmann, U., Gougoussis, C., Kokalj, A., Lazzeri, M., … and Wentzcovitch, R. M. (2009). Quantum Espresso: a modular and open-source software project for quantum simulations of materials. *Journal of Physics: Condensed Matter*, 21(39): 395502.
16. Giannozzi, P., Baseggio, O., Bonfà, P., Brunato, D., Car, R., Carnimeo, I., Cavazzoni, C., de Gironcoli, S., Delugas, P., Ferrari Ruffino, F., Ferretti, A., Marzari, N., Timrov, I., Urru, A. and Baroni, S. (2020). Quantum Espresso toward the exascale. *The Journal of Chemical Physics*, 152(15): 154105.
17. Gil, D. M., Defonsi Lestard, M. E., Estévez-Hernández, O., Duque, J. and Reguera, E. (2015). Quantum chemical studies on molecular structure, spectroscopic (IR, Raman, UV–Vis), NBO and Homo–Lumo analysis of 1-benzyl-3-(2-furoyl) thiourea. *Spectrochimica Acta Part A: Molecular and Biomolecular Spectroscopy*, *145*, 553-562.
18. Gopinath, K. P., Vo, D.-V. N., Gnana Prakash, D., Adithya Joseph, A., Viswanathan, S. and Arun, J. (2021). Environmental applications of carbon-based materials: a review. *Environmental Chemistry Letters*, 19(1): 557-582.

19. Griffiths, K., Dale, C., Hedley, J., Kowal, M. D., Kaner, R. B. and Keegan, N. (2014). Laser-scribed graphene presents an opportunity to print a new generation of disposable electrochemical sensors. *Nanoscale*, 6(22): 13613–13622.
20. Hossain, M. T., Alam, M. N. K. and Islam, M. R. (2016). Gate oxide dependent performance of graphene FET using quasi-ballistic transport model. *3rd International Conference on Electrical Engineering and Information Communication Technology (ICEEICT)*, pp. 1-5.
21. Hosseindokht, Z., Paryavi, M., Asadian, E., Mohammadpour, R., Rafii-Tabar, H. and Sasanpour, P. (2017). Pressure sensor based on patterned laser scribed reduced graphene oxide; experiment & modeling. *2017 International Conference on Orange Technologies (ICOT)*, pp. 15-17.
22. Jeon, C., Shin, H.-C., Song, I., Kim, M., Park, J.-H., Nam, J., Oh, D.-H., Woo, S., Hwang, C.-C., Park, C.-Y. and Ahn, J. R. (2013). Opening and reversible control of a wide energy gap in uniform monolayer graphene. *Scientific Reports*, *3*(1): 2725.
23. Jigmat Stondus. (2016). Study of single and few-layers MoS_2 crystals. Master of Science, Banaras Hindu University.
24. Ke, X., Hao, G., Rong, Y., Zhou, X., Liu, J., Xiao, L. and Jiang, W. (2016). A facile approach to the hydrothermal synthesis of graphene. *16th International Conference on Nanotechnology (IEEE-NANO)*, pp. 604-607.
25. Koay, H. W., Ruslinda, A. R., Hashwan, S. S. B., Fatin, M. F., Thivina, V., Tony, V. C. S., Md Arshad, M. K., Voon, C. H. and Hashim, U. (2016). Surface morphology of reduced graphene oxide-carbon nanotubes hybrid film for bio-sensing applications. *International Conference on Semiconductor Electronics (ICSE)*, pp. 320-323.
26. Kumar, R., Dias, W., Rubira, R. J. G., Alaferdov, A. V., Vaz, A. R., Singh, R. K., Teixeira, S. R., Constantino, C. J. L. and Moshkalev, S. A. (2018). Simple and fast approach for synthesis of reduced graphene oxide–MoS_2 hybrids for room temperature gas detection. *IEEE Transactions on Electron Devices*, 65(9): 3943-3949.
27. Lebedeva, I. V., Knizhnik, A. A., Popov, A. M., Lozovik, Y. E. and Potapkin, B. V. (2011). Interlayer interaction and relative vibrations of bilayer graphene. *Physical Chemistry Chemical Physics*, 13(13): 5687.
28. Lin, S.-P., Ciou, J.-Y., Lai, T.-Y. and Lin, T.-W. (2017). Impedimetric investigation of dual electrical properties of reduced graphene-oxide-based biosensors in the detection of dopamine. *39th Annual International Conference of the IEEE Engineering in Medicine and Biology Society (EMBC)*, pp. 4098-4101.
29. Liu, X.-S., Bo, Z.-M., Tu, W.-C., Lin, M.-Y. and Chen, S.-L. (2017). Enhanced performance of reduced graphene oxide photodetectors by Ag nanoparticles. *Eleventh International Conference on Sensing Technology (ICST)*, pp. 1-4.
30. Liu, Z., Suenaga, K., Harris, P. J. F. and Iijima, S. (2009). Open and closed edges of graphene layers. *Physical Review Letters*, 102(1): 015501.
31. Marguna, S., Sulthoni, M. A., Anshori, I., Yuliarto, B., Surawijaya, A. and Utari, L. (2019). Synthesis of zinc oxide (ZnO) – graphene nanocomposite as CO gas sensor application. *International Symposium on Electronics and Smart Devices (ISESD)*, pp. 1-4.
32. Mi, W.-T., Qi, H.-Y., Zhao, H.-M., Li, Y.-X., Yang, Y. and Ren, T.-L. (2016). Ultrasound-aided spray casting for graphene oxide deposition. *2016 IEEE International Nanoelectronics Conference (INEC)*, pp. 1-2.
33. Mucha-Kruczyński, M., Aleiner, I. L. and Fal'ko, V. I. (2011). Strained bilayer graphene: Band structure topology and Landau level spectrum. *Physical Review B*, 84(4): 041404.
34. Ng, W.-B. (2018). Graphene-based materials for biotransistor application. Doctoral thesis, Nanyang Technological University, Singapore.
35. Ojo, O. O., Jonnalagadda, S. B. and Martincigh, B. S. (2018). Synthesis of graphene oxide under differing conditions and its characterization. *8th International Conference Nanomaterials: Application & Properties (NAP)*, pp. 1-4.
36. Pang, Y., Yang, Z., Xie, X. and Tao, L.-Q. (2020). Graphene oxide modified porous graphene for aqueous alcohol detection. *IEEE Sensors Letters*, 4(2): 1-4.

37. Papadakis, I., Stathis, A., Karampitsos, N., Stavrou, M., Kyrginas, D. and Couris, S. (2020). UV Laser photo-reduction of graphene oxide and graphene fluoride for the efficient tuning of their nonlinear optical response. *22nd International Conference on Transparent Optical Networks (ICTON)*, pp. 1-4.
38. Pashangpour, M. and Ghaffari, V. (2013). Investigation of structural and electronic transport properties of graphene and graphane using maximally localized Wannier functions. *Journal of Theoretical and Applied Physics*, *7*(1): 9.
39. Quhe, R., Ma, J., Zeng, Z., Tang, K., Zheng, J., Wang, Y., Ni, Z., Wang, L., Gao, Z., Shi, J. and Lu, J. (2013). Tunable band gap in few-layer graphene by surface adsorption. *Scientific Reports*, 3(1): 1794.
40. Rai, S., Bhujel, R. and Swain, B. P. (2018). Electrochemical analysis of graphene oxide and reduced graphene oxide for super capacitor applications. *IEEE Electron Devices Kolkata Conference (EDKCON)*, pp. 489-492.
41. Rana, S., Sandhu, I. S. and Chitkara, M. (2018). Exfoliation of graphene oxide via chemical reduction method. *6th Edition of International Conference on Wireless Networks & Embedded Systems (WECON)*, pp. 54-57.
42. Rani, P. and Bhandari, R. (2013). DFT study of defects in graphene. *International Conference on Advanced Nanomaterials & Emerging Engineering Technologies*, pp. 237-239.
43. Rani, P., Dubey, G. S. and Jindal, V. K. (2014). DFT study of optical properties of pure and doped graphene. *Physica E: Low-Dimensional Systems and Nanostructures*, *62*: 28-35.
44. Razado-Colambo, I., Avila, J., Vignaud, D., Godey, S., Wallart, X., Woodruff, D. P. and Asensio, M. C. (2018). Structural determination of bilayer graphene on SiC(0001) using synchrotron radiation photoelectron diffraction. *Scientific Reports*, 8(1): 10190.
45. Rozhkov, A. V., Sboychakov, A. O., Rakhmanov, A. L. and Nori, F. (2016). Electronic properties of graphene-based bilayer systems. *Physics Reports*, 648: 1-104.
46. Ayyappan, S. & R.Nithya. (2018). Molecular structure, NBO and HOMO-LUMO analysis of quercetin on single layer graphene by density functional theory. *Digest Journal of Nanomaterials and Biostructures*, *13*(1): 97-105.
47. Seenithurai, S., Pandyan, R. K., Kumar, S. V., & Mahendran, M. (2013). Electronic Properties of boron and nitrogen doped graphene. *Nano Hybrids*, 5: 65-83.
48. Shruthi, G., Anshika, Baishali, G., Nella, N., Radhakrishna, V. and Rajanna, K. (2018). Investigation on reduced graphene oxide for radiation sensing application. *IEEE Sensors*, pp. 1-4.
49. Song, S., Zhao, H., Zheng, X., Zhang, H., Liu, Y., Wang, Y. and Han, B. (2018). A density functional theory study of the role of functionalized graphene particles as effective additives in power cable insulation. *Royal Society Open Science*, *5*(2): 170772.
50. Khan, T. T. (2017). Spectroscopic and microscopic analysis of graphene for sensor applications. The U niversity of Texas at El Paso.
51. Tencha, A., Fedoriv, V., Shtepliuk, I., Yakimova, R., Ivanov, I., Khranovskyy, V., Shavanova, K. and Ruban, Y. (2017). Synthesis of graphene oxide inks for printed electronics. *IEEE International Young Scientists Forum on Applied Physics and Engineering (YSF)*, pp. 155-158.
52. Thema, F. T., Moloto, M. J., Dikio, E. D., Nyangiwe, N. N., Kotsedi, L., Maaza, M. and Khenfouch, M. (2013). Synthesis and characterization of graphene thin films by chemical reduction of exfoliated and intercalated graphite oxide. *Journal of Chemistry*, 2013: 1-6.
53. Torrisi, L., Silipigni, L. and Cutroneo, M. (2018). Radiation effects of IR laser on graphene oxide irradiated in vacuum and in air. *Vacuum*, 153: 122-131.
54. You, T., Yang, N., Shu, Y. and Yin, P. (2019). A DFT study on graphene-based surface-enhanced Raman spectroscopy of Benzenedithiol adsorbed on gold/graphene. *Journal of Raman Spectroscopy*, 50(10): 1510-1518.

55. Zainal, N., How, J. F., Choo, X. H. and Soon, C. F. (2020). Synthesis and characterization of graphene oxide (GO) and reduced graphene oxide (rGO) using Modified Tour's method for sensing device applications. *2020 IEEE Student Conference on Research and Development (SCOReD)*: pp. 385-390.
56. Zhan, D. (2013). Structural and electronic properties of graphene and modified graphene. Doctoral thesis, Nanyang Technological University, Singapore.
57. Zhang, D., Liu, J. and Xia, B. (2016). Layer-by-layer self-assembly of zinc oxide/graphene oxide hybrid toward ultrasensitive humidity sensing. *IEEE Electron Device Letters*, *37*(7): 916-919.
58. Zhang, Y., Tang, T.-T., Girit, C., Hao, Z., Martin, M. C., Zettl, A., Crommie, M. F., Shen, Y. R. and Wang, F. (2009). Direct observation of a widely tunable bandgap in bilayer graphene. *Nature*, 459(7248): 820-823.
59. Vu, K. B., Le Phuc Nhi, T., Vu, V. V. and Tung Ngo, S. (2020). How do magnetic, structural, and electronic criteria of aromaticity relate to HOMO – LUMO gap? An evaluation for graphene quantum dot and its derivatives. *Chemical Physics,* 539: 110951.
60. Zhu, Z., Chutia, A., Sahnoun, R., Koyama, M., Tsuboi, H., Hatakeyama, N., Endou, A., Takaba, H., Kubo, M., Del Carpio, C. A. and Miyamoto, A. (2008). Theoretical study on electronic and electrical properties of nanostructural ZnO. *Japanese Journal of Applied Physics*, 47(4): 2999-3006.

Malaysian Journal of Analytical Sciences Vol 26 No 6 2022

Articles 1-9 are selected papers from the "The 9th International Conference on Sensors (AsiaSense 2021), 20-21 October 2021; organized by the Malaysian Society for Sensor Technology Development (Sensor Malaysia)".

Guest Editor: Jaafar Abdullah

Page

1. NANOPARTICLES FUNCTIONALIZED REDUCED GRAPHENE OXIDE THIN FILMS FOR DETECTION OF ACETIC ACID AT LOW CONCENTRATIONS 1158
Nor Syahira Mohd Tombel, Marmeezee Mohd Yusoff, Hasan Firdaus Mohd Zaki, Firzalaila Syarina Md Yakin, Siti Aishah Mohamad Badaruddin

2. ENHANCING THE HYDROGEN GAS SENSING PROPERTIES OF ZINC OXIDE DOPED WITH ALUMINUM PREPARED VIA THERMAL OXIDATION 1168
Naif H. Al-Hardan, Muhammad Azmi Abdul Hamid, Azlan Abdul Aziz, Naser M. Ahmed

3. ENZYME-BASED ELECTROCHEMICAL BIOSENSOR ON IMMOBILIZATION OF TYROSINASE ONTO CARBOXYL FUNCTIONALIZED CARBON NANOTUBE FOR DETECTION OF TYRAMINE 1179
Nurul Hana Masod and Syaza Azhari

4. DEVELOPMENT OF AN ELECTROCHEMICAL IMMUNOSENSOR STRIP FOR EARLY DETECTION OF RICE BACTERIAL LEAF BLIGHT (BLB) DISEASE AND ITS APPLICATION ON A PORTABLE DEVICE 1191
Hazana Razali, Norhafniza Awaludin, Nurul Hidayah Husin, Sahira Akmar Zulkepli, Rafidah Abd Rahman, Mohammad Rejab Ismail, Kogeethavani Ramachandran, Faridah Salam, Nur Azura Mohd Said

5. LABEL-FREE ELECTROCHEMICAL IMMUNOSENSOR DEVELOPMENT FOR MYCOTOXINS DETECTION IN GRAIN CORN 1205
Noor Sheryna Jusoh, Norhafniza Awaludin, Faridah Salam, Adlin Azlina Abdul Kadir, Nur Azura Mohd Said

6. CHARACTERIZATION OF CELLULOSE NANOCRYSTAL-GOLD NANOPARTICLES/CHITOSAN MODIFIED SCREEN-PRINTED CARBON ELECTRODE AND ITS APPLICATION IN THE FABRICATION OF ELECTROCHEMICAL BIOSENSOR FOR TETRACYCLINE DETECTION 1216
Nurul Shahirah Hasim, Nor Azah Yusof, Ruzniza Mohd Zawawi, Noordiana Nordin

7. CARBON DOTS/CHITOSAN MODIFIED SCREEN-PRINTED CARBON ELECTRODES FOR THE DETECTION OF BISPHENOL A 1227
Nor Faezah Mohd Daud, Jaafar Abdullah, Nor Azah Yusof, Putri Nur Syafieqah Zainal

8. THE APPLICATION OF ELECTRONIC NOSE COUPLED WITH 80:20 K-NEAREST NEIGHBORS CLASSIFICATION TECHNIQUE FOR AGARWOOD OIL QUALITY INDEX ESTABLISHMENT 1240
Sahrim Lias, Abd Majid Jalil, Mailina Jamil, Mohd Shafik Yuzman Tolmanan, Nurlaila Ismail, Mohd Nasir Taib

9. MODELING THE TIME RESPONSE OF CURRENT USING INTERDIGITATED ARRAYS IN A SHALLOW ELECTROCHEMICAL CELL 1249
Cristian F. Guajardo Yevenes and Werasak Surareungchai

10. FERROCENE MEDIATED AMPEROMETRIC BIOSENSOR FOR L-GLUTAMATE BASED ON L-GLUTAMATE OXIDASE IMMOBILIZED IN A PHOTOCURABLE METHACRYLIC FILM 1260
Noor Zuhartini Md Muslim, Musa Ahmad, Lee Yook Heng, Bahruddin Saad

11. SURFACTANT FUNCTIONALIZATION OF MAGNETIC NANOPARTICLES: A STUDY ON THE PARTICLE SIZE DISTRIBUTION AND ZETA POTENTIAL AS A NANOFLUID TO IMPROVE THERMAL CONDUCTIVITY 1274
Cheah Ching Wei, Noorashikin Md. Saleh, Nik Nur Atiqah Nik Wee, Beh Shiuan Yih, Ahmad Fazlizan, Farhanini Yusoff

12. OPTIMIZATION OF QUADRUPOLE TIME-OF-FLIGHT LIQUID CHROMATOGRAPHY MASS SPECTROMETRY (QTOF-LC/MS) CONDITIONS FOR DETERMINATION OF COLISTIN IN HUMAN PLASMA 1288
Mohd Shafie Zabidi, Ruzilawati Abu Bakar, Nurfadhlina Musa, Suzana Mustafa, Wan Nazirah Wan Yusuf

13. TRANSESTERIFICATION OF *Calophyllum inophyllum* OIL USING CaO-K_2CO_3 CATALYST FROM *Corbicula fluminea* SHELLS AND BANANA PEELS 1303

Lee Wei Zhen, Siti Norhafiza Mohd Khazaai, Gaanty Pragas Maniam, Liliwirianis Nawi

14. EFFECT OF FAT REPLACEMENT WITH DIFFERENT TYPES OF EGGPLANTS ON THE PHYSICOCHEMICAL AND SENSORIAL PROPERTIES OF CHICKEN SAUSAGES: A CHEMOMETRIC APPROACH 1313
Farra Nabilah Hamidon, Mohd Razali Faridah, Abu Bakar Asyrul-Izhar, Muhamad Shirwan Abdullah Sani, Mohammad Rashedi Ismail-Fitry

15. CHARACTERIZATION AND PHYSICOCHEMICAL STUDY OF β-CYCLODEXTRIN-ANGELWING CLAM HYDROLYSATE COMPLEXES 1332
Nurul Fasihah Razak, Atikah Mansor, Nur Adila Basari, Normah Ismail

16. MAGNETIC NANOPARTICLES AS EFFECTIVE ADSORBENTS FOR THE REMOVAL OF HEAVY METALS FROM WATER: A REVIEW OF SURFACE MODIFICATION (2015-2022) 1344
Gimba Joshua Dagil, Ng Nyuk-Ting, Aemi Syazwani Abdul Keyon, Sheela Chandren, Wan Aini Wan Ibrahim

17. A REVIEW ON LIPID OXIDATION IN EDIBLE OILS 1378
Radhika Loganathan, Azmil Haizam Ahmad Tarmizi, Shireene Ratna Vethakkan, Kim-Tiu Teng|

18. CHEMICAL SYNTHESIS OF METAL OXIDE NANOPARTICLES VIA IONIC LIQUID AS CAPPING AGENT: PRINCIPLE, PREPARATION AND APPLICATIONS 1394
Nurul Syafiqah Tapak, Mohd Azizi Nawawi, Ahmad Husaini Mohamed, Eddie Tan Ti Tjih, Yusairie Mohd, Ahmad Hazri Bin Ab Rashid, Jaafar Abdullah, Nor Azah Yusof, Nor Monica Ahmad

Malaysian Journal of Analytical Sciences (MJAS)
Published by Malaysian Analytical Sciences Society

NANOPARTICLES FUNCTIONALIZED REDUCED GRAPHENE OXIDE THIN FILMS FOR DETECTION OF ACETIC ACID AT LOW CONCENTRATIONS

(Filem Nipis Grafin Oksida Terkurang Berfungsi Nanopartikel untuk Pengesanan Asid Asetik pada Kepekatan Rendah)

Nor Syahira Mohd Tombel[1*], Marmeezee Mohd Yusoff[2], Hasan Firdaus Mohd Zaki[2,3], Firzalaila Syarina Md Yakin[4] and Siti Aishah Mohamad Badaruddin[5]

[1]Department of Computational and Theoretical Sciences, Kulliyyah of Science, International Islamic University of Malaysia, 25200, Kuantan, Pahang, Malaysia
[2]Kulliyyah of Engineering, International Islamic University Malaysia, Jalan Gombak, 53100, Kuala Lumpur, Malaysia
[3]Centre for Unmanned Technologies (CUTe), Kulliyyah of Engineering, International Islamic University of Malaysia, Jalan Gombak, 53100, Kuala Lumpur, Malaysia
[4]Advanced Devices Lab, MIMOS Berhad, Technology Park Malaysia, 57000 Kuala Lumpur, Malaysia

[*]Corresponding author: norsyahiramt@gmail.com

Received: 31 January 2022; Accepted: 23 April 2022; Published: 27 December 2022

Abstract

This research proposes reduced graphene oxide (rGO) functionalized with nanoparticles (NPs) from gold (Au), silver (Ag) and platinum (Pt) as a sensing material for the detection of acetic acid gas at low concentrations, from 1 to 5 part per million (ppm). The rGO was functionalized with NPs at different sputtering durations (15 sec and 75 sec) and relative frequency (RF) power (30W and 70W) to study the enhancement of sensing properties. The sensors were exposed to acetic acid from 1 to 5 ppm in the presence of 20% relative humidity (RH) and at 30 °C room temperature. In this work, the Au NPs/rGO (30W 15s), Ag NPs/rGO (30W 15s) and Pt NPs/rGO (70W 15s) sensors were reported to have a good response with sheet resistance, (R_s) at values: 327.2, 453.844 and 201.084 Ω/sq, respectively, compared with the reference sensor, rGO at only R_s, 529.614 Ω/sq. The three sensors had also recorded high R^2 values compared to the reference rGO (0.9448) with values of 0.993, 0.966 and 0.995 for Au/rGO (30W 15s), Ag/rGO (30W 15s) and Pt/rGO (70W 15s), respectively. Thus, the functionalization of rGO with nanoparticles can enhance the sensor's electrical properties and generate good responses for acetic acid gas detection at low concentrations.

Keywords: reduced graphene oxide, functionalization, nanoparticle, response, sensitivity, gas detection.

Abstrak

Penyelidikan ini mencadangkan grafin oksida terkurang (rGO) dan kefungsiannya dengan nanopartikel (NPs) daripada emas (Au), perak (Ag) dan platinum (Pt) sebagai bahan penderiaan untuk pengesanan gas asid asetik pada kepekatan rendah. NPs telah difungsikan dengan rGO pada tempoh percikan yang berbeza (15 saat dan 75 saat) dan kuasa frekuensi relatif (RF) (30W dan 70W) untuk mengkaji peningkatan sifat penderiaan peranti penderia. Penderia didedahkan dengan asid asetik dari 1 hingga 5 bahagian per juta (ppm) kepekatan dengan kehadiran 20% Kelembapan Relatif (RH) dan pada suhu bilik 30 °C. Dalam kerja ini, penderia Au NPs/rGO (30W 15s), Ag NPs/rGO (30W 15s) dan Pt NPs/rGO (70W 15s) dilaporkan mempunyai tindak balas yang baik dengan nilai rintangan lembaran, Rs yang diukur; 327.2, 453.844 dan 201.084 Ω/sq, masing-masing, dengan nilai yang lebih rendah daripada penderia rujukan, rGO sahaja iaitu 529.614 Ω/sq. Ketiga-tiga penderia itu juga mencatatkan nilai R^2 yang lebih tinggi berbanding rGO rujukan (0.9448) dengan nilai masing-masing 0.993, 0.966 dan 0.995 untuk Au NPs/rGO (30W 15s), Ag NPs/rGO (30W 15s) dan Pt NPs/rGO (70W 15s). Oleh itu, kefungsian rGO dengan nanopartikel boleh meningkatkan sifat elektrik sensor dan menjana tindak balas yang baik untuk pengesanan gas asid asetik pada kepekatan rendah.

Kata kunci: grafin oksida terkurang, kefungsian, nanopartikel, tindak balas, kepekaan, pengesanan gas

Introduction

Graphene is a two-dimensional crystalline material that has become a promising sensing element due to its unique properties of having high surface area [1], fast electrical transport, zero bandgap semiconductor [2] and high electron mobility at room temperature [3]. The properties of graphene demonstrate its potential for gas sensing applications with high sensitivity, which is mainly related to the resistivity and adsorption sites of the surface material.

Graphene oxide (GO) and reduced graphene oxide (rGO) derived from graphene can further improve the performance of a material as a sensing element [4]. GO and rGO have good electrical conductivity and sensitive surface adsorbates compared to graphene only due to the crystal defects and oxygen functionalization on its edge and basal [5-6]. A large number of functional groups and defects on rGO provide abundance adsorption sites [7]. Metal oxide nanoparticles such as gold (Au), silver (Ag) and platinum (Pt) have been functionalized with graphene or rGO to enhance the sensitivity of the surface material. Metal nanoparticles are reported to be an excellent catalyst due to their high ratio of surface atoms which increase the subsequent interaction of targeted gases with the absorbed oxygen species on the sensing surface [2,8].

In the medical field, the detection of a volatile organic compound (VOC) through breath analysis has been used as a quick and non-invasive diagnostic procedure to monitor human health. There are hundreds of VOCs used as preclinical biomarkers in diagnosing various pulmonary diseases as they are linked to metabolic activity in the body and provide information about an individual's health [9]. Many gasses were studied for VOC detection such as acetone, toluene, isoprene, acetaldehyde, ethanol, acetic acid, phenol and 2-propanol [10-11]. Acetic acid is a natural biomarker that is correlated with metabolic acids. It is an indicator of airways acidification for a patient with gastroesophageal reflux and cystic fibrosis disease [12]. Thus, a non-invasive approach for the detection of VOC as a breath biomarker is expected to improve health monitoring and early diagnosis [9].

In this study, we report the functionalized rGO with Au NPs, Ag NPs, and Pt NPs as a thin film on resistive VOC sensors for acetic acid detection. Different sputtering durations and powers during the deposition of the nanoparticle on the rGO thin film were tested to study the consequences on the sensing properties. The electrical parameters of the sensing materials, such as sheet resistivity and conductivity, were measured using hall effect measurement. Furthermore, the sensor sensing behavior was determined and studied from the detection of acetic acid gas (1 to 5 ppm) in the presence of 20% relative humidity (RH) at room temperature. The result from this study highlights the material that has suitable fabrication parameters with good performance and sensitivity to low concentrations of acetic acid at room temperature.

Materials and Methods

The rGO was derived from GO films as mentioned in [12]. The rGO layer was spin-coated and reduced at a

temperature of more than 700 °C. Then, the rGO was patterned as sensing material on top of a titanium/platinum (Ti/Pt) interdigitated electrode (IDE) that was deposited on a silicon dioxide/silicon (SiO_2/Si) substrate. The sensor was then loaded into a vacuum deposition chamber for Au NPs (99.99% purity) and sputtered at the duration of 15 sec and 75 sec. The sputtering was carried out in an Ar environment at 0.005 mbar with RF power of 30W and 70W. The lift-off process was done by soaking the sensors in acetone solutions where the photoresist on pads was removed. This process was repeated for Ag and Pt nanoparticles functionalization. The sensor's design is illustrated in Figure 1 and the details of the parameter are described in Table 1.

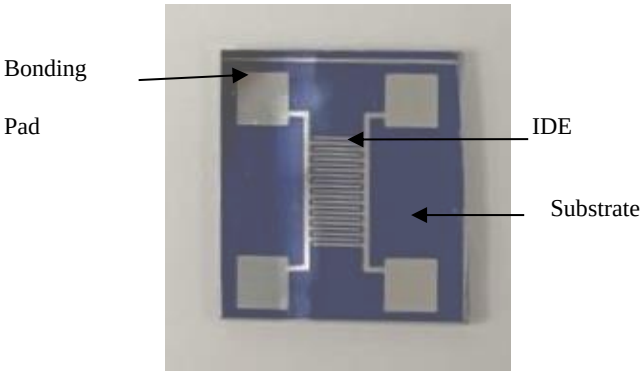


Figure 1. Image of the VOC sensor

Table 1. List of Samples and Parameters of the VOC Sensors

Sample No.	Nanoparticles	Power (WRF)	Time (sec)	Remarks
1	Reference rGO film			Bare rGO
2	Au	30	15	Au NPs/rGO (30W 15s)
3	Au	30	75	Au NPs/rGO (30W 75s)
4	Au	70	15	Au NPs/rGO (70W 15s)
5	Au	70	75	Au NPs/rGO (70W 75s)
6	Ag	30	15	Ag NPs/rGO (30W 15s)
7	Ag	30	75	Ag NPs/rGO (30W 75s)
8	Ag	70	15	Ag NPs/rGO (70W 15s)
9	Ag	70	75	Ag NPs/rGO (70W 75s)
10	Pt	30	15	Pt NPs/rGO (30W 15s)
11	Pt	30	75	Pt NPs/rGO (30W 75s)
12	Pt	70	15	Pt NPs/rGO (70W 15s)
13	Pt	70	75	Pt NPs/rGO (70W 75s)

***rGO= reduced graphene oxide, Au NPs = Gold nanoparticle, Ag NPs = Silver nanoparticle, Pt NPs = Platinum nanoparticle**

The electrical properties of the sensors were obtained using hall effect measurement (Ecopia HMS-5300) at room temperature before proceeding with the VOC gas detection test. The experimental setup for the gas sensing system is illustrated in Figure 2. The procedure was the same as mentioned in the previous study [13].

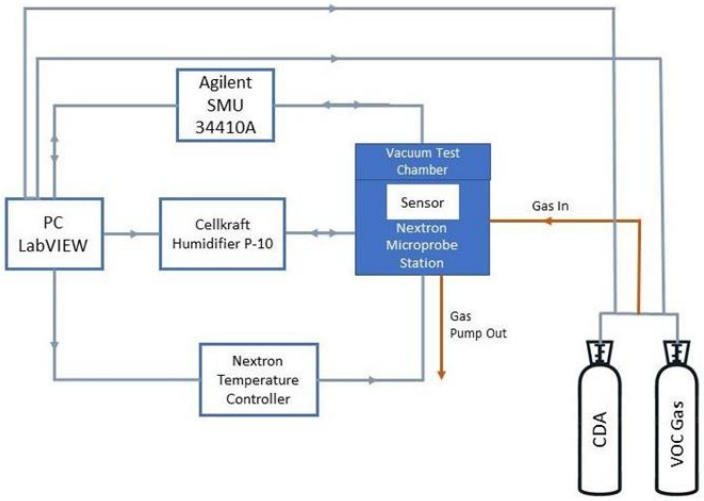


Figure 2. Schematic diagram of the experimental setup for gas detection system

The sensor was put on a sample stage in the Nextron microprobe station. Then, gas testing measurement was applied with a clean exposure method at 20% RH and at room temperature, 30℃. The flow of clean dry air (CDA) was maintained at 1 L/min for 3 min to stabilize the baseline reading for the sensor. Next, the VOC gas was exposed to the sensor at 1ppm for 30 sec. Then, the gas purged out and the CDA was allowed to flow again in 30 sec. The method was repeated by increasing the gas concentration with 1 to 5 ppm. Changes in resistance reading as the signal output were used to measure the sensor response and sensitivity (S) using the formula below [14, 15]:

$$\Delta R = R_{air} - R_{gas} \quad (1)$$

$$\text{Sensitivity (S)} = R_{air}/R_{gas} \quad (2)$$

$$\text{Response} = \frac{\Delta R}{R_{gas}} \times 100\ (\%) \quad (3)$$

Where R_{air} is an average resistance in CDA only, without VOC gas. R_{gas} is an average resistance with the exposure of VOC gas.

Results and Discussion

Surface morphology

Figure 3 shows the FESEM images of rGO thin film sputtered with Au NPs/rGO, Ag NPs/rGO and Pt NPs/rGO for parameters 30W 15 sec, 30W 75 sec, 70W 15 sec and 70W 75 sec with 200k applied magnification for each device. Based on Figure 3, the grain size was increased with the increase of time and power. Good particle formation can be found at 15 sec to 75 sec duration of nanoparticle sputtering. The nanoparticle size for Au and Ag had become bigger as the power and sputtering duration increased. Meanwhile, the grain size for Ag NPs/rGO at 70W began to agglomerate into large entities and become irregular in shape. This may be due to the coalescence of nanoparticles at a longer sputtering duration [16]. Pt NPs still showed a smaller size at 30W and 70W, and the grain size cannot be seen clearly as it was fully deposited onto the rGO thin film compared with Au and Ag NPs.

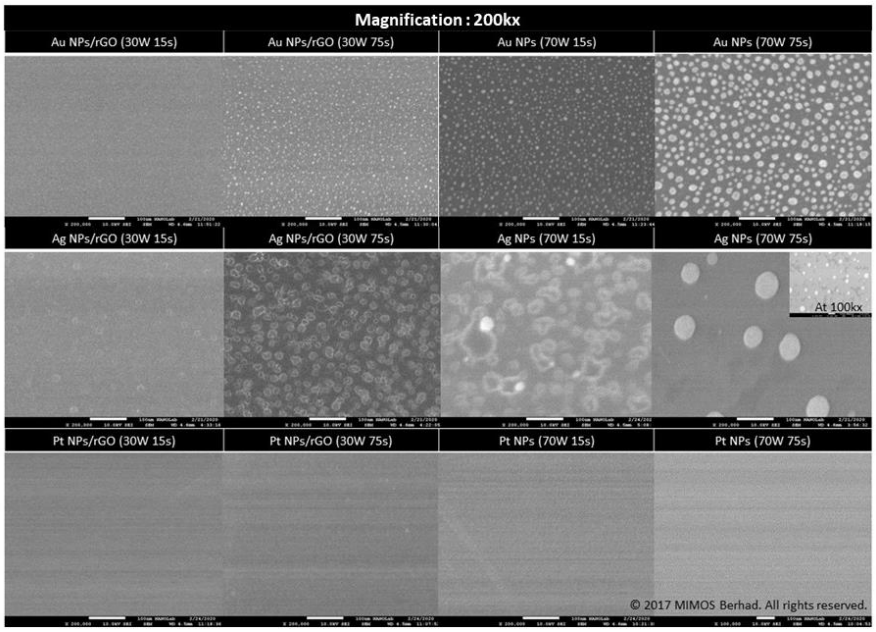


Figure 3. FESEM image of nanoparticle Au, Ag and Pt on rGO thin film after 15 sec and 75 sec sputtering at 30W and 70W

Hall effect measurement analysis

Electrical properties such as average sheet resistivity, Rs, average resistance, R and conductivity, σ of thin film on the samples were obtained from the hall effect measurement and are listed in Table 2. Functionalized NPs except Ag NPS/rGO at 70W had shown lower resistivity compared with the reference sensor, the thin film with rGO only. The NPs' functionalization on the rGO thin film was varied with power and sputtering duration. The variation caused defect concentrations on the thin film and increased the electrical properties of NPs functionalized rGO rather than the thin film of the rGO only [17].

Table 2. List of electrical properties for the VOC sensor

Sensor	Average Resistance Sheet, Rs, (Ω/sq)	Average Resistance, R (Ω)	Conductivity, σ (S/cm)
rGO	529.61	0.000201	4964.56
Au NPs/rGO (30W 15s)	327.20	0.000129	7732.44
Au NPs/rGO (30W 75s)	394.16	0.000154	6475.38
Au NPs/rGO (70W 15s)	394.43	0.000155	6471.26
Au NPs/rGO (70W 75s)	394.84	0.000154	6497.20
Ag NPs/rGO (30W 15s)	453.84	0.000176	5689.86
Ag NPs/rGO (30W 75s)	467.94	0.000181	5518.76
Ag NPs/rGO (70W 15s)	793.39	0.000300	3331.94
Ag NPs/rGO (70W 75s)	3641.00	0.001364	733.388
Pt NPs/rGO (30W 15s)	270.02	0.000109	9163.50
Pt NPs/rGO (30W 75s)	286.96	0.000116	8595.58
Pt NPs/rGO (70W 15s)	201.08	0.000085	11758.20
Pt NPs/rGO (70W 75s)	426.37	0.000166	6032.040

Figure 4 plots the average sheet resistivity, R_s value for Au NPs/rGO, Ag NPs/rGO and Pt NPs/rGO films at the different parameters. The bare rGO film marked as a reference sensor has a R_s value of 529.61 Ω/sq. Meanwhile, for rGO functionalized with Au, Ag and Pt, the NPs showed a decrease in the Rs value except for Ag NPs at 70 W. The sensor with thin film Au NPs/rGO, Ag NPs/rGO and Pt NPs/rGO at 30W and 15 sec had the R_s value decrease to 327.2, 453. 84 and 270.02 Ω/sq, respectively. However, Ag NPs/rGO at 70W at sputtering time 15 sec to 75 sec showed a gradual increase in the sheet resistivity from 793.39 Ω/sq to 3641.00 Ω/sq, which may be due to the increment of the grain size for Ag NPs at high power. The increment of power and sputtering time during functionalization had increased the grain size of the NPs (refer to Figure 3), thus increasing the sheet resistivity of the thin film. The increased grain size of the nanoparticle had affected the resistivity of the device as the grain boundaries act as scattering centers for the electron [18].

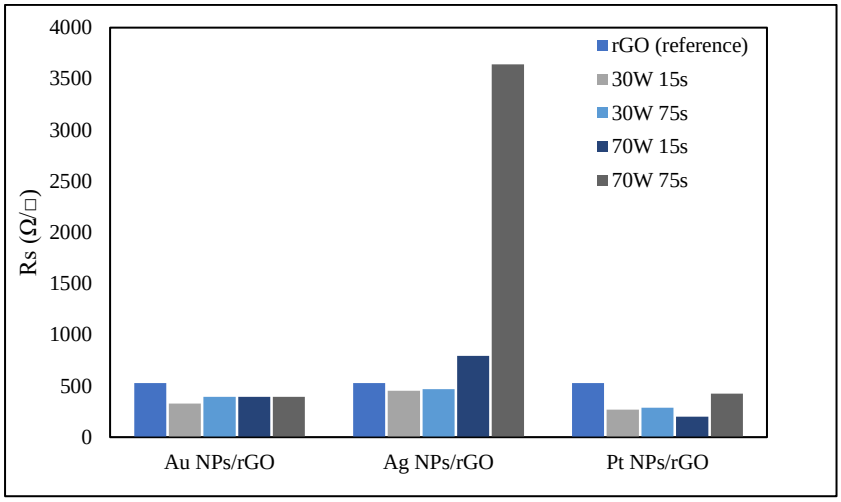


Figure 4. The sheet resistivity of the rGO and the functionalization with nanoparticles at four different parameters

Sensor response measurement

The response from the reference sensor during exposure to acetic acid is shown in Figure 5. At first, when the CDA was exposed to the chamber, the resistance increased due to the removal of electrons that took place by oxygen absorption in the depletion layer. At this phase, the sensor also showed a drift in baseline reading. Drift in sensor response occurs due to many factors, such as the age of the sensor or variation from environmental conditions. For this sensor, the source of the sensor drift may come from the temperature or humidity changes in the chamber [19].

Next, when the acetic acid was purged into the chamber, resistance from the rGO sensing layer began to decrease. This is because the gas molecules reacted with the adsorbed oxygen ions and the electrons were absorbed back into the conduction band [17]. The sensor with rGO and NPs functionalized rGO acted as an n-type semiconductor. Thus, the resistance decreased as the acetic acid acted as a reducing gas on the sensing element.

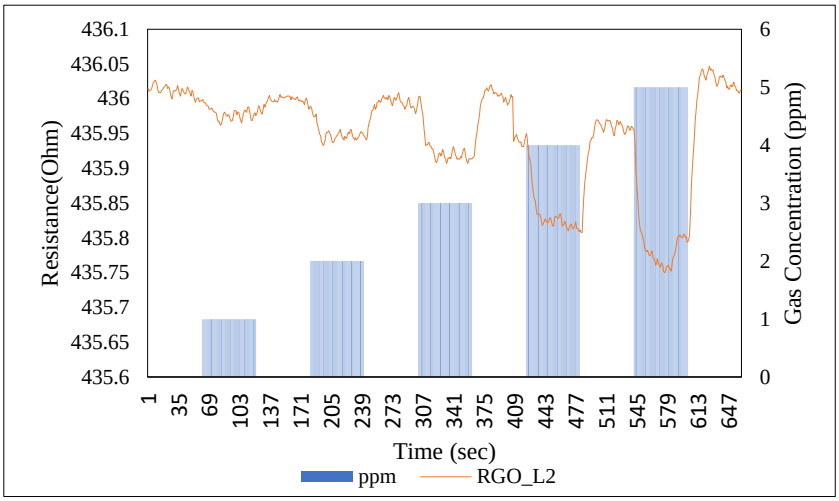


Figure 5. Response rGO thin film-based VOC Sensor on 1 to 5 ppm of acetic acid

Figure 6 shows the average sensitivity for functionalized rGO with a) Au NPs, b) Ag NPs and c) Pt NPs. The sensitivity of the sensor increased as the concentration increased. Meanwhile, Figure 7 showed the R^2 value for the linearity of the sensor response that corresponds with the gas concentration. For sensor selection, the sensor response and the R^2 value were compared for each sensor.

Based on the result in Figure 6a, the Au NPs/rGO sensors had low sensitivity with acetic acid compared with the reference sensor. However, the linearity of the sensor response based on Figure 7 showed that Au NPs/rGO at 30W and 15 sec had R^2 value 0.9869, which was the highest among the others, followed by Au NPs/rGO at 70W and 75 sec. The sheet resistivity for Au NPs was also the lowest at 30W and 15 sec at 327.20 Ω/sq. The sensor conductivity for Au NPs at 30W reached maximum at low sputtering duration, while at high sputtering duration, it was good at high power.

Next, for Ag NPs functionalization, parameter 70W and 75 sec showed a good response compared to the reference sensor. Even though the Ag NPs/rGO (70W 75s) sensor had the highest R_s with 3641 Ω/sq, the sensitivity of the sensors was higher based on the result in Figure 6b. The sensitivity of the Ag NPs functionalized rGO was higher than pure rGO because the attachment of the Ag nanoparticle onto the rGO led to more active sites such as defects and oxygen functional group for adsorption of VOC molecules [20]. Besides that, the agglomerate grain size of Ag NP on the rGO thin film caused it to become more sensitive with the acetic acid. Based on Chen Zhou et al. in their study in 2012, a decrease in the grain size of the nanoparticle on the thin film was reported to be low in electrical and thermal conductivities [21].

Next, for the Pt NPs/rGO sensor in Figure 6c, the sensitivity with the acetic acid was the same as Au NPs which is lower than the pure rGO. The grain size of the nanoparticle can be seen clearly as Ag NPs, however the R^2 value for the Pt NPs/rGO sensor at high power (70W) had a high R^2 value compared to the pure rGO and Pt NPs/rGO at 30W. Based on the hall effect measurement, Pt NPs had low R_s value compared to the pure rGO. However, a good linearity of the sensor response was observed at high power for Pt NPs at 15 sec and 75 sec with 0.9948 and 0.9842, respectively. The Rs value for Pt NPs/rGO at 30W 15 sec had increased from 270.02 to 286.96 Ω/sq. The lowest R^2 value for the Pt NPs at low power can be affected by the duration of sputtering. Pt is commonly used as an electrode as it has high chemical stability and is more stable at high temperature [17], thus, the sensor's sensitivity can be seen as good at high temperature.

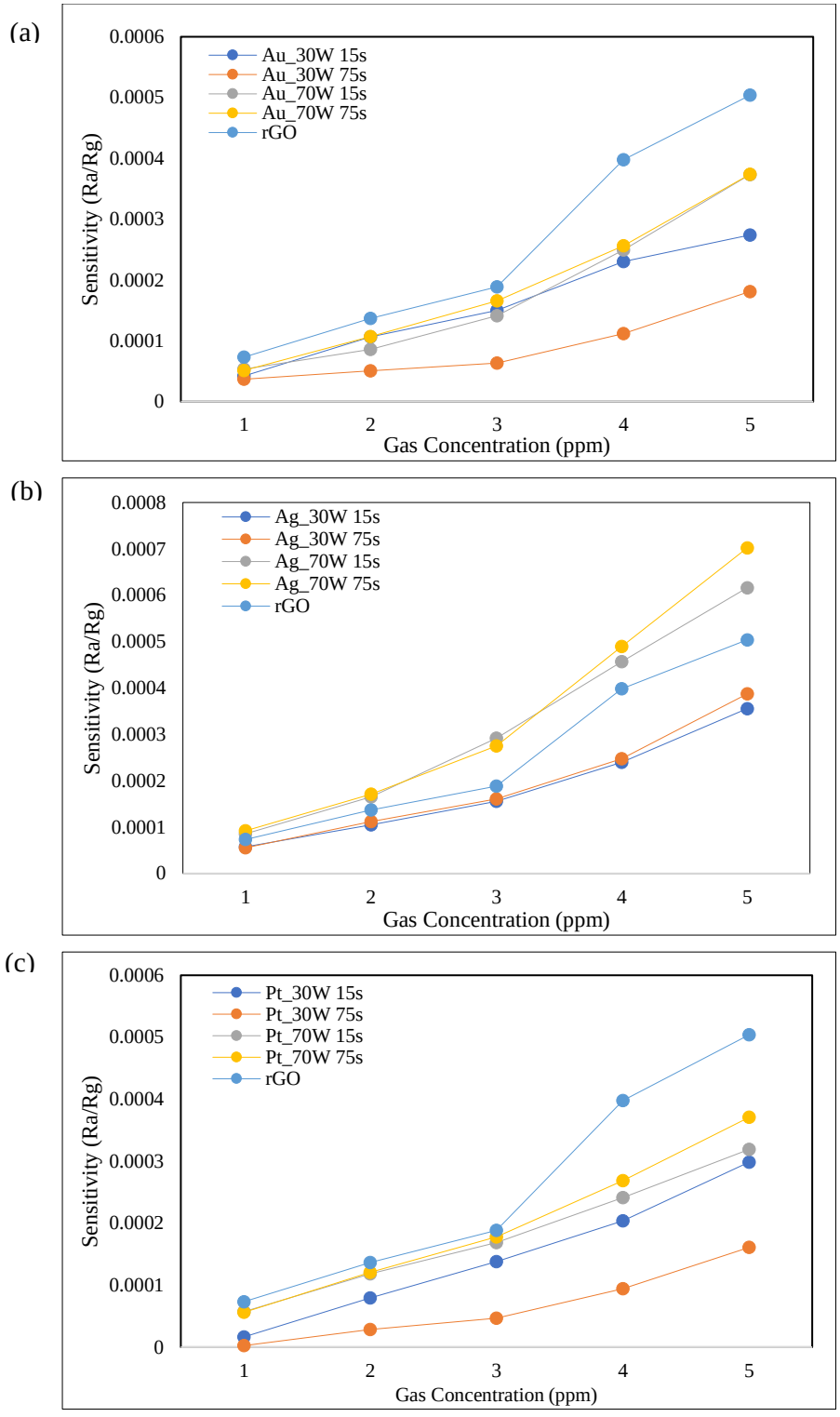


Figure 6. Sensitivity for functionalized rGO with a) Au NPs, b) Ag NPs and c) Pt NPs sensors

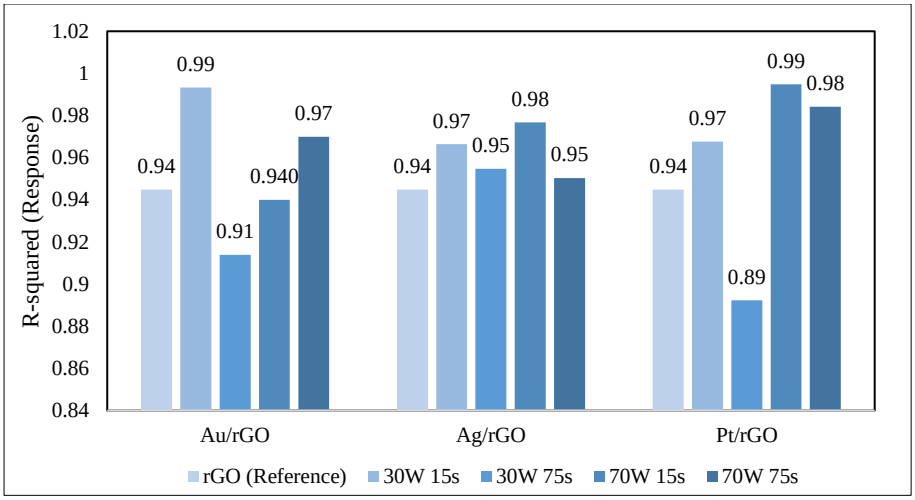


Figure 7. The R^2 value for the sensors on the detection of acetic acid

Conclusion

In this work, the n-type material was separately analyzed to detect reducing gas. The VOC sensors of rGO functionalized with NPs can detect low concentrations of acetic acid at a low operating temperature. The sensitivity results were compared between metal nanoparticles at different powers and durations. However, the cause of sensitivity for different types of nanoparticle functionalization rGOs were affected by different reasons. For Au NPs, the sensitivity of the sensor was influenced by the resistivity of the thin film, while for Ag NPs, the agglomerate of the grain size was more affected. For Pt NPs, high power made the sensor more sensitive to acetic acid. Hence, the study for these sensors can be taken further by varying the sputtering duration at each power and comparing it with more types of gas so that the effect of the nanoparticle on rGO thin film can be understood better and thus can be used for sensor selection.

Acknowledgement

This project is a collaboration between the International Islamic University Malaysia (IIUM) with the Centre of Unmanned Technologies, Kulliyyah of Engineering and Department of R&D, MIMOS Bhd. This research was partially sponsored by the Fundamental Research Grant Scheme (FRGS19159-0768) and MIMOS Berhad (SPG21-015-0015). We thank Dr. Ismahadi Syono for the main supervision.

References

1. Zhang, H., Li, Q., Huang, J., Du, Y. and Ruan, S. C. (2016). Reduced graphene oxide / Au Nanocomposite for NO_2 sensing at low operating temperature. *Sensor,* 16(2): 1-9.
2. Abdel-Karim, R., Reda, Y. and Abdel-Fattah, A. (2020). Review: Nanostructured materials-based nanosensors. *Journal of The Electrochemical Society,* 167: 037554.
3. Paula, M., Gil, G., Sandra, C., Nuno, A., Manoj, S., Jos, G. and Antnio, S. (2017), Functionalized graphene nanocomposites. *Advances in Nanocomposite Technology,* 2017: 11-15.
4. Behi, S., Bohli, N., Casanova-ch, J. and Llobet, E. (2020). Metal oxide nanoparticle-decorated few layer graphene nanoflake chemoresistors for the detection of aromatic volatile organic compounds. *Sensors,* 20: 3413:1-15.
5. Lipatov, A., Varezhnikov, A., Wilson, P. and Sysoev, V. V. (2013). Highly selective gas sensor arrays based on thermally reduced graphene oxide. *Nanoscale,* 5: 5426-5434.

6. Abdullah, M. F., Soriadi, N., Yakin, F.S.M, Badaruddin, S.A.M. and Syono, M. I. (2020). Materials science in semiconductor processing tuning the optoelectronic properties of the rGO-AuNPs hybrid film by pre-decoration and AuNPs-assisted thermal reduction. *Materials Science in Semiconductor Processing,* 112: 105017.
7. Wang, C., Lei, S., Li, X., Guo, S., Cui, P., Wei, X., Liu, W. and Liu, H. (2018). A reduced GO-graphene hybrid gas sensor for ultra-low concentration ammonia detection. *Sensors (Switzerland),* 18(9): 3147.
8. Mirzaei, A., Lee, J., Majhi, S. M., Weber, M., Bechelany, M. and Kim, H. W. (2019). Resistive gas sensors based on metal-oxide nanowires Resistive gas sensors based on metal-oxide nanowires. *Journal of Applied Physics,* 2019: 241102.
9. Malika, K., Kim, T., Losic, D. and Thanh, T. (2016). Recent advances in engineered graphene and composites for detection of volatile organic compounds (VOCs) and non-invasive diseases diagnosis. *Carbon,* 110: 97-129.
10. Ghimenti, S., Francesco, F. Di, Onor, M., Pleil, J. D., Stiegel, M. A., Sobus, J. R., Unterkofler, K., King, J., Mochalski, P., Pleil, J. D., Stiegel, M. A. and Risby, T. H. (2013), Clinical breath analysis : discriminating between human endogenous compounds and exogenous (environmental) chemical confounder. *Journal of Breath Research,* 7: 1-11.
11. Gaude, E., Nakhleh, M. K., Patassini, S., Boschmans, J., Allsworth, M., Boyle, B., and Van Der Schee, M. P. (2019), Targeted breath analysis: Exogenous volatile organic compounds (EVOC) as metabolic pathway-specific probe. *Journal of Breath Research,* 13(3): 032001.
12. Yakin, F. S. M., Abdullah, M. F., Badaruddin, S. A, Syono, M. I. and Soriadi, N. (2021), Surface modification and properties modulation of rGO film by short duration H_2 and NH_3 plasma treatment. *Materials Today: Proceedings,* 42: 2996-3001.
13. Tombel, N. S. M., Badaruddin, S. A. M., Yakin, F. S. M., Zaki, H. F. M. and Syono, M. I. (2021). Detection of low PPM of volatile organic compounds using nanomaterial functionalized reduced graphene oxide sensor. *AIP Conference Proceedings,* 2368: 020004.
14. Amiri, V., Roshan, H., Mirzaei, A., Neri, G. and Ayesh, A. I. (2020). Nanostructured metal oxide-based acetone gas sensors : a review. *Sensors,* 20: 3096.
15. Wang, C., Yin, L., Zhang, L., Xiang, D. and Gao, R. (2010). Metal oxide gas sensors: Sensitivity and influencing factors. *Sensors,* 10: 2088-2106.
16. Aniq, M., Mohammad, S., Wah, H., Bien, D. C. S., Hj, I., Azid, A., Woon, M. and Shukri, S. (2014). Surface morphology, resistivity, and magnetoresistance of Co, Fe, Ni, Co – Fe and Ni – Fe nanoparticles on TiN layers induced by hydrogen plasma treatment. *Thin Solid Films,* 550: 22-26.
17. Arun, K., Lekshmi, M. S and Suja, K. (2021). Performance analysis, modeling, and development of a signal conditioning unit of n-type metal oxide gas sensor for acetone gas detection. *Journal of Computational Electronics,* 20: 1938-1947.
18. Arshak, K., Moore, E., Lyons, G.M., Harris, J. and Clifford, S. (2004). A review of gas sensors employed in electronic nose applications. *Sensor Review,* 24: 181-198.
19. Vergara, A., Vembu, S., Ayhan, T., Ryan, M. A., Homer, M. L. and Huerta, R. (2012). Chemical gas sensor drift compensation using classifier ensembles. *Sensors and Actuators, B: Chemical,* 166-167: 320-329.
20. Gupta, S., Chatterjee, S., Ray, A. K. and Chakraborty, A. K. (2015). Graphene – metal oxide nanohybrids for toxic gas sensor : A review. *Sensors & Actuators: B Chemical,* 221(2): 1170-1181.
21. Zhou, C., Yu, J., Qin, Y. and Zheng, J. (2013). Grain size effects in polycrystalline gold nanoparticles. *Nanoscale,* 4(14): 4228-4233.

Malaysian Journal of Analytical Sciences (MJAS)
Published by Malaysian Analytical Sciences Society

ENHANCING THE HYDROGEN GAS SENSING PROPERTIES OF ZINC OXIDE DOPED WITH ALUMINUM PREPARED VIA THERMAL OXIDATION

(Meningkatkan Sifat Penderiaan Gas Hidrogen bagi Zink Oksida Terdop Aluminium yang Disediakan dengan Kaedah Pengoksidaan Terma)

Naif H. Al-Hardan[1*], Muhammad Azmi Abdul Hamid[1], Azlan Abdul Aziz[2], Naser M. Ahmed[2]

[1]Department of Applied Physics,
Faculty of Science and Technology,
Universiti Kebangsaan Malaysia, 43600 UKM Bangi, Selangor, Malaysia
[2]School of Physics,
Universiti Sains Malaysia, 11800 Penang, Penang, Malaysia

[*]Corresponding author: naifalhardan@ukm.edu.my

Received: 31 January 2022; Accepted: 19 May 2022; Published: 27 December 2022

Abstract

This work describes the gas sensing performance of undoped zinc oxide (ZnO) and ZnO doped with 2 atomic% aluminum (ZnO: Al 2% at.) prepared via the thermal oxidation of zinc (Zn) and Al metal. The prepared films exhibited a polycrystalline structure of the hexagonal ZnO structure. The element composition shows the presence of Zn, O and Al, with Al percentage of approximately 2.2% at. The current-voltage characteristic was used to study the effect of the low hydrogen (H_2) concentrations on the sensing properties of ZnO and ZnO: Al. The maximum response of the undoped ZnO was approximately 100 at an operating temperature of 400 ℃ and increased to approximately 2000 at an operating temperature of 300 ℃ after doping with 2% at. Al. The current study reveals the promising potential for the Al-doped ZnO for low H_2 gas concentrations, as there was an enhancement in the response and reduction in the operating temperature of the doped ZnO with Al.

Keywords: hydrogen gas sensors, doping process, ZnO:Al

Abstrak

Kerja ini menerangkan prestasi penderiaan gas untuk zink oksida (ZnO) tanpa dop dan ZnO terdop 2 atom% aluminum (ZnO: Al 2% at.) yang disediakan melalui pengoksidaan terma logam zink (Zn) dan Al. Filem yang disediakan mempunyai struktur polikristal iaitu struktur heksagonal ZnO. Komposisi unsur menunjukkan kehadiran Zn, O dan Al, dengan peratusan Al pada anggaran 2.2% at. Ciri Arus-Voltan telah digunakan untuk mengkaji kesan kepekatan hidrogen (H_2) rendah terhadap sifat penderiaan ZnO dan ZnO:Al. Gerakbalas maksimum ZnO tanpa dop dalam anggaran 100 pada suhu operasi 400℃ dan meningkat kepada 2000 pada suhu operasi 300℃ setelah didop dengan Al. Kajian semasa menunjukkan ZnO terdop Al mempunyai potensi baik pada kepekatan gas H_2 yang rendah, di mana pengayaan dalam respons dan pengurangan dalam operasi suhu terhadap ZnO didop Bersama Al.

Kata kunci: hidrogen penderia gas, proses doping, ZnO:Al

Introduction

Recently, metal oxide semiconductor gas sensors have attracted considerable attention due to their applications in integrated circuit processes [1-3]. It is known that semiconductor sensors have been widely used and studied owing to their low cost, small size, and reliability [4-6]. However, the performance of the gas sensors based on metal oxide semiconductors showed drawbacks, as they need high operating temperatures and show a relatively low sensitivity.

The modification and the improvements in the metal oxide semiconductor gas sensors performance can be approached with different paths. Surface modification [7, 8] and doping process [9, 10] are among them. Recently, extensive studies on the doping process and its effect on the gas sensing performance of the metal oxide semiconductor were conducted. Elements such as chromium [10], indium [11], magnesium [12] aluminum (Al) [13-16] and others [17] have been carried out for different gas sensing applications. Aluminium was the most studied element for doping ZnO for several applications, such as conductive transparent layers [18]. In addition, the Al is inexpensive metal and abundant as compared with the other doped elements.

There are many published reports on the application of aluminum as a dopant for ZnO based gas sensors. Paraguay et al. [19] prepared ethanol vapor sensors based on ZnO, and different metals such as tin, indium, Al, iron and copper were used as dopants. No difference in operating temperature was observed. However, the ethanol vapor sensor based on ZnO doped with tin shows the highest sensitivity for ethanol vapor. Hijri et al. [13] prepared ZnO doped with 1-5% atomic Al nanoparticles via sol-gel process. The working operating temperature was in the range of 250-300 ^{o}C. The sensors based on ZnO: Al manifested a higher response than the undoped ZnO sensor in carbon monoxide environment. Zan et al. [20] synthesized ZnO: Al (0.1/0.075/0.05/0.025 mol/L) via a hydrothermal method. Different nanostructure morphologies were prepared, and the operating temperatures of the prepared ZnO: Al nanostructures were almost the same, despite the fact that different nanostructure morphologies were prepared. However, the sensitivity of the disk shape structures was the heights compared to other nanostructure morphologies. Several gases were demonstrated in the study, such as ammonia, carbon monoxide, and H_2. The chemical bath deposition method was conducted to prepare ethanol vapor sensors based on undoped ZnO and doped ZnO: Al. The optimum performance of the prepared sensor was for the sample with Al concentration equal to 2.90 at% [21]. The prepared ethanol sensor was operated at 300^{o}C as a working temperature. Furthermore, Yoo et. al [16] reported on the sensing of acetone by Al-doped ZnO for breath analysis applications. It was reported that doping ZnO with 1 at% Al will enhance the detection performance of the ZnO nanoparticles.

Hydrogen is one of the most gasses demonstrated for their importance as one of the resources of clean energy [22, 23]. H_2 gas is considered as one of the flammable gasses with a wide range of flammability in the air, which is about 4–75% by volume. The lowest limit of H_2 concentration in the atmosphere to cause an explosion is 4.65%, making it one of the most flammable gasses [24]. Sensors with the ability to detect low levels of H_2 ranging from 0.1 ppm to 100 ppm are required for applications involving leak detection in hydrogen fuel systems [23, 25].

Currently, there are few studies regarding the gas sensing properties of ZnO films prepared by oxidation as well as the process of doping it. Furthermore, the effect of the applied bias voltage on the gas sensing performance of the undoped and doped ZnO:Al was not explored wildly. In this study, we prepared zinc oxide (ZnO) and aluminum doped zinc oxide (ZnO: Al) through the thermal oxidation of dc sputtered Zn metal. The aim of this study is to enhance the sensing properties of the ZnO gas sensor through the doping process for H_2 gas sensors.

Materials and Methods

Silicon n-type wafer with (1 0 0) orientation was used as a substrate. Initially, the cleaning process of the wafer is

according to the RCA (Radio Corporation of America) method [26]. A silicon dioxide (SiO_2) thick layer is grown through a thermal oxidation process. Platinum (Pt) is used as a heating element and electrode. The pattern of the heating element and electrodes was carried out using the photolithography technique. Zn metal and Zn + Al thin films were coated using the A306 dc sputtering unit from Edwards. The target was high purity Zn metal target with a purity of >99.99% (diameter 7.62 cm) from (Xiamen Advanced and High-tech Material Co. Ltd, China) for the first batch of samples, while a high purity 2 cm Al rod (99.99% from Sigma-Aldrich (M) Sdn Bhd, Malaysia) with a diameter of 2 mm attached on top of the Zn target for the doped Zn. After reaching a pressure below 1 x 10^{-5} mbar, Ar gas was introduced into the chamber through a needle valve. During this process, the working pressure was held constant at approximately 4.5 x 10^{-2} mbar, and the dc power was maintained at 250 W.

The oxidation process was performed using a controlled tube furnace from Lenton. Both samples were inserted at room temperature, which was subsequently raised up to 400 ℃ at the rate of 5℃.min^{-1} with a constant flow rate of high purity (99.98%) oxygen. The oxidation time was 30 min. The film's color changed to white after the oxidation process. The thickness of the produced films was (300 ± 20) nm as measured by Filmetrics F20 optical reflectometer (based on the optical interference method). PANalytical X-ray diffractometer (HR-XRD) is used to obtain the crystal structure of the prepared films. The diffraction angles were in the range of 20° - 60°. A scanning electron microscope (SEM JEOL model JSM-6460 LV) with an energy dispersion spectroscopy (EDS type INCAx from OXFORD instrument) was used for structure, surface morphology, and elemental analysis of the prepared samples. Atomic force microscope (AFM) was also used for the morphology of the prepared samples' surface.

The current-voltage (I-V) characteristic of the sensor was measured using a programmable KEITHLEY Electrometer – model 617, which also supplied the voltage V ranging from -2 to 2 volts. A DC power supply was used for supplying the voltage to the heating element at the operating temperature between 50 ℃ to 450 ℃. A calibrated K - type thermocouple was mounted on the device to determine the operating temperature of the sensor. After 3 min of turning on the gas flow, the measurements were commenced to ensure a homogeneous distribution of the gas under study inside the chamber. The output current was collected as a function of different H_2 concentration (0-120) ppm. The test chamber was made of stainless steel, creating a volume of about 8200 cm^3. Highly grade 2% H_2 balanced in nitrogen (MOX-LINDE GASES SDN BHD, Malaysia) was used as a test gas. The measurements were taken at room temperature at humidity and temperature of 62% and 25℃, respectively.

Results and Discussion

Structure and elements analysis

The X-ray diffraction patterns of the 30-min thermal oxidation of Zn metal and Al-doped Zn are depicted in Figure 1. The pattern shows the polycrystalline nature of the prepared samples. Furthermore, there was no evidence of Zn metal in both prepared undoped and doped ZnO films, which confirmed the complete conversion of Zn metal to ZnO. The Bragg angles appear at 31.8°, 34.3°, 36.2°, and 56.8°, which belong to the (100), (002), (101) and (102) phases of ZnO (JCPDS card no. 36-1451), respectively. The decrease in the peak's intensity after doping with Al is also worth noting. This might be attributed to the existence of Al_2O_3 grains that interrupt the nucleation of the structure growth [27]. The EDX values for ZnO and ZnO: Al are shown in Table 1, along with their corresponding elemental compositions. It is clear that the Zn:O ratio is almost identical, and that the Al concentration is approximately 2.2at%.

Table 1. The element percentage of the ZnO and ZnO:Al samples prepared through the 30-minute thermal oxidation of Zn and Zn:Al

Elements	Atomic (%)	
	ZnO	ZnO: Al
O	52.48	52.17
Zn	47.52	45.65
Al	-	2.20

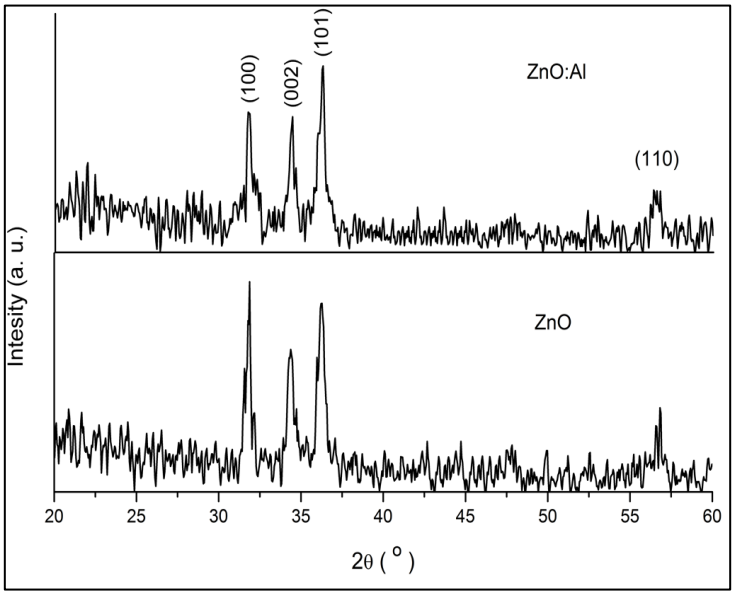


Figure 1. HR-XRD of ZnO and ZnO: Al samples after a 30-minute thermal oxidation at 400 ℃

The SEM and AFM micrographs of the surface of both sensors are depicted in Figure 2. It can be observed that the undoped ZnO surface appears to be more condensed as compared to the doped one, which demonstrated a porous microstructure with larger grains. The enhancement of the ZnO: Al grains size is due to the segregation of Al content into the grain boundaries [28]. The AFM micrograph also confirms that the doped ZnO possesses a rougher surface as compared to the undoped one. The root mean square of surface roughness measured by AFM for the undoped ZnO was 45 nm, which increased to 78 nm for the doped ZnO with 2.2at% Al. Surface roughness and less compact structure may be attributed to the migration of Al dopants towards the grain boundary, where they react with oxygen atoms and segregate as Al_2O_3 [29].

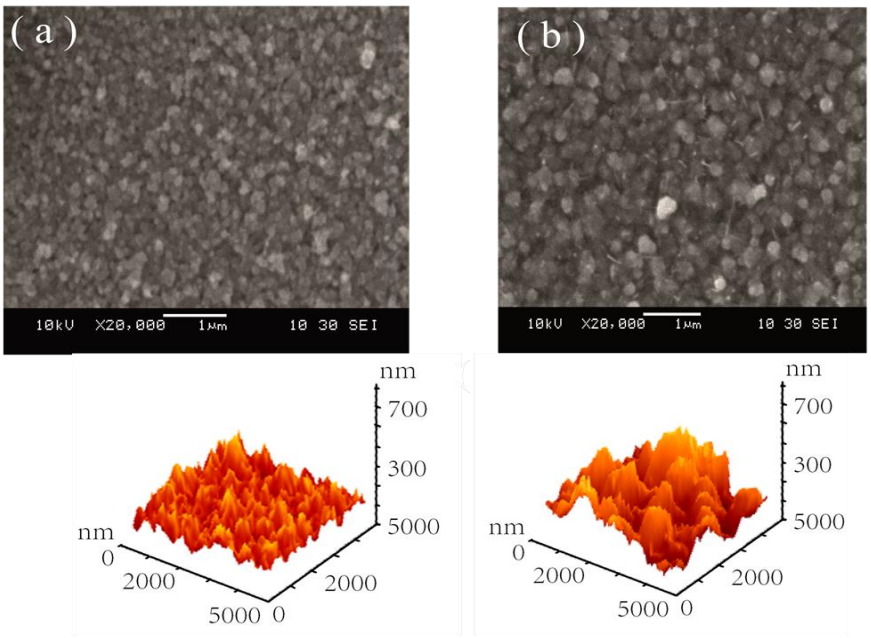


Figure 2. The SEM and AFM micrographs for both (a) ZnO and (b) ZnO: Al were prepared through the thermal oxidation of Zn metal; the bar length is 1 μm

The current-voltage characterization

The resistance of both prepared gas sensors samples in the temperature range starting from room temperature up to 450 ℃ is measured in an air atmosphere, and the results are shown in Figure 3. It is worth noting that the resistance of both sensing materials decreased along with the temperature. This indicates the semiconductor behavior of both prepared samples. Moreover, the resistance of the ZnO: Al was lower than that of undoped ZnO in the temperature range from 50 ℃ to around 250 ℃. The lower baseline resistance could be attributed to the higher charge carrier concentration resulting from the donor nature of the substitution of Al^{3+} on Zn^{2+} sites [28, 30]. These results are comparable with those published [13, 31]. The decrease in sheet resistance at 100-250 ℃ was due to the thermal excitation of electrons into the conduction band. Furthermore, it has been reported that undoped ZnO undergoes a reduction process as the temperature rises to form oxygen vacancies, which are immediately ionized to donate electrons to the conduction band [32, 33]. The next regime of the behavior (above 250℃) exhibited a positive temperature coefficient of resistance (PTCR) for the ZnO sample. However, for the ZnO: Al sample, PTCR appeared in the temperature ranging from 250 – 350 ℃ before giving way to the negative temperature coefficient (NTCR) of the resistance regime at temperatures above 350 ℃. The PTCR regime in the ZnO sample is probably due to the thermal desorption of the (OH^-) layer [34] or the adsorption of various oxygen molecules on the ZnO surface [30].

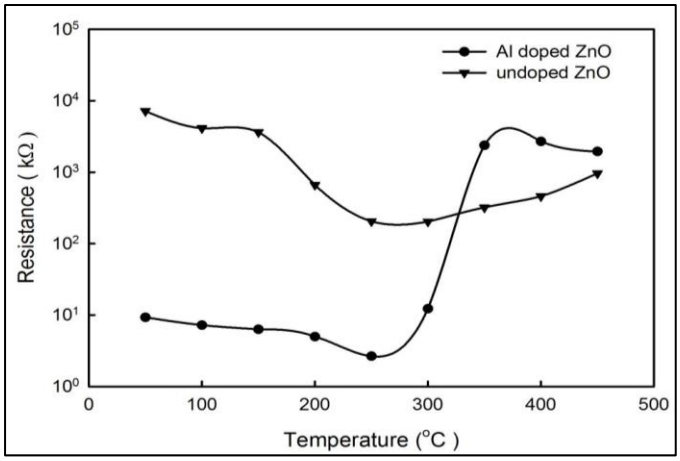


Figure 3. The electrical resistance behavior of the ZnO and ZnO: Al samples

In order to evaluate the quality of the manufactured sensors as well as determine the optimum operating temperature, both sensors were exposed to a fixed concentration of H_2 (100 ppm), while the temperature was varied between 100℃ and 450℃ with a step of 50℃ (there was the insignificant response at temperature lower than 100℃ for both samples). The quality levels of both ZnO and ZnO: Al sensors were estimated by measuring their response (Equation 1), which can be calculated by the ratio of the resistance in the air (Ra) and resistance in the hydrogen gas atmosphere (R_g) [34]:

$$S = \frac{Ra}{Rg} \quad (1)$$

Figure 4 (semi-log graph) reveals the response of both prepared sensors as a function of the operating temperatures. In both cases, the response to the 100 ppm H_2 was increased with the temperature. The maximum response of the undoped ZnO was approximately 100 and occurred at 400℃, and it was approximately 2100 at an operating temperature of 300℃ for the doped ZnO:Al gas sensors. It is, therefore, concluded that the optimum operating temperature is 400℃ and 300 ℃ for the undoped ZnO and doped ZnO:Al gas sensors, respectively.

The reaction rate between the gas under test with the surface absorbed oxygen species is low at low operating temperatures. This is probably due to the high activation energy barrier of the surface reaction. Increasing the operating temperature will enhance the sensor response, which probably is due to the sufficient thermal energy to overcome the barrier height. According to Krishnakumar et al. [35], Patil and Patil [36] and Barreca et al. [8], the adsorbed oxygen may desorb from the surface at higher temperatures (the adsorbed oxygen will not be enough to react with the gas). This will result in decreasing the gas response at higher temperatures. It is obvious that the ZnO: Al sensor has a much lower operating temperature and higher response than that of the undoped ZnO sensor.

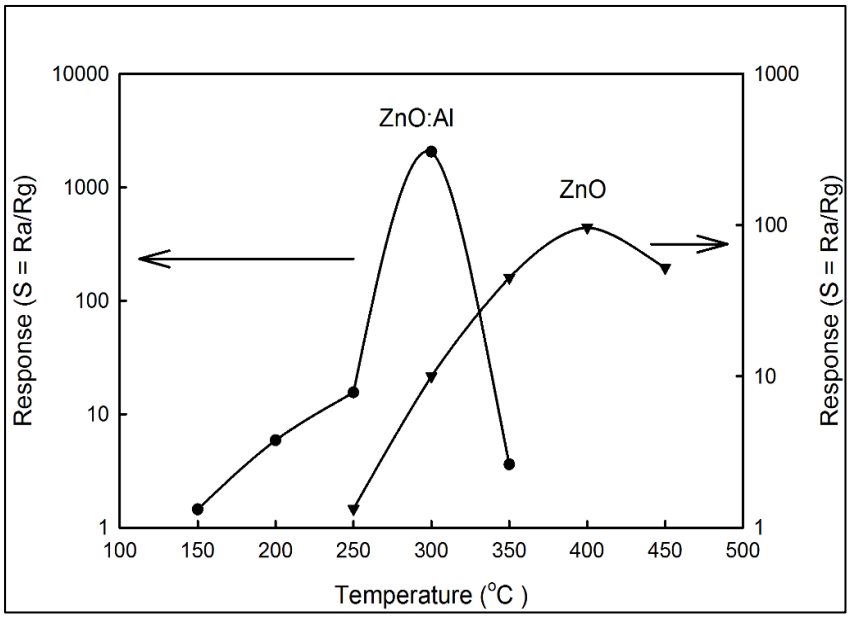


Figure 4. The operating temperature of the ZnO: Al and ZnO gas sensors.

We believe that the enhancement of the gas response at lower operating temperatures is due to the incorporation of the Al metal. Consequently, the surface activity is enhanced as Al has lower ionization energy than the Zn [10]. Furthermore, the modification in the surface nature may consider another factor that might enhance the response of the doped ZnO gas sensor. The increase in the roughness of the surface will result in an increase in the surface to volume ratio, which will allow the gas to penetrate more through the sensitive area of the oxide. On the other hand, the surface is usually dense for the undoped ZnO, and the sensing reactions are restricted to the surface.

Several authors [37, 38] have observed the occurrence of shifting operating temperature by doping; it was found that such an effect is related to the changes in the reaction equilibrium, which strongly depend on operating temperature [38]. Figure 5 shows the current-voltage characteristic of both the undoped and doped ZnO with 2% at. Al in H_2 atmosphere with the concentration ranging from 40 to 160 ppm. The operating temperatures were fixed at 400 ^oC and 300 ^oC for the undoped and doped ZnO, respectively. The figure shows that the current magnitude for both sensors increased as the gas concentrations increased. Furthermore, the current values of the doped ZnO are becoming higher than the undoped ZnO.

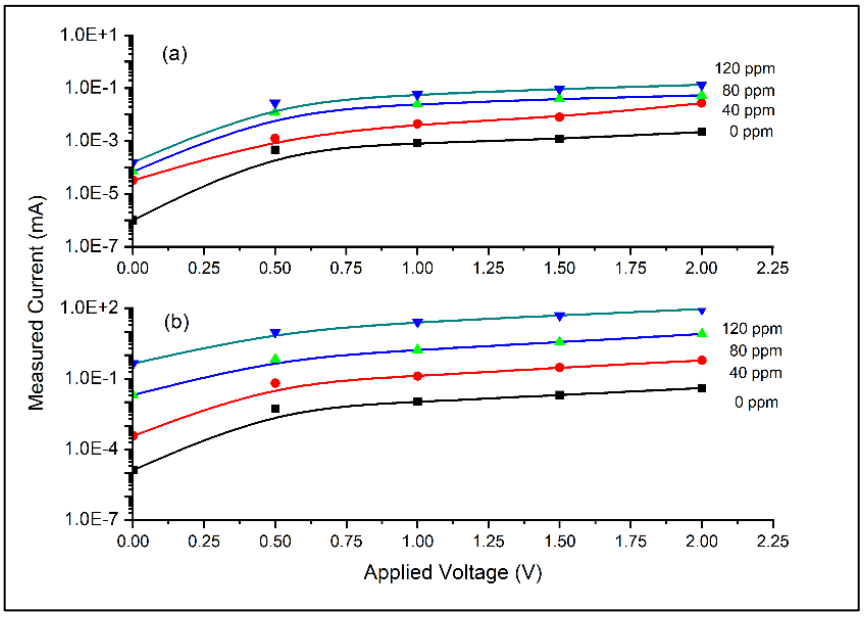


Figure 5. The I-V characteristic of (a) ZnO and (b) ZnO: Al in the H_2 atmosphere with concentration ranging from 40 to 160 ppm

It is well accepted that the detection of reduction gases over the metal oxide surface involves an adsorption−oxidation−desorption process [39]. Here, the oxygen molecules play an important role in this process. Upon the exposure of the metal oxide in the air at elevated temperatures (higher than 200℃, oxygen molecules are adsorbed over at surface of the oxide, and the formation of oxygen ions (O^-, O^{2-} or O^{-2}) will accrue (Equation 2-5), by attracting electrons from the conduction band of the metal oxide. The reaction can be summarized as follow [37];

$$O_2(gas) \Leftrightarrow O_2(adsorbed) \quad (2)$$

$$O_2(ads) + \bar{e} \Leftrightarrow O_2^-(ads) \quad (3)$$

$$O_2^-(ads) + \bar{e} \Leftrightarrow 2O^-(ads) \quad (4)$$

$$O^-(ads) + \bar{e} \Leftrightarrow O^{-2}(ads) \quad (5)$$

This will form a space-charge depletion layer on the surface of the oxide resulting in a reduction of the carrier concentration. When the sensors are exposed to a reducing gas (in this case is H_2), the H_2 gas reacts with the adsorbed oxygen ions on the sensor's surface, and as a result, the electrons will be released back into the conduction band, causing an increase in the produced current, as can be expected (Equation 6) from the following reaction between the hydrogen gas molecules and the adsorbed oxygen:

$$H_2 + O^- \rightarrow H_2O(gas) + e^- \quad (6)$$

As the doping content of Al increases the carrier concentration, this will result in a higher output current as compared to the undoped ZnO gas sensor. The behavior of both undoped ZnO and doped ZnO:Al with the H_2 concentrations from (0 - 120) ppm at a bias voltage of 2V is depicted in Figure 6. It can be observed

that the sensor's measured current increased when exposed to hydrogen up to 120 ppm with a good linearity that proves the suitability of using the ZnO for low hydrogen concentrations.

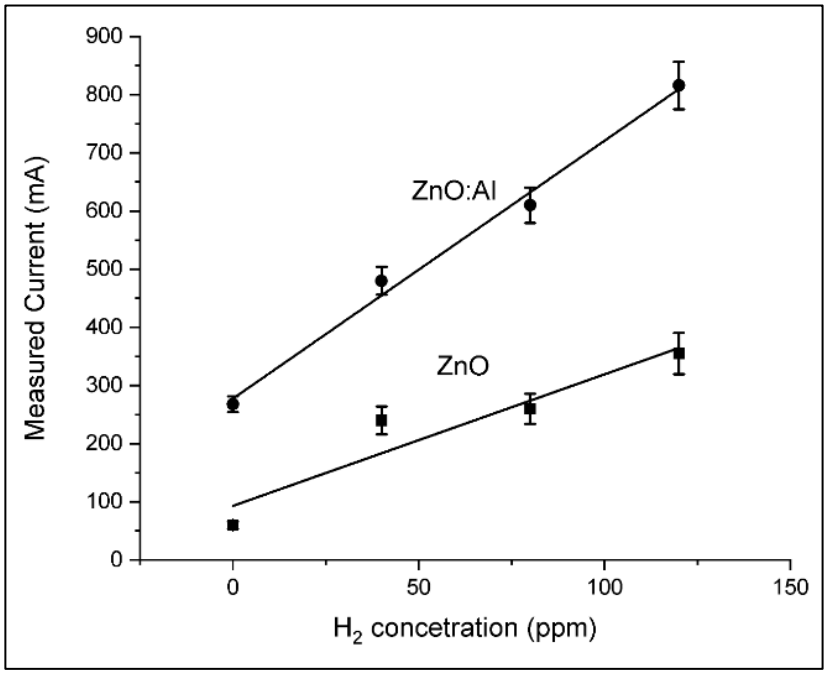


Figure 6. The response of the measured current for ZnO and ZnO: Al when exposed to the H2 atmosphere for different concentration levels. The operating temperature of the undoped and doped ZnO was 400 ℃ and 300 ℃, respectively, and the applied voltage was fixed at 2V

Conclusion

In this study, undoped ZnO and doped ZnO: Al gas sensors were successfully prepared by the thermal oxidation of the Zn metal at 400℃. It was also found that the operating temperature was reduced, and the sensitivity was higher for the doped ZnO: Al sensor. The I – V characteristic of both samples show a significant response for the measured H_2 concentration range. Due to the increase in the carrier concentration of the Al doped ZnO, the enhancement of response was noticed. The results show a potential application of the Al doped ZnO for low range H_2 concentration gas sensors.

Acknowledgement

The authors acknowledge the financial support of CRIM- Universiti Kebangsaan Malaysia (UKM), grant GGPM-2020-047. The authors also acknowledged the support of the school of physics Universiti Sains Malaysia (USM).

References

1. Müller, G., Friedberger, A., Kreisl, P., Ahlers, S., Schulz, O. and Becker, T. (2003). A MEMS toolkit for metal-oxide-based gas sensing systems. *Thin Solid Films*, 436(1): 34-45.
2. Tuller, H. L. and Mlcak, R. (2000). Advanced sensor technology based on oxide thin film-MEMS integration. *Journal of Electroceramics*, 4(2): 415-425.
3. Graf, M., Barrettino, D., Zimmermann, M., Hierlemann, A., Baltes, H., Hahn, S., ... and Weimar, U. (2004). CMOS monolithic metal-oxide sensor system comprising a microhotplate and associated circuitry. *IEEE Sensors Journal*, 4(1): 9-16.

4. Alenezi, M. R., Henley, S. J., Emerson, N. G. and Silva, S. R. P. (2014). From 1D and 2D ZnO nanostructures to 3D hierarchical structures with enhanced gas sensing properties. *Nanoscale,* 6(1): 235-247.
5. Al-Hardan, N. H., Abdul Hamid, M. A., Shamsudin, R., Othman, N. K. and Kar Keng, L. (2016). Amperometric non-enzymatic hydrogen peroxide sensor based on aligned zinc oxide nanorods. *Sensors*, 16(7): 1004.
6. Al-Khalqi, E. M., Hamid, M. A. A., Shamsudin, R., Al-Hardan, N. H., Jalar, A. and Keng, L. K. (2020). Zinc oxide nanorod electrolyte–insulator–semiconductor sensor for enhanced 2-methoxyethanol selectivity. *IEEE Sensors Journal*, 21(5): 6234-6240.
7. Law, J. B. K. and Thong, J. T. L. (2008). Improving the NH_3 gas sensitivity of ZnO nanowire sensors by reducing the carrier concentration. *Nanotechnology*, *19*(20), 205502.
8. Barreca, D., Bekermann, D., Comini, E., Devi, A., Fischer, R. A., Gasparotto, A., ... and Tondello, E. (2010). 1D ZnO nano-assemblies by Plasma-CVD as chemical sensors for flammable and toxic gases. *Sensors and Actuators B: Chemical*, 149(1): 1-7.
9. Basu, S. and Basu, P. K. (2009). Nanocrystalline metal oxides for methane sensors: role of noble metals. *Journal of Sensors,* 2009: 861968.
10. Al-Hardan, N. H., Abdullah, M. J. and Aziz, A. A. (2013). Performance of Cr-doped ZnO for acetone sensing. *Applied Surface Science,* 270: 480-485.
11. Hjiri, M., Dhahri, R., Omri, K., El Mir, L., Leonardi, S. G., Donato, N. and Neri, G. (2014). Effect of indium doping on ZnO based-gas sensor for CO. *Materials Science in Semiconductor Processing*, 27: 319-325.
12. Al-Khalqi, E. M., Abdul Hamid, M. A., Al-Hardan, N. H. and Keng, L. K. (2021). Highly sensitive magnesium-doped ZnO nanorod pH sensors based on electrolyte–insulator–semiconductor (EIS) sensors. *Sensors*, 21(6): 2110.
13. Hjiri, M., El Mir, L., Leonardi, S. G., Pistone, A., Mavilia, L. and Neri, G. (2014). Al-doped ZnO for highly sensitive CO gas sensors. *Sensors and Actuators B: Chemical*, 196: 413-420.
14. Yang, Z., Huang, Y., Chen, G., Guo, Z., Cheng, S. and Huang, S. (2009). Ethanol gas sensor based on Al-doped ZnO nanomaterial with many gas diffusing channels. *Sensors and Actuators B: Chemical*, 140(2): 549-556.
15. Navale, S. C., Ravi, V., Mulla, I. S., Gosavi, S. W. and Kulkarni, S. K. (2007). Low temperature synthesis and NOx sensing properties of nanostructured Al-doped ZnO. *Sensors and Actuators B: Chemical*, 126(2): 382-386.
16. Yoo, R., Güntner, A. T., Park, Y., Rim, H. J., Lee, H. S. and Lee, W. (2019). Sensing of acetone by Al-doped ZnO. *Sensors and Actuators B: Chemical*, 283: 107-115.
17. Darvishnejad, M. H., Firooz, A. A., Beheshtian, J. and Khodadadi, A. A. (2016). Highly sensitive and selective ethanol and acetone gas sensors by adding some dopants (Mn, Fe, Co, Ni) onto hexagonal ZnO plates. *RSC Advances*, 6(10): 7838-7845.
18. Lee, S. H., Han, S. H., Jung, H. S., Shin, H., Lee, J., Noh, J. H., ... and Shin, H. (2010). Al-doped ZnO thin film: a new transparent conducting layer for ZnO nanowire-based dye-sensitized solar cells. *The Journal of Physical Chemistry C*, 114(15): 7185-7189.
19. Miki-Yoshida, M., Morales, J. and Solis, J. (2000). Influence of Al, In, Cu, Fe and Sn dopants on the response of thin film ZnO gas sensor to ethanol vapour. *Thin Solid Films*, 373(1-2): 137-140.
20. Zan, L., Wei, Q. and Xiaohong, W. (2015). Controllable hydrothermal synthesis of Al-doped ZnO with different microstructures, growth mechanisms, and gas sensing properties. *RSC Advances,* 5(69): 56325-56332.
21. Yuliarto, B., Nulhakim, L., Ramadhani, M. F., Iqbal, M. and Nuruddin, A. (2015). Improved performances of ethanol sensor fabricated on Al-doped ZnO nanosheet thin films. *IEEE Sensors Journal,* 15(7): 4114-4120.
22. Fardindoost, S., Rahimi, F. and Ghasempour, R. (2010). Pd doped WO_3 films prepared by sol–gel process for hydrogen sensing. *International Journal of Hydrogen Energy,* 35(2): 854-860.

23. Grimes, C. A., Ong, K. G., Varghese, O. K., Yang, X., Mor, G., Paulose, M., ... and Mason, A. J. (2003). A sentinel sensor network for hydrogen sensing. *Sensors*, 3(3): 69-82.
24. Al-Salman, H. S., Abdullah, M. J. and Al-Hardan, N. (2013). ZnO thin film nanostructures for hydrogen gas sensing applications. *Ceramics International,* 39: S447-S450.
25. Boon-Brett, L., Bousek, J., Black, G., Moretto, P., Castello, P., Hübert, T. and Banach, U. (2010). Identifying performance gaps in hydrogen safety sensor technology for automotive and stationary applications. *International Journal of Hydrogen Energy*, 35(1): 373-384.
26. Kern, W. (1990). The evolution of silicon wafer cleaning technology. *Journal of the Electrochemical Society,* 137(6): 1887.
27. Jeong, S. H., Kho, S., Jung, D., Lee, S. B. and Boo, J. H. (2003). Deposition of aluminum-doped zinc oxide films by RF magnetron sputtering and study of their surface characteristics. *Surface and Coatings Technology,* 174: 187-192.
28. Ma, T. Y. and Lee, S. C. (2000). Effects of aluminum content and substrate temperature on the structural and electrical properties of aluminum-doped ZnO films prepared by ultrasonic spray pyrolysis. *Journal of Materials Science: Materials in Electronics,* 11(4): 305-309.
29. Lupan, O., Shishiyanu, S., Ursaki, V., Khallaf, H., Chow, L., Shishiyanu, T., ... and Railean, S. (2009). Synthesis of nanostructured Al-doped zinc oxide films on Si for solar cells applications. *Solar Energy Materials and Solar Cells,* 93(8), 1417-1422.
30. Haug, F. J., Geller, Z., Zogg, H., Tiwari, A. N., & Vignali, C. (2001). Influence of deposition conditions on the thermal stability of ZnO: Al films grown by rf magnetron sputtering. *Journal of Vacuum Science & Technology A: Vacuum, Surfaces, and Films,* 19(1): 171-174.
31. Sahay, P. P. and Nath, R. K. (2008). Al-doped ZnO thin films as methanol sensors. *Sensors and Actuators B: Chemical,* 134(2), 654-659.
32. Gurlo, A. and Riedel, R. (2007). In situ and operando spectroscopy for assessing mechanisms of gas sensing. *Angewandte Chemie International Edition,* 46(21): 3826-3848.
33. Nenov, T. G. and Yordanov, S. P. (2020). Ceramic sensors: technology and applications. CRC press.
34. Moseley, P. T. (1997). Solid state gas sensors. *Measurement Science And Technology,* 8(3): 223.
35. Krishnakumar, T., Jayaprakash, R., Pinna, N., Donato, N., Bonavita, A., Micali, G. and Neri, G. (2009). CO gas sensing of ZnO nanostructures synthesized by an assisted microwave wet chemical route. *Sensors and Actuators B: Chemical,* 143(1): 198-204.
36. Patil, D. R. and Patil, L. A. (2009). Cr_2O_3-modified ZnO thick film resistors as LPG sensors. *Talanta,* 77(4): 1409-1414.
37. Xia, H., Wang, Y., Kong, F., Wang, S., Zhu, B., Guo, X., ... and Wu, S. (2008). Au-doped WO_3-based sensor for NO2 detection at low operating temperature. *Sensors and Actuators B: Chemical,* 134(1), 133-139.
38. Ferro, R., Rodriguez, J. A. and Bertrand, P. (2005). Development and characterization of a sprayed ZnO thin film‐based NO_2 sensor. *Physica Status Solidi* (C), 2(10): 3754-3757.
39. Tian, S., Yang, F., Zeng, D. and Xie, C. (2012). Solution-processed gas sensors based on ZnO nanorods array with an exposed (0001) facet for enhanced gas-sensing properties. *The Journal of Physical Chemistry C,* 116(19): 10586-10591.

Malaysian Journal of Analytical Sciences (MJAS)
Published by Malaysian Analytical Sciences Society

ENZYME-BASED ELECTROCHEMICAL BIOSENSOR ON IMMOBILIZATION OF TYROSINASE ONTO CARBOXYL FUNCTIONALIZED CARBON NANOTUBE FOR DETECTION OF TYRAMINE

(Biosensor Elektrokimia Berasaskan-Enzim Diimobilasi Enzim Tirosinase Ke Karboksil Tiupnano Karbon Untuk Pengesanan Tiramin)

Nurul Hana Masód and Syaza Azhari*

Industrial Chemical Technology,
Faculty of Science and Technology,
Universiti Sains Islam Malaysia, Negeri Sembilan Nilai 71800, Malaysia

**Corresponding author: syaza@usim.edu.my*

Received: 12 February 2022; Accepted: 27 March 2022; Published: 27 December 2022

Abstract

Tyramine (TYR) in foods have been regarded as a quality indicator of food freshness for assessing microbial action, which potentially affects human health. Enzyme-based electrochemical biosensor technology represents an excessively massive field that significantly impacts food quality control with incredible potential and rapid tools. Thus, this study aimed to immobilize tyrosinase (tyro) over single-wall carbon nanotubes (SWCNTs) onto the screen-printed carbon electrode (SPCE) in the detection of TYR. The characteristics and electrochemical behaviour of the modified SPCEs were investigated by Fourier transformed infrared spectroscopy (FTIR), cyclic voltammetry (CV) and differential pulse voltammetry (DPV). Under optimum experimental conditions, Tyro-SWCNT-COOH/SPCE biosensor exhibit good performance at scan rate 50 mVs^{-1} (range of 10 to 500 mVs^{-1}), pH 8.0 (range of 7.0 – 10.0), 8 µL enzyme tyrosinase (range of 2 to 10 µL), and 0.5 mg/mL SWCNTs (range of 0.2 - 3.0 mg/ml). The modified SPCEs was successfully applied for tyramine (TYR) determination with a detection limit (LOD) of 0.02 mM.

Keywords: tyrosinase, tyramine, screen-printed electrode, single-walled carbon nanotube

Abstrak

Tiramin (TYR) dalam makanan telah dianggap sebagai penunjuk kualiti kesegaran makanan untuk menilai tindakan mikrob yang berpotensi menjejaskan kesihatan manusia. Teknologi biosensor elektrokimia berasaskan enzim mewakili bidang yang luas dimana mampu memberi kesan ketara terhadap kawalan kualiti makanan dengan potensi dan alat pantas yang luar biasa. Oleh itu, matlamat kajian ini adalah untuk mengalihkan tirosinase (tyro) ke atas tiubnano karbon berdinding tunggal (SWCNT) ke elektrod karbon bercetak skrin (SPCE) dalam pengesanan tiramin (TYR). Ciri-ciri dan tingkah laku elektrokimia SPCE yang diubah suai telah disiasat oleh spektroskopi inframerah (FTIR), voltammetri kitaran (CV) dan voltammetri nadi pembezaan (DPV). Di bawah keadaan percubaan optimum, biosensor Tyro-SWCNT-COOH/SPCE mempamerkan prestasi yang baik pada kadar imbasan 50 mVs^{-1} (julat 10 hingga 500 mVs^{-1}), pH 8.0 (julat 7.0 – 10.0), 8 µl enzim tirosinase (julat daripada 2 hingga 10 µl), dan 0.5 mg/ml

SWCNTs (julat 0.2 – 3.0 mg/ml). SPCE yang diubah suai telah berjaya digunakan untuk penentuan tiramine (TYR) dengan had pengesanan (LOD) sebanyak 0.02 mM.

Kata kunci: tirosinase, tiramin, elektrod bercetak skrin, tiub nano karbon berdinding tunggal

Introduction

Tyramine (TYR) is one of the most abundant compounds in a group of biogenic amines (BAs) that are present in a variety of foods due to their capability to show the activity of certain microorganisms such as *Enterobacteriaceae,* including *E. coli* [1–3]. Today, food safety and quality are the main concerns among consumers and health agencies worldwide [4]. Furthermore, TYR can affect human health by stimulating the release of catecholamines from the sympathetic nervous system, which can increase heart rate and blood pressure, which can lead to migraines, hypertension, cardiac failure, and cause serious intoxication effects when ingested in large quantities [5–8]. Due to their toxicity to human health, the optimization parameter for modification of the electrode in the detection of TYR is important.

The demand for safer food quality has promoted more research into BAs quantification over the past few years. Previous work deals with the development of a sensitive and easily fabricated electrochemical biosensor for TYR detection using tyrosinase (tyro) on a glassy carbon electrode [9], such as electrochemical deposition of poly-(8-anilino-1-naphthalene sulphonic acid) attached with gold nanoparticles (AuNP) on gold electrodes (AuE) by polymerization of the monomer [10,11]. However, amongst all of the modified electrodes, screen-printed electrode (SPCE) is the most suitable to be used based on electrochemical analysis in environmental, clinical or agricultural food areas due to its versatility of fabrication, affordability, nontoxic and customizability with nanomaterials and biological elements such as enzymes resulting in the high surface area of the modified electrode [12].

Nanomaterials such as single-wall carbon nanotubes (SWCNT) play an important part in the recent development of enzyme-based biosensors providing advantages such as high catalytic efficiency, rapid response times [13] and enzymes processed with nanoparticles employed to overcome the inherent drawbacks of enzymes [14]. SWCNT is also very good at adsorption, electrical, mechanical, and thermal properties, and it has a lot of surface area, which makes it a good material for the fabrication of electrochemical biosensors and allows them to stay in harsh chemical environments [15]. In addition, SWCNTs that functionalize with carboxylic acid groups (-COOH) help to mitigate this disadvantage by affording the possibility of further chemical derivatization [16].

Enzyme tyro is commonly used to determine analytes containing phenolic compounds [17–19]. Carbon nanotubes act as conductive material and have been commonly used as common approaches for the immobilization of tyro onto various substrates [20]. In previous work by Apetrei, an amperometric TYR biosensor has been developed by immobilizing enzyme tyro on SWCNT-COOH thin film of SPCE electrodes for detection of TYR level in fish products by using amperometric techniques [21]. Other than that, studied by da Silva, the same enzyme tyro was used using a modification of the glassy carbon electrode (GCE) [22].

However, there are only a few reports on tyro immobilized on SPCE with a synthesis of SWCNT-COOH on TYR determination. As a result, more detailed research on the immobilization of tyro over the activated surface of SWCNT-COOH modified SPCE in the detection of TYR is required to determine the best parameter for developing the novel electrode. Thus, in this study, the effect of various compositions on the modification of the electrode Tyro-SWCNT-COOH/SPCE in the detection of TYR was investigated. The optimization focused on the effect of scan rate, pH of the buffer, amount of enzyme and concentration of SWCNT-COOH that contributed to giving the optimum condition of the biosensor in the experiment.

Materials and Methods

Apparatus

Tyrosinase from mushroom (EC 1.14.18.1) ≥1000 unit/mg, carbon nanotube, and single-walled, ≥98%

carbon basis, n-hydroxysuccinimide (NHS), potassium hexacyanoferrate (III) reagentplus®, tyramine, sodium phosphate dibasic (Na_2HPO_4), sodium phosphate monobasic (NaH_2PO_4) were purchased from Sigma Aldrich (St. Louis, MO, USA). Nitric acid (HNO_3) (65%) and sulphuric acid (H_2SO_4) (95-98%) were purchased from R&M Chemicals. The 1-ethyl-3-(3-dimethylaminopropyl) carbodiimide hydrochloride (EDC) is from G-Bioscience, USA and potassium chloride (KCl) is from Friendemann Schmidt. The stock solution of enzyme tyrosinase and EDC/NHS coupling agent has been aliquoted and stored at -20°C. All reagents used in this research are analytical grade and used without further purification. Water purified with a Milli-Q system (Millipore Milli-Q, Badford, MA, USA) was used for the preparation of all aqueous solutions.

Chemicals and instrumentations

The weight balance and pH measurements (Mettler Toledo) using a pH meter were employed for all pH measurements and calibrated with buffer pH 4, 7 and 10. Elmasonic EASY 120 H was used for ultrasonication of solution, and Beckman counter centrifuges Allegra 64R was used in ultracentrifuge precipitate separation. The electrochemical measurements were obtained using the Autolab (Ecochemie, Utrecht, The Netherlands) potentiostat incorporated with a general-purpose electrochemical system (NOVA 2.1.4), connected to a computer for data processing. The characterization of SWCNT-COOH was carried out using Fourier transform infrared (FTIR) (Perkin Elmer).

Electrodes and electrochemical cell

The electrochemical experiments were carried out using a screen-printed carbon electrode (SPCE) purchased from Rapid Lab Sdn Bhd (Bangi, Malaysia), which was made up of carbon as the working electrode (diameter: 5 mm), silver chloride (AgCl) as the reference electrode and carbon as counter electrodes. Measurement and electrochemical characterization were carried out using cyclic voltammetry (CV), and differential pulse voltammetry (DPV). CV was registered from -0.6 to 1.0 V at a scan rate of 0.05 Vs^{-1} (except otherwise indicated). DPV was registered from 0.0 to 1.0 V with a scan rate of 0.05 Vs^{-1} and a potential of 0.5 V (except otherwise indicated).

Synthesis of SWCNT-COOH

The amount of 200 mg of SWCNTs was dissolved in 200 mL of concentrated sulphuric acid (H_2SO_4) and nitric acid (HNO_3) with a ratio of 3:1. The mixture then undergoes sonication for 6 hours at 60 °C. The solution was allowed to cool, then distilled water was added, and left overnight. The solution was then ultracentrifuged (35000 rpm), the sedimental black solution was collected, and distilled water was used to control the pH until it reached neutral pH 7. After that, the black sedimental solution was collected using a vacuum filtration assembly with (0.45 µm pore size) filter paper. The filtered SWCNT-COOH bedding was dried in an oven overnight at 50ºC, and the obtained SWCNT-COOH powder was characterized using FTIR.

Biosensor fabrication

The 12 µL of 0.5 mg/mL SWCNT-COOH solution was drop cast onto the pre-treated SPCE surface and dried at room temperature for 30 minutes. The 10 µL of 0.5 M EDC/NHS solution was dropped onto the dried SWCNT-COOH/SPCE. After 30 minutes, 10 µL of enzyme tyrosinase solution (2 mg/ml, 200 units activity) was dropped gently onto the SWCNT-COOH/SPCE at 4ºC for 15 minutes, and the electrode was rinsed with PBS to remove the unbonded enzyme. Each analysis was repeated three times.

Immobilization of tyrosinase on SWCNT-COOH/SPCE

Immobilized enzymes onto an SPCE using EDC/NHS coupling were prepared by dissolving 0.048 g of EDC (0.25 M) and 0.029 g of NHS (0.25 M) into a 1 mL polypropylene microcentrifuge tube and 0.05 M phosphate buffer solution (PBS) at pH 7.0 up until the mark. The prepared solution was then stored in the freezer.

Optimization procedure

The parameters that were investigated for the optimization of the modified electrode are the effect of pH of the electrolyte (pH 7.0, 8.0, 9.0 and 10.0), effects of SWCNT-COOH concentration (0.2, 0.5, 1.0. 1.5, 2.0 and 3.0 mg/mL) and the amount of enzyme (2, 4, 6, 8 and 10 µL) by keeping other parameters fixed and changing one factor at a time. All the measurements

were run three times, and the error bars show the standard deviation of the three measurements. The electrochemical response of the biosensor was carried out at 0.50 V in phosphate buffer solution (PBS) at 50 mM in the presence of tyramine (TYR) (0.05 M) using differential pulse voltammetry (DPV) by observing the peak current (ΔI_p) response. For the immobilization of the enzyme, tyro was prepared in a solution of 2 mg/ml as a stock solution (activity 2000 units) before being diluted to 0.2 mg/mL (200 units activity) as a working solution. Six different concentrations of enzyme tyro (≥1000 U/mg) ranging between 2, 4, 6, 8 and 10 µL were used in the fabrication of the biosensor and were directly immobilized onto SWCNT-COOH/SPCE after drop cast of EDC/NHS that act as an immobilization holder.

Result and Discussion

Biosensor fabrication

The biocatalytic performance of an immobilized enzyme system depends mostly on the intrinsic properties of both the biomolecule and its support. Single-walled carbon nanotubes (SWCNTs) possess unique features for tyrosinase (tyro) immobilization by adsorption after drop-casting as the first layer on a screen-printed carbon electrode (SPCE). Thus, the optimum concentration condition of SWCNT-COOH was studied on the DPV peak current (ΔI_p) response of modified electrode tyro-SWCNT-COOH/SPCE at 0.2, 0.5, 1.0. 1.5, 2.0 and 3.0 mg/mL SWCNT-COOH towards TYR determination. The resulting biosensor was denoted as Tyro-SWCNTCOOH/SPCE, as shown in Figure 1. The first layer of modification involves SWCNT-COOH to form a thin solid drop solution onto the flat surface of SPCEs, followed by evaporation of the solution. After that, the enzyme tyro was immobilized over SWCNT-COOH by an adsorption process.

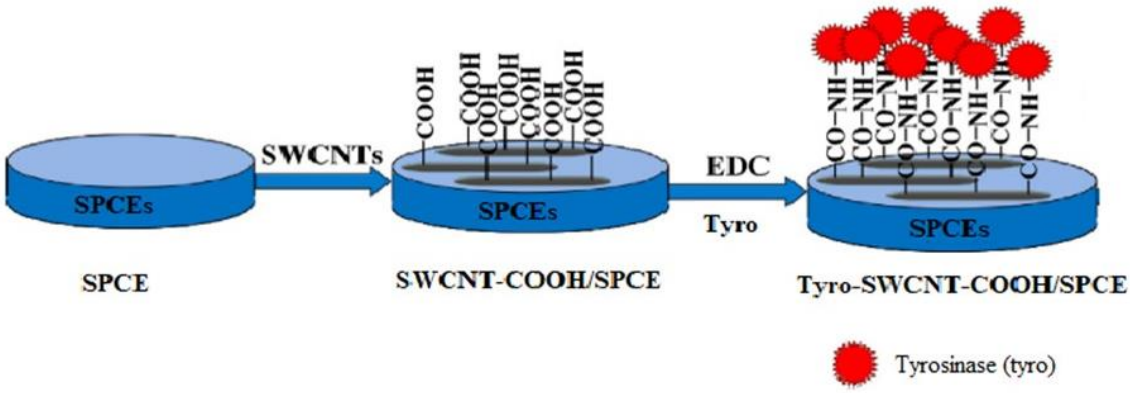


Figure 1. Proposed schematic reaction of the tyrosinase study on the single-walled carbon nanotube carboxyl functionalized (SWCNT-COOH) modified electrode for detection of tyramine (TYR)

Figure 2(a) shows carboxyl functionalized single-walled carbon nanotube (SWCNTCOOH) using the acid treatment method. Chemical manipulation becomes difficult when pristine CNTs are inherently insoluble in organic solvents. Thus, functionalizing the pristine CNTs with carboxylic acid groups will help to mitigate this disadvantage by affording the possibility of further chemical derivatization.

Effective immobilization of the enzymes is a crucial step in the development of high-performance biosensors. In this study, immobilization of tyro onto SWCNT-COOH/SPCE was employed using EDC/NHS coupling to activate the carboxyl groups of SWCNT-COOH that have been drop cast as the first layer of modification. The EDC/NHS activation method can minimize any adverse effects on the bioactivity of target molecules; thus, it was preferred due to its high conversion efficiency and excellent biocompatibility [23].

The EDC/NHS used in this study was 0.25/0.25 M, where the equal amount of EDC/NHS = 0.25/0.25 M shows the most effective concentration for the carboxyl group [24]. The -COOH functionalized groups on the sidewalk of the SWCNT will be used as the precursor for diimidation for the formation of amide bonds with the amine groups of the enzyme. This will be successfully achieved through the reaction of carboxylic acid groups with EDC/NHS to form an amine-reactive ester group that finally bonds to the -NH group in the enzyme, so that the enzyme is immobilized on the electrode. The conjugation of the enzyme reaction pathway onto SWCNTs is shown in the mechanism given in Figure 2(b).

2(a) 2(b)

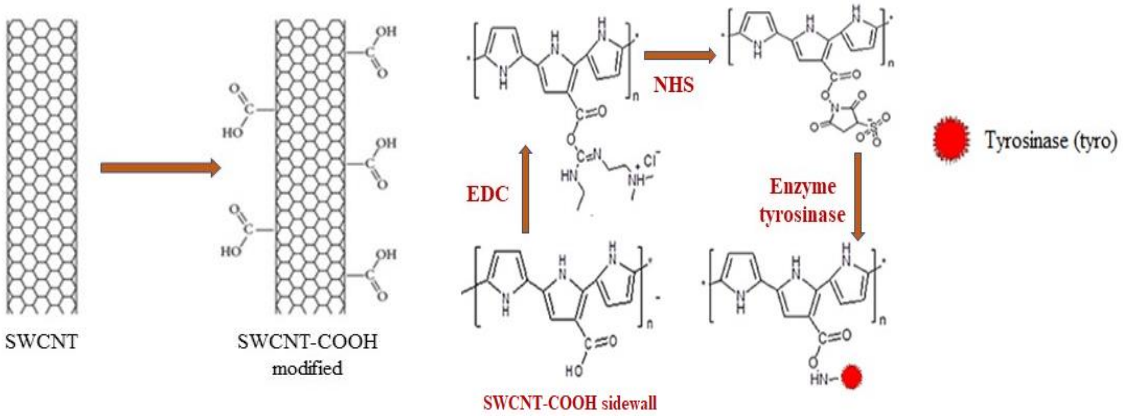


Figure 2. (a) Carboxyl functionalized single-walled carbon nanotube (SWCNT) using an acid treatment method, (b) The EDC/NHS coupling method's mechanism.

Characterizations of the modified electrode

Figure 3 shows the comparison of the total reflection infrared spectra in a range of 4000 - 1000 cm^{-1} for (a) pristine SWCNT and (b) functionalized SWCNT after being treated with H_2SO_4 and HNO_3 acid treatment method, producing SWCNT-COOH. It can be clearly shown that there is a broad peak representing the O-H stretching of hydroxyl groups from carboxyl groups (O=C-OH and C-OH) at about 3296 cm^{-1} [25]. During purification, the partial oxidation reaction occurs, causing the carboxyl group to be present on the surface of pristine SWCNT [26]. The apparent peaks at 1750 cm^{-1} and 1055 cm^{-1} are contributed by the presence of C=O and C-O stretching vibration of the carboxyl group (-COOH), respectively [27]. Meanwhile, the C-H stretch modes of H-C=O in the carbonyl group also indicate the presence of a long-chain alkyl molecule that is attributed to peak 2920 cm^{-1} [28].

FTIR spectra were used to ensure the presence of carboxyl functionalized group -COOH on SWCNT to indicate the successfulness of the synthesis of SWCNT to SWCNT-COOH using the acid treatment method in this study [29]. The functionalization method was used to improve interfacial interactions with nanotubes and to produce a well-dispersed SWCNT composition to drop the SWCNT-COOH dispersion on SPCE during the modification of the electrode. By comparing the FTIR absorption spectra of pristine and SWCNT-COOH, SWCNT oxidized by a mixture of H_2SO_4 and HNO_3 were successfully added with the carboxylic groups (-COOH) to the wall of SWCNT, improving the properties of carbon nanotubes.

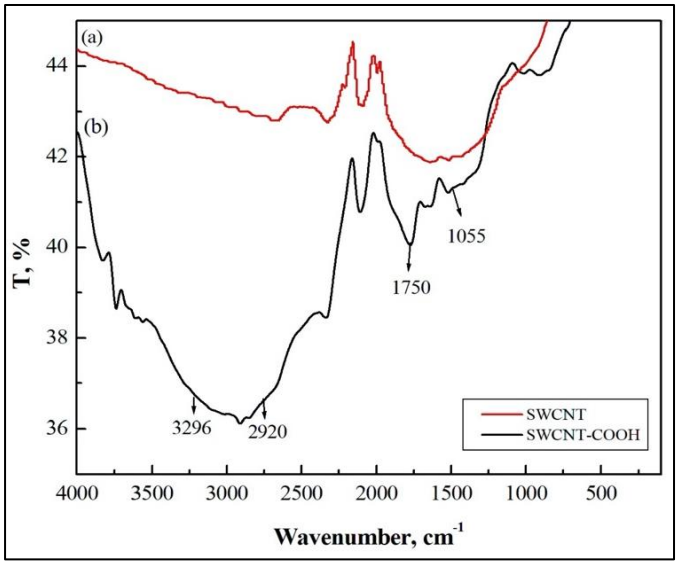


Figure 3. FTIR spectra of (a) pristine single-walled carbon nanotube, (b) functionalized single-walled carbon nanotube

Electrochemical characterization

Cyclic voltammetry (CV) was conducted at 0.50 V to characterize the electrochemical behavior of bare SPCE and modified SPCE. In this study, CV was performed on three different types of electrodes in 0.05 M ferrocyanide $(Fe(CN)_6)^{3-/4-}$ a solution containing 100 mM KCl as shown in Figure 4 (a) bare SPCE, (b) SWCNT-COOH/SPCE, and (c) Tyro-SWCNT-COOH/SPCE. When the surface of the electrode was modified, the ΔIp_a was increased from 34.86 µA at bare SPCE to 97.40 µA and 109.32 µA at SWCNT-COOH/SPCE and Tyro-SWCNT-COOH/SPCE, respectively. The increase in the peak current proves the electrode was successfully developed, which could be described by the transmission of electrons between the electrode and redox probe. The number of electrons transferred can be determined using the peak separation as a criterion for Nernstian behavior. The Randles-Sevcik equation was used to calculate the active surface area of SPCE.

$$I_{pa} = (2.69 \times 10^5)\, n^{3/2} ACD^{1/2} \nu^{1/2} . \quad (1)$$

Based on Equation (1), the real active surface area of the electrode was calculated by substituting the value of n (number of electrons) = 1 $[Fe(CN)^{3-/4-}$ system], A (electrode area) = (22/7) $(0.25\ cm)^2$ = 0.196 cm^2, C (concentration) = 0.05 mol L^{-1}, D (diffusion coefficient) = 7.6×10^{-6} $cm^2\ s^{-1}$ and ν (scan rate) = 0.05 Vs^{-1}. From the calculation, the value of the geometrical surface area of the electrode is 0.126 $cm^{2,}$ and the electrochemical surface area of the real electrode is much larger, as expected. As tabulated in Table 1, the active surface area of bare SPCE was calculated as 4.2091 cm^2 while it was 11.7604 and 13.1997 cm^2 after modification with SWCNT and enzyme tyro, respectively. Thus, higher electron transfer happened at a larger value of active surface area on the modified electrode [26]. This also proved that the modification was successfully improved at each layer of the electrode.

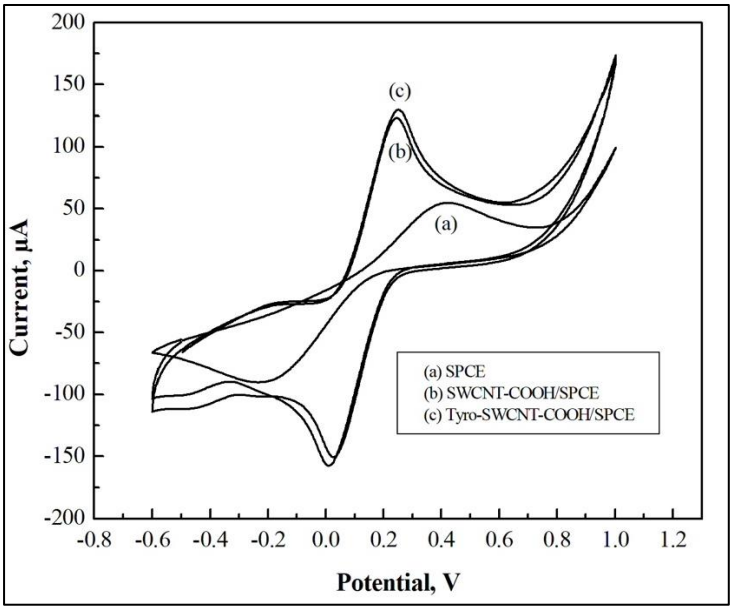


Figure 4. (a) CVs of (a) SPCE, (b) SWCNT-COOH/SPCE, (c) and Tyro-SWCNT-COOH/SPCE (0.05 M $(Fe(CN)_6)^{3-/4-}$ solution containing 100 mM KCl at 50 mVs^{-1})

Table 1: Electrochemical parameters obtained from voltammograms in Figure 4

Electrode	E_{Pc} (V)	E_{Pa} (V)	Ip_c (µA)	Ip_a(µA)	A (cm^2)	Current density (µA/cm^2)
SPCE	0.40	-0.19	-36.67	34.86	4.20	8.28
SWCNT-COOH/SPCE	0.23	0.03	-94.22	97.40	11.76	8.28
Tyro-SWCNT-COOH/SPCE	0.24	0.02	-99.03	109.32	13.19	8.28

Figure 5(a) compares the background current before (solid line) and after modification (dashes-line). The voltammogram of modified SWCNT-COOH/SPCE displayed an increase in peak current as compared to the bare electrode, which can be attributed to the redox behavior of SWCNT-COOH on the electrode surface. Similar voltammogram patterns for carboxyl functionalized on carbon nanotubes (CNT-COOH) were previously reported at different electrode surfaces [30].

The presence of SWCNT-COOH was also verified by CVs measurements in 0.05 M PBS solution containing 100 mM KCl between -0.2 and 1.0 V at a different scan rate of 10, 25, 50, 75, 100, 250, 300, 400 and 500 mVs^{-1}, as shown in Figure 5(b). From the observation, the same pattern is retained from 10 to 100 mVs^{-1} with the appearance of the oxidation peak at 0.1 V, while at a higher scan rate above 250 mVs^{-1}, the redox peak is less visible. According to Venton et al., the rate of diffusion-controlled of the Faradaic currents that occur at the surface of the electrode is proportional to the square root of scan rate resulting in, an increase of background current at a faster rate compared to the Faradaic currents [31]. Thus, the scan rate to be used in this study was at 50 mVs^{-1}.

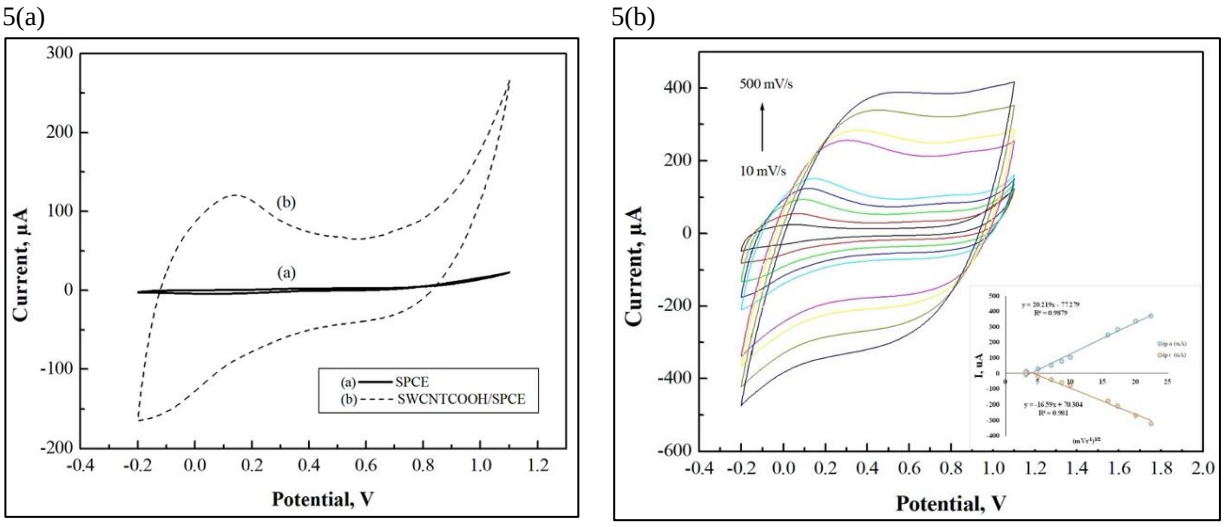


Figure 5: (a) CVs of bare SPCE and SWCNT-COOH/SPCE (50 mM PB buffer solution pH 8.0 containing 100 mM KCl) and (b) CVs of SWCNT-COOH/SPCE (0.05 M PBS solution containing 100 mM KCl) inset: plots of peak current vs square root of scan rate and recorded at 10, 25, 50, 75, 100, 250, 300, 400 and 500 mVs^{-1} inset: plots of peak current vs square root of scan rate.

Optimization of modified electrode composition for determination of tyramine

In this study, the effect of pH was analyzed in a wide range, starting from pH 3.0 to 11.0. Figure 6(a) shows the influence of pH in the detection of tyramine (TYR) at pH 7.0 to 10.0. However, no peak was observed at pH less than 6 and above pH 11 due to the deactivation of tyro under strong acid and alkaline conditions. It can be seen that the activity of tyrosinase (tyro) increased first up to pH 8 and then decreased until pH 10.0. The decreased response of the biosensor might be due to the absence of the biocatalytic activity resulting in enzyme denaturation [32]. Therefore, pH 8.0 was chosen as the optimum pH in all experiments in the electrochemical determination of TYR.

Figure 6(b) shows the effect of the SWCNT-COOH concentration on the modified electrode. This study is important to identify a suitable concentration of SWCNT-COOH on the modified electrode in which increasing performance is correlated with the small size of SWCNT-COOH, which enhanced the large surface area of the electrode. When the enzyme is added in the following stage, the electrode's high specific area allows for the immobilization of higher concentrations of bioreceptor units relative to the biosensor surface [33]. The graph shows an increased pattern starting at 0.2 mg/ml, and a higher reading was observed at 0.5 mg/ml. However, further increasing the concentration of SWCNT-COOH caused a decrease in biosensor response. This can be attributed to the thickness of the nanocomposites that will block the electric conductivity on the surface of the electrode [34]. Thus, 0.5 mg/ml of SWCNT-COOH was selected as the optimum concentration for biosensor fabrication of the SWCNT-COOH layer on SPCE.

Figure 6(c) depicts the effect of increasing the enzyme amount from 2, 4, 6 and 8 L. However, at 10 µL of tyro, a slight decrease in the biosensor response was observed, which can be attributed to the protein loading on the electrode surface rising due to mass transfer diffusion limitation through the electrode surface. Thus, the amount of enzyme at 8 µL was chosen as the optimum parameter in the modification of the biosensor.

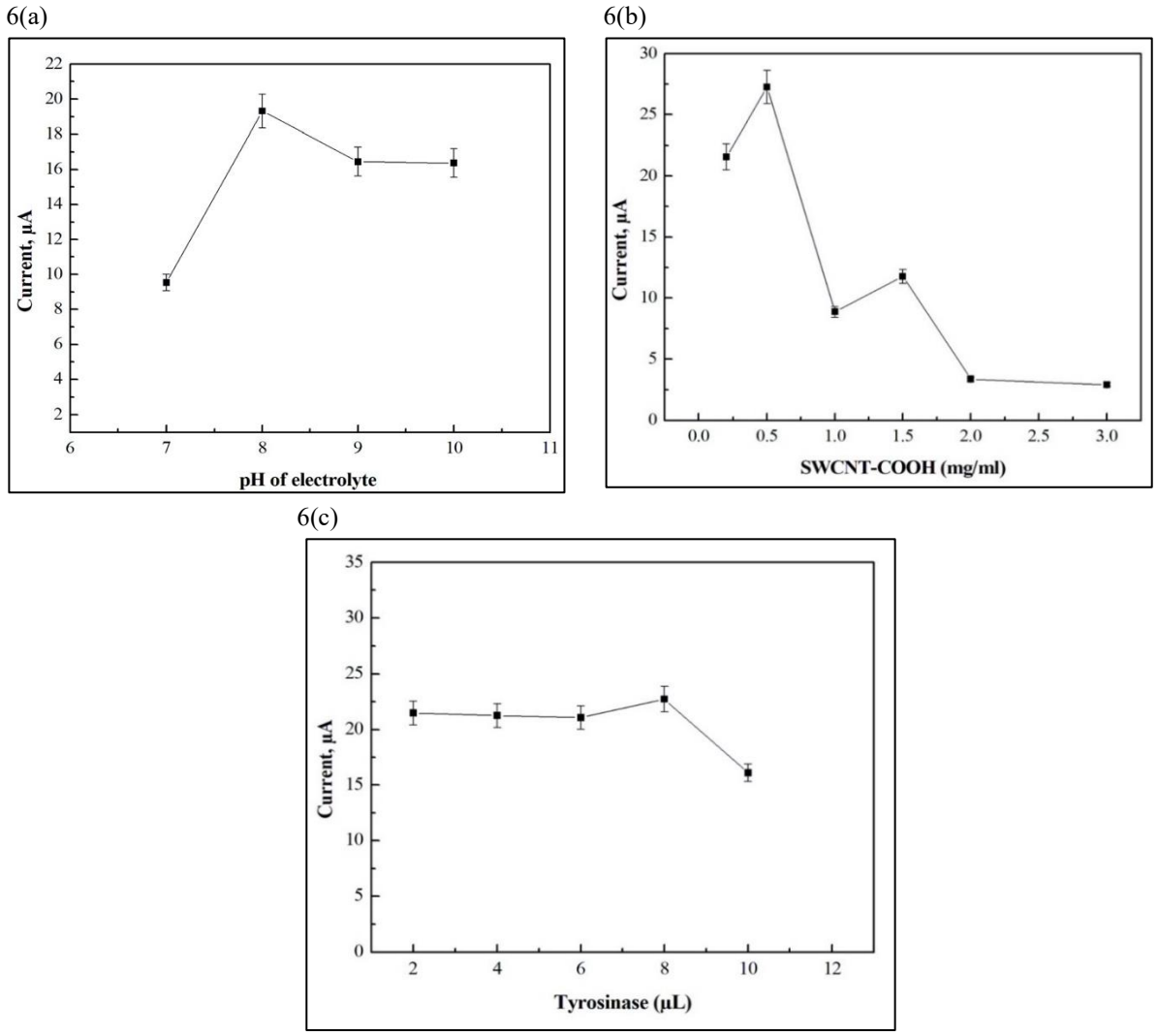


Figure 6. (a) The influence of pH value, (b) concentration of SWCNT-COOH, and (c) amount of tyrosinase on the response of Tyro-SWCNT-COOH/SPCE in 50 mM PB solution containing 0.05 M tyramine at +0.05 V

Figure 7(a) shows the CVs of three-electrode modifications in the presence of 0.05 M tyramine (TYR): bare SPCE (curve a), Tyro-SWCNT-COOH/SPCE (curve b), and SWCNT-COOH/SPCE (curve c) in 0.05 M PB solution pH 8.0, analyzed by CVs from -0.6 to 1.0 V at a scan rate of 100 mVs^{-1}. The peak potential of TYR at modified SWCNT-COOH/SPCE was observed at 0.67 V. While for bare SPCE, no oxidation peak was detected, showing that the modification of electrode SPCE using SWCNT-COOH and enzyme tyro was successfully fabricated. A similar peak potential for TYR oxidation was also reported previously [35].

The standard addition method was investigated to confirm the peak potential of TYR at Tyro-SWCNT-COH/SPCE using differential pulse voltammetry (DPV). Figure 7(b) showed the continuous successive additions of TYR in PBS (0.05 M, pH 8.0) ranging from 0.05 mM to 0.15 mM. The oxidation peak appeared at 0.67 V, and the peak current gradually increased with TYR concentration. From the calibration plot, the correlation coefficient (R^2) was found to be 0.9749 with

a low limit of detection (LOD) value of 0.02 mM. It can be concluded that the Tyro-SWCNT-COOH/SPCE is a sensitive biosensor for TYR detection, which offers lower detection limits.

7(a) 7(b)

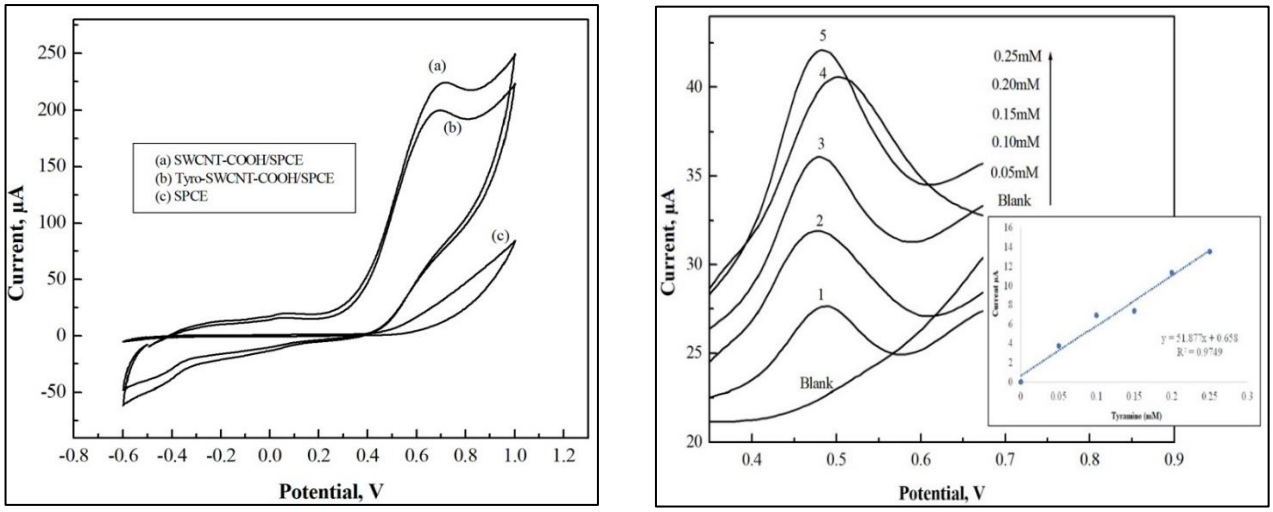


Figure 7. (a) CVs of SPCE, SWCNT-COOH/SPCE, Tyro-SWCNT-COOH/SPCE and in the presence of 0.05 M Tyramine in 0.05 M PB buffer solution pH 8.0. (b) Differential pulse voltammetry (DPV) response of tyro-SWCNT-COOH/SPCE in the presence of tyramine (0.05 to 0.15 mM) in 0.05 M PBS of pH 8.0 at a scan rate of 100 mVs^{-1}. Calibration plot of the current response vs the concentration of tyramine

Conclusion

In this work, a novel biosensor based on Tyro-SWCNT-COOH/SPCE was successfully fabricated, characterized, and optimized for tyramine (TYR) detection. Single-walled carbon nanotubes carboxyl functionalized (SWCNT-COOH) were successfully synthesized and used as a biocompatible matrix for tyrosinase (tyro) immobilization. The SWCNT functionalized -COOH contributed to a suitable microenvironment for immobilization of enzyme, thus retaining the bioactivity of a tyro. The optimum parameters used for this research for the Tyro-SWCNT-COOH/SPCE biosensor exhibit good performance at a scan rate of 50 mVs^{-1}, pH 8.0 of phosphate buffer solution (PBS), 8 µl enzyme tyrosinase and 0.5 mg/ml of SWCNTs. The developed biosensor showed a good lower correlation coefficient (R^2) 0.9749 and detection limits (LOD) of 0.02 mM. All these satisfactory results show that SWCNT-COOH and tyro have good properties as electroactive nanomaterials for biosensor surface modification in the determination of TYR. The biosensor developed could be used to determine TYR in real food sample analysis in the future.

Acknowledgement

This work was supported by the Ministry of Higher Education Malaysia (MOHE) for the financial support through Fundamental Research Grant Scheme for Research Acculturation of Early Career Researchers (FRGS-RACER) [Grant code: USIM/FRGS-RACER/FST/50919].

References

1. Lázaro, C.A., Conte-Júnior, C.A., Canto, A.C., Monteiro, M.L.G., Costa-Lima, B., Cruz, A.G. da, et al. (2015). Biogenic amines as bacterial quality indicators in different poultry meat species, *LWT - Food Science and Technology*, 60(1): 15-21.

2. Lázaro, C.A., Conte-Júnior, C.A., Cunha, F.L., Márcico, E.T., Mano, S.B. and Franco, R.M. (2013). Validation of an HPLC methodology for the identification and quantification of biogenic amines in chicken meat. *Food Analytical Methods*, 6(4): 1024-1032.
3. Durlu-Özkaya, F., Ayhan, K. and Vural, N. (2001). Biogenic amines produced by Enterobacteriaceae isolated from meat products. *Meat Science*, 58(2): 163-166.
4. Ruiz-Capillas, C. and Herrero, A.M. (2019). Impact of biogenic amines on food quality and safety. *Foods*, 31(12): 2368-2378.
5. Soares, I.P., da Silva, A.G., da Fonseca Alves, R., de Souza Corrêa, R.A.M., Ferreira, L.F. and Franco, D.L. (2019). Electrochemical enzymatic biosensor for tyramine based on polymeric matrix derived from 4-mercaptophenylacetic acid. *Journal of Solid State Electrochemistry*, 23 (3): 985-995.
6. Verma, N., Hooda, V., Gahlaut, A., Gothwal, A. and Hooda, V. (2019). Enzymatic biosensors for the quantification of biogenic amines: a literature update. *Critical Reviews in Biotechnology*, 2019: 1-14.
7. Khan, M.Z.H., Liu, X., Zhu, J., Ma, F., Hu, W. and Liu, X. (2018). Electrochemical detection of tyramine with ITO/APTES/ErGO electrode and its application in real sample analysis. *Biosensors and Bioelectronics*, 118(3): 1169-1198.
8. Cantarini, M. V., Painter, C.J., Gilmore, E.M., Bolger, C., Watkins, C.L., and Hughes, A.M. (2004). Effect of oral linezolid on the pressor response to intravenous tyramine. *British Journal of Clinical Pharmacology*, 58(5): 470-475.
9. Costa, D.J.E., Martínez, A.M., Ribeiro, W.F., Bichinho, K.M., Di Nezio, M.S., Pistonesi, M.F., et al. (2016). Determination of tryptamine in foods using square wave adsorptive stripping voltammetry. *Talanta*, 154: 134-140.
10. da Silva, W., Ghica, M.E., Ajayi, R.F., Iwuoha, E.I. and Brett, C.M.A. (2019). Impedimetric sensor for tyramine based on gold nanoparticle doped-poly(8-anilino-1-naphthalene sulphonic acid) modified gold electrodes. *Talanta*, 195: 604-612.
11. Wan, H., Sun, Q., Li, H., Sun, F., Hu, N., and Wang, P. (2015). Screen-printed gold electrode with gold nanoparticles modification for simultaneous electrochemical determination of lead and copper. *Sensors and Actuators, B: Chemical*, 209: 336-342.
12. Jewell, E., Philip, B. and Greenwood, P. (2016) Improved manufacturing performance of screen printed carbon electrodes through material formulation. *Biosensors*, 6(3): 30.
13. Rawat, K.A., Bhamore, J.R., Singhal, R.K. and Kailasa, S.K. (2017) Microwave assisted synthesis of tyrosine protected gold nanoparticles for dual (colorimetric and fluorimetric) detection of spermine and spermidine in biological samples. *Biosensors and Bioelectronics*, 88: 71-77.
14. Chen, M., Zeng, G., Xu, P., Lai, C. and Tang, L. (2017) How do enzymes' meet' nanoparticles and nanomaterials?. *Trends in Biochemical Sciences*, 42(11): 914-930.
15. Lan, L., Yao, Y., Ping, J., and Ying, Y. (2017). Recent advances in nanomaterial-based biosensors for antibiotics detection. *Biosensors and Bioelectronics*, 91: 504-514.
16. Apetrei, I.M. and Apetrei, C. (2013). Amperometric biosensor based on polypyrrole and tyrosinase for the detection of tyramine in food samples. *Sensors and Actuators, B: Chemical*, 178: 40-46.
17. Manan, F.A.A., Hong, W.W., Abdullah, J., Yusof, N.A. and Ahmad, I. (2019). Nanocrystalline cellulose decorated quantum dots based tyrosinase biosensor for phenol determination. *Materials Science and Engineering C*, 99: 37-46.
18. Camargo, J.R., Baccarin, M., Raymundo-Pereira, P.A., Campos, A.M., Oliveira, G.G., Fatibello-Filho, O. (2018). Electrochemical biosensor made with tyrosinase immobilized in a matrix of nanodiamonds and potato starch for detecting phenolic compounds, *Analytica Chimica Acta*, 1034: 137-143.
19. Montereali, M.R., Seta, L. Della, Vastarella, W. and Pilloton, R. (2010). A disposable Laccase-Tyrosinase based biosensor for amperometric detection of phenolic compounds in must and wine. *Journal of Molecular Catalysis B: Enzymatic*, 64 (3-4): 189-194.

20. Wang, B., Zheng, J., He, Y. and Sheng, Q. (2013). A sandwich-type phenolic biosensor based on tyrosinase embedding into single-wall carbon nanotubes and polyaniline nanocomposites. *Sensors and Actuators, B: Chemical*, 186: 417-422.
21. Apetrei, I.M. and Apetrei, C. (2015). The biocomposite screen-printed biosensor based on immobilization of tyrosinase onto the carboxyl functionalized carbon nanotube for assaying tyramine in fish products. *Journal of Food Engineering*, 149: 1-8.
22. da Silva, W., Ghica, M.E., Ajayi, R.F., Iwuoha, E.I. and Brett, C.M.A. (2019). Tyrosinase based amperometric biosensor for determination of tyramine in fermented food and beverages with gold nanoparticle doped poly(8-anilino-1-naphthalene sulphonic acid) modified electrode. *Food Chemistry*, 282: 18-26.
23. Ng, C.M., Loh, H.S., Muthoosamy, K., Sridewi, N. and Manickam, S. (2016). Conjugation of insulin onto the sidewalls of single-walled carbon nanotubes through functionalization and diimide-activated amidation. *International Journal of Nanomedicine*, 11: 1607-1614.
24. Guler, Z. and Sarac, A.S. (2016) Electrochemical impedance and spectroscopy study of the EDC/NHS activation of the carboxyl groups on poly(ε-caprolactone)/poly(m-anthranilic acid) nanofibers. *Express Polymer Letters*, 10(2): 96-110.
25. Rahman, M.J. and Mieno, T. (2014). Water-dispersible multiwalled carbon nanotubes obtained from citric-acid-assisted oxygen plasma functionalization. *Journal of Nanomaterials*, 2014: 508192.
26. Azri, F.A., Sukor, R., Hajian, R., Yusof, N.A., Bakar, F.A., and Selamat, J. (2017). Modification strategy of screen-printed carbon electrode with functionalized multi-walled carbon nanotube and chitosan matrix for biosensor development. *Asian Journal of Chemistry*, 29(1): 31-36.
27. Moraes, M.B., Cividanes, L., and Thim, G. (2018). Synthesis of graphene oxide and functionalized CNT nanocomposites based on epoxy resin. *Journal of Aerospace Technology and Management*, 10: 1-10.
28. Abuilaiwi, F.A., Laoui, T., Al-Harthi, M., and Atieh, M.A. (2010). Modification and functionalization of multiwalled carbon nanotube (MWCNT) via fischer esterification. *Arabian Journal for Science and Engineering*,. 29 (1): 31-36.
29. Tsai, P.A., Kuo, H.Y., Chiu, W.M. and Wu, J.H. (2013). Purification and functionalization of single-walled carbon nanotubes through different treatment procedures. *Journal of Nanomaterials*, 2013: 3-12.
30. Jacobs, C.B., Vickrey, T.L., and Venton, B.J. (2011). Functional groups modulate the sensitivity and electron transfer kinetics of neurochemicals at carbon nanotube modified microelectrodes. *Analyst*, 136 (17): 3557-3565.
31. Venton, B.J. and Cao, Q. (2020). Fundamentals of fast-scan cyclic voltammetry for dopamine detection. *Analyst*, 145(4): 1158-1168.
32. Rahimi-Mohseni, M., Raoof, J.B., Ojani, R., Aghajanzadeh, T.A., and Bagheri Hashkavayi, A. (2018). Development of a new paper based nano-biosensor using the co-catalytic effect of tyrosinase from banana peel tissue (Musa Cavendish) and functionalized silica nanoparticles for voltammetric determination of L-tyrosine. *International Journal of Biological Macromolecules*, 113: 648-654.
33. Tîlmaciu, C.M. and Morris, M.C. (2015). Carbon nanotube biosensors. *Frontiers in Chemistry*, 3: 1-21.
34. Muhammad, A., Yusof, N.A., Hajian, R., and Abdullah, J. (2016). Construction of an electrochemical sensor based on carbon nanotubes/gold nanoparticles for trace determination of amoxicillin in bovine milk. *Sensors (Switzerland)*, 16 (1): 1-13.
35. Chakkarapani, L.D. and Brandl, M. (2020). Carbon screen-printed electrode coated with poly (toluidine blue) as an electrochemical sensor for the detection of tyramine. *Engineering Proceedings*, 2(1): 51.

Malaysian Journal of Analytical Sciences (MJAS)
Published by Malaysian Analytical Sciences Society

DEVELOPMENT OF AN ELECTROCHEMICAL IMMUNOSENSOR STRIP FOR EARLY DETECTION OF RICE BACTERIAL LEAF BLIGHT (BLB) DISEASE AND ITS APPLICATION ON A PORTABLE DEVICE

(Pembangunan Strip Imunosensor Elektrokimia Untuk Pengesanan Awal Penyakit Hawar Daun Bakteria Padi dan Aplikasinya Pada Peranti Mudah Alih)

Hazana Razali[1], Norhafniza Awaludin[1], Nurul Hidayah Husin[1], Sahira Akmar Zulkepli[1], Rafidah Abd Rahman[1], Mohammad Rejab Ismail[1], Kogeethavani Ramachandran[2], Faridah Salam[1], Nur Azura Mohd Said[1*]

[1]Biotechnology & Nanotechnology Research Centre,
MARDI Headquarter, Persiaran MARDI-UPM, 43400 Serdang, Selangor, Malaysia
[2]Paddy& Rice Research Centre,
MARDI Seberang Perai, 13200 Seberang Perai, Pulau Pinang

[*]Corresponding author : nazurams@mardi.gov.my

Received: 8 February 2022; Accepted: 27 April 2022 ; Published: 27 December 2022

Abstract

We described here an electrochemical immunosensor strip based on a screen-printed carbon electrode (SPCE) for early detection of rice bacterial leaf blight (BLB) disease. The causal agent for this destructive disease has been identified as *Xanthomonas oryzae* pv. *oryzae* (*Xoo*). In order to circumvent the disease outbreak, an early detection system is required. Polyclonal antibody against *Xoo* was employed and immobilized on the SPCE strips modified with polypyrrole (PPy) and functionalized multi-walled carbon nanotube (fMWCNT) network. The anti-*Xoo* antibody is conjugated with horseradish peroxidase (HRP) as an enzyme label and used as the detection agent in the sensor development. Electrochemical detection was carried out via the chronoamperometry technique at a set potential of -200 mV. A fixed anti-*Xoo* antibody concentration at 0.03 mg/mL on the working electrode of the strip surface produced a standard linear curve for *Xoo* detection (R^2 = 0.9746). Two extraction methods for rice leaves (scissors-cutting and grinding) were compared for real samples application analysis. The scissors-cutting method had less matrix interference effect and gave a higher recovery rate than the grinding method. The optimal immunosensor configuration was then compared with the PCR technique for *Xoo* detection in inoculated leaves in a controlled environment. A good correlation of 92.7% was achieved between the two methods. The immunosensor strips were then tested on an Android-based portable biosensor device for on-site detection of BLB in hotspot areas at Bagan Terap, Selangor Northwest and Sg. Burong, Tanjung Karang. On-field detection has indicated that the immunosensor strips can detect BLB disease as early as 15 days after transplant (DAT) before symptoms appear.

Keywords: bacterial leaf blight, early detection, immunosensor, rice disease, *Xanthomonas oryzae* pv.*oryzae*

Abstrak

Satu strip imunosensor elektrokimia berasaskan elektrod karbon bercetak skrin (SPCE) untuk pengesanan awal penyakit hawar daun bakteria (BLB) pada pokok padi dilaporkan dalam kajian ini. Agen penyakit padi ini telah dikenalpasti disebabkan oleh bakteria *Xanthomonas oryzae* pv. *oryzea* (*Xoo*). Bagi mengekang penyebaran penyakit padi ini, satu sistem pengesanan awal penyakit padi adalah diperlukan. Antibodi poliklonal terhadap *Xoo* digunakan dalam kajian ini dan dipegunkan ke atas permukaan strip yang telah diubah suai dengan jaringan polipirol (PPy) dan nanotiub karbon berbilang dinding berfungsi (fMWCNT). Antibodi anti-*Xoo* dikonjugasikan dengan *horseradish peroxidase* (HRP) sebagai label enzim; dan digunakan sebagai agen pengesanan dalam pembangunan sensor. Pengesanan elektrokimia dilakukan dengan menggunakan teknik kronoamperometri pada set potensi -200 mV. Pada kepekatan antibodi 0.03 mg/mLyang dipegunkan pada permukaan elektrod bekerja strip, satu graf piawai linear untuk pengesanan *Xoo* berjaya dibangunkan (R^2 = 0.9746). Bagi aplikasi sampel sebenar, dua kaedah pengekstrakan daun padi (menggunting daun dan pengisaran daun) telah dibandingkan. Kaedah menggunting daun didapati memberikan kesan matriks yang lebih rendah dan kadar pulangan yang lebih tinggi berbanding kaedah pengisaran daun. Kaedah sensor ini kemudian dibandingkan dengan teknik PCR bagi analisis sampel daun teraruh dengan bakteria *Xoo* dalam persekitaran yang terkawal. Korelasi yang baik dengan nilai 92.7% telah dicapai bagi kedua-dua kaedah tersebut. Strip imunosensor ini kemudiannya diuji pada satu peranti biosensor mudah alih berasaskan Android untuk pengesanan BLB di lapangan di kawasan titik panas Bagan Terap, Barat Laut Selangor dan Sg. Burong, Tanjung Karang. Kajian lapangan menunjukkan bahawa strip pengesanan imunosensor ini berupaya mengesan penyakit BLB seawal hari ke-15 selepas transplan (HLT) sebelum kemunculan simptom penyakit.

Kata kunci: hawar daun bakteria, pengesanan awal, imunosensor, penyakit padi, *Xanthomonas oryzae* pv. *oryzae (Xoo)*

Introduction

Rice (*Oryza sativa* L.) is an important staple food in Malaysia and the Asia region. However, rice production has always been hampered by the recurrent attack of several rice diseases, causing massive yield and economic loss to the farmers and agricultural industry. In Malaysia itself, rice diseases in a susceptible variety's crop may cause yield reduction up to 70% [1] depending on the stage and duration of water deficit [2]. Bacterial leaf blight (BLB) disease is one of the major rice diseases in Malaysia. This destructive rice disease is caused by *Xanthomonas oryzae* pv.*oryzae (Xoo)*, a gram-negative bacterium. *Xoo* cells invade the rice plants through the wound opening on the leaves. At the initial stage, BLB symptoms appear as tannish-grey to white-yellowish lesions along the leaf's veins, and this alone causes yield losses up to 50% [3]. At advanced stages, however, BLB is difficult to distinguish from the bacterial leaf streak (BLS) disease, and although direct observation of the bacteria is preferred, the indication is not scientifically proven or confirmed.

Chemical control still remains the main method to reduce the infection of bacterial diseases incidence. However, in good plant disease management, the use of pesticides should be minimized. To prevent or control the spread of the disease, it is therefore crucial for farmers or extension agencies to detect the causal pathogens accurately at an early stage. Common practice for rice disease detection relies on the symptom's recognition by experienced plant pathologists or farmers. This technique, however is not scientifically validated. Other laboratory-based methods such as agar plate culture, polymerase chain reaction (PCR), and enzyme-linked immunosorbent assay (ELISA), albeit specific, still require skilled and trained operators to operate them [4]. Furthermore, these techniques are generally not suitable for on-site analysis.

Under this circumstance, there is a considerable need to develop a biosensor system for early and accurate pathogen detection for rice disease management. With this regard, biosensor technology lends itself well due to its attractive features such as rapid detection sensitivity, reliability, inexpensive, simple performance, and most importantly, its ability to provide real-time and on-field analysis [5, 6]. Antibody-based biosensor or immunosensor application for agricultural plant pathogens detection is reported to hold great potential as it allows detection in various sample matrices such as water and seeds [7]. In this study, an antibody-based electrochemical biosensor strip is developed for the early detection of BLB disease. Electrochemical immunosensor has gained much attention in recent

decades owing to their versatility with wide sensing range and high sensitivity [8, 9].

The electrochemical immunosensor works on the principle that the specific binding interaction between antibody and antigen on an electrode strip is sensed and the signal generated is measured and amplified. Surface functionalization on an electrode surface is generally performed using conducting electroactive polymers (CEPs) and/or nanomaterials to provide antibody binding sites and enhance the signal generated. Here, we employ polypyrrole as the CEPs with functionalized multi-walled carbon nanotubes (fMWCNTs) to serve those purposes. MWCNTs-modified biosensor has been widely used due to their superior performance [10], sensitivity, and, most importantly, suitability for biomolecules exposure. When performing an immunochemical reaction, the binding interaction between the biomolecules and their targeted analytes can be performed either by direct or indirect assay format. Herein, a sandwich assay enzyme-linked immunosorbent assay (ELISA) format was adapted and employed in the sensor development.

Following the successful development and performance of the biosensor strips as indicated in the inoculated samples study, the strips were then tested on an Android-based portable electrochemical device for on-site BLB detection in rice fields located at Selangor Northwest. This device is integrated with the Internet-of-Things (IoT) application that allows the analysed data to be stored on a cloud server and accessed by supervisors at different locations instantaneously. The biosensor strips application with a handheld Android device offers flexibility and portability in the IoT-biosensor system [11]. Ultimately, integrating IoT with the biosensor system will greatly change the way plant disease management control, particularly for the early warning system for rice disease detection. Hence the objective of this study is first to develop an immuno-based strip for early detection of BLB disease in rice plants, and secondly, to demonstrate the strips' viability when attached to a custom-made portable biosensor device for on-site application. To the best of our knowledge, the latter has not been reported and ventured by any researchers in rice/plant disease management though several reports on plant disease biosensors have been published [3, 7, 12, 13, 14].

Materials and Methods

Production of polyclonal antibody against *Xoo*

Polyclonal antibody against *Xoo* was raised and developed in-house at Biotechnology and Nanotechnology Research Centre, MARDI Serdang using local isolated cultures from Paddy and Rice Research Center, MARDI Seberang Perai (P0.0, P1.0, and P7.3 strains). The procedure for polyclonal antibody production has been granted with MARDI Animal Ethics Committee Approval (20171103/R/MAEC27). Antibody purification was conducted using the Akta-Prime protein purifier system (GE Healthcare).

Chemicals and reagents

Ethanolamine, phosphate buffer saline (PBS) tablets, pyrrole, sodium bicarbonate ($NaHCO_3$), sodium carbonate (Na_2CO_3), and *3,3',5,5'*-tetramethylbenzidine (TMB) substrate solution were purchased from Sigma-Aldrich, USA. *N*-(3-Dimethylaminopropyl) - *N*'-ethylcarbodiimide hydrochloride (EDC) and *N*-hydroxysuccinimide (NHS) were from Sigma-Aldrich, Japan. Functionalized multi-walled carbon nanotubes (MWCNT-COOH) were supplied from Dropsens, Spain. Plastic-based screen-printed carbon electrodes (SPCEs) were from BioGenes Technologies Sdn. Bhd., Malaysia. EZ-Link™ Plus Activated Peroxidase Kit was from Thermo-Scientific, USA. Phosphate buffered saline (PBS) solution was prepared by dissolving one PBS tablet in 200 mL deionized (DI) water yielding 0.01 M phosphate buffer. All solutions were prepared using DI water from a Milli-Q Ultrapure water system with a resistivity of 18.2 MΩcm.

Surface modification for antibody immobilization

Electrodeposition of polypyrrole and functionalized-MWCNT on the SPCE strip surface was achieved by a one-step electropolymerization of 0.075 M pyrrole in the presence of 0.1 mg/mL MWCNT-COOH via chronoamperometry technique. The mixtures were electrodeposited for 900 s in PBS at a fixed potential of 1.0 V. The strip was then rinsed with DI water and air-dried under nitrogen (N_2) flow. The carboxylic acid group of MWCNT-COOH was activated in a 10 µL

mixture of 0.4 M EDC and 0.1M NHS (1:1) for 15 mins. The excess was washed out using PBS, rinsed with distilled water, and N_2 dried. Next, 5 µL of anti-*Xoo* antibody was dropped on the electrode surface for 1 hour and washed with PBS. The remaining active sites on the SPCE surface were deactivated for 30 mins using 0.1% ethanolamine. *Xoo* cells or samples were placed on the SPCE's working electrode (WE) and incubated for 1 hour. The unbound antigen was washed away with PBS, and 5 µL of purified anti-*Xoo* antibody conjugated with HRP was dropped onto the working electrode and incubated for 30 mins, washed again with PBS. All modification steps were performed at room temperature.

Electrochemical set-up and measurements

Sensor characterization and analysis for the SPCEs were performed on an Autolab PGSTAT 20 potentiostat (Eco Chemie, Netherlands). Unmodified and modified SPCEs were characterized and compared using the cyclic voltammetry (CV) technique in a redox solution of 1 mM FCA in PBS 0.01 M, pH 7.4 (scan rates of 500 mV/s, potential window -0.1 to +0.6 V). Electrochemical measurements for the modified SPCEs with bounded antibody and *Xoo* cells were carried out by placing 50 µL of TMB solution onto SPCEs covering all three-electrode and measured using chronoamperometry at the optimized potential for 300 s.

The developed SPCEs are attached to a handheld Android-based biosensor device for on-site analysis. This portable device with internet-of-things (IoT) integration has been fabricated and developed with BioGenes Technologies Sdn. Bhd., Malaysia. Besides 4G connection with the built-in mobile application, it also has Global Positioning System (GPS) function to pinpoint the location of sampling. This portable electrochemical device consists of two connected hardware units enclosed in a plastic casing. The first unit is a touch-screen Android-based device with developed electrochemical software. The second unit is an electrochemical transducer that converts the signal from chemical reactions into readable and analysable data. The data collected are saved in a central cloud server and can be accessed through the website **https://provenpac.solutions/MARDI/padi** by authorized users. The detection of BLB disease in the rice fields was conducted with a simple extraction method.

Surface morphological study

The microscopic analysis was performed using field emission scanning electron microscopy (FESEM, JOEL JSM-7600F). Samples for FESEM were mounted on the stub, followed by coating with gold. The samples were visualized at 20 kV accelerating voltage with 20,000-60,000x magnification.

Polymerase chain reaction (PCR)

PCR reaction was carried out in a Bio-Rad thermocycler following the conditions: denaturation at 95°C for 5 min followed by 30 cycles of 95°C for 30 s, 58°C for 30 s, and 72°C for 30 s, and final elongation at 72°C for 1 min. The primer used in this study is described in Table 1 below.

Table 1. Primer for BLB disease detection using PCR method

Primer Name	Sequences (5' - 3')
JLXocF	CAAGACAGACATTGCTGGCA
JLXocR	GGTCTGGAATTTGTACTCCG

Results and Discussion

Sensor surface modification and characterization

A sandwich enzyme-linked immunosorbent assay (ELISA) format was adapted and employed in the sensor development. Polyclonal antibody against *Xoo* is first immobilized on the modified sensor strip surface, capturing the antigen (i.e.,*Xoo* bacteria) (Fig. 1). Then, a secondary antibody with horseradish peroxidase (HRP) enzyme label, which is associated with the other site of the antigen, is added. Electrochemical detection

was carried out using *3, 3', 5, 5'*-tetramethylbenzidine dihydrochloride (TMB)/H_2O_2 as the enzyme mediator/substrate system and conducted using chronoamperometry at an optimized set potential of -200mV. The enzyme's reaction and its substrate will produce a signal current whereby the intensity of the signal generated is directly proportional to the amount of analyte present in the sample.

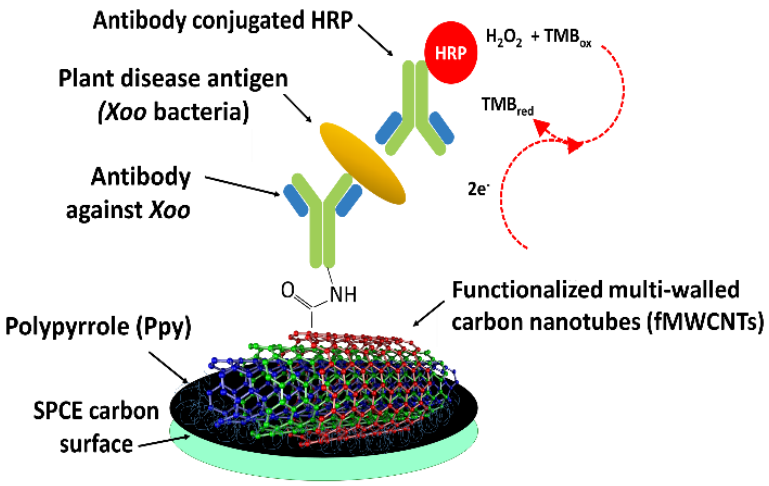


Figure 1. Schematic diagram of electrochemical immunosensor platform employing a sandwich immunoassay format for *Xoo* detection for bacterial leaf blight (BLB) disease

As can be seen from Figure 1, polypyrrole (PPy) and functionalized-multiwall carbon nanotube (MWCNT-COOH) were introduced to the sensor surface. By deliberately attaching or treating certain chemicals or nanomaterials on an electrode surface, the surface would take on the chemical properties of the attached compounds. As carbon material on the SPCE surface is inert, such modification will increase the sensor performance by enhancing the electrochemical properties on the electrode's surface [15]. The challenge of these modified electrodes, though is that they have to be durable and able to retain the activity of the biological receptors so that they do not denature easily and impair the chemical reaction activity. PPy was used in sensor platform modification due to its intrinsic chemical and electrical properties [16]. This type of conducting electroactive polymeris formed under mildly oxidative conditions from aqueous media. The mild conditions used for polymerizations are thus ideal for the immobilization of most of the biological elements in biosensor construction. PPy was incorporated with MWCNT-COOH to improve the sensitivity and selectivity of the biosensor besides providing a high surface area for antibody attachment owing to the carboxylic groups. Several unique properties of MWCNT, such as excellent mechanical strength, superior electrical conductivity, and electrochemically stable in aqueous and nonaqueous solutions, have received much attention in selecting the nanomaterial in sensor surface modification [17]. The EDC-NHS (1:1) was used to cross-link the COOH groups in the fMWCNT with the amine group of antibodies. Amine and carboxyl coupling are commonly achieved via carbodiimide chemistry that utilizes EDC with NHS esters; such has been reported to produce robust amide bond formation [18].

The performance of the modified electrode was characterized by cyclic voltammetry (CV). Figure 2 shows cyclic voltammograms of a bare (unmodified) and modified SPCE in the presence of 1mM ferrocenecarboxylic acid (FCA) in 0.01M PBS pH 7.4. After surface modification with electrodeposited PPy/MWCNT-COOH, peak current was found to increase due to the presence of PPy significantly. The modified electrode's oxidation and reduction peak currents increased two-fold more than the unmodified

electrode (Table 2). This indicates that active surface area has been successfully generated by incorporating the PPy/MWCNT-COOH. Such provides large binding sites and allows more antibody immobilization on the modified electrode surface. PPy has excellent conductivity, increasing the oxidation and reduction current [16] and improving electrochemical performance. On the other hand, MWCNTs incorporated with PPy have effective surface areas that act as supporting matrix for high density antibody attachment and provide a higher selectivity and sensitivity to the analyte of interest [19].

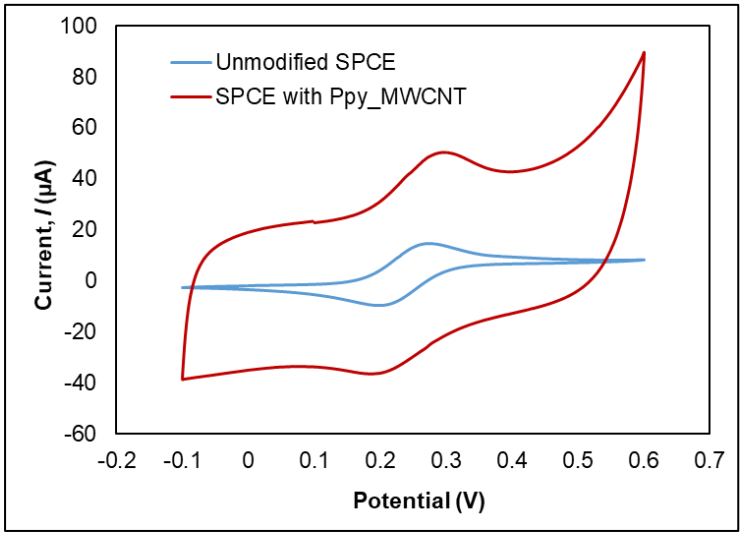


Figure 2. Cyclic voltammograms for an unmodified SPCE (blue line) and modified SPCE with electrodeposited PPy/MWCNT-COOH (red line)

Table 2. Electrochemical properties of unmodified and modified SPCE

	Peak Separation, ΔE(mV)	**Maximum i_{pa} (µA)**	**Maximum i_{pc} (µA)**	**Current Ratio (i_{pa}/i_{pc})**
Unmodified SPCE	63	19.0	-13.3	|0.98|
Modified SPCE	107	50.6	-38.5	|1.03|

Visual characterization of carbon surface prior to and after PPy/MWCNT electrodeposition was analyzed by FESEM. A scanning electron microscopic (SEM) image of the unmodified SPCE surface at 50,000x magnification showed a rough surface structure with the presence of a non-homogenous shape of carbon aggregate (Figure 3a). Following surface modification, typical cauliflower-like structures associated with successful PPy formation are observed (Figure 3b) [20]. Meanwhile, *Xoo* bacteria has rod-shaped cells with flagellum, where each cell has a width in the range of 300-400 nm.

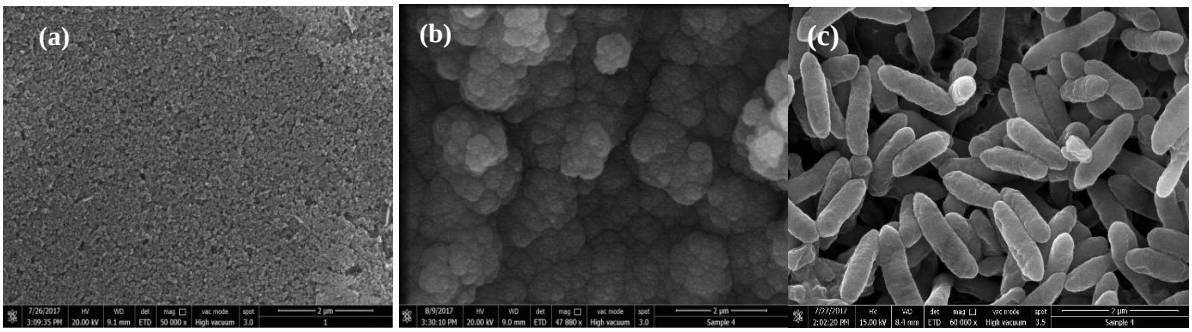


Figure 3. FESEM image of (a) unmodified working electrode (WE) on SPCE, (b) electrodeposited PPy on WE (Magnification of 50 000x); and (c) *Xoo* bacteria cells (Magnification 60,000x)

Development of electrochemical immunosensor

In order to obtain the best detection performance for biosensor development, the set potential was first optimized. Electrooxidative intermediate, produced by the enzyme-substrate interaction, is either oxidized or reduced by the potential applied to the biosensor. Set potential optimization was performed by scanning the potential from -0.6 V to +0.6 V for electrode coated with different concentrations of *Xoo* (i.e. 10^0, 10^2, 10^4, 10^6, 10^8 and 10^9 CFU/mL). The signal current to background current (S/B) ratio was measured. From Figure 4, we can see that the electrochemical current signal was optimum at -0.2 V with a significant S/B current ratio. Hence, -0.2 V was selected as set potential for further study.

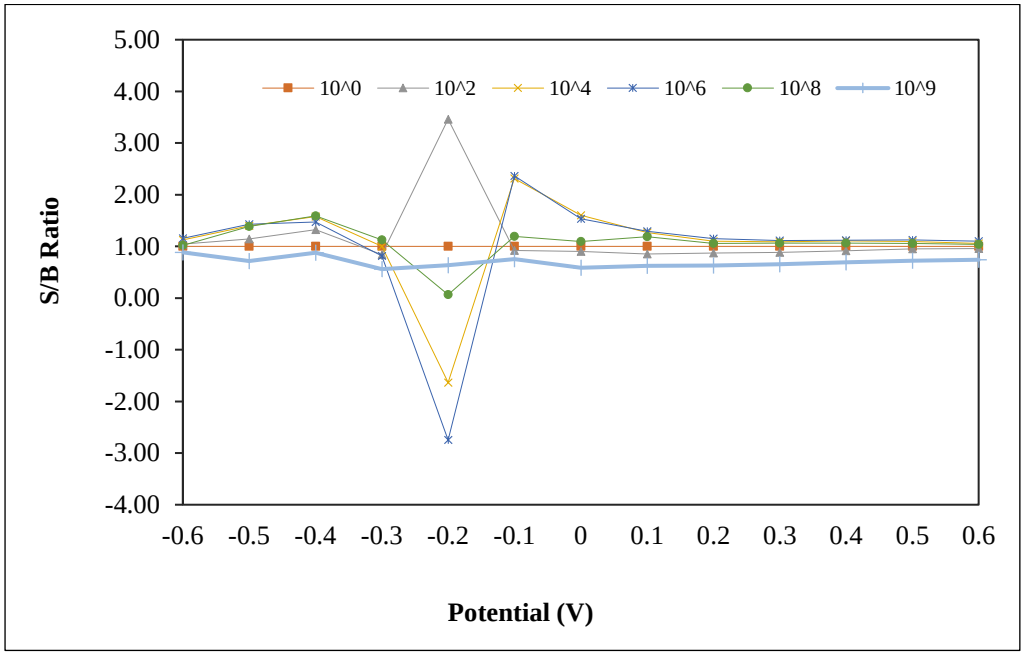


Figure 4. Set potential optimization by scanning the potential window from -0.6 V to +0.6 V

A standard graph was developed at optimized parameters using a mixed culture of *Xoo* (P0.0, P1.0, and P7.3) in carbonate-bicarbonate buffer, pH9.6. The current signal for each concentration of *Xoo* (0 - 10^9 CFU/mL) was recorded via chronoamperometry (CA) analysis at a set potential of -200mV for 300s.

Carbonate-bicarbonate buffer pH9.6 was used as blank control, accounted for 0 CFU/mL standard. An optimal *Xoo* antibody concentration of 0.3 mg/mL is immobilized on the SPCE as previously optimized [21]. The calibration plot of current generated against five concentrations of *Xoo* shows a linear current signal with a correlation coefficient of 0.926 for a linear regression graph (Fig. 5a). The immunosensor developed shows sensitivity with a limit of detection (LOD) at 10^2 CFU/mL. Several parameters have been optimized in order to reduce the non-specific binding in the sensor development, as reported before [22]. These include the dilution for *Xoo* cell cultures in 0.1 M carbonate-bicarbonate buffer, pH 9.6, and the utilization of 0.1% ethanolamine as a blocking buffer as opposed to 0.5% BSA [23].

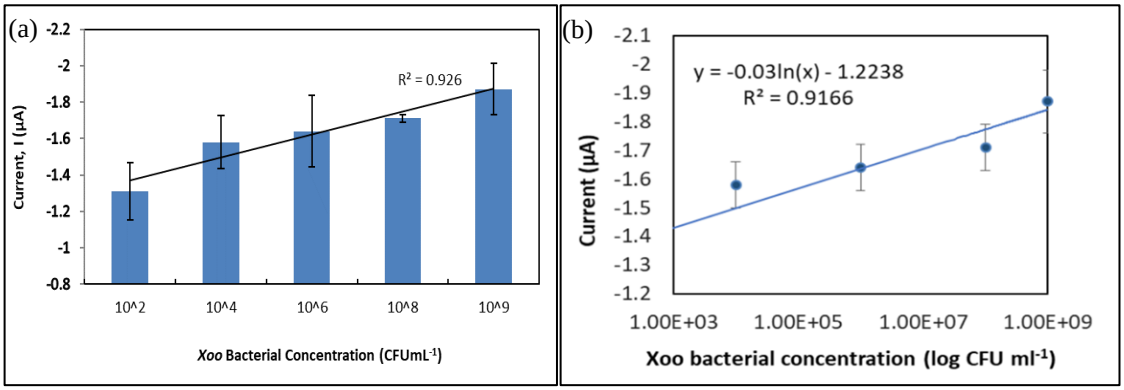


Figure 5. Calibration plot (a) linear regression graph and (b) logarithmic graph of *Xanthomonas oryzae* pv. *oryzae*(*Xoo*) using *Xoo* mixed culture of P0.0, P1.0, and P7.3

The matrix effect study was then performed to investigate the leaves effect in the electrochemical background current. *Xoo* with a concentration between 10^0 to 10^9 CFU/mL were studied in three different matrices, i.e pure culture, ground rice leaves, and cut (with scissors) rice leaves. Standard graph developed in the rice leaves cut using scissors showed excellent current increment response in accordance with the increasing concentration of *Xoo* up to 10^8 CFU/mL. Meanwhile, the standard plot in the grinded rice leaves matrix recorded the lowest current values compared to the other two matrices (Figure 6). Standard curve developed in cut rice leaves also showed good recovery besides exhibiting lower background current at 10^0 CFU/mL (i.e. blank control). Hence, cutting rice leaves with the scissors technique is selected for sample preparation and standard calibration plot development for the next biosensor studies with the real sample application.

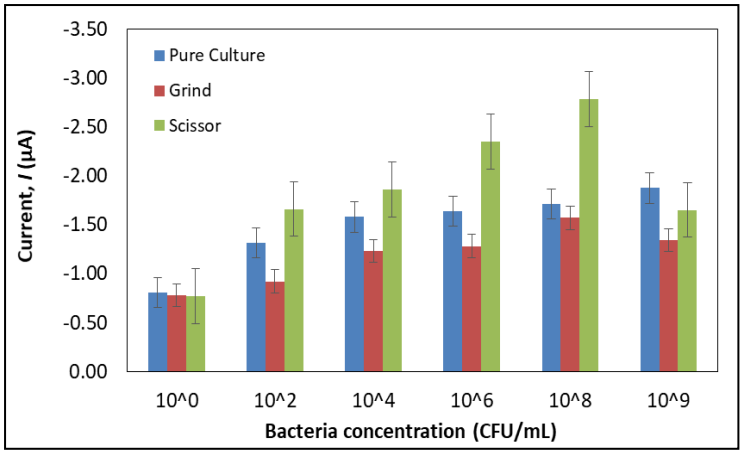


Figure 6. Matrix effect study and comparison of standard plot in different matrix

Performance of BLB disease immunosensor strips in a controlled environment

The performance of the developed electrochemical immunosensor was investigated by testing the strips on artificially infected rice leaves (MR 263 variety) with *Xoo* bacteria. Infection samples were prepared by inoculating *Xoo* in healthy rice leaves in a controlled environment. A total seven bacterial inoculation treatments (*n*=3) with two different inoculation techniques i.e.(i) brushing technique and (ii) scissors-cutting technique at a concentration of *Xoo* 0 CFU/mL (control study with sterile distilled water), 10^2, $10^{4,}$ and 10^8 CFU/mL were carried out. As presented in Table 3, only results from a second replicate (R2) are presented here. The results were determined from the standard calibration curve against the log concentration of *Xoo* cells (CFU/mL). T1R2 and T4R2 are the control study (blank) for brushing and scissors-cutting techniques. While T2R2 and T3R2 were inoculated with 10^4 and 10^8 CFU/mL of *Xoo* respectively by brushing techniques, and T5R2, T6R2, and T7R2 with 10^2, $10^{4,}$ and 10^8 CFU/mL respectively by scissors-cutting techniques.

The developed immunosensor was validated by PCR as a standard method. Table 3 shows the comparison between detection by electrochemical immunosensor strips and PCR for BLB disease detection in 41 inoculated samples. The immunosensor was able to detect the BLB disease as early as the third day of infection with disease agent for T5R2 (inoculation of 10^2 CFU/mL by scissors-cutting techniques) samples. For T3R2 and T7R2 samples, the immunosensor was able to detect the pathogens after 14 days. The results correlate with the PCR method for all the inoculated samples with a 92.7% correlation. This proves that the electrochemical immunosensor system developed has the potential as a bioanalysis tool for the early detection of bacterial leaf blight (BLB) disease and can be used in rice field areas.

Table 3. Detection of *Xanthomonas oryzae* pv. *oryzae* (*Xoo*) in artificially inoculated rice leaves with two different inoculation techniques; (a) brushing (T1R2 – T3R2) and (b) scissors-cutting (T4R2 – T7R2)

Sample	*DAI (Day)	Sensor	PCR
T1R2	0	**-ve**	**-ve**
	1	**-ve**	**-ve**
	3	**-ve**	**-ve**
	5	**-ve**	**-ve**

	7	**-ve**	**-ve**
	14	**-ve**	**-ve**
T2R2	0	**-ve**	**-ve**
	1	**-ve**	**-ve**
	3	**-ve**	**-ve**
	5	**-ve**	**-ve**
	7	**-ve**	**-ve**
	14	**-ve**	**-ve**
T3R2	0	**-ve**	**-ve**
	1	**-ve**	**-ve**
	3	**-ve**	**-ve**
	5	**-ve**	**-ve**
	7	**-ve**	**-ve**
	14	**+ve**	**+ve**
T4R2	1	**-ve**	**-ve**
	3	**-ve**	**-ve**
	5	**-ve**	**-ve**
	7	**-ve**	**-ve**
	14	**-ve**	**-ve**
T5R2	0	**-ve**	**-ve**
	1	**-ve**	**-ve**
	3	**+ve**	**-ve**
	5	**-ve**	**-ve**
	7	**+ve**	**-ve**
	14	**-ve**	**+ve**
T6R2	0	**-ve**	**-ve**
	1	**-ve**	**-ve**
	3	**-ve**	**-ve**
	5	**-ve**	**-ve**
	7	**-ve**	**-ve**
	14	**-ve**	**-ve**
T7R2	0	**-ve**	**-ve**
	1	**-ve**	**-ve**
	3	**-ve**	**-ve**
	5	**-ve**	**-ve**
	7	**-ve**	**-ve**
	14	**+ve**	**+ve**

**DAI=days after inoculation*

Application of immunosensor strips on an IoT-biosensor portable device

A portable biosensor device with internet-of-things integration (IoT-biosensor) was employed for on-site detection of BLB disease using simple sample preparation (Figure 7). The modified strips with antibodies against *Xoo* are attached to the portable reader for sample analysis. Two hotspots for BLB disease are selected for this study, namely rice fields in Sg. Burong, Tanjung Karang and Bagan Terap, Selangor Northwest. The objectives of this study are to investigate the viability of the strips with the handheld device and to simulate a real sample application scenario in the field for future reference. The developed IoT-biosensor device prototype could provide fast data acquisition besides holds potential as a smart biosensor device that can reduce the dependency on bulky instrumentation for detection purposes.



Figure 7. Simple sample preparation on rice field for BLB detection using the fabricated IoT-biosensor handheld device

Table 4 shows the result of on-site analysis on 11 plots of BLB hotspots in Sg. Burong, Tanjung Karang. Samples were collected and tested on the field days after transplant (DAT) of DAT-15 and DAT-25. The results were obtained within 200 s by using the IoT-biosensor device. Results are displayed on the screen and can be stored on a cloud server. The analyzed data and further configurations can be accessed through a dedicated web page https://provenpac.solutions/MARDI/padi. All results were validated by the ELISA method, which used antibody-based detection similar to the immunosensor system developed. The immunosensor strips integrated with the IoT-biosensor device can detect BLB disease at early stage (DAT-15) before the symptoms appear. However, the ELISA method could not detect *Xoo* cells in all DAT-15 samples. All rice plants in the plots were confirmed to have BLB disease at DAT-25, as indicated by both ELISA and IoT-biosensor.

Table 4. Comparison of BLB detection analysis in Sg. Burong, Tanjung Karang hotspot

*DAT	Detection Method	A4	A5	A6	A7	A8	A9	A10	A11	A12	A14	A15
DAT-15	ELISA	-ve										
	IoT-BIOSENSOR	-ve	-ve	-ve	-ve	-ve	+ve	+ve	+ve	+ve	+ve	+ve
DAT-25	ELISA	+ve										
	IoT-BIOSENSOR	+ve										

**DAT=days after transplant*

A second on-field analysis was also conducted in two rice plots in Bagan Terap, Selangor Northwest, late before harvest (i.e. HLT 90-100). As validated by ELISA, Table 5 showed a 100% correlation between IoT-Biosensor with ELISA technique for Plot 1 and 80 % correlation for Plot 2. IoT-Biosensor reader was able to detect the *Xoo* presence even at a very low concentration (sample 2E) when the ELISA technique was unable to detect *Xoo*. The results prove that the IoT-biosensor developed has successfully detected the presence of BLB disease agent below ELISA's detection limit. As reported by Awaludin et al. [14], ELISA methods have limitations where their detection limits are merely in the range of 10^4-10^5 CFU/mL where as our immunosensor strip can detect as low as possible 10^2 CFU/mL.

Table 5. Comparison of BLB detection analysis in Bagan Terap, Selangor Northwest hotspot

BLB Hotspot	IoT-Biosensor	ELISA
1A	+ve	+ve
1B	+ve	+ve
1C	+ve	+ve
1D	+ve	+ve
1E	+ve	+ve
2A	+ve	+ve
2B	+ve	+ve
2C	+ve	+ve
2D	+ve	+ve
2E	+ve	-ve

Compared to other findings on BLB detection using an immunological approach, a Western Blot method using polyclonal antibody against *Xoo* has reported detecting *Xoo* cells at 3.5 x 10^3 CFU/mL [24]. Immuno-based assay using monoclonal antibodies developed by Wu et al. [25] have LOD of 1×10^4 CFU/mL for ELISA and 1×10^5 CFU/mL for immunochromatographic. The immunosensor strips described and developed here are superior to those afore mentioned techniques as they have better and lower LOD of 10^2 CFU/mL. Although a fluorescence-based immunoassay for BLB detection employing the same antibody source as ours has a lower LOD of 22 CFU/mL [14], this method still requires a fluorescence spectroscopy to measure the wavelength thus, portability is a major hindrance.

Conclusion

Here, we have demonstrated the development of an electrochemical immunosensor strip for the early detection of *Xoo* bacteria, the causal agent for bacterial leaf blight disease (BLB) in rice. Early detection mechanism in an efficient plant disease management can reduce the damage and losses due to pathogenic infections. A sandwich assay enzyme-linked immunosorbent assay (ELISA) format was adapted and employed in the sensor development. Surface modification with electrodeposited polypyrrole and functionalized multi-walled carbon nanotube (PPy-fMWCNT) network has greatly improved the sensor strip's performance, as indicated by electrochemical characterizations. A standard calibration plot in pure mix culture of *Xoo* (P0.0, P1.0, and P7.3) has been developed with R^2=0.9166. Scissors cutting for rice leaves was chosen for sample preparation and used in the development of a standard calibration plot for a real sample application. The efficiency of the developed electrochemical strips were tested on inoculated rice leaves samples, and show good sensitivity and high correlation with the PCR method. The electrochemical immunosensor strips were then integrated with an Android-based IoT-biosensor device suited for on-site detection purposes. The system was successfully applied

and tested on rice fields in BLB hotspot areas in Selangor. By using the immunostrips, early detection of BLB has been identified on DAT-15 as indicated by later infection stage using both sensor and ELISA techniques. This Android-based portable handheld reader with the developed immunostrips for BLB disease will eventually be an innovative on-site rice disease detection tool prior to the appearance of any visual symptoms so that corrective measures can be taken to prevent the spread of disease.

Acknowledgement

We thank the Malaysian Agriculture Research and Development Institute (MARDI) for the research funding under the development project (RMK-11) and our appreciation to all the members who have been directly or indirectly involved in this project throughout the years.

References

1. Nurul Nahar, E., Adam, P., Mazidah, M., Roslan, I., and Rafii, Y. M. (2020). Rice blast disease in Malaysia: Options for its control. *Journal of Tropical Agriculture & Food Science*, 48(1): 11-23.
2. Shamsudin, N. A. A., Swamy, B. P. M., Ratnam, W., Cruz, M. T. S., Raman, A. and Kumar, A. (2016). Marker assisted pyramiding of drought yield QTLs into a popular Malaysian Rice Cultivar, MR219. *BMC Genet*. 17: 30.
3. Faizal Azizi, M. M. and Lau, H. Y. (2022). Advanced diagnostic approaches developed for the global menace of rice disease: A review. *Canadian Journal of Plant Pathology*, 44(5): 627-651.
4. Song, E.S., Noh, T.H. and Chae, S.C. (2014). PCR-based assay for rapid and specific detection of the new *Xanthomonas oryzae pv. oryzae* K3a race using an AFLP-derived marker. *Journal of Microbiology & Biotechnology*, 24(6): 732-739.
5. Thakur, M., Wang, B. and Verma, M. L. (2022). Development and applications of nanobiosensors for sustainable agricultural and food industries: Recent developments, challenges and perspectives. *Environmental Technology & Innovation*, 26: 102371.
6. Perez-Fernandez, B. and de la Escosura-Muniz, A. (2022). Electrochemical biosensors based on nanomaterials for aflatoxins detection: A review (2015-2021). .*Analytica Chimica Acta*, 1212: 339658.
7. Fang, Y. and Ramasamy, R. P. (2015). Current and prospective methods for plant disease detection. *Biosensors*, 5(3): 537-561.
8. Felix, F. S. and Angnes, L. (2018). Electrochemical immunosensors—a powerful tool for analytical applications. *Biosensors & Bioelectronic*, 102: 470-478.
9. Wen, W., Yan, X., Zhu, C. Du, D. and Lin, Y. (2017). Recent advances in electrochemical immunosensors. *Analytical Chemistry*, 89: 138-156.
10. Sireesha, M., Babu, V. J., Kiran, A. S. K. and Ramakrishna, S. (2018). A review on carbon nanotubes in biosensor devices and their applications in medicine. *Nanocomposites*, 4(2): 36-57.
11. Bianchi, V., Boni, A., Bassoli, M., Giannetto, M., Fortunati, S., Careri, M. and Munari, I. D. (2021). IoT and biosensors: A smart portable potentiostat with advanced cloud-enabled features. *IEEE Access*, 9: 141544-141554.
12. Uda, M. N. A., Hasfalina, C. M., Samsuzanaa, A. A., Faridah, S., Gopinath, S. C. and Parmin, N. A. (2019). A disposable biosensor based on antibody-antigen interaction for tungro disease detection. *Nanobiosensors for Biomolecular Targeting*, 2019: 147-164.
13. Mohd Said, N. A., Abu Bakar, N. and Lau, H. Y. (2020). Label-free Detection of *Erwinia mallotivora* DNA for papaya dieback disease using electrochemical impedance spectroscopy approach. *ASM Science Journal*, 13(4): 1-8.
14. Awaludin, N., Abdullah, J., Salam, F., Ramachandran, K., Yusof, N. A. and Wasoh, H. (2020). Fluorescence-based immunoassay for the detection of *Xanthomonas oryzae*pv. *oryzae* in rice leaf. *Analytical Biochemistry*, 610: 113876.
15. Shi, J. and Marshall Porterfield, D. (2014). Surface modification approaches for electrochemical biosensors. *Biosensors-Emerging Materials and Applications*, 2014: 642.

16. Sheikhzadeh, E.,Chamsaz, M., Turner, A. P. F., Jager, E. W. H. and Beni, V. (2016). Label-free impedimetric biosensor for *Salmonella typhimurium* detection based on poly [pyrrole-co-3-carboxyl-pyrrole] copolymer supported aptamer. *Biosensors & Bioelectronics*, 80: 194-200.
17. Ancuta, D. and Constantin, A. (2021). Development of polypyrrole modified screen-printed carbon electrode based sensors for determination of l-tyrosine in pharmaceutical products. *International Journal Molecular Science*, 22:7528.
18. Welch, N. G., Scoble, J. A., Muir, B. W., and Pigram, P. J. (2017). Orientation and characterization of immobilized antibodies for improved immunoassays. *Biointerphases*, 12(2): 301.
19. Li, W., Diao, K., Qiu, D., Zeng, Y., Tang, K. and Zhu, Y. (2021). A highly-sensitive and selective antibody-like sensor based on molecularly imprinted poly (L-arginine) on COOH-MWCNTs for electrochemical recognition and detection of deoxynivalenol. *Food Chemistry*, 350: 129229.
20. Hassanein, A., Salahuddin, N., Matsuda, A., Kawamura, G. and Elfiky, M. (2017). Fabrication of biosensor based on Chitosan-ZnO/Polypyrrole nanocomposite modified carbon paste electrode for electroanalytical application. *Materials Science & Engineering*: C, 80: 494-501.
21. Abd Rahman, R., Razali, H., Mohd Said, N. A., Masdor, N. A. and Salam, F. (2020). Determination of immunosensor parameters for a sensitive and rapid detection of *Xanthomonas oryzae* pv. *oryzae*. *Transactions of The Malaysian Society of Plant Physiology*, pp. 27.
22. Mohd Said, N. A., Razali, H., Abd Rahman, R., Masdor, N. A., Ismail, M. R. and Salam, F. (2018). Sensor optimizations for immunosensor development for the detection of *Xanthomonas oryzae* pv. *Oryzicola* in rice bacterial leaf streak. *Proccedings* of *National Conference on Agricultural and Food Mechanization 2018 (NCAFM 2018), 17-19 April, Pullman Kuching, Sarawak*, pp. 313-316.
23. Hazana, R., Nur Azura, M. S. and Faridah, S. (2019). Immunosensor development for the detection of *Xanthomonas oryzae* pv. *oryzicola* in rice bacterial leaf streak. *Transactions of The Malaysian Society of Plant Physiology*, 26: 315-319.
24. Guo, M., Lan, J., Mingli Guan, J. S., Shi, J., Guan, M., Wei, J., Liu, L., Li, L., Dou, S. and Liu, G. (2015). Western Blot detection of *Xanthomonas oryzae*pv. *Oryzae* in rice, *Journal of Plant Pathology & Microbiology*, 4:1-6.
25. Wu, X., Kong, D., Song, S., Liu, L., Kuang, H. and Xu, C. (2015). Development of sandwich ELISA and immune chromatographic strip methods for the detection of *Xanthomonas oryzae* pv. *Oryzae*. *Analytical Methods*, 7: 6190-6197.

Malaysian Journal of Analytical Sciences (MJAS)
Published by Malaysian Analytical Sciences Society

LABEL-FREE ELECTROCHEMICAL IMMUNOSENSOR DEVELOPMENT FOR MYCOTOXINS DETECTION IN GRAIN CORN

(Pembangunan Imunosensor Elektrokimia Tanpa Label untuk Pengesanan Mikotoksin dalam Jagung Bijian)

Noor Sheryna Jusoh, Norhafniza Awaludin, Faridah Salam, Adlin Azlina Abdul Kadir, Nur Azura Mohd Said*****

Biotechnology and Nanotechnology Research Centre,
Malaysian Agricultural Research and Development Institute,
MARDI Headquarter, Persiaran MARDI-UPM, 43400 Serdang, Selangor, Malaysia

**Corresponding author: nazurams@mardi.gov.my*

Received: 7 February 2022; Accepted: 23 April 2022; Published: 27 December 2022

Abstract

Mycotoxins have been a huge threat in the agriculture and poultry industries. In Malaysia, the presence of mycotoxins, particularly in grain corn, is not only detrimental to health; it may also have a detrimental effect on the economy, as we rely heavily on this source for animal feed. With this regard, a rapid detection method of mycotoxins on-site lends itself well in reducing the negative economic impact and strengthening the food safety aspect. We report here an electrochemical-based biosensor for mycotoxins detection in grain corn employing differential pulse voltammetry technique. Polyclonal antibodies against Aflatoxin B1 and Ochratoxin A were developed in-house and used in the sensor development. Cross-reactivity study with intra and interspecies proved the selectivity of developed antibodies. The antibodies were then immobilized on a screen-printed carbon electrode functionalized with gold nanoparticles and polyaniline. The developed immunosensor system showed significant performance in both phosphate buffer solution (PBS) and grain corn matrix systems. Excellent R^2 and low limit of detection (LOD) values were achieved in a broad working range for both buffer conditions. Aflatoxin B1 displayed R^2 of 0.9935 and LOD of 0.6 ppb in PBS; and R^2 of 0.978 and LOD of 1.81 ppb in grain corn matrix. Ochratoxin A displayed R^2 of 0.9962 and LOD of 0.87 ppb in PBS; and R^2 of 0.971 and LOD of 3.18 ppb in grain corn matrix. The LODs obtained for both detections are lower than the maximum residues limit (MRLs) permitted for grain corn (5 ppb). Both aflatoxin and ochratoxin biosensors exhibited acceptable recoveries in the 90% to 120% recovery range in grain corn matrix. This successful method could be applied and widened to other cereal grains and their processed food products.

Keywords: aflatoxin B1, ochratoxin A, immunosensor, differential pulse voltammetry, grain corn

Abstrak

Mikotoksin merupakan satu ancaman kepada industri pertanian dan ternakan. Di Malaysia, kehadiran mikotoksin terutamanya dalam jagung bijian bukan sahaja merbahaya kepada kesihatan, tetapi juga membawa kesan yang buruk kepada ekonomi berikutan kebergantungan sepenuhnya kepada jagung bijian sebagai sumber makanan haiwan. Dalam hal ini, kaedah pengesanan pantas mikotoksin di lapangan dapat mengurangkan kesan negatif kepada ekonomi di samping memperkasa aspek keselamatan makanan. Kami melaporkan biosensor berdasarkan elektrokimia untuk pengesanan mikotoksin dalam jagung bijian dengan menggunakan teknik voltametri denyut beza. Antibodi poliklonal terhadap Aflatoksin B1 dan Okratoksin A telah dibangunkan secara dalaman dan digunakan dalam pembangunan sensor. Kajian tindakbalas silang intra dan interspesies membuktikan selektiviti antibodi yang dibangunkan. Antibodi kemudian dipegunkan di atas elektrod skrin-bercetak karbon berfungsi dengan nanozarah emas dan

polianilin. Sistem immunosensor yang dibangunkan menunjukkan prestasi yang signifikan dalam kedua-dua sistem larutan penimbal fosfat (PBS) dan matriks jagung. Nilai R^2 dan had pengesanan rendah (LOD) yang baik dapat dicapai dalam julat bekerja yang luas bagi kedua-dua keadaan penimbal. Aflatoksin B1 menunjukkan R^2 0.9935 dan LOD 0.6 ppb dalam PBS; dan R^2 0.978 dan LOD 1.81 ppb dalam matriks jagung bijian. Ochratoxin A menunjukkan R^2 0.9962 dan LOD 0.87 ppb dalam PBS; dan R^2 0.971 dan LOD 3.18 ppb dalam matriks jagung bijian. LOD yang didapati bagi kedua-dua pengesanan adalah lebih rendah daripada had residu maksimum (MRL) yang dibenarkan untuk jagung bijian (5 ppb). Kedua-dua biosensor aflatoksin dan okratoksin menunjukkan perolehan yang boleh diterima dalam julat perolehan 90% to 120% dalam matriks jagung. Kaedah yang terbukti berjaya ini boleh digunakan dan diperluaskan kepada lain-lain bijian dan produk makanan terproses.

Kata kunci: aflatoksin B1, okratoksin A, imunosensor, voltametri denyut beza, jagung bijian

Introduction

Potent mycotoxins such as aflatoxins, ochratoxins, fumonisins, zearalenones and trichothecenes are produced by microfungi such as *Aspergillus* species, *Penicillium* species and *Fusarium* species, which are specific to certain mycotoxins [1]. The presence of those fungi on crops does not guarantee the production of harmful mycotoxins. However, poor aeration and high humidity during storage can accelerate mycotoxins production and eventually lead to serious crop contamination [2]. Natural weather or environmental changes in certain countries or regions also contribute to mycotoxins' occurrence. For instance, the natural tropical weather of Malaysia has led to manifestation of *Aspergillus* species and *Fusarium* species in soil, resulting in contamination of aflatoxins and *Fusarium* related mycotoxins in agricultural crops [3]. In addition, initial contamination can also take place during harvesting, followed by a lack of good processing, handling and transport practices [4]. Primary corn processing such as cleaning, dry milling, steeping and wet milling can help to reduce the level of mycotoxins in food samples but do not entirely eliminate them [5, 6]. Therefore, most of the food or products are already severely contaminated before being consumed by animals and humans. Figure 1 shows the distribution of mycotoxins from contaminated crops to animals and humans.

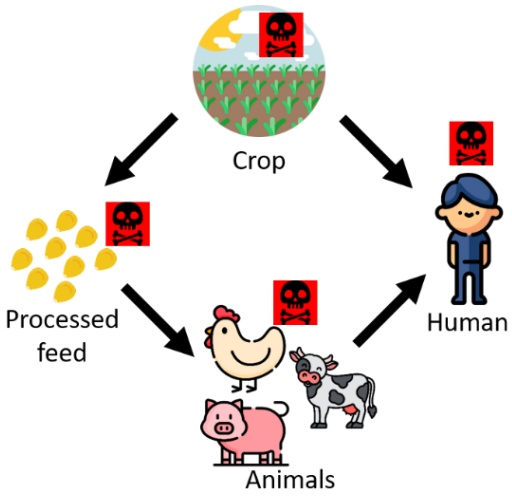


Figure 1. Distribution of mycotoxins from contaminated crops to animals and humans

Mycotoxins are not a minute problem as the occurrence of mycotoxins in food and feed is a global issue and not only subject to certain parts of the world. Even though most places have different natural weather and environment, mycotoxins always have their ways to exist. Ten years of research were conducted by Gruber-Dorninger and team in 2019 [7] to study the occurrence of mycotoxins in 15 regions around the globe. The commodities tested included feed, soybean (grains and meal), corn (silage and grains), wheat, barley and rice.

From the study, deoxynivalenol and fumonisin contaminations were collectively found to be dominating the toxins occurrence in the commodities. The other mycotoxins class also exceeded the maximum limit regulated for each region. Occurrence and contamination of mycotoxins from other studies were also in correspondence with the result obtained [8-12].

The concern for mycotoxins arises due to the alarming consequences of mycotoxin contamination. Crops yield, animal health and productivity, human health, economy and food security are the most affected area, and they are closely related to each other. Low crops productivity due to contamination can cause low income for farmers as no contaminated products are allowed in the market [13]. Consecutively, their well-being can be affected in many ways, such as accessibility to decent food and health care. This situation also applies to animals. Factors such as growth depression, low nutrient absorption, reproductive problems, and low egg production and hatchability result from low mycotoxin consumption of contaminated feed, which is highly associated with declining animal productivity [14]. High ingestion of mycotoxins can lead to acute health problems such as liver, kidney and gastrointestinal damage, haemorrhaging and, in the worst case – death. Since most mycotoxins are carcinogenic, human also shares similar health problems such as oesophageal and liver cancer, alimentary toxic aleukia, kidney disease, cardiac beriberi and death [15]. In terms of economic impact, the final consumer has to pay a high price for the finished products due to the low availability of feed and food in the market, processing and handling cost and regulatory services for monitoring mycotoxins [4]. The United States, Africa and South-East Asia recorded annual losses of around USD 1.68 billion, USD 750 million and USD 1 billion, respectively, as a result of aflatoxins contamination. Eventually, with all these arising problems, food security will be a major concern in the near future.

The most common and conventional mycotoxins detection methods are thin-layer chromatography, gas chromatography, liquid chromatography and real-time polymerase chain reaction [16,17]. Normally, gas and liquid chromatography analysis is often coupled with mass spectrometry to enhance the detection sensitivity [18]. Although these methods can detect multiple analytes in one measurement, the drawbacks (i.e., large sample volume, long sample preparation and analysis, expensive equipment and maintenance, laboratory-based analysis) have urged the development of simpler and easier analytical methods, with similar or better detection. The new approach to the mycotoxin detection method is a biosensor. Biosensor is a device where a reaction between biomolecules is translated into an electrical signal by a transducer, and the data can be recorded and displayed [19]. Biomolecules such as an antibody, aptamer, DNA and molecular imprinted polymer are commonly used as these biorecognition elements are highly sensitive toward their specific target analyte. Electrochemical transducers (potentiometry, voltammetry, amperometry and impedance) are widely used in biosensor development as these techniques offer high sensitivity and a wide working range with a variety of mycotoxins [20]. The combination of biomolecules and electrochemical measurement was proven to detect mycotoxins in the low detection range [21] successfully. Incorporation of nanomaterials (carbon nanotubes, graphene's, gold nanoparticles, quantum dots; to name a few) into the system can enhance the performance of developed biosensors, especially for electrochemical transducers [22, 23]. In addition to simple sample preparation and small sample volume, biosensor carries the potential for in-situ detection that end-users can carry out with moderate training.

Materials and Methods

Materials and instrumentation

Polyclonal antibodies against aflatoxin A (AB1) and ochratoxin A (OA) were produced in-house by the Biotechnology & Nanotechnology Research Centre (Animal Ethics Committee of MARDI approval number 20190215/R/MAEC00045). Phosphate buffer saline (PBS) tablet, dimethyl sulfoxide (DMSO) and OA standard were purchased from Sigma (USA, UK and Israel, respectively). Potassium chloride (KCl), acetonitrile (ACN, HPLC grade), methanol (MeOH, HPLC grade) and glacial acetic acid (GAA) were obtained from Merck (Germany). Potassium hexacyanoferrate (III) (ferricyanide) and potassium hexacyanoferrate (II) trihydrate (ferrocyanide) were

acquired from Sigma-Aldrich (USA and Japan, respectively). Polyaniline emeraldine salt (PANIs) and gold nanoparticle (AuNP) came from Aldrich (USA). AB1 standard, aflatoxin B2 (AB2), aflatoxin G1 (AG1), aflatoxin G2 (AG2), ochratoxin B (OB), fumonisin B1 (FB1), fumonisin B2 (FB2) and fumonisin B3 (FB3) standards were purchased from Romer Labs (Austria). Dry milk powder was obtained from Santa Cruz (USA). All reagents used were of analytical standard or higher, as stated.

Refrigerated centrifuge 5810 R (Eppendorf, Germany) was used during the extraction of corn samples. AUTOLAB Potentiostat (Metrohm, Switzerland) is equipped with Nova 1.10 software for cyclic voltammetry (CV) and differential pulse voltammetry (DPV) measurement. Screen-printed carbon electrode (SPCE) with three electrode system comprising working, counter and reference electrodes made from carbon was purchased from BioGenes Technologies (Malaysia). Chromatographic analysis of mycotoxins was conducted using isocratic high-performance liquid chromatography (HPLC, UVE LCTech, Germany) equipped with a fluorescence detector (Waters 2475 Multi λ Fluorescence Detector). RP C18 column (150 x 4.6 mm, LCTech) with guard column 8 x 4 mm and RP C18 column (125 x 3 mm; 3 µm; 120 A, LCTech) were used for aflatoxin and ochratoxin, respectively. Grain corn sample (GWG888) was obtained from a local source and stored at room temperature.

Modification of SPCE

Bare SPCE was modified with AuNP, PANIs (in DMSO) and a mixture of both to improve the surface performance. A 10 µL of each solution was deposited on a carbon working electrode for 30 minutes. Excess liquid was discarded and left dried at room temperature. A 100 µL 5 mM redox electrolyte (ferricyanide/ferrocyanide in 0.1 M KCl) was added to SPCE and an electrochemical measurement was conducted. The stability of the modified electrode was evaluated by measuring CV for 50 cycles.

Standard curve determination

Mycotoxins standard curve was determined by applying direct assay protocol on modified SPCE. A 10 µL AuNP-PANIs mixture was deposited on the working electrode and left for 30 minutes. After discarding the excess liquid, 10 µL 0.1 mg/mL mycotoxin antibody was immobilised for an hour. The SPCE was washed three times with 50 µL PBS followed by deionised water. A 50 µL blocking buffer (0.05% dry milk in 0.01 M PBS) was added and incubated for 30 minutes. The SPCE has washed again. A 10 µL serial dilutions of five different mycotoxins concentrations were immobilised on the working surface and allowed to incubate for 2 hours. The SPCE has washed again, and 100 µL of 5 mM redox electrolyte was added to the SPCE for the electrochemical measurement. The experiment was carried out at room temperature.

Cross-reactivity

Cross-reactivity of each mycotoxin was conducted by introducing mycotoxins of the same and different groups into the assay. Mycotoxins used were AB2, AG1, AG2, OB, FB2 and FB3. The concentration used was 5 ppb for both AB1 and OA.

Real sample analysis

The sensitivity of the developed electrochemical sensor was evaluated with a real extracted corn sample. The direct assay was conducted on the SPCE to construct a standard mycotoxin curve in a grain corn matrix. Mycotoxins were prepared in grain corn matrix instead of PBS during standard preparation. Then, the procedure was repeated with extracted spiked samples for the recovery study.

HPLC analysis

Prior to HPLC, mycotoxins first were extracted from grain corn samples. For aflatoxin analysis, 100 mL extraction solvent (60% MeOH) was added to 25 g ground corn and blended for 3 minutes or shaken for 60 minutes. 4 mL filtered extract was added to 12 mL PBS. For ochratoxin analysis, the extraction method was the same, except that the extraction solvent used was 80% MeOH.

Aflatoxin and ochratoxin analysis were conducted using isocratic HPLC with fluorescence detection in reverse phase analysis. For aflatoxin analysis, water:MeOH:ACN (60:30:15 v/v) was used as eluent.

Injection of sample volume was 10-100 µL at a flow rate of 1.2 mL/min through RP C18 column at a column temperature of 33 °C. Fluorescence detector; Ex.: 365 nm, Em.: 460 nm. For ochratoxin analysis, water:MeOH:ACN/GAA (40:55:5/1 v/v) was used as eluent. Injection of sample volume was 10-100 µL at a flow rate of 0.6 mL/min through RP C18 column at a column temperature of 40 °C. Fluorescence detector; Ex.: 395 nm, Em.: 440 nm.

Results and Discussion

Modification of SPCE

Figure 2 shows the modification and immobilisation of biomolecules on the electrode surface. Both AuNP and PANIs were used to enhance the electrical and electrochemical properties of the electrode. The immobilisation of the nanoparticles and conducting polymer has improved the conductivity of the carbon surface, and this has been proved by a significant increase in current reading in both voltammetric measurements (Figure 3). Besides, the peak separation of modified electrodes was much closer than bare (unmodified) electrodes, as shown in Figure 3(a), which implied that the redox reaction occurred at a fast pace with a stable rate. The AuNP-PANIs modified SPCE recorded the highest DPV current reading of 466 µA (Figure 3(b)) with low peak separation (100 mV) and a current ratio near 1 (1.04) (Table 1). AuNP played an essential role in enhancing the performance of carbon surfaces. In addition to contributing to the conductivity [24], AuNP also provides binding sites for antibodies. Antibodies can bind with reagents such as thiols and polymers, but they can also directly attach to gold [25,26]. Thus, more binding sites are available, and the developed biosensor's sensitivity will increase accordingly.

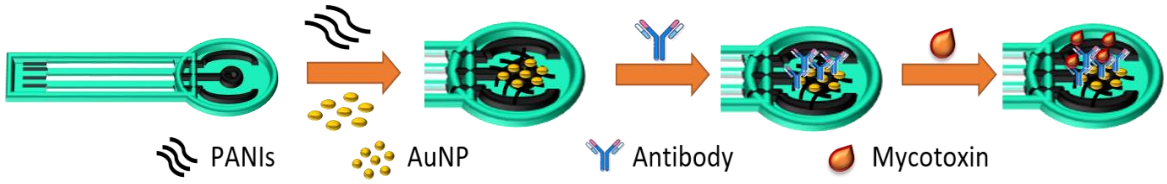


Figure 2. Modification and immobilisation of biomolecules on working SPCE surface

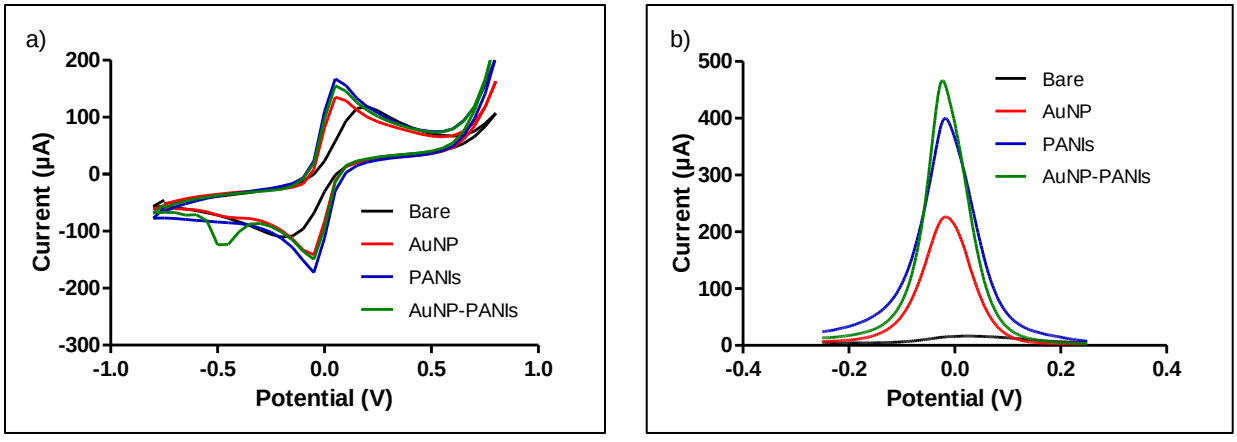


Figure 3. a) CV and b) DPV of bare and modified SPCE in 5 mM ferricyanide/ferrocyanide (in 0.1 M KCl). Scan rate; 50 mV/s (CV) and 2 mV/s (DPV)

Table 1. Electrochemical properties of bare and modified SPCE

	CV		DPV
	Peak Separation (mV)	**Current Ratio (i_a/i_c)**	**Peak Current (µA)**
Bare	400	1.08	16
AuNP	100	0.95	226
PANIs	100	0.97	400
AuNP-PANIs	100	1.04	466

The stability of the AuNP-PANIs-modified electrode has been investigated by allowing the electrode under CV measurement for 50 cycles. Anodic and cathodic peak current values were recorded and presented in Figure 4. A current increase was observed at anodic current starting from cycle 30 onwards. This might suggest that during the measurement, AuNP was fully stabilised by PANIs, resulting in the increased signal current [27]. Overall, the current reading of the modified surface was highly stable throughout the continuous electrochemical cycles, especially the cathodic current. This proved that the immobilised AuNP and PANIs were strongly attached to the carbon surface, and no leaching was detected from the voltammetric measurement.

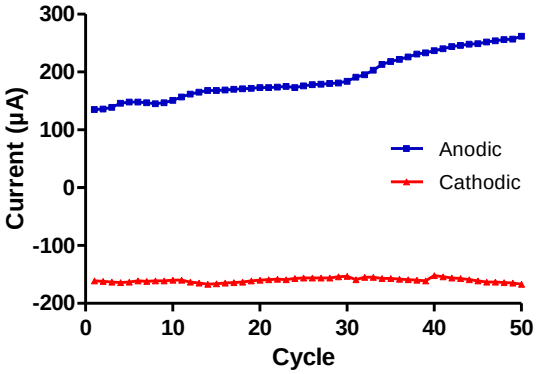


Figure 4. Stability of SPCE modified with 1 mg/mL PANIs and 20 nm AuNP under 50 cycles of CV

Standard curve determination

The sensitivity of developed AB1 and OA sensors were investigated at different concentrations of mycotoxin in PBS. The direct assay was conducted on the modified SPCE (Figure 2), and the sensor's sensitivity was measured using DPV, in terms of the current reading. Both AB1 and OA exhibited good linear correlation (high R^2 values) in a broad working range (Figure 5). Based on the plotted standard curve, the limit of detection (LOD) and limit of quantification (LOQ) were calculated and recorded in Table 2. Both mycotoxins showed lower LOD and LOQ values, which were much lower than the maximum regulation limit (MRL). Aside from contributing to conductivity and large surface area for binding, the combination of AuNP and PANIs also possesses high biocompatibility with antibodies [28]. This allowed more antibodies to be attached to the SPCE surface and maintained the binding stability throughout the assay process. This proved that the developed electrochemical sensor was highly sensitive in detecting the target analytes even in low concentrations.

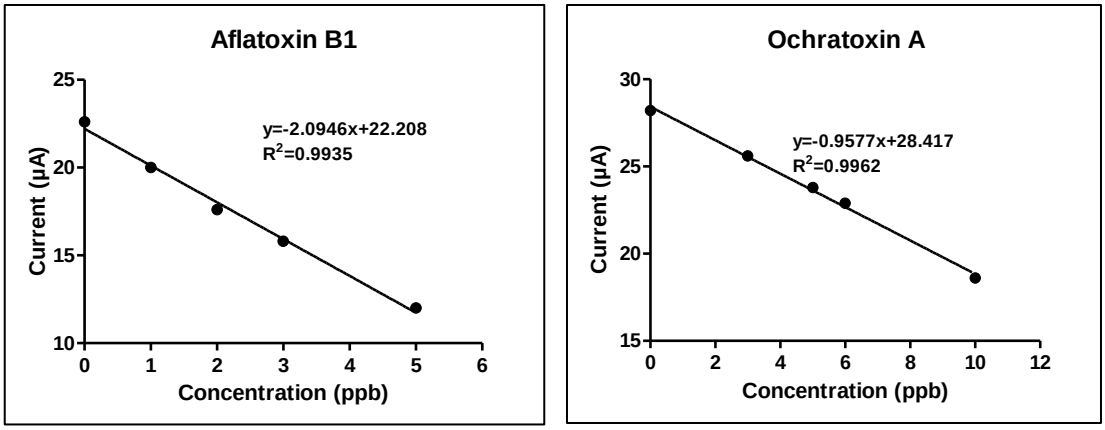


Figure 5. Standard curve of aflatoxin A (AB1) and ochratoxin A (OA) in PBS

Table 2. Calculated LOD and LOQ values for AB1 and OA in PBS

Mycotoxin	LOD (ppb)	LOQ (ppb)	MRL (ppb)
Aflatoxin B1	0.60	1.80	5
Ochratoxin A	0.87	2.63	5

Cross-reactivity

In order to investigate the selectivity of the developed antibody, the assay was tested with other mycotoxins of the same and different groups (Figure 6). AB1 antibody was cross-reacted with AB2, AG1 AG2, OA, OB, FB1, FB2 and FB3, while OA antibody was cross-reacted with OB, AB1, AB2, AG1 AG2, FB1, FB2 and FB3. The results showed that each developed antibody was strongly selective towards its targeted mycotoxin, where no significant electrochemical response was observed when tested against different mycotoxins, even in the same mycotoxin class. This was due to the vast difference in chemical structures between each mycotoxin (Figure 7). AB1 structure depicts stacked oxolane and aromatic rings, while the OA structure exhibits a few aromatic rings containing amine, carboxyl and hydroxyl functional groups. In contrast, the structure of FB1 is a long carbon chain with a number of hydroxyl functional groups, which contributes to its high polarity.

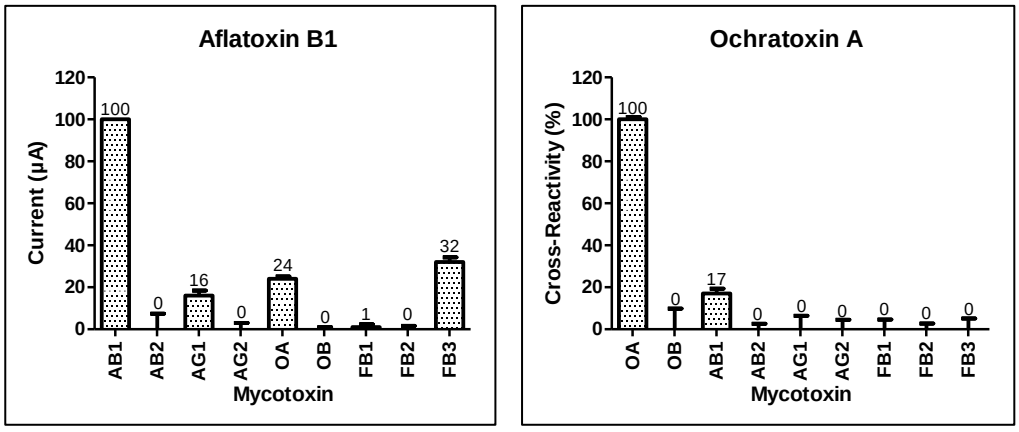


Figure 6. Intra and interspecies cross-reactivity of AB1 and OA

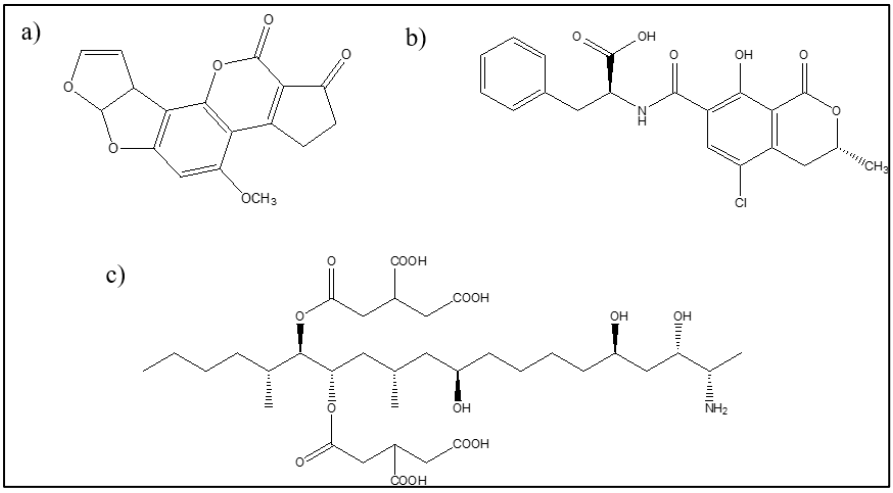


Figure 7. Chemical structure of a) AB1, b) OA, and c) FB1

Real sample analysis

The sensitivity of developed AB1 and OA sensors was also investigated in real grain corn samples. Grain corn is one of the main compositions of animal feed [29], and the inevitable occurrence of mycotoxins in unprocessed and processed grain corn hence gravely affects the animal feed industry. The analysis of samples employed the same direct assay, and the sensor's sensitivity was measured using DPV. Both AB1 and OA exhibited good R^2 values in a wider working range (Figure 8). The calculated LOD and LOQ values were also below the MRL (Table 3). This proved that the developed electrochemical sensor was highly sensitive in detecting the target analytes in the grain corn matrix.

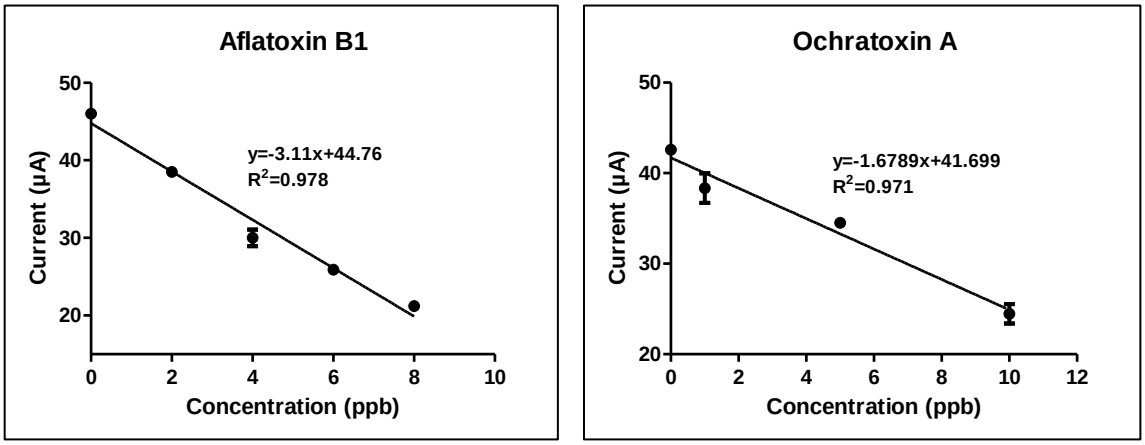


Figure 8. Standard curve of AB1 and OA in grain corn matrix

Table 3. Calculated LOD and LOQ values of AB1 and OA in corn matrix

Mycotoxin	LOD (ppb)	LOQ (ppb)	MRL (ppb)
Aflatoxin B1	1.81	5.48	5
Ochratoxin A	3.18	9.63	5

The recovery study was achieved by spiking several analytes' concentrations into grain corn and electrochemically measuring to detect the presence of mycotoxins in samples (Table 4). Overall, AB1 and OA exhibited good recovery in the range of 90-130%. Polar solvents such as ACN can work with a variety of mycotoxins, thus contributing to the success of mycotoxin extraction in corn samples [30]. The combination of water and the organic solvent was proven to increase polarity and helped in the effective extraction of solid samples [31].

Table 4. Recovery of spiked corn samples with AB1 and OA

Aflatoxin B1			Ochratoxin A		
Spiked (ppb)	**Found (ppb)**	**Recovery (%)**	**Spiked (ppb)**	**Found (ppb)**	**Recovery (%)**
2	1.92	96	5	5.24	105
6	5.52	92	10	12.56	126

Comparison with HPLC analysis

The viability of the developed electrochemical immunosensor for mycotoxins detection in grain corn was compared with chromatographic analysis. Results obtained from both techniques were recorded in Table 5. AB1 was detected lower than the MRL by both methods. AB1 was detected slightly higher from the developed biosensor may be due to the detection date being performed later than HPLC analysis. In contrast, both methods exhibited high OA concentration, which was above the regulated level. The difference in detected concentration between the sensor and HPLC was due to the fact that electrochemical-based detection has a base current limit. For example, the base current for OA was ±15 μA and is able to detect OA concentration in samples up to 15 ppb. The sensor cannot accurately determine the concentration of the target analyte but can determine if the concentration exceeds the MRL. The examined grain corn samples were contaminated by OA and were confirmed by both detection methods.

Table 5. Detected AB1 and OA using HPLC and developed electrochemical sensor

Mycotoxin	Detected Concentration (ppb)		MRL (ppb)
	HPLC	**Sensor**	
Aflatoxin B1	0.34	2.24	5
Ochratoxin A	25.82	15.78	5

Conclusion

The imbuement of AuNP coupled with PANIs onto the carbon working surface has greatly enhanced the properties of the sensor medium in terms of conductivity and as active binding sites. The AuNP-PANIs modified SPCE recorded the highest DPV current reading with low peak separation (100 mV) and a current ratio near 1 (1.04). The performance of the developed antibody-based biosensor has been proven via the sensitivity study in corn matrix and selectivity study with other mycotoxins using the electrochemical technique. Both AB1 and OA displayed high R^2 values in a broad working range with low LOD values. The developed antibodies (AB1 and OA) were exceptionally specific towards their target analyte and showed minimal cross-reactivity toward other mycotoxins. The detection of AB1 and OA in grain corn samples using the developed biosensor was at par with the instrumentation method. When evaluated using both developed electrochemical biosensor and chromatographic techniques, the tested grain corn sample was highly contaminated with OA compared to AB1. In future, AB1 and OA contamination in other food and feeds constituents such as rice, coffee beans, peanut, wheat and barley can be determined using this developed electrochemical biosensor.

Acknowledgment

This study was funded under *Sumber Rezeki Baru Jagung Bijian* (KRB-167) grant by the Ministry of Agriculture and Food Industries (MAFI). Authors would also like to thank Biotechnology and Nanotechnology Research Centre for all the facilities and materials.

References

1. Buszewska-Forajta, M. (2020). Mycotoxins, invisible danger of feedstuff with toxic effect on animals. *Toxicon*, 182: 34-53.
2. Adegbeye, M, J., Reddy, P. R. K., Chilaka, C. A., Balogun, O. B., Elghandour, M. M. Y., Rivas-Caceres, R. R. and Salem, A. Z. M. (2020). Mycotoxin toxicity and residue in animal products: Prevalence, consumer, exposure and reduction strategies – A review. *Toxicon*, 177: 96-108.
3. Afsah-Hejri, L., Jinap, S., Hajeb, P., Radu, S. and Shakibazadeh, S. (2013). A review on mycotoxins in food and feed: Malaysia case study. *Comprehensive Reviews in Food Science and Food Safety*, 12: 629-651.
4. Magnolia, A. P., Poloni, V. L. and Cavaglieri, L. (2019). Impact of mycotoxin contamination in the animal feed industry. *Current Opinion in Food Science*, 29: 99-108.
5. Schaarschmidt, S. and Fauhl-Hassek, C. (2021). The fate of mycotoxins during the primary food processing of maize. *Food Control*, 121: 107651.
6. Kumar, P., Mahato, D. K., Sharma, B., Borah, R., Haque, S., Mahmud, M. M. C., Shah, A. K., Rawal, D., Bora, H. and Bui, S. (2020). Ochratoxins in food and feed: Occurrence and impact on human health and management strategies. *Toxicon*, 187: 151-162.
7. Gruber-Dorninger, C., Jenkins, T. and Schatzmayr, G. (2019). Global mycotoxin occurrence in feed: A ten-year survey. *Toxins*, 11(375): 1-25.
8. Kebede, H., Liu, X., Jin, J. and Xing, F. (2020). Current status of major mycotoxins contamination in food and feed in Africa. *Food Control*, 110: 106975.
9. Luo, S., Du, H., Kebede, H., Liu, Y. and Xing, F. (2021). Contamination status of major mycotoxins in agricultural product and food stuff in Europe. *Food Control*, 127: 108120.
10. Agriopoulou, S., Stamatelopoulou, E. and Varzakas, T. (2020). Advances in occurrence, importance, and mycotoxin control strategies: Prevention and detoxification in foods. *Foods*, 9 (137): 1-48.
11. Chiotta, M. L., Fumero, M. V., Cendoya, E., Palazzini, J. M., Alaniz-Zanon, M. S., Ramirez, M. L. and Chulze, S. N. (2020). Toxigenic fungal species and natural occurrence of mycotoxins in crops harvested in Argentina. *Revista Argentina de Microbiologia*, 52 (4): 339-347.
12. Al-Jaal, B., Salama, S., Al-Qasmi, N. and Jaganjac, M. (2019). Mycotoxin contamination of food and feed in the Gulf Cooperation council countries and its detection. *Toxicon*, 171: 43-50.
13. Udomkun, P., Wiredu, A. N., Nagle, M., Bandyopadhyay, R., Muller, J. and Vanlauwe, B. (2017). Mycotoxins in Sub-Saharan Africa: Present situation, socio-economic impact, awareness, and outlook. *Food Control*, 72: 110-122.
14. Bryden, W. L. (2012). Mycotoxin contamination of the feed supply chain: Implications for animal productivity and feed security. *Animal Feed Science and Technology*, 173: 134-158.
15. Munkvold, G.P., Arias, S., Taschl, I. & Gruber-Dorninger, C. (2019). In Serna-Salvidar, S.O. (3rd Edition), Corn: Chemistry and Technology (pp. 235-287). AACC International & Elsevier Inc. Publisher.
16. Kaushik, A., Arya, S. K., Vasudev, A. and Bhansali, S. (2013). Recent advances in detection of ochratoxin A. *Open Journal of Applied Biosensor*, 2: 1-11.
17. Yao, H., Hruska, Z. and Mavungu, D. D. (2015). Developments in detection and determination of aflatoxins. *World Mycotoxin Journal*, 8(2): 181-191.
18. Roseanu, A., Jecu, L., Badea, M. and Evans, R. W. (2010). Mycotoxins: An overview on their quantification methods. *Romanian Journal of Biochemistry*, 47(1): 79-86.
19. Moina, C., & Ybarra, G. (2012). Fundamentals and applications of immunosensors. In N. H. L. Chiu (Ed.), Advances in immunoassay technology. Rijeka, Croatia: InTech: pp. 65–80.

20. Vidal, J. C., Bonel, L., Ezquerra, A., Hernandez, S., Bertolin, J. R., Cubel, C. and Castillo, J. R. (2013). Electrochemical affinity biosensors for detection of mycotoxins: A review. *Biosensors and Bioelectronics*, 49: 146-158.
21. Sharma, A., Goud, K. Y., Hayat, A., Bhand, S. and Marty, J. L. (2017). Recent advances in electrochemical-based sensing platforms for aflatoxins detection. *Chemosensors*, 5 (1): 1-15.
22. Tothill, I. E. (2011). Biosensors and nanomaterials and their application for mycotoxin determination. *World Mycotoxin Journal*, 4(4): 361-374.
23. Alhamoud, Y., Yang, D., Kenston, S. S. F., Liu, G., Liu, L., Zhou, H., Ahmed, F. and Zhao, J. (2019). Advances in biosensors for the detection of ochratoxin A: Bio-receptors, nanomaterials, and their applications. *Biosensors and Bioelectronics*, 141: 111418.
24. Ma, H., Sun, J., Zhang, Y., Bian, C., Xia, S. and Zhen, T. (2016). Label-free immunosensor based on one-step electrodeposition of chitosan-gold nanoparticles biocompatible film on Au microelectrode for determination of aflatoxin B1 in maize. *Biosensors and Bioelectronics*, 80: 222-229.
25. Shaikh, M. O., Srikanth, B., Zhu, P.-Y. and Chu, C.-H. (2019). Impedimetric immunosensor utilizing polyaniline/gold nanocomposite-modified screen-printed electrodes for early detection of chronic kidney disease. *Sensors*, 19(18): 3990.
26. Zhang, S., Shen, Y., Shen, G., Wang, S., Shen, G. and Yu, R. (2016). Electrochemical immunosensor based on Pd-Au nanoparticles supported on functionalized PDDA-MWCNT nanocomposites for aflatoxin B1 detection. *Analytical Biochemistry*, 494: 10-15.
27. Kabomo, T. M. and Scurrel, M. S. (2016). The effect of protonation and oxidation state of polyaniline on the stability of gold nanoparticles. *European Polymer Journal*, 82: 300-306.
28. Yagati, A. K., Chavan, S. G., Baek, C., Lee, M.-H. and Min, J. (2018). Label-free impedance sensing of aflatoxin B1 with polyaniline nanofibers/Au nanoparticle electrode array. *Sensors*, 18 (1320): 1-14.
29. Lee, N. A. and Rachmawati, S. (2006). A rapid ELISA for screening aflatoxin B1 in animal feed and feed ingredients in Indonesia. *Food and Agricultural Immunology*, 17(2): 91-104.
30. Nakhjavan, B., Ahmed, N. S. and Khosravifard, M. (2020). Development of an improved method of sample extraction and quantitation of multi-mycotoxin in feed by LC-MS/MS. *Toxins*, 12(462): 1-14.
31. Iqbal, S. Z. (2021). Mycotoxins in food, recent development in food analysis and future challenges; a review. *Current Opinion in Food Science*, 42: 237-247.

Malaysian Journal of Analytical Sciences (MJAS)
Published by Malaysian Analytical Sciences Society

CHARACTERIZATION OF CELLULOSE NANOCRYSTAL-GOLD NANOPARTICLES/CHITOSAN MODIFIED SCREEN-PRINTED CARBON ELECTRODE AND ITS APPLICATION IN THE FABRICATION OF ELECTROCHEMICAL BIOSENSOR FOR TETRACYCLINE DETECTION

(Percirian Elektrod Skrin Bercetak Karbon Terubahsuai Nanokristal Selulosa-Partikel Nano Emas/Kitosan dan Aplikasinya dalam Fabrikasi Penderia Bio Elektrokimia untuk Pengesanan Tetrasiklin)

Nurul Shahirah Hasim[1], Nor Azah Yusof[1,2], Ruzniza Mohd Zawawi[1], Noordiana Nordin[3*]

[1]Department of Chemistry,
Faculty of Science,
Universiti Putra Malaysia, 43400 Serdang, Selangor, Malaysia
[2]Functional Nanotechnology Devices Laboratory,
Institute of Nanoscience and Nanotechnology,
Universiti Putra Malaysia, 43400 Serdang, Selangor, Malaysia
[3]Laboratory of Food Safety and Food Integrity,
Institute of Tropical Agriculture and Food Security,
Universiti Putra Malaysia, 43400 Serdang, Selangor, Malaysia.

[*]Corresponding author: noordiana@upm.edu.my

Received: 10 February 2022; Accepted: 19 July 2022; Published: 27 December 2022

Abstract

Tetracycline is one of the antibiotics used therapeutically and as a growth promoter in animals. Tetracycline residues in food products of animal origin have raised concerns among consumers. Due to its adverse effects on human health, it is critical to develop a reliable analytical method for routine monitoring of tetracycline in foods. Biosensors are among the rapid analytical devices that are reliable because of their simple detection methodology, low cost, sensitivity and specificity. For an effective signal transformation of tetracycline residues, it is critical to completely attach the transducer to the biological component, so that a feasible biosensor can be constructed. In this study, the screen-printed carbon electrode (SPCE) was modified with cellulose nanocrystal–gold nanoparticles/chitosan composite (CNC–AuNPs/chitosan). The synthesized CNC–AuNPs composite was characterized using UV–Vis spectroscopy, X-ray diffraction, Fourier-transform infrared spectroscopy and high-resolution transmission electron microscopy. In addition, the electrochemical behavior of the modified SPCE was investigated by cyclic voltammetry, differential pulse voltammetry (DPV) and electrochemical impedance spectroscopy under optimized conditions. DPV showed a linear calibration within the range of 0.01 to1000 µM concentration of tetracycline with the detection limit of 0.07 µM. The developed biosensor also resulted in different peak currents measured after storage for 14 days at room temperature (53.07%) and under 4°C (89.28%). Therefore, with acceptable sensitivity and selectivity, the fabricated biosensor can be suggested as a potential detection method for tetracycline residues.

Keywords: Cellulose nanocrystal, gold nanoparticles, screen-printed carbon electrode, electrochemical biosensor, tetracycline

Abstrak

Tetrasiklin adalah salah satu antibiotik yang digunakan secara terapeutik dan sebagai penyokong pertumbuhan pada haiwan. Sisa tetrasiklin dalam produk makanan yang berasal dari haiwan telah menimbulkan kebimbangan di kalangan pengguna. Oleh kerana kesan buruknya terhadap kesihatan manusia, adalah sangat penting untuk membangunkan kaedah analisis yang boleh dipercayai untuk pemantauan rutin tetrasiklin dalam makanan. Penderia bio adalah antara peranti analisis pantas yang boleh dipercayai kerana kaedah pengesanannya yang mudah, menjimatkan kos, kepekaan dan kekhususannya. Untuk transformasi isyarat yang berkesan dari sisa tetrasiklin, adalah sangat penting untuk melampirkan transduser sepenuhnya ke komponen biologi, supaya penderia bio yang boleh dilaksanakan dapat dibina. Dalam kajian ini, penderia bio dengan pengubahsuaian elektrod skrin bercetak karbon (SPCE) telah melibatkan nanokristal selulosa-partikel nano emas/kitosan (CNC-AuNPs/kitosan). Komposit CNC-AuNPs yang disintesis telah dicirikan dengan menggunakan spektroskopi penglihatan-UV, pembelauan sinaran-X, spektroskopi inframerah transformasi Fourier dan mikroskopi penghantaran elektron. Di samping itu, tingkah laku elektrokimia SPCE yang diubahsuai telah disiasat oleh voltammetri berkitar, voltammetri pembeza denyut (DPV) dan spektrometer electrokimia impedans dibawah keadaan yang optima. DPV menunjukkan kalibrasi linear dalam julat kepekatan tetrasiklin 0.01 hingga 1000 μM dengan had pengesanan 0.07 μM. Penderia bio yang telah dibangunkan juga telah menghasilkan perbezaan dalam arus puncak yang diukur setelah disimpan selama 14 hari pada suhu bilik (53.07%) dan di bawah suhu 4°C (89.28%). Oleh itu, dengan sensitiviti dan selektiviti yang telah diperoleh, penderia bio yang dibangunkan disyorkan berpotensi sebagai kaedah pengesanan sisa tetrasiklin.

Kata kunci: nanokristal **s**elulosa, partikel nano emas, elektrod karbon tercetak, penderia bio elektrokimia, tetrasiklin

Introduction

Antibiotic residues in animal-derived foods, owing mostly to antibiotic abuse in animal husbandry, have become a global concern and a significant health risk for humans and animals [1]. Since the 1940s, tetracycline has played a significant role in veterinary medicine and feed additives because of its broad-spectrum antibacterial properties and economic benefits. In livestock agriculture, tetracycline is frequently used to stimulate growth through increased food intake, weight gain and herd health. This approach may result in the presence of trace levels of these medications in animal-derived products such as milk and eggs, posing substantial health hazards to humans. The presence of tetracycline residues in foods may result in the transmission of antibiotic-resistant pathogenic microorganisms via the food chain. Another effect identified is its potential to trigger allergic reactions in hypersensitive persons [2].

According to Food and Drug Administration summary reports, sales and distribution of antimicrobials authorized for use in food-producing animals totaled roughly 14.8 million kg in 2012, with tetracycline accounting for 40% of total sales [3]. This data demonstrates that tetracycline is widely employed in animal food production, placing it at the top of the list of antibacterial drugs. To assure food safety and protect consumers from exposure to these contaminants, national and international regulatory organizations have established a tolerance level for tetracycline. Maximum residue levels (MRLs) are the maximum permissible concentrations of food residues and/or hazardous metabolites in food and feed products [4]. Food and Agricultural Organization of United Nations/World Health Organization have determined MRLs for tetracycline to be 200 μg kg^{-1} in chicken muscle and 400 μg kg^{-1} in egg samples [5].

Due to the possible detrimental effects of tetracycline in food, it is vital to develop accurate analytical methods that are speedy, precise, cost-effective, time-saving and environmentally friendly for routine tetracycline monitoring in food. Biosensor technology is being implemented in the field of analytical chemistry and is rapidly gaining popularity among researchers. Biosensors are small, portable devices that enable the detection of analytes by converting the chemical reaction to a signal utilizing biological recognition elements adsorbed on the physicochemical transducer [6]. This signal may generate qualitative or quantitative information. Biosensors have become one of the most often used rapid analytical methods, owing to the advantages of being quick, simple and sensitive. As a

result, the integration of biosensors currently has not only enhanced research on food safety involving chemical and microbial contamination but also improved the preservation of food freshness through packaging methods [7].

One of the fundamental principles of the electrochemical biosensor is the correlation between the biological component and the transducer that may affect the specificity of detection. Several previous reports have utilized nanomaterials as a significant advancement in these areas [8–11]. In this study, we propose a novel cellulose nanocrystal–gold nanoparticles/chitosan (CNC–AuNPs/chitosan) as the modifier of the screen-printed carbon electrode (SPCE) to amplify the current signal measured. Using the modification, an electrochemical biosensor was fabricated to determine tetracycline residues. The differential pulse voltammetry (DPV) technique was used in the presence of a redox indicator during detection.

Materials and Methods

Reagents and apparatus

All the chemical reagents used in this study were of analytical grade and used without further purification unless stated otherwise. Dry CNC with 0.94 weight percentage of sulphur (Batch# 2014-FPL-CNC-065) was purchased from the University of Maine (USA). Chitosan, tetracycline hydrochloride and streptomycin sulphate were procured from Nacalai Tesque (Japan). Gold (III) chloride trihydrate ($HAuCl_4.3H_2O$), bovine serum albumin (BSA), trizma hydrochloride (Tris–HCl) and glutaraldehyde (GA) were obtained from Sigma-Aldrich (USA). Potassium chloride (KCl) was obtained from Bendosen Chemical (Malaysia). Potassium ferricyanide ($K_3Fe(CN)_6$) and phosphate buffer saline (PBS) were purchased from R&M Chemicals (Malaysia). Potassium ferrocyanide ($K_4Fe(CN)_6$) was purchased from Millipore (Canada). Synthetic oligonucleotides for amine-terminated ssDNA (tetracycline aptamer, TET-aptamer) were purchased (as lyophilized powder) from Apical Scientific (Malaysia) with the following sequence: 5'-NH_2–CCCC CGGC AGGC CACG GCTT GGGT TGGT CCCA CTGC GCGT-3' (anti-tetracycline). Electrochemical measurements were performed using an Autolab III Eco-Chemie (Netherland) voltammetric analyser with NOVA 1.11 software and an impedance potentiometric module FRA 32M (10 μHz to 32 MHz) (Netherland) with NOVA 2.4 software. The SPCE used for the analysis, which comprises a three-electrode system: a counter electrode, a carbon working electrode and an Ag/AgCl reference electrode, was purchased from Metrohm DropSens (Spain). The characterization was performed using UV–vis spectroscopy (Perkin Elmer), X-ray diffraction (XRD) (Philips), high-resolution transmission electron microscopy (HR-TEM) (JEOL) and Fourier-transform infrared spectroscopy (FTIR) (Shimadzu).

Synthesis and characterization of CNC-AuNPs

CNC–AuNPs were synthesized by mixing 1% sodium citrate solution with 0.2 mM $HAuCl_4$ solution and 0.1% CNC suspension. The volume of the mixture was made up of deionized water and heated at 80°C for an hour. The color changes were observed, and the final solution was then cooled to room temperature and kept in a fridge. The CNC–AuNPs were characterized using UV–vis spectroscopy, XRD, HR-TEM and FTIR.

Fabrication and characterization of modified SPCE

The SPCE was modified based on the layer-by-layer method. First, CNC–AuNPs were sonicated for 5 min. Then, 4 μL of CNC–AuNPs was drop cast on the SPCE (SPCE/CNC–AuNPs) and dried at ambient temperature. Chitosan solution was prepared by adding 0.5 g chitosan to 50 mL acetic acid (2%) and stirred for several hours until completely dissolved. Then, 4 μL chitosan solution was drop cast as the second layer (SPCE/CNC–AuNPs/chitosan) and air-dried. The bare and modified SPCE was characterized after each deposition layer using cyclic voltammetry (CV) at the potential range of –0.4 to 0.7 V for 20 cycles with a scan rate of 0.1 V/s in 1 mM $K_3Fe(CN)_6$ and 50 mM KCl. The electrochemical impedance spectroscopy was conducted at the frequency range of 0.01 to 10 000 Hz with an amplitude of 0.3 V in 5 mM $K_3Fe(CN)_6$, 5 mM $K_4Fe(CN)_6$ and 0.1 mM KCl.

Development of electrochemical biosensor

The modified SPCE was placed in 1% GA and washed. The GA acts as the linker between the DNA probe and

the modified SPCE. Various TET-aptamer concentrations ranging from 0.01 to 1000 nM were drop cast on the SPCE/CNC–AuNPs/chitosan and kept at room temperature at various incubation times ranging from 15 to 90 min. Optimum concentration and incubation time of the TET-aptamer were selected for further analysis. Tris–HCL buffer was used to wash the unbound aptamer on the SPCE/CNC–AuNPs/chitosan/TET-aptamer prior to measurement by DPV. Several concentrations of tetracycline ranging from 10 nM to 1 mM were drop cast on the SPCE/CNC–AuNPs/chitosan/TET-aptamer and incubated for an hour. Tris–HCL buffer was used to wash the unbound tetracycline. Prior to electrochemical measurement, the SPCE/CNC–AuNPs/chitosan/TET-aptamer was immersed in BSA to avoid non-specific binding. DPV was performed at the potential range of –0.6 to 0.7 V and a scan rate of 0.01 V/s in 1 mM $K_3Fe(CN)_6$ and 50 mM KCl.

Results and Discussion

Characterization of CNC-AuNPs

UV–vis spectroscopy was used to confirm the presence of AuNPs in CNC suspension. The CNC–AuNPs nanocomposite, as shown in Figure 1A, exhibited a distinct absorption peak around 525 nm, which can be traced back to the surface plasmon resonance band of AuNPs. The broad peak area is expected from the synthesis of AuNPs using a citrate-reduction method [12]. The cellulose nanocrystal structure of the synthesized CNC–AuNPs was determined using XRD. Figure 1B depicts the XRD patterns of CNC and CNC–AuNPs. The CNC showed a prominent peak at 2 theta at 15.2°, 22.6° and 34.5°, which were derived from the typical reflection planes (110), (200) and (040) of cellulose, respectively [13]. With the addition of those peaks, CNC–AuNPs displayed four new peaks in the vicinity of 39.1°, 44.2°, 64.9° and 77.8°, which were indexed to the (111), (200), (220) and (311) planes of gold lattice, respectively [14]. Consequently, the XRD pattern indicated that the metallic production of AuNPs did not change the crystallographic property of CNC. The FTIR technique was used to determine the chemical composition or structure of the sample. In most cases, the CNC is represented by a broad peak of O–H spanning between 3100 and 3700 cm^{-1} due to the hydrogen connection between the hydroxyl group and the carboxyl group. The presence of a hydrogen bond in the structure aids in the nucleation process that occurs during the synthesis of AuNPs [15]. As illustrated in Figure 1C, the CNC–AuNPs displayed peaks at roughly 2900 cm^{-1} and 1635 cm^{-1}, which were attributed to the C–H stretching and the C=C stretching of the cellulose structure, respectively, in the spectrum.

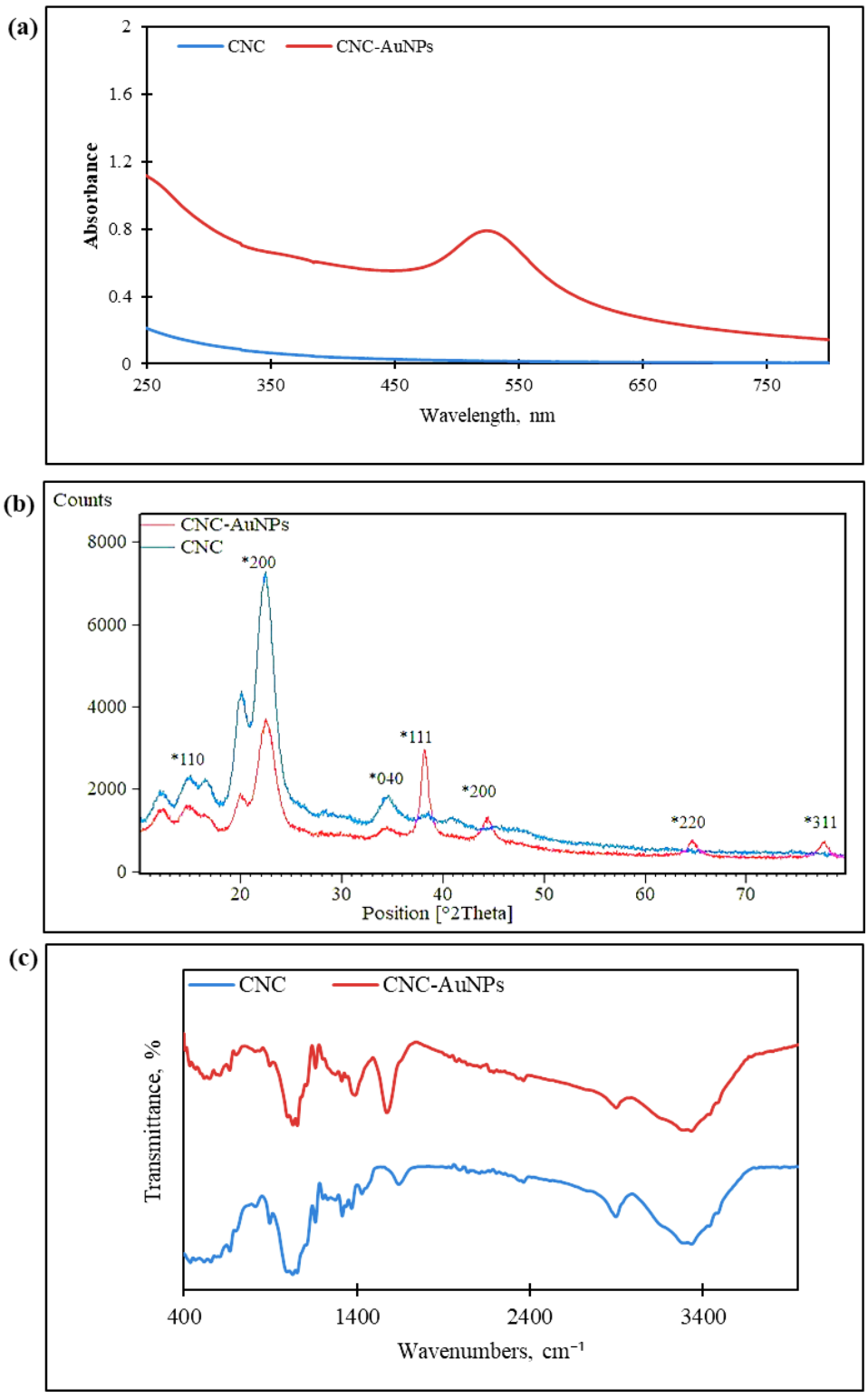


Figure 1. (a) UV-vis spectra, (b) XRD pattern and (c) FTIR spectra of CNC and CNC-AuNPs

The TEM images clearly revealed the production of the gold particles. In Figure 2a, CNC's TEM image revealed rod-like particles of cellulose crystalline with a diameter of less than 10 nm. The distribution showed that most of the cellulose crystals are about 6 to 7 nm. Meanwhile, Figure 2b reveals that there is a small populated zone of AuNPs with a diameter of around 20 nm. The agglomeration and the inconsistency in the particle size of the AuNPs may be due to the inefficient thermal process during the synthesis [16]. In addition, the CNC–AuNPs elemental spectra were obtained using the TEM–EDX. The EDX analysis revealed an abundance of gold particles with a weight percentage of 84.2, indicating that the production of AuNPs in the presence of CNC has occurred.

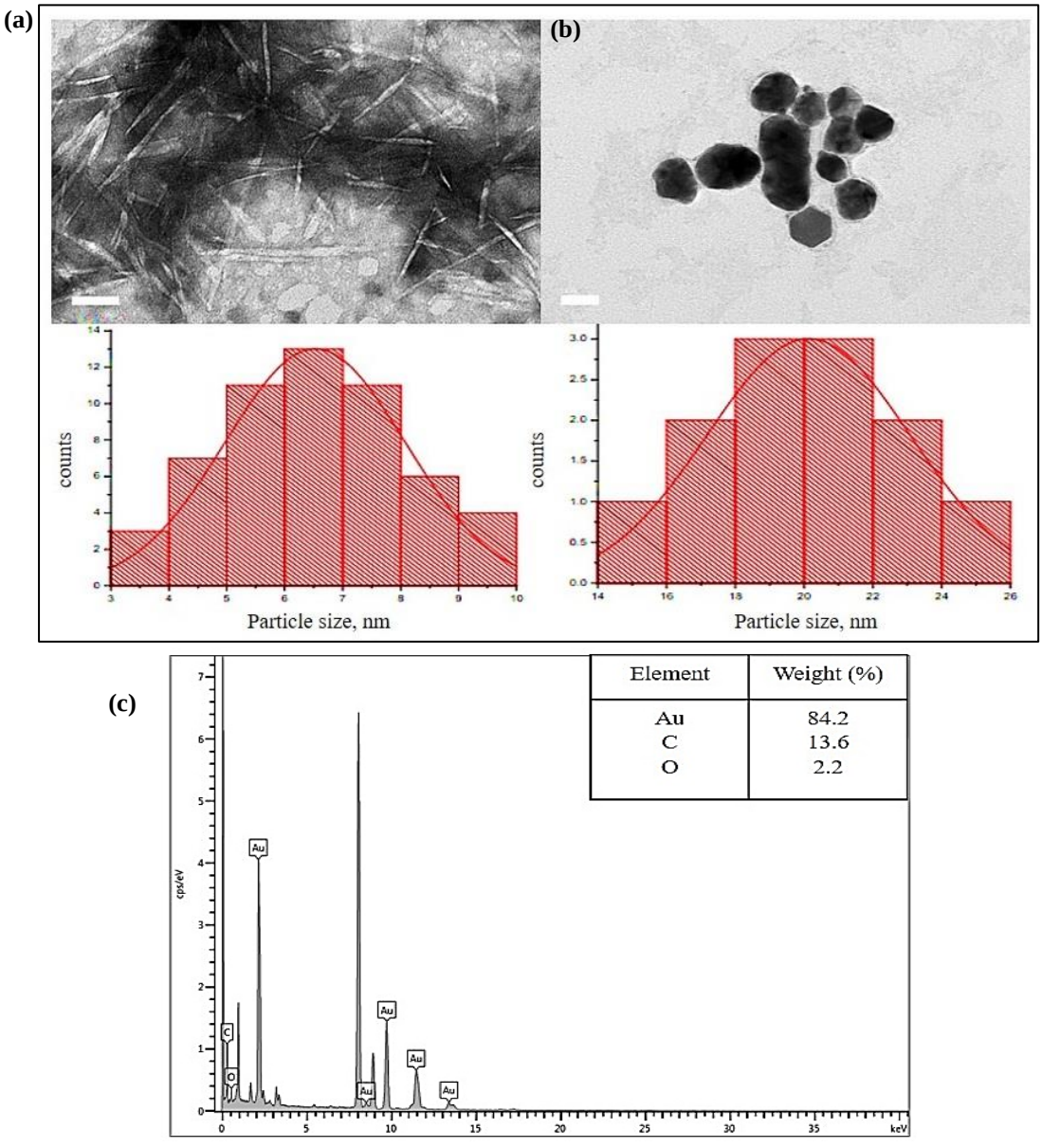


Figure 2. (a) TEM image of CNC, (b) TEM image CNC-AuNPs (50k magnification) and (c) TEM-EDX analysis of CNC-AuNPs (inset; elemental analysis)

Electrochemical properties of the modified electrode

For the modification of the SPCE, chitosan solution was drop cast on the CNC–AuNPs surface. CV was performed to investigate the bare SPCE and CNC–AuNPs/chitosan-modified SPCE, and the signals are shown in Figure 3a. The CNC–AuNPs/chitosan-modified SPCE demonstrated the highest anodic peak, measuring around 74.29 µA when compared with the CNC–AuNPs-modified SPCE. The increment of about sevenfold in the peak current may be due to the chitosan layer that acts as a hydrophobic barrier [17], allowing the CNC–AuNPs to remain intact on the surface of SPCE, thus allowing the amplification of the signal. By calculating the relative standard deviation (RSD), the repeatability and reproducibility of the modified SPCE were determined. The percent RSD for repeatability was 5.1% when five consecutive readings of the modified electrode were taken. Using the same approach on five individual electrodes resulted in a 6.4% RSD for reproducibility. As for the Nyquist plot from Figure 3b, it is proved that the measurement complimented the CV measurements as the resistance decreased for the modified electrode. The R_{ct} values recorded for bare and modified electrodes were 394.08 and 116.27 Ω, respectively. Therefore, it is believed that the modified electrode can improve conductivity while also providing reliable and reproducible measurements for the biosensor.

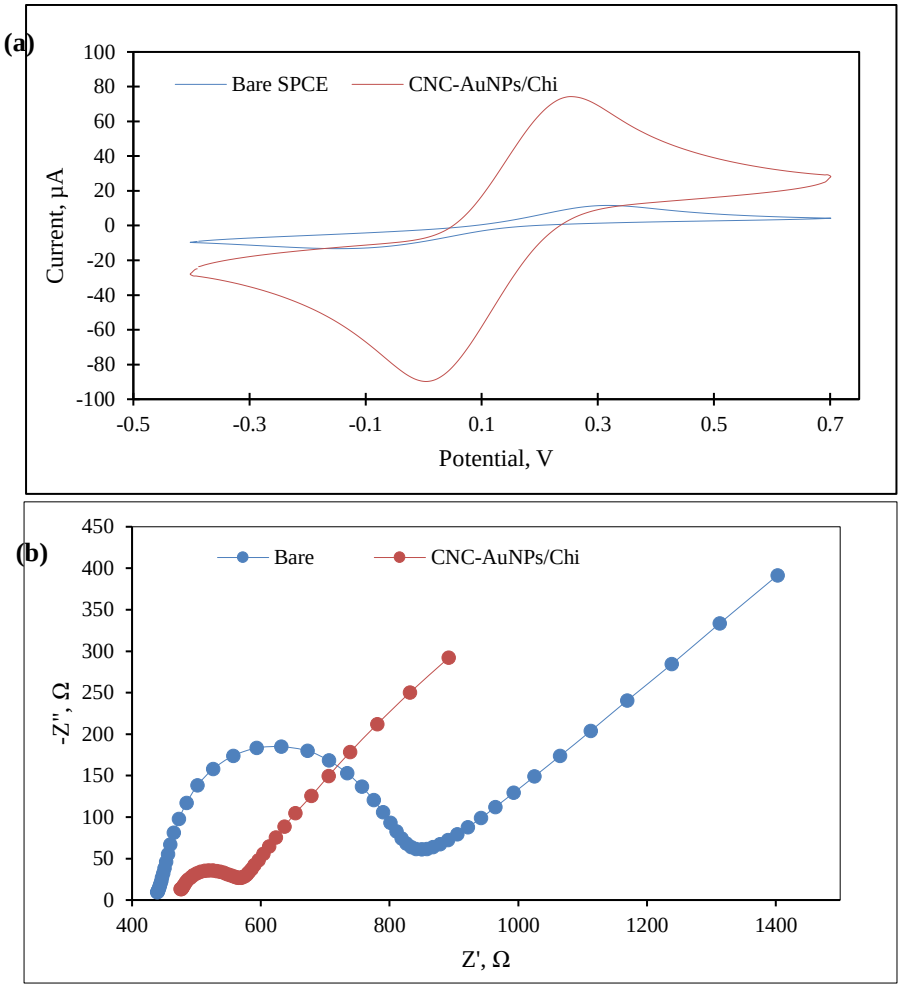


Figure 3. (a) Cyclic voltammogram and (b) Nyquist plot of bare SPCE and CNC-AuNPs/chitosan-modified SPCE

Optimization of the TET-aptamer

Several variables, including incubation duration and immobilized TET-aptamer concentration, were investigated to obtain the highest possible output from the biosensor. These parameters must be optimized because they have an impact on the binding of the TET-aptamer with the tetracycline as well as the peak current of DPV. To find the optimal concentration of the TET-aptamer, the CNC–AuNPs/chitosan-modified SPCE was pipetted with various concentrations (0.01 to 1000 nM) of the TET-aptamer for 30 min. Based on Figure 4a, the peak current increased as the concentration of the TET-aptamer increased from 0.01 to 1 nM. Nevertheless, the peak current began to decrease as the concentration increased from 10 to 1000 nM. This could be due to the too close proximity on the surface of the CNC–AuNPs/chitosan-modified SPCE that causes electrostatic repulsion. Hence, the optimized concentration of the TET-aptamer was found to be 1 nM. In addition, Figure 4b shows the effect of the incubation time of the TET-aptamer on the DPV peak current. The TET-aptamer (1 nM) was dropped on the CNC–AuNPs/chitosan-modified SPCE for 15 to 90 min. The findings showed that the peak current reached a maximum at 75 min yet decreased at 90 min, which might be due to the instability of the TET-aptamer after being left for a longer period on the electrode surface. Thus, the optimum incubation time of the TET-aptamer was selected at 75 min.

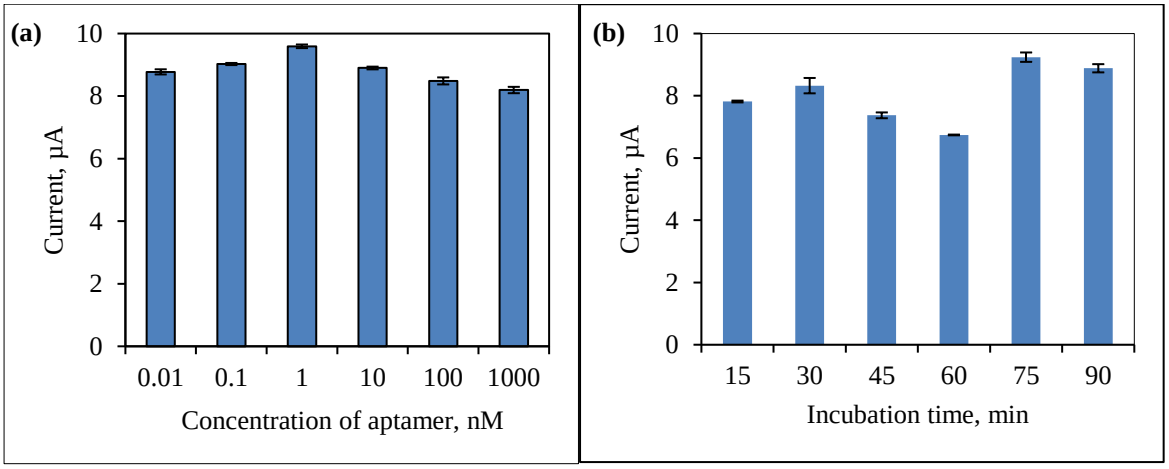


Figure 4. The effect of different **(A)** incubation times and **(B)** concentrations of the TET-aptamer at potential of -0.6 to 0.7 V

Detection of tetracycline

Under the optimal experimental conditions, the DPV response was recorded for the tetracycline detection. To validate the constructed biosensor, tetracycline was incubated on the immobilized TET-aptamer surface at multiple concentrations ranging from 10 nM to 1 mM. It can be observed in Figure 5a that the continuous drop of the DPV peak current was associated with the binding of the tetracycline to the TET-aptamer. These findings also can be compared with those of Zhao et al. [18], Benvidi et al. [19], and Tang et al. [20] who reported a decrease in DPV signals with the presence of tetracycline. In addition, the linear calibration was plotted between the log of different concentrations of tetracycline and the relative change in peak current ($\Delta I/I_0$) (Figure 5b). The biosensor demonstrated a linear regression, which was stated as $y = 0.70x + 4.65$ with a correlation coefficient of $R^2 = 0.9707$. From the linear slope, the limit of detection (LOD) was obtained at 0.07 µM of tetracycline concentration, which was calculated using the $3\sigma/s$ formula, where σ is the standard deviation of the blank and s is the slope of the calibration curve. The reproducibility of the developed biosensor was also evaluated from five individual electrodes and the resulted percent RSD was 4.1%. This proved the consistency of the signal measurements, which relate to the reliability of the fabricated biosensor.

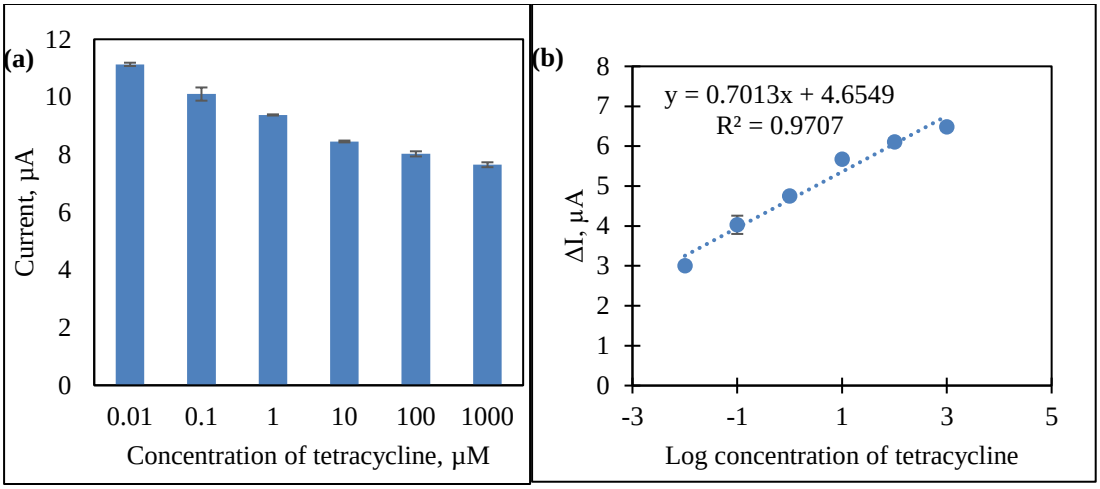


Figure 5. (a) DPV of the biosensor taken at different concentrations of tetracycline and (b) the calibration curve of the biosensor; LOD: 0.07 µM

The selectivity of the biosensor was investigated using several types of antibiotics to assess the specificity of the TET-aptamer binding to the tetracycline. DPV responses to tetracycline, ampicillin, streptomycin and oxytetracycline are demonstrated in Figure 6. The highest peak current (12.32 µA) was observed for ampicillin, owing to the various binding sites of the TET-aptamer that were used to capture it. Compared with the other antibiotics, tetracycline recorded the lowest peak current (10.10 µA). This demonstrates that the TET-aptamer is capable of distinguishing tetracycline from other distinct antibiotic molecules (ampicillin and streptomycin) as well as the structurally related derivative antibiotics (oxytetracycline). The stability of the developed biosensor was also analyzed using 100 µM tetracycline. The biosensor was stored for 14 days at room temperature and under 4 °C. The relative difference in peak current from the initial response for room temperature and under 4 °C was 53.07% and 89.27%, respectively. This indicates that the biosensors cannot be stored more than 2 weeks before use.

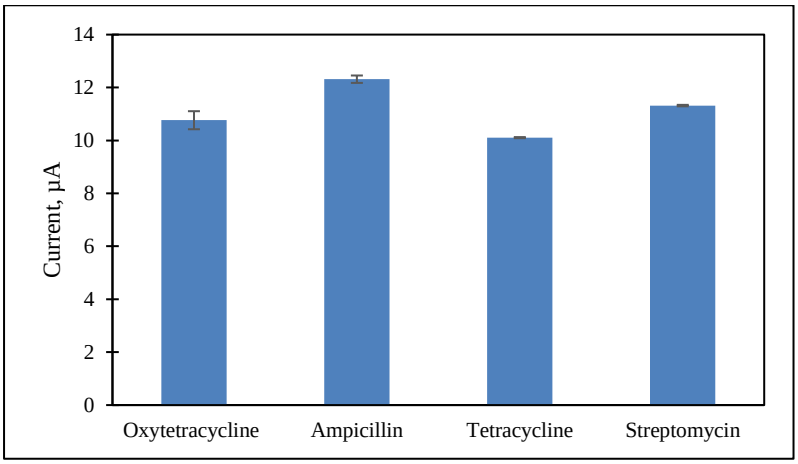


Figure 6. DPV responses of the tetracycline, ampicillin, streptomycin and oxytetracycline

Conclusion

In this study, CNC–AuNPs were synthesized, characterized and employed as the transducer element for the fabrication of a biosensor. After being modified in conjunction with chitosan, the modified SPCE demonstrated a significant current peak increment of sevenfold. With an acceptable percent RSD, the CNC–AuNPs/chitosan-modified SPCE showed a repeatable and reproducible result. With the chosen modified surface, the biosensor was developed for tetracycline detection. DPV recorded a decreasing current with an increasing concentration of tetracycline. From the analysis, it was found that the LOD for the detection was 0.07 μM (RSD = 4.1%). The findings of this study imply that using a combination of approaches to modify disposable SPCEs with CNC–AuNPs and chitosan for prospective use as a biosensor for tetracycline detection may be a potential alternative.

Acknowledgement

The authors gratefully acknowledge the financial assistance provided by the Ministry of Education Malaysia and Universiti Putra Malaysia under the Putra-IPM project (GP-IPM/2017/9580100).

References

1 . Ramchandani, M., Manges, A. R., DebRoy, C., Smith, S. P., Johnson, J. R. and Riley, L.W. (2005). Possible animal origin of human-associated, multidrug-resistant, uropathogenic *Escherichia coli. Clinical Infectious Diseases*, 40(2): 251-257.

2 . Landers, T. F., Cohen, B., Wittum, T. E. and Larson, E .L. (2012). A review of antibiotic use in food animals: Perspective, policy, and potential. *Public Health Reports*, 127(1): 4-22.

3 . Food Drug Administration (2014). 2012 summary report on antimicrobials sold or distributed for use in food-producing animals. Washington DC: Department of Health and Human Services, Food and Drug Administration, Center for Veterinary Medicine: pp. 1-56.

4 . Boyaci, I. H. and Mutlu, M. (2011). Amperometric biosensors in food processing, safety, and quality control. *Biosensors in Food Processing, Safety, and Quality Control,* 2011: 1-51.

5 . Codex Alimentarius (2018). Maximum residue limits (MRLs) and risk management recommendations (RMRs) for residues of veterinary drugs in food CX/MRL 2-2018. Access from http://www.fao.org/fao-who-codexalimentarius/codex-texts/dbs/vetdrugs/veterinary-drugs/en/.

6 . Mustafa, F. and Andreescu, S. (2018). Chemical and biological sensors for food-quality monitoring and smart packaging. *Foods*, 7(10): 168.

7 . Yan, W., Chen, C., Wang, L., Zhang, D., Li, A.J., Yao, Z. and Shi, L.Y. (2016). Facile and green synthesis of cellulose nanocrystal-supported gold nanoparticles with superior catalytic activity. *Carbohydrate Polymers*, 140: 66-73.

8 . Guo, Y., Shen, G., Sun, X. and Wang, X. (2015). Electrochemical aptasensor based on multiwalled carbon nanotubes and graphene for tetracycline detection. *IEEE Sensors Journal*, 15(3): 1951-1958.

9 . Ouyang, Q., Liu, Y., Chen, Q., Guo, Z., Zhao, J., Li, H. and Hu, W. (2017). Rapid and specific sensing of tetracycline in food using a novel upconversion aptasensor. *Food Control*, 81:156-163.

10 . Jahanbani, S. and Benvidi, A. (2016). Comparison of two fabricated aptasensors based on modified carbon paste/oleic acid and magnetic bar carbon paste/Fe_3O_4@oleic acid nanoparticle electrodes for tetracycline detection. *Biosensors and Bioelectronics*, 85:553-562.

11 . Le, T. H., Pham, V. P., La, T. H., Phan, T. B. and Le, Q. H. (2016). Electrochemical aptasensor for detecting tetracycline in milk. *Advances in Natural Sciences: Nanoscience and Nanotechnology*, 7(1): 015008.

12 . Brown, K. R., Walter, D. G. and Natan, M. J. (2000). Seeding of colloidal Au nanoparticle solutions: Improved control of particle size and shape. *Chemistry of Materials*, 12(2): 306-313.

13 . Zhao, H., Kwak, J. H., Conrad Zhang, Z., Brown, H. M., Arey, B.W. and Holladay, J. E. (2007). Studying cellulose fiber structure by SEM, XRD, NMR and acid hydrolysis. *Carbohydrate Polymers*, 68(2): 235-241.

14 . Krishnamurthy, S., Esterle, A., Sharma, N. C. and Sahi, S. V. (2014). Yucca-derived synthesis of gold nanomaterial and their catalytic potential. *Nanoscale Research Letters*, 9(1): 1-9.

15 . Lam, E., Hrapovic, S., Majid, E., Chong, J. H. and Luong, J. H. T. (2012). Catalysis using gold nanoparticles decorated on nanocrystalline cellulose. *Nanoscale*, 4(3): 997-1002.

16 . Kimling, J., Maier, M., Okenve, B., Kotaidis, V., Ballot, H. and Plech, A. (2006). Turkevich method for gold nanoparticle synthesis revisited. *Journal of Physical Chemistry B*, 110(32): 15700-15707.

17 . Jiang, Y. and Wu, J. (2019). Recent development in chitosan nanocomposites for surface-based biosensor applications. *Electrophoresis*, 40(16): 2084-2097.

18 . Zhou, L., Li, D.J., Gai, L., Wang, J. P. and Li, Y. Bin. (2012). Electrochemical aptasensor for the detection of tetracycline with multi-walled carbon nanotubes amplification. *Sensors and Actuators, B: Chemical*, 162(1): 201-208.

19 . Benvidi, A., Tezerjani, M. D., Moshtaghiun, S. M. and Mazloum-Ardakani, M. (2016). An aptasensor for tetracycline using a glassy carbon modified with nanosheets of graphene oxide. *Microchimica Acta*, 183: 1797-1804.

20 . Tang, Y., Liu, P., Xu, J., Li, L. Le, Yang, L., Liu, X., Liu, S. and Zhou, Y. (2018). Electrochemical aptasensor based on a novel flower-like TiO_2 nanocomposite for the detection of tetracycline. *Sensors and Actuators, B: Chemical*, 258: 906-912.

Malaysian Journal of Analytical Sciences (MJAS)
Published by Malaysian Analytical Sciences Society

CARBON DOTS/CHITOSAN MODIFIED SCREEN-PRINTED CARBON ELECTRODES FOR THE DETECTION OF BISPHENOL A

(Elektrod Karbon Bercetak Skrin Terubah Suai Karbon Titik/Kitosan untuk Pengesanan Bisfenol A)

Nor Faezah Mohd Daud[1], Jaafar Abdullah[1,2]*, Nor Azah Yusof[1,2], Putri Nur Syafieqah Zainal[1]

[1]*Department of Chemistry,*
Faculty of Science,
Universiti Putra Malaysia, 43400 UPM Serdang, Selangor, Malaysia
[2]*Institute of Nanoscience and Nanotechnology,*
University Putra Malaysia, 43400 Serdang, Selangor, Malaysia

[*]*Corresponding author: jafar@upm.edu.my*

Received: 10 February 2022; Accepted: 16 June 2022; Published: 27 December 2022

Abstract

Bisphenol A (BPA) is an organic compound in daily plastic products. The compound is primarily transferred from water bottles, food cans liners, and dental fillings into foods and beverages. The BPA is considered an endocrine-disrupting compound related to broad health concerns, such as reproduction problems and the development of various cancers. Consequently, developing a reliable analytical approach to determine BPA levels is urgent. The current study developed an electrochemical sensor from modified screen-printed carbon electrodes (SPCE) with carbon dots-chitosan (CDs-CS) to detect BPA. The CDs-modified SPCE provided a good electrocatalytic application with extraordinary electronic properties and significantly enhanced electrical conductivity. The modified SPCE/CDs-CS sensor was prepared through the drop casting technique. Subsequently, its BPA detection abilities were assessed via differential pulse voltammetry (DPV). In investigating the optimum parameters to elevate the performance of the developed sensors, 1% m/v CS concentration and 1:1 (v/v) CDs to CS ratio were recorded. The obtained CDs-CS/SPCE sensor demonstrated great electrocatalytic features for detecting BPA within the 0.4 and 10 µM concentration range with a sensitivity of 0.46 µA/µM (R^2 = 0.9911) and 0.37 µM limit of detection (LOD).

Keywords: Bisphenol A, carbon dots, chitosan, electrochemical sensor, environmental

Abstrak

Bisfenol A (BPA) adalah sebatian organik yang terdapat dalam produk plastik yang kita gunakan setiap hari. Sebilangan besarnya dipindahkan ke dalam makanan dan minuman termasuk botol air, lapisan tin makanan, dan tampalan gigi. BPA dianggap sebagai sebatian yang mengganggu endokrin yang berkaitan dengan pelbagai jenis masalah kesihatan seperti perkembangan barah dan masalah pembiakan. Oleh itu, pembangunan pendekatan analisis yang boleh dipercayai untuk mengesan BPA adalah isu mendesak. Dalam kajian ini, sensor elektrokimia berasaskan modifikasi elektrod karbon bercetak skrin (SPCE) dengan karbon titik-kitosan (CD-CS) telah diterokai untuk mengesan bisfenol A (BPA). SPCE yang diubahsuai dengan CD memberikan aplikasi elektro-pemangkin yang baik mempunyai sifat elektronik yang luar biasa dan peningkatan besar dalam kekonduksian elektrik. SPCE yang diubahsuai dengan CDs-CS disediakan dengan menggunakan teknik penyalutan titis. Pengesanan BPA pada sensor SPCE / CDs-CS dikaji dengan menggunakan voltammetri denyutan pembezaan (DPV). Parameter optimum pembangunan sensor seperti kepekatan CS 1% (m/v) dan nisbah CD-CS 1/1 (v/v) dikaji untuk meningkatkan prestasi sensor yang dibangunkan. Hasil kajian menunjukkan bahawa SPCE yang dimodifikasi dengan komposit CD-CS mempunyai ciri elektrokatalitik yang hebat untuk

mengesan BPA dalam julat kepekatan dari 0.4 μM hingga 10 μM dengan kepekaan 0.46 μA/μM (R^2 = 0.9911) dan had pengesanan (LOD) 0.37 μM.

Kata kunci: bisfenol A, karbon titik, kitosan, sensor elektrokimia, alam sekitar

Introduction

Bisphenol A (BPA) or 2,2-bis(4-hydroxyphenyl)propane is a compound predominantly employed as monomers in the synthesis of epoxy resins and polycarbonate (PC). A combination of BPA and other materials is utilised in plastic production. Products, such as packaging materials for food, beverages and wastewater samples and engineering plastics, contain BPA [1]. In 2015, the European Food Safety Authority (EFSA) proposed that the minimum amount of temporary tolerable daily intake (t-TDI) of BPA should not exceed 4 $\mu g\ kg^{-1}$ of body weight per day [2]. Minute amounts of BPA might endanger human health and, at worst, lead to prostate, testicular, or breast cancer, reproductive disorders, including low sperm quality, congenital disabilities, and impaired brain development [3]. Consequently, a rapid, simple, sensitive, and selective BPA detection technique is immediately demanded.

Commercialised techniques of BPA detection include high-performance liquid chromatography (HPLC), gas chromatography coupled with mass spectrometry (GC-MS) [4], and liquid chromatography-tandem mass spectrometry (LC-MS-MS) [5]. Although the methods are highly sensitive and offer low detection limits, the techniques involve several operational steps, making them time-consuming, and the procedure for processing the samples is tedious. Furthermore, the instrumentations required are intricate, expensive, and not convenient for on-site detection [6], hence the demand for a novel analytical technique to determine BPA levels.

The BPA is an electroactive species that contain phenolic hydroxyl groups that could be oxidised on electrode surfaces. Nonetheless, the direct determination of BPA with bare electrodes is infrequent due to its weak signal response, and its oxidation involves a relatively high overpotential [7]. Accordingly, to refine the selectivity and sensitivity of BPA detection, various materials have been recommended for the modification of SPCE, such as ionic liquids [8], enzymes, molecularly imprinted polymers [9], carbon materials, including carbon nanotubes [10], single-walled (SWCNT) [11], multiple-walled (MWCNT) [12], and graphene, [13] and metal nanoparticle-based composites, such as gold nanoparticles (AuNPs) [14] and ferroferric oxide nanoparticles (Fe_3O_4NPs) [15].

Carbon dots (CDs) were accidentally discovered during the electrophoretic purification of single-wall carbon nanotubes (SWCNTs) and were derived from its arc-discharge soot [16]. A novel carbon nanomaterial, the CDs has drawn considerable attention in recent years due to its excellent properties, including low toxicity [17], remarkable conductivity [18], large surface area, and high stability [19]. Recently, methods of synthesising CDs, including hydrothermal ultrasonic, laser ablation, and microwave synthesis, have been studied extensively, where the hydrothermal method was reported to be the most simple, environmentally friendly, and inexpensive [20]. The potential applications of CDs were demonstrated in numerous areas, including biosensing [21], chemical sensing [25–27], bioimaging, electrocatalysis, and photocatalysis [25]. Additionally, CDs have been employed in the electrochemical detection of dopamine [26], L-cysteine [27], and curcumin [28], demonstrating the prospects of applying CDs in the electrochemical field.

Chitosan (CS) is a linear polysaccharide composed of randomly distributed β-(1→4)-linked D-glucosamines (deacetylated units) and N-acetyl-D-glucosamines (acetylated units) [29]. The compound is a biocompatible, hydrophilic, cationic, and biodegradable biopolymer [30]. Consequently, CS could be utilised as a dispersant to form a stable film on the surface of electrodes with several kinds of modified materials due to its great film-forming ability, good adhesion, soaring permeability, nontoxicity, cheapness, and susceptibility to chemical modifications [29]. Furthermore, the compound is also applicable as energy storage materials [31], biosensors [29], and cell imaging [32], as it could

be electrodeposited on the broad surfaces of electrodes or conductive substrates to form coatings or patterns with precise spatial and temporal control [34-35]. Some biological materials (such as glucose oxidase and haemoglobin) and nanoparticles (for example, silver nanoparticles and carbon nanotubes) could also be deposited by employing CS [34], where the CS acts as a immobilisation matrix combined with CDs to modified electrodes and utilised as sensors [26].

In the present study, carbon dots-chitosan (CDs-CS) composite deposited on screen-printed carbon electrode (SPCE) for excellent catalytic performance and conductivity for BPA determination was explored. The nanocomposite offered several advantages, including remarkable conductivity, large surface area, good film-forming capabilities, and high stability. Furthermore, the CDs-CS based electrode provided an excellent electrocatalytic activity toward BPA oxidation, representing a new platform for electrochemical sensor development.

Materials and Methods

Reagents and materials

The BPA, potassium chloride (KCl), potassium ferricyanide ($K_3[Fe(CN)_6]$), citric acid, acetic acid, disodium hydrogen phosphate ($Na_2HPO_4.7H_2O$), and potassium dihydrogen phosphate ($NaH_2PO_4.H_2O$) were purchased from R&M Chemicals company (Petaling Jaya, Selangor, Malaysia). The CS was obtained from Sigma-Aldrich (Petaling Jaya, Selangor, Malaysia), while ethylenediamine was bought from Acros Organics (Geel W.Z.2., Geel, Belgium). In the current study, deionised water (18.2 MΩ·cm at 25 ℃, Milli-Q) was employed throughout the experiments.

The screen-printed carbon electrode (3 mm in diameter) consisted of a reference (AgCl), counter (carbon), and working (carbon) electrodes that were purchased from Rapid Labs Sdn. Bhd. (Bangi, Selangor, Malaysia). Each BPA standard solution was diluted with an 80:20 ethanol-to-water ratio in volume per volume (v/v) into a stock solution of 100 µM BPA. Electrochemical measurements were performed with Model Autolab Type III (Eco Chemie B. V., Netherlands). Cyclic voltammetry (CV) and differential pulse voltammetry (DPV) data analyses were conducted via the Nova 1.11 software.

The synthesis of CDs and preparation of CS

The hydrothermal method was employed to synthesise the carbon dots in the present study [35]. First, the citric acid (3.0 g) and ethylenediamine (1.875 mL) were dissolved in deionised distilled water (ddH_2O, 30 mL). The solution was then transferred to a reactor and heated in an oven for five hours at 150℃. Subsequently, the clear brownish solution formed was stored at 4°C and wrapped with aluminium foil to maintain a dark condition. The CS solution (1%, w/v) was then prepared by dissolving 0.5 g CS powder in 1% (w/v) aqueous acetic acid solution (50 mL). The mixture was continuously stirred vigorously overnight.

The preparation of BPA stock solution and supporting electrolyte

A 100 µM BPA was prepared by adding 228 mg of BPA into 80% ethanol and 20% ddH_2O in a 100 mL volumetric flask. The $K_3[Fe(CN)_6]$ (5 mM) and 0.1 M KCl mixture was utilised as a supporting electrolyte, where 0.1646 g $K_3[Fe(CN)_6]$ and 0.7455 g KCl were dissolved in 100 mL of ddH_2O in a 100 mL volumetric flask. Subsequently, a phosphate buffer solution (PBS) was prepared by adding disodium hydrogen phosphate ($Na_2HPO_4.7H_2O$) (2.0 g) and potassium dihydrogen phosphate ($NaH_2PO_4.H_2O$) (0.339 g) into 80 mL of deionised water in a 100 mL conical flask. Hydrochloric acid and sodium hydroxide were employed to adjust the solution to the desired pH.

Modification of SPCE

A mixture (7 µL) of 1:1 (v/v) CDs solution to chitosan (1%, w/v) was spread on the surface of the SPCE before being dried for approximately five hours at room temperature. The modified electrode is then denoted as the CDs-CS/SPCE.

The electrochemical method

The CV analysis was implemented within the −0.4 and 0.65 V potential range at a 100 mV/s scan rate for five cycles to evaluate the performance of the modified SPCE by employing 5 mM $K_3[Fe(CN)_6]$ and 0.1 M KCl. A redox probe consisting of $K_3[Fe(CN)_6]$ was employed to evaluate the electrochemical behaviour of the SPCE

post-modification with CDs-CS [36]. Differential pulse voltammetry (DPV) measurements were recorded within the 0.1 to 0.8 V potential range with PBS (pH 7.4). The assessment parameters were 0.2 V deposition potential, 60 s deposition time, and 10 mV/s scan rate.

Results and Discussion

Electrochemical behaviour of the modified electrodes

The electrochemical behaviours evaluation of the modified electrodes was performed with CV analysis. Figure 1 illustrates cyclic voltammograms of the bare SPCE, CS/SPCE, CDs/SPCE, and CDs-CS/SPCE electrodes. The pair of redox peaks exhibited by the bare SPCE demonstrated its electrochemical characteristics, which provided a rapid location of redox potentials of the electroactive species.

The modified CDs/SPCE recorded enhanced redox peak current at a calculated enhancement factor of 1.85, which might result from the wider active surface area and good electron transfer, as CDs are good conducting material. The electrochemical response of the CS-modified electrode documented a lower redox peak signal than the bare SPCE, indicating that the CS/SPCE was non-electroactive in the selected scanning region [37]. The CDs-CS/SPCE nanocomposites demonstrated synergistic electron transfer, as evidenced by the significant redox peak current signal enhancement at a factor of 4.17 due to the presence of CDs-CSs on the SPCE surface. The CDs were excellent conductors and more stable when CS was employed as a fixative agent on the electrode that opposed the easy dissolution of the CDs from the surfaces of the SPCE into the PBS solution [16]. The oxidation (*Epa*) and reduction (*Epc*) peak potentials were recorded at 0.31 and −0.04 V.

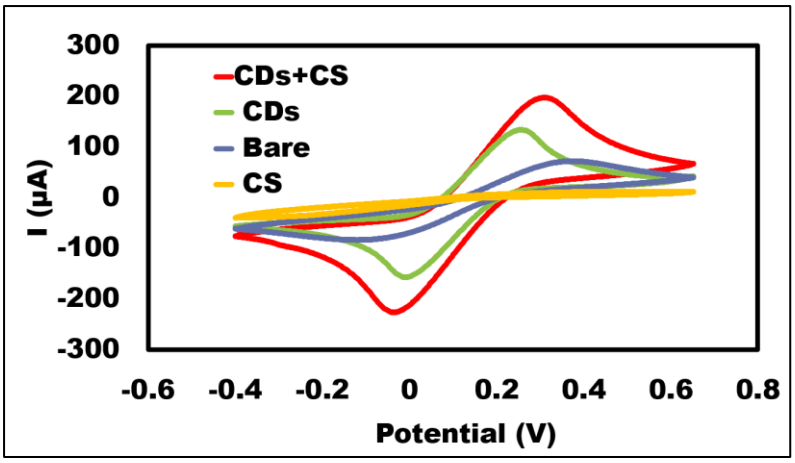


Figure 1. The cyclic voltammograms of the modified electrodes in 5 mM $K_3[Fe(CN)_6]$/0.1M KCl within the −0.4V to 0.65V range potential at 100 mV/s scan rate

Optimisation: The influence of CS concentration (%) and volume and the CDs to CS ratio on the SPCE

The current study determined the optimised parameters for modifying the SPCE surfaces through CV. The optimum percentage of CS mixed with CDs, which could affect the performance of the CDs-CS/SPCE sensor, was investigated. Varying concentrations of CS, 0.1 to 2.0% (w/v), were employed. The current response increased from 0.1 to 1%, and the optimum current response was observed at 1% (w/v) CS. At concentrations exceeding 1%, decreased current response was recorded [see Figure 2(a)]. The observations might be due to the increased resistance at the modified electrode surfaces with higher CS percentages [38]. Consequently, the present study employed 1% (w/v) CS concentration as the ideal percentage for the CDs-CS composite immobilisation onto the sensor.

The amount of CDs-CS composite immobilised on the surface of the SPCE affects the sensitivity of the developed sensor. Accordingly, different CDs-CS volumes (1 to 11 µL) were employed in the present study. The oxidation peak current was observed ascending with an increasing CD-CS volume up to 7 µL before slightly reducing [see Figure 2(b)]. The phenomenon might result from the thicker nanocomposite film formed with larger volumes of CDs-CS, which could obstruct the transfer of electrons and mass on the surface of the SPCE [38]. Consequently, the current study applied 7 µL CDs-CS in the fabrication of the sensor.

In the present study, the ratio of CDs to CS was varied (1:0.1, 1:0.5, 1:1, 1:1.5, and 1:2 v/v) to evaluate the optimum volume ratio of the CDs-CS composite. Figure 2(c) demonstrates that the oxidation current response increased from 1:0.1 to 1:1 before gradually dropping as the ratio rose to 1:2. The results could be due to the high volume of CS, which hindered electron transfer. Accordingly, a 1:1 (v/v) CDs to CS volume ratio was selected to fabricate the sensor developed.

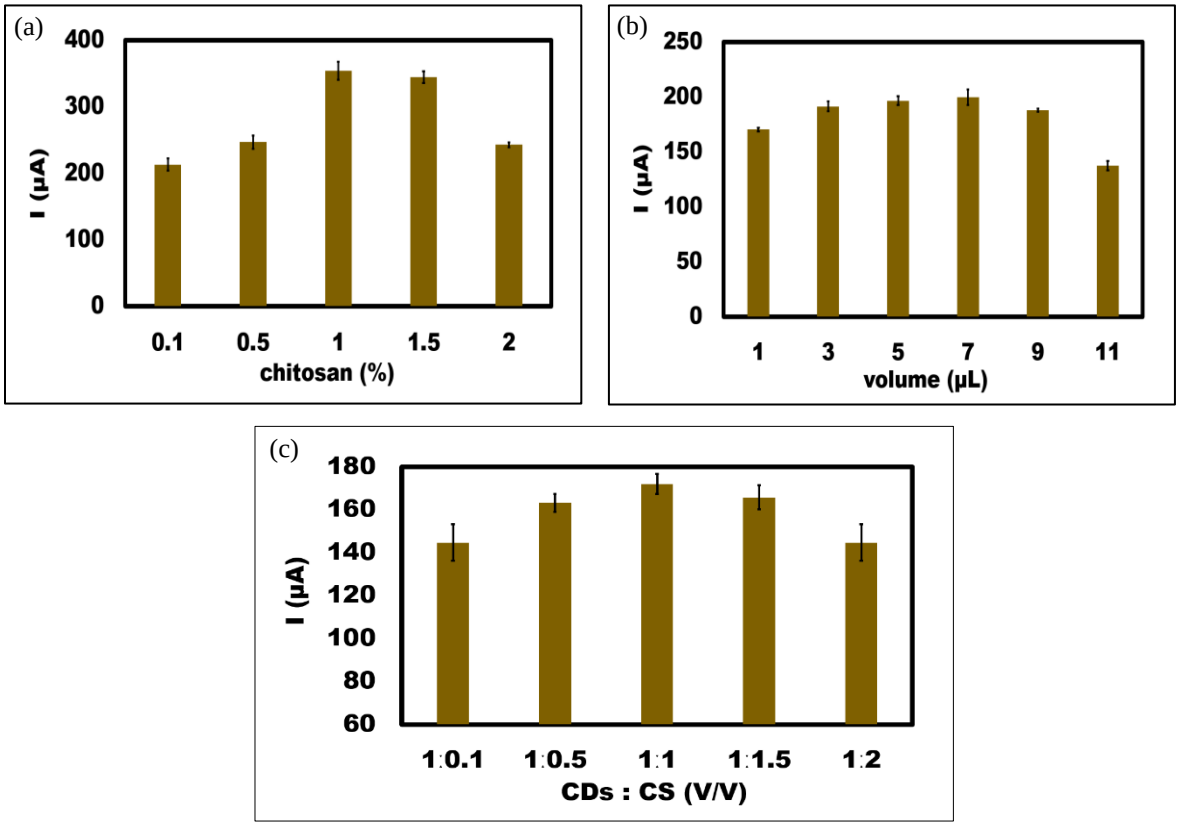


Figure 2. The influence of (a) CS concentration (%, w/v), (b) volume of CDs-CS (µL), and (c) CDs to CS (v/v) ratio mixed drop casted onto the SPCE in 5 mM $K_3[Fe(CN)_6]$/0.1 M KCl at 100 mV/s scan rate

The effects of the supporting electrolyte

Supporting electrolytes play a significant factor in electrochemical studies for detecting analytes. Hydrochloric acid-potassium chloride buffer (HCl-KCl) (pH 3), PBS (pH 7.4), and carbonate-bicarbonate buffer (CBBS) (pH 9) solutions were employed as the supporting electrolyte in the current study (see Figure 3). The buffers were selected due to their different pHs since BPA could be sustained at pHs 3-9 [39]. Nonetheless, numerous reports documented pH 7.4 as the ideal pH to determine BPA levels. The phenomenon might be due to the present form of BPA being affected

by the pH of the supporting electrolyte. In the present study, as 1 µM of BPA was added to PBS (pH 7.4), a 4.0 µA oxidation current was recorded, while HCl-KCl buffer and CBBS documented 2.14 and 2.62 µA, respectively. Consequently, PBS was selected for further analyses.

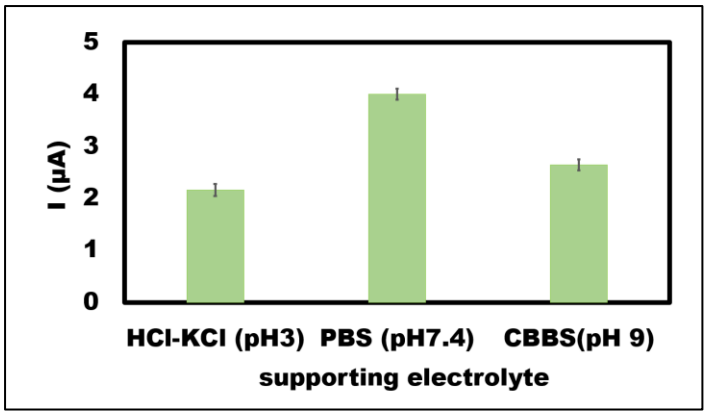


Figure 3. The effects of various supporting electrolytes on the sensor signals in the presence of 1 µM BPA

The effects of pH

Another vital criterion for evaluating the performance of sensors in detecting BPA is pH, and in the current study, the effects were assessed within the 6–8 pH range. The PBS was utilised as the suitable pH to sustain the BPA was reported to be slightly acidic to slightly basic [39]. The anodic peak (E_{pa}) and anodic current (I_{pa}) potentials of 1 µM BPA were examined. The I_{pa} increased from pH 6 to 7 and reached the highest value at pH 7.4. The I_{pa} value then gradually decreased as the pH rose to 8 [see Figure 4(a)]. The CDs could absorb the non-dissociated BPA more easily than the dissociated form in a neutral pH environment with the optimal pH value, which was lower than the pKa of BPA (pKa = 9.73) [35]. Moreover, the results agreed with previous reports that recorded pH 7.4 as the best pH for determining BPA levels [40–41]. Consequently, pH 7.4 was chosen as the optimum pH since it recorded the highest response from the sensor.

Figure 4(b) demonstrates the BPA E_{pa} shifting to a more negative value as the pH was increased due to deprotonation of BPA towards CDs-CS/SPCE [42]. At lower pHs, the H+ ions of the analyte tend to compete with the excess H+ ions originating from the supporting electrolyte. Consequently, a driving force (energy) is required for the BPA to be oxidised, resulting in the peak occurring at higher potentials. The equation Epa (V) = −0.0618 pH + 0.9032, R^2 = 0.9724 illustrates that the E_{pa} and pH possessed a better linearity with a high correlation coefficient. A shift of typically 61.8 mV per pH unit was very close to the Nernst theoretical value, which is 59.10 mV pH^{-1}. The value revealed that the deprotonation of BPA towards CDs-CS/SPCE occurred [42], revealing that equal numbers of proton and electron were present on the electrode that resulted from the electrochemical oxidation of BPA [43]. Accordingly, PBS at pH 7.4 was selected to determine BPA levels in the present study.

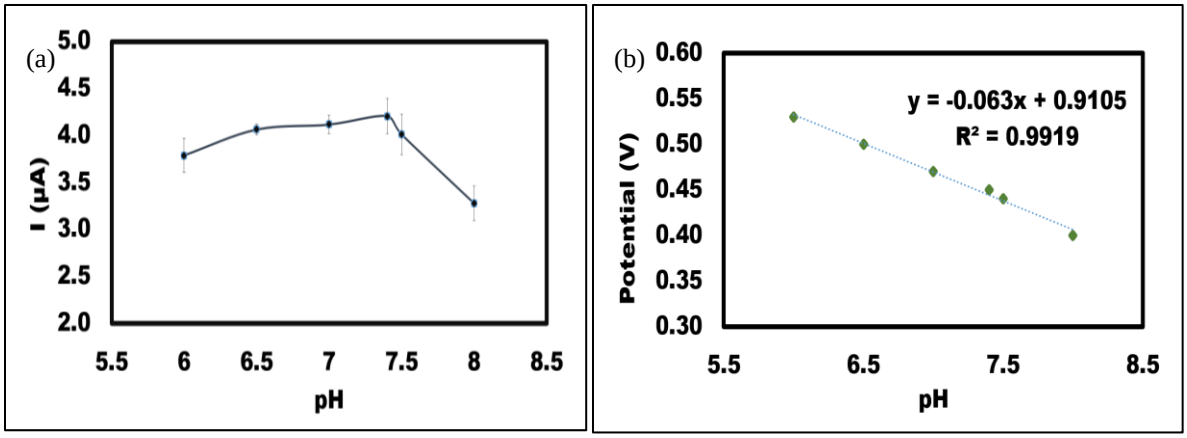


Figure 4. The effects of pH on the (a) oxidation peak current and (b) potential response of 1 µM BPA determined via DPV at 10 mV s^{-1} scan rate

The effects of deposition time and potential

Deposition time is one of the essential factors in improving BPA detection. The data measures the optimum period for the BPA to be deposited onto the surface of the CDs-CS/SPCE sensor. The DPV was employed to evaluate the factor in the presence of 1 µM BPA in PBS (pH 7.4) within a 20-140 s time frame. Figure 5(a) demonstrates the increment of the oxidation peak current at 60 s. At more than 60 s, the oxidation peak current started to descend due to the saturation of the active surface site on the electrode surfaces with BPA, which lessened the electron transfer rate between them. Consequently, 60 s was selected as the best deposition time to develop the sensor in the present study.

Figure 5(b) portrays the relationship between the BPA oxidation peak current signal and deposition potential. As the potential elevated from 0.1 to 0.2 V, the BPA oxidation peak current gradually increased. Conversely, the BPA deposited on the electrode surfaces decreased at deposition potentials exceeding 0.5 V. The phenomenon could be related to saturated adsorption of BPA on the SPCE surfaces. Accordingly, 0.2 V was selected as the optimal deposition potential for the present study.

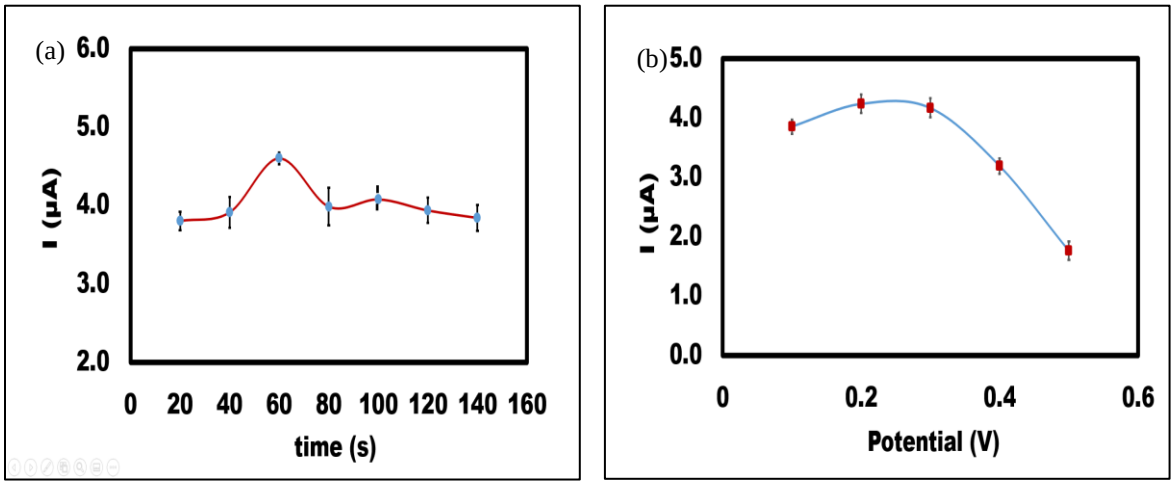


Figure 5. The effects of deposition (a) time and (b) potential on the 1 µM BPA oxidation peak current in PBS (pH 7.4)

Electrochemically active surface area

In the current study, the scan rate employed was within the 10 to 100 mV/s range in $[Fe(CN)_6]^{3-/4-}$ as the probe via the CV technique. By exploring the relationship between the anodic current response and the square root of scan rate, the electroactive surface area of the bare SPCE and the modified CDs-CS/SPCE was determined with the Randles-Sevcik equation (Eq. 1).

$$Ip = (2.69 \times 10^5)\, n^{3/2} A.D^{1/2} V^{1/2} Co \quad (1)$$

where Ip is the maximum current, n is the number of electrons transferred (n = 1), (A) is the electroactive surface area of the electrode (cm^2), D is 7.6×10^{-6} $cm^2 s^{-1}$, which is the diffusion coefficient of $[Fe(CN)_6]^{3-/4-}$ solution, Co is the concentration of $[Fe(CN)_6]^{3-/4-}$, and V is the scan rate (mV/s) [44].

Based on Figure 6(a), the current response constantly increased and shifted towards positive potential at higher scan rates (mV/s). The regression equations, Epa, obtained for the bare SPCE and modified SPCE were slope = 5.778, R^2 = 0.9627 and slope = 21.956, R^2 = 0.9987, respectively. Consequently, the calculated electroactive surface area for the bare SPCE was 0.0016 cm^2, while the CDs-CS/SPCE recorded 0.0049 cm^2, which was approximately 3-fold higher.

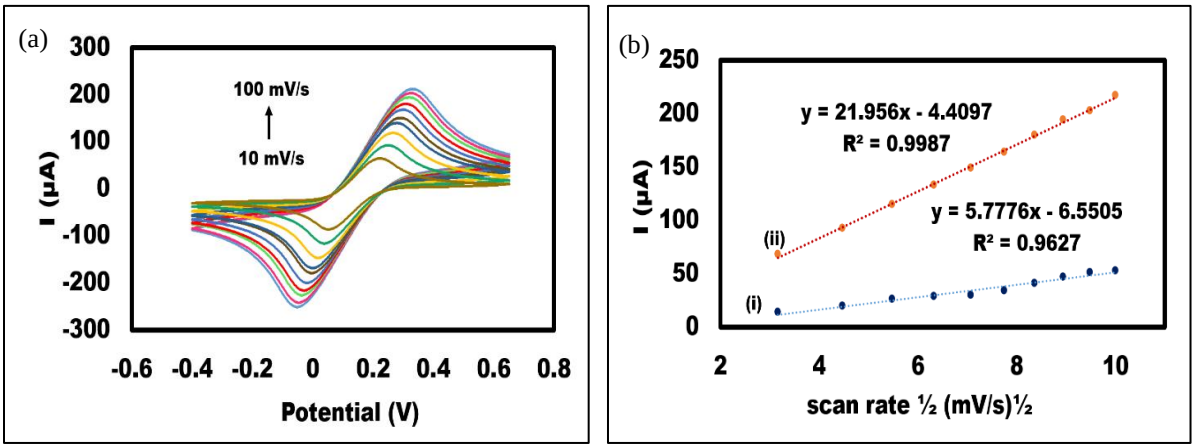


Figure 6. The (a) cyclic voltammograms of the modified electrode for scan rates between 10 and 100mV/s and (b) oxidation current response towards the square root of scan rate for the (i) bare and (ii) CDs-CS/SPCE electrodes

The electrochemical behaviour of BPA

Figure 7(a) illustrates the cyclic voltammograms of the single oxidation peak current of BPA (1 µM) in PBS (0.1 M, pH 7.4). The absence of reduction peak current indicated the irreversible process of BPA determination [45]. Nonetheless, as the cycle increased, the anodic current of BPA significantly decreased. The behaviour could be due to the formation of polymeric products by BPA, which blocked the surfaces of the electrode.

The electrochemical responses of BPA at varying modification conditions of the SPCE were also evaluated through DPV [see Figure 7(b)], consisting of 1 µM BPA in PBS (pH 7.4) and within the +0.2 to +0.7 V potential range. The oxidation peak was observed at the +0.45 V potential for the CDs-CS/SPCE, which was in agreement with previous studies that documented an anodic peak current of 4.23 µA. The BPA electrochemical response for the bare SPCE, CS/SPCE, and CDs/SPCE were observed at 0.48, 0.45, and 0.43 V potentials with anodic peak currents of 0.37, 2.37, and 2.94 µA, respectively.

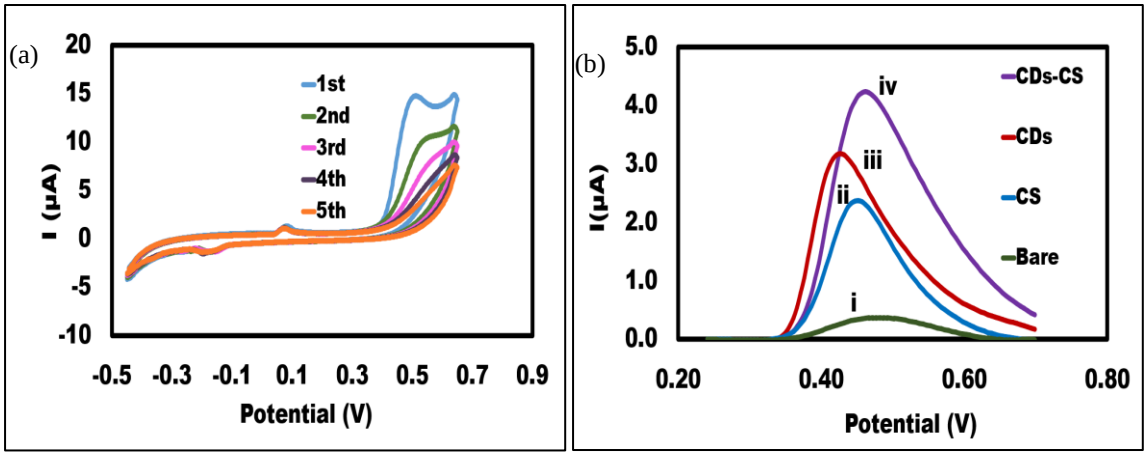


Figure 7. The (a) cyclic voltammograms of different cycles of CDs-CS/SPCE at 100 mV/s scan rate and (b) differential pulse voltammograms of the (i) bare (ii) CS (iii) CDs, and (iv) CDs-CS electrodes in 1 µM BPA with 0.1 M pH 7.4 PBS

The CDs-CS/SPCE sensor recorded an absolute-defined oxidation peak at the +0.45 V potential in DPV. Under optimised conditions, the behaviour of the electrochemical response of the sensor towards BPA in PBS (0.1 M, pH 7.4) as a supporting electrolyte was investigated. Figure 8 illustrates the oxidation peak current observed in varying concentrations of BPA, 0.4 µM to 10 µM, with a sensitivity of 0.4606 µA/µM (R^2 = 0.9911) and a limit of detection (LOD) of 0.37 µM.

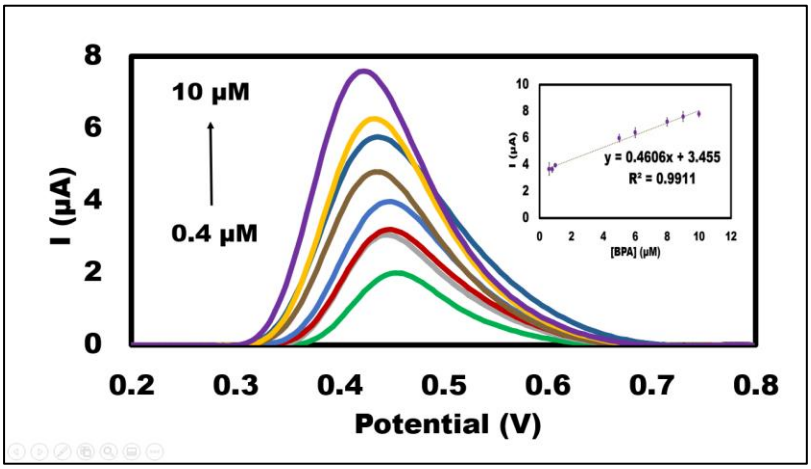


Figure 8. The differential pulse voltammograms of oxidation peak current in varying BPA concentrations (0.4– 10 µM) in PBS (0.1 M, pH 7.4) at 10 mV/s scan rate within 0.2 and 0.8 V potential range versus AgCl. *Note:* The inset diagram denotes the correlation between the current response (µA) and BPA concentration (µM)

Reproducibility, stability, and selectivity of the CDs-CS/SPCE electrodes

The reproducibility of the CDs-CS/SPCE sensor was examined with fabricated sensors prepared independently within similar parameters and evaluated with 1 µM BPA in PBS (pH 7.4). The relative standard deviation (RSD) was 3.66 % (n = 15), indicating good reproducibility. The developed sensor was stored in a

dark box at room temperature for the stability study. The performance of the sensor was evaluated every week in the presence of 1 µM of BPA in PBS (0.1 M, pH 7.4). The sensor retained its performance. Nevertheless, after one, two, and three weeks, the performance decreased to 91.3, 89.5, and 79.5% of its initial response after a month of storage. The selectivity of the developed sensor was also evaluated. Figure 9 demonstrates that the sensor recorded no significant current response towards phenol, 2,4-dinitrophenol, 4-chlorophenol, K^+,Cu^{2+}, Cl^-, and SO_4^{2-}. The compounds were employed at a concentration 10-fold higher (10 µM) than the BPA, proving that the developed sensor was selective towards BPA.

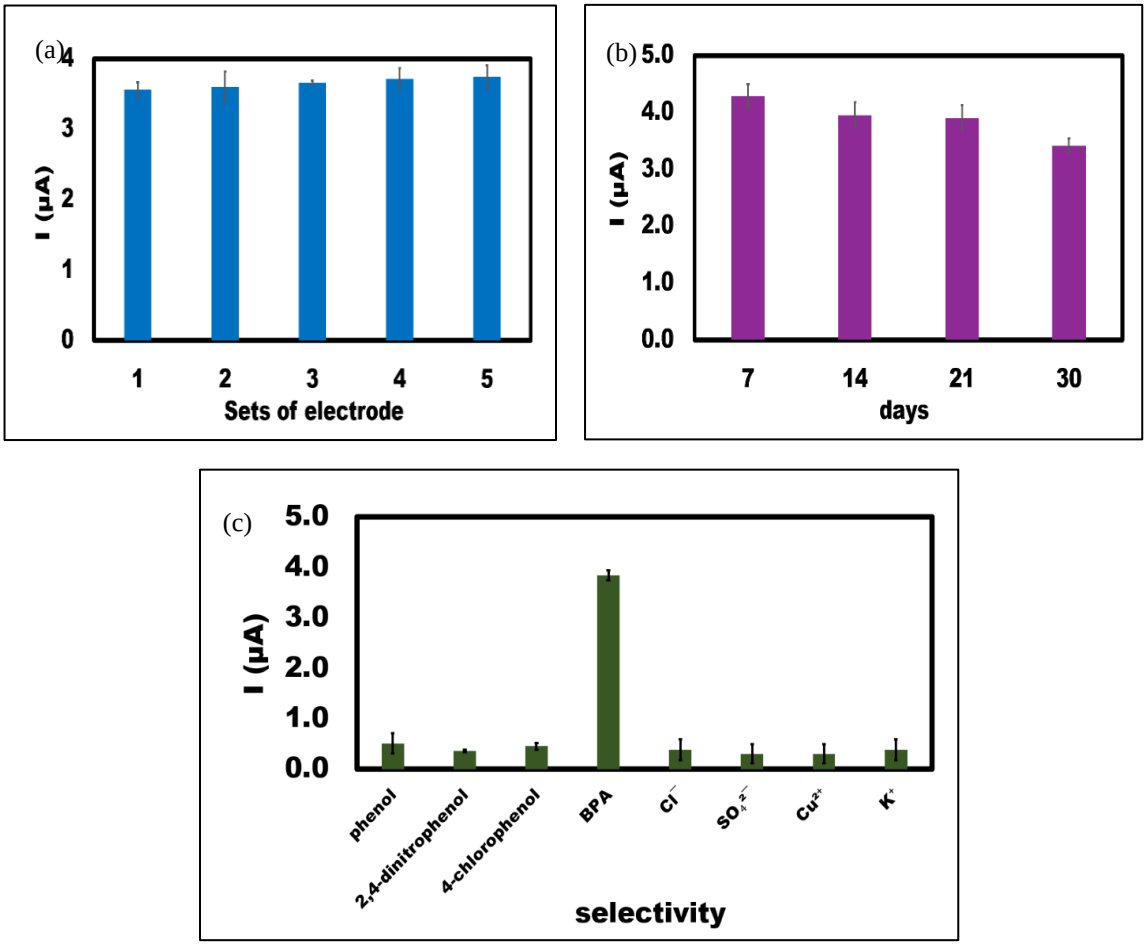


Figure 9. The current responses of (a) different sets of electrodes utilised in the reproducibility study, (b) electrodes analysed on different days in the stability study, and (c) various phenols and ions tested in PBS (pH 7.4) for the selectivity study

Conclusion

The present study successfully fabricated SPCE with CDs-CS to develop electrodes with good electrocatalytic performance to detect BPA. The CDs-CS/SPCE-based sensor exhibited good analytical performance in determining BPA within the 0.4 to 10 µM concentration range, with a sensitivity of 0.46 µA/µM (R^2 = 0.9911) and LOD 0.37 µM. The developed sensor also provided a large surface area for BPA adsorption and good conductivity and selectivity. Furthermore, the sensor demonstrated potential

applications for the sensitive and rapid determinations of BPA levels in aqueous systems.

Acknowledgement

The authors would like to express gratitude to Universiti Putra Malaysia for providing sponsorship under the Putra Grant (GPIPB/2016/9515403).

References

1. Santana, E. R., de Lima, C. A., Piovesan, J. V. and Spinelli, A. (2017). An original ferroferric oxide and gold nanoparticles-modified glassy carbon electrode for the determination of bisphenol A. *Sensors and Actuators B: Chemical*, 240: 487-496.
2. Shi, R., Yuan, X., Liu, A., Xu, M. and Zhao, Z. (2018). Determination of bisphenol a in beverages by an electrochemical sensor based on Rh_2O_3/reduced graphene oxide composites. *Applied Sciences*, 8(12): 2535.
3. Watabe, Y., Kondo, T., Morita, M., Tanaka, N., Haginaka, J. and Hosoya, K. (2004). Determination of bisphenol A in environmental water at ultra-low level by high-performance liquid chromatography with an effective on-line pretreatment device. *Journal of Chromatography A,* 1032(1-2): 45-49.
4. Cunha, S. C., Pena, A. and Fernandes, J. O. (2015). Dispersive liquid–liquid microextraction followed by microwave-assisted silylation and gas chromatography-mass spectrometry analysis for simultaneous trace quantification of bisphenol A and 13 ultraviolet filters in wastewaters. *Journal of Chromatography A*, 1414: 10-21.
5. ter Halle, A., Claparols, C., Garrigues, J. C., Franceschi-Messant, S. and Perez, E. (2015). Development of an extraction method based on new porous organogel materials coupled with liquid chromatography–mass spectrometry for the rapid quantification of bisphenol A in urine. *Journal of Chromatography A*, 1414: 1-9.
6. Yin, H., Zhou, Y., Xu, J., Ai, S., Cui, L. and Zhu, L. (2010). Amperometric biosensor based on tyrosinase immobilized onto multiwalled carbon nanotubes-cobalt phthalocyanine-silk fibroin film and its application to determine bisphenol A. *Analytica Chimica Acta,* 659(1-2): 144-150.
7. Farajzadeh, M. A. and Mogaddam, M. R. A. (2012). Air-assisted liquid–liquid microextraction method as a novel microextraction technique; Application in extraction and preconcentration of phthalate esters in aqueous sample followed by gas chromatography–flame ionization detection. *Analytica Chimica Acta*, 728: 31-38.
8. Nikahd, B. and Khalilzadeh, M. A. (2016). Liquid phase determination of bisphenol A in food samples using novel nanostructure ionic liquid modified sensor. *Journal of Molecular Liquids,* 215: 253-257.
9. Wang, J. Y., Su, Y. L., Wu, B. H. and Cheng, S. H. (2016). Reusable electrochemical sensor for bisphenol A based on ionic liquid functionalized conducting polymer platform. *Talanta,* 147: 103-110.
10. Goulart, L. A., de Moraes, F. C. and Mascaro, L. H. (2016). Influence of the different carbon nanotubes on the development of electrochemical sensors for bisphenol A. *Materials Science and Engineering: C*, 58: 768-773.
11. Moraes, F. C., Silva, T. A., Cesarino, I. and Machado, S. A. (2013). Effect of the surface organization with carbon nanotubes on the electrochemical detection of bisphenol A. *Sensors and Actuators B: Chemical*, 177: 14-18.
12. Li, Y., Gao, Y., Cao, Y. and Li, H. (2012). Electrochemical sensor for bisphenol A determination based on MWCNT/melamine complex modified GCE. *Sensors and Actuators B: Chemical*, 171: 726-733.
13. Fan, H., Li, Y., Wu, D., Ma, H., Mao, K., Fan, D., ... and Wei, Q. (2012). Electrochemical bisphenol A sensor based on N-doped graphene sheets. *Analytica Chimica Acta*, 711: 24-28.
14. Niu, X., Yang, W., Wang, G., Ren, J., Guo, H. and Gao, J. (2013). A novel electrochemical sensor of bisphenol A based on stacked graphene nanofibers/gold nanoparticles composite modified glassy carbon electrode. *Electrochimica Acta*, 98: 167-175.

15. Zhang, Y., Cheng, Y., Zhou, Y., Li, B., Gu, W., Shi, X. and Xian, Y. (2013). Electrochemical sensor for bisphenol A based on magnetic nanoparticles decorated reduced graphene oxide. *Talanta*, 107: 211-218.
16. Yu, L., Yue, X., Yang, R., Jing, S. and Qu, L. (2016). A sensitive and low toxicity electrochemical sensor for 2, 4-dichlorophenol based on the nanocomposite of carbon dots, hexadecyltrimethyl ammonium bromide and chitosan. *Sensors and Actuators B: Chemical*, 224: 241-247.
17. Zou, Y., Yan, F., Zheng, T., Shi, D., Sun, F., Yang, N. and Chen, L. (2015). Highly luminescent organosilane-functionalized carbon dots as a nanosensor for sensitive and selective detection of quercetin in aqueous solution. *Talanta*, 135:145-148.
18. Zuo, P., Lu, X., Sun, Z., Guo, Y. and He, H. (2016). A review on syntheses, properties, characterization and bioanalytical applications of fluorescent carbon dots. *Microchimica Acta*, 183(2): 519-542.
19. Baruah, U., Gogoi, N., Majumdar, G. and Chowdhury, D. (2015). β-Cyclodextrin and calix [4] arene-25, 26, 27, 28-tetrol capped carbon dots for selective and sensitive detection of fluoride. *Carbohydrate Polymers*, 117: 377-383.
20. Wei, Y., Zhang, D., Fang, Y., Wang, H., Liu, Y., Xu, Z., ... and Guo, Y. (2019). Detection of ascorbic acid using green synthesized carbon quantum dots. *Journal of Sensors*, 2019.
21. Hou, J., Dong, J., Zhu, H., Teng, X., Ai, S. and Mang, M. (2015). A simple and sensitive fluorescent sensor for methyl parathion based on l-tyrosine methyl ester functionalized carbon dots. *Biosensors and Bioelectronics*, 68: 20-26.
22. Wu, L., Ma, C., Zheng, X., Liu, H. and Yu, J. (2015). based electrochemiluminescence origami device for protein detection using assembled cascade DNA–carbon dots nanotags based on rolling circle amplification. *Biosensors and Bioelectronics*, 68: 413-420.
23. Qian, Z. S., Chai, L. J., Huang, Y. Y., Tang, C., Shen, J. J., Chen, J. R. and Feng, H. (2015). A real-time fluorescent assay for the detection of alkaline phosphatase activity based on carbon quantum dots. *Biosensors and Bioelectronics*, 68: 675-680.
24. Song, J., Zhao, L., Wang, Y., Xue, Y., Deng, Y., Zhao, X. and Li, Q. (2018). Carbon quantum dots prepared with chitosan for synthesis of CQDs/AuNPs for iodine ions detection. *Nanomaterials*, 8(12): 1043.
25. Abdullah, J., Ahmad, M., Heng, L. Y., Karuppiah, N. and Sidek, H. (2006). Stacked films immobilization of MBTH in nafion/sol-gel silicate and horseradish peroxidase in chitosan for the determination of phenolic compounds. *Analytical and Bioanalytical Chemistry*, 386(5): 1285-1292.
26. Yu, L., Yue, X., Yang, R., Jing, S. and Qu, L. (2016). A sensitive and low toxicity electrochemical sensor for 2, 4-dichlorophenol based on the nanocomposite of carbon dots, hexadecyltrimethyl ammonium bromide and chitosan. *Sensors and Actuators B: Chemical*, 224: 241-247.
27. Jiang, Y., Han, Q., Jin, C., Zhang, J. and Wang, B. (2015). A fluorescence turn-off chemosensor based on N-doped carbon quantum dots for detection of Fe^{3+} in aqueous solution. *Materials Letters*, 141: 366-368.
28. Kou, L. J., Liang, R. N., Wang, X. W., Chen, Y. and Qin, W. (2013). Potentiometric sensor for determination of neutral bisphenol A using a molecularly imprinted polymer as a receptor. *Analytical and Bioanalytical Chemistry*, 405(14): 4931-4936.
29. Guo, W., Pi, F., Zhang, H., Sun, J., Zhang, Y. and Sun, X. (2017). A novel molecularly imprinted electrochemical sensor modified with carbon dots, chitosan, gold nanoparticles for the determination of patulin. *Biosensors and Bioelectronics*, 98: 299-304.
30. Omidi, M., Yadegari, A. and Tayebi, L. (2017). Wound dressing application of pH-sensitive carbon dots/chitosan hydrogel. *RSC Advances*, 7(18): 10638-10649.
31. Hassan, S., Suzuki, M. and Abd El-Moneim, A. (2014). Synthesis of MnO_2–chitosan nanocomposite by one-step electrodeposition for electrochemical energy storage application. *Journal of Power Sources*, 246: 68-73.

32. Chowdhuri, A. R., Tripathy, S., Haldar, C., Roy, S. and Sahu, S. K. (2015). Single step synthesis of carbon dot embedded chitosan nanoparticles for cell imaging and hydrophobic drug delivery. *Journal of Materials Chemistry B*, 3(47), 9122-9131.
33. Liu, Y., Li, J., Tschirhart, T., Terrell, J. L., Kim, E., Tsao, C. Y., ... and Payne, G. F. (2017). Connecting biology to electronics: Molecular communication via redox modality. *Advanced Healthcare Materials*, 6(24): 1700789.
34. Wang, Y. H., Yu, C. M., Gu, H. Y. and Tu, Y. F. (2016). The hemoglobin-modified electrode with chitosan/Fe3O4 nanocomposite for the detection of trichloroacetic acid. *Journal of Solid State Electrochemistry*, 20(5): 1337-1344.
35. Omar, N. A. S., Irmawati, R., Fen, Y. W., Abdullah, J., Daud, N. F. M., Daniyal, W. M. E. M. M. and Mahdi, M. A. (2021). A sensing approach for manganese ion detection by carbon dots nanocomposite thin film-based surface plasmon resonance sensor. *Optik*, 243: 167435.
36. Muhammad, N., Abdullah, J., Sulaiman, Y. and Ngee, L. H. (2017). Electrochemical determination of 3-nitrophenol with a reduced graphene oxide modified screen printed carbon electrode. *Sensor Letters*, 15(2): 187-195.
37. Yin, H., Ma, Q., Zhou, Y., Ai, S. and Zhu, L. (2010). Electrochemical behavior and voltammetric determination of 4-aminophenol based on graphene–chitosan composite film modified glassy carbon electrode. *Electrochimica Acta*, 55(23): 7102-7108.
38. Fartas, F. M., Abdullah, J., Yusof, N. A., Sulaiman, Y. and Saiman, M. I. (2017). Biosensor based on tyrosinase immobilized on graphene-decorated gold nanoparticle/chitosan for phenolic detection in aqueous. *Sensors*, 17(5): 1132.
39. Rekos, K., Kampouraki, Z. C., Sarafidis, C., Samanidou, V. and Deliyanni, E. (2019). Graphene oxide based magnetic nanocomposites with polymers as effective bisphenol–a nanoadsorbents. *Materials*, 12(12): 1987.
40. Ashraf, G., Asif, M., Aziz, A., Wang, Z., Qiu, X., Huang, Q., ... and Liu, H. (2019). Nanocomposites consisting of copper and copper oxide incorporated into MoS_4 nanostructures for sensitive voltammetric determination of bisphenol A. *Microchimica Acta*, 186(6): 1-9.
41. Vikas, V., Swamy, B. K., Viswanath, C. C. and Naik, T. S. (2017). Electrochemical studies of bisphenol-A at sodium alpha olefin sulfonate modified carbon paste electrode: A voltammetric study. *Analytical & Bioanalytical Electrochemistry*, 9(2): 164-173.
42. Hou, C., Tang, W., Zhang, C., Wang, Y. and Zhu, N. (2014). A novel and sensitive electrochemical sensor for bisphenol A determination based on carbon black supporting ferroferric oxide nanoparticles. *Electrochimica Acta*, 144: 324-331.
43. Ulubay Karabiberoğlu, Ş. (2019). Sensitive voltammetric determination of bisphenol A based on a glassy carbon electrode modified with copper oxide-zinc oxide decorated on graphene oxide. *Electroanalysis*, 31(1): 91-102.
44. Yang, J. and Gunasekaran, S. (2013). Electrochemically reduced graphene oxide sheets for use in high performance supercapacitors. *Carbon*, 51: 36-44.
45. Pereira, G. F., Andrade, L. S., Rocha-Filho, R. C., Bocchi, N. and Biaggio, S. R. (2012). Electrochemical determination of bisphenol A using a boron-doped diamond electrode. *Electrochimica Acta*, 82: 3-8.

Malaysian Journal of Analytical Sciences (MJAS)
Published by Malaysian Analytical Sciences Society

THE APPLICATION OF ELECTRONIC NOSE COUPLED WITH 80:20 K-NEAREST NEIGHBORS CLASSIFICATION TECHNIQUE FOR AGARWOOD OIL QUALITY INDEX ESTABLISHMENT

(Kombinasi Aplikasi Hidung Elektronik Bersama Teknik Klasifikasi 80:20 K-Nearest Neighbors Untuk Pembangunan Indek Kualiti Minyak Gaharu)

Sahrim Lias[1, 2], Abd Majid Jalil[2], Mailina Jamil[2], Mohd Shafik Yuzman Tolmanan[2], Nurlaila Ismail[1], Mohd Nasir Taib[1]

[1] *Faculty of Electrical Engineering,*
University Teknologi Mara (UiTM), Shah Alam 40000, Selangor, Malaysia
[2] *Natural Products Division,*
Forest Research Institute Malaysia (FRIM), Kepong 52109, Selangor, Malaysia

**Corresponding author: sahrim@frim.gov.my*

Received: 3 February 2022; Accepted: 19 May 2022; Published: 27 December 2022

Abstract

Agarwood oil is highly valued with numerous uses and benefits to the user. However, traditional agarwood grading techniques are subjective, time consuming and labor intensive with poorly reproducible results, in our study, a commercial Fox4000 electronic nose (EN) with AlphaSOFT software was evaluated as a substitute for human nose sniff assessment. Eight pure agarwood oil samples were used: the JBD sample that was selected as the initial high-grade reference sample based on previous research, and seven samples new to the FRIM collection. All samples were subjected to the EN tests and the seven new samples compared with the JBD sample using the non-parametric Wilcoxon's signed-rank test. The REG sample that was closest in aroma profile to JBD was then chosen as the high-grade reference sample for subsequent tests. Varying volumes of REG were blended with gurjun balsam and sandalwood pure oils to produce nineteen blended samples containing increasing percentages of REG. The 19 samples were then used in the EN tests for database establishment. All 19 blended samples were subjected to the EN tests and resulting data transformed using a z-score scale to generate an Agarwood Oil Quality Index (AOQI) that was classified into three levels based on percentage volume of agarwood oil in the oil blend. The EN significant sensor selection process was conducted using Spearman's rho correlation (SRC) and stepwise multi linear regression (SMLR). Finally, the 80:20 k-Nearest Neighbors (kNN) classifier was used to evaluate the AOQI model with the confusion-matrix based performance measure (CMBPM) as the classifier performance evaluator. The results showed SRC with 11 selected sensors outperformed SMLR with 80:20 k-NN test accuracy equal to 89.5%.

Keywords: agarwood oil grading, electronic nose, 80:20 k-NN classifier

Abstrak

Minyak gaharu dikenali mempunyai harga yang tinggi dengan pelbagai kegunaan dan manfaat kepada pengguna. Walau bagaima napun, teknik penggredan gaharu secara tradisional adalah sangat terhad dari segi subjektiviti, kebolehulangan yang rendah, peng gunaan masa, dankos buruh yang mahal. Dalam kajian ini, Hidung Elektronik (EN) Fox4000 komersial dengan perisian AlphaS OFT telah digunakan bagi menggantikan penilaian menghidu menggunakan hidung manusia. Lapan sampel minyak gaharu tulen telah digunakan. Sampel JBD telah dipilih sebagai sampel rujukan bergred tinggi berdasarkan kajian terdahulu . Semua sampel te rtakluk kepada eksperimen EN dan dibandingkan dengan sampel JBD menggunakan ujian peringkat-bertanda Wilcoxon bukan pa rametrik untuk pemilihan sampel rujukan gred tinggi yang baharu. Sampel REG telah dipilih dan dicampur dengan sampel miny ak keruing dan cendana tulen . Kesemua 19 sampel campuran telah melalui ujian EN untuk penubuhan tiga tahap utama Indeks K ualiti Minyak Gaharu (AOQI) menggunakan skala skor-z. Proses pemilihan sensor EN yang signifikan telah dijalankan menggun akan teknik Spearman Rho Correlation (SRC) dan Stepwise Multi Linear Regression (SMLR). Akhirnya, teknik kelasifikasi 80:2 0 k-Nearest Neighbors (k-NN) telah digunakan untuk menilai model AOQI dengan teknik Confusion-Matrix Based Performance Measure (CMBPM) sebagai penilai prestasi pengelasan. Keputusan menunjukkan SRC dengan 11 sensor terpilih mengatasi prest asi SMLR dengan ketepatan ujian 80:20 k-NN bersamaan dengan 89.50%.

Kata kunci: penggredan minyak gaharu, hidung elektronik, pengelasan 80:20 k-NN

Introduction

The wood and essential oils of agarwood (Aquilaria spp.) command very high prices of up to USD90,000/kg for grade AAAAA wood and USD14,000/kg for super grade essential oil on the global market. In Malaysia, grade A agarwood is priced at MYR18,000/kg [1]. Grading methods traditionally used by traders involve assessing the color (shine and resin content estimation), size, shape, fragrance, thickness and density of the raw materials. These grading methods are subjective and can leave the harvesters' product undervalued [2]. To address this problem, better techniques used to grade and classify agarwood woodchips and essential oils have been developed based on wood colour scale template (grades A through C) [3], intended usage (aroma, block, classic, dust, extractable wood and fragrance) [4], wood extractive resin content (A, B, C and D), and electronic nose (EN) grading (high and low grades) for wood [1].

Not as easily accessible are scientific grading or quality assessment techniques offered to the agarwood industry as technical services, such as gas chromatography (GC), gas chromatography–mass spectrometry (GCMS), solid phase micro extraction (SPME) and EN approaches. These methods are typically used separately to identify the selected predefined quality of agarwood oils (pure and in oil blends) and for low and high grade classifications [5-13]. To date, no research has evaluated the use of EN combined with chemistry inputs in quantifying agarwood oil percentages in oil blends for export regulation (taxation or tax exemption) or for use by agarwood traders as an evaluation standard. This study proposes a technique to evaluate the established three levels of the agarwood oil quality index (AOQI) using the 80:20 k-NN classifier with Spearman's rho correlation (SRC) and stepwise multi linear regression (SMLR).

Materials and Methods

The overall research flow outlined in Figure 1 includes agarwood oil sample collection, EN tests, statistical ana lysis for selection of a high-grade reference sample, sam ple blending, EN features extraction, data scaling for A OQI and the 80:20 kNN classifier. The detailed methods for each step are described below.

Agarwood oil collection and high-grade reference sample selection

Eight agarwood oil samples and two common essential oils i.e., gurjun balsam (*Dipterocarpus* sp.) and sandalwood (*Santalum album*) were collected or purchased from local reputable traders of agarwood oil. The Johor Baharu Deluxe (JBD) agarwood sample was selected as the high-grade oil benchmark and reference sample (REFF) as it reportedly contains all significant c hemical compounds found in high-grade agarwood. A n ew high-grade agarwood oil reference (B1) was selecte d based on its EN fingerprint aroma, from seven new sa mples in the Forest Research Institute Malaysia (FRIM) collection (EXQ-OUDO30, HER-OUDO35, MAL1-O UDOI9, MAL2-OUDOI10, MAL3-OUDOI11, MAJ-O UDOI12 and REG-OUDOI13), and using statistical cor

relation of EN data with JBD EN data.

Sample blending processes and EN tests

Pure samples of the three selected reference oils: agarwood (B1), sandalwood (B2) and gurjun balsam (B3) were blended by volume in ratios as given in Table 1. A total of 19 samples (S1–S19) were blended. The blending formula in Table 1 was based on fixed volumes of B2 and B3 while the volume of B1 varied from 0% to 90%. S12 had an equal volume ratio for B1, B2 and B3 (33%:33%:33%). The percentage value of agarwood oil was represented by the percentage value of its volume in the blended oil samples. A commercial FOX4000 EN (Alpha-MOS, Toulouse, France) containing an 18-sensor array of metal oxide semiconductor (MOS) chemical sensors, bundled with AlphaSOFT version 12 data analysis software were used. The EN sensor chambers were divided into three types of high performance (HiP) chambers: chamber A containing doped metal oxide sensors (T30/1, P10/1, P10/2, P40/1, T70/2 and PA2), chamber B containing doped metal oxide sensors (P30/1, P30/2, P40/2, T40/2, T40/1 and TA2) and chamber CL2 containing undoped metal oxide sensors (LY2/AA, LY2/G, LY2/gCT, LY2/gCTl, LY2/Gh and LY2/LG). The carrier gas used was purified air grade (P = 5 psi). For each EN test, the sample was first prepared, heated, then injected via an injection port into the EN sample inlet, which recorded sensor response data into a main database. The EN was used to capture the uniqueness of each sample's scent and transform that information into sensor response data. The headspace generated from each heated sample was injected manually into the injection port using a gas-tight syringe. The system allowed the purified air as the headspace carrier gas to carry the sample headspace through all three chambers in the system and exit at the exhaust port. Simultaneously, the AlphaSOFT software recorded all EN raw data in the database. A total of 135 sample vials were used in the EN tests in developing the database.

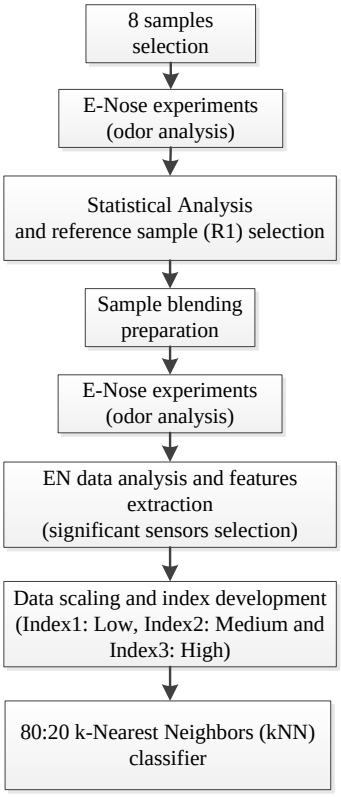


Figure 1. Overall research flowchart showing progression of samples in the electronic nose (EN) tests

Table 1. Ratios (by volume) of essential oil blends for samples used in the study; agarwood oil being the main reference

	Essential Oil Blend Ratio																			
	Sample No.	**S1**	**S2**	**S3**	**S4**	**S5**	**S6**	**S7**	**S8**	**S9**	**S10**	**S11**	**S12**	**S13**	**S14**	**S15**	**S16**	**S17**	**S18**	**S19**
Sandalwood, B3 (fixed)	%	50.0	49.5	49.0	48.0	47.0	46.0	45.0	42.5	40.0	37.5	35.0	33.3	32.5	30.0	25.0	20.0	15.0	10.0	5.0
	Gram (mg)	150.00	150.00	150.00	150.00	150.00	150.00	150.00	150.00	150.00	150.00	150.00	150.00	150.00	150.00	150.00	150.00	150.00	150.00	150.00
Gurjum balsam, B2 (fixed)	%	50.0	49.5	49.0	48.0	47.0	46.0	45.0	42.5	40.0	37.5	35.0	33.3	32.5	30.0	25.0	20.0	15.0	10.0	5.0
	Gram (mg)	150.00	150.00	150.00	150.00	150.00	150.00	150.00	150.00	150.00	150.00	150.00	150.00	150.00	150.00	150.00	0.15 00	0.15 00	0.15 00	0.15 00
Agarwood, B1 (variable)	%	0.0	1.0	2.0	4.0	6.0	8.0	10.0	15.0	20.0	25.0	30.0	33.3	35.0	40.0	50.0	60.0	70.0	80.0	90.0
	Gram (mg)	0.00	3.00	6.10	12.50	19.10	26.10	33.33	52.90	75.00	100.00	128.60	150.00	161.50	200.00	300.00	450.00	0.70 00	1.20 00	2.70 00
TOTAL (mg)		300.00	303.00	303.12	312.50	319.10	326.10	333.33	352.90	375.00	400.00	428.60	450.00	461.50	500.00	600.00	750.00	100 0.00	150 0.00	300 0.00

Agarwood oil quality index (AOQI) scaling and 80:20 k-nearest neighbors' classifier (kNN)

The AOQI scale is based on the conversion of B1 values (of 0% to 90%) in the sample blends (S1-S19) into a z-score scale using the z-score transformation. The z-score is a standard score method that normalises each score to its standard deviation from the mean score. For the z-score data scaling process in our study, the main EN database data were converted into x-scale values using Equation 1.

$$Z_{\text{score}} = \frac{X - \mu}{\sigma} = \frac{X - mean}{standard\ deviation} \quad (1)$$

Z-score conversion values (Table 2) produced two main threshold values that fell between -0.55 and -0.37 (closest to -0.5) and between 0.34 and 0.70 (closest to 0.5), which corresponded with 20% and 50% B1 volumes in the original data for the blended samples, respectively. Three indices were selected for AOQI with z-score and actual values as illustrated in Figure 2. As a result, three values for AOQI were established as represented in Equation 2.

$$\text{Agarwood oil quality index (AOQI)} = \begin{bmatrix} \text{INDEX 3: HIGH \% VOLUME} \geq 50\% \\ 20\% < \text{INDEX 2: MIDDLE \% VOLUME} < 50\% \\ \text{INDEX 1: LOW \% VOLUME} \leq 20\% \end{bmatrix} \quad (2)$$

Table 2. The Agarwood Oil Quality Index (AOQI) three scales based on z-score conversion values

		S1	S2	S3	S4	S5	S6	S7	S8	S9	S10	S11	S12	S13	S14	S15	S16	S17	S18	S19
B1 (Variable)	%	0.00	1.00	2.00	4.00	6.00	8.00	10.00	15.00	20.00	25.00	30.00	33.33	35.00	40.00	50.00	60.00	70.00	80.00	90.00
	z-score	-1.09	-1.05	-1.02	-0.95	-0.87	-0.80	-0.73	-0.55	-0.37	-0.20	-0.02	0.10	0.16	0.34	0.70	1.05	1.41	1.77	2.12
		INDEX $1_{z\text{-score}} \leq -0.37$ INDEX $1_{real} \leq 20\%$								$-0.37 <$ INDEX $2_{z\text{-score}} < 0.34$ $20\% <$ INDEX $2_{real} < 50\%$					INDEX $3_{z\text{-score}} \geq 0.34$ INDEX $3_{real} \geq 50\%$					

K nearest neighbor (kNN) is one of the simplest machine learning algorithms with a robust statistical-based supervised machine learning classification technique. The kNN classifier assigns samples that are unclassified to the class that most of its k-nearest neighbors belong to. Furthermore, it is a classifier that uses distance between a point and all its neighbors in an image to find nearest neighbors. The core idea of the kNN algorithm is to select the category of the sample with the most same categories among the K nearest samples in the feature space as the classification of the sample to be tested [14-18].

In our study, the 80:20 kNN was optimized with training and testing datasets constructed from 80% and 20% data partitioned from total EN data, respectively. Three AOQI indices represent three different classes (Figure 2) and the three indices previously defined with the z-score method therefore show 8, 6 and 5 samples falling under Index 1, 2 and 3, respectively.

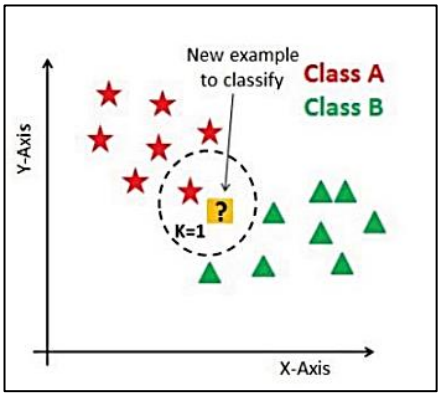


Figure 2. K-nearest neighbor (kNN) classifier illustration [17]

The 80% training dataset consisted of 64 data from Index 1, 48 data from Index 2 and 40 data from Index 3 for a total of 152 data (Table 3). All unique data patterns related to each index group were recorded in the kNN model. The remaining 20% testing data consisted of 16 data from Index 1, 12 data from Index 2 and 10 data from Index 3

for a total of 38 data. After that, the 20% testing data were projected to the kNN classifier training database to find the nearest matching index group. Finally, classifier accuracy was calculated using the confusion-matrix based performance measure (CMBPM; Equation 3) where TP = true positive, TN = true negative, FN = false negative and FP = false positive. The highest classifier accuracy is 100%.

$$80{:}20\ k-NN\ Accuracy\ (\%) = \frac{TP+TN}{TP+TN+FN+FP} \quad (3)$$

Table 3. The agarwood oil quality index (AOQI) three scales with electronic nose (EN) data distribution for 80:20 kNN classifiers

INDEX $1_{real} \leq 20\%$								**$20\% <$ INDEX $2_{real} < 50\%$**						**INDEX $3_{real} \geq 50\%$**				
S1	**S2**	**S3**	**S4**	**S5**	**S6**	**S7**	**S8**	**S9**	**S10**	**S11**	**S12**	**S13**	**S14**	**S15**	**S16**	**S17**	**S18**	**S19**
Data matrix size = [18 sensors x 5 vials x 8 samples] + 100% synthetic data = [80 x 18]								Data matrix size = [18 sensors x 5 vials x 6 samples] + 100% synthetic data = [60 x 18]						Data matrix size = [18 sensors x 5 vials x 5 samples] + 100% synthetic data = [50 x 18]				
$Training_{80\%}$ = 64 samples								$Training_{80\%}$ = 48 samples						$Training_{80\%}$ = 40 samples				
$Testing_{20\%}$ = 16 samples								$Testing_{20\%}$ = 12 samples						$Testing_{20\%}$ = 10 samples				

Results and Discussion

For the normal data distribution test, all samples were not normally distributed as all p and h values were < 0.05 and 1, respectively (Table 4). Thus, a non-parametric statistical test was selected. For EN data comparison between JBD with seven selected samples using the Wilcoxon rank sum test, REG had the highest p-value = 0.78293 and h = 0 indicating REG had almost the same odor data in continuous distribution as JBD (Table 5). The REG sample was then selected as the reference agarwood oil (B1) mixed with B2 and B3 to produce 19 oil blend samples. All 19 samples were subjected to EN testing and were stored in the main EN database.

Table 4. The results of the sample normality distribution test (Lilliefors test) for the eight agarwood oil samples

	JBD	**MAL2**	**MAL3**	**MAJ**	**REG**	**MAL1**	**EXQ**	**HER**
P-value	0	5.83E-05	0.005966499	6.67E-05	0	0.000617	0	0
h	1	1	1	1	1	1	1	1

Table 5. The Wilcoxon rank sum test comparison of the high-grade reference agarwood oil (JBD) against seven other agarwood oil samples

	JBD-MAL2	**JBD-MAL3**	**JBD-MAJ**	**JBD-REG**	**JBD-MAL1**	**JBD-EXQ**	**JBD-HER**
P-value	0.00424	0.0006	0.61824	0.78293*	0.0006	0.04161	0.0588
h	1	1	0	0*	1	1	0

*Note: P-value > 0.05 & h=0 ---> x1 and x2 are from the same continuous distribution

From Spearman's rho correlation (SRC) test in Table 6, all 11 less correlated sensors with p < 0.05 were selected including T30/1, P10/1, P10/2, P40/1, T70/2, PA/2, P30/1, P30/2, T40/2, T40/1 and TA/2. From MATLAB results in Figure 3, five EN sensors including LY2/LG, LY2/G, LY2/GH, P10/2 and P10/2 were selected by stepwise multi linear regression (SMLR). Both groups of selected sensors were then tested using the kNN 80:20 classifier and the result with the best classification accuracy was chosen.

Table 6. Spearman's rho correlation (SRC) results for the electronic nose 18-sensor array

		S7	S8	S9	S10	S11	S12	S13	S15	S16	S17	S18
		T30/1	P10/1	P10/2	P40/1	T70/2	PA/2	P30/1	P30/2	T40/2	T40/1	TA/2
S7	T30/1	1.000	FALSE	FALSE	FALSE	FALSE	FALSE	FALSE	FALSE	FALSE	FALSE	FALSE
S8	P10/1	FALSE	1.000	FALSE	FALSE	FALSE	FALSE	FALSE	FALSE	FALSE	FALSE	FALSE
S9	P10/2	FALSE	FALSE	1.000	FALSE	FALSE	FALSE	FALSE	FALSE	FALSE	FALSE	FALSE
S10	P40/1	FALSE	FALSE	FALSE	1.000	FALSE	FALSE	FALSE	FALSE	FALSE	FALSE	FALSE
S11	T70/2	FALSE	FALSE	FALSE	FALSE	1.000	FALSE	FALSE	FALSE	FALSE	FALSE	FALSE
S12	PA/2	FALSE	FALSE	FALSE	FALSE	FALSE	1.000	FALSE	FALSE	FALSE	FALSE	FALSE
S13	P30/1	FALSE	FALSE	FALSE	FALSE	FALSE	FALSE	1.000	FALSE	FALSE	FALSE	FALSE
S15	P30/2	FALSE	FALSE	FALSE	FALSE	FALSE	FALSE	FALSE	1.000	FALSE	FALSE	FALSE
S16	T40/2	FALSE	FALSE	FALSE	FALSE	FALSE	FALSE	FALSE	FALSE	1.000	FALSE	FALSE
S17	T40/1	FALSE	FALSE	FALSE	FALSE	FALSE	FALSE	FALSE	FALSE	FALSE	1.000	FALSE
S18	TA/2	FALSE	FALSE	FALSE	FALSE	FALSE	FALSE	FALSE	FALSE	FALSE	FALSE	1.000

```
mdl = LinearModel.stepwise(X_norm,y,'constant','upper','linear')
1. Adding x8, FStat = 31.3251, pValue = 2.19115e-07
2. Adding x9, FStat = 37.4543, pValue = 2.2613e-08
3. Adding x5, FStat = 20.6649, pValue = 1.67939e-05
4. Adding x2, FStat = 30.6164, pValue = 3.0622e-07
5. Adding x1, FStat = 5.6516, pValue = 0.019581
6. Adding x4, FStat = 9.2139, pValue = 0.0031586
7. Removing x5, FStat = 0.52906, pValue = 0.46893

mdl =


Linear regression model:
    y ~ 1 + x1 + x2 + x4 + x8 + x9

Estimated Coefficients:
                   Estimate     SE          tStat      pValue
    (Intercept)     1.8421     0.045282     40.681     2.7368e-59
    x1             0.76541     0.22417      3.4145     0.00096424
    x2             -1.9358     0.41402     -4.6756     1.0376e-05
    x4               2.906      0.3891      7.4685     5.2772e-11
    x8              2.1268     0.22559      9.4277     4.8863e-15
    x9             -1.7152     0.22532     -7.6123     2.6927e-11


Number of observations: 95, Error degrees of freedom: 89
Root Mean Squared Error: 0.441
R-squared: 0.723,  Adjusted R-Squared 0.708
F-statistic vs. constant model: 46.5, p-value = 2.18e-23
```

Figure 3. Electronic nose sensor selection using stepwise multi linear regression (SMLR) in MATLAB

The highest kNN 80:20 classifier training accuracy values for SMLR and SRC were from k = 1 and k = 2, respectively, while the highest kNN 80:20 classifier testing accuracy values for SMLR and SRC were from k = 4 and k = 1 same as k = 2, respectively (Figures 4 and 5). Between the two features extraction techniques, the best k-NN 80:20 classifier training and testing accuracy values were from SRC with values of 100.0% and 89.5%, respectively. While SMLR had a training accuracy of 100.0%, testing accuracy was only 82.5% (Table 7).

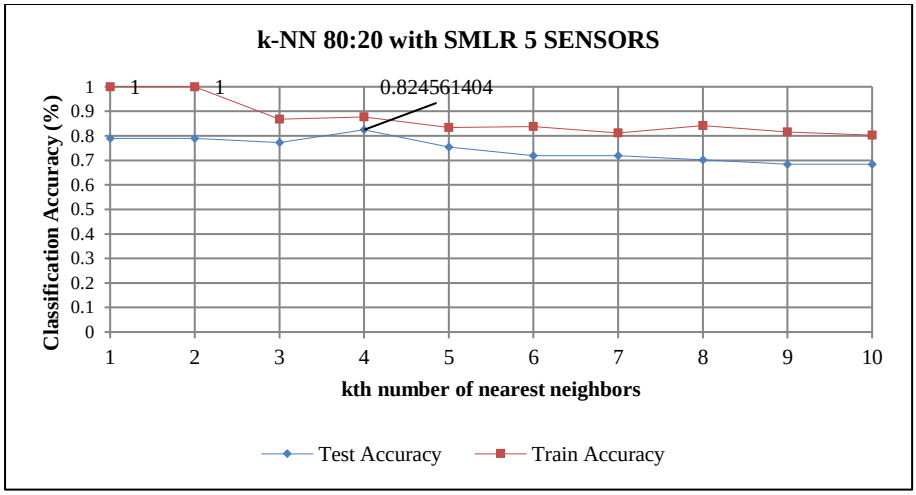


Figure 4. 80:20 k-nearest neighbors (kNN) training and testing classification accuracy with five selected sensors using the stepwise multi linear regression (SMLR) features extraction technique

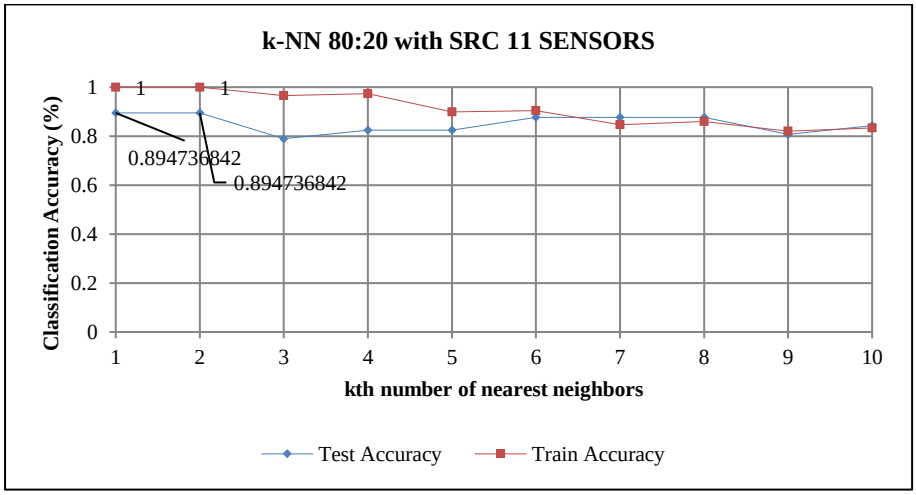


Figure 5. 80:20 k-nearest neighbors (kNN) training and testing classification accuracy with 11 selected sensors using Spearman's rho correlation (SRC) features extraction technique

Table 7. Summary of k-nearest neighbors (kNN) classifier training and testing accuracy for stepwise multi linear regression (SMLR) and Spearman's rho correlation (SRC) features extraction techniques

Classifier	**SMLR 5 Sensors**		**SRC 11 Sensors**	
	Train (Accuracy: %)	Test (Accuracy: %)	Train (Accuracy: %)	Test (Accuracy: %)
80:20 kNN	100.0	82.5	100.0	89.5

Conclusions

The REG sample was selected from among seven new samples in the FRIM collection as the high-grade reference (B1) in our study because it had an aroma profile closest to that of the JBD sample. Varying volumes of B1 were then mixed with B2 and B3 (in fixed, 1:1 ratios) to produce nineteen blended samples containing increasing percentages of B1. The 19 samples were then used in the EN tests for database establishment. The z-score-transformed EN data

successfully indexed the AOQI into three levels. The AOQI with 11 sensors selected by SRC was proven to generate a classification test accuracy that was 7% higher than the SMLR-selected 5 sensors (89.5% vs 82.5% respectively). Lastly, the kNN classifier only needed 11 significant sensors from 18 sensors to produce the best test accuracy. In conclusion, the 80:20 kNN classifier was proven to classify the percentage volume of pure agarwood oil in the oil blend into three groups with Index 1, 2 and 3 denoting AOQI low, medium and high percentage volumes of ≤ 20%, 20% < index < 50% and ≥ 50%, respectively.

Acknowledgement

The authors would like to thank the staff of the Natural Products Division, FRIM for their invaluable support. The study was funded by FRIM grant "PHSB: Membangunkan Strategi Pemuliharaan dan Menambahbaik Kualiti Hasil Spesies Aquilaria Terpilih Secara Lestari di Malaysia".

References

1. Yahya, A. Z., Wai Mun, H. and Hassan, N. H. (2018). KARAS (*Aquilaria malaccensis*) A plantation species in Peninsular Malaysia. Forest Research Institute Malaysia (FRIM). Kuala Lumpur, Malaysia.
2. Muhammad, I., Jusoh, M. Z. and Sajap, A. S. (2018). Gaharu Komoditi Ketiga Negara. University Putra Malaysia (UPM). Selangor, Malaysia.
3. Forestry Department Peninsular Malaysia (2015). Manual in grading of agarwood. Forestry Department Peninsular Malaysia (FDPM). Selangor, Malaysia.
4. Malaysian Timber industry Board (2014). Panduan pengkelasan produk gaharu Malaysia. Malaysian Timber industry Board (MTIB). Kuala Lumpur, Malaysia.
5. Lias, Sahrim, Ali, N. A. M., Jamil, M., Jalil, A. M. and Othman, M. F. (2016). Discrimination of pure and mixture agarwood oils via electronic nose coupled with k-NN kfold classifier. *Procedia Chemistry*, 20: 63-68.
6. Ismail, N., Rahiman, M. H. F., Taib, M. N., Ali, N. A. M., Jamil, M. and Tajuddin, S. N. (2013). Classification of the quality of agarwood oils from Malaysia using Z-score technique. *Proceedings - 2013 IEEE 3rd International Conference on System Engineering and Technology, 2*013: 78-82.
7. Haslina, E., Latib, A., Najib, M. S., Mohd, C., Che, A. and Tajuddin, S. N. (2018). Analysis of different quality agarwood oil (*Aquilaria malaccensis*) and sensory study. *Journal of Telecommunication, Electronic and Computer Engineering*, 10(1): 57-61.
8. Zubir, N. S. A., Abas, M. A., Ismail, N., Ali, N. A. M., Rahiman, M. H. F., Mun, N. K., Tajuddin, S. H. and Taib, M. N. (2017). Analysis of algorithms variation in multilayer perceptron neural network for agarwood oil qualities classification. *8th Control and System Graduate Research Colloquium, ICSGRC 2017 - Proceedings*: 122-126.
9. Ismail, N., Rahiman, M. H. F., Taib, M. N., Ali, N. A. M., Jamil, M. and Tajuddin, S. N. (2013). Analysis of chemical compounds of agarwood oil based on headspace-solid phase microextraction combined with gas chromatography mass-spectrometry. *9th International Colloquium on Signal Processing and Its Applications*: 215-218.
10. Ismail, S. N., Maulidiani, M., Akhtar, M. T., Abas, F., Ismail, I. S., Khatib, A., Mohamad Ali, N. A. and Shaari, K. (2017). Discriminative analysis of different grades of gaharu (*Aquilaria malaccensis* Lamk.) via1H-NMR-based metabolomics using PLS-DA and random forests classification models. *Molecules*, 22(10): 1612.
11. Lias, S., Mohamad Ali, N. A., Jamil, M., Tolmanan, M. S. Y. and Misman, M. A. (2018). A study on the application of electronic nose coupled with dfa and statistical analysis for evaluating the relationship between sample volumes versus sensor intensity of agarwood essential oils blending ratio. *MATEC Web of Conferences*, 2018: 201-02008.
12. Ismail, N., Rahiman, M. H. F., Taib, M. N., Ali, N. A. M., Jamil, M. and Tajuddin, S. N. (2014). Application of ANN in agarwood oil grade classification. *10th International Colloquium on Signal Processing and Its Applications, CSPA* 2014: 216-220.

13. Ismail, N., Rahiman, M. H. F., Taib, M. N., Ali, N. A. M., Jamil, M. and Tajuddin, S. N. (2014). A review study of agarwood oil and its quality analysis*, Jurnal Teknologi*, 1: 37-42.
14. Karimifard, S., Ahmadian, A., Khoshnevisan, M. and Nambakhsh, M. S. (2006). Morphological heart arrhythmia detection using hermitian basis functions and kNN classifier. *Annual International Conference of the IEEE Engineering in Medicine and Biology - Proceedings*, (4): 1367-1370.
15. Liang, K. and Wang, D. (2019). KNN _ SVM based information transmission method for renewable energy power generation. *IEEE Sustainable Power and Energy Conference, 2019:* 1671–1676.
16. Wasule, V. and Sonar, P. (2017). Classification of brain MRI using SVM and KNN classifier. *3rd IEEE International Conference on Sensing, Signal Processing and Security, 2017*: 218-223.
17. Bharate, A. A. and Shirdhonkar, M. S. (2020). Classification of grape leaves using KNN and SVM classifiers. *4th International Conference on Computing Methodologies and Communication,* 2020: 745-749.
18. Xu, M., Wang, J. and Gu, S. (2019). Rapid identification of tea quality by E-nose and computer vision combining with a synergetic data fusion strategy. *Journal of Food Engineering*, 241: 10-17.

Malaysian Journal of Analytical Sciences (MJAS)
Published by Malaysian Analytical Sciences Society

MODELING THE TIME RESPONSE OF CURRENT USING INTERDIGITATED ARRAYS IN A SHALLOW ELECTROCHEMICAL CELL

(Pemodelan Respons Arus Mengunakan Susunan Interdigital dalam Sel Elektrokimia Cetek)

Cristian F. Guajardo Yévenes[1,2,*] and Werasak Surareungchai[3,4]

[1]*Biological Engineering Program, Faculty of Engineering,*
[2]*Pilot Plant Development and Training Institute,*
[3]*Nanoscience and Nanotechnology Graduate Program,*
[4]*School of Bioresources and Technology,*
King Mongkut's University of Technology Thonburi,
49 Soi Thian Thale 25, Thanon Bang Khun Thian Chai Thale
Bangkok 10150, Thailand

[*]*Corresponding author: cristian.gua@kmutt.ac.th*

Received: 9 February 2022; Accepted: 25 July 2022; Published: 27 December 2022

Abstract

The interdigitated array of electrodes (IDAE) is a common choice for integration in small electrochemical sensors due to the amplified currents and fast response times. The design and assessment of IDAE performance in microfluidic cells require the use of mathematical models, in which the diffusion equation is widely applied. Analytical solutions for this equation are available for IDAEs in tall cells; however, they are not currently available for shallow cells, as is the case with microfluidic devices. The issue of whether it is possible to model the time response of IDAEs in shallow cells using simple exponential functions is addressed in this work. This is achieved by numerically solving the diffusion equation to obtain the time response of the current and later by applying non-linear regression to obtain exponential models. The current response is generally complex due to the many Fourier harmonics involved. However, the findings reveal that when the elapsed time is greater than some characteristic time, the current response can be approximated by an exponential curve. Furthermore, higher currents can be obtained at the expense of longer response times when the cell is tall, while shorter response times can be obtained at the expense of lower currents when the cell is shallow.

Keywords: Shallow electrochemical cell, Interdigitated arrays, Numerical simulation, Current response.

Abstrak

Elektrod susunan interdigital (IDEA) adalah pilihan biasa bagi intergrasi dalam sensor elektrokimia kecil berdasarkan arus teramplikasi dan respons masa yang pantas. Rekabentuk dan penilaian bagi prestasi IDEA di dalam sel mikrobendalir memerlukan pemodelan matematik, di mana persamaan resapan digunakan secara meluas. Penyelesaian analitikal bagi persamaan ini sesuai

bagi IDEA dalam sel tinggi; namun belum ada bagi sel cetek, khusus bagi kes bersama mikrobendalir. Isu terhadap kebarangkalian ia berhasil terhadap model respons masa di dalam sel cetek menggunakan fungsi eksponen mudah telah dikaji. Ia dicapai melalui penyelesaian berangka persamaan resapan untuk mendapatkan respons masa bagi arus dan kemudian digunakan bagi regresi tak linear untuk mendapatkan model eksponen. Respons arus secara umum adalah kompleks disebabkan oleh penglibatan harmonik Fourier. Namun, hasil kajian mendapati apabila masa berlalu lebih kuat berbanding masa pencirian, responsa arus boleh dianggar oleh lengkung eksponen. Selanjutnya, arus yang tinggi boleh diperolehi pada masa respons yang lebih lama apabila susunan sel adalah tinggi, sebaliknya masa respons yang lebih pendek diperolehi pada arus yang rendah di mana kedudukan sel adalah cetek.

Kata kunci: sel elektrokimia cetek, susunan interdigital, simulasi berangka, respons arus

Introduction

Microelectrodes are of interest in electrochemical detection due to their fast response, high current density, and reduced sample volumes [1]. Among these, the interdigitated array of electrodes (IDAE) is a common choice for integration in microfluidic electrochemical sensors due to the amplified currents obtained by redox cycling at multiple electrode bands and the fact that microfluidic devices and microelectrodes share similar fabrication techniques [2, 3].

Obtaining good designs or assessing the performance of IDAE in microfluidic electrochemical cells requires the use of mathematical models. In particular, the diffusion equation is a commonly used model and valid when the effects of convection and migration in the cell are negligible. An analytical solution of the diffusion equation is possible for IDAEs in very tall cells [4]; however, this is not currently available for shallow cells, as in the case of many microfluidic cells. For this reason, numerical simulations of the diffusion equation are commonly performed to obtain the concentration profile and subsequently the current through the cell for the device in question [5, 6].

The issue of whether it is possible to model the time response of the current using simple exponential functions is addressed in this research. This is achieved by numerically solving the diffusion equation for electrochemical cells of different heights containing an IDAE with bands and gaps of equal width. Once this has been done, non-linear regressions are performed on the simulated currents to obtain their fitting parameters, which correspond to the magnitude in steady state and the time constant (reciprocal of the exponential decay constant). The obtained exponential approximations are valid when the elapsed time is greater than some characteristic times. This model for the current shows that there is a trade-off between faster time responses and higher detection currents, depending on the dimensions of the electrochemical cell and IDAE.

Materials and Methods

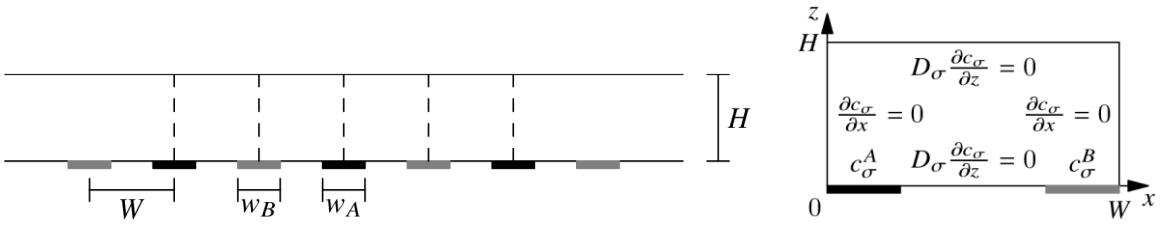
Model of the IDAE

Consider an IDAE located at the bottom of an electrochemical cell of height H (Figure 1a). The IDAE consists of two band arrays, A (black) and B (gray), where consecutive bands are separated by the distance W between their centers, have widths of w_A and w_B, and share a common length L which is in contact with the electrochemical solution in the channel. The electrochemical cell may also include a counter electrode, external to the IDAE, when each array is potentiostated independently with a bipotentiostat.

The solution comprises a mixture of oxidized (O) and reduced (R) species, in uniform initial concentrations $c_{O,i}$ and $c_{R,i}$, respectively, which are transported only by diffusion (with diffusion coefficient D) and react at the surface of the electrodes by exchanging n_e electrons.

$$O + n_e\, e^- \rightleftharpoons R \qquad (1)$$

For the sake of simplicity, reversible electrode reactions are assumed, and therefore, the Nernst equation is valid even when the current flows through the electrodes [7].



(a) Cross section of the full cell (b) One unit of symmetry (unit cell)

Figure 1. Shallow electrochemical cell with an IDAE. This cell can be regarded as an assembly of several unit cells. Here c_σ is the concentration of species σ (either O or R), and c_σ^A and c_σ^B are the concentrations applied at bands A and B, respectively

If the length L is sufficiently large, the fringing effects at the ends of each band can be neglected, and the electrochemical cell reduced to two dimensions. Moreover, if the number of bands is large enough, the fringing effects at both ends of the IDAE can also be neglected, allowing the IDAE to be represented as an assembly of two-dimensional *unit cells* (Figure 1b) due to its periodic arrangement [4, 8]. In the event of a counter electrode external to the IDAE, this is assumed to be located far away, such that the fringing effects at both ends of the IDAE are further avoided.

Under these conditions, the concentration profile inside a single unit cell is given by the diffusion equation

$$\frac{1}{D}\frac{\partial c_\sigma}{\partial t} = \frac{\partial^2 c_\sigma}{\partial x^2} + \frac{\partial^2 c_\sigma}{\partial z^2} \tag{2}$$

where $c_\sigma(x, z, t)$ is the concentration of species σ (either O or R), which is subject to the initial concentrations present in the electrochemical cell

$$c_\sigma(x, z, 0^-) = c_{\sigma,i} \tag{3}$$

as well as boundary conditions for insulation (top and bottom), symmetry (left and right), and applied concentrations c_σ^A and c_σ^B at the bands, as indicated in Figure 1b.

It should be noted that the concentrations applied at the surface of the bands E (which can be either A or B) are uniform. This is possible due to the validity of the Nernst equation

$$ln\left(\frac{c_O^E}{c_R^E}\right) = \frac{Fn_e}{RT}(V_E - V^{o\prime}) \tag{4}$$

where F is Faraday's constant, R is the universal gas constant, T is the temperature of the system, V_E is the potential applied at bands E, and $V^{o\prime}$ is the formal potential of the redox couple. Furthermore, the sum of concentrations at any point in the unit cell is constant and uniform [4, 8]

$$c_O(x, z, t) + c_R(x, z, t) = c_{O,i} + c_{R,i}$$

Both facts make the concentrations of species O and R at each band E (either A or B) uniform and dependent only on the potential applied at that same band

$$c_O^E = \frac{c_{O,i}+c_{R,i}}{1+e^{\frac{-Fn_e}{RT}(V_E - V^{o\prime})}} \tag{5}$$

$$c_R^E = \frac{c_{R,i}+c_{O,i}}{1+e^{\frac{+Fn_e}{RT}(V_E - V^{o\prime})}} \tag{6}$$

Once the concentration profile is known, the current at an individual band E (either A or B) can be obtained by integrating the current density on that band

$$i_E = \int_E \mp F\, n_e D \frac{\partial c_\sigma}{\partial z}(x, 0, t) L dx \tag{7}$$

where minus or plus signs should be used when the species σ corresponds to O or R, respectively.

Implementation of the simulations

All equations were normalized using the relations $\gamma_\sigma = [c_\sigma - c_\sigma{}^A]/[c_\sigma{}^B - c_\sigma{}^A]$, $\xi = x/W$, $\zeta = z/W$ and $\tau = \pi^2 Dt/W^2$, to make the results available for devices fabricated at different scales. In particular, the diffusion equation, its initial concentration, and the concentrations at the bands were transformed to

$$\pi^2 \frac{\partial \gamma_\sigma}{\partial \tau} = \frac{\partial^2 \gamma_\sigma}{\partial \xi^2} + \frac{\partial^2 \gamma_\sigma}{\partial \zeta^2} \quad (8)$$

$$\gamma_\sigma(\xi, \zeta, 0^-) = \gamma_{\sigma,i} = \frac{c_{\sigma,i} - c_\sigma^A}{c_\sigma^B - c_\sigma^A} \quad (9)$$

$$\gamma_\sigma(\xi, 0, \tau) = 0 \text{ for } \xi \in A \quad (10)$$

$$\gamma_\sigma(\xi, 0, \tau) = 1 \text{ for } \xi \in B \quad (11)$$

while the boundary conditions for insulation and symmetry remained equal to zero, and the normalized current at a single band resulted in

$$\frac{i_E/L}{\pi^2 F n_e D[c_\sigma^B - c_\sigma^A]} = \int_E \frac{\mp 1}{\pi^2} \frac{\partial \gamma_\sigma}{\partial \zeta}(\xi, 0, \tau) d\xi \quad (12)$$

where minus or plus signs should be used when the species σ corresponds to O or R, respectively.

Two cases were considered for initial concentrations: (i) The case $\gamma_{\sigma,i} = 0$, where the initial concentration of one species equals the concentration applied at one of the arrays $c_{\sigma,i} = c_\sigma{}^A$. This is a common setup for IDAEs, especially when $c_{\sigma,i} = 0$ and the concentration $c_\sigma{}^A$ is forced to zero by potentiostating at a fixed extreme potential [4], while the concentration at the other array $c_\sigma{}^B$ is potentiostated at will. This configuration requires a bipotentiostat with a counter electrode external to the IDAE.

(ii) The case $\gamma_{\sigma,i} = 0.5$, where the average concentration applied to the arrays is equal to the initial concentration $(c_\sigma{}^A + c_\sigma{}^B)/2 = c_{\sigma,i}$. This condition, together with bands of equal width ($w_A = w_B$), produces symmetrical concentration profiles, leading to equal currents at the arrays [8, 9]. This last situation corresponds to the case where a conventional potentiostat drives one of the arrays while the other array performs as a counter electrode, thus sparing the need for an external counter electrode.

In particular, IDAEs with bands and gaps of equal width ($w_A = w_B = W/2$) were considered for all simulations, since this is a common design choice, and also because it facilitates the display of results. This choice also simplifies the implementation of the meshes, chosen in this study to be of an exponential kind as shown in Figure 2. Each mesh used in the simulations consists of $n_x \times n_z$ elements, where the size of the smallest element is $\delta_x = \delta_z = \delta_0$, and the remaining elements increase in size according to the growth factor (stretching parameter) $r_x = r_z = r$ [10]. The resolution of the meshes was tested for diffusion in steady state with a unit cell with an aspect ratio $H/W = 1$ (Figure 2) and successively refined until the absolute error of the normalized current between two consecutive iterations was less than 0.0005, corresponding approximately to three decimal places of accuracy. The values obtained for the smallest element and the growth factor were $\delta_0 = 0.00025$ and $r \approx 1.2496$, respectively, and used for all simulations in this study.

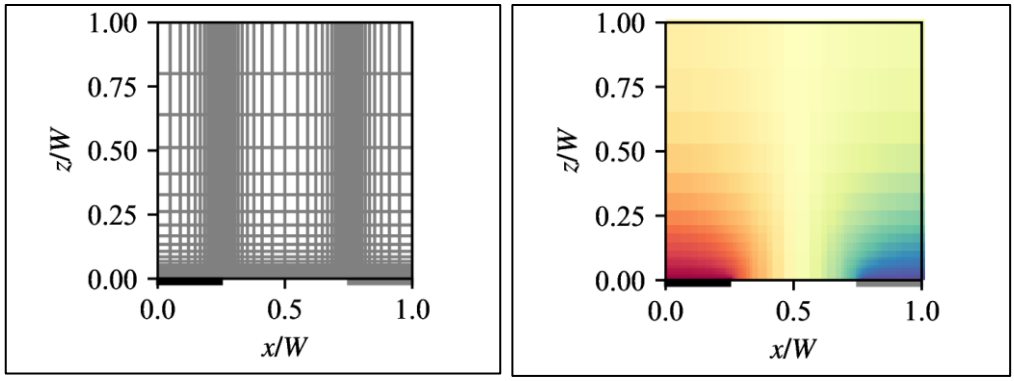


Figure 2. Exponential mesh (left) and normalized concentration in steady state (right) for the case $H/W = 1$. Number of elements is $n_x \times n_z = 100 \times 31$, and size of the smallest element $\delta_x = \delta_z = \delta_0 = 0.00025$ with a growth factor of $r_x = r_z = r \approx 1.2496$.

The simulations considered different aspect ratios $H/W = \{1, 1/2, 1/3, \ldots, 1/10\}$, and were solved numerically by writing the normalized diffusion equation, its boundary conditions, and the corresponding meshes in Python with the aid of the FiPy package [11]. These simulations can be downloaded from [12].

Exponential fits for the current response

The concentration profile in a shallow cell containing an IDAE evolves over time in a complex manner, with the addition of several Fourier harmonics to produce the right result. Each of these harmonics contains an exponential factor

$$exp\left(-\left[n^2 + k^2\frac{W^2}{H^2}\right]\frac{\pi^2}{W^2}Dt\right) \text{ for } \begin{matrix} n = 1,2,\ldots \\ k = 0,1,\ldots \end{matrix} \qquad (13)$$

which dampens the influence of the harmonic over time. Some of these harmonics will decay faster than others. In particular, the harmonic $(n, k) = (1, 0)$ is the slowest to decay and the only one remaining and contributing to the concentration for times $\pi^2 Dt/W^2 > 1$ and aspect ratios $H/W < 1/2$. The exponential factors of all other harmonics ($n \geq 1$ and $k \geq 1$) are less than $\exp(-[1^2 + 1^2 \times 2^2]) = \exp(-5) \approx 0.0067 = 0.67\%$ and therefore disappear quickly. This leads the concentration profile to behave like an exponential under the conditions stated previously [8].

The previous argument also suggests that the current may behave like an exponential after a certain time T

$$i_E = i_f + K\exp(-t/\tau_i) \quad \text{for } t \gtrsim T \qquad (14)$$

where i_f is the current of a single band in steady state, K is a real number, and τ_i is the *time constant* of the current response. However, this time T may not be equal to its counterpart obtained for the concentration.

After obtaining the time response of the current by numerically solving the diffusion equation, we searched for the time T and the parameters i_f, K and τ_i of the exponential curve. This was done in four steps (see Figure 3): (i) Search for the time t_{ss} where the current i_E and its steady state i_f differ by 0.67%. This gives a rough approximation of the time when an exponential decays to 0.67% (which corresponds to $5\tau_i$). (ii) Find the time $t_{ss}/5$. This gives a rough approximation of the time constant of the current τ_i. However, this time may be too soon for the current to behave exponentially. (iii) Find the time $T = 2t_{ss}/5$. This time gives a rough approximation of $2\tau_i$, where it is more likely for the current to start behaving exponentially. We could have also chosen $3t_{ss}/5$; however, $2t_{ss}/5$ gave good results for exponential fit. Times near $4t_{ss}/5$ or beyond are not advisable, since they would be too close to the time where the current reaches steady state, and thus the current would no longer be exponential but nearly constant. (iv) Once $T = 2t_{ss}/5$ is known, fit an exponential curve to the simulation data of the current between times T and t_{ss} to obtain the fitting parameters i_f, K, and τ_i. Since the model for the current is not linear

in its parameters, a non-linear fit needs to be performed. This procedure was also implemented in Python, whose script can be downloaded from [12].

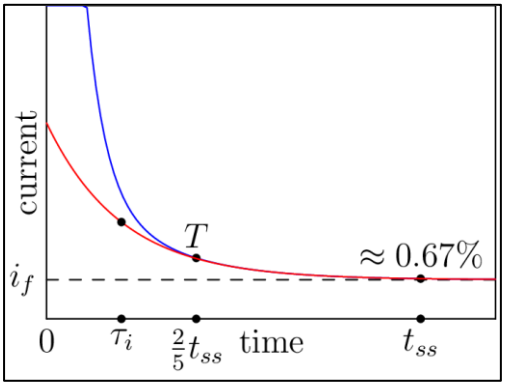


Figure 3. Process to obtain the exponential fit (red) for the time response of the current (blue). (i) Find t_{ss}, which corresponds to the time where the current i_E and i_f differ by 0.67%. (ii) Find $t_{ss}/5$, which gives a rough approximation of τ_i. (iii) Find $T = 2t_{ss}/5$, which gives a rough approximation of the time $2\tau_i$. (iv) Fit an exponential curve to the time response of the current i_E, by taking the simulation data between $T = 2t_{ss}/5$ and t_{ss}

Results and Discussion

The simulations of the currents and their respective exponential fits were performed for the cases involving external and internal counter electrodes, using a bipotentiostat and conventional potentiostat, respectively; the most common configurations to drive an IDAE. For both cases, electrochemical cells of different heights were used while fixing the width of the unit cell. The results are discussed below.

Case of external counter electrode ($c_{\sigma,i} = c_\sigma^A$)

For this case, we considered that the initial concentration of one species equals its concentration applied at one array $c_{\sigma,i} = c_\sigma^A$, achieved by potentiostating array A and forcing c_σ^A to be equal to $c_{\sigma,i}$, while array B is potentiostated at will. In practice, this requires the use of a bipotentiostat with a counter electrode external to the IDAE.

Under these conditions, several simulations were performed using different values of W/H. The simulations produced currents of different magnitude at bands A and B, as shown in Figure 4. This provides clear evidence of the need for a counter electrode, external to the IDAE, to be responsible for collecting the net current $i_{\text{net}} = i_A + i_B \neq 0$ produced in every unit cell, as indicated in Figure 5. However, as the simulations reach steady state, the net current tends to zero, meaning that the currents at both bands must be balanced in steady state $i_A = -i_B$. This is only possible under the assumption of a large number of bands and an external counter electrode far away from the IDAE.

As expected, all currents obtained by simulation (circles) can be approximated by exponentials (lines), as presented in Figures 4 and 5. In fact, in the case of currents at B in Figure 4, the exponential approximations show some deviation from their simulated counterparts for $t > \tau_i$, while improving considerably for $t > T$ (where T is roughly $2\tau_i$), and clearly showing a steady-state response for $t > 5\tau_i$. The parameters i_f, K, and τ_i obtained from all exponential fits are given in Table 1, such that the exponential approximations can be easily reconstructed as required.

In Figure 6, the magnitudes of currents at A and B are equal in steady state and decrease as the cell becomes shallower. This is because there are two main gradients

of concentration when the electrochemical cell is tall: (i) between the IDAE and the bulk concentration near the roof of the cell; and (ii) in between consecutive bands (Figure 2). However, when the cell becomes shallower, the gradient between the IDAE and the roof of the cell tends to disappear, leaving only the gradient of concentration between consecutive bands. The time constants of currents at A and B, as well as the net current, are all equal, decreasing as the cell becomes shallower. This is because the electrochemical species can escape to the region of bulk concentration near the roof of the cell when the cell is tall (Figure 2) and later diffuse to the external counter electrode. However, when the cell becomes shallower, the electrochemical species are forced to diffuse only between consecutive bands due to the low roof of the cell. Therefore, in the case of a shallow cell, the species diffuse through a shorter distance compared to the case of a taller cell.

The previous results show that there is a compromise between sensitivity (current) and response time (time constant) of the sensor. The taller the electrochemical cell, the more sensitive it becomes, but the longer the response time. Conversely, the shallower the electrochemical cell, the less sensitive it becomes, but the shorter the response time.

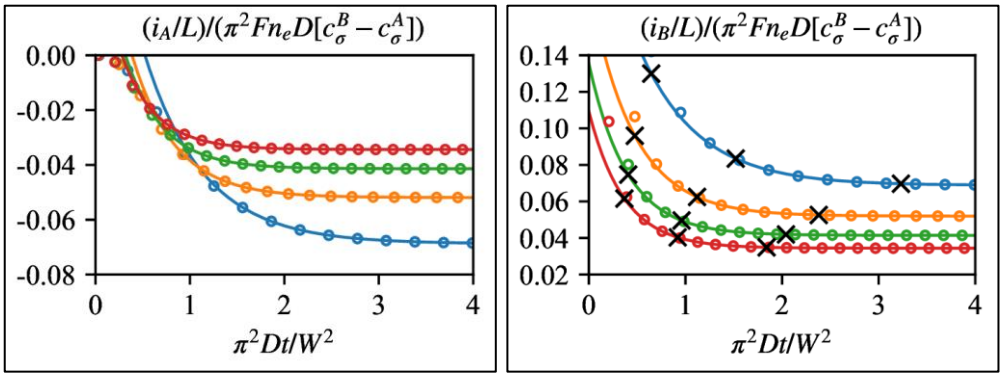


Figure 4. Normalized versions of the current through single bands i_A (left) and i_B (right) for selected aspect ratios W/H = {4, 6, 8, 10} (lines in order from blue to red) and initial concentration $c_{\sigma,i} = c_\sigma{}^A$. Circles correspond to the simulation points, while solid lines correspond to the exponential fit. Crosses on a line correspond to the times τ_i, T and $5\tau_i$ (in order from left to right)

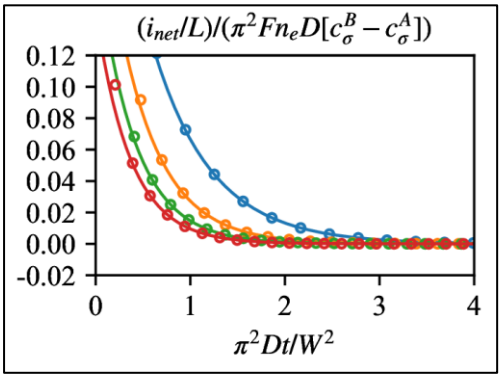


Figure 5. Normalized version of the net current $i_{net} = i_A + i_B$ for selected aspect ratios W/H = {4, 6, 8, 10} (lines in order from blue to red) and initial concentration $c_{\sigma,i} = c_\sigma{}^A$. Circles correspond to the simulation points, while solid lines correspond to the exponential fit

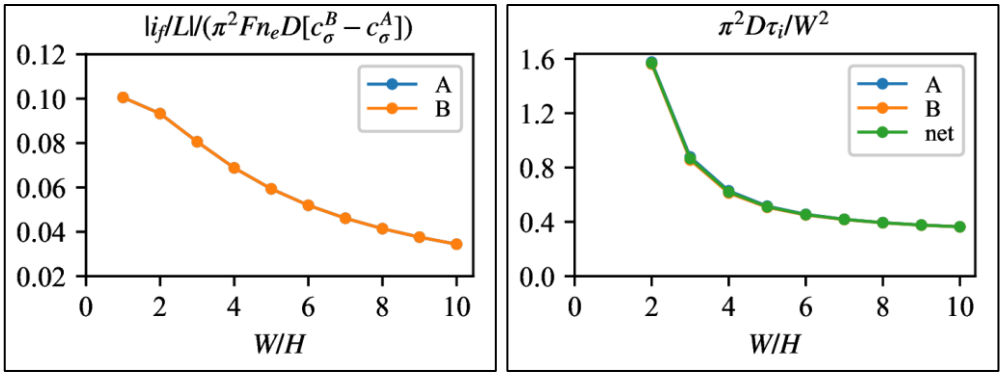


Figure 6. Normalized versions of the absolute value of the steady-state current $|i_f|$ (left) and the time constant of the current τ_i (right) for different aspect ratios W/H and initial concentration $c_{\sigma,i} = c_\sigma{}^A$. The case $W/H = 1$ has been omitted from the normalized time constant plot to maintain good visualization of the lower values

Table 1. Parameters resulting from the exponential fit of normalized currents for different aspect ratios W/H and initial concentration $c_{\sigma,i} = c_\sigma{}^A = 0$. The parameters p_0, p_1, and p_2 correspond to the normalized versions of i_f, K and τ_i, that is, $(i_f/L)/(\pi^2 F n_e D[c_\sigma{}^A - c_\sigma{}^B])$, $(K/L)/(\pi^2 F n_e D[c_\sigma{}^A - c_\sigma{}^B])$, and $\pi^2 D\tau_i/W^2$. The coefficient of determination was $R^2 > 0.9999$ for all cases

	A			*B*			net		
W/H	p_0	p_1	p_2	p_0	p_1	p_2	p_0	p_1	p_2
1	-0.1005	0.0878	5.1005	0.1005	0.0878	5.1002	0	0.1757	5.1003
2	-0.0933	0.1447	1.5761	0.0933	0.1446	1.5611	0	0.2943	1.5685
3	-0.0806	0.1643	0.8779	0.0806	0.1820	0.8549	0	0.3459	0.8662
4	-0.0688	0.1581	0.6287	0.0688	0.1759	0.6118	0	0.3336	0.6201
5	-0.0593	0.1406	0.5156	0.0593	0.1506	0.5065	0	0.2910	0.5110
6	-0.0519	0.1215	0.4554	0.0519	0.1266	0.4505	0	0.2480	0.4529
7	-0.0461	0.1054	0.4191	0.0461	0.1079	0.4165	0	0.2133	0.4178
8	-0.0414	0.0925	0.3945	0.0414	0.0941	0.3927	0	0.1865	0.3936
9	-0.0376	0.0823	0.3769	0.0376	0.0834	0.3756	0	0.1657	0.3763
10	-0.0344	0.0742	0.3638	0.0344	0.0749	0.3630	0	0.1491	0.3634

Case of internal counter electrode ($c_{\sigma,i} = [c_\sigma{}^A + c_\sigma{}^B]/2$)
In this case, the average concentration applied at the bands equals the initial concentration $(c_\sigma{}^A + c_\sigma{}^B)/2 = c_{\sigma,i}$, corresponding to the case where a conventional potentiostat drives one of the arrays while the other array performs as a counter electrode. Here, the potential (and therefore the concentration) of the counter electrode is regulated automatically by the potentiostat following the previous average condition, which can be rewritten as $[c_\sigma{}^B - c_{\sigma,i}] = -[c_\sigma{}^A - c_{\sigma,i}]$.

Under these conditions, several simulations were performed using different values of W/H. Unlike the case of the external counter electrode, these simulations

produced currents of the same magnitude at bands A and B, but with the opposite sign $i_A = -i_B$, and not only during steady state but for all simulation times (Figure 7). This means that all current generated by bands B is always collected by bands A, thus confirming the use of an internal counter electrode.

As before, all currents obtained by simulation (circles) can be approximated by exponentials (lines), as presented in Figure 7. For example, in the case of currents at bands B, the exponential approximations show some deviation for times $t > \tau_i$, but a considerable improvement for $t > T$ (roughly $2\tau_i$). All current responses reach steady state at times $t > 5\tau_i$. The parameters i_f, K, and τ_i obtained from all exponential fits are given in Table 2, such that the exponential approximations can be easily reconstructed as required.

In Figure 8, the magnitudes of the currents at bands A and B decrease as the cell becomes shallower, in the same way as in the case of the external counter electrode (at least for their normalized versions). In similarity to the case of the external counter electrode, this is due to the vertical gradient of concentration between the IDAE and the roof of the cell (Figure 2), which disappears as the cell becomes shallower. The time constants of the currents at bands A and B are equal, decreasing as the cell becomes shallower. However, the values obtained here are much shorter than those obtained for the external counter electrode (compared with Figure 6). This can be explained by the absence of an external counter electrode, and therefore, the species cannot escape far from the IDAE but diffuse only between consecutive bands, even in the case of a tall electrochemical cell.

Finally, as in the case of the external counter electrode, a compromise exists between the sensitivity (current) and response time (time constant) of the electrochemical sensor. The shallower the electrochemical cell, the less sensitive it becomes, but the shorter the response time. And vice versa in the case of tall cells.

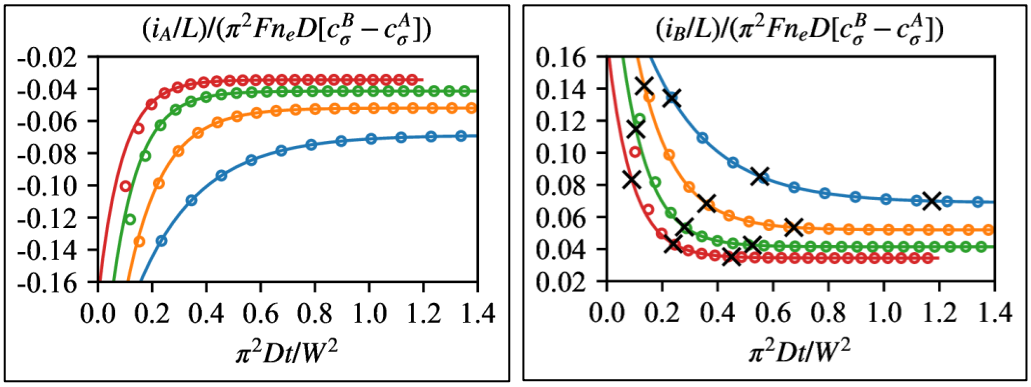


Figure 7. Normalized versions of the current through single bands i_A (left) and i_B (right) for selected aspect ratios W/H = {4, 6, 8, 10} (lines in order from blue to red) and initial concentration $c_{\sigma,i} = (c_\sigma^A + c_\sigma^B)/2$. Circles correspond to the simulation points, while solid lines correspond to the exponential fit. Crosses on a line correspond to the times τ_i, T, and $5\tau_i$ (in order from left to right)

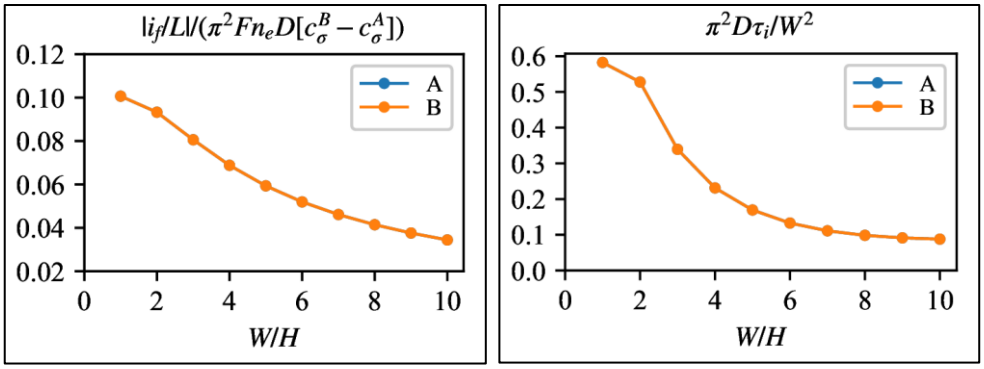


Figure 8. Normalized versions of the absolute value of the steady-state current $|i_f|$ (left) and the time constant of the current τ_i (right) for different aspect ratios W/H and initial concentration $c_{\sigma,i} = (c_\sigma^A + c_\sigma^B)/2$

Table 2. Parameters resulting from the exponential fit of normalized currents for different aspect ratios W/H and initial concentration $c_{\sigma,i} = (c_\sigma^A + c_\sigma^B)/2$. The parameters p_0, p_1, and p_2 correspond to the normalized versions of i_f, K, and τ_i, that is, $(i_f/L)/(\pi^2 F n_e D[c_\sigma^A - c_\sigma^B])$, $(K/L)/(\pi^2 F n_e D[c_\sigma^A - c_\sigma^B])$, and $\pi^2 D\tau_i/W^2$. The coefficient of determination was $R^2 > 0.9985$ for all cases

	A			*B*		
W/H	p_0	p_1	p_2	p_0	p_1	p_2
1	-0.1006	-0.0310	0.5825	0.1006	0.0310	0.5825
2	-0.0933	-0.0601	0.5277	0.0933	0.0601	0.5277
3	-0.0806	-0.1212	0.3392	0.0806	0.1212	0.3392
4	-0.0688	-0.1800	0.2312	0.0688	0.1800	0.2312
5	-0.0593	-0.2253	0.1694	0.0593	0.2253	0.1694
6	-0.0519	-0.2479	0.1328	0.0519	0.2479	0.1328
7	-0.0461	-0.2426	0.1111	0.0461	0.2426	0.1111
8	-0.0414	-0.2132	0.0984	0.0414	0.2132	0.0984
9	-0.0376	-0.1739	0.0913	0.0376	0.1739	0.0913
10	-0.0344	-0.1363	0.0877	0.0344	0.1363	0.0877

Conclusion

In this work, the main issue of whether the current response of an IDAE in a shallow electrochemical cell can be modeled by an exponential function has been addressed. The results show that a simple exponential function can approximate the time response of the current for elapsed times greater than approximately two-time constants, reaching steady state after approximately five-time constants. Normalized steady-state currents and time constants were tabulated for different aspect ratios (separation between bands with respect to height of the cell), such that they can be used for cells of different scales or dimensions.

When driving the IDAE with a bipotentiostat (both arrays perform as working electrodes), the net current at the arrays is non-zero during the transient state (approaching zero in steady state) and must be collected

by an external counter electrode. On the other hand, when driving the IDAE with a conventional potentiostat (one array performs as a working electrode, while the other performs as an internal counter electrode), the currents at the arrays are always of equal magnitude and opposite signs (during the transient and steady states).

In the cases of external and internal counter electrodes, the steady-state magnitude and time constant of the current decrease as the electrochemical cell becomes shallower. This shows a trade-off or compromise between sensitivity (in terms of current magnitude) and response time (in terms of time constant) for IDAEs in shallow cells. Higher currents can be obtained at the expense of longer response times when the cell is tall (compared to the separation between consecutive bands of the IDAE) and shorter response times at the expense of lower currents when the cell is shallow.

Acknowledgment

The authors gratefully acknowledge *Petchra Pra Jom Klao Ph.D. Scholarship* (Grant No. 28/2558), *King Mongkut's University of Technology Thonburi.* The authors also acknowledge the financial support provided by *King Mongkut's University of Technology Thonburi* and the *Research Network NANOTEC* (RNN) program (Grant No. P1851883) of the *National Nanotechnology Center* (NANOTEC), NSTDA, Ministry of Science and Technology, Thailand.

References

1. Karimian, N. and Ugo, P. (2019). Recent advances in sensing and biosensing with arrays of nanoelectrodes. *Current Opinion in Electrochemistry*, 16: 106-116.
2. Rackus, D. G., Shamsi, M. H. and Wheeler, A. R. (2015). Electrochemistry, biosensors and microfluidics: A convergence of fields. *Chemical Society Reviews*, 44: 5320-5340.
3. Gencoglu, A. and Minerick, A. R. (2014). Electrochemical detection techniques in micro- and nanofluidic devices. *Microfluidics and Nanofluidics*, 17: 781-807.
4. Aoki, K., Morita, M., Niwa, O. and Tabei, H. (1988). Quantitative analysis of reversible diffusion-controlled currents of redox soluble species at interdigitatedgitated array electrodes under steady-state conditions. *Journal of Electroanalytical Chemistry and Interfacial Electrochemistry*, 256. 269-282.
5. Kanno, Y., Goto, T., Ino, K., Inoue, K. Y., Takahashi, Y., Shiku, H. and Matsue, T. (2014). SU-8-based flexible amperometric device with IDA electrodes to regenerate redox species in small spaces. *Analytical Sciences*, 30: 305-309.
6. Heo, J.-I., Lim, Y. and Shin, H. (2013). The effect of channel height and electrode aspect ratio on redox cycling at carbon interdigitated array nanoelectrodes confined in a microchannel. *Analyst*, 138: 6404-6411.
7. Oldham, K. and Myland, J. (1994). Fundamentals of electrochemical science. Academic Press, UK. §5:8.
8. Guajardo, C., Ngamchana, S. and Surareungchai, W. (2013). Mathematical modeling of interdigitated electrode arrays in finite electrochemical cells. *Journal of Electroanalytical Chemistry*, 705: 19-29.
9. Morf, W. E., Koudelka-Hep, M., de Rooij, N. F. (2006). Theoretical treatment and computer simulation of microelectrode arrays. *Journal of Electroanalytical Chemistry*, 590: 47-56.
10. Britz, D. and Strutwolf, J. (2016). Digital simulation in electrochemistry. Springer International Publishing, Switzerland. §7.2.
11. Guyer, J. E., Wheeler, D. and Warren, J. A. (2009). FiPy: Partial differential equations with Python. Computing in Science and Engineering, 11(3): 6-5.
12. Guajardo Y., Cristian F. and Surareungchai, W. (2021). Simulations for the current's time response of interdigitated arrays in shallow electrochemical cells using FiPy. https://doi.org/10.5281/zenodo.5633322 [software].

Malaysian Journal of Analytical Sciences (MJAS)
Published by Malaysian Analytical Sciences Society

FERROCENE MEDIATED AMPEROMETRIC BIOSENSOR FOR L-GLUTAMATE BASED ON L-GLUTAMATE OXIDASE IMMOBILIZED IN A PHOTOCURABLE METHACRYLIC FILM

(Biosensor Amperometrik L-Glutamat berperantara Ferosena berasaskan L-Glutamat Oksida Terpegun dalam Fotosalutan Filem Metakrilik)

Noor Zuhartini Md Muslim[1*], Musa Ahmad[2], Lee Yook Heng[3], Bahruddin Saad[4]

[1]School of Health Sciences, Health Campus,
Universiti Sains Malaysia, 16150 Kubang Kerian, Kelantan, Malaysia
[2]Faculty of Science & Technology,
Universiti Sains Islam Malaysia, 71800 Bandar Baru Nilai, Negeri Sembilan, Malaysia
[3]School of Chemical Sciences and Food Technology,
Faculty of Science & Technology, Universiti Kebangsaan Malaysia, 43600 Bangi, Selangor, Malaysia
[4]Department of Fundamental & Applied Scinces,
Universiti Teknologi PETRONAS, Bandar Seri Iskandar, 32610 Perak, Malaysia

[*]Corresponding author: zuhartini@usm.my

Received: 24 May 2022; Accepted: 27 September 2022; Published: 27 December 2022

Abstract

L-glutamate is widely used as a flavour enhancer in various foodstuffs and seasoning in the form of monosodium glutamate (MSG). MSG has been linked to neurotoxic effects, metabolic disorders, headache, numbness and palpitation. In this work, an amperometric L-glutamate biosensor based on photocurable poly(2-hydroxylethyl methacrylate)-containing ferrocene film for the determination of L-glutamate in food samples is described. The sensor is fabricated based on simultaneous immobilization of both L-glutamate oxidase and ferrocene as a mediator during the deposition of poly(2-hydroxylethyl methacrylate) film via photocuring. Ferrocene was used to shuttle the electrons directly between the reduced enzyme and the electrode. From electrochemical studies, a linear response towards L-glutamate in the concentration range of 10-30 mM was obtained at applied potential of +0.25 V with the detection limit of 7.7 mM. The storage stability of the biosensor is up to 4 months under storage condition of 4 ^{o}C in refrigerator. The performance of the biosensor was applied to the determination of L-glutamate in food stocks from local supermarkets. Results from amperometric L-glutamate biosensor were further validated with HPLC method.

Keywords: photocurable, methacrylate polymers, ferrocene, L-glutamate biosensor

Abstrak

L-glutamat digunakan secara meluas dalam pelbagai bahan makanan dan perasa dalam bentuk mononatrium glutamat (MSG). MSG telah dikaitkan dengan kesan neurotoksik, gangguan metabolik, sakit kepala, rasa kebas dan berdebar-debar. Biosensor amperomerik L-glutamat berasaskan fotosalutan poli(2-hidroksiletil matakrilat)-mengandungi filem ferosena dihuraikan untuk

penentuan L-glutamat di dalam sampel makanan. Sensor ini direka berasaskan pemegunan secara serentak bagi L-glutamat oksida dan ferosena sebagai perantara semasa pemendapan filem poli(2-hidroksiletil metakrilat) menerusi fotosalutan. Ferosena digunakan sebagai perantara ulang-alik elektron secara langsung antara penurunan enzim dengan elektrod. Berdasarkan kajian elektrokimia, rangsangan linear terhadap L-glutamat diperoleh dalam julat kepekatan 10-30 mM pada keupayaan +0.25 V dengan had pengesanan 7.7 mM. Jangka hayat kestabilan biosensor penyimpanan dalam peti sejuk adalah mencapai sehingga 4 bulan pada suhu 4^{o}C. Prestasi biosensor diaplikasikan untuk penentuan L-glutamat dalam stok makanan daripada pasar raya tempatan. Keputusan daripada biosensor L-glutamat seterusnya disahkan dengan kaedah HPLC.

Kata kunci: fotosalutan, polimer metakrilat, ferosena, biosensor L-glutamat

Introduction

Glutamic acid is an important neurotransmitter of the central nervous system [1]. It is widely used as an additive to enhance the flavour in variety of foods prepared at home, restaurants, and by food processor in a form of monosodium glutamate (MSG). Glutamic acid exists both as free glutamate and bound with other amino acids in a protein. Only the free form of L-glutamate can enhance the food's flavour. The use of MSG in foods became controversial in the late 1960s when it was claimed to be the cause of a range of adverse reactions in people who had eaten foods containing the additive. Symptoms of MSG-sensitivity (called "Chinese restaurant syndrome") consist of numbness at the back of the neck and arms, weakness and palpitation. There is growing evidence linking the abnormalities of endogenous glutamate metabolism with certain diseases, such as Alzheimer's, Huntington's disease and Amyotrophic lateral sclerosis [2]. In Malaysia, the use of MSG must be in the form of 99.9% L-glutamate but there is no regulation on the limit of MSG that can be added into the food [3]. However, based on European Food Safety Authority (EFSA) panel after re-evaluating the safety of glutamate additives in 2017, the acceptable daily intake for glutamate additive has been set to 30 mg/kg bw/day [4].

There are several methods to determine the L-glutamate. Typically, separation techniques, in particular high-performance liquid chromatography [5, 6, 7], high-performance thin layer chromatography [8], thin layer chromatography and liquid chromatography-mass spectrometry [9] and capillary electrophoresis [10] are commonly used but require pre-concentration and sample derivatization. These techniques are also time consuming and need to be performed by highly trained operators. In contrast, simple and cost-effective spectrophotometric [11, 12, 13] and potentiometric [14] methods with chemical derivatization have been considered by some authors as an alternative for determination of L-glutamate in food. However, poor selectivity and interference from complex matrices in food may give inaccurate determination of L-glutamate. Therefore, enzymatic biosensors are gaining considerable attention due to their advantages of high selectivity and sensitivity towards L-glutamate**.** L-glutamate dehydrogenase [15, 16] and L-glutamate oxidase [17-23] had been widely used as a biological recognition to construct enzymatic sensors. Many enzymic methods have been used in conjunction with spectrophotometry [16, 19], potentiometry [20, 21] and amperometry [15, 17, 18, 22, 23] for the analysis of L-glutamate.

Enzyme electrodes have been proven to be the most widely applicable since it served to concentrate the enzyme activity in the vicinity of the sensor surface. A mixture of glutaraldehyde and bovine serum albumin (BSA) were usually used as a cross-linking reagent to immobilize the enzyme onto the electrode. A photo-cross linkable polymer polyvinyl alcohol bearing styrylpyridinium (PVA-SbQ) mixed with BSA and glutaraldehyde exposure has been reported for fabrication of an enzyme L-glutamate oxidase on a planar palladium electrode [18]. Hydrogen peroxide produced from the catalytic reaction by the L-glutamate oxidase which is proportional to the concentration of MSG was recorded at a potential of +400 mV versus Ag/AgCl reference electrode. The measurement range of L-glutamate was obtained between 50 nM - 100 µM. However, this method required a long procedure where glutaraldehyde in vaporized form was used instead of mixing directly to prevent enzyme deactivation during chemical attachment. Another approached was the

development of amperometric biosensor of L-glutamate based on the co-immobilization of L-glutamate dehydrogenase (GLDH) and salicylate hydroxylase (SHL) entrapped in a poly(carbamoyl) sulfonate (PCS) hydrogel and sandwiched between a dialysis membrane and a Teflon membrane on a Clark-type oxygen electrode [15]. Enzyme solution of GLDH and SHL was mixed with PCS and polymerization then achieved by adjusting the pH of the enzyme matrix through the addition of polyethylenimine (PEI). The mixture of the enzyme-PCS gel was spread over a Teflon membrane, followed by drying and storing at 4°C overnight. Simple immobilization technique through entrapment of the L-glutamate oxidase in chitosan film also required a few hours to complete the immobilization process [17].

In this work, the enzyme L-glutamate oxidase (Glox) was used as a biological recognition element to detect L-glutamate. The enzyme reactions with L-glutamate are illustrated in Equation 1. L-glutamate reacted with Glox producing H_2O_2, α-ketoglutarate, NH_3 and a reduced form of Glox. The product H_2O_2 is an electroactive species, which can be oxidized to yield current flow. However, due to the high oxidation potential of H_2O_2 which gives poor selectivity and interferences to the biosensor signal, therefore H_2O_2 was not used in the transduction process. Instead, ferrocene (Fc) was used as a mediator to shuttle electrons directly between the reduced enzyme and the electrode (Equation 2). The Fc diffused to the working electrode, oxidized or reduced at a fixed potential until it reached equilibrium (Equation 3). In this way, the current generated was directly proportional to the concentration of L-glutamate. The similar concept had been reported to construct glucose biosensor [24].

$$\mathrm{L-glutamate} + \mathrm{Glox_{oxidized}} \rightarrow \mathrm{Glox_{reduced}} + \alpha\mathrm{-ketoglutarate} + \mathrm{NH_3} + \mathrm{H_2O_2} \quad (1)$$

$$\mathrm{Glox_{reduced}} + 2\,\mathrm{Fc^+} \rightarrow \mathrm{Glox_{oxidized}} + 2\,\mathrm{Fc} \quad (2)$$

$$\text{At the working electrode: } \mathrm{Fc} \leftrightarrows \mathrm{Fc^+} + \mathrm{e^-} \quad (3)$$

A one-step procedure for fabrication of a L-glutamate biosensor film is using a photocuring technique. Briefly, both Fc mediator and Glox are immobilized in a polymer which is formed from photopolymerization of 2-hydroxylethyl methacrylate (HEMA). This is a simple and rapid technique for preparation of a biosensor, as compared with those described elsewhere [22, 23].

Materials and Methods

Materials and reagent

All chemicals used were of analytical grade and deionized water was used throughout for all solutions preparation. Ferrocene was obtained from Fluka (98% purity), 2-hydroxylethyl methacrylate (HEMA, 98%) purity) and L-glutamate oxidase (Glox) (≥ 5.0 unit/mg) were obtained from Sigma. Initiator 2,2-dimethoxy-2-phenylacetophenone (DMPP, 99% purity) was supplied by Aldrich and monosodium glutamate monohydrate was supplied by Acros Organic (99% purity). Phosphate buffer (0.1 M, pH 7.0) used as electrolyte in electrochemical measurements was prepared in 0.1 M NaCl.

Preparation of biosensors

Carbon-paste screen-printed electrodes (SPE) (Scrint Print Technology, Malaysia) were used as working electrodes with electrode surface 4 mm in diameter. Initially, a stock homogeneous solution of HEMA containing DMPP and Fc was prepared by mixing 1 mL of HEMA solution, 1.6 % DMPP (w/w) and 1 % Fc (w/w) in a dark bottle. The stock solution was stored at 4°C when not in used. The formulation was changed accordingly when certain experimental parameters were investigated. Then, appropriate amount of stock HEMA solution was mixed with Glox and a volume of 5 µL mixture solution of Fc/HEMA/Glox was deposited on the working electrode area and then exposed to UV radiation (λ = 365 nm, 15 W) under nitrogen gas in 8 minutes to form a solid thin layer membrane.

Electrochemical measurements

The electrochemical measurements were performed with an Autolab PGSTAT 12 Potentiostat/Galvanostat. A one compartment cell with a working volume of 4 mL 0.1 M phosphate/NaCl buffer was used. The working

electrode is a SPE coated with polymer-containing Fc film whereas silver/silver chloride (Ag/AgCl) and a glassy carbon electrode were used as reference electrode and auxiliary electrode respectively. The characterization of the potential-dependent behaviour of Fc with cyclic voltammetric (CV) was carried out by scanning between -0.5 - 0.7 V (versus Ag/AgCl) at a scan rate 5 mV/s in an unstirred 0.1 M phosphate/NaCl buffer pH 7. The effect of the detection potential on the electrode sensitivity was examined amperometrically for applied potentials varying between +0.1 - +0.4 V under a stirred solution of 4 mL 0.1 M phosphate/NaCl buffer pH 7.0, 30 mM L-glutamate.

The biosensor was optimized with regards to several parameters, namely, effect of pH, Fc and enzyme loading over the amperometric response of the electrode at an optimum applied potential of +0.25 V versus Ag/AgCl. For the determination of the effect of pH value on the biosensor response, 30 mM L-glutamate solution was prepared by adding 60 µL of 2 M L-glutamate with 4 ml of buffer with different pH (5 - 9). The stock pH 5 - 9 buffer solution was obtained by mixing 0.1 M phosphate solution with NaCl and pH was adjusted with NaOH or HCl. The effect of the Fc concentration used as a mediator on the biosensor response was tested by varying the concentration of Fc at 0.5%, 1% and 2% (w/w) and for enzyme loading, the amount of Glox was varied in the range of 20 - 160 U/g Fc/HEMA at the fixed amount of Fc and pH.

The stability of the biosensor for reusability (repetitive usage) was tested by preparing six different biosensors which three of them were used once a day and another three were used once in every two weeks. The performance for each biosensor was measured by using 20 mM standard L-glutamate. The biosensor performance of the first day was used as a reference and the percentage of the relative response was determined. After each usage the biosensors was stored in a closed container under dry storage at 4ºC. The reusability was carried out until the percentage relative response reached below 50% [25]. For the storage stability, another three biosensors were prepared and they were stored dry at 4ºC. The biosensors were tested periodically once a month for six months using 20 mM L-glutamate solution.

The calibration measurements were performed by placing the working electrode in 4 mL of a stirred 0.1 M phosphate/NaCl buffer (pH 7.0) at an applied potential of +0.25 V versus Ag/AgCl. When the background current reaching the steady value, an appropriate amount of L-glutamate solution was added into an electrochemical cell. After the addition, the current increased to a new steady value. The L-glutamate concentrations were added then plotted against the difference in current between before and after glutamate addition.

Biosensor at the optimum condition was applied to determine the concentration of the L-glutamate in food samples. The interference effect of the matrix in the samples was tested first by measuring any possible amperometric response after adding three possible interference species such as ascorbic acid, L-aspartate and D-glutamic acid into the samples. The interference study was also carried out by doing recovery study. For recovery studies, the biosensors were employed for the determination of L-glutamate in four different food samples such as fried rice seasoning, fish sauce, sour curry paste and concentrated chicken stock. Two set of food samples were prepared which one without spiked standard L-glutamate and the other one with spiked standard L-glutamate. Percent recovery was calculated by the formula below:

$$\% \text{ recovery} = (x-y)/z \times 100$$

x = average [L-glutamate] in spiked sample
y = average [L-glutamate] in non-spiked sample
z = average [L-glutamte] that was spiked in the sample

Food stocks were obtained from local supermarkets. Solid samples and pastes were dissolved in boiling water according to the manufacturer's instructions and treated as liquid samples. Samples were filtered using filter paper type Whatman Ashless before the determination. The liquid sample produced well-defined amperometric responses similar to those of L-glutamate standard.

HPLC method for L-glutamate determination

For HPLC method, the sample was centrifuged at 3000 rpm for 15 minutes and filtered using 0.4 µm membrane filter. L-glutamate levels were determined by isocratic liquid chromatographic using fluorescence detection after pre-column derivatization with o-phthaldialdehyde (OPA) [26]. OPA (108 mg) was dissolved in 1 mL of 99.5% ethanol. Borate buffer (0.4 M, pH 10.4) was added and followed by 20 µL of 2-mercaptoethanol and 20 µL of L-glutamate/sample made up to 10 mL. The derivatized L-glutamate solution was injected into the HPLC column within one minute after preparation. The HPLC analysis was carried out using a Jasco PV-1580 instrument with a ThermoHypersil-Keystone Hypersil ODS column (250 × 4.6 mm, 5 µm) at room temperature. The excitation and emission wavelengths of the Jasco FD-1520-Intelligent Fluorescence detector were set at 330 nm and 455 nm respectively to detect the derivatized L-glutamate. The volume of the derivatized sample injected was 20 µL. The analysis was carried out isocratically using a mobile phase of methanol-phosphate buffer (35:65, v/v) at pH 5.8.

Results and Discussion

The cyclic voltammetry study of immobilized ferrocene mediator in the biosensor

As shown in Figure 1, as the potential becomes more positive and the reduced form of the Fc is converted into the oxidized ferricenium species, hence there is appearance of the anodic peak in the range of +0.2 - +0.5 V. As the potential is reversed, a cathodic peak is detected in the range of +0.1 - +0.3 V attributed to the electrochemical activity of the ferricenium generated during the forward scan. The similar pattern was also observed in an earlier study using the similar polymer films with Fc as a mediator [24]. It can be shown that the immobilised Fc mediator demonstrated electrochemical reversible behaviour. Therefore, effect of applied potential on the biosensor response against L-glutamate was tested in the range of +0.1 – +0.5 V and the results are shown in Figure 2.

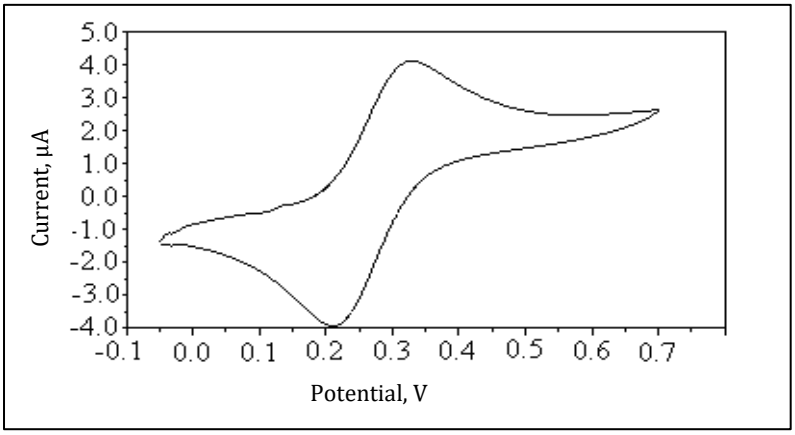


Figure 1. Cyclic voltammograms of Fc/HEMA/Glox biosensor versus Ag/AgCl electrode from -0.5 – +0.7 V with a scan rate of 5 mV/s in an unstirred 0.1 M phosphate buffer/NaCl pH 7

The biosensor response showed rapidly increasing with the applied potential until it reached at optimum potential of +0.25 V. At the potential higher than +0.25 V, the current was observed to decrease. The obtained potential was relatively low compared to reported potential by Liu et. al. [23] that was +0.6 V. The low applied potential was beneficial to avoid any interference from other electroactive species such as

ascorbic acid. Therefore, an applied potential of +0.25 V versus Ag/AgCl was carried out for all subsequent studies.

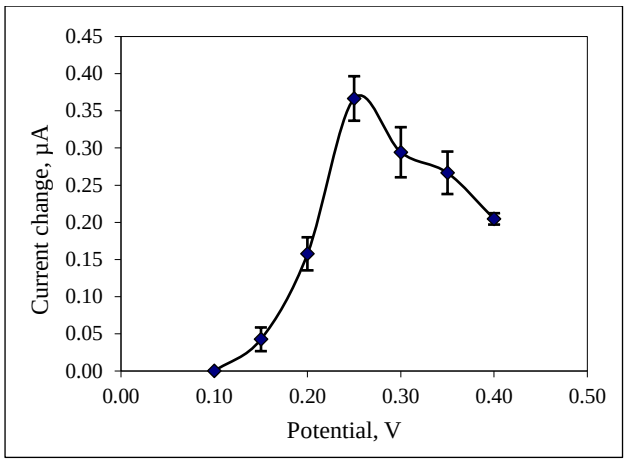


Figure 2. Effect of applied potential on the biosensor response studied for amperometric measurements for 25 mM L-glutamate in 0.1 M phosphate/NaCl buffer pH 7.0 versus Ag/AgCl electrode

Effect of pH

The influence of the buffer pH is very essential to the sensitivity of the biosensors because the pH does not only affect the electrochemical behavior of Fc but also the bioactivity of Glox. The bioactivity of the immobilized enzyme with Fc/HEMA/Glox that deposited on the electrode was influenced by the pH of the buffer used as shown in Figure 3. All buffers were solutions of 0.1 M phosphate buffer/NaCl. A plot of the current response to a fixed amount of L-glutamate as a function of pH change indicated that the response reached maximum value at pH 7.0. The behavior of the enzyme Glox was reported to be more stable in pH between 7.0 - 7.4 [27]. Therefore, further studies of the biosensor response with L-glutamate will be carried out at pH 7.0.

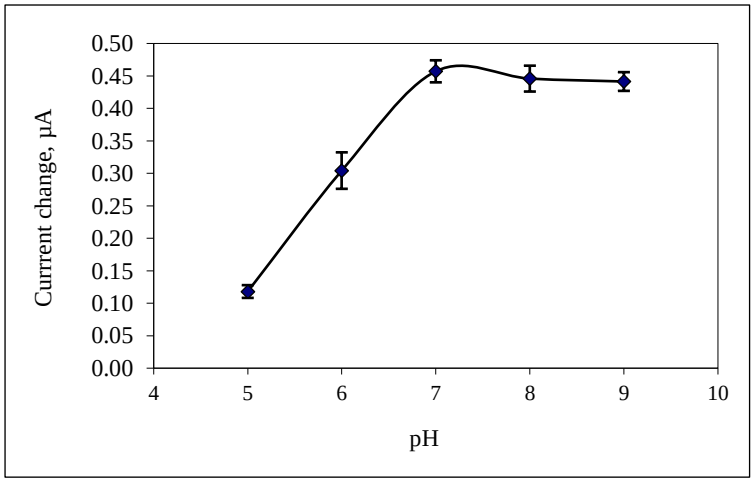


Figure 3. Effect of pH on the maximum response of the glutamate biosensor in 30 mM of L-glutamate at +0.25 V in 0.1 M phosphate/NaCl buffer pH 7.0 versus Ag/AgCl electrode

Effect of ferrocene concentration

Ferrocene as a mediator was used in this constructed biosensor. Ferrocene was immobilized together with Glox/HEMA deposited on the working electrode. In the absence of mediator, the biosensor did not demonstrate any response to the present of L-glutamate. This may be attributed to the non-existence of redox reaction of the H_2O_2 at the surface of the working electrode. In the presence of the Fc mediator, the one-electron oxidation of Fc to the stable ferricenium cation was a simple electron transfer reaction, where complications arising from adsorption or associated chemical reaction which were not expected [28]. Ferrocene has been used as the mediator for the determination of glucose using glucose oxidase as a biological sensing material [24]. Glucose oxidase and Glox belong to the same oxidase family with the same cofactor (FAD) with almost the same enzyme conformation [29].

The effect of varying concentration of immobilized mediator Fc on the biosensor response can be seen in Figure 4. The optimum concentration of Fc to give the best biosensor response to L-glutamate is at 1% of Fc by weighting of the biosensor film. The Fc concentration above 1% did not increase the biosensor response but instead resulting a decrease of response signal. This was probably due to the blockage of the access to the active site of the enzyme by excessive Fc molecules in the biosensor membrane. Ferrocene concentration of 0.5% was not enough to oxidize back the reduced enzyme and interact with L-glutamate substrate. These scenarios were agreeable with Wang et al. [30], when the mediator concentration was low, the biosensor response was limited by the enzyme-mediator kinetic whereas as the concentration was higher, the biosensor response was limited by the enzyme-substrate kinetics.

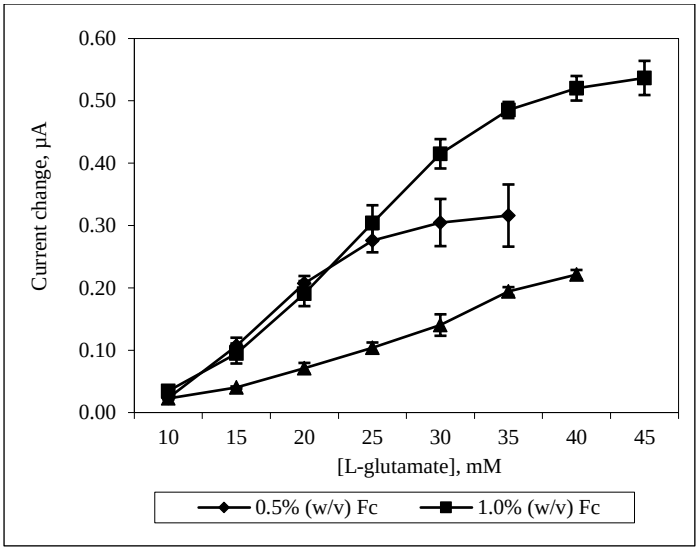


Figure 4. Effect of Fc concentration on the biosensor response at +0.25 V for a series of L-glutamate concentration in 0.1 M phosphate buffer/NaCl pH 7.0 versus Ag/AgCl electrode

Effect of enzyme loading

Enzyme loading also affected the performance of the biosensor. The Glox enzyme was used as a biological reagent for the detection of L-glutamate substrates in Fc/HEMA membranes. From the study of Glox enzyme loading (20 - 160 U/g Fc/HEMA), 120 U/g was enough to give the best performance for the biosensor (Figure 5). The insert graph was the plot enzyme loading versus current change in 40 mM L-glutamate. Reaction rates increased linearly with the increasing concentration of enzyme if the concentration of the substrate was in excess when compared with the amount of enzyme [31]. The sensitivity and the linear dynamic range of the biosensor increased with the increase amount of immobilized enzyme [32]. However, large immobilized enzyme loads were also considered unsuitable because

the limited space in the polymer caused the enzyme active site to be shielded and cannot be fully exposed to glutamate oxidation and reduction reactions [33]. Therefore, an enzyme load of 120 U/g HEMA was selected in this study for the preparation of all biosensors for further amperometry studies.

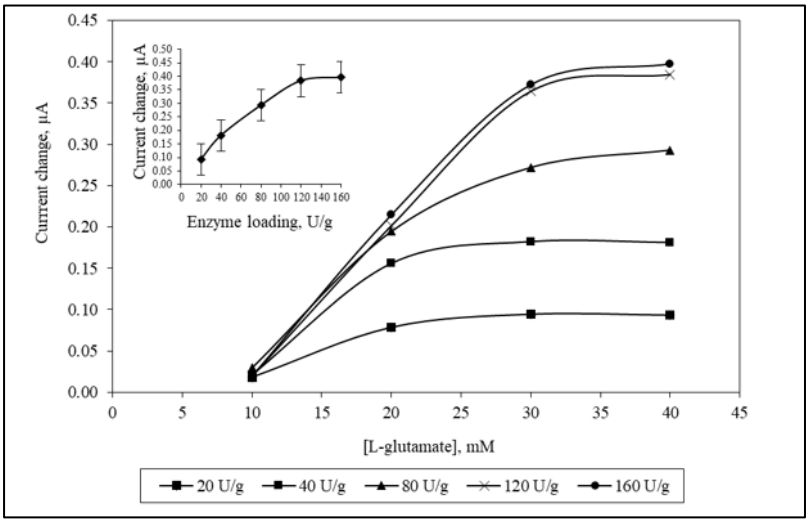


Figure 5. Effect of enzyme loading on the biosensor response at +0.25 V for a series of L-glutamate concentration in 0.1 M phosphate buffer/NaCl pH 7.0 versus Ag/AgCl electrode. The insert graph was the plot enzyme loading versus current change in 40 mM L-glutamate

The stability of L-glutamate biosensor

Stability characteristics related to reusability (repetitive usage) and shelf life are the important factors need to investigate. The stability of a biosensor was influenced by factors such as the method of enzyme immobilization and biosensor storage conditions. From the study of the stability by using the same biosensor for repeated measurement (Figure 6), the percent relative response showed an increasing trend from day 1 – 4 due to conditioning steps until its stabilized. This is associated with decreasing diffusional barriers of the analyte and membrane [25]. The percent relative response was very stable upon repeated injection from day 4 - 9, demonstrating that the membrane did not undergo fouling by the oxidation products. However, the percent relative response started to decrease from day 10 and reached below 50% at day 17. The decreasing trend of the biosensor may be due to hydrophilic property of the HEMA and its swell after it immersed in aqueous L-glutamate solution. The swelling process caused more L-glutamate substrate to penetrate the membrane. This condition would cause the enzyme activity to decrease due to the overexposure to the glutamate solution. Lim and Ang [31] also reported that the enzyme activity was decreased when exposing to high substrate concentrations. The swelling process of polymer membranes affected diffusion, surface properties, mechanical properties and surface movement [34].

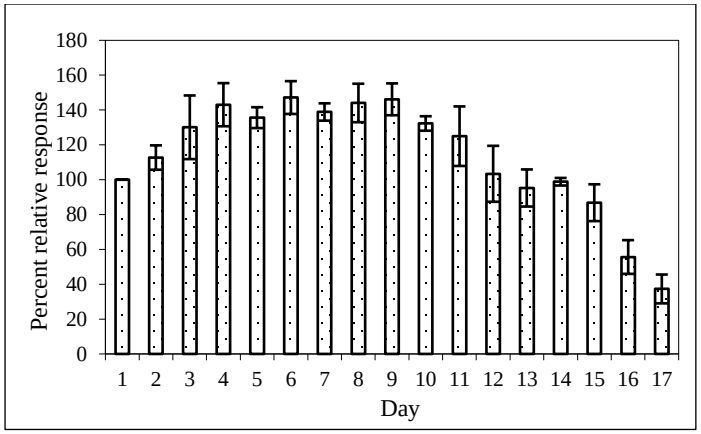


Figure 6. The stability of glutamate biosensor by using the same biosensor for reusability by taking the measurement once a day and kept dry at 4ºC while not in use

The stability of the biosensor was also tested by measuring the percent relative response in 2 weeks' time (Figure 7). The measurement on the first day was used as a reference and considered 100% performance. After measuring, the biosensor was stored dry at 4 ºC. The usage on the 75th day showed that the percent relative response decreased significantly by 41%. The finding showed that, if the biosensor did not use in everyday but only once in two weeks' time, the stability of the biosensor can be extended.

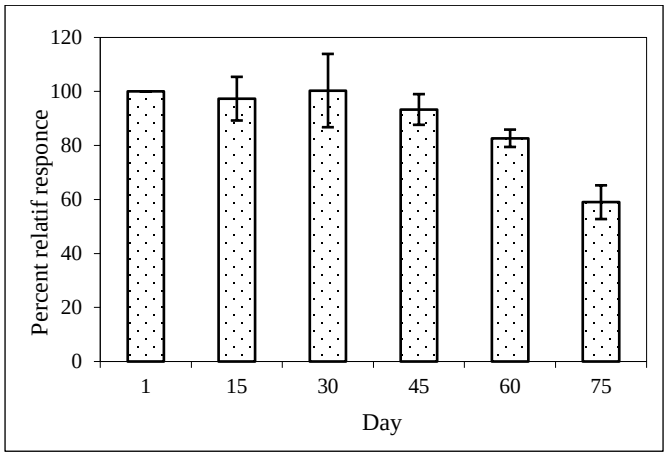


Figure 7. The stability of glutamate biosensor by using the same biosensor for reusability by taking the measurement once in two week's time and kept dry at 4ºC while not in use

Figure 8 showed the performance of a biosensor prepared in a similar preparation, stored at a temperature of 4ºC in a close container and dry state. According to Chang et al. [18], the storage stability of biosensors can be improved if the working electrode containing the immobilized enzyme is stored in a dry state (not dipped in a buffer solution). The first day measurement was used as a reference for the subsequence measurement. Biosensor using different Fc/HEMA/Glox membrane was measured only once at 1-month intervals and it showed a good performance up to 4 months of storage. A decrease in the performance of the biosensor after 4 months of storage, may be because of drying process of the membrane, even though it was not in used. Since the

biosensors were kept in drying state, continuous drying of the Fc/HEMA/Glox membrane in turn causing it to be unable to maintain enzyme activity. Water molecules was trapped in the Fc/HEMA/Glox membrane and were considered important in maintaining the enzyme activity.

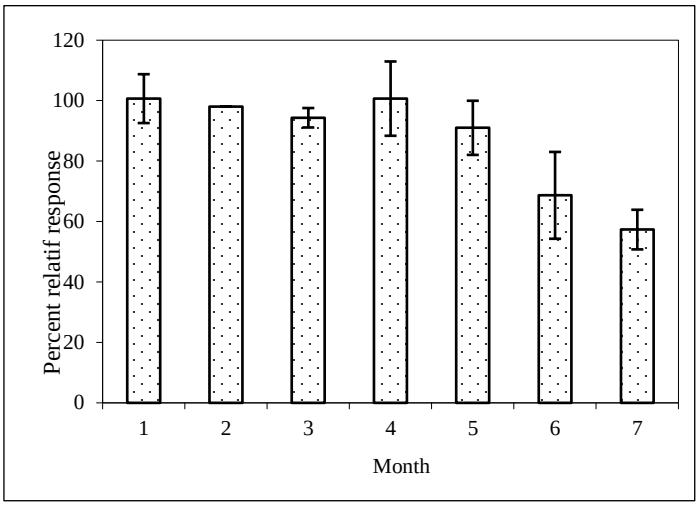


Figure 8. The storage stability of biosensor by taking the measurements once a month of different biosensor in 20 mM L-glutamate

The analytical performance of the L-glutamate biosensor

The electrochemical response of the biosensor to increasing concentration of L-glutamate is shown in Figure 9. A linear response to L-glutamate from 10 – 30 mM was demonstrated, with a sensitivity slope of 0.0173 μAmM^{-1} (R^2 = 0.984). The corresponding detection limit calculated from the L-glutamate concentration that producing an amperometric signal equals to the signal of the baseline plus three times of the standard deviation value [35] was 7.7 mM. The reproducibility of each data point had a relative standard deviation (RSD) value between 2.6% - 11.2% (n = 3) and this indicated that the biosensor showed reproducible responses.

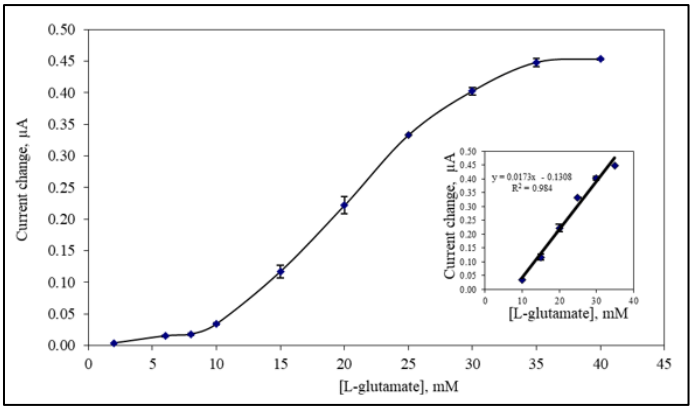


Figure 9. Response of the L-glutamate biosensor with changes in the concentrations of L-glutamate determined at applied potential +0.25 V versus Ag/AgCl electrode in stirred solution of 0.1 M phosphate/NaCl buffer pH 7. The linear range is also shown by the inset

The proposed glutamate biosensor was compared with the reported glutamate biosensor in literature. Performance of the proposed biosensor (Table 1) resulted the limit of detection which slightly higher than those of biosensors reported in literature. However, the proposed biosensor in terms of the fabrication is simple and faster. Moreover, the amount of L-glutamate in food sample was relatively high; in the range of 6.7 – 658 mg/100 g in fresh food to 0.05 – 6830 mg/100 g in processed food [36] and in food seasoning 4.8 – 21.3% [37]. Therefore, the proposed biosensor was practical to be used as a tool to detect the presence of L-glutamate in food.

Table 1. Characteristics of some glutamate biosensors reported in the literature

Type of Enzyme	Biosensor Configuration (Operational Mode)	Detection Mode	Linearity (mM)	LOD (mM)	Reference
Glox	Photocurable poly(2-hydroxylethyl methacrylate)/ferrocene	+0.25 V vs Ag/AgCl	10 – 30	7.7	Proposed
Glox	Absorption chitosan	+0.4 V vs Ag/AgCl	5×10^{-4} – 2×10^{-1}	1.0×10^{-4}	[17]
Glucose oxdase	Cross-linking glutaraldehyde/BSA/Nafion/ metal viologen	-0.65 V vs. SCE	Until 0.75	2×10^{-2}	[29]
Glox	Cross-linking glutraldehyde/BSA	+0.7 V vs Ag/AgCl	Until 0.8	3×10^{-3}	[38]
Glox	Nafion/Prussion blue	+0.0 V vs Ag/AgCl	1×10^{-4} – 1×10^{-1}	1×10^{-4}	[39]

The specificity of the biosensor to L-glutamate was evaluated by measuring a standard solution of possible interferents such as ascorbic acid, L-aspartate and D-glutamic acid under the same conditions. Ascorbic acid was chosen to represent any interference from carboxylic acid group species, L-aspartate for amino acid group and D-glutamate is a chiral to L-glutamate. No response was observed demonstrating that these substances did not interfere with the detection of L-glutamate.

Recoveries ranging from 98 –105% were obtained to the determination of L-glutamate using the L-glutamate biosensor in four different types of food matrices; this indicated that the complicated matrices of these food samples did not interfere with the performance of the glutamate biosensor.

The results of a comparative study for L-glutamate determination in some food samples using both the biosensor and standard HPLC procedure are shown in Table 2. When compared with the HPLC method, the content of L-glutamate determined in the selected food items which was analyzed by the biosensor and demonstrated a very close result. A statistical analysis (*t*-test) at 95% confidence level comparing the means of measurements obtained from the two methods of glutamate sensor and HPLC also showed no significant difference, indicating that the method developed was in good agreement with the established method.

Table 2. Comparison of L-glutamate level in food stocks obtained from local supermarkets by using the L-glutamate biosensor and HPLC method (n=3)

Type of Food	L-Glutamate Level (%)		
	Biosensor	HPLC	t-test
Anchovies stock cube	17.70 ± 0.27	17.73 ± 0.29	0.1
Fried rice mix-chicken seasoning	21.24 ± 0.46	21.38 ± 0.48	0.4
Vegetable soup seasoning	5.75 ± 0.09	5.66 ± 0.15	0.9
Fried vermicelli paste	5.47 ± 0.17	5.57 ± 0.06	1.0

Conclusion

The use of Fc mediator together with photocurable membrane technology in the fabrication of L-glutamate biosensor has successfully produced an amperometric L-glutamate biosensor (applied potential of +0.25 V versus Ag/AgCl, pH electrolyte 7.0, 1% ferrocene concentration, 120 U/g enzyme loading and with up to 4 months shelf life) that can be used to detect L-glutamate in food items. The photocurable technique in this work was simple and faster compared to covalent bonding or absorption technique reported in the literature. The biosensor exhibited a reproducible characteristic with acceptable RSD values. The biosensor had developed a linear dynamic range of 10 – 30 mM L-glutamate with LOD 7.7 mM. L-glutamate level in food samples determined from the biosensor was comparable to conventional HPLC method.

Acknowledgements

The authors greatly appreciate the instrumental and financial supports received from School of Health Sciences, Universiti Sains Malaysia (USM) and Universiti Kebangsaan Malaysia (UKM).

References

1. Borisova, T., Kucherenko, D., Soldatkin, O., Kucherenko, I., Pastukhov, A., Nazarova, A., Galkin, M., Borysov, A., Krisanova, N., Soldatkin, A. and El`skaya, A. (2018). An amperometric glutamate biosensor for monitoring glutamate release from brain nerve terminals and in blood plasma. *Analytica Chimica Acta*, 1022: 113-123.
2. Isoaho, N., Peltola, E., Sainio, S., Koskinen, J. and Laurila, T. (2018). Pt-grown carbon nanofibers for enzymatic glutamate biosensors and assessment of their biocompatibility. *Royal Society of Chemistry Advance*, 8, 35802-35812.
3. Malaysia and International Law Book Services (2015). Food act 1983 (Act 281) & regulations. International Law Book Services, Petaling Jaya.
4. EFSA Panel on Food Additives and Nutrient Sources added to Food. (2017). Re-evaluation of glutamic acid (E 620), sodium glutamate (E 621), potassium glutamate (E 622), calcium glutamate (E 623), ammonium glutamate (E 624) and magnesium glutamate (E 625) as food additives. *EFSA Journal*, 15: 4910-4999.
5. Lateef, M., Siddiqui, K., Saleem, M and Iqbal, L. (2012). Estimation of monosodium glutamate by modified HPLC method in various pakistani spices formula. *Journal- Chemical Society of Pakistan*, 34: 39-42.
6. Soyseven, M. and Arli, G. (2021). Method validation and rapid determination of monosodium glutamate in various food products by HPLC–fluorescence detection and method optimization of HPLC–evaporative light scattering detection approach without derivatization. *Journal of Chromatographic Science*, 122: 60(8):760-769.
7. Mustafa, S., Saleem, Y. and Hameed, S. (2015). Determination of monosodium glutamate content in selected traditional meat dishes. *International Journal of Scientific & Engineering Research*, 6: 569-572.
8. Krishna Veni, N., Karthika, D., Surya Devi, M., Rubini, M. F., Vishalini, M. and Pradeepa, Y. J. (2010). Analysis of monosodium l-glutamate in food products by high-performance thin layer chromatography. *Journal of Young Pharmacists*, 2: 297-300.

9. Ambusaidi, M. M. S. K., Pandian, S. B. S., Swaminathan, S. and Sudhakar, M. S. (2020). A survey on the monosodium glutamate occurrence in food products and it's analysis by thin layer chromatography and liquid chromatography-mass spectrometry from sultanate of Oman. *International Journal of Analytical and Bioanalytical Methods*, 2: 1-11.
10. Camila, D. M. C., Felix, G. R. R., Andreas, M. and José, A. F. (2019). On-line electroextraction in capillary electrophoresis: application on the determination of glutamic acid in soy sauces. *Electrophoresis*, 40: 323-329.
11. Nuradi and Widarti (2018). Analysis of monosodium glutamat level on meatballs snacks (BAKSO) sold in the Makassar and Parepare City of South Sulawesi Province with visible spectrophotometer. *International Journal of Sciences: Basic and Applied Research,* 38: 34-41.
12. Ali, H. M., Hammad, S. F. and El-Malla, S. F. (2021). Green spectrophotometric methods for determination of a monosodium glutamate in different matrices. *Microchemical Journal,* 169: 1-9.
13. Rachma, F. A. and Saptawati, T. (2021). Analysis tolerance of monosodium glutamate (MSG) in instant noodles with uv-vis spectrophotometry. *Journal of Science and Technology Research for Farmacy,* 1: 20-24.
14. Alonge, P. O., Idemudia, O. S. and Odokuma-Alonge, O. (2019). Direct assay of monosodium glutamate in multi-sourced bouillon cubes by first derivative potentiometric titration. *Journal of Applied Sciences and Environmental Management,* 23: 299-304.
15. Cui, Y., Barford, J. P. and Renneberg, R. (2007). Development of an interference-free biosensor for l-glutamate using a bienzyme salicylate hydoxylase/l-glutamate dehydrogenase system. *Enzyme and Microbial Technology*, 41: 689-693.
16. Lioe, H. N., Dyahpakarti, G. C., Zakaria, N. A., Sudrajat, H. R., and Rahayu, I. (2019). Exposure assessment of monosodium glutamate in prepared foods with frying, sautéing, grilling or baking process. *Proceedings of the 2nd SEAFAST International Seminar*, pp. 49-56.
17. Zhang, M., Mullens, C. and Gorski, W. (2006). Amperometric glutamate biosensor based on chitosan enzyme film. *Electrochimica Acta*, 51: 4528-4532.
18. Chang, K. –S, Chang, C. –K, Chou, S. –F., Han, H. –C. and Chen, C. –Y. (2007). Characterization of a planar l-glutamate amperometric biosensor immobilized with a photo-crosslinkable polymer membrane. *Sensors and Actuators B,* 122: 195-203.
19. Alnokkari, A., Ataie, M. and Alasaf, Z. (2013). Colorimetric determination of monosodium glutamate in food samples using l-glutamate oxidase. *Chinese Journal of Applied and Environmental Biology,* 19: 1069-1072.
20. Yılmaz, D. and Karakus, E. (2011). Construction of a potentiometric glutamate biosensor for determination of glutamate in some real samples. *Artificial Cells, Blood Substitutes, and Biotechnology,* 39: 385-391.
21. Mizutani, S., Okumura, Y., Horio, T., Iwata, T., Okumura, K., Takahashi, K., Murakami, Y., Dasai, F., Ishida, M. and Sawada, K. (2017). Development of glutamate sensor for neurotransmitter imaging. *Sensors and Materials,* 29: 253-260.
22. Soldatkina, O. V., Soldatkin, O. O., Ozansoy Kasap, B., Kucherenko, D. Yu., Kucherenko, I. S., Akata Kurc, B. and Dzyadevych, S. V. (2017). A novel amperometric glutamate biosensor based on glutamate oxidase adsorbed on silicalite. *Nanoscale Research Letters,* 12: 1-8.
23. Liu, J., Fan, Y., Chen, G. and Liu, Y. (2021). Highly sensitive glutamate biosensor based on platinum nanoparticles decorated MXene-$Ti_3C_2T_x$ for l-glutamate determination in foodstuffs. *LWT-Food Science and Technology*, 148: 1-8.
24. Sim Bean, L., Yook Heng, L., Yamin, B. M. and Ahmad, M. (2005). Photocurable ferrocene-containing poly(2-hydroxyl ethyl methacrylate) films for mediated amperometric glucose biosensor. *Thin solid Films*, 477: 104-110.
25. Sarika, C., Rekha, K. and Narasimha Murthy, B. (2015). Studies on enhancing operational stability of a reusable laccase-based biosensor probe for detection of ortho-substituted phenolic derivatives. *3 Biotech*, 5: 911-924.

26. Ryth-Rinder, M., Kerekes, N., Svensson, M. and Hökfelt, T. (2001). Glutamate release from adult primary sensory neurons in culture is modulated by growth factors. *Regulatory Peptides,* 102: 69-79.
27. Wachiratianchai, S., Bhumiratana, A. and Udomsopagit, S. (2004). Isolation, purification, and characterization of l-glutamate oxidase from *Streptomyces* sp. 18G. *Journal of Biotechnology*, 7: 277-284.
28. Haymond, S., Babcock, G. T. and Swain, G. M. (2003). Electron transfer kinetics of ferrocene at microcryctalline boron-doped diamond electrodes: Effects of solvent and electrolytes. *Electroanalysis*, 15: 249-253.
29. Maalouf, R., Chebib, H., Saïkali, Y., Vittori, O., Sigaud, M. and Jaffrezic-Renault, N. (2007). Amperometric and impedimetric characterization of a glutamate biosensor based on Nafion® and a methyl viologen modified glassy carbon electrode. *Biosensors and Bioelectronics*, 22: 2682-2688.
30. Wang, H.-S., Pan, Q.-X. and Wang, G. -X. (2005). A biosensor based on immobilization of horseradish peroxide in chitosan matrix cross-linked with glyoxal for amperometric determination of hydrogen peroxide. *Sensors*, 5: 266 -276.
31. Lim, P. E. and Ang, T. T. (1990). Enzim dan ilmu energetik sel. Pusat Pengajian Luar Kampus, Universiti Sains Malaysia, Pulau Pinang.
32. Deng, Q., Guo, Y. and Dong, S. (1996). Cyro-hydrogel for the construction of a tyrosinase-based biosensor. *Analytica Chimica Acta*, 319: 71-77.
33. Seidel, J. M. and Malmonge, S. M. (2000). Synthesis of polyHEMA hydrogels for using as biomaterials. bulk and solution radical-initiated polymerization techniques. *Material Research*, 3: 79-83.
34. Neumann, M. G., Schmitta, C. C., Catalina, F. and Goi, B. E. (2007). Material behaviour: The relation between the polymerization rates and swelling coefficients for copolymers obtained by photoinitiation. *Polymer Testing*, 26: 189-194.
35. Miller, J. N. and Miller, J. C. (2000). Statistics and chemometrics for analytical chemistry, 4th Edition, Pearson Education.
36. Janarthanan, C. and Mottola, H. A. (1998). Enzymatic determinations with rotating bioreactors: Determination of glutamate in food products. *Analytical Chimica Acta,* 369: 147-155.
37. Isa, I. M. and Ghani, S. A. (2009). A non-plasticized chitosan based solid state electrode for flow injection analysis of glutamate in food samples. *Food Chemistry*, 112: 756-759.
38. Upadhyay, S., Ohgami, N., Kusakabe, H., Mizuno, H., Arima, J., Tamura, T., Inagaki, K. and Suzuki, H. (2006). Performance characterization of recombinant l-glutamate oxidase in a micro GOT/GPT sensing system. *Sensors and Actuators B*, 119: 570 – 576.
39. Karyakin, A. A., Karyakina, E. E. and Lo Gorton. (2000). Amperometric biosensor for glutamat using prussion blue-based "artificial peroxidase" as a transducer for hydrogen peroxide. *Analytical Chemistry,* 72: 1720-1723

Malaysian Journal of Analytical Sciences (MJAS)
Published by Malaysian Analytical Sciences Society

SURFACTANT FUNCTIONALIZATION OF MAGNETIC NANOPARTICLES: A STUDY ON THE PARTICLE SIZE DISTRIBUTION AND ZETA POTENTIAL AS A NANOFLUID TO IMPROVE THERMAL CONDUCTIVITY

(Perfungsian Surfaktan Nanopartikel Magnet: Kajian Mengenai Taburan Saiz Zarah dan Potensi Zeta Sebagai Bendalir Nano untuk Meningkatkan Kekonduksian Terma)

Cheah Ching Wei[1], Noorashikin Md. Saleh[1*], Nik Nur Atiqah Nik Wee[1], Beh Shiuan Yih[1], Ahmad Fazlizan[2], Farhanini Yusoff[3]

[1,2]Department of Chemical and Process Engineering,
Faculty of Engineering and Built Environment, Universiti Kebangsaan Malaysia,
43600 UKM Bangi, Selangor, Malaysia
[2]Institute of Solar Energy,
Universiti Kebangsaan Malaysia, 43600 UKM Bangi, Selangor, Malaysia
[3]Faculty of Science and Marine Environment,
Universiti Malaysia Terengganu, 21030 Kuala Nerus, Terengganu, Malaysia

[*]Corresponding author: noorashikin@ukm.edu.my

Received: 18 May 2022; Accepted: 15 September 2022; Published: 27 December 2022

Abstract

Solar energy has gained increasing popularity in the last decade, resulting in the development of photovoltaic/thermal (PV/T) systems to improve photovoltaic cell efficiency. Working fluid is one of the most important components in a heat transfer system. In this study, Fe_3O_4@Sylgard 309 nanoparticles were synthesized for nanofluid preparation. The stability and particle size of the nanofluid were analyzed using the dynamic light scattering method. Water-based nanofluid at pH 7 had the highest zeta potential compared to the same water-based nanofluid at different pHs ranging from 5.2 to 9.4. The nanofluid synthesized using cetyltrimethylammonium ammonium bromide and sodium dodecyl sulfate as the surfactant achieved better stability than the nanofluid synthesized without the addition of the surfactant. Ethylene glycol (EG)-based nanofluid had the highest zeta potential value of -2.54 mV compared to the water-based and polyethylene glycol (PEG)-based nanofluids. Nanoparticles in the PEG-based nanofluid remained suspended for two days and were better than the water-based and EG-based nanofluids. The improvement of the thermal conductivity of the metal oxide nanofluid compared to the conventional base fluid in previous studies was reviewed. The results showed that the thermal conductivity of nanofluid was higher than the base fluid up to 49.4%, indicating the potential for nanofluid applications in PV/T systems if the stability of the nanofluid can be improved.

Keywords: Ferum(III) oxide, magnetic nanoparticle, nanofluid, thermal conductivity, thermophysical property

Abstrak

Popularitи tenaga suria semakin meningkat sejak sedekad yang lalu dan menghasilkan pembangunan sistem fotovolta/terma (PV/T) untuk meningkatkan kecekapan sel fotovolta. Bendalir kerja adalah salah satu komponen terpenting dalam sistem pemindahan haba. Dalam kajian ini, nanozarah Fe_3O_4@Sylgard 309 telah disintesis untuk menyediakan cecair nano. Kestabilan dan saiz zarah cecair nano dianalisis menggunakan kaedah penyerakan cahaya dinamik. Bendalir nano berasaskan air pada pH 7 mempunyai potensi zeta yang paling tinggi berbanding dengan cecair nano berasaskan air yang sama pada pH berbeza antara 5.2 hingga 9.4. Kestabilan cecair nano yang disintesis menggunakan setiltrimetilammonium bromida dan natrium dodesil sulfat sebagai surfaktan adalah lebih baik iaitu -2.54 mV daripada cecair nano yang disintesis tanpa penambahan surfaktan. Bendalir nano berasaskan etilena glikol (EG) mempunyai nilai potensi zeta yang paling tinggi berbanding dengan cecair nano berasaskan air dan polietilena glikol (PEG). Nanozarah dalam cecair nano berasaskan PEG kekal terampai selama dua hari dan lebih baik daripada cecair nano berasaskan air dan EG. Peningkatan kekonduksian terma bagi cecair nano oksida logam berbanding dengan cecair asas konvensional dalam kajian terdahulu telah dikaji semula. Keputusan menunjukkan bahawa kekonduksian terma cecair nano adalah lebih tinggi daripada cecair asas sehingga 49.4% dan mempunyai potensi aplikasi cecair nano dalam sistem PV/T sekiranya kestabilan cecair nano dapat dipertingkatkan.

Kata kunci: Ferum(III) oksida, nanozarah magnet, bendalir nano, termal kekonduksian, sifat termofizik

Introduction

As global warming worsens due to the emission of greenhouse gases, the demand for energy consumption is expected to increase, particularly in the industrial sector. According to the data obtained from the International Energy Agency, the growth of energy demand between 2017 and 2018 was 4% in 2018, which was equivalent to 900 TWh. The demand is expected to increase continuously as climate change increases the demand for air conditioning and consumption in the industrial sector [1-3].

Although solar energy can be converted into electrical energy using photovoltaic (PV) cells, long-term exposure will increase the temperature of the cells. Proton transfer rate is hindered in a commercial solar panel [4]. Meanwhile, 30% of the industrial process and heating, ventilation, and air conditioning (HVAC) systems require temperatures below 100 ℃, which can be achieved using commercial solar thermal collectors [3]. Working fluids (e.g., thermal oil, water, and glycols) have been implemented in HVAC systems but with poor efficiency.

Based on previous studies, PV electrical efficiency could be enhanced by integration with a heat collection system. The PV electrical efficiency of a photovoltaic/thermal (PV/T) system using silicon carbide (SiC) nanofluid under different solar irradiance levels (400–600 W) was enhanced significantly in the range of 13.3%-13.9% compared to the PV electrical efficiency of the reference PV module without a heat collection system in the range of 5.2%-10.52%. Another study on a PV/T system using SiC nanofluid reported an increase in the electrical efficiency up to 24.1% compared to the PV system alone [7]. A study on a PV/T system showed that the overall energy efficiency increased by 76.6% and achieved an overall energy efficiency of 16.9% using titanium dioxide (TiO_2) nanofluid compared to water [8]. These findings highlight the potential application of nanofluid in the PV/T system.

Magnetic nanoparticles possess magnetic properties that ease recycling and adsorption in the heat transfer process. Magnetic nanoparticles consist of iron oxides, iron alloys, and ferrite-based nanoparticles [9,10]. Nanofluid is the colloidal suspension of nanoparticles in the base fluid. Several types of nanofluid have been synthesized using carbon nanotube, metal oxide, and silica nanoparticles [11-25]. Surfactants such as cetyltrimethylammonium bromide (CTAB), sodium dodecyl sulfate (SDS), sodium dodecylbenzene sulfonate (SDBS), and acetic acid have been used to reduce agglomeration and improve the stability of nanofluids. The dispersion stability of the nanoparticles in the liquid will affect the commercialization of the nanofluid as the sedimented particles might cause scaling in the pump [26].

Ghadiri et al. synthesized Fe_3O_4 nanofluid with a nanoparticle concentration up to 3 wt. %. Acetic acid

was added to the nanofluid and ultrasonicated for 30 min to stabilize the nanofluid. The nanoparticle size was 45 nm and the nanofluid was stable for a month. The electrical and thermal efficiency of the PV/T system using 3 wt. % Fe_3O_4 nanofluid recorded an improvement of 4.8% and 35%, respectively, compared to the PV/T system using distilled water [27].

In the author's previous research, metal oxide nanofluid known as adsorbent MNP-Sylgard 309 was synthesized for the extraction of pollutants from environmental samples [11]. The excellent results allowed the metal oxide nanofluid to be applied in a new research field, which is the application for improving thermal conductivity. This is because the behavior of the synthesized metal oxide nanofluid has the tendency to increase the heat transfer rate in a heat exchanger without increasing its size. This is due to the higher thermal conductivity of the nanofluid. This improvement will lead to a lower temperature requirement in the thermal conductivity of a solar collector.

In this study, Fe_3O_4 nanoparticles were synthesized using the chemical co-precipitation method. Iron oxide nanoparticles were modified using 3-(triethoxysilyl)propylamine (APTES) and surfactant Sylgard 309. Fe_3O_4@Sylgard 309 nanoparticles were dispersed in the base fluid using ultrasonication to stabilize the nanofluid. Later, Fe_3O_4@Sylgard 309 nanoparticles were synthesized at different pHs using different base fluids. The nanoparticles and nanofluid synthesized were characterized using the dynamic light scattering (DLS) method. The stability of Fe_3O_4@Sylgard 309 nanoparticles in the water at different pHs was analyzed and compared. Furthermore, the stability of Fe_3O_4@Sylgard 309 nanoparticles in different base fluids (polyethylene glycol (PEG), ethylene glycol (EG), and water) at similar pH with the addition of different surfactants was compared. A review of previous studies regarding the thermal conductivity of metal oxide nanofluid in solar collectors was performed and summarized. Fe_3O_4@Sylgard 309 nanoparticles are feasible to be explored as the metal oxide nanofluid to be added to the solar collector for improving thermal conductivity.

Materials and Methods

Materials and reagents

Methanol (99.7%), ammonia hydroxide (25%), APTES, acetic acid, CTAB, polyethylene glycol (PEG 1500), EG, and SDS were purchased from Merck (Darmstadt, Germany). Iron(III) chloride hexahydrate ($FeCl_3 \cdot 6H_2O$) and iron chloride tetrahydrate ($FeCl_2 \cdot 4H_2O$) were supplied by R&M Chemicals (Essex, UK). Deionized water (18.2 MΩ cm^{-1}) used in the nanoparticles and nanofluid preparation was produced by a Sartorius Milli-Q system.

Synthesis of Fe_3O_4 nanoparticles

First, 3.1736 g of $FeCl_2 \cdot 4H_2O$ and 7.5709 g of $FeCl_3 \cdot 6H_2O$ were dissolved in 320 mL of deionized water and stirred under inert conditions for 1 h at 80 °C. Then, 40 mL of aqueous ammonia was added to the mixture and stirred for 1 h under inert conditions before being cooled to room temperature. The synthesized blackish liquid containing magnetic nanoparticles was decanted using a permanent magnet and washed using hot water five times to obtain Fe_3O_4 nanoparticles.

Surface modification of Fe_3O_4 nanoparticles using APTES and Sylgard 309

Next, the Fe_3O_4 nanoparticle surface was modified using APTES. A total amount of 4.2252 g of Fe_3O_4 was dissolved in 150 mL ethanol (50%) and sonicated for 30 min. Then, 17 mL of APTES was added to the mixture and stirred under inert conditions for 2 h at 40 °C before being cooled to room temperature. The modified nanoparticles were decanted and washed using ethanol and deionized water a few times prior to drying for 24 h at 70 °C under vacuum conditions. Finally, 0.2 g of the modified nanoparticles was dispersed in 8 mL of Sylgard 309 and stirred under inert conditions for 24 h at 60 °C before being cooled to room temperature. The final product was decanted and washed with deionized water and ethanol before being dried under vacuum conditions for 24 h at 70 °C. The synthesized nanoparticles were characterized using a Malvern Nano-ZS particle size analyzer to determine their hydrodynamic size and zeta potential. The synthesis of the Fe_3O_4@Sylgard 309 nanoparticle is shown in Figure 1.

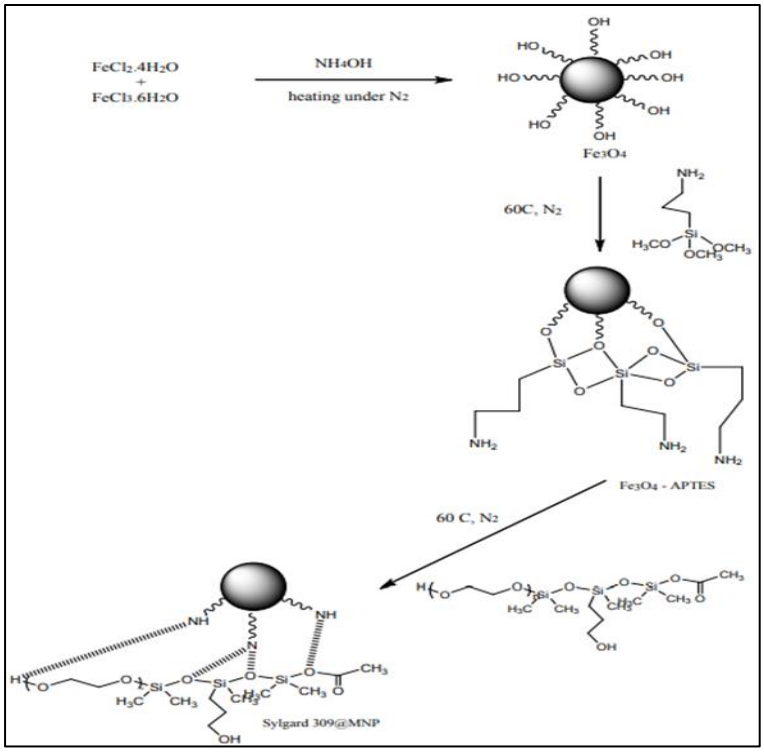


Figure 1. Synthesis of Fe_3O_4@Sylgard 309 nanoparticle [16]

Preparation of nanofluid

Nanofluid preparation was done by sonication (60 min) after adding the modified nanoparticles to the water with a concentration of 0.1 wt.%. Different types of nanofluids were synthesized using different base fluids (PEG, EG) and at different pHs (5.2, 5.9, 7.0, 8.4, 9.4). The dispersion stability and zeta potential of the nanofluids were determined using the Malvern Nano-ZS particle size analyzer.

Results and Discussion

Particle size distribution of synthesized nanoparticles

The results for the synthesis of Fe_3O_4 nanoparticles and surface modification of Fe_3O_4 nanoparticles using APTES and surfactant Sylgard 309 have been published [16]. The paper contains the results of the characterization of Fe_3O_4 nanoparticles coated with APTES and Sylgard 309. The current paper focuses on the application of Fe_3O_4 nanoparticles coated with APTES and Sylgard 309 by studying the particle size di stribution and zeta potential of the nanofluid to improve thermal conductivity. The particle size distribution result showed that the color of Fe_3O_4 changed from black to brown after modification using APTES. Then, the brown color of APTES-modified Fe_3O_4 nanoparticles using Sylgard-309 changed to dark brown. The surface-modified nanoparticle samples are shown in Figure 2. Changes in the color of Fe_3O_4 nanoparticles after surface modification were observed in previous studies [32, 33]. Fe_3O_4 surface modification was done without changing the nanoparticle core (i.e., Fe_3O_4). A study determined that the crystallinity was preserved even after surface modification based on the same peak intensity in the X-ray diffraction (XRD) diffractogram [16].

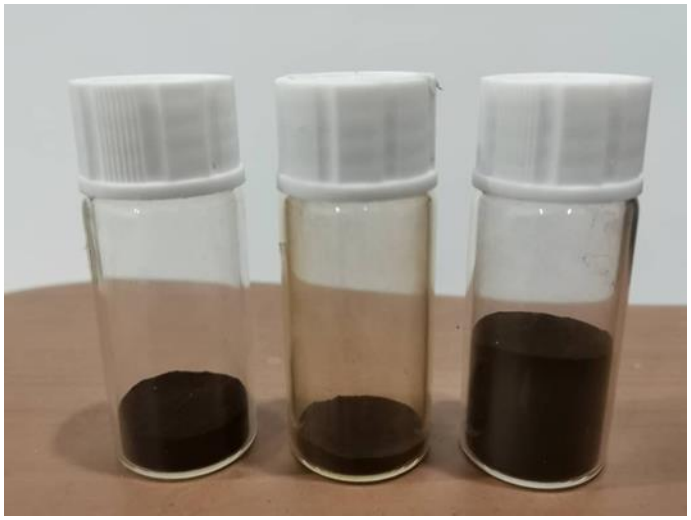


Figure 2. Fe_3O_4 nanoparticles synthesized (left) and modified using APTES (middle) and Sylgard 309 (right)

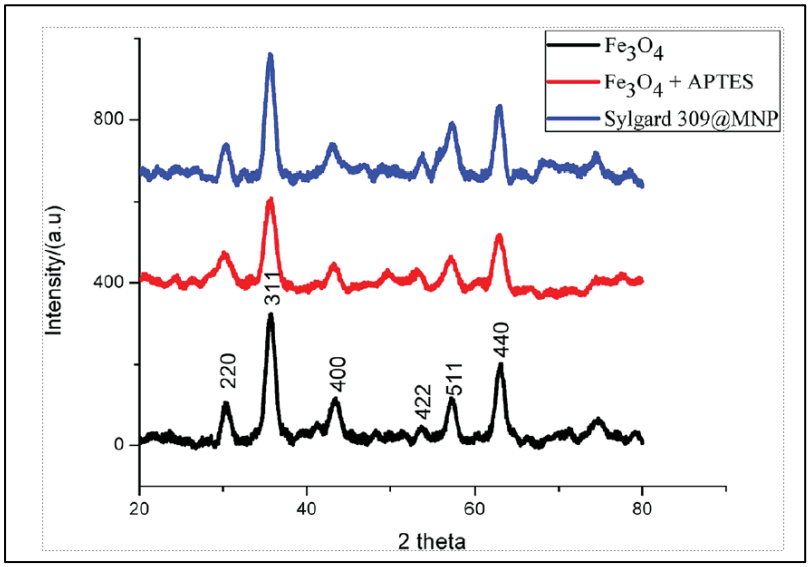


Figure 3. XRD patterns of Fe_3O_4 nanoparticles, Fe_3O_4 + APTES nanoparticles, and Sylgard 309@MNP [16]

In our previous study, XRD was used to identify the crystallinity of Fe_3O_4, Fe_3O_4 + APTES, and Sylgard 309@MNP. As shown in Figure 3, Fe_3O_4 exhibited good crystallinity with diffraction peaks appearing at the 2θ values of 30.42°, 35.59°, 43.59°, 53.63°, 57.50°, and 63.04°, which can be assigned to the (220), (311), (400), (422), (511), and (440) reflections of Fe_3O_4, respectively, which are similar to those of other previous studies [23, 24]. Furthermore, the spectra of Fe_3O_4 + APTES and Sylgard 309@MNP showed approximately identical characteristics of diffraction peaks, revealing that the surface modification of Fe_3O_4 did not change its crystalline phase. The lower intensity of the diffraction peaks was observed in the cases of Fe_3O_4 + APTES and Sylgard 309@MNP, which may be due to the presence of an amorphous layer of APTES and Sylgard 309 on Fe_3O_4 [16].

Based on the particle size distribution shown in Figure 4, the particle size of the synthesized Fe_3O_4 had two peaks, which were 862.2 nm with 89.1% of intensity and 90.53 nm with 10.9% of intensity. This revealed that the diameter of the synthesized nanoparticles was lower than 100 nm. However, there was another peak at 862.2 nm, which was due to agglomeration, and this increased the hydrodynamic size of the nanoparticles in the nanofluid.

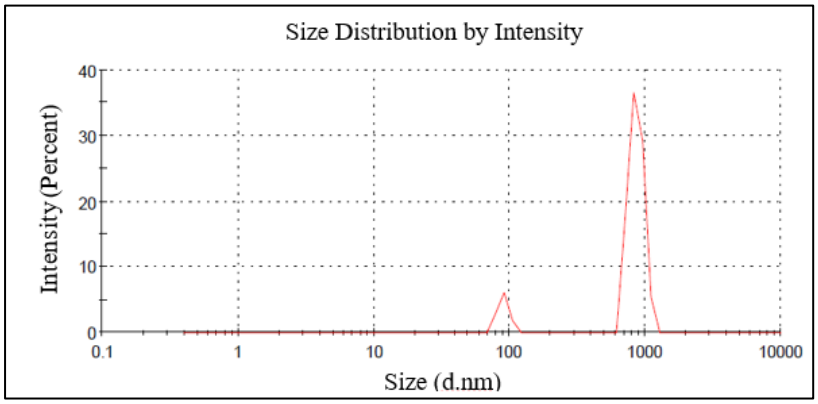


Figure 4. Particle size distribution of synthesized Fe_3O_4 nanoparticles

In the DLS method, an incident laser is generated, which is scattered by the nanoparticles in the colloidal suspension, causing constructive and destructive interference and also resulting in the fluctuation of the scattered light intensity. The fluctuation of the light intensity is then correlated to derive the hydrodynamic radius of the solid particle. The particle diameter detected using the DLS method is the hydrodynamic diameter of the solid particle, which is bounded by the slipping plane.

The slipping plane of the nanoparticle is affected by the aggregation and diffusion of the particle through the boundary of the hydrodynamic structure (slipping plane) into the internal layer [34]. Therefore, if the nanoparticle is not monodispersed in the nanofluid, then the particle size of each nanoparticle cannot be characterized accurately using the DLS method. This is due to the aggregation of nanoparticles in the colloidal suspension, which will result in inaccurate particle size measurement. The reported data of DLS and zeta potential were inaccurate in previous research of nanomedicine research [35].

In Figure 5, the result from DLS showed that the nanoparticles modified using APTES had a larger particle diameter of 1,817 nm. However, after the APTES-modified nanoparticles were characterized using Sylgard 309 (a non-ionic surfactant), the result in Figure 6 showed that the two peaks in the particle size were 73.32 nm with 7.8% of intensity and 482.4 nm with 92.2% of intensity. This proved that the particles modified using APTES caused the aggregation. The change in the particle size distribution could be affected by zeta potential and changes in the zeta potential might be caused by the shift of the slipping plane by molecules characterized on the core nanoparticle surface and also the displacement of the counter ion in the stern layer due to polymer adsorption on the core nanoparticles [36].

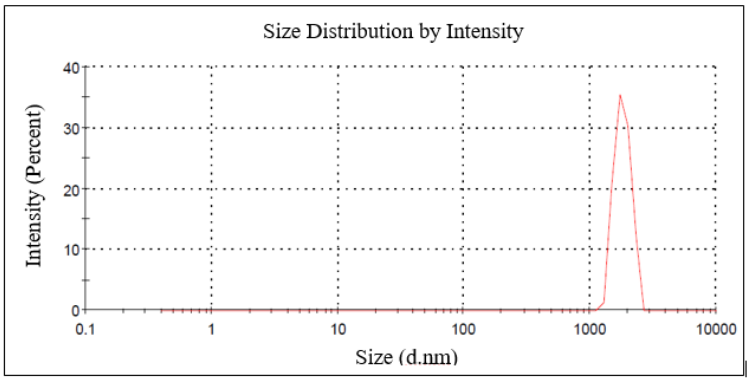


Figure 5. Particle size distribution of Fe_3O_4 nanoparticles modified using APTES

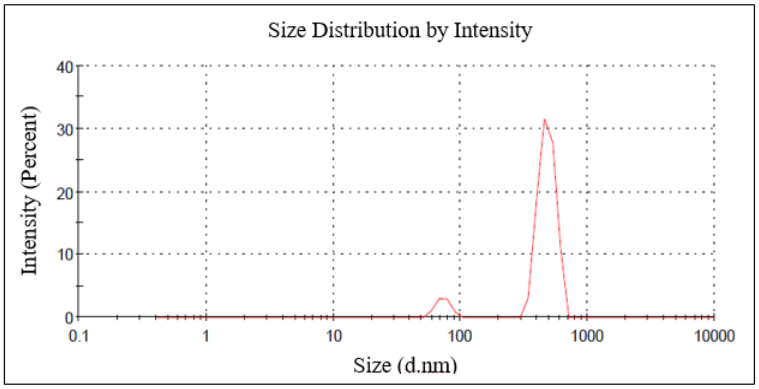


Figure 6. Particle size distribution of synthesized Fe_3O_4@Sylgard 309 nanoparticles

Zeta potential and stability of the synthesized nanofluid

Zeta potential is the parameter used to characterize the electric double layer on the solid/liquid interface. When an ionized solid particle is suspended in the liquid, it will be surrounded by liquid ions with the opposite charge to the surface of the solid particle. Both the solid particle and the liquid layer shell will move together through the liquid. The potential difference between the external liquid shell and the liquid is called zeta potential. Zeta potential is used to describe the behavior of the dispersion of particles in the colloidal system and the stability of the nanofluid [26, 37]. Abadeh et al. examined the effect of the type of surfactant, the amount of surfactant, and pH on nanofluid stability and magnetization [38].

This solid/liquid interface is the boundary of the hydrodynamic structure of the nanoparticles in the colloidal suspension and zeta potential is the potential difference between the internal layer and the external layer of the slipping plane, as shown in Figure 5 Zeta potential is an established parameter in determining the stability of nanoparticle dispersion in nanofluid against aggregation. Zeta potential higher than 30 mV or lower than -30 mV is considered a stable suspension due to charge stabilization between the nanoparticles with high electrostatic repulsive strength. Colloidal suspension with zeta potential higher than 40 mV or lower than -40 mV is considered as having good stability [34, 37].

Based on the zeta potential values measured using the DLS method in Table 1, it can be determined that none of the synthesized nanofluids had enough stability to be

considered as stable colloidal suspension. In the particle size distribution measurement, the results generated are similar to the particle size distribution in which the particle size is affected by the aggregation of the nanoparticles. This is because the particle size distribution increased as the aggregation increased. Furthermore, the pH value will affect the zeta potential of the nanofluid. The zeta potential will affect the dispersive ability of the nanoparticles in the nanofluid, resulting in nanoparticle aggregation. This is in good agreement with previous studies. Zeta potential is usually related to the time needed for the nanoparticles to sediment at the bottom of the nanofluid. The time needed for the nanoparticles to sediment in the nanofluid with a zeta potential value higher than 30 mV or lower than -30 mV is longer than the nanofluid with a zeta potential value closer to 0 mV.

Table 1. Zeta potential and nanoparticle size distribution of water-based nanofluids synthesized at different pHs

pH	**5.2**	**5.9**	**Intensity percentage (%)**	**7.0**	**Intensity percentage (%)**	**8.4**	**9.4**
Particle size, diameter (nm)	163.9	463.9	89.2	482.4	92.2	893.1	1,868
	-	111	10.8	73.32	7.8	-	-
Zeta potential (mV)	-5.56	-4.5	100	-12.4	100	-2.54	-2.62

The zeta potential value was the lowest at pH 7. As the pH value transitioned to a higher or lower value, the zeta potential increased and became closer to 0 mV. However, based on the observation, the sedimentation of the particles at pH 7 occurred earlier than other nanoparticles. This might be due to the nanoparticles being synthesized using Sylgard 309, which is a non-ionic surfactant. This result is in contrast with the statement that the closer the zeta potential value to 0 mV, the shorter the time needed for nanoparticle sedimentation to occur. However, it is still acceptable as the zeta potential of the synthesized nanofluid is not lower than -30 mV and is still considered an unstable nanofluid. The nanoparticles in all water-based nanofluids synthesized at different pHs were found to sediment at the bottom of the nanofluids in a day. Therefore, pH 9.4 was chosen as an optimum pH used for the subsequent study.

In Figure 7, the zeta potential of the water-based nanofluid without the addition of surfactant showed an apparent zeta potential of -5.8 mV, while the zeta potential of the water-based nanofluids synthesized with CTAB and SDS achieved the zeta potential values of 32.3 mV and -41.9 mV, as shown in Figures 8 and 9, respectively. Nanofluid stability improvement was achieved using CTAB and SDS as the surfactant. The zeta potential result of the synthesized nanofluid with CTAB was positive, while the zeta potential result with the addition of SDS was always negative. Both surfactants were able to stabilize the nanofluid as the zeta potential of the synthesized nanofluid was higher than 30 mV or lower than -30 mV. The zeta potential results are in good agreement with the data from previous studies. The time needed for nanoparticle sedimentation to occur in the nanofluids with the addition of CTAB and SDS was longer than the synthesized nanofluid without the addition of surfactant. However, the nanoparticles in the synthesized nanofluid were found to sediment at the bottom of the nanofluid in a day.

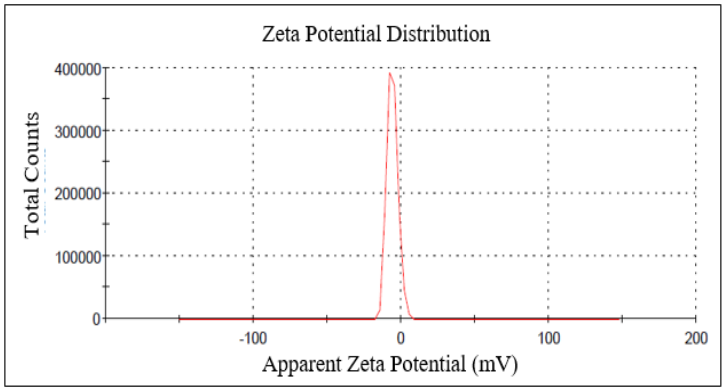


Figure 7. Zeta potential of water-based nanofluid synthesized without the addition of surfactant

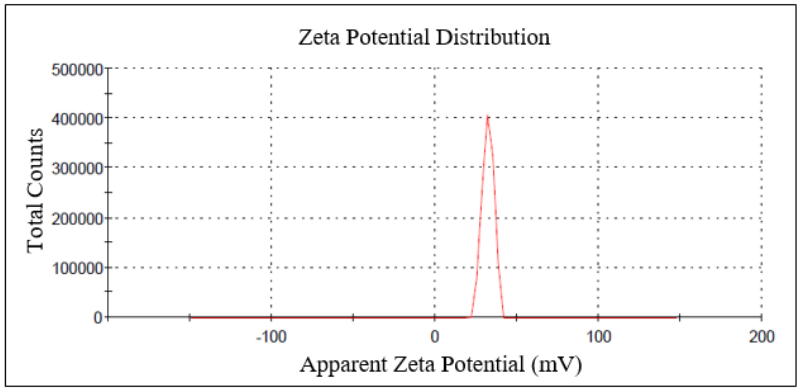


Figure 8. Zeta potential of water-based nanofluid synthesized with the addition of CTAB

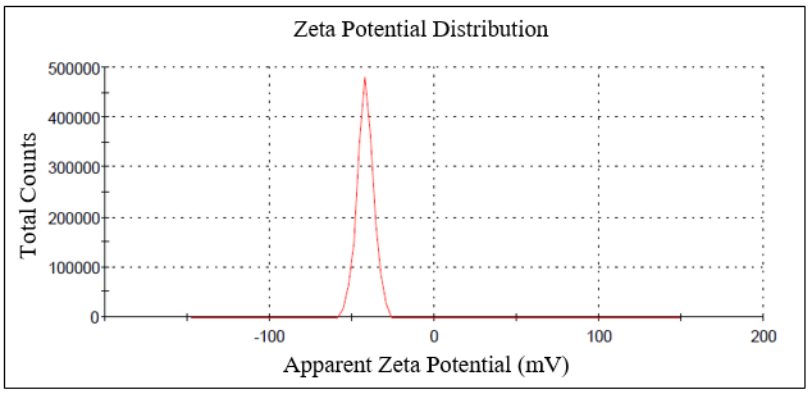


Figure 9. Zeta potential of water-based nanofluid synthesized with the addition of SDS

Nanofluids were synthesized using different base fluids of water, PEG, and EG without any addition of surfactant. Based on the data obtained in Table 2, it was found that the zeta potential value of water-based nanofluid was -2.62 mV, -14.7 mV for EG-based nanofluid, and 3.93 mV for PEG-based nanofluid. The water-based nanofluid recorded a zeta potential closest to zero, which means that it is highly unstable.

EG-based nanofluid was also highly unstable due to the similar zeta potential value to water-based nanofluid. EG-based nanofluid had a zeta potential value that was furthest away from 0 mV. However, based on the observation, nanoparticles in PEG-based nanofluid were able to remain suspended within two days, while the nanoparticles in water- and EG-based nanofluids were only able to remain suspended within one day. This is because PEG is a high viscosity base fluid. Sedimentation is caused by the resultant force acting on the nanoparticles from the stronger gravitational force than the drag force exerted on the nanoparticles by the base fluid [42].

The drag force in a high viscosity base fluid is stronger than a low viscosity base fluid. Therefore, the sedimentation time of the nanoparticles in PEG-based nanofluid was longer.

Table 2. Zeta potential values of nanofluids synthesized using different base fluids

Type of Base Fluid	Water-based at pH 9	EG-based	PEG-based
Zeta potential (mV)	-2.62	-14.7	3.93

Review of previous studies on nanofluid thermal conductivity in solar collectors

Based on previous studies, the application of metal oxide nanofluid in PV/T systems improved the energy generation efficiency compared to the PV/T system utilizing conventional base fluid or PV system alone. Several types of nanofluids from previous studies are summarized in Table 3.

Abareshi et al. synthesized Fe_3O_4 nanofluid using tetramethylammonium hydroxide as the surfactant. The study stated that nanofluid suspension with a zeta potential lower than -30 mV or higher than 30 mV was a stable nanofluid. The nanofluid had a zeta potential value of -41.7 mV, hence it was a stable nanofluid, and the thermal conductivity improvement was 11.5% when the volume fraction of the magnetic nanoparticles was 3 vol% at 40 °C [46].

Al-Shamani et al. prepared TiO_2 nanofluid to be implemented in a thermal collector system of an integrated PV/T module. Based on the results, the TiO_2 nanofluid had an improved thermal conductivity of 12.5% compared to water. The electrical efficiency of the PV/T system utilizing TiO_2 increased by 1% compared to the module utilizing water due to the lower module temperature after exposure to solar irradiation [6].

Based on the previous studies on thermal conductivity, it was shown that the PV/T system utilizing metal oxide nanofluid was able to gain up to 49.4% thermal conductivity improvement compared to the conventional base fluid. However, the results of thermal conductivity improvement of the nanofluid varied. This could be due to different methods used for measuring the thermal conductivity improvement of the nanofluid under different parameters, such as humidity and the surrounding temperature of the environment.

In previous research on magnetic actuated transfer systems, it was shown that it was possible to achieve overall exergy, heat transfer coefficient, and thermal efficiency improvement when the Fe_3O_4 nanofluid was under an alternating magnetic field. However, the difference in the data varied widely. Therefore, it is important to study this particular system to gain more data to determine if any additional factors may cause the discrepancies between these studies on magnetic nanofluids, as well as other nanofluids in heat transfer applications.

Table 3. Summary of thermal conductivity improvement of nanofluids in previous studies

Nanofluid	Concentration	Stabilization Process	Stabilization Analysis	Thermal Conductivity Improvement	Study
• Fe_3O_4/water	•1 wt.% •3 wt.%	• Surfactant – acetic acid • Ultrasonication – 30 min	• Stable in a month • Particle diameter = 45 nm	• No data	22
• TiO_2/water	•0.1 wt.%	• Surfactant – SDS • Ultrasonication bath – 3 h	• Stable in 3 days	• 1%	37
• TiO_2/water	•0.1 vol% •0.3 vol%	• Surfactant – PEG • Pressurized homogenization	• Stable for a month • Ratio of nanoparticle: surfactant = 1:2	• 6%	16
• Al_2O_3/water • CuO/water	•0.8 wt. %	• Surfactant –SDBS • pH: alumina = 8.0, Cu = 9.5	• Zeta potential higher than 40 mV	• Alumina: 15% • Cu: 18%	39
• Al_2O_3/water • CuO/water	•2–10 vol% •2–10 vol%	• Ultrasonication – 3 h	• Stable for a few days	• Alumina: 30% • Cu: 52%	40
• Fe_3O_4/water	•No data	• No data	• No data	• No data	41
• Fe_3O_4/ water	•0–3 vol%	• Surfactant – tetramethylammonium hydroxide	• No data	• 11.5% at 40 ℃	42
• TiO_2/water	•0–2 wt. %	• Ultrasonication	• No data	• 12.5%	6
• Fe_3O_4/water	•0%–0.1%	• No data	• Zeta potential = -46.3 mV	• 33.8% at 40 ℃	14

Conclusion

Fe_3O_4@Sylgard 309 nanoparticles were synthesized and used as the nanofluid to improve the stability and thermophysical properties of a solar collector. The stability and particle size of the nanofluid were analyzed using the DLS method. Water-based nanofluid at pH 7 had the highest zeta potential compared to the same water-based nanofluid at different pHs ranging from 5.2 to 9.4. The stability of the synthesized nanofluid using CTAB and SDS as the surfactant was better than the nanofluid synthesized without the addition of surfactant. EG-based nanofluid had the highest zeta potential value compared to the water- and PEG-based nanofluids. Nanoparticles in PEG-based nanofluid could remain suspended within two days, which were longer than water- and EG-based nanofluids. Therefore, PEG-based

nanofluid has the potential to be used in a solar collector because it has longer time to be effective as a fluid, which is related to the high conductivity in a solar system. The thermal conductivity improvement of the metal oxide nanofluid compared to conventional base fluid in previous studies was reviewed. The review showed that the thermal conductivity of nanofluid was higher than the base fluid up to 49.4%. This result highlights the potential of nanofluid applications in PV/T systems if the stability of the nanofluid can be improved.

Acknowledgement

We would like to express our gratitude to the Ministry of Higher Education Malaysia for the Fundamental Research Grant Scheme FRGS/1/2022/STG04/UKM/02/7.

References

1. IEA (2019). Global Energy & CO2 Status Report. 2019
2. Ritchie, H., and Roser, M. (2017). CO_2 and greenhouse gas emissions. *Renewable Energy.* 2017: pp. 1-10.
3. Dahlan, N. Y., and Ismail, M. F. A (2015). Review on solar thermal technologies for low and medium temperature industrial process heat. *Journal of Industrial Technology*, 23(1): 25-44.
4. Ibrahim, A., and El-Amin, A. (2012). Temperature effect on the performance of n-type c-Si film grown by linear facing target sputtering for thin film silicon photovoltaic devices. *Optoelectronics and Advanced Materials-Rapid Communications,* 6:73-77.
5. Jama, M., Singh, T., Gamaleldin, S. M., Koc, M., Samara, A., Isaifan, R. J. (2016). Critical review on nanofluids. *Journal of Nanomaterials,* 26: 6717624.
6. Al-Shamani, A. N., Sopian, K., Mat, S., Hasan, H. A., Abed, A. M., and Ruslan, M. (2016). Experimental studies of rectangular tube absorber photovoltaic thermal collector with various types of nanofluids under the tropical climate conditions. *Energy Conversion and Management,* 124: 528-542.
7. Al-Waeli, A. H., Sopian, K., Chaichan, M. T., Kazem, H. A., Hasan, H. A., and Al-Shamani, A. N. (2017). An experimental investigation of SiC nanofluid as a base-fluid for a photovoltaic thermal PV/T system. *Energy Conversion and Management,* 142, 547-558.
8. Said, Z., Sabiha, M., Saidur, R., Hepbasli, A., Rahim, N. A., Mekhilef, S., et al. (2015). Performance enhancement of a flat plate solar collector using titanium dioxide nanofluid and polyethylene glycol dispersant. *Journal of Cleaner Production,* 92: 343-353.
9. Yusoff, M. M., Yahaya, N., Saleh, N. M., and Raoov, M. (2018). A study on the removal of propyl, butyl, and benzyl parabens via newly synthesised ionic liquid loaded magnetically confined polymeric mesoporous adsorbent. *RSC Advances,* 8(45): 25617-25635.
10. Guo, T., Lin, M., Huang, J., Zhou, C., Tian, W., Yu, H., et al. (2018). The recent advances of magnetic nanoparticles in medicine. *Journal of Nanomaterials*, 2018: 7805147.
11. Noorashikin, M.S., Mohamad, S. and Abas, M. R. (2014). Extraction of parabens from water samples using cloud point extraction of non-ionic surfactant with beta-cyclodextrin as modifier. *Journal of Surfactants and Detergents*, 17: 747-758.
12. Yusoff, F., Khing, N. T., Hao, C. C., Sang, L. P., Muhamad, N. A. B., and Saleh, N. M. (2018). The electrochemical behavior of zinc oxide/reduced graphene oxide composite electrode in dopamine. *Malaysian Journal of Analytical Sciences,* 22(2): 227-237.
13. Noorashikin, M. S., Sohaimi, N. M., Suda, N., Aziz, H. Z., Zaini, S. R. M., Kandasamy, S., et al. (2017). The application of cloud point extraction in environmental analysis. *Journal Sustainability Science Management,* 12: 79-95.
14. Noorashikin, M., Mohamad, S., and Abas, M. (2016). Determination of parabens in water samples by cloud point extraction and aqueous two-phase extraction using high-performance liquid chromatography. *Desalination and Water Treatment,* 57(47): 22353-22361.

15. Norseyrihan, M. S., Noorashikin, M. S., Adibah, M., and Farhanini, Y. (2016). Cloud point extraction of methylphenol in water samples with low viscosity of non-ionic surfactant Sylgard 309 coupled with high-performance liquid chromatography. *Separation Science and Technology*, 51(14): 2386-2393.
16. Ariffin, M. M., Sohaimi, N. M., Yih, B. S., and Saleh, N. M. (2019). Magnetite nanoparticles coated with surfactant Sylgard 309 and its application as an adsorbent for paraben extraction from pharmaceutical and water samples. *Analytical Methods,* 11(32): 4126-4136.
17. Baker, I. (2018). Magnetic nanoparticle synthesis. *Nanobiomaterials*, 2018: 197-229.
18. Gonzalez-Carreno, T., Morales, M., Gracia, M., and Serna, C. (1993). Preparation of uniform γ-Fe_2O_3 particles with nanometer size by spray pyrolysis. *Materials Letters,* 18(3): 151-155.
19. Haiza, H., Yaacob, I., and Azhar, A. Z. A. (2018). Thermal conductivity of water-based magnetite ferrofluids at different temperature for heat transfer applications. *Solid State Phenomena,* 280: 36-42.
20. Moon, J.-W., Rawn, C. J., Rondinone, A. J., Love, L. J., Roh, Y., Everett, S. M., et al. (2010). Large-scale production of magnetic nanoparticles using bacterial fermentation. *Journal of Industrial Microbiology & Biotechnology*, 37(10): 1023-1031.
21. Safee, N. H. A., Abdullah, M. P., and Othman, M. R. (2010). Carboxymethyl chitosan− Fe_3O_4 nanoparticles: synthesis and characterization. *Malaysian Journal Analytical Sciences,* 14: 63-68.
22. Sugimoto, T., Wang, Y., Itoh, H., and Muramatsu, A. (1998). Systematic control of size, shape and internal structure of monodisperse α-Fe_2O_3 particles. *Colloids and Surfaces A: Physicochemical and Engineering Aspects,* 134(3): 265-279.
23. Sun, S., and Zeng, H. Size-controlled synthesis of magnetite nanoparticles. *Journal of the American Chemical Society*, 124(28): 8204-8205.
24. Wang, X., Zhuang, J., Peng, Q., and Li, Y. (2005). A general strategy for nanocrystal synthesis. *Nature*, 437(7055): 121-124.
25. Zhang, G., Liao, Y., and Baker, I. (2010). Surface engineering of core/shell iron/iron oxide nanoparticles from microemulsions for hyperthermia. *Materials Science and Engineering*, 30(1): 92-97.
26. Biehl, P., Von der Lühe, M., Dutz, S., and Schacher, F. H. (2018). Synthesis, characterization, and applications of magnetic nanoparticles featuring polyzwitterionic coatings. *Polymers*, 10(1): 91.
27. Ghadiri, M., Sardarabadi, M., Pasandideh-fard, M., and Moghadam, A. J. (2015). Experimental investigation of a PVT system performance using nano ferrofluids. *Energy Conversion and Management*, 103: 468-476.
28. Mohanraj, K., and Sivakumar, G. (2017). Synthesis of γ-Fe_2O_3, Fe_3O_4 and copper doped Fe_3O_4 nanoparticles by sonochemical method. *Sains Malaysiana***,** 46(10): 1935-1942.
29. Mufti, N., Atma, T., Fuad, A., and Sutadji, E. (2014). Synthesis and characterization of black, red and yellow nanoparticles pigments from the iron sand. In *AIP Conference Proceedings,* 1617: 165-169.
30. Song, K., Lee, S., Suh, C.-Y., Kim, W., Ko, K.-S., and Shin, D. (2012). Synthesis and characterization of iron oxide nanoparticles prepared by electrical explosion of Fe wire in Ar–O_2 gas mixtures. *Materials Transactions*, M2012186.
31. Nalle, F., Wahid, R., Wulandari, I., and Sabarudin, A. (2019). Synthesis and characterization of magnetic Fe_3O_4 nanoparticles using oleic acid as stabilizing agent. *Rasayan Journal of Chemistry,* 12(1): 14-21.
32. Xie, L., Qian, W., Yang, S., Sun, J., and Gong, T. (2017). A facile and green synthetic route for preparation of heterostructure Fe_3O_4@Au nanocomposites. *MATEC Web of Conferences*, *88*: 02001.
33. Zhou, J., Meng, L., Lu, Q., Fu, J., and Huang, X. (2009). Superparamagnetic submicro-megranates: Fe_3O_4 nanoparticles coated with highly cross-linked organic/inorganic hybrids. *Chemical Communications*, 42: 6370-6372.
34. Lowry, G. V., Hill, R. J., Harper, S., Rawle, A. F., Hendren, C. O., Klaessig, F., et al. (2016). Guidance to improve the scientific value of zeta-potential measurements in nanoEHS. *Environmental Science: Nano*, *3*(5): 953-965.

35. Bhattacharjee, S. (2016). DLS and zeta potential–what they are and what they are not?. *Journal of Controlled Release,* 235: 337-351.
36. Ostolska, I., and Wiśniewska, M. (2014). Application of the zeta potential measurements to explanation of colloidal Cr_2O_3 stability mechanism in the presence of the ionic polyamino acids. *Colloid and Polymer Science*, *292*(10): 2453-2464.
37. Salopek, B., Krasic, D. and Filipovic, S. (1992). Measurement and application of zeta-potential. *Rudarsko-geolosko-naftni zbornik, 4*(1): 147.
38. Abadeh, A., Passandideh-Fard, M., Maghrebi, M. J. and Mohammadi, M. (2019). Stability and magnetization of Fe_3O_4/water nanofluid preparation characteristics using Taguchi method. *Journal of Thermal Analysis and Calorimetry*, 135(2): 1323-1334.
39. Uskoković, V., Castiglione, Z., Cubas, P., Zhu, L., Li, W. and Habelitz, S. (2010). Zeta-potential and particle size analysis of human amelogenins. *Journal of Dental Research*, 89(2): 149-153.
40. Wang, T., Ni, M., Luo, Z., Shou, C., and Cen, K. (2012). Viscosity and aggregation structure of nanocolloidal dispersions. *Chinese Science Bulletin*, 57(27): 3644-3651.
41. Ghadimi, A., and Metselaar, I. H. (2013). The influence of surfactant and ultrasonic processing on improvement of stability, thermal conductivity and viscosity of titania nanofluid. *Experimental Thermal and Fluid Science*, 51: 1-9.
42. Gensdarmes, F. (2015). Methods of Detection and Characterization. *Nanoengineering,* 2015: 55-84.
43. Wang, L., Wang, X., Gu, R., Wang, H., Yao, L., Wen, L., et al. (2018). Observations of fine particulate nitrated phenols in four sites in northern China: concentrations, source apportionment, and secondary formation. *Atmospheric Chemistry and Physics*, 18(6): 4349-4359.
44. Li, C. H., and Peterson, G. (2006). Experimental investigation of temperature and volume fraction variations on the effective thermal conductivity of nanoparticle suspensions (nanofluids). *Journal of Applied Physics*, 99(8): 084314.
45. Şeşen, M., Tekşen, Y., Şendur, K., Pınar Mengüç, M., Öztürk, H., Yağcı Acar, H., et al. (2012). Heat transfer enhancement with actuation of magnetic nanoparticles suspended in a base fluid. *Journal of Applied Physics*, 112(6): 064320.
46. Abareshi, M., Goharshadi, E. K., Zebarjad, S. M., Fadafan, H. K. and Youssefi, A. (2010). Fabrication, characterization and measurement of thermal conductivity of Fe3O4 nanofluids. *Journal of Magnetism and Magnetic Materials*, 322(24): 3895-3901.
47. Yüksel, N. (2016). The review of some commonly used methods and techniques to measure the thermal conductivity of insulation materials. In A. Almusaed, & A. Almssad (Eds.), *Insulation Materials in Context of Sustainability*. IntechOpen.

Malaysian Journal of Analytical Sciences (MJAS)
Published by Malaysian Analytical Sciences Society

OPTIMIZATION OF QUADRUPOLE TIME-OF-FLIGHT LIQUID CHROMATOGRAPHY MASS SPECTROMETRY (QTOF-LC/MS) CONDITIONS FOR DETERMINATION OF COLISTIN IN HUMAN PLASMA

(Pengoptimuman Kondisi Kuadrupel Masa Penerbangan Kromatografi Cecair-Jisim Spektometri (QTOF-LC/MS) untuk Pengenalpastian Colistin di dalam Plasma Manusia)

Mohd Shafie Zabidi[1], Ruzilawati Abu Bakar[1], Nurfadhlina Musa[2], Suzana Mustafa[3], Wan Nazirah Wan Yusuf[1*]

[1]Department of Pharmacology,
School of Medical Sciences, Health Campus,
Universiti Sains Malaysia, Kubang Kerian, Kelantan, Malaysia
[2]Human Genome Centre, School of Medical Sciences, Health Campus,
Universiti Sains Malaysia, Kubang Kerian, Kelantan, Malaysia.
[3]Department of Pharmacy,
Hospital Raja Perempuan Zainab II, Kota Bharu, Kelantan, Malaysia

[*]Corresponding author: wnazirah@usm.my

Received: 27 July 2022; Accepted: 29 September 2022; Published: 27 December 2022

Abstract

Colistin is an antibiotic used as a last option to treat bacterial infections; it has a limited therapeutic window and needs to be monitored for dose optimization. This study aimed to optimize liquid chromatography-mass spectrometry conditions for colistin determination in human plasma. The parameters that affect the performance of liquid chromatography and mass spectrometry were investigated by modifying the composition of the mobile phase in isocratic and gradient elution mode, varying concentrations of acetonitrile and formic acid in the mobile phase, column temperature, ionization mode, and collision energy voltage. The gradient elution with water and acetonitrile, both containing 0.1% formic acid, was effectively used to separate the analytes on a Zorbax SB-C8 column maintained at 40°C. The retention times for colistin A, colistin B, and polymyxin B were 4.003, 3.810, and 4.047 min, respectively. Detection was performed with a quadrupole time-of-flight analyzer using electrospray ionization operated in the negative mode. The precursor–product ion pairs were identified at *m/z* 1123.7300/1079.7032 for colistin A, *m/z* 1109.7151/1065.6886 for colistin B, and *m/z* 1157.7159/1113.6889 for polymyxin B (internal standard). The optimum chromatographic condition for the separation and detection of colistin using quadrupole time-of-flight liquid chromatography mass spectrometry was established.

Keywords: colistin, high performance liquid chromatography, mass spectrometry, QTOF-LC/MS, human plasma

Abstrak

Colistin adalah antibiotik pilihan terakhir digunakan untuk rawatan jangkitan bakteria, ia mempunyai julat terapeutik yang sempit dan pemantauan diperlukan dalam mengoptimumkan dos rawatan. Kajian ini bertujuan untuk mengoptima kondisi kromatografi cecair-jisim spektrometri untuk pengenalpastian colistin di dalam plasma manusia. Parameter yang mempengaruhi prestasi kromatografi cecair dan spektrometri jisim dikaji dengan mengubah suai komposisi fasa bergerak dalam mod elusi isokratik dan kecerunan, perbezaan kepekatan acetonitril dan asid formik dalam fasa bergerak, suhu turus, mod pengionan dan pelangaran tenaga voltan. Kaedah kecerunan elusi dengan menggunakan air dan acetonitril di mana kedua-duanya mengandungi 0.1% asid formik digunakan untuk pemisahanan analit-analit pada turus Zorbax SB-C8 dengan suhu tetap 40 ºC. Masa retensi bagi colistin A, colistin B and polymyxin B adalah 4.003, 3.810, dan 4.047 minit. Penganalisa kuadrupel masa penerbangan digunakan untuk tujuan pengesanan dan dikendalikan menggunakan ionisasi semburan-elektro di dalam mod negatif. Pasangan ion prekursor-produk dikenalpasti di *m/z* 1123.7300, 1079.7032 untuk colistin A, *m/z* 1109.7151, 1065.6886 untuk colistin B dan *m/z* 1157.7159, 1113.6889 untuk polymyxin B (piawai dalaman). Kaedah kromatografik untuk pemisahan dan pengesanan colistin yang optimum menggunakan kuadrupel masa penerbangan kromatografi cecair-jisim sepectrometry telah berjaya dibangunkan.

Kata kunci: colistin, kromatografi cecair prestasi tinggi, spektrometri jisim, QTOF-LC/MS, plasma manusia

Introduction

Colistin, also known as polymyxin E, has re-emerged in the clinical setting for the treatment of multidrug-resistant (MDR) gram-negative organism infection due to limited available treatment options. Colistin dosing is difficult; nephrotoxicity remains a significant dose-limiting side effect, and adequate colistin plasma concentration is difficult to achieve, even though the recommendation of colistin dosing from the new guideline is followed [1–3]. Therefore, therapeutic drug monitoring is recommended to ensure safety and efficacy and to improve clinical outcomes [1]. Colistin is administered intravenously or nebulized into the lungs in the form of colistimethate sodium or colistin methanesulfonate sodium (CMS), an inactive prodrug of colistin [4]. CMS consists of two main components, CMS A and CMS B, which are hydrolyzed spontaneously *in vivo* and *in vitro* to form a mixture of partially sulfomethylated derivatives and then converted to the main active compounds colistin A and colistin B [4, 5]. The conversion of CMS to colistin is influenced by time, temperature, pH, and matrices [6–8]. CMS differs from colistin by additional sulfomethyl groups on each of the five diaminobutyric acid residues. Colistin possesses five free amino groups that can be adsorbed by many materials, such as plastic, polystyrene, and soda-lime glass [9]. The loss due to adsorption may lead to inaccurate results, hence misevaluating the amount of colistin. Colistin has poor ultraviolet absorption and no native fluorescence properties; therefore, derivatized prior analysis is required.

Separation techniques using liquid chromatography with fluorimetry detection or coupled with mass spectrometry detection are among the most frequently reported methods for colistin detection [10–14]. These techniques are sensitive and able to measure the concentration of colistin in the clinically relevant analytical range of 0.05-20 µg/mL [15]. Derivatization is necessary for liquid chromatography with fluorimetry detection, and the chromatographic run time is rather long. The liquid chromatography run time varies from 9 to 35 min in the fluorimetry detection method [16–18]. Liquid chromatography with mass spectrometry allows shorter run times and is also able to detect colistin levels 2–7 times lower than fluorimetry. Studies have reported three analytical methods for sample preparation in colistin assays: protein precipitation with solid-phase extraction (SPE) [13,16,19], protein precipitation [20], and SPE [12]. To achieve efficient analysis, sample pre-treatment should be as simple as possible. Complicated procedures should be avoided because of the high chances of the conversion of CMS to colistin during the procedure [12, 20]. The highly acidic protein precipitation may cause significant CMS hydrolysis [12, 21]. SPE's advantage over the protein precipitation procedure is that it can provide a clean extract and a sufficient concentration of analytes. The conversion of CMS to colistin can be minimized using a nonacidic SPE procedure [12].

In liquid chromatography with mass spectrometry (LC/MS) method development, it is critical to optimize

the various analytical columns, mobile phases, and chromatographic settings to improve the peak's shape and achieve effective colistin A and B separation. The strong interaction between the primary amines in colistin with silanol groups in the C18 column caused significant peak tailing and broadening of the mass spectrometry (MS) colistin chromatogram. Therefore, to enhance the chromatographic peak's shape, formic acid [19, 22, 23] or acetic acid [11, 21] were added to an organic solvent or deionized water in various proportions. Several studies have been conducted to overcome this interaction. Wan et al. [24], used gradient elution using a mixture of 0.1 percent formic acid in water and 0.1 percent formic acid in acetonitrile (5 to 70 percent) for the mobile phase. The low concentration of formic acid may improve the shape of the chromatographic peak by providing a proton donor so that the analytes can form a stable performed-ion. Whereas, Ma et al. [21] used one percent acetic acid in an isocratic elution that included acetonitrile and water (80:19). Jansson et al. [20] used a different mixture in the mobile phase consisted of a mixture of 0.03 percent trifluoroacetic acid (TFA) and 25 percent acetonitrile which demonstrated good separation of colistin A and colistin B. However, TFA was reported to reduce MS ionization [25, 26].

Acquisition parameters such as ionization, desolvation, ion transfer, collision cell fragmentation, and mass analysis provide the best signal for precursor and product ionization of colistin required for MS optimization [27]. The fragmentor voltage (FV) and collision energy (CE) are the common parameters used for optimization [23][11]. Other optimized MS parameters include (1) the nebulization process: ion spray voltage, capillary voltage, and nozzle voltage; and (2) the desolvation process: source temperature, drying/desolvation temperature, and gas flow [19][23][12]. Optimum fragmentation of analytes was measured using signal-to-noise ratio and variations in the fragmentation of colistin A and colistin B. The aim of the present study was to optimize liquid chromatography and mass spectrometry for colistin determination in human plasma using quadrupole time-of-flight liquid chromatography mass spectrometry (QTOF LC/MS).

Materials and Methods

Chemicals and reagents

The colistin sulphate, purchased from Toronto Research Chemicals (Canada) and polymyxin B (1 mg/mL) solution, purchased from Sigma-Aldrich were used as standard. HPLC grade acetonitrile and methanol were purchased from Merck (Darmstadt, Germany). Formic acid (Optima^{TM} LC/MS Grade) was purchased from Fisher Chemical (USA). The de-ionized water was obtained using water deionizer Mili-Q® water purification system. For the solid-phase extraction (SPE) procedures, OASIS hydrophilic-lipophilic balance (HLB) polymetric material cartridges were purchased from Waters (USA). The eluent was 0.1% formic acid in methanol and was prepared by an appropriate dilution of concentrated formic acid with methanol. Pooled drug-free human plasma was donated from Blood Bank, Hospital Universiti Sains Malaysia, Malaysia.

Instrumentation

The Agilent Technologies, 6545 Quadrupole Time-of-Flight Liquid Chromatography/Mass Spectrometry (Q-TOF LC/MS) system was used for detecting colistin in human plasma. The LC-MS system consisted of an Agilent Technologies 1260 high performance liquid chromatography (HPLC) equipped with a binary pump and an autosampler. Chromatographic analysis was performed using Agilent MassHunter Workstation System software (version B.04.00) on a Zorbax SB-C-8 column having 150 × 4.6mm ID and 5µm particle size. A precolumn, Agilent Zorbax Reliance Cartridge Guard-Columns having 12.5 × 4.6mm I.D and 5µm particle size was used to protect the analytical column and extend its lifetime. Mass spectrometry equipped with Dual Agilent Jet Stream electrospray ionization (AJS ESI) interface and Q-TOF mass spectrometer that uses a quadrupole, a hexapole (collision cell) and a time-of-flight unit to produce MS/MS spectra.

Drug standard and internal standard

The colistin sulfate standard contains two major components, colistin A and colistin B. Documented molecular mass of colistin A is 1169.46 ± 98.08g/mol with molecular formula $C_{53}H_{100}N_{16}0_{13}$, colistin B is

1155.43 ± 98.08g/mol with molecular formula $C_{52}H_{98}N_{16}0_{13}$ and polymyxin B is 1203.477g/mol with molecular formula $C_{56}H_{98}N_{16}O_{13}$. The composition percentages colistin A and colistin B reported from the manufacturer were 37.91% and 62.09% respectively.

Working solution and spiked plasma

Standard stock solution of 1000 µg/mL colistin sulphate was prepared in deionized water by appropriately weighing the drugs. The stock solutions of colistin sulphate were stored at -20ºC in polypropylene tube. Working solution of colistin sulphate was prepared by appropriately diluting the stock with deionized water. For the preparation of samples, blank plasma was added with appropriate amount of colistin sulphate working solution to obtain a concentration range of 0.5-10µg/ml.

Sample preparation

Prior to solid phase extraction (SPE), all plasma was centrifuged at 2500 rpm for 10 minutes. A 500 µL of plasma was diluted with 500 µL deionized water. A 10 µL of an internal standard (polymyxin B, 2µg) was added. Each SPE cartridge was pre-conditioned with 1 mL of methanol followed by 2 mL of deionized water. 1 mL of samples were loaded to the SPE and wash with 1 mL of deionized water. The analytes were eluted with 1 mL of 0.1% formic acid in methanol and collected in 1.5 mL analytical tube. The solvent was dried under a gentle nitrogen stream. The residue was reconstituted in 50 µL of formic acid 0.1% in deionized water. After the mixture was vortexed, the sample was directly introduced into the QTOF-LC/MS system after mixing.

Chromatographic optimization parameters

In order to determine the most optimum chromatographic condition, the effect of modifying composition of the mobile phase in isocratic (50%A:50%B, 30%A:70%B and 20%A:80%B), gradient elution mode (the linear of solvent B starting 5% to 100% gradient elution with increment 5-10% for 4-10min), varying concentration of formic acid (0.05%, 0.1% and 0.2%) in the mobile phase and column temperature (30, 40, 45 and 50ºC). Reverse phase chromatography was used for the separation of colistin A, colistin B and polymyxin B (internal standard).

Mass spectrometry optimization parameters

The ionization mode (positive or negative ionization) and collision energy voltage (CE) (range of 5v to 35v with 2.5v step up) were investigated for optimization of mass spectrometry. All parameter investigated and experiment conducted for optimization of QTOF-LC/MS conditions are listed in Table 1.

Table 1. Experiment conducted for optimization of QTOF-LC/MS conditions

Parameters	Variants
Type of mobile phase	Solvent A: Formic acid in deionized water Solvent B: Acetonitrile or Formic acid in acetonitrile
Composition of mobile phase in isocratic elution mode	50%A:50%B, 30%A:70%B and 20%A:80%B
Composition of mobile phase in gradient elution mode	The linear of solvent B starting 5% to 100% gradient elution with increment 5-10% for 4-10min.
Column temperature	30, 40, 45 and 50ºC
Ionization mode	Positive ionization (+ ESI) Negative ionization (- ESI)
Collision energy voltage (CE)	Range of 5v to 35v with 2.5v step up

%; percentage, + ESI; positive electrospray ionization, - ESI; negative electrospray ionization, v; volt; ºC; degree of Celsius

Extraction recovery

The recovery (RE) was determined by comparing peak area of colistin A, colistin B and polymyxin B (internal standard) spiked before extraction (α) with the results obtained from analytes spiked after extraction (β).
The formula was used:

$$RE\ (\%) = \alpha \div \beta \times 100 \quad (1)$$

The percentage extraction recovery was obtained for 3 different concentrations; 0.5 mcg/mL (Low), 5 mcg/mL (Medium) and 10 mcg/mL (High).

Precision

Precision was evaluated by replicate analysis of colistin A, colistin B and polymyxin at 3 different concentrations; 0.5 mcg/mL (Low), 5 mcg/mL (Medium), and 10 mcg/mL (High). Precision was expressed as the percentage of the coefficients of variation (CV) by each pool.

Results and Discussion

Sample preparation

The SPE was chosen for the sample pre-treatment of plasma samples to provide a fast and simple procedure. Protein precipitation is the simplest sample pre-treatment method, in which organic solvents such as methanol or acetonitrile are commonly used and mixed with acids such as trichloroacetic acid (TCA) or trifluoroacetic acid (TFA). Researchers have noted that using an acidic pretreatment to deproteinize causes a considerable amount of CMS hydrolysis [12]. Colistin is administered intravenously as the inactive prodrug colistin methanesulfonate sodium (CMS), which is metabolized in the body into a variety of partly sulfomethylated derivatives before being converted to colistin [4]. It is crucial to develop a simple, nonacidic sample pretreatment method due to CMS stability and to reduce the hydrolysis of CMS to colistin during analysis. In this study, a nonacidic solid phase extraction (SPE) method established by Gobin et al. [12] was replicated with some modifications. The Oasis HLB column was used in this study, as it can remove anionic CMS from plasma while retaining cationic colistin A and B. To improve the liquid chromatography analysis and mass spectrometry detection, further evaporation of the eluent is required.

In this study, the eluates were dried at room temperature under a moderate nitrogen stream instead of in a heating block at 45 °C. To obtain reproducible peak areas of colistin A and colistin B, the supernatant was later diluted with deionized water containing 0.1% formic acid. Formic acid was used to reduce peak tailing and improve mass spectrometry ionization efficiency. However, formic acid resulted in CMS hydrolysis [12]. To minimize hydrolysis of CMS after introduction of low acid concentration, the sample were run immediately and total time for workup procedure after the dried sample were diluted with deionized water containing 0.1% formic acid would be no more than 5 hours [12,20]. All precautionary measures taken in this study ensured minimizing the hydrolysis of CMS during the analysis.

Optimization of chromatographic condition: Isocratic and gradient elution

No peaks were detected for any of the mobile phase compositions tested in isocratic mode (50%A:50%B, 30%A:70%B, and 20%A:80%B) (Figure 1). Thus, we investigated a gradient concentration of acetonitrile of up to 100%. Initial gradient elution with water: acetonitrile (from 95:5 to 0:100, v/v, both mobile phases were added with 0.1% formic acid) for 10 min was used for the detection of both colistin and the internal standard. However, all of the analyte peaks were broadening and tailing (Figure 2). This phenomenon has been observed in previous studies [21,24] and has been attributed to the absorption of colistin on the stationary phase of the liquid chromatographic column, which causes significant peak tailing. Colistin is a polycationic peptide with hydrophilic and lipophilic moieties. The tailing effect, probably due to the terminal amine group (hydrophilic) and negative ion from the mild acidic mobile phase, may help to form ion pairs with the polar molecules, increase their hydrophobicity, change their charge status, and change the interaction between the analyte and the stationary phase [21,24].

Formic acid concentration

Different compositions of formic acid were added to the mobile phases, and the concentration of 0.1% formic

acid was sufficient to minimize the absorption of analyte to the stationary phase. Increasing the gradient elution from 10% to 100% of mobile phase B allowed the analyte to achieve good retention, and maintaining 100% of high organic content for 2 min helped achieve better ionization efficiency of the analyte and flush out the remnants of the sample residues (Figure 3).

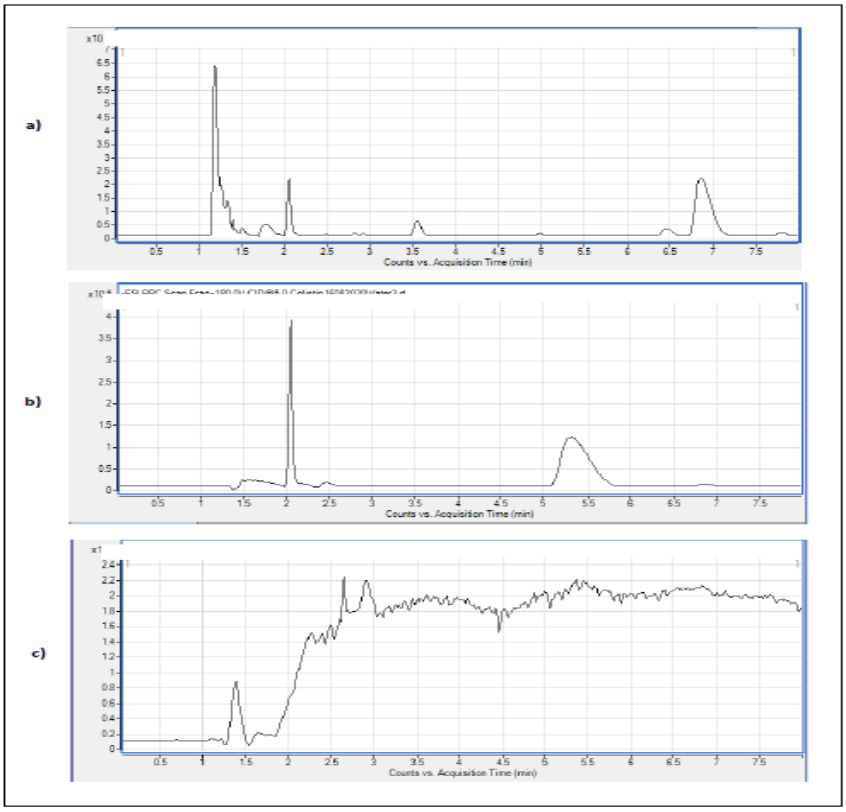


Figure 1. Mass spectrometry chromatogram of the mobile phase compositions tested in isocratic mode a) 50%A:50%B, b) 30%A:70%B, and c) 20%A:80%B

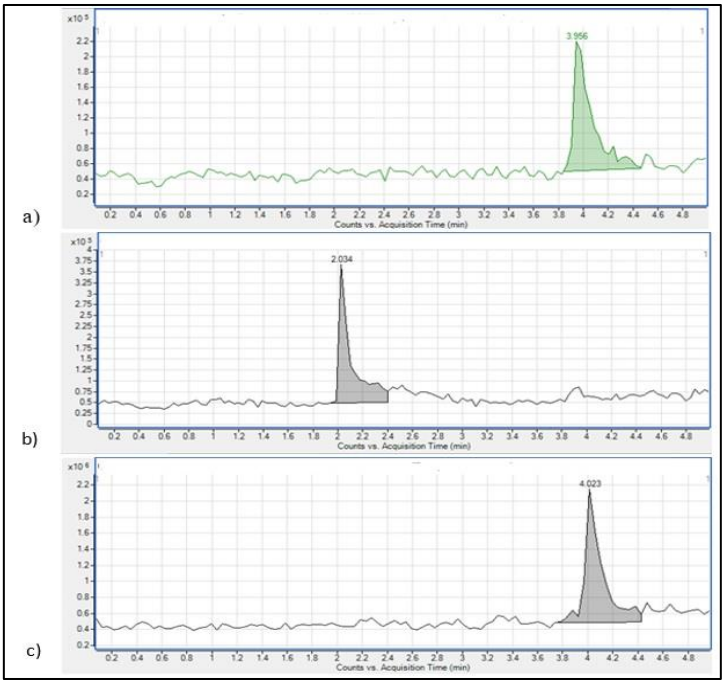


Figure 2. Mass spectrometry chromatogram of a) colistin A b) colistin B and c) polymyxin B (internal standard). Gradient elution 5% of solvent B (ACN-0.1% FA) to 80% for 4 min, total run time 5 min

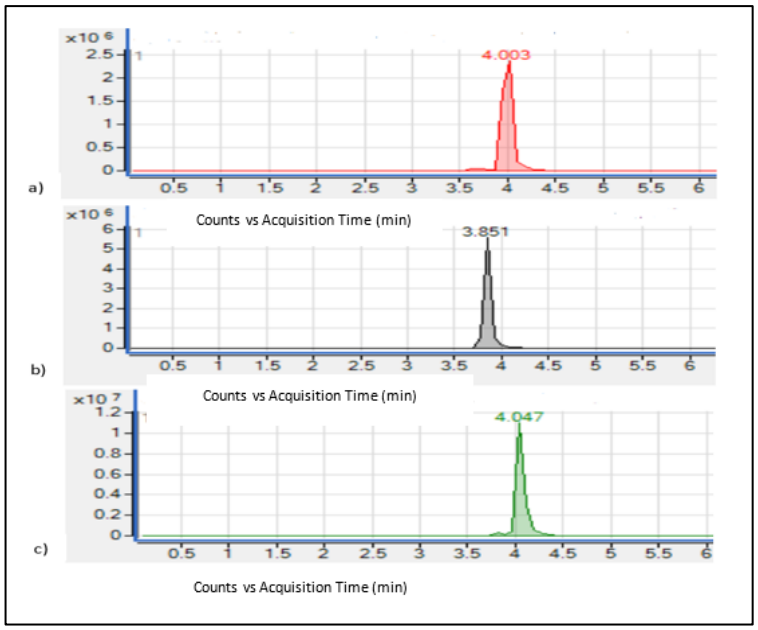


Figure 3. Mass spectrometry chromatogram of a) colistin A b) colistin B and c) polymyxin B (internal standard). Gradient elution 10% of solvent B (ACN-0.1% FA) to 100% for 10 min, total run time 18 min

Column temperature

The column temperatures of 30 ºC, 40 ºC, 45 ºC and 50 ºC were tested for their effects on colistin's peak retention time and area. Gradient elution was tested with mobile phase 5 percent of solvent B (ACN-0.1 percent FA) to 100 percent for 10 min. A higher column

temperature is usually able to produce a better peak shape and allows faster elution of the analytes. Further, it reduces the mobile phase solvent viscosity and, thus, lowers column pressure. However, no effect on the peak area or retention time was observed at high temperatures (Figure 4). Column temperature at 40 ºC was finally selected, as reported by a previous study [28]. The optimization of mobile phase composition, gradient elution program, and column temperature of 40 ºC were able to produce a better peak shape. Even though the mass spectrometry chromatogram peaks overlapped, the separation was done by mass, so the physical separation of the analytes by the chromatographic column was not required [12].

Optimization of mass spectrometry condition

The electrospray ionization (ESI) technique was used to generate precursor and product-ion spectra of the analytes for the identification of colistin A and colistin B. ESI is the preferred method of analysis for most drugs and applies to a broad range of polar to partially non-polar ions [29]. ESI generates positively or negatively charged ions of colistin A and B using positive ESI (+ESI) mode or negative (-ESI) mode. Most studies have reported LC-MS/MS with +ESI mode [13, 22, 30]. Other investigations, however, have reported using the -ESI mode in the LC-MS/MS method [11, 20]. Therefore, both +ESI and -ESI modes were tested for mass spectrometry optimization in this study. The MS-only method was run to identify precursor masses of colistin A and colistin B. After identifying the precursor masses of interest, the targeted MS/MS method was run to identify the precursor ion and product ion. For the acquisition of the full-scan mass spectra, the collision energy was set at 5 v to minimize colistin adduct formation while preventing the fragmentation of the molecular ion.

Formation and selection of precursor masses of Coli stin A and Colistin B

Full-scan mass spectra for both the analytes were acquired in continuum and centroid mode in the mass range of 90–1800 amu. Documented molecular masses from the certificates of analysis of colistin A, colistin B, and polymyxin B were 1169.46 ± 98.08, 1155.43 ± 98.08, and 1203.477, respectively, with molecular formula $C_{53}H_{102}N_{16}0_{16}S$ for colistin and molecular formula $C_{56}H_{100}N_{16}O_{17}S$ for polymyxin B. In +ESI mode, the identified molecular masses of colistin A and colistin B were 1168.78 and 1154.77, respectively. However, in -ESI mode, the identified molecular masses of colistin A, colistin B, and polymyxin B were 1169.5823, 1155.5155, and 1203.477, respectively. After identifying the precursor masses of interest, the targeted MS/MS method was run to identify the precursor ion and the product ion.

Formation and selection of precursor ions of Colistin A and Colistin B

In the +ESI mode, the dual ESI source generated molecular ions into multiple charges, giving rise to the singly charged molecular ions $[M+H]^+$ at *m/z* 1169.7919 and $[M+Na]^+$ at *m/z* 1191.7742 for colistin A. For colistin B, the singly charged ions were $[M+H]^+$ at *m/z* 1155.7762 and $[M+Na]^+$ at 1177.7589. The dominant ion peak in the scan mode mass spectrum was $[M+H]^+$. The precursor ions of colistin A at *m/z* 1169.79 and colistin B at *m/z* 1155.78 for colistin B were set as the targeted precursor ions for the analysis of colistin sulfate in standard solution. Targeted MS/MS method was run, and two dominant product ions were identified at *m/z* 1169.79 → *m/z* 302.1985/728.4976 for colistin A (Figure 5) and at *m/z* 1155.78 → *m/z* 302.1981/728.4963 for colistin B (Figure 5). This result is in contrast with a previous report that identified the product ions at *m/z* 1167.7559 → *m/z* 1123.7266/1079.7014 for colistin A and 1153.7385 → *m/z* 1109.7134/1065.5870 for colistin B [11].

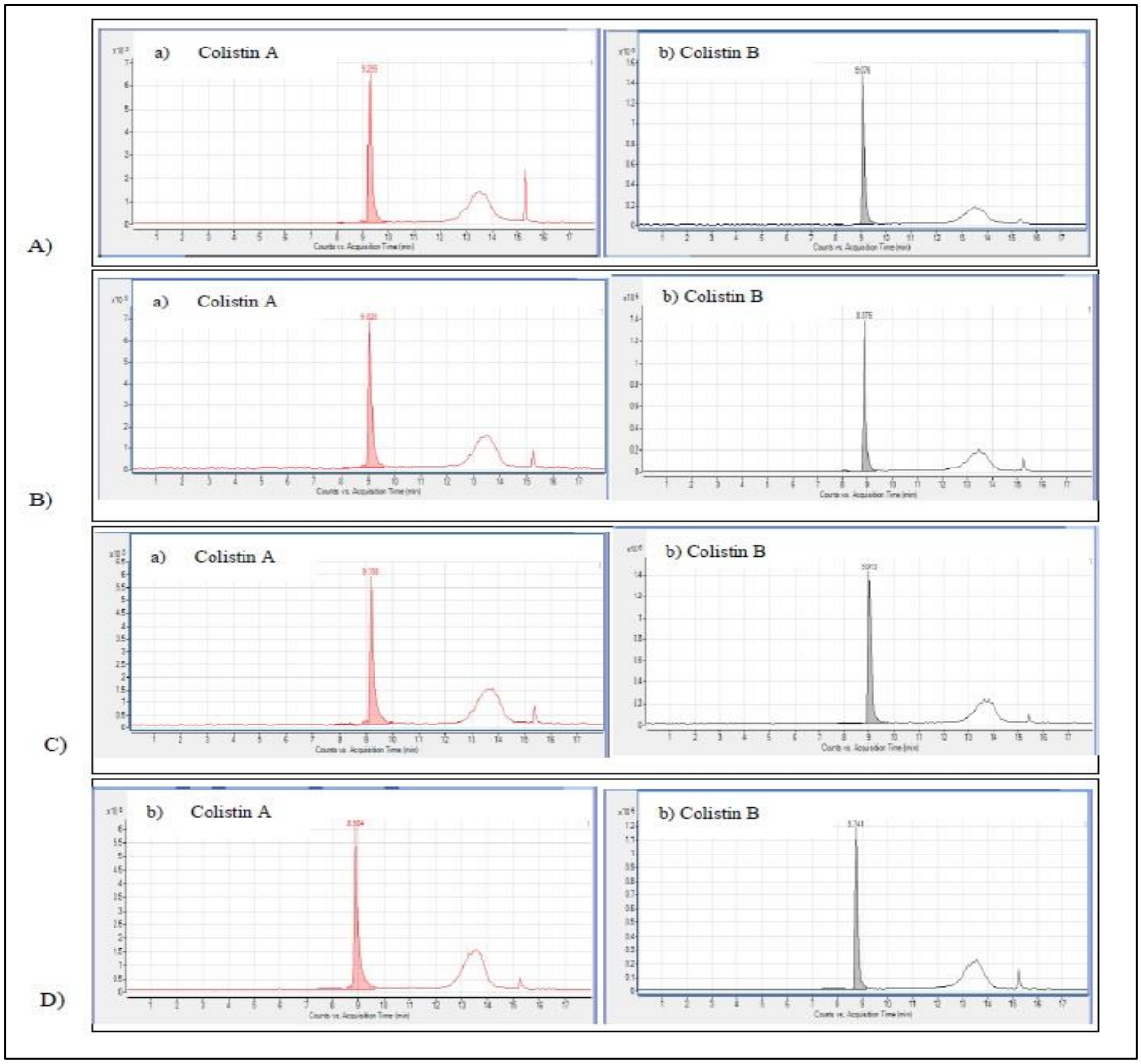


Figure 4. Mass spectrometry chromatogram of colistin A and colistin B when the column temperature was set A: 30ºC, B: 40ºC, C: 45ºC and D: 50ºC. Gradient elution 5% of solvent B (ACN-0.1% FA) to 100% for 10 min

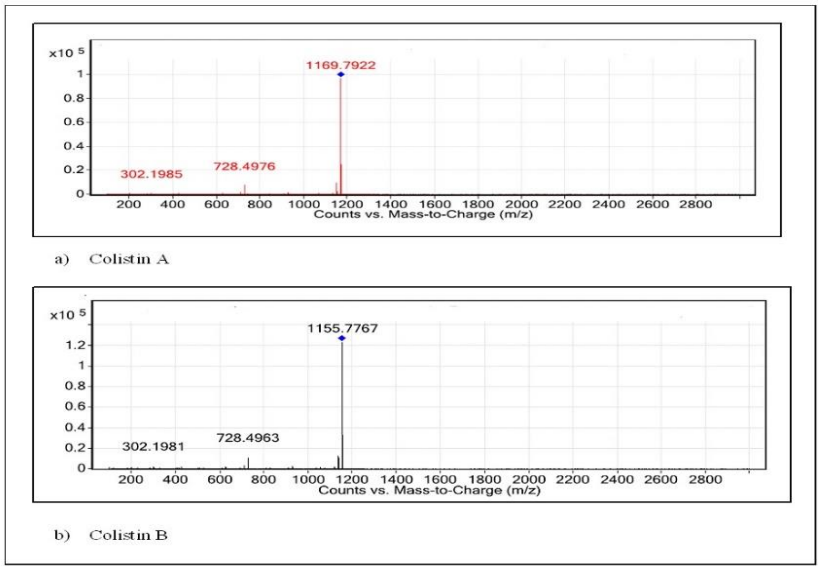


Figure 5. Mass spectrometry spectrum of precursor ion and product ion of a) colistin A, *m/z* 1169.79 → *m/z* 302.1985, 728.4976 and b) colistin B, *m/z* 1155.78 → *m/z* 302.1981, 728.4963 in positive ionization mode (ESI+)

In the -ESI mode, the dual ESI source generated molecular ions into multiple charges, giving rise to singly charged molecular ion $[M-H]^-$ at *m/z* 1167.7683 and doubly charged molecular ion $[M-2H]^{-2}$ at *m/z* 583.377 for colistin A**.** The singly charged ion $[M-H]^-$ for colistin was at *m/z* 1153.7526, with doubly charged molecular ions $[M-2H]^{-2}$ at 576.3714 and $[2M+CL]^-$ at *m/z* 2347.465. For polymyxin B, the singly charged ion $[M-H]^-$ was at *m/z* 1201.7579 and the doubly charged molecular ion $[M-2H]^{-2}$ was at 600.3749. The dominant ion peak in the scan mode mass spectrum was $[M-H]^-$. The $[M-H]^-$ ion, which had a higher intensity, was chosen as the precursor ion for the analytes (colistin A: *m/z* 1167.7683; colistin B: *m/z* 1153.7526; and polymyxin B: *m/z* 1201.7579). Targeted MS/MS method was run and dominant product ions were identified at *m/z* 1167.7683 → *m/z* 1123.7202/1079.697 for colistin A, *m/z* 1153.7526 → *m/z* 1109.7046/1065.6803 for colistin B, and *m/z* 1201.7579 → *m/z* 1157.73/1113.6791 for polymyxin B (Figure 6). This result is similar to a previous finding reported by Gikas et al. [11], in which these product ions arise from the successive loss of 44 Da, which is attributed to the side chain cleavage of CH_3CHO from the L-threonine (Thr) amino acid residue. Colistin A and colistin B presented greater ionization efficiency in -ESI than in +ESI; thus, the -ESI mode was selected for further analysis.

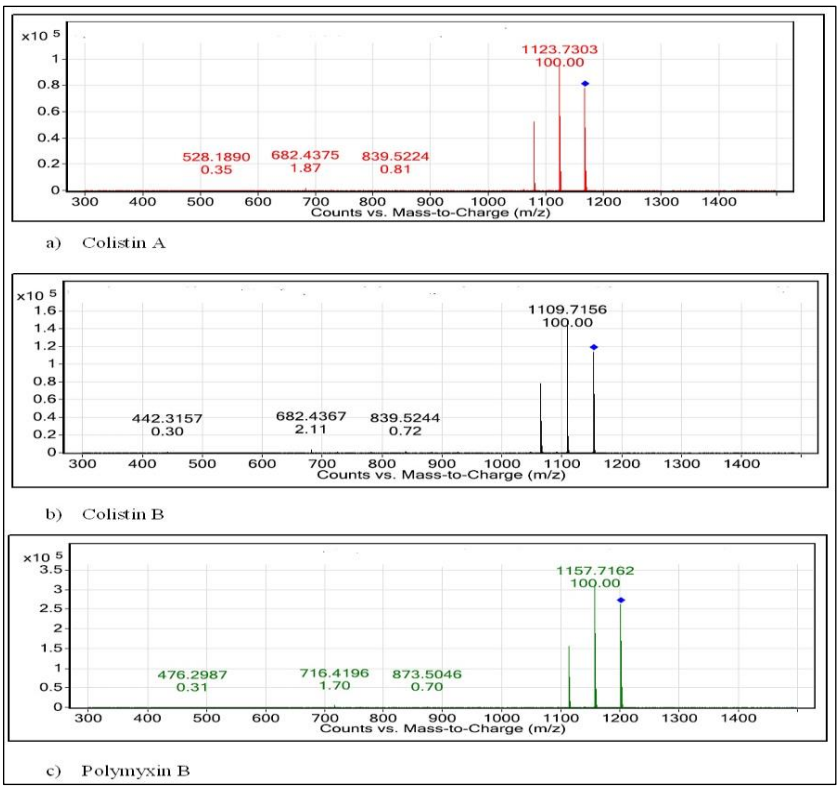


Figure 6. Mass spectrometry spectrum of precursor ion and product ion of a) colistin A, *m/z* 1167.7683 → *m/z* 1123.7202, 1079.697, b) colistin B *m/z* 1153.7526 → *m/z* 1109.7046, 1065.6803 and c) polymyxin B *m/z* 1201.7579 → *m/z* 1157.73, 1113.6791 in negative ionization mode (ESI-)

Optimization of collision energy voltage

The optimum value of collision energy for colistin A, colistin B, and polymyxin B was determined by studying collision energy from 15 to 30v. Figure 7 indicates that when the signal to noise ratio (SNR) for colistin A and colistin B was gradually increased from 18 to 20v, the SNR values became inconsistent with rising collision energy. It was found that 20v provided the best fragmentation of colistin A and colistin B, whereas 22v caused some fragmentation in the form of extra peaks with different m/z, indicating that high collision energy caused colistin A and colistin B to become more fragmented, lowering the detection limit.

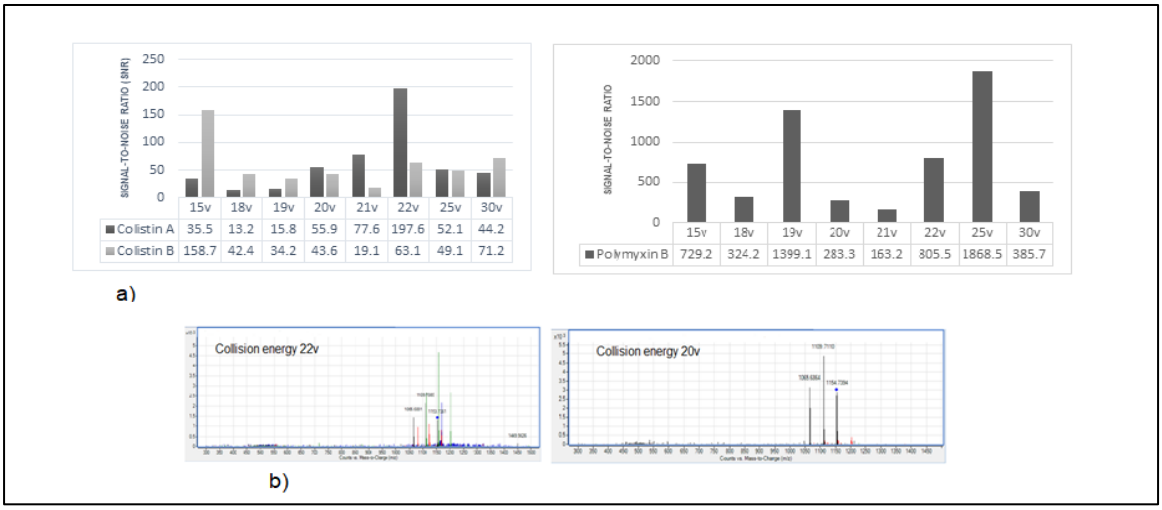


Figure 7. Optimization of Collision Energy Voltage. a) Signal-to-noise ratio of colistin A, colistin B and polymyxin B b) mass fragment for detection of colistin A, colistin B and polymyxin B

Final liquid chromatography and mass spectrometry conditions

A binary mobile phase gradient consisting of 0.1% aqueous formic acid (Solvent A) and acetonitrile with 0.1% formic acid (Solvent B) was selected for chromatographic separation. The gradient elution program used is shown in Table 2. The post run time was 2 min to equilibrate the column with the initial solvent proportions (80% solvent A and 20% solvent B). The injection volume was 5 µL and the column temperature of 40°C.

Table 2. Gradient of the elution program

Time (minutes)	Mobile Phase A (%)	Mobile Phase B (%)	Flow Rate (mL/min)
0	80	20	1
0-8	90-0	10-100	1
8 – 10	0	100	1
10 – 10.1	0 - 95	100 - 5	1.5
10.1 - 16	95	5	1.5

mL/min: milliliter per minutes; %: percentage

The mass spectrometer was operated in the negative-ion mode. The optimal mass spectrometry setup parameters were a 320 °C gas temperature, 8 L/min drying gas, 35 psig nebulizer, 350 °C sheath gas temperature, 11 L/min sheath gas flow, 3500 V Vcap, 3.416 microA capillary, 1000 V nozzle voltage (Expt), and 5.64 microA chamber. The collision energy was optimized as 20 v for colistin A, colistin B, and polymyxin B. For the acquisition of the full-scan mass spectra, the collision energy was set at 2 v to minimize colistin adduct formation while preventing the fragmentation of the molecular ion. Full-scan mass spectra for both the analytes were acquired in continuum and centroid mode in the mass range of 300–2000 amu.

Extraction recovery

Recovery represents the percentage of the analyte still present after sample workup compared with the amount of the analyte initially contained in the sample. The extraction recoveries of colistin A, colistin B, and

polymyxin B at the three concentrations are shown in Table 3. The recovery with various concentrations of the analytes ranged from 78–95%. The coefficients of variation (CV) for the analytes were less than 10% and within the acceptance limit [31].

Table 3. Results of the extraction recovery of colistin A, colistin B and polymyxin B

Concentration (mcg/mL)	Extraction Recovery (%)		
	Colistin A	Colistin B	Polymyxin B
0.5	80.8	82.8	79.7
5	95.4	86.8	83.1
10	78.8	81.8	75.6
Mean	85.00	83.80	79.47
SD	9.06	2.65	3.76
CV	3.6	1.1	1.6

CV: Coefficient of variation; mcg/ml: microgram per milliliter; SD: Standard deviation; %: Percentage

Conclusion

The quadrupole time-of-flight liquid chromatography mass spectrometry (QTOF-LC/MS) condition for the separation and detection of colistin A, colistin B, and polymyxin B was established successfully. The retention times for colistin A, colistin B, and polymyxin B were 4.003 min, 3.81 min, and 4.047 min, respectively. In this study, the separation of analytes was achieved in 18 min using the gradient mode.

Acknowledgement

This study was supported by USM Bridging Grant No: 304.PPSP.6316240 and GIPS-PhD Grant No: 311/PPSP/4404810. The first author was supported by Malaysia Ministry of Health Hadiah Latihan Persekutuan. The authors thank Dr Prof Madya Dr Maizan Mohamed (Faculty of Veterinar, Universiti Malaysia Kelantan, Pengkalan Chepa) and Dr. Chan Sue Hay (USAINS, USM Penang) for their cooperation in conducting the research. The authors also acknowledge staff members of laboratory Faculty of Veterinar, Universiti Malaysia Kelantan and staff members of laboratory department of Pharmacology, School of Medical Sciences, Universiti Sains Malaysia for their support and help.

References

1. Tsuji, B. T., Pogue, J, M., Zavascki, A. P., Paul, M., Daikos, G, L., Forrest, A., Giacobbe, D, R., Viscoli C., Giamarellou, H., Karaiskos, I., Kaye, D., Mouton, J. W., Tam, V. H., Thamlikitkul, V., Wunderink, R. G., Li, J., Nation, R. L. and Kaye, K. S. (2019). international consensus guidelines for the optimal use of the polymyxins: Endorsed by the American College of Clinical Pharmacy (ACCP), European Society of Clinical Microbiology and Infectious Diseases (ESCMID), Infectious Diseases Society of America (IDS). *Pharmacotherapy*, 39 (1): 10-39.
2. Nation, R., L., Garonzik, S. M., Thamlikitkul, V., Giamarellos-Bourboulis, E. J., Forrest, A., Paterson, D. L., Li, J. and Silveira, F. P. (2017). Dosing guidance for intravenous colistin in critically ill patients. *Clinical Infectious Diseases*, 64 (5): 565-571.
3. Ehrentraut, S. F., Muenster, S., Kreyer, S., Theuerkauf, N. U., Bode, C., Steinhagen, F., Ehrentraut, H., Schewe, J. C., Weber, M., Putensen, C. and Muders, T. (2020). Extensive therapeutic drug monitoring of colistin in critically Ill patients reveals undetected risks. *Microorganisms*, 8(3): 415.
4. Bergen, P. J., Li, J., Rayner, C. R. and Nation, R. L. (2006). Colistin methanesulfonate is an inactive prodrug of colistin against *Pseudomonas aeruginosa*. *Antimicrobial Agents Chemotheraphy*, 50(6): 1953-1958.

5. Li, J., Nation, R. L., Turnidge, J. D., Milne, R. W., Coulthard, K., Rayner, C. R. and Paterson, D. L. (2006). Colistin: the re-emerging antibiotic for multidrug-resistant Gram-negative bacterial infections. *Lancet Infectious Disease,* 6(9): 589-601.
6. Milne, R. W., Nation, R. L., Li, J., Coulthard, K. and Turnidge, J. D. (2003). Stability of colistin and colistin methanesulfonate in aqueous media and plasma as determined by high-performance liquid chromatography. *Antimicrobial Agents Chemotherapy*, 47(4): 1364-1370.
7. Dudhani, R. V., Nation, R. L. and Li, J. (2010). Evaluating the stability of colistin and colistin methanesulphonate in human plasma under different conditions of storage. *Journal of Antimicrobial Chemotherapy*, 65(7): 1412-1415.
8. Orwa, J. A., Govaerts, C., Gevers, K., Roets, E., Van Schepdael, A. and Hoogmartens, J. (2002). Study of the stability of polymyxins B(1), E(1) and E(2) in aqueous solution using liquid chromatography and mass spectrometry. *Journal of Pharmaceutical Biomedical Analysis,* 29(1-2): 2003-2012.
9. Karvanen, M., Malmberg, C., Lagerback, P., Friberg, L. E. and Cars, O. (2017). Colistin is extensively lost during standard in vitro experimental conditions. *Antimicrobial Agents Chemother*apy, 61(11): e00857-17.
10. Li, J., Milne, R. W., Nation, R. L., Turnidge, J. D., Coulthard, K. and Valentine, J. (2002). Simple method for assaying colistin methanesulfonate in plasma and urine using high-performance liquid chromatography. *Antimicrobial Agents Chemotheraphy*, 46(10): 3304-3307.
11. Gikas, E., Bazoti, F. N., Katsimardou, M., Anagnostopoulos, D., Papanikolaou, K., Inglezos, I., Skoutelis, A., Daikos, G. L. and Tsarbopoulos, A. (2013). Determination of colistin A and colistin B in human plasma by UPLC–ESI high resolution tandem MS: Application to a pharmacokinetic study. *Journal of Pharmaceutical and Biomedical Analysis*, 83: 228-236.
12. Gobin, P., Lemaître, F., Marchand, S., Couet, W. and Olivier, J. C. (2010). Assay of colistin and colistin methanesulfonate in plasma and urine by liquid chromatography-tandem mass spectrometry. *Antimicrobial Agents Chemotherapy,* 54(5): 1941-1948.
13. Cangemi, G., Barco, S., Castagnola, E., Tripodi, G., Favata, F. and D'Avolio, A. (2016). Development and validation of UHPLC–MS/MS methods for the quantification of colistin in plasma and dried plasma spots. *Journal of Pharmaceutical and Biomedical Analysis*, 129: 1-7.
14. Chepyala, D.,Tsai, I. L., Sun, H. Y., Lin, S. W. and Kuo, C. H. (2015). Development and validation of a high-performance liquid chromatography-fluorescence detection method for the accurate quantification of colistin in human plasma. *Journal of Chromatography B*, 980: 48-54.
15. Milne, R.W. (2019). Bioanalysis and stability of polymyxins. polymyxin antibiotics: From labarotory bench to bedside, advances in experimental medicine and biology. Springer Nature, Switzerland: pp. 73-87.
16. Li, J., Milne, R. W., Nation, R. L., Turnidge, J. D., Coulthard, K. and Johnson, D. W. (2001). A simple method for the assay of colistin in human plasma, using pre-column derivatization with 9-fluorenylmethyl chloroformate in solid-phase extraction cartridges and reversed-phase high-performance liquid chromatography. *Journal of Chromatography B,* 761(2): 167-175.
17. Le Brun, P. P., de Graaf, A. I. and Vinks, A. A. (2000). High-performance liquid chromatographic method for the determination of colistin in serum. *Therapeutic Drug Monitoring*, 22(5): 589-593.
18. Reed, M. D., Stern, R. C., O'Riordan, M. A. and Blumer, J. L. (2001). The pharmacokinetics of colistin in patients with cystic fibrosis. *Journal of Clinical Pharmacology*, 41 (6): 645-654.
19. Bihan, K., Lu, Q., Enjalbert, M., Apparuit, M., Langeron, O., Rouby, J., Funck-Brentano, C. and Zahr, N. (2016). Determination of colistin and colistimethate levels in human plasma and urine by high-performance liquid chromatography-tandem mass spectrometry. *Therapeutic Drug Monitoring,* 38(6): 796–803.

20. Jansson, B., Karvanen, M. Cars, O., Plachouras, D. and Friberg, L. E. (2009). Quantitative analysis of colistin A and colistin B in plasma and culture medium using a simple precipitation step followed by LC/MS/MS. *Journal and Pharmaceutical and Biomedical Analysis*, 49(3): 760-767.
21. Ma, Z., Wang, J., Gerber, J. P. and Milne, R. W. (2008). Determination of colistin in human plasma, urine and other biological samples using LC-MS/MS. *Journal of Chromatography B*, 862 (1-2): 205-212.
22. Leporati, M., Bua, R. O., Mariano, F., Carignano, P., Stella, M., Biancone, L. and Vincenti, M. (2014). Determination by LC-MS/MS of colistins A and B in plasma and ultrafiltrate from critically ill patients undergoing continuous venovenous hemodiafiltration. *Therapeutic Drug Monitoring,* 36(2): 182-191.
23. Tsai, I. L., Sun, H. Y., Chen, G. Y., Lin, S. W. and Kuo, C. H. (2013). Simultaneous quantification of antimicrobial agents for multidrug-resistant bacterial infections in human plasma by ultra-high-pressure liquid chromatography-tandem mass spectrometry. *Talanta*, 116: 593-603.
24. Wan, E. C., Ho, C., Sin, D. W. and Wong, Y. (2006). Detection of residual bacitracin A, colistin A, and colistin B in milk and animal tissues by liquid chromatography tandem mass spectrometry. *Analytical and Bioanalytical Chemistry*, 385(1): 181-188.
25. Mallet, C. R., Lu, Z. and Mazzeo, J. R. (2004). A study of ion suppression effects in electrospray ionization from mobile phase additives and solid-phase extracts. *Rapid Communications in Mass Spectrometry*, 18 (1): 49-58.
26. George, R., Haywood, A., Khan, S., Radovanovic, M., Simmonds, J. and Norris, R. (2018). Enhancement and suppression of ionization in drug analysis using HPLC-MS/MS in support of therapeutic drug monitoring: A review of current knowledge of its minimization and assessment. *Therapeutic Drug Monitoring*, 40 (1): 1-8.
27. Sargent, M., (2013). Guide to achieving reliable quantitative LC-MS measurements. RSC Analytical Methods Committee. United Kingdom. pp. 35-42.
28. Hanai, Y., Matsuo, K., Kosugi, T., Kusano, A., Ohashi, H., Kimura, I., Hirayama, S., Nanjo, Y., Ishii, Y., Sato, T., Miyazaki, T., Nishizawa, K and Yoshio, T. (2018). Rapid, simple, and clinically applicable high-performance liquid chromatography method for clinical determination of plasma colistin concentrations. *Journal of Pharmaceutical Health Care and Sciences*, 4: 1-9.
29. Adaway, J. E. and Keevil, B. G. (2012). Therapeutic drug monitoring and LC–MS/MS. *Journal of Chromatography B*, 883–884: 33–49.
30. Dotsikas, Y., Markopoulou, C. K., Koundourellis, J. E. and Loukas, Y. L. (2011). Validation of a novel LC-MS/MS method for the quantitation of colistin A and B in human plasma. *Journal of Separation Science*, 34(1): 37-45.
31. Food and Drug Administration (2018). Bioanalytical method validation guidance. Access from https://www.fda.gov/regulatory-information/search-fda-guidance-documents/bioanalytical-method-validation-guidance-industry. [Access online 29 April 2020].

Malaysian Journal of Analytical Sciences (MJAS)
Published by Malaysian Analytical Sciences Society

TRANSESTERIFICATION OF *Calophyllum inophyllum* OIL USING CaO-K_2CO_3 CATALYST FROM *Corbicula fluminea* SHELLS AND BANANA PEELS

(Transesterifikasi Minyak *Calophyllum inophyllum* Menggunakan Mangkin, CaO-K_2CO_3 daripada Cangkerang *Corbicula fluminea* dan Kulit Pisang)

Lee Wei Zhen[1], Siti Norhafiza Mohd Khazaai[2*], Gaanty Pragas Maniam[1], Liliwirianis Nawi[2]

[1]*Faculty of Industrial Sciences & Technology,*
Universiti Malaysia Pahang,
Lebuhraya Tun Razak, 26300 Gambang, Kuantan, Pahang, Malaysia
[2]*Faculty of Applied Sciences,*
Universiti Teknologi MARA Pahang, 26400 Jengka, Pahang, Malaysia

[*]*Corresponding author: ctnorhafiza03@yahoo.com*

Received: 10 May 2022; Accepted: 27 September 2022; Published: 27 December 2022

Abstract

Utilizing *Calophyllum inophyllum* oil (CIO) and waste-based calcium oxide-potassium carbonate (CaO-K_2CO_3) catalyst can bring down the biodiesel production cost and this has become the main issue. CIO is a non-edible feedstock that has the potential to be used as biodiesel feedstock. The acid value and free fatty acid (FFA) content of CIO were 124.54 mg KOH/g and 62.64%, respectively. The acid values were reduced to 11.21 mg KOH/g with 5.60% of free fatty acid (FFA) by acid-catalyzed esterification reaction using a 12:1 methanol to oil ratio. CIO had iodine value of 94.33 mg I_2/g, 1.37% moisture content, a density of 929.1 kg/m^3, and viscosity of 119.5 mm^2/s. It was extracted using a cold maceration method and was found to be predominantly made up of oleic acid. CaO-K_2CO_3 was used to avoid the problems faced by the single metallic catalysts (CaO and K_2CO_3). It was synthesized using physical mixing and used as a heterogeneous catalyst for the transesterification of CIO to produce biodiesel. The base heterogeneous catalyst was characterized and analyzed using TGA, FTIR, XRD, FESEM-EDX, BET, and Hammett indicators. These analyses have proven that calcium oxide (CaO) and potassium carbonate (K_2CO_3) were well incorporated catalyst. CaO-K_2CO_3 is a moderate catalyst with the basic strength of H ≤9.3. Two parameters, which are methanol to oil ratio and reaction time, were optimized to obtain a higher methyl ester yield. The maximum yield of methyl ester obtained from transesterification of CIO at 65 °C was 86.7% using 6 wt.% of 1:1 CaO- K_2CO_3 and 9:1 methanol to oil ratio within 4 h reaction time. CaO-K_2CO_3 appeared as a promising catalyst in converting CIO to biodiesel.

Keyword: banana peels, *corbicula fluminea* shells, methyl ester

Abstrak

Kegunaan minyak *Calophyllum inophyllum* (CIO) dan pemangkin kalsium oksida-potasium karbonat (CaO-K_2CO_3) berasaskan sisa boleh mengurangkan kos pengeluaran biodiesel yang telah menjadi isu utama. CIO adalah bahan mentah tidak boleh dimakan

yang berpotensi untuk digunakan sebagai bahan mentah biodiesel. Kandungan nilai asid dan asid lemak bebas bagi CIO adalah 124.54 mg KOH/g dan 62.64%. Penurunan nilai asid telah berkurang kepada 11.21 mg KOH/g dengan 5.60% of asid lemak bebas melalui tindakbalas esterifikasi asid dengan menggunakan metanol pada minyak (12:1). CIO mempunyai nilai iodin value 94.33 mg I_2/g, 1.37% kandungan lembapan, ketumpatan 929.1 kg/m^3, dan kelikatan 119.5 mm^2/s. Ia diekstrak dengan kaedah pemekatan sejuk dan kebanyakannya terdiri daripada asid oleik. CaO-K_2CO_3 digunakan untuk mengelakkan masalah yang dihadapi oleh pemangkin logam tunggal (CaO dan K_2CO_3). Ia disintesis dengan pencampuran fizikal. Pemangkin heterogen telah dicirikan dan dianalisis dengan menggunakan TGA, FTIR, XRD, FESEM-EDX, BET dan Hemmett. Analisis ini telah membuktikan bahawa kalsium oksida (CaO dan K_2CO_3) telah digabungkan dengan baik. CaO-K_2CO_3 merupakan mangkin sederhana dengan kekuatan alkali H_≤9.3. Dua parameter iaitu nisbah metanol kepada minyak dan masa tindak balas telah dioptimumkan untuk mendapatkan hasil metil ester yang lebih tinggi. Hasil maksimum metil ester yang diperoleh daripada transesterifikasi minyak biji CIO pada 65 °C ialah 86.7% menggunakan 6 wt.% CaO- K_2CO_3, nisbah metanol kepada minyak 9:1 selama 4 j masa tindak balas. CaO-K_2CO_3 sebagai mangkin yang dijanjikan dalam perubahan CIO kepada biodiesel.

Kata kunci: Kulit pisang, cangkerang *corbicula fluminea*, metil ester

Introduction

Nowadays, fossil fuels are the dominant energy source worldwide. Human relies heavily on fossil fuels for daily activities because of their reliability and energy efficiency. However, fossil fuels belong to non-renewable energy derived from the remains of ancient animals and plants buried millions of years ago. The burning of fossil fuels leads to an increased rate of environmental deterioration. To overcome this problem, biofuel, such as biodiesel, appears as a promising alternative to fossil fuel for diesel engines [1]. Biodiesel is a form of alternative fuel derived from vegetable oil or animal fat. Biodiesel production leads to a cleaner emission profile and higher energy efficiency compared to fossil fuel [1] and is the most outstanding biofuel due to several excellent properties such as non-toxic and high biodegradability. [2, 3]. The primary obstacle in commercializing biodiesel is the cost since the production of biodiesel from edible oil is not economically viable. The extensive use of edible oils, especially palm oil, for biodiesel production may cause a food crisis. As a result, biodiesel is very expensive to be used as a fuel due to the tremendous demand for edible oils [4]. These issues can be addressed by utilizing low-cost feedstock such as non-edible oil for biodiesel production.

Calophyllum inophyllum (CI), commonly known as Penaga Laut in Malaysia, is a medium-sized plant that grows up to 20 to 30 m high [5;6]. It thrives in sub-tropical, tropical climates, and can grow in harsh conditions [7]. CIO is a good candidate for green energy production due to its high oil content. The seed oil content of CI ranges from 40-75% (dry weight basis), which is greater than Jatropha seed oil (40-60%) and rubber seed oil (40-50%) [8]. CI grows in mixed cultures with minimal cultivation, thus minimum cultivation cost is required [9]. Since CIO is a non-edible oil, the utilization of CIO as a biodiesel feedstock will not interfere with food provision hence reducing the food crisis problem caused by edible oils. In terms of a heterogeneous catalyst, the monometallic catalyst exhibits low stability towards carbon dioxide and moisture. Even though CaO has high catalytic performance, it will leach out Ca^{2+} due to moisture from the surrounding. The leaching of Ca^{2+} deteriorates the quality of biodiesel by reacting with the FFA of the oil resulting in saponification and deactivation of catalyst function. Besides that, it also has low catalytic activity due to the poor basic site on the surface of the catalyst.

Therefore, in this research, a CaO-K_2CO_3 bimetallic catalysts (catalyst compose of two metals) heterogeneous catalyst is used to produce biodiesel. Bimetallic catalysts exhibit a synergistic effect that makes the catalysts superior to monometallic catalysts [10]. The two metallic elements can form an effective bimetallic catalyst although they do not mix each other to form an alloy. They have superior stability towards moisture and carbon dioxide, thus effectively increasing the lifetime of the catalyst [11]. In addition, bimetallic catalysts have a larger surface area and stronger basic strength resulting in better catalytic performance. Due to these reasons, researchers have mixed CaO or magnesium oxide (MgO) with other monometallic catalysts to increase the selectivity and catalytic activity

of the catalyst [12]. This study aims to investigate the possibility of using CaO-K_2CO_3 as a heterogeneous base bimetallic catalyst for biodiesel production from CIO. To the best of our knowledge, the synthesis of CaO-K_2CO_3 bimetallic catalyst in catalyzing the transesterification of CIO for biodiesel production has never been reported.

Materials and Methods

The CI fruits were collected from the UiTM landscape to obtain the seed oil as feedstock for fatty acid methyl ester production. Banana peels and *corbicula fluminea* were obtained from a local stall in Pahang. ACS grade of methanol, chloroform, Thin Layer Chromatography (TLC) plate, and isopropanol were purchased from Merck KGaA (Germany). AR grades of n-hexane, sulphuric acid and petroleum ether were obtained from Bendosen and Fisher Scientific, respectively. Iodine resublimed from R&M Chemical and potassium hydroxide (KOH) extra pure from Loba Chemie were also used in this study. HPLC grade n-heptane (99%) and C_{17} methyl heptadecanoate as the internal standard for methyl ester were purchased from Friedemann Schmidt. Phenolphthalein (H_= 9.3), 2,4-Dinitroaniline (H_= 15.0), and 4-nitroaniline (H_= 18.4) from Sigma-Aldrich were used as Hammett indicators.

CI fruits were dried under the sun for five days. The seeds were obtained from the crashed outer layers of the dried fruits and were washed with warm water to remove dirt and impurities. Then, the seeds were dried in an oven at 100℃ overnight to remove moisture content. The dried seeds were then ground into fine powder for further extraction [13, 14]. A total of 200 g of powdered seed was placed in a 500 mL beaker. The extraction solvent of n-hexane was then poured into the beaker until the powdered seed was completely covered. The beaker was sealed with aluminum foil and kept for 5 days. The seed oil was separated from the powdered seed by filtration. Subsequently, the seed oil was separated from n-hexane using a Buchi R-100 rotary evaporator at 70 °C. The extracted oil was then transferred to 30 mL vials and kept in the refrigerator.

The bimetallic catalyst was prepared in a 1:1 CaO/ K_2CO_3 molar ratio. The washed clamshells were dried under the sun for two days and crushed using a pestle and mortar. The *corbicula fluminea* shell fine powder was then calcined at 900 °C using a tube furnace. Banana peels that contained K_2CO_3 were sectioned and cut into several pieces. The peels were dried in an oven at 100 °C overnight before grounding the dried peels using a grinder. The banana peels fine powder was then calcined using a tube furnace at 550 °C. A bimetallic catalyst with a CaO/ K_2CO_3 molar ratio of 1:1 was prepared by physically mixing (ball milling) the same ratio of CaO and K_2CO_3. The catalysts were characterized and analyzed using Thermogravimetric Analysis (TGA), X-ray diffraction (XRD), Brunauer-Emmett-Teller (BET), Field Emission Scanning Electron Microscopy and Electron Dispersive X-ray (FESEM-EDX), and Fourier Transform Infrared Radiation (FTIR) analyses. Furthermore, Hammett indicators were also used to determine the basicity of the catalyst. High contents of FFA in CIO were converted to triglyceride using a sulfuric acid catalyst. The conversion of FFA was performed at 60 °C for 2 hours using methanol to oil ratio of 12:1 and 1 wt.% catalyst [13]. This procedure was repeated with the same methodology to reduce the acid value of the oil to less than 5 mg KOH/g oil.

The resulting mixture was transferred to centrifuge tubes to separate excess methanol and contaminants from triglyceride [14]. Transesterification reactions were carried out in a 50 mL round bottom flask equipped with a condenser, thermometer, and magnetic stirrer immersed in a water bath. A total of 5 g of CIO was added to the calcined catalysts and methanol mixture. The mixture was refluxed under constant 500-600 rpm magnetic stirring with a 1:1 CaO/ K_2CO_3 ratio, 6 wt.% catalyst loading, 65 °C reaction at varied reaction times (2 - 5 hours), and several methanol to oil ratios (7:1, 9:1, 11:1, 13:1 and 15:1). After the transesterification reaction, the product mixture was cooled to room temperature. Then, the product mixture was centrifuged at 4000 rpm for 5 min to separate the desired product from the by-products. The FAME content in the sample was analyzed using GC-FID. GC-FID (Agilent 7890A GC-System) with a polar capillary column (MEGA-Wax, 30 m length, 0.32 mm internal diameter, and 0.50 µm film thickness). Samples were prepared by mixing

20 mg of the methyl ester with 400 µL of internal standard using a micropipette. A total of 10 mg/mL of methyl heptadecanoate (C_{17}) was used as an internal standard. For each sample analysis, a sample volume of 1µL was injected into GC. The carrier gas was helium, which had a linear velocity of 40 cm s^{-1}. The initial oven temperature was 190 °C with a 2 min equilibration interval. The temperature of the oven was raised 10 °C per minute until it reaches 230 °C and held for 8 min. The methyl ester content was observed and calculated following the EN14103 European regulation procedure.

Results and Discussion

The characterization of CIO was performed based on acid value, FFA %, iodine value, moisture content, density, and viscosity to determine seed oil quality before transesterification reaction following standard test methods (ASTM D1298; ASTM D1298). The acid value and FFA content of CIO were 124.54 mg KOH/g and 62.64%, respectively in which the values reduced to 91% (acid value: 11.21 mg KOH/g, FFA: 5.60%) after the esterification reaction. It has an iodine value of 94.33 mg I_2/g, 1.37 % moisture content, a density of 929.1 kg/m^3, and viscosity of 119.5 mm^2/s. Oleic acid (73.21%) is predominantly found in the seed oil followed by linoleic acid (13.5%) and palmitic acid (11.7%) play a major FFA in CIO. A similar observation of abundant fatty acids was seen in previous research [8; 14].

Based on Figure 1(a), a weight loss occurred in a single stage ranging between 600 °C and 780 °C. The decreasing TGA thermal curve indicates the thermal decomposition of calcium carbonate ($CaCO_3$) to CaO [15]. The CaO product was stable after 780 °C in which 55% of the sample weight remained. About 44% of TGA weight was loss from $CaCO_3$ suggesting the elimination of carbon dioxide. Meanwhile, as shown in Figure 1(b), involving four stages of the decomposition phase. Firstly, 9.57% of weight loss between 41 °C and 194 °C was attributed to the dehydration of banana peels from the loss of moisture content [16;17]. In the second stage, the volatile matter contents such as hemicellulose, cellulose, and lignin were broken down [18]. This led to a drastic weight loss (39%) of the sample resulting in the lowest value in the DTA plot curve between 200 ℃ and 400 ℃. The final stage ranging between 800 °C and 1000 °C was associated with the solid decomposition of the sample.

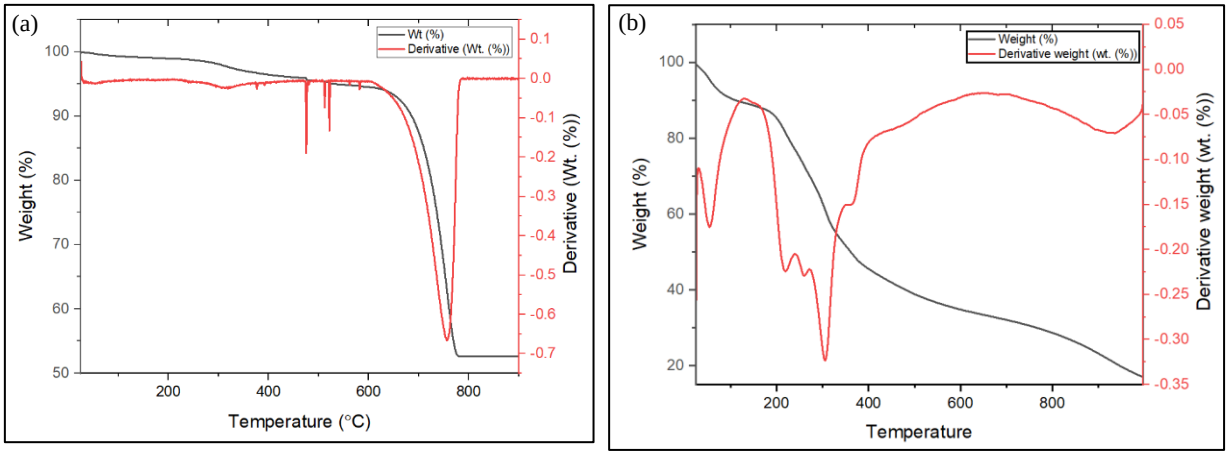


Figure 1. TGA/DTA curve of (a) uncalcined *corbicula fluminea* shells (UCFS) and (b) uncalcined banana peels (UBP)

Based on Figure 2, the peaks of calcined *corbicula fluminea* shells (CCFS) observed at 2θ = 32.484°, 37.635°, 54.109°, 64.404°, and 67.644° were attributed to lime (CaO). $CaCO_3$ was completely transformed into CaO. The appearance of sharp and narrow peaks in CCFS defined the highly crystalline structure of the catalysts [19]. The XRD pattern of calcined banana peels (CBP) presented the characteristic peaks associated with K_2CO_3. It was found that the species exhibited at 2θ value of 43° and 67.7° referred for UBP

and 2θ value of 32.48°, 40.679°, 50.326°, 57.94°, 66.513°, and 73.82° referred for CBP. After thermally calcined at 600 °C, it was observed that K_2CO_3 appeared as the main component of CBP. Compared to CBP, there were small and unclear peaks found in UBP, indicating the importance of the calcination process in producing catalysts with higher crystallinity. The XRD pattern revealed that the CCFS has higher crystallinity compared to CBP. The characteristic peaks of CaO-K_2CO_3 at 2θ = 29.80°, 40.694°, 50.298°, 50.89°, 66.54°, and 73.906° were attributed to K_2CO_3 while the peaks exhibited at 2θ = 32.379°, 37.553°, 54.035°, 64.403°, and 67.611° were assigned to CaO. CaO and K_2CO_3 were considered the principal constituents in the bimetallic catalyst.

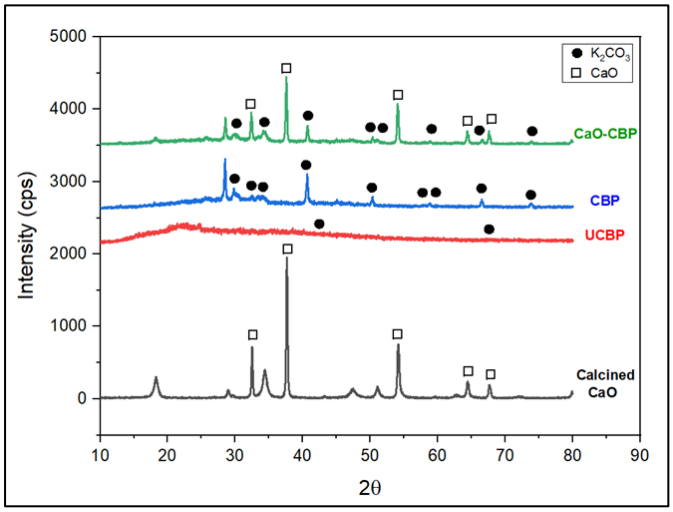


Figure 2. XRD pattern of CCFS, UBP, CBP and CaO-K_2CO_3

The FTIR spectra were used to identify the functional groups involved in CCFS, UBP, CBP, and CaO-K_2CO_3. The intense broad IR peaks at 3436.52 cm^{-1} (CCFS), 3420.60 cm^{-1} (CaO-K_2CO_3), 3436.63 cm^{-1} (CBP), and 3447.11 cm^{-1} (UBP) were assigned to the bending and stretching vibration of O-H bonds indicating the presence of water molecules on the surface of the catalysts [20]. The weak peaks observed at 874.43 cm^{-1} (CCFS), 869.48 cm^{-1} (CaO-K_2CO_3), 669.09 cm^{-1} (CBP), and 667.71 cm^{-1} (UBP) may be due to the stretching vibration of metal-O bonds. The peaks indicated the presence of carbonates in the catalysts at 1384.51 cm^{-1} (CaO-K_2CO_3), 1384.26 cm^{-1} (CBP) and 1384.58 cm^{-1} (UBP), which were assigned to C-O bending and stretching vibration. However, based on Figure 3, the peak at 1384 cm^{-1} was strong only in the calcined catalysts, CBP and CaO-K_2CO_3, representing K_2CO_3. The sharp characteristic bands at 3643.77 cm^{-1} (CCFS) and 3643.97 cm^{-1} (CaO-K_2CO_3) show the presence of the hydroxide (OH) group of calcium hydroxide ($Ca(OH)_2$). The production of this group may be via the hydration reaction between CaO and water molecules. The peak of 1419.83 cm^{-1} in CCFS was assigned to the symmetrical and unsymmetrical O-C-O stretching attached to CaO [21].

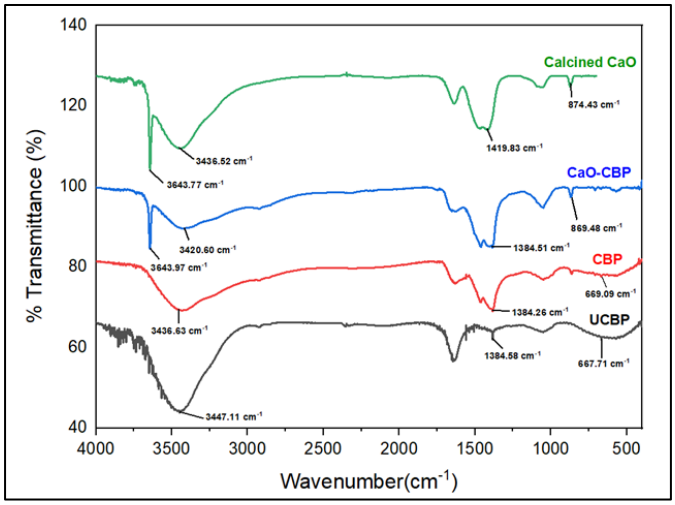


Figure 3. FTIR spectra for CCFS, UBP, CBP and CaO-K_2CO_3

The Hammett indicators used in this analysis are phenolphthalein (H_= 9.8), 2,4-dinitroaniline (H_= 15.0), and 4-nitroaniline (H_= 18.4). CaO-K_2CO_3 turned the colorless phenolphthalein into pink, but the yellow color of 2, 4-dinitroaniline and 4-nitroaniline remains unchanged indicating the basic strength within the range of 9.8 < H_ < 15.0. According to Ngaosuwan et al. [22] the La_2O_3/CaO developed from the eggshells by physical mixing indicated the basic strength within the range of 7.2 < H_ < 9.8. CaO-K_2CO_3 that was synthesized in this work showed higher basicity compared to bimetallic catalyst in the previous study.

The Brunauer-Emmett-Teller (BET) analysis was used to determine the BET surface area, pore volume, and pore size of the catalysts. It was observed that the BET surface areas of both calcined compounds, CCFS and CBP were greater than the uncalcined samples. Thus, it can be concluded that the calcining process contributes to the enhancement of the catalyst's surface area. The pore volume and pore size of the corbicula fluminea shell was discovered to be in an increasing trend from 0.0106 cm^3/g to 0.0358 cm^3/g and 155.8632 Å to 157.1291 Å, respectively after calcination process. The same trend was observed in banana peels, whereby the pore volume and pore size increased from 0.0031 cm^3/g to 0.0205 cm^3/g and 25.8222 Å to 51.3117 Å, respectively. This was expected to provide a better interaction between the oil sample and catalysts. On the other hand, CaO-K_2CO_3 was found to have a BET surface area of 22.5885 m^2/g demonstrating a greater surface area compared to CBP and CCFS. The bimetallic catalyst was expected to contain a greater catalytic property than a monometallic catalyst. However, the pore volume and pore size of CaO-K_2CO_3 were smaller compared to CCFS and CBP. It was suspected that the pore of the catalyst was blocked by CCFS on the CBP [23].

The agglomerated particles of CCFS with irregular shapes were observed in Figure 4 (a). In contrast, Figure 4(b) reveals the irregular structure of UBP with a smooth surface. Calcination plays a significant role in the morphology of banana peels. After the calcining process, the catalyst structure changes dramatically. Figure 4(c) demonstrates a porous morphology of CBP. The cross-sectional view of CBP shows the presence of multiple pores. The microstructure possesses a rough surface with aggregated particles on top of the surface. The binding of CaO on the surface of CBP is illustrated in Figure 4 (d). The agglomerated structures of CCFS fill the pores of CBP in which it binds with CBP forming a bimetallic catalyst. CaO serves as a medium to fill the available voids in CBP with the aim to enhance the surface area of the catalysts hence diminishing the pore volume. EDX analysis was performed to determine the surface elemental composition of the catalysts. Figure 5 shows the EDX spectra of CCFS, UBP, CBP, and CaO-

K_2CO_3 bimetallic catalyst. The spectra show a significant amount of carbon, oxygen, potassium, and calcium on the catalysts. CCFS has 55.36% of O, 30.87% of Ca, and 13.77% of C. UBP has 45.58% of O, 25.49% of K, and 24.67% of C whereas CBP has 51.83% of O, 29.57% of K, and 16.42% of C. CaO-K_2CO_3 consists of 47.32% O, 22.19% Ca, 20.26% C, and 10.24% K.

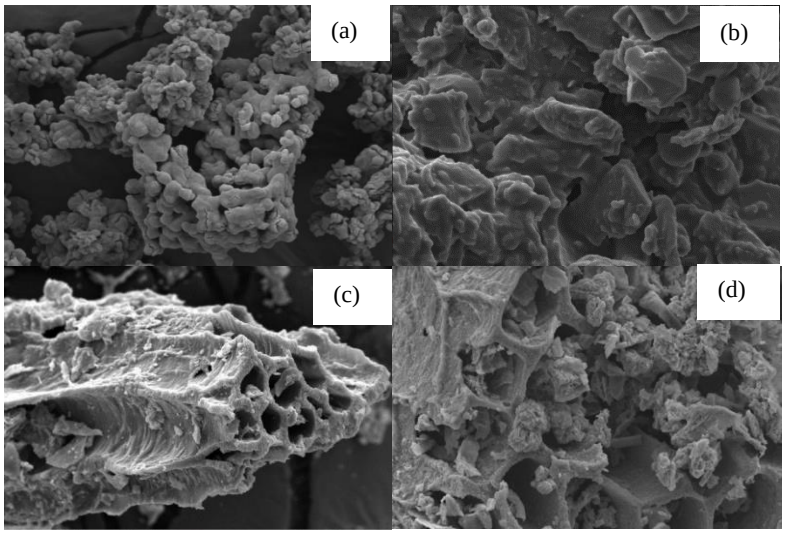


Figure 4. FESEM photographs of (a) CCFS, (b) UBP, (c) CBP and (d) CaO-K_2CO_3 under magnification of 5000

Since the stoichiometric molar ratio of methanol to oil for the transesterification process is 3:1, an excess amount of methanol is required to drive the equilibrium towards biodiesel production. Therefore, the 7:1 molar ratio was taken as the starting value for investigation [24]. As shown in Figure 6(a), the yields of the biodiesel increased as the methanol to oil ratio increased from 7:1 to 9:1. In this study, the molar ratio of 9:1 is determined as the optimum methanol to oil ratio with an 81.4% yield of methyl ester. When the methanol to oil ratio was further increased beyond the optimum ratio (9:1), the biodiesel yields gradually dropped. Glycerol, the side product of the transesterification reaction could dissolve in the excess of methanol and inhibit the reaction of methanol with triglyceride and catalyst. This reaction hampers the separation of glycerol from methyl ester and thus, reduces the methyl ester yield [24]. Therefore, methanol to oil ratio of 9:1 was used to optimize the transesterification of CIO since it produced the highest yield of methyl ester of 81.4 % at 65 ℃ using 6 wt.% 1:1 CaO-K_2CO_3 in 3 h reaction time.

The methyl ester yield increased as the reaction duration increased from 2 to 4 hours. However, after an optimal reaction duration, a further increase in the reaction time will reduce the methyl ester conversion. Since transesterification reaction is a reversible process, the backward or reverse reaction started when equilibrium has been achieved. This would lead to the loss of methyl ester and soap formation [25]. Thus, it is significant to determine the optimal reaction time to obtain a higher biodiesel yield [26]. Therefore, the optimal reaction time was 4 hours with 86.7% biodiesel yield at 65 ℃ using 6 wt.% of 1:1 CaO-K_2CO_3 and 9:1 methanol to oil ratio.

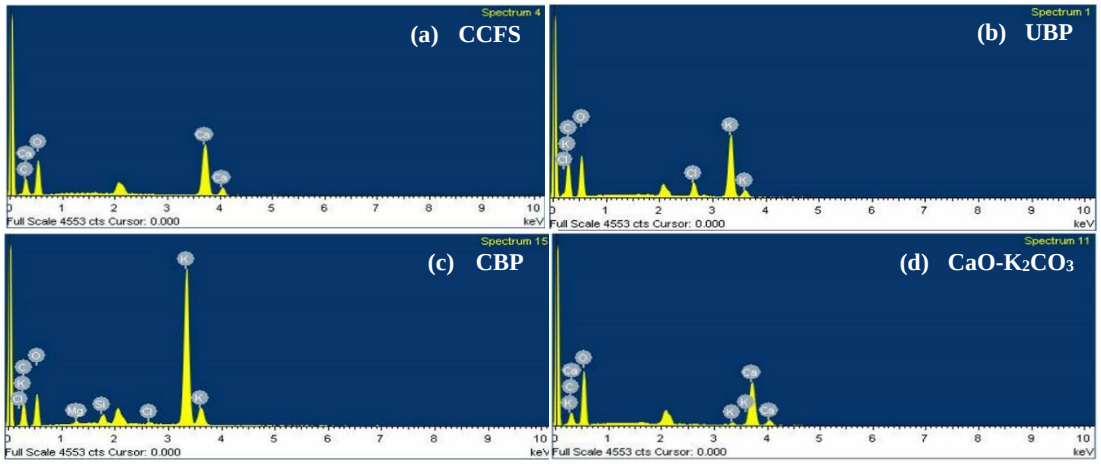


Figure 5. EDX spectra of (a) CCFS, (b) UBP, (c) CBP and (d) CaO-K_2CO_3 bimetallic catalyst

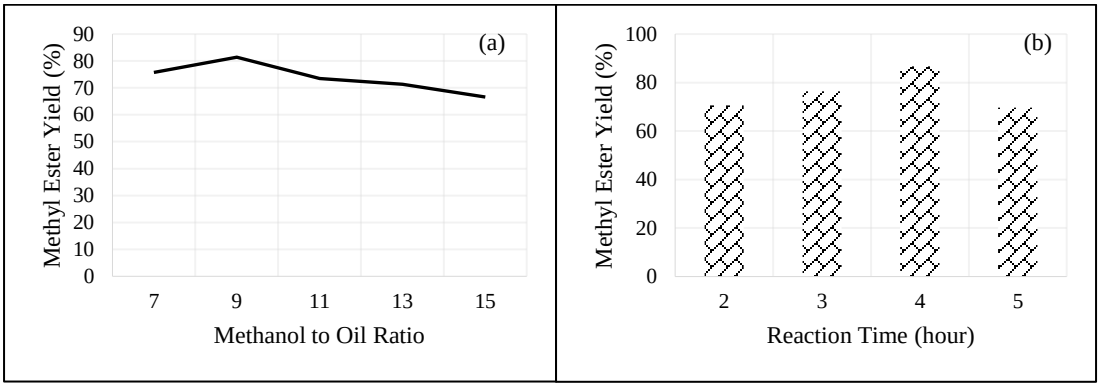


Figure 6. Effect of (a) methanol/oil molar ratio and (b) reaction duration

Conclusion

In this study, a heterogeneous CaO-K_2CO_3 bimetallic catalyst derived from *Corbicula fluminea* shell and banana peels was synthesized and successfully utilized in the transesterification of CIO for the conversion of biodiesel. Bimetallic catalyst CaO-K_2CO_3 was synthesized by physical mixing of CaO and K_2CO_3. Bimetallic catalysts CaO-K_2CO_3 characterized using TGA, XRD, FTIR, FESEM-EDX, BET, and Hammett indicators revealed the potential to be utilized as a solid catalyst in biodiesel conversion. A maximum of 86.7% of methyl ester yield could be obtained at 65 °C using a 9:1 methanol to oil ratio and 6 wt.% of 1:1 CaO-K_2CO_3 at 4 hours reaction time. Using waste materials is an eco-friendly approach that minimizes the cost of catalysts and adds value to these waste materials. Biodiesel from CIO is considered cost-effective renewable energy.

Acknowledgement

The authors would like to thank Ministry of Higher Education, Malaysia, Universiti Malaysia Pahang and Universiti Teknologi MARA Pahang for research project (600-TNCPI 5/3/DDN (06)(001/2020) and (FGRS/1/2019/STG01/UMP/02/2).

References

1. Ogunkunle, O. and Ahmed, N. A. (2019). A review of global current scenario of biodiesel adoption and combustion in vehicular diesel engines. *Energy Reports*, 5:1560-1579.
2. Hajjari, M. Ardjmand, M. and Tabatabaei, M. (2014). Experimental investigation of the effect of cerium oxide nanoparticles as a combustion-improving additive on biodiesel oxidative stability: Mechanism. *RSC Advances*, 4(28): 14352-14356.
3. Tabatabaei, M. Karimi, K. Kumar, R. and Horvátah, I. (2015). Renewable energy and alternative fuel technologies neural computation for rehabilitation. *BioMed Research International*, 2015: 2-4.
4. Demirbas, A. Bafail, A. Ahmad, W. and Sheikh, M. (2016). Biodiesel production from non-edible plant oils. *Energy Exploration and Exploitation,* 34(2): 290-318.
5. Friday, J. B. and Okano, D. (2006). *Calophyllum inophyllum* (kamani) *Clusiaceae* (syn. Guttiferae) (mangosteen family) species profiles for Pacific Island Agroforestry www.traditionaltree.org. Doc-Developpement-Durable.Org, April.
6. Niju, S. Vishnupriya, G. and Balajii, M. (2019). Process optimization of *Calophyllum inophyllum*-waste cooking oil mixture for biodiesel production using *Donax deltoides* shells as heterogeneous catalyst. *Sustainable Environment Research*, 1(1): 1-12.
7. Jahirul, M. I. Brown, R. J. Senadeera, W. Ashwath, N. Rasul, M. G. Rahman, M. M. Hossain, F. M. Moghaddam, L., Islam, M. A. and O'Hara, I. M. (2015). Physio-chemical assessment of beauty leaf (*Calophyllum inophyllum*) as second-generation biodiesel feedstock. *Energy Reports*, 1: 204-215.
8. Fadhlullah, M. Widiyanto, S. N. B. and Restiawaty, E. (2015). The potential of nyamplung (*Calophyllum inophyllum L.*) seed oil as biodiesel feedstock: Effect of seed moisture content and particle size on oil yield. *Energy Procedia*, 68 : 177-185.
9. Azam, M. M. Waris, A. and Nahar, N. M. (2005). Prospects and potential of fatty acid methyl esters of some non-traditional seed oils for use as biodiesel in India. *Biomass and Bioenergy*, 29(4): 293-302.
10. Koehle, M. and Mhadeshwar, A. (2013). Nanoparticle catalysis for reforming of biomass-derived fuels. In New and Future Developments in Catalysis: Catalysis by Nanoparticles. *Elsevier*.
11. García-Diéguez, M., Pieta, I. S. Herrera, M. C., Larrubia, M. A. and Alemany, L. J. (2010). Nanostructured Pt- and Ni-based catalysts for CO_2-reforming of methane. *Journal of Catalysis*, 270(1): 136-145.
12. Faruque, M. O. Razzak, S. A. and Hossain, M. M. (2020). Application of heterogeneous catalysts for biodiesel production from microalgal oil—a review. *Catalysts*, 10(9): 1-25.
13. Atabani, A. E. (2011). *Calophyllum inophyllum L* . as a potential feedstock for bio-diesel production. 6th International Green Energy Conference, 2011: 1-8.
14. Rajendran, N. Gurunathan, B. and I., A. E. S. (2021). Optimization and technoeconomic analysis of biooil extraction from Calophyllum inophyllum L. seeds by ultrasonic assisted solvent oil extraction. *Industrial Crops and Products*, 162: 113273.
15. Vaimakis, T. C. (2013). Thermogravimetry (TG) or thermogravimetric analysis (TGA). University of Ioannina, 4(7): 11419-11426.
16. Biswas, B. Singh, R. Kumar, J. Khan, A. A. Krishna, B. B. and Bhaskar, T. (2016). Slow pyrolysis of prot, alkali and dealkaline lignins for production of chemicals. *Bioresource Technology*, 213: 319-326.
17. Chaiwong, K. Kiatsiriroat, T. Vorayos, N. and Thararax, C. (2013). Study of bio-oil and bio-char production from algae by slow pyrolysis. *Biomass and Bioenergy*, 56: 600-606.
18. Sait, H. H. Hussain, A. Salema, A. A. and Ani, F. N. (2012). Pyrolysis and combustion kinetics of date palm biomass using thermogravimetric analysis. *Bioresource Technology*, 118: 382-389.
19. Lokman Nolhakim, M. A. H. Shohaimi, N. A. M. Mokhtar, W. N. A. W. Ibrahim, M. L. and Abdullah, R. F. (2021). Immobilization of potassium-based heterogeneous catalyst over alumina beads and powder support in the transesterification of waste cooking oil. *Catalysts,* 11(8): 976.

20. Correia, L. M. Saboya, R. M. A. de Sousa Campelo, N. Cecilia, J. A. Rodríguez-Castellón, E. Cavalcante, C. L. and Vieira, R. S. (2014). Characterization of calcium oxide catalysts from natural sources and their application in the transesterification of sunflower oil. *Bioresource Technology*, 151: 207-213.
21. Suprapto, Fauziah, T. R. Sangi, M. S. Oetami, T. P. Qoniah, I. and Prasetyoko, D. (2016). Calcium oxide from limestone as solid base catalyst in transesterification of Reutealis trisperma oil. *Indonesian Journal of Chemistry*, 16(2): 208-213.
22. Ngaosuwan, K. Chaiyariyakul, W. Inthong, O. Kiatkittipong, W., Wongsawaeng, D. and Assabumrungrat, S. (2021). La_2O_3/CaO catalyst derived from eggshells: Effects of preparation method and La content on textural properties and catalytic activity for transesterification. *Catalysis Communications*, 149: 106247.
23. Ruhul, A. M. Kalam, M. A. Masjuki, H. H. Fattah, I. M. R. Reham, S. S. and Rashed, M. M. (2015). State of the art of biodiesel production processes: A review of the heterogeneous catalyst. *RSC Advances*, 5(122): 101023-101044.
24. Degfie, T. A. Mamo, T. T. and Mekonnen, Y. S. (2019). Optimized biodiesel production from waste cooking oil (WCO) using calcium oxide (CaO) nano-catalyst. *Scientific Reports*, 9(1): 1-8.
25. Leung, D. Y. C. Wu, X. and Leung, M. K. H. (2010). A review on biodiesel production using catalyzed transesterification. Applied Energy, 87(4): 1083-1095.
26. Khazaai, S. N. M. Embong, N. H. Hasshim, H. Rahim, M. H. A. and Maniam, G. P. (2018). Transesterification of Karanja (*Pongammia Pinnata*) oil using barnacle derived CaO mixed ZnO. *AIP Conference Proceedings*, 2016: 020097.

Malaysian Journal of Analytical Sciences (MJAS)
Published by Malaysian Analytical Sciences Society

EFFECT OF FAT REPLACEMENT WITH DIFFERENT TYPES OF EGGPLANTS ON THE PHYSICOCHEMICAL AND SENSORIAL PROPERTIES OF CHICKEN SAUSAGES: A CHEMOMETRIC APPROACH

(Kesan Penggantian Lemak dengan Pelbagai Jenis Terung terhadap Sifat Fisikokimia dan Deria Rasa Sosej Ayam: Pendekatan secara Kemometrik)

Farra Nabilah Hamidon[1], Mohd Razali Faridah[1], Abu Bakar Asyrul-Izhar[1], Muhamad Shirwan Abdullah Sani[3,4], Mohammad Rashedi Ismail-Fitry[1,2*]

[1]Department of Food Technology,
Faculty of Food Science and Technology,
Universiti Putra Malaysia 43400 UPM Serdang, Selangor, Malaysia
[2]Halal Products Research Institute,
Universiti Putra Malaysia 43400 UPM Serdang, Selangor, Malaysia
[3]International Institute for Halal Research and Training (INHART),
Level 3, KICT Building,
International Islamic University Malaysia (IIUM), 53100 Jalan Gombak, Selangor, Malaysia
[4]Konsortium Institut Halal IPT Malaysia,
Ministry of Higher Education, Block E8, Complex E,
Federal Government Administrative Centre, 62604 Putrajaya, Malaysia

[*]Corresponding author: ismailfitry@upm.edu.my

Received: 25 May 2022; Accepted: 27 August 2022; Published: 27 December 2022

Abstract

Animal fat plays an important role in processed meat products as it is responsible for improving some physicochemical and sensorial qualities of the final products. However, consumption of high-fat food products is linked to a higher risk of various cardiometabolic diseases such as type 2 diabetes mellitus and cardiovascular diseases. Eggplant has the potential to be used as a fat replacer, but different types of eggplants could produce various results. Thus, this study aimed to produce reduced-fat chicken sausages re-formulated with five different types of eggplants [Round Asian Eggplant (RAE), Pearl Red Eggplant (PRE), Pea Eggplant (PE), Round Black Eggplant (RBE), and Green Thai Eggplant (GTE)] as the fat replacers. The chicken sausages were evaluated for physicochemical and sensorial properties and compared to sausage containing only chicken fat as the control. The RAE, PRE, and PE sausages had the lowest fat content at 4.34%, 6.30% and 7.64%, respectively, thus can be claimed as reduced fat chicken sausages. There were no significant differences among all formulations in terms of ash, moisture, protein, cooking loss, water holding capacity, springiness, and cohesiveness. The sensory analysis revealed that consumers accepted the RAE and PRE sausages compared to the control and the least preferred was PE. This was supported by the PCA, which positively proposed lower fat content (4.34%) and higher a^* value (3.21) while rejecting higher pH (6.35) and b^* values (15.88) of the reduced-fat-chicken sausages. In conclusion, eggplants can be used as fat replacers to produce reduced-fat chicken sausages with Round Asian Eggplant being the best option.

Keywords: chicken meat products, fat mimetics, fat replacers, healthier meat products, low-fat sausages

Abstrak

Lemak haiwan memainkan peranan penting dalam produk daging yang diproses kerana ia bertanggungjawab untuk menambah baik beberapa kualiti fizikokimia dan deria rasa produk akhir. Walau bagaimanapun, pengambilan produk makanan tinggi lemak dikaitkan dengan risiko yang lebih tinggi untuk pelbagai penyakit kardiometabolik seperti diabetes mellitus jenis 2 dan penyakit kardiovaskular. Terung mempunyai potensi untuk digunakan sebagai pengganti lemak, tetapi jenis terung yang berbeza boleh menghasilkan keputusan yang pelbagai. Oleh itu, kajian ini bertujuan untuk menghasilkan sosej ayam kurang lemak yang dirumus semula menggunakan lima jenis terung yang berbeza [*Round Asian Eggplant* (RAE), *Pearl Red Eggplant* (PRE), *Pea Eggplant* (PE), *Round Black Eggplant* (RBE), dan *Green Thai Eggplant* (GTE)] sebagai pengganti lemak. Sosej ayam telah dinilai untuk sifat fizikokimia dan deria rasa dan dibandingkan dengan sosej yang mengandungi hanya lemak ayam sebagai kawalan. Sosej RAE, PRE, dan PE mempunyai kandungan lemak terendah masing-masing pada 4.34%, 6.30%, dan 7.64%, oleh itu boleh diperakukan sebagai sosej ayam kurang lemak. Tiada perbezaan yang ketara antara semua formulasi dari segi abu, kelembapan, protein, kehilangan berat memasak, kapasiti memegang air, keanjalan dan kepaduan. Analisis deria rasa mendedahkan bahawa pengguna menerima sosej RAE dan PRE berbanding dengan kawalan dan yang paling tidak disukai adalah PE. Ini disokong oleh PCA, yang secara positif mencadangkan kandungan lemak yang lebih rendah (4.34%) dan nilai *a** yang lebih tinggi (3.21) sambil menolak nilai pH (6.35) dan *b** (15.88) yang lebih tinggi untuk sosej ayam dikurangkan lemak. Kesimpulannya, terung boleh digunakan sebagai pengganti lemak untuk menghasilkan sosej ayam kurang lemak dengan *Round Asian Eggplant* menjadi pilihan terbaik.

Kata kunci: produk daging ayam, lemak mimetic, pengganti lemak, produk daging yang lebih sihat, sosej rendah lemak

Introduction

The growing concerns about the potential health risks associated with the consumption of high-saturated fat have caused the meat industries to modify traditional meat products or develop new formulations with lower fat contents and better fatty acid profiles [1,2]. Fat contributes to the flavour, texture, colour, mouthfeel, and appearance, so it is not completely removed from meat product formulations [3], alternatively, the fat is replaced with plant-based ingredients that function similar to fat but reduce the total fat, calories, and cholesterol content [4,5]. According to the Nutrient Comparative Claims, a food product is claimed as reduced fat if it has at least a 25 per cent lower fat content than the original product [6].

Eggplant (*Solanum melongena)* also known as brinjal, berenjena, aubergine or melanzane is an edible fruit that originated in India [7] and is commonly cultivated in Asia, Europe, Africa, and the Near East [8]. The eggplants are grouped based on the fruit shape into three botanical types: dwarf (*S. melongena var. depressum*), egg-shaped (*S. melongena var. esculentum*) and long and slender in shape (*S. melongena var. serpentinum*) [9,10]. They are an excellent source of dietary fibre and vitamins such as vitamin B6, vitamin K, vitamin C, niacin, and folate in addition to minerals including potassium, copper, magnesium, manganese, and molybdenum [11, 12]. Eggplant fruits are suitable plant-based ingredients to be incorporated into meat products due to their characteristics. For example, Akesowan and Jariyawaranugoon [13] reported that the incorporation of 2.73% w/w of eggplant powder shows positive attributes towards shrinkage, cooking yield and firmness of chicken nuggets extended with white button mushroom. Ammar [11] proved that the addition of 5 to 10% w/w eggplant pulp can successfully produce high-fibre chicken nuggets with some positive attributes such as water holding capacity and cooking yield and sensory evaluation. Eggplant powder added to pork sausage formulations produced sausages with a higher moisture and protein content and lower fat content [14]. Zhu et al. [15] also reported that eggplant powder mixed with soybean oil and used as a fat replacer improved the water- and fat-binding, texture, and sensory properties of pork sausages.

However, no study has evaluated the different types of eggplants as fat replacers. In addition, the best variables to describe the meat products added with eggplants could further increase the understanding of eggplants' functionalities. Therefore, this study determined the

physicochemical and sensory properties of chicken sausages with five different eggplants: Round Asian Eggplant (RAE), Pearl Red Eggplant (PRE), Pea Eggplant (PE), Round Black Eggplant (RBE) and Green Thai Eggplant (GTE) as the fat replacers. The most discriminant variables of the newly formulated chicken sausages were selected by using a chemometric approach based on multivariate statistics. The outcomes are expected to highlight the potential of eggplants as fat replacers in the production of healthier meat products and could also be a reference for further research.

Materials and Methods

Preparation of chicken sausages

Five different types of eggplant fruits [Round Asian Eggplant (RAE), Pearl Red Eggplant (PRE), Pea Eggplant (PE), Round Black Eggplant (RBE) and Green Thai Eggplant (GTE)] were purchased from the local market in Bandar Sri Damansara, Selangor. The eggplants were separately rinsed with clean water and boiled for five minutes to make them softer and stop the enzymatic browning before being mashed using mortar and pestle into paste form. Frozen chicken breasts were purchased from a meat shop (Sri Ternak, Sri Kembangan, Selangor). The chicken breasts were ground using a mincer machine (Hobart 4822, USA). The control chicken sausage was formulated with 70% chicken meat, 10% fat, 10% corn starch, 1.25% salt, 0.5% sugar, 0.5% black pepper, 0.25% STPP and 7.5 % ice water. For the treatment of fat-replaced chicken sausages, the fat was replaced either by RAE, PRE, PE, RBE, or GTE at 10% of the total weight of the formulation. The minced chicken meat and other ingredients were placed into the bowl cutter (K3 Model-BenchType, Taiwan) and mixed for 10 minutes, then, added with the eggplant paste and continued mixing for another 6 minutes. The mixture was weighed into approximately 30 g portions and stuffed into the sausage casings, boiled for 10 minutes, taken out and cooled down in iced water. The casings were removed and the sausages were vacuum-packed in a polyethylene bag.

Proximate analysis

Proximate compositions of the chicken sausages were determined according to the AOAC methods [16]. Moisture content was determined by using the oven drying method where the chicken sausages were heated to 105 °C overnight and the moisture content was calculated based on the weight loss of the chicken sausages. Ash content was determined by igniting the chicken sausages at 550 °C using the furnace (Method No. 930.05). For crude fat, the Soxhlet extraction method was used where the weight of fat extracted petroleum ether was measured (Method No. 930.09). The crude protein content was determined by using the micro-Kjeldahl method (Method No. 978.04). The carbohydrate was calculated by the difference. The percentage of fat reduction was calculated based on the fat reduced in the newly formulated sausage against the fat of the control sample.

Water holding capacity (WHC)

Each chicken sausage was pre-weighed at 1.5 g and placed in a centrifuge tube with a filter paper (Whatman No. 1) and centrifuged for 15 minutes at 4000 g at 20°C using a centrifuge (KUBOTA 5800, Japan). The dried chicken sausages were then re-weighed, and the reading was recorded. WHC was determined using the following calculation [17]:

$$\text{WHC (\%)} = \frac{\text{(water weight before centrifuge - water weight after centrifuge)}}{\text{the sample weight}} \times 100 \quad (1)$$

Cooking loss

The chicken sausages were pan-fried evenly for 5 minutes using a non-stick pan with the internal temperature reaching 75°C. The cooking loss of the chicken sausages was determined by measuring the initial weight and final weight after cooking the sausages as follows [17]:

$$\text{Cooking loss (\%)} = \frac{\text{(initial weight – final weight) of chicken sausage}}{\text{the initial weight of chicken sausage}} \times 100 \quad (2)$$

pH analysis

The pH values were analyzed before the manufacture of chicken sausages. Five g of meat batter from each chicken sausage sample were homogenized with 40 mL of distilled water. Then the pH values of the chicken sausages were measured using a pH meter (Jenway Model 3505 pH meter, UK) [17].

Colour measurements

The colour of the chicken sausage was measured using a colourimeter (Minolta spectrophotometer CM 3500d, Japan) and the colour reading includes lightness (L^*), redness (a^*) and yellowness (b^*). The equipment was standardized using a white colour standard [17].

Texture analysis

The texture measurement of the chicken sausages was conducted using a computer-assisted TA-XT2i Texture Analyzer (Stable Micro Systems, UK). A compression test was used to determine hardness (g), cohesiveness (mm/mm), chewiness (g/m^3) and springiness (mm/mm). The test was carried out by using a 75 mm compression platen type probe with a 25 kg load cell at a pre-test speed of 2.00 mm/sec, test speed of 2.00 mm/sec and post-test speed of 5.00 mm/sec, a distance of 10.00 mm and auto-trigger type (5.0 g) [17].

Sensory analysis

A Hedonic test was conducted to evaluate the appearance, colour, texture, flavour, aroma and overall acceptability between the chicken sausages incorporated with different types of eggplant and against the control. A nine-point hedonic scale was used to evaluate the chicken sausages ranging from 9 (like extremely) to 1 (dislike extremely) by 30 untrained panellists [18].

Statistical analysis

Data obtained was analyzed using one-way ANOVA to identify significant differences among the means of various chicken sausages treatments using Tukey's test ($p<0.05$). The statistical program used was Minitab software, release 19 (Minitab Inc., Pennsylvania, USA). The results were expressed as means ± SD (standard deviation) of three replicates [18].

Dataset pre-processing

The distributions of (1) physicochemical properties, i.e., proximate, WHC, cooking loss, pH, colour measurement and texture values and (2) sensory properties were evaluated by developing the box and whisker plot (BWP) at a significant level (α) of 0.05 using XLSTAT-Pro (2017) statistical software (Addinsoft, Paris, France). The outlier presence of which values exceeded three times the box's height marked with a dot or '×' was evaluated to confirm the dataset variability. The BWP skewness was also examined to confirm the transformation of physicochemical and sensory properties as a whole dataset. The dataset distribution is deemed positively skewed or right-skewed when its mean value is larger than the median value, and vice versa; hence, the dataset is then subjected to transformation before correlation and principal component analyses (PCA) [19].

Correlation analysis

The correlation between the physicochemical and sensory properties was carried out using Pearson correlation to measure the strength (weak, moderate, or strong) and direction (positive and negative) of the linear relationship between two variables. In this study, the strong, weak, and moderate correlation were determined by correlation matrix (CM) value; $|0.000| < R < |0.300|$ for weak, $|0.300| < R < |0.700|$ for moderate and $|0.700| < R < |1.000|$ for strong CMs [20].

Principal component analysis

The PCA of Pearson correlation was carried out at α of 0.05 to (1) identify the variables with different factor loadings and (2) suggest the significant variables that might contribute to the formulations of chicken sausages. The dataset was transformed into smaller sets of new independent variables denoted as principal components (PCs). The cumulative variability of the PCs was examined to determine the percentage of the dataset explained in the formulations. At the same time, physicochemical properties and sensory properties variables were ranked based on their factor loadings: Strong for $FL \geq |0.750|$, moderate for $|0.500| < FL < |0.749|$ and weak for $FL \leq |0.499|$. Based on these FLs, the contribution of each physicochemical and sensory property and their intercorrelation in the formulations

were examined and further explained [20].

Results and Discussion

Proximate composition

Table 1 shows the proximate analysis of the fat-replaced chicken sausages compared to the control. There were no significant differences ($p<0.05$) between the sausages regarding the ash, moisture, protein and carbohydrate contents. Although the eggplants provide minerals such as calcium, magnesium, phosphorus, potassium, iron, copper and zinc [21], their addition to chicken sausages did not significantly increase the ash content, with fat-replaced chicken sausages containing between 1.27% w/w to 2.08% w/w ash compared to the control of 1.43% w/w. The moisture content was probably not affected due to the similar water-binding ability of the eggplants to chicken fat. The high-water retention properties of the eggplant fibres also contribute to the moisture content of the meat products [11], which is positive as fat controls moisture release from the inner layers of the meat products [21]. Cengiz and Gokoglu [23] also showed an insignificant ($p>0.05$) effect on moisture content for frankfurter-type sausages incorporated with citrus fibre and soy protein concentrate as fat replacers.

Table 1. The proximate composition of the fat-replaced chicken sausages with eggplants compared to the control with fat

Sample[1]	Ash (% w/w)	Moisture (% w/w)	Protein (% w/w)	Carbohydrate (% w/w)	Fat (% w/w)	Fat Reduced Against Original Formulation (% w/w)
Control	1.43 ± 0.07^{a}	67.62 ± 2.13^{a}	11.76 ± 0.89^{a}	3.21 ± 3.46^{a}	15.98 ± 1.42^{a}	Not related
RAE	1.75 ± 0.06^{a}	72.92 ± 2.03^{a}	12.25 ± 0.77^{a}	8.74 ± 2.00^{a}	4.34 ± 2.10^{c}	71.95 ± 15.94^{a}
PRE	1.27 ± 0.71^{a}	68.22 ± 7.96^{a}	10.89 ± 1.94^{a}	13.32 ± 7.62^{a}	6.30 ± 2.23^{c}	60.17 ± 14.77^{ab}
PE	1.68 ± 0.46^{a}	70.52 ± 2.47^{a}	11.38 ± 1.05^{a}	8.79 ± 3.46^{a}	7.64 ± 0.54^{bc}	51.78 ± 6.93^{ab}
RBE	1.69 ± 0.18^{a}	70.65 ± 1.15^{a}	11.86 ± 0.45^{a}	7.50 ± 0.37^{a}	8.30 ± 0.48^{bc}	47.61 ± 7.68^{ab}
GTE	2.08 ± 0.95^{a}	71.28 ± 2.36^{a}	10.89 ± 0.94^{a}	4.28 ± 3.75^{a}	11.47 ± 2.28^{ab}	28.25 ± 12.89^{b}

[1]RAE: Round Asian Eggplant, PRE: Pearl Red Eggplant, PE: Pea Eggplant, RBE: Round Black Eggplant, and GTE: Green Thai Eggplant.
[a-c]Mean ± SD with different letters is significantly different (P<0.05) within the same column.

According to San José et al. [24], although protein content varies in different types of eggplants, it is generally low with not less than 1 g per 100 g. There were no significant differences in the protein content of the sausages as expected. Similarly, there was no significant effect ($P>0.05$) on the carbohydrate content of the sausages, however, the carbohydrate content of the fat-replaced chicken sausages (4.28–13.32% w/w) was higher compared to the control (3.21% w/w), most probably due to the carbohydrate content of the eggplants. Similarly, Bunmee et al., [25] also observed an increase in carbohydrate content in beef patties incorporated with purple eggplant flour. The addition of carbohydrate-based components may contribute to a higher amount of carbohydrates in meat products [26]. Nevertheless, all fat-replaced chicken sausages produced had protein (7.03–14.14%) and carbohydrate (6.69–21.59%) contents similar to various commercially available chicken sausages [27].

All fat-replaced chicken sausages had a significantly reduced fat content, except for sausages incorporated with GTE (11.47% w/w), compared to the control (15.98% w/w), with chicken sausages incorporated with RAE (4.34% w/w) and PRE (6.30% w/w) having the lowest fat content. This agreed with the previous studies by Kahar et al. [28] and Ramle et al. [18], which reported that the replacement of animal fat with plant resources can lower the fat content of meat products. These results confirmed that the use of eggplants as a fat replacer reduces the fat content of meat products except for the addition of GTE. The RAE sausages had the highest ($p<0.05$) fat reduction compared to the control (71.95% w/w), while the GTE sample was the lowest (28.25%

w/w) (Table 1). All chicken sausages incorporated with different types of eggplants had more than 25% fat reduction, so according to the Food Regulations 1985 [6], they can be claimed as fat-reduced sausages.

Water holding capacity (WHC), cooking loss, and pH

WHC indicates the ability of the chicken sausages to bind water under no influence from outside forces and determines the juiciness in conjunction with the flavour, texture, and colour of meat products [29]. Table 2 shows no significant differences ($p>0.05$) in the WHC for all the chicken sausages. The fat in the control formulation could entrap water molecules thus retaining the WHC value, and eggplants can hold the water due to their hydrophilic nature and porous texture of the fibres [30]. In addition, eggplant particles may fill the space around the protein gel matrix and bind water within which also increases the WHC [31]. The WHC data was predicted to be directly proportional to the moisture content, with a higher WHC indicating stronger development of the protein network that entraps the water within the meat products due to the enhanced intermolecular cross-linking between myofibrillar proteins and eggplant [32].

Table 2. The water holding capacity (WHC), cooking loss and pH of the fat-replaced chicken sausages with eggplants compared to the control with fat

Sample[1]	WHC (% w/w)	Cooking Loss (% w/w)	pH
Control	99.97 ± 0.03[a]	10.75 ± 1.86[a]	6.36 ± 0.03[a]
RAE	99.58 ± 0.41[a]	8.24 ± 1.73[a]	6.26 ± 0.12[ab]
PRE	99.90 ± 0.03[a]	7.21 ± 1.67[a]	6.20 ± 0.06[b]
PE	99.41 ± 0.90[a]	7.12 ± 1.52[a]	6.35 ± 0.02[ab]
RBE	99.93 ± 0.05[a]	10.00 ± 3.33[a]	6.31 ± 0.02[ab]
GTE	99.66 ± 0.49[a]	12.83 ± 2.61[a]	6.33 ± 0.02[ab]

[1]RAE: Round Asian Eggplant, PRE: Pearl Red Eggplant, PE: Pea Eggplant, RBE: Round Black Eggplant, and GTE: Green Thai Eggplant.
[a-b]Mean ± SD with different letters is significantly different (P<0.05) within the same column.

Cooking loss is one of the important parameters to evaluate the quality of meat products and is defined as the percentage of weight loss due to heat treatment and cooking loss depends on the capacity of the gel matrix to immobilise fat and water in finely comminuted meat products [33]. There were no significant differences between the fat-replaced sausages compared to the control chicken sausages (Table 2). The cooking loss of the control sausages was attributed to moisture evaporation and fat leakage due to melting during cooking [34], whereas the cooking loss of the eggplants-incorporated sausages could be due to moisture loss. However, since no notable difference was observed between control and eggplant-incorporated sausages, it can be concluded that not much fat was released from the control sausages, while the eggplants used in this study had water retaining ability during cooking similar to the fat. Nevertheless, the GTE and RBE sausages both had high cooking losses near to the control's value, most probably due to the high-fat content as reported in Table 1. Cooking loss can be an indicator of the WHC of meat products that are mostly influenced by factors such as moisture, fat, protein content and processing methods (heating, cutting, grinding) [35, 36] and is supported by the cooking loss and WHC results, where both showed no significant difference among the chicken sausages. Through hydrogen bonding, the WHC of the myofibrillar protein improves promoting emulsion stability which contributes to the reduced cooking loss of low-fat sausages [31].

No significant difference in pH was observed between the control and all chicken sausages, except for the sausages incorporated with PRE. This indicated that eggplants did not affect the acidity of the sausages and eventually would not influence the taste. Various studies have shown that the replacement of fat with plant-based ingredients did not have a notable effect on the pH of meat products. For example, Das et al., [37] reported that the pH of the meat product was not significantly

affected by the addition of soy protein. The addition of other proteins like gelatin in low-fat sausages also did not affect the pH value of the low-fat sausages [38].

Colour and texture properties

Colour is an extrinsic factor that influences customer satisfaction and preferences for meat products [39]. Colour variation can result from the protein-fat interactions, structural proteins and the homogeneity of the cut surface [40]. The colour of the chicken sausages was significantly affected by the addition of different types of eggplant as the fat replacer (Table 3). The lightness (L^*) decreased significantly compared to the control, in line with the results reported by Park et al. [41]. The colour change may be caused by the hydration of the additional dietary fibre (hydrocolloids) as the added fibres were mostly white or egg-coloured [42]. According to Dingstad et al. [43], at least 60 per cent of consumers are willing to purchase sausages when the L^* value was between 62.3 and 68.5. The chicken sausages did not achieve the desired lightness and even become darker after heating, but the L^* values were in the range of commercial chicken sausages (44.42–65.54) [27] with RAE and PRE being most similar to the control. The other darker chicken sausages were influenced by the colour of the eggplant.

In terms of the redness (a^*) and yellowness (b^*), only PE showed a significantly lower value compared to the control, indicating that most eggplants used did not reduce the red colour and alter the yellowness of the chicken sausages. The redness (a^*) of meat products results from the presence of several heme proteins, haemoglobin and myoglobin in the meat and the red colour is the main attribute of meat products [44]. The degree of redness is the general metric used to indicate the freshness of meat and meat products, and meat sausages with higher a^* values usually are more attractive to consumers and have the best market approval rate [45]. Meanwhile, the yellow colour intensity could increase if the fat in sausages was replaced with yellow-coloured plants [46]. Thus, this showed that the colour characteristics of all the eggplants gave yellowness (b^*) values close to the control chicken sausage except for PE. To conclude, most of the eggplants used as the fat replacer did not alter the colour of the chicken sausages, especially RAE and PRE with lightness, redness and yellowness values similar to the control.

Table 3. The colour (L^*, a^*, b^*) and texture properties of the fat-replaced chicken sausages with eggplants compared to the control with fat

Sample[1]	Colour Measurements			Texture Properties			
	Lightness (L^*)	Redness (a^*)	Yellowness (b^*)	Hardness (g)	Springiness (mm/mm)	Cohesiveness (mm/mm)	Chewiness (g/m^3)
Control	55.14 ± 0.87^{a}	2.63 ± 0.16^{ab}	14.30 ± 0.67^{b}	10418 ± 1539^{b}	0.92 ± 0.02^{a}	0.40 ± 0.02^{a}	3835 ± 799^{b}
RAE	53.11 ± 0.37^{ab}	2.45 ± 0.11^{b}	13.20 ± 0.61^{b}	14998 ± 1286^{ab}	0.91 ± 0.02^{a}	0.39 ± 0.04^{a}	5269 ± 301^{ab}
PRE	53.05 ± 0.66^{ab}	2.69 ± 0.01^{ab}	13.55 ± 0.37^{b}	15654 ± 2706^{a}	0.90 ± 0.02^{a}	0.44 ± 0.02^{a}	6260 ± 1243^{a}
PE	50.40 ± 0.36^{c}	1.03 ± 0.30^{c}	15.88 ± 0.65^{a}	14767 ± 1669^{ab}	0.91 ± 0.02^{a}	0.43 ± 0.03^{a}	5778 ± 316^{ab}
RBE	51.97 ± 1.33^{bc}	2.89 ± 0.30^{ab}	14.68 ± 0.71^{ab}	12281 ± 1783^{ab}	0.91 ± 0.02^{a}	0.41 ± 0.02^{a}	4592 ± 658^{ab}
GTE	49.43 ± 1.50^{c}	3.21 ± 0.29^{a}	14.35 ± 0.29^{ab}	11108 ± 1605^{ab}	0.93 ± 0.01^{a}	0.41 ± 0.00^{a}	4274 ± 602^{ab}

[1]RAE: Round Asian Eggplant, PRE: Pearl Red Eggplant, PE: Pea Eggplant, RBE: Round Black Eggplant, and GTE: Green Thai Eggplant.

[a-c]Mean ± SD with different letters is significantly different (P<0.05) within the same column.

The texture of meat products often influences consumer preference. Table 3 shows the texture properties of the fat-replaced chicken sausages with eggplants against the control. Among the five different types of eggplants used, PRE-fat-replaced chicken sausage had significantly ($p<0.05$) high hardness (15654 g) and chewiness (6260 g/m^3) values compared to control, with no significant differences observed in both the hardness and chewiness of the other chicken sausages compared to the control. A similar result was found by Choe and Kim [47] that the addition of wheat fibre mixture increased the hardness of chicken sausages. Other studies also reported that the replacement of fat with various types of fibres increased the hardness of other

types of meat products [48, 49]. The meat proteins used in fat encapsulation were reduced when fat replacers were used to replace animal fat, thus more meat proteins should be utilised through the gel structure of the meat matrix to achieve an acceptable texture [50]. These changes in textural properties may be due to dietary fibre, which can bind water and absorb fat [5]. In addition, reducing the fat could lead to increased hardness and chewiness [49].

There were no significant differences in the springiness and cohesiveness of all the chicken sausages which indicates that the replacement of animal fat with different types of eggplants gave the same springiness and cohesiveness to the final products. Similar results were obtained by Choi et al. [51], for reduced fat chicken sausage containing brewer's spent grain dietary fibre with no significant difference in the value of cohesiveness among all the samples. To summarise, the eggplants did not change the textural properties of the fat-replaced chicken sausages compared to the control except for the PRE.

Sensory properties

Table 4 summarises the sensory analysis of the chicken sausage with different types of eggplant used as the fat replacer. The sensory attributes were appearance, colour, texture, flavour, aroma and overall acceptability and all play important roles in consumer preferences to determine the palatability of food products [39]. The panellists rated the PE chicken sausages the lowest compared to the other fat-treated chicken sausages and control, with the other fat-replaced chicken sausages scoring similarly to the control. These results agree with that obtained by Ammar [11], which indicates that the addition of eggplant pulp powder did not affect the sensory scores of chicken meat nuggets compared to the control. These results also suggested that there was no decrementing effect on the sensory properties of chicken sausages after the addition of different types of eggplants except for PE. This is a very important characteristic since additional ingredients could negatively affect the sensory properties of meat products owing to their strong taste and flavour [46], thus changing the attractiveness of food and affecting consumer choice [51].

Table 4. Sensory properties of the fat-replaced chicken sausages with eggplants compared to the control with fat

Sample[1]	Appearance	Colour	Texture	Flavour	Aroma	Overall Acceptability
Control	6.47 ± 1.33^{a}	6.20 ± 1.32^{ab}	6.60 ± 1.28^{a}	7.03 ± 1.16^{a}	6.70 ± 1.09^{a}	7.07 ± 1.20^{a}
RAE	6.37 ± 1.16^{a}	6.50 ± 1.31^{a}	6.23 ± 1.01^{ab}	6.80 ± 1.24^{a}	6.07 ± 1.44^{ab}	6.93 ± 0.94^{a}
PRE	6.43 ± 1.22^{a}	6.20 ± 1.27^{ab}	6.37 ± 1.33^{ab}	6.57 ± 1.17^{a}	6.50 ± 1.38^{a}	6.73 ± 1.11^{a}
PE	5.17 ± 1.62^{b}	5.40 ± 1.42^{b}	5.60 ± 1.20^{b}	4.97 ± 1.65^{b}	5.20 ± 1.56^{b}	5.03 ± 1.52^{b}
RBE	6.53 ± 1.04^{a}	6.33 ± 1.24^{ab}	6.33 ± 1.42^{ab}	6.57 ± 1.35^{a}	6.13 ± 1.47^{ab}	6.70 ± 1.06^{a}
GTE	6.10 ± 1.35^{ab}	6.13 ± 1.22^{ab}	6.43 ± 1.14^{ab}	6.67 ± 1.24^{a}	6.23 ± 1.52^{ab}	6.70 ± 1.39^{a}

[1]RAE: Round Asian Eggplant, PRE: Pearl Red Eggplant, PE: Pea Eggplant, RBE: Round Black Eggplant, and GTE: Green Thai Eggplant.
[a-b]Mean ± SD with different letters is significantly different (P<0.05) within the same column.

Correlation of physicochemical and sensory properties

Figure 1 (a) and 1 (b) depict the BWP of the physicochemical and sensory properties of the chicken sausages. Among the variables, carbohydrate, moisture, ash, WHC, cooking loss, pH, *a**, chewiness, cohesiveness, overall acceptability, aroma, flavour, texture, and appearance had outliers marked with a dot or (×), which indicated high variability within the dataset. The plus (+) sign in Figure 1 (a) and Figure 1 (b) indicates the mean value for each variable, where only ash, cooking loss, chewiness, cohesiveness, aroma and colour had a similar mean value compared to the median, indicating low or no skewness of the dataset distribution. Other variables showed right and left skewnesses in their dataset distribution, hence, they were transformed before correlation analysis.

The Pearson correlation test was used to determine correlations between two variables, i.e., the physicochemical and sensory properties (Table 5). The correlation matrix (CM) investigated the strength (weak, moderate, or strong) and direction (positive and negative) of the linear relationship between these two variables. Positive and negative correlations between two variables at $|0.700| < R < |1.000|$ indicated strong CM, $|0.300| < R < |0.700|$ for moderate CM and $3|0.000| < R < |0.300|$ for weak CM. From Table 5, hardness and chewiness had eight strong and moderate CMs followed by *a**, *b**, cooking loss, carbohydrate with seven, and pH, fat, and fat reduction with six strong and moderate CMs. All sensory evaluation variables had five overall strong and moderate CMs. Among these variables, several two matched variables had positive and strong CMs., e.g., hardness and chewiness (R = 0.92), flavour and overall acceptability (R = 0.85), appearance and colour (R = 0.77), cooking loss and springiness (R = 0.73), and carbohydrate and fat reduction (R = 0.70), which denoted that these variables had a proportional relationship to each other.

The positive correlation between hardness and chewiness is similar to a study by Varga-Visi et al. [53], which indicated that there was a strong CM between hardness and chewiness of low-fat turkey sausages. In addition, this result was also supported by De Angelis et al. [54] and is probably due to the addition of the fat replacer which contains fibre which increases the hardness and chewiness of the product [55]. The positive correlation between appearance and colour might be explained by the panellists rating the appearance based on the colour of the chicken sausages, which is supported by the sensory properties results tabulated in Table 4, which shows that PE scored the lowest value for both appearance and colour. A positive correlation between flavour and overall acceptability aligned with the results obtained by Andersen et al. [56], which explained that flavour is the main factor to determine product acceptability. The polymers present in the fat replacer might limit water mobility and inhibit water release during cooking, thus, affecting the texture profile analysis which includes the springiness of the meat product [57]. Furthermore, Garcia-Santos et al. [58] also showed that carbohydrate content significantly affects the fat reduction of sausage.

Fat and fat reduction (R = -0.99), pH and carbohydrate (R = -0.72) and fat and carbohydrate (R = -0.72) were negatively and strongly correlated indicating that these variables had an inverse proportional relationship. Jin et al. [59] showed that there are no significant changes in the pH in Pearson's correlation test on emulsion-type pork sausages. Generally, the pH of the meat product is affected by both the raw meat and the additives [60]. The incorporation of starch significantly decreases the fat percentage of emulsion-type sausage, and these ingredients may be able to replace the voids created by the reduced fat and give more high-molecular carbohydrates to the emulsion-type sausage [61]. Although these variables rendered strong and moderate CMs, the CM value only explained the correlation between two variables [20], so PCA was performed [62].

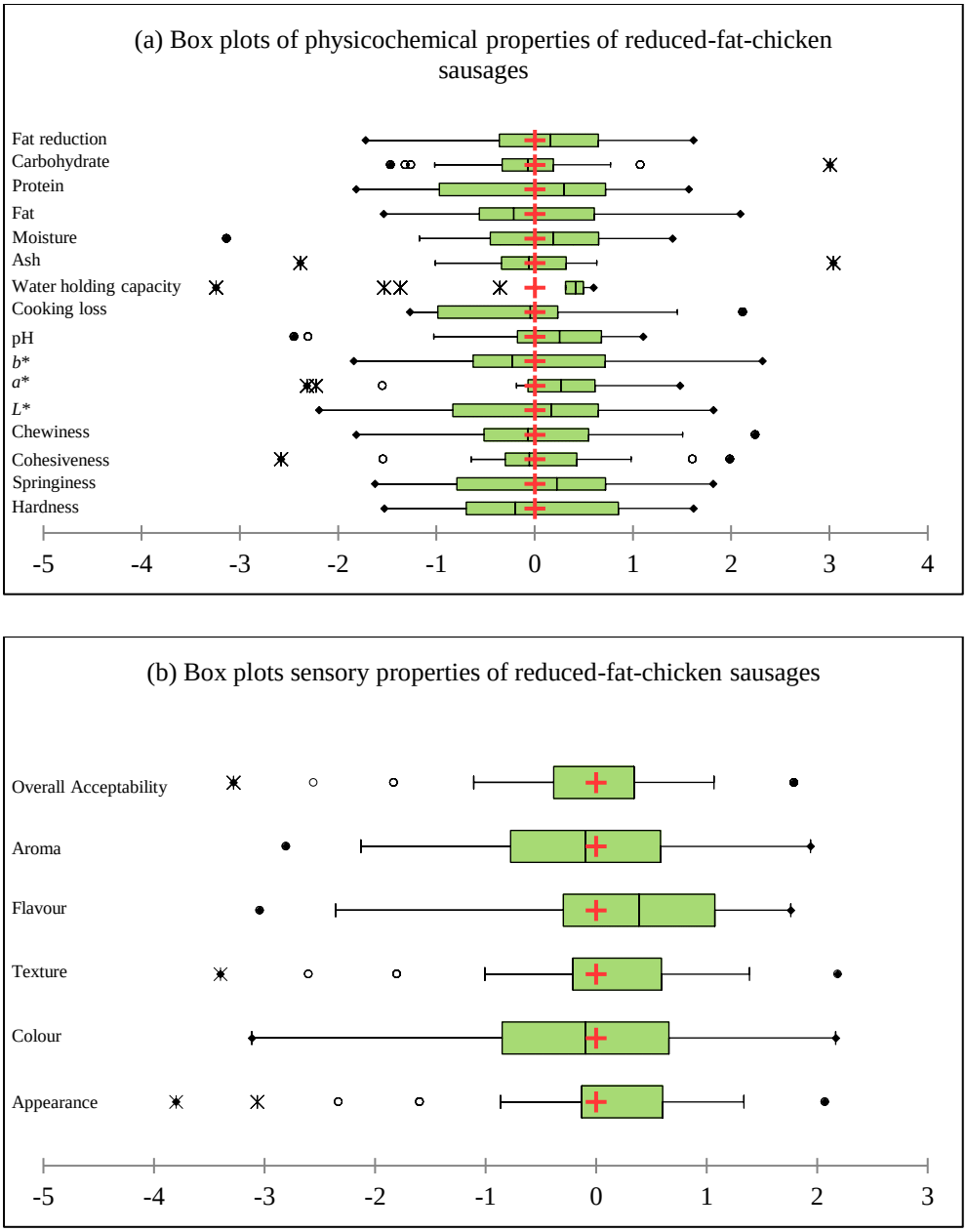


Figure 1. Box plots of (a) physicochemical properties and (b) sensory properties of reduced-fat-chicken sausages

Table 5. Correlation matrix of physicochemical and sensory properties

Variables	Correlation matrix[1,2]									
	Hardness	**Springiness**	**Cohesiveness**	**Chewiness**	***L****	***a****	***b****	**pH**	**Cooking loss**	**WHC**
Hardness	1.00	-0.13	0.07	**0.92**	-0.11	**-0.42**	**-0.30**	**-0.42**	**-0.55**	-0.08
Springiness	-0.13	1.00	-0.01	0.00	-0.26	**0.30**	-0.09	0.10	**0.73**	0.15
Cohesiveness	0.07	-0.01	1.00	**0.43**	-0.16	-0.19	**0.30**	-0.20	-0.12	-0.28
Chewiness	**0.92**	0.00	**0.43**	1.00	-0.17	**-0.41**	-0.16	**-0.46**	**-0.46**	-0.14
*L**	-0.11	-0.26	-0.16	-0.17	1.00	0.05	**-0.43**	-0.15	-0.18	0.29
*a**	**-0.42**	**0.30**	-0.19	**-0.41**	0.05	1.00	**-0.44**	-0.16	**0.51**	0.22
*b**	**-0.30**	-0.09	**0.30**	-0.16	**-0.43**	**-0.44**	1.00	**0.38**	-0.01	**-0.32**
pH	**-0.42**	0.10	-0.20	**-0.46**	-0.15	-0.16	**0.38**	1.00	0.21	-0.26
Cooking loss	**-0.55**	**0.73**	-0.12	**-0.46**	-0.18	**0.51**	-0.01	0.21	1.00	0.24
WHC	-0.08	0.15	-0.28	-0.14	0.29	0.22	**-0.32**	-0.26	0.24	1.00
Ash	-0.15	0.14	-0.29	-0.25	**-0.47**	0.11	0.08	0.20	0.11	0.19
Moisture	-0.11	-0.07	0.18	-0.06	-0.12	-0.02	0.07	0.23	0.08	**-0.42**
Fat	**-0.67**	0.24	-0.18	**-0.65**	0.23	0.21	0.17	**0.59**	**0.39**	0.12
Protein	0.13	-0.14	**-0.41**	-0.08	0.17	-0.09	-0.25	0.05	-0.13	0.02
Carbohydrate	**0.65**	-0.14	0.14	**0.65**	-0.10	-0.16	-0.15	**-0.72**	**-0.38**	0.19
Fat reduction	**0.66**	-0.19	0.23	**0.65**	-0.23	-0.21	-0.19	**-0.60**	**-0.38**	-0.11
Appearance	-0.12	-0.06	-0.07	-0.14	0.21	0.27	-0.21	-0.11	0.05	0.16
Colour	-0.05	-0.08	-0.12	-0.09	0.11	0.21	-0.15	-0.09	0.03	0.06
Texture	-0.17	-0.08	-0.02	-0.17	0.19	0.19	-0.14	-0.02	0.05	0.08
Flavour	-0.19	-0.02	-0.17	-0.24	0.29	**0.37**	**-0.30**	-0.10	0.14	0.19
Aroma	-0.09	0.06	-0.07	-0.09	0.19	0.23	-0.23	-0.07	0.09	0.25
Overall Acceptability	-0.18	-0.03	-0.21	-0.24	0.29	**0.40**	-0.33	-0.12	0.14	0.24
Number of strong and moderate CMs	8	2	3	8	2	7	7	6	7	2

[1]|0.000| < R < |0.300| = weak correlation, |0.300| < R < |0.700| = moderate correlation and |0.700| < R < |1.000| = strong correlation matrix.

[2]Correlation matrix with the bold value indicated strong and moderate correlations between two variables

Table 5. (Continued)

Variables	Correlation matrix[1,2]											
	Ash	**Moisture**	**Fat**	**Protein**	**Carbohydrate**	**Fat reduction**	**Appearance**	**Colour**	**Texture**	**Flavour**	**Aroma**	**Overall Acceptability**
Hardness	-0.15	-0.11	**-0.67**	0.13	**0.65**	**0.66**	-0.12	-0.05	-0.17	-0.19	-0.09	-0.18
Springiness	0.14	-0.07	0.24	-0.14	-0.14	-0.19	-0.06	-0.08	-0.08	-0.02	0.06	-0.03
Cohesiveness	-0.29	0.18	-0.18	**-0.41**	0.14	0.23	-0.07	-0.12	-0.02	-0.17	-0.07	-0.21
Chewiness	-0.25	-0.06	**-0.65**	-0.08	**0.65**	**0.65**	-0.14	-0.09	-0.17	-0.24	-0.09	-0.24
*L**	**-0.47**	-0.12	0.23	0.17	-0.10	-0.23	0.21	0.11	0.19	0.29	0.19	0.29
*a**	0.11	-0.02	0.21	-0.09	-0.16	-0.21	0.27	0.21	0.19	**0.37**	0.23	**0.40**
*b**	0.08	0.07	0.17	-0.25	-0.15	-0.19	-0.21	-0.15	-0.14	**-0.30**	-0.23	**-0.33**
pH	0.20	0.23	**0.59**	0.05	**-0.72**	**-0.60**	-0.11	-0.09	-0.02	-0.10	-0.07	-0.12
Cooking loss	0.11	0.08	**0.39**	-0.13	**-0.38**	**-0.38**	0.05	0.03	0.05	0.14	0.09	0.14
WHC	0.19	**-0.42**	0.12	0.02	0.19	-0.11	0.16	0.06	0.08	0.19	0.25	0.24
Ash	1.00	-0.14	-0.07	0.03	0.05	0.05	-0.04	-0.01	-0.02	0.02	0.11	0.03
Moisture	-0.14	1.00	-0.16	**-0.33**	**-0.53**	0.15	0.06	0.09	0.08	0.06	-0.13	0.04
Fat	-0.07	-0.16	1.00	-0.06	**-0.72**	**-0.99**	0.08	0.00	0.17	0.16	0.12	0.13
Protein	0.03	-0.33	-0.06	1.00	0.07	0.09	0.02	0.02	-0.07	-0.04	-0.03	0.00
Carbohydrate	0.05	**-0.53**	**-0.72**	0.07	1.00	**0.70**	-0.12	-0.08	-0.19	-0.18	-0.01	-0.15
Fat reduction	0.05	0.15	**-0.99**	0.09	**0.70**	1.00	-0.09	-0.04	-0.19	-0.20	-0.14	-0.16
Appearance	-0.04	0.06	0.08	0.02	-0.12	-0.09	1.00	**0.77**	**0.42**	**0.52**	**0.38**	**0.63**
Colour	-0.01	0.09	0.00	0.02	-0.08	-0.04	**0.77**	1.00	**0.40**	**0.50**	**0.32**	**0.59**
Texture	-0.02	0.08	0.17	-0.07	-0.19	-0.19	**0.42**	**0.40**	1.00	**0.62**	**0.56**	**0.62**
Flavour	0.02	0.06	0.16	-0.04	-0.18	-0.20	**0.52**	**0.50**	**0.62**	1.00	**0.58**	**0.85**
Aroma	0.11	-0.13	0.12	-0.03	-0.01	-0.14	**0.38**	**0.32**	**0.56**	**0.58**	1.00	**0.65**
Overall Acceptability	0.03	0.04	0.13	0.00	-0.15	-0.16	**0.63**	**0.59**	**0.62**	**0.85**	**0.65**	1.00
Number of strong and moderate CMs	1	2	6	2	7	6	5	5	5	5	5	5

[1]*|0.000| < R < |0.300| = weak correlation, |0.300| < R < |0.700| = moderate correlation and |0.700| < R < |1.000| = strong correlation matrix.*
[2]*Correlation matrix with the bold value indicated strong and moderate correlations between two variables.*

Association of the physicochemical and sensory properties of the chicken sausages

The PCA was performed to identify (1) variables with different factor loadings and (2) significant variables that might contribute to the formulation of the chicken sausages. Table 6 shows the factor loading (FL) of each variable in their respective principal component (PC). The number of PCs generated was based on the number of variables, and as the number of PC increased, the eigenvalue (EV) and dataset variability (DV) decreased, while cumulative explained variability (CEV) increased. This was evident as PC1 had the highest EV and DV and the lowest CEV. The increment of PC numbers indicated that more variables explained the dataset in this study,

hence, all physicochemical and sensory properties variables were explained until PC5. However, among these variables, those with strong (FL ≥ |0.750|) and moderate (|0.500| < FL < |0.749|) FL were the significant variables that explained the formulation of chicken sausages.

Table 6. Factor loading of variables in principal components (PCs) for the formulation of the reduced fat-chicken sausages

Variables	Factor Loading (FL)[1,2]				
	PC1	PC2	PC3	PC4	PC5
Hardness	**0.7659**	0.4100	-0.0111	0.0418	0.0342
Springiness	-0.2288	-0.2004	-0.4283	**-0.6014**	-0.2234
Cohesiveness	0.3453	-0.0790	0.4642	-0.3639	-0.4019
Chewiness	**0.7965**	0.3302	0.1056	-0.1631	-0.1777
*L**	-0.2674	0.3498	0.0079	**0.6245**	-0.5028
*a**	**-0.5383**	0.2240	-0.3175	-0.3652	-0.1716
*b**	0.0785	**-0.6133**	0.3528	-0.0712	0.2379
pH	-0.4154	**-0.6572**	0.1934	0.1667	0.2940
Cooking loss	**-0.5600**	-0.2546	-0.3509	**-0.5317**	-0.1818
Water holding capacity	-0.2412	0.3242	**-0.6157**	0.0492	-0.1284
Ash	-0.1087	-0.0932	-0.3650	-0.2796	**0.7500**
Moisture	-0.0657	-0.1640	**0.6587**	-0.3090	-0.0036
Fat	**-0.7573**	-0.4336	-0.0546	0.2486	-0.2132
Protein	0.0436	0.1265	-0.3232	**0.5457**	0.3173
Carbohydrate	**0.7015**	0.4784	-0.3424	-0.0697	0.0361
Fat reduction	**0.7681**	0.4101	0.0336	-0.2552	0.1723
Appearance	-0.4500	**0.5686**	0.2610	-0.0530	0.1166
Colour	-0.3812	**0.5443**	0.3047	-0.0824	0.2269
Texture	**-0.4904**	0.4567	0.3201	-0.0446	0.0660
Flavour	**-0.5969**	**0.5931**	0.1788	-0.0659	0.0590
Aroma	-0.4398	**0.5307**	0.0305	-0.0989	0.0807
Overall acceptability	**-0.6089**	**0.6591**	0.1536	-0.0724	0.1031
Eigenvalue (EV)	5.4867	4.0066	2.2880	1.9979	1.5487
Dataset variability (DV), %	24.9396	18.2118	10.4001	9.0813	7.0396
Cumulative explained variability (CEV), %	24.9396	43.1514	53.5515	62.6328	69.6724

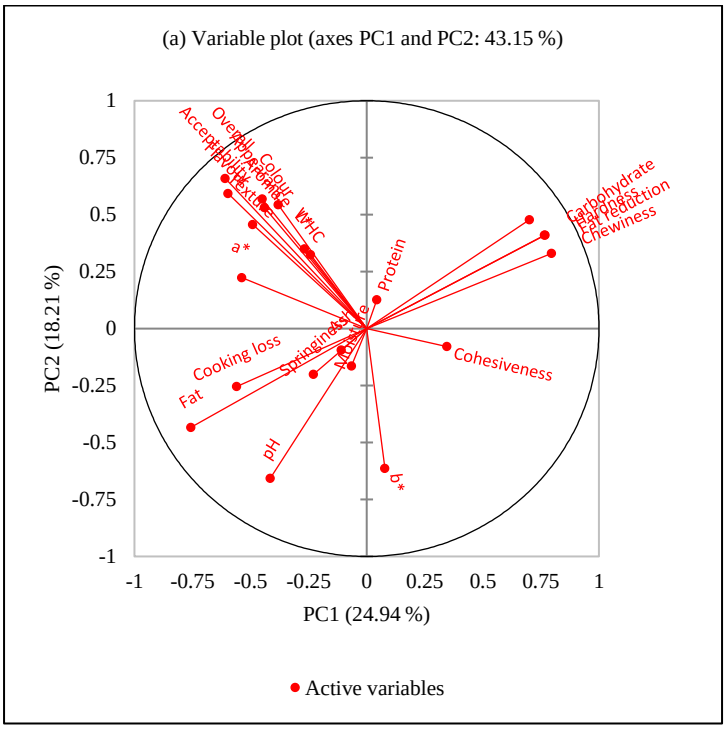
[1]*FL ≥ |0.750| = strong factor loading and |0.500| < FL < |0.749| = moderate factor loading*

[2]*Factor loading with bold value indicated strong and moderate factor loading in the principal component*

Chewiness (FL = 0.7965), hardness (FL = 0.7659), fat reduction (FL = 0.7681), fat (FL = -0.7573), carbohydrate (FL = 0.7015), overall acceptability (FL = -0.6089), flavour (FL = -0.5969), cooking loss (FL = -0.5600) and a* (FL = -0.5383) had strong and moderate FL in PC1 (Table 6). Texture with an FL value of -0.4904 was considered moderate FL since the FL value was nearer to |0.500|. Variables with the same positive or negative signs were positively correlated. For instance, chewiness, hardness, fat reduction, and carbohydrate were positively correlated, while fat, overall acceptability, flavour, cooking loss, *a** and texture had a similar correlation. Meanwhile, the chewiness, hardness, fat reduction, and carbohydrate had negative correlations to the latter, as shown in Figure 2(a), where chewiness, hardness, fat reduction, and carbohydrate are located nearer to each other, and the fat, overall acceptability, flavour, cooking loss, *a** and texture

resided in the opposite direction. Accordingly, it is proposed that chewiness, hardness, and carbohydrate content negatively affect the overall acceptability, flavour and texture of the RAE formulated sausages since these variables fell in the RAE group in Figure 2(b). Also, the fat content and *a** value related to the redness of the sausages rendered a positive effect on the overall acceptability and flavour of the GTE formulated sausages in Figure 2(b).

In PC2, the overall acceptability (FL = 0.6591), pH (FL = -0.6572), b* (FL = -0.6133), flavour (0.5931), appearance (FL = 0.5686), colour (FL= 0.5443), and aroma (FL= 0.5307) had strong and moderate FL. Likewise, these variables were positively correlated with (1) overall acceptability, flavour, appearance, colour and aroma, and (2) pH and *b**, while (1) and (2) were negatively correlated to each other. These correlations indicated that pH and *b** value of the sausages negatively affected the overall acceptability, flavour, appearance, colour and aroma (Figure 2a), especially in PE sausages and controls (Figure 2b). Moreover, the RAE and RBE formulations had the best overall acceptability, flavour, appearance, and colour since these variables were located in the RAE and RBE groups. No correlation was present for all variables in PC1 and PC2 since they were located at 90° in Figure 2(a). However, the overall acceptability had moderate FL in both PC1 and PC2.



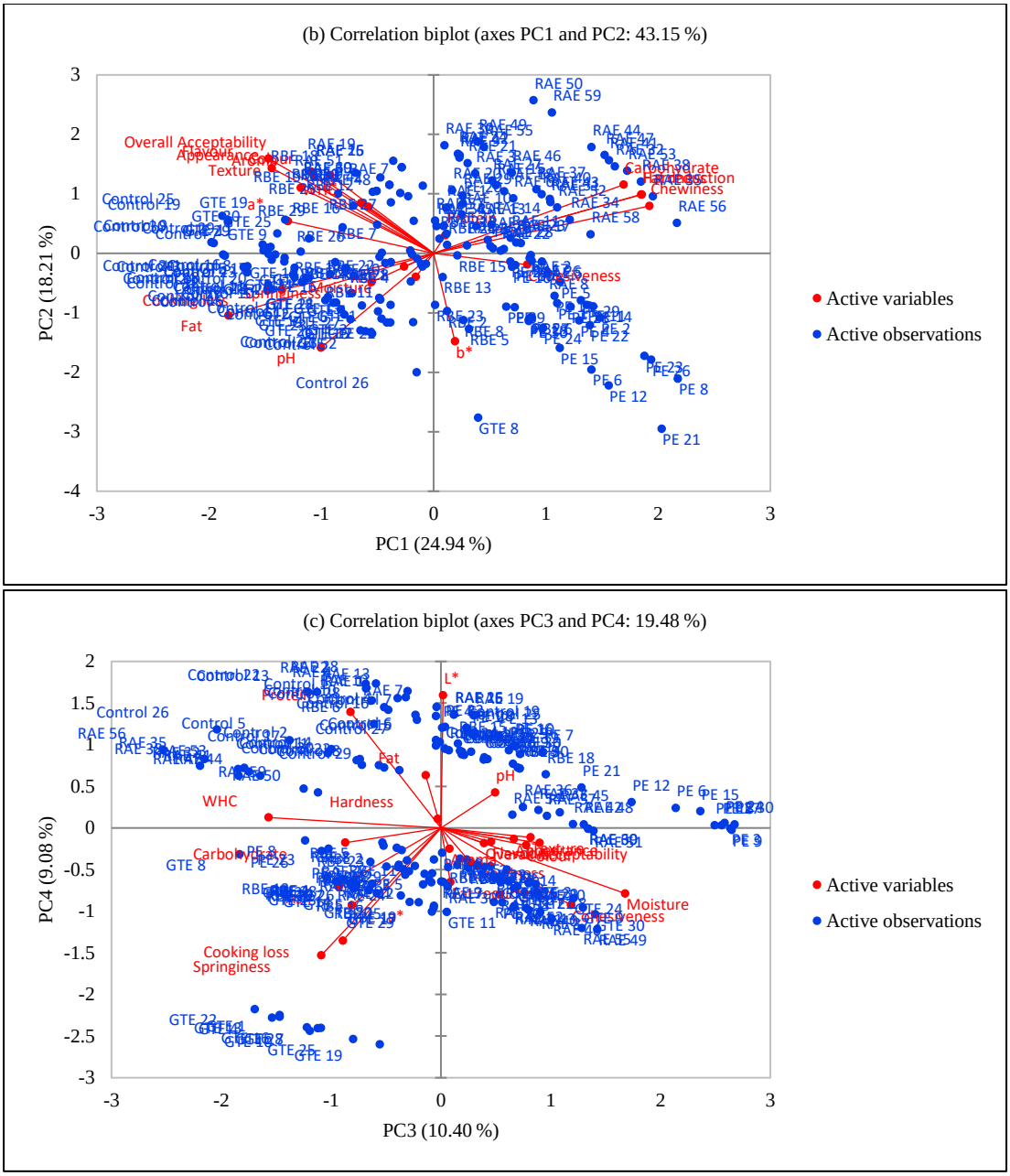


Figure 2. (a) Variable plot (PC1 and PC2), (b) correlation biplot of (PC1 and PC2) and (c) correlation biplot of (PC3 and PC4) of variables and formulations of reduced-fat-chicken sausage

WHC (FL = -0.6157) and moisture (FL=0.6587) in PC3 were negatively correlated while springiness (FL = -0.6014) and cooking loss (FL = -0.5317) in PC4 were positively correlated. Similarly, *L** (FL = 0.6245) and protein (FL = 0.5457) in PC4 were positively correlated. The WHC and moisture were dominant in RAE and GTE, respectively, while both springiness and cooking loss were dominant in GTE (Figure 2(c)). Figure 2(c) also depicted that both the *L** value and protein were dominant in the control, RAE and PE. The cohesiveness did not achieve moderate or strong FL, while ash was only found in PC5, indicating they were very unlikely to

affect the formulation. Nevertheless, although some variables in PC3, PC4 and PC5 had strong and moderate FL, they played less important roles in dictating their influences on the sensory evaluation since they were present in higher PC numbers with low DV. Based on the PCA, overall, the panellists rated the chicken sausages based on the most discriminant variables, which were the fat content (4.34% ± 2.10), *a** value (3.21 ± 0.29), pH (6.35 ± 0.02), *b** value (15.88 ± 0.65). The RAE sample was positively selected due to its low-fat content and high *a** value, while the PE sample was less preferred due to its high pH and *b** values.

Conclusion

In conclusion, the incorporation of eggplants as fat replacers in chicken sausages' production can be considered a successful strategy. Despite many positive results of the majority of the eggplants, three types of eggplants; the Round Asian Eggplant (RAE), Pearl Red Eggplant (PRE) and Pea Eggplants (PE) had lower fat values compared to the control, and therefore, can be claimed as reduced-fat meat products. Further analysis using the principal component analysis, the panellists were influenced to positively rate the sample with the lowest fat content and high *a** value, which represents the RAE sample while rejecting the PE sample due to high pH and *b** values. Therefore, based on the overall result, Round Asian Eggplant (RAE) can be considered the best eggplant type with the highest potential to be used as a fat replacer in the production of reduced-fat chicken sausages.

Acknowledgement

This work was supported by the Ministry of Higher Education of Malaysia (FRGS/1/2019/STG04/UPM/02/7) and the Faculty of Food Science and Technology, Universiti Putra Malaysia.

References

1. Asyrul-Izhar, A. B., Bakar, J., Sazili, A. Q., Meng, G. Y. and Ismail-Fitry, M. R. (2022). Incorporation of different physical forms of fat replacers in the production of low-fat/ reduced-fat meat products; which is more practical?. *Food Reviews International*, 2022: 1-33.
2. Grasso, S., Brunton, N. P., Lyng, J. G., Lalor, F. and Monahan, F. J. (2014). Healthy processed meat products-Regulatory, reformulation and consumer challenges. *Trends in Food Science & Technology,* 39(1): 4-17.
3. Felisberto, M. H. F., Galvão, M. T. E. L., Picone, C. S. F., Cunha, R. L. and Pollonio, M. A. R. (2015). Effect of prebiotic ingredients on the rheological properties and microstructure of reduced-sodium and low-fat meat emulsions. *LWT-Food Science and Technology,* 60(1): 148-155.
4. Cengiz, E. and Gokoglu, N. (2005). Changes in energy and cholesterol contents of frankfurter-type sausages with fat reduction and fat replacer addition. *Food Chemistry,* 91(3): 443-447.
5. Choi, Y. S., Choi, J. H., Han, D. J., Kim, H. Y., Lee, M. A., Kim, H. W., Jeong, J. Y. and Kim, C. J. (2009). Characteristics of low-fat meat emulsion systems with pork fat replaced by vegetable oils and rice bran fiber. *Meat Science,* 82(2): 266-271.
6. Food Act 1983 and Food Regulations 1985 (Act 281) (2014). International Law Book Services, Petaling Jaya: pp. 89-90.
7. Niño-Medina, G., Urías-Orona, V., Muy-Rangel, M. D. and Heredia, J. B. (2017). Structure and content of phenolics in eggplant (*Solanum melongena*)-a review. *South African Journal of Botany,* 111: 161-169.
8. Weese, T. L. and Bohs, L. (2010). Eggplant origins: out of Africa, into the Orient. *Taxon,* 59(1): 49-56.
9. Maroto, J. V. (2002). Parte Sexta: Hortalizas aprovechables por sus frutos. *Horticultura Herbácea Especial. 5ta. ed. Ediciones Mundi-Prensa, México DF, México,* 481-495.
10. Pua, E.C. and Davey, M.R. (Eds.). (2007). Biotechnology in agriculture and forestry, transgenic crops IV. Springer Verlag, Berlin, Heidelberg, Berlin, pp. 201-219.
11. Ammar, M. S. (2017). Producing of high fiber chicken meat nuggets by using different fiber sources. *Middle East Journal of Agriculture Research,* 6(2): 415-423.
12. Fraikue, F. B. (2016). Unveiling the potential utility of eggplant: a review. In *Conference Proceedings of INCEDI*: pp. 883-895.
13. Akesowan, A. and Jariyawaranugoon, U. (2021).

Optimization of salt reduction and eggplant powder for chicken nugget formulation with white button mushroom as a meat extender. *Food Research,* 5(1): 277-284.

14. Sembring, H. S. B. and Chin, K. B. (2021). Antioxidant activities of eggplant (*Solanum melongena*) powder with different drying methods and addition levels to pork sausages. *Food Science of Animal Resources,* 41(4): 715-730.
15. Zhu, Y., Zhang, Y. and Peng, Z. (2021). Effect of eggplant powder on the physicochemical and sensory characteristics of reduced-fat pork sausages. *Foods,* 10(4): 743.
16. Association of Officiating Analytical Chemists (AOAC) (2005). Official method of analysis of the AOAC. 18th ed. United States.
17. Ismail, N. A., Bakar, J., Sazili, A. Q. and Ismail-Fitry, M. R. (2021). Effect of different levels of fat, sodium chloride, and sodium tripolyphosphate on the physicochemical and microstructure properties of Jamnapari goat meat emulsion modelling system. *International Food Research Journal,* 28(5):916-925.
18. Ramle, N. A., Zulkunain, M. and Ismail-Fitry, M. R. (2021). Replacing animal fat with edible mushrooms: a strategy to produce high-quality and low-fat buffalo meatballs. *International Food Research Journal,* 28(5): 905-915.
19. Sharin, S. N., Sani, M. S. A., Jaafar, M. A., Yuswan, M. H., Kassim, N. K., Manaf, Y. N., Wasoh, H., Zaki, N. N. M. and Hashim, A. M. (2021). Discrimination of Malaysian stingless bee honey from different entomological origins based on physicochemical properties and volatile compound profiles using chemometrics and machine learning. *Food Chemistry,* 346: 128654.
20. Ismail, A. M., Sani, M. S. A., Azid, A., Zaki, N. N. M., Arshad, S., Tukiran, N. A., Abidin, S. A. S. Z., Samsudin, M. S. and Ismail, A. (2021). Food forensics on gelatine source via ultra-high-performance liquid chromatography diode-array detector and principal component analysis. *SN Applied Sciences,* 3(79): 1-19.
21. Uthumporn, U., Fazilah, A., Tajul, A. Y., Maizura, M. and Ruri, A. S. (2016). Physico-chemical and antioxidant properties of eggplant flour as a functional ingredient. *Advance Journal of Food Science and Technology,* 12(5): 235-243
22. dos Santos, B. A., Campagnol, P. C. B., Pacheco, M. T. B. and Pollonio, M. A. R. (2012). Fructooligosaccharides as a fat replacer in fermented cooked sausages. *International Journal of Food Science & Technology,* 47(6): 1183-1192.
23. Cengiz, E. and Gokoglu, N. (2007). Effects of fat reduction and fat replacer addition on some quality characteristics of frankfurter-type sausages. *International Journal of Food Science & Technology*, 42(3): 366-372.
24. San José, R., Sánchez, M. C., Cámara, M. M. and Prohens, J. (2013). Composition of eggplant cultivars of the Occidental type and implications for the improvement of nutritional and functional quality. *International Journal of Food Science & Technology,* 48(12): 2490-2499.
25. Bunmee, T., Setthaya, P., Chaiwang, N. and Sansawat, T. (2022). Effect of purple eggplant flour on physicochemical, lipid oxidation, and sensory properties of low-fat beef patties. *International Journal of Food Science*, 2022: 9753201.
26. Fan, R., Zhou, D. and Cao, X. (2020). Evaluation of oat β-glucan-marine collagen peptide mixed gel and its application as the fat replacer in the sausage products. *Plos One,* 15(5): e0233447.
27. Huda, N., Wei, L. H., Jean, A. T. and Ismail, I. (2010). Physicochemical properties of Malaysian commercial chicken sausages. *International Journal of Poultry Science,* 9(10): 954-958.
28. Kahar, S. N. S., Ismail-Fitry, M. R., Yusoff, M. M., Rozzamri, A., Bakar, J. and Ibadullah, W. Z. W. (2021). Substitution of fat with various types of squashes and gourds from the Cucurbitaceae family in the production of low-fat buffalo meat patties. *Malaysian Applied Biology,* 50(1): 169-179.
29. Feng, T., Ye, R., Zhuang, H., Rong, Z., Fang, Z., Wang, Y., Gu, Z. and Jin, Z. (2013). Physicochemical properties and sensory evaluation of Mesona Blumes gum/rice starch mixed gels as fat-substitutes in Chinese Cantonese-style sausage. *Food Research International,* 50(1): 85-93.
30. Figuerola, F., Hurtado, M. L., Estévez, A. M., Chiffelle, I. and Asenjo, F. (2005). Fibre concentrates from apple pomace and citrus peel as

potential fibre sources for food enrichment. *Food chemistry,* 91(3): 395-401.

31. Lee, C. H. and Chin, K. B. (2019). Evaluation of physicochemical and textural properties of myofibrillar protein gels and low-fat model sausage containing various levels of curdlan. *Asian-Australasian Journal of Animal Sciences,* 32(1): 144.
32. Morin, L. A., Temelli, F. and McMullen, L. (2004). Interactions between meat proteins and barley *(Hordeum spp.*) β-glucan within a reduced-fat breakfast sausage system. *Meat Science,* 68(3): 419-430.
33. Cao, L., Rasco, B. A., Tang, J., Niu, L., Lai, K., Fan, Y. and Huang, Y. (2016). Effects of freshness on the cook loss and shrinkage of grass carp (*Ctenopharyngodon idellus*) fillets following pasteurization. *International Journal of Food Properties,* 19(10): 2297-2306.
34. Moghtadaei, M., Soltanizadeh, N., & Goli, S. A. H. (2018). Production of sesame oil oleogels based on beeswax and application as partial substitutes of animal fat in beef burger. *Food Research International*, 108: 368-377.
35. Choe, J. H., Kim, H. Y., Lee, J. M., Kim, Y. J. and Kim, C. J. (2013). Quality of frankfurter-type sausages with added pig skin and wheat fiber mixture as fat replacers. *Meat Science,* 93(4): 849-854.
36. Zayas, J. F. (1985). Structural and water binding properties of meat emulsions prepared with emulsified and unemulsified fat. *Journal of Food Science,* 50(3): 689-692.
37. Das, A. K., Anjaneyulu, A. S. R., Gadekar, Y. P., Singh, R. P. and Pragati, H. (2008). Effect of full-fat soy paste and textured soy granules on quality and shelf-life of goat meat nuggets in frozen storage. *Meat Science*, 80(3): 607-614.
38. Lee, C. H. and Chin, K. B. (2016). Effects of pork gelatin levels on the physicochemical and textural properties of model sausages at different fat levels. *LWT-Food Science and Technology,* 74: 325-330.
39. Troy, D. J. and Kerry, J. P. (2010). Consumer perception and the role of science in the meat industry. *Meat Science,* 86(1): 214-226.
40. Kang, Z. L., Wang, T. T., Li, Y. P., Li, K. and Ma, H. J. (2020). Effect of sodium alginate on physical-chemical, protein conformation and sensory of low-fat frankfurters. *Meat Science*, 162: 108043.
41. Park, K. S., Choi, Y. S., Kim, H. Y., Kim, H. W., Song, D. H., Hwang, K. E., Choi, S. G. and Kim, C. J. (2012). Quality characteristics of chicken emulsion sausages with different levels of Makgeolli lees fiber. *Food Science of Animal Resources,* 32(1): 54-61.
42. Ferjančič, B., Kugler, S., Korošec, M., Polak, T. and Bertoncelj, J. (2020). Development of low-fat chicken bologna sausages enriched with inulin, oat fibre or psyllium. *International Journal of Food Science & Technology,* 56(4): 1818-1828.
43. Dingstad, G. I., Kubberød, E., Næs, T. and Egelandsdal, B. (2005). Critical quality constraints of sensory attributes in frankfurter-type sausages, to be applied in optimization models. *LWT-Food Science and Technology,* 38(6): 665-676.
44. Zhang, W., Xiao, S., Samaraweera, H., Lee, E. J. and Ahn, D. U. (2010). Improving functional value of meat products. *Meat Science,* 86(1): 15-31
45. Ch'ng, S. E., Ng, M. D., Pindi, W., Kang, O. L., Abdullah, A. and Babji, A. S. (2014). Chicken sausages formulated with gelatin from different sources: A comparison of sensory acceptability and storage stability. *World Applied Sciences Journal,* 31(120): 2062-2067.
46. Verma, A. K., Sharma, B. D. and Banerjee, R. (2010). Effect of sodium chloride replacement and apple pulp inclusion on the physico-chemical, textural and sensory properties of low-fat chicken nuggets. *LWT-Food Science and Technology,* 43(4): 715-719.
47. Choe, J. and Kim, H. Y. (2019). Quality characteristics of reduced fat emulsion-type chicken sausages using chicken skin and wheat fiber mixture as fat replacer. *Poultry Science*, 98(6): 2662-2669.
48. Fernández-Ginés, J. M., Fernández-López, J., Sayas-Barberá, E., Sendra, E. and Pérez-Álvarez, J. A. (2004). Lemon albedo as a new source of dietary fiber: Application to bologna sausages. *Meat Science,* 67(1): 7-13.
49. Salazar, P., García, M. L. and Selgas, M. D. (2009). Short-chain fructooligosaccharides as potential

functional ingredient in dry fermented sausages with different fat levels. *International Journal of Food Science & Technology,* 44(6): 1100-1107.

50. Kang, Z. L., Zhu, D. Y., Li, B., Ma, H. J. and Song, Z. J. (2017). Effect of pre-emulsified sesame oil on physical-chemical and rheological properties of pork batters. *Food Science and Technology,* 37(4): 620-626.
51. Choi, M. S., Choi, Y. S., Kim, H. W., Hwang, K. E., Song, D. H., Lee, S. Y. and Kim, C. J. (2014). Effects of replacing pork back fat with brewer's spent grain dietary fiber on quality characteristics of reduced-fat chicken sausages. *Korean Journal for Food Science of Animal Resources,* 34(2): 158.
52. Kılınççeker, O. and Kurt, S. (2018). Effects of inulin, carrot and cellulose fibres on the properties of raw and fried chicken meatballs. *South African Journal of Animal Science,* 48(1): 39-47.
53. Varga-Visi, É., Toxanbayeva, B., Andrássyné Baka, G. and Romvári, R. (2018). Textural properties of turkey sausage using pea fiber or potato starch as fat replacers. *Acta Alimentaria,* 47(1): 36-43.
54. De Angelis, D., Kaleda, A., Pasqualone, A., Vaikma, H., Tamm, M., Tammik, M. L., Squeo, G. and Summo, C. (2020). Physicochemical and sensorial evaluation of meat analogues produced from dry-fractionated pea and oat proteins. *Foods,* 9(12): 1754.
55. Souza, C. V. B., Bellucci, E. R. B., Lorenzo, J. M. and Barretto, A. C. D. S. (2019). Low-fat Brazilian cooked sausage-Paio-with added oat fiber and inulin as a fat substitute: effect on the technological properties and sensory acceptance. *Food Science and Technology,* 39: 295-303.
56. Andersen, B. V., Brockhoff, P. B. and Hyldig, G. (2019). The importance of liking of appearance,-odour,-taste and-texture in the evaluation of overall liking. A comparison with the evaluation of sensory satisfaction. *Food Quality and Preference,* 71: 228-232.
57. Huang, S., Mejía, S. M. V., Murch, S. J. and Bohrer, B. M. (2019). Cooking loss, texture properties, and color of comminuted beef prepared with breadfruit (*Artocarpus altilis*) flour. *Meat and Muscle Biology,* 3(1): 231.
58. Garcia-santos, M. D. S. L., Conceicao, F. S., Villas Boas, F., Salotti De Souza, B. M. and Barretto, A. C. D. S. (2019). Effect of the addition of resistant starch in sausage with fat reduction on the physicochemical and sensory properties. *Food Science and Technology*, 39: 491-497.
59. Jin, S. K., Ha, S. R., Hur, S. J., and Choi, J. S. (2016). Effect of the Ratio of Raw Material Components on the physico-chemical characteristics of emulsion-type pork sausages. *Asian-Australasian Journal of Animal Sciences,* 29(2): 263.
60. Puolanne, E. J., Ruusunen, M. H. and Vainionpää, J. I. (2001). Combined effects of NaCl and raw meat pH on water-holding in cooked sausage with and without added phosphate. *Meat Science,* 58(1): 1-7.
61. Pereira, J., Hu, H., Xing, L., Zhang, W. and Zhou, G. (2020). Influence of rice flour, glutinous rice flour, and tapioca starch on the functional properties and quality of an emulsion-type cooked sausage. *Foods,* 9(1): 9.
62. Idris, M. H. H., Manaf, Y. N., Desa, M. N. M., Hashim, A. M., Sani, M. S. A., Zaki, N. N. M., Yuswan, M. H., Kamaruddin, M. S., Hassan, M. S., Yusof, Y. A. and Mustafa, S. (2021). A conjunction of sn-2 fatty acids and overall fatty acid composition combined with chemometric techniques increase the effectiveness of lard detection in fish feed. *Chemometrics and Intelligent Laboratory Systems,* 213: 104308.

Malaysian Journal of Analytical Sciences (MJAS)
Published by Malaysian Analytical Sciences Society

CHARACTERIZATION AND PHYSICOCHEMICAL STUDY OF B - CYCLODEXTRIN- ANGELWING CLAM HYDROLYSATE COMPLEXES

(Pencirian dan Kajian Fisikokimia bagi β-Siklodekstrin-Mentarang Hidrolisat Kompleks)

Nurul Fasihah Razak*, Atikah Mansor, Nur Adila Basari, Normah Ismail

Department of Chemical and Food Technology,
Politeknik Tun Syed Nasir Syed Ismail, 84600 Pagoh, Johor, Malaysia

**Corresponding author:nurul.fasihah@ptsn.edu.my*

Received: 12 December 2021; Accepted: 23 November 2022; Published: 27 December 2022

Abstract

The formed β-cyclodextrin- angelwing complexes were characterized using Fourier transform infrared spectrometry (FTIR) and sodium dodecyl sulfate-polyacrylamide electrophoresis (SDS-PAGE) to mask the bitterness of angelwing clam protein hydrolysate. The shift of O-H stretching to a lower wavenumber and the reduction of the intensity of band C=O and C-H indicated the formation of β-cyclodextrin- angelwing clam hydrolysate complexes. SDS-PAGE analysis showed a lower number of band distributions, revealing the effects of β-cyclodextrin on the mobility of protein during gel electrophoresis. The physicochemical properties of angelwing clam hydrolysate (BH), kneading method hydrolysate (KMH), and physical mixture hydrolysate (PMH) were studied. When compared to functional properties, BH outperformed KMH and PMH. Meanwhile, KMH and PMH showed a higher water holding capacity and a lower oil holding capacity than BH. While the solubility, foaming properties and emulsifying properties of KMH and PMH were lower than BH, the values were still comparable with others of higher sources of protein hydrolysate. Therefore, KMH and PMH can be one of recent potential functional food ingredients.

Keywords: physicochemical analysis, functional properties, angelwing clam, β-cyclodextrin, inclusion complex

Abstrak

β-siklodekstrin-mentarang-hidrolisat kompleks yang terbentuk dicirikan menggunakan spektrometer transformasi inframerah Fourier (FTIR) dan elektroforesis gel poliakrilamida-sodium dodekil sulfat (SDS-PAGE). Peralihan peregangan bilangan gelombang O-H yang lebih rendah dan pengurangan intensiti pada gelombang C=O dan C-H menunjukkan pembentukan kompleks hidrolisat β-siklodekstrin-mentarang hidrolisat. Analisis SDS-PAGE menunjukkan jumlah pengedaran bilangan jalur yang lebih rendah membuktikan pengaruh β-siklodekstrin pada pergerakan protein dalam elektroforesis gel. Sifat fizikokimia mentarang hidrolisat (BH), Kaedah menguli hidrolisat (KMH) dan campuran fizikal hidrolisat (PMH) telah dikaji. Dalam membezakan ciri-ciri fungsi, BH menunjukkan ciri-ciri fungsi yang lebih baik daripada KMH dan PMH. KMH dan PMH menunjukkan daya tahan air yang lebih tinggi dan daya tahan minyak yang lebih rendah berbanding BH. Keterlarutan, sifat berbuih dan sifat pengemulsi KMH dan PMH adalah lebih rendah daripada BH, walaubagaimanapun nilainya masih boleh dibandingkan dengan sumber hidrolisat protein yang tinggi. KMH dan PMH dianggap sebagai salah satu potensi ramuan makanan.

Kata kunci: analisis fizikokimia, sifat kefungsian, mentarang, β-siklodekstrin, kemasukan kompleks

Introduction

Cyclodextrin molecules are cyclic oligosaccharides referred to as α, β, γ-cyclodextrin. They are composed of six, seven, and eight glucopyranose units, respectively linked by -1,4 linkage. Alpha cyclodextrin typically forms a complex with low molecular weight molecules and a compound with an aliphatic side chain. While γ-cyclodextrin can accommodate larger molecules such as steroids, the cost is expensive. β-cyclodextrin is the most accessible, cheap, and effective, as well as its cavity size is suitable for a wide range of guest molecules [1, 2]. Previous studies reported that among various flavor encapsulation techniques, molecular inclusions in β-cyclodextrin molecules are the most effective [1, 3]. Different types of guest molecules such as drugs, steroids, ionic liquids, and dyes have been used as host and guest interactions with β- cyclodextrin to change the properties of the guest molecules into the desired form. However, there is a lack of studies involved in the interactions of host and guest molecules between β-cyclodextrin and protein hydrolysates. Protein hydrolysates have been used for various purposes in foods such as flavor enhancers, protein supplements, and beverage stabilizers [4]. According to previous research, angelwing clam hydrolysate has the potential to be a good source of food ingredients because it consists of high protein content at 74.41%, low fat content at 3.43%, and high total essential amino acids, ranging from 32.94% to 54.17% [5].

Since the protein hydrolysate produced from angelwing clam species has a bitter flavor, its application for human consumption is limited [6]. Therefore, the study of inclusion complexes between β-cyclodextrin and angelwing clam protein hydrolysate is essential to mask the bitter taste. The inclusion complex of these host and guest systems occurred through various interactions such as hydrogen bonding, van der walls interaction, hydrophobic interactions, and electrostatic attraction, all of which alter the photochemical and photophysical properties of the guest molecules [7]. Thus, the physical, chemical, and biochemical properties of guest molecules will be changed [2]. The inclusion of cyclodextrins exerts a profound effect on the physicochemical properties of guest molecules [8]. However, it is still unknown whether entrapment in the internal cavity of β-cyclodextrins could affect their physicochemical properties since there is no information regarding the physicochemical properties of complex formation between protein hydrolysate and β-cyclodextrins. Thus, the current study focused on determining the characteristics and the effects of protein hydrolysate on its physical and chemical properties after forming a complex with β-cyclodextrin.

Materials and Methods

Materials

Angelwing clams were purchased from Pantai Remis, Selangor, Malaysia. The clams were placed on ice and transported to the laboratory. Upon arrival, the clams were washed and their flesh was separated manually before they were then stored at -20°C prior to further processing. Meanwhile, bromelain (1.5 AU/g) was obtained from Novozymes Sdn. Bhd., Malaysia and stored at 4°C until further used.

Preparation of angelwing clam hydrolysates

Angelwing clam hydrolysate was prepared according to the method described by Normah and Nurul Fasihah (2014). 500 grams of angelwing clam flesh was mixed with 531.33 mL of distilled water and then minced in a blender [5]. The mixture was transferred into 1 L beaker, then placed in a water bath. The water bath was set at 45°C and the pH of the mixture was adjusted to 6 using 1.0 N NaOH or 1.0 N HCl. Once the temperature and pH were constant, bromelain (enzyme substrate ratio of 3%) was added and hydrolysis was performed for two hours. The mixture was continuously stirred at the speed of 200 rpm using a stirring propeller. The pH was kept constant throughout the hydrolysis by the addition of 1.0 N NaOH. At the end of the hydrolysis, the reaction was terminated by heating the mixture at 90 ºC for 15 minutes in a water bath. Then, the mixture was centrifuged (Hettich ZENTRIFUGEN, UNIVERSAL 320R) at 10000 rpm and 4 ºC for 20 minutes. The supernatant was collected and freeze dried using biomedical freeze dryer (Alpha 1-4, Martin Christ). The resulting hydrolysate was named as Angelwing clam hydrolysate (BH).

Preparation of angelwing clam hydrolysate –β-cyclodextrin complexes

Angelwing clam hydrolysate and β-cyclodextrin were mixed in a ratio of 1:0.8 (v/w) using the following methods:

Physical mixing method

For the physical mixing method, the hydrolysate was prepared according to the procedure mentioned earlier, except that β-cyclodextrin was added to the supernatant at a ratio of 1:0.8 (v/w) at a temperature of 38.5±1 °C. The mixture was consistently agitated at 150 rpm for 12 minutes using an incubator shaker (Innova 4080 INCUBATOR SHAKER, United States). The product was then freeze dried using biomedical freeze dryer (Alpha 1-4, Martin Christ) [3]. The resulting hydrolysate was named as physical mixed hydrolysate (PMH).

Kneading method

The procedure for physical method was imitated. However, after agitation, the sample was placed in a mortar and grounded for 45 minutes. The product was freeze dried. The resulting hydrolysate was named as kneaded method hydrolysate (KMH).

Characterization

Angelwing clam hydrolysate- β-cyclodextrin were characterized using Fourier transform infrared spectroscopy (FTIR) and sodium dodecyl sulfate polyacrylamide gel electrophoresis (SDS-PAGE).

Fourier Transform Infrared spectroscopy

The functional group analysis was performed using FTIR (Avatar 360, Thermo Nicolet, USA) as according to Normah and Nurul Fasihah [9]. The sample was ground in an agate mortar until the particle size was measured approximately at 2.5 micron and the surface of the solid appeared shiny. 0.08 g of powdered potassium bromide (KBr) was added into the mixture and grounded for about 30 seconds. The mixture was scraped into the middle and grounded for another 15 seconds. The sample and KBr should be finely grounded to avoid the mixture from scattering infrared radiation excessively. The mixture was then placed in an evacuable mold and subjected to a pressure of 10 to 20 MPa. Perkin Elmer spectrum software was used to control the spectrometer and data were collected over the wavenumber range 4000-400 cm^{-1} with a resolution of 4 cm^{-1} and collection spectra of 16.

Sodium dodecyl sulfate polyacrylamide gel electrophoresis

One gram of hydrolysate was mixed with 10 ml deionized water and filtered using a membrane filter with a pore size of 0.45 µm. 6.5 µL of the solution was then mixed with 2.5 µL NuPAGE®LDS sample buffer (4X) and 1 µL NuPAGE® Reducing Agent (10X). The mixture was heated at 70 ºC for 10 minutes. 15 µL sample was loaded into each well of the SDS-PAGE system each comprised of a 12% resolving gel and a 5% stacking gel. Benchmark™ protein ladder with the range of 220 to 10 kDa was used as a marker. Electrophoresis was performed using the XCell Surelock electrophoresis cell (Bio-Rad Laboratories, Hercules, CA, USA). Electrophoresis was run for 50 minutes at 100-125 mA/gel. After the running process, the gels were washed with 100 mL of ultrapure water and were stained with Coomassie Brilliant Blue dye**.**

Solubility

Solubility, in this study, was determined according to the method by Klompong et al. [10]. A total of two hundred milligrams of samples were dispersed in 20 ml of deionized water, and the mixture's pH was adjusted between pH 2 and 10. The mixture was stirred at room temperature for 30 minutes and centrifuged at 7500 ×g for 15 minutes (5420, KUBOTA, JAPAN). The protein content of each supernatant was determined using Kjedhal (Vapodest 50s, Gerhardt, Germany). The following equation was used to calculate the nitrogen solubility index (NSI):

$$\text{NSI (\%)} = \frac{\text{Protein content in supernatant}}{\text{Total protein in sample}} \text{ x } 100 \quad (1)$$

Water holding capacity

The water holding capacity (WHC) was determined using the method outlined by Diniz and Martin [11]. Triplicate samples (0.5 g) were analyzed. Each sample was dissolved in 10 ml of distilled water in centrifuged tube and vortexes for 30 seconds. The dispersions were allowed to stand at room temperature for 30 minutes, and then centrifuged at 2800 ×g for 25 minutes (5420, KUBOTA, JAPAN). The supernatant was filtered, and the volume was accurately measured. The difference between the initial volumes of distilled water added to the protein sample and the supernatant volume was retrieved. The result was reported as the amount of water absorbed per gram (g) of protein hydrolysate in milliliter (mL).

Oil holding capacity

The oil holding capacity (OHC) was determined using the method described by Shahidi et al. with a slight modification. A 10 mL of soybean oil was added to 500 mg samples into a centrifuge tube [12]. The mixture was centrifuged for 25 minutes in 3800 ×g (5420, KUBOTA, JAPAN). The amount of oil absorption was determined by measuring the volume of oil before centrifugation and the amount of oil supernatant after centrifugation. The analysis was done in triplicate.

$$\text{OHC (mg/mL)} = \text{volume before centrifuge (mg/mL)} - \text{volume of supernatant (mg/mL)} \quad (2)$$

Emulsifying properties

The emulsifying activity index (EAI) and the emulsion stability index (ESI) were determined using the method described by Klompong et al. (2007) with a slight modification [10]. A total of 300 milligrams of sample was dissolved in 30 ml of deionized water. The solution was then mixed with 10 ml sunflower oil, and the pH was adjusted between 2 and 10. The mixture was homogenized (IKA T25 digital ULTRA-TURRAX) at the speed of 14000 rpm for 1 minute. 15 µl of aliquot emulsion was pipetted from the bottom of the container at 0 and 10 minutes after homogenization. After that, the sample was then mixed with 5 ml of 0.1 % sodium dodecyl sulphate solution. The absorbance of the diluted solution was measured at 500 nm using a UV-VIS spectrophotometer (Perkin Elmer Instrument Lambda 35, USA). This data calculated EAI and ESI using the following equation:

$$\text{EAI } (m^2/g) = (2 \text{ x } 2.303 \text{ x } A_{500})/(0.25 \text{ x protein weight (g)}) \quad (3)$$

where; A_{500} = the absorbance at 500 nm.

$$ESI \text{ (min)} = A_0 \, x \, \Delta t \, / \Delta A \quad (4)$$

Where; $\Delta A = A_0 - A_{10}$,

$\Delta t = 10 \, min, A_0$ is the absorbance at zero min and A10 is the absorbance at 10 min, at 500nm.

Foaming properties

Foaming capacity and stability of hydrolysate were measured using the method of Sathe and Salunkhe [13]. A set of 3-gram samples were dissolved in 100 ml of distilled water, with its pH was adjusted between 2 and 10. The protein solution was whipped at 16000 rpm for 3 minutes using a homogenizer (IKA T25 digital ULTRA-TURRAX) and poured into a 100 ml graduated cylinder. The total sample volume was taken at 0 minutes for foam capacity, and up to 60 minutes for foam stability. Foam capacity and stability were then calculated using the equation below:

$$\text{Foam capacity (\%)} = [(A - B)/B] \text{ x } 100$$

Where; A = the volume after whipping (mL) at 0 min and B = the volume before whipping (mL) at 0 min.

$$\text{Foam stability (\%)} = [(A - B)/B] \times 100$$

Where; A = the volume after standing (mlL) at 60 min and B = the volume before whipping (mL).

Statistical analysis

The data were analyzed using Analysis of Variance (ANOVA) to determine statistical significance at the 5% level. The Duncan Multiple Range Test (DMRT) was used to identify mean differences. Statistical analysis was performed using the Statistical Package for Social Science (IBM SPSS Statistics for Windows, Version 20.0. [14].

Results and Discussion

Fourier transform infrared spectroscopy

The complexation of Angelwing clam hydrolysate (BH) and β-cyclodextrin was investigated using FTIR. The formation of a complex between the mixture of β-cyclodextrin and BH is desired to gain a better product with a less bitter taste. As illustrated in Figure 1, the O-H stretching vibration of all samples exhibited a different profile. The peak of KMH and PMH were 3368.04 cm^{-1} and 3370.62 cm^{-1}, respectively, meanwhile β-cyclodextrin and BH were at 3400.70 cm^{-1} and 3375.25 cm^{-1}, respectively. The broad hydroxyl (O-H) peak shown in β-cyclodextrin indicated that β-cyclodextrin contained water molecules. However, it was found that this pattern was narrowed in the complexes of KMH and PMH, showing that this pattern gave a good indication of the formation of the inclusion complex. This study is in line with the study by Crupi et al., who observed a decrease in the frequencies of O-H bands during the formation of inclusion complexes, indicating a reduction of water molecules in the cyclodextrin cavity due to the entrance of guest molecules inside the cavity [15]. However, BH showed high frequencies at 3375.25 cm^{-1}. This is probably because the protein contents in BH have a high amount of hydrogen bonds formed between dipolar groups of carboxylic acid and amide [16].

The stretching regions of the C=O group can be found approximately 1650 cm^{-1} to 1540 cm^{-1}. As shown in Figure 1, the frequencies of β-cyclodextrin and BH were at 1647.33 cm^{-1} and 1640 cm^{-1}, respectively. KMH and PMH showed lower frequencies compared to their BH at 1642.01cm^{-1} and 1643.11 cm^{-1}, respectively. The intensity of this band appeared to be reduced, indicating that the carbonyl group was used for complexation.

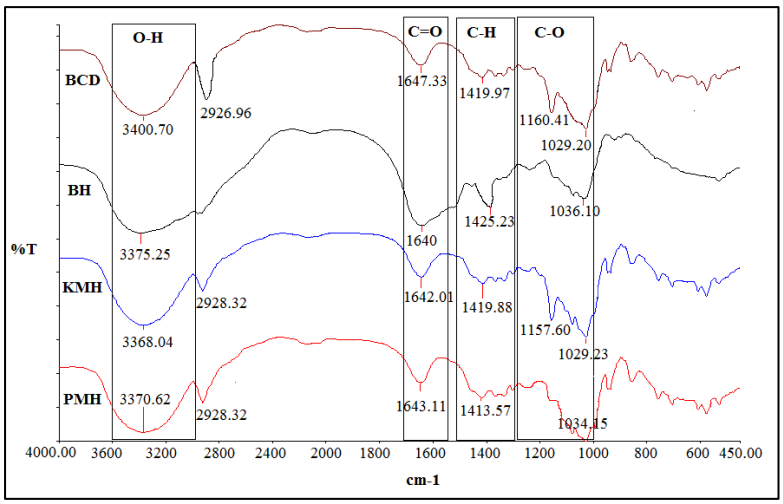


Figure 1. FTIR spectrums of (BCD) β-cyclodextrin, (BH) angelwing clam hydrolysate, (KMH) kneaded method hydrolysate and physical mixed hydrolysate (PMH)

The stretching region of alkane (C-H) were found between 1300 cm^{-1} and 1512 cm^{-1}. The wavenumbers for BH and β-cyclodextrin were 1425.23 cm^{-1} and 1419.97 cm^{-1}, respectively. While KMH and PMH had the peak frequencies at 1419.88 cm^{-1} and 1413.57 cm^{-1}, respectively. The intensity of this band appeared to be reduced for KMH and PMH. Thus, this indicated that the C-H group was also used in the complexation process.

The spectrums within the range of 1160 cm^{-1} to 1020 cm^{-1} were associated with the C-O stretching peaks. It can be seen in β-cyclodextrin and BH at frequencies of 1029.20 cm^{-1} and 1036.10 cm^{-1}, respectively. KMH and PMH peaks had lower frequencies compared to BH at 1029.23 cm^{-1} and 1034.15 cm^{-1}, respectively. The frequencies of modified hydrolysate and its constituent molecule showed a declining pattern, indicating the formation of an inclusion complex. The lower frequencies of KMH and PMH compared to BH were due to the new formation of intermolecular hydrogen bonding, which weakened the strength of interatomic C-O bonds [15]. Thus, C-O stretching of KMH and PMH is shifted to a lower wavenumber than BH [2].

The same pattern as for KMH and PMH in FTIR spectrum analysis reveals the formation of an inclusion complex between BH and β-cyclodextrin. However, the current study was insufficient to determine which method was better. Even though the patterns in the spectrum of KMH and PMH were similar, kneading is a more effective method for forming complexes between angelwing clam hydrolysate and β-cyclodextrin than physical mixing. This is supported by previous research which demonstrated that the morphology of BH- β-cyclodextrin complex was more distinct in KMH rather than PMH [6]. Although the FESEM image of the PMH confirmed the presence of crystalline hydrolysate, BH particles were observed either partially mixed or loosely adhered to the surface of β-cyclodextrin. On the contrary, a drastic change was observed in the morphology of BH and β-cyclodextrin in KMH complex, with both molecules losing their original shape [6].

Sodium dodecyl sulfate polyacrylamide gel electrophoresis

Figure 2 shows the SDS-PAGE patterns for Flesh, BH, KMH and PMH. There was a noticeable difference in SDS-PAGE profiles between samples. Following electrophoresis, BH showed more than eleven subunits at 160 kDa, 90 kDa, 80 kDa, 70 kDa, 50 kDa, 40 kDa, 30 kDa, 25 kDa, 20 kDa, 15 kDa, 10 kDa and <10 kDa. Whereas KMH showed only two subunits at 70 kDa and 60 kDa. Meanwhile, PMH showed more than three subunits at 50 kDa, 20 kDa and <10 kDa (see Figure 2). BH showed many bands distributions at lower molecular weights, which indicated the presence of hydrophobic peptides due to the high hydrophobic of proteins. This is bound to more SDS reagent and thus a faster migration in polyacrylamide gels [17]. However, KMH and PMH had the least bands distributions at lower molecular weights. This is the effect of inclusion complex formed by the hydrophobic peptide inserted into β-cyclodextrin cavity, which then reduced the denaturation effect on protein by SDS reagent.

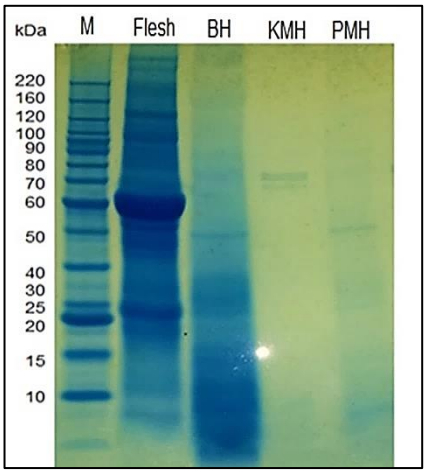


Figure 2. Molecular weight distribution of angelwing clam hydrolysate (BH), hydrolysate from kneading method (KMH) hydrolysate from physical mixing method (PMH)

The difference in SDS-PAGE profiles between samples also revealed the formation of the inclusion complex in KMH and PMH. Different bands distribution in Figure 2 shows that β-cyclodextrin influenced the mobility of proteins in polyacrylamide gel electrophoresis. The

least band presented in KMH indicated the low fragmentation of protein by anionic surfactant of sodium dodecyl sulfate (SDS). This is attributed to that β-cyclodextrin groups were possibly grafted covalently onto the surface of proteins and formed intramolecular inclusion complexes with nearby hydrophobic residues of the protein, thus reducing the denaturation of protein [18]. This study also corroborated with Rozema and Gellman, who found that β-cyclodextrin is one of the carbohydrate molecules that is known to stabilize protein folding and function as an artificial chaperone that refolds protein structure and inhibits aggregation [19].

Solubility

The pH-solubility profiles of BH, KMH and PMH proteins are shown in Figure 3. It was found that the protein solubility of BH, KMH and PMH in water at different pH (pH 2 to pH 10) showed the same pattern curve. Protein solubility of BH, KMH and PMH were significantly different ($p < 0.05$) and soluble over a wide pH range with a solubility of greater than 50%. BH, KMH and PMH presented minimum protein solubility at pH 4 with values of 86.03%, 65.27% and 70.79%, respectively, and a maximum protein solubility at pH 10 with values of 99.02%, 70.33% and 82.28%, respectively. This indicates that in general, protein's solubility decreases as the pH increases until it reaches the isoelectric points and then increases [20]. Proteins are amphoteric molecules, which means that when exposed to an acidic medium at pH lower than their isoelectric point, they behave as positive ions and repel each other, resulting in their good dispersity. ON the other hand, as the pH value approaches the isoelectric point, solubility decreases. Similarly in alkaline solutions, at pH values higher than the isoelectric point, protein molecules transform into negative ions, increasing their solubility [21]. However, not all protein hydrolysates have an isoelectric point at pH 4. Previous studies showed that peanut protein had an isoelectric point at pH 4.5, as seen from its drastically reduced solubility at this pH [22]. This result indicated that protein solubility is directly related to the pH of the solution and the isoelectric point of protein.

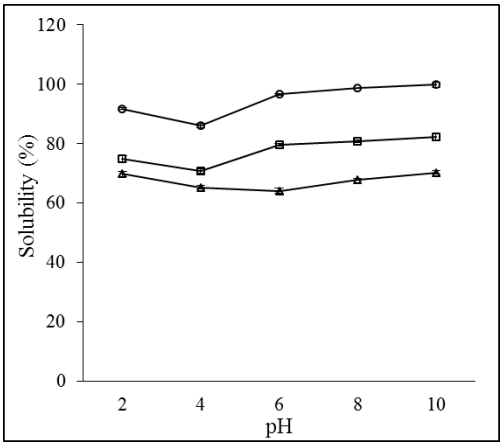


Figure 3. Solubility of Angelwing clam hydrolysate (BH =●), physical mixed hydrolysate (PMH =▲) and kneaded method hydrolysate (KMH = ■). Bars represent standard deviation from triplet determination

Solubility in BH was higher than KMH and PMH due to the lower molecular weight of peptides during hydrolysis which was generated by reducing the secondary structure in protein [23]. The solubility of KMH and PMH was slightly lower compared to BH which proved the formation of an inclusion complex between the guest and host compounds of BH and β-cyclodextrin. According to previous studies by Rahman [24] and Sanjoy et al. [25], the solubility of the inclusion complex is higher than the solubility of β-cyclodextrin if the guest molecules are highly soluble in water. However, the solubility of the inclusion complex is lower than β-cyclodextrin, but will have a higher solubility than its guest molecule if the guest molecule has poor solubility in water. This explains the reason for a lower solubility between KMH and PMH. To conclude, these studies revealed that a physicochemical property of a complex is different from that of β-cyclodextrin and its guest molecule.

Water holding capacity and oil holding capacity

According to Table 1, the water holding capacity of BH, KMH and PMH were significantly different ($p < 0.05$), with BH having lower water holding capacity than KMH and PMH at 4.60 mL/g, 5.349 mL/g and 5.572 mL/g, respectively. According to Amiza et al. water holding capacity values were influenced by the

solubility of the samples [23]. However, Tang et al. reveals the high protein solubility was not necessarily related to the high-water holding capacity. The lower water holding capacity of BH was probably related to its lower molecular weight, leading to a smaller interface surface area [22]. Besides, decreased water holding capacity might be attributed to the hydrolytic degradation of the protein structure, in which physical entrapment plays an important role in the adsorption of water [23].

Table 1: Water holding capacity and oil holding capacity of hydrolysate and the modified

Functional Properties	**BH**	**PMH**	**KMH**
Water Holding Capacity (mL/g)	4.60^{b}±0.24	5.35^{a}±0.17	5.57± 0.25
Oil Holding Capacity	5.16^{a}±0.05	3.96^{b}±0.04	3.44^{c}±0.01

Values are expressed as means ± standard deviation from triplicate determinations. Different letters within rows indicate significant difference at $p < 0.05$

The higher value of WHC in KMH and PMH indicated the effects of β-cyclodextrin on water holding capacity. The changes in water holding capacity in the samples were probably due to the inclusion complex between BH and β-cyclodextrin, which had changed the molecule structure of KMH and PMH. This study corroborated previous studies indicating that the binding strength of proteins was mainly dependent on their molecular structure [26]. Therefore, the changes in molecular structure produced from the complexes PMH may have significantly altered its water holding capacity in KMH and PMH.

The mechanism of fat absorption is mostly attributed to the physical entrapment of the oil. The oil holding capacity (OHC) obtained from BH was significantly ($p <0.05$) higher (5.16 mL/g) than KMH (3.44 mL/g) and PMH (3.96 mL/g) as shown in Table 1. This agrees with a previous study in which the oil holding capacities of BH possessed a higher oil holding capacity [27]. The high oil holding capacity of BH could be due to its higher surface hydrophobicity and degree of hydrolysis as suggested by Kristinsson and Rasco [28]. On the contrary, low oil absorption might be because the presence of a large proportion of hydrophilic groups and polar amino acids on the surface of the protein molecules after the complex was formed with β-cyclodextrin [13].

Foaming properties

The foaming capacity and stability were significantly ($p<0.05$) higher than KMH and PMH at all pH values (pH 2 to pH 10). The results suggested that BH had a more flexible protein structure in aqueous solutions and interacted strongly at the air–water interface to form more stable foams when compared to the KMH and PMH. In addition, hydrophobic had improved the foaming capacity and had made the protein more flexible [29]. Hydrophobic residues of protein in KMH and PMH were found less in SDS-PAGE studies. This is proved by less band distribution in polyacrylamide gels at lower molecular weights. This occurs due to sodium dodecyl sulphate (SDS) preferentially binds to hydrophobic regions of proteins. Therefore, hydrophobic proteins bind a higher amount of SDS than hydrophilic proteins, resulting in faster migration on SDS-PAGE [17]. This study revealed that β-cyclodextrin gave an effect on foaming properties by forming an inclusion complex with hydrophobic amino acids residues, thus causing hydrophobic residues to be hidden and less exposed.

The effect of pH on foaming capacity and foaming stability of BH, PMH and KMH are shown in Figures 4 (a) and (b). The lowest foam capacity and stability was observed at pH 4 among BH (74.33%, 70.33%), PMH (37.00%, 31.17%) and KMH (29.50%, 26.16%). The relationship between foaming properties and pH for BH, PMH and KMH was similar to the relationship between protein solubility and pH. In this study, the foaming

properties of the hydrolysate samples were found to decrease at pH 4, and to increase at pH 6. However, there was a slight decrease in alkaline pH. The changing foaming properties at different pH values showed that net charge had an influence on the adsorption of proteins at the air-,water-interface [9]. However, BH showed an increase in foaming properties as the pH continued to increase. This is agreed in previous studies, which demonstrated that as the pH increased, deprotonation of the acidic and basic groups occur, and when the net charge is increased, the foaming properties of protein are also enhanced [30].

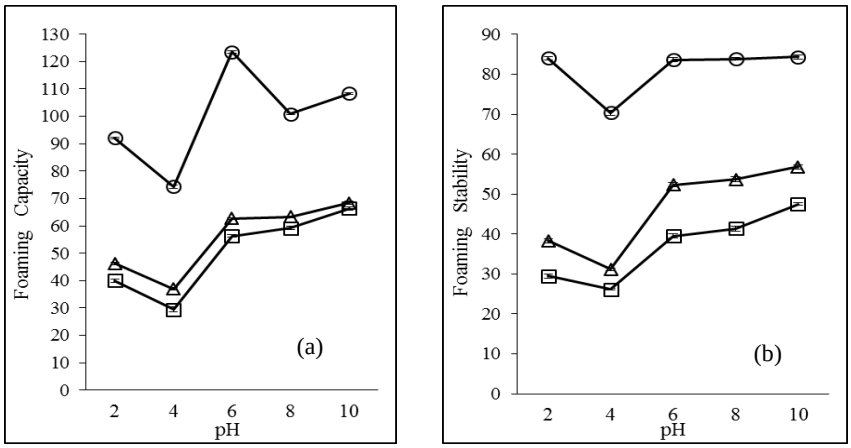


Figure 4. (a) Foaming Capacity and (b) Foaming Stability of Angelwing clam hydrolysate (BH=○), hydrolysate produced by physical mixing (PMH=Δ) and hydrolysate produced by kneading method (KMH= □). Bars represent standard deviation from triplicate determination

Emulsion properties

Emulsifying activity index (EAI) and emulsion stability index (ESI) of hydrolysate are shown in Figure 5. BH had a higher emulsion activity index at all pH values (pH 2 to pH 10) compared to KMH and PMH. This supports Mutilangi et al. as the higher solubility of hydrolysate results in higher EAI [29] because hydrolysate with higher solubility could rapidly diffuse and adsorb at the interface [10]. However, both KMH and PMH showed lower EAI across all pH ranges compared to BH, due to the complex formation between β-cyclodextrin and BH. This complex formation reduced the ability of the oil to form stable oil-in-water emulsions because β-cyclodextrin is not a surfactant, therefore, does not have the tendency to lower the surface tension between two liquids and thus, does not promote the oil-in-water emulsion. However, BH contains surface active material and promote oil-in-water emulsion due to the presence of hydrophilic and hydrophobic groups with their associated charge [31, 32]. Besides that, the lower EAI values in PMH and KMH are probably because of the extensive degradation of protein caused by further methods used to debitter the hydrolysate, such as kneading and rapid shaking in an incubator shaker.

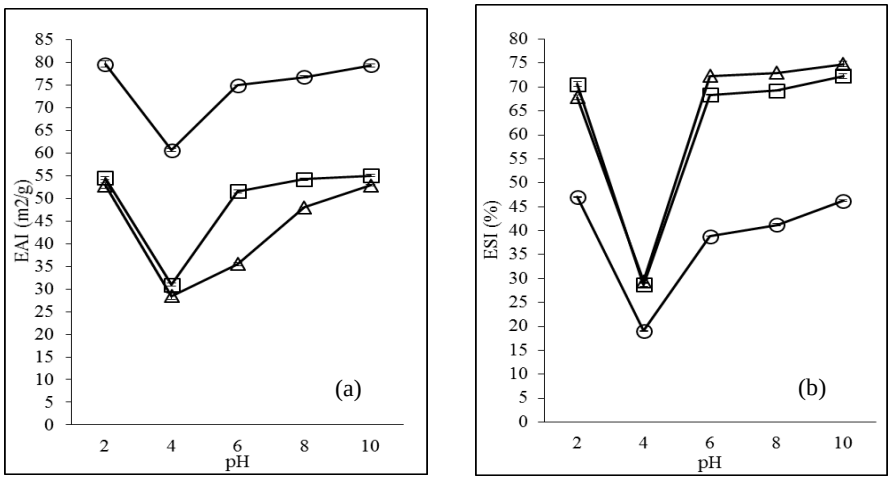


Figure 5. (a) Emulsifying activity index and (b) Emulsion stability index of Angelwing clam hydrolysate (BH=○), hydrolysate produced by physical mixing (PMH= Δ) and hydrolysate produced by kneading method (KMH= □)

At pH 10, the emulsion activity indexes of BH, PMH and KMH were significantly different ($p < 0.05$), with maximum values at 79.30%, 52.87% and 55.01%, respectively, whereas the emulsion stability index were at 46.55%, 74.81% and 69.63%, respectively. However, the minimum emulsion activity index in BH, PMH and KMH at pH 4 (isoelectric point) were 60.58%, 28.45% and 30.91%, respectively whereas the emulsion stability index was 19.01%, 29.41% and 28.71%, respectively. The results indicated that emulsion properties were pH-dependent, with alkaline pH significantly improving emulsion capacity over acidic pH. The tendency was similar to protein solubility (see Figure 3). For instance, protein solubility was low at pH of 4, implying that protein adsorption at the oil–water interface would be diffusion controlled. However, at pH range of 6 to 10, as protein solubility increased, the activation energy barrier prevented protein migration from taking place in a diffusion dependent manner. An increase in protein solubility facilitated interaction between the oil and aqueous phases [20]. The emulsion stability of BH was significantly lower than that of KMH and PMH due to its lower molecular weight (refer Figure 2). Although small peptides diffuse rapidly toward the interface are effective in producing emulsions, they are less efficient at stabilizing emulsions, because they may not readily agglomerate to produce a fat-globule membrane due to charge repulsions [33].

Conclusion

The characterizations of complex formation between BH and β-cyclodextrin are shown through FTIR analysis. The changes in the FTIR peak patterns of the complexes were compared with their corresponding peaks of pure BH and β-cyclodextrin. The difference in the peak patterns of O-H stretching profiles reveals the complexation formation in KMH and PMH. The low frequency in the C=O stretching vibration and C-H stretching vibration of KMH and PMH also reveals the formation of complex between BH and β-cyclodextrin. Low fragmentation of proteins in polyacrylamide gels in KMH and PMH is compared to BH, proving that the inclusion complex had formed by grafting the β-cyclodextrin molecule to the protein surface and reducing the denaturation of protein by SDS reagent. The physicochemical analysis shows that β-cyclodextrin influences the functional properties of hydrolysate. Despite that BH has a good quality of nitrogen solubility index, the solubility of BH is reduced when it forms a complex with β-cyclodextrin. As a result, the decreased solubility in KMH and PMH has an effect on their water and oil holding capacities, as well as foaming emulsifying properties. Even though, the functional properties of KMH and PMH are slightly reduced after the complex formation between BH and β-cyclodextrin,

their reducing values remain within the best ranges for all protein hydrolysates studied.

References

1. Del Valle. E. (2004). Cyclodextrins and their uses: a review. *Process Biochemistry*, 39: 1033-1046.
2. Sambasevam, K. P., Sharifah, M., Norazilawati, M. S. and Nor Atiqah, I. (2013). Synthesis and characterization of the inclusion complex of β-cyclodextrin and azomethine. *International Journal Molecular Science*, 14: 3671-3682.
3. Hou, L., Wang, J. and Zhang, D. (2013). Optimization of debittering of soybean antioxidant hydrolysates with β-cyclodextrin using surface response methodology. *Journal of Food Science and Technology* 50: 521-527.
4. Nazeer, R. A., Prabha, K. R., Divya Kumar, N. S., Sampath, G. and Jai, R. (2011). Isolation of antioxidant peptides from clam, *Meretrix casta* (Chemnitz). *Journal of Food Science and Technology* 50: 777-783.
5. Normah, I. and Nurul Fasihah, R. (2014). Sensory, amino acids composition and flavour compounds of angelwing clam (*Pholas orientalis*) hydrolysates produced using two different enzymes. *Science Letters*, 8:1, 25-33.
6. Normah, I. and Nurul Fasihah, R. (2017). Evaluation of β-cyclodextrin masking effect on the bitterness of angelwing clam (*Pholas orientalis*) hydrolysate. *International Food Research Journal*, 24(4): 1500-1506.
7. Szejtli J. (1998). Introduction and general overview of cyclodextrin chemistry. *Chemistry Reviews*, 98:1743-1753.
8. Schmid G. (1989). Cyclodextrin glucanotransferse production: yield enhancement by overexpression of cloned genes. *Trends Biotechnologies*, 7: 244-248.
9. Normah, I and Nurul Fasihah, R. (2016). Bitterness and physichochemical properties of angelwing clam (*Pholas orientalis*) hydrolysate. *Malaysian Journal of Analytical Sciences*, 20: 594-600.
10. Klompong, V., Benjakul, S., Kantachote, D and Shahidi. (2007). Antioxidative activity and functional properties of protein hydrolysate of yellow stripe trevally (*Selaroids leptolepis*) as influenced by the degree of hydrolysis and enzyme type. *Food Chemistry*, 102: 317-327.
11. Diniz, F. M. and Martin, A. M. (1997). Effects of the extent of enzymatic hydrolysis on the functional properties of shark protein hydrolysate. *Lebensmittel Wissenschaft and Technologies* 30: 266-272.
12. Shahidi, F., Xiao-Qing, H. and Synowiecki, J. (1995). Production and characteristics of protein hydrolysates from capelin (*Mallotus villosus*). *Food Chemistry* 53: 285-293.
13. Sathe, S. K. and Salunkhe, D. K. (1981). Functional properties of the Great Northern bean (*Phaseolus vulgaris* L.) proteins: emulsion, foaming, viscosity and gelation properties. *Journal of Food Science*, 46: 71-74.
14. IBM Corporation (2011). IBM SPSS Statistics for Windows, Version 20.0. Armonk, NY: IBM Corp.
15. Crupi, V., Ficarra, R., Guardo, M., Majolino, D., Stancanelli, R. and Venuti, V. (2007). UV-vis and FTIR-ATR spectroscopic technique to study the inclusion complexes of genistein with β-cyclodextrin. *Journal of Pharmaceutical and Biomedical Analysis*, 44: 110-117.
16. Simon, B. W., Adi, N. and Teti, E. (2011). Functional interaction components of protein isolates and glucomannan in food bars by FTIR and SEM studies. *African Journal of Food Science*, 5: 12-21.
17. Robinson, N. C. and Tanford, C. (1975). The binding of deoxycholate, triton X-100, sodium dodecyl sulfate, and phosphatidylcholine vesicles to cytochrome b5. *Biochemistry*, 14: 369-378.
18. Aachmann, F. L., Otzen, D. E., Larsen, K. L. and Wimmer, R. (2003). Structural background of cyclodextrin-protein interactions. *Protein Engineering,*16: 905-912.
19. Rozema, D and Gellman, S. H. (1996). Artificial chaperone-assisted refolding of carbonicanhydrase. *Biological Chemistry*, 271: 3478-3487.

20. Muo, X and Hua, Y. (2012). Composition, structure and functional properties of protein concentrates and isolates produced from walnut (*Juglans regia* L.). *International Journal of Molecular Sciences*, 13: 1561-1581.
21. Yin, Y. R., Liu, W. Q and Xiao, K. J. (1996). The study of Sesame protein solubility and emulsification. *Food Science*, 17: 3-6.
22. Tang, L., Sun, J., Zhang, H. C., Zhang, C. S., Yu, L. N. and Bi, J. (2012). Evaluation of physicochemical and antioxidant properties of peanut protein hydrolysate. *PLoS One* 7(5): e37863.
23. Amiza, M. A., Ow, Y. W. and Faazaz A. L. (2013). Physicochemical properties of silver catfish (*Pangasius* sp.) frame hydrolysate. *International Food Research Journal*, 20(3):1255-1262.
24. Rahman, M. S. (2007). Hand book of food preservation. 2nd edition, Boca Raton, FL, USA, CRC Press: pp. 519.
25. Sanjoy Kumar D., Rajabalaya, R., Sheba, D., Nasimul, G., Jasmina, K and Nanda, A. (2013). Cyclodextrins-the molecular container. *Research Journal of Pharmaceutical, Biological and Chemical Sciences*, 4: 1694-1720.
26. Chaplin, M. F. (2003). Fibre and water binding. *Proceeding of Nutritional Society*, 62: 223-227.
27. Popovic, l., Peričin, D., Vaštag, Z. and Popovic, S. (2011). Optimization of enzymatic hydrolysis of cucurbitin using response surface methodology: improvement of the functional properties. *International Journal of Food*, 7, 5: 1556-3758.
28. Kristinsson, H. G. and Rasco, B. A. (2000). Fish protein hydrolysates: Production, biochemical and functional properties. *Critical Reviews in Food Science and Nutrition*, 40: 43-81.
29. Mutilangi, W. A. M., Panyam, D. and Kilara, A. (1996). Functional properties of hydrolysates from proteolysis of heat-denatured whey protein isolate. *Journal of Food Science*, 61: 270-274.
30. Wagner, J. R., Sorgentini, D. A and Anon M. C. (2000). Relation between solubility and surface hydrophobicity as an indicator of modifications during preparation processes of commercial and laboratory-prepared soy protein isolates. *Journal of Agricltural Food Chemistry*, 48, 3159-3165.
31. Mentink, L. (1999). β-cyclodextrin emulsion: Mechanism of emulsification and application to the preparation of green metalworking fluids. Netherlands, Springers: pp. 693-696.
32. Gbogouri, G. A., Linder, M., Fanni, J, and Parmentier, M. (2004). The influence of hydrolysis degree on the functional properties of salmon byproducts hydrolysates. *Journal of Food Sciences*, 69: 615-622.
33. Cho, D-Y., Jo, K., Cho, S. Y., Kim, J. M., Lim, K., Suh, H. J and Oh, S. (2014). Antioxidant effect and functional properties of hydrolysates derived from egg-white protein. *Korean Journal Food Sciences of Animal Resources*, 34(3): 362-371.

Malaysian Journal of Analytical Sciences (MJAS)
Published by Malaysian Analytical Sciences Society

MAGNETIC NANOPARTICLES AS EFFECTIVE ADSORBENTS FOR THE REMOVAL OF HEAVY METALS FROM WATER: A REVIEW OF SURFACE MODIFICATION (2015-2022)

(Nanozarah Bermagnet Sebagai Penjerap yang Berkesan untuk Penyingkiran Logam Berat daripada Air: Tinjauan Kajian Pengubahsuaian Permukaan (2015-2022))

Gimba Joshua Dagil[1,2], Ng Nyuk-Ting[1], Aemi Syazwani Abdul Keyon[1,3*], Sheela Chandren[1,3], Wan Aini Wan Ibrahim[1,3*]

[1]Department of Chemistry,
Faculty of Science,
Universiti Teknologi Malaysia, 81310, Johor Bahru, Johor, Malaysia
[2]Department of Science, Plateau State Polytechnic, Barkin Ladi,
P.M.B 02023, Bukuru, Jos Nigeria
[3]Centre for Sustainable Nanomaterials,
Ibnu Sina Institute for Scientific and Industrial Research,
Universiti Teknologi Malaysia, 81310, Johor Bahru, Johor, Malaysia

**Corresponding author e-mail: aemi@utm.my; waini@utm.my*

Received: 17 July 2022; Accepted: 27 September 2022; Published: 27 December 2022

Abstract

The use of biopolymer composite materials in the usage of magnetic nanoparticles for the removal of heavy metal pollutants has received little attention, despite their remarkable physical and chemical properties that suggested their huge potential as promising adsorbents. . Therefore, various sorbents for heavy metals removal have been prepared including surface-modified magnetic nanoparticles (MNPs). MNPs are susceptible to oxidation in the air and agglomeration in solvents rendering them to lose their essential adsorbent properties. Silica coating has proven to prevent degradation of the MNP and functionalizes the surface with silanol groups. A fundamental understanding of various surface modifications would be beneficial for near future research as well as industrial applications. Thus, this article aims in reviewing the most recent advances for surface modification of MNPs materials, including biopolymer materials, focusing on the chemistry preparation, characterization, optimization, mechanisms of adsorption, isotherms and kinetic models in order to remove various metals in water.

Keywords: magnetic nanoparticles, functionalization, modification biopolymer, heavy metals, water environment

Abstrak

Pengunaan komposit bioplimer sebagai nanozarah bermagnet untuk penjerapan logam berat kurang mendapat perhatian, walaupun ianya mempunyai ciri fizikal dan kimia yang luar biasa yang menjadikan komposit bioplimer sebagai penjerap berkesan. Oleh itu, pelbagai penjerap untuk penyingkiran logam berat telah disediakan termasuk permukaan nanopartikel bermagnet yang diubah suai (MNPs). MNPs mudah teroksida di udara dan mudah bergumpal dalam pelarut menyebabkan bahan ini kehilangan ciri-ciri

penjerapan yang penting. Salutan silika telah dibuktikan menghalang kemerosotan MNPs serta menyebabkan permukaan tersebut berfungsi dengan kumpulan silanol. Pemahaman yang baik tentang pelbagai pengubahsuaian permukaan akan memberi manfaat untuk penyelidikan masa hadapan serta aplikasi industri. Maka, artikel ini bertujuan untuk membincangkan dengan lebih mendalam kemajuan terkini dalam pengubahsuaian permukaan MNP termasuk bahan biopolimer, fokus terhadap penyediaan secara kimia, pencirian, keadaan penjerapan optimum, mekanisme penjerapan, model isoterma penjerapan dan model kinetik yang digunakan untuk penyingkiran bahan pencemar ion logam yang berbeza dalam persekitaran air.

Kata kunci: nanopartikel bermagnet, kefungsian, biopolimer pengubahsuaian, logam berat, persekitaran air

Introduction

Pollution from heavy metals (lead, cadmium, and copper) poses a serious risk to human lives as well as the environment (water, soil, and air) across the world. Metallic elements with relative densities are greater than those of water, greater than or equal to 5 g/cm, and the potential to be hazardous even at low concentrations are referred to as heavy metals. [1]. These heavy metals (lead, cadmium, and copper) are non-biodegradable, and therefore, tend to bioaccumulate in the biological and ecological system over a prolonged period, potentially causing damage to living organisms. The discharge of a high concentration of heavy metals into the environment could be from mining, agricultural, domestic, and industrial activities [1, 2]. The dumping of effluents into water bodies could cause harm to aquatic environments. Thus, due to health threats of the heavy metals, the industries that have the potential in polluting the 'water bodies should treat their effluents sufficiently before releasing them to fit into the environmental guideline standard. To prevent long-term exposure, it is essential to monitor contamination levels from their drainage source. Non-essential heavy metals such as mercury (Hg), lead (Pb), arsenic (As), cadmium (Cd), and antimony (Sb) are listed in several regulatory bodies as contaminants in various water matrices. The World Health Organization (WHO) and the United States Environmental Protection Agency (USEPA) have stipulated regulatory limits for Pb to be 0.005 mg/L as well as 0.015 mg/L in drinking water, considering its dangerous impacts on the environment and humans [3, 4, 5]. The limits for Hg, Cd, and As in drinking water are 2, 5, and 100 µg/L, respectively [6]. Some heavy metals (i.e. zinc (Zn), copper (Cu), iron (Fe), and selenium (Se) are essential because they are required for various biological processes and physiochemical functions in most kinds of living organisms [7]. These categories of metal elements remain safe to all living organisms as long as their concentrations are within acceptable threshold values stipulated by regulatory bodies.

Several techniques for removing heavy metals from the water include precipitation [8], ion exchange [9], coagulation [10], and floatation [11]. However, these methods exhibited several disadvantages and limitations due to their high cost, low effectiveness, disposal of sludge, and inaptness to a wide variety of pollutants. The issue with the disposal of the resulting waste and/or sludge using these techniques makes adsorption a more promising choice due to its reusability of sorbents thus, being the more economical and easy separation method of materials because of the magnetic property of MNP full term? (MNPs). Adsorbents have been prepared from agricultural wastes [9, 12], clay [13], zeolite [14], activated carbon [15] and biopolymers [12]. A new class of material and organic-inorganic hybrid material have become more popular in creating high-performance adsorbents. Magnetic polymeric-based and/or silica-based nanoparticles showed the potential to remove metal through surface modifications. The modified hybrid materials have better properties than the original components. Thus, the surface coating of magnetic nanoparticles (MNPs) is one of the fundamental challenges that stands against researchers for the utilization of these materials for water purification. Recently, MNPs materials received greater attention due to their unique properties in terms of readiness to be modified and nontoxic properties. The MNPs were prepared and used as cores shells. Chemical co-precipit ation was mostly recommended since it was considered the easiest and the fastest method with less hazardous c hemical and procedure requirements. This method invol ved the preparation starting from the aqueous mixtures of solutions of Fe(II)/Fe(III) and salt solution by adding a base solution under an inert atmosphere at room temp erature with a slight increase in temperature [14, 15].

The MNPs have a high surface area which yields a lot of active sites for various modifications, but due to the setbacks of agglomeration, the active site could be reduced, and this was a major challenge for the preparation of MNPs. The surface coating with inorganic or organic surfactants can be an alternative method to remedy the agglomeration of the MNPs. For instance, the use of certain inorganic capping agents such as silica (SiO_2) has a unique physical and chemical property that could generally be applied during this process. Meanwhile, SiO_2 is more chemically stable in acidic media, thus, suitable to be used for surface coating of the MNPs. Thus, this could curb the process of agglomeration and serve as a protection for the MNPs in acidic environments. The surface coatings are done with the use of SiO_2 immediately as the next step after the preparations of MNPs. The SiO_2 layer is usually coated on the MNPs surface by the application of the Stober method whereby the SiO_2 were used to cover the surface of the MNPs to form the silica coated magnetite (Fe_3O_4/SiO_2) nanoparticle core-shell system [16]. After the SiO_2 coating, the next step was the functionalization of the MNPs surface. There are several techniques designed to functionalize MNPs surfaces. However, the easiest way is to graft the acid-functionalized group-containing compound with an organic mixture for example oleic acid [17] and n-octadecyl phosphonic acid [17], or it could be done directly onto the surface of MNPs dependent on Lewis acid/base interaction, which will change the MNPs into a hydrophobic adsorbent. Additionally, a silane coupling agent could be directly immobilized onto the surface of MNPs. For instance, amino-group functionalization of MNPs could be achieved through direct salinizing the MNPs with 3-aminopropyltriethoxysilane (APTES) or indirectly onto the surface of the silica-coated MNPs. This paper reviews the advancements in the synthesis of MNPs materials and surface modification with functional groups (e.g, $-NH_2$, -COOH, or -SH). The use of biopolymer organic components containing polysaccharides obtained from sporopollenin, alginate, chitin, and chitosan used as adsorbent composites for the removal of metal ions pollution in aqueous solutions were discussed. The focus was made on the preparation chemistry, characterization, and optimization, mechanisms of adsorption, isotherms, and kinetic models, for the removal of various metals in water.

Chitosan-based MNPs adsorbent

Chitosan (CS) is the major derivative of chitin which could be produced by the process of the deacetylation of the chitin in basic conditions, it is known for its good and outstanding properties such as biocompatibility, biodegradability, antibacterial properties, and non-toxic properties [18,19]. The structure of CS was composed of a linear-linked polysaccharide of randomly distributed (β-4)-linked-D-glucosamine (deacetylated unit) and N-acetyl-D-glutamine (acetylated unit). It has several commercial and biochemical uses [20]. In addition, it is known for its exceptional ability as an effective adsorbent due to its amino ($-NH_2$) and hydroxyl (-OH) functional groups in their molecules which served as attraction sites toward metal ions. The adsorbents prepared from chitosan-based MNPs for removing metal in water are tabulated in Table 1 [21-37]. In 2018, Song et al. [21] prepared a novel magnetic thiolated/quaternized/chitosan composite (Fe_3O_4/SH/CS) using an inverse suspension technique. The Fe_3O_4 was prepared as a precursor followed by the incorporation of the CS and the SH components. The purpose of the addition of CS was to boost the adsorbent's adsorption capacity through their functional groups. All results from this characterization confirmed the presence of -OH, -NH, and -SH in the composite, as well as the composition of the adsorbent, which revealed the synthesis process was successful. The composite showed high removal efficiency for Hg(II), Pb(II), As(V), Zn(II), As(III), Cu(II), and Cd(II) in basic conditions (pH 6 to 9). Pb(II) showed the highest adsorption capacity of 235.63mg/g while the maximum adsorption capacities values for the other metal ions were 66.27, 67.69, 28.00, 33.99,13.63 and 16.34 mg/g for As(V), As(III), Cu(II), Hg(II), Zn(II) and Cd(II) respectively. Additionally, the Freundlich isotherm was more fitted for all the metal ions due to the correlation coefficient (R^2) values ≥ 0.99, than the Langmuir, indicating heterogeneous adsorbate and multilayer adsorbent interaction sites. The kinetic process fitted best to pseudo-second order where the R^2 values were ≥ 0.99, indicating the chemisorption process. The adsorbent showed excellent reusability for Pb(II) (as model ion) where the removal efficiency for the Pb(II)

was achieved at 93% at 5 cycles.

A new adsorbent from attapulgite (ATP), ethylenediaminetetraacetic acid (EDTA), and chitosan to form the composite adsorbent (Fe_3O_4/ATP/ EDTA/CS) was performed by Sun and co-workers [22] The process of synthesis was done first by combining ATP and Fe_3O_4, followed by the addition of CS gel beads to the Fe_3O_4/ATP nanoparticles, where glutaraldehyde (GA) was employed as the cross-linker. Finally, gel beads-Fe_3O_4/ATP/CS were modified by EDTA to form the new Fe_3O_4/ATP/EDTA/CS adsorbent via amidation reaction (i.e., formation of amide through the reaction between carboxylic acid and amine by using a coupling agent such as EDTA) to further enhance removal efficiency. The magnetic material structural formation was confirmed by FTIR with Fe-O spectrum at 571 cm^{-1}, 1663 cm^{-1} (C=N) vibration that showed a reaction took place between CS and GA, 1631 cm^{-1} ($-COO^-$), 1398 cm^{-1} (C-O) indicating a carbonyl group had been introduced to EDTA and that the synthesis of the new adsorbent was successful. The maximum adsorption ability of the fabricated Fe_3O_4/ATP/EDTA/CS adsorbent material was 368.32, 267.94, and 220.31 mg/g, onto Pb(II), Cu(II), and Ni(II) in that order. The adsorption capacities of Fe_3O_4/ATP/ CS were 224.15, 144.47, and 105mg/g for Pb(II), Cu(II), and Ni(II), respectively, with lower values when compared to those of Fe_3O_4/ATP/EDTA/CS. These results demonstrated that the chelation by EDTA had greatly enhanced the adsorption capacity of the main adsorbent; Fe_3O_4/ATP/EDTA/CS. The procedure of adsorption better fitted the kinetics of pseudo-second data with R^2 values 0.9998, 0.9978, and 0.9967 for Pb(II), Cu(II), and Ni(II), respectively, indicating a chemisorption process. Additionally, the authors discovered that the adsorption mechanism to be homogeneous adsorbate and monolayer active sites interaction with high R^2 values 0.9995, 0.9950, 0.9958 Pb(II), Cu(II), and Ni(II), respectively, satisfying Langmuir isotherm than the Freundlichs' physisorption process. Consequently, the adsorbent could still demonstrate good adsorption capacity of repetitive use (5 cycles) by retaining its potential ability > 89% for Pb(II), Cu(II), and Ni(II), thus this indicated its capability to save cost. Chen et al. [23] explored Champ cellulose (*Millettia speciosa*) as well as chitosan to prepare magnetic hydrogels (MSCC/CS hydrogel) composite adsorbent for the removal of Cu(II). The purpose of adding CS was to enhance the adsorption process through the presence of amino-functional groups. The characterization results of functional groups involved in the synthesis process and the mechanisms of interactions demonstrated that electrostatic attraction was involved, with amino groups dominantly operating in the Cu(II) adsorption mechanism. The FTIR characterization showed the functional groups of -OH for cellulose at a broad peak at 3421 cm^{-1} and subsequent adsorption peaks at 2902 cm^{-1} and 1429 cm^{-1} for C-H stretching vibrations in methyl and methylene, respectively. Other peaks at 1429 cm^{-1} and 1371 cm^{-1} for C-H bending vibration as well as -NH_2 from CS were observed, indicating successful synthesis. The results from the adsorption kinetic process revealed the pseudo-first order kinetic process had a better match than the pseudo-second-order kinetic process, which had an R^2 value of 0.9822 for the adsorption of Cu(II). Therefore, physisorption dominated the process. The adsorption isotherm revealed that the Freundlich model had a higher R^2 value of 0.9975 than the Langmuir isotherm, indicating a heterogeneous and multilayer adsorption of Cu(II) onto the adsorbent. The results of the thermodynamic analysis showed that the Cu(II) adsorption process was spontaneous and endothermic, with values for G and H of -6.04KJ/mol and +18.79KJ/mol, respectively. The ΔS value was at +0.8KJ/mol which also implied the randomness of the process as well as endothermic. Furthermore, the increment in pH increased the adsorption capacity of MSCC/CS hydrogel due to the interaction of Cu(II) on the adsorbent's negative parts. On top of that, the authors reported that the adsorbent had reasonable reusability, with an adsorption efficiency of > 75% for 5 consecutive cycles.

Elanchezhiyan et al. [24] developed magnetic kaolinite (MKa) that immobilized in chitosan beads(CB) by a simple co-precipitation method (MKa/4%CB). The MKa was prepared first before CB was introduced into the mixture and applied for the removal of Cd(II) and Pb(II) from a wastewater ecosystem. The purpose of the modification with CB is to enhance the adsorption process through some amino functional group's

addition. Findings from FTIR characterization revealed the presence of Fe-O spectra between 580 and 630, a shift of spectra from 3430 cm^{-1}, 1629 cm^{-1}, 630 cm^{-1}, to 3438 cm^{-1}, 1631 cm^{-1}, 636 cm^{-1}, and 585 cm^{-1} for magnetic kaolinite. In addition, the peaks with chitosan shifted from 3430 cm^{-1}, 1639 cm^{-1}, 1596 cm^{-1}, and 142 cm^{-1}1 to 3457 cm^{-1}, 1655 cm^{-1}, 1676 cm^{-1}, and 1460 cm^{-1}, respectively, for -OH, -CH, -CN and -NH_2 vibration stretching, thus confirming successful synthesis process. The adsorption mechanism of both metals unto MKa/4%CB was through ion-exchange and coordination bonding, due to the more active sites of -NH_2 and -OH functional groups contributed by CB. The optimization factors were achieved at pH 6, initial concentration of the adsorbate of 20mg/L, adsorbent dosage as 100mg, temperature 25°C, and shaking speed at 200rpm. The adsorption isotherm studies fitted with Langmuir, which indicated homogeneous and monolayer adsorption sites were available as compared to heterogeneous sites. Additionally, the calculated adsorption capabilities were 90.9 and 88.5 mg/g for Pb(II) as well as Cd(II). The adsorption kinetic data plot demonstrated that both metal ions fitted into the pseudo-second order, thus demonstrating a chemisorption process. Synthesized adsorbents could be used for 4 cycles without any substantial adsorption capacity reduction. Huang et al. [25] prepared a phosphorylated(P), CS-coated Fe_3O_4/SiO_2 NPs adsorbent ($Fe_3O_4/SiO_2/CS/P$) and used it to remove Pb(II). The purpose of phosphorylating the adsorbent was to enhance the Pb(II) adsorption performance of the adsorbent and also alter the selectivity of other metals' adsorption. At pH 6.0, the researchers conducted multi-ions solution competitive assays. The results revealed that $Fe_3O_4/SiO_2/CS/P$ had a 10-fold greater ability to remove Pb(II) than other metals, with a distribution coefficient of 0.75 L/g, while $Fe_3O_4/SiO_2/CS$ exhibited highly discriminating sorption towards Ag, according to the multi-ions solution competitive trial. The removal of Pb(II) improved when compared to the uncoated silica adsorbent due to the presence of P. The $Fe_3O_4/SiO_2/CS/P$ could provide greater acidity protection against any probable Fe leaching after the acidity studies at pH 1. Furthermore, the XPS and FTIR spectral analyses showed that the exceptional adsorption process and the discriminatory tendency to remove Pb(II) were mostly manipulated by coordination connecting phosphate groups on the adsorbent surface of the material. The Langmuir adsorption capacities were 151.8, 131.8, 27.7 and 25.8mg/g for $Fe_3O_4/SiO_2/CS/P$, $Fe_3O_4/CS/P$, $Fe_3O_4/SiO_2/CS$, Fe_3O_4/CS, with the R^2 values 0.999, 0.986, 0.933 and 0.945, respectively; indicating a monolayer - surface-active sites interaction with a homogeneous adsorbate. The kinetic adsorption of Pb(II) unto $Fe_3O_4/SiO_2/CS/P$, $Fe_3O_4/CS/P$, $Fe_3O_4/SiO_2/CS$, and Fe_3O_4/CS revealed the best fit for pseudo-second order than the -pseudo-first order with R^2 > 0.992, thus indicating a chemisorption process.

Liu et al. [26] synthesized magnetic anaerobiotic granule sludge/chitosan (M/CS/AnGS) composite adsorbent and applied it for Pb(II) and Cu(II) removal from the water solution. The purpose of the modification is to enhance the process of adsorption through the addition of some functional groups. The FTIR revealed the presence of broad band spectra for -NH_2 and -OH were responsible for the adsorption and confirmed the success of the synthesis process. The optimum parameters influencing the adsorption capability of the CS/AnGS were an adsorbent dosage of 16 mg, pH 6, and a short contact time of 30 min. The highest adsorption capacities were 97.97 and 83.65 mg/g for Pb(II) and Cu(II), respectively. These were higher than the works of Zhang et al. [27] with 50.4 and 57.1mg/g for Pb(II) and Cu(II) in that order. The adsorption kinetics model of Pb(II) and Cu(II) is better suited to the pseudo-second order compared to the pseudo-first order with the R^2 values of 0.999 and 0.993, respectively, suggesting the chemisorption adsorption process. The Langmuir isotherm showed monolayer active site adsorption with R^2 of 0.9801 and 0.9920 respectively, indicating homogeneous adsorbate and a monolayer active site. Zhang et al. [24] prepared magnetic cyanoethyl chitosan beads (M/CNS/CS) and applied them for Co(II) removal from wastewater. The magnetite was prepared through co-precipitations and the cyanoethyl was used for the functionalization of the composite. The adsorption capacity towards Co(II) was enhanced by the grafting of cyanoethyl groups onto the CS. The FTIR revealed the presence of broad band spectra for -NH_2 and -OH around 3000-3700 cm^{-1} in chitosan, 1598 $cm^{-1,}$ and 1132 cm^{-1} for -NH_2, and a new band at 2250 cm^{-1} for -CN

spectrum due to the successful synthesis of M/CNS/CS. Hence, -CN, OH and -NH_2 were responsible for the removal of Co(II). The optimal factors were achieved at pH 6.72, contact time 4h, initial concentration of cobalt ions 500 mg/L, and temperature 308K. Additionally, the second-order model, as well as the Langmuir model data, were the best fittings with the coefficient of regression R^2 >0.99. This indicated that the chemisorption process and a monolayer surface-active sites interaction. The adsorption capability of 17.92 mg/g was less when compared to the adsorption capacity of 34.92mg/g obtained by Lee, et al. [42]. In that study, they used the same purpose of treatment of wastewater containing Co(II) heavy metal ions. The thermodynamic factors indicated endothermic and spontaneous process with the values as ΔH = +28.76KJ/mol, ΔS = +128.7J/mol and ΔG = -12.22KJ/molK.

Zhang et al. [27] synthesized a facile magnetic-responsive CNT/chitosan aggregate adsorbent (CNT/CS) and applied it for the removal of various contaminants via a two-step approach. The purpose of the modification is to enhance the adsorption process through the addition of some active sites due to functional groups. FTIR characterization revealed the spectra of 3450-3500 cm^{-1} for -OH stretching vibration in CNT, 1656 $cm^{-1,}$ and 1595 cm^{-1} due to carbonyl group of CNT, and 3480 cm^{-1} and 3375 cm^{-1} for -OH and -NH_2, respectively, which showed the formation of CS on top of CNT, thus confirming successful synthesis process of the adsorbent. The result of adsorption capacity for heavy metals by CNT/CS aggregate observed the order of Fe(III)>Cu(II)>Pb(II)>Zn(II), with adsorption capabilities of 68.8, 57.1, 50.4, and 16.6 mg/g in that order, perhaps due to electro positivity sequence. The mechanism of interaction was mainly du pi-pi stacking, cation-pi interactions, hydrophobic effect, and chelation tendencies of the metal ions. Meanwhile, the performance of CNT/CS was better than CNT alone due to the presence of the functional groups -OH, and -NH_2 on the CS which enhanced the removal of the contaminants. The isotherm kinetics for the metal ions well supported the kinetic isotherm model of pseudo-second order with $R^2 \geq 0.997$, close to unity implying a chemisorption adsorption process. Since the adsorbent could be reused as it could retain over 78% of its original worth, the CNT/CS material demonstrated great potential in the removal of multiple pollutants from aqueous mixtures.

The adsorbent's crosslinked CS/g/PMAM through the method of grafting CS with poly(methacrylamide (g/PMAM) was synthesized by Sutriman and co-workers. They applied for removal of Cu(II) and Cd(II) in aqueous solution [28]. The modified CS was to improve acid resistance and also enhance the adsorbent's adsorption capacity toward the removal of metal ions in aqueous solutions. FTIR characterization showed the presence of -OH and -NH_2 functional groups at spectral bands of 3423 cm^{-1} and 1615 cm^{-1} in chitosan and bands shifted to 3423 cm^{-1} and 1623 cm^{-1} to confirm the successful synthesis of the adsorbent CS/g/PMAM. By comparing the functional groups, C-O, C=O, -OH, -NH_2, and C-NH_2, the X-ray photoelectron spectroscopy (XPS) analysis revealed that adsorption of both metal ions occurred on the surfaces of the adsorbent by chelation via C-O, C=O, and C-NH_2 functional groups. The behaviors of crosslinked CS/g/PMAM from metals were investigated. It was revealed that the solution pH played a major role in adsorption Cu(II) and Cd(II) favored pH 4 and pH 5, respectively. Their Langmuir maximum adsorption capacities were 140.9 mg/g and 178.6 mg/g, respectively, with a better fit than the Freundlich isotherm data proposing monolayer adsorption than the Freundlich isotherm. Pseudo-second order indicated a better fit (R^2 = 0.999) than pseudo-first order, indicating that chemisorption or electron transfer was the dominant mechanism onto the crosslinked CS/g/PMAM. Additionally, the X-ray photoelectron spectroscopy (XPS) analysis revealed that adsorption of both metal ions occurred on the surfaces of the adsorbent by chelation via C-O, C=O, and C-NH_2 functional groups. Pooladi et al. [29] synthesized a new adsorbent of chitosan-hydroxyapatite-MNPs (CS/HAP/Fe_3O_4) and applied it for the removal of Cu(II) and Zn(II) from aqueous solutions. The purpose of the modification was to introduce some new functional groups active sites for the adsorption of the metal ions. The authors used chitosan and HAP because the two materials were low-cost and easily accessible, acquired from shrimp shells as well as bone ash, respectively. The adsorbent performances of CS/HAP/Fe_3O_4 were better than the

HAP/Fe_3O_4 due to the surface modification with the functional groups of the CS when compared. The FTIR characterization results showed the presence of the functional groups of -OH and -NH_2 to confirm the success of the synthesis process. The optimized removal experiment parameters employing fundamental composite design (CCD) together with response-surface-methodology (RSM) were 65 min contact time for Cu(II), initial concentration of 2.87 mg/L, Zn(II) initial concentration of 2.61 mg/L, pH 5.5 and adsorbent dosage 0.018g. The adsorption capabilities for Cu(II) and Zn(II) were 3.659 and 6.497mg/g, respectively. The authors attributed the low adsorption capacities that resulted to the synergistic negative influence of the cation on each other's adsorption behavior and perhaps their differences in the electrochemical series. The acquired adsorption isotherm data were well fit by the Temkin and Langmuir isotherms for Cu(II) and Zn(II), respectively, with coefficients of determination R^2 of 0.987 and 0.987, respectively, as compared to the Freundlich isotherm with R^2 of 0.912. The adsorption kinetics were pseudo-second order kinetic models for Zn(II) and Cu(II) with $R^2 \geq 0.99$ indicating that the adsorption was chemisorption and a spontaneous process.

Feng et al. [30] synthesized magnetic/chitosan/bentonite (Fe_3O_4/CS/BT) aggregate adsorbent using organic components materials and applied it for the remediation of acid mine drainage containing Cr(VI). The purpose of the modification was to enhance the adsorption process. FTIR characterization showed the presence of -OH and -NH_2 functional groups at spectral bands of 3423 cm^{-1} and 1615 cm^{-1} in CS and bands shifted to 3423 cm^{-1} and 1623 cm^{-1} to confirm the successful synthesis of Fe_3O_4/CS/BT. The authors discovered that the adsorbent aggregates had excellent magnetism (20.0emu/g), high stability, and good performance for the removal of Cr(VI) with the maximum adsorption capability of 62.1mg/g from the synthetic aqueous solutions. The adsorption isotherm fitted into the Langmuir isotherm proposing monolayer adsorption more than the Freundlich isotherm. Additionally, the kinetic information well fitted into the pseudo-second kinetics indicating the chemisorption process. On top of that, the thermodynamic factors demonstrated that Cr(VI) adsorption towards Fe_3O_4/CS/BT was exothermic as well as spontaneous in nature. The solution pH was an important factor for adsorption and was enhanced at pH 2.0 accordingly to the law of pKa. Besides that, Fe_3O_4/CS/BT was discovered to possess an exceptional adsorbent quality for actual acid mine drainage remediation of metals containing Ni, Zn, Fe, Cu, Cr, Pb, and Cd, with all their percentage removal > 84%. A study by Sun et al. [31] developed biopolymer chitosan/tannin (CS/TA) as an adsorption paper material for removing Cu(II) and Cd(II) from alkaline water solutions. The purpose of the chitosan was to promote flocculation on the paper material while both chitosan and tannin played the role of cross-linking on the paper material for modification. The FT-IR characterization revealed three distinct peaks at 1688, 1600, and 1200 cm^{-1}, which correspond to the stretching spectral vibrations of C=O, -C=C- of the benzene ring, as well as -C-O- in the tannin, correspondingly. As a result, CS could substantially encourage flocculation of tannin in the CS/TA adsorbent. The CS/TA adsorbent removal ability might have been primarily supported by a complexation formation mechanism, with the maximum adsorption capacity accomplished at pH 9. Langmuir isotherms accurately matched the adsorption data with an R^2 value of 0.9904, which was higher than Freundlich with an R^2 value of 0.984, thus indicating a favorable monolayer surface adsorption, with outstanding Cu(II) and Cd(II) adsorption capacities of 684.93 and 813.01mg/g, respectively. The adsorption of the various heavy metals unto CS/TA was preferential in the order of Cu(II) > Cd(II) and that Cu(II) competed with Cd(II) for active binding sites at concentrations more than or equivalent to 200 mg/L.

Huang et al. [32] prepared a new adsorbent sodium alginate/carboxymethyl chitosan (SA/CCS) hydrogel beads polyacrylamide (SA/CCS/P) and modified kaolin (SA/CCS/K) in which a simple polyacrylamide modification kaolin procedure was developed to enhance the adsorption performance towards the removal of Cu(II). FTIR results showed the presence of the functional groups of -OH, -NH_2, and -COOH which were responsible for the adsorption of Cu(II). The Langmuir adsorption capacities of adsorbents SA/CCS, SA/CCS/K, and SA/CCS/P, were 4.306, 4.621, and

5.515mg/g, respectively, showing that the modification due to polyacrylamide successfully enhanced the adsorption process and the increase due to presence of its functional groups. The increase proved that the adsorption of SA/CCS/P was better than the other adsorbents and therefore remained a good candidate for the removal of Cu(II) ions. The trend showed a substantially low removal ability which could be due to low interaction. The maximum adsorption capacity of Cu(II) onto SA/CCS/P was 5.516mg/g. Finding from both the kinetic and isothermal studies revealed that both Langmuir isotherm and pseudo-second were fitted into the adsorption process with both R^2 greater than 0.999. This indicated a homogeneous surface and monolayer as well as chemisorption process. Furthermore, adding kaolin was modified to reduce the tendency of coexisting ions interference. The adsorption capacity remained above 82% after 5 cycles of the reused adsorption-desorption experiment. Zhang et al. [33] synthesized a versatile adsorbent from EDTA and chitosan biofunctionalized magnetic bamboo biochar (E/CS/M/BB) and applied it for the removal of methyl orange (MO), Cd(II), and Zn(II). Magnetite was prepared by the co-precipitation method before the addition of the bamboo biochar, while GA served as a cross-linker between the magnetic chitosan and the bamboo biochar (BB) to form E/CS/M/BB. It was found that EDTA reacted with E/CS/M and BB via the amidation method to finally obtain the new adsorbent. By comparison of the adsorbent's adsorption performance, E/CS/M/BB was better than BB due to the electrostatic attractions pi-pi bond, and hydrogen bonding, which were enhanced via the $-NH_2$ and $-COO^-$ functional groups from EDTA. FTIR characterization results showed the functional groups of -OH, C=O, C=C, C-O, N-H, and $-NH_2$ to confirm the successful synthesis process. The maximum adsorption capacity at the optimum conditions were 305.4, 63.3, and 50.8 mg/g, for MO, Cd(II), and Zn(II), respectively. Pseudo-second order was more fitted with a R^2 value of 0.9895-0.9982 for MO, Cd(II) and Zn(II) than the pseudo-first order with R^2 values of 0.8541-0.9156, indicating chemisorption process. Additionally, the isotherm adsorption study revealed that Langmuir isotherm data was more fitted with the coefficient of determinations (R^2) value of 0.9981-0.9999 for MO, Cd(II) and Zn(II) than Freundlich with R^2 values of 0.7658-0.8701, indicating a homogeneous adsorbate surface interaction with a monolayer adsorbent active site. Adsorption-desorption experiment demonstrated that the efficiency of E/CS/M/BB towards MO was still retained after eight rounds but decreased for Cd(II) and Zn(II) by 16.8% and 19.5% respectively, indicating the cost efficiency of the adsorbent.

Similarly, Karimi et al. [34] prepared a magnetic-based chitosan/Al_2O_3/Fe_3O_4 (M/CS) nanocomposite adsorbent via ethylenediaminetetraacetic acid (EDTA) functionalization to improve the adsorption as new adsorbent (EDTA/M/CS). FTIR results showed a 1575-1639 cm^{-1} shift in peaks for EDTA/M/CS showing the presence of amino group on M-CS via the vibrational bending of the amide with C=O and $-COO^-$ on the surface of the adsorbent, thus confirming the successful synthesis process. By comparison, the EDTA functionalized M/CS adsorbent revealed that the adsorption capacity increased by about 14.3, 5.6, and 9.1 times towards Zn(II), Cu(II), and Cd(II), respectively indicating that EDTA/M/CS performed better than M-CS adsorbent. The maximum adsorption capacity of 43.93, 109.90, and 43.12mg/g for Zn(II), Cd(II), and Cu(II), respectively at pH 5.3. Finding from the isotherm studies revealed that Langmuir isotherm was mostly fitted into the isotherm data and could adequately explain the adsorption process with R^2 greater than 0.99, indicating a homogeneous adsorbate surface interaction with a monolayer adsorption active site. Additionally, the adsorption kinetics fitted the pseudo-second order with $R^2 > 0.99$ showing a chemisorption process. Furthermore, the thermodynamic study discovered that the adsorption process was exothermic and spontaneous with the values of ΔH, ΔG, and ΔS as -22.7KJ/mol, -10186.1J/mol, and 0.0451KJ/molK, respectively for Zn(II). Besides that, the values were -33.638 KJ/mol, -9797.21 J/mol and 0.0851J/molK, respectively for Cd (II). Additionally, -52.224 KJ/mol, -9129.58 J/mol and 0.1468J/molK, respectively for Cu(II) at 288K. Nasirimoghaddam et al. [36] synthesized a new adsorbent by immobilizing CS-coated magnetite (CS/Fe_3O_4) and applying it for the removal of Hg(II) from industrial aqueous and oily samples. The preparation of Fe_3O_4 was by co-precipitation of Fe(II)

and Fe(III) salts via NH_3 solution before immobilizing chitosan on its' surface to enhance the adsorption of the Hg(II). FTIR characterization results revealed the Fe-O bonds and the -OH and -NH_2 functional groups to confirm the successful synthesis process. The optimized parameters were temperature 289K, pH 6, adsorbent dose 10mg/ml, and 50mg/L initial concentration of adsorbates. The isotherm study revealed that the Langmuir isotherm was more fitted than the Freundlich isotherm with the R^2 value of 0.999 indicating homogeneous adsorbate and monolayer adsorbent surface interactions. The process at 298K was endothermic with ΔH value of +13,169.38KJ/mol, spontaneous with a ΔG value of -60.998Kj/mol, and ΔS as +41.969J/molK. This showed an increase in the randomness process, thus, suggesting that the solid/liquid interface interactions during the Hg(II) and the CS/Fe_3O_4. Furthermore, the adsorption-desorption study revealed that the adsorbent could retain it's 85% potential after a few recycle adsorption processes. Jiang et al. [37] synthesized a new adsorbent of functionalized SiO_2 coated MNPs with CS (Fe_3O_4/SiO_2/CS) to remove Cr(VI) in an aqueous mixture. Three steps were involved in the synthesis process. Firstly, the preparation of Fe_3O_4 by solvothermal reduction procedure, secondly, the preparation through silica coating of the Fe_3O_4 to form Fe_3O_4/SiO_2 and lastly, by immobilizing of chitosan via glutaraldehyde as the cross-linker to form Fe_3O_4/SiO_2-CS to increase the adsorption process. The FTIR characterization results showed the presence of the functional groups of -OH from adsorbed water molecules3436 cm^{-1} Fe-O at 585 cm^{-1} from Fe_3O_4, 1083 cm^{-1} for Si-O, from Fe_3O_4/SiO_2, and -NH_2 at 1640cm^{-1} from chitosan. The BET analysis showed Fe_3O_4 and Fe_3O_4/SiO_2 surface area as 24.0 and 121.0m^2/g, respectively, suggesting that porous silica was coated on top of magnetite to confirm the successful synthesis process. The possible adsorption mechanisms of the adsorbent towards Cr(VI) were reduction and electrostatic processes. The interferences adsorption experiment showed that the adsorbent had a strong affinity for Cr(VI) in the solution containing the ions of Zn(II), Cu(II), Cr(VI), Cd(II), and Ni(II). The researchers found that the adsorption capability of the adsorbent was high (336.7 mg/g) towards Cr(VI), which was enhanced effectively via a simple technique of cross-linking. The pseudo-second order dynamic model for the adsorption methods well-fitted more than the pseudo-first-order kinetics with R^2>0.999, thus indicating a chemisorption process. The Langmuir isotherm model fitted better with the adsorption process than the Freundlich isotherm with R^2 close to unity which showed a homogeneous phase with monolayer active sites. The recent advances in chitosan-based adsorbent materials for heavy metal removal [21-39] are summarized in Table 1.

Table 1. Chitosan-based adsorbent materials

Adsorbent	Metal Ions	q_{max} (mg/g)	pH	Isotherm/Kinetics	References
Fe_3O_4/SH/CS	Pb(II)	235.5	7.0	Langmuir Pseudo 2nd order kinetics	[21]
Fe_3O_4/ATP/ EDTA/CS	Pb(II) Cu(II) Ni(II)	368.3 267.9 220.3		Langmuir Pseudo 2nd order kinetics	[22]
MSCC/CS	Cu(II)	17.20	6.0	Langmuir Pseudo 2nd order kinetics	[23]
MKa/4%CB	Cd(II) Pb(II)	90.988.50	6.0	Langmuir Pseudo 2nd order kinetics	[24]
Fe_3O_4/SiO_2/CS/P	Pb(II)	0.75 L/g	1.0	Langmuir Pseudo 2nd order kinetics	[25]
M/CS/AnGC	Pb(II) Cu(II)	97.97 83.65	6.0	Langmuir Freundlich isotherms	[26]
CNT/CS	Fe(II) Cu(II) Pb(II) Zn(II)	68.8 57.1 50.4 16.6	5.0	Langmuir Pseudo 2nd order kinetics	[27]
CS/g/PMAm	Cu(II) Cd(II)	140.9 176.6	4-5	Langmuir Pseudo 2nd order kinetics	[28]
CS/HAP/Fe_3O_4	Cu(II) Zn(II)	3.659 6.497	5.50	Langmuir Pseudo 2nd order kinetics	[29]
Fe_3O_4/CS/BT	Cr(II)	62.01		Langmuir Pseudo 2nd order	[30]
CS/TA	Cu(II) Cd(II)	684.9 813.0		Langmuir	[31]
SA/CCS/P	Cu(II)	5.515		Langmuir Pseudo 2nd order	[32]
E/CS/M/BB	MO Cd(II) Zn(II)	305.4 63.3 50.8	5.0	Langmuir Pseudo 2nd order	[33]
EDTA/M/CS	Zn(II) Cu(II) Cd(II)	-	5.3	Langmuir Pseudo 2nd order	[34]
CS/Fe_3O_4	Hg(II)	-	3.0	Langmuir	[36]
Fe_3O_4/SiO_2/CS	Cr(VI)	336.7		Langmuir Pseudo 2nd order	[37]

Alginate-based adsorbents

Alginic acid or else its salt known as alginate is a biopolymer component of polysaccharides found in the colonies of a variety of algae species. It has a copolymer structure made up of layers of β-1,4-associated d-mannuronic acid (M-block) as well as α-1,4-linked l-guluronic acid (G-block) [38]. The existence of a 2 μm thick perforated holes wall of exine internal as well as the exterior surface of alginate, makes it easier for elements and compounds like heavy metals to adsorb. The recent advances in alginate-based adsorbent materials for heavy metal removal [39-44] are summarized in Table 2.

Ren et al. [39] produced new gel beads adsorbent from sodium alginate-carboxymethyl cellulose (SA/CMC) and utilized them to remove Pb(II) in a water mixture. The synthesis was successful via cross-linking of SA and CMC to enhance the adsorption of Pb(II). FTIR showed the functional groups of -OH and -COO in the complete synthesis of SA/CMC were responsible for complexation interactions with Pb(II). The authors verified parameters accountable for maximum adsorption of the Pb(II) and the results demonstrated that the initial adsorbate concentration was achieved at 5mg/L with adsorbent dose of 0.8g, and the temperature of 37 °C, and the vibration time of 18 hours. The adsorption experiment showed that Pb(II) adsorption unto the SA/CMC was greater than 99% under the optimum conditions. In addition, the author's comparative findings revealed that the Pb(II) removal efficiency of SA/CMC was significantly higher than that of traditional adsorbent CMC. Thus, they concluded that the SA could have improved the adsorption procedure possibly due to the functional groups on the SA. Additionally, the Pb(II) adsorption process unto the SA/CMC fitted the Langmuir adsorption isotherm, as well as the adsorption model depicted through a pseudo-second-order kinetic equation. Findings demonstrated that Langmuir R^2 value of 0.718, Freundlich value of 1.96, while the Temkin of R^2 was higher than 0.98. Thus, these demonstrated that both were homogeneous and heterogeneous adsorption sites of the adsorbent as well as both monolayer and multilayer surface sites were involved. The kinetic adsorption model also better fitted the pseudo-second order than the pseudo-first order indicating chemisorption than the physisorption process. Cordova et al. [40] developed a new adsorbent made of alginate (Alg) as a matrix with xanthation (XA) to form adsorbent (XA/Alg) and employed it to remove Cu(II)Zn(II). The purpose of introducing Alg was to enhance the adsorption of metal ions through its suitable functional groups. The important parameters were studied such as the effect of reaction time and findings demonstrated that time ranged (from 4-12 hours), the types of the base suitable to control the pH values were discovered to be (NaOH-KOH), and the quantity of carbon disulphide was (2-10%v/v) to obtain the green materials. NMR methods were used to analyze the XA/SA adsorbent and the evidence of β-removal was found at 5.45 ppm. The findings from the NMR experiment in solid-state revealed that a shoulder was achieved at 182 ppm attributed to the C-S group. The EDS mapping procedure also confirmed the existence of the thiol (S element), whereas XRD showed a semi-crystalline structure. The chemical shifts of δ(C=S) bands were at 863 to 805 cm^{-1}, and ν(C=S) bands were at 662 to 602 cm^{-1}. The findings showed that the maximum adsorption capabilities of Zn(II) and Cu(II) occurred up to 47.30 and 86.40 mg/g, respectively higher than for maximum adsorption capabilities of values were 6.497 and 3.659mg/g respectively for Zn(II) and Cu(II) obtained by Pooladi et al. [29]

Fuks et al. [41] synthesized a new adsorbent by the combination of Fe_3O_4 into calcium alginate gels (CaAlg) to form aggregate magnetic adsorbent material known as alginic ferrogels (Fe_3O_4/CaAlg), utilized for the removal of cationic radionuclides; Am(III), Sr(II), Cs(I) and Eu(III) from aqueous mixtures. The removal of cations of radionuclides was achieved through the direct dosing of the solution mixed with sodium alginate/iron carbonyl with a 2 hours continuous stirring. The purpose of introducing alginate was to improve the adsorption of radionuclides metals through the suitable functional groups of -OH and $-COO^-$ through the modification by CaAlg. The optimized factors were obtained at 15g/L of iron carbonyl suspended in 1 L of an aqueous solution of sodium alginate and the addition of about 20 g $CaCl_2$ to 1 L of the solution comprising the radioactive metals. These findings revealed that the percentage removals of the radionuclides were 30-100%. The author reported

the removal of cations of radionuclides were due to the calcium chloride ions exchange with Cs(I) which was less favorable because of the smaller charge of the ions except that it could be trapped in the adsorbent pores. On the other hand, the ions of Am(III) and Eu(III) could efficiently be removed from the aqueous solution much better than the monovalent Cs(I) and divalent Sr(II) ions. Consequently, the authors concluded that other metal salts could not considerably influence the removal efficiency as much as the roles played by the number of charges on the ions. Lee et al. [42] synthesized a new adsorbent by incorporating Ca/Alg, zinc-ferrocyanide (Zn/FC), and Cyanex 272 to yield an adsorbent composite beads of ZnFC-Cyanex 272-alginate (ZCA), which was then used to remove Cs(I) and Co(II) in water. The Ca/Alg beads were produced through the cation exchange and cross-linking between sodium alginate (Na/Alg) and calcium chloride ($CaCl_2.2H_2O$) in the presence of water. FTIR results showed the -OH, and -COO- in Ca/Alg, -CH stretching vibrations in ZnFC-Cyanex 272 as well as spectral peaks at 1164cm^{-1}, 960 cm^{-1}, representing the P=O and C-O-P stretching vibration respectively: thus, confirming the successful synthesis process. By comparing the adsorbent's performances (Ca-Alg and ZCA), the latter was greater than the former due to the presence of some suitable functional groups of -OH, and -COO- in ZCA adsorbents which were responsible for binding with the metal ions. The maximum adsorption capability for Cs(I) and Co(II) was 71.73, and 34.92 mg/g. respectively. The adsorption procedure fitted both Langmuir isotherm, as well as pseudo-second-order kinetics, to support the adsorption process, indicating the isotherm revealed homogeneous and monolayer surface interactions and a well-fitting chemosorption kinetic process. Additionally, the ZCA composite beads could demonstrate an exceptional selectivity toward Cs(I) and Co(II) despite the presence of competitive cations of K(I), Fe(II), Na(I), and Ni(II). Consequently, the authors concluded that ZCA composite beads could be reused 3 times after the adsorption-desorption studies and could still maintain their excellent potential for the selective removal of Co(II) and Cs(I) in contaminated water.

Song et al. [43] synthesized a new adsorbent of Ca/Alg and applied it for the removal of rare earth metals (i.e., La, Sr, and Li). The purpose of the composite through modification with alginate is to enhance the adsorption process. FTIR characterization showed the presence of -OH, -COO^-, and -C-O functional groups in the Ca/Alg. Findings revealed that the adsorption capacities of Ca-Alg adsorbent towards La(I), Sr(I), and Li(I) were 0.562. 6.695 and 8.625mg/g, respectively. However, the adsorption capacities were generally low because the amount of adsorption depended on the number of the valences of the metal ions which was related to electrostatic interaction. The kinetics model and the isotherm studies were explored for the adsorption process and the findings demonstrated that Li(I) did not fit into both the pseudo-second-order and the pseudo-first-order process at both high and low initial concentrations with the R^2 = 0.781 and 0.825 respectively, while data for Sr(I) and La(I) both matched the pseudo-first as well as the pseudo-second order with R^2 values 0.999 as well as 1.00 respectively. This favored at lower and higher concentrations suggesting that both were physisorption and chemisorption processes. Additionally, the Freundlich isotherm data were more fitted for the adsorption process for La(I), Sr(I), and Li(I) with an R^2 value of 0.981, 0.974, and 0.983, respectively, thus this was more than the Langmuir isotherm data with R^2 values of 0.928, 0.927 and 0.814 respectively, indicated a heterogeneous layer surface interaction. Furthermore, the presence of co-existing ions could not largely affect the adsorption process towards the removal of trace metal ions. Dai et al. [44] developed a unique polysaccharide-based thermos-receptive hydrogel adsorbent material made from SA as well as 2-hydroxy-3- isopropoxy propyl/starch (HIPS) to form (HIPS/SA) and utilized it for the Cu(II) removal. The complex and permeable structure, laden with carboxyl groups, was to provide enough adsorption sites necessary for Cu(II) removal. The FTIR characterization results clearly showed the presence of suitable functional groups of O-H, C-H, C-O-C, -COO- and C=O in SA, HIPS/SA to confirm the successful synthesis process. The BET surface area of HIPS/SA hydrogel was 2.7785 m^2/g, this was much greater than SA alone with 0.284 m^2/g surface area, thus indicating a good surface area for adsorption for HIPS/SA. The conditions for the adsorbent's thermal

reversible responsive swelling/shrinking actions of adsorbent were examined as well as the effects of pH as well as the initial amounts of Cu(II) on adsorption ability. These findings showed that adsorbent dosage of 50 mg, pH 5.5, shaking speed, 200 rpm, temperature, 20 °C, contact time of 48 hours, and initial amounts of 100 mg/L. The maximum adsorption capacities of SA gel, as well as HIPS/SA, were 21.11 and 25.80 mg/g respectively indicating that there was a significant increase in adsorption upon the modification of SA by the HIPS. The adsorption isotherms and kinetics of the adsorbent further demonstrated that the adsorption of Cu(II) onto the HIPS/SA adsorbent which was a better fit for the Langmuir as well as the pseudo-second-order models, with both R^2 as 0.999 and the maximum adsorption capacity for Cu(II) onto the HIPS/SA being 25.81 mg/g. Additionally, the adsorption studies revealed that the adsorbent could still be stable even after 5 cycles with the adsorption capacity of HIPS/SA decreasing from 19.83 to 15.23 mg/g.

Ahmed et al. [45] synthesized a new grafting polymer through the grafting of diphenylamine (DPA) on Na/Alg to form a composite (Na/Alg/g/DPA) adsorbent and applied it to remove Co(II) in wastewater solution. FTIR functional groups of -COOH, -COO-, -C-O, C=C, and C=N. From FTIR, they suggested a polymer structure, thus confirming that the grafting of DPA unto NaAlg in the synthesis process was successful. The adsorption performance of NaAlg-g-DPA was higher than NaAlg due to the existence of suitable functional groups as a result of the grafting of the DPA. The BET surface area of Na/Alg/g/DPA and Na/Alg was found to be 13.164 m^2/g and 2.4459 m^2/g, respectively, indicating that the grafting of DPA onto Na/Alg had greatly increased the surface area for the adsorption process, thus, making the adsorption of Co (II) more feasible. The enhancement of the external area for the one-step manufactured composite was linked to its mesoporous properties, which were crucial in Co(II) adsorption, according to the author's report. Additionally, the authors discovered that the best grafting efficiency was 97.5% at the initial concentration of 0.5M. The results of the kinetic study fitted well into the pseudo-second-order reaction mechanism of Na/Alg/g/DPA with adsorption capacity up to 17.2711 mg/g and an $R^2 = 0.9998$. Consequently, the linear plot, the second order kinetics model had $R^2 > 0.99$, indicating a chemisorption process. Additionally, the adsorption isotherms studies revealed that the Langmuir, Freundlich, and Temkin data were all fitted with a linear plot with the coefficient of determination, $R^2 > 0.9$ which indicated that the adsorption process was both homogeneous and heterogeneous surface interaction. Allouss et al. [46] used an ionotropic gelation approach to produce a new adsorbent from graphene-oxide (GO) combined with condensed carboxymethyl cellulose-Alginate (CMC/Alg) hydrogel nanoparticles as (CMC/Alg/GO) adsorbent and was applied to remove Cu(II) from water solution. FTIR results showed the presence of -OH, and -COOH functional groups in both graphene oxide and alginate to confirm the successful synthesis process and the functional groups were responsible for Cu(II) adsorption. The authors studied the adsorption of Cu(II) particles onto the adsorbent under various experimental settings and discovered that the best-optimized conditions were achieved at an adsorbent dosage of 2g/L, an initial amount of 150mg/L, a contact period of 90 minutes, a temperature of 398K, and a pH of 5. CMC, CMC/Alg, and CMC/Alg/GO were compared for the adsorbent's adsorption performances, thus results also demonstrated that embedded CMC-Alg/GO beads had a superior adsorption capacity to the natural CMC/Alg beads owing to a synergetic influence between the functional units of the GO and the CMC/Alg matrix. The adsorption capabilities at equilibrium for CMC/Alg, and CMC/Alg/GO, were 22.10 and 39.96 mg/g at 1% addition of GO. Subsequently, the adsorption capacity increases to 41.72 and 64.00 mg/g with the addition of 3 and 5% of GO, respectively, indicating that the adsorption capacity is GO dependent. It was clear that the modifications improved the adsorption process when the data were compared. Additionally, the pseudo-second-order adsorption kinetics was well fitted, with R^2 values varying from 0.7974 to 0.989 which was better than the values within the range of 0.953 to 0.995 fittings for the pseudo-first order. Furthermore, both the Langmuir isotherm model and the Freundlich isotherm showed the R^2 values of 0.999, indicating that both physisorption and chemisorption processes were the rate control mechanisms. The intraparticle distribution model was also investigated, with the conclusion that the

adsorption process was a progression of external adsorption as well as intraparticle distribution.

Hassan et al. [47] synthesized an efficient adsorbent by functionalizing a multi-walled carbon nanotube (CNT) ($CNT/CONH_2$) with an amide functional group ($CONH_2$) followed by an imprinted network of sodium alginate (NaAlg) containing hydroxyapatite (HAP) to form the new adsorbent (NaAlg/HAP/CNT). They then applied it to remove Co(II) from wastewater. The purpose of the $-CONH_2$ group addition and the modification was to enhance the metal adsorption process unto the adsorbent. The FTIR characterization revealed the presence of the functional group of -C-N from CNT, -CCOH from NaAlg, and the phosphate group from the HAP to confirm the successful synthesis process. The adsorption conditions were optimized and the findings revealed that the maximum adsorption capacity of Co(II) unto the NaAlg/HAP/CNT adsorbent was 394.5mg/g with a BET surface area of $163.4m^2/g$ greater than those of NaAlg/HAP with $33.1m^2/g$ and NaAlg/CNT with $72.9m^2/g$, indicating a good surface area for adsorption of Co(II). By comparing the adsorption capacities of adsorbents, it was discovered that NaAlg/HAP/CNT with 394.5 mg/g was greater than NaAlg/HAP with 355.2 mg/g and greater than NaAlg/CNT with 354.7 mg/g, indicating that that the adsorption capacities were enhanced through the modifications. Furthermore, the investigated kinetics model was found to be fitted into the pseudo-second-order and the Langmuir isotherm with the R^2 higher than 0.99 indicating a chemisorption process and a monolayer surface, respectively.

The adsorption process was both endothermic and spontaneous. The recent advances in alginate-based adsorbent materials for heavy metal removal [39-47] are summarized in Table 2.

Table 2. Alginate-based adsorbent materials for the removal of metal particles in aqueous mixtures

Adsorbent	Metal Ions	q_{max} (mg/g)	pH	Isotherm/Kinetics	References
SA/CMC	Pb(II)	-	5	Langmuir Pseudo 2nd order	[39]
XA/Alg	Zn(II) Cu(II)	47.30 86.40	7.0	-	[40]
Ca/Fe_3O_4/Alg	Sr (I)Cs (I) Eu(I)	30.00% 80.00% 71.73%	3.5-4.5	-	[41]
Ca/Alg/ZnFC	Cs(I) Co(II)	71.73 34.92	-	Langmuir Pseudo 2nd order	[42]
Ca/Alg beads	Cs(I) Sr(I) La(I)	01.64 93.82 99.30	7	Langmuir Freundlich	[43}
HIPS/SA	Cu(II)	25.81	4.5	Langmuir Pseudo 2nd order	[44
NaAlg/g/DPA	Co(II)	91.60	10.0	Temkin's Pseudo 2nd order	[45]
CMC/Alg/GO	Cu(II)	-	5.0	Langmuir Pseudo 2nd order	[46]
NaAlg/HAP/CNT	Co(II)	394.5	8.4-9.3	Freundlich Pseudo 2nd order	[47]

Sporopollenin-based adsorbents

Lycopodium clavatum (sporopollenin, (Sp)) is among the biopolymer materials which can be utilized as an adsorbent with an exceptionally safe biomacromolecule. It exists freely in nature as a segment of the external mass of spores and dust which makes it impervious to attacks by inorganic acids and soluble bases [49]. It possesses an exceptional property that can stay in topographical layers for more than a century while maintaining its full morphological qualities, and this proposed great steadiness of Sp at exceptional requirement. However, the complete chemical structure of the Sp is yet to be discovered, and it also has a stable inter-chain ring structure of aromatic compound containing carbon, hydrogen, and oxygen in a stoichiometry of $C_{90}H_{144}O_{27}$. Moreover, its functional group is the hydroxyl structure making it accessible for modification in huge quantities. Along these lines, the hydroxyl group fills in as anchorage targets for metal atom complexation just as an extension of the needed surface functional group and with the combination of different other materials with high affinity for metal [44]. MNPs can be manipulated with Sp to give magnetic sporopollenin (Msp). These manipulations of Msp have been reported to be utilized in the removal of a wide range of poisons, for example, metal ions pollutants [49].

The various Sp-based adsorbent materials for the removal of heavy metal particles in water solution are summarized in Table 3 [51-56]. Furthermore, Sayin, et al. [51] synthesized a new adsorbent calix[4]arene Sp-based on the adsorbent (SP-Calix) and applied it for the removal of Cr(VI) from an aqueous mixture. The adsorbent was made through the method of immobilization of dihydrazine amide derived from p-test-butylcalix [4] arene on the modified Sp. FTIR characterization. The results showed the presence of the required functional groups of carbonyl and isocyanate to confirm the successful synthesis process. The batch-wise adsorption method of analysis was used to optimize numerous experimental factors and the results were achieved at pH 5, shaking speed 175 rpm, initial concentration 1.0 x 10^{-4}mmol/dm^3, and temperature of 25 °C. Additionally, the maximum adsorption capability was calculated to be 28.07 mg/g. The isotherm study showed that among the three isotherms; Langmuir, Freundlich, and Dubinin-Radushkevich, Freundlich were all found to be the most suitable to describe the adsorption process with the R^2 value close to unity. Meanwhile, the R^2 value for Langmuir was 0.8945. Additionally, the thermodynamic study showed that the value for ΔH, ΔS, and ΔG were found to be +41.01, +222.48, and +30.88KJ/mol which indicated endothermic, randomness, and spontaneous sorption process. Ünlü & Ersoz, [52], synthesized the new adsorbent dithiocarbonate/sporopollenin (DTC/SP) and applied it for Pb(II), Cd(II) as well as Cu(II) metal ions removal. The purpose of introducing sporopollenin was to enhance the adsorption performance of the dithiocarbonate. FTIR results showed the presence of the functional groups of DTC-SP was well captured from the functional groups of DTC and Sp to confirm the successful synthesis process. DTC/SP could adsorb metal ions better than the DTC when comparing the adsorbents, due to the presence of the functional groups of Sp. The mechanism of interaction was that of the DTC/SP chelating exchanger process. The operating pH for Cd(II), Pb(II), as well as Cd(II) metal particles were 7, 5.5, and 4, respectively, and the contact period ranged from 30 min to 7 hours, according to the author's findings. The isotherms studies revealed the maximal adsorption capacities for disclosed Cd(II), Pb(II), and Cu(II) were 7.09, 94.73, and 17.35 mg/g, in that order. The Langmuir R^2 values for the metal ions of Cu(II), Pb(II), as well as Cd(II), were 1.00, 0.9976, and 0.9951, respectively indicating a good fit process, and a homogeneous adsorbate and a monolayer surface interaction. Additionally, the Freundlich correlation coefficients R^2 for Cd(II), Pb(II), and Cu(II) were 0.9225, 0.9949, and 0.9572 in that order, while the Dubinin-Radushkevich(D-RK) R^2 value for Cu(II), Pb(II), as well as Cd(II), were 0.9795,0.9992, and 0.949, respectively. Both Langmuir and D-R isotherms were foreseen by the isotherm with homogeneous and conventional surfaces, i.e., homogeneous, and heterogeneous surfaces of the adsorbate unto the monolayer and multilayer sites of the adsorbent, hence, both Langmuir and D-R isotherms were predicted. Furthermore, the kinetic forecast of the pseudo-second-order process with R^2 values of 0.9975, 0.9996, and 0.9997 for Cu(II), Pb(II), and Cd(II) respectively, outperformed the fit for the pseudo-first order process

with R^2 values of 0.9791, 0.9902, and 0.9548 for Cu(II), Pb(II), as well as Cd(II) in that order. Furthermore, the thermodynamic parameters ΔH^o, $\Delta S^{o,}$ and ΔG^o values were computed as endothermic, randomness, and spontaneous after the graphical reading of the investigational data for the adsorption of Pb(II), and Cu(II), as well as Cd(II) ions to the DTC-SP. On top of this, the mechanism for the process of adsorption was revealed to be an ion exchange process in which the DST/SP is behaving as a chelating exchanger because the functionality present on the DST and adsorption took place through the exchange of valences between the resin and the adsorbent.

Hassan et al. [53] synthesized a new effective adsorbent through APTES functionalized magnetic sporopollenin-based silica-coated ($MSp/SiO_2/NH_2$) and graphene oxide (GO) to form $GO/SiO_2/MSp/SiO_2/NH_2$ and applied for hazardous Pb(II) ions removal from aqueous solution. The purpose of the modification and functionalization of the GO was to hance the adsorption process. FTIR characterization results showed the presence of the -OH, and –COOH which confirmed the successful synthesis process, and these functional groups were responsible for the adsorption of the metal ions. The researchers discovered that the new adsorbent $GO/SiO_2/MSp/SiO_2/NH_2$ at the optimized experimental conditions of pH 6, with a 20 mg amount of adsorbent dosage, initial concentration of 100 mg/L the highest adsorption capabilities realized for Pb(II) was 323.5 mg/g. The adsorption process was studied by utilizing the Langmuir and Freundlich isotherms, and the kinetics with pseudo-first order along with pseudo-second-order models. Findings from this study revealed Langmuir isotherms with an R^2 value of 0.9994 fitted better than the Freundlich adsorption isotherm with an R^2 value of 0.5129. Meanwhile, the maximum adsorption capacity was found to be 323.5 mg/g for Pb(II). Additionally, findings showed that the pseudo-second order proved a better fitted with an R^2 value of 0.9999 for Pb(II) than the pseudo-first-order with R^2 values of 0.4262. In the same manner, the models affirmed a multilayer adsorption process followed by a chemisorption and physisorption model for the targeted metal ion. The thermodynamic study showed ΔH value of +99.901KJ/mol, ΔS value of +0.349KJ/mol, and ΔG value of -6.627KJ/mol indicating endothermic, randomness, and spontaneous process. The authors discovered that the generation studies showed that the potential of the adsorbent only decreased by 8.6% after the 10th round with adsorption capacity maintained at 295m/g thus showing a good recovery, eco-friendly and consequently concluded that the adsorbent shows good future potential to remove lead ions from wastewater.

Ren et al. [54] created a new modified EDTA/chitosan-SiO_2-Fe_3O_4 (EDCMS) adsorbent and used it for the removal of heavy metal ions (Pb(II), Cu(II), as well as Cd(II) from water solution. CMS was created by modifying the surface of chitosan-SiO_2-Fe_3O_4 with EDTA on top of the water/soluble carbodiimide as a cross-linker in a buffer blend. The purpose of EDTA was to enhance the adsorption process. FTIR characterization showed the functional groups of C=O, COO-, and N-H to confirm the successful synthesis process due to the combination of CMS and EDTA via the amide bonds. The most effective optimized conditions for the heavy metal ions removal by the EDCMS were achieved at pH 5, the dosage of 1.0g/L, and contact duration of 360 minutes. The maximal adsorption capacities of EDCMS for Cd(II), Pb(II), and Cu(II) ions were 64,41, 108.98, and 48.55 mg/g, respectively. The Langmuir isotherms investigation supported the sorption process with R^2 values of 0.996, 0.995, and 0.999 for Cd(II), Pb(II), as well as Cu(II), respectively, over Freundlich, with R^2 values of 0.812, 0.912, and 0.947 for Cu (II), Pb(II), and Cd (II) ions respectively. The kinetic study fitted well into the pseudo-second order with R^2 values of 0.999 for Cu(II), Pb(II), and Cd(II) ions, respectively, better than the pseudo-first order with R^2 values of 0.918, 0.980, and 0.906 for Cu(II), Pb(II), and Cd(II) ions correspondingly. Furthermore, both the EDCMS and CMS adsorption kinetics isotherm supported the mechanism of the pseudo-second-order kinetic model, and their equilibrium data were successfully matched with the Langmuir isothermal model. Additionally, at pH 5.0 (25 °C), the maximum adsorption capability of CMS was found to be 2.54, 9.32, and 55.64 mg/g for Cu(II), Pb(II), and Cd(II) ions, respectively, demonstrating the selective adsorption of Cu(II) ions, while the values of EDCMS were 64, 41, 108.98 and 48.55 mg/g, for Cd(II), Pb(II) and Cu(II) ions

correspondingly. The maximum adsorption capacities of EDCMS and CMS towards the removal of metal ions when compared clearly showed that the presence of EDTA enhanced the adsorption process through the modifications. Both EDCMS and CMS adsorption processes were endothermic, and the recycle studies demonstrated that after 12 rounds of reusability, EDCMS decreased by roughly 25% of its adsorption ability for heavy metal ions.

Recently, Bilgic et al. [55], prepared new adsorbent materials from a boron dipyrromethene (BODIPY) derivative which was immobilized on a sensor, then modified on 3-(Aminopropyltrimethoxysilane (APTES) to produce a microcapsule fluorescent sensor adsorbent (Sp/APTES/monoBODIPY) and applied it for Cu(II) the removal and selective sensitive detector. The Cd(II) used was from alkaline mixtures. FTIR results showed the presence of functional groups such as C=C, C=O, and -C=O, Si-O, OH, $-NH_2$ as well as the C-N bond present in both Sp-APTES and Sp-APTES-monoBODIPY adsorbent to confirm the successful synthesis process and the functional groups were responsible for the removal of Cu(II). The adsorbents Sp/APTES/monoBODIPY and Sp/APTES, when compared, in terms of adsorption performance, the former could adsorb Cu(II) better than Sp-APTES due to some suitable functional groups which was confirmed by FTIR. The maximum adsorption capacity of the Sp/APTES/monoBODIPY adsorbent unto Cu(II) was 25 mg/g. The authors reported that both the kinetics model and isotherms study revealed that pseudo-second-order kinetics and Langmuir adsorption were both fitted into the adsorption process with R^2 higher than 0.99.

Ahmad et al. [56] synthesized a new adsorbent of piperazine-functionalized/magnetic/sporopollenin hybrid adsorbent (MNPs/sp/HEP) and applied it used for the removal of Pb(II) as well as As(III) in water. The purpose of the functionalization with the HEP is to enhance the process of metal adsorption. FTIR results showed the presence of the functional groups of -OH. -COOH, C=N, and $-NH_2$ confirmed successful synthesis processes and the functional groups were also mainly responsible for the adsorption of the metal ions. The metal ions removal under optimized parameters was achieved through a batch-wise method with optimum adsorption capacities (q_m) be 13.36 mg/g and 69.85 mg/g for the Pb(II) and As(III), respectively. The experimental data analysis using the non-linear equations for the Langmuir and Freundlich isotherm model was additionally investigated. The findings revealed that the R^2 values of the linear for Pb(II) demonstrated higher for the non-linear plot for the analysis of both isotherms. However, the opposite results are shown in AS(III), where the R^2 values for the non-linear plot for both isotherms were relatively higher than the linear. Hence, AS(III) fitted better with the non-linear plots. The thermodynamic studies of the adsorption process revealed that the removal of both Pb(II) and As(III) ions was spontaneous and exothermic as ΔG and ΔH were both negative according to the findings by the researchers. This proved that the association of the adsorbate at the solid/solution interface was a random process. When comparing adsorbents performance, MNPs/sp/HEP showed a 119% rise in maximum adsorption capacity for Pb(II) as compared to MNPs/sp. This might be due to competition among the Pb(II) and As(III) ions for the insufficient active adsorption sites on MNPs/sp/HEP. Thus, based on the results the new adsorbent MNPs/sp/HEP proved to be an effective material for metal ions removal from aqueous solutions. Sargına et al. [57] synthesized natural polymers as biosorbents from two biomacromolecules and applied them for heavy metals removal. The components of the adsorbent were Cs, a versatile derivative of chitin, and Sp, a biopolymer with outstanding mechanical properties, and great resistance to chemical and biological reactions to form CS/Sp microcapsules which were prepared via a cross-linker. FTIR characterization showed the functional groups of hydroxyls, and carbonyl/carboxyl to confirm the combination of CS and Sp to form CS/Sp microcapsules. The adsorption performance of the microcapsules (CS/Sp) and the natural CS applied for the removal of Cu(II), Cd(II), Cr(III), Ni(II), and Zn(II) ions at various metal ions concentration, pH, amount of adsorbent, temperature, and contact time. The adsorption isotherm model fitted the Langmuir isotherm data and the adsorption capacity of the CS beads was found to be 85.16, 86.56, 51.47, 34.04, and 46.42 mg/g for Cu(II), Cd(II), Cr(III), Ni(II), and Zn(II), respectively. While,

the CS/Sp beads showed greater affinity for the ions at 92.78, 179.85, and 47.54 mg/g for Cu(II), Cr(III), and Ni(II), respectively, values of 16.86 and 16.34 mg/g for Cd(II), and Zn(II) were lower, respectively. Thus, the study revealed that the Sp enhanced ion sorption capacity of Cd(II) and Zn(II). Additionally, these findings from the adsorption isotherm studies revealed that both the Langmuir and the Freundlich isotherm fitted the adsorption process indicating both homogeneous and heterogeneous adsorbate and both monolayer and multilayer adsorbent interaction were involved. These authors stated that sporopollenin itself had an affinity for the metal ions due to the functional hydroxyl, carbonyl/carboxyl, and ether moieties present in its structure. Sargin et al. [58]synthesized bio-based sorbents, chitosan/sporopollenin (CS//Sp) especially by cross-linked chitosan (CS), with glutaraldehyde (GA) and combined with Sp to form (CS/GA/Sp) and applied for the removal of heavy metal. The metal adsorption behavior of chitosan-based sorbents was largely affected by the kind of cross-linking agent and degree of cross-linking. In the study, the authors described the preparation of chitosan/sporopollenin (CS/Sp) microcapsules cross-linked with various amounts of chitosan/glutaraldehyde (GA) ratios. The CS/GA/Sp were modified with 0.3, 0.9, and 1.5 mL of GA solution (in 25% water v:v) for 1.50 g of Cs. FTIR characterization. The results showed the presence of the functional groups of -OH, -C-N, -C=N, and -NH_2 to confirm the successful synthesis process. The adsorption performance of the microcapsules was studied for the removal of Cu(II) at different optimized conditions such as concentrations, contact time, amount of adsorbent, temperature, and pH. These findings showed that the maximum adsorption capacities of Cu(II) removal based on 0.3, 0.9, and 1.5mL GA impregnated CS microcapsules, which were 88.9, 100.4, and 80.7 mg/g, respectively. This indicated that the adsorption process could be best achieved at 0.9mL of GA. The outcomes of the investigation of the equilibrium adsorption isotherm data of the microcapsules demonstrated a better fit to the Freundlich isotherm model than the Langmuir isotherm data. Additionally, the affinity of the CS microcapsules towards Zn(II), Cd(II), Ni(II), and Cr(III) in presence of Cu(II) was revealed upon further investigation. Similarly, the findings revealed that the GA/Cs ratio could greatly affect the metal ions adsorption performance and the physicochemical nature of the microcapsules. Consequently, the results unveiled, implies that when CS microcapsules were cross-linked with 0.9 mL of GA solution, this could give a superior Cu(II) ion adsorption capacity and could be cost-effective sorbents in water treatment. The sporopollenin-based adsorbent materials for the removal of heavy metals in water solution are summarized in Table3 [48-60].

Tannic acid-based MNPs adsorbents

Tannic acid (TA) is a natural organic polyphenol comprising sugar esters. Researchers have been modifying MNP with tannic acid to enhance surface properties and adsorption capacity [61]. Tannic acid, a humic substance comprising carboxyl and hydroxyl functional groups was a well-established metal scavenger, due to the abundant phenolic hydroxyl and carbonyl functional groups on the framework. The complexation and precipitation of polyphenols with polyvalent cations in aqueous mixtures were well understood from the works of the earlier investigator that the nano adsorbent (Fe_3O_4/TA NPs) had possible applications to remove metals from aqueous systems [62]. While some other industrial application of TA is known to be an adsorbent to remove various kinds of chemical species, it is also known to contain hydroxyl groups which show affinity as adsorbents for metal ions recovery [62,63].

Table 3. Sporopollenin-based adsorbents

Adsorbent	Metal Ions	q_{max} (mg/g)	pH	Isotherm/ Kinetics	References
P-t-bCalix/Sp	Cr(VI)	-	1.5	Freundlich	[51]
DTC/SP	Cu(II) Pb(II) Cd(II)	-	4	Langmuir	[52]
MSp/ SiO_2/NH_2	Pb(II)	325.5	6.0	Langmuir	[53]
EDCMS	Cu(II) Pb(II) Cd(II)	-	5.0	Langmuir Pseudo-2nd order	[54]
Sp/APTES/ monoBODIPY	Cu(II)	25		Langmuir Pseudo-2nd order	[55]
MNPS/sp/ HEP	Pb(II) As(III)	-	6.5	Pseudo-2nd order	[56]
CS/Sp microcapsules	Cu(II) Cd(II) Cr (II) Zn(II) Ni(II)	-	-	Langmuir	[57]
CS/GA/Sp	Cu(II)	100.4	-	Freundlich	[58]

Zou et al. [64], used a simple coordination procedure to produce a novel TA-based adsorbent (TA/Zr) and used it for the removal of Pb(II). The purpose of the TA is to introduce some phenolic carboxyl functional groups to enhance the metal ions adsorption process. FTIR characterization results confirmed the presence of some prominent phenolic hydroxyl and carbonyl functional to show the successful synthesis process. Batch adsorption experiments were used to explore the effect of varied initial Pb(II) concentrations on the adsorption capabilities of TA/Zr. The author's findings, disclosed that the maximum adsorption capability was achieved as 99.0 mg/g at 25 °C and an initial Pb(II) concentration of 170 mg/L. The Langmuir, as well as Freundlich models R^2 value of 0.99, which were well fitted into the adsorption process showing monolayer Pb(II) adsorption on the surface of TA/Zr with the theoretical maximum adsorption capacity of 100 mg/g. The results explored for the kinetics of Pb(II) adsorption onto TA/Zr demonstrated that the pseudo-second-order > pseudo-first-order model, indicating that chemisorption was the dominant process. TA/Zr had adsorption selectivity for Pb(II) which was further investigated when mixed with binary solutions such as Zn(II), Cu(II), Co(II), Cd(II), Ni(II), and Pb(II) at a concentration of 150 mg/L. The Pb(II) removal was 64.62 mg/g significantly higher than the removal of other metal ions by the TA/Zr with values of 1.26, 3.68, 4.39, 1.14, 3.94 mg/g, for Zn(II), Cu(II), Co(II), Cd(II), Ni(II), respectively. Therefore, TA contributed substantially more to TA/Zr selectivity than the Zr species. Furthermore, the authors inferred that the presence of phenolic hydroxyl (e-OH) structures on the

surface of TA was responsible for the significant adsorption in which the hydroxyl groups of oxygen atoms synchronized with Pb(II), while hydrogen atoms of hydroxyl groups could be substituted and released as hydrogen ions, in this way showed, a proton exchange mechanism for the selective Pb(II) removal, as confirmed by the results of the characterization and batch adsorption assessments. Huang et al. [65] used a fast and scalable production strategy to produce tannin-based magnetic permeable organic polymers (TA/MOPs) adsorbent for the removal of methylene blue (MB) as well as Pb(II) from water mixtures by using workable tannin acid as construction blocks through an azo connection reaction without losing any phenolic eOH groups. FTIR characterization results showed the presence of some prominent phenolic hydroxyl and carbonyl functional to confirm the successful synthesis process. The results of VSM characterizations showed the value TA/MOPs saturation magnetization which was 17.6 emu/g. This indicated that the amount of MNPs separated throughout the reaction process could be controlled. For the BET surface area of TA/MOPs, results showed the presence of high unique surface areas of 110.7 m^2/g for adsorption process, and plentiful phenolic eOH groups which were capable of providing ultrahigh adsorption capacities and quick adsorption kinetics. The researchers also discovered that MB and Pb(II) adsorption equilibrium capacities of 1696mg/g and 252 mg/g, in that order, could be achieved in 10 min of contact time. The subsequent linear R^2 obtained from the pseudo-first-order model were 0.9425 and 0.9425 for MB and Pb(II), respectively. While the pseudo-second-order model, finely matched better with a high positive R^2 of 0.999 and 0.9908) for MB and Pb(II) respectively. Thus, the rate-controlling step for both Pb(II) and MB adsorption revealed chemical adsorption. The Langmuir isotherm data with an R^2 value of 0.999 was more suitably fitted than the Freundlich isotherm with an R^2 value of 0.9768 which indicated a monolayer chemisorption process governing the interactions of the components. Consequently, the outstanding stability and superparamagnetic attraction properties of the adsorbent could allow 5 cycles with great results without any substantial performance degradation (i.e., the adsorbent still retains over 90% of its adsorption potential), thereby justifying the low-cost efficiency.

Huang et al. [66], formulated an adsorbent from polyethylene polyamine (P/P) and tannic acid (TA) as (P/P/TA), and encapsulated them with Magaly-layered double hydroxide (LDH), to form an adsorbent (LDH-P-P/TA) and to remove Cu(II). The FTIR showed the broad spectral band at 3478cm^{-1} for -OH due to LDH, 3478 cm^{-1} spectra shifted to 3446 cm^{-1} due to the formation of LDH/PP/TA, while spectral bands at 2880-2960 cm^{-1} corresponded to C-H stretching vibration. New bands formed at 1707cm^{-1} and attributed to TA and new bands at 1500 cm^{-1} stand for C=C vibrational band in benzene and 1350 cm^{-1} for C-O stretching vibration for TA acid groups and 1199 cm^{-1} due to TA esters groups thus, confirming the successful synthesis process. The optimized conditions were all investigated as, contact time, solution pH, starting Cu(II) concentration, and temperature. The produced adsorbents LDH, PP/TA, and LDH/PP/TA gave the maximum adsorption of Cu(II) as 23.39, 27.78, and 41.56 mg/g respectively. Therefore, this indicated a progressive rise in the adsorption capacities with modifications. The adsorption ability of Cu(II) was considerably increased when LHD was added to the PP/TA polymer. Furthermore, the adsorption of Cu(II) onto the LDH/PP/TA was fitted into the pseudo-second order with an R^2 value of 0.997, as against the pseudo-first order with an R^2 value of 0.9766. In addition, the calculated qe full term? (qe) was close to the experimental with values of 42.62 and 41.56 mg/g in that order, indicating a good fit. Additionally, the isotherm favored the Langmuir isotherm over the Freundlich isotherm data, with an R^2 value of 0.9897 and 0.8488 respectively. Furthermore, the thermodynamic adsorption capacity was 58.70 mg/g with ΔG = -8.25KJ/mol and ΔH = 22.97KJ/mol, thus, revealing that the adsorption procedure was spontaneous as well as endothermic. The mechanisms of interaction were shown to be primarily mediated by electrostatic and complexation interactions towards the removal of Cu(II). Shi et al. [67], fabricated (TA/CS/MOF) a membrane-type adsorbent by blending and depositing chitosan, TA, and metal-organic structure (MOF, UIO-66) on the surface of polyether sulfone (PES) membrane. The adsorption-desorption of N_2 isotherm

demonstrated the specific surface area of TA/CS/MOF reduced from 598.2m^2/g to 135.77m^2/g after the addition of UIO-66 which reduced the pore volume to confirm the success of the modification in the synthesis process. FTIR characterization showed the presence of -OH, -C-O-C, and -NH_2 to confirm the synthesis process. The SEM images of MOF showed an open-pore surface, while TA/CS/MOF image confirm the successful coating. All these results showed that the MOF contributed a core to the disperse of the tannic acid/chitosan mixture in order to enhance the removal of pollutants. Additionally, under optimized conditions, the findings showed that when the proportion of MOF/Chitosan was combined, at 30%, pH at 3.5, and then the filtration for 200min, the pollutant removal achieved 99%. The improved driving force induced by the concentration polarity in the filtration was assumed to alter the capacity of the adsorbent in the dynamic filtration, which proved a pollutant load-up capacity was 3 times better than that of the static adsorption. The findings from the dynamic filtration process demonstrated that the data fitted both the pseudo-first order and pseudo-second order for most of the adsorption processes for the adsorbate with the $R^2 \geq 0.99$, suggested the process as a chemisorption rate-controlling step. Similarly, the Elovich model fitted the data with the value of $R^2 \geq 0.99$ which showed that the diffusion was also influenced by the adsorption process.

Liu et al. [68], produced adsorbents from, poly(tannin-hexamethylenediamine) (PTHA), by changing the mole proportion of TA as well as hexamethylenediamine (HA) in a one-pot combination to produce a new adsorbent (PEG/PTHA) to remove Cr(VI). The results given were based on the effectiveness of Cr(VI) removal versus all made adsorbents according to the mole ratio formulation. The PEG/PTHA demonstrated an excellent adsorption performance with the mole ratio at TA/HA as 1:12.5. FTIR characterization results showed the presence of some phenolic hydroxyl and carbonyl functional to confirm the successful synthesis process. The adsorption experiment's optimum conditions were achieved at 24 h, pH 2 to 6, and an initial amount of 100mg/L. The process of adsorption for the kinetic equation was demonstrated to conform to the pseudo-second-order isotherm model with an R^2 value of 0.99293 which was better than the pseudo-first-order kinetic, R^2 value of 0.97335. This showed the chemisorption process dominating. Additionally, the highest adsorption capacity for the removal of Cr(VI) was 283.29 mg/g at 30 °C, depending on the isothermal curve appropriately described by the Langmuir model. On top of that, findings from the isotherm analysis revealed that Langmuir isotherm proved superior (R^2 =0.9939) over Freundlich (R^2 = 0.9084) specified homogeneous adsorbate and monolayer as surface interactions. Meanwhile, the authors discovered and stated that the amount of highly toxic Cr(VI) had remained lowered to the less toxic Cr(III) for the duration of the adsorption process. Gao et al. [69], created a new adsorbent from TA/templated mesoporous silica nanoparticles (T/MSNs) by using a simple non-surfactant template technique. The dopamine functionalized T/MSNs to form (Dop/TMSNs) adsorbent, achieved by using a superficial and biomimetic coating approach and used to remove Cu(II). The purpose of functionalization of Dop on top of T/MSNs was to enhance the process of adsorption of the Cu(II) from an aqueous solution. FTIR characterization results showed the presence of some prominent phenolic hydroxyl and carbonyl functional to confirm the successful synthesis process. The results of the adsorption under optimized conditions were achieved at an initial concentration of 100 mg/L, a temperature of 298 K, a contact time of 180min, a pH of 5.5, and an adsorbent dose of 1.0mg/L. Additionally, the kinetic model investigation revealed that the pseudo-second-order model was better preferred (R^2 = 0.995), above the pseudo-first-order model (R^2 =0.827). Meanwhile, the calculated adsorption capacity for the pseudo-second-order model was 45.4 mg/g, close to the experimental value of 42.8 mg/g. Furthermore, the results of the adsorption isotherm model revealed that the Langmuir model had a better fit with an R^2 value of 0.994 as compared to the Freundlich model's R^2 value of 0.948. This implied a homogenous adsorbate process and a monolayer adsorbent active site interaction. Moreover, Langmuir model's adsorption capacity was 58.7 mg/g, which was close to the experimental value of 55.6 mg/g. As for the K(I) and Na(I) concentrations had only a little impact on the adsorption process. The adsorbent's adsorption capacity was maintained at 89.2% efficiency

even after four recycling rounds. Yun Zhang et al. [70], developed a novel adsorbent multi-functional polymer hydrogel (Zr/DETA/TS) with a three-dimensional network structure and used it for the removal of Pb(II), Hg(II), as well as CrO_2(IV) via organic-inorganic crosslinking. FTIR characterization results showed the presence of amino, hydroxyl, carbonyl, and phenolic hydroxyl in the as-prepared composite adsorbent to confirm the successful synthesis process, which was responsible for the metal adsorption process. The peak spectral band at 150cm^{-1} due to N-H bending vibrations of amino in the adsorbent was shifted to 1494 cm^{-1} as well as 1497 cm^{-1} after the adsorption of Pb(II) and Hg(II), respectively, indicated that ionic exchange and electrostatic interactions were the major adsorption mechanisms for Pb(II) as well as Hg(II) removal, while electrostatic attraction, inner-sphere complex, and esterification played a significant role in CrO_2(IV). The optimal parameters for Pb(II), Hg(II), as well as CrO_2(IV), were 200mg/L initial concentration, 780 min contact time, and pH 5, respectively. The Langmuir model adsorption capacity was 384.61, 416.66, and 125.00 mg/g for Pb(II), Hg(II), as well as CrO_2(IV), respectively. The Langmuir model, fitted better with R^2 values of 0.9957, 0.9930, and 0.9949 for Pb(II), Hg(II), as well as CrO_2(IV), than the Freundlich model, with R^2 values of 0.8314, 0.8817, and 0.8435, while the Dubinin-Radushkevich(DRK) isotherm model, with R^2 values of 0.9750, 0.9422, and 0.8940 for Pb(II), Hg(II), as well as CrO_2(IV). The pseudo-second order was also found to be better at fitting the data than the first order, as shown by the kinetic models, which had R^2 values of 0.9995, 0.9999, and 0.9973, respectively. This indicated a chemisorption process over the pseudo-first order model, which had values of 0.9598, 0.9728, and 0.8290 for Pb(II), Hg(II), and CrO2(IV), respectively.

Deng et al. [71], fabricated out of MnO_2(Mn), polyethyleneimine (PEI), and TA, which was a new adsorbent called (Mn/PEI/TA) and used it to remove Cu(II) and Cr(VI) from effluent solution. FTIR characterization showed phenolic hydroxyl groups on the surface of TA and O-N on the surface of functional groups on the MnO_2. This improved the removal of metal ions by complexation. According to the results of the experiment, the maximal adsorption capabilities of the Mn/PEI/TA adsorbent towards Cu(II) as well as Cr(VI) were 121.5 and 790.2 mg/g correspondingly. The physicochemical interaction mechanism in the process of Cu(II) and Cr(VI) co-adsorption on the Mn/PEI/TA was also described using the surface complexation structure model. The complexation, solvation action, electrostatic force, and adsorbate-adsorbate lateral interaction, could be the factors for spontaneous interactions. Although chemical action was the major force significant to adsorption equilibrium, physical electrostatic contact was discovered to be the dominant factor in the primary stage. The scientists then remarked, however, that studying the adsorption on the adsorbent's surface, demonstrated that the Cr(VI) reacted with a few reducing agents. These reducing agents converted it into Cr(III) with the help of functional groups (hydroxylamine-NH_2). The understanding of the adsorption mechanism could have aided in the advancement of heavy metal adsorbents and the addition of PEI/TA considerably aided the adsorption process, demonstrating that the Mn/PEI/TA adsorbent nanocomposite. Consequently, the authors discovered that the results from adsorption-desorption studies revealed that the adsorption capacity was reduced by 12% after recycling 5-times, showing favorable adsorbent for removing heavy metal ions. Zhu et al. [72] prepared TA-based on graphene aerogel adsorbent via the hydrothermal method by incorporating both graphene oxide(GO) and TA in a one-step method to form aerogel composite adsorbent (TRGA) and applied it to the removal of Pb(II) and Cd(II) from wastewater. FTIR results showed the presence of -OH broadband at 1120cm^{-1}, and spectral peaks in 1750, 1695 cm^{-1}, and 1614 cm^{-1}. They were due to the stretching vibration of the ester group and ketone groups. The spectral, C=O. 3383 cm^{-1} peak appeared for -OH groups while the peak at 1695 cm^{-1} and 1614 cm^{-1} disappeared to confirm that GO was present. BET surface area was confirmed to have a value of 122.2 m^2/g with high porosity to enable the adsorption of metal ions. The TRGA maximum adsorption capacity toward Pb (II) and Cd (II) was achieved at 803.84 mg/g and 395.80 mg/g, respectively at pH 4. Findings from the isotherm studies revealed that both Langmuir and Freundlich's isotherm could adequately explain the adsorption process with R^2 values of 0.9924 and 0.9741, respectively.

Ucer et al. [73], developed a new TA immobilized on activated carbon (TA/AC) adsorbent and used it for the removal of Fe(III), Mn(II), Zn(II), Cd(II), and Cu(II)FTIR characterization results. This showed the presence of -COOH and -OH functional groups which were known to be metal ions scavengers. The optimal adsorption parameters were achieved at pH 2-8, a contact period of 60 min, and an adsorbent dosage range of 0.02-2mg. The percent metal ions removed for Zn(II), Cd(II), Cu(II), Mn(II), as well as Fe(III) under optimum conditions were 49.0, 60.1, 89.0, 45.0, and 70.4%, respectively at pH ranging from 5-8. Furthermore, the isotherm adsorption data revealed, that both Langmuir and Freundlich could appropriately explain the adsorption process. Langmuir R^2 values for Zn(II), Cd(II), Cu(II), Mn(II), as well as Fe(III) were 0.989, 0.965, 0.992, 0.990, and 0.966, correspondingly, while Freundlich R^2 values for Zn(II), Cd(II), Cu(II), Mn(II), as well as Fe(III) were 0.978, 0.955, 0.905, 0.989, and 0.935 correspondingly. Furthermore, the order of attraction based on removal by TA/AC and natural carbon was similar, with Mn(II) < Zn(II) < Cd(II) < Fe(III) < Cu(II) and electronegativities values being identical. Furthermore, in separate systems, the adsorption capacity of TA/AC increasing order of Mn(1.13) < Zn(1.23) < Cd(1.51) < Fe(1.77) < Cu(2.23) and in Cu(II) mixed competitive systems, Mn(1.11) < Zn(1.19) < Cd(1.48) < Fe(1.56) also in increased order. Thus, the principal adsorption mechanisms participating in the binding of metal ions were a combination of complex formation, ion exchange, and surface adsorption activities. Findings from the reusability study showed that the adsorbed-desorbed metal ions efficiently ranged from 90.2 to 98.4% by utilizing 0.1 M HCl without damaging the improved adsorbent. In another development, a research conducted by Fan et al. [74] and core workers, a core-shell nano-structured MNPs biopolymer-based composite sorbent was synthesized by immobilizing persimmon-tannin (PT) on top of the overlay of Fe_3O_4/SiO_2 microspheres to produce (Fe_3O_4/SiO_2/PT) adsorbent and applied for the removal of Pd(II), as well as Au(III). The main purpose of PT immobilization of the Fe_3O_4/SiO_2 microspheres is to introduce the presence of some phenolic hydroxyl functional groups to enhance the adsorption of metal ions. FTIR findings showed spectra at 575-589cm^{-1} for Fe-O bond in Fe_3O_4, 794 $cm^{-1,}$ and 1082 cm^{-1} for Si-O-Si bond for coating of SiO_2 on top of Fe_3O_4, 3410 cm^{-1} for -NH due to PT functionalization on top of Fe_3O_4/SiO_2. 3396 cm^{-1} and 1446 cm^{-1} stretching vibrations were for O-H and C-C confirming the presence of phenolic -OH groups from tannin, thereby confirming the successful synthesis of the process. The adsorption capacities of the Fe_3O_4/SiO_2/PT unto Pd(II) and Au(III) under optimized conditions were shown to be 196.46 and 917.43 mg/g respectively, as applied for metal ions removal. The kinetic study revealed that pseudo-second-order with the correlation coefficient R^2 value 0.9969 and 0.9996 for Au(III) and Pd(II) respectively, proved superior over pseudo-first-order with R^2 0.9860 and 0.8712 for Au(III) and Pd(II). Hence, this indicated the chemisorption process. The Langmuir adsorption isotherm showed a better fit with R^2 values of 0.9940 and 0.9937 for Au(III) and Pd(II) respectively than the Freundlich model with R^2 values of 0.9279 and 0.8457 for Au(III) and Pd(II), thus, indicating a homogeneous adsorbate monolayer interaction surface site. The tannic acid-based adsorbent material for the removal of metal in an aqueous solution [61-74] is summarized in Table 4.

Table 4. Tannic acid-based adsorbents

Adsorbent	Metal ions	q_{max} (mg/g)	pH	Isotherm/Kinetics	References
CS /TA	Cu(II) Cd(II)	6810 84.93	9.0	Langmuir	[61]
TA/Zr	Pb(II)	170.0	3.3-3.7	-	[64]
TA/MOFs	Pb(II)	252.0	2-7	-	[65]
LDH/PP/TA	Cu(II)	41.56	-	Langmuir Pseudo 1st 2nd order	[66]
TA/CS/MOF	Cr(II)	99.0%	3.5	Pseudo 1st 2nd order	[67]
PEG/PTHA	Cr(IV)	283.3	2-6	Langmuir 2nd order	[68]
DOP/TMSNS	Pb(II)	58.70	5.5	-	[69]
Zr/DETA/TS	Pb(II) Hg(II) Cr (II)	384.6 416.7 125.0	3-5	Pseudo 1st 2nd order	[70]
Mn/PEI/TA	Cu (II) Cr(II	12.50 790.2	5.5	Langmuir	[71]
TRGA	Pb(II) Cd(II)	803.8 395.8	4.0	Langmuir Freundlich	[72]
TA/AC	Cu(II) Cd(II) Mn(II)	23.50 17.80 14.88 11.30	-	Langmuir Freundlich	[73]
Fe_3O_4/SiO_2/PT	Au(III) Pd(II)	917.4 196.4	5.0	Langmuir Freundlich Pseudo 1st 2nd order	[74]

Silica coated MNPs adsorbent

Numerous published works on the applications of the functionalized silica coated MNPs materials utilized as adsorbent raw material for heavy metal ions removal in aqueous media are readily available. For example, Zhang, et al. [75] produced a new MNPs adsorbent material of $Fe_3O_4/SiO_2/NH_2$ core-shell by the sol-gel controllable method and applied it to remove Pb(II) in contaminated natural water. The purpose of the functionalization of the SiO_2 coated MNPs materials was to enhance the adsorption capacity of the adsorbent due to sone suitable functional group. Fe_3O_4, Fe_3O_4/SiO_2, and $Fe_3O_4/SiO_2/NH_2$ were compared for the performances of adsorbents, the adsorption capacities towards Pb(II) which were 6.94, 42.85, 243.9 mg/g, respectively. These progressive increases were due to the adsorption of the -OH groups on $Fe_3O_4/SiO_2/NH_2$ caused by SiO_2 coating of Fe_3O_4 and the $-NH_2$ functionalization of the Fe_3O_4/SiO_2, to form $Fe_3O_4/SiO_2/NH_2$. FTIR characterization results showed the presence of the spectral bands at $1630cm^{-1}$ and $3430cm^{-1}$ corresponding to the O-H vibration from water molecules as well as the presence of NH_2 groups due to functionalization. BET results also showed the surface area of $77m^2/g$ for Fe_3O_4 and $138m^2/g$ for $Fe_3O_4/SiO_2/NH_2$ hence, confirming the coating of SiO_2 on top of Fe_3O_4 with its surface endowed with functionalization due to APTMS. Under optimum parameters for uniform core-shell formation with a relatively high loading amino functionality at 5.45%, with the use of TEOS and APTMS for the sol-gel process, the researchers were able to remove the metal ions were ease with the aid of an external magnet. More findings demonstrated that the adsorbent could effectively remove Pb(II) with an adsorption capability of 243.9 mg/g at 25 ℃. Both the Langmuir model and kinetic data were well fitted into the pseudo-second-order model with R^2 =0.994 against the Freundlich model with R^2 =0.9684. This, indicated homogeneous adsorbate and a chemisorption process, upon the interpretation of the adsorption equilibrium process results. Additionally, the thermodynamic study showed that ΔH = +18.058KJ/mol, ΔS = +73.237KJ/mol and ΔG = -5.233KJ/mol showed endothermic, randomness and spontaneous process.

Zhang, et al. [76] synthesized a novel adsorbent of thiol-functionalized MNPs materials ($Fe_3O_4/SiO_2/SH$) for effluent solutions. The surface-functionalized MNPs were exceptionally viable for the additional removal of Ag, Cd, Pb, Hg, As, and Ti metal ions from water solutions. The purpose of the surface modifications with the -SH group was to enhance the adsorption process through the functional groups. Findings from their experiments indicated that all metals bonded successfully with the -SH functional groups of the ligand, except for As, which binds more to the MNPs. Similarly, the MNPs materials were functionalized in conjunction with mesoporous silica, by further introducing an aminopropyl functional unit to produce the adsorbent ($Fe_3O_4/mSiO_2/NH_2$) and applied for the removal of Cr(III) as a liquid solution and this was achieved with greater recovery. The adsorption capacity of the adsorbent containing just mesoporous silica ($Fe_3O_4/mSiO_2$), was found to show an adsorption capacity of 36.91 mg/g at pH 5.4. However, further functionalization with aminopropyl ($Fe_3O_4/mSiO_2/NH_2$) resulted in the rise in the adsorption capacity to 108.14 mg/g. This showed the $-NH_2$ group enhanced the adsorption process. The mechanisms of interaction between the adsorbent and the metal ions were ascribed to be the coordination of Cr(III) with the amine functional groups ($-NH_2$) combined with the electrostatic impacts of the silica surface. Additionally, the results from the isothermal studies revealed that Freundlich isotherms were better fitted into the isotherm data than the Langmuir isotherms with the R^2 value of 0.99, indicating a heterogeneous solution and multilayer active surface interaction. Sabermahani et al. [77], reported the synthesis of a new adsorbent of polyaniline/maghemite magnetic nanocomposite (PANI/¥-Fe_2O_3/MNC) in which the polyaniline was used as an active agent by the method of polymerization of aniline and applied to remove Pb(II). The purpose of polymerization with aniline was to improve the adsorption process. FTIR characterization results confirmed the presence of some prominent amino-phenol functional groups to show the successful synthesis process. The batch method was used for the adsorption study and the findings showed at optimized conditions were achieved at pH 6.0, adsorbent dosage of 40mg, and the equilibrium contact time was enhanced at

90 min. Additionally, the Freundlich adsorption isotherms were revealed to have a better fit with an R^2 value of 0.97 than the Langmuir isotherm with an R^2 value of 0.80. They found that pseudo-second order (R^2 = 0.984) > the pseudo-first order (R^2 = 0.447). This proved that a chemisorption process more than heterogeneous adsorbate interacting with multilayer active sites.

Similarly, Lin et al. [78], produced a new adsorbent of amino-functionalized SiO_2 coated MNPs ($NH_2/SiO_2/Fe_3O_4$) to remove Cu(II) in water solution. An amino-functionalized SiO_2 magnetite was synthesized with N-(3-trimethoxypropyl) ethylenediamine (TPED) as the surface modifier to enhance the metal removal. The adsorption performances of the adsorbents, Fe_3O_4, SiO_2/Fe_3O_4, and $NH_2/SiO_2/Fe_3O_4$, when compared, was obvious that there was a progressive increase in that order due to the modification which was expected to enhance the adsorption process. FTIR characterization showed that the -NH_2 functional groups were key to the adsorption process. The optimum pH solution was achieved between the range of 5-6, and the maximum adsorption capacity was 10.41 mg/g. Adsorption isotherms studies revealed that equilibrium adsorption data were well fitted into the Langmuir isotherm equations with the R^2 value close to unity than the Freundlich isotherms, indicating homogeneous adsorbate and monolayer adsorbent surface-active sites. Additionally, the kinetic isotherm revealed that the pseudo-second order best explained the adsorption kinetics with the R^2 value close to unity than the pseudo-first order indicating the chemisorption process. The enthalpy energy ΔH was found to be endothermic with the value of +26.92 kJ/mol. The authors discovered that the optimum conditions for adsorption of Cu(II) with the adsorbent $NH_2/SiO_2/Fe_3O_4$ could also be better optimized by using the desorption solvent of a 0.1 M HNO_3 concentration.

Jin, et al. [79], synthesized new magnetic mesoporous SiO_2-coated core-shell nanoparticles (Fe_3O_4/m/SiO_2) adsorbents based on different Fe_3O_4 core sizes. This was to evaluate the impact of the magnetic core sizes on the adsorption capability of adsorbent and to remove Cu(II). Meanwhile, the adsorption capability was discovered to be 84.4m/g for Cu(II). The findings revealed that magnetic core sizes were pH-dependent and have an influence on the magnetic properties of the various adsorbents as well as the structure of the mesoporous silica, specific surface area, and the different interactions with the surface moieties. The adsorption kinetics study for the various adsorptions unto the adsorbent revealed to be fitted to the pseudo-second-order kinetic model. This had well-proven that the adsorption process was a chemisorption process. Nodeh et al. [80] synthesized a new modified magnetic graphene oxide composite adsorbent ($Fe_3O_4/SiO_2/GO$) and intended to remove As(III) and As(V) from ecological samples. The purpose of the modification with the GO was to enhance the adsorption process. Peaks in the FTIR spectrum for O-H at 3400 cm-1, C=O stretching vibrations at 1714 cm-1 for carboxylic groups, C-O vibrations at 1036 cm-1, and C=C aromatic vibrations in GO at 1437 cm-1 all indicated effective synthesis. The findings showed that the $Fe_3O_4/SiO_2/GO$ adsorbent exhibited a superior adsorption capacity towards As(III) along with As(V) with values of 7.51 and 11.40 mg/g, respectively. The adsorbent demonstrated the linearity of 0.05-2.0 ngml-1 and the magnetic solid-phase extraction (MSPE) procedure was used for the pre-concentrations of the metal ions. The Langmuir model was better fitted into the adsorption process with the coefficient of determination; R2 being 0.9992 and 0.9985) for the ions of As(III) and As(V), in that order, than the Freundlich model with R2 0.9256 and 0.9754 .The pseudo-second-order was better fitted with R^2 0.9984 and 0.9968 than the pseudo-first order with R^2 0.8181 and 0.9447 for As(III) as well as As(V), indicating the chemisorption process. The thermodynamic parameters gave correspondingly R^2 0.9990 and 0.9998 as well. The ΔH, ΔS, and ΔG were 29.27KJ/mol, 0.09KJ/mol, and -0.45J/molK for As(III) and 40.75KJ/mol, 0.14KJ/mol, and -2.15KJ/mol for As(V) accordingly indicating endothermic and spontaneous process. Both As(III) and As(V) adsorption on the adsorbent were spontaneously negative when the adsorbent material was applied using the lake, tap water, spring water, and river tap water. The technique could give good relative recoveries of 72.55-109.71% and RSD of 0.1- 4.3 %, with n = 3. The reusability studies showed that the adsorbent could be reused 15 times in

an adsorption-desorption experiment with about 80% potential, to prove that the adsorbent was economically feasible.

Purwanto et al. [81]., synthesized a new adsorbent of a composite of rice husk and ash/activated carbon (AC) made from coconut shell which was subsequently combined with silica gel(SG) and also modified with 3-aminopropyltrimethoxysilane (APTES), through the technique of sol-gel to form (SG/APTES/AC) adsorbent, and was used to remove Pb(II) in aqueous solutions. FTIR characterization showed the functional groups of Si-O-Si from silica gel and -NH_2 from APTES to confirm the successful synthesis process. BET surface area of the SG/APTES/AC adsorbent was 290.23m^2/g at 22°C, which showed a good surface area for adsorption. The results of the investigations revealed that the optimum pH for the adsorption was achieved at 5.0 and the adsorption equilibrium for Pb(II) was achieved within 20 min of the contact time. The Pb(II) adsorption unto the composite adsorbent was well fitted into the Langmuir isotherm model >Freundlich with the R^2 > 0.99 and the maximum and minimum adsorption capacity values were 46.94 mg/g and 29.72 mg/g, respectively.

Ahmad et al. [82] synthesized an adsorbent based on MNPs coated mixture of inorganic-organic material of nanocomposite (MNPs/SiO_2/TSD/TEOS) to remove Ni(II) and Pb(II). Meanwhile, the purpose of the TSD-TEOS was used as a modifier hybrid to enhance the adsorption of the metal ions pollutants. FTIR results showed the spectral peaks at 3405cm^{-1}, 2934 cm^{-1}, 2873 cm^{-1}, 1580 cm^{-1},1475 cm^{-1}, 1317 cm^{-1},1051 cm^{-1},788 cm^{-1}, and 578 cm^{-1} for the bonds of N-H, -CH_3, -CH_2, C-C, C-N, -NH_2, Si-O, Si-C and Fe-O respectively. Extra spectral peaks of 3294 cm^{-1}, 2934 cm^{-1}, 1580 cm^{-1}, 1317 cm^{-1}, and 788 cm^{-1} were observed for N-H, C-H, C-N, NH_2, and Si-C, thus, confirming the successful synthesis process. The researchers discovered that the new adsorbent MNPs/SiO_2/TSD/TEOS at the optimized experimental conditions of PH 5, with a 20 mg amount of adsorbent dosage, the highest adsorption capacity realized for Pb(II) and Ni(II) particles were 417, and 357 mg/g, respectively. The adsorption studies were conducted by utilizing the Langmuir and Freundlich isotherms. The results showed that the Freundlich adsorption isotherm fitted more with the value R^2 of 0.997. This was higher than the Langmuir isotherms with an R^2 value, of 0.871, indicating more heterogeneous adsorbate and multilayer adsorbent active sites interaction. Additionally, findings from the kinetic study showed that the pseudo-second-order proved a better fit with R^2values 1.00 and 0.998 for Pb(II) and Ni(II) respectively than the pseudo-first-order with R^2 values 0.666 and 0.641 for Pb(II) and Ni(II) indicating a chemisorption process. The authors then argued that the newly synthesized adsorbent was different in structure and ability from those most prepared sol-gel-based adsorbents. The results gave a higher adsorption capacity for Pb(II) and Ni(II). Wang, et al. [83] synthesized a new adsorbent of thiol SiO_2 shell coated onto MNPs (Fe_3O_4/SiO_2/SH) by the hydroxylation method of Na_2SiO_3 modified with thiol groups(-SH) and applied to remove Hg (II). The purpose of the -SH group is to enhance the metal adsorption process. FTIR revealed a Fe-O bond with an intense absorption band at 587cm^{-1}, then after the silica coatings, a Fe-O band appeared at 1087 cm^{-1} and for the thiol functionalization, a new spectral band appeared at 2586 cm^{-1} for the -SH bond, thus Fe_3O_4 was successfully coated by SiO_2 and functionalized by the -SH to confirm the success of the synthesis process. The researchers used SiO_2 shells as a protection to the iron core from being corroded or dispersed in acid solution. Their results have demonstrated that the adsorbent coating of the functionalized material, Fe_3O_4/SiO_2/SH showed an excellent adsorption property due to its superior adsorption capability with a rapid adsorption rate. The adsorbent exhibited a good adsorption capacity of 132.0 mg/g owing to the powerful interaction between the -SH group of the adsorbent material and the mercury. They were able to observe that the presence of the -SH groups and was also responsible for the step-up of the adsorption capacities model. The R^2 values were 1.00, 0.920, 0.985, and 0.934 for Langmuir, Freundlich, Temkin, and D-R isotherm models respectively. All R^2 > 0.920 implies that all four isothermal data could be used to explain the equilibrium adsorption process of the Hg(II) unto adsorbent. Additionally, the adsorption mechanisms depended mostly on the electrostatic interactions of the active sites of the adsorbent and the

Hg(II). Furthermore after five rounds of adsorption-desorption studies, the high adsorption capacity of the adsorbent was achieved in the first round and the subsequent values for the second to fifth rounds as 51.1, 42.3, 40.5, and 34.3 mg/g, respectively.

In another related development, Ghorbani et al.[84], a new adsorbent from magnetic-ethylene-diamine-modified graphene oxide (MEDFGO) was prepared to remove Cd(II) and Pb(II). The purpose of the modification with EDTA was to enhance the adsorption process through the $-NH_2$ functional groups. FTIR results showed the functional groups of C-O, C-N from amide, and C-N from amine at 1624, 1400 cm^{-1}, and 1045cm^{-1}, respectively, indicating the interaction between graphene oxide and ethylenediamine and the presence of a peak at 578 cm^{-1} from Fe_3O_4. This confirmed the successful binding of EDFGO and Fe_3O_4. The optimized parameters, namely pH, sorbent dosage, shaking rate, and desorption time, were found to be 6, 33.0 mg, 500 rpm, and 11 mins, respectively. The adsorption capacity of Pb(II) as well as Cd(II) onto the synthesized adsorbent was 10.9 and 10.3 mg/g, respectively. The pseudo-first order and pseudo-second-order equations, both well interpreted the kinetic process with R^2 (0.9102-0.9901) and R^2 (0.9584-0.9935) for Pb (II) and Cd (II), respectively. The Freundlich model data for the metal ions adsorption was better fitted with R^2 0.9719 and 0.9795 for Pb(II) and Cd(II), respectively. The Langmuir model with R^2 0.0100 and 0.9630 for Pb(II) and Cd (II), indicated a heterogeneous adsorbate and a multilayer active sites adsorbent interaction. The thermodynamic parameters were well fitted for both Pb(II) and Cd(II) with R^2 0.9908 and 0.9894 respectively. Meanwhile, the ΔH, ΔS, and ΔG were 37.50KJ/mol, 217.08J/molK, and -39.13KJ/mol and 31.82KJ/mol, 176.12J/molK, and -30.35KJ/mol for Pb(II) and Cd(II) respectively indicated and endothermic as well as the spontaneous process of adsorption. Furthermore, the metal ions removal was discovered to be 99.6 and 99.4% for Pb(II) and Cd(II) respectively recovery after six times of the adsorption-desorption experiment. Santhosh et al.[85] synthesized a new MNPs composite adsorbent of (SiO_2/Co/Fe_3O_4) nanoparticles, amine-functionalized with APTES (SiO_2/Co/Fe_3O_4/NH_2) adorned on graphene oxide by using solvothermal along with sol-gel processes to generate the adsorbent (SiO_2/Co/Fe_3O_4/NH_2/GO) and applied the adsorbent for the removal of organic (black dye 1) and inorganic pollutants (Cr(VI) in effluent solutions. The purpose of the modification with APTES was to enhance the adsorption process through the $-NH_2$ functional groups. FTIR characterization showed the presence of the functional groups of Si-O-Si in SiO_2 coating of Fe_3O_4, $-NH_2$ in APTES functionalization and (epoxides, -OH, and -COOH) groups from GO to confirm the successful synthesis process. The results showed that the synthesis processes were well captured in the characterization methods which showed that the SiO_2/Co/Fe_3O_4/NH_2/GO adsorbent was of good quality. Furthermore, black dye 1 and Cr(VI) had respective adsorption capacities of 130.7 and 136.4 mg/g on the SiO2/Co/Fe3O4/NH2/GO adsorbent, which were well fitted into the Langmuir isotherm than the Freundlich with R2 close to unity. . More so, the results showed that the adsorption was influenced by a maximum value of PH 2. Additionally, the kinetics study interpretation showed compliance with the pseudo-second-order kinetics model with a good fit for both pollutants. Furthermore, the adsorption-desorption studies demonstrated that SiO_2/Co/Fe_3O_4/NH_2/GO could retain its potential with 92% and 65% of Black dye 1 and Cr(VI), respectively even after five rounds to prove its worthiness as a material. Hence, it could be concluded that the material was good for the removal of organic and inorganic pollutants in effluent solutions.

Conclusion

The environmental safety of water supply and efficient management of wastewater remains one of the global concerns. It is discovered that over the last seven years, there have been more notable advances in the development of biopolymer and magnetic-based adsorbents for the removal of pollutants from water and wastewater. The formulation of the adsorbent and the mechanism of the adsorption i.e., chelation, ions exchange, coordination, chemisorption, and electrostatic attraction adsorptions isotherms models, kinetic models, and thermodynamic parameters was applied for the elimination of different heavy metal pollutants in an aqueous environment were specifically discussed. The impact of physicochemical factors on the

performance of these adsorbents was also reviewed. Meanwhile, these magnetic biopolymers sorbents offered a faraway benefit of chemical interaction due to the presence of functional groups like the -OH and -NH_2 groups and magnetic properties for the separation during heavy metal removal. Accordingly, it could be established that the types of functional groups, as well as the surface area presented in the adsorbents, play significant roles in the removal of metals in both aqueous and wastewater environments. It was also discovered in the review that good proportion removal and optimum adsorption capabilities were achieved at optimal conditions. Consequently, the adsorption of these metals was either one of Langmuir, Freundlich, or some additional linear plot adsorption isotherms models. In addition, pseudo-second and first-order kinetics were crucial in determining the nature of the adsorption processes. However, much of the adsorbent produced by the scientists was in an aqueous solution that comprises the heavy metal of concern without the real sample interferences. Therefore, the potential researchers must perform research in real samples as well as in the industrial natural environment.

Acknowledgment

We are grateful for the financial support of the work by Universiti Teknologi Malaysia via the Universiti Teknologi Malaysia Fundamental Research grant (UTMFR, Q.J130000.2554.20H98, reference number PY/2019/02057) and UTMShine grant (Q.J130000.2454.09G30, reference number PY/2020/03555). We would like to acknowledge Ms. Nur Shahz Ereena Zulkifli, Ms. Nur Idayu Mat Ghani, and Ms. Anis Nur Shasha Abdul Halim for their help with language and technical proofreading.

References

1. Sayato, Y. (1989). WHO guidelines for drinking-water quality. *Eisei Kagaku,* 35(5): 307-12.
2. WHO (2003). Lead in drinking-water: background document for development of WHO guidelines for drinking-water quality. WHO. Available from https://apps.who.int/iris/handle/10665/75370.
3. WHO (2017). Guidelines for drinking-water quality: first addendum to the fourth edition. World Health Organisation. Available from: https://apps.who.int/iris/bitstream/handle/10665/254636/9789241550017-eng.pdf
4. Ali, H., Khan, E. and Ilahi, I. (2019), Environmental chemistry and ecotoxicology of hazardous heavy metals: Environmental persistence, toxicity, and bioaccumulation. *Journal of Chemistry,* 2019: 6730305.
5. Zhang, Y. and Duan, X. (2020). Chemical precipitation of heavy metals from wastewater by using the synthetical magnesium hydroxy carbonate. *Water Science Technology*; 81(6):1130-1136.
6. Bashir, A., Malik, L. A., Ahad, S., Manzoor, T., Bhat, M. A., Dar, G. N., et al. (2019). Removal of heavy metal ions from aqueous system by ion-exchange and biosorption methods. *Environmental Chemistry Letters,* 17(2): 729-754.
7. Al-Shannag, M., Al-Qodah, Z., Bani-Melhem, K., Qtaishat, M. R. and Alkasrawi, M. (2015). Heavy metal ions removal from metal plating wastewater using electrocoagulation: Kinetic study and process performance. *Chemical Engineering Journal,* 260: 749-756.
8. Deliyanni, E. A., Kyzas, G. Z., Matis, K. A., (2017). Various flotation techniques for metal ions removal. *Journal Molecular Liquids,* 225: 260-264.
9. Yee, L. Y., Asrul, N. M., Kamarulzaman, F. F., Ali, T. G., Zulkifli, N. S. E., Kamaruddin, A. F., et al. (2021). Recent advances in agricultural waste-based adsorbents for the removal of pollutants in water (2017-2020). *Malaysian Journal Analytical Sciences,* 25(3): 415-431.
10. Fouda-Mbanga, B. G., Prabakaran, E. and Pillay, K., (2021). Carbohydrate biopolymers, lignin-based adsorbents for removal of heavy metals (Cd^{2+}, Pb^{2+}, Zn) from wastewater, regeneration, and reuse for spent adsorbents including latent fingerprint detection: A review. *Biotechnology Reports,* 30:e00609.
11. Cheng, T. H., Sankaran, R., Show, P. L., Ooi, C. W., Liu, B. L., Chai, W. S., et al. (2021). Removal of protein wastes by cylinder-shaped NaY zeolite adsorbents decorated with heavy metal wastes. *International Journal Biology Macromolecules,* 185(May):761-772.

12. Khalfa, L., Sdiri, A., Bagane, M. and Cervera, M. L. (2021). A calcined clay fixed-bed adsorption studies for the removal of heavy metals from aqueous solutions. *Journal Clean Production,* 278:123935.
13. Zhang, Z., Wang, T., Zhang, H., Liu, Y. and Xing, B. (2021). Adsorption of Pb(II) and Cd(II) by magnetic-activated carbon and its mechanism. *Science Total Environment,* 757:143910.
14. Liu, Z. H. and Yi, J. (2002), Falling film evaporation heat transfer of water/salt mixtures from roll-worked enhanced tubes and tube bundle. *Applied Thermal Engineering,* 22(1): 83-95.
15. Yaacob, S. F. F. S., Razak, N. S. A., Aun, T. T., Rozi, S. K. M., Jamil, A. K. M. and Mohamad, S. (2018). Synthesis and characterizations of magnetic bio-material sporopollenin for the removal of oil from aqueous environment. *Industrial Crops Production,*124(July): 442-448.
16. Abd Razak, N. F., Shamsuddin, M. and Lee, S. L. (2018). Adsorption kinetics and thermodynamics studies of gold(III) ions using thioctic acid-functionalized silica coated magnetite nanoparticles. *Chemical Engineering Research Design,* 130:18-28.
17. Ding, J., Gao, Q., Luo, D., Shi, Z. G. and Feng, Y. Q. (2010). n-Octadecylphosphonic acid grafted mesoporous magnetic nanoparticle: Preparation, characterization, and application in magnetic solid-phase extraction. *Journal of Chromatography A,* 1217: 7351-7358.
18. Shen, Y., Zhao, P. and Shao, Q., (2014). Porous silica and carbon derived materials from rice husk pyrolysis char. *Microporous Mesoporous Materials*, 188: 46-76.
19. Sutirman, Z. A., Sanagi, M. M., Abd Karim, K. J., Wan Ibrahim, W. A., Jume, B. H. (2018). Equilibrium, kinetic and mechanism studies of Cu(II) and Cd(II) ions adsorption by modified chitosan beads. *International Journal Biology Macromolecules,*116: 255-263.
20. Poon, L., Wilson, L. D. and Headley, J. V. (2014). Chitosan-glutaraldehyde copolymers and their sorption properties. *Carbohydrate Polymers,* 109: 92-101.
21. Song, X., Li, L., Zhou, L. and Chen, P., (2018). Magnetic thiolated/quaternized-chitosan composites design and application for various heavy metal ions removal, including cation and anion. *Chemical Engineering Research Design,* 136: 581-592.
22. Sun, P., Zhang, W., Zou, B., Zhou, L., Ye, Z. and Zhao, Q. (2021). Preparation of EDTA-modified magnetic attapulgite chitosan gel bead adsorbent for the removal of Cu(II), Pb(II), and Ni(II). *International Journal Biology Macromolecules,* 182:1138-1149.
23. Chen, X., Huang, Z., Luo, S. Y., Zong, M. H. and Lou, W. Y., (2021). Multi-functional magnetic hydrogels based on *Millettia speciosa* champ residue cellulose and chitosan: Highly efficient and reusable adsorbent for Congo red and Cu^{2+} removal. *Chemical Engineering Journal,* 423(5): 130198.
24. Elanchezhiyan, S. S., Karthikeyan, P., Rathinam, K., Hasmath Farzana, M. and Park, C. M. (2021). Magnetic kaolinite immobilized chitosan beads for the removal of Pb(II) and Cd(II) ions from an aqueous environment. *Carbohydrate Polymers,* 261(3):117892.
25. Huang, Y., Hu, C., An, Y., Xiong, Z., Hu, X., Zhang, G., et al. (2021). Magnetic phosphorylated chitosan composite as a novel adsorbent for highly effective and selective capture of lead from aqueous solution. *Journal Hazardous Materials*, 405(7): 124195.
26. Liu, T., Han, X., Wang, Y., Yan, L., Du, B., Wei, Q., et al. (2017). Magnetic chitosan/anaerobic granular sludge composite: Synthesis, characterization, and application in heavy metal ions removal. *Journal Colloid Interface Sciences,* 508:405-414.
27. Zhang, Q., Zhuang, S. and Wang, J. (2020). Biosorptive removal of cobalt(II) from aqueous solutions using magnetic cyanoethyl chitosan beads. *Journal Environmental Chemical Engineering*, 8(6):104531.
28 Sutirman, Z. A., Sanagi, M. M., Abd Karim, K. J., Wan Ibrahim, W. A. and Jume, B. H. (2018). Equilibrium, kinetic and mechanism studies of Cu(II) and Cd(II) ions adsorption by modified chitosan beads. *International Journal of Biological Macromolecules*, 116: 255-263.

29. Pooladi, A. and Bazargan-Lari, R. (2020). Simultaneous removal of copper and zinc ions by Chitosan/hydroxyapatite/nano-magnetite composite. *Journal Materials Resesearch Technology,* 9(6):14841-14852.
30. Feng, G., Ma, J., Zhang, X., Zhang, Q., Xiao, Y., Ma, Q., et al. (2019). Magnetic natural composite Fe_3O_4-chitosan@bentonite for removal of heavy metals from acid mine drainage. *Journal Colloid Interface Sciences,*538:132-141.
31. Sun, H., Xia, N., Liu, Z., Kong, F. and Wang, S. (2019). Removal of copper and cadmium ions from alkaline solutions using chitosan-tannin functional paper materials as adsorbent. *Chemosphere,* 236: 124370.
32. Huang, H., Yang, Q., Zhang, L., Huang, C. and Liang, Y., (2022). Polyacrylamide modified kaolin enhances the adsorption of sodium alginate/carboxymethyl chitosan hydrogel beads for copper ions. *Chemical Engineering Research Design,* 180 :296-305.
33. Zhang, H., Li, R. and Zhang, Z., (2022). A versatile EDTA and chitosan bi-functionalized magnetic bamboo biochar for simultaneous removal of methyl orange and heavy metals from complex wastewater. *Environmental Pollution,* 293(11):118517.
34. Karimi, F., Ayati, A., Tanhaei, B., Sanati, A. L., Afshar, S., Kardan, A., et al. (2022). Removal of metal ions using a new magnetic chitosan nano-bio-adsorbent; A powerful approach in water treatment. *Environmental Research,* 203(5): 111753.
36. Nasirimoghaddam, S., Zeinali, S. and Sabbaghi, S., (2015). Chitosan coated magnetic nanoparticles as nano-adsorbent for efficient removal of mercury contents from industrial aqueous and oily samples. *Journal Industrial Engineering Chemistry*, 27(2014): 79-87.
37. Jiang, Y., Cai, W., Tu, W. and Zhu, M., (2019). Facile cross-link method to synthesize magnetic Fe_3O_4@SiO_2-chitosan with high adsorption capacity toward hexavalent chromium. *Journal Chemical Engineering Data,* 64(1): 226-233.
38 Kim, H. S., Lee, C. G. and Lee, E. Y. (2011). Alginate lyase: Structure, property, and application. *Biotechnology and Bioprocess Engineering*, 16(5): 843-851.
39. Ren, H., Gao, Z., Wu, D., Jiang, J., Sun, Y. and Luo, C. (2016). Efficient Pb(II) removal using sodium alginate-carboxymethyl cellulose gel beads: Preparation, characterization, and adsorption mechanism. *Carbohydrate Polymers,* 137: 402-409.
40. Córdova, B. M., Venâncio, T., Olivera, M. and Huamani-Palomino, R. G. (2021). Xanthation of alginate for heavy metal ions removal. Characterization of xanthate-modified alginates and their metal derivatives. *International Journal Biology Macromoleclues,* 169: 130-142.
41. Fuks, L., Herdzik-Koniecko, I., Polkowska-Motrenko, H. and Oszczak, A. (2018). Novel procedure for removal of the radioactive metals from aqueous wastes by the magnetic calcium alginate. *International Journal Environmental Science Technology,* 15(12): 2657-2668.
42. Lee, H. K., Choi, J. W., Kim, J. H., Kim, C. R. and Choi, S. J. (2021). Simultaneous selective removal of cesium and cobalt from water using calcium alginate-zinc ferrocyanide-Cyanex 272 composite beads. *Environmental Science Pollution Ressearch,* 28: 42014-42023.
43. Song, D., Park, S., Kang, H. W., Park, S. and Bin Han, J. (2013). Recovery of lithium (I), strontium (II), and lanthanum (III) using Ca-alginate beads. *Journal Chemical Engineering Data,* 58: 2455-2464.
44. Dai, M., Liu, Y., Ju, B. and Tian, Y. (2019). Preparation of thermoresponsive alginate/starch ether composite hydrogel and its application to the removal of Cu(II) from aqueous solution. *Bioresource Technology*, 294(7):122192.
45. Ahmed, A., Mohamed, F., Elzanaty, A. M. and Abdel-Gawad, O. F. (2021). Synthesis and characterization of diphenylamine grafted onto sodium alginate for metal removal. *International Journal Biology Macromolecules,* 167:766-776.

46. Allouss, D., Essamlali, Y., Chakir, A., Khadhar, S. and Zahouily, M. (2020). Effective removal of Cu(II) from aqueous solution over graphene oxide encapsulated carboxymethylcellulose-alginate hydrogel microspheres: towards real wastewater treatment plants. *Environmental Science Pollution Ressearch,* 27(7):7476-7492.
47. Hassan, R. M. (2021). Novel synthesis of natural cation exchange resin by crosslinking the sodium alginate as a natural polymer with 1,6-hexamethylene diisocyanate in inert solvents: Characteristics and application. *International Journal Biology Macromolecules,* 184:926-935.
48. Córdova, B. M., Infantas, G. C., Mayta, S., Huamani-Palomino, R. G., Kock, F. V. C., Montes de Oca, J., et al. (2021). Xanthate-modified alginates for the removal of Pb(II) and Ni(II) from aqueous solutions: A brief analysis of alginate xanthation. *International Journal Biology Macromolecules,* 179:557-566.
49. Ibrahim, W. A. W., Hassan, A. A. M., Sutirman, Z. A. and Bakar, M. B. (2020). A mini review on sporopollenin-based materials for removal of heavy metal ions from aqueous solution. *Malaysian Journal of Analytical Sciences,* 24(3): 300-312.
50. Ahmad, N. F., Kamboh, M. A., Nodeh, H. R., Nadiah, S., Abd, B. and Mohamad, S. (2017). Synthesis of piperazine functionalized magnetic sporopollenin: a new organic-inorganic hybrid material for the removal of lead (II) and arsenic (III) from aqueous solution. *Environmental Science and Pollution Research,* 24(27): 21846-21858.
51. Sayin, S., Gubbuk, I. H. and Yilmaz, M. (2013). Preparation of calix[4]arene-based sporopollenin and examination of its dichromate sorption ability. *Journal of Inclusion Phenomena and Macrocyclic Chemistry*, 75(1–2):111-118.
52. Ünlü, N. and Ersoz, M., (2007). Removal of heavy metal ions by using dithiocarbamate-sporopollenin. *Separaction and Purification Technology,* 52(3): 461-469.
53. Hassan, A. M., Wan Ibrahim, W. A., Bakar, M. B., Sanagi, M. M., Sutirman, Z. A., Nodeh, H. R., et al. (2020). New effective 3-aminopropyltrimethoxy-silane functionalized magnetic sporopollenin-based silica coatedgraphene oxide adsorbent for removal of Pb(II)from aqueous environment. *Journal Environmental Management,* 253(10): 109658.
54 Ren, Y., Abbood, H. A., He, F., Peng, H., Huang, K. (2013). Magnetic EDTA-modified chitosan/SiO_2/Fe_3O_4 adsorbent: Preparation, characterization, and application in heavy metal adsorption. *Chemical Engineering Journal*, 226: 300-311.
55. Bilgic, A., Cimen, A., Bastug, E. and Kursunlu, A. N. (2022). Fluorescent sporopollenin microcapsule modified by BODIPY for sensitive&selective recognition and efficient removal of Cu(II) from aqueous solution. *Chemical Engineering Research Design,*178: 61-72.
56. Ahmad, N. F., Kamboh, M. A., Nodeh, H. R., Halim, S. N. B. A. and Mohamad, S., (2017). Synthesis of piperazine functionalized magnetic sporopollenin: a new organic-inorganic hybrid material for the removal of lead(II) and arsenic(III) from aqueous solution. *Environmental Science Pollution Research,* 24(27): 21846-21858.
57 Sargin I, Arslan G. (2015). Chitosan/sporopollenin microcapsules: Preparation, characterization, and application in heavy metal removal. *International Journal Biology Macromolecules,* 75: 230-238.
58. Sargin, İ. And Arslan, G., (2016). Effect of glutaraldehyde cross-linking degree of chitosan/sporopollenin microcapsules on the removal of copper(II) from aqueous solution. *Desalination Water Treatment,* 57(23): 10664-10676.
59. Şener, M., Reddy, D. H. K. and Kayan, B. (2014). Biosorption properties of pretreated sporopollenin biomass for lead(II) and copper(II): Application of response surface methodology. *Ecological Engineering,* 68: 200-208.
60. Ersoz, M., Pehlivan, E., Duncan, H. J., Yildiz, S. and Pehlivan, M. (1995), Ion exchange equilibria of heavy metals in aqueous solution on new chelating resins of sporopollenin. *Reaction Polymers,* 24(3): 195-202.

61. Bagtash, M., Yamini, Y., Tahmasebi, E., Zolgharnein, J. and Dalirnasab, Z., (2016). Magnetite nanoparticles coated with tannic acid as a viable sorbent for solid-phase extraction of Cd^{2+}, $Co^{2+,}$ and Cr^{3+}. *Microchimica Acta,* 183(1): 449-456.
62. Makeswari, M. (2013). Tannin gel derived from leaves of *Ricinus communis* as an adsorbent for the removal of Cu(II) and Ni(II) ions from aqueous solution. *International Journal of Modern Engineering Research,* 3(5): 3255-3266.
63. Kavitha, V. U. and Kandasubramanian, B. (2020). Tannins for wastewater treatment. *SN Applied Sciences,* 2: 1081.
64. Zou, L., Shao, P., Zhang, K., Yang, L., You, D., Shi, H., et al. (2018). Tannic acid-based adsorbent with a superior selectivity for lead(II) capture: Adsorption site and selective mechanism. Chemical Engineering Journal, 364: 160-166.
65. Huang, L., Shuai, Q. and Hu, S. (2019), Tannin-based magnetic porous organic polymers as robust scavengers for methylene blue and lead ions. *Journal Cleaner Production,* 215: 280-289.
66. Huang, Q., Zhao, J., Liu, M., Chen, J., Zhu, X., Wu, T., et al. (2018). Preparation of polyethylene polyamine@tannic acid encapsulated MgAl-layered double hydroxide for the efficient removal of copper (II) ions from aqueous solution. *Journal Taiwan Institute Chemical Engineering,* 82:92-101.
67. Shi, P., Hu, X., Duan, M. (2021). A UIO-66/tannic acid/chitosan/polyethersulfone hybrid membrane-like adsorbent for the dynamic removal of dye and Cr(VI) from water. *Journal Cleaner Production,* 290: 125794.
68. Liu, Q., Liu, Q., Liu, B., Hu, T., Li,u W. and Yao, J., (2018), Green synthesis of tannin-hexamethylenediamine based adsorbents for efficient removal of Cr(VI). *Journal Hazardous Materials,* 352(3):27-35.
69. Gao, J., Lei, H., Han, Z., Shi, Q., Chen, Y. and Jiang, Y., (2017). Dopamine functionalized tannic-acid-templated mesoporous silica nanoparticles as a new sorbent for the efficient removal of Cu^{2+} from aqueous solution. *Scientific Reports,* 7(7): 1-11.
70. Zhang, Y., He, F. and Li, X. (2016). Three-dimensional composite hydrogel based on polyamine zirconium oxide, alginate, and tannic acid with high performance for Pb(II), Hg(II), and Cr(VI) trapping. *Journal Taiwan Institute Chemical Engineering,* 65: 304-311.
71. Deng, X., Wang, L., Xiu, Q., Wang, Y., Han, H., Dai, D., et al. (2021). Adsorption performance and physicochemical mechanism of MnO_2-polyethyleneimine-tannic acid composites for the removal of Cu(II) and Cr(VI) from aqueous solution. *Frontier Chemical Science Engineering,* 15(3): 538-551.
72. Zhu, Y. H., Zhang, Q., Sun, G. T., Chen, C. Z., Zhu, M. Q. and Huang, X. H. (2022), The synthesis of tannin-based graphene aerogel by hydrothermal treatment for removal of heavy metal ions. *Industrial Crops and Production,* 176:114304.
73. Üçer, A., Uyanik, A. and Aygün, Ş. F. (2006). Adsorption of Cu(II), Cd(II), Zn(II), Mn(II), and Fe(III) ions by tannic acid immobilized activated carbon. *Separation Purification Technology,* 47(3): 113-118.
74. Fan, R., Min, H., Hong, X., Yi, Q., Liu, W., Zhang, Q., et al. (2019). Plant tannin immobilized Fe_3O_4@SiO_2 microspheres: A novel and green magnetic bio-sorbent with superior adsorption capacities for gold and palladium. *Journal Hazardous Materials,* 364:780-790.
75. Zhang, S., Zhang, Y., Liu, J., Xu, Q., Xiao, H., Wang, X., et al. (2013). Thiol modified Fe_3O_4@SiO_2 as a robust, high effective, and recycling magnetic sorbent for mercury removal. *Chemical Engineering Journal,* 226: 30-38.
76 Egodawatte, S., Datt, A., Burns, E. A. and Larsen, S. C. (2015) Chemical insight into the adsorption of chromium(III) on iron oxide/mesoporous silica nanocomposites. *Langmuir,* 31(27): 7553-7562.
77 Sabermahani F., Irannejad, L. and Mahani, N. M. (2018). Using polyaniline/maghemit magnetic nanocomposite for removal of lead from aqueous solutions. *Iranian Journal of Analytical Chemistry,* 5(1): 33-38.
78. Lin, Y., Chen, H., Lin, K., Chen, B. and Chiou, C., (2011). Application of magnetic particles modified with amino groups to adsorb copper ions in aqueous solution. *Journal Environmental Sciences,* 23(1):44-50.

79. Jin, S., Park, B. C., Ham, W. S., Pan, L. and Kim, Y. K. (2017). Effect of the magnetic core size of amino-functionalized Fe_3O_4-mesoporous SiO_2 core-shell nanoparticles on the removal of heavy metal ions. *Colloids Surfaces A Physicochemical Engineering Aspects,* 531(8):133-140.
80. Nodeh, H. R., Aini, W., Ibrahim, W. and Sanagi, M. M. (2016). Development of magnetic graphene oxide adsorbent for the removal and preconcentration of As (III) and As (V) species from environmental water samples. *Environmental Science Pollution Research*, 23: 9759-9773.
81. Purwanto, A., Putri, E. A. and Rosyidah, D. (2017). Adsorption of Pb (II) using silica gel composite from rice husk ash modified 3-aminopropyltriethoxysilane (APTES) - activated carbon from coconut shell. *AIP Conference Proceedings,* 1823: 020034.
82. Ahmad, N., Sereshti, H., Mousazadeh, M., Rashid Nodeh, H., Kamboh, M. A., Mohamad, S. (2019), New magnetic silica-based hybrid organic-inorganic nanocomposite for the removal of lead(II) and nickel(II) ions from aqueous solutions. *Materials Chemistry and Physics*, 226: 73-81.
83. Wang Z, Xu J, Hu Y, Zhao H, Zhou J, Liu Y, et al. (2015). Functional nanomaterials: Study on aqueous Hg(II) adsorption by magnetic Fe_3O_4@SiO_2-SH nanoparticles. *Journal Taiwan Institute Chemical Engineering,* 60: 394-402.
84. Ghorbani, M., Shams, A., l Seyedin, I. and Lahoori, O. N. (2018). Magnetic ethylene diamine-functionalized graphene oxide as a novel sorbent for removal of lead and cadmium ions from wastewater samples. *Environmental Science and Pollution Research*, 25: 5655-5667.
85. Santhosh, C., Daneshgar, E., Kollu, P., Peräniemi, S., Nirmala, G., A., Bhatnagar, A. (2017). Magnetic SiO_2@$CoFe_2O_4$ nanoparticles decorated on graphene oxide as efficient adsorbents for the removal of anionic pollutants from water. *Chemical Engineering Journal,* 322: 472-487

Malaysian Journal of Analytical Sciences (MJAS)
Published by Malaysian Analytical Sciences Society

A REVIEW ON LIPID OXIDATION IN EDIBLE OILS

(Ulasan Mengenai Pengoksidaan Lelemak salam Minyak Masak)

Radhika Loganathan[1,2*], Azmil Haizam Ahmad Tarmizi[1], Shireene Ratna Vethakkan[2], Kim-Tiu Teng[1]

[1] Malaysian Palm Oil Board,
Bandar Baru Bangi, 43000 Kajang, Selangor, Malaysia
[2] Department of Medicine,
Faculty of Medicine, University of Malaya, 50603 Kuala Lumpur, Malaysia

**Correspondence author: radhika@mpob.gov.my*

Received: 28 February 2022; Accepted: 3 July 2022; Published: 27 December 2022

Abstract

Lipid oxidation is the main quandary that causes deterioration of cooking oil quality resulting in off-flavours and an unpleasant odour called rancidity. Oxidative stability can directly affect oil quality and shelf life. Edible oil gets oxidised during processing and storage stages through auto- and photo-oxidations. In addition to this, cooking causes chemical reactions such as hydrolysis, oxidation, and polymerization. Hence, it is imperative to evaluate methods and measures that could maintain the quality of the oil. In addition, it is vital to evaluate the conditions or processes with potentially deleterious effects on oil quality and nutritional benefits to enable avoidance of these negative variables. The rate of oxidation depends on several factors including the presence of oxygen and light, unfavourable storage temperature, fatty acid composition, and cooking conditions and practices. This article reviews the mechanism of auto-oxidation and photo-oxidation, the role of pro-oxidants and antioxidants as well as chemical reactions induced by conventional heating techniques.

Keywords: lipid oxidation, storage conditions, thermal oxidation, oxidative stability, phytonutrient stability

Abstrak

Pengoksidaan lelemak adalah masalah utama yang menyebabkan kemerosotan kualiti minyak masak yang mengakibatkan rasa dan bau (tengik) yang tidak menyenangan. Kestabilan oksidatif secara langsung boleh menjejaskan kualiti minyak dan jangka hayat. Minyak masak akan teroksida semasa pemprosesan dan penyimpanan melalui auto- dan foto-oksida. Di samping itu, proses memasak melibatkan tindak balas kimia seperti hidrolisis, pengoksidaan, dan pempolimeran. Oleh itu, adalah penting untuk menilai kaedah dan langkah-langkah pencegahan bagi mengekalkan kualiti minyak masak. Tambahan lagi, adalah penting untuk menilai keadaan atau proses yang boleh menjejaskan kualiti minyak dan faktor nutrisi untuk mengelakkan pembolehubah negatif ini. Kadar pengoksidaan bergantung kepada beberapa faktor, diantaranya adalah kehadiran oksigen dan cahaya, suhu penyimpanan yang tidak sesuai, komposisi asid lemak, serta keadaan dan amalan memasak. Artikel ini mengkaji mekanisme auto-oksida dan foto-oksida, peranan pro-oksidan dan antioksida serta tindak balas kimia yang disebabkan oleh teknik masakan konvensional.

Kata kunci: pengoksidaan lelemak, keadaan penyimpanan, pengoksidaan terma, kestabilan oksidatif, kestabilan fitonutrien

Introduction

Lipid oxidation

Lipid oxidation is the main process of concern that causes quality deterioration in edible oil that contributes to off-flavors and an unpleasant odor due to oil rancidity. The ability of an oil to withstand oxidation is important, particularly under warm climate conditions in tropical countries, logistics and transportation, unfavorable storage conditions, cooking practices, and extended cooking processes. Oxidative stability is an important indicator of the quality and shelf life of products. Oxidative stability of edible oils is defined as resistance to oxidation during processing, storage, and cooking [1, 2]. The rate of oxidation depends on several factors including the availability of oxygen, the presence of light, and the temperature.

The oxidation process destroys essential fatty acids and promotes the formation of off-flavored and potentially toxic, mutagenic, and carcinogenic new compounds like diacylglycerols, monoacylglycerols, monomers, polymers, free fatty acids, and other oxidative substances. This induces a significant loss of oil quality that promotes changes in functional, sensory properties, nutritional attributes, and safety of oils and food products [3]. The time taken for secondary products to develop from primary oxidation products (hydroperoxides), varies between oils [1]. Oils with significant levels of unsaturated fatty acids are generally more susceptible to the oxidation process [4].

The results of our current review could imply that storage and cooking conditions as well as the choice of cooking oil can have economic ramifications both on a domestic and industrial scale and may potentially be of public health concern. At an industrial scale, current work will enable decisions to be made on storage/transport environments along the logistical supply chain as well as at wholesale and retail sites. The literature search on thermal stability with different cooking techniques and oil selections could serve as a benchmark to educate consumers on appropriate home practices in terms of better heating techniques, oil management and handling, optimum temperatures, and choice of cooking oil to preserve the wholesomeness of the oil. A good quality oil may spoil faster if consumers do not take appropriate measures to control oil integrity. Thus, consumers need to be educated on oil handling during domestic cooking. Such understanding is important to consumers, as any adverse storage and heating conditions will impinge on the shelf life and quality of the oil.

In the following context, the mechanism of auto- and photo-oxidations, the role of pro-oxidants and antioxidants as well as chemical reactions resulting from common heating techniques will be elaborated.

Mechanism of auto-oxidation

Lipid auto-oxidation is a free radical chain reaction, characterized by three stages; initiation, propagation, and termination [1].

Initiation: $RH \rightarrow R\bullet + H\bullet$

During initiation, an endothermic reaction by homolytic cleavage of the covalent bond in the C-H hydrocarbon chain of fatty acid (RH) molecule takes place with the formation of a free hydrogen radical (H•) and fatty acid radical (R•). This reaction may be catalysed the by presence of heat, metal ions, ultraviolet and visible light [1].

Propagation: $R\bullet + O \rightarrow ROO\bullet$

$ROO\bullet + RH \rightarrow ROOH + R\bullet$

Propagation of auto-oxidation generally occurs between oxygen and a highly reactive fatty acid radical (R•) which forms primary oxidative compounds that are highly reactive (peroxyl radical (ROO•)). The unstable peroxyl radical (ROO•) is capable of reacting with unsaturated fatty acids to form a hydroperoxide (ROOH) which is a marker for early oxidation and a newly developed reactive fatty acid radical (R•) that

could initiate further oxidation and a free radical chain reaction. The formation of peroxyl radical (ROO•) and hydroperoxides (ROOH) are dependent on the presence of oxygen and excessive heat [1]. Deterioration starts once the unstable primary oxidative products called peroxides are developed in the oil. This compound is tasteless and odorless.

In the presence of transition metals (like iron (Fe) and copper (Cu) in unrefined oils) and/or at high temperatures, antioxidants in the oils deplete, and unstable hydroperoxides (ROOH) readily decompose to alkoxy radicals (RO) which then form non-volatile secondary oxidation products such as aldehydes, ketones, acids, esters, alcohols, and short-chain hydrocarbons [5]. This reaction occurs rapidly and Fe^{2+} (or Cu^{+}) will degenerate but the regeneration of Fe^{2+} (or Cu^{+}) will be slow.

Fast reaction: Fe^{2+} (or Cu^{+}) + ROOH → Fe^{3+} (or Cu^{2+}) + RO• + OH^{-}
Slow reaction: Fe^{3+} (or Cu^{2+}) + ROOH → ROO • + Fe^{2+} (or Cu^{+}) + H^{+}

Termination: R• + R• → R-R
R• + ROO• → ROOR
ROO• + ROO• → ROOR + O2

In the termination stage of auto-oxidation, sufficiently free radicals interact with one another to form non-radical relatively stable products.

Primary antioxidants like phenols (AH) can promote the termination process hence shortening the propagation sequence in the auto-oxidation mechanism:

Propagation: ROO• + AH → ROOH + A•

Carotenes and vitamin E are extensive molecules (B) with extensively conjugated unsaturation.

Propagation: ROO• + B → ROOB•

The intermediate radicals (A• and ROOB•) are converted to either dimers or substitution products, most importantly these products are free of any undesirable properties [1].

Mechanism of photo-oxidation

Lipid oxidation is hastened by light, especially in presence of photo-sensitizers like chlorophylls [1]. Photo-oxidation generates aliphatic and aromatic oxidized compounds which include ketones, aldehydes, carboxylic acids, fatty acids, esters, epoxides, sulfoxides, sulfones, phenols, anhydrides, quinones, and alcohols.

Sensitizers are aromatic compounds (e.g., fluorescein dyes, methylene blue, and polycyclic aromatic hydrocarbons) that absorb electromagnetic radiation usually from the visible light spectrum. During the photosensitized oxidation process, the sensitizer in the stable ground (^{0}Sen) or singlet state (^{1}Sen) absorbs energy (hv) [that is transferred from light rapidly (in picoseconds)] and becomes excited (^{1}Sen*). This excited-state sensitizer returns to its stable ground state by releasing excess energy as non-radiative heat, electromagnetic radiation (fluorescence and phosphorescence), and other photochemical/ photophysical reactions [6].

Excitation and deactivation of sensitizer: ^{1}Sen + hv ↔ ^{1}Sen*

Reaction of triplet state sensitizers (^{3}Sen*) with substrates; -

Type 1: $^3Sen^* + RH \rightarrow$ (sensitizer H + R•) or ($•R^+ + •Sen^-$)
(Sensitizer H + R•) or ($•R^+ + •Sen^-$) + $^3O_2 \rightarrow$ ROOH

Excited triplet state sensitizers ($^3Sen^*$) can react with the C-H hydrocarbon chain of fatty acid (RH) molecule and form fatty acid free radical which in turn forms hydroperoxide (ROOH).

Type 2: $^3Sen^* + {}^3O_2 \rightarrow {}^1O_2$
$^1O_2 + RH \rightarrow$ ROOH

Excited triplet state sensitizers ($^3Sen^*$) can react with $^3O_2$ to form $^1O_2$. Then, $^1O_2$ reacts chemically or transfers its energy to an acceptor, unsaturated fatty acid, and causes the formation of a hydroperoxide (ROOH).

Pro-oxidants

There are several common physical conditions or environmental states that can promote lipid oxidation. This section will discuss several pro-oxidants that play a role in domestic storage conditions (Table 1) and common heating techniques (Table 2). These environmental parameters and physical conditions modulate the quality of the oil.

Oxygen

Oil degradation upon storage at temperate (-3 to 18 °C) or tropical temperatures commonly occurs due to the interaction of oxygen with fatty acid radical (R•). This involves only the early propagation step of the auto-oxidation mechanism and forms hydroperoxide (ROOH) which is a marker for the early oxidation stage. Daskalaki et al. conducted storage stability studies on virgin olive oils with 1 to 3% headspace (space of a closed bottle). These oils were stored in dark conditions for 15 months at home storage conditions (20±4 °C). It was reported that lower levels of peroxide values with higher retention of polyphenols can be attained with low oxygen (headspace) availability and lower polyunsaturated linoleic acid content [7].

Storage stability of palm, sunflower, and cottonseed oils exposed to light, air, or both light and air were studied for 4 consecutive days. In terms of stability, palm oil, with higher levels of saturation, was most stable followed by cottonseed oil and lastly sunflower oil. Oils exposed to both air and light were found to oxidise fastest. Moreover, the effect of photo-oxidation by light was greater than auto-oxidation by air. To avoid prolonged exposure to light and air, the authors recommend purchasing small packages of oil. In other words, lower oil to volume ratio has shorter exposure and faster use-up of the oil as compared higher oil to volume ratio packaging size [8].

Light

Photo-oxidation involves interaction between a double bond and a highly activated singlet oxygen ($^1O_2$) produced from ordinary triplet oxygen ($^3O_2$). Light has a greater influence and results in a quicker reaction on $^1O_2$ oxidation as compared to auto-oxidation. Exposure to light of shorter wavelengths (<300nm) (higher frequencies) which travels faster and has more energy, therefore leads to a faster oxidation rate of the oil as compared to longer wavelengths (>300nm) [9]. Packaging material and place of storage are therefore crucial to preserve the quality of the oil.

Storage stability of physically refined rice bran oil and binary blends with refined sunflower and safflower oil in different types of packaging (polyethylene terephthalate (PET), laminates, and glass bottles) were studied for 11 months storage period [10]. All the samples were still within limits after 11 months. Blended oils with higher levels of iodine value or saturation exhibited better stability. In terms of packaging, laminate pouches with no light interference were the best with minimum quality parameter changes followed by glass bottles and lastly PET bottles. Laminated pouches and glass bottles are more suitable for longer storage periods since there were no or minimal changes reported with regards to physio-chemical characteristics (peroxide value (PV), free

fatty acid (FFA), color, and p-anisidine value (AnV)) as compared to PET bottles [10].

Nutrient stability of sunflower oils stored in PET clear bottles and exposed to daylight at an ambient temperature of 25 °C were studied for a 10-month storage period [4]. Storage period and PET clear packaging were found to affect the shelf life of oils and result in a drastic loss of antioxidants (total tocopherols (52-64%) and beta-carotene (63-65%)). This implies a protective role of antioxidants against oxidative rancidity. The authors recommend the storage of oils in the dark and at a lower temperature to ensure longer shelf life [4].

Fatty acid composition of oils

Unsaturated fatty acids are more prone to oxidation compared to less unsaturated oils. The iodine value is commonly used as a measure of the relative degree of unsaturation in oil components. Storage stability of sesame oil (control), sesame: rice bran oil blends (80:20 and 20:80), and sesame: mustard oil blends (80:20 and 20:80) were studied for 12 months of storage. Sesame oil has predominantly poly-unsaturated fatty acid (PUFA)-C18:2 (46.74%) and mono-unsaturated fatty acid (MUFA)-C18:1 (37.4%). Blending with rice bran oil resulted in an increase in saturated fatty acid (SAFA)-C16:0 and MUFA-C18:1 as well as a reduction in PUFA-C18:2. Whereas, blending with mustard oil reduced SAFA-C16:0 further. Low SAFA content could be the reason why sesame: mustard oil blends were found to be the least stable based on physicochemical parameters evaluated. Sesame: rice bran oil blends were more stable compared to sesame oil itself [11].

Crude palm oil (CPO), sunflower (SFO), and sesame oils (SO) and their blends binary CPO+(SFO/SO) (3:1, 1:1, 1:3) and ternary CPO+SFO+SO (1:1:1, 2:1:1, 1:2:1, 1:1:2) were tested with regards to storage stability. These oils are unrefined oils purchased from local producers. Traditional processed CPO is obtained by primitive African village methods which involve boiling palm fruitlets, crushing the pulp, and extracting the crude oil. Two series of experiments were conducted. In the first set of experiments, the oils were subjected to heat at 120°C, for 3 hours per day for 60 days in the dark and the second experiment served as a control comparison with unheated oils in the dark for the same storage period. Based on oxidative parameter changes, binary blends of CPO with sesame oil or sunflower oil were most stable compared to the individual oil itself or ternary blends. This oxidative stability can be related to change/increase in saturation as reflected by iodine values [12].

Blends of soybean oil with sea buckthorn oil, camellia oil, rice bran oil, sesame oil, and groundnut oil were stored at accelerated degradation storage conditions of 60°C without the interference of air for 24 days. Blends of soybean oil with sea buckthorn oil responded best, followed by rice bran oil, camellia oil, sesame oil, groundnut oil, and lastly soybean itself. The oxidative stability of the blends increases as the degree of saturation increases [13].

Storage temperature

In a study on shelf-life stability of vitamin A fortified palm oils with varying initial values of PV (< 2, 4, or 9 mEq O_2/kg), oils were flushed with nitrogen in the headspace and stored in amber bottles in the dark at elevated temperatures of 60, 75 and 90°C. It was found that the vitamin A fortified oils in the form of retinyl palmitate oxidized faster in high PV oils with a shelf life ranging from a few days to 3 months based on PV standard (<10 mEq O_2/kg). This is due to the antioxidant nature of vitamin A which reacts against auto-oxidation of the oil. The authors also concluded that it was advisable to fortify oils with low PV value [14].

Following this study, Silalahi et al. studied vitamin A stability in RBD palm olein with PV values of less than 0.5 mEq O_2/kg. Effect of temperature (16-20 °C (cool), 24-29 °C (ambient), or 24-45 °C (seasonal)), as well as packing type (transparent PET bottle, nylon linear low-density polyethylene (LLDPE) (transparent and opaque) pouch or high-density polyethylene (HDPE) jerry can), were compared for 2 years storage period. Vitamin A content reduced to a greater extent at higher temperatures: 45-75% at 24-45°C, followed by 43-49% at 24-29 °C, and lastly 39-45% at 16-20 °C after 2

years of storage period. In terms of packaging material, opaque nylon LLDPE was the most stable followed by transparent PET bottles and lastly HDPE jerrycans. The samples did not have direct exposure to UV or sunlight. However, this deterioration may have occurred due to auto-oxidation by oxygen in the headspace of packaging materials which is highest in HDPE jerrycan followed by PET clear bottles and lastly opaque nylon LLDPE [15].

The solubility of oxygen in crude oil is higher than in refined oil. Crude oils contain transition metals that are reduced in refined oil. These transition metals in crude oil accelerate the oxidation of the oil. Storage stability of crude palm oils produced by either local companies, small producers, or industry was investigated for 3 months storage period at 2 different temperatures (20 and 30 °C). The PV of oils stored at 30°C was higher. Crude palm oil produced traditionally by the small producers had higher levels of FFA, moisture content, deterioration of bleachability index (DOBI), and PV due to poor handling and processing methods (i.e. low level of hygiene, fruitlet bruising during transportation as well as fermentation before threshing, clarification, and storage) compared to local companies and industries [16].

Antioxidants

Antioxidants are the best means of fending off oxidation. Antioxidants can be categorized as natural or synthetic, and differ in their mode of action. Only permitted antioxidants can be used in fats and food according to agreed standards. Butylated hydroxytoluene (BHT) and tert-butylhydroquinone (TBHQ) are common primary antioxidant compounds. The role of synthetic antioxidants (TBHQ, BHT, TBHQ+BHT) or control (without additive) in improving oxidative stability was studied in palm olein, soybean, and linseed oil. The oils were stored at room temperature or 70°C for 168 hours. Based on PVs, palm olein was found to be most stable (22-41% change from baseline), followed by linseed oil (26-43% change from baseline) and lastly soybean oil (320-500% change from baseline) after 168 hours storage period in their natural form. This is attributable to the oil's fatty acid composition, whereby the latter contains a higher amount of polyunsaturated fatty acid (PUFA). Longer storage periods and heat were found to affect the oxidative stability of the oils. In terms of antioxidant stability for palm olein, TBHQ was found to be the best followed by BHT and finally the mix. The mix of BHT and TBHQ was found to be superior for soybean oil and linseed oil compared to BHT and TBHQ by themselves [17].

Oxidative stability of sunflower, corn, extra virgin olive, grape seed, and walnut oils was studied after 5 days of storage at 50 °C. These oils are rich in natural antioxidants such as polyphenols, tocopherols, and vitamin C. Walnut oil was found to have the highest antioxidant capacity and chemical stability followed by olive oil, grape seed oil, corn oil, and lastly sunflower oil. High antioxidant levels were also associated with low PV and FFA content in the oils [18].

Crude oil refining removes toxic and undesirable substances such as mono- and diacylglycerols, pro-oxidants, moisture, FFAs, pigments, volatiles, and contaminants that are detrimental to the flavor, color, stability, or safety of the refined oils. The storage stability of crude and fully refined rice bran oil was studied over 8 months storage period at room temperature with and without the influence of light. Crude rice bran oil was found to have better oxidative stability based on the oil stability index as compared to refined rice bran oil. This is because crude rice bran oil contains a higher level of natural antioxidants such as vitamin E, sterols, and γ-oryzanol that have a synergistic effect with phosphatides. Both the oils were better stored in the dark and sensitive when exposed to daylight [19].

Table 1. Effects of storage conditions on physiochemical parameters of cooking oils

Oil Type	Duration	Storage Conditions	FFA	PV	AnV	TOTOX	extinction coefficients	FAC	Phenolic Compounds	Vitamin E	Carotenes	Antioxidant activity	Rancimat	Summary/ Comments	Ref.
Real storage conditions															
PO vs CSO vs SFO	4 days	Container conditions: 1) Sealed coloured (no light and air) vs 2) Sealed transparent (with light and no air) vs 3) Open transparent (with light and air)	X	X	X									– Stability: PO > CSO > SFO. – Condition stability: 1) no light and air > 2) with light, no air > 3) with light and air	[8]
Cold pressed peanut oil	20 day	Oil without antioxidant addition vs addition of rosemary extract (type Oxy' Less CS) vs ramDOPE vs hpDOPE vs α-tocopherol vs tocopherol mixture vs sage extract vs PG vs BHA		X										– Oxidative stability: PG (best) > rosemary > olive pomace (ramDOPE) > sage extract > olive pomace (hdDOPE) > tocopherol mixture/BHA > control without antioxidants > α-tocopherol	[20]
CPO vs SFO vs SO vs CPO+(SFO/SO) (3:1, 1:1, 1:3) vs CPO+SFO+SO (1:1:1, 2:1:1, 1:2:1, 1:1:2)	60 days	1) Heated at 120°C, 3hr/day x 60days, dark; 2) unheated, dark	X	X										– Storage stability: Binary (CPO+SO> CPO+SFO) > Single (CPO>SO>SFO) > Ternary blends	[12]
CPO (by local company vs small producer's vs industry)	3 months	20 & 30°C	X	X										– Stability: Oils from industry > local company > small producers – Deterioration: 30°C > 20°C	[16]
PO vs SBO vs LSO (TBHQ vs BHT vs TBHQ+BHT vs no additive)	168 hours	RT vs 70°C		X										– Oxidative stability: PO > LSO > SBO – Storage and heat: increase oxidation – Antioxidant stability: i. PO: TBHQ>BHT>mix, ii. SBO& LSO: mix>BHT>TBHQ	[17]
Crude vs refined RBO	240 days (8 months)	Transparent bottles; no exposure to atmospheric oxygen, kept in dark or exposed to daylight at ambient temperature	X					X		X			X	– Oxidative stability: crude > refined RBO – Antioxidant stability: γ-Oryzanol (most stable)> sterol esters > sterols > vitamin E (least stable) – Storage stability: keep in dark > light	[19]
SFO (n=4 with different country of origin)	307 days	Headspace: no protective atmosphere; PET bottles; 21-34°C								X	X		X	– Stability: no difference with different origins. – PET bottles not suitable for long storage period: reduces vitamin E & carotenes. – Advise: store at dark & low temperature for longer storage period	[4]

[a] Abbreviations: AnV: *p*-anisidine value, BHA: butylhydroxyanisole, BHT: butylated hydroxyl toluene, CPO: crude palm oil, CSO: cotton seed oil, DOPE: dry olive pomace extract, FAC: fatty acid composition, FFA: free fatty acid, LSO: linseed oil, PG: propyl gallate, PO: palm oil, PV: peroxide value, RBO: rice bran oil, SBO: soyabean oil, SFO: sunflower oil, SO: sesame oil, TBHQ: tert-Butylhydroquinone, TOTOX: total oxidation value

Table 1. Effects of storage conditions on physiochemical parameters of cooking oils (continued)

Oil Type	Duration	Storage Conditions	FFA	PV	AnV	TOTOX	extinction coefficients	FAC	Phenolic Compounds	Vitamin E	Carotenes	Antioxidant activity	Rancimat	Summary/ Comments	Ref.
RBO vs RBO+SAF (20:80) vs RBO+SFO (60:40)	11 months	Packaging materials: bottles (PET vs glass) vs laminated pouches; 25°C	X	X	X			X						– Stability: RBO+SAF > RBO+SFO > RBO. – Stability: Laminated pouches and glass bottles > PET bottles	[10]
SO vs blends SO+RBO vs SO+MO (80:20 & 20:80)	12 months	PET clear bottles at RT	X	X	X	X		X						– Blends of SAFA: MUFA: PUFA at 1:1:1 is recommended to increase stability.	[11]
VOO (Lianolia vs Koroneiki variety)	15 months	Headspace: 1-3%, Dark; 20± 4°C		X					X					– Oxygen exposure: increase in PV correlates with reduction in phenolic compounds and formation of oxidized phenolic compounds	[7]
PO+Vitamin A	16 & 24 months	1) Temperature:16-20°C(cool) vs 24-29°C(ambient) vs 24-45°C (seasonal); 2) Pack type: PET bottle vs nylon LLDPE pouch vs HDPE JC; 3) Packaging type: transparent PET vs opaque nylon vs LLDPE pouch		X							X			– Vitamin A Stability: 16-20°C > 16-20°C > 24-45°C; – Packaging stability: opaque nylon LLDPE > transparent PET > HDPE jerrycan	[15]
Schaal oven test															
Vitamin A fortified palm oil with varying PV values; 2 vs 4 vs 9 mEq O_2/kg		Headspace: flushed with N_2, amber bottles in dark; 60, 75 & 90°C		X							X			– Shelf life of RPO: 3-30days. – Increase in PV causes decrease in vitamin A retention. – Fortification of vitamin A should be done on low PV oils	[14]
SFO vs CN vs EVOO vs GSO vs COC vs WNO	5 days	50°C, light, atmospheric oxygen	X	X								X		– Antioxidant activity decreases as FFA and PV increase	[18]
SBO vs SBO+CAO vs SBO+SO vs SBO+RBO vs SBO+GNO vs SBO+SEBO	24 days	60°C, dark, no headspace		X	X		X							– Stability: SBO+SEA > SBO+RBO >SBO+CAO > SBO+SEBO > SBO+GNO > SBO	[13]

[a]Abbreviations: AnV: p-anisidine value, CAO: camellia oil, CN: corn oil, COC: coconut oil, EVOO: extra virgin olive oil, FAC: fatty acid composition, FFA: free fatty acid, GNO: groundnut oil, GSO: grape seed oil, HDPE: high density polyethylene, LLDPE: linear low density polyethylene, MUFA: mono-unsaturated fatty acid, MO: mustard oil, PET: polyethelene terephthalate, PO: palm oil, PUFA: poly-unsaturated fatty acid, PV: peroxide value, RBO: rice bran oil, RBO: rice bran oil, RT: room temperature, SAF: safflower oil, SBO: soyabean oil, SAFA: saturated fatty acid, SEBO: sea buckthorn oil, SFO: sunflower oil, SO: sesame oil, TOTOX: total oxidation value, VOO: virgin olive oil, WNO: walnut oil.

The addition effect of natural [rosemary extract, sage extract, DOPE-dry olive pomace extract (type hpDOPE and ramDOPE), α-tocopherol and mixtures of tocopherols] and synthetic antioxidants [propyl gallate (PG) and butylhydroxyanisole (BHA)] were evaluated with regards to the oxidative stability (PV) of cold-pressed peanut oil compared to control (oil without antioxidants) for 20 days. Propyl gallate provided the best antioxidant protection, followed by rosemary extract (type OxyLess CS), olive pomace (ramDOPE), sage extract, and olive pomace (hdDOPE), both tocopherol mixture and BHA had equal antioxidant capacity, followed by control oil without antioxidants and the least in the order was α-tocopherol [20].

Chemical reactions during cooking

Cooking oils are an essential part of our daily diet preparations. Some cooking oils are rich in heat-sensitive nutrients that offer varying health benefits. The nutritional content of the oils is affected by different cooking techniques such as deep-frying, pan-frying, conventional oven baking and roasting as well as microwave heating. Table 2 summarizes the effects of several heating techniques under real and simulated cooking conditions on several analytical parameters.

Frying is the oldest method of food preparation. There are different frying techniques namely pan-frying, deep-frying, shallow frying, and stir-frying. The difference lies in the amount of oil used, the latter using lesser oil [21]. The frying technique transfers heat through the convection of oil directly from a heating element [22]. Moving forward in history, the conventional oven revolutionized methods of cooking. The conventional oven operates by transferring heat through convection but uses air as a heat transfer medium [22]. Roasting and baking are common cooking techniques of the conventional oven, which primarily operates by convection of air and secondarily radiation from the oven walls and conduction from the baking pan. The roasting technique requires comparable amounts of fat compared to pan-frying but is highly prone to oxidation as a higher surface area is exposed to convection hot air and for a longer processing time [21]. The microwave oven is a modern technique for heating food through the conversion of electromagnetic energy to thermal energy. A microwave oven heats food faster due to the direct penetration of microwaves into food materials compared to conventional heating on a stove or oven. However, a major hitch to this technique is non-uniform heating that could be influenced by microwave cavity design, food physical properties, and food geometry [23]. Different cooking techniques and operation conditions undoubtedly will impact the physicochemical properties of the oil. The following section will discuss chemical reactions induced by heating which include hydrolysis, oxidation, and polymerization.

Hydrolysis

The FFA concentration is one of the most important indicators of oil deterioration during heating. The formation of FFA is due to the hydrolysis of triacylglycerol (TAG) and hydroperoxide (ROOH) decomposition in oil during heating in the presence of moisture and air. At simulated heating conditions, heating at 180 °C was reported to discourage major triacylglycerol hydrolysis [24, 25, 22]. However, in the presence of a food matrix, the acidity values rapidly increased with frying time probably due to moisture content in the presence of food [26, 27]. The formation of FFA is associated with smoke points [28]. An increase in FFA has an inverse association with the smoke point [3]. The smoke point of fats/oils decreases when the fat begins to break down into FFA, monoacylglycerols (MAG), diacylglycerols (DAG), and volatile compounds [28].

Table 2. Effects of different heating techniques on physiochemical parameters of cooking oils

Heating Technique	Oil Type	Food Matrix	Heating Conditions	FFA	PV	AnV	TOTOX	extinction coefficients	FAC	Polar compounds	Phenolics	Vitamin E	Carotenes	Rancimat	Summary/ Comments	Ref.
DF	EVOO vs VOO (Year 2004) vs VOO (Year 2005) vs refined OO+VOO blend vs SFO	Potatoes	170°C; 27 hr (9h/day); 120min X 10sessions/day; NR	X	X	X		X	X	X				X	Stability: SFO least, OO groups similar	[34]
DF	POo vs CO vs SBO vs MOO	Potatoes	185°C; 6 hr/day X 5 days; 75 sessions; FR				X		X	X					Stability: POo & MOO (high SAFA&MUFA oils) > SBO & CO (high PUFA oils)	[42]
DF	POo vs POo+BEO (200ppm) vs POo+BEO (500ppm)	Potatoes	180°C; 80 sessions/day x 5days; FR	X	X	X		X						X	Stability: POo+BEO (500ppm) > POo+BEO (200ppm) > POo	[35]
DF	PO vs HO-SFO+CO blend	Potatoes	170°C; 12 min/cycle x 60 session/day (12hr/day) X 5 days; 300 sessions; FR	X	X	X	X		X	X		X		X	Stability: PO > HO-SFO+CO blend	[32]
DF	POo vs SQPOo	Potatoes	180°C, 56 hr (8 hr/day); CR	X						X		X		X	Stability: POo similar to SQPOo	[2]
DF	POo vs PGE fortified POo(s) (PGE:0.1%vs 0.2% vs 0.3% vs 0.4%)	Potatoes	170°C; 16 cycles (8hr/day) X 5 days; 80 cycles; FR	X		X			X	X					Stability: POo> POo+PGE 0.1% > POo+PGE 0.2% > POo+PGE 0.3% > POo+PGE 0.4%)	[43]
DF	POo	Potatoes	180°C; 8 hr/day x 5 days; 80 sessions; FR; Frying protocols: 1) draining under vacuum (1.33kPa) vs 2) draining under atmospheric pressure	X		X			X			X			Stability: draining under vacuum > conventional draining under atmospheric pressure	[48]
DF	11 oils: (1) Singular oils: POo/SBO/CO/SFO vs (2) binary blends POo+ SBO/CO/SFO at (90:10)/(50:50) ratios vs (3) Tertiary blend POo+SBO+CO (40:50:10)	Potatoes	180°C; 8 hr/day x 9 days; 144 sessions; FR			X			X	X					Stability: POo blended oils > SBO/CO/SFO	[27]
DF	HO-LL-RAP vs HO-SFO vs MO-SFO vs LL-SBO vs POo	Potatoes, battered chicken, fish sticks	185°C; 8 hr/day x 6 days; 60 sessions; FR	X		X				X		X			Stabilty; HO-RAP > HO-SFO > POo > MO-SFO > LL-SBO	[47]

[a] Abbreviations:
AnV: *p*-anisidine value, BEO: basil essential oil, CO: canola oil, CR: continuous replenishment, DF: deep frying, EVOO: extra virgin olive oil, FAC: fatty acid composition, FFA: free fatty acid, FR: frequent replenishment, HO: high olein, LL: low linoleic, MO: mid oleic, MOO: moringa oleifera seed oils, MUFA: mono-unsaturated fatty acid, NR: null replenishment, OO: olive oil, PGE: polyglycerol fatty acid esters, PO: palm oil, POo: palm olein, PV: peroxide value, RAP: rapeseed oil, SAFA: saturated fatty acid, SBO: soybean oil, SFO: sunflower oil, SQPOo: special quality palm olein, TOTOX: total oxidation value, VOO: virgin olive oil.

Table 2. Effects of different heating techniques on physiochemical parameters of cooking oils (continued)

Heating Technique	Oil Type	Food Matrix	Heating Conditions	FFA	PV	AnV	TOTOX	extinction coefficients	FAC	Polar compounds	Phenolics	Vitamin E	Carotenes	Rancimat	Summary/ Comments	Ref.
DF	11 oils: (1) Singular oils: POo/SBO/CO/SFO vs (2) binary blends POo+ SBO/CO/SFO at (90:10)/(50:50) ratios vs (3) Tertiary blend POo+SBO+CO (40:50:10)	Potatoes	180°C; 8 hr/day x 9 days; 144 sessions; FR											X	Blending unsaturated oils with POo improved oxidative stability.	[31]
DF	RBD PO	chicken	150, 200 & 250°C; 1 day (8 hr/day); 10 min/ sessions (48 sessions)						X						Temperature >200°C causes PUFA isomerization and trans formation. FAC composition of chicken= oxidised oil: proves absorption of harmful compounds.	[45]
DF	15 EVOO samples	Gelatinized maize starch	180°C; 30min / session x 2												Long exposure to heat cause formation of toxic volatile compounds	[49]
DF	Palm products (RBD PO vs SFPO vs DFPO vs RPOo vs PBS) vs HOSFO	Simulation	180°C; 10 days (8 hr day-1), FR	X		X				X		X			RBD PO, SFPO and DFPO most stable	[3]
DF	EVOO Italian vs Portuguese	Simulated	180°C; 3hr		X						X	X			Fluorescence spectroscopy suitable for EVOO quality characterization	[39]
DF	VOO (Lianolia vs Koroneiki variety)	Simulated	180°C; 0-60mins	X	X			X			X				Thermal oxidation: increase in PV correlates with decrease in phenolic compounds & formation of oxidized phenolic compounds	[7]
DF vs PF	EVOO vs SFO+CSO+POo blend	Potatoes	170°C, 12min X 10sessions (1 day); NR	X	X			X	X	X	X	X		X	Stability: deep-fry > pan-fry; Oil stability: EVOO > SFO+CSO+POo blend	[30]
H	VOO (Lianolia vs Koroneiki variety)	Simulated	100°C; 1-4 hr	X	X			X			X				Phenolic compounds stable at 100°C	[7]
H	PO+Vitamin A (45ppm vs 225ppm)	Simulated	180°C; 5 minutes	X	X								X		Low level of oxidised oil is suggested for vitamin A fortification	[15]
MV	EVOO (NE Portugal) vs EVOO (Central Portugal) vs VOO (South Portugal)	Simulated	1000W, 0-15 minutes	X	X			X				X	X		Stability: EVOO>VOO	[25]
MV	4 types of OO	Simulated	1000W, 0-15 minutes	X	X			X			X		X		Microwave is encouraged only for short period of heating	[24]

[a]Abbreviations: AnV: *p*-anisidine value, CO: canola oil, CSO: cottonseed oil, DF: deep frying, DFPO: double fractionated palm olein, EVOO: extra virgin olive oil, FAC: fatty acid composition, FFA: free fatty acid, FR: frequent replenishment, H: heating, MV: microwave oven, NR: null replenishment, OO: olive oil, PF: pan frying, PO: palm oil, POo: palm olein, PV: peroxide value, PUFA: poly-unsaturated fatty acid, RBD: refined bleached deordarised, SBO: soybean oil, SFO: sunflower oil, SFPO: single fractionated palm olein, TOTOX: total oxidation value, VOO: virgin olive oil

Table 2. Effects of different heating techniques on physiochemical parameters of cooking oils (continued)

Heating Technique	Oil Type	Food Matrix	Heating Conditions	FFA	PV	AnV	TOTOX	extinction coefficients	FAC	Polar compounds	Phenolics	Vitamin E	Carotenes	Rancimate	Summary/ Comments	Ref.
MV vs. OVN	ROO vs EVOO	Simulated	MV:500W, 0-30 min		X			X	X						Microwave not significantly higher than conventional oven	[38]
			OVN:1200W, 0-30 min		X			X	X							
MV	SO vs SBO	Simulated	low power: 500W vs medium power:650W vs high power:800W, 0-20 minutes	X	X	X									Stability: SO > SBO; Higher power > degradation	[26]
		chips		X	X	X										
MV	S-LO vs NS-LO	Simulated	1000W, 0-5 min	X	X	X	X	X							Stability: S-LO < NS-LO, PUFA oils not suitable for heat treatment	[36]
MV	Pork lard vs SFO vs RAP vs GNO vs HO-GNO	Simulated	500W, 0-40 min	X				X							Stability: HO-GNO > pork lard > RAP > GNO > SFO. PUFA oil least stable	[33]
MV	POo vs SFO vs POo+SFO blend	Simulated	Medium power setting, 0-20 min	X	X	X	X	X	X	X					Stability: POo > POo+SFO > SFO	[41]
MV	SFO vs CO	Simulated	700W, 0-10 min (Magnetron pause of total heating time: 10% vs 30%)		X	X		X	X			X			Stability: CO > SFO Magnetron pause: 30% better than 10% (higher vitamin E & lesser oxidative compounds	[40]
MV vs. OVN	R-SFO vs R-SFO+GSE (200, 400, 600, 800 and 1000ppm) vs R-SFO+BHT (200ppm)	Simulated	MV: 900W, 0-240 min		X	X	X	X			X				Microwave had higher oxidation values than oven; R-SFO+GSE >600ppm better than SFO+BHT	[37]
			OVN: 1200W, 0-240 min		X	X	X	X			X					
MV vs. OVN	ROO vs EVOO	Simulated	MV: 500W, 0-30 min		X			X	X						Microwave not significantly higher than conventional oven	[38]
			OVN: 1200W, 0-30 min		X			X	X							
MV	4 types of OO	Simulated	1000W, 0-15 min	X	X			X			X		X		Microwave is encouraged only for short period of heating	[24]
DF vs MV vs OVN	RPOo vs POo	Simulated	170°C; 3 hr deep-fat fryer vs microwave oven vs conventional oven	X	X	X	X		X			X	X		Stability: POo>RPOo; POo: stable for all 3 heating techniques; RPOo: not suitable for prolonged heating when carotenes retention is of concern	[22]

[a]Abbreviations:
AnV: *p*-anisidine value, BHT: butylated hydroxytoluene, CO: canola oil, DF: deep frying, EVOO: extra virgin olive oil, FAC: fatty acid composition, FFA: free fatty acid, GNO: groundnut oil, GSE: grape seed extract, HO: high olein, MV: microwave oven, NS-LO: non-stripped linseed oil, OO: olive oil, OVN: conventional oven, POo: palm olein, PUFA: poly-unsaturated fatty acid, PV: peroxide value, RAP: rapeseed oil, ROO: refined olive oil, RPOo: red palm olein, R-SFO: refined sunflower oil, SBO: soybean oil, SFO: sunflower oil, S-LO: stripped linseed oil, SO: sesame oil, TOTOX: total oxidation value

Oxidation

Three types of oxidations take place during the heating process namely autoxidation, thermal oxidation, and photosensitized oxidation. The science behind thermal oxidation is principally similar to the mechanism of auto-oxidation that involves initiation, propagation, and termination. However, the rate of thermal oxidation is faster compared to autoxidation [29]. The induction period is the point where rapid changes occur as a result of oxidation, usually measured by the Rancimat method and expressed in hours. The time taken for secondary reaction products to appear is known as the induction time, induction period, or Oil Stability Index (OSI) [2]. The induction period of the oil was reported to decrease over time with heating [30, 31]. The reduction in the induction period is more prominent in oils containing high amounts of unsaturated fatty acids especially PUFAs [32]. Conjugated dienes are formed corresponding with the formation of linoleic acid hydroperoxide as an early indicator of lipid oxidation [33]. The UV-Vis extinction coefficients K_{232} and K_{270} are other analytical measures that relate to the content of conjugated dienes and trienes in the oil. High PUFA content oils were found to increase these coefficient values faster as compared to monounsaturated and saturated oils subjected to deep-frying [34, 35], pan-frying [30], microwave oven [24,33,36], and conventional oven [37, 38]. Conjugated dienes and peroxides are highly unstable primary intermediate oxidation products of oil which lead to the formation of a complex secondary mixture of volatile compounds such as aldehydes, ketones, hydrocarbons, alcohols, and esters [29]. A reducing trend of PV however was observed by Cheikhousman et al. proving the transformation of unstable primary oxidation products to secondary oxidation products [39]. Peroxides, therefore, are not a good index of oxidation measurement.

Anisidine values (AnV) represent the level of non-volatile aldehydes, primarily, measuring the presence of 2-alkenals and 2,4-alkadienals generated in the fat during the decomposition of hydroperoxides [5]. A progressive increase in AnV was observed with deep-frying [34, 35], microwave [36, 40, 41] and conventional oven [37, 22] heating. The total oxidation (TOTOX) value is an extension of AnV method given as the sum of two times PV and AnV, which is an important evaluation parameter for the overall oxidation state. At low temperatures and a short storage period, the formation of oxidation compounds is slow; hydroperoxides are the major compounds formed. Whereas during heating (high temperatures), the formation of secondary oxidation products is very rapid. Hence, AnV dominates TOTOX value during heating while PV dominates TOTOX value upon storage. Therefore increase in TOTOX value by deep-frying [42], microwave oven [36, 33, 41], and conventional oven [37, 22] is known to reflect a better approximation of the development of oxidative deterioration as it measures both hydroperoxides and secondary breakdown products.

Linoleic acid (C18:2) is highly susceptible to oxidation. The degree of oxidative deterioration is namely evaluated by the ratio of C18:2/C16:0 and is reported to decrease upon prolonged heating by deep-frying [32, 43, 44], pan-frying [30] and microwave oven [40, 41], with a greater degree of saturation. Oil degradation during heating decreases the levels of PUFA, increases the saturated fatty acid content [38, 40, 45, 34, 42], and increases C18 trans [45]. Trans fatty acids are produced from cis-unsaturated fatty acids upon heating of oils at high temperatures and by the hydrogenation process. The chemical structure of the carbon chain of trans fatty acids is more stable than that of cis fatty acids when exposed to heat [46]. The fatty acid composition of the food matrix was found to be similar to the immersed cooking oil during deep-frying, this study implied that harmful oxidative products would be absorbed by the food matrix [45].

Oxidative degradation of oils during heating depends on the fatty acid composition, especially PUFA content as well as the content of natural antioxidants [33]. Minor component losses were also reported by some authors with heat exposure. Antioxidants like polyphenols [30, 39, 7, 24, 37], vitamin E [39, 30, 47, 22], carotenoids [25, 24, 22], vitamin A [15] and chlorophylls [25] were found to degrade upon prolonged heat exposure.

Polymerization

Oil endures hydrolysis, oxidation, and polymerization upon heating, resulting in the formation of decomposition by-products such as non-volatile polar

compounds and triacylglycerol dimers and polymers. The total polar compounds characterize the fatty acid degradation products with higher polarity and molecular weight than initial triglycerides present in the oil with heat exposure. Total polar compounds are a widely accepted indicator to measure fat degradation [21]. Total polar compounds were found to increase with heating time and were greater in oils with a higher degree of unsaturation with heat exposure e.g. deep frying [34], microwave oven [41], and pan-frying [30]. A weak correlation was found between diacylglycerols and total polar compounds, this negates the concern that oils with high natural diacylglycerol content result in a higher rate of formation of total polar compounds upon heating [27].

Polymers are formed in heated oils [33, 47]. These polymers accelerate the oxidation of oil and lead to some physical changes in oil such as an increase in viscosity, color, and foam as well as a decrease in smoke point. An increase in polymers [29] or oil viscosity [48] causes high oil absorption in food. Viscosity was reported to increase with prolonged heating by deep-frying [48, 44] and microwave oven heating [41]. Additionally, prolonged exposure of PUFAs to heat also causes neo-formation of harmful volatile compounds such as acrolein and crotonal [49].

Conclusion

Translating the results of the current review into daily diet application/recommendations for the public's benefit, our research has demonstrated that consumers need to be educated and exposed that cooking oil should be placed away from heat and light to preserve oil quality and phytonutrient content. In addition, it is advisable to keep air to oil interface minimal in a closed handling system for both storage and heating purposes. Polyunsaturated oils are very susceptible to oxidation. Saturated or blended oils are recommended for long cooking processes to maximise the quality of oil and delay the onset of lipid oxidation. Antioxidants are desirable to increase the oxidative stability of the oil, but they degrade at unsuitable storage conditions and with prolonged heating.

Acknowledgements

The authors thank the director-general of the Malaysian Palm Oil Board for permission to publish this study.

References

1. Choe, E. and Min, D. B. (2006). Mechanisms and factors for edible oil oxidation. *Comprehensive Reviews in Food Science and Food Safety,* 5(4): 169-186.
2. Ahmad Tarmizi, A. H. and Ismail, R. (2008). Comparison of the frying stability of standard palm olein and special quality palm olein. *Journal of the American Oil Chemists' Society,* 85(3): 245-251.
3. Ahmad Tarmizi, A. H. and Siew, W. L. (2008). Quality assessment of palm products upon prolonged heat treatment. *Journal Oleo Science,* 57(12): 639-648.
4. Vrbiková, L., Schmidt, Š., Kreps, F., Tmakova, L., Čertík, M. and Sekretar, S. (2014). Degradation of selected nutrients in sunflower oils during long-term storage. *Czech Journal of Food Sciences,* 32(6): 595-600.
5. Gupta, M. K. (2005). Frying oils. Bailey's industrial oil and fat products, John Wiley & Sons Inc., New Jersey: pp 4: 1.
6. Saha, S. and Mondal, S. (2018). Photochemistry and photophysics: Fundamentals to applications: BoD–Books on Demand.
7. Daskalaki, D., Kefi, G., Kotsiou, K. and Tasioula-Margari, M. (2009). Evaluation of phenolic compounds degradation in virgin olive oil during storage and heating. *Journal of Food and Nutrition Research,* 48 (1): 31-41.
8. Henry, L. N. (2016). Effect of light and air on the quality and stability of selected vegetable oils. *International Journal of Innovative Research in Science, Engineering and Technology,* 5: 6609-6616.
9. Shankar, R., Shim, W. J., An, J. G. and Yim, U. H. (2015). A practical review on photooxidation of crude oil: Laboratory lamp setup and factors affecting it. *Water Research,* 68: 304-315.
10. Mishra, R. and Sharma, H. (2011). Effect of packaging materials on the storage stability of physically refined rice bran oil and its blends. *African Journal of Food Science,* 5(12): 676-685.
11. Gulla, S. and Waghray, K. (2011). Effect of storage on physico-chemical characteristics and fatty acid composition of selected oil blends. *Journal of Life Sciences,* 3(1): 35-46.
12. Ngassapa, F., Nyandoro, S. and Mwaisaka, T. (2012). Effects of temperature on the physicochemical properties of traditionally processed vegetable oils and their blends. *Tanzania Journal of Science,* 38(3): 166-176

13. Li, Y., Ma, W. J., Qi, B. K., Rokayya, S., Li, D., Wang, J. and Jiang, L. Z. (2014). Blending of soybean oil with selected vegetable oils: impact on oxidative stability and radical scavenging activity. *Asian Pacific Journal of Cancer Prevention,* 15(6): 2583-2589.
14. Andarwulan, N., Gitapratiwi, D., Laillou, A., Fitriani, D., Hariyadi, P., Moench-Pfanner, R. and Martianto, D. (2014). Quality of vegetable oil prior to fortification is an important criteria to achieve a health impact. *Nutrients,* 6(11): 5051-5060.
15. Silalahi, D. K. N., Yuliyanti, D., da Silva, M., Christianti, I., Mulyono, K. and Wassell, P. (2017). The stability of vitamin A in fortified palm olein during extended storage and thermal treatment. *International Journal of Food Science & Technology, 52*(8): 1869-1877.
16. Augustin, G., Anne, M. N., Armand, A. B. and Moses, M. C. (2015). Some physicochemical characteristics and storage stability of crude palm oils (*Elaeis guineensis* Jacq). *American Journal of Food Science and Technology, 3*(4): 97-102.
17. Azeez, O. T., Ejeta, K. O., Frank, E. O. and Gerald, N. E. (2013). Effects of antioxidants on the oxidative stability of vegetable oil at elevated temperature. *International Journal of Applied Science and Technology,* 3(5): 107-115.
18. Amariei, S., Sănduleac, E. and Ciornei, S. (2016). Comparative study of oxidative stability for different types of vegetable oils. *Food and Environment Safety Journal,* 12(2): 156-160.
19. Mezouari, S. and Eichner, K. (2007). Comparative study on the stability of crude and refined rice bran oil during long term storage at room temperature. *European Journal of Lipid Science and Technology,* 109 (3): 198-205.
20. Tihomir, M., Drago, Š., Jurislav, B., Antonija, Š., Dubravka, V. Č. and Antun, J. (2019). Production and stabilisation of peanut oil. *Nutrition and Dietetics,* 8(1): 40-45.
21. Santos, C. S., Cruz, R., Cunha, S. C. and Casal, S. (2013). Effect of cooking on olive oil quality attributes. *Food Research International,* 54(2): 2016-2024.
22. Loganathan, R., Tarmizi, A. H. A., Vethakkan, S. R. and Teng, K.-T. (2020). Retention of carotenes and vitamin E, and physico-chemical changes occurring upon heating red palm olein using deep-fat fryer, microwave oven and conventional oven. *Journal Oleo Sciences,* 69(3): 167-183.
23. Tang, J. and Resurreccion Jr, F. (2009). Electromagnetic basis of microwave heating. Development of packaging and products for use in microwave ovens. Elsevier. pp. 3-38e.
24. Yahyaoui, A., Rigane, G. and Salem, R. B. (2014). Microwave heating of different commercial tunisian olive oil: Regarding to exposure times on physical and chemical parameters properties. *Biochemistry and Physiology, 3*(2): 1-5.
25. Malheiro, R., Oliveira, I., Vilas-Boas, M., Falcão, S., Bento, A. and Pereira, J. A. (2009). Effect of microwave heating with different exposure times on physical and chemical parameters of olive oil. *Food and Chemical Toxicology,* 47(1): 92-97.
26. Ghosh, J., Banerjee, A., Gupta, S., Sengupta, A. and Ghosh, M. (2014). Comparative degradation effects of sesame and soybean oil during heating using microwave irradiation. *Journal of Scientific and Industrial Research,* 73(8): 547-552.
27. Ahmad Tarmizi, A. H., Hishamuddin, E. and Abd Razak, R. A. (2019). Impartial assessment of oil degradation through partitioning of polar compounds in vegetable oils under simulated frying practice of fast food restaurants. *Food Control, 96*: 445-455.
28. Ahmad Tarmizi, A. H., Ismail, R. and Kuntom, A. (2016). Effect of frying on the palm oil quality attributes–A Review. *Journal of Oil Palm Research,* 28(2): 143-153.
29. Choe, E. and Min, D. (2007). Chemistry of deep-fat frying oils. *Jornal Food Sciences,* 72(5): 77-86.
30. Andrikopoulos, N. K., Kalogeropoulos, N., Falirea, A. and Barbagianni, M. N. (2002). Performance of virgin olive oil and vegetable shortening during domestic deep-frying and pan-frying of potatoes. *International Journal of Food Science and Technology,* 37(2): 177-190.
31. Ahmad Tarmizi, A. H., Ahmad, K., Sahri, M. M. and May, C. Y. (2016). Rancimat test for measuring the oxidative stability of cooking oils upon prolonged frying. *Journal of Oil Palm Research,* 28(4): 531-535.
32. Hu, M., Pan;, K., Niu;, Y., Chen;, S., Yoong;, J. H., Tarmizi;, A. H. A. and Zhang, G. (2020). Comparative assessment of thermal resistance of palm stearin and high oleic blended oil when subjected to frying practice in fast food restaurants. *Journal of Oil Palm Research,* 32(1): 90-102.
33. Dostalova, J., Hanzlik, P., Reblova, Z., Pokorny, J. and Sakurai, H. (2005). Oxidative changes of vegetable oils during microwave heating. *Czech Journal of Food Sciences,* 23(6): 230-239.

34. Casal, S., Malheiro, R., Sendas, A., Oliveira, B. P. and Pereira, J. A. (2010). Olive oil stability under deep-frying conditions. *Food and Chemical Toxicology,* 48(10): 2972-2979.
35. Cardoso-Ugarte, G. A., Morlan-Palmas, C. C. and Sosa-Morales, M. E. (2013). Effect of the addition of basil essential oil on the degradation of palm olein during repeated deep frying of French fries. *Journal of Food Science,* 78(7): 978-984.
36. Megahed, M. G. (2011). Effect of microwave heating of linseed oil on the formation of primary and secondary oxidation products. *Agriculture and Biology Journal of North America,* 2: 673-679.
37. Poiana, M. A. (2012). Enhancing oxidative stability of sunflower oil during convective and microwave heating using grape seed extract. *International Journal of Molecule Sciences,* 13(7): 9240-9259.
38. Mahmoud, E. A. E.-M., Dostálová, J., Pokorný, J., Lukešová, D. and Doležal, M. (2009). Oxidation of olive oils during microwave and conventional heating for fast food preparation. *Czech Journal of Food Sciences,* 27: 173-177.
39. Cheikhousman, R., Zude, M., Bouveresse, D. J.-R., Léger, C. L., Rutledge, D. N. and Birlouez-Aragon, I. (2005). Fluorescence spectroscopy for monitoring deterioration of extra virgin olive oil during heating. *Analytical Bioanalytical Chemistry,* 382(6): 1438-1443.
40. Kreps, F., Vrbiková, L., Schmidt, Š., Sekretár, S. and Híreš, O. (2014). Chemical changes in microwave heated vegetable oils. *European Journal of Lipid Science and Technology,* 116(12): 1685-1693.
41. Ali, M. A., Nouruddeen, Z. B., Muhamad, I., Latip, R. and Othman, N. H. (2014). Effect of microwave heating on oxidative degradation of sunflower oil in the presence of palm olein. *Sains Malaysiana*, 43 (8): 1189-1195.
42. Abdulkarim, S. and Ghazali, H. (2012). Fatty acid ratios and their relative amounts as indicators of oil stability and extent of oil deterioration during frying. *Journal of Food, Agriculture and Environment,* 10: 33-38.
43. Ahmad Tarmizi, A. H., Abd Razak, R. A., Abdul Hammid, A. N. and Kuntom, A. (2019). Effect of anti-clouding agent on the fate of 3-monochloropropane-1, 2-diol esters and glycidyl esters in palm olein during repeated frying. *Molecules,* 24(12): 1-13.
44. Choi, H., Lee, E. and Lee, K.-G. (2014). Quality evaluation of noble mixed oil blended with palm and canola oil. *Journal of Oleo Sciences,* 63(7): 653-660.
45. Chen, W. A., Chiu, C. P., Cheng, W. C., Hsu, C. K. and Kuo, M. I. (2013). Total polar compounds and acid values of repeatedly used frying oils measured by standard and rapid methods. *Journal of Food and Drug Analysis,* 21(1): 58-65.
46. Liu, W. and Lu, G. (2018). Cis-trans isomerization of unsaturated fatty acids in edible oils to prepare trans fat. *Grasas y Aceites,* 69(3): 268.
47. Aladedunye, F. and Przybylski, R. (2014). Performance of palm olein and modified rapeseed, sunflower, and soybean oils in intermittent deep‐frying. *European Journal of Lipid Science and Technology,* 116 (2): 144-152.
48. Ahmad Tarmizi, A. H., Niranjan, K. and Gordon, M. (2013). Physico-chemical changes occurring in oil when atmospheric frying is combined with post-frying vacuum application. *Food Chemistry,* 136(2): 902-908.
49. Procida, G., Cichelli, A., Compagnone, D., Maggio, R. M., Cerretani, L. and Del Carlo, M. (2009). Influence of chemical composition of olive oil on the development of volatile compounds during frying. *European Food Research and Technology,* 230(2): 217-229.

Malaysian Journal of Analytical Sciences (MJAS)
Published by Malaysian Analytical Sciences Society

CHEMICAL SYNTHESIS OF METAL OXIDE NANOPARTICLES VIA IONIC LIQUID AS CAPPING AGENT: PRINCIPLE, PREPARATION AND APPLICATIONS

(Sintesis Kimia Logam Oksida Nanozarah Melalui Cecair Ionik Sebagai Ejen Pembekat: Prinsip, Penyediaan dan Aplikasi)

Nurul Syafiqah Tapak[1,2], Mohd Azizi Nawawi[2], Ahmad Husaini Mohamed[1], Eddie Tan Ti Tjih[3], Yusairie Mohd[2], Ahmad Hazri Bin Ab Rashid[4], Jaafar Abdullah[5*], Nor Azah Yusof [5], Nor Monica Ahmad[1,6*]

[1]School of Chemistry and Environment,
Faculty of Applied Sciences,
Universiti Teknologi MARA, Cawangan Negeri Sembilan, Kampus Kuala Pilah,
72000 Kuala Pilah, Malaysia
[2] School of Chemistry and Environment,
Faculty of Applied Sciences,
Universiti Teknologi MARA, 40450 Shah Alam, Malaysia
[3]School of Industrial Technology,
Faculty of Applied Sciences,
Universiti Teknologi MARA, Cawangan Negeri Sembilan, Kampus Kuala Pilah,
72000 Kuala Pilah, Malaysia
[4]Industrial Biotechnology Research Center SIRIM Berhad
No 1, Persiaran Dato' Menteri Section 2, PO Box 7035 40700 Shah Alam, Selangor
[5] Department of Chemistry,
Faculty of Science,
Universiti Putra Malaysia, Serdang, Selangor, Malaysia
[6] Biotechnology, Microbiology and Environment Collaborative Sciences,
Universiti Teknologi MARA, Cawangan Negeri Sembilan Kampus Kuala Pilah,
72000 Kuala Pilah, Negeri Sembilan, Malaysia

[*]Corresponding author: normonica@gmail.com , jafar@upm.edu.my

Received: 27 January 2022; Accepted: 10 June 2022; Published: 27 December 2022

Abstract

Wet chemical synthesis has received much attention to develop a wide array of metal oxide nanoparticles (MONPs) due to its low production cost, simplicity, and ability to produce ultrafine products. In recent years, room temperature ionic liquids (RTILs) as a superior solvent, have managed to produce excellent properties of MONPs that are gaining attention due to excellent physical properties such as small particle size, high surface area, and high porosity. To date, the abundance of available data on MONPs can now be used by researchers to establish suitable methods for producing high-performance materials particularly to suit specific applications. However, there is very limited information on the synthesis mechanisms and common characterization methods used in the preparation of MONPs using RTILs. Therefore, this paper aims to provide a comprehensive review on the MONPs synthesis methods using RTILs via sol gel, hydrothermal, microwave assisted, ultrasonic assisted, and precipitation method alongside the characterization by spectroscopic and microscopic techniques. In this article, various fabrication methods to synthesize MONPs with different morphologies and sizes are reviewed. Also, a step-by-step approach on the mechanisms to improve MONPs properties and impacts of RTILs on the formation of MONPs is highlighted. Finally, the potential of MONPs as antibacterial and catalyst are discussed.

Keywords: characterisation, ionic liquid, synthesis, metal oxide

Abstrak

Sintesis kimia basah telah mendapat banyak perhatian untuk membangunkan pelbagai jenis nanozarah oksida logam (MONPs) kerana kos pengeluarannya yang rendah, kesederhanaan dan keupayaan untuk menghasilkan produk ultrahalus. Dalam beberapa tahun kebelakangan ini, cecair ionik suhu bilik (RTILs) sebagai pelarut unggul, telah berjaya menghasilkan ciri-ciri terbaik MONPs yang mendapat perhatian kerana sifat fizikal yang sangat baik seperti saiz zarah yang kecil, luas permukaan yang tinggi, dan keliangan yang tinggi. Sehingga kini, banyaknya data yang tersedia mengenai MONPs kini boleh digunakan oleh penyelidik untuk mewujudkan kaedah yang sesuai untuk menghasilkan bahan berprestasi tinggi terutamanya untuk disesuaikan dengan aplikasi tertentu. Walau bagaimanapun, terdapat maklumat yang sangat terhad mengenai mekanisme sintesis dan kaedah pencirian biasa yang digunakan dalam penyediaan MONPs menggunakan RTILs. Oleh itu, kertas kerja ini bertujuan untuk memberikan ulasan komprehensif tentang kaedah sintesis MONPs menggunakan RTILs melalui sol gel, hidroterma, dibantu gelombang mikro, dibantu ultrasonik, dan kaedah pemendakan di samping pencirian oleh teknik spektroskopi dan mikroskopik. Dalam artikel ini, pelbagai kaedah fabrikasi untuk mensintesis MONP dengan morfologi dan saiz yang berbeza disemak. Juga, pendekatan langkah demi langkah mengenai mekanisme untuk menambah baik sifat MONPs dan kesan RTILs terhadap pembentukan MONPs diserlahkan. Akhir sekali, potensi MONPs untuk menghalang bakteria dibincangkan.

Kata kunci: pencirian, cecair ionik, sintesis, logam oksida

Introduction

Metallic elements can be transformed using various techniques to metal oxides nanoparticles (MONPs) with unique properties such as high surface to volume ratio, reduced surface imperfections, and superior magnetic, optical, electrical, and catalytic capabilities that are correlated to their size and distinct than their bulk materials [1-5]. MONPs are trendy in various applications, namely the health industry [6], textiles industry [7], in the cosmetic industry as antimicrobial agents [8] and the photocatalyst field [9, 10]. The designation of an experimental procedure for the synthesis of MONPs is an important aspect of nanotechnology with a size range of 1 to 100 nanometres (nm) [11]. With these demands, remarkable researches have been performed to prepare a variety of MONPs from d and f blocks elements in the periodic table such as iron oxide (Fe_2O_3) [12], magnesium oxide (MgO) [13], manganese oxide (MnO_2) [14, 15], zinc oxide (ZnO) [16], titanium oxide (TiO_2) [17], copper oxide (CuO) [18], zirconium oxide (ZrO_2) [19], silica oxide (SiO_2) [20], cerium oxide (CeO_2) [21], samarium oxide (Sm_2O_3), lanthanum oxide (La_2O_3) , ytterbium oxide (Yb_2O_3), and scandium oxide (Sc_2O_3). In general, there are two types of strategies to produce MONPs:

i) Top-down method: physical approaches which involve the fragmentation of bulk material into smaller fine particles up to nanoparticle sizes. This method uses several techniques such as ion and ball milling [22, 23], laser ablation [24, 25], chemical vapor, and deposition pulsed-laser deposition [26]. Moreover, this method requires the availability of tools or instruments and a competent operator to perform the specific techniques.

ii) Bottom-up method: tailor-made process using biological method such as plant extract [27, 28], fungi [29], and chemical method such as precipitation [30, 31] , sol–gel [32, 33], hydrothermal [34, 35], and microwave-assisted synthesis [36]. This method offers several advantages including a narrow size distribution, minimal energy usage, low processing temperatures for thermolabile materials, and low cost [37]. Moreover, these methods control the size and structures of MONPs by initiating kinetic energy within the particles to prevent clusters from accumulating [38, 39, 40].

Among the available methods to synthesize MONPs, the chemical method provides promising strategies owing to simpler procedures, ability to control reaction temperature, and high reproducibility [41]. The chemical method involves four main stages which are the formation of precursor, nucleation, growth, and ageing processes that can be controlled to obtain the desired size and shape [42]. To synthesize MONPs using the chemical method, a strong fundamental understanding of the method is required. Chemical methods have gained prominence for the synthesis of MONPs because of their mono-dispersive and non-agglomerative properties, which could be achieved by stabilising MONPs with capping agents especially during the growth stages [43]. This is because Ostwald ripening tends to occur during growth stages as it is a thermodynamically spontaneous process that leads to

agglomeration of the MONPs [44].Therefore, stabilizers or capping agents are needed for the synthesis of small MONPs as a protective layer that shields the particles from each other. Currently, several types of capping agents have been reported for the synthesis of MONPs such as tri-*n*-octyl phosphine oxide, dodecyle amine [45], aniline [46], polyethylene glycol [47], tetraoctyl ammonium bromide [48], hybrid poly(ethylene glycol), polyvinyl alcohols [49], octylamine [50], and room temperature ionic liquids (RTILs) to control the size of the MONPs.

The desired properties of RTILs are in terms of viscosity, conductivity, density, and thermal stability which could be regulated by altering the length of the alkyl chain of cations [51]. The synthesis of MONPs using RTILs has been proven to be environmentally friendly because RTILs can be reused and recycled for another cycle [52, 53]. Furthermore, due to their non-volatility characteristic, RTILs do not contribute to air pollution, and are deemed suitable and safe for industrial applications. The utilization of RTILs as a capping agent in the synthesis of MONPs has gained the attention of researchers due to their ability to produce an aggregation-free-end product, mainly due to the ionic liquid stabilization [54-58]. This is due to: (1) the unique structure of RTILs, cationic-anionic layers from RTILs surrounding the MONPs can generate a great electrostatic force between the MONPs [59], (2) the double-layered RTILs offer electrostatic interactions that can prevent MONPs from aggregating by balancing van der Waals interactions between the MONPs [60], (3) the alkyl side-chains of RTILs stretching far from the MONPs surface lead to a secondary steric stabilization to block the MONPs from approaching each other [61], and (4) the stabilization approach which involves hydrogen bonding from inter RTILs structure and intra RTILs-MONPs surfaces that may improve the synthesis of MONPs [62]. Common RTILs used as capping agents in the synthesis of MONPs involve groups from imidazolium [63], ammonium [30], choline [64], and pyrrole based RTILs [30, 65]. The use of RTILs as a capping agent has been proven to solve the agglomeration problem that usually occurs during the synthesis of MONPs. RTILs have been proven earlier as effective stabilizing agents in the formation of silver NPs [66], cadmium sulphide quantum dots [67], and silver/copper oxide/bentonite nanocomposites [68]. Moreover, RTILs can be used as a capping agent to control the size and shape of MONPs by manipulating the alkyl chain of cations or anions to achieve controllable physical properties [69, 70].

Numerous literature reviews have been published by researchers dedicated to the synthesis of MONPs concerning the utilization of RTILs. In 2011, Abbot et al. [71] provided a critical review on the processing metal and MONPs using RTILs. However, the review covered the role of RTILs in the extraction method to gain high purity metal and MONPs via physical synthesis only. In addition, review articles by Prechtl 2013 [72] and Seitkalieva et al. [73] on the synthesis of MONPs in RTILs covered the catalysis application and did not include a detailed mechanism on the formations of these MONPs in RTILs. Furthermore, there is limited information appertain to the roles of RTILs as a capping agent in the formation of MONPs in the chemical method, especially during the four important stages. In 2017, He and Alexandridis [2] reviewed the utilization of RTILs in MONPs, focusing on the hybrid benefits of MONPs and RTILs in the catalyst, electrochemical, and separation applications, The article only focussed on the emerging applications for the hybrid MONPs dispersed in RTILs. Furthermore, besides the essential contributions of RTILs in a variety of synthesis techniques and their excellent potential, the performances of MONPs in RTILs via chemical method should be emphasized. Therefore, attention must be given to the synthesis of MONPs via chemical method since these materials with smaller size are in great demand in various applications.

The present work will review the progress of the chemical method to synthesize MONPs using RTILs to produce excellent performances of MONPs. Subsequently, the characterization of MONPs involving transmission electron microscopy (TEM), scanning electron microscopy-energy dispersive X-ray (SEM- EDX), X-ray diffraction (XRD), ultraviolet visible (UV-Vis), and Fourier transforms infrared (FTIR) will be discussed herein along with the impacts and influences of RTILs in the MONPs synthesis. This review highlights the applications of MONPs in several sectors including antibacterial, catalysts, and others applications.

A step-by-step approach on the formation of MONPs via RTILs

As an alternative to the conventional organic molecular solvents, RTILs are used as a capping agent in the synthesis of MONPs. A capping agent is defined as an amphiphilic molecule consisting of a polar head

and a non-polar hydrocarbon tail. Both parts depend on the effectiveness of the capping agent, where the non-polar tail interacts with the medium around it, while the polar head coordinates with the metal atom [74]. A brief mechanism on the formation of zirconium oxide (ZrO2) NPs has been explained in our previous study [75]. Figure 1 depicts the reaction of the capping agent towards MONPs during the synthesis where each MONPs is well separated, thus reducing the risk of agglomeration. Typically, the formation of precursor molecules occurs during hydroxylation and hydrolysis reactions, creating a metal of zero charges [37]. Whereby, the metal hydroxides that are formed (formation of M-OH, where M is the metal) then take part in the condensation reactions lead to the nucleation of the solid material [76].

Nucleation is the second step in the preparation of MONPs, where the nuclei or seeds function as a template for crystal growth [1]. For example, the addition of reducing agent sodium hydroxide (NaOH) into the metallic precursor (zirconium chloride, $ZrCl_4$) solution causes the metal ion of Zr^{4+} to reduce to metal atom (Zr^0), creating supersaturated zirconium hydroxide (Zr-OH) that subsequently undergo nucleation [77]. Having said that, it is very important to control the concentration of NaOH in this step as it can indirectly affect the production of MONPs. For instance, if a lot of OH^- is produced in a short period, the metal ions in the solution will quickly precipitate due to the high pH environment, causing the metal ions to only have a minimal contribution to MONPs growth, prohibiting further growth of the MONPs [78]. Following nucleation, MONP's growth continues until the concentration of the precursor reaches equilibrium based on solubility [76]. Diffusion determines the growth rate of the particle; whereby smaller particles have recorded a larger growth rate compared to larger particles.

Next, the change in particle size occurs due to the ageing step that involves coarsening of the particle or also known as the Ostwald ripening process. Ostwald ripening is defined as a thermodynamically spontaneous process where larger particles are more energetically favored than smaller particles. Therefore, smaller particles diffuse in a solution before attaching themselves to the surface of larger particles. This step decreases the amount of smaller particles that are present in the solution. Meanwhile, agglomeration tends to occur rapidly for larger particles because larger particles tend to grow inappropriately due to lower surface energy [79]. The outcomes of the effect of RTILs structure in the MONPs synthesis could be observed through the morphologies and shape of the materials. The impact of the type of RTILs utilized and the exact reaction conditions on the particle size and shape of ZnO NPs were recently described by Alammar and Mudring [80]. It was discovered that increasing the length of the cation alkyl chain results in the creation of nanospheres rather than nanorods. This was explained by the steric effect of the longer alkyl chains of the RTILs with the ZnO NPs surface interaction which inhibit the growth of the particles for their typical creation of nanorods. It was also described that the longer cation chain contributes to smaller particle size with a diameter of 100 nm rather than shorter alkyl chain with a diameter of 400 nm. This was also agreed by other researches that also synthesized ZnO NPs that the length of the alkyl chain affect the morphology, size, and shape due to the steric hindrance [81, 82]. Similarly, the study on CeO NPs synthesis in RTILs reported that an exchange in RTILs cations would lead to a different morphology such that methylimidazolium $(C_3mimOH)^+$ and trishexyltetradecylphosphonium $(P_{66614})^+$ produced spherical-like and nanosheet assembly with particles size smaller than 10 nm.

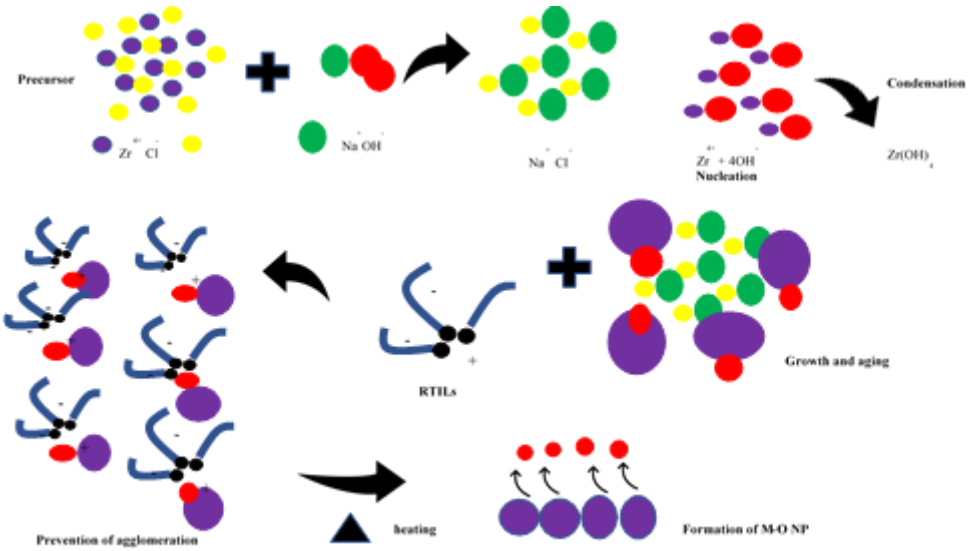


Figure 1. Proposed illustration for the steps in synthesis of MONPs using RTILs as capping agent. Source: [1, 37, 74-82].

Synthesis of MONPs using RTILs

Based on the evidence, the versatility of capping agents allows control over the agglomeration of particles from forming an anisotropic structure [83]. In addition, RTILs have been reported as effective capping agents in the synthesis of MONPs due to their peculiar structural properties. Therefore, the introduction of RTILs as a capping agent into the precursor solution allows the successful synthesis of many MONPs through bottom-up methods such as hydrothermal [84, 85], sol-gel [86], precipitation [30], microwave-assisted [36], and ultrasound-assisted [78] and their application as tabulated in Table 1. Of which, hydrothermal and sol-gel methods are most preferred because they are simpler and milder compared to microwave-assisted which requires special equipment to perform. In addition, sol-gel method is a green synthesize method that enables the recycling of RTILs, thus reducing the amount of chemicals used.

Table 1. Summary on methods and effects of RTILs on structure, properties, and application of MONPs

Method	RTILs	MONPs	Finding	[a]Size (nm) [b]Morphology	Application	Ref.
Sol-gel	Aliquat HTA-1	MnO_2	Good charging and discharging behavior at various current densities.	[a]20 [b]nanorod	Supercapacitor	[33]
	EMIMBr	TiO_2	The ratios of rutile to anatase in the products can be contro lled by altering the RTILs co ncentration.	[a]3.6-5.2 [b]nanorod	n.a	[32]
	$BMIMBF_4$	CeO_2	The formation of MONPs are successfully formed in RTILs acting as a soft-templating agent.	[a]15-20 [b]spherical	Auto-catalytic regenerative	[87]
	BMIMI	ZnO	May act as a template and very impactful on the structure and surface properties of ZnO NPs.	[a]9.13 [b]hexagonal	Antibacterial	[86]
	$BMIMBF_4$	MgO	RTILs formed an extended and lightly structured hydrogen bond network.	[a]30-50 [b]nanorod	n.a	[88]
	$BMIMPF_6$	TiO_2	Important in achieving a longer aging time for the formation of a stable sol-gel network.	[a]5 [b]sponge-like pore	n.a	[89]

Method	RTILs	MONPs	Finding	[a]Size (nm) [b]Morphology	Application	Ref.
	BMIMCl	Si-GO	Higher surface area with high crystalline phase.	[a]20-30 [b]spherical	Removal of heavy metal ions from water	[63]
	Benzimidazolium	ZnO	Good photocatalyst and antibacterial behavior.	[a]96.24 [b]n.a	Antibacterial	[90]
	$BMIMPF_6$	Nd_2O_3	Nd_2O_3-RTILs exhibited bactericidal activity yet at low concentrations and it is more effective drug for biomedical applications.	[a]48 [b]spherical, cubic, cuboic	Antibacterial	[91]
	TMPA-TFSI	Ag/Mn_3O_4/bent	Exhibited non-aggregated and displayed a significant amount of rod and spherical morphologies.	[a]10.4 [b]rod-like	Antibacterial	[92]
	$BMIMPF_6$	SrO/CeO_2	Controlled size of SrO/CeO_2 mixed MONPs exhibit antibacterial and antioxidant activity.	[a]5-55 [b]nanorod	Antioxidant and antibacterial	[93]
	$BMIMPF_6$	Ag-Au/Y_2O_3	RTILs controlled the growth and prevent the agglomeration of metal ions that give higher antibacterial and anticancer properties.	[a]30 [b]nanoflake=like	Biological	[94]
Hydrothermal	$BMIMBF_4$	Yb_2O_3	Less agglomeration due to the use of RTILs in the synthesis.	[a]35 [b] hexagonal, spherical, rectangular	Biological	[95]
	$BMIMPF_6$	Ag-rGO	Higher yields and better control over the diameter of the nanoparticles.	[a]10 [b] n.a	n.a	[96]
	TFSI	ZnO	Exhibited hexagonal shaped ZnO NPs in a very short period of reaction time.	[a]1500-2000 [b]hexagonal	n.a	[34]
	C_{16}MMIMBr	PtAg/rGO	Exhibited enhanced electrocatalytic performance, high methanol tolerant activity, and improved stability.	[a]31.5 [b]flower-like	Oxygen reduction	[97]
	$C_{10}MIMBF_4$ BMIM BF_4	ZnO	Difference alkyl chain length could affect the size of pore channels of hollow structure, the dispersivity and uniformity of ZnO NPs	[a]10 [b]ring-like	n.a	[98]
	C_3MIMBr	ZnO	Successfully synthesized ring-like ZnO NPs and promoted growth of tube-like structure.	[a]500 [b]ring-like hollow	Photoluminescence	[35]
	BDMIMCl	γ-Al_2O_3	Various morphologies successfully synthesis.	[a]90 [b]nanoleaves	n.a	[99]
	$BMIMPF_6$	Sm_2O_3	Particles are separated by distance without agglomeration.	[a]30-50 [b]cubic	Biomedical	[100]
	$BMIMBF_4$	WO_3	RTILs are important in the controlled synthesis of nanostructured materials.	[a]36 [b] spherical	NO_2 sensing	[85]
	HMIMBr	CeO_2– TiO_2	Large specific surface area and uniform pore size.	[a]3-4 [b]spherical	Photocatalytic	[101]

Method	RTILs	MONPs	Finding	[a]Size (nm) [b]Morphology	Application	Ref.
	BMIMCl	Fe_2O_3	Various morphologies of product yield.	[a]39.1 [b] hexagonal	n.a	[84]
	$BMIMBF_4$	TiO_2	Can prevent the production of brookite and favour the growth of the anatase phase.	[a]7.8 [b]n.a	Photocatalytic	[102]
	$BMIMBF_4$	ZnO	ZnO NPs with snowflake shape obtained as the RTILs used acted as a template which improved the sensitivity of NO_x sensor.	[a]600 [b]needle-like	Detection of NOx	[103]
	$BMIMPF_6$	La_2O_3	RTILs acts as a size and shape-directing agent contributes to good antibacterial and anti-inflammatory activities	[a]43 [b]spherical	Biomedical	[11]
Ultrasound-assisted	$EMIMBF_4$	Fe_2O_3	High conductivity with slightly increased viscosity and density.	[a]2-6 [b] quasi-spherical	Liquid marble	[78]
	$HMIMNTf_2$	ZnO	High yield and uniform diameter of small MONPs.	[a]60 [b]spherical	n.a	[104]
	Ionic liquid choline serinate	CeO_2	RTILs provide more stability to the MONPs and acts as cross-linking agent for collagen stabilization.	[a]19.95 [b]n.a	Biomedical	[105]
Precipitation	Poly (N- vinyl pyrrolidone)	ZnO	Increased efficiency in removing water pollutants.	[a]41.4 [b]spherical	Water treatment	[30]
	$BMIMNTf_2$	Fe_2O_3	MONPs exhibited well-controlled size and size distribution.	[a]10.6 [b]spherical	n.a	[31]
Microwave-assisted	$OMIMPF_6$	ZnO	No agglomeration, pure product.	[a]16 [b]spherica	Esterification reaction	[36]

1-ethyl-3-methyl-imidazolium bromide (EMIMBr), neodymium oxide (Nd_2O_3), N-trimethyl-N-propylammonium bis(trifluoromethanesulfonyl)imid (TMPA-TFSI), silver/manganese oxide/bentonite (Ag/Mn_3O_4/bent), lithiated sarcosine-trifluoromethyl sulfonyl imide (TFSI), silver nanoparticles-reduced graphene oxide (Ag-rGO), 1-hexadecyl-2,3-dimethylimidazolium bromide (C_{16}MMIMBr), bimetallic reduced graphene oxide (PtAg/rGO), 1-decyl-3-methylimidazolium tetrafluoroborate ($C_{10}MIMBF_4$), 1-propyl-3-methylimidazolium bromide (C_3MIMBr), 1-butyl-2,3-dimethyl imidazollium chloride (BDMIMCl), gamma-aluminium oxide (γ-Al_2O_3), lanthanum oxide (La_2O_3), Silver and gold decorated Y_2O_3NPs (Ag-Au/Y_2O_3), graphene oxide (GO), silica–graphene oxide nanocomposite (Si-GO), 1-ethyl-3-methylimidazolium bis (trifluoromethylsulfonyl)imide (EMIMTFSI), 1-butyl 3-methyl imidazolium Iodide (BMIMI)., n.a (not availbale).

Sol gel method

Among many available methods, sol-gel is an effective and the simplest chemical method to synthesize MONPs with the desired properties. This method involves various steps starting with the hydrolysis process, followed by polycondensation, gelation, and aging of the metal alkoxide in the presence of acid or base. From this mechanism, a pure and homogenous product would be formed in mild condition before subjected to drying, compaction, and crystallization steps that would improve the chemical homogeneity of the MONPs formed [106, 107]. The reaction of sol-gel through partial hydrolysis of the alkoxide, polycondensation of the hydroxyl, and polymerization of alkoxyl groups are explained using equations as follow [108]:

$$M(OCH_2CH_3)_{10} + x6H_2O \rightarrow M(OCH_2CH_3)_4(OH)_6 + 6CH_3OH \quad (1)$$

$$M\text{-}OH + HO\text{-}M \rightarrow M\text{-}O\text{-}M + H_2O \quad (2)$$

$$M\text{-}OCH_3 + HO\text{-}M \rightarrow M\text{-}O\text{-}M + CH_3OH \quad (3)$$

Fang and Song [87] synthesized CeO_2 NPs via the sol-gel method using cerium nitrate hexahydrate ($Ce(NO_3)_3.6H_2O$) as a precursor dispersed in water. During the synthesis activity, a capping agent of $BMIMBF_4$ was added to control the formation of MONPs. The RTILs in the supernatant solution was collected using a rotary evaporator and was reused in the next synthesis activity of CeO_2 NPs. The recycled

activity indicated that the capping agents used were environmentally friendly. The size of the obtained CeO_2 was between 15 nm to 25 nm after calcined at high temperature for 6 hours. The research was then expanded to study the formation of CeO_2/Chitosan composite. According to the UV-visible spectrum, adding cerium oxide nanoparticles to the chitosan polymer produced a high ability of catalytic oxidative recovery from spectrum shifting, which could be related to the material's tiny size which allowed the penetration into chitosan.

Pandiyan et al. [93] reported a simple and eco-friendly method using RTILs which assisted green synthesis of ceramic SrO/CeO_2 NPs via the sol-gel method. The prepared SrO/CeO_2 NPs were highly crystallized and purified when analyzed using XRD. Based on the investigation, the $BMIPF_6$ improved the surface morphology of the SrO/CeO_2 NPs as compared to the synthesis without BMIM]PF_6. This was due to the material that was uniformly distributed, and the growth and agglomeration activities that was controlled with the presence of $BMIMPF_6$.

Meanwhile, Sundarajan et al. [86] successfully prepared nanocrystalline ZnO NPs using the sol-gel method using 1-butyl 3-methyl imidazolium iodide ($[BMIM]^+ I^-$) as a capping agent. The product was calcinated at 400 ℃ to produce white colored ZnO NPs. To overcome the drawback, $[BMIM]^+ I^-$ was added which acted as a capping agent by adsorbing on the surface and covering the ZnO NPs during crystallization. The calculated average crystal size was found to be smaller with the presence of $BMIM]^+ I^-$ than that without RTILs, indicating the significant role of ($[BMIM]^+ I^-$) in influencing the structure and surface properties of ZnO NPs. During the application of ZnO NPs as an antibacterial agent, it was observed that the bacterial growth inhibition increased due to their small particles size and improved morphology which improved the uniform distribution of Zn^{2+} ions on the bacterial surface, indicating significant enhancement of antibacterial activity. In recent years, Sundarajan et al. [91] reported on the advanced synthesis of neodymium oxide nanoparticles using the sol-gel method by reacting neodymium chloride hexahydrate ($NdCl_3.6H_2O$) and $BMIMPF_6$ at room temperature. The final product was calcinated at a very high temperature (650 ℃) for 5 hours in a muffle furnace. As a result, a material highly improved surface smoothness was obtained due to the excellent roles of the capping agent ($BMIMPF_6$) to control the particles agglomeration as compared to the materials without RTILs. Moreover, they reported that the scavenging activity of Nd_2O_3 NPs synthesized in $BMIMPF_6$ was higher than that of Nd_2O_3 NPs, suggesting that they could be exploited as a viable treatment of diabetes disorders.

On the other hand, a similar method was investigated by Bharate et al. [33] to synthesize MnO_2 NPs in Aliquat HTA-1, whereby 1.5 g of manganese chloride (precursor) was dissolved into 25 mL of distilled water before the addition of Aliquat HTA-1. During the synthesis of MnO_2 NPs, weight ratio of MnO_2 NPs to Aliquat HTA-1 of 1:4 was added amidst the synthesis to ensure that all the particles were capped with the RTILs as it prevents agglomeration, which further prevents anisotropic growth of the particle. The amount of RTILs added was larger than most reported literature that used imidazolium based RTILs. In their work, a comparison study to investigate the effectiveness of RTILs was done where one of the MnO_2 NPs was synthesized without RTILs showing to form spherical shape in contra to nanorods. The RTILs used in this study was also used as an electrolyte during the supercapacitor application where they used 5% of Aliquat HTA.

Hydrothermal method

The hydrothermal method is another choice of method to synthesize MONPs that typically use Teflon-line stainless steel autoclaved reactor with temperature higher than 100°C and pressures above 1 atm [109]. Liu et al. [101] used RTILs to synthesize CeO_2 NPs. It was done by dissolving 0.005 mol of 1-hexadecane-3-methylimidazolium bromide ($C_{16}MIM^+Br^-$) in 15 mL distilled water through vigorous stirring at 40°C for 30 minutes. Then, tetrabutyl orthotitanate (TBOT) and cerium nitrate ($Ce(NO_3)_3$) were added to the solution. In their study, they reported for the first time a facile synthesis of hybrid MONPs of CeO_2–TiO_2 NPs with adjustable Ce/Ti percentages using RTILs, where the molar proportion of cerium (Ce) in the composition varied in the range of 5% to 30%. Upon the completion of stirring for 30 minutes, the pH of the solution was adjusted to 9 -10 using dropwise addition of ammonia solution followed by stirring for 2 hours. Then, the homogeneous sol was transferred to a 100 mL Teflon-line stainless steel autoclave at 100°C for 2 days. The finding from XPS spectra revealed that the Ce^{3+}concentrations decreased from 5% CeO_2–TiO_2 to 30% CeO_2–TiO_2 , indicating that the amount of Ce^{3+} in total Ce declined with the growing amount of CeO_2

NPs.

Zhang et al. [85] investigated the role of RTILs in improving the sensitivity of tungsten trioxide (WO_3) to NO_2 gas. In the synthesis of the material, different concentrations of $BMIMBF_4$ were added amidst the synthesis process. The surface composition of the material was studied using X-ray photoelectron spectroscopy (XPS), which revealed characteristic peaks corresponding to the C, O, W, and N elements in the materials, as well as the appearance of a N 1s peak at 400.2 eV, attributed to imine (=N-) derived from the imidazole ring in RTILs. When compared to WO_3 NPs generated without the addition of RTILs, the as-synthesized WO_3 NPs have significantly enhanced the sensing characteristics of NO_2. The phenomenon could be attributed to the high proportions of surface adsorption oxygen and the residue of C-N from $BMIMBF_4$, thus creating a large specific surface area.

On the other hand, Muthulakshmi et al. [100] used the same hydrothermal method in the synthesis of samarium oxide (Sm_2O_3) NPs. In their work, they utilized 1-butyl 3-methylimidazolium hexafluorophosphate ($BMIMPF_6$) to assist the synthesis route. In their findings, the particle size Sm_2O_3 NPs was between 50 nm and 80 nm as examined using dynamic light scattering method. Due to the superior properties of $BMIMPF_6$ as a capping agent, the particles were found well separated by a certain distance without agglomeration. The consistent particle size distribution and surface charge distribution visible in this finding could possibly explain the stability of Sm_2O_3 NPs produced in $BMIMPF_6$. Subsequently, the stability of the MONPs was proven by a high zeta potential (36.3 mV), indicating high stability of the synthesized Sm_2O_3 NPs. In the recent year, Muthulakshmi et al. [110] described the synthesis of ytterbium oxide (Yb_2O_3) NPs using the same capping agent ($BMIMPF_6$). It was discovered that the large agglomeration of NPs was minimized due to the addition of $BMIMPF_6$ in the synthesis process which was evidenced by using a particle size analyzer. The polydispersity index (P.I.) of the material was calculated to be 0.246 along with the superior electrophoretic mobility (0.000212 cm_2/Vs), indicating a homogeneous particle size distribution and surface charge. Furthermore, the stability of Yb_2O_3 NPs was excellent, making the potential of the material in medicinal field possible.

Microwave-assisted method

The microwave assisted method uses a domestic microwave oven to synthesis MONPs that involves efficient heating method which can significantly decrease the reaction time by the operation of electromagnetic waves between 300 MHz to 300 GHz [54]. For example, Kavya et al. [36] explored the microwave-assisted method to prepare ZnO NPs. 16 g of NaOH was added to 5.5 g zinc acetate dihydrate and 50 mL of distilled water while stirring. The suspension was placed in a microwave oven after adding 2 mL of $OMIMPF_6$ to 3 mL of the prepared solution (2.45 GHz, 850 W). The mixture was then irradiated for 2 minutes to 9 minutes in a loop using 30% of the microwave's output power (on 10 s; off 5 s). The formed spherical shape of the ZnO NPs was discovered to be greatly controlled by the initial production of nuclei by microwave irradiations, and then the subsequent role of the ionic liquid as a growth controller. A small particle size (16 nm) of ZnO NPs was obtained, making them suitable as a catalyst in the esterification between benzoic acid and methanol. The esterification reaction using 5 mol% ZnO NPs as an acid catalyst provided excellent yields in a short reaction time (2 hours), indicating that the produced ZnO NPs have outstanding potential as an alternative catalyst. The microwaved assisted method of MONPs synthesis in addition of RTILs as a capping agent can act as a microwave absorber and improve the induced uniform heating into the solution and maintain thermal homogeneity by an ionic conduction mechanism that lead to the formation of MONPs [42].

Precipitation method

Precipitation method is another synthesis method that is unique, cost-effective, simple, and involves controlling the pH of the medium [111]. The precipitation reaction process consists of five steps[112]:

(1) Dissociation of NaOH: $2NaOH_{(s)} \rightarrow 2Na^{+}_{(aq)} + 2OH^{-}_{(aq)}$

(2) Dissociation of precursor: $M(NO_3)_2{\cdot}XH_2O_{(s)} \rightarrow M^{2+}_{(aq)} + 2NO_3^{-}{}_{(aq)} + XH_2O$

(3) Formation of metal hydroxide: $M^{2+}{}_{(aq)} + 2OH^{-}_{(aq)} + XH2O_{(aq)} \rightarrow M(OH)^2{\cdot}XH_2O_{(s)}$

(4) Formation of colorless solution: $2Na^{+} + 2NO_3^{-} \rightarrow 2NaNO_3$

(5) Drying: $M(OH)_2{\cdot}XH_2O_{(s)} \rightarrow Zn(OH)_{2(s)} + XH_2O_{(g)}$ and

(6) Calcination: $M(OH)_{2(s)} \rightarrow MO_{(s)} + H_2O_{(g)}$

For instance, Atta et al. [30] synthesized ZnO NPs using the precipitation method. In brief, zinc nitrate hexahydrate (0.1 mol) was dissolved in 50 mL water and mixed with 4 g of poly-2-Acrylamido-2-methyl-1- propane sulfonic acid (PAMPSA) or poly-2-Acrylamido-2-methyl-1-propanesulfonic acid/N-vinyl pyrrolidone (PAMPSA/VP) under intense stirring until a clear solution was obtained. Then, 30 mL of NaOH (0.2 M in ethanol) was added to the reaction mixture and vigorously stirred until the pH of the solution reached 12.5. The pH is one of the important factors to be monitored as it has an impact on the product obtained. The number of H^+ or OH^- ions in the sol, which effectively dictates the polymerization of the metal–oxygen bonds, is well recognized to have a substantial influence on the morphology of the produced metal oxide precipitation/solution. The hydrolysis and condensation behavior of the solution during gel formation is affected by the pH of the precursor solution, thus affects the shape but does not affect much on the crystal quality of the MONPs [113]. Therefore, it is important to make sure the solution reach the desired pH to obtain the desired MONPs. Next, to produce a milky solution, the reaction temperature was increased to 45°C for 4 hours before letting it to rest. Then, the cooled reaction mixture was centrifuged at 15000 rpm for 10 minutes. To extract the aggregates and organic impurities, the precipitate was washed several times with distilled water and ethanol before drying for 5 hours at 150 °C.

Ultrasound-assisted method

The ultrasound-assisted method is a method that uses ultrasonic irradiation at frequencies ranging from 20 kHz to 500 MHz in sonochemical technologies to begin or modify chemical processes [54]. This method was described in two different studies to synthesize Fe_2O_3 NPs and ZnO NPs. For example, Zhang et al. [78] described the synthesis of Fe_2O_3 NPs through facile and energy saving (100 mW) ultrasonic decomposition of $Fe(CO)_5$ with 20 ml of $EMIMBF_4$ in a 50 mL round-bottomed flask in an ice bath. The ultrasound probe was placed 1 cm below the liquid surface, where the mixture was ultrasonicated for 1.5 hours at 100 mW. It was discovered that steric forces successfully stabilized the colloidal particles in $EMIMBF_4$, since the bulky structure of molecules/ions $EMIMBF_4$ strongly attached to the colloidal surfaces, allowing them to separate each colloidal surface in some circumstances. The nonpolar alkyl chains acted as a protective group and further inhibit the aggregation of the particles. Similarly, $EMIMBF_4$ enhanced the solvation force in the generation of MONPs, where the multi-layered structure created longer range repulsion and minimized agglomeration.

Whereas, Goharshadi et al. [104] prepared ZnO NPs by dissolving zinc acetate dihydrate into distilled water with dropwise of NaOH solution. The synthesis activity was magnetically stirred under room temperature, resulting in a clear $[Zn(OH)_4]^{-2}$ solution. Before subjected to 40 kHz of ultrasonication for 1 hour, HMIMNTf2 was added into the $[Zn(OH)_4]^{-2}$ solution until white precipitate of ZnO NPs was obtained. The total acoustic power injected into the sample solution was estimated at 50 W by a calorimetry. The white ZnO NPs precipitate was then centrifuged, washed, and dried for 10 hours in a vacuum oven at 40 °C. According to the analysis, both HMIMNTf2 and ultrasound posed a critical role during the formation of ZnO NPs. The obtained ZnO NPs were spherical in shape and well aggregated, consisting of numerous tiny nanoparticles with homogeneous diameters of about 60 nm. This could be possibly explained through the capping agent of HMIMNTf2 which consists of cation $[C6mim]^+$ and anion $[NTf2]^-$. Cation from $[C6mim]^+$ created the electrostatic attraction within the precursor solution comprising a large number of $[Zn(OH)_4]^{2-}$ ions. Due to the high polarization of $[C6mim]^+$, these cation–anion pairs were likely to dehydrate and produce ZnO NPs nuclei. Furthermore, $[C6mim]^+$ ions containing hydroxyl can still adsorb the negatively charged ZnO NPs nuclei's surface to restrict the activities of freshly produced ZnO NPs surfaces, causing the anisotropic development of ZnO NPs to be significantly controlled. The features and comparative analysis of different chemical synthesis methods for MONPs is displayed in Table 2.

Table 2. Comparative analysis of different chemical synthesis methods for MONPs

Synthesis Method	Specific Features	Advantages	Disadvantages
Sol gel method	1. A sol (or solution) grows slowly to form a gel-like system containing liquid and solid phases [114].	1. Possible recycling of RTILs. 2. Made at considerable low temperature below 100 ºC.	1. Product controlled by various parameters; where the final product obtained is affected by concentration of precursor, pH condition, and synthesis time during the sol-gel reaction [115].
Hydrothermal method	1. The action of water at elevated pressure and temperature under a sealed environment in an autoclave [116].	1. Highly nanostructured nanoparticles are controlled over pressure and temperature only [117]. 2. Zero-emission of toxic gases, since the reaction are in the closed system of autoclave [118].	1. Requires expensive equipment (autoclave).
Microwave-Assisted Method	1. Open vessel is simpler than closed vessels [119]. 2. The absorption of microwave radiation by the precursor followed by heat generation through dielectric heating [120].	1. Uniform heating. 2. Possible to use household microwave oven [121]. 3. Use scientific microwave oven. 4. Heats the target molecules directly. 5. Very short reaction time and high efficiency.	1. Requires expensive equipment (microwave oven).

Synthesis Method	Specific Features	Advantages	Disadvantages
Precipitation method	1. Synthesis begins with reaction between metal and alkaline solution or precipitating agent (NaOH, KOH, ammonia etc.) followed by aggregation and precipitate product is collected by filtration or centrifugation [122].	1. Simple. 2. Shape of the particle can be alter by changing the precursor, type of precipitating agent and quantity of organic phase [123]. 3. High crystallinity and homogeneity of product [124]. 4. Cost-effective and scalable [125].	1. pH sensitive. 2. Further thermal treatment is needed [122].
Ultrasound-assisted method	1. Involves energy in the form of heat, light, radiation, electric potential [126]. 2. Formation of bubbles due to the cavitation during ultrasonication [127].	1. More appropriate method for green and sustainable synthetic processes [128]. 2. Minimization of waste [129]. 3. Effective for nanoparticle formation as it yields high product.	1. Require expensive equipment (ultrasonic irradiation). 2. Various reaction parameters including temperature, time, energy input, and pressure must be controlled [126].

Characterization

Morphology and microscopy analysis

Microscopy analysis by transmission electron microscopy (TEM) and scanning electron microscopy (SEM) are carried out to study the morphology of MONPs such as quality, shape, density, diameter, thickness, length, size, and orientation of the as-grown nanostructure [130]. Both use a beam electron to view an image, whereby TEM image is displayed in a two-dimensional projection that passes through the sample while SEM image illustrates the surface morphology of the sample [131, 132].

Scanning electron microscopy

SEM is a microscopy technique that focuses the electron beam to a spot and interacts with the sample which then produces various signals that are combined to form an image. The formation of the image can be used to obtain information about the surface topography and composition depending on the scan pattern chosen [133]. In assessing the physical properties of MONPs, SEM imaging techniques are usually employed to observe their microstructure and morphological properties like size and shape distribution.

A previous study by Mahjoub et al. [134] who synthesized ZnO NPs using chiral ionic liquid (2[N-(n-But)$_4$]+[$C_2H_4(OH)_2(CO_2)_2$]$^{2-}$) (CIL) as a capping agent proved that the absence of CIL resulted in the agglomeration of flower-like ZnO NPs as demonstrated by the obtained SEM image. This shows that CIL plays an important role in morphology of the ZnO NPs. As for the growth of flower-like crystal, when [Zn $(OH)_4]^{2-}$ was decomposed, oxide nuclei developed quickly and served as the growth unit for the formation of ZnO NPs nuclei and epitaxial growth into the flower-like structures. This phenomenon can occur with the help of microwave heating. In general, each Zn^{2+} atom is surrounded by a tetrahedral group of four oxygen ions in hexagonal packing, making the CIL cations and anions easily absorbed on the of O^{2-} and Zn^{2+} surfaces by electrostatic force. However, the amount the CIL extensively affected the morphology of the ZnO NPs as the CIL presence was at 0.3 g, resulting in a narcis-like morphology of the ZnO NPs. A similar finding was also obtained by Kowsari and Karimzadeh [135] who synthesized BaO NPs using CIL, where the amount of CIL added into the MONPs affected the morphology of the product such that a low amount of CIL (0.15 g) formed a heterogenous butterfly-like and cubic like morphology while a higher amount of CIL (0.25 g) formed a cubic like morphology. Instead, they reported that decreasing concentration of CIL reduced the amount of ion carrying the OH group that were responsible for the growth of BaO NPs nuclei to navigate the surfaces forming both cubic and butterfly-like morphologies.

EDX analysis

The elemental mapping using EDX analysis is particularly important in proving the presence of metallic elements and other elements such as oxygen in the sample. This technique can be considered as qualitative and semi-quantitative analysis. The intensity of the peaks in the spectrum indicates the concentration of the respective element since every element has a specific set of peaks in the photoelectron which is determined by photon energy and the respective binding energies [136]. A study on the synthesis of silver NPs using three biodegradables protic ionic liquid (PILs) was reported by Tzani et al. [137], whereby the EDX spectra indicated the composition of the important elements. According to the EDX spectra, the Ag particle was the major element present in the composition with zero interruption from nitrogen element indicating that the NO_3^- ions were appropriately washed and perhaps it did not cap or adsorb in the Ag particles. Indeed, the PILs were successfully washed away using acetone, ethanol, and water. However, it did not interfere with the formation of the Ag NPs [137]. Similarly, a notable evidence of study specifically related to the EDX spectra of CeO_2/ZrO_2 core MONPs synthesized with $BMIMPF_6$ showing a well homogenous composition of cerium (25.95%), zirconium (8.325%), and oxygen (12.07%) due to the washing step during the synthesis using distilled water prior to the characterization technique [138]. However, they also emphasized on the significance of calcination of the MONPs core since the sintering of the particles would give a homogeneity of the MONPs product. Furthermore, another study [95] revealed similar results to the previous study where pure Yb_2O_3 NPs was synthesized using $BMIMPF_6$ in which the elemental composition percentages of ytterbium and oxygen peaks were 85.5% and 10.1%, respectively.

Transmission electron microscopy

TEM is used to observe the size distribution and morphology of the MONPs powder [139]. This analysis provides crystal or surface structure information along with the image up to a few angstrom resolutions. Determination of chemical composition is made possible when TEM is equipped with EDX since the working principle of TEM uses a high energy electron source of around 200 KeV [130]. A thin sample is irradiated with an electron beam of uniform current density passes through the samples to help visualize the size, shape (spherical, flower-like, rod-like or spindle-like structure), and effects of agglomeration [88]. Valuable information on the shape and particle size can provide the potential activity or quantify the distribution characteristics [140]. Moreover, the advantages of TEM include the ability to display the agglomeration of particles under a high-resolution image [141, 142].

As an alternative solvent to improve the properties of the MONPs, RTILs were used as capping agents in several studies [30, 33, 36, 78, 143]. Morphology of ZnO NPs synthesized using (TBA_2($_L$-Tar)) RTILs was elucidated using TEM that proved a flawless rose-like structure and were made up of self-assemble nanosheets with a length and width of several micrometers and a thickness of 30–40 nm with a preferred orientation due to the effect of tartrate anions that reformed the growth mechanism of the ZnO NPs [144]. This confirm that the CIL presence in the synthesis proscribed the 1D growth of the ZnO NPs nanostructures and rearranged the ZnO NPs to form 2D nanosheets that assemble into the hierarchical architectures like "roses." However, the author mentioned, generally the uses of basic imidazolium-based RTILs tends to formed a typical ZnO NPs in nanorods or nanowires structures based on the anisotropic growth of the crystal. In other words, RTILs can be soft templating to the formation of the MONPs structure that can be confirmed by TEM. This finding was found similar in other study where the CIL was acting as template in the formation of ZnO NPs and CuO NPs and the morphology reported a flower-shape with the particle size in the range of 100 – 200 nm for ZnO NPs and a needle-like shape for CuO NPs with a length of 400 – 500 nm and a diameter of 10 – 15 nm. Although the MONPs was synthesized using CIL, there was no significant change in morphology but when the CIL was not added in the MONPs synthesis, the TEM image showed an irregular size and shape. Probably, the presence of RTILs even as a simple additive in water can indeed affect the morphology of CuO NPs. This might be due to the strong electrostatic interactions between anions and cations, as well as π-π stacking and van der Waals interactions involving imidazolium cations perhaps can influence the formation of MONPs that are further characterized using TEM [145].

Moreover, $BMIMPF_6$ is one of the common RTILs used in the synthesis of MONPs to act as capping agent in order to prevent the agglomeration of the MONPs. A Previous study used $BMIMPF_6$ in the synthesis Nd_2O_3 NPs exhibited cubic and spherical shape with a diameter of 48 nm. The synthesis of Nd_2O_3 NPs was reported to exhibit more effective drug delivery for biomedical application [91]. Similarly, Pandiyan et al. also used the same RTILs to control and prevent the agglomeration of metal ions that contributed to nanoflake-like structures of Ag-Au/Y_2O_3 NPs with a diameter of 30 nm. The MONPs obtained were also suitable to be applied in antibacterial and anticancer applications [94]. In addition to this, Veerasingam et al. and Muthulakshmi et al. also reported a size of 43 nm and 50 nm for La_2O_3 NPs and Sm_2O_3 NPs, respectively based on their TEM micrographs. From the TEM image, the crystalite size of La_2O_3 NPs in the absence of $BMIMPF_6$ clearly showed agglomerated particles and while RTILs assisted of La_2O_3 NPs showed agglomeration free particles. Both study reported that $BMIMPF_6$ was able to act as shape-directing agent and the particle were well separated without any agglomeration [11, 100]. It is worth to point out that, $BMIMPF_6$ was suitable in synthesis of various MONPs as this RTIL have weak interaction of cation and anion when interacted with water that enabled the positively charged metal ions to interact with the negatively charged of the RTILs anion to control the growth of the MONPs. From the reported journal, it was noted that a morphology, size, crystal structure, qualitative, and quantitative analysis can all be done using these characterization techniques as this technique provides higher resolution than a light microscope [146].

Besides that, another alternative of RTILs used to prevent agglomeration of the synthesized MONPs was mentioned in previous study by Liu et al. [147] who used 1-hexadecane-3-methylimidazolium bromide (HMIMBr) as a template via the hydrothermal method to produce well-dispersed CeO-TiO_2 NPs. The TEM images demonstrated rod-like shape for 5% CeO-TiO_2 NPs, 10% CeO-TiO2, and 15% CeO-TiO_2 NPs, while

the spherical shape was observed for pure CeO NPs and 30% CeO-TiO_2 NPs at an approximate size of 15 nm. The prepared CeO-TiO_2 NPs was used in the photocatalytic degradation of p-chlorophenol that produced high photocatalytic activity under UV or visible irradiation [101].

Spectroscopic analysis

Fourier-transform infrared

FTIR spectroscopy is a technique used to obtain the absorption or emission spectrum of a solid, liquid or gas in the infrared region, where the spectrum promotes transition between the rotational or vibrational energy level of the ground electronic energy state [148]. Usually, FTIR is used to confirm the bonding and qualitatively detect the presence of functional groups in a nanostructure [139, 149]. FTIR spectroscopy is used to identify functional groups, main vibrational mode, impurities (if any), and determine the purity of MONPs that validates the structural unit and connectivity such as bridging and non-bridging of oxygen in the synthesis of MONPs [150, 151].

The synthesis of MONPs using RTILs has gained interest recently due to the advantages of RTILs. The interpretation of typical peak is still considered as highly divisive due to the difference in opinions expressed by many researchers. A slightly similar peak was almost found on every synthesis MONPs indicating the stretching vibration of O-H bond that are mainly from the alcohol residue. This statement was well supported by a few researchers that synthesized MONPs using RTILs. For instance, Nithya et al. who synthesised CeO_2/ZrO_2 NPs core synthesized using $BMIMPF_6$ reported a broad band at 3426 cm^{-1}. This was similarly found by Veerasingam et al. [11] who observed a broadband at 3453 cm^{-1}. However, Sundrarajan et al. indicated that a broadband located at 3437 cm^{-1} attributed to hydroxyl group of water molecule. Besides that, even though ZrO_2 NPs and CeO_2 NPs have typical absorption peaks at 600 cm^{-1} and 510 $cm^{-1,}$ respectively, the distortion of the peak was reported for CeO_2/ZrO_2 core synthesized using $BMIMPF_6$. The significant peaks were observed at 498 cm^{-1} (CeO_2 NPs) and 416 cm^{-1} (ZrO_2 NPs) mainly due to the effects of zirconia grafting on the cerium surface and was not affected by the $BMIMPF_6$ which enhanced the size and morphology of the MONPs without altering the environment [138]. This finding was then further supported by Fang and Song who synthesized CeO_2 NPs capped by $BMIMBF_4$, the FTIR spectrum manifested a single-phase crystalline CeO_2 NPs with band peaks at 640 cm^{-1} and 673 cm^{-1} representing the Ce-O-Ce stretching vibration. This study reported that the two peaks above 3000 cm^{-1} in the infrared (IR) spectra indicated diagnostic changes in the C-H-F hydrogen bonding between BF_4 anions and the position of hydrogen at 4,5 within the imidazolium ring [87]. This phenomenon revealed that the method employed to synthesize MONPs did not remove all RTILs, hence may require several modifications including calcination temperature and type of method to achieve excellent purity.

It was in contrary to another study that RTILS did not alter the significant functional group of MONPs as none of the RTILs peaks appeared in the FTIR for those MONPs synthesized in RTILs. Based on the results, peaks for Ag-Au doped RuO_2 NPs in $BMIMPF_6$ was determined at 476 cm^{-1} belonging to RuO_2 NPs [152]. Another peak identified in the spectrum corresponded to the hydroxyl group (O-H) indicating the presence of OH bonded alcohol and a phenolic compound that arose from the plant extract used in the synthesis of the MONPs [152]. Furthermore, Sundrarajan et al. [86] provided complementary results for the synthesis of ZnO NPs that reposted the finding of Zn-O stretching vibration at 418 cm^{-1} in the spectra. This study also reported the presence of several other peaks at 2956.97 cm^{-1}, 2404.04 cm^{-1}, 1764.93 cm^{-1}, 1388.00 cm^{-1}, and 1164.38 cm^{-1} indicating the presence of C–O and C–H stretching vibrations from the phenolic compounds within the plant extracts before calcination. While the peak at 1626.95 cm^{-1} maybe due to the presence of intramolecular hydrogen bonds of the ionic liquid. Following the calcination process, the peak at 3500 cm^{-1} remained due to O–H stretching vibration from moisture adsorption. In this study, ZnO NPs were synthesized with the absence and presence of BMIMI but the significant stretching vibration of Zn-O spectra appears at the same wavenumber whereby this indicate that the addition of the BMIMI does not alter the purity of the ZnO NPs. However, uses of another type of RTILs may contribute to peak shifting that may be attributed to changing properties of the synthesis ZnO NPs. For instance, the synthesis of ZnO NPs using chiral ionic liquid reported a strong adsorption peak at 544 cm^{-1} that can be assigned to the Zn–O stretching bonds. With comparison to the typical absorption spectra of ZnO NPs, this peak was shifted to a higher wavelength, and this feature

attributed speculatively to the distinctive structure of ZnO NPs formed in the presence of the RTILs [145].

On the other hand, in another study [99], FTIR was performed to assess the nature of bonds and absorbance of the peak in the prepared Sm_2O_3 NPs. A broad prominent peak was observed at 3444 cm^{-1} which corresponded to O-H stretching vibration, indicating the presence of a water molecule. While the absorption peaks at 1109 cm^{-1} indicated C-O stretching vibration. Also, significant peaks were observed at 749 cm^{-1} and 657 cm^{-1} for Sm-O stretching vibration. In summary, Table 3 lists the functional groups and wavenumber range for the MONPs discussed in this section.

Table 3. Main Functional Groups of MONPs and Wavenumber.

MONPs	Wavenumber (cm^{-1})	Vibrational Mode	Ref.
CeO_2	673	Stretching	[52]
	450	Stretching	[153]
	674 and 545	Stretching	[21]
ZnO	418	Stretching	[86]
	501	Stretching	[112]
ZrO_2	595	Stretching	[138]
	492.73	Stretching	[19]
	473	Stretching	[154]
TiO_2	490	Stretching	[155]

UV-visible spectroscopy

The UV–Vis spectra of MONPs provide significant information regarding their optical characteristics. UV–Vis spectroscopy is also used to investigate the defect energy states induced by various doping agents in MONPs [156, 157]. Besides, for MONPs, UV-vis is commonly used to characterize supported single MONPs and it is widely known that absorption edge energies reduce as oxide domain size increases [158].

Bharate et al. [33] reported that the MnO_2 synthesized with aliquat HTA-1 had a significant absorption at λ_{max} 395 nm that showed smaller bathochromic shift, whereas MnO_2 NPs prepared without aliquat HTA-1 had absorption at λ_{max} 386 nm which could be due to its size and form. The MnO_2 NPs with aliquat HTA-1 had a smaller bathochromic shift than MnO_2 without aliquat HTA-1, which could be due to its size and form. These results show that Aliquat HTA-1, an RTIL, functioned as a surfactant and regulated the size and form of nanoparticles. Similarly, the UV–visible spectra of ZnO NPs showed the excitonic absorption peaks at 222 nm in the presence of BMIMI while 227 nm in the absence of BMIMI. As for the absorption band, it was moved to the lowest wavelength and the blue shift of the quantum confinement effect indicating the production of ZnO NPs [86]. Another study that used $BMIMBF_4$ to synthesize the rare earth MONPs showed that by using UV-Vis spectrum data, the insertion of CeO_2 NPs into the chitosan polymer has a high ability of catalytic oxidative recovery. This can be confirmed by the spectrum shifting from lower to higher and higher to lower energy range with hydrogen peroxide aid. In addition, the valence states of cerium oxide (3^+ and 4^+) on the surface of nanoparticles fundamentally function as an antioxidant, which had been trapping free radicals in the culture medium that was validated using UV-Vis data [52] the sharp absorption band arise from the transition of valence band to conduction band of the MONPs. One can also notice that the absorption band of the maximum wavelength from the UV-vis spectra indicates that the RTILs affected structure formation of the particles as well as the optical properties of the synthesized MONPs. The absorption band showed a blue shift peak due to smaller particles size owing to the use of RTILs as capping agent in the synthesis of MONPs. However, there were studies that show a red shift region when they used RTILs in their synthesis due to the formation of mixed morphology (hexagonal, rectangular, and spherical) of the MONPs product or changing in the shape or structure of the particles such as from spherical to nanarod in the absence and presence of RTILs as a templating agent, respectively [110, 159].

Crystallinity analysis

X-ray powder diffraction

The XRD is a common technique used to study the crystal structures and atomic spacing based on the

constructive interference of monochromatic X-rays. A crystalline sample using XRD consist of three basic elements, namely an X-ray tube, a sample holder, and an X-ray detector [160, 161]. Moreover, XRD is suitable for various types of material such as fluids, metals, minerals, polymers, catalysts, plastics, pharmaceuticals, thin-film coatings, ceramics, solar cells, and semiconductors since it is a non-destructive method [160].

Also, XRD is a fingerprint technique used to study the crystallographic structures, purity, and atomic spacing of the MONPs, whether it is an amorphous or crystal structure based on the constructive interference of monochromatic X-rays and samples. The main distinctive peaks in XRD diffractograms that fit the experimental data of MONPs structure can be used to confirm the presence of MONPs [162, 163]. Meanwhile ZnO/CdO NPs rodlike particles were successfully synthesized by using the hydrothermal method in the ionic liquid medium (4-methylpyridine,2,2,2- trifluoroacetate) and can be clarified using XRD pattern after dried in air at 150 °C. The diffraction peaks were observed at 2θ = 34.0°, 35.0°, 37.05°, 48.04°, 57.03°, 68.02°, 69.00° correspond to (100), (002), (101), (102), (110), (112), and (201), respectively, these peaks are attributed to ZnO nanorod. Therefore, the as-synthesized products have great purity and crystallinity, as evidenced by the sharp and strong diffraction peaks from XRD pattern [163]. In addition to this, the synthesis of ZnO NPs with different pH by aqueous solution growth technique also successfully obtained ZnO NPs using Benzyltrimethylammoiumhydroxide (BTMAH) RTILs at different concentration and various pH. The micro/nanorods were extremely crystalline, as evidenced by XRD patterns with large, high-intensity peaks extending over the 2θ dimension. In this study, crystal planes were only reported at 100, 002, 101, 102, 110, 103, 200, 112, 201, 004 and 202. It was reported that due to the effect of ionic liquid concentration and pH the crystallite size was reduced with good crystallinity [165]. Similarly, Kowsari and Abdpour [166] also reported peaks at 2θ = 34.0, 35.0, 37.05, 48.04, 57.03, 63.04, 65.01, 68.02, 69.00 which corresponded to 100, 002, 101, 102, 110, 103, 200, 112, 201, respectively. The results show that the product is entirely made up of pure phase, with no impurity reflection peaks that indicates the hexagonal wurtzite structures of ZnO NPs when synthesis with functional RTILs, which are consistent with standard JCPDS: 792205 card ICSD#: 067454 [166]. From the reported journals, the synthesis of ZnO NPs using different type of RTILs as capping agents contribute to different crystal systems and a variety of MONPs structures as well as crystallite sizes.

Other than that, in the synthesis of TiO_2 N Ps using $BMIMBF_4$ was also investigated where the crystal plane was observed to be 101, 004, 200, 105, 204 indicated to anatase phase of the TiO_2 NPs without any trace of brookite and rutile phase detected. Based on this study there was a presence of brookite phase during the absence of the $BMIMBF_4$ where the XRD pattern showed a diffraction peak at 2θ=30.8º and disappeared when $BMIMBF_4$ were added amidst the synthesis of MONPs and a sharp diffraction appeared and increased at 2θ=25.4º with increasing amount of RTILs added [102]. A similar observation was also reported by Zheng et al. [32] who synthesis TiO_2 using different concentration EMIMBr and the XRD pattern showed a crystallite phase evolution of the synthesis TiO_2. The absence of EMIMBr gave about a 92% of anatase with minimal brookite phase in the system showing a crystal plane of 101, 004, 200, 105, and 211. The increasing of EMIMBr concentration led to growing of pure rutile phase in the crystal system with crystal plane of 110, 101, 200, 111, 210, 211, and 220. It is worth to noted that, different concentration of RTIL added into the reaction synthesis will provide diversity of crystal system. Therefore, researcher can utilize the amount of RTILs in order to obtain a desired crystal system of the TiO_2 NPs to make sure the suitability of the MONPs products for a curtained application.

Recent and future applications of MONPs synthesized in RTILs

The excellent properties of MONPs that are produced using RTILs as a capping agent were reported in many sectors including water treatment [30], super capacitance [33], catalyst [36], and antibacterial applications.

Antibacterial application

MONPs has drawn researchers interest due to their broad spectrum in antibacterial activities. New developments of antibacterial products or agents are in ominous need due to the resistance of microbial towards antibiotics through mutation process [167]. To investigate the antibacterial activity, the mechanism steps involved between MONPs and microbial are as follows [90, 167, 168, 169, 170, 171]. The MONPs adsorb on the surface of cell wall,

penetrating into the cell, therefore further modify the replication and respiration leading to cell death as reported previously

1. Promote the formation of reactive oxygen species (ROS) from the MONPs that can interact with proteins and/or intercalate between the purine and pyrimidine components that are present in DNA involving further damage in the cell membrane, and
2. Causing a cell death by disrupting the signal transduction pathways of the cells.

Muthulakshmi et al. [110], examined the uniform size of Yb_2O_3 NPs synthesized in the $BMIMPF_6$ as a capping agent during the formation of Yb_2O_3 NPs. The suitable concentrations Yb_2O_3 NPs (150 µg/mL) was added carefully on the plates containing gram positive of *S. aureus* and gram negative of *E. coli* which were cultured in the nutrient agar. After 24 hours, the inhibition zone of Yb_2O_3 NPs synthesized in $BMIMPF_6$ was found to be higher compared to Yb_2O_3 NPs synthesized without $BMIMPF_6$. On *E. coli*, the inhibition zones of Yb_2O_3 and RTIL-Yb_2O_3 NPs were 5 and 8 mm, respectively while the zone of inhibition of Yb_2O_3, RTILs-Yb_2O_3 NPs, on *S. aureus* was at 4 and 7 mm. The effectiveness of inhibition activities of Yb_2O_3 NPs due to formation of uniform size coverage on the bacterial systems, which allow metal cations to be released from MONPs to damage the cell wall by adhering to the bacteria's surface and interacting with cell wall amino acids [39]. A similar investigation has been performed by Sundarajan et al. [91], where $BMIMPF_6$ assisted Nd_2O_3 NPs acting as antibacterial agents pathogenic bacteria like *E. Coli* and *S. aureus*. Even at a very low concentration (10 µg/mL), Nd_2O_3 NPs assisted $BMIMPF_6$ to display a relevant zone of inhibitions indicateing a potential in bactericidal activity.

According to their finding, inhibition zone of gram-negative bacteria (*E. coli*) containing Nd_2O_3 NPs was found at 2 mm while double zone inhibitions were found at Nd_2O_3 NPs- $BMIMPF_6$ (4 mm). Similar observation was reported for the zone of inhibition of the Nd_2O_3 NPs (5 mm) against *Staphylococcus aureus* where the zone inhibition was found larger using Nd_2O_3- $BMIMPF_6$ (7 mm).

Likely, Sundrarajan et al. [86] examined an inhibition zone of ZnO NPs against gram negative of *E.coli* by different methods such as the zone of inhibition, growth curve and biofilm formation. In their finding, the improved morphologically material exhibited very good antibacterial activity against the gram-negative. The ZnO NPs (50 µg mL^{-1}) without RTILs after calcination produced maximum diameter of inhibition zone (2.2 cm) while a same concentration of ZnO NPs synthesized in BMIMI produced larger inhibition zones with a diameter of 3.2 cm, indicating stronger antibacterial activity. Furthermore, upon test on *E. coli* bacterium's biofilm architecture on glass, the control demonstrated biofilm bacterial strains' significant adhering capacity after incubation. However, confocal fluorescence micrograph revealed that ZnO NPs in BMIMI were more effective and active in reducing adhesion and biofilm formation, and that they inhibited bacterial growth better than ZnO NPs without BMIMI. These effective bactericidal capabilities could be attributed to the tiny particle size and enhanced shape of the synthesized material, which allowed for uniform distribution of Zn^{2+} ions on the bacterial surface, resulting in substantial antibacterial activity.

Another MONPs nanocomposite have been synthesis for biological activities has been studied by far to inhibit the growth of *Staphylococcus aureus* (Gram-positive) and *Escherichia coli* (Gram-negative) bacteria such as Ag-Au/Y_2O_3 NPs in $BMIMPF_6$ [93], Ag-Au doped RuO_2 NPs synthesized in $BMIMPF_6$ [151], silver/manganese oxide/bentonite nanocomposite synthesized in N-trimethyl-N-propylammonium bis(trifluoromethanesulfonyl) imide [91]. Different physiological features including shape, size, charge, and morphology have a significant impact on the antibacterial activity of MONPs aided RTILs. Small particles have a larger surface area than bulk material, allowing them to pass through the bacterial wall more quickly. MONPs with a smaller crystalline size are more effective at releasing ions and inhibiting bacterial growth by entering cell membranes and reacting with sulfhydryl inside the cell membranes. As a result, the MONPs break the membrane and render proteins inactive, causing the bacterial cell to die [94].

Catalyst

Researchers are interested in developing photocatalysts with a mesoporous shape to produce high photocatalytic activity and promote quick intraparticle molecular transfer. To acquire higher photocatalyst characteristics, bigger surface area particles are necessary to improve light harvesting and adsorption for reactant molecules. For example, Liu et

al., [102] described the synthesis of TiO_2 NPs in $BMIMBF_4$ where the addition of $BMIMBF_4$ encouraged the formation of anatase TiO_2 NPs. The material was very thermally stable which enabled the preservation of anatase phase even after calcination at 900 °C. The photocatalytic activity of TiO_2 prepared with $BMIMBF_4$ was higher than that of the sample prepared without RTILs attributed to a larger surface area, good anatase crystal mesostructured and small particles size of synthesized material.

Subsequently, Liu et al. [147] investigated the photocatalytic activity of CeO_2–TiO_2 NPs produced in $C_{16}MIMBr$ for the degradation of p-chlorophenol aqueous solution under UV and visible-light irradiation using well-crystallized CeO_2–TiO_2 NPs. During the research, they discovered that 10% CeO_2–TiO_2 NPs had the maximum photoactivity under UV and visible light irradiation, with degradation rates of 95.3% and 57.5%, respectively. This activity was supported by the greater surface area, higher Ce^{3+} concentration, highest surface hydroxyl group concentration, and strongest light absorbance due to the smaller particle size (11–16 nm) formed in the synthesis. Meanwhile, Kayva et al. [36] reported the use of ZnO NPs synthesized in $OMIMPF_6$ (capping agent) to reduce the agglomeration via microwave irradiation method in esterification. Due to its good reproducibility, ZnO NPs as the smart material acts as a solid acid catalyst in the esterification process as it can be used up to four cycles. The authors discovered that the catalysts managed to enhance the percentage yield of primary alcohol to almost 80%.

Other applications

According to Atta et al., ZnO NPs are environmentally friendly nanocomposites for water treatment applications due to their antimicrobial and superior properties. In their work, poly-IL (PIL) based quaternary ammonium salts of 2–acrylamido-2-methyl propane sulfonic acid homopolymer and its copolymer, N-vinyl pyrrolidone, were used as capping agents to control the shapes and sizes of ZnO NPs. The prepared ZnO NPs were successfully crosslinked to 2–acrylamido-2-methyl propane sulfonic acid-co-acrylonitrile nanocomposites, which were used as adsorbents for methylene blue dye, as one of the efforts to reduce a hazardous organic pollutant found in water. The enhanced properties of ZnO NPs showed high removal rates than that used without ZnO NPs [30]. Bharate et al. [33] synthesized MnO_2 NPs in IL for supercapacitor application as an electrode material. The study revealed that MnO_2 NPs displayed different morphology in the presence of nanorod-shaped RTILs and the absence of spherical-shaped RTILs. As for the supercapacitor study, cyclic voltammetry and charge-discharge analysis were performed using an electrode modified with MnO_2-capped RTILs. The electrode generated substantial pseudo-capacitance reaching a maximum value probably due to the supercapacitor assembled with RTILs capped MnO_2 NPs, as positive and negative electrodes, resulting in high specific capacitance and better rate capability. Based on the available literature, remarkably excellent properties have been reported in studies of MONPs synthesized in RTILs in various fields. Therefore, the synthesis of other materials could be now investigated in the RTILs to obtain improved physiological properties.

Conclusion

In conclusion, he synthesis of MONPs commonly involve chemical methods which include sol-gel, hydrothermal, ultrasound-assisted, precipitation, and microwave-assisted. This paper provided a comprehensive review of the common techniques of preparation and characterization of MONPs using RTILs. In general, the MONPs could be prepared using various RTILs by chemical method followed by calcination and characterization to get the desired structure and morphology of the MONPs. SEM/EDX and TEM were used to study the structure and morphology of the synthesized MONPs, whereas XRD was used to study the crystallinity and purity of the synthesized MONPs. Meanwhile, FTIR and UV-VIS were used to study the shifting of the functional group of the MONPs and the maximum wavelength shifting of absorbance of the synthesis MONPs. Based on the studies, various structure and morphology of the MONPs have been reported and can be tailor-made using different RTILs for the synthesis of specific MONPs. On the other hand, the impacts of RTILs on the formation of MONPs which reduces the agglomeration during the growth steps was also extensively discussed in this review. Moreover, this review recapitulated the applications of MONPs synthesized using RTILs with enhanced properties in antibacterial, catalyst, and other applications. For example, in antibacterial application, the inhibition zone of bacteria for MONPs that were synthesized using RTILs were doubled rather than the MONPs that were not synthesized using RTILs. In short, this review would be beneficial for manufacturers custom-made materials of MONPs using RTILs with effective properties. Finally, it is hoped that this review will not

only exhibit the recent progress in the synthesis of MONPs using RTILs, but also embark further research to explore insightful and green methods for the preparation of MONPs.

Acknowledgement

The authors gratefully acknowledge the financial support by Ministry of Education Malaysia (Fundamental Research Grant Scheme FRGS/1/ 2019/STG05/UITM/03/3). The authors acknowledge Faculty of Applied Science UiTM Shah Alam and Centre for Research and Instrumentation Management (CRIM) for the analytical services given.

References

1. Thanh, N. T. K., Maclean, N. and Mahiddine, S. (2014). Mechanisms of nucleation and growth of nanoparticles in solution. *Chemical Reviews*, 114(15): 7610-7630.
2. He, Z. and Alexandridis, P. (2017). Ionic liquid and nanoparticle hybrid systems: Emerging applications. *Advances in Colloid and Interface Science*, 244: 54-70.
3. McNamara, K. and Tofail, S. A. M. (2017). Nanoparticles in biomedical applications. *Advances in Physics: X*, *2*(1): 54-88.
4. Nikolova, M. P. and Chavali, M. S. (2020). Metal oxide nanoparticles as biomedical materials. *Biomimetics*, 5(2): 27.
5. Stankic, S., Suman, S., Haque, F. and Vidic, J. (2016). Pure and multi metal oxide nanoparticles: Synthesis, antibacterial and cytotoxic properties. *Journal of Nanobiotechnology*, 14(1): 1-20.
6. Andreescu, S., Ornatska, M., Erlichman, J. S., Ana, E. and Leiter, J. C. (2011). Biomedical applications of metal oxide nanoparticles. In *Fine Particles in Medicine and Pharmacy*. (Egon Matijević Editor). Springerlink Book: pp. 57-100.
7. Joshi, M. and Roy, A. (2018). Antimicrobial textiles based on metal and metal oxide nano-particles. *Nanomaterials in the Wet Processing of Textiles*, 2018: 71-111.
8. Raghunath, A. and Perumal, E. (2017). Metal oxide nanoparticles as antimicrobial agents: a promise for the future. *International Journal of Antimicrobial Agents*, 49(2): 137-152.
9. Nagajyothi, P. C., Prabhakar Vattikuti, S. V., Devarayapalli, K. C., Yoo, K., Shim, J. and Sreekanth, T. V. M. (2020). Green synthesis: Photocatalytic degradation of textile dyes using metal and metal oxide nanoparticles-latest trends and advancements. *Critical Reviews in Environmental Science and Technology*, 50(24): 2617-2723.
10. Khan, M. M., Adil, S. F. and Al-Mayouf, A. (2015). Metal oxides as photocatalysts. *Journal of Saudi Chemical Society*, 19(5): 462-464.
11. Veerasingam, M., Murugesan, B. and Mahalingam, S. (2020). Ionic liquid mediated morphologically improved lanthanum oxide nanoparticles by Andrographis paniculata leaves extract and its biomedical applications. *Journal of Rare Earths*, 38(3): 281-291.
12. Cheng, Z., Tan, A. L. K., Tao, Y., Shan, D., Ting, K. E. and Yin, X. J. (2012). Synthesis and characterization of iron oxide nanoparticles and applications in the removal of heavy metals from industrial wastewater. *International Journal of Photoenergy*, 2012: 608298.
13. Zhu, D., Chen, Y., Yang, H., Wang, S., Wang, X., Zhang, S. and Chen, H. (2020). Synthesis and characterization of magnesium oxide nanoparticle-containing biochar composites for efficient phosphorus removal from aqueous solution. *Chemosphere*, 247: 125847.
14. Dang, T. D., Cheney, M. A., Qian, S., Joo, S. W. and Min, B. K. (2013). A novel rapid one-step synthesis of manganese oxide nanoparticles at room temperature using poly(dimethylsiloxane). *Industrial and Engineering Chemistry Research*, 52(7): 2750-2753.
15. Dawadi, S., Gupta, A., Khatri, M., Budhathoki, B., Lamichhane, G. and Parajuli, N. (2020). Manganese dioxide nanoparticles: synthesis, application and challenges. *Bulletin of Materials Science*, 43: 227.
16. Mahamuni, P. P., Patil, P. M., Dhanavade, M. J., Badiger, M. V., Shadija, P. G., Lokhande, A. C. and Bohara, R. A. (2019). Synthesis and characterization of zinc oxide nanoparticles by using polyol chemistry for their antimicrobial and antibiofilm activity. *Biochemistry and Biophysics Reports*, 17(9): 71-80.
17. Elbushra, H., Ahmed, M., Wardi, H. and Eassa, N. (2018). Synthesis and characterization of TiO_2 using sol-gel method at different annealing temperatures. *MRS Advances*, 3(42–43): 2527-2535.
18. Singh, P. K., Kumar, P., Hussain, M., Das, A. K. and Nayak, G. C. (2016). Synthesis and characterization of CuO nanoparticles using strong base electrolyte through electrochemical discharge process. *Bulletin of Materials Science*, 39(2): 469-478.

19. Fathima, J. B., Pugazhendhi, A. and Venis, R. (2017). Synthesis and characterization of ZrO_2 nanoparticles-antimicrobial activity and their prospective role in dental care. *Microbial Pathogenesis*, 110: 245-251.
20. Dubey, R. S., Rajesh, Y. B. R. D. and More, M. A. (2015). Synthesis and Characterization of SiO_2 nanoparticles via sol-gel method for industrial applications. *Materials Today: Proceedings*, 2(4–5): 3575-3579.
21. Sakthiraj, K. and Karthikeyan, B. (2020). Synthesis and characterization of cerium oxide nanoparticles using different solvents for electrochemical applications. *Applied Physics A: Materials Science and Processing*, 126(1): 1-10.
22. Wang, C., Xu, H., Wang, C., Liu, T., Yang, S., Nie, Y., Guo, X., Ma, X. and Jiang, X. (2021). Preparation of VO2 (M) nanoparticles with exemplary optical performance from VO2 (B) nanobelts by ball milling. *Journal of Alloys and Compounds*, 877: 159888.
23. Malevu, T. D. (2021). Ball Milling synthesis and characterization of highly crystalline TiO_2-ZnO hybrids for photovoltaic applications . *Physica B: Condensed Matter*, 621(7): 413291.
24. Rashid, T. M., Nayef, U. M., Jabir, M. S., and Mutlak, F. A. H. (2021). Synthesis and characterization of Au:ZnO (core:shell) nanoparticles via laser ablation. *Optik*, 244(7): 167569.
25. Altuwirqi, R. M., Albakri, A. S., Al-Jawhari, H. and Ganash, E. A. (2020). Green synthesis of copper oxide nanoparticles by pulsed laser ablation in spinach leaves extract. *Optik*, 219(4): 165280.
26. Menazea, A. A. and Awwad, N. S. (2020). Pulsed Nd:YAG laser deposition-assisted synthesis of silver/copper oxide nanocomposite thin film for 4-nitrophenol reduction. *Radiation Physics and Chemistry*, 177(5): 109112.
27. Shreema, K., Mathammal, R., Kalaiselvi, V., Vijayakumar, S., Selvakumar, K. and Senthil, K. (2021). Green synthesis of silver doped zinc oxide nanoparticles using fresh leaf extract *Morinda citrifoliaand* its antioxidant potential. *Materials Today: Proceedings*, 47: 2126-2131.
28. Ramzan, M., Obodo, R. M., Mukhtar, S., Ilyas, S. Z., Aziz, F. and Thovhogi, N. (2019). Green synthesis of copper oxide nanoparticles using Cedrus deodara aqueous extract for antibacterial activity. *Materials Today: Proceedings*, 36: 576-581.
29. Khan, M. F., Ansari, A. H., Hameedullah, M., Ahmad, E., Husain, F. M., Zia, Q., Baig, U., Zaheer, M. R., Alam, M. M., Khan, A. M., Alothman, Z. A., Ahmad, I., Ashraf, G. M. and Aliev, G. (2016). Sol-gel synthesis of thorn-like ZnO nanoparticles endorsing mechanical stirring effect and their antimicrobial activities: Potential role as nano-Antibiotics. *Scientific Reports*, 6(5): 1-12.
30. Atta, A. M., Al-Lohedan, H. A., Ezzat, A. O., Tawfik, A. M. and Hashem, A. I. (2017). Synthesis of zinc oxide nanocomposites using poly (ionic liquids) based on quaternary ammonium acrylamidomethyl propane sulfonate for water treatment. *Journal of Molecular Liquids*, 236: 38-47.
31. Wang, Y., Maksimuk, S., Shen, R. and Yang, H. (2007). Synthesis of iron oxide nanoparticles using a freshly-made or recycled imidazolium-based ionic liquid. *Green Chemistry,* 10: 1051-1056.
32. Zheng, W., Liu, X., Yan, Z. and Zhu, L. (2009). Ionic liquid-assisted synthesis of large-scale TiO_2 nanoparticles with controllable phase by hydrolysis of TiCl4. *ACS Nano*, *3*(1): 115-122.
33. Bharate, B. G., Hande, P. E., Samui, A. B. and Kulkarni, P. S. (2018). Ionic liquid (IL) capped MnO_2 nanoparticles as an electrode material and IL as electrolyte for supercapacitor application. *Renewable Energy,* 126: 437-444.
34. Sivanantham, A., Firoz Babu, K., Anbu Kulandainathan, M., Babu, S. G., Suresh Bapu, R. H. and Sreedhar, G. (2014). Capping and catalytic behaviour of lithiated sarcosine TFSI on the formation of hexagonal ZnO micro rods using hydrothermal method. *Materials Letters*, 128: 195-198.
35. Qi, K., Yang, J., Fu, J., Wang, G., Zhu, L., Liu, G. and Zheng, W. (2013). Morphology-controllable ZnO rings: Ionic liquid-assisted hydrothermal synthesis, growth mechanism and photoluminescence properties. *CrystEngComm*, 15(34): 6729-6735.
36. Kavya, S. H., Kumar, V. V., & Kumar, C. R. (2018). Synthesis and characterization of stable ZnO nanoparticles using imidazolium-based ionic liquids and their applications in esterification reaction. *Indian Journal of Chemistry, 57*: 1112-1120.
37. Ahmadi Tehrani, A., Omranpoor, M. M., Vatanara, A., Seyedabadi, M. and Ramezani, V. (2019). Formation of nanosuspensions in bottom-

up approach: theories and optimization. *DARU Journal of Pharmaceutical Sciences*, 27(1): 451-473.

38. Jalab, J., Abdelwahed, W., Kitaz, A. and Al-kayali, R. (2021). Green synthesis of silver nanoparticles using aqueous extract of Acacia cyanophylla and its antibacterial activity. *Heliyon, 7*(9): e08033.
39. Khan, M. A. R., Shamim, M., Mamun, A. and Hosna, M. (2021). Review on platinum nanoparticles : Synthesis , characterization , and applications. *Microchemical Journal*, 171(9): 106840.
40. Devatha, C. P. and Thalla, A. K. (2018). Chapter 7 - green synthesis of nanomaterials (pp. 169-184). Elsevier.
41. Alam, M. M., Asiri, A. M. and Rahman, M. M. (2021). Wet-chemically synthesis of SnO_2-doped Ag_2O nanostructured materials for sensitive detection of choline by an alternative electrochemical approach. *Microchemical Journal*, 165(2): 106092.
42. Nikam, A. V., Prasad, B. L. V. and Kulkarni, A. A. (2018). Wet chemical synthesis of metal oxide nanoparticles: A review. *CrystEngComm*, 20(35): 5091-5107.
43. Zhou, Y. (2006). Recent advances in ionic liquids for synthesis of inorganic nanomaterials. *Current Nanoscience*, 1(1): 35-42.
44. Irfan, M., Ahmad, T., Moniruzzaman, M., Bhattacharjee, S. and Abdullah, B. (2020). Size and stability modulation of ionic liquid functionalized gold nanoparticles synthesized using *Elaeis guineensis* (oil palm) kernel extract. *Arabian Journal of Chemistry*, 13(1): 75-85.
45. Nishad, K K., Manthrammel, M. A., Shkir, M., AlFaify, S. and Pandey, R. K. (2022). Effect of organic capping on defect induced ferromagnetism in ZnO nanoparticles. *Physica B: Condensed Matter*, 624: 413379.
46. Rostami-Tapeh-Esmaeil, E., Golshan, M., Salami-Kalajahi, M. and Roghani-Mamaqani, H. (2021). Synthesis of copper and copper oxide nanoparticles with different morphologies using aniline as reducing agent. *Solid State Communications*, 334-335(5): 114364.
47. Yong, N. L., Ahmad, A., & Mohammad, A. W. (2012). Synthesis and characterization of silver nanoparticles by a sonochemical method. *Xiyou Jinshu Cailiao Yu Gongcheng/Rare Metal Materials and Engineering*, 41(10): 1700-1705.
48. Saraji, M. and Alijani, S. (2021). A molecularly imprinted polymer on chromium (III) oxide nanoparticles for spectrofluorometric detection of bisphenol A. *Spectrochimica Acta - Part A: Molecular and Biomolecular Spectroscopy*, 255: 119711.
49. Sedlák, J., Kuřitka, I., Machovský, M., Šuly, P., Bažant, P. and Sedláček, T. (2015). Zinc oxide nanoparticles with surface modified by degradation of capping polymers in situ during microwave synthesis. *Advanced Powder Technology*, 26(4): 1064-1071.
50. Bomila, R., Venkatesan, A. and Srinivasan, S. (2018). Structural, luminescence and photocatalytic properties of pure and octylamine capped ZnO nanoparticles. *Optik*, 158: 565-573.
51. Hajipour, A. R. and Rafiee, F. (2015). Recent progress in ionic liquids and their applications in organic synthesis. *Organic Preparations and Procedures International*, 47(4): 1-60.
52. Fang, X. and Song, H. (2019). Synthesis of cerium oxide nanoparticles loaded on chitosan for enhanced auto-catalytic regenerative ability and biocompatibility for the spinal cord injury repair. *Journal of Photochemistry and Photobiology B: Biology*, 191: 83-87.
53. Sundrarajan, M., Jegatheeswaran, S., Selvam, S., Sanjeevi, N. and Balaji, M. (2015). The ionic liquid assisted green synthesis of hydroxyapatite nanoplates by *Moringa oleifera* flower extract: A biomimetic approach. *Materials and Design*, *88*: 1183-1190.
54. Łuczak, J., Paszkiewicz, M., Krukowska, A., Malankowska, A. and Zaleska-Medynska, A. (2016). Ionic liquids for nano- and microstructures preparation. Part 2: Application in synthesis. *Advances in Colloid and Interface Science*, 227: 1-52.
55. Migowski, P., Machado, G., Texeira, S. R., Alves, M. C. M., Morais, J., Traverse, A. and Dupont, J. (2007). Synthesis and characterization of nickel nanoparticles dispersed in imidazolium ionic liquids. *Physical Chemistry Chemical Physics*, 9(34): 4814-4821.
56. Vollmer, C. and Janiak, C. (2011). Naked metal nanoparticles from metal carbonyls in ionic liquids: Easy synthesis and stabilization. *Coordination Chemistry Reviews*, *255*(17-18): 2039-2057.
57. Scheeren, C. W., Machado, G., Teixeira, S. R., Morais, J., Domingos, J. B. and Dupont, J. (2006). Synthesis and characterization of Pt(0) nanoparticles in imidazolium ionic liquids.

Journal of Physical Chemistry B, 110(26): 13011-13020.

58. Zhao, M., Li, N., Zheng, L., Li, G. and Yu, L. (2008). Synthesis of well-dispersed NiO nanoparticles with a room temperature ionic liquid. *Journal of Dispersion Science and Technology,* 29(8): 1103-1105.
59. Sakai, K., Okada, K., Uka, A., Misono, T., Endo, T., Sasaki, S., Abe, M. and Sakai, H. (2015). Effects of water on solvation layers of imidazolium-type room temperature ionic liquids on silica and mica. *Langmuir*, 31(22), 6085–6091.
60. Ninham, B. W. (1999). On progress in forces since the DLVO theory. *Advances in Colloid and Interface Science*, 83(1): 1-17.
61. Obliosca, J. M., Arellano, I. H. J., Huang, M. H. and Arco, S. D. (2010). Double layer micellar stabilization of gold nanocrystals by greener ionic liquid 1-butyl-3-methylimidazolium lauryl sulfate. *Materials Letters*, 64(9): 1109-1112.
62. He, Z., & Alexandridis, P. (2015). Nanoparticles in ionic liquids: Interactions and organization. *Physical Chemistry Chemical Physics*, 17(28): 18238-18261.
63. Barik, B., Kumar, A., Nayak, P. S., Achary, L. S. K., Rout, L. and Dash, P. (2020). Ionic liquid assisted mesoporous silica-graphene oxide nanocomposite synthesis and its application for removal of heavy metal ions from water. *Materials Chemistry and Physics*, 239(8): 122028.
64. Das, M., Aswathy, T. R., Pal, S. and Naskar, K. (2021). Effect of ionic liquid modified graphene oxide on mechanical and self-healing application of an ionic elastomer. *European Polymer Journal*, 158(7): 110691.
65. Kargar, S., Elhamifar, D. and Zarnegaryan, A. (2021). Ionic liquid modified graphene oxide supported Mo-complex: A novel, efficient and highly stable catalyst. *Surfaces and Interfaces*, 23(1): 100946.
66. Husanu, E., Chiappe, C., Bernardini, A., Cappello, V. and Gemmi, M. (2018). Synthesis of colloidal Ag nanoparticles with citrate based ionic liquids as reducing and capping agents. *Colloids and Surfaces A: Physicochemical and Engineering Aspects*, 538(11): 506-512.
67. Sadeghi, S. and Olieaei, S. (2019). Capped cadmium sulfide quantum dots with a new ionic liquid as a fluorescent probe for sensitive detection of florfenicol in meat samples. *Spectrochimica Acta - Part A: Molecular and Biomolecular Spectroscopy*, 223: 117349.
68. Krishnan, B. and Mahalingam, S. (2017). Improved surface morphology of silver/copper oxide/bentonite nanocomposite using aliphatic ammonium based ionic liquid for enhanced biological activities. *Journal of Molecular Liquids*, 241: 1044-1058.
69. Ahmad, T., Bustam, M. A., Irfan, M., Moniruzzaman, M., Samsudin, M. F. R., Asghar, H. M. A., Muhammad, N., Iqbal, J. and Bhattacharjee, S. (2019). Effect of gold and iron nanoparticles on photocatalytic behaviour of titanium dioxide towards 1-butyl-3-methylimidazolium chloride ionic liquid. *Journal of Molecular Liquids*, 291: 2–6.
70. Verma, C., Ebenso, E. E. and Quraishi, M. A. (2019). Transition metal nanoparticles in ionic liquids: Synthesis and stabilization. *Journal of Molecular Liquids*, 276: 826-849.
71. Abbott, A. P., Frisch, G., Hartley, J. and Ryder, K. S. (2011). Processing of metals and metal oxides using ionic liquids. *Green Chemistry*, 13(3): 471-481.
72. Prechtl, M. H. G. and Campbell, P. S. (2013). Metal oxide and bimetallic nanoparticles in ionic liquids: Synthesis and application in multiphase catalysis. *Nanotechnology Reviews*, 2(5): 577-595.
73. Seitkalieva, M. M., Samoylenko, D. E., Lotsman, K. A., Rodygin, K. S. and Ananikov, V. P. (2021). Metal nanoparticles in ionic liquids: Synthesis and catalytic applications. *Coordination Chemistry Reviews*, 445: 213982.
74. Gulati, S., Sachdeva, M. and Bhasin, K. K. (2018). Capping agents in nanoparticle synthesis: Surfactant and solvent system. *AIP Conference Proceedings*, 2018: 1953.
75. Tapak, N. S., Nawawi, M. A., Tjih, E. T. T., Mohd, Y., Ab Rashid, A. H., Abdullah, J., ... and Ahmad, N. M. (2022). The synthesis of zirconium oxide (ZrO2) nanoparticles (NPs) in 1-butyl-3-methylimidazolium trifluoroacetate (BMIM CF_3COO) for an amperometry phenol biosensor. *Materials Today Communications,* 33: 104142.
76. Oskam, G. (2006). Metal oxide nanoparticles: Synthesis, characterization and application. *Journal of Sol-Gel Science and Technology*, 37(3): 161-164.
77. Hu, H., Huang, X., Deng, C., Chen, X. and Qian, Y. (2007). Hydrothermal synthesis of ZnO nanowires and nanobelts on a large scale. *Materials Chemistry and Physics*, 106(1): 58-62.

78. Zhang, S., Zhang, Y., Wang, Y., Liu, S. and Deng, Y. (2012). Sonochemical formation of iron oxide nanoparticles in ionic liquids for magnetic liquid marble. *Physical Chemical Chemistry Physics,* 15: 5132-5138.
79. Janiak, C. (2013). Ionic liquids for the synthesis and stabilization of metal nanoparticles. Zeitschrift Fur Naturforschung - Section B Journal of Chemical Sciences, 68(10): 1059-1089
80. Alammar, T. and Mudring, A. V. (2011). Sonochemical synthesis of 0D, 1D, and 2D zinc oxide nanostructures in ionic liquids and their photocatalytic activity. *ChemSusChem*, 4(12): 1796-1804.
81. Wang, L., Chang, L., Zhao, B., Yuan, Z., Shao, G. and Zheng, W. (2008). Systematic investigation on morphologies, forming mechanism, photocatalytic and photoluminescent properties of ZnO nanostructures constructed in ionic liquids. *Inorganic Chemistry*, 47(5): 1443-1452.
82. Zhu, H., Huang, J. F., Pan, Z. and Dai, S. (2006). Ionothermal synthesis of hierarchical ZnO nanostructures from ionic-liquid precursors. *Chemistry of Materials*, 18(18): 4473-4477.
83. Ma, B. Z., Yu, J. and Dai, S. (2010). Preparation of inorganic materials using ionic liquids. *Advance Materials,* 130012: 261-285.
84. Lian, J., Duan, X., Ma, J., Peng, P., Kim, T., & Zheng, W. (2009). Hematite (α-Fe_2O_3) with various morphologies: ionic liquid-assisted synthesis, formation mechanism, and properties. *ACS Nano, 3*(11): 3749-3761.
85. Zhang, Y., Cheng, X., Zhang, X., Major, Z., Xu, Y., Gao, S., Zhao, H. and Huo, L. (2019). Ionic liquid-assisted synthesis of tungsten oxide nanoparticles with enhanced NO_2 sensing properties at near room temperature. *Applied Surface Science*, 2: 144533.
86. Sundrarajan, M., Jegatheeswaran, S., Selvam, S., Gowri, R., Balaji, M. and Bharathi, K. (2017). Green approach : Ionic liquid assisted synthesis of nanocrystalline ZnO in phyto medium and their antibacterial investigation. *Materials Letters*, 201: 31-34.
87. Fang, X. and Song, H. (2019). Synthesis of cerium oxide nanoparticles loaded on chitosan for enhanced auto-catalytic regenerative ability and biocompatibility for the spinal cord injury repair. *Journal of Photochemistry and Photobiology B: Biology*, 191: 83-87.
88. Sundrarajan, M., Gandhi, R. G. R., Suresh, J., Selvam, S. and Gowri, S. (2012). Sol-gel synthesis of MgO nanoparticles using ionic liquid-[BMIM]BF_4 as capping agent. *Nanoscience and Nanotechnology Letters*, 4(1): 100-104.
89. Yoo, K., Choi, H. and Dionysiou, D. D. (2004). Ionic liquid assisted preparation of nanostructured TiO_2 particles. Chemical Communications, 17: 2000-2001.
90. García Rojas, L. M., Huerta-Aguilar, C. A., Tecuapa-Flores, E. D., Huerta-José, D. S., Thangarasu, P., Sidhu, J. S., Singh, N. and de la Luz Corea Téllez, M. (2020). Why ionic liquids coated ZnO nanocomposites emerging as environmental remediates: Enhanced photo-oxidation of 4-nitroaniline and encouraged antibacterial behavior. *Journal of Molecular Liquids*, 319: 114107.
91. Sundrarajan, M. and Muthulakshmi, V. (2021). Green synthesis of ionic liquid mediated neodymium oxide nanoparticles by Andrographis paniculata leaves extract for effective bio-medical applications. *Journal of Environmental Chemical Engineering*, *9*(1): 104716.
92. Sundrarajan, M., Bama, K., Selvanathan, G. and Prabhu, M. R. (2018). Ionic liquid-mediated: Enhanced surface morphology of silver/manganese oxide/bentonite nanocomposite for improved biological activities. *Journal of Molecular Liquids*, 249: 1020-1032.
93. Pandiyan, N., Murugesan, B., Sonamuthu, J., Samayanan, S. and Mahalingam, S. (2019). [BMIM]PF_6 ionic liquid mediated green synthesis of ceramic SrO/CeO_2 nanostructure using *Pedalium murex* leaf extract and their antioxidant and antibacterial activities. *Ceramics International*, 45(9): 12138-12148.
94. Pandiyan, N., Murugesan, B., Arumugam, M., Chinnaalagu, D., Samayanan, S. and Mahalingam, S. (2021). Ionic liquid mediated green synthesis of Ag-Au/Y_2O_3 nanoparticles using leaves extracts of Justicia adhatoda: Structural characterization and its biological applications. *Advanced Powder Technology*, 32(7): 2213-2225.
95. Muthulakshmi, V. and Sundrarajan, M. (2020). Green synthesis of ionic liquid assisted ytterbium oxide nanoparticles by Couroupita guianensis abul leaves extract for biological applications. *Journal of Environmental Chemical Engineering*, 8(4): 103992.
96. Shen, J., Shi, M., Yan, B., Ma, H., Li, N. and Ye, M. (2011). One-pot hydrothermal synthesis of

Ag-reduced graphene oxide composite with ionic liquid. *Journal of Materials Chemistry,* 21(21): 7795-7801.

97. Lv, J. J., Feng, J. X., Li, S. S., Wang, Y. Y., Wang, A. J., Zhang, Q. L., Chen, J. R. and Feng, J. J. (2014). Ionic liquid crystal-assisted synthesis of PtAg nanoflowers on reduced graphene oxide and their enhanced electrocatalytic activity toward oxygen reduction reaction. *Electrochimica Acta*, 133: 407-413.
98. Zhang, J., Wang, J., Zhou, S., Duan, K., Feng, B., Weng, J., Tang, H. and Wu, P. (2010). Ionic liquid-controlled synthesis of ZnO microspheres. *Journal of Materials Chemistry*, 20(43): 9798-9804.
99. Kim, T., Lian, J., Ma, J., Duan, X. and Zheng, W. (2010). Morphology controllable synthesis of γ-alumina nanostructures via an ionic liquid-assisted hydrothermal route. *Crystal Growth and Design*, 10(7): 292-2933.
100. Muthulakshmi, V., Balaji, M. and Sundrarajan, M. (2020). Biomedical applications of ionic liquid mediated samarium oxide nanoparticles by *Andrographis paniculata* leaves extract. *Materials Chemistry and Physics*, 242(11): 122483.
101. Liu, H., Wang, M., Wang, Y., Liang, Y., Cao, W. and Su, Y. (2011). Ionic liquid-templated synthesis of mesoporous CeO_2–TiO_2 nanoparticles and their enhanced photocatalytic activities under UV or visible light. *Journal of Photochemistry & Photobiology, A: Chemistry, 223*(2–3): 157-164.
102. Liu, H., Liang, Y., Hu, H. and Wang, M. (2009). Hydrothermal synthesis of mesostructured nanocrystalline TiO 2 in an ionic liquid – water mixture and its photocatalytic performance. *Solid State Sciences*, 11(9): 1655-1660.
103. Gao, R., Gao, S., Wang, P., Xu, Y., Zhang, X., Cheng, X., Zhou, X., Major, Z., Zhu, H. and Huo, L. (2020). Ionic liquid assisted synthesis of snowflake ZnO for detection of NOx and sensing mechanism. *Sensors and Actuators, B: Chemical*, 303: 127085.
104. Goharshadi, E. K., Ding, Y., Namayandeh, M. and Nancarrow, P. (2009). Ultrasound-assisted green synthesis of nanocrystalline ZnO in the ionic liquid [hmim][NTf_2]. *Ultrasonics Sonochemistry*, 16: 120-123.
105. Inbasekar, C. and Fathima, N. N. (2020). Collagen stabilization using ionic liquid functionalised cerium oxide nanoparticle. *International Journal of Biological Macromolecules*, 147: 24-28.
106. Ellateif, T. M. A. and Mitra, S. (2017). Sol gel synthesis and characterization of zirconia containing hydrophobic silica nanoparticles. *Journal of Advances in Nanomaterials*, *2*(4): 185-196.
107. Lu, Y., Dong, W., Ding, J., Wang, W. and Wang, A. (2019). Hydroxyapatite nanomaterials: synthesis, properties, and functional applications. In *Nanomaterials from Clay Minerals*. Elsevier Inc.
108. Lim, H. S., Ahmad, A. and Hamzah, H. (2013). Synthesis of zirconium oxide nanoparticle by sol-gel technique. *AIP Conference Proceedings*, 1571: 812–816.
109. Behbahani, A., Rowshanzamir, S. and Esmaeilifar, A. (2012). Hydrothermal synthesis of zirconia nanoparticles from commercial zirconia. *Procedia Engineering*, 42: 908-917.
110. Muthulakshmi, V., Kumar, P. and Sundrarajan, M. (2021). Green synthesis of Ionic liquid mediated Ytterbium oxide nanoparticles by *Andrographis paniculata* leaves extract for structural, morphological and biomedical applications. *Journal of Environmental Chemical Engineering*, 9(4): 105270.
111. Jolivet, J. P., Cassaignon, S., Chanéac, C., Chiche, D., Durupthy, O. and Portehault, D. (2010). Design of metal oxide nanoparticles: Control of size, shape, crystalline structure and functionalization by aqueous chemistry. *Comptes Rendus Chimie*, 13(1–2): 40-51.
112. Kotresh, M. G., Patil, M. K. and Inamdar, S. R. (2021). Reaction temperature based synthesis of ZnO nanoparticles using co-precipitation method: Detailed structural and optical characterization. *Optik*, 243(6): 167506.
113. Wahab, R., Kim, Y. S. and Shin, H. S. (2009). Synthesis, characterization and effect of pH variation on zinc oxide nanostructures. *Materials Transactions*, 50(8): 2092-2097.
114. Nair, P. A. K., Vasconcelos, W. L., Paine, K. and Calabria-Holley, J. (2021). A review on applications of sol-gel science in cement. *Construction and Building Materials*, 291: 123065.
115. Danks, A. E., Hall, S. R. and Schnepp, Z. (2016). The evolution of 'sol–gel' chemistry as a technique for materials synthesis. *Materials Horizon,* 2: 91-112.
116. Shandilya, M., Rai, R., Singh, J., Shandilya, M.,

Rai, R. and Singh, J. (2016). Review: hydrothermal technology for smart materials. *Advances in Applied Chemistry,* 115: 354-376.

117. Sahoo, S., Pazhamalai, P., Mariappan, V. K., Veerasubramani, G. K., Nam-Jin Kim, Kim, S.-J. and A. (2020). Hydrothermally synthesized chalcopyrite platelets as electrode material for symmetric supercapacitors. *Inorganic Chemistry Frontiers*, 2020: 1-30.
118. Yadav, S. and Sharma, A. (2021). Importance and challenges of hydrothermal technique for synthesis of transition metal oxides and composites as supercapacitor electrode materials. *Journal of Energy Storage*, 44: 103295.
119. Ng, H. K. M., Lim, G. K. and Leo, C. P. (2021). Comparison between hydrothermal and microwave-assisted synthesis of carbon dots from biowaste and chemical for heavy metal detection : A review. *Microchemical Journal*, 165: 106116.
120. Medeiros, T. V. de, Manioudakis, J., Noun, F., Macairan, J.-R., Victoria, F. and Naccache, R. (2019). Microwave-assisted synthesis of carbon dots and their applications. *Materials Chemistry C*, 2019: 1-20.
121. Jusuf, B. N., Sambudi, N. S., Isnaeni, I. and Samsuri, S. (2018). Microwave-assisted synthesis of carbon dots from eggshell membrane ashes by using sodium hydroxide and their usage for degradation of methylene blue. *Journal of Environmental Chemical Engineering*, 6(6): 7426-7433.
122. Wang, X., Ahmad, M. and Sun, H. (2017). Three-dimensional ZnO hierarchical nanostructures: solution phase synthesis and applications. *Materials*, 10(11): 1-23.
123. Kołodziejczak-radzimska, A., Markiewicz, E. and Jesionowski, T. (2012). Structural characterisation of ZnO particles obtained by the emulsion precipitation method. *Journal of Nanomaterials,* 2012: 656353.
124. Kurian, M. and Nair, D. S. (2013). Effect of preparation conditions on nickel zinc ferrite nanoparticles : a comparison between sol – gel auto combustion and co-precipitation methods. *Journal of Saudi Chemical Society*, 20(1): 557-522.
125. Sepulveda-guzman, S., Reeja-jayan, B., Rosa, E. De and Torres-castro, A. (2009). Synthesis of assembled ZnO structures by precipitation method in aqueous media. *Materials Chemistry and Physics,* 115: 172-178.
126. Bhosale, M. A., Chenna, D. R. and Bhanage, B. M. (2017). Ultrasound assisted synthesis of gold nanoparticles as an efficient catalyst for reduction of various nitro compounds. *ChemistrySelect,* 2(3): 1225-1231.
127. Deshmukh, A. R., Gupta, A. and Kim, B. S. (2019). Ultrasound assisted green synthesis of silver and iron oxide nanoparticles using fenugreek seed extract and their enhanced antibacterial and antioxidant activities. *Biomed Research International,* 2019: 1714358.
128. Cravotto, G. and Cintas, P. (2006). Power ultrasound in organic synthesis : moving cavitational chemistry from academia to innovative and large-scale applications. *Chemical Society Review,* 2:180-196.
129. Naeimi, H. and Farahnak, M. (2018). A facile one-pot ultrasound-assisted green synthesis of tetrahydrobenzo[b]pyrans catalyzed by gold nanoparticles supported on thiol - functionalized reduced graphene oxide. *Research on Chemical Intermediates*, 44(5): 3227-3247.
130. Hussain, M. (2014). Synthesis, characterization and applications of metal oxide. Dissertation Linköping University.
131. Khaldakar, M. and Butala, D. (2017). The synthesis and characterization of metal oxide nanoparticles and its application for photo catalysis. *International Journal of Scientific and Research Publications*, *7*(3): 499.
132. Tushar G, R. and Babita R, A. (2019). Transmission electron microscopy- an overview. *International Research Journal for Inventions in Pharmaceutical Sciences*, 1(2): 1-7.
133. Inkson, B. J. (2016). Scanning electron microscopy (SEM) and Transmission electron microscopy (TEM) for materials characterization. In *Materials Characterization Using Nondestructive Evaluation (NDE) Methods*. Elsevier Ltd.
134. Mahjoub, A. R., Movahedi, M., Kowsari, E. and Yavari, I. (2014). Narcis-like zinc oxide: Chiral ionic liquid assisted synthesis, photoluminescence and photocatalytic activity. *Materials Science in Semiconductor Processing*, 22(1): 1-6.
135. Kowsari, E. and Karimzadeh, A. H. (2012). Fabrication of fern-like, fish skeleton-like, and butterfly-like BaO nanostructures as nanofillers for radar-absorbing nanocomposites. *Materials Letters*, 74: 33-36.
136. Mourdikoudis, S., Pallares, R. M. and Thanh, N. T. K. (2018). Characterization techniques for

nanoparticles: Comparison and complementarity upon studying nanoparticle properties. *Nanoscale*, 10(27): 12871-12934.

137. Tzani, A., Koutsoukos, S., Koukouzelis, D. and Detsi, A. (2017). Synthesis and characterization of silver nanoparticles using biodegradable protic ionic liquids. *Journal of Molecular Liquids*, 243: 212-218.
138. Nithya, P., Balaji, M., Jegatheeswaran, S., Selvam, S. and Sundrarajan, M. (2017). Facile biological synthetic strategy to morphologically aligned CeO_2/ZrO_2 core nanoparticles using *Justicia adhatoda* extract and ionic liquid: Enhancement of its bio-medical properties. *Journal of Photochemistry & Photobiology, B: Biology*, 2017:1-34.
139. Padovini, D. S. S., Pontes, D. S. L., Dalmaschio, C. J., Pontes, F. M. and Longo, E. (2014). Facile synthesis and characterization of ZrO_2 nanoparticles prepared by the AOP/hydrothermal route. *RSC Advances*, 4(73): 38484-38490.
140. Lu, X., Tao, L., Song, D., Li, Y. and Gao, F. (2018). Bimetallic Pd @ Au nanorods based ultrasensitive acetylcholinesterase biosensor for determination of organophosphate pesticides. *Sensors & Actuators: B. Chemical*, 255: 2575-2581.
141. Shyamala, S., Kalaiarasi, S., Karpagavinayagam, P., Vedhi, C., Muthuchudarkodi, R. R., Kulandaivel, S., and Lakshmi, A. (2021). Synthesis of metal oxide nanoparticles doped poly 3 anisidine nanocomposites with enhanced electrocatalytic activity for methanol oxidation. *Materials Today: Proceedings*, 2021: 3-10.
142. Rakhimol, K. R., Thomas, S., Kalarikkal, N. and Jayachandran, K. (2020). Casein mediated synthesis of stabilized metal/metal-oxide nanoparticles with varied surface morphology through pH alteration. *Materials Chemistry and Physics*, 246: 122803.
143. Itoh, H., Naka, K. and Chujo, Y. (2004). Synthesis of gold nanoparticles modified with ionic liquid based on the imidazolium cation. *Journal of American Chemical Society,* 26(1): 3026-3027.
144. Kowsari, E. and Bazri, B. (2014). Synthesis of rose-like ZnO hierarchical nanostructures in the presence of ionic liquid/Mg2+ for air purification and their shape-dependent photodegradation of SO_2, NOx, and CO. *Applied Catalysis A: General*, 475: 325-334.
145. Husanu, E., Cappello, V., Pomelli, C. S., David, J., Gemmi, M. and Chiappe, C. (2017). Chiral ionic liquid assisted synthesis of some metal oxides. *RSC Advances*, 7(2): 1154-1160.
146. Pulskamp, K., Diabaté, S. and Krug, H. F. (2007). Carbon nanotubes show no sign of acute toxicity but induce intracellular reactive oxygen species in dependence on contaminants. *Toxicology Letters*, 168(1): 58-74.
147. Liu, H., Wang, M., Wang, Y., Liang, Y., Cao, W. and Su, Y. (2011). Ionic liquid-templated synthesis of mesoporous CeO2-TiO 2 nanoparticles and their enhanced photocatalytic activities under UV or visible light. *Journal of Photochemistry and Photobiology A: Chemistry*, 223(2-3): 157-164.
148. Ismail, A. A., van de Voort, F. R. and Sedman, J. (1997). Chapter 4 Fourier transform infrared spectroscopy: Principles and applications. *Techniques and Instrumentation in Analytical Chemistry*, 18(C): 93-139.
149. Bodade, A. B., Taiwade, M. A. and Chaudhari, G. N. (2017). Bioelectrode based chitosan-nano copper oxide for application to. *Journal of Applied Pharmaceutical Research,* 5: 30-39.
150. Alomairy, S., Al-Buriahi, M. S., Abdel Wahab, E. A., Sriwunkum, C. and Shaaban, K. S. (2021). Synthesis, FTIR, and neutron/charged particle transmission properties of Pb_3O_4–SiO_2–ZnO–WO_3 glass system. *Ceramics International*, 47(12): 17322-17330.
151. Kumar, A. (2020). Sol gel synthesis of zinc oxide nanoparticles and their application as nano-composite electrode material for supercapacitor. *Journal of Molecular Structure*, 1220: 128654.
152. Nithya, P., Balaji, M., Mayakrishnan, A. and Jegatheeswaran, S. (2020). Biogenic approach for the synthesis of Ag-Au doped RuO_2 nanoparticles in BMIM-PF_6 ionic liquid medium: Structural characterization and its biocidal activity against pathogenic bacteria and HeLa cancerous cells. *Journal of Molecular Liquids*, 312: 113245.
153. Goharshadi, E. K., Samiee, S. and Nancarrow, P. (2011). Fabrication of cerium oxide nanoparticles: Characterization and optical properties. *Journal of Colloid and Interface Science*, 356(2): 473-480.
154. Rajesh, G. and Nagar, A. (2018). Efficacy of calcination on the optical, structural and photocatalytic properties of Zirconium Oxide via facile precipitation method. *Journal of Emerging Technologies and Innovative Research, 5*(10): 575-585.

155. Devanand Venkatasubbu, G., Ramasamy, S., Ramakrishnan, V. and Kumar, J. (2013). Folate targeted PEGylated titanium dioxide nanoparticles as a nanocarrier for targeted paclitaxel drug delivery. *Advanced Powder Technology*, 24(6): 947-954.
156. Ramzan, M., Obodo, R. M., Mukhtar, S., Ilyas, S. Z., Aziz, F. and Thovhogi, N. (2019). Green synthesis of copper oxide nanoparticles using Cedrus deodara aqueous extract for antibacterial activity. *Materials Today: Proceedings*, 36: 576-581.
157. Garg, S., Gautam, S., Pal, J., Kandasami, A. and Goyal, N. (2021). Materials Characterization Characterizing the defects and ferromagnetism in metal oxides : The case of magnesium oxide. *Materials Characterization*, 179(5): 111366.
158. Nair, H., Liszka, M. J., Gatt, J. E. and Baertsch, C. D. (2008). Effects of metal oxide domain size, dispersion, and interaction in mixed WOx / MoOx catalysts supported on Al_2O_3 for the partial oxidation of ethanol to acetaldehyde. *Journal Physical Chemistry,* 112: 1612-1620.
159. Bharate, B. G., Hande, P. E., Samui, A. B. and Kulkarni, P. S. (2018). Ionic liquid (IL) capped MnO_2 nanoparticles as an electrode material and IL as electrolyte for supercapacitor application. *Renewable Energy*, 126: 437-444.
160. Bunaciu, A. A., Udriştioiu, E. gabriela, and Aboul-Enein, H. Y. (2015). X-ray diffraction: Instrumentation and applications. *Critical Reviews in Analytical Chemistry*, 45(4): 289-299.
161. Connolly, J. R. (2005). Introduction to X-ray powder diffraction. *Spring*, 2005: 1-9.
162. Zangaro, G. A. C., Carvalho, A. C. S., Ekawa, B., do Nascimento, A. L. C. S., Nunes, W. D. G., Fernandes, R. P., Parkes, G. M. B., Ashton, G. P., Ionashiro, M. and Caires, F. J. (2019). Study of the thermal behavior in oxidative and pyrolysis conditions of some transition metals complexes with Lornoxicam as ligand using the techniques: TG-DSC, DSC, HSM and EGA (TG-FTIR and HSM-MS). *Thermochimica Acta*, 681(8): 178399.
163. Amaya, S. L., Alonso-Núñez, G., Díaz De León, J. N., Fuentes, S. and Echavarría, A. (2021). Synthesis and characterization of metal oxides complexes with potential application in HDS reactions. *Materials Letters*, 291: 129562.
164. Kowsari, E. and Abdpour, S. (2016). Investigation performance of rod-like ZnO/CdO composites, synthesized in ionic liquid medium as photocatalytic for degradation of air pollutants (SO_2 and NO_X). *Optik*, 127(23): 11567-11576.
165. Singh, N. and Haque, F. Z. (2016). Synthesis of zinc oxide nanoparticles with different pH by aqueous solution growth technique. *Optik*, 127(1): 174-177.
166. Kowsari, E. and Abdpour, S. (2017). In-situ functionalization of mesoporous hexagonal ZnO synthesized in task specific ionic liquid as a photocatalyst for elimination of SO2, NOx, and CO. *Journal of Solid State Chemistry*, 256(9): 141-150.
167. Salleh, A., Naomi, R., Utami, N. D., Mohammad, A. W., Mahmoudi, E., Mustafa, N. and Fauzi, M. B. (2020). The potential of silver nanoparticles for antiviral and antibacterial applications: A mechanism of action. *Nanomaterials*, 10(8): 1-20.
168. Issn, O. P. and Sarkar, S. (2020). Silver nanoparticles with bronchodilators through nebulisation to treat Covid-19 patients. *Journal of Current Medical Researcg and Opinion*, 3(4): 449-450.
169. Shereen, M. A., Khan, S., Kazmi, A., Bashir, N. and Siddique, R. (2020). Covid-19 Infection: Origin, transmission, and characteristics of human coronaviruses. *Journal of Advanced Research*, 24: 91-98.
170. El-Shishtawy, R. M., Asiri, A. M., Abdelwahed, N. A. M. and Al-Otaibi, M. M. (2011). In situ production of silver nanoparticle on cotton fabric and its antimicrobial evaluation. *Cellulose*, 18(1): 75-82.
171. Jia, M., Zhang, W., He, T., Shu, M., Deng, J., Wang, J., Li, W., Bai, J., Lin, Q., Luo, F., Zhou, W. and Zeng, X. (2020). Evaluation of the genotoxic and oxidative damage potential of silver nanoparticles in human NCM460 and HCT116 cells. *International Journal of Molecular Sciences*, 21(5): 1618.